Biswajeet Pradhan · *Editor*

GCEC 2017

Proceedings of the 1st Global Civil Engineering Conference

Springer

Lecture Notes in Civil Engineering

Volume 9

Series editors

Marco di Prisco, Politecnico di Milano, Milano, Italy
Sheng-Hong Chen, School of Water Resources and Hydropower, Wuhan
University, Wuhan, China
Giovanni Solari, University of Genoa, Genova, Italy
Ioannis Vayas, National Technical University of Athens, Athens, Greece

Lecture Notes in Civil Engineering (LNCE) publishes the latest developments in Civil Engineering - quickly, informally and in top quality. Though original research reported in proceedings and post-proceedings represents the core of LNCE, edited volumes of exceptionally high quality and interest may also be considered for publication. Volumes published in LNCE embrace all aspects and subfields of, as well as new challenges in, Civil Engineering. Topics in the series include:

– Construction and Structural Mechanics
– Building Materials
– Concrete, Steel and Timber Structures
– Geotechnical Engineering
– Earthquake Engineering
– Coastal Engineering
– Hydraulics, Hydrology and Water Resources Engineering
– Environmental Engineering and Sustainability
– Structural Health and Monitoring
– Surveying and Geographical Information Systems
– Heating, Ventilation and Air Conditioning (HVAC)
– Transportation and Traffic
– Risk Analysis
– Safety and Security

More information about this series at http://www.springer.com/series/15087

Biswajeet Pradhan
Editor

GCEC 2017

Proceedings of the 1st Global Civil
Engineering Conference

Springer

Editor
Biswajeet Pradhan
Department of Civil Engineering
University Putra Malaysia
Serdang
Malaysia

and

School of Systems, Management and Leadership,
  Faculty of Engineering and IT
University of Technology Sydney
Ultimo, NSW
Australia

Preface

This Lecture Note in Civil Engineering (LNCE) book contains contributions presented at Global Civil Engineering Conference 2017 (GCEC 2017) on *Steering Global Sustainability through Civil Engineering* which was held at Kuala Lumpur, Malaysia, from 26 to 28 July 2017. The conference was organized into 21 sessions and many of them running in parallel sessions.

The 110 papers were carefully reviewed and selected from more than 300 submissions describing up-to-date applications of state-of-the-art techniques and tools in various disciplines of civil engineering and geosciences to solve real-world problems. This book entails interdisciplinary research, experimental and/or theoretical studies yielding new insights that advance civil engineering methods. The book covers the following areas: structural and construction engineering, geospatial engineering, geotechnical engineering, highway and transportation engineering, water engineering and construction management-related applications.

Each contribution of the conference has been peer-reviewed by at least two members of the scientific technical committee. Their efforts have contributed to the high quality of the final book contributions, and therefore, their reviewing activity is acknowledged and appreciated.

The organizers would like to thank the authors, presenters, session organizers and session chairs for their participation in the GCEC 2017.

Finally, I express my sincere thanks to Dr. Loyola D'Silva, publishing editor at Springer for LNCE Series, and Mr. Ayyasamy Gowrishankar, Mr. Sooryadeepth Jayakrishnan and Ms. Beate Siek at Springer for their great support during the preparation of the final book.

I do hope that the reader will find the book a source of inspiration for both research and professional life.

Kuala Lumpur, Malaysia   Distinguished Professor Biswajeet Pradhan
Sydney, Australia
May 2018

Peer Review Members

Abang Abdullah Abang Ali
Abdul Halim Ghazali
Aidi Hizami Ales
Azlan Abdul Aziz
Badronnisa Yusuf
Balqis Mohamed Rehan
Biswajeet Pradhan
Bujang Kim Huat
F. N. A. A. Aziz
Farzad Hejazi
F. M. Jakarni
Haslinda Nahazanan
H. Z. M. Shafri
Husaini Omar
Hussain Hamid
Izian Abd. Karim
Law Teik Hua
Mohd Saleh Jaafar
Mohd. Shahrizal b. Ab Razak
Nabilah Abu Bakar
Nik Norsyahariati Nik Daud
Nor Azizi Safiee
Noor Azline Mohd. Nasir
Nuzul Azam Haron
R. Muniandy
R. S. M. Rashid
S. Hassim

Shattri Mansor
Syazwani Idrus
Z. M. Yusoff
Zed Diyana Zulkafli

Contents

Part VI   Construction Management

Part I
Structural and Construction Engineering

Influence of Polyethylene and Stainless Steel Fibres on Compressive and Tensile Behaviour of High-Performance Fibre-Reinforced Cementitious Composites

J. A. A. Salvador Filho, D. Lavorato, A. V. Bergami, J. R. Azeredo, C. Nuti and S. Santini

Abstract High-Performance Fibre-Reinforced Cementitious Composites (HPFRCC) is a class of materials studied extensively for applications in structural rehabilitation of existing structures and in design of new structures. These materials have high mechanical strength, pseudo-strain-hardening behaviour and low porosity due to a highly dense microstructure of the cementitious matrix. Furthermore, they guarantee great durability by adding microfibres in the proper ratio, which limits the crack opening. This paper deals with the mechanical properties assessment of HPFRCC mixtures designed with locally available materials. Different HPFRCC mix designs were considered with a very compact cementitious matrix reinforced with two different types of microfibres: high-density polyethylene fibres and hooked stainless steel fibres considering 1% or 2% of the volume contents. The influence of the fibre contents on the compressive and tensile strengths, the strain-hardening performance and the fracture energy are discussed.

Keywords Cementitious composites · Fibre reinforcement · Mechanical properties · Concrete repair

J. A. A. Salvador Filho (✉)
Department of Civil Engineering, Federal Institute of Education Science and Technology of São Paulo, Campus Caraguatatuba, Alameda Bahia, Caraguatatuba, SP 1739, Brazil
e-mail: jasalvador@ifsp.edu.br

D. Lavorato · A. V. Bergami · J. R. Azeredo · C. Nuti · S. Santini
Department of Architecture, Università Degli Studi Roma Tre, via Segre, 4/6, Rome, Italy

1   Introduction

Ordinary Concrete (OC) is notoriously known as a fragile material in tensile (Fig. 1a), while Fibre-Reinforced Concrete (FRC) presents higher ductility and strain-softening behaviour after first cracking (Fig. 1b). The proper use of certain types of fibre in high strength cementitious matrixes produced with small dimensions aggregates, high pozzolanicity powders and specific admixtures can increase the support capacity in tensile even after first cracks opening, so that a pseudo-strain-hardening behaviour (Fig. 1c). Materials with such properties are termed in literature as Very High Strength Concrete (VHSC), Engineered Cementitious Composites (ECC), High Strength High Ductility Concrete (HSHDC), Strain-Hardening Cementitious Composites (SHCC) or High-Performance Fibre-Reinforced Cementitious Composites (HPFRCC). In this work is adopted the last denomination.

HPFRCC and UHPFRCC are materials for repair, strengthening and/or retrofit of damaged reinforced concrete (rc) structures. Kobayashi and Rokugo [2] presented a study on loaded reinforced concrete beams using HPFRCC under chloride
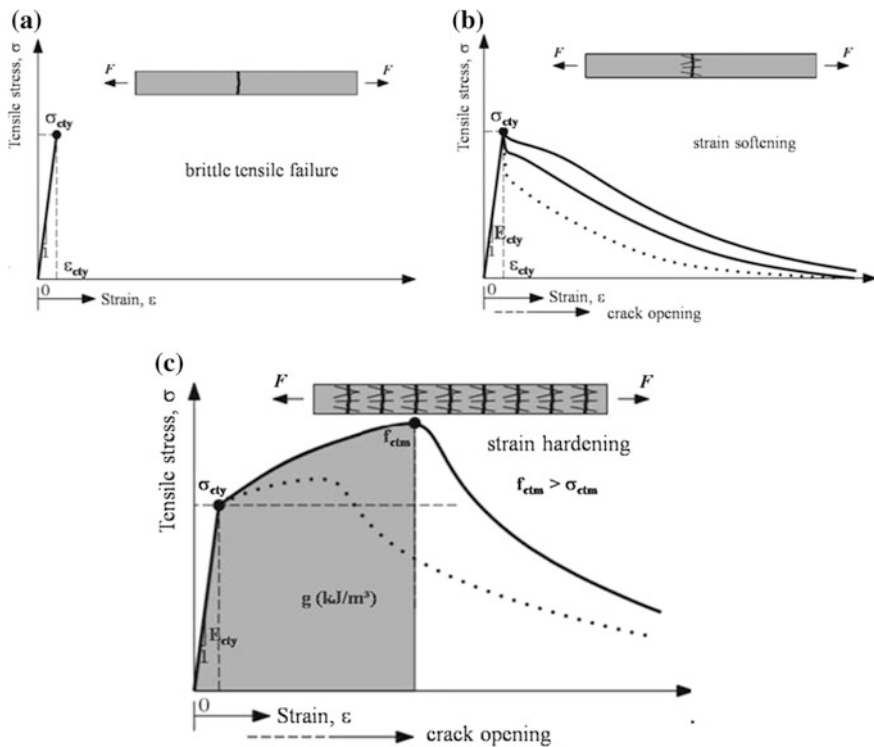
Fig. 1 Stress–strain curves for **a** plain concrete, **b** fibre-reinforced concrete and **c** UHPFRCC (adapted from Ranade et al. [1])

attack. The experimental results indicate that even after the formation of multiple cracks after loading, the HPFRCC remains waterproof due to the small width of the cracks. Similar results were obtained by Meda et al. [3] on rc columns retrofitted with UHPFRCC.

In the literature [4–8], there are different mix proportions and fabrication methods for HPFRCC materials. Each HPFRCC shows peculiar material characteristics which depend on the properties of the available materials used to produce the cementitious matrix in different parts of the world and on the type, size and properties of the fibres.

For that reason, it is much important to define proper methods for obtaining matrices and composites with specific mechanical and chemical characteristics using the locally available components.

The present study is part of an experimental programme with the aim to produce first guidelines useful to produce HPFRCC and UHPFRCC for rapid repair and/or strengthening to improve structural security on damaged rc structures, as plastic dissipation and shear strength [9, 10]. The effect of different volumes and types of fibres on the mechanical properties of HPFRCC is investigated experimentally using locally available materials in the region of Rome (Italy).

The mechanical properties of different mixes design of HPFRCC were studied by experimental tests at Roma Tre University Lab: on $40 \times 40 \times 40$ mm cubic specimens according to EN 12190-3 for evaluating the compressive strength; on $160 \times 40 \times 40$ mm cubic specimens for evaluating flexural strength according to EN 1015-11; on $160 \times 40 \times 40$ mm specimens for evaluation of the modulus of elasticity according to EN 13412 and according to the CNR-DT 204/2006 for plain matrix without fibres addiction.

2 Experimental Programme

The selection criteria of constituent materials for the preparation of HPFRCC was adapted from Nicolaides et al. [5]: (i) fine aggregates (max. 1.2 mm) to improve homogeneity; (ii) silica fume to improve cement paste—aggregate interface and reduce voids or defects; (iii) limestone filler to improve plasticity and cohesion of the mixture in fresh state; (iv) low water/cement ratio by inclusion of high-range water reducer admixture; (v) improvement of thixotropic consistency by inclusion of thixotropizer admixture; (vi) incorporation of small-sized fibres to enhance ductility. Although many HPFRCC in literature have quartz sand in composition due to its pozzolanic potential, this material cannot be found in the region of Rome, and in this study, limestone sand substituted it.

The cement used is Ordinary Portland Cement (OPC) CEM I 52.5 R, provided by Buzzi Unicem Spa (Italy). This cement contains at least 95% of clinker and up to a maximum of 5% of minor constituents, not considering the additions of calcium sulphate and additives. Silica fume (Addiment Spa, Italy) is used as pozzolanic material, and limestone powder (Buzzi Unicem Spa. Italy) is used as filler. Both
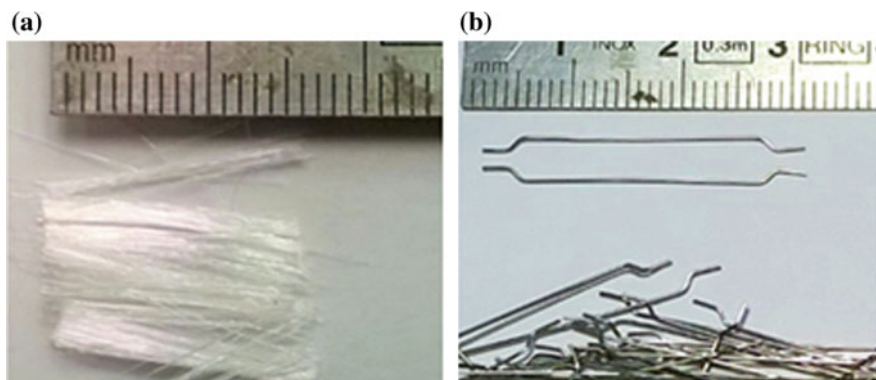
Fig. 2 Polyethylene **a** and stainless steel **b** fibres

Table 1 Geometry and physical/mechanical properties of the fibres used for HPFRCC

Fibre	Polyethylene	Stainless steel
Notation	P	S
Form	Straight	Hooked
Specific gravity (g/cm^3)	0.97	7.66
Length (mm)	15	30
Diameter (mm)	0.0042	0.38
Aspect ratio	3571.4	78.9
Tensile strength (MPa)	2570	2000
Young's modulus (MPa)	73,000	210,000

materials were added in volumetric substitution of cement. A limestone sand is used in fraction of 0–1.2 mm (Buzzi Unicem Spa. Italy). An acrylic-based high-range water reducer (Addiment Spa, Italy) is used to adjust the workability of cementitious composites. A thickener admixture (SI-KA) is used to achieve a thixotropic consistency for patching repair. Two different types of small-sized fibres were used: polyethylene (Honeywell, USA), Fig. 2a; and stainless steel (Bekaert, Italy), Fig. 2b. The main information about the fibres is summarized in Table 1.

2.1 Mix Design and Preparation

HPFRCC is considered an expensive material due to its high cement content (around 1000 kg/m^3). For practical and economic feasibility applications, it was designed a preliminary mix for a plain cementitious matrix with high volumes of filler substitution with locally available materials. After several trial-and-error attempts, it was decided to maintain the silica fume and limestone powder proportions in 15 and 20% in volume substitution of cement, respectively, to reach a

Table 2 Mixture proportion for base HPFRCC material matrix

Main parameters		
Binder composition (vol%)		
Portland cement type I, 52.5	65%	
Silica fume	15%	
Limestone filler 0–75 μm	20%	
Binder consumption	727.7 kg/m^3	
Water/binder ratio	0.37	
Aggregate/binder ratio	1.5	
Material	Consumption (Kg/m^3)	Proportions
Cement	505.68	1.00
Silica fume	89.32	0.18
Limestone powder	136.07	0.27
Sand < 1.2 mm	1279.36	2.53
Water	272.29	0.54
Water reducer admix	12.64	0.025
Anti-shrinkage admix	5.06	0.010
Thixotropizer agent	5.06	0.010

minimum water/binder ratio of 0.37. This ratio is likely to have produced a denser and stiffer mix with the desired thixotropic consistency for patching. The mixture proportions and properties of base materials are detailed in Table 2.

The production of cementitious composites was performed according to the following steps: (i) cement, silica fume and limestone filler were dry-mixed for 1 min in low velocity; (ii) water and water reducer admixture was added, and this paste mixed for 5 min; after a pause of 3 min, the mix was resumed for 2 min; (iii) the sand was added and mixed for 2 min; (iv) thickener agent and anti-shrinkage admixture were added and mixed for 2 min; (v) for fibre-reinforced mixtures, the fibres were added slowly for a good dispersion into the cementitious matrix and them mixed for 2 min for a perfect homogeneity. Referential plain concrete mixture is named R0, and mixtures reinforced with Polypropylene 1 and 2 vol%, and Stainless-steel 1 and 2 vol% are named P1, P2, S1 and S2, respectively.

2.2   Evaluation of Mechanical Properties

The mechanical properties of the selected HPFRCC mixes were investigated experimentally according to EN 12190-3 for compressive strength of 40 × 40 × 40 mm cubic specimens; EN 1015-11 for flexural strength of 160 × 40 × 40 mm cubic specimens; and EN 13412 for evaluation of the modulus of

elasticity in compression for $160 \times 40 \times 40$ mm. According to the CNR-DT 204/ 2006, it was evaluated the modulus of elasticity just for plain matrix without fibres addiction.

The tensile behaviour of the HPFRCC was studied using the equipment for the uniaxial tension tests presented in Fig. 3. The dog-bone HPFRCC samples have shape defined according to of CNR [11] and JSCE [12] recommendations.

The average extension of the dog-bone specimen was measured over the central part using an extensometer with base measure range of 50 mm placed on a side of the mounting frame clamped to the sample as shown in Fig. 3b. The uniaxial tensile load was applied with a 500 kN capacity MTS universal testing machine. The samples were fixed at both ends of the testing machine by an apparatus designed specifically for this work. Load–displacement data were recorded using a data acquisition system.

The tensile test was conducted according to the recommendations of CNR [11] and JSCE [12] for the direct displacement-controlled tension testing of dog-bone samples at a displacement rate of 0.5 mm/min.

The first crack stress or yield stress (σ_{cty}), the tensile strength f_{ctm} and corresponding strain in tension (ε_{ctm} and ε_{ctm}, respectively) were determined on the experimental stress–strain curve to evaluate the condition described in Eq. (1) to determine the pseudo-strain-hardening behaviour:

$$f_{ctm} > \sigma_{cty} \tag{1}$$
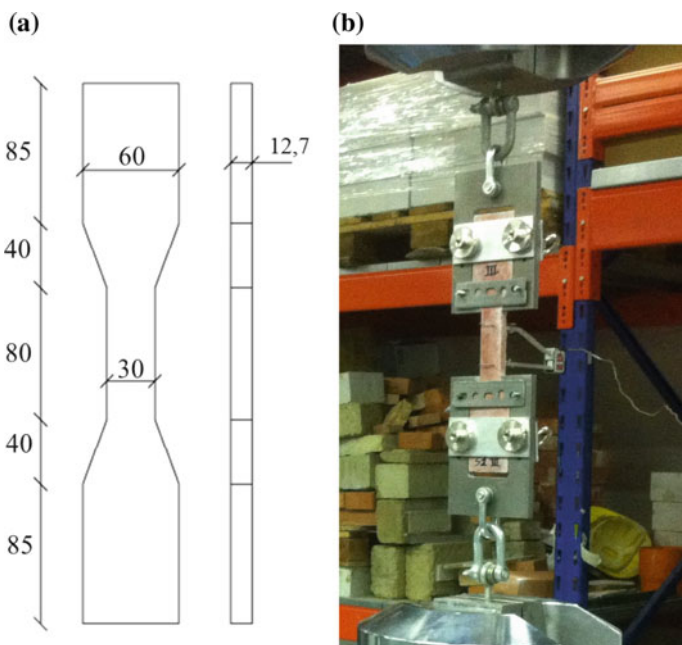
Fig. 3 JSCE dog-bone specimen dimensions (**a**), and axial tensile test setup (**b**)

Furthermore, the number of cracks within the gauge length of the samples was counted, and the average crack spacing was calculated by dividing the gauge length (80 mm) by the number of cracks. The energy-absorption capacity g of the HPFRCC was calculated as the area under the stress–strain curve from zero strain to the strain corresponding to the maximum tensile stress ε_{ts} according to Eq. 2. The energy absorption corresponding to the strain-softening area after ε_{ts} is not investigated in this work.

$$g = \int_{0}^{\varepsilon} ts \, \sigma(\varepsilon) d\varepsilon \qquad (2)$$

3 Experimental Results and Discussion

3.1 Mechanical Properties

The average results of four 40 mm cubes under axial compression, three $160 \times 40 \times 40$ mm prisms under three-point flexure test and six dog-bone specimens tested under direct uniaxial tension for each batch (mix proportions in Table 2) are presented in Figs. 4, 5 and 6. The elastic modulus of three $160 \times 40 \times 40$ mm prisms under compression was determined just for plain cementitious matrix. The mechanical properties obtained for the plain matrix and the UHPFRCC are shown in Table 3.
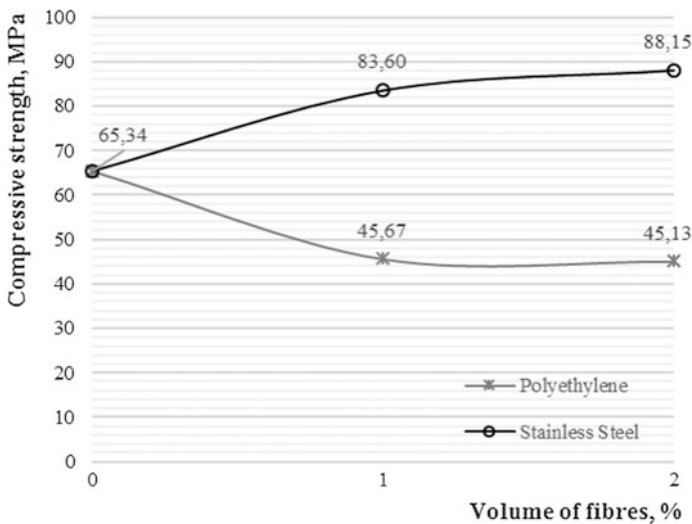
Fig. 4 Compressive strength results about UHFRCC plain matrix (R0) and UHFRCC mixtures with polyethylene fibres (P1, P2) or steel fibres (S1, S2)
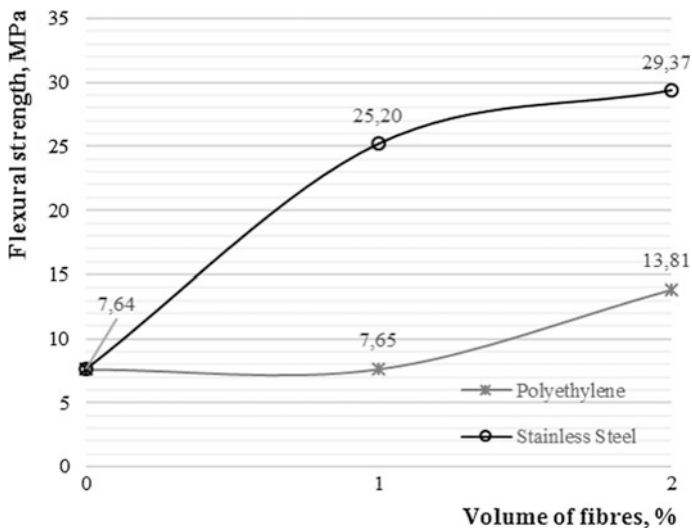
Fig. 5 Flexural strength results about UHFRCC plain matrix (R0) and UHFRCC mixtures with polyethylene fibres (P1, P2) or steel fibres (S1, S2)
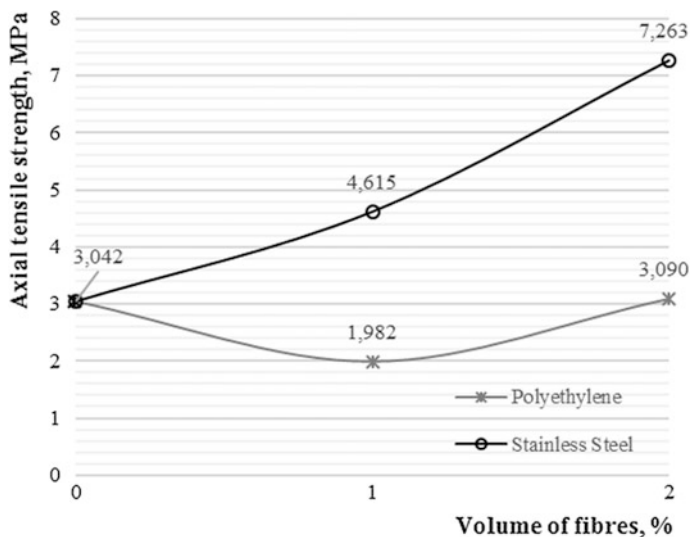
Fig. 6 Axial direct tensile strength results about UHFRCC plain matrix (R0) and UHFRCC mixtures with polyethylene fibres (P1, P2) or steel fibres (S1, S2)

In Fig. 4 are presented the results about the compressive strength of cubic specimens for each batch of mixtures. The compressive strength in case of polyethylene fibre mixtures P1 and P2 was reduced by 30.1 and 30.9% with respect to

Table 3 Experimental tests results: mechanical properties of plain matrix R0 and UHFRCC mixture with polyethylene fibres (P1, P2) or stainless steel fibres (S1, S2)

Code	R0	P1	P2	S1	S2
Compressive strength, R_{cm} (MPa)	65.34	45.67	45.13	83.60	88.15
Modulus of elasticity, E_{cm} (GPa)	25.99	–			
Flexural strength, f_{cfm} (MPa)	7.64	7.65	13.81	25.20	29.37
Axial tensile strength, f_{ctm} (MPa)	3.042	1.982	3.090	4.615	7.263

the one measured in case of the plain cementitious matrix (R0). The incorporation of 1.0 and 2.0 vol% of stainless steel fibres in the plain matrix improved the compressive strength by 27.9 and 34.9%, respectively, in case of S1 and S2 mixes.

The incorporation of 1.0 vol% of polyethylene (P1) fibres in the plain matrix maintained the flexural strength of UHFRCC around $\sim$7.5 MPa as well as the one of the plain cementitious matrix (R0). Mixtures with incorporation of 1.0 vol% of stainless steel (S1) fibres presented flexural strength 230% higher than the one of plain cementitious matrixes (R0). The incorporation of 2.0 vol% of polyethylene (P2) and stainless steel (S2) fibres increased the flexural strength of plain matrix by 82 and 285%, respectively (Fig. 5).

The axial direct tensile test results are presented in Fig. 6. These results show that the tensile strength of the UHFRCC plain cementitious matrix (R0) increases using stainless steel (S1 and S2) fibres mixtures. The higher results were achieved with 2.0 vol% incorporation of stainless steel fibres (7.3 MPa). The incorporation of 1.0 vol% of polyethylene fibres (P1) reduced the axial tensile strength by 35%, and 2.0 vol% (P2) increased by 2%.

3.2 Stress–Strain Curves

The tensile stress–strain curves of all the tested samples of HPFRCC are illustrated in Fig. 7a through (d) for mixtures P1, P2, S1 and S2, respectively. The mean curve obtained starting from all the available samples for each mixture are shown as thicker lines. The stress–strain curves show an increase in the stresses between σ_{cty} and f_{ctm} in case of each sample of each mixture. It is possible to identify a strain-hardening behaviour also in case of P1 and P2 samples despite the decreasing of the compressive strength in function of the fibre content as described above (Fig. 7c, d).

The values of the yield stress σ_{ty}, the yield strain ε_{cty}, the maximum stress and the maximum strain ε_{ctm} were selected on each curve and shown in Table 4.

The influence of the different types and volumes of fibres on the stress–strain behaviour of HPFRCC can be observed by the mean curves relative to the tensile tests shown in Fig. 8. In this figure, the yield stress σty is assumed as the stress
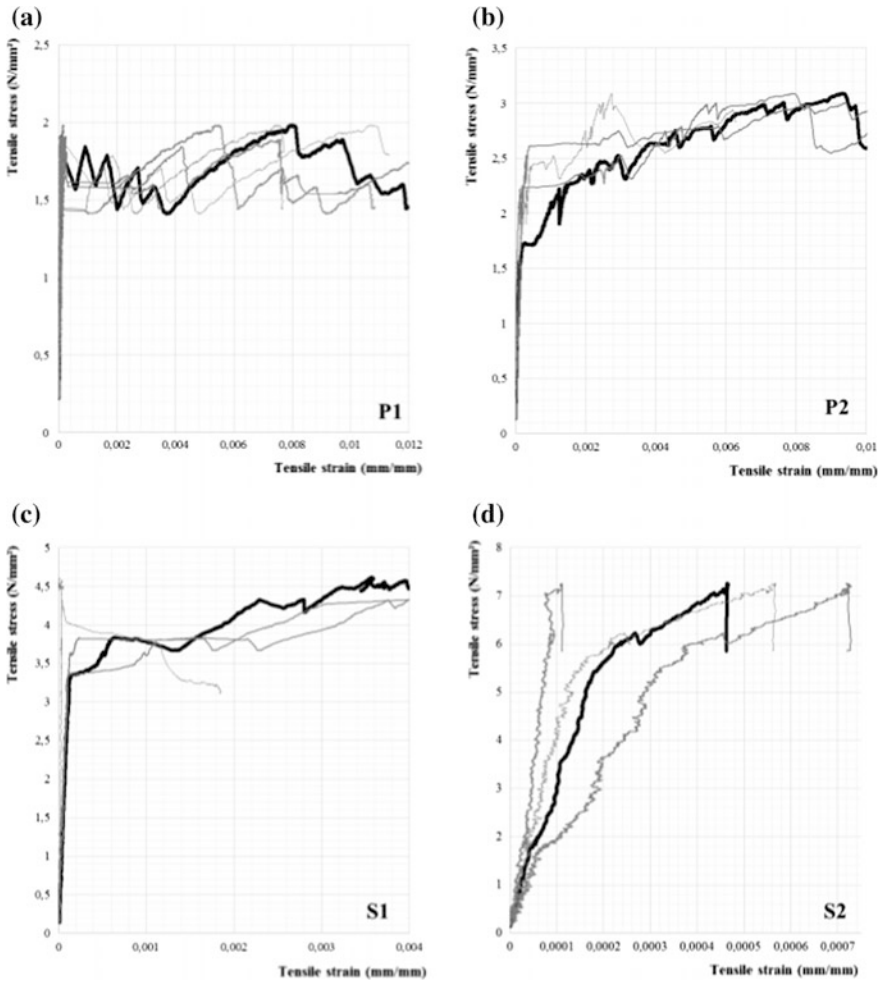
Fig. 7 Tensile stress–strain curves of UHFRCC mixtures with polyethylene fibres (P1, P2) or steel fibres (S1, S2)

Table 4 Yield stress and strain, axial tensile strength and maximum axial strain measured during the tests on UHFRCC with different mixtures [polyethylene fibres (P1, P2) or steel fibres (S1, S2)]

Mixture	P1	P2	S1	S2
Pre-cracking				
Yield stress, σ_{cty} (MPa)	1.887	1.731	3.353	4.396
Yield strain, ε_{cty} (mm/mm)	8.8826E-05	2.6105E-04	1.4880E-04	7.7784E-05
Post-cracking				
Axial tensile strength, f_{ctm} (MPa)	1.982	3.090	4.615	7.263
Max. axial strain, ε_{ctm} (mm/mm)	0.00792954	0.00744774	0.00357204	0.00122039
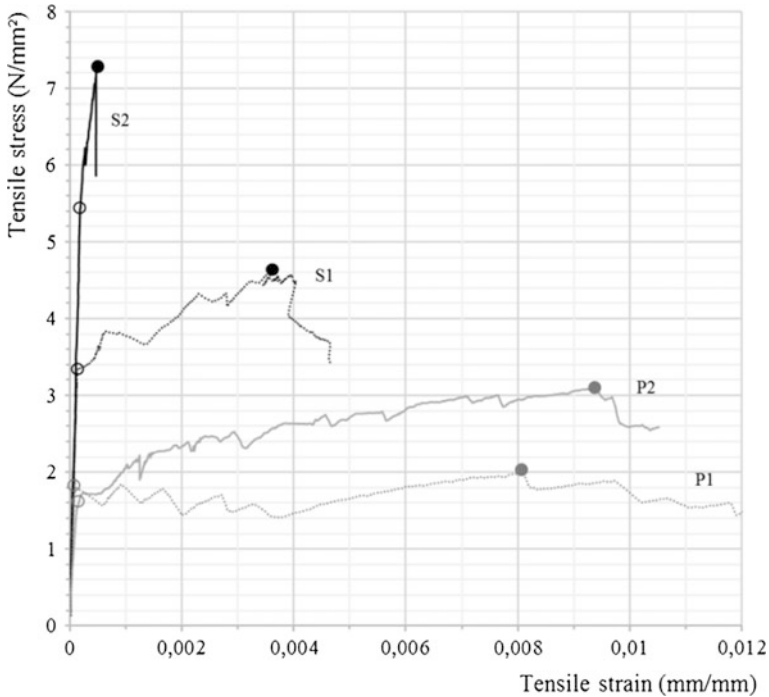
Fig. 8 Mean tensile stress–strain curves of UHFRCC mixtures with polyethylene fibres (P1, P2) or steel fibres (S1, S2); σ_{ty} yield stress (open circle); maximum tensile stress f_{ctm} (solid circle)

value that triggers the nonlinear deviation of the stress–strain curve for each curve (open circle). The maximum tensile stress f_{ctm} is indicated by a solid circle on the same curve.

HPFRCC mixtures reinforced with polyethylene fibres P1 and P2 presented, respectively, 0.81 and 0.94% on deformation corresponding to the axial strength (ε_{ctm}). These results are greater than the observed in case of HPFRCC reinforced with stainless steel fibres S1 (0.40%) and S2 (0.046%). Also, its observed that a greater amount of polyethylene fibres (2 vol%) has increased the deformations in comparison with the mixtures with 1 vol% of the same fibre. The opposite behaviour occurred with the mixtures reinforced with stainless steel fibres.

3.3 Energy Absorption and Multiple Cracking

The number of cracks and the crack spacing were visually evaluated once a dominant crack had become localized and the loading tests were completed. Typical examples of cracking patterns are shown in Fig. 9. To make the cracks more visible, water was sprayed on the surface before taking the photos. The cracking

Fig. 9 Mean tensile stress–strain curves of UHFRCC mixtures with polyethylene fibres (P1, P2) or steel fibres (S1, S2); σ_{ty} yield stress (open circle); maximum tensile stress f_{ctm} (solid circle)

Table 5 Energy absorption and average cracking spacing results

Mixture	P1	P2	S1	S2
Energy absorption, g (kJ/m^3)	13.833	24.985	15.907	2.468
Average cracking spacing (mm)	25.00	6.04	45.71	64.00

pattern of HPFRCC was clearly influenced by the type and volume of fibres. The number of cracks increased, and the average crack spacing decreased, as the volume of polyethylene fibres increased. On the other hand, the opposite behaviour was observed with stainless steel fibres, as shown in Table 5.

4   Summary and Conclusions

This paper presents the mix design and mechanical properties assessment for a High-Performance Fibre-Reinforced Cementitious Composite (HPFRCC). The design of the cementitious matrix is based on the achievement of low cement consumption and a thixotropic consistency for practical and economic feasibility as repair material. From the presented results, the following conclusions are drawn:

– The addition of polyethylene and stainless steel fibres presented microcrack pattern and ductile failure. It was detected the pseudo-strain-hardening behaviour for all samples.
– Polyethylene fibres mixtures presented lower compressive strength ($\sim$30%) compared to the plain cementitious matrix. Other properties were not significantly affected by this type of fibre except an improvement on flexural strength with 2.0 vol%.

– Mixtures reinforced by hooked stainless steel fibres achieved higher strengths for all assessed mechanical properties, except for energy absorption. The maximum compressive, flexural and tensile strengths at 28 days for mixtures with stainless steel fibre in 2.0 vol% reached, respectively, about 88, 29 and 7 MPa.
– HPFRCC mixtures reinforced with polyethylene fibres P1 and P2 presented, respectively, 0.81 and 0.94% on deformation corresponding to the axial strength (ε_{ctm}). These results are greater than those observed in case of HPFRCC reinforced with stainless steel fibres S1 (0.40%) and S2 (0.046%).
– The higher amount of polyethylene fibres (2 vol%) has increased the deformations and consequently the energy absorption of the cementitious matrixes in comparison with the mixtures with 1 vol% of the same fibre.
– The opposite behaviour occurred with the mixtures reinforced with stainless steel fibres.

References

1. Ranade, R., Stults, M.D., Li, V.C., Rushing, T.S., Roth, J., Heard, W.F.: Development of high strength high ductility concrete. In: 2nd International RILEM Conference on Strain Hardening Cementitious Composites. Rio de Janeiro, RILEM (2011)
2. Kobayashi, K., Rokugo, K.: Mechanical performance of corroded RC member repaired by HPFRCC patching. Constr. Building Mater. Yanagido **39**, 139–147 (2013)
3. Meda, A., Mostosi, S., Rinaldi, Z., Riva, P.: Corroded RC columns repair and strengthening with high performance fiber reinforced concrete jacket. Mater. Struct. **49**, 1967–1978 (2016)
4. Kim, S.W., Park, W.S., Jang, Y.I., Feo, L., Yun, H.D.: Crack damage mitigation and shear behaviour of shear-dominant rein-forced concrete beams repaired with strain-hardening cement based composite, composites part B (2015)
5. Nicolaides, D., Kanellopoulos, A., Christou, A.M.P.: Development of UHPFRCC with the Use of Materials Available in Cyprus. FIB Symposium. Prague, FIB (2011)
6. Vitek, J.L., Coufal, R., Citek, D.: UHPC—development and testing on structural elements. Procedia Eng. **65** (2013)
7. Wille, K., El-Tawil, S., Naaman, A.E.: Properties of strain hardening ultra-high performance fibre reinforced concrete (UHP-FRC) under direct tensile loading. Cem. Concr. Compos. **48** (2014)
8. Yu, R., Spiez, P., Brouwersm, H.J.H.: Mix design and properties assessment of ultra-high performance fibre reinforced concrete (UHPFRC). Cem. Concr. Res. **56** (2014)
9. Lavorato, D., Bergami, A.V., Nuti, C., Briseghella, B., Tarantino, A.M., Santini, S., Huang, Y., Xue, J.: Seismic damaged Chinese RC bridges repaired and retrofitted by rapid intervention to improve plastic dissipation and shear strength. In: Proceedings of 16WCEE 2017. Santiago Chile, 9th–13th Jan 2017

10. Lavorato, D., Wu, J., Huang, Y., Xue, J., Bergami, A.V., Briseghella, B., Nuti, C., Tarantino, A.M., Santini S.: New solutions for rapid repair and retrofit of RC bridge piers CINPAR 2016. In: XII International Conference on Structural Repair and Rehabilitation. Porto, Portugal, 26–29 Oct 2016
11. National Reseach Council: CNR-DT 204/2006—Guide for the Design and Construction of Fiber-Reinforced Concrete Structures. CNR, Rome (2007)
12. JSCE Concrete Committee: Recommendations for Design and Construction of High Performance Fiber Reinforced Cement Composites with Multiple Fine Cracks (HPFRCC) (2008)

RC Column Repaired with HPFRCC and Confined with CFRP: Numerical Analyses to Evaluate the Column Section Capacity

D. Lavorato, J. Azeredo, A. V. Bergami, J. A. A. Salvador Filho,
C. Nuti, S. Santini and B. Briseghella

Abstract This paper presents a numerical study to evaluate the behavior of reinforced concrete (RC) columns with circular section repaired and retrofitted by high-performance fiber-reinforced cement composites (HPFRCC) jackets and external carbon fiber-reinforced polymer (CFRP) wrapping. The column damage is due to degradation of concrete and steel rebars for effect of the corrosion. Different HPFRCC mix designs were considered to repair the column assuming different fiber types (polyethylene, stainless steel) and volume contents (1% or 2%). These HPFRCC concretes were developed and tested experimentally at the lab of the University of Roma Tre (Salvador Filho et al. in Mechanical properties of HPFRCC reinforced with different types and volumes of fibres [1]). The numerical analyses were conducted by means of fiber models using the software *OpenSees* (OpenSees structural software [computer software]. Pacific Earthquake Engineering Research Center, University of California, Berkeley, CA, [2]) applying a vertical load and a displacement history (section rotation). The analyzed sections represent the undamaged section, the section damaged for effect of rebar corrosion, and the repaired and retrofitted sections. The first numerical results about the section strength capacities for each type of repair material are discussed.

Keywords Repair · Confined section · Push-over analysis · Finite element method · HPFRCC

D. Lavorato (✉) · J. Azeredo · A. V. Bergami · C. Nuti · S. Santini
Department of Architecture, Roma Tre University,
Largo Giovanni Battista Marzi, 10, Rome, Italy
e-mail: davide.lavorato@uniroma3.it

J. A. A.Salvador Filho
Department of Civil Engineering, Federal Institute of Education Science
and Technology of São Paulo, Campus Caraguatatuba, Alameda Bahia,
Caraguatatuba 1739, Brazil

B. Briseghella
College of Civil Engineering, Fuzhou University, University Town,
2 Xue Yuan Road, Fuzhou, China

1   Introduction

Many reinforced concrete (RC) structures built in aggressive environment present deterioration problems, both for the phenomena related to the maintenance and for the effects linked to aggressive agents of the atmosphere. The lack of proper maintenance of structures during their service life can originate pathological phenomena such as deterioration of concrete and steel, which manifest before the time provided in the structural design, often with serious consequences and great damage.

The reinforcement corrosion is one of the first direct consequences of reinforced concrete deterioration, which can cause a reduction of the structures' performance. Rehabilitation interventions on these structures, which aim to recover or increase structural capacity, can result difficult on construction site.

In this paper, repair techniques were considered to restore the concrete and steel rebar parts damaged by corrosion phenomena.

The nonlinear behavior of a circular RC column damaged by the corrosion of the steel reinforcement and then repaired and/or retrofitted by HPFRCC materials and CFRP wrapping was investigated by numerical analyses.

Different fiber section models were built in *OpenSees* [2] to study the behavior of the undamaged section before the corrosion: the section damaged by corrosion of the steel rebar, the section repaired by HPFRCC jacket which is used to restore the removed damaged concrete parts, and the section repaired by HPFRCC and retrofitted by an external CFRP wrapping. The HPFRCC materials with polyethylene or stainless steel fibers were considered to repair the damaged concrete parts. These HPFRCC concretes were developed and tested experimentally at the lab of the University of Roma Tre [1]. The first results of this numerical analysis about the section capacity are discussed to evaluate the effectiveness of the proposed interventions.

2   HPFRCC Materials

Plain concrete is a brittle material with low tensile strength but fibers may be added in the cementitious composite to improve its mechanical behavior. Besides the contribution in terms of tenacity, the fibers develop an important contribution for a better distribution of cracks in the concrete when this material is subjected to increasing loads until failure.

High-performance fiber-reinforced cementitious composites (HPFRCC) are a class of material characterized not only by high strength and low permeability but also by pseudo-ductility post-cracking behavior (consequently high deformability) and development of micro-cracks under tensile stress (Fig. 1). These characteristics are achieved due to the highly dense microstructure of cementitious matrix combined with use of microfibers that in adequate proportion can limit the width of the
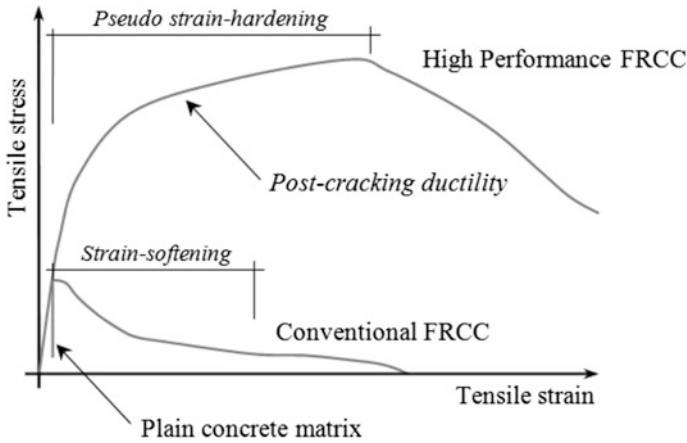
Fig. 1 Typical stress–strain curves (under tensile stress) for comparison between conventional FRCC (fiber-reinforced concrete) and high-performance FRCC behavior

cracks. These effects are described by several researches [3–6]. These materials are obtained by a combination of high-strength concrete and short fibers with an improved homogeneity, because traditional coarse aggregates are replaced with fine sand.

Pseudo strain-hardening behavior of HPFRCC under direct uniaxial tensile stress is an increase in tensile stress after first cracking (Fig. 1). On the other hand, conventional fiber-reinforced cementitious composites (FRCC) exhibit a decrease in tensile stress after first cracking that is called strain-softening, as generally seen in cement-based materials such as mortar and concrete.

An extensive experimental investigation was carried at Roma Tre University Lab to produce UHPFRCC with locally available materials and the effect of different volumes and types of fibers on mechanical properties. The main results from this study are shown in Table 1.

Table 1 Experimental tests results: mechanical properties of plain cementitious matrix and UHFRCC mixtures reinforced with polyethylene fibers and stainless steel fibers [1]

Mixtures	Plain matrix	Polyethylene		Stainless steel	
		1%	2%	1%	2 %
Compressive strength, R_{cm} (MPa)	65.34	45.67	45.13	83.60	88.15
Modulus of elasticity, E_{cm} (GPa)	25.99	–			
Flexural strength, f_{cfm} (MPa)	7.64	7.65	13.81	25.20	29.37
Axial tensile strength, f_{ctm} (MPa)	3.042	1.982	3.090	4.615	7.263

3   Case of Study: RC Cantilever Column

The numerical investigation was carried out considering a cantilever column tested experimentally before and after repair and retrofitting interventions by Lavorato et al. [7–18].

In this study, an RC cantilever column of 420 mm in diameter and 1170 mm in height represents a 1/6 scaled specimen of a bridge pier (Fig. 2). The steel reinforcement was composed of 12 bars with diameter D_s = 12 mm (longitudinal rebars), clear cover thickness of C = 30 mm, and transverse reinforcement with diameter D_{st} = 6 mm provided at 120 mm of spacing (Table 1). The mean compressive strength (f_{cm}), the modulus of elasticity (E_c), and the tensile strength (f_{ctm}) of the undamaged column concrete are given in Table 2.

The yield strength of the longitudinal reinforcing steel (f_{ym}), the yield strength of the transverse reinforcing steel (f_{ytm}), and the rebar elastic modulus (E_s) are given in Table 2.

The damage due to corrosion assumed in the RC section is shown in Fig. 3 where it is evident: the concrete spalling due to rush expansion, the steel stirrups rupture, and the reduction of the longitudinal rebar diameter. The rebar mass loss is assumed equal to 10%, and the rebar steel characteristics were calculated by formulations presented in Kashani et al. [19, 20]: the reduced rebar diameter is 11.38 mm, the yield strength in tension is equal to 545.65 MPa, and the yield strength in compression is equal to 502.57 MPa.

Fig. 2 Case of study: AS built columns with corroded rebars
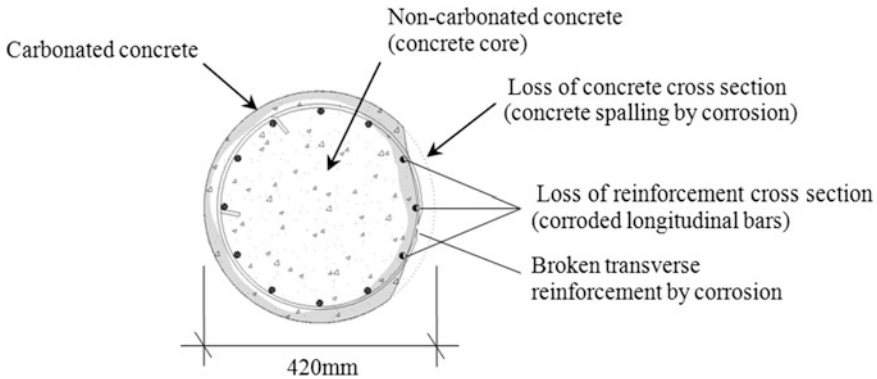
Fig. 3 Damage due to corrosion of the rebars assumed for the studied RC column section: damage of the concrete part and steel reinforcement

4 Numerical Investigation of the Behavior of Repaired and Retrofitted RC Sections

Some numerical simulations were performed to evaluate the bearing capacity of RC structural elements damaged by corrosion of the steel rebars and then repaired and retrofitted using HPFRCC materials. The numerical analyses were conducted considering: the undamaged column section, the column section damaged for effect of the rebar corrosion phenomena, the column section repaired by means of HPFRCC after the removing of the damaged concrete parts, and the column section repaired by HPFRCC and retrofitted by CFRP wrapping [17, 18, 21].

4.1 Numerical Models

The analysis about the nonlinear behavior of the circular reinforced concrete (RC) section of the column studied in [7–16, 22] was conducted by a fiber model using *OpenSees* software framework [2].

The fiber section (Fig. 4) was divided into several concrete and steel parts (fibers). The discretization of the section is illustrated in Fig. 4. Thirteen radial and 16/32 tangential divisions were employed for the concrete parts of the section whereas the longitudinal rebars are simulated by single steel fibers. This level of discretization is used to lead accurate results based on a convergence study not reported here.

To assess the performance level of the column base section, four numerical models were considered: the undamaged section before corrosion phenomena (Fig. 5), the damaged section with corroded steel rebars and degraded concrete parts due to corrosion (Fig. 6), the section repaired by HPFRCC to restore the
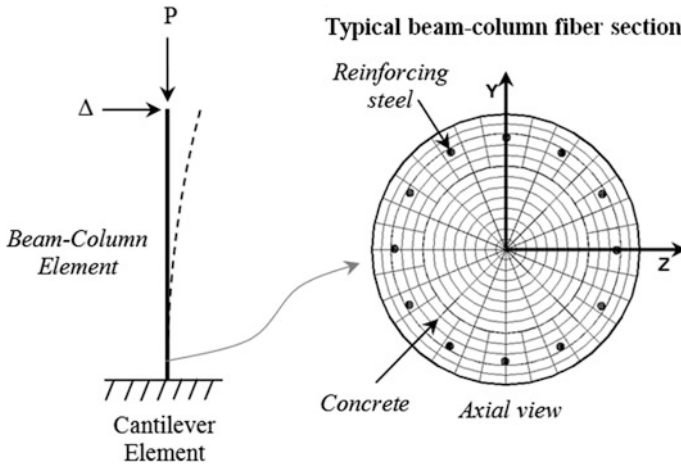
Fig. 4 Fiber model of the RC column section (FEM model in *OpenSees* [2])
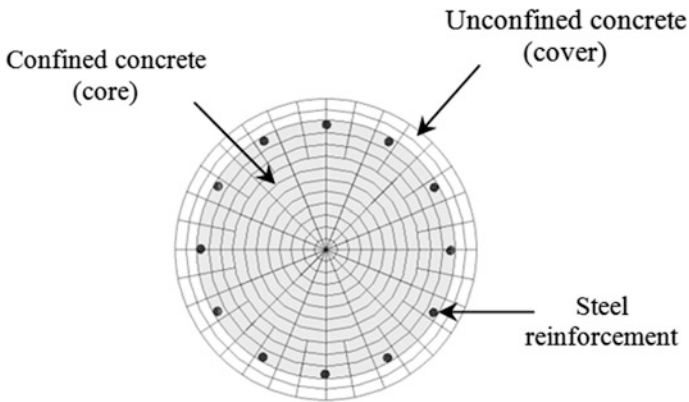
Fig. 5 Fiber section model in *OpenSees*: the undamaged base column section before corrosion phenomena

removed damaged concrete parts (Fig. 7), and the section repaired by HPFRCC and retrofitted by CFRP wrapping (Fig. 8).

The section model of the undamaged column had the geometries and steel reinforcement characteristics shown in §3.

The section model of the damaged column (Fig. 6) due to corrosion was built starting from the model of the undamaged section (Fig. 5):

– removing the deteriorated external part of the concrete section (Fig. 3),
– assuming no stirrup confinement effect on the section core concrete (broken stirrups),
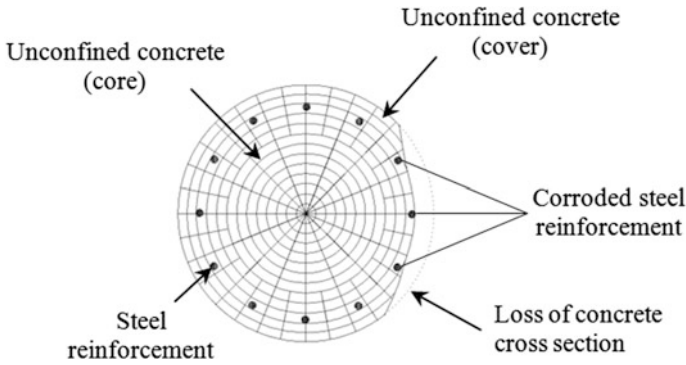
Fig. 6 Fiber section model in *OpenSees*: the damaged base column section due to corrosion phenomena

Fig. 7 Fiber section model in *OpenSees*: the repaired base column section by HPFRCC
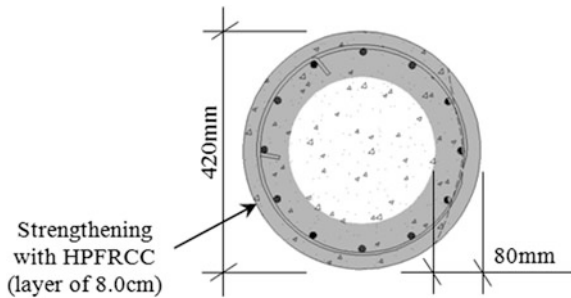
Fig. 8 Fiber section model in *OpenSees*: the repaired and retrofitted base column section by HPFRCC and CFRP wrapping
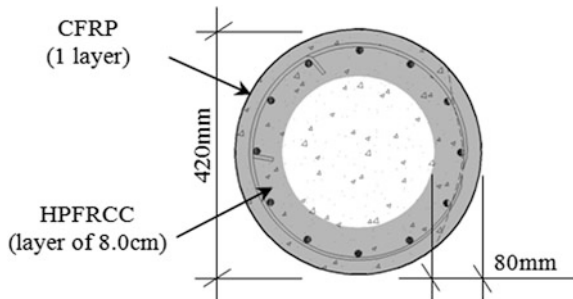
– reducing the longitudinal rebar diameter and the steel mechanical properties as in Kashani et al. [19, 20] considering a mass loss of 10% (§3).

The section model of the repaired column had an external part (8.0 cm, Fig. 7) built by HPFRCC to restore the damaged concrete parts removed along the external part of the RC section. Two HPFRCC mixtures were considered with polyethylene

or stainless steel fibers and 1% or 2% of fiber content. These HPFRCC materials were tested experimentally in [1] to define the concrete characteristics.

The section model of the repaired and retrofitted column had an external part built by HPFRCC to restore the damaged concrete parts (8.0 cm, Fig. 8). The CFRP wrapping used to retrofit the column was not modeled but its confinement effect on the section core concrete was evaluated during the material properties definition. The mechanical characteristics of CFRP system were obtained from the commercial products specifications (f_{fk} = 4700 N/mm^2; E_f = 240000 N/mm^2; ε_f = 1.8%; t_f = 0.167 mm).

Proper concrete and steel material models (stress–strain relation) were associated with each fiber in the section considering the material properties given in §3. The mechanical characteristics of the corroded rebar were calculated by Kashani et al. model [19, 20] considering the residual capacity of the corroded rebars (§3). The model presented by Hosotani et al. [23, 24] simulated the behavior of the confined concrete by stirrups or CFRP.

The HPFRCC material behavior was defined considering the mechanical characteristics obtained from the experimental investigation explained in Salvador Filho et al. [1].

Each material model was simplified by a multilinear model to use the hysteretic material model available in *OpenSees* [2]. This approximation can be considered valid for the aims of these first analyses.

Nonlinear analyses were carried out applying a vertical load (266 kN) and a monotonic deformation history (section rotation) on the fiber section model to evaluate the corresponding moment–rotation behavior.

4.2 Numerical Results

The monotonic moment–rotation curves obtained by the numerical analysis in *OpenSees* for the undamaged, the damaged, the repaired, and the repaired and retrofitted sections are given in Figs. 9, 10 and 11. The comparison about the capacity curve for each type of section is given in Table 3 in terms of maximum moment (M_{max}) and performance factor (F_p) calculated by the ratio between the maximum moment of the section and the maximum moment of the undamaged section.

Fig. 9 Numerical moment–rotation capacity curve for the undamaged (original condition), the damaged (deteriorated current time), and the repaired by HPFRCC with polyethylene or stainless steel fiber using a fiber content of 1%
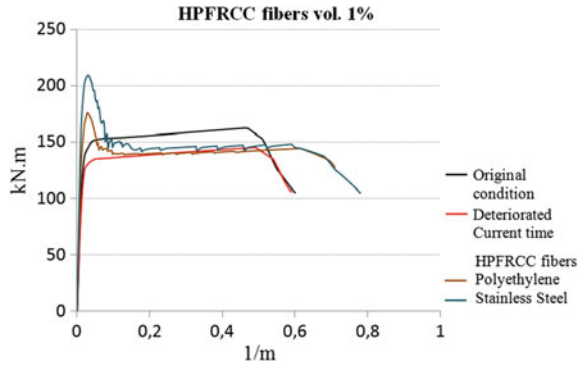
Fig. 10 Numerical moment–rotation capacity curve for the undamaged (original condition), the damaged (deteriorated current time), and the repaired by HPFRCC with polyethylene or stainless steel fiber using a fiber content of 2%
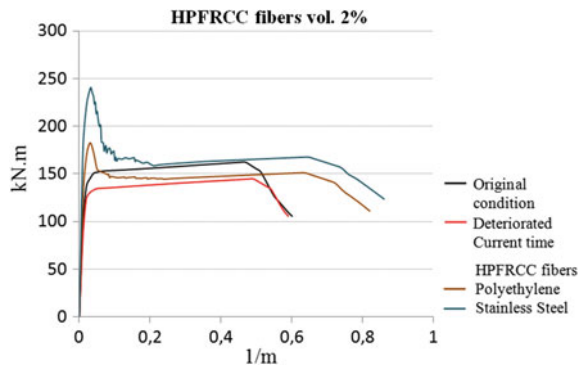
Fig. 11 Numerical moment–rotation capacity curve for the undamaged (original condition), the damaged (deteriorated current time), and the repaired by HPFRCC with polyethylene or stainless steel fiber using a fiber content of 2% and retrofitted by one layer of CFRP
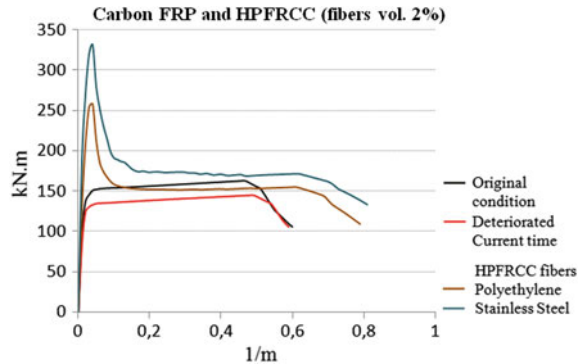
5 Result Discussion and Conclusions

The nonlinear behavior of a circular RC column damaged by the corrosion of the steel reinforcement and then repaired and/or retrofitted by HPFRCC materials and CFRP wrapping was investigated by means of monotonic numerical analyses.

Table 2 Key information about the section geometries and the materials characteristics for the studied undamaged RC column

Concrete				
D	C	f_{cm}	f_{ctm}	E_c
(mm)	(mm)	(MPa)	(MPa)	(GPa)
420	30	20	2.21	22.36

Longitudinal bars				Transverse bars			
D_s		f_{ym}	E_s	D_{st}	s	f_{ytm}	E_s
(mm)	n	(MPa)	(GPa)	(mm)	(mm)	(MPa)	(GPa)
12	12	574.37	200	6	120	445.46	200

Note D = cross section diameter; C = concrete cover thickness; f_{cm} = concrete cylinder strength; f_{ctm} = concrete tension strength; E_c = elastic modulus of concrete; D_s = diameter of longitudinal bars; n = number of longitudinal steel bars; f_{ym}, f_{ytm} = yield stress of steel bars; E_s = elastic modulus of steel; D_{st} = diameter of transverse steel bars; s = spacing of transverse steel bars

Table 3 Comparison between moment–rotation curves in terms of maximum moments (M_{max}) obtained for the undamaged (original condition), the damaged (deteriorated current time), the repaired by HPFRCC with polyethylene or stainless steel fiber, and the repaired and retrofitted by CFRP wrapping (one layer) and performance factor (F_p)

Column section			M_{max} (kN m)	F_p
Original condition not damaged			163	1.00
Deteriorated current time			145	0.89
Repaired with HPFRCC	Polyethylene	(1%)	176	1.08
		(2%)	183	1.12
	Stainless steel	(1%)	209	1.28
		(2%)	241	1.48
Repaired and retrofitted CFRP and HPFRCC	Polyethylene	(2%)	258	1.58
	Stainless steel	(2%)	331	2.03

Note Fibre volume fraction (%) M_{max} = maximum moment; F_p = performance factor (in relation to the maximum moment of the original section—not damaged)

A detailed fiber section model was implemented in *OpenSees* program taking in account different section conditions: the undamaged section, the section damaged by corrosion of the steel rebar, the section repaired by HPFRCC jackets used to restore the removed damaged concrete, and the section repaired by HPFRCC and retrofitted by an external CFRP wrapping. HPFRCC materials with different fiber types (polyethylene, stainless steel) and volume contents (1% or 2%) studied during the experimental campaign in [1] were considered to repair the damaged concrete parts.

The first comparison of the results of the numerical analyses performed for each type of section in terms of maximum moment showed:

– The corrosion of the steel rebars reduces the section capacity. It is obvious because the longitudinal rebar diameter is reduced for effect of the corrosion and the damaged concrete part does not give contribution to the resistant moment capacity.
– The sections repaired by means of a modest layer of HPFRCC (8.0 cm) with polyethylene or stainless steel fibers after the damaged concrete removal showed an improved section capacity. The HPFRCC with polyethylene fiber can improve the section capacity of about 8% or 12% with respect to the one of the original undamaged sections using 1% or 2% of fiber content, respectively. The HPFRCC with stainless steel fiber can improve the section capacity of about 28% or 48% with respect to the one of the original undamaged sections using 1% or 2% of fiber content, respectively.
– The section repaired by means of a modest layer of HPFRCC (8 cm) with polyethylene or stainless steel fibers and retrofitted by one layer of CFRP wrapping can increase the section capacity. The HPFRCC with polyethylene fiber (2%) can improve about the 58% the resisting moment capacity of the section with respect to the one of the original undamaged sections. The HPFRCC with stainless steel fiber (2%) can improve about the 103% the resisting moment capacity of the section with respect to the one of the original undamaged sections.

One aspect considered relevant was the possibility of applying these techniques without changing the geometry of the elements and improving the durability of the structure, due to the presence of microfibers and the low porosity of the HPFRCC material. In this case, polyethylene fibers could be used in HPFRCC for the repair that requires a better distribution of finer cracks in the structure, consequently improving its resistance in relation to the entrance of aggressive agents. Proper anchorage of the new concrete jacket should be garanteed but it is not investigated here. This study is in progress and the anchorage problem will be discussed in a next paper.

References

1. Salvador Filho, J.A.A., Nuti, C., Santini, S., Lavorato, D., da Azeredo, J.R.: Mechanical properties of HPFRCC reinforced with different types and volumes of fibres. In: Anais do 58º Congresso Brasileiro do Concreto, CBC2016–58CBC (2016)

2. OpenSees structural software [computer software]. Berkeley, CA, Pacific Earthquake Engineering Research Center, University of California (2001)
3. Ranade, R., Stults, M.D., Li, V.C., Rushing, T.S., Roth, J., Heard, W.F.: Development of high strength high ductility concrete. In: 2nd International RILEM Conference on Strain Hardening Cementitious Composites. Rio de Janeiro, RILEM (2011)
4. Kim, S.W., Park, W.S., Jang, Y.I., Feo, L., Yun, H.D.: Crack damage mitigation and shear behavior of shear-dominant rein-forced concrete beams repaired with strain-hardening cement based composite. Compos. Part B (2015)
5. Wille, K., El-Tawil, S., Naaman, A.E.,:Properties of strain hardening ultra-high performance fibre reinforced concrete (UHP-FRC) under direct tensile loading. Cem. Concr. Compos. **48** (2014)
6. Yu, R., Spiez, P., Brouwersm, H.J.H.: Mix design and properties assessment of ultra-high performance fibre reinforced concrete (UHPFRC). Cem. Concr. Res. **56** (2014)
7. Lavorato, D., Nuti, C.: Pseudo-dynamic tests on reinforced concrete bridges repaired and retrofitted after seismic damage. Eng. Struct. **94**, 96–112 (2015)
8. Albanesi, T., Lavorato, D., Nuti, C., Santini, S.: Experimental program for pseudodynamic tests on repaired and retrofitted bridge piers. Eur. J. Environ. Civil Eng. **13**(6), 671–683 (2009) (Paris: Lavoisier)
9. Zhou, Z., Lavorato, D., Nuti, C., Marano, G.C.: A model for carbon and stainless steel reinforcing bars including inelastic buckling for evaluation of capacity of existing structures. COMPDYN 2015—5th ECCOMAS Thematic Conference on Computational Methods in Structural Dynamics and Earthquake Engineering, pp. 876–886 (2015)
10. Lavorato, D., Nuti, C.: Pseudo-dynamic testing of repaired and retrofitted RC bridges. fib Symposium PRAGUE 2011: Concrete Engineering for Excellence and Efficiency, Proceedings, 1, pp. 451–454 (2011)
11. Albanesi, T., Lavorato, D., Nuti, C., Santini, S.: Experimental tests on repaired and retrofitted bridge piers. In Proceedings of the International FIB Symposium, pp. 673–678 (2008)
12. Lavorato, D., Bergami, A.V., Nuti, C., Briseghella, B., Xue, J., Tarantino, A.M., Marano, G.C., Santini, S.: Ultra-high-performance fibre-reinforced concrete jacket for the repair and the seismic retrofitting of Italian and Chinese RC bridges. COMPDYN 2017—Proceedings of the 6th International Conference on Computational Methods in Structural Dynamics and Earthquake Engineering, 1, pp. 2149–2160 (2017)
13. Lavorato, D., Nuti, C.: Seismic response of repaired bridges by pseudodynamic tests. In: Bridge Maintenance, Safety, Management and Life-Cycle Optimization—Proceedings of the 5th International Conference on Bridge Maintenance, Safety and Management, pp. 11–15. Pennsylvania, USA (July 2010)
14. Lavorato, D., Nuti, C., Santini, S.: Experimental investigation of the seismic response of repaired R.C. bridges by means of pseudodynamic tests. In: IABSE Symposium, Large Structures and Infrastructures for Environmentally Constrained and Urbanised Areas, pp. 22–24. Venice (Sept 2010)
15. Lavorato, D., Nuti, C., Briseghella, B., Santini, S., Xue, J.: A Repair and retrofitting intervention to improve plastic dissipation and shear strength of Chinese RC bridges. In: Proceedings of IABSE Conference—Structural Engineering: Providing Solutions to Global Challenges. Geneva, Switzerland (2015)
16. Albanesi, T., Lavorato, D., Nuti, C., Santini, S.: Experimental tests on repaired and retrofitted bridge piers. Proceedings of the International FIB Symposium 2008—Tailor Made Concrete Structures: New Solutions for our Society, p. 151 (2008)
17. Imperatore, S., Lavorato, D., Nuti, C., Santini, S., Sguerri, L.: Shear performance of existing reinforced concrete T-beams strengthened with FRP. Proceedings of the 6th International Conference on FRP Composites in Civil Engineering, CICE 2012 (2012)
18. Imperatore, S., Lavorato, D., Nuti, C., Santini, S., Sguerri, L.: Numerical modeling of existing RC beams strengthened in shear with FRP U-sheets. Proceedings of the 6th International Conference on FRP Composites in Civil Engineering, CICE 2012 (2012)

19. Kashani, M.M., Crewe, A.J., Alexander, N.A.: Nonlinear stress–strain behavior of corrosion-damaged reinforcing bars including inelastic buckling. Eng. Struct. **48**, 417–429 (2013)
20. Kashani, M.M., Lowes, L.N., et al.: Phenomenological hysteretic model for corroded reinforcing bars including inelastic buckling and low-cycle fatigue degradation. Comput. Struct. **156**, 58–71 (2015)
21. Imperatore S., Lavorato D., Nuti C, Santini S, Sguerri L.: Shear behavior of existing RC T-Beams strengthened with CFRP. IABSE Symposium Report 99 (18):958–965 (2013)
22. Zhou, Z., Nuti, C., Lavorato, D.: Modeling of the mechanical behavior of stainless reinforcing steel. Proceedings of the 10th fib International PhD Symposium in Civil Engineering, pp. 515–520 (2014)
23. Hosotani, J., Kawashima, K. et al.: Discussion by Kappos, A.J. Stress-strain model for confined reinforced concrete in bridge piers. J. Struct. Eng. **124**(10), 1228–1230 (1998)
24. Hosotani, J., Kawashima, K., et al.: Stress-strain model for confined reinforced concrete in bridge piers. Member, ASCE. J. Struct. Eng. **123**(5), 624–633 (1997)

Overall Significance's Rank of Leadership Factors Amongst Critical Success Factors for Construction Projects

N. A. N. Nasaruddin and I. A. Rahman

Abstract Previous studies had identified several construction's critical success factors (CSFs) in their hierarchical order, and one of these factors is leadership. Eleven academic articles were found that produced list of these construction's CSFs in ranking order based on the significance of these factors towards the project success. Thus, this paper presents the average level of significance of leadership factors amongst CSFs. Level of significance for each leadership factor was determined based on formula presented in this paper. It was found that leadership factor was averagely 74.2% significance amongst to the CSFs. This implies the need of strong leadership role in ensuring construction project success which should be emphasized to parties involved in undertaking construction projects.

Keywords Critical success factors (CSFs) · Leadership · Construction project success

1 Introduction

Naturally, construction projects are complex, fragmented, resources-driven [1, 2] and sometimes require large and sophisticated plants for the operation. The need for construction projects is to fulfil the increase of living standard through improvement of infrastructure projects, consumption habit's pattern and naturally with the growth in population [3]. Hence, in the maiden stage of construction, parties involved have to be appointed to execute the project as stipulated in the contract document. Previously, several studies had indicated that many construction projects failed to adhere to main criteria for project success, which are within the contract time and cost, acceptable quality and safety on site [4, 5]. Relating to this issue, there are few aspects to be considered during construction project life cycle such as

N. A. N. Nasaruddin (✉) · I. A. Rahman
Faculty of Civil and Environmental Engineering,
Universiti Tun Hussein Onn Malaysia, Johor, Malaysia
e-mail: nurain_ngah@yahoo.com

financial, clients, value added and operational which related to construction project success [6]. Each aspect provides idea and direction towards the way to carry out construction project successfully. Consequently, all parties involved should be able to notify and manage the critical success factors (CSFs) well.

Amongst the important factors is leadership in manoeuvring construction's project success. Hence, this paper is intended to determine the degree of significance of leadership towards construction project success.

2 Importance of Leadership in Construction Project Success

Achieving successful construction project completion requires supporting of many parties in managerial position of leadership. Basically, managing construction project requires four basic management functions that comprise planning, organizing, directing and controlling [7]. While handling the project, there are problems and challenges from socioeconomic issues, limited resources, organizational drawback and incapable to deal with critical situations [8] and these can be rendered with construction leader not only good in managing but also smart in tackling these issue from getting worse. Hence, it is important to include leadership elements as a value added to the management function for successful construction project delivery [9].

In the construction industry, leadership is obviously synonym with key project management practitioners who play a vital role to keep construction project on track and driven to project success orientation. Construction leaders have to deal with various peoples, trades and attitudes so as their instructions can be imparted and followed throughout the project life cycle [10]. Moreover, good construction leaders should able to provide direction and motivation to subordinates in the organizational hierarchy and construction labours [11]. A review on previous studies indicates that a good leadership practice has contributed to 76% of projects success [12]. Hence, good leadership requires construction leader to possess a set of distinctive qualities to be applied in different circumstances of project complexity for success actual construction. Amongst principal good leadership attributes are team building, communication, visionary, planning and strategy, and decision-making [13].

3 Leadership Factor in Construction's Critical Success Factors

In this paper, critical success factor (CSF) is a term used to demonstrate inputs to construction project management system which will directly increase the potential of project success [14]. CSFs are important means to speed construction progress

Table 1 Leadership factors in construction's CSFs

References	Numbers of identified CSFs	Numbers of groups for CSFs	Font size and style
[16]	39	4	Competent project manager
[17]	80	8	Leadership and team management
[18]	22	–	Top management support
[19]	15	7	Team leader competent
[20]	57	–	Leadership of management
[21]	39	10	Leadership skills of project manager
[9]	12	–	Leadership and commitment of top management
[22]	46	–	Team leader's competence
[23]	71	7	Experience of project manager
[24]	12	–	Project manager efficiency
[7]	6	–	Leadership skills of the project manager

and guide the organization in facing pitfalls that might slow initiatives to project performance improvement [15]. There are many studies on identifying CSFs in ensuring construction project success and amongst these factors is leadership. The list of leadership factors extracted from 11 academic articles of construction's CSFs are summarizing as Table 1.

Table 1 indicates that there are 11 references that had identified CSFs for construction project. Based on this table, only five articles classified the CSFs in groups which varies between from 4 to 10 groups. It also shows the leadership factors which was highlighted in their identified CSFs to achieve construction project success.

4 Rank of Leadership Factor in CSFs

Besides identifying leadership factors as in Table 1, the articles also identified the hierarchical position of leadership in rank of all CSFs. The level of significance of leadership factor in construction's CSFs was extracted and illustrated as in Table 2. Significant percentage (SP) for leadership factor is calculated by the process of normalization using the following established formula:

$$\text{Significance percentage (SP)} = \left[\frac{(\text{no.of critical success factors - rank of leadership})}{\text{no.of critical success factors}} \right] \times 100$$

Table 2 Significance level of leadership factors in construction's CSFs

Leadership's factor in CSFs	Ranks of leadership factor in CSFs	Significance level of leadership factor (%)
Competent project manager	3rd in 39	92.3
Leadership and team management	30th in 80	62.5
Top management support	4th in 22	81.8
Team leader competent	5th in 15	66.7
Leadership of management	2nd in 57	96.5
Leadership skills of project manager	2nd in 41	95.1
Leadership and commitment of top management	1st in 12	91.7
Team leader's competence	13th in 46	71.7
Experience of project manager	36th in 71	49.3
Project manager efficiency	3rd in 12	75.0
Leadership skills of the project manager	4th in 6	33.3
Mean %		74.2

Table 2 illustrates the degree of significance of leadership in the construction's CSFs extracted from previous articles. Leadership factor in CSFs shows maximum and minimum significance percentage with 96.5 and 33.3%, respectively. The mean value of 74.2% is perceived as high and this indicates quality leadership is important to ensure the success of the construction project.

5 Conclusion

Leadership is seemingly significant to ensure the success of the construction project. It should be emphasized to construction practitioners on the importance of leadership aspect in managing their construction projects. Thus, it needs an outstanding construction leader with strong quality leadership criteria to faced project challenges in minimizing the risk of construction project failure. This study is as an initial step in determining the dominant characteristics of leadership towards construction project success.

References

1. Hussin, J.M., Rahman, I.A., Memon, A.H.: The way forward in sustainable construction: issues and challenges. Int. J. Adv. Appl. Sci. **2**(1), 15–24 (2013)
2. Subramani, T., Sruthi, P.S., Kavitha, M.: Causes of cost overrun in construction. IOSR J. Eng. **4**(6), 1–7 (2014)
3. Nagapan, S., Rahman, I.A., Asmi, A., Memon, A.H., Latif, I.: Issues on construction waste: the need for sustainable waste management. Colloquium Humanit. Sci. Eng. Res (CHUSER), pp. 325–330 (2012)
4. Zuofa, T., Ochieng, E.G.: Project failure: the way forward and panacea for development. Int. J. Bus. Manage. **9**(11), 59–71 (2014)
5. Olaniran, O.J.: The effects of cost-based contractor selection on construction project performance. J. Financ. Manage. Property Constr. **20**(3), 235–251 (2015)
6. Satankar, P.P., Jain, A.P.S.: Study of success factors for real estate construction projects. Int. Res. J. Eng. Technol. **2**(4), 804–808 (2015)
7. Amade, B., Ubani, E.C., Omajeh, E.O.M., Anita, U., Njoku, P.: Critical success factors for public construction delivery: a case of Oweri, Imo state. Int. J. Res. Manage. Sci Technol. **3**(1), 11–12 (2015)
8. Yadollahi, M., Mirghasemi, M., Zin, R.M., Singh, B.: Architect critical challenges as a project manager in construction projects: a case study. Adv. Civil Eng. **205310** (2014)
9. Taner, M.T.: Critical success factors for six sigma implementation in large-scale turkish construction companies. Int. Rev. Manage. Mark. **3**(4), 212–225 (2013)
10. Mouchi, G., Olabode Rotimi, J., Ramachandra, T.: The skill sets required for managing complex construction projects. Bus. Educ. Adm. **3**(1), 89–100 (2011)
11. Jung, Y., Mills, T.: Learning leadership skills from professionals in the construction industry. In: 3rd International Conference on Construction Engineering and Management (2009)
12. Nauman, S., Khan, A.M.: Patterns of leadership for effective project management. J. Qual. Technol. Manage (2008)
13. Nasaruddin, N.A.N., Rahman, I.A.: Leadership quality for Malaysia construction leader to steer a success construction project. MATEC Web Conf. **47** (2016)
14. Garbharran, H., Govender, J., Msani, T.: Critical success factors influencing project success in the construction industry. Afr. J. Online **19**(2), 90–108 (2012)
15. Alias, Z., Zawawi, E.M.A., Yusof, K., Aris, N.M.: Determining critical success factors of project management practice: a conceptual framework. Procedia-Social Behav. Sci. **153**, 61–69 (2014)
16. Toor, S.R., Ogunlana, S.O.: Critical coms of success in large-scale construction projects: evidence from Thailand construction industry. Int. J. Project Manage. **26**(4), 420–430 (2008)
17. Park, S.H.: Whole life performance assessment: critical success factors. J. Constr. Eng. Manage. **135**(11), 1146–1161 (2009)
18. Ogwueleka, A.: The critical success factors influencing project performance in Nigeria. Int. J. Manage. Sci. Eng. Manage. **6**(5), 343–349 (2011)
19. Yong, Y.C., Mustaffa, N.E.: Analysis of factors critical to construction project success in Malaysia. Eng. Constr. Architectural Manage. **19**(5), 543–556 (2012)
20. Von Meding, J., Maidi, D.P., Spillane, J., Bruen, J., McGrath, R.: Critical success factors of construction project quality in Brunei Darussalam. In: The International Conference on Sustainable Built Environment for Now and the Future (2012)
21. Omran, A., Abdulbagei, M.A., Gebril, A.O.: An evaluation of the critical success factors for construction projects in Libya. Int. J. Econ. Behav, 17–25 (2012)

22. Yong, Y.C., Mustaffa, N.E.: Critical success factors for Malaysian construction projects: an empirical assessment. Constr. Manage. Econ. **31**(9), 959–978 (2013)
23. Neringa, G., Audrius, B.: Prioritizing critical success factors influencing construction projects performance in Lithuania. Int. J. Adv. Manage. Econ. **3**(4), 19–25 (2014)
24. Varajao, J., Dominguez, C., Ribeiro, P., Paiva, A.: Critical success aspects in project management: similarities and differences between the construction and software industry management: industry. Tehnicki Vjesnik **21**(3), 583–589 (2014)

Relationship of Microcrack Pattern and the Shear Strength of Granitic Rock

M. P. Nur Irfah, M. R. Mohd Shahril and O. Husaini

Abstract Granitic rock can be found in abundance at the Banjaran Titiwangsa main range as the most dominant geology. The granitic slope with the fracture surface has produced the microcrack pattern that can affect the stability of the slopes at the Pos Selim area, which is located at the Banjaran Titiwangsa. The relationship of the microcrack pattern and the shear strength of the granitic rock is investigated as to know the behavior of the crack pattern with the shearing force. The granitic samples are collected at Pos Selim area which is identified as grade II slightly weathered conditions. The samples which are then tested using rock shear box test are applied with increasing normal load of 5, 10, 20, 30, and 40 kN, respectively. The microcrack pattern is observed using SEM image. The analysis of SEM image shows that the behavior of microcrack starts from the crack initiation with the small point at the center. The microcrack length extends into a larger crack and transverse from the center toward the side of the sample. When stress increases, the microcrack length tends to also increase until it reaches the peak point. Finally, further addition of shear stress will result in a decrease of microcrack length. The relationship of microcrack length and the shear stress is in the form of polynomial curve with second order ($R^2 = 0.955$). In conclusion, based on the relationship of microcrack pattern and shear strength, the highest shear stress is 6 MPa producing the 200 μm of microcrack length.

M. P. Nur Irfah (✉)
Civil Engineering Department, College of Engineering, Universiti Tenaga Nasional, Jalan UNITEN-IKRAM, 43009 Kajang, Selangor, Malaysia
e-mail: irfah@uniten.edu.my

M. R. Mohd Shahril
UEM Construction Sdn. Bhd, No 21-1, 22-1, First floor, Jalan Impian Mahkota 1, Taman Saujana Impian, 43000 Kajang, Selangor, Malaysia

O. Husaini
Faculty of Engineering, Universiti Putra Malaysia, 43400 UPM Serdang, Selangor, Malaysia

1   Introduction

The microcrack pattern occurs mainly within the mineral compositions. For example, granite rock consists of mica, feldspar, and biotite minerals. Thus, it can be seen that the cracks occurred within feldspar and oriented parallel to the drill core axis. The cracks are less abundant in feldspar because there is a disturbance of the crystal lattice if the feldspar is altered. Furthermore, the crack propagation is improved in micas and opaque due to the difference in the mechanical strength and E-modulus [1].

The shear strength where the slip surface of the rock tends to slides has effected the microcrack pattern. Microcrack highly dependents on the mineralogy, fabric, and microstructure of a given rock type. The deformed granite has about twice the crack density (crack length per unit area) as compared to undeformed granite. Based on its microcrack densities, the densities of microcracks have increased tremendously at the fracture tip, and the magnitude of fracture increases more in deformed rock as compared to undeformed rock [2].

The shear failure of brittle rock can be more complicated process involving a number of stages of damage accumulation rather than tensile failure. It is generally accepted that brittle fracture results from the interaction of microcrack within a rock mass [3]. In this study, the microcrack pattern is analyzed based on its macroscopic image during pre-shear and post-shear stage. The microcrack length and the crack pattern are analyzed and measured at pre-shear and post-shear stage.

2   Microcrack Pattern of Granitic Rock

Granitic rock, which consists of biotite, feldspar, quartz, and mica minerals, has a unique microcrack pattern. The granitic rock has a crack initiations pattern that starts from the small point and extended to a larger crack. The larger crack was then split the samples into two. As compared to limestone rock, the microcrack pattern in limestone starts from small micropores. The micropores start to extend, and it propagates into microcrack length. The microcrack length is then transverse from the left side to the right side. Some of the micropores from limestone tend to dissolve [4].

Based on the granite microcracking pattern studied by [5], they observed the transgranular microcracks are formed in a plane perpendicular to the core axis. To know the degree of stress-induced core damage, the ratio horizontal to axial transgranular microcracking could be an indicator. The dominant mode of microcracks can be termed as naturally occurring for the core depth less than 200 m. The stress-induced microcracks are linearly proportional to the grain boundary, intergranular, and transgranular microcracks, which are constant regardless of any depth

of the core. The indicator of the degree of stress induced in core damage is depending on the ratio of horizontal to axial transgranular microcrack. Most of the transgranular microcracks are formed in a plane perpendicular to the core axis [5].

Based on [6], the initiation and propagation of microcracks in granitic rock under stress are highly dependent upon the mineralogical and textural characteristic of the various lithotypes. Detailed observation and quantification of microcracks before and after uniaxial compression test were conducted. During uniaxial compression, the intergranular microcrack, which is the dominating crack type, is gradually transformed or organized into transgranular cracks. Knowledge of the mineralogical and textural characteristics may assist in the prediction of potential development of failure surfaces of an ultrabasic rock in service.

It can be summarized that the microcracking behavior based on the literature, the microcrack is stress induced, and its initiation and propagation are highly dependent upon the mineralogical and textural characteristics of the various lithotypes. Microcrack starts in feldspar and oriented parallel to the drill core axis. However, if the feldspars are altered, cracks are less abundant because of the disturbance of the crystal lattice.

3 Methodology of Research

The methodology of the research starts from identifying the problem statement. In Malaysia, especially at the mountainous, areas such as Cameron Highland area have many landslide events. The landside of rock slope is caused by the fracture of the rock which extends into rock slope failure. The fracture which is studied in the microscopic scale with stress induced as to get the microcrack pattern analysis is the main objective of this research. The behavior of microcrack pattern of granitic rock is reviewed in the literature review. Two experimental works are conducted such as Robertson direct shear box test and scanning electron microscope. Granite core samples were collected at Pos Selim area 20 km away from Cameron Highland. For the direct shear box test, the shear stress is applied to the rock with increasing normal stress. The applied normal stress are 5, 10, 20, 30, and 40 kPa. The SEM image is taken before the direct shear test and after the direct shear test. The microcrack pattern for pre-shear and post-shear was recorded and analysis has been done. SEM is scanning electron microscope which used the electron to magnify the microcrack on the rock surface. The correlations of the microcrack with the stress induced are obtained from the analysis of the result. The detailed methodology of the research is shown in Fig. 1.
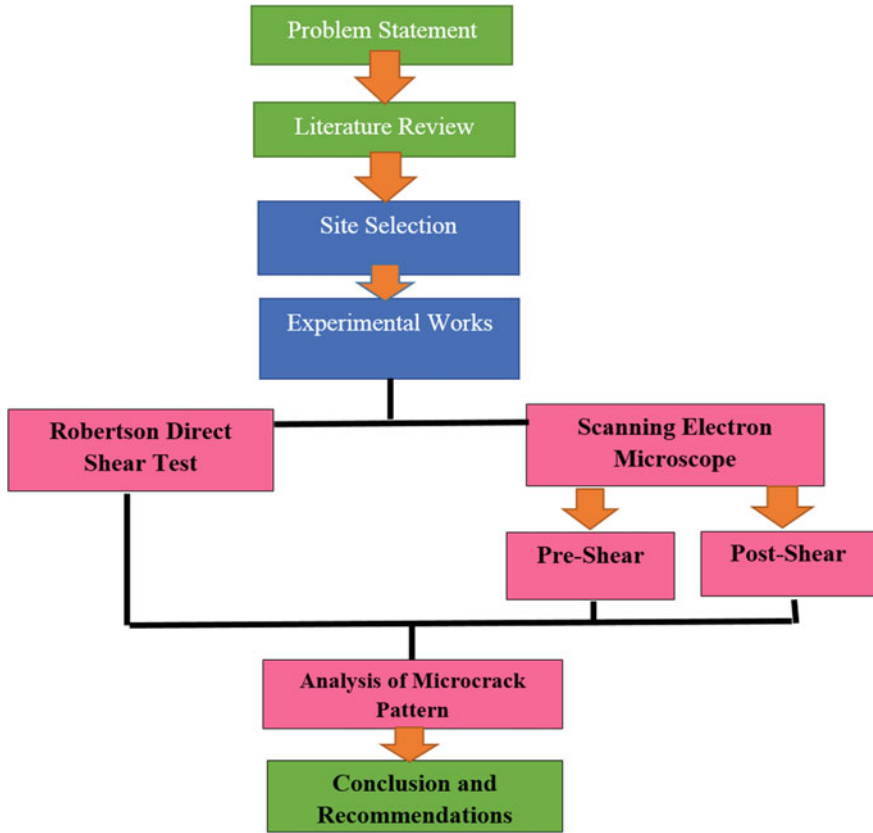
Fig. 1 Methodology of research

4 Results of the Microcrack Pattern and Shear Strength

4.1 Microcrack Pattern for Grade II

The results of SEM image for grade II of weathered granite are shown in Figs. 2 and 3. Figure 2 shows the microcrack pattern before applying the shear stress, and Fig. 3 shows the microcrack pattern after the shear stress test. Table 1 shows the SEM image analysis, and Table 2 shows the shear strength and microcrack pattern. Figure 4 gives the graph of shear stress versus microcrack length.

Grade II
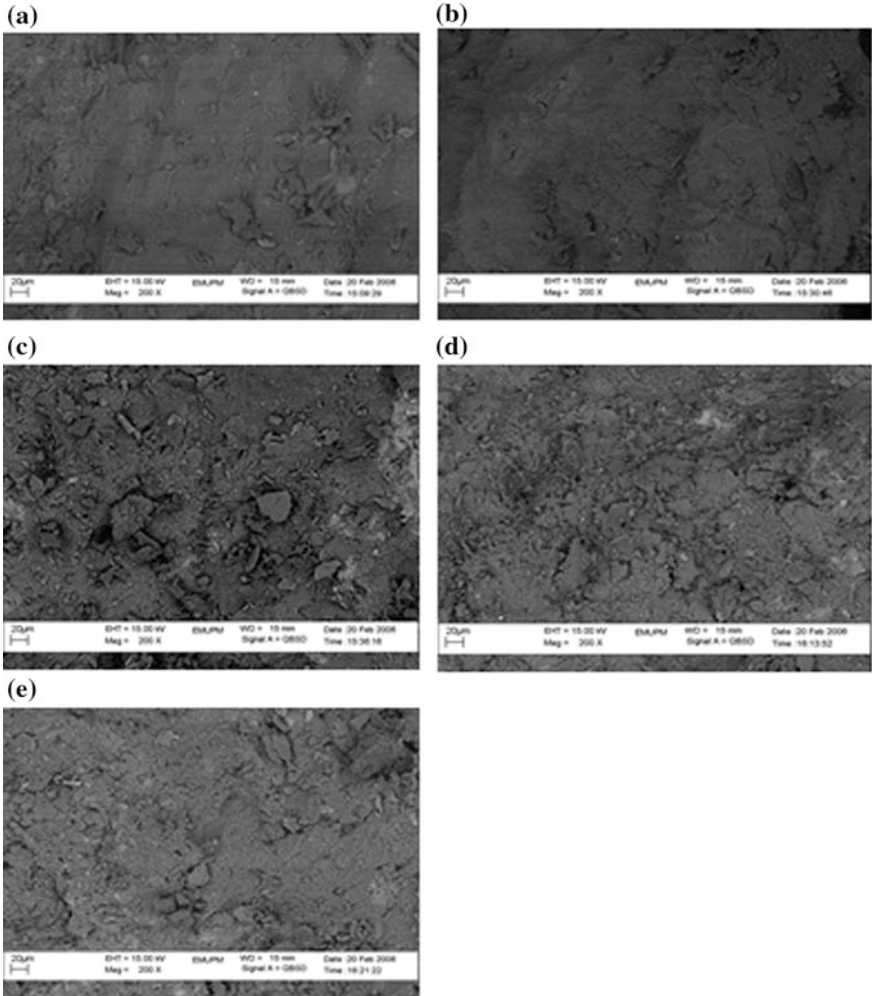
Fig. 2 Pre-shear SEM image of microcrack pattern of grade II granitic rock

5 Discussion of Shear Stress and Microcrack Length

The results for sample S21–S25 during the pre-shear stress show that the shear surface is slightly fractured with no transgranular crack. After the sample is sheared by applying the normal stress of 2.7 MPa, there is a presence of open crack at the top and below of the specimen. The SEM image is shown in Fig. 3. The open crack occurs along the feldspar area, and the intergranular crack has gradually become the transgranular crack. As the normal stress is increased to 5.9, 11.4, 16.6, and 21.8 MPa, the optimum microcrack length is at 30 kN loading with the longest

Grade II

(a) Loading 5 kN
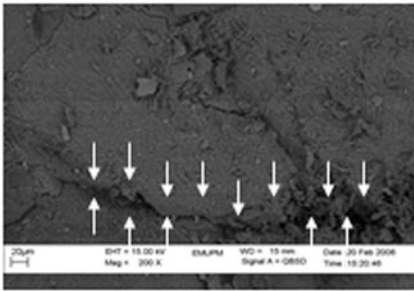
(b) Loading 10 kN
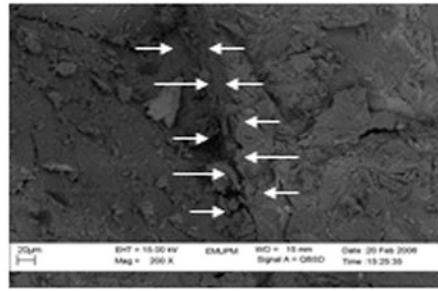
(c) Loading 20 kN
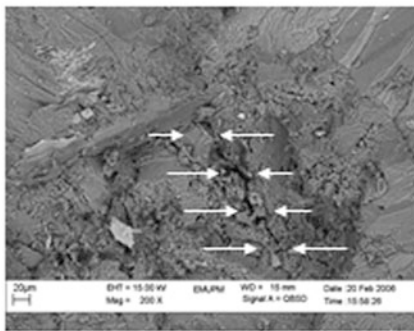
(d) Loading 30 kN
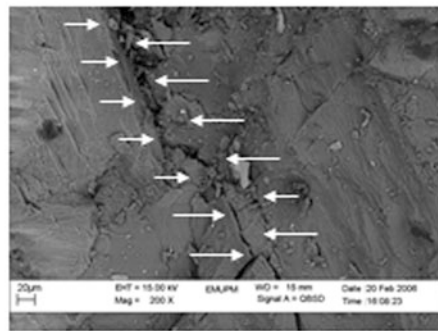
(e) Loading 40 kN
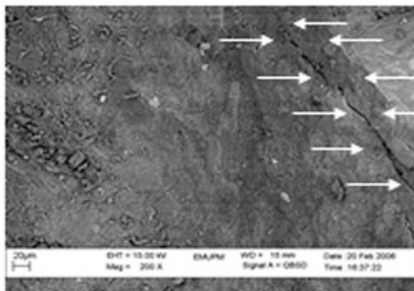
Fig. 3 Post-shear SEM image of microcrack pattern of grade II granitic rock

microcrack length of 260 μm. The largest crack which started from one side travels to another side. The presence of large transgranular crack at the center enlarging toward the outer of the sample. As the normal stress is at the maximum, which is 21.8 MPa, the crack length reduces to 200 μm. Based on the SEM image, only small fracture presence and the open crack at the outer of the specimen.

Table 1 SEM analysis data (sample S21–S25 in grade II)

Sample no	Normal load (kN)	Crack length (μm)		Percentage of sheared surface (%)		Microscopic fracture characteristics	
		Pre-shear	Post-shear	Pre-shear	Post-shear	Pre-shear	Post-shear
S21	5	0	300 (below) 120 (top)	0	45	The surface is slightly fractured with no transgranular crack	The presence of open crack on the surface at the top and below of the specimen
S22	10	20	140 (top) 60 (center)	0	50	The is small fracture on the surface, smooth surface	Open crack at the top and center of the specimen
S23	20	0	140	0	55	Presence of small fracture area	Presence of transgranular crack which starts from outer toward the center of the specimen
S24	30	20	260	0	60	Small crack on the specimen, surface undulating	Presence of large transgranular crack at the center enlarging toward the outer
S25	40	40	200	0	65	Small fracture presence	Open crack at the outer of the specimen

Table 2 Shear strength and microcrack length

Sample no	Normal load (kN)	Normal stress (MPa)	Shear stress (MPa)	Microcrack length (μm)
S21	5	2.7	2.1	300
S22	10	5.9	3.6	140
S23	20	11.4	3.1	140
S24	30	16.6	4.2	260
S25	40	21.8	6.0	200

The graph in Fig. 4 shows the shear stress against the microcrack length for granitic sample. The shear stress and microcrack length have a polynomial with second-order relationship which can be described as follows, Eq. (1):

Fig. 4 The shear stress versus microcrack length for granitic samples
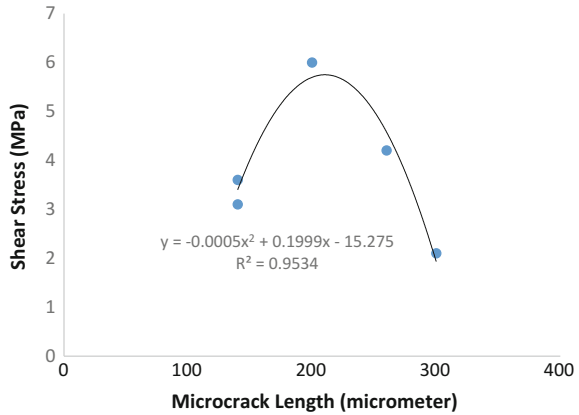
$$y = -0.0005x^2 + 0.199x - 15.275 \qquad (1)$$

where x is the microcrack length, and y is the shear stress values. The shear stress increases with the microcrack length. The shear stress increases until it reaches the peak point. The shear stress reduces with the increase of microcrack length. This has been proven from the graph shown in Fig. 4. The microcrack length at the 2.7 MPa normal stress gives the microcrack length of 300 µm. The maximum normal stress of 21.8 MPa gives the microcrack length of 200 MPa and shear stress of 6.0 MPa. The bell-shaped curve with the optimum microcrack length at 260 µm is obtained from the shear stress and microcrack pattern analysis.

6 Conclusion

In conclusion, the microcrack pattern has been observed using SEM image, and the crack length started with the small intergranular crack and extended into larger cracks. The crack pattern was then transverse into boundary grain between the minerals. The microcrack length of the granitic rock increases with the increase of shear stress, and it reaches the maximum point. The maximum normal stress of 21.8 MPa gives the microcrack length of 200 MPa and shear stress of 6.0 MPa. The optimum microcrack length is 260 µm. The knowledge from this relationship will give the indications for the crack pattern with the shear strength as to study its behavior that will affect the stability of slopes. The weak surface of the rock is at the weak mineral components such as feldspars and followed by mica, biotite, and quartz.

References

1. Urban, A., Jan, H., Jimmy, S.: Characterisation of microcracks in the bohus granite, western Sweden caused by uniaxial cyclic loading. J. Eng. Geol. **72**(1–1), 131–142 (2004)
2. Moore, D.E., Lockner, D.A.: The role of microcracking in shear-fracture propagation in granite. J. Struct. Geol. **17**(1), 95–111, 113–114 (1995)
3. Moore, D.E., Lockner, D.A., Reches, Z.: Microcrack interaction leading to shear failure. In: The 33th US Symposium on Rock Mechanics (1992)
4. Nur Irfah, M.P., Husaini, O., Bujang, K.H., Halina, M., Zainuddin, M.Y.: Microcrack pattern propagation and rock quality designation of Batu Caves limestone. Electron. J. Geotech. Eng. **16F**, paper 2011–045, 591–603 (2011)
5. Seong, S.L., Derek, C.M., Urban, A.: In-situ stress and micro-cracking in granite cores with depth. J. Eng. Geol. 147–148 (2012)
6. Ioannis, R., Basilios, T., Panagiotis, P., Konstantin, H.: Microcracks in ultrabasic rocks under uniaxial compressive stress. J. Eng. Geol. **117**(1–2), 104–113 (2011)

Causes of Delay and Cost Overrun in Malaysian Construction Industry

Muhammad Muhammad Tahir, Nuzul Azam Haron,
Aidi Hizami Alias and Ikechukwu A. Diugwu

Abstract The construction industry in Malaysia drives the economic growth and development of the country. However, the industry is plagued with delays and cost overrun which transforms what should have been successful projects to projects incurring additional costs, disagreements, litigation and in some cases abandonment of projects. This research studied the causes of delays and cost overrun in the industry and ranked them according to their perceived importance to the contractors, with a view to establishing those to be addressed by the contractors. Online questionnaires were used for data collection for this research. A total of 69 responses were analysed using principal component analysis (PCA) (factor analysis) to identify the main causes. The result of the analysis showed that delay in preparation of design document, poor schedule and control of time, delay in delivery of material to site, lack of knowledge about the different defined execution methods, shortage of labour and material in market, and changes in scope of work were the main causes of delay and cost overrun. The identified causes if properly addressed would reduce the rate of delays and cost overrun in construction projects, thus enhancing the economic growth and development of the country.

Keywords Cost overrun · Construction industry · Delays

M. M. Tahir (✉) · N. A. Haron (✉) · A. H. Alias
Department of Civil Engineering, University Putra Malaysia, Serdang, Malaysia
e-mail: Mtahir1129@gmail.com

N. A. Haron
e-mail: nuzul@upm.edu.my

A. H. Alias
e-mail: aidihizami@upm.edu.my

I. A. Diugwu
Project Management Technology Department, Federal University
of Technology Minna, Akure, Nigeria
e-mail: i.diugwu@aim.com

1 Introduction

The Malaysian construction industry accounted for between 11.9 and 13.1% of the national gross domestic product (GDP) of Malaysia in the four quarters of 2016 [1]. The construction industry in Malaysia plays a vital role in its economic growth. It offers job opportunities and increment to the people's quality of life by providing essential socio-economic infrastructures, such as offices, roads, houses and schools. Malaysia is progressively marching towards industrialization and the construction industry role is been enhanced at the same time with the aim of bringing to reality the needs and aspiration of its population [2].

Although this indicates that the infrastructural development and the economic growth in Malaysian which is been driven by the construction industry often experience delays and cost overruns. Consequently, the level of impact on the economy is affected due to the incurred cost that was not budgeted for, differences resulting from disagreements, litigations and abandonment in some cases [3].

Cost and time control in construction project has been one of the most important issues in construction since the emergence of the industry [4]. A successful project, in addition to satisfying quality output standards, must also satisfy time and budget objectives. Time and cost performance are fundamental criteria used in the assessment of how successful a project is. However, it is very common in the construction industry that projects are rarely completed on time which is as a result of issues emanating from ineffective cost and time controls [5]. Similarly, [6] stated that the two major concerns in managing construction projects are cost and time control. Most of the features of projects that give rise to delay and cost overruns vary most times alongside with the project type, location, sizes and scopes. However, construction projects are becoming more complex as they now involve many stakeholders from different disciplines. The management and control of cost and time in construction is fundamental to the success of many projects. A study that was carried out on cost overrun by Chartered Institute of Building (CIOB) in 2008 reported that 90% of public works projects have issues associated with cost overruns [7]. This shows that delay and cost overrun are global issues.

Specifically, the Malaysian construction industry has experienced numerous cases of project delays and cost overruns that have led to additional project costs and impacted negatively on the sector [8]. For instance, the industry, when compared to other industries in the country, has suffered approximately 20–25% decline in the last few years [9]. As a result, the Malaysian construction industry is regarded as the industry facing poor performance leading to failure in achieving effective and efficient cost and time management [10, 11].

Presently, a number of tools that can be used for cost and time control have been developed [12]. However, there are variations in functions, with some designed specifically for particular type of projects [13]. Some of these tools include Earned Value Management (EVM), Gantt Bar Charts, Critical Path Method (CPM) and Program Evaluation and Review Technique (PERT) [14, 15]. In addition to the development of these tools, software packages have been developed to assist in the

use of these project control tools such as Microsoft Project, Primavera, Asta Power Project, etc. But, in spite of the development and use of these tools and software packages, construction projects still suffer delays and cost overruns.

Existing studies on the causes of delay and cost overrun in Malaysian construction industry have shown that time and cost performance are an important issue that needs to be addressed in the industry [2, 3, 16–19].

2 Related Studies

Previous researches conducted have shown that project delays are common and costly, and occur in almost every construction project, though to varying degrees and magnitude [2]. This makes the study of the causes of these delays imperative, if there were to be effective project management. As a result of the overriding importance of time for both the owner (in terms of performance) and the contractor (in terms of money), it is the source of frequent disputes and claims, often leading to litigations.

In Malaysia, the construction industry contributes to the economic expansion of the country and serves as an engine of growth [18, 20, 21]. However, the construction industry's contributions are been threatened by escalating cost and time overruns [17, 19, 22–24]. The delay factors most times vary from project to project [8]. Below are some of the causes of delay and cost overrun (Table 1).

This has shown that there have been several studies conducted on project delays and cost overruns globally. These studies, continuous research and advancement in technology for controlling delays and cost overrun in the industry, notwithstanding, delays and cost overrun still occur. This makes it an important issue to be studied frequently in order to develop means to solving this phenomenon. This research seeks to identify the major causes of delay and cost overrun in Malaysian construction industry from the viewpoint of contractors.

3 Methodology

This study adopted a quantitative methodology in the identification of the different causes of delay and cost overrun in Malaysian construction industry. A questionnaire survey was used as a data gathering tool. A draft copy of the questionnaire on causes of delay and cost overrun in the industry was developed and given to lecturers and postgraduate students. A revised questionnaire based on the above was then given to 10 respondents. These two steps helped in ensuring both face and content validity of the questionnaire, and ensured questions asked would be understood by respondents to the main questionnaire. Published tables were used for determining the sample size. The sampling frame for the study comprised of the G7 rated civil engineering construction companies that are registered with CIDB in the Klang region of

Table 1 Causes of delay and cost overrun

S. no.	Causes	Source
1	Poor site management and supervision, unforeseen ground conditions, project team slow rate in making decisions, changes in scope caused by initiated and necessary variations of work by the project sponsors	[25]
2	Changes initiated by the designers, weather, client requirement, late deliveries, site condition and economic conditions	[26]
3	Poor management of site, unforeseen ground conditions, change orders and poor decision-making	[25, 27]
4	Changes in design, poor planning and labour productivity. Poor site management, late payment, labour supply, improper planning, lack of experience, problems with subcontractors and shortage of materials	[18]
5	Client organisations delay in payments, modification of contracts, economic hardship, procurement materials, design changes, staffing issues, lack or unavailability of working equipment, poor supervision, mistakes during construction, poor site coordination, specification changes and labour disputes	[28]
6	Poor design, resource and labour shortages, poor project planning, inefficient contractor management, financial difficulties and change orders	[29]
7	Change in design	[30]
8	Financial problems and coordination problems	[2]
9	Delay factors such as shortage of materials, change orders, delay in payment of suppliers, poor management of site and late submission of drawings are the main causes of delay	[17]
10	Labour productivity, slow decision-making, inflation, material delivery and insufficient equipment	[31]
11	Contractors and factors associated with finance	[3]

Malaysia. Thus, sampling was confined to specific groups of construction companies who could provide the desired information set by the researchers. According to CIDB Malaysia (2016), there are 187 registered G7 rated construction companies in Klang region. From the published table used [32], the minimum sample size for the population study was set at 67 at ±10% precision level. Data collection was carried out using questionnaires, while SPSS version 23 was used for data analysis which focused on frequency distribution and descriptive analysis. While principal component analysis (PCA) using factor analysis was used in identifying the key causes of cost overrun and delays from the responses, the test for reliability of response items was based on Cronbach's alpha test.

4 Result and Discussion

The respondents of the questionnaire survey who are representatives of the different G7 rated companies had different backgrounds in terms of job positions, level of education, working experience and working experience with BIM. The distribution

of these variables was analysed using descriptive analysis. The summary of the respondents' distribution is shown in Table 2.

The result of the analysis of respondents' job position shows that (33.3%) been the highest percentage of respondents are engineers, followed by project managers with (20.2%), while only (7.2%) of the respondents were directors in their companies. More also, the frequency distribution of the respondents' level of education indicated that (49.3%) of the respondents have masters' degree (M.Sc.), and (40.6%) had B.Sc. educational qualifications. The result from the frequency distribution table (Table 2) also showed that (52.2%) of the respondents have more than 10 years working experience in the construction industry, and (30.4%) of the respondents have less than 5 years working experience in the industry. While only (17.4%) of the respondents have industry working experience between 5 and 10 years. The three characteristics of the respondents' (job position, level of education and industry working experience) showed that the respondents are qualified to answer the questions contained on the questionnaires used for this research. Most of the respondents are well educated and have substantial working experience in the industry which makes them valid respondents for the questionnaire administration.

The reliability and internal consistency of the questions were tested using Cronbach's alpha test. The scale reliability and internal consistency for the 19 items tested which is the alpha coefficient was 0.904. Similarly, Kaiser-Meyer-Olkin measure of sampling adequacy was 0.776, which is above the commonly suggested value of 0.600, while the Bartlett's test of sphericity was significant (χ^2 (171) = 697.262, $p < .01$). Table 3 shows the commonalities were all above 0.5, an indication that all the items have some common variance with one another. In view of the results of the above analyses, all the items (19) are suitable for the analysis. The principal component analysis was used for the analysis, because the principal aim of the analysis is to ascertain the main causes of cost overrun and delays in Malaysian construction industry.

Table 2 Frequency distribution of respondent's demographic characteristics

Variable	Level	Frequency	Percentage
Job position	Director	5	7.2
	Project manager	14	20.2
	Technical officer	7	10.1
	Engineer	23	33.3
	Architect	7	10.1
	Others	13	18.8
Level of education	B.Sc.	28	40.6
	M.Sc.	34	49.3
	Ph.D.	2	2.9
	Other	5	7.2
Industry working experience	Less than 5 years	21	30.4
	Between 5 and 10 years	12	17.4
	More than 10 years	36	52.2

Table 3 Communalities

S. no.	Items	Initial	Extraction
1	Poor schedule and control of time	1.000	.777
2	Delay in preparation of design documents	1.000	.765
3	Ineffective communication between stakeholders	1.000	.683
4	Changes in laws and regulations	1.000	.677
5	Low productivity of labour	1.000	.682
6	Lack of knowledge about the different defined execution methods	1.000	.793
7	Adherence to outdated/old construction methods	1.000	.799
8	Extreme weather and environmental conditions	1.000	.714
9	Delay in delivery of materials to site	1.000	.829
10	Poor budget and cost control	1.000	.762
11	Inaccurate estimates	1.000	.703
12	Lack of contractor/subcontractor's experience	1.000	.775
13	Error in technical documents	1.000	.740
14	Error during construction	1.000	.751
15	Changes in scope of work	1.000	.714
16	Poor contract management and experience of consultant	1.000	.778
17	Financial issues	1.000	.760
18	Shortage of labour and materials in market	1.000	.792
19	Low level of productivity of labour	1.000	.685
Extraction method: principal component analysis			

Six components with eigenvalues greater than one were found. The eigenvalues and total variance explained by the six components are shown in Table 4. The eigenvalues after Varimax rotation showed that the first factor explained (37.5%) of the variance, the second factor (10.12%) of the variance, the third factor (8.28%) of the variance, the fourth factor (7.23%) of the variance, fifth factor (6.12%) of the variance, while the sixth factor explained (5.37%) of the variance. These six factors explain (74.61%) factor structure of the total variance among the items.

The 'Varimax rotational matrix' in Table 5 shows the correlation of each of the items with the six components with eigenvalues greater than (1) that were selected. The correlation relationship ranges from (−1) to (+1) indicating the strength of the relationship. The minimum criteria for the correlation of the variables with the extracted components are set at 0.4. None of the items were eliminated as they all contribute to the simple factor structure and meet the minimum criteria of having a correlation of 0.4 with at least one of the extracted components. All of the variables have an acceptable positive correlations coefficient with at least one of the components. The variables with the highest correlation with each of the components can be named after the components as they show very high positive correlation with the components when compared to the other items [33].

Table 4 Total variance explained

Component	Initial eigenvalues			Extraction sums of squared loadings			Rotation sums of squared loadings		
	Total	% of variance	Cumulative %	Total	% of variance	Cumulative %	Total	% of variance	Cumulative %
1	7.125	37.498	37.498	7.125	37.498	37.498	2.794	14.708	14.708
2	1.923	10.119	47.617	1.923	10.119	47.617	2.438	12.833	27.541
3	1.573	8.278	55.895	1.573	8.278	55.895	2.378	12.515	40.056
4	1.374	7.233	63.128	1.374	7.233	63.128	2.324	12.229	52.285
5	1.162	6.117	69.244	1.162	6.117	69.244	2.296	12.085	64.370
6	1.020	5.369	74.614	1.020	5.369	74.614	1.946	10.243	74.614
7	.694	3.650	78.264						
8	.652	3.431	81.695						
9	.577	3.035	84.729						
10	.563	2.961	87.691						
11	.438	2.307	89.998						
12	.387	2.036	92.034						
13	.335	1.762	93.795						
14	.311	1.634	95.430						
15	.264	1.387	96.817						
16	.201	1.060	97.876						
17	.179	.945	98.821						
18	.131	.690	99.511						
19	.093	.489	100.000						

Extraction method: principal component analysis

Table 5 Rotated component matrix

S. no.	Items	Component					
		1	2	3	4	5	6
1	Poor schedule and control of time		.826				
2	Delay in preparation of design documents	.841					
3	Ineffective communication between stakeholders			.680			
4	Changes in laws and regulations				.371		.595
5	Low productivity of labour			.647			
6	Lack of knowledge about the different defined execution methods					.842	
7	Adherence to outdated/old construction methods					.816	
8	Extreme weather and environmental conditions		.382	.622			
9	Delay in delivery of materials to site			.830			
10	Poor budget and cost control	.397	.692				
11	Inaccurate estimates	.530	.471				.385
12	Lack of contractor/subcontractor's experience		.436		.612	.449	
13	Error in technical documents	.477					.558
14	Error during construction		.595		.357		.355
15	Changes in scope of work						.799
16	Poor contract management and experience of consultant	.764					
17	Financial issues	.626			.389		
18	Shortage of labour and materials in market				.811		
19	Low level of productivity of labour				.737		

Extraction method: principal component analysis
Rotation method: Varimax with Kaiser normalisation

The first component had positive significant correlations with six (6) of the variables and had its highest correlation with the item 'delay in preparation of design documents'. The late submission of drawings, change orders and poor site management are among the main causes of cost overrun and delays in Malaysian construction industry [17]. The findings of this research have shown that this issue still exists in the industry.

More also, the second component had positive significant correlations with six (6) of the variables also and had its highest correlation with the item 'poor schedule and control of time'. Similar researches by Alaghbari et al. [2] and Kaliba and Muya [28] are in agreement with the findings of this research. Both authors

identified poor schedules and control of time as an important issue that needs to be addressed in order to reduce delays and cost overrun in the industry.

Similarly, the third component had positive significant correlations with four (4) of the variables and had its highest correlation with the item 'Delay in delivery of materials to site'. This is in agreement with the findings of Al-Momani [26] and Al-Tmeemy and Abdul-Rahman [31] that stated in their separate researches that the delay in the delivery of materials to the site is among the main causes of delay in construction projects.

While the fourth component had positive significant correlations with six (6) of the variables and had its highest correlation with the item 'shortage of labour and materials in market'. This is similar to the findings of Sambasivan and Soon [18] that shortage of materials in market and labour were among the main causes of delay and cost overrun in Malaysia.

The lack of knowledge about different defined execution models, poor contract management by consultant, governmental inefficiencies and mistakes in technical documents among others were findings of Abd El-Razek and Bassioni [34] on the causes of delay and cost overrun in Malaysian construction industry. This concurs with the result from the fifth component that had positive significant correlations with only three (3) of the variables and had its highest correlation with the item 'Lack of knowledge about the different defined execution methods'.

This is contrary to the findings of Alaghbari et al. [2] who conducted a study on the causes of delay in construction projects in Malaysia and found that 'financial problems' and 'coordination problems' were the two most important factors causing delay in construction projects in Malaysia. The sixth component had positive significant correlations with five (5) of the variables and had its highest correlation with the item 'changes in scope of work'. This concurs with findings of other researchers who conducted similar studies on the causes of delay in Malaysia and other countries. Changes in design (change in scope) are regarded as the most significant cause of poor time and cost control from practitioners point of view [30]. Similarly, Sambasivan and Soon [18] stated that predominantly, delays occur as a result of changes in scope, poor schedule and planning, and labour productivity. More also, in Thailand, the main causes of delay were identified to include poor project planning and control, change orders and many more [29]. The result of the study confirms the findings of these researchers and many more in stating that changes in the scope of work are among the main causes of delay in construction projects.

5   Conclusion

The result from the analysis showed delay in preparation of design document, poor schedule and control of time, delay in delivery of material to site, lack of knowledge about the different defined execution methods, shortage of labour and material in market, and changes in scope of work as the main causes of delay and cost overrun.

This implies that even with the advancement of technology, the Malaysian construction industry still faces set back due to the occurrence of these causes of delay and cost overrun. However, studies have shown that the use of advanced technologies such as Industrialised Building Systems (IBS) and Building Information Model (BIM) reduces the occurrence of these causes. The industry in collaboration with the government will need to put in more effort in creating awareness and the need for the use of these advanced technologies in order to reduce the occurrence of these causes of delay and cost overrun. More also, the identified causes if properly addressed using the suggested advanced technologies, should reduce the occurrence of delays and cost overrun. This will in turn increase the economic growth and development of the country at large.

References

1. Department of Statistics (DOSM): National Accounts: Quarterly Gross Domestic Product (Fourth Quarter 2016). Department of Statistics, Editor. 2017, Department of Statistics, Malaysia: Kuala Lumpur (2017)
2. Alaghbari, W.E., et al.: The significant factors causing delay of building construction projects in Malaysia. Eng. Constr. Architectural Manag. **14**(2), 192–206 (2007)
3. Shehu, Z., Endut, I.R., Akintoye, A.: Factors contributing to project time and hence cost overrun in the Malaysian construction industry. J. Financ. Manage. Property Constr. **19**(1), 55–75 (2014)
4. Minchin Jr., R.E., et al.: Comparison of cost and time performance of design-build and design-bid-build delivery systems in Florida. J. Constr. Eng. Manage. **139**(10), 04013007 (2013)
5. Forbes, L.H., Ahmed, S.M.: Modern Construction: Lean Project Delivery and Integrated Practices (2010) (CRC Press)
6. Rasdorf, W.J., Abudayyeh, O.Y.: Cost-and schedule-control integration: issues and needs. J. Constr. Eng. Manage. **117**(3), 486–502 (1991)
7. Flyvbjerg, B., Holm, M.S., Buhl, S.: Underestimating costs in public works projects: error or lie? J. Am. Plann. Assoc. **68**(3), 279–295 (2009)
8. Enshassi, A., Al-Najjar, J., Kumaraswamy, M.: Delays and cost overruns in the construction projects in the Gaza Strip. J. Financ. Manage. Property Constr. **14**(2), 126–151 (2009)
9. JBIM: Official publication of the national BIM standard (NBIMS) and the national institute of building science. J. Build. Inf. Model (2007) (Washington D.C.)
10. Ismail, I., et al.: Comparative Study on Time Management Practices in Construction Industry Between Kedah and Kelantan (2013)
11. Rahman, I.A., et al.: Time and cost performance of costruction projects in southern and cenrtal regions of Penisular Malaysia. In: 2012 IEEE Colloquium on Humanities, Science and Engineering (CHUSER) (2012)
12. Mohd-Nor, M., Grant, M.P.: Building information modelling (BIM) in the malaysian architecture industry. WSEAS Trans. Env. Dev. **10**, 264–273 (2014)
13. Yamin, R.A., Harmelink, D.J.: Comparison of linear scheduling model (LSM) and critical path method (CPM). J. Constr. Eng. Manage. **127**(5), 374–381 (2001)
14. John, N.: Project Management for Business and Technology. Prentice Hall (2003)
15. Lester, A.: Project Planning and Control. Butterworth-Heinemann (2003)
16. Bazjanac, V.: Virtual Building Environments (VBE)-Applying Information Modeling to Buildings (2006)

17. Ramanathan, C., Potty, N.S., Idrus, A.B.: Analysis of time and cost overrun in Malaysian construction. In: Advanced Materials Research. Trans Tech Publications (2012)
18. Sambasivan, M., Soon, Y.W.: Causes and effects of delays in Malaysian construction industry. Int. J. Project Manage. **25**(5), 517–526 (2007)
19. Ting, S., Khoo, H., Wong, S.: Project Management Development in Malaysia: A Case Study. Department of Civil Engineering, Faculty of Engineering, University Malaysia (2009)
20. Doloi, H., et al.: Analysing factors affecting delays in Indian construction projects. Int. J. Project Manage. **30**(4), 479–489 (2012)
21. Memon, A.H., et al.: BIM in Malaysian construction industry: status, advantages, barriers and strategies to enhance the implementation level. Res. J. Appl. Sci. Eng. Technol. **8**(5), 606–614 (2014)
22. Kaming, P.F., et al.: Factors influencing construction time and cost overruns on high-rise projects in Indonesia. Constr. Manage. Econ. **15**(1), 83–94 (1997)
23. Ofori, G.: Programmes for improving the performance of contracting firms in developing countries: A review of approaches and appropriate options. Constr. Manage. Econ. **9**(1), 19–38 (1991)
24. Ofori, G.: Research on construction industry development at the crossroads. Constr. Manage. Econ. **11**(3), 175–185 (1993)
25. Chan, D.W., Kumaraswamy, M.M.: A comparative study of causes of time overruns in Hong Kong construction projects. Int. J. Project Manage. **15**(1), 55–63 (1997)
26. Al-Momani, A.H.: Construction delay: a quantitative analysis. Int. J. Project Manage. **18**(1), 51–59 (2000)
27. Chan, D.W., Kumaraswamy, M.M.: Compressing construction durations: lessons learned from Hong Kong building projects. Int. J. Project Manage. **20**(1), 23–35 (2002)
28. Kaliba, C., Muya, M., Mumba, K.: Cost escalation and schedule delays in road construction projects in Zambia. Int. J. Project Manage. **27**(5), 522–531 (2009)
29. Toor, S.U.R., Ogunlana, S.O.: Problems causing delays in major construction projects in Thailand. Constr. Manage. Econ. **26**(4), 395–408 (2008)
30. Olawale, Y.A., Sun, M.: Cost and time control of construction projects: inhibiting factors and mitigating measures in practice. Constr. Manage. Econ **28**(5), 509–526 (2010)
31. Al-Tmeemy, S.M.H., Abdul-Rahman, H., Harun, Z.: Contractors' perception of the use of costs of quality system in Malaysian building construction projects. Int. J. Project Manage. **30**(7), 827–838 (2012)
32. Cochran, W.G.: Sampling Techniques. Wiley (2007)
33. Neill, J.: Writing up a Factor Analysis, 7 p. Retrieved 7 Sept 2008
34. Abd El-Razek, M., Bassioni, H., Mobarak, A.: Causes of delay in building construction projects in Egypt. J. Constr. Eng. Manage. **134**(11), 831–841 (2008)

Efficient Structural Sandwich Wall Panels Devoid of Thermal Bridges

Sani Mohammed Bida, F. N. A. A. Aziz, Mohd Saleh Jaafar, Farzad Hejazi and Abu Bakar Nabilah

Abstract Reinforced concrete sandwich wall panels are developed to reduce the effect of thermal transmission across the wall systems. The reduction of the thermal transmission is achieved through incorporation of an insulating layer. However, this insulating layer led to a reduction of structural performance. The provision of shear connection in the sandwich system improved its structural integrity and increased with increase in a number of shear connectors. However, if the shear connectors are placed directly across the layers of the concrete wythes, it will decrease its thermal efficiency. The thermal and structural performance works in contrary effect to an increasing number of shear connectors. Hence, optimizing both structural and thermal efficiencies simultaneously in reinforced concrete sandwich system has been a challenge for a very long time. Therefore, this paper presents an alternative approach focusing on the thermal path method to produce an optimum shear connector used. This approach eliminates the direct transmission path between the two wythes and, at the same time, avoids the use of alternative materials such as fibre-reinforced polymers which could be uneconomical. With this method, both thermal and structural efficiencies are optimized using only conventional concrete and steel materials.

Keywords Precast concrete sandwich panel · Shear connection
Thermal performance

S. M. Bida (✉) · F. N. A. A. Aziz · M. S. Jaafar · F. Hejazi · A. B. Nabilah
Department of Civil Engineering, Faculty of Engineering, Housing Research Centre,
Universiti Putra Malaysia, Serdang, Selangor, Malaysia
e-mail: informsani@yahoo.com

F. N. A. A. Aziz
e-mail: farah@upm.edu.my

M. S. Jaafar
e-mail: msj@upm.my

F. Hejazi
e-mail: farzad@fhejazi.com

A. B. Nabilah
e-mail: nabilah@upm.edu.my

1   Introduction

Interest in high-rise structural buildings in urban centres is on the increase due to the competition for the scarce available spaces. These structural buildings are made up of either beam–column frameworks or wall–slab systems. The wall–slab systems are structurally very efficient, but exhibit high thermal transmission. The thermal radiation through the surface of the wall of the buildings transfers heat into the building as a result of difference in temperature between the internal and external areas of the building environment. The heat absorbed into the building is determined by the thermal conductivity of the materials used [1]. Usually, the temperature rise due to heat transmission across buildings is overcome through provision of air-conditioning system for thermal indoor comfort or provision of heaters in the case of buildings in cold regions. Unfortunately, the mechanical air-conditioning system is one of the highest energy consuming equipment in buildings, thus, the need to renew the wall design systems towards sustainable development becomes highly imperative.

Substantial percentage of world's total energy consumptions and greenhouse emissions result from building sector due to high HVAC equipment usage [2, 3]. In America, a significant share of energy consumption comes from housing with about 50–70% coming from heating and cooling and air-conditioning [4]. In Europe, buildings account for about 30% of energy use which could be more in hotter parts of the word. This has led to global warming which has become a challenging phenomenon with far-reaching consequences. Attempts to curb this challenge in other areas of research include recycling and reducing fossils fuel consumption [5].

In the construction industry and modern architecture, emphasis on sustainable green infrastructural development through minimization of thermal transfer between outside and inner parts of buildings has been the principal focus of research. This is achieved through the provision of insulation layer between the building components, thus, leading to the paradigm shift to precast concrete sandwich systems (PCSS). This approach has helped significantly in producing thermally efficient non-structural components. Al-Ajlan [6] reported that the use of insulation layer in building elements is considered the most effective way of conserving energy. Hacker [7], also emphasized that utilizing insulation in household components would minimize annual energy requirement both for heating and cooling.

Therefore, this global renewed interest in energy conservation has called for demand in energy efficiency in building components such as precast concrete sandwich panels (PCSP) system. This technology is a product of industrialized building system (IBS) that have gained popularity in civil engineering applications due to its thermal performance [8, 9]. PCSP offers better thermal efficiency than other traditional masonry or solid wall building construction methods due to the insulation layer created between the concrete wythes. The two sides of the separated wythes are required to be connected through the insulation layer. The connection points cause thermal transfer from one side of the panel to the other and is referred

to as thermal bridges [10–13]. Since the choice of insulation, shear connection and wythes materials significantly affects the PCSP behaviour in terms of strength and thermal performances, a paradigm shift in the material used for PCSP system from conventional concrete and steel to foamed concrete and fibre-reinforced polymers (FRP) for wythes and shear connection design, respectively, has been observed. These approaches are quite expensive, and the availability in commercial quantity for turnkey projects is still in doubt.

Precast concrete sandwich panel is a sustainable and environmentally friendly building composite system due to their thermal performance, though with reduced structural performance. This paper presents thermal path approach to insulated precast concrete sandwich panel using the conventional reinforced concrete system. The shear connectors are staggered between the two faces of the panels to avoid direct thermal transfer.

2 Experimental Programme

2.1 Materials

The precast concrete sandwich panels (PCSP) were produced from combinations of concrete for wythes and shear studs, reinforcement bars for shear connections and BRC steel wire mesh for wythes reinforcement. Specimen size $500 \times 500 \times 150$ mm was designed and produced as shown in Fig. 1, and the thickness of each wythe is 40 mm. The shear stud 150×50 mm was used as connection point. Figure 2 shows the shear connector locations which are staggered to prevent direct thermal bridges and the spacing of the connectors were varied between 200, 300,
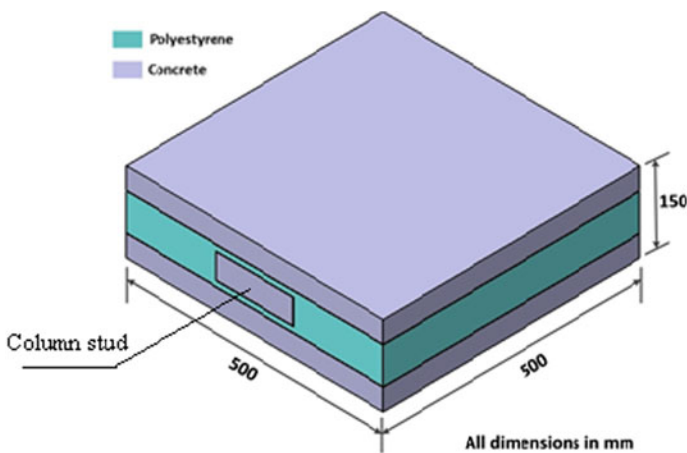
Fig. 1 Specimen used for the thermal transmission experiment

Fig. 2 Section through the
column stud shear connection
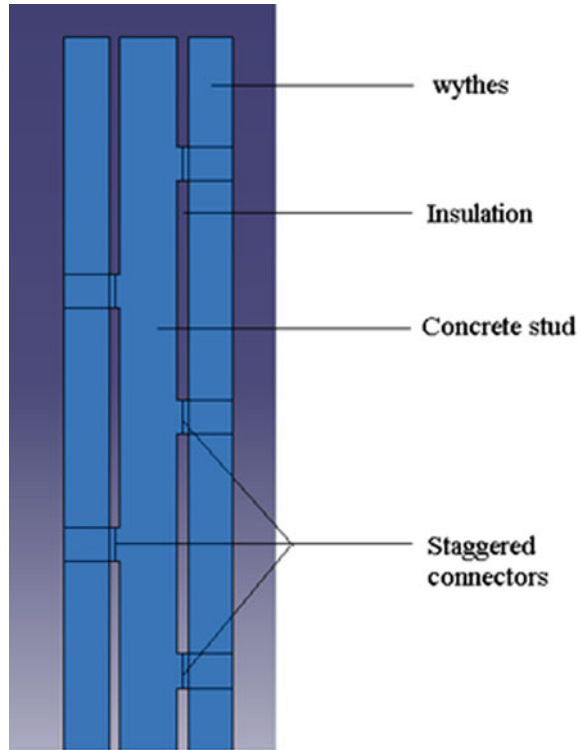
400 mm and the control specimen and designated as P200, P300, P400 and P0,
respectively. A ready mix concrete of 28 days target strength 40 MPa was used
using 10 mm maximum aggregate size. BRC steel wire mesh 6 mm diameter and
100×100 mm opening was used as vertical and horizontal reinforcement in each
wythe. Polystyrene insulation material was used between the wythes in other to
minimize the thermal transmission. The choice of insulation material was based on
the combined properties such as thermal resistance, water absorption, economy and
availability in local markets. In this regard, 70 mm thick polypropylene was used as
insulation material between the column studs. The column stud positions comprise
10–50–10 mm section for insulation–concrete–insulation, respectively. All the
polystyrene materials are glued to the dry surfaces of the precast concrete panels
after curing using polystyrene friendly adhesives.

2.2 Methodology

A steady-state thermal conductivity test using calibrated hot box method (CHB) in
conformity with ASTM C 1363 [14] was used to measure the hot and cold tem-
peratures of both air and surfaces of the PCSP assembly system. The specimen
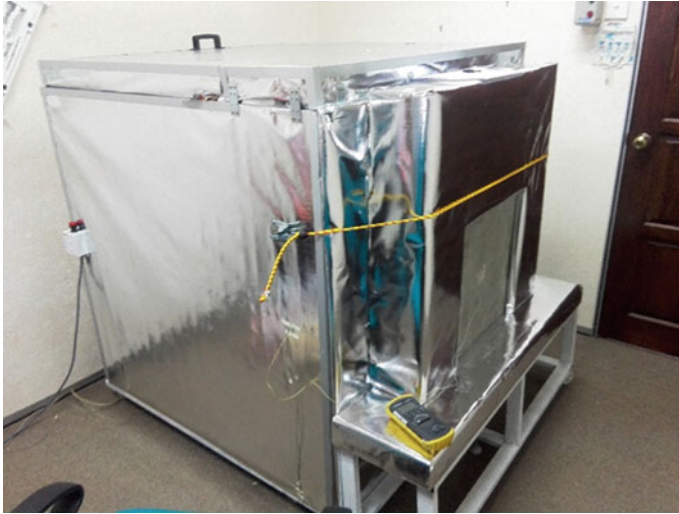
Fig. 3 Hot box apparatus

comprises two sides which are set up as hot and the cold side. The hot side is made up of hot chamber or box while the room where the box is located represents the cold side. Each face of the specimen contains surface thermocouple attached to the concrete surface of the specimen. Additional one thermocouple in each chamber was used to measure the air temperature until steady state is reached. All the devices were attached to the data logger and configured before the commencement of the experiment. The experiment was carried out for a period of 600 min with a maximum steady temperature of 60–65 °C, and the hot box apparatus is shown in Fig. 3. The wall specimens were designed with shear connectors spaced at 200, 300, 400 mm and the control designated P200, P300, P400 and P0, respectively.

3   Results and Discussion

The temperature profile for the cold surfaces was recorded until the change in temperature becomes negligible or attained steady-state conditions. The experiment was carried out for a period of 600 min when the steady state was attained as shown in Fig. 4. The cold surface temperature of the in the cold chamber was observed to decrease gradually before it begins to rise for all the specimens except the control which shows linear increment in surface temperature. The reduction in the surface temperatures on the respective samples is due to the thermal path which is design parallel to the ambient surface receiving the heat energy. The thermal transmission parallel to the sample surface is slower than the transmission perpendicular to the ambient surface. This is consistent with the 'thermal conductivity' as provided in
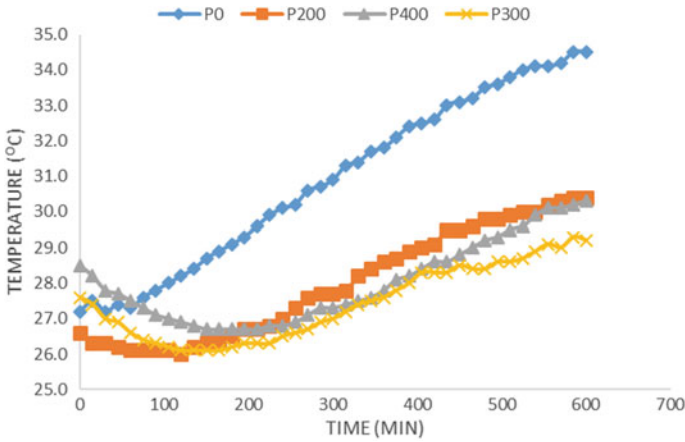
Fig. 4 Cold surface temperature of the samples
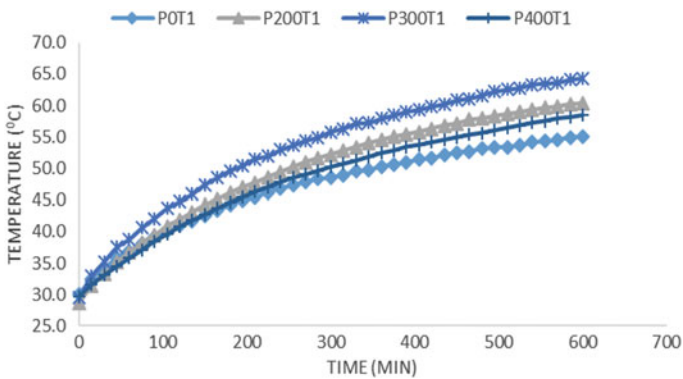
Fig. 5 Hot surface temperature of the samples

American Society of Heating, Refrigeration and Air-conditioning Engineer's handbook ASHRAE [15]. Also, as shown in Fig. 4, the result reveals that the delay in the heat transmission increases with increase in the length of the thermal path. Despite the difference in the initial cold surface temperature, delays in heat transmission of 120, 165 and 210 min were recorded for shear connection spacing designs of 200, 300 and 400 mm, respectively. On the other hand, the control shows higher cold surface temperature and increases linearly although other specimens had reached the steady state.

Figure 5 shows temperature profile of hot surface of all the specimens under consideration. It could be observed that the control specimen recorded the lowest hot surface temperature because, most of the heat is transmitted to the cold side much more than the other specimens design using the thermal path approach (P200,

P300 and P400). The result shows that the hot surface temperature increases with increase in thermal path length for control, 200 and 300 mm spacing. However, the 400 mm design is inconsistent with the expected result which falls between 200 and 300 mm shear spacing designs. This behaviour is due to the higher initial temperature of the cold surface at the start of the experiment. It was deduced that the more the difficulty of the heat to transfer to the other side of the wall, the higher the hot surface temperature.

Figure 6 shows the difference in temperature between the hot and the cold surfaces of the specimens. The temperature difference is one of the major determinants of thermal conductivity. The higher the temperature difference the lower the thermal conductivity. In this experiment, the temperature difference increases with increase in shear connection thermal path length. The differences of up to 75% were recorded between the control and the 300 mm shear connection design. This approach helps in optimizing the thermal efficiency and will be further research to determine the structural capacity of the panel system before it can be utilized as structural component.

In line with the provision of ASTM C1363 [14], the air temperature profile in both hot and cold chambers is recorded as shown in Fig. 7. It was observed that the
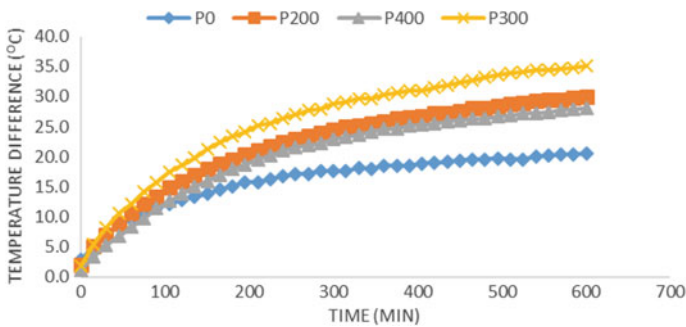
Fig. 6 Temperature difference between hot and cold sample surfaces
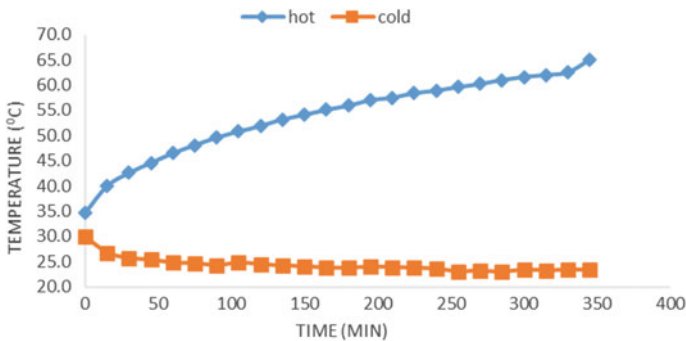
Fig. 7 Air temperatures in the hot and cold chambers

temperature falls between 23 and 65 °C which is within the limits provided in the aforementioned code of between −40 and 85 °C.

4 Conclusions

This experiment was carried out to determine the thermal performance of insulated precast concrete sandwich panels using hot box method under constant temperature refers to as steady-state conditions. Based on the results obtained and subsequent analysis, the following conclusions were drawn:

1. The thermal transmission across the specimen is directly proportional to the length of the thermal path.
2. The time lag for heat transfer depends on the direction of the thermal path, either parallel or perpendicular to the ambient surface of the panel system. The heat transmittance is slower for thermal path parallel to the ambient surface of the wall system making it more efficient.
3. Delay in the heat transfer of about 60 min is achieved for every 100 mm thermal path design parallel to the surface of the heat source (hot side).

References

1. Hata, R.M., Hassan, R., Idayu, H., Arshad, F.: The thermal conductivity of selected tropical timber species using hot box method. Jurnal Teknologi **78**(5–4) (2016)
2. Jelle, B.P.: Traditional, state-of-the-art and future thermal building insulation materials and solutions–properties, requirements and possibilities. Energy Build. **43**(10), 2549–2563 (2011)
3. Buratti, C., Belloni, E., Lunghi, L., Borri, A., Castori, G., Corradi, M.: Mechanical characterization and thermal conductivity measurements using of a new'small hot-box'apparatus: innovative insulating reinforced coatings analysis. J. Build. Eng. **7**, 63–70 (2016)
4. Al-Homoud, M.S.: Performance characteristics and practical applications of common building thermal insulation materials. Build. Environ. **40**(3), 353–366 (2005)
5. Sukontasukkul, P.: Use of crumb rubber to improve thermal and sound properties of pre-cast concrete panel. Constr. Build. Mater. **23**(2), 1084–1092 (2009)
6. Al-Ajlan, S.A.: Measurements of thermal properties of insulation materials by using transient plane source technique. Appl. Therm. Eng. **26**(17), 2184–2191 (2006)
7. Hacker, J.N., De Saulles, T.P., Minson, A.J., Holmes, M.J.: Embodied and operational carbon dioxide emissions from housing: a case study on the effects of thermal mass and climate change. Energy Build. **40**(3), 375–384 (2008)
8. Bai, F., Davidson, J.S.: Analysis of partially composite foam insulated concrete sandwich structures. Eng. Struct. **91**, 197–209 (2015)

9. Benayoune, A., Samad, A.A.A., Trikha, D., Ali, A.A.A., Ashrabov, A.: Structural behaviour of eccentrically loaded precast sandwich panels. Constr. Build. Mater. **20**(9), 713–724 (2006)
10. Kim, Y.J., Allard, A.: Thermal response of precast concrete sandwich walls with various steel connectors for architectural buildings in cold regions. Energy Build. **80**, 137–148 (2014)
11. Lee, B.J., Pessiki, S.: Thermal performance evaluation of precast concrete three-wythe sandwich wall panels. Energy Build. **38**(8), 1006–1014 (2006)
12. Lee, B.J., Pessiki, S.:Thermal behavior of precast prestressed concrete three-wythe sandwich wall panels. Build. Integr. Solutions, 1–15 (2006)
13. Theodosiou, T., Papadopoulos, A.: The impact of thermal bridges on the energy demand of buildings with double brick wall constructions. Energy Build. **40**(11), 2083–2089 (2008)
14. ASTM C1363-11: Standard Test Method for Thermal Performance of Building Materials and Envelope Assemblies by Means of a Hot Box Apparatus. Annual Book of ASTM Standards, ASTM International, West Conshohocken, PA (2011)
15. ASHRAE Handbook: American Society of Heating, Refrigerating and Air-Conditioning Engineers, pp. 3–3.24. Ashrae Inc. Atlanta (1997)

Application of Wood Waste Ash in Concrete Making: Revisited

Check for updates

Muktar Nuhu Danraka, F. N. A. A. Aziz, Mohd Saleh Jaafar, Noorazline Mohd Nasir and Suraya Abdulrashid

Abstract Portland cement production is a carbon dioxide trigger responsible for almost 5% of the worlds CO_2 emissions. Pozzolanic inclusions could contribute to sustainability particularly if they are derived from waste. Managing solid waste is increasingly becoming a global challenge as a result of increasing volume of accumulated waste from industrial and agricultural by-products. Environmental concerns as well as economic implications related with disposal of these wastes have prompted many researches in order to provide viable solutions. Recycling of these waste materials into the construction industry seems to be a more promising and viable alternative most especially in the manufacturing of greener and sustainable concrete material. Wood ash (WA) is a by-product derived from incineration of wood as well as its products such as sawdust, wood bark and chips. This paper presents an overview on investigations performed on the applicability of this material in mortar and concrete making. Specifics on physical, chemical,

F. N. A. A. Aziz (✉)
Faculty of Engineering, Department of Civil Engineering, Housing Research Centre,
Universiti Putra Malaysia, Serdang, Selangor, Malaysia
e-mail: farah@upm.edu.my

M. N. Danraka · M. S. Jaafar · N. M. Nasir
Faculty of Engineering, Department of Civil Engineering, Universiti Putra Malaysia,
Serdang, Selangor, Malaysia
e-mail: mndanraka@gmail.com

M. S. Jaafar
e-mail: msj@upm.edu.my

N. M. Nasir
e-mail: nazline@upm.edu.my

S. Abdulrashid
Faculty of Engineering, Department of Chemical and Environmental Engineering,
Universiti Putra Malaysia, Serdang, Selangor, Malaysia
e-mail: suraya_ar@upm.edu.my

M. N. Danraka
Faculty of Engineering, Department of Civil Engineering, Abubakar Tafawa Balewa
University, Bauchi, Nigeria

mineralogical and elemental characteristics of the waste material are discussed. It highpoints the impact of wood ash on workability, compressive and flexure strengths, water absorption, drying shrinkage, carbonation, alkali–silica reaction (ASR) and chloride permeability of concrete.

Keywords Concrete · Recycling · Wood ash · Mechanical properties Durability · Supplementary cementitious material

1 Introduction

Annually, more than 1 m^3 of concrete is estimated to be produced globally per person [1] making it the most widely used construction material. Portland cement which is the main ingredient in concrete is mostly criticized due to its environmental influence arising from the clinker production [2, 3]. Currently, about 3 billion tonnes of cement is consumed world over [4]. In fact, up to 1.5 billion tonnes of CO_2 is released into the atmosphere yearly by cement production plants arising from the manufacture of portland cement amounting to almost 5% of CO_2 emissions worldwide and if this unwanted trend lingers, the result will likely increase to 6% by the year 2015 [5, 6]; hence, all efforts to fight this ugly scenario become imperative.

More so, the tremendous increase in demand for energy especially in developing countries has led to search for renewable energy source as alternatives to fossil fuels due to outcry by environmentalist in order to compensate for the available ones.

A recent survey by [7] has projected an increase in world energy consumption of 47% from 2007 to 2035. In Malaysia, total electricity generated using renewable energy sources in 2009 amounts to only 5.5% while 94.5% was generated through fossil fuels like coal, oil and natural gas. The Malaysian timber processing sector stands to be a prospective candidate as a source of renewable energy in order to compliment the electricity demand as it is regarded to be among the largest unexploited biomass resource in Malaysia [8]. Biomass from wood, namely, wood chips, sawdust and cut-offs represents the main waste material resulting from timber manufacturing industries [9]. Wood wastes remain the most preferred fuel for biomass kilns than herbaceous and agricultural waste because the combustion of wood wastes produces quite lesser residual and fly ash [10]. While the above said practices offers a practical solution to managing of the solid waste produced from the wood residues, a major problem associated with their prevalent usage as a fuel is the residual ash generated in substantial quantities of which the industry is yet to find widespread empirical applications regarding the recycling of this ash material [11].

In this light, several investigations have established the success of wood ash as material replacing cement to fabricate structural concrete possessing adequate mechanical as well as durability characteristics [11–14]. These research findings

could provide twofold answers regarding the solid waste management issue and enhancing the sustainability of the construction industry.

2   Properties of Wood Ash

The beneficial use of wood waste ash is strongly governed by their chemical and physical characteristics which vary considerably depending on several factors [13]. These characteristics are mostly influenced by the tree species, conditions and areas where the trees are grown, temperature and means of incineration as well as the method employed during the collection of ash [15, 16]. Thus, this necessitates the appropriate characterisation of the ash before its utilization as a constituent material in blended cement and concrete.

The chemical composition as well as the quantity of wood ash produced is strongly governed by the temperature of combustion in the furnace. Incinerating at higher temperatures above 1000 °C results in a lower yield of wood ash generated while at same time results to a significant reduction in the amount of carbonate mainly arising from the chemical disintegration of the above-mentioned chemical compound. The physical properties of the resulting ash after incineration are influenced significantly by the various types of combustion technologies adopted. Generally, the resulting wood ash generated in fluidized furnaces is largely fine fly ash while those generated in the grate-fired incinerators are coarser in nature which tends to reside in the combustion unit as bottom ash. The chemical properties of the resulting wood ash after incineration of wood waste is reliant on the tree species from which it was obtained. The chemical composition of SiO_2, Al_2O_3, Fe_2O_3 and CaO, which determines the acceptability of wood ash as pozzolana, differs greatly from one tree species to another [11]. Differences in the chemical characteristics of wood ash generated from various tree species are shown in Table 1.

2.1   Physical Properties

The pozzolanic as well as hydraulic reactivity of wood waste ash is significantly affected by physical properties of the ash; hence, variations in these properties demand proper characterization of the wood ash obtained from various sources before use as cement replacing material for concrete production.

Cheah and Ramli [12] assessed the physical properties of high calcium wood ash (HCWA) used as partially replacing cement. The specific gravity, surface area and median size d_{50} were found to be 2.52, 1087.1 m^2/kg and 5.16 μm, respectively. In a different research to study the transport properties of (HCWA)—densified silica fume (DSF) hybrid mortar, Cheah and Ramli [24] reported that the wood ash had a surface area and median size d_{50} of 8.39 μm and 611 m^2/kg. The fine grading of the wood ash is attributed to an efficient grinding action.

Table 1 Summary of differences in chemical composition of wood ash

Author/compound	SiO_2	Al_2O_3	Fe_2O_3	CaO	MgO	TiO_2	K_2O	Na_2O	SO_3	C	P_2O_5	LOI (%)
Elinwa and Mahmood [17]	67.2	4.09	2.26	9.98	5.8	–	–	0.08	0.45	–	0.48	4.67
Udeoyo and Dashibil [18]	78.92	0.89	0.85	0.58	0.96	–	–	0.43	–	17.93	–	8.4
Elinwa and Ejeh [19]	67.2	4.09	2.26	9.98	5.8	–	–	0.08	0.45	–	0.48	4.67
Naik et al. [20]	32.4	17.1	9.8	3.5	0.7	0.7	1.1	0.9	2.2	–	–	31.6
	13	7.8	2.6	13.7	2.6	0.5	0.4	0.6	0.9	–	–	58.1
	50.7	8.2	2.1	19.6	6.5	1.2	2.8	2.1	0.1	–	–	6.7
	30	12.3	14.2	2.2	0.7	0.9	0.5	0.5	2.1	–	–	35.3
	8.1	7.5	3	25.3	4.5	0.3	3.3	3.3	12.5	–	–	32.8
Abdullahi [21]	31.8	28	2.34	10.53	9.32	–	10.38	6.5	–	–	–	27
Rajamma et al. [22]	41	9.3	2.6	11.4	2.3	0.4	3.9	0.9	–	–	0.9	–
	28	6.2	2.2	25.4	5	0.3	3.2	3.3	–	–	0.9	–
Cheah and Ramli [12]	28	4.1	2.5	39	10	0.13	7.4	1	1	2	3.9	7.22
Esteves et al. [23]	52.1	13.3	5.3	15.9	3.31	–	4.14	–	0.45	–	–	10.4
	25.1	11.3	5.18	40.1	6.63	–	2.07	–	1.12	–	–	3.5
Ramos et al. [14]	73.01	11.93	3.38	2.64	1.03	0.48	4.14	3.81	<0.05	–	0.59	1.47
Cheah and Ramli [24]	2.7	1.3	1.3	61	8.7	0.11	12	–	2.8	6.7	2.7	18
Berra et al. [25]	20.03	5.04	2.44	63.03	1.35	0.22	1.12	1.04	3.36	–	0.13	2.4

Esteves et al. [23] determined the particle size and specific surface (BET) of two wood ashes, namely, BFA1 and BFA2 in his study to assess the influence of the wood ashes in mitigating the effect of ASR. The reported values of particle size and surface areas for BFA1 are 17 μm and 28.52 m^2/g while for BFA2 are 21 μm and 1.74 m^2/g, respectively. Although both samples have similar size distributions but the surface areas was completely different. The greater value for BFA1 could be explicated by the higher quantity of unburnt carbon and the irregularity pattern in the shape of the particle.

Berra et al. [25] reported the average particle sizes and densities of three wood ashes WBFA1, WBFA2 and WBFA3 for use as cement-based material as 135, 86 and 179 μm while the densities of the wood ashes ranged between 2.35 and 2.76 g/cm^3, respectively. The densities of the wood ashes were similar to that achieved by coal fly ash and considerably lesser than those of standard cement. Hence, by partially replacing cement with wood ash, the weight of the blended material could be considerably reduced.

2.2 Chemical Properties

The chemical composition of biomass fly ash is an essential parameter which governs its suitability to be adopted as pozzolan in blended cement mixtures; hence, adequate characterisation is required. X-ray fluorescence (XRF) tests conducted in numerous researches had established substantial amounts of calcium and silica in samples of the ash investigated (Table 1). In some of these studies, the wood ash could be classified as possessing pozzolanic reactivity while in others they might be regarded as possessing hydraulic reactivity.

Cheah and Ramli [12] analysed the chemical composition of HCWA to be used as cement replacing material. Results obtained by X-ray diffraction (XRD) analysis revealed the main chemical phase to be Monticellite ($CaMgSiO_4$), Arkemanite ($CaMgSiO_2$) and Pectolite ($HNaCaSi_3O_9$). The presence of these compounds is in accordance with the results obtained from the XRF examinations (Table 1) which showed the presence of considerable amounts of CaO, MgO and SiO$_2$ in the ash. The XRD pattern which shows a diffuse broadband between 24° and 37° on the 2θ scale is indicative of the glassy nature of the silicate minerals.

Esteves et al. [23] reported the principal crystalline phases on BFA2 are quartz, periclase and calcite while those present in BFA1 are quartz, microcline and calcite. Variations are due to the differences in the chemical characteristics as shown in Table 1. The ashes can both be classified as type C in relation to those of coal incineration as they both contain more than 10% CaO as well as react both hydraulically and pozzolanically. XRD analysis performed by [25] revealed the existence of large quantity of amorphous phase of lime, calcite and quartz as the main crystalline phases.

3 Properties of Mortar and Concrete Incorporating Wood Ash

3.1 Standard Consistency

Cheah and Ramli [9] detected that the incorporation of HCWA at increasing percentages of cement replacement achieved a negligible rise in water demand of blended mixtures. This scenario could be mainly ascribed to similarity in the particle grading of the HCWA and OPC.

Cheah et al. [26] observed that as HCWA is gradually added into the blended system of HCWA-PFA geopolymer there is a corresponding rise in the water demand so as to attain standard consistency for the blended HCWA-PFA geopolymer paste This may be explained based on the porous nature and angular shape of the HCWA particles in comparison to PFA particles which normally exhibits a smooth and spherical nature.

3.2 Setting Time (Initial and Final)

According to [12], the addition of HCWA at levels of cement replacement up to 20% extends the initial and final setting times of the DSF cement paste. This situation could be advantageous as it gives more time for activities of transporting, placing and consolidation of the mortar or concrete. Cheah et al. [26] studied the synergistic effect of HCWA and PFA blended geopolymer binders with different arrangement ratios of between 0 to 100 and 100 to 0, respectively at 10% step increase for the purpose of fabricating building block. They concluded that increasing the mass proportion of HCWA leads to a significant increase in water demand of the blended paste. Also, paste having equal quantity of wood ash and fly ash exhibited a greater degree of both final and initial setting characteristics relative to blended paste containing either fly ash or wood ash only. This phenomenon is as a result of superior rate of reactivity in the former paste resulting in a quicker development of geopolymeric products that resulted in the subsequent stiffening of the paste.

3.3 Slump

Abdullahi [21] investigated the effect of wood ash on concrete slump by replacing cement with wood ash at varying proportions (0, 10, 20, 30 and 40%) with a mix design of 1:2:4. The result is presented in Table 2. Result depicts that mixes with higher contents of wood ash require a higher amount of water to attain satisfactory workability.

Table 2 Wood ash concrete slump test result [21]

HCWA content (%)	0	10		20	30	40
Water/binder actual ratio	0.6	0.66		0.67	0.68	0.69
Slump (mm)	30	35		40	40	35

Table 3 Slump of mortar with HCWA as cement replacement [9]

HCWA content (%)	0	5	10	15	20	25
Superplasticizer dosage (%)	1.85	1.85	1.85	1.98	1.98	1.98
Slump (mm)	90	70	50	50	50	50

Cheah and Ramli [9] reported the results of slump test of mortar samples incorporating different percentages of HCWA (0, 5, 10, 15, 20 and 25%) by weight of cement. The results are shown in Table 3.

From the results, it is clear that as cement replacement levels increases, there is a reduction in the slump of the mixes. As increment in the amount of HCWA continued, a higher dosage of superplasticizer was needed to retain the slump according to the desired range. Mixes with 15, 20 and 30% levels of HCWA addition achieved the same slump values at a constant dose of superplasticizer of 1.98%. These outcomes could be clarified due to the marginal higher surface area of HCWA compared to OPC.

3.4 Compressive Strength

Cheah and Ramli [12] studied the strength in compression of mortar mixes incorporating HCWA up to 90 days with HCWA content of 5, 10, 15, 20 and 25%. They concluded that the targeted strength of 40 MPa was attained for mortar mixtures having contents of HCWA up to 20%. Also, mortar mix incorporating 15% of HCWA achieved higher strength in compression than the control after extended curing regime of 90 days. Mortar having up to 25% HCWA exhibited compressive strength beyond 90% of control mix. Also, Cheah and Ramli [9] investigated the compression strength of HCWA-DSF hybrid mortar containing a constant amount of DSF (7.5% of cement weight) and varying proportions of HCWA ranging from 2 to 20% at step increment of 2%. They concluded that the strength in compression of mortar having HCWA contents of 2 and 4% was improved considerably at early and later curing periods. Mortar mix containing HCWA amount up to 14% in blend with 7.5% DSF by binder weight achieved comparable strength as the control mixture at 364 days.

3.5 Flexural Strength

The strength in flexure of mortar mixes incorporating HCWA up to 90 days with HCWA content of 5, 10, 15, 20 and 25% was investigated by [12]. They established that an increase in flexural strength is achieved at 5% HCWA content at all ages relative to the control mix. Cheah and Ramli [9] studied the flexural strength of HCWA-DSF hybrid mortar containing a constant amount of DSF (7.5% of cement weight) and varying proportions of HCWA ranging from 2 to 20% at step increment of 2%. They established that mortar mix having up to 8% HCWA in parallel with 7.5% DSF achieved higher flexural strength in comparison with the control mix. Also, up to 20%, HCWA could be utilized together with 7.5% DSF to obtain comparable flexure strength relative to control mortar.

3.6 Drying Shrinkage

Cheah and Ramli [12] examined the drying shrinkage of mortar mixes fabricated by replacing cement with HCWA at varying percentages (5, 10, 15, 20 and 25%) of the total weight of binder. They reported that the utilization of HCWA at 10% as supplementary cementing material lead to the decline in overall drying shrinkage of mortar on exposure to air curing.

3.7 Carbonation

Cheah and Ramli [12] examined the effect of HCWA on the resistance to carbonation of mortar mixes fabricated by replacing cement with HCWA at varying percentages (5, 10, 15, 20 and 25%) of the total weight of binder. The result indicated that the resistance to carbonation of mortar mix having 5% HCWA was enhanced upon comparison with the control, and that the inclusions of above 5% HCWA could result to a lesser degree of carbonation. In another study [24], examined the resistance to carbonation of mortar mixtures produced by replacing cement with HCWA at varying percentages (2, 4, 6, 8, 10, 12, 14, 16, 18 and 20%) in combination with 7.5% DSF of total weight of binder weight. They reported that an optimum level HCWA replacement to achieve enhanced carbonation resistance is 10%. This enhancement could be attributed to the refinement in pore structure of the mortar mix with HCWA compared to the control mortar.

Ramos et al. [14] conducted research on the carbonation resistance of mortar produced with 0, 10 and 20% WWA obtained from a power plant as replacement for cement. They, however, concluded that the depth of carbonation for the blended mixtures was higher than the control and that depth of carbonation increases with an increase in WWA levels. They attributed this trend to possible reduction in portlandite resulting in a decrease in pH.

3.8 Alkali–Silica Reaction

Ramos et al. [14] conducted research on the influence of WWA on resistance of alkali–silica reaction of mortar produced with 0, 10 and 20% WWA obtained from a power plant as replacement for cement. From the obtained results, it is evident that the control set had exhibited possible detrimental expansion in accordance with ASTM 1567 (greater than 0.1% beyond 14 days in sodium hydroxide) for the related type of cement and sand used. They concluded that WWA was successful in inhibiting the expansion due to ASR and that higher content of WWA could lead to lesser expansion.

4 Conclusions

- Wood ash quality and quantity are depended mainly on the temperature as well as the technology of combustion and the tree species the wood biomass is derived. Thus, appropriate characterisation of wood ash becomes imperative before its implementation in cement-based materials.
- Incorporating wood ash as a cement replacing material negatively affects workability of concrete.
- Presently, code of practice regarding the usage of wood ash is non-existent. However, characteristics of wood ash demonstrate that ASTM C 618 'Standard specification for coal fly ash and raw or calcined natural pozzolan for use as mineral admixture' can be adopted for wood ash.
- Generally, the inclusion of wood ash in cement-based mixtures decreases the mechanical strength of the mixtures.
- Improved durability performance could contribute to sustainability in construction.

References

1. Scrivener, K.L., Kirkpatrick, R.J.: Innovation in use and research on cementitious material. Cem. Concr. Res. **38**(2), 128–136 (2008)
2. Schneider, M., Romer, M., Tschudin, M., Bolio, H.: Sustainable cement production—present and future. Cem. Concr. Res. **41**(7), 642–650 (2011)
3. Ahmari, S., Zhang, L.: Production of eco-friendly bricks from copper mine tailings through geopolymerization. Constr. Build. Mater. **29**, 323–331 (2012)
4. Zampini, D.: Future developments of concrete in the construction materials industry. ICE Manual Constr. Mater. **1**, 251–258 (2009)
5. Davidovits, J.: Global warming impact on the cement and aggregates industries. World Res. Rev. **6**(2), 263–278 (1994)

6. Damtoft, J.S., Jacques, L., Duncan, H., Danielle, S., Martin, G.E.: Sustainable development and climate change initiatives. Cem. Concr. Res. **38**(2), 115–127 (2008)
7. Conti, J., Paul, H., Doman, L.E., Smith, K.A., Sullivan, J.O., Vincent, K.R., Barden, J.L., Martin, P.D., Mellish, C.M.L., Kearney, D.R.: International Energy Outlook 2011. US Energy Information Administration, Technical Report No. DOE/EIA-0484 (2011)
8. Shafie, S.M., Mahlia, T.M.I., Masjuki, H.H., Ahmad-Yazid, A.: A review on electricity generation based on biomass residue in Malaysia. Renew. Sustain. Energy Rev. **16**(8), 5879–5889 (2012)
9. Cheah, C.B., Ramli, M.: The engineering properties of high performance concrete with HCWA–DSF supplementary binder. Constr. Build. Mater. **40**, 93–103 (2013)
10. Vassilev, S.V., David, B., Andersen, L.K., Vassileva, C.G.: An overview of the chemical composition of biomass. Fuel **89**(5), 913–933 (2010)
11. Cheah, C.B., Ramli, M.: The implementation of wood waste ash as a partial cement replacement material in the production of structural grade concrete and mortar: an overview. Resour. Conserv. Recycl. **55**(7), 669–685 (2011)
12. Cheah, C.B., Ramli, M.: Mechanical strength, durability and drying shrinkage of structural mortar containing HCWA as partial replacement of cement. Constr. Build. Mater. **30**, 320–329 (2012)
13. Siddique, R.: Utilization of wood ash in concrete manufacturing. Resour. Conserv. Recycl. **67**, 27–33 (2012)
14. Ramos, T., Matos, A.M., Sousa-Coutinho, J.: Mortar with wood waste ash: mechanical strength carbonation resistance and ASR expansion. Constr. Build. Mater. **49**, 343–351 (2013)
15. Etiegni, L., Campbell, A.: Physical and chemical characteristics of wood ash. Biores. Technol. **37**(2), 173–178 (1991)
16. Wiegand, P.S., Unwin, J.P.: Alternative management of pulp and paper industry solid wastes. Tappi J. **77**(4), 91–97 (1994)
17. Elinwa, A.U., Mahmood, Y.A.: Ash from timber waste as cement replacement material. Cement Concr. Compos. **24**(2), 219–222 (2002)
18. Udoeyo, F.F., Dashibil, P.U.: Sawdust ash as concrete material. J. Mater. Civ. Eng. **14**(2), 173–176 (2002)
19. Elinwa, A., Ejeh, S.: Effects of the incorporation of sawdust waste incineration fly ash in cement pastes and mortars. J. Asian Archit. Build. Eng. **3**(1), 1–7 (2004)
20. Naik, T.R., Kraus, R.N., Siddique, R.: Controlled low-strength materials containing mixtures of coal ash and new pozzolanic material. ACI Mater. J. **100**(3) (2003)
21. Abdullahi, M.: Characteristics of wood ash/OPC concrete. Leonardo Electron. J. Practices Technol. **8**, 9–16 (2006)
22. Rajamma, R., Richard, B.J., Tarelho, L.A.C., Allen, G.C., Labrincha, J.A., Ferreira, V.M.: Characterisation and use of biomass fly ash in cement-based materials. J. Hazard. Mater. **172**(2), 1049–1060 (2009)
23. Esteves, T., Rajamma, R., Soares, D., Silva, A.S., Ferreira, V.M., Labrincha, J.A.: Use of biomass fly ash for mitigation of alkali-silica reaction of cement mortars. Constr. Build. Mater. **26**(1), 687–693 (2012)
24. Cheah, C.B., Ramli, M.: The fluid transport properties of HCWA–DSF hybrid supplementary binder mortar. Compos. B Eng. **56**, 681–690 (2014)
25. Berra, M., Mangialardi, T., Paolini, A.E.: Reuse of woody biomass fly ash in cement-based materials. Constr. Build. Mater. **76**, 286–296 (2015)
26. Cheah, C.B., Part, W.K., Ramli, M.: The long term engineering properties of cementless building block work containing large volume of wood ash and coal fly ash. Constr. Build. Mater. **143**, 522–536 (2017)

Comparative Study on Change Orders in Building Projects

Jerome Jordan F. Famadico and Melito A. Baccay

Abstract This research aimed to contribute to the small but growing empirical literatures and studies on Change Orders in building construction industry in selected cities in the National Capital Region (NCR), Philippines. Using descriptive/survey research method specifically expert sampling method, key informant interviews, actual site observations and desk reviews of project documents (e.g., contract documents, plans and specifications, etc.), this study investigated and compared the causes and effects of Change Orders in public and private building construction projects and formulated recommendations and guidelines in order to address the problems brought about by Change Orders. Moreover, the existing change order management control practices being implemented by the contractors, consultants, and clients in response to the issuance of construction Change Orders were also identified and investigated. Based on the results of the study, it was found out that the major causes of Change Orders in building construction projects in the Philippines were related to change of plans and scope by the owner, adjustment of schedule, unpredictable weather conditions, unforeseen site conditions, change of schedule by the owner, long waiting time for approval of construction drawings, complexity of construction projects and external factors which are beyond the control of the contractors, consultants, and clients. Consequently, Change Orders have resulted to project time extension and delay in project completion, increase in the overall cost of the project, changes in the cash flow and loss of earnings, additional payments to the contractor, and increased time and material related charges. Generally, the management control practices being undertaken by both the public and private sector in dealing with Change Orders were as follows: (i) all changes in the design documents were checked, reviewed, and justified by the designers and consultants; (ii) coordination and cooperation

J. J. F. Famadico (✉)
Civil Engineering Department, Adamson University, Manila, Philippines
e-mail: jeromefamadico@yahoo.com

M. A. Baccay
Graduate School, Technological University of the Philippines, Manila, Philippines

among the contractors, consultants, and clients were encouraged; (iii) project personnel take proactive measures to promptly settle, authorize, and execute Change Orders in construction projects; (iv) involvement of knowledgeable persons or representatives during the change order negotiation and approval (v) a written approval of both parties should be made with clear scope of change before executing the requested changes or variations; and (vi) the use of various techniques in order to track cost of changes.

1 Introduction

Nowadays, one of the most important problems in the construction industry is change or variation in plans and specifications [22]. According to Rodriguez [19], the change occurs in every building construction project and the magnitude of which varies considerably from project to project. Alnuaimi et al. [3] cited that developing countries like the Philippines have experienced more Change Orders brought about by the needs of the owner in the course of the design or construction as compared to those projects in the developed countries. Changes in construction projects are primarily due to three main causes as follows: design errors and omissions, change in field conditions, and owner-initiated changes.

Change Order is defined by Clare [5] as a "written agreement between the owner, contractor and architect on the specific change in the work and any adjustment in the contract or the contract time". It is being issued by both parties to correct or modify the original design or scope of work. The corrections or modifications are carried out for many reasons like for instance: the changes in scope made by the client; and the result of change requests made by the consultant due to design errors or new findings during the courses of implementation. Change Orders are inevitable in most construction projects and may result to big number of claims, disputes and may eventually lead to legal battles if not been resolved immediately using the formalized change management process according to Rodriguez [19] and Aneesa et al. [4].

In the Philippines, Change Order is classified as one form of a Variation Order. Presidential Decree 1594 (PD 1594) [18] defines Variation Order as a document being issued in order to cover any change in plans and specifications, increase or decrease in quantities, deleted items and introduction of new work items that are not in the original contract. A Variation Order may either be in the form of a Change Order, Extra Work Order, or a Supplemental Agreement. Change Order, according to this decree, is issued in order to cover any increase or decrease in quantities of original work items in the contract. Extra Work Order, on the other hand, is issued to cover the introduction of new work items. Finally, Supplemental Agreement is

issued if the aggregate amount of Change Orders and extra work orders exceeds 25% of the escalated contract price. And among these three, Change Order is encountered the most due to a number of changes in the plans as well as in the project design and specifications.

According to the Philippine Daily Inquirer 2015 report, the construction industry was identified as one of the sectors that contributed significantly to the country's robust economy. However, the efficiency of construction projects are greatly affected by the magnitude and frequency of the Change Orders that are being filed during construction. Given the limited funding available for building projects, it is therefore imperative that these projects shall be undertaken in the most efficient way to properly and effectively manage these construction Change Orders. Numerous studies and articles by Aneesa et al. [4], Alnuaimi et al. [3], Rodriguez [19], and Ibbs [9] have written articles on Change Order and change management in the field of construction industry and have reported that improving the administrative process of Change Orders is beneficial in terms of reducing the cost and risk for all the project participants and it encourages more trustful relationship between the contractor and the client.

Based on the foregoing, there is a need for the study and better understanding on the impact of Change Orders, particularly their causes and effects in construction projects. Given the above, this study aimed to investigate the prevailing causes and effects of construction Change Orders. Moreover, this study also aimed to look into the management practices being implemented in order to minimize or mitigate the effects of these inevitable Change Orders in the construction industry. Thus, recommending alternative courses of action and guidelines that would be of help to construction professionals, engineers, and architects in efficiently and effectively managing Change Orders in their respective projects.

2 Literature Review

Change Order is inevitable in every construction project. It is defined as a written agreement between the owner, consultant, and contractor on any modification to the original scope of the construction contract. Change Orders are classified into three: (a) in terms of the initiator of changes [1, 14]; (b) in terms of the net effect on the scope of the project [1, 21]; and (c) in terms of the procedures used in introducing them [6, 17]. Alnuaimi et al. [3] and Ijaola & Iyagba [11] found out that the most important factors causing these Change Orders were related to the owner's instruction for additional works and modification to design and non-availability of construction manuals and procedures. Agreeing with this finding, Ibn-homaid et al. [10] also concluded that change of the project scope due to owner's requirements as the most frequent and important cause of Change Orders followed by inadequate field investigation.

Various studies [3, 4, 11] revealed that the most important effects of Change Orders are delays in the project schedule, claims and disputes, and cost overruns. Osman et al. [17] and Ibn-homaid et al. [10] further explained that aside from these identified effects, interruption of continuous work, additional payment to the contractor and increase in overhead expenses are also being experienced due to occurrence of Change Orders. Even though Change Orders cause a lot of problems, several empirical researches show that only few people believe that no one is benefitting from them. In the study of Alnuaimi et al. [3], they identified that the contractor is the party benefitting the most from Change Orders followed by consultants and then clients.

Ijaola and Iyagba [11] identified that the most important remedy for Change Orders is having a specialized quantity surveyor and project manager in large construction projects. Alnuaimi et al. [3], on the other hand, concluded that the most important remedy is the review of registration and technical capability of the consultants. Even though these research findings differ in description, they mean the same idea that these suggested remedies were consultant-related and these show how consultants could prevent changes during construction.

For Egan et al. [6], there are no generic standards related to change order management process because of the uniqueness of each project. However, Hwang and Low [8] and Molly [15] identified relevant steps in managing Change Orders which include: (1) identify the change, (2) evaluate the change, (3) document the change, and (4) resolve/implement changes. Motawa et al. [16] further explained that inconsistent management of the change process can result in many disruptive effects, contract disputes and project failure.

3   Research Objectives

The objectives of this study were as follows:

1. To identify the prevailing causes and effects of construction Change Orders in public and private building projects.
2. To identify the existing management control practices being implemented by the contractors, consultants, and clients to address construction Change Orders in public and private building projects.
3. To determine the significant differences in the perception with regards to the causes and effects of Change Orders (a) between public and private sectors, and (b) among clients, consultants, and contractors.
4. To recommend alternative courses of actions and/or guidelines in order to minimize/mitigate the issues and problems related to construction Change Orders.

4 Conceptual Framework

To attain the objectives of the study, this research has been conceptualized to determine the major causes and effects of building construction Change Order together with the existing management control practices in the selected construction firm in the Philippines. Figure 1 presents the Conceptual Framework.

As shown in Fig. 1, the inputs of this study consist of the prevailing causes and effects of construction Change Orders in the construction projects and the existing management control practices implemented by the contractors, consultants, and clients. These inputs were subjected to statistical treatment of data and served as the basis for the in-depth analysis of the research findings, conclusions, and recommendations.

The process portion of this study constitutes the conduct of an evidence-based empirical research process using researcher-made questionnaire, desk review or documentary analysis for secondary data; conduct of key informant interviews and analysis of the research findings. The output of this study is a management model based on the findings of the study that would serve as guidelines or model by the contractors, consultants, construction industry professionals, and owners in controlling or minimizing the effects of construction Change Orders.
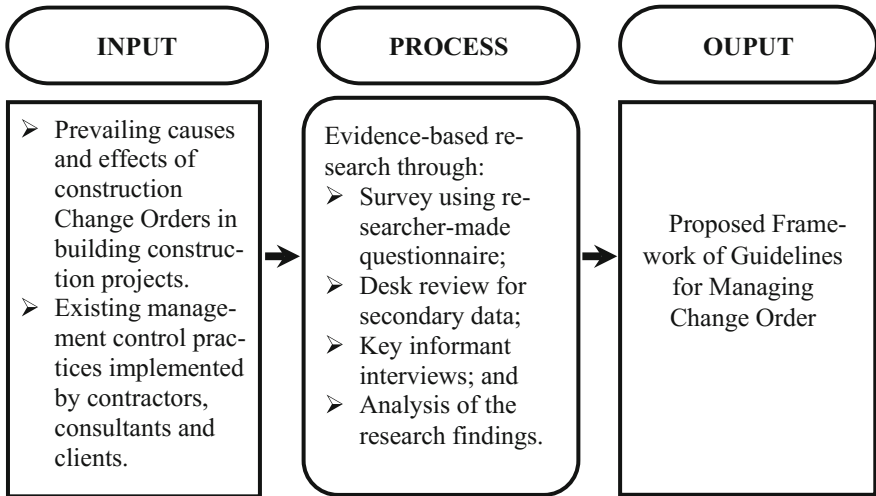
Fig. 1 Conceptual framework of the study

5   Significance of the Study

The findings of the study will prove beneficial to the following:

1. Philippine Building Construction Industry. This research will provide valuable information to the building construction industry in the Philippines with regard to the current situation and status of Change Order management in the country. This study will also serve as a basis for developing recommendations and guidelines for minimizing Change Order as well as possible recommendations on how to manage, control, and minimize the problems related to Change Orders which can have major impacts in the overall project performance.
2. Clients, Consultants, and Contractors. It is hoped that the research findings and suggested remedies will be helpful to various project stakeholders particularly the clients, consultants, and contractors. The results of this study will provide recommendations and alternative courses of action or Change Order guidelines that would help them to minimize and or mitigate the issues and problems related to Change Order.
3. Project Planners, Engineers, and Decision Makers. This study will also help these industry professionals in planning effectively prior to starting a project and even during the design phase in order to minimize and control changes and change effects. The results and findings will be used by project managers in making decisions and necessary actions to minimize various problems brought about by Change Orders.

6   Scope and Delimitations of the Study

This study covered the analysis of main causes, potential effects, and management control practices in the building construction Change Orders in selected cities and municipalities in the NCR based on the specific research questions indicated in the statement of the problem. The unit of analysis was based solely on the perceptions or opinions of the respondents, namely, Contractor, Consultant, and Owner or Client coming from different companies. The first limitation was related to the data used for building construction projects which were limited to only seven (7) selected cities and municipalities of the NCR and was not able to cover the entire cities and municipalities of the NCR due to the difficulty in the retrieval of questionnaires. Hence, the statistical strength of the total sample was relatively moderate, especially when Change Orders were examined by the type of building construction projects. The moderate statistical strength was likely attributable to the relatively small sample size among group of respondents in the analyses since more data would be needed to confirm the research findings. Nevertheless, the perceptions and opinions gathered and generated from the three groups of respondents in a way represented the entire population of the study.

7 Methodology

7.1 Research Design

This study employed descriptive or survey research method. According to Fraenkel and Wallen [7] a descriptive survey involves asking the same set of questions prepared in written questionnaire of a large number of individuals and could be administered to the target samples either by mail, by telephone, or in person. Moreover, a survey research was used to obtain data from the population (or a sample) to determine the current status with respect to variables or subject under investigation which in this study is to identify the primary causes and effects of Change Orders [7, p. 12].

7.2 Research Locale

This research was conducted in the National Capital Region specifically in Metro Manila. Aside from accessibility, the NCR is also the ideal location for this study because of its diverse or different kinds of building construction projects implemented. It is also one of the best places/locations where one can find the biggest and the most complicated building construction projects in the Philippines. Thus, lots of Change Orders have been encountered from the owners according to some professional engineers. Moreover, it is also a site for many building construction companies; consultancy and engineering design companies, as well as owners whose projects are located and extended to different regions and provinces across the country.

7.3 Sample and Sampling Techniques

The data used in the study were gathered from Consultants, Clients/Owners, and Contractors coming from the different building construction firms in NCR prime cities such as Manila, Mandaluyong City, Pasig City, Pasay City, Quezon City, Las Piñas, and Taguig City using purposive sampling. Purposive Sampling was utilized in this study in order to choose the specific or group of experts within the population of the construction company.

Specifically, this research utilized the expert sampling method because this study requires assessment or getting opinions of experts (i.e., contractors, engineers, architects, consultants, project managers, clients/owners) which requires a relatively high level of knowledge and expertise in the field of building construction industry and experts who are heavily involved in managing and/or addressing Change Orders in their respective companies.

Table 1 Distribution of respondents

Respondents	Public	Private	Total	%
Contractors	34	34	68	68.00
Clients	16	7	23	23.00
Consultants	0	9	9	9.00
Total	50	50	100	100.00

In this study, a total of one hundred (100) respondents were surveyed (50 each from both the public and private sectors). Table 1 presents the distribution of respondents from both public and private sector, as follows:

As shown in Table 1, a total of thirty four (34) respondents represents the Contractors in the private sector and the other thirty four (34) Contractors represents the public sector. Sixteen (16) respondents were Clients/Owners in the public sector and seven (7) respondents came from Clients/Owners in the private sector. The remaining nine (9) respondents came from the Consultants in the private sector. It is interesting to note that in the public sector, the Clients/owners also act as the project Consultants; hence, there were no consultant respondents for the public sector. Majority of these respondents were male with less than 30 years working experience in both public and private building construction projects in NCR.

7.4 Data Gathering Instruments

To gather data and answer the research questions indicated in this research, a questionnaire was developed tailor-fit for this study to assess the perceptions of clients, consultants, and contractors on the causes and effects of Change Orders. This questionnaire was composed of four (4) parts. Part I contained the demographic profile of the respondents such as experience, profession, and specialty of their projects. Part II, III, and IV pertains to the survey questions relative to the causes, effects, and management control practices of Change Orders in building construction projects in the Philippines.

7.5 Data Gathering Process

Before distributing the questionnaires to the target respondents, a dry run or pilot test was administered to selected engineers and architects in building construction industry. The objectives of the pilot test were to determine the reliability and validity of the specific questions and to determine whether it was easy to accomplish or not. After the pilot testing, the validated questionnaires were administered to the selected sample respondents, namely, Consultants, Clients/Owners, and Contractor of both public and private sector. To ensure a high retrieval rate,

the researcher personally handed and administered the questionnaires with a cover letter explaining the purpose and importance of the study.

Aside from the questionnaire, the researcher also conducted key informant interviews (KIIs) to the selected respondents in order to obtain firsthand information about the background and history of the project as well as to gain some insights about the building construction projects. In addition, the researcher also conducted actual site observations to gain more insights on how other companies responded to Change Orders. The valuable piece of information derived from the interviews were used as evidence-based information which greatly helped the researcher in terms of analyzing and interpreting the findings on the actual causes of Change Orders in the building construction projects in the Philippines. Moreover, project documents were also collected particularly those pertaining to the commercial and contractual aspect of the project of the selected construction companies and were utilized during the desk review of secondary data to substantiate the research findings.

The data collected from the administered questionnaires were tallied, classified, categorized, and analyzed according to the research objectives. These gathered data were analyzed and interpreted using different statistical analysis methods, utilizing Statistical Program for Social Science (SPSS) software version 19 for this purpose. Interpretations were arbitrarily assigned for the purpose of interpreting the findings, as follows:

Lowest score	Highest score	Interpretation
4.21	5.00	Very often
3.61	4.20	Often
2.41	3.60	Sometimes
1.81	2.40	Seldom
1.00	1.80	Never

7.6 Statistical Treatment of Data

In order to answer the research questions, the researchers floated the questionnaires to the target respondents. The data collected from the administered questionnaires were tallied, classified, categorized, and analyzed according to the research objectives. The descriptive statistics used in this study were as follows:

Percentage. This was utilized in the study for computation of the percentage for numerical analysis and for comparing magnitudes. This was applied "to determine the ratio of frequencies of responses to the total number of respondents expressed in percentile" [13]. It was expressed by the following formula:

$$P = \frac{f}{N} \times 100\%, \tag{1}$$

where,

P percentage
f frequency of response
N total number of cases

Weighted Mean. The weighted mean was used in determining the mean scores per item in the specific causes and effects of Change Order. Specifically, it determined the mean value of the perception of respondents on certain items related to the research questions and was expressed by the following formula:

$$\bar{x} = \frac{\sum f_x}{N}, \tag{2}$$

where,

$\bar{x}$ computed value of the weighted mean
$\sum$ summation symbol
f frequency
x unit weight
N total number of respondents

One-way Analysis of Variance (ANOVA). The one-way ANOVA was used to determine the significant differences in terms of perceptions between the public and private group of respondents with regards to the causes and effects of Change Orders. The following is the formula for computing the one-way ANOVA:

$$F = \frac{\text{MST}}{\text{MSE}} \tag{3}$$

where

F ANOVA coefficient
MST   Mean sum of squares due to treatment
MSE   Mean sum of squares due to error

Formula for MST:

$$\text{MST} = \frac{\text{SST}}{p - 1} \tag{4}$$

$$\text{SST} = \sum n(x - \bar{x})^2, \tag{5}$$

where

SST Sum of squares due to treatment
p Total number of population
n Total number of samples

Formula for MSE

$$MSE = \frac{SSE}{N - p} \tag{6}$$

$$SSE = \sum (n - 1)S^2, \tag{7}$$

where

SSE Sum of squares due to error
S Standard deviation of the samples
N Total number of observations.

8 Research Findings and Results

8.1 Causes of Change Orders

Table 2 presents the results of the comparative survey research findings with regard to the causes of Change Orders between the selected public and private construction projects in NCR. As shown in the table, the top five (5) most common causes of Change Orders in the public sector were related to change of plans and scope by the owner ($M = 3.39$, SD = 1.04); followed by change in the project design ($M = 3.22$, SD = 0.94); unpredictable weather conditions ($M = 3.17$, SD = 1.15); unforeseen site conditions ($M = 3.17$, SD = 0.99), and change of schedule by the owner ($M = 3.11$, SD = 1.18).

Compared to the public sector, the same major causes of Change Orders were also reported by the private sector respondents and these includes: change in the design ($M = 4.25$, SD = 0.89), followed by change of plans change and scope by the owner ($M = 3.93$, SD = 1.12), the change of schedule by the owner ($M = 3.61$, SD = 1.13), except however for the two identified causes which pertains to the long waiting time for approval of construction drawings ($M = 3.57$, SD = 0.92) and the complexity of project ($M = 3.54$, SD = 0.74).

Based on the results, the change of plans or scope of work by the owner is one of the most significant causes of Change Orders in building construction as reported by the public and private sector respondents. The same finding was also revealed in various literatures and studies (e.g., [20]) and in the documentary analyses conducted on Change Orders. This change in scope of work and plans is normally due to the expansion of the contracted work as a result of enhancements to the design or reduction because of budget considerations and value engineering.

Table 2 Comparison on the causes of Change Orders in the public and private building construction projects

Public sector					Private sector				
Causes	Mean	SD	Rank	Interpretation	Causes	Mean	SD	Rank	Interpretation
Change of plans and scope by the owner	3.39	1.04	1	Sometimes	Changes in the design	4.25	0.89	1	Very often
Changes in the design	3.22	0.94	2	Sometimes	Change of plans and scope by the owner	3.93	1.12	2	Often
Unpredictable weather conditions	3.17	1.15	3	Sometimes	Change of schedule by the owner	3.61	1.13	3	Often
Unforeseen site conditions	3.17	0.99	4	Sometimes	Long waiting time for approval of construction drawings	3.57	0.92	4	Sometimes
Change of schedule by the owner	3.11	1.18	5	Sometimes	Complexity of Project	3.54	0.74	5	Sometimes
Average	3.21	1.06		Sometimes	Average	3.78	0.96		Often

The next major cause of Change Order as identified by both public and private sectors has something to do with changes in the design. According to the key informant interviews (KIIs) and based on the experience of this researcher, changes in design happen in any building projects especially when a construction project commences before the design has been finalized. Changes in design may also happen when the design has been reviewed by the consultant who has a different opinion or perspective with that of the designer and recommended making some changes.

Based on the foregoing exposition, while these identified major causes of Change Order often happen in private sector building projects, however, these causes only happen sometimes or occasionally in the public sector as signified by their average mean of 3.21 and a standard deviation of 1.06. When validated with the respondents during the KIIs as to why the above-mentioned top major causes happen only sometimes in the public sector, one of the reasons cited was that unlike in private sector, Change Orders in public construction projects are only limited to 10% of the original project cost. And public sector building projects do not usually allow or encourage Change Orders because they believe that they will cause more delays in project schedule which is disadvantageous to the end-users.

It is also interesting to note that the top three (3) major causes of Change Orders as identified by both the public and private respondents were confirmed by the study of Alaryan et al. [2], Al-Dubaisi [1] which also reported that the change of plans by the owners/clients, problems related to project site, errors and omission in the design, change of project scope by owners/clients, and new government regulations were the major Causes of Change Order in construction projects in Kuwait and Saudi Arabia. While the former study was conducted in a different setting, however, it seems that regardless of the location, the same causes were observed with regards to the causes of Change Order.

8.2 Effects of Change Orders

As shown in Table 3, the respondents from the public sector identified the five major effects of Change Orders as follows: (1) time extension ($M = 3.50$, SD = 0.79), (2) delay in project completion ($M = 3.44$, SD = 0.92), (3) increase in the overall cost of the project ($M = 3.44$, SD = 0.83), (4) changes in the cash flow and (5) loss of earnings ($M = 3.22$, SD = 0.65). When compared to the private sector respondents, the same findings were also reported particularly on the top three effects of Change Orders particularly (1) time extension ($M = 3.86$, SD = 0.97), (2) delay in the project completion ($M = 3.86$, SD = 1.11), and increase in the overall cost of the project ($M = 3.64$, SD = 1.13). However, the remaining top two effects identified by the private sector respondents were different from that of the public sector responses, specifically on the issues related to additional payments to the Contractor ($M = 3.75$, SD = 1.17), and increased time- and material-related charges ($M = 3.68$, SD = 1.06). The standard deviation of 1.09 for the private sector respondents is still widely

Table 3 Comparison on the effects of Change Orders in the public and private building construction projects

Public sector					Private sector				
Effects	Mean	SD	Rank	Interpretation	Effects	Mean	SD	Rank	Interpretation
Time extension	3.50	0.79	1	Sometimes	Time extension	3.86	0.97	1	Often
Delay in project completion	3.44	0.92	2	Sometimes	Delay in project completion	3.86	1.11	2	Often
Increase in the overall cost of the project	3.28	0.83	3	Sometimes	Additional payments to the contractor	3.75	1.17	3	Often
Changes in the cash flow	3.22	0.65	4	Sometimes	Increased time and material related charges	3.68	1.06	4	Often
Loss of earnings	3.22	0.65	5	Sometimes	Increase in the overall cost of the project	3.64	1.13	5	Often
Average	3.33	0.77		Sometimes	Average	3.76	1.09		Often

dispersed and reflects that there is a wide variation of opinions among all the respondents involved.

In terms of the degree of occurrence, it is quite different since the identified five major effects of Change Orders are often or regularly happening in the private sector but are only happening sometimes or occasionally in the public sector according to the data. It was also observed that more Change Orders are being issued in private building projects due to the freedom of the owners/clients to initiate changes as stipulated in the contract unlike in public building projects wherein Change Orders are only limited up to 10% of the original project cost thus limiting the possible effects.

It can be deduced from the research findings that both public and private sector respondents rated time extension, delay in project completion, and increase in the overall project cost as three of the most significant effects of Change Orders. This indicates that they are mostly concerned on the additional days or months that may be incurred by the project due to delay in some of the construction activities brought about by these Change Orders. An increase in the overall cost was also expected since any delay or extension in the project duration would normally result to additional project costs. These findings were corroborated by the study of Al-Dubaisi [1], Osman et al. [17] and Ismail [12] which also reported that the five common effects of Change Orders were related to delay in completion schedule, increase in the project duration, increase in the project cost, increase in overhead expenses, and delays in payment.

8.3 Management Control Practices of Change Orders

As shown in Table 4, the top five (5) management and control of Change Orders identified by the respondents which happened frequently or "Often" in the public sector are: (1) changes in the design documents are checked and reviewed for justifications ($M = 3.67$, SD = 1.08); (2) encourage coordination and cooperation among the contractors, consultants, and clients ($M = 3.61$, SD = 0.85), (3) personnel involved in the building construction project take proactive measures to promptly settle, authorize, and execute Change Orders ($M = 3.55$, SD = 0.86); (4) Change Order is negotiated by knowledgeable persons ($M = 3.50$, SD = 0.92); and (5) changes are not made without appropriate written approval ($M = 3.44$, SD = 1.25). When compared to the top three management and control of Change Orders identified by the private sector respondents, the same findings were also revealed in the public sector except however for the remaining top two control mechanisms which pertains to the implementation of the policy of having a clear scope of the change ($M = 4.00$, SD = 0.94) and the use of various techniques (e.g., work breakdown structure) which are being implemented in order to track cost of any possible changes ($M = 3.96$, SD = 1.10).

Interestingly, almost all of the respondents from both public and private sectors agreed that changes in the contract documents need to undergo a thorough review and checking by authorized persons prior to their issuance and implementation at

Table 4 Comparison on the management control practices being implemented in the public and private building construction projects

Public sector					Private sector				
Management control practices	Mean	SD	Rank	Interpretation	Management control practices	Mean	SD	Rank	Interpretation
All changes to design documents are checked and reviewed for justifications	3.67	1.08	1	Often	All changes to design documents are checked and reviewed for justifications	4.21	0.83	1	Very often
Encourage team effort among all parties	3.61	0.85	2	Often	Change order is negotiated by knowledgeable persons	4.04	1.00	2	Often
Project personnel take proactive measures to promptly settle, authorize, and execute Change Orders on any project in your organization	3.56	0.86	3	Sometimes	Project personnel take proactive measures to promptly settle, authorize, and execute Change Orders on any project in your organization	4.04	1.00	3	Often
Change order is negotiated by knowledgeable persons	3.50	0.92	4	Sometimes	The scope of change is made clear	4.00	0.94	4	Often
Changes are not made without appropriate approval in writing	3.44	1.25	5	Sometimes	Work breakdown structure (WBS) or other techniques are used to track cost of changes	3.96	1.10	5	Often
Average	3.56	0.99		Sometimes	Average	4.05	0.98		Often

the project site. This management practice can eliminate a lot of problems such as errors and omissions in the design, unclear scope of work, and conflicts between contract documents, among others. This research finding was confirmed by the study of Al-Dubaisi [1] and Alaryan et al. [2] which also reported that reviewing and checking of design prior to change approval is one of the most important practices for managing and controlling Change Orders in various building construction projects in the different countries in the world. Moreover, the study also revealed that both public and private sector respondents perceived team effort and collaboration as the second most important change management and control practice. Finally, the data also revealed that public and private sector respondents both agreed that Change Orders must be reviewed, settled, and discussed by authorized and competent key personnel only. This management practice is very important in order to prevent errors in the design and decision blunders which can lead to further mistakes and more Change Orders. The same findings were also observed from various empirical findings conducted in different countries relative to management and control practices of Change Orders [2, 1, 10].

8.4 One-Way Analysis of Variance (ANOVA)

The researcher hypothesized that there is no significant difference between the public and private respondents' responses with regards to the causes of Change Orders in building construction projects in the Philippines. And in order to answer this question, Table 5 presents the results of the One-way ANOVA on the differences in perceptions between the public and private sectors respondents. A 0.05 level of confidence has been used to determine if there is indeed significant difference between public and private sector respondents' responses.

The results in Table 5 revealed that there were significant differences on the perceptions of both public and private sector respondents on the three identified factors causing Change Orders particularly project-related causes ($p = 0.025$), design-related causes ($p = 0.0005$), and contractor-related causes ($p = 0.033$). The significant differences in perceptions indicated that public and private sectors do not agree with each other that these are the major factors that cause Change Orders in building construction projects. However, they do agree that Change Orders are mostly caused by the client ($p = 0.116$) and other external factors ($p = 0.501$) such as unforeseen site conditions and force majeure among others.

From the foregoing exposition, it is safe to assume that the differences in perception between the respondents in public and private sectors on the three out of five factors which cause Change Orders was due to the differences in the setting and contract conditions that the two sectors are engaged with. While it is true that the private sector usually engaged in contracts which allow them to issue unlimited number of Change Orders, however public sector is usually engaged in various contracts which limit themselves to issue Change Orders up to 10% only of the original contract cost as stipulated in Republic Act 9184 (RA 9184). And because

Table 5 Differences in perceptions between the public and private sector respondents with regard to the causes of change order

Causes of Change Orders		Sum of squares	df	Mean square	F	Sig.
Project-related causes	Between groups	2.39	1.00	2.39	5.40	**0.025***
	Within groups	19.49	99.00	0.44		
	Total	21.88	100.00			
Client-related causes	Between groups	2.94	1.00	2.94	2.57	0.116
	Within groups	50.37	99.00	1.14		
	Total	53.30	100.00			
Design-related causes	Between groups	5.76	1.00	5.76	14.16	**0.0005***
	Within groups	17.90	99.00	0.41		
	Total	23.66	100.00			
Contractor-related causes	Between groups	3.21	1.00	3.21	4.86	**0.033***
	Within groups	29.04	99.00	0.66		
	Total	32.24	100.00			
External factors	Between groups	0.25	1.00	0.25	0.46	0.501
	Within groups	23.41	99.00	0.53		
	Total	23.66	100.00			

*Significant at 0.05 level of confidence

of this, the public sector is more cautious when it comes to creating changes to contract documents (Table 6).

The ANOVA revealed that there were no significant differences between the public and private sector with regards to the effects of the Changes Orders in the building construction projects in almost all of the top five reported effects of Change orders, except for risk-related effects which differ in their perceptions. But taken collectively, it is safe to assume that both public and private sector respondents have agreed that the most frequent effects of Change Orders are very much related to: time and schedule ($p = 0.061$); project cost ($p = 0.132$); productivity ($p = 0.118$); and other effects ($p = 0.623$) such as loss of morale, quality degradation, etc. The ANOVA results also revealed that the same effects are being experienced in every construction project. However, public and private sector respondents differs on how often risk-related effects ($p = 0.04$) such as accelerating the project, and site congestion are happening as a result of Change Orders.

Table 6 Differences in perceptions between the public and private sector respondents with regard to the effects of change order

Effects of Change Orders		Sum of squares	df	Mean square	F	Sig.
Time-related effects	Between groups	1.97	1.00	1.97	3.69	0.061
	Within groups	23.48	99.00	0.53		
	Total	25.45	100.00			
Cost-related effects	Between groups	1.47	1.00	1.47	2.36	0.132
	Within groups	27.51	99.00	0.63		
	Total	28.98	100.00			
Productivity-related effects	Between groups	1.55	1.00	1.55	2.55	0.118
	Within groups	26.71	99.00	0.61		
	Total	28.26	100.00			
Risk-related effects	Between groups	1.93	1.00	1.93	4.46	**0.040***
	Within groups	18.99	99.00	0.43		
	Total	20.92	100.00			
Other effects	Between groups	0.14	1.00	0.14	0.25	0.623
	Within groups	24.28	99.00	0.55		
	Total	24.41	100.00			

*Significant at 0.05 level of confidence

In this study, it was hypothesized that there were no significant differences between clients', consultants', and contractors' perceptions on the causes and effects of Change Orders. And in order to test this hypothesis, a one-way ANOVA test was done and is presented in Table 7.

The data revealed that there were no significant differences with regards to the factors related project-related causes ($p = 0.429$), design-related causes ($p = 0.722$), and external factors ($p = 0.266$) which have p-value greater than 0.05. These findings confirmed that indeed the clients, consultants, and contractors were in agreement with the identified factors causing Change Orders in the building construction projects in the Philippines. However, there were significant differences in perceptions with regards to the factors related to client ($p = 0.04$) and contractor ($p = 0.017$). Both have p-values less than 0.05, which indicated that there was a different view on these identified factors that causes Change Orders. Based on the foregoing exposition, clients, consultants, and contractors have differed in their

Table 7 Differences in perceptions between consultants, contractors, and clients/owners with regard to the causes of change order

Causes of Change Orders		Sum of squares	df	Mean square	F	Sig.
Project-related causes	Between groups	0.84	2.00	0.42	0.86	0.429
	Within groups	21.04	98.00	0.49		
	Total	21.88	100.00			
Client-related causes	Between groups	7.41	2.00	3.71	3.47	**0.040***
	Within groups	45.89	98.00	1.07		
	Total	53.30	100.00			
Design-related causes	Between groups	0.36	2.00	0.18	0.33	0.722
	Within groups	23.31	98.00	0.54		
	Total	23.66	100.00			
Contractor-related causes	Between groups	5.59	2.00	2.80	4.51	**0.017***
	Within groups	26.65	98.00	0.62		
	Total	32.24	100.00			
External factors	Between groups	1.41	2.00	0.71	1.37	0.266
	Within groups	22.24	98.00	0.52		
	Total	23.66	100.00			

*Significant at 0.05 level of confidence

perceptions as to who causes the Change Orders in both public and private building construction projects. Hence, to validate the above findings a Post Hoc analysis in ANOVA using Fisher's Least Significant Difference (LSD) was utilized in this study. LSD was used to compare the means and get the relationships between groups of respondents. Table 9 presents the results of the LSD.

As shown in Table 8, there were significant differences existed: (a) between contractors' and consultants' ($p = 0.043$) perceptions that causes of Change Order are client-related; and (b) between the contractor and client ($p = 0.007$) that the contractor is one of the major initiators of Change Orders. However, there were no significant differences with regards to the other causes of Change Orders. These findings indicate that there is a difference in the responses when identifying which party causes change order. Clients and their consultants deny that clients cause Change Orders as reflected by their low mean scores compared to that of the contractors which say otherwise. Furthermore, with regards to the contractor-related

Table 8 Differences in perceptions of consultants, contractors and clients/owners with regard to the causes of Change Orders (post hoc Analysis)

Causes of Change Orders (dependent variable)	(I) Type	(J) Type	Mean difference (I − J)	Std. error	95% confidence interval		Sig.
					Lower bound	Upper bound	
Project-related causes	Contractor	Consultant	−0.281	0.337	−0.960	0.399	0.410
		Client	−0.293	0.254	−0.806	0.220	0.256
	Consultant	Contractor	0.281	0.337	−0.399	0.960	0.410
		Client	−0.012	0.383	−0.785	0.760	0.974
	Client	Contractor	0.293	0.254	−0.220	0.806	0.256
		Consultant	0.012	0.383	−0.760	0.785	0.974
Client-related causes	Contractor	Consultant	1.039	0.498	0.035	2.043	**0.043***
		Client	0.739	0.376	−0.019	1.496	0.056
	Consultant	Contractor	−1.039	0.498	−2.043	−0.035	**0.043***
		Client	−0.300	0.566	−1.441	0.841	0.599
	Client	Contractor	−0.739	0.376	−1.496	0.019	0.056
		Consultant	0.300	0.566	−0.841	1.441	0.599
Design-related causes	Contractor	Consultant	0.215	0.355	−0.501	0.930	0.548
		Client	0.172	0.268	−0.368	0.712	0.524
	Consultant	Contractor	−0.215	0.355	−0.930	0.501	0.548
		Client	−0.043	0.403	−0.856	0.770	0.916
	Client	Contractor	−0.172	0.268	−0.712	0.368	0.524
		Consultant	0.043	0.403	−0.770	0.856	0.916
Contractor-related causes	Contractor	Consultant	−0.563	0.379	−1.328	0.202	0.145
		Client	−0.813	0.286	−1.391	−0.236	**0.007***
	Consultant	Contractor	0.563	0.379	−0.202	1.328	0.145
		Client	−0.250	0.431	−1.120	0.620	0.565
	Client	Contractor	0.813	0.286	0.236	1.391	**0.007***
		Consultant	0.250	0.431	−0.620	1.120	0.565
External factors	Contractor	Consultant	0.517	0.347	−0.182	1.216	0.143
		Client	−0.112	0.262	−0.639	0.416	0.672
	Consultant	Contractor	−0.517	0.347	−1.216	0.182	0.143
		Client	−0.629	0.394	−1.423	0.166	0.118
	Client	Contractor	0.112	0.262	−0.416	0.639	0.672
		Consultant	0.629	0.394	−0.166	1.423	0.118

*Significant at 0.05 level of confidence

causes, the same finding was observed between contractors and clients. During the KIIs, it was revealed that contractors and clients strongly disagree with each other. Clients said that contractors often cause Change Orders, whereas contractors say otherwise as revealed by their lower mean scores.

Based on these findings, it seemed that there is a blaming game as to who initiated or causes Change Orders in building construction projects. Clients placed more blame on the contractors than themselves and vice versa. And this disparity in their perceptions often leads to various claims, conflicts, and disputes.

The data presented in Table 9 revealed that there were no significant differences in the perceptions of respondents coming from consultants, contractors, and clients or owners with regards to the effects of Change Orders except however for other effects (e.g., poor professional relations, quality degradation, and loss of morale) which has a *p*-value of 0.045. They have different views as to how often these other effects particularly poor professional relations, quality degradation, and loss of morale happen in building construction projects. And this can be attributed due to varying conditions wherein one party may encounter these other effects, but the other party may not.

Table 9 Differences in perceptions between the consultants, contractors, and clients/owners with regard to the effects of change order

Effects of Change Orders		Sum of squares	df	Mean square	*F*	Sig.
Time-related effects	Between groups	0.36	2.00	0.18	0.31	0.734
	Within groups	25.09	98.00	0.58		
	Total	25.45	100.00			
Cost-related effects	Between groups	0.58	2.00	0.29	0.44	0.645
	Within groups	28.40	98.00	0.66		
	Total	28.98	100.00			
Productivity-related effects	Between groups	0.39	2.00	0.20	0.30	0.740
	Within groups	27.87	98.00	0.65		
	Total	28.26	100.00			
Risk-related effects	Between groups	0.38	2.00	0.19	0.40	0.672
	Within groups	20.54	98.00	0.48		
	Total	20.92	100.00			
Other effects	Between groups	3.29	2.00	1.64	3.35	**0.045***
	Within groups	21.12	98.00	0.49		
	Total	24.41	100.00			

*Significant at 0.05 level of confidence

In order to validate the above findings and further evaluate these differences among the three groups of respondents, a Post Hoc analysis in ANOVA using Fisher's Least Significant Difference (LSD) was utilized in this study. LSD was used to compare the means and get the relationships between groups of respondents. Table 10 presents the results of the LSD.

Table 10 Differences in perception of consultants, contractors and clients/owners with regard to the effects of Change Orders (post hoc Analysis)

Effects of Change Orders (dependent variable)	(I) Type	(J) Type	Mean difference (I − J)	Std. error	95% confidence interval		Sig.
					Lower bound	Upper bound	
Time-related effects	Contractor	Consultant	0.04	0.37	−0.70	0.79	0.91
		Client	−0.21	0.28	−0.77	0.35	0.46
	Consultant	Contractor	−0.04	0.37	−0.79	0.70	0.91
		Client	−0.25	0.42	−1.09	0.59	0.55
	Client	Contractor	0.21	0.28	−0.35	0.77	0.46
		Consultant	0.25	0.42	−0.59	1.09	0.55
Cost-related effects	Contractor	Consultant	0.11	0.39	−0.68	0.90	0.78
		Client	−0.24	0.30	−0.84	0.35	0.41
	Consultant	Contractor	−0.11	0.39	−0.90	0.68	0.78
		Client	−0.36	0.45	−1.25	0.54	0.43
	Client	Contractor	0.24	0.30	−0.35	0.84	0.41
		Consultant	0.36	0.45	−0.54	1.25	0.43
Productivity-related effects	Contractor	Consultant	0.21	0.39	−0.57	1.00	0.58
		Client	−0.13	0.29	−0.72	0.46	0.66
	Consultant	Contractor	−0.21	0.39	−1.00	0.57	0.58
		Client	−0.34	0.44	−1.23	0.55	0.44
	Client	Contractor	0.13	0.29	−0.46	0.72	0.66
		Consultant	0.34	0.44	−0.55	1.23	0.44
Risk-related effects	Contractor	Consultant	0.14	0.33	−0.53	0.81	0.67
		Client	−0.17	0.25	−0.68	0.33	0.49
	Consultant	Contractor	−0.14	0.33	−0.81	0.53	0.67
		Client	−0.32	0.38	−1.08	0.45	0.41
	Client	Contractor	0.17	0.25	−0.33	0.68	0.49
		Consultant	0.32	0.38	−0.45	1.08	0.41
Others effects	Contractor	Consultant	0.30	0.34	−0.38	0.98	0.38
		Client	−0.57	0.25	−1.08	−.05	**0.03***
	Consultant	Contractor	−0.30	0.34	−0.98	0.38	0.38
		Client	−0.87	0.38	−1.64	−0.09	**0.03***
	Client	Contractor	0.57	0.25	0.05	1.08	**0.03***
		Consultant	0.87	0.38	0.09	1.64	**0.03***

*Significant at 0.05 level of confidence

As shown in Table 10, the results of the ANOVA revealed that there were significant differences in the responses between the clients and contractors and also between clients and consultants on other effects (e.g., poor professional relations, quality degradation, loss of morale) as signified by the p-value of 0.03 which is less than the 0.05 level of confidence. This means that contractors and consultants are losing morale due to a number of Change Orders being issued at site. However, clients may not experience the same thing and may perceive the issuance of Change Orders as a good opportunity to enhance their construction project.

8.5 A Proposed Framework of Guidelines for Managing Change Orders

The researcher designed a research-validated framework or a set of guidelines which was based on the synthesis of several change process models reviewed in several literatures and on the actual site conditions of selected building construction projects in NCR. This framework was presented to construction professionals in selected building construction projects in NCR and was found to be reliable, acceptable, and can be recommended for proper implementation. This framework consists of procedures which were revised and improved continuously throughout the study especially after carrying out key informant interviews and analyzing the results of the survey. As shown in Fig. 2, this framework is composed of nine (9) stages or steps in managing Change Orders. This steps include: (1) Evaluate the Contract Documents; (2) Identify the Change; (3) Notify all the concerned parties; (4) Initiate and Propose; (5) Review and Evaluate the Change Order Request; (6) Approve the Change Order Request; (7) Implement or Execute the Change Order Request; (8) Settle Unresolved Change Orders and Claims; (9) Document the Change.

Thus, the following paper is hereby presented.

8.5.1 A Research-Validated Set of Guidelines for Managing Change Orders in Building Construction Projects in the Philippines

Implementing Guidelines for Managing Change Orders

Step 1. Evaluate the Contract Documents

- *Contractors, consultants, and clients should thoroughly review and understand contract requirements and provisions regarding conflicts and discrepancies in contract documents and any other risks before the project starts*
- *Contract documents should contain a change clause which would allow for changes to the scope of work and allows the contractor an equitable adjustment to the contract price or schedule as a result of a change.*

Step 2. Identify the Change

- *The second step in successful change order management is to identify the change, which can be defined as any anticipated or actual deviation from the scope, schedule, or price/budget/cost.*

Step 3. Notify All the Concerned Parties

- *The contractor should notify the owner through a Change Notice that a change has been spotted or had already happened.*
- *It is highly suggested that Change Notices reflecting the details of extra work to be performed shall be prepared and shall be submitted to the Client within seven (7) days to officialize the change.*

Step 4. Initiate & Propose
    A. Client/Owner Initiates the CO Proposal

- *When a change order is initiated by the client/owner, the process should begin with a request for proposal (RFP).*
- *The RFP should present all the needed information so that the contractor can make a reasonable and realistic estimate of the costs and the time required in order to implement the change.*

    B. Contractor Initiates the CO Proposal

- *When a change order is initiated by the contractor, the contractor should prepare a Change Order Request/Proposal, in a prescribed professional format, just after submitting the Change Notice.*
- *This request should contain a full description of the change and its corresponding production costs.*
- *Additionally, change requests should effectively use graphics and numbers to communicate the desired information to the intended audience. It should also establish a link or cause–effect relationship between the entitlement and the damages.*

Step 5. Review and Evaluate the Change Order Request
    A. Contractor's representative reviews request and submits to Consultant

- *The Contractor should review first their change order request in order to check any errors and/or omissions in it before submitting to the Consultant*

    B. Consultant reviews the CO request and recommends to the Client/Owner

- *The Consultant should check the rationality and validity of the Contractor's request and submit the request to the Client/Owner*

    C. Client/Owner reviews merits of the proposed Change Order

- *The client should perform a detailed review and evaluation of the change documents in order to assess the rationality of the proposed change order and its possible impacts.*

- *The client should also evaluate the contractor's entitlement to recover additional costs or time by determining whether or not a change has occurred and if a remedy for the change exists in the contract documents.*

Step 6. Approve the Change Order Request
   A. If Client denies Change Order request

- *If the Client does not find the CO request to be reasonable, it should be returned to the Contractor with denied authorization.*

   B. If Client approves the Change Order request.

- *Consultant should request from Contractor quotations/price proposal of the change order.*
- *Contractor should estimate time and cost and submit signed Change Order proposal to the Consultant*
- *Consultant should review time/cost proposal and negotiate terms.*

a. *If the Consultant determines that the Contractor is entitled to recover costs and/ or time associated with change, they should measure the effect of the change by calculating the additional costs and/or time extension required and compare and negotiate them to the impacts quantified in the contractor's change order request/proposal.*
b. *If Consultant and Contractor do not agree on the time and cost implications of the change, attempt to renegotiate the terms. Otherwise, if still disapproved, confer immediately with Legal/Contracts for assistance in securing reconsideration, arbitration or filing of a Claim*

Step 7. Implement/Execute the Change Order Request
   A. Client/Owner signs Change Order

- *The client, should approve the Change Order preferably within fifteen (15) days from the receipt of the CO request, or as specified in relevant contract provisions.*
- *If the approval of Change Order was not obtained from the client within the specified time, the contractor may have the option to hold or stop the change order in process.*

   B. Contractor begins Change Order work

- *The contractor should proceed with the execution of the change order works immediately right after the approval of the change order request/proposal to avoid further damages and delays.*
- *It is very important that change order work should begin after the client or client's representative issues a written authorization to proceed. Verbal authorization should be avoided.*

Step 8. Settle Unresolved Change Orders and Claims

- *All work items including all the issued Change Orders should be verified technically by the Client and/or Consultant whether those were completed correctly and satisfactorily.*
- *Moreover, all the remaining Change Orders and any other potential Change Orders should also be identified and resolved in a timely manner before the project close-out.*
- *Clients, consultants, and contractors should be proactive in settling all the claims and resolving all the issues and disputes regarding Change Orders in order to avoid unnecessary surprises in the future.*

Step 9. Document the Change

- *A complete documentation of the change should be created in order to provide the necessary data to prove and substantiate the occurrence of the changes.*
- *Appropriate supporting records and documents, including a written copy of the change directive, should also be maintained with the change order package.*
- *A checklist of documents and records that should be kept and maintained includes but may not be limited to: actual progress photos, project correspondences, minutes of meetings, original and revised construction drawings, construction contract and other legal documents.*

```
                          ┌─────────────────────────┐
                          │          START          │
                          └─────────────────────────┘
                                      │
  EVALUATE                 ┌─────────────────────────┐
                          │ Evaluate contract documents │
                          └─────────────────────────┘
                                      │
  IDENTIFY                 ┌─────────────────────────┐
                          │     Identify the Change    │
                          └─────────────────────────┘
                                      │
                          ┌─────────────────────────┐
                          │ Notify all concerned parties │
                          └─────────────────────────┘
  INITIATE &
  PROPOSE
```

EVALUATE

Evaluate contract documents

IDENTIFY

Identify the Change

Notify all concerned parties

INITIATE & PROPOSE

| Client initiates CO Proposal | Contractor initiates CO Proposal |

| Client prepares Request for Proposal (RFP) | Contractor prepares Change Order Request/ Proposal |

REVIEW

Consultant reviews and recommends proposal to Client

Client reviews merits of the proposed Change Order

APPROVE

Change recommended by Client?

YES — Consultant prepares cost estimates and revised schedule — A

NO — CO Request returned to Contractor with authorization denied — END

Fig. 2 Flow chart of procedures for managing change order

A

Consultant requests CO price proposal from Contractor

Contractor estimates time and cost and submits signed CO proposal to Consultant

Consultant reviews time & cost proposal and negotiates terms

NEGOTIATE

Agree on Time and Cost?

YES

NO

Client signs Change Order

Attempt re-negotiation. If still disapproved, confer with Legal/Contracts Office for assistance in securing reconsideration, arbitration or filing of a Claim.

IMPLEMENT

Contractor begins CO works

SETTLE/ RECONCILE

Settle unresolved CO and claims

DOCUMENT

Document the Change

END

Fig. 2 (continued)

9   Conclusions

In the light of the foregoing findings, the following conclusions were drawn:

1. The common major causes of Change Orders in public and private building construction projects in the Philippines were related to clients' requests particularly changes in the plans and scope of work, changes in the design, and change in project schedule. The common major effects as reported by both the public and private respondents were related to project time extension, delay in project completion, and increase in the overall cost of the project.
2. The most common management control practices being undertaken by both public and private sector respondents were: (i) all changes in the design documents are checked and reviewed for justifications, (ii) project personnel take proactive measures to promptly settle, authorize, and execute Change Orders, and (iii) Change Order is negotiated by knowledgeable persons.
3. The results revealed that there were significant differences between the public and private sector respondents' responses on the causes of Change Orders particularly on project-related causes, design-related causes, and contractor-related causes. However, there were no significant differences between the public and private sector with regards to the effects of Changes Orders in building construction projects in the Philippines in almost all of the top five reported effects of Change orders, except for risk-related effects which differ in their perceptions.
4. There were significant differences on the respondents perception: (a) between contractor and consultant on the perception that Change Order are client-related causes; (b) between the contractor and client that the contractors are one of the major originators of Change Orders. However, there were no significant differences between clients, consultants, and contractors with regards to their perceptions on the major effects of Change Orders, except for the other effects of Change Orders such as poor professional relations and quality degradation.
5. The research-validated framework or set of guidelines that was developed in this study was found to be acceptable to the construction industry and can be used to minimize and or mitigate the issues and problems related to Change Orders in building construction projects.

10   Recommendations

In the light of the foregoing findings and conclusions, the following recommendations are offered:

1. To conduct thorough review and finalization of all designs, construction plans and specifications, scope of work and project schedule prior to the commencement of the project.

2. To conduct complete and meticulous site investigations such as soil surveys and geotechnical studies. Likewise, weather conditions should be recorded on a daily basis in order to support and justify claims for time extensions due to uncontrollable factors.
3. To require contractors to submit catch-up revised schedule to clients and consultants in order for them to adjust and recover from the effects of Change Orders in the overall project duration.
4. Clients, consultants, and contractors should discretely track the cost as well as schedule impacts in order to have a greater chance of recovery from cost overruns and underruns. This can be implemented by creating a unique cost code to capture the costs associated with the proposed change.
5. Inasmuch as three of the most common identified management practices being implemented to address Change Orders were related to checking and reviewing of design documents, proactively settling, authorizing and executing Change Orders, and proper negotiation by knowledgeable persons, it is recommended that these management practices be adopted in all public and private building construction projects.

References

1. Al-Dubaisi, A.H.: Change orders in construction projects in Saudi Arabia, Master's thesis. Available from Dissertations and Theses database (UMI No. 1399744) (2000)
2. Alaryan, A., Elshahat, A., Dawood, M.: Causes and effects of change orders on construction projects in Kuwait. Int. J. Eng. Res. Appl. **4**(7), 1–8 (2014)
3. Alnuaimi, A.S., Taha, R.A., Mohsin, M.Al, Al-harthi, A.S.: Causes, effects, benefits, and remedies of change orders on public construction projects in Oman. J Constr. Eng. Manage. **136**, 615–623 (2010)
4. Aneesa, M.M., Mohamed, H.E., Abdel, R.: Evaluation of change management efficiency of construction constructors. HBRC J. **9**, 77–85 (2013)
5. Clare, B.S.: Reviewing change orders 101. AACE Int. Trans., 1–5 (2008)
6. Egan, J.J., Seder, J.E., Anderson, D.L.: Practices in construction change order management. Cost Eng., 12–17 (April 2012)
7. Fraenkel, J., Wallen, N.: How to design and evaluate research in education, 8th edn. McGraw-Hill Education, New York (2007)
8. Hwang, B.G., Low, L.K.: Construction project change management in Singapore: status, importance and impact. Int. J. Project Manage. **30**(7), 817–826 (2012). https://doi.org/10.1016/j.ijproman.2011.11.001
9. Ibbs, C.: Change's impact on construction productivity. J. Constr. Eng. Manage. **123**(1), 89–97 (1997)
10. Ibn-homaid, N.T., Eldosouky, A.I., Al-ghamdi, M.A.: Change orders in Saudi linear construction projects. Emirates J. Eng. Res. **16**(1), 33–42 (2011)
11. Ijaola, I.A., Iyagba, R.O.: A comparative study of causes of change orders in public construction project in Nigeria and Oman. J. Emerg. Trends Econ. Manage. Sci. **3**(5), 495–501 (2012)
12. Ismail, A., Pourrostam, T., Soleymanzadeh, A., Ghouyounchizad, M.: Factors causing variation orders and their effects in Roadway construction projects. Res. J. Appl. Sci. Eng. Technol. **4**(23), 4969–4972 (2012)

13. Levin, J.A., Fox, J.A.: Elementary statistics in social research: essentials, 3rd edn. Northeastern University, Boston (1997)
14. Love, P.E., Holt, G.D., Shen, L.Y., Li, H., Irani, Z.: Using systems dynamics to better understand change and rework in construction project management systems. Int. J. Proj. Manag. **20**(6), 425–436 (2002)
15. Molly, K.K.: Six steps for successful change order management. Cost Eng. **49**(4), 12–20 (2007)
16. Motawa, I., Anumba, C., Lee, S., Peña-Mora, F.: An integrated system for change management in construction. Autom. Construc. **16**(3), 368–377 (2007)
17. Osman, Z., Omran, A., Foo, C.K.: The potential effects of variation orders in construction projects. J. Eng. Ann. Fac. Eng. Hunedoara **2**, 141–152 (2009)
18. Philippine Domestic Construction Board: A primer on PD no. 1594 and its implementing rules & regulations as amended. Philippine Domestic Construction Board, Makati, Metro Manila (1989)
19. Rodriguez, J.: Five (5) situations that might trigger a change order request. Retrieved from: http://construction.about.com/od/Claims-Management/a/Common-Causes-For-A-Change-Order.htm (2016)
20. Serag, E., Oloufa, A., Malone, L., Radwan, E.: Model for quantifying the impact of change orders on project cost for U.S. roadwork construction. J. Constr. Eng. Manage. **136**, 1015–1027 (2010)
21. Sun, M., Meng, X.: Taxonomy for change causes and effects in construction projects. Int. J. Project Manage. **27**(6), 560–572 (2009). https://doi.org/10.1016/j.ijproman.2008.10.005
22. Sundaram R.: Managing change order costs in construction projects: how owners can stay on top. Retrieved from https://www.fgould.com/americas/articles/managing-change-order-costs-construction-projects (2012)

Numerical Modelling for Twin Horizontal Circle Tunnels Under Static and Dynamic Loads

Jaafar Mohammed and Eva Hrubesova

Abstract According to recent studies and observed failures of underground structures, many researchers have addressed the design and construction of tunnel lining against static/dynamic loads and earthquake vibration to get the safety of these structures. Therefore this paper includes the study of the behavior of tunnel lining due to static and dynamic loads. Inner diameter of tunnel is D m. Concrete lining of thickness 0.3 m. The depth of the tunnel centre line from the ground level is 10 D below the surface of the ground, the twin tunnel centre are 3D. After tunnel model is created in the software MIDAS GTS NX, the model is run to analyze the tunnel stability and deformation in static and dynamic conditions by calculating the value of each mesh node based on 3D finite element method and were undertaken to investigate the seismic tunnel response conditions to compare the results in the displacement, stresses, forces and bending moments acting on the tunnel lining. Due to the application of the static load the stress–strain state around the tunnel periphery is changed, the primary stress state is disrupted and the potential of instability increases, otherwise the result shows that the applied dynamic stress is not negligible for underground structure, but it is less dangerous in comparison with the others.

Keywords Static load · Dynamic load · Tunnel · Earthquake · FEA
Displacement

J. Mohammed (✉) · E. Hrubesova
Department of Geotechnics and Underground Engineering,
Faculty of Civil Engineering, VSB-Technical University of Ostrava,
L. Podeste1875, 708 33 Ostrava-Poruba, Czech Republic
e-mail: jaafar.brifkani@uod.ac

E. Hrubesova
e-mail: eva.hrubesova@vsb.cz

1   Introduction

This case study deals with the static and dynamic analysis of twin circle tunnels that use shield Tunnel Boring Machine (TBM) are predicted, the construction stages and parameters such as gravity, drilling or excavation pressure, jack thrust are applied on the shield excavation, the shield external pressure and segment external pressure are applied around the tunnel which are simulated in a 3D finite elements analysis utilizing MIDAS G1TS NX software and both the face and grout pressures are the most influencing parameters. After tunnel modelling the calculation is run to analyze the tunnel stability by calculating the value of each mesh node based on 3D finite element method, to simulate the effect of earthquake on tunnel stability and displacement. Most of researchers explain that shallow tunnels suffer higher damage compared to deep structures. Many numerical analyses were carried out in order to verify and compare the stresses, forces and bending moments acting on the tunnel lining according with the seismic design. In this subject, twin tunnel were studied by more authors like [1–13].

Response spectrum analysis expresses the natural period, natural angular frequency or natural frequency at the maximum physical quantity response as a function when a dynamic load is applied to the structure. The analysis can be expressed as a displacement response spectrum, pseudo-rapidity response spectrum or pseudo-acceleration response spectrum [14].

Understanding the behavior of tunnel structures during seismic load is one of the most interesting challenges in geotechnical engineering. While tunnels generally performed during earthquakes better than structures on the ground surface, some examples of damage, some of these important structures during previous earthquake events, that is, the 1995 Kobe, Japan earthquake, the 1999 Chi Chi, Taiwan earthquake, the 1999 Bolu, Turkey earthquake, the 2004 Baladeh, Iran earthquake, the 2008 Sichuan, China earthquake, and recently the 2014 Valparaiso, Chile earthquake, highlights the need to account for seismic loading in the design of underground structures [15].

In static analysis, when analyzing a model with infinite material such as ground, boundaries are set far enough from main analysis area. But in dynamic analysis since effect of waves reflection occurs, if boundaries are set in the same way as static analysis, big error may occur [14].

Static and dynamic plane strain finite element (FE) analyses were undertaken to investigate the seismic tunnel response at two sections and to compare the results with the post-earthquake field observations. The predicted maximum total hoop stress during the earthquake exceeds the strength of shotcrete in the examined section. The occurrence of lining failure and the predicted failure mechanism compare very favourably with field observations [16].

In recent years, many tunnels have been built in urban environments; this often involves the construction of twin tunnels in close proximity to each other. In addition, in many cases, the new tunnel is often excavated adjacent to an already existing one. Most of them are twin horizontal tunnels. However, in some cases, the

twin tunnels are stacked over each other in order to avoid the pile foundations of existing building on the ground surface [15].

2 Definition of Ground and Structural Materials

This paper studies the 3D model with gravity in Z direction. The thickness of concrete lining is 0.3 m. Distance between the tunnel centre line and ground surface is 10 D. Water table was not considered in the calculation. Tunnel simulation had 47 stage sets. Tables 1, 2 and 3 are presented the mechanical and physical properties of material for ground and structure used in modelling for tunnels. Applied static loads [gravity, drilling or excavation pressure (200 kN/m^2), and the jack thrust (−4500 kN/m^2), are applied on the shield excavation face. The shield external pressure (50 kN/m^2) and segment external pressure (1000 kN/m^2)] are applied around the tunnel as shown in Fig. 15 [14]. The dimension of the model are ($x = 210$, $z = 210$, $y = 80$) m.

Table 1 Ground materials

Name	Soft rock	Segment
Material	Isotropic	Isotropic
Model type	Elastic	Elastic
Elastic modulus (E) [kN/m^2]	20,000	20,000,000
Poisson's ratio (ν)	0.4	0.2
Unit weight (γ) [kN/m^3]	18	24
Drainage parameters	Drainage	Drainage

Table 2 Structure materials

Name	Steel	Grout
Material	Isotropic	Isotropic
Model type	Elastic	Elastic
Elastic modulus (E) [kN/m^2]	25,000,000	15,000,000
Poisson's ratio (ν)	0.25	0.3
Unit weight (γ) [kN/m^3]	78	23

Table 3 Ground properties

Material	Soil	Segment
Type	3D	3D

3   Simulation and Calibration of the Numerical Model

The overview of modelling steps consists of: (1) definition of input parameters and constitutive models for ground, segment, shield and grout, (2) geometry generation using solid elements for ground and tunnel segments, (3) mesh generation using auto meshing, (4) load definition (gravity, drilling or excavation pressure, jack thrust, shield external pressure and segment external pressure), (5) setup construction sequence, (6) define construction stage analysis control, and final run, (7) created eigenvalue and (8) created response spectrum. The construction process can be divided in construction stages with a length of a tunnel ring about 2 m long, in each of these stages the same steps are repeated. The calculation consists of a number of stages, each of which models the same parts of the excavation process. The support pressure at the tunnel face needed to prevent active failure at the face, the installation of the tunnel lining and the grouting of the gap between the soil and the newly installed lining. Construction stage that will be considered as the in situ condition and check the displacement reset condition consideration.

The calculated in situ stress is in equilibrium with the self-weight and the same boundary conditions are used in singular analysis for analysis. The default damping ratio is applied to all modes that have a lower priority than the specified mode. If the input damping ratio is different from the damping ratio of the response spectrum function, the spectrum data is adjusted with reference to the input damping ratio and used for analysis [14].

4   Three-Dimensional FEM Modelling

The FE mesh of the soil and tunnel lining are shown in Figs. 1, 2, 3, 4, 5 and 6. An 80 m long tunnel has been modelled in soft rock with tunnel lining thickness of 300 mm; the depth of tunnel centre line from the ground surface is 140 m.

Gravity 9.81 m/s^2 is applied globally on the model, while the two tub tunnels are subjected to static loads [gravity, drilling or excavation pressure, jack thrust are applied on the shield excavation face, the shield external pressure and segment external pressure are applied around the tunnel]. A 20,000 kN/m^2 of elastic modulus and a Poisson's ratio of 0.4 are used.

Eigenvalue analysis is used to analyze the inherent dynamic properties of the ground/structure including damping parameters, and this can be used to obtain the natural mode (mode shape), natural period (natural frequency), modal participation factor, etc., of the ground/structure. These properties are determined on the basis of the mass and stiffness of the structure. In other words, if a structure is determined, the natural frequency and vibration mode (natural mode) are also determined and the number of properties is the same as the degree of freedom of the structure. For real cases, the structure does not vibrate at a single mode shape and multiple modes overlap to display a complex vibration shape [14].
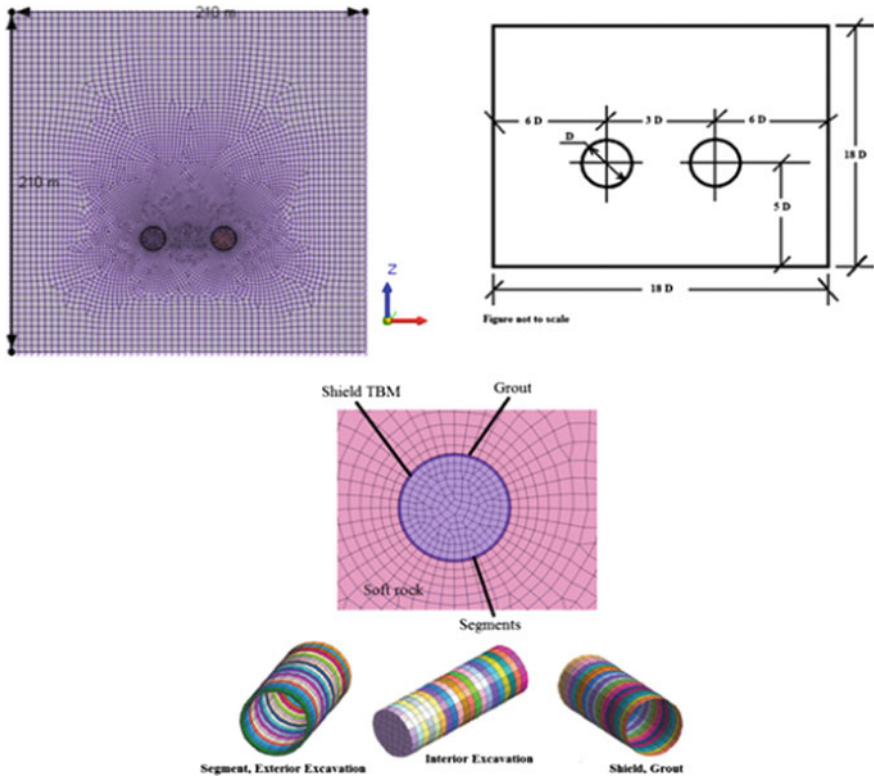
Fig. 1 Mesh tunnel profile
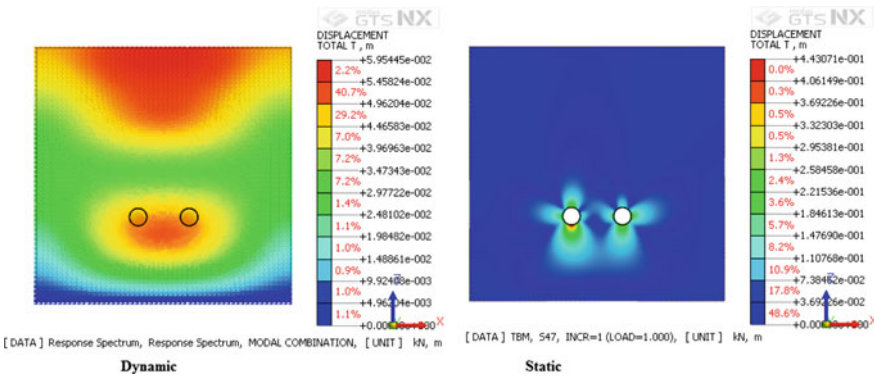
Fig. 2 Total displacement distribution in static and dynamic analysis
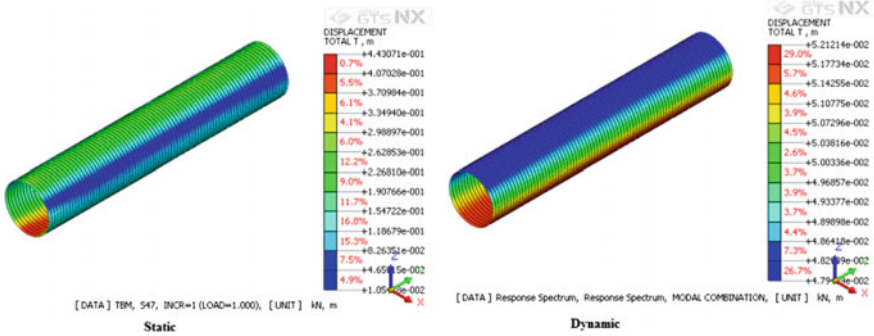
Fig. 3 Total displacement distribution in static and dynamic analysis on the shield of first tunnel
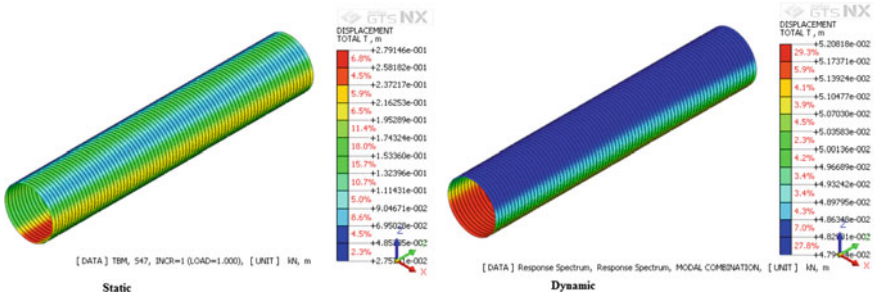
Fig. 4 Total displacement distribution in static and dynamic analysis on the shield of second tunnel
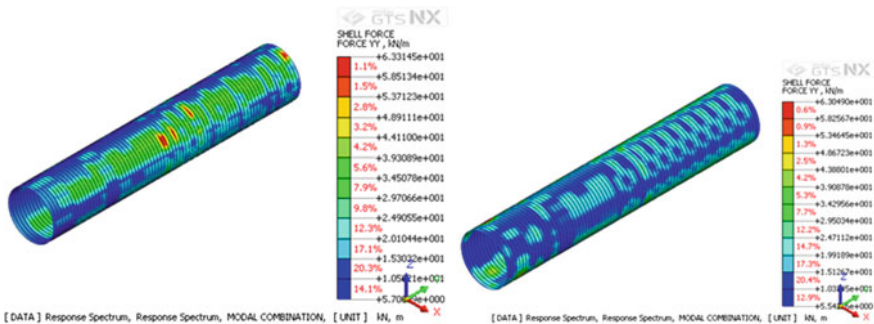
Fig. 5 Force distribution in dynamic analysis on the shield of first and second tunnel

In Figs. 7, 8, 9, 10, 11, 12, 13 and 14, the distribution of (displacement, force, bending moment and shear) in static and dynamic analysis for both tunnels is shown (Fig. 15). Due to the application of the static/dynamic loads on tunnel the distribution on periphery is changed, therefore the balance is disrupted and the
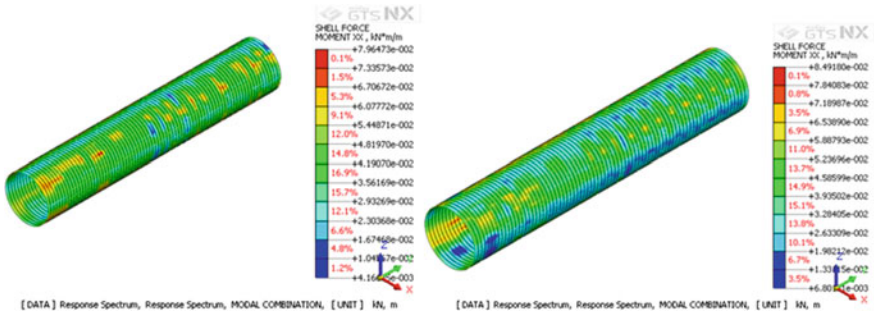
Fig. 6 Bending moment distribution in dynamic analysis on the shield of first and second tunnel
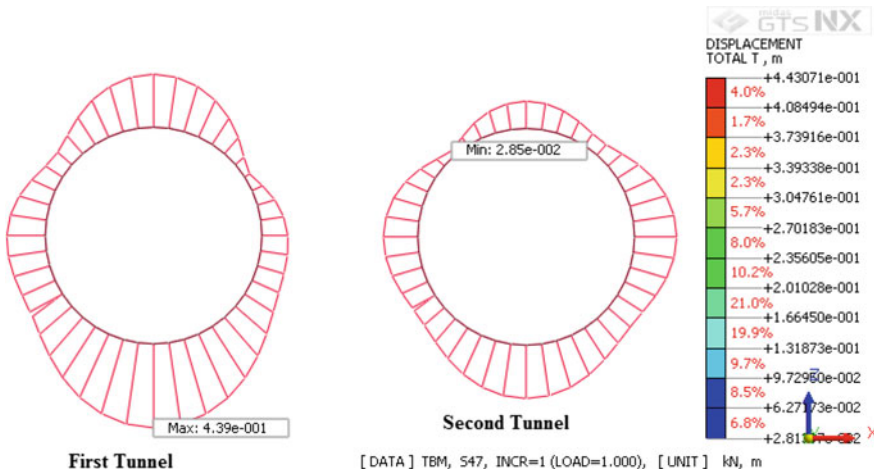
Fig. 7 Displacement distribution in static analysis on the face of shield tunnel
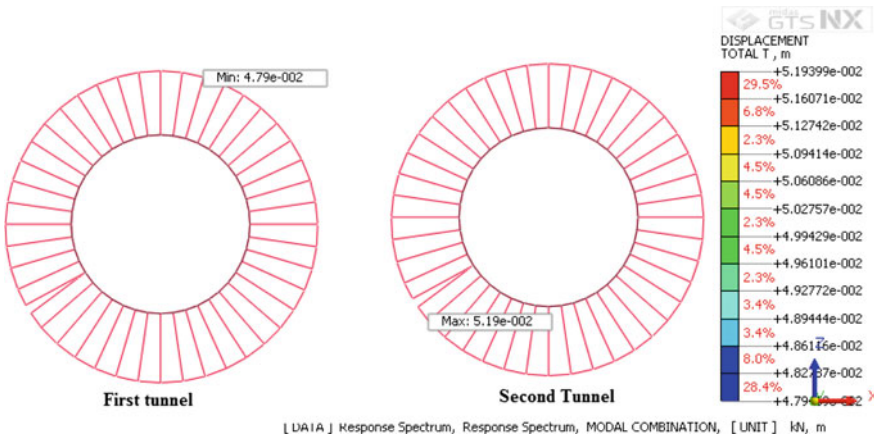
Fig. 8 Displacement distribution in dynamic analysis on the face of shield tunnel
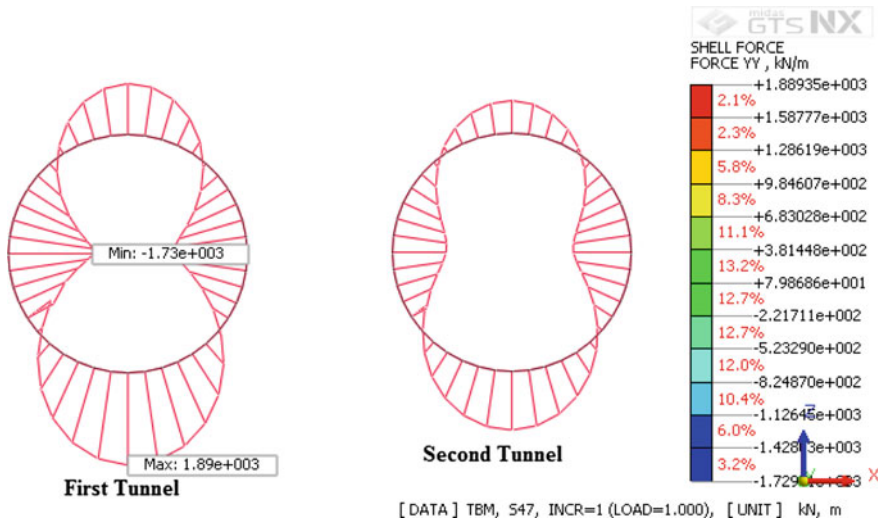
Fig. 9 Force distribution in static analysis on the face of shield tunnel
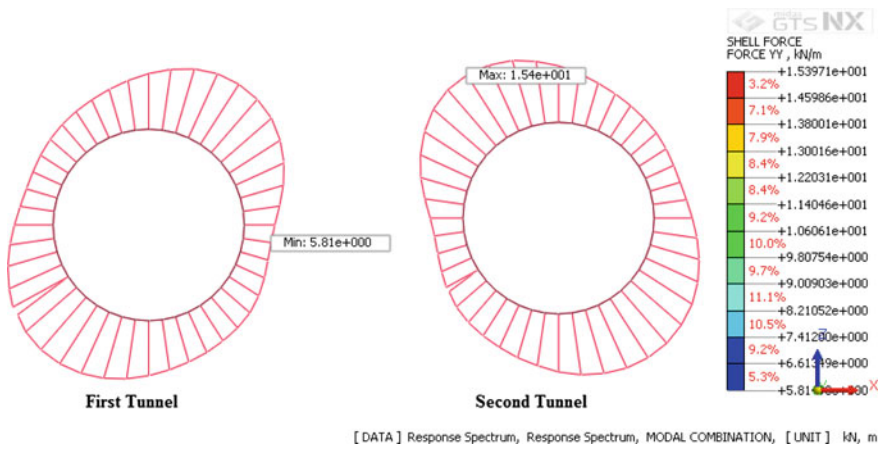
Fig. 10 Force distribution in dynamic analysis on the face of shield tunnel

potential of instability increases, otherwise the result show briefly in Tables 4, 5, 6 and 7. Design Response Spectrum of UBC (1997) is used as seismic response spectrum as shown in Fig. 16.
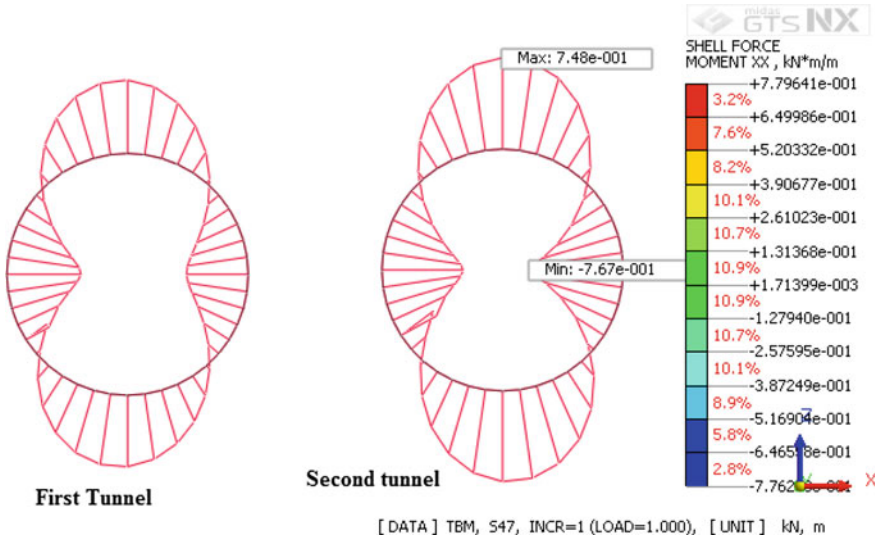
Fig. 11 Bending moment distribution in static analysis on the face of shield tunnel
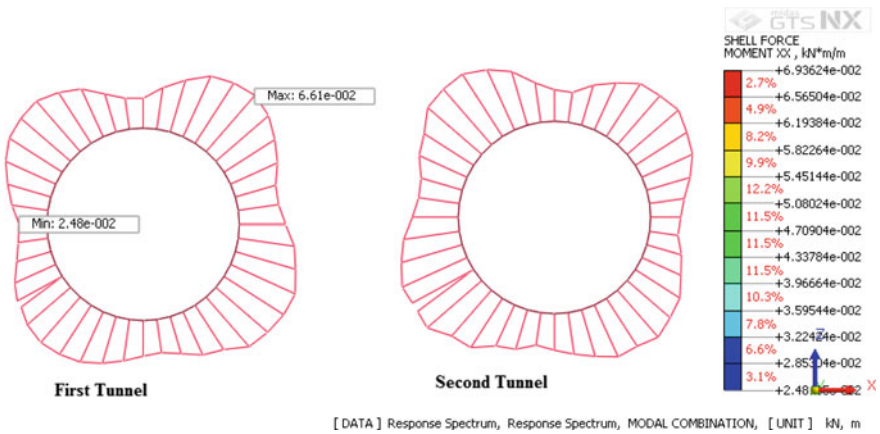
Fig. 12 Bending moment distribution in dynamic analysis on the face of shield tunnel
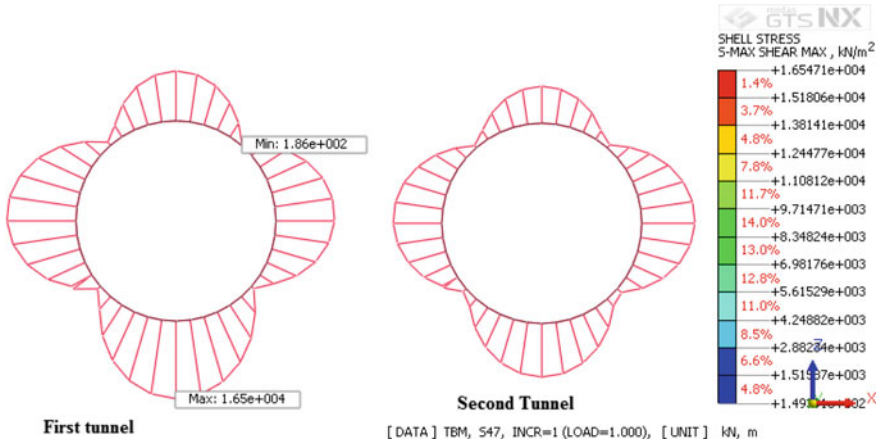
Fig. 13 Shear distribution in static analysis on the face of shield tunnel
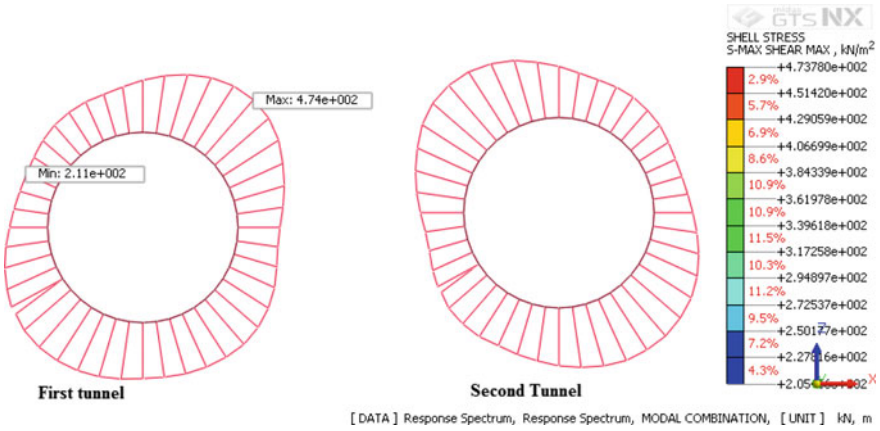
Fig. 14 Shear distribution in dynamic analysis on the face of shield tunnel
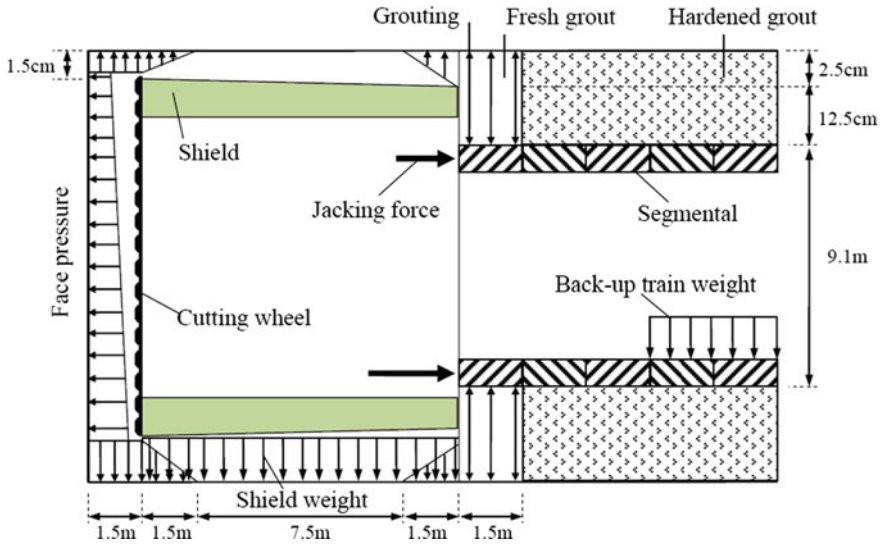
Fig. 15 Layout of the proposed TBM model (not scaled) [15]

5   Conclusions

Based on the tunnel modelling using software MIDAS GTS NX, the 3D analysis of the tunnel response under static and dynamic conditions was performed to investigate the seismic tunnel response to compare the results of the displacement, stresses, forces and bending moments acting on the tunnel.

They provide very good results when tunnelling conditions are known by using numerical analysis. During the shield TBM excavation, it is assumed that the excavation pressure and the jack thrust are applied on the shield excavation face. The shield external pressure and segment external pressure are applied around that face.

The effects of different factors on circular tunnels lining, including elasticity modulus (E), Poisson's ratio (v), unit weight (γ), rock conditions, and tunnel diameters (D), etc., are studied through the numerical analysis solution. In this study, the following conclusions are drawn: Figs. 2, 3 and 4 show the displacement in static and dynamic conditions. Due to the application of the static load, the stress–strain state around the tunnel periphery is changed, the primary stress state is disrupted and the potential of instability increases.

In Figs. 5, 6, 7, 8, 9, 10, 11, 12, 13 and 14, the distribution of (displacement, force, bending moment and shear) in static and dynamic analysis for both tunnels is shown. Due to the application of the static/dynamic loads on tunnel the distribution on periphery is changed, therefore the balance is disrupted and the potential of instability increases, the result is shown briefly in Tables 4, 5, 6 and 7, otherwise

Table 4 The result of distribution in static analysis on both tunnels

Case	First tunnel	Second tunnel
Displacement	Has the Maximum value which is (0.439 m). Bottom is more affected than top. Left side more affected	Has Minimum value which is (0.0285 m). Bottom is more affected than top. Right side more affected
Force	Have maximum (1890 kN/m) and minimum (−1730 kN/m) value. Bottom is more affected than top	Bottom is more affected than top
Bending moment	Approximate the distribution is in uniform	Have maximum (0.748 kN m/m) and minimum (−0.767 kN m/m) value. Approximate the distribution is in uniform
Shear	Have maximum (16500 kN/m^2) and minimum (186 kN/m^2) value. Bottom is more affected than top. Left is more affected	Bottom is more affected than top. Approximate the distribution is in uniform
Unit weight (γ) [kN/m^3]	78	23

Table 5 The result of distribution in dynamic analysis on both tunnels

Case	First tunnel	Second tunnel
Displacement	Has the minimum value (0.0479 m). Approximate the distribution is in uniform	Has maximum value (0.0519 m). Approximate the distribution is in uniform
Force	Have minimum value (5.81 kN/m). Approximate the distribution isn't in uniform	Have maximum value (15.4 kN/m) value. Approximate the distribution isn't in uniform
Bending moment	Have Minimum value (0.0661 kN m/m) and Minimum value (0.0248 kNm/m). Approximate the distribution isn't in uniform	Approximate the distribution isn't in uniform
Shear	Have maximum value (474 kN/m^2) and minimum value (211 kN/m^2). Approximate the distribution isn't in uniform	Approximate the distribution isn't in uniform

Table 6 The maximum value for both shield tunnels

Case	First tunnel (left)			
	Displacement (m)	Force (kN/m)	Bending moment (kNm/m)	Shear (kN/m^2)
Static	0.443071	1889.35	0.600271	16547.1
Dynamic	0.0521214	63.3145	0.0796473	498.198
Case	Second tunnel (right)			
	Displacement (m)	Force (kN/m)	Bending moment (kNm/m)	Shear (kN/m^2)
Static	0.279146	1201.32	0.779046	11435.1
Dynamic	0.0520818	63.049	0.084918	515.513

Table 7 The minimum value for both shield tunnels

Case	First tunnel (left)			
	Displacement (m)	Force (kN/m)	Bending Moment (kNm/m)	Shear (kN/m^2)
Static	0.0105478	−1731.63	−0.607041	2.25958
Dynamic	0.0479459	5.70099	0.00416665	185.678
Case	Second tunnel (right)			
	Displacement (m)	Force (kN/m)	Bending Moment (kNm/m)	Shear (kN/m^2)
Static	0.0275741	−1178.71	−0.77524	2.25897
Dynamic	0.0479454	5.54226	0.00680181	189.299
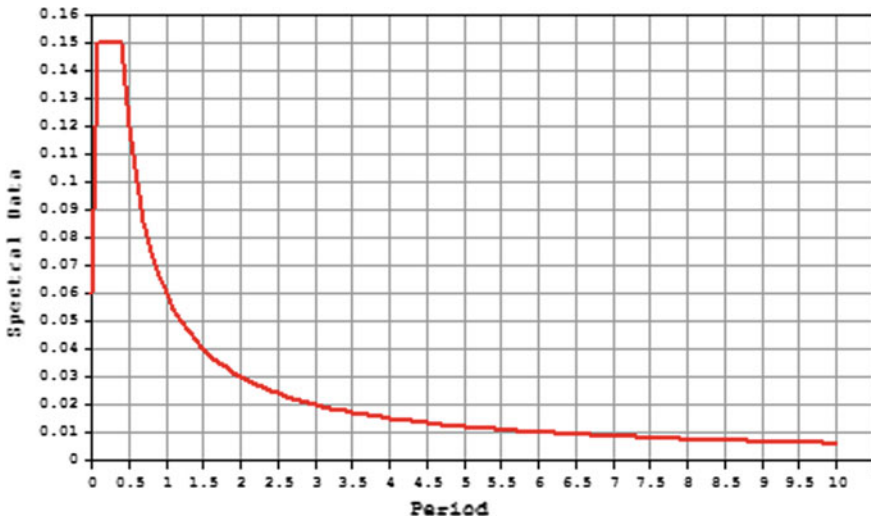
Fig. 16 Modified response spectrum using UBC (1997); damping ration = 0.05; seismic coefficient: Ca = 0.06 Cv = 0.06; normalized acceleration [14]

the result shows that the applied dynamic stress is not negligible for underground structure, but it is less dangerous in comparison with the superstructure.

References

1. Hashasha, Y.M.A., Hook, J.J., Schmidt, B., John, I., Yao, C.: Seismic design and analysis of underground structures. Tunnel. Undergr. Space Technol. **16**(2001), 247–293 (2001)
2. Hosseini, N., Oraee, K., Gholinejad, M.: Seismic analysis of horseshoe tunnels under dynamic loads due to earthquakes. In: Aziz, N (ed.) 10th Underground Coal Operators' Conference, University of Wollongong & the Australasian Institute of Mining and Metallurgy, 140–145 (2010)
3. Lanzano, G., Bilotta, E., Russo, G.: Tunnels under seismic loading: a review of damage case histories and protection methods. Strat. Reduction Seismic Risk, 65–75. (2008)
4. Bilotta, E., Lanzano, G., Russo, G.: Pseudostatic and dynamic analyses of tunnels in transversal and longitudinal directions. In: 4th International Conference on Earthquake Geotechnical Engineering, Paper No. 1550, June 25–28, 2007
5. Akhlaghi, T., Nikkar, A.: Effect of vertically propagating shear waves on seismic behavior of circular tunnels, Hindawi Publishing Corporation. Sci World J. **2014**, 10 (2014). Article ID 806092
6. Zurlo, M.A.: Seismic response of circular tunnels—Numerical validation of closed form solutions. In: 1st Civil and Environmental Engineering Student Conference, Imperial College London, 25–26 June 2012
7. Wang (Joe), J.N.: Parsons Brinckerhoff Quade & Douglas, Seismic Design of Tunnels a Simple State of the Art Design Approach (1993)
8. Fahimifar, A., Vakilzadeh, A.: Numerical and analytical solutions for ovaling deformation in circular tunnels under seismic loading. Int. J. Recent Trends Eng. **1**(6), 30–35 (2009)
9. Shaalan, O.A., Salem, T.N., El shamy, E.A., Mansour, R.M.: Dynamic analysis of two adjacent tunnels. Int. J. Eng. Innovative Technol. (IJEIT) **4**(4) (October 2014)
10. Li, Z., Grasmick, J., Mooney, M.: Influence of slurry TBM parameters on ground deformation, ITA WTC 2015 Congress and 41st General Assembly, Lacroma Valamar Congress Center, Dubrovnik, Croatia, 2015
11. El-Naiem, M.A.A.: Effect of damping on the behavior of tunnel lining under seismic loads. J. Eng. Sci. Assiut Univ. **34**(6), 1727–1742 (2006)
12. Demagh, R., Emeriault, F., Hammoud, F.: 3D modelling of tunnel excavation using pressurized tunnel boring machine in over consolidated soils. Studia Geotechnica et Mechanica **XXXV**(2), 3–17 (2013). https://doi.org/10.2478/sgem-2013
13. Tshering, T.: The impact of earthquakes on tunnels in different rock mass quality Q—A numerical analysis, Master thesis (2001)
14. Midas Engineering Software—Tutorial
15. Anh Do, N.: Numerical analyses of segmental tunnel lining under static and dynamic loads, Civil Engineering. INSA de Lyon, 2014. English. NNT: 2014ISAL0042 (2014)
16. Kontoe, S., Zdrakovic, L., Potts, D.M., Menkiti, C.O.: Case Study on Seismic Tunnel Response (2008)

Composite Slab Numerical Strength Test Method Under Partial Connection Approach

Kachalla Mohammed, Izian Abd Karim and F. N. A. A. Aziz

Abstract The present uneconomic strength determination approach for profiled composite slab (PCS) constitutes a serious challenge that contributed significantly to design conservatism. This study seeks to address this challenge by developing and a subsequent experimental validation of a numerical strength determination function for PCS through implementing a rational-based approach. Hence, a procedural algorithm lead to the development of PCS determination function using longitudinal shear estimation method by considering section slenderness and deck characteristics. The strength test performance between the developed scheme and the experiment-based test results indicates high similarity, demonstrating the viability of the proposed strength determination methodology developed.

Keywords Composite slab · Strength load · Longitudinal shear

1 Introduction

Profiled composite slab application in the construction industry has many advantages due to its construction simplicity in comparison to other flooring system. The sheeting deck serves as shuttering by shouldering the concrete weight, for example. This construction method gained popularity due to the elimination of the time-consuming temporary forms—erection and subsequent removal [1–5]. However, investigations [1, 6–8] show the behavior of profiled deck composite slab

K. Mohammed (✉)
Civil and Water Resources Engineering Department, University of Maiduguri, Maiduguri, Nigeria
e-mail: engrkachalla@unimaid.edu.ng; engrkachalla@gmail.com

I. A. Karim (✉) · F. N. A. A. Aziz
Civil Engineering Department, Universiti Putra Malaysia, Seri Kembangan, Malaysia
e-mail: izian_abd@upm.edu.my

F. N. A. A. Aziz
e-mail: farah@upm.edu.my

Fig. 1 PCS failure regions
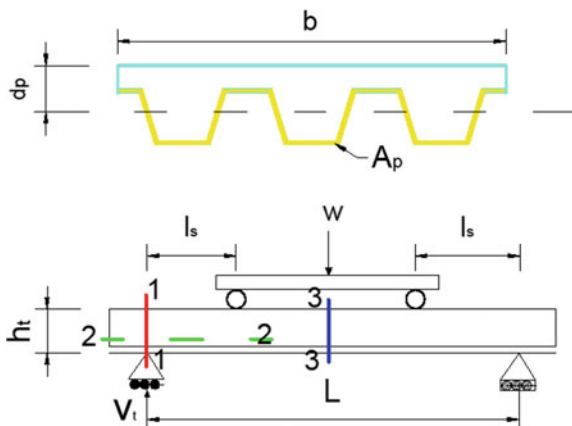
is affected by the bond failure in the longitudinal direction (see Sect. 2.2 in Fig. 1) more than the other associated failure forms. Intuitively, longitudinal shear capacity defines the ultimate strength of profiled composite slab; typical example is shown in Fig. 1 that demonstrates the three associated failure points [9]. However, a number of issues are known to affect the longitudinal shear capacity; for example the type and level of embossment, the steel strain, shear span length, etc. [10]. These issues have greatly constraint the development of deterministic-based strength capacity for profiled composite slab (PCS) that will replace the current challenge of uneconomic strength determination method. This study is necessitated to address the serious challenges faced especially with the complex interface between the profiled sheeting deck and concrete [11]. Hence, this paper presents a simplified PCS numerical strength function devoid of any complex experimental test, and equivalent experimental validation of the strength determination function.

2 Safety Determinant

Safety indices determination is through the application of a reliability concept through which the failure probability (p_f) is determined. Intuitively, the higher material strength R-value than the demand load Q; this will definitely guarantee some degree of structural safety than otherwise (unwanted situation). Hence, treating the R and Q as random variables [12], the unforeseen chances for the unwanted scenario is by

$$p_f = R - Q < 0 = p(k < 0) \tag{1}$$

The limit state function k delineates between the desired boundary condition from the failure state condition. The (p_f) value is a real nonnegative number between 0 and 1, but it is usually expressed using reliability index or safety index (β) [3, 13] with the application of the First-Order Reliability Method (FORM).

2.1 Partial Connection Method

Partial connection method for the longitudinal shear strength of PCS takes into account a complete redistribution of longitudinal shear at the concrete-sheeting deck interface [14]. The shear connection degree $\xi\,(N_c/N_{cf})$ gives the level of redistribution; $\xi = 0$ signifying no composite action and $\xi = 1$ indicating full shear connection while slip and strain values are zero under this case. Similarly, for ξ value between 0 and 1 shows partial shear connection between the sheeting deck and the concrete. The expression given in Eq. (2) returns the longitudinal shear τ_u value in this study, according to literature [15].

$$\tau_u = \frac{\xi_{test} N_{cf}}{b(l_s + l_o)} \tag{2}$$

The parameters l_o and l_s are the overhang and shear span lengths for a given profiled deck width, b that has a yield force value of $N_{cf} = 0.85 A_p f_{yp}$ (see Fig. 2). The depth of neutral axis position (x) within the system is as shown by the expression in Eq. (3).

$$x = \frac{N_{cf}}{0.85 f_{ck} b} \leq h_c \tag{3}$$

The parameter h_c in Eq. (3) stands for the concrete thickness. Hence, the design bending resistance $m_{p,Rd}$ is

$$m_{p,Rd} = N_{cf} + m_{pr} \tag{4}$$

The plastic resistance moment m_{pr} and the lever arm z functions in Eq. (4) are as follows:

$$\begin{aligned} m_{pr} &= 1.25 m_{pa}(1 - \xi) \leq m_{pa} \\ z &= h_c - e_p - 0.5x + (e_p - e)\xi \end{aligned} \tag{5}$$

The deck plastic moment of resistance is m_{pa}, while e and e_p are the centroids distance (see Fig. 2).

Fig. 2 Stress–strain diagram
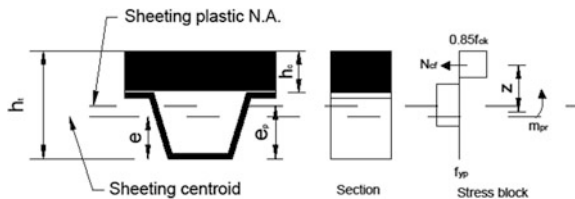
Fig. 3 Partial-connection interaction curve
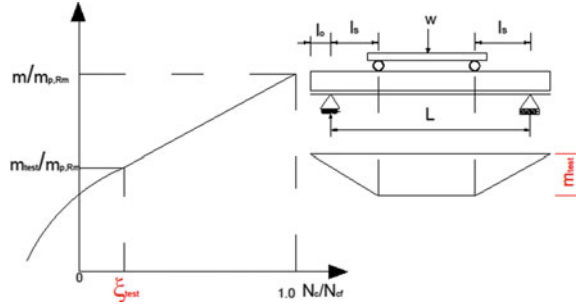
Figure 3 shows the partial interaction curve for the determination of the degree of shear connection. While all the other parameters in that figure are previously explained, the experimental bending m_{test} value is from laboratory test results.

2.2 Performance Function

This study performance function for the determination of the safety index value with the application of FORM method is from the material strength capacity and design load estimation from the shear resistance of composite slab as

$$Q_m - \frac{m_{p,Rd}}{0.5l_s} = R - Q, \tag{6}$$

where Q_m stands for the nominal resistance (Strength tests value over span length), and has a bias factor of 1.0. Furthermore, on the basis of Ellingwood and Galambos [16], the COV and statistical distribution type for the b and l_s parameters are 0.17 and log-normal distribution (Bias factor is 1.0 for both parameters). Additionally, the nominal resistance value for the safety value determination is from the literature. Hence, the detailed test specimens properties and their laboratories performance can be found in Marimuthu et al. [2] and Hedaoo et al. [17].

2.3 Numerical Strength Determination Function

Load ratio l_r in this study is defined as the ratio of experimental PCS strength load (FTL) over design load ζ_{dl}. Hence, the establishment of best-fit relation between the l_r function and the deck performance estimation is highly essential in developing the numerical strength determination function as shown with Fig. 4. The figure provides the mean p_{fmean} value of 0.69 ($\beta = -0.513$). This value led to the development of numerical strength load P_{ftl} for predicting PCS performance as shown with Eq. (7) [18].
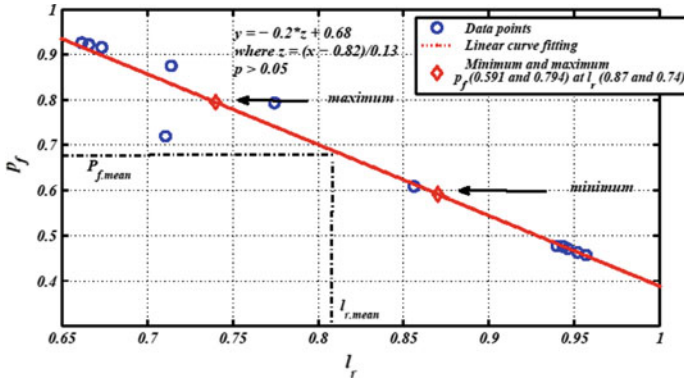
Fig. 4 PCS load-ratio effect on performance

$$P_{ftl} = 0.41(A_p f_{yp} d_p / l_s - 3.1) \tag{7}$$

Equation (7) expression computes the performance of PCS without the rigors of the costlier experimental works. However, how good the function can only be confirm if there is close-matched up with an experimental test results for PCS. Therefore, the following section provides details on the experimental validation work.

3 Experimental Test Set-up

This study experimental test scope consisted of testing four PCS that includes two specimens for both long and short shear span lengths; 228, 243 mm, and 305, 320 mm, respectively. Hence, these specimens are identified using notations SS and LS; for example, SS-228 and LS-305 represents short and long specimen with shear span length of 228 and 305 mm, respectively. A similar notation also applies to the other test-shear span lengths.

3.1 Materials Properties and Concreting

The metal deck thickness is about 0.47 mm, and it is 1829 mm long (*L*), having width (*b*) value of 820 mm as shown in Fig. 5. Normal grade concrete is prepared using 20 mm aggregate for 120 mm thick concrete. For hydration control, 5.1 mm mild bars are mesh through at 220 mm both ways, and placed 20 mm above the metal deck.

Fig. 5 Test specimen profile
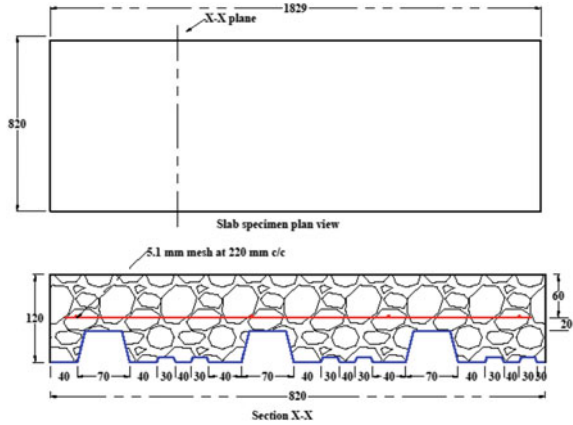
The required necessary laboratory checks on the concrete mix design prior to concreting are fully adhered to according to the ACI-318 standard, and the mix design found to be workable. Moreover, cubes for the determination of the compressive strength from the batch mixes for testing after 28 days by covering concrete surface with Gunny bags, and shows an average compressive strength of 28.5 MPa.

3.2 Test Set-up

Hydraulic jack load is applied upon the test specimen with a two spreader roller weighing about 10 kg each which are placed on top of the slab specimen with the intention of applying the two point load from cross beam that also weigh about 70 kg (Fig. 6). The overhang length is 100 mm from both ends. In determining the slab failure mode during the test procedure, linear variable displacement transducers (LVDT) were at the edges of the decking sheet and the concrete as depicted in Fig. 7. Similar LVDT placements are provided at the mid-span, and a data logger-TDS-530 records all the values for the end-slip, the mid-span deflection

Fig. 6 Specimen set-up
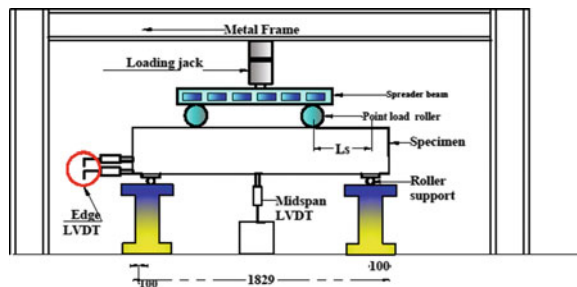
value including the test loads. The testing is halted when the maximum applied load drops by about 20%, or the mid-span deflection value is approaching $l/300$ [19].

The experimental test results are to validate the numerical solution estimation derived as shown with the Eq. (7) for the strength capacity determination of PCS. Hence, possible closeness between the compared results will validate the suitability of the developed model for strength capacity estimation of PCS.

4 Results and Discussion

Figure 8 shows experimental performance of this study's tested slab specimens. The figure provides maximum FTL sustained under each respective shear span length value. A maximum strength tests value of 45.97 kN is recorded with the shortest shear span length, and the lengthiest shear span test value gives 27.97 kN. After the maximum peak failure load, an average of 50% unloading peak load results in a high deflection value. This explains why there is a large jump beyond the peak load values.

Table 1 shows the PCS capacity test results between the experimental test load and approximate estimation from the developed strength test function. The comparative result shows an equal variance between the experimental results and approximate estimation values ($t = -1.67$, dof $= 6$, $p > 0.05$). This implies that the statistical p-value indicates closeness between the strength values. Hence, this paper concludes that the developed numerical strength function will significantly determines the performance of PCS without the rigors of the costly experimental testing procedure that posed serious challenges.

Fig. 7 LVDT arrangements
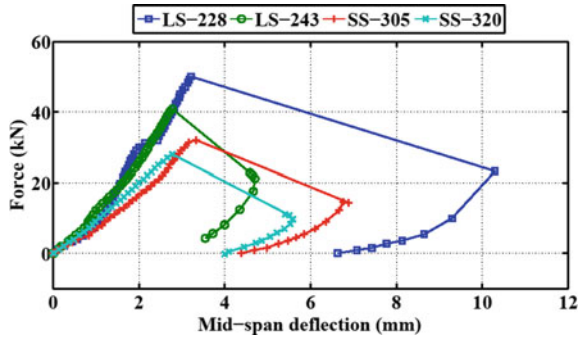
Fig. 8 PCS experimental test performance

Table 1 Experimental and approximate failure test load comparisons

Label	A_p (mm^2)	f_{yp} (MPa)	d_p (mm)	l_s (mm)	l (m)	Experimental FTL (kN)	p_{ffl} FTL (kN)
LS-228	496.71	340	100	228	1.83	45.97	41.28
LS-243				243		41.73	52.17
SS-305				305		33.50	41.03
SS-320				320		27.97	38.94

5   Conclusion

This paper shows a development of a rational-based function for profiled deck composite slab strength determination through longitudinal shear capacity using partial connection method. This study aims to addresses the challenge of costly experimental procedure for PCS strength determination. This leads to develop a numerical strength determination function, and an experimental validation test for confirmation. The litmus strength values comparisons between the experimental results and the numerical estimations of PCS strength capacities shows similar variance indicating the prospect of this study developed model for determining PCS strength capacity.

References

1. Chen, S.: Load carrying capacity of composite slabs with various end constraints. J. Constr. Steel Res. **59**(3), 385–403 (2003)

2. Marimuthu, V., et al.: Experimental studies on composite deck slabs to determine the shear-bond characteristic values of the embossed profiled sheet. J. Constr. Steel Res. **63**(6), 791–803 (2007)
3. Degtyarev, V.: Reliability-based evaluation of U.S. design provisions for composite steel deck in construction stage. J. Struct. Eng. **138**(3), 308–317 (2012)
4. Gholamhoseini, A., et al.: Longitudinal shear stress and bond–slip relationships in composite concrete slabs. Eng. Struct. **69**, 37–48 (2014)
5. Abdullah, R., et al.: Characterization of shear bond stress for design of composite slabs using an improved partial shear connection method. J. Civil Eng. Manage. **21**(6), 720–732 (2015)
6. Tsalkatidis, T., Avdelas, A.: The unilateral contact problem in composite slabs: Experimental study and numerical treatment. J. Constr. Steel Res. **66**(3), 480–486 (2010)
7. Burnet, M.J., Oehlers, D.J.: Rib shear connectors in composite profiled slabs. J. Constr. Steel Res. **57**(12), 1267–1287 (2001)
8. Tenhovuori, A.I., Leskelä, M.V.: Longitudinal shear resistance of composite slabs. J. Constr. Steel Res. **46**(1–3), 228 (1998)
9. Marčiukaitis, G., Jonaitis, B., Valivonis, J.: Analysis of deflections of composite slabs with profiled sheeting up to the ultimate moment. J. Constr. Steel Res. **62**(8), 820–830 (2006)
10. Tzaros, K.A., Mistakidis, E.S., Perdikaris, P.C.: A numerical model based on nonconvex–nonsmooth optimization for the simulation of bending tests on composite slabs with profiled steel sheeting. Eng. Struct. **32**(3), 843–853 (2010)
11. Abdullah, R., Samuel Easterling, W.: Determination of composite slab strength using a new elemental test method. J. Struct. Eng. **133**(9), 1268–1277 (2007)
12. Adrzej, S.N., Anna, M.R., Ewa, K.S.: Revised statistical resistance model for reinforced concrete structural component. ACI **284**, 1–16 (2012)
13. Okasha, N., Aichouni, M.: Proposed structural reliability-based approach for the classification of concrete quality. J. Mater. Civ. Eng. **0**, 04014169 (2014)
14. Stephen, H.: Composite slab, in EN 1994—Eurocode 4: Design of Composite Steel and Concrete Structures 2008, The Steel Construction Institute: Silwood park, Ascot, Berkshire, SL5 7QN, United Kingdom (2008)
15. Johnson, R.P.: Composite Structures of Steel and Concrete. Beams, Slabs, Columns and Frames for Building, vol. 1, 2nd edn, p. 228. Blackwell Publishing, London (2004)
16. Ellingwood, B., Galambos, T.V.: Probability-based criteria for structural design. Struct. Saf. **1**(1), 15–26 (1982)
17. Hedaoo, N., Gupta, L., Ronghe, G.: Design of composite slabs with profiled steel decking: a comparison between experimental and analytical studies. Int. J. Adv. Struct. Eng. **4**(1), 1 (2012)
18. Mohammed, K., Karim, I.A., Hammood, R.A.: Composite slab strength determination approach through reliability analysis. J. Build. Eng. **9**, 1–9 (2017)
19. Rana, M.M., Uy, B., Mirza, O.: Experimental and numerical study of end anchorage in composite slabs. J. Constr. Steel Res. **115**, 372–386 (2015)

Critical Crack-Tip Opening Displacement of SCLC

Moosa Mazloom and Mohammad Karamloo

Abstract The aim of this study is to consider the effects of water/binder ratio on fracture behavior of self-compacting lightweight concrete (SCLC). To do so, four mixes with constant nominal size of aggregate (d_a = 12.5 mm) have been prepared such that the weight of aggregate and portion of coarse aggregate to fine aggregate were designed to be constant. Forty-eight notched beam specimens were tested under displacement-controlled condition to achieve the maximum tolerable loads of beams under three-point bending configuration. Afterwards, the results were analyzed according to size effect method to realize the influences regarding water/binder ratio. Test results showed that as the water/binder ratio increased from 0.35 to 0.50, the fracture energy and toughness decreased by 65.8 and 54.5%. Moreover, the water/binder ratio had apparent influences on the values of critical crack-tip opening displacement.

Keywords Self-compacting lightweight concrete · Fracture energy
Fracture toughness · Material properties · Water to binder ratio
Crack-tip opening displacement

1 Introduction

In recent years, more attention has been paid to develop a generation of concrete, which has the ability to fill the formworks without external vibration, bleeding, and segregation, as well as having a low density [1, 2]. This demarche is the integration of technical knowledge, economy, and environmental protection, since this category of mix compositions could reduce the waste demolish and self-weight of

M. Mazloom (✉) · M. Karamloo
Department of Civil Engineering, Shahid Rajaee Teacher Training
University, Lavizan, Tehran, Iran
e-mail: mazloom@srttu.edu

M. Karamloo
e-mail: m.karamloo@srttu.edu

structures along with the air CO_2, which is a byproduct of cement industry. SCLC is a good example of these types of concrete, which usually consists of lightweight coarse aggregate and normal weight river sand. The use of lightweight aggregate (LWA) is reported to have the ability to reduce the autogenous shrinkage [3] due to internal curing [4, 5]. With recent trend toward using lightweight aggregate in concrete, some researches have been conducted all over the world to reveal the advantages and disadvantages of LWA. For instance, it is reported that the use of LWA could reduce the water permeability since its internal structure is not inter-connected and holds water [6]. The porous structure of LWA leads to lower ion concentration and besides the decrease of chloride penetration [7, 8], it could decrease the influences of water expansion due to freezing, and consequently, could enhance the freeze and thaw resistance [9]. Instead, lower modulus of elasticity in comparison to normal weight concrete (NC), increases the risk of creep [10].

Even before cracking, concrete exhibits nonlinear response [11] and fracture parameters are the means that should be used to explain the behavior of cracked concrete members [12]. Although the knowledge about the fracture behavior of NC is sufficient, there are still debates on the issue of fracture behavior of SCLC due to use of high amounts of ultra-fine particles and LWA as a coarse aggregate. Therefore, structural application of SCLC necessitates an understanding of the material fracture behavior. In this regard, this study considers the effects of water to binder ratio on fracture energy (G_f), toughness (K_{IC}), and critical crack-tip opening displacement ($CTOD_C$) of SCLC.

2 Introduction

The literature introduces some approaches for determination of fracture parameters of concrete. Work-of-fracture method (WFM) is one of the most popular methods, which has been introduced in RILEM 50-FMC [13]. The method uses three-point bending test on notched beam specimens to determine the fracture energy of the concrete. However, it is proved that the method has the drawback of size dependency [14, 15]. Based on WFM, the size dependent fracture energy (G_F) could be obtained as [13]:

$$G_F = \frac{W_F}{b(d - a_0)} \qquad (1)$$

where W_F is the area under load displacement curve, b is the beam width, d is the depth of the beam, and a_0 is the notch length. Apart from the size dependency, which is mainly attributed to weight of specimen [16], conducting a stable test is too hard and needs special conditions such as very stiff universal testing machine.

The other method is boundary effect model (BEM), which is based on local fracture energy definition, and has been originally proposed by Duan et al. [17–19].

According to this concept, one could determine the size-dependent fracture energy as [19, 20]:

$$G_{\mathrm{F}}\left(\frac{a}{d}\right) = \frac{1}{d-a} \int_0^{d-a} g_f(x)\mathrm{d}x \tag{2}$$

in which a is crack length and g_f is the local fracture energy. The variation of local fracture energy along the crack path was described by a bilinear approximation proposed by Hu and Wittman [21] (see Fig. 1). Accordingly, by defining the intersection of these two asymptotes as a transition ligament size (a1), the Eq. (2) has been solved to determine the size independent fracture energy (G_f) as

$$G_{\mathrm{F}} = \begin{cases} G_f\left(1 - 0.5\frac{\frac{a_1}{d}}{(1-\frac{a}{d})}\right) & 1 - \frac{a}{d} > \frac{a_1}{d} \\ G_f\left(0.5\frac{1-\frac{a}{d}}{\frac{a_1}{d}}\right) & 1 - \frac{a}{d} \le \frac{a_1}{d} \end{cases} \tag{3}$$

In this method, for each concrete mix, two series of specimens, having pre-cracks with a/d ratios of 0.1 and 0.6, should be tested using work-of-fracture method to determine the values of G_F and a_1 [21, 22]. Afterwards, by using Eq. (3), one determines the size-independent fracture energy of the composition. Although this method looks simple, it has some drawbacks such as a need to special testing equipment. Besides, this method is not introduced in any guidelines. Therefore, the Bazant's size effect method (SEM) is preferable.

Bazant and Pfeiffer proposed a model [23] which subsequently became a basis for size effect method. According to this model, RILEM published a guideline to introduce SEM to researchers and practitioners [24]. In this method, geometrically similar specimens are tested to determine the peak loads. Subsequently, by extrapolating these peak loads to a specimen with infinite dimension, along with using the Bazant's size effect law (SEL), the fracture parameters could be determined. The SEL is a nonlinear fracture mechanics' relation between the depth of specimen and nominal failure stress σ_N as

Fig. 1 Bilinear model for local fracture energy
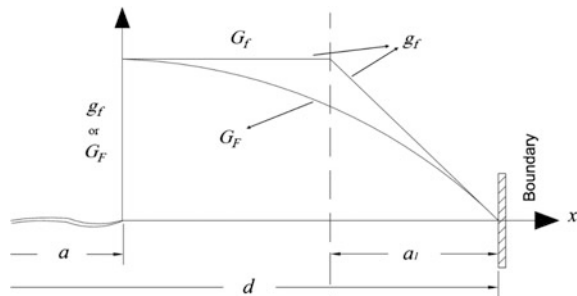
$$\sigma_N = B(1 + \beta)^{-0.5}, \tag{4}$$

where β is brittleness number and B is an empirical parameter.

The brittleness number, introduced by Bazant and Kazemi [25], is a tool for ductility assessment of the concrete using fracture mechanics. Besides, it indicates the design criterion of the structure. In other words, when $\beta > 10$, the behavior of specimen approaches brittle behavior and should be designed according to linear elastic fracture mechanics' constitutive relations [25]. Instead, the plastic limit criterion should be used for specimens with $\beta \leq 0.1$. For $0.1 \leq \beta \leq 10$, nonlinear fracture mechanics' constitutive relations should be used [2]. The brittleness number could be calculated as

$$\beta = {}^{d}\!/\!_{d_0} \tag{5}$$

in which d is the beam depth and d_0 is an empirical constant to be found from the experiments.

The SEM uses linear regression for extrapolation as

$$Y = AX + C, \tag{6}$$

where A and C are the slope and intercept of the fitted line, respectively. X and Y are the abscissae and ordinates of a coordinate system as

$$\begin{cases} X = d \\ Y = \dfrac{1}{\sigma_N^2} \end{cases} \tag{7}$$

The SEM recommends the least size range ratio of 1:4 to avoid data scattering. In addition, based on the LEFM theory, the size-independent fracture energy could be found as [1, 2]

$$G_f = g\left(\frac{a_0}{d}\right) E^{-1} A^{-1} \tag{8}$$

Generally, in order to avoid scattering data, the size range of the test specimens is chosen to have at least the scale ratio of 1:4. Besides, since the fracture of the specimen with infinite size follows the LEFM theory, the fracture energy and the effective length of fracture process zone can be determined as

$$C_f = \frac{C g_f(\alpha_0)}{A g'_f(\alpha_0)} \tag{9}$$

in which $g(a_0/d)$ is non-dimensional energy release rate, which could be found in many references such as [26, 27], A is the angular coefficient of the fitted line, and

E is the modulus of elasticity. Since the method uses extrapolation method to determine the fracture energy in an infinitely large specimen, the LEFM governs. Hence, the other fracture parameters of interests could also be found as [24]:

$$K_{IC} = d_0^{0.5} B \sqrt{g\left(\frac{a_0}{d}\right)} \tag{10}$$

$$CTOD_C = 3.19 \frac{K_{IC}}{E} \sqrt{c_f}, \tag{11}$$

where c_f is the effective length of fracture process zone and could be found on RILEM FMT-89.

The size effect method is a globally accepted method, which is to be implemented in this study. However, it should be noted that this method is not suitable for specimens, which are not geometrically similar. Recently, Hu and Duan claimed that their model (BEM) could circumvent this drawback [28]. While, Hoover and Bazant experimentally proved that this model does not fit the results [29].

3 Materials and Testing Method

3.1 Materials

In this study, ordinary Portland cement, provided from Tehran cement factory, has been used. The coarse aggregate was lightweight expanded clay aggregate (LECA), whose specific gravity was about 583 kg/m^3. For all compositions, same river sand was provided whose fineness modulus was about three. According to ASTM C494 specifications [30], type G poly carboxylate-based super plasticiser was used to reach the desired workability. Moreover, limestone powder had a role of viscosity modifying agent.

Four composition with water/binder ratios of 0.35, 0.4, 0.45, and 0.5 have been prepared in which LECA/sand ratio has been kept constant at 0.294. The total weigh of aggregate was constant and equal to 1100 kg/m^3. The detailed mix design parameters and fresh state test results could be found in [2]. Moreover, the maximum nominal size of coarse aggregate was 12.5 mm for all mixes.

3.2 Curing and Casting of Notched Beam Specimens

For each mix, 12 specimens with four different sizes of $38.1 \times 38.1 \times 102$ mm^3, $38.1 \times 76.2 \times 203$ mm^3, $38.1 \times 152.4 \times 407$ mm^3 and $38.1 \times 304.8 \times 814$ mm^3, were casted according RILEM recommendations [24]. For each specimen, a pre-crack with a_0/d ratio of 0.2 was made during the casting by using 3 mm acrylic plate. All specimens have been demolded after 1 day and cured under water at $20 \pm 20C$.

3.3 Test Method

In order to reach the desired accuracy, a closed-loop servo-electro-controlled testing machine with the highest capacity of 150 kN, provided from Zwick/Roell, was used. All tests have been carried out under displacement-controlled condition such that the peak loads were achieved in about 1 min. Afterwards, the peak loads were recorded and the effects of specimen weights were compensated according to RILEM recommendations. The test setup configuration could be found in [1, 2].

4 Results and Discussions

RILEM FMT-89 proposed a method for weight compensation in which the effect of weight are being excluded from the analysis by RILEM FMT-89 [24]:

$$P_0 = P + \frac{2S_n - L_n}{2S_n} mg, \tag{12}$$

where P_0 is corrected peak load, P is recorded maximum load of specimen, S_n is the span of the specimen and is considered to be $S_n = 2.5d$, Ln is length of the beam specimen and based on RILEM recommendations is equal to 2.67d, m is mass of specimen, and g is gravitational acceleration, which is assumed to be about 9.81 m/s^2. Figure 2 shows the corrected peak loads versus specimens' depth.

As stated previously, the results of each series should be extrapolated to a specimen with infinite dimensions. In this regards, the procedure has been carried out for all compositions. To illustrate the method, Fig. 3 shows the fitted line for W50.
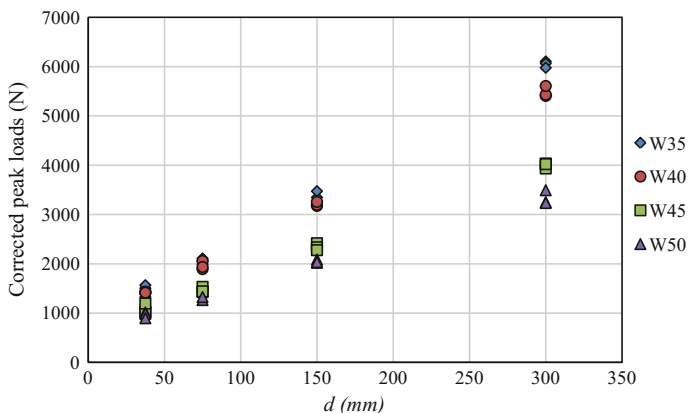
Fig. 2 Corrected peak loads of each mix versus depth of specimens
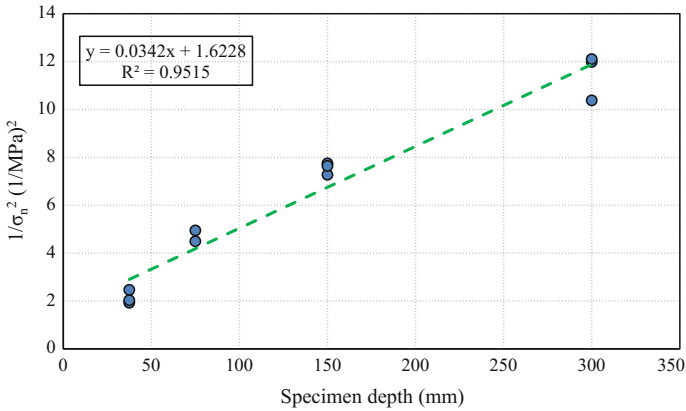
Fig. 3 Fitting a line for W50 mix

As can be seen, the values of slope and intercept of the fitted line are 0.0342 mm^{-1} MPa^{-2} and 1.6228 MPa^{-2}, respectively. Subsequently, in order to determine the fracture parameters Eqs. (8)–(10) were used. Figure 4 shows the variation of fracture energy and toughness versus water/binder ratio. It is apparent that by increasing the value of water/binder both values of fracture energy and toughness decrease. These findings could be attributed to probable increase in porosity of paste and interfacial zone. In addition, the critical crack-tip opening displacement has been affected by water/binder ratio (see Fig. 5). As can be seen, 27.4% variation in water/binder ratio caused 49.3% variation of fracture toughness along with 47.7% variation of fracture energy, and 3.2% of CTOD$_C$.
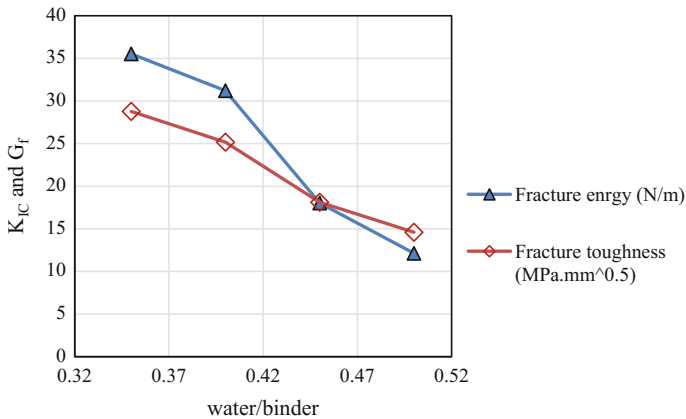
Fig. 4 Fracture energy and Fracture toughness versus water/binder ratio
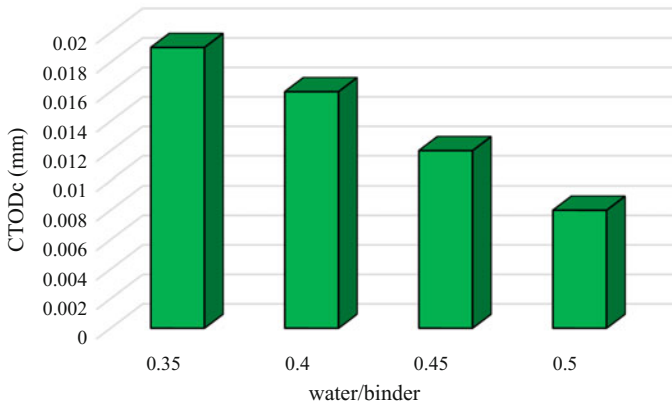
Fig. 5 Variations of critical crack-tip opening displacement versus water/binder ratio

5 Conclusions

The following conclusions could be drawn from the study:

1. The fracture energy has been influenced by water/binder ratio. In other words, as the water/binder ratio decreased, the fracture energy increased.
2. The decrease of water/binder ratio increased the fracture toughness of self-compacting lightweight concrete.
3. As the water/binder ratio increased, the critical crack-tip opening displacement decreased.

References

1. Karamloo, M., Mazloom, M., Payganeh, G.: Effects of maximum aggregate size on fracture behaviors of self-compacting lightweight concrete. Constr. Build. Mater. **123**, 508–515 (2016)
2. Karamloo, M., Mazloom, M., Payganeh, G.: Influences of water to cement ratio on brittleness and fracture parameters of self-compacting lightweight concrete, Part A. Eng. Fract. Mech. **168**, 227–241 (2016)
3. Kaszynska, M., Zielinski, A.: Effect of lightweight aggregate on minimizing autogenous shrinkage in self-consolidating concrete. Procedia Eng. **108**, 608–615 (2015)
4. Famili, H., Saryazdi, M.K., Parhizkar, T.: Internal curing of high strength self consolidating concrete by saturated lightweight aggregate - effects on material properties. Int. J. Civil Eng. **10**, 210–221 (2012)
5. Golias, M., Castro, J., Weiss, J.: The influence of the initial moisture content of lightweight aggregate on internal curing. Constr. Build. Mater. **35**, 52–62 (2012)
6. Khandaker, M.A.H., Saifuddin, A.: Lightweight concrete incorporating volcanic ash-based blended cement and pumice aggregate. J. Mater. Civ. Eng. **23**, 493–498 (2011)

7. Haque, M.N., Al-Khaiat, H., Kayali, O.: Strength and durability of lightweight concrete. Cement Concr. Compos. **26**, 307–314 (2004)

8. Kockal, N.U., Ozturan, T.: Durability of lightweight concretes with lightweight fly ash aggregates. Constr. Build. Mater. **25**, 1430–1438 (2011)

9. Kucharczyková, B., Keršner, Z., Pospíchal, O., Misák, P., Vymazal, T.: Influence of freeze–thaw cycles on fracture parameters values of lightweight concrete. Procedia Eng. **2**, 959–966 (2010)

10. Yehia, S., AlHamaydeh, M., Farrag, S.: High-strength lightweight SCC matrix with partial normal-weight coarse-aggregate replacement: strength and durability evaluations. J. Mater. Civil Eng. **26**, 04014086-1–04014086-11 (2014)

11. Sim, J.I., Yang, K.H., Lee, E.T., Yi, S.T.: Effects of aggregate and specimen sizes on lightweight concrete fracture energy. J. Mater. Civ. Eng. **26**, 845–854 (2014)

12. Gettu, R., Bazant, Z.P., Karr, M.E.: Fracture properties and brittleness of high-strength concrete. ACI Mater. J. **87**, 608–618 (1990)

13. RILEM FMC-50: Determination of the fracture energy of mortar and concrete by means of three-point bend tests on notched beams. Mater. Struct. **18**, 287–290 (1985)

14. Bažant, Z.P., Yu, Q.: Size-effect testing of cohesive fracture parameters and nonuniqueness of work-of-fracture method. J. Eng. Mech. **137**, 580–588 (2011)

15. Bazant, Z.P., Kazemi, M.T.: Size dependence of concrete fracture energy determined by RILEM work-of-fracture method. Int. J. Fract. **51**, 121–138 (1991)

16. Elices, M., Guinea, G.V., Planas, J.: On the measurment of concrete fracture energy using 3-point bend tests. Mater. Struct. **30**, 375–376 (1997)

17. Duan, K., Hu, X., Wittmann, F.H.: Scaling of quasi-brittle fracture: Boundary and size effect. Mech. Mater. **38**, 128–141 (2006)

18. Hu, X., Duan, K.: Influence of fracture process zone height on fracture energy of concrete. Cem. Concr. Res. **34**, 1321–1330 (2004)

19. Duan, K., Hu, X., Wittmann, F.H.: Boundary effect on concrete fracture and non-constant fracture energy distribution. Eng. Fract. Mech. **70**, 2257–2268 (2003)

20. Duan, K., Hu, X.Z., Wittmann, F.H.: Size effect on fracture resistance and fracture energy of concrete. Mater. Struct. **36**, 74–80 (2003)

21. Hu, X.Z., Wittmann, F.H.: Fracture energy and fracture process zone. Mater. Struct. **25**, 319–326 (1992)

22. Alyhya, W.S., Abo Dhaheer, M.S., Al-Rubaye, M.M., Karihaloo, B.L.: Influence of mix composition and strength on the fracture properties of self-compacting concrete. Constr. Build. Mater. **110**, 312–322 (2016)

23. Bazant, Z., Pfeiffer, P.: Determination of fracture energy from size effect and brittleness number. ACI Mater. J. **84**, 463–480 (1987)

24. RILEM FMT-89: Size-effect method for determining fracture energy and process zone size of concrete. Mater. Struct. **23**, 461–465 (1990)

25. Bazant, Z.P., Kazemi, M.T.: Determination of fracture energy, process zone length and brittleness number from size effect, with application to rock and concrete. Int. J. Fract. **44**, 111–131 (1990)

26. Mazloom, M., Karamloo, M.: Applied Fracture Mechanics (in persian), 1st edn. Shahid Rajaee Teacher Training University Press, Tehran, Iran (2016)

27. Anderson, T.L.: Fracture Mechanics: Fundamentals and Applications, 3rd Edn. Taylor & Francis; 6000 Broken Sound Parkway NW, Suite 300, Boca Raton, FL 33487-2742 (2005)

28. Hu, X., Duan, K.: Mechanism behind the size effect phenomenon. J. Eng. Mech. **136**, 60–68 (2010)

29. Hoover, C.G., Bažant, Z.P.: Comparison of the hu-duan boundary effect model with the size-shape effect law for quasi-brittle fracture based on new comprehensive fracture tests. J. Eng. Mech. **140**, 480–486 (2014)

30. ASTM C494: Standard Specification for Chemical Admixtures for Concrete. American Society of Testing Materials (ASTM), Pennsylvania (2001)

Numerical Analysis of Multilayer Geosynthetic-Reinforced Bed Over Stone Columns-Improved Soft Clay

Mobin Afzalirad, Mehran Naghizadehrokni, Martin Ziegler and Mojtaba Razaghnia

Abstract Installation of stone columns is recognized as a usual procedure for the treatment for soft clay soils. In the current research, three-dimensional finite-element analyses were performed to simulate the behavior of multilayer geosynthetic-reinforced granular bed over stone column-reinforced soft soil using the ABAQUS. An extensive research was conducted for better understanding of the mechanism of load transfer in ordinary stone columns (OSCs) and geosynthetic-encased columns (GECs) installed under a concrete foundation. Parametric studies were also carried out to investigate the effects of factors such as hardness of the geosynthetic encasement and the region replacement proportion on the overall behaviour of the GECs group. The results designated that utilizing of more than one geosynthetic reinforcement with stone columns is not so effective to reduce the maximum settlement. But, a multilayer reinforcement system is efficient to decrease the maximum settlement when stone columns are not used. It was also shown that there is a large growth in the amount of stress concentration proportion with the presence of geosynthetic reinforcement in comparison with the amount when there is no geosynthetic reinforcement present.

Keywords Stone column · Geosynthetic-Reinforced bed · Soft soil
Finite-element method · 3D analysis

1 Introduction

Large segments, particularly along the beach, are covered with thick soft marine clay deposits which have very low shear strength and high compressibility. Stone columns, one of the most commonly used soil improvement technique, have been

M. Afzalirad · M. Razaghnia
Institute of Civil Engineering, University of Azad, Qaemshahr, Iran

M. Naghizadehrokni (✉) · M. Ziegler
RWTH Aachen University, Geotechnical Engineering, Aachen, Germany
e-mail: Naghizadehrokni@geotechnik.rwth-aachen.de

utilized throughout the world to enhance the bearing capacity of the soft soils and decrease the settlement of superstructures constructed on them. Utilizing the stone columns also increases the rate of the consolidation of the soft clay.

The stone column technique was adopted in European Countries in the early 1960s. Stone columns in compressive loads fail in different modes, such as bulging [1], general shear failure [2], and sliding [3]. But, the most usual failure mode for stone columns in soft clays is bulging [4].

A granular layer of sand or gravel, 0.3 m or more in thickness, is usually placed over the top of the stone columns for catering a drainage route and spread the stresses coming from the superstructures. Selecting a proper diameter, stiffness, and spacing of the stone columns is very important to improve an existing soft soil. Studies have shown that maximum settlement decreases as the stiffness of the stone column raises, however differential settlement which is the settlement difference between the center of the stone columns and the mid-span of the column spacing, increases [5, 6]. Thus, a suitable level of stiffness must be utilized to gain an optimum amount of the maximum and the differential settlement of the improved ground. It has been further seen that the rate of the stabilization of the soft soil increases as the stiffness of the stone column increases [7]. The maximum and differential settlement increases as the spacing-to-diameter ratio increases [5], whereas the rate of consolidation decreases as this ratio increases.

Horizontal geosynthetic-reinforcement sheets can be used in the granular columns to increase the load-carrying capacity as well as decrease the bulging of the columns [4, 8]. Van Impe proposed the concept of covering the stone column by wrapping with geotextile in the year 1985 [9]. Geosynthetic encasement can also be used to extend the use of stone columns for extremely soft soil condition [10–14]. The first projects started successfully in Germany around 1995 [15].

The granular bed can be further reinforced with the geogrid to boost the load-carrying capacity and decrease the settlement of the stone column-improved soft clay. Han and Gabr [8] carried out a numerical analysis of geosynthetic-reinforced and pile-supported earth platforms over soft soil. Based on lumped parameter modeling approach, models have been expanded for single layer [5, 16]. Deb et al. [17] have been done a laboratory model test on single-stone column to study the effect of reinforcement diameter and thickness response, bearing volume and construction of the stone column. The published literature on the performance of reinforced granular fill over soft soil with stone columns group is limited.

In the present study, the results of 3D numerical analyses of different aspects of the performance of multilayer geosynthetic-reinforced granular bed over stone column-reinforced soft soil were presented using the finite-element program ABAQUS. The calibration of the methods utilized in the numerical analyses was performed by modeling the experimental results presented by Ambily and Gandhi [18]. A comprehensive study was carried out to better understanding the load-transfer mechanism of a group of Geosynthetic Encased Columns (GECs) and the multilayer geosynthetic-reinforced granular bed over stone column-reinforced. The results of the numerical study conducted for the effect of multilayer

geosynthetic-reinforced granular fill over soft soil with stone columns on settlement response, bearing capacity and bulging of the stone column were reported.

2 Validation of Finite-Element Model

In order to calibrate the numerical procedure used in the present research, the settlement results gained from the current finite-element analyses were compared with the experimental results presented by Ambily and Gandhi [18]. The model tests were performed on a group of seven stone columns arranged in a triangular pattern as illustrated in Fig. 1. The diameter of the stone columns utilized in the model test was 100 mm and spacing between the stone columns was taken as 300 mm. The diameter was 835 mm and load was applied through a 16 mm thick mild steel plate with stiffeners to ensure negligible constructional deformation. A 30 mm thick sand bed was located between the stone columns and the footing. The length of the stone columns was equal to the depth of the soft soil (450 mm). The clay, sand, and stones material behaviors were simulated using Mohr–Coulomb's criterion. The finite-element mesh was expanded utilizing eight-node linear brick elements for the stone columns, clay, and sand, displayed in Fig. 2. At the bottom boundary of the finite-element mesh, the displacements are set to zero in the z direction. The displacements in the x and y directions were set to zero on the circumferential boundary of the soft soil zone. In following model test, footing was loaded up to 4.6 mm settlement. Figure 3 compares the results obtained from the model test and based on the current FEM analysis, which matches well. This comparison shows that the predicted values from the settlement using the present analysis have acceptable correspondence with the experimental results.
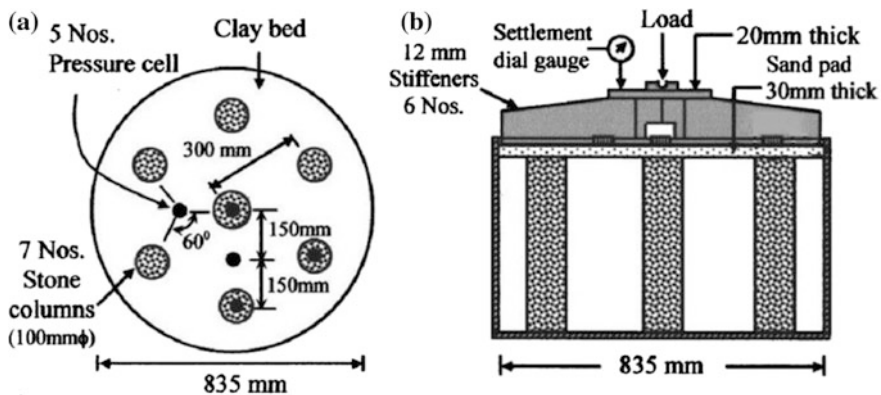
Fig. 1 Group test arrangement: **a** plan view; and **b** section of test tank Ambily and Gandhi [18]
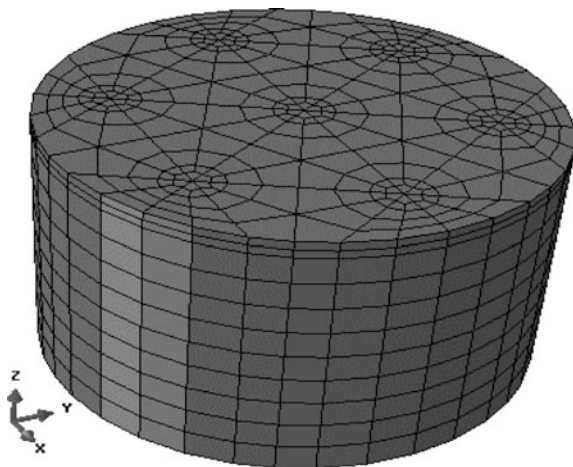
Fig. 2 Finite-element mesh used for the calibration analyses
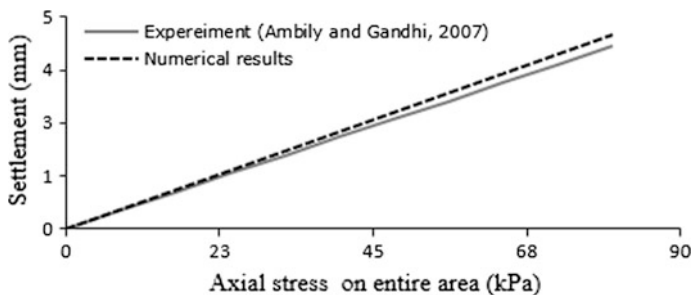
Fig. 3 Comparison of maximum settlements for the calibration analyses

2.1 Numerical Modeling

Finite-element analyses were carried out by the ABAQUS Program. Since there are two planes of symmetry in the zone of interest, it was only vital to numerically model the behavior of the system over a quarter of the domain. In all of the numerical analyses that were carried out, the thickness of the soft soil and length of the stone columns were assumed to be 10 m. A 300 kPa surcharge pressure was applied in 100 increments on the stone columns group through a 1 m thick, linear-elastic concrete foundation. A multilayer geosynthetic-reinforced granular fill resting on soft soil with stone columns can be seen in Fig. 4 [19].

At the bottom boundary of the finite-element mesh, the displacements were set to zero in the z direction. The displacements in the x and y directions were set to zero on the circumferential boundary of the soft soil zone. On the planes of symmetry,

Fig. 4 Multilayer geosynthetic-reinforced granular fill resting over soil with stone columns
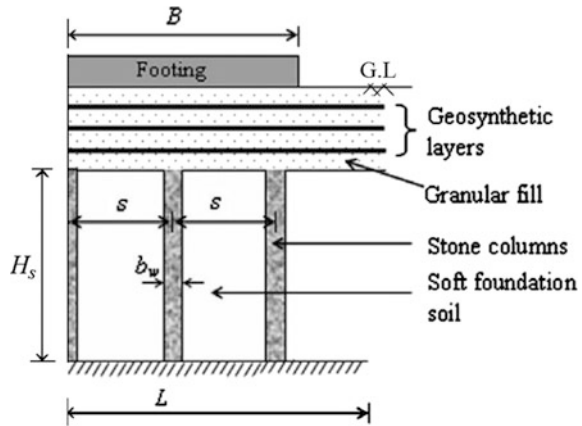
normal displacement was restricted. The diameter of geogrid reinforcement was chosen as two times the diameter of the footing.

Figure 5 shows a typical finite-element mesh used in the analyses. The finite-element mesh used in the numerical simulations was developed using eight-node Linear Brick elements for both the stone column, sand and soft soil. For constitutive modeling, the clay soil was represented by the modified Cam clay (MCC) material while the linear-elastic, perfectly plastic model (the Mohr–Coulomb failure criterion) was used to model the crushed stone, and sand. It should be noted that the MCC parameters considered in this study were inferred from the geotechnical parameters of soft soils encountered in a recent soft ground improvement project [20]. The Mohr–Coulomb parameters used in the numerical analyses were based on the material properties that Ambily and Gandhi [18] used in their tests, and are presented in Table 1.
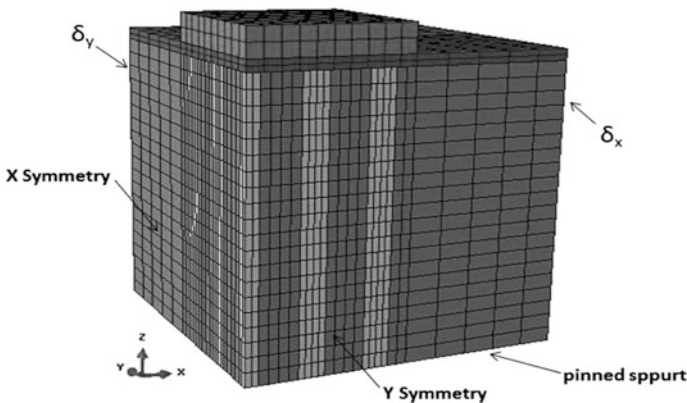
Fig. 5 Typical finite-element mesh used in the analyses

Table 1 Material properties used in the numerical models

Material properties	Stone column	Soft soil	Sand
Sat. unit weight (kN/m^3)	–	17	–
Dry. unit weight (kN/m^3)	16.62	–	15.50
Young's modulus (kPa)	55,000	–	20,000
Poisson's ratio	0.3	0.3	0.3
Cohesion (kPa)	0	–	0
Friction angle (deg)	43	–	10
Dilation angle (deg)	10	–	4
Critical state stress ratio (M)	–	1.3	–
logarithmic hardening constant for plasticity (λ)	–	0.3	–
logarithmic bulk modulus for elastic material behavior (κ)	–	0.02	–
Initial void ratio (eo)	0.62	1.5	0.74

The geosynthetic was modeled using four-node quadrilateral, decreased integration membrane elements. The geosynthetic was assumed to be an isotropic linear-elastic material, with an assumed Poisson's ratio of 0.3 [21]. Based upon the results of a prior comprehensive numerical study [14], to avoid adversely influencing the numerical results, and knowing that the encasement did not carry vertical (compressive) load, the "No Compression" option that is available in ABAQUS was utilized to more appropriately characterize the behavior of the geosynthetics.

Alexiew [22] documented that design values of tensile modulus (J) between 2000 and 4000 KN/M were required for the geosynthetic used to encase stone columns on a number of different projects. Consequently, a circumferential elastic modulus of 4000 KN/M was used in the numerical analyses. The circumferential elastic modulus (E) of the geosynthetic was derived from the relationship $J = Et$, where t is the thickness of geosynthetic, which was assumed to be 5 mm for all of the numerical analyses performed. The various stone columns are referred to use the column numbers which are shown in Fig. 6.

3 Numerical Results Multilayer Geosynthetic-Reinforced Sand Bed Resting Over Soil with Stone Columns

In this section, effects of various design parameters on the performance of multi-layer geosynthetic-reinforced sand bed resting over soil with stone columns installed under a concrete foundation are examined. The settlement and lateral deformation and force of stone columns obtained from the analyses were selected as representatives of the group behavior.

Fig. 6 Stone column numbers used in numerical modeling
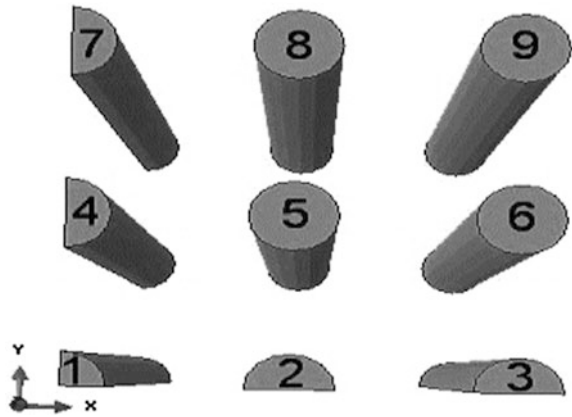
3.1 Load-Settlement Characteristics

Figure 7 shows the variation of maximum settlement with load for multilayer geosynthetic-reinforced sand bed with 1 m thick over soft soil. It has been observed that if the soft soil is not improved with stone columns, the reduction of the maximum settlement at the center of the loaded region as compared to the unimproved soil is 16, 22, and 27% as the number of geosynthetic layers increases from 1 to 3 respectively. The maximum settlement reduction is 37% if only stone columns are used. Thus, it can be said that the use of multilayer reinforcement system is effective to reduce the maximum settlement when stone columns are not used.
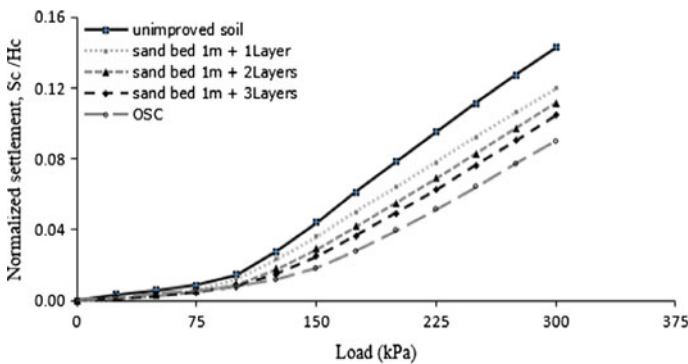
Fig. 7 Load-settlement characteristics of reinforced sand bed layers

3.2 Lateral Deflections of Stone Column

Figure 8 which is contour lateral displacement is shown the results from the full 3D analyses for a group of OSC. As it can be seen, the incidence of failure mechanisms is clearly visible and the maximum lateral displacement in the stone columns, the columns of the upper elements circumferential ring, occurs. So the pattern lateral displacement of the stone columns is important. In the field, most constructed stone columns have equal ratios of length-to-diameter and a bulging failure usually develops depending on whether the tip of the column is floating in soft soil or resting on a firm bearing layer [23].

The effect of unreinforced and geosynthetic-reinforced sand bed placed over stone column on bulging behavior of the column has been studied. The lateral deflection of column number 25 obtained from the analyzed models are presented in Fig. 9. In the case of only stone column-improved soft clay, a maximum bulge of 145 mm has been observed at a depth of 3 m from top of stone column. As compared to the only stone column-improved soil, 5.5% reduction in maximum bulge diameter of the stone column has been observed when sand bed is placed over the stone column-improved soft clay. Additional 20% reduction in maximum bulge diameter has been observed when geosynthetic reinforcement is placed within the sand bed. It can be concluded that the maximum bulge diameter of stone column reduces and the depth of bulge increases with the application of sand bed. Inclusion of geosynthetic reinforcement further reduces the bulge diameter and increases the bulge depth.

Shahu et al. [24] shows that adequate thickness of granular mat reduces the load carried by granular pile both at the top and bottom and helps to reduce the failure of the granular pile due to bulging of the pile. Very high stress concentration has been observed near the top of the columns, which causes high bulging. However, when

Fig. 8 Contour plots lateral displacement of stone columns
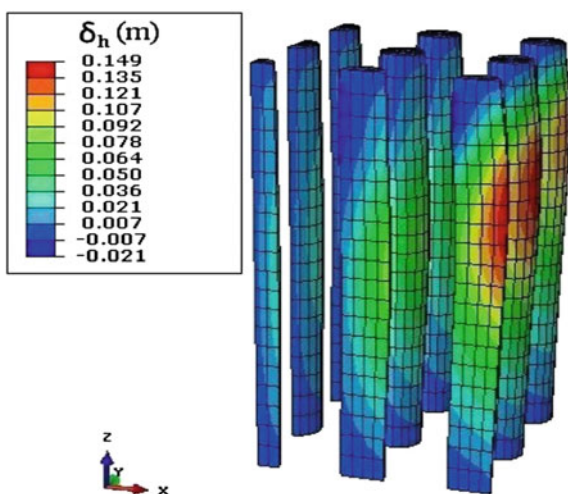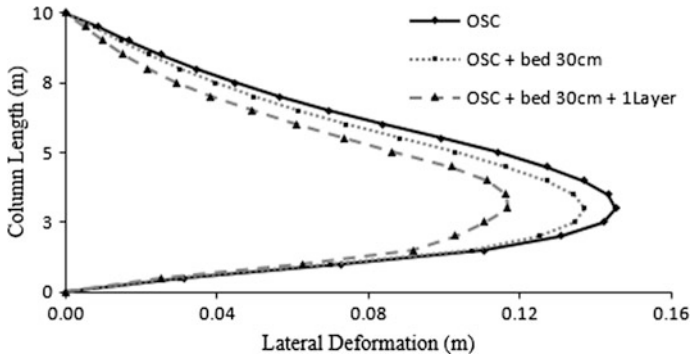
Fig. 9 Lateral deflections of the stone column 6 when soft clay has been improved with stone column alone, unreinforced and geosynthetic-reinforced sand bed over stone column-improved soft clay

sand bed is placed over the stone column-improved soft clay, significant reduction in stress concentration on top of the column has been observed and the variation of stress concentration with depth is more uniform. Thus, placement of sand bed on top of the stone column-improved soft clay reduces the bulge diameter and increases the bulge depth of the stone column.

3.3 Optimal Thickness of the Geosynthetic -Reinforced Sand Bed

Figure 10 shows the load-settlement characteristics of the geosynthetic-reinforced sand bed of different thicknesses where it is placed over stone column-improved clay. It has been observed that as the ratio of thickness of sand bed to the diameter
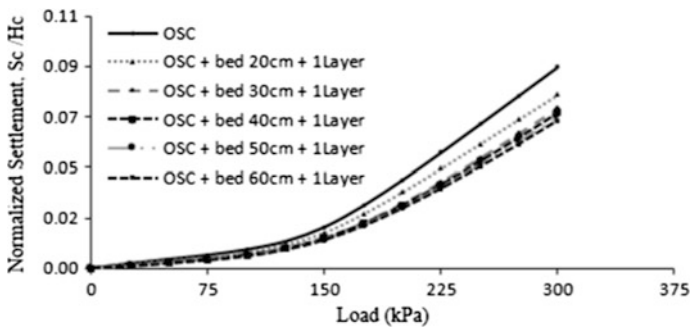
Fig. 10 Load-settlement characteristics of reinforced sand bed of different thicknesses over stone column-improved soft clay

of the footing (H_s/D ratio) increases, the load-carrying capacity also increases up to a value of 0.3. Whereas beyond this value, the load-carrying capacity decreases by increasing the thickness of the sand bed. Thus, the optimum thickness of geosynthetic-reinforced sand bed is 0.3 times the diameter of the footing.

The vertical component of the tensile force acts in the geosynthetic reinforcement partially counterbalances by the overlying soil. As a result, the vertical stress is reduced in the zone due to combined action of mobilized tension in the reinforcement and membrane action in its curvature [25–27]. However, when the sand bed thickness increases such that $H_s/D > 0.3$, a major portion of the shear failure zone of the soil is developed above the reinforcement layer and the deflection of the reinforcement also decreases [27]. This phenomenon reduces the effectiveness of the geosynthetic layer causing reduction in bearing capacity. Thus, the stone column under geosynthetic-reinforced sand bed having $H_s/D = 0.4$ produces less bearing capacity than that under geosynthetic-reinforced sand bed having $H_s/D = 0.3$. This is due to the fact that as the thickness of the reinforced sand bed increases, the deflection of the reinforcement decreases and the effectiveness of the reinforcement also decreases [17].

The effect of tensile stiffness of the geosynthetic on the settlement response has been studied for multilayer-reinforced soil. It is seen that irrespective of the number of reinforcement layer, the maximum settlement decreases (Fig. 11) as the stiffness of the geosynthetic layers increases up to the range of 4000–5000 kN/M, beyond which the rate of change in settlement is negligible. The reduction in the values of settlement is 22, 25.6, and 28% for one, two and three layers case, respectively.

3.4   Load Transfer

To investigate the effects of the geosynthetics-reinforced sand bed of 1, 2, and 3 reinforced layers on the end-bearing behavior, load-transfer curves of stone column
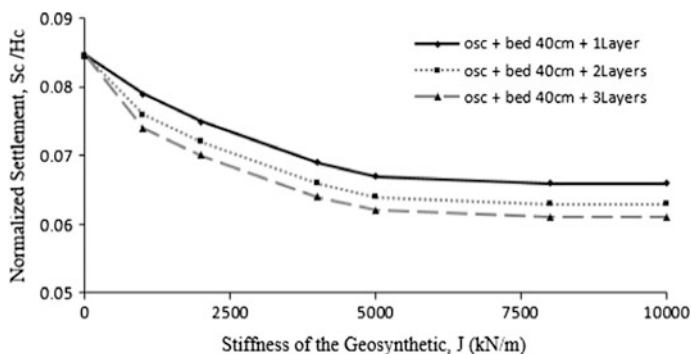
Fig. 11 Effect of geosynthetic tensile stiffness on maximum settlement geosynthetic -reinforced sand bed over stone column-improved soft clay

at a 300 kPa surcharge pressure are shown in Figs. 12 and 13 show the load transfer of column 1 and 6, respectively. The force of columns number 1 and 6 has been increased by 116 and 112% when the soil is improved by stone columns along with unreinforced sand bed, respectively. Use of single layer geosynthetics-reinforcement with stone columns increases the value of column force at surface by 135% whereas the increment is 143 and 148% if two and three layers of geosynthetics-reinforcement are used with stone columns, respectively.
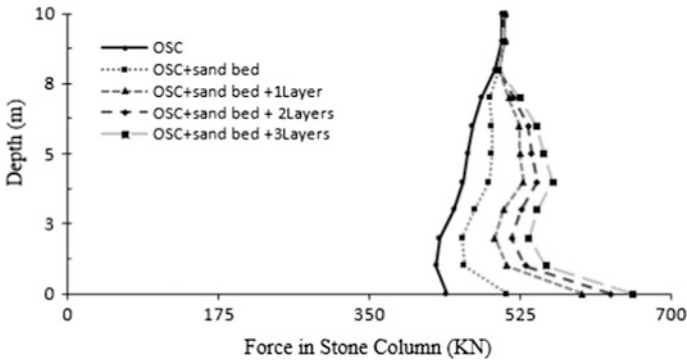
Fig. 12 Load-transfer curves of column 1 for geosynthetic-reinforced sand bed over stone column-improved soft clay
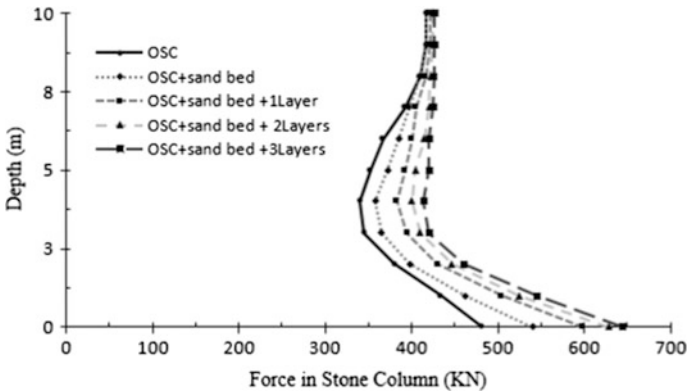
Fig. 13 Load-transfer curves of column 6 for geosynthetic-reinforced sand bed over stone column-improved soft clay

4 Mechanism of GECs Behavior

Mechanisms governing GECs behavior (in relation to the influencing factors) are presented in the following sections.

4.1 *Load Transfer*

In stone column-reinforced ground, stress concentration occurs in stone columns due to the higher relative stiffness of the column to soil, the degree of which can be quantified using the stress concentration ratio (SCR), which is defined as the ratio of the stress on the stone column, $\sigma'_{v,SC}$, to that on the soil, $\sigma'_{v,cl}$. As the degree of load transfer between the column and the soil depends largely on the modulus ratio between the stone column and the soil, the SCR is thus expected to be larger for a GECs than for a OSCs.

Figure 14 shows the vertical stress in the stone column-normalized settlement (S_c/H_c) displacement response for both a GECs and OSCs. Increased encasement stiffness also increases the vertical stress in the stone column $\sigma'_{v,SC}$, such that at a settlement of 390 mm, the mobilized vertical stress on top of the GECs with $J = 10,000$ KN/M is 2.4 times greater than that of OSCs.

The use of encasement can noticeably enhance the load-carrying capacity of OSCs (Fig. 12), it is instructive to more comprehensively study the load-transfer mechanism of both OSCs and GECs.
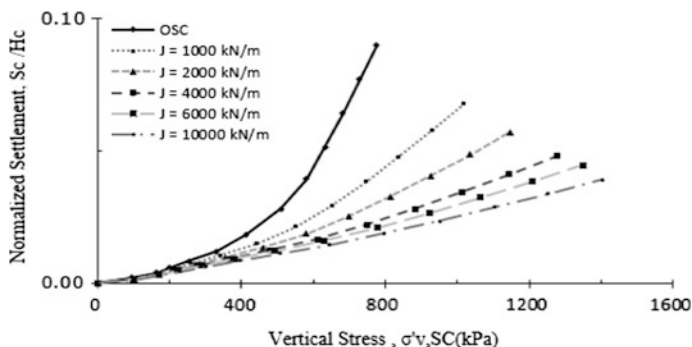
Fig. 14 Effect of encasement on vertical effective stress in stone column

4.2 Force in Stone Column

The end-bearing capacity of columns is another component that should be considered when the overall load-transfer behavior of these systems is studied. To investigate the effects of column encasement on the end-bearing behavior, load-transfer curves of an OSC and GECs at a 300 kPa surcharge pressure are shown in Figs. 15 and 16. Figures 15 and 16 show the load transfer of column 1 and 6, respectively.

The distributions of computed column force with depth are presented in Fig. 15. The column force increased with depth until a maximum value of 720 kN was achieved at about mid-depth. This is due to negative drag-down from the surrounding clay that tends to settle more than that of the stone column.
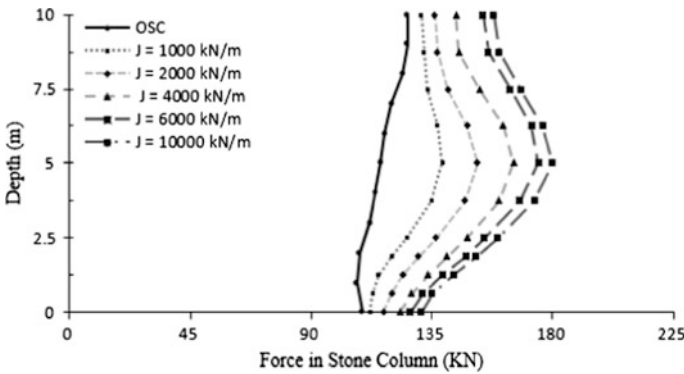
Fig. 15 Load-transfer curves of stone column 1 obtained from models with various encasement stiffness
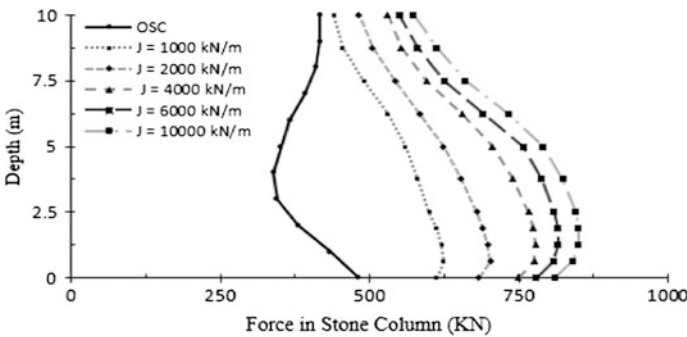
Fig. 16 Load-transfer curves of stone column 6 obtained from models with various encasement stiffness

From Fig. 16, it can be seen that both the OSCs and GECs are primarily end-bearing columns as 86 and 70% of the loads applied at the ground surface are transferred to the tip of the columns, respectively. As shown in Fig. 16, the amount of load transferred to the tip of the GECs is much greater than that of the OSCs at a given settlement, because the encasement makes the GECs a stronger and more rigid element.

4.3 Settlement

These results demonstrate that the geosynthetic encasement can significantly reduce the settlement of the soft ground by decreasing the degree of surcharge load transferred to the clay layer and increasing the stiffness of the stone column.

Stone column encasement also increases the stiffness of the stone column-clay composite ground. Figure 17 shows the variations of surcharge pressure (P_{sur})-normalized settlement (S_c/H_c) relationships for different values of encasement stiffness. Note that S_c represents the settlement at the top of GECs. As one would expect, the slope of $P_{sur} - S_c/H_c$ curve, K, representing the stiffness of the GECs-reinforced ground, increases with increasing J, indicating that the stiffness of the GECs-reinforced ground also increases as the encasement stiffness increases. For example, K increases from 3350 kPa for the OSC to 7672 kPa for the GECs with $J = 10,000$ kN/M, demonstrating approximately a 230% increase in the capacity for the GECs-reinforced ground.

4.4 Lateral Deflection

Figures 18 and 19 show the lateral deflections (δ_h) of column 6 and the associated geosynthetic hoop strains (ε_g), respectively, for different values of encasement
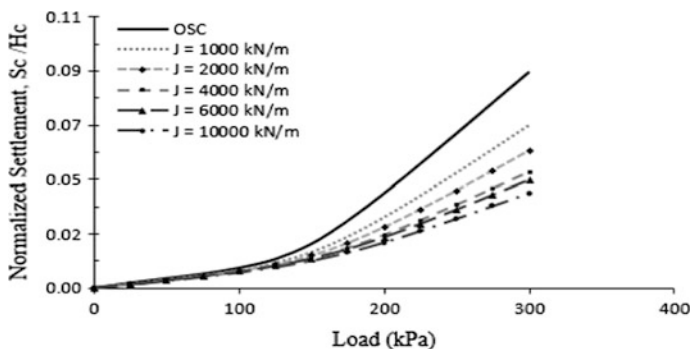
Fig. 17 Effect of encasement on global stiffness of GECs-clay composite ground
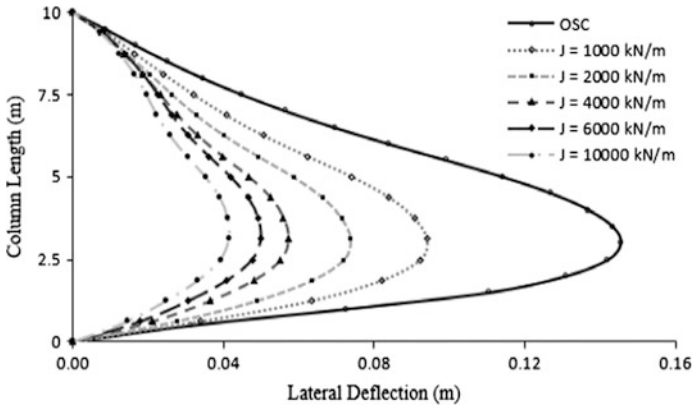
Fig. 18 Lateral deflections of stone column 6 obtained from models with various encasement stiffnesses
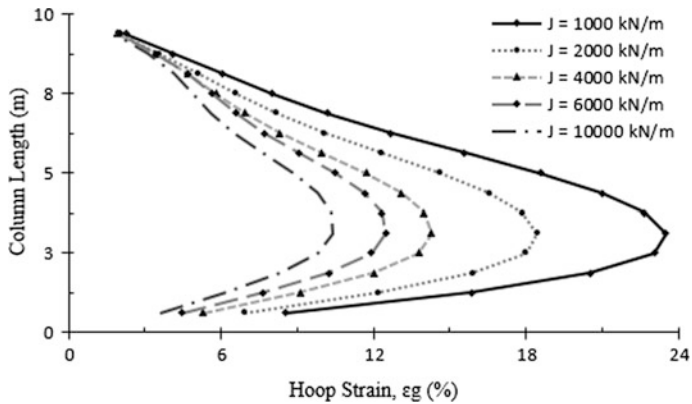
Fig. 19 Geosynthetic hoop strain of stone column 6 obtained from models with various encasement stiffness

stiffness. In Fig. 18, it can be seen that lateral deflection of the stone column tends to sharply increase with length, by up to 145 mm at $3.5D_{sc}$, where D_{sc} = stone column diameter, after which it decreases with length when no encasement is provided. This is attributed to mobilization of more load on top of the GECs (Fig. 14), and the subsequent transmission of greater loads to higher depths in the case of the GECs.

The geosynthetic hoop strain (ε_g) profiles, shown in Fig. 19, tend to follow the general trend observed in the δ_h profiles with a tendency of decreasing ε_g with increasing J, showing a maximum hoop strain of 23.5% occurring at $3.5D_{sc}$ below the top of the stone column for J = 1000 kN/M.

The confining effect provided by the geosynthetic encasement can be quantified using the ring tension force (ΔF_r) developed in the geosynthetic encasement. The ring tension force can be expressed as $\Delta F_r = J \cdot \varepsilon_g$ where ε_g = hoop strain, when assuming linear-elastic material behavior with stiffness J. The additional confining stress provided by the geosynthetic encasement $\Delta\sigma_{h,geo}$ can then be computed as $\Delta\sigma_{h,geo} = \Delta F_r / r_{geo}$ where r_{geo} = radius of the encasement [28]. Substituting $\Delta F_r = J \cdot \varepsilon_g$ into $\Delta\sigma_{h,geo} = \Delta F_r / r_{geo}$ yields

$$\Delta\sigma_{h,geo} = \frac{J \cdot \varepsilon_g}{r_{geo}} \tag{1}$$

Figures 20 and 21 show $\Delta\sigma_{h,geo}$ profiles along the stone column for various cases, computed using the results of FE analyses together with Eq. (2) for a 300 kPa surcharge pressure. As one would expect, it can be seen in Fig. 20 that a stiffer encasement provides greater $\Delta\sigma_{h,geo}$, showing $(\Delta\sigma_{h,geo})_{max}$ = 500–2600 kPa
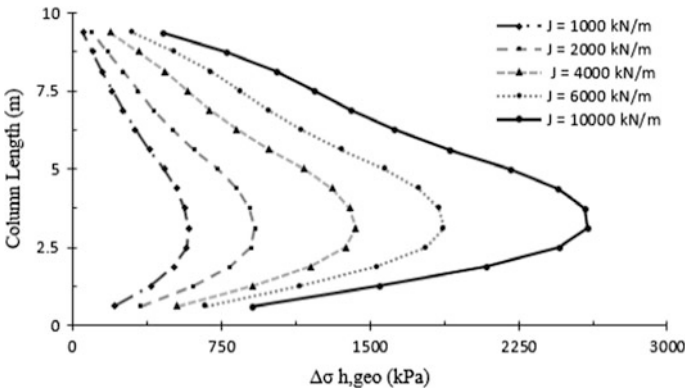
Fig. 20 Variation of $\Delta\sigma_{h,geo}$ with influencing factors: effect of J
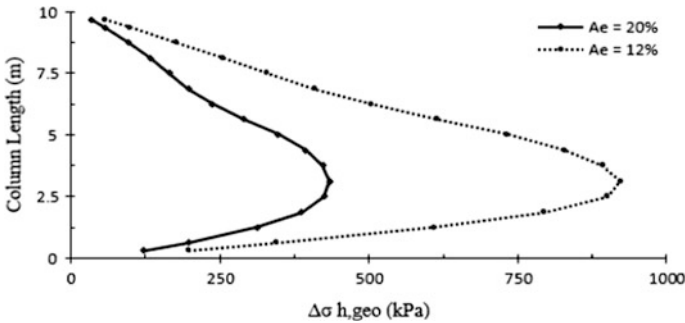
Fig. 21 Variation of $\Delta\sigma_{h,geo}$ with influencing factors: effects of a_E

depending on J. Figure 21 also indicates that the confining stress provided by the encasement depends on the encasement stiffness. For example, as shown in Fig. 21, for J = 2000 kN/M, larger $\Delta\sigma_{h,geo}$ are developed when the area replacement ratio a_E is lower and/or the ground is weaker, showing $(\Delta\sigma_{h,geo})_{max}$ = 920 kPa for a_E = 10% as opposed to $(\Delta\sigma_{h,geo})_{max}$ = 434 kPa for a_E = 20%, depending on the soil consistency. These results in fact suggest that the encasement has a greater impact when a_E is smaller, i.e., a lager spacing of GECs is weaker.

4.5 Effect of Encasement Stiffness the GECs Performance

The encasement stiffness J is important design item as they directly affect the cost of GECs. The effects of J on the GECs performance are examined. Figure 22 presents the variations of settlement ratio β with the encasement stiffness for GECs with a_E = 12, 20% for a 300 kPa surcharge pressure. As one would expect, it can be seen that in all cases the settlement ratio β decreases rapidly with J up to J = 2000 KN/M after which it decreases at a decreased rate. Another trend shown in these figs is that the $\beta - J$ relationships are practically the same for a given area replacement ratio.

4.6 Stiffness Improvement Factor

Figure 23 shows the variations of stiffness improvement factor (SIF), defined as the ratio of the stiffness of GECs-reinforced ground (K_{GECs}) to that of untreated ground ($K_{untreated}$), with the encasement stiffness and the area replacement ratio. Note that the stiffness values of the GECs-reinforced and untreated ground, i.e., K_{GECs}, and $K_{untreated}$ are obtained from the respective $P_{sur} - S_c/H_c$ curves given in Fig. 16 as
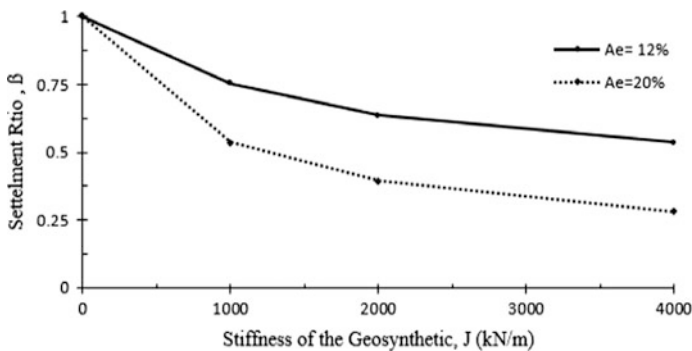
Fig. 22 Variation of settlement ratio with of geosynthetic tensile stiffness
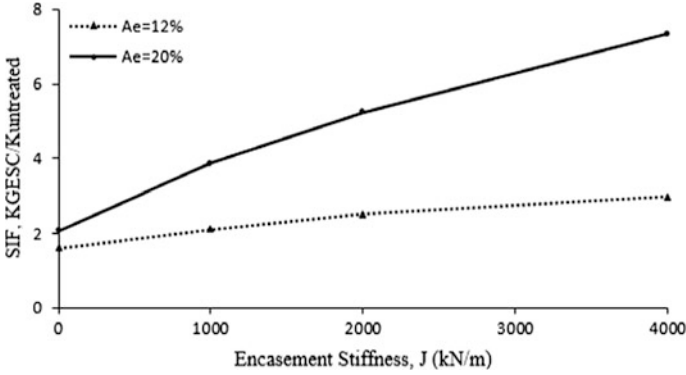
Fig. 23 Variation of SIF with J and a_F

average slopes. As shown, an eightfold increase in the stiffness of the ground can be achieved for the GECs with $J = 4000$ kN/M and $a_E = 20\%$ compared to that of the untreated ground. As before, cases with larger column spacing tend to yield greater SIF values for a given encasement stiffness, supporting the trend observed earlier.

Figure 23 can be used to make a preliminary estimate of the settlement of GECs-reinforced ground. For example, the settlement of GECs-reinforced ground $(S_c/H_c)_{\text{GECs}}$ under a given surcharge P_{sur} can be obtained using the settlement of untreated ground $(S_c/H_c)_{\text{untreated}}$ and the SIF given in Fig. 20, since SIF can be written, by definition, as

$$\text{SIF} = \frac{K_{\text{GESC}}}{K_{\text{untreated}}} = \frac{[p_{\text{sur}}/(S/H_c)]_{\text{GESC}}}{[P_{\text{sur}}/(S/H_c)]_{\text{untreated}}} = \frac{(S/H_c)_{\text{untreated}}}{(S/H_c)_{\text{GESC}}} a_F \tag{2}$$

The settlement of GECs-reinforced ground $(S_c/H_c)_{\text{GECs}}$ under a given embankment surcharge P_{sur} can then be expressed as

$$\left(\frac{S}{H_c}\right)_{\text{GESC}} = \frac{1}{\text{SIF}} \cdot \left(\frac{S}{H_c}\right)_{\text{untreated}} \tag{3}$$

Since (S_c/H_c) untreated can be computed as (S_c/H_c) untreated $= m_y \cdot \Delta\sigma'$, where m_v = coefficient of volume compressibility of untreated ground and $\Delta\sigma'$ = effective stress increase, $(S_c/H_c)_{\text{GECs}}$ can be computed as (S_c/H_c) GECs $= m_y \cdot p_{\text{sur}}/\text{SIF}$ assuming a constant mv and $\Delta\sigma' = p_{\text{sur}}$.

5   Stress Concentration Ratio

The SCR versus normalized surcharge pressure $p_{\text{sur}}/E_{\text{imp}}$ relationships are shown in Figs. 24. Note that the normalized surcharge pressure, $p_{\text{sur}}/E_{\text{imp}}$ is used in this
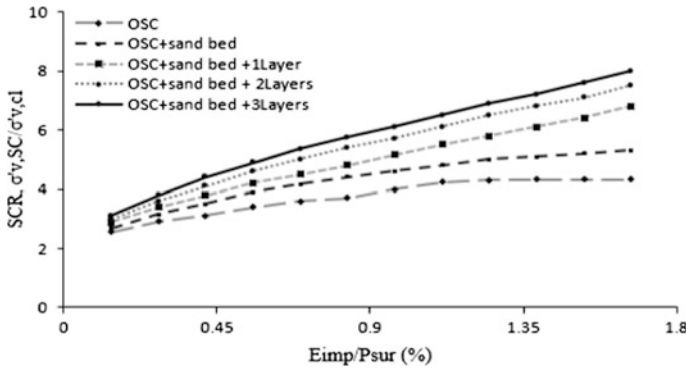
Fig. 24 Variation of stress concentration ratio with surcharge pressure for multilayer geosynthetic-reinforced system

figure, where E_{imp} = elastic modulus of the stone column-soil composite ground, computed based on the area replacement ratio as

$$E_{imp} = (A_s + A_{sc}) = E_{sc}A_{sc} + E_sA_s, \tag{4}$$

where A_{SC} and A_S are the surrounding soil and the cross-section areas of the stone column, respectively, and E_{sc} and E_s are the surrounding soil and elastic moduli of the stone column, respectively. Note that the elastic moduli of the untreated soils are computed using the following as:

$$E_s = \frac{3(1 - 2v)(1 + e_0)p'}{k}, \tag{5}$$

where p' = mean effective stress.

Figure 24 shows variation of stress concentration ratio with surcharge pressure for multilayer geosynthetic-reinforced sand bed with 40 cm thick placed over stone column. It can be seen, changes in the vertical effective stresses both in the stone column and in the clay layer caused by the multilayer geosynthetic-reinforced result in eight times larger SCR values for the three layers of geosynthetics-reinforcement than that for the OSC. The multilayer of geosynthetics-reinforcement transfers the stress from soil to stone columns due to stiffness difference between the soft soil and stone columns which reduce the possibility of soil yielding above stone columns. Thus, it can be said that there is a large increase in the values of stress concentration ratio in comparison to the values with the presence of geosynthetics-reinforcement when there is no geosynthetics-reinforcement present.

These changes in the vertical effective stresses both in the stone column and in the clay layer caused by the encasement result in nine times larger SCR values for the GECs with $J = 10,000$ kN/M than that for the OSCs as shown in Fig. 25. The SCR tends to increase with the surcharge pressure load. Thus, it can be said
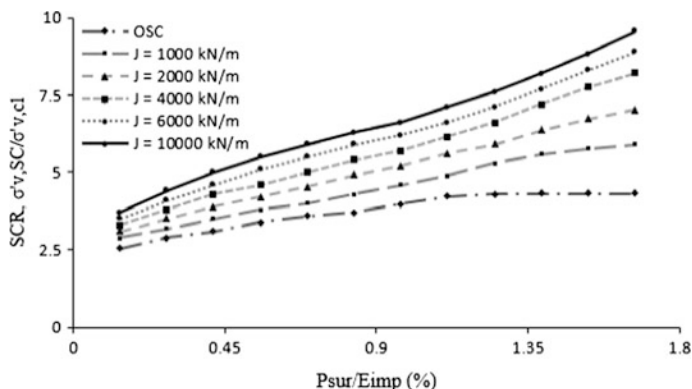
Fig. 25 Variation of SCR with surcharge pressure at depth 2.5 m for GECs with various encasement stiffness

that use of GECs with an increase in the encasement tensile stiffness helps the stress transfer process and causes further reduction of stress on the soft soil.

6   Conclusions

In this paper, three-dimensional numerical analyses were performed to study the settlement response of multilayer geosynthetic-reinforced granular fill over stone column-reinforced soil. Finite-Element Analyses were carried out to compare the group performance of GECs with OSCs.

A detailed study was implemented to better understand the mechanism of load-carrying capacity in a group of GECs and OCSs. Based on the results gained from present research, the following conclusions can be found:

It has been observed that the use of multilayer geosynthetics-reinforcement with stone columns is not very effective to reduce the maximum settlement. The multilayer-reinforced system is very much effective to reduce the maximum settlement when stone columns are not provided in the soft soil. However, single-layer reinforcement with stone columns is very effective to reduce the maximum settlement.

The optimum thickness of geosynthetic-reinforced sand bed is 0.3 times the diameter of the footing. Decreases in bulge diameter in depth of bulge have been observed due to placement of sand bed over stone column-improved soft clay. Further decrease in maximum bulge diameter and increase in depth of bulge have been observed due to application of geosynthetic.

More stress concentration means more stress is transferred from soil to stone columns due to stiffness difference which helps to reduce the possibility of soil yielding above the stone columns. The use of geosynthetic reinforcements

significantly helps the stress transfer process and causes further reduction of stress on the soft soil.

When encasing the stone column, the lateral bulging is considerably decreased due primarily to the added confinement by the encasement. The confinement stresses inferred from the ring tension force developed in the geosynthetic encasement are larger when the area replacement ratio is smaller.

Increase in the stiffness of the geosynthetic encasement of the stone columns leads to increasing the column stiffness, the hoop tension force mobilized in the encasement, and the lateral confinement provided to the column, leading to substantial enhancement in the performance of the GECs group.

The critical geosynthetic encasement stiffness, beyond which no further benefit can be achieved, was found to be approximately $J = 2000$ KN/M and it appears to be independent of the area replacement ratio and the surcharge pressure load intensity for the conditions analyzed.

Encasing stone columns increased the end-bearing capacity. Encasement also allowed for greater load transfer to deeper depths, which was led to corresponding increases in loads that were transferred to the tip of the column.

References

1. Hughes, J., Withers, N., Greenwood, D.: A field trial of the reinforcing effect of a stone column in soil. Geotechnique **25**, 31–44 (1975)
2. Madhav, M., Vitkar, P.: Strip footing on weak clay stabilized with a granular trench or pile. Can. Geotech. J. **15**, 605–609 (1978)
3. Aboshi, H., Ichimoto, E., Enoki, M., Harada, K.: The compozer—a method to improve characteristics of soft clays by inclusion of large diameter sand columns. Proc. Int. Conf. Soil Reinforcement ENPC **1**, 211–216 (1979)
4. Madhav, M., Miura, N.: Stone columns. In: Proceedings of the International Conference on Soil Mechanics and Foundation Engineering-International Society for Soil Mechanics and Foundation Engineering, pp. 163–163 (1994)
5. Deb, K.: Modeling of granular bed-stone column-improved soft soil. Int. J. Numer. Anal. Meth. Geomech. **32**, 1267–1288 (2008)
6. Deb, K.: Soil-structure interaction analysis of beams resting on multilayered geosynthetic-reinforced soil. Interact. Multiscale Mech. **5**, 369–383 (2012)
7. Han, J., Ye, S.-L.: Simplified method for consolidation rate of stone column reinforced foundations. J. Geotech. Geoenviron. Eng. **127**, 597–603 (2001)
8. Han, J., Gabr, M.: Numerical analysis of geosynthetic-reinforced and pile-supported earth platforms over soft soil. J. Geotech. Geoenviron. Eng. **128**, 44–53 (2002)
9. Van Impe, W.F.: Soil Improvement Techniques and Their Evolution (1989)
10. Malarvizhi, S., Ilamparuthi, K.: Load versus settlement of clay bed stabilized with stone and reinforced stone columns. In: Proceedingns of GeoAsia–2004, Seoul, Korea, pp. 322–329 (2004)
11. Ayadat, T., Hanna, A.: Encapsulated stone columns as a soil improvement technique for collapsible soil. Proc. Inst. Civ. Eng. Ground Improv. **9**, 137–147 (2005)
12. Murugesan, S., Rajagopal, K.: Geosynthetic-encased stone columns: numerical evaluation. Geotext. Geomembr. **24**, 349–358 (2006)

13. Gniel, J., Bouazza, A.: Improvement of soft soils using geogrid encased stone columns. Geotext. Geomembr. **27**, 167–175 (2009)
14. Khabbazian, M., Kaliakin, V.N., Meehan, C.L.: 3D numerical analyses of geosynthetic encased stone columns. In: 2009 International Foundation Congress and Equipment Expo (2009)
15. Kempfert, H., Göbel, C., Alexiew, D., Heitz, C.: German recommendations for reinforced embankments on pile-similar elements. In EuroGeo3-Third European Geosynthetics Conference, Geotechnical Engineering with Geosynthetics, pp. 279–284 (2004)
16. Deb, K., Basudhar, P., Chandra, S.: Generalized model for geosynthetic-reinforced granular fill-soft soil with stone columns. Int. J. Geomech. **7**, 266–276 (2007)
17. Deb, K., Samadhiya, N.K., Namdeo, J.B.: Laboratory model studies on unreinforced and geogrid-reinforced sand bed over stone column-improved soft clay. Geotext. Geomembr. **29**, 190–196 (2011)
18. Ambily, A., Gandhi, S.R.: Behavior of stone columns based on experimental and FEM analysis. J. Geotech. Geoenviron. Eng. **133**, 405–415 (2007)
19. Deb, K., Sivakugan, N., Chandra, S., Basudhar, P.: Numerical analysis of multi layer geosynthetic-reinforced granular bed over soft fill. Geotech. Geol. Eng. **25**, 639–646 (2007)
20. Yoo, C.: Performance of geosynthetic-encased stone columns in embankment construction: numerical investigation. J. Geotech. Geoenviron. Eng. **136**, 1148–1160 (2010)
21. Liu, H., Ng, C.W., Fei, K.: Performance of a geogrid-reinforced and pile-supported highway embankment over soft clay: case study. J. Geotech. Geoenviron. Eng. **133**, 1483–1493 (2007)
22. Alexiew, D., Brokemper, D., Lothspeich, S.: Geotextile encased columns (GEC): load capacity, geotextile selection and pre-design graphs. In: Proceeding of the Geo-Frontiers 2005 Congress, Austin, Texas, pp. 1–14 (2005)
23. Barksdale, R., Bachus, R.: Design and Construction of Stone Columns, Appendixes, vol. II. Federal Highway Administration, Washington DC, USA (1983)
24. Shahu, J., Madhav, M., Hayashi, S.: Analysis of soft ground-granular pile-granular mat system. Comput. Geotech. **27**, 45–62 (2000)
25. Basudhar, P., Dixit, P., Gharpure, A., Deb, K.: Finite element analysis of geotextile-reinforced sand-bed subjected to strip loading. Geotext. Geomembr. **26**, 91–99 (2008)
26. Burd, H.: Analysis of membrane action in reinforced unpaved roads. Can. Geotech. J. **32**, 946–956 (1995)
27. Lee, K., Manjunath, V., Dewaikar, D.: Numerical and model studies of strip footing supported by a reinforced granular fill-soft soil system. Can. Geotech. J. **36**, 793–806 (1999)
28. Raithel, M., Kempfert, H.-G.: Calculation models for dam foundations with geotextile coated sand columns. In: ISRM International Symposium (2000)

New Empirical Relationship Between Probabilistic and Deterministic Procedures Using a Genetic Algorithm

Mehran Naghizadehrokni and Asskar Janalizadechoobbasti

Abstract This article analyses the reliability based on the deterministic method and acceleration attenuation in the Chalus City, as well as, obtaining the density function of probability distribution and statistics for cyclic stress ratio (CSR). The density function of probability distribution and the cycle resistance ratio (CRR) can be concluded from the possibility of the cycle of resistance curves. The proposed first-order, second-moment procedure is used to determine the relationship between three factors including, the probability of liquefaction, the safety factor and the reliability index. In this study, the numerical approach of genetic algorithm is utilized to minimize the function of the reliability index. The usage of genetic algorithm model provides a reliable mechanism suitable for a computer program. Two empirical relationships based on P_L, N_{SPT}, and CSR with a correlation coefficient and mean error of 95 and 10%, respectively, and the relationship between P_L and Fs with a correlation coefficient of 0.887 are provided. Accuracy is measured by comparing the results with those of previous studies. The results of the present study show that a safety factor greater or smaller than 1 does not mean safety and/or liquefaction; to assure liquefaction probability, a reliability-based method should be used for analyses. Moreover, the designed algorithm in this study can be extended by keeping its generalities and having required information from other regions.

Keywords Liquefaction potential · Reliability procedure · Genetic algorithm

M. Naghizadehrokni (✉)
RWTH Aachen University, Geotechnical Engineering,
Aachen, Germany
e-mail: Naghizadehrokni@geotechnik.rwth-aachen.de

A. Janalizadechoobbasti
Geotechnical Engineering, Babol Noshirvani University
of Technology, Babol, Iran
e-mail: Asskar@nit.ac.it

1   Introduction

Iran lies on an earthquake belt, and the soil in many areas represents a high liquefaction potential under the dynamic load effects of earthquakes. Liquefaction can be one of the most important phenomena during an earthquake which causes damage to buildings and lifelines on sandy alluvium. If a vibration, like an earthquake, is imposed upon a sandy soil, the soil tends to decrease in volume and become compacted. If the soil is saturated and the speed of the movement caused by the vibration is very fast, the soil will become compacted with the same speed. The incidence of such conditions causes an outbreak of large deformations in the soil, and the soil becomes liquefied; such a situation is called liquefaction [1, 2].

The first step in assessing the risk of liquefaction is usually to evaluate liquefaction potential; if the soil has the least criteria for being liquefied, areas of liquefaction and the effects of its occurrence should be examined. Most empirical methods are based on deterministic analysis and parameters such as soil resistance and the load caused by the earthquake are considered without dispersion and error and changes are not considered [3, 4]. In addition, there is no exact correlation between the safety factor and probability of liquefaction. A new and comprehensive approach to investigate and resolve the issue as well as entering uncertainties in the calculations is statistical analysis, especially the analysis of reliability. Different methods of reliability analysis such as Advanced First-Order Second-Moment (AFOSM), the First-Order Second-Moment (FOSM), Monte Carlo Simulation (MCS), Point Estimating (PEM) and the new method which is a combination FOSM-PEM can be used in assessing soil liquefaction potential. In 1999 and 2002, Boulanger et al. studied this area based on CPT tests and shear wave velocity (Vs) [5, 6]. In 2004, Hwang et al. proposed relationships using statistical analysis based on observations of liquefaction and non-liquefaction zones at the Chi-Chi earthquake site. Due to the large amount of field data from the standard penetration test in Iran and the development of statistical methods, standard penetration test data is used for this study [7]. The results of 220 pieces of data related to 18 boreholes in the area of Chalus are controlled and compared by statistically proposed procedure based on reliability analysis with the results of other techniques that are based on observed data. The comparison results shows the efficacy of the proposed method.

2   Liquefaction Assessment by Using SPT Results

The use of N_{SPT} is introduced as a factor for evaluating liquefaction for the first time since a devastating earthquake occurred in 1964. Many researchers such as Boulanger and Idriss [6], NCEER (2001), Cetin (2000, 1990), Ishihara (1979), Seed et al. [11] and Yoshimi, Tokimatso, Iwasaki et al. (1982) have attempted to find the relationship between the seismic conditions causing liquefaction and N_{SPT}. Figure 1 generally offers a plan for liquefaction assessment based on N_{SPT} at geotechnical boreholes [8–12].
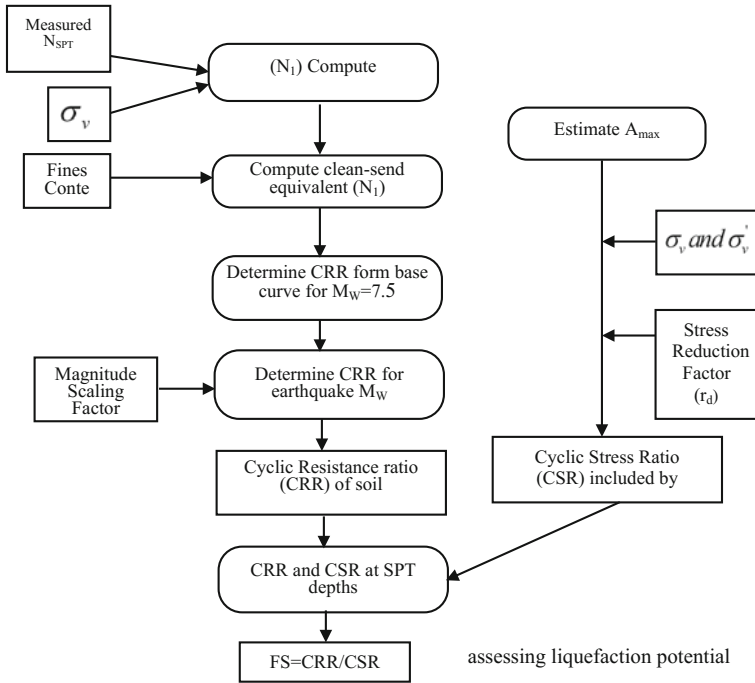
Fig. 1 The process of assessing liquefaction potential based on N_{SPT}

The simplified procedure of Idriss and Seed has been used in almost all lique-faction studies to estimate the cycle stress ratio in the critical layer, as in Eq. 1 [11]:

$$CSR_{7.5} = 0.65(A_{max}/g)(\sigma_v/\sigma_v')(r_d) \qquad (1)$$

In the above equation, A_{max} which is the maximum horizontal acceleration at ground level (PGA); g which is the acceleration of gravity; σ_v which is the total stress layer desired; σ_v' which is the effective stress layer desired and r_d is the shear mass participation nonlinear coefficient (coefficient reduced stress) (Z is a function of depth). In this paper, r_d is calculated with an equation provided by the National Center for Earthquake Engineering Research (NCEER) [10].

$$r_d = \frac{(1 - 0.4113z^{0.5} + 0.0405z + 0.001753z^{1.5})}{(1 - 0.4177z^{0.5} + 0.05729z - 0.0062z^{1.5} + 0.0012z^2)} \qquad (2)$$

Seed and Idriss used the SPT blow count (N1) in studying soil resistance against liquefaction that is determined by the CRR. In this study, CRR is the cycle resis-tance ratio obtained using the following equation [10, 11]:

$$\mathrm{CRR}_{7.5} = \frac{1}{34 - (N_1)_{60}} + \frac{(N_1)_{60}}{135} + \frac{50}{[10(N_1)_{60} + 45]^2} - \frac{1}{200} \tag{3}$$

In this equation, it should be supposed that the soil has good density and is not prepared to liquefy. For considering the effect of values (FC) in CRR, the following equation is presented by Seed et al. [11]:

$$(N_1)_{60cs} = a + b(N_1)_{60} \tag{4}$$

where a and b should be considered as the constant parameters and $(N_1)_{60}$ is a modified blow count for clean sand. The percentage of FC is calculated according to the following equation in the sand to define a and b:

$$a = \begin{cases} 0.0 & \mathrm{FC} \le 5\% \\ \exp\left[1.76 - \left(190/\mathrm{FC}^2\right)\right] & 5\% < \mathrm{FC} < 35\% \\ 0.5 & \mathrm{FC} \ge 35\% \end{cases} \tag{5}$$

$$b = \begin{cases} 1.0 & \mathrm{FC} \le 5\% \\ \left[0.99 + \left(\frac{\mathrm{FC}^{1.5}}{1000}\right)\right] & 5\% < \mathrm{FC} < 35\% \\ 1.2 & \mathrm{FC} \ge 35\% \end{cases} \tag{6}$$

Equivalent values $(N_1)_{60}$ for clean sand are obtained by using the above two equations [8].

3 Reliability Concept and Its Application in Geotechnical Engineering

The concept of probabilistic analysis becomes clearer when it is proposed and discussed against deterministic analysis. When there are uncertainties and errors in the measurement of parameters that can reduce the validity of calculations, using the probabilistic analysis approach is an appropriate solution to ensure the accuracy of calculated assessment results [13].

3.1 Reliability Method (FOSM)

In this method, the uncertainty of an independent variable is estimated as a function of input variable variances. To calculate the CSR, the average value (μ_{CSRN}) and the coefficient of variation related to it are calculated with Eqs. 7 and 8 [14]:

$$\mu_{\text{CSRN}} = 0.65 \frac{\mu_{a_{\max}}}{g} \cdot \frac{\mu_{\sigma_v}}{\mu_\sigma} \cdot \frac{\mu_{r_d}}{\mu_{\text{MSF}}} \tag{7}$$

$$V_{\text{CSRN}}^2 = V_{a_{\max}}^2 + V_{\sigma_v'}^2 + V_{\sigma_v}^2 + V_{r_d}^2 + V_{\text{MSF}}^2 - 2\rho_{\sigma_v \sigma_v'} V_{\sigma_v'} V_{\sigma_v} \tag{8}$$

In these equations μ, v and $\sigma_v \sigma_v'$ represent the mean, coefficient of variation and correlation coefficient between total and effective stresses, respectively. MSF is the earthquake intensity classifying factor. Uncertainties in the parameters of $A_{\max}$, MSF and r_d lead to uncertainties in CSR parameters. The covariance (COV) related to CRR is achieved from Eq. 9 [15]:

$$\text{COV}_{\text{CRR}} = \frac{\Delta_{\text{CRR}}}{2\mu_{\text{CRR}}} \tag{9}$$

Δ_{CRR} consists of $\mu_{(N_1)_{60}}$ and $\sigma_{(N_1)_{60}}$ which, respectively, represent the mean and standard deviation of soil resistance parameters.

In order to analyse reliability, the performance function (Z) is defined as Z = CRR-CSR; for smaller values of Z, instability is created and liquefaction will occur, and if Z = 0, restricted mode performance function is placed on the boundary between the two states and the non-occurrence of liquefaction. From the P_L parameter which is defined as the probability of liquefaction, the liquefaction risk will be calculated as in Eq. 10 [16]:

$$P_L = 1 - \phi(\beta) \tag{10}$$

where $\phi(\beta)$ is the standard normal cumulative probability and β is the reliability index. One way to calculate β is to specify the average amounts and standard deflection of the performance function by using all parameters which assume a normal distribution or a lognormal for performance function; it is, therefore, not required to assume distribution function to deduct CRR and CSR. Then, the log-normal reliability index β_{LN} is obtained from Eq. 11 in which μ_{FS} and V_{FS}, respectively, represent the mean and covariance of the safety factor:

$$\beta_{\text{LN}} = \frac{\ln\left[\frac{\mu_{\text{FS}}}{\sqrt{(1 + V_{\text{FS}}^2)}}\right]}{\sqrt{\ln(1 + V_{\text{FS}}^2)}} \tag{11}$$

In his research, J. H. Hwang provided Eq. 12 for calculating the possibility of liquefaction [17]. Table 1 represents the parameters that Hwang used in his obtained equation and these parameters are used for comparison with the present study.

Table 1 Parameters used by Hwang [7]

Parameter	β_0	β_1	β_2	β_3
Regression results	10.4	−0.2283	−0.001927	3.8

$$P_L = \frac{1}{1 + \exp\{-[\beta_0 + \beta_1 (N_1)_{60cs} + \beta_2 (N_1)^2_{60cs} + \beta_3 \ln(CSR)]\}} \tag{12}$$

3.2   Use of Genetic Algorithm Method in Minimizing β

Several optimization methods are used for minimizing the reliability index function, which is useful for reliability optimization problems. One optimization technique is the new genetic algorithm method. The genetic algorithm (GA) method is considered as a search procedure in computer science for finding a comprehensive solution for optimization and solving problems. GA is a special kind of evolutionary algorithm used in evolutionary biology techniques. It requires information related to the quality of each response, while most optimization methods also need derivatives of the problem, which may not be easy to obtain. The genetic algorithm does not need the details of the problem, so, it is more flexible than other optimization methods. Other advantages of this method are its easy mechanism in using a computer. In the present study, it is done with problem simulation using Matlab Software [18].

3.3   Probability of Liquefaction and Safety Factor

The reliability procedure is mostly utilized to calculate probability of liquefaction behind a specific safety factor, which can be evaluated quantitatively. Figure 2 shows a probability of liquefaction related to the calculation of the safety factor based on the different coefficients. Clearly, in the range of $Fs < 1$, the coefficient of variation is higher than the probability of liquefaction. In the range of $Fs > 1$, however, the coefficient of variation is lower than the probability of liquefaction. Therefore, to assess the various coefficients CRR and CSR of the potential of liquefaction, factors have a greater impact on probabilistic analysis [16, 19].
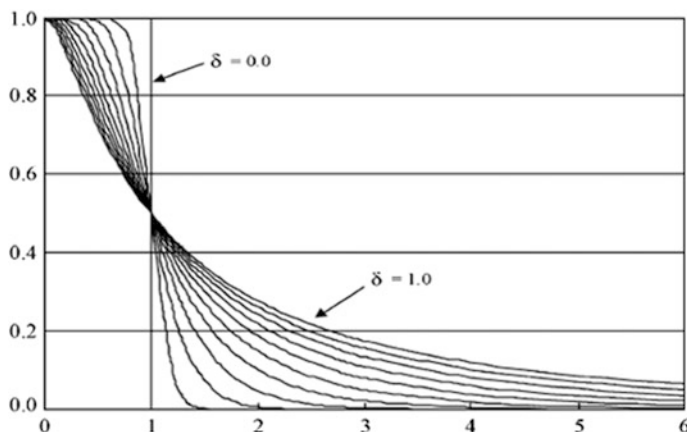
Fig. 2 Relation of liquefaction probability with the safety factor for different coefficients of variation

4 Use of Reliability Method in Assessing Liquefaction in the Study Area

The current study investigated the potential of liquefaction in the city of Chalus. This city is located at 36.6459°N, 51.4070°E, and south of the Caspian Sea. Active and effective faults around the town are shown in Table 2.

The most important of these faults are the Alborz north faults, the Caspian, and the lineaments of Amol and Babol that have high seismic potential. Because the liquefaction phenomenon is possible in high seismic areas and saturated sandy soils, the evaluation of the risk of the earthquake has great importance in Chalus.

The analytical method calculated a major earthquake (MN) equal to 3.6 on the Richter scale and a maximum horizontal acceleration (A_{max}) of 0.32 g. This amount is achieved based on Iranian seismic design code (2800 standard) for Chalus area in a 500-year return period event [20–24].

Table 2 Properties of active faults

Fault	Fault length (km)	Effective length (km)	Amax	Magnitude
Khazar	250	13	0.28	7.7
North Alborz	360	23	0.19	7.8

4.1 Coefficient of Variation and Correlation Related to Vertical Effective Stress and Total Tension

According to the records of 220 cases in the Chalus area and because of changes in the special weight of soil which generally varies between 15 and 21 Kn/m^3 in the studied area, the values of uncertainty for total stress and effective stress of 10 and 15%, respectively, are obtained through statistical calculations. The correlation between these two parameters is 95%. Clearly, the uncertainty related to effective stress is greater than that related to total stress because of changes in groundwater levels.

4.2 Uncertainty Related to the Effective Parameters in Liquefaction

Table 3 is provided random variables which are considered in this study with details. The mean values of the variables $(N_1)_{60cs}, \sigma'_v, \sigma_v$ are calculated based on the 220 case studied records.

The correlations between input variables are calculated and shown in Table 4.

Table 3 Random variables and considered characteristics

Random variable	β	Average	Coefficient of variation	Distribution function
$(N_1)_{60}$	X1	20	0.3	Normal
σ_v	X2	Depending on depth	0.1	Normal
σ'_v	X3	Depending on depth	0.15	Normal
A_{max}	X4	0.36	0.15	Normal
MW	X5	6.3	0.05	Normal

Table 4 The correlation coefficient between variables

	$(N_1)_{60}$	σ_v	σ'_v	A_{max}	MW
$(N_1)_{60}$	1	0.95	0	0	0
σ_v	0.95	1	0.95	0	0
σ'_v	0	0.95	1	0	0
A_{max}	0	0	0	1	0.9
MW	0	0	0	0.9	1

4.3 Flowchart Provided for Liquefaction Potential Assessment

A computer program is developed in MATLAB to evaluate the liquefaction potential based on the reliability approach for 220 case studied records. Figure 3 presents a written flowchart program for analysing the reliability of liquefaction. First, in this program, seismic information from the studied area, mean values and the coefficient of variation related to the effective parameters in evaluating liquefaction and parameters related to the genetic algorithm are presented to the program as constant input parameters. Then the geotechnical data required for liquefaction assessment, including groundwater levels, soil bulk density, soil layer depth, soil type, SPT number and the percentage of fine material passing from a No. 200 sieve, are given to the program as variable input parameters. The program is designed based on the flowchart-calculated reliability index values at different borehole depths and the probability of liquefaction in these depths is evaluated.

4.4 Evaluate of Liquefaction Incidence Possibility in Boreholes

In the studied areas, several boreholes are drilled for each project. The boreholes are selected for reliability analysis and the zoning areas where liquefaction is more likely to occur in terms of distribution size and groundwater level (low density, sand, high groundwater). In this study, the dataset contains about 220 records related to the 18 boreholes which are drilled at different locations and depths to investigate the potential of liquefaction. In each case, the CSR, CRR, values of reliability index and probability of liquefaction are investigated at all depths. Table 5 is presented a summary of calculation.

As seen in Table 5, Fs related to borehole 17 is greater than one that represents the absence of liquefaction at borehole location, although at this point probability of liquefaction based on the designed procedure equals 38% according to Chen's classification.

In boreholes 3 and 20, the Fs values are 0.87 and 0.85, respectively, and the probabilities of liquefaction are 54 and 50%. Thus, a higher safety factor does not indicate a safe area or one with less risk. This can also be seen in boreholes 17 and 12. A low-safety factor does not necessarily mean disintegration or liquefaction incidence. The probability of disintegration may be placed in the range of acceptable, even if the safety factor is relatively low. This case is shown in Fig. 4.

Based on the cases considered, a reduction in the amounts of Fs can lead to increasing the probability of disintegration, regardless of the method of calculation for Fs. The reliability index, the probability of failure and safety factor should be examined at the same time so that the results could be used in practical engineering projects.
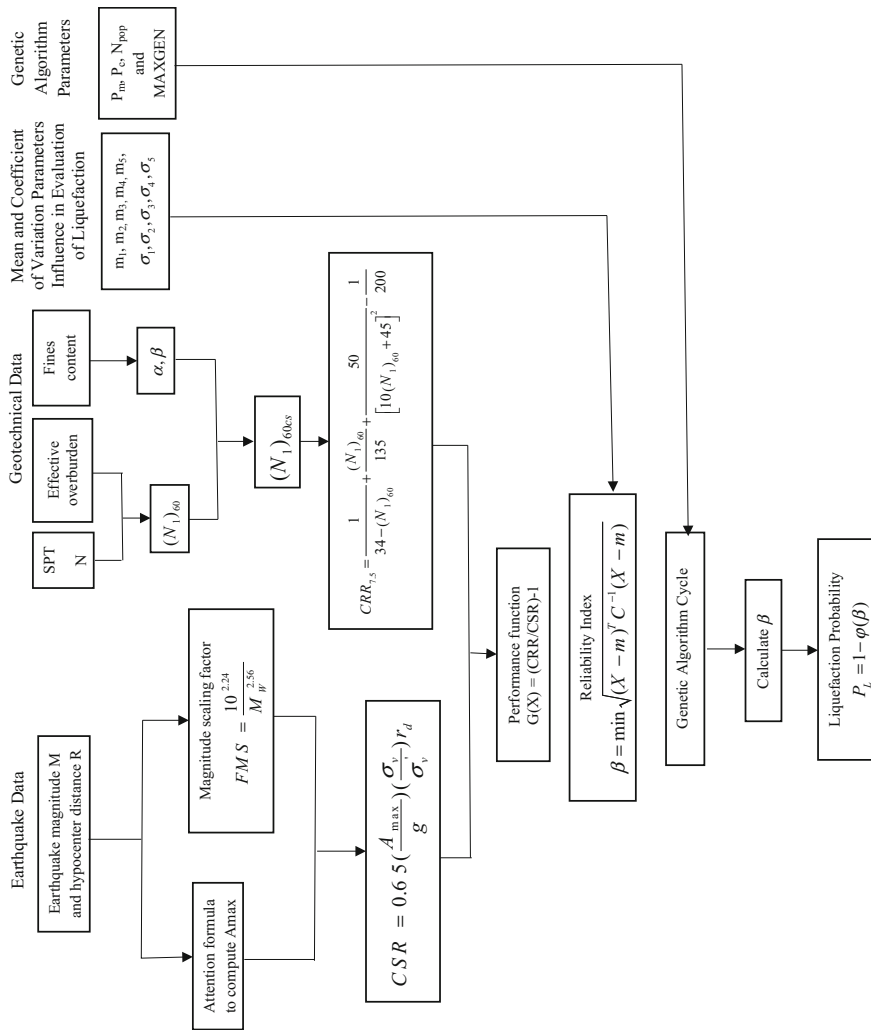
Fig. 3 Flowchart of the written program

Table 5 Summary of information and calculations for liquefaction potential in the study area

P_L (%)	β	F_S	CSR	CRR	MW	A_{max}	$(N_1)_{60}$	$T/m^2\sigma'_v$	$T/m^2\sigma_v$	Soil type	Depth (M)	Row
81	−0.88	0.71	0.2	0.14	6.3	0.36	13	4.5	6	SP-SM	2.5	1
87	−1.14	0.85	0.27	0.23	6.3	0.36	21	2.99	5.49	SP	3	2
54	−0.1	0.87	0.2	0.18	6.3	0.36	17	5.04	7.04	SP	3.5	3
82	−0.9	0.72	0.18	0.13	6.3	0.36	12	6.35	7.8	SP	4	4
77	−0.75	0.77	0.17	0.13	6.3	0.36	12	6.59	7.82	SM	4.5	5
97	−1.9	0.45	0.19	0.09	6.3	0.36	7	6	8	SP	5	6
27	0.62	1.08	0.19	0.21	6.3	0.36	19	7.5	10	SP	5.5	7
99	−2.53	0.31	0.24	0.07	6.3	0.36	5	4.35	7.05	SP-SM	6	8
26	0.65	1.09	0.2	0.21	6.3	0.36	20	5.59	11.82	SM	6.5	9
76	−0.7	0.78	0.2	0.15	6.3	0.36	14	9.5	13	SM	7	10
96	−1.8	0.43	0.22	0.1	6.3	0.36	8	9	14	SP	8	11
32	0.5	1	0.22	0.21	6.3	0.36	20	13	19	SP-SM	10	12
94	−1.59	0.52	0.21	0.11	6.3	0.36	9	14	22	SP-SM	11	13
19	0.86	1.12	0.21	0.24	6.3	0.36	22	14	21.9	SP-SM	11.5	14
56	−0.15	0.82	0.23	0.19	6.3	0.36	18	13	23.4	SP	12	15
77	−0.73	0.74	0.19	0.14	6.3	0.36	13	19	31.9	SP-SM	16	16
38	0.3	1.03	0.15	0.16	6.3	0.36	15	22.7	32	SP-SM	16.5	17
16	1	1.17	0.19	0.22	6.3	0.36	21	18.7	34.19	SM	17	18
12	1.18	0.3	0.19	0.25	6.3	0.36	22	19	36	SP-SM	18	19
50	0	0.85	0.2	0.17	6.3	0.36	16	15.1	33.6	SM	19	20

Fig. 4 Probability density
function for R and S
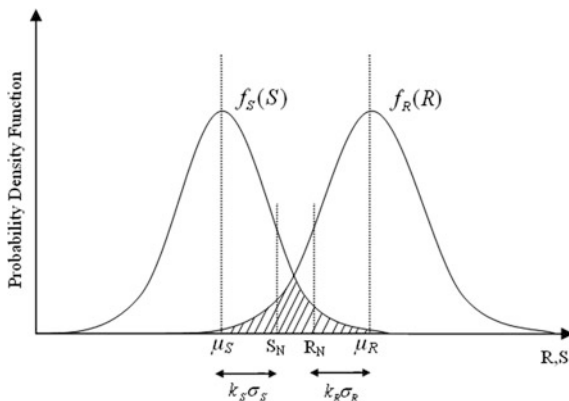
4.5 Proposed Equation for Probability of Liquefaction by Using the N-SPT and CSR

The two main parameters $(N_1)_{60cs}$ and CSR which indicate two groups of soil strength parameters and seismic parameters have been chosen for the investigation of potential liquefaction. To express the equation, the probable analysis will be considered for every borehole. This analysis begins with a reliability index calculation and continues by specifying parameters such as the probability of liquefaction, CRR, CSR and Fs. Eventually, these parameters end with nonlinear analysis and a regression coefficient that leads to the correlation regression equation.

The computer program is created based on this method. Records are entered into the program and calculations are done by comparing the data obtained in boreholes. Regression coefficients are calculated as part of the program based on this data. Regression analysis results are expressed by the following equation:

$$P_1 = \frac{1}{1 + \exp[-(13.7431 + 0.413\,(N_1)_{60\,CS} + 4.483\ln(CSR))]} \tag{13}$$

The correlation coefficient and mean error are 95 and 10%, respectively. Recent studies have been conducted to test the validity of the above equation. Hwang et al. considered the equation based on the non-liquefaction zone in the Chi-Chi earthquake. This equation is considered the basis of comparison in the above equation. The results of the comparison are summarized in Table 6.

The results presented in Table 6 reflect the close relationship between the presented equation and Hwang's equation. It can also be concluded that the data collected have both accuracy and a good match.

Two boreholes, including Chalus building and an office building on Azadi street, and the data related to them are selected for further comparison. Liquefaction possibility is shown in the Fig. 5 for two boreholes. These figures investigated and

Table 6 A comparison of the probability of liquefaction using the proposed and Hwang formula

Borehole number	$(N_1)_{60}$	CSR	Probability of liquefaction (%) reliability method	Probability of liquefaction (%) Hwang method	Error rate
1	13	0.2	81	73	0.1
2	21	0.2	23	20	0.13
3	17	0.2	54	46	0.15
4	12	0.18	82	70	0.15
5	12	0.17	77	66	0.14
6	7	0.19	97	92	0.05
7	19	0.19	27	28	0.04
8	5	0.24	99	98	0.01
9	20	0.2	26	26	0
10	14	0.2	76	67	0.12
11	8	0.22	96	94	0.12
12	20	0.22	32	30	0.03
13	9	0.21	94	91	0.03
14	22	0.21	19	18	0.05
15	18	0.23	56	52	0.07
16	13	0.19	77	69	0.1
17	15	0.15	38	34	0.11
18	21	0.19	16	17	0.06
9	22	0.19	12	13	0.8
20	16	0.2	50	53	0.06
The mean percentage of error					0.08

compared the liquefaction possibility based on the reliability index on and Hwang's approach. Figure 5 confirms a match between the two methods.

The comparison of a probable correlation is provided by Youd et al. for liquefaction potential assessment. They also extended the method used in this study and shown in the Fig. 6.

There is a collation of about 95% between the two methods.

In Fig. 7, the comparison of probable correlations for liquefaction potential assessment conducted in the current study and studies conducted by Seed et al. are shown.

Idriss and Boulanger suggested that the possible methods are damaged in liquefaction communication studies due to the lack of constant review of CRR and $(N_1)_{60cs}$ values.
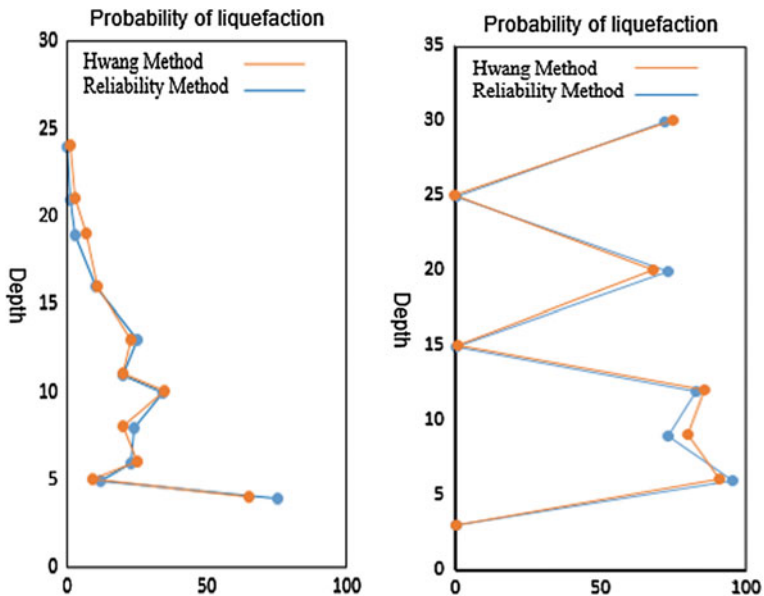
Fig. 5 A comparison of the proposed reliability method and Hwang procedure

Fig. 6 A comparison of the proposed method by Youd method
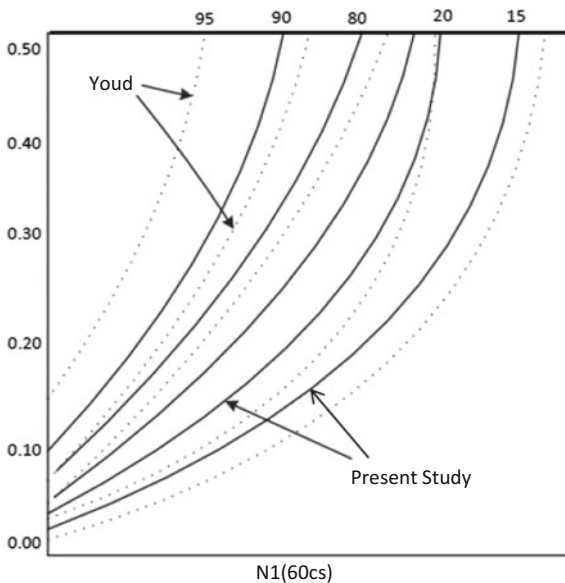
Fig. 7 A comparison of the proposed method by Seed method
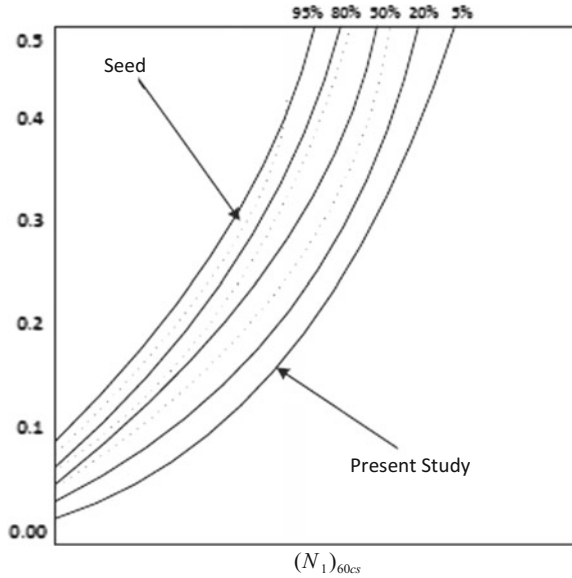
4.6 Potential for Liquefaction Incidence and Safety Factor

Reliability analysis not only proposes a logical framework for the consideration of uncertainties in load and resistance, but it also examines systematic procedures for selecting the Fs in special circumstances that may be related to it. The outstanding benefits of the reliability theory in the study of liquefaction potential allow Fs to be used in the quantitative analysis of liquefaction probability. The probability of liquefaction for the Fs related to the studied records is calculated and is shown in the Fig. 8.

Regression analysis results are obtained from the Eq. 14 for the relationship between P_L and F_S:

$$P_L = \frac{1}{1 + (F_S/0.783)^{6.63}} \tag{14}$$

The obtained correlation coefficient of 0.887 shows an acceptable relationship between the data and the used methods. According to the Fig. 8 and results of the Eq. 14, a maximum safety factor of 2.2 can be seen when the probability of liquefaction approaches zero. This case represents a non-economic design in engineering. A safety factor between 1 and 1.5, however, shows the probability of liquefaction according to computations. If the probability of liquefaction is less than 15%, liquefaction incidence is improbable, and this is equivalent to a safety factor of 1.15.
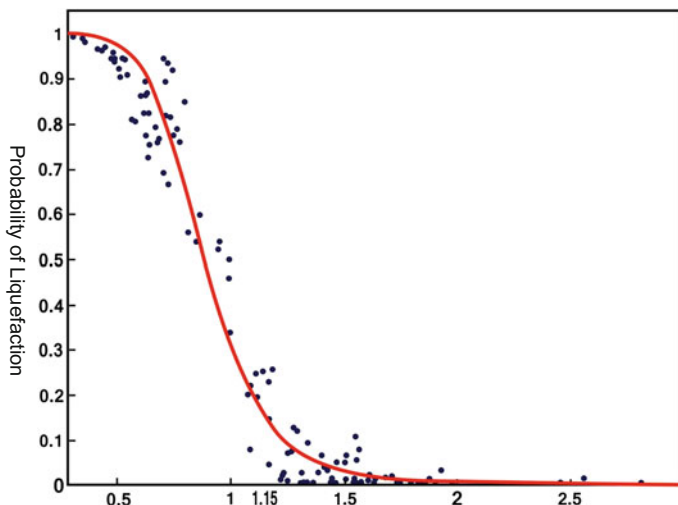
Fig. 8 Chart of the probability of liquefaction variation with a factor of safety

5 Conclusion

In this study, information is collected about boreholes in the city of Chalus, Iran. The data is used by the selected model to achieve the liquefaction potential in different layers. Surveys are carried out based on the genetic algorithm process and using the first-order, second-moment procedure to check reliability through process analysis and optimization. The study is considered a logical framework for liquefaction assessment that can be utilized as a practical procedure in geotechnical engineering. Based on the relationships used in this research, the liquefaction potential can be directly estimated by calculating P_L, CSR and, $(N_1)_{60cs}$ and it is possible that the mean error is less than 10%. The greatest advantage of the assumed relationship is the relationship between the probability of liquefaction and the safety factor. The decision can be made based on the risk of liquefaction when the measured values are close together. This case is very important for geotechnical engineering that uses normal methods to assess liquefaction. A high-safety factor against liquefaction does not always mean there is a safe mode analysis of reliability. The final evaluation should be done based on the values obtained from the liquefaction probability and reliability analysis.

The judgment criteria are based on the percentage of probability of liquefaction and control of errors in practical studies that should be considered. This algorithm can be allocated elsewhere, but its application is not related to the study area. The results achieved for the probability of liquefaction are compared with results obtained by other researchers; in some cases, there is a good versatility, but results are different in others. The results show the efficiency of the method used in this study. With regard to the relationship between CSR and the probability of

liquefaction and $(N_1)_{60cs}$, the probability of liquefaction can be calculated with an average error of less than 10% towards the practical considerations.

References

1. Zahmatkesh, A., Choobbasti, A.J.: Calibration of an advanced constitutive model for Babolsar sand accompanied by liquefaction analysis. J. Earthq. Eng. **21**, 679–699 (2016)
2. Ardeshiri-Lajimi, S., Yazdani, M., Assadi Langroudi, A.: A Study on the liquefaction risk in seismic design of foundations. Geomech. Eng. **11**, 805–820 (2016)
3. Bán, Z., Katona, T.J., Mahler, A.: Comparison of empirical liquefaction potential evaluation methods. Pollack Periodica **11**, 55–66 (2016)
4. Maurer, B.W., Green, R.A., Cubrinovski, M., Bradley, B.A.: Evaluation of the liquefaction potential index for assessing liquefaction hazard in Christchurch, New Zealand. J. Geotech. Geoenviron. Eng. **140**, 04014032 (2014)
5. Jha, S.K.: Reliability Analysis of Soil Liquefaction using Semi Anallytical and Numerical Method (FEM) (2013)
6. Boulanger, R.W., Idriss, I.: Probabilistic standard penetration test–based liquefaction–triggering procedure. J. Geotech. Geoenviron. Eng. **138**, 1185–1195 (2012)
7. Hwang, J.-H., Yang, C.-W., Juang, D.: A practical reliability-based method for assessing soil liquefaction potential. Soil Dyn. Earthq. Eng. **24**, 761–770 (2004)
8. Cetin, K.O., Seed, R.B., Der Kiureghian, A., Tokimatsu, K., Harder Jr., L.F., Kayen, R.E., et al.: Standard penetration test-based probabilistic and deterministic assessment of seismic soil liquefaction potential. J. Geotech. Geoenviron. Eng. **130**, 1314–1340 (2004)
9. Boulanger, R.W., Idriss, I.M.: Evaluating the Potential for Liquefaction or Cyclic Failure of Silts and Clays. Citeseer, New Jersey (2004)
10. Youd, T., Idriss, I., Andrus, R.D., Arango, I., Castro, G., Christian, J.T., et al.: Liquefaction resistance of soils: summary report from the 1996 NCEER and 1998 NCEER/NSF workshops on evaluation of liquefaction resistance of soils. J. Geotech. Geoenviron. Eng. **127**, 817–833 (2001)
11. Seed, H.B., Idriss, I., Arango, I.: Evaluation of liquefaction potential using field performance data. J. Geotech. Eng. **109**, 458–482 (1983)
12. Shibata, K., Ishihara, S.: Initial 87Sr/86Sr ratios of plutonic rocks from Japan. Contrib. Miner. Petrol. **70**, 381–390 (1979)
13. Hwang, J.-H., Chen, C.-H., Juang, C.H.: Liquefaction hazard analysis: a fully probabilistic method. In: Proceedings of the Sessions of the Geo-Frontiers 2005 Congress (2005)
14. Juang, C.H., Fang, S.Y., Khor, E.H.: First-order reliability method for probabilistic liquefaction triggering analysis using CPT. J. Geotech. Geoenviron. Eng. **132**, 337–350 (2006)
15. Juang, C.H., Fang, S.Y., Tang, W.H., Khor, E.H., Kung, G.T.-C., Zhang, J.: Evaluating model uncertainty of an SPT-based simplified method for reliability analysis for probability of liquefaction. Soils Found. **49**, 135–152 (2009)
16. Jha, S.K., Suzuki, K.: Reliability analysis of soil liquefaction based on standard penetration test. Comput. Geotech. **36**, 589–596 (2009)
17. Hwang, J.-H., Yang, C.-W.: Verification of critical cyclic strength curve by Taiwan Chi-Chi earthquake data. Soil Dyn. Earthq. Eng. **21**, 237–257 (2001)
18. Cammarata, G., Fichera, A., Guglielmino, D.: Optimization of a liquefaction plant using genetic algorithms. Appl. Energy **68**, 19–29 (2001)
19. Juang, C.H., Ching, J., Luo, Z., Ku, C.-S.: New models for probability of liquefaction using standard penetration tests based on an updated database of case histories. Eng. Geol. **133**, 85–93 (2012)

20. Yaghmaei-Sabegh, S., Mohammad-Alizadeh, H.: Improvement of Iranian Seismic Design Code Considering the Near-Fault Effects. Int. J. Eng. Trans. C: Aspects **25**, 147 (2012)
21. Naghizadehrokni, M., Choobbasti, A.J., Naghizadehrokni, M.: Liquefaction maps in Babol City, Iran through probabilistic and deterministic approaches. Geoenvir. Disast. **5**(1) (2018)
22. Naghizade, M., Janalizade, A.: Estimate the potential of liquefaction in sandy soils with reliability method in Chalos city (2010)
23. Naghizadehrokni, M.: A developed procedure for predicting the risk of liquefaction: a case study of rasht city. Inter. J. GEOMATE (2017)
24. Choobbasti, A., Naghizaderokni, M., Naghizaderokni, M.: Reliability analysis of soil liquefaction based on standard penetration: a case study in Babol city. In 2015 International Conference on Sustainable Civil Engineering (ICSCE 2015) (2015)

Mechanical Properties of Timber Dried Using Radio Frequency–Vacuum System

A. W. Mohd-Jamil and A. R. Zairul

Abstract Radio frequency–vacuum (RFV) is an alternative technique to dry solid timbers. The method was demonstrated to be effective in drying large dimension planks. Experimental results proved that the method considerably reduced drying period and successfully dried timber with fewer defects. An assessment was conducted to evaluate the effect of RFV system on some mechanical properties of timber. The timbers were classified as difficult to dry and require great consideration against rapid drying. This article discusses the mechanical properties of refractory timbers dried using an RFV drying system. The modulus of rupture, modulus of elasticity, Janka hardness and specific gravity of a selected Malaysian hardwood were analysed. Test results showed that the modulus of rupture and modulus of elasticity of RFV specimens were lower than the conventional kiln-dried timbers. On the other hand, the Janka hardness of RFV specimens was slightly higher. Comparison with kiln-dried timbers suggested that RFV process had no adverse effect on the specific gravity.

Keywords Wood drying · Modulus of rupture · Janka hardness

1 Introduction

The conventional method of air drying of timber to achieve equilibrium moisture content is a time-consuming and uneconomical process. The rate of drying highly depends on the dimension of planks, timber species and the climatic condition of the environment. For example, it could take from several months to more than a year to dry a 25 mm by 100 mm cross-section timber to below 20% moisture content. Technically, the drying period will be much longer for higher density timbers. The months-long process produces uncertainty to the procurement schedule and increases the cost of inventory management.

A. W. Mohd-Jamil (✉) · A. R. Zairul
Forest Research Institute Malaysia, 52109 Kepong, Selangor, Malaysia
e-mail: mohdjamil@frim.gov.my

The kiln drying method is normally recommended to speed up the drying process. For example, timber boards of 25-mm thick can be kiln dried to 12% moisture content in a few weeks. However, even with the kiln drying system, most of the heavy hardwoods are considered as difficult to dry, which is also referred to as refractory timbers. These timbers require great consideration against rapid drying for minimum defects [1]. High-density timbers are prone to critical defects such as end-splitting and warping. Excessive drying defects on structural components could affect the integrity of the strength. Besides, such physical defects are certainly undesirable for architectural members, e.g. floor strips and staircase boards. Thus, in practice, refractory timbers of more than 30 mm thick are usually air dried.

Studies demonstrated that radio frequency–vacuum (RFV) can effectively dry refractory timbers of large dimensions. The RFV process heats timber using a high-frequency wave in a vacuum condition, where the boiling point of water is lower. In the vacuum state, water is vapourised at a relatively low temperature hence reduces the tendency of timber to split. The RFV method greatly reduced drying time to days or weeks depending on the permeability of the timber [2]. Timbers dried using RFV were reported with lower shrinkage, lower residual stress and dimensionally more stable [3]. However, due to the uneven heating temperature, RFV drying showed a substantial variation in the final moisture content [4]. Thus, the imbalance of moisture content will directly influence the strength and stiffness of the timber. Besides, some studies reported that RFV drying slightly reduced the strength properties of the timber [5, 6].

Radio frequency–vacuum drying is a potential technique to dry large sized timbers. The system was demonstrated to be a successful and practical approach to drying timbers with considerably fewer defects. This study focused on the mechanical properties of timbers dried using an RFV drying system. The discussion highlights the modulus of rupture, modulus of elasticity, Janka hardness and specific gravity of a selected refractory timber of Malaysian hardwood species.

2 Materials and Methods

Timbers of kekatong (*Cynometra* spp.) were selected as samples. Kekatong is classified as heavy hardwood with air-dry density ranging from 880 to 1155 kg/m^3. The timber dries very slowly and prone to end-splitting and warping. Air drying of 15 mm $\times$ 40 mm boards took 3–5 months to reach approximately 17% moisture content. The timber is suitable for heavy constructional applications, heavy duty flooring and railway sleepers. Kekatong is classified as a refractory timber and requires considerable attention against drying defects. Kekatong planks were cut into test samples of 30 mm by 120 mm cross-section and 1600 mm long.

2.1 Radio Frequency–Vacuum Drying

The process of drying the timbers was performed using a radio frequency–vacuum (RFV) dryer with a capacity of 0.54 m^3. The system comprised of a drying chamber, a radio-frequency generator (the frequency was set at 6.7 MHz with 6.0 kW maximum output), a vacuum pump, a condenser and a chiller. The samples were arranged in the chamber without stickers and flanked between aluminium plates as illustrated in Fig. 1. The pressure and heating temperature were set to 50 Torr and 40 °C respectively. Drying process took approximately 14 days to achieve 12% moisture content.

2.2 Static Bending Test

Test was conducted based on BS 373 [7] method. The nominal size of the specimens was 20 mm × 20 mm × 300 mm. Force was applied based on three-point loading method with a span of 280 mm. A constant loading speed was applied at 6.6 mm min^{-1}. The arrangement of static bending test is illustrated in Fig. 2. Modulus of elasticity (MOE) and modulus of rupture (MOR) were calculated using the following formulae:

Fig. 1 Stacking of the timber samples in the RFV chamber
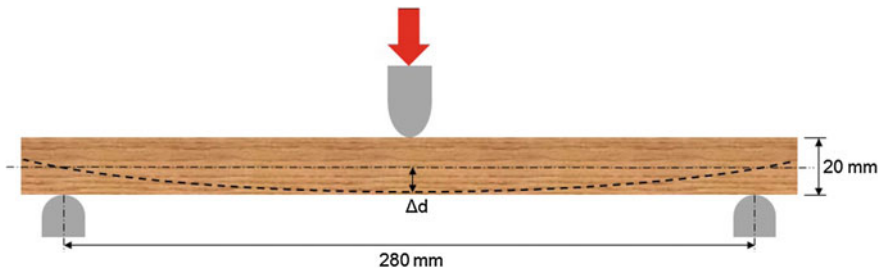
Fig. 2 Arrangement for static bending test

$$\text{MOE} = \Delta F/\Delta d \times s^3/4wt^3 \tag{1}$$

$$\text{MOR} = 3F_{\max}s/2wt^2 \tag{2}$$

where $\Delta F/\Delta d$ is the slope of the graph (N mm^{-1}), s is the bending span (mm), w is the width of the specimen (mm), t is the thickness of the specimen (mm) and $F_{\max}$ is the maximum bending load (N).

2.3 Janka Hardness Test

The test was conducted using the specimens of static bending test. A constant force of 6.35 mm min^{-1} was applied through a steel bar of a semi-circular end with a diameter of 11.28 mm. The Janka hardness value of a specimen was the resultant load at 5.64 mm penetration. The arrangement of Janka hardness test is illustrated in Fig. 3.
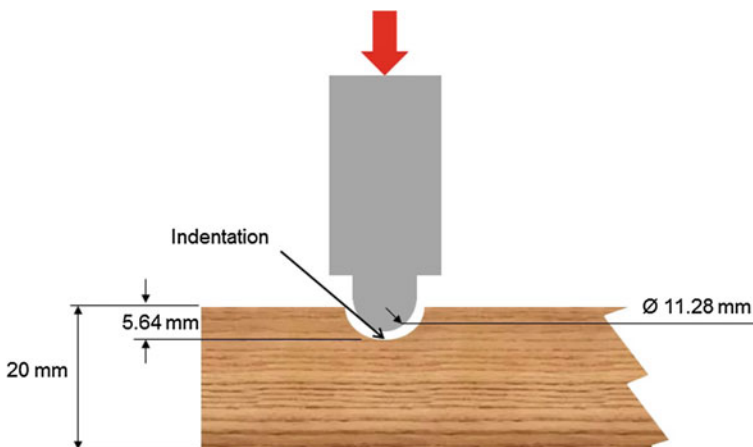
Fig. 3 Arrangement for Janka hardness test

2.4 Specific Gravity

The nominal size of the specimens was 20 mm × 20 mm × 60 mm. The specific gravity (SG) was calculated using the formula:

$$SG = m_{od}/V\rho_{H_2O} \tag{3}$$

where m_{od} is the oven-dried mass of the specimen (kg), V is the volume of the specimen at test (m³) and ρ_{H_2O} is the density of water (kg m⁻³).

3 Results and Discussion

The mechanical properties of radio frequency–vacuum (RFV) specimens were compared with standard kiln-dried (KD) specimens. The test results are shown in Table 1. All values were measured at an approximately 14% moisture content. Slight differences in mechanical properties between RFV and KD specimens were observed. KD specimens were considered as control specimens indicating a common method for drying of timber. Based on the values of KD specimens, the MOR and MOE of RFV were 3 and 2% lower respectively. On the other hand, the Janka hardness of RFV was 2% higher. From the engineering perspective, the differences of MOR, MOE and hardness between RFV and KD specimens were trivial. In theory, a minor variation of mechanical properties is expected even among specimens of the same origin.

A graph of MOR versus SG indicating modes of fracture is shown in Fig. 4. Generally, modes of fracture in the static bending test were observed as splintering, cross-grained, simple tension and brash (Fig. 5). The graph evidently showed that lowest strength specimens failed by brash. Straight-grained specimens indicated by splintering fracture gave high MOR values.

Observation of the modes of fracture also explained the differences of MOR and MOE between RFV and KD specimens. Two RFV specimens failed by brash plus

Table 1 Mechanical properties of RFV and KD samples

	Radio frequency–vacuum		Kiln dry	
	Mean	Standard deviation	Mean	Standard deviation
Modulus of rupture (N mm⁻¹)	154.5	32.0	159.2	21.1
Modulus of elasticity (N mm⁻¹)	16,915	2874	17,194	1717
Janka hardness (kN)	10.8	1.2	10.6	1.1
Specific gravity	0.897	0.026	0.874	0.033
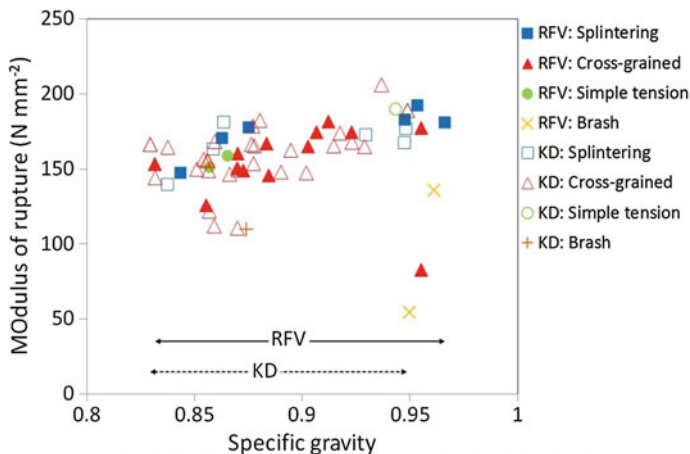
Fig. 4 Graph of MOR versus SG and modes of failure
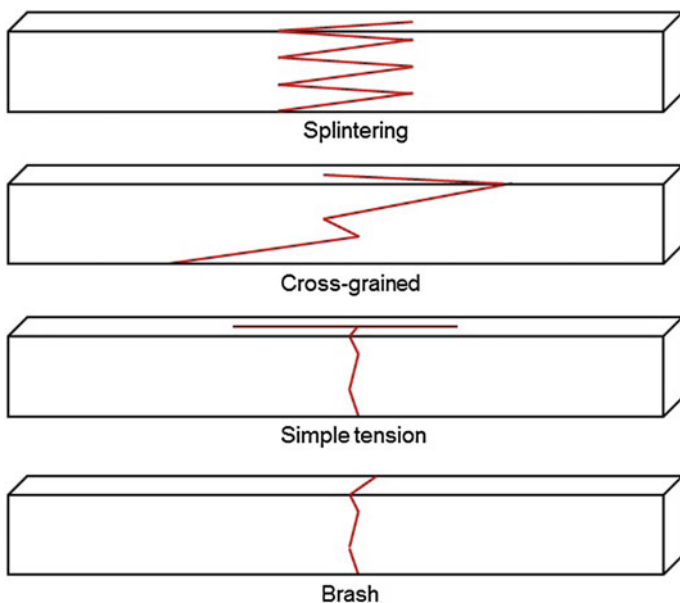
Fig. 5 Facies of static bending test failure (bottom view)

one cross-grained specimen resulted in very low MOR values despite having a comparatively high SG. Two values of the MOR were far-off below the average. The values gave outlying results which pinned down the means of MOR and MOE. Consequently, RFV specimens showed higher SD of MOR and MOE. Statistically,

high standard deviation indicated that the mechanical properties of RFV specimens were distributed over a wider range of values.

Brittle characteristic due to the RFV procedure was not demonstrated in the present study. Brittle wood is characterised by an abrupt breakage across the grain without splinters. The defect is normally indicated by brash fracture at maximum stress in the static bending test. Although a few specimens failed by brash, the influence of the RFV to the amount of brash failure was not significant.

The comparison of MOR, MOE, Janka hardness and specific gravity between RFV and KD specimens are presented in cumulative distribution function in Fig. 6a–d. The MOR and MOE of RFV specimens were slightly lower than KD despite having higher SG. The values of Janka hardness between RFV and KD specimens were comparable and showed a uniform distribution. The SG distribution graph was consistent with the higher RFV values than KD.

The average SG of RFV samples was 3% higher than the SG of KD specimens. The values of SG of RFV specimens were in the range of 0.832–0.966, whereas the values of SG of KD specimens were in the range of 0.829–0.949. Though the percentage of difference was observed, from a scientific point of view, this variation is not significant. In theory, the specific gravity of timber should be equivalent regardless of the duration of drying since it is measured at practically zero moisture content. Nevertheless, variations of specific gravity were normally observed even from the same sample. Mohd-Jamil and Khairul [8] demonstrated that the specific gravity of timber in a 15-year-old tropical tree varied from 0.418 to 0.488 along the height. Thus, the comparable SGs of the present study indicated that RFV process
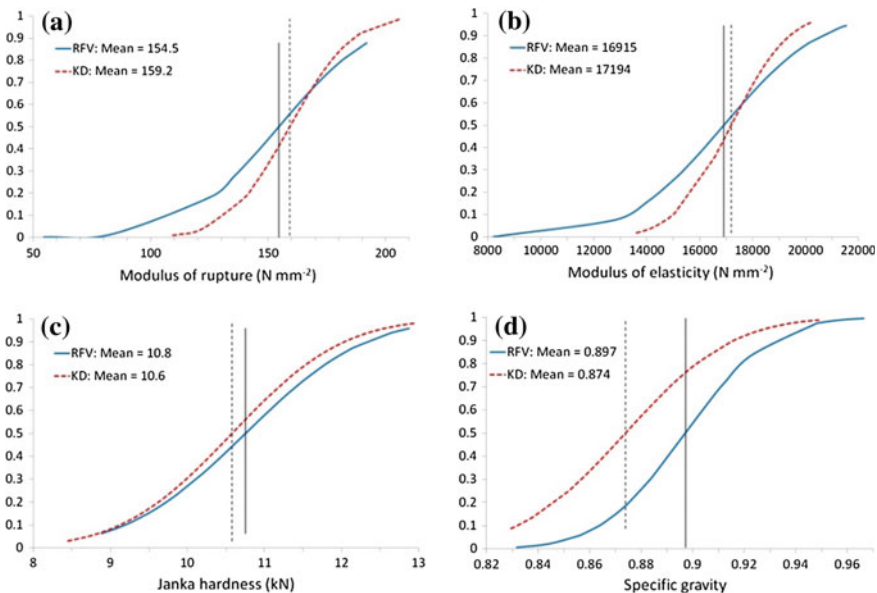
Fig. 6 Cumulative distributions of MOR, MOE, Janka hardness and SG

has no adverse effect on the cellular structures of the timber. However, the hypothesis requires analyses at a microscopic level hence it is unable to be confirmed at the moment.

The present tests were conducted using a selected hardwood species. Therefore, the results may be not the same for other species. Besides, the evaluation was limited to only four properties, i.e. MOR, MOE, Janka hardness and SG. Additional tests of other properties such as compression parallel to the grain, compression perpendicular to the grain, shear, tensile, etc., are essential and recommended for future study.

4 Conclusions

The MOR and MOE of RFV specimens were 3 and 2% lower than KD specimens respectively. On the other hand, Janka hardness of RFV was 2% higher. From the engineering perspective, the differences of MOR, MOE and hardness between RFV and KD specimens were trivial. The average SG of RFV samples was 3% higher than the SG of KD specimens.

References

1. Grewal, G.S.: Air Seasoning Properties of Some Malaysian Timbers, Trade Leaflet No. 41. Malaysian Timber Industry Board, Kuala Lumpur (1979)
2. Resch, H.: High-frequency electric current for drying of wood—historical perspectives. Maderas Ciencia Tecnologia **8**, 67–82 (2006)
3. Harris, R.A.: Dimensional stability of red oak and eastern white pine dried by radiofrequency/vacuum and conventional drying process. For. Prod. J. **38**, 25–26 (1988)
4. Lamb, F.M., Wengert, E.M.: Comparison of lumber drying quality between two vacuum drying systems and a conventional predryer and dry kiln system. Proc. Vac. Drying Wood **93**, 251–256 (1993)
5. Wengert, E.M., Lamb, F.M.: A comparison of conventional and new drying methods. Joint production division meetings of the National Association of Furniture Manufacturers and the Southern Furniture Manufacturers Association (1982)
6. Taniguchi, Y., Nishio, S.: High frequency electric power-vacuum drying of wood IV. Comparison of physical and mechanical properties of lumber dried by several drying methods. J. Jpn. Wood Res. Soc. **37**, 405–414 (1991)
7. BSI (British Standards Institution). BS 373: Methods of Testing Small Clear Specimens of Timber. BSI, London (1957)
8. Mohd-Jamil, A.W., Khairul, M.: Variations of mechanical properties in plantation timbers of jelutong (Dyera costulata) and khaya (Khaya ivorensis) along the radial and vertical positions. J. Trop. For. Sci. **29**, 114–120 (2017)

A Parametric Study and Design Equation of Reinforced Concrete Deep Beams Subjected to Elevated Temperature

Hend S. Zayan, Jamal A. Farhan, Akram S. Mahmoud and Juma'a A. AL-Somaydaii

Abstract Reinforced concrete may be subjected to temperature due to climatic change or fire. However, deep beams can be exposed to various temperatures. This study will be treated and focused on the criteria of thermal analysis of deep beams. Many lectures are verified by nonlinear finite element method. Also, a parametric study is carried out to investigate the effect of some factors on the behavior of deep beams exposed to elevated temperature. The models are analyzed by the finite element method using (ANSYS) package. These factors are temperature, concrete compressive strength, and the shear span-to-effective depth (a/d) ratio. The results show that when the temperature increases with constant compressive strength and (a/d) ratio, the load capacity and deflection at failure are decreased, while when compressive strength increased, the load capacity and deflection at failure are increased for the same (a/d) ratio and the same temperature. Finally, the results show that the load capacity decreases and deflection increases with an increase in (a/d) ratio for the same temperature and same compressive strength. In addition to the parametric study, the proposed model to predict the strength of the deep beams exposed to high temperature is derived using artificial neural network by MATLAB and SPSS facilities. The error (R) had been (0.99) and square value ($R^2 = 0.98$). This means that the model is efficient and the error is very small.

Keywords Deep beams · Elevated temperature · ANSYS · Parametric study Artificial neural networks

1 Introduction

The deep beam is a beam when effective span-to-depth ratio (a/d) is 4 or less as defined by ACI code [1, 2]. The Euro-International Concrete Committee defined deep beam if span length to hole depth (L/H) < 2 for simply supported beam and

H. S. Zayan (✉) · J. A. Farhan · A. S. Mahmoud · J. A. AL-Somaydaii
Civil Engineering Department, University of Anbar, Ramadi, Iraq
e-mail: areesakhs@gmail.com
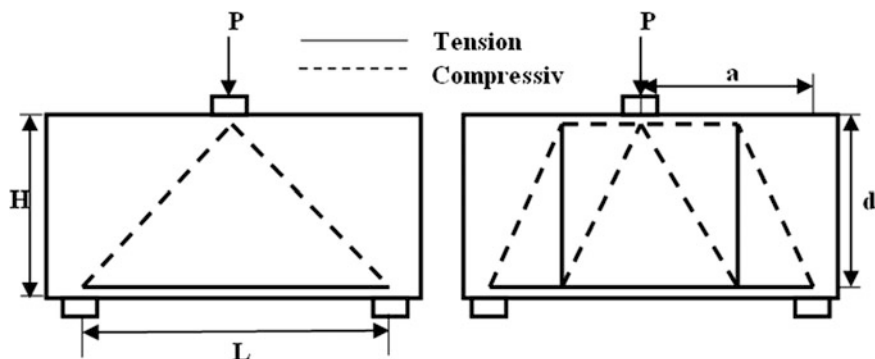
Fig. 1 Strut and Tie method details [5]

(*L/H*) < 2.5 for continuous beam [3], As shown in Fig. 1. Deep beam has various uses such as transfer deep girders, wall footing, foundation pile caps, bunkers, foundation beams, floor diaphragms, and shear walls. It fails usually by shear, there are two types of shear failure [4] (1-diagonal compression failure: occur nearly along the line joining the load point and the support point, 2-diagonal tension failure: occur by clean fracture near along the line joining support with the nearest loading point) as shown in Fig. 1.

High temperature has significant effects on behavior and strength of deep beams. When temperature increases, in ultimate load and failure deflection are clearly decreasing [6–8]. In this paper, the deep beam models were analyzed by finite element analysis using ANSYS package, then the parametric study was carried out for the models (i.e., some factors are changed with respect to others) where three different factors are varying. The first one is temperature (*T*), and seven temperatures are considered (20, 100, 300, and 500) °C. The second factor is compressive strength (f_c'), and five strengths are considered (30, 50, and 70) MPa. The third factor is load span-to-length (*a/d*) ratio, and three values are considered (1, 2, and 3). One hundred and five (105) samples are investigated to evaluate these changes.

2 Modeling

The model dimensions were the width (*b* = 100) mm, height (h = 225) mm, and length varied as (750, 1150, and 1550) mm, for *a/d* ratios (1, 2, and 3) respectively. The concrete cover was (25) mm in all specimens. The reinforcement configurations are the same for all the samples as shown in Fig. 2. Tables 1 and 2 show the details of the analyzed samples. Their results showed clearly the deterioration in properties and ultimate load with high temperature. Theoretical model is adequate by comparing it with experimental works from the literature research [9].
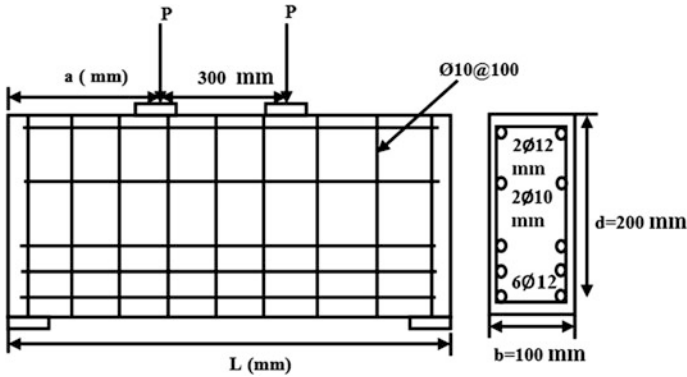
Fig. 2 Deep beam specimen details

Table 1 Sample properties

Structural component	Open shear transfer coefficient	Closed shear transfer coefficient	Compressive strength (MPa)	Yield stress (MPa)	Young's modulus (MPa)	Tangent modulus (MPa)	Area (mm^2)
Symbols	β_t	β_c	f_c'	f_y	E	E_T	BA
Concrete	0.4	0.9	30	–	21,153	–	–
			50		30,836		
			70		39,574		
Steel reinforcement (Ø 12 mm)	–	–	–	838	195,150	19,515	113
Steel reinforcement (Ø 10 mm)	–	–	–	408	204,850	20,485	78.5

Table 2 Thermal properties of tested specimen

Structural component	Symbol	$T = 100$ °C	$T = 300$ °C	$T = 500$ °C
Concrete	K	1.765	1.361	1.042
	C	900	1050	1100
	ρ	2331	2284	2237
Steel reinforcement	K	60	60	60
	C	500	500	500
	ρ	7850	7850	7850

3   Parametric Study of Elevated Temperature Effect

Seven stages in temperature are made in this study to evaluate the concrete behavior under different degrees of temperature for each compressive strength and (*a*/*d*) ratio. These temperatures are (20, 100, 300, and 500) °C. From Figs. 3, 4, 5, 6, 7, 8, 9, 10, and 11, the results show that by increasing the temperature for the samples, the load capacity and deflection at failure are decreased. Each curve shows the load–deflection relation for constant compressive strength and (*a*/*d*) ratio. Also, from these curves, it can be noticed that for *a*/*d* = 1, curves are not distinguished like curves with *a*/*d* = 3. That means with increasing length, deep beam samples will be more clear in the behavior [10, 11].

The sample of specimens included as DT (temp. *a*/*d*), where DT means deep beam exposed to elevated temperature, (temp.) is the value of temperature (°C), (compressive strength of concrete (MPa), (*a*/*d*) shear span-to-effect depth ratio. The mark (#) means various values of a parameter which is studied.

Fig. 3 Load–deflection behavior for DT(#).30.1
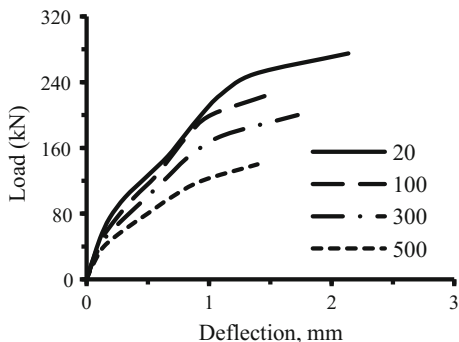
Fig. 4 Load–deflection behavior for DT(#).30.2
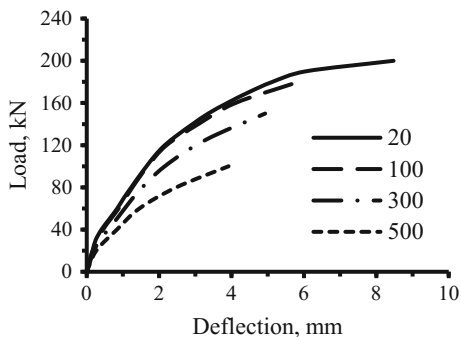
Fig. 5 Load–deflection behavior for DT(#).30.3
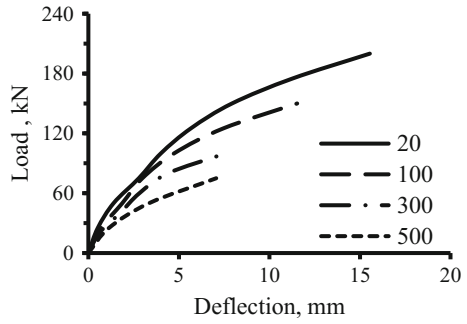
Fig. 6 Load–deflection behavior for DT(#).50.1
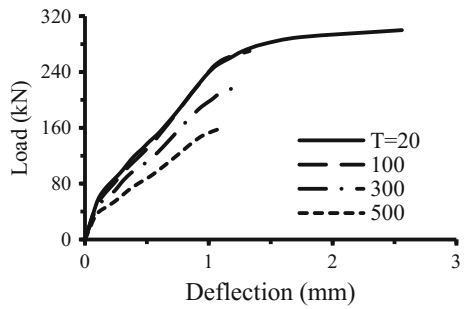
Fig. 7 Load–deflection behavior for DT(#).50.2
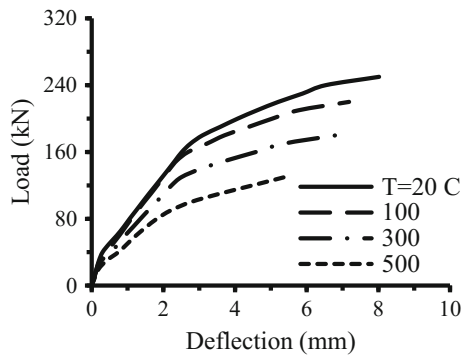
For specimens having concrete compressive strength more than 40 MPa, the behavior of samples with $a/d = 1$ will be more distinguished just like $a/d = 2$ and $a/d = 3$. This means that for high-strength concrete, the effect of high temperature had less effect on concrete, not as for normal concrete.

Fig. 8 Load–deflection
behavior for DT(#).50.3
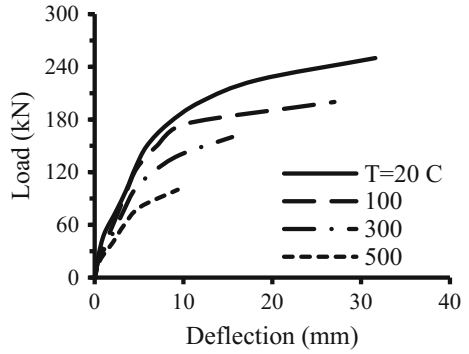
Fig. 9 Load–deflection
behavior for DT(#).70.1
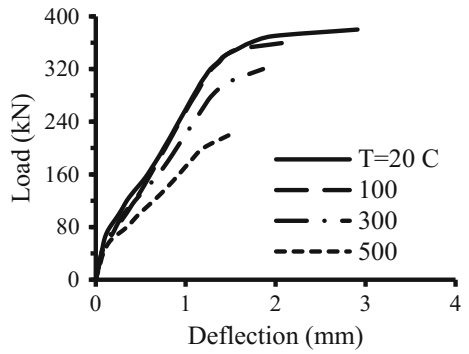
Fig. 10 Load–deflection
behavior for DT(#).70.2
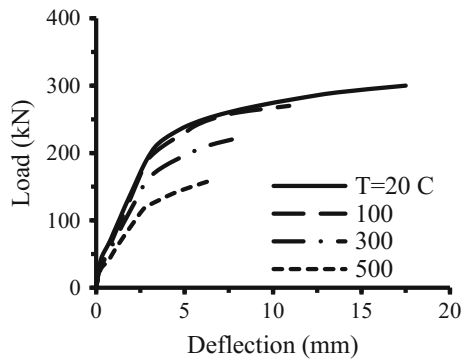
Fig. 11 Load–deflection behavior for DT(#).70.3
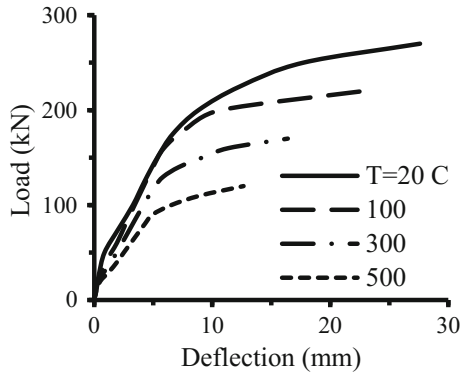
4 Effect of Concrete Compressive Strength

In this study, five types of models are considered to evaluate the behavior of concrete with respect to different temperature strengths. The five strengths are (30, 50, and 70) MPa. They are selected to show the behavior of normal, moderate, and high-strength concrete. Figures 12, 13, 14, 15, 16, 17, 18, 19 and 20 show this behavior. The results show that by increasing the compressive strength for the samples, the load capacity and deflection at failure are increased with the same (a/d) ratio and same temperature (Figs. 21, 22 and 23).

For ($a/d = 1$) and temperature (20) °C, the increase of compressive strength about (3.5) times leads to an increase in ultimate load about (1.90) times. But for temperature (250) °C, the ultimate load increases to about (2.61) times. And for a temperature of (500) °C, the ultimate load increases to about (2.2) times.

That means by increasing the temperature, the percentage of ultimate load increases and then decreases as shown in Fig. 24. Because, at first, the water in the open voids is drying, so the disjoining pressure is going away and increase the strength of the concrete that leads to the increase in the ultimate load [8, 12–14]. Then with temperature raises, the water in closed voids is drying leading to thermal shrinkage and the strength decreases that reduces the ultimate load.

Fig. 12 Load–deflection behavior for DT20.(#).1
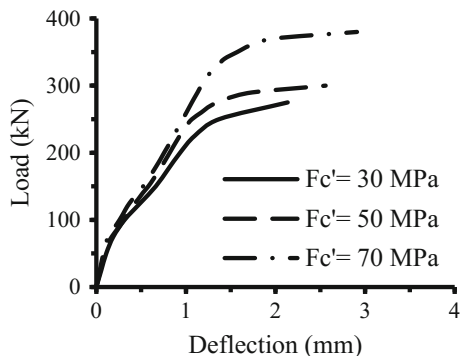
Fig. 13 Load–deflection
behavior for DT20.(#).2
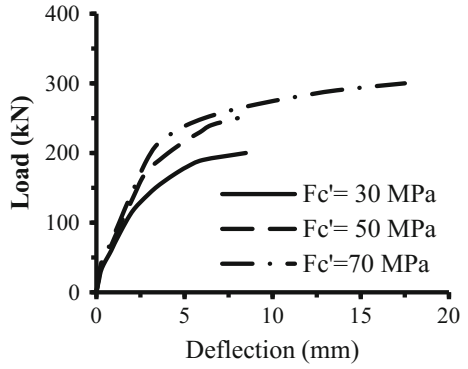
Fig. 14 Load–deflection
behavior for DT20.(#).3
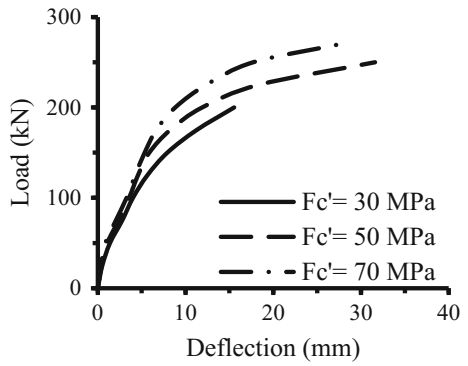
Fig. 15 Load–deflection
behavior for DT100.(#).1
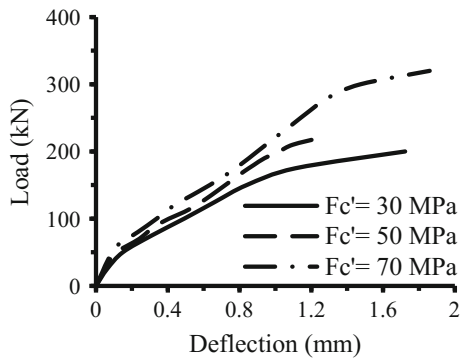
Fig. 16 Load–deflection behavior for DT100.(#).2
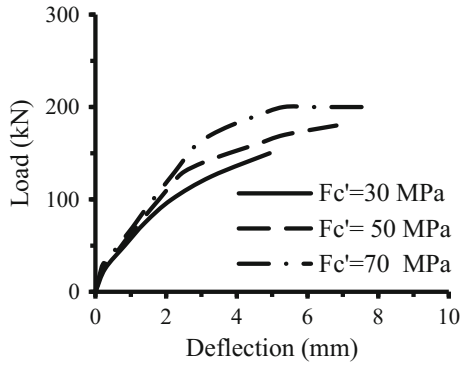
Fig. 17 Load–deflection behavior for DT100.(#).3
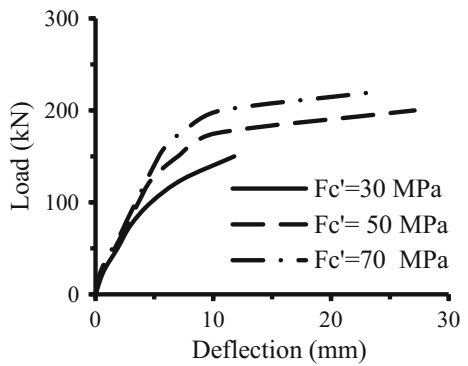
Fig. 18 Load–deflection behavior for DT300.(#).1
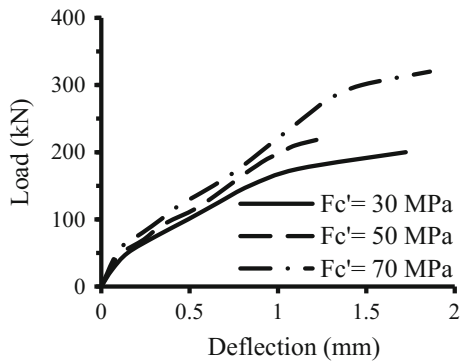
Fig. 19 Load–deflection behavior for DT300.(#).2
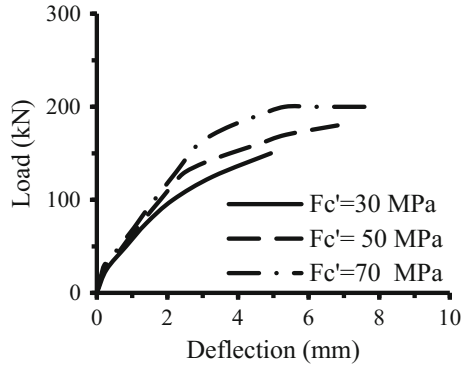
Fig. 20 Load–deflection behavior for DT300.(#).3
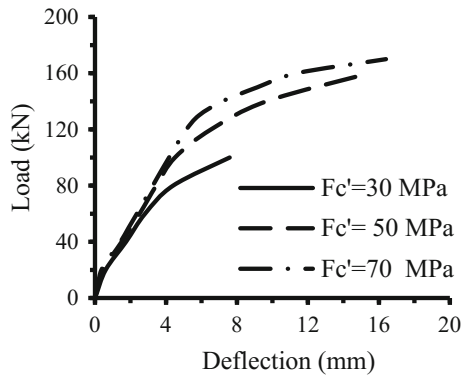
Fig. 21 Load–deflection behavior for DT500.(#).1
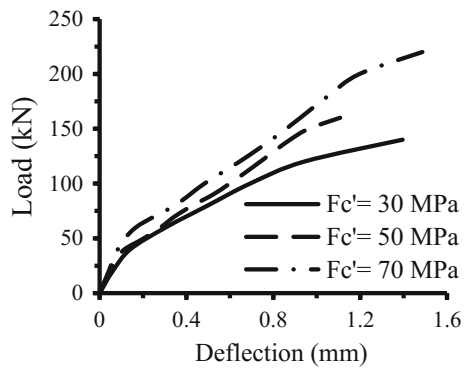
Fig. 22 Load–deflection behavior for DT500.(#).2
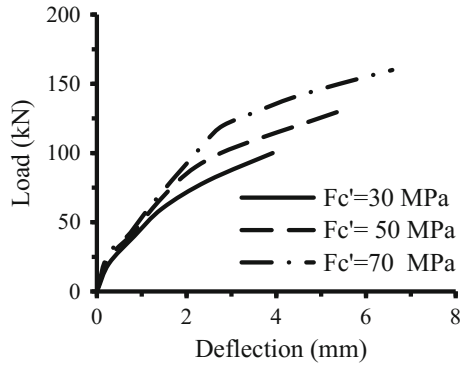
Fig. 23 Load–deflection behavior for DT500.(#).3
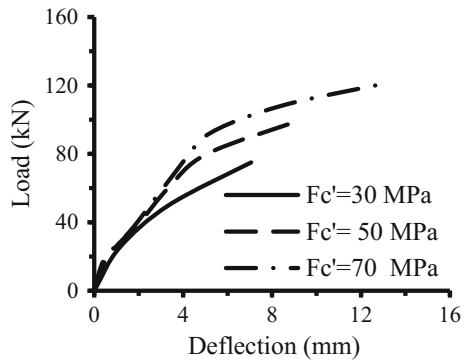
Fig. 24 Ultimate load percentage with temperature
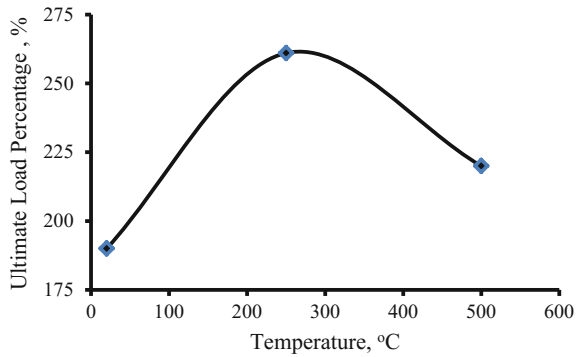
5 Effect of Length to Effective Depth Ratio (*a/d*)

For this study, three types of models are evaluated for analyzing the behavior of deep beams for different (*a/d*) ratios. These ratios are (1, 2, and 3). Figures 25, 26, and 27, show that the load capacity decreases and deflection at failure increases with the increase in the (*a/d*) ratio. This means that deep beams behave like normal beams with increasing in length. In addition, increase in midspan deflection can be noticed when the length increases [5].
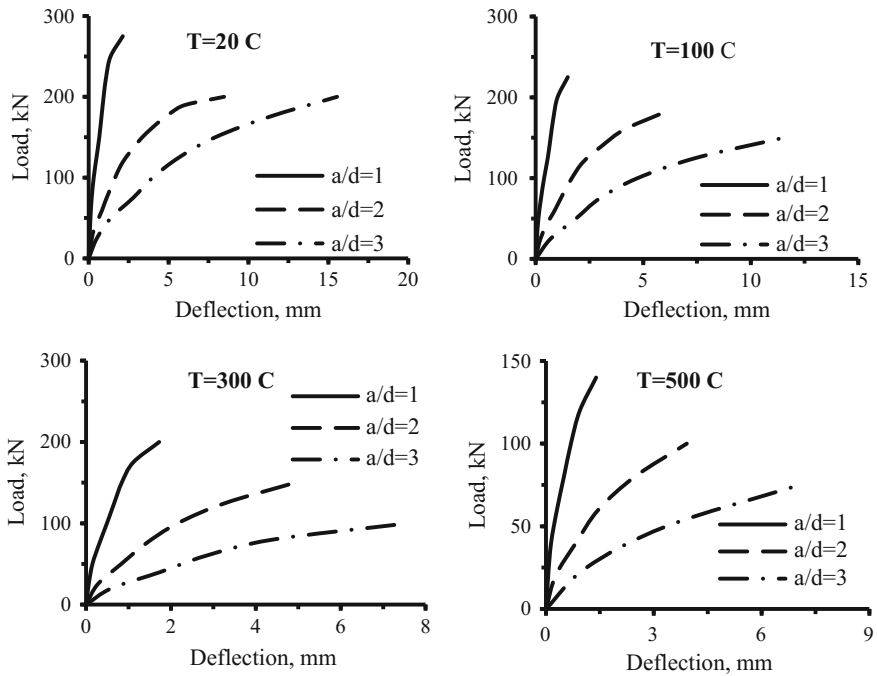
Fig. 25 Load–deflection behavior for deep beams have f_c' = 30 MPa
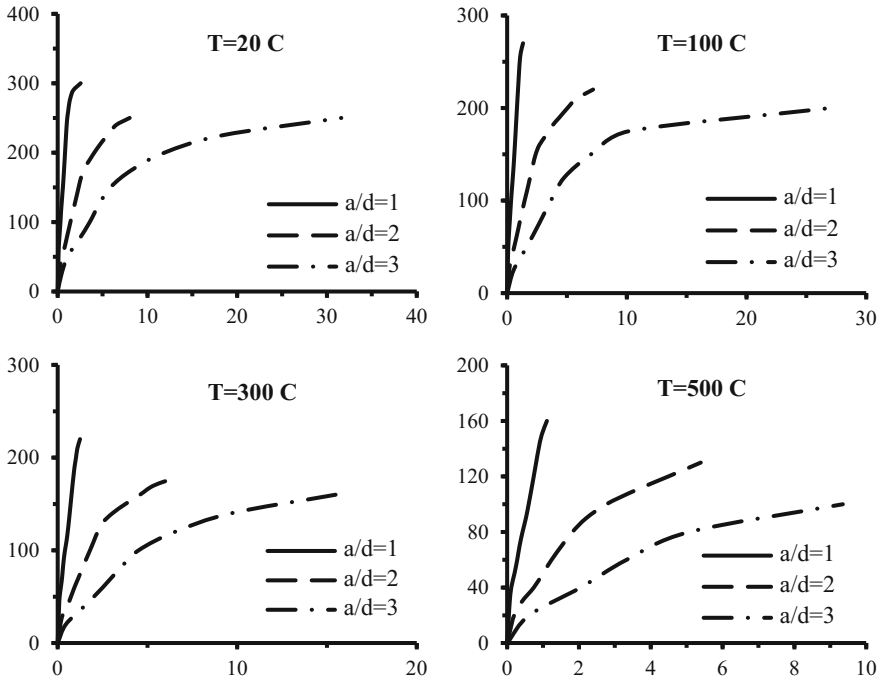
Fig. 26 Load–deflection behavior for deep beams have $f_c' = 50$ MPa

6 Artificial Neural Networks by MATLAB and SPSS for the Proposed Model

6.1 Introduction

Due to the difficulty of analytical solutions for thermal analysis of concrete members, the results of parametric study are simulated using artificial neural networks (ANNs) to evaluate the proposed model that can be used to estimate the ultimate load of R.C. deep beams subjected to elevated temperature. The ANNs model is worked using MATLAB and SPSS facilities.

6.2 Neural Network by MATLAB of Proposed Model

In order to find the percentage of error and the efficiency of the proposed model, the results are divided into input matrix and output matrix, then dealing with neural network (ANN) with training (80%), testing (10%), and validation (10%). The error (R) was (0.99) and the square value was ($R^2 = 0.98$). So, the model is efficient and
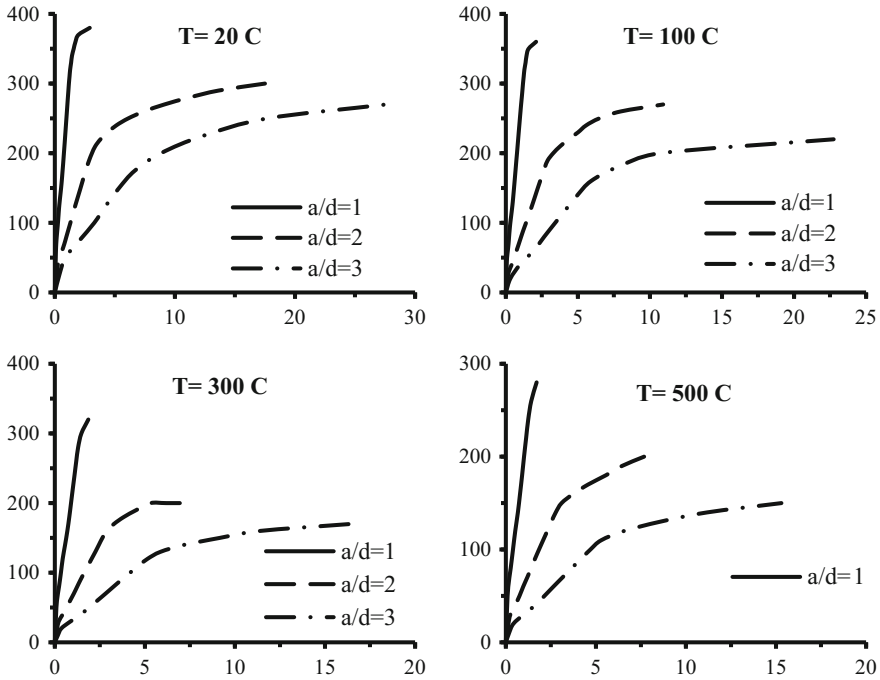
Fig. 27 Load–deflection behavior for deep beams have $f_c' = 70$ MPa

the error is very small. So that, the models from the parametric study can be used for making the relation curves between inputs (temperature, compressive strength, and *a/d* ratio) and output (ultimate load) [15–18]. Figures 28 and 29 show neural network results.

6.3 Proposed Model of R.C. Deep Beams Including Temperature Effect

The results of the parametric study for (105) specimens have been given as input in SPSS Skelton, eight properties that were changed in the specimens were taken and analyzed in neural networks simulations. The output window shows the results for the models with different details as well as the error percentage, and the weights (this is the most important in this study). From the weights, the equation for the ultimate load can be written. The figures show the results as shown in Tables 3, 4, 5, and 6; also, the Figs. (30, 31, and 32). All these results are illustrated and summarized the validated data for a proposed model of this study.
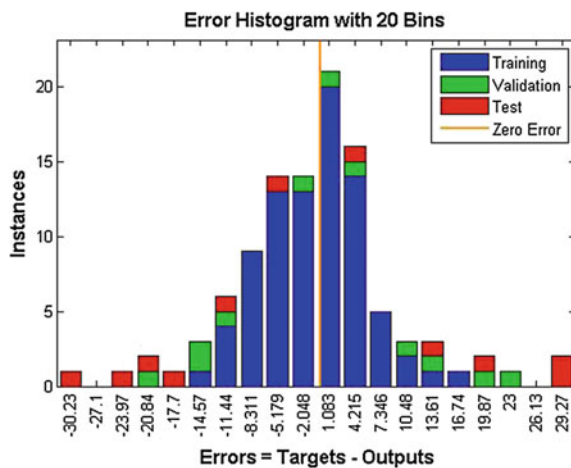
Fig. 28 Error histogram for the models
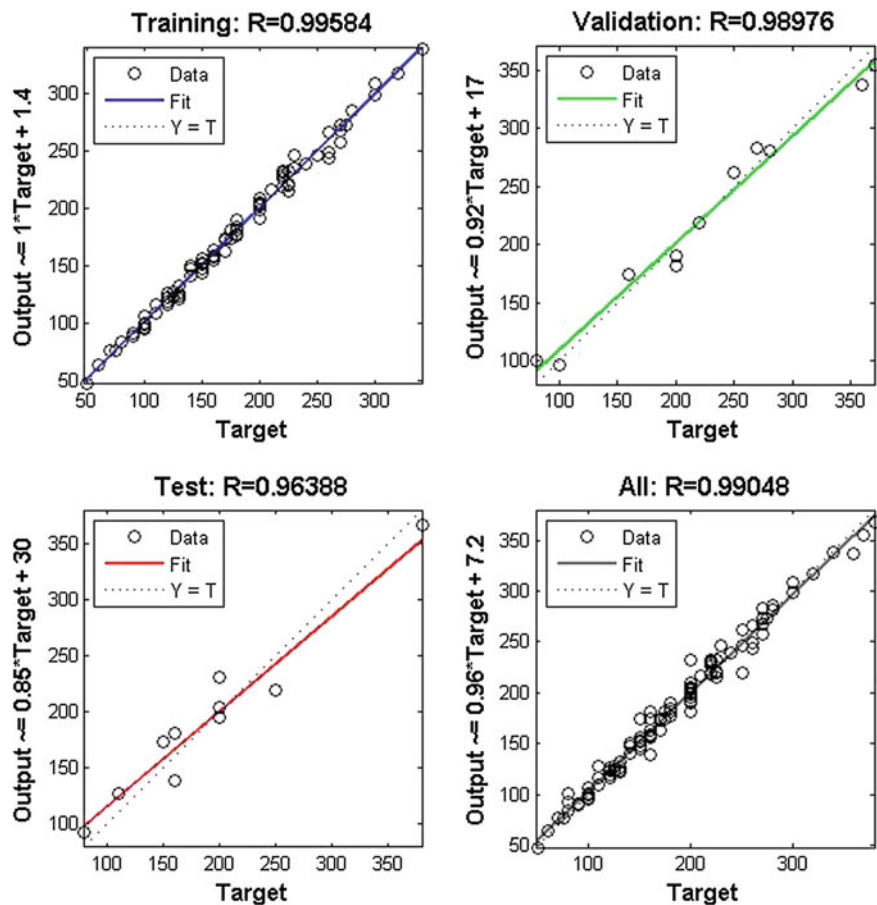
Fig. 29 Regression for the models

Table 3 Case processing summary

		N	Percent
Sample	Training	78	74.3%
	Testing	17	16.2%
	Holdout	10	9.5%
Valid		105	105
Excluded		0	0
Total		105	105

Table 4 Model summary

Training	Sum of squares error	.613
	Relative error	.073
	Stopping rule used	1 consecutive step(s) with no decrease in error[a]
	Training time	0:00:00.02
Testing	Sum of squares error	.106
	Relative error	.079
Holdout	Relative error	.380

Dependent variable: Pu

[a]Error computations are based on the testing sample

Table 5 Independent variable importance

	Importance	Normalized importance (%)
f_c	.098	29.1
E_c	.105	31.0
f_t	.338	100.0
a_d	.107	31.8
T	.228	67.5
E_{sl}	.096	28.4
E_{sv}	.027	8.0

The most important result is the last figure that shows the skeleton of the modeling and the last table that shows the parameter weights that are given as input in the equation. The equation is

$$y = \frac{1}{1 + e^{-\theta_2 + w_7 \tan h(x)}} \tag{1}$$

where

$$x = \theta_1 + \sum_{n}^{i=1} w_i v_i \tag{2}$$

Table 6 Parameter estimates

Predictor		Predicted	
		Hidden layer 1	Output layer
		H (1:1)	Pu
Input layer	(Bias)	.232	
	f_c	.172	
	E_c	.182	
	f_t	−.641	
	a_d	.182	
	T	.359	
	E_{sl}	.170	
	E_{sv}	−.042	
Hidden layer 1	(Bias)		−.004
	H (1:1)		−1.367
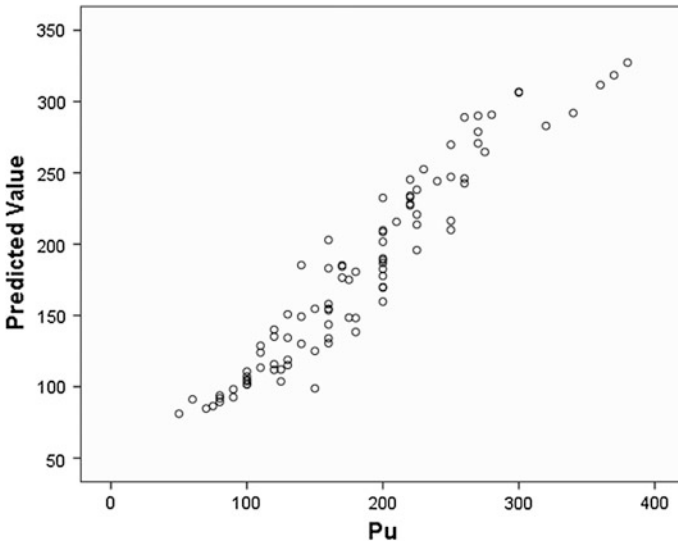
Fig. 30 Finite element versus predicted results of max flexural capacity loads

In this study, x is

$$x = 0.232 + \left(0.172 * f_c'\right) + (0.182 * E_c) - (0.641 * f_t) + \left(0.182 * \frac{a}{d}\right)$$
$$- (0.359 * T) + (0.17 * E_{sl}) - (0.042 * E_{sv}) \tag{3}$$
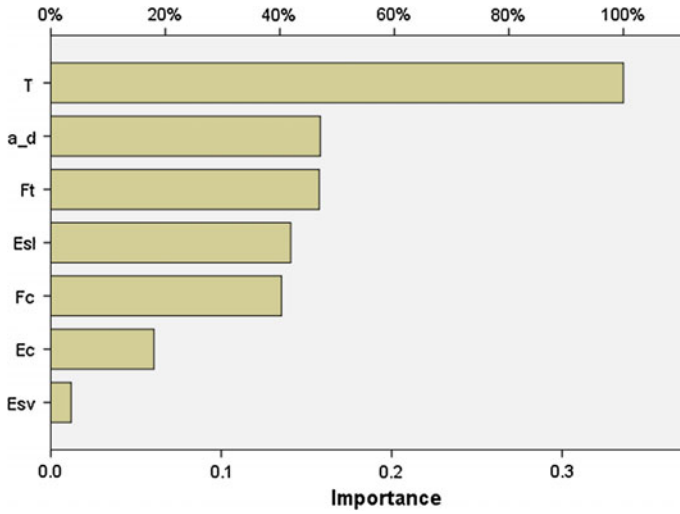
Fig. 31 Normalized importance of ANN Model
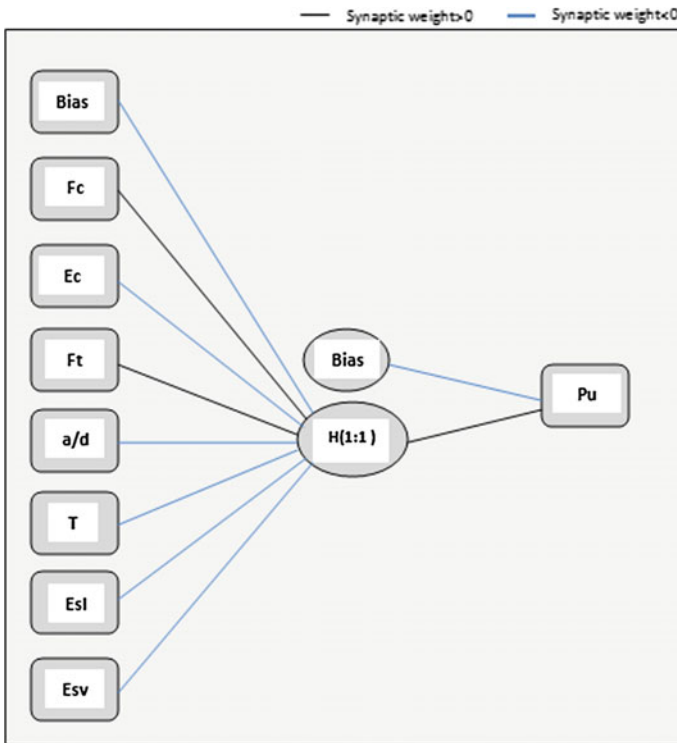
Fig. 32 The skeleton of the modeling

where

f_t splitting strength of concrete (MPa)
$\frac{a}{d}$ effective length span-to-depth ratio
T temperature (°C)
E_{sl} modulus of elasticity for longitudinal steel reinforcement (MPa)
E_{sv} modulus of elasticity for vertical steel reinforcement (MPa)

So Eq. (1) is

$$y = \frac{1}{1 + e^{0.004 - 1.367 \tan h(x)}} \qquad (4)$$

The values of ultimate load (y) from Eq. (4) are between (0–1) and not the real values. For getting the real values, variable weights must be corrected by using Eq. (5) as follows:

$$x = \frac{x - x_{\min}}{x_{\max} - x_{\min}} \qquad (5)$$

So, the real ultimate load will be calculated from Eqs. (6) and (7) as follows:

$$y = \frac{230}{1 + e^{0.004 - 1.367 \tan h(x)}} + 50 \qquad (6)$$

where $y = P_{\text{estimate}}$, and x is

$$x = 0.232 + \left(0.172 * \frac{f'_c - 20}{50}\right) + \left(0.182 * \frac{E_c - 21{,}153}{18{,}421}\right) - \left(0.641 * \frac{f_t - 2.77}{2.41}\right)$$
$$+ \left(0.182 * \frac{\frac{a}{d} - 1}{2}\right) - \left(0.359 * \frac{T - 400}{100}\right) + \left(0.17 * \frac{E_{sl} - 117{,}090}{19{,}515}\right) - \left(0.042 * \frac{E_{sv} - 122{,}910}{20{,}485}\right) \qquad (7)$$

The mean absolute percentage error (MAPE) is

$$\text{MAPE} = \text{ABS}\left(\frac{P_{\text{actual}} - P_{\text{estimate}}}{P_{\text{actual}}}\right) \qquad (8)$$

And, average accuracy percentage (AA%) is

$$\text{AA} = 100 - \text{MAPE} \qquad (9)$$

The coefficient of correlation (R) and the coefficient of determination (R^2) are shown in Table.

Fig. 33 Comparison
between load from FEA and
loads from SPSS
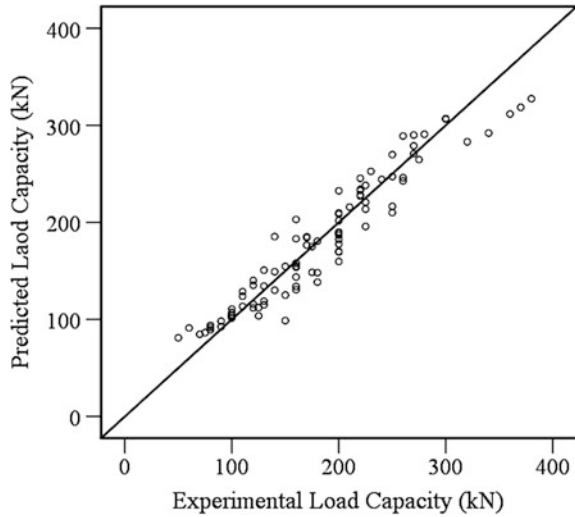
Name	Percentage
MAPE	76.20
AA	99.23
R	96.83
R^2	93.76

This means that the comparison between finite element models and ANN models are so good. This can be seen in Fig. 33.

7 Conclusions

The following conclusions are drawn based on the numerical analysis:

1. Nonlinear finite element procedure using ANSYS features to simulate reinforced concrete deep beams subjected to elevated temperature is used.
2. For checking the efficiency of the models, using neural network error R was about (99%) and square error R^2 (98%).
3. The deep beam samples that have compressive strength more than 40 MPa with $a/d = 1$, their behavior is more distinguished when $a/d = 2$ and $a/d = 3$. This means that for high-strength concrete, the effect of high temperature had less effect on concrete.
4. Deep beams having $a/d = 1$ and temperature (20) °C, compressive strength that increase by about (3.5) times lead to increase in ultimate load about (1.9) times. But for temperature (250) °C, the ultimate load increase about (2.61) times. And for temperature (500) °C, the ultimate load increase by (2.2) times.

5. This study takes deep means for behavior of concrete with temperature changes in seasons, or in the same day between day and night, and even in the same hour between outside and inside the room if (cooling/heating) turned on. In ACI code take the large factor of error as 40%, the results from these samples exceed half of it. That makes the temperature change an important factor for concrete durability.

6. For deep beams behavior, when the length increased lead to increase in midspan deflection. And by increasing the length the deep beams behave like normal beams.

Notations

Symbol	Descriptions
β_t	Open shear transfer coefficient
β_c	Closed shear transfer coefficient
f_c'	Compressive strength (MPa)
f_y	Yield stress (MPa)
E	Young's modulus (MPa)
E_T	Tangent modulus (MPa)
A	Area (mm^2)
K	Thermal conductivity (W/m °C)
C	Specific heat (J/kg °C)
ρ	Density (kg/m^3)

References

1. ACI Committee 318: Building Code Requirements for Structural Concrete. American Concrete Institute, Farmington Hills, USA (2011)
2. ACI Committee 318M: Building Code Requirements for Structural Concrete. American Concrete Institute, Michigan, USA (2014)
3. Ama'ash, H.: New model for shear resistance of simple supported reinforced concrete deep beam. Kufa J. Eng. **3**(1) (2011) (In Arabic)
4. Chen, W.F.: Plasticity in Reinforced Concrete. McGraw-Hill, USA. https://doi.org/10.1016/0045-7825(82)90016-0
5. Osman, B.H.: Shear in R.C. deep beams. M.Sc. thesis, University of Khartoum, Sudan (2008)
6. ANSYS, Copyright: ANSYS Help, Release 11.0. (2007)
7. Abdul Razzaq, K.S.: Effect of heating on simply supported reinforced concrete deep beams. Diyala J. Eng. Sci. **08**(02), 116–133 (2015)
8. Felicetti, R., Gambarova, P.G., Semiglia, M.: Residual capacity of HSC thermally damaged deep beams. J. Struct. Eng. **125**(3), 319–327 (1999). https://doi.org/10.1061/(ASCE)0733-9445(1999)125:3(319)
9. American Concrete Institute: Building Code Requirements for Reinforced Concrete. Detroit, ACI-381-14 (2014)
10. Antony, N.K., Ramadass, S., Ramanujan, J.: Parametric study on the shear strength of concrete deep beam using ANSYS. Am. J. Eng. Res. (AJER) **4**, 51–59 (2013)

11. Eurocode 2: Design of Concrete Structures, Part 1-2; General Rules—Structural Fire Design. Brussels (1996)
12. European Committee for Standardisation (CEN): Eurocode 3: Design of Steel Structures, Part 1.1: General Rules and Rules for Buildings, DD ENV 1-1.EC3 (1993)
13. European Committee for Standardisation (CEN): Eurocode 4: Design of Composite Steel and Concrete Structures, Part 1.1: General Rules and Rules for Buildings, DD ENV 1-1 (1994)
14. Guo Z.: Experiment and Calculation of Reinforced Concrete at Elevated Temperatures. Tsinghua University Press. Published by Elsevier Inc., The Netherlands (2011). https://doi.org/10.1016/c2010-0-65988-8
15. Al-Zwainy F.M.: The use of artificial neural networks for productivity estimation of finishing stone works for building projects. Eng. Dev. J. **16**(2), 42–60 (2012)
16. Landau, S., Everitt, B.S.: A Handbook of Statistical Analyses using SPSS. Chapman & Hall/CRC Press LLC, UK (2004)
17. Mahmood A.S.: Predicting of torsional strength of prestressed concrete beams using artificial neural networks. Int. J. Sci. Eng. Res. **6**(2), 1222–1230 (2015)
18. Rasheed F.: Artificial neural network circuit for spectral pattern recognition. M.Sc. thesis, Texas A&M University (2013)

3D FEM to Predict Residual Stresses of Press-Braked Thin-Walled Steel Sections

Ayad Mutafi, N. Yidris, M. R. Ishak and R. Zahari

Abstract Cold-formed steel sections are normally produced by cold work manufacturing processes. The amount of cold work to form the sections may have induced residual stresses in the section especially in the area of bending. Hence, these cold work processes may have significant effects on the section behaviour and load-bearing capacity. There was a lack of studies in investigating the effects of residual stresses raised by press-braking operations unlike the roll-forming operation. Therefore, a 3D finite element simulation was employed to simulate this forming process. This study investigated the magnitude of the maximum residual stresses along the length of the corner region and through-thickness residual stress variations induced by the press-braking forming process. The study concluded that residual stresses are not linear longitudinally (along the corner region). Maximum residual stresses exist near the middle surface of the plate. The comparison of the 3D-FE results with the 2D-FE results illustrate that 3D-FE has a variation in transverse and longitudinal residual stresses along the plate length. In addition, 2D-FE results overestimate the residual stresses along the corner region.

Keywords Cold-formed steel · FEM · Residual stresses

1 Introduction

Cold-formed steel sections are produced by cold work manufacturing processes. It is known that these processes have significant effects on the section behaviour and load-bearing capacity. This is due to the amount of cold work to form the sections that produce residual stresses. The high amounts of the residual stresses reduce the load capacity of the section, as stated by Quach [1].

There were many attempts to measure the residual stresses. These attempts varied between the experimental and numerical methods. Batista and Rodrigues [2]

A. Mutafi (✉) · N. Yidris · M. R. Ishak · R. Zahari
Department of Aerospace Engineering, Universiti Putra Malaysia, Selangor, Malaysia
e-mail: ayad2motafi@live.com

215

indicated that sections produced by the roll-forming process have residual stresses higher than the press-braking process. Their experiment measured the longitudinal stresses of both processes of the same section geometry. Moreover, Weng and Peköz [3] attempted to measure the longitudinal residual stresses of cold-formed sections. Their experiment showed that residual stresses at corner regions are higher than the flat ones. Also, their findings stated that the inner surface is subjected to compressive residual stresses while the outer one is subjected to tensile residual stresses. Weng and White [4] have conducted an experimental study to measure surface residual stresses. The study also measured through-thickness residual stresses on thick cold bent steel plates using the sectional method. It was reported that through-thickness residual stress distribution was of the zigzag type and the maximum residual stress either occurs at the inside surface of the bend or near the neutral surface of the plate.

Numerical attempts to predict the residual stresses have been done by few researchers [5–9]. These works were intended to introduce alternatives in measuring the residual stresses because measurements by destructive methods have limitations in accuracy and are time-consuming. Moen et al. [5] presented an analytical method for predicting residual stresses in sections formed by the roll-forming process. The study also included several analytical approaches for determining residual stress distribution through the thickness of rolled sheet. Their motivation of the study is to define residual stresses of cold formed steel at its initial state. Quach et al. [6, 7] established a closed-form analytical method for predicting residual stresses and equivalent plastic strains from coiled, uncoiled, and mechanical flattening of carbon steel sheets. Then he implemented the finite element 2D technique for press-braked sections as an alternative of laboratory measurements to predict residual stresses distribution. The outcomes showed good agreement with experimental values.

Most of the studies investigated the effects of roll-forming operations on steel section behaviours. Press-braking was not of much interest to many researchers except for [7–9]. These studies confirmed the residual stresses variation through the thickness by 2D FE model. However, Quach et al. [1, 10] stated that stress distribution changes in a narrow region close to the member edges which are free of stresses. Therefore, this makes the 2D-FE insufficient for determining the residual stresses distribution. This study aims to investigate the residual stresses along the corner region by simulating a 3D finite element model. The main motivation of this study is to establish a comparison between 2D and 3D FEM in the determination of the maximum residual stresses.

2 Simulation of Press-Braking Process

2.1 Scope

Press-braking is a simple section forming process where flat sheet material is placed between a punch and die and folded along the length of the member as shown in Fig. 1. The investigation into the finite element modelling technique for estimating residual stresses introduced by the press-braking process is restricted to the corner region where it experiences the stamping force due to punch movement. Residual stresses at the flat regions are introduced by coiling and uncoiling. This study simulated a section tested by Weng and Peköz [3]. Their experiment results are important to validate finite element results.

2.2 Model Description

An explicit finite element code in ABAQUS [11] was employed to simulate the forming process (Press-braking process). As mentioned earlier, finite element modelling is restricted to the corner region where it experiences the stamping force due to punch movement. Residual stresses at the flat regions are raised by coiling and uncoiling. The implementation of explicit analysis is more effective in quasi-static problems such as metal forming.

The model contains three parts: Punch, Die, and Steel sheet. The punch and die were modelled by an analytical model and the steel sheets were deformable shells with a four-node, quadrilateral, stress/displacement shell element with reduced integration and a large-strain formulation (S4R) [11]. This element can handle large strains and rotations. Simpson's rule with 11 integration points was used for integration across the shell wall thickness. The interaction between the model parts was simulated by general contact.

Fig. 1 Press-braking process of cold formed steel
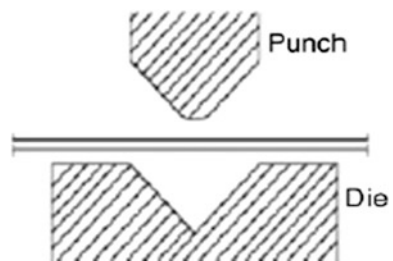
2.3 Geometrical Properties

The section properties were extracted from [3]. A thin-walled lip channel section with 3.96 mm corner radius was investigated for residual stress distribution through thickness. Full details on geometrical properties of the section are presented in Table 1, Fig. 3.

2.4 Material Properties

The modelling of material nonlinearity in ABAQUS [11] required the definition of a true stress—logarithmic plastic strain relationship up to the ultimate point, which was converted from the nominal stress–strain data. Figure 2 shows the nominal stress–strain curves, true stress–strain curves and true stress-logarithmic plastic strain curves that were extracted from the following equations. Regarding Ref. [3] experiment, specimen PBC14 did not provide experimental stress–strain curves [7]

$$\sigma = E\varepsilon, \quad \varepsilon \leq \sigma_y/E \tag{1}$$

Table 1 Geometrical and material properties of lipped channel sections

Specimen	t (mm)	a (mm)	b (mm)	c (mm)	R (mm)	σ_y (MPa)	σ_u (MPa)	$\varepsilon_y (\times 10^{-6})$	E (GPa)	n $(\times 10^{-2})$	$\varepsilon_u^a \%$
PBC 14	1.80	76.23	41.45	15.37	3.96	250.1	345	1230	203.3	9.56	33

Where R is the corner radius, σ_y is yield stress, σ_u is ultimate stress, ε_y is yield strain, ε_u is ultimate strain and E is modulus of elasticity
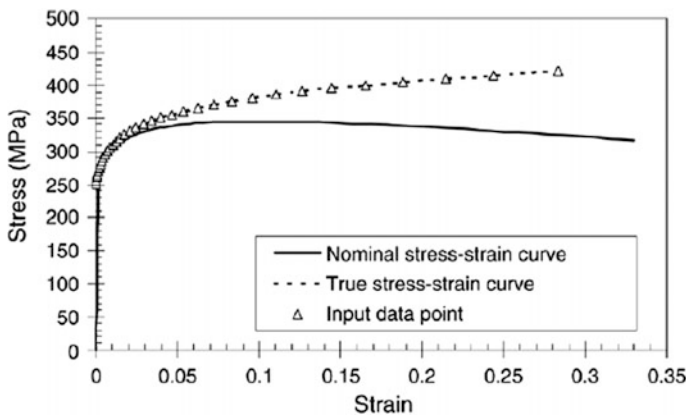
Fig. 2 Weng and Peköz specimen PBC14 [7]
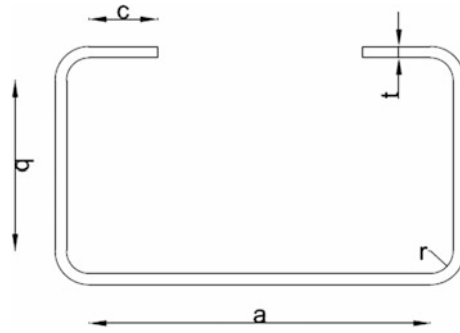
Fig. 3 Dimensions of a lipped channel section
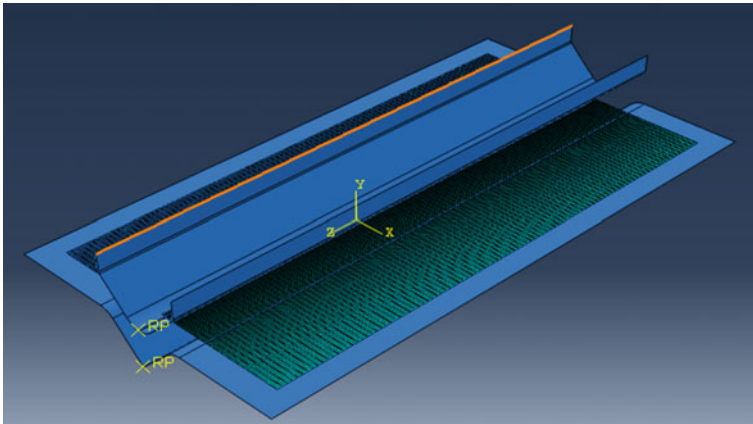
Fig. 4 FE model

$$\sigma = \sigma_y \left(\frac{E_\varepsilon}{\sigma_y} \right)^n, \quad \varepsilon > \sigma_y / E \tag{2}$$

Full details on geometrical, material properties of the section and FE model are presented in Table 1, Figs. 3 and 4.

2.5 Mesh Convergence Study

Mesh convergence studies have been performed for a rectangular metal sheet subjected to metal forming by press-braking in order to determine the optimal density of mesh in the sheet metal model. Four mesh densities were examined and the residual stresses of the steel sheets were noted. The shorter edge of the plate had

Fig. 5 The selected
longitudinal lines
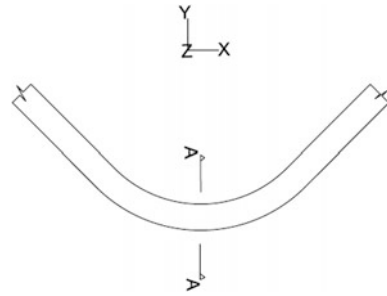
number of seeds that was higher than the longer edge as at this location, the metal
sheet had interaction with the punch and the die, hence experienced large bending.

In this study, the stress results of three longitudinal node lines—mid-corner line
A-A was monitored and shown in Fig. 5. The steel sheet can be divided into three
regions: a corner region and two flat regions. The location of point A is at the
middle of the bend curve. This location was selected in order to verify the finite
element results with those of Refs. [3, 7].

In this convergence study, maximum compressive residual stresses are taken into
account as these stresses have influence in the section buckling strength [12]. This
study examined the stresses at the mid-corner line (A-A) only. Table 2 summarizes
the results on the convergence test.

From Table 2, a mesh of 300×150 is taken as a reference to evaluate the
accuracy of the other three meshes. It can be seen that the mesh with 200×150
showed results closer to the reference mesh. Therefore, the mesh with 200×150 is
the adopted mesh for this study.

Table 2 Comparison of maximum compressive stresses for PBC14 at mid-corner line (A-A)

Mesh	No. of elements	Max. compressive residual stresses			
		$\sigma_{Tran.}$ (MPa)	Diff. %	$\sigma_{Long.}$ (MPa)	Diff. %
(150×100)	15,000	278.74	0.75	164.58	0.22
(200×100)	20,000	275.95	−0.26	164.35	0.08
(200×150) Adopted	30,000	276.83	0.06	162.66	−0.95
(300×150)	45,000	276.66	0.0	164.22	0.00

3 Results and Discussions

3.1 Validation of the Results

When performing numerical simulations, it is essential that the results from the finite element analyses be compared with independent published work. Consideration has been given to the work of Weng and Peköz [3] and also Quach's 2D finite element simulation [7]. Quach et al. [6] concluded that the magnitudes of residual stresses were sensitive to the coiling radius and the yield stress of the material; the larger the radius the smaller the stresses. Hence, this study assumed that residual stresses arising from the coiling and uncoiling process is negligible by considering that the coil diameter has the magnitude of 1100 mm [7].

The residual strain at flat regions were determined by the closed-form analytical solution presented in [6] that predicts residual stresses and equivalent plastic strains from the coiling-flattening process. Transverse to longitudinal stress ratio is expressed as a function of the distance from the mid-plane and the material behaviour is assumed to be elastic-perfectly plastic.

Figure 6 shows a good agreement between this study and results of plastic strain in Refs. [3, 7]. Therefore, the 3D FE results of this study are validated. Comparing the results in Fig. 6, 3D-FE longitudinal strains give a good prediction than the results in 2D-FE.

3.2 Results Comparison

Previous numerical studies agreed that maximum residual stresses location is near the middle surface of the corner region [3, 5, 7]. Earlier experimental study suggested that the magnitude of longitudinal residual stresses at the corner area is in the
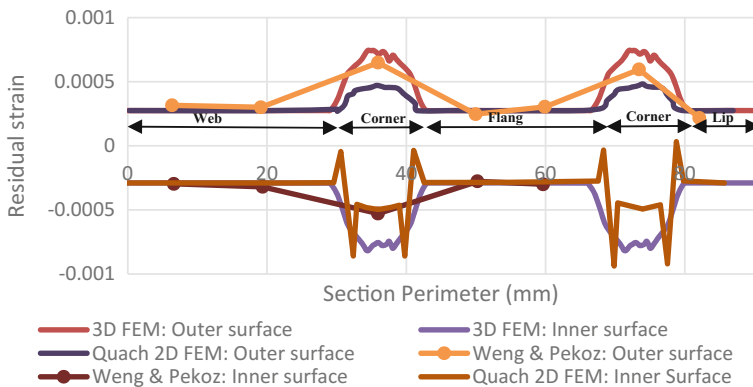
Fig. 6 Comparison of residual strain of section PBC14

Table 3 Comparison of residual stresses (PBC14 Specimen)

	A-A (Mid-corner)			
	σ_z/σ_y		σ_x/σ_y	
	Tensile	Comp.	Tensile	Comp.
Experiment [3]	0.25–0.7	0.25–0.7	–	–
2D-FE [7]	0.5	0.9	0.8	1.4
3D-FE	0.68	0.65	1.28	1.11

range of 0.25–0.7σ_y yield stress [3]. Also, compression residual stresses were found at the inner surface and tensile residual stresses found at the outer surface. Meanwhile the 2D-FE analysis results in [7] showed that peak longitudinal and transverse compression residual stresses at the mid-corner (A-A) were 0.9σ_y and 1.4σ_y respectively and peak longitudinal and transverse tensile residual stresses were 0.5σ_y and 0.8σ_y at the mid-surface.

In the present study, maximum residual stresses were located near the middle layer of the plate. At the mid-corner, maximum longitudinal compressive and tensile residual stresses are about 0.68σ_y and 0.65σ_y respectively and are located near the mid-layer of the plate. Additionally, peak transverse compressive and tensile residual stresses are found near the mid-layer and they are 1.28σ_y and 1.11σ_y respectively. The summary of the comparison between the current work and Refs. [3, 7] is shown in Table 3.

Figure 7 shows that the 2D-FE results predicted residual stresses to be linear along the corner region. However, 3D-FE shows that residual stresses are not linear especially near the plate edges where it is lower than the rest of the plate.

4 Future Work

There will be future work implementing the same finite element technique to investigate the effects of geometrical properties (Corner radius and sheet thickness) on the prediction of maximum residual stresses.

a) Maximum Transverse residual stresses

b) Maximum Longitudinal residual stresses
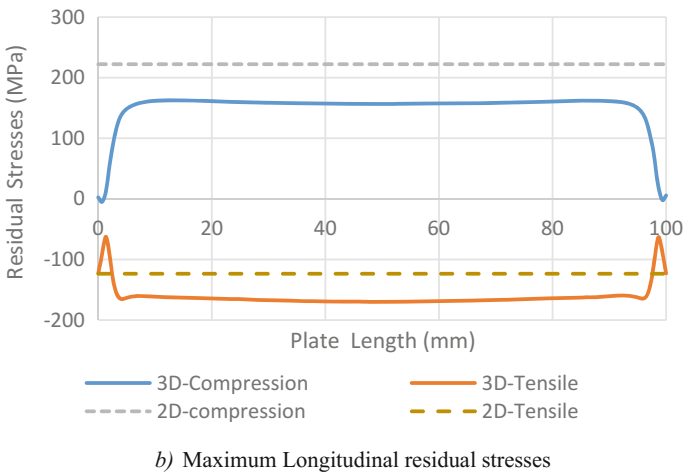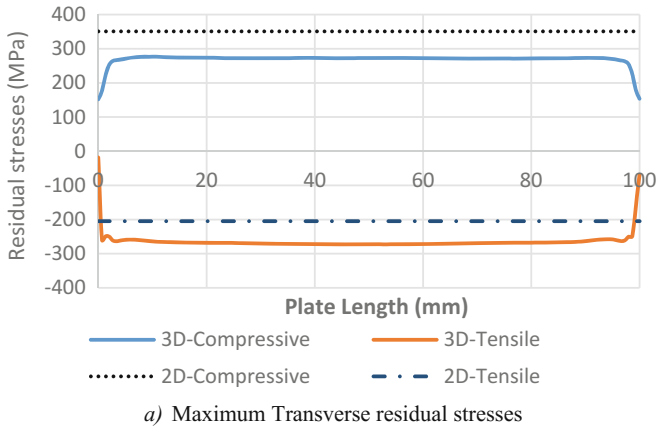
Fig. 7 Maximum residual stresses in 3D-FE versus 2D-FE

5 Conclusion

Cold formed steel sections are normally produced by cold work manufacturing processes. The amount of cold work to form the sections may have induced residual stresses in the section especially in the area of bending. Studies by researchers in the past on the effects of local buckling on the failure mechanics of thin-walled compression members have shown that ultimate failure will occur when the yielding has reached most of the middle surface in the corner region of the sections. Hence, these cold work processes may have significant effects on the section behaviour and load-bearing capacity. Most of the studies have investigated the effects of residual stresses arising from roll-forming operations and its influence on steel section

behaviour. Press-braking has not been of much interest to researchers. Therefore, a 3D finite element simulation was employed to simulate this forming process. This study investigated the magnitude of the maximum residual stresses along the length of the corner region and through-thickness residual stress variations induced by the press-braking forming process. The study concluded that residual stresses are not linear longitudinally (along the corner region). Maximum residual stresses exist near the middle surface of the plate. The comparison between the 3D-FE results with existing 2D-FE results illustrate that 3D-FE results show a variation in transverse and longitudinal residual stresses along the plate length. In addition, 2D-FE results overestimated the residual stresses along the corner region.

References

1. Quach, W.M., Teng, J.G., Chung, K.F.: Effect of the manufacturing process on the behaviour of press-braked thin-walled steel columns. Eng. Struct. **32**(11), 3501–3515 (2010)
2. Batista, E.D.M., Rodrigues, F.G.: Residual stress measurements on cold-formed profiles. Exp. Tech. **16**(5), 25–29 (1992)
3. Weng, C.C., Pekoz,T.: Residual stresses in cold-formed steel members. J. Struct. Eng. **116**(6), 1611–1625 (1990)
4. Weng, C.C., White, R.: Residual stresses in cold-bent thick steel plates. J. Struct. Eng. **116**(1), 24–39 (1990)
5. Moen, C.D., Igusa, T., Schafer, B.W.: Prediction of residual stresses and strains in cold-formed steel members. Thin-Walled Struct. **46**(11), 1274–1289 (2008)
6. Quach, W.M., Teng, J.G., Chung, K.F.: Residual stresses in steel sheets due to coiling and uncoiling: a closed-form analytical solution. Eng. Struct. **26**(9), 1249–1259 (2004)
7. Quach, W.M., Teng, J.G., Chung, K.F.: Finite element predictions of residual stresses in press-braked thin-walled steel sections. Eng. Struct. **28**(11), 1609–1619 (2006)
8. Quach, W.M., Teng, J.G., Chung, K.F.: Residual stresses in press-braked stainless steel sections, I: coiling and uncoiling of sheets. J. Constr. Steel Res. **65**(8–9), 1803–1815 (2009)
9. Quach, W.M., Teng, J.G., Chung, K.F.: Residual stresses in press-braked stainless steel sections, II: press-braking operations. J. Constr. Steel Res. **65**(8–9), 1816–1826 (2009)
10. Abambres, M., Quach, W.-M.: Residual stresses in steel members: a review of available analytical expressions. Int. J. Struct. Integrity **7**(1), 70–94 (2016)
11. ABAQUS 6.13-4: Dassault Systèmes Simulia Corp., Providence, RI (2013)
12. Loughlan, J., Yidris, N., Cunningham, P.R.: The effects of local buckling and material yielding on the axial stiffness and failure of uniformly compressed I-section and box-section struts. Thin-Walled Struct. **49**(2), 264–279 (2011)

Probabilistic Study of the Undrained Bearing Capacity of Strip Footings

N. Brahmi, M. Mellas, A. Mabrouki, D. Benmeddour and M. Y. Ouahab

Abstract The undrained bearing capacity of strip footings has been extensively studied in the literature by a deterministic manner where the soil is assumed uniform. In practice, the spatial variability of random soil affects the ultimate bearing capacity of strip footings. This paper focuses on a probabilistic study using adaptive finite element limit analysis combined with random field theory to investigate the bearing capacity of strip footings subjected to vertical and centric inclined loads, on a cohesive soil with spatially variable distribution of the undrained shear strength. A parametric study is performed using OptumG2 to investigate the effects of diverse probabilistic parameters associated in the problem of undrained bearing capacity of strip footings.

Keywords Bearing capacity · Strip footing · Random field · Cohesive soil

1 Introduction

Classical methods of bearing capacity evaluation for shallow foundations consider that the soil beneath the foundation is uniform, which involves a deterministic analysis, using representative values for different soil parameters. These values are generally the averages or the most conservative values obtained from in situ or laboratory tests. These methods apply a global safety factor to take into account the uncertainties of soil properties; this factor is obtained based on experience.

The sources of uncertainties associated with geotechnical engineering practice can be classified in three main groups [1]: inherent variability or the natural

N. Brahmi (✉) · M. Mellas · A. Mabrouki (✉) · D. Benmeddour · M. Y. Ouahab
Civil Engineering Laboratory, Biskra University, BP 145, 07000 Biskra, Algeria
e-mail: narimanebrahmi@outlook.fr

A. Mabrouki
e-mail: a.mabroukii@yahoo.fr

heterogeneity, measurement errors, and model transformation uncertainties. The present study is concerned only with the spatial variability, which can be modelled as random field.

The assumption of homogeneous soil ignores some possible failure mechanisms and may lead to an overestimation of the bearing capacity of the foundations. In order to investigate the influence of randomly distributed undrained shear strength, the bearing capacity of a strip rough footing has been studied using elasto-plastic finite element analyses combined with random field theory [2]. It was found that the mean bearing capacity for spatially random soil is always lower than the deterministic bearing capacity. Also, the Random Finite Element Method (RFEM) was used to investigate the effect of the variation in the shear strength, on the bearing capacity of strip footing under combined loading [3]. The results showed that the mean bearing capacity for separate vertical, horizontal or moment loading, decreases with increasing soil variability; it was demonstrated that most of the failure envelopes are found inside the deterministic one, which means that soil variability can reduce the bearing capacity. Furthermore, the bearing capacity of buried footings was studied by using the elasto-plastic finite element method and the limit analysis method with its two bounding theorems (upper and lower bounds) [4]. It was found that the bearing capacity factors for a footing in random soils are all smaller than the corresponding bearing capacity factor in homogeneous soils.

Recently, the Random Adaptive Finite Element Limit Analysis (RAFELA) for probabilistic applications was used [5], it was found that the proposed method reduces the gap between the upper and lower bound solutions comparing with the equivalent uniform meshes. The RAFELA method has been also adopted to study the effect of spatial correlation distance in the undrained shear strength on an eccentrically loaded strip footing [6]. It was demonstrated that the greatest reduction in the bearing capacity is for pure vertical loads; moreover, the greatest reduction is obtained for the smaller correlation lengths with a critical value that represents the greatest reduction in the bearing capacity.

This paper investigates the effect of the spatial variability in the undrained shear strength of clays, on the bearing capacity of strip footings under vertical and inclined loads, using Random Adaptive Finite Element Limit Analysis (RAFELA).

2   Problem Presentation

In this paper, the finite element program OptumG2 [7] was used to study the bearing capacity of rough strip footings of width $B = 1$ m, founded on a spatially varying cohesive soil and subjected to vertical and inclined loads (Fig. 1). The soil domain of width 8B and height 3B is modelled with a perfectly plastic constitutive model and the material failure is defined by the Tresca criterion. The undrained Young's modulus and the unit weight of the soil are kept constant ($Eu = 30$ MPa and $\gamma = 16$ kN/m^3) while the undrained cohesion is spatially variable.
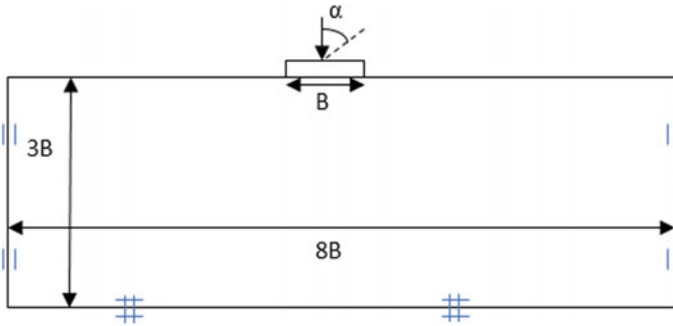
Fig. 1 Problem geometry

The footing is modelled as a rigid plate and the boundary conditions are shown in Fig. 1. The vertical sides of the model were constrained horizontally, while the base of the model was constrained in all directions.

The bearing capacity evaluation for the strip rigid footing with OptumG2 is based on subdividing the soil into a number of elements, using Finite Element Limit Analysis. Limit analysis is a powerful tool for analyzing the bearing capacity of foundations. The bounding theorems, considers the soil to be perfectly plastic and follows an associated flow rule. The bearing capacity is obtained by applying a multiplier load which is amplified until a state of incipient collapse is attained. In this study, the adaptive meshing in finite element limit analysis is used to reduce the gap between the lower and upper bounds.

Spatial variability can be characterized by a trend refers to the mean value and residual variation representing the variability about the trend. At two different points in the space, the residuals are statistically correlated to one another. This correlation is described by the autocorrelation function [6]:

$$\rho((x_1, y_1)(x_2, y_2)) = \exp\left(\frac{-|x_1 - x_2|}{\theta_x}\right) \exp\left(\frac{-|y_1 - y_2|}{\theta_y}\right) \tag{1}$$

The integral of this function represents the scale of fluctuation; this latter also called correlation length is defined as the distance over which the correlation of the properties is relatively strong.

Soil spatial variability is modelled as random field which is described by the coefficient of variation of the property (representing the percentage of dispersion in data) and by the scale of fluctuation.

In the present study, a lognormal distribution is assumed for the undrained shear strength with a mean value $\mu_{Cu} = 10$ kPa, a coefficient of variation (COV), a vertical and horizontal correlation distances which are assumed to be isotropic $CL_x = CL_y$.

Spatial variability is modelled using random field theory in conjunction with finite element limit analysis and Monte Carlo simulations.

3   Results and Discussion

3.1   Bearing Capacity Factor for Vertically Loaded Strip Footing

The limit load of strip footing on clay is evaluated through the bearing capacity factor N_c is well known to be $\pi + 2$ [8]. In the present study, this factor is calculated as follows:

$$N_C = \frac{q_u}{\mu_{Cu}} \tag{2}$$

Where q_u: the bearing capacity, and μ_{Cu}: the mean value of the undrained shear strength.

Deterministic analyses. The bearing capacity factor was first investigated by a deterministic analysis, for a uniform soil with a value of 10 kPa for the undrained shear strength.

Table 1 shows the results for the upper and lower bound solutions using both uniform meshes and adaptive refinement, it can be seen that mesh adaptivity reduces the gap between the upper and lower bounds, the average bearing capacity factor is in a very good agreement with the exact solution [8].

Probabilistic analyses. A parametric study was investigated to explore the influence of stochastic parameters on the mean bearing capacity factor. For each analysis, four parameters are required to describe the log-normally distributed random field of Cu:

- Mean value μ_{Cu} (kPa)
- Coefficient of variation COV_{Cu} (%)
- Horizontal correlation length CL_x (m)
- Vertical correlation length CL_y (m).

Spatial correlation length is assumed to be isotropic ($CL_x = CL_y$), the dimensionless spatial correlation length is then: $\Theta = CL_x/B = CL_y/B$.

The mean value is kept constant in all analysis $\mu_{Cu} = 10$ kPa, while the coefficient of variation and the spatial correlation lengths are varied respectively as follows:

$COV_{Cu} = 10, 20, 30, 40$ and 50%.

$\Theta = 0.125, 0.25, 0.5, 1, 2, 3$ and 4.

The cumulative probability distributions for all COVs are illustrated in Fig. 2 for $\Theta = 1$. It is worthwhile noting that the bearing capacity factors in this figure are the

Table 1 Deterministic results

N_c	UB	LB	Average	Analytical
Uniform mesh	5.45	4.982	5.22	5.14
Adaptive mesh	5.206	5.082	5.144	
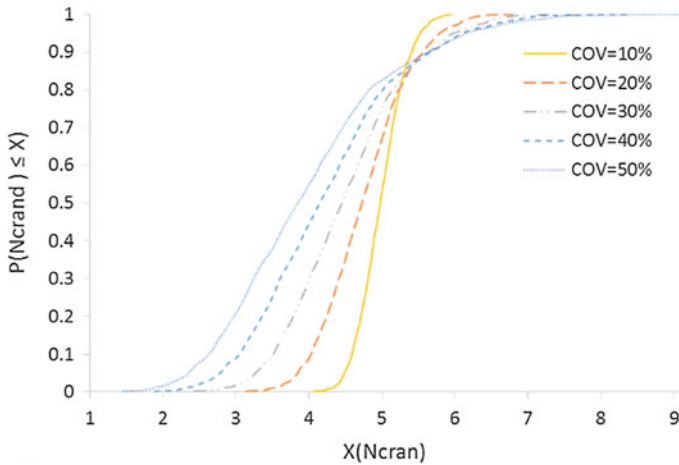
Fig. 2 Cumulative probability of bearing capacity factors N_c (for $\Theta = 1$)

averages between the upper and lower bounds. It is clear that the mean bearing capacity with all values of COV_{Cu} is less than 5.144 (the average deterministic value of N_c).

Figure 3 shows the variation of the mean bearing capacity factor normalized by the deterministic bearing capacity factor ($\mu N_c/N_{cdet}$) with COV_{Cu}. It can be seen that increasing spatial variability (COV from 10 to 50%) decreases the mean bearing capacity factor. The same result is found by Griffiths et al. [2] and Cassidy et al. [3].

The variation of the mean bearing capacity factor normalized by the deterministic bearing capacity factor ($\mu N_c/N_{cdet}$) with spatial correlation length is shown in Fig. 4. It can be seen that for all correlation lengths, the value of $\mu N_c/N_{cdet}$ is less than 1 which implies that the mean bearing capacity factor for random soils is always less than the deterministic value. Also, the mean bearing capacity factor decreases with decreasing the value of the correlation length with a critical value of $\Theta = 0.25$ that correspond to the greatest reduction of N_c. The obtained results are in a good agreement with those of Abid et al. [6] and Griffiths et al. [2].

3.2 Effect of Load Inclination on the Bearing Capacity of Strip Footing

A parametric study was carried out to explore the effect of spatial correlation distance on the bearing capacity of a strip footing, subjected to inclined loading with different load inclinations (α): $\alpha = 0°$ (pure vertical load), 5°, 10°, 15°, 20°, 30°, 60° and 90° (pure horizontal load).

The bearing capacity is expressed in terms of failure envelopes defined in VH space for different spatial correlation lengths. Failure envelopes shown in Fig. 5 are
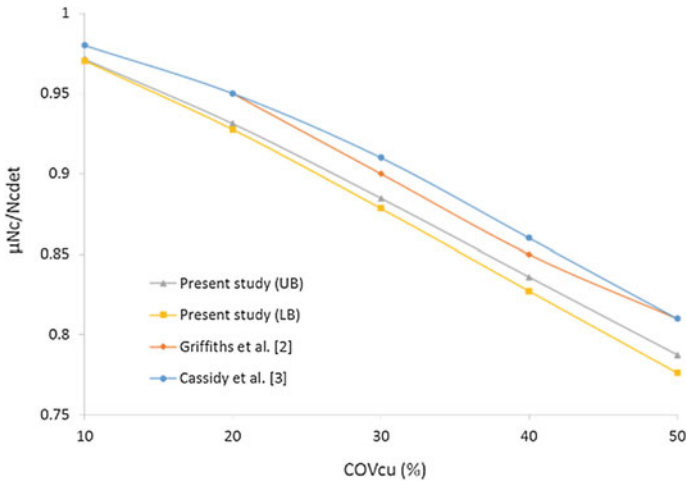
Fig. 3 Influence of varying COV_{Cu} on the mean normalized bearing capacity factor
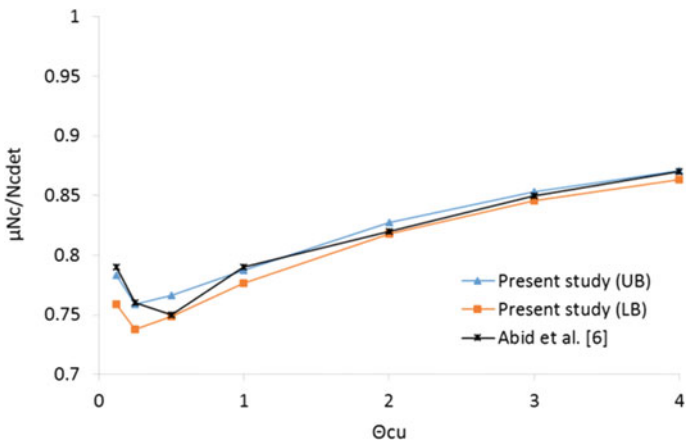
Fig. 4 Influence of varying Θ on the mean normalized bearing capacity factor

plotted for mean normalized loads (each value of $\mu V_u/BC_u$ and $\mu H_u/BC_u$ is the average between the upper and lower bounds). It is seen that the size and shape of failure envelopes change with the variation of spatial correlation length.

Figure 6 shows the influence of spatial correlation length on the normalized combined bearing capacity (the average between upper and lower bounds), for different load inclinations. It can be seen that the decrease of load inclination, increases the reduction of the bearing capacity, as observed, the greatest reduction
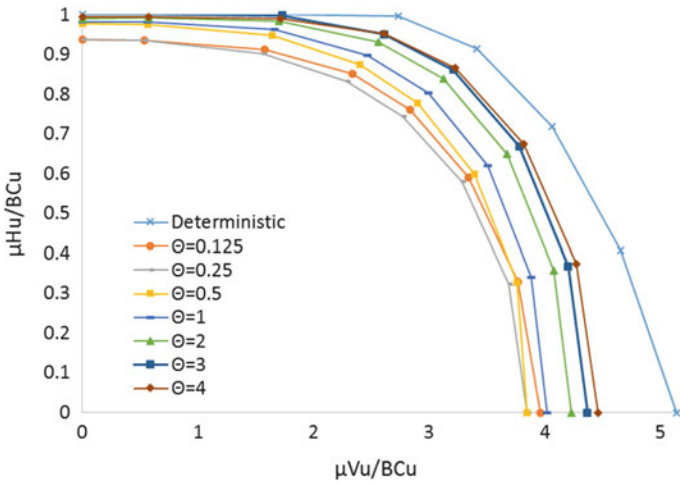
Fig. 5 Mean normalized VH failure envelope
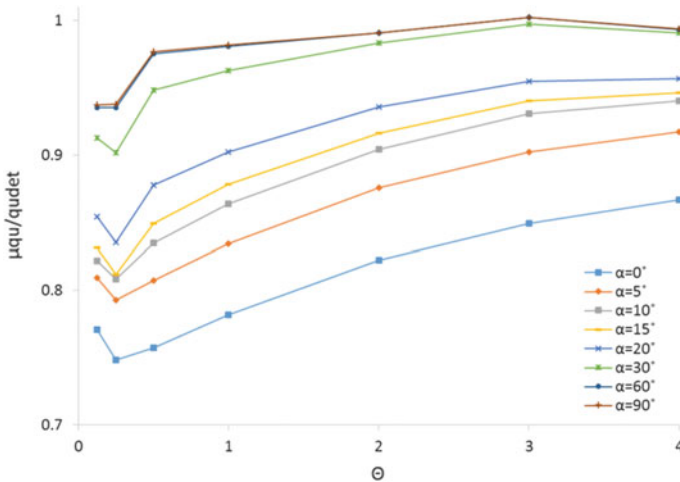
Fig. 6 Effect of spatial correlation length on the normalized combined bearing capacity

occurs when the load is vertical, while the least reduction occurs for horizontal loads. As the spatial correlation length decreases the reduction of the bearing capacity increases (for all load inclinations). In addition, the critical spatial correlation length is 0.25.

3.3 Failure Mechanism

The failure mechanism associated with each spatial correlation length is shown in
Fig. 7. It can be observed that the shear path follows zones where the soil is weak,
resulting unsymmetrical failure mechanism especially for the greater correlation
length in contrast to the symmetrical failure mode in uniform soils. This result is
already observed by Li et al. [4], therefore the spatial variability in soil properties
changes considerably the bearing capacity and the failure mechanism.
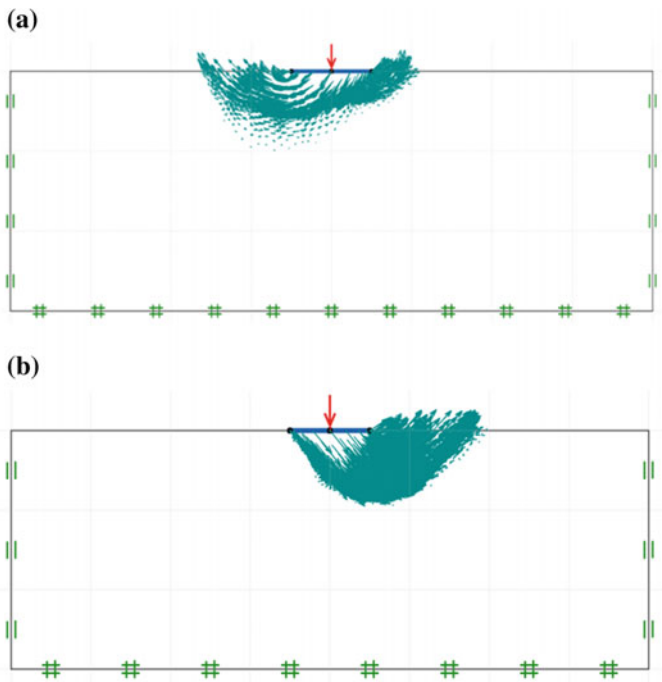
Fig. 7 Failure mechanism associated with **a** Θ = 0.125 and **b** Θ = 4

4 Conclusion

The influence of the probabilistic parameters (coefficient of variation and correlation length for the undrained shear strength) was investigated for the bearing capacity factor N_c of strip footings using RAFELA. It was found that random bearing capacity factors are always lower than the deterministic value for vertical loading. The mean N_c of the 1000 Monte Carlo simulations decreases with increasing COV_{Cu} and with decreasing Θ, also in all cases is lower than the deterministic value. This result demonstrates that the bearing capacity of the foundation is reduced when the soil is spatially variable; a critical value of $\Theta = 0.25$ was observed for the greatest reduction of N_c. The failure envelopes for inclined loading change with the variation of correlation length.

References

1. Phoon, K.K., Kulhawy, F.H.: Characterization of geotechnical variability. Can. Geotech. J. **36**(4), 612–624 (1999)
2. Griffiths, D.V., Fenton, G.A., Manoharan, N.: Bearing capacity of rough rigid strip footing on cohesive soil: probabilistic study. J. Geotech. Geoenvironmental Eng. **128**(9), 743–755 (2002)
3. Cassidy, M.J., Uzielli, M., Tian, Y.: Probabilistic combined loading failure envelopes of a strip footing on spatially variable soil. Comput. Geotech. **49**, 191–205 (2013)
4. Li, J.H., Cassidy, M.J., Tian, Y., Huang, J., Lyamin, A. V., Uzielli, M.: Buried footings in random soils: comparison of limit analysis and finite element analysis. Georisk. Assess. Manage. Risk Eng. Syst. Geohazards **10**(1), 55–65 (2015)
5. Abid, A., Lyamin, A.V., Huang, J., Li, J.H., Cassidy, M.J., Sloan, S.W.: Probabilistic stability assessment using adaptive limit analysis and random fields. Acta Geotech. **12**(4), 937–948 (2017)
6. Ali, A., Lyamin, A.V., Huang, J., Sloan, S.W., Cassidy, M.J.: Effect of spatial correlation length on the bearing capacity of an eccentrically loaded strip footing. In: 6th Asian-Pacific Symposium on Structural Reliability and its Applications, Shanghai, China (2016)
7. Krabbenhoft, K., Lyamin, A.V., Krabbenhoft, J.: Optum Computational Engineering (Optum G2), (2015), www.optumce.com
8. Prandtl, L.: Uber die Harte plastischer Korper, Nachrichten von der Koniglichen Gesellschaft der Wissenschaftenzu Gottingen. Math. Phys. KI **12**, 74–85 (1920)

Glass Footbridge

Yazmin Sahol Hamid and Gerard Parke

Abstract When a footbridge is made of glass, it shows to the pedestrians the wonder and uniqueness of itself, i.e., its transparent characteristic. However, the perceived unwanted characteristics, such as the brittleness of glass may make it unsuitable, if used for a load-bearing structural member. But, using a toughened and laminated glass panel as the primary structural member can be practical because this toughened glass has a higher failure strength and is considerably safer when compared to ordinary glass. This paper began with an architectural drawing of a glass footbridge. Each primary beam of the footbridge was made from a large-sized glass panel. The bridge was modeled using beam finite elements and analysed using the finite element program, SAP 2000. The model was initially formed in 2D and analysed using two different support conditions. The analysis was repeated for a 3D model. The results of maximum moments, shear forces and deflections produced using both the 2D and 3D models and also using different support conditions are compared. The maximum stress was calculated and checked with the failure strength of toughened glass. The maximum deflection was also checked with the limiting value given in standard codes of practice. Connectors have been designed to connect the glass sub-panels together which have been used to form the large size glass panels, namely, the primary beams. The connectors have been designed and the stress level in the connection checked. Modal analyses using 2D and 3D models were also carried out to give frequencies and mode shapes of the footbridge under vibration. The frequencies are checked against the minimum value required

Y. S. Hamid (✉)
Faculty of Civil Engineering, Universiti Teknologi MARA (UiTM)
Selangor, Shah Alam, Selangor, Malaysia
e-mail: yazminsahol@salam.uitm.edu.my; minbelle@yahoo.com

G. Parke
Department of Civil and Environmental Engineering,
University of Surrey, Guildford, UK
e-mail: g.parke@surrey.ac.uk

according to standard codes of practice. All of the above checks were found to satisfy the relevant design criteria, and consequently the footbridge is now considered to be safe and ready for construction.

1   Introduction

Over the last years, architects and interior designers have been busy creating new innovative structural designs using new types of materials. Laminated glass has driven a growing number of architects and engineers to work with elements in unconventional ways. To exploit the unique characteristics of glass, it should be used as the structural material for a closed room which will allow the sun, moon, and stars to be viewed, while protecting the room from rain, wind and cold, which is only becomes possible by using structural glass. In this paper, a footbridge made from glass was investigated. The idea came from an architectural drawing by an architect named Joris Luchinger, which is displayed in Nijsse [1]. The property of transparency is a valued feature in this glass footbridge.

It certainly takes a leap of faith to cross a glass footbridge where there is no visible framing, but which is only made of toughened laminated glass panels supported by toughened laminated glass beams. So far, only a small number of designers are willing to participate in using glass as the structural material because of its unpredictability and potential to injure people in the case of a breakage or falling shards. Glass acts in a significantly diverse manner compared to other materials like, for example, steel. The failure of an annealed glass beam is brittle, unlike a steel beam which may fail exhibiting large deformations. If an annealed glass beam is over loaded it would fracture and break completely, thus causing sudden failure of the beam. However, recent use of glass as a structural material has not only given us great exposure but has helped people realize that laminated glass can be used safely and successfully in working situations as proven by certain architects and engineers, where three panels of glass glued together can make a safe structural beam element.

As engineers, our paramount responsibility is the safety of people using the structure. An engineer naturally has to assume the obligation to analyse all possibilities of unwelcome effects of the proposed innovation. In this study, as mentioned above, a study of the behavior of the proposed glass footbridge structure drawn by Joris Luchinger (Nijsse 2002) was investigated. From a model analysis, the maximum moment, shear force, deflection and stresses of the glass panels were obtained. Then a modal analysis was conducted in order to obtain frequencies and mode shapes of the glass footbridge model. The model was created in the form of 2D and 3D to investigate the behavior of the proposed glass footbridge and also to have a comparison between the two models. However, in the 2D analysis, horizontal and torsional mode shapes are restricted which can only be obtained from a

3D analysis. Since the bridge has not been constructed and only a detail architectural drawing was given, a model and linear elastic analysis of this glass footbridge was undertaken in order to determine the behavior of the proposed glass footbridge structure.

1.1 Strength of Glass

Generally, loading on a structure induces bending moments and shear forces in the structural members. The bending moments are analysed and assessed. In order that the benefits of the analysis can be realized, the values of the bending moments must be used to check the stress levels developed in the members subjected to the load. Hence, a check for safety on the value of the maximum bending stress initiated from the maximum bending moment value used on the basis of factored loading not exceed the design stress.

For a structure made of glass, the undesirable characteristics of this material, i.e., its brittle character can cause fracture especially where there are flaws on the surface of the glass which normally leads to stress concentrations. Hence, the possibility of the formation of stress concentration cannot be overlooked and must be considered in the design procedure whenever glass is used. Table 1 shows the design stresses of different types of glass, such as float glass, heat-strengthened glass and toughened glass. The values of the design stresses are for use with factored loads and, where appropriate, for nonlinear analysis. In this paper, toughened glass is used and therefore the maximum bending stress value obtained from the glass footbridge analysis were compared with the design stress/strength of toughened glass given in Table 1.

Table 1 Design stresses (Concept Ritchlijn: Construction glass (Holland), October 1996)

Type of glass	Permanent loads	Medium-term loads	Short-term (gust) loads
Float glass	7 N/mm^2-single 7 N/mm^2-single	17 N/mm^2-single 14 N/mm^2-double	28 N/mm^2-single 24 N/mm^2-double
Heat-strengthened glass	22 N/mm^2-single 19 N/mm^2-double	24 N/mm^2-single 21 N/mm^2-double	37 N/mm^2-single 32 N/mm^2-double
Toughened glass	50 N/mm^2-single 43 N/mm^2-double	53 N/mm^2-single 46 N/mm^2-double	56 N/mm^2-single 48 N/mm^2-double

1.2   Vibration

Over the past years there are several cases of footbridges experiencing severe vibration due to pedestrian loading. On the opening day in June 2000 the Millennium Footbridge, London experienced horizontal vibration induced by horizontal synchronized pedestrian load which was caused by 8000–10,000 people crossing the bridge. As a result, dampers were fitted to the Millennium Footbridge to lessen the "sway" caused by high pedestrian densities. Generally, structures like pedestrian footbridges are subject to static and also dynamic loading. If magnitude of the vibration coincides with natural frequency of the footbridge, resonance occurs and the structure can become unsafe [2]. Hence, footbridges must be designed so as not to be susceptible to vibrations. For the analysis of structural vibrations is necessary to calculate the natural frequencies of the structure and then determine the response to the expected excitation. In this way it can be determined whether a particular structure will fulfill its intended function. Conventional beam footbridges of spans greater than 25 m are likely to have a fundamental natural frequency within the range of the input excitation caused by pedestrians crossing the structure. A valuable closed-form approximation is given in BS5400 Part 2, [3]. According to Hauksson [4], many footbridges have vertical and horizontal frequency of 1.4–2.4 Hz and 0.7–1.2 Hz respectively. When walking over a bridge pedestrians are more tolerant of vertical vibration than horizontal vibration. Based on BD37/01, [5] the total minimum range of allowable vertical and horizontal frequencies are 5 and 1.5 Hz respectively. Therefore, bridges are susceptible to suffer excessive vibration under pedestrian action if the frequency is below the minimum range mentioned. It is also essential to consider both the horizontal and vertical excitation arising from pedestrians using the structure.

2   Model Analysis of Glass Footbridge

Figure 1 shows a detailed model of a glass footbridge that has not been constructed yet. This model was taken from a book titled Glass in Structures (Nijsse 2002). The concept was by Joris Luchinger, a graduating student, who drew and sent the drawing as shown in Fig. 2 for his project submission in a design competition. The goal of the competition was to propose a structure that can be used to cross the wide waters in the Florida area in The Netherlands. Joris Luchinger proposed a complicated footbridge, entirely made of glass. The footbridge has six large glass beams used as its primary girders. The beams are tapered in the middle of the span to create their "just not meeting" appearance. Each glass beam comprises of three longitudinal panels, and each panel is formed from four layers of 15 mm thick toughened glass, laminated by resin. Meanwhile, for each secondary beam which spans between the primary beams, their height is 150 mm and consists of 2×10 mm annealed laminated glass rectangular plates. These secondary beams
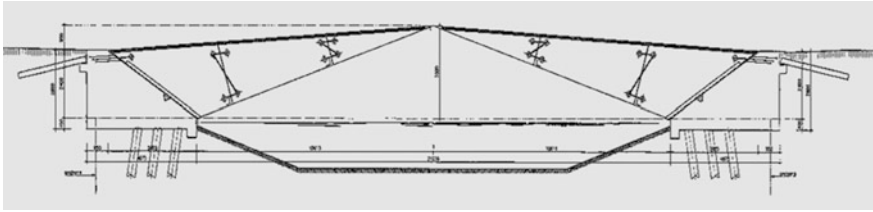
Fig. 1 Architectural drawing of a glass footbridge (Nijsse 2002)
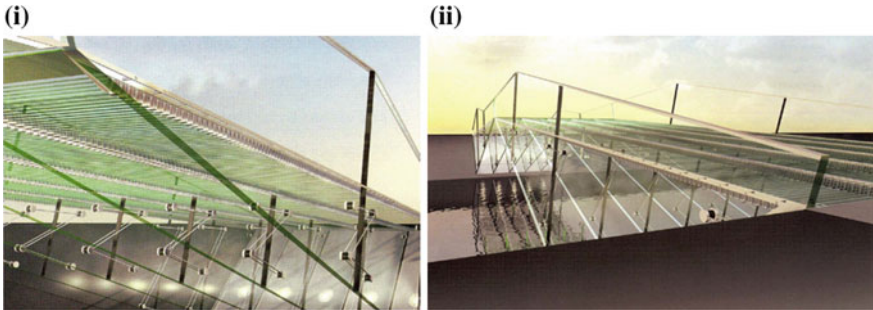
Fig. 2 **i** Closeup view of glass footbridge. **ii** Side view of glass footbridge (Nijse 2002)

are at 30 mm center to center making a total of 300 beams forming the floor of the bridge. The primary beams which are also known as the main girders are connected to the secondary beams by a stainless steel shoe fastened in an inverted U-profile. The small secondary beams are ensured of lateral stability by providing tensioned steel cables in the plan of the bridge deck.

3 Modeling Approach

The use of glass as a structural material has undergone a marked changed in the world of structural engineering. To create safe structures, it is necessary and common in any engineering design to analyse the structure before it is constructed. It is also wise to think ahead during early stage of conceptual design, making approximate calculation in the process, so that problems that may occur in the structure can be minimized. Therefore, it is good practice to develop a realistic Finite Element (FE) model for structural simulations before construction.

For this study the analysis, using a general purpose structural analysis programme, i.e., SAP 2000 has been performed. This programme is suitable for the analysis of structures subject to static and dynamic loadings. In this investigation, the structural response of the model in terms of its displacement and resulting forces due to the excitation of loads was determined.

In using SAP 2000, values of the material and section properties, support and loading conditions and dimensions of the model become the input data for the programme in order to determine the behavior of the model. Using this numerical model different types of support conditions were investigated. Thus, the maximum and minimum bending moment, shear force and deflection were obtained. Also the frequency and deflection limits of the glass footbridge were determined in order to satisfy the design code limits for footbridges as specified in BD 37/01, [5].

For the combination values, the dead load Gk and imposed load Qk, a partial factor of safety of $\gamma f = 1.0$ was applied to all load combinations at serviceability limit state. The glass footbridge finite element model carries a uniformly distributed dead load from deck slab of 1.47 and 0.74 kN/m and a uniformly distributed imposed load of 5 and 2.5 kN/m for the inner and edge girders respectively.

3.1 Formation of the 2D Model

To carry out the analysis, a 2D model of an inner girder was created using SAP 2000. In order to create a simple 2D model, the structural plan in a 3D view is first considered, before a typical 2D structure can be isolated. As stated earlier, the original bridge of the structure consists of six large panels arranged to be 1.0 m apart from each other. There are 300 small secondary beams placed perpendicular to the panels, where each beam is 1.0 m in length and 60 mm in depth, forming the floor of the bridge. However, for this investigation, the length and depth of the secondary beams was converted into an equivalent width and depth of a flat slab, 1.0 m and 60 mm respectively. The six large glass panels were modeled using beam finite elements. The above consideration simplified the input data for SAP 2000.

The beam was modeled to include a hinge at the middle of the span. This non-prismatic girder was divided into seven elements. As shown in the finite element model in Fig. 3, the seven elements labeled as FSEC1, FSEC2, FSEC3, FSEC4, FSEC5, FSEC6, and FSEC7, define the finite beam elements of the main girder under investigation.
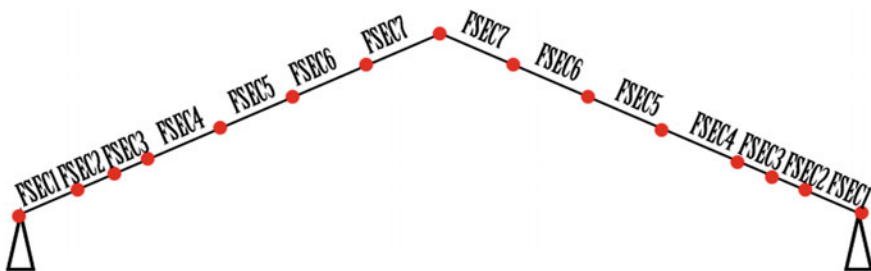
Fig. 3 Finite element model of girder (2D view)

Every beam element has a constant width, 60 mm, but with different heights and lengths thus creating different values of longitudinal sectional area, volume, and mass. The other important input data necessary for a finite element model is the material properties of its elements. Therefore, all beam elements were given a Modulus of Elasticity, density and Poisson's ratio as 70 kN/m^3, 2500 kg/m^3 as 0.22 respectively. These values have been taken from a book titled Structural use of glass in buildings (Institute of Structural Engineering), and are typical for annealed glass.

3.2 Formation of the 3D Model

For the formation of this 3D model, the structure is modeled into six large glass panels joined together with a deck slab, 60 mm thick. Hence, the main beam (or girder) defined in the 2D modal analysis is duplicated into five other girders which are at 1 m center to center, making a total of six girders all together. However, for the 3D model analysis, the uniformly distributed dead and imposed loads from deck slab, which are transferred to the outer or edge girder, differs from the inner girder by a half, since the edge girder only carries half of the deck slab width. In the 2D model analysis, only beam finite elements of the primary girder are taken into consideration. In contrast, in the 3D model analysis, both primary and secondary beam finite elements are defined in the Programme SAP. Each secondary beam is modeled as seven beam elements to simulate the solid deck of 60 mm thick. As shown in the finite element model in Fig. 4, the seven beam finite elements labeled as FSEC8, FSEC9, FSEC10, FSEC11, FSEC12, FSEC13, and FSEC14, define the finite elements of the secondary beams under investigation. All components in the 3D model, i.e., primary and secondary beams exhibit the same material properties of glass as specified in Sect. 3.1. For this specific analysis, every secondary beam had a constant height and length of 60 and 1000 mm respectively. However, their widths are different, thus creating different values of section properties.

4 Comparison Between the 2D and 3D Numerical Models

The aim of carrying out the 2D and 3D finite element analysis was to investigate the response of the glass bridge structure due to static loads. The behavior using different types of support conditions, i.e., pinned-pinned (ModelPP) or fixed-fixed (ModelFF) supports were also investigated. Hence, FEA using both types of supports were conducted and the results are compared. The analysed models produced values and locations of maximum bending moment, shear force and deflection. Tables 2, 3 and 4 compare the maximum moment, shear force, and deflections obtained from the 2D and 3D models. In the 2D analysis all the moments are carried by the primary beams, hence the moments are slightly higher than in the 3D
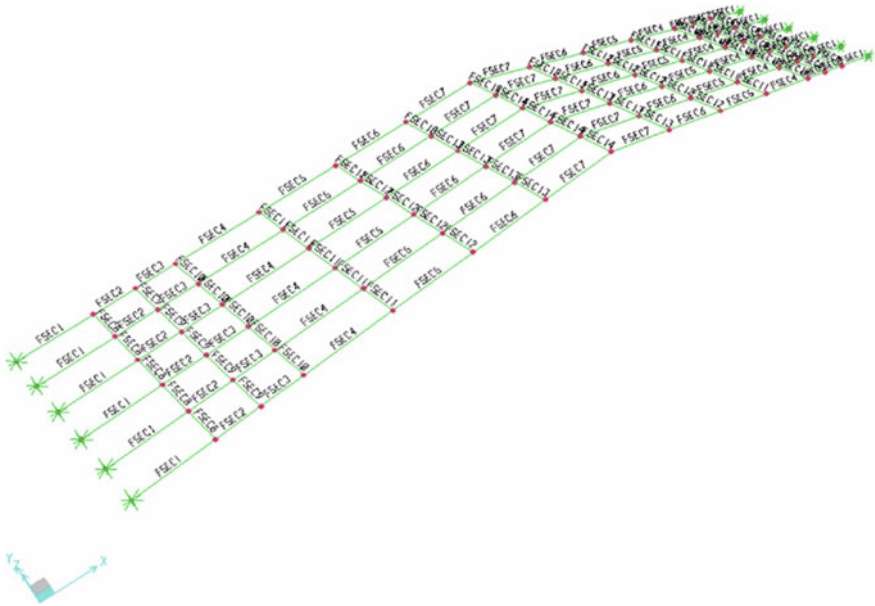
Fig. 4 Finite element model of glass footbridge (3D view)

Table 2 Comparison of maximum moment between 2D and 3D model

Supports	Max moment 2D model		Max moment 3D model		Max moment, % difference between models
	Value kNm	Location	Value kNm	Location	
ModelPP	173.2 (+ve)	At quarter span	164.2 (+ve)	At quarter span	4.2
ModelFF	499.3 (−ve)	At support	449 (−ve)	At support	10.9

analysis because in 3D the secondary beams also help in carrying part of the moments. The 2D analysis is expected to give the maximum deflection due to the fact that the maximum moments were obtained from this model there by giving the maximum deflection. Whereas, the 3D had the maximum shear force because the secondary beams will also contribute part of the shear and total shear will be carried by the primary beam. While in the 2D model there will not be any contribution from the secondary beams.

Table 3 Comparison of maximum shear force between 2D and 3D model

Supports	Max shear force 2D model		Max shear force 3D model		Max shear force, % difference between models
	Value kN	Location	Value kN	Location	
ModelPP	58.3 (−ve)	At support	64.4 (−ve)	At support	10.5
ModelFF	97.5 (−ve)	At support	98.4 (−ve)	At support	0.9

Table 4 Comparison of maximum deflection between 2D and 3D model

Supports	Max deflection 2D model		Max deflection 3D model		Max deflection, % difference between models
	Value mm	Location	Value mm	Location	
ModelPP	28.3	Near middle span	24.6	Near middle span	13.1
ModelFF	3.1	Near middle span	2.7	Near middle span	12.9

(i) 1st horizontal mode   (ii) 2nd horizontal mode   (iii) 3rd horizontal mode

(iv) 1st vertical mode   (v) 2nd vertical mode   (vi) 3rd vertical mode
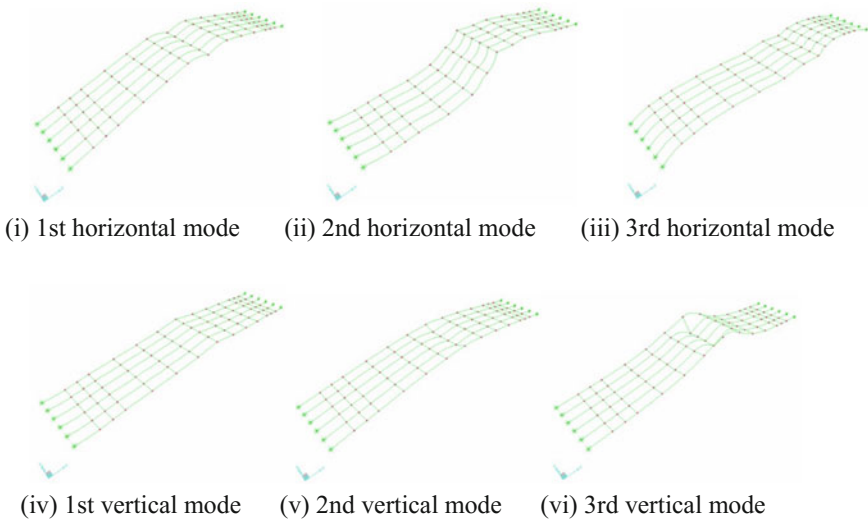
Fig. 5 The first three horizontal and vertical modes of the model with pinned-pinned supports

Fig. 6 Torsional mode of the model with pinned-pinned supports

(i) 1st horizontal mode   (ii) 2nd horizontal mode   (iii) 3rd horizontal mode

(iv) 1st vertical mode   (v) 2nd vertical mode   (vi) 3rd vertical mode
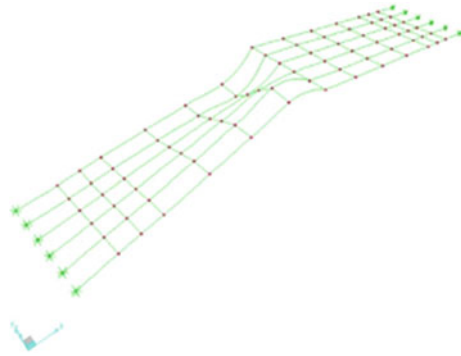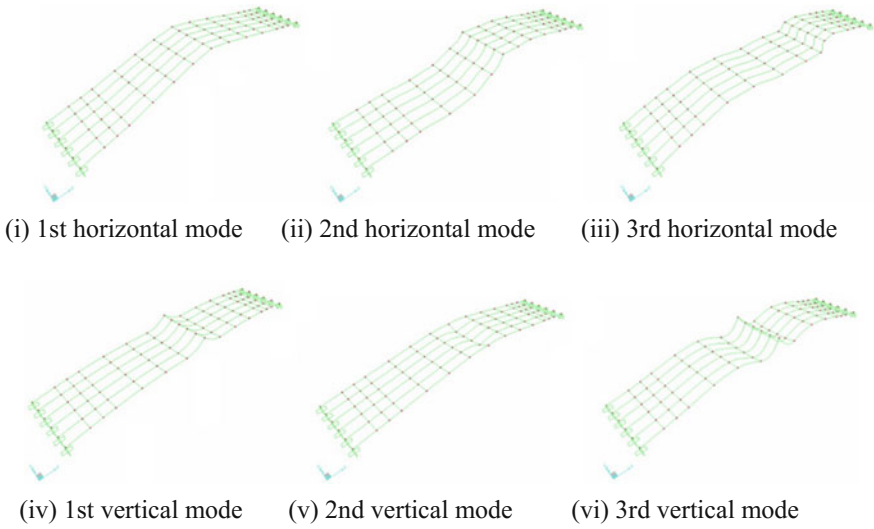
Fig. 7 The first three horizontal and vertical modes and frequencies of the model with fixed-fixed supports

Fig. 8 Torsional mode of the model with fixed-fixed supports
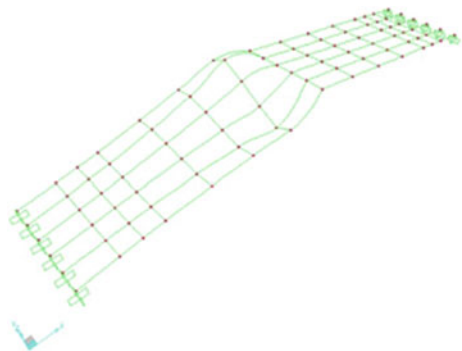
5 Frequencies and Modes of Vibration on the Models

Generally, a 3D modal analysis gives three types of mode shapes, i.e., horizontal, vertical and torsional as, compared to a 2D modal analysis which can produce only two types of mode shape, namely vertical and horizontal. Figures 5 and 7 show the first three horizontal and vertical modes and frequencies of the 3D model with pinned-pinned and fixed-fixed supports respectively. Figures 6 and 8 show the torsional mode and frequencies of the model with pinned-pinned and fixed-fixed supports respectively.

BS5400 states that if the fundamental frequency of vertical and horizontal vibration is less than 5 and 1.5 Hz respectively, the risk of upwards and lateral movements of unacceptable magnitude may occur and should be considered in the design. However, for this specific analysis of the glass footbridge the results obtained clearly shows that frequencies obtained for both conditions are within the required limits. A comparison of the vertical vibration criteria using pinned-pinned and fixed-fixed support conditions is presented in Tables 5 and 6 respectively. A comparison of the vertical vibration criteria indicates that the frequency obtained from the 3D model is only slightly higher than the values obtained from the 2D model by factors not exceeding more than 5.4%. This also indicates that there is a good agreement between the 2D and 3D model with a maximum difference in the order of 5%.

Table 5 Comparison of the frequency and mass participation factor between the 2D and 3D models for the pinned-pinned supports

No. of mode	2D model		3D model		Maximum frequency, % difference between models
	Calculated frequency [Hz]	Mass participation factor (%)	Calculated frequency [Hz]	Mass participation factor (%)	
1st vertical mode	5.68	76.8	5.9	76.7	3.9
2nd vertical mode	31.2	77.4	32.4	77.3	3.8
3rd vertical mode	41.6	87.9	42.7	84.7	2.6

Table 6 Comparison of the frequency and mass participation factor between the 2D and 3D models for the fixed-fixed supports

No. of mode	2D model		3D model		Maximum frequency, % difference between models
	Calculated frequency [Hz]	Mass participation factor (%)	Calculated frequency [Hz]	Mass participation factor (%)	
1st vertical mode	18.6	50.7	19.6	50.3	5.4
2nd vertical mode	32.4	51.0	33.5	50.5	3.4
3rd vertical mode	58.5	70.6	60.9	70.1	4.1

6 Connections

For steel connection design calculations, the average bearing stress, shear and tensile stress is required. However, for a brittle material like glass, the approach for its connection design procedure is comparatively more rigorous. Besides needing the value of the average bearing, shear and tensile stress, the design calculation also needs the value of the localized tensile stress concentration to ensure a safe design. In the process, forces developed should be properly and smoothly transferred between the glass members through the steel plates and bolts of the connections.

Due to the large size of each glass panel, being almost 10.5 m in length with a variable depth up to 2.8614 m, each panel needs to be subdivided into at least three smaller size panels which are connected with each other at Node 3 and Node 5 as shown in Fig. 9. Each sub-panel is formed from four layers of 15 mm thick toughened glass. Figure 10 shows the detail connection where the sub-panels are fixed together. At the connection, two connecters are used to transfer the bending
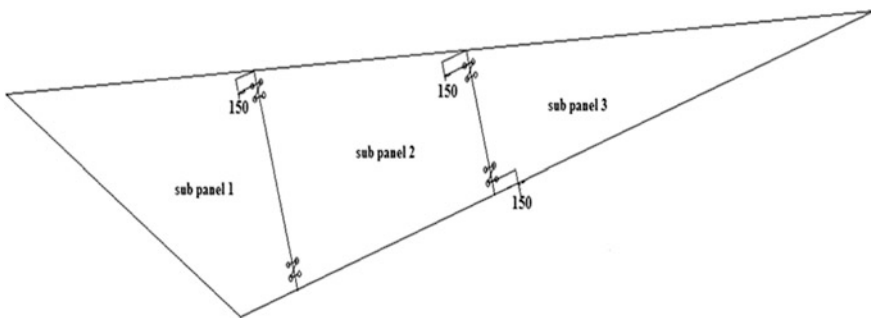
Fig. 9 Sub panel with connections
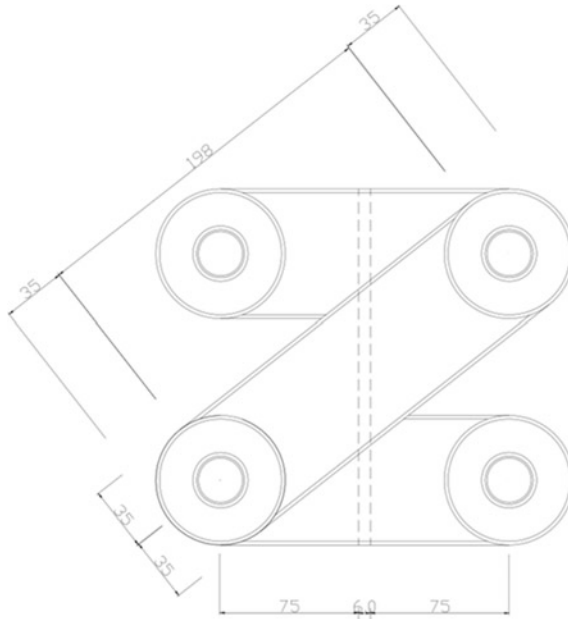
Fig. 10 Connection details Adopted from Nijsse (2002) (All dimensions are in mm)

Table 7 Stresses at connection

Type of support	Maximum moment, M (kNm)	Vertical distance, d (mm)	$F_{tension} = M/d$ (kN)	Tensile area A (mm²)	Stress in one strap = (Ftension/A)/2 (N/mm²)
Model PP	238.2	1325.4	179.7	480	187.0
Model FF	691.8	2770.7	249.7	480	260.1

moment between the sub-panels. For the purpose of designing the connecters at Node 5, the maximum bending moment value along the panel is used as the design moment acting on the connection. Hence, for Model PP the maximum bending moment in the large panel at this location is 238.15 kNm as given in Table 7. Once the connecters have been selected, stress levels in the connection will be checked.

The following shows the procedure adopted for the design of the connection.

Step1: To determine the force and type of bolt at Node 5 for Model PP;

$$\text{Moment acting on the connection,} \, M = 238.2 \text{ kNm}$$
$$= 238.2 \times 10^3 \text{ kNmm}$$

Vertical Distance, $d = $ (Height of beam at node 5) $- (2 \times$ Height of the *connecter*) $= 1625.4 - 2 \times 150 = 1325.4$ mm

Note that the vertical distance d, is defined as the total height of the beam at node 5, minus the height of the two connecters. (Each connecter is 150 mm high.) Horizontal shear force acting on the connection,

$$
\begin{aligned}
\text{Ftension} &= M/d \\
&= (238.2 \times 103 \text{ kNmm}) \\
&= 1325.4 \text{ mm} \\
&= 179.7 \text{ kN}
\end{aligned}
$$

The above implies that the shear capacity of the connection bolts should be more than 179.6 kN for a safe design. Hence, consider a total of 8, M20 Grade 8.8 bolts in accordance with BS 4395: Parts 1 & 2 with an individual shear capacity of 184 kN in double shear.

Total shear capacity from two bolts is $2 \times 184 = 368$ kN and as $179.7 < 368$ kN the connection is OK!

Step2: To check the stress level;

Select steel plate 150 mm height, 70 mm wide and 10 mm thick.

Tensile area $= (70 - (20 + 2))$ mm $\times 10$ mm $= 480$ mm^2

where diameter of bolt $= 20$ mm and

clearance hole $= 22$ mm

$$
\begin{aligned}
\text{Stress} &= (\text{tensile force}/\text{tensile area}) \\
&= (179.6 \times 103 \text{ N})/(480 \text{ mm}^2) \\
&= 374.2 \text{ N/mm}^2
\end{aligned}
$$

However, as there are two straps carrying this load, one each side of the glass beam this strap force can be divided by two; hence the tensile stress in each strap is 187 N/mm^2. Since the steel grade S275 and the stress in one strap is less than 275 N/mm^2, therefore the selected strap is adequate. Therefore, two connectors with bolts size M20 Grade 8.8 are placed at Node 3 and Node 5 in Model PP. The above steps are repeated when designing the connection at Node 3 and Node 5 in Model FF, where the maximum moment 691.8 kNm for the panel is taken to be the moment acting at the connection.

7 Discussion, Conclusion, and Recommendations

This paper presents the investigation into the behavior of a glass footbridge as shown in Fig. 2. The footbridge is made of toughened glass, has six primary beams or panels and 3000 secondary beams which act as the floor deck. The 2D finite

element model shown in Fig. 3 is created using the Program SAP 2000, which is a finite element general purpose program. The model is formed using beam finite elements. The model having pinned-pinned supports, Model PP was analysed and the analysis was repeated with model having fixed-fixed support conditions, Model FF. Values in Table 4 indicate that the type of supports, influence the analytical results, where Model PP has comparatively higher maximum deflection whereas Model FF has higher maximum moment and shear force.

Maximum stresses for the models are calculated, where for Model PP and Model FF are 18.1 and 7.32 N/mm^2 respectively. Since these values are less than the tensile failure strength of toughened glass, typically 43–50 N/mm^2, the footbridge using this type of toughened glass is considered to be safe. Tables 1, 2 and 3 compare the maximum moment, shear force and deflection obtained from the 2D and 3D models. In the 2D analysis all the moments are carried by the primary beams, hence the moments are slightly higher than in the 3D analysis because in the 3D model the secondary beams also helps in carrying part of the moments. The 2D analysis is expected to give the maximum deflection due to the fact that the maximum moments were obtained from this model there by giving the maximum deflection. Whereas, the 3D had the maximum shear force because the secondary beams will also contribute part of the shear and total shear will be carried by the primary beam. While in the 2D model there was no contribution from the secondary beams. The maximum deflection was 28.3 and 3.1 mm for model PP and Model FF respectively. Since these values are lower than the limiting value of 82.0 mm calculated based on code of practice, therefore the footbridge is safe.

Due to the large size of the glass panel (representing the primary beam), it was subdivided into smaller size panels which needed to be connected together. At the connections, connectors using steel bolts and steel straps were selected. The stress levels at the connections were checked and found to be adequate.

Although the analytical results using the 2D model was expected not to be very different from the 3D model, this investigation proves that this was in fact true, because the results differ only slightly as shown in Tables 2, 3 and 4. Modal analysis was carried out to determine the frequencies and mode shapes due to the vibrations of the footbridge. Modal analysis using the 2D model produces frequencies in a vertical mode only, whereas using the 3D model frequencies in three different modes can be obtained, vertical, horizontal, and torsional. Because the frequencies of vertical and horizontal vibrations of this footbridge are higher than the minimum value required as specified in the standard, therefore vibrations of an unacceptable magnitude would not occur in this footbridge. Because, the checks carried out indicate that the footbridge satisfies the design criteria, the footbridge design is considered to be safe and the structure is almost ready to be constructed.

Although a large portion of the glass bridge has been designed in this investigation there remains addition work which needs to be undertaken before the structure can be fabricated and erected. Further consideration has to be given to the connections, especially the support connections, which are subject to high shear loads and also to the bearing stresses in the glass adjacent to the bolts. Because the main beams are laminated careful consideration has to be given to the material

chosen to use between the individual laminations. It is important that the laminated beam acts as one complete unit and that stresses are uniformly distributed throughout the thickness of the beam otherwise the outer laminations may become overstressed and fail prematurely.

As the proposed glass footbridge is a novel structure, if finance is available it would be sensible to either construct a model of the structure or preferably to monitor the actual structure to check that the measured stresses under full load are in accordance with those calculated from the finite element analysis. In addition, the fundamental frequency of the structure could be obtained by dynamically exciting the structure and this could also be checked against the calculated value.

In the future it is expected that more glass structures with maximum transparency will be developed. Such structures free engineers from building masonry walls and steel frames and beams, which allow for more space and freedom.

References

1. Nijsse, R.: Glass in Structures, Birkhäuser, Berlin (2002)
2. Smith, J.W.: Vibration of Structures: Applications in Civil Engineering Design. Chapman and Hall, Bristol (1998)
3. Maguire, J.R., Wyatt, T.A.: ICE Design and Practice: Dynamics: An Introduction for Civil and Structural Engineers, 2nd edn. Thomas Telford Publishing, London (2002)
4. Hauksson, F.: Dynamic behavior of footbridges subjected to pedestrians-induced vibrations. Master Dissertation, Lund University (2005). Retrieved 17 Dec 2007, from Lund University Digital Library
5. BD37/88: Departmental Standard—Loads for Highway Bridges. Highway and Traffic Agency, London (1989)

Performance Criterion for Selecting Columns to Be Removed in the Alternate Load Path (ALP) Analysis for Progressive Collapse Assessment

Hazrina Mansor, Peter Disney and Gerard Parke

Abstract The alternate load path (ALP) method is an event-independent approach in analysing robustness against progressive collapse, where the actual load arising from the complicated triggering event is not considered. The method proposes the removal of one or more load-bearing elements of a structure, such as a column, and the consequences following from the location of removed column onto the investigated structure will be analysed in terms of its ability to redistribute the gravity loads to the remaining intact structural elements. Since the assessment of structural robustness using the ALP method is highly dependent on the location of the lost column, it is important that selection of the critical column position that needs to be removed for detail progressive collapsed assessment is undertaken with care. If this is not the case, the results generated will not be able to show the actual level of the robustness of the structure. In this paper, a new, performance criterion namely, the computation of the total number of overstressed remaining members was introduced to determine the most critical column location for further evaluation of the structural resistance against progressive collapse. SAP2000 structural design software and MATLAB were used as tools for the collapse analysis. A ten-storey moment-resisting steel frame structure was used to demonstrate the implementation of the proposed criterion. It can be concluded that the proposed criterion has the potential to be a useful and quick indicator to determine the critical column location for a more detail progressive collapse analysis of a structure.

Keywords Progressive collapse · Quantitative algorithm · Alternate load path

H. Mansor (✉)
Universiti Teknologi Mara (UiTM), 40450 Shah Alam, Selangor, Malaysia
e-mail: hazrina.uitm@gmail.com

P. Disney · G. Parke
University of Surrey (UniS), Guildford GU2 7XH, UK
e-mail: P.Disney@surrey.ac.uk

G. Parke
e-mail: g.parke@surrey.ac.uk

1 Introduction

The provisions which address the progressive collapse issue was first documented in an approved document A3 in the United Kingdom Building Regulations document, 2000 [1]. The recommendation for the progressive collapse issue was initiated in the document after the Ronan Point collapse incident in 1968 and further encouraged after the IRA bombing campaign in the UK in the 1970s and 1980s. The regulations recommended the tying approach, the key element approach and the alternate load path approach to ensure that structures have a minimum level of strength to resist accidental loading. The tying approach requires members in the structure to be horizontally and vertically tied together to enhance continuity, ductility and structural redundancy between the structural elements. Meanwhile, ALP approach is designed to allow for bridging over the lost, untied, member and upon removal, the collapse is limited to at most 70 m^2 or 15% of the area of each floor, whichever is the smallest. Whilst, the key element approach is recommended when the structural members failed to bridge over the loss of untied members; therefore, the member should be designed as a key member and ought to be able to withstand a pressure of 34 kN/m^2. The three robustness strategies were then to be applied to a building depending on the class of the building.

The implementation and scope of the proposed strategies given in the United Kingdom Building regulation, Approved document A3 are very similar with the Eurocode robustness requirements, which have been adopted in BS EN 1991-1-7:2006 [2] with only a slight modification. The Eurocode document provides two general design strategies based on accidental design situations. The first strategy is based on an identified accidental action while the second type of strategy is based on unidentified accidental actions. The strategy which is based on identified accidental actions, recommended three design strategies; these are (i) Design for sufficient minimum robustness, (ii) Prevent or reduce action and, (iii) Design to sustain action. In BS EN 1991-1-7:2006 the Eurocode document, these strategies of identified accidental actions can be found in clause 3.2. In addition, the implementation of the first form of strategy might also provide adequate robustness for the structure against some unidentified actions depending on the exact nature of the strategy. As for the second form of strategy which is based on unidentified accidental actions, the strategies include various possible events and are also linked to strategies based on limiting the spread of localised failure. The strategy which is based on unidentified accidental actions, recommended three design strategies; these are: (i) Enhanced redundancy, (ii) Design to resist notional accidental actions and (iii) Prescriptive rule. It should be noted that the sufficiency of the implemented strategies is highly dependent on the actual characteristics of the accidental actions. These design strategies can be found in BS EN 1991-1-7:2006 clause 3.3(1).

To conclude, the Approved Document A3 provided the initial idea to enhance the overall structural integrity for buildings where its strategy in mitigating progressive collapse for a building is based on the requirement and the level of importance of the building under consideration. Therefore, different progressive

collapse design assessment approaches and robustness strategies are applied to different classes of structure, which is quite cost-effective in terms of actual implementation. However, in terms of the implementation of the notional element removal and key element approaches, it should be stressed that there is a lack of information in the document on how such approaches should be implemented to evaluate the potential risk of collapse for a building.

Unlike the UK and Eurocode design guidelines, the General Service Administration (GSA) and Department of Defence (DoD) recommend several locations on the ground floor to be considered for column removal. These recommendations include an exterior column near the middle of both the long and short side of the building, a column located at the corner of the building, an interior column near to the perimeter column and other positions where the geometry of the structure changes [3, 4]. The documents also come with the outline procedures on how to carry out progressive collapse assessment via linear or nonlinear static and dynamic analyses. These recommendations have been widely adopted by researchers investigating progressive collapse, among them are Kwasniewski [5] and Liu [6, 7]. Although these column locations have been recommended by GSA and DoD, there is still a possibility that other columns might also be critical as has been found by Fu [8] and Tavakoli [9]. Nevertheless, in certain aspects, the approach given in the UK and Eurocode design guidelines does have a great advantage since the evaluation process covers the removal of all supporting elements in the structure, thus providing a more comprehensive view on the structure's robustness. Therefore, more detailed information is required with regards to the procedure on how such notional element should be removed by utilising the idea of removing all supporting members as suggested in the UK and Eurocode design guidelines and the types of analysis required for such an approach, which is the focus of this paper.

2 Proposed Quantitative Column Removal Approach

The quantitative method proposed in this study comprises of four major steps, these are (1) Structural design (2) Member removal process with subsequent analysis (3) Determination of the critical column location and (4) Classification of the column removal cases. First, the proposed structure is modelled and designed with the appropriate dimensions, material properties, section sizes, support restraints and loading in accordance with the general design procedure. In this study, the author used the SAP 2000 finite element analysis software is used to design and model the proposed structure. For the member removal process, the first step is the determination of the designed structural members that must be eliminated one at a time when assessing the robustness of the structure and the second step is the elimination process of the individual designed structural members that have been determined. The type of structural members that need to be removed is highly dependent on the design of the building. In this procedure, the selection of the members to be removed is based on the UK and Eurocode design guideline; these are columns and

the transfer beams supporting columns. To reduce the computational time taken during the elimination process (i.e. when removing and analysing the structure), an 'auto-operation' technique is proposed with the aid of SAP 2000 finite element analysis software version 15 and MATLAB. The general procedure used for the elimination process is presented in the flowcharts shown in Fig. 1. The next stage is the determination of the critical column location. The critical column location is determined based on the proposed performance criterion achieved by counting the total number of overstressed members for each case of column removal, where any remaining intact member which has a Demand Capacity Ratio (DCR) value exceeding 1.0 is overstressed. Finally, the classification of column removal cases which will indicate the critical column location is carried out based on the proposed performance criteria.

2.1 Demand Capacity Ratio

Force interaction criteria for cross-section resistance of a member

For the cross-section of a member which is subjected to combined axial force and bending moment, the interaction equations in accordance with clause 6.2.1(7), 6.2.9 of the Eurocode 3 1993-1-1 [10] will be applied;

(a) Class 1 and class 2 cross sections

For I section, the summation of the utilisation ratios for each force component is as follows:

$$\text{DCR} = \left[\frac{M_{y,\text{Ed}}}{M_{N,y,\text{Rd}}}\right]^{\alpha} + \left[\frac{M_{z,\text{Ed}}}{M_{N,z,\text{Rd}}}\right]^{\beta} \leq 1 \qquad (\text{EC3cl.6.2.9.1(6)})$$

where

$$\alpha = 2 \text{ and } \beta = 5n \geq 1$$

$$M_{N,y,\text{Rd}} = M_{pl,y,\text{Rd}}\left(\frac{1-n}{1-0.5a}\right) \qquad (\text{EC3cl.6.2.9.1(5)})$$

$$M_{N,z,\text{Rd}} = \begin{cases} M_{pl,z,\text{Rd}}, & \text{for } n < a \\ M_{pl,z,\text{Rd}}\left[1 - \left(\frac{n-a}{1-a}\right)^2\right], & \text{for } n < a \end{cases} \qquad (\text{EC3cl.6.2.9.1(5)})$$

where

$$n = \left(\frac{N_{\text{ED}}}{N_{\text{Pl,Rd}}}\right) \qquad (\text{EC3cl.6.2.9.1(5)})$$
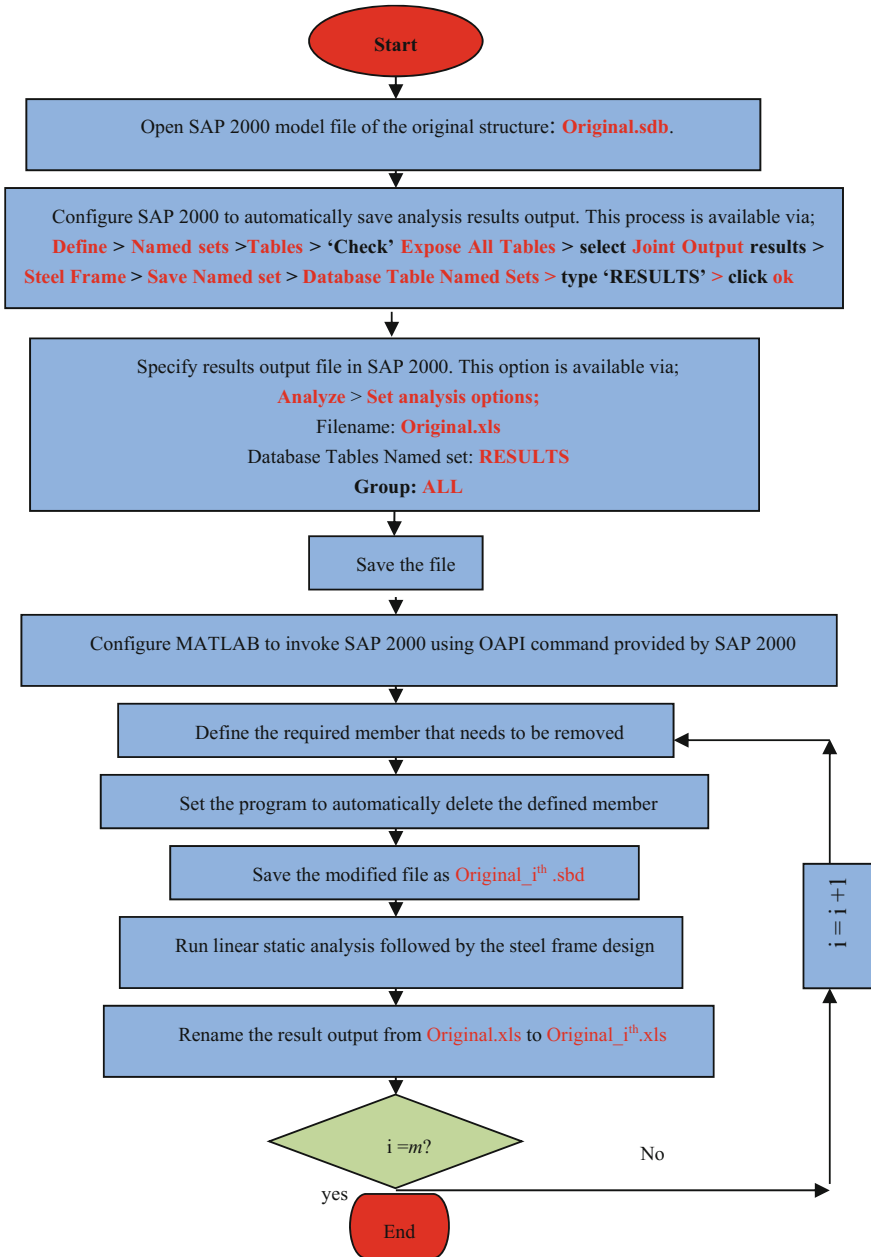
Fig. 1 Auto-removal process

However,

$$M_{N,y,\text{Rd}} = M_{\text{pl},y,\text{Rd}} \quad \text{if} \quad N_{\text{ED}} \leq 0.25 N_{\text{pl,Rd}}$$

and

$$N_{\text{ED}} \leq 0.5 \frac{h_w t_w f_y}{\gamma_{m0}} \qquad\qquad (\text{EC3cl.6.2.9.1(4)})$$

Furthermore,

$$M_{N,y,\text{Rd}} = M_{\text{pl},z,\text{Rd}} \text{ if } N_{ED} \leq 0.5 \frac{h_w t_w f_y}{\gamma_{m0}} \qquad\qquad (\text{EC3cl.6.2.9.1(4)})$$

(b) Class 3 cross sections

For all shapes, the combined axial force and bending is conservatively calculated by taking the linear summation of the utilisation ratios for each force component as follows:

$$\text{DCR} = \frac{N_{\text{Ed}}}{N_{\text{Rd}}} + \frac{M_{y,\text{Ed}}}{M_{y,\text{Rd}}} + \frac{M_{Z,\text{Ed}}}{M_{Z,\text{Rd}}} \leq 1.0 \qquad\qquad (\text{EC3Cl.6.2.1(7)})$$

Force interaction criteria for buckling resistance of a member

For a member that is subjected to a combined effect of axial compression and bending with special emphasis on flexure and lateral torsional buckling, the demand capacity ratio is defined by calculating the utilisation ratios obtained from the interaction equation given in clause 6.3.3(4) of Eurocode 3 1993-1-1 [10], which is given as follows:

$$\text{DCR} = \frac{N_{\text{Ed}}}{\frac{\chi_y N_{\text{Rk}}}{\gamma_{M1}}} + k_{yy} \frac{M_{y,\text{Ed}}}{\chi_{LT} \frac{M_{y,\text{Rk}}}{\gamma_{M1}}} + k_{yz} \frac{M_{Z,\text{Ed}}}{\frac{M_{Z,\text{RK}}}{\gamma_{M1}}} \leq 1.0 \qquad (\text{EC3Cl.6.3.3(4)})$$

$$\text{DCR} = \frac{N_{\text{Ed}}}{\frac{\chi_z N_{\text{Rk}}}{\gamma_{M1}}} + k_{zy} \frac{M_{y,\text{Ed}}}{\chi_{LT} \frac{M_{y,\text{Rk}}}{\gamma_{M1}}} + k_{zz} \frac{M_{Z,\text{Ed}}}{\frac{M_{Z,\text{RK}}}{\gamma_{M1}}} \leq 1.0 \qquad (\text{EC3cl.6.3.3(4)})$$

2.2 Computation of the Total Number of Overstressed Members Based on Their Demand Capacity Ratio (DCR)

The severity of the effect of a column removal on the structure is quantified by counting the total number of remaining overstressed structural members. It is believed

that the probability of a structure experiencing progressive collapse after a sudden loss of a column is highly dependent on the number of failed or overstressed members remaining in the structure. Therefore, the highest count is expected to indicate that the structure is most susceptible to experience progressive collapse. Whilst, the lowest count indicates the structure has the lowest tendency to collapse. The column removal cases are first sorted according to the total number of overstressed members from the highest to the lowest. The cases are then categorised into three classes, which are a low number of overstressed members, a medium number of overstressed members and a high number of overstressed members. The range between low, medium and high categories can be determined by using the following formula:

$$\text{Range} = \frac{N_{\text{max, overstressed}} - N_{\text{min, overstressed}}}{3} \tag{1}$$

where

$N_{\text{max, overstressed}}$ is the maximum total number of remaining overstressed members considering all the removal cases and

$N_{\text{min, overstressed}}$ is the minimum total number of remaining overstressed members considering all the removal cases.

3 Implementation of the Proposed Approach

3.1 Proposed Structure

A ten storeys moment-resisting frame of a commercial office building was proposed to demonstrate the effectiveness of the proposed method. The beam-column joints were rigid, where all the translational and rotational movements are restrained. Figure 2 illustrated the structural plan of the structure. All the storeys are 4.0 m in height, apart from the ground to first floor which has a height of 5.5 m (refer to Fig. 4). Figure 3 shows the three-dimensional and plan views of the moment resisting ten-storey steel frame building respectively.

3.2 Member Removal Process

The proposed ten-storey moment-resisting steel frame building shown in Fig. 3 does not include any transfer beams which would support a series of columns, thus in this case, only the removal of individual column sections needs to be considered. Bearing in mind, that the direction of the wind load, floor arrangement, section sizes, and geometrical structural stiffness of the designed structure were symmetrical in their global x-x axis, only columns which are located between the regions of
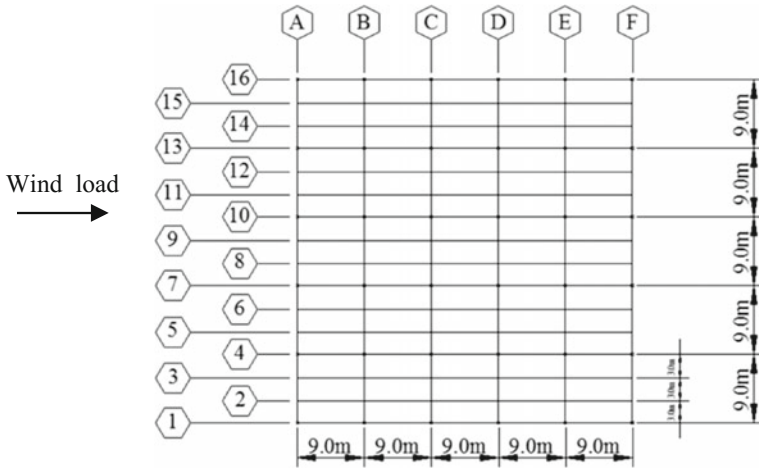
Fig. 2 Plan view with wind load direction
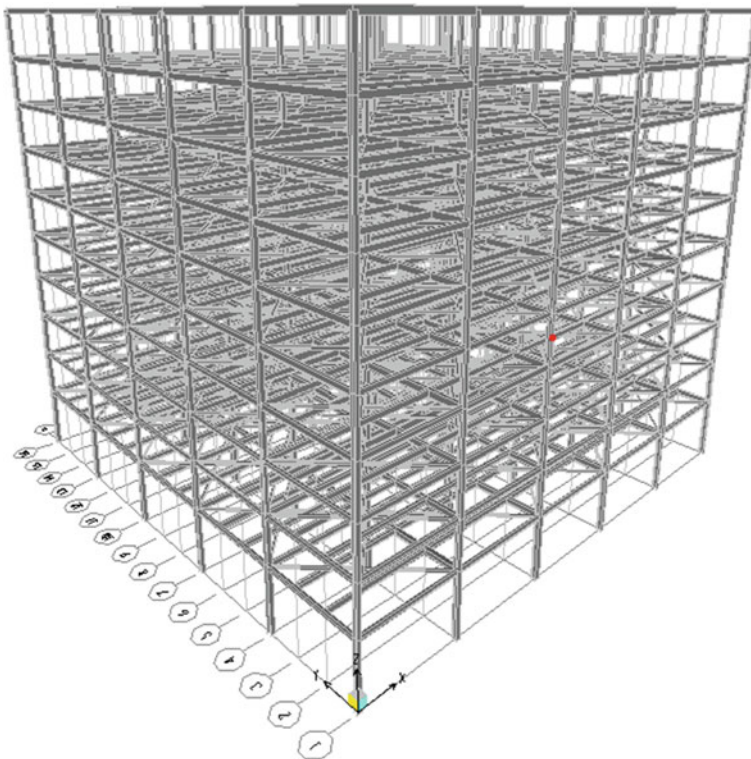
Fig. 3 Three-dimensional view of the proposed frame
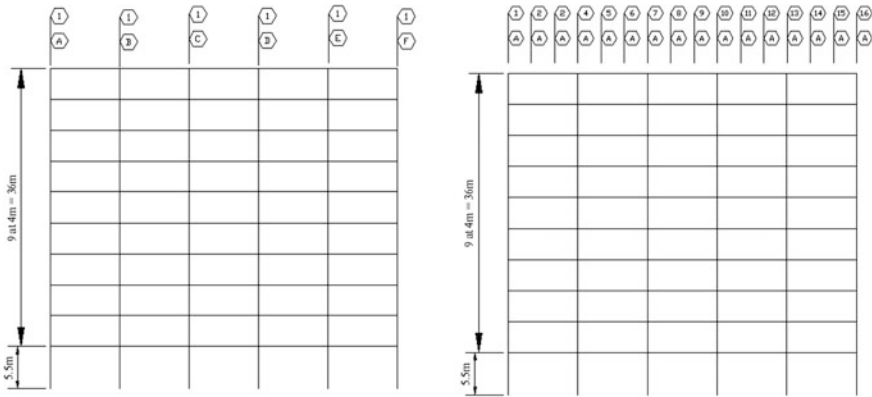
Fig. 4 Dimension of the moment frame in elevation

grid 1 to grid 8 throughout levels 1–10 of the building were considered for removal in this study. Overall, the total number of column locations for removal, one at a time, equals 180, creating 180 individual cases to be analysed. Next, is the elimination process for each of the chosen columns. The elimination process was carried out using the 'auto-operation' method. The location of the column that needs to be removed and its element identification are determined and presented in Fig. 5a, b and c. To execute the auto-operation, a MATLAB program has been written. The columns were removed one by one where the sequence of column removal for grid 1 started from column element id 1 which was then followed by columns 11, 21, 31, 41, 51, 2, 12, 22 until element id 60. In addition, the same column removal sequence was also applied to grid 4 and grid 7. At the start of the elimination process, the designer must request the required results' outputs such as joint output and steel frame design data, so that the results will be automatically generated. As a result of this auto-removal process, a total number of 180 configuration models have been generated together with their results output into an Excel file. The numbering of the 180 column removal cases was defined by its removal sequence as shown in Fig. 6a, b and c. Case 1, Case 2, Case 3 and Case 4 and until Case 180 in Fig. 6a, b and c represents the cases of columns with element identification 1, 11, 21, 31 and until element identification number 180 were removed respectively.

3.3 Determination of the Critical Column Location

The requested DCR value for each member before and after removal must be extracted from the 180 result sets output generated in Excel files in Sect. 3.2. To simplify this process, a program has been written in MATLAB. Thereafter, the results were then sorted according to the procedure explained in Sect. 2.2. The results, based on the proposed performance criterion, are presented in detail in subsequent sections.
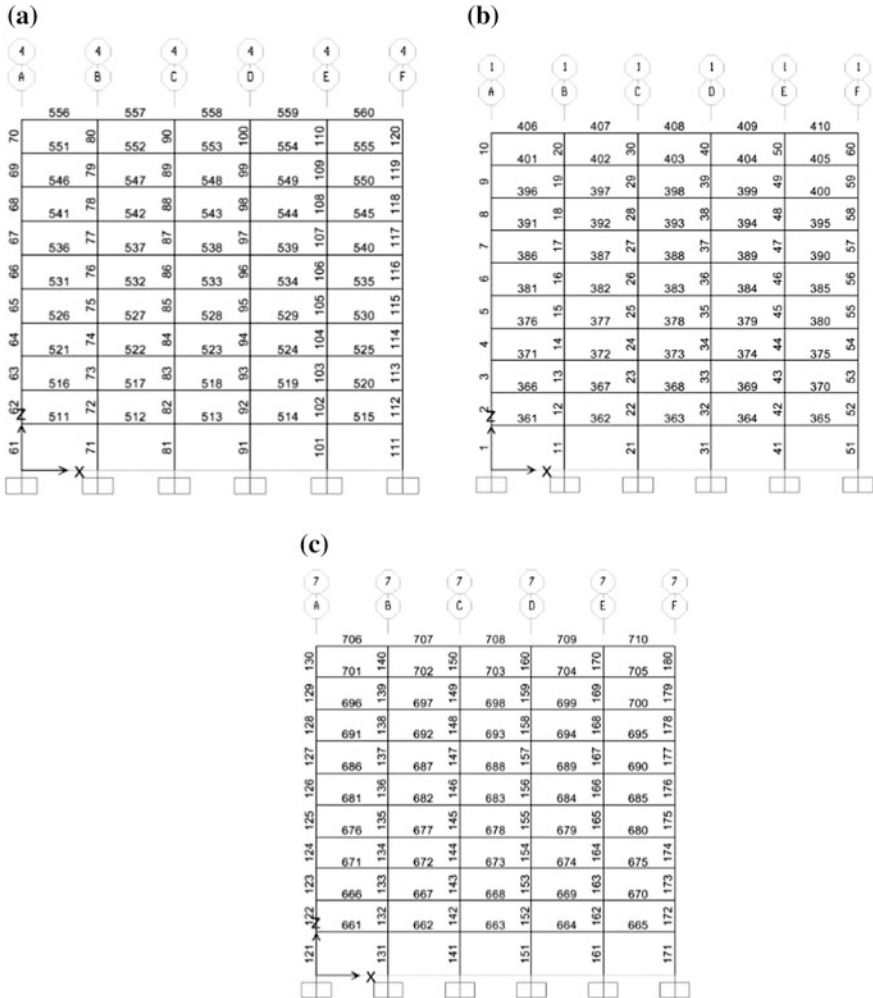
Fig. 5 a Element id for member in grid 1, **b** element id for members in grid 4, **c** element id for members in grid 7

4 Results

In this section, the results for all column removal cases in terms of their total number of overstressed members have been determined and sorted in descending order from the highest to the lowest. From the results produced by the algorithm, the sudden loss of a column in case 65 causes the maximum number of remaining overstressed member in the structure, which is 124 members. Meanwhile, the minimum total number of remaining overstressed members upon the sudden removal of a column is determined from case 180 with only 2 overstressed
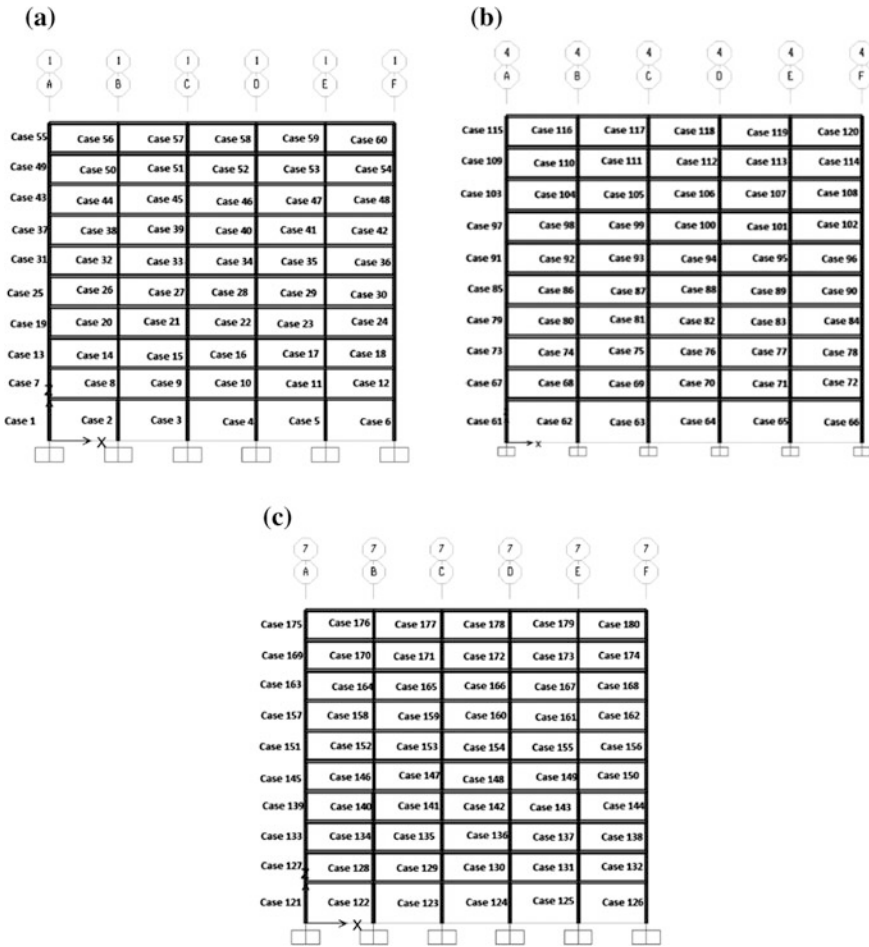
Fig. 6 **a** Column removal cases in grid 1, **b** column removal cases in grid 4, **c** column removal cases in grid 7

members. All the 180 column removal cases were then divided into three categories which are (1) highest number of total overstressed members, (2) medium number of total overstressed members and (3) lowest number of total overstressed members. Therefore, using Eq. 1, the ranges of these categories are calculated as follows:

$$\text{Range} = \frac{N_{\text{max, overstressed}} - N_{\text{min, overstressed}}}{3}$$

$$= \frac{124 - 2}{3} = 40.67 \approx 41 \tag{1}$$

Table 1 Categories of column removal cases based on the total number of overstressed members

Category	Limit of total number of overstressed members
Low	2–43
Medium	44–85
High	86–127

where

$N_{max, overstressed}$ is the maximum number of remaining overstressed members considering all of the removal cases and

$N_{min, overstressed}$ is the minimum number of remaining overstressed members considering all of the removal cases.

Using the range value of 41 for each category, the limits for high, medium and low categories are listed in Table 1.

Utilising the calculated limit for each category as presented in Table 1, all column removal cases were placed in their corresponding category as presented in Table 2.

5 Analysis and Discussion

In all 180 column removal cases applied to this structure, the case with the highest total number of overstressed members is column removal case 65, while column removal case 180 has the lowest number of overstressed members. Based on the total number of overstressed members in all cases, utilising Eq. 1, the limits for the high, medium and low categories are 2–43, 44–85 and 86–127 respectively (refer Table 1). In terms of the number of cases per category, it has been found that 29 out of 180 cases are in the high category, 67 cases are in the medium category and 84 cases are in the low category (refer Table 2). For the column removal cases in the high category, most of the removed columns are in the interior of the structure and also near to the perimeter. This can be seen in Figs. 7 and 8 whereby the location of columns which have been categorized under the high category is highlighted in red. Due to their interior location, they have more members spanning on to them. Upon their removal, it is expected that the connected beams will have a small capability to effectively redistribute loads from the loss of the column as the unsupported length would have doubled and the loss of the column would have induced forces into the beams that were not considered in the original design. Therefore, this effect significantly increases the applied load on the surrounding members. It is understood that the total of axial loads carried by a column will be decreasing as the storey levels increases. Since many columns in the high category are situated at level 1–5, they are normally subjected to high axial loading compared to the columns at higher storey location. Consequently, their removal will substantially increase the vertical

Table 2 Categorisation of column removal cases based on the proposed criterion

Category	Column removal cases (no. of overstressed members)
High	Case 65 (124), Case 62 (120), Case 71 (116), Case 63 (112), Case 68 (112)
	Case 64 (109), Case 77 (109), Case 122 (109), Case 125 (109), Case 74 (106)
	Case 128 (103), Case 131 (103), Case 69 (101), Case 123 (101), Case 124 (100)
	Case 70 (99), Case 83 (98), Case 80 (96), Case 134 (96), Case 137 (96)
	Case 75 (94), Case 76 (91), Case 89 (91), Case 129 (91), Case 130 (90)
	Case 135 (87), Case 140 (87), Case 143 (86)
Medium	Case 86 (85), Case 81 (84), Case 136 (84), Case 146 (82), Case 82 (81)
	Case 149 (80), Case 5 (79), Case 95 (79), Case 92 (78), Case 155 (77)
	Case 141 (76), Case 11 (75), Case 2 (74), Case 152 (74), Case 142 (73)
	Case 8 (71), Case 87 (71), Case 17 (69), Case 88 (69), Case 3 (67)
	Case 4 (66), Case 66 (66), Case 101 (66), Case 14 (64), Case 98 (64)
	Case 147 (64), Case 72 (63), Case 126 (63), Case 148 (62), Case 9 (61)
	Case 23 (61), Case 61 (61), Case 161 (61), Case 10 (60), Case 78 (60)
	Case 67 (59), Case 93 (59), Case 121 (59), Case 132 (59), Case 158 (59)
	Case 20 (58), Case 15 (57), Case 16 (56), Case 94 (56), Case 127 (56)
	Case 73 (55), Case 29 (54), Case 138 (54), Case 84 (52), Case 21 (51)
	Case 26 (51), Case 133 (51), Case 153 (51), Case 22 (50), Case 144 (49)
	Case 154 (49), Case 79 (47), Case 27 (46), Case 35 (46), Case 107 (46)
	Case 28 (45), Case 104 (45), Case 90 (44), Case 99 (44), Case 100(44)
	Case 150 (44)
Low	Case 32 (43), Case 139 (43), Case 6 (42), Case 1 (41), Case 167 (41)
	Case 12 (40), Case 33 (40), Case 34 (39), Case 156 (39), Case 164 (39)
	Case 159 (38), Case 160 (38), Case 7 (37), Case 18 (37), Case 85 (37)
	Case 24 (36), Case 38 (35), Case 41 (35), Case 145 (35), Case 13 (34)
	Case 96 (33), Case 30 (32), Case 105 (32), Case 106 (31), Case 19 (30)
	Case 39 (30), Case 40(30), Case 165 (30), Case 166 (30), Case 91 (29)
	Case 36 (27), Case 151 (27), Case 162 (27), Case 25 (26), Case 113(25)
	Case 44 (24), Case 47 (24), Case 102 (24), Case 110 (24), Case 31 (22)
	Case 45 (22), Case 46 (22), Case 173 (21), Case 157 (20), Case 170 (20)
	Case 37 (18), Case 42 (18), Case 97 (18), Case 48 (15), Case 43 (14)
	Case 50 (14), Case 51 (14), Case 53 (14), Case 111 (14), Case 112 (14)
	Case 168 (14), Case 52 (13), Case 108 (13), Case 103 (12), Case 172 (12)
	Case 163 (11), Case 171 (11), Case 49 (10), Case 54 (9), Case 174 (8)
	Case 114 (7), Case 116 (7), Case 119 (7), Case 176 (7), Case 179 (7)
	Case 109 (6), Case 169 (6), Case 56 (5), Case 59 (5), Case 117 (4)
	Case 118 (4), Case 177 (4), Case 178 (4), Case 55 (2), Case 57 (2)
	Case 58 (2), Case 60 (2), Case 115 (2), Case 120 (2), Case 175 (2)
	Case 180 (2)

load on the surrounding columns. Furthermore, as the removed columns are at the low levels, their removals are likely to initiate a cascading failure of all members above the removed column. As for the column removal cases in the medium category, the loss of these columns will induce the same detrimental effects on the surrounding members, as experienced by the column removal cases in the high category. The distribution of the cases which fell into this category is highlighted in yellow and can be found in Figs. 7, 8 and 9. However, the total number of over-stressed member in this category is slightly lower due to two main factors. First, some of the cases in the medium category are distributed in grid 1, where they are mostly at level 1–5. Since these columns are located at the perimeter, they have fewer connectivity members compared to those in the interior. Therefore, the resultant total number of overstressed members occurring when these columns are removed will be lower as fewer members were connected to the removed column. Second, the column removal cases in this category can also be found in grids 4 and 7, where the position in term of storey level varies from level 3 to level 7. Due to the reduction in the number of supported storeys for these columns, their carried load is reduced compared to columns at lower storey level such as columns posi-tioned at ground floor. Thus, the amount of load being redistributed is lower on the removal of these columns. Finally, the column removal cases in the low category show a significant reduction in their total number of overstressed members, where the majority of them are located at the higher level and at the corner of the structure (refer to Figs. 7, 8 and 9). To be more specific, they are located between level 6 and level 10. As has been described before, a reduction in the number of supported storeys which in turn reduces the vertical load in these columns has indirectly lowered the number of overstressed members upon the removal of the considered column.
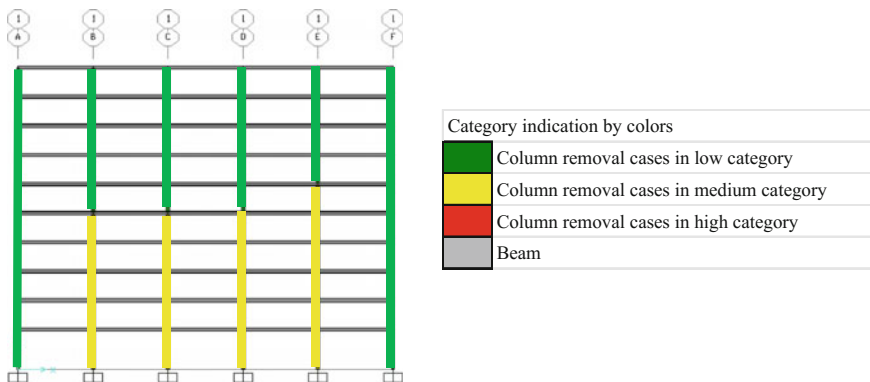
Fig. 7 Location of column removal cases in high, medium and low categories in grid 1
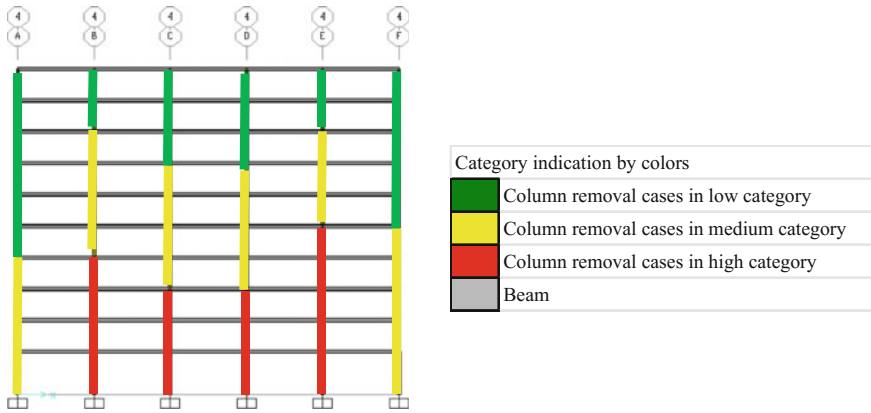
Fig. 8 Location of column removal cases in high, medium and low categories in grid 4
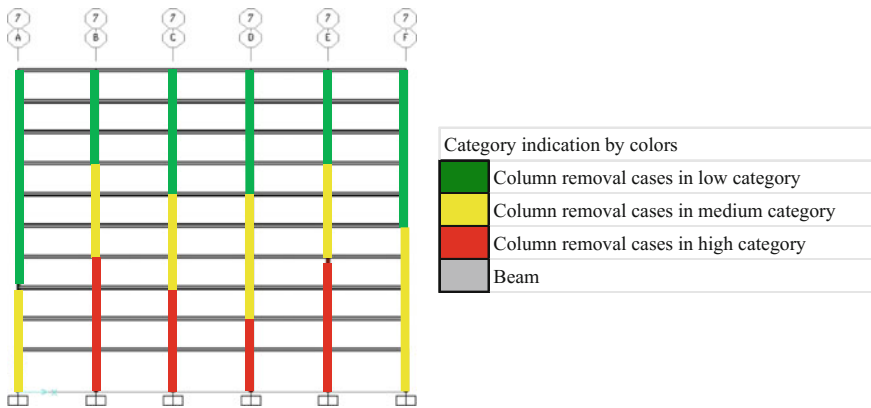
Fig. 9 Location of column removal cases in high, medium and low categories in grid 7

6 Conclusion

This paper has illustrated a quick approach to determine the critical columns for removal in a ten-storey moment resisting steel frame structure for ALP analysis. The proposed method utilised a new criterion, which is the computation of the total number of overstressed intact members remaining. The advantages of the proposed approach are that it utilises the basic idea of Approved Document A by the UK Building Regulation and Eurocodes, where both the documents require transfer beams supporting columns and all columns are to be removed one at a time in assessing the consequences of the removed column on the remaining structure, and the auto-operation technique proposed herein is able to speed up the column elimination process. Although the proposed method has been carefully constructed,

there will still be limitations existing within the method. First, the proposed removal method was designed without considering the possible effects of impact loads from the upper floors upon the removal of each column. Because of this, all the removal processes were undertaken by neglecting this dynamic effect. In addition, it is also highlighted that the determination of the critical column location implemented in this study is based solely on linear static analysis where the effect of nonlinearities such as material and geometric nonlinearities are excluded. Although this type of analysis may not realistically represent the actual behaviour of the structure, still it is believed that this is the best compromise in analysing each individual column when selecting the most vulnerable column location. To justify the accuracy of the selection of the critical column location, it has been decided that the proposed criterion will be compared with other performance criterion and a more comprehensive nonlinear dynamic analysis would be carried out for selected locations, which will be presented in the future companion papers.

References

1. Approved Document A—Structure. Office of the Deputy Prime Minister (2013)
2. Eurocode 1: Actions on structures. British Standard Institution (2006)
3. Progressive Collapse Analysis and Design Guidelines. General Service Administration (2003)
4. Design of Structures to Resist Progressive Collapse UFC 4-023-03. Department of Defense, United State of America (2015)
5. Kwasniewski, L.: Nonlinear dynamic simulations of progressive collapse for a multistory building. Eng. Struct. **32**(5), 1223–1235 (2010). ISSN 0141-0296
6. Liu, J.L.: Preventing progressive collapse through strengthening beam-to-column connection, part 1: theoretical analysis. J. Constr. Steel Res. **66**(2), 229–237 (2010)
7. Liu, J.L.: Preventing progressive collapse through strengthening beam-to-column connection, part 2: finite element analysis. J. Constr. Steel Res. **66**(2), 238–247 (2010)
8. Fu, F.: 3-D nonlinear dynamic progressive collapse analysis of multi-storey steel composite frame buildings—parametric study. Eng. Struct. **32**(12), 3974–3980 (2010)
9. Tavakoli, H.R., Rashidi Alashti, A., Abdollahzadeh, G.R.: 3-D nonlinear static progressive collapse analysis of multi-story steel braced buildings. In: 15th World Conference in Earthquake Engineering (2012)
10. Eurocode 3: Design of Steel Structures—Part 1-1: General Rules and Rules for Buildings. European Committee for Standardization (2005)

Effect of Clinoptilolite on Fresh and Early Strength Properties of Self-Compacting Concrete

Khalid Mohammed Breesem, Manal M. Abood and A. B. M. Amrul Kaish

Abstract The type of concrete called Self-compacting concrete (SCC) is well accepted nowadays by construction industries because of its flowability. In this study, the effect of natural zeolite (NZ) (Clinoptilolite) on the behaviour of self-compacting concrete was observed. Different percentages of NZ (5, 10 and 15%) by weight of cement were used in replacing cement. Water to powder (w/p) ratio was chosen 0.36, 0.38 and 0.4. Slump flow and V-funnel tests were used in investigating the concrete's fresh properties; and the compressive strength was investigated at 3 and 7 days of curing. Results showed that the flowability decreases with an increasing amount of NZ. It was also observed that the specimens which had clinoptilolite had lower compressive strengths than that of the control specimens within the period of 3 days. However, after 7 days, strengths of SCC become closer to the strength of control specimens. It can be considered as a clear improvement in strength after 7 days for mixes containing NZ up to 10% compared to control mixes. Therefore, it can be said that NZ can be utilised up to 10% to replace cement in the production of SCC.

Keywords Self-Compacting concrete · Natural zeolite · Early compressive strength · V-Funnel test

K. M. Breesem (✉) · M. M. Abood · A. B. M. A. Kaish
Department of Civil Engineering, Infrastructure University Kuala Lumpur,
43000 Kajang, Malaysia
e-mail: khalidbreseem@yahoo.com

K. M. Breesem
Al-Mussaib Technical Institute, Al-Furat Al-Awsat Technical University,
Babylon 51009, Iraq

1 Introduction

Nowadays, the use of supplementary materials in concrete is very common. These materials improve one or more properties of concrete [1]. Using waste materials in self-compacting concrete (SCC) lead to mitigating the massive quantities generated waste from various industries, and the construction works becoming friendly to the environment [2, 3]; as well as enhancing the quality of concrete [4, 5]. There are three major criteria for achieving a good SCC and they include; filling ability, passing ability and stability (segregation resistance). Clinoptilolite as natural zeolite has been used in building and construction sector since a long time [4].

The investigations of the usage of NZ to make SCC as a replacement of cement have been conducted by many researchers [5–7]. Also the enhancement of the microstructure of paste [8], early hydration [9] and engineering as well as durability properties of both cement and concrete [10, 11]. Canpolat et al. stated that sometimes the strength of the concrete can be improved by Clinoptilolite just like fly ash and silica fume which are better than cement in terms of improving the strength of the concrete [12, 13].

Despite several studies performed in incorporating of NZ in SCC, limited research has been published about the early strength behaviour. This study aims at investigating the fresh properties and early strength of SCC. For this target, slump flow, V-funnel and compressive strength were determined to evaluate fresh and hardened properties of SCC mixes containing varying percentage of NZ. Results have significance as an indicator to a related property in both of the casting and the early strength properties.

2 Materials and Methodology

Self-compacting concrete samples consist of cement, fine aggregate, coarse aggregate and superplasticizer. The use of Ordinary Portland cement (OPC) with a certain gravity (SG) of 3.1 and fineness of 328 kg/m^2 was employed; Fine Aggregate has SG and fineness modulus of 2.67 and 2.84, respectively. 10 mm crushed gravel with SG and water absorption of 2.67 and 0.63, respectively, was used as coarse aggregate. Concrete mixes consist of total powder of 500 kg/m^3. The proportion of fine to total aggregate content was kept 50.46% of the total aggregate content. The water to powder (w/p) ratio was 0.36, 0.38 and 0.40. Three control mixes used OPC only, and the rest mixes were replaced OPC by NZ at 5, 10 and 15% weight of cement. The slump flow and V-funnel tests were conducted and compared with EFNARC proposed limits. The compressive strength test was carried out using $100 \times 100 \times 100$ mm^3 cube specimens after 3 and 7 days of wet curing based on (BS EN 12390-3, 2002). The descriptions of mixtures are shown in Table 1.

Table 1 Mix proportion for SCC (kg/m^3)

Mixes	OPC	NZ	Sand	Gravel	SP	w/p
C36	500	0	855.90	840.60	6.5	0.36
C38	500	0	840.00	824.60	5.9	0.38
C40	500	0	826.80	811.30	4.5	0.40
M36Z5	475	25	855.90	840.60	10.0	0.36
M36Z10	450	50	855.90	840.60	11.3	0.36
M36Z15	425	75	855.90	840.60	11.3	0.36
M38Z5	475	25	840.00	824.60	11.1	0.38
M38Z10	450	50	840.00	824.60	11.0	0.38
M38Z15	425	75	840.00	824.60	11.0	0.38
M40Z5	475	25	826.80	811.30	10.8	0.40
M40Z10	450	50	826.80	811.30	11.0	0.40
M40Z15	425	75	826.80	811.30	12.8	0.40

C = control mix; M = concrete mix with NZ; 36, 38, 40 = "water to powder ratio of 0.36, 0.38, and 0.40"; Z5, Z10, and Z15 = NZ at 5, 10, and 15%; SP = superplasticizer

3 Result and Discussion

3.1 Fresh Properties of SCC

Table 2 presents the effects of NZ substitution on the fresh properties of SCC. As shown in the table, concrete which contains NZ satisfies slump flow. However, the using of a higher level of NZ resulted in a higher demand for SP to preserve the necessary flowability. Cement replacement by NZ led to a high viscosity that offers an essential stability and high segregation resistance required for SCC [14]. Concrete mixes with NZ shows a slump flow in the range of 693–652 mm, 761–788 mm and 843–813 mm for w/p ratios of 0.36, 0.38 and 0.40, respectively compared to 725, 756 and 843 mm for C36, C38 and C40, respectively. The findings can be attributed to that of the behaviour of this pozzolanic material involving reactive SiO_2 and Al_2O_3 as well as reducing the free water content and increasing the concentration of fine particles which may enhance the cohesion and viscosity.

V-funnel time was also recorded in the range of 6–13.98 s. Similarity was observed between Tendency noted in T_{50} flow time and V-funnel times of SCC mixes which were commonly increased when NZ was included. The finding supports the observation by Raggiotti et al. [15] who stated that because of the high surface area of NZ and the higher paste volume of the mixtures by the inclusion of NZ, the viscosity of fresh concrete increases. Based on the NZ content, the effect of w/p ratio of 0.36 is around 11.76–51.5% higher than that of w/p ratio of 0.40.

Table 2 Data recorded from of slump flow and V-funnel tests

Mix ID	Data of slump flow test		Data of V-funnel test	
	Slump (mm)	T50 cm (s)	Flow (s)	Time funnel at T_5 min
C36	725	4.00	6.80	7.41
M36Z5	693	4.16	8.15	9.70
M36Z10	655	4.22	8.78	11.10
M36Z15	652	4.46	13.98	16.10
C38	756	2.97	6.20	6.76
M38Z5	661	3.11	6.50	8.30
M38Z10	680	3.18	7.20	8.75
M38Z15	688	3.43	8.66	11.20
C40	843	2.36	6.00	6.76
M40Z5	838	2.58	6.40	8.16
M40Z10	829	2.80	6.50	9.19
M40Z15	813	2.95	7.10	10.07

3.2 Early Compressive Strength

Compressive strength is a significant property that reflects the quality of concrete. In this study, the compressive strength properties at early ages of concrete containing NZ was compared with the control mixes. Figure 1 shows the SCC compressive strength at 3 and 7 days. It indicates that the specimens' compressive strength increased with age at a specific w/p ratio. Specimens with clinoptilolite showed lower compressive strengths than that of the control SCC specimens, especially at 3 days. However, after 3 days the compressive strengths of the SCC with NZ at 5, 10 and 15% of weight are close to the strength of control concrete
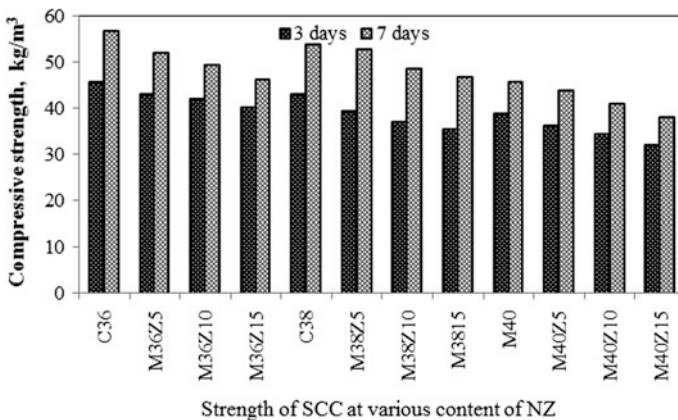
Fig. 1 SCC compressive strength at early ages compressive strength at early ages

(namely C36, C38 and C40). It is mentioned by several researchers that the NZ has a positive effect on the strength of the concrete specimens with the high specific surface area [10, 12, 16].

At the age of 3 days, the compressive strengths of the SCC specimens of M36 with 5 and 10% NZ content are lower than that of the C36 by 5.7, 7.9%, respectively.

The reduction is because of the lack of $Ca(OH)_2$ in the process of hydration at early ages even after an increase in reactive clinoptilolite phases in concrete [17]. However, there was an increment from 3 to 7 days by 17.38% in strength for M36, while 31.47% increment for M38, and 19.24% increment for M40. Therefore, it could be said that the secondary C-S-H gel is produced by reacting silicon dioxide (present in NZ) with the $Ca(OH)_2$ (from the hydration of OPC). However, 10% NZ replaced cement increases the strength over of 10%; and the compressive strength decreases considerably beyond this limit.

4 Conclusion

The following conclusions are drawn based on the findings of this study:

- The flowability of SCC mixes decreases with an increased in the NZ content.
- It was noted a link between the reduction rate of slump flow and the NZ amount; which is an increased dose of SP is needed for the maintenance of the self-compacting property of concrete.
- NZ shows slower reactivity at an early age which is reflected by the lower compressive strength of SCC compared to control mix. In addition to that, this decrease becomes higher with high replacement levels.
- The compressive strength of SCC increases with the reduction in the water–powder ratio.

Finally, the study is a concept that reflects environmentally friendly materials used in the manufacture of concrete. Using of clinoptilolite in this research, the goals are achieved, one of them is to improve mechanical properties of concrete to achieve the best performance and reduce the amount of cement used and reduce CO_2 emissions and then reduce energy consumption.

References

1. Batayneh, M., Marie, I., Asi, I.: Use of selected waste materials in concrete mixes. Waste Manage. **27**, 1870–1876 (2007)
2. Persson, B.: A comparison between mechanical propel-ties of self-compacting concrete and the corresponding properties of normal concrete. Cem. Concr. Res. **31**, 193–198 (2001)
3. Sakir, S., Raman, S.N., Kaish, A.B.M.A., Mutalib, A.A.: Self-flowing mortar for ferrocement in strengthening applications. Perspect. Sci. **8**, 673–676 (2016)
4. Sabet, F.A., Libre, N.A., Shekarchi, M.: Mechanical and durability properties of self consolidating high performance concrete incorporating natural zeolite, silica fume and fly ash. Constr. Build. Mater. **44**, 175–184 (2013)
5. Ramezanianpour A.A., Kazemian, A., Sarvari, M., Ahmadi, B., Moghadam, M.A.: Investigation of long term durability of natural incorporated Eco-SCC zeolite. In: 10th International Congress on Advances in Civil Engineering, pp. 17–19 (2012)
6. Grigaliunas, P., Rudzionis, Z.: Investigation and comparison of SCFRC properties incorporating fly ash and zeolitic additives. J. Sustain. Archit. Civ. Eng. **9**, 35–49 (2014)
7. Akçaözoğlu, K., Fener, M., Akçaözoğlu, S., Öcal, R.: Microstructural examination of the effect of elevated temperature on the concrete containing clinoptilolite. Constr. Build. Mater. **72**, 316–325 (2014)
8. Caputo, D., Liguori, B., Colella, C.: Some advances in understanding the pozzolanic activity of zeolites: the effect of zeolite structure. Cem. Concr. Compos. **30**, 455–462 (2008)
9. Perraki, T., Kakali, G., Kontoleon, F.: The effect of natural zeolites on the early hydration of Portland cement. Microporous Mesoporous Mater. **61**, 205–212 (2003)
10. Bilim, C.: Properties of cement mortars containing clinoptilolite as a supplementary cementitious material. Constr. Build. Material **25**, 3175–3180 (2011)
11. Ahmadi, B., Shekarchi, M.: Use of natural zeolite as a supplementary cementitious material. Cem. Concr. Compos. **32**, 134–141 (2010)
12. Canpolat, F., Yilmaz, K., Köse, M.M., Sümer, M., Yurdusev, M.: Use of zeolite, coal bottom ash and fly ash as replacement materials in cement production. Cem. Concr. Res. **34**, 731–735 (2004)
13. Breesem, K.M., Faris, F.G., Abdel-Magid, I.M.: Behavior of self-compacting concrete using different sludge and waste materials—a general overview. Int. J. Chem. Environ. Biol. Sci. **2**, 151–156 (2014)
14. Uzal, B., Turanli, L., Yücel, H., Göncüoğlu, M.C., Çulfaz, A.: Pozzolanic activity of clinoptilolite: a comparative study with silica fume, fly ash and a non-zeolitic natural pozzolan. Cem. Concr. Res. **40**, 398–404 (2010)
15. Raggiotti, B.B., Positieri, M.J., Locati, F., Murra, J., Marfil, S.: Zeolite, study of aptitude as a natural pozzolan applied to structural concrete. Rev. la Constr. **14**, 14–20 (2015)
16. Najimi, M., Sobhani, J., Ahmadi, B., Shekarchi, M.: An experimental study on durability properties of concrete containing zeolite as a highly reactive natural pozzolan. Constr. Build. Mater. **35**, 1023–1033 (2012)
17. Chan, C.F., Mitsuda, T.: Formation of 11 Å tobermorite from mixtures of lime and colloidal silica with quartz. Cem. Concr. Res. **8**, 135–138 (1978)

Characterization of Homogeneity of Asphalt Concrete Using 2D Cross-Sectional Images

Ayhan Oner Yucel and Murat Guler

Abstract Asphalt concrete is fabricated from a three-phase mixture consisting of aggregate, asphalt binder, and air voids. Homogeneity of asphalt mixtures affects performance characteristics of asphalt concrete pavements. In this study, homogeneity is determined from 2D vertical section images of gyratory compacted specimens. Because the aggregate structure dominates the performance of asphalt concrete, the mixture homogeneity is determined via statistical distribution of aggregate particles. The cross-sectional images are obtained using a flatbed scanner and then processed to detect various particle shape parameters and locations. Aggregate shape parameters are used for the purpose of determining aggregate gradation curves based on 2D cross-section images of asphalt concrete specimens. An algorithm is developed to detect all the particles in the cross-sections, and then the detected aggregates are redistributed at random orientations and locations to create synthetic images of the same cross-sections. In this way, a large number of sectional images representing the distribution of the same aggregate size fractions are generated. Statistical analyses are performed on four different mixture specimens to determine the range of particle size distributions functions. Results show that the particle distribution of the specimens fall within the range of distribution functions for homogenous mixtures.

Keywords Asphalt mixtures · Homogeneity · Image processing and analysis

1 Introduction

Homogeneity has many effect on performance-related properties of asphalt concrete pavements [1–5]. Mixture homogeneity is of primary importance in terms of expected performance properties of asphalt concrete pavements [6]. Previous

A. O. Yucel (✉) · M. Guler
Department of Civil Engineering, Middle East Technical University,
Ankara 06800, Turkey
e-mail: ayucel@metu.edu.tr

studies show that mixture segregation during lay-down process can significantly reduce the stiffness, tensile strength, and fatigue life of asphalt concrete [6]. Asphalt mixture consists of three major components: asphalt binder, aggregate, and air voids. Asphalt mixture homogeneity can be evaluated based on aggregates distribution because the distribution of other components depends mainly on aggregates structure [5, 7].

There are many approaches to evaluate the homogeneity of asphalt mixture components [7–9]. In this study, homogeneity of asphalt mixtures was studied using 2D cross-sectional digital images obtained from asphalt concrete specimens after applying a series of image-processing techniques. The analysis procedure started with determining the aggregate gradation using various particle shape parameters in order to approximate the actual aggregate gradation. The mixture homogeneity was then evaluated for four different asphalt concrete specimens based on their vertical cross-sectional images.

2 Aggregate Size Distribution of Asphalt Mixtures

2.1 Image Acquisition and Enhancement

Transferring images to computer memory is the initial step of digital image processing [10]. This operation is named as image acquisition. The acquisition can be done via different types of devices but in this study a 2D flatbed scanner was used. The scanning resolutions was set to 600 dpi to capture small-size particles enough for the minimum aggregate size necessary in the study. Flatbed scanners are functional and easy to use for capturing 2D cross-sectional images from asphalt concrete samples [11]. After acquiring and storing the images, next step is the image enhancement before starting the particle shape analyses.

The output format of the digital cross-section images was lossless bitmap with 24-bit RGB color scale. The original images from the flatbed scanner have to be converted to binary images using an appropriate thresholding method to conduct further image analysis techniques. In the binary conversion operation some information about the image can be lost [12]. To be able to prevent this problem, image enhancement should be carried out considering minimum loss of information. For instance, color variations between aggregates or in a single particle surface become difficult problems to tackle in particle recognition. In this study, enhancement operations like smoothing and histogram equalization were used to increase the success of particle recognition. Figure 1 shows an original RGB image and its binary equivalent for a vertical section of one of the asphalt concrete specimens.
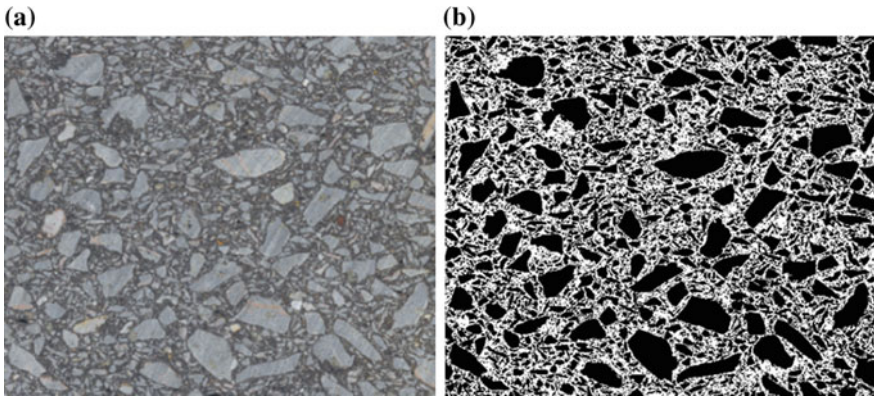
Fig. 1 Vertical section image. **a** Original image, **b** binary image

2.2 Shape Parameters

This study was conducted using four different asphalt concrete specimens with two gradations and two aggregate types, which are basalt and limestone. Table 1 shows the properties of mixtures and Table 2 shows the selected gradations.

Because of the limitation in the resolution of the scanner used, it is, in general, difficult to detect fine particles in the 2D surface section images. Based on the analyses of several images taken at different resolution levels, it is discovered that the detection of particles smaller than 0.425 mm in size practically not possible. Therefore, the image analyses for particle detection were limited to 0.425 mm and the calculated size distributions were corrected for the undetected size portion using an appropriate procedure as discussed in the below section.

Ozen and Guler [13] determined that the maximum Feret diameter is an optimal shape parameter to estimate the size distribution of aggregates in concrete samples. There are also other shape parameters used for particle shape analysis such as particle area, equivalent circle diameter, equivalent ellipse major axis, polygon

Table 1 Properties of mix designs

Mix design	1	2	3	4
Gradation	Type-1	Type-2	Type-1	Type-2
Aggregate type	Basalt	Basalt	Limestone	Limestone

Table 2 Gradation of asphalt mixtures

Sieve sizes (mm)		19	12.5	9.5	4.75	2	0.425	0.18	0.075
Percent passing	Type-1	100	88	72	42	25	10	7	3
	Type-2	100	100	90	72	53	28	16	8
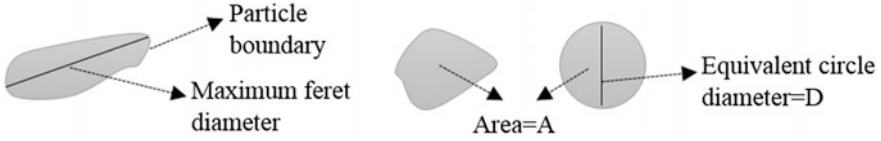
Fig. 2 Maximum Feret diameter and equivalent circle diameter of aggregate particles

diameter, major axis length, minor axis length in the literature [14]. In this study, the size distribution of aggregates was estimated by using the maximum Feret diameter and the equivalent circle diameter of aggregate particles. Both the horizontal and vertical cross-sections of laboratory prepared specimens were used for the size distribution analyses. For each specimen, only one vertical section image and one horizontal section image were used in the image analyses.

In the particle shape analysis, maximum Feret diameter is a line segment connecting the two perimeter points with the farthest distance between them. The diameter of an equal area circle is called equivalent circle diameter as shown in Fig. 2.

2.3 Size Distribution Analysis of Aggregates

In mechanical sieving, mass of particles is used in the calculation of particle size distribution, however, the area of particles can only be used in the digital image analysis of aggregate particles. As in the size distribution analysis procedure implemented in our study, maximum Feret diameters and equivalent circle diameters were calculated and compared with the standard diagonal sieve sizes and the square sieve sizes, respectively, to determine the percent retaining aggregates from which to calculate the passing of each size fraction.

2.4 Results of Size Distribution Analyses

Retaining percentages on each sieve were found by calculating the ratio of the particle areas retaining on the corresponding sieve to the total aggregate area. To eliminate the effect of undetected small aggregates, minimum size was determined and the particles smaller than this value were ignored in the distribution analyses using Eq. (1).

$$P_e = \frac{(100 - P_f)}{100} P_i,$$

(1)

Table 3 Results of gradation analysis

Sieve size (mm)	Actual	Horizontal (s)		Vertical (s)		Horizontal (s)		Vertical (s)	
		Max. Feret	Eq. dia.	Max. Feret	Eq. dia.	Max. Feret	Eq. dia.	Max. Feret	Eq. dia.
		Mix-1				Mix-3			
19	100	100	100	100	100	100	100	100	100
12.5	88	89.9	84.1	89.7	90.7	90.8	89.6	95.1	94.8
9.5	72	71.3	71.4	76.7	76.7	78.6	76.4	86.1	82.4
4.75	42	40.6	42.2	43.7	44.7	44.1	41.4	45.9	44.6
2	25	23.1	24.1	23.4	24.7	24.1	23.7	25	25.3
0.425	10	10	10	10	10	10	10	10	10
		Mix-2				Mix-4			
12.5	100	100	100	100	100	100	100	100	100
9.5	90	89.6	88.3	92.1	94.4	90.9	89.2	94.6	95.1
4.75	72	70.3	71.1	72.9	74.5	72.3	72.4	77.6	76.9
2	53	48.9	49.9	51	53.4	52.8	53.4	54.1	54.4
0.425	28	28	28	28	28	28	28	28	28

where P_e = normalized percent retaining; P_f = percentage of excluded particles from the image analysis; and P_i = percent retaining as computed from the image analysis.

The results of gradation analyses are given in Table 3 for four mixtures of horizontal and vertical cross-sections.

Analysis results show that maximum Feret diameter and equivalent circle diameter can be successfully used to approximate the actual size distribution of mixtures' aggregates.

3 Homogeneity Test

3.1 Homogeneity Index

To establish the characteristics of aggregate size distribution and the range of relevant distribution functions for a 2D cross-section image, a MATLAB® algorithm was developed. The algorithm can detect all the particles in the cross-sections, and then detected particles are redistributed to create synthetic cross-sectional images. In this way, a large number of sectional images using the particles of the original cross-sections can be generated. In the developed algorithm, aggregates are sorted from large to small sizes according to their maximum Feret diameters and then relocated into the new image without any overlapping problem. The center
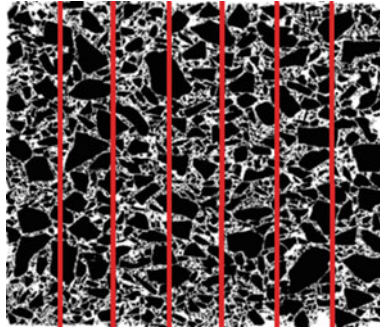
Fig. 3 Vertical section divided into strips of same dimension

coordinates and the orientation of each particle are randomly determined in the synthetic images.

In the redistribution process, input is the binary image of the compacted specimen vertical or horizontal cross-section and the output is the image of the same size as the original image but with redistributed aggregates.

Homogeneity index has been developed based on the relative frequency distribution of aggregates. One of the cut surfaces of the asphalt concrete specimens was divided into vertical strips of the same dimension as shown in Fig. 3. Number of strips was selected according to the maximum aggregate size exist in the cross-section.

In the homogeneity analyses, cross-section images were divided into seven strips and five size intervals were used in the calculation of relative frequency distribution. Table 4 shows relative frequency distribution of particles calculated for mixture-1. It can be seen that the sum of all relative frequency values is equal to 1.

Size limits shown in the table represent maximum Feret diameter of the cross-section particles. Particles with maximum Feret diameter smaller than 70 pixels are ignored in the homogeneity index evaluation.

Homogeneity index was calculated based on the absolute difference between average relative frequencies of 1000 synthetic images created using the developed algorithm and the relative frequency distribution of the original specimen particles. As many as 1000 runs were implemented for each mixture type using the

Table 4 Relative frequency distribution

Size (pixel)/location	P-1	P-2	P-3	P-4	P-5	P-6	P-7
>230	0.0144	0.0224	0.0160	0.0176	0.0160	0.0192	0.0224
190–230	0.0080	0.0064	0.0096	0.0096	0.0224	0.0128	0.0048
150–190	0.0192	0.0160	0.0144	0.0192	0.0176	0.0160	0.0128
110–150	0.0224	0.0337	0.0417	0.0256	0.0288	0.0208	0.0224
70–110	0.0865	0.0577	0.0737	0.0785	0.0577	0.0689	0.0641

redistribution algorithm. The test statistics of four asphalt mixture specimens was calculated and compared with their critical values to evaluate homogeneity index.

3.2 Statistics for Critical Values

It is important to determine critical values for the evaluation of mixture's homogeneity. To obtain critical statistic, probability distribution of homogeneity index should be determined. It is necessary to regenerate as many sectional images as possible using the redistribution algorithm to find the critical values of homogeneity index. In this study, 1000 synthetic images were created for each type of mixtures, and then critical values were determined. Three different levels of significance, which are 10, 5, and 1% (with cumulative probabilities of 90, 95, and 99%), were considered because the importance of homogeneity might be different for different specimens. In the calculation of the cumulative distribution functions, it is assumed that the test statistic has standard normal distribution. Figure 4 shows these cumulative probabilities for homogeneity indexes of four mixtures.

Critical statistics were determined for three levels of significance by the help of cumulative distribution functions. The critical values were found from the upper tail of the distributions. Table 5 shows critical values, homogeneity indexes which were calculated for original specimens and probability levels. Probability level means cumulative probability value corresponding to homogeneity index. In general, cumulative distribution functions of four mixtures show that the test index has
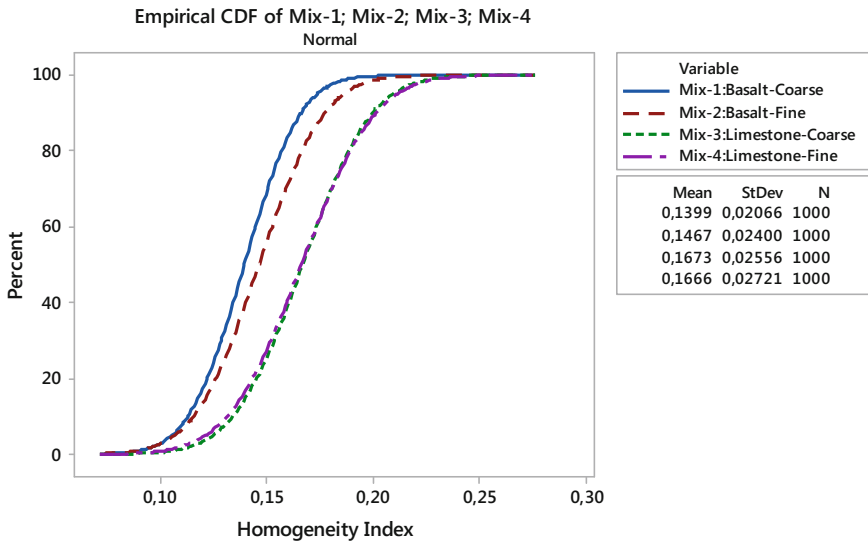
Fig. 4 Cumulative distribution functions of test mixtures

Table 5 Homogeneity index and critical values of specimens

Specimen/level of significance	Critical values			Homogeneity index	Probability levels
	10	5	1		
Mix-1	0.1664	0.1739	0.1879	0.1598	83.3
Mix-2	0.1775	0.1862	0.2026	0.1542	62.2
Mix-3	0.2000	0.2093	0.2267	0.1757	62.9
Mix-4	0.2015	0.2114	0.2299	0.1701	55.1

standard normal distribution and the standard deviations of homogeneity indexes of regenerated images are very close to each other for four mixtures.

According to Table 5, it can be seen that all of the specimens are homogeneous because the homogeneity indexes are smaller than their critical values, however, the homogeneity index of the first mixture is very close to critical value at 10% significance level. Probability level of mix-1 is also significantly higher comparing to the others.

According to cumulative distribution functions, mix-3 and mix-4 have almost same probability distribution. Mix-3 and mix-4 were prepared using same type aggregate with different gradations. Probability distributions of mix-1 and mix-2 are also very close to each other. Again mix-1 and mix-2 were prepared using same type aggregate with different gradations. Cumulative probability distributions of mixtures 1 and 2 are very far from distributions of mixtures 3 and 4. These results show that aggregate type seems to have more effect on probability distribution of test indices than aggregate gradation.

An experimental study conducted by Sun [6] investigated effect of aggregate gradation and aggregate type on asphalt mixture homogeneity. In this study, it was concluded that both aggregate gradation and aggregate type influence the index of homogeneity at different extents. In our study, effect of aggregate type on probability distribution of test indices is obvious, but a significant effect of aggregate gradation on test indices was not detected from the probability distributions.

4 Conclusion

The study has presented a testing method of homogeneity of asphalt mixture specimens by the help of image analysis and processing methods. Homogeneity index of asphalt concrete specimens was calculated based on relative frequency distributions of aggregate particles. Critical statistics were determined from regenerated synthetic cross-sectional images representing the distribution of the same aggregate size fractions as the original cross-sections. Homogeneity of four different mixtures was evaluated by dividing the vertical section images into vertical panels.

Results show that all of the tested specimens homogenous according to the controlled significance levels. Probability level corresponding to first mixture as considerably larger than probability levels of other tree mixtures, so it can be concluded that the first mixture is more segregated than others. Proposed test method can be developed for the further studies to determine homogeneity of asphalt concrete specimens using different distribution parameters.

References

1. Cross, S.A., Brown, E.R.: Effect of segregation on performance of hot-mix asphalt. Transp. Res. Rec. **1417**, 117–126 (1993)
2. Khedaywi, T.S., White, T.D.: Development and analysis of laboratory techniques for simulating segregation. Transp. Res. Rec. **1492**, 36–45 (1995)
3. NCHRP Report 441: Segregation in hot-mix asphalt pavements. Transportation Research Board-National Research Council (2000)
4. Cross, S.A., Hainin, M.R., Adu-Osei, A.: Effects of segregation on mix properties of hot mix asphalt. Report No. K-TRAN:KU-96-6. Kansas Department of Transportation (1998)
5. Peng, Y., Sun, L.J.: Towards an index of asphalt mixture homogeneity. In: Road Materials and Pavement Design, vol. 10, no. 3, pp. 545–567 (2009)
6. Sun, L.: Structural Behavior of Asphalt Pavements, p. 821. Elsevier Inc., (2016)
7. Azari, H.: Effect of aggregate inhomogeneity on mechanical properties of asphalt mixtures. Ph.D. thesis, University of Maryland at College Park, UMI Number: 3201993 (2005)
8. Hunter, A.E., Airey, G.D., Collop, A.C.: Aggregate orientation and segregation in laboratory-compacted asphalt samples. In: Transportation Research Record: Journal of the Transportation Research Board, No. 1891, TRB, pp. 8–15. National Research Council, Washington, D.C. (2004)
9. Saadeh, S., Tashman, L., Masad, E., Mogawer W.: Spatial and directional distribution of aggregates in asphalt mixes. J. Test. Eval. **30**(6), Paper ID JTE11147_306 (2002)
10. Yadav, A., Yadav, P.: Digital image processing. University Science Press, New Delhi-Boston USA (2009)
11. Coenen, A.R.: Image analysis of aggregate structure parameters as performance indicators of rutting resistance. Ph.D. thesis, University of Wisconsin-Madison, UMI Number: 3488710 (2011)
12. Koul, A.: Impact of global and adaptive thresholding: methods on Urdu documents, Advances in Computer Vision and Information Technology, pp. 894–897. I. K. International Publishing, India (2007)
13. Ozen, M., Guler, M.: Assessment of optimum threshold and particle shape parameter for the image analysis of aggregate size distribution of concrete sections. Opt. Lasers Eng. **53**, 122–132 (2014)
14. Yue, Z.Q., Morin, I.: Digital image processing for aggregate orientation in asphalt concrete mixtures. Can. J. Civ. Eng. **23**, 480–489 (1996)

Risk Analysis of the In Situ Production of Precast Concrete Members

Jeeyoung Lim, Seunghyun Son, Youngju Na and Sunkuk Kim

Abstract The precast concrete (PC) method has been preferred for reasons of shortening of construction time, quality assurance, and cost reduction. In addition, in situ production of PC members under equivalent production conditions can save costs while ensuring quality equal to or better than in-plant production. Despite these advantages, in situ production is being avoided due to possible risks from project management. Therefore, in order to generalize the in situ production of PC members, it is necessary to clarify the causes of the possible risks and establish responses. Therefore, the purpose of this study is to analyse the in situ production risks of PC members. The results of this study can be used to establish a systematic response plan for possible risks in the in situ production of PC members.

Keywords Precast concrete members · In situ production · Risk analysis
Risk identification

1 Introduction

The precast concrete (PC) method has been preferred for reasons of shortening of construction time [1], quality assurance [2], and cost reduction [3–5] and is growing constantly by new technology development and investment [6]. At this time that equipment and material costs are reduced while labour cost is increased, capital-intensive PC method is great advantage [7].

In addition, under equivalent production conditions, in situ production of PC members can save costs while ensuring quality equal to or better than in-plant production [8]. Despite these advantages, in situ production is being avoided due to possible risks from project management. However, if risk factors are analysed systematically before the in situ production of PC members and countermeasures are devised, the concerned risks can be overcome.

J. Lim · S. Son · Y. Na · S. Kim (✉)
Kyung Hee University, Yongin-si/Gyeonggi-do, Republic of Korea
e-mail: kimskuk@khu.ac.kr

A study on in situ production is surveyed. Lim et al. [9] analysed the problems of as-is plywood form and requirements for development of in situ production form of composite PC frame. Lee [10] presented the management factors and requirements for in situ production of composite PC members, developed a management model and applied them to the case site.

Park et al. [11] developed concrete manufacturing technologies for ultra-high strength concrete pile. And for this study, it measured the strength using pilot-produced elements and proposed optimum production conditions. Won et al. [12] conducted a study on energy-efficient of the steam curing for the in situ production of PC members. Although these studies explored details about production method of in situ production and the effect of application of the case site, further research is needed to study on risks analysis of in situ production of PC members.

In order to generalize the in situ production of PC members, it is necessary to clarify the causes of the possible risks and establish responses. Therefore, the purpose of this study is to analyse the in situ production risks of PC members. For conducting this study, in situ production members are columns and beams only. And risks set limit to negative aspects such as loss, damage and lack, except in positive aspects such as profit, gain and opportunity.

For this purpose, the in situ production process of PC members is analysed and the factors of in situ production risk are analysed. These risk factors can be used to establish a systematic response plan for possible risks in the in situ production of PC members.

2 Analysis on Influence Factors for In Situ Production of PC Elements

As shown with Table 1, conditions are assumed for analysis of in situ production risk factors. First of all, because PC slabs require a lot of space in production as well as relatively large facilities, it is assumed to procure the slabs only by in-plant production. However, PC columns and beams are relatively slender elements, and

Table 1 Conditions for analysis of risk factors

Condition	Description
1	PC slabs are procured only by in-plant production
2	If the site conditions are not satisfactory and all PC columns and beams are difficult to produce in site, some of them would be procured by in-plant production
3	In situ produced PC members have better cost and quality than in-plant produced, and thus they are assigned to in situ production by priority
4	Schedule for in situ production of PC members is satisfied with erection schedule

thus smaller area and simpler facilities are required for production of them. Therefore, this study is only for in situ production of columns and beams.

However, if the site conditions are not satisfactory and all PC columns and beams are difficult to produce in site, some of them would be procured by in-plant production. Because in situ produced PC members are better cost and quality than in-plant produced, it is assumed to assign to in situ production by priority. Schedule for in situ production of PC members is dependent on erection schedule. Therefore, this study is to analyse risks for in situ production of PC members satisfied with erection schedule [13].

As shown in Fig. 1, influence factors of in situ production are analysed based on assumed conditions. Production and installation of PC members are reflected both of duration and quantity simultaneously. Production of PC members is influenced by production plan and production plan is composed of in situ production plan and in-plant production plan. Because the sum total of quantity of in situ production and in-plant production is in concordance with total quantity of installation of PC members, production and installation affect each other.

In situ production plan is influenced by available production area in construction site, the number of moulds determining production members per production cycle, and production cycle included production time and production process. Available production area is determined by layout plan included moulds, curing facilities and stacking area [14]. Adequacy of production plan should be examined by the match logic between production and installation plan.
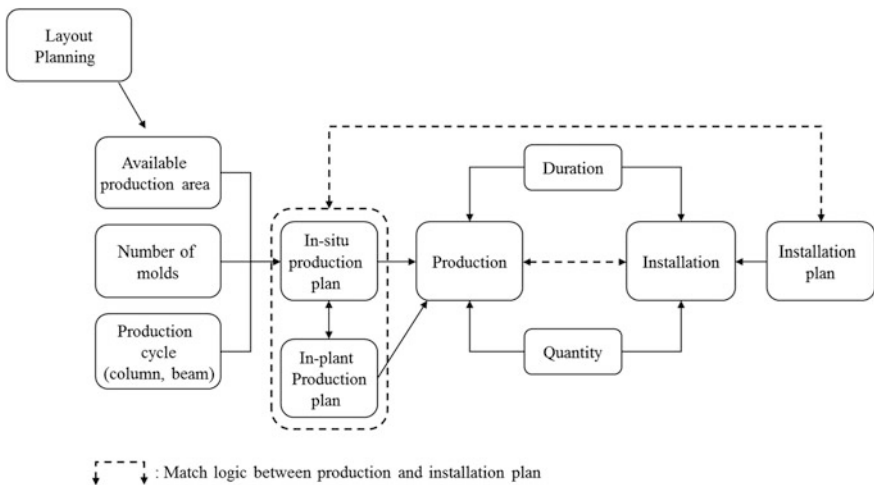
Fig. 1 Analysis on influence factors for in situ production

3   Analysis on In Situ Production Process of PC Elements

Risk identification is the process to analyse types and characteristics of risk factors related to the project, classify systematically these and weight these according to their importance [15]. In addition, only for risks selected at risk identification, analysis and response are conducted, and thus all of risk factors related the project should be identified thoroughly [15]. Therefore, for analysing correctly risk factors, the process for in situ production of PC members should be established.

As shown with Fig. 2, the process for in situ production of PC members is composed of establishment of in situ production plan, execution of in situ production and installation of PC members. While establishing in situ production plan, first of all, quantity of in situ production of PC members is calculated from total quantity of them. Some of them would be procured by in-plant production, if the site conditions are not satisfactory and all PC columns and beams are difficult to produce in site such as complex structural system of PC members and difficulty of assuring available production area.

Subsequent to determining quantity for in situ production, project duration is estimated, and the start and the completion of installation of PC members are calculated from this duration. Deciding the duration of installation work, and then time difference between the start of in situ production and the start of installation is calculated so that lead time is determined.

In addition, the completion of production is calculated from curing and transport time of PC members, and then time lag about the completion of production and the completion of installation is determined. After calculating in situ production duration, detailed plans are established such as deciding production cycle process, production time per production cycle, available production area, layout plan and the number of moulds.

If establishment of in situ production plan is completed, layout plan of in situ production is conducted to reflect minimizing interference of other works and transport time of members. In-plant produced bent rebar should be procured before the beginning of concreting, and is used by crane to instal on accurate position according to shop drawing. Concreting and curing is completed, and then PC members is inspected according to quality regulations and stacked in the order of installation.
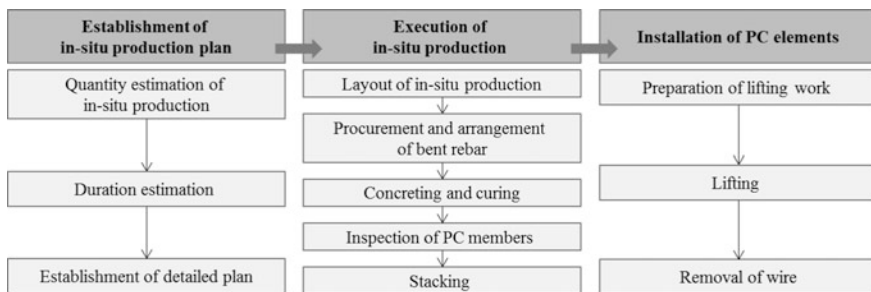
Fig. 2 Analysis on in situ production process

Subsequent to in situ production, lifting work of PC members is prepared such as connecting work with members in order of stacking. After PC members are lifted, moved and installed by positioning, they are dismantled promptly the connecting part. If duration and quantity are not matched each other between in situ production and installation, reproducing PC members or delayed happen.

4 Risk Identification for In Situ Production of PC Elements

In situ production of PC elements should be satisfactory in aspects of time, cost, quality and safety. Thus risk factors are classified into four sections as shown with Table 2, and analysed by three stages of in situ production process as mentioned.

Table 2 Risk identification for in situ production of PC elements

Phase	Risk factors	
Establishment of in situ production plan	Composite item	Difficulty to establish in situ production plan due to a lack of experience
	Time	Decision delay
		Difficulty to get lead time influenced the start
		Difficulty to estimate lead time and time lag, if production cycle information can't be obtained
Execution of in situ production	Composite item	Limited and small space. (requirement for curing and stacking area)
		Interference with other works
		Complex construction site due to employing labour and equipment for in situ production of PC members
		Variable climatic conditions
		Discordance between plans and site conditions
	Time	Time increase in comparison with in-plant production
		Procurement delay of materials such as bent rebar for in situ production
	Cost	Cost increase in comparison with in-plant production while in situ production partly
		Operation of independent in situ production manager
	Quality	Difficulty for quality assurance of PC members
		Lack of quality regulation
Installation of PC elements	Composite item	Discordance of quantity between production and installation
		Installation process errors due to stacking without regard to installation process
	Time	No match logic between in situ production and installation time. (Difficulty of producing timely PC members)

When planning in situ production, risk factors are classified with time and composite item concerned in general aspects of time, cost, quality and safety. If production manager and the persons concerned have a lack of experience related to in situ production of PC members, it is difficult that whole plans are established correctly. PC members should be completed to produce before installing, and thus assurance of the lead time is important. Therefore, if lead time cannot be ensured because of decision delay or the construction start delay, delay of the completion happens. In addition, if manager cannot obtain production cycle information, it is difficult to estimate lead time and time lag because he do not know accurate production period.

When executing in situ production, risk factors are classified with composite item, time, cost and quality. Since construction site has limited space, during in situ production, interference with production works happens as well as it is too small to conduct other works. In addition, employing labour and equipment for producing PC members is the cause of complex construction site. In situ production is important to climatic conditions in comparison with in-plant, and re-establishing in situ production plan could happen due to discordance between plans and site conditions.

In terms of time, production members per production cycle are limited, and so there is concern about longer period increase of in situ production than in-plant. And the project completion delay happens due to procurement delay of materials such as bent rebar for in situ production. In terms of cost, unit cost increase happens if in situ production partly is conducted, and due to operation of independent in situ production manager, labour cost increase happens in comparison with in-plant production. In addition, in terms of quality, there are difficulty for quality assurance of PC members in comparison with in-plant and the lack of quality regulation of PC members.

At installation, risk factors related to in situ production are classified with composite item and time. Due to duplicate or missing PC members of in situ and in-plant production, quantity discordance between production and installation can happen. If stacking is conducted without regard to installation process, installation process errors becomes delay and cost increase problems. In terms of time, due to no match logic between in situ production and installation time, difficult situation of ensuring stacking space or complete delay can happen.

Through identifying risk factors, it is confirmed that risk management is necessary in general aspects of time, cost, quality and safety. And, it is confirmed that three great division is more useful than detailed division for risk identification.

5   Conclusion

In this study, influenced factors for in situ production of PC members are analysed and risk identification by phase is conducted. The following conclusions were derived:

First, through analysis on influence factors for in situ production of PC elements, it is confirmed how in situ production and installation are related with each factor such as available production area, the number of moulds and production cycle information. Adequacy of production plan should be examined by whether logic between production and installation plan are matched or not.

Second, in situ production consists of three phases such as establishing in situ production plan, executing in situ production and installing PC members. And detailed works conducted by phase and considerations is confirmed.

Third, influence factors on each phase are analysed and it is confirmed that it is necessary to manage risks in aspects of time, cost, quality and safety.

Risks analysed in this study have dynamic relationships in aspects of time, cost and quality. Therefore, causal loop diagram should be drew for defining risks' relation. Then, risk management model should be conducted using system dynamics. Finally, the results of this study are used for developing enterprise system to manage risks systematically, as well as provide the basis for productivity improvement of in situ production of PC members academically.

References

1. Chan, W.T., Hu, H.: Constraint programming approach to precast production scheduling. J. Constr. Eng. Manage. **128**, 513–521 (2002). https://doi.org/10.1061/(ASCE)0733-9364 (2002)128:6(513)
2. Eastman, C.M., Sacks, R.: Relative productivity in the AEC industries in the United States for on-site and off-site activities. J. Constr. Eng. Manage. **134**(7), 517–526 (2008). https://doi.org/ 10.1061/(ASCE)0733-9364(2008)134:7(517)
3. Badir, Y.F., Abdul Kadir, M.R., Hasim, A.H.: Industrialized building systems construction in Malaysia. J. Archit. Eng. **8**(1), 19–23 (2002). https://doi.org/10.1061/(ASCE)1076-0431 (2002)8:1(19)
4. Kale, S., Arditi, D.: Diffusion of ISO 9000 certification in the precast concrete industry. Constr. Manage. Econ. **24**(5), 485–495 (2006). https://doi.org/10.1080/01446190600601594
5. Polat, G.: Factors affecting the use of precast concrete systems in the united states. J. Constr. Eng. Manage. **134**(3), 169–178 (2008). https://doi.org/10.1061/(ASCE)0733-9364(2008)134: 3(169)
6. Kang, H.J.: A study of ship design process optimization in a concurrent engineering environment. Master's thesis, Seoul National University (2008)
7. Oh, O.J.: A model for production and erection integration management (PEIM) of large scale pc structures using system dynamics. Doctor's thesis, Kyung Hee University (2017)
8. Hong, W.K., Lee, G., Lee, S., Kim, S.: Algorithms for in-situ production layout of composite precast concrete members. Autom. Constr. **41**, 50–59 (2014). https://doi.org/10.1016/j.autcon. 2014.02.005
9. Lim, C., Joo, J.K., Lee, G.J., Kim, S.: Basic analysis for form system of in-situ production of precast concrete members. In: 2011 Autumn Annual Conference of Construction Engineering and Management, vol. 12, no. 1, pp. 137–138 (2011)

10. Lee, G.J.: A study of in-situ production management model of composite precast concrete members. Doctor's thesis, Kyung Hee University (2012)
11. Park, S.H., Lim, C.Y., Lee, W.J., Kim, D.S., Jung, Y.S.: The experimental study on concrete manufacturing technologies for ultra high strength concrete pile. In: 2013 Spring Annual Conference Korea Concrete Institute, vol. 25, no. 1, pp. 67–68 (2013)
12. Won, I., Na, Y., Kim, J.T., Kim, S.: Energy-efficient algorithms of the steam curing for the in situ production of precast concrete members. Energy Build. **64**, 275–284 (2013). https://doi.org/10.1016/j.enbuild.2013.05.019
13. Lim, J., Cho, W., Lee, T.O., Kim, S.: A basic study of process and layout for in-situ production of precast concrete members. In: 2016 Autumn Annual Conference of The Architectural Institute of Korea, vol. 36, no. 2, pp. 945–946 (2016)
14. Lim, C.: Construction planning model for in-situ production and installation of composite precast concrete frame. Doctor's thesis, Kyung Hee University (2016)
15. Kim, I.H.: Risk management in the construction projects. Kimoondang, pp. 51–52 (2001)

Risk Identification of Innovative Composite Precast Concrete Structure Applied to Heavy-Loaded- and Long-Span Buildings

Seunghyun Son, Jeeyoung Lim, Oumjung Oh, Jeong Tai Kim and Sunkuk Kim

Abstract Most of the heavy-loaded- and long-span buildings are being constructed with pin-joint PC method. For pin joints, adequate erection time is needed to ensure the structural stability of the joint. Since the SMART frame developed to solve this problem is moment-jointed, structural stability is ensured at the same time as the PC member is assembled. In addition, if SMART frame is used for heavy-loaded- and long-span building projects, it will be possible to shorten erection time, secure quality, and reduce costs. However, in order to apply the SMART frame in practice, it is necessary to predict in advance the risks that may arise during project execution. Therefore, the purpose of this study is to identify the risk identification of an innovative composite precast concrete structure with heavy-loaded- and long-span buildings. The results of this study will be used as basic data for systematic risk management when SMART frame method is applied.

Keywords Composite precast concrete structure · Heavy-loaded- and long-span buildings · Construction site application · Risk analysis · Risk identification

1 Introduction

Most long-span- and heavy-loaded buildings such as large distribution centers are constructed in steel frame or PC structure. In case of the conventional PC structure, beams are simply placed on top of columns and they are pin-jointed. Such joint part cannot deliver moment. Thus, a large shear wall or RC structure core must be installed to support the lateral load [1]. Yet, it may be one of the biggest burdens on the client because of its tremendous amount of installation cost and it is the cause of delayed construction for it is a critical process of the framework. Additionally, simply mounting beams on columns may cause collapse accidents. SMART frame method developed to complement these problems is a composite precise concrete

S. Son · J. Lim · O. Oh · J. T. Kim · S. Kim (✉)
Kyung Hee University, Yongin-si/Gyeonggi-do, Republic of Korea
e-mail: kimskuk@khu.ac.kr

structure system that applies the advantages of steel frame and reinforced concrete [2]. Several studies have confirmed that the SMART frame method is effective in terms of structural stability, constructability and economic feasibility as well as superior to the conventional frame systems [3].

In particular, the innovative advantage of SMART frame is that it ensures structural stability once it is installed with moment-joint [1]. When SMART frame with such advantage is applied to long-span- and heavy loaded buildings like large distribution centers, it is expected to show significant improvement in construction period, quality, safety, and ultimately, cost reduction when compared to the existing PC structure. For verification, it is necessary to compare it with the conventional PC structure method and analyze the risk and opportunity of SMART frame in terms of construction period, quality, safety and cost. Therefore, the purpose of this study is for risk identification of an innovative composite precast concrete structure applied to heavy-loaded- and long-span buildings. The study procedure is described as below.

First, a theoretical study is conducted regarding the conventional PC structure and SMART frame which is the composite PC structure. Characteristics of each construction method are identified through this theoretical consideration. Second, the identified characteristics of each type (SMART frame vs. PC structure) are compared and analyzed. Their advantages and disadvantages upon implementation of long-span- and heavy-loaded building projects are drawn. Third, the opportunity of SMART frame is identified in comparison with the existing PC structure and its risks in terms of construction period, cost, quality and safety are investigated.

2 Theoretical Consideration

2.1 Conventional PC Construction Method

PC construction method is one of the assembly methods in which members are fabricated at factories and transported to sites for assembly. However, when installing the members, they are simply mounted which makes it rather difficult to ensure continuity in joints of the structure. Such disadvantage is the main cause of reduced constructability. Especially, Seo Soo-il [4] analyzed the characteristics of PC construction through a case study on PC construction of Jeonju World Cup Stadium. Several consideration points were identified through the study, including reviews on temporary building materials for structural stability, necessity of skilled engineers for installation of members and treatment of each member joint. However, they are related to the characteristics of pin-joint PC construction method, and it has limits in reducing defects. To solve this, it is necessary to use a structure system that simplifies construction and stably ensures quality of joints, and composite PC members.

2.2 SMART Frame

Moment-joint is used to restrain rotation of beam members by fastening both H-shaped steel webs and flanges with bolts or welding. SMART frame that is considered in the study is composed of columns and beams which integrated the advantages of reinforced concrete and steel frame, and its joint is a moment-joint. As shown in Fig. 1, the composite PC column of SMART frame consists of the steel frames for beam–column connection and for PC column–PC column connection, and reinforced concrete columns. In case of the composite PC beam, it is composed of steel frame and reinforced concrete, and there are several types of PC beams depending on the steel frame installation method [3].

3 Comparative Analysis of the Conventional PC Structure and SMART Frame

This section compares the characteristics of the conventional PC structure and SMART frame, studied in the previous section, when applied to long-span- and heavy-loaded buildings. Accordingly, the advantages of SMART frame method against PC method are identified. The comparative analysis of two methods is shown in Table 1.

Notable advantages of SMART frame that are identified in Table 1 when compared with the conventional PC structure are as follows. First of all, it is easy to assemble using bolts for the joint, and the moment-joint ensures structural stability
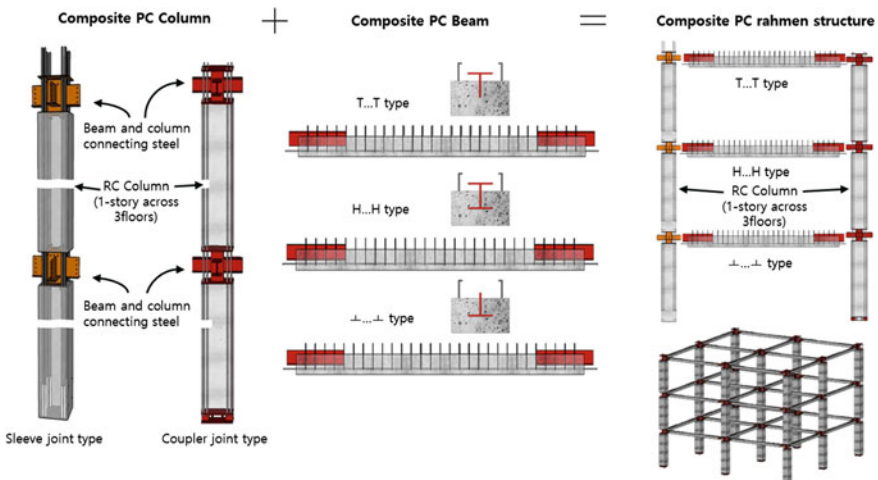
Fig. 1 SMART frame composition [1, 3]

Table 1 Conventional PC structure versus SMART frame

Classification	PC structure	SMART frame
Main member	General PC(RC)	Composite PC(SRC)
Joint structure	Pin-joint	Moment-joint
Core role	Shear wall supporting the lateral load	Simple vertical passage
Construction safety	Lateral stiffening like braces needed	Lateral stiffening not needed
Lateral load resisting system	Shear wall (wet), core wall (wet), brace and etc. needed	Installation not needed
Slab system	Expensive PC slab required (Double-T, RPS and etc.)	Inexpensive deck plate system can be used (Deep deck and etc.)
Installation method	Floor-by-floor method must be applied	Floor-by-floor, section or frame type upward method can be all applied (same as the framework)
Critical process	Mainly RC core	PC member assembly
Equipment operation plan	Limited equipment flow planning owing to the floor-by-floor method	Diversity of equipment movement planning owing to the section method

and construction stability immediately after the assembly. Thus, no additional lateral load resisting system is needed, resulting in cost reduction. Second, the slab installation process is not critical and inexpensive slabs, including deed deck plates can be used, which contributes to reduction of construction duration and cost. Third, unlike the conventional PC structure that must be applied with the floor-by-floor method, SMART frame may be applied with floor-by-floor, section and/or upward method. This makes it possible for SMART frame to reduce the construction period.

4 Risk Analysis

This section analyzes potential risk and opportunity when SMART frame is applied to long-span- and heavy-loaded buildings. It is shown in Table 2.

When it comes to the construction period, the expected risk of SMART frame is the increased time for member installation or reproduction of members as the joint quality degrades. Upon fabrication of members, there may be errors and member installation may be impossible. Steel forms can be used to make members and minimize construction errors. The expected risk in relation to cost is the increased material cost due to an increased amount of steel frames when compared to the

Table 2 Risk & opportunity of SMART frame

Classification	Conventional PC structure	SMART frame	
		Opportunity	Risk
Construction period	1. Additional lateral load resisting systems such as braces and shear walls are needed; 2. Upper floor construction cannot be done until the joint is cured	1. Construction period is reduced because additional lateral load resisting system is not needed 2. Construction period may be reduced by modular frame installation	1. Member installation time may increase or members may need to be reproduced as the joint quality degrades
Cost	1. Input of temporary members; 2. Input of additional manpower; 3. Additional lateral load resisting system (shear wall, RC core)	1. Reduced temporary members; 2. Reduced (skilled) manpower; 3. Reduced cross-section of members	1. Increased material cost because of increased quantity of steel frame; 2. Increased cost for renting a crane as the member weight increases upon modular frame installation
Quality	1. Potential quality degradation due to additional processes such as pouring for joints and lateral load resisting system	1. Outstanding quality maintained even during the joint processing; 2. Same performance for construction work even when unskilled engineers are input	1. Inaccuracy upon steel frame joint connection
Safety	1. Existing risk of removal as beams are simply mounted on top of columns	1. Stability of the joint secured because of the moment-joint; 2. Risk factors may decrease owing to improved working environment as temporary structures are reduced	1. Increased anxiety as the member weight increased during the modular frame installation; 2. Risk factors may increase depending on the lifting method

quantity used in the conventional PC structure. Additionally, a large-capacity crane should be used for installation of modular frames that are two-floor-one-section and three-floor-one-section because the member weight increases. This results in increased cost for renting a crane. However, one of the advantages of SMART frame is quick installation, which shortens the renting period of crane, and consequently may reduce cost. Any expected risk related to quality is inaccuracy of steel frame connection when SMART frame is adopted. Such inaccuracy may be caused by errors in member production accuracy, including the position of steel frames. Furthermore, unskilled engineers may make construction errors. The expected safety risk is the increased anxiety upon installation of modular frames that are two-floor-one-section, three-floor-one-section and so forth.

5 Conclusion

The study was conducted to identify risk that may occur during execution of the project to apply SMART frame that is developed to improve the problems of the conventional pin-joint PC method. The study performed the following analyses.

First, it reviewed studies on the conventional pin-joint PC structure and moment-joint composite PC structure, SMART frame, and arrived at the conclusion that it is necessary to have an improved structural system.

Second, it analyzed the structural characteristics of and differences between the conventional pin-joint PC structure and SMART frame, and identified the advantages and disadvantages of each structural system.

Third, after verifying the opportunity of SMART frame when applied to long-span- and heavy-loaded buildings, its corresponding risk was investigated.

The risks identified in the study have dynamic relations that are mutually interfering in the aspects of construction period, cost, quality and safety. Thus, the study result will be used to draw a causal loop diagram for dynamic analysis. Moreover, it will be used as the basic data to build a risk management system when applying the SMART frame method to long-span- and heavy-loaded buildings.

References

1. Hong, W.K., Park, S.C., Lee, H.C., Kim, J.M., Kim, S.I., Lee, S.G., Yoon, K.J.: Composite beam composed of steel and precast concrete (modularized hybrid system). Part III: application for a 19-storey building. Struct. Des. Tall Spec. Build. **19**(6), 679–706 (2010). https://doi.org/10.1002/tal.507
2. Lee, S.H., Kim, S.E., Kim, G.H., Joo, J.K., Kim, S.K.: Analysis of structural work scheduling of green frame-focusing on apartment buildings. J. Korea Inst. Build. Constr. **11**(3), 301–309 (2011). https://doi.org/10.5345/JKIC.2011.06.3.301
3. Hong, W.K., Kim, J.M., Park, S.C., Kim, S.I., Lee, S.G., Lee, H.C., Yoon, K.J.: Composite beam composed of steel and pre-cast concrete. (Modularized Hybrid System, MHS) Part II: analytical investigation. Struct. Des. Tall Spec. Build. **18**(8), 891–905 (2009). https://doi.org/10.1002/tal.484
4. Seo, S.I.: Precast concrete construction for Chounju soccer field. J. Korea Concr. Inst. **14**(4), 86–88 (2002)

The Use of Polystyrene as Substitute of Sand in Pontoon Concrete

Norpadzlihatun Manap, Jung Sem Wong and Noor Shahifah Syahrom

Abstract The construction industry in Malaysia has been growing over the years. In order to fulfil the demand, new land needs to be opened and developed. However, this could be an issue as opening and developing a new land causes adverse effects to the environment as these leads to the Green House effect. One of the solutions is to design pontoon-type concrete structure. Pontoon-type concrete structure refers to the artificial pontoon-type structure made from concrete. However, designing a pontoon-type structure requires a special mixture of concrete and infill material. It is profitable to use sustainable material including polystyrene. This research aims to determine the strength of pontoon type concrete partially made from polystyrene and to compare the strength of it with M20 mix concrete. A laboratory testing has been conducted and it can be concluded that the strength of concrete made from polystyrene were lesser than conventional M20 concrete. These may come from the fact that the smooth surface of polystyrene tends to have a weak bonding in the cement paste. It can be concluded that the concrete made from polystyrene could be used for pontoon concrete for non-structural application. This result is significant for the construction industry as it produces new sustainable material for construction industry.

1 Introduction

Pontoon-type concrete structure refers to the artificial pontoon-type structure made from concrete. Pontoon concrete structure have been developed for a variety of purposes such as floating bridges, floating plant, floating terminal and floating cities [10]. The designing concept of pontoon type concrete structure aims to solve the insufficient land problems. Pontoon-type concrete structure is one of the

N. Manap (✉) · J. S. Wong · N. S. Syahrom
Department of Construction Management, Faculty of Technology
Management and Business, Universiti Tun Hussein Onn,
Parit Raja, Malaysia
e-mail: padzliha@uthm.edu.my

technologies that support future large human habitation on the sea. The concept of floating cities had been introduced by Pernice in 2009 [9].

The construction industry is growing over the years, therefore in order to fulfil the demand, new land needs to be opened and developed to provide spaces for building and facilities. However, this lead to insufficient land-use issues. One of the solutions is to design pontoon-type concrete structure. The pontoon-type concrete structure is a type of concrete structure that allows the building floats on the water. However, designing a pontoon-type structure requires a special mixture of concrete and infill material [8].

The construction industry in Malaysia is expanding as more construction works have been done over the years. The value of the construction work has shown an increase in the past few years. In order to fill the demand, new land need to be developed for building and facilities. However, this could be an issue as opening a new land has adverse effects to the environment. Green House effects will occur due to demolishment of forest for construction purpose. Destruction of natural habitat for several species of animals and plants is the main concern regarding the opening of new city.

One of the solutions is to design pontoon-type concrete structure. The pontoon concrete is a type of concrete structure that allows the building float on the water. The application of pontoon-type concrete structure is an innovative solution to encounter insufficient land issue. However, the conventional concrete with high density is very low in floatability. Moreover, the issue is to design a pontoon-type structure requires a special concrete [8]. Basically, the concrete used in the pontoon concept are concrete made from lightweight aggregate. However, lightweight aggregate concrete is expensive than conventional concrete. The extra cost consists of material cost, cost for storing, placing, curing, reinforcement details, including protection from contamination of the water [5]. Therefore, there is a necessity to seek new material instead of using lightweight aggregate. Polystyrene with very lightweight property and cheap price are very suitable for replacing lightweight aggregate in producing the pontoon-type concrete.

The objectives for this research are to determine the strength of pontoon-type concrete made partially from polystyrene and to compare the strength of between pontoon-types concrete made partially from polystyrene with M20 mix concrete. Pontoon-type concrete will be produced and tested in the Construction Material laboratory in the Faculty of Technology Management and Business, Universiti Tun Hussein Onn Malaysia. There are many benefits to perform the research of pontoon-type concrete made from recycled materials. Basically, it can be classified into the environment and the construction industry. Designing the pontoon-type concrete using discarded polystyrene is a good way to manage high volume of trash for a long period of time. Through the usage of polystyrene, the industry can seek for a new resource in production of pontoon type concrete.

2 Literature Review

Historically, construction activities have been associated with the process of industrial and urban development since the Industrial Revolution period. A number of studies have confirmed that approximately half of the investment in gross fixed capital formation is contributed by the construction sector in most developing countries. The construction industry and its activities have great impact on all aspects of human life [2, 3]. As the urbanization expand, the land reclamation is carried out to ease the pressure on existing heavily used land and underground spaces. However, land reclamation has its limitation [7]. Moreover, it can damage the marine environment [4]. Design of pontoon concrete is an attractive way as a solution for artificial land on the sea [10].

Concrete is most widely used in construction industry today. The main ingredients of concrete are fine aggregate, course aggregate, cement and water. Special additives are also added to enhance or modify its properties. The fine aggregate and course aggregate constitute the most of the volume in concrete as it is an economical filler material that improves the durability of the concrete. When cement is mixed with water, it acts as a hydrates agent to bind the mixtures to form a hard substance when dried which called concrete. Concrete is a good construction material and it is suitable to be used for construction of strong structural building with a relatively low cost as compared with the use of timber. Besides that, concrete can be easily shaped to fill the needs while it in the fresh concrete form. Moreover, several of finishers such as tiles can be applied to it for aesthetic value.

Although concrete has a higher compressive strength, concrete relatively are low in tensile strength. However, this can be solved with adding the reinforcement in concrete to enhance the tensile strength of it. In addition, conventional concrete has a higher density compared with other materials. Concrete is one of the highest durability construction materials. It only requires little maintenance and it is a very good thermal-resistance material. The properties of the concrete can be affected by the amount of ingredients in the concrete. Exceeding of water content will drop the strength of concrete. On the other hand, the properties of concrete can be improved with some special additive such as plasticizers and air-entraining material. The properties of concrete include low-cost parameter, high compressive strength, low tensile strength, high density and high thermal resistance. The strength of concrete refers to its load affordability. Concrete is a comparatively brittle material which is relatively weak in tension. Therefore, reinforced concrete is designed to equally bear the compressive strength and tensile strength. Basically the concrete will go through a curing process at the age of 7th and 28th days for the purpose of studying the strength developments of concrete. The differences of design of concrete mixtures are to establish specific concrete characteristic and to select the proportion of available materials to produce concrete with required properties.

In addition, density of the typical foamed concrete being used in construction engineering generally ranges from 500 to 1200 kg/m^3, are very suitable in designing the concrete pontoon to sustain the structure float on the water [6].

Compared to normal classified into two categories, which are used due to its characteristic to reduce its weight and density. In construction industry, foamed concrete had been applied in concrete, the most distinct characteristics of thermal conductivity. Lightweight concrete is generally lightweight aggregate concrete with its low density and high thermo-insulating. The main properties of the lightweight concrete are the low density and low capacity. Lightweight aggregate concrete is used for construction of super high-rise building with giving the benefits by reducing self-weight. Due to the high porosity of the lightweight aggregate, lightweight aggregate concrete is more insulating than normal concrete [1].

Pontoon concrete is a concrete floating berth which carries a certain amount of weight. For the pontoon to stay afloat on the water, the design concept is usually hollow in core. But there is also exception that is filled with foam or other lighter materials in the pontoon. This design concept is to make sure the pontoon light as it is designed to displace a large amount of water. Generally, the concrete pontoon consists of two parts, which are the concrete mixtures and the inner system. So it is a necessity to design a lightweight concrete so that the pontoon can stay afloat on the water. The pontoon concrete is design based on the concept of Archimedes' Principle. Thus, the inner system inside the concrete affects the floatability of the pontoon. Basically the design of the pontoon is based on the idea of submarine.

The pontoon concrete normally is designed as a hollow system inside the core. The pontoon will stay afloat on the water surface as long as the load applied on the pontoon do not exceed the maximum load capacity. On the other hand, the design of the pontoon should use lightweight expanded clay aggregate, and raisin had been used in designing the concrete for the pontoon. Those materials have a lesser density than water. Therefore, several researches had been conducted to seek lighter material in designing the pontoon concrete. Materials such as coconut fibre and aluminium foil can be an option.

3 Methodology

Eighteen concrete cubes were produced which six of it made from 25% of polystyrene as substitute for course aggregate; six of it made from 50% of polystyrene as substitute for course aggregate and the rest of the cubes were made from 75% of polystyrene as substitute for course aggregate. The cement used was Ordinary Portland Cement (OPC) which manufactured locally; the water used is obtain from pipe water; the fine aggregate and course aggregate used was obtained from a nearby quarry; polystyrene used was recyclable. A small capacity of concrete mixer was used in the experiment as only a small amount of concrete needed to cast the specimens.

The concrete was mixed using concrete mixer. Ready mix concrete was poured carefully into the formwork of test cube with dimension 100 mm × 100 mm × 100 mm. Cube test was carried out once the cube is being removed from the formwork. The cube specimens were cured in a water tank and compression test

were conducted on 7th days and 28th days after casting. A total number of 18 cube specimens were tested for 7th and 28th days.

The compressive strength of the sample was recorded and presented in graphs. The collected data will be compared against the targeted value, which is M20 mix of concrete. The type of M20 mix concrete will give 20 N/mm^2 compressive strength after 28 days curing process. Basically, after curing period of 7 days, the concrete will achieve around 65–70% of the M20 mix concrete strength.

4 Result and Discussion

4.1 Strength of Concrete Made from 25% of Course Aggregate Replaced with Polystyrene

Figures 1 and 2 shows the strength of concrete made by replacing 25% of course aggregate with polystyrene for a curing period of 7 days and 28 days, respectively. When 25% of course aggregate was replaced by polystyrene, the concrete produced a compressive strength that is almost similar to the normal strength of the M20 concrete mix. The compressive strength of the concrete recorded an average of 11.0 N/mm^2 after 7 days curing process (Fig. 1) and an average of 19.3 N/mm^2 after 28 days curing process (Fig. 2).

Fig. 1 Strength of concrete made with replacing 25% of course aggregate with polystyrene—7 days curing
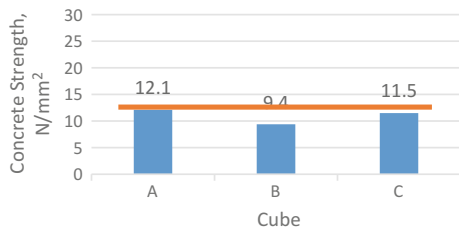
Fig. 2 Strength of concrete made with replacing 25% of course aggregate with polystyrene—28 days curing
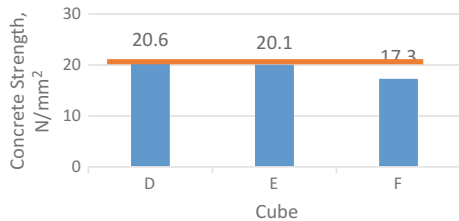
4.2   Strength of Concrete Made from 50% of Course Aggregate Replace with Polystyrene

Figures 3 and 4 shows the strength of concrete made with replacing 50% of course aggregate with polystyrene for a curing period of 7 days and 28 days respectively. When 50% of course aggregate was replaced by polystyrene, the concrete produced a compressive strength that is only achieved almost half of the normal strength of the M20 concrete mix. The compressive strength of the concrete recorded an average of 7.9 N/mm^2 after 7 days curing process (Fig. 3) and an average of 9.2 N/mm^2 after 28 days curing process (Fig. 4). The concrete shows a difference of −5.1 and −10.8 N/mm^2 in strength respectively.

4.3   Strength of Concrete Made from 75% of Course Aggregate Replace with Polystyrene

Figures 5 and 6 shows the strength of concrete made with replacing 75% of course aggregate with polystyrene for a curing period of 7 days and 28 days respectively.

Fig. 3 Strength of concrete made with replacing 50% of course aggregate with polystyrene—7 days curing
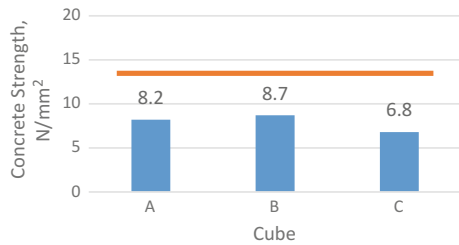
Fig. 4 Strength of concrete made with replacing 50% of course aggregate with polystyrene—28 days curing
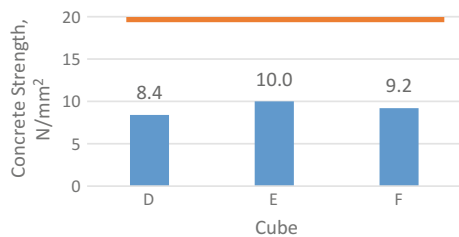
Fig. 5 Strength of concrete made with replacing 75% of course aggregate with polystyrene—7 days curing
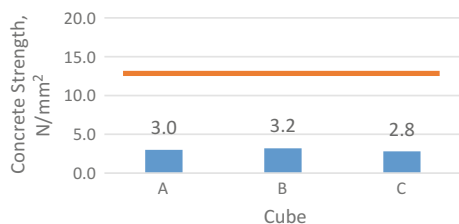
Fig. 6 Strength of concrete made with replacing 75% of course aggregate with polystyrene—28 days curing
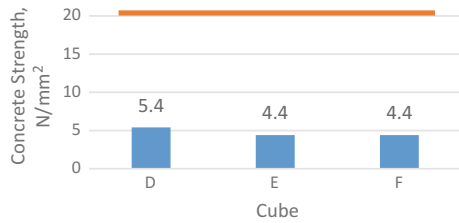
When 75% of course aggregate was replaced by polystyrene, the sample concrete shows huge difference in compressive strength as compared with normal strength of the M20 concrete mix. The compressive strength of the concrete recorded an average of 3.0 N/mm^2 after 7 days curing process (Fig. 5) and an average of 4.7 N/mm^2 after 28 days curing process (Fig. 6). The concrete shows a very huge difference in compressive strength which were −10.0 and −15.3 N/mm^2 in strength respectively.

4.4 Comparison of Strength of Concrete with Course Aggregate Replaced with Polystyrene

Figure 7 shows that the increase of the polystyrene content in the mix will directly decrease the compressive strength of the concrete cube. The mix with 25% of course aggregate replaced with polystyrene was the only mix that is able to produce the required strength of 20.0 N/mm^2 after 28 days curing process. The mix with 50% of course aggregate replaced with polystyrene shows the least of increased strength between 7 and 28 days, which was only 16.5%, while 75% of course aggregate replaced with polystyrene shows increase of 56.7, and 25% of course aggregate replaced with polystyrene shows the highest increase of 75.5%.

After comparison of normal concrete with the samples, it can be concluded that the strength of concrete made from polystyrene was lesser than normal concrete (M20 mix concrete). These may come from the fact that the smooth surface of polystyrene tends to have a weak bonding in the cement paste. Because of the poor

Fig. 7 Strength of concrete made with polystyrene as substitute for course aggregate
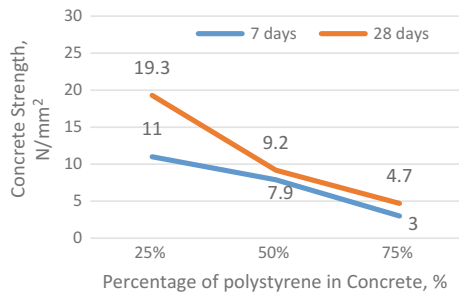
bonding, failure takes place in the cement paste, hence affecting the compressive strength which tends to be lesser when polystyrenes contents increase. Besides that, polystyrene could be used for pontoon concrete for non-structural application due to its properties that is lower density than normal concrete.

5   Conclusion

A conclusion can be made that the increasing of the proportional of polystyrene replaced with course aggregate in the concrete mixture will directly decrease the compressive strength of the concrete cube. The strength of concrete made with 25% of course aggregate replacing with polystyrene showed an average of 11.0 N/mm^2 for 7 days curing process and 19.3 N/mm^2 for 28 days curing process. Meanwhile, with the increasing of polystyrene contents to 50% in the concrete mixtures, the strength of the samples shows an average of 7.9 N/mm^2 for 7 days curing process and 9.2 N/mm^2 for 28 days curing process. For the concrete cube that replacing 75% of course aggregate with polystyrene, the strength of the samples shows an average of 3.0 N/mm^2 for 7 days curing process and 4.7 N/mm^2 for 28 days curing process. It can also be concluded that the samples recorded show the strength of concrete made from polystyrene was lesser than normal concrete (M20 mix concrete). The result shows the strength of concrete made with 25% of course aggregate replaced with polystyrene was the only sample that almost achieved the targeted value as 28 days curing period. The strength of the samples recorded an average of 19.3 N/mm^2 which was slightly weaker than normal concrete after 28 days curing process. Meanwhile, for concrete made with 50 and 75% of coarse aggregate replaced with polystyrene gives an average of compressive strength of 9.2 and 4.7 N/mm^2 respectively. The result showed a huge difference in terms of compressive strength when the samples were compared to the control (M20 mix concrete). The research helps to improve the way of waste management towards polystyrene waste as well as enhancing the environmental health in the construction industry. However, concrete made from polystyrene was suggested for future research to be designed and tested for its plasticity limit.

References

1. Kwang, S.Y., Yeon, J.J., Erie Seong, H.H, Tae, S.Y.: Experimental investigation on annual changes in mechanical properties of structural concretes with various types of lightweight aggregates. Constr. Build. Mater. 442–451 (2014)

2. Manap, N., Raja Bedali, R.A.A., Sandirasegaran, K., Masrom, M.A.N., Yahya, M.Y.: Strength of concrete made from dredged sediments. J. Teknol. **78**(3), 111–116 (2016)
3. Manap, N., Polis, S., Sandirasegaran, K., Masrom, M.A.N., Goh, K.C., Yahya, M.Y.: Strength of brick made from dredged sediments. J. Teknol. **78**(3), 87–92 (2016)
4. Manap, N., Voulvoulis, N.: Data analysis for environmental impact of dredging. J. Clean. Prod. **137**(11), 394–404 (2016)
5. Manap, N., Voulvoulis, N.: Environmental screening method for dredging in contaminated river. Appl. Mech. Mater. **567**, 50–55 (2014)
6. Pan, Z., Li, H., Liu, W.: Preparation and characterization of super low density foamed concrete from Portland cement and admixtures. Constr. Build. Mater. 256–261 (2014)
7. Sandirasegaran, K., Manap, N.: Impacts of dredging and reclamation projects. J. Teknol. **78** (3), 139–143 (2016)
8. Starr, P., Wainwright, D.A.: Design and construction of a concrete floating berth. J. Eng. Struct. **18**(11), 837–841 (1996)
9. Wang, C.M., Tay, Z.Y.: Very Large Floating Structures: Applications, Research and Development. J. Procedia Eng. **14**, 62–67 (2011)
10. Watanabe, E., Wang, C.M., Utsunomiya, T., Mon, T.: Very Large Floating Structures: Applications, Analysis and Design. National University of Singapore, Singapore (2004)

LEED and Green Building Designs

Walaa Mohamed Metwally

Abstract Scientific consensus agrees that global climate changes over the past centuries until today are due to human activities. And it is a growing threat to environment in the society. With this in mind building industries need to contribute their efforts to encourage a healthier life style and to live in a healthier environment. One contribution devoted to preventing harm to the environment is the (LEED). LEED is a body that provides certifications for Environmental and energy Design from architectural industry to the applicants. It is the only rating system for the green building design that communicates with global sustainable development practices and projects. LEED certification is based on the overall score that is achieved for any given project. This certification will measure the impact of the green building design and sustainability, and it will provide the project with one of the LEED rating levels (platinum, gold, silver and certified), also it will help the project's owner and operators to measure the building's performance. Projects from office towers to single family homes have registered for LEED certification. Some of them have submitted registration for the LEED certification, as a result of the continuous growth that has spurred the recent pricing structure changes. This is a clear indication of LEED's continued strength and value to the growing market places. This paper aims to

1. Recognize and celebrate high-quality "green" building.
2. Measure the "green" building solution which is based on sustainable building practices.
3. Explain how to register a project.
4. Raise awareness of the efficiency of staff performance in the work place.

The research focuses on two studies in order to reach its aims

1. First is the theoretical part which is divided into many factors

   - What is the LEED?
   - What is the LEED certified to?

W. M. Metwally (✉)
Prince Sultan University, Riyadh, KSA, Saudi Arabia
e-mail: Wmetwally@psu.edu.sa

- What are the LEED measures?
- Why certify?
- Why are the LEED professional credentials changing?
- What are the eligibility requirements for the LEED professional credentials?
- How to register a project with the LEED?

2. Second is the applied part

- This part includes the projects submitted for LEED certification, and one is selected for the case studies in Saudi Arabia. Thereafter, the study ends with important conclusions and recommendations.

Keywords LEED · Green building · Sustainability · Energy and environmental design

1 Introduction

Our economy is changing based on the development of new technology. The environmental sustainability field is one that has entered a period of rapid expansion that directs the economic and political indicators that determine growth in the near future to creating a health and environmental buildings and homes for humans.

LEED has become a professional, long-term investment in the promotion of a healthy planet. Moreover, LEED is furnished with skills that are in demand by many sectors of the architectural industry. It is internationally marketable and engages clients in activities which aim to transform the globally built environment to a firm hold on professional and beneficial skills in the environment.

2 An Overview of the Issue of Concern

This study was produced in 2009 by (UNEP) the United Nations Environment program, which lead to increase the sustainable projects and products in future; this study is based on the changing of climate and building and The enormous scale of the global in the built environment.

The study's result stated that 30% of global annual greenhouse gas attributed to the building sector, which represents up to 40% of global energy usage. The climate change and their negative effects and the public pressure can be solved by transforming the globally built environment to green and sustainable environment considering how much and how it will take to change it to this value.

LEED is an asset that can aid negative effects in the building industry, by transforming the built environment and meeting its demands for sustainable and green projects. These environmental sustainability products are growing and supporting a long-term professional investment in the community and also helping

professionals grasp the limitless possibilities associated to serve all professionals engaged in construction activities and transforms our built environment in the years to come.

3 Green Building Design and Sustainability

Since the 1990s, the media has often talked about "green" or "sustainable" buildings [1].

Green building or sustainability can be defined as

"Eliminates negative environmental impact completely through skilful, sensitive design" [2].

Green building is also responsible for the environmental process in the building life-cycle starting from the building design, building construction, building operation, building maintenance, renovation, and demolition. Also attempts to reduce the environmental impacts (heating, electricity use, carpet cleaning, etc.). During the building production, construction process, as well as during the building life.

Also this green design will emphasize in practice, the efficiency of cooling and heating system, recycled or reused material in the building, solar technology, wind power, and on-site management.

All of these require a strong cooperation between the project's responsible: Client, design team, architects, engineers, they will be responsible in all the project's stages starting from the site selection, project's formation, material selection and project's implementation [3].

A building will be a "green" design with the following:

- Reducing the consumption of natural resources for its construction, for example, control the use of wood that are available in the forest.
- Reusing the recycled materials in the building construction instead of sending to landfill.
- Reducing the cost and the consumption of water uses and energy.
- The development footprint is limited, open space is restored and enhanced, and landscape architecture is designed to provide wildlife habitat, storm water management, and beauty with minimal water consumption and maintenance.
- Minimizing or eliminating the heat for the site and the building designs in walkways design and construction, parking area, asphalt and other non-reflective materials on the building roof which absorbs much solar heat that effects on the air condition, ventilation and heating system, and landscape irrigation system needs.
- Having natural day lighting and outdoor views in majority of the interior spaces.
- Applying high efficient systems for the materials like paint, flooring, and furniture are used to improve the indoor environmental air quality.
- Using recycled materials starting from the building structure to choosing the furniture and carpeting.

4 Benefits of Green Building and Sustainable Development[1]

There are many benefits of "green" building that effect and improve the people's health in the environment The "green" building can reduce the building impact in the long run during the degradation of the environment.

On the other hand, the sustainable environment has financial and personal benefits, for example, reduced water bills, using the water-efficient fixtures, In addition, reducing the heating costs in the use of insulation with a high heat resistance rating.

The "Green" architecture features can be found in

- Designing the ventilation, heating, and cooling systems for the building designs.
- Using the lighting and appliances with full energy-efficiency.
- Applying the water and plumbing fixtures in right ways
- Planning the landscapes design by considering to maximize the passive solar energy
- Using alternate sources such as solar or wind power
- Using non-synthetic, non-toxic materials which are found in the environment.
- Obtaining the local stone and woods and eliminating the cost of the transportation instead of long-hauls
- Using the woods which are available (Harvested)
- Reusing the older building and constructions,
- Using recycling materials for architectural salvage
- The space use (ensuring efficiency)
- Choosing the locations—enabling optimal locations and maximizing sunlight, winds, and natural sheltering.

** Most "green" buildings do not have all of these features, however, in order to achieve sustainability or do "green" the highest goal is to be fully sustainable.

5 LEED

There is a promotion for green and green building. Since 1993, over time and by the year 2000, the U.S. "Green" Building Council created a new rating system for buildings to develop the project to sustainability and pursing for LEED certifications by earning points across several area. These areas will be scored according to address sustainability issues for one of the four LEED rating level of certifications.

---

[1]Reference [4].

Any building project from homes to corporate headquarters[2] can be assigned for the LEED certification which comes a fee; The US "Green" Building Council rating system develop the products to include the following steps: The technical development by committee, pilot testing, a public comment period, approval by council membership, and then the release for public use.

In the event that major renovations are performed, high standards are maintained for certifying the design and construction of various commercial projects or institutional buildings. In order to deliver architecturally sustainable designs the following categories are considered

– Minimizing the impact of water resources and using sustainable sites (SS)
– Reducing the Water efficiency (WE).
– Innovation in using the Energy and Atmosphere (EA)—using different strategies.
– Reducing the waste of Material and Resources (MR—using sustainable building materials.
– Designing better Indoor Environmental Quality (IEQ)—using daylight and view.
– Innovation in Design (ID)—sustainable building expertise.
– Regional priority (RP)—regional environmental priorities.

The architectural industry has embraced the concept of designing sustainable buildings. Moreover, its vast interest has led architects to become accredited LEED professionals [5].[3]

5.1 Guidelines to Achieve the Certification for LEED-Commercial[4]

Step 1—**Register** the project by submitting the registration details and the payment (Fig. 1).

In preparation for the registration, it is very important to ensure that the project meets the requirements. First, the applicant must comply with the project size requirements, second, they should be informed about specifics on the minimum project requirements, and (this information can be found by visiting the credit library). Third, the applicant must select the appropriate rating system for their project from the LEED guide manual.

The commercial rating systems for LEED 2009 and LEED v4 can be certified in any of the following:

---

[2]Reference [4].

[3]Reference [5].

[4]Green Building Council, 2017, [6].

Fig. 1 Diagram for guidelines to achieve LEED certification

– LEED certification for Homes and Midrise
– Certification for Building Design and Construction (LEED BD + C)
– Certification for Interior Design and Construction (LEED ID + C)
– Certification for Operations and Maintenance (LEED O + M)

Now applicants are ready to apply. Applicants must visit the LEED website. Then they should submit the information for their project, complete, and submit the application and payment then sign the certification agreement. The application will be accessible on the LEED website.

Re-certification (LEED O + M only)

It is required for the projects that already has been certified with LEED O + M to recertify within 5 years of the previous LEED certification to remain as currently certified. Also this project is eligible for re-certification after 12 months and can be re-certified every 12 months.

Step 2—Apply for the LEED certification online and pay a review fee.

The applicants can submit all the project's documents through LEED website, they should upload their documents and make sure with the quality check of the entire application before submitting for review after receiving these documents by GBCI, they will be ready to review the project with their team members, then they will collect all the information, analyse the project's data and calculate the performance in order to identify the LEED credits.

Step 3—Reviewed by GBCI

GBCI will conduct a technical review. This review will vary from one project to another and it depends on the type of the project and its needs, and also the level of the certification rating system which the projects will register for.

If the applicants feel that the result is incorrect, they can appeal for their project (CIR appeal) by contacting GBCI

Step 4—Certified: The certification decision is received. Success applicants will be notified of the LEED certification.

In the event that the project team is not satisfied with the final certification report they have the right to appeal to the GBCI. Once the applicant has accepted the final certification report, it is deemed "closed out" which means that the applicant has lost the right to re-appeal for the certification or even review their decisions.

5.2   The Level of the LEED Certification

The entire project can be assigned in one of four LEED level certification and the degree of the project that will be achieved as follows:

– The project earned 40–49 points can be certified as LEED Certified™
– The project earned 50–59 points can be certified as LEED Silver®
– The project earned 60–79 points can be certified as LEED Gold®
– The project earned 80+ points can be certified as LEED Platinum®

5.3   Certification fees

The fee will be charged per building or project and it based on the project's scale and which rating system will be register for.

5.4   LEED-Certified Projects

Over 62,000 projects around the world have been certified for LEED in more than 150 countries, and every day around 2 million square feet of LEED space certified, all of these statistical numbers and the increase in numbers indicate the importance of becoming LEED for many countries and projects. Also the professionals are positioning themselves to remain competitive in an increasing economy by acquiring skills that are in demand and internationally profit-making.

(KAFD)—King Abdullah Financial District is one of the most important projects for prestigious urban developments. Located in Riyadh, it is noticeably an ambitious, distinguished project that has earned its position as a substantial addition to the economic sector (Fig. 2).

5.5   Introduction to King Abdullah Financial District (KAFD) project

The KAFD is an under construction project located on King Fahad Road in Al Aqeeq area of Riyadh, Saudi Arabia (New York Times 2006) [7].[5]

---

[5]Reference [7].

Fig. 2 General view for King Abdullah financial district

On Tuesday, 9/5/2006, King Abdullah bin Abdulaziz laid the foundation stone of King Abdullah Financial District (KAFD) as the biggest urban edifice in Riyadh city which includes the most important official financial institutions and other financial bodies.[6]

KAFD project master plan was designed and overseen by Danish Architect "Henning Larsen" and the development of this project was headed by Waleed Al Eisa the CEO. Additional designs will be provided individually for each sub project by their own designers.

There are many staffs were working in the KAFD project: designers, engineers, manager's team, observers, workers who are working together and spare no effort around the clock to accomplish the project to make sure that the work is maintained according to the preset plans as agreed, The project is led by engineers team from Al-Ra'idah Investment Company and they are the main contractor of the KAFD project, Hill International.[7] Also the contractors assigned are working 24 h a day to stay on target (Fig. 3).

KAFD was the largest project in the world that seeking green building accreditation in 2011. The project built on 1.6 million square meters and includes 59 towers in the site.

The project is designed to meet the growing demand for class-A offices which equipped with high tech and modern capabilities. The KAFD Financial Academy is expected to meet all the domestically high demand for manpower qualified in the financial domain and in modern investment management.

The project has a direct route to the King Khalid Riyadh airport, and is served by many main roads which lead to many regions. In addition, it is near to al-Olaya Region which contains many commercial areas located in.

The project includes various uses with three million square meters, and can be divided to

- Accommodation area for 12,000 residents
- Parking spaces
- KAFD also contains the headquarters of the Financial Market (Tadawul)[8]
- Financial academy

---

[6]*ALRA'IDAH*, 2017 [8].

[7]See Footnote 6.

[8]Reference [9].

Fig. 3 KAFD construction work in progress

– Numerous banks equate to 62,000
– Other financial institutions
– Alongside financial service companies and other multinational corporations.

5.6 KAFD's Vision and Mission

The KAFD vision is to establish a project for generations and the generations to come,

KAFD entrenches well-established pillars meant to put into effect this vision, which accords with the aspirations of the upcoming generations,

The project will ensure the development and continuity of the pioneering role of the Kingdom of Saudi Arabia, as the country with the largest economy Gulf region (Fig. 4).[9]

---

[9]See Footnote 6.

Fig. 4 Picture of KAFD illustrates the future generation

5.7 Project's Aims and Objectives[10]

The KAFD project aims to establish several economic gains by contributing to the economic growth and development. The projects objective is to enable Riyadh to witness with different fields which are follows:

- Combining the working in the financial sector and the agencies
- Developing the Saudi economy by raising the contribution of all the financial sector in KSA with its available capabilities required
- Attracting the largest companies in financial investments field.
- providing many job offers for professionals and for Saudi national force
- Setting up a financial academy to meet the demands and needs of training and professional development for employees (Fig. 5).

---

[10]Reference [10], 2017.

Fig. 5 KAFD and the economic growth

5.8 KAFD and Design Concept

KFAD was setting up as financial academy to meet the demands and needs of training and professional development for employees. It has been designed to be a smart, elegant, and self-sufficient center with the global standards.

The project has been designed that facilitates include the places for the financial work practice and investment in the KSA, the projects contains many international banks, several prestigious local, varies of investment companies, and professional services area needed for the financial field work In order to become one of the biggest and effective economy and financial city that serve the professionals in the financial field.

5.9 Activities and Components of the Project

KAFD consists of the main headquarter, "Capital Market Authority", Tadawul Center which is the "Stock Exchange" headquarter, academy financial project, and several national banks and other companies and institutions. Also it Included the components of any projects required with each sector: accounting, legal auditing, and the consulting and financial institutions.

Further components includes, different services and facilities: five stars hotels, residential projects and neighborhood, conference and showroom halls, recreational and sporting activity places, and modern means of transportation.

The project's activities and work areas:

- **Work places**: are designated for the financial companies and institutions. This is considered as very important area in the project, as it includes the "Capital Market Authority" (main headquarters), Famous banks, and companies. All of these are collectively intended to secure the Kingdom's leading role in its capacity as the region's hugest economy and financial status. Work place area will also accommodate high-qualified employees and workers that will be working in the financial sectors.
- **Education**: An educational institution, pioneered by the financial academy, will be a part of the center. It will deal with courses' trainers, financials specialties, and the people working in financial institutions.
- **Mosque**: A number of mosques have been designed for the center which will welcome local Muslims and other Muslim visitors. The comfortable, relaxing

and convenient environment will make their worship experience peaceful. One of the mosques was awarded the global award for Islamic architectural distinction for the tremendous achievement which demonstrates the outstanding quality and creativity of the efforts towards uniqueness.

- **Housing**: Part of the center a residential compound for financial projects' workers and for educational services, this area was designed with the global standard to provide suitable future human needs.
- **Meeting Places**: these areas were designed to create meeting points for the compound's inhabitants for exchanging the ideas and opinions also to create entertainments areas for different activities which include many attraction and recreation areas such as: aquarium, center of earth's climate, Vally park (AL Wadi), environmental and science Museums, also many recreation and educational facilities and projects.
- **Transportation**: KFAD was designed to provide different kinds of transportation for their users

  – The transporting of cars were designed to make the projectways move smoothly and comfortably and it includes self-contained infrastructure.
  – The attraction areas were designed to move between the project's buildings by suspended monorail that connects all the different area in the project with each other.
  – Skywalk area was designed to wander on foot in safe and smooth way, passing with well-designed environmental passages and landscape required for entertainments.

- **Services and Facilities**: KFAD is considering one of the most important self-contained financial centers in the world which includes many services and facilities needed for the twenty-first-century specifications.

The project provides large number of hotels (5 stars), showroom center, conference building, administrative offices, many towers for financials sectors, and these buildings are provided with modern and creative equipments and prerequisites.[11]

In the front of each building in the project, car parks were designed according to global standards and added with special valet services for their user's car and securing till they exit the project.

5.10 *LEED/Master Plan and Design Concept*[12]

The project master plan was designed by architect Henning Larsen, his concept is based on sustainability and all the master plans were designed to achieve LEED certificate.

---

[11]See Footnote 10.
[12]Reference [11] P 1.

Most of the individual buildings were designed also to achieve either Silver or Gold LEED certifications. And for that the architect Henning Larsen will consult during the building design and implementation phases, to ensure that the proposed scheme achieves a standard for LEED certification and sustainable development.

Henning designed the master plan to create modern metropolis project style which unites the Arabian urban traditions which will give the Saudi capital, Riyadh a different kind of a project that includes open and public space and a skyline with a new outstanding landmark. These project will be the heart of Wadi Hanifa Area as an attractive urban project in Saudi Arabia, and also included different areas and activities: residential area, commercial and recreation projects, restaurants, hotels, conferences, and sport facilities as an active and creative compound in Riyadh city.

The project based on the following important environmental achievements can be applied for any sustainable projects:

- Optimizing the proportion of each building in the project for lower outside temperature by 6–8 °C
- Using suitable materials in the building's facades, many water features, and covering with vegetation in the landscape design to avoid the high humidity and achieve lower temperature.
- Controlling the heat of daylight to create the well-designed environmentally controlled outdoors by designing the transparencies of the project's facades.
- Respecting the orientation that effected on designing the project's facades to save more energy.
- Reducing the energy consumption by using local materials reduce energy consumption for different transportation ways.
- Minimize the project's maintenance and using high-quality materials which have a long lifetime to maintain it.
- Using the solar cells as environmental treatment placed on roofs and integrated into the facades.
- Reducing cooling loads to lower outdoor temperature but using shading of the project's facades.
- Using roofs capes in order to achieve sustainable objectives.
- Designing the skywalks which used to connect between the different project's areas and buildings, it was affected on reducing the needs of the car transportation; this skywalk was designed to save the energy by using powdered solar energy.
- Reducing the energy consumption by using "Intelligent" lighting, KFAD was designed to be a smart, elegant, and self-sufficient (Fig. 6).

6   Brief conclusion

- Sustainable Architectural Designs aims to assist teacher and designer to create buildings that help the community to meet their needs.

Fig. 6 KAFD Facades are orientated in order to enhance energy saving

- Support development with "green" to reduce future operation and maintenance costs.
- Create sustainable green buildings that become durable value to the society and culture and also users which have been built to them.
- Save energy and use renewable energy by incorporating energy efficiency into projects and assessing the efficiency of existing equipment.
- Integrate sustainable green building which includes the efficiency of energy, conservation of water, increase the quality of out and in door spaces and areas and increases the value and environmental integrity in the design projects.
- Expand green building education and outreach services in the architectural, environmental, and construction fields to include more green building projects. In addition, consider program standards to a higher level of performance.
- Keep current projects with the green building rating systems and participate in the ongoing development of green building rating systems.
- Use certified and qualified contractors. Consider standards for building construction through LEED, and with green school design.
- Encouraging architects to become LEED-accredited professionals. As the LEED certifications are considered now not as US market leader, but it becomes the most widely used rating system by federal and state agencies, it also helps the building projects to communicate with other sustainability design projects achievements [5].[13]
- Set a minimum goal of LEED certification to achieve as many points possible for water and energy conservation.

---

[13]Reference [5].

References

1. Beaver, R.: Mainstream Green sustainable Design, p 10. LPA, Australia (2005)
2. McLennan, J.F.: The Philosophy of Sustainable Design, Forward by Bob Berkebil. no date (2004). ISBN-10: 0974903302. http://www.epa.gov/greenbuilding/pubs/about.htm
3. Ji, Y., Plainiotis, S.: Design for Sustainability. China Architecture and Building Press, Beijing (2006). ISBN 7-112-08390-7
4. Karpilo, J.: Sustainable Development Promotes Environmentally Friendly Buildings. In: Sustainable Development, Geography Intern, updated 28 Feb 2017
5. Lyengar, K.: Sustainable Architectural Design, An overview, pp. 239–240. Routledge, New York and London (2015)
6. www.usgbc.org/articles/5-reasons-its-worth-it-become-leed-professional
7. Saudis Plan Middle East Financial Center. New York Times, 10 May 2006
8. http://www.kafd.com.sa/
9. King Abdullah Financial District now the world's biggest green development. MEED, 16 Oct 2011
10. http://www.alraidah.com.sa/sites/En/MediaCenter/News/Pages/1-11.aspx
11. https://stateofgreen.com/en/profiles/henning-larsen-architects/solutions/king-abdullah-financial-district

Regression Analysis of OPC-MK-RM-Based Ternary-Blended Concrete Based on Its Experimental Results

Rathan Raj Rajendran and E. B. Perumal Pillai

Abstract The performance and strength needs are not adequately satisfied by the advancement in concrete technology as well as the development of new materials and components. Part replacement of cement by mineral admixtures in concrete overcomes many problems and leads to improvement in the strength as well as durability of concrete. This paper deals with the regression analysis of various experimental results on compressive strength of Ordinary Portland Cement (OPC)-Metakaolin (MK)-Red Mud (RM)-based ternary-blended concrete with different water-binder ratios (*w/b*) 0.40, 0.38, 0.36, and 0.33. For all *w/b* ratios, the compressive strength was determined at different days of curing. In all the *w/b* ratios the regression analysis using SPSS software and the regression curve had been carried out by replacing 0–14% of the mass of OPC with MK and RM separately and a combination of MK:RM of different proportions of 50:50, 60:40, 70:30, and 80:20. The analysis was also done using neural network. From the experimental results the strength activity index was high in 8% replacement of OPC by MK and 4% by RM whereas in the combination of MK:RM at 10% for the proportion 80:20 shows the highest strength activity index.

Keywords Metakaolin · Red mud · Strength activity index · Regression models

1 Introduction

Concrete, the utmost popular and the powerful building material is being used nowadays for all types of infrastructural projects. Bearing in mind, the worldwide use of concrete for most of the constructions and its increasing demand for new

R. R. Rajendran (✉)
Department of Civil Engineering, Vels University, Chennai, India
e-mail: r.rathanraj@gmail.com

E. B. Perumal Pillai
Department of Civil Engineering, Veltech Dr. RR & Dr. SR University,
Chennai, India

structures, the technical advantages of materials such as mineral admixtures and waste materials from industries are further complimented by other economic, ecological, and environmental considerations. Concrete provides a safe haven to many of the toxic elements present in industrial wastes through chemical binding. Technical solution to handle and dispose waste materials will cause less harm to our environment. However, in spite of the overwhelming technical, environment, and economical benefits derived from the use of mineral admixtures and waste materials in concrete, there is still a considerable misinformation on their use in concrete. The integrity and durability of concrete structures are closely linked with the characteristics of these materials used, but there is no clear understanding of this interrelationship between material characteristics and structural performance.

In this paper, a brief investigation about the utilization of Metakaolin (MK) as mineral admixture and Red mud (RM) as waste material in cement concrete were studied and the results are presented.

Several researches have proposed modifications to conventional methods. Within the limit of available raw materials, the selection of the suitable materials, proportions and mixes conducted in the field and laboratory have typically proven adequate concrete characteristics [1, 2]. With adequate mechanism of proportion and replacement of materials, concrete with compressive strengths of 60 MPa is possible in construction.

The increase in concrete strength when metakaolin partially replaces cement in concrete under three elementary factors namely cement hydration, pozzolanic activity, and relative strength [3]. The strength development of Jamaican red mud formed by the addition of hydrated lime, condensed silica fume and lime stone was preliminarily investigated [4]. The investigation results provide a suitable composites construction material without Portland cement as binder to the construction industry.

2 Experimental Investigation

2.1 Materials Used

The following are the materials that were used in this investigation:

- Ordinary Portland Cement confirming by BIS: 12269-1987.
- Metakaolin in dry densified form conforming to ASTM C 1240.
- Red mud is a byproduct in dry densified form.
- NSF-based Superplasticizer confirming by BIS: 9103 [5] and ASTM C-494 [6].
- Broken granite stones confirming by BIS: 383 [7].
- River sand confirming by BIS: 383 [7].
- Portable water used for concreting and curing.

2.2 Mix Proportions

A formulated mix design procedure by combining the BIS, ACI method, and the available literatures on HSC was used in this investigation. The formulation of mix and detailed design procedure [8] is explained by the author in his previous publication.

Based on the published mix design procedure, a HSC mixture proportions with a characteristic target mean compressive strength of 30, 40, 50, and 60 N/mm^2 were designed without any mineral admixtures. However, the use of several trial mixtures is important in the design of HSC. Therefore, to get the optimum proportions, trial mixes were arrived by replacing 0, 2, 4, 6, 8, 10, 12, and 14% of the mass of cement by MK and RM separately also in the proportion ratios of MK:RM (50:50, 60:40, 70:30, and 80:20) respectively. In all the above combinations, a super-plasticizer by name CONPLAST SP430 was used at 1% by weight of the binder for obtaining workable concrete. The quantities of different material requirement per m^3 of concrete for the trial mixes of different w/b ratios are available in the author another publication [9].

3 Results and Discussions

3.1 Effects of Metakaolin on Cube Compressive Strength

The variation of rate of development of cube compressive strength of concrete with metakaolin in terms of strength activity index is measured for the four w/b ratios of 0.40, 0.38, 0.36, and 0.33 is given in Fig. 1. The rate of development of strength of metakaolin concrete in compression increases monotonically with a raise in metakaolin level at all four w/b ratios and at all curing times. The strength activity index is maximum for mixes with 8% replacement of cement by metakaolin in all w/b ratios. The same was observed by other researchers [10, 11]. The development of compressive strength in terms of strength index increases as the metakaolin content increases from 0%, the compressive strength gradually increases up to 8% and thereafter, it gradually falls off.

Figure 2 shows the regression analysis of experimental results on various concrete mixes with MK of all water-binder ratios. The relationship between 28 days compressive strength of concrete and w/b ratio of metakaolin based concrete was obtained as

$$f_{ck} = 1.569(w/b)^{-3.52} \tag{1}$$

where,

f_{ck} Cube compressive strength of concrete at the age of 28 days in N/mm^2 and
w/b water-binder ratio
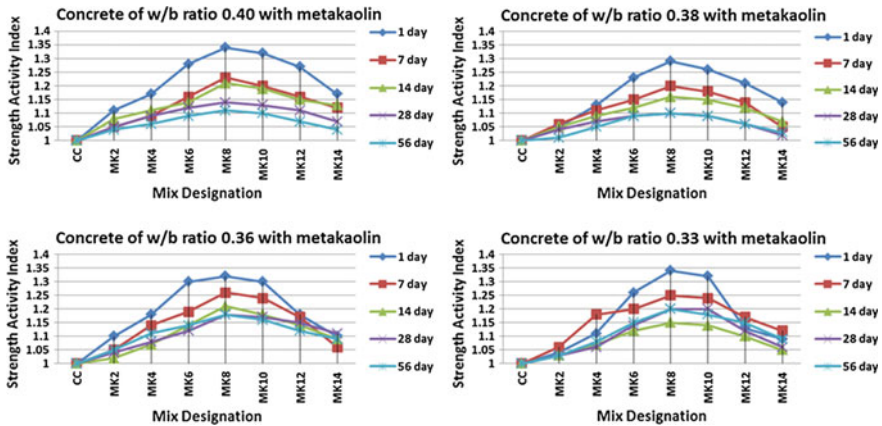
Fig. 1 Variation of strength activity index concrete with metakaolin

Fig. 2 Relationship between compressive strength and *w/b* ratio of metakaolin based concrete
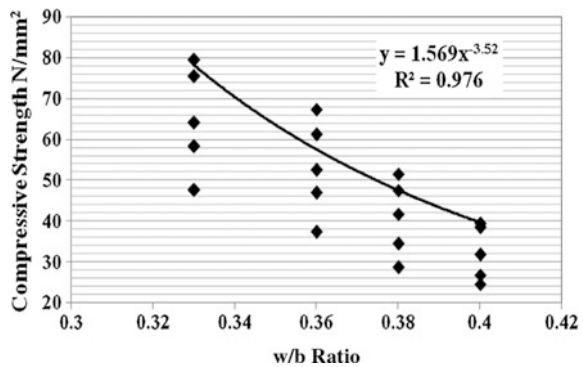
Hence it was experiential that the compressive strength of concrete with addition of MK and different *w/b* ratios also varied like conventional concrete and their best fit curves also obey Abram's law for conventional concrete, compressive strength $f_{ck} = A/(Bw/c)$.

3.2 Effects of Red Mud on Cube Compressive Strength

Figure 3 shows the variation of rate of development of compressive strength of concrete with red mud in terms of strength activity index for the four water-binder ratios. The rate of development of compressive strength of red mud-based concrete increases up to 4% replacement of red mud in all *w/b* ratios. However beyond 4% the strength starts decreasing for all mixes. The increase in the rate of development
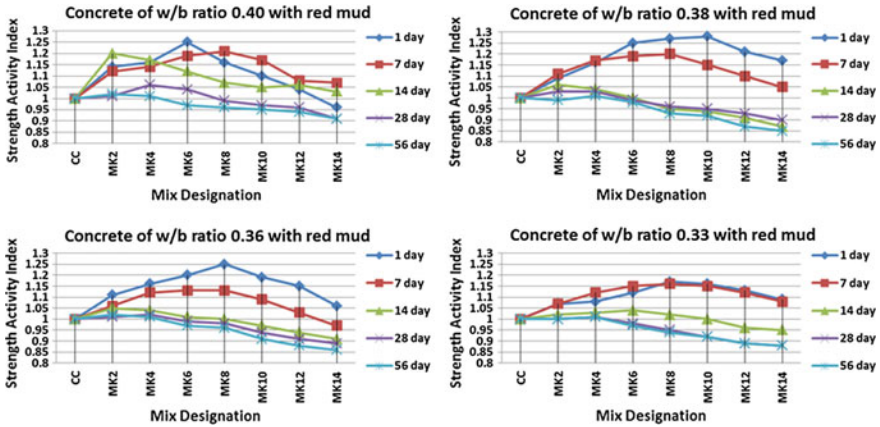
Fig. 3 Variation of strength activity index concrete with red mud

of compressive strength may be due to the fact that the cement replacement of around 4% increases the finer particles in the mix, which increases its density by filling the voids.

Another reason for increase in strength may be due to extra availability of Al_2O_3, SiO_2, and TiO_2 whose presence up to certain percentage increases the strength of concrete by combining with other constituents of cement during the progress of hydration. The compressive strength of concrete obtained from cement and neutralized red mud increases up to 5% replacement for constant water to (cement + red mud) ratio [12].

Figure 4 shows the regression analysis based on the experimental results of various concrete mixes with red mud of all water-binder ratios. The relationship between 28 days compressive strength and water-binder ratio of red mud based concrete was obtained as

$$f_{ck} = 2.493\,(w/b)^{-2.94} \tag{2}$$

Fig. 4 Relationship between compressive strength and *w/b* ratio of red mud based concrete
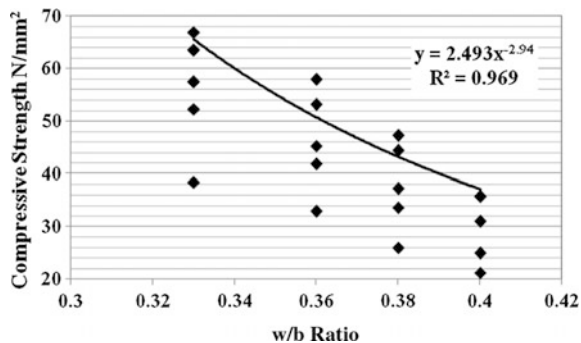
3.3 Effects of Metakaolin and Red Mud Blend on Cube Compressive Strength

The influence on cube compressive strengths in terms of strength activity index for the four *w/b* ratios of concrete containing various MK and RM blends of MK:RM of different proportions of 50:50, 60:40, 70:30, and 80:20 as partial cement replacement at various ages is shown in Fig. 5. The rate of development of strength increases with the metakaolin content of the blend. In all the *w/b* ratios at 10% of total replacement, a maximum of strength occurs at 80% metakaolin and 20% red mud. The increase in strength is associated with acceleration of the hydration reactions of metakaolin; the red mud particles are acting as a filler materials in concrete, and this phenomena is same for all the mixes. Also in all the replacement levels and of different MK:RM proportions the variations of the strength activity indexes are very small. Beyond the 10% replacement levels there are remarkable reductions in the strength activity index, it shows that 10% replacement is acting as the optimum replacement level which gave higher strengths.

Figure 6 shows the regression analysis based on the experimental results of various concrete mixes with a combination of Metakaolin and red mud of all *w/b* ratios. The relationship between 28 days compressive strength water-binder ratio of MK-RM blend based concrete was obtained as

$$f_{ck} = 2.508(w/b)^{-2.99} \tag{3}$$
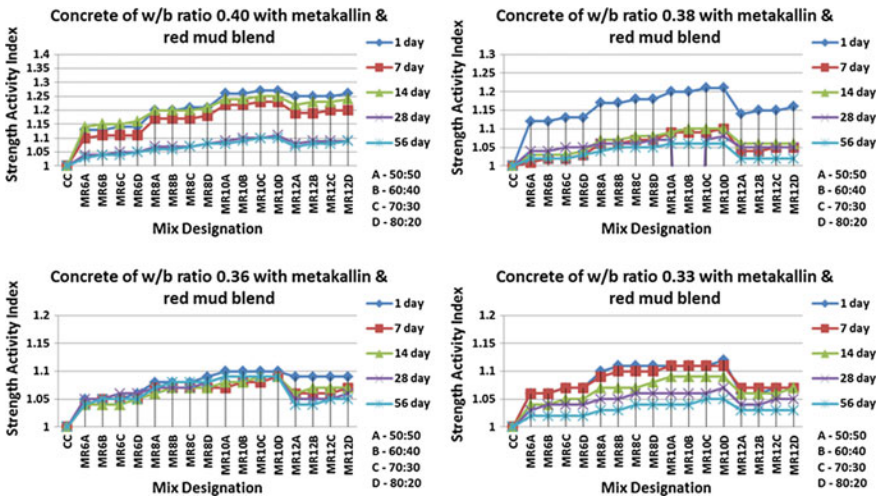
Fig. 5 Variation of strength activity index concrete with metakaolin-red mud blend

Fig. 6 Relationship between compressive strength and *w/b* ratio of metakaolin-red mud blend
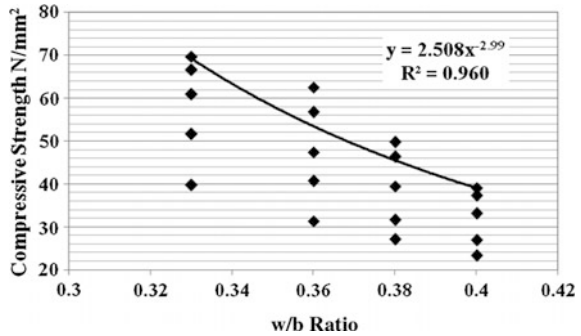
3.4 Relationship Between Cube Compressive Strength and the Independent Variables

The regression analysis was carried out using SPSS software and the regression curve was drawn. This analysis was calculated based on the experimental results of various concrete mixes with cement replacement by MK, RM, and MK-RM blend of all *w/b* ratios. The following independent variables such as *w/b* ratio (*w/b*), cement (*C*), MK, RM, and curing days (*D*) were considered to prepare the regression fit with the compressive strength (f_{ck}) as the dependent variable. The relationship between compressive strength of concrete with MK, RM, and MK-RM blend and the independent variables was obtained as follows:

$$f_{ck} = 478.38 - 820.56 \, (w/b) - 0.363 \, (C) - 0.283 \, (MK) + 0.428(D)$$
$$f_{ck} = 355.76 - 624.85 \, (w/b) - 0.229(C) - 0.283 \, (MK) + 0.318(D)$$
$$f_{ck} = 311.80 - 566.73 \, (w/b) - 0.180(C) - 0.110 \, (MK) - 0.137(RM) + 0.415(D)$$

Which is subjected to upper and lower bounds of examination indicates below:

$$0.33 < w/b < 0.4 \qquad 311.75 < C < 439.39 \quad 7.25 < MK < 61.52$$
$$7.25 < RM < 61.52 \quad 1 < D < 56$$

The analysis was also done using neural network. The results obtained from regression analysis and neural network analysis were found to be closer to each and the points fit on the regression curve and the neural network curve were found to be very much coinciding with the experimental results. Figures 7, 8 and 9 show the influence of metakaolin, red mud, and metakaolin-red mud blend on the cube compressive strength based on regression analysis and neural network analysis.
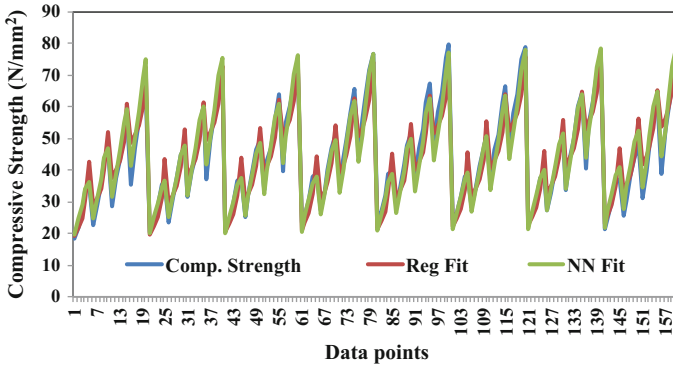
Fig. 7 Influence of metakaolin on cube compressive strength based on regression and neural network analysis
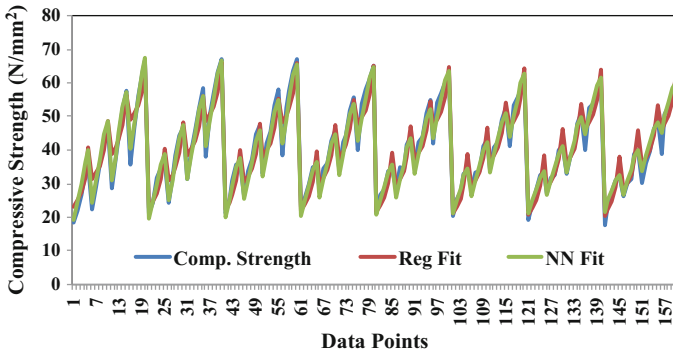
Fig. 8 Influence of red mud on cube compressive strength based on regression and neural network analysis
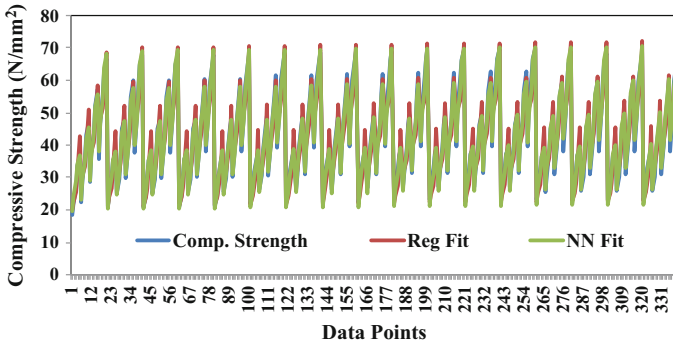
Fig. 9 Influence of metakaolin-red mud blend on cube compressive strength based on regression and neural network analysis

4 Conclusion

Based on the studies on concrete with metakaolin, red mud, and MK-RM combinations the following are the conclusions were drawn.

- The optimum percentage replacement of cement by metakaolin and red mud for all *w/b* ratios of concrete mixes was found to be 8 and 4% for achieving the maximum strength activity index at the age of 28 days. For metakaolin-red mud blend the optimum percentage replacement was found to be 10% with MK:RM ratio 80:20.
- Based on regression analysis the relationship between strength and *w/b* ratio was arrived at, for cement with metakaolin, red mud and metakaolin-red mud blend are as follows.

$$f_{ck} = 1.569 \, (w/b)^{-3.52}$$
$$f_{ck} = 2.493 \, (w/b)^{-2.94} \quad \text{and}$$
$$f_{ck} = 2.508 \, (w/b)^{-2.99}$$

- For all the replacement levels and for different MK:RM proportions, the strength activity index variations are insignificant. The increases in strength activity index due to these replacements were never more than 20%.
- In all the *w/b* ratios with all MK:RM proportions replacement, the little raise in compressive strength is due to pozzolanic and acceleration of hydration reactions of MK alone. Hence it is not suggested that the secondary cementitious materials should be used for enhancing the strength

References

1. Mehta, P.K., Aitcin, P.C.: Principles underlying production of high performance concrete. Cem. Concr. Compos. **12**(2), 70–78 (1990)
2. ACI 363 R-92 State-of-the-art report on high strength concrete. In: ACI Manual of Concrete Practice, Part 1, Materials and General Properties of Concrete, pp. 55 (1993)
3. Wild, S., Khatib, J.M., Jones, A.: Relative strength, pozzolanic activity and cement hydration in superplasticised metakaolin concrete. Cem. Concr. Res. **26**(10), 1537–1544 (1996)
4. Gordon, J.N., Pinnock, W.R., Moore, M.M.: A preliminary investigation of strength development in Jamaican red mud composites. Cem. Concr. Compos. **18**, 371–379 (1996)
5. BIS: 9103 (1999) Concrete Admixtures—Specifications. Bureau of Indian Standards, New Delhi, India
6. ASTM C 494: Standard specification for chemical admixtures for concrete. In: Annual Book of American Society for Testing Materials Standard (1992)
7. BIS: 383 (1970) Specification for coarse and fine aggregate from natural sources for concrete. Bureau of Indian Standards, New Delhi, India

8. Rathan Raj, R., Perumal Pillai, E.B., Santhakumar, A.R.: Evaluation and mix design for ternary blended high strength concrete. ELSEVIER (SciVerse ScienceDirect) Procedia Eng. **51**, 65–74 (2013)
9. Rathan Raj, R., Perumal Pillai, E.B., Santhakumar, A.R.: Studies on strength and diffusion characteristics of blended cement concrete. Indian Concr. Inst. J. **13**(4), 7–16 (2013)
10. Brooks, J.J., Johari, M.A.M.: Effects of metakaolin on creep and shrinkage of concrete. Cem. Concr. Compos. **23**(6), 495–502 (2001)
11. Roy, D.M., Arjunan, P., Silsbee, M.R.: Effect of silica fume, metakaolin, and low-calcium fly ash on chemical reaction of concrete. Cem. Concr. Res. **3**, 1809–1813 (2001)
12. Kumar, V., Nautiyal, B.D., Jha, A.K.: Use of neutralized red mud in concrete. Indian Concr. J. 505–507 (1989)

Comparative Study on Various Behaviours of an RC Structure with Prestressed Concrete Structure

Jasim Anamangadan, J. Visuvasam and Anoj Kumar Dubey

Abstract Aesthetics of a structure are given primary importance in the present days and this demands new and challenging designs with large spans and complicated designs. The role of a structural engineer becomes more significant because of these structural irregularities. This makes it necessary to have advanced technologies like post-tensioning if we are not ready to compromise in the aesthetics. Generation of such irregular structures will form varying mass and stiffness distribution which imparts to the effect of torsion. This paper deals with the various structural behaviour of a multi-storied RC Convention Centre building having large spans of around 32 m. The effect on the structure due to these large spans is compared with both RC and prestressed concrete. The roof slab of the auditorium portion of the structure is designed with normal RCC and compared with Slabs resting on Prestressed Post-tensioned Girders using the software Adapt Builder 2016. A comparative study between RCC and prestressed concrete is also done. Diaphragm action of the structure is considered for seismic design in order to provide a monolithic action and hence to counteract the effect of torsion. A comparative study is done with and without considering the effect of torsion into account and the results shows that in higher seismic zones the effect of torsion is predominant and proper care should be given to extreme columns and corner columns which are more vulnerable to failure. Response spectrum analysis of the structure is done in STAAD.Pro and storey response plots are obtained.

Keywords Post-tensioning · Stiffness · Diaphragm

J. Anamangadan (✉) · J. Visuvasam
School of Civil and Chemical Engineering, VIT University, Vellore, India
e-mail: jasimspm@gmail.com

A. K. Dubey
NBCC Engineering Consultancy Limited, New Delhi, India

1 Introduction

The architectural demands are changing day by day and new designs are being implemented in buildings which creates irregular structures. This study deals with the various structural behaviour of an RC Convention Centre building. The structure is in New Delhi having auditoriums, office space, library, assembly halls, conference rooms, etc. The main feature of the project is that in certain portions like the auditorium, there are large spans of around 32 m. The larger spans are first designed with RCC and the sizes of the members are noted and they are again designed with advanced technologies like Post-Tensioning and the new sizes of the members are noted and are compared.

The irregularity in the structure will lead to varying distribution of mass and stiffness which imparts to the effect of torsion. Torsion is predominant in higher seismic zones and proper care should be given to extreme columns and corner columns which are more vulnerable to failure. Diaphragm action of the structure is considered for seismic design in order to increase the strength and monolithic action and hence to counteract the effect of torsion.

In India, IS Code: 1893-2002 provides suitable provisions for earthquake resistant design. In usual design practice, the effects of torsion are not considered but as the location is in high seismic zone, additional provisions are provided for torsion so as to check the consequences like partial or entire failure of the structure. The roof portion is assigned as a rigid diaphragm with the cut-outs being removed. The roof slab of the auditorium of the structure is designed with normal RCC and it is compared with RC slabs resting on Prestressed Post-Tensioned Girders and a comparative study between RCC and prestressed concrete is also done.

2 Methodology

A multi-storied structure is selected in a high seismic zone and the Response Spectrum Analysis was performed to check the performance of the model. Storey response plot as well as the effect of torsion in the structure was found out. The critical spans of the model were identified and designed the structure with normal RCC. The same critical spans were analysed manually using post-tensioned design using the design code for Prestressed Concrete IS 1343 and found out the required section for the design. The structure is then analysed and designed in post-tension analysing software Adapt Builder 2016. The results were noted and the deflections, bending moments coming on the structure were noted and they were compared with the RC structure. A comparative study between the sizes of the structure with RC and prestressed concrete is performed [1–3].

3 Prestress Analysis

The technology in which the high yield strength and elasticity of the steel bars and high compressive strength of concrete are utilised together with some new technology which is capable of more load resisting capacity than normal concrete is termed as prestressing. Basically there are two methods of prestressing, they are pre-tensioning and post-tensioning. In pre-tensioning, the tension is applied through the jacks before the casting of concrete. And in post-tensioning the cables are stressed only after acquiring adequate strength to the casted concrete. The minimum cube strengths used for pre-tensioning and post-tensioning are M40 and M35 respectively [4].

In this study the top portion of the auditorium is to be considered as RC slab resting on large spanned post-tensioned girders.

3.1 Load Balancing Methodology

The analysis is done by load balancing methodology in which "Prestressing balances a certain portion of gravity loads so that the flexural members like Beams, slabs, girders will not subject to bending stress under given loading".

In this method, approximately 65–80% of the load will be balanced by tendons. These are effective for indeterminate structures. The other methods for prestress analysis are elastic stress and the ultimate strength methods. Unlike the other methods of analysis, load balancing method is more advantageous in case when dealing with flat slabs and other thin-shelled structures [5].

4 Torsional Analysis

Torsion or the twisting action is a major cause for failure of the structures. The structures with various constraints like irregularity, non-uniformity, unequal distribution of masses, etc. have developed the irregular distribution of mass, strength and stiffness tend to cause serious damages to the structure. During earthquake, as the structure vibrates the inertial force acts through the Centre of Mass while the force developed due to the resisting action acts through the centre of rigidity of the structure. This creates a lateral-torsional-coupling due to the eccentricity created between the centre of mass and centre of rigidity of the structure (Fig. 1) [6, 7].
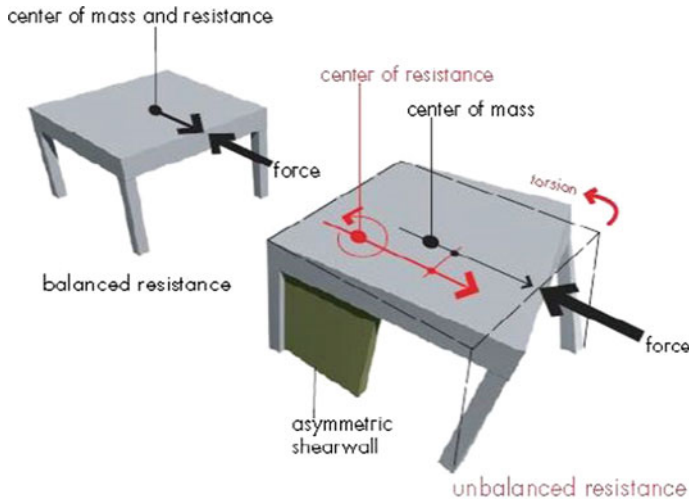
Fig. 1 Generation of torsion [7]

4.1 Eccentricity Consideration

As per Indian Seismic Design Standard Code, the seismic loads are added by taking four load cases for earthquake as per Clause 7.9.2 of IS:1893-2002. The clause states that

The design eccentricity e_{di} to be used at the floor i shall be taken as

$$e_{di} = 1.5\ e_{di} + 0.05\ b_i$$

Or

$$e_{di} = e_{di} - 0.05\ b_i$$

Whichever of these gives the more severe effect in the shear of any frame where

e_{di} = Static eccentricity at floor i defined as the distance between centre of mass and centre of rigidity.

b_1 = Floor plan dimension of floor i, perpendicular to the direction of force.

The factor 1.5 represents dynamic amplification factor while the factor 0.05 represents the extent of accidental eccentricity.

The loads are added in four cases as of the above clause with the coefficients as 1.5 and 0.05 for the positive X and Z directions and 1.0 and −0.05 for the negative X and Z directions (Fig. 2) [8].

Fig. 2 Seismic load
definition for torsion
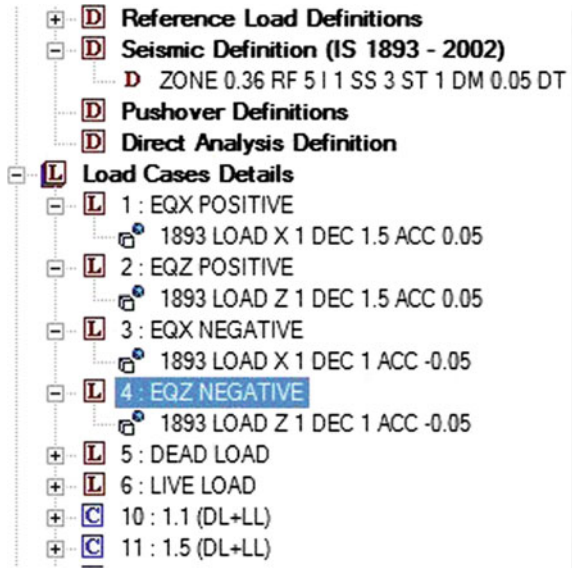
4.2 Diaphragm Consideration

The structure is modelled by assigning rigid diaphragms at the floor level and the whole structure acts monolithically as a single unit which increases the seismic resisting capacity and helps to increase the stiffness of the structure. In Staad the diaphragm can be assigned by taking the General > Specifications > Node > Floor Diaphragm. The range for the location of the diaphragms has to be specified by removing the cut-outs from the structure. Removal of cut-out is mandatory because which may provide additional stiffness which is actually not there in the structure [9, 10].

4.3 Seismic Load Consideration

In spite of doing normal methodology for accounting torsion, we shall go for a separate method in which two reference loads R1 and R2 were created. Reference loads can be created from Load definitions > Reference Loads > add new Reference Load. The first reference load R1 is to account for the modal masses which will be acting in all the three directions with a positive magnitude. The loads acting on the structure are considered by removing the negative magnitude and added them in all three directions X, Y and Z. While defining the load case for R1 the loading type has to be set into Mass to account for the seismic mass of the structure. R2 has to be assigned similarly but the change is that R2 is with loading type as gravity and only the load in the Y direction has to be considered and that too with the real sign (Fig. 3).

Fig. 3 Reference loads
definition
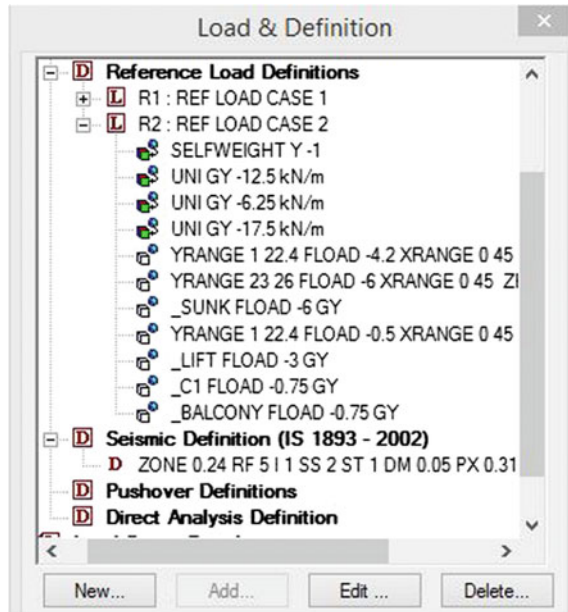
5 Model Description

The structure is modelled as several 3D frame elements. Frame element is modelled as a straight line connecting two points each with 3° of freedom at ends. Each element will be prismatic and having its own local coordinates system for defining sectional properties and loads. Each frame element is loaded by gravity load. Element internal forces are produced at the ends of each element. Sections are defined independently of the frame elements, and are assigned to the elements.

Building is designed for Gravity load and seismic load as per the Indian Standard Codes IS 456 and IS 1893-2002, which includes Dead load, Live load and seismic load without taking the effect of torsion and the other case with considering the effect of torsion which includes the provisions for accidental eccentricity as per IS 1893-2002. The Lateral force applied using "Equivalent Static Analysis" in which the lateral forces are calculated manually and lumped at each floor (Fig. 4) [11].

As per the irregularity conditions mentioned in IS 1893-2002 Part I, the structure will exhibit vertical irregularity if A/L ratio exceeds 0.15.

Here for our structure the value of A coming is 13.4 m.

And the base length L for the structure is 83.5 m.

Hence

$$\frac{A}{L} \text{ Ratio} = \frac{13.4}{83.5} = 0.160,$$

Which is greater than 0.15.

Hence the structure is showing vertical geometric irregularity.

Fig. 4 Vertical geometric
irregularity
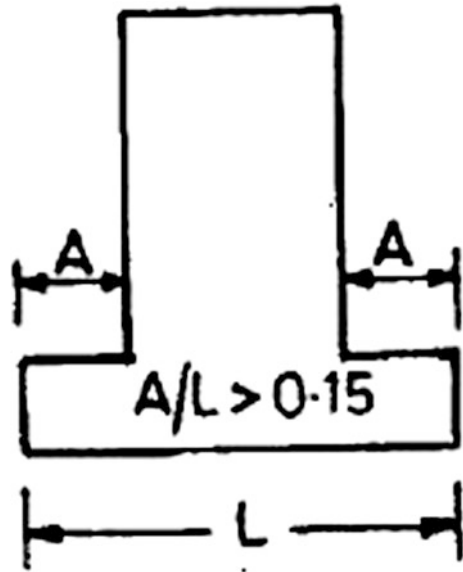
The main auditorium capable of occupying 700 persons having a span of 32 m × 32m which is having a clear height of 10 m. The auditorium portion having large spans is designed both in RCC and Prestressed concrete (Fig. 5).

Adapt Builder 2016 is a prestressing analysis and design software used for pre tensioned and post-tensioned members like PT girders PT slabs, etc. The whole structure of auditorium above which the library is there is modelled and the loads are applied accordingly (Fig. 6; Table 1).

6 Results and Discussions

6.1 Storey Drift

Storey drift is defined as the ratio of displacement of two consecutive floors to height of that floor. It is the drift of one level of a multi storey building relative to the level below.

As per IS 1893(Part 1):2002, "the storey drift shall not exceed 0.004 times the storey height". Here in this study the floor height considered is 5 m and the maximum value of permitted storey drift is 0.02 mm.

The storey drifts are plotted for various floor levels and it can be seen that the maximum drift coming in this structure is around 0.014 coming in the second floor which is less than 0.02 mm the permissible limit (Fig. 7) [11, 12].
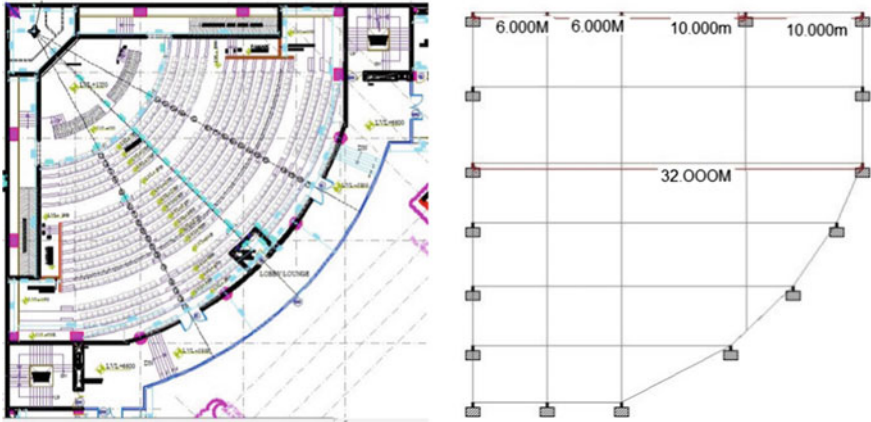
Fig. 5 Architectural plan and layout of the auditorium portion
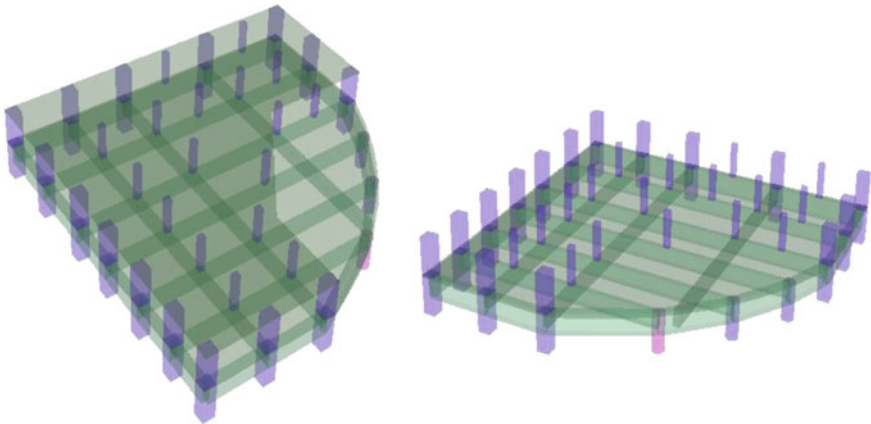
Fig. 6 3D Model of the auditorium

6.2 Torsional Design Results

When the Torsional analysis was carried out it can be seen that certain columns at critical locations like re-entrant columns have adverse effect due to Torsion. Hence those columns in the structure tend to fail. The bar graph with blue colour represents the area of steel required for the column design when torsion was not considered. When torsion was considered, in all these cases the area of steel are revised and shown in red colour which is slightly higher than the previous reinforcement. The two graphs represent the columns C1–C5 and C6–C10 with area of steel on the Y axes. It can be seen that there is around 20% increment in the percentage of steel

Table 1 Loads considered in the design

Dead load	Magnitude (KN/m^2)	Live load	Magnitude (kN/m^2)
Typical floor	7.15	Parking	5.0
Terrace	6.0	Auditorium	4.0
Parapet	7.0	Library	6.0
Partition wall	14.0	Staircase	4.0
Landscaping	1.5	Fire tender	20.0

Fig. 7 Storey drift
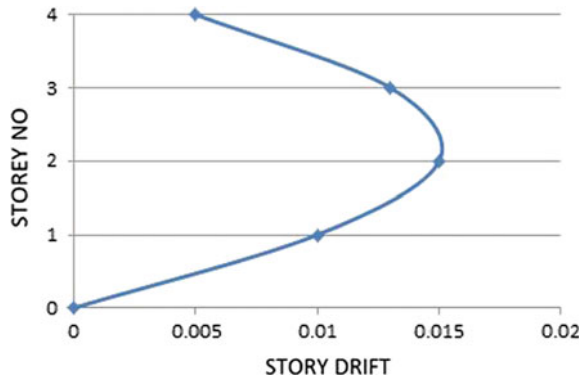
consumed at re-entrant columns and an increase of around 10–15% at other critical locations (Fig. 8) [6, 8, 13].

6.3 RC and PT Design Results

Prior to the design in PT, the structure was modelled and designed in Staad.Pro and the design outputs were noted for the critical portion, i.e. near to the auditorium. The largest span of around 32 m is coming in the structure above the auditorium portion.

Table 2 represents the reinforced concrete design results and our aim is to optimise and economise the section and the reinforcement by using the advanced prestressing technology. Thus the structure is modelled in Prestressing analysis and design software called Adapt Builder and a comparative study is conducted between normal RC and Prestressed Concrete. The same complicated portion of the structure with a span 32 m which is having a beam dimension of 750 mm 1750 mm by RC design has designed manually for the same loading conditions using prestress design and it is found that the new optimised section designed as Post-Tensioned Girder coming is 600 mm × 1300 mm (Fig. 9).
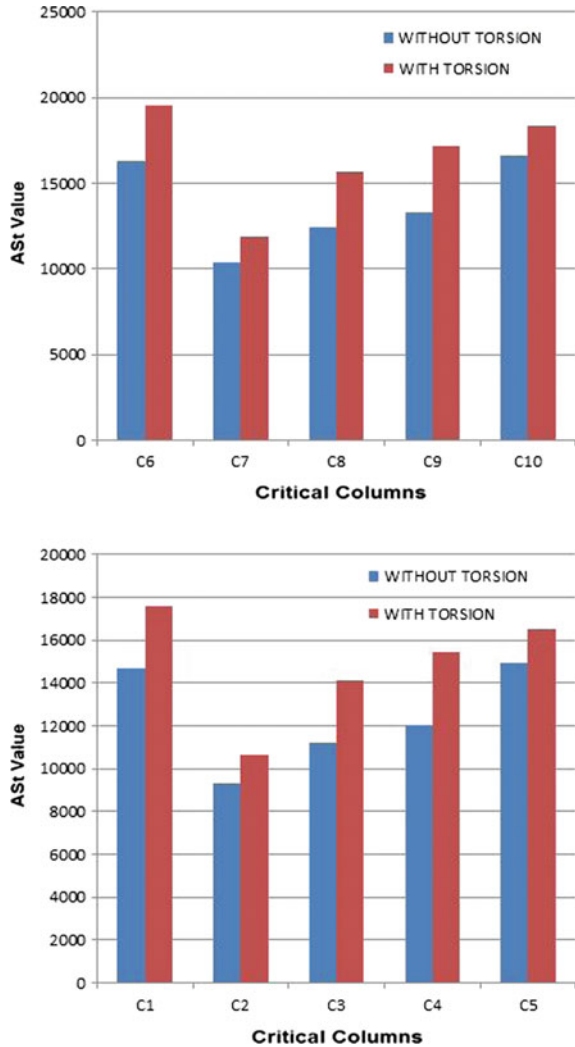
6.4 Comparison of RCC with PSC

The entire structure is modelled and analysed in the software Adapt Builder and various behaviours of the structure are compared for both RC and Prestressed concrete.

Deformation. The auditorium portion of the structure alone is considered and is modelled in Adapt builder with the new optimised size of beams as 600 mm
 1300 mm and the first fig represents the deformation of the auditorium portion with post-tensioned girders and the second one with the normal RC girders. The

Table 2 Beam design and reinforcement details

Beam dimension	Span (m)	Reinforcement	
B1 1200 mm × 2100 mm	10	Top	7#32 mm bars
		Bottom	7#32 mm bars
B2 1800 mm × 2000 mm	15	Top	10#32 mm bars
		Bottom	10#32 mm bars
B3 1500 mm × 2000 mm	20	Top	12#32 mm bars
		Bottom	12#32 mm bars
B3 750 mm × 1750 mm	32	Top	12#32 mm bars
		Bottom	12#32 mm bars
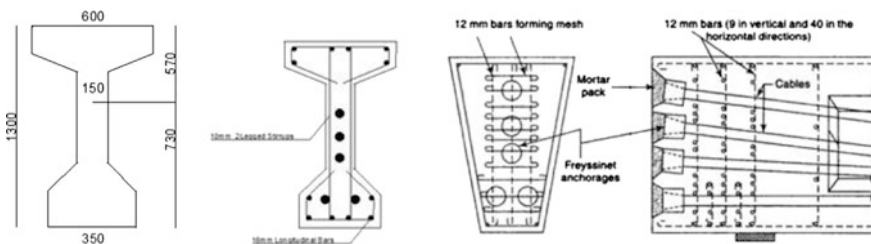
Fig. 9 PT design results
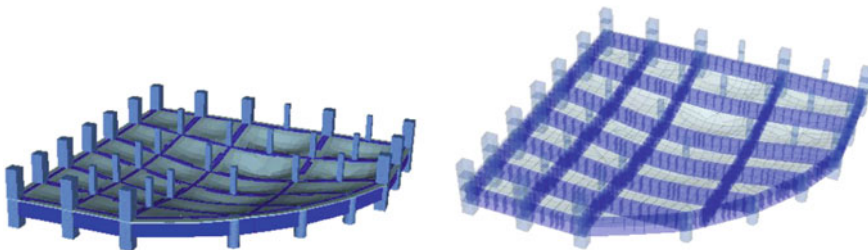
Fig. 10 Deformation comparison

deformations for the second case is very much higher as there is no PT tendons in this case and also the span is more hence the deformation (Fig. 10).

Bending Moment. When the beams are designed as Post-Tensioned girders with the new dimension of 600 mm × 1300 mm, the maximum bending moment coming for the structure is around 3400 kNm. But we can see from the manual calculations that the maximum moment carrying capacity of the section is up to 3900 KNm. Hence the moments are within the permissible limits only (Fig. 11).

Deflection. The first figure representing the deflection contour of the auditorium when the structure is modelled as PT and the following second figure represents the
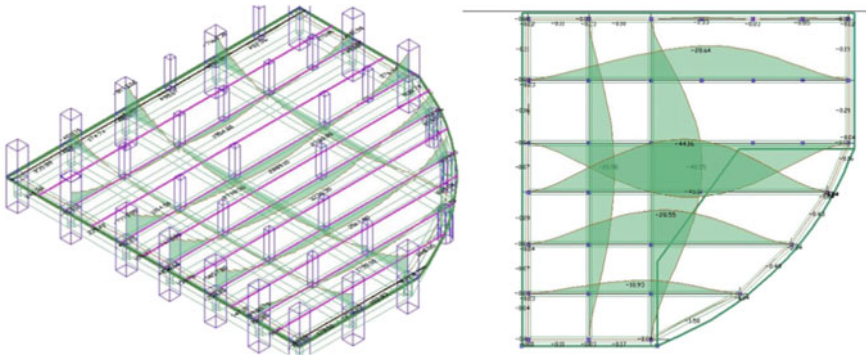
Fig. 11 Bending moment representation
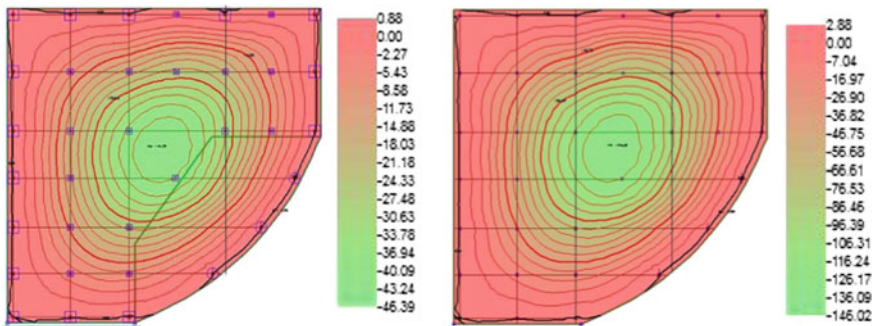
Fig. 12 Deflection comparison

deflection contour of the structure without PT tendons with the girder dimensions as the reduced dimensions, i.e. 600 mm × 1300 mm. In the first case it can be seen that the deflection range is from 0 to 46.39 mm and the maximum deflection is lying with in the permissible limit. While the second case the deflection is beyond the maximum limit of 120 mm (Fig. 12).

The deflections permitted are represented graphically for the two cases with the limiting deflection as a cut off level. It can be clearly seen that the deflection is beyond the limit when the reduced dimension of PT, i.e. 600 mm × 1300 mm is applied to the RC. In order to keep the deflection with in the limit the RC structure must be designed with a larger size that is 750 mm × 1750 mm (Fig. 1).

Area of Steel required and Volume of Concrete. The areas of steel required for both prestress and RC were found out and they were compared and represented graphically. It can be seen that there is a reduction of around 50% in the area of steel used for the structure when Prestressed Concrete is employed and also there is considerable amount of reduce in concrete as the size of the section decreases drastically (Fig. 14) [6, 8, 13].
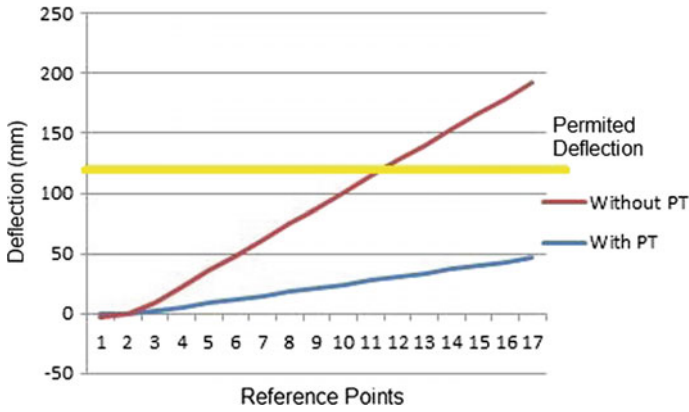
Fig. 13 Deflection graph
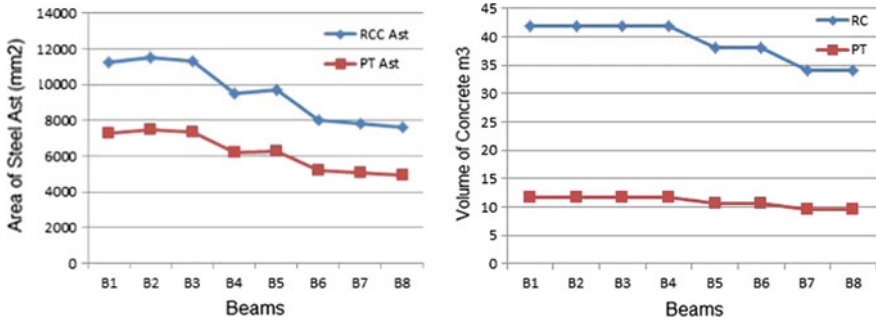
Fig. 14 Area of steel and volume of concrete graph
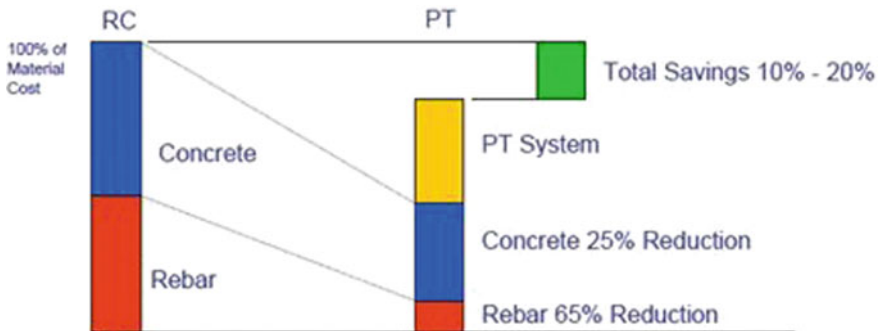
Fig. 15 Cost comparison

Cost Comparison. The reduction in size, early form work removal, less volume of concrete, less area of steel requirement, etc. contributed to a reduction in cost of the structure. But it is to be noted that this economy can be achieved only if the span of the structure is greater than 7 m otherwise the cost of jacking and stressing operations will be more. Compared to normal RC works the operation and installation of PT needs skilled and qualified labour hence if the span is less instead of having cost saving the price may be more (Fig. 15) [5].

7 Conclusion

Based on the work the following point-wise conclusions are drawn:

- The torsional design is mandatory for structures in high seismic zones with edge and re-entrant corner columns with more care.
- Proper ductile detailing has to be done for these structures, as we are focussing on strong column weak beam methodology more importance has to be given for the column reinforcements.
- For members with large spans the structure has to be designed in prestress to make use of the advantages like economic sections, less deflections, early form work removal, etc.
- The size of the critical sections coming in RCC are more than that of prestressed concrete both of which are supposed to carry the same load.
- The deflections are coming within the limit for a smaller section in case of post-tensioned girders
- The prestressing will be effective when the span is beyond 7 m otherwise the stressing will cause more when compared to that of the RC structure.
- Bending moment is within the limit when it comes to the prestressed concrete with reduced dimension.
- Stresses of the members are within the permissible limits only.

References

1. IS 456-2000. Indian Standard for plain and reinforced concrete code of practice. Bureau of Indian Standards, New Delhi
2. Park, R., Paulay, T.: Reinforced concrete structures, Wiley, New York (1975)
3. Park Y.J., Ang A.H.S., Wen Y.K.: Seismic damage analysis of reinforced concrete buildings. J. Struct. Eng. ASCE. **111**(4), 740–757 (1985)
4. IS: 1343-1980, Indian standard code of practice for prestresse concrete. Bureau of Indian Standards, New Delhi
5. Lin, T.Y.: Load balancing for design and analysis of prestressed concrete structures. J. American Concr. Inst. **60**(6), (1963)

6. Dutta, S. C.: Effect of strength deterioration on inelastic seismic torsional behaviour of asymmetric Rc buildings, Build. Environ. **36**(0), 1109–1118 (2013)
7. Fajfar, P., Marušić, D., Peruš, I.: Torsional effects in the pushover-based seismic analysis of buildings. J. Earthquake Eng. **9**(06): 831–854 (2005)
8. Wakchaure, M.R., Y.U. Nagare.: Effect of torsion consideration in analysis of multi storey frame. Int. J. Eng. Res. App. (IJERA) ISSN (2013): 2248–9622
9. Jain, S.K: Earthquake engineering: problems and prospects. Indian Concr. J. **68**(11), (1994)
10. Goud, S.S., Kumar, R.P.: Seismic design provisions for ductile detailed reinforced concrete structures. (2014)
11. IS 1893 (Part-1)-2002. Criteria for earthquake resistant design of structures. bureau of indian standards. New Delhi
12. Murty, C.V.R., Pradeep Kumar, R.: Critical review of indian seismic code IS 1893:2002. In: International colloquium on architecture and structure interaction for sustainable development. (2013)
13. Maske, S.G., Dr Pajgade, P.S.: Torsional behaviour of asymmetrical buildings. Int. J. Mod. Eng. Res. ISSN (2013): 2249–6645

Performance of Cold-Formed Steel Frames In-filled by Polystyrene Light Weight Concrete Subjected to Lateral Load

Hossein Parastesh, Mohammad Rezaeian Pakizeh and Farzad Hejazi

Abstract Today, it is very important to apply innovative technologies and materials for the purpose of constructing lightweight buildings, reducing time built, and improving the performance and earthquake resistance of buildings. In such walls, the empty spaces are normally filled with stone wool and polystyrene blocks. To this end, lightweight concrete (LWC) can also be used, which results in an improvement in behavior of these frames; it makes the walls considerably stiffer and reduces the local buckling of sections. This research was carried out for evaluating the performance of cold-formed steel frame in-filled by polystyrene lightweight concrete using ABAQUS software. In this study, three cold-formed steel frames were introduced with 2.4 m length, 1.4 m height, and 5 cm thickness and analyzed under lateral load. The first specimen was consisted of studs and runners with semi-rigid connections and without bracing. The second specimen consisted of studs and runners with X-shaped bracings. Finally, the third one was similar to the first one except that the cavity between members was filled using Polystyrene lightweight concrete. To achieve the best type of LWC and explore the optimum mix design with efficient concrete consistent with the frame system, testing was done on totally 30 samples of perlite and polystyrene concrete and compared with each other. Based on the results, in comparison with strap bracing, because of high stiffness of in-filled frames, they could act as the main lateral load-bearing system, hence attracting more portions of the lateral excitations.

Keywords Cold-formed steel · Polystyrene · Lightweight concrete

H. Parastesh · M. R. Pakizeh (✉)
Department of Civil Engineering, University of Science and Culture,
Tehran, Iran
e-mail: mp.rezaeian@yahoo.com

H. Parastesh
e-mail: Parastesh@usc.ac.ir

F. Hejazi (✉)
Department of Civil Engineering, University Putra Malaysia,
Putrajaya, Malaysia
e-mail: farzad@fhejazi.com

1 Introduction

Nonstructural components, e.g., in-fill walls, have a significant effect on the structural seismic response; they also improve the lateral stiffness and reduce drifts and displacements [1]. Cold-formed lightweight steel frames are increasingly applied to current industrial constructions in seismic zones. Three issues have promoted the use of cold-formed thin steel elements: cost reduction, economical-geographical conditions, and limitations of the resources required to supply the construction materials. In general, in countries such as North America, Europe, Japan, China, and Australia, to build low-rise residential and commercial constructions for load-bearing and enclosure systems, the structures that are framed by means of cold-formed steel (CFS) containing lightweight sheathing and CFS members are employed instead of timber structures. These structures generally come with a number of advantages, including lightweight, workability, dimensional stability, full recyclability, and cost effectiveness. They are normally consisted of steel frames—which include tracks, studs, bracing members, and blocking members —and lightweight sheathing connected to CFS members by means of self-drilling screw connections. Typically, shear walls give support to vertical loads that are transferred from roofs and floors of the building and also to seismic loads and horizontal winds. Under horizontal loads, these structures usually have a complex mechanical behavior.

The American Iron and Steel Institute (AISIS213) [2] gives its standards on the basis of results of remarkable cyclic and monotonic tests carried out by Serrette et al. [3–5] on CFS-framed shear walls. Due to light weight of CFS frames and their weakness against lateral forces, e.g., earthquake forces, it is helpful to use light-weight concrete in order to fill out CFS frame since they have light weight and appropriate insulation against heat and sound. It results in unit weight decrease of concrete and at the same time, preserving adequate strength [6].

The literature shows that replacing the Ordinary Portland Cement with Perlite Powder slightly reduces compressive strength of concrete; though, it considerably enhances the lightness and permeability [7]. Because in these types of structures, the cross-sections of wall were filled using thermal and acoustic insulators, all through the exploration, it was associated with negative impacts produced by the hollow walls. Nevertheless, developing these types of structures in high-seismic regions by means of in-filled walls using combinatorial and light materials can effectively optimize the buildings. As a result, these systems can be developed by filling the walls with light materials like perlite concrete or polystyrene foam concrete. For the purpose of simplifying the detailing of frames; enhancing the acoustic, thermal, and fire resistance performance; and improving the load-bearing capability and stability of the structures, the present study recommends the application of lightweight concrete to filling out cavities that exist between members. This system outperforms the braced type regarding not only improvement of structural behavior, but also architecture and the use of structures; this leads to improving the structural performance and increasing the buildings' level of safety.

In addition, it enjoys an entire and has no problem concerning cavity walls sprayed with lightweight concrete that generally suffer from problems with installation procedures of attached parts.

In the present study, at first, different mix designs of polystyrene and perlite concrete were examined in order to identify the best type of lightweight concrete (LWC) and explore the optimum mix design with capable and effective concrete consistent with the frame system. To this end, totally 30 samples (comprising 10 mix designs each of which had 3 samples) were prepared and tested. After that, some experiments were conducted on structural composition of the CFS frame, which was in-filled with lightweight concrete, and the results were compared with those obtained from a case to which strap bracing had been applied. In addition, the failure modes, lateral stiffness, ductility, load-bearing capacity, and strain variation in the CFS frame specimens were completely analyzed.

2 State of the Art

The application of CFS members to construction industry was started in the 1850s in both the UK and the US [8]; though, these components were not broadly used in buildings until 1946. The publish of a variety of new editions of codes suggested for designing the structural components of CFS structures by American Iron and Steel Institution (AISI) accelerated the development process of steel structures with thin cold-formed cross-sections. During the early nineteenth century, these thin steel elements were applied to the bridge constructions; then, with the development of aircraft industry in the early twentieth century, the industry section also applied them [9].

The light steel structures were meanwhile applied to commercial buildings across the world. In the US, statistics indicate that over 60% of light steel frames are nonstructural, and in this type of frames, walls are not generally designed [10]. Two last decades have witnessed the growth of light steel frames application to residential housing in Australia. Considering different advantages of this system, in 2005, the National Association of Steel-Framed Housing INC (NASH) prepared a comprehensive standard titled "*Light Residential Braced Steel Frames*" [11].

3 Review of Experimental Studies

3.1 Cold-Formed Steel

Adham [12], in 1990, was the pioneer in experimental research on steel frames in which five tests were carried out where cyclic loading was used in CFS walls and studs were fixed together by means of diagonal clamps at the end, in a back to back

form. The clamps to frames were designed with overhead gusset plates so that they can inhibit failure in connection. In addition, two gypsum plates with 16 mm in thickness were positioned in each side of the wall [12]. Each sample was simultaneously put under cyclic lateral and vertical loads. In the samples that had higher lateral stiffness, local buckling occurred by crippling at the top of braces, and drift and tracks were then observed more than 0.8%. Furthermore, when the area of braces increased, the capacity of panels enhanced, too. In 2004, Fulop and Dubina examined three samples. At each side of the samples, cross braces with the length to width ratio of 1.5 were positioned and the samples were exposed to cyclic and monotonic loadings. Double studs were applied in corners, and connection of the brace to frame occurred according to the yield tension. In spite of a rise in the studs' length on the braces, the results did not demonstrate the ductility capacity of braces completely since the fracture increased at the corner, and lateral deformations took place because of stretches in the braces [13]. In 2006, Kim carried out shaking table experiment in order to examine the operation of CFS in structures with two stories. This test demonstrated the yielding in nonlinear behavior in clamps of the first story in addition to yielding phenomenon near the track. In the studs, due to local buckling, any flexibility was not shaped [14]. Afterward, in 2007, an experimental research was performed in Germany to test the behaviors of shear walls that were made up of CFS with sheathing on one or both sides under vertical and horizontal loads. According to the obtained results, a design process was provided in such a way that it can allow the design of walls to carry both horizontal and vertical loads. In addition, this research indicated the effects and significance of the presence of sheathing for cold-formed section in the mechanism of failure in shear walls [9].

Pan and Shan [15] conducted a number of experiments on structural strength of CFS-framed shear walls sheathed in gypsum boards, calcium silicate boards (CSBs), and OSB panels. While designing the test specimens, two aspect ratios, i.e., 1.0 and 2.0, were considered. Regarding the highest ultimate strength, the CFS walls that had OSB panels ranked the first; the second in the ranking were the walls with CSB panels and the CFS walls that had gypsum boards. For the same aspect ratio, the ultimate strength of the wall specimens with one-sided sheathing was around 50% of those specimens that were sheathed on both sides. The design ductility ratios of 6.6, 3.9, and 3.8 were introduced for CFS-framed walls sheathed with gypsum boards, OSB panels, and CSB panels, respectively. A number of tests were performed by Nithyadharan [16] on eight various CFS-framed shear walls that had been sheathed in CSB panels. As shown by findings, the failure process included bearing, titling, and pull-through of the screws; then, entire separation took place following by rigid body rotation of the CSB panels. The increase of the board thickness and distance of the screw edge led to increase of the ultimate strength and energy dissipation. Compared to the walls panels with Type A board arrangement (a single board across which the shear was transferred), the walls panels with Type B board arrangement (two boards with a discontinuity at the intermediate stud) were subjected to a remarkably greater deformation. The reason was excessive relative slippage at the screws in the interior studs of the former.

Several cyclic tests were conducted by Liu [17] on the full-scale CFS walls sheathed by the OSB panels; which demonstrated that the most important mechanism of energy dissipation occurred at the fastener-to-sheathing connections, which involved bearing, tilting, and pull-through. The interior gypsum boards were applied to improve the initial stiffness and make a modest enhancement on the strength, whereas the other behaviors were similar to behaviors seen in cases with ledger track and with no interior gypsum board. Typically, the hysteretic behaviors of the CFS wall panels involved a serious pinching response. Two models, namely Pinching 4 fitted to the tested data and Equivalent energy elastic plastic (EEEP), were suggested to be used for nonlinear history analysis.

Zeynalian [18] made use of fiber-cement boards (FCBs) to apply cyclic lateral loading to sheathed CFS-framed shear walls to study their structural behavior. It was revealed that under cyclic loading, the walls showed reasonable lateral resistance to ductility and shear strength; as a result, the design was proved appropriate to be applied to regions with seismic actions. On the other hand, with elimination of the FCB panels from one side, a reduction occurred in both the strength and the ductility of the wall. Such modification could be made effectively for those diagonal stud elements that were applied to corners of the wall. To design CFS-framed shear walls, the US Army Corps of Engineers (USACOE) (the publisher of TI809-07 [19]) made available some guidelines that were more stringent than the AISI Standards [2]. The USACOE standards suggest that to calculate the shear capacity of a CFS wall, the sheathing contribution to both sides should be ignored and just the strength of the CFS frame should be relied on. Zeynalian [20–22] carried out numerical and experimental research on CFS frames with knee elements and reported that the CFS frames demonstrated relatively high maximum drifts; though, their strength was lower than the strength of X-shaped bracing systems. As a result, the knee-stud bracing systems can be applied merely to low-seismic-activity regions in which there is a low requirement for lateral resistance capacity. In another research, Moghimi [23] studied the shear behavior of CFS frames with steel-strap X-shaped bracing, and the results showed the incidence of distortional and local buckling of frame members in stable modes; in addition, the strap-braced CFS frames were shown capable of providing a substantial shear capacity level after incidence of the first buckling signs. Attaching brackets to four corners of a CFS frame made a considerable improvement on the lateral performance of the frame assemblies. Through selecting suitable perforated straps, strap alongside the distributed holes could be created so that they could reach yielding, which prevented tear of the strap at the tension unit location or the strap-to-frame connection. A number of experimental and theoretical studies were conducted by Iuorio and Macillo [24, 25] in order to examine the seismic behaviors of CFS-strap-braced stud walls, and it was reported that a reasonable agreement existed between the experimentally determined and theoretically predicted behaviors of the walls and the connection systems in terms of the shear capacity. In addition, the necessity for cautiously designing the wall corners was emphasized as their behaviors showed significant effect on the overall wall's response. Furthermore, behavior factor values stated by AISIS213 [1] were confirmed by experiments, with the code values that

were corresponded to lower limits of experimental results. Several scholars have introduced new sheathing and connecting techniques to enhance the shear resistance of CFS-framed shear walls. Serrette [26, 27] made use of structural adhesive and steel pins in order to attach structural wood sheathing, and the shear capacity was demonstrated approximately comparable to the shear capacity obtained by self-drilling screws. To further reduce the needed thickness of CFS-framed shear walls, Yu [28, 29], DaBreo [30], Shakibanasab [31], and Mohebbi [32] investigated the shear behaviors of such walls by means of plain steel sheathing and reported that they were substantially stiff and strong.

Vigh [33] employed low-profile corrugated steel sheets, as a replacement for plain steel sheathing, in order to decrease the out-of-plane deformation of sheathing. The corrugated shear wall was proved to have proper ductility as well as higher shear strength. Moreover, Mowrtage [34] introduced a novel sheathing technique wherein shotcreted ribbed steel sheets were used to enhance load-bearing capacity and stability of the walls. Lateral load-bearing capacity of the walls sheathed by means of the proposed technique was also shown almost two times more than that of the walls sheathed using conventional boards. To satisfy the thermal, acoustic, and fire resistance needs, complex detailing of CFS-framed shear walls should be provided. Traditionally, a thermal insulator in the shape of expanded polystyrene (EPS) boards, extruded polystyrene (XPS) boards, or insulation cotton are placed inside cavities or on the external surfaces of the steel frames. Furthermore, breathable papers and waterproof membranes are used in external facades in a way to minimize the energy loss through exchanging vapor between walls and external environment.

3.2 Lightweight Concrete

Many studies carried out in recent decades have focused on the utilization of concrete with lightweight aggregate in building construction. More specifically, many reports have been released in regard to application of lightweight concrete to road infrastructures and railways subgrade [35]. In recent years, lightweight concrete has been encouraged primarily because of quick developments occurred in construction of high-rise buildings and concrete structures with large dimension and long spans. Light concrete has shown more improved insulation, higher energy absorption, and lower density compared to conventionally used concrete. It can decrease both weight and cost of construction; though, its strength level cannot satisfy the minimum level of strength required as a structural member, which has resulted in being rejected as a load-bearing and structural member. Currently, researchers of this field have been focused on making a concrete with low density and acceptable properties so that it can be dependably utilized as a structural member and a load-bearing structure. This type of concrete makes a significant decrease in weight of buildings, hence reducing considerably the effective earthquake force on the buildings that, in tu rn, reduces damage to the buildings. In order

to create a structural lightweight concrete, mineral aggregates and lightweight industrial must be used as replacements for the common aggregates in a way to preserve the compressive strength while the density decreases. A number of tests were done by Li et al. [36] on mechanical properties of lightweight concrete that contained polystyrene aggregates, which resulted in proposing some solutions to existing defects. They also tested the compressive strength, density, and stress–strain behavior of lightweight concrete and introduced the most effective mixture design with polystyrene aggregates. As proved by the obtained results, the volume of polystyrene aggregates had significant effects on the compressive strength and ratio of water to cement in lightweight concrete. It was also revealed that the most important problem of this concrete was the segregation of polystyrene aggregates from the concrete matrix; the segregation could be evaded by molding.

Madandoust et al. [37] made use of some methods like the slump flow, V-shaped funnel test, T50, and L-shaped concrete block to investigate the properties of lightweight self-compacting EPS concrete in the fresh stage. Findings indicated that the mixture design with a high density could generally satisfy the criterion of self-compacting concrete.

Chen et al. [38] studied the impact of superplasticizers on workability of lightweight EPS concrete. Furthermore, they studied the impact of curing conditions and the ratio of superplasticizers to cement on the bending strength of lightweight EPS concrete. Results showed that the strength of lightweight EPS concrete that contained superplasticizers was meaningfully dependent on curing conditions. Additionally, the superplasticizers could improve the bending strength of lightweight concrete. Babu et al. [39] examined the relationship between the size of polystyrene aggregates, humidity characteristics, and lightweight concrete. It was shown that the concrete containing smaller sizes of polystyrene aggregates had higher compressive strength in comparison with concrete with larger sizes of polystyrene aggregates. In addition, the use of EPS aggregates led to beginning of gradual fracturing process under loading despite brittle fracturing of common concrete. Their study showed that if EPS is used, it results in humidity characteristics (e.g., evaporation), and absorption will become more desirable.

Miled et al. [40] conducted also a research on the compressive behavior of concrete containing EPS aggregate and the impacts of polystyrene size upon fracture mode of the concrete. As confirmed by the obtained results, the EPS aggregate size had effect on the compressive strength. In addition, it was demonstrated that the concrete that had less porousness was affected much less than that with more porousness. The fracture mode examination was used to propose a new model for prediction of the compressive strength of lightweight EPS concrete with a variety of aggregates sizes. The shrinkage and mechanical properties of lightweight EPS concrete was examined by Tang et al. [41]. It was reported that in lightweight concrete, the polystyrenes possessed adequate ductility; though, due to low strength, it could not be utilized as a structural member. They made use of polystyrene aggregates to form lightweight concrete; then, they tested it with a density ranging from 2247 to 2270 kg/m^3. Findings showed high dependency of density and modulus of elasticity on the type and size of the polystyrene aggregates. EPS

concrete and perlite concrete were compared by Bagon [35] regarding their application to marine vessels. With a specific density; the modulus of rupture, compressive strength, and modulus of elasticity of EPS concrete were 25, 50, and 100%, respectively, higher than those of the perlite concrete. Ray et al. [42] made a test on the mixture design and mechanical properties of concrete with very low density. To make lightweight concrete, polystyrene aggregates were employed. As demonstrated by the obtained results, if smaller sizes of EPS are used, it will result in higher compressive strength. Perry et al. [43] carried out research on behaviors and mixture designs of EPS concrete. They examined a concrete containing polystyrene with volumetric percentages of 40, 50, and 60. The level of density and strength of the samples were measured. In addition, the stress–strain relationship of lightweight EPS concrete was investigated. Bischoff et al. [44] investigated the behavior of EPS concrete under tough impact; the impact was made by free-fall of a hammer from a certain height. They also formed three groups of samples and tested them with compressive strengths ranging from 4 to 12 MPa. Finally, a comparison was made between the obtained results and the static penetration tests. The samples commenced destruction from the crushing zone under the impact. This type of concrete was proved to have low crushing resistance while having enough capacity to be appropriately compacted and shaped.

A research was carried out by Babu et al. [45] on behavior of lightweight concrete that comprised microsilica and EPS. They employed EPS as lightweight aggregates and microsilica as cement supplementary material. The study was primarily focused on the workability, durability, and strength of lightweight concrete containing polystyrene. Findings confirmed that increasing the percentage of microsilica resulted in enhancing the concrete strength.

In the present study, a variety of mix designs of polystyrene and perlite concrete were examined in order to attain the best type of lightweight concrete and explore the optimum mix design with effective concrete in consistency with frame system. To this end, totally 30 samples (i.e., 10 mix designs each of which had 3 samples) were taken into account.

4   Tests Program

We took into consideration the frame system and their lightness, and to obtain a proper application in these frames, lightweight concrete was utilized in a way to fill out the cavities existed between the members. First, a number of experimental tests were carried out on various lightweight concretes to attain an optimum mix design. Such concrete was chosen to have a low level of density and a satisfactory compressive strength (associated with low density). After that, the ABAQUS software was applied to analysis of behaviors of CFS frames in three models under lateral loads and the obtained results were compared to each other (see Fig. 1).
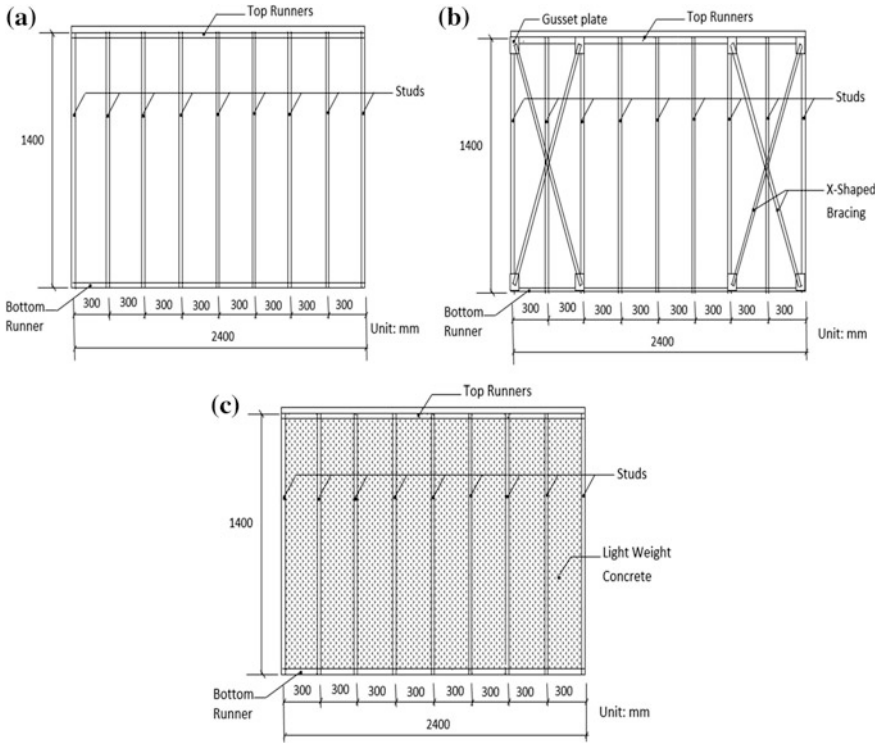
Fig. 1 Configuration of CFS frames: a CFS frame without bracing, b CFS frame with X-shaped bracings, c CFS frame in-filled by light weight concrete

(a) Frame with no bracing and with semi-rigid connections (the first specimen). For this specimen laboratorial model was manufactured and verified by Abaqus model.

(b) Frame with both X-shaped bracing and semi-rigid connections (the second specimen).

(c) Frame with no brace, but in-filled with lightweight concrete (the third specimen).

4.1 Lightweight Concrete

The present research tested both polystyrene and perlite concretes in order to identify the best type of concrete and explore the optimum mix design with effective concrete in consistency with the frame system. To the end of this paper, a total of 30 samples (i.e., 10 mix designs each of which had 3 samples) were examined.

Table 1 Properties and result of perlite concrete

Mix design	1	2	3	4	5
Cement (kg)	250	250	300	375	475
Perlite (kg)	110	55	100	110	246
Water (kg)	130	130	150	300	190
Polystyrene (kg)	–	5.5	0	–	–
Gravel (kg)	–	–	–	–	125
Sand (kg)	–	–	100	–	38
Density (kg/m^3)	1155	561.2	737	1261	1157
Compressive strengths (MPa)	4.01	0.88	1.32	5.77	2.0
	3.87	0.86	1.4	5.69	2.16
	4.13	0.89	1.27	5.84	1.87
Average compressive strengths (MPa)	4.0	0.88	1.33	5.77	2.01
Age (day)	7	7	7	7	30

The present research made use of the weight method taking into consideration other studies previously conducted on this field. Though, since low density is the criteria of operation, the method of trial and error was used. For the perlite concrete, rate of water absorption and density of materials were computed prior to mixing; furthermore, the utilized perlite was entirely dried to remove any humidity. Samples in different ages were examined and varied mix design and test results were attained for the perlite concrete (see Table 1).

On the other hand, for the polystyrene concrete, to reduce the weight of concrete as far as possible, polystyrene granules were used as granule or filler; they showed much less density compared to that of the perlite concrete. In addition, microsilica contents of the polystyrene concrete were more than that of the conventional concretes. Typically, the volume of microsilica is freed out since the alkali reaction with concrete is 10–15% of the weight of cement and the rest of it plays the role of a filler. This reaction considers the empty spaces between polystyrene particles, and this way, it enhances the compressive strength of the concrete. Table 2 presents the mix design and the results obtained from the tests conducted on different polystyrene concretes.

4.1.1 Selection of the Optimum Mix Design

Various mix designs made high efficiency and low density. The observations done based on designs are

1. The perlite concrete had higher level of density in comparison with the polystyrene concrete; this property was because of high density of the perlite granules.
2. The perlite showed high sensitivity to percussion and with long mixing time, it broke out and its granulating varied, which resulted in increase of cement and water usage, hence leading to having high density.

Table 2 Properties and result of polystyrene concrete

Mix design	1	2	3	4	5
Cement (kg)	300	200	350	350	375
Polystyrene (kg)	5.4	5	10	10	40
Water (kg)	200	120	180	116	250
Sand (kg)	0	80	0	0	0
Polypropylene (kg)	–	–	–	–	4.5
Microsilica (kg)	–	–	–	–	150
Superplasticizer (kg)	–	–	–	–	5
Density (kg/m^3)	608.3	736.6	1348	651.5	585
Compressive strengths (MPa)	0.86 0.85 0.92	0.64 0.72 0.78	1.14 1.18 1.19	1.31 1.38 1.28	2.04 1.93 1.97
Average Compressive strengths (MPa)	0.88	0.71	1.17	1.33	1.98
Age (day)	7	7	7	7	30

Table 3 Properties of appropriate final mix design

Cement (kg)	375
Polystyrene (kg)	40
Water (kg)	250
Sand (kg)	4.5
Polypropylene (kg)	150
Microsilica (kg)	5
Superplasticizer (kg)	585
Density (kg/m^3)	587
Compressive strength (MPa)	2.03

3. It was obvious that the polystyrene dosage and water cement ratio most significantly affected the compressive strength of the lightweight concrete [46].
4. When microsilica concrete was used with polystyrene granules, it not only enhanced the strength (because of the alkali reaction with concrete), but also acted as a filler due to the existence of empty spaces between polystyrene granules; it positively affected the strength. The proper final mix design to make the lightweight concrete for this study is presented in Table 3 and its stress–strain graph is displayed in Fig. 2.

4.2 Test Specimens of CFS Frames

The test specimens were produced on 1/2 scale of the real model designed on the basis of the Iranian CFS code [47] and constructed in Pardis of Tehran, Iran

Stress–Strain curve of
appropriate final mix design
samples
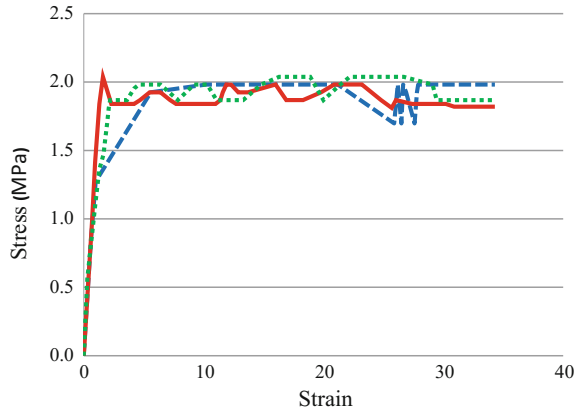
(see Fig. 3). Table 4 presents the material properties of the CFS members. Each test specimen was 2400 mm in width and 1400 mm in height, and the CFS studs were spaced at 300 mm. Configurations of the CFS frames are displayed in Fig. 1. As demonstrated in Fig. 4, each CFS frame comprised runners (0.75 mm thickness, 25 mm flange, and 50 mm web), studs (0.75 mm thickness, 25 mm flange, 50 mm web, and 8 mm lip), and strap bracing members (0.75 mm thickness, 1500 mm length, and 100 mm width) (Fig. 4).

Fig. 3 Actual model of CFS in Pardis of Tehran

Table 4 Properties of Cold-Formed Steel

Nominal thickness (mm)	Yield stress (Fy) (MPa)	Ultimate stress (Fu) (MPa)	Elongation (%)
0.75	270	326	36
1	280	338	39
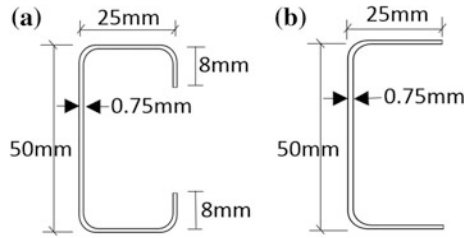
Fig. 4 Cross-sectional dimension of CFS frame; a stud, b runner
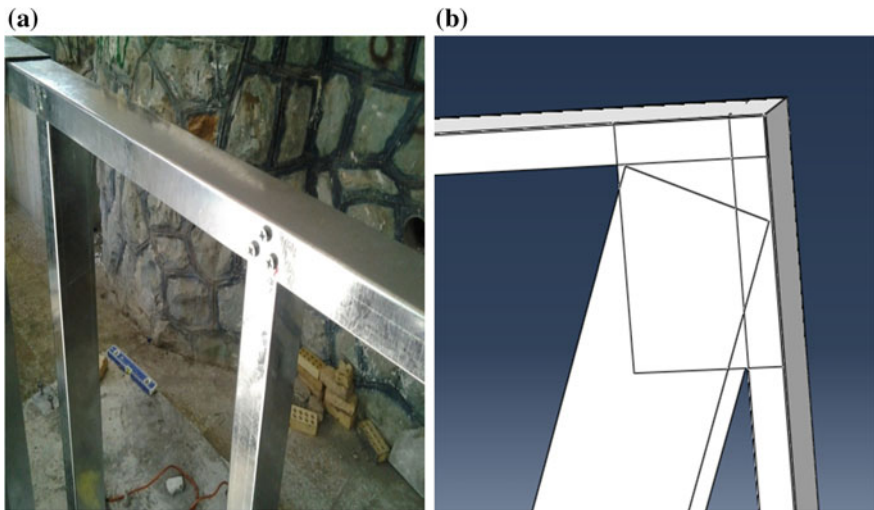
Fig. 5 Details of connections: a Connection of stud to runner in laboratorial model of first specimen b connection of X-shaped bracings to gusset plate and end studs of second specimen in Abaqus software

For the laboratorial model of the first specimen (Fig. 6a), three self-drilling screws were provided for the semi-rigid connection between runners and studs in each direction (see Fig. 5a). Seven base plates were applied to connecting the bottom runner to the foundation. In each base plate, two NO, #20 bolts with 550 mm length were installed (with 100 mm distance). In case of the CFS frame with X-shaped bracings (Fig. 6b), gusset plates (0.75 thickness, 150 mm length,

Fig. 6 a Laboratorial and FE models of first specimen: Frame without bracing but with semi-rigid connections b second specimen: Frame with X-shaped bracing and with semi-rigid connections and c third specimen: Frame without brace but in-filled with lightweight concrete

and 100 mm width) were applied to strengthening the connection with the help of X-shaped bracings (see Fig. 5b). The CFS-framed shear wall specimen (Fig. 6c) comprised studs and runners with properties of the first and the second specimens, with no bracing. Cavities between members in this type of specimen (Fig. 6c) were entirely filled using proper lightweight concrete (Table 3).

4.3 Loading Protocols

The displacement control method (which was based on the Method B of the ASTM Standard [48]) was applied to the horizontal cyclic loading protocol for the laboratorial specimen. The reason of choosing this method was relatively low lateral stiffness and shear capacity of the specimen. A hydraulic jack with 10 tons of
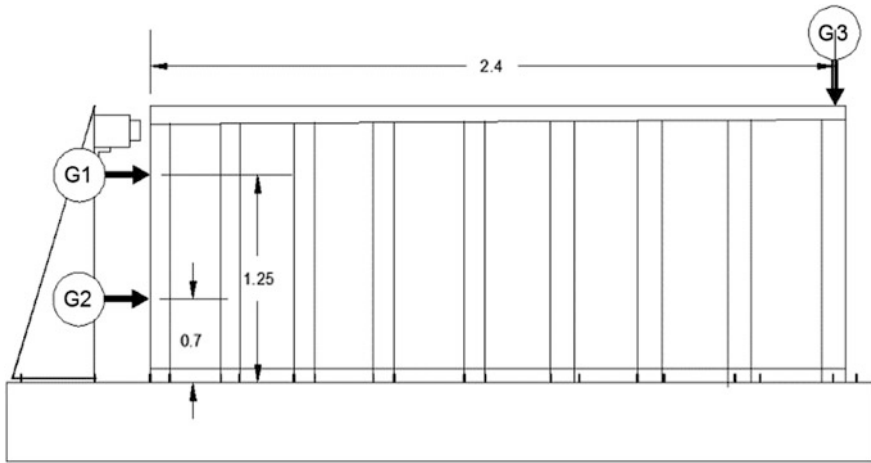
Fig. 7 Frame of loading

weight was utilized in this experiment to apply the pushover load. Loading of the frame was done in a unidirectional form, and as shown in Fig. 7, the hydraulic jack was positioned at the top of the frame designed previously for the purpose of this test. Three linear variable differential transformers (LVDTs) (G1, G2, and G3) were applied to the tests as displayed in Fig. 7. Two LVDTs (i.e., G1, G2) measured the horizontal displacement at the height of 0.7 and 1.25 m, respectively, and one LVDT (i.e., G3) measured the vertical displacement.

5   Results and Discussion

Several tests were carried out on the forces-displacement curves, deformation in height of wall, lateral resistance, and their failure mechanism, and the obtained results were compared to each other. The following subsections explain the advantages of lightweight concrete in lateral performance of the walls compared to strap bracing.

5.1   *Initial Hardness of Specimens*

According to the results obtained after the specimens' displacement, the gradient of load-displacement curve was taken into consideration as an initial hardness in the specimen and displayed in Fig. 8. The hardness level of the third specimen made up of lightweight concrete was clearly four times higher than that of the second specimen that had utilized strap brace.
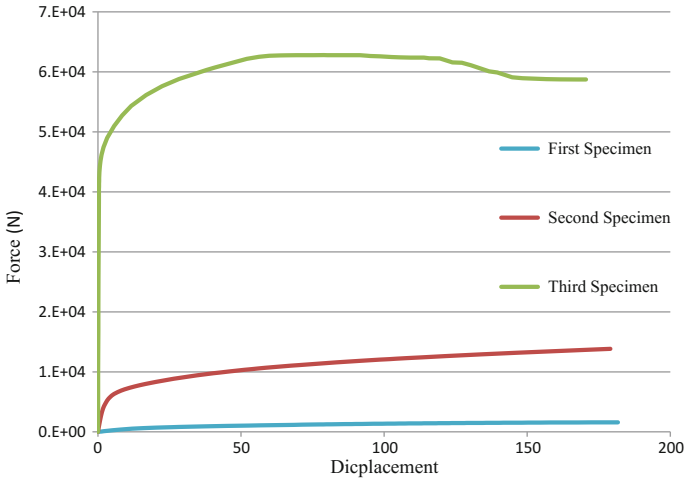
Fig. 8 Force-Displacement curve of specimens

5.2 Failure Mechanism

5.2.1 First Specimen

Since this frame did not have strong connections, the frame showed insufficient tolerance, and while the force was reaching 200 N, in connection of upper runner and stud No.2, a case of local buckling occurred (Fig. 9), and even with constancy of the force, the displacement augmented. After unloading, the frame moved 1 cm towards its first position and 9 cm permanent deformation occurred (see Fig. 10).

Fig. 9 Local buckling of connection in first specimen
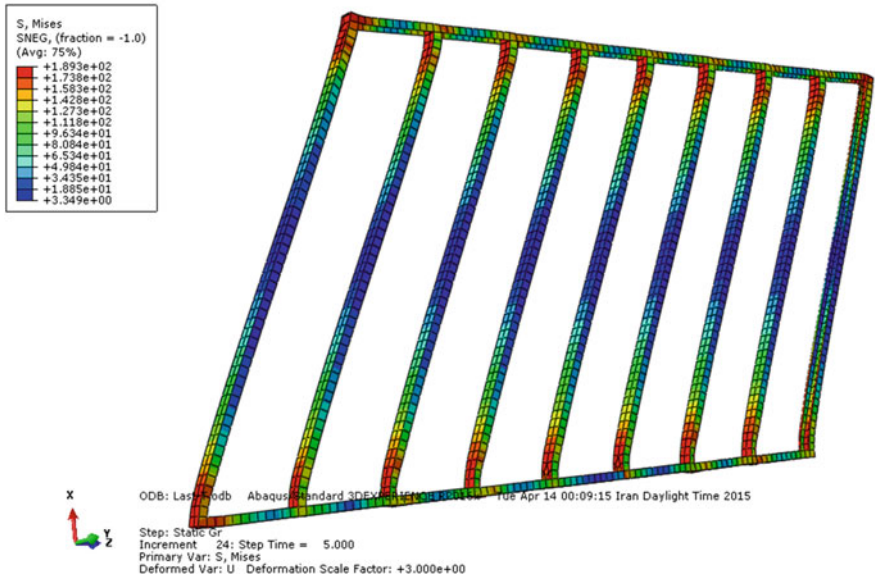
Fig. 10 Permanent deformation in first specimen

Fig. 11 Buckling of braces and sinus shape of deformation in second specimen

5.2.2 Second Specimen

At this specimen, after influencing the lateral forces in the, the frame deformation began and the first and last span (braced) turned clockwise in connection of the lower runner with stud numbers 1 and 7. As Fig. 11 displays, with around 3100 N force, buckling happened in the compression brace. In addition the upper runner shape changed in the sinus formation. At the time when force was reaching close to 3000 N, in connection of upper and lower runner with stud number 7, not only buckling, but also crippling took place, and a decrease was observed in the load-bearing of the frame (see Fig. 12). At this stage, the ultimate displacement of G1, G2, and G3, was 70, 39, and 10.7 mm, respectively.

5.2.3 Third Frame Specimen

For the third frame filled with polystyrene lightweight concrete, when the concrete was loaded, its age was 30 days, and the mix design was selected based on the chosen mix design and the production procedure presented in Table 3. Following the application of lateral load, due to high stiffness of the in-filled frame, the frame rotation was rigid, but lateral buckling took place and the final frame deformation was similar to sinus; though, it was much slighter than a braced frame. When loading ended, the concrete was not damaged, the frame was safe, and the problem was related to failure of CFS frame (see Figs. 13 and 14).
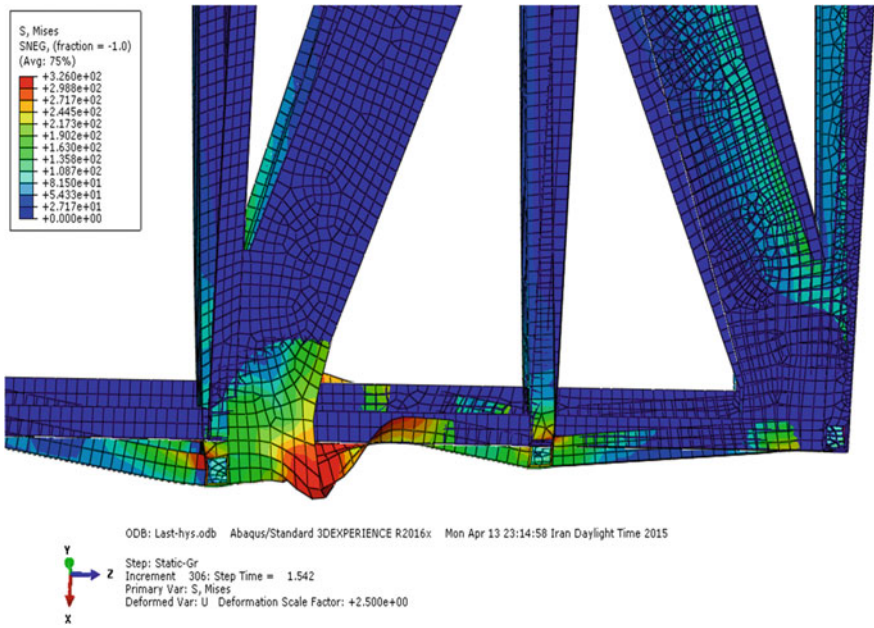
Fig. 12 Buckling and crippling in connection of bottom runner in second
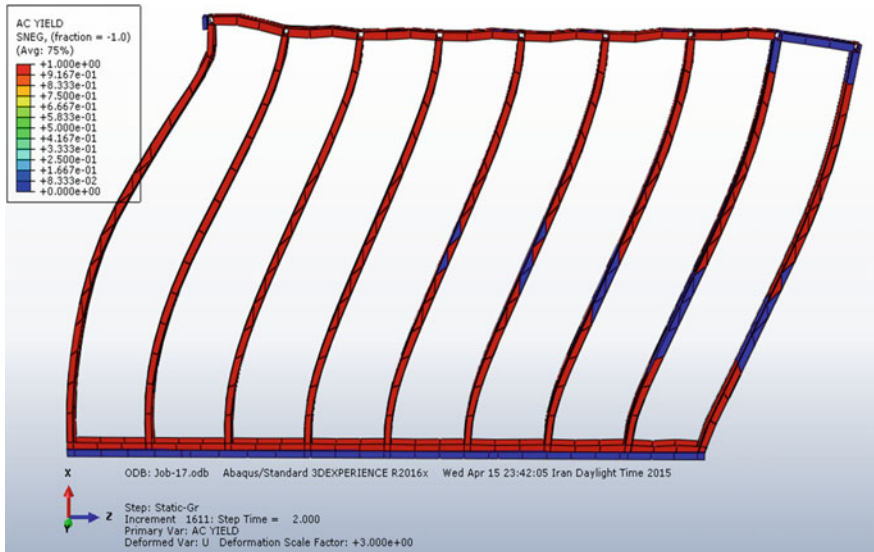
Fig. 13 Deformation of CFS frame in third specimen
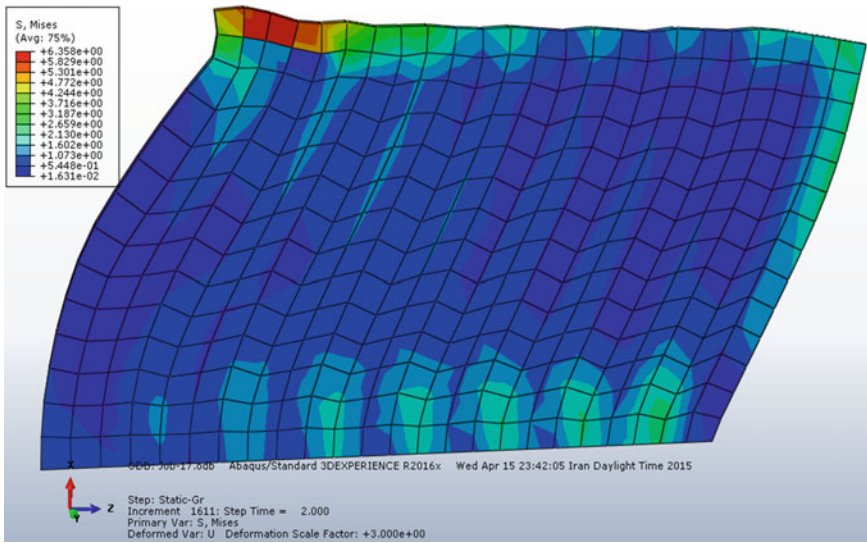
Fig. 14 Deformation of concrete in third specimen

6   Conclusions

This research tested one specimen and analyzed three ½ scale specimens, comprising one CFS frame in-filled by lightweight concrete, one bare CFS frames, and one CFS frame with x-shaped bracing using ABAQUS software. The conclusions drawn through the tests are as follows:

(1) As one of the most important parameters was the thinness of the CFS members (that may cause tearing), increasing the number of self-drilling screws did not lead to increase of the connection rigidity, and the connection performance was comparable to that of the pin.

(2) The initial hardness of materials was another parameter studied here. As revealed by findings, if lightweight concrete is used, the lateral stiffness of CFS frame increases significantly.

(3) Utilization of lightweight concrete as a replacement for strap brace led to an enhancement in the lateral load-bearing of the frame up to 84.6%.

(4) The rate of energy absorption of CFS frame with the use of lightweight concrete was shown 68% higher than the braced frame.

(5) CFS frame filled by polystyrene concrete in comparison with strap bracing, because of high stiffness of in-filled frames, they could act as the main lateral load-bearing system.

References

1. Rezaeian, P., Marsono, A.: Structural system of safe house against tornado and earthquake. Key Eng. Mater., 594–595 (2014)
2. American Iron and Steel Institute (AISI): North American Standard for Cold-Formed Steel Framing Lateral Design. AISIS213, Washington, DC, USA (2007)
3. Serrette, R.L., Nguyen, H., Hall, G.: Shear Wall Values for Light Weight Steel Framing. Report No.LGSRG-3-96, Department of Civil Engineering, Santa Clara UniversitySantaClara, CA, USA (1996)
4. Serrette, R.L.: Additional Shear Wall Values for Light Weight Steel Framing. ReportNo. LGSRG-1-97, Department of Civil Engineering, Santa Clara University Santa Clara, CA, USA (1997)
5. Serrette, R.L.: Performance of Cold-Formed Steel-Framed Shear Walls: Alternative Configurations. Report No. LGSRG-06-02, Department of Civil Engineering, Santa Clara University Santa Clara, CA, USA (2002)
6. Farghal Maree, K.: Hilal Riad Analytical and experimental investigation for bond behavior of newly developed polystyrene foam particles' lightweight concrete. Eng. Struct. **58**, 1–11 (2014)
7. Ramezanianpour, A.A., Karein, S.M.M., Vosoughi, P., Pilvar, A., Isapour, S., Moodi, F.: Effects of calcined perlite powder as a SCM on the strength and permeability of concrete. Constr. Build. Mater. **66**, 222–228 (2014)
8. CFSEI: Cold Formed Steel Engineering Institute
9. Lange, J., Naujoks, B.: Behaviour of cold—formed steel shear walls under horizontal and vertical loads. Thin Wall Struct. **44**(12), 1214–1222 (2007)
10. Restrepo, J.I., Bersofsky, A.M.: Performance Characteristics of Light Gage Steel Stud Partition Walls Thin-Walled Structures, vol. 49, issue id 2, p. 317 (2011)
11. Moghimi, Hassan, Ronagh, Hamid R.: Performance of light—gauge cold—formed steel strap—braced stud walls subjected to cyclic loading. Eng. Struct. **31**(1), 69–83 (2009)
12. Adham, S.A., Avanessian, V., Hart, G.C., Anderson, R.W., Elmlinger, J., Gregory, J.: Shear wall resistance of lightgage steel stud wall systems. Earthq. Spectra. **6**(1), 1–14 (1990)
13. Fulop, L.A., Dubina, D.: Performance of wall-stud cold—formed shear panels under monotonic and cyclic loading. Thin Walled Struct. **42**(2), 321–338 (2004)
14. Kim, T.W., Wilcoski, J., Foutch, D.A., Lee, M.S.: Shake table test of cold—formed steel shear panel. Eng. Struct. **28**(10), 1462–1470 (2006)
15. Pan, C.L., Shan, M.Y.: Monotonic shear tests of cold-formed steel wall frames with sheathing. Thin Walled Struct. **49**(2), 363–370 (2011)
16. Nithyadharan, M., Kalyanaraman, V.: Behavior of cold-formed steel shear wall panels under monotonic and reversed cyclic loading. Thin Walled Struct. **60**(11), 12–23 (2012)
17. Liu, P., Peterman, K.D., Schafer, B.W.: Impact of construction details on OSB-sheathed cold-formed steel framed shear walls. J. Constr. Steel Res. **101**, 114–123 (2014)
18. Zeynalian, M., Ronagh, H.R.: Seismic performance of cold formed steel walls sheathed by fibre-cement board panels. J. Constr. Steel Res. **107**, 1–11 (2015)
19. U.S. Army Corps of Engineers, Engineering and Construction Division, Directorate of Military Program, Technical Instructions: Design of Cold-formed Load Bearing Steel Systems and Masonry Veneer/steel Stud Walls, TI809-07, Washington, DC, USA (2006)
20. Zeynalian, M., Ronagh, H.R.: A numerical study on seismic characteristics of knee-braced cold formed steel shear walls. Thin Walled Struct. **49**(12), 1517–1525 (2011)
21. Zeynalian, M., Ronagh, H.R., Hatami, S.: Seismic characteristics of K-braced cold-formed steel shear walls. J. Constr. Steel Res. **77**(10), 23–31 (2012)
22. Zeynalian, M., Ronagh, H.R.: An experimental investigation on the lateral behavior of knee-braced cold-formed steel shear walls. Thin Walled Struct. **51**(2), 64–75 (2012)

23. Moghimi, H., Ronagh, H.R.: Better connection details for strap-braced CFS stud walls in seismic regions. Thin Walled Struct. **47**, 122–135 (2009)
24. Iuorio, O., Macillo, V., Terracciano, M.T., Pali, T., Fiorino, L., Landolfo, R.: Seismic response of CFS strap-braced stud walls: experimental investigation. Thin Walled Struct. **85**, 466–480 (2014)
25. Macillo, V., Iuorio, O., Terracciano, M.T., Fiorino, L., Landolfo, R.: Seismic response of CFS strap-braced stud walls: theoretical study. Thin Walled Struct. **85**, 301–312 (2014)
26. Serrette, R., Lam, I., Qi, H., Hernandez, H., Toback, A.: Cold-formed steel frame shear walls utilizing structural adhesives. J. Struct. Eng. ASCE **132**(4), 591–599 (2006)
27. Serrette, R., Nolan, D.P.: Reversed cyclic performance of shear walls with wood panels attached to cold-formed steel with pins. J. Struct. Eng. ASCE **135**(8), 959–967 (2009)
28. Yu, C.: Shear resistance of cold-formed steel framed shear walls with 0.686, 0.762, and 0.838 mm steel sheet sheathing. Eng. Struct. **32**(6), 1522–1529 (2010)
29. Yu, C., Chen, Y.: Detailing recommendations for 1.83 m wide cold-formed steel shear walls with steel sheathing. J. Constr. Steel Res. **67**(1), 93–101 (2011)
30. DaBreo, J., Balh, N., Ong-Tone, C., Rogers, C.A.: Steel sheathed cold-formed steel framed shear walls subjected to lateral and gravity loading. Thin-Walled Struct. **74**, 232–245 (2014)
31. Shakibanasab, A., Attari, N.K.A., Salari, M.: Astatistical and experimental investigation into the accuracy of capacity reduction factor for cold-formed steel shear walls with steel sheathing. Thin Walled Struct. **77**(4), 56–66 (2014)
32. Mohebbi, S., Mirghaderi, R., Farahbod, F., Sabbagh, A.B.: Experimental work on single and double sided steel sheathed cold-formed steel shear walls for seismic actions. Thin Walled Struct. **91**, 50–62 (2015)
33. Vigh, L.G., Liel, A.B., Deierlein, G.G., Miranda, E., Tipping, S.: Component model calibration for cyclic behavior of a corrugated shear wall. Thin Walled Struct. **75**(2), 53–62 (2014)
34. Mowrtage, W., Hasan, N., Pekmezci, B., Atahan, H.N.: Loadingcarryingcapacity enhancement of cold-formed steel walls using shotcreted steel sheets. Thin Walled Struct. **60**(11), 145–153 (2012)
35. Bagon, C., Frondistou-Yannas, S.: Marine floating concrete made with polystyrene expanded beads. Mag. Concr. Res. **28**, 225–229, 320 (1976)
36. Xu, Y., Jiang, L., Xu, J., Li, Y.: Mechanical properties of expanded polystyrene lightweight 321 aggregate concrete and brick. Constr. Build. Mater. **27**(1), 32–38, 322 (2012)
37. Madandoust, R., Ranjbar, M.M., Mousavi, S.Y.: An investigation on the fresh 323 properties of self-compacted lightweight concrete containing expanded polystyrene. Constr. Build. Mater. **25**(9), 3721–3731, 325 (2011)
38. Chen, B., Liu, J.: Mechanical properties of polymer-modified concretes containing expanded 326 polystyrene beads. Constr. Build Mater. **21**(1), 7–11, 327 (2007)
39. Babu, D.S., Babu, K.G., Tiong-Huan, W.: Effect of polystyrene aggregate size on 328 strength and moisture migration characteristics of lightweight concrete. Cem. Concr. Compos. **28**(6), 520–527, 330 (2006)
40. Miled, K., Sab, K., Le Roy, R.: Particle size effect on EPS lightweight concrete compressive 331 strength: experimental investigation and modeling. Mech. Mater. **39**(3):222–40, 332 (2007)
41. Tang, W.C., Lo, Y., Nadeem, A.B.I.D.: Mechanical and drying shrinkage properties of structural graded 333 polystyrene concrete. Cement Concr. Compos. **30**, 403–409, 334 (2008)
42. Le Roy, R., Parant, E., Boulay, C.: Taking account the inclusions size in lightweight concrete compressive 335 strength prediction. Cem. Concr. Res. **35**(4), 770–5 (2005)
43. Perry, S.H., Bischoff, P.H.,0 Yamura, K.: Mix details and material behaviour of polystyrene aggregate 337 concrete. Mag. Concr. Res. **43**, 71–6, 338 (1991)
44. Bischoff, P.H., Yamura, K., Perry, S.H.: Polystyrene aggregate concrete subjected to hard impact. Proc. Inst. Civil Eng. **89**(2), 225–39, 340 (1990)

45. Babu, K.G., Babu, D.S.: Behaviour of lightweight expanded polystyrene concrete 341 containing silica fume. Cem. Concr. Res. **33**(5), 755–762 (2003)
46. Yi, Xu, Jiang, Linhua, Jinxia, Xu, Li, Yang: Mechanical properties of expanded polystyrene lightweight aggregate concrete an brick. Constr. Build. Mater. **27**(1), 32–38 (2012)
47. The building and housing research center of Iran, cold formed steel design code, 1st edn. (2001)
48. American Society for Testing and Materials (ASTM), Standard Test Methods for Cyclic (Reversed) Load Test for Shear Resistance of Walls for Buildings, ASTM E2126-07, West Conshohocken, USA (2007)

Shear Behavior of Strengthened Beams

Abdesselam Zergua and Sabiha Barour

Abstract Strengthening the reinforced concrete elements using polymer fibers continues to interest many researchers. In this context, an experimental study has been completed to evaluate the reinforcement on shear behavior of beams. Different fiber band positions were applied to beams in nodal zones. The four-point bending tests have been performed. The results have shown that the inclined bands by 45° with respect to the beam axis provide better results compared to those obtained by orthogonal bands (90°), in strength, stiffness, and ultimate load, as well as deformations. In addition, the use of these bands increases the bearing capacity by reducing the arrow and limits crack widths and ensures better behavior of these structures.

Keywords Strengthing of beams · Shear behavior · Band fiber reinforcement

1 Introduction

Using externally bonded fiber-reinforced polymer (FRP) sheets to strengthen structural elements as columns and beams has been reported by many authors [1–3]. This reinforcing method presents many advantages related to FRP material such a good corrosion resistance, light weight, high-strength-to-weight ratio, easy to install, non-conductive and resistance to the chemicals [4].

Externally bonded FRP reinforcement is used to wrap the beam cross-section with fibers and thus enhances its shear resistance [5–9].

Flexural behavior of reinforced concrete (rc) beams can be well predicted. However, up to date, just a few studies have been focused on the shear strengthening with FRP. The prediction of shear behavior of rc beams is so difficult because of the complexity on shear transfer mechanism [10].

A. Zergua (✉) · S. Barour
Department of Civil Engineering, Université des Frères Mentouri
Constantine 1, Constantine, Algeria
e-mail: Zergua.abdesselam@umc.edu.dz

It has been reported that the brittle nature of rc beams causes their shear failure which is the most disastrous failure mode. In general, shear failure should be avoided. The strengthening is achieved by having FRP reinforcement to limit the development of cracks and thus reduces their intensification into the compression zone.

This study focuses on the shear performance and failure mode of rc beams strengthened with different configurations of externally bonded FRP sheets. To fulfill this objective, 20 rc beams specimens were constructed and strengthened with three FRP configurations. The beams were loaded until the failure and the load displacement curves were recorded.

2 Material and Test Procedure

A total of 20 rc beams were grouped into four series called as P0, P1, P2, and P3. The beams consisted of a 1000 mm simply supported span. The cross-section of all tested beams was a rectangular with a total depth of 150 mm and a width of 100 mm. They were reinforced for flexure using four steel bars 8 mm steel strands with high yield strength. They were designed to fail in shear while the flexural reinforcement is within the elastic range to simulate the linear behavior of FRP. The concrete used had average 28-day compression strength of 50 MPa and an average tensile strength of 4 MPa, based on splitting test of concrete cylinders.

In series P0, five rc beams were tested without shear reinforcement. They were used as a control beams. Those of series P1 and P2 were reinforced for shear by FRP sheets oriented at 90°, spaced of 50 mm and 100 mm, respectively. However, the last five beams were reinforced by FRP oriented at 45° spacing 50 mm for series P3.

Details of the tested beams are summarized in Table 1.

The simply supported beams were tested monotonically under four-point bending by means of a universal testing machine. Each beam was loaded continuously to failure with each load increments approximately 5% from its theoretical ultimate load.

3 Results and Discussion

All beams were tested and loaded till failure. Table 2 and Fig. 1 show the experimental results for different beams.

From the experimental data, the control beams (series P0, without FRP sheets) showed that shear cracks (or diagonal cracks) appeared initially at load 20 kN (about 39% of its ultimate load). They appeared at the bottom part near the support point. However, flexural cracks occurred later at load 29 kN (at about 55% of the ultimate load). Further new cracks developed at the tension zone of the mid-span

Table 1 Configuration of reinforcement

Beams series	Configurations
P1	
P2	
P3	

Table 2 Experimental results

Beams series	Load for first crack (kN)	Failure load (kN)	Gain in strength (%)	Max displacement (mm)
P0	20	52	0	5.2
P1	27	55	5.8	9.61
P2	22	53	2.0	10.55
P3	27	56	7.7	10.4

area during the occurrence of the shear crack. Diagonal cracks are located near the supports. They were caused by excess applied shear forces. As load was increased, they propagated to the beam compression zone. However, in cases of wrapped beams P1, P2, and P3 series, flexural cracks appeared initially at load 27, 22, and 27 kN respectively. They started from the bottom of the beam and widened to the top part (the compression zone). This is because the FRP limits and restricts the shear cracks development. That is the effectiveness of the FRP wrapping. As the load continues increasing, new cracks appeared at the tension zone, near the support point. They widened and propagated to the compression zone. At the outer shear span, several diagonal cracks were also observed. As the load increases, new cracks began to appear at the tension zone which widened and propagated to the compression zone of the beam.

Beams P0   Beams P1

Beams P2   Beams P3
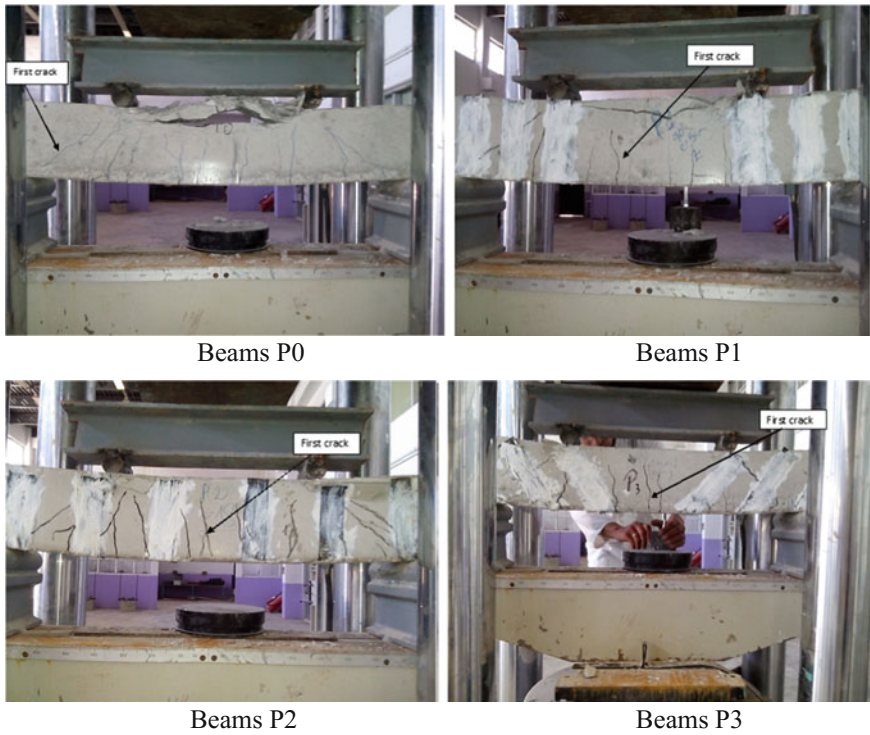
Fig. 1 Cracks and failure modes of beams

For the wrapped specimens, gains in strength of 2–7.7% were achieved. In addition, the FRP reinforcement effectiveness was influenced by the configuration. It increases with decreasing the space between the sheets.

A longitudinal crack formed on the top surface of the specimen before the failure. The crack initiated close to the applied load position. They extended towards the support then the failure occurred on a vertical plane by concrete splitting.

Figure 1 presents the curve load versus vertical displacement for beams series. P0 series shows a linear behavior until the appearance of the first shear crack corresponding to 20 kN load and 0.175 mm displacement. Then the cracks widened and propagated until the failure at 52 kN and displacement of 5.2 mm. However, these curves are highly similar for all the beams. Three steps are then observed. The first one concerns the linear part characterized by the absence of cracks. The stiffness of the reinforced beams is greater than those with no reinforcement. The second part is the beginning of the damage. It is characterized by the appearance of flexural cracks in case of reinforced beams and shear cracks in beams without reinforcement. This part is longer in case of reinforced beams because of the effectiveness of FRP. The third part is also highly similar for all the beams (Fig. 2).
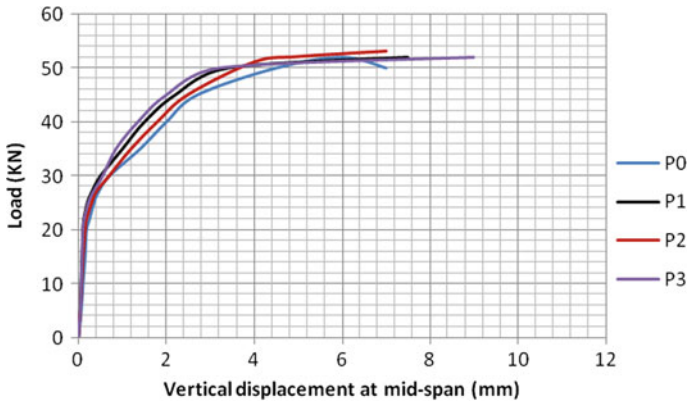
Fig. 2 Load versus displacement for beam series

4 Conclusion

The experimental results allow the following conclusions:

Externally bonded FRP reinforcement can be used to enhance the shear capacity of RC beams. This enhancement depends on the wrapped configuration.

The failure mode of the strengthened specimens was flexural failure, while the failure of the control specimens was shear compression failure mode.

The flexural capacity of the strengthened specimens was less than their shear capacity. The strength gain ranges from 2 to 7.7%. For those specimens, the failure mode was dominant by flexural.

The load versus the mid-span deflection curves of the tested beams are shown in Fig. 2. For all test series, the strengthened specimens showed a higher failure load compared to the control specimens. In Series P1, P2, and P3, the mid-span deflection of the strengthened specimens ultimate load was about 2.5 respectively, which corresponds to three times the deflection of the control specimen.

The control specimen had a more ductile behavior than the strengthened specimens. The specimen P1, completely wrapped FRP sheets showed a large ductility.

Shear reinforcement prevents failure in shear, increases beam ductility, and subsequently the sudden failure will be reduced.

References

1. Khalifa, A., Gold, W.J., Nanni, A., Abdel Aziz, M.I.: Contribution of externally bonded frp to shear capacity of flexural members. ASCE-J. Compos. Constr. **2**, 195–203 (1998)
2. Benmokrane, B., El-Salakawy, E., El-Gamal, S.E., Sylvain, G.: Construction and testing of an innovative concrete bridge deck totally reinforced with glass frp bars: valalain bridge on highway 20 east. ASCE, J. Bridge Eng. **12**, 632–645 (2007)

3. Machial, R.M., Shahria, A.M., Rteil, A.: Shear strength contribution of transverse FRP reinforcement in bridge girders. IABSE-JSCE joint conference on advances in bridge engineering-II, August 8–10, Dhaka, Bangladesh (2010)
4. Mallinson, J.H.: Corrosion resistant plastic composites in chemical plant design, p. 592. CRC Press, USA, (1987)
5. Chajes, M.J., Januska, T.F., Mertz, D.R., Thomson, T.A., Finch, W.W.: Shear strengthening of reinforced concrete beams using externally applied composite fabrics. ACI Struct. J. **92**(3), 295–303 (1995)
6. Taerwe, L., Khalil, H., Matthys, S.: Behavior of RC beams strengthened in shear by external cfrp sheets. In: Non—Metallic (FRP) reinforcement for concrete structures. proceedings of the third symposium, 1, 483–490 (1997)
7. Triantafillou, T.C.: Shear Strengthening of Reinforced Concrete Beams Using Epoxy Bonded FRP Composites. ACI Struct. J. **95**(2), 107–115 (1998)
8. Adhikary, B.B., Mutsuyoshi, H.: Behavior of Concrete Beams Strengthened in Shear with Carbon Fiber Sheets. J. Compos. Constr. ASCE **8**, 258–264 (2004)
9. Teng, J.G., Lam., L., Chen, J.F.: Shear strengthening of RC beams with FRP composites. Struct. Eng. Mater. **6**, 173–184 (2004)
10. Sundarraja, M.C., Rajamohan, S.: Strengthening of RC beams in shear using GFRP inclined strips—an experimental study. Constr. Build. Mater. **23**, 856–864 (2009)

Probabilistic Analysis of Slopes by Finite Element Method

Imene Bougouffa, Mekki Mellas and Mohamed Baheddi

Abstract A 2D deterministic stability analysis of the frictional slope is done in order to estimate the coefficient of security using the finite element limit analysis. The methodology makes use of the Optum G2 software. Hence, a 2D probabilistic study was considered by the finite element analysis with the random field theory according to the Monte Carlo simulation by the Karhunen–Loeve approach, the spatial variability and the local averaging of the soil's random variables were addressed into the analysis to determine the effect of their random log-normal distribution in a parametric study, while considering the rest of the slope's parameters as constants. Hence, the choice of the stochastic parameters of the slope (coefficient of variation COV, correlation lengths θ) is taken into account to evaluate the probability of failure. The analysis was repeated until obtaining stable statistics of the output utilizing 1000 Monte Carlo runs, and then representing the analysis results via the familiar software Microsoft Excel 2013. It is found that the mean value of the coefficient of security decreases with the raise of the spatial variability (COV), thus, it presents a reduction in the standard deviation. However, the probability of slope failure increases with COV for a corresponding high factor of security; and large values of the correlation lengths provide more smoothly varying field.

Keywords Finite element $\cdot$ Monte Carlo simulation $\cdot$ Probability
Slope stability $\cdot$ Spatial variability

I. Bougouffa (✉) · M. Mellas
Faculty of Science and Technology, Department of Civil Engineering
and Hydraulic, Mohamed Khider University, 07000 Biskra, Algeria
e-mail: bougouffa-imene@hotmail.com

M. Mellas
e-mail: m_mellas@yahoo.fr

M. Baheddi
Faculty of Technology, Department of Civil Engineering, Batna University,
05000 Batna, Algeria
e-mail: Baheddi_md@yahoo.fr

1 Introduction

In general, the physical and hydraulic properties of the soil vary spatially in vertical directions, while the horizontal directions are less significant in many of the geotechnical analyses; the inherent variability of the soil's properties depends on the heterogeneity of the soil and the statistical uncertainty of its in situ measurements, the soil's geological formation history and its variation by nature, laboratory equipment and random tests on the soil mass, especially when the results are transformed into a model of soil properties through empirical models or correlation ones.

The deterministic analysis gives only approximate solutions near to the actual ones; for this reason, the probabilistic analysis is carried out recently. It has started spreading in the 1970s, and it has been followed by some studies of the failure of a cohesive slope by finite elements, in which the resulting probability of failure can be unconservative while neglecting the spatial variability which causes a decrease in the factor of safety [1]. Others have referred to the importance of simple circular stability charts in the determination of the probability of failure without running Monte Carlo simulation [2]. A good agreement has been found between the perturbation finite element method and the spectral stochastic finite element method SSFEM, in which they can handle the second-moment analysis of the slope stability [3]. It has been noted via the random finite element method that the spatial correlation length conducts to a minimum reliability of the slope [4]. The use of the modified code mFEM has been studied to prove that reinforcing constructed slopes by geosynthetics can lead to small probabilities of failure and the soil friction angle can affect the outcomes [5]. And others have searched for the spatial variability impact of normally consolidated slopes with linearly increasing strength with depth and inspected their probability of failure [6].

This paper has determined the effect of the randomly log-normally distributed parameters $(C - \varphi)$ on the coefficient of security utilizing Optum G2 software, taking into consideration the same $C - \varphi$ slope in a previous study [7] without the reinforcing system, in which an elastoplastic analysis according to the method of shear strength reduction was utilized to locate the slip surface. In addition, the same slope was calculated [8] with the difference finite analysis according to the method of the shear strength reduction utilizing the Flac3D. Both of these studies showed a critical slip surface according to the maximum shear strength in the pile while neglecting the maximal shear deformation in the soil, which is considered to be unreasonable. The study was carried out in the present paper by the finite element limit analysis with the random field theory according to the Monte Carlo simulation by the Karhunen–Loeve approach. The results were presented statistically.

The parameters that do not represent any significant variation in the analysis are treated as constants and analysed deterministically; while the others are taken into account as random variables and will be analysed stochastically; knowing that, the stochastic parameters are chosen according to the intervals of Phoon [9].

2 Finite Element Limit Analysis

The finite element method principle is to transform a continued problem into a discretized one consisting of many elements of the geometry; thus, transforming the system of partial derivative equations into a system of algebraic equations to make the problem less complicated by solving it in one procedure. Hence, in slopes the finite element method necessitates taking into account the shear strength parameters of the soil under drained and undrained conditions, and the time scope of the analysis (long or short terms) to give pretty accurate results of the factor of safety F_s according to the failing zones where the shear strength is unable to sustain shear stresses [10].

In order to simplify the field generation and to distribute the shear strength parameters (C and φ) the use of one thousand triangle mesh element (3 Gauss points per element) is available; Figs. 1 and 2 show a slope's adaptive mesh with 1000 lower or upper bound triangle elements. Moreover, the mesh adaptivity is chosen in order to avoid the noticeable differences between the outputs obtained from the upper and the lower bounds of the limit analysis and it takes into consideration all of the necessary zones of plasticity in the failing mechanism of the slope to achieve a high level of accuracy; more details about the comparison between a uniform and an adaptive meshing was explained in an earlier study [11]. The principle of the upper and lower bounds is based on the virtual work principle Eq. (1). The upper bound is defined by an admissible kinematic velocity field that refers to the possible failure mechanism (the kinematic discontinuities are presented as the failing surface), taking into account that the admissible word refers to the rate of the resulted deformation that should satisfy the flow rule; the latter is defined as in Eq. (2).

$$\int_v \sigma^T \dot{\varepsilon}^p \, dV - \int_v b^T \dot{U} dV - \alpha \int_{S_r} t^T \dot{U} dS = 0. \tag{1}$$

$$F\dot{\lambda}_b = \dot{\varepsilon}_a^p. \tag{2}$$

where σ^T is the stress field vector, $\dot{\varepsilon}^p$ is the plastic strain rates (time derivative), V is the solid of volume, b^T are the body forces vector, $\dot{U}$ is the exact velocity field, α is

Fig. 1 Linear triangle element
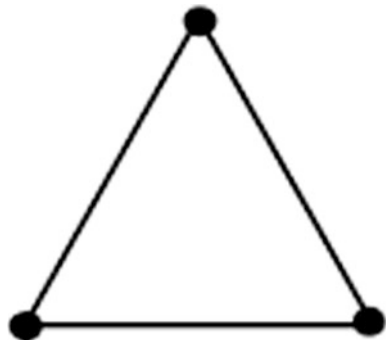
Fig. 2 Adaptive 1000
triangle mesh elements of a
2D slope
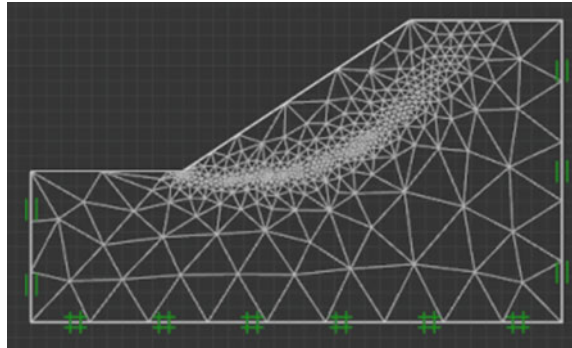
the load multiplier, Sr is the part of the boundary S subjected to tractions, t is the traction vector. However, the velocity field, in general, is expressed as follows:

$$\nabla \dot{U} = F\dot{\lambda} = \dot{\varepsilon}^p. \tag{3}$$

where F is the yield function, $\dot{\lambda}_b$ is the plastic multiplier in a considered stress field of σ_b, and $\dot{\varepsilon}_a^p$ is the plastic strain rates in a considered stress field of σ_a, ∇ is the matrix of the partial derivative. However, in the upper bound theorem, the coefficient of security is found according to the equity between the rate of total work W done by external body forces or volumetric forces, and the rate of dissipated work inside of the failure mechanism D as planes (straight lines) in case of $\varphi \geq 0$, and log spirals (circles) in case of $\varphi = 0$

$$W = \int_s t_i v_i \mathrm{d}S + \int_{S_t} b_i v_i \mathrm{d}S_t. \tag{4}$$

$$D = \int_{S_t} \sigma_{ij} \dot{\varepsilon}_{ij} \mathrm{d}S_t + \int_L t_i [v_i] \mathrm{d}L. \tag{5}$$

where S_t refers to the discontinued velocity surface, and L is the velocity discontinuity line. The associated flow rule provides equity between the rates of strains and stresses according to the yield condition as shows Eq. (6). However, the Mohr–Coulomb criterion and the associated flow rule, take the consideration of all surfaces of a rigid block as an admissible velocity discontinuity line, so the velocity jump vector should be inclined at an angle φ on the velocity discontinuity line in the 2D and the 3D analysis as shows Eq. (7)

$$\dot{\varepsilon}_{ij} = \dot{\lambda} \left(\frac{\partial F(\sigma_{ij})}{\partial \sigma_{ij}} \right). \tag{6}$$

$$[v_n] = [v_t] tg\varphi. \tag{7}$$

where $\dot{\varepsilon}_{ij}$ is the rate of strain, $\dot{\lambda}$ is the plastic multiplier and $\partial\sigma_{ij}$ is the stress according to the yield condition $\partial F(\sigma_{ij})$ with respect to its partial shear strength parameters that might cause the yielding of the soil. Moreover, $[v_n]$ and $[v_t]$ are the normal and tangential velocity jump vector components respectively. Thus, according to the finite element method, the F_s is defined according to the parts resulting from the division of the failing surface

$$F_s = \frac{\sum_{i=1}^{n}(c + \sigma_i tg\varphi)\triangle l_i}{\sum_{i=1}^{n}\tau_i\triangle l_i}. \tag{8}$$

where σ_i and τ_i are the normal stress and the shear stress corresponding to each segment; $\triangle l_i$ is the length of a segment corresponding to the failing surface in the ith element. In the middle of the ith segment, τ_i and σ_i are expressed in terms of $\sigma_x, \sigma_y,$ and σ_{xy}

$$\tau_i = 0.5(\sigma_y - \sigma_x)\sin(2\alpha) + \sigma_{xy}\cos(2\alpha). \tag{9}$$

$$\sigma_i = \sigma_x\sin^2(\alpha) + \sigma_y\cos^2(\alpha) - \sigma_{xy}\sin(2\alpha). \tag{10}$$

where α is the inclination angle of the element to the horizontal. Taking into account that a value of F_s inferior of 1.5 indicates failing of slopes in which is considered risky for people's lives; thus, it is necessary to obtain a value equals or superior of 1.5 to assure high stability and less hazards [12].

3 Random Field and the Inherent Variability

Spatial variability is taken into account in natural soils, in which the parameters in situ are randomly distributed according to the random field of Gauss–Laplace [1]. The soils parameters which influence the coefficient of safety are the cohesion, and the friction angle; whereas the others which influence the calculated stabilization are the Young's modulus E, the Poisson's ratio v, and the unit weight γ. Thus, in the present study, the cohesion and the friction angle are considered as random variables, while the others are maintained as constants.

The spatial variability of the random parameters is distributed log-normally. Thus, the stochastic parameters that define the inherent variability are the mean μ_x, the standard deviation σ_x, the coefficient of variation COV and the horizontal and vertical correlation lengths respectively (scale of fluctuation) $\theta_{(h)}, \theta_{(v)}$, who represents the correlation between a set of measured values of the parameter at a specific spatial point with the adjacent point, however, they are obtained by statistical analysis [9].

Table 1 Values of the coefficient of variation COV% corresponding to the cohesion and the friction angle adopted for this paper

Geotechnical parameter	Type of soil	The mean value KN/m²	COV (%)	Source
φ	Sandy–Clayey soil	$\mu = 20°- 40°$	5–15	Lab measurements
C	Clayey soil	$\mu = 5\text{–}400$	10–40	Field measurements (Vane shear test)

$$\mu_x = e^{\mu_y + \frac{\sigma_y^2}{2}}. \tag{11}$$

where $y = lnx$, x is the random variable.

$$\sigma_x = \mu_x \sqrt{\exp\left(\sigma_y^2\right) - 1} = \mu_x \cdot \frac{COV}{100}\% \tag{12}$$

$$\theta_{(v)} = [2 - 6]\,\text{m}; \quad \theta_{(h)} = [40 - 60]\,\text{m}. \tag{13}$$

And the COV (%) is chosen according to the interval as represented in Table 1 Or it can be obtained from a simplified expression as the following:

$$COV = \frac{\sigma_x}{\mu_x}. \tag{14}$$

4 Monte Carlo Simulation (Karhunen–Loeve Expansion)

The Monte Carlo simulation according to the Karhunen–Loeve expansion is carried out to generate the log-normal random field based on its nodal coordinates by entering the set of statistical parameters (input) of COV and θ corresponding to the probabilistic field which has a specific expansion degree N of the normal standard variables. Moreover, this number of terms was chosen equal to 1000 based on an earlier study [13], and it increases whenever θ decreases. Hence, the output is in the form of statistics of the coefficient of security F_s, the mean, the standard deviation, its probabilistic distribution function PDF and its cumulative distribution function CDF. Hence, the two latter parameters are defined by the following expressions respectively.

$$f(x) = \begin{cases} \frac{1}{x\sigma_y\sqrt{2\pi}}\exp\left[-\frac{1}{2}\left(\frac{lnx - \mu_y}{\sigma_y}\right)^2\right], & x > 0. \\ 0, & \text{if not.} \end{cases} \tag{15}$$

$$F(x, \mu, \sigma) = \frac{1}{2} \text{erfc}\left(-\frac{\ln x - \mu_y}{\sigma_y \sqrt{2}}\right). \tag{16}$$

where erfc is the complementary error function. Thus, the PDF can be defined in terms of the CDF Eq. (17). However, the probability of the slope's failure will be estimated, in which a random variable X is inferior of a particular value of x Eq. (18); in other words, the collapse happens while the algorithm is enabled to converge and remains stable for any given Monte Carlo realization. The Karhunen–Loeve expansion discretizes the random anisotropic field in 2D, taking into account the minimal number of the shear strength random parameters that are distributed log-normally for reasons of accuracy. The process of discretization is based on the spectral decomposition of the autocorrelation function.

$$f_{F_s}(y_i) = \frac{\text{CDF}(y_i) - \text{CDF}(y_{i-1})}{y_i - y_{i-1}}. \tag{17}$$

$$P_f(X < x) = \Phi\left(\frac{\ln X - \mu_{\ln X}}{\sigma_{\ln X}}\right). \tag{18}$$

where Φ is a cumulative standard normal distribution function.

5 Case of Study

The slope considered in this study [7, 14] is frictional, yielding to the Mohr–Coulomb criterion. The parameters of the soil are represented in Table 2, as well as the geometry in Fig. 3 in which, the pile reinforcement was not taken into account in this paper. Moreover, a boundary condition representing full fixity in the base and a tangential one on the side boundaries. The deterministic 2D limit analysis gave a factor of safety F_s equals to 1.18; which is in good agreement with the previous studies since it was considered by the authors in the reasonable interval of the factor of safety $\{1, 18 - 1, 2\}$. Then, the 2D probabilistic analysis was performed for the log-normally distributed cohesion and friction angle, with the following stochastic parameters: Horizontal and vertical correlation lengths,

Parameters	Soil
Unit weight γ (kN/ m³)	20
Cohesion C (kPa)	10
Friction angle φ (°)	20
Elastic modulus E (MPa)	200
Poisson's ratio υ	0.25

Table 2 Parameters of the C – φ slope in two dimensions
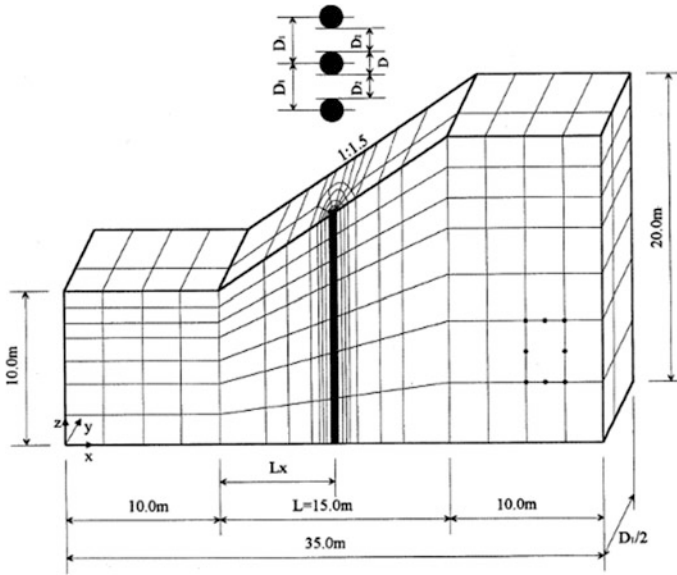
Fig. 3 Slope's geometry with embedded row of piles [7], in which the reinforcement is not taken into account in this paper

respectively, in which they were held constants for the following analysis $\theta_{c(h)} = 50$ m; $\theta_{c(v)} = 2$ m, and $\theta_{\varphi(h)} = 50$ m; $\theta_{\varphi(v)} = 2$ m.

The parametric study was performed for the coefficient of variation, which is varying for the cohesion and the friction angle as represented in Table 3. Thus, the influence of Monte Carlo realizations on the mean and the standard deviation of the security factor for the four sets of input variables are represented in Fig. 4 with respect to the average values of the upper and lower bounds of the limit analysis, these analyses (a, b, c, d) give a decreasing mean value of F_s μ_{F_s}, respectively, equals to 1.176; 1.141; 1.106; 1.072 corresponding to the following decreasing standard deviation of F_s σ_{F_s}, respectively, 0.154; 0.342; 0.465; 0.517 and a probability of failure equals to $P_f(Fs < 1.5) = 97, 87, 86, 85\%$. From Fig. 5, as expected the probability of failure decreases as F_s increases and decreases with the increase of COV for ($F_s < 1.5$). The opposite of this trend happens for ($F_s > 1.5$) and it results of high probability of failure for an opposite influence of spatial

Table 3 Values of the coefficient of variation corresponding to the cohesion and the friction angle, respectively, of the C – φ slope for the parametric study

Coefficient of variation	Analysis 1 (%)	Analysis 2 (%)	Analysis 3 (%)	Analysis 4 (%)
COV_c	10	25	30	40
COV_φ	5	10	15	15
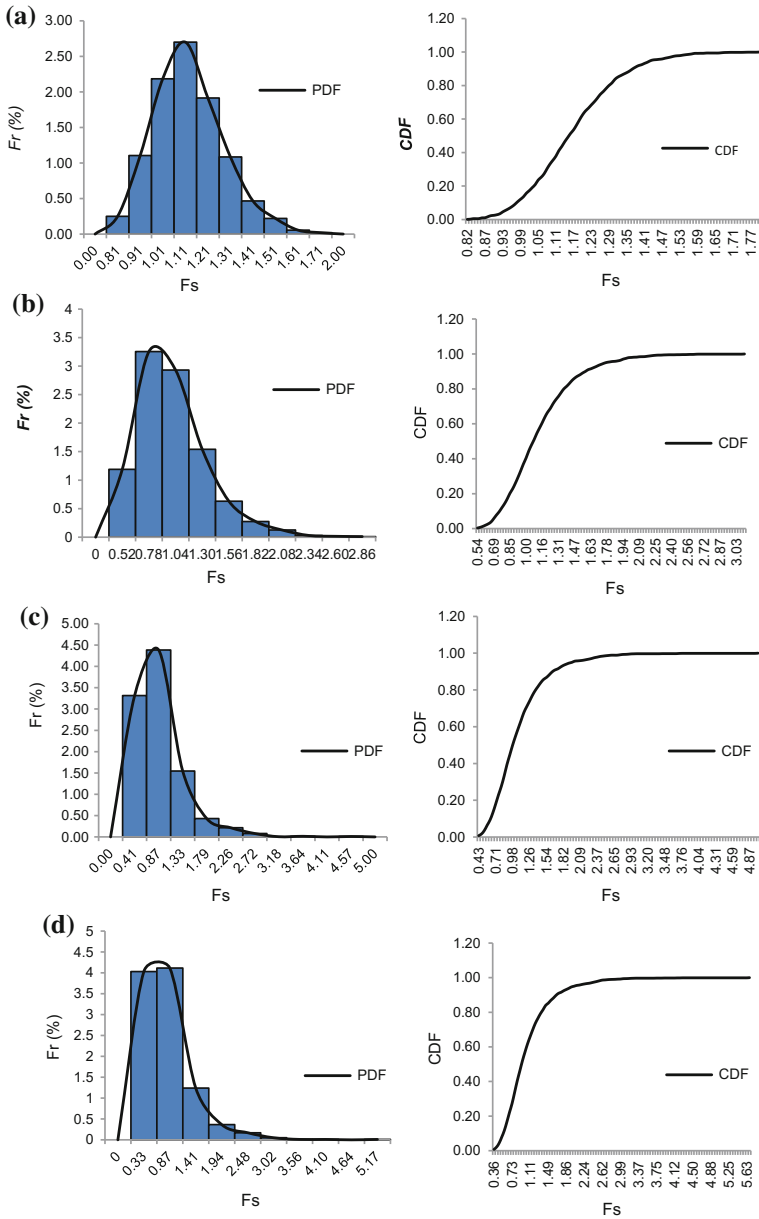
Fig. 4 Resulting parametric PDF and CDF of the factor of safety obtained by Optum G2 for the 4 analyses respectively
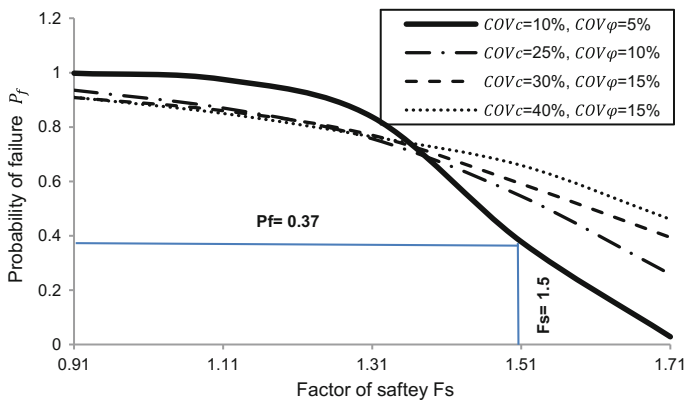
Fig. 5 Probability of failure versus factor of safety based on the variation of COV
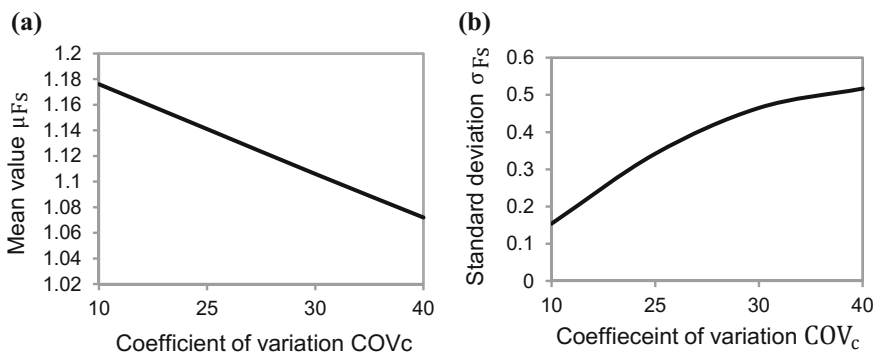
Fig. 6 Mean value μ_{F_s} and standard deviation σ_{F_s} of the factor of safety versus the COV of C in (**a**) and (**b**) respectively

variability and decreasing values of COV. Moreover, for a mean value of F_s as high as $\mu_{F_s} = 1.5$ (corresponding to $COV_c = 10\%$, and $COV_\varphi = 5\%$), the soil leads to a probability of failure of $P_f = 0.37$, which indicates a rarely failing system.
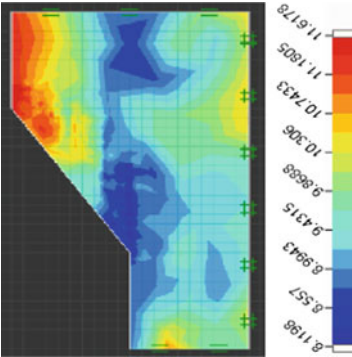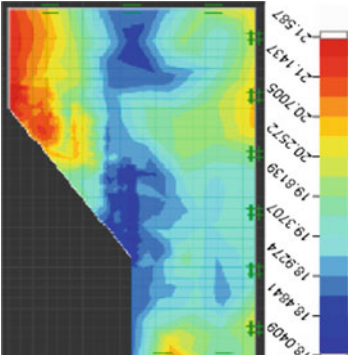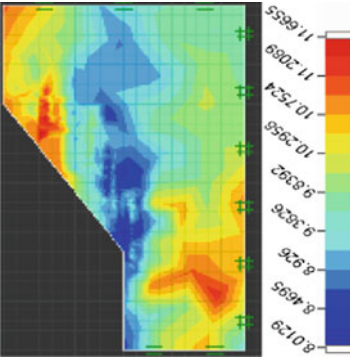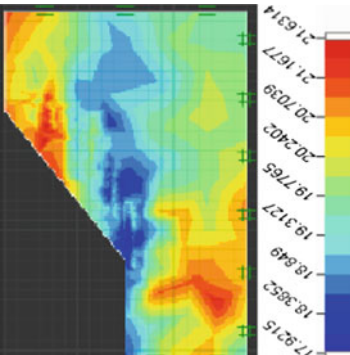
Figures 6 and 7, deduce the effect of different spatial variabilities on the standard deviation and the mean value of the factor of security, the latter increases as the corresponding spatial variability COV of the soil strength parameters decreases. Thus, it presents an increase in the standard deviation, in which it tends to a constant value for $COV_c > 40\%$, and $COV_\varphi > 15\%$.
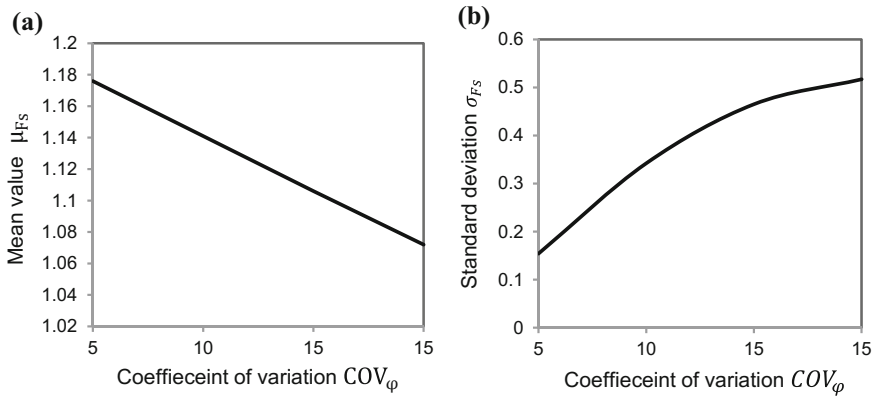
Fig. 7 Mean value μ_{F_s} and standard deviation σ_{F_s} of the factor of safety versus the COV of φ in (a) and (b) respectively

The second part of the parametric study, is to maintain the coefficient of variation values constants $COV_c = 10\%$; $COV_\varphi = 5\%$, and varying the correlation lengths of the cohesion in an anisotropic way in order to estimate whether the random field is ragged or smoothly varying. From Table 4; we can conclude that large values of correlation lengths provide more smoothly varying fields which lead to larger values of the coefficient of security, thus the probability of failure decreases; and the vice versa, whereas it compares well with the frictional field, in which the correlation lengths are varying in the same way. Moreover, Fig. 8 shows that the probability of failure is sensitive to spatial correlation lengths, thus, it decreases with the increase of F_s and with the increase of θ for ($F_s < 1.5$). The opposite of this trend happens for ($F_s > 1.5$) and it results in high probability of failure for an opposite influence of spatial variability and decreasing values of θ. Hence, the crossover refers to the feeblest path through the soil, and it happens for $F_s = 1.37$ with a $P_f = 0.61$.

Table 4 Random fields of the cohesion and the friction angle, respectively, corresponding to the upper bound of the finite element limit analysis

Figure of random C field corresponding to the upper bound	Figure of random φ field corresponding to the upper bound
$\theta_{c(h)} = 60$ m $\theta_{c(v)} = 6$ m we have: $\mu_{F_s} = 1.19$ P_f (Fs ; 1.5) = 91.9%	
$\theta_{c(h)} = 40$ m $\theta_{c(v)} = 2m$ we have: $\mu_{F_s} = 1,179$ P_f (Fs < 1.5) == 97%	
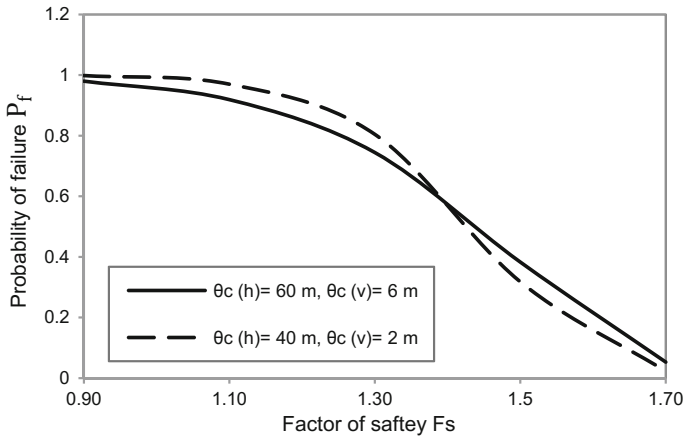
Fig. 8 Probability of failure versus factor of safety based on the variation of θ

6 Conclusion

This paper introduces a deterministic analysis of a frictional slope to investigate its factor of safety; in which it is in good agreement with the previous studies. The analysis was carried out using the finite element limit analysis in two dimensions via the Optum G2 program. Hence, the probabilistic analysis was performed considering the slope as a random field with log-normally distributed random variable (cohesion and friction angle). The study showed the influence of the coefficient of variation and the correlation lengths on the resulting mean and standard deviation of the factors of safety, and the probability of failure in a parametric study. However, the probability of failure was estimated as the probability that the factor of safety be inferior of 1.5. Moreover, the parametric analysis showed that low values of the coefficient of variation COV for both of the slope's random variables, give a mean value of the factor of safety tends to the deterministic one. In other words, as lower as the factor of safety can get, the slip surface becomes deeper and the probability of the slope's failure becomes higher. Thus, the sensitivity of the probability of failure to the spatial correlation was investigated, in which it decreases with the increase of the correlation lengths θ.

References

1. Griffiths, D., Fenton, G.: Probabilistic Slope Stability Analysis by Finite Elements. J. Geotech. Geoenviron. Eng. **130**, 507–518 (2004). https://doi.org/10.1061/(asce)1090-0241(2004)130:5 (507)
2. Javankhoshdel, S., Bathurst, R.: Simplified probabilistic slope stability design charts for cohesive and cohesive-frictional (c – φ) soils. Canadian Geotech. J. **51**:1033–1045 (2014). https://doi.org/10.1139/cgj-2013-0385

3. Farah, K., ltifi, M., Hassis, H.: A study of probabilistic FEMs for a slope reliability analysis using the stress fields. Open Civ. Eng. **9**, 196–206 (2015)

4. Allahverdizadeh, P., Griffiths, D., Fenton, G.: The Random Finite Element Method (RFEM) in probabilistic slope stability analysis with consideration of spatial variability of soil properties. IFCEE (2015). https://doi.org/10.1061/9780784479087.178

5. Luo, N., Bathurst, R., Javankhoshdel, S.: Probabilistic stability analysis of simple reinforced slopes by finite element method. Comput. Geotech. **77**, 45–55 (2016). https://doi.org/10.1016/j.compgeo.2016.04.001

6. Zhu, D., Griffiths, D., Huang, J., Fenton, G.: Probabilistic stability analyses of undrained slopes with linearly increasing mean strength. Géotech. **67**, 733–746 (2017). https://doi.org/10.1680/jgeot.16.p.223

7. Cai, F., Ugai, K.: Numerical analysis of the stability of a slope reinforced with piles. Soils Found. **40**, 73–84 (2000). https://doi.org/10.3208/sandf.40.73

8. Won, J., You, K., Jeong, S., Kim, S.: Coupled effects in stability analysis of pile–slope systems. Comput. Geotech. **32**, 304–315 (2005). https://doi.org/10.1016/j.compgeo.2005.02.006

9. Phoon, K., Kulhawy, F.: Evaluation of geotechnical property variability. Can. Geotech. J. **36**, 625–639 (1999). https://doi.org/10.1139/t99-039

10. Duncan, J.: State of the art: limit equilibrium and finite-element analysis of slopes. J. Geotech. Eng. **122**, 577–596 (1996). https://doi.org/10.1061/(asce)0733-9410(1996)122:7(577)

11. Ali, A., Lyamin, A., Huang, J., et al.: Probabilistic stability assessment using adaptive limit analysis and random fields. Acta Geotech. **12**, 937–948 (2016). https://doi.org/10.1007/s11440-016-0505-1

12. Bishop, A., Morgenstern, N.: Stability Coefficients for Earth Slopes. Géotech. **10**, 129–153 (1960). https://doi.org/10.1680/geot.1960.10.4.129

13. Huang, J., Lyamin, A., Griffiths, D., et al.: Quantitative risk assessment of landslide by limit analysis and random fields. Comput. Geotech. **53**, 60–67 (2013). https://doi.org/10.1016/j.compgeo.2013.04.009

14. Wei, W., Cheng, Y.: Strength reduction analysis for slope reinforced with one row of piles. Comput. Geotech. **36**, 1176–1185 (2009). https://doi.org/10.1016/j.compgeo.2009.05.004

15. Shen, J., Priest, S., Karakus, M.: Determination of Mohr-Coulomb Shear Strength Parameters from Generalized Hoek-Brown Criterion for Slope Stability Analysis. Rock Mech. Rock Eng. **45**, 123–129 (2011). https://doi.org/10.1007/s00603-011-0184-z

Building Information Modelling—Development and Validation of Implementation Framework for Improving Performance of Subcontractors

M. Sodangi

Abstract Recent problems related to design and poor performance of many indigenous subcontractors in Saudi Arabia are clear calls for action to improve the overall performance of the subcontractors to be highly competitive; deliver high quality service to clients and wider society, minimize the rate of disputes and push the local industry forward. With the exclusive ability of Building Information Modelling (BIM) to enhance organization amongst operators, contractors and design teams; its implementation reduces project time, cost, material consumption and carbon emissions while improving contractors and subcontractors' productivity and quality performance. The technology to implement BIM is readily obtainable and quickly evolving. However, many subcontractors in the Kingdom are perceived to be slow in embracing the BIM revolution due to widespread lack of BIM knowledge, lack of will amongst the subcontractors to implement BIM. There is also apparent confusion due to lack of clear methodologies for BIM processes in the Kingdom. Thus, this paper made attempt to develop and validate a framework that could assist the relevant authorities to prepare regulatory guidelines that could encourage subcontractors' full utilization of building information modelling in their construction projects and seek to raise their general capabilities. Expert validation was used to authenticate the framework. The high relative importance indices rated by the participants for most of the functions in the framework strongly indicate that the various functions (activities) are significant in influencing the adoption of BIM in projects and improving subcontractors' performance. This paper provides original contribution to knowledge through a methodical investigation of the awareness and readiness levels of the subcontracting sector of the Saudi Arabian construction industry in applying the functions of BIM technology for construction projects. The paper also determined the critical success factors that are critical in the decision of adopting BIM. Above all, the paper presented a concise methodology for the development and validation of the BIM implementation framework for improving

M. Sodangi (✉)
Department of Civil & Construction Engineering, Imam Abdulrahman Bin Faisal University
(Formerly University of Dammam), Dammam, Saudi Arabia
e-mail: misodangi@iau.edu.sa; sodangimahmoud@gmail.com

subcontractors' performance. The outcomes of this study could be useful to regulators of the Saudi Arabian construction industry for preparing guidelines to improve the general level of BIM adoption and expertise within the industry.

Keywords Building information modelling · Framework · Subcontractors Saudi Arabia

1 Introduction

The BIM is an automated illustration of the physical and functional features of a facility. Thus, BIM functions collaborative knowledge source for information about a facility, establishing a consistent platform for decision making during the service life of a facility from initial inception to demolition [16]. Recent problems with design and poor performance of subcontractors in Saudi Arabia necessitate for urgent action to reposition and enhance the local construction industry to be highly competitive; deliver high quality service to clients and society as a whole, minimize the frequency of disputes as well as move the industry forward. The BIM technology is a relatively evolving approach to project design, construction as well as operations and facilities management. It facilitates the building development, construction and building operation [6]. It is gradually changing how construction projects are being executed worldwide. This new technology has unique capacity to improve coordination between design teams, construction contractors and operators. Thus, BIM implementation reduces project time, cost, material consumption and carbon emissions while improving contractors' productivity and quality performance, Mom and Hsieh [15]. The BIM's cost-effectiveness and its apparent efficiency are generally recognized worldwide. Developed nations in Asia, Europe and North America are at present enjoying the numerous benefits of BIM implementation in construction project delivery, operations and facilities management. Conversely, the GCC region in particular is perceived to be slow in embracing the BIM revolution. The region may as well fall further behind in the global construction industry.

Despite the obvious benefits and readiness of BIM software, Issa [13] pointed out that BIM adoption has been slower than anticipated in the GCC region. The author further highlighted that the few 'big' construction companies that use BIM in their major projects generally apply it to some basic functionalities. This indicates that the industry is to a large extent lacking the requisite proficiency in BIM application. Not that alone, considerable number of the region's construction subcontracting organizations hardly use BIM in their projects, which is attributed to lack of clear implantation guidance. Similarly, Baldwin [7] acknowledged shortfall in local BIM knowledge. Besides, there is apparent confusion due to lack of clear methodologies for BIM processes in the region. He further emphasized on the need for the region's regulatory authorities to advocate for industry-wide BIM adoption and the industry must seek to improve its proficiency level.

2 Related Study

A construction industry-based BIM framework that focuses on the areas of technology, process, as well as policy, was introduced by Succar [21]. However, the framework lacks any measure for evaluating and enhancing performance. Few years after, a much improved framework was developed by Jung and Joo [14] that identified promising areas and driving factors for BIM in practice. Still, the framework lacked the clear guidance on how construction subcontracting companies should implement BIM and falls short in providing strategies for improving performance and productivity. In an attempt to position BIM adoption in the industry, a collective BIM decision framework was developed by Gu and London [10]. The authors focused on analyzing the preparedness of the construction industry with respect to the people, process and products. Yet, the analysis presented mainly highlighted the mapping process and not the much desired performance appraisal as well as enhancement. Remarkably, BIM strategies, protocols, and integrated project delivery methods were introduced by prominent bodies [1, 3, 4, 17] to define the needs, requirements, and obstacles for BIM implementation. Nonetheless, a Multi-Criteria Decision Making Model for selecting of BIM tools was not provided. A more improved attempt was made by Succar [22] when he developed a maturity matrix for BIM performance appraisal and enhancement. Yet, the study was limited to the conceptual phase; more work was required to authenticate the findings through a construction industry-wide survey.

Recently, Gerges et al. [9] determined the present position of BIM adoption in the Middle East by analyzing the level of BIM implementation among relevant stakeholders in the construction industry. Findings of the survey reveal that the extent of BIM adoption in the region is not satisfactory. They further affirmed that nearly 20% of construction organizations apply BIM in any capacity whereas the remaining 80% are neither applying the technology nor involved in its implementation process in whatever way. Similarly, Hassan [11] conducted a study on BIM implementation, practices and barriers in the GCC construction industry. The author acknowledged the application of the technology in selected construction projects in UAE and Kuwait though there are no published sources to ascertain the real status of BIM implementation in the entire GCC. Key among the findings of his study was the evidence of low implementation rate for BIM in construction projects in the GCC construction market and the lack of BIM awareness, and unwillingness of the stakeholders in accepting to change the existing work practices. In a related attempt by [2], their study was aimed at evaluating the awareness and experience levels of 4D planning and BIM technology in the industry in Qatar as well as identifying the likely challenges to the general implementation of BIM. The evaluation was undertaken through an industry wide survey administered to related experts in Qatar.

The research findings reported by Issa [13] and Baldwin [7] on the use of BIM in the Middle East region have plainly emphasized a lack of guidance on how construction subcontracting companies in the GCC region and Jordan should

implement BIM. This lack of guidance is one of the reasons why the construction subcontracting companies are disinclined to adopt BIM. Therefore, this research is aimed at developing a framework to support the implementation of Building Information Modeling (BIM) for improving subcontractors' project-level performance.

2.1 Study Objectives

The central goal of the study is to propose a framework for implementing BIM that would support the enhancement subcontractors' project-level performance in Saudi Arabia.

The goal will be achieved through the following objectives:

- To determine the subcontractors' awareness and preparedness for implementing Building Information Modeling in their construction projects.
- To prioritize the critical success factors for practical use of BIM for construction projects.
- To develop and validate the framework for implementing BIM.

3 Methodology

3.1 Objective 1—Determining the Subcontractors' Awareness and Preparedness for Implementing Building Information Modeling in Their Construction Projects

A Saudi Arabian construction industry wide survey was conducted to examine subcontractors' awareness and preparedness for implementing BIM in their construction projects. Judgmental sampling was adopted in carefully selecting the subcontracting companies for the survey. The sampling frame for the targeted subcontracting companies predominantly have their core business operations in the areas of architectural engineering, structural engineering, geotechnical engineering, and building services (mechanical and electrical works). The sample was generated from a recent list made available to the researchers by the Saudi Arabian Ministry of Housing & Public Works. Initial information on the subcontractors was obtained from the Ministry. A total of one hundred and twenty six questionnaires were distributed to the subcontracting construction companies. Electronic mail based questionnaire was used for the survey considering its considerable short response time, better response quality, low costs and internet access to the participants.

Severity index analysis was used to rank the subcontractors' levels of awareness and preparedness, while reliability test was run to ascertain how reliable the questionnaire method was.

3.2 Objective 2—Prioritizing the Critical Success Factors for Practical Use of BIM for Construction Projects

A GCC regional construction industry wide questionnaire survey was undertaken to identify and rank the critical success factors that are critical in the decision of adopting BIM. Also, the factors' level of contribution in the decision to adopt BIM was identified and ranked. In this survey, Judgmental sampling was also be adopted to carefully select the Architectural, Engineering and Construction companies that have set the pace in the use of BIM in their design and construction projects. The selection was based on information obtained from Building SMART ME.

3.3 Objective 3—Developing and Validating the Framework for Implementing BIM

The proposed framework was developed according to the empirical results and discussions. Key among the building blocks for developing the framework are the factors for practical adoption of BIM in the construction industry. Interview was used during the expert validation process to authenticate and validate the framework.

4 Results and Discussion

4.1 Determining Subcontractors' Awareness and Preparedness for Implementing BIM in Construction Projects

Respondents for this survey have their core business operations in the areas of architectural engineering, structural engineering, geotechnical engineering, and building services (mechanical and electrical works). This implies that the survey participants have the proficiencies to give dependable and consistent response to the survey questions. Since BIM serves an information center to provide better communication among construction team members, the responses from these professionals in their respective positions would be valuable for the outcomes of this paper. The essential information given by the competent participants is considered

reasonably consistent and vital for this survey. In order to prioritize the factors for evaluating the levels of awareness and preparedness, frequency and the below severity index formula were used:

$$\text{S.I} = \sum_{i=1}^{5} w_i * \frac{f_i}{n} * \left. 100 \right/ (a * 100) \tag{1}$$

The index of severity varies from zero to one. The five levels indicating the awareness and readiness extent of the respondents are transformed to severity index values: very high awareness/readiness (0.80–1.00); high awareness/readiness (0.70–0.79); moderate awareness/readiness (0.50–0.69); Low awareness/readiness (0.20–0.49) and very low awareness/readiness (0.0–0.19). From the transformed severity indices mentioned above, it could be inferred that a factor's higher value of severity index suggest higher level of awareness/readiness for that particular factor. Conversely, the lower the severity index value for any factor the lower level of awareness/readiness for that particular factor [12, 20].

Figure 1 shows the severity level of BIM Awareness among subcontractors in all the Project Stages. It could be seen that all the four respective Construction Project Stages have low severity indices values (0.20–0.49), which indicates low BIM awareness among the respondents in the entire project stages presented for the survey.

The implication of the low BIM awareness in the 'in-use and maintenance stage' is that most of these subcontractors do not know the BIM's ability to minimize energy waste, obtain maintenance and repair cost pre-estimation, carry out maintenance and repair at the appropriate time and to recover building data for planned intervention works.

As for the low BIM awareness in the 'Construction stage', it can be affirmed that the subcontractors are not quite aware of the capabilities of the BIM to simplify and improve project-level construction processes and only a small group of the respondents are conversant with the powers of BIM application in construction
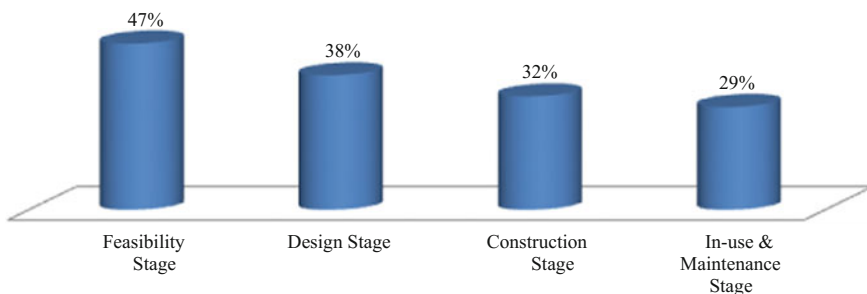
Fig. 1 Severity level of BIM awareness among subcontractors in project stages

industry. The low BIM awareness in the 'feasibility stage' seems to suggest that only a small number of these subcontractors know the BIM's ability to showcase a model for the project during the feasibility stage in order to produce enhanced visualisation to all concerned parties to the project. This great ability of BIM, which allows project owners and designers to easily make modifications to the project model and analyse the subsequent cost implications accordingly is to a high extent not well known among the subcontractors. As for the implication of the low BIM awareness in the 'design stage', it goes to show that the subcontractors have poor knowledge of the BIM's ability to provide better communication among construction team members, reduce discrepancies between architect & engineer drawings, reduce discrepancies between drawings and bill of quantities and to decrease tendering duration by eliminating the taking off process. This finding obviously points to the fact that other important BIM's functions in the design stage are not well known among the subcontractors.

Figure 2 presents summary of the severity indices of factors used in assessing the respondents' level of preparedness in implementing BIM in construction project. A closer observation in Fig. 3 would reveal that all the four respective readiness aspects have low severity indices values (0.20–0.49), which indicates low level of readiness for BIM implementation in construction among the respondents. This seeks to emphasize clear lack of will and motivation amongst the subcontracting companies towards using BIM for construction works. This may be linked to the fact that there are some drawbacks to BIM implementation across subcontracting sector of Saudi Arabian construction industry. These drawbacks or difficulties could be related to poor knowledge of the BIM technology amongst the subcontracting companies; lack of obvious proof of financial benefits, high cost of training, shortfall on government guidelines and strategies, social and typical refusal to accept change and most importantly, construction clients are not demanding the usage of BIM on construction projects.
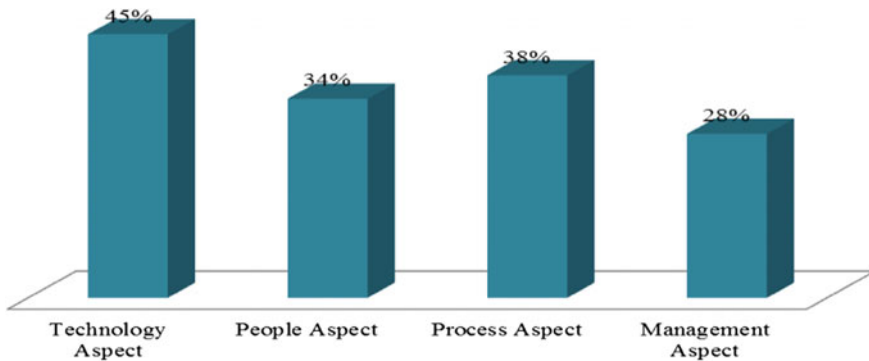
Fig. 2 Severity level of subcontractors' readiness to implement BIM in construction
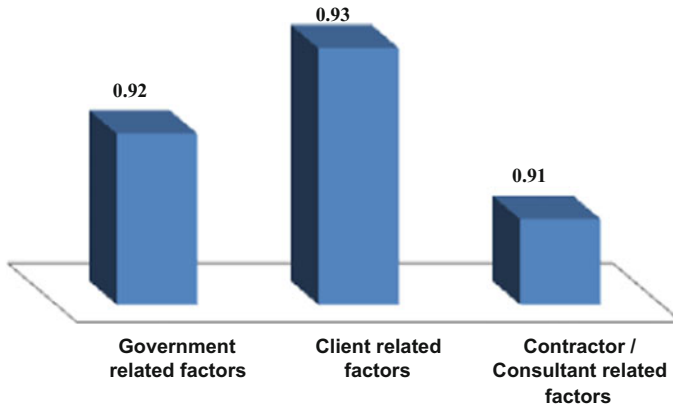
Fig. 3 Relative importance index and ranks of critical success factors for BIM adoption

4.2 Prioritizing the Critical Success Factors for Practical Adoption of Building Information Modeling in the Construction Industry

In total, seventy five questionnaires were distributed to selected companies and sixty (80%) were returned and analysed. The response rate is regarded satisfactory and acceptable for questionnaire survey. In relation to similar surveys in this field of study, twenty one percent is considered satisfactory and acceptable by Proverbs et al. [18]. Thus, 80% response rate is considered to be very good. The participants were required to rate the significance level of the factors for practical adoption of BIM in the construction industry based on a five-point Likert scale. The scale was pre-defined to them as; 1 = not at all important; 2 = slightly important; 3 = important; 4 = very important and 5 = extremely important. The explanation of rating scale was done in such a way that if a participant rated a factor extremely important; the equivalent score for that factor will be five. Therefore, the 5-point Likert-scale was then converted to Relative Importance Indices (RII) for each factor. The index varies from zero to one. Enshassi et al. [8], Sodangi et al. [19], Tam et al. [23], Zeng et al. [24] pointed out that an RII value of 0.80 is rated high. Therefore, any factor that scores an RII value of 0.80 (80%) is regarded as highly important factor.

Figure 3 shows the RII values and ranks of critical success factors for adoption of BIM in construction industry. Most of the respondents considered the three categories of the Critical success Factors as being very significant in influencing the adoption of BIM in construction industry. This is indicated by the aggregated relative importance indices for the three categories, (0.91, 0.93 and 0.92) which are excellent scores since 1.0 is the maximum value on the scale. The prioritization of these factors influenced the development of the framework for BIM implementation.

4.3 Develop Framework for Using BIM in Construction Projects

The BIM implementation framework for improving subcontractors' performance evolved based on earlier obtained empirical results, findings and discussions. Prominent among the building blocks for developing the proposed conceptual framework (Fig. 4) are the critical success factors for practical adoption of BIM in the construction industry.

From Fig. 4, it could be seen that the BIM Implementation Framework consists of three major components (critical success factors) namely; the expected roles of the Client, Government (regulatory authorities) and Contractor/Consultant's companies. These components form parts of the philosophy and criteria for practical use of BIM for construction projects.

The meticulous arrangement of the critical success factors i.e. the expected roles of the Client, Government (regulatory authorities) and Contractor/Consultant's
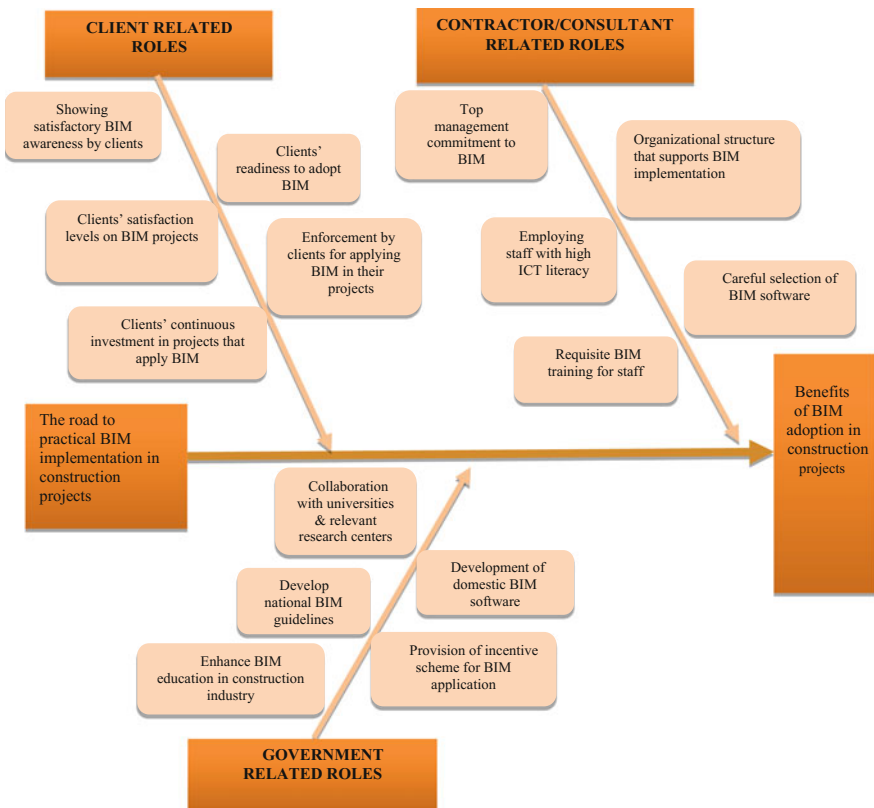
Fig. 4 BIM implementation framework for improving subcontractors' performance

companies in the framework provides a gradual procedure for preparing the implementation framework. This indicates that the BIM implementation framework for improving subcontractors' performance was tactically and consistently envisaged and initiated. The framework is shown in Fig. 4. The authors are hopeful that it could function as a tool for preparing national BIM guidelines for construction companies to implement BIM in construction projects. Expert validation was used to authenticate and approve the framework. The validation statistics is presented in Table 1.

The displayed results in Table 1 reveal that not a single participant assessed any of the factors slightly or not at all important. Nearly all the entire participants rated the BIM implementation framework as being very important in influencing the adoption of BIM in construction projects and improving subcontractors' performance. This is supported by the mean RII of 0.95(95%). Going by results of the validation, an RII value of 0.87 is the least value among all the factors in Table 1.

Table 1 Distribution of validation statistics

Stakeholders for BIM adoption	Functions/roles	Importance scores					RII	Mean RII
		1	2	3	4	5		
Contractor/ consultant	Top management commitment to BIM implementation	0	0	0	4	8	0.93	0.95
	Organizational structure that supports BIM implementation	0	0	0	1	11	0.98	
	Employing staff with high ICT literacy	0	0	0	3	9	0.95	
	Requisite BIM training for staff	0	0	0	0	12	1.00	
	Careful selection of BIM software	0	0	0	2	10	0.97	
Clients	Showing satisfactory BIM awareness by clients	0	0	0	4	8	0.93	
	Enforcement by clients for applying BIM in their projects	0	0	0	1	11	0.98	
	Clients' readiness to adopt BIM	0	0	0	5	7	0.92	
	Clients' satisfaction levels on BIM projects	0	0	0	3	9	0.95	
	Clients' continuous investment in projects that apply BIM	0	0	1	6	5	0.87	
Government	Enhance BIM education in construction industry	0	0	1	1	10	0.95	
	Develop national BIM guidelines	0	0	0	0	12	1.00	
	Provision of incentive scheme for BIM application	0	0	0	0	12	1.00	
	Collaboration with universities & relevant research centers	0	0	0	2	10	0.97	
	Development of domestic BIM software	0	0	0	6	6	0.90	

For that reason, the high RII values obtained by all the factors strong indicate that the various factors significant in influencing the adoption of BIM in projects and improving subcontractors' performance.

5 Conclusion

This section draws together the major themes of the paper. Survey findings on the assessment of subcontractors' awareness and preparedness level for implementing BIM in construction projects in Saudi Arabia reveal a widespread lack of BIM knowledge across subcontracting sector and emphasize clear lack of will and motivation amongst the subcontracting companies towards implementing BIM in construction projects. On the other hand, findings of the GCC regional construction industry wide survey identified and ranked the critical success factors that are critical in the decision of adopting BIM i.e. Government-related, Client-related and Contractor/Consultant-related factors. Also, the factors' level of contribution in the decision to adopt BIM was found to be very high (over 90%). Thus, the main critical success factors and their sub-factors are considered as being very significant in influencing the adoption of BIM in construction industry. The BIM implementation framework for improving subcontractors' performance was developed based on the empirical findings and discussions. The framework consists of three major components (critical success factors) namely; the expected roles of the Client, Government (regulatory authorities) and Contractor/Consultant's companies. These components form parts of the philosophy and criteria for practical use of BIM for construction works. The arrangement of the expected roles of the Client, Government (regulatory authorities) and Contractor/Consultant's companies in the framework suggests that the BIM implementation framework for improving subcontractors' performance was tactically and consistently envisaged and initiated. The framework could serve as a tool for preparing national BIM guidelines for construction companies to implement BIM in construction projects. The framework was validated by panel of specialists. The specialists rated the framework as being significant in influencing the adoption of BIM in construction projects and improving subcontractors' performance.

This paper provides original contribution to knowledge through a methodical investigation of the awareness and readiness levels of the subcontracting sector of the Saudi Arabian construction industry in applying the functions of BIM technology in construction related works. Also, the paper determined the critical success factors that are critical in the decision of adopting BIM. Above all, the paper presented a concise methodology for the development and validation of the BIM implementation framework for improving subcontractors' performance. The outcomes of this study could be useful to regulators of the Saudi Arabian construction industry for preparing guidelines to improve the general level of BIM adoption and expertise within the industry.

References

1. AGC.: The AGC contractors' guide to BIM, 1st edn. Available online: http://www.agcnebuilders.com/documents/BIMGuide.pdf(2006). Accessed: Nov 2013
2. Ahmed, S.M., Emam, H.H., Farrell, P.: Barriers to BIM/4D Implementation in Qatar. The 1st international conference of cib middle east & north africa conference, pp. 533–547, Abu Dhabi, UAE, Dec 2014
3. AIA.: AIA Document E202–2008: Building information modelling protocol exhibit, 2008. Available online: http://www.revit3d.com/files/ipd/Revit3D%20E202-2008_eSample_Blank%20Property%20of%20AIA.pdf. Accessed: Oct 2013
4. AIACC.: AIA California council, integrated project delivery: a guide, version 1, 2007. Available online: http://www.aia.org/aiaucmp/groups/aia/documents/document/aiab085539.pdf. Accessed Oct 2013
5. Aibinu, A.A., Jagboro, G.O.: The effects of construction delays on project delivery in Nigerian construction industry. Int. J. Project Manage. **20**, 593–599 (2002)
6. Aranda-Mena, G.; Crawford, J.; Chevez, A.; Froese, T.: Building information modeling demystified: does it make business sense to adopt BIM? In: Paper presented at W078—Information technology for construction: 25th international conference on information technology in construction, Santiago, Chile, July 15–17, (2008)
7. Baldwin, M.: BIM in the Middle East—a need for open BIM Guides, Standards and Manuals. Internet: http://iug.buildingsmart.org/resources/. Mar 21–Dec 21, 2013
8. Enshassi, A., Mohamed, S., El Karriri, A.: Factors affecting the bid/no bid decision in the palestinian construction industry. J. Financ. Manage. Property Constr. **15**(2), 118–142 (2010)
9. Gerges, M., Austin, S., Mayouf, M., Ahiakwo, O., Jaeger, M., Saad, A., Gohary, T.E.: An investigation into the implementation of Building Information Modeling in the Middle East, ITcon. **22**, 1–15 http://www.itcon.org/2017/1 (2017). Accessed 20 Apr 2017
10. Gu, N., London, K.: Understanding and facilitating BIM adoption in the AEC industry. Autom. Constr. **19**, 988–999 (2010)
11. Hassan, M. A.: Implementation of building information modeling (BIM): practices and barriers in construction industry in gcc. Master of Science Dissertation, http://www.academia.edu/14046998/module_code_d31zz_implementation_of_building_information_modelling_bim_practices_and_barriers_in_construction_industry_in_gcc (2012). Accessed 20 Apr 2017
12. Idrus, A.B., Newman, J.B.: Construction related factors influencing the choice of concrete floor systems. J. Constr. Manage. Econo. **20**, 13–19 (2002)
13. Issa, R.: Survey findings, BIM in the Middle East—The Reality and the Way Forward. http://www.bimjournal.com/wp-content/ (2013). Accessed 20 Apr 2014
14. Jung, Y., Joo, M.: Building information modelling framework for practical implementation. Auto. Constr. **20**(2), 126–133 (2011)
15. Mom, M.; Hsieh, S.: Toward performance assessment of BIM technology implementation, 14th *International Conference on Computing in Civil and Building Engineering*. Moscow, Russia, June, 2012
16. National Institute of BUILDING SCIENCES.: National BIM Standard-United States. https://www.nationalbimstandard.org/files/NBIMS-US_FactSheet_2015.pdf (2015). Accessed 20 Apr 2017
17. Ohio DAS.: State of Ohio Building Information Modelling (BIM) protocol. Available online: http://das.ohio.gov/LinkClick.aspx?fileticket=VD8N3VDCjno%3D&tabid=305. (2010). Last accessed Nov 2013

18. Proverbs, D.G., Holt, G.D., Olomolaiye, P.O.: Factors influencing the choice of concrete supply methods. Build. Res. Inf. **25**(3), 116–126 (1999)
19. Sodangi, M., Khamidi, M.F., Idrus, A., Hammad, D.B., Umar, A.A.: Best practice criteria for sustainable maintenance management of heritage buildings in Malaysia. Procedia Eng. **77**, 11–19 (2014)
20. Sodangi, M., Salman, A.F., Shaawat, M.E.: Exploring the Challenges in Utilization of BIM in Maintenance Management of Mosques. Proceedings of the first international conference on mosque architecture, pp. 31–48, University of Dammam, Saudi Arabia, 2016
21. Succar, B.: Building information modeling framework: a research and delivery foundation for industry stakeholders. Auto. Constr. **18**(3), 357–375 (2009)
22. Succar. B.: Building information modeling maturity matrix. In: Underwood, J., Isikdag, U. (eds.) Handbook of Research on Building Information Modelling and Construction Informatics: Concepts and Technologies. Information Science Reference, pp. 65–102. IGI Publishing (2010)
23. Tam, C.M., Deng, Z.M., Zeng, S.X., Ho, C.S.: Quest for continuous quality improvement for public housing construction in Hong Kong. Constr. Manage. Econ. **18**(4), 437–446 (2000)
24. Zeng, S.X., Tian, P., Tam, C.M.: Quality assurance in design organizations: a Case Study in China. Manag. Aud. J. **20**(7), 679–690 (2005)

Use of Concrete Wastes as the Partial Replacement of Natural Fine Aggregates in the Production of Concrete

Suman Saha, C. Rajasekaran and K. Vinay

Abstract Due to rapid development of construction industries in various dimensions, demand for construction materials is also gaining high momentum. Therefore, availability of natural sources of construction materials is going to be in decreasing trend to cope up with the high demand. Again currently, quantity of construction and demolition waste is also going too high day by day. Reuse of these construction and demolition waste is one of the promising solutions to protect natural fine aggregates. This study aims at investigations the possibility of the usage of these construction and demolition wastes to produce the fresh concrete with desirable properties. Natural fine aggregates (river sand) are replaced by the recycled fine aggregates by the different percentage levels for the production of fresh concrete. A comparative interpretation on the strength characteristics of the concrete produced with Ordinary Portland Cement and Portland Pozzolana Cement is also presented and discussed in this paper.

Keywords Recycled fine aggregates · Compressive strength · Flexural strength Splitting tensile strength · Concrete

1 Introduction

Concrete is the most commonly used construction material in the world and it is basically consists of 70–80% of aggregates. In the recent years, due to the increase in demand for construction activities resulted in two major problems namely lack of

S. Saha (✉) · C. Rajasekaran · K. Vinay
Department of Civil Engineering, National Institute of Technology Karnataka,
Surathkal 575025, Mangalore, India
e-mail: Sumansaha.civil@gmail.com

C. Rajasekaran
e-mail: bcrajasekaran@nitk.edu.in

K. Vinay
e-mail: vinaykudlur1@gmail.com

aggregates or raw materials for construction purpose and generation of millions of tonnes of construction and demolition wastes (C&DW), which creates environmental disposal problems. There is a need of finding a solution to the above problems. There are several experimental works carried out that were related to using of alternative materials in construction especially in concrete. The solution for such problems is the utilization of recycled aggregates from C&DW, which will give a solution to both the problems which are causing environmental problems. It has been stated that approximately 40% of C&DW is of concrete wastes and conducted an experimental study to investigate the possibility of using these concrete wastes for the production of fresh concrete [1]. An experimental study was done to determine the possibility of incorporating fresh concrete waste as recycled aggregate in concrete both fine and coarse aggregates [2]. In order to determine performance of mortar where the recycled concrete aggregates were used as a replacement to natural fine aggregate, an experimental investigation was conducted [3]. A series of experiments were conducted to determine the long-term performance of concrete produced with fine recycled concrete aggregates obtained from an original concrete and concluded that the replacement of recycled fine aggregate in concrete gives feasible durability conditions for smaller percentage of replacement, i.e. up to 30% and also suggested to use the binders other than Ordinary Portland cement to get higher acceptable the replacement ratio, which could compensate the presence of fine recycled concrete aggregates [4]. To assess the performance of demolished waste as fine aggregate in concrete, experiments were conducted and concluded that the recycled aggregate concrete may be an alternative to the conventional concrete [5]. Another experimental investigation was done on the properties of concrete by replacing crushed fine stone, furnace bottom ash and fine recycled aggregate with natural fine aggregates [6]. The reasons behind the increasing trend of the generations of huge quantity construction and demolition wastes has been stated and conducted investigation on the incorporation of recycled coarse aggregates in concrete mixes [7, 8]. 15–30% reduction in strength for concrete containing crushed concrete and 10% reduction in strength for concrete containing 100% crushed brick as fine aggregate were observed in this study [9]. Difficulties with respect to durability view were observed for the 100% replacement of the natural fine aggregates by RFA in a concrete mix [10].

2 Experimental Programme

2.1 Materials

The materials used in the present investigation were Ordinary Portland Cement (OPC), Portland Pozzolana Cement (PPC), Natural Coarse Aggregates (NCA), Recycled Fine Aggregates (RFA), Natural Fine Aggregates (NFA) and Water. The properties of these materials have been discussed in the following sections:

Ordinary Portland Cement (OPC). OPC 43 grade cement conforming to IS: 8112-1989 [11] was used for the experimental work. The following tests were conducted to obtain properties of cement and the results are tabulated in Table 1.

Portland Pozzolana Cement (PPC). PPC is generated by inter grinding OPC clinker with 15–35% of pozzolanic material. In the present experimental work, fly ash based Portland Pozzolana cement conforming to IS: 1489-1991 (Part 1) [12] was used. The results of the various tests on PPC properties are given in Table 1.

Natural Coarse Aggregate (NCA). Coarse aggregate was procured from locally available resources and in this work, 20 mm was used as the maximum size of aggregate. The properties of natural coarse aggregate were determined as per the guidelines given by IS:2386-1963 [13] and presented in Table 2. Particle size distribution of NCA is shown in Fig. 1.

Natural Fine Aggregates (NFA). The aggregate material which passes through 4.75 mm IS sieve and retained on 75 µ IS sieve is termed as fine aggregate. The sand used for the experimental works was procured from local resources and conformed to grading zone II (IS: 383-1970) [14]. Table 3 represents the properties of fine aggregates used in this study.

Recycled Fine Aggregates (RFA). The RFA was produced from the available old tested concrete specimens (cubes, cylinders, beams, etc.) in the concrete laboratory of Department of Civil Engineering, National Institute of Technology Karnataka, Surathkal. The specimens without reinforcement were first crushed by hydraulic machine and then manually using hammer broken down into small pieces. Then fine aggregate was separated from the coarse aggregate by sieving through 4.75 mm sieve. The aggregate materials, which passed through the IS sieve size 4.75 mm and retained on 150 µ sieve, were considered as RFA. After separations of aggregates were kept separately in a dry place till it had been used in the concrete. The properties of RFA are presented in Table 3. To maintain particle size distribution curve (as shown in Fig. 1) of the RFA similar to that of the natural fine

Table 1 Properties of OPC and PPC

Characteristics	OPC	PPC	Standard values
Normal consistency	29%	31%	–
Initial setting time	80 min	55 min	Not to be less than 30 min
Final setting time	225 min	170 min	Not to be greater than 600 min
Fineness	1.90%	1.73%	Not to be greater than 10%
Specific gravity	3.10	2.83	–

Table 2 Properties of natural coarse aggregates

Characteristics	NCA
Type	Natural
Specific gravity	2.72
Water absorption	0.5%
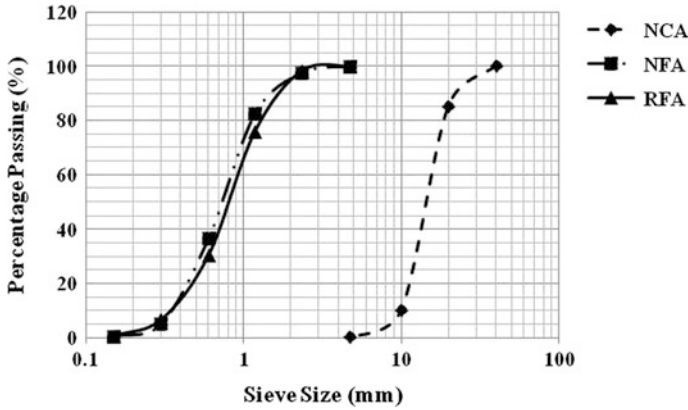
Fig. 1 Particle size distribution curve of NCA, NFA and RFA

Table 3 Properties of fine aggregates

Characteristics	Value	
Type	Sand (NFA)	RFA
Specific gravity	2.61	2.25
Grading zone	II	II
Water absorption (%)	1.0	10.2

aggregate, the different sizes of RFA were mixed in a suitable proportion during the production of fresh concrete.

Water. Tap water was used for the purposes of mixing and curing both. The pH value of the water, which was used for the present study, was 8.32. According to IS 456: 2000 [15], pH value of water should not be less than 6.

2.2 Concrete Mixes

In this study, the mix proportions of the concrete were calculated according to the guidelines given in IS: 10262-2009 [16]. Concrete mixes had been designed by keeping the water–cement ratio as 0.5. NFA were replaced by RFA as per desired replacement level. Extra quantity of water was added to take care of the water absorption properties of RFA. For both types of concrete, mixes with zero percentage of RFA were taken as the control mixes. The quantity of the different materials required for one cubic metre of concrete is tabulated in the Table 4 for OPC-based concrete and in Table 5 for PPC based concrete.

Table 4 Quantity of Materials per m³ OPC based concrete

Mix name	W/C ratio	Replacement of NFA (%)	Cement (kg)	NCA (kg)	NFA (kg)	RFCA (kg)	Water (kg)	Extra water (kg)	Total W/C
$MOPC_0$	0.50	0	372	1170.3	688.40	0	186	12.73	0.53
$MOPC_{10}$		10			629.02	59.34		18.19	0.54
$MOPC_{20}$		20			569.52	118.78		23.66	0.56
$MOPC_{30}$		30			510.13	178.17		29.12	0.58
$MOPC_{40}$		40			450.74	237.56		34.58	0.59

$MOPC_0$ Concrete mix with zero percentage of RFA (Control Mix); $MOPC_{10}$ Concrete mix with 10% of RFA; $MOPC_{20}$ Concrete mix with 20% of RFA; $MOPC_{30}$ Concrete mix with 30% of RFA; $MOPC_{40}$ Concrete mix with 40% of RFA; *W/C* water–cement ratio; *NFA* Natural Fine Aggregates; *NCA* Natural Coarse Aggregate; *RFA* Recycled Fine Aggregate

Table 5 Quantity of Materials per m³ PPC based concrete

Mix name	W/C ratio	Replacement of NFA (%)	Cement (kg)	NCA (kg)	NFA (kg)	RFA (kg)	Water (kg)	Extra water (kg)	Total W/C
$MPPC_0$	0.45	0	372	1151.13	677.0	0	186	12.52	0.53
$MPPC_{10}$		10			618.64	58.36		17.88	0.54
$MPPC_{20}$		20			560.28	116.72		23.25	0.56
$MPPC_{30}$		30			501.92	175.08		28.62	0.57
$MPPC_{40}$		40			443.56	233.44		34.00	0.59

$MPPC_0$ Concrete mix with zero percentage of RFA (Control Mix); $MPPC_{10}$ Concrete mix with 10% of RFA; $MPPC_{20}$ Concrete mix with 20% of RFA; $MPPC_{30}$ Concrete mix with 30% of RFA; $MPPC_{40}$ Concrete mix with 40% of RFA; *W/C* water–cement ratio; *NFA* Natural Fine Aggregates; *NCA* Natural Coarse Aggregate; *RFA* Recycled Fine Aggregate

2.3 Tests on Concrete Mixes

Cubes of size 150 mm × 150 mm × 150 mm were cast to study the compressive strength, cylinders having dimension 150 mm (diameter) × 300 mm (height) were cast to study the splitting tensile strength and prismatic beams, having dimension 100 mm × 100 mm × 500 mm were cast to study the flexural strength of various concrete mixes. After careful demoulding, the specimens, i.e. cubes, cylinders and beams were kept for curing in normal tap water at the room temperature in the laboratory. Cast specimen samples were tested after moist curing of 7 days and 28 days as per standard guidelines [17, 18].

3 Results and Discussion

3.1 Compressive Strength

Figures 2 and 3 show the variation of compressive strength at 7 and 28 days respectively for OPC- and PPC-based concrete mixes. The compressive strength of the cubes cast with OPC- and PPC-based concrete mixes having RFA was observed to be in increasing trend till the percentage level of replacement of NFA by RFA is 20%. Even with 30% of RFA, concrete specimens also showed higher strength than that of control mixes.

Increase in compressive strength may be due to the additional cementitious materials present in the recycled aggregates, which will increase the amount of binder materials to the mixes. Furthermore, with increase of replacement percentage the strength decreases due to the high water absorption property of RFA. In order to compensate high water absorption capacity of RFA, extra water was added to the mixes, which results total water–cement ratio in concrete mixes high.

Fig. 2 Compressive strength at 7 days
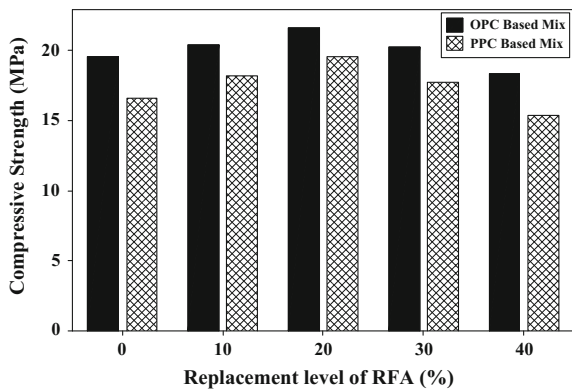
Fig. 3 Compressive strength at 28 days
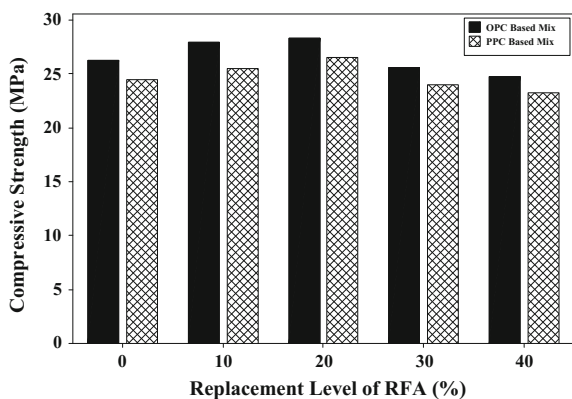
3.2 Flexural Strength

Flexural strength of OPC-based concrete mixes with RFA was observed to be increased up to 20% replacement of NFA by RFA whereas for PPC-based concrete mixes up to 10% replacement of NFA by RFA. Variation of flexural strength of prismatic beam specimens at 7 and 28 days are shown in the Figs. 4 and 5 respectively. Bonding between binders and recycled aggregates at high percentage replacement may be weaker. Increment in flexural strength of OPC-based concrete mixes produced with RFA was found higher than that of PPC-based concrete mixes.

Fig. 4 Flexural strength at 7 days
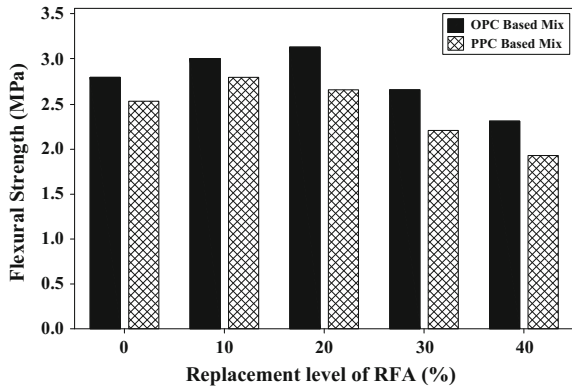
Fig. 5 Flexural strength at 28 days
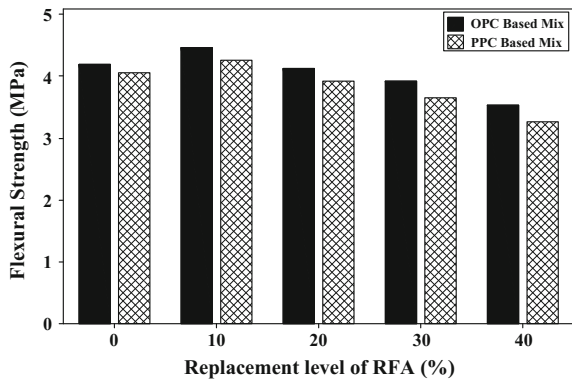
3.3 Splitting Tensile Strength

Splitting tensile strength of cylindrical specimens at 7 and 28 days are shown in
Figs. 6 and 7 respectively. It was observed that splitting tensile strength of OPC-
and PPC-based concrete mixes increased with the increment of RFA up to 10% in
the mixes. Increment of splitting tensile strength of OPC based concrete mixes with
10% RFA was found higher than that of PPC-based concrete mixes with 10% RFA.
When the replacement percentage level is higher than 10%, decrement in splitting
tensile strength was observed for both types of mixes.

Fig. 6 Splitting tensile strength at 7 days
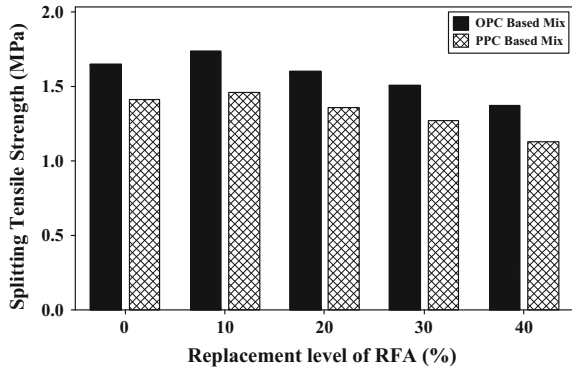
Fig. 7 Splitting tensile strength at 28 days
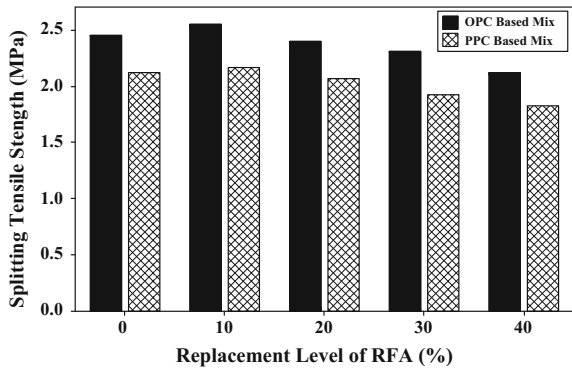
4 Conclusions

In this paper, results of experimental investigations to determine strength of recycled aggregate concrete using Ordinary Portland Cement and Portland Pozzolana cement are presented and discussed. From this study, the following conclusions can be made:

- Water absorption capacity of RFA was observed to be significantly higher than the NFA. Due to this, desired workability of concrete mixes may not be achieved. Water absorption capacity of RFA was noticed ten times more than that of NFA (sand). This study also reported similar results from their work [19].
- With 20% RFA, concrete mixes showed 10.58% increase in compressive strength after 7 days for OPC-based concrete whereas for PPC-based concrete mixes increment is 17.84% with respect to control mixes. Increase in compressive strength after 28 days were observed to be 7.89% for OPC mixes and 8.47% for PPC mixes with 20% RFA. When the replacement level of NFA by RFA is 40%, decrease of compressive strength after 7 and 28 days was found to be 6.53 and 5.68% respectively for OPC mixes and 7.11 and 4.87% for PPC mixes.
- Increment in flexural strength of concrete after 7 days was noticed to be 11.78% for OPC mixes and 5.13% for PPC-based mixes with 20% RFA. Flexural strength of concrete mixes with 10% RFA after 28 days were increased by 6.19% for OPC mixes and 4.92% for PPC mixes.
- Splitting tensile strength of concrete after 7 days and 28 days was found to be increased 5.54 and 4.08% respectively for OPC mixes and 3.54 and 4.22% respectively for PPC mixes when NFA is replaced 10% by RFA.
- Compressive strength, flexural strength and splitting tensile strength of concrete were observed to be decreased than that of control concrete mixes when NFA is replaced 40% by RFA.

In order to overcome the problems related to procure natural fine aggregates (sand) and to protect natural resources, environmental systems, etc. RFA can be used as alternative materials for sand in concrete mixes with limited percentage even though strength decrement was observed with higher quantity of RFA in mixes. Same conclusions made by several researchers [5, 20].

References

1. Saha, S., Rajasekaran, C.: Strength characteristics of recycled aggregate concrete produced with portland slag cement. J. Constr. Eng. Technol. Manage. **6**(1), 70–77 (2016)

Early Strength Properties of Concrete Incorporating Plastic Fibers Derived from Waste Plastic Bags

Asset Turlanbekov and A. B. M. A. Kaish

Abstract Malaysia alone generates approximately 30,000 tons of rubbish every day containing around 13% of solid plastic waste. Besides conventional recycling and landfilling, an alternative disposal of this waste is required for sustainable development. Adding plastic waste as a fiber in concrete would play an important role to reduce plastic waste. This study investigates the 7 days test results of properties of concrete containing plastic fibers derived from waste bags. In this study, polyethylene waste plastic bags were manually cut into fibers of two different lengths (5–12 mm and 20–35 mm). Nine concrete mixtures were prepared with quantities of 0.1, 0.2, 0.3, 0.4% of both types of plastic fibers. Workability, compressive strength, splitting tensile strength, and flexural strength were tested at 7 days and compared with conventional concrete. The addition of plastic fibers significantly improved concrete properties. Research results showed that depending on quantity of plastic fibers, concrete may achieve different strengths. The test results proved that the utilization of plastic fibers derived from waste plastic bags in concrete is possible and it can improve the properties of concrete.

Keyword Plastic wastes · Plastic fibers · Green technology
Fibre reinforced concrete

1 Introduction

Plastic waste worldwide is increasing and especially in Malaysia it is become critical. Plastic waste takes years to decompose which make the issue more critical. According to the Association of Plastic Manufactures, low-density polyethylene is

A. Turlanbekov · A. B. M. A. Kaish (✉)
Department of Civil Engineering, Infrastructure University Kuala Lumpur,
43000, Kajang Selangor, Malaysia
e-mail: amrul.kaish@iukl.edu.my; amrul.cuet@gmail.com

A. Turlanbekov
e-mail: asset.turlanbekov@gmail.com

the biggest waste contributor with approximately 23% (plastic bags). The world's usage of plastics increased from five million tons in the middle of twentieth century to one hundred million tons at the beginning of twenty-first century [1]. Since the twentieth century, plastics have been used increasingly, in 2012 45.9 million of tons of plastics were used only in Europe [2]. According to the Environment Agency up to 80% of waste plastics are sent to landfills. Malaysia is not an exception and they also have the same challenge.

As a developing country with a population of over 30 million people, it uses huge amounts of different types of plastic bags. All these waste plastic bags are nowadays being disposed in landfill sites and thus increasing the threat to the environment. Therefore, we need to study some alternative disposal ways for these plastic bags. These waste plastic bags can be utilized in the production of concrete.

With the addition of plastic fibers, they enhance the mechanical properties of concrete, because polypropylene fibers inhibit the cracking growth that occurred in the concrete [3]. Polypropylene fibers mixed with steel can significantly decrease the plastic shrinkage as well as drying shrinkage cracking. It also minimizes the degradation of compressive strength of the concrete after exposure to elevated temperatures [4]. With the addition of polypropylene fibers also improve the durability properties of concrete [5]. Hsie [6] studied the effects of polypropylene fibers in concrete. Results show positive effects when it was compared with pure concrete. It was found that drying shrinkage decreases with the increase of fiber content [6]. Naaman [7] stated that the usage of waste polypropylene fibers positively affect the flexural strength of concrete. The presence of fibers in concrete controls the crack and fibers bridging cracks reducing concrete permeability [8].

However, previous researchers did not focus on the utilization of waste plastic bags in concrete. For this reason, because of a lack in information about developing Plastic Fiber-Reinforced Concrete (PFRC) incorporating plastic fibers derived from waste plastic bags, a study is required to develop a new way of utilizing waste plastic bags in concrete as fiber to minimize its disposal problem. This research would help us to understand an alternative way of utilizing plastic bags.

2   Experimental Program

Ordinary Portland cement, aggregates, water and waste plastic bags were used to prepare plastic fiber-reinforced concrete (PFRC). River sand with a specific gravity of 2.68 was used as a fine aggregate. 20 mm downgraded crushed stone was used as coarse aggregate in this study.

The experimental program of concrete properties was conducted in two phases, in fresh and a hardened condition. The slump test was conducted immediately after the preparation of concrete mix using a slump cone according the BS 1881:102 standard. After the slump test, concrete was cast in standard molds of cube, cylinder, and beam to determine the hardened properties. The concrete was de-molded after 24 h of casting and placed in water for curing until the date of

testing. İn the second phase of experimental test, the compressive strength test based on BS EN 12390-3:2009, flexural strength test based on BS EN 12390-5:2009 and splitting tensile strength test was conducted.

3 Experimental Program

3.1 Slump

Figure 1 shows the slump test results. When the addition of fibers increased, the mix became stiffer. The slump test showed that short fibers PFRC workability was better than long fibers PFRC. With the addition of fibers the workability of concrete decreased. Both types of fibers with the amounts of 0.3 and 0.4% had low workability results.

3.2 Compressive Strength

Table 1 shows the average compressive strength of PFRC at 7 days. The results show the compressive strength of control mix (CM), PFRC 0.1%, PFRC 0.2%, PFRC 0.3%, PFRC 0.4%. For each concrete mix 3 specimens was tested and only the average results are reported here. The compressive strength of plain concrete was 20.94 Mpa. However, the average strength of PFRC with 0.1% of long plastic fibers is 20% greater than that of CM specimens. This increased strength might be attributed to the crack bridging action by the fibers. For the rest of the specimens, compressive strength gradually decreases with the increase of fiber content. However, PFRC with 0.4% fiber showed lower strength than CM specimens.
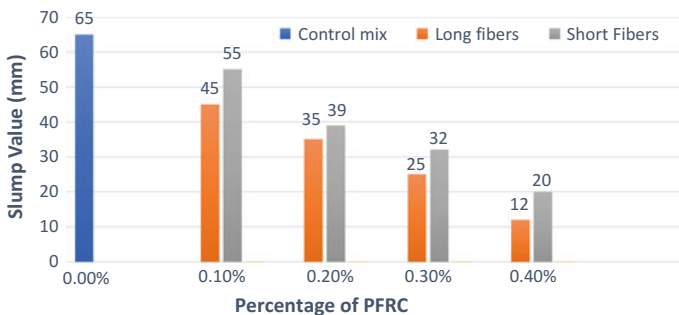
Fig. 1 Slump test results

Table 1 Compressive strength of specimens

Mix design	Compressive strength (Mpa)
Control mix	20.95
PFRC 0.1% (20–35 mm)	24.02
PFRC 0.2% (20–35 mm)	22.50
PFRC 0.3% (20–35 mm)	20.7
PFRC 0.4% (20–35 mm)	20.4
PFRC 0.1% (5–12 mm)	22.35
PFRC 0.2% (5–12 mm)	21.95
PFRC 0.3% (5–12 mm)	21.6
PFRC 0.4% (5–12 mm)	19.9

3.3 Splitting Tensile Strength

Figure 2 shows the results of the splitting tensile strength. It is clear from the figure that the concrete specimens with the addition of plastic fibers achieved better results than conventional concrete. PFRC specimen with 0.3% of short fibers shows the highest tensile strength of 3.21 Mpa. However, when the quantity of fibers were increased the tensile strength of specimens decreased, because of the low workability of concrete.

3.4 Flexural Strength

During flexural test, PFRC was more durable than the control mix design. Specimens with long fibers content showed higher flexural strength than specimens
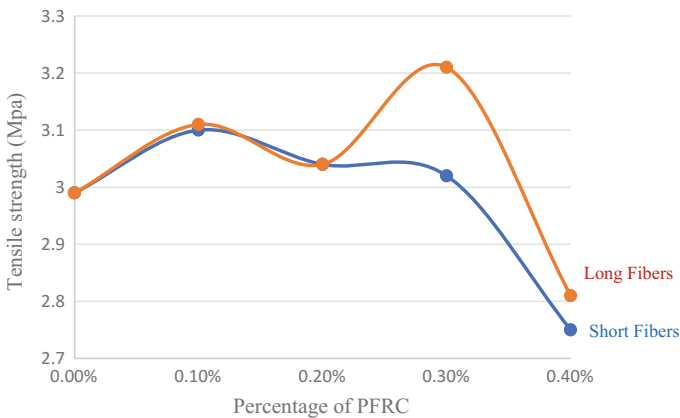
Fig. 2 Splitting tensile strength test results

Table 2 Flexural strength test results

Mix design	Flexural strength (Mpa)
Control mix	2.95
PFRC 0.1% (20–35 mm)	3.30
PFRC 0.2% (20–35 mm)	3.25
PFRC 0.3% (20–35 mm)	3.05
PFRC 0.4% (20–35 mm)	3.00
PFRC 0.1% (5–12 mm)	3.00
PFRC 0.2% (5–12 mm)	3.1
PFRC 0.3% (5–12 mm)	3.02
PFRC 0.4% (5–12 mm)	3.01

with short fibers content (Table 2). All the PFRC specimens show better flexural strength that of CM specimens at any replacement level. The highest result was obtained in the case of specimens 0.1% long fibers. However, flexural strength decreases with the increase in fiber content. This decrement is more prominent in the case of PFRC with long fibers (Table 2).

4   Conclusion

Our global problem of waste plastic bags and its catastrophical increasing makes its disposal a very critical problem. Current study was done to observe the feasibilities of utilizing waste plastic fibers in concrete. Test results show that the utilization of plastic fibers derived from waste plastic bags in concrete is possible; and it can enhance the properties of concrete in terms of compressive, split tensile, and flexural strengths. This type of concrete can also be utilized in seismically active areas, since PFRC showed positive strength in terms of flexural and split tensile strength compared to plain concrete. However, further studies about PFRC utilizing waste plastic bags is required to warrant its field application.

References

1. Siddique, R., Khabit, J., Kaur, L.: Use of recycled plastic in concrete: a review. Waste Manag. **28**, 1835–1852 (2007)
2. Gu, L., Ozbakkaloglu, T.: Use of recycled plastic in concrete. Waste Manag. **51**, 19–42 (2016)
3. Jameran, A., Ibrahim, Izni S., Hamizah, S., Rahim, A.: Mechanical properties of steel-polypropylene fibre reinforced concrete under elevated temperature. Procedia Eng. **125**, 818–824 (2015)

4. Hadithi, A.I., Hilal, N.N.: The possibility of enhancing some properties of self-compacting concrete by adding waste plastic fibers. J. Build. Eng. 20–28 (2016)
5. Ardeshana, A.L., Dr Desa, A.K.: Durability of fiber reinforced concrete of marine structures. Int. J. Eng. Res. 215–219 (2012)
6. Hsie, M., Tu, C., Song, P.S.: Mechanical properties of polypropylene hybrid fiber-reinforced concrete. Mater. Sci. Eng. 153–157 (2008)
7. Naaman, A. E., Garcia, S., Korkmaz, M., Li, V. C.: Investigation of the use of carpet waste PP fibers in concrete. ASCE 782–791 (1996)
8. Yehia, S., Douba, A., Abdullahi, O., Farrag, S.: Mechanical and durability evaluation of fiber-reinforced self-compacting concrete. Constr. Build. Mater. 120–133 (2016)

Numerical Analysis on Lateral Distortional Buckling of Octagonal Castellated Steel Beams

M. Mimoune and S. Siouane

Abstract A numerical model is suggested to predict the behavior of alveolar beams to multiple octagonal openings up to failure taking into account material and geometric nonlinearities in calculation. This research is interested in the effect of web distortions in a lateral distortional buckling mode of the I-beams on simply supported subjected to a load concentrated in the middle of the beam. Analytical expressions obtained from previous works have been adapted to these alveolar beams in order to study the influence of thick flanges, stocky flanges, slender webs, and slender beams. The study was carried out in order to compare the numerical and analytical results in addition to the design method of the EC-3.

Keywords Analytical results · Castellated beam · FEA · Web-post

1 Introduction

Castellated beams are beams containing different forms of holes. The technical importance of this dispositive is to decrease the weight and to increase the bending stiffness (inertia moment) of the beam. These openings significantly affect considerably the shear and buckling resistance of the girder leading to failure. Six potential failure modes were obtained [1] depending on the geometrical settings, positions and type of loading and supports conditions. The ruin of this type of beams often manifests itself as lateral torsional buckling and local buckling. In castellated beams, the existence of web openings results in a reduction in the stiffness of the web plate which increases the level of web deformations. As a result local web distortions are more likely to accompany the lateral torsional buckling deformation leading to the occurrence of lateral distortional buckling mode. Several studies have been carried out on lateral and distortional buckling of castellated

M. Mimoune (✉) · S. Siouane
Civil Engineering Department, Faculty of Engineering, University in Constantine,
Constantine, Algeria
e-mail: mmimoune@gmail.com

beams [2, 3, 4, 5]. In this paper, the lateral distortional buckling of octagonal steel beams is studied to show the impact of the potential failure modes of those beams. The analytical equations applied, gave different values which will be used for comparison with the Eurocode 3 [6] values.

2 Design Method

The inelastic Lateral Torsional Buckling solutions for beams with solid web proposed by Bradford and Trahair [7], then modified for the case of lateral distortional buckling by Pi and Trahair [4] and Kalkan and Buyukkaragoz [3], has shown that the stiffness of the steel I-beam is influenced by the large deformations due to the buckling of the web, are used herein. These solutions are adapted and applied to castellated beams. We introduce the previous concept of reduced rigidities, while calculating the geometrical characteristics of the sections in mid-length of the opening of the alveolar beams, as recommended in the Eurocode Annex N [6].

A comparison is made between analytical results and numerical resultants calculated by Ansys. Table 1 resumes the data and results that depend on calculation inelastic domain of beams.

3 Modeling by Finite Element

We used the numerical software ANSYS version 12.1 [8] to realize the modeling of the beam, this software of research is special in the numeric simulations by finite elements it offers a wide range of options for the graphical interface. Solid webs, web-posts, and flanges were modeled by shell elements SHELL43 with four nodes, with six degrees of freedom at each node with a capacity of plastic deformation in great displacement (Fig. 1).

The precision of the results around the openings is obtained by finer meshes. The calculation model was used as a whole and loading about the upper girder flange at mid-span of beams. In this work, we take the same support conditions and loading of beams used in the tests of [5], at illustrated in Fig. 2.

The steel of beams used was modeled as an isotropic bilinear material, elastic perfectly plastic behavior (in tension and in compression) taking Von Mises

Table 1 Results of calculation plastic

Specimen	h_t (mm)	t_w (mm)	Class	β_w	M_{pl} (kN m)	L_r (m)	σ_v (LB) (MPa)
IPE-B900	900	10.2	2	1.0	941.1	5.410	626.4
IPE-B900$_t$			2		1156.8		
HEB-B900	900	14.5	2	1.0	2087.6	8.914	1,338.8
HEB-B900$_t$			1		2394.3		
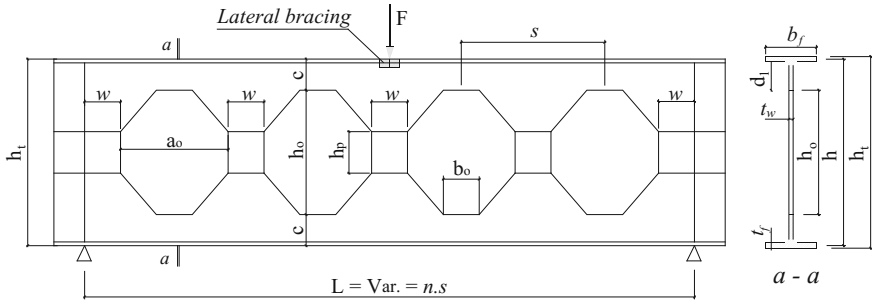
Fig. 1 Castellated beam with octagonal openings
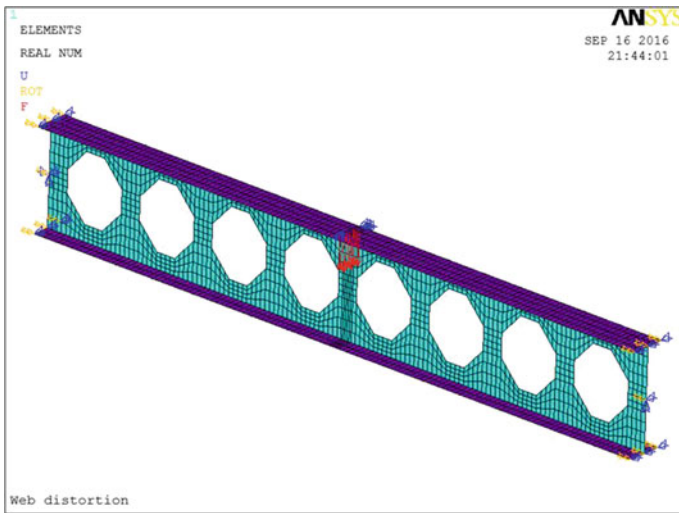
Fig. 2 FE model for octagonal openings beam ($n = 8$)

criterion. The Young's modulus $E = 210$ GPa, the Poisson's ratio $\upsilon = 0.3$ and the yield strength $f_y = 235$ MPa.

A 3D numerical model was obtained on the basis on 04 series studied beams of varied lengths from 2 to 86 s (opening pairs varying from 2 to 86, which correspond to lengths varying from 1575 m to 60,375 m), these series composed:

- 02 series of alveolar beams of octagonal openings to basis of the profiles IPE500 and HEB500.
- 02 series of solid-web beams (even previous alveolar beams with closing of the openings). These beams are denominated: IPE-B900$_t$ and HEB-B900$_t$, Fig. 1 and Table 2.

Table 2 Geometric properties of alveolar beams in mm

Specimen	L	b_f	t_f	d_I	t_w	a_o	b_o	w	c	s	h_p	h_o	h	h_t
IPE-B900	Var.	200	16	134	10.2	525	175	175	150	700	200	600	884	900
HEB-B900	Var.	300	28	122	14.5	525	175	175	150	700	200	600	872	900

4 Validation of Finite Element Model

The references of Zirakian and Showkati (2006) [5] and [9] were used as the basis for validation, and ANSYS software for analysis. The tested beams were loaded so that the lateral torsional buckling is favored. The load is applied at the upper of flange in the mid-span of the beam. The vertical stiffeners at the supports will make it possible to eliminate the deformations in the ends of the beam.

The studied beams failed by lateral torsional buckling, lateral distortional buckling, or web-post buckling effect. The numerical model by FE developed for alveolar beams has been validated with the results available in the literature [5, 9]. Table 3 summarizes the comparison of the results obtained.

5 Analysis and Comparison of Results

The purpose of this research concerns the influence of slenderness of the octagonal castellated beams on the lateral buckling moment and the failure modes under concentrated middle loading. Among factors influencing the behavior (elastic, inelastic) of alveolar beams are the lateral torsional buckling moment to plastic moment ratio, the slenderness of the web d_w/t_w, and the slenderness of the beams. The parameters, which are considered in the present study also the thickness and width flanges, the length of beam between lateral supports and the dimensions of the octagonal opening web. The numerical analysis was carried on 63 octagonal castellated beams and 63 solid-web beams. The theoretical study took into account the experimental parameters. The slenderness of the web h_t/d_w varies from 0.60 to

Table 3 Comparison of experimental, FEA and EC-3 critical loads

Beam	L	(1) P_{cr} [5]	(2) P_{cr} [9]	(3) P_{cr} [6]	(4) PFEA	$|\Delta^a|\%$	$|\Delta^b|\%$
C180-3600	3.60	21.58	/	18.36	21.65	−0.32	−15.20
C180-4400	4.40	15.63	/	13.59	16.65	−6.31	−18.38
C210-3600	3.60	37.22	/	35.52	36.08	3.16	−1.55
C210-5200	5.20	24.90	/	20.16	26.03	4.34	−22.5
2.94 [9][a]	2.94	/	32.8	30.64	31.38	4.53	−2.36
4.20 [9][a]	4.20	/	14.9	13.24	13.77	8.21	−3.85

[a]*Beams not contain braced*; $\Delta^a = (1;2) - (4)/(4)$; $\Delta^b = (3) - (4)/(4)$; Unit: kN, m
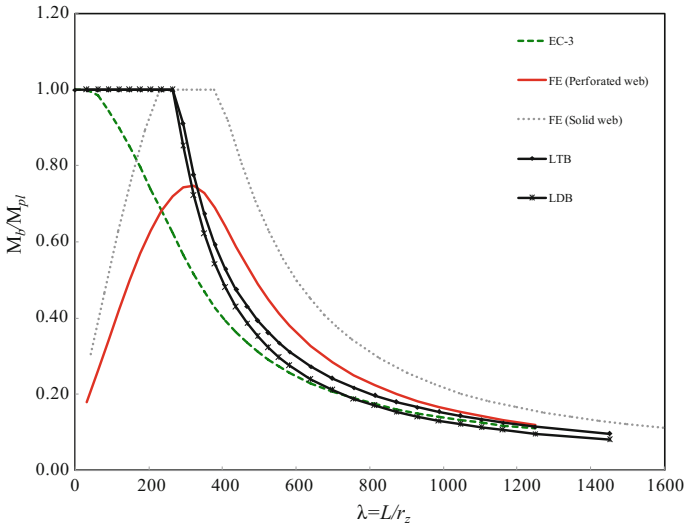
Fig. 3 Comparison: analytical, FEA and EC-3 results (IPE-B900)

0.70; the results obtained are shown in Figs. 3 and 4. These results obtained are compared with those calculated with the formulas developed by Kalkan and Buyukkaragoz [3] and according to EC-3 [6], for the different cases envisaged of alveolar beams manufactured on the basis of the profiles IPE500 and HEB500 and/ or without closing of the web openings.

In Fig. 3, the results of the comparison of the moments obtained for the different ratios of the slenderness L/r_z are presented in the same conditions of supports and loading as the specimen C210-3600 of Zirakian and Showkati [5]. For IPE-B900 beams, it can be seen that the moment calculated by FEA solution is nearly equal to the theoretical critical moment for slenderness $\lambda \geq 600$, analytical solutions underestimate the buckling moments, particularly for L/r_z ratios less than 600 the curves diverge. It is clear from this figure that the EC-3 result gives more conservative estimates. It is also observed that the beams whose slenderness is weak (less than 200) failed at elastic state. We can note that the FEA values obtained for solid-web beams are higher than those of the castellated beams.

For the short beams, the instability is manifested by buckling of the web-post and local buckling web, before reaching the plastic moment. It can also be noted that the EC3 code limits the influence of the local buckling or web-post buckling in both flexion and compression by the classification of the cross-sections by the mean of calculation of the slenderness of elements. In this study the beams studied are considered of class 1 and 2 (Table 1), which is able to reach their full plastic moment. The EC-3 [6] gives a high moment of resistant of lateral buckling moment for the short beams whereas the failure beams intervenes by buckling of the web-post for the castellated beams and by buckling of the web for the solid-web beams.
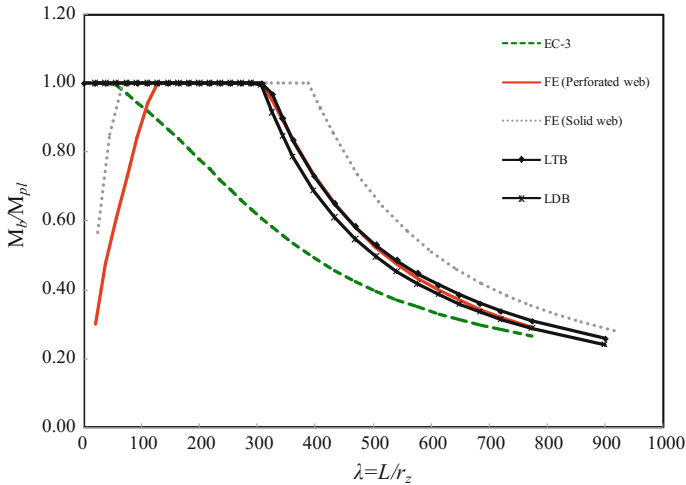
Fig. 4 Comparison with analytical, FEA and EC-3 results (HEB-B900)

The curves also indicate that the percentage difference is less than 10% between the lateral buckling moments and the lateral distortional buckling moments for slenderness $\lambda \leq 500$, which shows that the web distortion has no important effect on the ultimate load of the beams with low slenderness. When the slenderness λ increases beyond 500, the effect of web distortion increase slightly. Consequently, it is clear that the slender web is not affected by the distortion particularly between lateral fixing points with large distances (length of the unmaintained span increases). The influence of the web distortion decreases for wide and thick flanges corresponding to HEB profile. It is also noted that the gap between FEA results, EC-3 results and analytical results increase in this case (Fig. 4).

Figure 5 shows clearly the huge effect of the flange thickness on the plastic moment of beams, on the other hand the slenderness of web-post or solid web appears to be of secondary importance. The increase in the flange thickness of the beam seems to play a role in reducing the web distortion. Intermediate cases may occur where instability occurs as a result of the lateral torsional buckling of beams accompanied by local buckling of web or web-post buckling in the case of less wide and thin flanges (Fig. 6).
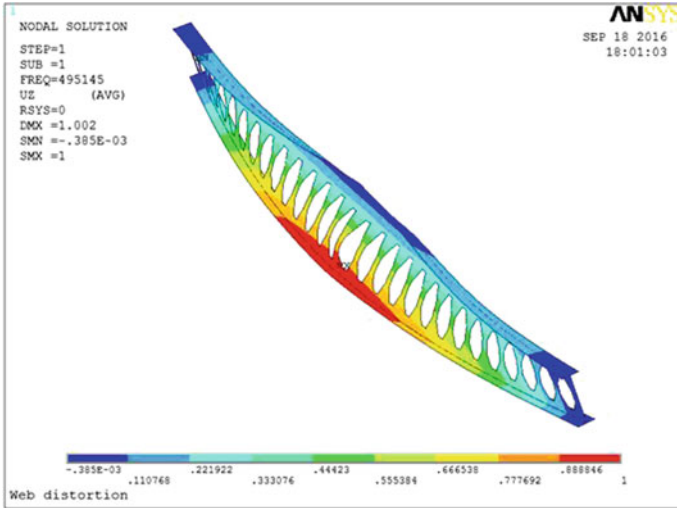
Fig. 5 Lateral distortional buckling of castellated beam. HEB-B900 (*L* = 19.775 m)
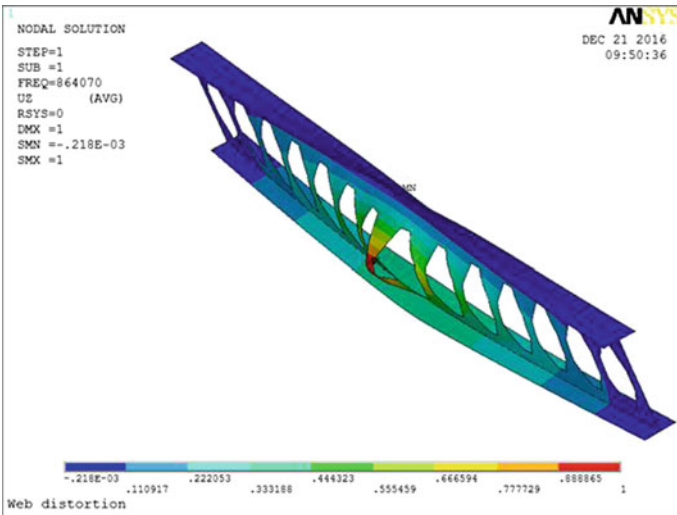
Fig. 6 Lateral distortional buckling of castellated beam. HEB-B900 (*L* = 9.975 m) P_{cr} = 864 kN

6　Conclusion

Numerical model was suggested to estimate moment capacity resistance of octagonal castellated beams. The analytical expressions applied to castellated beams give interesting results. The main conclusions of the comparative study were

- In alveolar beams the ruin occurs by buckling in the web-post contrary to solid web.
- Eurocode give more conservative results compared to numerical model results and analytical result.
- It has been found that the reductions in the buckling moments of octagonal castellated beams since web distortions produce an increase when the slenderness of the web increases.
- Lateral distortional buckling solutions given in this study is very close to numerical model results (FEA) for alveolar beams with wide and thick flanges.
- The web distortion has no influence on the ultimate load of the I-beams with low slenderness and with thick flanges.

References

1. Kerdal, D., Nethercot, D.A.: Failure modes for castellated beams. J. Constr. Steel Res. **4**, 295–315 (1984)
2. Bradford, M.A.: Lateral-distortional buckling of steel I-section members. J. Constr. Steel Res. **23**, 97–116 (1992)
3. Kalkan, I., Buyukkaragoz, A.: A numerical and analytical study on distortional buckling of doubly-symmetric steel I-beams. J. Constr. Steel Res. **70**, 289–297 (2012)
4. Pi, Y.L., Trahair, N.S.: Distortion and warping at beam supports, ASCE. J. Stru. Eng. **126**, 1279–1287 (2000)
5. Zirakian, T., Showkati, H.: Distortional buckling of castellated beams. J. Constr. Steel Res. **62**, 863–871 (2006)
6. ENV (1993)-1-1Eurocode 3: Design of steel structures-Part 1–1: general rules and rules for buildings, 1992, and amendment A2 of Eurocode Annex N 'Openings in Webs' (1993)
7. Bradford, M.A., Trahair, N.S.: Distortional buckling of I-beams, ASCE. J. Struct. Div. **107**, 355–70 (1981)
8. ANSYS: Manuel Mechanical APD, version 12.1 (2009)
9. Mohebkhah, A.: The moment-gradient factor in lateral-torsional buckling on inelastic castellated beams. J. Constr. Steel Res. **60**, 1481–1494 (2004)
10. Bradford, M.A.: Inelastic distortional buckling of I-beams. Comput. Struct. **24**, 923–33 (1986)
11. Liu, T.C.H., Chung K.F.: Steel beams with large web openings of various shapes and sizes: finite element investigation. J. Constr. Steel Res **59**, 1159–1176 (2003)
12. Soltani, M.R., Bouchaïr, A., Mimoune, M.: Nonlinear FE analysis of the ultimate behavior of steel castellated beams. J. Constr. Steel Res. **70**, 101–114 (2012)
13. Redwood, R., Zaarour, W.: Web buckling in thin webbed castellated beam. J. Stru. Eng. **08**, 860–866 (1996)
14. Redwood, R., Demirdjian, S.: Castellated beam web buckling in shear. J. Stru. Eng. **10**, 1202–1207 (1998)
15. Tsavdaridis, K.D., Galiatsatos, G.: Assesment of cellular beams with transverse stiffeners and closely spaced web openings. Thin-Wal. Struct. **94**, 636–650 (2015)
16. Zirakian, T.: Elastic distortional buckling of doubly symmetric I-shaped flexural members with slender webs. Thin-Wal. Stru **46**, 466–475 (2008)

Implementation of Construction Safety Knowledge Management via Building Information Model

Kongphon Chunko and Vacharapoom Benjaoran

Abstract Occupational safety and health is the most important concern of construction companies because both direct and indirect losses impact the companies. In addition, knowledge management can help raise safety awareness in the companies. Therefore, this research aims to develop Building Information Model for Construction Safety Knowledge Management (BIM-CSKM), which implements construction safety knowledge management and uses the building information modeling software for storing and presenting safety knowledge. The test results show safety knowledge for each of the five risky areas in the construction project, i.e., floor openings, radius of tower cranes, material stockpiles, scaffolding structures, and excavations.

Keywords Knowledge management · Construction safety · Building information model

1 Introduction

Knowledge management is one of the powerful management methods of a modern organization that has currently received attention. Kanjananit et al. [1] stated that knowledge management helps create new knowledge systematically by using the prior knowledge of the people in the organization. According to Malhotra pointed in [2], the organization needs to integrate the capability of information technology with the ability of people appropriately. The characteristics of each construction project are unique and result in different new work experiences and knowledge of people in the company, one important of this is safety knowledge. Lin and Lee [3] have developed a tool (method) to capture and share knowledge among a group of

K. Chunko · V. Benjaoran (✉)
School of Civil Engineering, Suranaree University of Technology,
Nakhon Ratchasima, Thailand
e-mail: vacharapoom@sut.ac.th

engineers, using online discussions as a channel for exchanging their acknowledged problems and mistakes with an attempt to gain mutual solutions or preventions.

Building Information Model (BIM) is a tool for managing construction project information throughout the project life including design and construction processes. Many successful applications of BIM in construction can be found in the literature. For example, Ding et al. [4] have developed a tool for risk management in the construction project by using BIM. It visually presents risk information and safety issues in construction projects.

Safety management is one of the most important missions to which construction companies should give priority and great attention. This research aims to develop a novel method for capturing and presenting existing implicit safety knowledge of the company, and implement the knowledge management process guided by the Office of The Public Sector Development Commission [5]. Therefore, Building Information Model-based Construction Safety Knowledge Management (BIM-CSKM) is initiated.

2   Research Methodology

This research is divided into the following three tasks:

Task 1: Exploration of the present safety knowledge management

The interview sessions are performed with a group of people involved in construction safety including one project manager, four safety officers, two project engineers, two foremen, and one worker. The interview agenda is about the details of the practical safety knowledge management in terms of safety activities and protocols, measures for accident preventions or corrections, collaborations among the team, and dissemination and presentation of the knowledge discovered. Results are characteristics of the practical knowledge management implementing on construction companies, and these are then used for the development of BIM-CSKM.

Task 2: Development of BIM-CSKM

BIM-CSKM consists of five steps. They are the knowledge search tool, knowledge identification, knowledge analysis, knowledge access, and learning BIM-CSKM, which captures and analyzes the safety knowledge resulting from the individual experiences and uses SketchUp version 2017 by Trimble companies for visually presenting this safety knowledge. These five steps are assigned to a particular person (e.g., chief safety officer) as a knowledge agent [6] who is responsible for reducing the knowledge gap and sharing knowledge among people in different positions of the construction company.

Task 3: Test of BIM-CSKM

After the development, BIM-CSKM is tested on a selected construction project as a case study. All five steps of BIM-CSKM are performed to prove if any new knowledge can be captured and diffused. Furthermore, the test also includes the evaluation of learning. A panel of the interviewees is asked for comments after the presentation of safety knowledge through BIM-CSKM.

3 Results

3.1 Task 1 Result

From the interviews with 10 samples, nine of them pointed that the safety talk is the main activity and channel for sharing present safety information and they are interested in joining this weekly event. Eight of them reported that individual safety knowledge transferred through talks while working. All interviewees unanimously agreed that the companies lacked a tool or technology for managing valuable tacit safety knowledge and they are positively interested in implementing a contemporary information technology for the knowledge management.

3.2 Task 2 Result

The development of BIM-CSKM is initiated. Its process of knowledge management for construction safety consists of the following five steps:

Step 1: Knowledge Search Tools. A chief safety officer is responsible for creating a formal questionnaire which is used as a knowledge search tool. The questionnaire includes a set of closed-ended questions for collecting individual experiences about one's occupational injuries and the other set of open-ended questions for collecting safety knowledge, especially, accidents caused by working over workers' capability [7], for example, take a shortcut on an operation, and ignore safety rules or disciplines. The construction project is distinguished into five risky operational areas namely floor openings, radius of tower cranes, material stockpiles, scaffolding structures, and excavations.

Step 2: Knowledge Identification. The chief safety officer then uses the questionnaire for interviewing people of various ranks on site. The interviewees answer the closed-ended questions according to their work and accident experiences. The interviewer also uses a structured interview approach as the open-ended questions to capture individual experiences.

Step 3: Knowledge Analysis. The chief safety officer analyzes the results of interviews using the inductive method which considers similar characteristics of problems or accidents occurred in the construction project. In addition, the results

of the analysis have to present accident causations and accident protections for the five risky areas that are further formulated with a suitable building information model software.

Step 4: Knowledge Access. Tacit knowledge is difficult to document [8]; therefore, it has to be presented through a visualization with a use of building information model. An assist of a competent draftsman is required to employ the SketchUp program for storing, presenting, and accessing safety knowledge. The details of the formation of building information model for this process are as follows:

Process 1: Model the constructing buildings on the positions as placed in the site layout plan along with some other temporary facilities such as site office, tower cranes, and fences.

Process 2: Specify the five risky areas in the construction project and model them as shaded blocks as shown in Fig. 1. They are the floor opening area (represented by number 1), e.g., elevator shaft, the swing radius of tower crane (represented by number 2), the stockpile area (represented by number 3), e.g., stack of steel bars, the scaffolding area (represented by number 4), and excavations (represented by number 5), e.g., underground water tank.

Process 3: Add the component attributes function for inputting the captured safety knowledge for the five risky areas into the model. An example of safety knowledge as the input data to the component attributes pop-up is shown in Fig. 2.
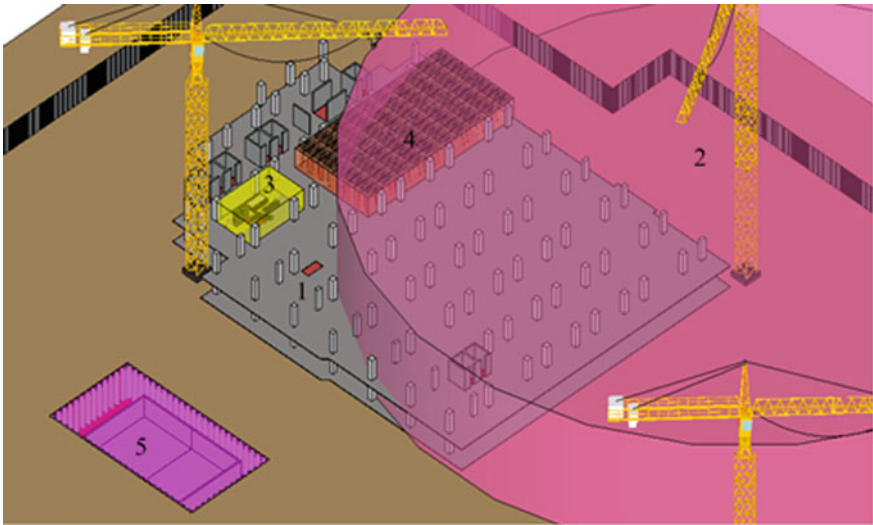
Fig. 1 The specified five risky areas in the case study of the construction project
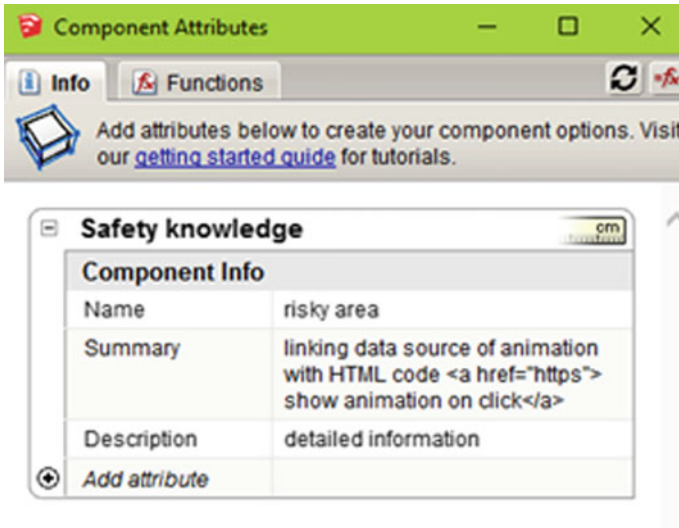
Fig. 2 An example of safety knowledge input into component attributes

Process 4: Use the scene function to simulate and animate the related activity, safety precaution, and accident prevention. This is to raise safety awareness for people involved.

Process 5: Use the component options function for presenting safety knowledge of each of the five risky areas.

3.3 Task 3 Result

The test results show safety knowledge for each of the five risky areas in the construction project used as a case study. That is as follows:

Project manager who has more than 10 years of construction work experience told that the safety flag instead of safety guardrail installation around floor openings cannot prevent anyone from falls. He reported a real case that a worker carried the materials carelessly and fell from floor openings with the safety flag around.

Foreman who has more than 10 years of work experience in construction. He reported that the materials transportation with a use of a crane. An improper materials bundle with different sizes and types, which causes some materials get loosed and could slip out of the bundle and fall.

Safety officer has 1–3 years of work experience in construction. He said that storing materials onto the stockpile untidily without sorting the type of materials out requires more time for searching for what we want and increases the risk of other materials falling onto him.

Project engineers have 6–10 years of work experience in construction. He reported that a use of plywood sheets instead of the walking panels on the scaffolding structures and their unsuitable supports can cause a movement or slip of the plywood sheets and people fall from the scaffolding structures.

Worker has more than 10 years of work experience in construction. He said that a construction scrap from working above and nearby an excavation can fall on people working within the excavation.

This captured safety knowledge and likely accident details are then presented component options function as shown an example in Fig. 3. 3D animations are also formulated and visually presented as well. These 3D animations help characterize and simulate the details of accident scenes which were directly experienced and learnt by the knowledge contributors.

The presentation of information of BIM-CSKM has been evaluated by a panel of interviewees who gave some comments on their learning. The result showed that the presentation of safety knowledge through the animation and visualization from the building information modeling software can help audiences understand a greater detail of information, and gain their attention to learn. It can also help the learners raise a safety awareness and agree to abide the safety rules of the company. Nevertheless, the presentation of BIM-CSKM has some limitations such as the language used in the communication where audiences may currently be the
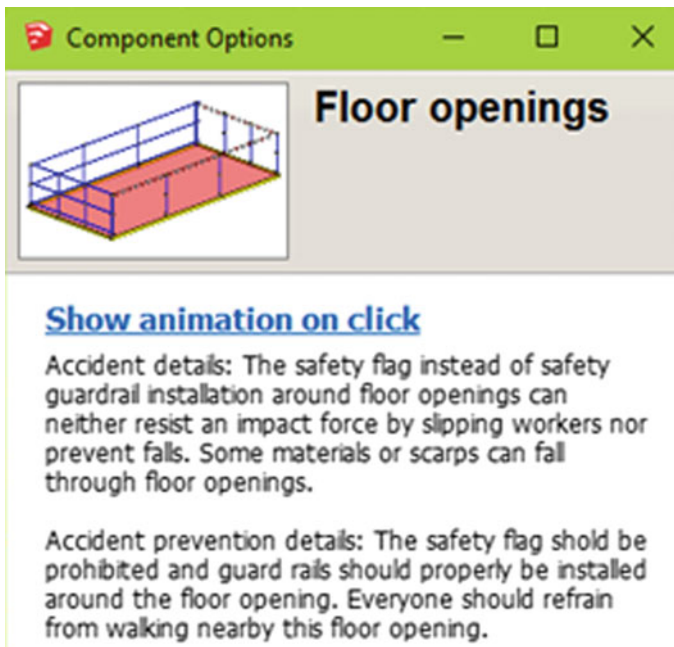
Fig. 3 An example of the presentation of safety knowledge through the component options pop-up

diversified workforce, a variety of activities at different stages of the construction, the nature of the construction project, and the availability of equipment used for the presentations.

4 Conclusion

This research has developed BIM-CSKM, which is the method for storing and presenting safety knowledge. The test results show the characteristics of various safety knowledge captured from different positions and experienced individuals in the company. The evaluation results show that the presentation with animation and visualization can assist the learners to efficiently understand the details of the safety knowledge so that they can implement and follow the safety knowledge correctly. The construction company can apply this method for sharing safety knowledge to other people in the company. It helps facilitate learning and fully utilizing that valuable knowledge to prevent similar problems or accidents happen again. The knowledge management for construction safety by BIM-CSKM cannot be successful if top management does not support and people in the company do not cooperate and accept changes.

References

1. Kanjananit, P., Ninphan, P., Prasatkhetragarn, N.: Knowledge Management: To Enhance the Quality Cycle. Office of the Higher Education Commission, Bangkok (2003)
2. Singapore Productivity and Standards Board: Primer on Knowledge Management. Integrated Press, Singapore (2001)
3. Lin, Y.-C., Lee, H.-Y.: Developing project communities of practice-based knowledge management system in construction. Autom. Constr. **22**, 422–432 (2012). https://doi.org/10.1016/j.autcon.2011.10.004
4. Ding, L.Y., Zhong, B.T., Wu, S., Luo, H.B.: Construction risk knowledge management in BIM using ontology and semantic web technology. Saf. Sci. **87**, 202–213 (2016). https://doi.org/10.1016/j.ssci.2016.04.008
5. Office of the Public Sector Development Commission (OPDC): Organization Improvement Toolkits. Vision Print and Media, Bangkok (2008)
6. Chaikrongrag, P., Angkasith, V.: Organizing knowledge creation: the implementation of SECI model in slider fabrication in hard disk drive industry. KMUTT Res. Dev. J. **33**(3), 215–222 (2010)
7. Sooksil, N., Benjaoran, V.: Model for predicting impact of loss due to task demand exceeded capability of construction workers. KMUTT Res. Dev. J. **38**(2), 117–131 (2015)
8. O'Dell, C., Grayson, C.J., Essaides, N.: If Only We Knew What We Know: The Transfer of Internal Knowledge and Best Practice. The Free Press, New York (1998)

Finite Element Analysis of the Loading Position Effects to the Bending Behaviour of Triangular Web Profile Steel Section

F. De'nan, K. K. Shoong and N. S. Hashim

Abstract Loading position effect on the bending behaviour of triangular web profile (T_{RI}WP) steel section is presented in this paper. A T_{RI}WP steel section was made by the connection two flanges to a web plate triangular profile, which were analysed using LUSAS finite element software. The study involved 3000, 4000 and 4800 mm span of T_{RI}WP steel sections with size $200 \times 100 \times 6 \times 3$ mm and $180 \times 75 \times 5 \times 2$ mm, respectively. Three types of loading positions were studied: the middle of the slanting part, the upper corner and the lower corner (of the corrugation profile). It was observed that the middle of the inclined part loading position contributes lower deflection compared to the others loading position. This was true for both deflection in major axis of T_{RI}WP1 and T_{RI}WP2 steel section. This was due to the middle position (inclined part) of the web section, which is more stiffen between the upper and lower positions of the web. Meanwhile, for the minor axis, the deflection value of inclined part is nearly close to the upper and lower loading position results, although the deflection value of the inclined part is the highest compared to the other loading positions.

Keywords Finite element analysis · Bending behaviour · Triangular web profile

1 Introduction

Economic design is achieved by changing the web into a corrugation profile. Through web corrugation profile, it is increased the stability against buckling. Besides that, corrugation web profile possible to reduce the raw material and cost of

F. De'nan · K. K. Shoong · N. S. Hashim (✉)
School of Civil Engineering, Universiti Sains Malaysia,
Engineering Campus, 14300 Nibong Tebal, Penang, Malaysia
e-mail: wani_a02@yahoo.com

F. De'nan
e-mail: cefatimah@usm.my

K. K. Shoong
e-mail: cekkc@usm.my

web stiffeners. It is estimated more than 30% compared with standard I-beams and about 10–30% compared with conventional built-up sections. By comparing with a truss system, high strength-to-weight ratio section is achieved and reduces the cost and steel, as the clear spans increase. In addition, it is reduced the erection cost. Lifting equipment are not required when lifting and unloading the beam because over the weak axis bending and rotation, the corrugation in the web makes the section high on bending resistance. The necessity for brace angles or tubes against rotation resistance is reduced, further erection cost and time also reduced [1].

Bending behaviour almost the mainly structural action for each section. Other effects such as bearing and shear are also presented. Therefore, it is important that the stiffness properties of the section are adequate to avoid any excessive deflection.

Previous researchers had conducted several tests to investigate structural properties of the vertically trapezoidal corrugation such as bending and shear mode and including compressive patch loads. It was found that local buckling on the web for coarse corrugation and global buckling on the web for dense corrugation was the main failure effects under shear loading [2]. Since early 60s, the studies on the behaviour of trapezoid web profile beam are conducted and only on 1980, the full capacity of trapezoid web profile has been explored in detail [3–5].

According to the previous study, when the trapezoidal web girder is loaded at the centre of the oblique corrugation part, the highest strength value is achieved. Meanwhile, when it is applied at the centre of the flat corrugation part, the girder has the lowest strength value [6, 7]. With a Ramberg–Osgood strain-hardening model for webs, the ultimate strength of girder is about 8–12%, which was higher than the ultimate strength of an elastic-perfectly plastic analysis. Through block distribution analysis, it was found that the degree of strain hardening and yield stress for the small region material at the corner of the web profile is higher than in other regions. However, the ultimate and the shear capacity post-buckling increase by the increment of web thickness. The corrugation depth did not affect the ultimate shear capacity but affected the buckling mode localization degree. Thus, in order to increase the bending behaviour of corrugated steel section, a new shape of steel section known as triangular web profile ($T_{RI}WP$) steel section has been studied in this paper.

This triangular web profile ($T_{RI}WP$) steel section eliminated the eccentric stiffeners as in trapezoidal web steel section. The transition model from trapezoidal web steel section to triangular web profile ($T_{RI}WP$) steel section are clearly figured in Fig. 1. This type of steel section was used to study the effect of the loading position to the bending behaviour in major (I_x) and minor (I_y) axes of $T_{RI}WP$ by finite element analysis.

Generally, without carrying any axial stresses due to flexure, prestressing, creep, the corrugated webs can withstand shearing forces. Thus, only pure shear stresses appear in the corrugated webs. As a result, by using corrugated webs, alternative attractive to composite bridges girder is obtained [8–11].

Ordinary plane web I-beam was tested experimentally to analyse the strength effects on a beam web corrugation. The comparison between the results obtained from both methods, for the plane web type, shows 3.1–7.1% differences and for the
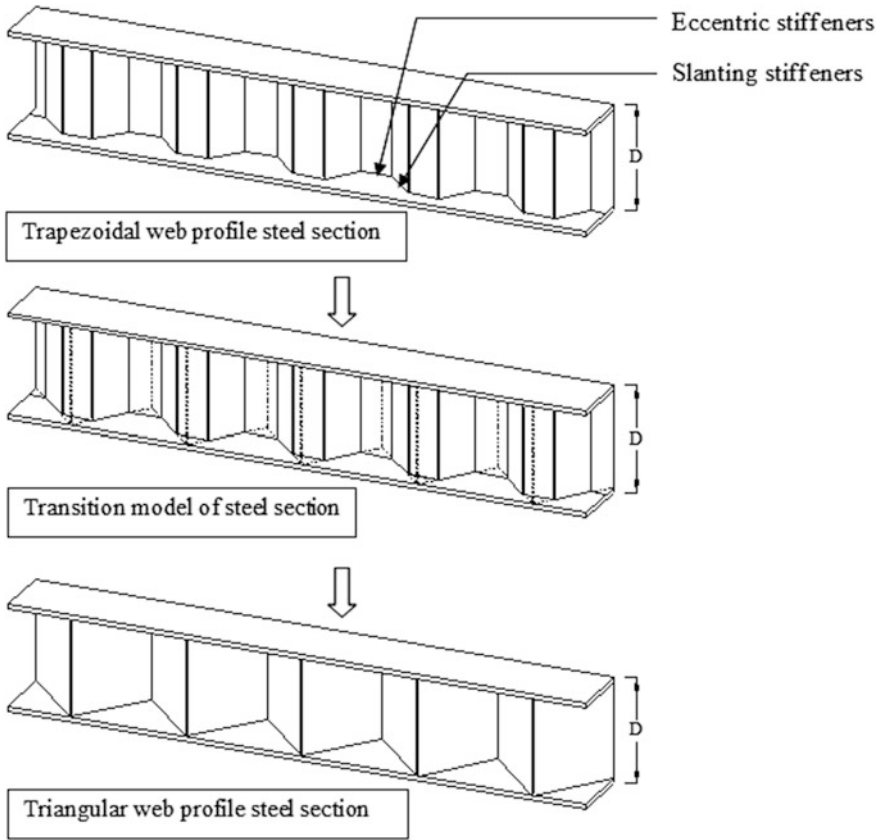
Fig. 1 The transition model from TWP steel section to T_{RI}WP steel section

beams with vertical corrugated web, 38.8–54.4% able to stand higher moments than the horizontal type. The vertical corrugated web provides a more resistance to the flange buckling, between the plane and horizontal corrugated web types and the same results for the other three radiuses. Moreover, corrugated web beams with larger corrugation radius could resist higher bending moment, and it is true for the sizes used. 10.6% reduction in weight for the vertical corrugated web compared to the FW beam [12]. However, the compression flange yielded and vertically buckled into the crippled web [13]. Besides that, larger radius corrugation was able to resist high bending until the yielding stage. This affected the increment of the second moment of area (I) that controls the bending stresses (σ_{zz}).

In addition, the panel width had the most significant effect on the mode of buckling. An ideal ratio between the inclined panel width and the horizontal panel width for a trapezoidal corrugation profile is proposed to be 1.0 [14]. Besides that, global buckling mode governs the instability behaviour for significantly small corrugation width b (dense corrugation), and the local buckling mode governs the

behaviour for significantly large values of b. The corrugation angle also affects the interactive critical stress for small panel widths, b where the behaviour is controlled by either pure global buckling or interaction between global buckling and steel yielding. The numerical analysis reveals that after web buckling has occurred, corrugated web girders still continue carrying the load. The width of panel clearly affected the post-buckling strength. For corrugated webs with bigger panel widths, the strength of post-buckling reached 53% for a 400 mm panel width. For such girders, the lateral torsion-flexure buckling resistance is 12–37% higher than the traditional plane webs plate girders [15].

In web, the shear force caused some varying buckling modes such as local, global and interactive shear buckling. However, the shear force due to accordion effects was overcome by using corrugated web [16]. In particular, the interactive shear buckling among local and global modes was clearly discussed [17].

It was found that the critical moment increases from constant web to corrugation web [18]. About 21–29% the elastic lateral-torsional buckling strength of the I-girder with trapezoidal web corrugations higher than the I-girder with flat webs [19].

For I-girder with corrugated webs in a plastic and elastic stage, as the section became elastic section, the effect of bracing stiffness decreased and increased as the lateral unbraced length increases [20]. It means modified slenderness of I-girder is one of the factors that affected the stiffness of the restraint. Moreover, numerical simulations indicated that when the loading length increases, the load carrying capacities increased linearly. However, the load carrying capacity decreases for the high web or fold ratios. Besides that, when the corrugation angle increases, the patch loading resistance increases and the failure mode in the parameter range of bridges is mainly local buckling [21].
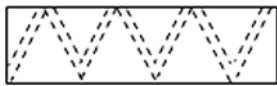
Throughout this investigation, a triangular web profile ($T_{RI}WP$) steel section was selected. Parametric studies were carried out on $T_{RI}WP$ to investigate the loading position effects to the bending behaviour.

2 Parametric Study

Two types of mild sections were studied, namely, $T_{RI}WP1$ ($200 \times 100 \times 6 \times 3$ mm) and $T_{RI}WP2$ ($180 \times 75 \times 5 \times 2$ mm). A parametric study by FEA on the $T_{RI}WP$ was analysed to obtain the loading position–deflection graphs of the bending behaviour for $T_{RI}WP$ steel sections. For this analysis, no initial imperfectness and load eccentrically occurred were assumed. Table 1 shown the dimensions for each type of section.

The maximum deflection, δ for elastic condition of a simply supported beam as shown in Fig. 1, can be calculated by using Eq. 1, if a point load, P, is applied at the mid-span:

Table 1 The detail properties of $T_{RI}WP$ and FW specimens

Case	Plan view		Size
$T_{RI}WP1$	L = 3000, 4000, 4800 mm		200 × 100 × 6 × 3 mm
$T_{RI}WP2$	L = 3000, 4000, 4800 mm		180 × 75 × 5 × 2 mm

$$\delta = \frac{PL^3}{48EI} \tag{1}$$

where I = second moment of area, P = applied point load, L = length of span, E = elastic modulus of steel, and δ = vertical deflection at midspan.

A linear relationship between the load (P) and deflection (δ) can be obtained from a load–deflection graph [22]. In this study, each surface of $T_{RI}WP$ models is formed by 4 nodal lines. Thin shell element in 3D dimension was selected to represent the model element type. Each of $T_{RI}WP$ steel section was assigned ungraded mild steel with Young's modulus, E, of 209×10^3 N/mm^2, shear modulus, G, of 79×10^3 N/mm^2 and Poisson ratio of 0.3. Throughout the analysis, the material properties remain constant.

The boundary and loadings situation have to represent the actual situation of triangular web profile for its application. Throughout this analysis, the total global distributed load is assigned in the middle of the span. The nodes at the support are constrained in its x, y and z translation at both sides of the support to make sure the load is applied entirely the whole web. The boundary and loading conditions assigned to the model in the minor and major axis are shown in Fig. 2. The support condition enlargement to the model was shown in the respective figure.

3 Convergence Study

Increased mesh density and higher order elements were inputted in each part of the model simultaneously to get the suitable mesh for $T_{RI}WP$ steel section model. It is clearly indicated that from the Model 1 to Model 6, the displacement increment becomes smaller. It is observed that a convergence mesh is obtained when the number of elements is 234. Therefore, elements size 20 is used in following analyses.

(a) The loading and support situation in major axis

(b) The loading and support situation in minor axis
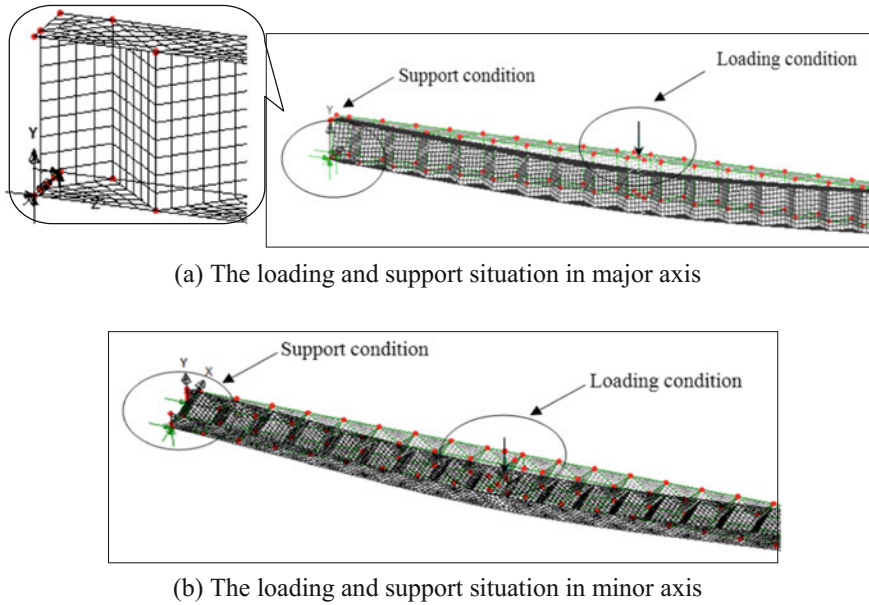
Fig. 2 Mode of deflection of a $T_{RI}WP$ model

4 Results and Discussion

The effects of the stated three loading positions on bending behaviour as shown in Fig. 3 were investigated. The aim of this analysis is to know the best loading point for use in design work.

The results of analysis due to the loading position effects under point load 14 kN in major axis and 3 kN in minor axis are listed in Table 2 for the $T_{RI}WP1$ steel section and Table 3 under point load 8 kN in major axis and 1 kN in minor axis for the $T_{RI}WP2$ steel section, and are shown in Figs. 4 and 5. From Figs. 4a and 5a, it was noted that the loading position at the middle of the inclined part gives minimum deflection compared to the others loading position. This was true for both

(a) The middle of the slanting   (b) The lower corner   (c) The upper corner
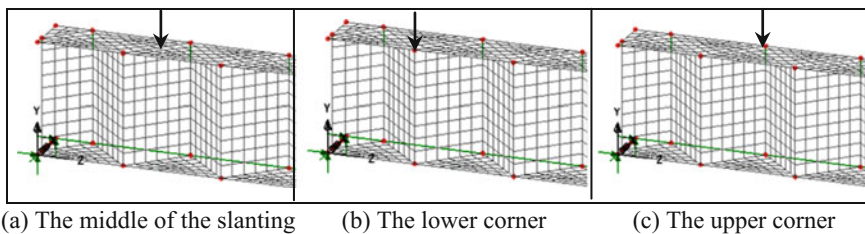
Fig. 3 Types of loading position

Table 2 Deflection in minor and major axis for section 200 × 100 × 6 × 3 mm

Loading position	Span (mm)	Deflection in major axis, δ_{major} (mm)	Deflection in minor axis, δ_{minor} (mm)
At the upper corner	3000	10.47	3.74
	4000	19.04	11.70
	4800	26.95	21.93
At the lower corner	3000	20.76	3.72
	4000	28.19	11.75
	4800	35.38	21.99
At the middle of the slanting part	3000	5.40	5.54
	4000	8.81	11.79
	4800	12.62	22.02

Table 3 Deflection in minor and major axis for section 180 × 75 × 5 × 2 mm

Loading position	Span (mm)	Deflection in major axis, δ_{major} (mm)	Deflection in minor axis, δ_{minor} (mm)
At the upper corner	3000	11.52	3.47
	4000	22.05	11.97
	4800	27.36	18.98
At the lower corner	3000	17.87	3.50
	4000	21.97	11.95
	4800	32.32	19.01
At the middle of the slanting part	3000	4.95	3.90
	4000	8.81	12.36
	4800	13.75	19.23

deflections in the major axis of $T_{RI}WP1$ and $T_{RI}WP2$ steel section. This was due to the middle position (inclined part) of the web section, which is more stiffen between the upper and lower positions of the web. Meanwhile, for the minor axis, the deflection value of inclined part is nearly close to the upper and lower loading position results, although the deflection value of the inclined part is the highest compared to the other loading positions (see Figs. 4b and 5b).

In this section, parametric studies were presented to investigate how loading position influences the bending behaviour in minor and major axis of $T_{RI}WP$ steel section. For conclusion, the best loading point in bending about the major axis is in the middle of the slanting part. Deflection due to bending in minor axis is found more or less same of each loading point.

The comparison between maximum deflection results of the experimental and theoretical analysis for FW and $T_{RI}WP$ steel section was presented [22] and tabulated in Tables 4 and 5. It was found that the deflections in major axis for $T_{RI}WP$ steel section is higher compared to that of FW steel section. However, deflection in minor axis for $T_{RI}WP$ steel section is lesser compared to that of FW steel section.
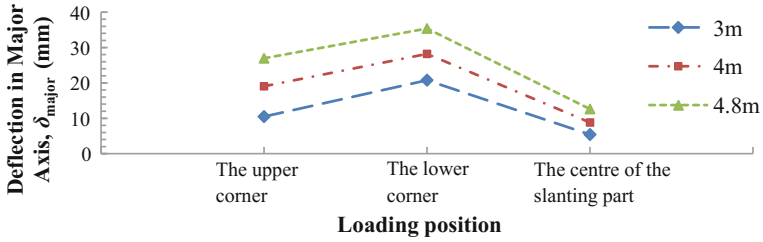
(a) Major axis (I_x) under point load 14 kN
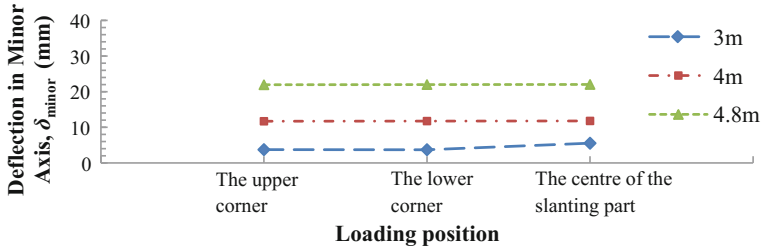
(b) Minor axis (I_y) under point load 3 kN

Fig. 4 Deflection, δ versus loading position (section 200 × 100 × 6 × 3 mm)
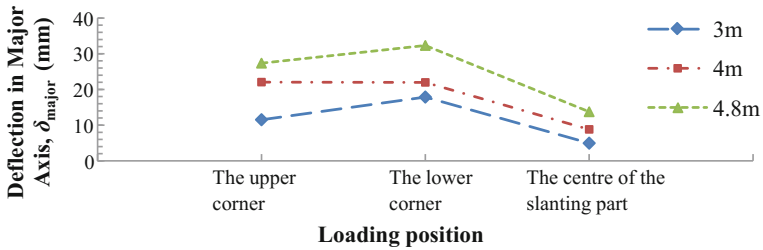
(a) Major axis (I_x) under point load 8 kN
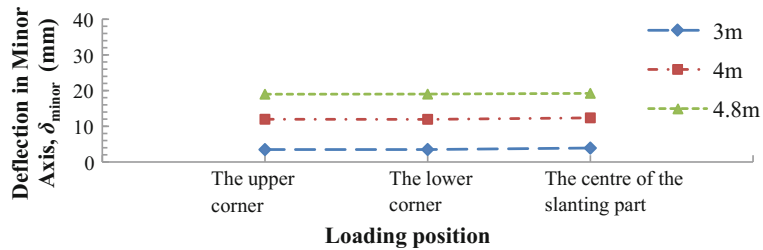
(b) Minor axis (I_y) under 1 kN point load

Fig. 5 Deflection, δ versus loading position (section 180 × 75 × 5 × 2 mm)

Table 4 Deflections for $T_{RI}WP1$ and FW1 steel section ($200 \times 100 \times 6 \times 3$ mm)

Span (mm)	Major axis			Minor axis		
	$\delta_{T_{RI}WP}$ (mm)	δ_{FW} (mm)	δ_{THEORY} (mm) Equation 1	$\delta_{T_{RI}WP}$ (mm)	δ_{FW} (mm)	δ_{THEORY} (mm) Equation 1
3000	5.403	3.088	2.908	5.536	8.057	8.071
4000	8.806	6.924	6.894	11.789	17.283	19.130
4800	12.616	13.100	11.913	22.015	32.776	33.060

Table 5 Deflections for $T_{RI}WP2$ and FW2 ($180 \times 75 \times 5 \times 2$ mm)

Span (mm)	Major axis			Minor axis		
	$\delta_{T_{RI}WP}$ (mm)	δ_{FW} (mm)	δ_{THEORY} (mm) Equation 1	$\delta_{T_{RI}WP}$ (mm)	δ_{FW} (mm)	δ_{THEORY} (mm) Equation 1
3000	4.951	3.636	3.281	3.900	7.710	7.654
4000	8.811	7.856	7.777	12.362	18.343	18.140
4800	13.754	13.502	13.440	19.230	30.858	31.346

It means in minor axis, the $T_{RI}WP$ steel section is stiffer compared to that of FW steel section. Therefore, in minor axis, $T_{RI}WP$ steel section has a higher bending resistance than FW steel section.

The load versus deflection of experimental and analytical study for both types of steel section was plotted. It was observed the entire data is returned to zero when the applied load being unloaded. It means the section returns to the original shape after the loading being unloaded. This proved that bending tests were carried in elastic condition only.

In major axis, the maximum deflection of $T_{RI}WP$ was higher than that of the FW steel section. The web section with triangular profile acted as stiffeners was not effected the bending behaviour in major axis. However, in minor axis, the maximum deflection of $T_{RI}WP$ steel section was lower than that of the FW steel section.

In summary, the deflection in minor axis for $T_{RI}WP$ for both sizes is lower than FW steel section. It shows that $T_{RI}WP$ steel section is stiffer compared to FW steel section in minor axis. Meanwhile, the deflections in major axis for $T_{RI}WP$ is higher than that of FW steel section.

5 Conclusions

In general, the study of corrugated steel section and literature on the previous research were reviewed in this paper. It was concluded that the bending behaviour of FW and TWP sections research is early discussed. However, the bending

behaviour research of $T_{RI}WP$ steel section is not available yet. From the previous analysis, it was identified that bending behaviour of trapezoidal web girder is dependent on loading position. Therefore, investigation of the effects of loading position was studied in detail because it may influence the bending behaviour of $T_{RI}WP$ steel section.

A parametric study was done by using LUSAS software. Bending behaviour for both sizes of $T_{RI}WP$ due to the effects of section properties was observed and investigated. It was observed from the parametric study results that the best loading point in bending about major axis is at the middle of the slanting corrugation part. Deflection due to bending about minor axis is found to be approximately the same regardless of position of the loading point. For economic design consideration in bending, appropriate loading position should be early considered.

References

1. AISC: Modern Steel Construction. American Institute of Steel Construction, Chicago, IL (1999)
2. Elgaaly, M., Hamilton, R.W., Seshadri, A.: Shear strength of beams with corrugated webs. J. Struct. Eng. **122**(9), 390–398 (1996)
3. Elgaaly, M., Seshadri, A., Hamilton, R.W.: Bending strength of steel beams with corrugated webs. J. Struct. Eng. **123**(6), 772–782 (1997)
4. Johnson, R.P., Cafolla, J.: Corrugated webs in plate girders for bridges. Proc. Inst. Civ. Eng. Struct. Buildings **122**(2), 157–164 (1997)
5. Johnson, R.P., Cafolla, J.: Local flange buckling in plate girders with corrugated webs. Proc. Inst. Civ. Eng. Struct. Buildings **122**(2), 148–156 (1997)
6. Luo, R., Edlund, B.: Ultimate strength of girders with trapezoidally corrugated webs under patch loading. Thin-Walled Struct. **24**(2), 135–156 (1996)
7. Luo, R., Edlund, B.: Shear capacity of plate girders with trapezoidally corrugated webs. Thin-Walled Struct. **26**(1), 19–44 (1996)
8. Sayed-Ahmed, E.Y.: Behaviour of steel and (or) composite girders with corrugated steel webs. Can. J. Civ. Eng. **28**, 656–672 (2001)
9. Hassanein, M.F., Kharoob, O.F.: Behaviour of bridge girders with corrugated webs: (I) real boundary condition at the juncture of the web and flanges. Eng. Struct. **57**, 554–564 (2013)
10. Hassanein, M.F., Kharoob, O.F.: Behaviour of bridge girders with corrugated webs: (II) shear strength and design. Eng. Struct. **57**, 544–553 (2013)
11. Ko, H.-J., Moon, J., Shin, Y.-W., Lee, H.-E.: Non-linear analyses model for composites box-girders with corrugated steel webs under torsion. Steel Compos. Struct. **14**(5), 409–429 (2013)
12. Chan, C.L., Khalid, Y.A., Sahari, B.B., Hamouda, A.M.S.: Finite element analysis of corrugated web beams under bending. J. Constr. Steel Res. **58**(11), 1391–1406 (2002)
13. Khalid, Y.A., Chan, C.L., Sahari, B.B., Hamouda, A.M.S.: Bending behaviour of corrugated web beams. J. Mater. Process. Technol. **150**(3), 242–254 (2004)
14. Sayed-Ahmed, E.Y.: Plate girders with corrugated steel webs. AISC Eng. J. First Quarter, 1–13 (2005)

15. Sayed-Ahmed, E.Y.: Lateral torsion-flexure buckling of corrugated web steel girders. Proc. Inst. Civ. Eng. Struct. Buildings **158**(1), 53–69 (2005)
16. Moon, J., Yi, J., Choi, B.H., Lee, H.-E.: Shear strength and design of trapezoidally corrugated steel webs. J. Constr. Steel Res. **65**(5), 1198–1205 (2009)
17. Yi, J.-W., Gil, H., Youm, K., Lee, H.: Interactive shear buckling behavior of trapezoidally corrugated steel webs. Eng. Struct. **30**(6), 1659–1666 (2008)
18. Korrani, H.R.K.N., Molanaei, S.: The effects of the corrugation profiles of the web on the lateral-torsional buckling strength of the inelastic I-girder. World Appl. Sci. J. **8**(5), 527–530 (2010)
19. Nguyen, N.D., Kim, S.N., Han, S.-R., Kang, Y.-J.: Elastic lateral-torsional buckling strength of I-girder with trapezoidal web corrugations using a new warping constant under uniform moment. Eng. Struct. **32**(8), 2157–2165 (2010)
20. Korrani, H.R.K.N.: Lateral bracing of I-girder with corrugated webs under uniform bending. J. Constr. Steel Res. **66**(12), 1502–1509 (2010)
21. Kövesdi, B., Braun, B., Kuhlmann, U., Dunai, L.: Patch loading resistance of girders with corrugated webs. J. Constr. Steel Res. **66**(12), 1445–1454 (2010)
22. De'nan, F., Hashim, N.S.: Experimental study on bending behaviour of triangular web profile steel beam section. Int. J. Res. Eng. Technol. **2**(10), 384–390 (2013) | eISSN: 2319-1163 | pISSN: 2321-7308

Comparative Analysis of Progressive Collapse of Regular and Irregular RC Building

Moinul Haq and Ashish Agarwal

Abstract Progressive collapse analysis of three 20-storey regular building with/ without central atrium and irregular RC frame buildings using linear elastic static and nonlinear static methodologies is carried out using SAP2000 software. Irregularity is provided by taking stepped-type geometry in elevation along shorter bay. Each procedure of the performed analysis is investigated thoroughly and DCR values are quantified, described in brief with advantages and disadvantages, comparing significantly according to GSA guidelines. The purpose of this research is to investigate structural linear and nonlinear behaviour of different building structures and develop design rules and strategies to economically design structures resistant to progressive collapse. Using nonlinear static analysis, rotation and displacement of plastic hinges are observed along with percentage GSA load attempt caused due to sudden removal of primary load-bearing column member of ground floor from different positions.

Keywords Progressive collapse · LSA · NSA · Multi-storeyed RC building GSA

1 Introduction

A structure encounters progressive collapse in condition when an essential basic member collapse because of man-made or natural causes, the loads from the lost member are transferred to connecting members, and afterward adjoining member fails because of the redistributed loads, and the process repeats until a disproportionate amount of the structure is damaged or collapses. The term initiating damage refers to local damage that sparks progressive collapse [1].

M. Haq (✉) · A. Agarwal
Civil Engineering Department, Aligarh Muslim University, Aligarh, India
e-mail: mmhaq2010@gmail.com

Progressive collapse includes nonlinear mechanism in which members of structure are stressed beyond their elastic limit to failure [2]. The objective of this study is to identify a methodology for determining the potential of a structure to progressive collapse using different analysis techniques. Static Linear analysis and Static Nonlinear (Pushover Analysis) techniques are considered in contrast for analyzing the structure [3].

1.1 Building Geometry

Three 20-storey RC Frame building, i.e. without atrium, with atrium and stepped along shorter span are considered for analysis (Fig. 1). Size of all buildings is 40 m × 32 m with 4 m × 4 m panel size in plan with overall height of 57 m. Storey height for top 17 floors are 3 m and lowest three are of 2 m height utilized for parking spaces.

The size of beam and column is taken as 250 mm × 300 mm and 450 mm 450 mm respectively with 150 mm slab thickness. M25 concrete and Fe415 & Fe250 steel grade is used for material properties. Dead load of structure with walls on periphery of building and live load of 3 kN/m^2 is taken into account for design of building according to IS 456-2000.

For building with central atrium (Fig. 1b), the size of atrium is 16 m × 16 m, whereas in stepped building stepping is done along shorter span after 7th and 12th storey (Fig. 1c).
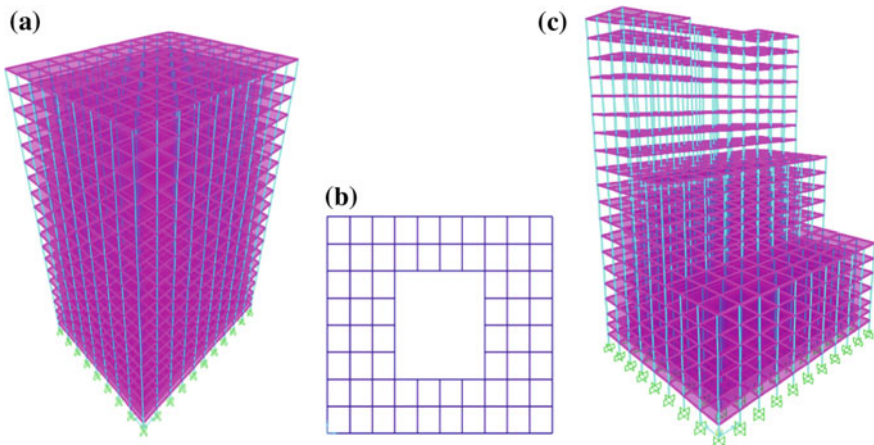
Fig. 1 **a** Regular building with no atrium. **b** Regular building plan with atrium & **c** Irregular building with stepped elevation

2 Linear Static Analysis

In linear static analysis (LSA), different cases of column removal from the specified location of ground floor are considered in geometry (Fig. 2) and analysis with the gravity load given by Eq. 1 imposed on the structure has been carried out. From the analysis results, Demand Capacity Ratio (DCR) is calculated for each structural member after observing demand at critical locations in each building. These DCR values as calculated from this analysis will ultimately assist to ascertain the potential against progressive collapse [4].

While performing a static linear analysis, the vertical load case applied to the structure is taken as

$$Load = 2(DL + 0.25LL) \tag{1}$$

The GSA 2003 proposed the use of the DCR, the ratio of the member force and the member strength, as a criterion to determine the failure of main structural members by the linear analysis procedure [5]

$$DCR = Q_{UD}/Q_{CE}, \tag{2}$$

where, Q_{UD} is the influential force (demand) deduced in components (moment, axial force and shear, etc.); and Q_{CE} is the expected ultimate capacity of the component (moment, axial force, shear, etc.). At any section, capacity of the member is calculated as per IS456:2000 from the obtained reinforcement details after analysis and design [6].

The permissible DCR values according to GSA guidelines for primary and secondary structural members are
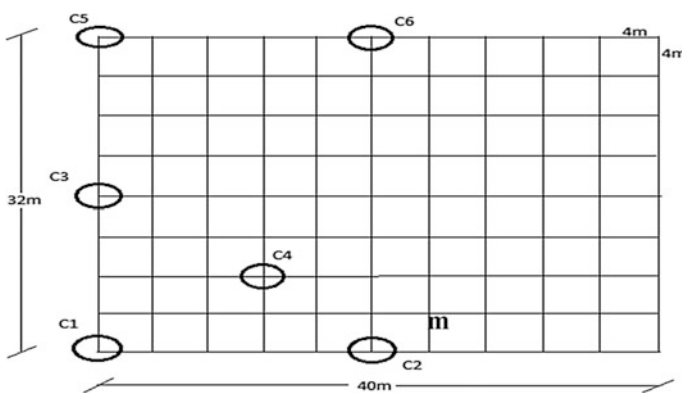
Fig. 2 Building plan grid showing various positions from where ground floor column is removed in different structures

DCR < 2.0; for Regular Buildings
DCR < 1.5; for Irregular Buildings

If the DCR of a member at any section exceeds the acceptance criteria in shear and flexure as stated above, the member is considered as failed.

The steps followed in LSA according to GSA 2003 guideline. [7]

1. The space models for different structural geometry are prepared followed by concrete design and reinforcement check which ultimately helps to calculate the capacity of the member in flexure. Strength increase factor is considered during PCA.
2. Before performing LSA, DCR values are generated by calculating demand and capacity as per Indian Standard codes provision for each members considering column loss scenario by removing ground floor column from the specified locations as mentioned above one at a time.
3. These calculated DCR values are checked for acceptance criteria along with the comparison in corresponding storeys of structure provided in GSA 2003 [8].

The moment's diagrams for different types of RC frame building with no column removal and column removal from C1, C2, C3 and C4 locations are shown in Figs. 3, 4 and 5. The unsymmetrical distribution of moments over the collapsed ground floor column to the top floor is observed in all column removal cases which impart more tendencies to fail in progressive collapse [9].

3 Static Nonlinear Analysis (NSA)

In NSA nonlinear behaviour of structural members attaining maximum load (load-controlled) or maximum displacement (displacement controlled) by applying increasing loads in steps is examined. NSA is also known as "pushover analysis". Ductility of structural components can be quantified by using this method under lateral load conditions. It is a measure which is expressed as the ratio of maximum deformations and yield deformations. Generally, the ability of the structure to attain large ductility results in better performance under earthquake loading. In well-designed structures, pushover analysis engages many structural elements and generally ensures balanced design (strong columns and weak beams, for example) [10]. In most cases, vertical pushover analysis would be load-controlled, since, in analyzing for progressive collapse potential, structural performance under normal service loads is evaluated [11]. Vertical pushover analysis for the evaluation of progressive collapse will lead to overly conservative ductility values. The advantage of this method is that it includes material nonlinear behaviour and the disadvantages of this method are it does not consider dynamic effects such as amplification factors, inertia and damping forces [2].
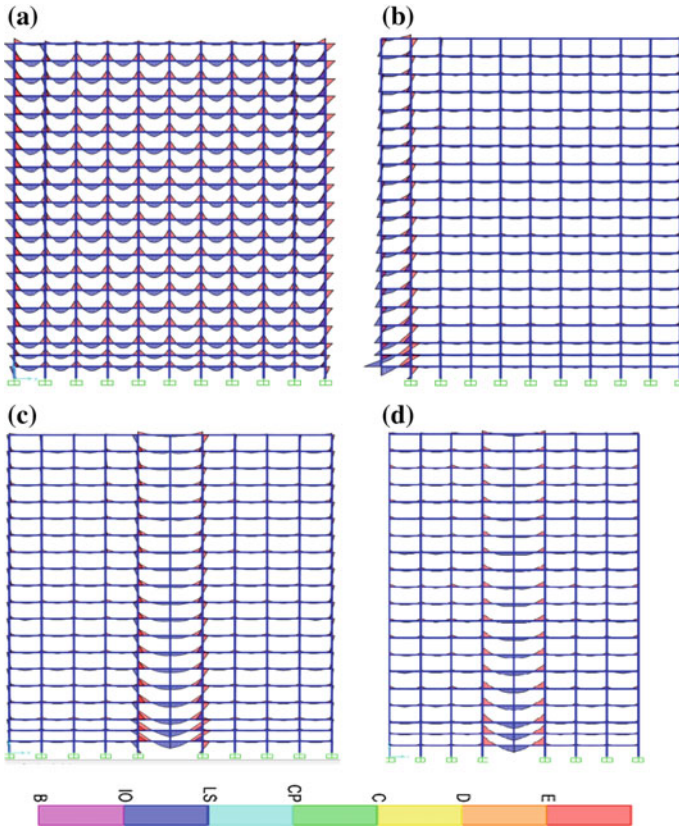
Fig. 3 Moments distribution in regular building when **a** No column removed, **b** Column C1 removed, **c** Column C2 removed, **d** Column C3 removed

The steps followed in NSA according to GSA 2003 guideline [8].

1. The space models for different structural geometry are prepared that consecutively undergo concrete design and reinforcement check which ultimately helps to calculate the capacity of the member in flexure. Strength increase factor is considered during PCA.
2. Before performing NSA, M3 and V2 plastic hinges are assigned at both the ends of beam whereas P-M2-M3 hinges are assigned to columns at both the ends in SAP2000 uses Tables 5-6 of FEMA-356 [12].
3. Perform the analysis after defining the load combination as per GSA for nonlinear case. Hinge formations are observed till failure [7].

Load case defined for static nonlinear analysis is same as static linear analysis. For nonlinear analysis automatic hinge properties are assigned to each frame element.
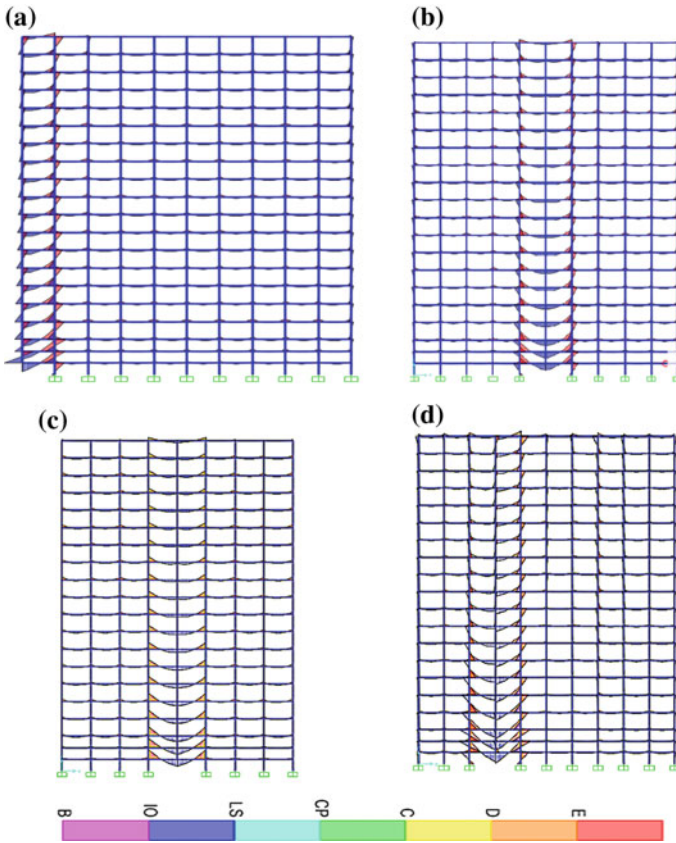
Fig. 4 Moments distribution in building with atrium when, **a** column C1 removed, **b** column C2 removed, **c** column C3 removed, **d** column C4 removed

Figures 6, 7 and 8 shows hinge formed along longer bay in horizontal and traverse direction in different buildings geometry.

It is observed from the pushover analysis results shown in Figs. 6, 7 and 8 that corresponding joints over collapsed column shows excessive deformation, and it should be compulsory to ensure beam–column joint have sufficient strength and ductility so as to ensure permissible hinges formation before opting for pushover analysis.

4 Results

4.1 DCR Values

A plot of DCR values in flexure on ordinate with number of storey on abscissa of Regular Building, Building with atrium and Irregular Building with stepped elevation is shown below in Figs. 9, 10 and 11 respectively.
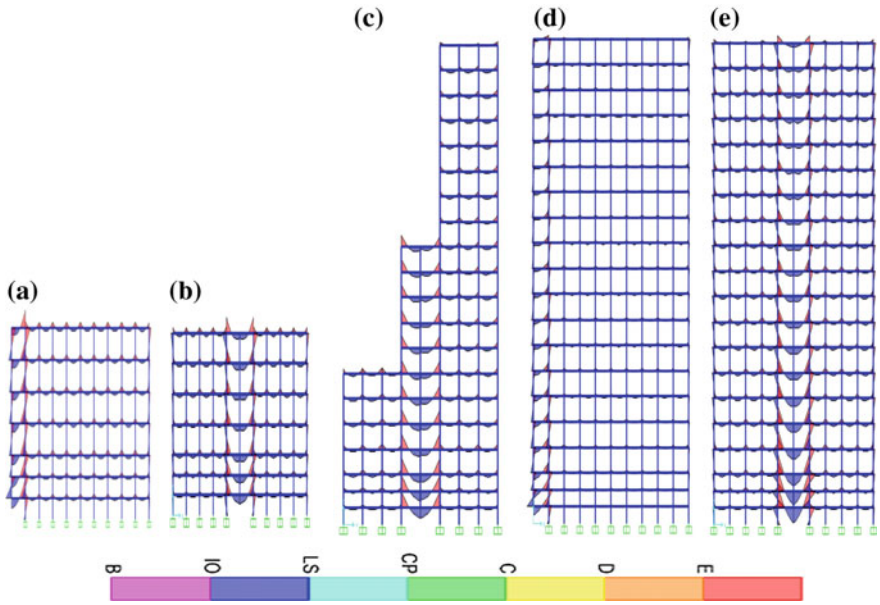
Fig. 5 Moments distribution in irregular building with stepped elevation along shorter span when **a** column C1 removed, **b** column C2 removed, **c** column C3 removed, **d** column C5 removed, **e** column C6 removed
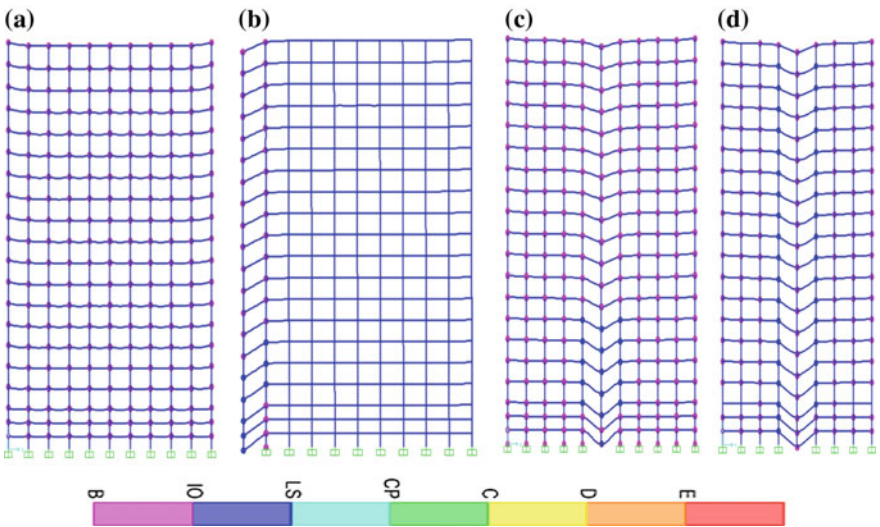
Fig. 6 Hinges formation in regular building when **a** no column removed, **b** column C1 removed, **c** column C2 removed, **d** column C3 removed
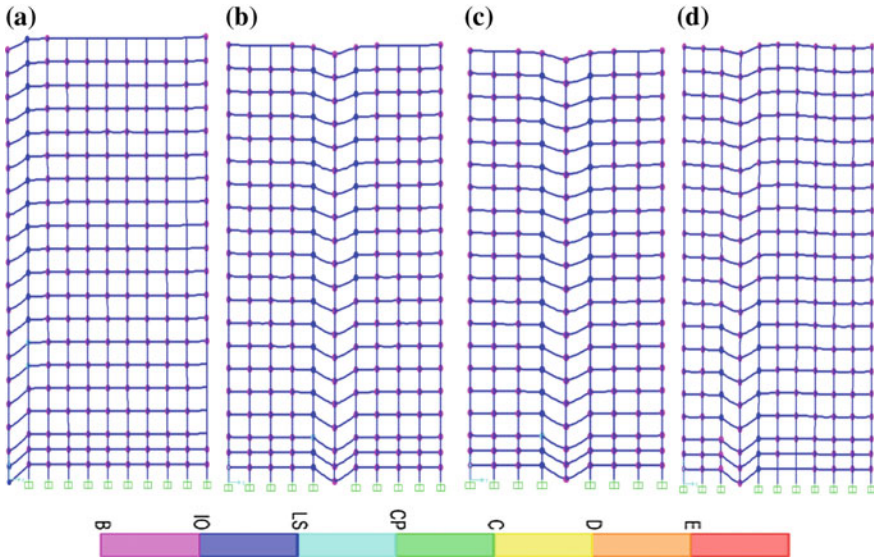
Fig. 7 Hinges formation in building with atrium when, **a** column C1 removed, **b** column C2 removed, **c** column C3 removed, **d** column C4 removed
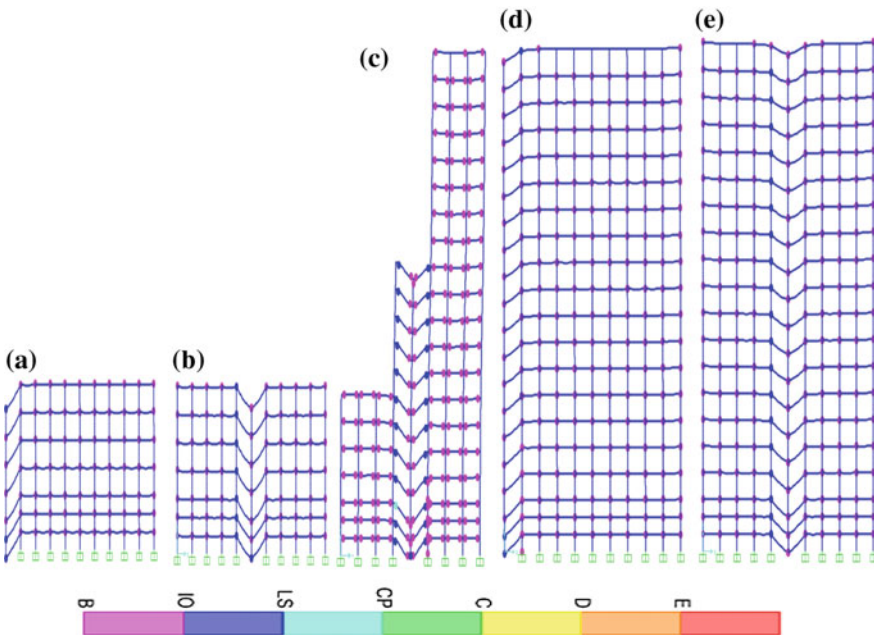
Fig. 8 Hinges formation in Irregular building with stepped elevation along shorter span when **a** column C1 removed, **b** column C2 removed, **c** column C3 removed, **d** column C5 removed, **e** column C6 removed
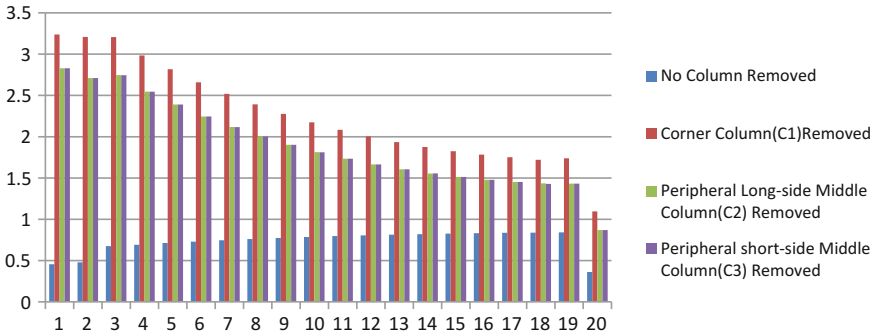
Fig. 9 Plot of DCR values with number of storeys in regular building
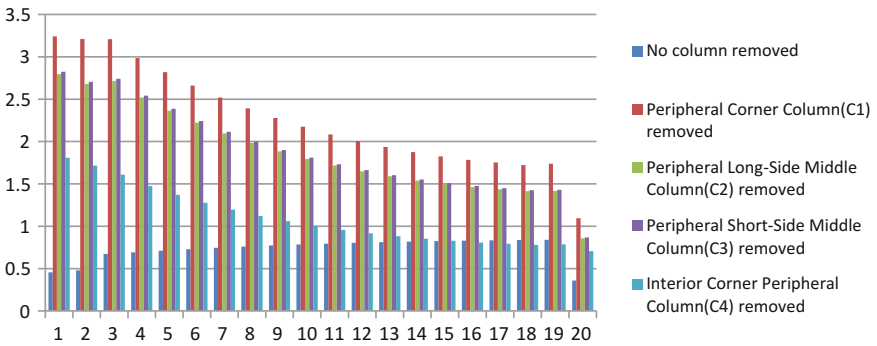
Fig. 10 Plot of DCR values with number of storeys in regular building with atrium
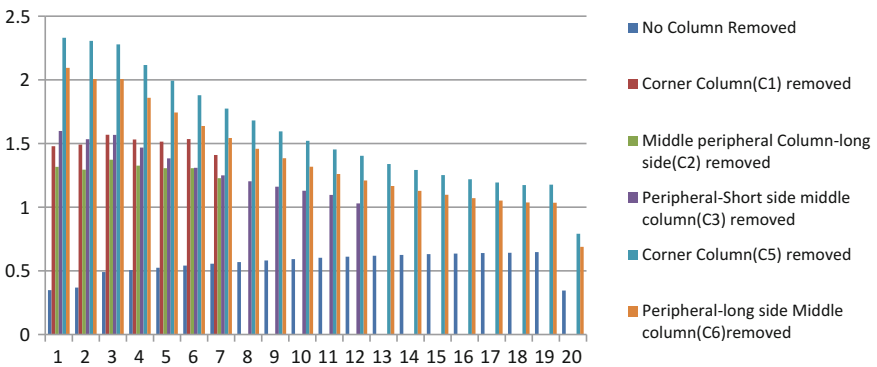
Fig. 11 Plot of DCR values with number of storeys in irregular building

It is seen from shown plots that the corner column collapse in all the buildings shows critical results followed by peripheral column removal case along shorter bay as the DCR values exceeds the permissible limits as per GSA guidelines [8]. In all cases the failure of beam–column joint will initiate above the fully damaged column which will continue to impart to top floor. To resist this failure special consideration in design is given to beam–columns joints of lower 12 storeys in given building structures by taking heavy sections to resist progressive collapse at these critical locations.

4.2 Percentage GSA Load Attempt

Percentage of load attempt is calculated as ratio of summation of the reactions obtained at the supports of the structure for each analysis step and total load applied. In NSA a building is considered to have enough resistance against progressive collapse if the percent load sustained by the building after loss of column in each case exceeds 50% [7].

Percent load attempt in all the column removal cases of regular building are near to permissible limit of 50%. This is due to heavy dead loads of tall building regular structure (Table 1) as compared to building with atrium or stepped elevated building (Tables 2 and 3). In irregular building with stepped elevation the critical value of percent GSA load attempt is due to collapse of corner column of full height building span.

Table 1 GSA load attempt in NSA for regular building

Column removal case	GSA loading condition	%GSA load attempt
Column C1	2(DL + 0.25LL)	66.73
Column C2	2(DL + 0.25LL)	67.78
Column C3	2(DL + 0.25LL)	60.16

Table 2 GSA load attempt in NSA for building with atrium

Column removal case	GSA loading condition	%GSA load attempt
Column C1	2(DL + 0.25LL)	88.05
Column C2	2(DL + 0.25LL)	74.26
Column C3	2(DL + 0.25LL)	74.75
Column C4	2(DL + 0.25LL)	87.25

Table 3 GSA load attempt in NSA for irregular building with stepped elevation

Column removal case	GSA loading condition	%GSA load attempt
Column C1	2(DL + 0.25LL)	75.84
Column C2	2(DL + 0.25LL)	84.62
Column C3	2(DL + 0.25LL)	91.97
Column C5	2(DL + 0.25LL)	54.67
Column C6	2(DL + 0.25LL)	83.97

5 Conclusions

In this research observed data from analysis is compared with the proposed methods to further evaluate accuracy and improve the assumptions and simplifications. Various factors such as different structural geometry, different position of column removal as well as different methods of analysis are considered in this study. The effects of using different bay sizes, atrium space and irregularities on the model should also be investigated to determine how the simplified models stiffness of building changes.

It is observed that high rise RC frame structures has more tendencies to redistribute moments after collapse and consequently offer more resistance to progressive collapse. Maximum consideration to peripheral corner beam–column joint sections in lower storeys above the collapsed column joint should be given for design progressive collapse resistant building as DCR value passed across the permissible limits according to GSA 2003 guidelines. The critical hinges formation in all buildings due to overcoming gravity loads is examined. The ultimate goal of this study is to give insight into ways to help prevent progressive collapse of structures.

References

1. Buscemi, N., Marjanishvili, S.: SDOF model for progressive collapse analysis. In: *Structures Congress* 2005 (2005)
2. Marjanishvili, S.M.: Progressive analysis procedure for progressive collapse. J. Perform. Constructed Facil. **18**(2), 79–85 (2004)
3. Shefna, L. S., Binu, P., Girija, K.: Progressive collapse analysis of a reinforced concrete frame building. Int. J. Civ. Eng. Technol. (IJCIET) **5**(12), 93–98 (2014)
4. Joshi, D. D., Patel, P. V., Tank, S. J.: Linear and nonlinear static analysis for assessment of progressive collapse potential of multistoried building. Structures
5. Kim, J.: Assessment of progressive collapse resisting capacity of steel moment frames. J. Constr. Steel Res. 200901
6. Karuna, S., Yashaswini, S.: Assessment of progressive collapse on a reinforced concrete framed building. Int. J. Emerg. Technol. Adv. Eng. **5**(6) (2015)
7. Ashna, T. E., Nivya J.: Progressive collapse analysis of regular structure. Int. J. Adv. Res. Eng. Manage. (IJAREM) **01**(07), 90–95 (2015). http://ijarem.org/papers/v1-i7/13.pdf

8. General Services Administration (GSA): Progressive Collapse Analysis and Design Guidelines for New Federal Office Buildings and Major Modernization Projects. Office of Chief Architect, GSA, Washington, DC (2003)
9. Sadek, F., Main, J.A., Lew, H.S., Bao, Y.: Testing and analysis of steel and concrete beam column assemblies under a column removal scenario. J. Struct. Eng. **137**, 881–892 (2011)
10. FEMA274: NEHRP Commentary on the Guidelines for the Seismic Rehabilitation of Buildings. Federal Emergency Management Agency, Washington, DC (1997)
11. Bhavik, R. P.: Progressive collapse analysis of RC buildings using non-linear static and non-linear dynamic method. Int. J. Emerg. Technol. Adv. Eng. **4**(9) (2014)
12. FEMA273: NEHRP Guidelines for the Seismic Rehabilitation of Buildings. Federal Emergency Management Agency, Washington, DC (1997)

Nonlinear Analysis of Triangular Web Profile Steel Section Under Bending Behaviour

F. De'nan, K. K. Shoong, N. S. Hashim and Chin Wai Ken

Abstract Corrugated web profiles have been introduced by researchers to increase the stiffness of the web. A triangular web profile (TriWP) steel section is a section of joining slanting stiffeners at a certain corrugation angle forming a triangular web profile. In this research, the nonlinear bending behaviour of TriWP steel section in major axis is analysed by finite element analysis and experimental. From the finite element analysis and experimental testing, it is observed that in major axis FW section shows a higher bending capacity compared to that of TriWP section. Parametric study is carried out to analyse the effects of web thickness, depth, corrugation angle, flange thickness and loading position to bending behaviour of TriWP section. Result of parametric study shows that by the increment of web thickness, flange thickness and depth of section, the bending capacity of TriWP steel section is increased. Moreover, larger corrugation angle also improves the bending capacity as the number of slanting stiffener increases throughout the span as the corrugation angle increased.

Keywords Triangular web profile · Bending capacity · Web thickness
Flange thickness · Corrugation angle · Finite element analysis

F. De'nan (✉) · K. K. Shoong · N. S. Hashim · C. W. Ken
School of Civil Engineering, Universiti Sains Malaysia,
Nibong Tebal, Penang, Malaysia
e-mail: cefatimah@usm.my

K. K. Shoong
e-mail: cekkc@usm.my

N. S. Hashim
e-mail: wani_a02@yahoo.com

C. W. Ken
e-mail: chinwaiken@gmail.com

1 Introduction

Structural element such as beam is capable to withstanding load especially by bending resistance. The induced bending moment on the beam is generally from the external loads, span, weight. It is revealed that I-shaped section is effective to sustain both bending and shears loads into the plane web [1].

The I-section or H-piles are commonly used in design works. Original shapes of these beams are made from two parallel web and flanges which about 30–40% of the whole weight of a medium narrow and width flange is contributed by the web part. In construction application, the web normally resists the compressive stress and transfers the shear in the beam while the flanges bear the most external loads. Thus, cost-saving is achieved by using higher part for the flanges and thinner web material, without affecting the load-carrying capability of the beam [2]. The beams with wholly corrugated web (WCW) are introduced and could economize on materials used and stronger in strength than the conventional beams. The effects of the corrugation parameters and beams' dimensions to the bending performance are still scarce [3] especially for Triangular Web Profile (TriWP) steel section.

Overall construction cost and substantial savings in steel weight is achieved by the use of partial strength or semi-rigid connections. It is concluded that the connection use of extended end-plate has contributed to significant reduction to the deflection and significant increment to moment resistance of the beam compared to that of flush end-plate connection [4].

However, due to the location of the cut out in the parallel parts, local buckling is always crucial. The ratio between 0.18 and 0.7 of corrugation depth (b_t) to length of parallel parts (a_1) leads to higher shear resistance. For the corrugated webs with cut out, the ratio of the length of parallel parts (a_1) to the length of diagonal parts (a_2), $\beta > 1.0$ slightly increases the buckling coefficient. Lower sher resistance is occured if the horizontal eccentricity of cut out was increased. However, the vertical eccentricity is not effected on shear resistance [5].

The resistance of steel girders subjected to applied concentrated forces is called patch load. Through geometric imperfections of nonlinear analysis, failure mode and ultimate load is determined. It was found that by the increment of loading length, flange thickness and flange width is increased by the patch loading resistance. Meanwhile when the fold ratio increased and web ratio is decreased of the load-carrying capacity if failure mode is local buckling [6].

For the case of pure shear force, the failure mode was shear buckling of the web (case $V_1/V_2 = 1$) and the failure mode was local web crippling (case $V_1/V_2 = -1$) for the case of pure patch loading, where V_1 and V_2 are shear forces at the two sides of shear panel. There is no strict limit drawn in the interaction zone under patch loading and bending, however a uniform transition between the two failure modes can be observed [7].

It can be summarized that most of behaviours of corrugated steel section with Trapezoidal Web Profile (TWP) is reviewed by researchers. Study on behaviours of TWP such as bending [8], shear [9], secondary bending moment, lateral torsional

buckling [10, 11], patch loading, partial strength connection, TWP with cut out and combined shear, bending and patch loading is carried out. The advantages of trapezoidal corrugated webs section is verified through the researches.

An alternative built-up section with Triangular Web Profile (TriWP) has been introduced and analysed. A TriWP steel is corrugated at regular interval into triangular shape along the span. This construction improves the ratio of section weight to strength compared to conventional section. In Trapezoidal Web Profile (TWP), the highest ultimate load is applied at the middle of the oblique part, whereas the girder has the lowest ultimate load when it is applied to the middle of the flat part of webs [12]. The introduction of TriWP steel section aborts the use of eccentric stiffeners as used in TWP but maintain the use of slanting stiffeners joining one to each other at a certain corrugation angle forming a triangular web profile [13].

The change in stiffness is small in the shape and material properties are assumed to be the same throughout the deformation process. This is called the elastic deformation. When the applied stresses exceed the yield strength, the beam will deform permanently. This is called plastic deformation. Through nonlinear analysis, the moment capacity of TriWP steel section is determined. The importance of experimental study is to verify the finding through finite element analysis.

2 Methodology

Two approach methods are used to achieve the objective of this analysis including finite element analysis (modelling) and experimental study. For detailed visualization of stresses distribution and displacement, finite element analysis (FEA) is used. Experimental study is carried out to verify the findings of FEA. Parametric study by using LUSAS software to investigate the web thickness, depth, corrugation angle, flange thickness and loading position effects to bending behaviour of TriWP section is done.

3 Test Procedures

3.1 Experimental Study

At the both end, the beam is simply supported and restrained from any side way movement to ensure the bending is uniaxial. The load cell is placed right at the mid span. Two cylindrical loading noses with a spacing one-third of the support span are placed at the centre. Meanwhile, three vertical displacement transducers (LVDT1, LVDT2 and LVDT3), load (P) is applied and increased consistently through the load cells. At each load increment, the readings of the vertical displacement are recorded by the data logger. The test is continued until the beam reaches its ultimate strength. The actual experiment setup is shown in Fig. 1.

(a) FW Section   (b) TriWP Section
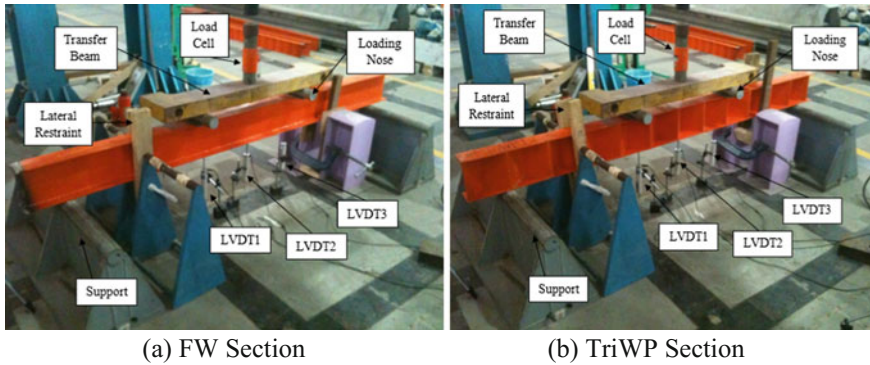
Fig. 1 Actual experiment setup

3.2 Finite Element Analysis

For this analysis, the model properties used are $200 \times 100 \times 6 \times 3$ mm which 200 mm is the depth of the web (D), 100 mm is the flange width (B), 6 mm is the flange thickness (t_f) and 3 mm is the web thickness (t_w). There are several steps to conduct finite element analysis using LUSAS software. First, a new model is created by define the origin of the model and insert the coordinate of the model based on the properties of the model respectively. After that, surfaces are created on the model starting from the flange and the web of the model. Then, meshing, geometry, material, support included the loading are defined and assigned to the section. Nonlinear control option is set up before analysis started.

4 Results and Discussion

4.1 Experimental Study

Laboratory testing has been carried out to determine the moment capacity of TriWP steel section and FW section. Four specimens (TriWP1C, TriWP1D, FW1C and FW1D) with identical geometric parameters such as $D = 200$ mm, $B = 100$ mm, $t_w = 3$ mm and $t_f = 6$ mm are tested. Figures 2 and 3 show the load deflection curves of TriWP section and FW section respectively while Tables 1 and 2 summarize the results of experimental testing and finite element analysis.

The sections behave elastically until it reaches the yield load (P_y) when $P < P_y$, further increase in load (P) results in significant increase in deflection (δ). The peak of the load deflection curve is known as the ultimate load (P_u). From the experiment results, by comparing the yield moment (M_y) and ultimate moment (M_u) of TriWP and FW section, it is found that FW sections has higher bending capacity than
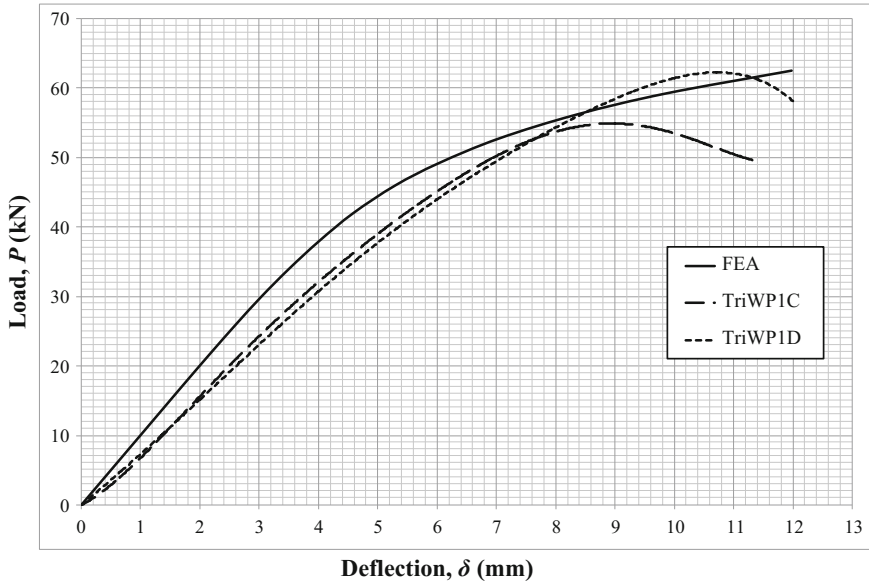
Fig. 2 Load deflection curves of TriWP section (200 × 100 × 6 × 3 mm)
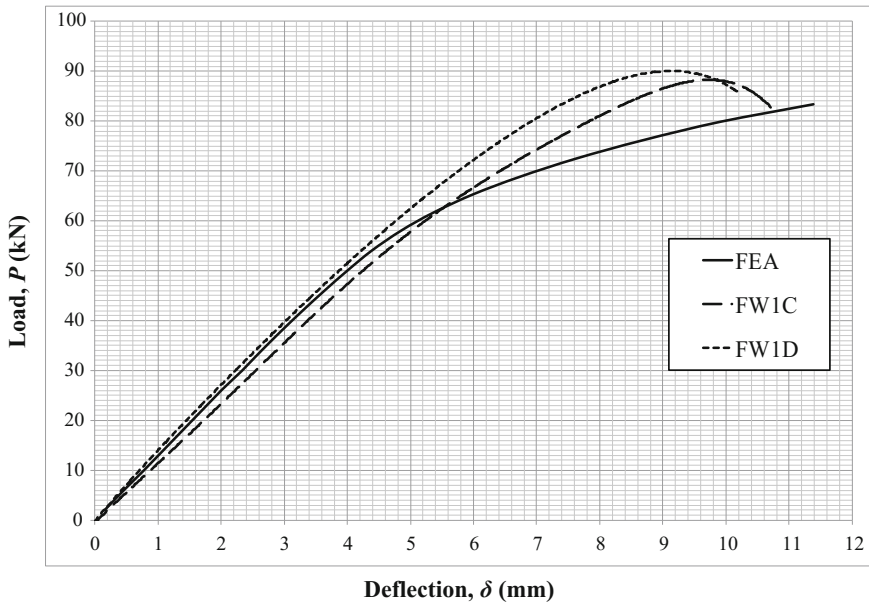
Fig. 3 Load deflection curves of FW section (200 × 100 × 6 × 3 mm)

Table 1 Comparison of experimental results between TriWP and FW sections

Section	TriWP	FW	$(M_{\text{TriWP}})/(M_{\text{FW}})$
Yield moment, M_y (kNm)	11.15	15.35	0.726
Ultimate moment, M_u (kNm)	21.04	31.71	0.664

Table 2 Comparison of yield moment, M_y between experimental and finite element analysis results

Method		Lab testing (a)	FEA (b)	% Difference $\left[\frac{(b)-(a)}{a} \times 100\% \right]$
Yield moment, M_y	TriWP	15.35	15.40	0.33
	FW	11.15	10.85	2.69

TriWP section in major axis. The yield moment, M_y of TriWP section is 27.4% less than FW section while the ultimate moment, M_u of TriWP section is 33.6% less than FW section (Table 1). The failure load could not be determined from the finite element results where strain hardening properties were used. Nevertheless, by comparing load deflection curves, it shows a good agreement between the both FEA and experimental testing results Moreover, by comparing the yield moments, the percentage of differences are only 2.7% for TriWP section and 0.3% for FW section (Table 2). Figures 4 and 5 shows the deformed sections after failure while the failure modes of finite element models as shown in Fig. 6.

From the deformed shapes, it is noticed that deformed shapes of the specimen after failure are well predicted by the finite element analysis models. From the modes of failure, it can be concluded that FW section tends to fail by bending while TriWP section tends to fail by local buckling.

Generally, the vertical loading induced bending of the beam. This results in longitudinal stresses in one-half of the beam and compressive in the other. As the

(a) FW1C　　　　　　　　　　　　　　　(b) FW1D

Fig. 4 Deformed FW sections after failure

(a) TriWP1C　　　　　　　　　　　(b) TriWP1D
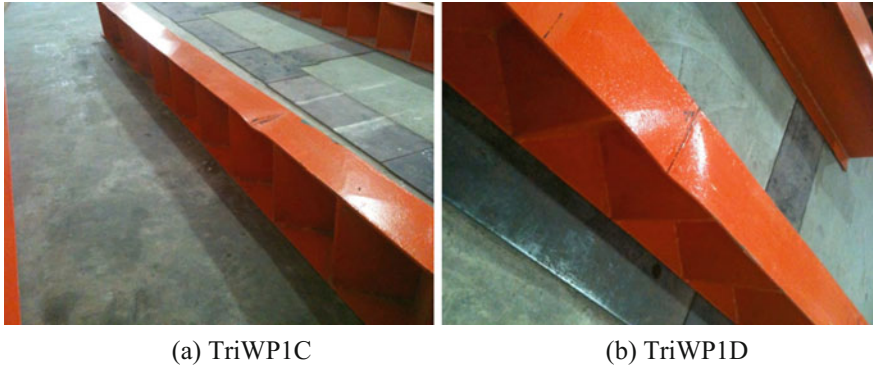
Fig. 5 Deformed TriWP sections after failure

(a) FW Section　　　　　　　　　　(b) TriWP Section
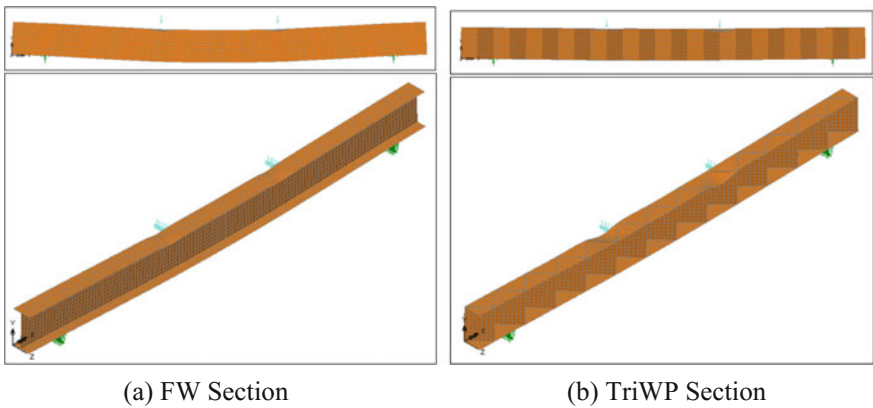
Fig. 6 Failure modes of finite element analysis models

bending moment increases, the steel reaches its yield stress. Eventually, across the entire cross-section of the beam, the steel yields in tension or compression. At this point the beam cross-section has become plastic at the point of maximum moment induced by the loading.

4.2 Parametric Study

Parametric study is carried out to analysed the web thickness (t_w), depth (D), corrugation angle (θ) and flange thickness (t_f) effects to the bending behaviour of TriWP section. Figure 7a shows the load deflection curves of TriWP sections with various web thickness (t_w) while Fig. 7b shows the load deflection curves of TriWP sections with various depth (D).

(a) Web thicknesses (t_w)

(b) Depths (D)

Fig. 7 Load deflection curves of TriWP sections

(a) Corrugation angles (θ)

(b) Flange thickness (t_f)
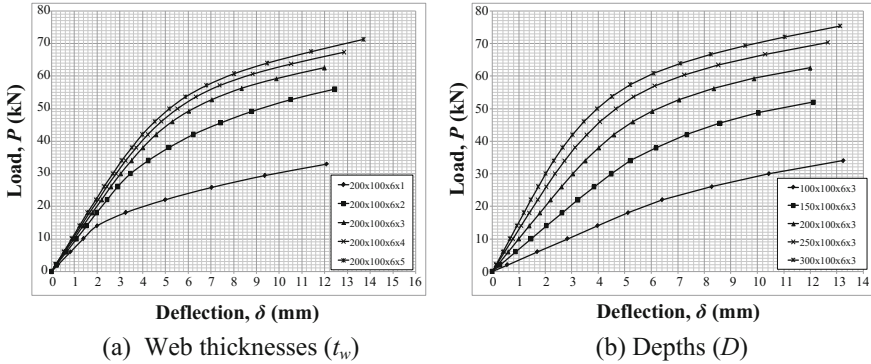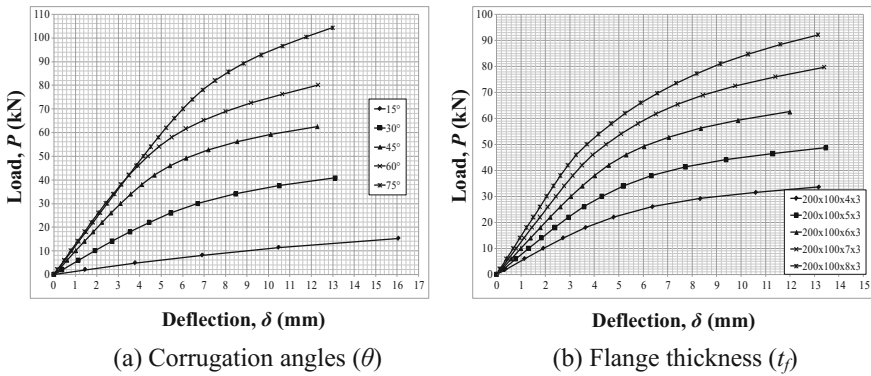
Fig. 8 Load deflection curves of TriWP sections

Figure 8a shows the load deflection curves of TriWP sections with various corrugation angles (θ). In the design of steel section, larger corrugation angles (θ) results in a higher bending capacity, however larger corrugation angles (θ) may not be economical since the weight of the section and the amount of material used is increased as the corrugation angle (θ) becomes larger. Figure 8b shows the load deflection curves of TriWP sections with various flange thickness (t_f).

The result of parametric study shows that a thicker web and flange thickness increase the bending capacity of TriWP steel section. A deeper section also results in a higher bending capacity. Besides, larger corrugation angle improves the bending capacity as the number of slanting stiffener increases throughout the span as the corrugation angle increased.

5 Conclusions

In conclusion, FW section has a higher bending capacity as compared to TriWP steel section. The yield moment, M_y of TriWP section is 27.4% less than FW section while the ultimate moment, M_u of TriWP section is 33.65% less than FW section. The results of experimental study and the finite element analysis showed a good agreement. By comparing the yield moment (M_y) obtained for both experimental testing and finite element modelling, the percentage of differences is only 0.3% for FW section and 2.7% for TriWP section.

Parametric study shows that by the increment of web thickness, flange thickness and depth of section, the bending capacity of TriWP steel section increased. Moreover, larger corrugation angle improved the bending capacity because the number of slanting stiffener increased throughout the span as the corrugation angle increased.

As for conclusion, when beam is subjected to bending, the flanges mostly resist the bending, the top flange will undergo compression where the bottom flange will undergo tension. The shear force is resisted by the web of the beam. Therefore, the web of the beam must be able to withstand the shear force to prevent excessive deflection due to the applied loading.

References

1. McKenzie, W. M. C.: Design of Structural Elements. Palgrave Macmillan Limited, UK (2004)
2. Khalid, Y.A., Chan, C.L., Sahari, B.B., Hamouda, A.M.S.: Bending behaviour of corrugated web beams. J. Mater. Process. Technol. **150**(3), 242–254 (2004). https://doi.org/10.1016/j.jmatprotec.2004.02.042
3. Chan, C.L., Khalid, Y.A., Sahari, B.B., Hamouda, A.M.S.: Finite element analysis of corrugated web beams under bending. J. Constr. Steel Res. **58**(11), 1391–1406 (2002). https://doi.org/10.1016/S0143-974X(01)00075-X
4. Tahir, M.M., Sulaiman, A., Saggaff, A.: Structural behaviour of trapezoidal web profiled steel beam section using partial strength connection. Electron. J. Struct. Eng. **8**, 55–66 (2008)
5. Romeijin, A., Sarkhosh, R., De Hoop, H.: Basic parametric study on corrugated web girders with cut outs. J. Constr. Steel Res. **65**(2), 395–407 (2009). https://doi.org/10.1016/j.jcsr.2008.02.006
6. Kovesdi, B., Braun, B., Kuhlmann, U., Dunai, L.: Patch loading resistance of girders with corrugated webs. J. Constr. Steel Res. **66**(12), 1445–1454 (2010). https://doi.org/10.1016/j.jcsr.2010.05.011
7. Kovesdi, B., Dunai, L., Kuhlmann, U.: Interacting stability behaviour of steel I-girders with corrugated webs. Thin-Walled Struct. **61**, 132–144 (2012). https://doi.org/10.1016/j.tws.2012.05.005

8. Elgaaly, M., Seshadri, A., Hamilton, R. W.: Bending strength of steel beams with corrugated webs. J. Struct. Eng. **123**(6), 772–782 (1997). https://doi.org/10.1061/(ASCE)0733-9445

9. Driver, R. G., Abbas, H. H., Sause, R.: Shear behavior of corrugated web bridge girders. J. Struct. Eng. **132**(2), 195–203 (2006). https://doi.org/10.1061/(ASCE)0733-9445

10. Korrani, H.R.K.N.: Lateral bracing of I-girder with corrugated webs under uniform bending. J. Constr. Steel Res. **66**(12), 1502–1509 (2010). https://doi.org/10.1016/j.jcsr.2010.06.003

11. Denan, F., Osman, M.H., Saad, S.: The study of lateral torsional buckling behaviour of beam with trapezoid web steel section by experimental and finite element analysis. Int. J. Res. Rev. Appl. Sci. **2**(2), 232 (2010)

12. Luo, R., Edlund, B.: Ultimate strength of girders with trapezoidally corrugated webs under patch loading. Thin-Walled Struct. **24**(2), 135–156 (1996). https://doi.org/10.1016/0263-8231 (95)00029-1

13. Denan, F., Hashim, N. S.: Study on bending behaviour of triangular web profile steel section by finite element analysis. Appl. Mech. Mater. **94**, 1539–1544. https://doi.org/10.4028/www. scientific.net/AMM.94-96.1539

Constitutive Relations for Concrete Properties Under Acid Environment

Irma Aswani Ahmad, Nurlita Pertiwi
and Nur Anny Suryaningsih Taufieq

Abstract The relationships between concrete properties (strength, porosity, and carbonation) and time attacked by acid environment were studied. Current environmental condition with acid rain caused air, soil, and water is acidic. It threats the degradation building with concrete construction. Two groups were organized in this research. One of them which was defined as control specimen was immersed in water curing. The other one was immersed in a solution of 5% sulfuric acid (PH_3) for the purpose of simulating the acidic environment in the laboratory. Different from other reports, the cubes were not previously immersed in water for 28 days but directly immersed in acid solution after being demoulded for one day. Furthermore, the constitutional equations from laboratory experiment were validated by embedding the specimens in acid soil (real acid condition) with similar PH. The results showed that due to immersion in sulphuric acid 5%, concrete had a decreased strength, increased porosity and the occurrence of carbonation at the age of 3–90 days. The result from laboratory experiment for compressive strength was similar with that of a field experiment. Furthermore the relationship between the age of concrete and its porosity considered valid for the age of under 14 days. However, the relationship between the age of concrete and carbonation event judged invalid with that from a field experiment. The results established that the constitutive relations of the properties of concrete in the acid environment were considerably divided by the type of the acid environment.

Keywords Porosity · Carbonation · Compressive strength

I. A. Ahmad (✉) · N. Pertiwi · N. A. S. Taufieq
Engineering Faculty, Universitas Negeri Makassar, Makassar,
South Sulawesi, Indonesia
e-mail: irma.aswani.ahmad@unm.ac.id

1   Introduction

Deterioration of concrete properties under acid environment shows due to decreased strength of concrete and increased corrosion of reinforcing steel. In the past few decades, special acid-resistant cement was used for buildings located in acidic environments. However, the acidic soil, air, and water conditions are difficult to avoid, so we need to think another way to improve structural quality. This research examined the magnitude of the structural degradation due to the influence of acidic environment in both laboratory and field experiments.

Several previous researchers have studied about the deterioration of concrete due to acid attack. Concrete damage often occurs due to internal and external influences, which are an aggregate expansion, salt weathering, carbonation, and leaching. Furthermore, the corrosion affected the performance of concrete reinforcement. Specifically for foundation construction, it is complicated to monitor the extent of deterioration. Thus when designing of the concrete mixture, it is necessary to concern all harmful impacts effects both on concrete and its reinforcement [1]. The strength of concrete was reduced by 17.7% after kept in sulfuric solution for 180 days [2]. Furthermore, it implied that sulfate ions in sulfuric acid solution might penetrate into concrete and produce gypsum by the reaction with CH. The gypsum is known to be a border of concrete deterioration [3]. The degradation of compressive strength and modulus of elasticity of concrete exposed to sulfuric acid depend on the degree of microcracking which can be identified by the relative dynamic elastic modulus. The compressive strength decreased to 84 and 76% after 28 and 90 days immersion in acid solution respectively [4, 5]. Another property of concrete which is carbonation was also studied by several researchers. When concretes previously carbonated and then attacked by chlorides, the chlorides penetration were higher and much deeper into the concrete [6, 7]. Specimens which reached higher compressive stress had a slower rate of carbonation. However, those which reached higher tensile stress had a faster rate of carbonation. [8, 9]. Strength losses of concrete immersed in a solution of 3% of sodium sulfate were 3.91% and 5.12% at 7 and 28 days, respectively [10].

To circumvent above problems, previous researchers have proposed to use waste as cementitious materials such as slag, fly ash, rice husk ash to increase concrete durability against acid attack [11–15]. However, the purpose of this research was to determine the damage caused by the acid environment. There were two differences from other researchers. First, in the previous research, the concrete was immersed in acid solution after being cured completely for 28 days. Specimens in this research were directly immersed in acid solution after demoulded. This condition is similar to what happened in real concrete construction. Second, in the previous research, the study was conducted only in the laboratory. While in this study the results of studies in the laboratory were verified by embedded specimens in acid soil in the field. Constitutive relations of concrete properties attacked by acid solution were proposed to explain the relationship. There were compressive strength, porosity and carbonation models which had been verified to use in the acid environment.

These models were capable of giving information about the actual degradation due to the acid solution. Experts and designer easily estimated the grade of concrete for mixture under acid environment by recognizing the decrease of concrete properties.

2　Experimental Program

2.1　Materials

Materials in this study were coarse aggregate, fine aggregate, cement, and water. The coarse aggregate used in this research was crushed granite. Maximum size and specific gravity of the coarse were maximum 20 and 2.32 mm, respectively. The fine aggregate was natural siliceous river sand. Its fineness modulus and specific gravity were 2.56 and 2.41, respectively. The type of cement was Portland composite cement (PCC).

2.2　Mixture Proportion

The concrete mixture was made by using the volume proportions of (1) portland cement: (2) fine aggregate: (3) coarse aggregate. Water–cement ratio (w/c) used for all specimens was 0.46.

2.3　Preparation of Test Specimens

Cube specimens of $15 \times 15 \times 15 \text{ cm}^3$ were made for observation of compressive strength, porosity, and carbonation. Slump test was conducted to evaluate workability of mixtures according to [16]. Pouring of fresh concrete into the mold was done for three layers. Compaction by using a bar compaction was done each layer. Furthermore, the compaction was conducted by uniformly distributed strokes. After each layer was completely compacted, the surface should be flattened with a trowel until flush with the top side of the mold. After one day, the specimens were demoulded. Two groups were organized in this research. One of them which was defined as control specimen was immersed in water curing. The other one was immersed in a solution of 5% sulfuric acid (PH_3) for the purpose of simulating the acidic environment in the laboratory. The sulfuric acid solution was controlled every week to ensure that the solution retained at PH_3. The tests were conducted at 3, 7, 14, 21, 28, 45, 75, and 90 days. Porosity and compressive strength of concrete were measured in agreement with [17, 18]. Percentages of carbonation could be measured using phenolphthalein. If this solution was sprayed onto the surface of the concrete, then the color changes according to the level of acidity [19].

Furthermore, a field experiment was conducted to verify the results from a laboratory experiment. The specimens were not immersed in 5% sulfuric acid solution but were embedded in acid soil in the field with approximately similar PH.

3   Results and Discussion

3.1   Compressive Strength

Figure 1 shows the results of compressive strength of concrete both in water curing and acid solution at various ages. It was indicated that the compressive strength enlarged with time. It happened because, during the water curing, hydration process continued to form a hard compound. For example, specimens in water curing reached a compressive strength of approximately 10.408 and 27.029 MPa at 3 and 90 days, respectively. Then specimens in acid solution showed a lower compressive strength than those in water curing. The compressive strengths were about 10.204 MPa at three days and increased to 22.268 MPa at 28 days.

However, after immersion 28 days, the compressive strength decreased slowly to 20.907 MPa at 90 days. This result illustrated that acid environment started to affect the concrete strength after attacked by over 28 days. It may occur as a result of non-curing before immersion in acid solution. The hydration process was not perfect at the time of the attack by acid. The reactions that occurred between Ca $(OH)_2$ and the acid formed a less hard compound, thus lowering the strength.

Table 1 shows differences in compressive strength and strength ratio for both conditions. The differences increased gradually from 0.204 to 0.907% at 3 and 28 days, respectively. However, the differences increased rapidly from 2.256 to 6.122% at 45 and 90 days, respectively. Strength ratios of specimens in acid solution were slightly higher than those in a water curing for less than 28 days.

Fig. 1 Effect of environment on compressive strength
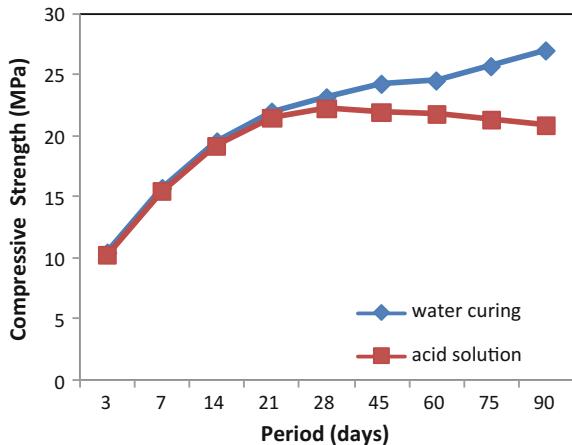
Table 1 Differences and strength ratio

Period (days)	Compressive strength (MPa)		Differences (%)	Strength ratio	
	Water	Acid		Water	Acid
3	10.408	10.204	0.204	0.449	0.458
7	15.714	15.419	0.295	0.678	0.692
14	19.547	19.229	0.318	0.843	0.864
21	21.996	21.485	0.510	0.949	0.965
28	23.175	22.268	0.907	1.000	1.000
45	24.286	22.029	2.256	1.048	0.989
60	24.558	21.769	2.789	1.060	0.978
75	25.737	21.338	4.399	1.111	0.958
90	27.029	20.907	6.122	1.166	0.939

Fig. 2 Relations between periods of immersion with compressive strength differences
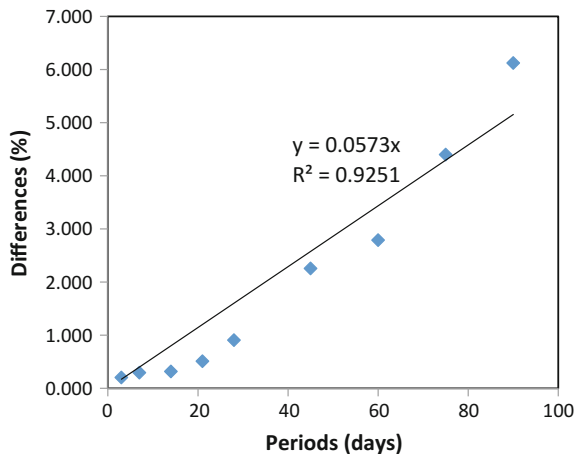
Otherwise, strength ratios of specimens in acid solution were slightly lower than those in a water curing for over than 28 days. For instance, the ratio of the specimen for 3 days in water curing was 0.449 and slightly increased to 0.458 in acid solution. However, the ratio of the specimen for 90 days in water curing was 1.166 and slightly decreased to 0.939 in acid solution.

The graph shown in Fig. 2 shows a model of compressive strength differences between water curing and acid solution. The proposed relation was appropriately evidenced by the higher value of regression coefficient (R_2). Figure 2 shows the result of regression analysis was a linear equation with 0.925 values of R_2.

Regression equation in Fig. 2, $y = 0.057x$, with x is immersion periods, and y is differences of compressive strength, was verified by embedded the specimens into the acid soil in the field. The result of field condition was described in Fig. 3. It indicated that new equation $y = 0.053x$ from the field condition was similar with that from acid solution.

Fig. 3 Validation of model
relation of compressive
strength

$$y = 0.0532x$$
$$R^2 = 0.8928$$
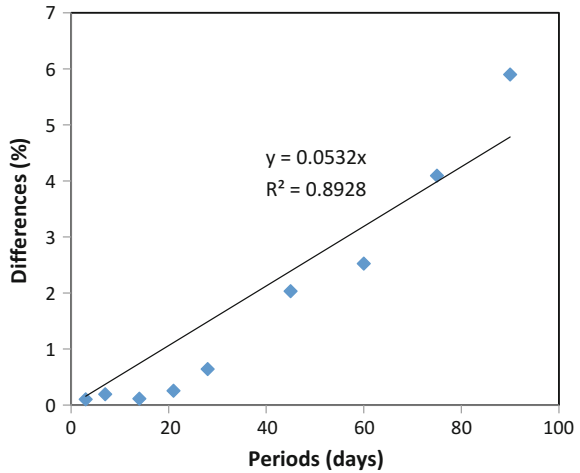
3.2 Porosity

Figure 4 described the results of porosity of concrete both in water curing and acid solution at various ages. It was indicated that the porosity of specimens cured in water declined with time. Otherwise, the porosity of them immersed in acid solution increased with time. For example, specimens in water curing showed a porosity of about 4.97 and 4.05% at 3 and 90 days, respectively. On the other hand, specimens in acid solution showed a porosity of about 5.02% for 3 days and increased to 5.12% for 90 days. The graph of porosity had the same tendency with that of compressive strength. However, the degradation of porosity was higher than that of compressive strength.

Fig. 4 Effect of environment on porosity
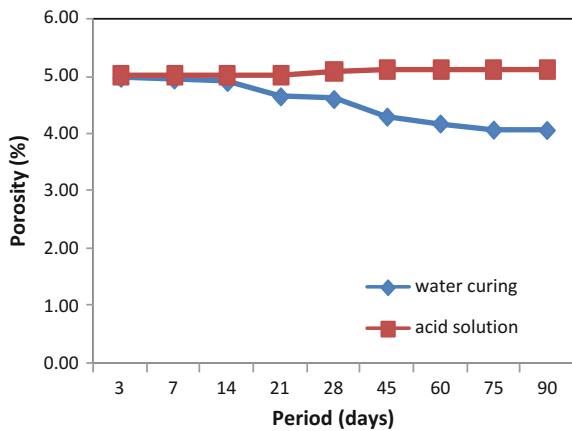
Table 2 Differences and strength ratio

Period (days)	Porosity (%)		Differences (%)
	Water	Acid	
3	4.97	5.02	0.92
7	4.94	5.03	1.70
14	4.90	5.03	2.65
21	4.65	5.03	8.29
28	4.60	5.10	10.81
45	4.29	5.10	18.96
60	4.17	5.11	22.61
75	4.06	5.11	25.94
90	4.05	5.12	26.20

Fig. 5 Relations between periods of immersion with porosity differences
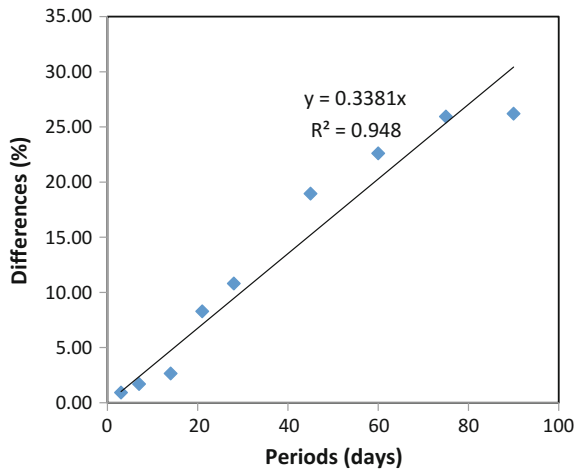
For 3 days, the difference in porosity was 0.92%; whereas, for 90 days, the difference increased to 26.20% (Table 2). The differences increased gradually from 0.92 to 2.65% at 3 and 14 days, respectively. However, the differences increased rapidly from 8.29 to 26.20% at 21 and 90 days, respectively.

The graph shown in Fig. 5 shows a model of porosity differences between water curing and acid solution. The proposed relation was appropriate evidenced by the higher value of regression coefficient (R^2). Figure 5 shows the result of regression analysis was a linear equation with 0.948 values of R^2.

Regression equation in Fig. 6, $y = 0.338x$, with x is immersion periods, and y is differences of porosity, was verified by embedded the specimens into the acid soil in the field. The result of field condition was described in Fig. 3. It indicated that new equation $y = 0.330x$ from the field condition was similar with that from acid solution.

Fig. 6 Validation of model relation of porosity
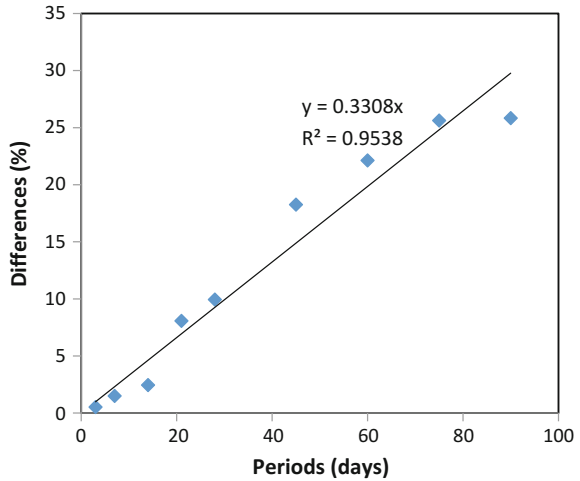
3.3 Carbonation

Figure 7 described the results of carbonation in acid solution at various ages. It was observed that the carbonation increased with a period of immersing in acid solution. For example, the percentages of carbonation were 25.19% at 3 days and dramatically rose to 97.49% at 90 days.

Figure 7 shows a model of carbonation differences between water curing and acid solution. The proposed relation was appropriate evidenced by the higher value of regression coefficient (R^2). Figure 7 shows the result of regression analysis was a linear equation with 0.908 values of R^2.

Regression equation in Fig. 7, $y = 10.33x$, with x is immersion periods, and y is differences of carbonation, was not verified by embedded the specimens into the

Fig. 7 Effect of environment on carbonation
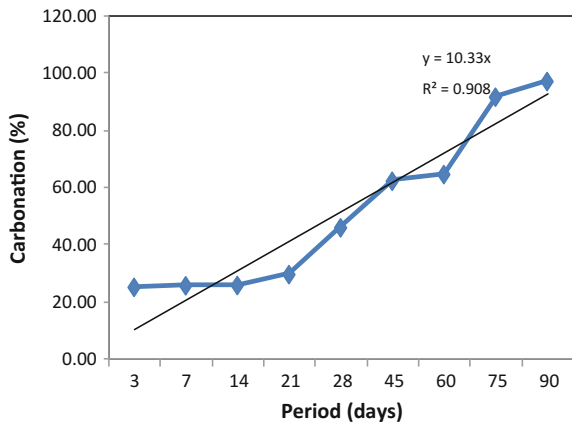
Fig. 8 Validation of model relation of carbonation
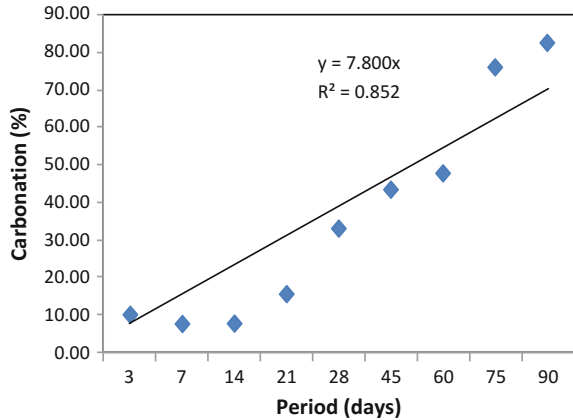
acid soil in the field. The result of field condition was described in Fig. 3. It indicated that new equation $y = 7.800x$ from the field condition was different from that from acid solution (Fig. 8).

Carbonation is a chemical reaction in the concrete, so it is strongly influenced by the acid content. Therefore, differences in acid content between laboratory treatments with on-site treatment caused a different level of carbonation. Carbonation is also affected by the oxygen content present in the environment. This condition was certainly different between laboratory treatments with on-site treatment.

4   Conclusions

Following conclusions can be delivered from this research:

1. The constitutive relation between immersion time and compressive strength in the acidic environment was obtained by the equation $y = 0.057x$. The variable x is the immersion time, while the variable y is the compressive strength.
2. The constitutive relation between immersion time and porosity in the acidic environment was obtained by the equation $y = 0.338x$. The variable x is the immersion time, while the variable y is the porosity.
3. The constitutive relation between immersion time and porosity in the acidic environment was not obtained. The result of the validation analysis with the value obtained in the field gave an illustration that the equation was invalid.

References

1. Zoran, B., Gordana, T.C., Nebojca, D., Jelena, S.: Damage of concrete and reinforcement of reinforced-concrete. Procedia Eng. **117**, 411–418 (2015). https://doi.org/10.1016/j.proeng.2015.08.187
2. Ahcene, M., Fattoum, K.: Pozzolan concrete durability on sulphate attack. Procedia Eng. **123**, 145–152 (2015). https://doi.org/10.1016/j.proeng.2015.08.035
3. Keisuke, T., Yoshiki, Y., Yuko, O., Kenji, K.: Deterioration of concrete immersed in sulfuric acid for a long term. Key Eng. Mater. **711**, 659–664 (2016). https://doi.org/10.4028/www.scientific.net/kem.711.659
4. Saiful, H., Cut, N.: Mechanical properties of concrete in compression exposed to sulfuric acid. Key Eng. Mater. **711**, 302–309 (2016). https://doi.org/10.4028/www.scientific.net/kem.711.302
5. Ahmad, I.A., Parung, H., Tjaronge, M.W., Djamaluddin, R.: Durability of concrete using rice husk ash as cement substitution exposed to acid rain. Int. J. Eng. Res. Appl. **4**(5)(version 4), 144–149 (2014)
6. Wang, Y., Nanukuttan, S., Baic, Y., Basheerd, P.A.M.: Influence of combined carbonation and chloride ingress regimes on rate of ingress and redistribution of chlorides in concrete. Constr. Build. Mater. **140**, 173–183 (2017). https://doi.org/10.1016/j.conbuildmat.2017.02.121
7. Eehab, A.B.K., Anwar, M.: Carbonation of ternary cementitious concrete systems containing fly ash and silica fume. Water Sci. **29**, 36–44 (2015). https://doi.org/10.1016/j.wsj.2014.12.001
8. Ren, Y., Huang, Q., Liu, X.L., Tong, Z.J.: A model of concrete carbonation depth under the coupling effects of load and environment. Mater. Res. Innovations **19**(SUPPL 9), 224–228 (2015). https://doi.org/10.1179/1432891715z.0000000001970
9. Hyunjin, J., Jae-Yuel, O., Kyung, J.L., Kyung, W.H., Kang, S.M.: Estimation of concrete carbonation depth considering multiple influencing factors on the deterioration of durability for reinforced concrete structures. Adv. Mater. Sci. Eng. **2016**, 1–18 (2016). https://doi.org/10.1155/2016/4814609
10. Dharma, P.R., Sreevidya, V., Jenifar, M.J.: Flexural behaviour and durability study of concrete on using low density aggregates. J. Pol. Directory Res. J. **09**(03), 466–470 (2016)
11. Chen, M.C., Wang, K., Xie, L.: Deterioration mechanism of cementitious materials under acid rain attack. Eng. Fail. Anal. **27**, 272–285 (2013). doi: https://doi.org/10.1016/j.engfailanal.2012.08.007
12. Ferraro, R.M., Nanni, A.: Effect of off-white rice husk ash on strength, porosity, conductivity and corrosion resistance of white concrete. Constr. Build. Mater. **31**, 220–225 (2012). doi: https://doi.org/10.1016/j.conbuildmat.2011.12.010
13. Ramadhansyah, P.J., Salwa, M.Z., Mahyun, A.W., Bakar, B.H.A., Johari, M.A.M., Che Norazman, C.W.: Properties of concrete containing rice husk ash under sodium chloride subjected to wetting and drying. Procedia Eng. **50**, 305–313 (2012). https://doi.org/10.1016/j.proeng.2012.10.035
14. Ahmad, I.A., Parung, H., Tjaronge, M.W., Djamaluddin, R.: Corrosion of conrete using portland composite cement and rice husk ash under simulated acid rain environment. Adv. Mater. Res. **789**, 511–514 (2013). https://doi.org/10.4028/www.scientific.net/amr.789.511
15. Seshasayee, V., Bharatkumar, B.H., Gajalakshmi, P.: Influence of fly ash on durability and performance of concrete. J. Pol. Directory Res. J. **09**(03), 341–346 (2016)
16. ASTM C 143-197: Standard Test Method for Slump of Hydraulic Cement Concrete. American Society for Testing and Materials, Annual Book (1998)

17. ASTM C39: Standard Test Method for Compressive Strength of Cylindrical Concrete Specimens. ASTM International, West Conshohocken, PA (2014)
18. ASTM C20: Standard Test Methods for Apparent Porosity, Water Absorption, Apparent Specific Gravity, and Bulk Density of Burned Refractory Brick and Shapes by Boiling Water. ASTM International, West Conshohocken, PA (2014)
19. Lee, H.J., Kim, D.G., Lee, J.H., Cho, M.S.: A study for carbonation degree on concrete using a phenolphthalein indicator and fourier-transform infrared spectroscopy. Int. J. Civil Environ. Struct. Constr. Architectural Eng. **6**(2), 95–101 (2012)

Nonlinear Analysis of Reinforced Concrete Hollow Beam with GFRP Bars and Stirrups Using Finite Element Method Under Cyclic Load

Sarah Jabbar, Farzad Hejazi and R. S. M. Rashid

Abstract Insufficient knowledge on using fibre-reinforced polymer (FRP) materials in hollow members limits their application. Torsional load results in the less efficient hollow section that plays an important role in hollow members. This load is generated on the members by an external load. The torsional load in hollow members that are reinforced longitudinally with FRP has been discussed for years. However, research on high-strength concrete (HSC) reinforced with glass fibre-reinforced polymer (GFRP) is scarce. Therefore, in this study, the behaviour of hollow beam internally reinforced with GFRP bars under cyclic load is investigated. For this purpose, the HSC-reinforced concrete hollow beam with GFRP bars and hollow beam with normal reinforcement are considered and finite element model is developed and nonlinear dynamic analysis has been conducted by applying cyclic loads to the developed models. In addition, reinforced concrete (RC) solid beam with HSC material is tested experimentally in order to verify and validate the ability of finite element software to predict the result. The analysis results are investigated in terms of the hysteresis loop, stress and strain distribution in the beam and it is indicated that the performance of hollow beam reinforced with GFRP bars and stirrups has improved in comparison with HSC beam with GFRP bars and also HSC beam with normal steel reinforcement. Therefore, based on this research, it is recommended to implement GFRP bars and stirrup for strengthening the concrete members in the high humidity areas where use of normal steel is not feasible due to corrosion threat.

S. Jabbar · F. Hejazi (✉) · R. S. M. Rashid
University Putra Malaysia, Seri Kembangan, Malaysia
e-mail: farzad@fhejazi.com

S. Jabbar
e-mail: sarahsaleem2015@gmail.com

R. S. M. Rashid
e-mail: raizal@upm.edu.my

S. Jabbar
Ministry of Municipalities, Baghdad, Iraq

1 Introduction

The cost incurred in applying beams with high-strength concrete (HSC) is higher than using normal-strength concrete (NSC). However, such beams are still widely applied in building structures and bridges because of their distinctive features. The beams with HSC present four basic faults depending on reinforcements when under torsional load [14]. The main failures of these beams are brittle fracture caused by inadequate reinforcement, a crisp failure because of insufficient strength of concrete, and corner cracking that leads to fragile and ductile failures. The increase in the strength of concrete cans intensifies the failure. Bernardo et al. [3] conducted a plastic analysis and evaluated the twist capacity of HSC hollow beams under pure torsion. They reported that the increase in the compressive strength of concrete slightly decreases the plastic twist capacity.

Corrosion can deteriorate the structure of beam and can thus cause cracking and spalling of concrete such that the maintenance cost increases [15]. Hejazi et al. [8] showed that weakness in the RC beam and columns may lead to reduce lateral stiffness of a floor and cause to appear soft story in the structure. Therefore, various techniques, such as applying fibre-reinforced polymer (FRP) materials, have been developed to prevent the problem of corrosion. FRP has become an important material in numerous applications because of its high specific strength and deterrence to corrosion. Fibre-reinforced composite materials are new industrial materials that can substitute concrete, metal or wood; these materials exhibit high elasticity and high strength [17] and can be used to establish new materials. Tavares et al. [18] studied the behaviour of reinforced concrete (RC) beams with glass FRP (GFRP) bars under bending load. The results indicated that the capacity is lower than that of the steel-reinforced beam. Similar flexural capacity can be achieved for the steel- and GFRP-RC beams by controlling the stiffness and tension force of the GFRP bars. Chansawat et al. [6] developed finite element (FE) model for RC beams with GFRP and carbon fibre-reinforced polymer (CFRP) bars and indicated that the FE simulations are an effective tool for analysing such a complex behaviour. Hii and Al-Mahaidi [9] investigated experimental and numerical realizations on the torsional strengthening of RC solid and hollow beams with the external bonding of CFRP, which can increase the crack and ultimate strengths up to 40 and 78%, respectively. El Maaddawy and Sherif [7] studied shear strengthening of concrete deep beams with the external bonding of CFRP in the opening, and they found that the shear strengthening of the external bonding of CFRP around the opening effectively improves the shear strength of RC deep beams.

Prabaghar and Kumaran [16] compared concrete beams reinforced internally with an equal percentage of GFRP with concrete beams reinforced with steel reinforcements under torsional load. The results indicated that the torsional

capacities are reduced by 20% for high-grade concrete and high percentage of steel while approximately 30% for low-grade concrete beams. Metwally [15] conducted nonlinear analysis using FE method for concrete deep beam reinforced with GFRP and CFRP bars. The findings showed that the behaviour of deep beam reinforced with GFRP bars differs from that of beam reinforced with CFRP bars. The difference is due to the low elastic modulus of the GFRP bars, there by dramatically increasing the deflection. Li et al. [13] studied the GFRP of a one-span pedestrian bridge in Taiwan using FE analysis (FEA). The deflection results from FEA showed that the pedestrian bridge meets the deflection criteria, and the external bonding of FRP composites on the concrete structures shows an effective and efficient way of strengthening concrete structures. Inoue and Egawa [10] examined the flexural and shear behaviour of hollow beam under cyclic load. The results indicated that the ultimate deformation and energy dissipation capacity of the hollow beam are smaller than those of the solid beam and that the ultimate failure is brittleness. In addition, the diagonal crack can be generated in the early stages such that the strain of stirrups considerably increases. Jabber et al. [11] studied the effect of web opening in RC hollow beam under flexural, torsional, and cyclic loads with different materials (HSC and ultra-high-performance concrete (UHPC). The findings revealed that the web opening decreases the capacity of beam, and the twisting capacity of UHPC beams is twice that of HSC beams. Torsional force is generated in hollow members by external force and weakens the hollow section; such phenomenon is rarely studied [19]. Burningham et al. [4] presented a repair method for RC deep beams incorporated with externally unbounded post-tensioned CFRP rods. The above-mentioned studies have insufficiently discussed the torsional behaviour of hollow members with longitudinal steel or GFRP reinforcement. Therefore, the present study investigates the behaviour of hollow beam internally reinforced with GFRP (bars, stirrups, and their combination) under cyclic load compared with hollow beam with steel reinforcement.

2 Hollow Beams with GFRP

FRP is an extraction of structural evolution of concrete material. This material is recommended for concrete components under ACI codes. The harsh environmental effects can be deterred using such materials of high strength and durability. FRP materials are available in various forms, such as cables, sheets, and plates. FRPs can be obtained in the form of bars via pultrusion, and FRP bars are employed as internal reinforcements and can be used as an alternative to the conventional steel reinforcements. The manufacture of FRP bars can cause various surface imperfections, which provide desirable coning between the bar and the surrounding concrete. The application of FRP bars in structural concrete flexural elements has attracted much attention from researchers. These applications include slabs, beams, and the flexural hollow section with HSC and UHPC. These hollow sections are used as passages for electrical and mechanical utilities, and they decrease story

height, material, and construction costs. The inadequate study has caused non-availability of specific provisions regarding minimum reinforcement amount for ensuring the ductile behaviour of beams under flexural loading. ACI [2] is based on empirical testing and provides information regarding the minimum amount of reinforcement. The Canadian Standards Association model code [5] in Mississauga identified the minimum amount of reinforcement for shear; this specification provides sufficient flexibility for the hollow section under cyclic loads. Applying FRP or GFRP is challenging but obtains a good result; this topic has been scarcely investigated. Therefore, the present study analyses the behaviour of hollow beam with internal reinforcement of GFRP under cyclic load.

2.1 Geometry of Considered Beam

Four beams are developed and analysed for validation purposes. All the models have the same cross-section dimensions of 600 mm × 600 mm with a length of 6000 mm [14] to consider the failure criteria in beams during the loading (Fig. 1). The concrete damage plasticity for Grade 50 is defined during the modelling. All parameters for damaged plasticity are considered following the experimental test by Jankowiak and Lodygowski [12] as listed in Table 1. Moreover, damage analysis is conducted by considering principal stresses and strains and comparing with yield

(a) Cross-section (mm).

(b) Longitudinal view (mm).
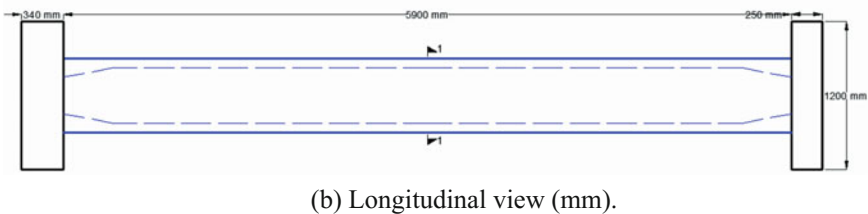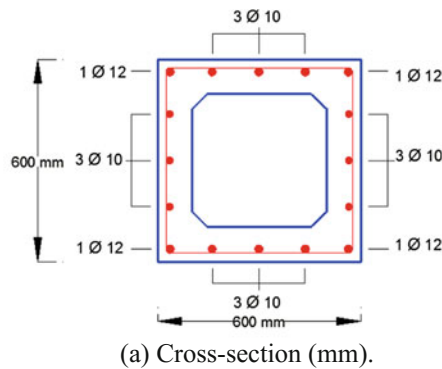
Fig. 1 Reinforced concrete beam [14]

Table 1 Material parameters of the CDP model for the B50 concrete class [12]

Material's parameters	Parameters	The parameters material's of CDP model	
		β	38°
Concrete elasticity		m	1
E [GPa]	19.7	$f = f_{b0}/f_c$	1.12
v	0.19	γ	0.666
Concrete compression hardening		Concrete compression damage	
Stress [MPa]	Crushing strain [-]	DamageC [-]	Crushing strain [-]
15	0	0	0
20.1978	7.47E−05	0	7.47E−05
30.00061	9.88E−05	0	9.88E−05
40.30378	0.000154	0	0.000154
50.00769	0.000762	0	0.000762
40.23609	0.002558	0.195402	0.002558
20.23609	0.005675	0.596382	0.005675
5.257557	0.011733	0.894865	0.011733
Concrete tension stiffening		Concrete tension damage	
Stress [MPa]	Cracking strain [-]	DamageT [-]	Cracking strain [-]
1.99893	0	0	0
2.842	3.33E−05	0	3.33E−05
1.86981	0.00016	0.406411	0.00016
0.862723	0.00028	0.69638	0.00028
0.226254	0.000685	0.920389	0.000685
0.056576	0.001087	0.980093	0.001087

stress in reinforcement and concrete and maximum yield strain. In this study, the yield stress (fy) for reinforcement and concrete are 400 and 50 MPa, respectively. The three-dimensional (3D) two-node first-order truss elements (T3D2-Truss) are used to model the GFRP reinforcing bars in the FE model of concrete beam specimens. Therefore, the GFRP with 19 mm diameter, 37,900 MPa modulus of elasticity and 0.26 Poisson's ratio is used as presented in the study of Metwally [15]. 3D tetrahedral element is used to model the beam in this study. The reason is that the solid (or continuum) elements in ABAQUS can be used for the linear and complex nonlinear analyses of contact, plasticity, and large deformations of hollow beam with GFRP (bars and combined bars and stirrups) under cyclic load. The interaction between GFRP bars and surrounding concrete using embedded region and truss elements is explored to represent the GFRP reinforcement bars, which are embedded in the "host" continuum solid elements (concrete). Embedding means that the translational degrees of freedom at the nodes of the embedded element is eliminated and constrained to the corresponding interpolated values in the host continuum element. The solid parts with embedded reinforcement approach assume perfect bond only at the embedded nodes. The parametric study is conducted to

investigate the effect of using GFRP (bars, stirrups, and their combination) as a replacement of steel reinforcement on the capacity of hollow beam under cyclic load with simply supported boundary conditions.

3 Verification of Finite Element Method

In this study, in order to verify finite element model and analysis two verifications have been conducted as explained in follow:

As mentioned in above to verify and validate the software result, one RC solid beam with grade 50 as shown in Fig. 2 is numerically modelled and analysed using FEM program and experimentally tested in the laboratory.

(a) Cross-section (mm).

(b) Longitudinal view (mm).
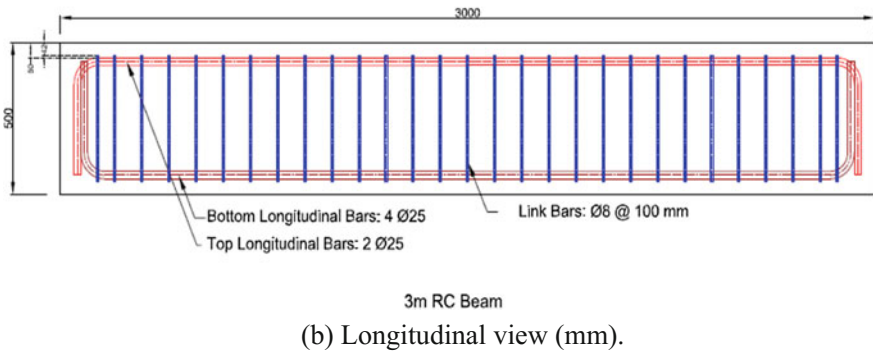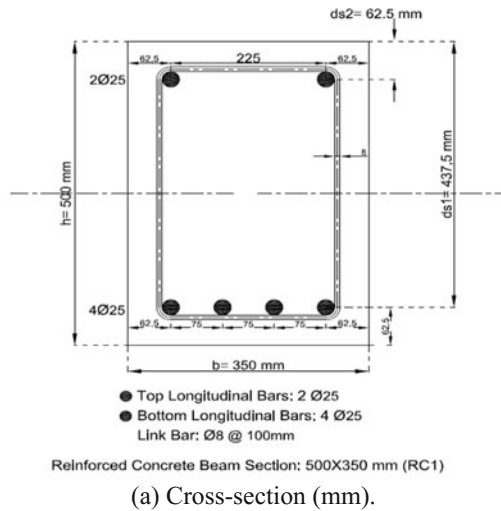
Fig. 2 **a**, **b** RC cross-sectional detailing

3.1　Verification for RC Solid Beam by Conducting

3.1.1　Experimental Testing

A pin and a roller support are prepared to be used in experimental test. Three LVDTs are used to measure the displacement. Figure 3 shows the test setup.

Figure 4 is illustrating the experimental testing setup of RC beam in the lab. The roller support, at the left side, and pin support at right side are selected. Four-point
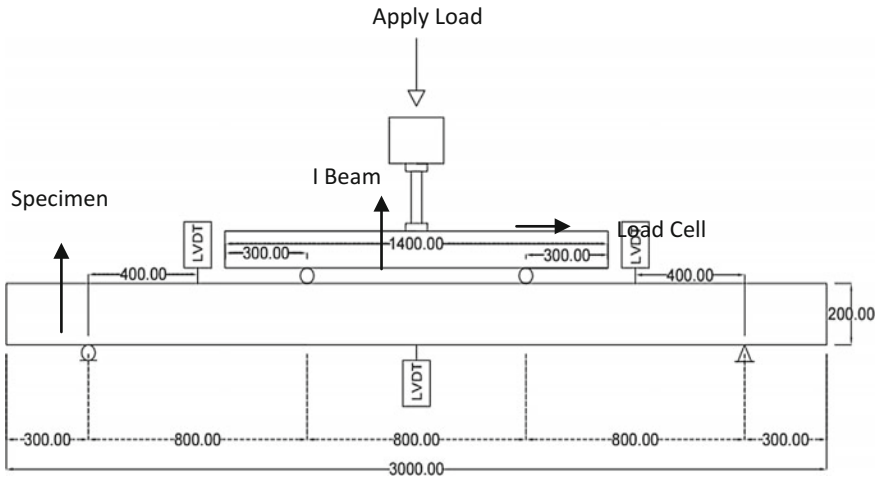
Fig. 3　Beam setup, all dimensions are in mm

Fig. 4　RC grade 50 test setup

bending test is performed for the test. I beam is used for the purpose of distribution of load into two points which located at 800 mm away from supports.

Figure 5 showing the crack pattern of RC beam subjected to monotonic loading. It can be noted that plenty of cracks appeared in different locations of beam. At first micro-cracks occurred in the bottom face of the midspan of beam at 200 kN applied load which is 44.64% of ultimate load.

From observation, many cracks appeared once applied force up to 300–350 kN, 62.5% of ultimate load, in 800 mm away from support, exactly at location of applied load. Besides that, as applied load increased to 550 kN, 98.21% of ultimate load, shear cracks also appeared diagonally near support location. Most of cracks continued to propagate towards the point load. The ultimate load of RC grade 50 beam was 560 kN.

3.1.2 Numerical Analysis for RC Solid Beam Grade 50

The same beam as the tested specimen in laboratory as shown in Fig. 6 is modelled by using ABAQUS software [1] and monotonic loading has been applying for verifying the result of experimental test.

The displacement applied to middle of beam is started from zero and continuously increased by 1 mm increment to reach to 150 mm. Pin and roller supports are chosen to model the boundary condition of the beam.

3.1.3 Comparison the Result of Experimental and Numerical

Figure 7 presented the load–displacement curve of experimental test compared with load–displacement curve obtained by numerical analysis.

Table 2 listed the result obtained based on the experimental and numerical analysis. It can be noted that the percentage of error is less than 20% which lead to prove the ability of software in predict the result.

3.2 Verification Study for Hollow Beam

The dimensions and properties of the concrete hollow beam (H) considered in this study are the same as those in the experimental study by Lopes and Bernardo [14] and the numerical investigation by Jabbar et al. [11]. Therefore, the validation of modelling in this study is conducted by comparing the results of the present study with the results of the abovementioned studies. Then, the hollow beam with steel reinforcement is compared with hollow beam with GFRP bars and stirrups and hollow beam with GFRP bars only with normal steel stirrups (Table 3). The RC

(a) RC crack pattern front view

(b) RC crack right view

(c) RC crack left view

Fig. 5 Crack pattern of RC beam
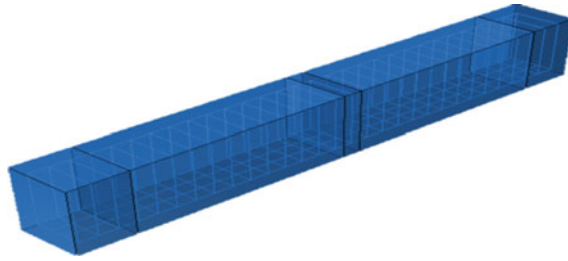
Fig. 6 Finite element model of RC beam
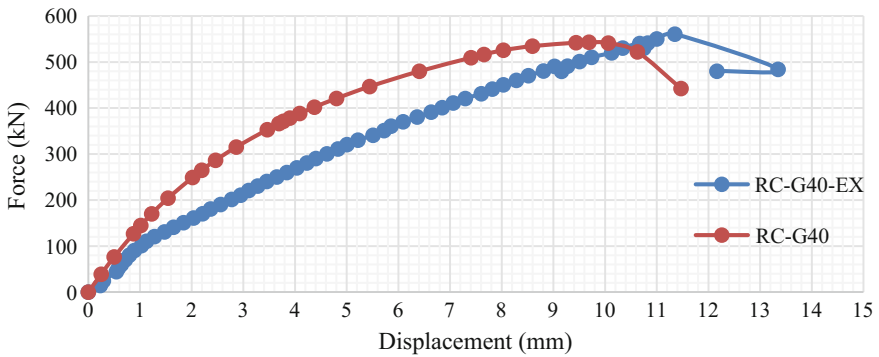
Fig. 7 RC result under monotonic loading

Table 2 Experimental and numerical result for RC beam

Beam type	RC-G50-Exp.	RC-G50-FEM.	$(RC_{Exp} - RC_{FEM})/RC_{Exp}$ (%)
F_u (kN)	560.60	543.08	3.12
Δ_u (mm)	13.30	11.6	12.78

Table 3 Verification study result

Beams	Torsion (KN m)	Increasing (%)
H experimental with normal reinforcement work [14]	254.8	–
H numerical work with normal reinforcement [11]	212	16
H with GFRP bars and stirrups	725	184
H with GFRP bars only with steel stirrups	402	57
H GFRP bars at web only and steel stirrups	579	127

hollow beams with GFRP showed higher torsional load than the beam with conventional reinforcements which is about 57, 127, 184%. This result is primarily due to a lower elastic modulus and higher tensile strain values for GFRP reinforcements than the steel reinforcements.

3.2.1 Beams Subjected to Cyclic Load

All models are loaded symmetrically by two-point loads with a distance of 1000 mm from the centre of the beam in evaluating the effect of a hollow section with normal reinforcement and with a GFRP reinforcement subjected to dynamic loading as the cyclic displacement. The amplitude of applied displacement is 100 mm, and the time history of displacement is presented in Fig. 8. The boundary conditions are applied to the support nodes and roller and pinned supports in the other end of the beam, as shown in Fig. 9.

In the modelling, all the elements are purposely assigned with the same mesh size. The beam models are meshed with a 100-mm element, as shown in Fig. 10.

The hysteresis graph for the HSC beam with GFRP (bars and combined bars and stirrups) under cyclic load is presented in Fig. 11. The load–deflection curves of the hollow beam with normal reinforcement differed from those of hollow beam with GFRP reinforcement. In addition, the capacity of hollow beam with normal reinforcement was less than that of the hollow beam with GFRP reinforcement bars or combined bars and stirrups.

The results in Table 4 indicate that the ultimate load capacity of the hollow beam with steel reinforcement was 213 kN, that for the hollow beam with GFRP bars was 677.9 kN, and that for the hollow beam with GFRP bars and stirrups was 2169 kN, although the capacity of hollow section was increased to 790 kN in terms of using GFRP bars at web only.

Therefore, using the GFRP bars and stirrups in beams increased the ultimate load by 918% compared with the hollow beam with normal reinforcement under cyclic load. Furthermore, using the GFRP bars and normal stirrups in beams increased the
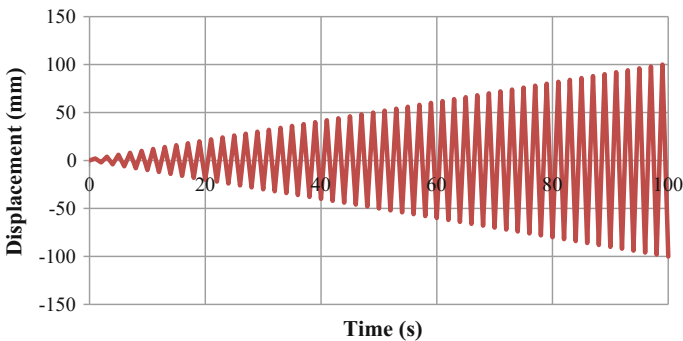
Fig. 8 Relative displacement versus time
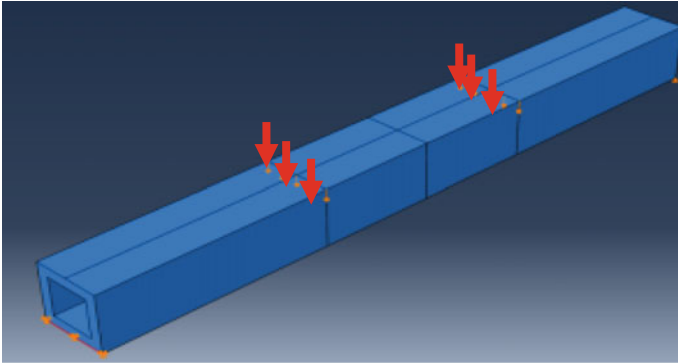
Fig. 9 Cyclic load applied on beams
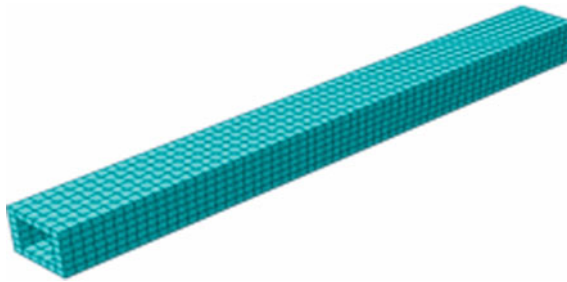
Fig. 10 Meshing for beams
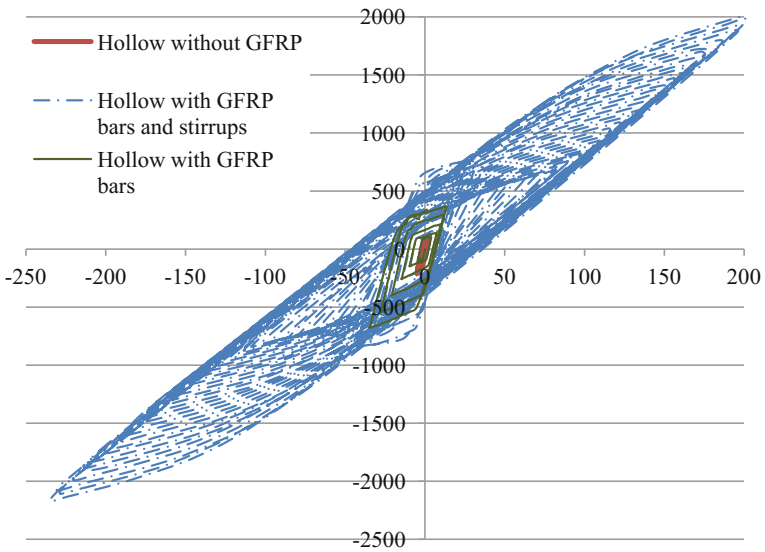
Fig. 11 Load–deflection graph for considered models

Table 4 HSC beams under cyclic load

Beam		H with normal reinforcement	H GFRP bars and steel stirrups	H GFRP bars and stirrups	H GFRP bars at web only and steel stirrups
Load	Load (KN)	213	677.9	2169	790
	Increasing (%)	–	218	1743	270
Energy dissipation	Area	10842493	86036408	1.68E+10	1.55E+08
	Increasing (%)	–	69	1584	1329
Displacement (mm)	At maximum force	5	34.7	235	70
	At 0.85 from maximum load	3.9	15.4	153	27
Ductility		1.3	2.25	1.5	2.5
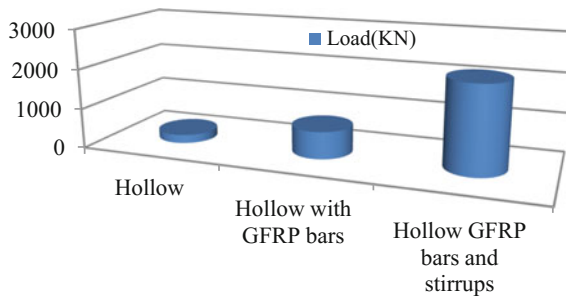
Fig. 12 Hollow beams capacity with GFRP

ultimate load by 218% compared with the hollow beam with normal reinforcement under cyclic load.

The area under curve of load displacement for hollow section beams with normal reinforcement and with GFRP bars substantially increased by 69%; such increase indicates a noticeable reduction in the beam performance. However, the increase was approximately 1584% for the beam with GFRP bars and stirrups compared with the hollow beam. In addition, the area under the curve of load displacement for the hollow beam with GFRP bars at web only was developed to 1329%. The ductility for the hollow beam was 1.3, which was smaller than that for the beam with GFRP bars at 2.25 and for the beam with GFRP bars and stirrups at 1.5 and about 2.5 for the beam with GFRP bars at the web only. Figure 12 shows the capacity of hollow beam reinforced with normal and GFRP bars.

The stress and strain distributions at the failure stage for all the studied beams are presented in Fig. 13. The stress in the beam reinforced with GFRP bars increased, and the stress distribution at the bottom was high. The maximum values of the

(1) Stress   (1) Stress

(2) Strain   (2) Strain

(a) Stress strain for hollow   (c) Stress strain for hollow beam with
beam with GFRP bars   GFRP bars only at web.

(1) Stress   (1) Stress

(2) Strain   (2) Strain

(b) Stress strain for hollow beam with   (d) Stress strain for hollow beam
GFRP bars and stirrups   with steel reinforcement.
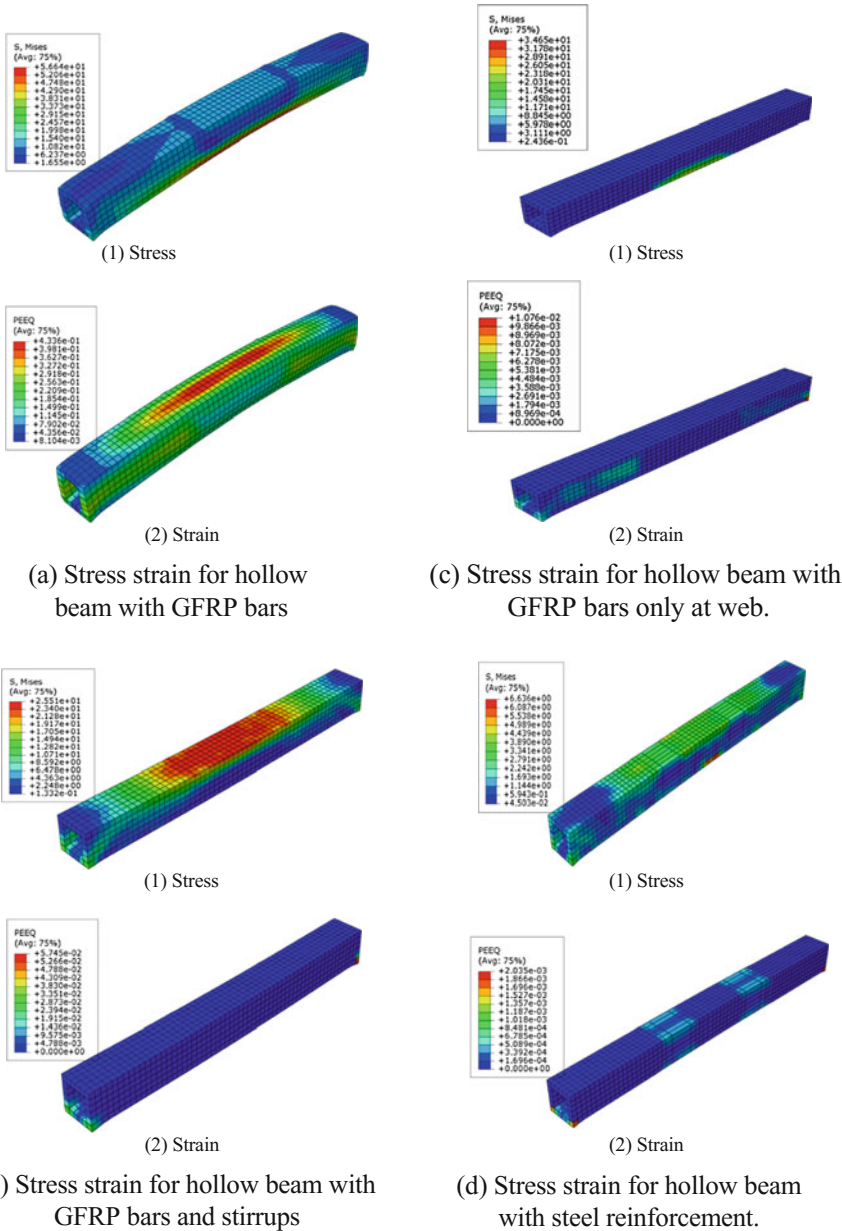
Fig. 13 Stress–strain for hollow beams (**a**, **b**, **c**, **d**)

Table 5 Maximum stress–strain for hollow beams with GFRP under cyclic load

Beam	Stress (MPa)	Strain (MPa)	Increasing
H with normal reinforcement	6.64	0.002	–
H GFRP bars and steel stirrups	56.6	0.433	7.52
H GFRP bars and stirrups	25.5	0.0574	2.84

principal stress in all modelled beams are listed in Table 3. The values of stress were 6.64, 56.6 and 25.5 MPa for the hollow beam without GFRP, the hollow beam with GFRP bars, and the hollow beam with GFRP bars and stirrups, respectively. The type of failure was described by the crushing of concrete because of the failure in the flexural compression zone.

Nonlinear strain distribution dominated the performance of hollow beams with GFRP reinforcements; therefore, FEA is the most appropriate technique for the analysis and design of such beams. The maximum amount of strain in different beams is presented in Table 5. The amounts of strain were 0.433, 0.002 and 0.0574 for the beam with GFRP bars, the beam with steel reinforcement, and the beam with GFRP bars and stirrups, respectively (Table 3). This nonlinearity of strain distribution is due to the shear deformations.

4 Conclusions

This study investigates the effect of implementing GFRP in hollow beams as bars and stirrups under cyclic load. For this purpose, the FE model of hollow beam with and without GFRP is developed, and the nonlinear FEA is conducted to predict the behaviour and strength of concrete hollow beams reinforced with GFRP (bars and combined bars and stirrups). On the other hand, RC solid beam with HSC material is tested experimentally in order to verify and validate of the finite element software to predict the result. It can be highlighted that the percentage of error is less than 20% in the comparison between the experimental and numerical result, which lead to prove the ability of software in predicts the result. On the basis of the numerical simulation results in terms of hollow section beams, the following conclusions are obtained.

The behaviour of hollow beam reinforced with GFRP bars and stirrups differed from that of hollow beam reinforced with steel bars and stirrups. The deflection of the beam reinforced with GFRP bars and stirrups was 10 times more than the hollow beam with steel reinforcement and three times more than the hollow beam reinforced with GFRP bars under cyclic load. The stress and strain increased for the hollow beam reinforced with GFRP bars and decreased for the hollow beam with steel reinforcement and the hollow beam with GFRP bars and stirrups. This study

proves that implanting GFRP bars can increase the performance of hollow beam and applying GFRP as bars and stirrups can considerably improve the action of the hollow beam under cyclic load.

References

1. ABAQUS: Standard Version 6.13-4. The ABAQUS Software is a product of Dassault Systèmes. Simulia Corp, Hibbitt Karlsson & Sorensen Inc, USA (2014)
2. ACI Committee: Building Code Requirements for Structural Concrete and Commentary (ACI 318). ACI, Farmington Hill, Michigan (2005)
3. Bernardo, L., Lopes, S.: Plastic analysis and twist capacity of high-strength concrete hollow beams under pure torsion. Eng. Struct. **49**, 190–201 (2013). https://doi.org/10.1016/j.engstruct.2012.10.030
4. Burningham, C.A., Pantelides, C.P., Reaveley, L.D.: Repair of reinforced concrete deep beams using post-tensioned CFRP rods. Compos. Struct. **125**, 256–265 (2015). https://doi.org/10.1016/j.compstruct.2015.01.054
5. Canadian Standards Association: Design of Concrete Structures (A23.3-04), Canadian Standards Association, Mississauga, Ontario, Canada (2004)
6. Chansawat, K., Potisuk, T., Miller, T.H., Yim, S.C., Kachlakev, D.I.: FE models of GFRP and CFRP strengthening of reinforced concrete beams. Adv. Civil Eng. (2009). https://doi.org/10.1155/2009/152196
7. El Maaddawy, T., Sherif, S.: FRP composites for shear strengthening of reinforced concrete deep beams with openings. Compos. Struct. **89**(1), 60–69 (2009). https://doi.org/10.1016/j.compstruct.2008.06.022
8. Hejazi, F., Jilani, S., Noorzaei, J., Chieng, C. Y., Jaafar, M. S., & Ali, A. A.: Effect of soft story on structural response of high rise buildings. In IOP Conference Series: Materials Science and Engineering, vol. 17(1), p. 012034 (2011)
9. Hii, A.K., Al-Mahaidi, R.: An experimental and numerical investigation on torsional strengthening of solid and box-section RC beams using CFRP laminates. Compos. Struct. **75**(1), 213–221 (2006). https://doi.org/10.1016/j.compstruct.2006.04.050
10. Inoue, S., and Egawa, N.: Flexural and shear behavior of reinforced concrete hollow beams under reversed cyclic loads. Paper presented at the proceedings of 11th world conference on earthquake engineering (1996)
11. Jabbar, S., Hejazi, F., Mahmod, H.M.: Effect of opening in reinforced concrete hollow beam web under torsional, flexural, and cyclic loadings. Lat. Am. J. Solids Struct. ABCM **13**(8), 1576–1595 (2016)
12. Jankowiak, T., Lodygowski, T.: Identification of parameters of concrete damage plasticity constitutive model. Found. Civil Environ. Eng. **6**(1), 53–69 (2005)
13. Li, Y.F., Badjie, S., Chen, W.W., Chiu, Y.T.: Case study of first all-GFRP pedestrian bridge in Taiwan. Case Stud. Constr. Mater. **1**, 83–95 (2014). https://doi.org/10.1016/j.cscm.2014.05.001
14. Lopes, S., Bernardo, L.: Twist behavior of high-strength concrete hollow beams–formation of plastic hinges along the length. Eng. Struct. **31**(1), 138–149 (2009). https://doi.org/10.1016/j.engstruct.2008.08.003
15. Metwally, I.M.: Nonlinear analysis of concrete deep beam reinforced with GFRP bars using finite element method. Malays. J. Civil Eng. **26**(2), 224–250 (2014)
16. Prabaghar, A., Kumaran, G.: Theoretical study on the behaviour of rectangular concrete beams reinforced internally with GFRP reinforcements under pure torsion. Int. J. Civil Struct. Eng. **2**(2), 579–603 (2011)

17. Sawaki, Y., Watanabe, J., Nakanishi, E., Isogimi, K.: Dynamic tensile behavior of aramid FRP using split hopkinson bar method. Fracture of Nano and Engineering Materials and Structures, pp. 523–524. Springer, Netherlands (2006)
18. Tavares, D.H., Giongo, J.S., Paultre, P.: Behavior of reinforced concrete beams reinforced with GFRP bars. Ibracon Struct. Mater. J. **1**(3), 285–295 (2008). https://doi.org/10.1590/S1983-41952008000300004
19. Torii, A.J., Machado, R.D.: Structural dynamic analysis for time response of bars and trusses using the generalized finite element method. Latin Am. J. Solids Struct. **9**(3), 1–31 (2012). https://doi.org/10.1590/s1679-78252012000300001

Investigation of Infill Wall Effect on Inelastic Response of Structures

Doaa Talib Hashim, Farzad Hejazi and Mohd Saleh Jaafar

Abstract Experience of recent earthquake proved that infill wall contributes to the behaviour of structures subjected to earthquake or any vibration loads. Although the infill wall is not considered during design process, as it is not a structural element. However, the function of infill wall during vibration of building has not been investigated comprehensively. Therefore, in this study, the influence of RC infill wall on seismic performance of the RC building during earthquake excitation is evaluated. For this purpose, a four-storey building; with and without RC infill wall elements is considered and finite element model is developed to study the influence of this RC infill wall in seismic response of building. Linear static, linear dynamic, nonlinear static (push over) and nonlinear dynamic (time history) analyses were all applied to the specified model for developing the finite element model of this building. On the other hand, an experimental study was carried out to verify the influence of the RC infill wall on the RC frame. The results indicated that utilizing RC infill wall can improve the response of the framed structure effectively during earthquake occurrence. It was also observed that adding infill wall in the outside bays of the four-storey building decreased the displacement of the structural nodes both in x and y directions and decreased their rotation around they and z axis. In addition, addition of RC infill walls reduced the axial forces in the columns and beams in the whole structure. Besides, a clear reduction in the shear forces was observed in the columns and beams. The moment around the beams and columns along the z axis was reduced after addition of the RC infill walls.

Keywords RC infill walls · ARC3D software · RC frame · Experimental work

D. T. Hashim · F. Hejazi (✉) · M. S. Jaafar
Department of Civil Engineering, Universiti Putra Malaysia,
43400 Serdang, Selangor, Malaysia
e-mail: farzad@fhejazi.com

D. T. Hashim
e-mail: doaatalib7@gmail.com

M. S. Jaafar
e-mail: msj@upm.my

1   Introduction

Earthquake phenomena are increasing covering more countries that have never experienced it before. Since earthquake involves huge damage of properties and loss of life, it is necessary to develop structural-resistant building [1]. Infill walls are non-structural elements that have significant contribution as lateral load resistance in frame structural system. It has been used in the construction of reinforced concrete structures to provide accommodation to the teaming population living in developing countries susceptible to seismic activity [4]. Also, infilled walls are used to provide weather protection, enclosure or as sub-division in large space in reinforced concrete frames. In addition, the infill walls are designed to restrain movement of frame systems and strengthen building subjected to horizontal loads. Faulty design and unsymmetrical arrangement of infill walls cause damage and subsequent failures of infill walls due to the effect of earthquake load [11].

RC infill walls are similar to reinforced concrete walls in terms of configuration to the shear wall but, with less thickness. Mostly, infill walls are considered as a pin and do not bond to the beam and column as in shear wall system. Generally, the infill walls are non-structural elements and are mostly not considered in the design. In fact, the infill walls are like a precast element and are used to fill the spaces. However, infill walls give good effect by increasing the stiffness of the structure. Besides, increasing the stiffness decreases the displacement at the same time and it helps to control the dynamic magnification that may occur in earthquakes [8]. Usually, the stiffness decreases with the increase in the number of floors due to the top floor columns carrying less weight compared with the lower floor columns [7].

Since the vibration most probably passes through the infill wall, it provides a good contribution in transferring the earthquake load and deformation to the members of the structure with lesser effect. In the past few decades, scientific community has been extensively involved in the investigation of the interaction between infill masonry walls and RC frames in the seismic structural system. Existing buildings, especially those designed for only vertical loads, in most cases lack adequate seismic provisions. In particular, infill masonry panels were not designed, assuming that there is no structural interaction with the surrounding frames [6].

The design of resistance structures to the earthquake is complicated as the phenomenon of earthquake is complicated. Many parameters are required to be considered while designing this type of building such as the height, shape, and materials. The most effective factor to be considered in earthquake-resistant construction method is the ground motion. The violent ground motion pushes the building rapidly from one direction to another which makes it difficult for the superstructure to constantly balance its load as a result of the inertial effects. According to previous studies, columns can bend during the intensified swaying motion and the building would be snapped and collapsed like matchsticks. Using RC infill walls is one of the most important and famous techniques in constructing more resistant buildings subjected to earthquake hazard. An

experimental and analytical study has been carried out by Ju et al. [10] to illustrate the effect of RC infill walls with and without slit separation. The work involves four one-bay-by-one-storey steel moment frame specimens along with push over analysis of multistorey frame models. The results indicated that the stiff RC wall would fail at a relatively small drift ratio before the steel moment frame developed to its full capacity. As a result, the author proposed to add slit-separation features at the edges of the RC infill walls in the construction of a steel moment frame. The slit-separated wall was isolated to be free from damage under small lateral storey drifts. In addition, the designed width prevents soft storey from failure and also increases the lateral resistance without inhibiting the ductility of the steel moment frame under large earthquake attack.

In order to enhance the sustainability of structures against seismic excitation, the constitutive law of viscous wall damper system (VWDs) has been formulated and integrated to develop a finite element model of VWD compatible with the reinforced concrete (RC) structure analytical model [9]. The finite element algorithm has been developed for inelastic analysis of RC buildings equipped with VWD devices capable of detecting damage to both structural members and damper connections under dynamic loading. This energy dissipation system succeeds by substantially diminishing and dissipating a structure induced by seismic responses. The results revealed that VWD device offers an effective earthquake energy dissipation system for multistorey buildings. Besides, a reduction of displacement in the time history analysis showed that the presence of VWD can substantially enhance the structural seismic performance. The results also revealed a noticeable reduction in the number of plastic hinges in the beam and column members. Shear forces and moments experienced in the column fluctuated with increases in the damping force.

This study aimed to investigate the linear and nonlinear behaviour of RC infill walls under static and dynamic loads. Also, to develop finite element model for RC structures with RC infill wall and evaluate the seismic response and damage in the RC frames with infill walls and make a comparison with RC frame without infill wall.

2 The Structure Under Consideration

A multistorey RC building of four storeys was considered in this study in order to investigate the effect of RC infill wall on the seismic response of the RC building. The building under consideration is used as a gym centre "Synergy fitness" at Selangor/Malaysia as shown in Fig. 1. The building consists of four levels, three bays in each direction as indicated in Fig. 2 focused on the maximum deflection of the infill wall structure.

The infill wall frame models have been analysed to investigate the overall response of infill wall element using ARC3D software program. The major aim of this study is to investigate the effect of RC infill walls in the linear static behaviour,

Fig. 1 The proposed building for the study
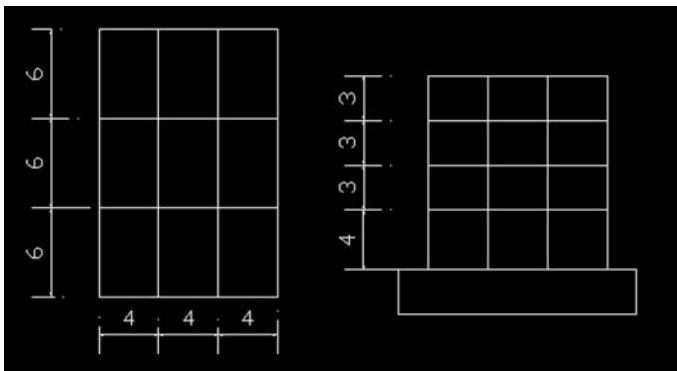
Fig. 2 The layout of the proposed building

under the push over load, and under the time history loading. The defined material properties and the section geometry in the finite element program are illustrated in Figs. 3a, b and 4a, b, respectively, in accordance with Euro code.

The structure has been analysed for two cases: (i) with and (ii) without infill walls. A comparison was made between the results of the two cases to find the effect of adding RC infill walls. The RC structure model without infill walls was subjected to 15 kN point load on each column of the top floor. In addition, the structure was subjected to 13kN/m D.L and L.L on all the beams of the whole structure as shown in Fig. 5a. Four RC infill walls were added on two bays on each
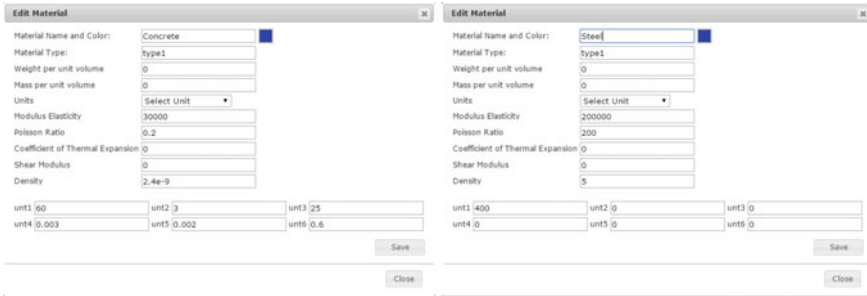
(a) Concrete properties   (b) Steel properties

Fig. 3 Material properties
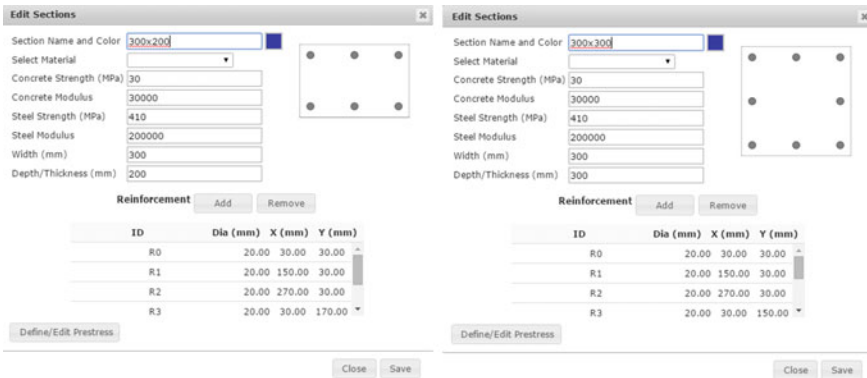
(a) Beam section geometry   (b) Column section geometry

Fig. 4 Section geometry

side in all the storeys of the building as presented in Fig. 5b. The thickness of the infill walls is 200 mm and reinforced with 20Ø20-207 c/c steel reinforcement. The dimensions and the spacing details are given in Fig. 6.

3 Numerical Analysis

In order to investigate the behaviour of RC infill wall in the seismic response of the structure, linear and nonlinear analyses were carried out by using ARC3D software for the aforementioned building in both the cases with and without infill walls. An attempt was made to demonstrate the generality and versatility of the developed code to study the response of reinforced concrete structures under earthquake excitation.

(a) The considered building without infill walls

(b) The considered building with infill walls
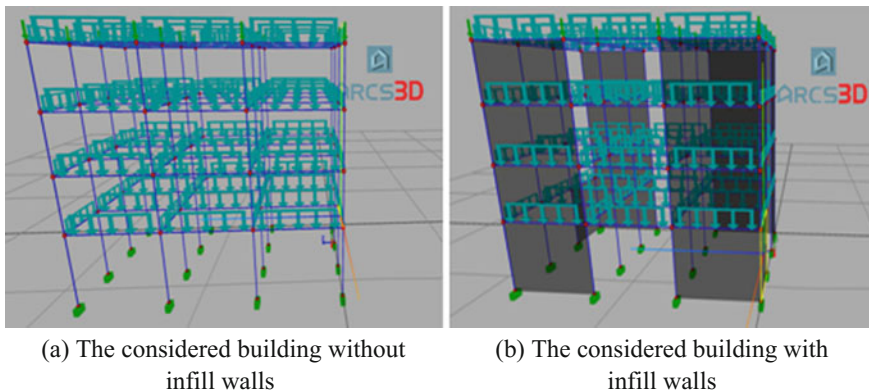
Fig. 5 The considered building with and without infill walls subjected to dead loads, live loads and point loads on the columns

Fig. 6 RC Infill walls details

Three analyses procedures have been conducted on the four storey building for with and without infill walls.

3.1 Linear Static Analysis

Linear static analysis was conducted on the building under consideration to investigate the influence of the RC infill walls in the building under static load.

Linear static analysis is the most basic type of analysis. The term linearly is related to the applied force and the term "static" means that the forces do not vary with time or, that the time variation is insignificant and can, therefore, be safely ignored. The static force is the dead load of the building. This model was subjected to 13 kN/m dead load in addition to the live load and 15 kN concentrated load on all the columns at the roof level.

Static analysis results showed that addition of RC infill walls elements has clearly decreased the node's displacement in X direction. The top floor's displacement in X direction of the building under the static linear analysis was observed to be decreased by about 67.5% compared with response of the structure without RC infill walls system as shown in Fig. 7a. Moreover, using the RC infill walls elements have reduced the displacement of the top floor in Z direction by about 84% compared with the response of the same building without infill walls elements as presented in Fig. 7b. Besides, the study revealed that the node displacement in Y direction was efficiently reduced by about 49.8% compared with a response without infill walls system as given in Fig. 7c.

Moreover, the average rotation of the outside nodes of the structure without RC infill walls around X axis was 6.54E-04θ clockwise. However after the addition of the infill walls, the outside's nodes average rotation around X axis was 6.69E-04θ clockwise for the same structure. During the comparison between the results, it was found that the rotation around X axis for with and without infill walls is almost same as shown in Fig. 8a. On the other hand, the average node's rotation around Y axis in the structure without infill walls is −4.08E-06θ counterclockwise. While the node's rotation around Y axis is 5.02E-09θ clockwise after addition of the RC infill walls as presented in Fig. 8b. Based on these results, the addition of the RC infill walls at the corners of the structure has decreased the rotation of the nodes around Y axis by 97.4%. During the linear static analysis, the average rotation of the nodes of the without infill walls structure around Z axis is −1.48E-06θ counterclockwise. After addition, the RC infill walls to the considered structure the average rotation of the

(a) Displacement in X direction

(b) Displacement in Z direction

(c) Displacement in Y direction
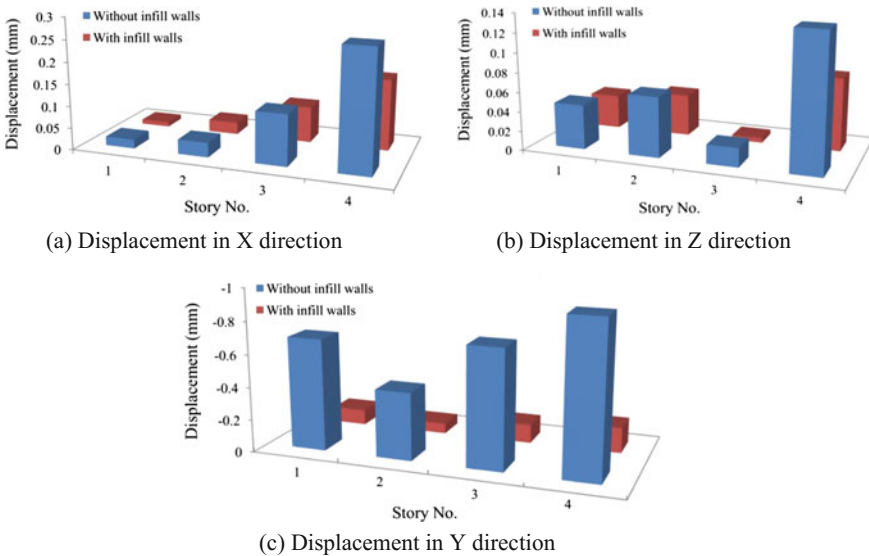
Fig. 7 The displacement results comparison with and without infill walls

(a) Rotation around X axis

(b) Rotation around Y axis

(c) Rotation around Z axis
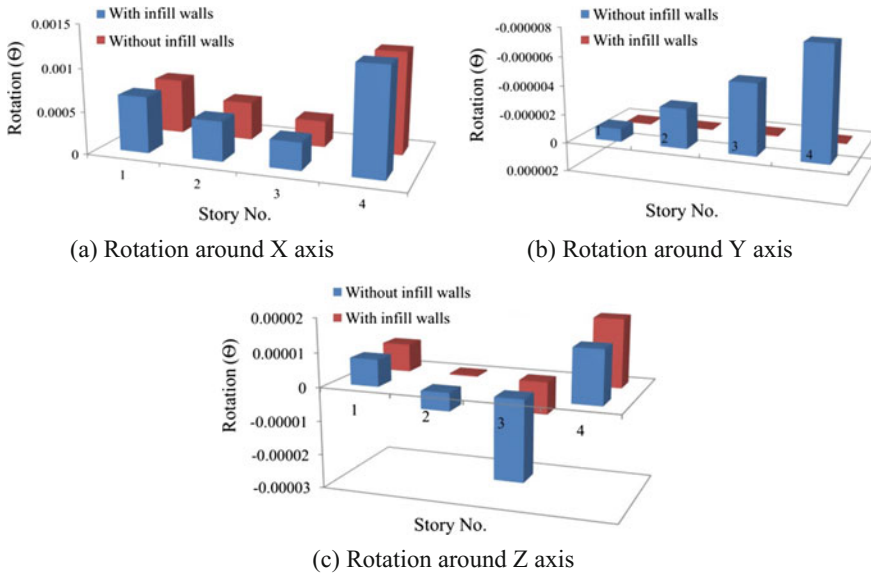
Fig. 8 The rotation results comparison for with and without infill walls

nodes around Z axis is 4.70E-06θ clockwise as given in Fig. 8c. It was concluded that the addition of RC infill walls at the structure corners decreases rotation at the middle of nodes around Z direction by 33.5%.

Moreover, adding the RC infill walls has decreased the generated forces in the columns in all the buildings' floors during the linear static analysis test. According to the numerical results, adding the RC infill walls has reduced the column's axial forces by 93.1% in Y axis as shown in Fig. 9a. Whereas, the columns shear forces in the Z axis have been reduced by 0.33% after adding the RC infill walls as given in Fig. 9b. Besides, after adding the RC infill walls the generated shear forces in the corner columns have been reduced by 2.2% in the X axis as shown in Fig. 9c.

Also, addition of RC infill walls to the considered structure decreased the torsional moment in the structure's corner columns. The maximum decrease in the torsional moment was at the first storey's column by 25.7% as shown in Fig. 10a. In contrast, adding RC infill walls at the structure's corners has decreased the bending moment around the X axis only in the first storey's corner column by 0.26% as shown in Fig. 10b. However, the RC infill walls have decreased the bending moment of the structure corner's columns around the Z axis, the maximum decreasing in bending moment around the Z axis was at the top storey's corner column by 64.2% as shown in Fig. 10c.

(a) Axial forces

(b) Shear forces in Z axis

(c) Shear forces in X axis
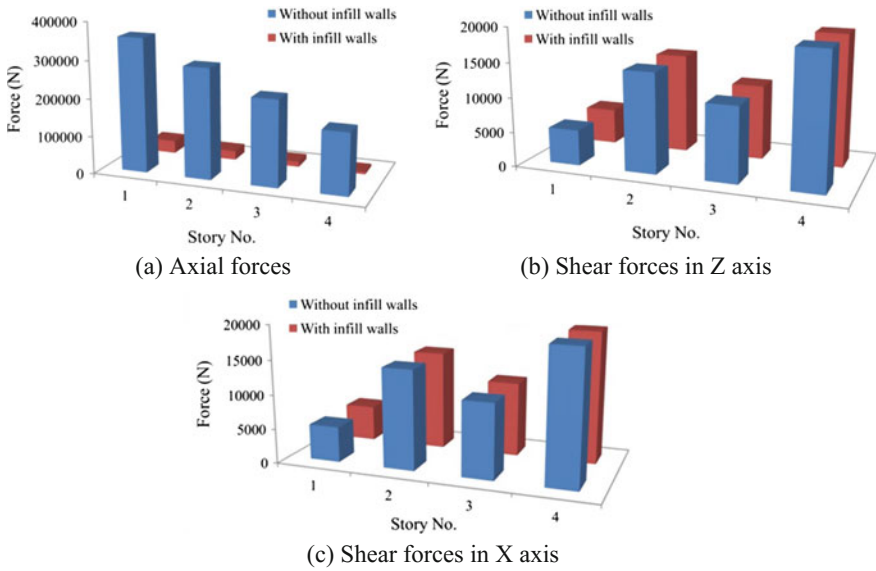
Fig. 9 Members forces results comparison for with and without infill walls

(a) Torsion moment results

(b) Bending moment results around X axis

(c) Bending moment results around Z axis
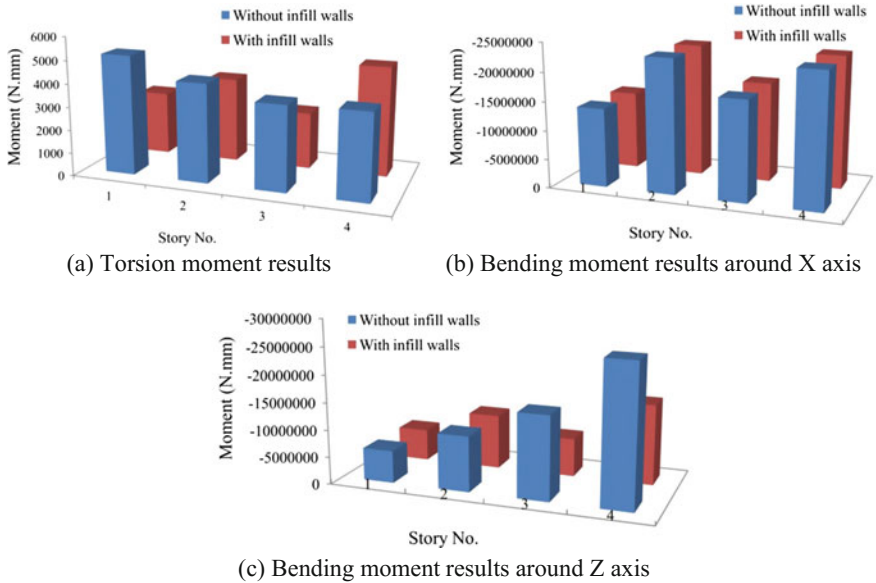
Fig. 10 Linear static moment results

3.2 Nonlinear Analysis of 3D RC Frame Structure with and Without Infill RC Walls

However, the static push over analysis has no exact theoretical foundation, it depends on the assumption of the response of structure related to the response of an equivalent single degree of freedom (SDOF) of the system. In this case, push over test of load 159,000 N was applied on each of the nodes (66 & 67) and the results of the analysis were calculated in nodes (78 & 79) by ARCS3D program and combine them together.

The horizontal displacement of the target nodes under the nonlinear static analysis is shown in Fig. 11. The peak horizontal displacement of the targeted nodes in the structure with infill wall system was decreased by about 4.37% compared with the response without infill wall system. Also, it can be observed in Fig. 12 that using RC infill walls does not affect the nodes' rotation severely. The peak rotation amplitude of the target nodes under the nonlinear static analysis was reduced by only 0.6% compared with the response without RC infill walls.

According to the nonlinear static analysis, the member forces result of the first column at the corner in each floor of the structure in both cases are shown in Fig. 13. Based on the nonlinear static analysis, using the RC infill walls elements has effectively reduced the axial force in the targeted members due to the applied push over load on one node. The peak axial force of the targeted members in the structure with infill wall system was decreased by about 77.45% compared with the response of the same building without infill wall elements.

Moreover, adding the RC infill walls to the building under consideration have clearly reduced the horizontal shear force in the member in the X direction, due to the applied push over load on one node only as shown in Fig. 14. The maximum shear force in the X direction of the targeted member in the structure with RC infill walls elements was observed to be decreased by about 11.6% compared with the response of without infill walls system. On the other hand, it was observed that the

Fig. 11 Displacement in the Z direction (mm)
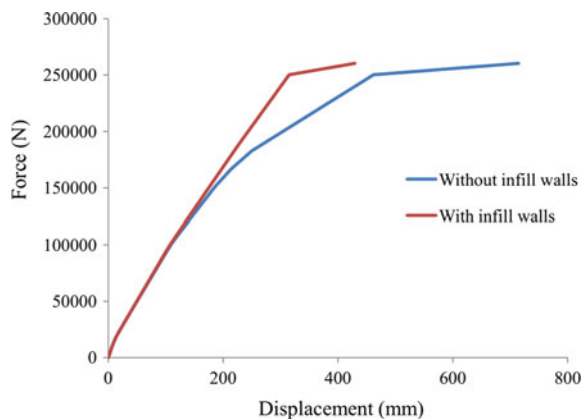
Fig. 12 Rotation around the
Z axis (θ)
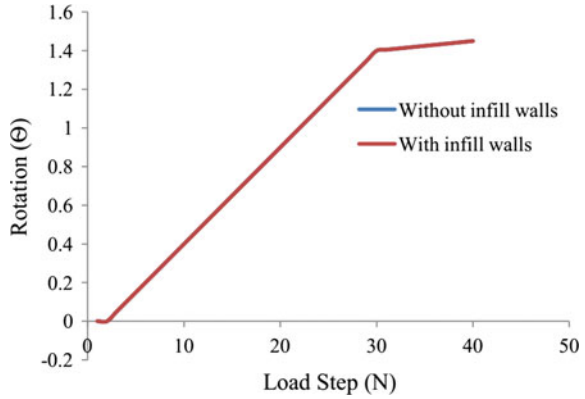
Fig. 13 Axial force results
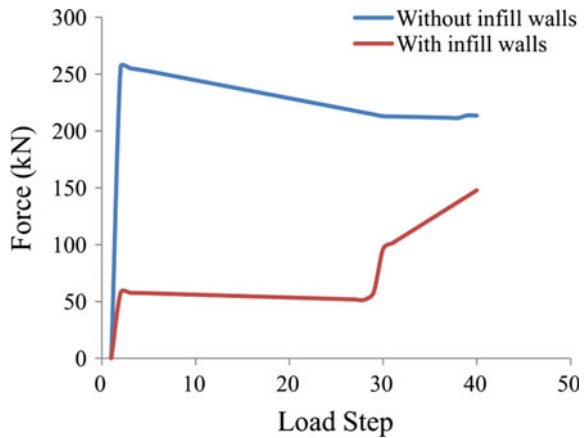
nonlinear static results using the RC infill wall elements have reduced the shear force in the considered members in the Z direction as shown in Fig. 15. The amplitude shear force in the Z direction of the target member under the nonlinear static analysis was decreased by about 1.12% due to the applied push over load on one node only compared with the response of the structure without RC infill wall elements.

The push over results showed that the generated torsional moments in the targeted element of the structure with RC infill wall is less than the generated one in the structure without RC infill walls under the nonlinear static analysis as illustrated in Fig. 16. The graph indicated that using RC infill walls elements has effectively reduced the torsion in the members by 31.44% compared with the response of the structure without infill wall elements due to applied push over load.

Besides, it was observed that addition of RC infill wall elements to the considered structure has reduced the generated bending moment around X axis as shown in Fig. 17. The push over results revealed that addition of the RC infill walls

Fig. 14 Shear forces in the *X* direction
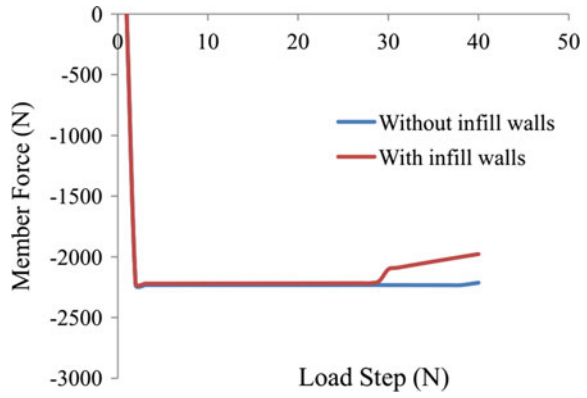
Fig. 15 Shear force in the *Z* direction
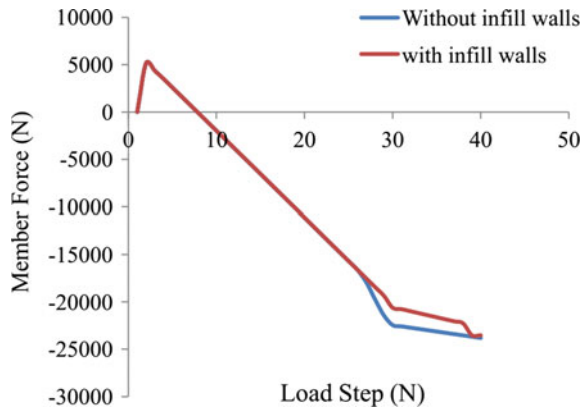
Fig. 16 Torsion results
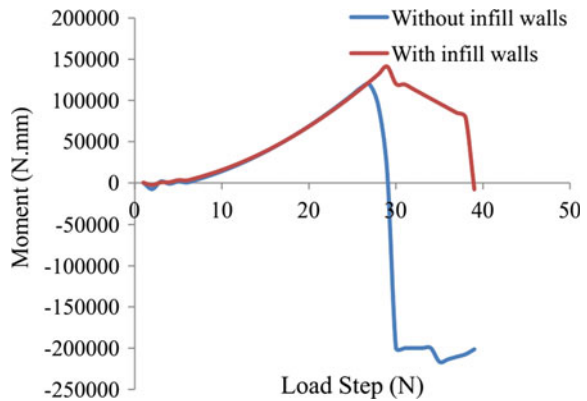
Fig. 17 Bending moment
around the X axis
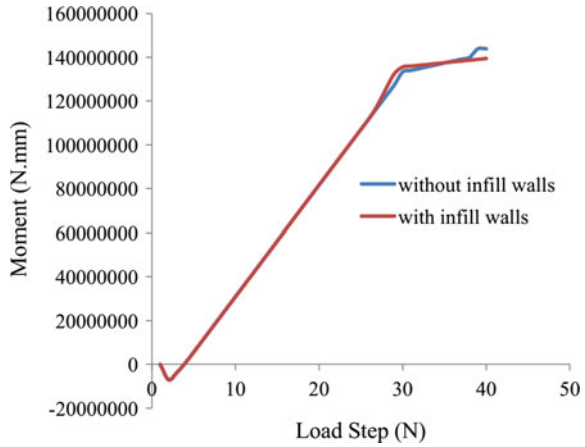
Fig. 18 Bending moment
around the Z axis
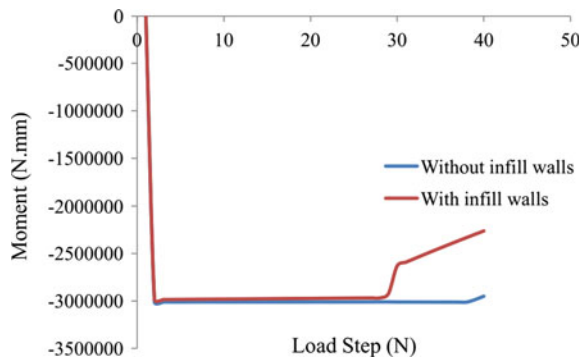
to all the corners and floors of the building has reduced the maximum generated bending moment around X axis in the corner columns by 3.1%. In addition, it was noticed that the generated bending moments around Z axis in the same columns has been minimized after addition of RC infill wall elements to the building under consideration as described in Fig. 18. By comparing the push over results of the structure with RC infill walls and similar structure without RC infill walls, it was observed that addition of the RC infill wall elements has reduced the maximum bending moment of the considered columns around the Z axis by 29.22%.

According to the force–displacement results of the push over analysis, it was observed that using RC infill walls has effectively reduced the considered nodes displacement in the Z direction by 41.2% compared with the response of the structure without RC infill wall system as shown in Fig. 19. Besides, it has found from the numerical results that the maximum force and displacement in the column attached to the RC infill walls were 231 kN and 336 mm respectively.

Fig. 19 Push over results
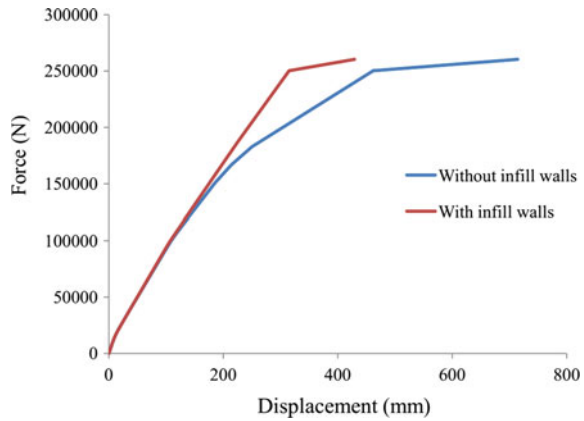
3.3 Nonlinear Dynamic Analysis of 3D Frame Structure with and Without RC Infill Walls

Since many and relatively strong earthquakes take place in many parts of the world, the study of the acceleration spectra for the earthquakes becomes of paramount importance [5]. The time history analysis shows the displacement results of the node (78). A corner column in the first floor has been considered for this analysis. The time–displacement results of the considered node in the X direction for both cases are shown in Fig. 20. It was observed that the displacement of node (78) in X direction was decreased by 99.5% after addition of the RC infill walls.

It was also noticed in Fig. 21 that using the RC infill walls had reduced the displacement in the Y direction. The peak displacement amplitude in the Y direction of the target node under the nonlinear dynamic analysis is reduced by about 50% compared with the response of the same structure without infill walls system.

Figure 22 shows that using the infill walls elements had reduced the displacement of the building in the Z direction. The peak displacement of the building in the

Fig. 20 Node's displacement in the X direction
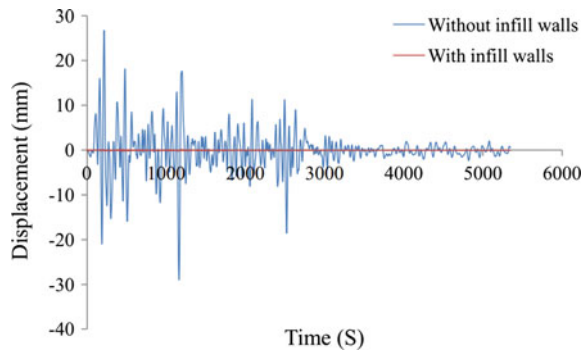
Fig. 21 Node's displacement results in the Y direction
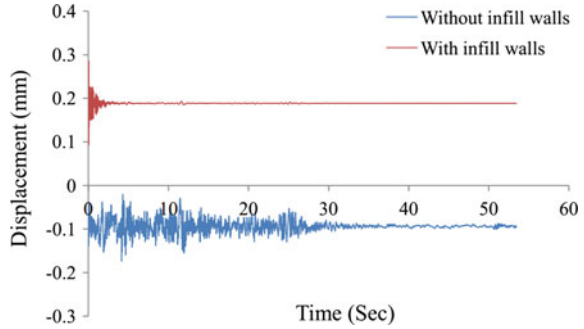
Fig. 22 Node's displacement in the Z direction
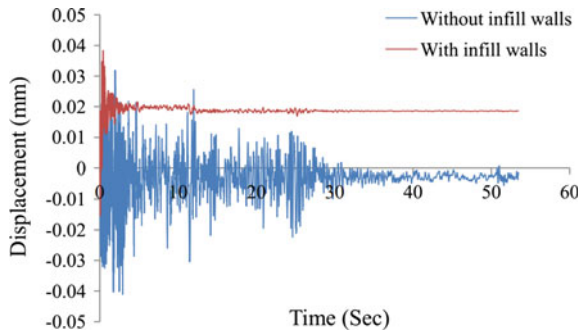
Z direction of the targeted node was reduced by about 16.9% compared with the response of without infill walls system.

The rotation around X axis due to the time history loading is shown in Fig. 23. It was observed that using the infill wall elements had effectively reduced the rotation around X axis. The peak rotation around X axis for the targeted node using infill walls was reduced by about 31% compared with the response of the same structure without infill walls.

The time history rotation results around Y axis of the node during the earthquake have been plotted as shown in Fig. 24. In addition to the rotation around the X axis, the result also shows that using infill wall elements effectively reduced structural rotation around Y axis. The peak rotation of the node around Y axis has been reduced by about 34.5% due to the contribution of the infill walls elements in the stiffening of the structure against the earthquake effect. Figure 25 shows that using the RC infill wall elements decrease the rotation of the considered nodes around the Z axis. The peak rotation of that node around the Z axis was reduced by about 96.4% compared with the response of the structure without infill wall elements.

Fig. 23 Node's rotation around the *X* axis
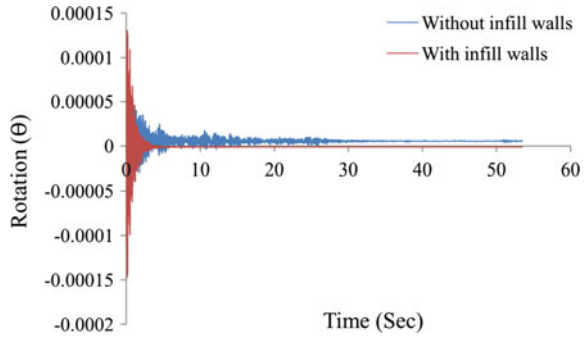
Fig. 24 Node's rotation around the *Y* axis
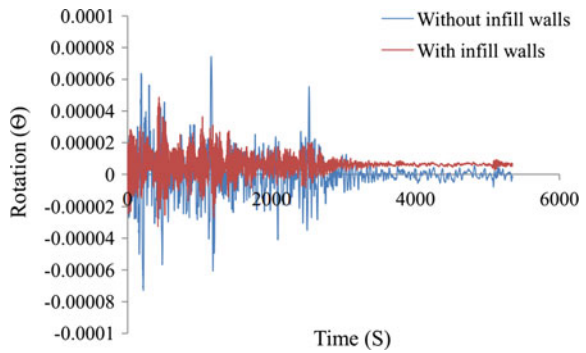
Fig. 25 Node's rotation around the *Z* axis
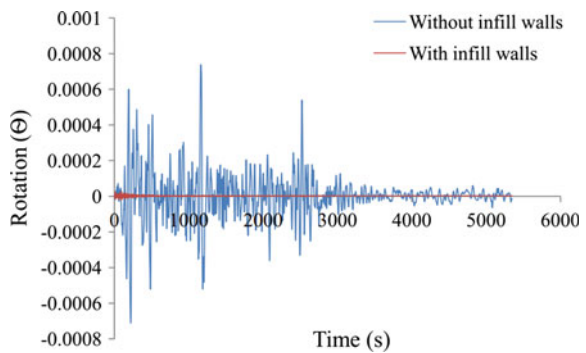
4 Experimental Testing

Figure 26 shows the RC frame designed that was produced in line with the provision of BS 8110-1 [2]. The RC frame samples were fitted with VSB devices and are designated as RC 1 and 2 for RC bare frame and VSB fitted RC frames respectively. The beam and column sections in all the samples were provided with 25 mm concrete cover to all reinforcements which are more than the required

minimum concrete cover provided in the code aforementioned. Figure 26 shows beam and column sections which are designed square shaped of 200 mm dimensions. Reinforcement bars 4 numbers (2 number each) size 14 and 20 mm diameter were used as longitudinal bars in the beams and columns. The shear links were designed and spaced at 80 mm interval along the column except for the base zones which contain stirrup spaced at 40 mm. This was carried out to avoid early failure due to high values of shear force concentration in the area. The same effective heights of 2000 mm and a free beam length of 1800 mm were used for all the specimens. The shear stirrups in the beams were also spaced at 80 mm distributed evenly along the length. All the shear links in both the columns and beams were designed as 8 mm diameter in all samples and the connection details are shown in Fig. 27. The bracing elements used were 14 mm diameter stainless steel and a minimum breaking load of 120 KN was used. The cables were used to brace the plates and jaw/jaw heavy-duty turnbuckles, alloy screw pin shackles, and wire rope thimbles fastened with steel clips were used as device hooks and the turnbuckles were used to pull the cable slack. In order to transfer and change the direction of the brace load into the devices, two pulleys provided at bottom plates were fitted with ball bearings. Four (4) high-strength hex bolts and nuts of 30 mm diameter were used as anchor device to the steel box at the base.
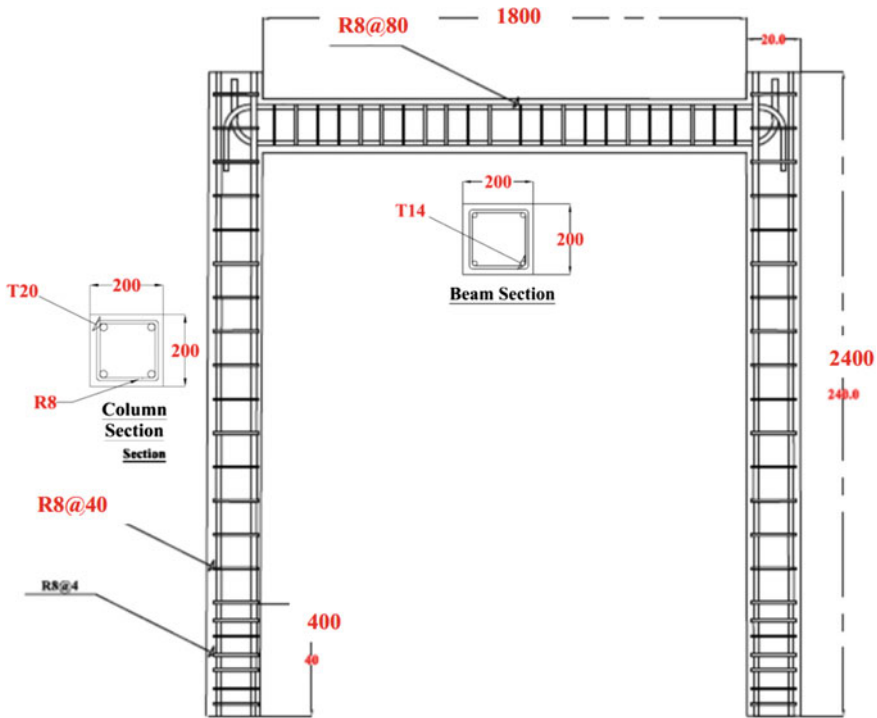
Fig. 26 Layout of bars in RC bare frame
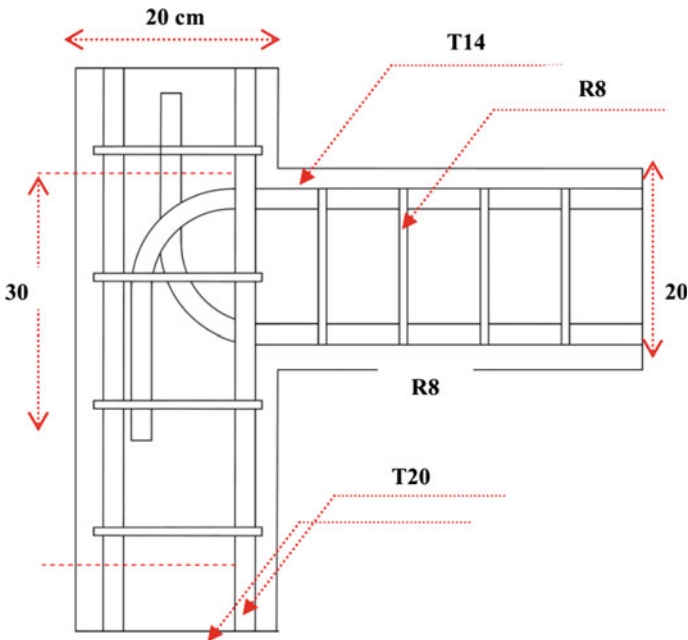
Fig. 27 Column–beam joint details

The anchorage length and the bending curvature of the longitudinal bars at the top and bottom of the beam were designed in line with the specification and requirement of the aforementioned code of practice. The connector bolts of 22 mm diameter mm were embedded in beam and columns samples separately before casting the concrete into the formwork and the VSB devices were attached to the concrete frames with the aid of exterior steel plates after the curing period. The top connection plates were then installed and tightened to the frame using the hex nuts. The anchorage length, bond stress, and bend radius were calculated based on the requirement of the code under consideration. Finally, high-strength wire of 14 mm diameter was used to connect the turnbuckle and shackled to the top plate and device rods.

4.1 Material Properties of RC Specimens

Mild and high-yield steel bars were used for shear links and longitudinal reinforcement in this experiment respectively. The mild steel and the high-yield longitudinal steel bars recorded yield strengths of 250 MPa and 460 MPa, respectively, this is in line with the provision of BS 8666 [3]. For instance, T20 represents deformed bar Type 2, with a yield strength of 460 MPa and diameter of

20 mm while, the mild steel bar of diameter 8 mm has a yield strength of 250 MPa. All the reinforcement bars were free from rust, grease, and any other coating that may cause de-bonding effects between the steel and the concrete.

The frame was constructed using a concrete of 30 MPa target compressive strength based on the recommendation of the code of practice for the concrete mix design as shown in Table 1. The aggregates used were about 75% of the concrete volume and were selected from a well-graded mixture of natural gravel, crushed stones, and sand from natural rock available in the Malaysian market. Portland Cement Type 2 commercially available in the local market was used in this experiment and potable pipe bone water was used for both the mixing and curing of the samples. Workability of fresh concrete plays a vital role in determining the level of compaction of in formwork in such a manner to avoid segregation. Slump test was conducted on the fresh concrete to evaluate the workability of the concrete matrix in the laboratory. Cubes samples of 50 numbers with size 150 mm × 150 mm × 150 mm was taken for assessment of the concrete compression strength at different age stages. During the casting phase, fresh concrete was placed in formwork in two layers and each layer was vibrated using a vibrator. A compression test was performed at 3, 7, 14, and 28 days and at the cyclic test day. The mean compression strength of the concrete cubes was 15.5, 18.5, 20.7, and 24.1 at 3, 7, 14, and 28 days, respectively. Also, the mean compression strength at the cyclic test day was 28.9 MPa. All specimens were covered and kept wet by spraying water over the samples regularly for 10 days, as recommended by the code. After 7 days, all formworks were removed, and the specimens were kept in the laboratory until testing period.

Three formworks were produced using plywood of 14 mm thickness and braced properly to avoid any deformation during the casting of the concrete. The formwork dimensions, shape, levels, angles, verticality and finishing height were checked during the formwork preparation. The formwork was prepared in a well-fitted situation and was sealed to prevent any possible leakage during concrete pouring. The formwork was properly cleaned and the internal surfaces were greased with oil to enable easy removal of the formwork before casting. Forklift and crane were used to relocate the samples after curing to the testing zone. All samples were painted white to enable easy detection of crack propagation.

Table 1 Concrete mix design (per metre cube)

Concrete grade (F_{cu})	30 MPa
Water	190 kg
Cement	425 kg
Fine aggregate	660 kg
Coarse aggregate	1135 kg

4.2   Monotonic Displacement History in Cyclic Test

Figure 28 shows the cyclic displacement history of the frames that was applied to all RC and steel frame specimens. The patterns of displacement history show a cyclic trend with progressively increasing amplitudes. The amplitudes increments started from 2.5 mm and gradually increased until failure. Figure 29a shows the location of the strain gauges mounted on the steel reinforcements in the RC frame and similar locations were chosen for all the RC frame sample as shown in Fig. 29b. Eight steel 10 mm length strain gauges were attached to the samples at different locations on the longitudinal reinforcement and the shear links. At the base of the left and the right columns, strain gauges designated S1 and S3 were attached to longitudinal reinforcements and S2 was connected to the column link. At the top longitudinal bars in the beam, two strain gauges S6 and S7 were connected and symmetrically located at 400 mm distance from the inner side of columns. Also, strain gauges S8 and S5 were attached to the bottom reinforcements and the shear link in the beam, respectively. All strain gauges were attached with the aid of glue and were wrapped by a waterproof tape. Figure 29b illustrates the position of strain gauges on the concrete surface in all RC frame models. Six 67 mm concrete strain gauges were attached to the smooth concrete surface by using standard rapid glue. Two strain gauges C9 and C14 were placed horizontally at the lower part of the columns. At the beam surface, four stain gauges C10, C11, C12 and C13 were attached symmetrically in the horizontal and vertical directions.

4.3   Results of Cyclic Dynamic Experimental Test on RC Frames

Figure 30 shows the actuator-deformed shape of the RC bare frame when subjected to maximum positive and negative displacements. The cracks occurred at the column–beam joint of the tensile side of the column cross section at a load of 29 kN.
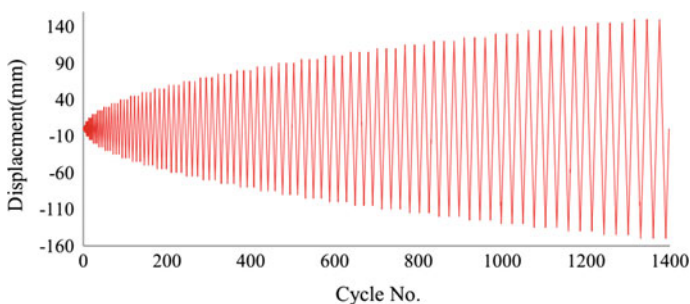
Fig. 28 Monotonic displacement history for RC model

(a) strain gauges on steel bars   (b) strain gauges on concrete surface
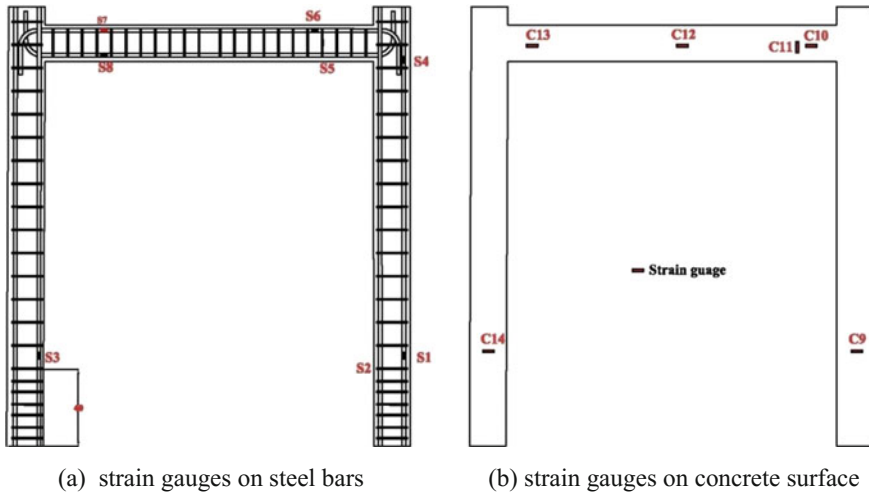
Fig. 29 Location of strain gauges at the RC models, **a** strain gauges on steel bars, **b** strain gauges on concrete surface

Fig. 30 Deformed shape of the RC bare frame under cyclic movement

These cracks opened and closed due to the effect of lateral cyclic loads applied to the frame during testing. Another crack emanated at the column–base connection when the load reached 47.1 kN. The cracks on the column sections were mainly due to the cyclic moment in the frame. Also, diagonal cracks of width more than 3 mm were observed on the beam–column joints which propagate as the displacement continuous. Failure was observed at the column end of the beam–column connection area as shown in Fig. 31.

The force–displacement diagram and skeleton curve of the RC bare frame is shown in Fig. 32. The maximum capacity of the RC bare frame and the displacement in the skeleton curve was observed to be 47.5 kN and 51 mm respectively. Despite the continuation of the experiment up to 100 mm displacement as

Fig. 31 Crack propagation in the RC bare frame column and connection zone
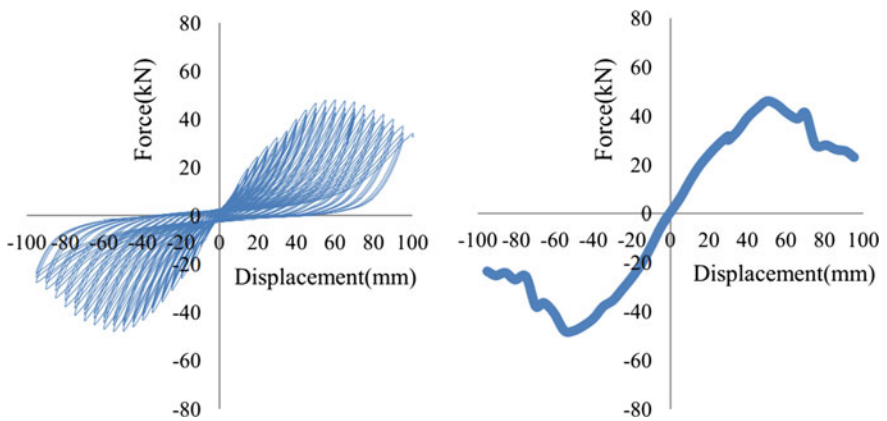
Fig. 32 Force–displacement relation and skeleton curve of the RC bare frame under dynamic test

Fig. 33 Numerical model of the RC frame with RC infill wall
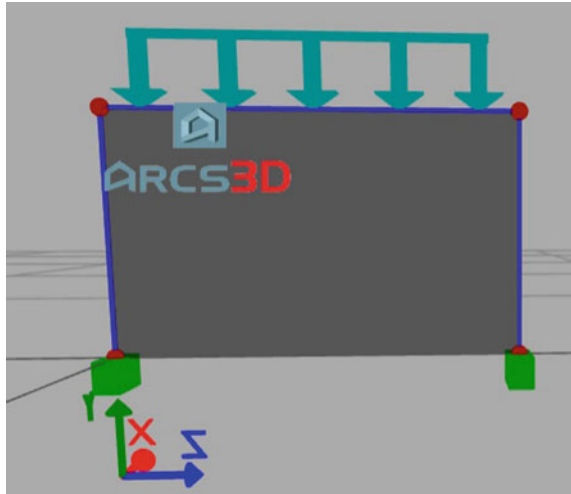
Fig. 34 Comparison between the experimental and the numerical results
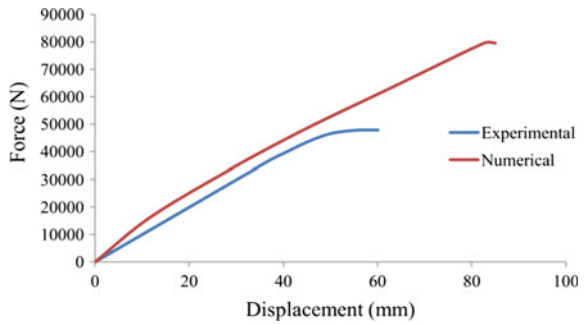
indicated in the skeleton curve, the capacity of the frame remains unchanged due to the failure already experienced at the joint location.

A comparison was made between the maximum force and displacement of the numerical results of the frame with RC infill walls as shown in Fig. 33 and the experimental result of the frame without RC infill walls. The comparison showed that addition of the RC infill walls to the considered RC structure has increased the maximum force capacity of the RC structure by 33% compared with the original structure as shown in Fig. 34. Moreover, the capacity of the RC structure with RC infill walls against the lateral displacement was increased by 36.4% compared with the same RC structure without RC infill walls as given in Fig. 34.

5 Conclusion

In this study, a finite element method for linear, nonlinear static analysis and nonlinear dynamic analysis of reinforced concrete structure equipped with RC infill walls subjected to seismic excitation was developed. An infill wall element with suitable reinforced detailed was used as a stiffener element in a reinforced concrete structure. ARCS3D, a finite element program was used to modify and analyse the reinforced concrete model with and without RC infill walls. This program is able to perform static, dynamic, linear and nonlinear type analyses for 3D reinforced concrete structures. In order to investigate the performance of RC infill walls in reinforced concrete structure, a comparison was made between the analysis's results of the model with and without RC infill walls that was obtained by ARCS3D program. In addition, an experimental test was carried out on RC frame without infill walls to investigate the performance of the RC frame without RC infill walls. Furthermore, an existing building was considered for analysis by the program in order to find the effect of the RC infill walls on the behaviour of the building in the normal case, under push over and seismic loads. In this study, the seismic response and the damage in RC frame with RC infill walls have been evaluated and a comparison between the behaviour of RC frame without RC infill wall and with RC infill wall was made. It was concluded that RC infill wall elements exhibit good resistance to structure and also increase the rigidity of the frame thereby decreasing the displacement and the rotation. Moreover, the displacement results of the nonlinear dynamic analysis showed that using RC infill walls elements had effectively reduced the displacement of the targeted node in X, Y and Z direction compared to the response of the same structure without RC infill wall system. Also, using infill walls system have reduced the rotation around X, Y and Z axes compared to the response of the without infill walls system. Furthermore, the member force in the nonlinear static analysis showed that using RC infill wall elements have decreased the axial forces in the Y axis, shear forces in the X direction and shear forces in the Z direction. More so, using RC infill wall elements have effectively reduced torsion, bending moment around the X axis and bending moment around Z axis.

References

1. Bell, D.K., Davidson, B.J.: Evaluation of earthquake risk buildings with masonry infill panels In: NZSEE Conference, Technical Conference, Future Directions: A Vision for Earthquake Engineering in New Zealand. New Zealand Society for Earthquake Engineering, Taupo New Zea, pp. 1–9 (2001)

2. BSI, B.S. 8110-1: Structural Use of Concrete–Part 1: Code of Practice for Design and Construction (1997)
3. British Standards Institution: British Standard 8666, BSI, London (2005)
4. Dorji, J.: Seismic performance of brick infilled RC frame structures in low and medium rise buildings in Bhutan. Doctoral dissertation, Queensland University of Technology (2009)
5. Drennov, A.F., Dzhurik, V.I., Serebrennikov, S.P., Bryzhak, E.V., Drennova, N.N.: The basic parameters of acceleration spectra for M > 5 earthquakes in the Baikal Rift zone. Russ. Geol. Geophys. **56**(2015), 773–781 (2015)
6. Fiore, A., Porco, F., Raffaele, D., Uva, G.: About the influence of the infill panels over the collapse mechanisms actived under pushover analyses: two case studies. Soil Dyn. Earthq. Eng. **39**, 11–22 (2012)
7. Hejazi, F., Jilani, S., Noorzaei, J., Chieng, C.Y., Jaafar, M.S., Ali, A.A.: Effect of soft story on structural response of high rise buildings. IOP Conference Series: Mater. Sci. Eng. **17**, 1–012034 (2011)
8. Hejazi, F., Noorzaei, J., Jaafar, M.S., Thanoon, W., Ali, A.A.A.: Optimization of active variable stiffness system for controlling structural response of a building under earthquake excitation. J. Struct. Eng. **36**(4), 235–242 (2009)
9. Hejazi, F., Shoaei, M.D., Tousi, A., Jaafar, M.S.: Analytical model for viscous wall dampers. Comput. Aided Civ. Infrastruct. Eng. **31**(5), 381–399 (2016)
10. Ju, R.S., Lee, H.J., Chen, C.C., Tao, C.C.: Experimental study on separating reinforced concrete infill walls from steel moment frames. J. Constr. Steel Res. **71**, 119 (2012)
11. Yatağan, S.: Damages and failures observed in infill walls of reinforced concrete frame after 1999 Kocaeli earthquake. A|Z ITU J. Fac. Architect. **8**(1), 219–228 (2011)

Fire Resistance of Bearing Walls in Light Steel Frame (LSF) Structures Including Various Insulation Filler Materials by Finite Element Method

Hossein Parastesh, Nima Ostovar and Farzad Hejazi

Abstract Using prefabricated structure in lightweight construction is the new method in both industry and civil engineering. Lightweight Steel Frame (LSF) becomes more valuable in the construction industry due to low cost, low weight, high speed of installation and resistance to environmental conditions. Cold-rolled form lightweight load-bearing wall is consisting of a thin sheet of steel with C-shaped sections (STUD), thermal insulation filler and cover sheets (Plaster Board). However, regardless of existing plasterboard protection the thin-walled steel sections heat up quickly and lose their strength under fire conditions. The main goal of the current study is an evaluation of thermal capacity and bearing strength of lightweight walls in terms of cellulosic fire condition analytically. The variable parameters are insulation filler materials (polystyrene, polystyrene concrete) and axial load. The Abaqus finite element software was used for modeling and analyzing of fire loads. Lightweight concrete fillers increase the axial bearing capacity of walls sustainably and polystyrene filler improved the fire resistance of walls.

Keywords Light gauge steel frame walls · Insulation filler · Polystyrene Fire resistance · Finite element analysis

H. Parastesh · N. Ostovar
Department of Civil Engineering, University of Science and Culture,
Tehran, Iran
e-mail: parastesh@usc.ac.ir

N. Ostovar
e-mail: nima_osv@yahoo.com

N. Ostovar · F. Hejazi (✉)
Department of Civil Engineering, University Putra Malaysia,
Serdang 43400, Malaysia
e-mail: farzad@upm.edu.my

1   Introduction

LSF was used initially as nonstructural, non-load-bearing member but they gradually have been used as bearing components in building constructions. Considering the novelty of using LSF as a load-bearing member it would be important to check its resistance in a fire condition. Empty space between two gypsum boards can be filled with various materials such as polystyrene, polystyrene concrete; therefore, studying these fillers and their effects on fire conditions are essential.

It is reported by many researchers that using finite element analyses (FEA) to study the behavior of LSF wall systems under fire conditions and to determine their FRR has advantages over full-scale fire tests of LSF walls [1–3]. It is less time consuming, cheaper and easier to perform. Many researchers used finite element analysis (FEA) for the study and it has advantages over full-scale fire tests of LSF walls. Many researchers studied the fire behavior of LSF wall panels due to its important role in the construction industry. Feng et al. [4] claims that to improve the fire resistance LSF wall panels interior (cavity) insulation can be used. On the other hand, other studies show that higher fire resistance can be achieved without cavity insulation [5, 6].

To assess the load-bearing LSF wall FRR, various full-scale fire tests were performed. In Gunalan et al. [7], demonstrated that some fillers are more efficient to be used in LSF walls as an inner cavity.

In this work, we investigate the numerical studies which are validated based on the full-scale fire test results in [8] and [9]. The aim of current study is to improve the efficiency of the complex structures and LSF wall fire behavior.

2   Method of Fire Protection

There are different methods to protect the structure in fire conditions, therefore, it is needed to test structures in fire conditions. Usually, these experiments are expensive and time consuming, instead, finite element method can be used to investigate the resistance of LSF walls in fire conditions under various load function such as axial constant loads or dynamic loads.

Abaqus is software which is used for finite element analysis to predict the structural behavior of thin-walled members. In this research, Abaqus provides results of LSF wall studs under different loadings with high accuracy. Additionally, this software is able to model mechanical properties and boundary conditions with high precision.

2.1 System Components

The main components of LSF which are stud and track (Rrunner) are shown in Fig. 1.

Runner in LSF walls is located horizontally on the floor and roof, it conducts the wall and connects the floor to the roof. Vertical members (studs) are located every 600 mm in runners, their height were 2400 mm and attached them as shown in Fig. 1.

Plasterboard is made of gypsum which is positioned between two thick layers of paper or cardboard and it is used as a separator in building the interior walls and roofs.
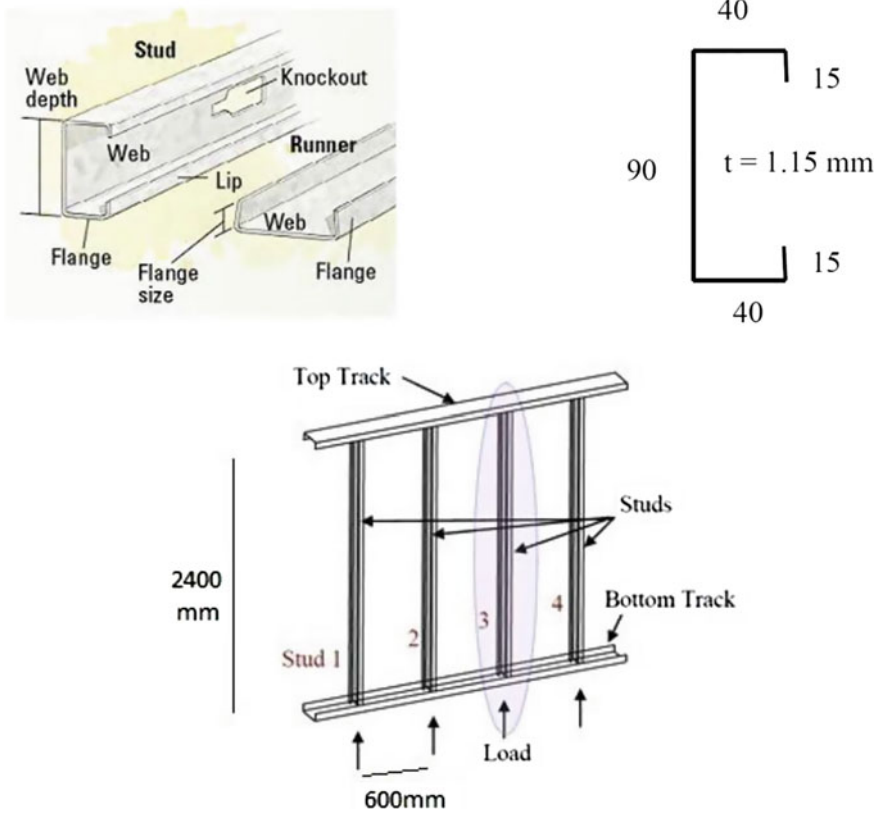
Fig. 1 LSF components (runner and stud)

2.2 Finite Element Analysis

Steel behavior models are divided into linear and nonlinear, which means that after reaching the yield stress, an increase in tension will be seen; Since the target of study is the behavior of the system against fire, it is necessary to study behavioral changes of steel in the case of heat in the model which would cause decrement in elasticity modulus, yield stress reduction and expansion.

3 Material Properties

Thermal properties of materials that are used in the models are shown in Table 1.

In modeling, steel behavior was considered as completely elastoplastic and modulus of elasticity and yield stress varies according to the temperature.

The thermal expansion coefficient of steel in accordance with the Eq. (1) varies with temperature as follows:

$$\alpha = 1.2 \times 10^{-5} + 0.4 \times 10^{-8}T - 2.416 \times 10^{-4}T \quad \text{for } 20\,^\circ\text{C} \le T \le 750\,^\circ\text{C} \quad (1)$$

In Table 2, steel mechanical and thermal properties are observed in the software. Steel density was considered as 7850 kg/m^3.

4 Verification

To validate the model, we used two experimental test models from Mahendran and Gunalan tests in 2013 [7]. They used a LSF STUD with external dimensions of 40 × 90 mm and thickness of 1.15 mm (Fig. 2) and they were evaluated in fire tests. They used 10 models to check their performance against fire. Models are shown in Table 3.

Table 1 Thermal properties of materials

Fillers	Thermal properties		
–	Density (Kg/m^3)	Conductivity (W/m C)	Specific heat (J/Kg C)
Steel	7850	43	450
Foam concrete	600	19/0	540
Polystyrene	30	03/0	1400
Polystyrene concrete	250	075/0	1060
Plaster board	800	17/0	1090
Air	225/1	024/0	1005

Table 2　Steel mechanical and thermal properties

Young's modulus	Poisson's ratio	Yield stress	Plastic strain	Expansion coefficient alpha	Temp
230769	0.3	583	0.002526336	0	20
209790	0.3	589	0.002807569	9.98E−06	100
184276	0.3	587	0.003185439	1.16E−05	200
164000	0.3	569	0.003469512	1.24E−05	300
146073	0.3	539	0.003689936	1.26E−05	330
125903	0.3	422	0.003351787	1.30E−05	400
106044	0.3	241	0.002272642	1.35E−05	500
79120	0.3	72	0.00091001	1.40E−05	600
37606	0.3	46	0.001223209	1.45E−05	700
10604	0.3	20	0.001886081	1.47E−05	800

Fig. 2　Test specimen before fire test
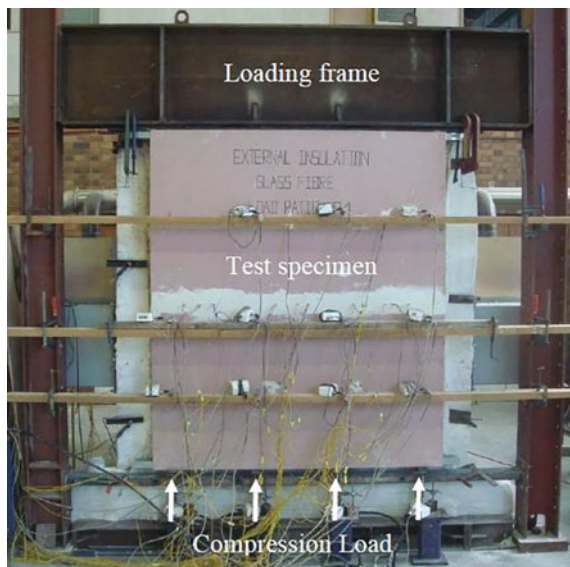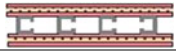
In the first validation test which is number 1 specimen in Table 3, one side of the wall panels was loaded with fire and one fiberglass layer between two plasterboards is used. As shown in Fig. 3, results of this work were similar to the results of steady-state condition in the test.

And also comparing results with the second verification, the similar results are achieved as shown in Fig. 4.

Number 2* specimen in Table 3, which had two plasterboard layers in both sides of STUDs without the cavity.

As it is shown in Figs. 3 and 4, it could be concluded that results of this work were similar to the benchmark method in steady-state condition [7].

Table 3 Details of tested LSF wall specimens (1–3)—tests conducted by Gunalan [9], (1*–7*)—tests conducted by Kolarkar [10]

Test	Configuration	Insulation	Load ratio	Test failure time (FRR) (min)	Vertical plasterboard joints
1		Glass fiber	0.2	118	Studs 1 and 3
2		Glass fiber	0.4	108	Studs 1 and 3
3		Rock fiber	0.4	134	Studs 2 and 4
1*		None	0.2	53	Studs 2 and 4
2*		None	0.2	111	Studs 2 and 4
3*		Glass fiber	0.2	101	Studs 2 and 4
4*		Rock fiber	0.2	107	Studs 2 and 4
5*		Cellulose fiber	0.2	110	Studs 1 and 3
6*		Rock fibre	0.2	136	Studs 2 and 4
7*		Cellulose fiber	0.2	124	Studs 2 and 4
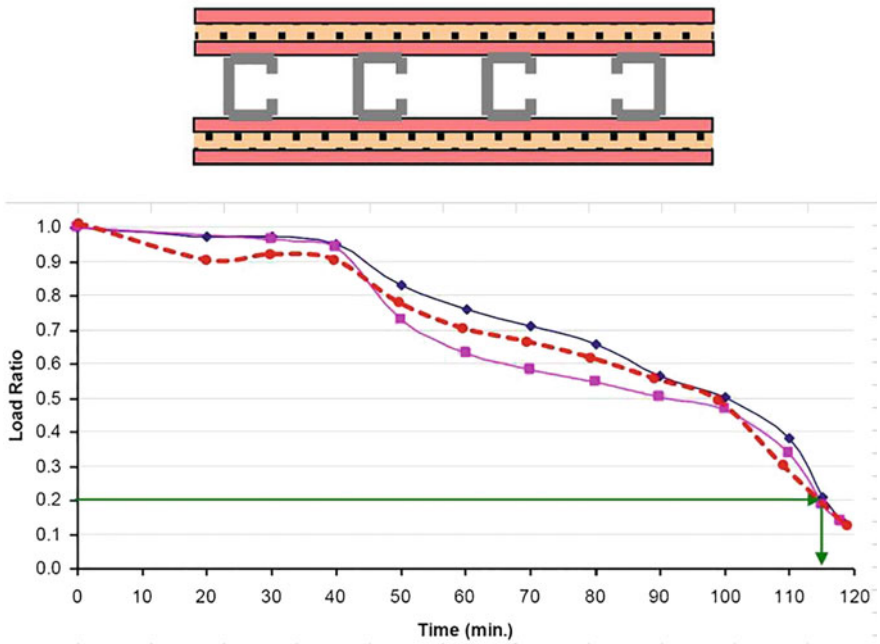
Fig. 3 Wall specimen number 1 verification (one fiberglass layer between two plasterboards and its result graph, red dashed lines belong to the verification result graph)
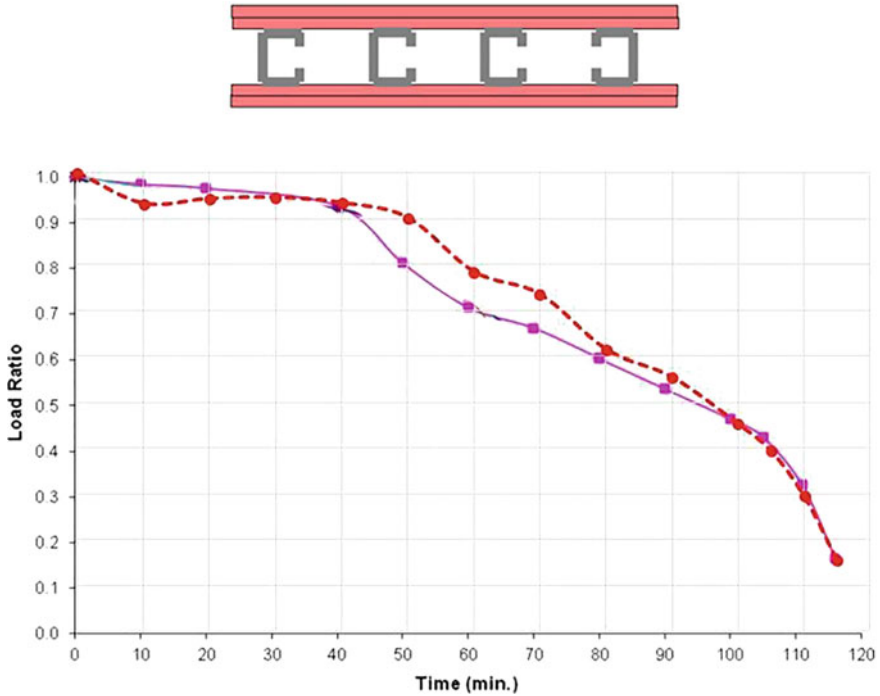
Fig. 4 Wall specimen number 2* verification (two plasterboards without a cavity and its result, red dashed line belongs to the verification result graph)

5 Modeling Description

Walls were modeled in Abaqus finite element modeling software. Shell elements (4nods S4R) was used for making the sections meshing which able to consider the buckling and deformation perfectly. Rigid plates were placed at the opposite ends of studs and they were attached to their upper and downward supports were hinged. Deformation within the confinement of Plasterboards studs at intervals of 30 cm was closed.

In Table 4, the variation of gap fillers and isolations which should be used in walls as shown. The height of stud and thickness of plasterboard should be assumed as 90 and 13 mm respectively. Top movements were closed and forces were applied to the downside. The hot flanges and cold one's heat was considered uniformly and in the web longitude was linearly, as shown in Fig. 5.
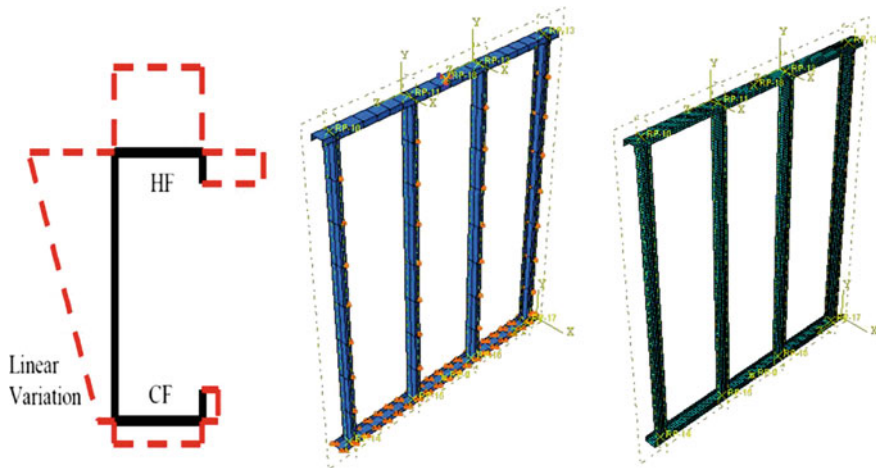
Fig. 5 The figure of Studs and description of heat transfer in stud section

6 Loading

The first step in the process of modeling and analyzing techniques is to expose one side of the wall to the fire standard condition (cellulosic fire condition) and extract the hot flange and cold flange temperature. Then the extracted temperature was applied and the web temperature which changes linearly between the hot flange and cold flange to the separate model to achieve their maximum load bearing at different times from the start point of firing (loads cannot be applied immediately after thermal analysis to the software). We achieved the ratio of the bearing walls with fillers and without fillers and thermal loading and named it as load ratio. Initial geometric imperfection is not allowed by thermal bowing to have any significant influence on the resistance of LSF wall studs.

There are two types of loading under fire condition in finite element analysis for steel members: 1. transient state 2. steady state.

In steady-state condition, the nonuniform temperature distributions in the steel section is heated up to a specific level and then remained steady. In the next step, loading would be added until failure.

In transient state condition, first the aimed load (for instance 0.2 of the ultimate load) is applied to give a specific LR (load ratio), after that nonuniform temperature distributions are inserted in a time frame in stud. In this research, transient state condition is used to analyze the models.

Graphs in Fig. 6 show the growth in temperature of hot and cold flanges during the specified time for different samples. In graphs, the solid curve corresponds to the standard cellulose fire temperature which exposes to the one side of the wall, dashed and dotted curves are related to the hot flange and cold flange respectively. It is assumed that one side of wall faces fire and the other side is exposed to open air

Table 4 Modelling variation of fillers and location of plasterboards (P is one layer of plasterboard, 2P is two layers of plasterboards, PSC is polystyrene concrete, and PS is polystyrene)

	Model code	Model figure
1	2P	
2	2x2P	
3	2P-PSC	
4	2x2P-PSC	
5	2x2P-PS	
6	2xP-PS-P	
7	2xP	
8	2xP-PSC	

condition, where walls transfer heat. So, if there are less materials between the wall and open air, wall would cool down earlier and the reduction in the bearing of the wall would be less (Table 4).

7 Analyzing Result of Charts

When one side of the wall uses plasterboard and the other side is exposed to the open air, the increasing ratio of temperature is lower, thus the reduction of resistance would be less. So, while plasterboard was on one side and not filled with any

filler, the temperature increase would be less; but it is not practicable since the wall did not have any coverage. It seems the best condition can be achieved using one layer of polystyrene between two plasterboards, since it was more practicable and its weight was less than concrete fillers (Fig. 6).

The usage of polystyrene as a filler did not have any sufficient result, since it worked as an isolation besides the hot flange which had resulted in heat focus on that area. The increase in the temperature in both concrete specimens did not have any obvious differences, but it should be considered that one of them (foam concrete) had more resistance and the other one had lower weight (polystyrene concrete). Therefore, the selection of the type should be decided based on the requirements.

If the heat transfer coefficient of materials was lower than air, then it was not suitable to be used as a filler. Since it caused heat concentration on one side, it would be more appropriate to use them as a coverage on walls.

It should be mentioned that because the specific heat capacity represents the amount of energy required to increase the temperature of a unit mass of material; it cannot be calculated if a material is appropriate to be used as isolation because density would also be effective. For instance, although the specific heat capacity of plasterboard and air are close to each other, it would have a low performance due to low density.

8 System Resistance with Various Fillers

In the next step, we will compare the strength decrease of studs. In the wall specimens with concrete fillers, the strength of concrete was added to the wall resistance. It should be noted that this strength would be decreased by an increase in temperature. In addition, while the concrete reached its maximum resistance, studs became confined, since the graphs of these walls were acquired in both confined and unconfined conditions. Then confined and unconfined graphs were added. When the concrete got its maximum strain displacement, confined graph and unconfined graph should be used respectively.

The maximum strength of walls at different times from the beginning of the fire with a maximum resistance of species without fillers and temperature were compared. "Load Ratio" for walls with concrete filler could be more than "one". For illustration, one curve of force and displacement without heat and fillers was shown Fig. 7 (the basic graph was used to acquire the load ratio).

In Fig. 8, the ratio of the strength of walls and the basic strength is indicated. To achieve these graph the model of each species analyzed six times. Every time the temperature of studs at various times was used to reach the maximum tolerated load which is extracted from samples.

The "Load Ratio" is acquired by dividing the maximum tolerated load on the sample loads without resistance and temperature. Every point of these curves is the result of a separate analysis.
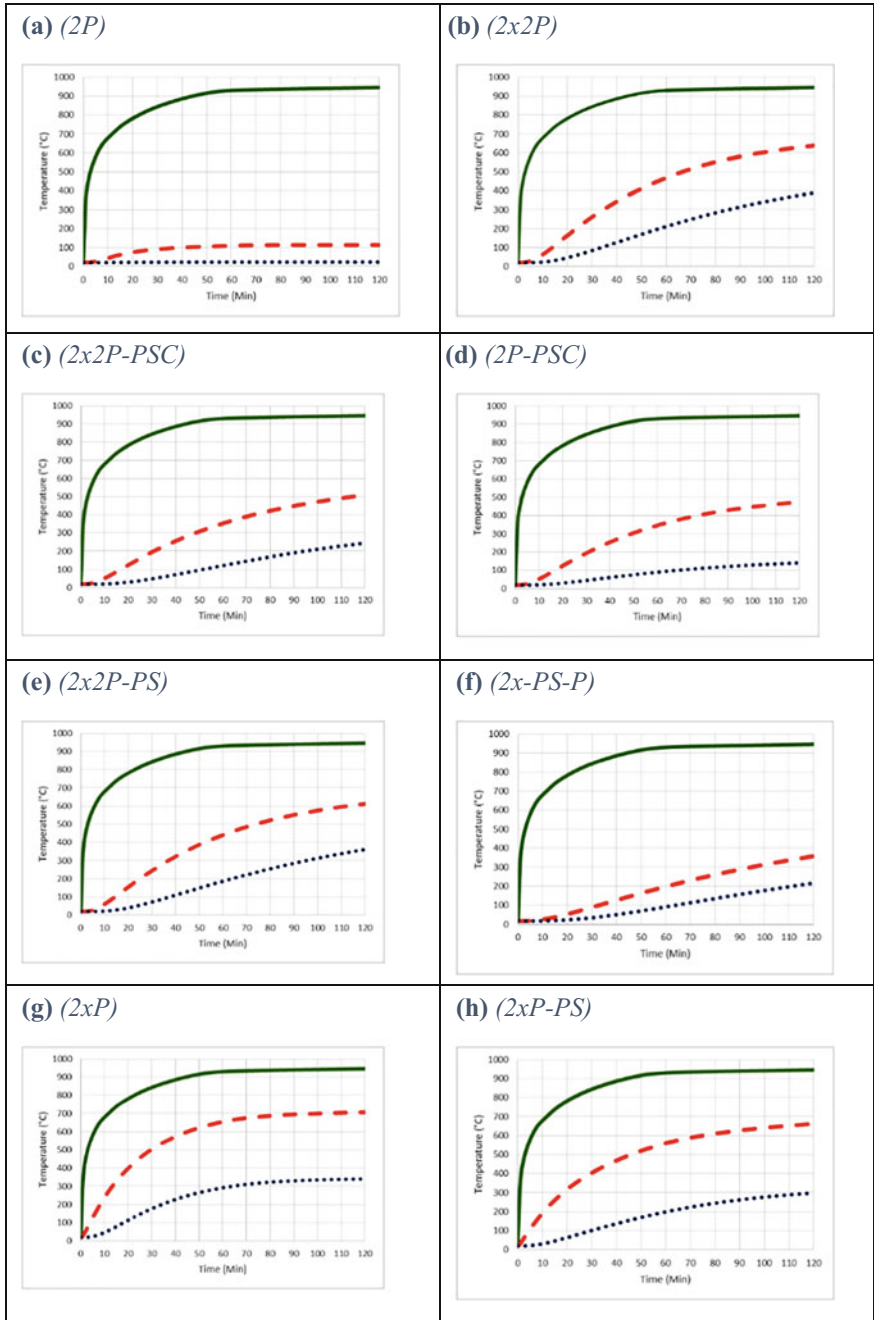
Fig. 6 Results of analyzing temperature–time and bearing-time growth temperature in both hot flanges and cold flanges. a–g stands for rows in Table 4
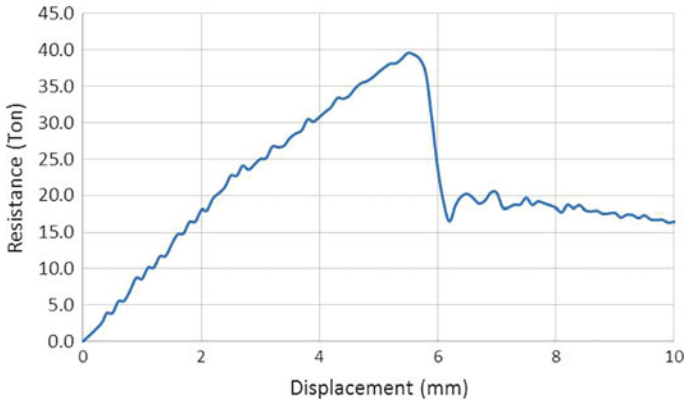
Fig. 7 Basic force–displacement graph without heat and loads
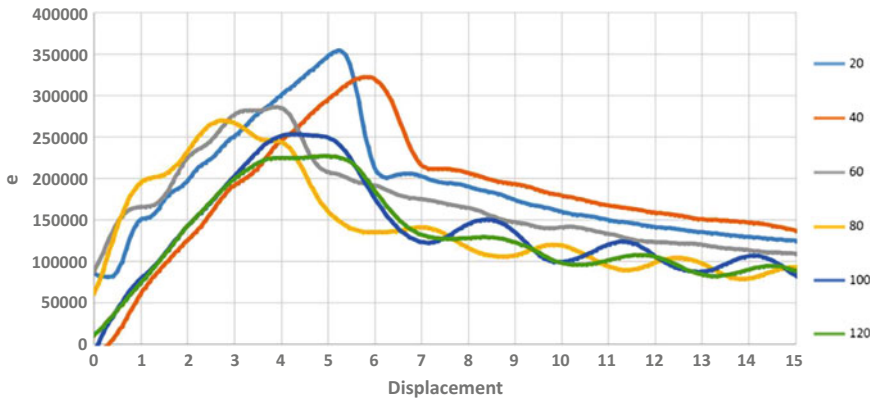
Fig. 8 Force–displacement graph for the 2x2P-PSC

As it can be seen in Fig. 9, species with concrete filler has the most strength as the bearing of concrete is also calculated in the total resistance. The effects of plasterboards are minimum in these samples. Also as the number of layers of the studs increase, the temperature has more pathway to reach flanges, as a result, better performance was achieved. When the heat flanges, it is better to set the conditions such that flanges can release the heat into the open air.
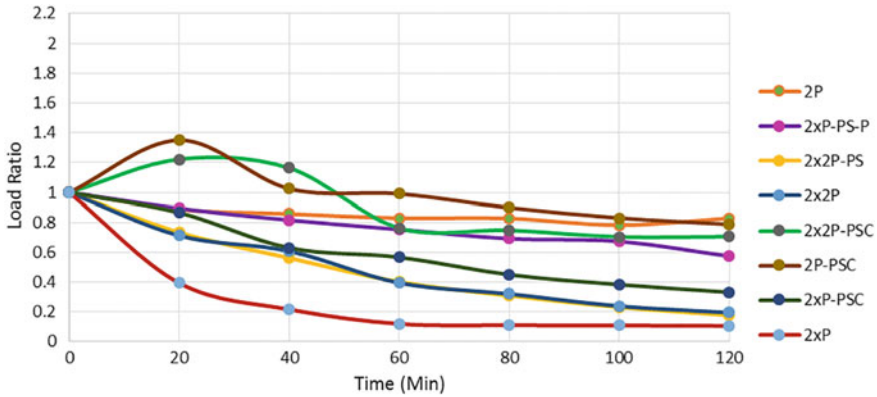
Fig. 9 Specimens load ratio

9 Conclusions

– Considering the weight and density in various concretes and exceptions from the structure, we can choose the efficient filler in construction.
– Considering limitations of dead load and live load, concrete fillers make structures heavier.
– The best performance is achieved by using one layer of polystyrene between plasterboards.
– In case of lateral walls, it is better to reduce the external layers to have a better heat exchange with open air and prevent the confined heat in walls.
– The usage of concrete fillers is appropriate when it is needed to increase the bearing of walls. Since steel's high thermal conductivity causes heat to get to the flange of studs, consequently it increases the temperature of the whole element, so these kinds of fillers would not be effective.

References

1. Kaitila, O.: Finite Element Modelling of Cold-Formed Steel Members at High Temperatures. Helsinki University of Technology, Espoo (2002)
2. Feng, M., Wang, Y.C., Davies, J.: Axial strength of cold-formed thin-walled steel channels under non-uniform temperatures in fire. Fire Saf. J. **38**(8), 679–707 (2003)
3. Zhao, B., et al.: Calculation rules of lightweight steel sections in fire situations. EUR **21426**, 1–226 (2005)
4. Feng, M., Wang, Y.C.: An experimental study of loaded full-scale cold-formed thin-walled steel structural panels under fire conditions. Fire Saf. J. **40**(1), 43–63 (2005)
5. Kodur, V., Sultan, M.: Factors influencing fire resistance of load-bearing steel stud walls. Fire Technol. **42**(1), 5–26 (2006)

6. Alfawakhiri, F.: Behaviour of Cold-Formed-Steel-Framed Walls and Floors in Standard Fire Resistance Tests. National Library of Canada/Bibliothèque nationale du Canada, Ottawa, Canada (2003)
7. Gunalan, S., Mahendran, M.: Finite element modelling of load bearing cold-formed steel wall systems under fire conditions. Eng. Struct. **56**, 1007–1027 (2013)
8. Kolarkar, P., Mahendran, M.: Thermal Performance of Plasterboard Lined Steel Stud Walls (2008)
9. Gunalan, S.: Structural Behaviour and Design of Cold-Formed Steel Wall Systems Under Fire Conditions. Queensland University of Technology, Brisbane (2011)
10. Kolarkar, P.: Structural and fire behaviour of a new steel stud wall system using composite panels (Doctoral dissertation, PhD thesis). Queensland University of Technology, Brisbane, Australia (2010)

Performance of Various Connection System for IBS Structure Subjected to Cyclic Load

Iman Sadeq, Farzad Hejazi and Sarah Jabbar

Abstract Nowadays, application of precast constructions is increasing, due to benefit of the industrialized building systems, specially the performance of this type of construction structures when effects of dynamic loads are considered. Precast beam column connection is mostly the critical part in the structures to resist the loads, so that the attention must be paid while designing such connections. Therefore, the aim of this study is to evaluate the efficiency of the precast concrete beam–column connection comparing with the conventional joints. Three-dimensional nonlinear analysis was conducted using finite element method with five beam–column connections under the effect of cyclic load, bearing pad, steel dowel, and steel angle cleat were used to improve the connections performance. The results indicated that the using of steel angle cleat and dowel together and doubling angle cleat have improved the lateral resistance of the precast connections as well as the lateral stiffness and the ability to dissipate damage energy when comparing with the conventional joint performance.

Keywords Precast concrete structures · Beam–column connection
Finite element analysis · IBS structure · Cyclic load

1 Introduction

Precast concrete construction is the widely used in Industrialized Building System. So many countries have headed towards using this type of construction due to many benefits provided by adopting prefabricated concrete elements in terms of speed of

I. Sadeq · F. Hejazi (✉) · S. Jabbar
Universiti Putra Malaysia, Serdang, Malaysia
e-mail: farzad@fhejazi.com

I. Sadeq
e-mail: imansadeq1980@yahoo.com

S. Jabbar
e-mail: sarahsaleem2015@gmail.com

erection, reduce wasteful materials, clean and safe environment, decrease the demand for workers and access to high-quality concrete away from climate's bad effect, nowadays, in many countries because it offers a package of benefits summarized in economic benefits in terms of shortening construction time, reducing reinforcing steel and wet concrete in site work wastages [15].

The strength of RC beam–column connections play a remarkable function in the durability of the structure while insufficient joints, which have ineligible joint transverse reinforcement and incompetent anchorage of the beam bottom reinforcement were the main reason of the observed damages in the structures over the years. Luk and Kuang [11] studied the performance of conventional beam–column joint and two wide beam–column joint with different beam width through numerical analysis subjected to quasi-static cyclic loading. The results indicated that the using of wide beam column joint reduced the stiffness and the lateral strength and increased the shear stress while less crack opening was noticed comparing with the conventional one. Bedirhanoglu et al. [4] examined the seismic performance of incomplete RC exterior beam–column connection modified with precast panels made of High-Performance Fiber Reinforced Cementitious Composites. Four full scales of beam–column connections were tested under cyclic action. It was found that modifying RC joints with (HPFRCC) panels increased the shear strength of the connection, slowed down the joint deformation, and prevent sliding of beam reinforcement due to proper welding for the bars hook in the connection zone.

Oinam et al. [14] investigated the Cyclic Response of non-ductile RC frame with steel fibers at beam–column joints and plastic hinge regions, the result indicate that the addition of steel fibers improved the damage tolerance, lateral load resisting capacity, lateral stiffness, ductility, and energy dissipation of the frame. On the other hand, Chidambaram and Agarwal [5] reported the performance of hybrid fiber reinforced beam–column connection under cyclic load through six exterior joints one is conventional concrete joint and the other made of concrete mixed with different kinds of composites in the connection zone and reinforced with three kinds of fiber: polypropylene fiber, brass-coated steel fiber, and hooked end steel fiber. The findings observed from this investigation showed improvement in joints performance with (HPFRCC) specially in connection strength comparing with conventional joint while connection with hooked steel fiber showed 50% increase in compressive strength than other modified joints as well as there were recognizable improvement in joints' stiffness, dissipated energy, less cracks were appeared in horizontal shape finally ductility was increased by 2–3 times than conventional joint. Frictional connections are considered to resist vertical loads only while it may fail due to loss of support which may occur in medium seismic areas because of its low resistance to horizontal loads, where the failure mechanism of the friction beam-to-column connections (excluding mechanical devices) depends only on the friction resistance between the connected elements. Banisheikholeslami et al. [3] studied the performance of steel beam–column connection with bearing pad under cyclic load in two steps—the first step fixing the rubber pad without bolts and the

second step with steel bolts. Using steel bolts with small pre-tensioned enhanced the ability to dissipate energy as the hysteresis loop was wider than the hysteresis loop of the connections without bolts fixing, as well as the pinching in the hysteresis loop was reduced in the second step. Ercolino et al. [8] conducted numerical study to evaluate the damage of the actual precast beam–column frictional connection with neoprene pad in industrial structure located in Emilia-Romagna. The numerical analysis showed an agreement with the real action where no collapse occurred in beam–column connection but the damage was due to roof collapse.

Resisting lateral loads needs adding some mechanical devices such as dowels connection where dowel is projected from the precast column and lied into sleeves cast inside the beams and filled with wet concrete. Performance of dowel connection is related to the behavior of several materials (concrete and steel), through creating contacts between elements (e.g., column concrete-to-dowel and wet concrete inside the sleeves-to-dowel contacts) as well as by the performance of the linked precast elements. Psycharis and Mouzakis [16] investigated the performance of the precast beam–column connection with two dowels as pinned joint under lateral monotonic and cyclic load. To study the shear ductility of the connection through changing some parameters which are dowel number, diameter D, their distance from edges in different directions d and the filler grout strength. It was found that for small ratio of d/D strength in pull direction was very low and increasing the number of dowels may enhance the performance in case of the monotonic load, while no significant effect in case of cyclic load. Magliulo et al. [12] studied the shear performance of precast beam–column connection with tow dowels projected vertically from the column and lied in the beam holes by applying monotonic horizontal load. A FEM connection was modeled to compare between numerical and experimental performance and the comparison showed a good agreement in case of shear strength which was increasing to 0.52%. Zoubek et al. [20] investigated the behavior of using dowel and neoprene pad in precast in beam–column with corbel joint in order to study the cyclic failure of the connection with comparing the result of experimental and FEM analyzing. Standard theory which proposed that failure mechanism is started as a result of dowel yield and concrete crush was proven, decreasing the plastic hinge length in the dowel reduced connection strength, using neoprene pad increased the strength of the connection and cyclic resistance; cyclic resistance represented 60% of monotonic resistance and a good matching between experimental and numerical results was found. Hawileh et al. [9] conducted nonlinear finite element analysis of a precast hybrid beam–column joint subjected to cyclic load with the effect of using post-tensioning strands to ensure the continuity of the connection. Although, the nonlinear action of the non-shrink grout between beam and column interface was investigated and analytical results showed very good coincidence with the experimental results the post-tensioned strands played a good rule in restoring the frame to its original condition during applying cyclic load. Maya et al. [13] experienced the cyclic performance of four interior prefabricated beam–column connections where top and

bottom channels were cast inside the beam to enable connecting splices bars with longitudinal reinforcement of the beam through the joint and then fill the gaps with Ultra-High Performance Fiber Reinforced Concrete. Cyclic load was applied at the column bottom and the results observed from the test show that increasing in the length of the splice bars led to increase the joint strength as well as provide proper shear strength and reduce the cracks in the joint region.

Angle cleat could be added to dry mechanical connections with dowel to restrain the precast beam from rotation movements and reduced forces induced on dowel as it tends to follow the shear forces direction when distorted so as shear forces will spread over the cleat itself. On the other hand, adding angle cleat on the top of the beam can control the initial vertical displacement of precast beam due to its self-weight. Leong [10] carried out an experimental study on precast beam–column with corbel connections using (dowel, angle cleat, stiffened angle cleat with one bolt and with two bolts) by applying vertical static incremental load on the pre-fabricated beam in order to examine the moment resisting, the failure mode and the load capacity of the connections. The result showed that the using of angle cleat improved joints strength while stiffened angle cleat reduced the joint strength comparing with ordinary cleat and stiffened angle cleat with two bolts showed enhancement in connection strength versus both connections with ordinary and stiffened cleat with one bolts. Vidjeapriya and Jaya [17] conducted an experiment to study the behavior of prefabricated beam–column connection as exterior joints for three specimens; RC joints as a benchmark, and two prefabricated beam-column joints with dowel, and with dowel plus angle cleat. Cyclic displacement load was applied and the precast joint with dowel and cleat behaved better than dowel joint and lesser than RC joint in terms of load carrying capacity, energy dissipation and hysteresis loop shape, whereas precast joint with dowel and cleat was the most ductile joint. Welded connections are extensively used by the precast concrete industry to ease construction [7]. Yuksel et al. [19] examined the demeanor of two types of exterior prefabricated beam–column connection, by using industrial and residential connections constructed with normal strength concrete and developed the connections (in terms of reinforcement welded to base steel plate in the beam around joint zone) under monotonic load before tested under cyclic displacement action. The results showed a regular load-displacement cycles and an acceptable behavior due to cyclic load up to 2.0% drift angle. The development of the rein-forcement detailing enhanced the displacement endurance and strength of the industrial type connection, and the post-peak behavior and damage distribution in the connection zone of residential connections. Babu et al. [2] investigated the behavior of three different types of beam–column connections under the effect of displacement-cyclic load. The first connection was monolithic joint, the second connection was precast beam with conventional column connected by a steel plate cast in the beam and welded to horizontal dowels cast in the column and the last connection was precast beam–column with corbel joint where wet concrete was cast on the top of beams to ensure continuity. The result showed acceptable shear

strength in case for all joint connection, however, conventional joint was better in case of energy dissipation and precast joint suffered from crack and damages. Choi et al. [6] investigated the demeanor of prefabricated beam–column connections using steel connectors consist of steel tube and steel plates with engineered cementitious composite used to fill the gaps, and compared with conventional monolithic joint through applying cyclic load. The results showed an acceptable seismic performance of the precast specimens that were ductile as areas on the developed connection, while the precast connections strength was 1.15 times more than the monolithic.

Wahjudi et al. [18] investigated the performance of prefabricated beam–column joint with U and L-bent anchorages which were put out of the column panel to enhance the seismic resistance of the joint whereas the conventional connection was used for comparison purpose. These specimens were tested under cyclic displacement action while their performance was stable at 5% drift angle; this gives an estimate that the specimens can resist cyclic load until 6% or 7% drift angle. Even though, the prefabricated connections have shown less strength, little high ductility, and less energy dissipation comparing with the conventional concrete connection. Aninthaneni and Dhakal [1] conducted a conceptual study to propose a demountable precast beam–column connection using dry connectors. This proposed building system consist of two systems—the first system to resist gravity load where the beam connected to the column by mechanical pin joint and the second system to resist lateral loads using double cleats and found that the damaged parts after an earthquake can be replaced by double cleats system also the strength can be increased. The review of literature shows that the using of dowel and cleat can increase the lateral strength of the precast connection. The behavior of precast beam–column connection has not been completely examined. Therefore, this study is focused on evaluating the effect of using welded angel cleat to steel plate for both sides in beam and column under cyclic load.

2 Various Connection System for IBS Beam Column Connection

As the dynamic loads consider the most danger loads which may lead to building collapse, it is very important to investigate the dynamic performance of precast beam–column joint in order to find new tools to enhance dynamic response of this connection therefore it is necessary to design precast beam–column connections considering all types of loading [1]. The conventional reinforced concrete beam–column joints is the fastest failure part in RC-framed building as assemblage of compressive, tensile and shear forces are transferred through these joints from column to beam. The carrying load capacity of these joints is affected by the

longitudinal and shear reinforcements. Under the effect of earthquake, the conventional beam–column joint may behave inelastically without any loss in its strength while due to cyclic effect of earthquake; the joints may fail as a reason of shear with spalling of concrete and loss of bond between the embedded reinforcement and concrete panels. While the efficiency of precast concrete frames in resisting all the loads impacts in IBS building depends on connection type such as bearing pad, dowel, angle cleat to resisting gravity and lateral loads.

3   Geometric Beam–Column Connections

In this work, half-scale monolithic RC beam–column joint is considered as benchmark connection for evaluating the dynamic performance of precast beam connections in comparison of conventional connection. The RC beam has the dimensions of $200 \times 200 \times 1900$ mm while the column dimensions are $200 \times 200 \times 2000$ mm as shown in Fig. 1. Also four precast frames with different connections as shown in Fig. 2 shows were modeled with beams dimension $200 \times 200 \times 1900$ mm, $200 \times 200 \times 2000$ mm and a clear span (Lc), depth (d), and width (b) of 6000, 600, and 600 mm for columns dimensions.

As shown in Fig. 3, four different precast beam–column with corbel connections were considered: the precast beam–column connection with bearing pad (PCBP), precast beam–column connection with dowel (PCD), precast beam–column connection with dowel and angle cleat (PCDAC), and precast beam–column connection with double angle cleat (PC2AC), as listed in Table 1. The frames were modeled using ABAQUS software with material of normal concrete grade 30, and all connections were subjected to cyclic load.

In this study, all the parts were meshed with 50 mm element, as shown in Fig. 3.

The embedded constraint is considered for all reinforcement interaction while bearing pad, dowel, and angle cleat are tied for concrete surface. Figure 4 showed the interactions in the precast connections.

Fig. 1 RC frame with normal connection

(a) PCBP: Precast beam-column connection with bearing pad.

(b) PCD: Precast beam-column connection with dowel.

(c) PCDAC: Precast beam-column connection with dowel and angle cleat.

(d) PC2AC: Precast beam-column connection with double angle cleat
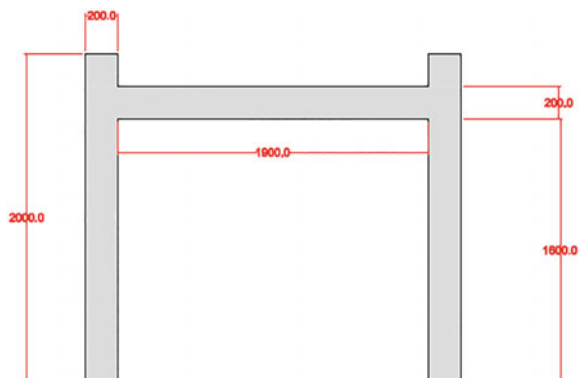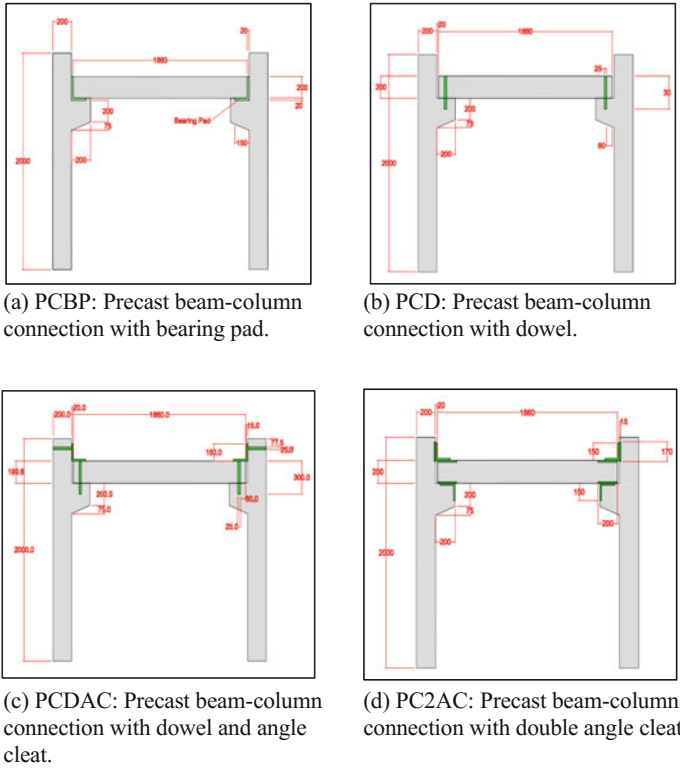
Fig. 2 Modeled connections

4 Results and Discussion

4.1 Precast Beam–Column with Corbel Connections Subjected to Cyclic Loading

To evaluate the performance of precast connections subjected to dynamic loading, all considered models were subjected to cyclic displacement. The amplitude of displacement applied was 100 mm for the connections and applied laterally at the column back parallel to the connection zone. The history of displacement is presented in Fig. 5a. The boundary conditions were applied to the bottom end of columns as fixed supports, as shown in Fig. 5b.

The hysteresis analysis for the cyclic loading of the connections is presented in Fig. 6. A marked difference is indicated between the load-deflection curves of the

(a) PCBP connection

(b) PCD connection

(c) PCDAC connection

(d) PC2AC connection
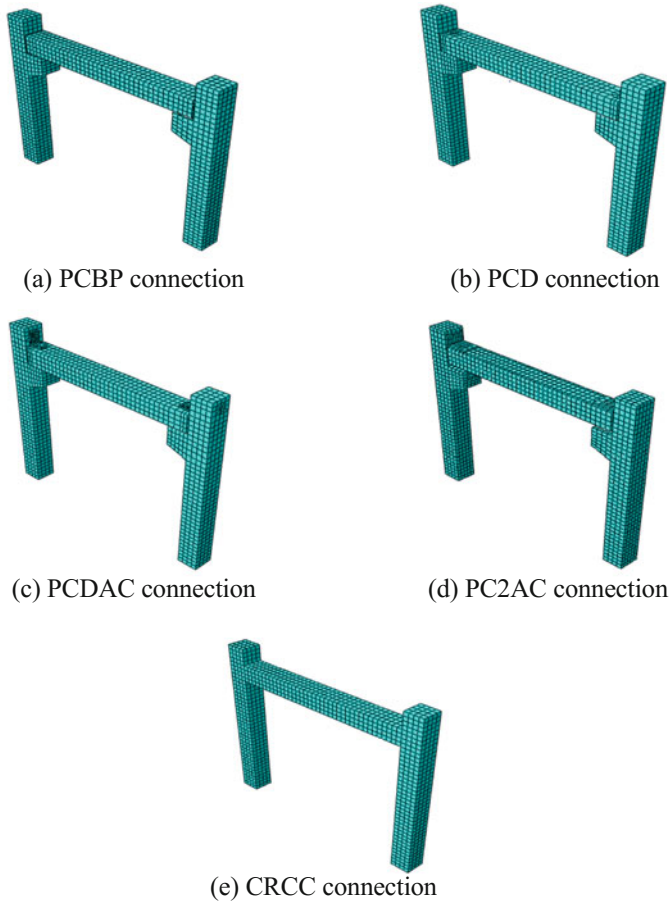
(e) CRCC connection

Fig. 3 Meshing for connections

Table 1 Varies type of beam considered

Notation	Connection type
CRCC	Conventional RC beam-column connection
PCBP	Precast beam–column connection with bearing pad
PCD	Precast beam–column connection with dowel
PCDAC	Precast beam–column connection with dowel and angle cleat
PC2AC	Precast beam–column connection with double angle cleat

connections compared with the conventional RC connection. In addition, the load capacity of the precast connections (PCDAC and PC2AC) was increased with the using of the steel angle cleat.

(a) PCBP: Precast beam-column
connection with bearing pad.

(b) PCD: Precast beam-column
connection with dowel.

(c) PCDAC: Precast beam-column
connection with dowel and angle cleat.

(d) PC2AC: Precast beam-column
connection with double angle cleat.
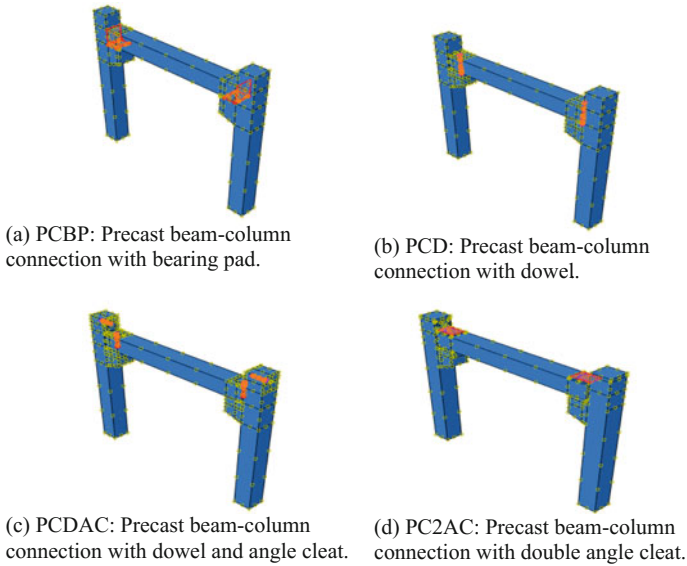
Fig. 4 Interaction for connections

The results listed in Table 2 indicated that the ultimate loads for the bench mark CRCC was 63.76 kN and for the precast connections PCBP, PCD, PCDAC and PC2AC were 43, 41.66, 78.3 and 75.26, respectively. Therefore, the use of the steel angle cleat increased the ultimate load by 22.8% for PCDAC and 18% for PC2AC, While PCBP and PCD showed reduction in the ultimate load capacity by 32.56 and 34.67% respectively. As earlier, it can be noticed that the effect of using angle cleat in the connection between the precast beam and column on enhancement the lateral strength of the precast connections.

The lateral stiffness of CRCC was 8.54×10^5 kN/m, it can be noticed that a huge increase in the lateral stiffness of the precast connection with double cleat PC2AC of 167% and that because of the high rigidity of the connection as beam is linked with the column via angle cleat in both top and bottom edges. The precast connection with dowel and cleat PCDAC showed an increase in the lateral stiffness of 42.2% comparing with conventional connection. The precast connection with bearing pad PCBP attained rise in stiffness of 16.5% while the precast connection with dowel PCD exhibited decreasing in the lateral stiffness of 34% based on the conventional connection stiffness. From above it can be noticed that the usage of the cleat in the connection between precast beam and column can increase the lateral stiffness of the joint while doubling the cleat lead to raise the lateral stiffness by three times.
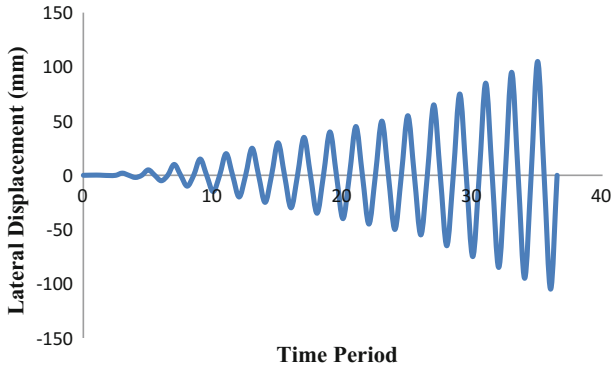
(a) Relative Displacement Vs time.

(a) CRCC connection   (b) PCBP connection

(c) PCD connection   (d) PCDAC connection

(e) PC2AC connection
(b) boundary conditions and applied cyclic load
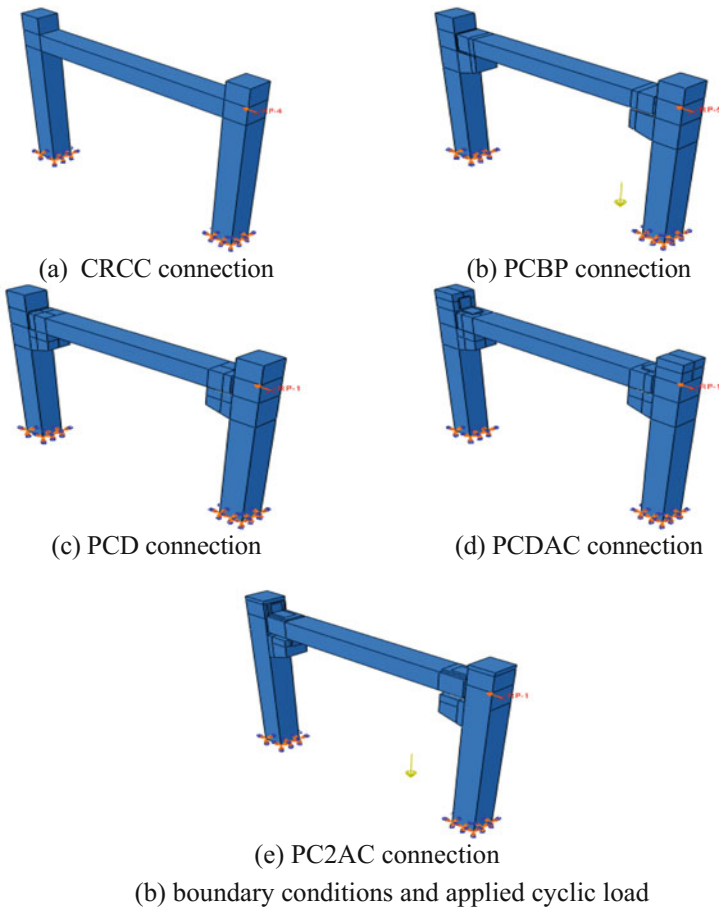
Fig. 5 Boundary condition for connections
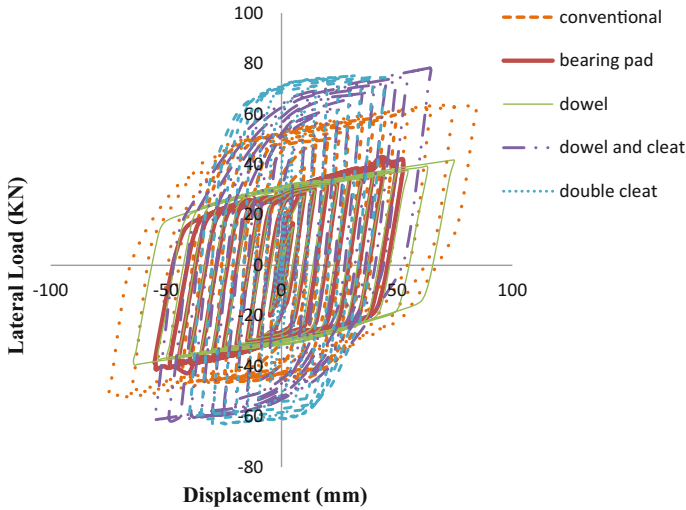
Fig. 6 Hysteresis loop of the connections

Table 2 Beam–column connections under cyclic load

Connections	CRCC	PCDAC	PC2AC	PCBP	PCD
Lateral strength (kN)	63.76	78.3	75.26	43	41.66
Variance of lateral strength (%)	0	22.80	18	32.56	34.67
Lateral stiffness (N/m)	8.54×10^5	12.14×10^5	22.8×10^5	9.95×10^5	5.64×10^5
Variance (%)	0	167	42.20	16.50	34
Lateral displacement at maximum-force (mm)	74.63	64.5	33	43.2	73.77
Variance (%)	0	13.60	55.80	42.11	1.15
Lateral displacement at 0.85 from-maximum (mm)	25.58	24.5	19.2	27	40.11
Ductility	2.9	2.63	2.27	1.6	1.84
Energy dissipation (kJ)	494.73	528.811	314.64	66.22	104.93
Variance (%)	0	6.88	36.40	86.60	78.80

Based on the conventional connection ability to dissipate energy, the precast connections showed different performance presented by a small increasing in energy dissipation of the precast connection with dowel and cleat as 6.88% higher than the conventional model. Precast connection with double cleat attained decreasing in energy dissipation of 36.4% due to the high lateral stiffness of this connection, as well as a huge decreasing in energy dissipation in both the precast

connection with dowel which exhibited 78.8% and precast connection with bearing pad of 86.6% lesser than the conventional connection. Figure 7 presented the energy dissipation of the connections.

Meanwhile, the ductility index for the maximum value which belong to conventional connection of 2.9, where closed value of ductility was found for precast connection with dowel cleat and precast connection with double cleat of 2.63 and 2.27 respectively, while precast connections with dowel and bearing pad show poor performance for connection ductility by 1.84 and 1.6 respectively.

The stress distributions for all studied beam–column connections at the failure stage are presented in Fig. 8. As shown in Fig. 9, the stress was distributed in the columns near the fixed end in high percentage while a considerable amount was generated in the connection region. The maximum principal stress values in all modeled connections are listed in Table 3. The results of the connections were almost identical and achieved high percentage of the concrete compressive strength which is 30 MPa. Principal stress in CRCC was 28.23 MPa, the precast connection for double cleat and dowel is about 28.55, 28.19 MPa. Due to high stiffness attained the highest value of stresses as which is 1.13% higher than the CRCC, while the stress distribution for dowel cleat and bearing pad is about 22.11, 24.75 MPa with decreasing 21.7, 12.32% respectively.

Figure 9 presented the plotted strain distributions of all considered beam–column connections. Similar to stress, the maximum plastic strain was noticed at the fixed supports at the bottom ends of the columns, whereas a small amount of plastic strain was generated in the connections area in conventional connection, precast connection with dowel cleat and precast connection with double cleat according to the rigidity of these connections. Strain occurring in the connections during applying cyclic displacement load represented the combination between steel and concrete deformation where the values of the plastic strain presented in Table 3 showed that the maximum value attained in the conventional connection of 0.81486 as a reason of the large displacement that exhibited in this connection and it was the

(a) CRCC connection

(b) PCBP connection

(c) PCD connection

(d) PCDAC connection

(e) PC2AC connection

Fig. 8 Stress distribution of the connections

(a) CRCC connection

(b) PCBP connection

(c) PCD connection

(d) PCDAC connection

(e) PC2AC connection
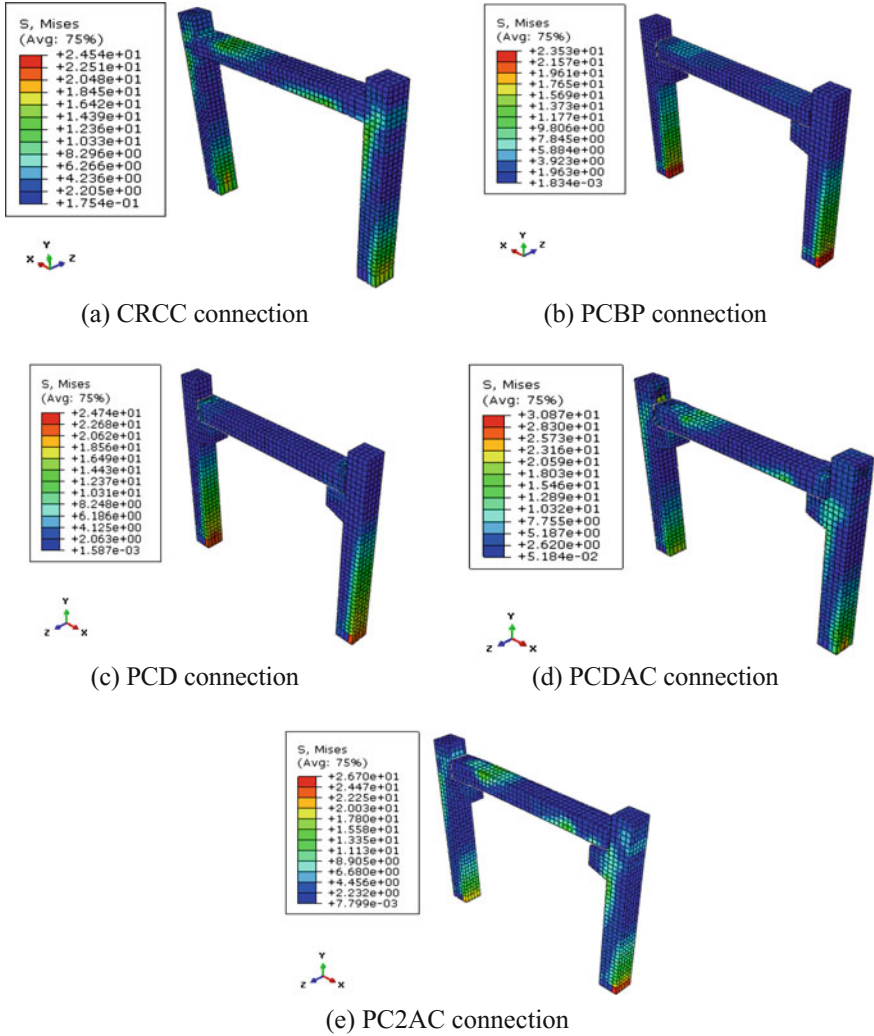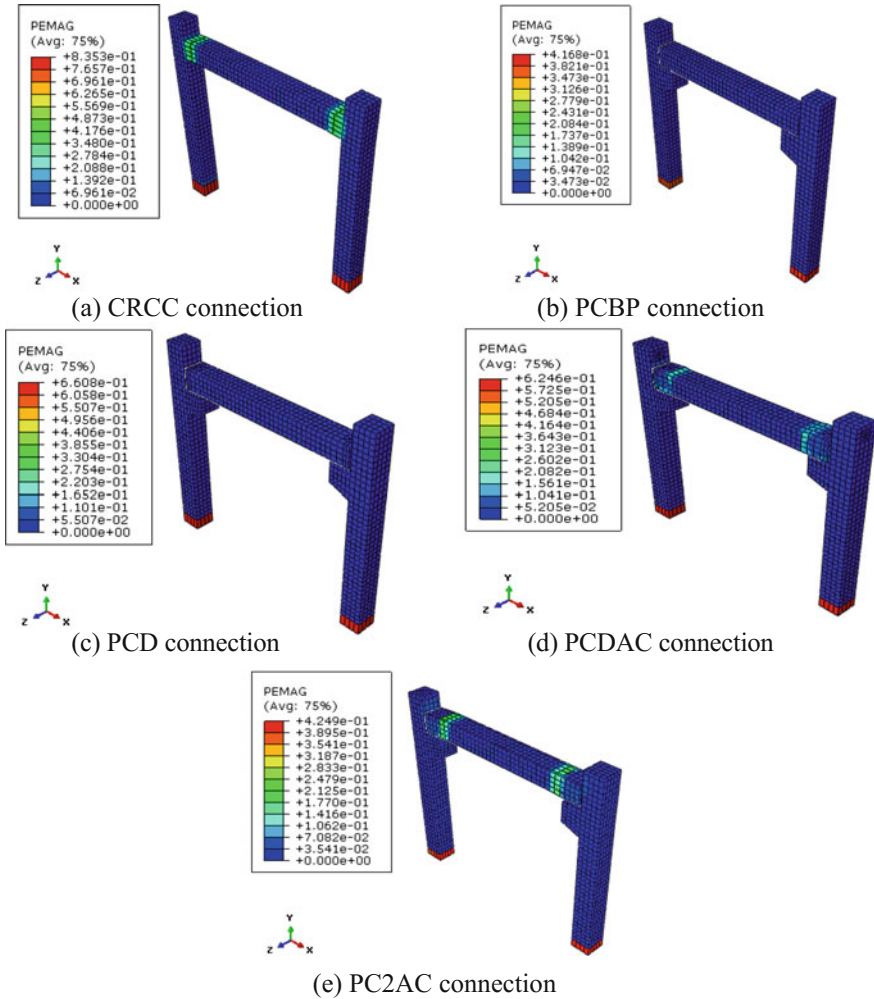
Fig. 9 Strain distribution for the connections

Table 3 Stress distribution of the connections

Connections	Stresses (mPa)	Variance %	Strain	Variance %
Conventional connection	28.23	0	0.81486	0
Precast connection with dowel	28.19	0.14	0.65322	19.8
Precast connection with dowel and cleat	22.11	21.7	0.61694	24.3
Precast connection with double cleat	28.55	1.13	0.4064	50.13
Precast connection with bearing pad	24.75	12.32	0.3892	32.56

largest value between the connections. Precast connection with dowel exhibited plastic strain only at the fixed supports as 19.8% lower than the conventional connection followed by the precast connection with dowel and cleat which showed decreasing in plastic strain as 24.3% from the maximum value. The precast connection with double cleat attained decreasing in plastic strain of 50.13% lower than the conventional connection. The lowest value of plastic strain occurs in the precast connection with bearing pad with decreasing in plastic strain as 52.24% comparing with the maximum value.

It can be noticed that the plastic strain attained by precast connection with double cleat is half of that for conventional connection and that because of the using angle cleat in the connection between beam and column. As strain is a function of displacement, decreasing in displacement value will lead to decrease in the strain, so we can see that the maximum displacement of precast connection with double cleat is 33 mm and it is approximately half of conventional maximum displacement which was 74.63 mm.

5   Conclusions

The behavior of precast beam column with various connection type (bearing pad, dowel, and angle cleat) is evaluated in this study in comparison of conventional connection under cyclic load by using numerical analysis and the result indicate that

1. precast connection with bearing pad and dowel presented poor performance to resist cyclic load in comparison of conventional connection, the ultimate strengths was decreasing to 32.56, 34.67% respectively, while the using of down cleat and double cleat increases the connection performance to 22.8, 18% respectively in comparison of conventional connection.
2. the result also shows that the reduction in capacity (energy dissipation) for bearing pad, dowel, and double cleat precast connections in comparison of conventional connection capacity is about 86.6, 78.8, and 36.4%, respectively, while precast concrete shows increasing in energy dissipation by 6.88%.
3. precast connection with (double cleat and dowel) shows almost near behavior fortress strain distribution with conventional connection while it was decreasing for dowel cleat and bearing pad link. However, the ductility was decreasing for all precast connection in comparison of conventional type.

References

1. Aninthaneni, P.K., Dhakal, R.P.: Conceptual development: low loss precast concrete frame building system with steel connections. In NZSEE Conference (2014)

2. Babu, V.R., Nakulesh, B., Siddhartha, P., Rao, A.V., Kumar, B.C.: Study on prefabricated concrete beam and column connections. Int. J. Appl. Sci. Eng. Manag. **2**(2), 41–45 (2013)

3. Banisheikholeslami, A., Behnamfar, F., Ghandil, M.: A beam-to-column connection with visco-elastic and hysteretic dampers for seismic damage control. J. Constr. Steel Res. **117**, 185–195 (2016). https://doi.org/10.1016/j.jcsr.2015.10.016

4. Bedirhanoglu, I., Ilki, A., Kumbasar, N.: Precast fiber reinforced cementitious composites for seismic retrofit of deficient RC joints—a pilot study. Eng. Struct. **52**, 192–206 (2013). https://doi.org/10.1016/j.engstruct.2013.02.020

5. Chidambaram, R.S., Agarwal, P.: Seismic behavior of hybrid fiber reinforced cementitious composite beam-column joints. Mater. Des. **86**, 771–781 (2015). https://doi.org/10.1016/j.matdes.2015.07.164

6. Choi, H.K., Choi, Y.C., Choi, C.S.: Development and testing of precast concrete beam-to-column connections. Eng. Struct. **56**, 1820–1835 (2013). https://doi.org/10.1016/j.engstruct.2013.07.021

7. Crisafulli, F.J., Restrepo, J.I.: Ductile steel connections for seismic resistant precast buildings. J. Earthq. Eng. **7**(4), 541–553 (2003). https://doi.org/10.1080/13632460309350463

8. Ercolino, M., Magliulo, G., Manfredi, G.: Failure of a precast RC building due to Emilia-Romagna earthquakes. Eng. Struct. **118**, 262–273 (2016). https://doi.org/10.1016/j.engstruct.2016.03.054

9. Hawileh, R.A., Rahman, A., Tabatabai, H.: Nonlinear finite element analysis and modeling of a precast hybrid beam-column connection subjected to cyclic loads. Appl. Math. Model. **34**(9), 2562–2583 (2010). https://doi.org/10.1016/j.apm.2009.11.020

10. Leong, D.C.P.: Behaviour of pinned beam-to-column connections for precast concrete frames (2006)

11. Luk, S.H., Kuang, J.S.: Seismic behaviour of RC exterior wide beam-column joints. In 15th World Conference on Earthquake Engineering (2012)

12. Magliulo, G., Ercolino, M., Cimmino, M., Capozzi, V., Manfredi, G.: FEM analysis of the strength of RC beam-to-column dowel connections under monotonic actions. Constr. Build. Mater. **69**, 271–284 (2014). https://doi.org/10.1016/j.conbuildmat.2014.07.036

13. Maya, L.F., Zanuy, C., Albajar, L., Lopez, C., Portabella, J.: Experimental assessment of connections for precast concrete frames using ultra high performance fibre reinforced concrete. Constr. Build. Mater. **48**, 173–186 (2013). https://doi.org/10.1016/j.conbuildmat.2013.07.002

14. Oinam, R.M., Sahoo, D.R., Sindhu, R.: Cyclic response of non-ductile RC frame with steel fibers at beam-column joints and plastic hinge regions. J. Earthq. Eng. **18**(6), 908–928 (2014). https://doi.org/10.1080/13632469.2014.916239

15. Precast concrete frames guide: Dublin, Ireland: Irish Precast Concrete Association. Precast concrete Irish Precast Concrete Association Unit 8, Newlands Business Park, Clondalkin, Dublin 22 (2003)

16. Psycharis, I.N., Mouzakis, H.P.: Shear resistance of pinned connections of precast members to monotonic and cyclic loading. Eng. Struct. **41**, 413–427 (2012). https://doi.org/10.1016/j.engstruct.2012.03.051

17. Vidjeapriya, R., Vasanthalakshmi, V., Jaya, K.P.: Performance of exterior precast concrete beam-column dowel connections under cyclic loading. Int. J. Civil Eng. **12**(1 A), 82–94 (2014)

18. Wahjudi, D.I., Suprobo, P., Sugihardjo, H.: Behavior of precast concrete beam-to-column connection with U-and L-bent bar anchorages placed outside the column panel-experimental study. Proc. Eng. **95**, 122–131 (2014). https://doi.org/10.1016/j.proeng.2014.12.171

19. Yuksel, E., Karadogan, H.F., Bal, İ.E., Ilki, A., Bal, A., Inci, P.: Seismic behavior of two exterior beam-column connections made of normal-strength concrete developed for precast construction. Eng. Struct. **99**, 157–172 (2015). https://doi.org/10.1016/j.engstruct.2015.04.044
20. Zoubek, B., Isakovic, T., Fahjan, Y., Fischinger, M.: Cyclic failure analysis of the beam-to-column dowel connections in precast industrial buildings. Eng. Struct. **52**, 179–191 (2013)

Preventing Seismic Pounding of Adjacent Structures Using Viscous Wall Damper Device

Navid Salami Pargoo, Farzad Hejazi and Sarah Jabbar

Abstract Today, a number of researchers are broadly studying the effective implementation of supplemental seismic energy dissipation systems to improve seismic behavior of structures during earthquakes. The current article studies the impacts of employing Viscous Wall Damper devices to couple two adjacent structures on seismic response of the new system. An exclusive finite element algorithm capable of modeling and analyzing structures equipped with special damper systems was used in order to perform a nonlinear time history analysis subjected to seismic excitation. Two ten-story RC framed structures are modeled adjacently in 11 different cases, each representing existence or damping coefficient of the Viscous Wall Damper device. A parametric study has been conducted in each case to assess the effectiveness of implementing Viscous Wall Damper devices on improving seismic behavior of the coupled structure. The considered metrics include rotation and displacement amplitude, plastic hinge formation, and induced element forces. It has been proved that the proposed damper system substantially diminishes and dissipates induced seismic response of the system. Also, it is indicated that the extent to which Viscous Wall Damper device contributes in mitigating seismic responses is highly correlated with the damping coefficient.

Keywords Viscous wall damper · Passive control · Adjacent structures
Seismic response mitigation · Finite element

N. S. Pargoo
Department of Civil Engineering, University of Science and Culture,
Tehran, Iran
e-mail: n.salamipargoo@usc.ac.ir

F. Hejazi (✉)
Department of Civil Engineering, University Putra Malaysia,
Selangor, Malaysia
e-mail: farzad@fhejazi.com

S. Jabbar
Housing Research Centre, University Putra Malaysia, Selangor, Malaysia
e-mail: sarahsaleem2015@gmail.com

1   Introduction

Seismic Pounding is defined as collision of two adjacent buildings during an earthquake [1]. As a couple of structures in close proximity with unlike properties (in terms of heights, structural systems, materials, etc.) are exposed to a quake, there will be a likelihood of occurring pounding within them. Pounding between proximate structures is an extremely complicated fact making the analysis of the equivalent problem tangled. A number of analytical models have been developed to explain the behavior of adjacent structures throughout a ground motion. Wolf and Skrikerud [2] investigated the pounding prompted on account of a small gap between the structure of a nuclear reactor and a nearby construction. Structural pounding issue is rather unfavorable than profitable proved by Efraimiadou et al. [3] when the collision between adjacent reinforced concrete (RC) buildings under multiple earthquakes was examined. Tapashetti and Swamy [1] demonstrated that the use of pounding prevention techniques such as incorporating new RC walls, bracing systems, dampers, combined system of RC wall and bracing, combined system of RC wall and dampers, and combined system of bracing and dampers between adjacent buildings are effective in mitigating the pounding due to earthquakes. Elwardany et al. [4] presented a finite element analysis for multi-story buildings to research the impacts of adding infill panels on the response of imposed mutual pounding of the structures during earthquakes.

An approach to control pounding is to couple adjacent structures via elastic or damping elements. Considering current concerns in earthquake-resistant design approaches, structures are likely to undergo significant damage but prevent collapse. While this attitude has been a standard for many decades, novel design methods and innovative devices are receiving more notice and being developed comparing with conventional approaches. Plenty new mechanical systems have been suggested in last two decades in order to improve structural behaviors during dynamic excitations. They are all recognized as "protective devices" and include supplemental viscoelastic dampers, viscous fluid dampers, frictional dampers, hysteretic dampers, tuned-mass dampers, and base isolation systems. A semi-active control scheme of joined structures has been suggested by Christenson et al. [5], and different coupled structural configurations have been studied and experimentally verified the effectiveness of employing such vibration control systems based on acceleration feedback. The usefulness of implementing evenly distributed viscous dampers between a couple of elastic parallel structures, excited by a same quake, in order to mitigate the consequent responses was investigated by Luco and De Barros [6], Zhang and Xu [7]. It has been confirmed that the seismic behavior of adjacent structures was improved through application of adjoining dampers.

The influence of position, quantity as well as linking arrangements of fluid dampers are investigated by Lu et al. [8] in order to strengthen two adjacent structures against seismic motions. Then, the obtained outcomes are compared with the use case of rigid rods.

Kageyama et al. [9] studied a passive vibration control procedure in which two adjacent structures were interconnected through dampers. Kim et al. [10] researched the impacts of implementing viscoelastic dampers at connections between a building and a sky-bridge as well as across the seismic joints. According to the outcomes of the conducted analysis, they found that the proposed procedure plays a significant role in reducing the displacements while no such improvement was observed considering the base shear. A new adjustable damping device as a coupling component consisting two dampers positioned between two structures was considered in theoretical and numerical simulations in order to verify the positive seismic behavior of the suggested protective system during a series of remarkable quakes [11]. Since a principal aim of proceeding in cutting-edge technologies of structural engineering is to improve the seismic behavior of structures, implementing a suitable supplemental energy dissipation system can contribute to a great deal [12, 13]. The impact of different characteristic parameters of supplemental viscous dampers on the behavior of RC structures was assessed through a parametric study, which preceded a design for an optimum viscous damper based on the anticipated performance to meet the different levels of demand for a given building [14]. Hejazi et al. [15] developed a 3D elastoplastic viscous damper element well-matched with the constitutive model to strengthen RC structures during earthquake excitations by finite element method. Hejazi et al. [16] developed a multi-objective optimization method to be used in structural passive control schemes according to a genetic algorithm. They also applied the model to a 3D RC framed building, whose structural seismic responses have been investigated. Kandemir-Mazanoglu and Mazanoglu [17] developed an optimization technique to determine the capacity of viscous dampers bearing one-sided structural pounding between two adjoining structures under seismic ground motions.

Although the above-mentioned research on mitigation of earthquake-induced pounding of adjacent structures provide some data about the impacts of different damper systems and their associated responses, the importance of the subject prompts a need to investigate the problem in depth, considering state-of-the-art damper systems as well a range of governing parameters. Hence, the current paper studies the effectiveness of implementing Viscous Wall Dampers, as an advanced system, between adjacent structures in order to attenuate the pounding consequences. In particular, this paper conducts a research on the influence of implementing Viscous Wall Dampers with different damping characteristics on a range of certain structural parameters in order to optimize the associated pounding ramifications in design and practice.

2 Nonlinear Analysis of the Adjacent RC Structures

A two-dimensional finite element model considering all nonlinearity possibilities present in the framed structural system has been generated in order to calculate the response of the structure using a combination of incremental iterative approach and

the Newton–Raphson practice. The aim is to investigate the effects of equipping two adjacent structures with Viscous Wall Damper (VWD) device in terms of reduction in dynamic responses due to earthquake excitations. Figure 1 illustrates the geometry and property details of the adjacent structures.

The model is generated in an exclusive finite element algorithm developed for nonlinear analysis of RC structures supplied with earthquake energy dissipation devices exposed to dynamic excitation. The program is capable of modeling and analyzing structures in order to detect plastic hinges in structural members under seismic excitations.

In order to perform a nonlinear time history analysis, the North-South component of El Centro earthquake record has been used as dynamic excitation (Fig. 2). The structures are bearing static loads as well, whose details are presented in Fig. 3. Figure 3 also represents how VWD device is employed to connect the structures in order to improve the seismic behavior of the connected structures. The damping force imposed to a VWD device is calculated by

$$F_{\text{VWD}} = \hat{C}_{\text{VWD}} \times V^{\eta}, \tag{1}$$

where F_{VWD} is the damping force, C_{VWD} stands for the damping coefficient of the VWD device, V represents the relative velocity of the damper, and η is exponential coefficient belonging to velocity. Velocity exponential coefficient of 1 introduces a linear behavior of the VWD device while any other values reveal a nonlinear behavior of the damper.
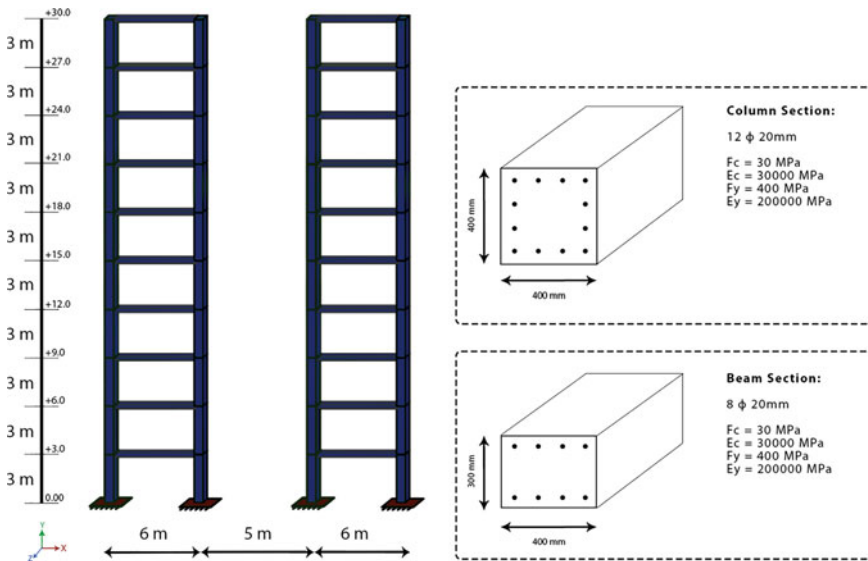
Fig. 1 Adjacent structures 2D geometric model and section properties

Fig. 2 Earthquake acceleration record (North–South component) of El Centro (Imperial Valley Irrigation District, USA-1940)
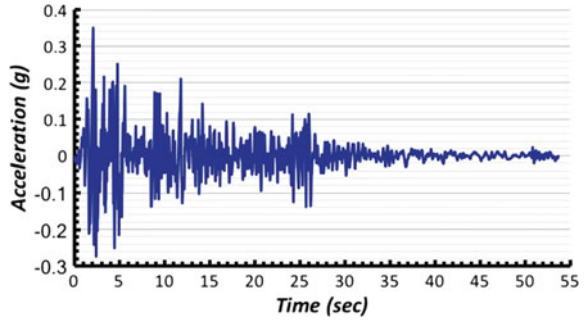
Fig. 3 Static loading details and coupling details of the two adjacent structures
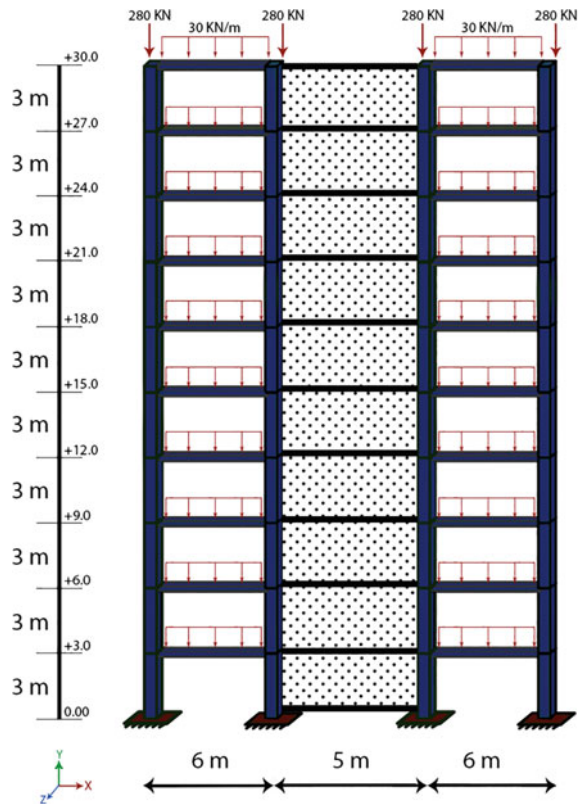
According to the above-mentioned equation, the governing factor to relieve the seismic responses of such structures is the damping coefficient. Thanks to the existence of dampers with a wide range of damping coefficients, there are options for implementing a proper damper with a given damping coefficient based on the requirement of structural design process.

3   Verification of the Developed Numerical Model

In order to verify the current numerical model of VWD device in terms of its influence on seismic behavior of a given system, two entirely identical 3D RC structures, which were investigated in an experimental study by Lu et al. [18], as seen in Fig. 4a, have been nominated for nonlinear dynamic analysis. The considered excitation for dynamic analysis has been El Centro earthquake record with an acceleration amplitude of 0.05 g as an intensity factor. The two structures of 1:2 length scale were built, one with VWD device implemented and the other without any; in order to compare the effectiveness of implementing such device with the case of no supplemental damping device employed. Among the two models, the second one was empowered with VWD device whose damping coefficient was 20 KN s/m. Furthermore, in order to assess the mechanical performance of the proposed device an exclusive test setup was designed and built, as seen in Fig. 5.

The three-story RC structures consisted of a single bay along the X direction and two bays along the Y direction, forming a plan of 2.4 m × 3.6 m. Elevation-wise, the buildings contained three stories of 2 m height. The geometrical properties of the frame are depicted in Fig. 4b. Furthermore, the section dimensions of considered columns are 150 mm in width and 150 mm in height, while beams are formed as a cross-section of 80 mm in width and 150 mm in height and each floor plates have a thickness of 55 mm. The exceptions are the beams connected to VWD
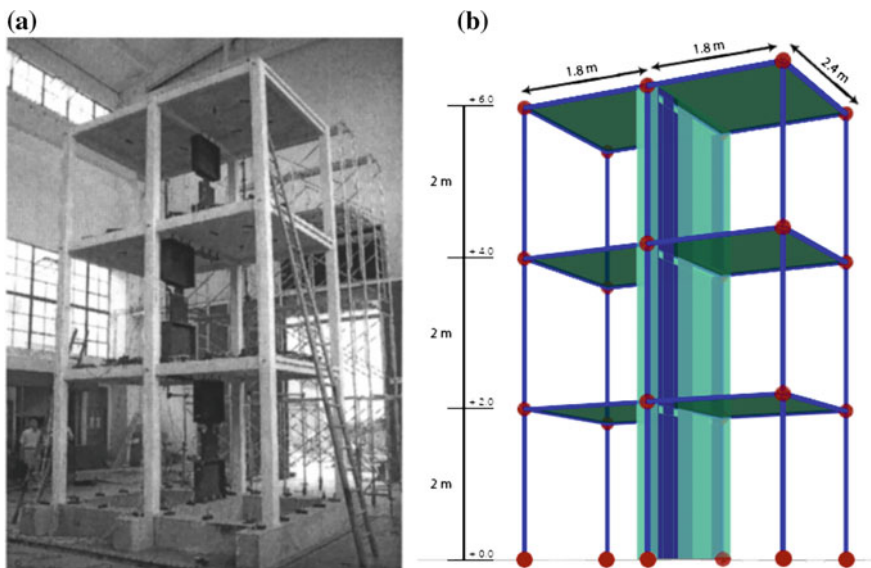
Fig. 4 Three dimensional RC frame equipped with VWD device. **a** Large-scaled model by Lu et al. [18], **b** Numerical model used in verification of the current study and its geometrical properties
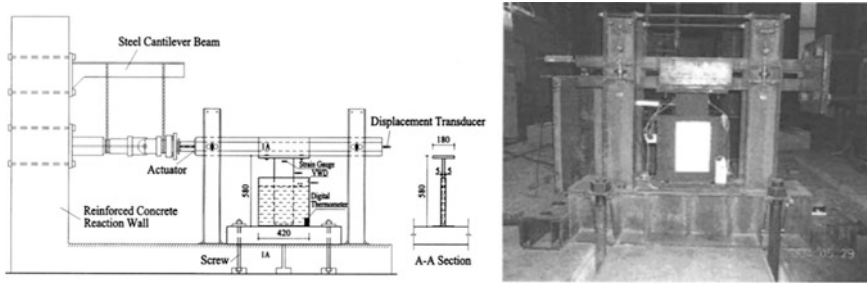
Fig. 5 Exclusive test setup and composition of VWD device

devices, whose dimension includes a width of 100 mm and a height of 150 mm. The geometrical, reinforcement, and material details of structural sections are illustrated in Fig. 6.

The structure enjoys of an inherent damping of 5%, while VWD device roles as an additional damping source. It has been assumed that VWD device functions in a linear behavior, due to taking exponential coefficient equal to one.

In order to verify the results, time history analysis was performed on numerical models of both structures and the subsequent displacements were compared with results of the experimental test by Lu et al. Figure 7a represents the recorded displacement outcomes for both cases of with and without VWD device implemented, achieved in the experiment by Lu et al. Likewise, Fig. 7b displays how both numerical models react to the imposed excitation in each story level. The comparison of the two graphs reveal that the proposed numerical model, to a large extent, is compatible with the experimental test of Lu et al. on the large-scaled structures.

4 Parametric Study

A numerical study has been conducted to assess the effectiveness of adding supplemental damper devices in controlling vibrations and seismic responses of adjoining structures. Hence, the impacts of damper damping coefficient on the mentioned systems have been studied through a nonlinear time history analysis of the simplified system excited by El Centro earthquake. In the current study, 11 different cases of VWD characteristics in terms of damping coefficient have been investigated, as seen in Table 1. Nonlinear time history analysis was performed for all 11 cases and the desired criteria (structural displacement, plastic hinge formation, and induced column forces) were evaluated in details.

Fc = 20 MPa   Ec = 25,000 MPa   Fy = 530 MPa   E y = 196,000 MPa
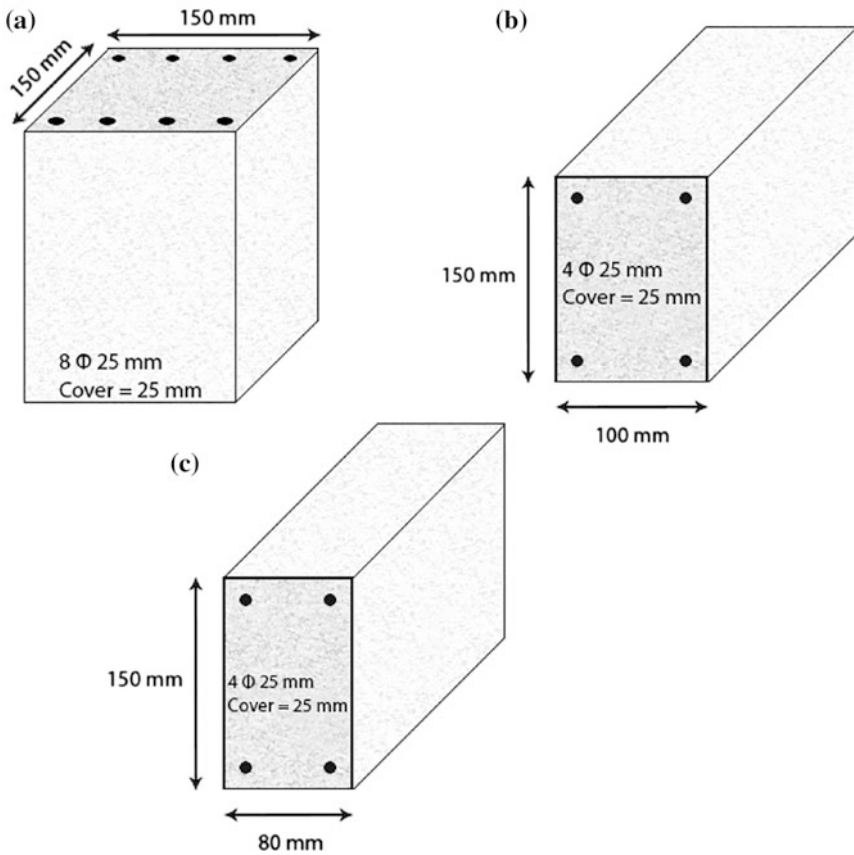
Fig. 6 Geometrical, reinforcement, and material specifications of structural sections. **a** Columns, **b** beams connected to VWD, **c** other beams
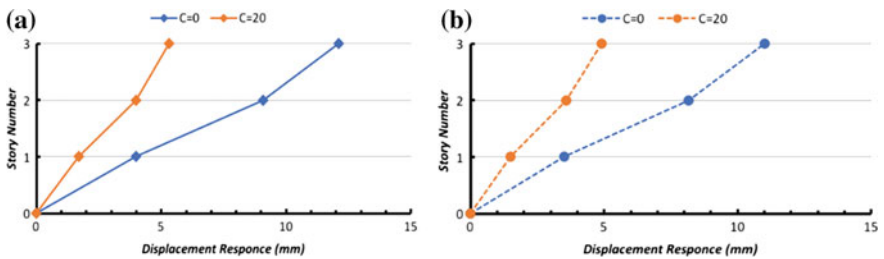
Fig. 7 Verifying the proposed numerical model in terms of displacement. **a** Experimental test by Lu et al. **b** the numerical model proposed in the current study

Table 1 Considered cases of damping coefficient

Case no.	I	II	III	IV	V	VI	VII	VIII	IX	X	XI
Damping coefficient (KN s/m)	0	20	40	60	80	100	150	200	250	300	350

4.1 Structural Displacement Criterion

The maximum structural displacement and rotation is associated with structural element demands. Therefore, the proposed structural system has been investigated under 11 damping characteristic cases. The first case considers the circumstance in which no VWD device is implemented, while other cases are representatives of different characteristics of VWD devices. Figure 8 shows the effectiveness of adapting VWD devices on maximum displacement and rotation at each story level in such proposed structural systems. Furthermore, the detailed values of displacements and rotations are listed in Table 2.

Figure 8 illustrates that the increase in VWD damping coefficient leads to a drop in structural displacement. According to Fig. 8a, VWD devices contributed the structure in decreasing the displacement in X direction. The ultimate reduction was from 39.18 to 14.83 mm while a VWD device with $C = 350$ KN s/m was employed. This represents a total reduction of 62% in structural displacement, as presented in Table 2.

Figure 8b demonstrates the effects of using VWD devices in reducing structural rotation in each story level. The highest reduction was recorded from 0.0019789 to 0.00149478 rad by 24% while a VWD device with damping coefficient of $C = 250$ KN s/m was adopted. Table 2 elaborates on the values concisely.

The comparison of induced displacement as well as rotation in the plain structure and the one equipped with VWD devices with damping coefficients of 20, 100, 200, and 350 KN s/m are demonstrated in Figs. 9, 10, 11, and 12, respectively, in terms of time history based graphs in X and over Z directions. These figures are
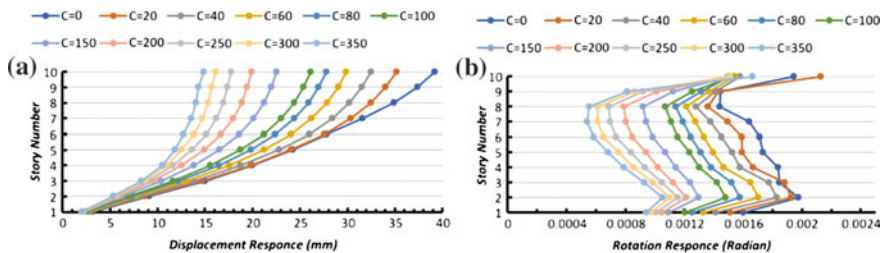
Fig. 8 Maximum displacements and rotations at each story heights: **a** displacement at X direction, **b** rotation over Z direction

Table 2 Displacement and rotation reduction rates in each damping coefficient case

Damping coefficient (KN s/m)	Maximum displacement in X direction (mm)	Displacement reduction in X direction (%)	Maximum rotation in Z direction (rad)	Rotation reduction in Z direction (%)
0	39.1804	0	0.0019789	0
20	35.1529	10	0.00212977	−8
40	32.4729	17	0.00182994	8
60	29.8901	24	0.00170446	14
80	27.7745	29	0.00158127	20
100	26.1154	33	0.00152677	23
150	22.5332	42	0.00150247	24
200	19.8808	49	0.00151433	23
250	17.7346	55	0.00149478	24
300	16.1191	59	0.00151919	23
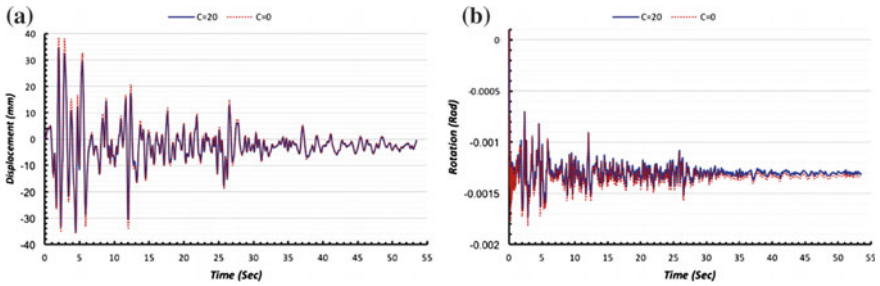
Fig. 9 Induced displacement and rotation versus time in X and over Z directions for C = 20 KN s/m **a** displacement, **b** rotation
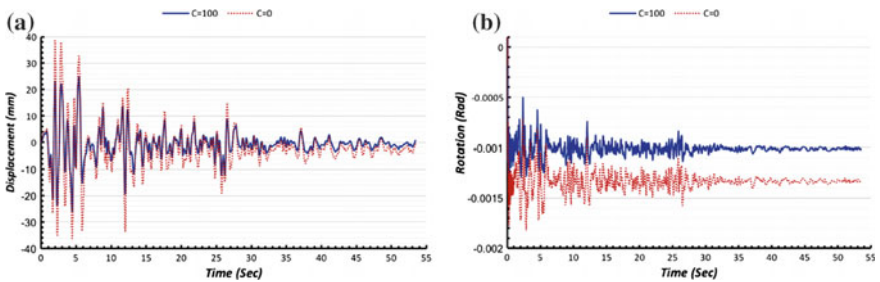
Fig. 10 Induced displacement and rotation versus time in X and over Z directions for C = 100 KN s/m **a** displacement, **b** rotation
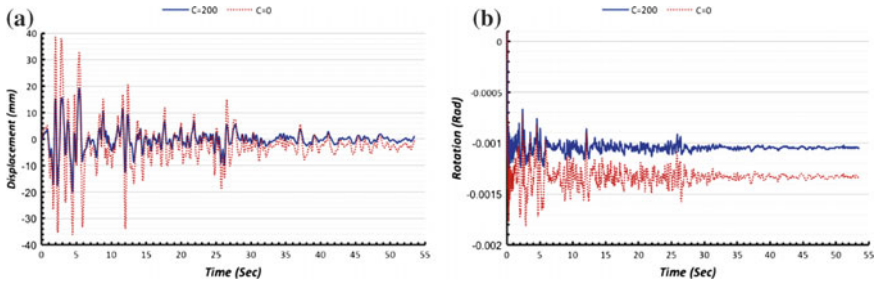
Fig. 11 Induced displacement and rotation versus time in X and over Z directions for $C = 200$ KN s/m **a** displacement, **b** rotation
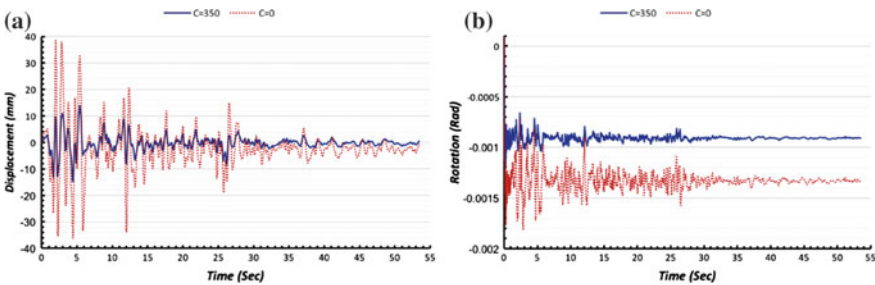
Fig. 12 Induced displacement and rotation versus time in X and over Z directions for $C = 350$ KN s/m **a** displacement, **b** rotation

confirming the efficiency of VWD device regarding the decrease in structural displacement amplitude and rotation.

4.2 Plastic Hinge Formation Criterion

This criterion studies the number of structural members undergone a plastic hinge, i.e., a failure due to the earthquake excitation.

Figure 13 exhibits the number of sections which experienced a plastic hinge (as distinct structural members) as well as the total number of induced plastic hinges (as summation of all plastic hinges) in all structural members during the excitation while VWD devices with distinctive characteristics of damping coefficient were mounted.

According to Fig. 13, increasing damping coefficient decreases the number of sections experiencing a plastic hinge from 24 in the unreinforced frame to 20 in the frame enhanced by a 20 KN s/m VWD, while further increase in damping coefficient to 40 KN s/m leads to a higher number of sections endured plastic hinge. As the damping coefficient rises to 200 KN s/m, the graph represents a descending
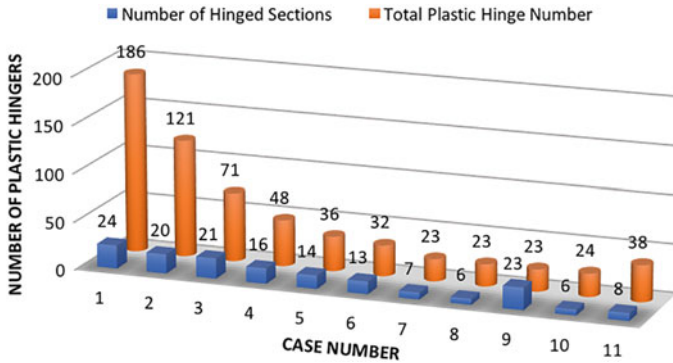
Fig. 13 Number of distanced hinged members and summation of all plastic hinge formations for different cases

trend reaching to a minimum of 6 hinged sections, which shows a 75% decrease in comparison with the case 1. Afterwards, a sudden surge in the number of hinged sections is recorded at $C = 250$ KN s/m. The graph ends up by a fluctuation at higher damping coefficients.

Similarly, the total number of plastic hinges signifies a sloping trend from 186 at case 1 leading to a constant value of 23 at the damping coefficients of 150, 200, 250 KN s/m. Ultimately, an escalating trend in the total number of plastic hinges is seen reaching to 38 at $C = 350$ KN s/m.

In nutshell, VWD devices with low values of damping coefficient show almost no significant improvement in the seismic behavior of the structure. This might be in accordance with an increase in the weight of the structure due to implementing VWD devices. However, higher values of damping coefficient improve performance and efficiency of VWD devices in diminishing induced forces due to seismic excitations.

4.3 Induced Column Forces

As identified in Fig. 14, a corner column has been selected to investigate the effectiveness of adopting VWD devices in dissipating induced column forces, including axial force, bending moment, and shear force.

Figures 15, 16, and 17 illustrate the efficiency of supplemental VWD devices with different damping coefficients in terms of diminishing imposed axial force, bending moment, and shear force, respectively.

According to Fig. 15, it can explicitly be outlined that low values of damping coefficient not only does not moderate the induced axial force, but also may magnify the axial force in some circumstances. However, higher values of damping coefficient lead to a sliding trend in induced axial force, although with little absolute impacts.
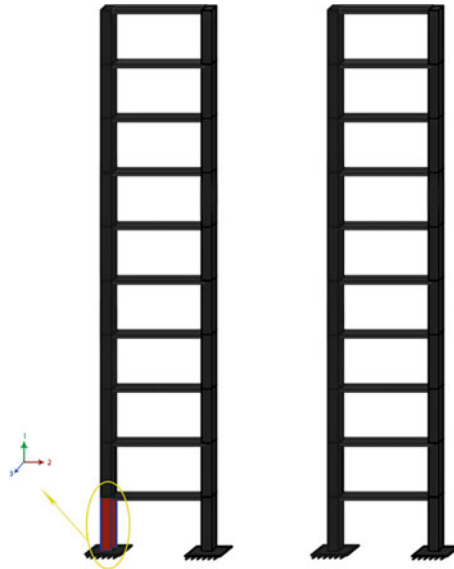
Fig. 14 The considered column of the structure and local coordinate system
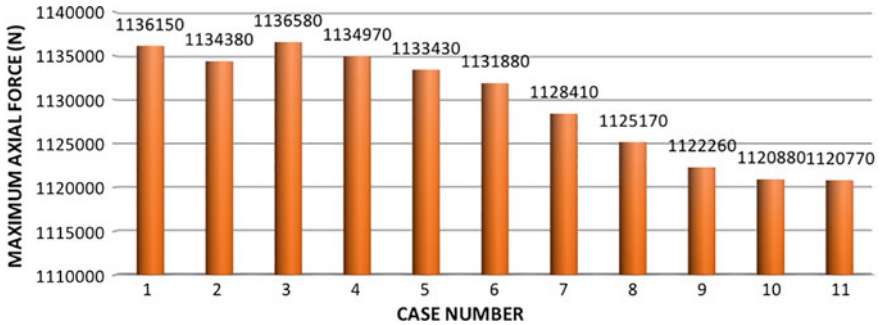
Fig. 15 Induced axial force of the specified column in each case

Considering the impacts on bending moment, Fig. 16 demonstrates a gentle descending trend with a plateau at higher values of damping coefficient. The same trend applies to the impacts of VWD devices on induced shear force. However, the slopping rate proceeds swiftly prior to the plateau bot with lesser positive absolute impacts, as seen in Fig. 17.
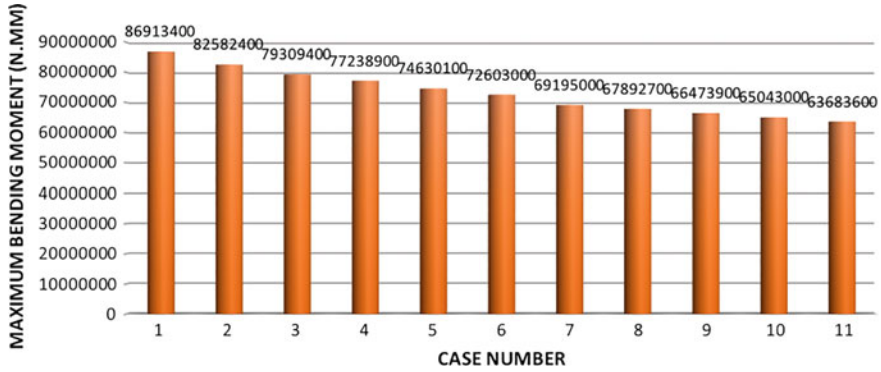
Fig. 16 Induced bending moment of the specified column in each case
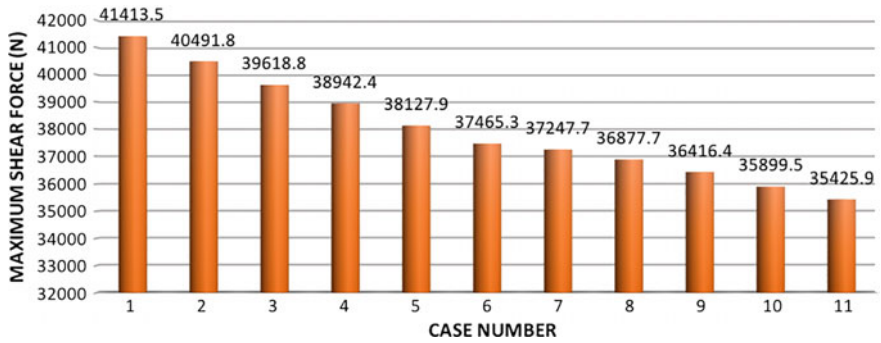
Fig. 17 Induced shear force of the specified column in each case

4.4 Overall Performance of VWD Device

Table 3 includes detailed performance index for response of the structures in all defined cases. In addition, an average of reduction for each case is presented based on displacement, rotation, plastic hinge formation, and element forces results. The average of reduction is taken into account as an overall performance of Viscous Wall Damper device.

As tabulated in Table 3, VWD devices with low values of damping coefficient, rolling as connector devices, have partial impacts on the seismic behavior of two adjacent structures. Therefore, higher rates of displacement, rotation, plastic hinge occurrence, and induced element forced are resulted. This mostly applies to VWD devices wither a damping coefficient lower than 60 KN s/m.

Conversely, VWD devices with damping coefficients higher than 60 KN s/m appear to be more impactful in diminishing the seismic behavior of two adjacent structures. Among 11 test cases, the ones with damping coefficients of 200 and

Table 3 Overall performance of Viscous Wall Damper device

Damping coefficient (KN s/m)	Displacement reduction in X direction (%)	Rotation reduction in X direction (%)	Section plastic hinge reduction (%)	Total plastic hinge reduction (%)	Axial force reduction (%)	Bending moment reduction (%)	Shear force reduction (%)	Average of reductions
0	0	0	0	0	0	0	0	0
20	10	−8	17	35	0	5	2	9
40	17	8	13	62	0	9	4	16
60	24	14	33	74	0	11	6	23
80	29	20	42	81	0	14	8	28
100	33	23	46	83	0	16	10	30
150	42	24	71	88	1	20	10	37
200	49	23	75	88	1	22	11	39
250	55	24	4	88	1	24	12	30
300	59	23	75	87	1	25	13	40
350	62	16	67	80	1	27	14	38

300 KN s/m present the most dissipating attribute in terms of seismic responses with average reduction rates of 39 and 40%, respectively.

Table 3 enables determining an optimum option in designing a connector VWD device between two adjacent structures, based on a given metric index, in order to mitigate seismic responses.

5   Conclusion

This study investigates the effectiveness of implementing supplemental Viscous Wall Damper devices to link a couple of adjacent structures in order to relieve seismic responses. Hence, a time history nonlinear analysis of two adjacent ten-story structures excited by a ground motion has been conducted.

The outcomes suggest that connecting adjacent structures with VWD devices lead to a noticeable reduction of seismic responses, including displacement amplitude, rotation, plastic hinge, and induced element forces. Moreover, the correlation between damping coefficient of VWD devices and dissipated seismic energy indicates a direct relationship with two exceptions. The first exception is a fluctuation in seismic responses corresponding with VWD devices with low values of damping coefficient. This might be a result of an increase in structural weight due to implementing VWD devices leading to more seismic demands, which cannot be overcome by little positive impact of VWD devices with low damping coefficient. The second exception occurs while damping coefficient rises so high, where improvements on seismic behavior deteriorate. This might be a result of an over damping circumstance triggered by the higher values of damping coefficient.

Apart from the exceptions, all seven metrics (displacement, rotation, section plastic hinge, total plastic hinge, axial force, bending moment, and shear force) indicate a downward trend. The trends relating to total plastic hinge, bending moment, and shear force relatively drop more swiftly comparing with other trends, which experience gentle cutbacks.

In perspective, employing VWD devices in connecting two adjacent structures successfully diminish earthquake actions and improve seismic behavior of the structure.

References

1. Tapashetti, A.S., Vijaya, S., Shivakumara Swamy, B.: Seismic pounding effect in building. Int. J. Adv. Eng. Technol. Manage. Appl. Sci. **2**, 2863–2868 (2014)

2. Wolf, J., Skrikerud, P.: Mutual pounding of adjacent structures during earthquakes. J. Nucl. Eng. Des. **57**, 253–275 (1980). https://doi.org/10.1016/0029-5493(80)90106-5

3. Efraimiadou, S., Hatzigeorgiou, G.D., Beskos, D.E.: Structural pounding between adjacent buildings: the effects of different structures configurations and multiple earthquakes. In: Proceedings of the 15th World Conference on Earthquake Engineering, Lisbon, Portugal, pp. 24–28 (2012)

4. Elwardany, H., Seleemah, A., Jankowski, R.: Seismic pounding behavior of multi-story buildings in series considering the effect of infill panels. Eng. Struct. **144**, 139–150 (2017). https://doi.org/10.1016/j.engstruct.2017.01.078

5. Christenson, R.E., Spencer Jr., B.F.: Coupled building control using smart dampers. In: Proceedings of the 13th ASCE Engineering Mechanics Division Conference, Baltimore, Maryland (1999)

6. Luco, J., De Barros, F.: Optimal damping between two adjacent elastic structures. J. Earthquake Eng. Struct. Dyn. **27**, 649–659 (1998). https://doi.org/10.1002/(sici)1096-9845(199807)27:7<649:aid-eqe748>3.0.co;2-5

7. Zhang, W., Xu, Y.: Dynamic characteristics and seismic response of adjacent buildings linked by discrete dampers. J. Earthquake Eng. Struct. Dyn. **28**, 1163–1185 (1999). https://doi.org/10.1002/(SICI)1096-9845(199910)28:10<1163:AID-EQE860>3.0.CO;2-0

8. Lu, X., Xu, Y., et al.: Seismic control of adjacent buildings using fluid dampers: experimental study. J. Adv. Build. Technol. **3**, 973–985 (2002)

9. Kageyama, M., Yasui, Y., Suzuki, T., Seto, K.: A study on optimum design of joint dampers connecting two towers: The case of connecting two same height towers at multiple points. In: Proceedings of the 2nd World Conference on Structural Control, Kyoto, Japan, pp. 1463–1472 (2004)

10. Kim, J., Ryu, J., Chung, L.: Seismic performance of structures connected by viscoelastic dampers. Eng. Struct. **28**, 183–195 (2006). https://doi.org/10.1016/j.engstruct.2005.05.014

11. Cundumi, O., Suárez, L.E.: Numerical investigation of a variable damping semi-active device for the mitigation of the seismic response of adjacent structures. Comput. Aided Civ. Infrastruct. Eng. **23**, 291–308 (2008). https://doi.org/10.1111/j.1467-8667.2007.00537.x

12. Basili, M., Angelis, D.E.M.: A reduced order model for optimal design of 2-mdof adjacent structures connected by hysteretic dampers. J. Sound Vib. **306**, 297–317 (2007). https://doi.org/10.1016/j.jsv.2007.05.012

13. Ok, S., Song, J., et al.: Optimal design of hysteretic dampers connecting adjacent structures using multi-objective genetic algorithm and stochastic linearization method. J. Eng. Struct. **30**, 1240–1249 (2008). https://doi.org/10.1016/j.engstruct.2007.07.019

14. Hejazi, F., Noorzaei, J., Jaafar, M.S., Abdullah, A.A.: Earthquake analysis of reinforce concrete framed structures with added viscous dampers. Int. J. Appl. Sci. Eng. Technol. **65**, 284–293 (2009)

15. Hejazi, F., Shoaei, M. D., Tousi, A., Jaafar, M.S.: Analytical model for viscous wall dampers. Comput. Aided Civ. Infrastruct. Eng. **31**, 381–399 (2015). https://doi.org/10.1111/mice.12161

16. Hejazi F., Toloue I., Jaafar, M., Noorzaei, J.: Optimization of earthquake energy dissipation system by genetic algorithm. Comput. Aided Civ. Infrastruct. Eng. **28**, 796–810 (2013). https://doi.org/10.1111/mice.12047

17. Kandemir-Mazanoglu, E.C., Mazanoglu, K.: An optimization study for viscous dampers between adjacent buildings. Mech. Syst. Sig. Process. **89**, 88–96 (2017). https://doi.org/10.1016/j.ymssp.2016.06.001

18. Lu, X., Zhou, Y., Yan, F.: Shaking table test and numerical analysis of RC frames with viscous wall dampers. J. Struct. Eng. **134**, 64–76 (2008). https://doi.org/10.1061/(ASCE)0733-9445(2008)134:1(64)

Seismic Behaviour of Prestressed and Normal Reinforcement of Communication Tower with Ultra-High Performance Concrete, High Strength Concrete and Normal Concrete Materials

Sarah Jabbar, Farzad Hejazi, Mohd Saleh Jaafar and R. S. M. Rashid

Abstract Nowadays, advances in telecommunications and broadcasting have led to the implementation of communication towers for installing network equipment. These towers are designed to go as high as possible in order to cover large area and avoid obstructions. However, there exist many challenges faced by engineers in relation to design of the tall and slender structures such as the complexity configuration of the structure. The nonlinear dynamic analysis is the only method that describes the actual behaviour of a structure during earthquake. Therefore, this study aims to investigate the behaviour of ultra-high performance concrete (UHPFC), high-strength concrete (HSC) and normal concrete communication tower with 30 m height located in Malaysia under seismic excitation. Also, to provide strength, stiffness and stability for the slender structures due to their sensitivity to dynamic load such as earthquake and vibration forces. For this propose, the finite element model of the tower is developed and time history analysis of communication tower under seismic load was conducted. In addition, the effect of using prestress instead of conventional reinforcement was investigated. The result indicated that prestressing of tower had lesser effect on the lateral displacement of tower under earthquake excitation. Although, the tower with UHPFC and HSC material

S. Jabbar · F. Hejazi (✉)
Universiti Putra Malaysia, Serdang, Malaysia
e-mail: farzad@fhejazi.com

S. Jabbar
e-mail: sarahsaleem2015@gmail.com

M. S. Jaafar · R. S. M. Rashid
Department of Civil Engineering, Universiti Putra Malaysia,
Serdang 43400, Malaysia
e-mail: msj@upm.my

R. S. M. Rashid
e-mail: raizal@upm.edu.my

shows lower lateral peak displacement against earthquake load compared to the normal concrete, which led to the increase in the use of these materials in lateral stiffness of the tower structure.

1 Introduction

Recently, the use of Ultra-high performance concrete (UHPC) and High-strength concrete (HSC) in new structures have been witnessed. HSC as the name implies exhibits has higher compressive compared with normal-strength concrete (NSC), however, with consequences of higher production cost. HSC is used in many construction works, particularly in bridge due to its strength advantages [11]. UHPC is another special kind of concrete that is gaining more popularity in civil engineering constructions due to its extraordinary properties such as strength and durability performance. It is a leading technology and up-to-date knowledge in concrete production [4]. Jabbar et al. [8] noted that the capacity of UHPC beams for twisting was twice that of HSC beams. Although, some new types of bridge member employing UHPCC was applied such as Shepherds Creek Bridge in Australia [3], FHWA short span bridge in the USA and Wapello Bridge in Iowa, USA [6], Kuyshu High Speed Bridge in Japan [14]. Also, there is a report about the application of UHPCC in hybrid beams and Wind Turbine tower. Wu et al. [21] carried out research program on Post-tensioned Ultra-High Performance concrete using cementitious composites with a target compressive strength of 200 MPa for hybrid wind turbine tower using different cases of wall thickness and prestressing tendons, and found that the wall thickness has effect on the displacement. In addition, the prestress can effectively reduce the stress and improve stability of the tower. Preciado et al. [18] proposed a method for reducing seismic vulnerability of masonry towers using externally prestressed devices and the result showed that a medium level prestressed system could increase bending capacity without reduction in ductility. In the highly prestressed system, degree of displacement of the tower was slightly reduced which indicates less ductility. Furthermore, the connection of discrete elements in precast concrete structures is important for overall continuity of the building [19]. The economic advantages of precast concrete structures are better than in situ concrete structures. The existing benefits include improved finishing, quality control, curing and concrete casting [20].

Earth tremor sets buildings in motion with different intensities and frequencies at different locations. This results to different degree of damages in structures located in the affected region. Therefore, it is highly imperative to construct an earthquake-resistant structure that is capable of resisting high-magnitude earthquake. In other to achieve this goal, time history analysis which is the behaviour of a structure during an earthquake could be employed to develop a sustainable and

cost-effective method. Qin et al. [7] studied the dynamic characteristic and seismic response of a Shanghai tower in China by developing finite element model under time history analysis. The result indicate that the time history analysis is a useful tool for seismic design for tall buildings. Lu et al. [12] carried out nonlinear dynamic time history analysis to investigate the behaviour of high-rise building structure with setbacks in elevation under rare earth tremor. The structure demonstrated sufficient seismic and ductility capacity to resist earthquake. Patil and Kumbhar [15] studied nonlinear dynamic analysis by developing finite element model for reinforced concrete framed building with 10 storey considering different seismic intensities. The result showed that time history analysis of multi-storeyed RCC structure is required to ensure resistance to earthquake excitation. Patil et al. [16] studied the structural behaviour of 80 m wind turbine tower under heavy ground motions and seismic fragility analysis. It was observed that the turbine tower is susceptible to overturning moment if subjected to earthquake. More so, the structure could fail due to permanent deformation and global buckling. Esfahani et al. [5] studied the seismic behaviour of IBS frames and partially prestressed concrete PPC. The time history analysis results revealed that IBS and PPC frames exhibits better seismic performance when compared with the conventional RC frames. Nguyen and Kima [13] presented a procedure for nonlinear inelastic time history analysis procedure for space semi-rigid six-storey steel frames under dynamic loads. It was observed that flexibility plays an important role in estimating the actual behaviour of steel frames connections. Alembagheri [2] studied the seismic behaviour of slender freestanding towers by considering an idealized hollow intake tower submerged under horizontal and vertical components of the El Centro earthquake test. The author observed that the interaction of water–structure affects the seismic behaviour of the tower. Paultre et al. [17] investigated seismic damage response of a moment resisting high-strength concrete frame by subjecting it to a repeated pseudo-dynamic vibration. The author developed methodology with regularization that showed that it is an effective approach to be used in predicting localization and level of damage in structures subjected to earthquakes excitation.

The review of literature indicates that the dynamic analysis is important in defining response of structures; although, the use of prestress concrete enhanced the tensile capacity of structures. But, there exist insufficient knowledge regarding towers' structure located in high seismicity environment. Therefore, this paper comprises of two major parts. First, finite element analysis model of communication tower is developed using ABAQUS software developed from HSC, UHPC and normal concrete material properties with prestress and conventional reinforced concrete. Then, time history analysis with different peak ground accelerations (El Centro USA and Malaysia excitation) is imperative in order to evaluate the performance of the different material (UHPC, HSC, normal concrete) under the aforementioned condition.

2 Dynamic Response of Tower Under Earthquake Excitation

Seismic response of a building is investigated using time history analysis under different earth tremor forces. This includes a chronological procedure of analysis for the dynamic response of a structure under specified loading that varies with time. Both acceleration and displacement responses are required in order to understand and visualize the dynamic behaviour of the system when subjected to the earth quake excitation. In this study, an attempt has been made to investigate the behaviour of different towers subjected to seismic excitation. For this purpose, two earthquake records of El Centro (USA, 1940) as moderate earthquake and Malaysian record a low intensity earthquake record have been implemented. The deflection is considered critical, it may be limited to height/500 [10]. In this case, the maximum allowable deflection at the tip of the tower is 60 mm.

3 Description of the Tower

The communication tower that used in this study is UHPFC with 30 m height located in Malaysia and consider three segments each segments with 10 m height. The tower system is considered as a rigid hollow column (cantilever) which is able to stand against horizontal load through its lateral stiffness which is provided through tower component such as the prestress tendons inside the segmental that can help to increase the resistance against lateral load. It consists of three segments each segment with 10 m height. The segments linked to each other by using bolts and nuts. The length the bolts and diameter is about 1000, 25 mm respectively for segmental connection. While it is about 1000 mm length with 32 mm diameter for foundation and first segmental connection. Each segment is arranged with eight tendons and each connection is arranged with eight holes for bolts. The three segments is fixed to a reinforcement concrete foundation block with 4.00 × 4.00 m cross section and 1 m in deep as showed in Fig. 1. Each segment is arranged with eight tendons and each connection is arranged with eight holes for bolts. Strand with 15.2 mm diameter with 260 MPa yield stress is prestressed with the tower with 1200 MPa prestresses force. In addition, the material properties for HSC material are reported by Jankowiak and Lodygowski [9] and for UHPFC by Chen and Graybeal [4].

Fig. 1 UHPFC communication tower located in Malaysia

4 Development of FEM Model

The Finite element analysis software ABAQUS [1] was used to develop and analyse 3-D model of the communication tower as shown in Fig. 2. In other to evaluate the behaviour of the communication tower, UHPFC, HSC and normal concrete material properties were used to develop the model and time history analysis was carried out. An eight-node linear brick of 3-D integration element (C3D8R) was used to simulate concrete parts and two-node linear 3-D truss elements (T3D2) was used to model the reinforcing bar elements and prestressing tendon element which are embedded in the concrete.

4.1 Nut and Screws

Nut and Screws were used to assemble the various components of the developed proposed connection. In this study, the length and the bolts diameter is about 1000, 25 mm respectively for segmental connection. While the diameter of bolts for the

Fig. 2 Developed FEM for
communication tower

Fig. 3 Bolt and nut geometry
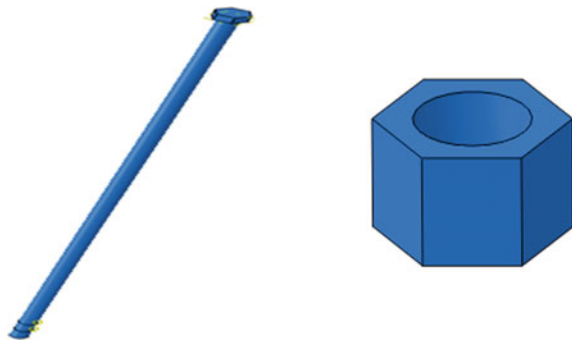
foundation and first segmental connection is about 32 mm. The screw and nut were
reproduced as solid elements using FEM software as shown in Fig. 3.

4.2 Interactions

All reinforcements were constraint as embedded in model while the
surface-to-surface contact was considered in the interaction for the outer and inner
nuts and bolt surfaces of the concrete which were eventually tied together.

4.3 Meshing

The structured and sweep technique is employed for meshing. All models are meshed with 150 mm of mesh size as shown in Fig. 4.

4.4 Load and Boundary Condition

The simulation models adopted in this work is as simple cantilever column. A fixed boundary condition is applied at the tower foundation as shown in Fig. 5. The definition of the boundary condition is given in Eq. 1.

$$U1 = U2 = U3 = UR1 = UR2 = UR3 = 0 \tag{1}$$

The time history analysis was conducted using the El Centro (USA, 1940) and Malaysia earthquake acceleration as shown in Fig. 6a, b.

Fig. 4 Tower mesh

Fig. 5 Applying load and
boundary condition

5   Result and Discussion

5.1   Time History Displacement

Time history analysis is performed for UHPFC, HSC, and normal concrete communication towers with prestress and normal reinforcement.

Records of the El Centro (USA, 1940) and Malaysia earthquakes are used for the time history analysis.

The comparison of displacements and accelerations from the response history analysis with the recorded of the precast communication towers is shown in the following figures to compare the response of the towers with different materials and with prestress and normal reinforcement during earthquake excitation.

The time history analysis responses displacement versus the time and the acceleration versus the time graphs for normal, HSC and UHPFC communication tower are shown in Fig. 7.

Based on the results of the fluctuating trend of the displacements it shows that the maximum deflection is reduced to 18.56, 5, 7.14% for tower with UHPFC, HSC and normal concrete, respectively, with using the prestress instead of normal reinforcement under time history analyses with El Centro earthquake due to less amount of damage.
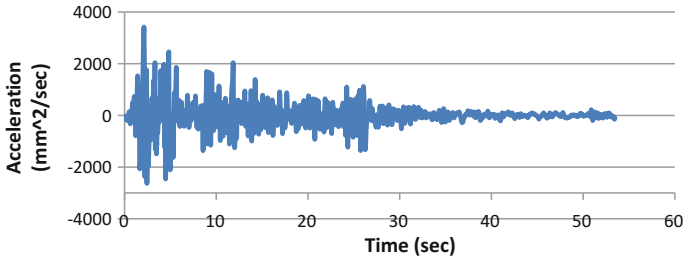
(a) Acceleration–time record forEl Centro earthquake
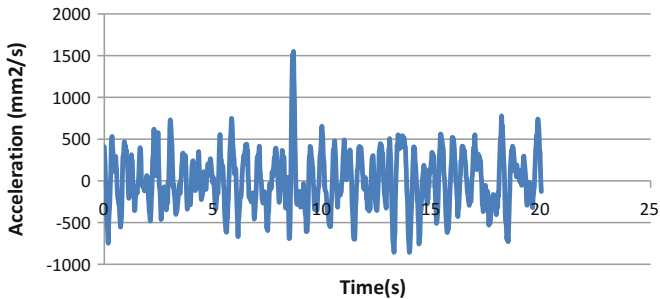
(b) Acceleration–time hisory record for Malaysia earthquake

Fig. 6 Earthquake acceleration–time history record

Figure 8 shows the maximum deflection and maximum relative acceleration for the UHPFC, HSC and normal concrete towers under Malaysian earth quake and the result indicates that using of the prestress can reduce the maximum deflection to 10.16, 11.26 and 6.4%, respectively in comparison of using the normal reinforcement for UHPFC, HSC and normal concrete communication towers.

Tables 1 and 2 represent the maximum relative responses (maximum relative displacement and maximum relative acceleration) of UHPFC, HSC and normal concrete of both prestressed and normal reinforcement communication towers subjected to El Centro and Malaysia earthquakes. Furthermore, the reduction percentage of the different dynamic responses is calculated.

5.2 Comparison Between UHPFC, HSC and Normal Concrete Prestressed Tower Under Time History Analysis

The relative displacement versus the time graph based on the time history analysis for normal concrete, HSC and UHPFC communication tower are shown in Fig. 9. Based on the results of the fluctuating trend of the displacements and acceleration
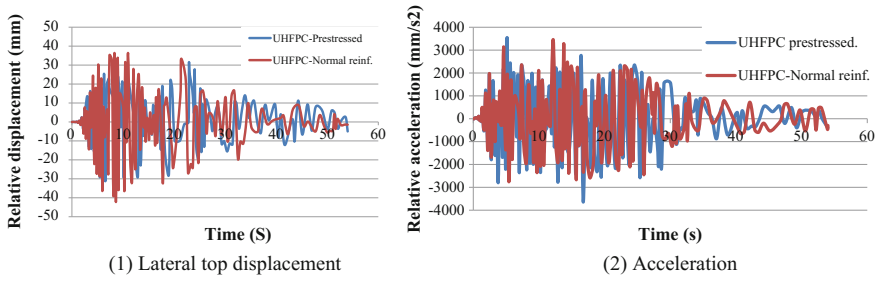
(1) Lateral top displacement

(2) Acceleration

(a) UHPFC tower with prestress and normal reinforcement (1) Lateral top displacement (2) Acceleration

(1) Lateral top displacement

(2) Acceleration

(b) HSC tower with prestress and normal reinforcement (1) Lateral top displacement (2) Acceleration
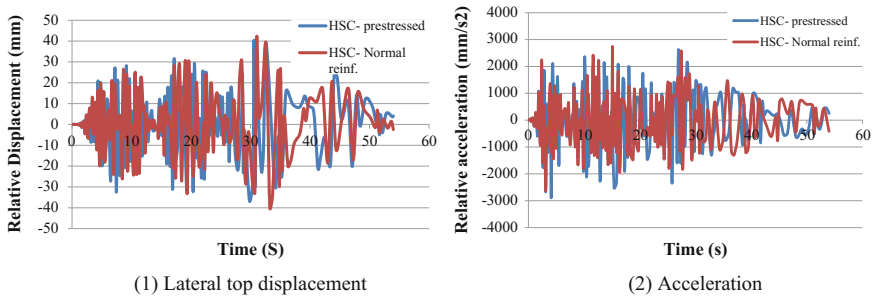
(1) Lateral top displacement
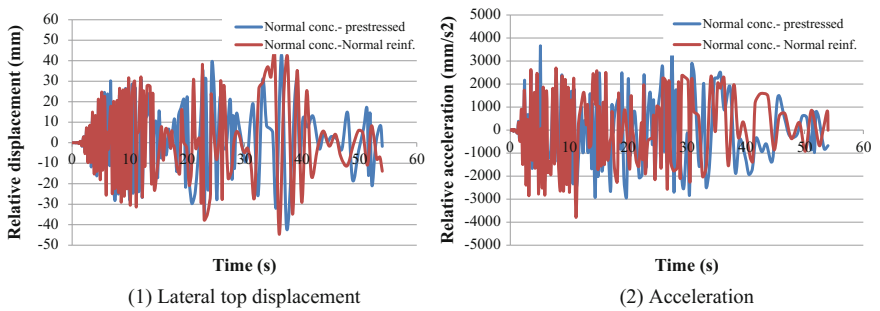
(2) Acceleration

(c) Normal concrete tower with prestress and normal reinforcement (1) Lateral top displacement (2) Acceleration

Fig. 7 Towers response under El Centro earthquake

the tower with UHPFC and HSC material, the result shows lower lateral peak displacement against earthquake loading which is about 30.7 and 40 mm respectively, while for conventional concrete, it is about 42 mm due to the initial low stiffness.
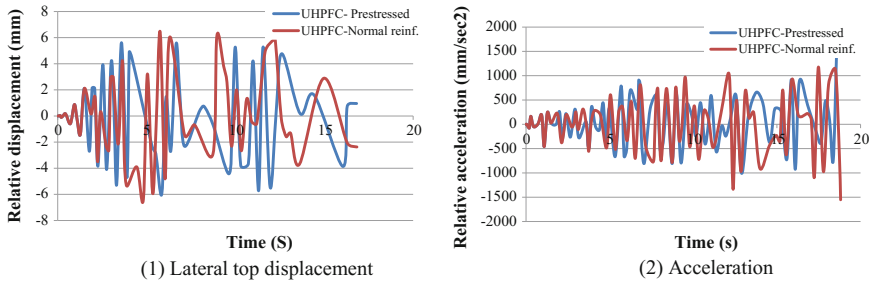
(1) Lateral top displacement   (2) Acceleration

(a) UHPFC tower with prestress and normal reinforcement (1) Lateral top displacement (2) Acceleration
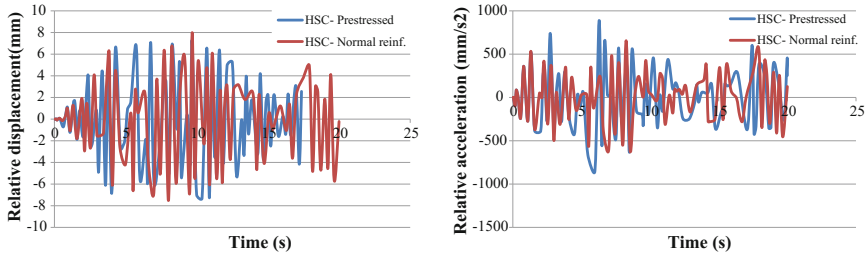
(1) Lateral top displacement   (2) Acceleration

(b) HSC tower with prestress and normal reinforcement (1) Lateral top displacement (2) Acceleration
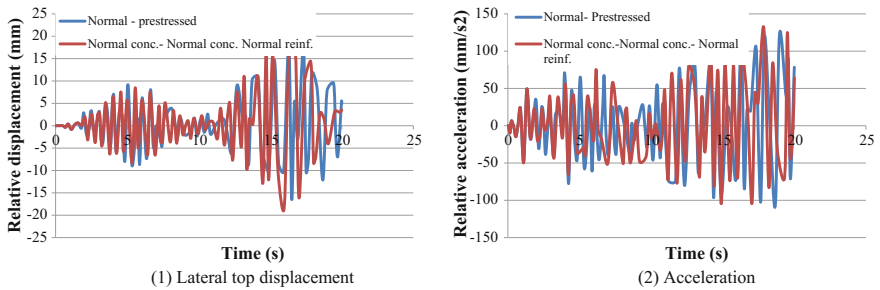
(1) Lateral top displacement   (2) Acceleration

(c) Normal concrete tower with prestress and normal reinforcement (1) Lateral top displacement (2) Acceleration

Fig. 8 Towers response under Malaysia earth quake

Although the deflections of the precast communication tower with (normal, HSC, UHPFC) material are compared under the other earthquake records (Malaysia) in Fig. 10. Where tower with normal concrete exhibit a larger lateral peak displacement 17.3 than HSC and UHPFC tower which is about 7.1, 5.9 mm respectively.

Table 1 Time history result for prestress and normal reinforcement tower under El Centro earthquake

Tower	Acceleration (mm/s^2)	Displacement (mm)	Reduction of displacement %
UHPFC—prestressed	3607	30.7	18.56
UHPFC—normal reinforcement	3462	36.4	
HSC—prestressed	2894	40	5
HSC—normal reinforcement	2747	42	
Normal concrete—prestressed	3663	42	7.14
Normal conc—normal reinforcement	3770	45	

Table 2 Time history result for prestress and normal reinforcement tower under Malaysia earthquake

Malaysia tEQ	Acceleration (mm/s^2)	Displacement (mm)	Reduction of displacement %
UHPFC—prestressed	1553	5.9	10.16
UHPFC—normal reinforcement	1552	6.5	
HSC—prestressed	889.4	7.1	11.26
HSC—normal reinforcement	656	7.9	
Normal concrete—prestressed	1230	17.3	6.4
Normal concrete—normal reinforcement	1046	18.4	

6 Conclusions

In this study, the dynamic behaviour of communication towers with different type of materials such as conventional, HSC and UHPFC under different seismic excitation was investigated. Therefore, a communication tower (30 m) height with different material properties (UHPFC, HSC and normal concrete) under prestressed condition is considered. Three-dimensional nonlinear finite element models were proposed to ascertain the nonlinear dynamic reactions in seismicity zones.
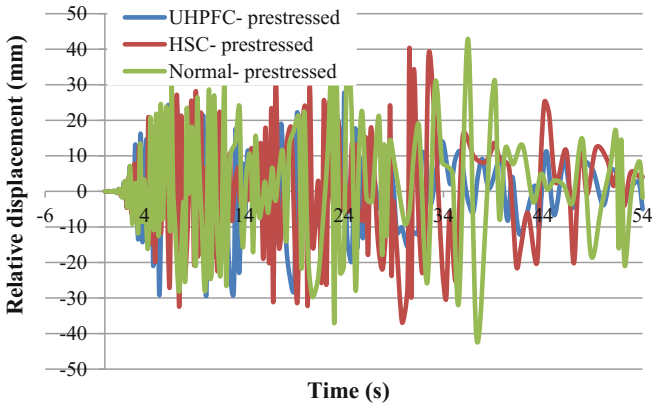
(a) comparison between UHPFC, HSC and Normal concrete tower in terms of lateral top displacement
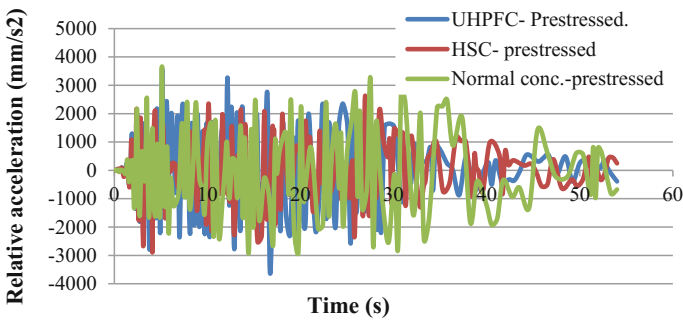
(b) Comparison between UHPFC, HSC and Normal concrete tower in terms of acceleration

Fig. 9 Towers response under El Centro earthquake

An earthquake records with different peak ground acceleration El Centro and Malaysia earthquake were applied to examine the performance of communication towers. The results indicated that using prestressed concrete in tower with UHPFC, HSC and conventional concrete material instead of normal reinforcement led to a reduced acceleration when subjected to any dynamic load. Also, less damage and increasing the strength were observed in the tower after testing. On the other hand, the tower with UHPFC and HSC material exhibits higher seismic performance in comparison to the conventional RC tower.
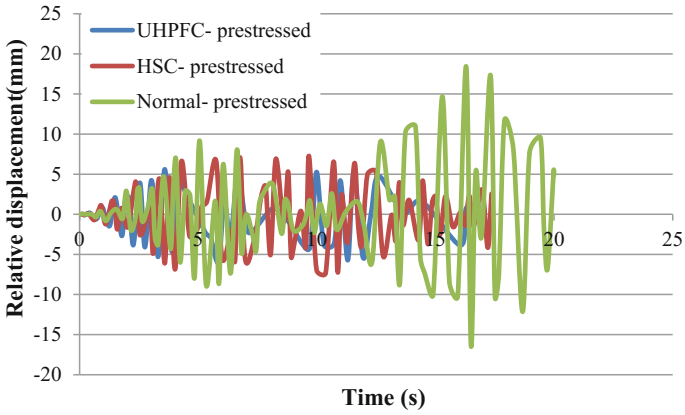
(a) comparison between UHPFC, HSC and Normal concrete tower in terms of lateral top displacement
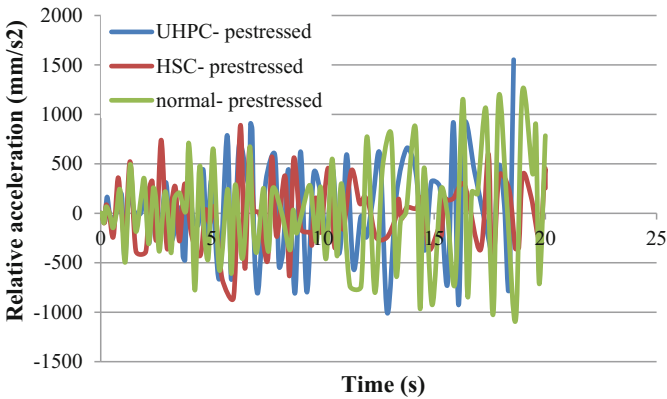
(b) Comparison between UHPFC, HSC and Normal concrete tower in terms of acceleration

Fig. 10 Towers response under Malaysian earthquake

References

1. ABAQUS.: Standard Version 6.13-4. The ABAQUS Software is a Product of Dassault Systèmes Simulia Corp. Hibbitt Karlsson & Sorensen Inc. US (2014)
2. Alembagheri, M.: Earthquake response of solitary slender freestanding intake towers. Soil Dynam. Earthq. Eng. **90**, 1–14 (2016). https://doi.org/10.1016/j.soildyn.2016.08.024
3. Cavill, B., Chirgwin, G.: The world's first Ductal road bridge Sherpherds gully creek bridge. In NSW, 21st Biennial Conference of the Concrete Institute of Australia, Brisbane (2003). http://worldcat.org/isbn/0855886986
4. Chen, L., Graybeal, B.A.: Modeling structural performance of ultrahigh performance concrete I-girders. J. Bridge Eng. (2011). https://doi.org/10.1061/(asce)be.1943-5592.0000305
5. Esfahani, M.H., Hejazi, F., Karimzadeh, K., Siang, T.K.: Seismic behavior of partially prestressed concrete structures. In Dynamics of Civil Structures, vol. 2, pp. 255–264. Springer International Publishing (2016). https://doi.org/10.1007/978-3-319-29751-4_26
6. Graybeal, B., Hartamann, J., Perry, V.: Ultra-high performance concrete for highway bridge. In FIB Symposium, Avignon, 26–28 April (2004)
7. Hao, Q., Xianzhong, Z., Yiyi, C., Bin, W.: Elasto-plastic-time history analysis of the shanghai tower under rare earthquakes. In CTBUH, Seoul Conference (2011)
8. Jabbar, S., Hejazi, F., Mahmod, H.M.: Effect of opening in reinforced concrete hollow beam web under torsional, flexural, and cyclic loadings. Latin Am. J. Solids Struct. ABCM J. **13**(8), 1576–1595 (2016)
9. Jankowiak, T., Lodygowski, T.: Identification of parameters of concrete damage plasticity constitutive model. Found. Civil Environ. Eng. **6**(1), 53–69 (2005)
10. Joint Technical Committee: Australian/New Zealand Standard, Structural design actions, Part 2: wind actions, AS/NZS 1170.2. Sydney, Standards Australia International Ltd.; Wellington, Standards New Zealand (2002)
11. Lopes, S., Bernardo, L.: Twist behaviour of high-strength concrete hollow beams—formation of plastic hinges along the length. Eng. Struct. **31**(1), 138–149 (2009). https://doi.org/10.1016/j.engstruct.2008.08.003
12. Lu, X., Su, N., Zhou, Y.: Nonlinear time history analysis of a super-tall building with setbacks in elevation. Struct. Des. Tall Spec. Build. **22**(7), 593–614 (2013). https://doi.org/10.1002/tal.717
13. Nguyen, P.C., Kim, S.E.: Second-order spread-of-plasticity approach for nonlinear time-history analysis of space semi-rigid steel frames. Finite Elem. Anal. Des. **105**, 1–15 (2015). https://doi.org/10.1016/j.finel.2015.06.006
14. Okuma, H.A., Nishikawa, K., Iwasaki, I., & Morita, T.: The first highway bridge applying ultra high strength fiber reinforced concrete in Japan. In 7th International Conference on Short and Medium Span Bridge, Montreal, Canada (2006)
15. Patil, A., Kumbhar, P.: Time history analysis of multistoried RCC buildings for different seismic intensities. Int. J. Struc. Civil Eng. Res. ISSN 2319-6009 (2013)
16. Patil, A., Jung, S., Kwon, O.-S.: Structural performance of a parked wind turbine tower subjected to strong ground motions. Eng. Struct. **120**, 92–102 (2016). https://doi.org/10.1016/j.engstruct.2016.04.020
17. Paultre, P., Weber, B., Mousseau, S., Proulx, J.: Detection and prediction of seismic damage to a high-strength concrete moment resisting frame structure. Eng. Struct. **114**, 209–225 (2016). https://doi.org/10.1016/j.engstruct.2016.02.013

18. Preciado, A., Sperbeck, S.T., Ramírez-Gaytán, A.: Seismic vulnerability enhancement of medieval and masonry bell towers externally prestressed with unbonded smart tendons. Eng. Struct. **122**, 50–61 (2016). https://doi.org/10.1016/j.engstruct.2016.05.007
19. Taheri, H., Hejazi, F., Vaghei, R., Jaafar, M.S., Ali, A.A.A.: New precast wall connection subjected to rotational loading. Periodica Polytech. Civil Eng. **60**(4), 547 (2016). https://doi.org/10.3311/ppci.8545
20. Vaghei, R., Hejazi, F., Taheri, H., Jaafar, M.S., Ali, A.A.A.A.: new precast wall connection subjected to monotonic loading. Comput. Concr **17**(1), 1–27 (2016). https://doi.org/10.12989/cac.2016.17.1.001
21. Wu, X.-G., Yang, J., Mpalla, I.B.: Innovative Post-tensioned Hybrid Wind Turbine Tower Made of Ultra High Performance Cementitious Composites Segment (2013)

Seismic Response of Shear Wall with Viscous Damping System

Farzad Hejazi, Nima Ostovar and Abdilahi Bashir

Abstract Seismic response behavior of the shear wall buildings has been investigated since last few years in the seismic zones using laboratory experimental testing and commercial package analysis. Three-dimensional analysis of shear wall structure under multiple direction of seismic excitation is a challenging work in the design of earthquake resistance structure, but the most challenging task is the analysis of the shear wall equipped with viscous damper at the middle of the shear wall using three dimensions of time history earthquake excitations. The main objective of this research is to find out the optimum shear wall location under three dimensions of earthquake excitation using commercial package ETABS. For this purpose two models of shear wall locations have been adapted in this research. Model type one, the shear wall is located at the middle span of three spans frame. Model type two, the shear wall is located at the corner spans of the same frame. The other objective of this research is to find out the optimum viscous damper location under three dimensions of earthquake excitation using commercial package ETBS. So, four different location of the viscous damper has been adapted in both two different shear wall models where the viscous damper embedded cut out of shear wall. The result of the peak deflection and structural member forces of the both shear wall models with and without implementation of viscous damper has been obtained successfully and compared their results accordingly. The result indicates the best performance of the shear wall goes to model type two. On the other hand, when the viscous damper located at the top of the shear wall frame structure has achieved the highest percentage reduction of the tip deflection and structural member forces of the shear wall frame and it is optimum location of viscous damper under 3D earthquake.

Keywords 3D earthquake · Shear wall · Viscous damper · Time history

F. Hejazi (✉) · N. Ostovar · A. Bashir
Department of Civil Engineering, Universiti Putra Malaysia, Serdang 43400, Malaysia
e-mail: farzad@upm.edu.my

1 Introduction

Earthquake is most destructive natural hazards that occur in almost all contents. The occurrence of the earthquake is result of the release energy from earthquake through shallow or less deep of the parts of the earth's interior which creates seismic waves [1]. The seismic waves move from inner of the crust to the surface of the earth with different speeds and frequencies. When the seismic waves reach on the surface of the earth where towns and cities locates, the seismic waves shakes the ground and moves little apart. The movement of the earth destroyed the buildings and structures on that surface of the earth. The damage that the structures receive depends upon the speed and the frequency of the seismic waves. Since the motion of the ground cause the destruction of the structures, it is necessary to identify some way to prevent the destruction of the structures during the ground movements. To achieve earthquake-resistant structures, seismic retrofitting and re-habitation of the buildings, three methods have been identified to dissipate the energy of earthquake and reduce effect of lateral load on the buildings [2]. These methods are; base isolation, energy absorption at plastic hinges, and use of mechanical devices to provide structural control system during earthquake as it can be seen in Fig. 1. The implementation of viscous dampers in the building structures as energy dissipation device has been chosen in this study to achieve earthquake-resistant structures.

The usage of the energy dissipation device in the building structures have been developed in the past decades [7, 8]. It has been utilized in different buildings with different devices to protect the buildings from excessive energy of seismic excitation. There are numerous types of dampers available commercially, which has been tested to different buildings. The viscous dampers are one of the energy dissipations that have been utilized in the building structure, which most commonly used of the frame structures, but the usage of the viscous dampers into the shear wall building are new in the seismic design field.

In 2003, Madsen carried the study on the effects of damping systems to improving the seismic design performance of multi storey buildings structures [3]. Madsen used ABAQUS in this study as finite element program package to analysis and obtain the response of the structure under seismic. The dampers are located within cutout sections of shear walls and then analysis has been taken on nine-storey building models to evaluate the effectiveness of the damper placement by subjecting seismic excitation. The result of this model studies on the nine-storey buildings showed that the ground floor placement of the damper has achieved the highest reduction of the tip deflection and tip acceleration.

In 2006, Julius Marko was carried a time history analysis of the shear wall model by observing the effects of the three types of damping devices on the seismic response of shear wall structures using ABAQUS/Standard version 6.3 [4]. The three types of the damping devices that Julius used his investigation were friction dampers, viscous elastic dampers, and hybrid dampers. The best performance was achieved in structure where damper installed in all three parts of the model with an overall reduction of 24.7%. The second best performance was achieved for model
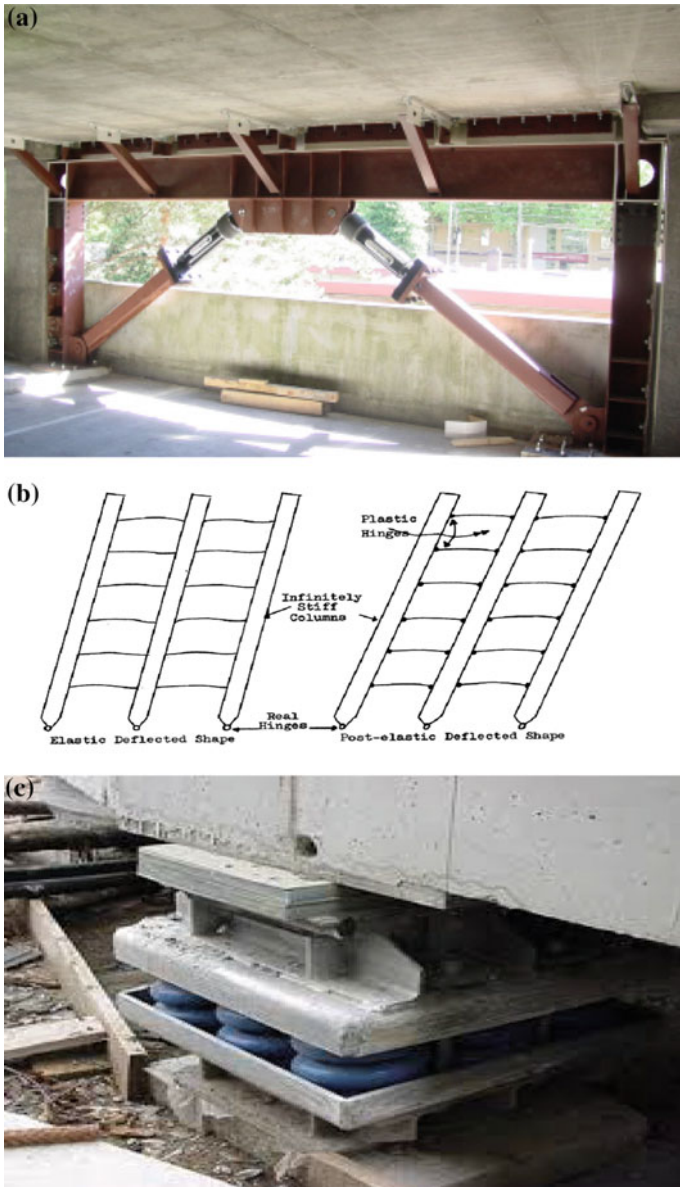
Fig. 1 a Mechanical devices viscous damper method **b** energy absorption at plastic hinges method **c** base isolation method

where dampers placed in the upper part of the structure with an overall reduction of 19.9% and following by when the dampers placed in the middle part of the structure with an overall reduction of 19.1%. Finally dampers placed in the lower part of the model achieved the lowest reduction of 8.5%.

Mostly the researchers have has done an investigation on implementation passive energy dissipation devices into frame structures system but rare investigation have been done towards the implementation of the viscous damping devices imbedded into shear walls of the building and investigation of the effect of dampers within shear wall in behavior of the building during earthquake [5–9]. This study is concentrating the investigation of the response of the shear wall buildings subjected to seismic loads with viscous damping devices strategically embedded into shear wall. This research is representing the fulfillment of the research gaps which have not done before in the structural and earthquake engineering field and this gaps are summarized as below: (a) There is no study on 3D analysis of the shear wall structural members with embedded dampers under multiple direction of seismic excitation. (b) There is no investigation on three direction Time history analysis of the shear wall structures with different location of the viscous dampers. (c) There is no many detailed study on response of the shear wall structural member in different locations under multiple direction of seismic excitation. (d) There is lack of information about the efficiency of damping system under multiple dimension of earthquake excitation.

The main objective of this study is to generate fundamental research information on the performance of the building equipped damping devices within shear wall during three-dimensional seismic excitations. The other supplementary objectives are: (a) To investigate the effects of the viscous damper locations in response of structure under multiple direction of seismic excitation. (b) To investigate the effects of the shear wall location under three dimension of seismic excitation. (c) To use the research findings to propose most effective damping shear wall during three dimension of seismic excitation for response performance of the structures.

This research is concentrated on the model analysis of RC shear wall structure equipped with damper devices in order to investigate the effect of implementation of viscous damper on seismic response of the shear wall buildings. This study is focusing the maximum deflection of the shear wall frame structure and structural member forces after applied the 3D seismic load to the structure. The shear wall frame models have been analyzed using three dimensions of earthquake records to investigate the overall response of the shear wall members using finite element program ETABS.

2 Methodology

A three-storey shear wall frame structure was modeled in two different types of the structural model in this research to investigate the response of the structure under seismic excitation. The two types of models are designated by Model Type One and Model Type two and each type of the models has been equipped a viscous damper in four locations as it is illustrated in Figs. 2 and 3. The Model Type One is represented by a symmetric three-storey frame with three spans in each side and the shear wall located at the middle span of each side. A diagonal viscous damper was

Fig. 2 Model type one
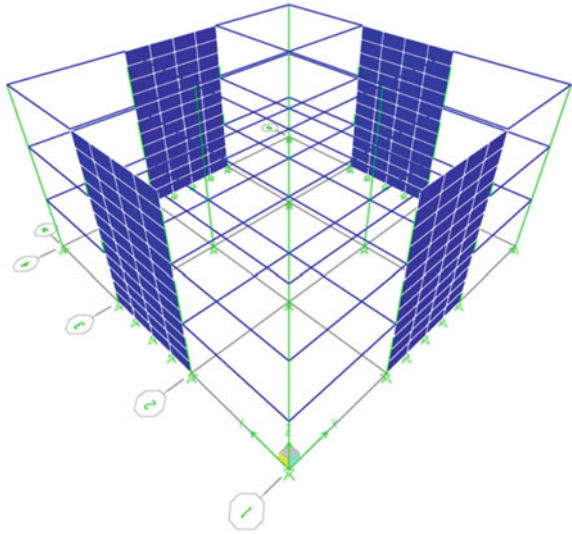
Fig. 3 Model type two
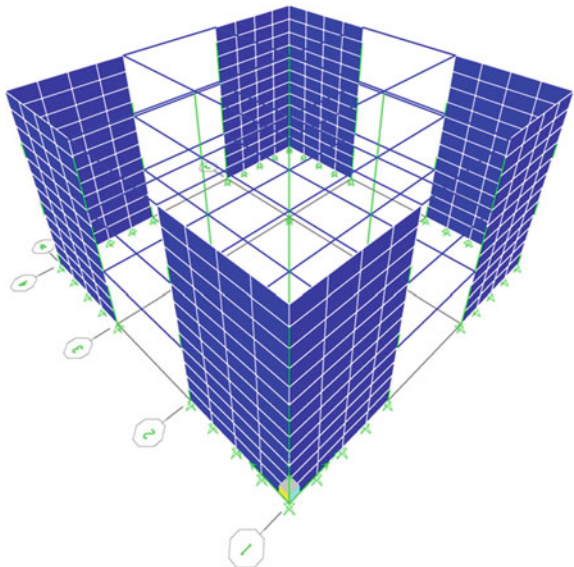
installed within cut out of shear wall at four different placements, namely bottom of the structure, middle of the structure, top storey of the structure and all storey of the frame-shear wall structure Fig. 1. The Model Type Two is represented by a symmetric three-storey frame with three spans in each side and the shear wall located at the corner spans of each side. A diagonal viscous damper was installed within cut out of shear wall at four different placements, namely bottom of the structure,

Fig. 4 Viscous damper usage in shear wall

middle of the structure, top storey of the structure and all storey of the frame-shear wall structure Fig. 4. The dimensions of the shear wall in model type one and type two is 10.5 m height, 6 m width and 0.15 m thick. Where the dimension of the beams is 400×250 mm and the columns are 150×150 mm. The frame only carries the self-weight and 7.21 kN brick wall loads.

The diagonal configuration of the viscous damper was considered for both types of models (Fig. 5). Furthermore, four different damper placements were considered to study the influence of the location on the seismic response of these buildings. Detail of the diagonal viscous damper located within the cut out of the shear wall is shown in Fig. 6. The properties of the viscous damper that has been utilized for all models of shear wall are Kd = 10×103 N/mm and Cd = 10×105 N/mm.

The El Centro three-dimensional earthquake records is selected for implementation to analysis as the multiple dimensions earthquake excitations in order to investigate the seismic response of shear wall frame structures with and without equipped viscous dampers. The three dimensions of El Centro (1940) earthquake records are shown in Fig. 7.

The overall schematic view of this research is presented a flow chart in Fig. 8.
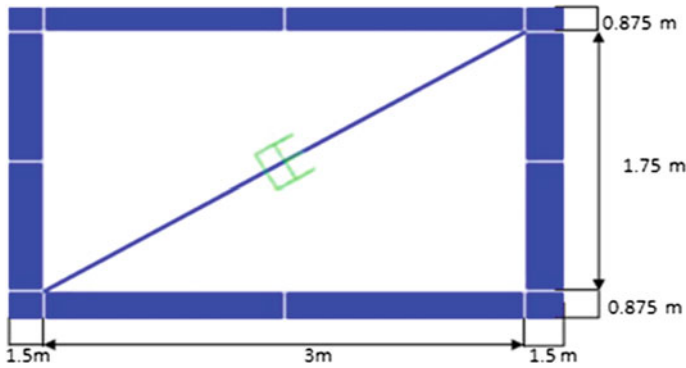
Fig. 5 Viscous damping equipped in shear wall structures
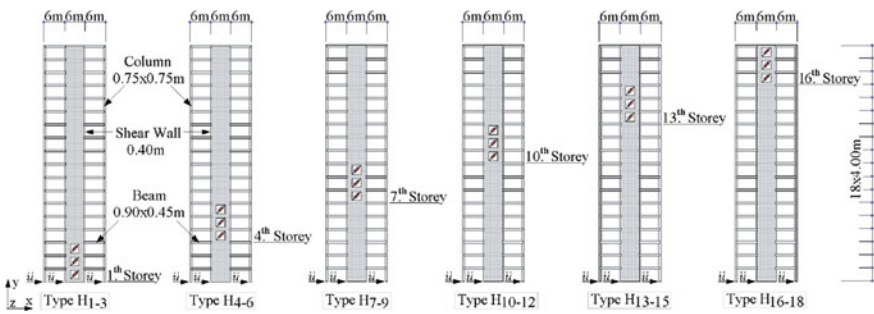
Fig. 6 Placement of dampers within 18-storey frame-shear wall structures [4]
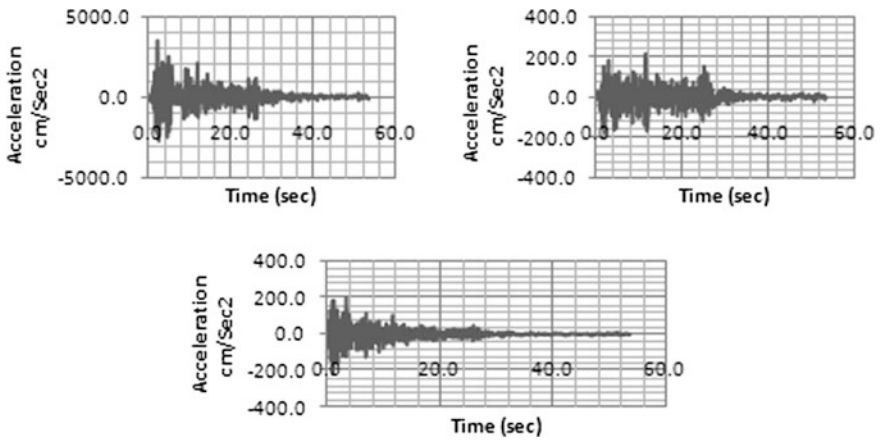
Fig. 7 El Centro (1940) earthquake record
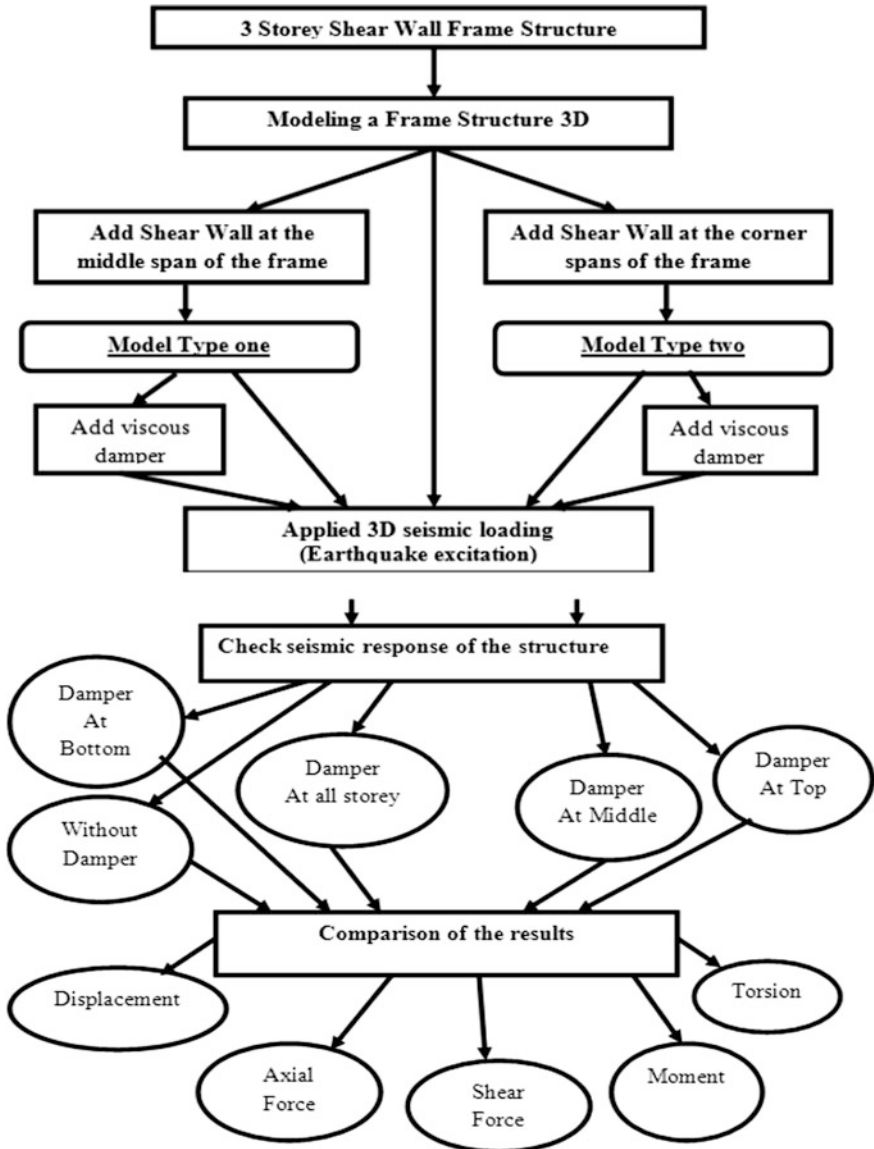
Fig. 8 Flow chart of the stages of analyzing a three-storey shear wall frame structure

3 Result and Discussion

Figure 9 shows the overall result of one frame and five shear wall frame models, which shows a different response performance, some of the models show good response performance under earthquake excitations, while the others show weak
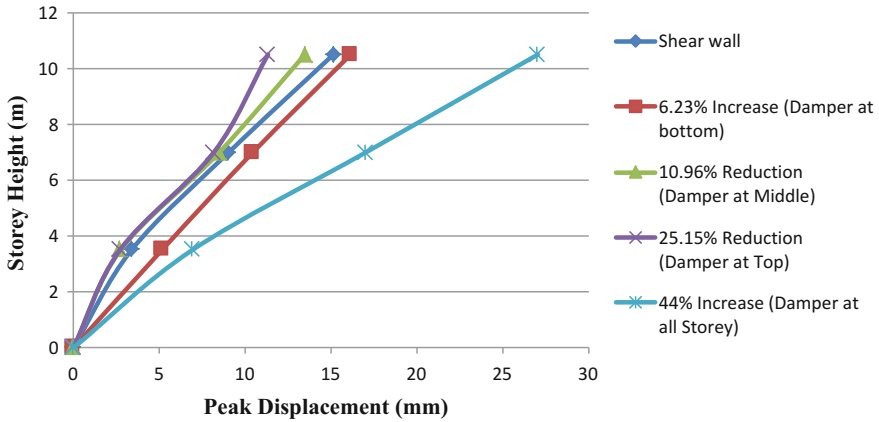
Fig. 9 Comparison of average peak storey displacements of shear wall with and without viscous damper model type one

response performance under earthquake excitation. The shear wall frame with viscous damper at the top of the structure achieved best performance compared to the frame-shear wall and those have viscous damper. The average peak deflection of shear wall frame equipped viscous damper at the top of the structure is reduced 25.15% compared to the shear wall without damping systems as shown in Fig. 7. Equipped viscous damper at top of the shear wall frame is the optimum location of the viscous damper in shear wall frame under three dimension of earthquake excitation. The result shows 17.9% reduction of the axial forces after equipped viscous damper at the all middle of the shear wall frame structure. The moment at the base of the shear wall frame structures is also reduced 20.65%, while the torsion and base shear of the building is also reduced 14.2 and 7.1% respectively as it is shown in Table 1.

The overall result of peak deflection and structural member force of the frame agreed the optimum location of the viscous damper in the shear wall frame is at the top of the frame structure, where the peak displacement achieved the highest reduction and all structural member forces are reduced.

The shear wall frame with viscous damper at the top of the structure achieved best performance compared to the frame-shear wall and those have viscous damper. Average maximum structure member forces of shear wall frame equipped viscous damper at the top of the structure in Fig. 10 reduced all forces compared to the shear wall without damping systems. The result shows 26.84% reduction of the axial forces after equipped viscous damper at the all top of the shear wall frame structure. The moment at the base of the shear wall frame structures is also reduced 32.79%, while the torsion and base shear of the building is also reduced 29.58 and 54.76% respectively as shown in Table 1, compared to the shear wall without damping systems. Based on the reduction of structural member forces of the shear wall frame, the optimum location of the viscous damper in shear wall frame under three dimension of earthquake excitation is the top of the shear wall frame.

Table 1 Comparison of maximum structural member forces of shear wall model type one and model type two

Structural member forces	Reduction (%)				
Model type one	Shear wall	Shear wall damper at bottom	Shear wall damper at middle	Shear wall damper at top	Shear wall damper at all storey
Axial force	176.2 kN	−28.94	−17.9	−2.16	29.1
Shear force	9233.93 kN	5	−7.1	−2.76	23.2
Torsion	83110 kN m	5.33	−14.2	−5.9	23.47
Moment	76260 kN m	−8.1	−20.65	−8.12	21.74
Structural member forces	Reduction (%)				
Model type two	Shear wall	Shear wall damper at bottom	Shear wall damper at middle	Shear wall damper at top	Shear wall damper at all storey
Axial force	75.23 kN	42.8	42.43	−26.84	69.31
Shear force	4054 kN	−2.58	−68.27	−54.76	17.43
Torsion	36320 kN m	0.14	12.14	−29.58	23.3
Moment	31960 kN m	−3.89	19.26	−32.79	19.88
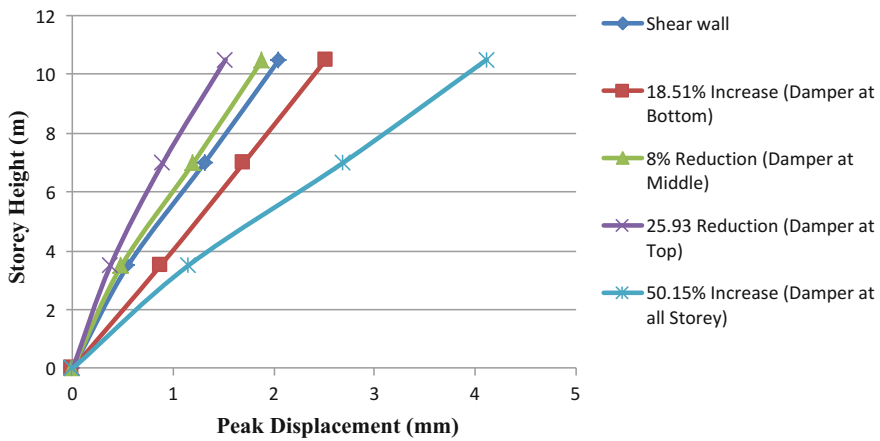
Fig. 10 Comparison of average peak storey displacements of shear wall with and without viscous damper model type two

The overall result of peak deflection and structural member force of the frame agreed the optimum location of the viscous damper in the shear wall frame is at the top of the frame structure. The peak displacement and all structural member forces are achieved at the highest reduction value when the viscous damper located at the top of the frame structure under three direction earthquake excitation.

The average result in Fig. 11 shows the highest peak displacement reduction in both models. Viscous damper equipped at top of the shear wall frame structure achieved highest peak displacement in both models. The average percentage peak deflection reduction achieved by shear wall equipped viscous damper at the top of the shear wall frame structure is 25.15 and 25.93% reduction of model type one and type two respectively. As conclusion the equipped viscous damper at top is optimum location of the damper under three direction of earthquake excitation.

Table 1 is illustrating the structural member force of shear wall frame structures under three direction of earthquake excitation. Model type one achieved the highest reduction of all structural member forces when the viscous damper located at the middle of the shear wall frame structure. Model type two achieved the highest reduction of all structural member forces when the viscous damper located at the top of the shear wall frame structure.

As the overall conclusion the location of the damper, which the two models have agreement the reduction of both peak deflection and structural member forces is a top of the shear wall frame structure. The optimum location of the diagonal viscous damper equipped in the shear wall frame is the top of the shear wall frame structure.
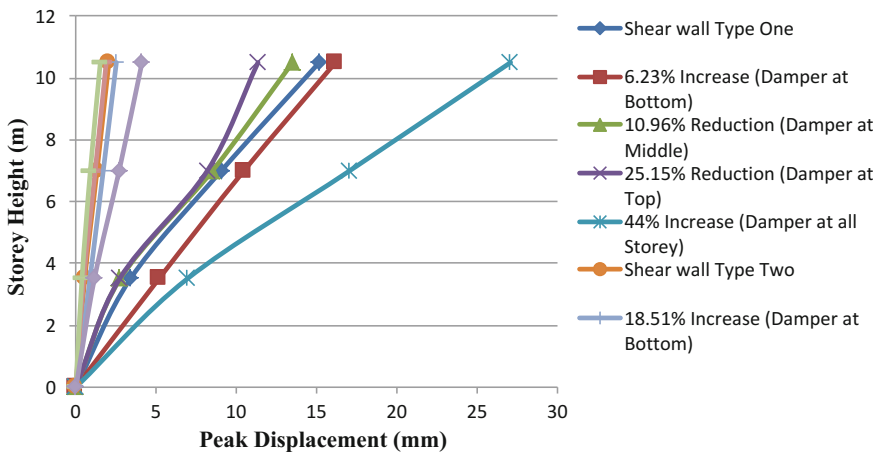
Fig. 11 Comparison of average peak storey displacements of shear wall type one and shear wall type two

4 Conclusion

The first objective of this research is to investigate the effect of the damper location inside the shear wall under three-dimensional of earthquake excitations. Two different models designated by model type one (shear wall at middle span) and model type two (shear wall at corner spans) is considered in this research and each model equipped viscous damper in different locations.

The average peak displacement reduction in both models with and without viscous damper has compared. The damper at top of the shear wall frame structure is achieved highest peak displacement in both models. As conclusion the equipped viscous damper at top is optimum location of the damper under three direction of earthquake excitation.

The second objective of this research is to investigate the effect of the shear wall location under the three-dimensional of earthquake excitations. Both shear walls has achieved high percentage peak displacement reduction compared with the frame. The model type two achieved highest earthquake energy dissipation compared with the shear wall type one. So that, the shear wall type two is optimum location of the shear wall under three direction of earthquake excitation.

The third objective is to propose the most effective damping shear wall during three dimension of seismic excitation. The shear wall achieved highest reduction when the viscous damper is located at the top of shear wall frame structure in model type two. The optimum location of the viscous damper equipped in the shear wall frame is the top of the model type two shear wall frame structure.

References

1. Deierlein, G.G., Reinhorn, A.M., Willford, M.R.: Nonlinear structural analysis for seismic design, a guide for practicing engineers, NEHRP seismic design technical brief no. 4, national earthquake hazards reduction program (NEHRP), NIST GCR 10-917-5
2. Federal Emergency Management Agency-FEMA: NEHRP guidelines and commentary for the seismic rehabilitation of building. Report no. 273/274, Building Seismic Council Washington, DC (1997)
3. Madsen, L.P.B., Thambiratnam, D.P., Perera, N.J.: Seismic response of building structures with dampers in shear walls. Comput. Struct. **81**(2003), 239–253 (2003)
4. Marko, J., Thambiratnam, D., Perera, N.: Study of viscoelastic and friction damper configurations in the seismic mitigation of medium-rise structures. J. Mech. Mater. Struct. **1**(6) (2006)
5. Hejazi, F., Noorzaei, J., Jaafar, M.S., Thanoon, W., Ali, A.A.A.: Optimization of active variable stiffness system for controlling structural response of a building under earthquake excitation. J. Struct. Eng. **36**(4), 235–244 (2009)

6. Hejazi, F., Kojouri, S.J., Noorzaei, J., Jaafar, M.S., Thanoon, W.A., Abang Abdullah, A.A.: Inelastic seismic response of RC building with control system. Key Eng. Mater. **462–463**, 241–246 (2009)
7. Constantinou, M.C., Soong, T.T, Dargush, G.T.: Passive energy dissipations system for structural design and retrofit, monograph no. 1. Multidisciplinary Centre for Earthquake Engineering Research, Buffalo, NY (1998)
8. Abbas, H., Kelly, J.M.: A methodology for design viscoelastic dampers in earthquake—resistance structures. Report no. UCB/EERC 93/09, Earthquake Engineering Research centre, University of California at Berkeley (1993)
9. Constantinou, M.C., Sigaher, A.N.: Energy dissipation system configurations for improved performance. In Proceeding of the 2000 Structures Congress and Exposition, ASCE, May 8–10, 2000, Philadelphia, PA (2000)

Part II
Geospatial Engineering

Identification of Geomorphic Anomaly and Morphotectonic Signature to Study the Seismotectonic Activity and Its Impact on Infrastructure Development Through Integrated Remote Sensing and GIS Techniques

Snehasish Ghosh and Ramamoorthy Sivakumar

Abstract The anomalous nature of basin morphological characteristics produces significant geomorphic anomaly which is the indicator of seismotectonic activity. In recent years, the increasing frequency of earthquakes and subsequent damages to infrastructures in Indian sub-continent reveal to study the seimotectonic earthquake. Hence, the present research focuses to identify the geomorphic anomaly and morphotectonic signature to study the seismotectonic activity and its impact on infrastructure development through integrated remote sensing and GIS techniques. The various geomorphic indices have been computed and superimposed curves have been analysed to identify the geomorphic anomaly. Also, the morphotectonic features have been recognized by analysing satellite images and field observation data to find out the active tectonic signature. Finally geomorphic anomaly and morphotectonic signature have been integrated to study the seismotectonic activity and compared with existing infrastructures to understand its seismic vulnerability. The analysis reveals that the neotectonic deformations, drainage anomaly, elongated basin, tilted surface and structural influence are the major geomorphic anomaly and significant evidences for seismotectonic activity in the study region. The various morphotectonic signatures such as narrow valley, knick point, alluvial terraces, triangular facets, river meander in resistance surface and uplifted topography are the great signatures of seismotectonic activity. The various infrastructures such as heritage, educational, private, administrative, residential buildings, communication bridges and roads have been

S. Ghosh (✉) · R. Sivakumar
Earthquake Research Cell, Faculty of Engineering and Technology, SRM Institute of Science and Technology, Kattankulathur, India
e-mail: snehasishghosh.s@ktr.srmuniv.ac.in; snehasishghosh.s10@gmail.com

R. Sivakumar
e-mail: sivakumar.r@ktr.srmuniv.ac.in

S. Ghosh · R. Sivakumar
Department of Civil Engineering, Faculty of Engineering and Technology, SRM Institute of Science and Technology, Kattankulathur, India

developed in various towns which are associated with significant geomorphic anomaly and morphotectonic features are more vulnerable during seismic activity. Also, the seismic retrofitting techniques have been suggested for existing infrastructures to protect them during seismic activity.

Keywords Geomorphic anomaly · Morphotectonic signature · Seismotectonic activity, infrastructures · Remote sensing and GIS

1 Introduction

Seismotectonic zones are recognized along the active faults which may be displaced due to continued deformation of rock masses and associated with frequent occurrences of earthquake and significant magnitude [1]. Most of the time, deformation of rock produces cracks and fractures in the subsurface along which displacement takes place [2]. The movement of faults in recent geological period resembles with significant geomorphic anomaly [3, 4]. The analysis of morphometric parameters can identify geomorphic anomaly which is the key indicators of seismotectonic activity [5–7]. Several researchers have studied different morphometric parameters for the identification of geomorphic anomaly. Mahmood and Gloaguen [8] have analysed hypsometric integral, stream-length gradient index, fractal dimension, basin shape index, valley floor width-to-height ratio to identify the geomorphic anomaly and active tectonic significance in Hindu Kush region. Similarly, Shukla et al. [9] have studied different morphotectonic parameters of Alakananda river basin for investigating past seismic evidences. The drainage morphometry has been also studied to find out the Geomorphic Signatures of Active Tectonics in drainage basins in the Southern Bolkar, mountain region [10]. Further, Bahrami [11] have discussed hierarchal anomaly index, asymmetry factor, basin shape, geomorphic parameters for identifying drainage system anomaly of Zagros basins.

The evidences of active tectonics have been also identified from tectonic geomorphic landforms. Jami et al. [12] have studied neotectonic evidences along the Gourband fault and found fault scarps and channel displacements which are important geomorphologic indicator for active tectonics. Similarly, Chen et al. [13] have identified geomorphic evidences of surface rupture, fault scarps, terraces for recent tectonics. The investigation of geomorphic evidences towards active tectonic in Wheeler Ridge, California have identified wind gap, fault scarp which are the important geomorphic evidences of tear faults [14]. Fault scarp, narrow valley and triangular facets have also been traced along the active faults in the Himalayan foothill by investigating Quaternary deformation along the North-Western Himalayan Frontal Zone, India [15].

In order to secure lives and properties from seismic disaster, the performance of the structures must be improved and thus it is required to design of seismic retrofitting structures for various existing infrastructures [16]. Nishikawa et al. [17] have proposed seismic retrofitting techniques for steel bridge columns to further

improve the seismic performance of steel column from compressive axial and cyclic lateral loads. The suitable reinforced concrete piers seismic retrofitting structures have been adopted for highway road in Japan [18]. Also, the seismic retrofitting techniques have been used to protect existing RC frame buildings from medium to high seismic activity [19, 20]. Further, Shakya et al. [21] recommended suitable retrofitting techniques of the ancient heritage of Nepalese Pagoda temples in Himalayan terrain. Similarly, Lignola et al. [22] also proposed a method of seismic retrofitting to protect adequately historical structures and artistic assets. In recent days, glass fibre-reinforced polymer (GFRP) has been globally endorsed to develop seismic retrofitting structure for traditional masonry walls, beam and columns to restore the functionality of deteriorated concrete frame [23].

Geoinformatics is the significant technique which has a capability to store huge number of databases and can analyse the spatial data for identifying geomorphic anomaly towards seismotectonic activity [24, 25]. The analysis of geomorphic anomaly is based on the quantitative measurement of morphometric parameters and identification of morphotectonic signature which can be derived from topographic maps, digital elevation data, aerial photographs, satellite images and fieldwork [3, 26]. In the past, the topographical map and aerial photograph have been used for morphotectonic analysis [27] while with the advancement of satellite remote sensing, digital elevation data (DEM) and satellite images have been endorsed for the identification of geomorphic anomaly and morphotectonic signature [8, 9].

In recent geological period, the increasing frequency of earthquakes and its subsequent damages to infrastructures in Himalayan region of Indian sub-continent reveals the essentiality to study the seimotectonic earthquake. Hence, the main aim of the present research is to identify the geomorphic anomaly and morphotectonic signature by the analysis of morphometric parameters for better understanding the seismotectonic activity and its impact on existing infrastructures in the study area through integrated remote sensing and GIS techniques. Also recommendations have been given by integrating geospatial and field observation data to further improve the strength of infrastructures.

2 Study Area

The Lower Tista sub-basin is selected as a study area which is a part of Brahmaputra basin. Tista is the major river in the study area which flows in south and south-east direction and joins with many numbers of tributaries. The tributaries in upper course are Rangit, Dik chhu, Rani khola, Rill, Rathong chhu while in lower course Gish, Lish, Chel, and Dharla are the major tributaries. Physiographically, it belongs to a part of Himalayan mountain and peneplain surface. The study area has been divided into 24 micro-basins on the basis of major segmentation of drainage network as shown in Fig. 1.
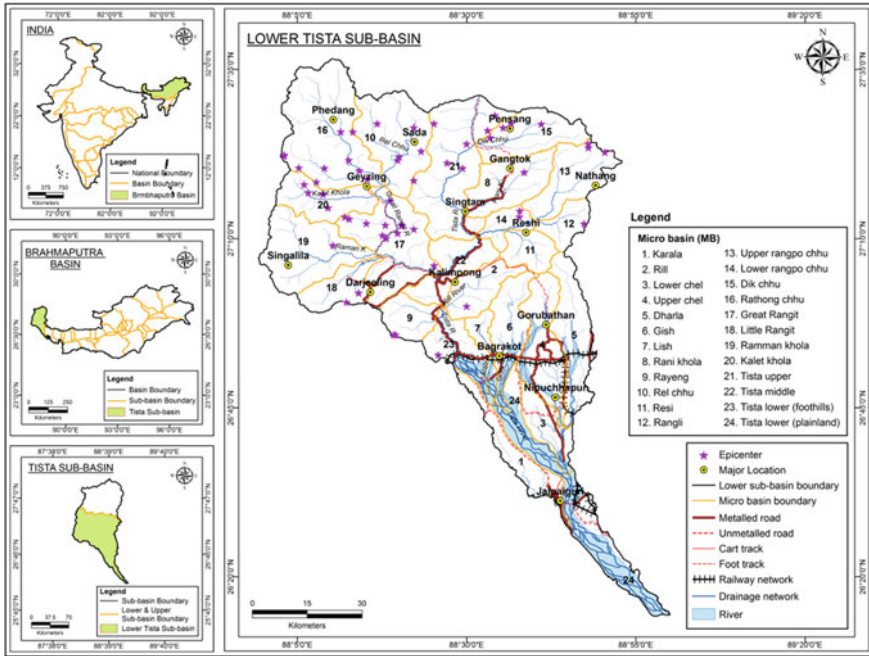
Fig. 1 Location map of the study area

3 Geology and Seismotectonic Characteristics

The database of geological formation has been prepared using geological and mineral maps of Sikkim and West Bengal [28, 29] (Fig. 2a). Kanchenjunga gneiss, Chunthang, Kanchenjunga augen gneiss and Cainozoic formations are found in the Greater Himalayan sequence. These formations are covered mainly in Kallet khola, Rathong chhu, Rel chhu, Ramman khola micro-basin whereas the major rock types are Biotite Gneiss, Sillimanite, Granite gneiss and Mica schist.

Gorubathan formation is the dominant geological formation in the Lesser Himalayan sequence which is found in the central part of study region covering maximum portion of Tista upper, middle micro-basin and lower Rangpo chhu micro-basin. Further, Buxa, Reyang, Ranjit pebble slate group, Damuda, Lingtse gneiss, Phuentsholling formations are enclosed in Ramgarh thrust region in this sequence. The Siwalik groups of formations are recognized in lower Tista (foothills), Gish and Lish micro-basin region which consist of fine to medium pebble sediments, sandstone, conglomerate and shale. The Baikunthapur, Chalsa and Matiali formation are the quaternary group of formations which have originated in very recent geological period occupying the micro-basin of Karala, Tista lower (plainland), Gish, Lish, Dharala, Karala upper and lower Chel.
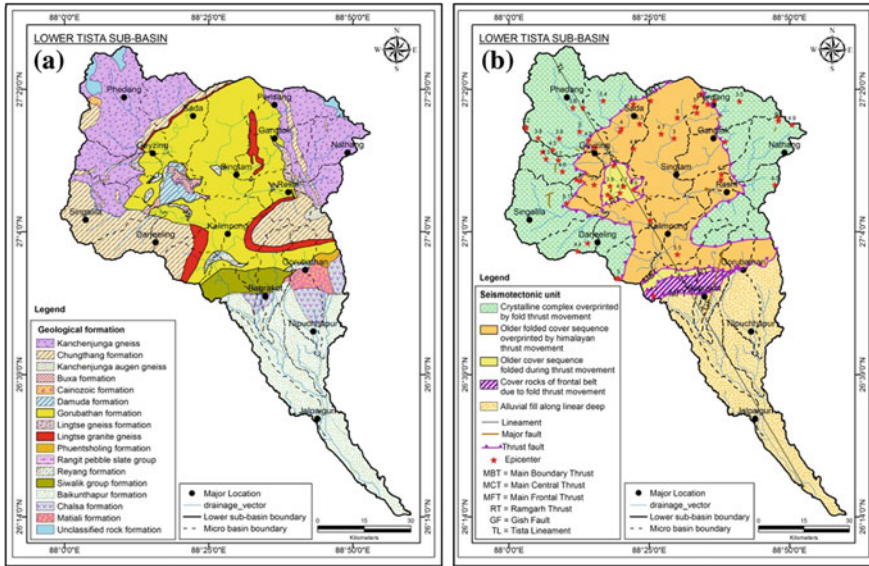
Fig. 2 **a** Geological formation. **b** Seismotectonic characteristics

Seismotectonic database has been prepared using seismotectonic atlas of India [30] and updated with seismological data (Fig. 2b). Crystalline complex is observed in Rathong chhu, Rel chhu, Kalet khola and Rangali micro-basin. Older folded cover sequence is separated from crystalline complex by MCT which covers the micro-basin of Tista upper, Tista middle, Rel chhu and Klalet khola. Older cover sequence folded during thrust movement in Great Rangit micro-basin and partially in upper part of Lish, Tista lower (foothills) and middle portion of Gish micro-basin area surrounded by Ramgarh thrust (RT). Alluvial fill along with linear deep tectonic unit is extended in Karala, Tista lower (plain land), Lower Chel, lower portion of Dharla, Lish Gish and upper chel below MFT.

4 Materials and Methods

In the present study, three stages methods have been adopted as shown in the flow chart (Fig. 3). These stages are data acquisition, identification of geomorphic anomaly and active tectonic signature and impact of seismotectonic activity on existing infrastructure.

4.1 Data Collection

In the present study, various spatial and non-spatial data have been acquired from different sources for geodatabase generation and analysis. The topographical map
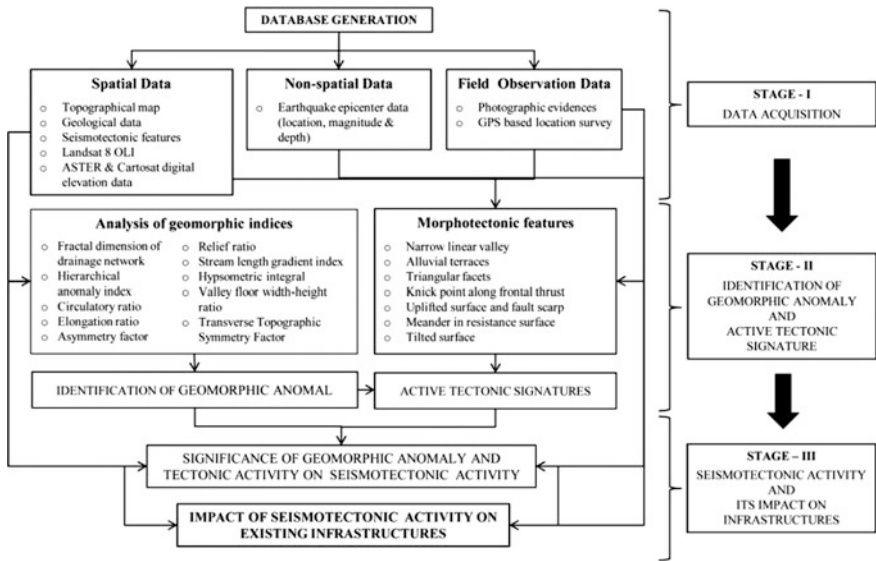
Fig. 3 Flow chart of methodology

has been collected from Survey of India (SOI) while Geology and seismotectonic data have been collected from the Geological Survey of India (GSI). The elevation data such as ASTER and Cartosat DEM have been collected from USGS earth explorer and NRSC Bhuvan respectively to retrieve elevation and surface drainage for the analysis of geomorphic anomaly. In addition, Landsat 8 OLI satellite image has been acquired from USGS Earth Explorer to identify the morphotectonic features in the study area. The seismological data mainly hypocenter distance and magnitude of epicenters have been acquired for the period between 1964 and 2015 from various published seismological catalogues.

The GPS based location survey and photographic evidences of morphotectoic features with existing infrastructures have been collected during field study.

4.2 Computation of Geomorphic Indices

4.2.1 Fractal Dimension of Drainage Network

The drainage patterns always represent irregularities and produces fractal nature in its courses which is defined as the ratio between natural logarithmic of bifurcation ratio and stream-length ratio [8] as shown in Eq. (1).

$$FD = \frac{\ln BR}{\ln SLR} \qquad (1)$$

where, *FD* is Fractal dimension of drainage network, *BR* is bifurcation ratio, *SLR* is stream-length ratio.

4.2.2 Hierarchical Anomaly Index

The drainage network follows a hierarchical order which produces the sequence of $1 \rightarrow 2$, $2 \rightarrow 3$ and $3 \rightarrow 4$ junctions whereas stream hierarchical anomalies occurs while the stream order produces the anomalous stream junction of $1 \rightarrow 3$, $1 \rightarrow 4$, $2 \rightarrow 4$, etc. which is the indicator of tectonic activity [11]. Hierarchical anomaly index is defined as the ratio between hierarchical anomaly number of whole basin and total number of first-order stream as given in Eq. (2) to measure the degree of perfectness of drainage hierarchical order.

$$HAI = \frac{Ha_{\mathrm{n}}}{\sum N_{\mathrm{so1}}} \qquad (2)$$

where, *HAI* is the hierarchical anomaly index; $\sum N_{\mathrm{so1}}$ is total number of first order stream; Ha_{n} is hierarchical anomaly number of whole micro-basin.

4.2.3 Geometry of River Basin

The geometry of river basin explains the different shapes of drainage basin which depends on main stream length, basin perimeter and area. The basin shapes are controlled by active tectonic process [27] and produces different indices.

Circulatory ratio is expressed as the ratio of basin area to the area of circle having circumference equal to the perimeter of the basin [8] as show in Eq. (3).

$$CR = \frac{4\pi A_{\mathrm{b}}}{P_{\mathrm{b}}^2} \qquad (3)$$

where, *CR* is Circulatory ratio; A_{b} is Area of the basin, P_{b} is Perimeter of the basin.

Elongation ratio is defined as the ratio between the diameter of the circle having equal area to the basin and the longest length of the basin [8] as shown in Eq. (4).

$$ER = \frac{2\sqrt{\frac{A_{\mathrm{b}}}{\pi}}}{L_{\mathrm{b}}} \qquad (4)$$

where, ER is Elongation ratio, A_{b} is basin area, L_{b} is the longest length of basin.

4.2.4 Transverse Topographic Symmetry Factor

Transverse Topographic Symmetry Factor is defined as the ratio between the distance of basin midline to drainage midline and distance of basin midline to basin divide [5] and expressed in Eq. (5).

$$TTSF = \frac{D_a}{D_d} \tag{5}$$

where, *TTSF* is Transverse Topographic Symmetry Factor, D_d is distance of basin midline to basin divide, D_a is distance of basin midline to drainage midline.

4.2.5 Asymmetry Factor

The asymmetry factor (AF) is the measurement of tectonic tilt of a drainage basin [3, 8] which is the ratio of right side area of the basin towards downstream to the total area of the basin as shown in Eq. (6).

$$AF = \frac{A_r}{A_t} \tag{6}$$

where, *AF* is Asymmetry factor, A_r is right side area of the basin of a downstream facing river, A_t is total area of the drainage basin.

4.2.6 Relief Ratio

Relief ratio is defined as the ratio between local reliefs to longest length of the basin [9] as shown in Eq. (7).

$$RR = \frac{E_{max} - E_{min}}{L_b} \tag{7}$$

where, *RR* is Relief ratio, E_{max} is maximum elevation of the basin, E_{min} is minimum elevation of the basin, L_b is longest length of the basin.

4.2.7 Stream-Length Gradient Index

The stream-length gradient index is defined as the ratio between elevation and length difference in a reach around the selected measure point to the multiplication with length of the river from source to measure point [8] as expressed in Eq. (8).

$$SLGI = \frac{\Delta h}{\Delta l} \times L_s \tag{8}$$

where, *SLGI* is Stream-length gradient index, Δh is changes in elevation of the reach around the selected point A, Δl is length of the channel in between the selected elevation contour, L_s is longest length of the channel from the drainage divide to the selected point of the reach.

4.2.8 Hypsometric Integral

Hypsometric integral is defined as the ratio of mean and minimum elevation differences to local relief [9] as expressed in Eq. (9).

$$HI = \frac{E_{\text{mean}} - E_{\text{min}}}{E_{\text{max}} - E_{\text{min}}} \tag{9}$$

where, E_{max} is maximum elevation, E_{min} is minimum elevation and E_{mean} is mean elevation of the basin.

4.2.9 Valley floor width-height ratio

Valley floor width-to-height ratio is defined as the ratio of twice width of valley floor to the addition of left and right side valley height difference from valley floor [8] as shown on the Eq. (10).

$$VFWHR = \frac{2W_{\text{f}}}{(E_{\text{ls}} - E_{\text{vf}}) + (E_{\text{rs}} - E_{\text{vf}})} \tag{10}$$

where, *VFWHR* is valley floor width–to-height ratio, W_{f} is width of the valley floor, E_{ls} is left side elevation of the valley divides, E_{rs} is right side elevation of the valley divides, E_{vf} is elevation of the valley floor.

5   Results and Discussions

5.1   Analysis of Geomorphic Anomaly and Its Seismotectonic Relation

The geomorphic anomaly has been identified by the analysis of morphometric parameters as shown in (Fig. 4; Table 1,2). The result shows that the hierarchical anomaly index (HAI) curve have significant peak and average fractal dimension of drainage network (AFDDN) curve have anomalous trough in Great rangit, Tista upper and Lish micro-basin (Fig. 4a) which indicates anomalous drainage network, structural influence on drainage development, intense neotectonic deformation [8, 11]. Similarly, asymmetry factor (AF) and average transverse topographic
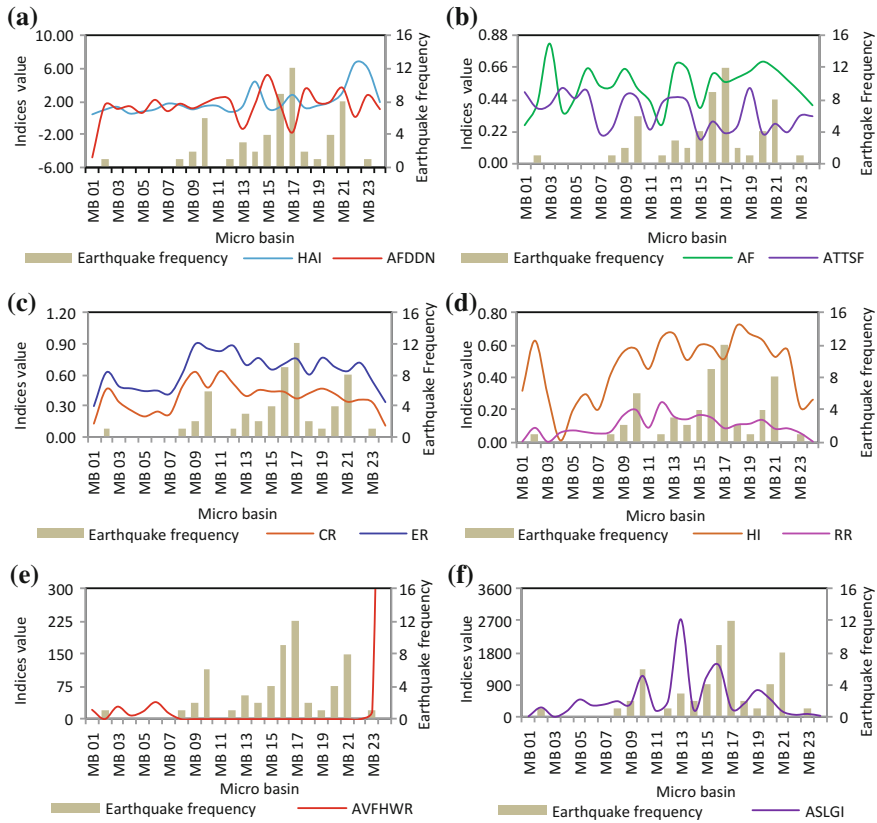
Fig. 4 Identification of seismotectonic evidences through geomorphic and morphotectonic anomaly

symmetry factor (ATTSF) curve shows significant peak in Gish, Raying, Lower rangpo chhu, Upper chel and Karala micro-basin micro-basin (Fig. 4b) which signifies an evidence of tectonic tilt. Further, Elongation ratio (ER) and Circulatory ratio (CR) curve represents anomalous trough in Karala, Lower and Upper chel, Dharala, Gish and Lish micro-basin in the foothills zone (Fig. 4c) signifying the presence of structurally controlled elongated basin which may evolve due to tectonic compression [9]. It is also observed that Rill, Rel chhu represents significant higher value and peak in Hypsometric integral (HI) and Relief ratio (RR) curve (Fig. 4d) which signifies steepness of relief, the presence of more resistant rock with less erosion, Youthful topography indicating high tectonic activity [3, 8]. The significant peak in Avg. Stream-length gradient index (ASLGI) curve with higher value (Fig. 4e; Table 2) and anomalous trough with lower value in average valley floor width-height ratio (AVFWHR) curve are observed in Rel chhu, upper rangpo chhu, Dik chhu and Rathong chhu micro-basin (Fig. 4f; Table 2) indicating the presence of high resistant hard rock with narrow valley [8, 9].

Table 1 Computation of linear and areal morphometric parameters

MB code	Micro-basin name	AFDDN	HAI	CR	ER	AF	ATTSF
MB 01	Karala	−4.80	0.43	0.13	0.30	0.26	0.49
MB 02	Rill	1.55	0.99	0.46	0.63	0.41	0.38
MB 03	Lower Chel	1.09	1.34	0.34	0.49	0.83	0.40
MB 04	Upper Chel	1.42	0.53	0.25	0.47	0.36	0.52
MB 05	Dharla	0.61	0.78	0.20	0.44	0.45	0.45
MB 06	Gish	2.19	1.02	0.25	0.45	0.65	0.50
MB 07	Lish	0.82	1.74	0.22	0.42	0.53	0.21
MB 08	Rani khola	1.72	1.57	0.49	0.62	0.53	0.25
MB 09	Rayeng	1.16	1.03	0.63	0.90	0.65	0.47
MB 10	Rel chhu	1.80	1.44	0.48	0.85	0.52	0.45
MB 11	Resi	2.42	1.46	0.64	0.83	0.43	0.23
MB 12	Rangli	2.19	0.73	0.52	0.88	0.27	0.42
MB 13	Upper Rangpo chhu	−1.34	1.36	0.40	0.70	0.68	0.46
MB 14	Lower Rangpo chhu	1.64	4.42	0.45	0.76	0.65	0.43
MB 15	Dik chhu	5.22	1.20	0.44	0.65	0.38	0.17
MB 16	Rathong chhu	1.72	1.32	0.44	0.71	0.62	0.29
MB 17	Great Rangit	−1.78	2.80	0.37	0.76	0.56	0.21
MB 18	Little Rangit	3.50	1.22	0.42	0.60	0.59	0.26
MB 19	Ramman khola	1.88	1.49	0.47	0.77	0.64	0.52
MB 20	Kalet khola	1.95	1.89	0.42	0.68	0.70	0.21
MB 21	Tista upper	3.67	3.08	0.34	0.64	0.65	0.27
MB 22	Tista middle	0.12	6.68	0.36	0.72	0.57	0.22
MB 23	Tista lower (foothills)	2.78	6.10	0.33	0.53	0.49	0.33
MB 24	Tista lower (plainland)	1.05	1.91	0.11	0.34	0.40	0.33

The seismological study reveals that the higher frequency of earthquake is observed in Kalet khola and Rathong chhu and Great rangit micro-basin where AF, ATTSF, RR, HI, AVFWHR, ASLGI parameters have greater influence. The study suggests that the tectonic tilt and stream migration, steep high resistance narrow valley, youthful topographic surface are the signatures for seismotectonic activity in these micro-basins. Micro-basin located in the foothills zones which have not resembles with any strong earthquake in the recent past shows symbolic geomorphic and morphotectonic anomaly indicating seismotectonic activity.

5.2 Morphotectonic Signature and Its Seismotectonic Significance

The different tectono-geomorphic landforms have been identified by integrating satellite images and field observation data to identify the morphotectonic signature

Table 2 Computation of relief morphometric parameters

MB code	Micro-basin name	RR	HI	AVFWHR	ASLGI
MB 01	Karala	0.003	0.32	21.61	21.11
MB 02	Rill	0.087	0.63	0.20	270.20
MB 03	Lower Chel	0.001	0.29	28.76	11.62
MB 04	Upper Chel	0.057	0.01	8.67	161.85
MB 05	Dharla	0.071	0.20	17.46	490.91
MB 06	Gish	0.061	0.30	39.25	328.53
MB 07	Lish	0.052	0.20	14.22	356.37
MB 08	Rani khola	0.064	0.42	0.08	445.41
MB 09	Rayeng	0.165	0.56	0.15	350.59
MB 10	Rel chhu	0.198	0.58	0.07	1154.96
MB 11	Resi	0.088	0.45	0.08	185.96
MB 12	Rangli	0.245	0.64	0.07	456.36
MB 13	Upper Rangpo chhu	0.157	0.67	0.08	2741.17
MB 14	Lower Rangpo chhu	0.140	0.51	0.12	218.74
MB 15	Dik chhu	0.167	0.60	0.07	1106.64
MB 16	Rathong chhu	0.149	0.59	0.10	1454.35
MB 17	Great Rangit	0.085	0.51	0.09	236.79
MB 18	Little Rangit	0.107	0.72	0.12	379.27
MB 19	Ramman khola	0.112	0.67	0.07	755.22
MB 20	Kalet khola	0.136	0.63	0.12	519.67
MB 21	Tista upper	0.081	0.53	0.07	161.52
MB 22	Tista middle	0.084	0.57	0.08	64.72
MB 23	Tista lower (foothills)	0.055	0.21	19.09	88.13
MB 24	Tista lower (plainland)	0.002	0.26	1659.53	36.66

and its importance on seismotectonic activity. The important feature like Knick point which reveals sudden break in channel gradient along the fault plane is observed along the frontal surface of the Tista lower (foothills), Lish, Gish, Upper chel and Dharala micro-basin region. The drainage pattern has been changed from dendritic to linear along the knick point (Fig. 5a, a′) which reveals the deviation of river longitudinal profile implying tectonic upliftment in the dynamic river system.

The presence of terraces at different levels in alluvial surface indicates past evidence of channel shift and continuous upliftment of the terrain [31]. It is observed in Tista lower, Lish, Gish micro-basin region (Fig. 5b, b′). The occurrence of alluvial terraces in various levels in the alluvial surface signifies the neotectonic deformation and presence of active faults.

Narrow valley in the micro-basin of Tista lower, Upper chel, Lish, Gish is observed in the Himalayan foothills zone while it becomes much wider in the plain land (Fig. 5c, c′). The influences of frontal and main boundary thrust are significant in this region.
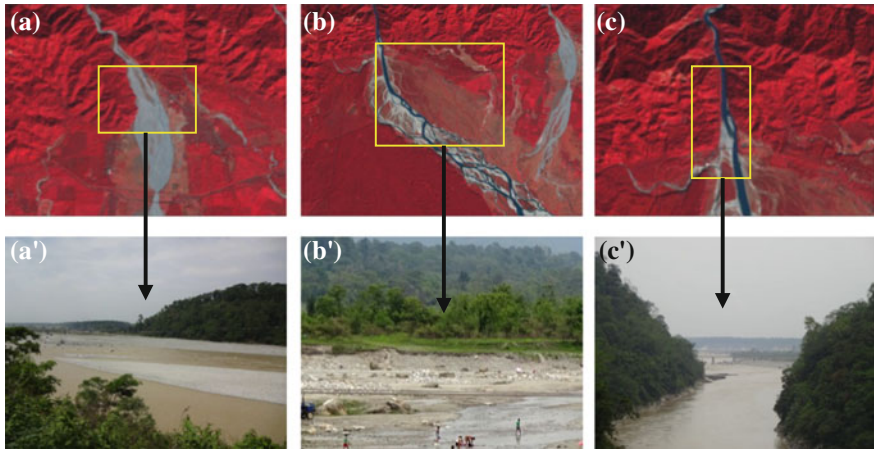
Fig. 5 Morphotectonic signature—**a**, **a′** knick point; **b**, **b′** neotectonic deformation; **c**, **c′** narrow linear valley along MFT

Compressed meander in river course is observed in resistance Himalayan surface (Fig. 6a, a′) which is the significant morphotectonic features in the study area. It is found that the little Ranjit, Great Rangit and Tista river produces more number of meander belts along their courses which have been segregated by numerous fault and lineament. The meander belt in resistance surface originated due to tectonic compression of thrust fault.

Fault scarp is formed due to tectonic force along the MFT (Fig. 6b, b′). It is a steep slope caused by the faulting of crustal rocks [32]. It is observed along the river
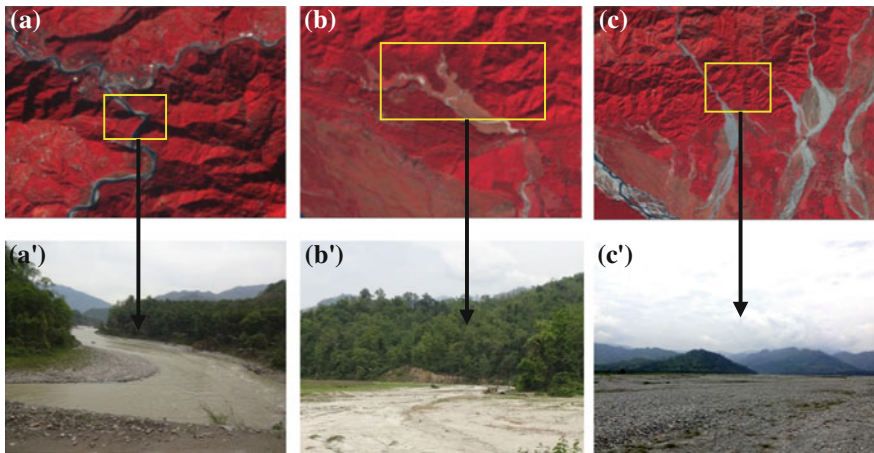
Fig. 6 Morphotectonic signature—**a**, **a′** compressed meander in resistance surface valley; **b**, **b′** fault scarp along MFT; **c**, **c′** triangular facets

basin of Tista, Lish, Gish and Upper chel. The young deformation recorded by fault scarp suggests recent movement and continuous upliftment along the frontal belt [5].

Triangulated facets are the dissected triangular front along the frontal surface (Fig. 6c, c′). It is observed in all foothills micro-basins along the MFT. It is the indicator of surface uplift and the presence of active thrust fault. The height of facets depends on the uplifted rate of elevated surface.

5.3 Impact Assessment of Geomorphic Anomaly and Seismotectonic Activity on Existing Infrastructures and Recommendations

Public and private infrastructures such as hotels, lodges and residential houses are located in different parts of the study area. One of the major towns is Darjeeling which is located in the transition zone of Great and Little Rangit micro-basin (Fig. 7a). Neotectonic deformation, anomalous drainage network and compressed meander in resistance surface are major geomorphic anomaly in this region. The field observation shows that the column and beam framed concrete structures are built in this region without any strong base which are associated with weak geological surface. It can be improved by adopting steel bracing structures for RC buildings to improve the seismic resistant power of the building [18].

Transportation infrastructures specifically road network is situated in Tista middle micro-basin as shown in Fig. 7b. Anomalous drainage networks and narrow

Fig. 7 Existing infrastructure: **a** settlement in Himalayan terraces, **b** highway in hilly terrain associated with landslide, **c** multi-storied infrastructure in Sikkim, **d** social infrastructure—educational institute, **e** cultural heritage infrastructure, **f** communication bridge on Tista river

valleys are the major active tectonics evidences in this region. The field observation reveals that the roads are located in the elevated steep slope and associated with frequent landslides. It is required retaining wall and jacketing of reinforced concrete or fibre sheets [18] to protect from landsides and seismic activity.

Multi-storied infrastructures have shown in Fig. 7c are located in Rani khola micro-basin region. It is located in Lesser Himalayan sequence where resistance rock, tectonic compression and dissected drainage basin are the significant geomorphic anomaly. The field study shows that the buildings are built with high column frame structure without any strong base. Strong base is required for all buildings in Himalayan region to protect them from crack development and failure during seismic activity [19].

Social infrastructure such as educational institute is located in Tista upper micro-basin region as shown in Fig. 7d. It is also a part of Lesser Himalayan sequence and has greater influence of MCT in eastern side of the study area. This micro-basin resembles with slight tectonic tilt, narrow valley and anomalous gradient index indicating the presence of the significant signature of active tectonics. The field observation reveals that the social infrastructure is built as a multi-storied concrete building supported by columns at base and required GFRP wrapping in columns to make the strong base of the structure [23].

Cultural heritage are observed in Rani khola micro-basin near Gangtok as shown in (Fig. 7e). This region is also a part of lesser Himalayan sequence and associated with frequent earthquake epicenter. Resistance rock, narrow valley with structural controlled, tectonic compression and frequent landslides are the major geomorphic anomaly in this region. Wooden structures can be anchored by metal elements in roofs and floors [21] to protect structures during seismic activity.

Communications bridges are found on the Tista rives as shown in Fig. 7f. It is located in between Siwalik and Quaternary formations which are separated by numerous thrust faults. The elongated basin, uplifted surface, triangular facets, terraces, etc. are the major morphotectonic signature which suggests the region is seismically active. The field study shows that the bridge is supported by columns in both side and probability of column failure during an earthquake. It is required to adopt single- or multi-column bent, fibre wrapping to prevent column during seismic activity [17].

6 Conclusions

In the present research, geomorphic anomaly and morphotectonic signature have been recognized by the analysis of remote sensing and GIS with field observation data. The analysis reveals that Kalet khola, Rathong chhu, Upper Rangpo chhu, Great Rangit micro-basin region shows significant geomorphic anomaly and where frequent earthquake occurrences with significant magnitude are observed. Even though, Lish, Gish, Dharala and other foothills micro-basin shows significant morphotectonic signatures and anomaly have not produced any significant

earthquake in the past. The various infrastructures have been developed in various towns which are associated with significant geomorphic anomaly and morphotectonic features are more vulnerable during seismic activity. The suitable seismic retrofitting techniques have been suggested for various existing infrastructures by considering present geological, seismotectonic conditions with the incorporation of field analysis data to protect infrastructures during seismic activity and also require detail investigation of structural engineering aspects before implementation of the provided suggestions.

References

1. Kuk, V., Prelogovi, E., Dragieevic, I.: Seismotectonically active zones in the Dinarides. Geol. Croat. **53**(2), 295–303 (2000)
2. Delic, M., Radojicic, Z.: Seismicity as a multidimensional stochastic process. In: The 7th Balkan Conference on Operational Research. Bacor 05. Constanta (2005)
3. Keller, E.A., Pinter, N.: Active tectonics. Uplift, and Landscape, Prentice Hall, New Jersey, Earthquakes (2002)
4. Verma, M., Bansal, B.K.: Seismic hazard assessment and mitigation in India: an overview. Int. J. Earth Sci. **102**, 1203–1218 (2013)
5. Cox, R.T.: Analysis of drainage-basin symmetry as a rapid technique to identify areas of possible quaternary tilt-block tectonics: an example from the Mississippi Embayment. Geol. Soc. Am. Bull. **106**(5), 571–581 (1994)
6. Perez-Pena, J.V., Azor, A., Azanon, J.M., Keller, E.A.: Active tectonics in the Sierra Nevada (Betic Cordillera, SE Spain): insights from geomorphic indexes and drainage pattern analysis. Geomorphology **119**, 74–87 (2010)
7. Tsodulos, I.M., Koukouvelas, I.K., Pavlides, S.: Tectonic geomorphology of the easternmost extension of the Gulf of Corinth (Beotia, Central Greece). Tectonophysics **453**, 211–232 (2008)
8. Mahmood, S.A., Gloaguen, R.: Appraisal of active tectonics in Hindu Kush: insights from DEM derived geomorphic indices and drainage analysis. Geosci. Front. **3**(4), 407–428 (2012)
9. Shukla, D.P., Dubey, C.S., Ningreichon, A.S., Singh, R.P., Mishra, B.K., Singh, S.K.: GIS-based morpho-tectonic studies of Alaknanda river basin: a precursor for hazard zonation. Nat. Hazards **71**, 433–1452 (2014)
10. Altın, T.B.: Geomorphic signatures of active tectonic in drainage basins in the Southern Bolkar Mountain, Turkey. J Ind. Soc. Remote Sens. **40**(2), 271–285 (2012)
11. Bahrami, S.: Analyzing the drainage system anomaly of Zagros basins: Implications for active tectonics. Tectonophysics **608**, 914–928 (2013)
12. Jami, M., M-khatib, M., Farimani, M.A., Mehrpouyan, M.: Study on Gourband fault activity on the basis of neotectonic evidences (Northeast of Torbat—e—Jam). Ind. J. Sci. Technol. **5** (11), 3642–3646 (2012)

13. Chen, Y., Chen, W., Wang, Y., Lo, P., Liu, T., Lee, J.: Geomorphic evidence for prior earthquakes: lessons from the 1999 Chichi earthquake in central Taiwan. Geology **30**(2), 171–174 (2002)
14. Karl, M., Talling, P.: Geomorphic evidence for tear faults accommodating lateral propagation of an active fault-bend fold, Wheeler Ridge, California. J. Struct. Geol. **19**(3), 397–411 (1997)
15. Malik, J.N., Nakata, T.: Active faults and related late quaternary deformation along the Northwestern Himalayan Frontal Zone, India. Annal. Geophys. **46**(5), 917–936 (2003)
16. Navya, G., Agarwal, P.: Seismic retrofitting of structures by steel bracings. Proc. Eng. **144**, 1364–1372 (2016)
17. Nishikawa, K., Yamamoto, S., Natori, T., Terao, K., Yasunami, H., Terada, M.: Retrofitting for seismic upgrading of steel bridge columns. Eng. Struct. **20**(4), 540–551 (1998)
18. Ogata, T., Osada, K.: Seismic retrofitting of expressway bridges in Japan. Cem. Concr. Compos. **22**, 17–27 (2000)
19. Mazza, F., Vulcano, A.: Displacement-based design procedure of damped braces for the seismic retrofitting of RC framed buildings. Bull. Earthq. Eng. **13**, 2121–2143 (2015)
20. Sengupta, A.K., Reddy, C.S., Badarinarayanan, V.T., Asokan, A.: Seismic analysis and retrofit of existing multi-storeyed buildings in India-an overview with a case study. In: 13th World Conference on Earthquake Engineering, Vancouver, B.C., Canada, paper no. 2571 (2004)
21. Shakya, M., Varum, H., Vicente, R., Costa, A.: Seismic vulnerability and loss assessment of the Nepalese Pagoda temples. Bull. Earthq. Eng. **13**(7), 2197–2223 (2015)
22. Lignola, G.P., Sarno, L.D., Ludovico, M.D., Prota, A.: The protection of artistic assets through the base isolation of historical buildings: a novel uplifting technology. Mater. Struct. **49**(10), 4247–4263 (2016)
23. McCuaig, L., Reginato, L., Soudki, K.: GFRP retrofit for facades in a Toronto school. Constr. Buil. Mater. **22**, 61–69 (2008)
24. Bhatta, B.: Remote Sensing and GIS. Oxford University Press, New Delhi (2008)
25. Lo, C.P., Yeung, A.K.W.: Concepts and Techniques of Geographic Information System, Upper Saddle River. Prentice Hall, NJ (2007)
26. Venkatesan, A., Jothibasu, A., Anbazhagan, S.: GIS based quantitative geomorphic analysis of fluvial system and implications on the effectiveness of river basin environmental management. In: Ramkumar, M., et al. (eds.) Environmental Management of River Basin Ecosystems, Springer Earth System Sciences (2015)
27. Ramírez-Herrera, M.T.: Geomorphic assessment of active tectonics in the Acambay Graben, Mexican Volcanic Belt. Earthq. Surf. Proc. Land. **23**, 17–332 (1998)
28. GSI.: Geology and mineral resources of Sikkim, Report, Geological Survey of India, West Bengal, Kolkata, (2012)
29. GSI.: Geology and mineral resources of West Bengal, Report, Geological Survey of India, West Bengal, Kolkata (2013)
30. Dasgupta, S., Pande, P., Ganguly. D., Iqbal, Z., Sanyal, K., Venkataraman, N.V., Sural, B., Harendranath, L., Mazumdar, K., Sanyal, S., Roy, A., Das, L.K., Misra P.S., Gupta, H.K.: Seismotectonic Atlas of India and its environs. In: Narula, P.L., Acharyya, S.K., Banerjee, J. (eds.) Special Publication Geological Survey of India, p. 86 (2000)
31. Nakata, T.: Geomorphic history and crustal movements of the foothills of the Himalayas. In: Tohoku University Science Reports, 7th Ser. (Geography), vol. 22, pp. 39–177 (1972)
32. Singh, S.: Geomorphology. Prayag Pustak Bhawan, Allahabad, India (2005)

Quantification of Geomorphic Indices for Identifying Water Retaining Problem in Basaltic Terrain and Preparation of Water Resource Management Plan Through Integrated Remote Sensing and GIS Techniques

Sandeep Mahajan and Ramamoorthy Sivakumar

Abstract Water is an essential resource for the existence of life on earth. The storage capacity of the water depends on the physiography, soil, slope and geomorphic characteristics of the region. The analysis of geomorphic indices can signify the relationship between topographic characteristic and water retaining capacity which helps in identifying the water shortage problem and its solution. Most of the coastal watersheds in Deccan trap region in India face water scarcity problem during non-monsoonal season as they are covered mostly by basaltic hard rock terrain which is less porous in nature. The main focus of the present research is the analysis of geomorphic indices to address the water retaining problem and to suggest water resource management plan through integrated Remote Sensing and GIS techniques. To achieve this goal, the spatial data has been collected from different sources which is incorporated with field observation data. The thematic databases such as geology and geomorphology have been prepared to understand the topographical characteristic of the study area. The various geomorphic indices have been quantified with the help of satellite image and ASTER GDEM in GIS platform. The comparative geomorphic indices curves have been prepared to understand the topographic and geomorphic factors for addressing the water recharge problems. The analysis of geomorphic indices shows that the water retaining capacity is very low in the Upper gad and Janvali sub-watershed due to the influence of hard (Basaltic) rock, steep slope and has greater structural control. Further, hard rock terrain, rugged topography and surface roughness have been observed during field study which has great influence on water retaining capacity.

S. Mahajan (✉) · R. Sivakumar
Department of Civil Engineering, SRM Institute of Science and Technology,
Kattankulathur, India
e-mail: isandeepmahajan@gmail.com

R. Sivakumar
e-mail: sivakumar.r@ktr.srmuniv.ac.in

The suitable artificial recharge techniques have also been suggested for sustainable development of water resource in the study area.

1 Introduction

Water is an essential resource for human being for survival on the earth. The water can be stored either in the form of surface or ground water. The ground water recharge through surface water exchange depends on lithological characteristics, soil properties, geomorphic and morphological variables. The alluvial surface is highly potential for ground water recharge [1] while the hard rock basaltic terrain which is associated with low porosity, impermeable lithology and characterised by massive basalt is not suitable for ground water recharge [2]. The study of water resources potentiality and identification of geomorphic constrains can be helpful for the practical solutions of water recharge in basaltic terrain to conserve it for its sustainable use.

Several researchers have analysed morphometric parameters to investigate the geomorphic constrains for ground water recharge especially in hard rock impermeable terrain. Chandniha and Kansal [3] have investigated hydrological characteristics of sub-watersheds based on the analysis of morphometric parameters using geospatial technique in Piperiya watershed, India. The significance of morphometric parameter has been studied for better understanding the groundwater potentiality in a structurally controlled terrain [4]. Similarly, the morphometric characteristics has been analysed to identify the interrelationship between hydraulic parameters and geomorphologic characteristics for Northern Foreland of Peninsular India using satellite remote sensing and GIS techniques [5]. Also, Chopra et al. [6] have studied morphometric parameters of sub-watersheds in Gurdaspur District, Punjab to understand the relationship between geomorphic constrains and water recharge capability. Similarly, Reddy et al. [7] have discussed about drainage morphological characteristics and its influence on dynamic changes of fluvial landforms for ground water recharge in a basaltic terrain of Central India.

Most of the coastal watersheds in Deccan trap region in India receives high rainfall during monsoon and it drains out to Arabian sea without any adequate groundwater recharge due to lithological and geomorphic constrains which leads to water scarcity problem during non-monsoonal season. Several researchers have identified different factors of water recharge problems based on geophysical survey, geological investigations and physiographic potentiality study [8, 9] while less work has been carried out by investigating drainage morphological characteristics and geomorphic constrains to identify the water recharge problem in basaltic terrain. Hence, the main aim of the present research is the quantification of geomorphic indices and comparative analysis of different morphological curves to address

the water retaining problem in basaltic terrain. Further, several artificial recharge methods have been suggested in the study for sustaining water resource in future.

2 Study Area

The Gad watershed is selected as a study area which is extended between 16°3′ to 16°24′ N latitude and 73°26′–73°57′ E longitude covering a geographical area of ∼ 1001.35 km^2 (Fig. 1). Gad is the major river in the study area which originates from the Sahyadri hills in the east and merges into Arabian Sea in the west. The maximum area involved in Deccan Trap region which is a well-known basaltic hard rock terrain face major problem of water resource during non-monsoonal season.

Physiographically, the region is divided into three divisions which include Sahyadri hill ranges, flat-topped hills and coastal plain. It falls under sub-tropical climatic region and receives sufficient rainfall in Monsoon season which varies between 1500 and 4000 mm. The Gad watershed is segregated into five sub-watersheds namely Upper Gad, Janvali, Middle Gad, Kasal and Lower Gad.
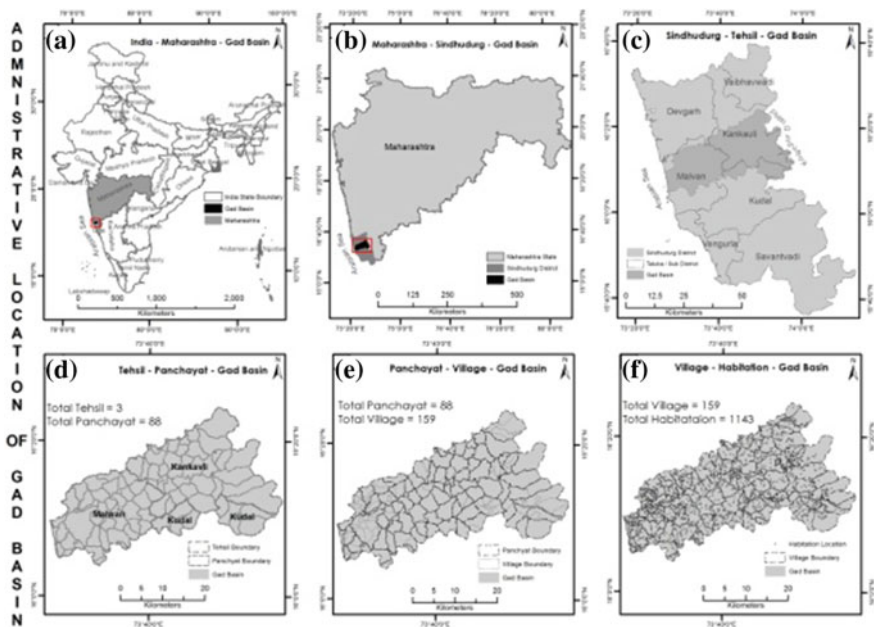
Fig. 1 Location map of the study area

3 Lithology and Geomorphological Set up

Lithological map of study area has been prepared using district resource map published by Geological Survey of India (GSI) with limited field studies (Fig. 2). The study area covered with different rock formations which formed in between Archaean to Quaternary geological period. Upper Gad and Janvali sub - watersheds are dominated by a Meta basaltic rocks, AA flows, Mega cryst flow, Quartz Chlorite Amphibole schist and Granite rocks. Also Shale, quartzite are observed in north eastern part of Janvali sub-watershed while southern part of Upper Gad shows few patches of laterite terrain. Middle gad is covered by Quartzite, Laterite, Schist and minor patches of Meta basalt with AA flows. Quartz Chlorite Amphibole schist is also dominant in Kasal sub-watershed along the river valley while laterite terrain occupies in upper catchment of kasal sub-watershed. Few patches of granite are also recognized in this sub-watershed Region. Lower gad sub-watershed is mainly covered by shale, lateritic rocks and quartz along the river while quartzite is dominant in coastal area the geomorphic map has been prepared using Landsat 8 satellite image and updated with the recent high-resolution Quick Bird satellite imagery with field observation. The study area is divided into different geomorphic unit based on the distribution of sub-watersheds. Coast line, Beach, coastal dunes, coastal plains and Lateritic upland are found in the lower Gad sub-watershed. Pediplain along with alluvial plains, residual hills, undulating lateritic upland and denudational hills are recognized in Middle Gad and Kasal sub-watershed.
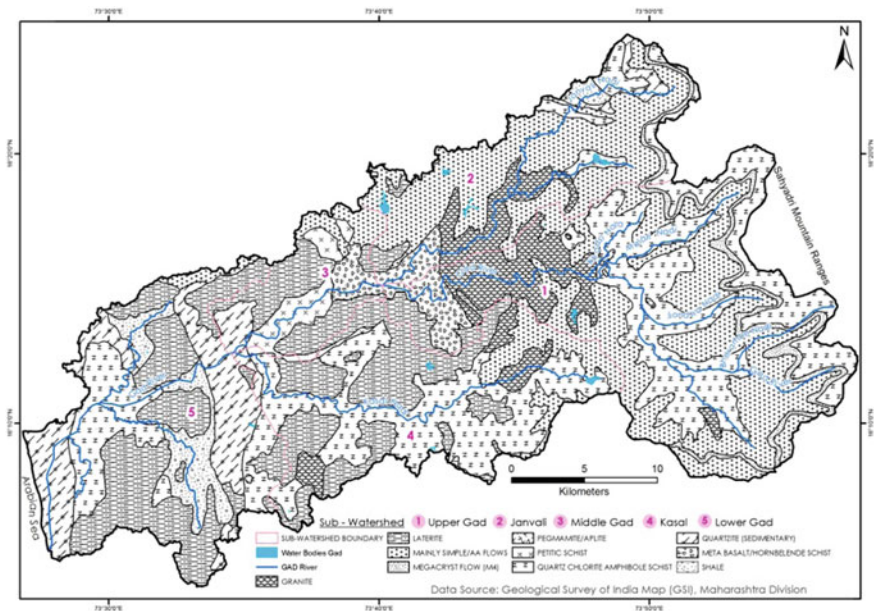
Fig. 2 Geology map of study area
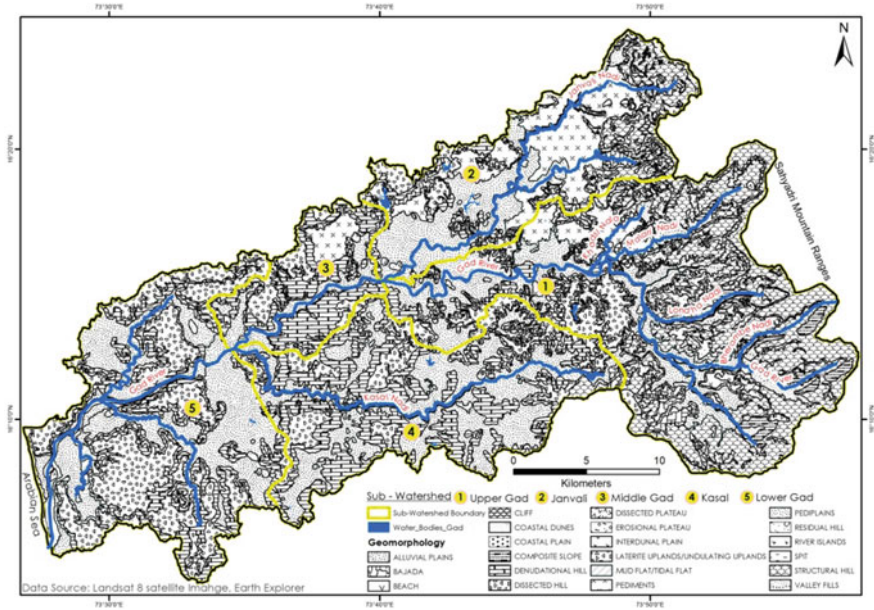
Fig. 3 Geomorphology of the study area

Structural hills, valley fills, cliff, Composite slope, Bajada, Pediplains and pediments are the prominent geomorphological features observed in Upper Gad and Janvali sub-watershed (Fig. 3).

4   Materials and Methods

4.1   Data Collection

The various spatial data has been collected from different source for the preparation of geo-database. Topographical map in the scale of 1:50,000 is acquired from Survey of India (SOI) to extract the basic information of the study area. Landsat 8 (30 m) satellite image has been collected from USGS Earth Explorer for the preparation of thematic database. Also it has been incorporated with high resolution Quick Bird image for better interpretation which has been visually interpreted from Google Earth with available resolution. The elevation data namely ASTERGDEM (30 m) along with Cartosat DEM is procured from USGS earth Explorer and NRSC, ISRO Indian data portal respectively and have been used for the analysis of geomorphic indices. District resource geology map has been collected from GSI (Geological Survey of India) for the preparation of lithological databases. Further,

Field based analysis has been carried out to collect evidences of geomorphic constrains and to identify water retaining problem in the study area.

4.2 Quantification of Geomorphic Indices

Bifurcation Ratio
Bifurcation ratio identifies the segregation of drainage network which is influenced by subsurface lithology and structural features [3, 4]. It is defined as the ratio between number of stream in given order and number of stream in next higher order [10] as expressed in Eq. (1). Mean bifurcation ratio of each sub-watershed has been achieved by computing average bifurcation ratio of different order.

$$R_b = \frac{N_u}{N_u + 1},$$
(1)

where, R_b is bifurcation ratio and N_u is number of stream in given order.

Drainage Density
Drainage density explains the nature of subsurface geological strata and its influence on ground water recharge [5]. It is computed by the total stream length per unit area divided by area of drainage basin 10 as expressed in Eq. (2).

$$D_d = \frac{T_{sl}}{A},$$
(2)

where, D_d is drainage density, T_{sl} is total stream length and A is area of sub-watershed.

Stream Frequency
Stream frequency measures the nature of stream network and the influence of bed rock properties on drainage development [5]. It is defined as the ratio between total number of stream and basin area [11] as shown in Eq. (3).

$$F_s = \frac{T_{ns}}{A},$$
(3)

where, F_s is stream frequency, T_{ns} is total number of stream, A is Area of sub-watershed.

Drainage Texture
Drainage texture explains the infiltration capacity and significant of lithological variables during surface recharge [7]. It is computed with the help of drainage density and stream frequency of the respective sub-watershed [12] as shown in Eq. (4)

$$T = D_d \times F_s \tag{4}$$

T is Drainage texture, D_d is drainage density and F_s is stream frequency.

Length of Overland Flow

Length of overland flow determines the nature of slope and lithological resistance on ground water storage [5]. Overland flow is the reciprocal of twice drainage density [11] as shown in Eq. (5)

$$L_g = \frac{1}{2D_d}, \tag{5}$$

where L_g is length of overland flow and D_d is drainage density.

Form Factor

Form factor determines the nature of surface flow by changing lithological characteristics and surface gradient [6]. It is expressed as the ratio between area and square of longest basin length [11] as mentioned in Eq. (6)

$$F_r = \frac{A}{L_b^2} \tag{6}$$

F_f is form factor, A is area of sub-watershed, L_b is longest length of the sub-watershed.

Relative Relief

Relative relief describes the denudational characteristics in different physiographic regions and its influence on ground water storage [4, 5]. It is the difference between highest and lowest elevation of a particular sub-watershed [13] as shown in Eq. (7)

$$R = H - h \tag{7}$$

R is Relative relief, H is highest elevation and h is lowest elevation.

5 Results and Discussions

5.1 Analysis of Geomorphic Indices for Identifying Water Recharge Problems

The geomorphic indices have been computed and comparative superimposed curves have been prepared to identify the geomorphic constrains for ground water recharge in the study area (Fig. 4; Table 1). The analysis of drainage density, stream frequency, stream texture and relative relief curve shows higher value with significant peak in upper Gad sub-watershed which indicates availability of sufficient surface water while it drains out due to high gradient and higher runoff leading
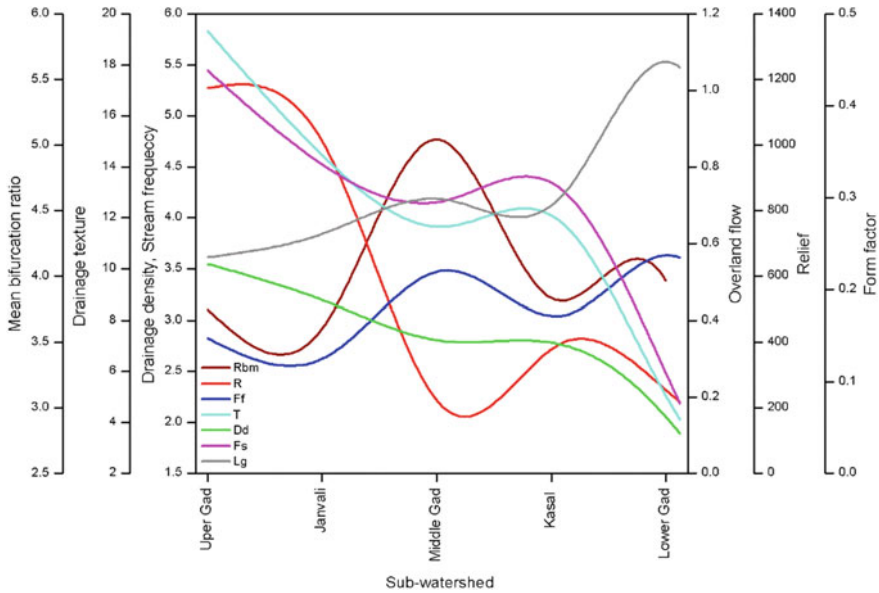
Fig. 4 Comparative morphological curve geomorphic constrains

Table 1 Quantification of morphometric parameters

SW code	Sub-watershed name	R_{bm}	D_d	F_s	T	F_f	L_g	R
SW 01	Upper gad	3.75	3.55	5.45	19.32	0.15	0.56	1173
SW 02	Janvali	3.60	3.18	4.50	14.33	0.13	0.63	992
SW 03	Middle gad	5.04	2.80	4.17	11.65	0.22	0.72	200
SW 04	Kasal	3.83	2.76	4.28	11.81	0.17	0.72	398
SW 05	Lower gad	3.97	1.89	2.18	4.12	0.23	1.06	218

to less water recharge [3]. Similarly, increasing trend in form factor and bifurcation ratio curve and declining trend in overland flow curve are also observed in Upper gad sub-watershed suggesting geological influence and structural control on drainage network in homogeneous basaltic hard rock (Fig. 5a) and maximum surface flow due to higher gradient [3, 4].

Stream frequency, stream texture drainage density, and relative relief curves represent peak with higher value in Janvali sub-watershed reflecting bed rock influence on fine texture drainage which produces higher runoff due to higher altitude. Also, form factor and bifurcation ratio curve shows significant trough with lower value in Janvali sub-watershed indicating sufficient water in river which can not be percolated and stored in the subsurface due to higher peak flow in less time and existence of less permeable [5] lithological structure (Fig. 5b).

Fig. 5 **a** Basaltic impermeable terrain, **b** Lithological resistance structural hills, **c** Piedmont zone, **d** Costal mudflat

Higher peak in bifurcation ratio and form factor curves along with significant trough in relative relief, stream texture and stream frequency curves have been observed in Middle Gad sub-watershed which indicates less influence of bed rock and lack of structural control on drainage network leading to minimum amount of water recharge in laterite and quartz surface [5] while higher slope in impermeable granitic terrain are responsible for high peak flow of drainage water with less infiltration [14].

Further, analysis shows that the relative relief, stream texture and stream frequency curve represent significant peak in Kasal sub-watershed indicating possibility of high runoff and soil erosion due to higher altitudinal variation in plateau region which leads to less water recharge [7]. Similarly form factor, bifurcation curve shows trough with lower value in sedimentary terrain of Kasal sub-watershed indicating higher availability of surface water and less flow in longer duration due to the presence of less resistance with low gradient topography [6].

The declining trend of drainage density, stream frequency, stream texture and relative relief and bifurcation ratio in lower gad sub-watershed indicating structural influence are negligible [14] where poor stream network are developed due to the presence of permeable laterite, shale, quartzite lithological structure. The significant increasing trend in overland flow curve is recognized in the same sub-watershed signifying less surface flow with high rate of infiltration in low gradient coastal mud flat and alluvial plain and pediment surface (Fig. 5c, d).

5.2 Water Resource Management Plan

Ground water recharge mainly depends on the two components namely source water availability and fishable structure to transfer source water into ground water [15]. The analysis of morphological parameters and GIS-based integration study identifies various geomorphological constraints for natural recharge in the study area. Even, geological investigation- and field-based study also shows that the study area is mostly covered by Basaltic hard rock terrain where infiltration is very less and recharge is low. Hence, it is required the preservation/conservation of water in the study region for future use. In this purpose, the following artificial recharge technique can be applied in the study area.

1. Minor irrigation tanks
   Upper gad and Janvali sub-watersheds are mostly involved in hard rock basaltic terrain. Steep slope and impermeable subsurface is not attributing much with surface water as well as ground water for agriculture activities. So the minor irrigation tanks are better option in these areas.
2. Afforestation
   Kasal sub-watershed areas with less vegetation cover should be considered for afforestation to reduce soil erosion and increase the water recharge capacity in the watershed.
3. Spreading method
   Middle Gad and Kasal sub-watershed is mainly flat terrain topography with extensive soil depth in comparison to other parts of study area. This region can be used for making of spreading basins which will help rapid percolation of water to the aquifers.
4. Ground water Dams
   Ground water dams are very effective in the basaltic hard terrain areas where ground water storage at a particular point for use in non-monsoon time when water shortage is at its peak. There is lot of examples in the Gad area for this kind of practices.
5. Nala banding, contour banding, and contour trenching
   In steep slope areas of the watershed these techniques are very important to check the water run off and to reduce the soil erosion.
6. Check dam
   Small check dam can be constructed in the areas of Janvali and Kasal sub-watershed region to reduce soil erosion and to let the water recharge.
7. Percolation tanks
   Percolation tanks can be implemented in the areas where sub surface is suitable for infiltration and bed rock is permeable to compliment the ground water recharge.

6 Conclusion

In the present study, the morphometric parameters have been analysed to address the water retaining problem. The result shows that the water retaining capacity is very low in the Upper gad and Janvali sub-watershed due to the influence of Basaltic rock, steep slope and great structural control. The field observation analysis also shows areas with impermeable lithology, rugged topography, surface roughness and structural control on drainage development which have great influence on water recharge capacity. The various artificial recharge techniques such as minor irrigation tanks, Spreading method, Ground water Dams, Nala banding, Check dam, percolation tanks for sustainable development of water resource.

References

1. Sophocleous.: Interactions between groundwater and surface water: the state of the science. Hydrogeol. J. **10**, 52–67 (2002)
2. Saraf, A.K., Choudhury, P.R.: Integrated remote sensing and GIS for groundwater exploration and identification of artificial recharge sites. Int. J. Remote Sens. **19**(10), 1825–1841 (1998)
3. Chandniha, S.K., Kansal, M.L.: Prioritization of sub-watersheds based on morphometric analysis using geospatial technique in Piperiya watershed, India. J. Appl. Water Sci. **7**(1), 329–338 (2017)
4. Sreedevi, P.D., Owais, S., Khan, H.H., Ahmed, S.: Morphometric analysis of a watershed of South India using SRTM data and GIS. J. Geol. Soc. India. **72**, 543–552 (2009)
5. Yadav, S.K., Singh, S.K., Gupta, M., Srivastava, P.K.: Morphometric analysis of upper tons basin from Northern Foreland of Peninsular India using CARTOSAT satellite and GIS. Geocarto Int. (2014). https://doi.org/10.1080/10106049.2013.868043
6. Chopra, R., Dhiman, R.D., Sharma, E.K.: Morphometric analysis of sub-watersheds in Gurdaspur district, punjab using remote sensing and GIS techniques. J. Ind. Soc. Remote Sens. **33**, 4 (2005)
7. Reddy, G.P.O., Maji, A.K., Gajbhiye, K.S.: Drainage morphometry and its influence on landform characteristics in a basaltic terrain, Central India—a remote sensing and GIS approach. Int. J. Appl. Earth Obs. Geoinf. **6**, 1–16 (2004)
8. Berthold, S., Bentley, L.R., Hayashi, M.: Integrated hydrogeological and geophysical study of depression focused groundwater recharge in the Canadian prairies. Water Resour. Res. **40**, W06505 (2004)
9. Geoffrey, N. D., Healy, R.W., Lorenz, D.L., Nimmo, J.R.: Comparison of local- to regional-scale estimates of ground-water recharge in Minnesota, USA. J. Hydrol. **334**, 231–249 (2007)
10. Horton, R.E.: Drainage basin characteristics. Trans. Am. Geophys. Union, **13**, 350–361 (1932)
11. Horton, R.E.: Erosional development of streams and their drainage watersheds hydro-physical approach to quantitative morphology. Bull Geol. Soc. Am. **56**, 275–370 (1945)

12. Smith, K.G.: Standards for grading texture of erosional topography. Amer. J. Sci **248**, 655–668 (1950)
13. Hadley, R.F., Schumm, S.A.: Sediment sources and drainage watershed characteristics in upper Cheyenne River Watershed. USGS Water Suppl. Paper, **1531-B** (1961)
14. Verstappen, H.T.H.: The applied geomorphology. Int. Ins. Aer. Surv. Earth Sci. (ITC). Enschede (1983)
15. Central Ground Water Board (CGWB): Government of Indian website for list of River basins and sub basins (2016). Available at http://cgwb.gov.in/watershed/cdbhatsol.html. Accessed 21 July 2016

Geospatial Risk Communication and Visualization of Natural Hazards Using Augmented Reality Constructs

S. N. Kundu and Muhammad Nawaz

Abstract GIS-based maps are currently the norm for risk visualization and communication of natural hazards. With advances in geospatial visualization and spatial interface technologies, interactive and dynamic risk visualization is now possible. Augmented reality adds another dimension to realistic visualization of natural hazards like floods and volcanic flows which can be achieved through spatial risk visualization and communication simulations in virtual reality mode. Communicating the knowledge to the most vulnerable communities which are residing in the risk zones is very useful for local stakeholders as they are mostly needful of the adaptation strategies. The current article experiments the use of an Augmented Reality Construct for developing a risk visualization interface, which delivers spatially aware geovisualization simulations. We propose the Augmented Reality Sandbox for educating and engaging the local community through simulated visualization of hazard risk and vulnerability with an aim to achieve holistic learning. This construct has a great potential for developing interactive and location-aware three-dimensional real-world simulations and visualization. We suggest that such applications be more prevalently used as we found it to be more effective than static 3D visualization constructs like hazard maps in communicating the risk potential from natural hazards like floods and volcanic lava flows.

Keywords Geographical information systems · Hazard maps · Augmented reality Risk visualization

S. N. Kundu (✉) · M. Nawaz
Department of Geography, National University of Singapore,
Singapore, Singapore
e-mail: snkundu@gmail.com

M. Nawaz
e-mail: geomn@nus.edu.sg

1   Introduction

Communication and visualization of geospatial risk is an important component of disaster risk management (DRM). The way the risk is visualized and communicated shapes the risk perception and actions in preparedness in response to an imminent disaster. Risk visualization and its effective communication can also influence the intervening decisions all across the disaster management cycle. Geospatial risk communication and visualization, therefore, plays an important role in assimilating the disaster risk and its credibility before the disaster strikes.

Disaster preparedness involves several organizations, which include both government and voluntary agencies alike, which mostly operate with a top-down perspective [1]. Communication of the risk is primarily through non-spatial actionable content addressing the hazard risk with an aim of identifying and informing the vulnerable community. Visualization of the disaster risk is normally a spatial representation of the static or dynamic simulation involving the geospatial analysis of the causative factors.

The risk communication framework (Fig. 1) is an iterative two-way process, where local people convey their needs and concerns to the specialists who address the risk information through spatial modelling and convey the results and associated situations [2]. The information generators or senders are government agencies, universities or research institutions who possess the skills, knowledge, technology and the political mandate to assess the risk and implement the DRM measures. The information receivers are represented by communities, businesses, and individuals who have good knowledge of the local area but lack the understanding of the technicalities involving the severity and scale of impact of the event.

Successful risk communication and visualization depend on the knowledge gap between the specialists and the local people (Fig. 2). In developing nations, this knowledge gap is very wide and is primarily due to the urban–rural setting leading to differential access to education and technology. Specialists, who operate from urban settings, are skilful in the use of technology and tools for hazard risk modelling but unlike local people, lack local knowledge. Local people, on the other

Fig. 1 The risk communication framework [2]
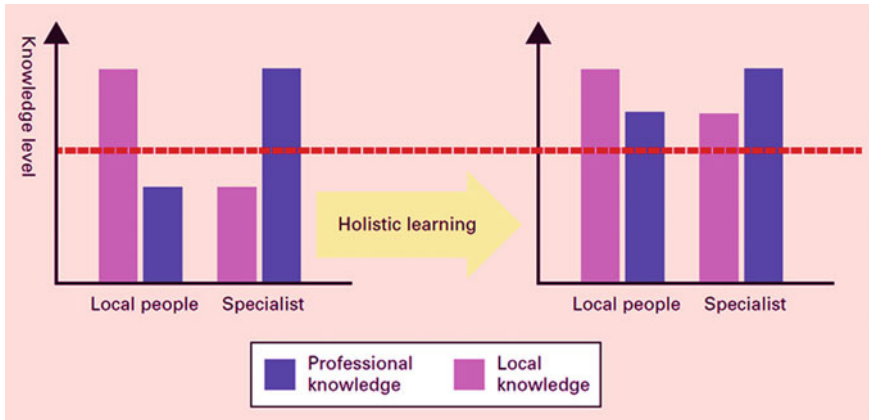
Fig. 2 The concept of holistic learning

hand, have little understanding of the professional expertise needed for under-standing geospatial risk from natural hazards. This gap needs to be addressed for a DRM to be successful. Instruments for risk communication and visualization in the form of hazard maps, booklets and videos, currently are the instruments for holistic learning which attempts to reduce this knowledge gap between specialists and local people.

Affordable Information and Communications Technology (ICT) tools and their increased accessibility to all have provided a means on which holistic learning can be achieved more effectively. Static hazards maps now can be replaced with interactive simulations which are more effective in visualizing disaster risks from natural hazards. Augmented reality (AR) which integrates Virtual reality (VR) with the real world has the potential for effective and enhanced holistic learning. The current chapter looks at the prevalently used instruments for risk visualization and communication and discusses the potential for augmented reality constructs as future risk communication and visualization tool.

2 Disaster Risk Management (DRM)

Disaster Risk Management (DRM) is an integral part of disaster management and primarily consists of four distinct phases (Fig. 3). The first two phases are miti-gation and preparedness, which involves simulation, training or information visu-alization for precautionary steps in the event of a future disaster. The following two phases involve decision-making in response to catastrophe and for restoring the impacted area back to normalcy.

Capacity development is important in DRM. Capacity building equips people, organizations and societies with the requisite capabilities to take effective decisions

Fig. 3 The disaster
management process
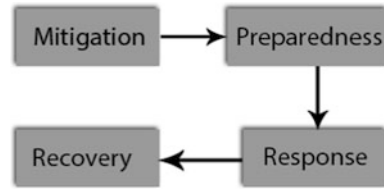
and actions to mitigate the disaster risk. Little formal and empirical research is available on capacity building for disaster risk management (DRM), which mostly resulted from the lack of robust, evidence-based guidance on how the capacity for DRM can be effectively generated at national and local levels.

However, continuous earth observation and geospatial analysis in Geographical Information Systems (GIS) have supported the preparation of hazard maps, where regions are classified based on the risk of exposure and severity of impact in the event of a future disaster.

2.1 Hazard Mapping and Vulnerability Assessment

Vulnerability to natural hazards has many components [3] and its assessment requires ample information that can be analysed in a Geographic Information System (GIS). Digital elevation models are used to characterize geomorphology [4] and serve as a basis for overlaying other information collected from field or satellite platforms. The nature of the threat, its probable occurrence and extent, its intensity and timing, and the sections of society vulnerable are the outputs from geospatial analytical models. Vulnerability to natural hazards is about exposure to various natural disasters. It also depends on its capacity to prepare for, respond to and recover from shocks resulting from natural hazards and extreme events.

The aim of hazard mapping and vulnerability assessment is to produce hazard maps which highlight the areas that are affected by or vulnerable to a particular natural hazard like earthquakes, volcanoes, landslides, flooding and tsunamis. Hazards maps are the de facto instruments for geospatial disaster risk communication and visualization which identify and represent the geospatial aspects of the exposure and severity of a local community. Hazard maps, therefore, are very useful for local people who are in need of adaptation strategies.

2.2 Issues with Hazard Maps

Many countries use hazard maps as a policy and decision-making tool. Hazard maps are used to assess and re-assess the vulnerability of people and property to
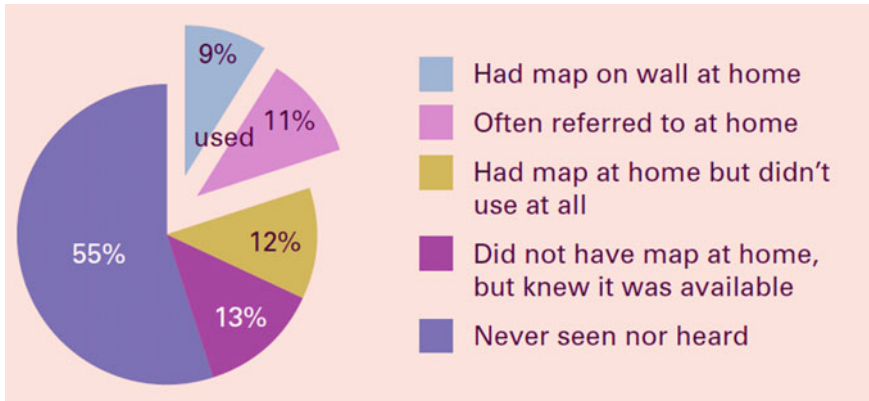
Fig. 4 Usage of hazard maps

natural hazards on a regular basis. The effectiveness of a hazard map depends on its accuracy and, the way it is communicated to local people and on how these maps are understood in a holistic manner.

The major issue with hazard maps is that its usability cannot be determined beforehand. Focus discussion groups and surveyors, local people and other stakeholders provide perceptions of the usability of disaster maps, albeit post the disaster. Although risk information and visualization maps are currently preferred by different decision-makers for risk mitigation activities [5], yet a study in 2011 [6] found that only around 20% local people had effectively used a hazard map and 55% has no idea that such a thing ever existed (Fig. 4).

3 Virtual Reality (VR)-Based Disaster Preparedness

Supported by the advances in information and communications technology, virtual reality-based disaster preparedness is increasingly being recognized as a novel alternative to traditional disaster risk communication and visualization. Virtual reality has long been used as an educational tool in natural science, examples of which are internet based portals for Virtual Field Trips [7], and other handheld devices like headgears and 3D goggles which provide immersive and experiential learning platforms [8–10]. The ubiquity and simplicity of these examples facilitate greater interaction among participants as compared to other traditional or conventional methods. Integration of VR with the real world has led to the birth of Augmented Reality (AR), which provides a more experiential platform and holds great potential for holistic learning especially in disaster management.

3.1 Augmented Reality

Caudell and Mizell [11] coined the term "Augmented Reality (AR)" to describe overlaying computer-generated and computer-presented information onto the real world. AR has been defined as "blending (augmenting) virtual data—information, rich media, and even live action—with what we see in the real world, for the purpose of enhancing the information we can perceive with our senses" [12]. It is a fast emerging technology that augments on top of the real world with continuous and implicit user control of the point of view and interactivity [13]. AR has been successfully used in military, medicine, engineering design, robotics and manufacturing [14] but its potential for smarter disaster management is yet to be realized. In Milgram's reality–virtuality continuum (Fig. 5), AR is founded on the real world with draped virtual components.

3.2 Enabling Technologies

AR utilizes several approaches to integrate the virtual world to the real world which makes use of several developing and emerging technologies. Four such enabling technologies relevant to the development of rich AR applications are positioning technologies, natural user interfaces, connected cloud computing environment and portable mobile devices [16]. Posture and location of objects in three dimensions are enabled by positioning technologies like Global Positioning Systems (GPS). An increasing number of AR applications use gesture and kinesthetic control [17, 18] which are integrated into the natural interfaces users commonly identify with. Size, weight and processor speeds make it more spontaneous and the internet connectivity to rich data enables simulation and interactivity.

4 Augmented Reality Sandbox for Risk Visualization

The Augmented Reality or AR Sandbox is an exhibit which can simulate some land surface processes. Its components include a depth-sensing 3D camera which senses the real-time changes to the sand surface and beams back the computed colour-coded contours via a screen projector. Natural earth processes like
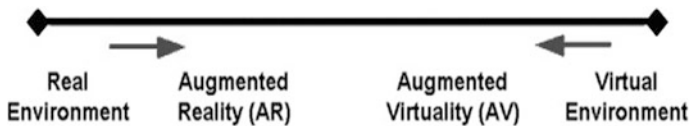
Fig. 5 Milgram's reality–virtuality continuum [15]

precipitation and volcanic flow can be simulated. The intensity of these events and the topography of the sand surface are controlled by the user thereby providing a learner-centric experiential and holistic learning.

4.1 Design

The constraints of the sandbox are based on the projector's projection space and camera's capabilities and specifications. The software behind the computational processes are all open source and hence free for all. Ideally, if all the components are at one's disposal, the AR Sandbox can be prepared in a day's time. Detailed instructions on how to build the AR sandbox is available at the AR sandbox forum available online at https://arsandbox.ucdavis.edu/forums/forum/ar-sandbox-forum/. The schematics of the AR Sandbox is presented in Fig. 6.

4.2 Applications

Supported by availability of online resources on constructing an AR Sandbox [19–22], more than 150 AR Sandboxes have been built in Europe and in the Americas ever since its inception in 2012 (Fig. 7). In 2017, an AR sandbox was built at National University of Singapore (NUS) to impart experiential education to geoscience undergraduates. Most AR Sandboxes in the world are primarily built for providing an experiential visualization of earth processes like precipitation, flooding and volcanic hazards in educational and research setups. It is for the first time that we extend its utility beyond to address holistic learning in disaster risk visualization and communication space.

Fig. 6 The design of the AR sandbox [19]
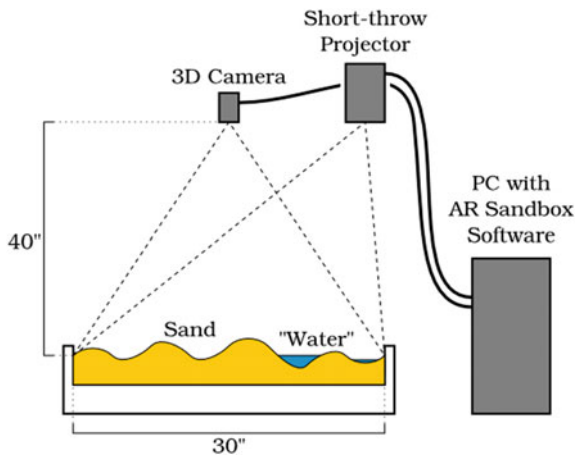
Fig. 7 AR sandboxes around the world (modified from [19])

4.3   Scope for Disaster Risk Visualization

With climate-change and global warming disrupting the precipitation patterns of many places, extreme events like incessant rains are most likely to cause extensive and intense flooding in vulnerable regions. Modelling precipitation and run-off on different topographies are possible in the current version of the AR Sandbox making it ideal for flood risk visualization and communication.

4.3.1   Flood Risk Visualization

Real-world topography of an area can be recreated using a pre-existing digital elevation model in the AR sandbox. On this topographic model, precipitation event with a given intensity and duration can be simulated triggering run-off and floods. The flooded regions in the topography can be visualized and users can see for themselves the impact of such a disaster. The various stages of such a simulation experiment are depicted in Fig. 8. One must note that the construct allows the user to control both the precipitation intensity and duration and the run-off distribution of water which is important in communicating the concept of severity and extent to the less technologically ignorant local people.

4.3.2   Communicating Flood Risk

While the AR sandbox construct facilitates real-time visualization of the flood and volcanic hazards, its practical use as a communication instrument is often challenging because it is heavy ($\sim$100 kg) and therefore not portable. However, such
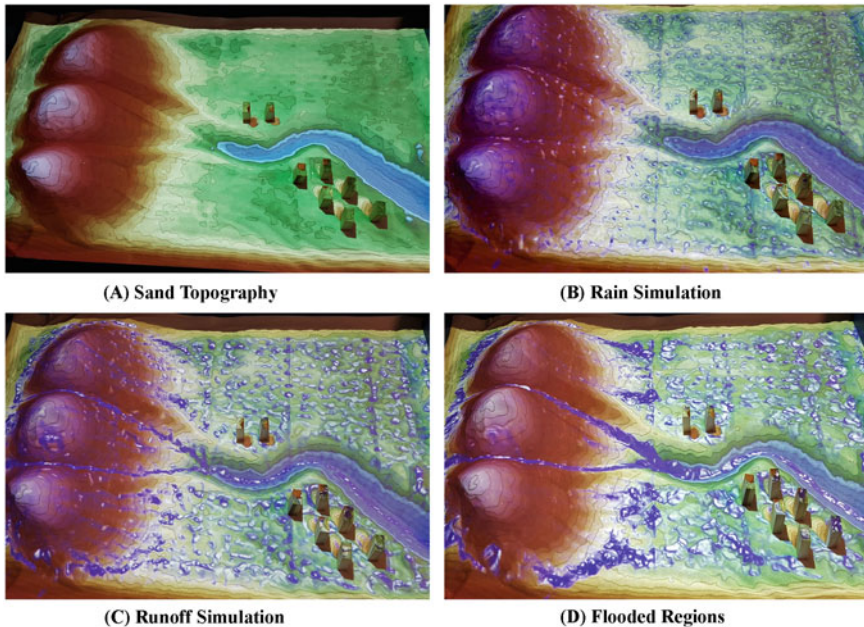
Fig. 8 Simulation and visualization using AR sandbox at NUS

sandboxes can be built in a week at regional centres, so that hazard simulations can be carried out for achieving holistic learning of the local people. The cost of the technology is expected to reduce thereby making an AR sandbox affordable to most. More so, new AR constructs can be conceived for modelling other types of hazards, e.g. earthquakes and landslides, and be used for visualization and communication of associated risks and hazards. Despite its current limitations, the AR sandbox has a great potential to be used as a risk communication tool.

5 Conclusion

Managing disaster risks would become a normal part of managing a country's economy and finances [23]. Linking disaster risk to other kinds of risk using inundation models [24], produces hazard maps which form the de facto instruments for DRM. GIS-based interactive simulation and visualization tools have also been experimented and implemented for disaster management practitioners [25]. However, with the AR sandbox construct, the hazard process could be simulated and visualized in relation to a real-world model. This provides a dynamic, experiential approach to the improved understanding of the precipitation and flooding event. This achieves holistic learning and therefore would be more emphatic in gaining the trust of the local people.

The AR sandbox construct is a step ahead as it provides a handle for the user to control the intensity and duration of the event and visualize the impacts on a real physical model. Such a construct shall be helpful to convince the local people of the perils through real-time simulation of the event. AR technology based constructs are now available as smartphone applications. Constructs using AR applications, if tailored to specific disasters in different geomorphic regions, has all the ingredients to be a successful instrument for disaster risk visualization and communication.

References

1. Scott, Z., Wooster, K., Few, R., Thomson, A., Tarazona, M.: Monitoring and evaluating disaster risk management capacity. Disaster Prev. Manage. **25**(3), 412–422 (2016)
2. Kikkawa, T.: Risk Communication: Aiming at Mutual Understanding and Better Decision Making. Fukumura Press, p. 197 (1999)
3. Opach, T., Rød, J.K.: Cartographic visualization of vulnerability to natural hazards. Cartograph. Int. J. Geograph. Inform. Geovisual. **48**(2), 113–125 (2013)
4. Kundu, S.N., Pattnaik, D.S.: Geomorphic characterization of seafloor using digital elevation model derivatives—a case study around Bombay high, Western Indian offshore. Geocarto Int. **29**(2), 185–197 (2014)
5. Schubert, J., Cheung, W.H., Luke, A., Gallien, T., Aghakouchak, A., Feldman, D., Matthew, R., Sanders, B.F.: Making Coastal Flood Hazard Maps to Support Decision-Making—What End Users Want. American Geophysical Union, Fall Meeting, Washington, DC (2015)
6. Cabinet Office.: Current Status of Efforts Toward Revision of Disaster Management Measures in Light of Lessons Learned from the Great East Japan Earthquake (2012)
7. Kundu, S.N.: Designing an effective virtual field trip for e-Learning. In: IEEE International Conference on Teaching, Assessment and Learning for Engineering (TALE 2016), Bangkok, 7–9 Dec 2016
8. Freeman, K.M., Thompson, S.F., Allely, E.B., Sobel, A.L., Stansfield, S.A., Pugh, W.M.: A virtual reality patient simulation system for teaching emergency response skills to U.S. Navy medical providers. Prehosp. Disaster Med. (2001)
9. Kizakevich, P.N., Culwell, A., Furberg, R., et al.: Virtual simulation-enhanced triage training for Iraqi medical personnel. Stud. Health Technol. Inform. **125**, 223–228 (2007)
10. Wilkerson, W., Avstreih, D., Gruppen, L., Beier, K.P., Wooliscroft, J.: Using immersive simulation for training first responders for mass casualty incidents. Acad. Emerg. Med. **15**, 1152–1159 (2008)
11. Caudell, T.P., Mizell, D.W.: Augmented reality: an application of heads-up display technology to manual manufacturing processes. In: Proceedings of 1992 IEEE Hawaii International Conference on Systems Sciences, pp. 659–669 (1992)
12. Johnson, L.F., Witchey, H.: The 2010 horizon report: Museum edition. Curator Mus. J. **54**(1), 37–40 (2011)
13. Kesim, M., Ozarslan, Y.: Augmented reality in education: Current technologies and the potential for education. Proc. Soc. Behav. Sci. **7**, 297–302 (2012)
14. Azuma, R., Baillot, Y., Behringer, R., Feiner, S., Julier, S., MacIntyre, B.: Recent Advances in Augmented Reality. IEEE, Los Alamitos (2001)

15. Milgram, P., Kishino, F.: A taxonomy of mixed reality visual displays, IEICE (Institute of Electronics, Information and Communication Engineers). Trans. Inform. Syst. (Special Issue on Networked Reality) (1994)
16. Chi, H., Kang, S., Wang, X.: Research trends and opportunities of augmented reality applications in architecture, engineering, and construction. Autom. Constr. **33**, 116–122 (2013)
17. White, S., Lister, L., Feiner, S.: Visual Hints for Tangible Gestures in Augmented Reality (2007)
18. Juang, J.R., Hung, W.H., Kang, S.C.: SimCrane 3D.sup.+: a crane simulator with kinesthetic and stereoscopic vision. Adv. Eng. Inform. **27**(4), 506 (2013)
19. Kreylos, O.: Augmented Reality Sand Box. https://arsandbox.ucdavis.edu/
20. Doc-Ok.org: A Developer's Perspective on Immersive 3D Computer Graphics. http://doc-ok.org/?p=164
21. Do-It-Yourself: Augmented Reality Sandbox. http://www.instructables.com/id/Augmented-Reality-Sandbox/
22. iSandbox: Augmented Reality Sandbox. http://ar-sandbox.com/index.php
23. Lavell, A., Maskrey, A.: The future of disaster risk management. Environ. Hazards **13**(4), 267–280 (2014)
24. Zhang, S., Pan, B.: An urban storm-inundation simulation method based on GIS. J. Hydrol. (Amsterdam) **517**, 260–268 (2014)
25. Leskens, J.G., Kehl, C., Tutenel, T., Kol, T., Haan, G.D., Stelling, G., Eisemann, E.: An interactive simulation and visualization tool for flood analysis usable for practitioners. Mitig. Adapt. Strat. Glob. Change **22**(2), 307–324 (2017)

Remote Sensing Imagery-Based Analysis of the Relationship Between Land Cover Changes and Suspended Sediments

S. N. Kundu

Abstract Anthropogenic activities like rapid urbanisation and commercial farming are driving land cover changes. South East Asia alone has witnessed large-scale changes in our environment and biodiversity due to forest conversion into commercial palm, cocoa and rubber plantations. In West Kalimantan of Indonesian Borneo, exponential increase in commercial palm plantation acreage at the cost of depleting rainforests was witnessed in the last three decades. The spatio-temporal variability of such land cover changes are effectively studied by using remote sensing techniques. The impact of such changes on hydrological processes at watershed scales can be established through change analysis. In this chapter, Landsat TM, MSS and ETM+ data between 1992 and 2013 were used to study land cover changes and estimate suspended sediment concentration from river waters. Normalised Difference Vegetation Index (NDVI) was computed for characterising vegetation land cover which was then classified as per the Food and Agricultural Organization schema. Both statistical and spatial change analysis were performed in a Geographical Information System (GIS). The results show a strong relationship between the observed land cover changes and estimated suspended sediment concentrations in the watershed which established a strong relationship between deforestation and erosion. This case study also presents an alternative methodology to link increased erosion to deforestation, especially in regions where applicability of Soil Loss Equation (SLE) based models are not possible due to lack of field collected datasets.

Keywords Remote sensing · Land cover · Suspended sediment concentration Change analysis · Erosion · Deforestation

S. N. Kundu (✉)
Department of Geography, National University of Singapore, Singapore, Singapore
e-mail: snkundu@gmail.com

1 Introduction

Conversion of tropical forests for resource utilisation has led to deforestation, soil loss, water quality issues and have even caused economic/political instability [1, 2]. Rapid deforestation and forest conversion is driving environmental change [1], impacting the energy, water and carbon cycles [3, 4]. Destruction of animal habitats, increased soil erosion and water pollution, disposal of biomass and air pollution are some of the prime environmental concerns arising out of such activities [5]. South East Asia has witnessed unprecedented increase in defor- estation and land conversion for commercial rubber and palm plantations over the last few decades [6].

Deforestation and forest degradation has been widely researched [7–10] using field collected and satellite remote sensing data. Erosion studies integrate spatial information on topography, soil, rainfall and land cover in Soil Loss Equations (SLEs) models [11]. Several studies [1, 12, 13] and reviews [14] have indicated the influence of deforestation on erosion. However, in the South East Asian tropics, SLE-based models are not feasible owing to lack of necessary spatial datasets and those available are of poor resolution and quality. Also, some researchers [15] have suggested that SLE-based models are inappropriate for the tropical regions. In such cases, analysis of temporal remote sensing provides a means for high-resolution data for change analysis that can be applied to study land cover and erosion. Multi-temporal change mapping is an established tech- nique [16] and use of Geographical Information Systems (GIS) adds a spatial dimension to the analysis.

Various approaches exist for exploiting multispectral reflectance information for land cover classification from remote sensing data. Normalised Density Vegetation Index (NDVI), which was initially devised for determining vegetation vigour, has also been used for land cover classification [17–19]. FAO [20] presents a land cover classification schema for the whole globe and its ubiquitous use has sup- ported comparative evaluation of land cover at regional and global scales. Availability of satellite data from various platforms (like NOAA AVHRR, SPOT, MODIS and MERIS) have aided several regional and global forest cover mappings [21–23]. Sediments originating from sheet and gully erosion end up in drainage systems in watersheds and end up as bedload and suspended sediments. The suspended sediments, concentration of which can be estimated using satellite data, are therefore representative of soil erosion at watershed scale. In the past, satellite data has supported the estimation of Suspended Sediment Concentration (SSC) from both rivers and oceans [16, 24–26].

Study of changes in land cover and suspended sediments in rivers can establish the relation between deforestation and erosion. The increasing availability of global imagery from Landsat Multispectral Scanner (MSS), Thematic Mapper (TM), and Enhanced Thematic Mapper (ETM+) and Operational Land Imager (OLI), coupled with the enhanced confidence in extracting and estimating surface environmental variables, have largely aided multi-temporal and multi-variate change studies.

The Landsat platform presents a rich data archive ever since it was launched in the 1970s. Its fortnightly repeat imaging capability and global coverage has strengthened its candidature for change analysis studies [27]. The current case study demonstrates the use of Landsat data for analysing and relating changes in land cover and suspended sediment concentration in a tropical watershed in the western part of Indonesian Borneo.

2 The Study Area

Sambas watershed, the study area, is located at the Sambas regency in West Kalimantan (Fig. 1). The regency has an area of 6716 km^2 and shares its border with the East Malaysian province of Sarawak at its north. The official census in January 2014 stands at 513,100 which yields a population density of 75 persons per km^2. This region has witnessed widespread deforestation and land conversion into commercial oil palm plantations, which makes it a perfect site for testing the hypothesis of this study.
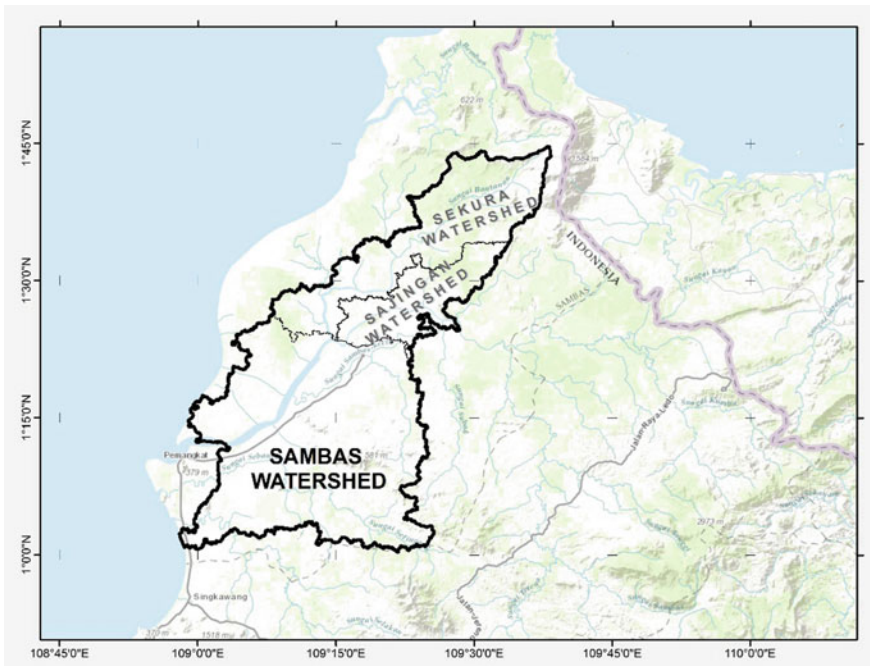
Fig. 1 Location map of the study area

2.1 Topography and Hydrology

Based on Aster Global Digital Elevation (GDEM), the Sambas watershed consists of mostly plains which are located at the southern part. The river basin has a total area of 2750 km^2 of which 70% area has slope lower than 150. Hilly regions (slope > 400) are located in the north, north-east and south-eastern parts and comprise only 5% of the total area of the watershed. The river system, which extends to about 233 km in length, originates from the north-eastern hills and flows south-west draining into the South China Sea.

2.2 Forest Conversion and Plantation History

Statistics from the Indonesian Statistical bureau (Fig. 2) reveal that oil palm plantations in Indonesia almost doubled to 11 million hectares in the last decade only. Since 2004, in Borneo alone, about 240,000 ha of land out of the total of 400,000 ha had been handed out to several palm oil companies. Most of these lands were tropical rainforests, which are now either cleared or are at different stages of the palm plantation cycle.

Fig. 2 Indonesia plantation statistics (data sourced from Statistik Perkebunan Indonesia 2015)

2.3   Land Use Practice for Palm Plantation

Land undergoes several stages of transformations before it converts into a mature palm plantation. Forests are cleared and then palm saplings are planted which grow into immature palms and eventually into producing mature palms (Fig. 3). Therefore the land cover at each stage can be classified as forests (rainforests), barren land (cleared land), grasslands (palm saplings), shrubs (immature palm trees) and forests (mature palm plantations). Different parts of the Sambas watershed are at different stages of this palming cycle. With more land being allocated for plantations, the proportion of non-forest land are constantly on the rise. Erosion in generally at high levels in the tropics and forest clearings add to the problem as they expose soil to eroding agents.

3   Data and Methods

Temporal Landsat data were used for this study which were processed and interpreted for classifying land cover and estimating suspended sediment concentration. An Aster Global Digital Elevation Model (GDEM) for the study area was used to delineate watershed and catchments which provided a general understanding of the
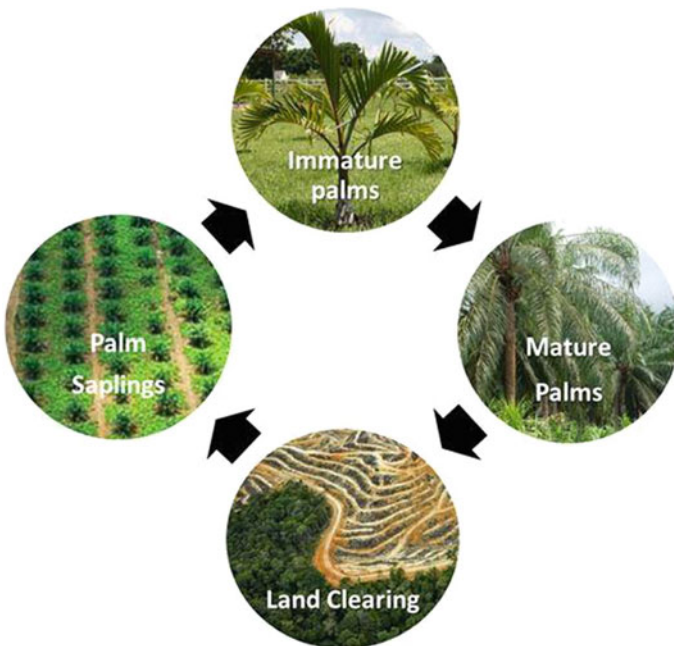
Fig. 3 Land transformation stages of palm plantations

geomorphology of the study area. GIS-based tools and algorithms were used for multispectral and multi-temporal analysis which involved NDVI calculation, land cover classification, suspended sediment estimation and spatio-temporal change analysis.

3.1 Topographic Analysis and Hydrology

3.1.1 Watershed Delineation

Watersheds are the natural boundaries in a fluvial-erosional system and can be computed programmatically from digital elevation models [28, 29]. The Aster GDEM was processed in ArcGIS (www.arcgis.com) to extract the whole watershed of the Sambas river system and the catchments of its main tributaries, namely Sekura and Sajingan (Fig. 1). Watershed and catchment extents were the natural boundaries within which temporal dynamics of land cover and suspended sediments were confined to.

3.2 Landsat Image Acquisition

Landsat imageries were sourced from the archives of the USGS Global Land Cover facility (www.landcover.org), details of which are provided in Table 1. False Colour Composites (FCC) for the watershed extent of the imageries were prepared for visual interpretation of change (Fig. 4).

3.3 Image Pre-processing

The ortho-rectified and geo-referenced imageries were pre-processed. This included the conversion of radiance values into reflectance. This process was succeeded by

Table 1 Details of landsat data used for the study

Platform	Bands used	Spectral wavelength (μm)	Spatial resolution (m)	Acquisition date
Landsat 8 OLI	B4 (RED) B5 (NIR)	0.64–0.67 0.85–0.88	30	22/6/2013
Landsat 7 ETM+	B3 (RED) B4 (NIR)	0.63–0.69 0.77–0.90	30	18/7/2002
Landsat 5 TM	B3 (RED) B4 (NIR)	0.63–0.69 0.77–0.90	30	9/7/1990
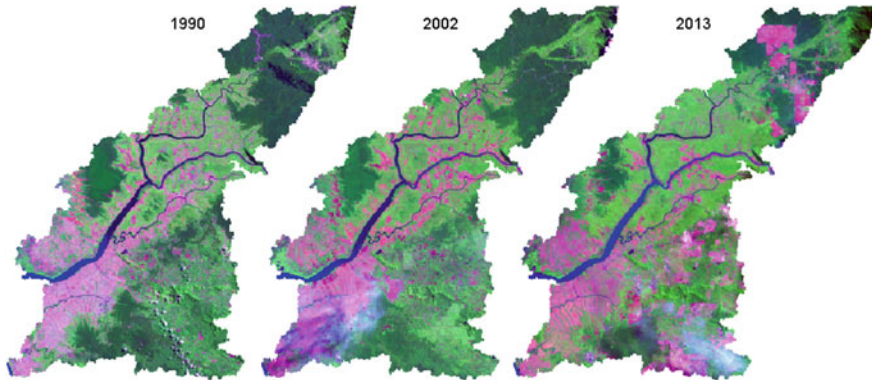
Fig. 4 Landsat false colour composites of the study area

atmospheric correction. The study area, being located in the tropics, is endemic to cloud cover. This makes it difficult to find an imagery which is completely devoid of cloud cover. The pixels belonging to clouds were assigned to the closest land cover class using the nearest-neighbour method.

3.3.1 Reflectance from Radiance

The imageries stored Digital Numbers (DN) in each pixel for each spectral band which represented radiance back from earth. In order to derive NDVI and SSC, the radiance was required to be converted to reflectance. This was done using sensor parameters provided in the metadata for each downloaded Landsat image. The approach to retrieve reflectance from radiance is elaborated in the User's Handbook for respective Landsat platform.

3.3.2 Atmospheric Correction

Deep water bodies have zero reflectance in the infrared band. Reflectance values for water bodies in the infrared bands serve as a means to eliminate the path reflectance (energy component reflected back to space by the atmosphere). The atmospheric correction involved estimation of this component through statistical analysis of reflectance values of water bodies in the study area and its deduction from the imagery.

3.3.3 False Colour Composite (FCC) Generation

False colour composites aid visual inspection of land cover. Red, blue and green colour were used for bands 6, 4 and 3, respectively to bring forth a contrast in the vegetation cover in the watershed (Fig. 4). A clear distinction between vegetated

(shades of green), water (blue-black) and barren lands (in pink) and the spatio-temporal variations can be observed from the FCCs. The increase of barren land and the decrease of forests (deep green) can be observed from 1990 to 2013.

3.4 Land Cover Classification

Deforestation being one prime aspect of this study, NDVI thresholds were used to classify land cover in this study. A classification accuracy was done using Google Earth where high-resolution imagery was available for 2013.

3.4.1 NDVI

The use of NDVI is prevalent in regional and global forest cover mapping and change detection [30]. Since its advent in 1973, NDVI had been used as an index to characterise phenology of vegetated landscapes [31]. The spectral contrast exhibited by vegetation in the red (VIS) and near infrared (NIR) bands of Landsat imagery is exploited to derive NDVI as below

$$NDVI = \frac{(NIR - VIS)}{(NIR + VIS)} \tag{1}$$

NDVI ranges from −1 to 1 and a supervised approach was adopted to define thresholds for each land cover class since fixed ranges were not found to be uniform across imageries of different vintages (Fig. 5).
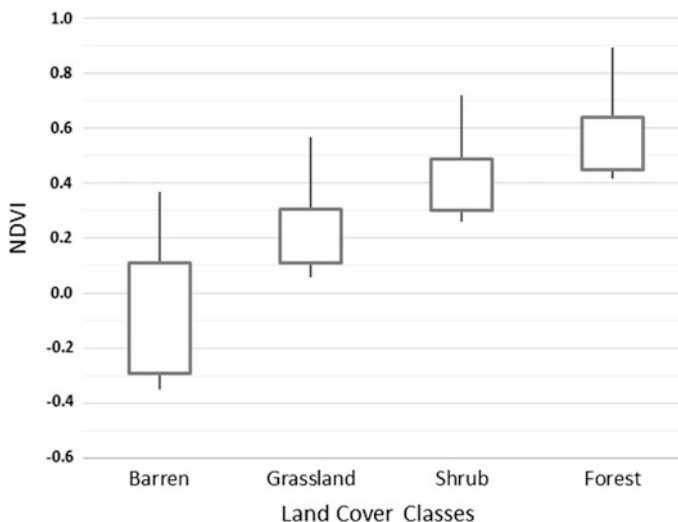
Fig. 5 NDVI variability among various land cover classes

Among the four land cover classes, NDVI variability was highest for barren lands. This could be attributed to the likelihood of varying moisture in the soil. Grasslands, shrubs and forests displayed low variability and high separability amongst themselves.

3.4.2 Land Cover Classification and Accuracy Assessment

Land cover is the observed bio-physical cover on the earth's surface. Food and Agricultural Organization (FAO) has developed the Land Cover Classification System (LCCS), a hierarchical classification schema which is detailed in Fig. 6. Out of the FAO-defined 17 global land cover classes, only 9 (including water) were found to exist in the study area. These were then generalised into five simplified land cover classes, namely forests, shrubs, grasslands, barren land and water. An accuracy assessment of the classification was performed for 2013 image against high resolution imagery from Google earth. Land cover classes for a hundred random locations were overlaid on to Google earth for manual inspection. This resulted a classification accuracy of 96%. As high resolution imagery for 1990 and 2002 were not available in Google earth, it was not possible to estimate the classification accuracies of the 1990 and 2002 images. As the same classification process was utilised for the earlier images, it was safe to assume that the accuracy would not vary significantly from the classification accuracy of the 2013 imagery.
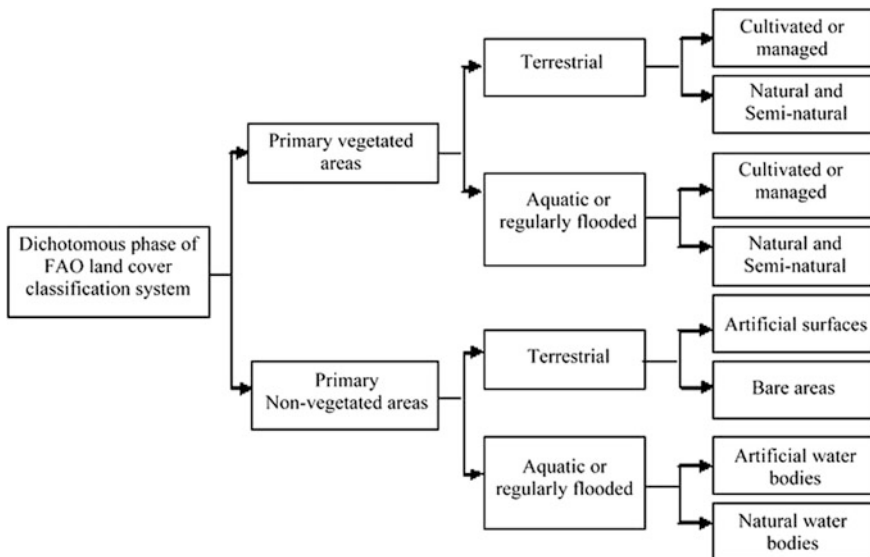
Fig. 6 Hierarchical structure FAO land cover system

3.5   Suspended Sediment Concentration (SSC)

SSC can be estimated from satellite imagery as the reflectance in the infrared band correlates well with turbidity in the water resulting from suspended sediments. A remote sensing and field validation research on turbid waters of Yangtze River yielded a relationship through regression analysis [32]. The equation developed by [32], is as below.

$$\ln(\text{SSC}) = 3.18236 * \ln(p_{w,4}) - 1.40060, \tag{2}$$

where SSC is in mg/l and $p(w, 4)$ is band 4 (NIR) reflectance.

4   Results and Discussion

4.1   Deforestation and Land Cover Changes

Deforestation is defined as a reduction of the forest cover and can be quantified statistically through change analysis of land cover. Conversion of forest cover into another land cover type like barren land, grasslands or shrubs can be determined in a GIS for estimating spatial change. Statistical and spatial land cover change was analysed for the whole Sambas watershed and the catchments of its tributaries. A visual inspection (Fig. 7), evidences that forest cover was significantly reduced between 1990 and 2013 and deforestation activities which were confined to the
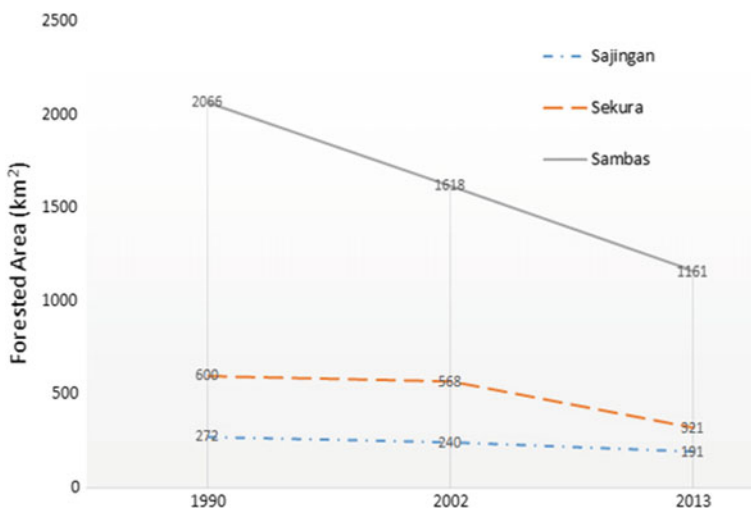
Fig. 7 Forest cover change in the Sambas watershed
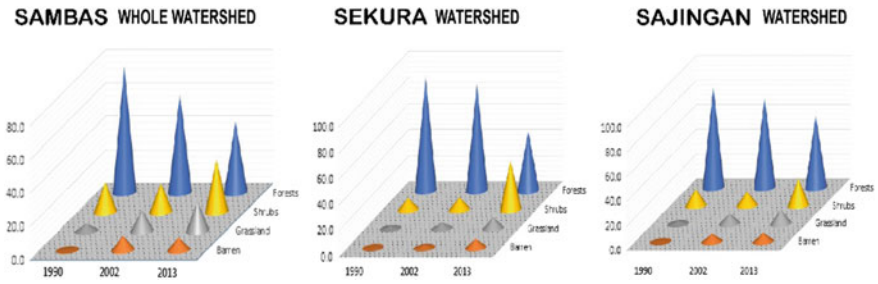
Fig. 8 Forest cover change in the Sambas watershed
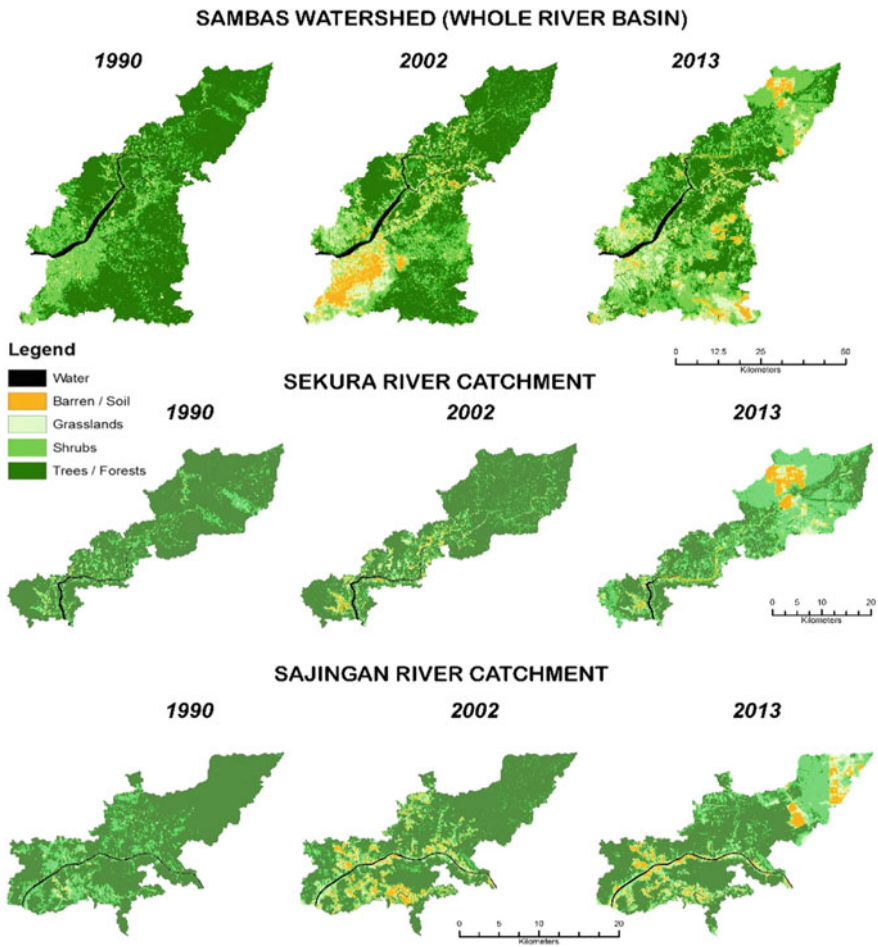
Fig. 9 Land cover changes in the Sambas watershed and tributary catchments

plains between 1990 and 2002 were evident in the northern parts of the watershed between 2002 and 2013.

In 2013, the forest cover in the Sambas watershed was reduced to 50% of the acreage in 1990. Between 1990 and 2002, deforestation and land conversion was limited to the plains as evident from Sekura and Sajingan forest cover (Fig. 8). However, from 2002 onwards, the activities extended into the upper parts of the watershed with Sajingan catchment witnessing relatively lesser levels of defor- estation as compared to the Sajingan catchment. Spatially, at different parts of the watershed, forest cover was being replaced with grasslands and barren land (Fig. 9), which is clearly attributed to the land use practice associated with palm plantations.

4.2 Erosion and SSC Changes

Eroded soil is transported by river systems in the confines of the watershed. Eroded matter is transported into river waters by streams and channels primarily as sus- pended and solution load. Spectral reflectance of clear water in the near-infra red wavelength is zero. Turbidity caused by suspended sediments make it reflective, concentration of which can be deduced from spectral reflectance information of remote sensing imagery (Eq. 2). SSC is therefore considered as an estimate of soil erosion. In 2013, the SSC levels were found to be much higher than the levels estimated in 1990 and 2002 (Fig. 10) although the increase was higher in the latter period (2002–2013).

SSC values, at equal interval sampling locations, along the rivers for the three years of observation were plotted (Fig. 11). The Sambas River had witnessed consistent increase in SSC levels during the study period indicating that erosion levels had increased between 1990 and 2013. It was however observed that the increase was significant between 2002 and 2013 only for Sekura and Sajingan catchments. For the same period of observation, SSC levels in Sajingan and Sekura were marginally higher that the main river (Sambas) watershed as rivers running at higher slopes can carry more material into suspension. In 2002, the Sambas River

Fig. 10 Suspended sediment concentration in waters of the river basin
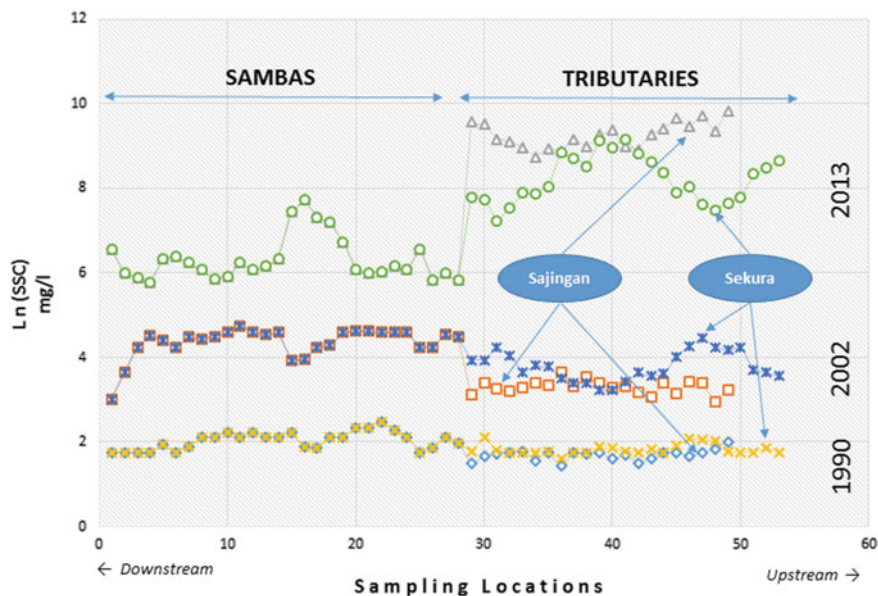
Fig. 11 SSC profile along the rivers in the Sambas watershed

Table 2 SSC and % forest cover for the Sambas river basin and sub-catchments

	Variables	Year 1990	Year 2002	Year 2013	Area (km^2)
Sambas watershed	%Forests	75.2	58.9	42.3	2747.7
	Ln(SSC)	1.87	3.86	7.78	
Sajingan river catchment	%Forests	82.6	72.9	58.1	329.4
	Ln(SSC)	1.69	3.29	9.25	
Sekura river catchment	%Forests	86.7	82.0	46.3	692.6
	Ln(SSC)	1.83	3.78	8.2	

section had higher SSC than its tributaries and this was unusual and requires further investigation as to whether it was driven by any extreme climatic event around the time.

4.3 Relationship Between Land Cover and Suspended Sediments

Influence of deforestation on runoff generation and soil erosion has long been studied at watershed scale [33]. With the hypothesis that deforestation leads to
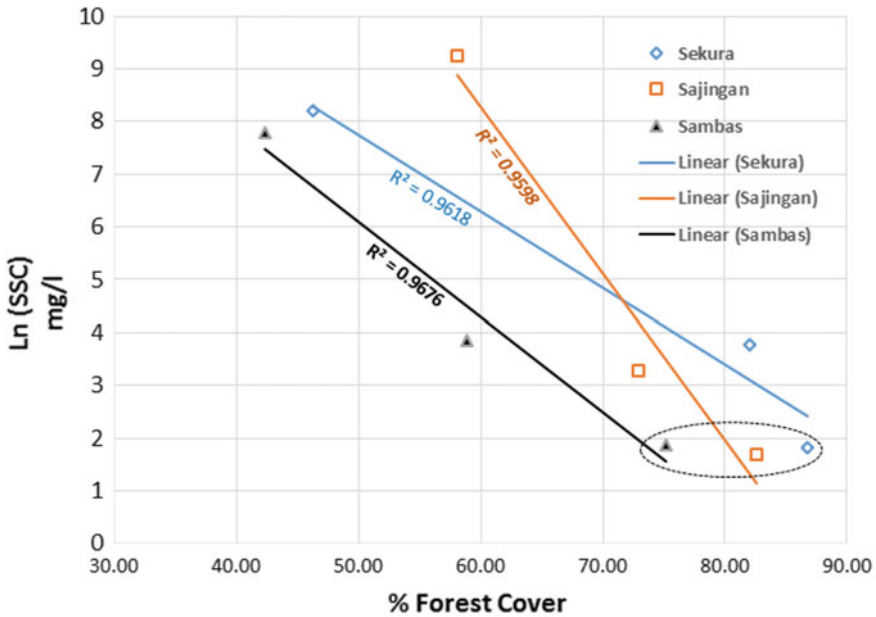
Fig. 12 Crossplot between SSC and % forest cover in the study area

increased erosion, reduction of forest cover should result in increased SSC levels. Table 2 lists the percentage of forest cover and Log of SSC for the different catchments and watersheds determined from this study.

Land use and vegetation are important factors in erosion and runoff generation. The relationship between deforestation and erosion can be established through the regression analysis of SSC levels and % forest cover (Fig. 12). Across the Sambas watershed and its tributary catchments, it was found that reduction of forest cover was associated with high SSC levels. From this regression study a consistent relationship emerged which reflected the strong association between land cover changes (deforestation) and suspended sediments (erosion).

5 Conclusion

The study used qualitative and quantitative analyses using remote sensing data to establish the relationship between land cover changes and suspended sediments in river waters. Deforestation for commercial plantation is a land use practice which exposes soil to eroding forces through removal of protective vegetated cover, thereby aiding erosion. The case study made use of suspended sediments as an indicator of erosion and NDVI as a means to characterise land cover. It also establishes the use of multi-temporal Landsat satellite imagery for change analysis

making it an indispensable tool for monitoring and measuring environmental change in a tropical watershed.

One of the prime constraints of this study was the assumption that there was no extreme climatic episode which may have influenced vegetation cover or suspended sediments in the waters. Also the SSC levels were estimated based on an algorithm that was tested in Yangtze River waters at a different time and location. Availability of weather data could have improved the confidence of the study and a field validation could have established the accuracy of the study. Despite these limitations, the results correlate well with other research based on SLE models and therefore has strong implication for the regional environmental studies [34]. This includes the likes of geohazards mapping [35], agriculture and forestry, climate change and urban development.

References

1. Kull, C.A.: Deforestation, erosion, and fire: degradation myths in the environmental history of Madagascar. Environ. Hist. **6**(4), 423–450 (2000)
2. Koh, L.P., Ghazoul, J.: Biofuels, biodiversity, and people: understanding the conflicts and finding opportunities. Biol. Conserv. **141**(10), 2450–2460 (2008)
3. Bonan, G.B.: Forests and climate change: forcings, feedbacks, and the climate benefits of forests. Science **320**, 1444–1449 (2008)
4. Malmer, A., Murdiyarso, D., Bruijnzeel, L.A., Ilstedt, U.: Carbon sequestration in tropical forests and water: a critical look at the basis for commonly used generalizations. Glob. Change Biol. **16**, 599–604 (2010)
5. Environmental Conservation Department (ECD): Environmental Impact Assessment (EIA) Guidelines Oil Palm Plantation Development. ECD, Sabah, Malaysia (2002)
6. Langner, A., Miettinen, J., Siegert, F.: Land cover change 2002–2005 in Borneo and the role of fire derived from MODIS imagery. Glob. Change Biol. **13**, 2329–2340 (2007)
7. Hosonuma, N., Herold, M., De Sy, V., De Fries, R.S., Brockhaus, M., Verchot, L., Romijn, E.: An assessment of deforestation and forest degradation drivers in developing countries. Environ. Res. Lett. **7**(4) (2012)
8. Asner, G.P., Knapp, D.E., Balaji, A., Paez-Acosta, G.: Automated mapping of tropical deforestation and forest degradation: CLASlite. J. Appl. Remote Sens. **3**(1), 33543 (2009)
9. Mukul, S.A., Herbohn, J.: The impacts of shifting cultivation on secondary forests dynamics in tropics: A synthesis of the key findings and spatio temporal distribution of research. Environ. Sci. Policy **55**, 167–177 (2016)
10. Lawrence, D., Vandecar, K.: Effects of tropical deforestation on climate and agriculture. Nat. Clim. Change **5**(1), 27–36 (2015)
11. Terranova, O., Antronico, L., Coscarelli, R., Iaquinta, P.: Soil erosion risk scenarios in the Mediterranean environment using RUSLE and GIS: an application model for Calabria (Southern Italy). Geomorphology **112**(3), 228–245 (2009)
12. Karamage, F., Shao, H., Chen, X., Ndayisaba, F., Nahayo, L., Kayiranga, A., Omifolaji, J.K., Liu, T., Zhang, C.: Deforestation effects on soil erosion in the Lake Kivu Basin, D.R. Congo-Rwanda. Forests **7**(11), 281 (2016)

13. Anselmetti, F.S., Hodell, D.A., Ariztegui, D., Brenner, M., Rosenmeier, M.F.: Quantification of soil erosion rates related to ancient Maya deforestation. Geology **35**(10), 915–918 (2007)

14. Labrière, N., Locatelli, B., Laumonier, Y., Freycon, V., Bernoux, M.: Soil erosion in the humid tropics: a systematic quantitative review. Agric. Ecosyst. Environ. **203**, 127–139 (2015)

15. Cohen, M.J., Shepherd, K.D., Walsh, M.G.: Empirical reformulation of the universal soil loss equation for erosion risk assessment in a tropical watershed. Geoderma **124**(3), 235–252 (2005)

16. Kundu, S.N., Sahoo, A.K., Mohapatra, S., Singh, R.P.: Change analysis using IRS-P4 OCM data after the Orissa super cyclone. Int. J. Remote Sens. **22**(7), 1383–1389 (2001)

17. El-Gammal, M.I., Ali, R.R., Samra, R.A.: NDVI threshold classification for detecting vegetation cover in Damietta governorate, Egypt. J. Am. Sci. 2014 **10**, 8 (2014)

18. Shao, Y., Lunetta, R.S., Wheeler, B., Iiames, J.S., Campbell, J.B.: An evaluation of time-series smoothing algorithms for land-cover classifications using MODIS-NDVI multi-temporal data. Remote Sens. Environ. **174**, 258–265 (2016)

19. Kong, F., Li, X., Wang, H., Xie, D., Li, X., Bai, Y.: Land cover classification based on fused data from GF-1 and MODIS NDVI time series. Remote Sens. **8**(9), 741 (2016)

20. FAO: Global forest resources assessment 2015. http://www.fao.org/forestry/fra/76871/en/. Accessed 13.06.16

21. DeFries, R.S., Hansen, M.C., Townshend, J.R.G., Janetos, A.C., Loveland, T.R.: A new global 1 km dataset of percent tree cover derived from remote sensing. Glob. Change Biol. **6**, 247–254 (2000)

22. Friedl, M.A., McIver, D.K., Hodges, J.C.F., Zhang, X.Y., Muchoney, D., Strahler, A.H., Woodcock, C.E., Gopal, S., Schneider, A., Cooper, A., Baccini, A., Gao, F., Schaaf, C.: Global land cover mapping from MODIS: algorithms and early results. Remote Sens. Environ. **83**(1), 287–302 (2002)

23. Fuller, D.O., Jessup, T.C., Salim, A.: Loss of forest cover in Kalimantan, Indonesia, since the 1997–1998 El Nino. Conserv. Biol. **18**, 249–254 (2003)

24. Walker, T.R., Grant, J., Cranford, P., Lintern, D.G., Hill, P., Jarvis, P., Barrell, J., Nozais, C.: Suspended sediment and erosion dynamics in Kugmallit Bay and Beaufort Sea during ice-free conditions. J. Mar. Syst. **74**(3), 794–809 (2008)

25. Suif, Z., Fleifle, A., Yoshimura, C., Saavedra, O.: Spatio-temporal patterns of soil erosion and suspended sediment dynamics in the mekong river basin. Sci. Total Environ. **568**, 933–945 (2016)

26. Marttila, H., Kløve, B.: Dynamics of erosion and suspended sediment transport from drained peatland forestry. J. Hydrol. **388**(3), 414–425 (2010)

27. Tucker, C.J., Grant, D.M., Dykstra, J.D.: NASA's Global orthorectified landsat data set. Photogram. Eng. Remote Sens. **70**(3), 313–322 (2004)

28. Chockalingam, L., Daya Sagar, B.S.: Mapping of sub-watersheds from digital elevation model: a morphological approach. Int. J. Pattern Recognit. Artif. Intell. **17**(2), 269–274 (2003)

29. Kundu, S., Pattanaik, D.: Mapping Onland river channels up to the seafloor along the west coast of india. Current Science (Bangalore) **101**(7), 958–962 (2011)

30. Lunetta, R.S., Knight, J.F., Ediriwickrema, J., Lyon, J.G., Worthy, L.D.: Land-cover change detection using multi-temporal MODIS NDVI data. Remote Sens. Environ. **105**(2), 142–154 (2006)

31. Huete, A.R.: Vegetation indices, remote sensing and forest monitoring. Geogr. Compass **6**(9), 513–532 (2012)

32. Wang, J.J., Lu, X.X., Liew, S.C., Zhou, Y.: Retrieval of suspended sediment concentrations in large turbid rivers using Landsat ETM+: an example from the Yangtze River, China. Earth Surf. Proc. Land. **34**, 1082–1092 (2009)

33. Gholami, V.: The influence of deforestation on runoff generation and soil erosion (Case study: Kasilian Watershed). J. For. Sci. **59**(7), 272–278 (2013)
34. Foster, W.A., Snaddon, J.L., Turner, E.C., Fayle, T.M., Cockerill, T.D., Ellwood, M.F., Broad, G.R., Chung, A.Y., Eggleton, P., Khen, C.V., Yusah, K.M.: Establishing the evidence base for maintaining biodiversity and ecosystem function in the oil palm landscapes of South East Asia. Phil. Trans. R. Soc. B **366**, 3277–3291 (2011)
35. Kundu, S.N.: Geohazards modelling using remote sensing & GIS. In: Sengupta, D., Agrahari, S. (eds.) Modelling Trends in Solid and Hazardous Waste Management. Springer Nature, USA (2017)

The Impact of Different International Terrestrial Reference Frames (ITRFs) on Positioning and Mapping in Malaysia

Nur Adilla Zulkifli, Ami Hassan Md Din and Abdullah Hisam Omar

Abstract In Malaysia, Geocentric Datum of Malaysia 2000 (GDM2000) is connected to the International Terrestrial Reference Frame 2000 (ITRF2000). In comparison with the previous models, ITRF2014 represents a significant improvement in datum definition and realization. Nevertheless, the improvement causes a frame difference between ITRF2000, ITRF2008 and ITRF2014. Due to earthquakes that hit Sumatra region of Indonesia in the years 2004, 2005 and 2007 followed by post-seismic and co-seismic activities, Malaysia no longer lies on a stable continent. The movement on tectonic plate caused a shifting in geodetic datum of Malaysia to become non-geocentric. Thus, this factor gives impacts on positioning and mapping in Malaysia particularly in the realm of cadastral. Therefore, to measure the effect, the coordinates for positioning and mapping based on different International Terrestrial Reference Frames were analysed. To achieve the aim, this study is categorized into three phases. In the first phase, Global Positioning System (GPS) data was processed with respect to different reference frames (ITRF2000, ITRF2008 and ITRF2014) by Precise Point Positioning (PPP) Waypoint software. The result derived from the first phase was then be used

N. A. Zulkifli · A. H. M. Din (✉) · A. H. Omar
Faculty of Geoinformation and Real Estate, Geomatic Innovation
Research Group (GIG), Universiti Teknologi Malaysia, 81310 Johor Bahru,
Johor, Malaysia
e-mail: amihassan@utm.my

N. A. Zulkifli
e-mail: dillazulkifli@gmail.com

A. H. Omar
e-mail: abdullahhisham@utm.my

A. H. M. Din
Faculty of Geoinformation and Real Estate, Geoscience and Digital Earth
Centre (INSTEG), Universiti Teknologi Malaysia,
81310 Johor Bahru, Johor, Malaysia

A. H. M. Din
Institute of Oceanography and Environment (INOS), Universiti Malaysia
Terengganu, Kuala Terengganu, Terengganu, Malaysia

in the next phase, where the coordinate was analysed based on different reference frames. In the third phase, the reliability of coordinate with different ITRFs was assessed specifically for cadastral purposes. In order to analyse the coordinates, a point at helipad of Universiti Teknologi Malaysia (UTM) was observed by using GPS static technique, and the data was processed differently according to the frames by PPP. The coordinates processed were used as a base station for fast static GPS observation. To process the data, Trimble Total Control (TTC) software was used resulting in three different coordinates of each point observed. The coordinates were assessed with respect to the existing Cassini-Soldner geocentric coordinates and coordinates derived from network-based Real-Time Kinematic (RTK) observation. The results show that ITRF2014 has small value of standard deviations with the mean of 0.0010, 0.0003 and 0.0020 m for latitude, longitude and height for point positioning. Whereas for mapping, the differences between coordinates from PA 40225—ITRF2000, PA 40225—ITRF2008 and PA 40225—ITRF2014 in general range from −0.277 to −0.209 m for northing and from 0.424 to 0.515 m for easting. In conclusion, GDM2000 has to be revised frequently with respect to the latest version of ITRF in order to give a better positional accuracy, and a fix geocentric mapping datum needs to be opted for cadastral integrated purposes in Malaysia.

Keywords International terrestrial reference frames · Geocentric datum of Malaysia · Datum · Positioning and mapping

1 Introduction

Malaysia is using datum GDM2000, and it is connected to ITRF2000. ITRF2000 is a combination of unconstrained space geodesy solutions free from any tectonic plate model. It was the most accurate that has been established by 800 stations located at about 500 sites with better distributions around the world compared to the previous ITRF models. However, due to the dynamic Earth, ITRF2000 is no longer reliable to use especially with the realization of other reference frames such as ITRF2008 and ITRF2014. There may occur differences in frames between those models that gives impacts on positioning and mapping in Malaysia especially in the field of cadastral. According to Wei et al. [1], there is a frame difference between ITRF2000 and ITRF2005 models, which may impact GNSS data processing, and it is considered more accurate to adopt the latest ITRF and to align old GNSS results into the latest frame. Meanwhile, Kang [2] also mentioned that some problem might occur when considering distinct characteristics of old cadastral surveying like a reinstatement using WGS (World Geodetic System) if there are republished national control points related to ITRF version and tectonic deformation, etc. Thus, to manage the cadastral data based on WGS in Korea, Kang suggested on developing nationwide mathematical model by installing it in GPS receiver firmware to calibrate the differences between old and new coordinates automatically.

Furthermore, from the study conducted by Satirapod et al. [3], there is also significant diversion when comparing coordinates results between different ITRFs in north and east components. Hence, due to widespread deformation and other expected post-seismic motion, they recommended updating the Thai coordinate reference frame to ITRF2005. Globally, over the past 15 years, there have been four major earthquakes that hit Sumatra region of Indonesia in the years 2004, 2005, 2007 and 2012 affected GDM2000 to no longer be geocentric. The motion of most of Sundaland has also been moved towards the west [4]. Thus, it is inevitable that this aspect affects many applications particularly on positioning and mapping purpose in Malaysia, which require accurate coordinates in accordance with the latest ITRF. Therefore, Gill [5] conducted a study to develop a datum transformation model in relation to the tectonic motion in Malaysia in order to maintain the geocentric element of GDM2000 with respect to time.

Based on previous studies conducted in China, Korea, Thailand and also Malaysia, these differences affected the coordinate systems of countries and it is compulsory to update the systems with respect to the latest global frame. Hence, this research presents an effort to analyse the coordinates particularly for positioning and mapping in Malaysia with respect to different International Terrestrial Reference Frames. The frames chosen were ITRF2000, ITRF2008 and ITRF2014, where observations were conducted to specifically study the impact on a certain point positioning and cadastral mapping in Johor Bahru.

1.1 GDM2000

Geodetic datum is a framework that enables us to define geodetic coordinates system. It includes the ellipsoid and the three-dimensional Cartesian system consists of X-axis, Y-axis and Z-axis as well as their translation, rotation and scale parameters. In order to describe positions on Earth accurately, a geocentric datum is required where the origin is at the mass centre of the Earth. In Malaysia, GDM2000 was adopted by the Department of Survey and Mapping Malaysia (DSMM) to establish a global and standardized coordinate system countrywide [6] where it was realized with respect to ITRF2000 at epoch 1st January 2000.

GDM2000 was realized through a permanent network of active GPS stations known as Malaysia Active GPS System (MASS) stations. In the year 1998, 15 MASS stations were established and operated where eight of the stations are located in Peninsular Malaysia and the other seven are in Sabah and Sarawak. Figure 1 shows the distribution of MASS stations across Malaysia.

GDM2000 was realized by the long baseline connection between MASS stations and 11 IGS stations from nearby regions. Four years span GPS data of 15 MASS stations and 11 IGS stations were used in the Bernese GPS processing software to determine the MASS stations coordinate on International Terrestrial Reference Frame (ITRF) [7]. In addition, according to Kadir et al. [7], GDM2000 is defined on ITRF2000 at 1–2 cm accuracy level. However, all sites coordinates used to realize
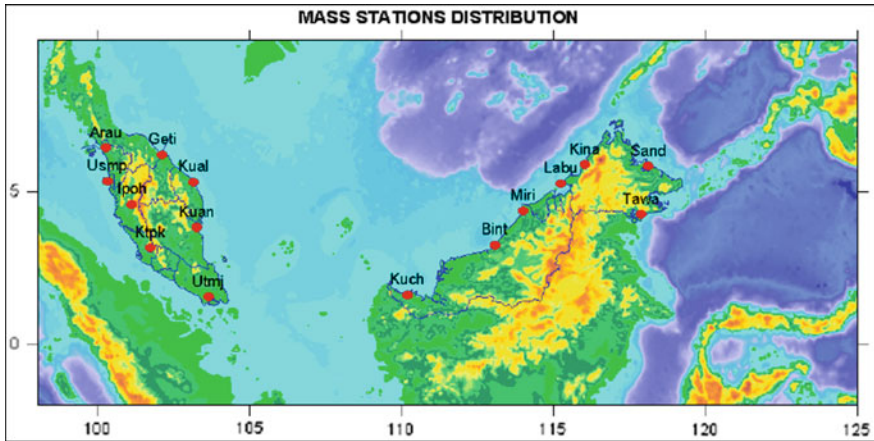
Fig. 1 Distribution of MASS stations throughout Malaysia in 1998 [7]

GDM2000 are assumed unchanged with time opposite to the fact that Earth is actually dynamic with the motion of plate tectonic.

Currently, MASS stations have been upgraded to Malaysian Real-Time Kinematic GNSS network (MyRTKnet) stations. MyRTKnet stations are the Continuously Operating Reference Station (CORS) established in Malaysia and they are broadly used in numerous positioning applications such as surveying, navigation, engineering, geodynamic and scientific studies. With the existing of MyRTKnet stations, the reliability of GDM2000 can be assessed by analysing the datum shifts via the displacements of the MyRTKnet stations caused by tectonic movements as well as the displacement induced by reference frame effects [6]. Due to earthquake that hits Sumatra region in the year 2004, a revision of GDM2000 was conducted in epoch 2006 known as GDM2000 (2006). The coordinates of four reference stations were fixed in the final local combined adjustment with respect to the original GDM2000 [8].

1.2   International Terrestrial Reference Frame (ITRF)

International Terrestrial Reference Frame (ITRF) is a set of points located on the Earth surface with their three-dimensional Cartesian coordinates and point's velocities that realize an ideal reference system. It can be used to measure plate tectonics and to represent the Earth when measuring its motion. Presently, there are 13 ITRF models realized with the aim to obtain a homogeneous reference frame for all geodetic and Earth scientific activities and applications starting with ITRF89 and ending with ITRF2014.

The combinations of space-based geodetic techniques such as Very Long Baseline Interferometry (VLBI), GPS, Satellite Lase Ranging (SLR) and Doppler Orbitography and Radiopositioning Integrated by Satellite (DORIS) have become a common practice to determine the global reference frames. Basically, the three ITRFs used the same techniques to define origin, scale and orientation. ITRF2000 combines unconstrained space geodesy solutions free from any tectonic motion model where the network consists of 800 stations located about 500 sites [9]; meanwhile, ITRF2008 is defined based on the reprocessed solutions of VLBI, SLR, GPS and DORIS spanning 29, 26, 12.5 and 16 years observation, respectively. This network comprises 934 stations located at 580 sites in northern and southern hemisphere [10]. According to Altamimi et al. [11], ITRF2014 is generated with an enhanced in modelling of nonlinear station motion including seasonal signals of station positions and post-seismic deformation for certain sites. It is defined by using VLBI, SLR, Global Navigation Satellite System (GNSS) and DORIS by using reprocessed time series weekly from SLR and DORIS, daily from GNSS and 24 h session-wise from VLBI. With an advance in technology, the reference frames are gradually improved in time giving a better accuracy to user.

1.3 Cadastral System in Malaysia

Previously, cadastral work and topographic mapping in Peninsular Malaysia were carried out by using Cassini-Soldner (Cassini) and Rectified Skew Orthomorphic (RSO) projection system, respectively. Besides, there are ten state Cassini-coordinate systems, and the northing and easting of the origins are not referred to a single triangulation system [7]. Figure 2 shows the origins of Cassini throughout Peninsular Malaysia.

Therefore, a homogeneous coordinate system with referenced to the global datum is required to accommodate future requirements in cadastral and mapping integrated purposes [12]. Currently, Peninsular Malaysia is adopting National Digital Cadastral Database (NDCDB) through a Coordinated Cadastral System project. As the datum origin is at the mass centre of the Earth, data integration can be done globally. However, the datum used which is GDM2000 is connected to ITRF2000. A non-geocentric datum will affect positioning and mapping specifically in the realm of cadastral. Hence, a fix geocentric mapping datum is required for cadastral purposes in Malaysia.

2 Data and Methods

2.1 Research Area Identification

The areas of study involved in this research have been narrowed down to the helipad area of Universiti Teknologi Malaysia (UTM) and Kampung Pasir, Johor
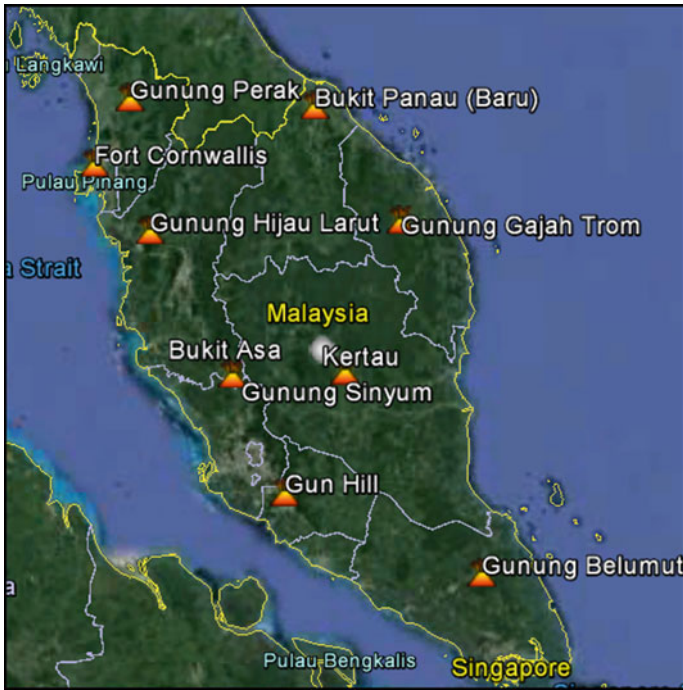
Fig. 2 Origins of Cassini across Peninsular Malaysia

Bahru where GPS static, fast static and network-based RTK observations were done, respectively. The GPS fast static observation was conducted on a point at helipad in order to do the analysis on point positioning. Meanwhile, the technique of GPS fast static and network-based RTK were implemented on cadastral lot, Lot 4199, Kampung Pasir, Mukim Pulai, Daerah Johor Bahru for the assessment in cadastral mapping.

2.2 Data Acquisition and Processing

Point Positioning. In this phase, 10 hours of GPS static observation on a point at helipad of Universiti Teknologi Malaysia (UTM) was carried out for 3 days to generate daily solution. The data was collected by using Topcon GR-5 and the data obtained was in Receiver Independent Exchange Format (RINEX) file containing Observation (O) and Navigation (N) files. The gathered data were then used for processing by using Waypoint software and Australian Surveying and Land Information Group (AUSLIG) Online GPS Processing System (AUSPOS).

The input data in Waypoint Processing Program is divided into two main parts. They are RINEX files and precise satellite orbit and clock data. The processing

Table 1 Processing parameters and models for GPS data processing by using Waypoint

Processing parameter	Processing strategy
Elevation mask angle	10°
Processing interval	1 s
Orbits/clock	Precise orbit and clock
Reference frames	ITRF2000, ITRF2008 and ITRF2014
Ionosphere	Double difference ionosphere-free linear combination
Tropospheric	Kalman filter (medium)
Processing method	PPP (multipass)
Type of solution	Float

mode used to process the data collected was Precise Point Positioning (PPP). PPP is an autonomous positioning method which does not use base station data. As no base station data was used to reduce correlated errors such as tropospheric delay, it was solved within Kalman filter whereas the ionospheric error was reduced by using linear combination (ionosphere-free) of L1 and L2. The format of input data used by Waypoint software is Waypoint Raw GNSS Data (.gpb). By using GNSS Data Converter, the data collected in RINEX format were converted into Waypoint's own format. In the meantime, precise orbit and clock data were automatically downloaded by GrafNav while running the program from ftp server of cddis.gsfc.nasa.gov. The 3 days of GPS static data were processed according to chosen reference frames (ITRF2000, ITRF2008 and ITRF2014), and the average of each coordinate was calculated. Table 1 shows the summary of processing parameters and models for GPS data processing by using Waypoint.

AUSPOS is a free online GPS data processing facility provided by Geoscience Australia [13]. The input data format for AUSPOS is in RINEX format which it only needs observation file. In order for AUSPOS to do the processing, it needs more than 1 hour data. AUSPOS follows the computation system in Bernese GNSS Software Version 5.2, which is double difference for baselines processing as well as the IGS orbits and IGS network stations. The reference stations chosen as fiducial stations are IGS and Asia-Pacific Reference Frame (APREF) stations. The coordinates computed are based on the IGS realization of the ITRF2008 reference frame and all the coordinates refer to a mean epoch of the site observation data. The 3 days data were processed by AUSPOS using different reference stations for each day, and the mean coordinates of 3 days data were calculated. Table 2 shows the summary of processing parameters and models for GPS data processing by using AUSPOS.

Mapping Purposes. In this part, fast static GPS and network-based RTK observations were conducted on five boundary stones at Lot 4199, Kampung Pasir. GPS fast static observation was carried out for 30 min with a base station established on the point at helipad whereas network-based RTK observation was carried out three times for every 10 epochs on each stone, respectively.

Table 2 Processing parameters and models for GPS data processing by using AUSPOS

Processing parameter	Processing strategy
Elevation cut-off angle	7°
Sampling rate	30 s
Orbits/EOP	IGS final orbits and EOP (Earth Orientation Parameter)
Reference frame	ITRF2008
Ground antenna phase centre calibration	IGS08 absolute phase centre variation model
Atmospheric loading	Applied
Ionosphere	Double difference ionosphere-free linear combination
Tropospheric model	GMF mapped with DRY-GMF
Tropospheric estimation	WET-GMF mapping function in 2 h interval
Tropospheric mapping function	GMF
Ambiguity solution	Code-based strategy for 180–6000 km baselines, phase-based L5/L3 strategy for 18–200 km baselines, Quasi-Ionosphere-Free (QIF) strategy for 18–2000 km baselines and direct L1/L2 strategy for 0–20 km baselines

In order to process the fast static data, TTC software was used. GPS import data of TTC are parted into two categories. They are the GPS data of base station and rover station in RINEX format. Coordinates of the base station were derived from the processing program of Waypoint based on ITRF2000, ITRF2008 and ITRF2014. Meanwhile, to attain the coordinates of rover stations, the fixed baseline processing and three-dimensional (3D) adjustment were done individually for each boundary stone. The coordinates obtained from network-based RTK were taken as average for assessment with other coordinates. Table 3 shows the summary of processing parameters and models for GPS data processing by using TTC.

Table 3 Processing parameters and models for GPS data processing by using TTC

Processing parameter	Processing strategy
GPS cut-off angle	10° and 20°
Processing interval	1 and 10 s
Orbits	Broadcast orbit
Ionosphere	Double difference ionosphere-free linear combination (more than 5 km baseline)
Atmospheric model	MSIS90
Tropospheric delay model	Saastamoinen

3   Results and Discussion

3.1   Coordinates of Point at Helipad by Precise Point Positioning (PPP)

From the Waypoint processing software, the coordinates of the point at helipad for 3 days data were derived in ITRF2000, ITRF2008 and ITRF2014. The mean for each reference frame was also calculated. The Standard Deviation (STD) for coordinates of 3 days data based on different reference frames is in mm level where the standard deviation of horizontal components is within 1 and 2 mm for vertical component. The result for vertical component is acceptable for 2 mm of standard deviation as according to Berber et al. [14], the height information in a GPS measurement is determined two to three times worse than the horizontal coordinate information, and this is because satellite configuration is more appropriate for horizontal coordinate determination. The coordinates of the point at helipad in different frames for 3 days data with their means are tabulated in Table 4 followed by the time series plot of residual coordinates for 3 days data based on three different reference frames in Fig. 3. The residual throughout the three different frames typically ranges from −0.0057 to 0.0135 mm for horizontal component (latitude and longitude) and −0.006 to 0.007 mm for vertical component (up).

From the coordinate derived based on different reference frames, the mean of horizontal and vertical coordinates between ITRF2014 and ITRF2008 shows a small difference compared to ITRF2000. This could probably tell that the earthquake that hits Sumatra region of Indonesia in the years 2004, 2005 and 2007

Table 4 Coordinates of the point at helipad with respect to ITRF2000, ITRF2008 and ITRF2014

	Latitude	STD (m)	Longitude	STD (m)	Height (m)	STD (m)
ITRF2000						
Day 1	1 33 29.59578	0.001	103 38 13.36570	0.000	42.256	0.002
Day 2	1 33 29.59536	0.001	103 38 13.36670	0.001	42.251	0.002
Day 3	1 33 29.59550	0.001	103 38 13.36637	0.000	42.263	0.002
Mean	1 33 29.59554		103 38 13.36626		42.257	
ITRF2008						
Day 1	1 33 29.59712	0.001	103 38 13.36570	0.000	42.239	0.002
Day 2	1 33 29.59670	0.001	103 38 13.36670	0.001	42.235	0.002
Day 3	1 33 29.59685	0.001	103 38 13.36636	0.000	42.247	0.002
Mean	1 33 29.59689		103 38 13.36625		42.240	
ITRF2014						
Day 1	1 33 29.59707	0.001	103 38 13.36576	0.000	42.237	0.002
Day 2	1 33 29.59664	0.001	103 38 13.36676	0.001	42.232	0.002
Day 3	1 33 29.59679	0.001	103 38 13.36642	0.000	42.244	0.002
Mean	1 33 29.59683		103 38 13.36631		42.238	
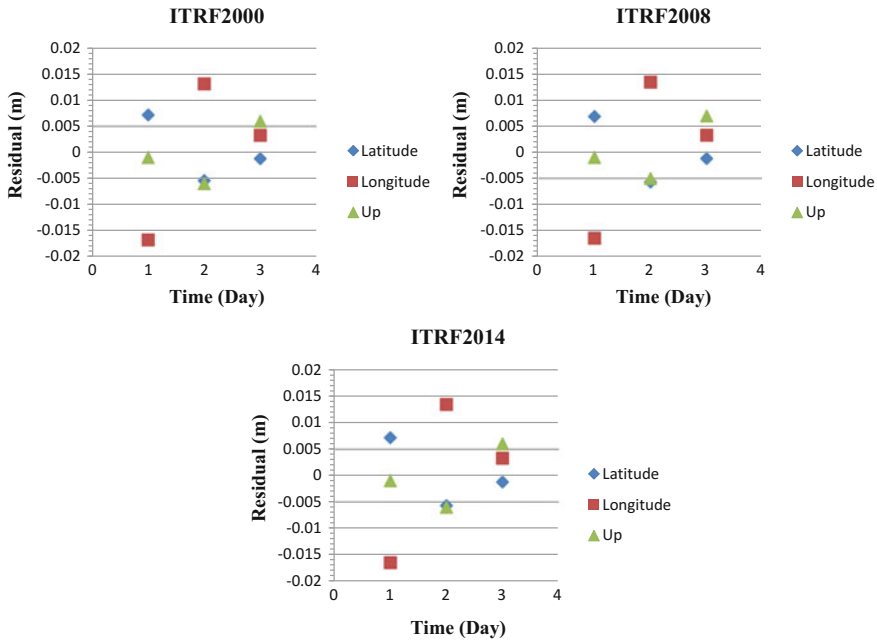
Fig. 3 Residual coordinates of 3 days data in ITRF2000, ITRF2008 and ITRF2014

triggered the movement on tectonic plate, hence causing a shifting in geodetic datum of Malaysia. Even though the differences in height between frames are up to cm level, it is still allowable as the altitude error is always considerably worse than the horizontal.

3.2 Coordinates of Point at Helipad by AUSPOS

AUSPOS used the maximum number of 15 nearby reference stations for processing, which consist of IGS stations as well as APREF stations. However, the chosen stations used for processing on day 1 differed to days 2 and 3. For day 1, only 11 stations (10 IGS + 1 APREF) were used while days 2 and 3 used 14 reference stations (11 IGS + 3 APREF) for processing. This could probably be due to data availability for that particular day on certain stations. Figure 4 shows the distribution of fiducial stations used to process the 3 days data in AUSPOS.

Table 5 shows the coordinate of the point at helipad with respect to ITRF2008 derived by using AUSPOS followed by the time series plot of residual coordinates for the 3 days data in Fig. 5. The standard deviations for the 3 days data are up to cm level with the smallest value in longitude, which is 6 mm, and the biggest value in height, which is 25 mm. Based on Fig. 5, the residual of the coordinates ranges
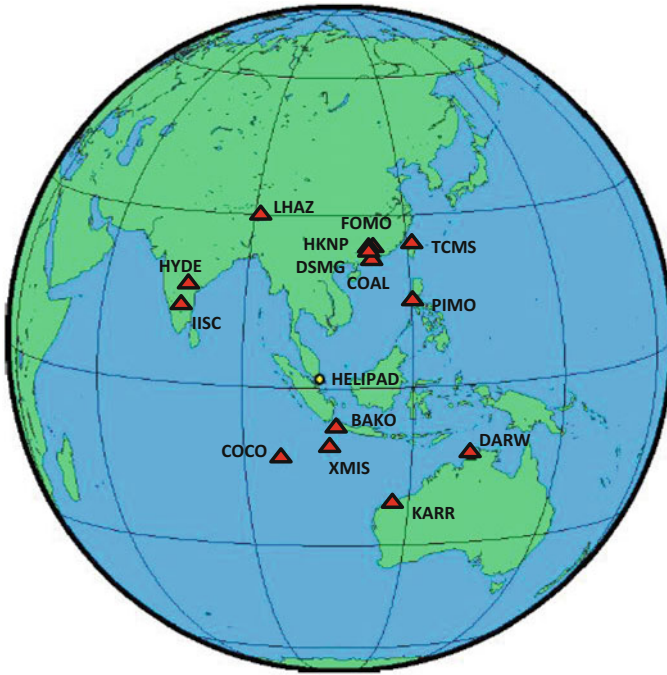
Fig. 4 Distribution of reference stations used in AUSPOS

from −0.0006 to 0.0057 mm for horizontal component (latitude and longitude) and −0.0075 to 0.0153 mm for vertical component (up). In the meantime, by referring to the data presented in Table 6, there is a small difference in horizontal component between the mean coordinates derived by AUSPOS and PPP which are −1.5 mm in latitude and −6.3 mm in longitude. Meanwhile, for the height coordinates, the difference is 24 cm, and it is considered tolerable as the standard deviation for this component is still within the range. To summarize the coordinate difference between AUSPOS and PPP, Fig. 6 portrays the residual differences for 3 days data along with the Root Mean Square Deviation (RMSD) of each component. The RMSD of horizontal components is 0.0047 m for latitude and 0.0115 m for longitude whereas the RMSD of the up component is 0.0061 m. These RMSDs indicate the differences or better known as residuals for evaluation of data.

AUSPOS processing strategy to resolve ambiguity is divided into four. They are code-based (180–6000 km baselines), phase-based L5/L3 (18–200 km baselines), Quasi-Ionosphere-Free (QIF) (18–2000 km baselines) and direct L1/L2 (0–20 km baselines) strategies. The strategy to resolve ambiguity for each baseline was chosen according to baseline length where the shortest baseline between stations COAL-DSMG (4.306 km) was resolved by using direct L1/L2, and the longest baseline between stations HKNP-HYDE (3679.651 km) was resolved by using Code-Based strategy. According to Tables 7, 8 and 9, the average ambiguity

Table 5 Coordinate of the point at helipad derived by AUSPOS based on ITRF2008

	Latitude	STD (m)	Longitude	STD (m)	Height (m)	STD (m)
ITRF2008						
Day 1	1 33 29.59682	0.009	103 38 13.36600	0.006	42.007	0.020
Day 2	1 33 29.59668	0.010	103 38 13.36608	0.006	41.988	0.023
Day 3	1 33 29.59703	0.010	103 38 13.36603	0.006	42.007	0.025
Mean	1 33 29.59684		103 38 13.36604		42.000	
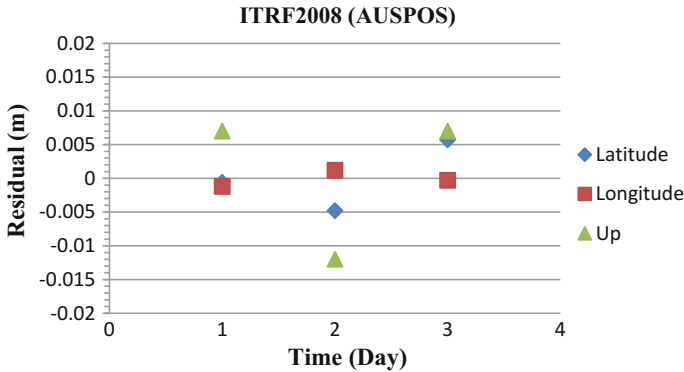
Fig. 5 Residual coordinates of 3 days data in ITRF2008 derived by AUSPOS

Table 6 Coordinate difference between AUSPOS and PPP

	Latitude (m)	Longitude (m)	Height (m)
Day 1	−0.0090	0.0090	−0.232
Day 2	−0.0006	−0.0186	−0.247
Day 3	0.0054	−0.0099	−0.240
Mean	−0.0015	−0.0063	−0.240

resolution for day 1, day 2 and day 3 shows the success rate of 72.3, 72.3 and 72.5%, respectively. The percentage of ambiguities resolved with the rate of 50% or better for a baseline formed by a user site indicates a reliable solution. However, the baseline between stations BAKO-HKNP shows a low percentage of ambiguities resolved for the 3 days, which are 25.9, 19.2 and 8%, respectively, compared to the other longer baseline. This might probably happened due to the data problem during those 3 consecutive days.
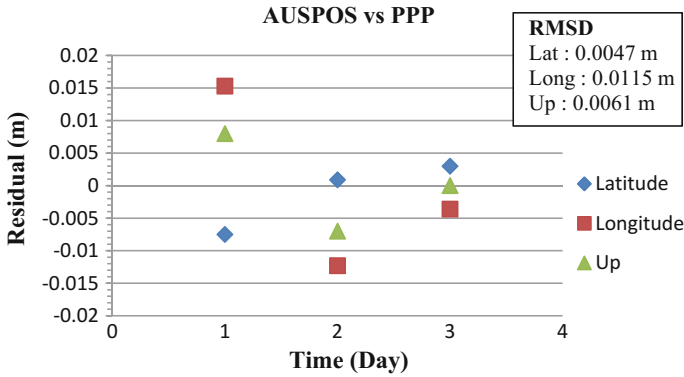
Fig. 6 Residual coordinates difference between AUSPOS and PPP

Table 7 Ambiguity resolution per baseline for day 1

Baseline	Ambiguities resolved (%)	Baseline length (km)
BAKO—HKNP	25.9	3234.634
HKNP—TCMS	82.6	776.860
HKNP—LHAZ	40.0	2406.585
BAKO—HELA	74.1	985.072
KARR—XMIS	83.4	1682.678
DARW—KARR	81.8	1738.492
HKNP—PIMO	76.0	1132.048
FOMO—HKNP	95.5	36.679
HYDE—LHAZ	87.0	1856.740
BAKO—XMIS	66.6	456.023
COCO—XMIS	82.6	984.535
Average	72.3	1387.577

3.3 Coordinates of Boundary Stones at Lot 4199

Coordinates of Cassini-Soldner Geocentric from PA 40225. Cadastral system in Johor, Malaysia used Cassini-Soldner geocentric with respect to ITRF2000 as its reference to carry out cadastral works. With the existing of NDCDB, integration of data can now be done globally as the origin of GDM2000 is at the mass centre of the Earth. According to PA 40225, the coordinates of boundary stones at Lot 4199 are tabulated as shown in Table 10. In order to assess the coordinates of point with different frames, the coordinates of boundary stones from the certified plan (PA 40225) are considered as true values.

Network-based RTK versus PA 40225. Similarly to coordinates from PA 40225, coordinates derived by the technique of network-based RTK are also in

Table 8 Ambiguity resolution per baseline for day 2

Baseline	Ambiguities resolved (%)	Baseline length (km)
BAKO—HKNP	19.2	3234.634
HKNP—TCMS	86.4	776.860
HKNP—LHAZ	30.0	2406.585
COCO—XMIS	86.4	984.535
BAKO—HELB	65.4	958.072
COAL—HKNP	90.9	37.121
COAL—DSMC	93.8	4.306
KARR—XMIS	76.0	1682.678
DARW—KARR	72.0	1738.492
HKNP—PIMO	82.6	1132.048
DSMG—FOMO	93.8	5.048
HYDE—LHAZ	77.3	1856.740
BAKO—XMIS	64.0	456.023
HYDE—IISC	75.0	497.626
Average	72.3	1126.483

Table 9 Ambiguity resolution per baseline for day 3

Baseline	Ambiguities resolved (%)	Baseline length (km)
HKNP—HYDE	35.3	3679.651
BAKO—HKNP	8.0	3234.634
HKNP—TCMS	85.0	776.860
COCO—XMIS	85.7	984.535
BAKO—HELC	62.9	958.072
COAL—HKNP	86.4	37.121
COAL—DSMC	95.8	4.306
KARR—XMIS	85.0	1682.678
DARW—KARR	85.7	1738.492
HKNP—PIMO	80.0	1132.048
DSMG—FOMO	97.7	5.048
HYDE—LHAZ	74.1	1856.740
BAKO—XMIS	57.1	456.023
HYDE—IISC	76.2	497.626
Average	72.5	1217.417

Cassini-Soldner geocentric connected to ITRF2000. This is because of the base stations used; they are the MyRTKnet stations and in Malaysia, MyRTKnet stations use GDM2000 as their datum with ITRF2000 as their reference frame. Table 11 shows the mean coordinates of points at cadastral lot by network-based RTK. The observations were done three times for every 10 epochs, and the mean coordinates

Table 10 Coordinates in Cassini-Soldner geocentric according to PA 40225

Boundary stone	Northing (m)	Easting (m)
3	−60757.255	15434.181
4	−60778.149	15418.435
5	−60765.888	15453.547
12	−60727.827	15253.414
14	−60743.953	15222.431

Table 11 Mean coordinates of points at Lot 4199 by network-based RTK

Boundary stone	Observation status	Northing (m)	Easting (m)
3	Fixed	−60757.317	15434.258
4	Fixed	−60778.217	15418.508
5	Fixed	−60765.945	15453.648
12	Float	−60726.348	15254.409
14	Fixed	−60743.942	15222.455

Table 12 Coordinates difference between network-based RTK and PA 40225

Boundary stones	Northing (m)	Easting (m)
3	−0.062	0.077
4	−0.068	0.073
5	−0.057	0.101
12	−1.479	0.995
14	−0.011	0.024
RMSD	0.0544	0.0742

of each point were calculated. For boundary stones 3, 4, 5 and 14, the ambiguities were managed to be fixed; meanwhile, for boundary stone 12, the observation status was float. This could probably be due to the position of the stone itself as it is located under the roof.

From the coordinate's difference between network-based RTK and PA 40225 as tabulated in Table 12, the differences vary between different points where the biggest difference is for boundary stone 12 and the smallest difference is for boundary stone 14, which are −1.479 m N, 0.995 m E and −0.011 m N, 0.024 m E, respectively.

ITRF2000 versus PA 40225. From the GPS fast static observation, coordinates of boundary stones were derived according to three different frames. TTC software provides coordinates in 3D geographical coordinates (latitude, longitude and height) along with their standard deviations as shown in Tables 13, 16 and 19. In order to do the assessment of coordinates between different frames and coordinates from PA 40225, map projection from 3D to two-dimensional (2D) (northing and easting) needs to be transformed as tabulated in Tables 14, 17 and 20. GDTS (Geodetic Datum Transformation System) software was used to transform

Table 13 Coordinates of points in ITRF2000

	Latitude	STD (m)	Longitude	STD (m)	Height (m)	STD (m)
ITRF2000						
3	1 29 35.10426	0.0181	103 41 59.15239	0.0157	11.9309	0.0267
4	1 29 34.42370	0.0134	103 41 58.64322	0.0160	11.0045	0.0231
5	1 29 34.82358	0.0128	103 41 59.78015	0.0138	11.8215	0.0202
12	1 29 36.05986	0.0667	103 41 53.30243	0.0666	09.5515	0.1131
14	1 29 35.53963	0.0141	103 41 52.30066	0.0137	09.6729	0.0222

Table 14 Coordinates in Cassini-Soldner geocentric based on ITRF2000

Boundary stones	Northing (m)	Easting (m)
ITRF2000		
3	−60757.521	15434.626
4	−60778.426	15418.916
5	−60766.141	15454.057
12	−60728.181	15253.821
14	−60744.162	15222.855

Table 15 Coordinates difference between ITRF2000 and PA 40225

Boundary stones	Northing (m)	Easting (m)
3	−0.266	0.445
4	−0.277	0.481
5	−0.253	0.510
12	−0.354	0.407
14	−0.209	0.424
RMSD	0.2526	0.4662

coordinates in ITRF2000, ITRF2008 and ITRF2014 to Cassini-Soldner geocentric and the state selection was Johor as the boundary stones are all located in Johor.

According to Tables 13, 16 and 19, the overall standard deviations for the horizontal components (latitude and longitude) of the boundary stones 3, 4, 5 and 14 are less than 2 cm whereas the standard deviation for the vertical component (height) is up to 2.7 cm with the biggest values on point 3, which are 1.81, 1.57 and 2.67 cm, respectively. However, for the boundary stone 12, the values of standard deviations for all components are slightly bigger than other points which are up to 11 cm. This could probably be due to the location of boundary stone. Due to multipath, the elevation cut-off to process the fast static data for point 12 is set up to 20° in order to obtain a fixed baseline compared to other points the elevation cut-off is set as default which is 10°. Therefore, boundary stone 12 is excluded from the assessment of coordinates between different frames. Based on Table 15, the coordinate differences between ITRF2000 and PA 40225 are generally range from −0.277 to −0.209 m for northing and from 0.424 to 0.510 m for easting along with

Table 16 Coordinates of points in ITRF2008

	Latitude	STD (m)	Longitude	STD (m)	Height (m)	STD (m)
ITRF2008						
3	1 29 35.10561	0.0181	103 41 59.15238	0.0157	11.9139	0.0267
4	1 29 34.42505	0.0134	103 41 58.64321	0.0160	10.9874	0.0231
5	1 29 34.82493	0.0128	103 41 59.78014	0.0138	11.8044	0.0202
12	1 29 36.06122	0.0666	103 41 53.30242	0.0665	09.5335	0.1129
14	1 29 35.54097	0.0141	103 41 52.30065	0.0137	09.6558	0.0222

Table 17 Coordinates in Cassini-Soldner geocentric based on ITRF2008

Boundary stones	Northing (m)	Easting (m)
ITRF2008		
3	−60757.479	15434.654
4	−60778.384	15418.916
5	−60766.099	15454.060
12	−60728.139	15253.820
14	−60744.120	15222.855

Table 18 Coordinates difference between ITRF2008 and PA 40225

Boundary stones	Northing (m)	Easting (m)
3	−0.224	0.473
4	−0.235	0.481
5	−0.211	0.513
12	−0.311	0.406
14	−0.167	0.424
RMSD	0.2108	0.4738

their RMSD, 0.2526 and 0.4662 m, respectively. Moreover, the differences of each point between coordinates derived from network-based RTK and PA 40225 is smaller for point 3, 4, 5 and 14 compared to differences of coordinates derived by single-based fast static GPS observation (ITRF2000) and certified plan. This could possibly tell that by using network-based RTK, the network correction is applied on each point can reduce the distance-dependent error (Tables 16 and 17).

ITRF2008 versus PA 40225. As Malaysia is using GDM2000 connected to ITRF2000, there would be bigger differences in coordinates between ITRF2008 and PA 40225 compared to ITRF2000 and PA 40225. However, for the northing component, differences of ITRF2008—PA 40225 are smaller where it ranges from −0.235 to −0.167 m except for easting component the differences are slightly bigger as it ranges from 0.424 to 0.513 m, and these differences are shown in Table 18 as well as their RMSD, which are 0.2108 m (northing) and 0.4738 m (easting) (Tables 19 and 20).

Table 19 Coordinates of points in ITRF2014

	Latitude	STD (m)	Longitude	STD (m)	Height (m)	STD (m)
ITRF2014						
3	1 29 35.10555	0.0181	103 41 59.15244	0.0157	11.9119	0.0267
4	1 29 34.42499	0.0134	103 41 58.64327	0.0160	10.9855	0.0231
5	1 29 34.82487	0.0128	103 41 59.78020	0.0138	11.8024	0.0202
12	1 29 36.06116	0.0666	103 41 53.30248	0.0665	09.5315	0.1129
14	1 29 35.54091	0.0141	103 41 52.30071	0.0137	09.6538	0.0222

Table 20 Coordinates in Cassini-Soldner geocentric based on ITRF2014

Boundary stones	Northing (m)	Easting (m)
ITRF2014		
3	−60757.481	15434.656
4	−60778.386	15418.918
5	−60766.101	15454.062
12	−60728.141	15253.822
14	−60744.122	15222.857

ITRF2014 versus PA 40225. As already mentioned in previous section, there should also be bigger differences in coordinates between ITRF2014 and PA 40225 compared to ITRF2000 and PA 40225. But then again, differences in coordinates of ITRF2014—PA 40225 for northing component are smaller within the range of −0.237 to −0.169 m. Aside from easting component, the differences in coordinates are also slightly bigger as it ranges from 0.426 to 0.515 m. The coordinate's differences between ITRF2014 and PA 40225 are tabulated in Table 21. These differences can also be evaluated from the RMSD of each component, which are 0.2128 and 0.4758 m for northing and easting.

The precision of coordinates for each boundary stone can be evaluated from the standard deviations on each component. Figure 7 summarizes the standard deviation of points 3, 4, 5, 12 and 14 based on ITRF2000 from the processing by using TTC software. In general, point 12 has the least precise coordinates, which are 0.0666, 0.0665 and 0.1129 m for latitude, longitude and height due to the location of the boundary stone whereas point 5 has the most precise coordinates with the value of standard deviation of 0.0128, 0.0138 and 0.0202 m, respectively.

Table 21 Coordinates differences between ITRF2014 and PA 40225

Boundary stones	Northing (m)	Easting (m)
3	−0.226	0.475
4	−0.237	0.483
5	−0.213	0.515
12	−0.314	0.408
14	−0.169	0.426
RMSD	0.2128	0.4758
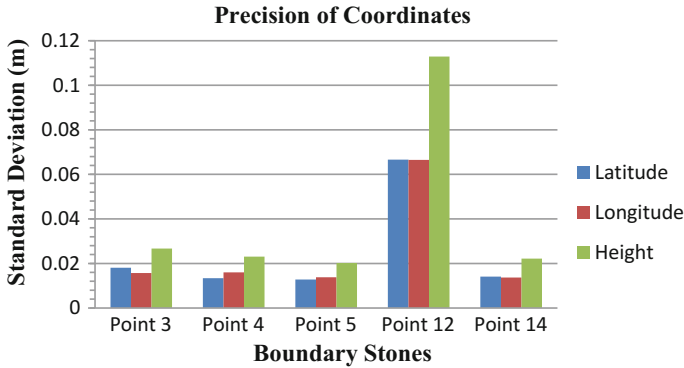
Fig. 7 Standard deviation of coordinates derived by using TTC based on ITRF2000

4 Conclusions

As comprehensively discussed in this paper, the 3 days data is successfully being processed by using Waypoint software in PPP mode with respect to different International Reference Frames (ITRF2000, ITRF2008 and ITRF2014). Undoubtedly, the coordinates derived with respect to the latest frame which is ITRF2014 are the most reliable to be adopted for positioning as they have small value of standard deviation. Moreover, according to Altamimi et al. [11], ITRF2014 is generated with an enhanced modelling of nonlinear station motions, including seasonal signals of station positions and post-seismic deformation for sites that were subject to major earthquake, so it is expected that ITRF2014 will provide a better positional accuracy compared to the previous version of ITRF. Due to dynamic Earth and Post-seismic Deformation (PSD), the origin of reference frames will gradually change across time affecting the position of points on Earth. However, with the existence of ITRF2014 that take into account the PSD by modelling it, the stations that are more prone to earthquake have the potential to accurately describe their actual trajectories. Contrarily, in cadastral survey, a homogenous coordinate system with reference to the global datum is required in mapping integrated purpose. Differences in ITRF give different coordinates for boundary stones on cadastral lot.

In conclusion, GDM2000 has to be revised frequently with respect to the latest version of ITRF in order to give a better positional accuracy and a fix geocentric mapping datum needs to be opted for cadastral integrated purposes in Malaysia.

References

1. Wei, Z., Shuang, Z., Bo, Y., Yanqiang, W., Zhiguang, L., Xiangang, M.: Effects of the differences between the ITRF2000 and ITRF2005 models in GNSS data processing. Geodesy Geodyn. **4**(4), 46–50 (2013)
2. Kang, S.G.: Establishing efficient cadastral surveying plan in accordance with introducing world geodetic reference system in Korea. Mod. Environ. Sci. Eng. **1**(6), 299–303 (2015)
3. Satirapod, C., Simons, W.J.F., Panumastrakul, E., Trisirisatayawong, I.: Updating the Thai coordinate reference frame to ITRF2005 using GPS measurements: observation on a diversion between ITRF2000 and ITRF2005 in Southeast Asia region. In: Proceeding of 7th FIG Regional Conference Spatial Data Serving People: Land Governance and the Environment Building the Capacity, pp. 19–22. Vietnam (2009)
4. Jhonny, J.: Post-seismic earthquake deformation monitoring in Peninsular Malaysia using global positioning system. Master thesis, Universiti Teknologi Malaysia, Faculty of Geoinformation Science and Engineering (2010)
5. Gill, J. S.: Development of a datum transformation model in relation to the tectonic motion in Malaysia. Master thesis, Universiti Teknologi Malaysia, Faculty of Geoinformation and Real Estate (2016)
6. Shariff, N.S.M., Musa, T.A., Omar, K., Othman, R.: The geocentric datum of Malaysia: preliminary assessment and implications. In: Rahman, A.A., Boguslawski, P., Anton, F., Said, M.N., Omar, K.M. (eds.) Geoinformation for Informed Decisions, pp. 71–83. Springer, Switzerland (2014)
7. Kadir, M., Ses, S., Omar, K., Desa, G., Omar, A.H., Taib, K., et al.: Geocentric datum GDM2000 for Malaysia implementation and implications. In: Seminar on GDM2000, 28 August 2003, Department of Surveying & Mapping Malaysia, Kuala Lumpur
8. Department of Survey and Mapping Malaysia (DSMM) (2009): Technical guide to the coordinate reference systems. Pekeliling Ketua Pengarah Ukur dan Pemetaan Bilangan 1/2009, Kuala Lumpur (2003)
9. Altamimi, Z., Sillard, P., Boucher, C.: ITRF2000: a new release of the international reference frame for earth science applications. J. Geophys. Res. **107**(B10), 1–19 (2002)
10. Altamimi, Z., Collilieux, X., Metivier, L.: ITRF2008: an improved solution of the international terrestrial reference frame. J. Geodesy **85**(8), 457–473 (2011)
11. Altamimi, Z., Rebischung, P., Metivier, L., Collilieux, X.: ITRF2014: a new release of the international terrestrial reference frame modelling nonlinear station motions. J. Geophys. Res. Solid Earth **121**(8), 6109–6131 (2016)
12. Kadir, M., Ses, S., Desa, G., Tong, C.W., Teng, C.B.: Towards the implementation of coordinated cadastral system in Malaysia: large cadastral network adjustments. Aust. Surveyor **45**(1), 37–46 (2012)
13. Australian Government Geoscience Malaysia. http://www.ga.gov.au/scientific-topics/positioning-navigation/geodesy/auspos. Last accessed 2017/04/20
14. Berber, M., Ustun, A., Yetkin, M.: Comparison of accuracy of GPS techniques. Measurement **45**(7), 1742–1746 (2012)

Monitoring the King Tide Phenomenon Over Malacca Straits and South China Sea from Space Geodetic Missions

Wan Ahmad Syauqi Wan Abd Latiff, Ami Hassan Md Din and Abdullah Hisam Omar

Abstract At the end of year 2016, the west coast of Peninsular Malaysia has been hit by the flood. The low-lying area along the coastline was flooded with seawater causes the villagers to be moved to the relief centre, while the flood caused a lot of loss and damage to their properties. This flood happened because the phenomenon called king tide had occurred during that day. This king tide is formed when the Moon is very close to the Earth (at its closest perigee) and in the New Moon or Full Moon phase. This has brought sudden increase in tide magnitude. This phenomenon can be studied in order to help the early decision-making and proper planning to be rolled out. There are bunch of technologies that are made available which can be used to study the tide efficiently. One of the following technologies is by using space geodetic technique, the satellite altimeter. Satellite altimeter is the geodetic space technique which is designed for the study of the ocean. Compared to the conventional method of observing tide using tide gauge, this satellite altimeter can give the larger spatial coverage on tide especially on deep ocean region and near coastal region. In this research, sea level data is processed and derived using Radar Altimeter Database System (RADS). Altimetry-derived sea level data is used

W. A. S. Wan Abd Latiff · A. H. Md Din (✉) · A. H. Omar
Faculty of Geoinformation and Real Estate, Geomatic Innovation
Research Group (GIG), Universiti Teknologi Malaysia,
81310 Johor Bahru, Johor, Malaysia
e-mail: amihassan@utm.my

W. A. S. Wan Abd Latiff
e-mail: ahmadsyauqi93@gmail.com

A. H. Omar
e-mail: abdullahhisham@utm.my

A. H. Md Din
Faculty of Geoinformation and Real Estate, Geoscience
and Digital Earth Centre (INSTEG), Universiti Teknologi
Malaysia, 81310 Johor Bahru, Johor, Malaysia

A. H. Md Din
Institute of Oceanography and Environment (INOS), Universiti Malaysia
Terengganu, Kuala Terengganu, Terengganu, Malaysia

to monitor the king tide phenomenon in order to see their pattern and magnitude by comparing to the normal perigee days on the past year. This satellite altimeter is utilized to study the area of interest, which is at Malacca Strait and South China Sea. The result clearly shows that the perigee phenomenon which occurred on November 14 gave a significant impact on the tidal magnitude. The verification process between the satellite altimetry and tidal data also indicates a good argument for the root-mean-square error and correlation coefficient. The outcomes show that the satellite altimeter can be used as a tool to observe and monitor the king tide phenomenon particularly in large-scale area.

Keywords King tide phenomenon · Sea level · Space geodetic
Radar altimeter database system

1   Research Background

Malaysian has been shocked by the news that several places along the west coast of Peninsular Malaysia have been flooded by the seawater. This high tide flooded the low-lying areas in Selangor, Kedah, and Perak in September 2016. Two hundred and twenty-four people from 53 families in Selangor, 76 people from 15 families in Kedah, and 132 people from 30 families in Perak were evacuated during the king tide phenomenon in September 2016. These phenomena rarely occur throughout the years and have been called by the name of "King Tide" and in 2016, it strikes the west coast of Peninsular Malaysia unusually [1].

When the moon is close to earth, called perigee, the tidal force is stronger. This large tide is known as perigee tide or perigean tide which repeats itself every 27.55 days. When the moon is farthest from earth called apogee, the tidal acceleration decreases about 30% respect to its perigee value. For the spring tide, it is actually the higher high tides and the lower low tides which occur at new and full moon [2].

At the new or full moon, the earth, sun, and moon are aligned such that the pull of the sun on the ocean adds the pull of the moon on the oceans king tide is actually a perigean spring tide which is combination of both perigean tide and spring tide that coincide together [3]. The king tide which is the peak of astronomical tide happens several times a year. Especially when the Moon's perigee (its closest point to Earth during its 28-day elliptical orbit) coincides with a spring tide (when the earth, sun, and moon are nearly aligned every 2 weeks). The perigean spring tide is shown in Fig. 1.

When the king tide hits the west coast of Peninsular Malaysia in September 2016, it is recorded that the Port Kelang Tide Gauge Station reading was at 5.6 m which is exceptionally high than normal day which is only at 3.6 m. Today, there are several technologies which have been used to observe and monitor every ocean
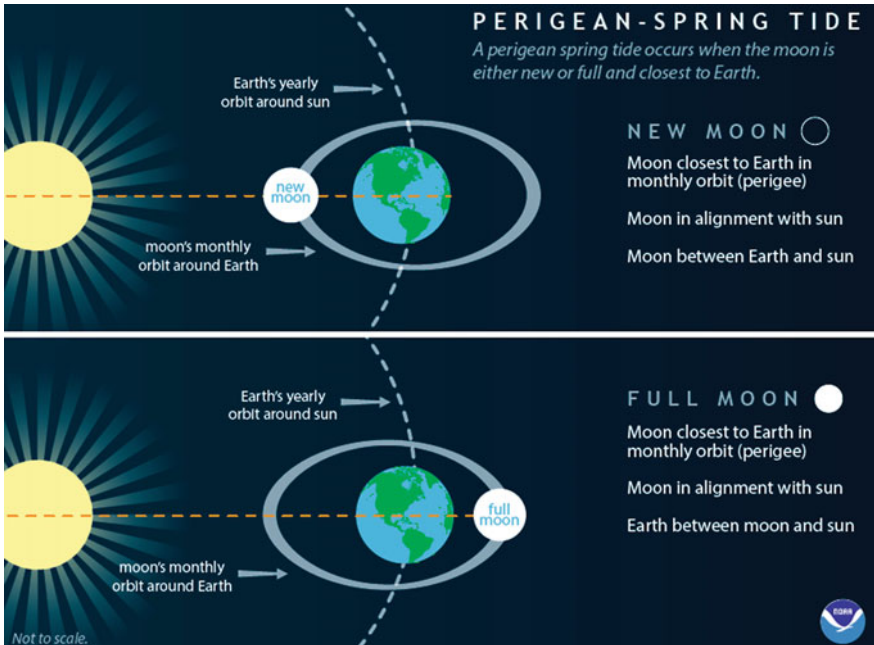
Fig. 1 The perigean spring tide illustration [4]

event precisely. One of the technologies is by using Satellite Altimeter (SA) approach method rather than only using the tide gauge station alone. By using this technology, the king tide event can be monitored and observed.

1.1 Principle of Satellite Altimeter

Satellite Altimeter (SA) is categorized as a remote sensing technique. Generally, there are two basic geometric measurements that are involved in this satellite altimeter in order to observe and provide data. First, the distance between the satellite and the sea surface is determined from the round-trip travel time of microwave pulses emitted downward by the satellite's radar and reflected back from the ocean.

Second, independent tracking systems are used to compute the satellite in three-dimensional positions relative to a fixed earth coordinate system. Combining these two measurements yields profiles of sea surface topography, or sea level, with respect to the reference ellipsoid. An altimeter operates by sending out a short pulse of radiation and measuring the time required for the pulse to return from the sea surface. This measurement is called altimeter range; R gives the height of the

instrument above the sea surface. The R from the satellite to mean sea level is estimated from the round-trip travel time.

Doppler Orbitography and Radiopositioning Integrated by Satellite (DORIS), Laser Ranging Station, and onboard Global Positioning System (GPS) are independent tracking system that is used to determine the position of satellite relative to earth fixed coordinate system. However, to get the value of the height of the water is not as easy as perceived.

There are several factors that have to be taken into account such as atmospheric correction (ionosphere, dry troposphere and wet troposphere), orbital altitude (altimeter range and instrument corrected), pole tide, solid earth tide, ocean tide loading, ocean tide, electromagnetic bias, sea state bias, and a dynamic atmosphere [5]. Figure 2 illustrates the satellite altimetry concept and principle.

Ordinarily, for sea surface height variation studies, it is more appropriate to refer the sea surface height to the Mean Sea Surface (MSS) rather than to the geoid surface, thus forming the SLA, h_{sla}, [5]:

$$h_{sla} = H - R_{obs} - \Delta h_{dry} - \Delta h_{wet} - \Delta h_{iono} - \Delta h_{ssb} - h_{MSS} - h_{tides} - h_{atm} \qquad (1)$$

where $R_{obs} = c\ t/2$ is the computed range from the travel time, t observed by the onboard Ultra-Stable Oscillator (USO), and c is the speed of the radar pulse neglecting refraction approximate 3×10^8 m/s
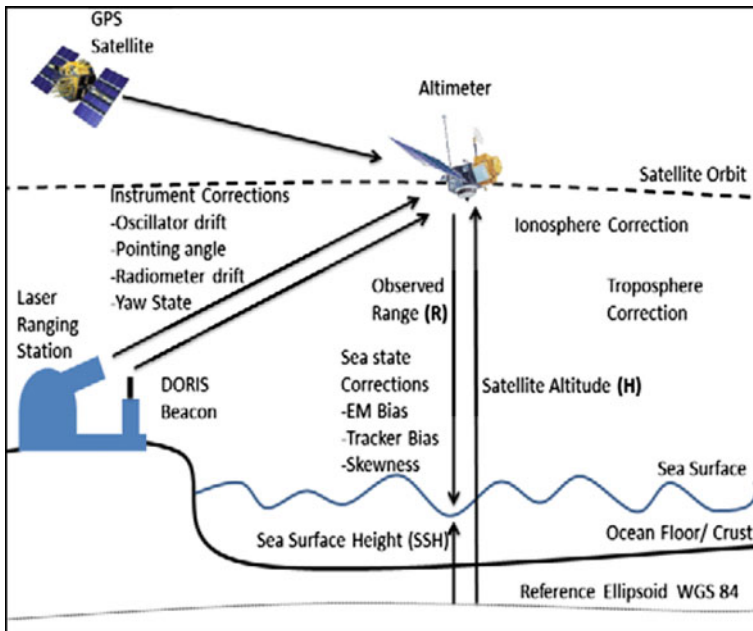
Fig. 2 The principle of satellite altimeter measurement [12]

Δh_{dry}	Dry tropospheric correction
Δh_{wet}	Wet tropospheric correction
Δh_{iono}	Ionospheric correction
Δh_{ssb}	Sea-state bias correction
h_{mss}	Mean sea surface
h_{tides}	Tides correction
h_{atm}	Dynamic atmospheric correction.

From this equation, the height of Sea Level Anomalies (SLA) will be used in this study as it is aimed at the study of king tide phenomenon.

2 Study Approach

2.1 Study Area and Data Processing

This study is being focused on Peninsular Malaysia which involved Malacca Strait and South China Sea. It ranges between 0°N ≤ Latitude ≤ 14°N and 95°E ≤ Longitude ≤ 108°E comprising the entire Peninsular Malaysia region as shown in Fig. 3.

Within the time span of 4 years and focused on the king tide event, the sea level trend is quantified from sea level anomalies data from the satellite altimeter technique. By the help of Radar Altimeter Database System (RADS) as the processing software, it will provide user to select the most suitable correction which will be applied to the data. Then, selected tidal data from Permanent Service of Mean Sea Level (PSMSL) are used as ground truth data in verification purpose for altimetry data in order to produce comparable result [6].

2.2 Data Verification

The monthly sea level data for data verification are acquired from the Permanent Service for Mean Sea Level (PSMSL) website. The comparison of sea level from altimetry and tidal data was carried out by extracting monthly SLA average at the altimeter track and tide gauge locations which are located near to each other.

The pattern and correlation of sea level anomalies of both measurements are evaluated over the same period in each area. Figure 4 shows the selected tide gauge, namely, Port Klang and Lumut for Malacca Straits and Geting and Pulau Tioman for South China Sea.
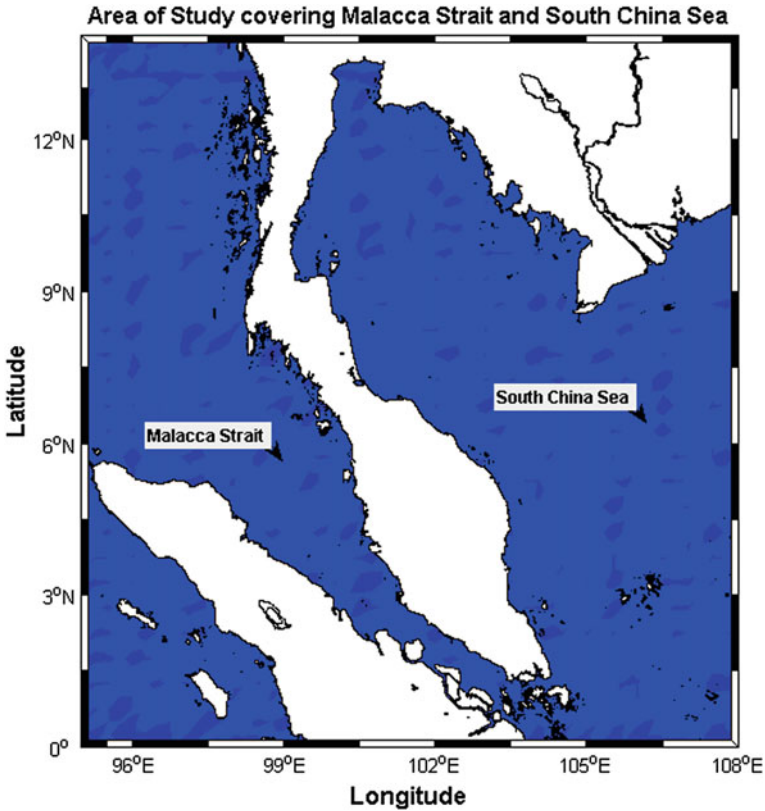
Fig. 3 The area of study conducted for this research which covers the Malacca Strait and South China Sea

2.3 Multi-mission Altimetry Data and Processing

Using the Radar Altimeter Database System (RADS) software, the SLA data is extracted and the data is applied with corrections. There are a lot of Satellite Altimeter (SA) data that are made available to be extracted but only the certain satellite altimeters are selected according to the time frame for this research which only covers from year 2013 until year 2016.

The involved satellite altimeters are Jason-2, Jason-3, Saral, and Cryosat. Table 1 shows the altimetry data selected for this study and the characteristic of the chosen altimeter satellites in Table 2.

In RADS processing, several steps are involved to execute the extraction of the sea level anomalies data. The processing starts from crossover adjustment for every multi-mission satellite and followed by data gridding for smoothing the data. Then, proceed with daily solution data for each multi-mission satellite and lastly extract
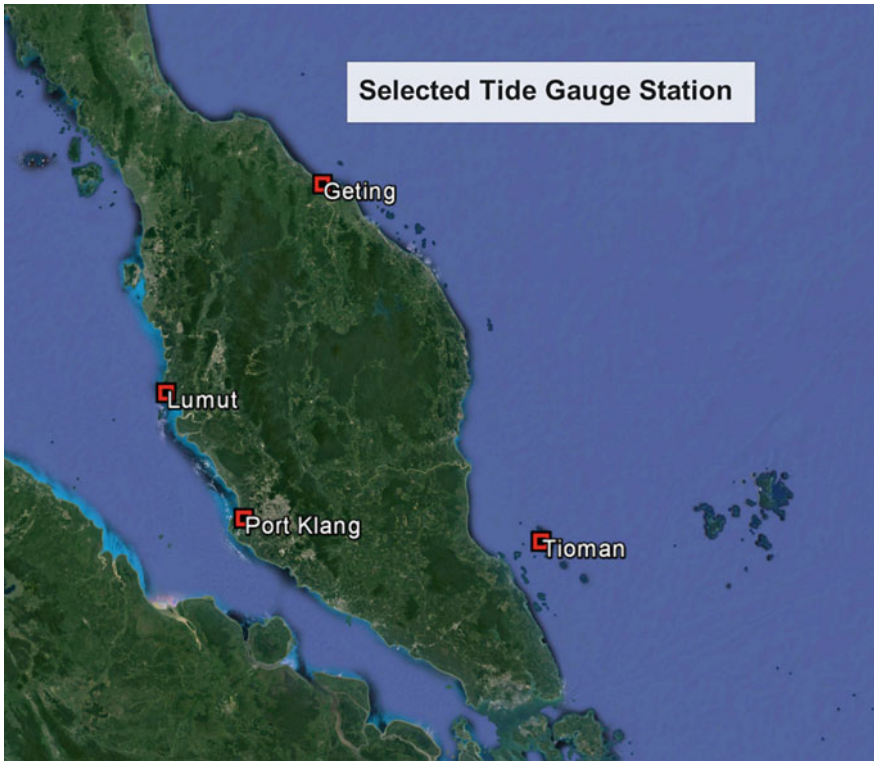
Fig. 4 The selected tide gauge station used for data verification for altimeter satellite

Table 1 The altimetry data selected for this study

Satellite	Period	Cycle
Jason-2	Jan 2013–Dec 2016	166–312
Jason-3	Jan 2016–Dec 2016	1–35
SARAL	Mac 2013–Dec 2016	1–39
CryoSat	Jan 2013–Dec 2016	37–86

Table 2 The characteristic of the chosen altimeter satellites [7]

Satellite	Agency	Launch on	Altitude (km)	Inclination (°)	Repeatability (days)
Jason-2	NASA CNES	20/06/2008	1336	66	10
Jason-3	NASA CNES NOAA	17/01/2016	1336	66	10
SARAL	ESA CNES	25/02/2013	~ 800	98.55	35
CryoSat	ESA	08/04/2010	717	92	30
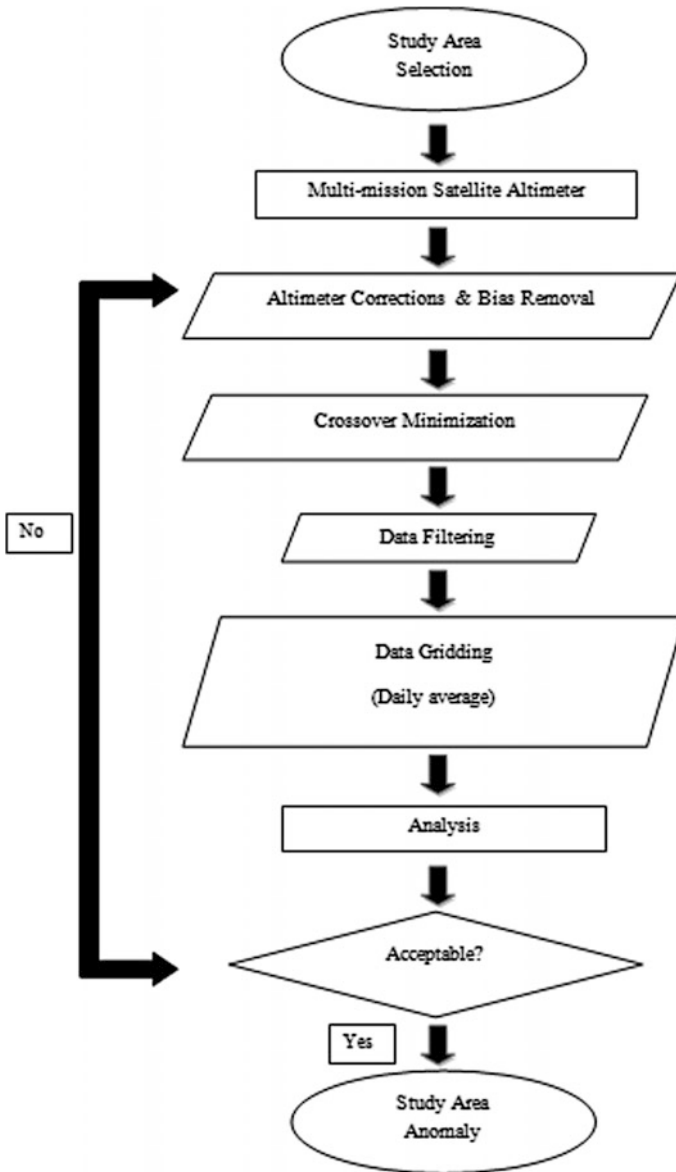
Fig. 5 The workflow of the RADS processing to retrieve the altimeter data

the sea level anomalies data for every selected point. Figure 5 shows the overview of RADS processing strategies.

The crossover adjustment is performed to integrate the data processing for the stated satellite altimeter that is used. Crossover adjustment is processed to adjust the
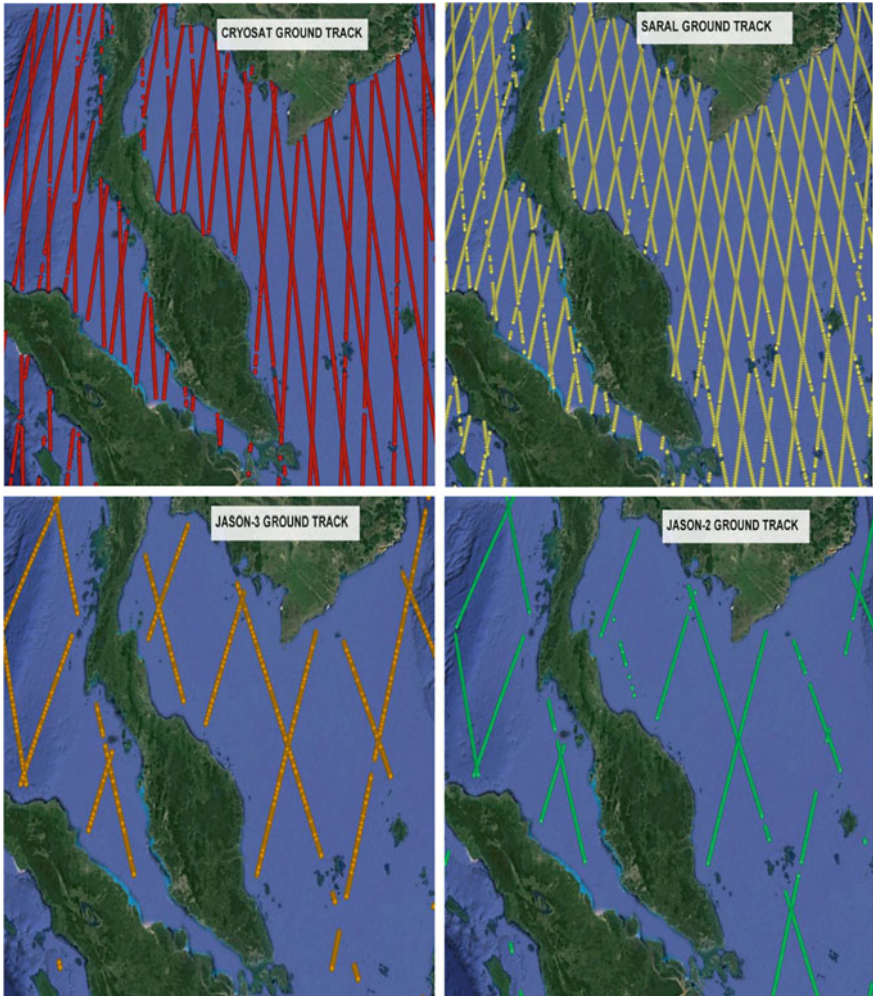
Fig. 6 The ground track for CryoSat, SARAL, Jason-3, and Jason-2

different satellite missions to a standard surface because of the disparity in the satellite orbit frame and orbit error and in this case, all four satellite altimeters are through the crossover adjustment process in order to achieve higher accuracy. Figure 5 shows the ground track for each of the selected satellite altimeter, and Fig. 6 shows the overall crossover for those selected satellites.

After crossover adjustment has been done successfully, data gridding and smoothing took place. During this stage, SLA data are filtered and gridded to grid size bin ($0.25° \times 0.25°$) using Gaussian weighting function with 1.5 sigma. A shell script to run the data gridding and smoothing is used.

Table 3 The details of perigean day date used to extract the data

Perigean dates			
Year	Month	Day	Length (km)
2013	June	23	356,989
2014	August	10	356,896
2015	September	28	356,876
2016	September	18	361,893
2016	October	16	357,859
2016	November	14	356,511

Both daily and monthly solutions are used in the data extraction. The extraction of sea level anomalies data for perigean days is performed using daily solution. The perigean day dates are taken from the Fourmilab website which provided the lunar perigee and apogee calculator for user to search the perigee and apogee dates [8]. Table 3 shows the details of perigean day dates which are extracted.

Then, the monthly solutions are used only to equate with the monthly tidal data solution for selected tide gauge station in order to see the correlation among these solutions for data verification purposes.

The satellite altimeter is subjected to errors and uncertainties. To increase the accuracy and reliability, many corrections are made on the processed data. The updated geophysical corrections and latest environmental are applied in the RADS processing. The corrections included are orbital altitude, sea state bias, dry and wet delay, electromagnetic bias, ocean tides and solid earth tide. The correction is done by assigning specific model for the selected satellite altimeter in RADS. This correction can be reviewed in Table 4.

Table 4 The applied correction in RADS processing [9]

Correction/model	Editing (m)		Description
	Min	Max	
Orbit/gravity field			All satellites: EIGEN-GL04S:
			DGM-E04/D-PAF
Dry troposphere	−2.4	−2.1	All satellites: atmospheric pressure grids
Wet troposphere	−0.6	0.0	All satellites: radiometer measurement
Ionosphere	−0.4	0.04	All satellite: smoothed dial-freq, ERS: NIC09
Dynamic atmosphere	−1.0	1.0	All satellites: MOG2D
Ocean tide	−5.0	5.0	All satellites: GOT 4.8
Load tide	−0.5	0.5	All satellites: GOT 4.8
Solid earth tide	−1.0	1.0	Applied (elastic response to tidal potential)
Pole tide	−0.1	0.1	Applied (tide produced by Polar Wobble)
Sea state bias	−1.0	1.0	All satellites: CLS nonparametric
			ERS: BM3/BM4 parametric
Reference	−1.0	1.0	DTU13 mean sea surface height
Engineering flag			Applied
Applied reference frame			Jason-2 and Jason-3

3   Result and Discussion

3.1   Data Verification

The sea level anomalies data from satellite altimeter is compared with the ground truth data which is the tidal data for the verification purpose. Four selected areas are picked for the verification process as stated earlier in Fig. 4. These selected tide gauge stations compromise east and west coast of Peninsular Malaysia. The results of the sea level verification are focused on the pattern and the correlation analysis between altimetry and tidal sea level anomalies.

The pattern for both datasets has been evaluated over the same time period in each area in order to produce a comparable result starting from year 2013 until year 2015. Figure 7 shows the sea level pattern at Geting and Pulau Tioman which evaluated for data from South China Sea and Fig. 8 shows the pattern for Port Klang and Lumut representing the Malacca Strait.

Figure 7 for Geting and Pulau Tioman shows a similar pattern of sea level variations with a more or likely regular annual cycle indicating that the chosen range and geophysical correction are well suited for these areas. Figure 8 for Lumut and Port Klang also shows the same pattern when the tide gauge sea level anomalies are compared with the altimeter sea level anomalies but because of missing on several tide gauge data, the pattern of sea level anomalies for Port Klang tide gauge looks distorted.
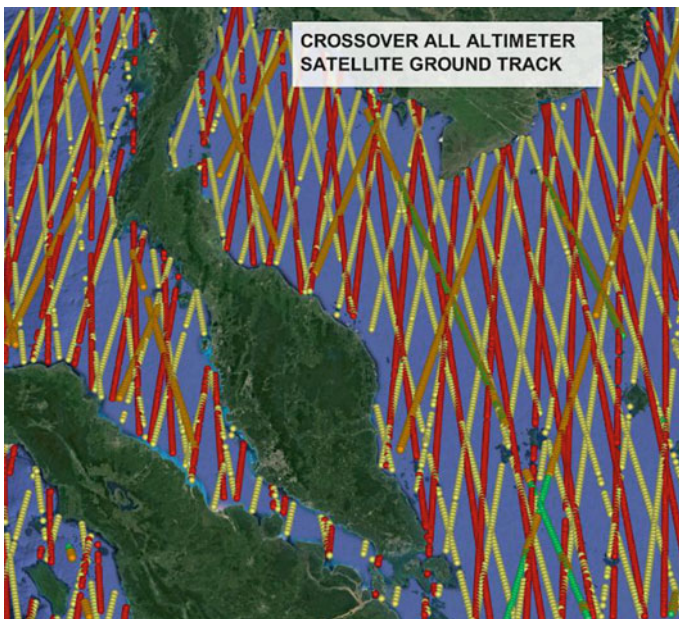
Fig. 7   The overall crossover for those four selected satellite altimeters
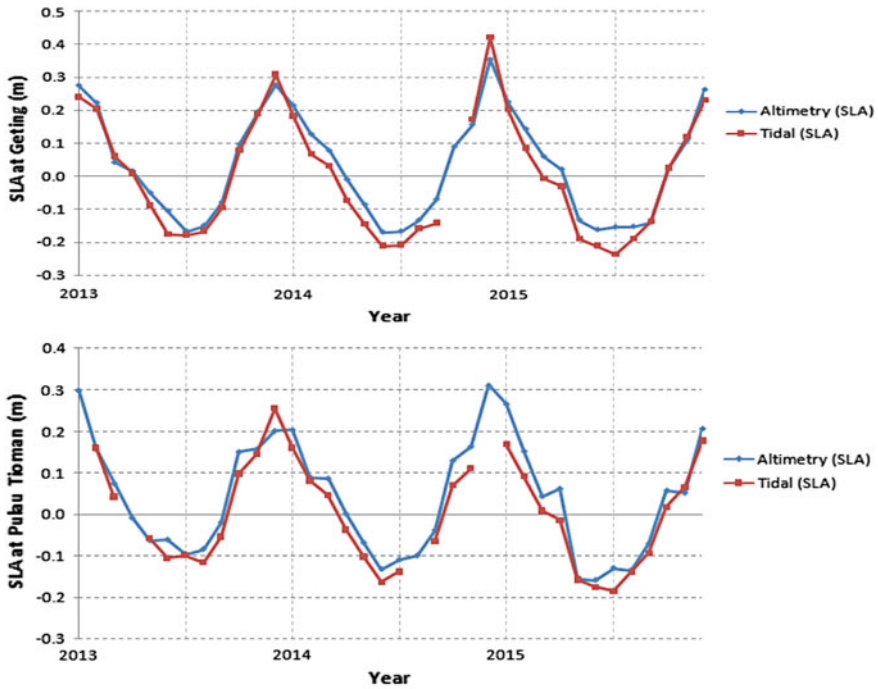
Fig. 8 The pattern of sea level anomalies at Geting and Pulau Tioman which represent the South China Sea

Next, the correlation analysis is performed. The correlation coefficient, R^2, is measured for the strength of the linear relationship between two inputs or variables. The higher the value of the correlation, the stronger the relationship between those two variables in positive relationship or negative relationship.

In order to validate the sea level anomalies from satellite altimeter, the tide sea level anomalies are also used; therefore, the value of R^2 is needed to see the relationship between two variables as shown in Figs. 9 and 10.

The value of correlation coefficient can be categorized as follows: 1 is perfect, 0.7–0.9 is strong, 0.4–0.6 is moderate, and less than 0.3 is a weak correlation [10]. All results are shown in Figs. 9 and 10.

The correlation values for both Geting and Pulau Tioman represented from the South China Sea are about 0.972 and 0.948, respectively. These values indicate the strong correlation between the tidal sea level anomalies and satellite altimeter sea level anomalies (Figs. 11, 12, and 13).

Overall, all of the stations give a confident result with the value of R^2 all above 0.6. The lowest correlation is at Pelabuhan Kelang. This is due to missing tide gauge data for several months as mentioned in description of Fig. 8. This highest correlation is at Geting station which is 0.972.
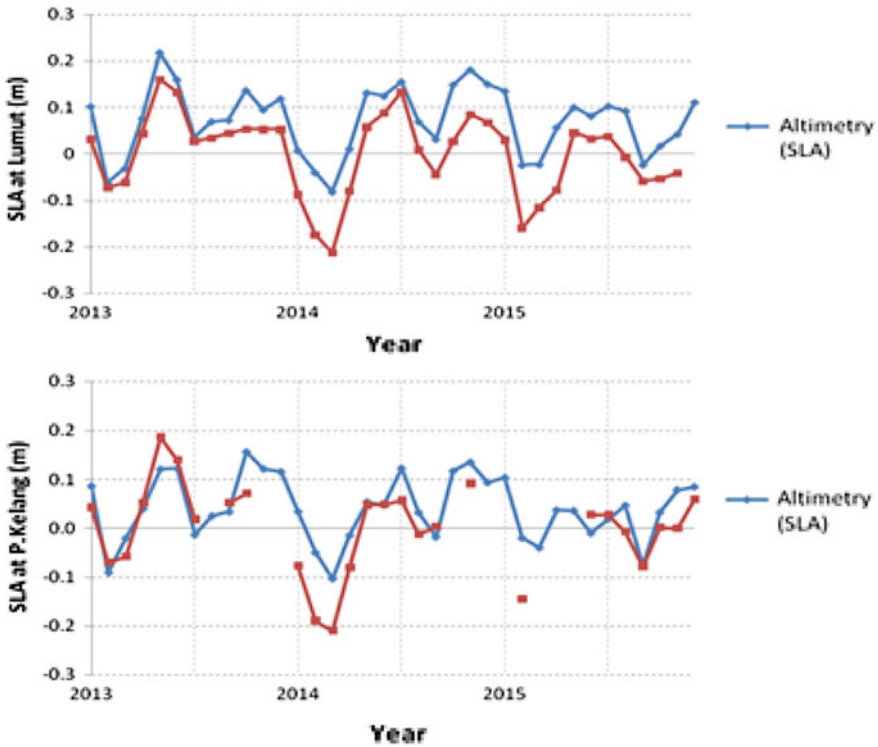
Fig. 9 The pattern of sea level anomalies at Lumut and Port Kelang which represent the Malacca Strait

The next validation process is by looking at Root-Mean-Square Error (RMSE) of the anomaly between the SLA altimeter and SLA tide gauge. RMSE indicates the magnitude of derivation for this study to determine either the data are acceptable or not. The RMSE is considered good enough if it has small value.

The RMSE values for every station are shown in Table 5. Based on results, the RMSE is very good for the Geting and Pulau Tioman station with the Pulau Tioman having the lowest RMSE at 0.0405 m followed by Geting at 0.0425 m. The RMSE for Lumut is at 0.0784 m, and Pelabuhan Klang at 0.0613 m shows the highest among those stations.

The unavailability of tidal data on certain months for Pelabuhan Klang and the location of the Lumut tide gauge station which is a little bit far from the altimeter tracks have led to the increase in RMSE value.
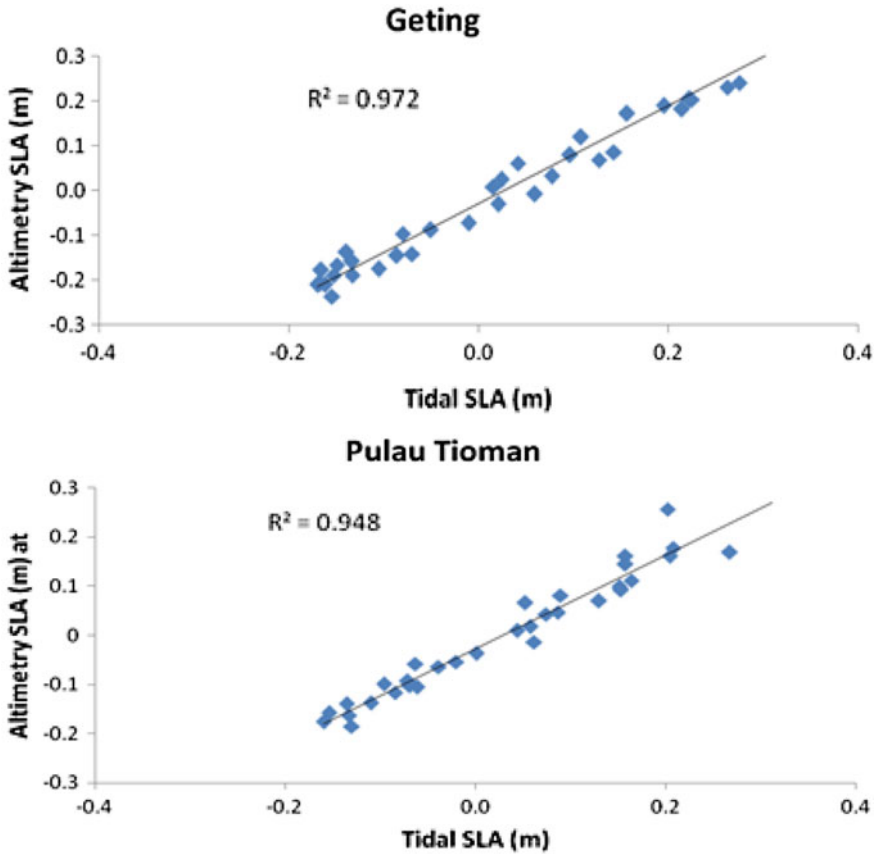
Fig. 10 The correlation plots for Geting and Pulau Tioman with the R^2 showing 0.972 and 0.948, respectively, indicating strong correlation value

3.2 Sea Level Pattern During King Tide Events

For the analysis purpose, the map of sea level anomalies over the Malacca Straits and South China Sea from satellite altimeter is produced, respectively. These maps are produced in comparison between the normal days on perigean day and during the king tide event which occurs during 2016. Offshore or deep ocean areas are the points chosen when extracting points from altimeter because the residual of SLA increases when it is closer to the coast because of the increased sea level variability in shallow depth water [11].

The outcomes from the pattern maps clearly show that the sea level anomalies pattern is changing and rising from place to place over the Malacca Straits and South China Sea during the king tide phenomenon on those 3 months in 2016 (see Fig. 14). The sea level varies and gradually increases during the event. Meanwhile,
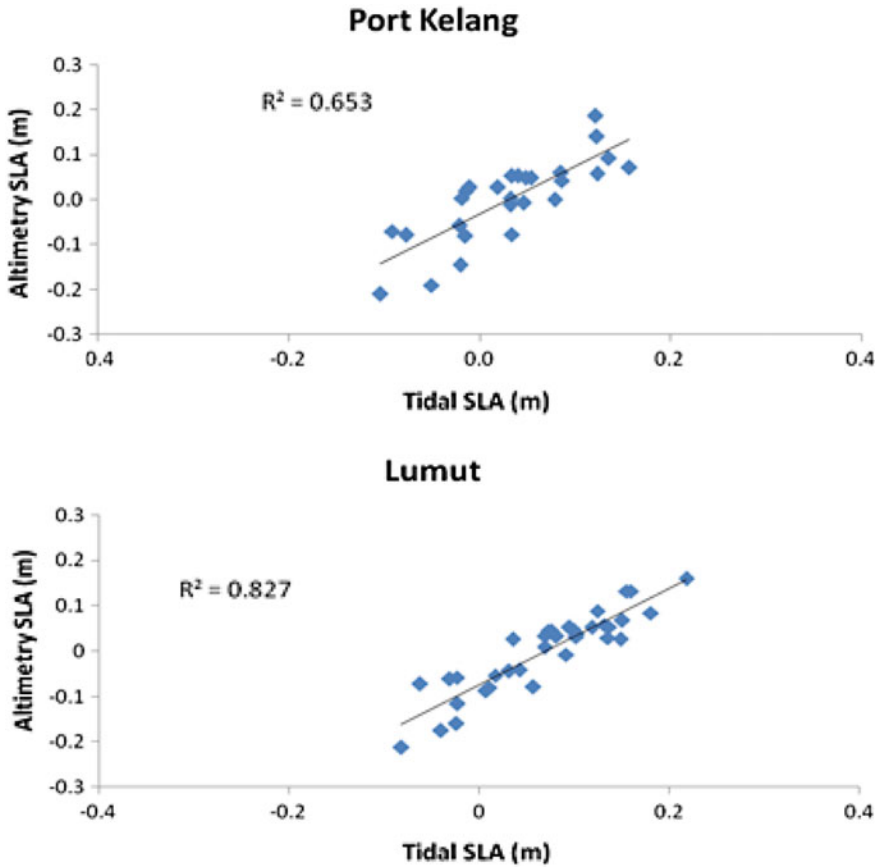
Fig. 11 The correlation plots for Port Kelang and Lumut with the R^2 showing 0.653 and 0.827, respectively

for the past perigean day in 2013, 2014, and 2015, the tide level shows a slight increase but not significantly as high as the 2016 king tide event (see Fig. 15).

Comparing the Malacca Straits and South China Sea, the Malacca Straits clearly affected during the perigean spring tide phenomenon when the map pattern showed the higher magnitude than the South China Sea. This is because the Malacca Straits is an enclosed strait as it is isolated from the open ocean unlike the South China Sea which showed a little changes only [12].

From all the years, it clearly shows that on November 14, 2016 (see Fig. 14), the sea level increased gradually as the length of moon from earth is only 356,511 km which is closest to the earth since 68 years ago [13] (see Table 3).

After that, on the day when the flood event occurs on September 18, 2016 at west coast of Peninsular (see Fig. 14), the sea level map pattern also shows a significant higher value compared to the other day. Looking at Table 3, the length
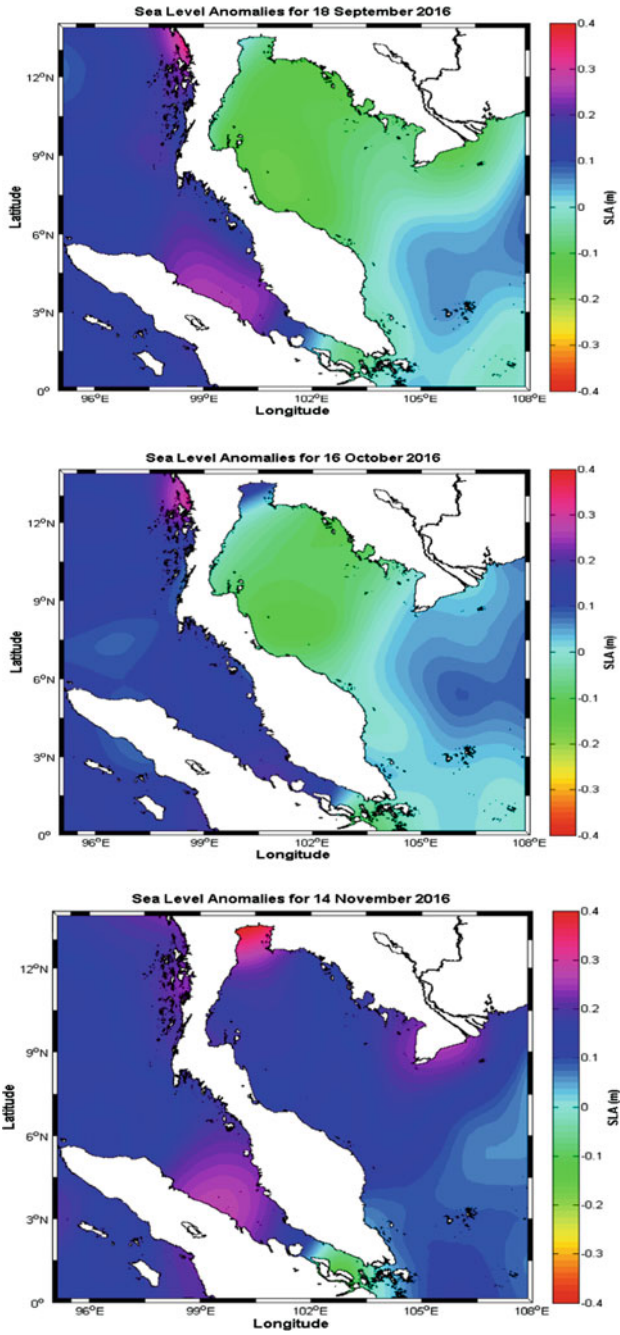
Fig. 12 The map pattern for the king tide event on 2016
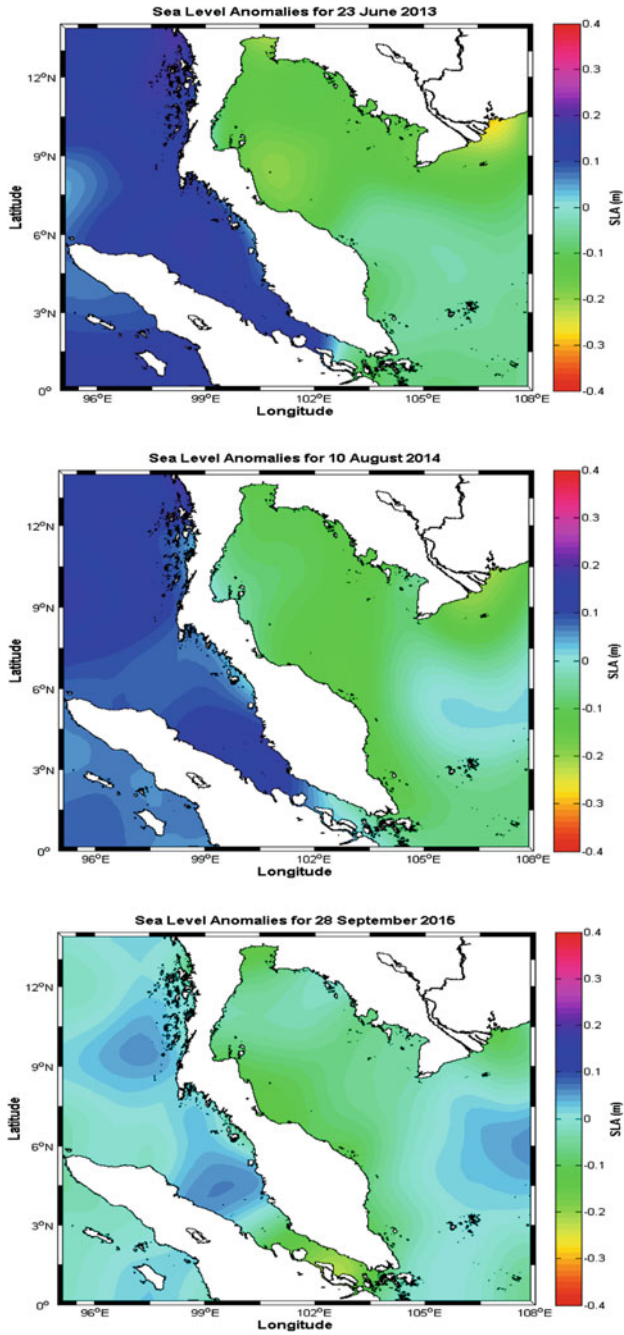
Fig. 13 The map pattern for normal perigean past year on 2013, 2014, and 2015

Table 5 The RMSE value for all the station

Station	RMSE value (m)
Geting	0.0425
Pulau Tioman	0.0405
Port Kelang	0.0613
Lumut	0.0784
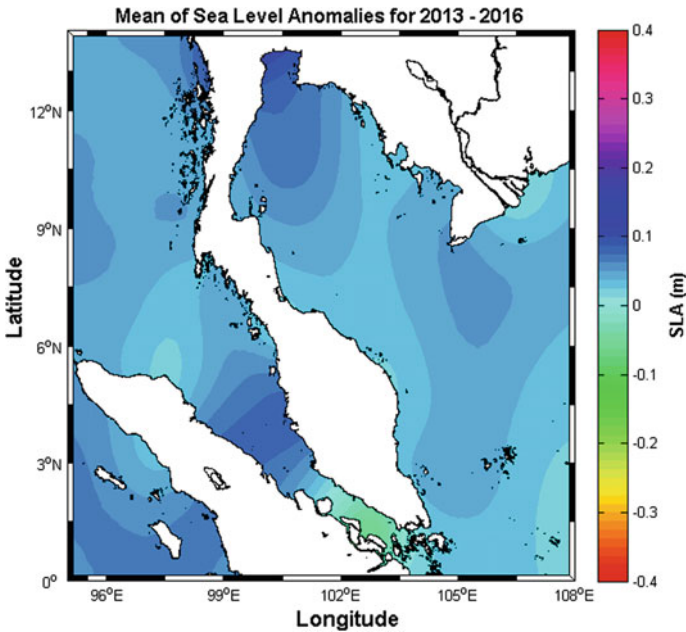
Fig. 14 The map pattern of mean sea level anomalies of year 2013 to 2016

of moon from earth at that time is only 361,893 km which is the farthest among those days from year 2013 to 2016.

3.3 The Residual Map Pattern

The further analysis is to see residual of sea level anomalies map pattern. This is done by simply subtracting the data of SLA during the king tide with the mean of sea level anomalies of the research area. The purpose of doing this is to produce a clear and comparable map to see the changes of the tide during the king tide event by eliminating the mean of sea level in that place. Figure 16 shows the mean of sea level anomalies for both Malacca Straits and South China Sea. Figures 15 and 16 show the residual pattern produce during the event.
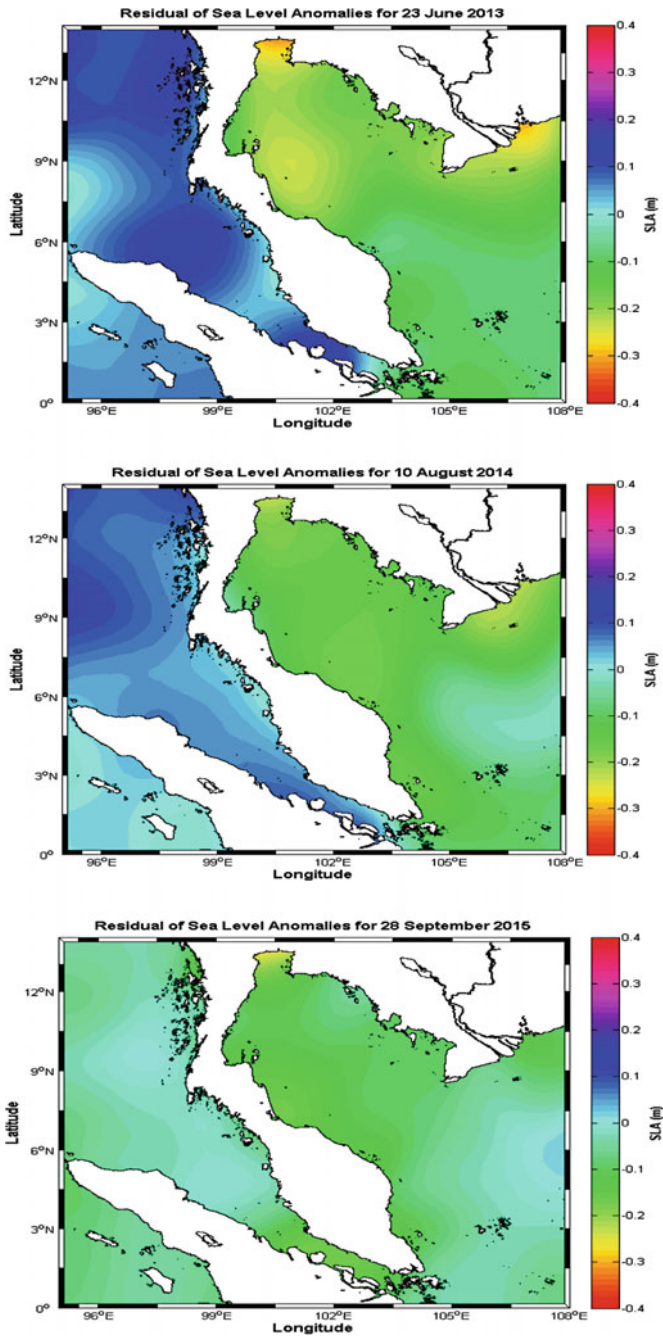
Fig. 15 The residual sea level anomalies during 2013, 2014, and 2015 perigean day
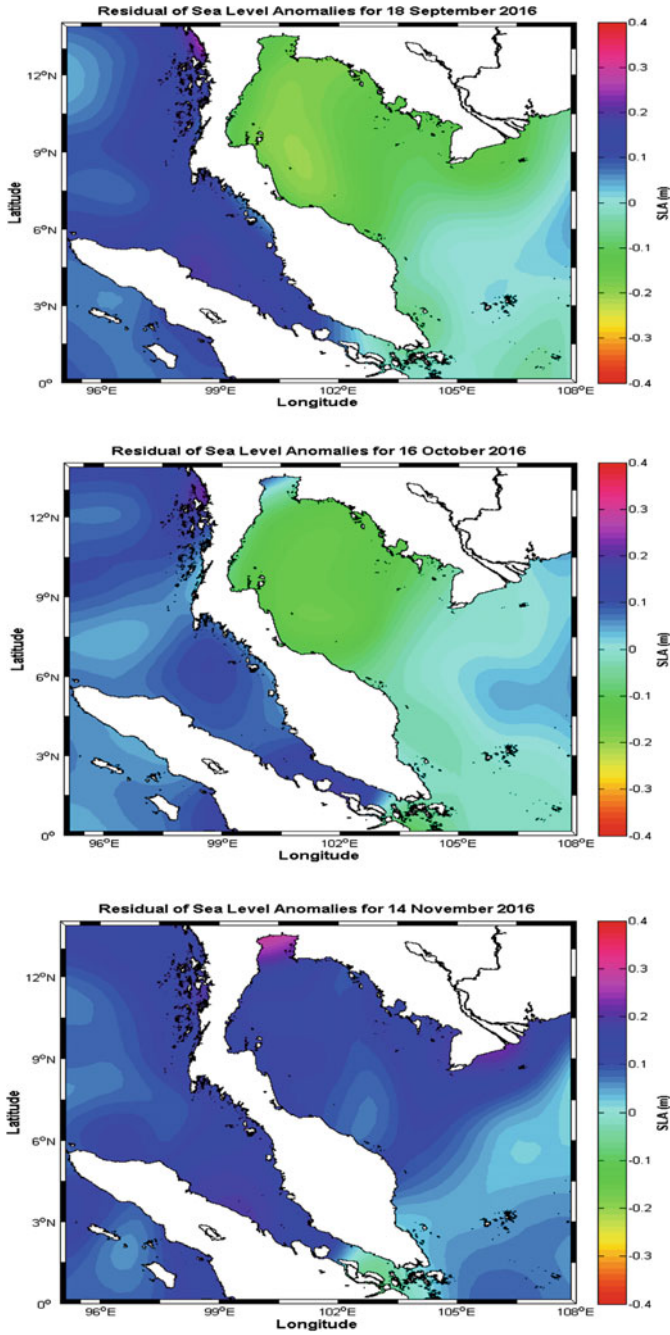
Fig. 16 The residual sea level anomalies during king tide event on 2016
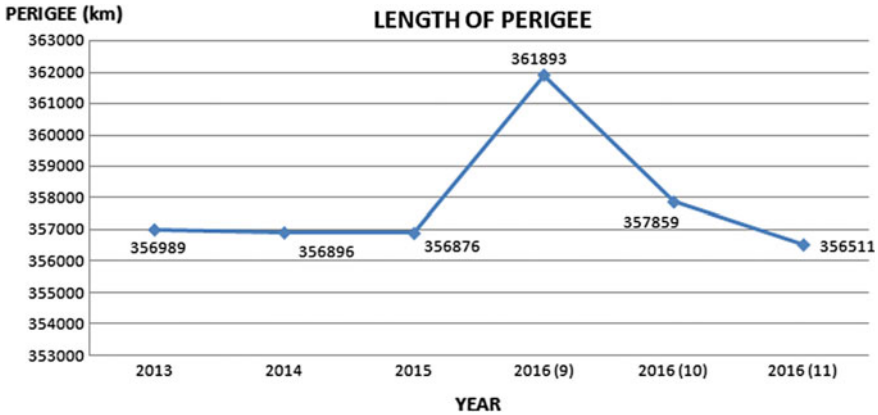
Fig. 17 The length of perigee from year 2013 until year 2016

From Figs. 17 and 18, when they are compared together, it clearly shows that the lunar perigee affected the pattern of tide and the November 14, 2016 is the greatest among them. The shortest perigee which occurs during this day has induced the tide to be greater than usual as the moon is one of the tidal influence factors [14]. Figure 17 shows the length of perigee when plotted in graph.
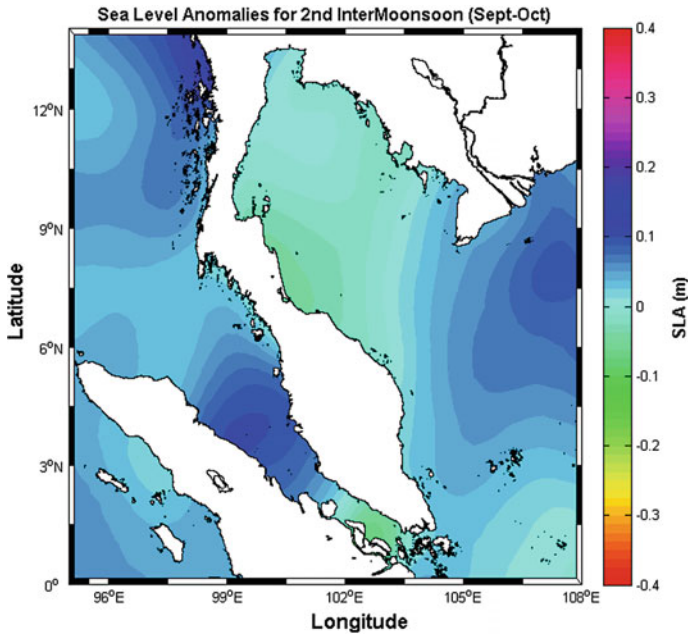
Fig. 18 The map of sea level anomalies for second inter-monsoon which occur on September to October every year

From Fig. 17, it has to be alerted that the king tide phenomenon which occurs in September and October 2016 is not a phenomenon totally caused by the perigee of the moon because the distance of the moon from earth is not in a close range compared to the other days.

The flood happened on those 2 days is because of the strong southwesterly wind with a speed of between 40 and 50 kmph, which occur during this period with the wave height about 3.5 m and at the same time during the full moon event [15]. Figure 18 shows the map of second inter-monsoon which occurs during September to October every year. According to the Fourmilab website, the November 14, 2016 is the perigee for 2016 and the shortest since 68 years ago [8].

4   Conclusion

From this study, it is proved that satellite altimeter can serve as a good tool to conduct a study on the oceanography especially on the tidal when it shows a very good argument with the tide gauge station. This technology can provide a good temporal and spatial coverage as an alternative for the tide gauge station. The king tide phenomenon occurs in late 2016 especially on November it shows that the lunar perigee gave a great impact on the tidal magnitude. The coincidence of lunar perigee and weather condition will make the tide-generating force become greater results in the tide to become higher, which cause the flood in September 2016.

References

1. BERNAMA: High-Tide Phenomenon, over 1000 People are Evacuated (21 Sept 2016)
2. Edwin, A.: Perigean spring tides versus apogean spring tides and their implication in pelagic mixing in the next 1.4 billion years. Ocean Physic Education (2016)
3. Marine Extension Bulletin: Perigean spring tide. Sea Grant Program (1998)
4. National Oceanic and Atmospheric Administration (NOAA): Perigean Spring Tide. https://www.oceanservice.noaa.gov/facts/perigean-spring-tide.html. 2016/5/11
5. Fu, L.L., Cazenave, A.: Altimetry and Earth Science, A Handbook of Techniques and Applications, Vol 69 of International Geophysics Series (2001)
6. CLS: Validation of Altimeter Data by Comparison with Tide Gauge Measurement. CLS. DOS/NT/12-259 Iss: 1.1 2013/3/14
7. AVISO: AVISO Satellite Altimetry Data. http://www.aviso.altimetry.fr/en/missions.html. 2017/5/10

8. Fourmilab: Lunar Perigee Apogee Calculator. https://www.fourmilab.ch/earthview/pacalc.html. 2017/4/24
9. Radar Altimeter Database System (RADS). https://rads.tudelft.nl/rads/data. 2016/5/10
10. Dancey, C.P., Reidy, J.: Statistic Without Maths for Psychology, 5th edn. ISBN: 9780273726029
11. Andersen, O.B., Scharroo, R.: Range and geophysical correction in coastal regions: and implications for mean sea surface determination. In: Coastal Altimetry. Springer, Berlin. https://doi.org/10.1007/978-3-642-12796-0 (2011)
12. Din A.H.M.: Sea level rise interpretation in Malaysia using multi-sensor techniques. Ph.D. thesis, Universiti Teknologi Malaysia, Skudai (2014)
13. Agensi Angkasa Negara (ANGKASA), Press Statement: Supermoon Terbesar Sejak 1948 Akan Berlaku Pada 14 November 2016. https://www.angkasa.gov.my/?q=node/1677
14. Richard, D.R., David, E.C.: Times of peak astronomical tides. GJI Mar. Geosci. Geophys. J. Int. **168**, 999–1004 (2007)
15. Ministry of Science, Technology and Innovation (MOSTI), Press Statement: Ombak Besar di Pantai Barat Semenanjung Malaysia

Climate Change—Causes, Impacts, Mitigation: A Review

Mahmoud Khazalah and Baskar Gopalan

Abstract Understanding the climate change is the main theme in this paper by reviewing the existing literature available so far. A detailed discussion has been highlighted on the causes like greenhouse effect, human activity and solar irradiance. The evidences such as change in sea level rise in global temperature, warming oceans, shrinking ice sheets, declining Arctic sea ice, glacial retreat, extreme events, ocean acidification and decreased snow cover have been discussed at great length. The consequences are rise in temperature, increase in frost-free season, change in precipitation pattern, more droughts and heat waves, and intense hurricanes. The mitigation, adaptation and the need of climate change research is also an important aspect in this review.

Keywords Climate change · Greenhouse effect · Precipitation pattern
Adaptation · Mitigation

1 Introduction

Short-term events, say, daily or weekly temperature and precipitation, are referred by weather. Long-term pattern of weather in earth is known as climate, say wet, dry, hot, cold. Climate system includes Earth's atmosphere, water cycle, soil, ice and living components. Climate change is variableness of the climate system. The basic element of study is green house effect that is contributed by green house gases. Most important green houses gases are carbon dioxide, water vapour and methane.

This paper attempts to review the recent researches done by scientists on evidences, consequences and solutions. The scope of this review paper is limited to only recent research findings done by scientists.

M. Khazalah (✉) · B. Gopalan
Shinas College of Technology, Al-Aqur, Shinas, Sultanate of Oman
e-mail: Mahmoud.Khazalah@shct.edu.om

B. Gopalan
e-mail: Baskar.Gopalan@shct.edu.om

2 Role of International Organisation on Climate Change

The responsibility of any international organisation to protect environment with respect climate change is quite a challenging task.

Intergovernmental Panel on Climate Change was formed by World Meteorological Organization and United Nations Environment Programme to present policymakers about impacts, risks, adaptation and mitigation. International Union for Conservation of Nature was founded to provide the knowledge and tools with 1300 Member organisations and 16,000 experts which comprises around 900 staff in more than 50 countries.

United Nations Framework Convention on Climate Change was framed to lessen release of greenhouse gas. Greenpeace presence is in more than 55 countries, with 2.8 million supporters worldwide in order to save the environment. Climate Action Network International is working on climate change with autonomous and independent members around the world. Climate Reality is to catalyse a global solution to the climate crisis. Citizen's Climate Lobby exists to create the political will for climate solutions by enabling individual breakthroughs. The Youth Climate Movement is to mobilise a generational movement to take positive action.

3 Climate Change Evidences

The evidences are extreme weather, heavy rainfall, floods, droughts, land loss, ocean warming, ocean acidification, reduction in agriculture output, rise in surface water temperature and decline in ice sheet.

The climate-induced risks for infrastructure posed by sea level rise have been studied. Drawbacks in response prioritisation task have been analysed by Gibbs [1]. Ways based on knowledge from decision theory were presented as solution. The occurrence of droughts and floods occur in the same year particularly in low lying areas results in crop losses. In addition, the prevalence and sternness of diseases have amplified over time. Dislodgment, wound and bereavement of people and damage to housing are consequent effects due to extreme events. Work productivity was decreased due to sickness. Malnutrition happened because of losses in crop. Financial demand increased for rebuilding of houses. These interacted impacts were studied by Yiran and Stringer [2]. Razavi et al. [3] made an attempt to study on extreme weather development and its level of uncertainty. Intense precipitation and temperature were analysed using global climate models. The results showed that the rising trend in extreme temperature indices and falling trend in forest days and ice days in 2020s, 2050s, 2080s.

Lehmann et al. [4] found that 12% more record-breaking rainfall events occurred globally due to climate change.

Land loss due to sea level rise effected by own emissions in intrinsic risk. Land loss due sea level rise affected by global emissions in extrinsic risk. Extrinsic risk is

27 and 15% of land loss in two non-island countries respectively as examined by Hardy [5].

Yang et al. [6] found that 7.1 and 17.5% reduction in winter wheat and spring wheat respectively due to heat stress as resulted by General Circulation Models (GCMs) in China.

Butcher et al. [7] found that 77% increase in surface water temperature in 27 lake 'archetypes' in U.S. as resulted by LISSS, a one-dimensional dynamic thermal simulation model.

Williams et al. [8] found that 17% decrease in cotton yield by 2030 n Southern Queensland and Northern NSW, eastern Australia as resulted by biophysical simulation model APSIM (Agricultural Production Systems sIMulator).

Jorgenson [9] projected net change of 6 and 17% resulted in time and temperature respectively by a three-state transition model developed in 60 ecotypes area involving 243 potential transitions during three 30 year periods.

Active fire spread days increase with impact of future climate change as suggested by Wang et al. [10] in Canadian forests. They found this increase of 35–400% by 2050 through modelling annual frequency of fire spread days across 16 fire regime zones of Canada.

In northern and southern states of US, physical activity may raise during the winter and decline during the summer respectively as the data on over 1.9 million respondents shown by Obradovich and Fowler [11].

Climate-induced changes model studied by Shimizu-kimura [12] that projected contraction due to exceeding current range of average temperature for endangered rainforest plant Triunia robusta, endemic to southeast Queensland, Australia. A 3.36-year cycle and a 22.6-year cycle connect to the El Niño–Southern Oscillation cycle and the Hale sunspot cycle respectively by studying England temperature (CET) dataset with the use of slow feature analysis and wavelet analysis done by Wang et al. [13]. Test results of a laboratory-scale minimal model that mimicking climate change indicated the nature of connections between external forcing and climate variability as shown by the study Vincze et al. [14]. Research on finding evidences of climate change is a continual process.

4 Consequences of Climate Change

The consequences of climate change are water scarcity, snow melt, changes in hydropower development, damages by extreme events, mortality in aquatic life, reduction in agriculture revenue, outbreak of diseases and changes in forest dynamics.

Bobojonov et al. [15] made an attempt to study on farm revenues. The decision to choose the type of crop to be planted was analysed by using a spatially explicit stochastic optimization model. Twenty five percent drop in income of farmers as the temperature increases to 3.2 °C. 46% increase in income of farmers as the temperature increases more conservatively.

Ranson et al. [16] found that 63% increase in hurricane damages where 2.5 °C in global surface air temperature in North Atlantic basin as predicted by multi-model.

Turunen et al. [17] tried to model the future snow conditions in particular snow pack especially deep snow and late snow melt. In addition they examined how the herders cope with the impact of extreme snow conditions. Forage availability is more during longer snow less season and thin snow cover. Extreme snow condition affects forage availability in turn intensified by low lichen biomass. Herders start supplementary feeding to reindeers. Coping capacity of herders could be aided not only by sustainable use of pastures but also through diversification of livelihood and mitigating the adverse effects of climate change.

Shrestha et al. [18] examined the related climate change related danger in hydro power development projects. Representative concentration pathways were applied for predicting rainfall and temperature. Any change in precipitation can cause effect on stream flow in turn affects the energy production. The study found that expectation of a mild to moderate risk.

Ross River virus became intense during climate change in Tasmanian as studied by Lyth and Holbrook [19]. Ouzeau et al. [20] used the EURO-CORDEX regional multi-model ensemble that simulates heat waves. The risk of deficient corn nitrogen has been estimated by probability model developed by Anderson and Kyveryga [21].

Alternative management scenarios for in-season nitrogen management for each risk attitudes can be explored by growers for nitrogen fertiliser management for corn. Benefit for cold-origin populations and decline for warm-origin populations are the growth response of black spruce (*Picea mariana*) and jack pine (*Pinus banksiana*) in future forest dynamics as identified by Pedlar and Mckenney [22].

A study by Russo [23] shows that climate-induced pumping variability is resulted in annual response to local precipitation in deep aquifers in the USA.

Zhao [24] made a study on statistical models, local crop models and global gridded crop models that predicted substantial rice yield loss under warming. Substantial rice yield loss under warming are suggested as possible mitigation strategies. A study by Lam [25] found that global fisheries revenues could drop by 35% more than the projected decrease in catches by the 2050s under high CO_2 emission scenarios.

The findings on consequences due to change in climate is still evolving and research is in continual process.

5   Solutions for Climate Change

The solutions for climate change are mitigation, adaptation, evacuation, social awareness, food security, climate services, participatory approach, climatization, boundary chains concept, water harvesting techniques, development of climate models and research on climate change.

Liu et al. [26] made a study on evaluation of economic returns to climate resilient development (CRD). Three models, say, house hold benefit cost model, diffusion model, regional model, were used in evaluation framework. The analyzers can be applied in developing countries. The results found the variables that significantly change the economic returns of the strategies. Phadke [27] developed a neighbourhood-based model used to fetch new opinions on climate change adaptation concerns and priorities which might help local climate adaptation planning decisions. Cvitanovic [28] made a study on linkage of climate adaptation and food security.

Khul et al. [29] suggested that evacuation as coastal flood management strategy due to climate change. Regional Climate Models have been used to find the change in climate which will positively affect central and northern Europe as the results shown by the study conducted by Grillakis et al. [30]. Hugh Brammer conducted a study which results that the adoption of appropriate measures based on knowledge of the physical geography of potentially affected areas could significantly reduce the currently predicted displacement of many millions of people; and the impacts of a slowly rising sea level are currently.

A multi-stage sampling process is applied to select to interview with a semi-structured questionnaire. Erratic precipitation, occurrence of flood, change in rainfall onset and cessation are the evidences of climate change. New diseases in livestock, crop failure, change in availability of pasture are the consequent effects. Shifting livestock, veterinary drugs purchase are responsive measures taken to tackle climate risk. This study by Egeru [31] recommended an integrated early warning system that captures perceptions and perceptions would raise the reliability of the climate risk information that disseminated. Mase et al. [32] conducted a study which addresses farmers' beliefs, perceived risks and attitudes toward adaptation with respect to climate change done through a survey of nearly 5000 corn farmers across 22 Midwestern U.S. Watersheds. Perception on current and future climate risks is influenced by past experiences. This aspect is confirmed through in-person interviews with 159 Midwest farmers done by Wilke and Morton [33].

Far stronger connections between researcher-driven and participatory approaches and cycling between exploratory and normative perspectives exist in scenario planning climate change adaptation and policy. The study conducted by Star et al. [34] expressed that mixed methods are most effective for decision-making in the context of climate change challenges. Boundary chains concept link science and decision-making as per the study by Kirchhoff [35]. To prevent disastrous effects over dry lands, it is must to keep global warming within 1.5 °C as the results indicate that warming of 3.2–4.0 °C over dry lands could occur when global warming reaches 2.0 °C as per the study conducted by Huang et al. [36]. Ferrant et al. [37] stated that water harvesting systems as developing measures to manage with impacts to keep ground water level in South India region. The research on the solutions for adaptation and mitigation for climate change is going on globally by scientists.

6 Conclusion

It is not easy to stop climate change since the pollution stays in the atmosphere for hundreds of years even though stopping of emitting carbon pollution. Global warming to no more than 2 °C is possible by using clean energy rather than fossil fuel instead. A warning trend is shown by results of analyses of surface temperature data sets around the world. It is confirmed by declining snow cover, glacier mass, and sea ice, rising atmospheric humidity, sea level, ocean temperature.

Research on mitigation and adaptation techniques must be expanded. Funding for production of clean energy must be increased. Any existing international political solution must be continued. World leaders seem to finally agree that urgent action is necessary. The stakeholders work together to make the climate solutions a reality. They support when world leaders take action to cur emission and stop rising global temperature.

References

1. Gibbs, M.T.: Pitfalls in coastal climate adaptation responses. Clim. Risk Manage. **8**, 1–8 (2015)
2. Yiran, G.A.B., Stringer, L.C.: Spatio-temporal analyses of impacts of multiple climatic hazards in a savannah ecosystem of Ghana. Clim. Risk Manage. **14**, 11–26 (2016)
3. Razavi, T., et al.: Regional climate change trends and uncertainty analysis using extreme indices: a case study of Hamilton, Canada. Clim. Risk Manage. **13**, 43–63 (2016)
4. Lehmann, J., et al.: Increased record-breaking precipitation events under global warming. Clim. Change **132**, 501–515 (2015)
5. Hardy, D.: Global sea-level rise: weighing country responsibility and risk. Clim. Change **137**, 333–345 (2016)
6. Yang, X., et al.: The impacts of increased heat stress events on wheat yield under climate change in China. Clim. Change **140**, 605–620 (2017)
7. Butcher, J.B., et al.: Rapid response of modern day ice sheets to external forcing. Earth Planet. Sci. Lett. **257**, 1–13 (2007)
8. Williams, A., et al.: Quantifying the response of cotton production in eastern Australia to climate change. Clim. Change **129**, 183–196 (2015)
9. Jorgenson, M.T.: Projected changes in diverse ecosystems from climate warming and biophysical drivers in northwest Alaska. Clim. Change **130**, 131–144 (2015)
10. Wang, X., et al.: Increasing frequency of extreme fire weather in Canada with climate change. Clim. Change **130**, 573–586 (2015)
11. Obradovich, N., Fowler, J.H.: Climate change may alter human physical activity patterns. Nat. Hum. Behav. **1**(5), 0097 (2017)
12. Shimizu-Kimura, Y., et al.: The relationship between climate change and the endangered rainforest shrub Triunia robusta (Proteaceae) endemic to southeast Queensland, Australia, 1–10. Sci. Rep. **7**, 46399 (2017). http://doi.org/10.1038/srep46399, http://www.nature.com/scientificreports/
13. Wang, G.: Identification of the driving forces of climate change using the longest instrumental temperature record, 1–7. Sci. Rep. **7**, 46091 (2017). http://doi.org/10.1038/srep46091, http://www.nature.com/scientificreports/

14. Vincze, M., et al.: Temperature fluctuations in a changing climate: an ensemble based experimental approach, 1–9. Sci. Rep. **7**, 254 (2017). http://doi.org/10.1038/s41598-017-00319-0, http://www.nature.com/scientificreports/

15. Bobojonov, I., et al.: Income and irrigation water use efficiency under climate change: an application of spatial stochastic crop and water allocation model to Western Uzbekistan. Clim. Risk Manage. **13**, 19–30 (2016)

16. Ranson, M., et al.: Tropical and extratropical cyclone damages under climate change. Clim. Change **127**, 227–241 (2014)

17. Turunen, M.T., et al.: Coping with difficult weather and snow conditions: reindeer herders' views on climate change impacts and coping strategies, Clim. Risk. Manage. **11**, 15–36 (2016)

18. Shrestha, S., et al.: Assessment of risks due to climate change for the upper Tamakoshi hydropower project in Nepal. Clim. Risk Manage. **14**, 27–41 (2016)

19. Lyth, A., Holbrook, N.J.: Assessing an indirect health implication of a changing climate: Ross river virus in a temperate island state. Clim. Risk Manage. **16** (2015)

20. Ouzeau, G., et al.: Heat waves analysis over France in present and future climate: application of a new method on the EURO-CORDEX ensemble. Clim. Serv. **4**, 1–12 (2016)

21. Anderson, C.J., Kyveryga, P.M.: Combining on-farm and climate data for risk management of nitrogen decisions. Clim. Risk Manage. **14**, 1–42 (2016)

22. Pedlar, J.H., Mckenney, D.W.: Assessing the anticipated growth response of northern conifer populations to a warming climate. Sci. Rep. **7** (2017)

23. Russo, T.A.: Depletion and response of deep groundwater to climate-induced pumping variability. Nat. Geo Sci. **10**, 105–108 (2017)

24. Zhao, C.: Plausible rice yield losses under future climate warming. Nat. Plants **3**(1), 16202 (2016)

25. Lam, V.W.Y., et al.: Projected change in global fisheries revenues under climate change. Sci. Rep. **3** (2016)

26. Liu, S., et al.: Evaluating economic costs and benefits of climate resilient livelihood strategies. Clim. Risk Manage. **12**, 115–129 (2016)

27. Phadke, R., et al.: Making it personal: diversity and deliberation in climate adaptation planning. Clim. Risk Manage. **9**, 62–76 (2015)

28. Cvitanovic, C., et al.: Linking adaptation science to action to build food secure Pacific Island communities. Clim. Risk Manage. **11**, 53–62 (2016)

29. Khul, L., et al.: Evacuation as a climate adaptation strategy for environmental justice communities. Clim. Change. **127**, 493–504 (2014)

30. Grillakis, M.G., et al.: Implications of 2 °C global warming in European summer tourism. Clim. Serv. 30–38 (2016)

31. Egeru, A., et al.: Climate risk management information, sources and responses in a pastoral region in East Africa. Clim. Risk Manage. **11**, 1–14 (2016)

32. Mase, A.S., et al.: Climate change beliefs, risk perceptions, and adaptation behavior among Midwestern U.S. crop farmers. Clim. Risk Manage. **15**, 8–17 (2017)

33. Wilke, A.K., Morton, L.W.: Analog years: connecting climate science and agricultural tradition to better manage landscapes of the future. Clim. Risk Manage. **15**, 32–44 (2017)

34. Star, J., et al.: Supporting adaptation decisions through scenario planning: enabling the effective use of multiple methods. Clim. Risk Manage. **14**, 88–94 (2016)

35. Kirchhoff, C.J.: Narrowing the gap between science and adaptation action: the role of boundary chains. Clim. Risk Manage. **14**, 1–5 (2016)

36. Huang, J., et al.: Accelerated dry land expansion under climate change. Nat. Clim. Change **6**, 166–171 (2015)

37. Ferrant, S., et al.: Projected impacts of climate change on farmers' extraction of groundwater from crystalline aquifers in South India. Sci. Rep. **4** (2014)

The Development of Computational Routine for Deformation Modelling and Analysis: A Case for Two-Dimensional Geodetic Technique

Nur Khalilah Bidi, Zainal Abidin Md Som, Ami Hassan Md Din and Abdullah Hisam Omar

Abstract Nowadays, deformation monitoring survey includes numerous tasks, for example monitoring of engineering structures such as dam and bridges, land subsidence, earthquakes and other related applications. As a result, many professional groups such as surveyors and structural engineers, besides geophysics and geologists study the deformation analysis as a rigorous subject. Deformation measurements and analysis using geodetic method is one of the complicated and challenging works that need to be undertaken by land surveyors. The result of deformation analysis is to be used by other professions such as engineers, geodesists and geophysics as well. However, they are not really interested in the geometrical analysis (i.e. coordinate difference). Actually, they required the result of deformation modelling which is the deformation parameter that related to their field of study. Here shows the importance of information on deformation modelling

N. K. Bidi · Z. A. M. Som (✉) · A. H. M. Din · A. H. Omar
Faculty of Geoinformation and Real Estate, Geomatic Innovation
Research Group (GIG), Universiti Teknologi Malaysia, Johor Bahru,
Johor, Malaysia
e-mail: zainalabidin@utm.my

N. K. Bidi
e-mail: nkhalilah3@gmail.com

A. H. M. Din
e-mail: amihassan@utm.my

A. H. Omar
e-mail: abdullahhisham@utm.my

A. H. M. Din
Faculty of Geoinformation and Real Estate, Geoscience and Digital
Earth Centre (INSTEG), Universiti Teknologi Malaysia, Johor Bahru,
Johor, Malaysia

A. H. M. Din
Institute of Oceanography and Environment (INOS), Universiti Malaysia
Terengganu, Kuala Terengganu, Terengganu, Malaysia

instead of geometrical analysis and when its need to be performed. This study focused on the development of deformation modelling computational routine and subsequently been incorporated into an existing deformation analysis package. Deformation modelling is the stage to produce the right mathematical model from the result of deformation analysis (trend analysis) with relevant deformation parameter. The computational routine developed to analyse survey data obtained by the conventional geodetic technique in 2 dimension. In order to do deformation analysis, MATLAB program has been used to solve all the computation process. As a result, the 'best' model has been selected among the five models tested. The best model showed what type of deformation occurs on the body of the simulation network. The outcomes of the research have also improved from previous software and the results obtained were good and practicable to this study.

1 Introduction

The tasks of monitoring survey and its subsequent deformation analysis have long been entrusted to land surveyors. Being an expert in positioning, surveyors are able to determine the deformation in the form of changes in shape or position of points surveyed. Deformation survey requires survey network that has been established which consists of reference control points and monitoring points been position on the object of interest at strategic locations. The survey network together with the monitoring points will be observed repeatedly with a minimum of two epochs. The coordinates of all surveyed points will be computed by least squares adjustment in each epoch separately and deformation analysis will be followed if the adjustment results showed any coordinate difference. A more exhaustive coverage on deformation survey and geodetic deformation analysis can be found in publications [1, 2]. A more recent publication on this same topic can be found in [3].

Essentially, geodetic monitoring networks are usually divided into absolute network and relative network. The absolute network consists of object points and reference points. Its reference points or pillar are located at the pre-selected location and the stability must be proven mathematically. Deformation occurs in objects or engineering structures such as dams, bridges and tunnels. However, the relative network established with its point was located at susceptible locations. It consists of object points and the reference pillars were subject to movement. They are all treated as object points. In the relative network, there is no assumption regarding the stability of any particular group of network stations. Deformation occurs on the earth physical surface such as land subsidence, tectonic movement and earthquakes.

Technological approaches and the improvements in the measurement methods lead to deformation monitoring as a crucial task in geodetic applications. Today, Global Positioning System (GPS) which is a space-based positioning technology

offers one of the effective monitoring approaches for the high-risk areas, such as landslide phenomena, land subsidence and deformation structure. Besides, a newly developed technique that is Terrestrial Laser Scanning (TLS) can accumulate thousands of data points in a couple of minutes, with capable applications to tunnel deformation monitoring [4].

Geodetic Deformation Analysis (GDA) is a crucial task in deformation survey. It is one of the challenging tasks need to be undertaken. Analysis of deformation methods has also been upgraded with the computers of high capacities that allow us to employ complex mathematical algorithms. Method of deformation analysis has been studied by International Federation of Surveyors. The surveying principle is still similar even though deformation analysis is now around 35 years old and there are a lot of approaches, techniques and methods [5].

The analysis of deformation geodetic network includes the geometrical analysis and physical interpretation. The deformation analysis requires several computational procedures to be fulfilled. There are several GDA software available at FGHT which was developed by UTM researchers such as DETECT [6] and COMPUT [7] and the latest is GDA package [8]. This study used GDA package to process the survey data. This package includes computation on least squares adjustment, pillar stability analysis and trend analysis in which the analysis was implemented using Robust S-Transformation method. However, GDA package is not complete yet, because it does not include the procedure of deformation modelling and physical interpretation. The previous package can only be used until trend analysis stage that shows the results of deformation analysis in a graphical representation. Figure 1 shows the interface of GDA package developed by Aisyah [8].
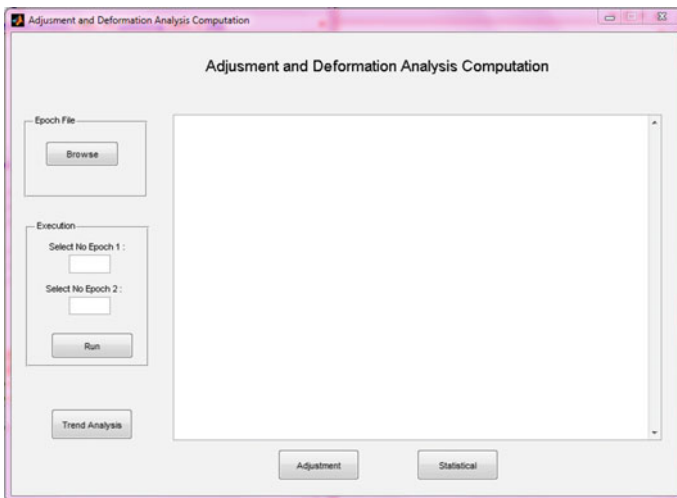
Fig. 1 Interface of Geodetic Deformation Analysis (GDA) package created using MATLAB program

Therefore, this study will continue to complete some procedure in GDA package. This paper presents an advance procedure for deformation analysis which is deformation modelling. This procedure is frequently used in practice. In the stage of analysing the deformation, surveyors are able to solve the geometry analysis which is the trend analysis. If the deformation occurred, the deformation parameters (deformation modelling) need to be established. The detection of deformation is also used by other professions such as engineers and geophysics. However, they do not require information on trend analysis. The result required is the parameter of the deformation that is related to their field of study. This paper will focus on geometrical analysis in which the method of deformation modelling will be used in order to describe deformation network. For more details, it also discusses the importance of deformation modelling and when it is needed to be performed.

The paper is organized as follows. Sections 2 and 3 give a detailed description of procedure related to geodetic deformation analysis and deformation modelling procedure via an integrated method. In Sect. 4, the result from the simulation survey and their analysis are discussed. The outline conclusions and future work are in Sect. 5.

2 Procedure of Geodetic Deformation Analysis

There are seven procedures required for fulfilling the deformation analysis. The stages of work are as shown in Fig. 2. However, not all the procedures will be considered to be fulfilled. The data acquisition can still be obtained if the pre-analysis is not done. Deformation modelling and physical interpretation will not be done if deformation does not occur in the objects or study area.

2.1 Least Squares Adjustment (LSA)

Measurements of deformation may contain an observables combination such as distance, azimuths, coordinates, directions, coordinate difference, etc. In order to determine the unknown quantities or parameters, the observations number normally more than a requirement of the minimum number [9]. In geodetic surveying, the coordinates of the points are the unknown quantities. The redundant observations are handy for gross error checking or outlier in the measurements, precision of the unknown quantities and network quality. Least Squares Adjustment (LSA) method is a significant tool in calculating the unknown parameters from redundant observation.

Basically, the LSA principle minimizes the sum of squares of the weighted residuals,

Fig. 2 Procedure of Geodetic Deformation Analysis (GDA)
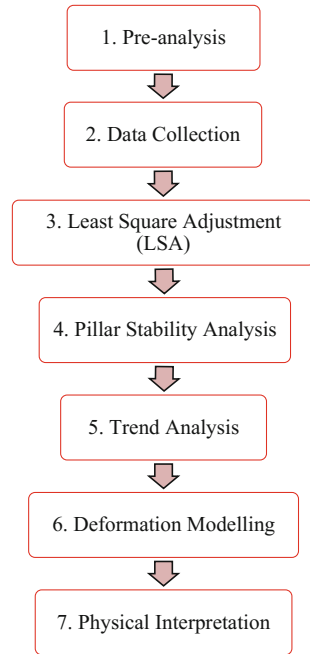
$$V^T PV = \text{minimum variance estimation} \tag{1}$$

where V is the residual vector and P is the weight matrix for the observation.

Other important aspects of LSA are errors and quality. Observations are subjected to systematic, gross and random errors [10]. It is assumed that observations are free from systematic errors. The global test (Chi-square) and local test (Tau test or Baarda method) are used for checking LSA results and screening of gross errors. The magnitude of random errors may be estimated using the method of simplified variance component estimation. Quality of the LSA results in terms of precision, accuracy, and reliability analysis can be estimated during pre-analysis.

2.2 Pillar Stability Analysis (PSA)

After the computation of Least Square Adjustment (LSA) is done in both epochs, the next process is to do the analysis of the pillar either it is stable or not. The pillar stability analysis is very important in implementing the deformation analysis. From that, the result of the pillar stability can produce the truth result of deformation analysis [11].

When LSA is used, it involves the selection of a data by selecting a specific control point in the network of deformation as reference or data. As the data

selected are unknown of its stability, then an analysis of pillar stability need to be performed for validation of its stabilization and suitable for the data. Choosing a wrong data or unstable control point will cause a big mistake in the analysis [8]. Therefore, all unstable points of reference network must be determined before posterior deformation analysis of the structure may be considerably twisted [1].

2.3 Trend Analysis

Trend analysis is a graphical representation that illustrates the outcomes of deformation analysis for the deformation network survey. The graphical representation is very helpful means to obtain the first impression of existing deformations. There are two important elements in trend analysis which are displacement vectors and error ellipse of control points and object points in the deformation network.

From Fig. 3, deformation can be detected by differencing the magnitude of displacement with the size of error ellipse produced. If the displacement magnitude in the range of size of ellipse errors, then deformation does not exist and the deformation will occur when the displacement magnitude is bigger than the size of ellipse errors.

Unfortunately, the displacement vectors depend on the geodetic datum, so that their interpretation has to be done with caution [1]. According to Jafari [12], the significance of the deformation analysis of the structures based on the monitoring measurements due to many contributions is clear. The trend analysis then forms a beginning for initial identification of the deformation models during modelling of deformation.

Fig. 3 Trend analysis for displacement vector versus error ellipse
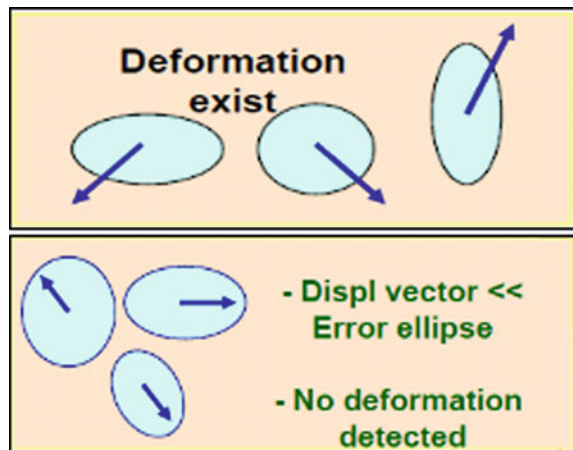
2.4 Deformation Modelling

The aim of deformation modelling is to represent the occurrence deformation by using geometrical and mathematical relationship. In order to complete this task, correct deformation parameter and the right mathematical model need to be identified in describing the deformation occurred.

a. Typical examples of deformation models in two dimensions are specified as follows:
b. Single-point movement (Rigid body displacement)
c. Homogenous strain
d. Combination of single-point movement and homogenous strain.

Single-point movement

The single-point movement can only be modelled in a relative sense where a point in block A has performed deformation into block B as shown in Fig. 4. Other points in block A have not performed any displacement. According to Zainal [13], this model does not contribute to the strain field and does not affect the stresses (i.e. it consists of only translation component and no strain parameter involves).

Homogenous strain

Homogenous strain is where the deformation has occurred in a block uniformly as shown in Fig. 5. All the points in block A are performing changes and create a new block that is block B. In this model, the element of orientation exists where it changes the orientation of the block A to block B.

Combination of single-point movement and homogenous strain

Figure 6 shows the model is a combination of single-point movement and homogenous strain. This combination show a deformable figure with one

Fig. 4 Single-point movement and parameter
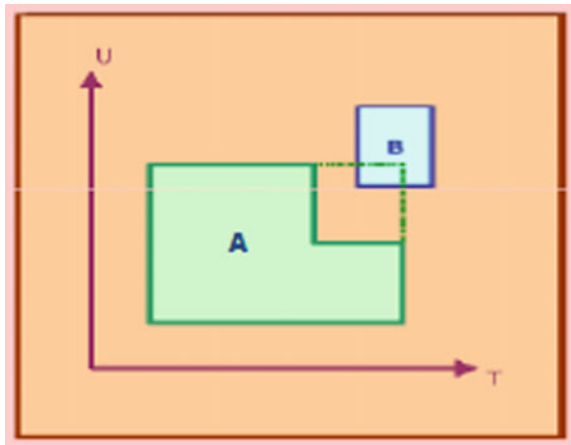
Fig. 5 Homogenous strain with parameter
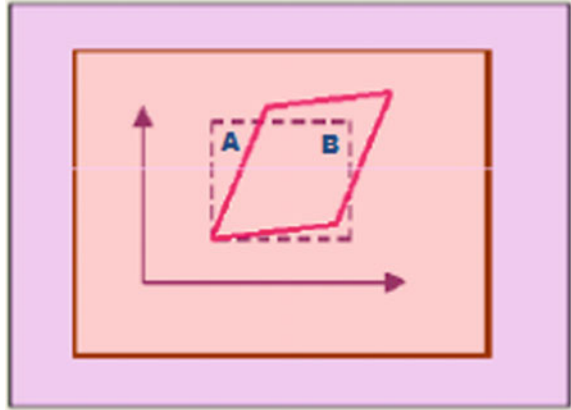
Fig. 6 Single-point movement and homogenous strain
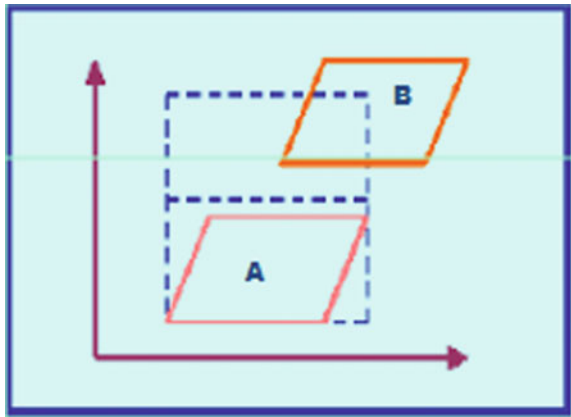
discontinuity between blocks A and B with dissimilar linear deformations in every block plus a single-point movement of the block B with respect to the block A. The deformation with this characteristic is known as discontinuity deformation. One straight line acts as divider of blocks A and B [13].

3 Methodology of Deformation Modelling

The deformation modelling procedure in this study is based on the famous generalized method established at University of New Brunswick, Canada [14]. Modelling of deformation can be implemented by using either the observation differences method or displacement (coordinate differences) method. However, the displacement method only will be focused in this study.
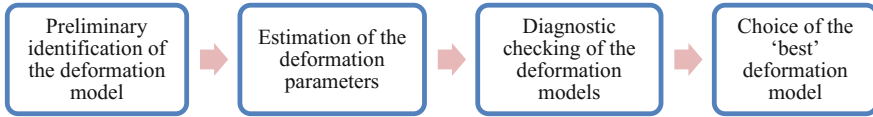
Fig. 7 Basic procedure of deformation modelling

The generalized method as shown in Fig. 7 generally involves several rudimentary processes.

3.1 Preliminary Identification of the Deformation Model

As for a choice of deformation model, it is influenced by a priori information that is obtainable, particularly from whatever trend or variation is showed by the measurements. In analysis of deformation, the entire region enclosed by the deformation survey is treated as a non-continuous deformable body that consists of different deformable blocks continuously [2]. In the 2D analysis, consideration of deformation parameters is as follows:

i. Two components of rigid body displacement $(\alpha_o \text{ and } b_o)$.
ii. A rotation parameter in xy axes $(\omega(x, y))$.
iii. Two normal strain components in x and y axes $(\varepsilon_x(x, y) \text{ and } \varepsilon_y(x, y))$ and shearing strain in xy axes $(\varepsilon_{xy}(x, y))$.

3.2 Estimation of the Deformation Parameters

The deformation modelling is done by process of least squares fitting based on Gauss–Markov model, which can be written as Eq. 1 [5, 15]:

$$d + v = Be \tag{2}$$

where

d is the displacement vector $(n \times 1)$
v is the vector of residual $(n \times 1)$
B is the design matrix $(n \times u)$
e is the vector of deformation parameter $(u \times 1)$—unknown parameter

The number of known displacements of the common points required should be equal to the number of unknown deformation parameters to determine the vector e

in the deformation model. If the number of displacements d is more than that of the unknown deformation parameters, then the vector e is calculated over LSA computation.

Then, the solution is acquired by Eq. 2 [5, 15]:

$$e = \left(B^T Q_d^{-1} B\right)^{-1} B^T Q_d^{-1} d \tag{3}$$

where Q_d is the covariance matrix for displacement vector.

3.3   Diagnostic Checking of the Deformation Model

In general, the model of deformation is not fully understood or it may even be completely unknown. The main objective of diagnostic checking of deformation model is to check the appropriateness of a postulated deformation model [5]. This includes the goodness of fit of the model on a global test and assessment on the significance of individual deformation parameters.

In certain case, the tested parameters are considered significant. If insignificant parameters are detected, these parameters are then deleted from the deformation model and new model is re-estimated and re-examined [2]. This procedure continues until accepted on the global test and all the parameters associated are statistically significant.

In this study, we will use F-distribution in the statistical test. This test is performed to determine the best model for deformation modelling. All the hypothesis testings are done under the assumption the null hypothesis is true. This ratio of sample variances will be examined with the statistic used. If the statistic does not go beyond the critical value (i.e. $T \leq F(\alpha, v_1, v_2)$), the null hypothesis is accepted at the significance level α (normally $\alpha = 0.05$). Hence, if the statistics go beyond the critical value (i.e. $T > F(\alpha, v_1, v_2)$), the null hypothesis is failed. The model of deformation is acceptable if the null hypothesis does not fail at a significance level α.

3.4   Choice of the Best Deformation Model

Subsequently, the performance of the deformable body is generally not fully identified, there is frequently more than one model that perhaps is suitable [10]. Selection of the 'best' model if the global test passes with a satisfactory probability and all the parameters involved are statistically significant. Then, if in excess, one deformation model passes the global test, hence the model with the least significant parameters is chosen.

Thus, the 'best' model should possess at least one or a combination of the following characteristics [16].

- Significance of the coefficients
- Minimal error of fitting
- Fewer number of coefficients consistent with reasonable error
- Based on physical reasons that are logical.

4 Result and Discussions

This section will highlight the computational result of deformation models that have been selected. The specific procedures involved are the LSA computation, geodetic deformation analysis involving pillar stability analysis and computation of displacement vector (trend analysis). Observation data used in this study is obtained by using simulation deformation geodetic network carried out at the field of Universiti Teknologi Malaysia (UTM).

A survey network consists of eight control stations established as shown in Fig. 8. There are two epochs of simulation data used for this study. Eight stations were observed and 28 distances were produced and 56 angles of observation data triangulation are obtained. The second epoch performs simulations by varying the position of stations as 7 and 8. After all specific procedures are done, the existing GDA program can be applied to determine the displacement vector, covariance matrix and the graphical plan for displacement vector and error ellipse. From the all data obtained, the trend analysis is generated. The deformation analysis direct result is the displacement vector d of all analysed points in the monitoring network and validating its significance. The evaluation of the significance of displacement for a single point consists of checking if the displacement vector of each point does not exceed the boundary of the error ellipse in the determination of their vector [17]. Figure 9 shows the trend analysis of computation between two epochs. In Fig. 9, it shows that stations 7 and 8 perform deformation according to the displacement vector and error ellipse.

Fig. 8 Simulation of deformation network control survey
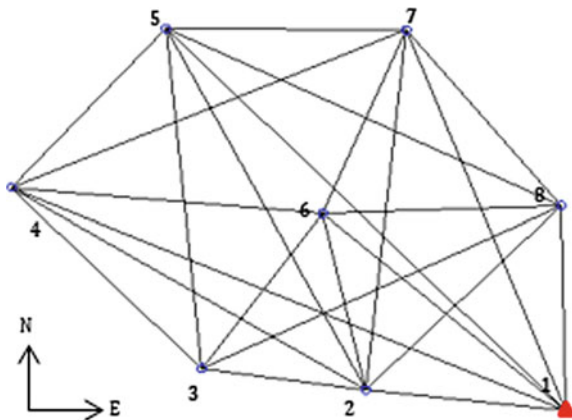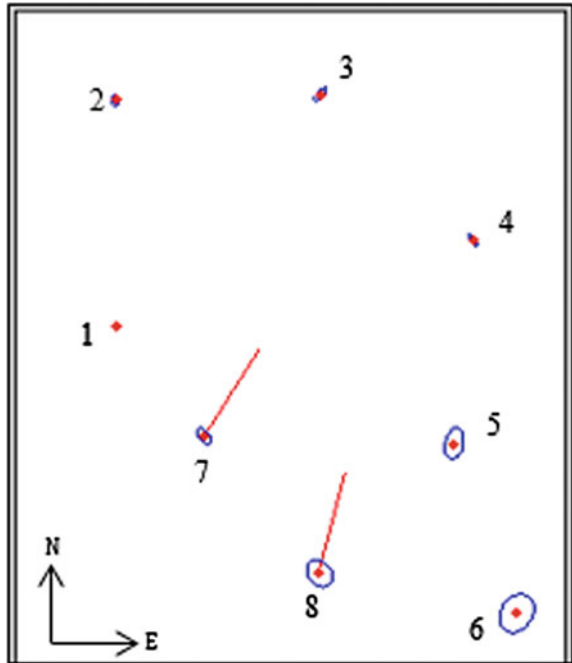
In order to achieve the aim of this study, the existing MATLAB package of deformation analysis has been upgraded to an advanced level which is modelling of deformation. There are five types of deformation models chosen from the simulation network. The models are as follows:

  i. Rigid body displacement at point 7
 ii. Rigid body displacement at point 8
iii. Rigid body displacement at point 7 and 8
 iv. Homogenous strain
  v. Combination of rigid body displacement and homogenous strain.

4.1 Model (i): Rigid Body Displacement at Point 7

The result was made on the first model of the displacement at point 7 as shown in Fig. 10. Example object point is good enough in representing the deformation of the whole network. Based on the result of separate adjustment, it shows that the point 7 moved independently, other points in the network remain stable. From the solution by least squares fitting,

Fig. 10 Deformation model
of rigid body displacement at
point 7 as Model (i)
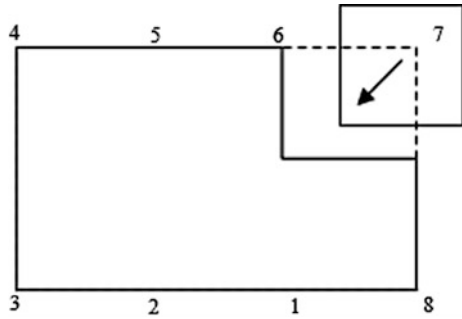
(i) Deformation parameter is

$$\mathbf{a} = 0.146 \, \text{m}$$
$$\mathbf{b} = 0.251 \, \text{m}$$

(ii) Global test result

$$T^2 = \frac{V^2 Q d^{-1} V}{(2p - d - u)\sigma_0^2} < F(2p - d - u, f, 0.95) \tag{4}$$

Substitute

p total point in the network as 8,
d datum defect as 2,
u number of parameter as 2,
f sum of degrees of freedom of epoch 1 and epoch 2.

$$\therefore \quad T^2 = 28.517 > 1.82 (F - \text{Test Failed})$$

Local test—significance test:

$$\bar{e}i = \frac{ei}{Qei} \quad F(1, f, 0.95) \tag{5}$$

Substitute ei, individual parameter,
Qei, correlation coefficient.

Significance level:

$$y = cdf(F, ei, v_1, v_2) \tag{6}$$

where cdf, cumulative distribution function,

ei, individual parameter,

v_1, numerator of degrees of freedom (1),

v_2, denominator of degrees of freedom (142).

As previously mentioned in (Sect. 3.3), this test is performed to determine the best model for deformation modelling. The statistical local test result and significance level have been arranged in Table 1.

The result of the selected deformation models is shown in Table 2. Based on the computation performed by MATLAB program, the result shows that Models (iii) and (v) only passed the global test from all the models tested. Then, Model (iii) was chosen as the 'best' model since the result passed the global test and the entire group of deformation parameters is significant statistically.

Based on the result of the Model (i), the calculation showed that the model failed in the global test. Hence, such model cannot be accepted to represent the deformation in the survey area. Since the model tested has failed the global test, significance test on each parameter is no longer needed. But for the purpose of completeness, significance test have been done as to know the significance level of each deformation parameter.

The selection of the best deformation model should possess at least one or a few combination of the characteristics which are (i) the significance of the coefficients, (ii) the fewer number of coefficients consistent with reasonable error, (iii) a minimal error of fitting and lastly (iv) based on physical grounds that is rational. Therefore, it can be summarized that points 7 and 8 were experiencing the rigid body movement. There is no homogeneous strain occuring to the body.

4.2 Improvement into Existing GDA Package
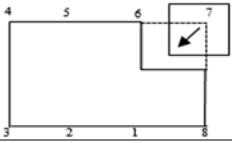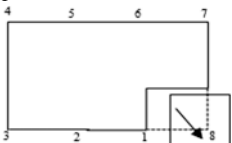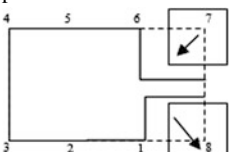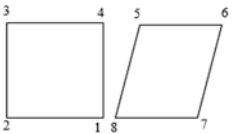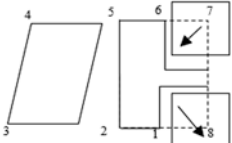
The main window is added to the previous GDA package as for some enhancement. The function of this window is to proceed with the geodetic deformation analysis computation. The figure of the main window is shown in Fig. 11.

As to achieve the second objective of this study, the MATLAB source codes of deformation modelling are added to the previous GDA computation package. These prove the deformation analysis package is almost complete by upgrading an advanced level procedure to be more effective for this study. A modelling analysis button was added and the result of the computation will be shown in the display window (see in Fig. 12).

Table 1 Result of local test

	ei	$F(1, f, 0.95)$	Significance level (%)
a	14.63 mm	0.999	99.99
b	25.09 mm	1.000	100

Table 2 Result of the selected deformation models from the simulation network

Type of model	Deformation parameters (m)	Significance $(1 - \alpha)$	Global test
i. Rigid body displacement at point 7	$a = 0.1463$ $b = 0.2509$	Significance (0.99) Significance (1.00)	Failed 28.517 > 1.821
ii. Rigid body displacement at point 8	$a_o = 0.3273$ $b_o = -0.2236$	Significance (1.00) Non-significance (0.00)	Failed 148.621 > 1.821
iii. Rigid body displacement at points 7 and 8	$a = 0.1463$ $b = 0.2509$ $a_o = 0.0685$ $b_o = 0.2884$	Significance (0.99) Significance (1.00) Significance (0.97) Significance (0.99)	Passed 0.029 < 1.898
iv. Homogenous strain	$\varepsilon_x = 0.0017$ $\varepsilon_y = 0.0012$ $\varepsilon_{xy} = -0.0013$ $w = 0.0003$	Significance (1.00) Significance (0.99) Non-significance (0.00) Significance (0.99)	Failed 62.65 > 1.898
v. Combination of rigid body displacement and homogenous strain	$a = 0.146235$ $b = 0.252252$ $a_o = 0.068902$ $b_o = 0.289512$ $\varepsilon_x = -0.000026$ $\varepsilon_y = -0.000013$ $\varepsilon_{xy} = 0.000019$ $w = -0.000007$	Significance (0.99) Significance (1.00) Non-significance (0.94) Significance (0.99) Non-significance (0.00) Non-significance (0.00) Non-significance (0.35) Non-significance (0.00)	Passed 0.020 < 2.163
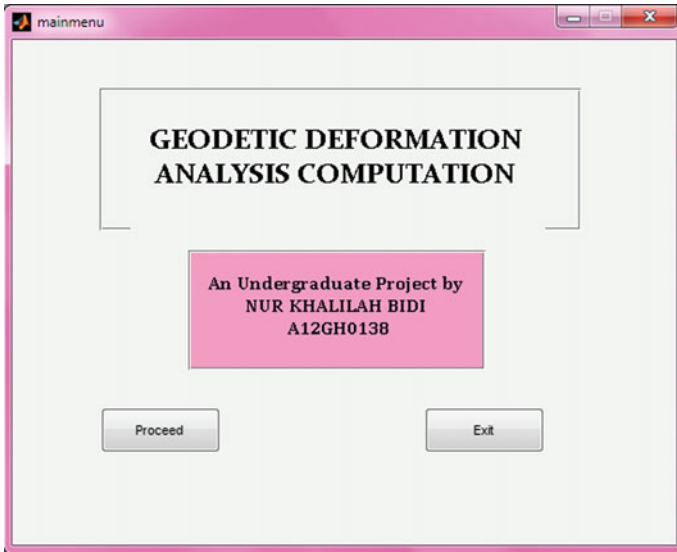
Fig. 11 Main menu of new version of GDA package
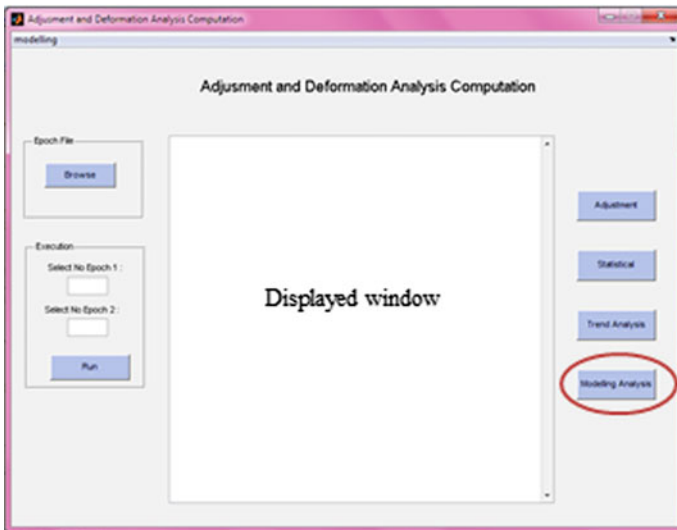
Fig. 12 New interface of GDA computation generated from GUIDE

5 Conclusions

This paper presented the deformation analysis procedure, which includes least squares adjustment of the network in each epoch, trend analysis and deformation modelling. The procedures are arranged in a systematic way, which is step-by-step analysis and can be practiced either on reference or relative monitoring networks.

Based on the results and analysis, the aim of this study was successfully achieved. Deformation modelling is one of the advanced procedures involve in geodetic deformation analysis. By adding this procedure, the GDA computation package almost achieves completeness.

The purpose of deformation modelling is a representation of the deformation occurred by using geometrical and mathematical relationship. The displacement of the points can be shown graphically by the selected models. The selected models involved are rigid body displacement at the move points, homogenous strain and the combination of rigid body displacement and homogenous strain. The five common deformation models selected in this study were created to be optimum sufficient in defining the behaviour of the body or object under investigation.

Besides, this study also has been a success to fulfil the second objective which is incorporating the developed routine and adding few improvements to an existing MATLAB package of GDA package. The improvement also makes the GDA program to solve the study of deformation network in 2 dimension. Perhaps in the future, the GDA computational package can be improved with the capability in GPS surveying in the 3-dimensional network can be added up.

References

1. Caspary, W.F.: Concepts of Network and Deformation Analysis, 1st edn. Monograph 11, School of Surveying, The University of New South Wales, Australia (1987)
2. Kuang, S.: Geodetic Network Analysis and Optimal Design: Concept and Applications. Ann Arbor Press Inc, Chelsea, Michigan (1996)
3. Ogundare, J.O.: Deformation monitoring and analysis. Geodetic techniques. In: Precision Surveying, The Principles and Geomatics Practice. Wiley, Hoboken, NJ, USA (2015)
4. Xiongyao, X., Xiaozhi, L.: Development of a 3D modelling algorithm for tunnel deformation monitoring based on terrestrial laser scanning. In: Underground Space. Department of Geotechnical Engineering, Tongji University, Shanghai, China (2017)
5. Setan, H., Singh, R.: Deformation Analysis of a Geodetic Monitoring Network. Center for Industrial Measurement and Engineering Surveying, Universiti Teknologi Malaysia (2001)
6. Setan, H.: Functional and stochastic models for geometrical detection of spatial deformation in engineering: a practical approach, Ph.D. Thesis. Department of Civil Engineering, City University, London (1995)

7. Singh, R.: Analisis Deformasi 2-D dengan kaedah Ujian Kongruensi. Bachelor Degree Project, Faculty of Geoinformation Science and Engineering, Universiti Teknologi Malaysia, Johor Bahru (1997)
8. Aisyah, R.: The Trend Analysis of Geodetic Monitoring Network by Use of Robust S-Transformation method. Bachelor Degree Project, Faculty of Geoinformation and Real Estate. Universiti Teknologi Malaysia (2014)
9. Ghilani, C.D., Wolf, P.R.: Adjustment Computations. Wiley, New York (2006)
10. Setan, H.: An Optimal Solution for Managing the Deformation Behavior of Engineering Structures. Pusat Pengurusan Penyelidikan, Universiti Teknologi Malaysia (2006)
11. Rosly, A.: Development of an Extended Version of Fredy03 Software for Deformation Analysis. Bachelor Degree Project, Faculty of Geoinformation and Real Estate, Universiti Teknologi Malaysia (2011)
12. Jafari, M.: Deformation modelling of structures enriched by inter-element continuity condition based on multi-sensor data fusion. Appl. Math. Model. **40**(21–22), 9316–9326 (2016)
13. Zainal, A.M.S.: Deformation Survey. Lecture Note Faculty of Geoinformation and Real Estate. Universiti Teknologi Malaysia (Unpublished) (2016)
14. Chen, Y.Q.: Analysis of deformation surveys—a generalized method. Technical Report No. 94. Department of Surveying Engineering, University of New Brunswick, Fredericton, N. B (1983)
15. Majudi, N.: Pemilihan model deformasi bagi jaringan geodetik. Projek Sarjana Muda, Fakulti Geinformasi dan Harta Tanah, Universiti Teknologi Malaysia (1999)
16. Chrzanowski, A.: Geotechnical and other non-geodetic methods in deformation measurements. In: Proceedings of the Deformation Measurement Workshop, pp. 112–153. Boston, Massachusetts, 31 November, Massachusetts Institute of Technology, Cambridge, M.A. (1986)
17. Kamiński, W., Nowel, K.: Local variance factors in deformation analysis of non-homogenous monitoring networks. Surv. Rev. **45**(328), 44–50 (2013)

A Review of GIS-Based and Multi-criteria Evaluation Method for Sustainable Landfill Site Selection Model

Habiba Ibrahim Mohammed, Zulkepli Majid, Norhakim Bin Yusof and Yamusa Bello Yamusa

Abstract The most used methods for the disposal of solid waste in majority of developed and developing municipalities are the landfilling method. Solid waste management plays a vital role in urban planning. However, selection of landfill site is very complicated and tedious task mainly because there are many factors and strict regulations involved in the identification and selection process. The main purpose of landfill site selection process is to identify the areas that will drastically reduce the negative impacts of the landfill to the immediate environment and the public health. Different site selection and identification studies made used of Geographic Information Systems (GIS) and Multi-Criteria Evaluation (MCE) methods. Also, the integration of these methodologies provides an environment to the decision-makers in siting suitable locations using land suitability analysis procedures. This paper proposes a conceptual model toward sustainable landfill site selection with the desegregation of GIS-based and multi-criteria decision analysis considering several criteria that are missed out to evaluate and identify the most suitable site for landfill. The outcome of this research would be of

H. I. Mohammed (✉) · Z. Majid · N. B. Yusof
Faculty of Geoinformation and Real Estate, Universiti Teknologi Malaysia,
81310 Skudai, Johor, Malaysia
e-mail: mydearhabiba@yahoo.com

Z. Majid
e-mail: zulkeplimajid@utm.my

N. B. Yusof
e-mail: norhakim@utm.my

Y. B. Yamusa
Faculty of Civil Engineering, Universiti Teknologi Malaysia,
81310 Skudai, Johor, Malaysia
e-mail: yamusabello@gmail.com

Y. B. Yamusa
Department of Civil Engineering, Nuhu Bamalli Polytechnic,
810001 Zaria, Nigeria

significant help to the waste management authority both local and international levels in siting a landfill toward sustainable solid waste management system.

Keywords Geographic information systems · Multi-criteria evaluation Landfill site selection

1 Introduction

The process of selecting landfill site is very complicated because it involves acquaintance of facts about many factors, parameters, rules, and regulations to be considered [1]. One of the crucial tasks regarding Municipal Solid Waste Management (MSWM) systems is the landfill site selection process because of the outcome occurring for the natural environment and the social opposition that landfill siting may evoke [2]. According to Kharat et al. [3], it is important to properly plan for the available land resources due to the present waste generation increase along with the scarcity of land. A lot of factors must be considered and mindfully evaluated in order to achieve the best site for landfill which will cause no or less negative impacts to the environment, society, and economy also conforming with the rules and regulations [4]. Examples of such factors include social and environmental factors, geomorphological features, and technical parameters. Waste disposal sites must preserve the ecological system in the surrounding environment [5–7]. Economic factors, which include the cost of acquiring land as well as development and operation costs, must also be considered [8]. Presently, the technological advancement has brought into the existence of the use of Geographic Information System (GIS) in landfill site selection study which has given rise to spatial data display and makes the selection process easier. The GIS allows data to be displayed and managed efficiently from variety of sources, and it reduces the time and cost in the siting process [9, 10]. GIS has matured into a powerful tool that can integrate driven types of spatial data and perform a variety of spatial analysis.

Technical literature has shown that GIS-based multi-criteria decision analysis provides a framework for land development and is helpful to engineers, decision-makers, and planners [11]. Many researchers have demonstrated the advantages of using GIS and multi-criteria methods in landfill site selection [11–17]. Suitable sites for waste disposal are evaluated by a numerous criterion such as land cost, surface- and groundwater, distance to settlement, waste production centeres, site capacity, road access, railways, airport, archaeological heritage, soil properties, and public acceptance. But the geotechnical properties should also be considered in the landfill siting. This paper proposes a conceptual model toward sustainable selection of landfill site with the integration of GIS-based and multi-criteria decision analysis considering the geotechnical factors to evaluate and identify the most suitable and appropriate site for landfilling.

2 Landfill Site Selection

A broad search especially in the journals, conferences, and articles published provided a good literature concerning selection of suitable site for landfill problem over the years. Most of these researchers found that MCA is one of the good techniques that can be used and combined with GIS to conduct site selection or site suitability analysis. In order to identify the most suitable disposal site for solid waste disposal, a wide and vigorous evaluation process must be considered such as economic, environmental, health, and social impacts [18–20].

The process of evaluating and selecting a new solid waste disposal site is very complicated and tedious as it involves diverse environmental and social fields of knowledge including science, economics, geology, geography, land survey, and sociology. Furthermore, the methodology required in evaluating new solid waste disposal site must consider certain factors and criterion such as distance to urban centers, water bodies, airports, infrastructures, and soil permeability. Therefore, there is a need for processing significant amount of spatial data, regulations, and acceptance criteria before siting a new solid waste disposal site. The site selection procedure, however, should make maximum use of the available information and ensure that the outcome of the process is acceptable by most stakeholders and thus landfill siting generally requires processing of a variety of spatial data [21].

A similar study has also been done by [22] where they discussed the integration of GIS and decision support system and its efficiency in solving the landfill site selection in Konya, Turkey. According to Chabuk et al. [5], GIS is considered as a powerful tool in assisting selection for a waste disposal site through its ability to deal with a huge amount of data from different sources. The MCDA techniques can be applied to solve any complex problem in a variety of fields of many practical situations. However, with GIS map analysis tools, maps can be easily and efficiently manipulated with a computer, also georeferenced data can be converted into computerized maps [21]. Table 1 shows an outline of the site selection criteria employed by various researchers from different parts of the world. Also from the table, the most frequently used criteria are the road and water bodies due to their high level of importance. Furthermore, this paper proposes a conceptual model emphasizing on the geotechnical properties of the soil that the landfill is to be sited.

3 GIS-Based and Multi-criteria Decision Analysis in Spatial Problems

The combination of GIS-based tools and decision analysis techniques has widened tremendously in various fields of research over the last few decades. This technology has given the distinctive capability of automating and analyzing a variety of spatial data including urban planning and development, environmental pollution, natural, and forest resources [11]. The negative impacts of solid waste disposal site

Table 1 Landfill site selection criteria from different researchers

S/No	Criteria	[23]	[24]	[25]	[26]	[27]	[22]	[28]	[29]	[30]	[31]	[32]	[33]	[34]	[13]	[35]	[36]	[14]	[17]	[5]	[37]	[15]
1	Land use/land cover	*	*	*		*	*	*	*	*	*	*	*	*	*			*	*	*	*	*
2	Road accessibility	*	*	*		*	*	*	*	*	*	*		*	*	*		*	*	*	*	*
3	Surface water		*	*	*	*		*	*	*	*	*	*	*	*	*		*	*	*	*	*
4	Groundwater	*		*	*	*		*	*	*		*	*	*	*		*	*	*	*	*	*
5	Slope		*			*	*	*		*	*	*	*	*	*	*	*	*	*	*		
6	Soil properties	*		*			*	*		*		*	*		*	*	*		*	*		
7	Elevation		*											*		*				*	*	*
8	Railway		*				*							*				*	*	*		
9	Waste generation	*				*				*		*						*	*			
10	Airports		*			*								*				*			*	
11	Residential areas		*	*		*			*	*	*		*	*	*	*		*	*	*		*
12	Wind														*							*
14	Cost of land					*																
15	Historical areas						*			*				*			*	*				
16	Infrastructures		*								*			*								
17	Agricultural areas						*				*									*		
18	Wetlands		*	*							*											
19	Sensitive areas							*		*		*	*	*					*			
20	Population			*	*				*													
21	Flooding																*					
22	Soil permeability							*														
23	Geotechnical properties																					

*The criteria was employed from the researchers in their study

to the public health cause difficulty in the site selection process. Most suitable landfill sites should be selected using multi-criteria evaluation techniques based on the nature of the study area. The purpose of integrating GIS and MCDA is to investigate different possible choices when it comes to multiple criteria decision-making and conflicting objectives [38]. This process provides various collections of methodology and procedures to bring out preferences to decision-makers and to incorporate them into GIS-based decision-making. GIS-based MCDA is used in analyzing geographic events where the results of the analysis depend on the spatial arrangement of the events [39].

A lot of studies on landfill site selection have been done using the combination of GIS coupled with MCDA methods, and examples of such studies [5, 13, 15, 17, 40, 41] can be mentioned. Furthermore, the MCDA, Analytical Hierarchy Process (AHP) has been popularly employed in landfill site selection in recent years. Ahmad et al. [16] carried out a research for identification of site for landfill in Punjab, Pakistan. Alavi et al. [32] identified a solid waste disposal site for the municipality of Mahshahr city, Iran using AHP and GIS. Rathore et al. [41] identified landfill sites in Lahore using the suitability model, Pakistan. Abujayyab et al. [42] using an intelligent system based (neural networks) focused on mapping suitability of landfill sites. Ohri et al. [14] demonstrated the detection of the most suitable landfill site in Varanasi, India using GIS-based overlay analysis and MCDA. Also, Moeinaddini et al. [10] implemented their study based on the evaluation the most suitable site in Karaj by combining Spatial Multi-Criteria Evaluation (SMCE) and GIS in their methodology. Latinopoulos and Kechagia [43] provided a framework for the evaluation of best sites for wind farm development projects which was based on the combination of GIS and spatial multi-criteria decision analysis. This process provided a decision-making tool for planning a wind farm at regional level. They developed a procedure which involved various siting criteria including social, environmental, economic, and technological for the identification of most suitable site for wind farm installation.

Sharifi et al. [44] conducted a study of MCDA for GIS-based hazardous waste landfill siting in Kurdistan Province, western Iran. Two-stage analysis was employed in their study which produced a spatial decision support system tool for hazardous waste management under developed region. Lawal et al. [45] conducted a research in Universiti Teknologi Malaysia which they proposed new recreational park. Their purpose of study was to investigate if the present recreational parks are effectively functioning in terms of distances, locations, and facilities. Datasets of the study area were created using GIS tools making it to be the set of criteria. These criteria were then combined into the Multi-Criteria Decision Process (MCDP). The Analytical Hierarchy Process (AHP) was used for the pair-wise comparison of the criteria thereby assigning weight to each criterion. After all these, the final output of the research was able to identify the most suitable sites to locate the proposed recreational park.

Youssef et al. [46] recommended the use of GIS-based multi-criteria analysis AHP approach as the most appropriate methods of evaluating land suitability analysis in any urban developed environments. Also, AHP provides an efficient site

suitability determination in different aspects or fields of development, which include urban development, industrial, and tourist. Khan and Samadder [47] evaluated environmentally suitable landfill sites in their study area which they implemented GIS-based and MCDA approaches. The Analytical Hierarchy Process (AHP) was used for the pair-wise comparison of the criteria thereby assigning weight to each criterion. Suitable landfill sites map was produced applying a Weighted Linear Combination (WLC) in GIS environment. According to El Baba et al. [48], landfill site selection can be done using Multi-Criteria Decision Analysis (MCDA) with the help of the AHP method. In their studies in Gaza Strip, new suitable landfill sites were selected using the above-mentioned methodology coupled with GIS. They employed different thematic layers and finally came out with the most suitable sites of about 5.5% of the study area. Table 2 shows the GIS-based and multi-criteria evaluation techniques in landfill site selection studies. Literature has shown that the use of GIS-Based MCDA using AHP has provided an acceptable method of landfill siting. Therefore, it should be employed to evaluate the geotechnical aspect as well.

Table 2 Landfill site selection using GIS-MCDA methods

S/No	Authors	Study area	Application	Methods
1	[24]	Ankara, Turkey	Landfill site selection	GIS/MCDA
2	[23]	Giroft, Iran	MSW Landfill site selection	AHP/GIS
3	[27]	Beijing, China	Landfill site selection	SIT/AHP
4	[49]	Nakuru, Kenya	Landfill suitability	GIS/MCDA
5	[29]	Colombia	Methodology for landfill location	GIS
6	[30]	Northern Cyprus	Sanitary landfill	GIS/AHP
7	[50]	Ramjerd, Iran	MSW Landfill site selection	GIS/AHP
8	[32]	Mahshahr, Iran	MSW Landfill site selection	GIS/AHP
9	[13]	Tafresh town, Iran	MSW Landfill site selection	AHP/GIS
10	[51]	Johor, Malaysia	Landfill site selection	GIS/AHP
11	[34]	Konya, Turkey	MSW Landfill site selection	GIS/AHP
12	[14]	Varanasi, India	Sanitary landfill site selection	GIS/AHP
13	[16]	Punjabi, Pakistan	Landfill site identification	GIS/MCE (AHP)
14	[40]	Antalya, Turkey	Landfill site selection	MCDA/GIS
15	[41]	Lahore, Pakistan	Landfill identification	GIS/AHP
16	[52]	Selangor, Malaysia	Landfill site selection model	GIS/AHP/WLC
17	[15]	Iranshahr, Iran	Landfill site selection	GIS/Fuzzy AHP
18	[17]	Behbahan, Iran	Landfill site selection	GIS/AHP
19	[5]	Babylon, Iraq	Landfill site selection	GIS/AHP
20	[3]	Mumbai, India	Modeling landfill site	Fuzzy MCDA

4   Geotechnical Criteria in Landfill

Geotechnics deals with the investigation of the engineering behavior of soil/rock. These investigations are used to design and build foundations, earth structures, pavement sub-grades, and landfill soil liners. In the time of early landfill siting and its development, the type of liner to be constructed must be determined. The compacted clay liner should have the tendency to minimize the downward movement of leachate. This liner in addition must have an adequate strength to support any superimposed load. Likewise, it can be able to withstand the seasonal variation that might cause swelling and shrinkage. The liner material can be classified as unsuitable, marginal, and suitable. Plasticity index below 6% is classified as unsuitable, between 6 and 12% are classified as marginal, and the materials which have plasticity index above 12% are classified as suitable [53].

The criteria in most regulatory agencies (guidelines) and researches specified a value of 1×10^{-9} m/s maximum hydraulic conductivity, a maximum of 4% volumetric shrinkage, and minimum of 200 kN/m^2 shear strength are required for hydraulic barrier systems [54–56]. Therefore, to set up a conceptual model toward a sustainable landfill siting, geotechnical properties of the soil have a vital role to play.

5   Conceptual Model Toward Sustainable Landfill Siting

Presently, there are several researches that have worked on addressing the issues related to landfill siting and their solutions, yet only few of these models can be employed for an optimal landfill site selection with only a little of available data [36]. Figure 1 describes the proposed model to efficiently select the best site for landfill. The main criteria and set of sub-criteria were determined depending on several local and international literatures. After that, it was classified into groups which are physical, environmental, geological, and socioeconomic.

The development of this model is to enhance the social, economic, environmental, and government regulatory setup. The AHP methods of pair-wise comparisons will be used to assign weights to each criterion and rank them, while weighted linear combination will be employed to rank the alternatives. This is because of their efficiency and accuracy when it comes to solid waste disposal site selection. Afterward, the geotechnical criteria to select the most feasible site are then employed to provide the best possible site for sanitary landfilling. Also, with this modeling, an accurate landfill site can be produced reducing the cost and time required compared to other methods. Following the model developed, the unpredictable error especially the geotechnical aspect in the decision-making process can be represented and analyzed.
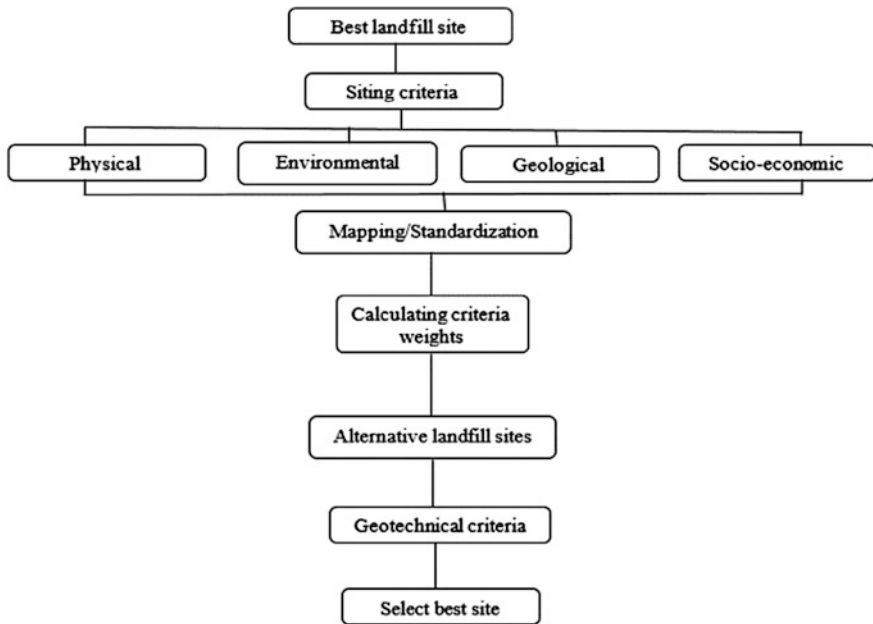
Fig. 1 Conceptual model for best site selection

6 Concluding Remarks

Achieving best site for landfill site selection/suitability using GIS coupled with MCDA tools has been described in this paper. The combination of these tools ensures efficiency and accuracy in the site selection studies. This paper demonstrated a conceptual model toward a sustainable site selection of landfill putting into consideration physical, socioeconomical, environmental, geological, and geotechnical criteria. This can be achieved with the combination of GIS-based and multi-criteria decision analysis methodology to identify and select the best site because MCDA enhances and provides a distinctive and reliable final decision. The outcome of this research would be of significant help to the waste management authority both local and international levels in siting a landfill toward sustainable solid waste management system.

References

1. Djokanović, S., Abolmasov, B., Jevremović, D.: GIS application for landfill site selection: a case study in Pančevo, Serbia. Bull. Eng. Geol. Environ. **75**(3), 1273–1299 (2016)
2. Demesouka, O., Vavatsikos, A., Anagnostopoulos, K.: GIS-based multicriteria municipal solid waste landfill suitability analysis: a review of the methodologies performed and criteria implemented. Waste Manage. Res. **32**(4), 270–296 (2014)
3. Kharat, M.G., et al.: Modeling landfill site selection using an integrated fuzzy MCDM approach. Model. Earth Syst. Environ. **2**(2) (2016)
4. Ahmad, S.Z., Ahamad, M.S.S., Yusoff, M.S.: A comprehensive review of environmental, physical and socio-economic (EPSE) criteria for spatial site selection of landfills in Malaysia. Appl. Mech. Mater. **802**, 412–418 (2015)
5. Chabuk, A., et al.: Landfill site selection using geographic information system and analytical hierarchy process: a case study Al-Hillah Qadhaa, Babylon, Iraq. Waste Manag. Res. **34**(5), 427–437 (2016)
6. Baban, S.M., Flannagan, J.: Developing and implementing GIS-assisted constraints criteria for planning landfill sites in the UK. Plann. Pract. Res. **13**(2), 139–151 (1998)
7. Önüt, S., Soner, S.: Transshipment site selection using the AHP and TOPSIS approaches under fuzzy environment. Waste Manag. **28**(9), 1552–1559 (2008)
8. Yesilnacar, M.I., Cetin, H.: An environmental geomorphologic approach to site selection for hazardous wastes. Environ. Geol. **55**(8), 1659–1671 (2008)
9. Delgado, O.B., et al.: Analysis of land suitability for the siting of inter-municipal landfills in the Cuitzeo Lake Basin, Mexico. Waste Manage. **28**(7), 1137–1146 (2008)
10. Moeinaddini, M., et al.: Siting MSW landfill using weighted linear combination and analytical hierarchy process (AHP) methodology in GIS environment (case study: Karaj). Waste Manag. **30**(5), 912–920 (2010)
11. Chandio, I.A., et al.: GIS-based analytic hierarchy process as a multicriteria decision analysis instrument: a review. Arab. J. Geosci. **6**(8), 3059–3066 (2013)
12. Shahabi, H., et al.: Evaluating Boolean, AHP and WLC methods for the selection of waste landfill sites using GIS and satellite images. Environ. Earth Sci. **71**(9), 4221–4233 (2013)
13. Elahi, A., Samadyar, H.: Municipal solid waste landfill site selection using analytic hierarchy process method for Tafresh Town. Middle-East J. Sci. Res. **22**(9), 1294–1307 (2014)
14. Ohri, A., Maurya, S.P., Mishra, S.: *Sanitary Landfill Site Selection by Using Geographic Information System* (2015)
15. Torabi-Kaveh, M., et al.: Landfill site selection using combination of GIS and fuzzy AHP, a case study: Iranshahr, Iran. Waste Manag. Res. (2016)
16. Ahmad, A., et al.: Landfill sites identification using GIS and multi-criteria method: a case study of intermediate city of Punjab, Pakistan. J. Geogr. Inf. Syst. **08**(01), 40–49 (2016)
17. Rahmat, Z.G., et al.: Landfill site selection using GIS and AHP: a case study: Behbahan, Iran. KSCE J. Civ. Eng. **21**(1), 111–118 (2016)
18. Al Sabbagh, M.K., et al.: Resource management performance in Bahrain: a systematic analysis of municipal waste management, secondary material flows and organizational aspects. Waste Manage. Res. **30**(8), 813–824 (2012)
19. Allesch, A., Brunner, P.H.: Assessment methods for solid waste management: a literature review. Waste Manage. Res. **32**(6), 461–473 (2014)
20. Wilson, D.C., et al.: Using research-based knowledge to underpin waste and resources policy. Waste Manage. Res. **25**(3), 247–256 (2007)
21. Khan, D., Samadder, S.R.: Municipal solid waste management using geographical information system aided methods: a mini review. Waste Manag. Res. **32**(11), 1049–1062 (2014)
22. Nas, B., et al.: Selection of MSW landfill site for Konya, Turkey using GIS and multi-criteria evaluation. Environ. Monit. Assess. **160**(1–4), 491–500 (2010)

23. Javaheri, H., et al.: Site selection of municipal solid waste landfills using analytical hierarchy process method in a geographical information technology environment in Giroft. J. Environ. Health Sci. Eng. **3**(3), 177–184 (2006)
24. Şener, B., Süzen, M.L., Doyuran, V.: Landfill site selection by using geographic information systems. Environ. Geol. **49**(3), 376–388 (2005)
25. Chang, N.B., Parvathinathan, G., Breeden, J.B.: Combining GIS with fuzzy multicriteria decision-making for landfill siting in a fast-growing urban region. J. Environ. Manage. **87**(1), 139–153 (2008)
26. Zamorano, M., et al.: Evaluation of a municipal landfill site in Southern Spain with GIS-aided methodology. J. Hazard. Mater. **160**(2–3), 473–481 (2008)
27. Wang, G., et al.: Landfill site selection using spatial information technologies and AHP: a case study in Beijing, China. J. Environ. Manage. **90**(8), 2414–2421 (2009)
28. Babalola, A., Busu, I.: Selection of landfill sites for solid waste treatment in Damaturu town-using GIS techniques. J. Environ. Prot. **02**(01), 1–10 (2011)
29. Mejía, Z., et al.: A methodology for landfill location using geographic information systems: a Colombian regional case. Ingeniería Inv. **32**(1), 64–70 (2012)
30. Kara, C., Doratli, N.: Application of GIS/AHP in siting sanitary landfill: a case study in Northern Cyprus. Waste Manag. Res. **30**(9), 966–980 (2012)
31. Yildirim, V.: Application of raster-based GIS techniques in the siting of landfills in Trabzon Province, Turkey: a case study. Waste Manag. Res. **30**(9), 949–960 (2012)
32. Alavi, N., et al.: Municipal solid waste landfill site selection with geographic information systems and analytical hierarchy process: a case study in Mahshahr County, Iran. Waste Manag. Res. **31**(1), 98–105 (2013)
33. Ebistu, T.A., Minale, A.S.: Solid waste dumping site suitability analysis using geographic information system (GIS) and remote sensing for Bahir Dar Town, North Western Ethiopia. Afr. J. Environ. Sci. Technol. **7**(11), 976–989 (2013)
34. Uyan, M.: MSW landfill site selection by combining AHP with GIS for Konya, Turkey. Environ. Earth Sci. **71**(4), 1629–1639 (2013)
35. Isa, M.Z., Saidu, A.V.: *Identification of Suitable Site for Solid Waste Disposal in Yola, Nigeria Using GIS Method* (2014)
36. Eskandari, M., et al.: Optimizing landfill site selection by using land classification maps. Environ. Sci. Pollut. Res. Int. **22**(10), 7754–7765 (2015)
37. Abujayyab, S.K., et al.: A new framework for geospatial site selection using artificial neural networks as decision rules: a case study on landfill sites. ISPRS Ann. Photogrammetry Remote Sens. Spat. Inf. Sci. **2**(2), 131 (2015)
38. Voogd, H.: Multicriteria Evaluation for Urban and Regional Planning, vol. 207. Pion, London (1983)
39. Cowen, D.J.: GIS versus CAD versus DBMS: what are the differences? Photogramm. Eng. Remote Sens. **54**(11), 1551–1555 (1988)
40. Aksoy, E., San, B.T.: Using Mcda and Gis for landfill site selection: central districts of Antalya Province. ISPRS Int. Arch. Photogramm. Remote Sens. Spat. Inf. Sci. **XLI-B2**, 151–157 (2016)
41. Rathore, S., Ahmad, S., Shirazi, S.: Use of the suitability model to identify landfill sites in Lahore-Pakistan. J. Basic Appl. Sci. **12**, 103–108 (2016)
42. Abujayyab, S.K., et al.: GIS modelling for new landfill sites: critical review of employed criteria and methods of selection criteria. In: IOP Conference Series: Earth and Environmental Science. IOP Publishing, Bristol (2016)
43. Latinopoulos, D., Kechagia, K.: A GIS-based multi-criteria evaluation for wind farm site selection. A regional scale application in Greece. Renew. Energy **78**, 550–560 (2015)
44. Sharifi, M., et al.: Integrating multi-criteria decision analysis for a GIS-based hazardous waste landfill sitting in Kurdistan Province, western Iran. Waste Manag. **29**(10), 2740–2758 (2009)
45. Lawal, D.U., Matori, A.N., Balogun, A.L.: A geographic information system and multi-criteria decision analysis in proposing new recreational park sites in Universiti Teknologi Malaysia. Mod. Appl. Sci. **5**(3), 39 (2011)

46. Youssef, A.M., Pradhan, B., Tarabees, E.: Integrated evaluation of urban development suitability based on remote sensing and GIS techniques: contribution from the analytic hierarchy process. Arab. J. Geosci. **4**(3–4), 463–473 (2011)
47. Khan, D., Samadder, S.: Application of GIS in landfill siting for municipal solid waste. Int. J. Environ. Res. Dev. **4**(1), 37–40 (2014)
48. El Baba, M., Kayastha, P., De Smedt, F.: Landfill site selection using multi-criteria evaluation in the GIS interface: a case study from the Gaza Strip, Palestine. Arab. J. Geosci. **8**(9), 7499–7513 (2014)
49. Kirimi, F.K., Waithaka, E.H.: Determination of suitable landfill site using geospatial techniques and multi-criteria decision analysis: a case study of Nakuru Town, Kenya. Int. J. Sci. Res. (IJSR) **3**(11), 2319–7064 (2014)
50. Eskandari, M., et al.: Integrating GIS and AHP for municipal solid waste landfill site selection. J. Basic Appl. Sci. Res. **3**(4), 588–595 (2013)
51. Mohd Yunus, M.Z., et al.: Integrating and utilizing AHP and GIS for landfill site selection. Appl. Mech. Mater. **773–774**, 100–104 (2015)
52. Ismail, S.: The challenge of future landfill: a case study of Malaysia. J. Toxicol. Environ. Health Sci. **5**(6), 86–96 (2013)
53. Jones, R., et al.: Selection of clays for use as landfill liners. Waste Disposal Landfill-Green **93**, 433–438 (1995)
54. Osinubi, K.J., Nwaiwu, C.M.: Design of compacted lateritic soil liners and covers. J. Geotech. Geoenviron. Eng. **132**(2), 203–213 (2006)
55. Bello, A.: Acceptable zone for reddish brown tropical soil as liner material. Pac. J. Sci. Technol. **16**(1) (2015)
56. Daniel, D.E., Wu, Y.K.: Compacted clay liners and covers for arid sites. J. Geotechn. Eng. **119**(2), 223–237 (1993)

Assessing the Reliability and Validity of Satellite Altimetry-Derived Wet Delay in Peninsular Malaysia

Mohamad Aswad Mohd Azman, Ami Hassan Md Din,
Tajul Ariffin Musa, Suhaila Salihin and Abdullah Hisam Omar

Abstract Water vapor is known as a gas state of water. The nature of the water vapor is invisible, which means it cannot be seen but can be sensed by the humidity in the air. As the climate is warming due to the increase of carbon dioxide and other anthropogenic greenhouse gases, water vapor is expected to increase rapidly as models broadly conserve relative humidity. Water vapor consists of two components, namely, dry and wet delay. Only wet delay will be highlighted in this study due to which the dry delay can be modeled easily. The wet delay in the atmosphere needs to be monitored as to detect and predict changes in earth's climate particularly for weather forecasting. There are many methods that can be used to measure the wet delay such radiosonde and Global Positioning System (GPS). But both of them had their limitations; for example, they were point-based solutions means that the wet delay can be derived at a certain area. Radiosonde method needs to be launched twice daily, and for a single launch, cost a lot. This study presents an effort to extract the wet delay measurement from radiometer system using satellite

M. A. Mohd Azman · A. H. M. Din (✉) · T. A. Musa · S. Salihin · A. H. Omar
Geomatic Innovation Research Group (GIG), Johor Bahru, Malaysia
e-mail: amihassan@utm.my

M. A. Mohd Azman
e-mail: aswadazman@yahoo.com

T. A. Musa
e-mail: tajulariffin@utm.my

S. Salihin
e-mail: suhailasalihin@gmail.com

A. H. Omar
e-mail: abdullahhisham@utm.my

A. H. M. Din
Geoscience and Digital Earth Centre (INSTEG), Faculty of Geoinformation
and Real Estate, Universiti Teknologi Malaysia, 81310 Johor Bahru,
Johor, Malaysia

A. H. M. Din
Institute of Oceanography and Environment (INOS),
Universiti Malaysia Terengganu, Kuala Terengganu, Terengganu, Malaysia

altimeter. The advantage of using satellite altimeter is that the wet delay parameter can be retrieved on land and marine areas. Thus, it can improve the spatial resolution for wet delay retrieval. This study employs the altimetry-derived wet delay trend based on multi-mission satellite altimeter in the Peninsular Malaysia for 1-year data, in 2014. Two altimeter missions were used, namely, Jason-2 and Saral. Radar Altimeter Database System (RADS) was used to extract the water vapor data. Altimetry-derived water vapor was verified with GPS-derived Zenith Wet Delay (ZWD) at six GPS Continuously Operating Reference System (CORS) stations. The verification results showed that the RMSE between the altimetry-derived wet delay and GPS-derived wet delay was about 3–12 cm. Furthermore, the data from the satellite altimeter is in a good shape with the seasonal variation of precipitation according to the climatic classification of the region. Besides that, the observed data also give reasonable values when considered for the wet and dry seasons because the value from the CORS and satellite altimeter only had a slight difference. In conclusion, altimetry-derived wet delay is promising to be used in climate and weather research in the future.

1 Introduction

Water vapor is known as a gas state of water. The nature of the water vapor is invisible, which means it cannot be seen but can be sensed by the humidity in the air. Water vapor consists of two components, namely, dry and wet delay. Only wet delay will be highlighted in this study due to which the dry delay can be modeled easily. The wet delay data or information can be used in climate and weather research. The wet delay in the atmosphere needs to be monitored as to detect and predict changes in earth's climate. It is relevant that a long-period variation in the volume of wet delay in the atmosphere to be tracked. The reason is to predict changes in the earth's climate as well as enhancing the weather forecasting [1].

There are many methods that can be used to measure the wet delay. Some uses radiosonde to observe wet delay data and some use Global Positioning System (GPS). Both of them have advantages and disadvantages. For example, radiosonde is quite an expensive instrument and it will always be launched at a certain station and usually it is launched twice daily (one in the morning and one at night). Ground truth data such as GPS can be done at any GPS CORS in a network. But the data from GPS eliminate some errors by using double-differencing technique. Besides that, the data from the GPS is a station-based data which means the data will be limited by the location of the GPS station.

In the previous study, started in 1992, scientists have been exploring the use of GPS for the wet delay measurement [2]. There are a lot of advantages in studying the wet delay. Regarding the space-borne systems, the wet delay lowers the propagation pace of the signals, procrastinating the time needed to hit the ground

[3]. For GPS methods, the propagation delay happened in the troposphere also known as Zenith Path Delay (ZPD) that can be estimated through the GPS data processing. But the main point of this research is to yield the information of the Zenith Wet Delay (ZWD).

In this study, satellite altimeter uses to extract wet delay data. The satellite missions that been used were Jason-2 and Saral. The data provided by the satellite altimeter has sufficient spatial and temporal resolutions. The aim of this research is to study the wet delay for Peninsular Malaysia by using multi-mission satellite altimeter. The advantage of using satellite altimetery-derived wet delay that combined with the other methods is that it can derive the amount of wet delay data over the marine areas.

1.1 Concept of Water Vapor

Water vapor is also known as a gas state of water. The word vapor stands for describing the gaseous state that recurs as a liquid or solid. The nature of the water vapor is invisible, which means that it cannot be seen but can be sensed by the humidity in the air. The production of the water vapor usually happened by the evaporation process. In other way, it can also be produced by the sublimation of the ice. Figure 1 shows the process of the water cycle.
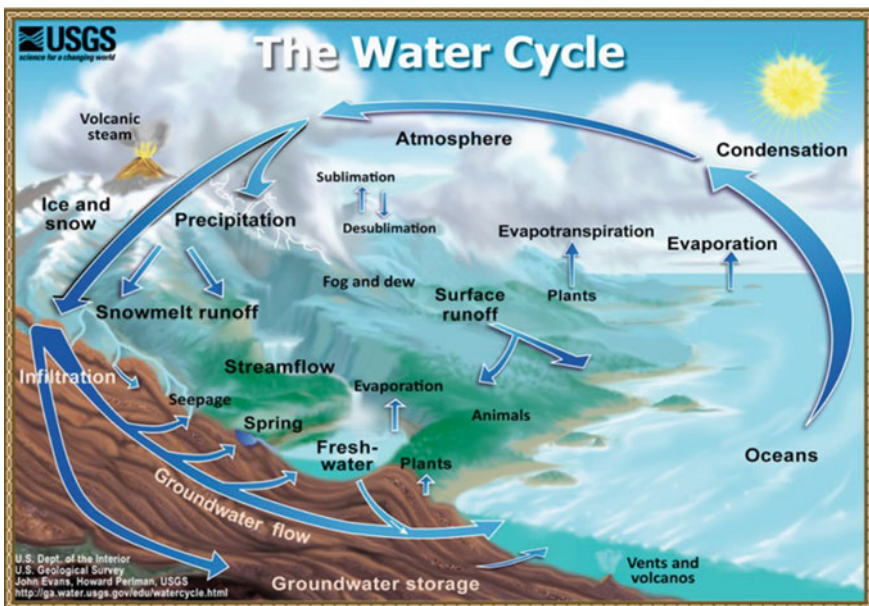
Fig. 1 Water cycle process [16]

Although water vapor is produced by water in gaseous state, it is the uttermost vital greenhouse gases. A reason for this statement is that the heat radiated from the Sun to the Earth's surfaces is particularly absorbed by the water molecules which are then radiated to all directions. As the climate is warming due to increasing carbon dioxide, other anthropogenic greenhouse gases of water vapor are expected to increase rapidly as models broadly conserve relative humidity [4]. In surveying, the water vapor and other dry gases such as carbon dioxide and nitrogen that contained in the layer of troposphere will contribute the error especially in GPS surveying, because it can delay the signal propagation from GPS satellite to the receiver on the ground. In high-precision practice essentially by GPS or InSAR, delayed radio signal propagation is known to be a major source of error [5].

Water vapor can also boost the warming effect of other greenhouse gases, such that the warming brought about by increased carbon dioxide allows more water vapor to enter the atmosphere. More water vapor in the air also gives rise to an increase in the formation of clouds in the troposphere. Clouds do consist of small water droplets, though, and, hence, they do absorb radiation [6].

1.2 Satellite Altimeter Principle

Satellite altimetry also known as a microwave sensor can give various kinds of information. The data is known as a raw data that need to do some corrections regarding the usage of the data. During the flight, the propagation of the signals, the signals will pass through the atmosphere and contain so many errors such as refraction, reflection, and time bias. Thus, with all the errors, it can delay the signal path. Any interference with the radar response signal needs to be taken ahead up. There are numbers of factors that can affect the data or signal path. One of them is wet delay. It can disturb the signal round-trip time, and thus these factors will be lead to distort the range measurements. To overcome these issues, we can apply the corrections for these interference effects on the altimeter signal by measuring them at certain frequencies. Now most of satellite altimetry equipped with the water vapor radiometer system.

The radiometer works by observing the brightness temperatures to extract the wet zenith delay. The water vapor from radiometer is calibrated using tipping curve measurements [7]. The reason for adopting a time average surface temperature is to give a better resemblance to the mean temperature of the wet troposphere than is administered by the direct surface temperature, which has large diurnal variations [8]. In order to get a definite wet path delay, errors need to be eliminated; in this point, cloud issuance needs to be discarded. To achieve that, use two frequencies of water vapor radiometer.

2 Research Approach

2.1 *Study Area*

In this study, the assessment of wet delay measurement was carried out over the Peninsular Malaysia region (tropical region). The areas of interest cover the Malacca Straits, South China Sea, and land area of Peninsular Malaysia as shown in Fig. 2.

2.2 *Data Processing*

Altimetry-Derived Wet Delay. In this study, two (2) satellite altimeter missions are selected: Jason- 2 and Saral to extract the wet delay data. The time period of satellite altimetry data is from January 2014 to December 2014. The Radar Altimeter Database System (RADS) is used as processing software for altimetry data. RADS has been set up for over 15 years, first built in Delft University of Technology, recently at the National Oceanic and Atmospheric Administration (NOAA) and altimetrics. RADS now assists as a model for a central climate data

Fig. 2 Peninsular Malaysia, South China Sea, and Malacca Straits

record for sea level. By virtue of the numerous user participated in auditing the data and the constant updates to the base, RADS is one of the uttermost accurate and complete databases of satellite altimeter [9].

RADS gives the user to be able to define the most suitable corrections that need to be applied to the data. To make it run within the needed specifications, user can create a getraw.nml command. The reason to create the getraw.nml is to ease the user to characterize their wanted geographical region by latitude and longitude along with other relevant parameter. The altimeter data extracted in this study ranges between $0°N \leq Latitude \geq 8°N$ and $96°E \leq Longitude \geq 108°E$ that covers Peninsular Malaysia, Malacca Straits, and South China Sea.

The missions move by the along track technique, where the satellite will pass over the same spot in different times. Thus, the data will be redundant. In this research, as mentioned, two satellite missions will be used, Jason-2 and Saral. Figure 3 shows the altimeter track for Jason-2 and Saral, respectively.

Based on Fig. 3, both the missions covered the Malacca Straits and South China Sea; Saral covered the land areas and Jason-2 only covered the nearest coastline to the Peninsular Malaysia. According to Fig. 3b, Saral altimeter track is denser which means the satellite mission will pass the same location in very short time compared with the Jason-2 altimeter track which is less dense. Hence, Saral altimeter mission will provide more data within the stated period than Jason-2. Table 1 shows the satellite altimeter's spatial and temporal characteristics. Figure 4 shows the

(a) Jason - 2   (b) Saral
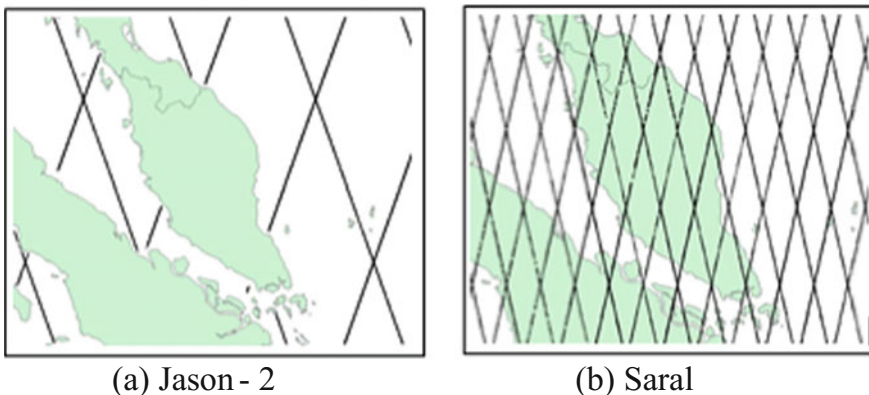
Fig. 3 Satellite altimeter's track for Jason-2 (**a**) and Saral (**b**)

Table 1 The satellite altimeter's temporal and spatial characteristics

Satellite mission	Agency	Track spacing (km)	Repeat cycle (days)
Jason-2	NASA	315	10
Saral	ESA & ISRO	75	35

Fig. 4 Multi-mission altimeter Track: Jason-2 combines with Saral
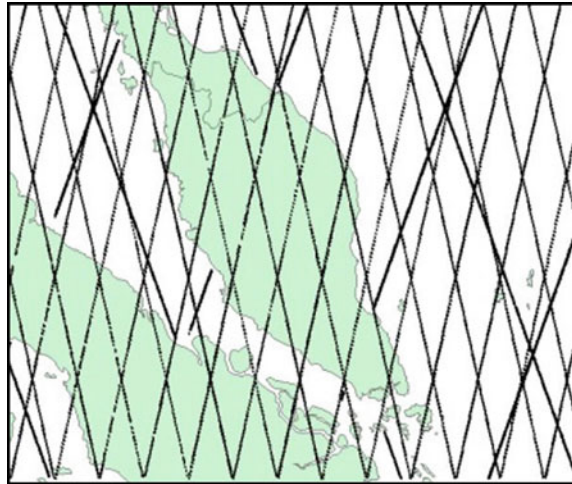
multi-mission track from Jason-2 and Saral. By combining these two satellite missions, the spatial and temporal resolutions of the data can be improved in the area of interest.

GPS-derived Zenith Wet Delay (ZWD)

Theory of GPS-derived ZWD Estimation. There are two delay experiences by GPS signal when passes through the atmosphere layer which are tropospheric delay and ionospheric delay. However, this study will focus on the tropospheric delay or called as Zenith Path Delay (ZPD) in order to derive Zenith Wet Delay (ZWD). Tropospheric delay is a non-dispersive medium to the GPS signal. This tropospheric delay can be computed through the integration along the signal path through the troposphere using the following expression [10]:

$$d^{\text{trop}} = \int (n - 1) \mathrm{d}s \tag{1}$$

where n is the refractive index of the troposphere.

The tropospheric delay can be divided into two components which are hydrostatic or dry and wet components. In zenith direction, total tropospheric delay can be simplified as

$$\text{ZPD} = \text{ZHD} + \text{ZWD} \tag{2}$$

where ZPD is the zenith path delay, ZHD is the zenith hydrostatic delay, and ZWD is the zenith wet delay.

The ZHD from (2) can be modeled as follows [11]:

$$\text{ZHD}_{\text{model}} = (2.2779 \pm 0.0024)\frac{\rho s}{f(\theta, h)} \tag{3}$$

where ρs is the surface pressure and (θ, h) is given by

$$(\theta, h) = 1 - 0.00266\cos(2\theta) - 0.00028h \tag{4}$$

where θ is the latitude and h is the height above ellipsoid. The ZWD can be retrieved by subtraction of ZHD from ZPD:

$$\text{ZWD} = \text{ZPD} - \text{ZHD} \tag{5}$$

In this study, 30 s interval of GPS data for six GPS CORS in Peninsular Malaysia was used (see Fig. 5). Bernese 5.0 software was utilized to estimate ZPD parameter after resolving and careful modeling for all the errors such as orbital errors of the satellites, the receiver position errors, phase cycle ambiguities, ionospheric delays, and clock errors. Hence, by using equation in (5), ZWD can be estimated.

To validate the altimeter techniques, the Root-Mean-Square Error (RMSE) of the wet delay will be calculated between the two techniques. The RMSE will be used to

Fig. 5 The distribution of the GPS CORS for ground truth data verification

check the accuracy of altimetry-derived wet delay. A graph will be plotted to evaluate the magnitude and pattern between these two sets of data.

2.3 Altimetry Data Processing

In RADS processing, several steps must be followed in order to extract the wet delay data. A distance-weighted gridding was applied to filter the noise in the data through losing a slight data as possible but yet can derive essential ideals for grids points located between tracks. The use of weighting function is to provide the points close to the center to be important and points far from the center to be relatively irrelevant. The weighting function is based on Gaussian distribution [12]. Then, the daily wet delay data from the missions are then filtered and gridded using Gaussian weighting function with Sigma 2.0. This step employs both temporal and spatial by selecting a square mesh with block size 0.25° (spatial) and cut-off at 9 days (temporal). The cut-off is also known as the moving windows. Figure 6 shows the steps of the altimeter processing need to be done before deriving the wet delay data.

3 Result and Discussion

3.1 Wet Delay Data Mapping

A yearly wet delay data map for 2014 was produced. Through this map, it showed the pattern of the wet delay for year 2014 starting from January 1, 2014 until December 31, 2014. Jason-2 and Saral satellite missions are used to produce the wet
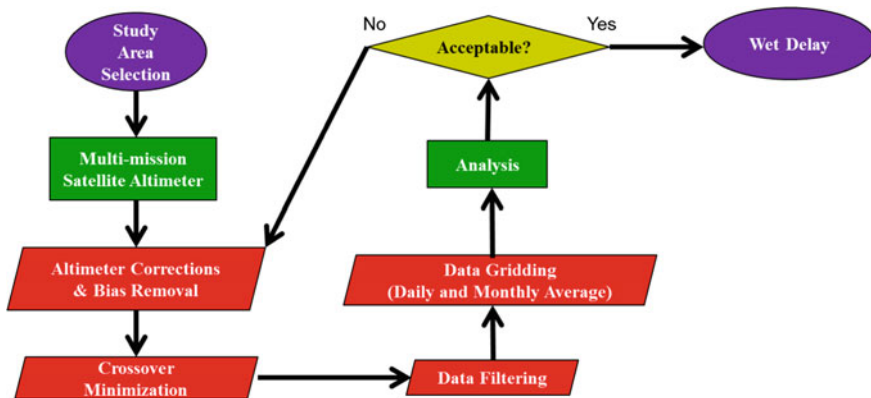
Fig. 6 Flow process for extracting wet delay data in RADS
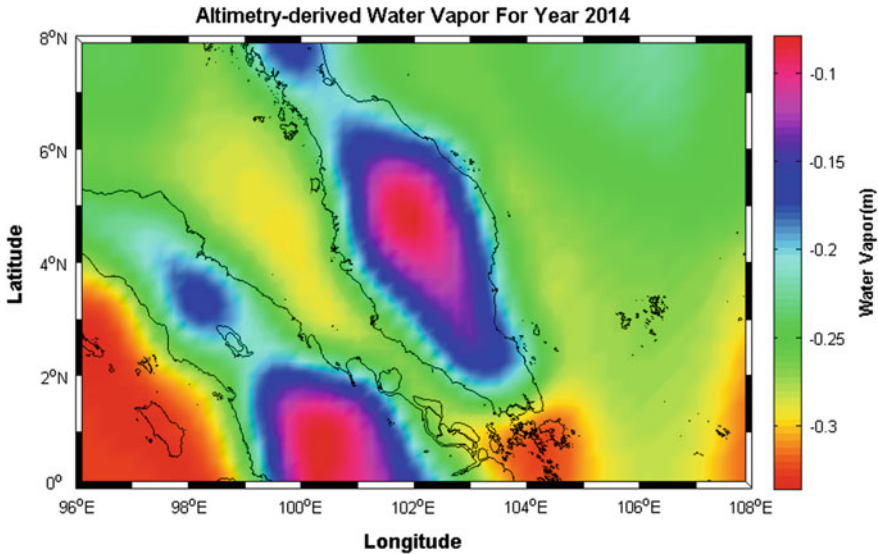
Fig. 7 Altimetry-derived wet delay for year 2014

delay map. The coverage of the research involves Peninsular Malaysia, Malacca Straits, and South China Sea. Based on Fig. 7, the wet delay ranges between −0.05 and −0.35 m over the study area.

From the map in Fig. 7, it showed that the area near to the coastline had higher values of the wet delay compared with the area far from the coastline. One factor that might affect the reading was due to the evaporation of water that occurs near to the coastline could increase up to the wet delay reading. As the areas that are far from coastline had lowered the value of data wet delay, the areas were at the developing areas and also had lowered the value of annual rainfall. The average value for wet delay over marine areas is about ∼0.25 m.

3.2 Data Verification: Wet Delay from Altimetry and GPS Data

In this section, the monthly mean wet delay data from altimeter and GPS were evaluated. From the line chart, the data illustrates the wet delay pattern along the year 2014. Then, both of the data are calculated for their RMSE to determine the differences of the wet delay value. In this research, GPS CORS was assumed as a reference value to the satellite altimeter. In the present research, it was laid out that GPS data can be taken on account for the affirmation of imitated wet delay values in like manner for quality control of GPS and pressure stations. The median diversity within the water vapor radiometer and the GPS approximated zenith wet delays was

6 mm with a standard deviation of 9 mm [13]. Many successful studies have been published either by using dedicated altimeter products or by, e.g., using in situ data sources to derive the corrections, such as surface pressure (for the dry correction) and wet tropospheric corrections derived from Global Navigation Satellite Systems (GNSS) stations [14]. Figure 8 shows the wet delay pattern between GPS CORS and satellite altimeter based on the chosen areas, namely, JUML, BABH, BANT, GETI, KROM, and KUAL (see Fig. 9).

Figure 10 depicts the pattern and RMSE for the chosen stations: BABH, BANT, JUML, GETI, KROM, and KUAL. They were all located in Peninsular Malaysia along the coastline region. Through all the patterns, it noticed that all the shapes of
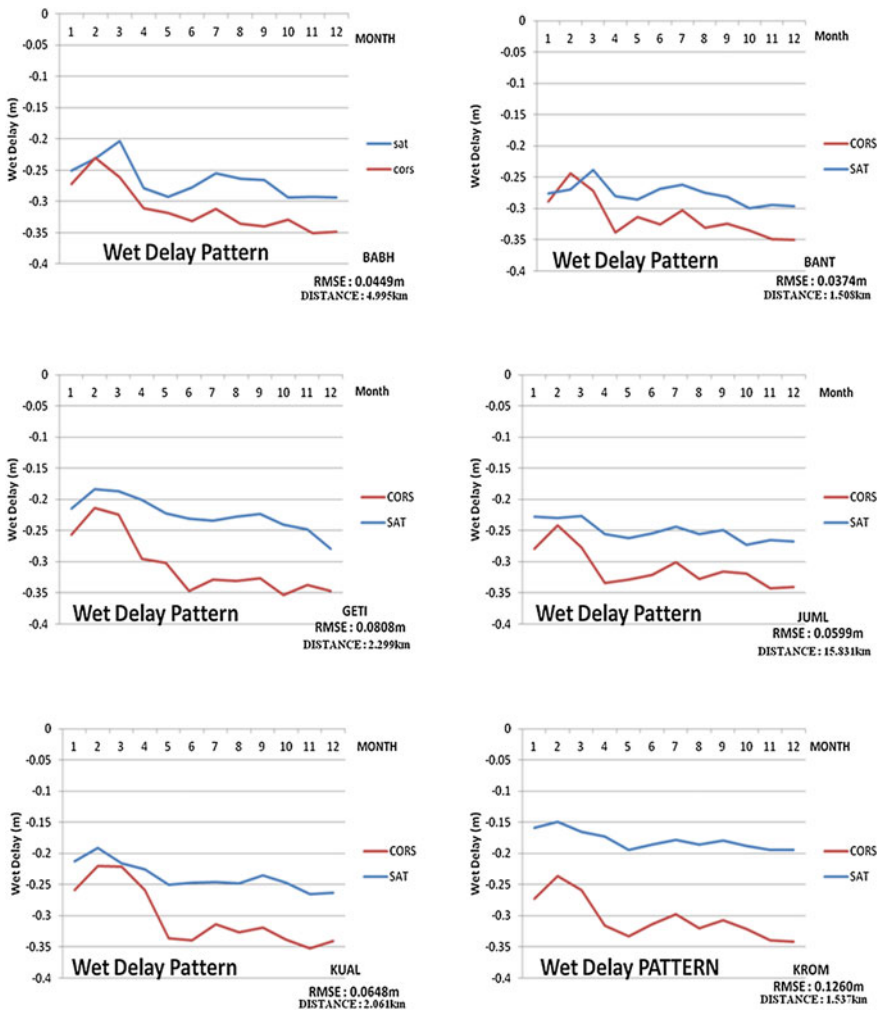
Fig. 8 Wet delay pattern for year 2014 at chosen area for both altimetry and GPS
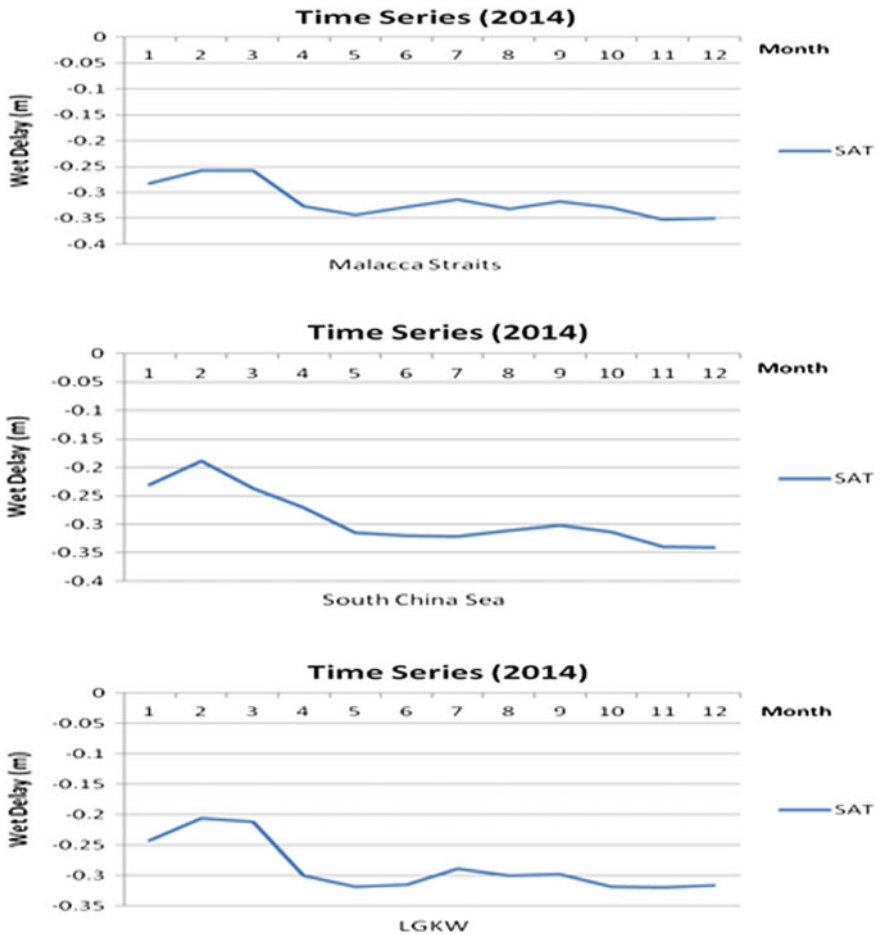
Fig. 9 Time series of altimetry-derived wet delay for year 2014

the pattern between the GPS and altimetry-derived wet delay were almost the same and yet the value of the RMSE was between 0.03 and 0.12 m. The distance from the CORS stations to the altimeter track was calculated, and the range was from 1.5 to 16 km.

The distance was calculated by using the ArcMap 10.2 software. From the patterns, it showed that the highest values of the wet delay that had been derived by both techniques were mostly between November and December, and the lowest values were between February and March.
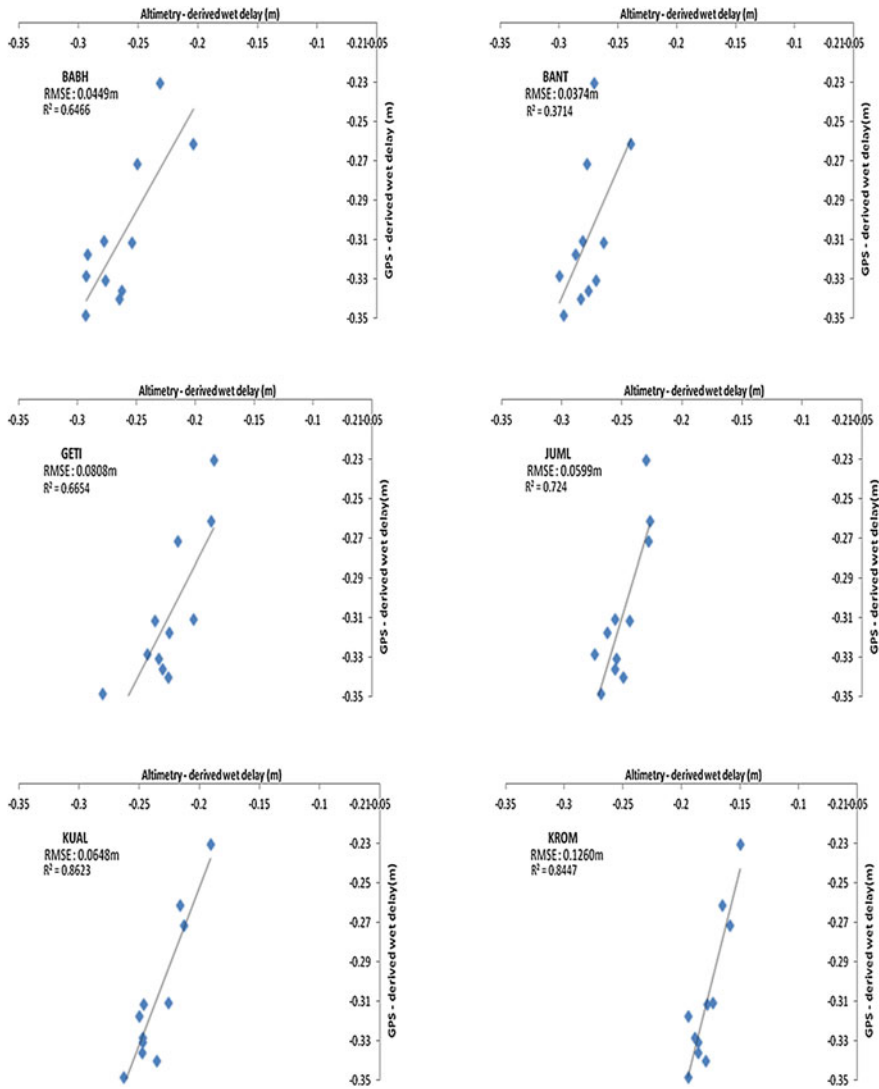
Fig. 10 The altimetry and GPS correlation analysis at chosen areas: BABH, BANT, GETI, JUML, KROM, and KUAL

3.3 Wet Delay Pattern Using Time Series Analysis

Time series shows the pattern of the wet delay data in a line chart. Figure 9 shows the satellite altimeter wet delay data for the year 2014 that it was extracted using RADS. The time series chart shows at three different areas involving the Malacca Straits, South China Sea, and at the LGKW CORS. The Malacca Straits' and South China Sea's data extracted by using point based. The latitudes and the longitudes are shown in Table 2 for both locations. These data are represented for the marine areas, while LGKW CORS is presented for land area. The data were extracted based on daily solution. In this study, the mean for each month was calculated. Then, the annual mean of wet delay data for 2014 was calculated. For South China Sea, the annual mean was −0.291 m and for the Malacca Straits it was about −0.316 m. Meanwhile, the annual mean for LGKW CORS was at −0.287 m. From Fig. 9, the month of November yields the highest monthly mean of wet delay while the lowest monthly mean for the wet delay data was in February. The Northeast Monsoon is known as the wet season because from November till December, the wet delay was recorded at the highest value compared with other months.

As we know, the wet delay is actually distributed by the clouds and also by the rainfall. In this study, the seasonal variation has been stressed on to evaluate in which month or season, the wet delay content was at the highest or at the lowest point. Seasonal variations will affect the wet delay content in the air. In this research, the highest wet delay content was from month of May until August which was known as Southwest Monsoon. Then, it was followed by the second inter-monsoon which was from September to October. Next is the Northeast Monsoon, from November to February. And the least mean for the seasonal variations was through the first inter-monsoon which is from May until April.

Figure 10 shows that the most of the chosen areas, JUML, GETI, BABH, KROM, and KUAL, are in good relationship with the correlation coefficient, R^2 value more than 0.6 except for BANT. Based on Fig. 10, the correlation analysis for KUAL and KROM yield confidence result with the R^2 value more than 0.8 which is close to 1. Thus, both of the techniques, satellite altimeter and GPS data, have strong positive correlation. In addition, the RMSE from these two areas shows a great result with 3–12 cm. Meanwhile, the correlation for GETI and BABH is 0.6 and for JUML is 0.7. For BANT, the correlation for altimetry and GPS-derived water vapor data shows a bad relationship between them, i.e., 0.3, but the RMSE shows a good result, that is, 0.037 m.

Table 2 Latitude and longitude of the point based on extracting altimetry-derived wet delay

Region	Latitude (°N)	Longitude (°E)
Malacca Straits	4.00	100.00
South China Sea	6.43	103.00

3.4 Wet Delay Variations Due to Seasonal Effects

In Malaysia, there are two types of monsoon that will occur annually. They are Northeast Monsoon and Southwest Monsoon. In this study, the seasonal variation will be categorized into four categories. The idea of this concept was to determine the interchange of wet delay data in each season. To make it easier, the data were mapped into colored map, where each color will represent the intensity of wet delay in the specific region. Figure 11 shows the mapped wet delay data according to the Northeast and Southwest Monsoon; meanwhile, Fig. 12 shows the mapped data for first and second inter-monsoon.

Based on Fig. 11, the Northeast monsoon happened from November until February while Southwest monsoon happened from May until August. The legend on the right of the figure shows the color scale that indicates the wet delay value. The highest value recorded for Northeast Monsoon was in November at −0.292 m and started to decrease month by month, until February at −0.2134 m. The average value in this season was −0.259 m. Meanwhile, for Southwest Monsoon, the average of the recorded wet delay data was −0.292 m and the highest value was in June, −0.305 m.

Figure 12 shows mapped data for first and second inter-monsoon. The first inter-monsoon in March gave higher wet delay value by −0.258 m than in April at
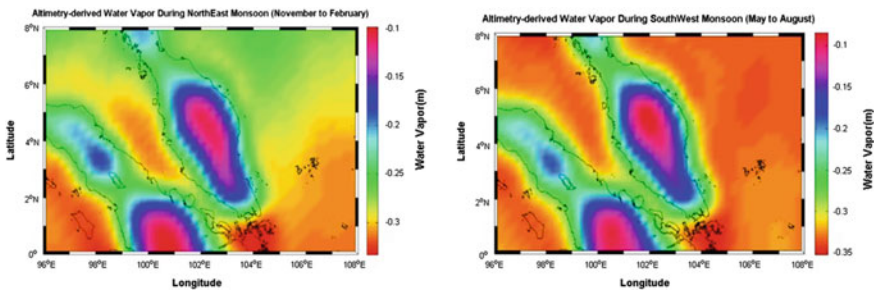
Fig. 11 Altimetry-derived wet delay during Northeast and Southwest Monsoon
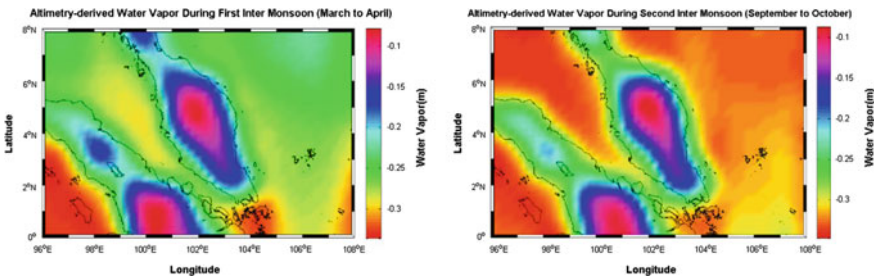
Fig. 12 Altimetry-derived wet delay during inter-monsoon

−0.228 m. The average value for the first inter-monsoon was at −0.274 m. Next, after the first inter-monsoon, was the second inter-monsoon that took place from September to October. The reading of the wet delay data collected in October was higher than in September.

Based on Figs. 11 and 12, the area near within the coastline recorded the highest value of wet delay compared to the area that is far from the coastline. This happened because the area near the coastline was near to the sea, and thus it had higher intense of humidity as we know that water molecules that evaporated from the sea will be in the air in gaseous state. While the area far from the coastline had lower value of the wet delay, it has lower humidity of air.

4   Conclusions

In this study, the data from the CORS was assumed to be the reference in order to verify the wet delay data from the satellite altimeter. The result of this study showed that the Root-Mean-Square Error (RMSE) between the satellite altimeter wet delay data and Continuously Operating Reference System (CORS) by Global Positioning System was at 3–12 cm. Furthermore, the data from the satellite altimeter is in a good shape with the seasonal variation of precipitation according to the climatic classification of the region. Besides that, the observed data also give a reasonable value when considered for the wet and dry seasons because the value from the CORS and satellite altimeter only had a slight difference.

On top of that, Fig. 8 shows that the wet delay pattern between the satellite altimeter and GPS was nearly the same. As shown in Fig. 8, the data from the satellite altimeter had the same characteristics, when the data from the CORS went down, and the data from the satellite also went down, despite on the RMSE values. From the results that had been yielded, the wet delay figurations deriving out of the satellite altimeter can be used to study the inconsistency of the atmospheric wet delay content in the region.

The advantage of using satellite altimeter as a method to determine the wet delay content is satellite altimeter that has a temporal and spatial solution; meanwhile, the GPS CORS stations are only a point-based reference. It means that wet delay data from the satellite altimeter can cover a bigger area than GPS CORS stations even over the marine areas. GPS and radiosonde cannot retrieve the wet delay data over the marine areas. Satellite altimetry is absolutely advantageous to observe the water level variety of big marine areas upon a long time series [15]. The satellite altimeter technique is flexible compared to the radiosonde because by the radiosonde technique, it is highly recommended to launch twice a day. In addition, a radiosonde method is expensive compared to the satellite altimeter. To launch the balloon, we need to hire staff to launch it and the balloon itself very costly. In conclusion, altimetry-derived wet delay is promising to be used in climate and weather research in the future.

References

1. Carnicer, K.M.R., Vallar, E.A., Galvez, M.C.D.: A preliminary study on the precipitable water vapor (PWV) from the Davao radiosonde station for 2014 (2016)
2. Bevis, M., Businger, S., Herring, T.A., Rocken, C., Anthes, R.A., Ware, R.H.: GPS meteorology: remote sensing of atmospheric water vapor using the global positioning system. J. Geophys. Res. Atmos. **97**(D14), 15787–15801 (1992)
3. Alshawaf, F., Fuhrmann, T., Heck, B., Hinz, S., Knoepfler, A., Luo, X., Westerhaus, M.: Atmospheric water vapour determination by the integration of INSAR and GNSS observations. In: Proceedings of fringe 2011 workshop, ESA SP-697 (2012)
4. Ruf, C.S., Dewan, R.P., Subramanya, B.: Combined microwave radiometer and altimeter retrieval of wet path delay for the GEOSAT follow-on. IEEE Trans. Geosci. Remote Sens. **34**(4), 991–999 (1996)
5. Schneider, E.K., Kirtman, B.P., Lindzen, R.S.: Tropospheric water vapor and climate sensitivity. J. Atmos. Sci. **56**(11), 1649–1658 (1999)
6. Hogg, D.C., Guiraud, F.O., Decker, M.T.: Measurement of excess radio transmission length on earth-space paths. Astron. Astrophys. **95**, 304–307 (1981)
7. Ojo, C.: Haloe v2. 0 Upper Tropospheric Water Vapor Climatology
8. Elgered, G.: Tropospheric radio-path delay from ground-based microwave radiometry. In: Atmospheric remote sensing by microwave radiometry, pp. 215–258. Wiley, New Jersey (1993)
9. Linfield, R., Bar-Sever, Y., Kroger, P., Keihm, S.: Comparison of global positioning system and water vapor radiometer wet tropospheric delay estimates. TDA Progress Report, pp 42–130 (1997)
10. Hofmann-Wellenhof, B., Lichtenegger, H., Collins, J.: Global positioning system: theory and practice, 6th edn. Springer, New York (2001)
11. Elgered, G., Davis, J.L., Herring, T.A., Shapiro, I.I.: Geodesy by radio interferometry: water vapor radiometry for estimation of the wet delay. J. Geophys. Res. **96**, 6541–6555 (1991)
12. Basu, A., Singh, M., Mandal, M.: Robust KLT tracking with Gaussian and Laplacian of Gaussian weighting functions. Pattern recognition, International Conference on (ICPR), pp. 661–664. Cambridge, UK (2004)
13. Coster, A.J., Niell, A.E., Burke, H.H.K., Czerwinski, M.G.: The westford water vapor experiment: use of GPS to determine total precipitable water vapor (1997)
14. Cretaux, J.F, Berge-Nguyen, M., Calmant, S., Romanovski, V.V., Meyssignac, B., Perosanz, F., Tashbaeva, S., Arsen, A., Fund, F., Martignago, N., et al.: Calibration of Envisat radar altimeter over Lake Issykkul. Adv. Space Res. 51, 1523–1541 (2013)
15. Crétaux, J.F., Jelinski, W., Calmant, S., Kouraev, A., Vuglinski, V., Berge-Nguyen, M., Gennero, M.C., Nono, F., Abarca Del Rio, R., Cansenave, A., Maisongrande, P.: SOLS: a lake database to monitor in the near real time water level and storage variations from remote sensing data. Adv. Space Res. **47**, 1497–1507 (2011)
16. USGS. https://water.usgs.gov/edu/watercyclesummary.html, last accessed 2017

Sea Level Impact Due to El Nino and La Nina Phenomena from Multi-mission Satellite Altimetry Data over Malaysian Seas

**Mohd Amiruddin Khairuddin, Ami Hassan Md Din
and Abdullah Hisam Omar**

Abstract The El Nino and La Nina phenomena indirectly provide dramatic changes to the sea level that can be caused by floods and drought, and affect various marine activities. For the past centuries, the main approach to measure sea level changes is by using coastal tide gauges. However, there is inconsistency in observing sea level variations using tide gauge data for the Malaysian country. The inconsistency is due to irregular geographical distributions of tide gauge stations established at coastal areas and there are no long-term tide records for the deep sea. An alternative method in order to solve this issue is by measuring the absolute sea level from space, i.e., satellite altimeter technique. Satellite altimeter implements excellent potential as an integral mechanism to the conventional coastal tide gauge instruments for monitoring sea level variation of Malaysian seas, especially for the deep sea. The aim of this research is to study the sea level pattern due to the effects of El Nino and La Nina phenomena using a combination of multi-mission satellite altimeters in the Malaysian seas. Radar Altimeter Database System (RADS) is used for retrieval and reduction of sea level data from satellite altimeter. Then, sea level data from tide gauge was used to verify satellite altimeter derive the sea level data.

M. A. Khairuddin · A. H. M. Din (✉) · A. H. Omar
Geomatic Innovation Research Group (GIG), Faculty of Geoinformation
and Real Estate, Universiti Teknologi Malaysia, 81310 Johor Bahru,
Johor, Malaysia
e-mail: amihassan@utm.my

M. A. Khairuddin
e-mail: termernator92@gmail.com

A. H. Omar
e-mail: abdullahhisham@utm.my

A. H. M. Din
Geoscience and Digital Earth Centre (INSTEG), Faculty of Geoinformation
and Real Estate, Universiti Teknologi Malaysia, 81310 Johor Bahru,
Johor, Malaysia

A. H. M. Din
Institute of Oceanography and Environment (INOS), Universiti Malaysia
Terengganu, Kuala Terengganu, Terengganu, Malaysia

The result of this research shows that satellite altimetry is reliable in other to monitor changes in sea level. It also shows that El Nino and La Nina phenomena can also contribute as one of the factors to sea level changes around Malaysian seas. Hence, this research will specifically help in the determination of sea level in Malaysia and to the professionals who have authority in governmental, environmental planning, agriculture, marine engineering, and economics.

1 Introduction

Nowadays, sea level change is one of the most current scientific topics. It is due to the consequence that is related to climate change, both for environment and for the societies. Variations in sea level materialize over a broad range of temporal and spatial scales, with the numerous contributing elements making it an integral measure of climate change [1, 2]. The primary contributors to contemporary sea level variation are the extension of the ocean as it warms and the transfer of water currently stored on land, especially from land ice (glaciers and ice sheets) [2].

Furthermore, El Nino and La Nina phenomena also contribute dramatic changes to sea level caused by floods and drought, and affect various marine activities. Generally, El Nino is known as unusually warm water episodes, which also produces extraordinary changes in sea level. Thus, the impact of the La Nina gives the similar effect as El Nino, but opposite to El Nino nature. However, La Nina effect is less extensive and damaging than El Nino. El Nino and La Nina are the powerful climate variations in the temporary climatic timescale range, and caused by variation in temperature between ocean and atmosphere in the east-central equatorial Pacific. These derivations from normal surface temperature caused large impact particularly on ocean process of global weather and climate.

Moreover, changes in sea level have conventionally been measured at a number of fixed tide gauge stations around the world, but with the increased accuracy of satellite altimetry, this now attempts the perfect opportunity for developing our learning on global and regional sea level change [3]. However, there is inconsistency in observing sea level changes using tide gauge data for the Malaysia country. The inconsistency is due to irregular geographical distributions of tide gauge stations established at coastal areas and there are no long-term tide records for the deep sea [4, 5].

Thus, satellite altimeter technique can be implemented as an alternative method to solve this issue by measuring absolute sea level from space. Furthermore, satellite altimeter implements excellent potential as an integral mechanism to the conventional coastal tide gauge instruments in order to monitor the sea level change of Malaysia seas, especially for the deep ocean.

Hence, this research is to study the magnitude and trend of sea level due to El Nino and La Nina phenomena by using multi-mission satellite altimeter. The area of interest covers Malaysian seas, namely, Malacca Strait, South China Sea, Sulu Sea, and Celebes Sea. Then, sea level data derived from satellite altimeter are verified with tidal data from tide gauge.

1.1 Principle of Satellite Altimeter

Satellite altimetry technique is invented to study about the ocean criterion such as determination of divergent sea surface and ice sheet, ocean tide, sea level rise, and marine geoid determination based on gravitational equipotential surface [close to sea surface height (SSH)] [6]. One of the essential contributions of satellite altimeter is the capability to provide wide spatial data all over the world ocean where the tide gauge is crucial to be achieved. This technique is capable of providing the long-term sea level data which is required to monitor the dynamics of the ocean which cannot be provided by tide gauge for a long period.

Generally, radar altimetry is a technique among the easier of remote sensing methods for measuring height. There are two main essential geometric calculations that are involved in satellite altimeter. First, based on radar range (R), radar altimeter on board of satellite permanently transmits signals to Earth and received the signal reflected from the sea surface. Information from the round-trip travel time between microwave pulses emitted downward by satellite's radar and reflected back from the ocean are used to determine the distance between satellite and sea surface. Second, the three-dimensional (3D) position relative to the earth fixes the coordinate system that is determined by the independent tracking system [3, 7]. By connecting, these two measurements produced profiles of sea surface topography, or sea level, with respect to the reference ellipsoid.

Satellite altimetry presents the rigorous SSH measurements. Based on the SSH estimation and mean sea surface data, sea level anomaly (SLA) is produced. SLA is important to describe the sea level changes. The SLA data provides the knowledge about the large-scale ocean circulation, including El Nino and La Nina phenomena [8]. Hence, SLA data are compatible with other to study the changes of sea level due to El Nino and La Nina events. Figure 1 shows the principle of satellite altimetry. By adopting a similar concept from [3], the SLA, h_{sla} given as

$$h_{sla} = H - R_{obs} - \Delta R_{dry} - \Delta R_{wet} - \Delta R_{iono} - \Delta R_{ssb} - h_{tides} - h_{atm} - h_{MSS} \quad (1)$$

where

H	Satellite altitude
R_{obs}	Altimeter range measurement
ΔR_{dry}	Dry tropospheric correction
ΔR_{wet}	Wet tropospheric correction
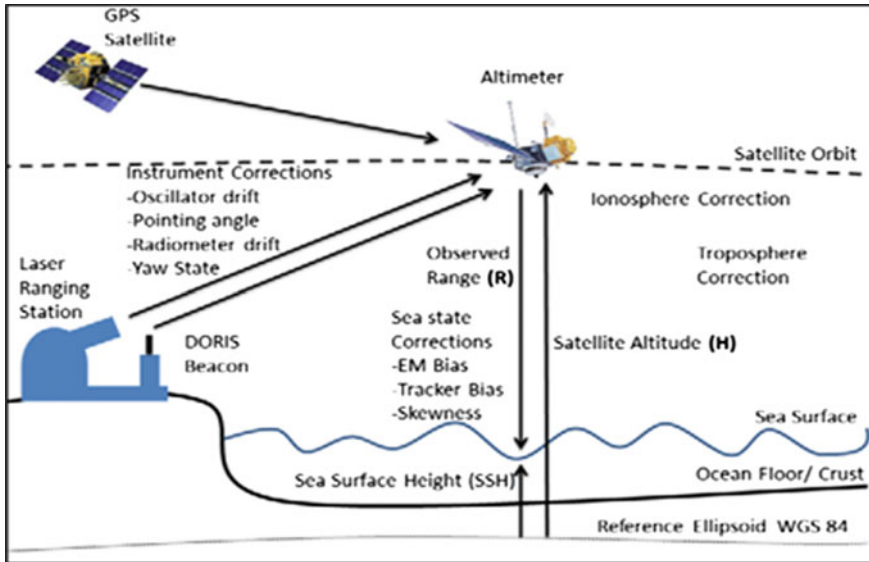
Fig. 1 Schematic view of satellite altimeter measurement (adapted from [9])

ΔR_{iono}	Ionospheric correction
ΔR_{ssb}	Sea-state bias correction
h_{tides}	Tides correction
h_{atm}	Dynamic atmospheric correction
h_{MSS}	Mean sea surface correction.

2 Research Approach

2.1 Research Area Identification and Data Processing

The area of interest covers Malaysian seas namely Malacca Strait, South China Sea, Sulu Sea, and Celebes Sea. It ranges between $0°\text{N} \leq \text{Latitude} \geq 14°\text{N}$ and $95°\text{E} \leq \text{Longitude} \geq 125°\text{E}$ that covers Malaysian seas. This research presents an intention to specify and describe the El Nino and La Nina phenomena impact on the sea level pattern within a 24-year period. The duration is from January 1993 to December 2016 around the Malaysian seas based on sea level information from SLA data obtained from the multi-mission satellite altimeter. The Radar Altimeter Database System (RADS) is funded by the Dutch government known as an internet facility for exploitation of remote sensing expertise and data. In the frame of RADS, the Delft Institute for Earth-Oriented Space Research (DEOS) is building a database that contains validated and verified altimeter data products that are consistent and

uniform in format, correction, accuracy, and reference system parameter [10]. Hence, RADS presents processing software for altimeter data processing. Beforehand, data verification is performed between altimetry data with selected tidal data in order to produce the comparable result.

2.2 Tidal Data

Permanent Service Mean Sea Level (PSMSL) has been accountable for the collection, publication, analysis, and interpretation of sea level data from the global network of tide gauge [11]. Thus, monthly tidal data are collected from PSMSL. There are eight tide gauge stations involved in this research, namely, P. Langkawi, Port Kelang, Geting, P. Tioman, Bintulu, Kota Kinabalu, Sandakan, and Tawau. Sea level from satellite altimeter is compared with tidal data by extracting monthly SLA average at the tide gauge locations and the altimeter tracks that are nearby the tide gauge station. The period of data starts from January 1, 1993 up to December 1, 2015. Hence, the pattern and correlation of sea level anomalies from both measurements are evaluated.

2.3 Multi-mission Altimetry Data and Processing

Nine (9) satellite altimeter missions are selected: TOPEX, Jason-1, Jason-2, Jason-3, ERS-1, ERS-2, ENVISAT, Cryosat, and Saral to derive SLA data. The time period of satellite altimetry data is from January 1993 to December 2016, while RADS presents as processing software for altimeter data processing. Figure 2 shows the overview of altimetry data processing in RADS.

The sea level data obtained are corrected for orbital altitude, altimeter range corrected for instrument, sea state bias, ionospheric delay, dry and wet tropospheric
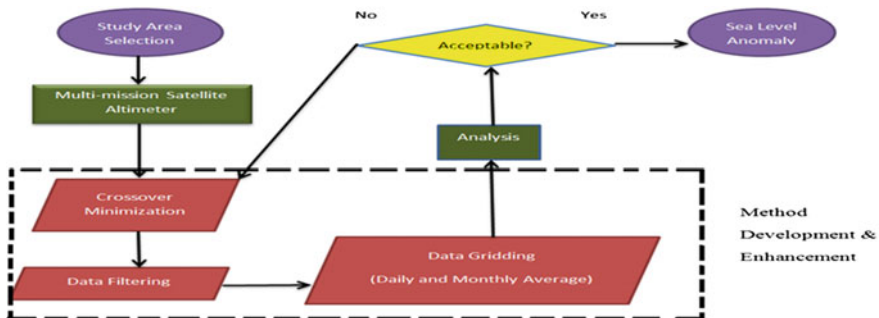
Fig. 2 Overview of altimetry data processing in RADS

Table 1 Corrections and models applied to altimeter processing in RADS

Correction/model	Editing (m)		Description
	Min	Max	
Orbit/gravity field	−2.4	−2.1	All satellites: EIGEN GL04C ERS: DGM-E04/D-PAF
Dry troposphere	−0.6	0.0	All satellites: atmospheric pressure grids (ECMWF)
Wet troposphere	−0.4	0.04	All satellites: radiometer measurement
Dynamic atmosphere	−1.0	1.0	All satellites: smoothed dual-frequency, ERS: NIC09
Ocean tide	−5.0	5.0	All satellites: GOT4.10
Load tide	−0.1	0.1	All satellites: GOT4.10
Solid earth tide	−1.0	1.0	Applied (elastic response to tidal potential)
Pole tide	−0.1	0.1	Applied (tide produced by polar wobble)
Sea state bias	−1.0	1.0	All satellites: CLS nonparametric
Reference	−1.0	1.0	DTU13 mean sea surface
Engineering flag			Applied
Reference surface			Jason-1 Jason-2 TOPEX

corrections, solid earth and ocean tides, ocean tide loading, pole tide electromagnetic bias, and inverse barometer corrections as displayed in Eq. 1 [12]. The bias is reduced by using specific models for each satellite altimeter mission in RADS as shown in Table 1.

Next, after extraction of sea level data from RADS, crossover adjustments are performed to integrate data processing for multi-mission satellites. This is due to the factors, for instance, orbital errors and inconsistency of satellite orbit frame; hence, the SSH from each satellite missions needs to be adjusted to a "standard" surface [13]. The general concept of multi-mission satellite is shown in Fig. 3.

The minimization was achieved with the orbit of the National Aeronautics and Space Agency (NASA) class satellites held fixed and those of European Space Agency (ESA) class satellites adjusted concurrently since NASA class satellite surpasses the accuracy of the orbits and measurements of the ESA class satellites [7]. The details of satellite altimeter used are characterized in Table 2.

The study area limits for crossover adjustment are between range −10° S ≤ Latitude ≥ 24°N and 85°E ≤ Longitude ≥ 135°E. In order to have sufficient crossover point, study area for crossover adjustment needs to be larger than actual study area.

Next, in order to ensure the quality of satellite altimeter data, the distance-weighted gridding need to be applied. A distance-weighted gridding is used to filter the noise in the data through losing a little information as possible while still obtaining important values for grids points located between tracks. The objective of weighting function is to arrange the points that are close to the center to

(a) Jason 1

(b) Jason 2

(c) Cryosat

(d) Saral

(e) Multi-mission satellites
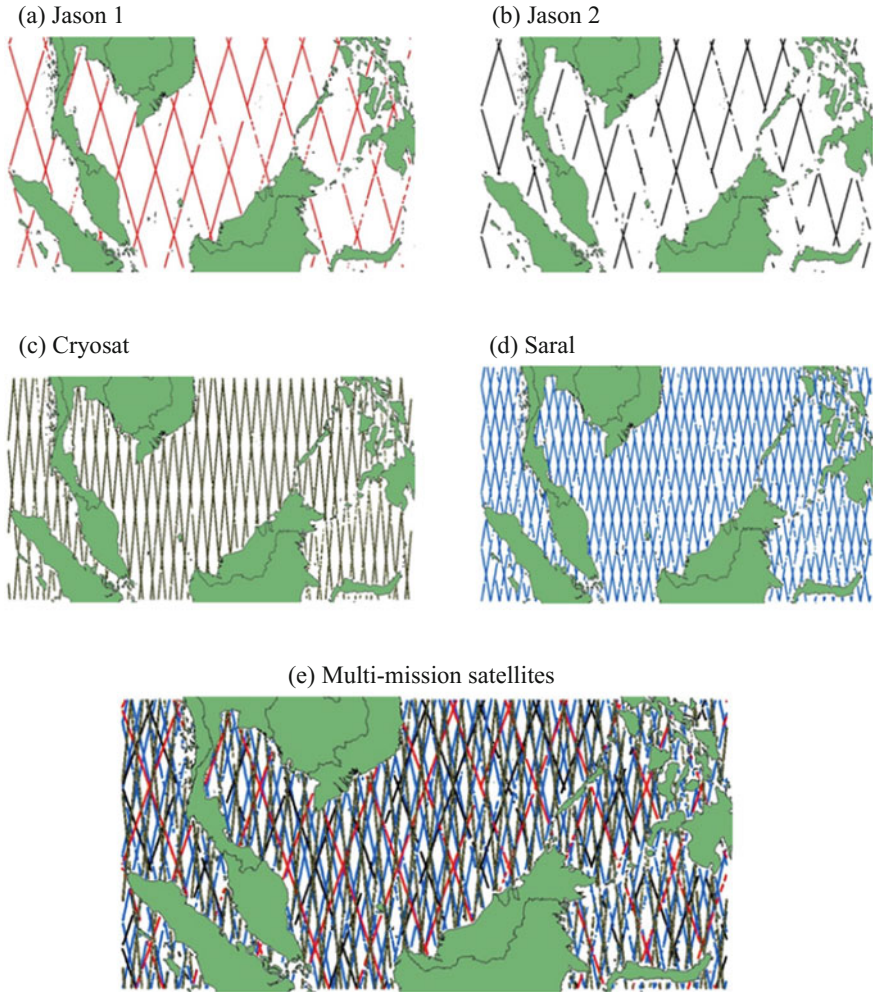
Fig. 3 Single track satellite altimeter compared to multi-mission satellite

Table 2 Satellite altimeter's spatial and temporal characteristic

Satellite mission	Agency	Track spacing (km)	Repeat cycle (days)
Topex	NASA	315	10
Jason 1	NASA	315	10
Jason 2	NASA	315	10
Jason 3	NASA	315	10
ERS-1	ESA	80	35
ERS-2	ESA	80	35
Cryosat	ESA	75	28
Saral	ESA & ISRO	75	35

be essential while points that are far or off the center to be approximately unimportant. The weighting function is based on Gaussian distribution [14].

Then, by using Gaussian weighting function with Sigma 2.0, the daily data from multi-mission satellite altimeters are then filtered and gridded to SLA bins. Gridding involves both temporal and spatial by selecting a square mesh with block size of 0.25° (spatial) and cut-off at 9 days (temporal).

After that, the daily solutions for sea level anomalies are then combined to the monthly average solutions. This step is done in other to uniform or compatible the final monthly altimeter solution with the monthly tide gauge solution.

3 Result and Discussion

3.1 Data Verification: Altimeter Versus Tide Gauge

The SLA from satellite altimeter data is compared with SLA from tide gauge (as a benchmarked) to analyze the pattern, correlation, and root-mean-square error (RMSE) of satellite altimeter data measurement. Eight (8) tide gauge data are selected covering east and west coast of Peninsular Malaysia and East Malaysia. Data verification is accomplished by extracting the monthly SLA average at the tide gauge locations and the altimetry track that are nearby the tide gauge stations. The patters of both measurements are evaluated over the same period in each area in order to produce comparable result starting from January 1, 1993 to December 31, 2015. The comparison between satellite altimetry data and tide gauge data is categorized into four (4) of Malaysian Seas that is Malacca Strait, South China Sea, Sulu Sea, and Celebes Sea. This is due to the tide gauge position that is selected for this research.

Malacca Strait. Based on Fig. 4, it shows the similarity in pattern of sea level from altimeter and the gauge determined good compliance at Pulau Langkawi and
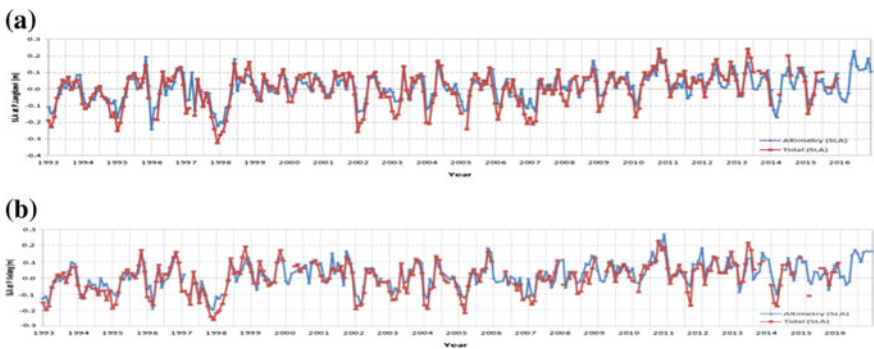
Fig. 4 Sea level comparison between altimetry and tidal data at P. Langkawi (**a**) and P. Kelang (**b**) of Malacca Strait

Port Kelang, respectively. The effect of El Nino on the sea level was clearly visible from both satellite altimeter and tide gauge data in late 1997 where the sea level suddenly decreases abnormally and reverted to normal after 1998 while in late of 2010 to early 2011, there is sudden rise caused by the effect of La Nina.

Furthermore, based on the RMSE analysis, it shows that measurement of satellite altimeter, respectively, to tide gauge measurement varies from 4 to 5 cm at both stations. Besides that, the correlation analysis at both stations is also in good relationship with the R^2 value more than 0.7 (see Fig. 5).

South China Sea. Sea level pattern of South China Sea is demonstrated by analyzing Geting, Pulau Tioman, Bintulu, and Kota Kinabalu as illustrated in Fig. 6. All tide gauge stations in Fig. 6 show a similar pattern of sea level variations with more or less regular annual cycle that the chosen range and geophysical corrections are well suitable for these areas. However, unlike Malacca Straits area, the effect of El Nino and La Nina events over South China Sea is hardly noticed because South China Sea is an open sea.

Time series pattern of sea level between altimetry and tidal SLA shows a good comparable result. Furthermore, based on Fig. 7, the correlation analysis for Geting, Pulau Tioman, Bintulu, and Kota Kinabalu produced confident result in the R^2 value more than 0.8 close to 1 that show both variables satellite altimeter and tide gauge data have strong positive correlation. Besides that, the RMSE analysis for altimetry data at these four locations shows a magnificent result with 3–4 cm, respectively.

Sulu and Celebes Seas. Based on Fig. 8, the sea level pattern at Tawau did not match very well where the altimetry data is slightly higher than tidal data. The correlation for Tawau station as shown in Fig. 9 is 0.7238 where the dispersion of data at the graph does not accumulate well, however, still suitable for sea level determination while correlation in Sandakan is 0.8298. The RMSEs for both stations are 5–6 cm, which shows that satellite altimeter is reliable for measurement of sea level around Malaysia Seas. An unusual drop at the late 1997 also causes the El Nino effect. This due to the Sulu and Celebes Seas is semi-closed sea. For this region, this shows that in the case of Malaysian Seas, the closed and semi-closed seas may reflect the effects of El Nino and La Nina events.
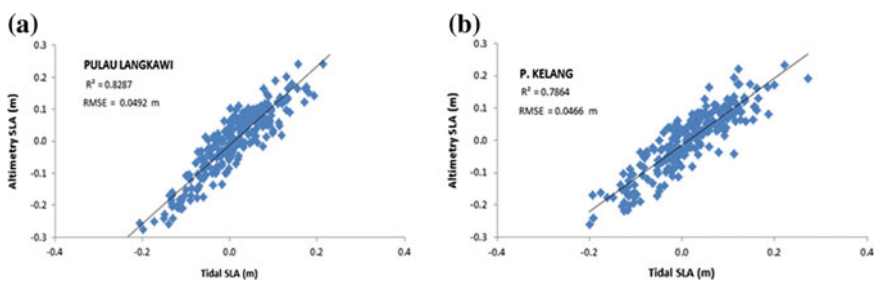
Fig. 5 The altimetry and tidal sea level correlation analysis at the P. Langkawi (**a**) and P. Kelang (**b**)
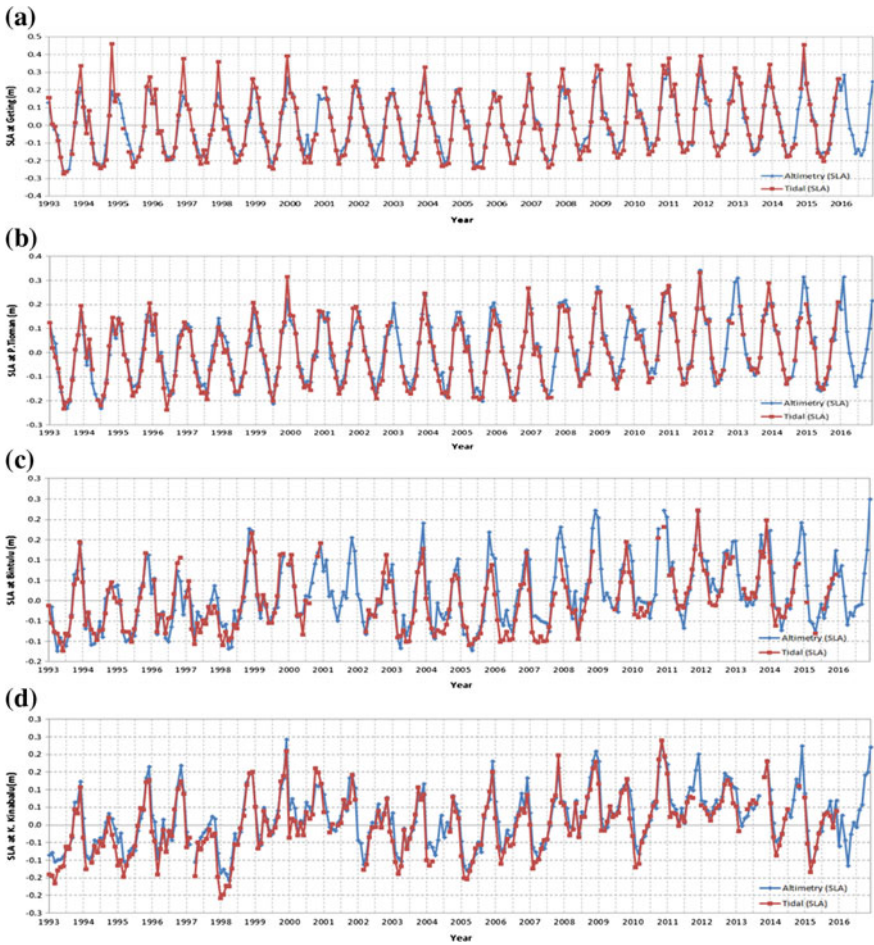
Fig. 6 Sea level comparison between altimetry and tidal data at Geting (**a**), P. Tioman (**b**), Bintulu (**c**), and K. Kinabalu (**d**) of South China Sea

All the graphs show the similarity in the pattern of sea level from altimeter, and tide gauge indicates good agreements for all station accordingly. Besides that, all altimetry data achieved an astonishing RMSE difference when compared with tidal data that range from 0.0341 to 0.0606 m. The correlation analysis for all location produced confidence results in the R^2 value that ranges from 0.7238 to 0.9476. The results proved that the altimeter processing was executed well in this research; hence, the altimetry data has a good probability of sea level determination in this region. The summary of R^2 and RMSE difference at each station is displayed in Table 3.
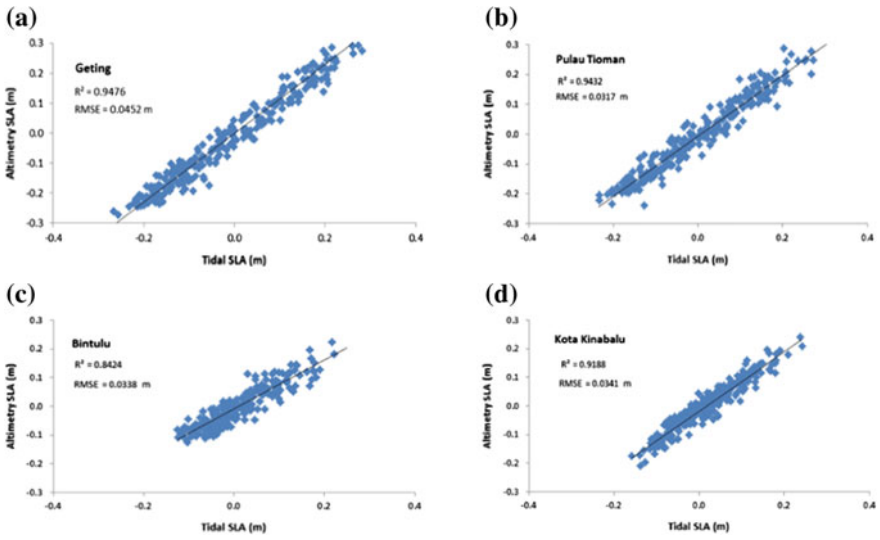
Fig. 7 The altimetry and tidal sea level correlation analysis at the Geting (**a**), P. Tioman (**b**), Bintulu (**c**), and K. Kinabalu (**d**)
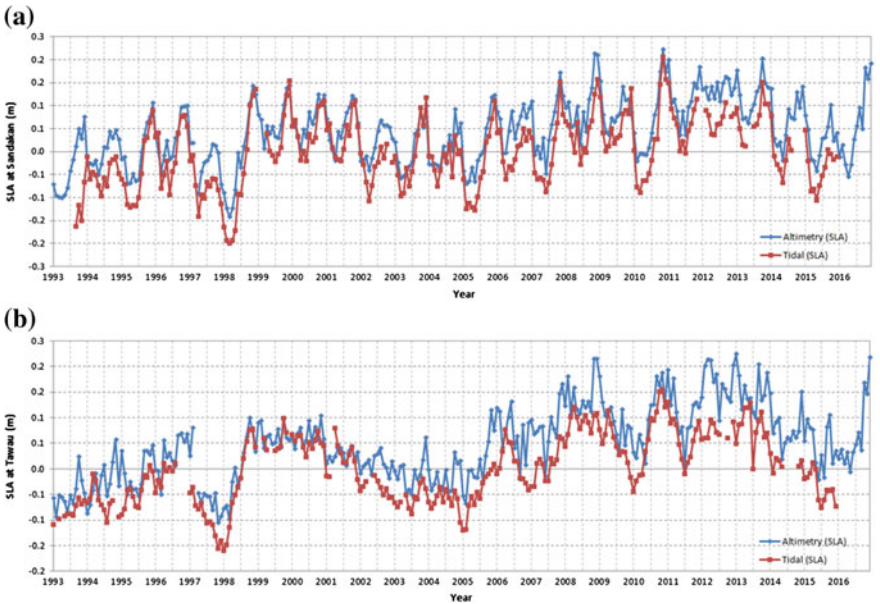
Fig. 8 Sea level comparison between altimetry and tidal data at Sandakan (**a**) and Tawau (**b**) of Sulu and Celebes Seas
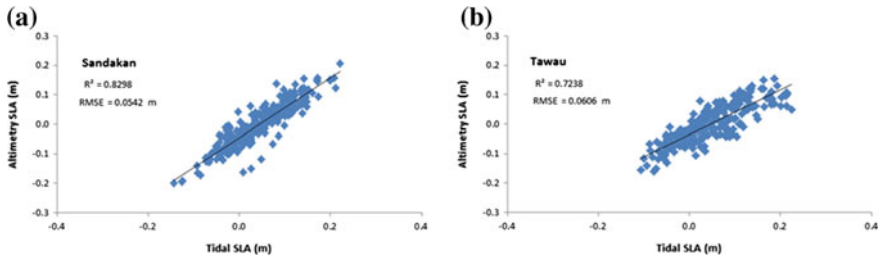
Fig. 9 The altimetry and tidal sea level correlation analysis at the Sandakan (**a**) and Tawau (**b**)

Table 3 R^2 and RMSE difference value

Stations	R^2	RMSE difference (m)
P. Langkawi	0.8287	0.0492
Port Kelang	0.7864	0.0466
Geting	0.9476	0.0452
P. Tioman	0.9432	0.0317
Bintulu	0.8424	0.0338
K. Kinabalu	0.9188	0.0341
Sandakan	0.8298	0.0542
Tawau	0.7238	0.0606

3.2 Analysis of Sea Level Variation Due to Seasonal Effects

There are a lot of factors that can contribute to variation of sea level such as global warming, climate, and others. However, in Malaysian region, there are four (4) types of monsoons that bring the different effects especially in weather, that is, Northeast Monsoon (November to February), Southwest Monsoon (May to August), first inter-monsoon (March and April), and second inter-monsoon (September and October). Hence, altimetry data was employed to produce climatology data to analyze sea level variation over Malaysian seas due to seasonal effects.

Climatology of sea level variation from 1993 to 2016 is illustrated in Fig. 10. Based on the result, it shows that sea level climatology for Malacca Strait, South China Sea, and Sulu Sea remain positive with a range from 0 to 0.04 m and indicated in green color scale on map, while some parts of Celebes Sea are slightly increased in sea level with 0–0.05 m (green to blue).

Hence, this map will act as (normal) sea level variation for climatology and will be used as reference to compare the sea level changes according to four (4) types of monsoons in Malaysian region.

Northeast Monsoon. Northeast Monsoon (November–February) originates in China and north Pacific. Furthermore, Northeast Monsoon brings heavy rainfall especially to the east coast of Peninsular Malaysia and western Sarawak. Figure 11 shows the sea level variation during Northeast Monsoon around Malaysian seas
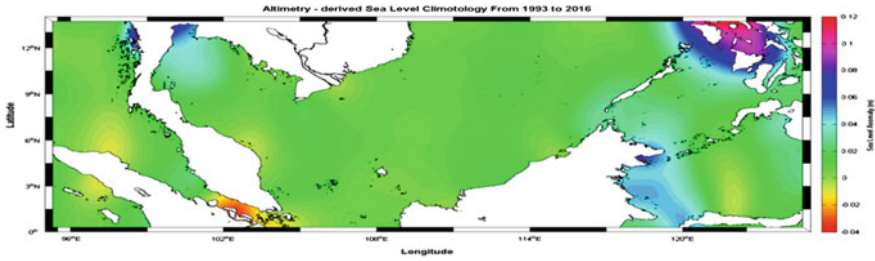
Fig. 10 Sea level anomaly climatology from 1993 to 2016
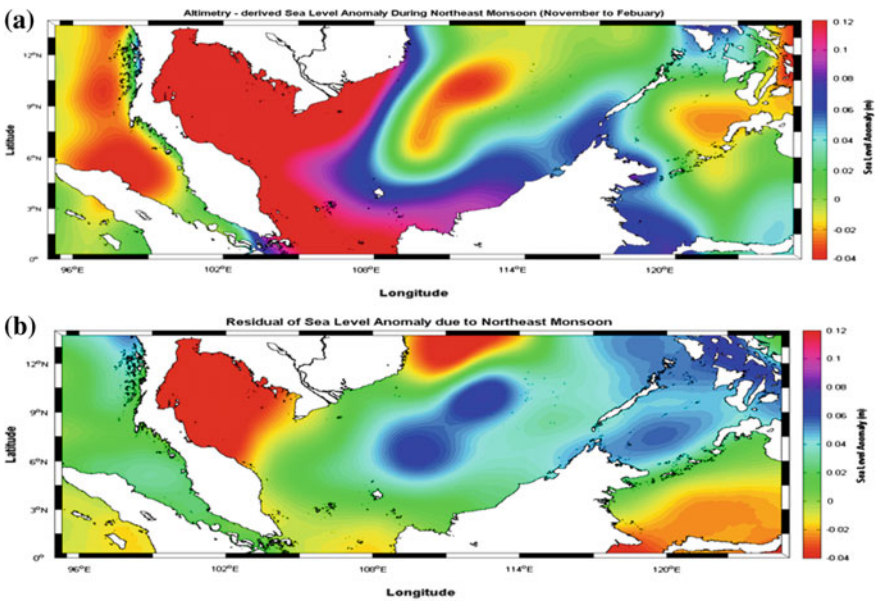
Fig. 11 Sea level anomaly during Northeast Monsoon (**a**) and residual of sea level anomaly during Northeast Monsoon (**b**)

with the residual that is compared to the map before as mentioned in Sect. 3.2. Based on the result, only Malacca Strait sea level variations remain stable with (0–0.04 m). However, for South China Sea, Sulu, and Celebes seas, there are significant changes in sea level variation. In South China Sea, there is some part that is decreased in sea level, while some other remains stable and increases the sea level. Meanwhile, for Sulu Sea, the sea level trends are increasing with 0.04–0.06 m, while Celebes Sea slightly decreased with 0–0.02 m. All the analysis is focused on the map residual of SLA due to Northeast Monsoon.

Southwest Monsoon. Southwest Monsoon (May–August) originates from deserts of Australia and signifies as drier season or weather with impact minimum
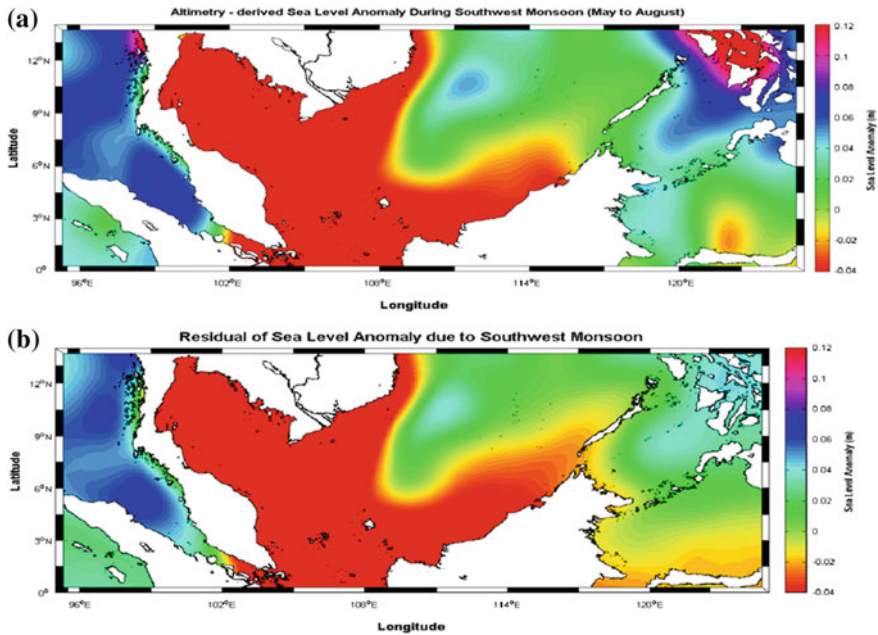
Fig. 12 Sea level anomaly during Southwest Monsoon (**a**) and residual of sea level anomaly during Southwest Monsoon (**b**)

rainfall throughout the country except for Sabah in East Malaysia. Based on the result, there is a significant variation in sea level around Malaysian seas; for Malacca Strait, the sea level slightly increased with range 0.04–0.06 m, while Sulu and Celebes Seas both slightly decreased with a range from 0 to −0.02 m. However, for South China Sea, the sea level dominantly decreased in sea level with a range from 0 to −0.04 m. All the result is shown in Fig. 12 and the analysis focused on the residual map.

First and Second Inter-Monsoon. First inter-monsoon (March–April) and second inter-monsoon (September–October) are the transition period between Northeast Monsoon and Southwest monsoon. During these two inter-monsoons, fair frequent rain occurs. Same for Northeast and Southwest monsoon, these two inter-monsoons are analyzed on variation of sea level around Malaysian seas and focus on the residual map. Based on result in Fig. 13, during first inter-monsoon, most of the area of Malaysian seas are gradually decreased in sea level with a range from 0 to −0.04 except for Celebes Sea that remains normal with range 0–0.02 m.

Next, during second inter-monsoon, Malacca Strait sea level variations remain stable with (0–0.04 m). However, for South China Sea, Sulu, and Celebes seas, there are significant changes in sea level variation. In South China Sea, there is some part that decreased in sea level, while some other remains stable and is increased in sea level. Meanwhile, for Sulu Sea, the sea level trends are increasing with 0.04–0.06 m, while Celebes Sea slightly decreased from 0 to −0.02 m.
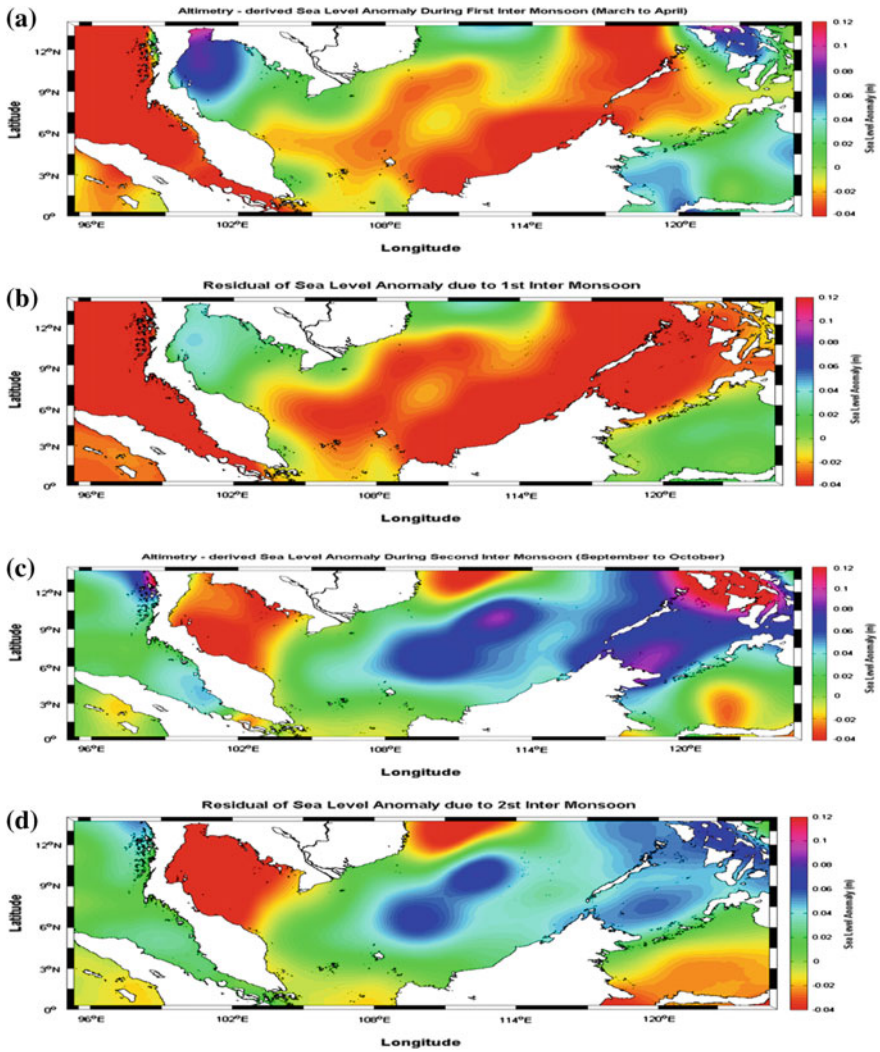
Fig. 13 Sea level anomaly during first inter-monsoon (**a**), residual of sea level anomaly during first inter-monsoon (**b**), sea level anomaly during second inter-monsoon (**c**), and residual of sea level anomaly during second inter-monsoon (**d**)

3.3 Analysis of Sea Level Fluctuation of Malaysian Seas

In this section, SLA data are selected at each of Malaysian Seas: Malacca Strait, South China Sea, Sulu, and Celebes Seas to analyze the magnitude or fluctuation of sea level at each area. Based on the results in Fig. 14, the sea level in Malacca Strait, Sulu, and Celebes Seas suddenly decreased significantly in late 1997 and

Fig. 14 The sea level fluctuation of Malacca Strait (**a**), Sulu Sea (**b**), Celebes Sea (**c**), and South China Sea (**d**)

back to normal after 1998 caused by El Nino effect. Meanwhile, in the late of 2010 to early 2011, there is sudden rise caused by the effect of La Nina.

However, for South China Sea, the abnormal pattern of sea level does not occur. Hence, the El Nino and La Nina events are hardly noticed because South China sea is an open sea. Hence, this shows that for Malaysian Seas, the closed and semi-closed seas may reflect the effect of El Nino and La Nina events.

3.4 Analysis of Sea Level Trend During El Nino and La Nina Events

By using altimetry data, the mean SLA map was produced over Malaysia Seas from 1993 to 2016 as illustrated in Fig. 15. As can be seen, the result shows that for the
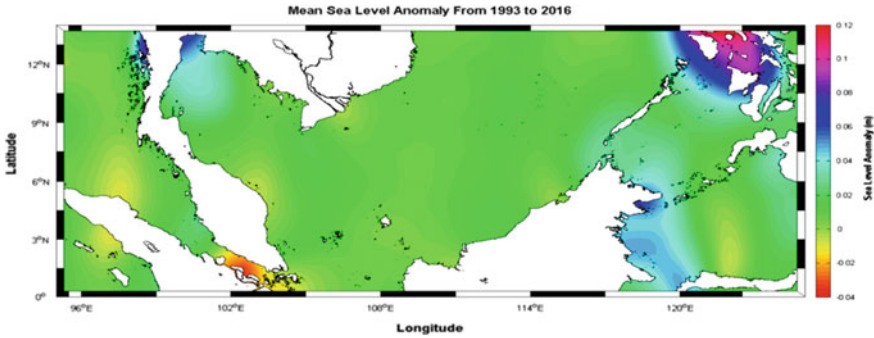
Fig. 15 Mean sea level anomaly from 1993 to 2016 using altimetry data

past 24 years sea level trends around Malaysia region remain positive with the range from 0 to 0.04 m that represents green color scale on the map. Hence, this map will act as (normal) sea level trend and used as a benchmark for the map produced for the El Nino and La Nina events.

El Nino and La Nina year events selected for this research are taken based on the record of Oceanic Nino Index (ONI) [15]. The ONI is one of the primary indices used to monitor the El Nino and La Nina events. The ONI is calculated by averaging sea surface temperature anomalies in an area of the east-central equatorial Pacific Ocean, region (5S to 5N; 120W to 170W). Hence, the next analysis is focused on El Nino and La Nina events selected from ONI that are summarized in Table 4.

Very Strong El Nino (1997–1998 and 2015–2016). Based on the results in Fig. 16, it shows that during very strong El Nino (1997–1998) the sea level trend around Malaysia seas significantly decreased from −0.01 to −0.04 m. Besides that, the map totally contrasts with the normal sea level trends as mentioned in Sect. 3.3 with dominant scale color change between green to red during El Nino event.

However, during very strong El Nino (2015–2016), the results are contrast; the sea level trends do not drop while remaining positive with significant increase in sea level especially at Malacca Strait with range 0.06–0.08 m. They are several factors that induce this result happened, first the selected El Nino event from ONI based on the sea surface temperature from east-central Pacific Ocean. Second, it may have relation with ocean circulation.

Strong El Nino (2002–2003 and 2009–2010). The sea level trend during 2002–2003 shows that around the Malacca Strait, Sulu, and Celebes Seas are the most affected with drop in sea level between 0 and 0.025 m (see Fig. 17). However, the

Table 4 Selected El Nino and La Nina events

El Nino		La Nina
Very strong	Moderate	Moderate
1997–1998	2002–2003	2007–2008
2015–2016	2009–2010	2010–2011
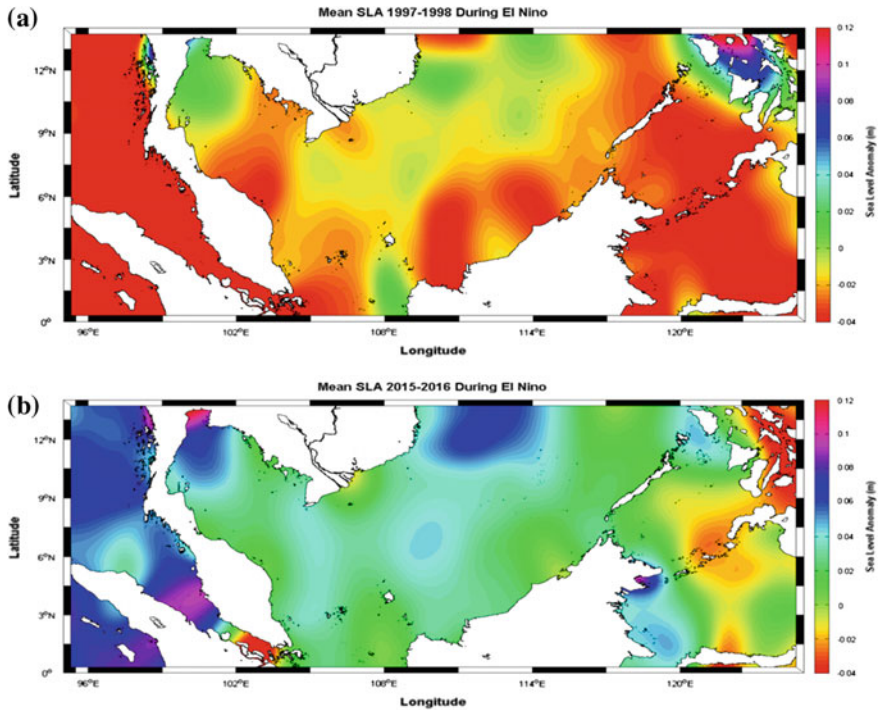
Fig. 16 Mean sea level anomaly from 1997 to 1998 (**a**) and 2015 to 2016 (**b**) using altimetry data during very strong El Nino event

trend of sea level around South China Sea remains normal with 0–0.02 m. This is due to the factor that South China Sea is the open sea, while Malacca Strait, Sulu, and Celebes Seas are closed or semi-closed seas that exposed to have more effect during this event.

However, during strong El Nino from 2009 to 2010, there is significant rise in sea level around all Malaysia seas with 0.04–0.10 m, which is indicated from blue to magenta color scale. This result indicated that the strong El Nino from 2009 to 2010 was insignificantly influenced the sea level variation over Malaysian seas.

Moderate La Nina (2007–2008 and 2010–2011). Based on ONI record, strong La Nina event happens before 1993, while Satellite Altimeter fully starts operation from 1993. That is why there is no altimetry data and analysis on strong La Nina. Based on the result in Fig. 18, the Moderate La Nina event during 2007–2008, the sea level trends are constant (normal) at Malacca Strait and South China Sea with 0–0.04 m. However, at Sulu and Celebes seas, there is a drastic increase in sea level from 0.04 to 0.10 m.
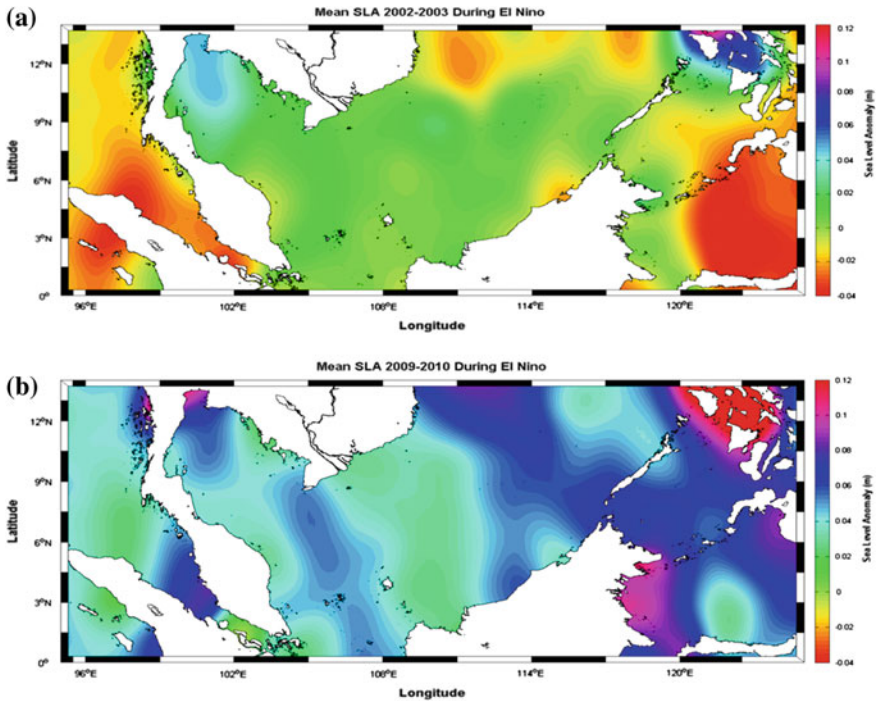
Fig. 17 Mean sea level anomaly from 2002 to 2003 (**a**) and 2009 to 2010 (**b**) using altimetry data during strong El Nino event

Next, during la Nina event from 2010 to 2011, the sea level trends around Malaysia seas are significantly rising with the range from 0.04 to 0.11 m. Hence, it can be concluded that sea level around Malaysia seas during La Nina event either remains stable or slightly increased in sea level. The summary of the analysis on El Nino and La Nina events is shown in Table 5.
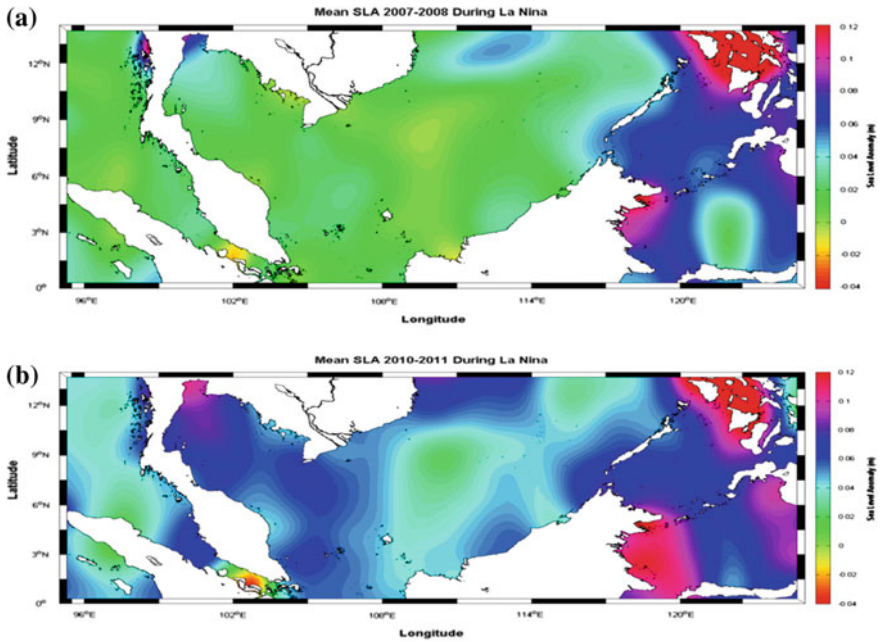
Fig. 18 Mean sea level anomaly from 2007 to 2008 (**a**) and 2010 to 2011 (**b**) using altimetry data during moderate La Nina event

Table 5 Summary of sea level range during El Nino and La Nina events

Event/Malaysia Seas	El Nino			
	Very strong		Strong	
	1997–1998	2015–2016	2002–2003	2009–2010
Malacca Strait	−0.03 to −0.04 m	0.06–0.08 m	−0.02 to −0.04 m	0.04–0.08 m
South China Sea	0 to −0.02 m	0–0.02 m	0–0.02 m	0.04–0.08 m
Sulu Sea	−0.02 to −0.04 m	−0.02 to 0.02 m	0 to −0.04 m	0.06–0.08 m
Celebes Sea	−0.02 to −0.04 m	−0.02 to 0.02 m	0 to −0.04 m	0.06–0.10 m

Event/Malaysia Seas	La Nina	
	Moderate	
	2007–2008	2010–2011
Malacca Strait	0–0.02 m	0.04–0.08 m
South China Sea	0–0.02 m	0.04–0.08 m
Sulu Sea	0.06–0.08 m	0.06–0.10 m
Celebes Sea	0.06–0.08 m	0 06–0.10 m

4 Conclusion

Based on this research, altimetry data provide a good result on analysis of sea level variation at Malaysian seas. Up to date, sea level always measured by tide gauge but with the Satellite Altimeter alternative method there is more research or study that can be done especially in deep seawater that can help other agencies to make decision or planning in their project of development and coastal protection management in Malaysia.

Hence, satellite altimeters are reliable and advanced technology that can be used to monitor sea level changes around our coastal area and can harmony cooperate with tide gauge stations.

Based on all the analysis, generally sea level trends will drop during El Nino while increase during La Nina event around Malaysian Seas. However, this analysis needs to be a further study on the other elements such as Seasonal Variation, Rainfall Variation, Sea Surface Temperature, and other elements that can give impact on the variation on sea level especially around Malaysia region.

Furthermore, El Nino and La Nina events are categorized as one of the climate change events that can contribute to changes in sea level that can cause floods and drought, and affect various marine activities especially at area around coastal. This issue must be taken into consideration by all people especially government have to give the uttermost attention in all aspect of planning in order to avoid any unwanted disaster will occur.

References

1. Milne, G.A., Gehrels, W.R., Hughes, C.W., Tamisiea, M.E.: Identifying the causes of sea-level change. Nat. Geosci. **2**(7), 471–478 (2009)
2. Church, J.A., Gregory, J.M., White, N.J., Platten, S.M., Mitrovica, J.X.: Understanding and projecting sea level change. Oceanography **24**(2), 130–143 (2011)
3. Fu, L.-L., Cazenave, A.: Satellite Altimetry and Earth Sciences: A Handbook of Techniques and Applications, vol. 69. Academic Press (2000)
4. Mohamed, A.: An Investigation of the vertical control network of peninsular malaysia using a combination of levelling, gravity, GPS and tidal data. Doctor Philosophy, Universiti Teknologi Malaysia, Skudai (2003)
5. Din, A.H.M.: Sea level rise estimation using satellite altimetry technique. M.Sc. Thesis, Universiti Teknologi Malaysia, Skudai (2010)
6. Morrow, E.: Estimates of land ice changes from sea level and gravity observations. Doctoral Dissertation (2014)
7. Din, A.H.M.: Sea level rise estimation and interpretation in Malaysian region using multi-sensor technique. Doctor Philosophy, Universiti Teknologi Malaysia, Skudai (2014)

8. Niedzielski, T., Kosek, W.: Analysis and prediction of altimetric sea level variations during El Niño, La Niña, and normal conditions. In: Proceedings of the 16th International Workshop on Laser Ranging, 305–310 (2009)
9. Watson, C.S.: Satellite altimeter calibration and validation using GPS buoy technology. Doctoral Dissertation, University of Tasmania (2005)
10. Naeije, M., Schrama, E., Scharroo, R.: The radar altimeter database system project rads. Paper presented at the IEEE 2000 International Geoscience and Remote Sensing Symposium. In: Proceedings of the IGARSS 2000 (2000)
11. Holgate, S.J., Matthews, A., Woodworth, P.L., Rickards, L.J., Tamisiea, M.E., Bradshaw, E., Pugh, J.: New data systems and products at the permanent service for mean sea level. J. Coastal Res. **29**(3), 493–504 (2013)
12. Din, A.H.M., Abazu, I.C., Pa'suya, M.F., Omar, K.M., Hamid, A.I.A.: The impact of sea level rise on geodetic vertical datum of peninsular malaysia. Int. Arch. Photogrammetry Remote Sens. Spat. Inf. Sci. **42** (2016)
13. Cazenave, A., Champollion, N., Paul, F., Benveniste, J. (eds.): Integrative study of the mean sea level and its components, vol. 58. Springer (2017)
14. Singh, M., Mandal, M.K., Basu, A.: Robust KLT tracking with Gaussian and Laplacian of Gaussian weighting functions, vol. 4. Paper presented at the ICPR (2004)
15. Oceanic Nino Index: http://ggweather.com/enso/oni.htm. Last accessed 20 Apr 2017

Applications of Deep Learning in Severity Prediction of Traffic Accidents

Maher Ibrahim Sameen, Biswajeet Pradhan, H. Z. M. Shafri and Hussain Bin Hamid

Abstract This study investigates the power of deep learning in predicting the severity of injuries when accidents occur due to traffic on Malaysian highways. Three network architectures based on a simple feedforward Neural Networks (NN), Recurrent Neural Networks (RNN), and Convolutional Neural Networks (CNN) were proposed and optimized through a grid search optimization to fine tune the hyperparameters of the models that can best predict the outputs with less computational costs. The results showed that among the tested algorithms, the RNN model with an average accuracy of 73.76% outperformed the NN model (68.79%) and the CNN (70.30%) model based on a 10-fold cross-validation approach. On the other hand, the sensitivity analysis indicated that the best optimization algorithm is "Nadam" in all the three network architectures. In addition, the best batch size for the NN and RNN was determined to be 4 and 8 for CNN. The dropout with keep probability of 0.2 and 0.5 was found critical for the CNN and RNN models, respectively. This research has shown that deep learning models such as CNN and RNN provide additional information inherent in the raw data such as temporal and spatial correlations that outperform the traditional NN model in terms of both accuracy and stability.

Keywords Traffic accidents · Recurrent neural networks · CNN
GIS · LiDAR

M. I. Sameen · B. Pradhan · H. Z. M. Shafri · H. B. Hamid
Department of Civil Engineering, Faculty of Engineering,
Geospatial Information Science Research Center (GISRC),
University Putra Malaysia, 43400 Serdang, Malaysia

B. Pradhan (✉)
Faculty of Engineering and Information Technology, School of Systems,
Management and Leadership, University of Technology Sydney,
Building 11, Level 06, 81 Broadway, PO Box 123, Ultimo, NSW 2007, Australia
e-mail: Biswajeet.Pradhan@uts.edu.au

1   Introduction

Future prediction is one of the fascinating topics for human endeavor and is identified to be a vital tool in transportation management. Understanding the whole network of transportation is much difficult than on a single road. The main purpose of this effort is to provide a better route with high safety level and support the traffic managers in managing road network in an efficient manner.

Recent studies have predicted that in 2030, traffic accidents will be the fifth leading cause of death worldwide [1]. Besides, the costs of fatalities and driver injuries due to traffic accidents have a significant impact on the society. This issue has led to investigating various aspects of traffic accident data and modeling in numerous geographic regions. In general, two research methods have dominated studies in traffic crash forecasting, statistical methods, and the neural networks. Statistical techniques such as K-Nearest Neighbors (KNN) [2], Support Vector Machine (SVM) [3, 4], and Logistic Regression (LR) [5] for predicting the frequency and the injury severity of traffic accidents have been applied. For the implementation of flexibility, generalizability, and strong forecasting power, Artificial Neural Networks (ANN) is used [6, 7]. Furthermore, previously, large amount of high-resolution data have been generated on freeway networks using traffic sensors for predicting traffic crashes. However, the theory of deep learning gradually began to exhibit superiority over the other techniques.

The advents of artificial intelligence have made deep learning to experience more patronage most especially with the aid of high-speed computing machines. The use of computational intelligence methods has encouraged paradigm shift from the conventional traffic forecasting to short-term traffic forecast based on deep learning approaches. The use of deep learning principle can resolve many issues related dimensionality with the aid of distributed calculation [8]. Many successes have been recorded from the use of deep learning most especially in the computer vision domain such as speech recognition, natural language processing, and many others [9–11]. With the aid of deep learning theory, several alternatives to neural network have been developed to ease the process of traffic prediction. Some of these alternatives are Feedforward Neural Network (NN), Recurrent Neural Network (RNN), and Convolutional Neural Network (CNN).

Therefore, deep learning models play a pivotal role in traffic accident forecast, even though, with some drawbacks. The primary drawback of deep learning models is the requirement of large datasets to train and low explanatory power. The basic aim of deep learning is to develop the representation of the actual predictor vector so that transformed data can be used for classification or linear regression. Thus, the aim of this study is to analyze and discuss the difference between the three basic network architectures: NN, CNN, and RNN, in predicting the severity of injuries in traffic accidents on high-speed highways.

2 Deep Learning Models

2.1 Feedforward Neural Networks (NN)

In machine learning, neural networks are a family of biological learning models. A simple NN model is an interconnection of neurons or nodes, which comprises three layers namely inputs, hidden, and output layers. In this study, the model represents a nonlinear mapping between the input values (accident predictors) and the output parameters (injury severity levels). Neurons are systematic connection of weight vectors, which are usually structured in layers with full connections between successive layers. The output signal is a function of the inputs to the node, which is modified, by a simple activation function [12, 13].

What has attracted the research fraternity the most in neural networks is the possibility of learning. The most common learning algorithm for neural networks is the backpropagation developed by Paul Werbos in 1974, which was later rediscovered by Rumelhart and Parker. The algorithm was designed to reduce the error function by using an iterative approach as shown in Eq. 1. Despite the success of such neural networks in remote sensing applications, a significant limitation of this model is the fact that their computational complexity is quite high and it has a drawback of overlearning [14, 15].

$$E = \frac{1}{2}\sum_{i=1}^{L}\left(d_j - o_j^M\right)^2 \tag{1}$$

where d_j and o_j^M denote output and current response, respectively, of the node "j" in the output layer, and "L" represents the number of nodes in the output layer. In this approach, corrections are made to weight parameters and added to the preceding values as shown in Eq. 2:

$$\begin{cases} \Delta w_{i,j} = -\mu \frac{\partial E}{\partial w_{i,j}} \\ \Delta w_{i,j}(t+1) = \Delta w_{i,j} + \alpha\,\Delta w_{i,j}(t) \end{cases} \tag{2}$$

The $w_{i,j}$ denotes parameter between node i and j, Δ is the learning rate which controls the amount of adjustment, α is a momentum factor between 0 and 1 and "t" represents the number of iterations. The parameter α refers to smoothing factor due to its ability to take care of the rapid changes between the weights [16].

2.2 Convolutional Neural Networks

Another effective neural network in areas of computer vision and classification is the Convolutional Neural Networks (CNN) [9]. The first CNN was developed by
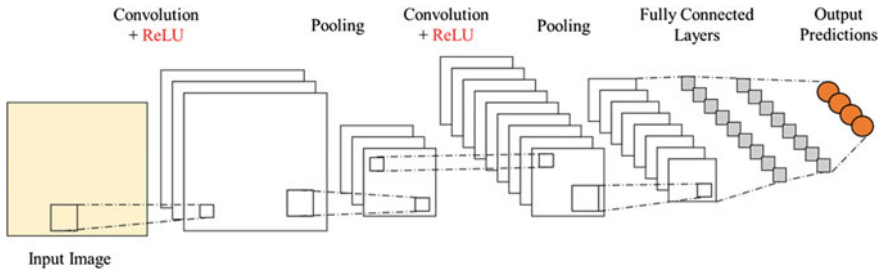
Fig. 1 The typical CNN model architecture

Yann LeCun (Fig. 1) which has contributed immensely in many works in computer vision and deep learning environment. This method is also referred as LeNet and was used in the early years mainly for character recognition works like zip digits, codes, and handwriting. It can also process data in multiple arrays format (color images, signals, sequences, audio, and video) depending on the dimensions of the convolution operations (1D, 2D, or 3D) [17].

Typically, four processes are involved in CNN operations: convolution, pooling or sub-sampling, nonlinearity (ReLU), and classification (fully connected layer) [17]. These aforementioned operations comprise the building blocks of CNN. Features can be extracted from input data such as image and time series using convolution operation. It preserves the spatial interactions between the input sample data through learning small subsets of the input files. ReLU (Rectified Linear Unit) is an additional nonlinear operation used after every convolution operation in networks. ReLU yield output in an element-wise manner, which substitutes negative values in the feature map with zero, and resolves real-world problems by utilizing its nonlinearity in the network. Furthermore, sub-sampling or down-sampling is also referred as spatial pooling that is used to reduce the dimensionality of each feature map but retains the most significant information. Max, Average, or Sum is some of the different types of spatial pooling available. The Max pooling uses the biggest element within the rectified feature map in any defined spatial neighborhood. Average pooling could also be taken instead of the biggest element or the sum of all elements in that window, although, according to Schindler and Van Gool [18], Max pooling has proven to be better than the average pooling.

Furthermore, in a traditional multilayer perceptron, connected layer uses a softmax activation function in the output layer. The output from the convolutional and pooling layers represents high-level features of the input data. The main reason behind the implementation of the fully connected layer is its capability in classifying features in input data into different classes based on the training dataset.

2.3 Recurrent Neural Networks

Recurrent Neural Networks (RNNs) are neural networks with feedback connections specifically designed to model sequences. They are computationally more powerful and biologically more reasonable than feedforward networks (no internal states). The feedback connections provide memory of past activations to the RNN, which enables it to learn the temporal dynamics of sequential data. RNN uses contextual information making it powerful for mapping between input and output sequences. However, the traditional RNNs have a problem called vanishing gradient or exploding gradient. However, Hochreiter and Schmidhuber [18] proposed Long Short-Term Memory (LSTM) to resolve such problems.

Hidden units are substituted by memory blocks in LSTM that contains self-connected memory cells and three multiplicative units (input, output, and forget gates). The gates enable reading, writing, and resetting operations in the memory block and control the behavior of the memory block. Figure 2 shows a diagram representing a single LSTM unit.

Let c_t be the sum of inputs at time step t and its previous time step activations, the LSTM updates for time step i given inputs x_t, h_{t-1}, and c_{t-1} are [19]

$$i_t = \sigma(W_{xi} \cdot x_t + W_{hi} \cdot h_{t-1} + W_{ci} \cdot c_{t-1} + b_i) \tag{3}$$

$$f_t = \sigma(W_{xf} \cdot x_t + W_{hf} \cdot h_{t-1} + W_{cf} \cdot c_{t-1} + b_f) \tag{4}$$

$$c_t = i_t \cdot \tanh(W_{xc} \cdot x_t + W_{hc} \cdot h_{t-1} + b_c) + f_t \cdot c_{t-1} \tag{5}$$
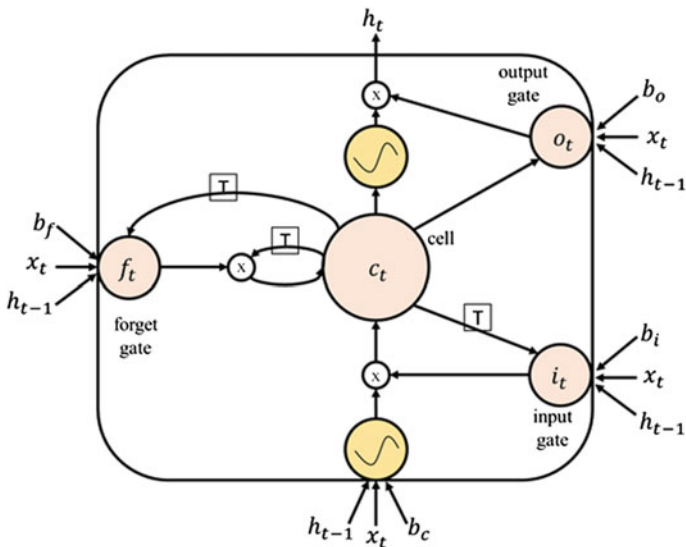
Fig. 2 The structure of a memory cell in LSTM-RNN

$$o_t = \sigma(W_{xo} \cdot x_t + W_{ho} \cdot h_{t-1} + W_{co} \cdot c_t + b_o) \qquad (6)$$

$$h_t = o_t \cdot \tanh(c_t) \qquad (7)$$

where σ is an element-wise nonlinearity such as a sigmoid function, W is the weight matrix, x_t is the input at time step t, h_{t-1} is the hidden state vector of the previous time step, and b_i denotes the input bias vector.

3 The Proposed Models

This study proposed three different network architectures based on a simple NN, CNN, and RNN models. Figure 3 shows the architecture of the NN model with two hidden layers of 50 hidden units. The model takes a vector of eight variables as inputs and predicts the severity of traffic accidents as only property damage, possible/evident injury, or disabling injury/fatality. The total parameters of this network are 3225 distributed as 72, 450, 2550, and 153 for the network layers, respectively. The backpropagation algorithm trained the model with the Nadam optimizer and a batch size of 4. The parameters of the network were selected via a grid search and a 10-fold cross-validation assessment.

The second proposed model is based on a CNN as shown in Fig. 4. In this model, the input data is transformed into a new feature representation through some convolution and pooling operations. A one-dimensional convolution operation is applied to handle the sequence accident data. The maximum pooling operations are applied to abstract the rectified features. Then, the features are flattened to be used
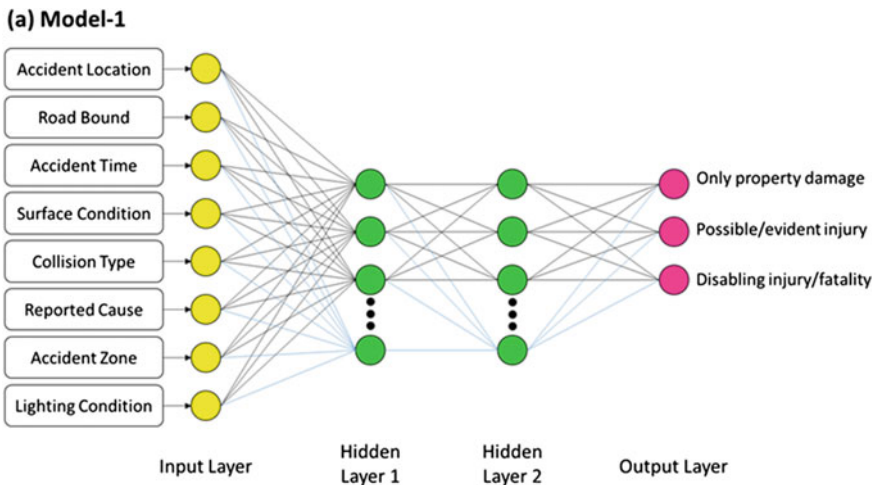
Fig. 3 The proposed NN model for injury severity prediction of traffic accidents
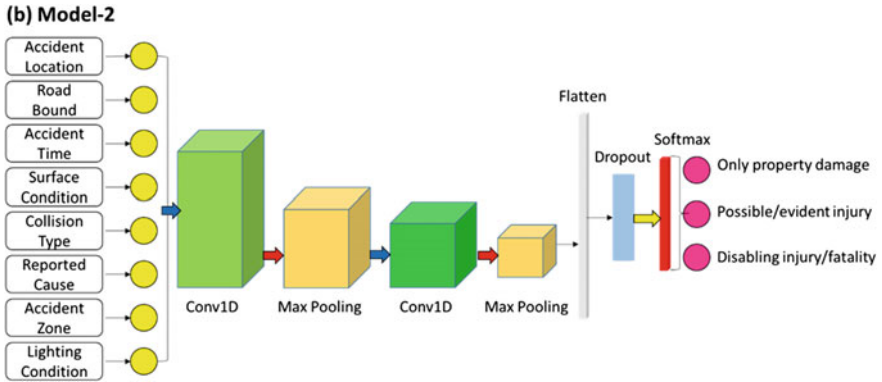
Fig. 4 The proposed CNN model for injury severity prediction of traffic accidents

for classification. A dropout layer is added to avoid overfitting. Finally, the injury severity of traffic accidents is predicted by the softmax layer. The total number of parameters of the CNN model is 4739.

On the other hand, the third model is based on an RNN, which was designed for sequence problems. An RNN can be thought as the addition of loops to the architecture. For example, in a given layer, each neuron may pass its signal latterly in addition to forward to the next layer. The output of the network may feedback as an input to the network with the next input vector, and so on. Figure 5 shows the proposed network architecture based on the RNN model. Similarly, the network takes a vector of eight variables as inputs and produces probabilities for three
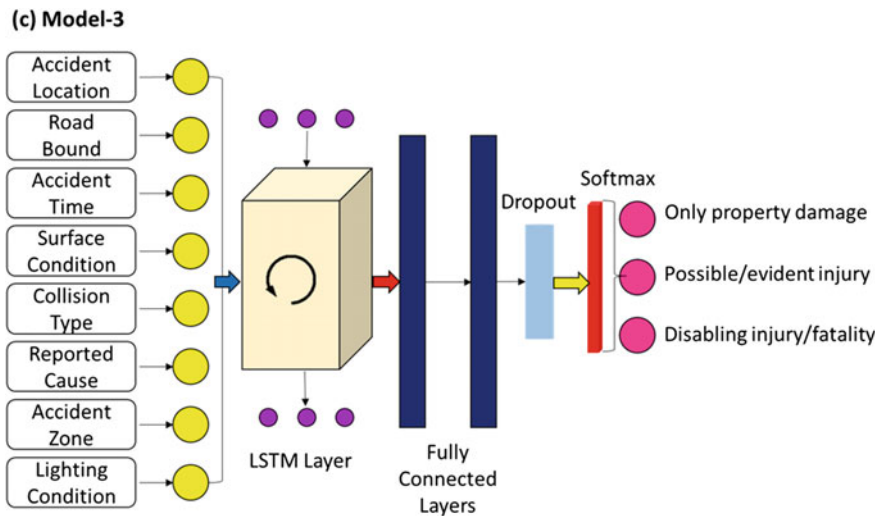
Fig. 5 The proposed RNN model for injury severity prediction of traffic accidents

severity classes of traffic accidents such as only property damage, possible/evident injury, or disabling injury/fatality. The network consists of an LSTM layer with 100 hidden units, two fully connected layers, a dropout layer, and a softmax layer. The total number of parameters of the RNN model is 82,755.

A dropout layer was applied to avoid overfitting of the CNN and the RNN models. Since the neural networks learn its weights from the training dataset, it is possible to overfit them and does not perform well when given new examples. The dropout layer sets some randomly selected activations to zero, and by this, it helps to alleviate the overfitting problem. It is used only during training time and not during test time. The number of activations that are dropout is controlled by the parameter known as keep probability.

4 Experimental Results

The models were implemented in Python using the open-source tensor flow deep learning framework developed by Google recently [20]. Tensor flow has automatic differentiation and parameter sharing capabilities, which allows a broad range of architectures to be easily defined and executed [20].

4.1 Dataset

The 2009–2015 traffic accident data for the North–South Expressway (NSE), Malaysia were used in this study. The NSE is the longest expressway (772 km) operated by Projek Lebuhraya Usaha Sama (PLUS) Berhad (i.e., the largest expressway operator in Malaysia) and links many major cities and towns in Peninsular Malaysia. The data were obtained from the PLUS accident databases. The files used in this study were accident frequency and accident severity files in the form of Excel spreadsheet. The accident frequency file contains the positional and descriptive accident location and the number of accidents in each road segment of 100 m. The accident records were separated according to the road bound (south, north). In contrast, the accident severity file contains the general accident characteristics such as accident time, road surface and lighting conditions, collision type, and the reported accident cause. To link the two files, the unique identity field (accident number) was used.

The section of NSE employed in this study has a length of 15 km running from Ayer Keroh (210 km) to Pedas Linggi (225 km) (Fig. 6). The accident severity data showed that the last section (220–225) of the NSE experienced several accidents resulting in serious injury (82) than the other sections (Table 1). Most accidents have occurred in the main route and southbound of the expressway. During the accident events, the actual accident causes were documented. The data showed that lost control, brake failure, and obstacles were the main accident causes in the NSE.
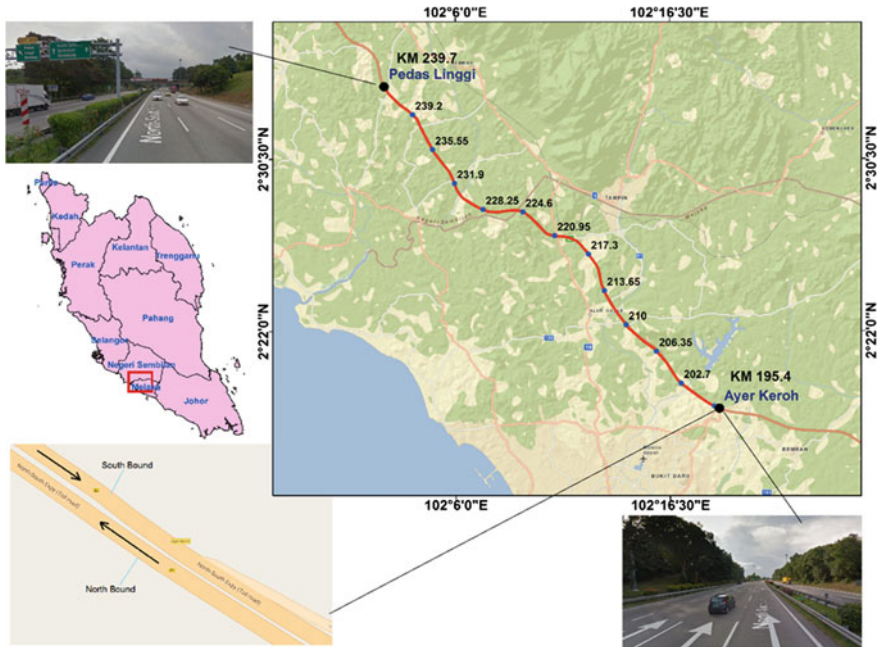
Fig. 6 Location of the NSE section analyzed in this study

Regarding lighting and surface conditions, the most accidents occurred in daylight condition and dry road surface. The main collision types in the accident records are out of control and rear collision. In addition, the accident time factor showed that 91.68% of the accidents occurred during the daytime. On the other hand, the data demonstrated that two car accidents, single heavy car with an object, and motorcycle with objects were mostly involved in the recorded crashes in the NSE.

4.2 Model Performance

The proposed models were tested by a 10-fold cross-validation method on the testing dataset. Table 2 and Fig. 7 show the accuracy of the NN, CNN, and RNN models. The RNN model has achieved the best accuracy (73.76%) compared with the CNN (70.30%) and the NN (68.79%) models. However, the CNN model slightly outperformed the RNN model regarding accuracy stability across different folds of the testing dataset. The standard deviations of the accuracies achieved by the CNN and RNN models are 0.53 and 1.24%, respectively. This result indicates the high stability of the CNN and the RNN models in predicting the injury severity of the traffic accidents. However, the NN model has low accuracy stability with a standard deviation of 2.21%.

Table 1 Driver injury severity distribution according to accident-related factors

Factor	Property damage only	Evident injury	Disabling injury	Total
Location				
210–214	185	172	58	415
215–219	234	47	56	337
220–225	238	58	82	378
Road bound				
South	453	99	139	691
North	287	73	79	439
Accident zone				
Interchange	14	3	0	17
Junction				
Lay-by	2	0	1	3
Main route	666	155	209	1030
Northbound entry ramp	8	2	0	10
Northbound exit ramp	4	2	0	6
Rest and service area	21	4	2	27
Southbound entry ramp	2	0	1	3
Southbound exit ramp	7	1	3	11
Toll plaza	16	5	2	23
Accident reported cause				
Bad pavement condition	0	1	0	1
Brake failure	6	2	1	9
Bump–bump	37	12	27	76
Dangerous pedestrian behavior	0	0	1	1
Drunk	0	0	1	1
Loss of wheel	1	0	2	3
Lost control	75	18	22	115
Mechanical	5	1	0	6
Mechanical/electrical failure	11	0	1	12
Obstacle	43	12	6	61
Other bad driving	15	1	4	20
Other human factor/over load/ over height	3	0	0	3
Over speeding	345	61	91	497
Parked vehicle	4	4	10	18
Skidding	1	0	0	1
Sleepy driver	134	44	42	220
Stray animal	13	1	2	16
Tire burst	47	15	8	70

(continued)

Table 1 (continued)

Factor	Property damage only	Evident injury	Disabling injury	Total
Lighting condition				
Dark with street light	47	6	8	61
Dark without street light	225	74	89	388
Dawn/dusk	35	9	9	53
Daylight	433	83	112	628
Surface condition				
Dry	460	146	190	796
Wet	280	26	28	334
Collision type				
Angular collision	9	2	0	11
Broken windscreen	2	0	0	2
Cross direction	2	0	1	3
Head-on collision	0	1	4	5
Hitting animal	12	1	2	15
Hitting object on road	44	12	7	63
Others	20	0	6	26
Out of control	457	92	107	656
Overturned	33	11	7	51
Rear collision	137	48	81	266
Right angle side collision	11	1	1	13
Side swipe	13	4	2	19
Accident time				
Daytime	677	156	203	1036
Nighttime	63	16	15	94
Vehicle type				
Car–bus	7	3	6	16
Car–car	499	68	60	627
Car–heavy car	51	11	14	76
Car–motorcycle	4	7	22	33
Heavy car	131	23	25	179
Heavy car–bus	2	3	3	8
Heavy car–heavy car	24	9	15	48
Heavy car–motorcycle	0	1	6	7
Heavy car–taxi	2	0	0	2
Motorcycle	11	42	60	113
Motorcycle–taxi	0	1	1	2
Motorcycle–van	0	0	2	2
Taxi	1	0	1	2
Van	8	4	3	15

Table 2 The average cross-validation accuracy of the proposed models	Model	10-fold cross-validation accuracy
	Model-1 feedforward	68.79% (±2.21%)
	Model-2 convolutional	70.30% (±0.53%)
	Model-3 recurrent	73.76% (±1.24%)

Fig. 7 The accuracy of the models tested by a 10-fold cross-validation method
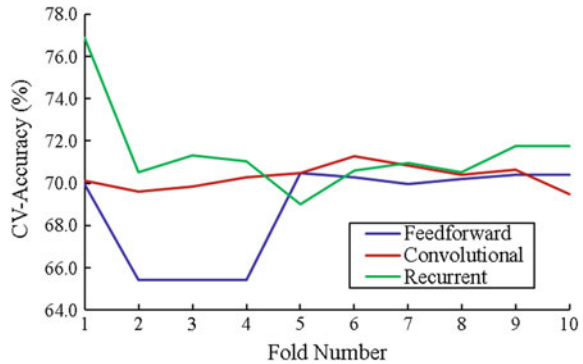
4.3   Optimization and Sensitivity Analysis

Since deep learning models largely depend on the type of data and the processing task, the network architecture should be optimized rather than just using some standard parameters. The data can vary by size, complexity, and the type of relationships between the predictors and the dependent variable. Therefore, in this study, the architectures of the NN, CNN, and the RNN networks were optimized via a grid search implemented in Scipy python. This technique explores and finds the right combinations of hyperparameters that can best predict the injury severity of traffic accidents from the eight predictors given to the networks as inputs.

Regarding the optimizer, the best algorithm was found to be Nadam for all the three models. The Nadam optimizer with its default parameters achieved the accuracy of 0.66, 0.70, and 0.73, for the NN, CNN, and RNN models, respectively (Fig. 8). Adam and Rmsprop optimizers also performed well for all the models. On the other hand, although the Adamax and Adadelta methods achieved relatively good accuracy in CNN model, their performance was significantly poor in the NN and RNN models. Overall, the Nadam algorithm is suggested to be used for analyzing traffic accident data.

Batch size refers to the number of training examples over which optimization update is computed. It has significant effects on the accuracy of the models. Figure 9 shows how the accuracy of the NN, CNN, and the RNN models changes on increasing the batch size from 2 to 64. Regarding the NN model, the performance of the model is decreasing with the growth of the batch size and the best accuracy was obtained when the batch size is equal to 4. Similarly, the batch size of 4 achieved the best accuracy in the RNN model. However, the CNN model performed best with the batch size of 8.

Fig. 8 Effects of optimization algorithm on the accuracy of the proposed models
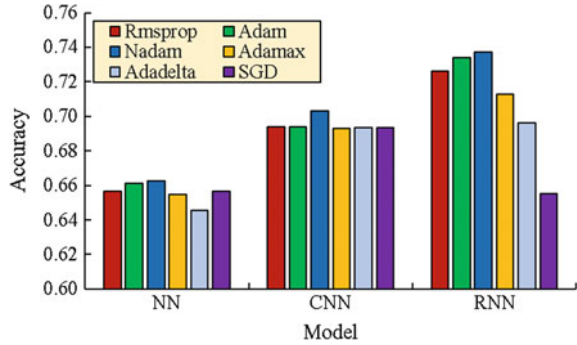
Fig. 9 Effects of the batch size on the accuracy of the proposed models
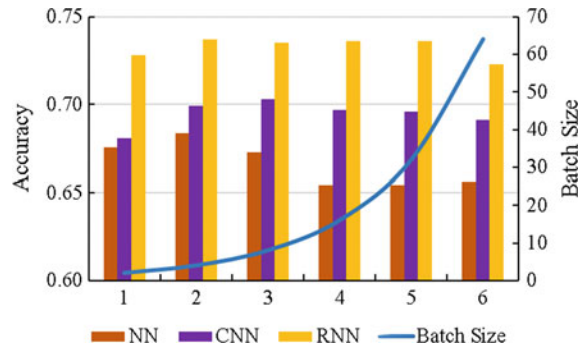
In addition, due to a high number of parameters in the CNN and RNN models, the dropout plays a major role in avoiding overfitting. Figure 10 shows the sensitivity analysis of the use of dropout layer with different keep probability parameters in the CNN and RNN models. The analysis shows that the best dropout rates are 0.2 and 0.5 for the CNN and RNN models, respectively. As selecting dropout rate has a significant effect on the accuracy of the deep learning models and it is widely dependent on the number of parameters in those models, this keep probability should be selected for each dataset and processing task by a grid search.

Fig. 10 Effects of the dropout rate on the CNN and RNN models
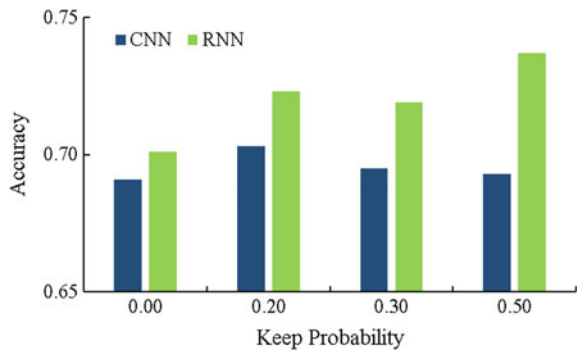
5 Discussion

In general, CNN models learn data representations to recognize patterns across space. In other words, a CNN model is best to use for recognizing components of an image or 2D array of numbers (e.g., line, curve, and objects). However, when traffic accident features transformed from the 1D vector into a 2D array, the CNN model can learn the spatial relationships between the features of different observations (accident events). Thus, it is expected to perform better than the traditional NN model, which does not take into account this additional feature in the data.

On the other hand, the RNN models learn data representations to recognize patterns across time. Therefore, comparing the CNN and RNN models can reveal the critical component (space or time) for forecasting traffic accidents. In this study, the two models found to be better regarding prediction accuracy than the NN model, meaning to say that including additional spatial and time features can improve the model performance than not using them at all. Having the accuracy of RNN found higher than that achieved by the CNN model, it seems that the temporal component of accident data is greater than the spatial structure of the data. This could be because of traffic, weather, and driving conditions (traffic volume, the speed of vehicles, and raining status); variations appear at different periods.

Furthermore, since the RNN models have memories where computations derived from the earlier input are fed back into the network, they can find relationships among the accident events that are difficult to be found by traditional methods or experts. Thus, they automate the feature identification and representation processes, which give significant advantages to the accident forecasting models. However, RNN models require complex training algorithms than the CNN required which sometimes limit their applications especially with very limited datasets or data without temporal features (e.g., time of the accident).

6 Conclusion

Predicting the injury severity of traffic accidents with high accuracy can improve the ability to manage roads in ways that are more efficient and provide safer roads for drivers. This study explored the accuracy performance of three deep learning architectures (feedforward, convolutional, and recurrent networks). First, an initial network architecture was selected by an empirical analysis, and then the network hyperparameters were optimized through grid search method. A sensitivity of the parameters was analyzed to understand their effects on the accuracy of the models.

The findings suggested that the RNN model performs best with an average accuracy of 73.76% compared to the CNN and NN models in which their accuracies were 70.30 and 68.79%, respectively. The sensitivity analysis showed that the best optimization technique for all the three models is Nadam. The best batch

sizes ranged from 4 to 8, and a dropout with 0.2 and 0.5 keep probability was found to be necessary for the CNN and RNN models.

Although this research has shown that the deep learning models such as RNN and CNN could be promising tools for road safety assessment, few points need to be analyzed in future works. First, the universal optimization of the networks needs to be established. Assessing of the networks on larger datasets can help transforming the deep learning models to the industry to be used in practice. Finally, the models such as RNN and CNN can be integrated into a unified deep learning framework to help other applications of road safety assessment.

References

1. Sameen, M.I., Pradhan, B.: Assessment of the Effects of Expressway Geometric Design Features on the Frequency of Accident Crash Rates Using High-Resolution Laser Scanning Data and GIS, pp. 1–15. Geomatics, Natural Hazards and Risk (2016)
2. Lv, Y., Tang, S., Zhao, H.: Real-time highway traffic accident prediction based on the k-nearest neighbor method. In: 2009 IEEE International Conference on Measuring Technology and Mechatronics Automation ICMTMA'09, vol. 3, pp. 547–550 (2009)
3. Li, X., Lord, D., Zhang, Y., Xie, Y.: Predicting motor vehicle crashes using support vector machine models. Accid. Anal. Prev. **40**(4), 1611–1618 (2008)
4. Li, Z., Liu, P., Wang, W., Xu, C.: Using support vector machine models for crash injury severity analysis. Accid. Anal. Prev. **45**, 478–486 (2012)
5. Al-Ghamdi, A.S.: Using logistic regression to estimate the influence of accident factors on accident severity. Accid. Anal. Prev. **34**(6), 729–741 (2002)
6. Delen, D., Sharda, R., Bessonov, M.: Identifying significant predictors of injury severity in traffic accidents using a series of artificial neural networks. Accid. Anal. Prev. **38**(3), 434–444 (2006)
7. Moghaddam, F.R., Afandizadeh, S., Ziyadi, M.: Prediction of accident severity using artificial neural networks. Int. J. Civil Eng. **9**(1), 41 (2011)
8. Ma, X., Yu, H., Wang, Y., Wang, Y.: Large-scale transportation network congestion evolution prediction using deep learning theory. PLoS ONE **10**(3), e0119044 (2015)
9. Krizhevsky, A., Sutskever, I., Hinton, G.E.: Imagenet classification with deep convolutional neural networks. In: Advances in Neural Information Processing Systems, pp. 1097–1105 (2012)
10. Graves, A., Mohamed, A.R., Hinton, G.: Speech recognition with deep recurrent neural networks. In: 2013 IEEE International Conference on Acoustics, Speech and Signal Processing (ICASSP), pp. 6645–6649 (2013)
11. Sarikaya, R., Hinton, G.E., Deoras, A.: Application of deep belief networks for natural language understanding. IEEE/ACM Trans. Audio Speech Lang. Process. (TASLP), **22**(4), 778–784 (2014)
12. Gardner, M.W., Dorling, S.R.: Artificial neural networks (the multilayer perceptron)—a review of applications in the atmospheric sciences. Atmos. Environ. **32**(14), 2627–2636 (1998)
13. Mokhtarzade, M., Zoej, M.V.: Road detection from high-resolution satellite images using artificial neural networks. Int. J. Appl. Earth Obs. Geoinf. **9**(1), 32–40 (2007)
14. Baczyński, D., Parol, M.: Influence of artificial neural network structure on quality of short-term electric energy consumption forecast. IEE Proc-Gener. Transm. Distrib. **151**(2), 241–245 (2004)

15. Mia, M.M.A., Biswas, S.K., Urmi, M.C., Siddique, A.: An algorithm for training multilayer perceptron (MLP) for Image reconstruction using neural network without overfitting. Int. J. Sci. Techno. Res. **4**(2), 271–275 (2015)
16. Yang, G.Y.C.: Geological Mapping from Multi-Source Data Using Neural Networks. University of Calgary, Geomatics Engineering (1995)
17. LeCun, Y., Bengio, Y., Hinton, G.: Deep learning. Nature **521**(7553), 436–444 (2015)
18. Hochreiter, S., Schmidhuber, J.: Long short-term memory. Neural Comput. **9**(8), 1735–1780 (1997)
19. Donahue, J., Hendricks, L.A., Guadarrama, S., Rohrbach, M., Venugopalan, S., Saenko, K., Darrell, T.: Long-term recurrent convolutional networks for visual recognition and description. In: Proceedings of the IEEE Conference on Computer Vision and Pattern Recognition, pp. 2625–2634 (2015)
20. Abadi, M., Agarwal, A., Barham, P., Brevdo, E., Chen, Z., Citro, C., Corrado, G.S., Davis, A., Dean, J., Devin, M., Ghemawat, S.: Tensorflow: Large-Scale Machine Learning on Heterogeneous Distributed Systems (2016)

Spatiotemporal Variations of Earth Tidal Displacement over Peninsular Malaysia Based on GPS Observations

**Nur Surayatul Atikah Alihan, Dudy Darmawan Wijaya,
Ami Hassan Md Din, Brian Bramanto and Abdullah Hisam Omar**

Abstract Malaysia, which geographically located in the Sunda Plate, is exposed to various types of natural hazards such as land subsidence, landslides, and natural deformation phenomena. This study is conducted to investigate both the spatial and temporal variations of Earth tidal displacement over Peninsular Malaysia using a Kinematic Precise Point Positioning (KPPP) GPS analysis. The continuous GPS observation over a 1-year period has been utilized to observe the diurnal, semi-diurnal, and long-term periods. The KPPP GPS solutions correlate well with prediction from the theoretical Earth tidal model that consists of both ocean tide loading and solid Earth body tide model with average positive correlation 0.9810 and average mean biased −1.2997 cm. Results have widened the understanding of Earth tidal variations in equatorial regions, thus beneficial for Earth tidal modeling and improving quality of space geodetic measurements.

N. S. A. Alihan · A. H. M. Din · A. H. Omar
Geomatic Innovation Research Group (GIG), Geoscience and Digital Earth
Centre (INSTEG), Faculty of Geoinformation and Real Estate,
Universiti Teknologi Malaysia, 81310 Johor Bahru, Johor, Malaysia
e-mail: nsatikah99@gmail.com

A. H. M. Din
e-mail: amihassan@utm.my

A. H. Omar
e-mail: abdullahhisham@utm.my

D. D. Wijaya (✉) · B. Bramanto
Geodesy Research Group, Faculty of Earth Sciences and Technology,
Institute of Technology Bandung, Bandung, Indonesia
e-mail: dudy@gd.itb.ac.id

B. Bramanto
e-mail: brian.bramanto@gmail.com

A. H. M. Din
Institute of Oceanography and Environment (INOS), Universiti Malaysia
Terengganu, Kuala Terengganu, Terengganu, Malaysia

1   Introduction

Since the Earth is an elastic body, the changes of gravitational force imposed by the Sun and the Moon along with the variable weight of the ocean tide trigger the deformation in the solid Earth [1, 2]. These geophysical loadings referred to as solid Earth tide or Earth body tide and ocean tide loading which commonly measured by various instruments that can measure the precise of tidal response such as sensitive gravimeters, strain meter, and tilt observations. However, the rising cost of operation, the less data provided, the sparse distribution of station, and the difficulty of accessing the best location for low-noise site causes inconsistent observations to expose the spatial diversity of the solid Earth tidal field [3]. With the advent of precise space geodetic techniques such as very long baseline interferometry (VLBI) and GPS, there have been several studies that utilize GPS to determine geophysical characteristics of tidal deformations, i.e., Earth tide (the sum of Earth body tide and ocean tide loading), ocean tide loading, and Earth body tide [2–4]. Furthermore, according to Yuan et al. [5], this technology has achieved millimeter-level accuracy in tidal measurements which have better precision than superconducting gravimeter [5].

The deformations of the Earth tide, Earth body tide, and ocean tide loading depend on the location of the site, tidal frequency or constituents and sidereal time. Both Earth tide and Earth body tide have the largest effect compared to the ocean tide loading which it can reach in centimeter (cm) level, about 5 cm in the horizontal plane and 20–30 cm in the height components [6–10]. Nevertheless, the loading effect of the ocean tide loading can be large as the geodetic stations very close to the shore [11]. Agnew [1] verifies that there are three parts of tidal deformations in geophysics. First, the facts about the Earth will be obtained from the measurement of the tidal deformations. Second, the tidal effects against the geodetic measurement can be eliminated by using the models of the tidal deformations. Third, these models can be used to examine the impact of the tidal fluctuations toward the geophysical phenomenon such as earthquakes, tsunami, and volcanic activity [1]. In this study, the GPS observed Earth body tide, ocean tide loading, and Earth tide to investigate the characteristics of Earth tidal displacements over the Peninsular Malaysian region.

2   Observation Data and Processing Method

A total of 45 stations of the Malaysian Real-Time Kinematic GNSS Network (MyRTKnet) operated by the Department of Surveying and Mapping Malaysia (DSMM) along the year 2013 was utilized. This study used Kinematic Precise Point

Positioning (KPPP) method in order to estimate the Earth tidal signal in GPS observations, in which these approaches can determine the position of the GPS stations for every 30 s at the centimeter level of accuracy [3]. An open-source software RTKLIB with Comment User Interface (CUI) is used to process the KPPP GPS data. This software is compatible for scientific research studies in the fields of surveying that require the standard and precise positioning. The processing strategy includes the data preparation of the 30s data sampling with 10° elevation mask angle, the International GNSS Service (IGS) final ephemerides, IGS final clock with sampling rate 30s, and Differential Code Bias (DCB). Subsequently, the measurement model was applied in the KPPP GPS processing such as the satellite and receiver antenna phase variation, phase windup correction, Ionosphere-free linear combination with dual frequency and estimated zenith total delays, and horizontal gradient parameters for troposphere correction. The continuously static integer ambiguities are estimated and resolved using fix and hold strategy. There are three configurations that have been used in the processing to determine the Earth tidal signal contained in the GPS observations. First, the processing strategy is without any Earth tidal correction. Second, the processing strategy is with Earth body tide correction and finally the processing strategy with Earth tide that includes Earth body tides and ocean tide loading correction.

3 The Correlation of the Earth Tide Signals Based on KPPP GPS with the Predictions from Theoretical Earth Tidal Model

This study analyzed about 1-year data, from January 1 until December 31, 2013 for 45 stations of MyRTKnet which is located in Peninsular Malaysia. The Earth body tide observed by the GPS was estimated by the difference of KPPP GPS solutions between the configuration of the processing strategy without any Earth tidal correction and the configuration processing with Earth body tide correction. Meanwhile, the ocean tide loading observation was estimated by the difference of KPPP GPS solutions between the configuration of processing with Earth body tide correction and the configuration processing with both Earth body tide and ocean tide loading correction. The total signal of Earth body tides and ocean tide loading is defined as the Earth tide signal. Then, these Earth body tide and ocean tide loading observations have been validated by the predictions from the theoretical Earth tidal model, including Earth body tide and ocean tide loading model obtained by IERS2003 and NAO.99b, respectively. The IERS2003 model is based on the effective values of Love number and Shida number, whereas the NAO.99b model depends on the assimilation of 5 years altimeter data from the TOPEX/POSEIDON into barotropic hydronomical model with a spatial resolution 0.5 by 0.5° grid [12, 13].

Figures 1, 2, and 3 exhibit the time series of the Earth tidal variation between the Earth tide signal based on GPS observations and the theoretical Earth tidal model
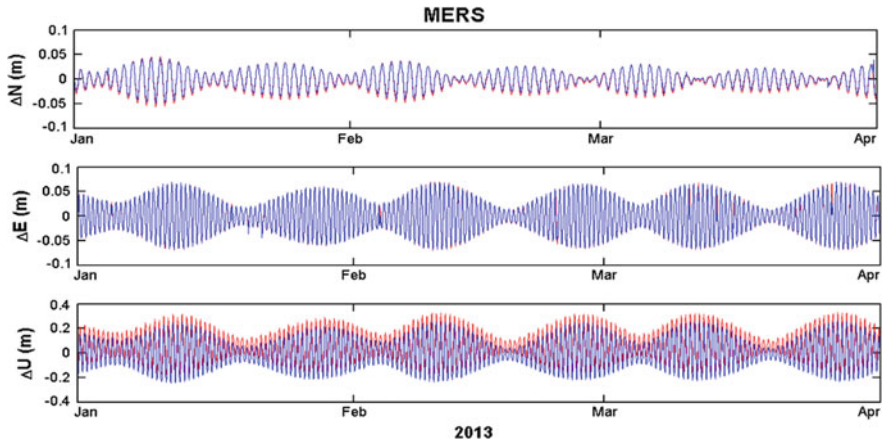
Fig. 1 The time series of Earth body tide variation at the MERS station. Blue and red lines are the Earth body tide observations and the Earth body tide model, respectively
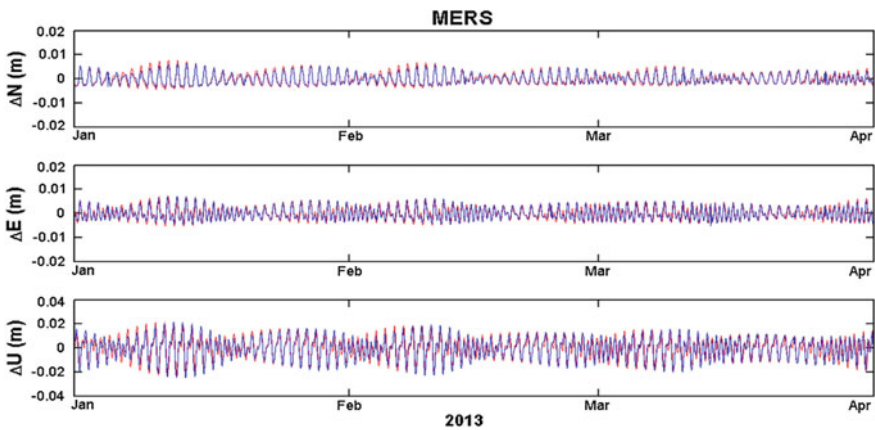
Fig. 2 The time series of ocean tide loading at the MERS station. Blue and red lines are the ocean tide loading observations and the ocean tide loading model, respectively

that consist of the Earth body tide, ocean tide loading, and Earth tide, respectively. The selected station, MERS, has been used with the period from January 1 until March 31, 2013 to easily observe the tidal variation precisely. Based on Figs. 1, 2, and 3, the observation signals from the GPS correspond with the theoretical Earth tidal model at northing, easting, and up components. The amplitude of up component is the largest compared to the northing and easting components which are over 20 cm in both Earth body tide and Earth tide variations, meanwhile over 2 cm in ocean tide loading. The comparison between the observations and theoretical models delineates a similar pattern for all component and it has been analyzed using
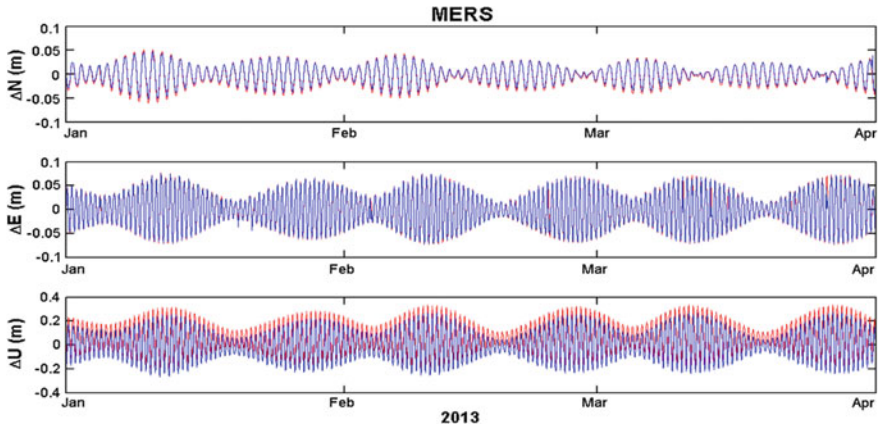
Fig. 3 The time series of Earth tidal variation at the MERS station. Blue and red lines represent the Earth tide observations and the theoretical Earth tidal model, respectively

linear regression methods to determine the correlation coefficient. The statistical comparison between the observations and model is listed in Table 1 in which the computation is based on the observation from the 45 stations along the year 2013.

The coefficient of correlation indicates the strength of the relationship between the observations and models. Generally, the correlation less than 0.5 is defined as weak, while the correlation greater than 0.8 is defined as strong correlation. Based on Table 1, the observations of Earth body tide, ocean tide loading, and Earth tide have a strong correlation with the theoretical model as the value of correlation coefficient is over than 0.9 and close to +1 in northing, easting, and up components. The mean biased was obtained based on the average difference between the theoretical model and observations which around 0.3 cm (N–S), 6×10^{-4} cm (E–W) and −6 cm (Up) at both Earth body tide and Earth tide, while the mean biased of ocean tide loading has the small value around 4×10^{-5} cm (N–S), 2×10^{-5} cm (E–W) and 5×10^{-4} cm (Up). The standard deviation of the difference between all the observations and the theoretical models is smaller in northing and easting components which is less than 1 cm, while the standard deviation in up component is around 1 cm.

3.1 Spectral Analysis

The tidal spectral analysis using Fast Fourier Transform (FFT) method was performed to determine the characteristic of geophysical loadings in GPS observations. Figures 4, 5, and 6 show the spectral analysis of 1 year of the Earth body tide, ocean tide loading, and Earth tide observations from the GPS and the theoretical models at MERS station. Both observations and models obtained the pattern of the periods in the diurnal, semi-diurnal, and long-term constituents.

Table 1 Summary of statistical comparison between the KPPP GPS solutions and theoretical models

Geophysical loadings	Comp.	Correlation coefficient			Mean biased (cm)			Std. deviation (cm)		
		Min	Max	Mean	Min	Max	Mean	Min	Max	Mean
Earth body tide	N–S	0.9912	0.9981	0.9947	0.1030	0.5340	0.3340	0.2626	0.4105	0.3412
	E–W	0.9887	0.9955	0.9926	1.5×10^{-4}	8.9×10^{4}	6.4×10^{4}	0.4476	0.7033	0.5679
	Up	0.9946	0.9982	0.9966	-6.2900	-6.0200	-6.1900	1.0254	1.1774	1.3891
Ocean tide loading	N–S	0.9523	0.9744	0.9604	1.6×10^{-5}	8.1×10^{-4}	4.9×10^{-5}	0.0591	0.1425	0.0865
	E–W	0.9315	0.9578	0.9493	-6.4×10^{-5}	1.2×10^{-4}	2.9×10^{-5}	0.0893	0.1604	0.1121
	Up	0.9407	0.9624	0.9536	8.3×10^{-5}	8.6×10^{-4}	5.5×10^{-4}	0.2347	0.5449	0.3724
Earth tide	N–S	0.9863	0.9978	0.9939	0.0996	0.5386	0.3339	0.2708	0.4847	0.3761
	E–W	0.9774	0.9953	0.9914	7.4×10^{-5}	9.4×10^{-4}	6.7×10^{-4}	0.4899	0.9875	0.6277
	Up	0.9927	0.9982	0.9963	-6.3187	-6.0478	-6.1770	1.0870	2.1437	1.4831
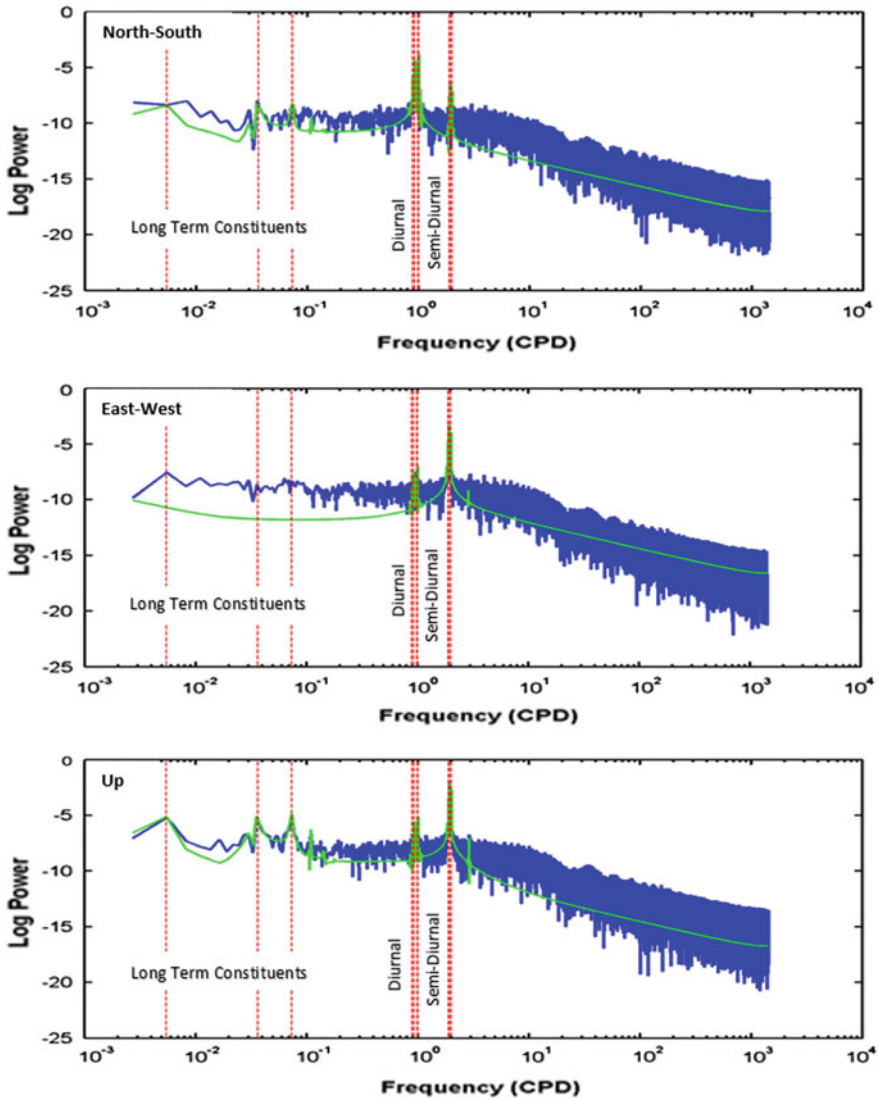
Fig. 4 The spectral comparison between Earth body tide observations (blue) and Earth body tide model (green)

In this study, a total of 11 tidal constituents Ssa, Mm, Mf, Q1, O1, P1, K1, N2, M2, S2, and K2 are well produced by the Earth body tide, ocean tide loading, and Earth tide observations as can be shown in Fig. 7. The summary of amplitude and phase of the primary tidal constituents for all observations are listed in Table 2. These values are based on the average of amplitude and phase for 45 MyRTKnet stations.
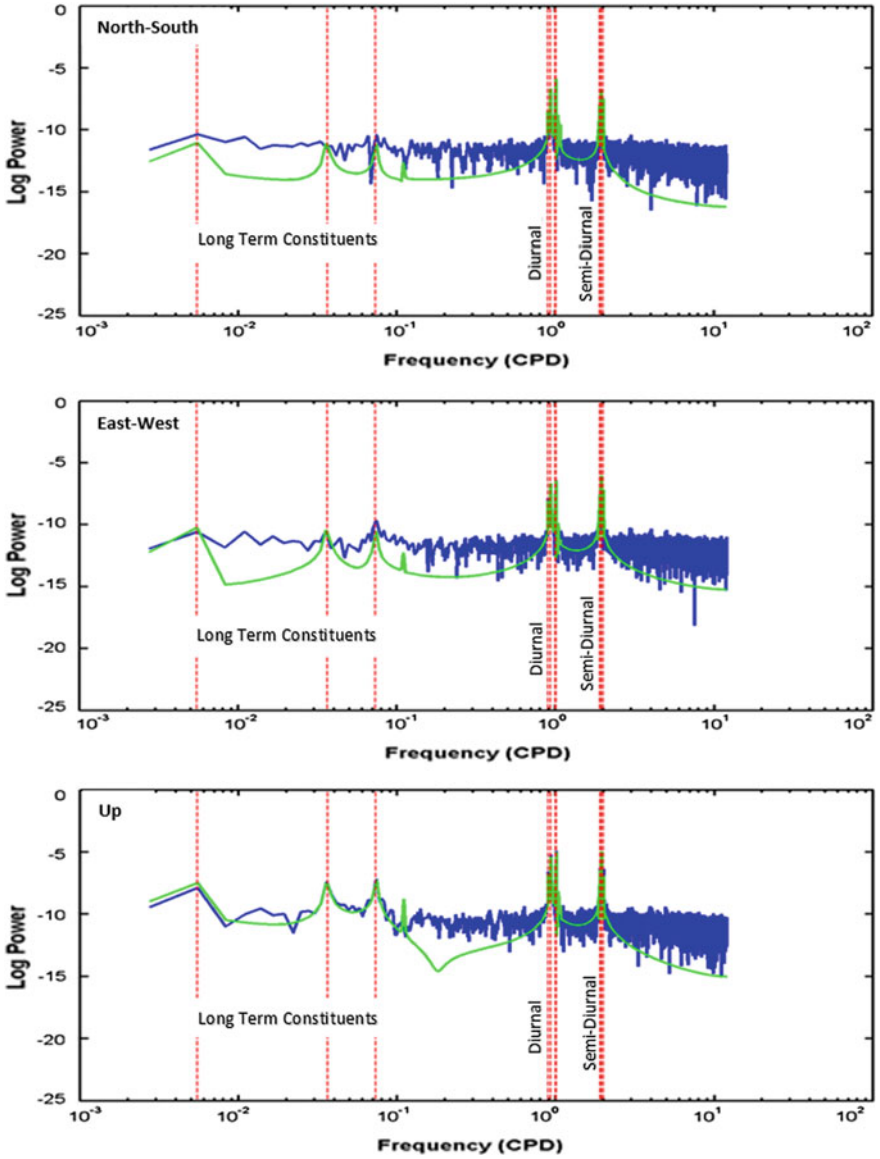
Fig. 5 The spectral comparison between ocean tide loading observations (blue) and ocean tide loading model (green)

Based on Table 2, the dominant signals show in Earth body tide observation is diurnal constituents (Q1, O1, P1, and K1) at northing component with the range amplitude 0.27–2.11 cm, whereas both easting and up components dominated by the semi-diurnal constituents (N2, M2, S2, and K2) with the range amplitude
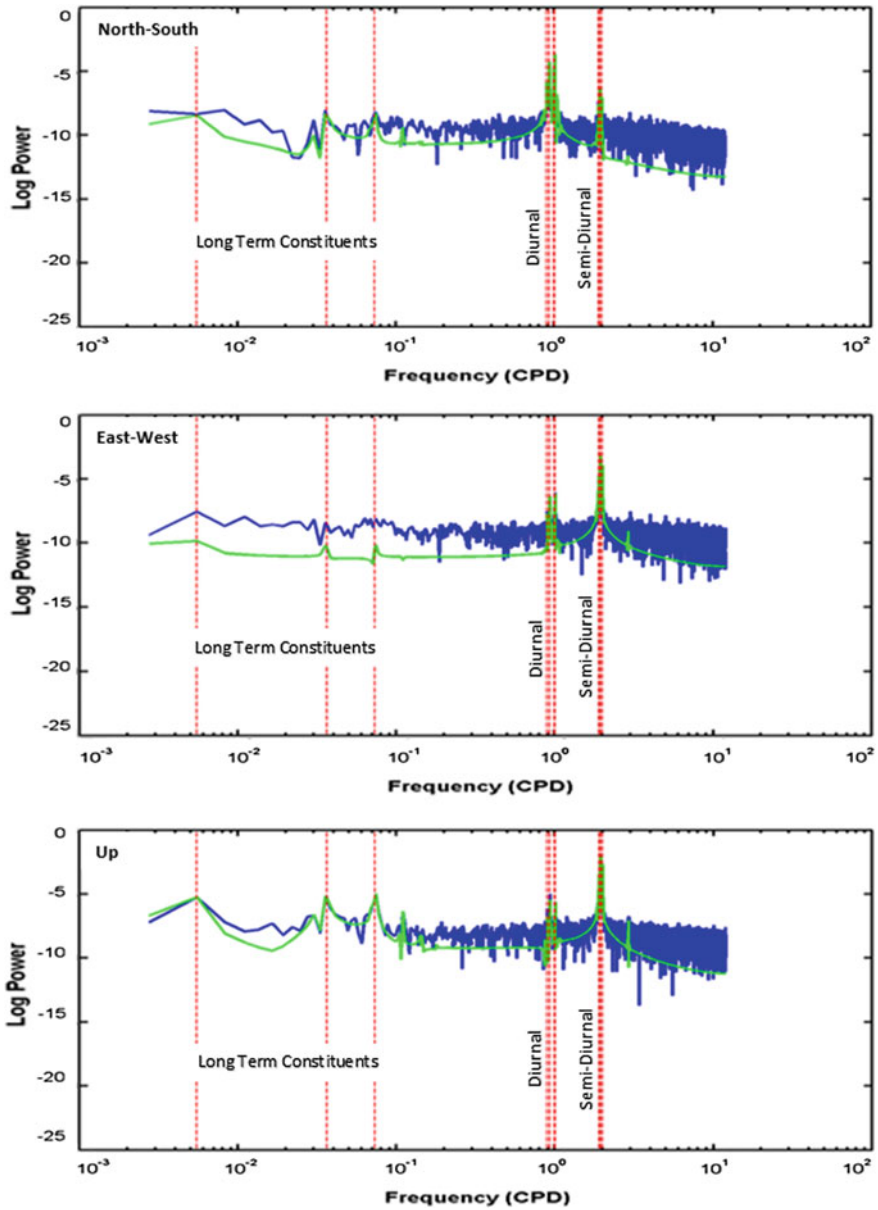
Fig. 6 The spectral comparison between Earth tide observations (blue) and Earth tide model (green)
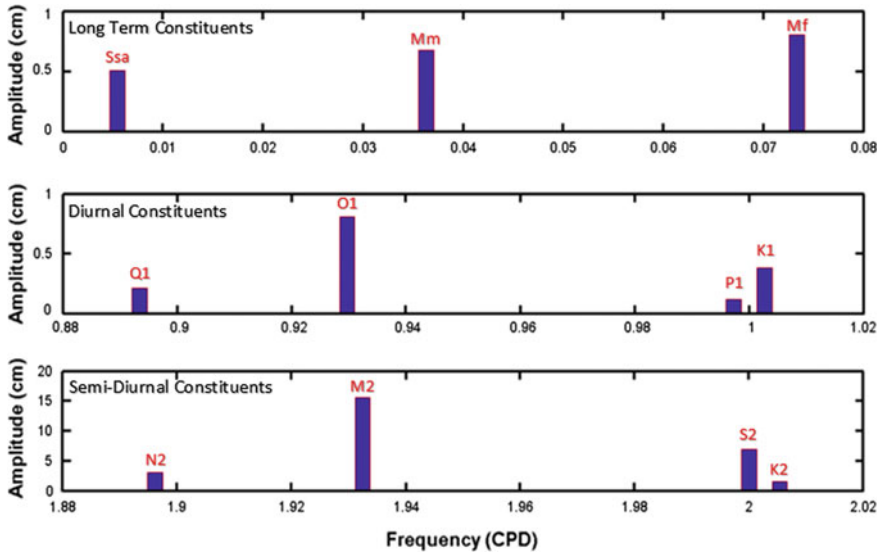
Fig. 7 The Earth tide observations (Up component) consist of a series of partial tides at long-term periods, diurnal periods, and semi-diurnal periods

0.39–4.17 cm and 1.48–14.84 cm, respectively. The diurnal constituents have periods close to 24 h and also be known as the phenomena that occur one cycle per day, while the semi-diurnal constituents have periods close to 12 h and the phenomena of semi-diurnal occur two cycles per day. The significance tidal constituents in ocean tide loading observation are semi-diurnal constituents (M2) at both northing and easting components with the amplitudes 0.22 and 0.25 cm, respectively, while at up component dominated by K1 and M2 constituents with the amplitude 0.64 and 0.56 cm, respectively. Similarly with Earth body tide observation, Earth tide observation delineates the diurnal constituents as the dominant signal at northing component, whereas semi-diurnal constituents at both easting and up components. The M2 constituent is the most dominant at the up component that can reach to 14.84 cm (Earth body tide observation), 0.57 cm (ocean tide loading observation), and 15.27 cm (Earth tide observation).

4 The Spatiotemporal of Earth Tidal Displacement in Peninsular Malaysia

The hourly snapshots of displacement at 45 stations which covers the Peninsular Malaysia have been generated to investigate the spatial and temporal variations of Earth tidal displacement along the year 2013 as shown in Figs. 8 and 9. These displacements contain all the Earth tidal signals including Earth body tide and ocean tide

Table 2 Summary of the amplitude and phase of the 11 major tidal constituents of Earth body tide, ocean tide loading, and Earth tide observations

		Earth body tide			Ocean tide loading			Earth tide		
		N–S	E–W	Up	N–S	E–W	Up	N–S	E–W	Up
Ssa	Amp.	0.0285	0.0392	0.5591	0.0034	0.0113	0.0542	0.0272	0.0660	0.5182
	Phase	−27.6661	−39.1147	165.0801	16.7861	1.7919	−13.9446	−29.9010	−7.2293	165.1521
Mm	Amp.	0.0519	0.0093	0.7376	0.0018	0.0046	0.0637	0.0527	0.0186	0.6801
	Phase	−114.2214	−32.7127	69.8326	−8.0922	−23.4238	−86.4520	−115.4883	56.6535	67.8235
Mf	Amp.	0.0491	0.0191	0.8489	0.0030	0.0117	0.0891	0.0499	0.0376	0.8021
	Phase	163.1403	−4.1703	−18.5872	25.1493	−106.3944	−140.8877	164.1045	−92.1327	−23.8906
Q1	Amp.	0.2697	0.0284	0.1485	0.0116	0.0298	0.1070	0.2609	0.0564	0.2434
	Phase	12.8468	−65.1848	6.5512	−53.6204	−107.8349	42.1188	11.3109	−74.9512	22.6570
O1	Amp.	1.4053	0.0949	0.7658	0.0627	0.1267	0.4886	1.3766	0.2164	1.1064
	Phase	83.1840	−7.6903	85.4877	34.5549	−21.5377	143.9422	81.3332	−14.0987	110.1912
P1	Amp.	0.7431	0.0530	0.3787	0.0454	0.0579	0.1990	0.7519	0.1061	0.2863
	Phase	−100.7370	163.0687	−105.3407	−86.3626	−124.4300	30.8204	−100.9802	33.2936	−65.8301
K1	Amp.	2.1055	0.1494	0.9461	0.1350	0.1819	0.6434	2.1263	0.2971	0.6658
	Phase	−110.3942	162.7421	−109.1919	−88.2800	−153.1626	30.8209	−109.4321	−132.9671	−59.4507
N2	Amp.	0.0633	0.7999	2.8745	0.0506	0.0504	0.1270	0.0833	0.7922	2.9364
	Phase	80.3060	168.2905	−101.5628	95.3805	77.5451	−122.4462	117.3444	165.3938	−103.5904
M2	Amp.	0.2850	4.1665	14.8369	0.2153	0.2517	0.5653	0.2923	4.2332	15.2731
	Phase	130.8511	−138.7168	−18.5672	−120.5240	16.2943	−71.1237	−2.7935	−141.2510	−49.3674
S2	Amp.	0.1275	1.8626	6.7403	0.0833	0.0907	0.1894	0.0687	1.8936	6.8674
	Phase	−19.9127	66.6442	157.0485	133.6344	77.2648	32.1988	36.7328	67.3184	157.2069
K2	Amp.	0.0243	0.3976	1.4798	0.0541	0.0649	0.0656	0.0494	0.4214	1.5195
	Phase	123.0963	−151.0415	−58.4875	−82.7865	−95.9216	−24.0920	−37.2946	−119.1241	−58.2626

Amp Amplitude of the observations in unit centimeter (cm). *Phase* Phase of the observations in unit degree of angle
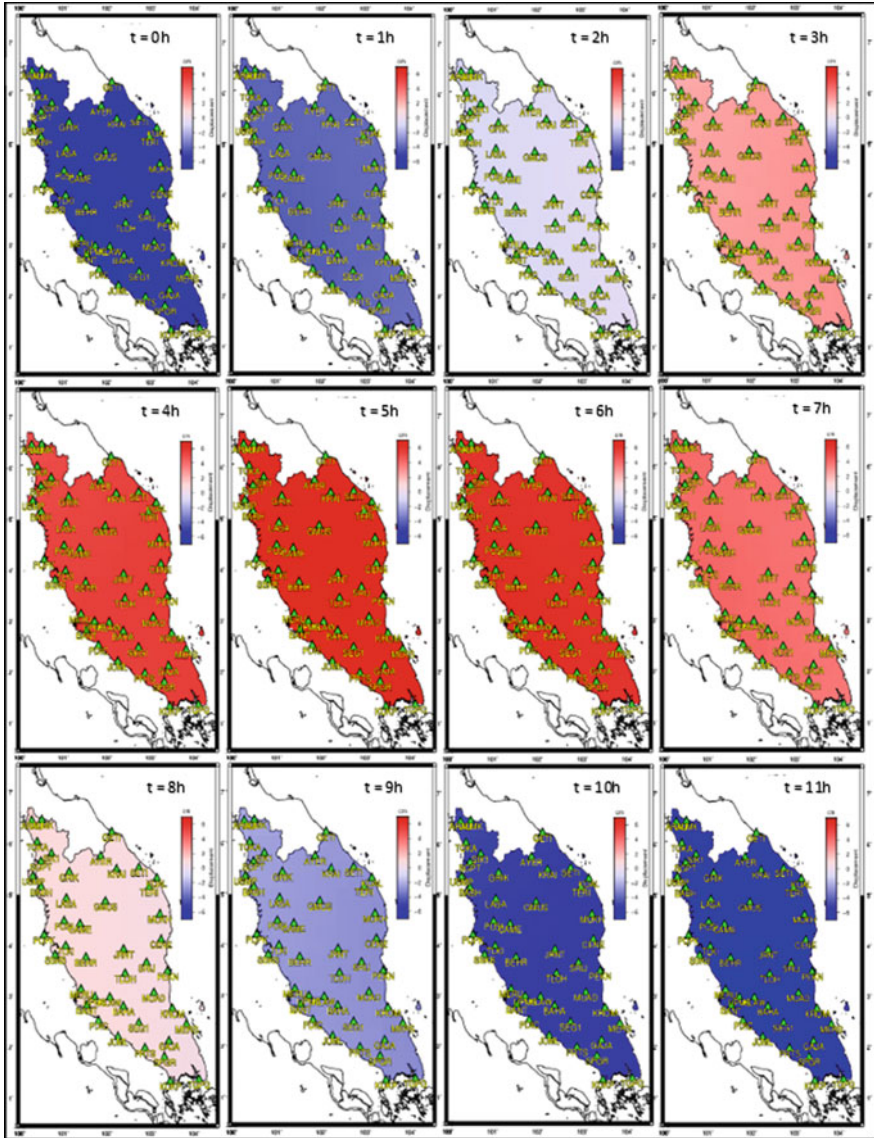
Fig. 8 Hourly Earth tide displacement from 0 h until 11 h on the Peninsular Malaysia. Blue and red colors represent the subsidence and uplift of MyRTKnet stations, respectively

loading, and it have been focused on up component as the up component is more affected by the Earth tide signals. The computation of hourly displacement is based on the average displacement of 1-year data. Based on Figs. 8 and 9, the MyRTKnet stations are displaced around −6 cm at time 0 h, around −3 cm at time first hour, around −1 cm at time second hour and around 2 cm at time third hour.
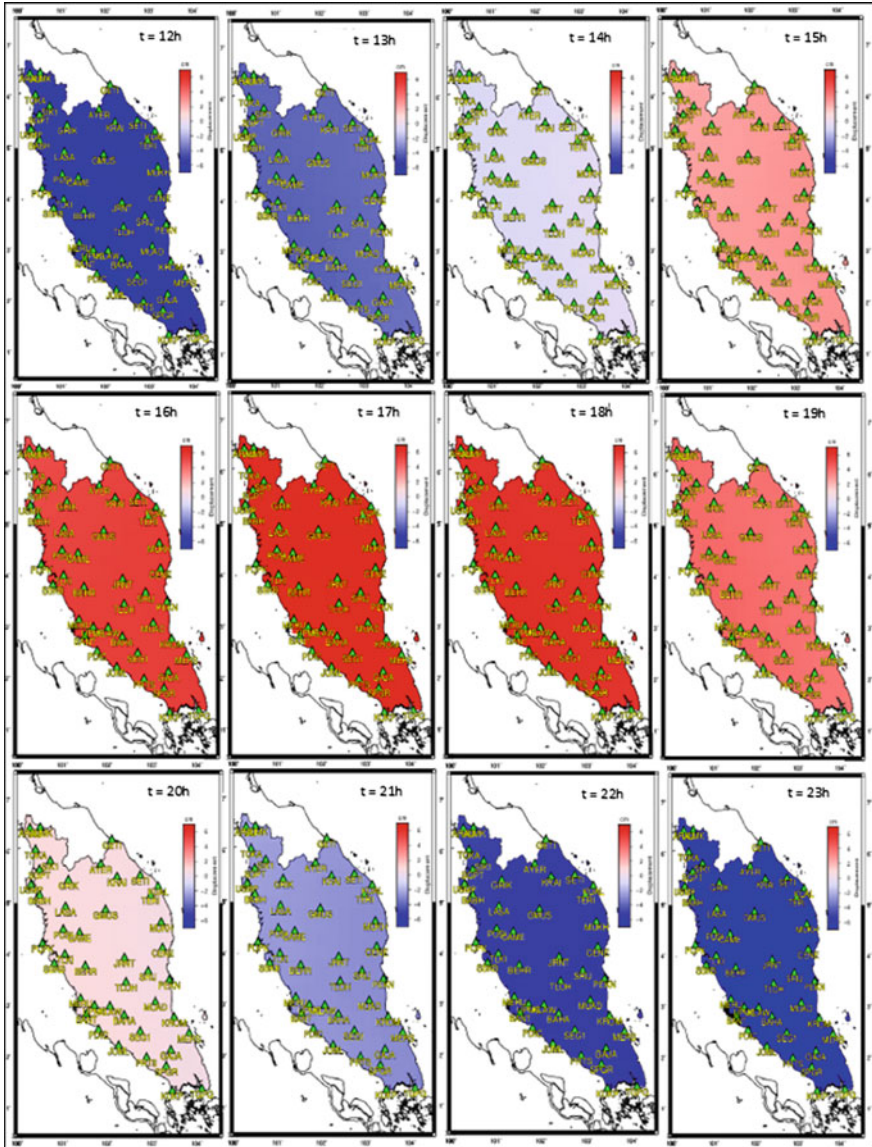
Fig. 9 Hourly Earth tide displacement from 12 h until 23 h on the Peninsular Malaysia. Blue and red colors represent the subsidence and uplift of MyRTKnet stations, respectively

Then, the stations are uplift at time 4 until time 6 h with displacement around 4–6 cm and the stations are slightly subsidence at time 7 until time 11 h with displacement around 3 cm until −6 cm. The Earth tide displacement at time 12 until 23 h shows the same pattern of variation with the previous time and it was indicated that the Earth tide displacements dominated by semi-diurnal constituents at up component.

5   Conclusion

In this study, the spatiotemporal of Earth tide response was generated in Peninsular Malaysia. The KPPP GPS solutions correlate well with the theoretical Earth tidal model that includes both Earth body tide and ocean tide loading. The diurnal, semi-diurnal, and long-term constituents are well detected by the observations. From the results, all the observations dominated by the semi-diurnal constituents at up components as the up component has the largest effect of Earth tidal signals that can reach until 20–30 cm.

References

1. Agnew, D.C.: Treatise On Geophysics: Geodesy, vol. 3. Elsevier, USA (2007)
2. Bos, M.S., Penna, N.T., Baker, T.F., Clarke, P.J.: Ocean tide loading displacements in western Europe: 2. GPS-observed anelastic dispersion in asthenosphere. J. Geophys. Res.: SolidEarth **120**, 6540–6557 (2015)
3. Ito, T., Okubo, M., Sagiya, T.: High resolution mapping of earth tide response based on GPS data in Japan. J. Geodyn. 253–259 (2009)
4. Vey, S., Calais, E., Llubes, M., Florsch, N., Woppelmann, G., Hinderer, J., Amalvict, M., Lalancette, M.F., Simon, B., Duquenne, F., Haase, J.S.: GPS measurements of ocean loading and its impact on zenith tropospheric delay estimates: a case study in Brittany, France. J. Geodesy **76**, 419–427 (2002)
5. Yuan, L., Chao, B.F., Ding, X., Zhong, P.: The tidal displacement field at Earth's surface determined using global GPS observations. J. Geophys. Res.: Solid Earth **118**, 2618–2632 (2013)
6. Bastos, L., Bos, M., Fernandes, R.: Sciences of Geodesy-I: Advances and Future Directions. Springer, New York (2010)
7. Cai, C.: Precise Point Positioning Using Dual-Frequency GPS and GLONASS Measurements. Degree of Master Science. Thesis/Dissertation. Department of Geomatics Engineering, University of Calgary, Alberta (2009)
8. Héroux, P., Kouba, J.: GPS precise point positioning using IGS orbit products. Phys. Chem. Earth Part A. **26**, 573–578 (2001)
9. Schureman, P.: Manual of Harmonic Analysis and Prediction of Tides. Special Publication No. 98. U.S. Department of Commerce, Coast and Geodetic Survey (1971)
10. Zheng, Y.: Generation of Network-Based Differential Corrections for Regional GNSS Services. Degree of Doctor of Philosophy. Thesis/Dissertation. Faculty of the Built Environment and Engineering, Queensland University of Technology, Australia (2006)

11. Pagiatakis, S.D.: Ocean Tide Loading on a Self-Gravitating, Compressible, Layered, Anistropic, Viscoelastic and Rotating Earth with Solid Inner Core and Fluid Outer Core. Technical Report. Department of Surveying Engineering, University of New Brunswick, Fredericton, N. B. Canada (1988)
12. Matsumoto, K., Takanezawa, T., Ooe, M.: Ocean tide models developed by assimilating TOPEX/POSEIDON altimeter data into hydro-dynamical model: a global model and regional model around Japan. J. Oceanogr. **56**, 567–581 (2000)
13. McCarthy, D.D., Petit, G.: IERS Conventions (2003). Volume 32 of IERS Technical Note. Defense Technical Information Center (2004)

Optimized Hierarchical Rule-Based Classification for Differentiating Shallow and Deep-Seated Landslide Using High-Resolution LiDAR Data

Mustafa Ridha Mezaal, Biswajeet Pradhan, H. Z. M. Shafri, H. Mojaddadi and Z. M. Yusoff

Abstract Landslide is one of the most devastating natural disasters across the world with serious negative impact on its inhabitants and the environs. Landslide is considered as a type of soil erosion which could be shallow, deep-seated, cut slope, bare soil, and so on. Distinguishing between these types of soil erosions in dense vegetation terrain like Cameron Highlands Malaysia is still a challenging issue. Thus, it is difficult to differentiate between these erosion types using traditional techniques in locations with dense vegetation. Light detection and ranging (LiDAR) can detect variations in terrain and provide detailed topographic information on locations behind dense vegetation. This paper presents a hierarchical rule-based classification to obtain accurate map of landslide types. The performance of the hierarchical rule set classification using LiDAR data, orthophoto, texture, and geometric features for distinguishing between the classes would be evaluated. Fuzzy logic supervised approach (FbSP) was employed to optimize the segmentation parameters such as scale, shape, and compactness. Consequently, a correlation-based feature selection technique was used to select relevant features to develop the rule sets. In addition, in other to differentiate between deep-seated cover under shadow and normal shadow, the band ration was created by dividing the intensity over the green band. The overall accuracy and the kappa coefficient of the hierarchal rule set classification were found to be 90.41 and 0.86%, respectively, for site A. More so, the hierarchal rule sets were evaluated using another site named site B, and the overall accuracy and the kappa coefficient were found to be 87.33 and 0.81%, respectively. Based on these results, it is demonstrated that the proposed methodology is highly effective in improving the classification accuracy.

M. R. Mezaal · B. Pradhan (✉) · H. Z. M. Shafri · H. Mojaddadi
Z. M. Yusoff
Department of Civil Engineering, Faculty of Engineering,
Universiti Putra Malaysia, 43400 Serdang, Selangor, Malaysia
e-mail: Biswajeet24@gmail.com; Biswajeet.Pradhan@uts.edu.au

B. Pradhan
Faculty of Engineering and Information Technology,
School of Systems, Management and Leadership,
University of Technology Sydney, Building 11,
Level 06, 81 Broadway, PO Box 123, Ultimo, NSW 2007, Australia

The LiDAR DEM data, visible bands, texture, and geometric features considerably influence the accuracy of differentiating between landslide types such as shallow and deep-seated and soil erosion types like cut slope and bare soil. Therefore, this study revealed that the proposed method is efficient and well-organized for differentiating among landslide and other soil erosion types in tropical forested areas.

Keywords Landslide · GIS · Fuzzy logic · LiDAR · Remote sensing

1 Introduction

Landslide, a destructive natural disaster, causes serious damage to lives and properties in many parts of the world. Landslides are naturally widely distributed and greatly endanger the safety and property of inhabitants. The main factors that trigger landslide are intense rainfall, volcanic eruption, earth tremor, changes in water level, and snowmelt. The occurrence of these natural disasters calls for the need for landslide inventory maps. The inventory maps could help in acquiring information such as magnitude of a landslide in an area, perform the initial steps in analysing its susceptibility, hazard, and risk of the landslide, study the patterns, distributions, shape, and type of landslides, and the evolution of landscape affected by landslides [1–4]. Rapid vegetation growth in tropical regions poses a serious challenge in producing a landslide inventory map, because it is hard to ascertain landslide location using the conventional recognition techniques due to the effect of vegetation cover, thus, the need for a rapid and accurate approach. However, visibility in heavy vegetation is a challenging issue in geomorphical mapping in tropical region [5]. Several techniques exist for detecting surface processes and fault reactivations in remote sensing [6]. Light detection and ranging (LiDAR) is a relatively new technique of remote sensing compared with other methods [2]. Compared to traditional techniques, LiDAR data makes use of active laser transmitters and receivers to obtain data of elevations more rapidly and accurately [6]. Normally, LiDAR data offers better performance over other remote sensing data due to its ability to penetrate areas with dense vegetation and provide important information on terrain with a high point density [2]. Useful information regarding topographic feature can be obtained by using high-resolution LiDAR-derived DEM. It depicts the ground surface and provides important information landslides covered by vegetation [7]. According to Whitworth et al. [8], LiDAR is a powerful and promising tool for detecting landslides and map feature under dense vegetation. Furthermore, LiDAR imagery has the capacity to study many small landslides that occurred in the past and present, and its effectiveness in mapping landslides formed by naked slopes and its vulnerability to future landslides [9]. The identification of three parameters is necessary for multiresolution segmentation algorithm namely, shape, scale, and compactness. However, it is time-consuming to determine these parameters using trial-and-error method [2]. To determine the optimal parameters automatically, various optimization techniques have been proposed and applied to

multiresolution segmentation algorithms [10–13]. Pradhan et al. [2] proposed a new optimization technique refers to as Taguchi method for landslide identification. In this work, the segmentation parameter optimization known as fuzzy-based segmentation parameter [FbSP] optimizer developed by Zhang et al. [14] was utilized to produce the optimized parameters at different segmentation levels. Depending on its movement characteristics and volume, landslides are classified as shallow or deep-seated [1]. In any case, both types differ in terms of volume, size, and damage influence, even though it is difficult to evaluate landslide mass volume [15]. Large-scale deep-seated landslides mostly result from the interaction between natural denudation processes and long-term rainfall while the shallow landslides are associated with short high-intensity rainfalls [15]. Several research works have been carried out to identify different landslide types using LiDAR data [1, 6, 16–21]. Valuable and significant information have been obtained for active geological process like landslide that reshapes topography. Therefore, it is highly imperative to differentiate between various types of landslides by investigating the geomorphological development of hillsides and the mitigation of landslide hazards [22]. Recently, Pradhan and Mezaal [23] differentiated between shallow and deep-seated landslides based on optimizing rule set.

Li et al. [24] reported that irrelevant features can be removed effectively using feature selection algorithms in order to improve the accuracy of classification. Overfitting may result when dealing with large feature numbers due to irrelevant input feature [24]. In contrast, the selection of a small possibly minimal feature set would result in the best possible classification [25]. Important feature should be selected to improve the results of landslide identification in a particular area [25]. According to Van Westen et al. [3], selecting relevant feature is highly imperative in distinguishing between landslides and non-landslides and in classifying them. Improved accuracy is observed after reducing feature [26]. Investigations have shown that the feature selection techniques have been used for identifying the locations of landslide and higher performance can be achieved with relevant feature [25–29]. A hierarchical algorithm can be efficient and robust when sample data and relevant features are incorporated in the classification, and delineation of image objects within a number of different scales [26]. Kurtz et al. [29] proposed a top-down hierarchical region-based framework to segment and classify multiresolution images from the lowest to the highest resolution, and extract complex patterns from VHR images. In 2014, Kurtz et al. [29] introduced a hierarchical approach for landslide detection from multiresolution sets of images. The results showed the efficiency of the proposed method with different hierarchical levels. In the same year, Rau et al. [18] proposed the use of three types of remote sensing data, multilevel segmentation, and hierarchical classification scheme. It was inferred that this approach could optimize the accuracy of landslide recognition and user accuracy.

However, due to the limitation of the research knowledge, none of the aforementioned studies have used LiDAR data only in hierarchical approach to differentiate types of landslide. Therefore, this paper employs only very high-resolution LiDAR data in hierarchical rule-based classification to accurately discriminate

between landslide types. In other to achieve this objective, it is imperative to optimize the multiresolution segmentation parameters and select the most relevant features from the high-resolution airborne laser scanning data.

2   Study Area

Cameron Highlands is one of the several rainforest areas characterized by a dense vegetation cover subject to landslide re-occurrences. This region encompasses an area of 26.7 km^2 and is located in the northern part of Peninsular Malaysia. It is situated at a latitude range of 4° 26′ 09″N–4° 27′ 30″N and a longitude range of 101° 23′ 02″E–101° 23′ 47″E (see Fig. 1). The average annual rainfall in the area is recorded to be approximately 2,660 mm with an average temperature of approximately 24 and 14 °C during daytime and nighttime, respectively. About 80% of the area is forest and has relatively flat landforms in the range of 0°–80°.

Figure 1 shows the two sites selected for analysis in this proposed method. In this model, site "A" was used to develop the proposed method for differentiating among two types of the landslide and other soil erosion, while site "B" was used to evaluate the hierarchal developed rule sets putting all features in both sites into considerations for avoidance of missing classes.

3   Methodology

Several steps were conducted in this study, which includes the LiDAR data and landslide inventories preprocesses to eliminate the noise and outliers from the LiDAR point cloud in preparation for the dataset in the subsequent stages. LiDAR point clouds were used to generate high-resolution (0.5 m) DEM and then drive other LiDAR-derived products. The LiDAR DEM data are slope, hillshade, aspect, and so on. Intensity is one of the most important attributes of LiDAR data. Height feature was derived by digital surface model (DSM) from digital elevation model (DTM). Afterward, LiDAR-derived products and orthophotos were combined by correcting their geometric distortions by integrating them into a coordinate system, which is then prepared in a GIS for feature extraction. Subsequently, the FbSP optimizer developed by Zhang et al. [14] was used to select the parameters such as scale, shape, and compactness at different levels of segmentation. A stratified random method was selected to obtain the training samples and the relevant features were obtained by using correlation feature selection algorithm. In this work, the hierarchical rule-based classification was applied to develop the rule sets in line with data obtained from site "A". The difference between four types of soil erosion
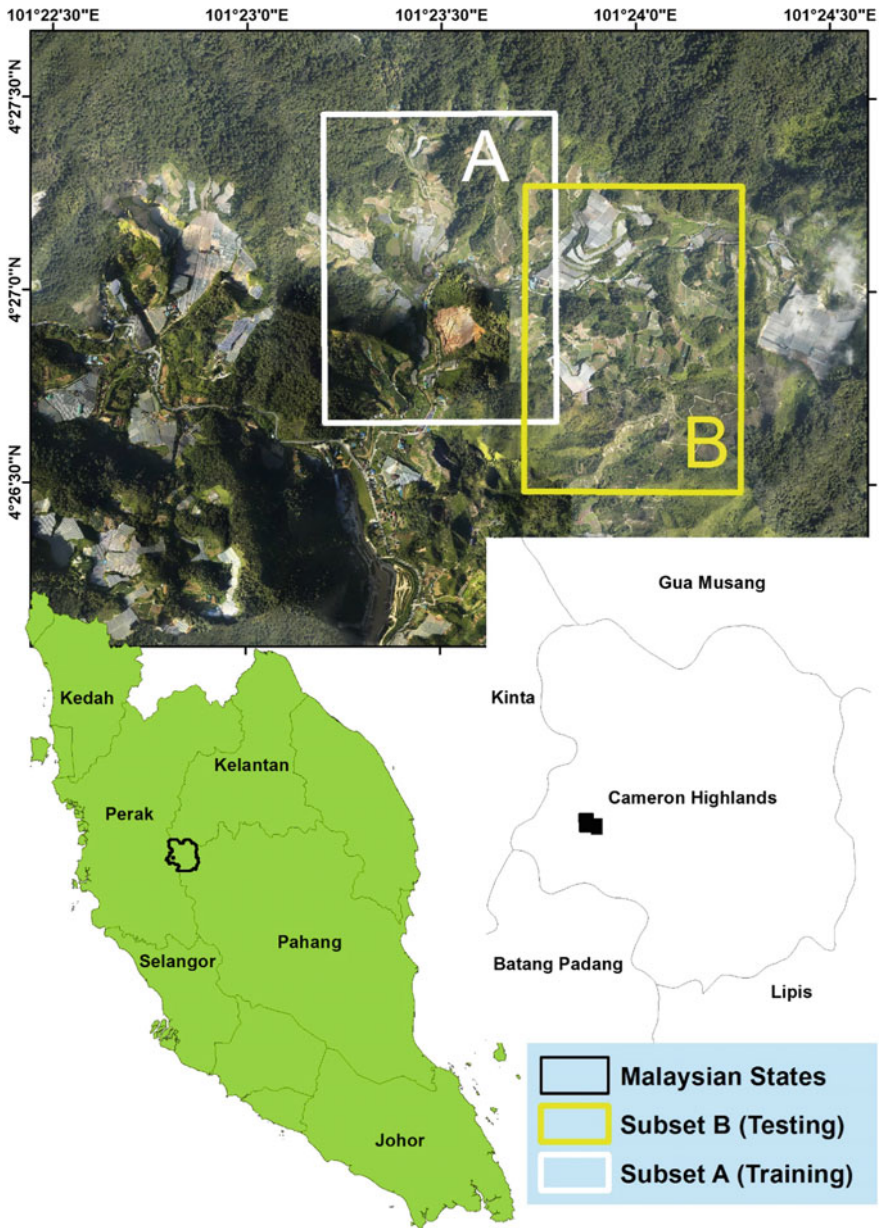
Fig. 1 Locations of the site A and B in Cameron Highland, Malaysia

namely bare soil, cut slope, shallow, and deep-seated was obtained. The evaluation of hierarchal developed rule sets was carried out in another site "B". The results were validated using confusion matrix for examining the classification map based on the reliability and efficiency (see Fig. 2).
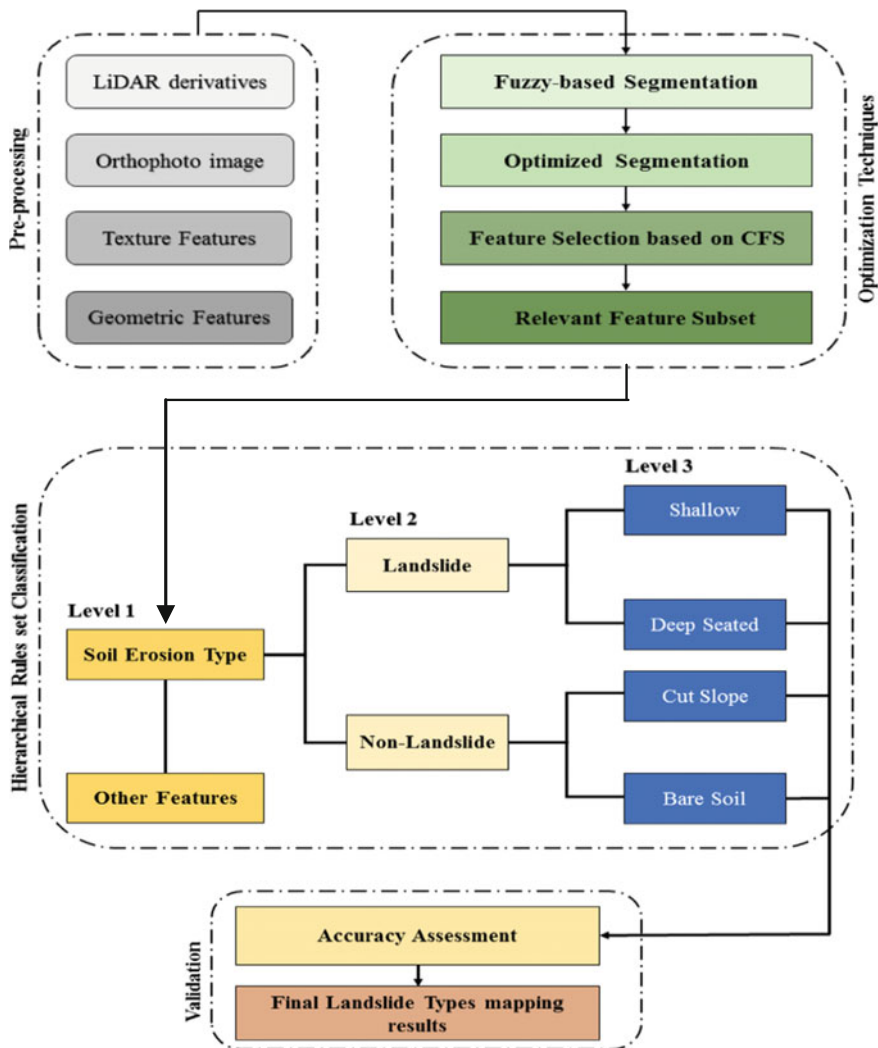
Fig. 2 The flowchart illustrates the overview of the proposed method

3.1 Data Used

The LiDAR point cloud data were collected in an area of 26.7 km² over the Ringlet and surrounding area of the Cameron Highlands at a flying height of 1510 m. The LiDAR data were captured on January 15, 2015. The point density was 8 points per square meter, and the pulse rate frequency was 25,000 Hz. The absolute accuracy of the LiDAR data must be restricted to meet the root-mean-square errors of 0.15 and 0.3 m in the vertical and horizontal axes, respectively. The same system for the

collection of LiDAR point cloud data in the study area was used to collect the orthophotos. A DEM with 0.5 m spatial resolution was interpolated from the LiDAR point clouds after the non-ground points were removed using inverse distance weighting (IDW), with GDM2000/Peninsula RSO as the spatial reference. Subsequently, the LiDAR-based DEM was used in generating a number of derived layers to facilitate the detection of landslides and their characteristics [30]. The slope is considered an important factor of land stability because of its direct impact on landslide phenomenology [31]. Moreover, the slope is the principal factor affecting the landslide occurrences [32]. Hillshade map provides a good image showing terrain movement, and this map facilitates landslide mapping [33]. The accuracy of DEM accuracy and its capability to represent the surface are affected not only by terrain morphology and sampling density but also by the interpolation algorithm [34]. The texture and geometric features contributed to increase the accuracy of landslide identification [24]. In addition, the intensity derived from the LiDAR data and texture significantly affects the accuracy of differentiating shallow from deep-seated landslides [23]. In this research, hillside, intensity, height (nDSM), slope, and aspect were derived from the LiDAR–DEM data (Fig. 3), orthophotos, and texture features and used for differentiating between the landslides types (i.e., shallow and deep-seated) and other types of soil erosion (cut slope and bare soil).

3.2 Image Segmentation

Image segmentation is the initial and prerequisite step in object-based analyses because it determines the size and shape of image objects [35]. The selection of the appropriate parameters of image segmentation relies on the selected application, the environment under analysis, and the underlying input imagery [35]. In segmentation, the image is generally subdivided into homogeneous regions [2]. The multiresolution segmentation algorithm is extensively used in various studies on eCognition software [35]. Three parameters (scale, shape, and compactness) should be identified in this algorithm. The values of these parameters can be determined using the traditional trial-and-error method, which is time-consuming and demands extensive work [2]. Therefore, various automatic and semiautomatic methods to identify the optimal parameters have been exploited [10–12, 31]. The Taguchi optimization method proposed by Pradhan et al. [2] and the fuzzy logic supervised approach presented by Zhang et al. [14] are among the advanced methods used for the automatic selection of segmentation parameters. Nevertheless, delineating image objects at various scales remains a challenge. Furthermore, not all selected features are completely exploited using a particular segmentation scale. Accordingly, an automatic method should be directly implemented.
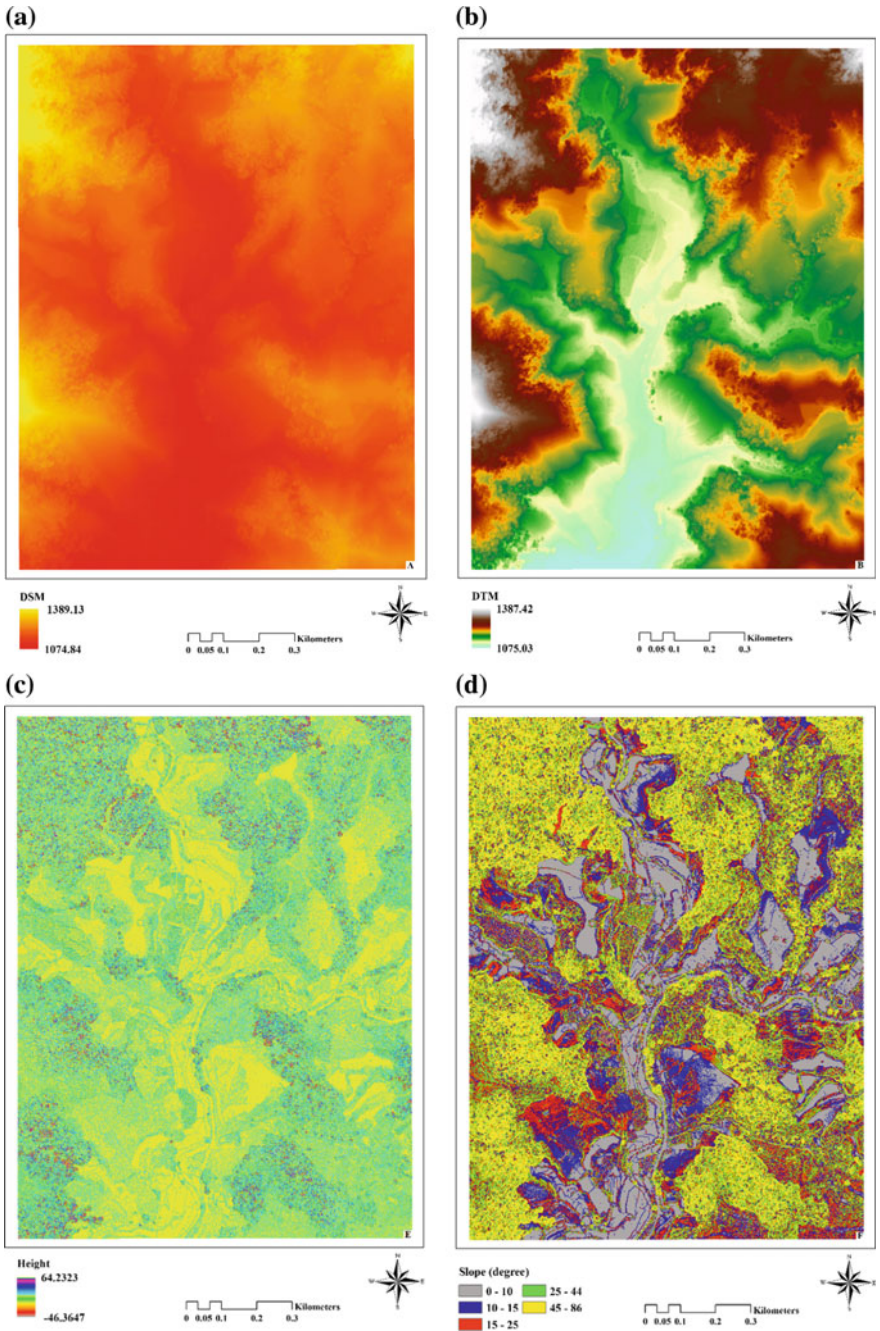
Fig. 3 Shows LiDAR-derived data **a** DSM, **b** DTM, **c** Intensity, **d** Hillshade, **e** Height, **f** Slope, **g** Aspect

(e)

Intensity
65535

0

0 0.05 0.1 0.2 0.3 Kilometers

(f)

Hillshade
254

0

0 0.05 0.1 0.2 0.3 Kilometers

(g)

Aspect
Flat | East | Southwest
North | Southeast | West
Northeast | South | Northwest
North

0 0.05 0.1 0.2 0.3 Kilometers
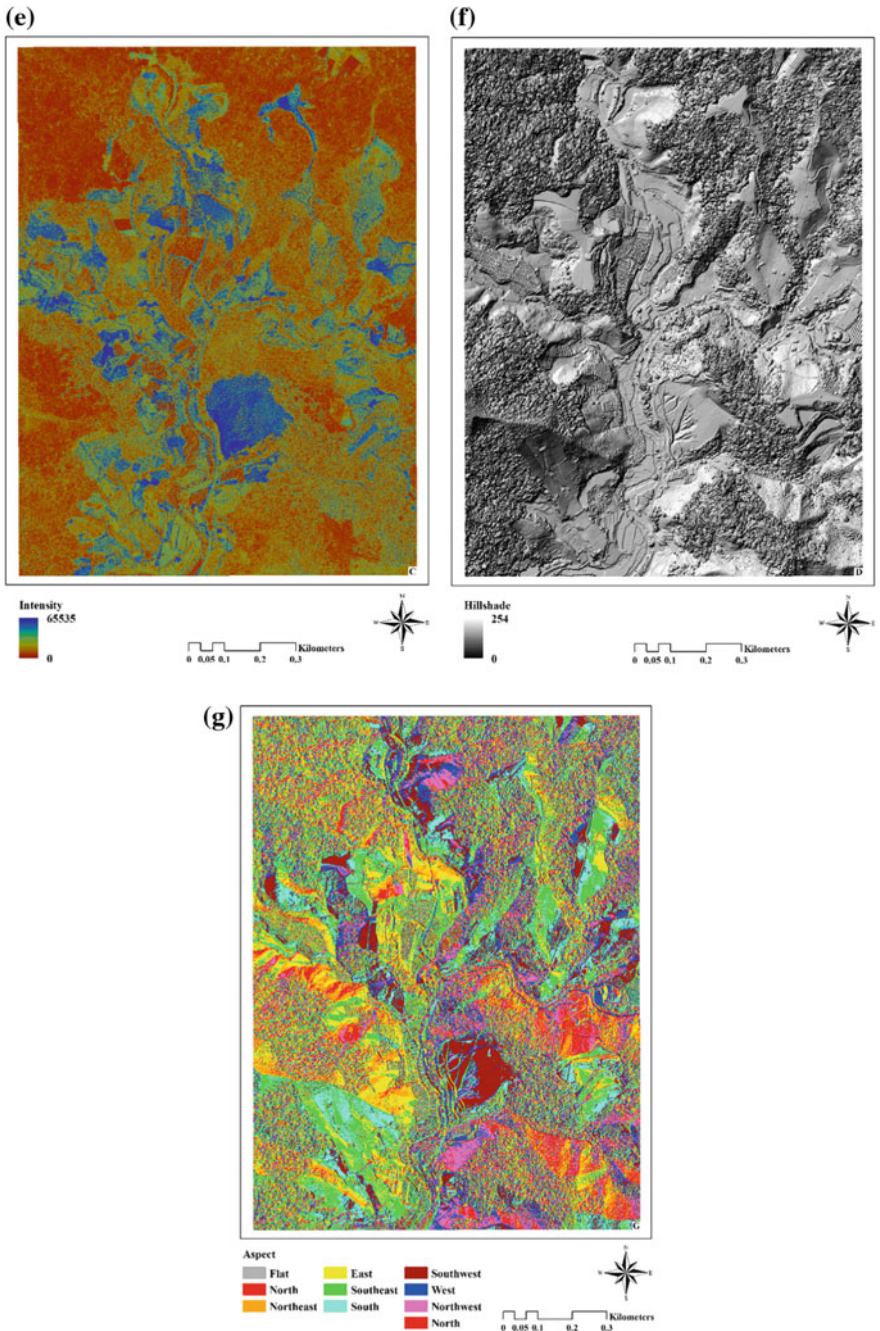
Fig. 3 (continued)

3.3   Correlation-Based Feature Selection

Selecting only the relevant attributes enhances the quality of landslide identification and classification in a particular area [25], working with a large number of features generates several problems. First, the algorithms are slowed down because numerous resources have to be considered [25]. Second, a higher number of features than the number of observations results in low accuracy. Third, irrelevant input features may lead to overfitting [24]. Therefore, important features should be selected to improve the accuracy of the feature extraction results. In the current study, CFS was performed using Weka 3.7 software to select the relevant features. The method established by Li et al. [36] was adopted in this study. The CFS algorithm was applied to all the LiDAR-derived data and orthophoto and the additional texture and geometric features. CFS was performed for determining the feature subsets to be used for developing the rules for differentiating landslide and non-landslide types. The CFS method has two basic steps: ranking the initial features and eliminating the least important features through an iterative process.

4   Results

4.1   Optimized Segmentation Based on FbSP Optimizer

The FbSP optimizer was used for optimizing the parameters of multiresolution segmentation such as scale, shape, and compactness. The optimized parameters contributed in distinguishing between landslides types (shallow and deep-seated) and non-landslides (bare soil and cut slope). It rapidly increases the classification accuracy to the highest level. These parameters improve the delineation of the segmentation boundaries in the classes. The use of this optimized segmentation parameters also enables us to exploit the spatial and textural features in differentiation of the landslide and non-landslides types. In the proposed method, an accurate segmentation was necessary to perform the preceding steps. The optimized segmentation parameters were identified using adequate number of training samples that include landslide and non-landslide classes. The selected values for the three parameters, for instance, the initial input parameters in the FbSP optimizer were 50, 0.1, and 0.1 for scale, shape, and compactness, respectively, as shown in Fig. 4a. After little iteration (3–5 iterations), the optimal results obtained by the FbSP optimizer were 70, 0.4, and 0.5, for scale, shape, and compactness, respectively, as illustrated in Fig. 4b. The results of segmentation reveal that the boundaries of landslide objects are delineated correctly in site A and the rule sets are facilitated and can be transferred to other site B.

Initial Segmentation   Optimized Segmentation
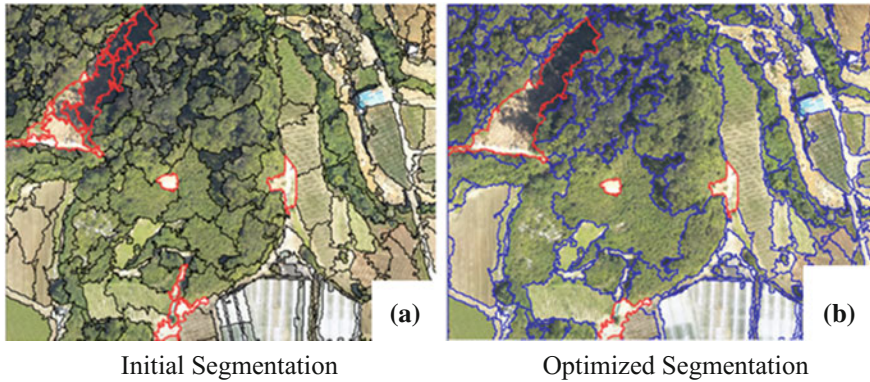
Fig. 4 Shows the process of optimization segmentation

4.2 Feature Selection Using CFS Method

Table 1 shows the results of a feature selection based on CFS algorithm for site A at scale of 70. The features input include LiDAR-derived DEM, orthophoto, texture, and geometric features. In this paper, the selection of the optimal combination was carried out based on several experimental steps. The experiment commenced from 2 to 100% of the 50 features and the optimal features were obtained at 100 iterations in accordance with the procedure proposed by Sameen et al. [37]. The result showed that the high classification accuracy was achieved at 10 features out of the 50 selected features. In the other features, the results indicated that there is no significance in the differentiation between the classes. It also revealed that using irrelevant features could result in low accuracy. Table 1 shows that the features such as intensity, GLCM Homogeneity, and mean red are ranked higher among others, even though LiDAR data, spectral, and geometric feature also contribute in distinguishing between the landslide and non-landslides types.

Table 1 Features selected based on CFS algorithm

Feature	Iteration	Rank
Intensity	20	1
GLCM homogeneity	18	2
Mean red	20	3
Slope	20	4
Height	17	5
Length/width	20	6
Mean green	20	7
Mean blue	18	8
Area	15	9
Mean DTM	20	10

4.3 Developed Rule Sets Based on Hierarchal Classification

Figure 5 shows the structure of soil erosion types such as landslide (i.e., shallow and deep-seated) and non-landslide (i.e., cut slope and bare soil). It is problematic to differentiate between the abovementioned classes due to their similarity in characteristics. Using trial-and-error method to optimize and develop, rule set is time-consuming and optimum rule sets are difficult to identify. The rule sets were automatically developed using data mining algorithm that refers to DT algorithm and was implemented in MATLAB R2015b. The advantage of using the MATLAB software is because it uses Gini's index as the separation criterion [38]. Hence, this work applies data mining algorithm called decision tree (DT) and important features to develop the rule sets. The 15 rule sets developed were used to differentiate between landslide and non-landslides types as described in Table 2. Three hierarchical levels were conducted to differentiate among the aforementioned classes: at the first level, site A was classified into soil erosion and other features. Then, at the second level, soil erosion was divided into landslide and non-landslide. In the third level, landslide class was subdivided into two subgroups namely shallow and deep-seated, while non-landslide was classified into cut slope and bare soil, and at all levels of hierarchal rule sets, the hierarchical rule sets developed to yield the best classification accuracy.

The classification results demonstrate the robustness and efficiency of the proposed method as shown in Fig. 6. Although very few misclassifications occurred during the process of classification, because most of the misclassification appeared in bare soil class with shallow landslide due to similarity in their characteristics such as form. The overall accuracy and kappa coefficient were 90.41 and 0.86%,
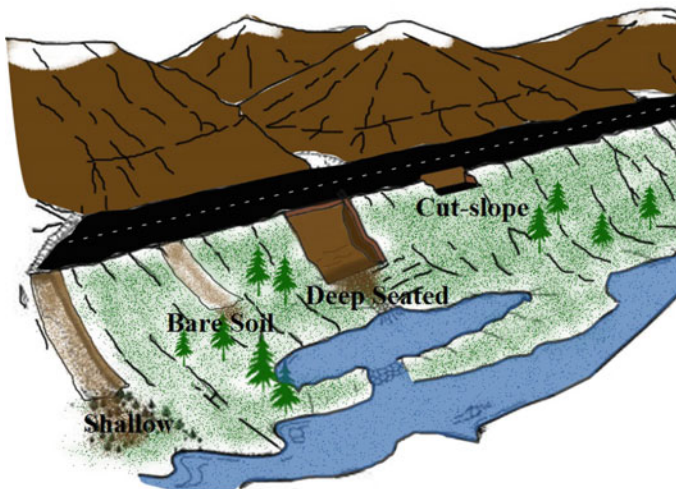
Fig. 5 Illustrates the structure of different types of soil erosion

Table 2 Rule sets developed by the DT algorithm using the important feature subset

Class	Rules	Description
Bare land	Height < 0.7	To distinguish from build-up area
	Slope < 18	To distinguish from landslides
	180 < mean blue	To separate from agricultural and vegetation lands
Cut slope	Length/width > 3	To distinguish from landslides
	Slope > 22	To distinguish from secondary soil road (bare lands)
	Mean red < 152	To separate from agricultural lands and vegetation lands
Shallow	Slope > 25	To distinguish from bare soil
	Intensity > 30,000	To detect the covered landslides with forest
	130 < mean green	To separate from agricultural lands and other features
Deep-seated	Slope > 30	To distinguish from bare lands
	Intensity > 25,000	To separate from agricultural lands and other features
	7000 > area > 1300	To distinguish from shallow
	170 < intensity/mean green < 486	To detect the covered landslides with forest and surrounding neighbor objects
	Length/width < 3	To distinguish from cut slope
	GLCM homogeneity < 0.06	To distinguish from shallow

respectively, as presented in Table 3. This shows that hierarchal rule-based classification is a promising approach for landslide inventory, disaster management, and urban planning.

The developed rules showed the contributions of the LiDAR data, visible band, geometric, and texture feature to differentiate among aforementioned classes due to the values of these features. Accordingly, the minimum value of the intensity feature enables separation between the bare soil and other classes such as cut slope or landslide as shown in Fig. 7a. Texture feature (GLCM homogenous) contributes to the differentiation between the deep-seated class and other classes as shown in Fig. 7b. The values of averaged RGB of the orthophoto were varied along with the classes which helped in distinguishing between the bare soil and other classes, although there was overlap in value between the bare soil and the shallow classes which can be solved by using another feature as shown in Fig. 7c. Moreover, the shadow and canopy forest affects the classification accuracy due to the total covering of the landslide. Therefore, this study creates a new band ratio by dividing the intensity feature and mean green for detecting landslides under shadow and canopy coverage that cannot be identified. Table 2 shows that slope, GLCM homogeneity, intensity feature, mean green, area, length/width can effectively differentiate shallow and deep-seated landslides from most similar landscape objects.
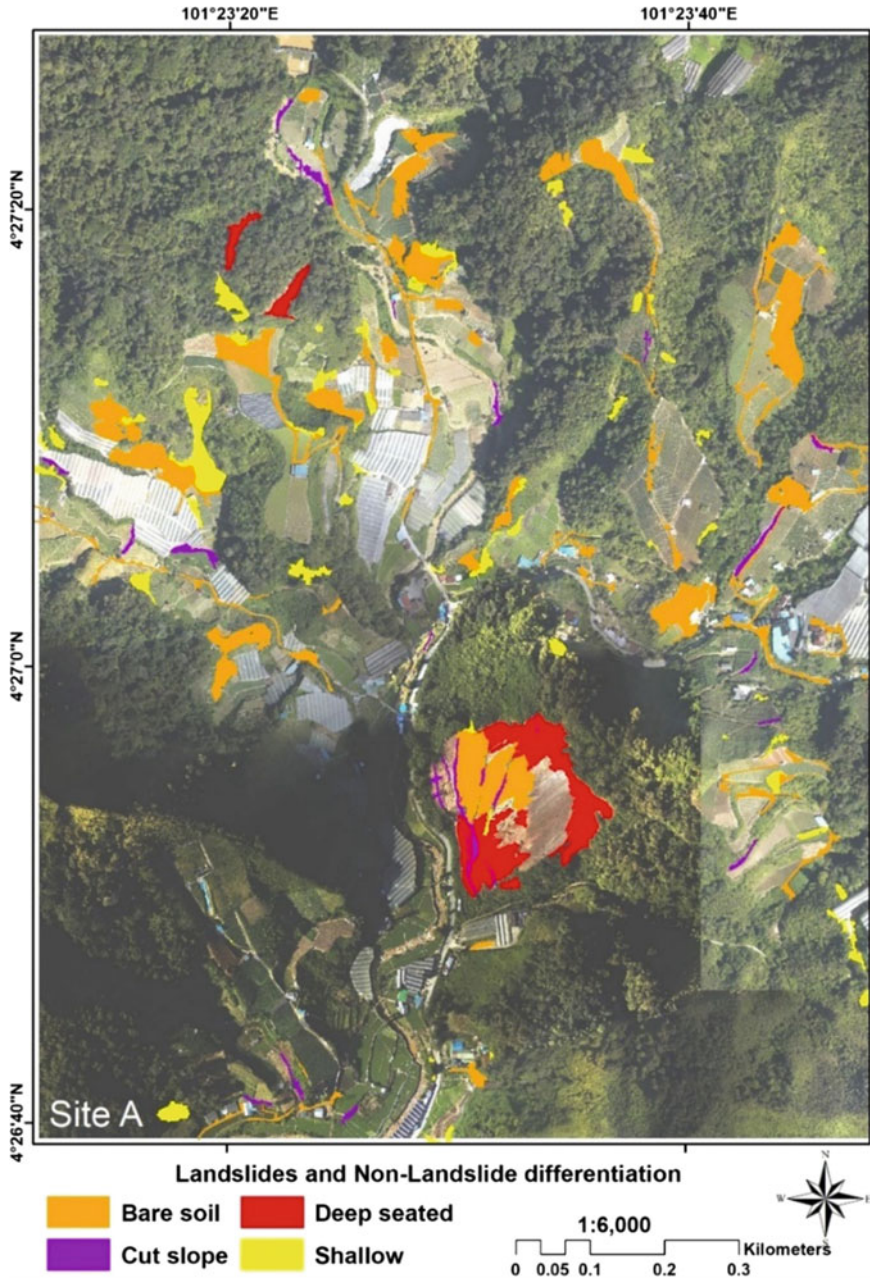
Fig. 6 Results of hierarchal rule set classification at site "A"

Table 3 Shows the results of overall accuracy, kappa coefficient, user's accuracy, and producer's accuracy for site A

LU/LC class names	Bare land	Cut slope	Shallow	Deep-seated	User accuracy	Commission error
Bare land	59	1	2	2	92.2%	7.8%
Cut slope	0	14	0	1	93.3%	6.7%
Shallow	3	1	41	2	87.2%	12.8%
Deep-seated	0	1	1	18	90.0%	10.0%
Total	62	17	44	23	Accuracy	
Producer's accuracy	95.2%	82.4%	93.2%	78.3%	Overall accuracy	Kappa coefficient
Omission error	4.8%	17.6%	6.8%	21.7%	90.41%	0.86

4.4 Evaluation of the Hierarchal Rule Sets

In this research, Cameron Highlands, Malaysia was used as case study to develop and evaluate rules using LiDAR dataset for site B. All the existing objects in the aforementioned site were put into considerations. The segmentation parameters were optimized using FbSP optimizer approach, noting that the generalization of the features selection is important for a transferable model. A technique developed by Bartels et al. [38] was employed by using a 10-fold cross-validation in order to have high accuracy prediction. Thus, the overall accuracy and kappa coefficient were found to be 87.33 and 0.81%, respectively. The result revealed that the hierarchal classification enables differentiation between landslide and other soil erosion types accurately in the site "B" as shown in Fig. 8, although there was a decline in accuracy due to differences in landslide characteristics and environmental conditions as presented by [35, 39]. Moreover, variations in the illumination conditions, sensors used, spatial resolutions of images, etc. are some other challenges that could influence the result as stated in a recent study by [19, 35].

4.5 Effect of Using Intensity on the Image Segmentation and Deep-Seated Landslide

Intensity feature contributes immensely to the process of differentiating between landslide types as shown in Fig. 9. The figure revealed the influence of intensity in identifying landslides under shadow and canopy vegetation. The yellow polygons in the figure show the boundaries of landslide, which were based on optimized segmentation in conjunction with intensity weightage (0.01). This is to show the influence of intensity in enhancing the landslide segmentation under shadow and canopy where it is impossible to identify using only visible bands. Furthermore, the classification of deep-seated class was highly improved whenever the intensity
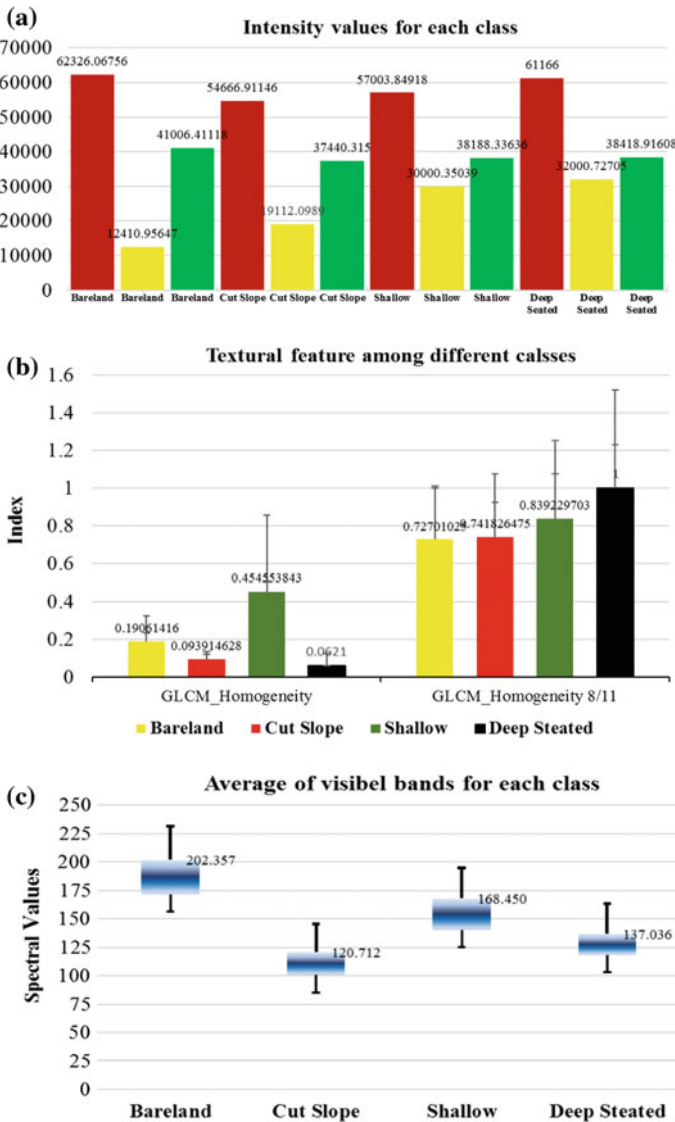
Fig. 7 Shows the values of **a** Texture, **b** Intensity, **c** Average of visible bands, which they contributed in distinguish between the classes (shallow, deep-seated, cut slope, and bare soil)

feature is used. The red polygon shows the shallow landslide that can be seen in visible band due to their lower depth despite their shadow cover. The significant role of band ratio such as intensity over green layers is also highlighted in order to differentiate between normal shadow and deep-seated shadow cover. The results

Fig. 8 Results of hierarchal rule set classification at site "B"
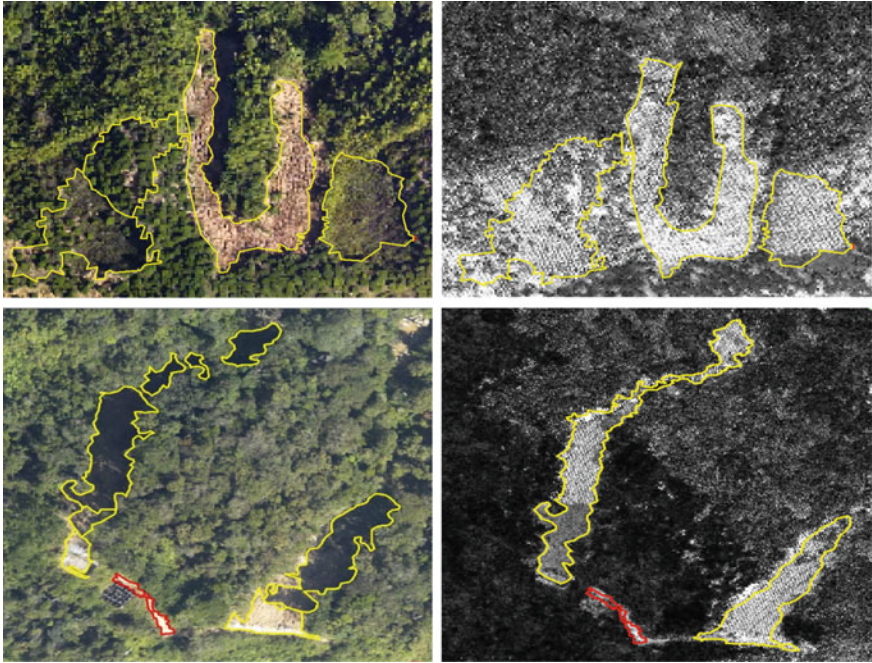
Fig. 9 Shows the amount of intensity value involved in landslide

have proven the importance of intensity in improving the segmentation of the objects and distinguishing between the deep-seated and the shadow landslides.

4.6 Validation

Stratified random sampling method was used to select the segment object in other to carry out the accuracy assessment. The classification results were based on the segments object on orthophoto image, intensity, height, and inventory map to select the reference data (landslide and non-landslide types). Subsequently, the reference data was compared with the results of the classification using confusion matrix [2]. Highest overall accuracy and kappa coefficient were achieved by using this proposed method and the overall accuracy and kappa coefficient of the hierarchal classification were 90.41 and 0.86%, respectively. Meanwhile, the user and producer accuracy were obtained for shallow class as 87.2 and 93.2%, respectively, while for deep-seated class, 90.0 and 78.3% were obtained, respectively, for site "A" as presented in Table 3. The lower user accuracy for shallow class was obtained due the similarity in characteristics of shallow landslide with bare soil class in some locations.

Table 4 Shows the results of overall accuracy, kappa coefficient, user's accuracy, and producer's accuracy for site B

LU/LC class names	Bare land	Cut slope	Shallow	Deep-seated	Total GCPs	User's accuracy	Commission error
Bare land	61	1	5	1	68	89.7%	10.3%
Cut slope	0	11	0	1	12	91.7%	8.3%
Shallow	4	0	38	2	44	86.4%	13.6%
Deep-seated	0	1	4	21	26	80.8%	19.2%
Total GCPs	65	13	47	25	150	Accuracy	
Producer's accuracy	93.8%	84.6%	80.9%	84.0%	Overall accuracy		Kappa coefficient
Omission error	6.2%	15.4%	19.1%	16.0%	87.33%		0.81

The accuracies of site B are presented in Table 4, and the overall accuracy and kappa coefficient were observed to be 87.33 and 0.81%, respectively. The user and producer accuracies for shallow class were obtained as 86.4 and 80.9%, respectively, while 80.8 and 84.0% were achieved for user and producer accuracies in deep-seated class, respectively. The results of accuracy assessment indicated that hierarchal rule-based classification system is effective and efficient for differentiation between landslide and other erosion types. The accuracies of user and producer for deep-seated class were observed to be decreased which is due to the variation in the characteristics of deep-seated such as deep and run out.

5 Discussion

The differentiation between types of landslide (shallow and deep-seated) and types of soil erosion (cut slope and bare soil classes) in densely vegetated areas like the Cameron Highlands is a challenging issue due to the presence of similarity in dense vegetation, shadow, and hilly areas. This research proposes a method that automatically differentiates between types of landslide by using high-resolution airborne laser scanning data (LiDAR) as well as visible band, texture, and geometric features. This research also showed that optimizing the segmentation parameters such as scale, shape, and compactness with the aid of the FbSP optimizer was satisfactory in distinguishing between landslide and non-landslide types. Optimized segmentation parameters enable generation of accurate objects segment and utilize spatial, texture, and geometric features for differentiating between the aforementioned classes. Since the landslides can be classified according to their features, accurate segmentation is necessary for differentiating between the classes.

The selection of relevant optimal features for landslide depends on the level of experience of the analysts. Therefore, it is highly imperative to establish a feature selection method that differentiates among landslides and non-landslide types.

The rule sets used to optimize features selected are simplified when CFS algorithm is employed in distinguishing between the aforementioned classes. In addition, the optimized features used to differentiate between the aforementioned classes are LiDAR DEM data (slope, height, and intensity), visible band, texture features (GLCM StdDev and GLCM homogeneity), and the geometric features. The result shows the contribution of the features such as LiDAR DEM data (intensity, slope, and height), texture feature (GLCM Homogeneity), spectral features (red, green, and blue), geometric features (length/width and area) for distinguishing between the types of landslides, and other types of soil erosion. The band ratio intensity feature over green band also helps in differentiating between the deep-seated classes under shadow and normal shadows. Moreover, the intensity feature contributed in delineating the boundary of landslide and differentiated between deep-seated classes. The proposed rule set has minimized the over-reliance on the analyst experience and computation time to a larger extent when compared with the existing complex rule sets of the image classification system.

Classification maps are significantly improved when the classification techniques are used. There exist many classification algorithms and each category has its own merits and demerits. In this research, three hierarchal levels were used and the result indicated that using this proposed method yield better accuracy. Besides, using optimized methods for segmentation parameters and feature selection with the aid of high-resolution LiDAR, orthophotos, texture, and geometric feature contributed to the simplification in the development of hierarchical rule sets and improve the transferability model. The hierarchal rule sets were developed based on site "A" and the same rules may not yield optimum values in other locations. Therefore, the developed rules were used in site "B" and high accuracy was achieved.

6 Field Investigation

Field investigation method was used to further ascertain the reliability of the proposed approach. A handheld GPS device (GeoExplorer 6000) was used to identify the locations of the landslides, as shown in Fig. 10. The data acquired from the field measurements enable assessment of the precision and reliability of the produced landslide inventory map. However, the field investigation result confirms the hierarchal classification detected on the landslides. Therefore, this method can conveniently identify landslide locations, differentiate between types of landslide, and produce reliable landslide inventory map for the Cameron Highlands, Malaysia.

Fig. 10 Shows the field photos in some locations of landslide at **a** Tanah Runtuh, **b** Tanah Rata

7 Conclusion

It is difficult to differentiate between two types of landslides (shallow and deep-seated) and types of soil erosion (cut slope and bare soil) by using conventional approach. Therefore, this research proposes a hierarchal rule-based classification that aids to differentiate between the classes of landslides in Cameron Highlands, Malaysia. A high-resolution airborne LiDAR data and fuzzy logic supervised approach (FbSP) were used as the main data sources and optimization segmentation parameters, respectively. Correlation-based feature selection (CFS) was used to obtain the important features subset. Hierarchal rule-based classification LiDAR DEM data, orthophoto, texture features, and geometric features were used to improve the classification accuracy. The optimization of the segmentation parameters and the selection of features improved the computational efficiency of the workflow and enhanced the transferability of the hierarchal rule sets into different spatial subsets within the Cameron Highlands in Malaysia. The overall accuracy and the kappa index of the hierarchal approach in site "A" are 90.41 and 0.86%, respectively. Furthermore, the overall accuracy and the kappa index for the site B are 87.33 and 0.81%, respectively. This indicated that developing hierarchal rule sets based on optimized techniques with the aid of VHR airborne LiDAR DEM data, spectral, and spatial features are effective in differentiating different types of landslides and soil erosion in tropical regions. This method offers future solution to geospatial issues in managing landslide hazards and risk assessments.

References

1. Guzzetti, F., Mondini, A.C., Cardinali, M., Fiorucci, F., Santangelo, M., Chang, K.-T.: Landslide inventory maps: new tools for an old problem. Earth-Sci. Rev. **112**(1), 42–66 (2012)

2. Pradhan, B., Jebur, M.N., Shafri, H.Z.M., Tehrany, M.S.: Data fusion technique using wavelet transform and Taguchi methods for automatic landslide detection from airborne laser scanning data and quickbird satellite imagery. IEEE Trans. Geosci. Remote Sens. **54**(3), 1610–1622 (2016)

3. Van Westen, C.J., Castellanos, E., Kuriakose, S.L.: Spatial data for landslide susceptibility, hazard, and vulnerability assessment: an overview. Eng. Geol. **102**(3), 112–131 (2008)

4. Parker, R.N., Densmore, A.L., Rosser, N.J., De Michele, M., Li, Y., Huang, R., Petley, D.N.: Mass wasting triggered by the 2008 Wenchuan earthquake is greater than orogenic growth. Nat. Geosci. **4**(7), 449–452 (2011)

5. Chen, R.F., Lin, C.W., Chen, Y.H., He, T.C., Fei, L.Y.: Detecting and characterizing active thrust fault and deep-seated landslides in dense forest areas of southern taiwan using airborne LiDAR DEM. Remote Sens **7**(11), 15443–15466 (2015)

6. Guzzetti, F., Cardinali, M., Reichenbach, P., Cipolla, F., Sebastiani, C., Galli, M., Salvati, P.: Landslides triggered by the 23 November 2000 rainfall event in the Imperia Province, Western Liguria, Italy. Eng. Geol. **73**(3), 229–245 (2004)

7. Tarolli, P., Arrowsmith, J.R., Vivoni, E.R.: Understanding earth surface processes from remotely sensed digital terrain classifiers. Geomorphology **113**(1), 1–3 (2009)

8. McKean, J., Roering, J.: Objective landslide detection and surface morphology mapping using high-resolution airborne laser altimetry. Geomorphology **57**(3), 331–351 (2004)

9. Whitworth, M., Giles, D., Murphy, W.: Airborne remote sensing for landslide hazard assessment: a case study on the Jurassic escarpment slopes of Worcestershire, UK. Q. J. Eng. Geol. Hydrogeol. **38**(3), 285–300 (2005)

10. Schulz, W.H.: Landslide susceptibility revealed by LIDAR imagery and historical records, Seattle, Washington. Eng. Geol. **89**(1), 67–87 (2007)

11. Anders, N.S., Seijmonsbergen, A.C., Bouten, W.: Segmentation optimization and stratified object-based analysis for semi-automated geomorphological mapping. Remote Sens. Environ. **115**(12), 2976–2985 (2011)

12. Belgiu, M., Drăguţ, L.: Comparing supervised and unsupervised multiresolution segmentation approaches for extracting buildings from very high resolution imagery. ISPRS J Photogramm Remote Sens. **96**, 67–75 (2014)

13. Drăguţ, L., Tiede, D., Levick, S.R.: ESP: a tool to estimate scale parameter for multiresolution image segmentation of remotely sensed data. Int. J. Geogr. Inf. Sci. **24**(6), 859–871 (2010)

14. Esch, T., Thiel, M., Bock, M., Roth, A., Dech, S.: Improvement of image segmentation accuracy based on multiscale optimization procedure. IEEE Geosci. Remote Sens. Lett. **5**(3), 463–467 (2008)

15. Zhang, Y., Maxwell, T., Tong, H., Dey, V.: Development of a supervised software tool for automated determination of optimal segmentation parameters for ecognition: na (2010)

16. Zêzere, J.L., Trigo, R.M., Trigo, I.F.: Shallow and deep landslides induced by rainfall in the Lisbon region (Portugal): assessment of relationships with the North Atlantic Oscillation. Nat. Hazard Earth Sys. **5**(3), 331–344 (2005)

17. Deng, S., Shi, W.: Semi-automatic approach for identifying locations of shallow debris slides/flows based on lidar-derived morphological features. Int. J. Remote Sens. **35**(10), 3741–3763 (2014)

18. Lin, C.-W., Tseng, C.-M., Tseng, Y.-H., Fei, L.-Y., Hsieh, Y.-C., Tarolli, P.: Recognition of large scale deep-seated landslides in forest areas of Taiwan using high resolution topography. J. Asian Earth Sci. **62**, 389–400 (2013)

19. Rau, J.Y., Jhan, J.P., Rau, R.J.: Semiautomatic object-oriented landslide recognition scheme from multisensor optical imagery and DEM. IEEE Trans. Geosci. Remote Sens. **52**(2), 1336–1349 (2014)

20. Kasai, M., Ikeda, M., Asahina, T., Fujisawa, K.: LiDAR-derived DEM evaluation of deep-seated landslides in a steep and rocky region of Japan. Geomorphology **113**(1), 57–69 (2009)

21. Van Den Eeckhaut, M., Poesen, J., Verstraeten, G., Vanacker, V., Moeyersons, J., Nyssen, J., Van Beek, L.P.H.: The effectiveness of hillshade maps and expert knowledge in mapping old deep-seated landslides. Geomorphology **67**(3), 351–363 (2005)
22. Passalacqua, P., Tarolli, P., Foufoula Georgiou, E.: Testing space scale methodologies for automatic geomorphic feature extraction from lidar in a complex mountainous landscape. Water Resour. Res. **46**(11) (2010)
23. Dou, J., Chang, K.-T., Chen, S., Yunus, A.P., Liu, J.-K., Xia, H., Zhu, Z.: Automatic case-based reasoning approach for landslide detection: integration of object-oriented image analysis and a genetic algorithm. Remote Sens. **7**(4), 4318–4342 (2015)
24. Li, X., Cheng, X., Chen, W., Chen, G., Liu, S.: Identification of forested landslides using LiDar data, object-based image analysis, and machine learning algorithms. Remote Sens. **7**(8), 9705–9726 (2015)
25. Chen, W., Li, X., Wang, Y., Chen, G., Liu, S.: Forested landslide detection using LiDAR data and the random forest algorithm: a case study of the Three Gorges, China. Remote Sens. Environ. **152**, 291–301 (2014)
26. Stumpf, A., Kerle, N.: Object-oriented mapping of landslides using random forests. Remote Sens. Environ. **115**(10), 2564–2577 (2011)
27. Borghuis, A., Chang, K., Lee, H.: Comparison between automated and manual mapping of typhoon-triggered landslides from SPOT-5 imagery. Int. J. Remote Sens. **28**(8), 1843–1856 (2007)
28. Danneels, G., Pirard, E., Havenith, H.-B.: Automatic landslide detection from remote sensing images using supervised classification methods. In: Paper Presented at the 2007 IEEE International Geoscience and Remote Sensing Symposium (2007)
29. Moine, M., Puissant, A., Malet, J.-P.: Detection of landslides from aerial and satellite images with a semi-automatic method. In: Application to the Barcelonnette Basin (Alpes-de-Hautes-Provence, France). Paper Presented at the Landslide Processes-from Geomorphologic Mapping to Dynamic Classifierling (2009)
30. Kurtz, C., Stumpf, A., Malet, J.P., Gançarski, P., Puissant, A., Passat, N.: Hierarchical extraction of landslides from multiresolution remotely sensed optical images. ISPRS J. Photogramm. Remote Sens. **87**, 122–136 (2014)
31. Miner, A., Flentje, P., Mazengarb, C., Windle, D.: Landslide recognition using LiDAR derived digital elevation classifiers-lessons learnt from selected Australian examples (2010)
32. Martha, T.R., Kerle, N., Van Westen, C.J., Jetten, V., Kumar, K.V.: Segment optimization and data-driven thresholding for knowledge-based landslide detection by object-based image analysis. IEEE Trans. Geosci. Remote **49**(12), 4928–4943 (2011)
33. Pradhan, B., Lee, S.: Regional landslide susceptibility analysis using back-propagation neural network classifier at Cameron Highland, Malaysia. Landslides **7**(1), 13–30 (2010)
34. Olaya, V.: Basic land-surface parameters. Dev. Soil Sci. **33**, 141–169 (2009)
35. Mezaal, M.R., Pradhan, B., Sameen, M.I., Mohd Shafri, H.Z., Yusoff, Z.M.: Optimized neural architecture for automatic landslide detection from high resolution airborne laser scanning data. Appl. Sci. **7**(7), 730 (2017)
36. Blaschke, T.: Object based image analysis for remote sensing. ISPRS J. Photogramm. Remote Sens. **65**(1), 2–16 (2010)
37. Li, M., Ma, L., Blaschke, T., Cheng, L., Tiede, D.: A systematic comparison of different object-based classification techniques using high spatial resolution imagery in agricultural environments. J. Appl. Earth Obs. Geoinf. **49**, 87–98 (2016)
38. Hamedianfar, A., Shafri, H.Z.M.: Integrated approach using data mining-based decision tree and object-based image analysis for high-resolution urban mapping of WorldView-2 satellite sensor data. J. Appl. Remote Sens. **10**(2), 025001 (2016)
39. Pradhan, B., Mezaal, M.R.: Optimized rule sets for automatic landslide characteristic detection in a highly vegetated forests. Laser Scanning Applications in Landslide Assessment, pp. 51–68. Springer International Publishing, New York (2017)
40. Kursa, M.B., Rudnicki, W.R.: Feature selection with the Boruta package. J. Stat. Softw. **36**, 1–3 (2010)

41. Barbarella, M., Fiani, M., Lugli, A.: Application of LiDAR-derived DEM for detection of mass movements on a landslide. Int. Arch. Photogramm. Remote Sense Spat. Inf. Sci. **1**(3), 89–98 (2013)
42. Sameen, M.I., Pradhan, B., Shafri, H.Z., Mezaal, M.R., bin Hamid, H.: Integration of ant colony optimization and object-based analysis for LiDAR data classification. IEEE J-STARS **10**, 2055 (2017)
43. Bartels, M., Wei, H.: Threshold-free object and ground point separation in LIDAR data. Pattern Recognit. Lett. **31**(10), 1089–1099 (2010)

Assessing Vertical Accuracy and the Impact of Water Surface Elevation from Different DEM Datasets

Ernieza Suhana Mokhtar, Biswajeet Pradhan, A. H. Ghazali
and H. Z. M. Shafri

Abstract Digital elevation models (DEMs) are essential to provide continuous terrain elevation for water surface elevation (WSE) with a variety of horizontal and vertical accuracies in flood inundation modelling. The WSE forecasting depends on the appropriateness of the DEM data used. The comparative methodology is applied to various DEM sources: LiDAR and IFSAR DEM based on different types of land use at each of the cross-sectional lines. The accuracy of the IFSAR DEMs was assessed with LiDAR data, which is a high-precision DEM and was applied in hydraulic modelling to simulate the WSE in Padang Terap, Kedah, Malaysia. Furthermore, Bjerklie's model is used as predicted discharge to support the analysis. The relationship of the DEMs is established by natural logarithm (ln). Then, the equation is interpolated on the original and resampled IFSAR DEMs to improve the medium-resolution data for WSE delineation. Next, the WSE was validated with observed WSE obtained along the upstream (Kuala Nerang) to the downstream parts (Kampung Kubu) Kedah using R^2, mean absolute error (MAE), and root-mean-square error (RMSE). By applying this method, the WSE can be improved by considering uncertainties and lead to produce a better flood hazard map using medium-high-resolution images.

E. S. Mokhtar · B. Pradhan · A. H. Ghazali · H. Z. M. Shafri
Department of Civil Engineering, Faculty of Engineering,
Universiti Putra Malaysia (UPM), 43400 Serdang, Selangor, Malaysia

E. S. Mokhtar
Department of Surveying Science and Geomatics, Faculty of Architecture,
Planning and Surveying, Universiti Teknologi MARA (Perlis),
02600 Arau, Perlis, Malaysia

B. Pradhan (✉)
Faculty of Engineering and Information Technology, School of Systems,
Management and Leadership, University of Technology Sydney, Building 11,
Level 06, 81 Broadway, PO Box 123, Ultimo, NSW 2007, Australia
e-mail: Biswajeet.Pradhan@uts.edu.au

1 Introduction

Topography data or also known as digital elevation model (DEM) is an essential data source to forecast flood inundation using one- or two-dimensional models. The DEM can be acquired using detail surveying, Shuttle Radar Topography Mission (SRTM), light detection and ranging (LiDAR) and IFSAR. Many researchers have explored the potentials of DEM in different data sources such as hydraulic and hydrology applications [1–5]. Yan et al. [6] had reviewed the capabilities of low-medium remote-sensed data, which has coarse spatial and low vertical resolution in flood modelling.

DEM significantly relates to data resolution and resampling techniques. Extensive studies have been conducted to examine the impact of changing DEM resolution to flood inundation. Many researchers focused on resampling DEM data from fine to coarse resolution, which is in the range of 3–1500 m mapping using various DEMs such as SRTM, Advanced Space-borne Thermal Emission and Reflection Radiometer (ASTER), Global Multi-resolution Terrain Elevation Data (GMTED) and LiDAR [7–9]. To enhance flood inundation mapping, the elevation error (RMSE) obtained from different resampled DEMs and LiDAR DEM was substituted to all resampled DEMs [7]. In another study, Tan et al. [9] assessed the use of resampling techniques (nearest neighbour, bilinear interpolation, cubic convolution and majority) and found that nearest neighbour and majority performed best. By maximizing the cell size or vice versa, the time processing significantly influences the computation spatial analysis. However, some information will be eradicated when the resampled DEM changes from coarse to fine resolutions [8]. Earls and Dixon [10] revealed that the resolution of the land-use map influences the hydraulic output. As recommended by literature, an analysis using finer resolution up to 1 m with different DEM sources should be performed [9]. However, to what extent the resampled image will affect the elevation of the land-use feature representation and water surface elevation in hydraulic analysis still needs more investigation.

The question is how to optimize low-medium DEM resolution dataset used in flood mapping? This study will examine the effects of resampled DEM data on each of the land-use type's elevation, establish the relationship between LiDAR and IFSAR DEMs as well as assess the sensitivity of DEMs on the water surface elevation (WSE) acquired from HEC-RAS model.

2 Study Area

This study was focused on the main river, Padang Terap River, which flows from Kuala Nerang Town to Kampung Kubu, Kedah, Malaysia (Fig. 1). The majority of the land in Padang Terap District is used as agriculture and forest land. The economic activities of the residents are rubber tapping and farming. The river had
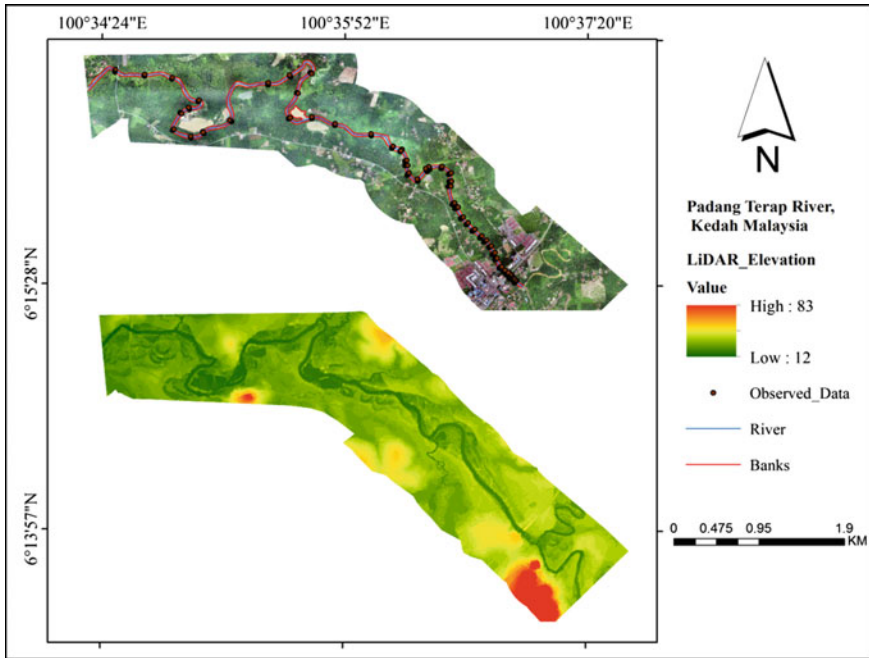
Fig. 1 Elevation and LiDAR orthophoto present study area, Padang Terap River, Kedah, Malaysia

contributed to the flood occurred in the year 2010 due to the river confluence of three main rivers: Padang Terap, Pedu and Ahning Rivers. On October 31, 2010, Padang Terap catchment consists of five rainfall stations: Durian Burung, Padang Sanai, Kuala Nerang, Kampung Kubu and Naka, which had received heavy rainfall volume (mm) of 197, 146, 114, 95 and 64, respectively. The next day, it increased drastically at all stations with 211, 159, 175 and 122 mm except for the Durian Burung station that reduced to 158 mm. The readings are categorized as heavy rain, which is more than 60 mm as stated in the DID (2010) report. Water level stations are only established at Padang Sanai, Kuala Nerang, Kampung Kubu and Kepala Batas and recorded as high water stages at 36.15, 20.62, 13.94 and 4.33 m, respectively. This study area was chosen because it is always exposed to the flooding and crop yield losses. Besides that, observation data is available to support the analysis.

3 Data Acquisition

Land-use map is used and consists of five classes of the land-use types such as bare land, cultivated and brush, developed area, forest and water features with an estimated area of 3, 44, 7, 0.8 and 4 km^2, respectively. The only area covered is within

8 km² due to the limitations of the DEM data. The land-use map was provided by Department of Town and Country Planning, Malaysia, for the year of 2009 (Fig. 2a). Figure 2b shows the vector features consisting of rivers, riverbanks, flow paths and cross-sectional lines generated from DEM data. A detailed explanation of the development river morphologies in vector format will be discussed in the next section. Two different DEMs such as IFSAR (Fig. 2d) and LiDAR DEM (Fig. 2c) datasets with several spatial resolutions were obtained on different dates, January 2009 and December 2015, respectively. The spatial resolution for the original IFSAR and LiDAR DEM data was 5 m and 15 cm, respectively. The elevation ranges of the study area are between 10 and 82 m. In the area of Kuala Nerang, water level gauge stations near the Padang Terap River situated at upstream area recorded the WSE during ground measurement data collection. The known WSE was recorded on 14 April 2014 at two stations: Kuala Nerang (upstream) and Kampung Kubu (downstream) as 15.440 m and 9.980 m, respectively (Fig. 3).

Hydraulic modelling has been carried out along 8 km of Padang Terap River between Kuala Nerang and Kampung Kubu, Kedah using a one-dimensional (1-D) HEC-RAS model (www.hec.usace.army.mil). In HEC-RAS, river networks, riverbanks and flow paths were digitized by referring to the IFSAR orthorectified radar image (ORI). For predicted cross-sectional (CS) lines, HEC-RAS provides a tool for auto-generation that only required CS interval as input. About 49 of the
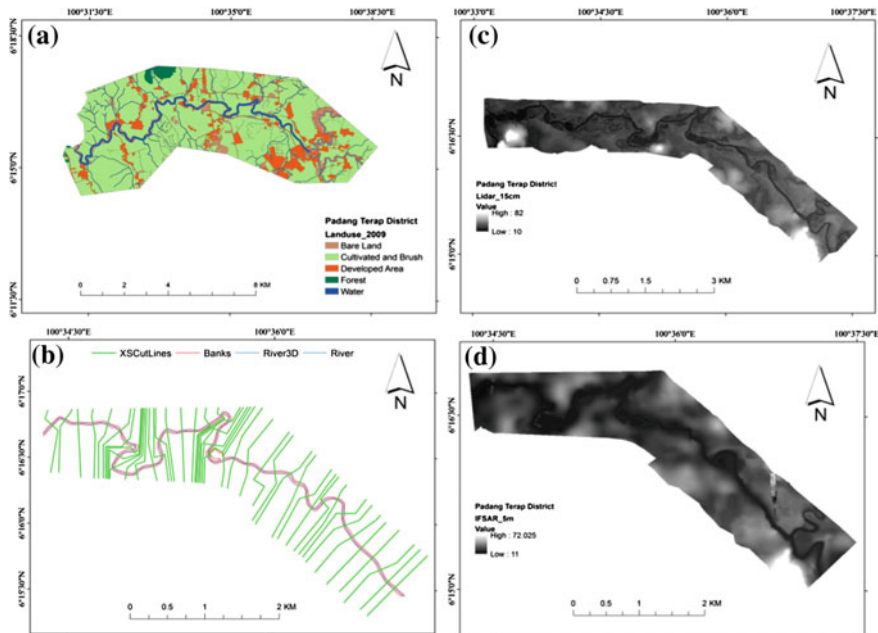
Fig. 2 **a** Land-use map, **b** LiDAR DEM, **c** river morphologies in vector format and **d** IFSAR DEM
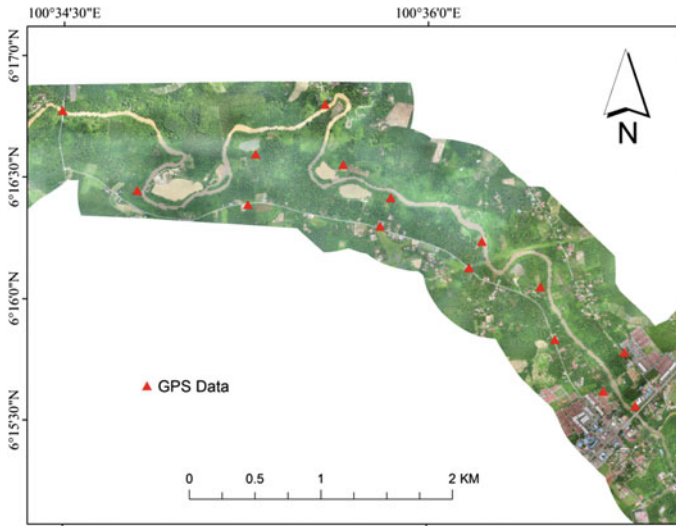
Fig. 3 GPS control points

observed cross-sectional lines were surveyed across the river and the total observed points are 585 points. The cross-sectional depth was measured using the Q-Liner equipment and global positioning system (GPS), which was used for positioning and WSE measurement purposes. The boundary condition of the steady flow at the downstream area is assigned by a friction slope which will be decided after the calibration is carried out.

4 Methodology

The methodology of this study involves three phases; (i) evaluate DEM data quality, (ii) model and calibrate DEM and (iii) predict WSE using DEM and optimize DEM. All errors between predicted and measured readings were quantified using the 'Extract Multi Values to Points' tool in ArcGIS software [4].

4.1 DEM Datasets Evaluation

The elevation accuracy was evaluated by a comparison analysis between LiDAR with 15 cm resolution ($LiDAR_{15\ cm}$) and two different DEMs: (i) original IFSAR ($IFSAR_{5\ m}$) and ii) resampled IFSAR with 1 m resolution ($IFSAR_{1\ m}$). The ground control points (GCP) observed by the global positioning system (GPS) were used to measure the accuracy of elevation obtained from the DEMs. About 14 observed

points were established along the Padang Terap River. The total number of the GCP was half, as suggested by Jung et al. [12]. This is because the area is difficult to assess as the area is covered by dense forestry and lack of open space areas. However, the GCPs are well distributed over the study area.

The LiDAR data was used as a reference to measure the degree of vertical accuracy for IFSAR DEM datasets based on different land-use classes. A total of 160 sampling points were created randomly on different land-use types at each of the cross sections, which are perpendicular to the river. Furthermore, the IFSAR DEM which was originally 5 m was resampled to 1 m using the nearest neighbour method [9]. The study compared the effects of $IFSAR_{5\ m}$ and resampled $IFSAR_{1\ m}$ DEMs on the elevation data for each of the land-use types different from Dixon and Earls' [8] that assessed the influences of DEMs on the land-use area. The error of elevation was determined by calculating the coefficient of determination (R^2), mean absolute error (MAE), root-mean-square error (RMSE) and Nash–Sutcliffe efficiency (NSE) for each DEM raster with respect to the original LiDAR for the entire area [9, 13]. In addition, the relationship between the $LiDAR_{5\ m}$ and the two DEMs ($IFSAR_{5\ m}$ and $IFSAR_{1\ m}$) was developed. The equation from the relationship between two parameters was interpolated on both IFSAR DEM images to optimize the DEM's elevation to enhance WSE prediction.

4.2 Discharge Model and DEM Calibration

The estimated discharge (Qp) was computed using Bjerklie's model (Eq. 1), which includes width (W), cross-sectional depth (Y) and channel slope (S):

$$Qp = 7.22\, W^{1.02} Y^{1.74} S^{0.35} \tag{1}$$

To calibrate the discharge model, the Monte Carlo (MC) analysis was carried out to find significant combined hydraulic parameter sets [3, 14–16]. About 8100 simulation sets [16] were run with different variable combinations such as width (W), river depth (Y) and channel slope (S) associated with the surface roughness (Manning's n) for five land-use classes. The river width was estimated on ORI data, while channel slope was computed based on two different elevations on LiDAR and IFSAR DEMs. For the cross-sectional water depth, the elevation was taken from the difference between the observed WSE recorded by MADA telemetry station (Kuala Nerang) and elevation of the IFSAR channel. In addition, the uniform distribution of the Manning-n was presented [14]. The Manning's n for floodplain and channel was assumed in different feasible ranges. Using a 95% confidence interval, the values of all variables in the lower, mean and upper bounds were chosen. On the other hand, only the IFSAR DEMs in both spatial resolutions (5 and 1 m) were calibrated using the natural logarithm (ln) equation. Raster calculator in ArcGIS was used to apply the equation over IFSAR elevation cells.

4.3 Water Surface Elevation Estimation

The WSE was estimated using the 1D HEC-RAS model. First, the river morphologies in the vector data need to be prepared using the Hec-GeoRAS and the detailed procedures that have been discussed in a previous study [17]. The Manning's *n* was substituted to the land-use types before delineating the WSE. In HEC-RAS, the discharge calculated by Bjerklie's model was assigned at the first cross-sectional line. Then, the boundary conditions at the downstream area [14, 18] were retrieved from the combined parameters using 95% confidence level. Lastly, the WSE and water extent were delineated in grid and vector formats, respectively. The observed WSE points were overlaid on the IFSAR and LiDAR DEM data, and a comparison analysis was carried out.

5 Result and Analysis

5.1 Assessing Vertical Accuracies on Different Land-Use Types

In this study, features such as bare land, building, grassland, paddy field, road, tree and water were chosen to evaluate the elevation discrepancies between $LiDAR_{15\ cm}$, $IFSAR_{5\ m}$ and resampled $IFSAR_{1\ m}$ DEMs. The LiDAR data was selected as data calibration in assessing errors in elevation of these two DEM sources.

Table 1 shows a topographic statistic of each DEM for original LiDAR (15 cm), resampled $LiDAR_{1\ m}$, original $IFSAR_{5\ m}$ and resampled $IFSAR_{1\ m}$. In general, it can be seen that no changes occurred when the resampling techniques were applied over the DEMs. However, the maximum slope changed substantially from 83.992° for fine resolution ($LiDAR_{15\ cm}$) to 76.579° with resampled $LiDAR_{1\ m}$ DEMs. In contrast, a similar pattern was found between the LiDAR DEM data and the $IFSAR_{5\ m}$ where the slope changed from 51.772° to 81.254° with fine resolution (resampled $IFSAR_{1\ m}$ DEM). Although no changes were found, specific impacts on the land-use types need to be assessed to obtain detail topography uncertainties.

Table 2 presents the likelihood functions for the whole random points in mixed land-use classes. The findings show the implication of the resampling process to the

Table 1 Ranges of elevation and slope value of original and resampled DEMs data

Model	Elevation (m)		Slope (°)	
	Min	Max	Min	Max
$LiDAR_{15\ cm}$	10	82	0	83.992
$LiDAR_{1\ m}$	10	82	0	76.579
$IFSAR_{5\ m}$	11	72.025	0	51.772
$IFSAR_{1\ m}$	11	72.025	0	81.254

Table 2 Elevation comparison between LiDAR and original and resampled IFSAR data based on likelihood measures

	GCP-LiDAR$_{15\ cm}$	GCP-IFSAR$_{5\ m}$	LiDAR$_{15\ cm}$-IFSAR$_{5\ m}$	LiDAR$_{15\ cm}$-IFSAR$_{1\ m}$
MAE	0.288	2.012	0.639	0.647
RMSE	0.321	2.380	0.818	0.845
R^2	0.982	0.738	0.930	0.926

IFSAR data where it reduced vertical accuracy about 1–3% in terms of MAE and RMSE. Although both DEM data were in various resolutions, the high correlation between LiDAR and IFSAR data was significantly shown at $R^2 = 90\%$. These errors are quite low because the area is mostly covered by agriculture land and low-lying areas. The result presented that the errors in elevation of the resampled IFSAR$_{1\ m}$ DEM that was converted to higher spatial resolution do not increase the results significantly [8]. However, the RMSE between the observed GCP and three different DEMs (LiDAR, original and resampled IFSAR DEM) showed better results compared to the DEM used in Tan et al. [9].

Figure 4 shows the residual distribution of the elevation between (i) original LiDAR$_{15\ cm}$ and IFSAR$_{5\ m}$ (Fig. 4a) and (ii) LiDAR$_{15\ cm}$ and resampled IFSAR$_{1\ m}$ (Fig. 4b) DEMs based on detailed land-use classes. The error distribution of road and area covered by tree elevation was increased to 2–3 m after applying over the resampled IFSAR$_{1\ m}$ DEM. This might be caused by the inclination of the DEM resolution causing the slope to increase concurrently, which directly influences the elevation of terrain surface. However, the lowest error distribution was identified at the paddy field area, which indicated an error of fewer than 0.5 m before and after the resampling process was employed. This might be because the paddy field is an open space and no obstacle distraction during the image scanning. At the same time, the elevation errors on the land-use type of the building and grassland were declined with the resampled IFSAR$_{1\ m}$ DEM and indicated better elevation estimations. The elevation of both features was increased with IFSAR$_{1\ m}$ while the slope decreased. Nevertheless, the error distribution for other features seems to be consistent with the estimated of about 1 m. This result presented that not all input DEM resolutions produce similar outputs and by reducing the cell size to increase the DEM resolution, the DEM accuracy does not improve [8]. The elevation errors cannot be disregarded and careful action needs to be taken while the resampling process is applied in flood modelling.

5.2 Calibration of Discharge Model and DEM Dataset

Using the Monte Carlo simulation sets and 95% confidence interval, the combined parameters *W*, *Y* and *S* were substituted into Bjerklie's model to estimate the river discharge (Table 3). The LiDAR data provides minimum discharge as compared to
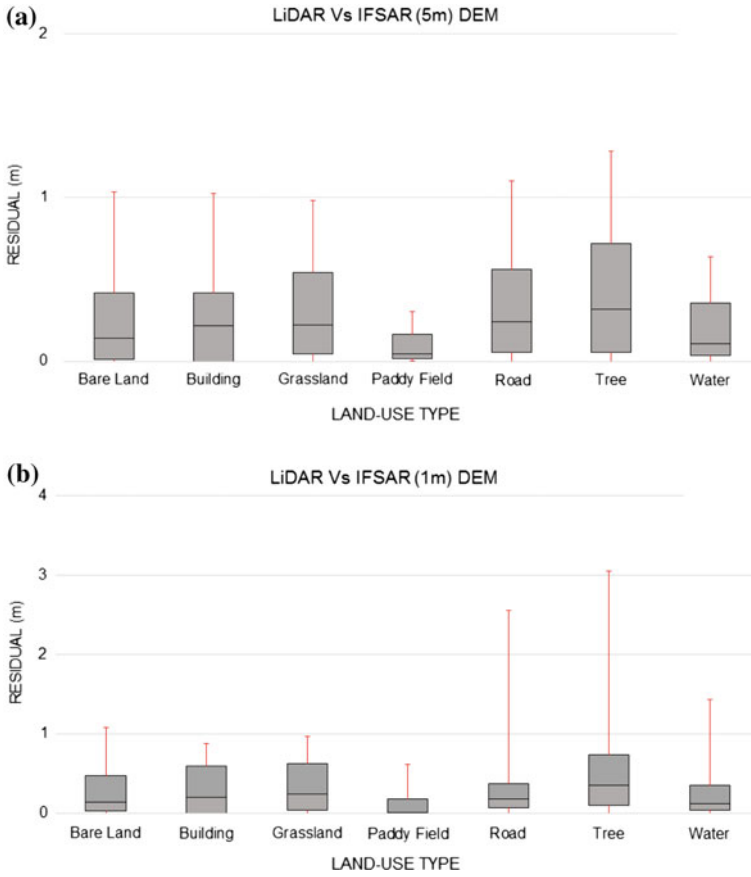
Fig. 4 Box plot showing the comparison of error distribution on different land-use types

Table 3 Combined hydraulic variables in discharge calculation

DEM	Conf. level	Bound	Hydraulic variables			
			W	Y	S	Q
LiDAR$_{15 cm}$		Lower	43.719	1.439	0.000342	39.265
	95%	Mean	43.829	1.442	0.000343	39.574
		Upper	43.939	1.446	0.000344	39.885
IFSAR$_{5 m}$		Lower	43.736	1.736	0.000218	46.507
	95%	Mean	43.845	1.740	0.000218	46.829
		Upper	43.955	1.745	0.000219	47.228
IFSAR$_{1 m}$		Lower	43.786	1.737	0.000276	50.639
	95%	Mean	43.896	1.742	0.000277	51.035
		Upper	44.006	1.746	0.000278	51.433

the other DEM datasets. This study found that the cross-sectional depth (*S*) significantly increased concurrently with the discharge value. It can be seen that the steepness of the channel slope and the wideness of the river did not affect the increment of the discharge value. However, the DEM resolution and accuracy affect more by small reaches with steeper channel slopes [7]. The channel slope increased as the original IFSAR DEM resolution (5 m) was resampled to 1 m resolution and vice versa as reported by [8].

Table 4 shows the parameter sets of the Manning-n based on different land-use types using 95% confidence interval. The bare land, cultivated and brush, developed area and forest presented surface roughness for floodplain while water feature is for channel roughness.

Figure 5 shows a scatter plot between $LiDAR_{15\ cm}$ and the original and resampled IFSAR DEMs. From the random elevation points on different land-use types, the relationship between LiDAR and IFSAR with 5 m resolution presented better results of approximately $R^2 = 0.97$ as compared to the resampled $IFSAR_{1\ m}$ DEM; $R^2 = 0.96$ (Fig. 3) with natural logarithm selected for the trend lines of Eqs. 2 and 3. Therefore, the established equation was applied to the DEM for optimization purposes in water surface elevation estimation.

Table 4 Manning-n of floodplain and channel areas

	Land-use types				
	Bare land	Cultivated and brush	Developed area	Forest	River
Manning-*n*	0.0398	0.0399	0.1741	0.1502	0.0398
	0.0400	0.0401	0.1753	0.1509	0.0400
	0.0401	0.0403	0.1766	0.1516	0.0402
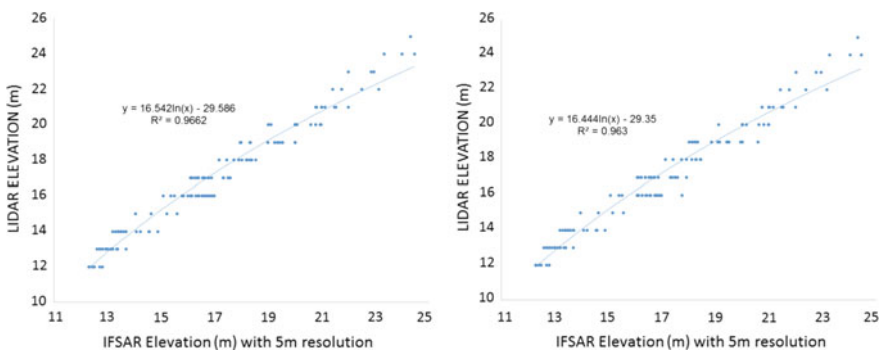
Fig. 5 Scatterplot between LiDAR and different IFSAR DEM resolutions

$$\text{IFSAR DEM}_{\text{Optimised}} = 16.542 \ln(\text{IFSAR}_{\text{Elevation}}) - 29.586 \tag{2}$$

$$\text{IFSAR DEM}_{\text{Optimised}} = 16.444 \ln(\text{IFSAR}_{\text{Elevation}}) - 29.35 \tag{3}$$

5.3 Comparison of Water Surface Elevation Between Different DEMs and Optimized DEM Datasets

To identify the capability of IFSAR in determining the WSE, the IFSAR DEM and resampled IFSAR DEM were optimized using Eqs. 2 and 3, respectively. Table 5 presents the comparison between observed WSE and predicted WSE obtained using the HEC-RAS model over different DEMs using likelihood measures. The findings show that the optimized IFSAR$_{5\ m}$ DEM presented fewer errors and enhanced the WSE prediction compared to the other DEM datasets. Based on NSE, about 7% has inclined from 45 to 52% when optimized with IFSAR DEM compared to the original IFSAR DEM. The WSE over the resampled LiDAR with 1 m resolution did not generate due to similar values of the combined hydraulic variables as original LiDAR DEM. The original DEMs did not produce similar results when compared to the resampled DEMs [8]. For example, the LiDAR$_{15\ cm}$ resampled to 1 m did not show similarities to the resampled IFSAR$_{1\ m}$. Figure 6 presents water surface elevation of 95% confidence interval (CI).

Table 5 Error comparison between measured and predicted WSE

DEM	Likelihood measures	Original DEM bound (95% CI)			DEM optimized bound (95% CI)		
		Lower	Mean	Upper	Lower	Mean	Upper
LiDAR$_{15\ cm}$	MAE	0.816	0.822	0.826			
	RMSE	1.114	1.118	1.122			
	NSE	0.478	0.474	0.471			
IFSAR$_{5\ m}$	MAE	0.839	0.838	0.836	0.786	0.785	0.784
	RMSE	1.149	1.149	1.149	1.071	1.071	1.072
	NSE	0.446	0.445	0.445	0.518	0.518	0.517
IFSAR$_{1\ m}$	MAE	0.840	0.839	0.838	0.790	0.789	0.787
	RMSE	1.149	1.149	1.150	1.071	1.072	1.072
	NSE	0.445	0.445	0.444	0.518	0.517	0.517
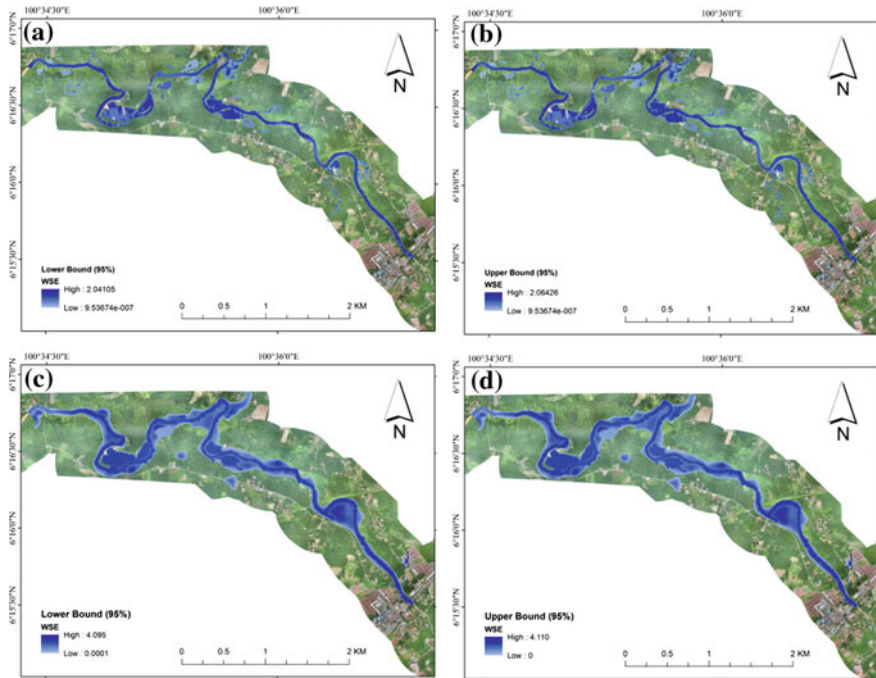
Fig. 6 WSE prediction from HEC-RAS model based on combined parameter sets using 95% confidence level at upper and lower bound using (**a**, **b**) LiDAR and (**c**, **d**) optimized IFSAR DEM with 5 m resolution

6   Conclusion

In flood mapping, prediction of the water surface elevation is essential to estimate the inundated area using remote-sensed data. The accuracy of the DEM data needs to be established prior to the WSE delineation. In this study, the effects of resampled DEMs (LiDAR and IFSAR) on the surface elevation and slope on each of the land-use types were assessed. The road and area were covered by trees highly sensitive to the DEM resolution, while paddy fields, buildings and grasslands presented less residual using the resampled IFSAR DEM. In addition, the maximum elevation of resampled $IFSAR_{1\ m}$ is insensitive to the DEM resolution. In contrast, the slope influences the DEM resolution as finer resolutions produce higher slopes compared to coarse DEM grid sizes.

Furthermore, R^2 of 90% was found in the relationship between original LiDAR and original and resampled IFSAR DEMs. In addition, the equations were established to calibrate the original IFSAR DEM to obtain the best results in water surface elevation prediction. No doubt that the LiDAR DEM can give the best results in any applications. However, surprisingly, optimized IFSAR DEM with 5 m resolution shows good estimation in WSE and can potentially be used in flood

inundation mapping whereas by resampling the IFSAR DEM, the errors slightly increased. Based on the likelihood measures, MAE (RMSE) for the optimize IFSAR5 m and resampled IFSAR1 m were presented as averages of 0.785 (1.071 m) and 0.789 m (1.072 m), respectively.

This study proposes DEM optimization that has shown results of better water surface elevation compared to the LiDAR DEM data. The suggested methodology can be tested on different sources of DEMs in flood inundation mapping for further analysis.

References

1. Qi, S., Brown, D.G., Tian, Q., Jiang, L., Zhao, T., Bergen, K.M.: Inundation extent and flood frequency mapping using LANDSAT imagery and digital elevation models. GISci. Remote Sens. **46**(1), 101–127 (2009)
2. Quyen, N.T.N., Liem, N.D., Loi, N.K.: Effect of land use change on water discharge in Srepok watershed, Central Highland, VietNam. Int. Soil Water Conserv. Res. **2**(3), 74–86 (2014)
3. Schumann, G., Matgen, P., Cutler, M.E.J., Black, A., Hoffmann, L., Pfister, L.: Comparison of remotely sensed water stages from LiDAR, topographic contours and SRTM. ISPRS J. Photogramm. Remote Sens. **63**(3), 283–296 (2008)
4. Coveney, S., Roberts, K.: Lightweight UAV digital elevation models and orthoimagery for environmental applications: data accuracy evaluation and potential for river flood risk modelling. Int. J. Remote Sens., 1–22 (2017)
5. Patro, S., Chatterjee, C., Singh, R., Raghuwanshi, N.S.: Hydrodynamic modelling of a large flood-prone river system in India with limited data. Hydrol. Process. **23**, 2774–2791 (2009)
6. Yan, K., Di Baldassarre, G., Solomatine, D.P., Schumann, G.J.P.: A review of low-cost space-borne data for flood modelling: topography, flood extent and water level. Hydrol. Process. **29**(15), 3368–3387 (2015)
7. Saksena, S., Merwade, V.: Incorporating the effect of DEM resolution and accuracy for improved flood inundation mapping. J. Hydrol. **530**, 180–194 (2015)
8. Dixon, B., Earls, J.: Resample or not? Effects of resolution of DEMs in watershed modeling. Hydrol. Process. **23**, 1714–1724 (2009)
9. Tan, M.L., Ficklin, D.L., Dixon, B., Ibrahim, A.L., Yusop, Z., Chaplot, V.: Impacts of DEM resolution, source, and resampling technique on SWAT-simulated streamflow. Appl. Geogr. **63**, 357–368 (2015)
10. Earls, J., Dixon, B.: Influence of resolution on the SWAT model: examining neighbouring basins. In AWRA Specialty Conference, pp. 1–7 (2006)
11. DID: Ringkasan Laporan Banjir Tahunan Bagi Tahun 2010/2011. Malaysia (2010)
12. USGS: Part 3 Quality Control (1998)
13. Tate, N.J., Fisher, F.: Causes and consequences of error in digital elevation models. Prog. Phys. Geogr. **30**(4), 467–489 (2006)
14. Jung, Y., Merwade, V., Asce, M.: Uncertainty quantification in flood inundation mapping using generalized likelihood uncertainty estimate and sensitivity analysis. J. Hydrol. Eng. **17**(4), 507–520 (2012)
15. Horritt, M.S.: A methodology for the validation of uncertain flood inundation models. J. Hydrol. **326**(1–4), 153–165 (2006)

16. Di Baldassarre, G., Schumann, G., Bates, P.D., Freer, J.E., Beven, K.J.: Flood-plain mapping: a critical discussion of deterministic and probabilistic approaches. Hydrol. Sci. J. **55**(3), 364–376 (2010)
17. Mokhtar, E.S., Pradhan, B., Ghazali, A.H., Shafri, H.Z.M.: Comparative assessment of water surface level using different discharge prediction models. Nat. Hazards (2017)
18. Jung, Y., Merwade, V., Yeo, K., Shin, Y., Lee, S.O.: An approach using a 1D hydraulic model, landsat imaging and generalized likelihood uncertainty estimation for an approximation of flood discharge. Water **5**, 1598–1621 (2013)

Improved Building Roof Type Classification Using Correlation-Based Feature Selection and Gain Ratio Algorithms

M. Norman, H. Z. M. Shafri, Biswajeet Pradhan and B. Yusuf

Abstract Of late, application of data mining for pattern recognition and feature classification is fast becoming an essential technique in remote sensing research. Accurate feature selection is a necessary step to improve the accuracy of classification. This process depends on the number of feature attributes available for interactive synthesis of common characteristics that discriminate different features. Geographic object-based image analysis (GEOBIA) has made it possible to derive varieties of object attribute for this purpose; however, the analysis is more computationally intensive. The aim of this study is to develop feature selection technique that will provide the most suitable attributes to identify different roofing materials and their conditions. First, the feature importance was evaluated using gain ratio algorithm, and the result was ranked, leading to selection of the optimal feature subset. Then, the quality of the selected features was assessed using correlation-based feature selection (CFS). The classification results using SVM classifier produced an overall accuracy of 83.16%. The study has shown that the ability to exploit rich image feature attribute through optimization process improves accurate extraction of roof material with greater reliability.

M. Norman · H. Z. M. Shafri (✉) · B. Pradhan · B. Yusuf
Department of Civil Engineering, Faculty of Engineering,
Universiti Putra Malaysia (UPM), 43400 Serdang, Selangor, Malaysia
e-mail: hzms04@gmail.com

B. Pradhan
e-mail: biswajeet24@gmail.com

H. Z. M. Shafri · B. Pradhan
Geospatial Information Science Research Centre (GISRC), Faculty of Engineering,
Universiti Putra Malaysia (UPM), 43400 Serdang, Selangor, Malaysia

M. Norman
Department of Surveying Science and Geomatics, Faculty of Architecture,
Planning and Surveying, Universiti Teknologi MARA (Perlis),
02600 Arau, Perlis, Malaysia
e-mail: ayunorman@gmail.com

1 Introduction

In remote sensing applications, roof identification and extraction is challenging due to similarities in geometric pattern, variation in physical and chemical properties and spatial heterogeneity. Geographic object-based image analysis (GEOBIA) has been widely used as it can generate numerous feature attributes of the image object for better feature classification. OBIA exploits the spectral, shape and texture characteristics of the images to partition it into features in vector form. It has been reported to provide better feature extraction capabilities compared to traditional pixel-based image classification techniques that accord it the widespread popularity among the remote sensing practitioners [1, 2]. Moreover, its feature attribute extraction oriented output facilitates data mining applications for pattern recognition [3]. To achieve a high degree of automation process, combination of quantitative attribute-based feature selections and machine learning classification are very significant.

Due to the high frequency of image objects and effect if illuminations versus sensor look angle, particularly in urban area, it is always difficult to group pixels belonging to the same object within a single image segment. This problem is more pronounced when unblended segmentation parameters are used [4, 5]. This causes numerous numbers of segments especially in high-resolution imagery making analysis of feature more computationally intensive and prone to error in classification.

Several feature selection algorithms have been used in the past to select relevant feature for different applications. Novack et al. [6] applied four different types of feature selection algorithms: Info-Gain, Relief-F, Fast Correlation-Based Filter (FCBF) and Random Forest, to provide ranking of variable importance. They found out that the features selected from the four algorithms are the same for each class group. This is because most of the algorithms consider not only the relevance of the features but also redundancy among each other. Recently, Li et al. [7] applied correlation-based feature selection (CFS) to measure the quality of a subset of features for land-use land-cover classification. The result shows that combining feature selection with classifiers such as Random Forest, the technique improved the accuracy of the classification. In this research, we present an effective means of extracting roof materials and their conditions using multispectral World-View 3 imagery through the process of feature attribute exploration.

2   Study Area and Datasets

This study was carried out over Universiti Putra Malaysia (UPM) and its surrounding, covering about 2.7 km² area (Fig. 1). This comprises residential type building setting with different roof materials including metal roof, concrete roof and asbestos roof, which are categorized according to their materials and conditions (new and old). The landscape presents mixture pervious and impervious surfaces such as water, road, trees, grass and bare land. High spatial resolution World-View 3 with panchromatic image with 0.31 spatial resolution and multispectral image with 1.24 m resolution were used for the investigation. This satellite was successfully launched on 13 August 2014. It is the first multi-payload, super-spectral, high-resolution commercial satellite sensor operating with eight multispectral bands (coastal, blue, green, yellow, red, red-edge, NIR 1 and NIR 2).

3   Methodology

3.1   Preprocessing and Segmentation

The World-View 3 image was corrected for radiometric and atmospheric effects to create a more faithful representation of the original scene. Subsequently, the image was segmented using the multiresolution segmentation algorithm in eCognition v9.1 [8]. With the define segmentation parameters, over-segmentation occurred leaving some features being represented by many image objects. This was corrected
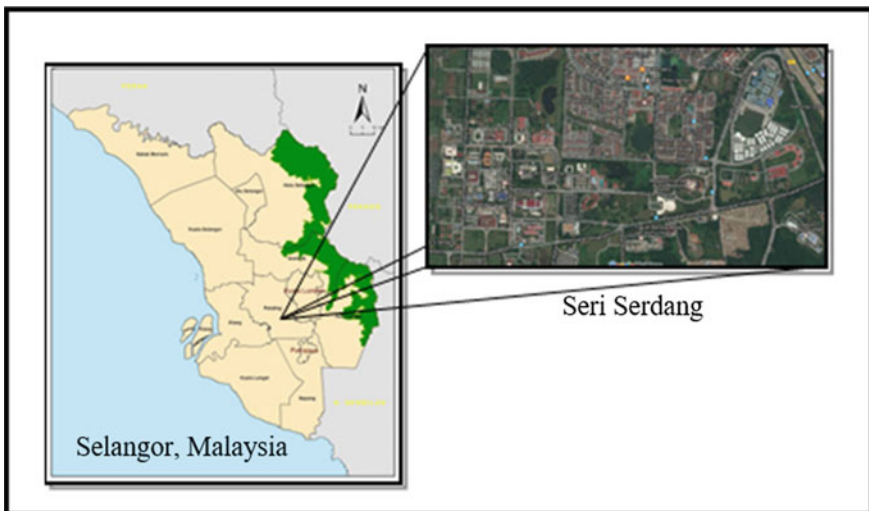
Fig. 1   Study area
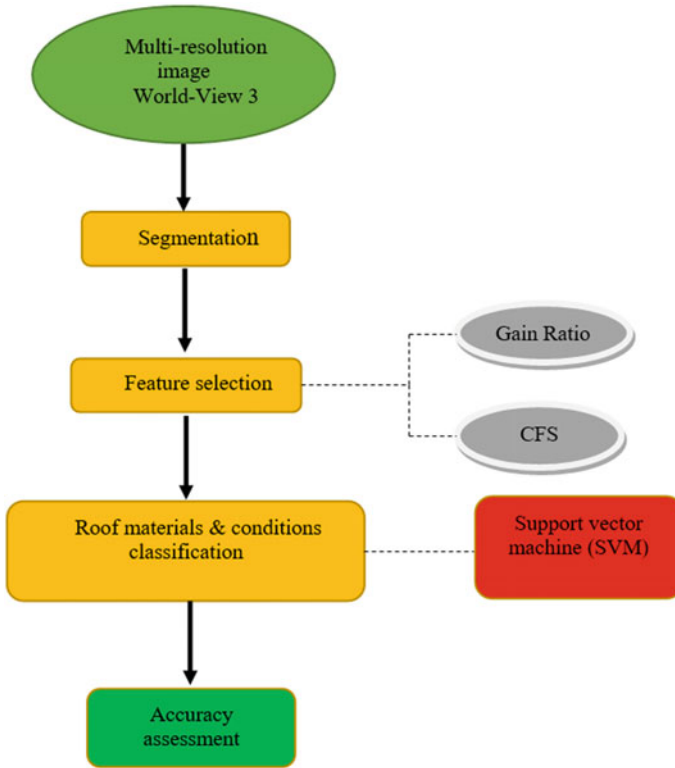
Fig. 2 Framework of the overall process

by merging contiguous segments into larger segment representing object entity based on the spectral similarity threshold. Schematic flow of data processing is presented in Fig. 2.

Five levels of segmentation parameters were defined using five different scale parameters (60, 70, 80, 90 and 100). Similarly, the shape and compactness parameters were set as 0.1, 0.3, 0.5, 0.7 and 0.9. These parameters were optimized using Taguchi method. The results of the experiment obtained the optimal parameter combinations 80:0.7:0.1 for scale, shape and compactness, respectively.

3.2 Features Selection

The advantage of OBIA is the ability to extract multiple attributes about the image objects, which allows intricate data exploration for object classification. However, processing the huge attribute data generated is computationally intensive. So, gain ratio (GR) algorithm (Eq. 1) [9] was used to assess the importance of the features attributes so as to select most important one in order minimizes the computational requirements. GR eliminates bias towards tests with many outcomes (large attribute values) by measuring information. The information gain measures interaction of attribute selection by employing decision tree, which computes the difference among the predicted information requirement, and then classifies a tuple in tuples for update information prerequisite. The greater the gain ratio, the more significant it represents features [10]. GR is expressed as

$$\text{Gain Ratio (A)} = \frac{\text{Gain (A)}}{\text{Split Info}_A(D)} \tag{1}$$

Having obtained the degree of importance of feature attributes with GR, correlation-based feature selection (CFS) (Eq. 2) was utilized to evaluate the quality of the features subset from which only the significant features for roof materials and conditions discrimination were selected. CFS simply evaluates the worth of a set of features using a heuristic assessment function based on the correlation of the features. A good feature subset contains features highly correlated with classes and highly uncorrelated to each other [11].

$$\text{Merits} = \frac{k\bar{r}_{\text{cf}}}{\sqrt{k + k(k-1)r_{\overline{\text{ff}}}}} \tag{2}$$

where f indicates the feature, c is the class, $\bar{r}_{\text{cf}}$ denotes the mean feature correlation with classes, $r_{\overline{\text{ff}}}$ indicates the average feature intercorrelation and k denotes the number of the attributes in the subset.

3.3 Classification and Accuracy Assessment

The image object represents unclassified features. In this study, support vector machine (SVM) was used to assign feature class to the image objects. SVM is based on statistical computational process that identifies the optimal hyperplane as a decision function in high-dimensional space [12]. The previous study shows that the number of features selected will determine the accuracy of SVM classification [13]. 12 classes, namely, tree, grass, water, road, shadow, bare land, new metal, old metal, new concrete, old concrete, new asbestos and old asbestos were extracted in

the process. The accuracy of the classification was evaluated using standard confusion matrix [14].

4   Result of Roof Materials and Conditions Discrimination

The results (Fig. 3a–c) indicate the rank of roof materials and conditions features according to gain ratio value from three categories, spectral, shape and texture. They have been ranked from the highest value to the lowest.

Table 1 shows that 11 features selected as the most suitable for classification.

The accuracy was calculated using standard confusion matrix method, whereby the results for classification were represented by this matrix (Fig. 4). Thus, the overall accuracy can be computed as well as individual class accuracy.

Figure 5a shows that new metal misclassified with old asbestos and after suitable features applied, the misclassification improves to be as new metal for the whole object (Fig. 5b). Meanwhile, there are three objects misclassified in Fig. 5c. Feature selection approach successfully solves the misclassification problem, whereby each object has been classified into its true class, such as new concrete re-classified as old concrete, old metal as new concrete and old metal as new metal (Fig. 6).

Result shows the classification of roof materials and conditions within UPM Serdang main campus and its surrounding area using SVM classifier. It proved that the result is much better after using the selected features to classify the image. As a result, overall accuracy for roof materials and conditions classification using SVM classifier is 83.16% and kappa coefficient is 0.81. After classification using selected features applied to the images, the results obviously show the improvement of misclassification.
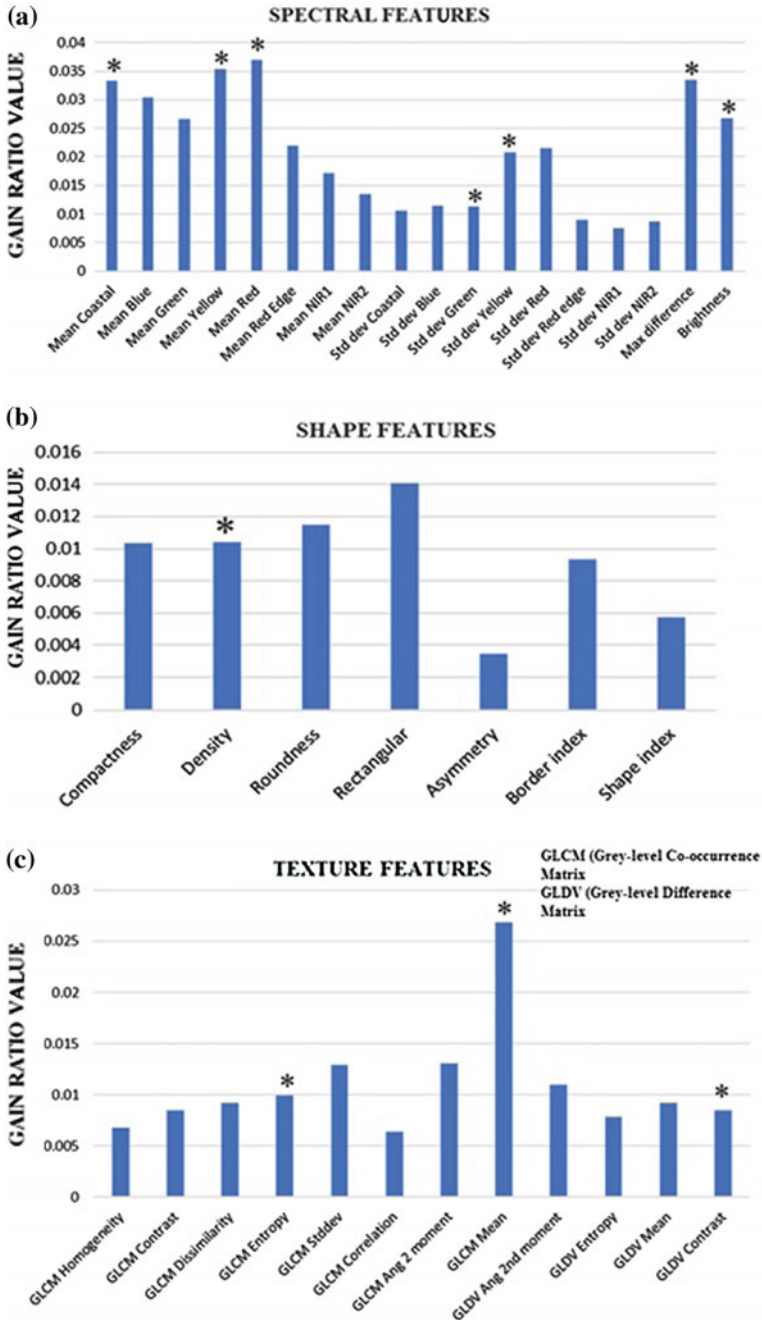
Fig. 3 Relative contributions of roof materials and conditions features based on gain ratio index

Table 1 Selected features

No.	Feature	Category
1	Mean coastal	Spectral
2	Mean yellow	Spectral
3	Mean red	Spectral
4	Brightness	Spectral
5	Maximum difference	Spectral
6	Standard deviation green	Spectral
7	Standard deviation yellow	Spectral
8	Density	Shape
9	GLCM entropy	Texture
10	GLCM mean	Texture
11	GLDV contrast	Texture

Classess	Confusion Matrix		Accuracy		Totals	
	Classified	Unclassified	Producer	User	KIA	Overall(100%)
New metal	19	2	0.9	1	0	90
Old metal	18	5	0.78	1	0	78
New concrete	9	4	0.69	1	0	69
Old concrete	15	5	0.75	1	0	75
New asbestos	2	1	1	1	Undefinied	100
Old asbestos	1	5	0.12	1	0	12
Water	7	3	0.7	1	0	70
Grass	21	0	1	1	Undefinied	100
Tree	25	0	1	1	Undefinied	100
Road	12	1	0.92	1	0	92
Shadow	16	0	1	1	Undefinied	100
Bare land	13	7	0.65	0	0	65

Fig. 4 Accuracy for each class
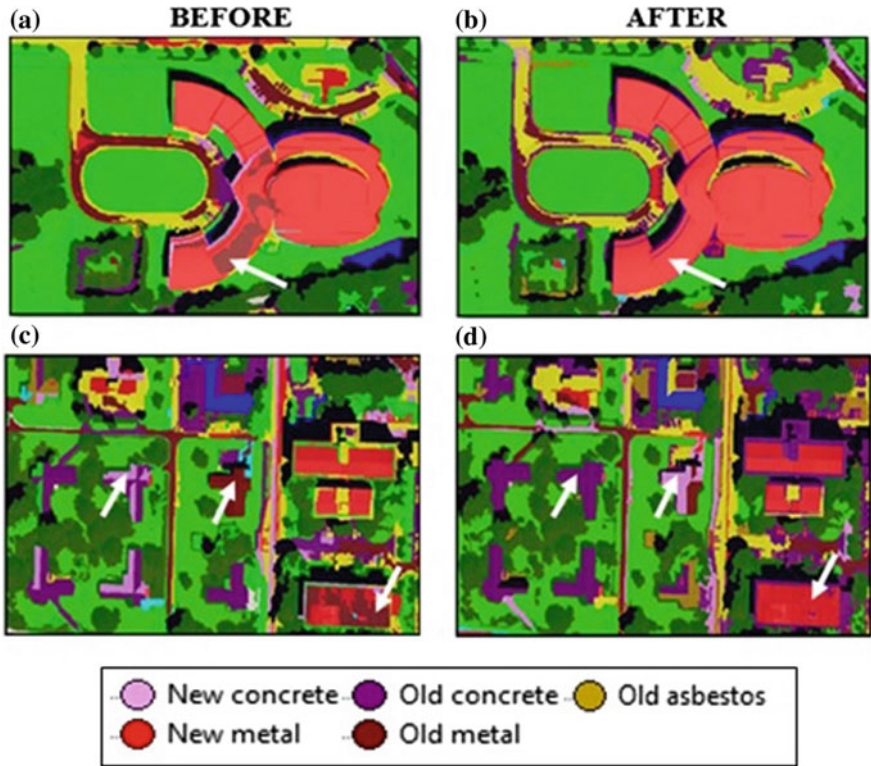
Fig. 5 Example of an improved classification for roof materials and conditions after suitable features applied
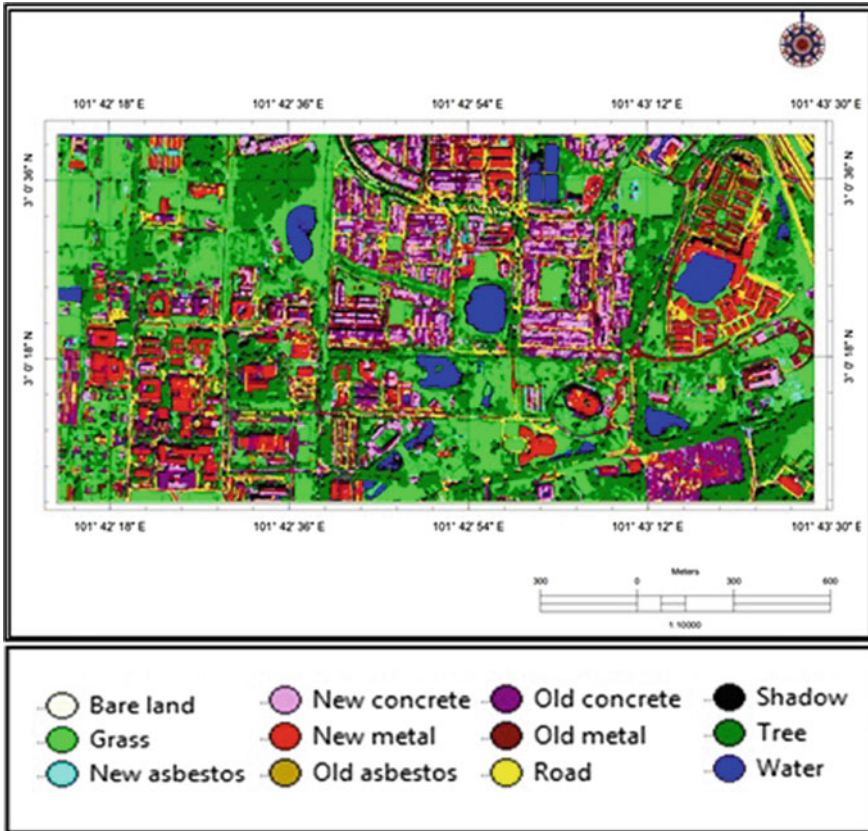
Fig. 6 Distribution of roof materials and conditions using SVM classifier

5   Conclusion

This study aimed to develop feature selection technique to verify the most suitable features to be used for the discrimination of roofing materials and conditions based on different feature algorithms available. The performance assessment was done, giving satisfied accuracy and error confusion matrix. Experimental results demonstrate that SVM based on significant features can improve the quality of classification and reduce the misclassification especially between road and concrete, shadow and water, old concrete and old metal as well. Those misclassifications are due to the similar spectral reflectances between each material.

As a result, the systematic feature selection approach can significantly contribute to roof materials and condition discrimination besides increase its accuracy. The application of gain ratio algorithm in this study is effective for reducing the misclassification problem of roof material classification.

Future research should be conducted by comparing several features selection algorithms, and further assessment of different classifiers is required.

References

1. Blaschke, T., et al.: Geographic object-based image analysis—towards a new paradigm. ISPRS J. Photogramm. Remote Sens. **87**, 180–191 (2014)
2. Radoux, J., Bogaert, P.: Accounting for the area of polygon sampling units for the prediction of primary accuracy assessment indices. Remote Sens. Environ. **142**(February), 9–19 (2014)
3. Dash, M., Liu, H.: Feature selection for classification. Intell. Data Anal. **1**(3), 131–156 (1997)
4. Kim, M., Warner, T.A., Madden, M., Atkinson, D.S.: Multi-scale GEOBIA with very high spatial resolution digital aerial imagery: scale, texture and image objects. Int. J. Remote Sens. **32**(10); **1161**(10), 2825–2850 (2011)
5. Zhang, X., Xiao, P., Song, X., She, J.: Boundary-constrained multi-scale segmentation method for remote sensing images. ISPRS J. Photogramm. Remote Sens. **78**(May), 15–25 (2013)
6. Novack, T., Esch, T., Kux, H., Stilla, U.: Machine learning comparison between WorldView-2 and QuickBird-2-simulated imagery regarding object-based urban land cover classification. Remote Sens. **3**(10), 2263–2282 (2011)
7. Li, D.T.M., Ma, L., Blaschke, T., Cheng, L.: A systematic comparison of different object based classification techniques using high spatial resolution imagery in agricultural environments. Int. J. Appl. Earth Obs. Geoinf. **49**, 87–98 (2016)
8. Weise, C.: eCognition Essentials, pp. 1–2 (2016)
9. Quinlan, J.R., Improved use of continuous attributes in C4. 5. l Artif. Intell. Res. Artif. Intell. Res. **4**, 77–90 (1996)
10. Ma, L., et al.: Evaluation of feature selection methods for object-based land cover mapping of unmanned aerial vehicle imagery using random forest and support vector machine classifiers. Int. J. Geo-Inform. **6**(51), 1–21 (2017)
11. Hall, M.A., Holmes, G.: Benchmarking attribute selection techniques for discrete class data mining. IEEE Trans. Knowl. Data Eng. **15**(6), 1437–1447 (2003)
12. Bazi, Y., Melgani, F.: Toward an optimal SVM classification system for hyperspectral remote sensing images. Geosci. Remote Sens. IEEE Trans. **44**(11), 3374–3385 (2006)
13. Hamedianfar, A., Shafri, H.Z.M.: Development of fuzzy rule-based parameters for urban object-oriented classification using very high resolution imagery. Geocarto Int. **29**(3), 268–292 (2014)
14. Congalton, R.G., Green, K.: Assessing the Accuracy of Remotely Sensed Data: Principles and Practices (2009)

Wave Height Climatology Assessment from Multi-mission Satellite Altimeter for Renewable Energy

Marith Banati Barata, Ami Hassan Md Din and Abdullah Hisham Omar

Abstract The fact that we will lose the source of fossil fuel in the future is undeniable. Hence, it is crucial to find the replacement of this resource. In present day, wave energy is found to be one of the sources of renewable energy. This chapter is proposing to assess the wave height climatology over the Malaysian seas in order to support renewable energy. The key step in the assessment of wave height climatology over Malaysian seas, South China Sea, Malacca Straits, Sulu Sea and Celebes Sea, is by acquiring an accurate and reliable wave height data. The Radar Altimeter Database System (RADS) was used to extract the 24 years of significant wave height data from January 1993 to December 2016. Altimetry-derived wave height data were validated with ground truth observation from wave buoy and Acoustic Doppler Current Profiler (ADCP). The wave height magnitude and pattern were then analysed particularly to see its characteristic during monsoon season. The monthly average of altimetry significant wave height from January 1993 to December 2016 was mapped in this study. The findings clearly show that the Northeast monsoon has the most significant effect of wave height variation over Malaysian seas, while the Southwest monsoon has minimal effect. The reliability of satellite altimetry also proved based on the RMSE and correlation results, which are 0.2515 m and 0.9396, respectively. This study offers useful wave height information especially related to renewable energy in the Malaysian seas for future studies.

M. B. Barata · A. H. M. Din (✉) · A. H. Omar
Geomatic Innovation Research Group (GIG), Faculty of Geoinformation
and Real Estate, Geoscience and Digital Earth Centre (INSTEG),
Universiti Teknologi Malaysia, 81310 Johor Bahru, Johor, Malaysia
e-mail: amihassan@utm.my

M. B. Barata
e-mail: marithbanati@yahoo.com

A. H. Omar
e-mail: abdullahhisham@utm.my

A. H. M. Din
Institute of Oceanography and Environment (INOS), Universiti Malaysia
Terengganu, Kuala Terengganu, Terengganu, Malaysia

1   Introduction

Fossil energy is being attributed as one of the main sources of global warming event. This further supports the need for replacement of this source. Various wave, tidal and current energy converters have been invented to explore the big potential of marine power, especially wave energy. Other than the only well-known water grounded source is hydroelectric dams, waves from the ocean also have the same potential to be a widely utilisable. Wave energy has a number of significant benefits including predictable source, profusion, massive load aspect and low eco-friendly effect and accessibility compared to other renewable energy sources [1].

Assessments have been done in verifying the potential of wave height as a source of renewable energy in various regions [2]. Previously, a study regarding wave energy and wave height in Malaysian Seas was conducted by Aziz [3]. The difference of wave heights within the monsoon seasons enables this environmental phenomenon to make an impact on the wave energy produced. The ocean wave rose up by gaining energy transformed from sun and wind. The wind that created by solar energy blows in the middle of the sea, which then transferred the energy to the ocean surface in order to convert winds energy to wave energy [4]. After the energy is transformed, it can mobilise thousand miles with low energy loss. Basically, the wave energy produced by the waves relies on the wind energy received.

The aim of this study is to produce the map of wave height climatology over the Malaysian seas in order to support renewable energy. Therefore, wave data plays the most important role in wave energy assessment. Acquiring the reliable and accurate wave height climatology is one of the essential phases in the evaluation of wave height. The wave height data from satellite altimeter needs to be verified by in situ measurements using offshore buoy in order to evaluate the quality of altimetry-derived wave height. There are limitations in the verification process since the measurements from a buoy are point-based while the satellite data produces measurements in a form of sets of gridded data with interpolation. A research was done by Shanas et al. [5] as resulted that the altimeter measurements represent a good data source to enhance our understanding of the variability even near the coast [5]. Satellite altimeter also has a wide coverage of data which makes the data more reliable for the climatology purposes. In this study, the satellite altimetry data are verified using two in situ measuring instruments which are offshore buoy and Acoustic Doppler Current Profiler (ADCP).

The 24 years of wave height data used in mapping the climatology of wave height over Malaysian seas from January 1993 to December 2016. The wave height data are mainly taken from satellite altimetry that has been known as a reliable data source over the years [6]. Studies from Abdullah et al. [7] and Aziz et al. [8] proved that the satellite altimetry is a reliable device to collect the wave height data and it

only has a few centimetres discrepancy in terms of accuracy. Satellite altimeter works by emitting a small pulse of microwave radiation with identified strength towards the sea surface. Then, the interaction of sea surface and the emitted pulse will be reflected back to the satellite altimeter. From the interaction, the travel time is measured precisely. In determining the wave height, several corrections like the behaviour of the radar pulse through the atmosphere, sea state bias and other geophysical signals have to be done [9].

1.1 Principle of Satellite Altimeter

Theoretically, satellite altimeter is a nadir-pointing instrument that measured the time travel of transmitted microwave radiation to be reflected back to the satellite. From the computed round trip radar pulse time, the wave height is obtained. 1700 pulses per second emitted in the interaction between ocean wave height and the reflected back satellite signal [10]. The range R from the satellite to ocean wave surface is predicted from the round trip travel time of

$$R = R^{\wedge} - \sum \Delta R_J \tag{1}$$

$R^{\wedge} = ct/2$ is the range calculated by ignoring the refraction based on speed of light c and ΔR_J, $J = 1, \ldots, N$ is the correction for the numerous biases between mean reference wave height and mean electromagnetic scattering surface. It also applies the correction for the numerous components of the atmosphere. The predicted range of orbit height and the wave height which are relative to the centre of the Earth varies along the satellites orbit from along-track dissimilarity. The height h of the targeted ocean wave which is relative to reference ellipsoid (Earth fit earth centre) is the result of the range measurements as follows:

$$R = H - R^{\wedge} = H - R^{\wedge} + \sum \Delta R_J \tag{2}$$

The radar target to the wave height is given by (2) that relative to the reference ellipsoid is affected by the uneven surface of the geoid, variation of wave height (types of tides) and atmospheric pressure loading response by the sea surface. The pulses are transmitted as footprints that were described as beam-limited footprint. It will specify the target surface area of wave height within the transmitted footprint. The design of the beam-limited altimeter limitation can be overcome by transmitting a very short pulse with duration of a few nanoseconds using a small antenna [11]. Figure 1 illustrates the schematic diagram of satellite altimeter system and its principle.

Practically, the situation is far more complicated. Several factors have to be taken into consideration in order to reduce the errors in getting the travel time such as the orbital error and hardware problem like electronic time delay, clock drift,
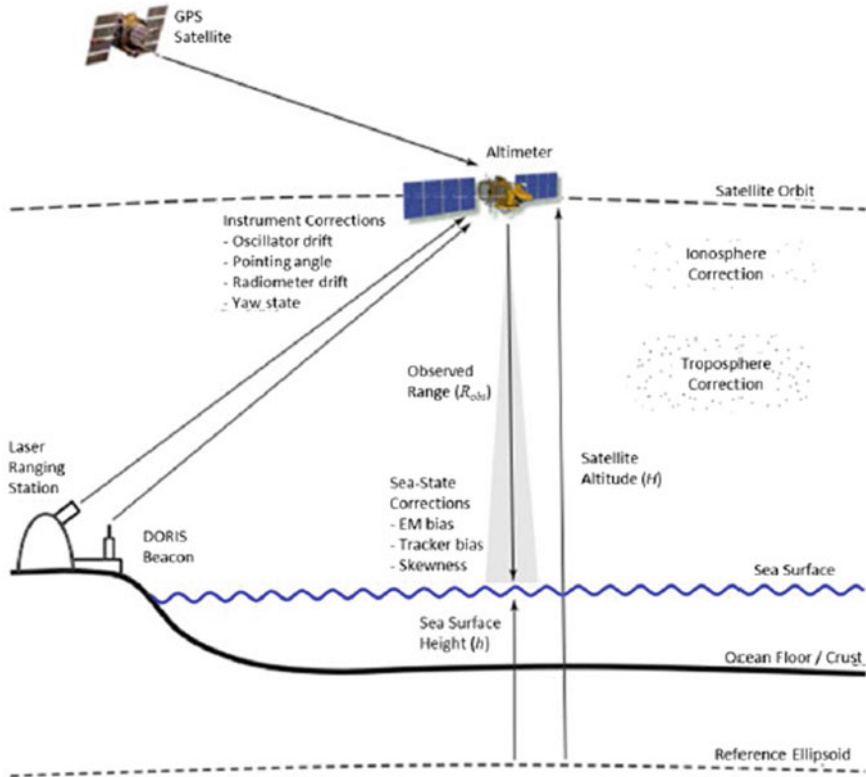
Fig. 1 Schematic view of satellite altimeter measurement [12]

offset antenna phase centre, centre of gravity, time lagging of observations, doppler shift error and more [8].

2　Research Approach

2.1　Area of Study

This study covers the Malaysian seas which includes South China Sea, Malacca straits, Sulu Sea and Celebes Sea (see Fig. 2). The South China Sea indicates the great possibility of producing high wave energy. This is because the location exposes to the Northeast monsoon from November until February for each year. The monsoon season will let winds to transfer the high energy to the ocean wave. Consequently, the wave height will increase rapidly.

Fig. 2 Study area of wave height distribution in Malaysian seas

2.2 Altimetry Data

Nowadays, altimetry data are distributed through many agencies like NOAA, AVISO, EUMETSAT and PODAAC. Besides, the Delft Institute for Earth-Oriented Space Research (DEOS) for Satellite Altimetry and the NOAA laboratory cooperate in the development of Radar Altimeter Database System (RADS). The RADS is well-known as a harmonised, certified and cross-calibrated sea-level database from all satellite altimeter missions [8]. In RADS, the latest corrected range and geophysical state of the ocean wave are able to access by the users [1]. They can also produce their own altimetry products based on their particular interests [9]. The altimetry data (RADS) products were verified and validated by DEOS. Besides, RADS database also consistently updates and makes corrections to their system, verify accuracy format and reference system parameters. This system also provides the need of scientists and operational users to have ready value-added sea-level data [1]. Presently, RADS allows users to extract the data from some present and past satellite altimeter missions. In this study, the satellite altimetry data used are data from January 1993 to December 2016. This study employs the gridded data from nine satellite altimeters, which are TOPEX, ENVISAT, ERS-1. ERS-2, JASON-1, JASON-2, JASON-3, SARAL and CRYOSAT. The monthly average wave height data set was used in the mapping process.

2.3 In Situ Data

Buoy and ADCP were used in this study for the validation process of satellite altimetry data. Acoustic Doppler technology is flexible in the measurement of sea
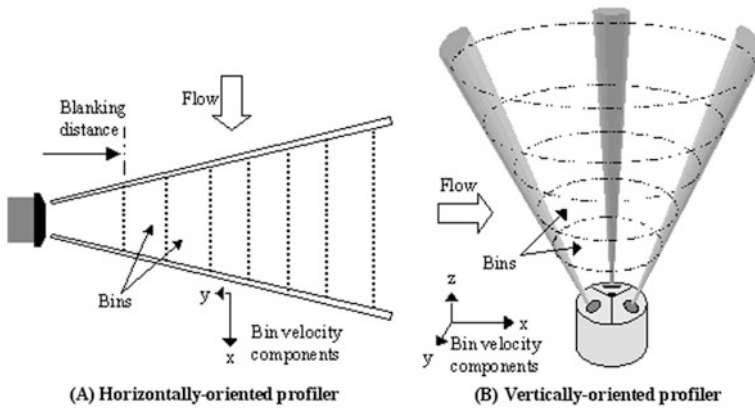
Fig. 3 The ADCP physical profile orientation [14]

conditions. However, this technology can be limited and it is less effective at measuring the small-scale kinematic fluctuations caused by waves and turbulence. The ADCP is equipped with acoustic transducers which ping at a minimal frequency rate of 2 Hz [13] (see Fig. 3). It is noted that the ADCP measures wave height through sounds energy of which may be absorbed by the water each time it pings. Therefore, the data collected may not be very accurate. The acoustic transducer will be tilted 20° away from its vertical in order to measure the wave height pattern. The Doppler Shift in the returned signal estimated in order to compute the velocity of the beams. From the calculated retuned signal, the wave height estimation is attained.

The ADCP data was provided by the Institute of Oceanography and Environment (INOS), Universiti Malaysia Terengganu, which includes monthly data from 2012 to 2016, but there were gaps in the data for several months.

The buoy is equipped with accelerometers to measure vertical heaves, or up and down movements to measure wave heights and swell period. The accelerometer will then calculate the data and interpret it in the form of wave height at the point where it is obtained. Figure 4 shows the schematic buoy mooring set up at 37 m depth of water level.

The buoy data were provided by oil and gas company who positioned the buoys at Sabah and Sarawak. The 24 years worth of wave height data from Malaysian seas that was retrieved from RADS is compared with offshore buoy and ADCP for the validation purposes. This is to evaluate the satellite data with the in situ measurement.
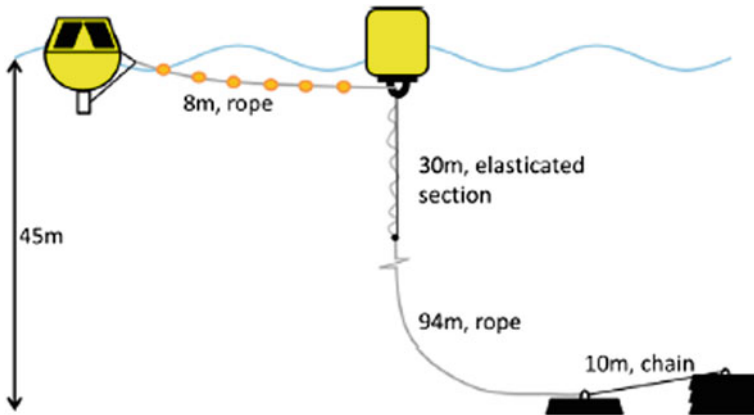
Fig. 4 A schematic of the buoy tie up setup during the installation in 37 m water depth, not to scale [15]

3 Result and Discussion

3.1 Data Verification: Altimetry-Derived Wave Height Versus Ground Truth-Derived Wave Height

There are two points of offshore buoy which consist of wave height data set located in Sabah and Sarawak. The other point of ground truth observation is ADCP in Terengganu. All these points were used as a benchmark in validating the satellite altimetry data. The points are located in Sabah waters at 5.83 latitude and 114.39 longitude and in Sarawak waters at 5.15 latitude and 111.82 longitude. The ADCP is located at 05.44 latitude and 103.16 E longitude (Refer Fig. 1).

In this validation process, it was evaluated with four types of moving windows which are 9, 5, 2 and 1 days. The altimeter data was gridded in 0.25° × 0.25° for spatial resolution. The verification process used the monthly data from January 1993 until December 2016. The root mean square error (RMSE) and correlation of the ground truth and altimetry observations are evaluated.

Based on the results, the RMSE and the correlation coefficients for all three verification points can be calculated. All three verification points show the different results for the best moving windows average. The Sarawak buoy data that were used in this verification was from October 1995 until January 2012. Based on Fig. 5, the smallest of RMSE for Sarawak buoy is by applying 9 days moving windows with 0.25145 m. However, it shows the opposite results for the best correlation coefficient analysis with 1 day moving windows giving the best results with 0.95992. In Sabah area, 5 days moving windows showed the best results for RMSE and correlation with 0.1845 m and 0.8664, respectively (see Fig. 6). The duration of buoy data in Sabah was from November 2004 until December 2007.

Fig. 5 The RMSE (m) and correlation results for Sarawak buoy
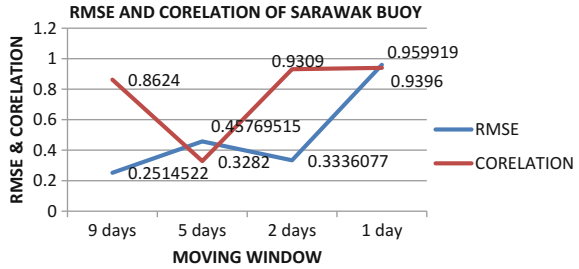
Fig. 6 The RMSE (m) and correlation results for Sabah buoy
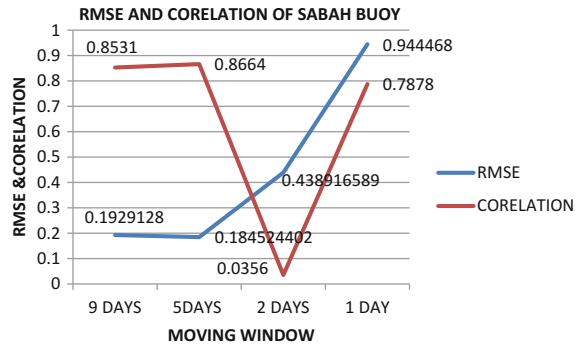
Next, Fig. 7 showed the result of reliability of ADCP in Terengganu with the 1 day moving windows as the best result for RMSE and 5 days for correlation. The RMSE value is 0.860332 m and the correlation is 0.3659. The ADCP data duration is from June 2012 until June 2016. This shows that ADCP has the latest result compared to the buoys but ADCP only provides data for several months in each year.

In producing climatology maps, the best moving window has to be chosen. Therefore, the readings from the Sarawak offshore, 9 days moving window was chosen to produce the wave height climatology maps. This is because the in situ data is the longest among the three points which is more reliable in this validation process. The agreement of the in situ measurement can be seen through the trends graph. The altimeter data was obtained from $0.25° \times 0.25°$ grids.

Fig. 7 The RMSE (m) and correlation results for ADCP in Terengganu
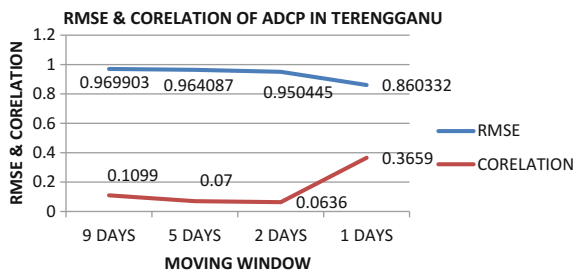
Fig. 8 The trend graph of Sarawak buoys and satellite altimeter based on 9 days moving windows
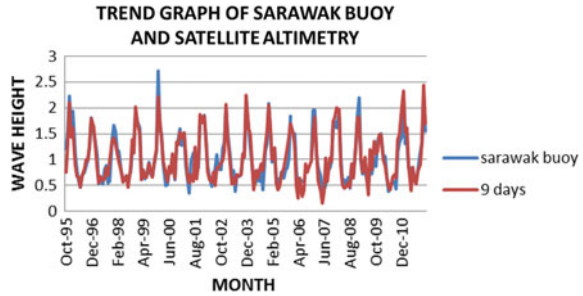
Based on Fig. 8, the wave height data from altimetry and buoy showed a similar trend and pattern. This result gave a good indicator of the reliability and validity of altimetry-derived wave height data. The differences of wave height between these two instruments were around less than 0.5 m. However, there are a few months in 1997, 2001, 2003, 2004 and 2010 showing the agreement of satellite altimeter and buoy quite loose, where the buoy data did not follow the pattern of satellite data. The satellite data in that particular year were taken from Topex, ERS-2 and Envisat. As informed, these satellites have already been improved in its accuracy like the Topex is a dual frequency satellite that is used to remove the path delay being caused by the ionospheric-free electron and also equipped with experimental sensor. Envisat also equipped with multiple sensors and developed an environmental satellite for the mapping of earth change. So, the accuracy of satellite was not doubted. The disagreement on these several months can be related to the hardware problem of the buoy. It can be seen that the unfollow pattern of buoy happened in the low wave height where we can justify that the buoy did not cope with low depth measurement.

On the other hand, as shown in Fig. 9 Sabah's buoy did not achieve the pattern like the one in Sarawak but the ascending and the descending trends show the reading is still following the pattern. The satellite track is affecting the trends since the benchmarking data from satellite is an interpolation point. It is different with buoy because the buoy is a point-based measurement which will give a better reading at its point. At some point, there are slight differences in the pattern of Sabah buoy trend. In February 2005, February 2006 and August 2007, the wave

Fig. 9 The trend graphs of Sabah buoy and satellite altimeter based on the 9 days moving window
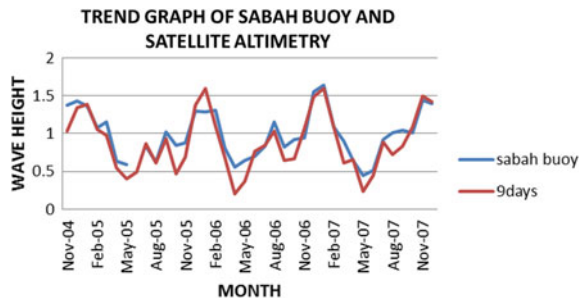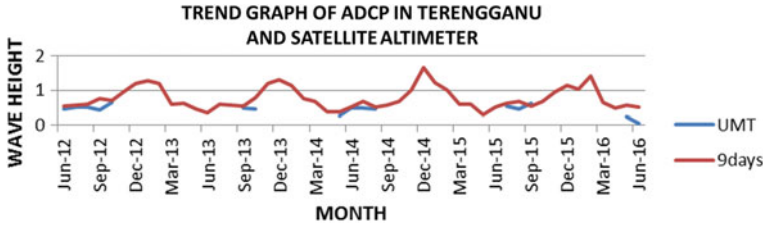
Fig. 10 The trend graph of ADCP in Terengganu and satellite altimeter based on the 9 days moving window

height pattern from the buoy was slightly different from the pattern of satellite altimetry. In this duration, the satellites that provide the wave height data are from Topex and Jason-1. Jason-1 is similar to Topex that emits dual frequency to the target wave which gets the orbit determination from GPS.

Next, the trend of ADCP with altimetry at Terengganu area was as shown in Fig. 10. There is a major gap between months for each year. It can justify that the data gap affecting the reliability of RMSE and correlations result in the verification process. The ADCP physical operations usually will innate single-ping measurement uncertainty of 0.30 ms^{-1}. This reduces to about 0.025 ms^{-1} uncertainty in the 5-min ($N > 100$) of the whole profile approximates. The Doppler Shift also happened since the ping travels in the water. The average of these uncertainties is further calculated during the 1000-km integration [16]. By comparing the location of ADCP and the buoys, it can clearly be seen that the ADCP is deployed in the nearshore area. This location has many disturbances like the high volume of bubble in nearshore area may cause the turbulence that will affect the accuracy of ADCP.

3.2 Mapping of Wave Height Climatology from 1993 to 2016 Over Malaysian Seas

The climatology of wave height over Malaysian seas from 1993 to 2016 was shown in Fig. 11. In general, the wave height climatology shows a constant result in all areas for the past 24 years over Malaysian seas. In the nearshore area, the climatology shows a stable calm wave where the height only between 0 and 1 m are shown in the blue colour. The yellow colour on the map indicates a high value of the wave height average in the middle South China seas which reached about 1.7 m. The monsoon seasons are affecting the wave heights in South China Seas since this area is quite open to the wind currents. So, the winds of the monsoon seasons are affecting the wave heights average in that particular area.
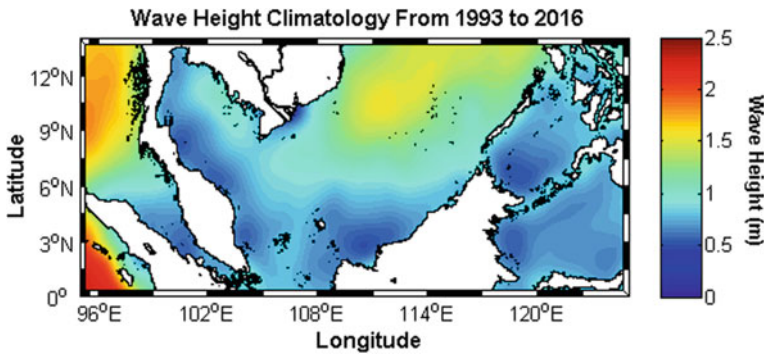
Fig. 11 The wave height climatology over Malaysian seas from 1993 to 2016

3.3 Time Series of Wave Height Over Malaysian Seas

Basically, these four seas are having three different tidal events, where Sulu Sea and Celebes Sea are facing mixed tides, South China Sea are having semi-diurnal tides and Malacca strait is having diurnal tides event. These events are affecting the wave height data in that particular area. As seen in the Fig. 12, in Malacca strait, there was actually a quite high wave height documented in 1996 and it became lower in the other three years but increased back in 2000. In the South China Sea, the same event also happened in 1996 but the wave height lowered after that and it has not been stable since that (see Fig. 13). The wave height has not been stable until 2002 and the same event happens again from 2009 until 2016. The variety of wave height data can also be seen in Fig. 14, where the Sulu Sea had the most drastic changes of waves compared to the other seas. Based on Fig. 2, the Sulu and Celebes seas are in a closed area, and both have had mixed tides but the pattern of wave heights time series are quite different. In Celebes Sea (see Fig. 15), the drastic changes of wave heights only happened in 2001 and 2007.
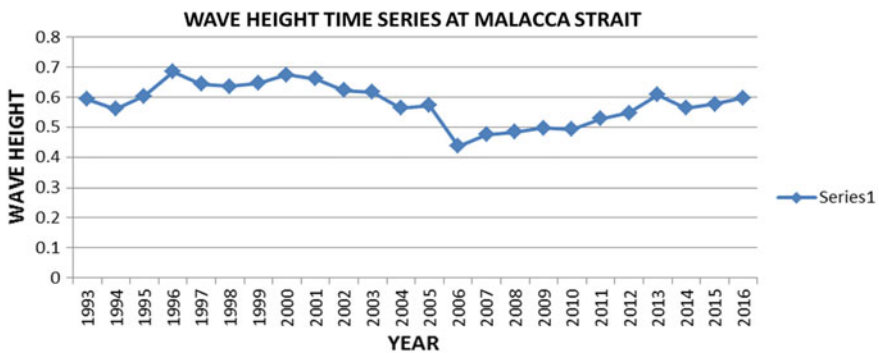
Fig. 12 Time series of monthly wave height for the Malacca Straits from 1993 to 2016
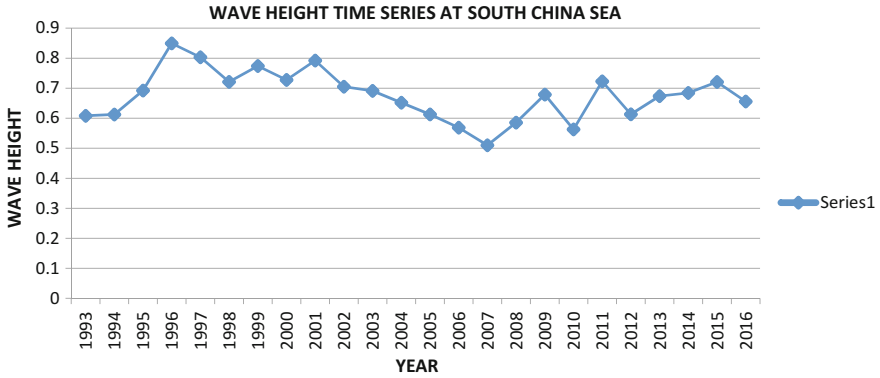
Fig. 13 Time series of monthly wave height for South China Sea from 1993 to 2016
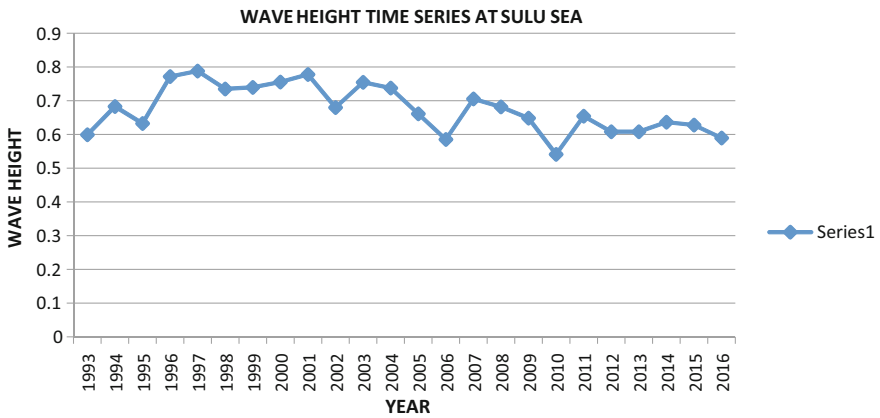
Fig. 14 Time series of monthly wave height for the Sulu Sea from 1993 to 2016
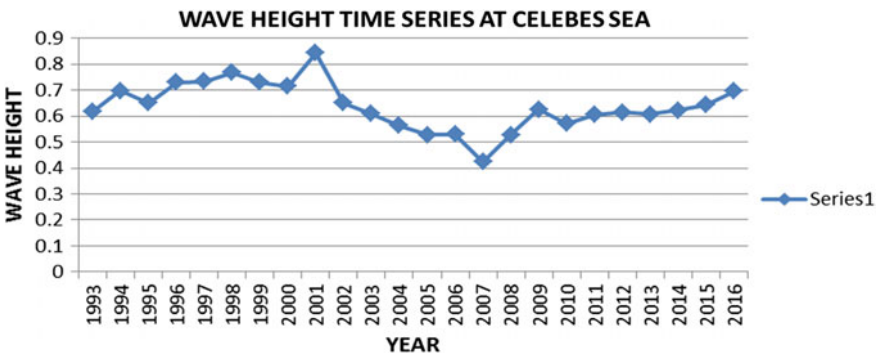
Fig. 15 Time series of monthly wave height for the Celebes Sea from 1993 to 2016

3.4 Wave Height Pattern Due to Seasonal Effects

Every year, Malaysian seas will experience four types of monsoon seasons, which will affect the wave height pattern. The monsoon seasons are as follows:

- First Inter-monsoon Season (March–April)
- Southwest Monsoon Season (May–August)
- Second Inter-monsoon Season (September–October)
- Northeast Monsoon Season (November–February)

First Inter-Monsoon. First inter-monsoon is a season that marks the transition between Northeast monsoon and Southwest monsoon. During inter-monsoon season, usually the wave height and wind are very mild, the wind direction is also flexible and the patterns tend to be in a disordered manner [17]. During this season also, the wind tension induces persistent coastal upwelling. Based on Fig. 16, it is noticeable that the wave height during first inter-monsoon is not more than 1 m, except on certain isolated areas such as in Sarawak shores and around Terengganu shores that have a reading of wave height around 1 m. Other than that all of the areas of Malaysian seas show a very calm of the wave climate.

Southwest Monsoon. During the Southwest monsoon, strong wind will travel from Indian Ocean and it will hit the west coast of Peninsular Malaysia. However, this case has never happened because of Sumatra Island (Indonesia) that has blocked the path of the strong wind. As the result in Fig. 17, the wave height around Malacca straits during this period does not rise as it happens in East coast of peninsular Malaysia. The wave climate in Malacca straits during this period is still a little bit higher than during the first inter-monsoon season. Some part of the South China Sea rises during the Southwest monsoon but, in the Celebes Sea and the Sulu Sea, the wave heights have lowered a little bit than during the first inter-monsoon. Wave height around the North or entrance of Straits of Malacca has been recorded to be at 1.5 m. This shows that it does not have a good protection from the Southwest monsoon compared to the other areas of Straits of Malacca at the south [12].
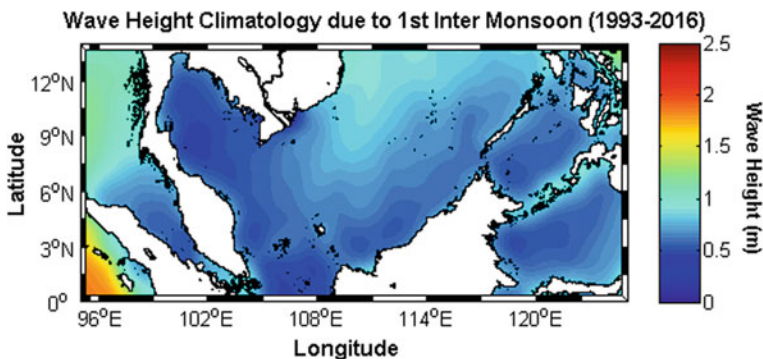
Fig. 16 The average of significant wave height first inter-monsoon season over Malaysian seas
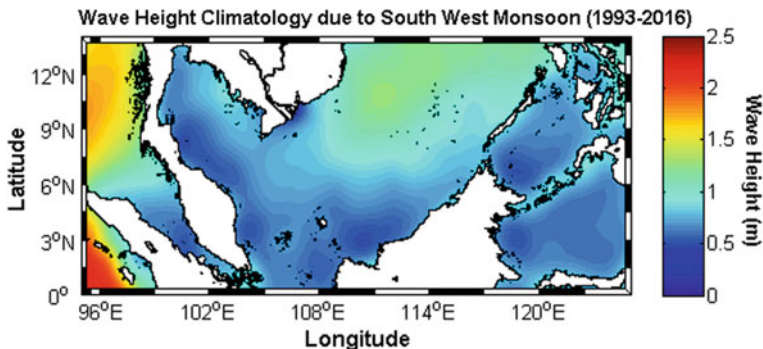
Fig. 17 The average of significant wave height Southwest monsoon season over Malaysian seas

Second Inter-Monsoon. Second inter-monsoon is the transition period of Southwest monsoon and Northeast monsoon. Figure 18 shows the Second inter-monsoon phase in Malaysian seas. During this season, the wave height is not as calm as the first inter-monsoon season. It can be seen in the middle of South China Sea, where the wave rose to be as high as 1.5 m. Only a few spots are below 1 m while the other areas of the seas are facing an increase of the wave height. The high wave starts to travel from Philippine towards East Coast, Sarawak and Sabah. It shows that the Northeast monsoon is on its way to Malaysia especially on the East Coast of Peninsular Malaysia.

Northeast Monsoon. November is the starting point for Northeast monsoon. However, sheltered area like Malacca straits remains calm during this time. The average of wave height for most of the Malacca straits areas is below 0.8 m. During this period of time, wave height in Malaysian seas starts to rise rapidly, especially in the open seas. Figure 19 shows that in East Coast of peninsular Malaysia, Sarawak shores and Sabah shores have the average wave height of above 1 m. On average, the wave height in the offshore areas is around 1.8 m and can be up to 2.5 m.
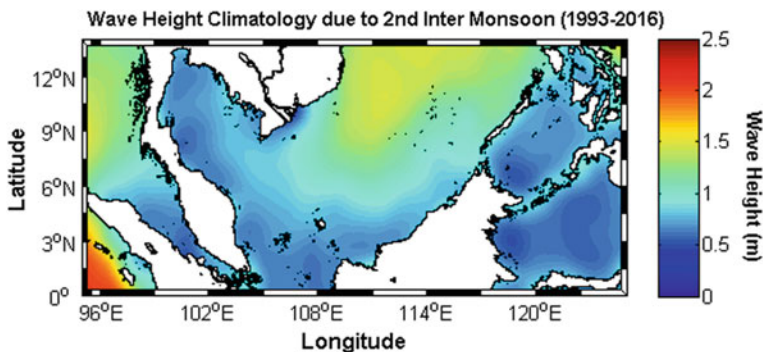
Fig. 18 The average of significant wave height second Inter-monsoon season over Malaysian seas
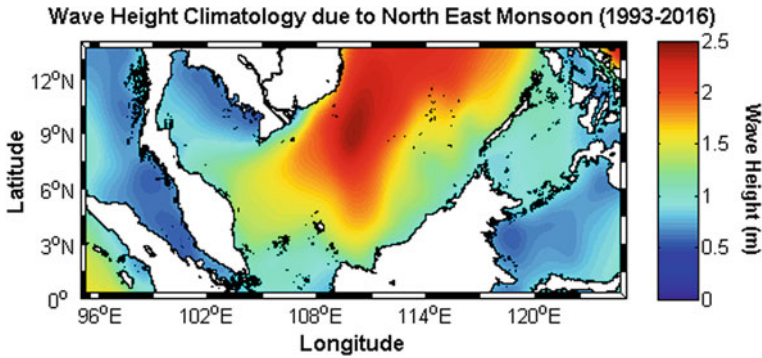
Fig. 19 The average of significant wave height Northeast monsoon season over Malaysian seas

From the result, it is clearly seen that there are several places that can be taken into consideration in implementing the renewable energy, which are in the areas of Terengganu shores and Sabah shores because both regions have a consistent measurement of wave height. The regions are facing a firm wave height for every year which is 1 m and above. Based on previous researches, the stronger the wind speed will produce the stronger the wave height.

4   Conclusions

The main purpose of the study is to provide the information on wave height climatology over Malaysian seas, where the climatology of wave height was made and analysed. The map shows the wave height of Malaysian seas throughout the 24 years evaluated in this study. The study also provides important information which can be used in the decision of developing the potential wave energy technology in Malaysia. The reliability of satellite altimeter data in wave height studies over Malaysian seas was also evaluated. The correlation of satellite altimeter and in situ measurement shows a good relative relationship because all of the correlation results are more than 0.7 for altimetry versus buoy using 9 days moving windows. The 24 years of satellite altimeter data that was taken from 1993 until 2016 are used to analyse the wave height climatology over Malaysian Seas. The effects of monsoon events towards the characteristics of the seas and wave height are also observed and analysed. From the results, it is shown that the wave heights in Malaysian seas are not very consistent because of the effect of the monsoon seasons. In conclusion, there are a few potential areas for the renewable energy from wave height such as in Terengganu and Sabah shores can be proposed for the future study.

References

1. Yaakob, O., Hashim, F.E., Omar, K.M., Din, A.M., Koh, K.K.: Satellite-based wave data and wave energy resource assessment for South China Sea. In: International Conference on Marine Technology Kuala Terengganu, Malaysia, 359–371 (2012)
2. Zheng, C.W., Li, C.Y.: Variation of the wave energy and significant wave height in the China Sea and adjacent waters. Renew. Sustain. Energy Rev. **43**, 381–387 (2014)
3. Aziz, W.A.: Wave height and wave energy mapping in Malaysian seas using satellite altimetry data. Master thesis, University Teknologi Malaysia (2014)
4. Samrat, N.H., Rahaman, M.H., Mamun, A., Adib, R., Ahmed, M.T.A.B.M.I.: Wave energy in Bangladesh, ECERE2015-P005 (2015)
5. Shanas, P.R., Sanil Kumar, V., Hithin, N.K.: Comparison of gridded multi-mission and along-track mono-mission satellite altimetry wave heights with in situ near-shore buoy data. Ocean. Eng. **83**, 24–35 (2014)
6. Fernando, S.P., Helen, A.F., Laurie, P.: Constructing improved decadal records of Antarctic ice shelf height change from multiple satellite radar altimeters. Remote Sens. Environ. 192–205 (2016)
7. Jarihani, A.A., Callow, J.N., Johansen, K., Gouweleeuw, B.: Evaluation of multiple satellite altimetry data for studying inland water bodies and river floods. J. Hydrol. **505**, 78–90 (2013)
8. Aziz, W.A.W.A., Yaakob, O., Omar, K.M., Din, A.M.: Satellite altimeter ocean wave height data in South China Sea. In: International Conference on Marine Technology, Kuala Terengganu, Malaysia (ID: MTP-21) (2012)
9. Andersen, O.B., Scharroo, R.: Coastal Altimeter. Springer, Berlin (2010)
10. Rosmorduc, V., Benveniste, J., Bronner, E., Dinardo, S., Lauret, O., Maheu, C., Milagro, M., Picot, N., Ambrozio, A., Escolà, R., Garcia-Mondejar, A., Restano, M., Schrama, E., Terra-Homem, M.: Radar altimetry tutorial. In: Benveniste, J., Picot, N. (eds.) ESA & CNES (2016)
11. Guido, V.: Model and Its Application to Cassini Mission. Department of Aerospace and Mechanical Engineering, Second University of Naples, Aversa, Italy (2007)
12. Liong, P.C.: Hydrography of the straits of Malacca. Malays. Agric. J. **49**(3), 381–391 (1974)
13. Work, P.A.: Nearshore directional wave measurements by surface-following buoy and acoustic Doppler current profiler. Ocean. Eng. Elsevier, **35**, 727–737, https://doi.org/10.1016/j.physletb.2003.10.071. (2008)
14. OSW Hydroacoustics: Acoutic Doppler profiler homepage. https://hydroacoustics.usgs.gov/indexvelocity/instruments.shtml#adp, last accessed 13 May 2017
15. Ashton, I.G.C., Johanning, L.: On errors in low frequency wave measurements from wave buoys. Ocean. Eng. **95**, 11–22 (2014)
16. Worst, J.S., Donohue, K.A., Rossby, T.A.: Comparison of vessel-mounted acoustic doppler current profiler and satellite altimeter estimates of sea surface height and transports between New Jersey and Bermuda along the CMV oleander route. J. Atmos. Oceanic Technol. **31**, 1422–1433 (2014)
17. Corrigan, C.E., Ramanathan, V., Schauer, J.J.: Impact of monsoon transitions on the physical and optical properties of aerosols. J. Geophys. Res. **111**, 1–15, D18208, https://doi.org/10.1029/2005JD006370. (2006)

Real-Time Precise Point Positioning (RT-PPP) for Positioning and Mapping

Duraisamy Ramachandran, Ami Hassan Md Din, Siti Aisah Ibrahim and Abdullah Hisam Omar

Abstract Real-Time Precise Point Positioning (RT-PPP) has started to develop among Global Positioning System (GPS) community due to some reasons, such as reference stations are required, very economical and easy to operate from everywhere. By using a dual-frequency receiver with the support from GPS precise products, RT-PPP has proven to give centimetre to decimeter positioning accuracy. Recently, the position can be obtained in real time using the real-time GPS precise products provided by many national geodetic agencies. Current real-time GPS positioning systems also allow accurate positioning by carrier phase-based double differencing approach. However, the limitation of using the differential approach is the process needs simultaneous data collection from common satellites at the reference station and the rover. Directly, the data acquisition process will become more difficult and this will decrease the suitability of this technique in other potential applications. The aim of this research is to analyse the current performance of RT-PPP technique using Hemisphere Atlas for positioning and mapping. This research also assessed the positioning accuracy between RT-PPP and static GPS techniques. Then, the reliability of RT-PPP for cadastral purposes is also evaluated. Methodologically, RT-PPP used Hemisphere Atlas, which is a dual-frequency receiver for position determination by processing raw pseudorange and carrier

D. Ramachandran · A. H. M. Din (✉) · A. H. Omar
Geomatic Innovation Research Group (GIG), Universiti Teknologi Malaysia,
81310 Johor Bahru, Johor, Malaysia
e-mail: amihassan@utm.my

A. H. M. Din
Faculty of Geoinformation and Real Estate, Geoscience and Digital
Earth Centre (INSTEG), Universiti Teknologi Malaysia,
81310 Johor Bahru, Johor, Malaysia

A. H. M. Din
Institute of Oceanography and Environment (INOS),
Universiti Malaysia Terengganu, Kuala Terengganu, Terengganu, Malaysia

S. A. Ibrahim
AV Tech Resources, Tingkat Atas, Lot 3281-B, Kampung Jaya,
Jalan Tengku Ma'asum, Pasir Hor, 15100 Kota Bharu, Kelantan, Malaysia

891

phase observations with the support from precise GPS orbit and clock information. The results of this research show that the coordinate for both positioning and mapping purposes using Hemisphere Atlas are within centimetre-level accuracy, i.e. below 10 cm for positioning and below 30 cm for cadastral purposes. Therefore, this study anticipates that RT-PPP has the potential to offer better operational flexibility that will guide for the full implementation of this technology particularly in surveying and mapping in the future.

1   Introduction

Nowadays, accessing accurate real-time satellite ephemeris and clock data has begun to receive increased attention among the scientific users of Global Navigation Satellite System (GNSS). The purpose of this improvement is for encouraging real-time-precise point positioning (PPP) solutions. As a result, all issues and development about IGS real-time infrastructure were handled by the IGS Real-Time Working Group (RTWG) [1]. The main advantage of this achievement is, it enables RT-PPP operations. The concept for RT-PPP is to use a single receiver and process raw code and carrier phase measurements. By applying this method, it proposes a backup plan to double differencing approach which is more precise and straightforward as in [2, 3]. RT-PPP is currently used in plate's movement scientific studies, real-time monitoring such as landslide and natural disasters' early warning systems [4]. Even though RT-PPP does not need reference stations but the user must keep in mind that accurate data of the satellite's orbit (ephemeris) and clocks are always required.

Presently, most of the GPS positioning systems only use carrier phase-based double differencing approaches. We cannot deny that this technique is able to provide high accuracy of positioning in real time, but to get this type of accuracy the differential process requires observation of the same GNSS satellites at the reference station (known precise coordinate) and rover stations. The disadvantages are, it will complicate the data collection process and will reduce the potential of this idea in many other practices. Furthermore, establishing a reference station in an area will always increase the expenses in labour and equipment. Besides, the idea of using the differential Real-Time Kinematic (RTK) solutions are restricted by the distance limitation between the base and rover.

Precise Point Positioning (PPP) processing of undifferenced smoothed pseudo-ranges with fixed precise satellite orbits and clocks has been used by Geodetic Survey Division (GSD) since 1992 [5]. By combining precise IGS satellite clocks at 15 min intervals with 30-s recording information from preferred reference stations with constant atomic clocks, 30-s precise satellite clocks are also produced [6]. These products can give metre-level precision that only will satisfy certain users

and only can be used in certain applications. The researches about PPP by using post-processed precise orbit and clock products have been studied in several papers, e.g. [1, 2, 7, 8]. As for current real-time practices only precise post-processed absolute positioning is implemented with the help of global reference stations network and IGS precise products [9].

The aim of this paper is to analyse the current performance of Real-Time Precise Point Positioning (RT-PPP) technique using Hemisphere Atlas for positioning and mapping. The proper place for conducting this research to analyse the positioning is around Universiti Teknologi Malaysia's (UTM) Johor Bahru Campus, particularly in the helipad. Apart from that, this research work was also used to evaluate the reliability of RT-PPP using Hemisphere Atlas for mapping purposes. So, data observation is conducted on the nearby cadastral lot. With its great potential, RT-PPP can replace or as an improvement to geodesy and existing GPS techniques, especially to the Malaysian survey community since it can give a millimetre to centimetre accuracy [10].

1.1 Principle of Carrier Phase-Based Differential Method

The simple basic concept to GPS data processing is to construct new observables by differencing because this way can eliminate or reduce most of the clock biases and the impact of several other measurement biases. The carrier phase-based differential GPS is capable of achieving higher positioning accuracy. The word 'kinematic' is used when the rover is moving from one location to other location. Commonly, the differential processing approach involves the use of at least one stationary reference receiver and at least one stationary or moving receiver, called a rover.

All information and data from reference receiver are transmitted to the roving receiver via communication links such as ground-based radio. The roving receiver will combine this data to form double difference observables and this will cancel the highly correlated errors. It follows the knowledge where the value of the positional error at the reference receiver is knowable when compared to the known value. This process will compute the 3D position vector from the base receiver to the rover. Therefore, the determined position of the rover is dependent upon the accuracy of the coordinates of the reference station and the accuracy of the computed 3D vector. The visualization of the single and double differencing are shown in Fig. 1.

1.2 Principle of Real-Time Precise Point Positioning (RT-PPP)

Real-time positioning is very complicated when compared with post-processing operation. The most critical problem that must be taken into concern is only a
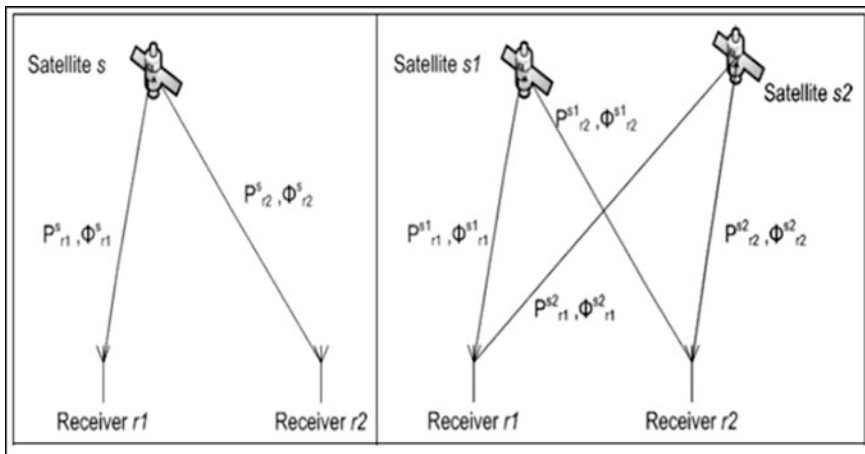
Fig. 1 Visualization of a single (left) and double (right) differencing [11]

wireless communication link is used to transfer the observation data in a short period of time. Generally, the satellite's position can be determined by using few types of data which are broadcast ephemeris, precise ephemeris and Almanac data [12]. During traditional PPP, only raw pseudorange and carrier phase measurements from the user's receiver are required.

However, to perform in real time the user's receiver must have the knowledge of accurate information about the satellite ephemeris and clock corrections. The time delay for the correction to be transferred must be only in few seconds, which is a very short period. On the other hand, the most common disadvantage of traditional absolute positioning by using a single receiver is the need of long convergence time in order to resolve the ambiguity so the positioning given is in centimetre level of accuracy [13].

Recently, with the introduction of a third frequency such as the L5 signal on the GPS constellation and equivalent third frequency on the Galileo constellation, the latency to initialize the ambiguities on a PPP solution has been reduced and now it is comparable to differential positioning techniques [14]. On the other hand, a network of ground reference station facilities is needed to calculate the GPS precise products (satellite's orbit and clock information). Then, the data analysis process can be done at the master control stations with relevant knowledge and then transmit the correction to users all over the world.

For the past 2 years, the International GNSS Service (IGS) Real-Time Working Group has been investigating the issues associated with real-time CORS infrastructure and data products by running the Pilot Project [15]. During the year 2012, IGS has begun a Real-Time Service (IGS-RTS) for supporting real-time positioning operation. Besides, IGS is also one of the agencies that always provide GPS orbit and clock information in different accuracies and latencies as shown in Table 1.

Table 1 IGS products [16]

Type		Accuracy	Latency	Updates	Sample interval
Broadcast	Orbits	∼100 cm	Real time	–	daily
	Sat. clocks	∼5 ns RMS			
		∼2.5 ns SDev			
Ultra-rapid (predicted half)	Orbits	∼5 cm	Real time	At 03, 09, 15, 21 UTC	15 min
	Sat. clocks	∼3 ns RMS			
		∼1.5 ns SDev			
Ultra-rapid (observed half)	Orbits	∼3 cm	3−9 h	At 03, 09, 15, 21 UTC	15 min
	Sat. clocks	∼150 ps RMS			
		∼50 ps SDev			
Rapid	Orbits	∼2.5 cm	17–41 h	At 17 UTC daily	15 min
	Sat. and Stn. clocks	∼75 ps RMS			5 min
		∼25 ps SDev			
Final	Orbits	∼2.5 cm	12–18 days	Every thursday	15 min
	Sat. and Stn. clocks	∼75 ps RMS			Sat.: 30 s
		∼20 ps SDev			Stn.: 5 min

However, several matters must be addressed for the implementation of RT-PPP. The issues that must be taken into consideration are the format of the correction and the mode to transmit the precise orbit and clock information in real time to user's receiver. The most important condition to encourage the user to use RT-PPP is the real-time PPP algorithms must be implemented inside the GNSS receiver and the proper way to do this is by developing a suitable RTCM standard for receiving and using the GPS precise products for the positioning determination [13].

Even though the "ultra-rapid (predicted)" orbit information by the IGS are available hours in advance to be used by the user in real time, but the predictability of the clock adjustment is really poor. Therefore, to improve the quality of the satellite clock estimation in RT-PPP, the time delay taken in transferring the correction from analysis centre to the user must be shortened. The working concept of RT-PPP using Hemisphere Atlas is illustrated in Fig. 2. The correction transmitted to the user is H10 service level, which can give the position accuracy of 8 and 4 cm of RMS error.
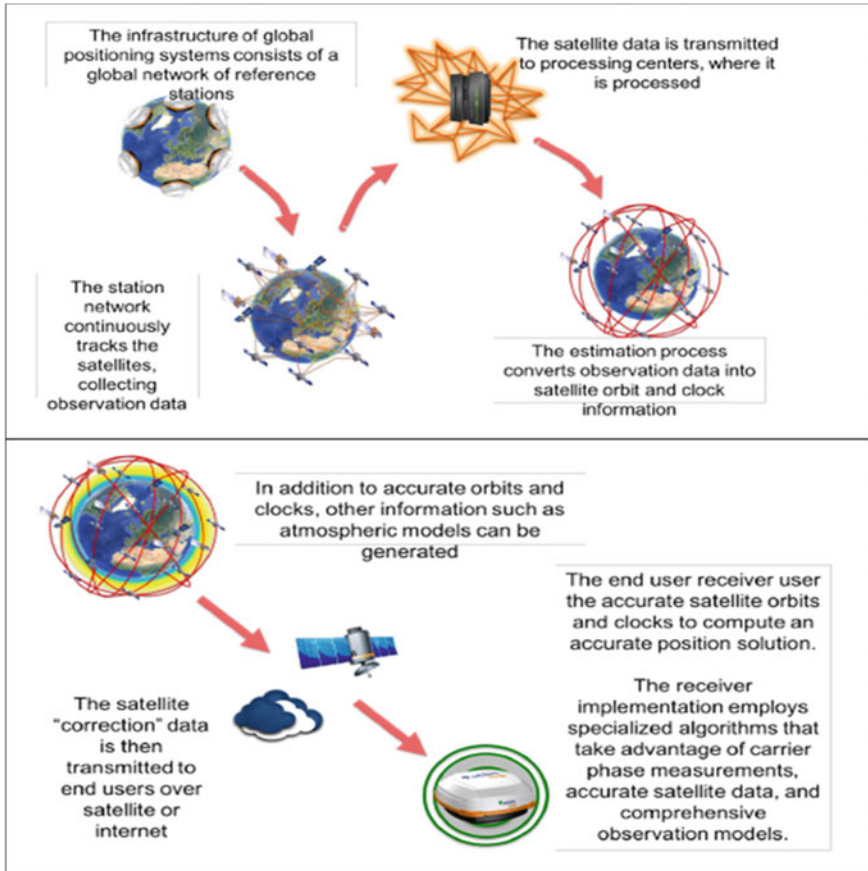
Fig. 2 The global correction services concept of Hemisphere Atlas [17]

2 Research Approach

2.1 Research Area Identification and Data Acquisition

The primary area of interest covers around Universiti Teknologi Malaysia's (UTM) Johor Bahru Campus particularly in the helipad (1° 33′ 29.60″N, 103° 38′ 13.37″E) for analysing the positioning. This research is also tested for mapping purposes, so the proper place will be a nearby cadastral lot (1° 29′ 59.86″N, 103° 41′4 7.03″E) which is Lot 119,110, Kampung Pasir, Mukim Pulai, Daerah Johor Bahru, Johor. Figure 3 shows the plot of the certified plan (PA 40225) for the study area used for mapping purpose which is in Kampung Pasir.

The coordinate for each boundary stones used in Kampung Pasir cadastral lot is listed in Table 2. All the coordinates are in Cassini–Soldner Geocentric data.
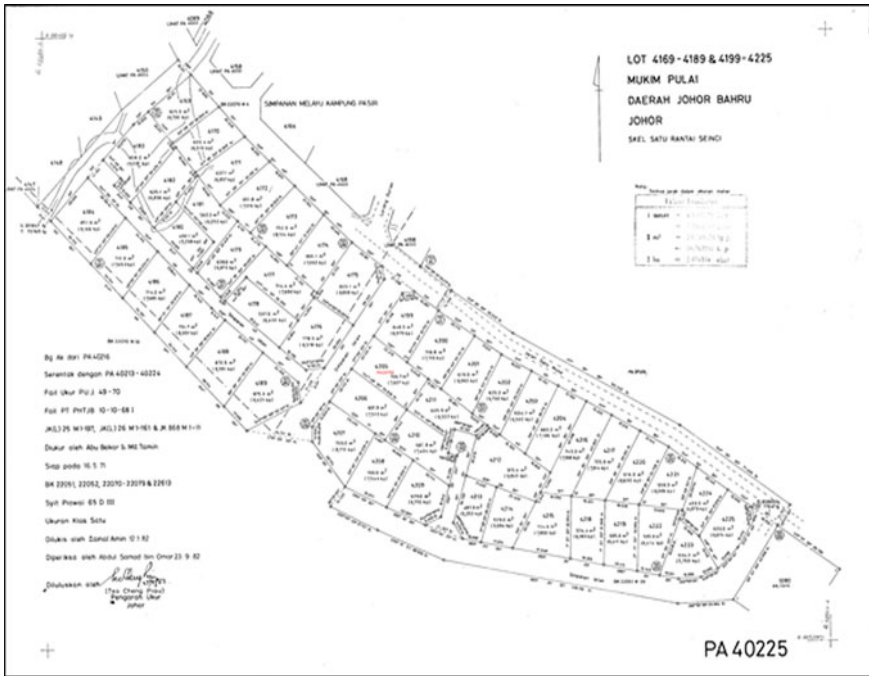
Fig. 3 The certified plan (PA 40225) of study area used for mapping purpose

Boundary stone	Cassini–Soldner Geocentric Johor	
	Northing (m)	Easting (m)
3	−60,757.255	15,434.181
4	−60,778.149	15,418.435
5	−60,765.888	15,453.547
12	−60,727.827	15,253.414
14	−60,743.953	15,222.431

Table 2 The coordinate of the boundary stones used in Kampung Pasir cadastral lot

Figure 4 shows the location of the two study areas. The distance between this two study areas is around 9.23 km.

There are two methods used in this positioning data acquisition phase. The first one is by using static GPS technique on the helipad UTM Johor Bahru. The static data is collected for almost 10 h each day for 3 days. Static data is collected for 3 days because to find the differences between the daily solution. The instrument used for this data collection is Topcon GR-5. The coordinate value after the post-processing acted as "ground truth value". Figure 5 shows the data collection using Topcon GR-5 in UTM helipad. The second method is by using RT-PPP GPS technique. The data is collected in real time by using Hemisphere Atlas instrument.

Fig. 4 The location of UTM helipad (1° 33′ 29.60″N, 103° 38′ 13.37″E) and Kampung Pasir (1° 29′ 59.86″N, 103° 41′ 47.03″E)

Fig. 5 The data collection for static mode using Topcon GR-5 in UTM helipad
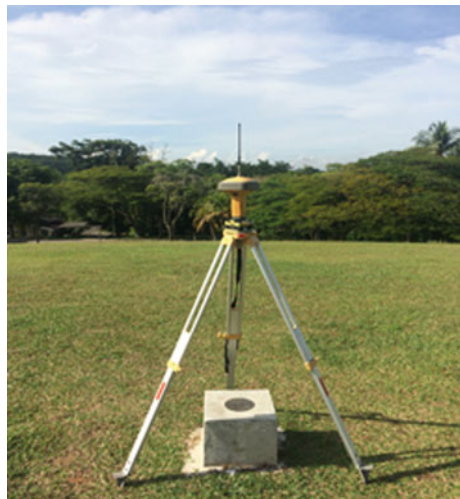
The GPS observation has been made by 15 epochs on the UTM helipad. The observation is done 15 epochs because to get the average coordinate value. The average coordinate value from real time is compared with the coordinate value that acts as the ground truth value from the static GPS technique. Figure 6 shows the data collection using Hemisphere Atlas for positioning purpose in UTM helipad.

Fig. 6 The data collection for RT-PPP mode using Hemisphere Atlas in UTM helipad
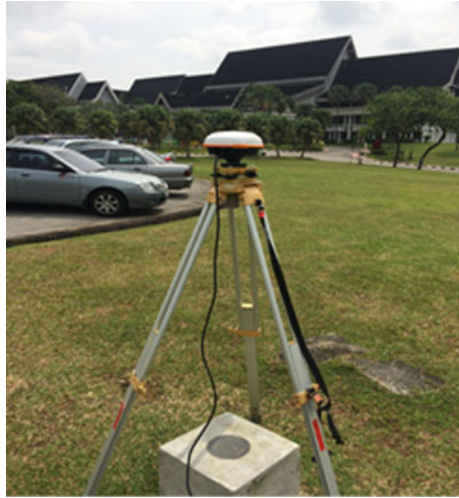
The RT-PPP technique is also tested for mapping purpose. So, data observation is conducted for at least 5 boundary stones on the nearby cadastral lot, Kampung Pasir (1° 29′ 59.86″N, 103° 41′ 47.03″E). For mapping purpose, three GPS techniques were used which are fast static (at least 30 min) and network-based RTK (Malaysian Real-Time Kinematic GPS Network) technique using Topcon GR-5 and RT-PPP using Hemisphere Atlas. The RT-PPP observation is made 5 epochs for each boundary stone to get an average value. The fast static technique is used for post-processing PPP. Figure 7 shows the data collection using Topcon GR-5 in Kampung Pasir, while Fig. 8 shows the data collection using Hemisphere Atlas in Kampung Pasir. The coordinate values from both techniques are gone through the

Fig. 7 The data collection for static mode using Topcon GR-5 in UTM helipad

Fig. 8 The data collection
for RT-PPP mode using
Hemisphere Atlas in
Kampung Pasir

transformation approach so that the new coordinate value (Geocentric Cassini–Soldner Johor) can be compared with the boundary stones coordinate value. The coordinate value for the boundary stones can be referred in the certified plan of this lot (PA 40225). By comparing these two values, it is easy to evaluate the reliability of RT-PPP for the cadastral purpose.

2.2 Positioning Data and Processing

During this phase, static data that collected on the helipad for 3 days using Topcon GR-5 undergone post-processing mode by using two different approaches which are by using AUSPOS and Waypoint software. The data that collected using Hemisphere Atlas does not need post-processing because it already gives real-time coordinates. AUSPOS is handled by Geoscience Australia and it is used freely for online GPS data processing. AUSPOS can work with any GPS RINEX data with the support from the network of IGS stations and IGS precise products. The coordinate computation is undertaken using the "Bernese 5.2" GNSS software so the reference frame used is International Terrestrial Reference Frame 2008 (ITRF2008) and double differencing approach is used [18]. The reference stations used for the processing for each day are different with one another and at least 10 reference stations are used for the processing. The result which is the average coordinate from 3 days only can be compared with the coordinate that used ITRF2008 in RT-PPP.

The Waypoint software has two functions, which are GrafNav and GrafNet. GrafNav is a post-processing function that can be used for static and moving GNSS processing. Apart from that, it also can be used with several receiver formats and
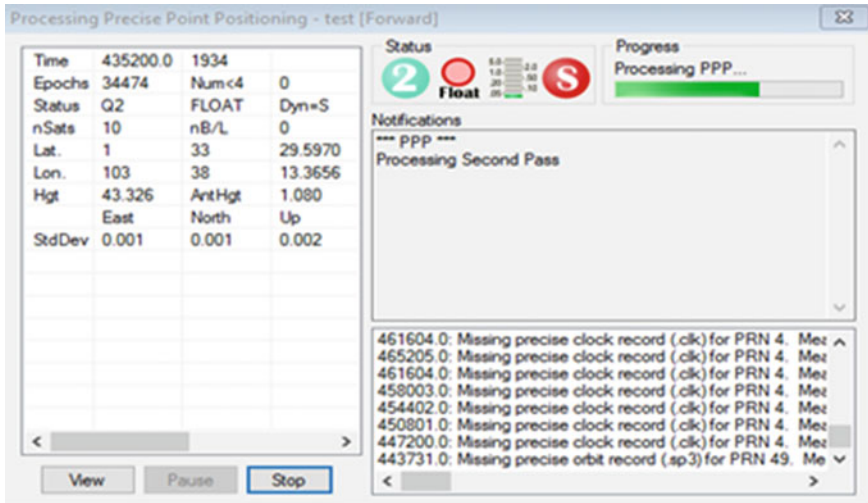
Fig. 9 Waypoint interface

support many types of processing such as PPP and multi-baseline (MB) processing. While GrafNet is largely used for network processing and adjustment. The function that used in Waypoint for this study is GrafNav and the processing method is PPP approach. PPP is an autonomous positioning method, which requires dual-frequency data as well as precise orbit and clock information. Hence, the precise information is downloaded from FTP site cddis.gsfc.nasa.gov. The static data is processed in three different reference frames which are ITRF2000, ITRF2008 and ITRF2014. Figure 9 shows the screenshot of the Waypoint software during the PPP processing.

The coordinate for each different frame is the average value from 3 days of observation. The elevation mask used is 10° and the processing interval is 1 s. Other processing parameters and processing strategies are summarized in Table 3.

2.3 Mapping Data and Processing

As already mentioned in research area identification and data acquisition section, the RT-PPP technique using Hemisphere Atlas is also tested for mapping purpose. So, the data is collected using Hemisphere Atlas in Kampung Pasir does not need any post-processing because the coordinate given is already in real-time Cassini–Soldner Johor state data. Besides, the data collected using Topcon GR-5 by applying the network-based RTK (MyRTKnet) technique also does not need post-processing because the coordinate given is already corrected by double differencing approach and the data used is GDM2000. The data collected using the

Table 3 Parameters and strategies used for Waypoint processing

Processing parameters	Processing strategy
Input data	Daily
Process data type	Automatic
Elevation cut off angle	10°
Sampling rate	1 s
Orbits	IGS final orbits (SP3)
Clocks	IGS final clocks
Reference frame	ITRF2000, ITRF2008, ITRF2014
Ionosphere	Ionospheric free (IF) linear combination (L3)
Troposphere	A priori Saastamoinen model
Tropospheric settings	Spectral density (medium)
L1 lock time cutoff	4 s
Time range (GMT)	Process entire time range
Velocity estimation	Doppler
Measurement standard deviations	Code: 7 m Carrier phase: 0.020 m Doppler: 1 m/s
Measurement usage	Enable GLONASS processing

fast-static technique for all boundary stones have undergone post-processing mode using Waypoint. The processing technique used is PPP and the data used is ITRF2000. The elevation mask used is 10° and the processing interval is 1 s. Other processing parameters and strategies are the same as in Table 3. Another data needed for the mapping verification is coordinate from the certified plan (PA 40225). The coordinate is in Cassini–Soldner Geocentric Johor state, which consists of Northing and Easting.

3   Results and Discussion

3.1   Data Verification for Positioning

During this phase, the real-time coordinate from RT-PPP using Hemisphere Atlas is compared with several post-processing approaches to analyse the performance of RT-PPP on the positioning. The coordinate status for RT-PPP is in fixed status for all the positioning. The post-processing coordinate by using AUSPOS is considered as "ground truth value" or data in order to do the comparison because AUSPOS processing strategy is based on double differencing, also normally known as relative positioning. The strategy of this processing is by determining the baseline vectors between two receivers or more but the main condition is the receivers must be observed simultaneously. The accuracy of the double difference technique depends

on the satellite ephemeris accuracy and the baseline length between the base station and rover [19]. Furthermore, AUSPOS is using scientific software, "Bernese 5.2" as the processing engine which can give a high accurate positioning by applying the double differencing approach.

RT-PPP versus AUSPOS. As for the quality control in AUSPOS, there are two outputs that need to be taken into account. The first one is the list and the amount of IGS stations used and the second one is the percentage of the resolved ambiguity. The list and the amount of the IGS stations needed for each day processing are different with one another. Table 4 shows the list of IGS stations used as a reference during the processing for each day. From Table 4, the number of IGS reference stations used for first-day processing is 11 stations, while second- and third-day processing used 14 stations. Table 5 shows the ambiguity resolution percentage results for 3 days. The ambiguity resolution has shown good results as its average is higher than 70%.

The average positioning after post-processing using AUSPOS is shown in Table 6 and the accuracy statistics is given in Fig. 10. The result shows that the precision of both components (horizontal and vertical) is only in millimetre level between the 3 days. The standard deviations of the coordinate (latitude, longitude, and ellipsoidal height) between 3 different days are almost the same which is consistent during that period.

Table 7 shows the positioning of RT-PPP using Hemisphere Atlas for 15 epochs in UTM helipad. The average value is taken in order to do the comparison. The coordinate is in real time and the data used is ITRF2008. The time taken to get the fixed solution is around 10 min. The surrounding of the helipad is an open area, which is free from obstacles that can cause multipath.

The positioning differences between RT-PPP and double difference solutions using AUSPOS are shown in Table 8. The result indicates that accurate positioning has been obtained in real-time using PPP method which is in centimetre level. The differences between the horizontal components are around 11 cm, which is around 7 cm for latitude and around 11 cm for longitude while for vertical is around 17.5 cm.

RT-PPP versus Waypoint. The position from the RT-PPP is also compared with the result from the Waypoint software by using PPP approach. The software used final orbit and clock information to process the data. Different types of data used in the processing but only result from ITRF2008 data can be compared with the position from the RT-PPP. The coordinate status for all the positioning after

Table 4 The list of IGS reference stations used for each day

	Day 1	Day 2	Day 3
Reference stations	BAKO, COCO, DARW, FOMO, HKNP, HYDE, KARR, LHAZ, PIMO, TCMS, XMIS	BAKO, COAL, COCO, DARW, DSMG, FOMO, HKNP, HYDE, IISC, KARR, LHAZ, PIMO, TCMS, XMIS	BAKO, COAL, COCO, DARW, DSMG, FOMO, HKNP, HYDE, IISC, KARR, LHAZ, PIMO, TCMS, XMIS

Table 5 The percentage of the resolved ambiguity for 3 days

Days	Ambiguity resolved		Average (%)
Day 1	BAKO-XMIS	66.6%	72.3
	HKNP-TCMS	82.6%	
	HKNP-LHAZ	40.0%	
	BAKO-HKNP	25.9%	
	KARR-XMIS	83.4%	
	DARW-KARR	81.8%	
	HKNP-PIMO	76.0%	
	FOMO-HKNP	95.5%	
	BAKO-BASE	74.1%	
	HYDE-LHAZ	87.0%	
	COCO-XMIS	82.6%	
Day 2	BAKO-XMIS	60.0%	70.7
	HKNP-TCMS	81.8%	
	HKNP-LHAZ	30.0%	
	COCO-XMIS	95.4%	
	COAL-HKNP	86.4%	
	COAL-DSMG	93.8%	
	BAKO-HKNP	19.2%	
	KARR-XMIS	76.0%	
	DARW-KARR	68.0%	
	HKNP-PIMO	78.3%	
	BAKO-BASE	64.0%	
	DSMG-FOMO	93.8%	
	HYDE-LHAZ	72.7%	
	HYDE-IISC	70.0%	
Day 3	HKNP-HYDE	35.3%	72.5
	BAKO-XMIS	57.1%	
	HKNP-TCMS	85.0%	
	COCO-XMIS	85.7%	
	COAL-HKNP	86.4%	
	COAL-DSMG	95.8%	
	BAKO-HKNP	8.0%	
	KARR-XMIS	85.0%	
	DARW-KARR	85.7%	
	HKNP-PIMO	80.0%	
	BAKO-BASE	62.9%	
	DSMG-FOMO	97.7%	
	HYDE-LHAZ	74.1%	
	HYDE-IISC	76.2%	

Table 6 The average positioning of AUSPOS processing

AUSPOS (ITRF2008)	Latitude	Longitude	Ellipsoidal height
Day 1	+1° 33′ 29.59682″	+103° 38′ 13.36600″	42.007
Day 2	+1° 33′ 29.59685″	+103° 38′ 13.36608″	41.993
Day 3	+1° 33′ 29.59703″	+103° 38′ 13.36603″	42.007
Average	+1° 33′ 29.59690″	+103° 38′ 13.36604″	42.002
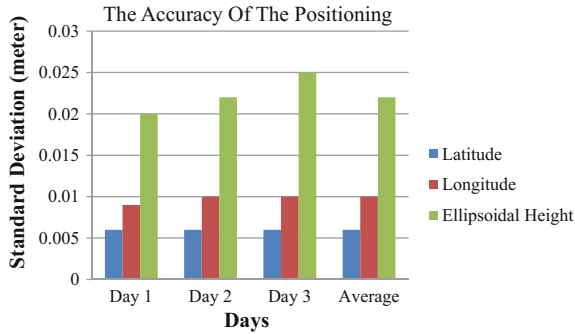
Fig. 10 The accuracy statistics (standard deviation) of the positioning

Table 7 The positioning of RT-PPP using Hemisphere Atlas in ITRF2008 data

No.	Latitude	Longitude	Ellipsoidal height
1	+1° 33′ 29.60,140,242″	+103° 38′ 13.36163264″	41.7343
2	+1° 33′ 29.60115408″	+103° 38′ 13.36305742″	41.7406
3	+1° 33′ 29.60089396″	+103° 38′ 13.36379924″	41.7675
4	+1° 33′ 29.59812506″	+103° 38′ 13.36562326″	41.8706
5	+1° 33′ 29.59709736″	+103° 38′ 13.36495736″	41.9275
6	+1° 33′ 29.59807062″	+103° 38′ 13.36795912″	41.9789
7	+1° 33′ 29.59753402″	+103° 38′ 13.37043870″	41.9245
8	+1° 33′ 29.59722854″	+103° 38′ 13.36883296″	41.9015
9	+1° 33′ 29.59776478″	+103° 38′ 13.36730746″	41.8772
10	+1° 33′ 29.59691902″	+103° 38′ 13.36502672″	41.8327
11	+1° 33′ 29.59660798″	+103° 38′ 13.36478150″	41.8175
12	+1° 33′ 29.59636030″	+103° 38′ 13.36463854″	41.7830
13	+1° 33′ 29.59651350″	+103° 38′ 13.36543972″	41.8301
14	+1° 33′ 29.59652454″	+103° 38′ 13.36579574″	41.8501
15	+1° 33′ 29.59670158″	+103° 38′ 13.36612532″	41.8160
Average	+1° 33′ 29.59927″	+103° 38′ 13.36569″	41.8270

Table 8 The differences between RT-PPP and AUSPOS positioning

RT-PPP versus AUSPOS	Latitude (m)	Longitude (m)	Ellipsoidal height (m)
Differences	0.0711	−0.0105	−0.1753

processing is a float. The coordinate from ITRF2008 is shown in Table 9 and the accuracy statistics for the position in illustrated in Figs. 11 and 12. The coordinate values for the 3 data are different slightly with one another.

Table 9 The positioning in the ITRF2008 data

Post-process (Waypoint-ITRF2008)	Latitude	Longitude	Ellipsoidal height
Day 1	+1° 33′ 29.59712″	+103° 38′ 13.36570″	42.239
Day 2	+1° 33′ 29.59670″	+103° 38′ 13.36670″	42.235
Day 3	+1° 33′ 29.59685″	+103° 38′ 13.36636″	42.247
Average	+1° 33′ 29.59689″	+103° 38′ 13.36625″	42.240
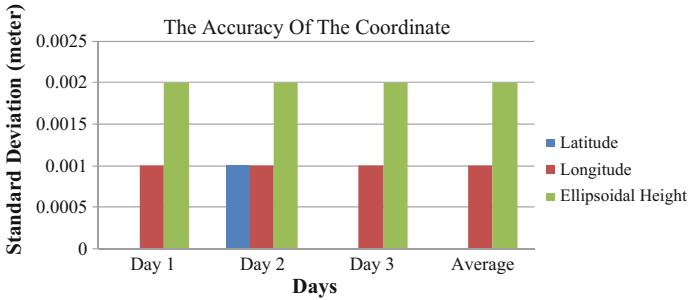
Fig. 11 The accuracy statistics (standard deviation) of the coordinate in the ITRF2008 data
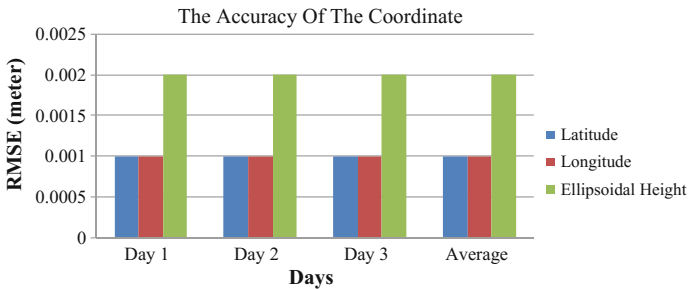
Fig. 12 The accuracy statistics (RMSE) of the coordinate in the ITRF2008 data

Figures 11 and 12 show that the standard deviation and RMS error value for the data is only in millimetre level. It indicates that the precision of the coordinate is having only small differences.

As shown in Table 10, centimetre accurate positioning results have been achieved. The key to achieving this level of accuracy is by using real-time precise orbit and clock products in the RT-PPP. The differences between RT-PPP and Waypoint post-processing in only in centimeter level for both horizontal and vertical. The latitude difference is around 7 cm and for longitude is around 17 cm.

Table 10 The positioning differences between RT-PPP and Waypoint

RT-PPP versus Waypoint	Latitude (*m*)	Longitude (*m*)	Ellipsoidal height (*m*)
Differences	0.0714	−0.0168	−0.4133

Table 11 The positioning in the ITRF2000 data

Post-process (Waypoint-ITRF2000)	Latitude	Longitude	Ellipsoidal height
Day 1	+1° 33′ 29.59578″	+103° 38′ 13.36570″	42.256
Day 2	+1° 33′ 29.59536″	+103° 38′ 13.36670″	42.251
Day 3	+1° 33′ 29.59550″	+103° 38′ 13.36637″	42.263
Average	+1° 33′ 29.59550″	+103° 38′ 13.36626″	42.257

Table 12 The positioning in the ITRF2014 data

Post-process (Waypoint-ITRF2014)	Latitude	Longitude	Ellipsoidal height
Day 1	+1° 33′ 29.59707″	+103° 38′ 13.36576″	42.237
Day 2	+1° 33′ 29.59664″	+103° 38′ 13.36676″	42.232
Day 3	+1° 33′ 29.59679″	+103° 38′ 13.36642″	42.244
Average	+1° 33′ 29.59683″	+103° 38′ 13.36631″	42.238

However, the ellipsoidal height for the two approaches is slightly higher than a horizontal component which is 41 cm.

Table 11 shows the coordinate values using ITRF2000 and Table 12 shows the coordinate values using ITRF2014. In order to do the comparison between different reference frames, the average value is taken. Besides, the precision of the positioning for ITRF2000 and ITRF2014 are also in millimetre level.

The differences of the positioning between three different reference frames which are ITRF2000, ITRF2008 and ITRF2014 using Waypoint is illustrated in Table 13. The table indicates that the differences between the horizontal components are only in centimetre level. The biggest differences that can be seen are in latitude component for ITRF2000 which is around 42 cm compared with ITRF2008 and around 40 cm compared with ITRF2014. Besides, the differences for longitude component are only in cm level and the biggest differences are in ITRF2014 which

Table 13 The differences of positioning between three different frames

Post-process (Waypoint)	Latitude	Longitude	Ellipsoidal height
ITRF2000	+1° 33′ 29.59550″	+103° 38′ 13.36626″	42.257
ITRF2008	+1° 33′ 29.59689″	+103° 38′ 13.36625″	42.257
ITRF2014	+1° 33′ 29.59683″	+103° 38′ 13.36631″	42.257

Table 14 The positioning differences between AUSPOS and Waypoint

AUSPOS versus Waypoint	Latitude (*m*)	Longitude (*m*)	Ellipsoidal height (*m*)
Differences	0.0003	−0.0063	−0.2380

is 2 cm compared with ITRF2000 and ITRF2008. As for ellipsoidal height, the value remains constant for three reference frames which are 42.257 m.

AUSPOS versus Waypoint. The results from two post-processing mode are also compared to see the differences. As mentioned earlier in positioning data and processing section, AUSPOS is using double differencing approach, while Waypoint is using the PPP method. So, the positioning from AUSPOS is more accurate than the Waypoint result. The differences are shown in Table 14 which indicates that latitude and longitude differences are only in millimetre level while ellipsoidal height differences are around 23.8 cm. By processing the data with accurate information about the satellite orbit and clock, high accuracy of positioning always can be achieved.

3.2 Data Verification for Mapping

This research is also to analyse the performance of RT-PPP using Hemisphere Atlas on cadastral purpose. The mapping projection used for real-time data collection is Cassini–Soldner Geocentric (Johor) which only consists of Northing and Easting. The coordinate is compared with other results from different techniques to find the differences. The real-time coordinate is collected for 5 boundary stones which are boundary stones 3, 4, 5, 12 and 14. Some of the boundary stone is under the house roof (boundary stone 12) or near to the fence or tree (boundary stones 3 and 4). So, the coordinate is in autonomous or float status. The RT-PPP coordinate for boundary stone 3 is in autonomous, boundary stones 4 and 12 are in float status and boundary stones 5 and 12 are in fixed status.

RT-PPP versus Waypoint. The RT-PPP coordinates that are taken for each boundary stone are shown in Table 15. The coordinate is only in 2D which consists of Northing and Easting. Boundary stones are located in a different location so the

Table 15 The coordinate of the boundary stones using RT-PPP

Boundary stone	Coordinate status	Cassini–Soldner Geocentric (Johor)	
		Northing (m)	Easting (m)
3	Autonomous	−60,757.1983	15,434.3748
4	Float	−60,778.5130	15,418.1127
5	Fixed	−60,766.1231	15,453.3525
12	Float	−60,728.5327	15,251.7930
14	Fixed	−60,744.0074	15,222.7516

Table 16 The coordinate of boundary stones using Waypoint post-processing

Boundary stone	Coordinate status	Waypoint (ITRF2000)	
		Northing (m)	Easting (m)
3	Float	−60,757.470	15,434.650
4	Float	−60,778.369	15,418.773
5	Float	−60,766.095	15,454.015
12	Float	−60,728.241	15,254.028
14	Float	−60,744.100	15,223.002

Table 17 The coordinate differences between RT-PPP and Waypoint

Boundary stone	RT-PPP versus Waypoint (m)		RMSD (m)	
	Northing	Easting	Northing	Easting
3	0.272	−0.275	0.144	0.450
4	−0.144	−0.660		
5	−0.028	−0.662		
12	−0.292	−2.235		
14	0.093	−0.250		

real-time coordinate taken are in different status depends on the condition of the location.

The GPS data is also collected in fast-static technique using Topcon GR-5. The data is processed using Waypoint in ITRF2000 data. The ambiguity status for all coordinates is float. The coordinate for each boundary stone is shown in Table 16.

The differences between the RT-PPP and Waypoint coordinate for all the boundary stones are only in centimetre level and the result is illustrated in Table 17. The smallest differences that can be achieved are around 3 cm for Northing on boundary stone 5 and around 25 cm for Easting on boundary stone 14. The coordinate status for both these boundary stones is fixed. The significant difference that can be seen is for Easting coordinate on boundary stone 12 which is around 2 m. The difference is so big because the boundary stone is located under the house roof. Moreover, the coordinate that collected is in float status. The table also shows the value for RMS deviation is around 14 cm for Northing which is smaller compared with Easting that shows around 45 cm. The RMS deviation is only in cm level because the difference for Easting component for boundary stone 12 is excluded for the RMS deviation calculation because of the float status and big differences with RT-PPP coordinate.

RT-PPP versus Network-Based RTK (MyRTKnet). The RT-PPP is also compared with the coordinate from network-based RTK (MyRTKnet), which uses GDM2000 as data. The MyRTKnet coordinate for each boundary stones is taken for 3 epochs so the coordinate given in Table 18 is the average value. The number of epochs for each coordinate is the average from 30 readings. Only one boundary stone gives a float status coordinate which is from boundary stone 12.

Table 18 The average coordinate readings using network-based RTK (MyRTKnet)

Boundary stone	Coordinate status	MyRTKnet (GDM2000)	
		Northing (m)	Easting (m)
3	Fixed	−60,757.317	15,434.258
4	Fixed	−60,778.217	15,418.508
5	Fixed	−60,765.945	15,453.648
12	Float	−60,726.348	15,254.409
14	Fixed	−60,743.942	15,222.455

Table 19 The coordinate differences between the RT-PPP and network-based RTK (MyRTKnet)

Boundary stone	RT-PPP versus MyRTKnet (m)		RMSD (m)	
	Northing	Easting	Northing	Easting
3	0.118	0.117	0.186	0.294
4	−0.296	−0.395		
5	−0.178	−0.295		
12	−2.184	−2.616		
14	−0.066	0.296		

The coordinate differences between the RT-PPP and network-based RTK (MyRTKnet) technique for most of the boundary stones are only in centimetre level and the differences are shown in Table 19. The most significant difference that can be seen for Northing and Easting components are on boundary stone 12 which is around 2 m for each of them. The difference is so big because the boundary stone is located under house roof. Moreover, the coordinate that collected is in float status. The smallest differences that can be achieved are around 7 cm for Northing on boundary stone 14 and around 12 cm for Easting on boundary stone 3. The constant differences for both Northing and Eating are for boundary stone 3 which are around 12 cm. Besides, the result also shows the RMS deviation for both Northing and Easting is below 30 cm. The RMS deviation for Northing is 19 cm which is smaller than Easting that shows around 30 cm. The differences for boundary stone 12 are excluded during the RMS deviation computation due to float solution.

RT-PPP versus Cassini–Soldner Geocentric (Johor). The coordinate for 5 of the boundary stones used are taken from certified plan (PA 40225). All the coordinates for each boundary stones are in Cassini–Soldner Geocentric of Johor state and the coordinate is shown in Table 20.

As can be seen, the differences between the RT-PPP and Cassini–Soldner Geocentric coordinate for most of the boundary stones are only in centimetre level and the differences are shown in Table 21. The big differences between both of them are for boundary 12 which give 71 cm for Northing and 1.6 m for Easting. The difference is so big because the coordinate collected is in float status. The smallest differences that can be achieved are around 6 cm for Northing on boundary

Table 20 The coordinate of each boundary stones from PA 40225

Boundary stone	Cassini–Soldner Geocentric (Johor)	
	Northing (m)	Easting (m)
3	−60,757.255	15,434.181
4	−60,778.149	15,418.435
5	−60,765.888	15,453.547
12	−60,727.827	15,253.414
14	−60,743.953	15,222.431

Table 21 The coordinate differences between RT-PPP and Cassini–Soldner Geocentric (Johor)

Boundary stone	RT-PPP versus Cassini–Soldner Geocentric Johor (m)		RMSD (m)	
	Northing	Easting	Northing	Easting
3	0.057	0.194	0.197	0.238
4	−0.364	−0.322		
5	−0.235	−0.194		
12	−0.706	−1.621		
14	−0.054	0.321		

stone 3 and 14 and around 20 cm for Easting on boundary stone 3 and 5. The table also indicates that the RMS deviation for Northing is around 20 cm and for Easting is 24 cm. The differences on boundary stone 12 for Northing component is around 71 cm and for Easting component is around 1.6 m so the RMS deviation is calculated by excluding the differences.

4 Conclusion

The performance of Real-Time Precise Point Positioning (RT-PPP) has been assessed by using Hemisphere Atlas under different dynamic environments. The results describe that Hemisphere Atlas can achieve centimetre accuracy for positioning by using precise orbit and clock information, which is an alternative way to traditional double differencing positioning. Apart from that, the results also indicate that the Hemisphere Atlas also can be used for mapping purpose because the coordinate accuracy is at centimetre level only. But the accuracy of the coordinate using RT-PPP for both positioning and mapping are influenced by the condition of the surrounding environment.

The results and analysis shown in this research prove the capacity of RT-PPP using Hemisphere Atlas for both positioning and mapping purpose. The main benefit of the RT-PPP approach is there are no differential approaches applied, so the need of local base stations are not required and this method can be used

anywhere on earth such as in urban or rural areas which have sparse GPS network [20]. Besides, this method will give greater operational flexibility in the future because it can reduce the cost of equipment and labours for maintaining the GPS base stations.

References

1. International GNSS Service Real Time Working Group. http://www.rtigs.net/rtigswg/. Accessed 3 Mar 2017
2. Zumberge, J.F., Heflin, M.B., Jefferson, D.C., Watkins, M.M., Webb, F.H.: Precise point positioning for the efficient and robust analysis of GPS data from large networks. J. Geophys. Res. Solid Earth **102**(B3), 5005–5017 (1997)
3. Kouba, J., Héroux, P.: Precise point positioning using IGS orbit and clock products. GPS Solutions **5**(2), 12–28 (2001)
4. El-Mowafy, A., Deo, M., Kubo, N.: Maintaining real-time precise point positioning during outages of orbit and clock corrections. GPS Solutions **21**, 1–11 (2016)
5. Héroux, P., Caissy, M. and Gallace, J.: Canadian active control system data acquisition and validation. In: Proceedings of the 1993 IGS (International GPS Service for Geodynamics), Workshop, University of Bern, pp. 49–58 (1993)
6. Héroux, P., Kouba, J.: GPS precise point positioning with a difference. Natural Resources Canada, Geomatics Canada, Geodetic Survey Division (1995)
7. Gao, Y., Shen, X.: A new method for carrier-phase-based precise point positioning. Navigation **49**(2), 109–116 (2002)
8. Gao, Y., Chen, K., Shen, X.: Real-time kinematic positioning based on un-differenced carrier phase data processing. In: Proceedings of ION National Technical Meeting. Anaheim, California (2003)
9. Mullerschoen, R., Bar-Server, Y.W. Bertiger, D. Stowers.: NASA's Global DGPS for High-Precision Users. GPS World, 14–20 January 2001
10. Bisnath, S., Gao, Y.: Current state of precise point positioning and future prospects and limitations. In: Sideris M.G. (eds) International Association of Geodesy Symposia Observing our Changing Earth, vol. 133. Springer, Berlin, Heidelberg (2009)
11. Eissfeller, B.: Real time kinematic and precise point positioning: status and trends. Ger. J. GPS **87**, 131–148 (2012)
12. Elsobeiey, M., Al-Harbi, S.: Performance of real-time precise point positioning using IGS real-time service. GPS Solutions **20**(3), 565–571 (2016)
13. Rizos, C., Janssen, V., Roberts, C., Grinter, T.: Precise point positioning: is the era of differential GNSS positioning drawing to an end (2012)
14. Grinter, T., Roberts, C.: Real time precise point positioning: are we there yet. In: IGNSS Symposium (2013)
15. International GNSS Service Real Time Pilot Project. http://kb.igs.org/hc/en-us/articles/115001975467-IGS-Real-Time-Pilot. Accessed 21 Jan 2017
16. International GNSS Service. http://www.igs.org/products/data. Accessed 15 Jan 2017

17. Hemisphere GNSS Whitepaper.: Global correction services for GNSS. [Brochure]. Arizona, USA (2015)
18. AUSPOS—Online GPS Processing Service. http://www.ga.gov.au/scientific-topics/positioning-navigation/geodesy/auspos. Accessed 5 Feb 2017
19. Leick, A.: GPS satellite surveying, 3rd edn. John Wiley and Sons Inc, New Jersey (2004)
20. Gao, Y., Chen, K.: Performance analysis of precise point positioning using real-time orbit and clock products. J. Global Pos. Syst. **3**(1–2), 95–100 (2004)

Identification of Debris Flow Initiation Zones Using Topographic Model and Airborne Laser Scanning Data

Usman Salihu Lay and Biswajeet Pradhan

Abstract Empirical multivariate predictive models represent an important tool to estimate debris flow initiation areas. Most of the approaches used in modelling debris flows propagation and deposit phases required identifying release (starting point) area or source area. Initiation areas offer a good overview to point out where field investigation should be conducted to establish a detailed hazard map. These zones, usually, are arbitrarily chosen which affect the model outputs; hence, there is a need to have accurate and automated means of identifying the release area. In addition to this, the resolution of the terrain dataset also affects the results of the detection of source areas. In this study, airborne laser scanning (ALS) data was used because of its robustness in providing detailed terrain attributes at high resolution. Primary and secondary conditioning parameters were derived from digital elevation model (DEM) as input into the modelling process. Three models were executed at different spatial resolution scales: 5, 10 and 15 m, respectively. MARSpline multivariate data mining predictive approach was implemented using morphometric indices and topographical derived parameter as independent variables. A statistics validation was calculated to estimate the optimal pixel size, 1200 randomly sample data were generated from existing inventory data. Debris flows and no-debris flows were categorized, and the transform to continuous integer (1 and 0), respectively. To achieve this, the data set was divided into two, 70% (840) for the training dataset and 30% (360) for validation. The best model was selected based on the model performance using the generalized cross validation (GCV) and the receiver operating characteristic (ROC) curve/area under curve (AUC) values. Conditioning parameters were numerically optimized to identify the arbitrarily maximum model

U. S. Lay
Department of Civil Engineering, Geospatial Information Science Research
Center (GISRC), Faculty of Engineering, University Putra Malaysia,
UPM, 43400, Serdang Seri Kembangan, Malaysia

B. Pradhan (✉)
Faculty of Engineering and Information Technology, School of Systems,
Management and Leadership, University of Technology Sydney, Building 11,
Level 06, 81 Broadway, Sydney, NSW PO Box 123, 2007, Australia
e-mail: Biswajeet.Pradhan@uts.edu.au; Biswajeet24@gmail.com

915

basis function for eleven variables, using MARSplines analysis (algorithm). The three most influencing topographic parameters identified are topographic roughness index (TRI), slope angle, and specific catchment area (SCA) with the percentage values of participation in the model of 100, 93, and 86%, respectively. The chosen function appeared to describe the analysed correlation sufficiently well. Consequently, three stages of optimization were made to determine the optimized source areas is possible with 10 m pixel size, 200 maximum basis functions and 3 maximum interactions, resulting into 82% ROC train and 80% test, GCV 0.189 and 85% correlation coefficient. The result will be of great contribution to the advancement of a broad understanding of the dynamics of debris flows hazard and mitigations at regional level which; that is resourceful for comprehensive slope management for safe urban planning decision-making process and debris flow disaster management.

Keywords LiDAR · Debris flow · GIS · Remote sensing · Malaysia

1 Introduction

Debris flows are dangerous natural hazard in countries with mountainous terrain. Different definition of debris flows exists in the literature; the prominent criteria associated with debris flow definition were fluids and solid sediments. Spencer et al. [34] defined debris flows as flows of sediments and water that verve down to a valley floor along traditional water paths or along slopes through new routes. This type of event develops following the sudden influx of large amounts of water on loose soils, particularly frequent in high-mountain regions. Also, Iverson [20] mentioned that debris flows occur when masses of poorly sorted sediment, agitated and saturated with water, surge down slopes in response to gravitational attraction. Further, they pointed that both solid and fluid forces extremely influence the motion, distinguishing debris flows from related phenomena such as rock avalanches and sediment-laden water floods. In comparison, solid grain forces dominate the physics of avalanches, and fluid forces dominate the physics of floods, solid and fluid forces must act in concert to produce a debris flow. Interaction of solid and fluid forces not only distinguishes debris flows physically but also gives them unique destructive power.

Other criteria for defining debris flows emphasize sediment concentrations, grain size distributions, flow front speeds, shear strengths and shear rates [2], but the requisite of interaction between solid and fluid forces makes a broader, more mechanistic distinction. By this rationale, many events identified as debris slides, debris torrents, debris floods, mudflows, mudslides, mud spates, hyper concentrated flows and lahars may be regarded as debris flows [22]. The diverse nomenclature reflects the varied origins, compositions, and appearances of debris flows, from calmly streaming, sand-rich slurries to tumultuous surges of boulders and mud.

Like avalanches of solids, debris flows can occur with little warning as a consequence of slope failure in continental and seafloor environments, and they can exert great impulsive loads on objects they encounter. Like water floods, debris flows are fluid enough to travel long distances in channels with modest slopes and to inundate vast areas. Large debris flows can exceed 10^9 m^3 in volume and release more than 10^{16} J of potential energy, but even commonplace flows of $\sim 10^3$ m^3 can denude vegetation, clog drainage ways, damage structures and endanger humans [32]. An avalanche path which holds to debris flows consists of three different zones: the *start zone, the track and the end zone*. At the end usually the debris flow deposits are poorly selected and are recognized on the ground because they make up typical banks and lobes.

The unpredictable timing and magnitude of debris flows hamper some investigations, often raised significance mitigating threat to man and his infrastructures. A number of tragic events related to this occurred resulting in loss of lives and properties. For example, it was estimated that 200,000 people died in 1920 from an earthquake-induced loess flow in Kansu Province China [15]. Also, 4000 people died after an earthquake-induced debris avalanche occurred at north peak of Nevados Huascaran, in Peru in 1962 [15].

Usually, different mechanisms triggers debris flows but the prominent in tropical Malaysia is the transformation of landslide to strip fast fluid sediments trigger by torrential rainfall. Debris flow is an important form landslide along the Cameroun Highland, often being the major source of havocs and debris transports into rivers. In Malaysia, debris flows induced disasters have the potential of causing far-reaching devastating catastrophes; landslides occur 2006–2009, and 2015 in places like Penang island, Cameron Highland, Peninsular and Karak [26]. In Malaysia scenario, debris flow incidents are only investigated and reported when human lives and/or infrastructures are impacted. Based on the newspaper reports and literature survey, there was at least 15 cases of killer debris flow tragedies from 1994 to 2012 and at least 137 people were killed. Currently, research on debris flows in Malaysia is still very limited to post-disaster investigation within the scene of the event. The catastrophes eventually cause heavy economic loses and human casualties.

Considering the scale of these events (debris flows), they are basically unpreventable. The most reliable way to harness these menace is to re-examine the morphology, and the complex environmental effects of the hazard. Application of modern monitoring and modelling technology, such as remote sensing and geographic information system (GIS), will reduce the number of waste of lives and property. Elsewhere justice has been done in this field specifically on debris flow, to date, no research has been performed on this specific study in Malaysia.

Various systems constitute the process and development of debris flow initiation, travel either through steep open slope or channelized type and possibly define their routes. Basically, the situation that warrants the occurrence of acute debris flow lied on certain parameters which include slope angle, water and presence of sediment [36]. The intricacy of debris flow field investigation is considered tedious and labourious [11, 37] due to the topographic setting of the area, these hinder

reconnaissance survey. Globally, research on this aspect of mass movement has been increased in the past decades, hence little have been reported on this topic especially in the tropical Malaysia despite the increase in research in environment-related hazards; yet there is vacuum open for further research. Debris flow initiation (source area) model is an essential aspect and filament for debris flows modelling (susceptibility, run out). Rickenmann [31], stated that the automated depiction of debris flow is governed by the two-phase mixtures and physical configuration. Similarly, Yu (2011) identified high rainfall intensity and the existence of sufficiently moveable materials as vital conditions that initiate debris flow.

Prediction of debris flow source area and susceptibility mapping shows a triumph in mitigating shallow landslide (debris flows). A number of models and approaches such as empirical, dynamics, heuristic, data mining and statistical have been reported realistically in different parts of the world [12, 16, 18, 19, 21, 25, 27, 29]; in mandate to expand our understanding on the progressions and phases of debris flow. Nowadays, data mining approaches and multivariate statistical techniques (Random Forest-RF, Classification and Regression Tree-CART, Support Vector Machine-SVM; Regression-SVR, Artificial Neural Network- ANN, Multivariate Adaptive Regression Splines-MARSplines, Logistic Multiple Regression-LMR, etc.) proved to have positive results in mass movement related predictions occurrence [5, 6, 8, 10, 17, 23, 25, 26, 35]. Among these, no model is superior over another in reality, but single or combination of two can be considered for certain mission; probably could be due to its/or their prospective ability to account for different control management practices and requires less data than other models. Huge amount of data is needed to implement multivariate techniques, this reveals as a short-fall link with the model; meanwhile data mining is established on the learning patterns in analysing bulky datasets. Lack of high spatial resolution terrain data is mostly limited to topography [9]. The major controlling features for debris flow modelling are detailed topography and channel constituent [27]. Topography influences the initiation and advancement of debris flow because it controls the entrainment strength of the flow. The catchment areas are determined by topography changes, while slope gradient controls flow velocity [9].

The accessibility of terrain data with high spatial resolution is not readily available in ample amount. Precise, open source spatial data especially DEM can be obtained in a coarse pixel size from different remotely sensed platforms. In recent past, advancement in the industry and the advent of laser scanning (LiDAR) tools endorsed accurately the simulations of debris flows and other mass movement related hazard better than ever.

Laser scanning data has been popurarily used for detecting the debris flow in tropical terrain; through a computerized LiDAR DEM-derived parameters a dynamic surface morphology can be estimated and debris flows initiation (source area) possibly be spotted. Numerous studies have demonstrated the application of LiDAR DEM data for simulating debris flow by matching multiple datasets and resolutions acquired over time [4].

Numerous researchers considered the notion of topographic threshold modelling different forms of landslides [21] and environmental hazards [30], most of their finding are tangential from the reality, note mention, the threshold is dynamic and its intensity depends on the nature of the surface and other factors. Local slope stability controls different terrain hazards at diverse scale level.

This paper is developed based on the postulation that high-resolution DEM data and accurately derived topographic variables are capable to replicate the impact of scale factors, and thus used to predict the optimal debris flow initiation locations. This research aims at detecting the debris flow source areas; this is achieved through these specific objectives: to assess the likelihood of creating spatial multivariate model for predicting the incident of debris flows in tropical Malaysia using only ALS-Lidar DEM to derive topographic variables and identify important variables for debris flow modelling for the tropical zone. It is believed that in different locations, debris flow is absolutely control by slope gradient; hence, we defined a threshold in slope angle between 15 and 35° which was used as a bench mark to all input variables and was selected based on this cardinal edge. Multivariate Adaptive Regression Spline (MARSpline) Friedman [13] approach was chosen for the modelling because we are interested in the traditional regression equation; this is a nonparametric method, known to have produced profound and noble results in modelling intricate phenomenon. Compared to other data mining approaches, MARS has proven to have limited runs time with simple output. In order to select the best model, we optimized the attributes of the selected algorithm.

2 Methodology and Study Area

2.1 Study Area

Cameroun Highland is one of the districts of Pahang state, Malaysia was considered in this research work (Fig. 1a). The study area is selected, because frequent occurrences landslides and is situated; to the north it borders with Kelantan, to the west partly border with Perak and located at the north-western angle of Pahang state. In contrast to other district in Malaysia, the Cameron Highlands has a distinctive serene that accommodate diverse species of flora and fauna with extensive ecosystem. The area is positioned between latitudes 04° 22′ 52″N to 04° 24′ 45″N and longitudes 101° 22′ 30″E to 101° 23′ 30″E (Fig. 1); it occupies a total area of 712 km^2. One of the unique physiognomies of the study area is mountain ranges oriented/extending from–(east). A slope angle ranges from 0 to 56° and altitude from 1071 to 1676 m.a.s.l. (Fig. 1b).

The geology of the area is dominantly granites, but patches of meta-sediments also exist. Like other tropical climate regions, Cameroun Highlands witnesses two articulated seasons wet and dry seasons annually, September to December and February to May [26]. The rainy season in the area has double peak periods, high in
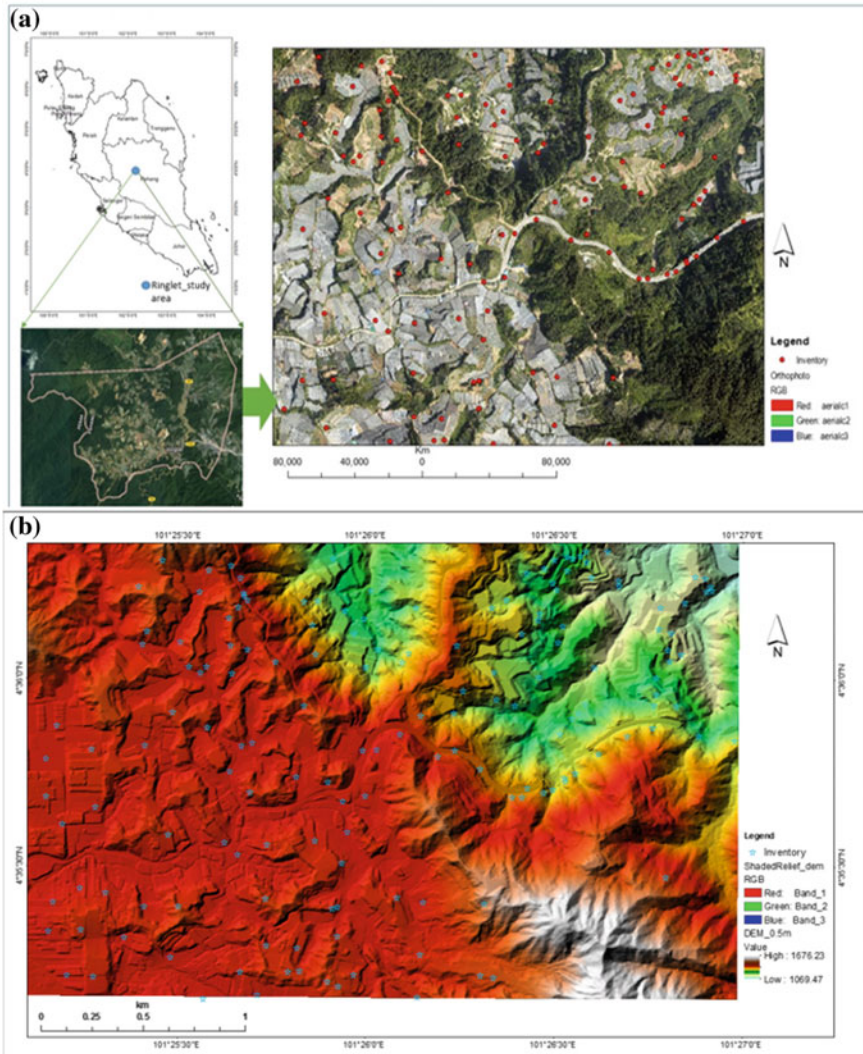
Fig. 1 **a** The study area. **b** DEM Shaded Relief data (5 cm pixel size)

March to May and November to December. This hilly area is recorded with a mean annual rainfall ranging from 2500 to 300 mm and annual temperature around 18°, day and night temperatures are 25° and 9° respectively. For details, see Pradhan et al. [29]. At the peak rainy season due to excessive down pour, many rivers tend to spill off their channels, possibly causing flood, slope instability, erosion and different forms of landslides (debris flows). Conventional approach or field detection of debris flows initiation/source area, in a rugged terrain like Cameron Highlands, is very difficult, sometimes impossible. Combining topographic

parameters from LiDAR DEM with geospatial science is adopted to accurately predict the source area in Cameroun Highlands.

2.2 Methodology

2.2.1 Data Type

The LiDAR data yielded high-resolution Laser scanning DEM data (5 cm) spatial resolution (Fig. 1b). The Airborne Laser Scanning (ALS) was acquired on 23 March, 2015, four return signals were noted by the sensor; the raw data is stored in LAS file format (version 1.1). A filter selection was employed to select the ground return (last return) from a number of levels of pulses return (non-ground) classes. The selected return point cloud density class (ground return) is up to 4 points per m^2, point density was interpolated using kriging approach with nearest neighbour function, the Malaysia Peninsula spatial reference system (GDM200 Peninsula_RSO) was adapted. The scale control menace was modelled based on neighbourhood size and grid resolution. The strength of LiDAR data is its ability to pierce through mountainous, dense forest canopy areas, like Cameron Highlands. Compare to other remotely sensed platform with DEM-derived products has a great persistence uncertainty [5, 6]; Laser scanning data provides high-resolution information. In a debris flow circumstance, the representation of terrain features such as the plain Earth surface is achieved in a metre scaled airborne LiDAR. To select suitable resolutions for the model, we 5 cm × 5 cm pixel size resampled the LiDAR DEM into multi-scales (5, 10 and 15 m) pixel sizes. From the LiDAR data, we used the local slope angles threshold (range 15–35°) as driven factor to deduce the model conditioning parameters. These DEMs were used to generate the primary and secondary debris flow conditioning parameters or model predictors variables.

A systematic combination of few variables is pertinent for initiating debris flow. Literature diverges with regards to the minimal contributing area for debris flows initiation. The slope angle that favours debris flows initiations varies for different areas: >15° as the lower starting edge [16], ≥20°–25° he mentioned that >34–37° there is decrease in debris flows because of the presence of resistance rocks, ≥25–40° noted that at slope angle ≥40° no debris flows; in Malaysia [27] used slope angle of >15°. Though, observed a direct relationship between amounts of debris flows with the slope gradient. We considered slope angle threshold ≥1° slope ≤35° being the minimum and values for the initiation, slope angle in this study formed the major cardinal parameter terrain stability. The plan curvature was used to identify the concave curvatures as possible source areas based on the assumption that debris flows tend to occur in gullies where the curvature is concave. There is no established threshold value for curvature in the literature.

2.2.2 Data Preparation

The step-by-step process used to achieve the research objectives is summarized in (Fig. 2). The landslide inventory map was used for various purposes: 1) preparing training and testing data; 2) DEM generation; 3) deriving primary and secondary geomorphic variables; and 4) landslide verification on the field with the aid of aerial orthophotos (Fig. 1a) were all obtained from Department of Mineral and Geosciences, Malaysia; was used in this research. Generating accurate and reliable debris flow source detection often depends on the scale and detailing. Therefore, the LiDAR data was processed to generate 5, 10 and 15 m DEM resolutions that reflect the multi-scaled dataset to produce the conditioning variables [28]. Different pixel sizes were used purposely to ascertain the best suitable size for the model process. Ultimate influence of pixel size on the accuracy modelling results has been reported in the literature. This pixel size used in this research is followed from the literature [14, 27, 29].

Detail facts on terrain properties are one of the vital prerequisites for different environmental engineering modelling [10]. The bounds for the variables were achieved from the threshold of slope (≥ 15 slope ≤ 35). Twelve types of topographic variables were generated from the multi-scale DEM layers using an open source Whitebox Geospatial Analysis tools version 3.4 software environments www.uoguelph.ca/hydrogeo/whitebox/. Consequent analyses were implemented in Salford Predictive Modeler software suite www.salford-system.com and ArcGIS 10.4 software www.esri.com for advance analyses and presentation of results. DEM-derived continuous variable, comprised of not restricted to slope angle, slope aspect, elevation, curvatures known as primary conditioning variables and secondary variables includes topographic wetness index (TWI), relative stream power index (RSPI), stream transportation index (STI), flow accumulations/specific catchment area (SCA)/upper course discharge, etc. (Fig. 3a–k), which are revealed to be active hazard predictors at different spatial scales [16, 25–29]. Equations adopted for generating these continuous topographic conditioning variables were demonstrated in Table 1.

In all the predictors or independent continuous variables, some have higher scale values, while others contained very low, float, and negative values. Higher values tend to control the model outcomes, to resolve this problem, data standardization becomes imperative, to support in the statistical strength. The derived topographic conditioning parameters were reclassified into ten classes using natural break, in order to have a standard scale for the model process (Fig. 4).

Furthermore, the multi-scales conditioning parameters were combined for different pixel sizes into a composite images using ArcMap software environment for training point. The training points were extracted from the composite image using multiple point extraction tool in ArcMap; corresponding points for each conditioning parameter are extracted and stored in attribute table and ready for further
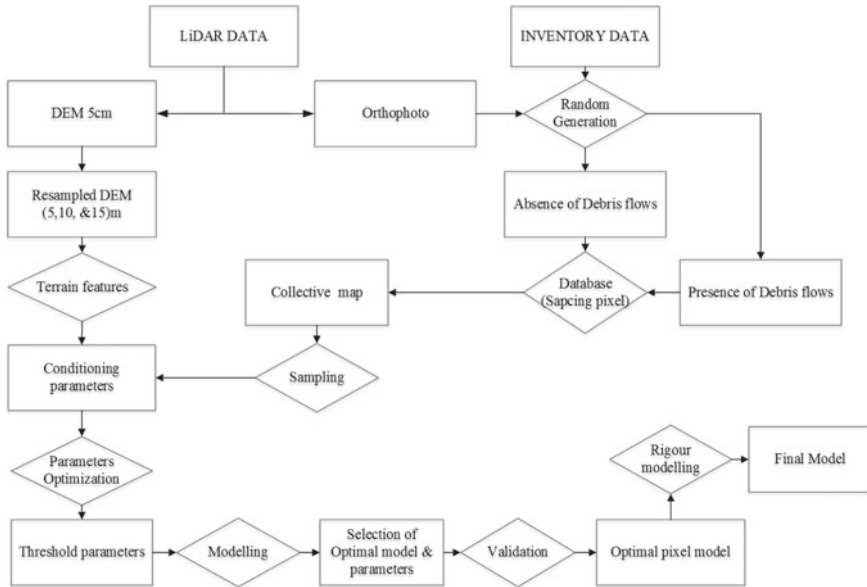
Fig. 2 The work flow chart

processes, though, they are the considered to be the independent variables or pre-dictors. The terrain was trained into a binary set 'debris flows' and 'no-debris flows' represented as 1 and 0 respectively; about 1200 points were generated, 600 for each variable and this class is considered as the dependent variable for the modelling. Figure 3: the conditioning parameters (a) Elevation, (b) Slope angle, (c) Plan curvature, (d) Profile curvature, (e) Specific catchment area, (f) Slope aspect, (g) Topographic position Index (TPI), (h) Total curvature, (i) Stream transportation index (STI), (j) Relative stream power index (RSPI), (k) Topographic wetness index (TWI) are demonstrated below.

2.2.3 Data Training

Occurrence of landslides/mass movement makes a significant constrain to development in Malaysia, notably through the inadvertent reactivation of the ancient landslides. It is obvious that there is no existing debris flow inventory data for the highly prone vulnerable areas in Malaysia. The landslide inventory map was also checked with the preceding work of [26]. We utilized this data to train and validate the performances of our models; about 306 landslide points were provided on an inventory map.
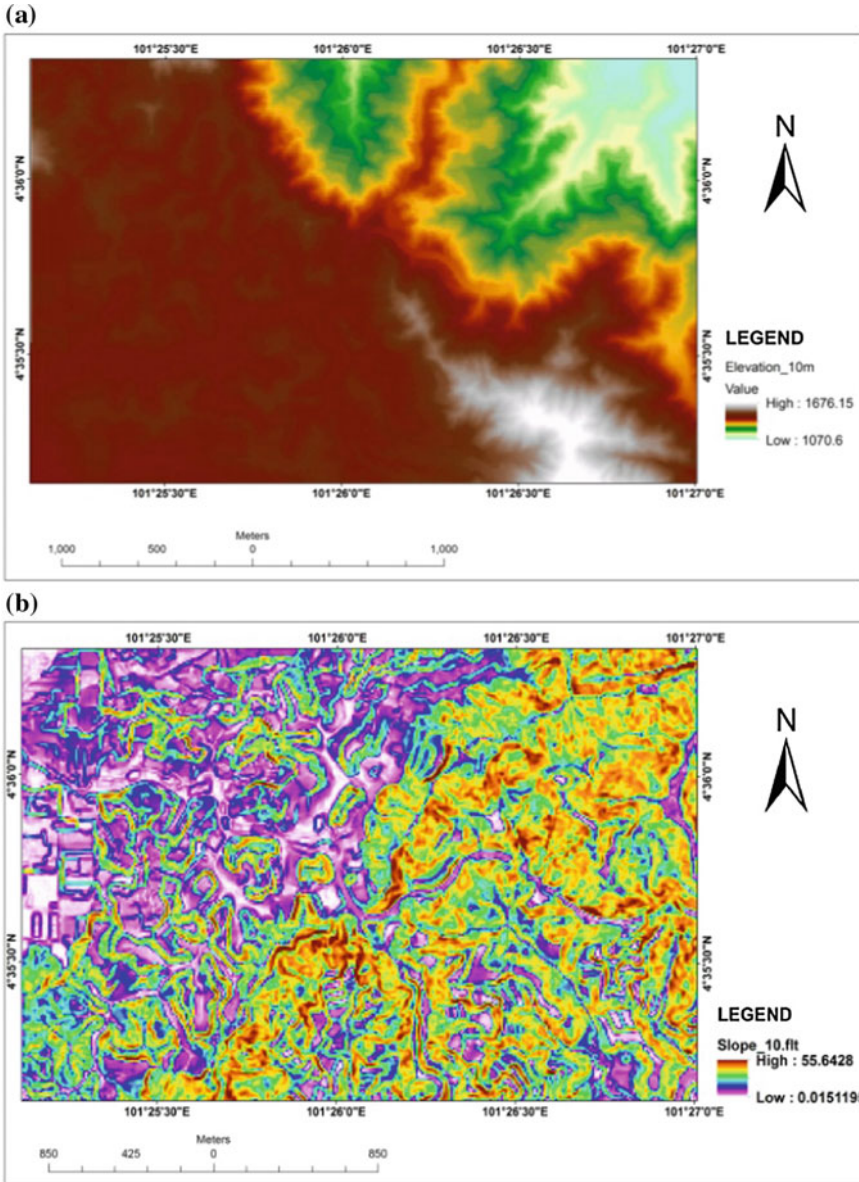
Fig. 3 **a** Elevation. **b** Slope angle. **c** Plan Curvature. **d** Profile curvature. **e** Specific catchment area. **f** Slope aspect. **g** Topographic position index (TPI). **h** Total curvature. **i** Stream transportation Index (STI). **j** Relative stream power index (RSPI). **k** Topographic wetness index (TWI)

(c)

(d)

Fig. 3 (continued)

(e)

(f)

Fig. 3 (continued)

(g)

(h)
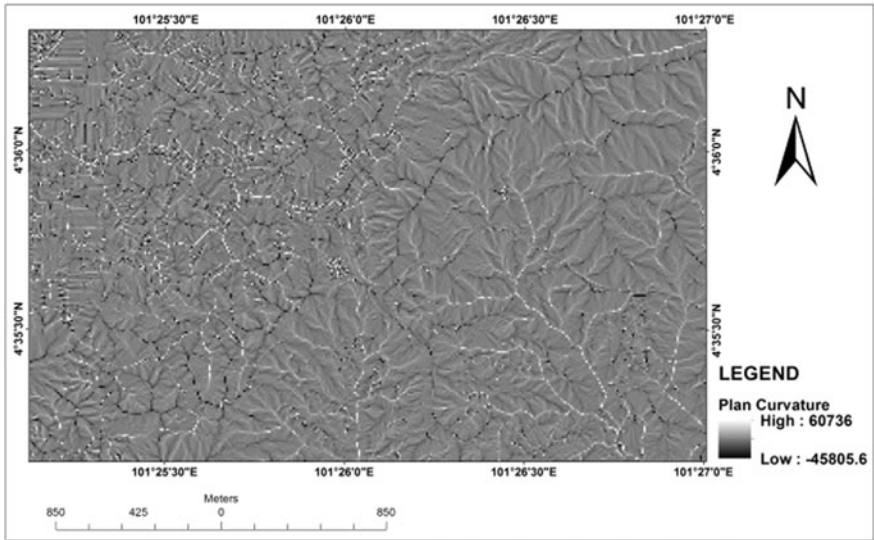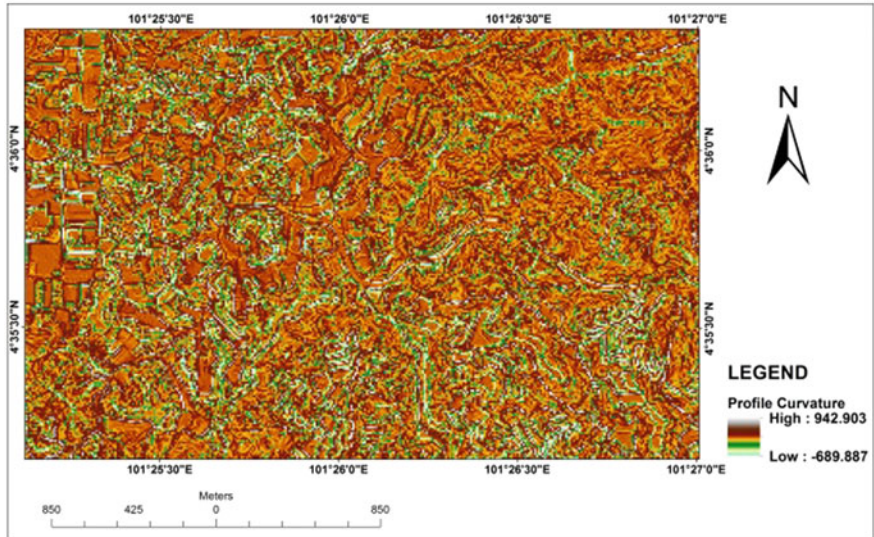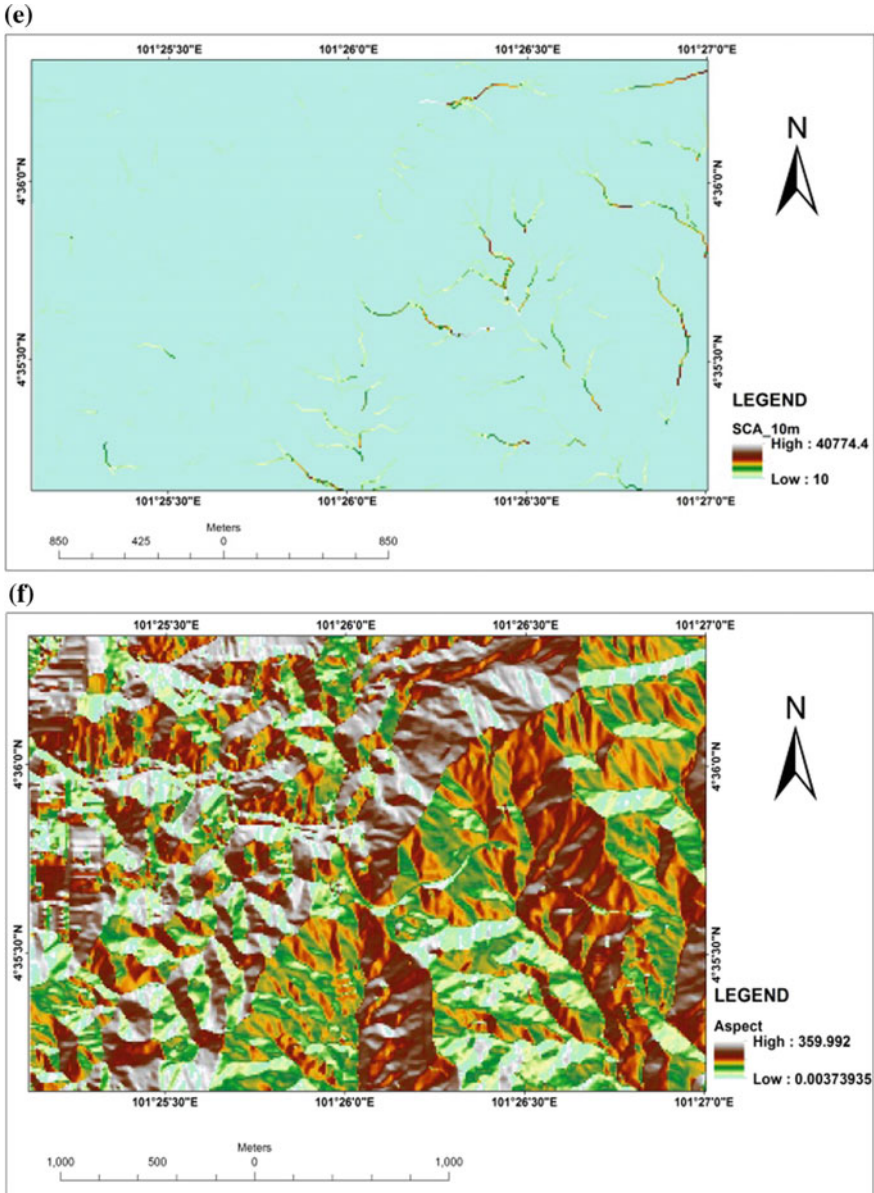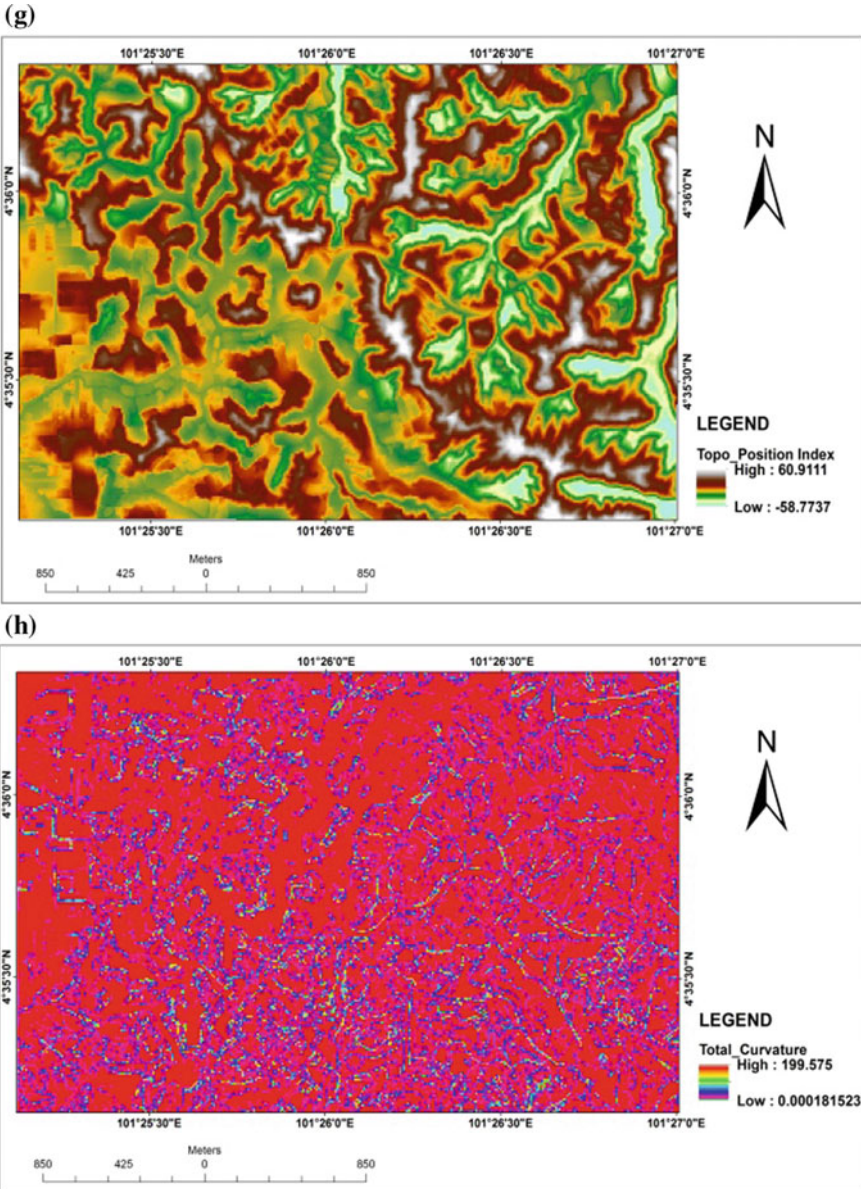
Fig. 3 (continued)

(i)
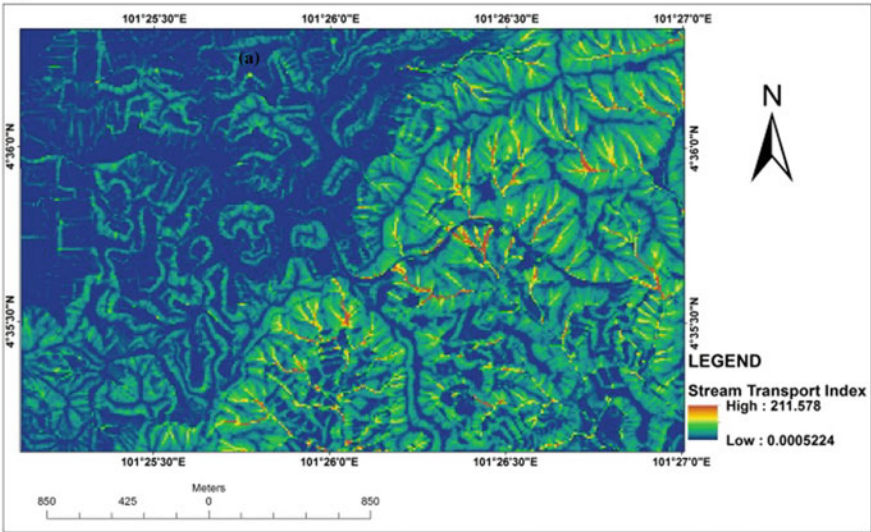
(j)
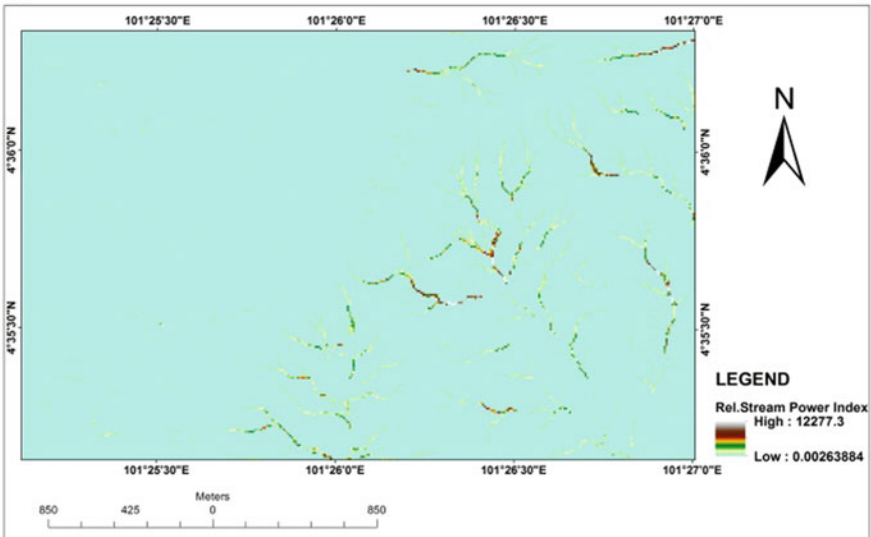
Fig. 3 (continued)

(k)
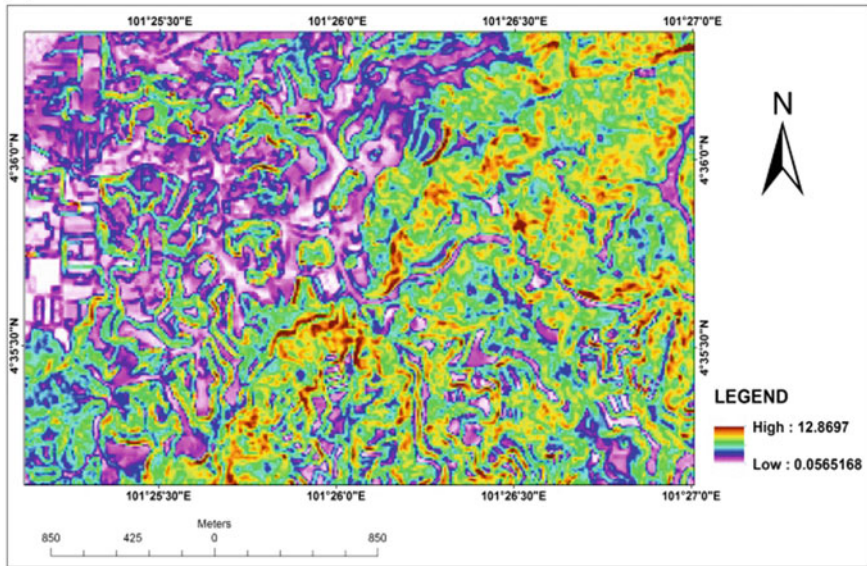
Fig. 3 (continued)

Table 1 Models input continuous variables

Parameters	Equations	Description
Topographic wetness index (TWI)	$\mathrm{TWI} = \ln\frac{\mathrm{Ac}}{\tan\beta}$	Purinton and Bookhage (2017)
RSP	$\mathrm{RSP} = \mathrm{Ac}^{\rho} * \tan\beta$	[24]
Stream transport index (STI)	$\mathrm{STI} = (M+1) * \left[\frac{\mathrm{Ac}}{22.12}\right]^{m} * \left[\sin\frac{\beta}{0.0896}\right]^{n}$	[3]
Topographic position index (TPI)	$\mathrm{DEV}_D = \frac{Z_o - Z_D}{S_D}$	[24]

Variable Importance		
Variable	Score	
RCLASTRI_1	100.00	
RCLASLOPE_	93.53	
RCLASSCA_1	85.53	
RCLASSTI_1	62.91	
RCLASPROFC	59.24	
RCLASTWI_1	57.51	
RCLASPLANC	44.97	
RCLASDEMEL	35.57	
RCLASTOTCV	27.61	
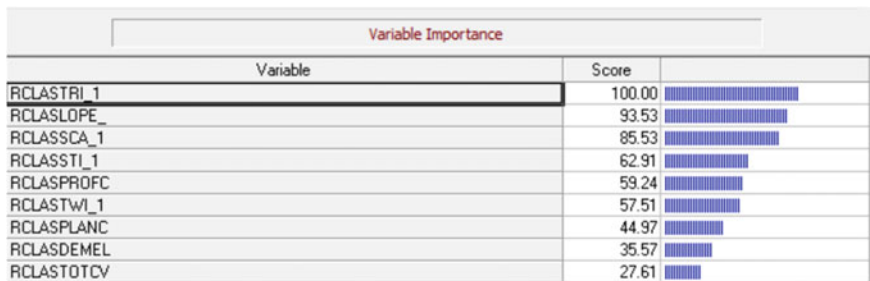
Fig. 4 Importance variable

2.2.4 Parameter Optimization

One of the important problems associated with the conditioning factors in a mass movement related hazard modelling is the optimization of the conditions simulations. In this paper, we computationally optimized some attributes of the selected data mining algorithms MARS [scales, maximum basis functions (MBF) and maximum values of interactions (MI)]. Previous work [14] has reported different methods for parameters optimization system selection. The method developed here is simpler and can be applied in the case of large number factors. A total of 50–200 MBF values with mi values of 1–3 were tested on multi-scale variables. The optimum parameter was selected based on lower GCV estimate and error rate.

Thirty-three experiments were executed on different pixel sizes, maximum basic functions and variable's maximum interaction; all participated optimally. The best combination is nominated, established on the outcomes of ROCs and GCVs in the experiments (Table 2). MARS algorithm is capable of identifying important variable(s) from input predictor continuous variables.

2.3 Identify Importance Variables for Debris Flow Modelling for the Tropical Zone

The major challenge confronting quantitative analyses in natural hazards modelling is the choice of conditioning factors [7]; but other models like physical based are governed by topographic attributes, and the object characteristics. To achieve accurate numerical model, it is necessary to use a perfect DEM data. It has been proved that coarse resolution DEM may omit significance topographic features whereas excessive fined resolutions DEMs may result to wide range of running time and possible inappropriate modelling output [1, 7]. The DEM with optimum pixel size is selected for further model process.

2.3.1 Multivariate Adaptive Regression Splines (MARS) Modelling Approach

This model was promoted by Friedman [13] to resolve classification and regression challenges; the focal of his determination was to predict continuous dependent variable from a set of independent continuous variables.

This is an automated regression modelling of data mining approach, elastic in nature, binary perfectly model and handle continuous dependent variables. MARS is a nonparametric without any assumption. The approach outshines at identifying optimal variable alterations and prospective interaction in all regression-related modelling result; it unveiled significant data forms and difficult interactions that are intolerable exposed by other approaches. Collection of model's continuous

Table 2 Generalized cross validation (GCV) and Area under curve (AUC) values for generated multi-scale resolutions

S/ no	Pixel size	Max. BF	Max. INTEG	ROC test	ROC train	GCY	MSE
1.	5	200	1	0.7174	0.7749702	0.2341	0.1919
2.			2	0.7564	0.7552624	0.2190	0.2032
3.			3	0.7348064	0.7323420	0.219	0.210
4.		**100**	1	0.732	0.7825470	0.2250	0.1900
5.*			**2**	**0.7648963**	**0.7642636**	**0.21777**	**0.19999**
6.			3	0.7204386	0.7310829	0.22060	0.20928
7.			1	0.7174495	0.7749702	0.234	0.19193
8.		300	2	0.7555324	0.7583317	0.21757	0.19997
9.			3	0.6524970	0.7322456	0.22193	0.20949
10.		50	1	0.7175320	0.7687986	0.22049	0.19460
11.*			**2**	**0.7334853**	**0.7702727**	**0.21337**	**0.19513**
12			3	0.7391994	0.7512288	0.21288	0.20216
13	10	300	1	0.7915015	0.8097793	0.20163	0.17855
14			2	0.7767043	0.7889721	0.19354	0.18576
15			3	0.7971165	0.8079112	0.18941	0.17776
16		200	1	0.7915015	0.8097793	0.19549	0.17855
17			2	0.8037554	0.7832248	0.19755	0.18984
18*			**3**	**0.8026985**	**0.8171384**	**0.18931**	**0.17301**
19		100	1	0.7785870	0.8008662	0.19294	0.18019
20			2	0.7484972	0.8027618	0.19432	0.18093
21			3	0.7858370	0.7569155	0.20814	0.20234
22	15	100	1	0.6714787	0.6849927	0.23787	0.22148
23			2	0.6971763	0.6714787	0.23926	0.21948
24*			**3**	**0.6779783**	**0.7184917**	**0.23219**	**0.21038**
25		200	1	0.6614369	0.6609249	0.23514	0.22727
26			2	0.6718129	0.6578139	0.23751	0.22790
27			3	0.5991312	0.6004857	0.24125	0.23542
28		300	1	0.6614369	0.6609249	0.23768	0.22727
29			2	0.6532331	0.6252022	0.242112	0.23674
30			3	0.6450627	0.6754549	0.24323	0.22519
31		50	1	0.6916124	0.6820727	0.23459	0.22350
32			2	0.6482206	0.6504661	0.23715	0.23176
33			3	0.6791145	0.6844873	0.23296	0.22286

The bold values show the significant values

variables and basis function are combined to produce the predictions given the inputs. Integration of inputs, continuous variables and basis functions yielded response prediction. BF provides analytical machinery to express Knot using intense search and effective degree of freedom (df) is a measure applied to justify for this quest [13]:

$$\frac{\text{Max}(0, x - c)}{\text{Max}(0, c - x)}. \tag{1}$$

This is a continuous transformation of actual value X into X*; value C defines the Knot placement for any data value (range from 0 to 100). The attributes resistance to multicollinearity is because each uses BF results to a different number of 0 s in a transformed variable. Multiple linear equations are built around the BF; this gives an idea on how the variable interacts. BFs should not exceed 200, the process stops once a user defines or specifies that the upper limit is reach. Linear dependency is handled automatically by discarding redundant BFs (Salford 2016).

Hastie et al. (2001) summarize the MARS model equation as:

$$y = f(x) = \beta_0 + \sum_{m-1}^{M} \beta_m h_m(X). \tag{2}$$

where

y　　　 function of the predictors variables (X) and their interactions;
β_0　　 intercept parameter;
β_m　　 weighted intercept parameter;
M　　　 terms of summation in the model;
$h_m(X)$　 m of number basic functions.

h is a function defined as:

$$h_{km}(X_{v(k,m)}) = \prod_{k-1}^{k} h_{km} \tag{3}$$

where $v(k, m)$ = the predictor in the kth of mth product; in order of interactions: when $k = 1$ is addictive model while $k = 2$ is pairwise interactive.

The BF is defined by the researcher; it was stated that the maximum interactive value should not exceed 3; except in rare cases. In this research paper, we explored the range (1–3) in search of the ideal interaction criterion. Also, maximum basis functions were calibrated ranging from 50 to 300 (Table 2) to identify the optimum value that is suitable for the models, capable of maximizing the model accuracy, and minimizes the GCV errors.

Generalized Cross Validation (GCV)

GCV trade-off goodness-of-fit against model complexity (overfitting). To choose the best subset, backward pass uses GCV to compare the performance of model subsets.

$$GCV = \frac{RSS}{\left(N * \left(1 - \text{Effective number of parameter}/N\right)^{\wedge 2}\right)} \quad (4)$$

where

RSS	Residual sum of squares, measure on training data,
N	Number of observation (number of row in X matrix)
Effective number of parameter	number of MARS terms and penalty *(number of MARS term—1)/2.

In any form of the basis function selections, a pruned was used to filter signal–noise basis functions, in which measure of goodness-of-fit was calculated (square and GCV errors).

GCV error is a measure of degree of model fitness both residual errors and model complexity. We admitted GCV error values in selecting the optimal model in debris flows source area prediction, the smaller the GCV the better you model (Table 2). Thus, GVC equation is given in STATISTICA (2016) tutorial as follows:

$$GCV = \frac{\sum_{i-1}^{N} (y_i - f(x_i))^2}{\left(1 - \frac{C}{N}\right)^2} \quad (5)$$

where

$C = 1 + cd$
N the number of cases in the dataset
d the effective degree of freedom (the same as the number of independent basis functions)
C the penalty for adding basis functions

Existing landslides inventory data for the study area is utilized for source areas training and validation, in the absence of debris flow historical records. As a form of landslide, it has some peculiar characteristics of it occurrences/initiations (triggering factors, rheology, one or two-phase flow etc.). In this research, we considered landslide inventory data and the derived multi-scale conditioning variables threshold; which were subsequently utilized as inputs data in running MARS model and validations. Primarily, the concerts of the all models were evaluated using GCV and ROC curve.

The predictive strength of the final results was subjected to the dataset validation assessments using ROC curves. According to Gómez-Gutiérrez [14], the ROC

curve is a graphical representation of ratio of positive issues appropriately predicted (true-positive/sensitivity) to the proportion of positive issues erroneously predicted (false-positive/1-specificity), on the potentially benchmark. In this paper, we specified that the MARSplines attributes are (maximum basis functions 50–200; interactions 1–3; df-3); increasing to higher BFs values will create more chance for nonlinearity in the data. Selection of optimal model was based on modern and legacy approaches; based on the test performance and based on GCV criterion. The best model with lowest GCV and highest ROC was nominated for final analysis, because the arbitrary choice threshold does not influence the AUC value they are used as a pointer of the model performance. The scale is between 1 and 0; if approaching 1 is a faultless model while towards 0.5 indicates fallacy in the model [14]. Heuristic approach was adopted to select the best attributes combination, which produced the best model, with lowest GCV, and highest AUC values. MARS algorithm in the Salford Predictive Modeler software (www.Salfordsystem.com) was employed to run the models. Successively, the final models were accomplished in the ArcGIS software environment to generate the outputs source area map.

BF Regression model

In order to generate the final debris flow source statistically; the regression (6) model was simulated in raster calculator with the basis functions (BF) generated from the model, as a coefficient of the model known as knot or independent variables; the output is shown in (Fig. 6).

Y = 0.458993 + 0.0566091 * BF13 + 0.0585988 * BF19 − 0.0194275 * BF75 + 0.0099626 * BF85 + 0.182283 * BF87 − 0.0250806 * BF110-0.0928679 * BF130 + 0.0035632 * BF186. (6)

Y = Dependent variable, i.e. the debris flow source areas detection

BF = indicated cells basis functions.

3 Results and Discussions

Selecting an optimal resolution is important for successful application of remote sensing. The leading contributing parameters used in the model were the shown in Fig. 3, chosen from the initial 12. A better result was generated using MARS model, tested the efficiency of the model using multi-scale resampled LiDAR data. Figure 6 displays a satisfactory result, selected from the best combination on different experiments conducted (Table 3). The optimal pixel size that is suitable for the developed modelled is 10 m spatial resolution; other identified optimum parameters area MBF = 200, mi = 3 about 82% AUC, 0.189 (19%) GCV and 0.173 (17%) MSE (Table 2).

3.1   Variable Importance

The variable importance was segregated and expressed in relative scale (0–100), the utmost variables have a score value of 100; other variable were adjusted to reveal their contributions compare to the highest scored variable (Fig. 4). In this paper, nine conditioning parameters were clearly identified as importance variables in the model development, the most contributed variable is topographic roughness index (TRI) with a 100 score value, followed by slope gradient with 94 score values; the least is the total curvature with 26 score values. While the remaining that is not selected are believed to have low impacts or possibly returned arbitrary noise behaviours (Salford tutorial 2013). Though, few variables have been proven in debris flows detection [16] this proved the assertions of (Salford tutorial 2013), 'that three criteria in a critical combination are relevant for debris flows initiation'; they recognize terrain slope, sediment available and water input (SCA). Amongst the optimized variables, three major parameters used in FLOW-R software were identified automatically and incorporated in the processes by MARS algorithm (Fig. 2).

3.2   Optimal Model Performance and Spatial Resolution

The outcomes of the GCV, ROC/AUC and MSE values achieved for the 33 models (Table 2) revealed that the GCV Values ranged from 0.189 to 0.243, the lowest and highest were observed on 10 and 15 m DEM, respectively. The MARS attributes value return best results with maximum basis function criteria 200 and worst with 300 values. The optimal AUC training result is 0.817 and agrees with the best GCV values and pixel size (10 m). Meanwhile, the high spatial resolution (5 m) did not turn out to produce the optimal model performance, with the GCV (0.213) and lowest AUC (0.733 tests and 0.770 training) values. Quantitatively, the disparity in low resolution performance is apparently greater than 10 m pixel size being (0.189) GCV values and AUC (0.802 test and 0.817 training) values (Table 3). The 10 m resolution yielded the best model results, this is similar to the model obtained by Chen [13], Horton et al. [16] and Gómez-Gutiérrez [14]. The GCV values are attested to be sensitive to pixel sizes, degree of interactions and basis functions (Table 2).

Table 3 Summary of models attributes optimizations

S/ No	Max BFs	Pixel size	Max. Integration	ROC/ AUG teat	ROC/ AUG train	Learn GCV	MSE
1.	50	5	2	0.7334853	0.7702727	0.21337	0.19513
2.	**200**	**10**	**3**	**0.8026985**	**0.8171384**	**0.18931**	**0.17301**
3.	100	15	3	0.6779783	0.7184917	0.23219	0.21038

The bold values show the significant values

Gómez-Gutiérrez et al. [14] established the model's vigour related to the training dataset modifications. The best model was considered to prepare the model, and is presented in Fig. 5.

The optimized model was simulated with the use of topographic conditioning factors and the result is shown in Fig. 5. It is indicated that about 80% of the source areas in detected and clustered at debris flows than in the contiguous terrain at the southern region of the map, started from down south-western (bottom left) of the map diagonally towards the north-eastward (top right) (Fig. 5) believed to have linkages with landform type (gully) and stream network of the area. Sparse traces of debris flow were detected in the Northern parts of the map; while in the north-west region of the map no indication of the hazard was establish, due to the present of man-made structures and low terrain elevation.

The general concert of the debris flows source area model based on the topographic LiDAR data was verified and proved excellent with 0.817 (82%) AUC values; supported by the ROC curve (Fig. 6). It was observed that ROC curve demonstrated a thoughtful inconsistency at the upper graph. The validation showed that the source area map obtained is adequate to be integrated into susceptibility, hazard and mitigation modelling.

4 Conclusion

In this research, variables were optimally transformed and automatically chosen. The harmful effect by debris flow is common in mountainous area, particularly in the Cameroun Highlands.

In this paper, the capability of LiDAR data is demonstrated in modelling debris flows source areas, by using an empirical approach. Imperatively, to improve our
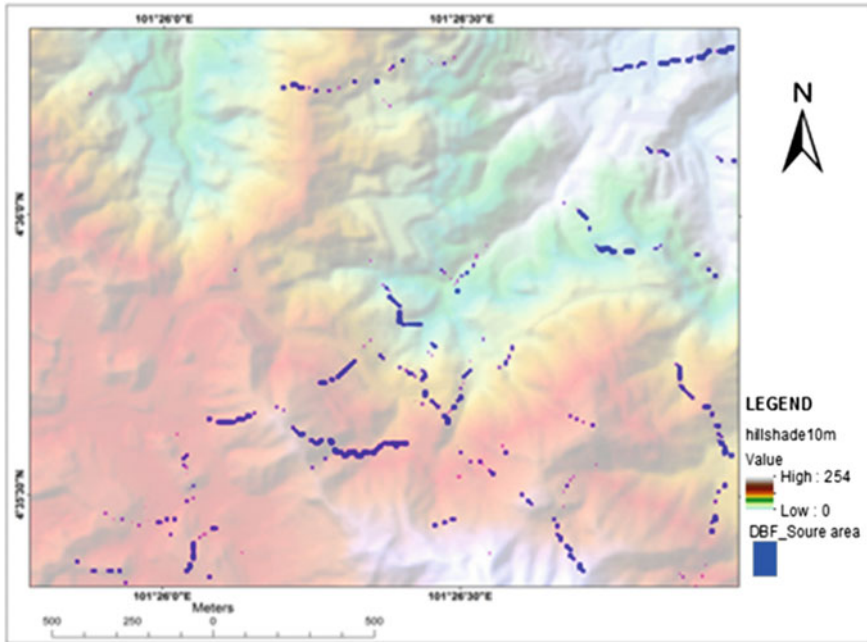
Fig. 5 Debris flow source areas

understanding of the behaviour of this menace in the area, detailed topographic data are handled and optimized.

Series of statistical models were accomplished, in search of optimum parameters or variable and processes combine to detect the debris flow source in a rugged area. Out of the four situations, the 10 m spatial resolution proves to be the best instance for a substantial and satisfactorily modelling of debris flow source areas. Both stream transport index and slope gradient were found to be the most important contributing factors, the attributes of the approach used has illustrated impact on the accuracy of the model outcome. Hence, the use of evolutionary optimization will be required to improve the attribute values and variables selection; in direction to attain tentative data which may tip up the performance to a reliable event replication.

Fig. 6 The model ROC curve
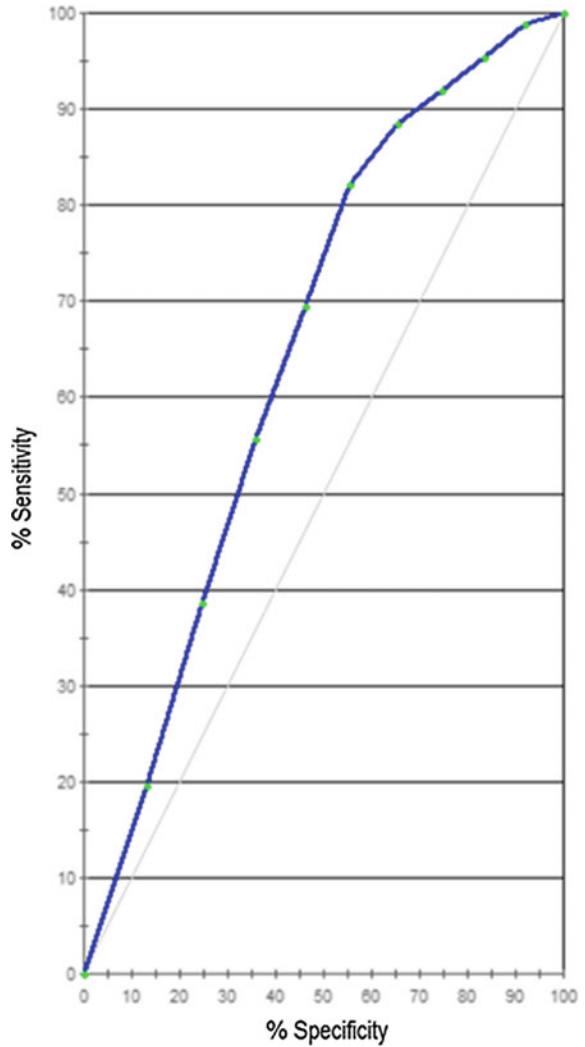
References

1. Bühler, Y., Christen, M., Kowalski, J., Bartelt, P.: Sensitivity of Snow Avalanche Simulations to Digital Elevation Model Quality and Resolution RID B-9859-2011. Ann. Glaciol. **52**(58), 72–80 (2011)
2. Carrara, A., Cardinali, M., Detti, R., Guzzetti, F., Pasqui, V., Reichenbach, P.: GIS techniques and statistical models in evaluating landslide hazard. Earth Surf. Proc. Land. **16**(5), 427–445 (1991)
3. Chen, H.X., Zhang, S., Peng, M., Zhang, Limin: A physically-based multi-hazard risk assessment platform for regional rainfall-induced slope failures and debris flows. Eng. Geol. **203**, 15–29 (2016). https://doi.org/10.1016/j.enggeo.2015.12.009

4. Chen, CY., Yu, F.C.: Morphometric analysis of debris flows and their source areas using GIS. Geomorphology **129**(3–4): 387–97. (2011). http://linkinghub.elsevier.com/retrieve/pii/S0169555X1100122X

5. Chen, W., Pourghasemi, H.R., Naghibi, S.A.: Prioritization of landslide conditioning factors and its spatial modeling in shangnan county, China using GIS-Based data mining algorithms. Bulletin Eng. Geol. Environ. 1–19 (2017a)

6. Chen, W., Pourghasemi, H.R., Zhao, Z.: A GIS-based comparative study of dempster-shafer, logistic regression and artificial neural network models for landslide susceptibility mapping. Geocarto Int. **32**(4): 367–85. (2017b). https://www.tandfonline.com/doi/full/10.1080/10106049.2016.1140824

7. Christen, M. et al. Integral hazard management using a unified software environment numerical simulation tool 'RAMMS.' Congress Interpraevent 77–86 (2012)

8. Conoscenti, C., et al.: Gully erosion susceptibility assessment by means of gis-based logistic regression: a case of sicily (Italy). Geomorphol **204**, 399–411 (2014). https://doi.org/10.1016/j.geomorph.2013.08.021

9. Conoscenti, C., Angileri, S. E., Rotigliano, E., Schnabel, S.: Using topographical attributes to evaluate gully erosion proneness (susceptibility) in two mediterranean basins : advantages and limitations (2015)

10. Ehsani, Amir Houshang, Quiel, Friedrich: Geomorphometric feature analysis using morphometric parameterization and artificial neural networks. Geomorphol **99**(1–4), 1–12 (2008)

11. Elkadiri, R., Sultan, M., Youssef, A.M., Elbayoumi, T., Chase, R., Bulkhi, A.B., Al-Katheeri, M.M.: A Remote Sensing-Based Approach for Debris-Flow Susceptibility Assessment Using Artificial Neural Networks and Logistic Regression Modeling. IEEE J. Sel. Top. Appl. Earth Obs. Remote Sens. **7**(12), 4818–4835 (2014)

12. Fischer, L., Rubensdotter, L., Sletten, K., Stalsberg, K., Melchiorre, C., Horton, P., Jaboyedoff, M.: Debris flow modeling for susceptibility mapping at regional to national scale in Norway. In Proceedings of the 11th International and 2nd North American Symposium on Landslides, pp. 3–8, (2012)

13. Friedman, J. H.: Multivariate adaptive regression splines. Ann. Stat. 1–67 (1991)

14. Gómez-Gutiérrez, Á., Conoscenti, C., Angileri, S.E., Rotigliano, E., Schnabel, S.: Using topographical attributes to evaluate gully erosion proneness (susceptibility) in two mediterranean basins: advantages and limitations. Nat. Hazards **79**(1), 291–314 (2015)

15. Hansen, J. E., Sue, D. Y., Wasserman, K.: Predicted values for clinical exercise testing 1–3. Am. Review Respir. Dis. **129**(2P2), S49–S55 (1984)

16. Horton, P., Jaboyedoff, M., Rudaz, B., Zimmermann, M.: Flow-R, a Model for Susceptibility Mapping of Debris Flows and Other Gravitational Hazards at a Regional Scale. Nat. Hazards Earth Syst. Sci. **13**(4), 869–885 (2013)

17. Hughes, A.O., Prosser, I.P., Stevenson, J., Scott, A., Lu, H., Gallant, J., Moran, C.J.: Gully erosion mapping for the national land and water resources audit. CSIRO Land Water Canberra Tech. Rep. **26**, 01–20 (2001)

18. Hungr, O., Morgan, G.C., Kellerhals, R.: Quantitative analysis of debris torrent hazards for design of remedial measures. Can. Geotech. J. **21**(4), 663–677 (1984)

19. Hussin, H.Y., Quan Luna, B., Van Westen, C.J., Christen, M., Malet, J.P., Van Asch, ThWJ: Parameterization of a Numerical 2-D debris flow model with entrainment: a case study of the faucon catchment, southern french alps. Nat. Hazards Earth Syst. Sci. **12**(10), 3075–3090 (2012)

20. Iverson, R.M.: The physics of debris flows. Rev. Geophys. **35**(3), 245–296 (1997)

21. Jaboyedoff, M., Oppikofer, T., Abellán, A., Derron, M.H., Loye, A., Metzger, R., Pedrazzini, A.: Use of LiDAR in landslide investigations: a review. Nat. Hazards **61**(1), 5–28 (2012)

22. Johnson A.M., Rodine J.R.: Debris flow. In: Brundsen, D., Prior, D.B. (eds.) Slope Instability, 257–361. (1984)

23. Kheir, R.B., Wilson, J., Deng, Y.: Use of terrain variables for mapping gully erosion susceptibility in Lebanon. Earth Surf. Proc. Land. **32**(12), 1770–1782 (2007)

24. Lindsay, J.B., Cockburn, J.M.H., Russell, H.A.J.: An integral image approach to performing multi-scale topographic position analysis. Geomorphology **245**(15), 51–61 (2015)
25. Pradhan, B., Lee, S.: Regional landslide susceptibility analysis using back-propagation neural network model at cameron highland, Malaysia. Landslides **7**(1), 13–30 (2010)
26. Pradhan, B.: A comparative study on the predictive ability of the decision tree, support vector machine and neuro-fuzzy models in landslide susceptibility mapping using GIS. Comput. Geosci. **51**, 350–365 (2013)
27. Pradhan, B., Bakar, S.B.A.: Debris flow source identification in tropical dense forest using airborne laser scanning data and Flow-R model. In: Pradhan, B. (ed.) Laser Scanning Applications in Landslide Assessment. pp. 85–112, Springer International Publishing, (2017)
28. Pradhan, B., Seeni M. I., Nampak, H.: Integration of LiDAR and quickBird data for automatic 685 landslide detection using object-based analysis and random forests. In: Laser Scanning Applications in Landslide Assessment, pp. 69–81. Springer, Cham. (2017)
29. Pradhan B., Kalantar B., Abdulwahid M.W. Dieu B.T.: Debris Flow Susceptibility Assessment Using Airborne Laser Scanning Data. In: Pradhan, B. (ed.) Laser Scanning Applications in Landslide Assessment. pp. 276–296, Springer International Publishing, (2017)
30. Quan Luna, B., Blahut, J., van Westen, C.J., Sterlacchini, S., van Asch, T.W.J., Akbas, S.O.: The application of numerical debris flow modelling for the generation of physical vulnerability curves. Nat. Hazards Earth Syst. Sci. **11**, 2047–2060 (2011). https://doi.org/10.5194/nhess-11-2047-2011
31. Rickenmann, D.: Methods for the quantitative assessment of channel processes in torrents (Steep Streams). CRC Press, (2016)
32. Salzmann, N., Kääb, A., Huggel, C., Allgöwer, B., Haeberli, W.: Assessment of the hazard potential of ice avalanches using remote sensing and GIS-modelling. Norsk Geografisk Tidsskrift-Norwegian J. Geo. **58**(2), 74–84 (2004)
33. Schneider, R.R., Hamann, A., Farr, D., Wang, X., Boutin, S.: Potential effects of climate change on ecosystem distribution in Alberta. Can. J. For. Res. **39**(5), 1001–1010 (2009)
34. Spencer, T., Slaymaker, O., Embleton-Hamann, C.: Landscape, landscape-scale processes and global environmental change: synthesis and new agendas for the twenty-first century. In: Cambridge, U. (ed.) Geomorphology and Global Environmental Change, pp. 403–423. Press, Cambridge (2009)
35. Svoray, T., et al.: Predicting gully initiation: comparing data mining techniques, analytical hierarchy processes and the topographic threshold. Earth Surf. Proc. Land. **37**(6), 607–619 (2012)
36. Takahashi, T.: Debris flow mechanics, prediction and countermeasurements (2007)
37. Takahashi, T.: Debris flow: mechanics, prediction and countermeasures. 2nd edn. ISBN: 1138000078, 9781138000070 (2014)
38. Varnes, D.J.: Slope movement types and processes. In: Schuster, R.L., Krizek, R.J. (eds.) Landslides, Analysis and Control, Special Report 176: Transportation Research Board, pp. 11–33. National Academy of Sciences, Washington, DC. (1978)

Drought Monitoring in the Coastal Belt of Bangladesh Using Landsat Time Series Satellite Images

**Afzal Ahmed, Eshrat Jahan Esha, A. S. M. Sadique Shahriar
and Iftekhar Alam**

Abstract Drought is a recurrent phenomenon in Bangladesh but it received very little attention in terms of early warning, detection, preparedness and mitigation of droughts. To manage all these aspects, an effective drought monitoring system is the prime pre-requisite. Till date, scientists worldwide have put several efforts to develop drought mapping and monitoring system using indices, which are derived from meteorological and satellite data. This study presents a method for spatio-temporal monitoring of drought in the coastal region of Bangladesh. Standardized Precipitation Index (SPI), which is based on meteorological data, is used in a GIS environment to generate drought hazard maps in the study area. On the other hand, time series Landsat satellite images were used to calculate various remote sensing based indices such as NDVI, VCI, TCI, VHI and NDWI in order to determine the extent of drought. Each of the indices produced a raster map, which is then reclassified to produce binary images with "drought" and "no-drought" classes. Finally, accuracy assessment of drought detection capability of the indices was done by formulating a comparison matrix from a set of values of randomly generated points within the study area. The result showed that NDVI and VCI are the most reliable indices for drought mapping for the study area based on the SPI values as standard. This study enabled a process of drought mapping basing on remote sensing indices and a comparative assessment of the performance of different indices as well. Inadequate numbers of meteorological stations in Bangladesh as well as missing rainfall data in some of those stations made the calculation of SPI values less accurate. As a consequence, the accuracy level of index based drought

A. Ahmed (✉) · E. J. Esha (✉) · A. S. M. Sadique Shahriar · I. Alam
Faculty of Civil Engineering, Military Institute of Science
and Technology, 1216 Dhaka, Bangladesh
e-mail: afzal.ahmed2008@gmail.com

E. J. Esha
e-mail: eshaeshratjahan@gmail.com

A. S. M. Sadique Shahriar
e-mail: sadiquehahriar40@yahoo.com

I. Alam
e-mail: iftekhar7101@gmail.com

identification has been deteriorated. Moreover, lack of ground truth data imposed a drawback on the accuracy assessment process. In spite of the aforementioned shortcomings, the methodology adopted in this study is capable of mapping the spatio-temporal pattern of drought from time series Landsat Satellite images with acceptable accuracy. This study recommends further research on assessing the suitability of all other drought indices for Bangladesh, formulation of drought definition policy and development of integrated drought monitoring system comprising meteorological, statistical, observational and remote sensing data.

Keywords Remote sensing · Landsat · Drought monitoring · Standardized Precipitation Index (SPI) · Normalized Difference Vegetation Index (NDVI) Vegetation Condition Index (VCI) · Temperature Condition Index (TCI) Vegetation Health Index (VHI) · Normalized Difference Water Index (NDWI)

1   Introduction

Drought is a recurring climate event and is one of the major natural calamities, which causes negative impacts on the environment as well as on agriculture and economy worldwide. Among various natural hazards i.e., floods, cyclones, and earth-quakes, drought possesses certain unique features. For example, it is difficult to determine the beginning and the end of drought. Besides, the effects of drought may build up slowly over a substantial period of time and may continue for several years after the cessation of the event [1]. Also, the geographical extent of drought impacts is quite large as compared to the damaged area that results from other natural [2]. Drought is a normal phenomenon of climatic events, which can occur in virtually all climatic regimes. Drought has become a common phenomenon in some parts of Bangladesh in the recent decades. Meteorologically drought can be classified into three types: permanent drought, which can be seen in the arid climate; seasonal drought—occurs due to irregularities in recognized rainy and dry seasons; and contingent drought—caused by irregularities in rainfall. In Bangladesh, the last two types are more rampant, which occurs mostly in pre-monsoon and post-monsoon periods., Bangladesh has suffered about 20 severe drought conditions during the last 50 years, which raised serious concern about food security as well as water security of the country [3]. Traditional drought monitoring was based entirely on rainfall data. For this purpose, several indices have been developed, which takes into account time-series statistical observation on rainfall, stream flow and other water-supply indicator. But such approach has several limitation e.g., limited number of metrological stations, missing climatic data, error in measurement etc. Besides, these indices are unable to address spatial variation because the index calculated at one location is only valid for that particular location. This situation is aggravated if the meteorological stations are sparsely distributed, which may affect the reliability of the drought indices [4]. Due to high spatial and temporal resolution of satellite images, satellite derived drought indicators have been widely

used to study droughts. Normalized Difference Vegetation Index (NDVI), Vegetation Condition Index (VCI), and Temperature Condition Index (TCI) are some of the extensively used vegetation indices, which could be used for drought monitoring. In this context, the objective of this study is to a remote sensing based drought mapping and monitoring system for Bangladesh with a view to facilitate the effort in effective drought management system for the country. Specific objectives of this study are as follows:

(a) Drought mapping of coastal belt of Bangladesh by applying a set of selected remote sensing based indices on Landsat time series satellite images.
(b) Comparison of remote sensing indices basing on Standardized Precipitation Index (SPI) values.
(c) Assessment of accuracy of the remote sensing indices in determination of drought.

2 Study Area

The geographical extent of the study area (Fig. 1) is between 22° 42′ and 22° 51′ North latitudes and 84° 54′ to 90° 44′ East longitudes, which extends inside from the coast up to 150 km.

The winter is warm and the average temperature during this period ranges between 18 and 32 °C. The temperature during summer ranges from 34 to 41 °C. Average annual rainfall in this area is above 2000 mm of which 90–95% occurs during the period from June to September. This area is affected by widespread flooding during monsoon. On the other hand, waterlogging problem persists on some part of this area during the dry season. Water security and food security in this area is severely challenged by the salinity in water as well as in soil.
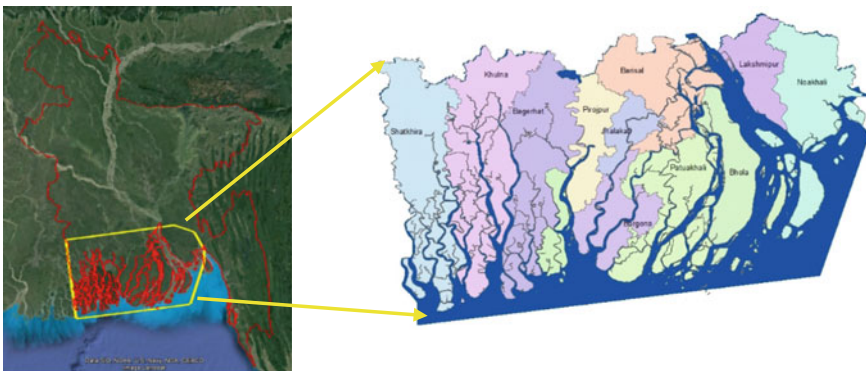
Fig. 1 Study area

3   Methodology

This study is an approach for drought monitoring in the coastal belt of Bangladesh by using Landsat time series satellite images. A drought monitoring system based on remote sensing and geographical information system technology has been proposed and its suitability in the context of Bangladesh has been evaluated. Landsat images of three years (2000, 2005 and 2010) covering the coastal belt of Bangladesh are used in this study. Historical rainfall data is used to evaluate the meteorological index of drought, which is then compared with the remote sensing indices to evaluate the effectiveness of the drought monitoring system. The meteorological index used here is the Standardized Precipitation Index (SPI) and a drought map is produced from the SPI values indicating various levels of severity with different color code in order to enable the visualization of drought over the study area.

On the other hand, a number of selected remote sensing indices have been calculated from Landsat time-series images. The SPI maps and the RS index maps were reclassified to obtain binary images showing drought and no-drought condition. Following that, a pixel to pixel comparison is done between the SPI drought maps and RS indices drought maps using a set of random points. Such comparison among the binary images provides a basis of accuracy assessment. The detailed methodology of this study is shown in the Fig. 2.

3.1   Data Collection

3.1.1   Meteorological Data Collection

For this study, the historical rainfall data of 34 meteorological stations of Bangladesh is downloaded from the website of Bangladesh Agricultural Research Council [5]. The data contains monthly average rainfall of the stations for the years from 1970 to 2013. The list of all the rain gauge stations is shown in the Table 1 [6]. This table is imported into ArcMap environment and a point feature map has been created using the latitudes and longitudes values of each stations. By overlaying the shapefile of the study area with this point feature map, it is found that total 8 stations (with highlighted rows) are located within the study area.

3.1.2   Image Acquisition

For each year, six tiles of Landsat images with path/row of 136/44, 137/44, 138/44, 136/45, 137/45, 138/45 have been downloaded. These images are freely downloadable from the US Geological Survey (USGS) [7]. These data are Level 1 Terrain Corrected (L1T) product, which are pre-georeferenced to UTM zone 46

Fig. 2 Flow chart of the methodology

North projection using WGS-84 datum. Table 2 represents some of the most useful technical specifications of the downloaded images.

3.2 Data Pre-processing and Database Preparation

The collected rainfall data is customized for software input and the downloaded Landsat images are taken through levels of pre-processing, customization and transformation and classification. The details are described below.

Table 1 List and locations of meteorological stations of Bangladesh

Station	Longitude (X)	Lattitude (Y)	Station	Longitude (X)	Lattitude (Y)
Barishal	*90.4*	*22.67*	Madaripur	90.22	23.18
Bhola	*90.67*	*22.33*	*Maijdi*	*91.13*	*22.83*
Bogra	89.42	24.83	*Mongla*	*89.67*	*22.417*
Chandpur	90.67	23.2	Mymensing	90.42	24.77
Chittagong	91.87	22.32	*Potuakhali*	*90.37*	*22.33*
Chuadanga	88.87	23.67	Rajshahi	88.58	24.33
Comilla	91.2	23.45	Rangamati	92.22	22.58
Cox's Bazar	92.03	21.42	Rangpur	89.3	25.7
Dhaka	90.4	23.68	Sandwip	91.42	22.42
Dinajpur	88.62	25.58	*Satkhira*	*89.17*	*22.68*
Faridpur	89.87	23.58	Sitakunda	91.58	22.53
Feni	91.4	23	Srimongol	91.67	24.3
Ishwardi	89.17	24.17	Syedpur	88.83	25.77
Jessore	89.23	23.17	Sylhet	91.83	24.9
Khepupara	*90.23*	*21.93*	Tangail	89.83	24.17
Khulna	*89.58*	*22.83*	Teknaf	92.33	20.83
Kutubdia	91.83	21.83			

3.2.1 Customization of Rainfall Data and SPI Calculation

The SPI is a powerful and flexible index yet simple to calculate, which was developed by the American scientisit McKee, Doesken and Kleist in 1993. SPI is designed to quantify the precipitation deficit for multiple timescales. Drought condition may pose impact on various water resources at different timescales. For example soil moisture condition may be affected by precipitation anomalies at relatively short time scale. Whereas, the deficiency in groundwater, streamflow and reservoir storage may be due to longer-term precipitation anomalies. For these reasons, the SPI is calculated for 3, 6, 12, 24 and 48 month timescales [8]. Mathematically, SPI can be calculated using the following equation:

$$\text{SPI} = \frac{X_i - X_m}{\sigma}$$

where, X_i is monthly rainfall record of the station; X_m is rainfall mean of the historical data; and σ is the standard deviation [9]. A software named spi_sl_6.exe was used to calculate SPI in this study. The customized rainfall data of different stations are converted in. cor format by renaming the file extensions. These. cor files were used as inputs and SPI-1, SPI-3, SPI-6, SPI-9, SPI-12, SPI-24 and SPI-48 are calculated for each station. The outputs are produced in.txt format by the software

Table 2 Specification of Landsat TM images

Year	Satellite	Sensor	Path/row	Julian day of acquired image	Spatial resolution (m)	Wavelength (μm)
2000	Landsat-5	TM (Thematic Mapper)	136/44	364 (2000)	30	Band 1: 0.45–0.52 Band 2: 0.52–0.60 Band 3: 0.63–0.69 Band 4: 0.76–0.90 Band 5: 1.55–1.75 Band 7: 2.08–2.35
			136/45	364 (2000)		
			137/44	355 (2000)		
			137/45	021 (2001)		
			138/44	314 (2000)		
			138/45	314 (2000)		
2005			136/44	329 (2005)		
			136/45	329 (2005)		
			137/44	320 (2005)		
			137/45	320 (2005)		
			138/44	311 (2005)		
			138/45	311 (2005)		
2010			136/44	359 (2010)		
			136/45	327 (2010)		
			137/44	318 (2010)		
			137/45	350 (2010)		
			138/44	309 (2010)		
			138/45	357 (2010)		

which was subsequently converted in tabular format for input in ArcGIS for SPI mapping.

3.2.2 Landsat Image Pre-processing

Before conducting image classification as well as calculating the remote sensing indices, each band of every image has gone through various steps of pre-processing e.g., radiometric corrections, mosaicking, clipping etc. These steps are described in brief in the following sub-sections:

Null Value Elimination

Each Landsat scene accompanies null data surrounding it, which must be removed before performing mosaicking or other image processing function on the scene [10]. In order to remove the null values, a Boolean raster has been created. This raster is then reclassified and multiplied with the original raster. Figure 3 shows a sample output of this process.

(a) Original Image   (b) Boolean raster   (c) Raster after eliminating
                                                    null value
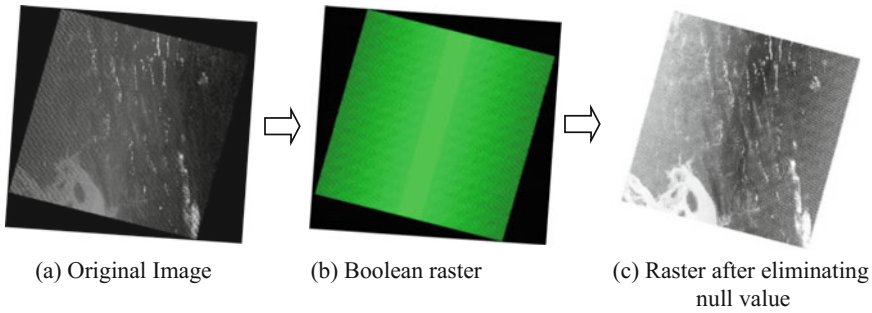
Fig. 3 Null value elimination

Radiometric Correction of Image

When the change detection is examined, it's important to normalize the images so that one can make comparisons between them [11]. For each band of every image, the radiometric correction is conducted in the following two steps: (a) conversion of digital number to radiance and (b) conversion of radiance to reflectance. Necessary equations for radiometric corrections are given below. Values of different parameters of the equations can be found from the metadata files (MTL files), which is available for each band for each Landsat scene. Radiance can be calculated from the digital number of a band from the following equation:

$$L_\lambda = \left(\frac{LMAX_\lambda - (LMIN_\lambda)}{QCALMAX - QCALMIN} \right) * ((BAND\ LAYER - (QCALMIN)) + LMIN_\lambda)$$

where, L_λ = Spectral radiance, $L_\lambda MAX$ and $L_\lambda MIN$ = highest and lowest possible values of radiance, QCALMAX and QCALMIN = calibrated maximum and minimum cell values. Conversion of Radiance to Reflectance can be done using the following equation:

$$\rho_\lambda = \left(\pi * L_\lambda * d^2 \right) / (ESUN_\lambda * \cos \theta_s)$$

where, ρ_λ = Top of atmosphere (TOA) reflectance of each pixel, L_λ = spectral radiance at the sensor aperture, d = distance from the earth to the sun in astronomical unit, $ESUN_\lambda$ = mean solar exoatmospheric irradiance, θ = angle between the sun and the satellite. Figure 4 shows the output of radiometric correction process.

Image mosaicking and study area delineation

In this study band wise mosaicking was done for each year's data. Six tiles (as mentioned in Table 2) are required to cover the entire study area and the mosaicking process is performed in ArcCatalog environment. The study area is then clipped from this mosaic using a region of interest (ROI) as shown in Fig. 5.

(a) Original Image   (b) DN to Radiance   (c) Radiance to Reflectance
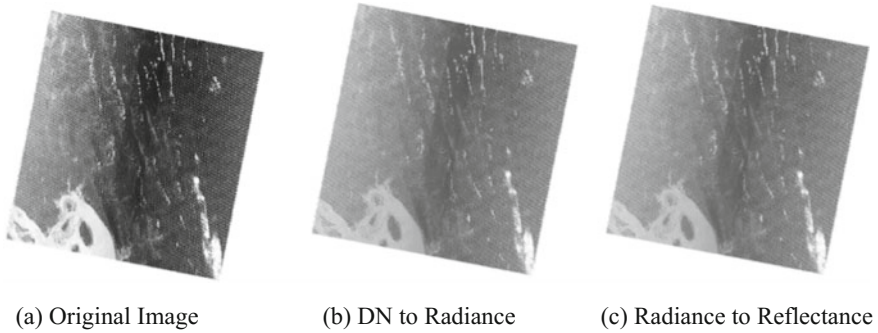
Fig. 4 Radiometric correction
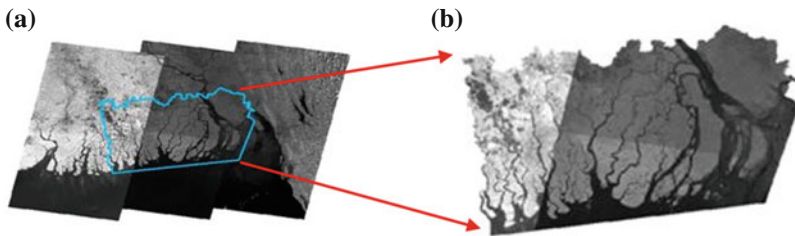
Fig. 5 **a** Mosaicking (Band 4, Year: 2000); **b** Delineated study area

3.3 Image Transformation—Application of RS Indices

There are a number of remote sensing indices for drought monitoring and assessment. Among these, the most commonly used index is the Normalized Difference Vegetation Index (NDVI), which is based on differences in absorption and reflectance in the visible and near-infrared (NIR) spectrums, respectively. The Vegetation Condition Index (VCI) compares the current NDVI of a particular period to the NDVI of previous years of the same period, where lower values indicate bad vegetation condition and higher value indicates good vegetation state. Temperature Condition Index (TCI) is used to determine stress on vegetation caused by temperatures and excessive wetness. Conditions are estimated relative to the maximum and minimum temperatures and modified to reflect different vegetation responses to temperature. The Vegetation Health Index (VHI) is a weighted average of VCI [12] and TCI [13] and is used globally for drought monitoring. In our study various remote sensing indices have been calculated as shown in Table 3.

Table 3 Different indices for drought monitoring

Index	Equation	Remarks
Normalized Difference Vegetation Index	$\mathrm{NDVI} = \dfrac{\mathrm{NIR - RED}}{\mathrm{NIR + RED}}$	It varies from +1 to −1. Water has negative value
Vegetation Condition Index	$\mathrm{VCI} = 100 * \dfrac{\mathrm{NDV - NDVI_{min}}}{\mathrm{NDVI_{max} - NDVI_{min}}}$	Expressed in percentage. 5–15%: extreme drought event
Temperature Condition Index	$\mathrm{TCI} = 100 * \dfrac{\mathrm{TB_{max} - TB}}{\mathrm{TB_{max} - TB_{min}}}$ $\mathrm{TBI} = \dfrac{K_2}{\ln\left(\frac{K_1}{L_\lambda}\right) + 1}$	TB = The brightness temperature of the thermal band, K_1 = Calibration constant (607.76), K_2 = Calibration constant (1260.56), L_λ = Spectral radiance
Vegetation Health Index	$\mathrm{VHI} = \dfrac{\mathrm{VCI + TCI}}{2}$	Value <10 represents extreme drought event
Normalized Difference Water Index	$\mathrm{NDWI} = \dfrac{\mathrm{NIR - SWIR}}{\mathrm{NIR + SWIR}}$	Water has positive value

3.4 Data Analysis

In this phase, the SPI point data has been used to generate SPI map by spatial interpolation (inverse distance weighted, IDW) technique within the ArcMap environment. As SPI is a month based indicator, the months for mapping SPI were chosen basing on the acquisition dates of Landsat images so that they both fall in the same time frame. After performing the spatial interpolation method, the ROI of the study area is used to clip the desired extent of the SPI maps. All the SPI maps as well as the remote sensing index images are reclassified into two classes, namely 'drought' and 'no drought'. The reclassification scheme is shown in Table 4 as follows:

For pixel to pixel comparison among the reclassified RS index maps with the SPI maps, a set of 1000 random points were generated within the study area. The corresponding pixel values for these points are then extracted. Thus, for a particular pixel of each reclassified image, a set of 'drought' and 'no drought' (1 = drought, 0 = no drought) values were obtained.

3.5 Accuracy Assessment

A comparison matrix was compiled which indicates the similarity or difference of the RS indices' values with/from the SPI values for a particular pixel. From the matrix, accuracy of various RS indices in comparison with SPI was calculated using the following formula:

Table 4 Reclassification schemes for indices

Index	Scheme for mapping		Reclassification for comparison	
	Value	Category	Value	Class
SPI	2.0>	Extremely wet	−1.00<	No drought
	1.50 to 1.99	Very wet		
	1.00 to 1.49	Moderately wet		
	−0.99 to 0.99	Near normal		
	−1.00 to −1.49	Moderately dry	≤ −1.00	Drought
	−1.5 to −1.99	Severely dry		
	−2<	Extremely dry		
NDVI			≤ 0	Drought
			0<	No drought
VCI	0–5	Exceptional	0–50	Drought
	5–15	Extreme		
	15–25	Severe		
	25–35	Moderate		
	35–50	Abnormally dry		
	50 ≤	Non-drought	50 ≤	No drought
TCI			10<	Drought
			≤ 10	No drought
VHI	<10	Extreme drought	≤ 40	Drought
	10–20	Severe drought		
	20–30	Moderate drought		
	30–40	Mild drought		
	>40	No drought	>40	No drought
NDWI			≤ 0	Drought
			0<	No drought

$$Accuracy(\%) = \frac{\text{number of points with similar class}}{\text{total number of random points}} \times 100$$

4 Results and Discussion

Sample outputs of SPI map and RS index images are shown in Fig. 6.

The reclassified maps showing drought and no-drought conditions for all year are shown in the subsequent figures.

The spatio-temporal variation of drought condition is evident from Fig. 7. From the SPI map we find that in 2000, the western part of the study area, the Satkhira district, was moderately wet in December while in 2010 the place became
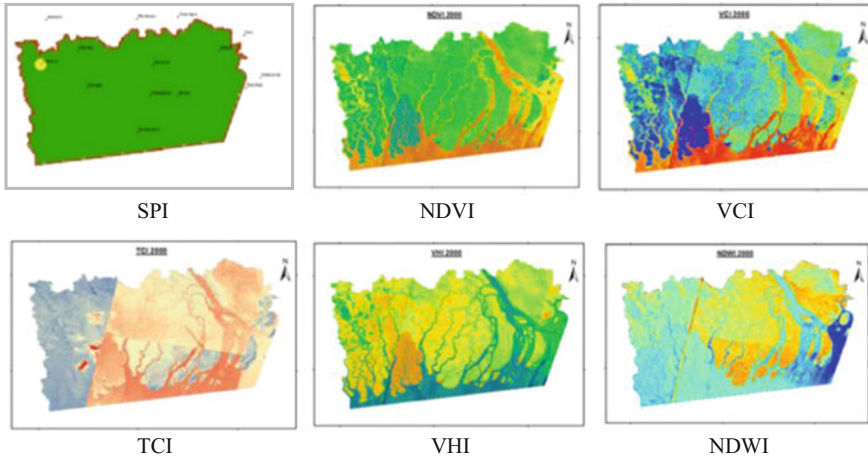
Fig. 6 Drought map of various indices

moderately dry. The spatial extent of drought condition also increased significantly in 2010. Reclassified images from remote sensing index images e.g. NDVI, VCI etc. also address similar variation.

A comparison matrix, as shown in Table 5, has been generated to assess the performance of each RS index with respect to the SPI map. The accuracy in drought identification has been calculated for each index and reported in percentage. A graph was generated comprising accuracy values of each RS index. Figure 8 shows a bar diagram where the relative accuracy of the RS indices can be observed. VCI and NDVI have higher accuracy compared to the other indices. Accuracy level has drastically reduced for the year 2010.

5 Discussion

In this study, an approach to monitor drought in the coastal belt of southern part of Bangladesh is proposed by utilizing meteorological data and Landsat time series satellite images. The meteorological index used here is the Standardized Precipitation Index (SPI) and the RS indices calculated are NDVI, VCI, TCI, VHI and NDWI. A drought map is produced for the study area that incorporates SPI values of each meteorological station that fall within the study area. This SPI map is a raster map with the same spatial resolution (30 m) of the Landsat images as well as the RS indices such that pixel to pixel comparison is possible. Before calculating RS indices, a series of pre-processing steps i.e., radiometric correction, null-value elimination, mosaicking and clipping is performed. Both the SPI map and the RS indices maps are then reclassified to produce binary images with 'drought' and
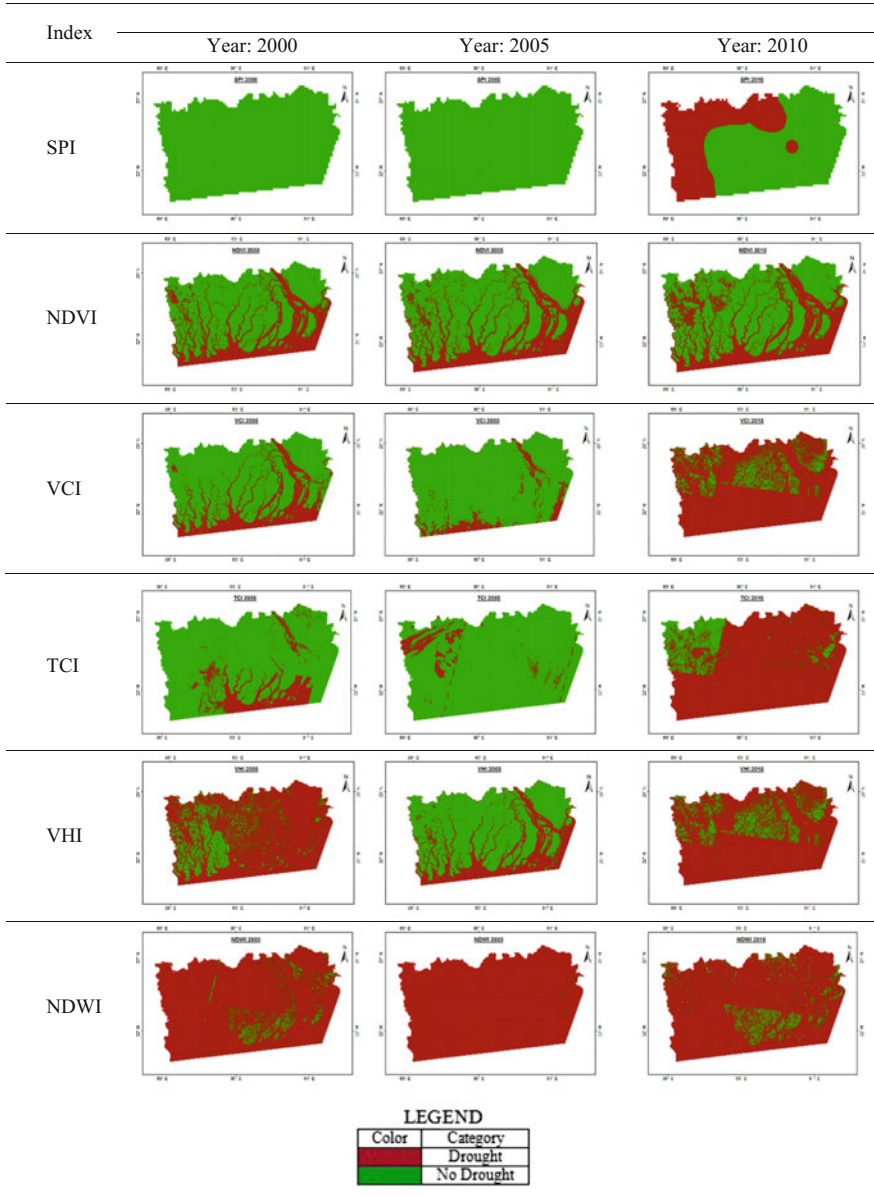
Fig. 7 Reclassified drought index map

'non-drought' classes for the purpose of pixel to pixel comparison. Here the SPI map is used as the basis of evaluating the accuracy of various RS indices. From Table 5 or Fig. 8, it is evident that NDVI and VCI have higher accuracy compared to the other RS indices. However, the accuracy level for all indices falls drastically

Table 5 Comparison matrix for SPI with all RS indices

Index		SPI		Total simillar points	Overall accuracy (%)	Remarks
		Drought (D)	No drought (ND)			
Year—2000						
NDVI	D	0	309	681	68.77	10 random points are outside of the boundary of the study area
	ND	0	681			
VCI	D	0	262	728	73.53	
	ND	0	728			
TCI	D	0	846	144	14.54	
	ND	0	144			
VHI	D	0	740	250	25.25	
	ND	0	250			
NDWI	D	0	901	89	8.98	
	ND	0	89			
Year—2005						
NDVI	D	0	314	675	68.25	11 random points are outside of the boundary of the study area
	ND	0	675			
VCI	D	0	97	892	90.19	
	ND	0	892			
TCI	D	0	47	942	95.25	
	ND	0	942			
VHI	D	0	300	689	69.67	
	ND	0	689			
NDWI	D	0	980	9	0.91	
	ND	0	9			
Year—2010						
NDVI	D	111	236	468	47.18	8 random points are outside of the boundary of the study area
	ND	288	357			
VCI	D	317	509	401	40.42	
	ND	82	84			
TCI	D	267	566	294	29.64	
	ND	132	27			
VHI	D	315	506	402	40.52	
	ND	84	87			
NDWI	D	111	236	468	47.18	
	ND	288	357			
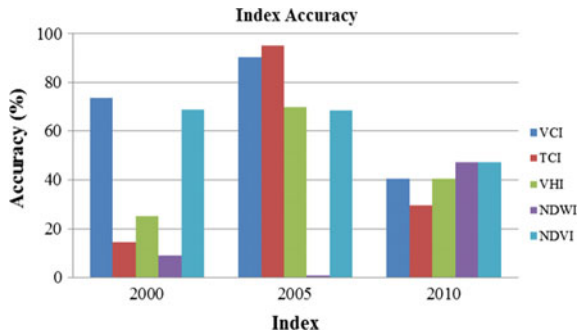
Fig. 8 Bar diagram showing accuracy level of various RS indices

during the year 2010. This may be attributed to the fact that the interpolated SPI values could not differentiate the land features like water, vegetation or build up areas. As a result, a less accurate SPI map could be produced.

A notable characteristic of the indices is that, almost all of them identified water bodies with larger depth (Bay of Bengal, rivers and canals) as drought areas. This may be due to the fact that indices usually utilize the reflectance from vegetation covers to identify drought conditions. As the deep water behaves unlike the vegetation cover, it is considered as absence of vegetation, which is drought in other words.

There were certain limitations of the study. Insufficient number of meteorological stations as well as missing rainfall data made the SPI map less accurate. As a result, the accuracy level of indices is also poor. Besides, due to budget constrain, high resolution satellite images could not be procured and ground data could not be collected.

References

1. Narasimhan, B., Srinivasan, R.: Development and evaluation of soil moisture deficit index and evapotranspiration deficit index for agricultural drought monitoring, **133**, 69–88 (2005). https://doi.org/10.1016/j.agrformet.2005.07.012
2. Sivakumar, M., Motha, R., Wilhite, D., Wood, D. (eds.): Agricultural drought indices proceedings of an expert meeting, p. 205. World Meteorological Organization (2004)
3. Banglapedia, http://en.banglapedia.org/index.php?title=Drought
4. Brown, J.F., Wardlow, B.D., Tadesse, T., Hayes, M.J., Reed, B.C.: The vegetation drought response index (VegDRI): a new integrated approach for monitoring drought stress in vegetation. GIScience Remote Sens. **45**(1), 16–46 (2008). https://doi.org/10.2747/1548-1603.45.1.16
5. Bangladesh Agricultural Research Council (BARC) (http://climate.barcapps.gov.bd)
6. N.Islam, M.N., Islam, A.K.M.S., Hayashi, T., Terao, T., Uyeda, H.: Application of a method to estimate rainfall in Bangladesh using GMS-5 Data, **24**(2), 83–89 (2002)
7. Global Visualization Viewer.: USGS (2016). http://doi.org/2016-04-26-glovis.usgs.gov

8. Ren, G., Zhou, Y., Chu, Z., Zhou, J., Zhang, A., Guo, J., Liu, X.: Urbanization effects on observed surface air temperature trends in North China. J. Clim. **21**, 1333–1348 (2008). https://doi.org/10.1175/2007JCLI1348.1

9. Murad, H., Islam, A.K.M.S.: Drought assessment using remote sensing and gis in north-west region of bangladesh (2011)

10. Graham, J.: Lesson 2 : How to bring Landsat data into ArcGIS, Mosaic and Clip Scenes (2010)

11. Mcgee, J., Campbell, J., Parece, T.: Remote sensing in an ArcMap environment (2015)

12. Bayarjargal, Y., Karnieli, A., Bayasgalan, M., Khudulmur, S., Gandush, C., Tucker, C.J.: A comparative study of NOAA-AVHRR derived drought indices using change vector analysis. Remote Sens. Environ. **105**(1), 9–22 (2006). https://doi.org/10.1016/j.rse.2006.06.003

13. Kogan, F.N.: World droughts in the new millennium from AVHRR-based Vegetation Health Indices. Eos EOS Trans. **8**(4), 3–7 (2002). https://doi.org/10.1029/2002EO000382

Assessment of Heavy Metal Contamination in Soil of Waste Disposal Site in Bangladesh: Implication of Spatial, Seasonal Variation and Indices

Kanij Fahmida and Md. Rafizul Islam

Abstract This study illustrates the extent of contamination for presence of heavy metal in soil of a selected waste disposal site at Rajbandh, Khulna, Bangladesh. Thus, this research was executed to assess the vulnerability associated with heavy metals in soil using integrated indices containing potential contamination (Cp), contamination factor (CF), pollution load index (PLI), modified contamination degree (mCD), numerical integrated contamination factor (NICF), enrichment factor (EF), geo-accumulation index (I_{geo}) and potential ecological risk index (PERI). To these endeavours, soil samples were collected from 60 selected locations of the disposal site in two different seasons; dry season (April, 2016) as well as rainy season (June, 2016). The relevant concentrations of Al, Fe, Mn, Cr, Cu, Pb, Zn, Ni, Cd, As, Co and Sc were measured in the laboratory through the standards method by atomic absorption spectrophotometer (AAS). The results of study can be concluded as most of the indices, i.e. CF, mCD, I_{geo} and PERI, indicated that the soil was polluted by heavy metals of Cd and Sb as well as Pb and As which is detrimental for the surrounding area. Pearson correlation analysis was performed to estimate the degree of association among the variable metals present in soil. Finally, the outcomes of this study will provide some useful insights for making appropriate management strategies to prevent or decrease soil pollution by metals around waste disposal site.

Keywords Disposal site · Contamination · Spatial distribution
Seasonal variation · Indices

K. Fahmida (✉) · Md. Rafizul Islam
Department of Civil Engineering, Khulna University of Engineering
and Technology, Khulna, Bangladesh
e-mail: kanijfahmida@yahoo.com

1   Introduction

Most common practice to deal with huge quantity of waste produced every day in developing countries is landfill. The term 'landfill' is defined as a single action for the final abandoning of MSW on a certain plot designed and constructed aiming the minimum effect to the adjacent atmosphere [1]. This continuous input of waste containing heavy metal elements could affect the soil and water quality around the landfill area [2]. Mostly, the complex biological and physicochemical processes of the enormous amount of waste make the adjacent areas vulnerable caused by the constant release of toxic heavy metal compounds from the decomposed waste, leachate and soil from the waste disposal sites [3–5]. These deadly metal releasing causes human health problems by entering the food chain through accumulating in plants from contaminated soil and polluted environment [6, 7].

In the present day, soil pollution by means of heavy metals is one of the biggest threats to the human race on the earth since soil is a fundamental component of the natural environment as well as has great involvement in human health. As well as metallurgical process, some natural process and anthropogenic activities are also root causes of soil pollution by metals [8]. Indiscriminate disposal of solid waste including industrial effluents and other toxic wastes are initiated by the rapid growth of industrialization and urbanization. Basically, the extent of ecological threats as a result of heavy metal in soil has increased prominently since the rapid growth of industries and daily use of constituents having these metals [9, 10].

Bioaccumulation of toxic heavy metals in soil and adjoining water contamination by leachate are the two main distresses regarding waste disposal on land [11]. These heavy metals cause severe health effects including cancer tempted tumour promotion when consumed by contained food and cannot metabolized by the body and accumulate in the soft tissues of human physique [12–14]. Moreover, non-biodegradable nature and long biological half-lives of heavy metals and toxic elements are the fundamental cause of destruction to the environment [15].

Khulna metropolitan city is the third among prime cities of Bangladesh. At the present time, Rajbandh waste disposal site is the only official dumping site. The presence of noxious heavy metals in soil in the surrounding area of waste dumping site may create an acute pollution of the underlying soil layer and water as well as also may pose health hazards to the city people. For the above-mentioned reasons, there is need for a comprehensive study of metal contamination of the soils in the region of the Rajbandh disposal site to discover the soil contamination level of the area. So, this study was directed to investigate the seasonal and spatial variation of different metals (Fe, Mn, Cr, Cu, Pb, Zn, Ni, Cd, As, Hg, Co Na, K, Ca, Al, Ti, Sb, Sc, Sr, V and Ba) concentrations and level of contamination of these metals around the waste dumping site at Rajbandh, Khulna, Bangladesh. These assessments are done by statistical analysis, integrated index analyses approach containing contamination factor (CF), potential contamination (Cp), pollution load index (PLI), modified contamination degree (mCD), numerical integrated contamination factor

(NICF), enrichment factor (EF), geo-accumulation index (I_{geo}) and potential ecological risk index (PERI). In addition, Pearson's correlation analysis was done for soil quality assessment.

2 Materials and Method

2.1 Geological Setting of Study Area

Khulna is a district among total 64 districts in Bangladesh. Besides, the Khulna city is in the northern part of the district, acknowledged as third largest among ten metropolitan cities of Bangladesh. Geographically, Khulna lies between 22° 47′ 16″ to 22° 52′ 0″ north latitude and 89° 31′ 36″ to 89° 34′ 35″ east longitude. This city is situated on the Rupsha and Bhairab riverbanks. At present, the city covers an area of 45.65 km^2 with a population about 1.5 million. The municipal solid waste of Khulna city is dumped in the Rajbandh disposal site with the purpose of accumulates and disposes it in the landfill. So, this waste disposal site was chosen as sampling place to explore and assess the soil quality and the contamination level. Figures 1 and 2 depicted the location map of Rajbandh, Khulna, Bangladesh and a map showing the sampling points at the Rajbandh waste disposal site zone.

2.2 Sampling

In this study, totally 60 soil samples were collected from the distinct locations of the waste disposal site as shown in Fig. 2. All the samples were collected at a depth of 0–30 cm from the existing ground surface. In the total 60 soil samples, 40 samples were collected in dry season (April, 2016) then rest 20 samples were collected in rainy season (June, 2016). In dry season, the sampling points were selected maintaining gradual addition of about 10 m distance from the first borehole (BH-1) by the subsequent boreholes. The first sampling point, BH-1 is located at the centre of the waste disposal site. On the other hand, the first borehole of rainy season (BH-41) is about 30 m apart from BH-1 which is the centre of the site and maintains a gradual addition of about 15 m in selecting other following boreholes.

2.3 Laboratory Investigation

To measure the concentration of heavy metals in soil, laboratory work was done following the standard test method. In laboratory investigation, at first, 10 g of each
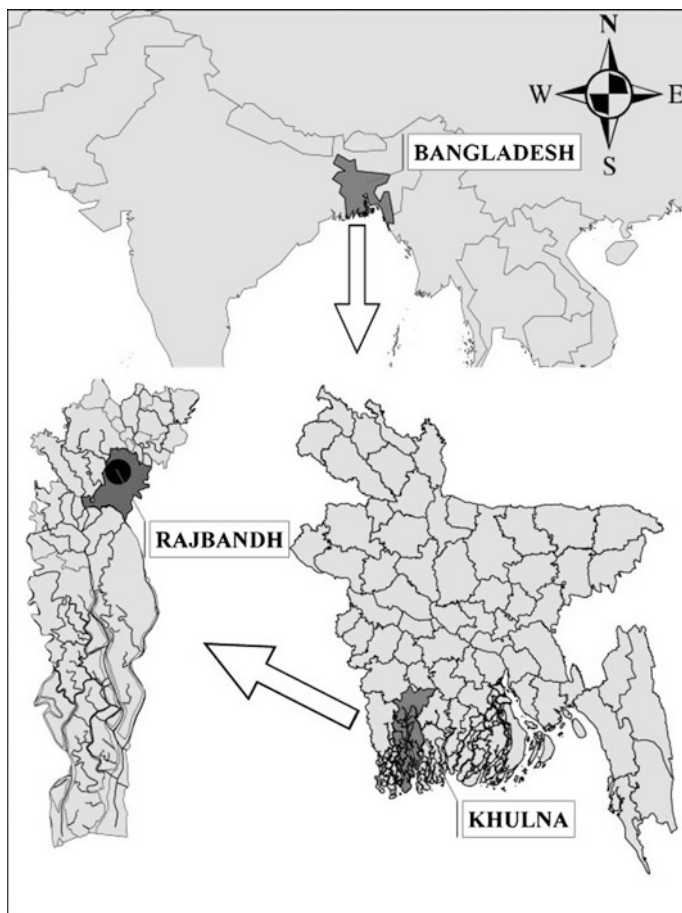
Fig. 1 Location map of Rajbandh at Khulna city of Bangladesh

soil sample was taken into a 100 mL conical flask. Already, the flask had been washed with deionized water prepared by adding 6 mL $HNO_3/HClO_4$ acid in ratio 2:1 and left overnight. Each sample was kept into the temperature of 150 °C for about 90 min. Later, temperature was raised to 230 °C for 30 min. Subsequently, HCl solution was added in ratio 1:1 to the digested sample and redigested again for another 30 min. The digested sample was washed into 100 mL volumetric flask and mixture obtained was cooled down to room temperature. After performing the digestion procedure, heavy metals in this digested solution were determined using atomic absorption spectrophotometer (AAS) and the amount of each heavy metal was deduced from the calibration graph. The relevant concentrations of Ca, Al, Fe, Mn, Cr, Cu, Pb, Zn, Ni, Cd, As, Co, Ti, Sb, Sr, Sc, V, Ba, Hg, Na and K in mg/kg were measured in the laboratory.
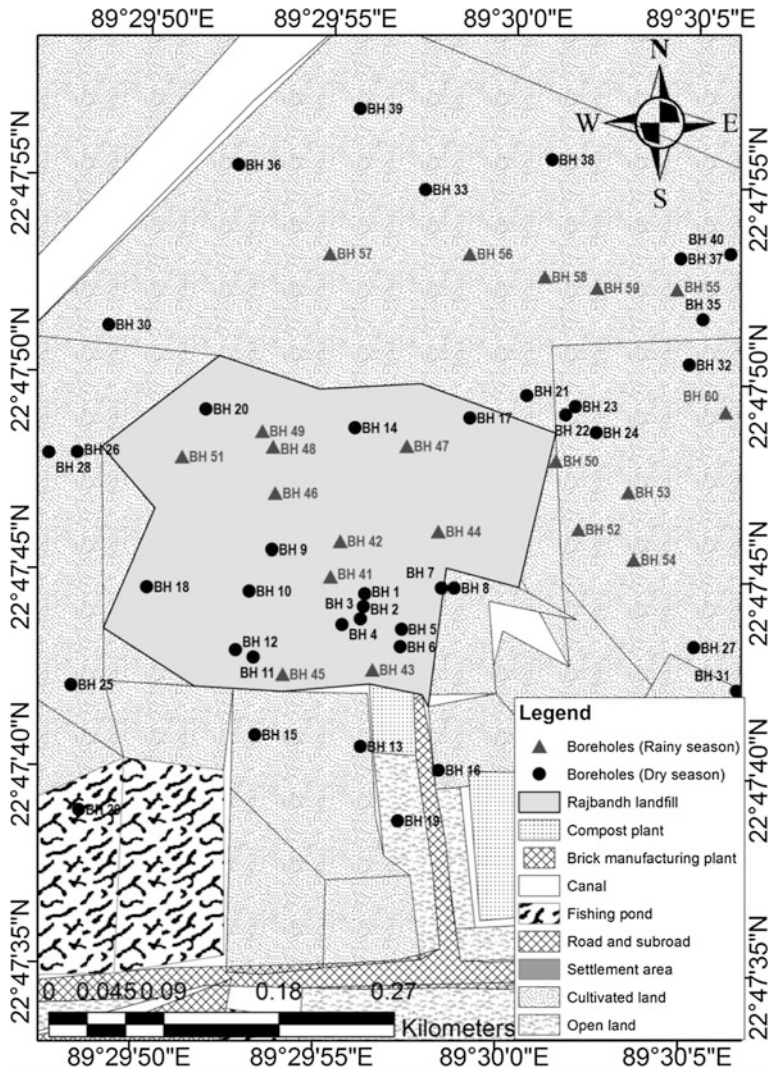
Fig. 2 Soil sampling location in waste disposal site at Rajbandh

2.4 Assessment of Soil Contamination by Indices

Potential Contamination. The potential contamination index (Cp) is used to estimate the amount of metallic elements detectable from soil analysis. The potential contamination index could be calculated by Eq. (1) [16, 17].

$$C_p = \frac{\text{Metal}_{\text{max}}}{\text{Metal}_{\text{background}}} \tag{1}$$

where $\text{Metal}_{\text{max}}$ is the maximum concentration of metal in soil, and $\text{Metal}_{\text{background}}$ is the average value of the same metal in a background level. The crustal abundance values of metals [18] were used as background data in the calculation of Cp and other following indices.

Contamination Factor. The contamination factor (CF) of a particular heavy metal is the ratio of metal concentration in the soil and the background value of the same metal [19]. The CF is computed using Eq. (2).

$$CF = \frac{C_{\text{metal}}}{C_{\text{background}}} \tag{2}$$

The classes according to the values of CF are as CF < 1 indicate low contamination; 1 < CF < 3 is moderate contamination; 3 < CF < 6 is considerable contamination and CF > 6 is very high contamination [20].

Pollution Load Index. The pollution load index (PLI) is calculated based on a different index, contamination factor (CF). The PLI of a definite area is calculated by finding the nth root of the numbers of CFs that was calculated for considered heavy metals in soil. Hence, Eq. (3) is used to compute the PLI [21].

$$PLI = \sqrt[n]{CF_1 \times CF_2 \times \cdots \times CF_n} \tag{3}$$

where, CF = contamination factor, n = number of heavy metals. There are two classes according to PLI value, if PLI > 1 is polluted; whereas <1 indicates no pollution [22].

Modified Contamination Degree. The degree of contamination is an index to estimate the pollution range of soil by heavy metals. Equation (4) was used to calculate mCD [23].

$$mCD = \frac{1}{n} \sum_{i=n}^{1} CF_i \tag{4}$$

In the equation, mCD is the modified contamination degree, n is the total number of metal elements considered and CF is the contamination factor as defined above. mCD is a improved and comprehensive form of the degree of contamination (CD) expressed in Eq. (5) [19].

$$CD = \sum_{i=n}^{1} CF_i \tag{5}$$

Computing values of CD is essential to suggest an extent of the overall contamination of surface layers in a sampling area. The definite formula of the CD is

Table 1 Classification of modified degree of contamination

mCD classes	Contamination level
mCD < 1.5	Nil to very low
$1.5 \leq$ mCD < 2	Low
$2 \leq$ mCD < 4	Moderate
$4 \leq$ mCD < 8	High
$8 \leq$ mCD < 16	Very high
$16 \leq$ mCD < 32	Extremely
mCD > 32	Ultra high

reserved to the seven specific metals (As, Cd, Cu, Cr, Hg, Pb, Zn) and the organic chemical polychlorinated biphenyl (PCB) [19]. However, mCD is more suitable for this study hence PCB was not analysed here. For classifying the level of contamination based on mCD, Table 1 was followed.

Nemerow Integrated Contamination Factor. Nemerow integrated contamination factor method is an integrated method compatible with extreme value, which not only considers the role of single elements but also highlights the importance of element with the most serious contamination. Nemerow integrated contamination factor (NICF) is computed using Eq. (6).

$$NICF = \sqrt{\frac{CF_{i(avg)} + CF_{i(max)}}{2}} \tag{6}$$

where, NICF is the nemerow contamination factor, CF_{avg} indicates the average value of contamination factor and CF_{max} represents the maximum value of a single contamination factor in soil pollutant measured in certain site. The classifications based on NICF value are presented in Table 2.

Enrichment Factor. Enrichment factor (EF) is used to obtain the level of pollution by anthropogenic actions based on heavy metal accumulation by soil [24]. The EF is computed using the relationship shown in Eq. (7).

$$EF = \frac{(C_x/C_{ref})_{sediment}}{(C_x/C_{ref})_{background}} \tag{7}$$

where C_x is the concentration of element x, and C_{ref} is the concentration of the reference element in sediment (s) and the earth's crust, respectively [20].

Table 2 Classification of nemerow integrated contamination factor (NICF)

NICF range	Class of contamination
NICF $\leq$ 0.7	Non-contaminated
0.7 < NICF $\leq$ 1	Warning line of contamination
1 < NICF $\leq$ 2	Low level of contamination
2 < NICF $\leq$ 3	Moderate level of contamination
NICF > 3	High level of contamination

Table 3 Classes of enrichment factor based on their value [26]

EF value	Designation of quality
>50	Extremely severe enrichment
25–50	Very severe enrichment
10–25	Severe enrichment
5–10	Moderately severe enrichment
3–5	Moderate enrichment
1–3	Minor enrichment
<1	No enrichment

These indexes of potential contamination are calculated by the normalization of one metal concentration in the top soil with respect to the concentration of a reference element. By the normalization, one metal concentration with respect to a reference element concentration in soil EF is calculated. In addition, a reference element is almost stable compared to other elements based on anthropogenic effect in the soil [25]. Typical elements used in many studies are Al, Fe, Mn and Rb. Significance of EF is provided in Table 3.

Geo-accumulation Index. The geo-accumulation index (I_{geo}) is used to estimate the grade of soil contamination by metals. The I_{geo} is defined as in Eq. (8) [27, 28].

$$I_{geo} = \log_2(C_n/1.5B_n) \tag{8}$$

where C_n is the measured concentration of a specific metal element and B_n is the geochemical background value (average shale value) of the same element. 1.5 as constant value is used in the index calculation to account for the natural variations in the environment and small anthropogenic influences. In Table 4 classes of I_{geo} are presented briefly.

Potential Ecological Risk Index. In this research work, the potential ecological risk index (PERI) was calculated as a pointer of modification in natural by soil pollution in terms of metal concentration [19]. This strategy for assessing natural hazard extensively considers the cooperative energy, poisonous level, concentration of heavy metals and biological affectability of those metals [30–32]. PERI is formed by three basic parts: contamination factor (CF), toxic response factor (TR) and

Table 4 Contamination classes for I_{geo} values [29]

I_{geo}	Value I_{geo}	Class designation of soil quality
>5	6	Extremely contaminated
4–5	5	Strongly to extremely contaminated
3–4	4	Strongly contaminated
2–3	3	Moderately to strongly contaminated
1–2	2	Moderately contaminated
0–1	1	Uncontaminated to moderately contaminated
0<	0	Uncontaminated

Table 5 Toxic response factor (TR) values for several metals [10, 19]

Metals	Zn	Cr	Cu	Pb	Hg	Cd	As	Ni	Co
TR	1	2	5	5	10	30	10	5	5

Table 6 Classification based on ecological risk index (ER) and potential ecological risk index (PERI)

ER	Pollution degree	PERI	Risk degree
ER < 30	Slight	<40	Slight
$30 \leq ER < 60$	Medium	$40 \leq RI < 80$	Medium
$60 \leq ER < 120$	Strong	$80 \leq RI < 160$	Strong
$120 \leq ER < 240$	Very strong	$160 \leq RI < 320$	Very strong
$ER \geq 240$	Extremely strong	$RI \geq 320$	–

potential ecological risk factor (ER). According to this technique, the ER and PERI were calculated using Eqs. (9) and (10).

$$ER = TR \times CF \tag{9}$$

$$PERI = \sum ER \tag{10}$$

where CF is measured by Eq. (2) stated as earlier. ER indicates the potential ecological risk index of a particular element; PERI means a comprehensive potential ecological risk index and TR is the toxic response factor of a single element, which was used provided in Tables 5 and 6.

3 Results and Discussion

3.1 Descriptive Statistical Analysis of Metals

The descriptive statistical analysis for heavy metals in soil of waste disposal site for two different seasons was performed using statistical package for the social sciences (SPSS) version 16.0. In this study, mean, median, 95% UCL, standard deviation, standard error, variance, coefficient of variance, skewness and kurtosis of heavy metals in soil were analysed. 95% UCL is helpful for defining upper end or a limit of concentrations of a certain heavy metal in soil. It is used to statistically demonstrate that no more than 95% of heavy metal concentrations are less than this standard with some confidence. Besides, skewness and kurtosis support by giving primarily recognition of overall characteristics about the distribution of all data. The values of skewness indicated the degree to which the analysed data are not symmetrical and kurtosis specifies exactly how the peak and tails of a distribution fluctuate from the normal distribution.

The statistical data of heavy metal concentration in soil for dry season is provided in Table 7. The table reveals the mean concentration of 1363.94, 15.69, 6.03, 6.20, 37.61, 34.57, 4.83, 4.55, 4.15, 4.63, 7.00, 68.30, 292.00, 183.80, 490.25, 1221.22, 6.07, 12.16, 27.53, 43.44 and 65.25 mg/kg for Fe, Mn, Cr, Cu, Pb, Zn, Ni, Cd, As, Hg, Co Na, K, Ca, Al, Ti, Sb, Sc, Sr, V and Ba, respectively during the dry season.

In contrast, based on the statistical analysis, the mean concentration was found to be 365.79, 5.41, 1.94, 2.55, 17.54, 17.58, 2.58, 2.03, 1.56, 1.72, 5.11, 25.74, 126.86, 100.16, 239.76, 707.89, 3.41, 7.73, 16.92, 21.43 and 39.58 mg/kg for Fe, Mn, Cr, Cu, Pb, Zn, Ni, Cd, As, Hg, Co Na, K, Ca, Al, Ti, Sb, Sc, Sr, V and Ba, respectively, in soil for the rainy season. So, the trend of heavy metals according to mean concentration in the dry season was: Fe > Ti > Al > K > Ca > Na > Ba > V > Pb > Zn > Sr > Mn > Sc > Co > Cu > Sb > Cr > Ni > Hg > Cd > As. While, in the rainy season the trend was: Ti > Fe > Al > K > Ca > Ba > Na > V > Zn > Pb >

Table 7 Statistical data of metal concentration in soil in dry season ($n = 40$)

[a]ME	Mean	median	[b]UCL	[c]SD	[d]SE	Variance	[e]CV	[f]Skew	[g]Kurt
Fe	1363.94	1386.50	1472.46	350.15	8.75	122,605.26	25.67	−0.08	−1.20
Mn	15.69	14.16	17.14	4.68	0.12	21.90	29.82	1.72	2.88
Cr	6.03	5.83	6.48	1.43	0.04	2.03	23.63	0.87	0.14
Cu	6.20	4.82	7.34	3.68	0.09	13.58	59.41	1.60	1.43
Pb	37.61	33.94	41.84	13.67	0.34	186.80	36.34	1.91	5.16
Zn	34.57	34.64	36.94	7.65	0.19	58.45	22.11	0.64	0.03
Ni	4.83	4.71	5.33	1.60	0.04	2.55	33.02	0.42	−0.95
Cd	4.55	4.4`6	4.90	1.14	0.03	1.29	24.99	0.40	−0.44
As	4.15	3.42	4.78	2.03	0.05	4.10	48.79	0.76	−0.64
Hg	4.63	4.01	5.27	2.07	0.05	4.27	44.63	0.83	−0.36
Co	7.00	6.67	7.75	2.42	0.06	5.84	34.50	0.41	−0.99
Na	68.30	77.89	77.36	29.22	0.73	853.63	42.78	−0.53	−1.34
K	292.00	316.37	324.56	105.06	2.63	11,037.03	35.98	−0.43	−0.90
Ca	183.80	173.19	202.91	61.67	1.54	3803.00	33.55	0.60	−0.74
Al	490.25	458.46	551.49	197.61	4.94	39,048.96	40.31	0.32	−0.66
Ti	1221.22	1223.83	1347.12	406.26	10.16	165,044.80	33.27	0.17	−1.20
Sb	6.07	5.76	6.75	2.19	0.05	4.79	36.04	0.82	0.73
Sc	12.16	11.67	13.18	3.27	0.08	10.70	26.89	0.47	−0.52
Sr	27.53	26.62	30.11	8.35	0.21	69.69	30.33	0.90	1.11
V	43.44	40.83	47.93	14.49	0.36	209.88	33.35	0.77	0.47
Ba	65.25	60.61	72.81	24.38	0.61	594.31	37.36	0.69	−0.64

[a]Metal element
[b]95% UCL (normal)
[c]Standard deviation
[d]Standard error
[e]Coefficent of variance
[f]Skewness
[g]Kurtosis

Sr > Sc > Mn > Co > Sb > Ni > Cu > Cd > Cr > Hg > As.   The   variation   of heavy metal concentration in soil for two seasons is caused by the heavy metal infiltrates in soil through rain water in rainy season. The higher variations in heavy metal distributions from the point source of discharge to the adjacent areas were disclosed by the higher values of standard deviation.

3.2   Spatial and Seasonal Variation of Metal Contents in Soil

Variations of metal concentrations (Fe, Pb, Cd and Sb) in dry and rainy season with respect to distance are shown in Figs. 3, 4, 5 and 6, respectively. Spatial variation is shown in the range of 30–300 m. In Fig. 3, the Fe distribution pattern reveals that the concentration is 2.5-fold higher in dry season than rainy season. Subsequently, in the study area, spatial and seasonal variation of Pb (Fig. 4) shows that the concentration is uniform in rainy season when concentration in dry season had abrupt rise and fall. Then, Pb contamination in soil is 2–2.8 times greater in dry season.

The graphical representation of Cd concentration depicts that the dry seasonal concentration is 1.75 times higher than rainy seasonal concentration and the change of concentration has a similar pattern in two seasons (Fig. 5). In Fig. 6, concentration of another toxic metal Sb gradually decreases in relation to the changes of distance in both the dry and rainy seasons where in dry season, concentration was threefold greater than that of rainy season. From this analysis of spatial and seasonal variation, it was clear that the metal concentration was found to be higher in dry season and all metal had reducing concentration with respect to distance.
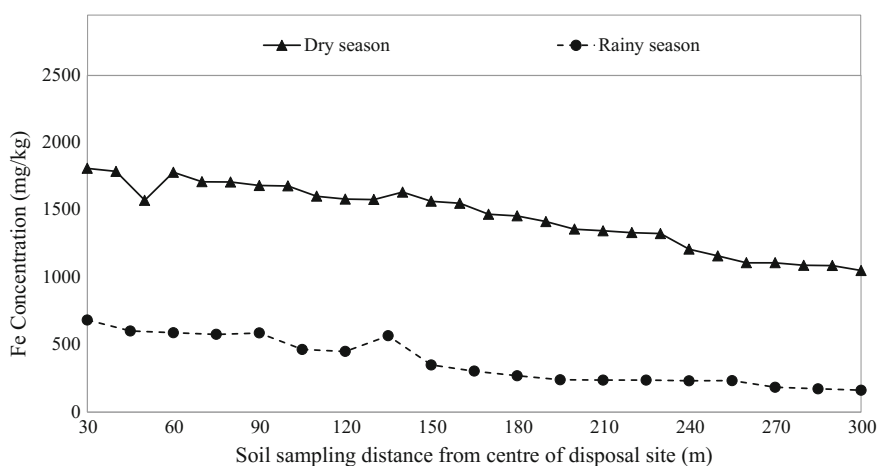
Fig. 3 Spatial and seasonal variation of Fe concentration in soil
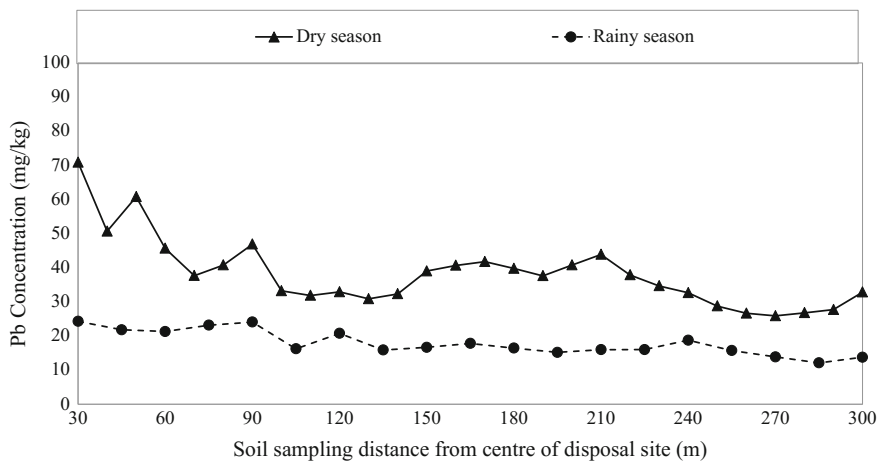
Fig. 4 Spatial and seasonal variation of Pb concentration in soil
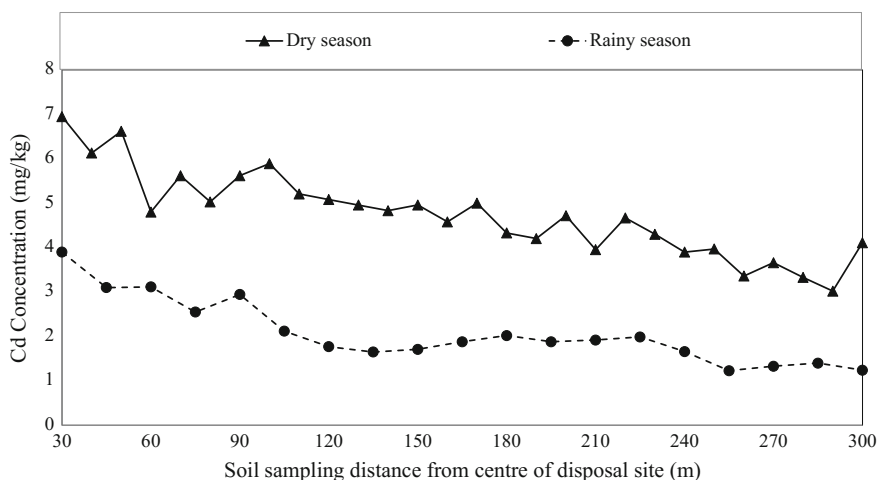
Fig. 5 Spatial and seasonal variation of Cd concentration in soil

Figures 7 and 8 illustrate the distribution pattern of four different metal element in soil using ArcGIS. In these figures, dark to light colour represents the highest to lowest value of concentration in soil. Based on Fig. 7, the distribution patterns of Fe, Cd and Sb concentrations in soil of dry season represent that they were almost the same. But, pattern for Pb distribution was to be different than that of other parameters. Additionally, comparing with map soil sampling location at study area (Fig. 2), all these patterns depict that the highest concentration lies around BH-1 and BH-2, which point towards centre of the waste disposal site.
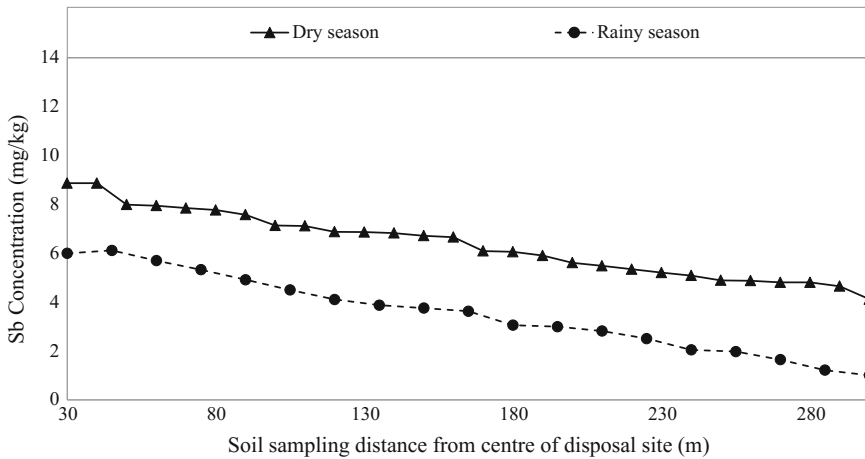
Fig. 6 Spatial and seasonal variation of Sb concentration in soil

Figure 7 depicts that the distribution patterns of Fe, Cd, Pb and Sb concentrations in soil of rainy season were found to be almost the same. Moreover, comparing with map of soil sampling location at study area (Fig. 2), all these patterns
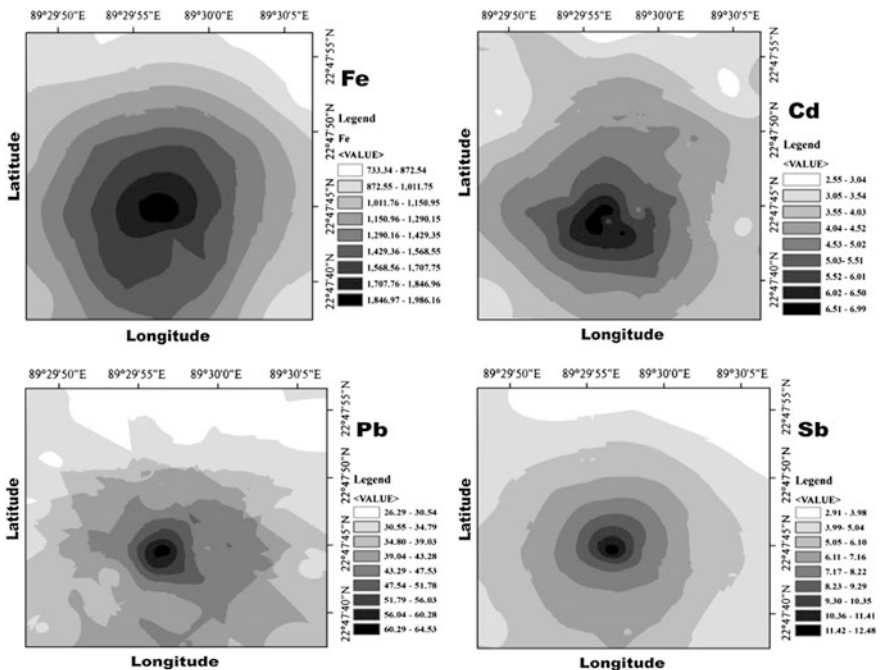
Fig. 7 Surface spatial distribution of Fe, Cd, Pb, Sb concentration in soil in dry season
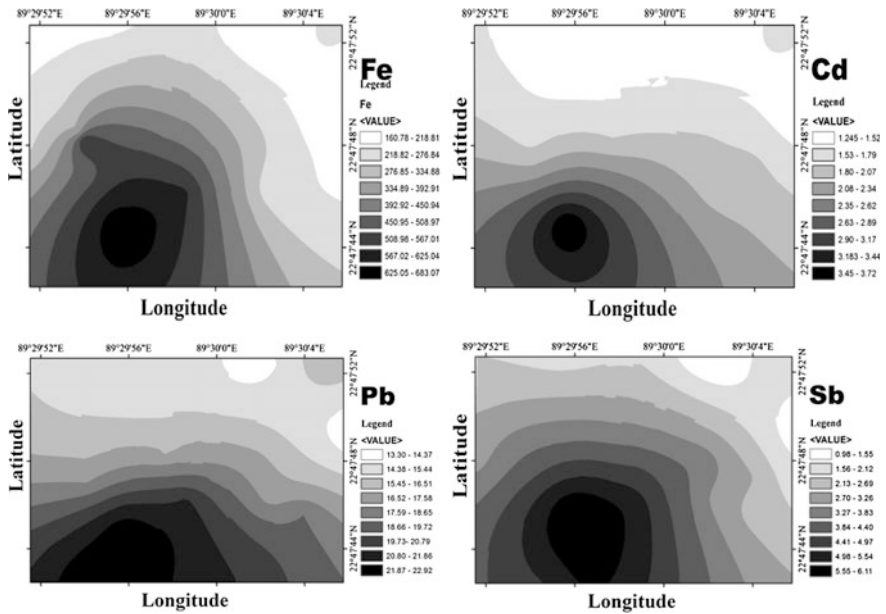
Fig. 8 Surface spatial distribution of Fe, Cd, Pb, Sb concentration in soil of rainy season

illustrate that the highest concentration lies around BH-41, BH-42 and the lowest concentration of metals lies around BH-59, BH-60. It also indicates that the centre of the waste disposal site is more contaminated by metals and gradually concentration of metals reduces with the increasing of distance from the centre of waste disposal site.

3.3 Assessment of Soil by Index Analysis

Potential Contamination Index. The potential contamination index (Cp) for 21 studied metals for all boreholes of two seasons is presented in Fig. 9. In Fig. 9, Cp value for the metals of Cd and Sb in both seasons as well as of Pb and As in dry season cross the dashed line of Cp = 3. As a result, Cp of Pb and As in dry season indicates severe contamination in soil. Correspondingly, for Cd and Sb, Cp of both seasons show severe contamination too. The value of Cp for Cd in dry season and rainy season was found to be 35.15 and 19.50, respectively. Similarly, the value of Cp for Sb in both seasons was 62.74 and 30.60. The value of Cp for the other metal that lies below the dashed line shows no contamination according to Cp classification.

Contamination Factor. The statistics of the computed values of contamination factor (CF) in soil are presented in Figs. 10 and 11, respectively for dry and rainy
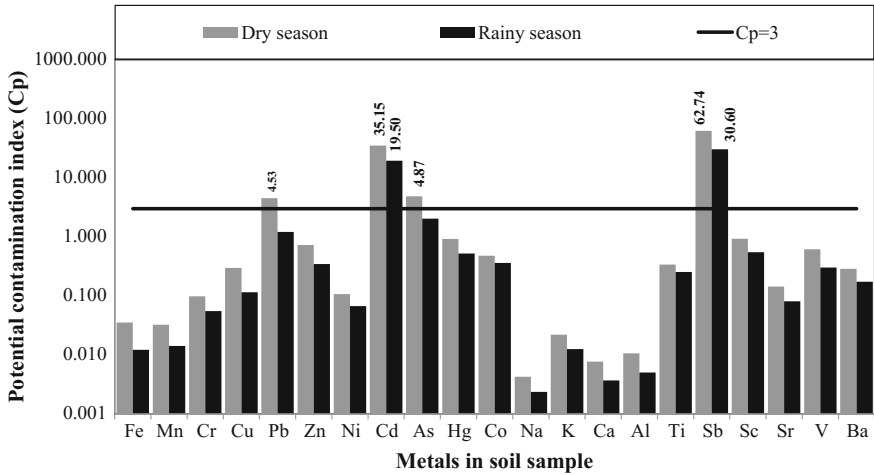
Fig. 9 Potential contamination index (Cp) of studied metals in two seasons

season. Figure 10 represents that the CF values of the metals of Fe, Mn, Cr, Cu, Zn, Ni, Hg, Co Na, K, Ca, Al, Ti, Sc, Sr, V and Ba were found to be less than 1 and hence indicated the low level of contamination. The values of CF for Pb indicated the contamination by Pb ranges moderate ($1 < CF < 3$) to be considerable ($3 < CF < 6$). Similarly, values of CF indicated the contamination by As ranges from low ($CF < 1$) to considerable ($3 < CF < 6$) though the mean of CF stands in moderate contamination class. Accordingly, the entire values of CF for Cd and Sb indicated the high level of contamination ($CF > 6$).
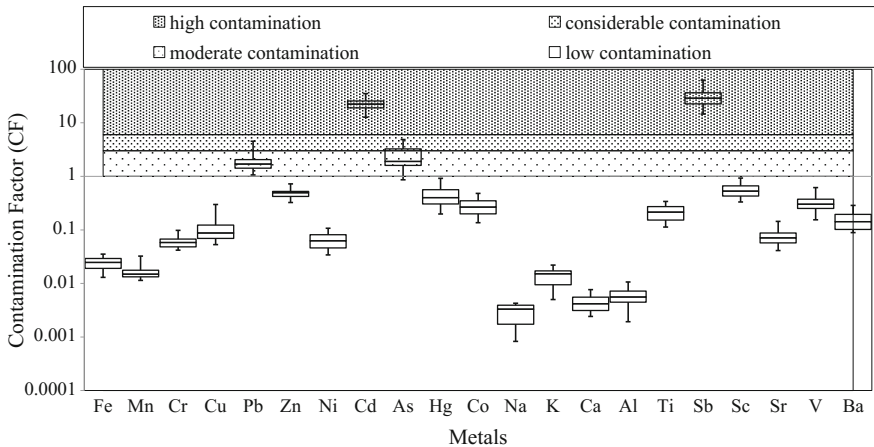
Fig. 10 Statistics of contamination factor (CF) of metals in soil in dry season
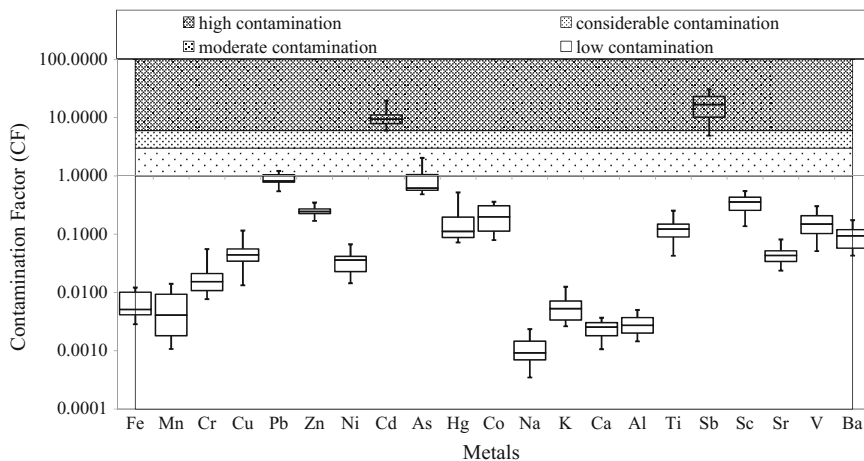
Fig. 11 Statistics of contamination factor (CF) of metals in rainy season

Figure 11 represents CF values for the metals of Fe, Mn, Cr, Cu, Zn, Ni, Hg, Co Na, K, Ca, Al, Ti, Sc, Sr, V and Ba in rainy season indicated the low level of contamination as dry season. Although, the most of the values of CF indicated the low level of contamination, nevertheless, the maximum value of CF for Pb and As indicated the moderate level of contamination in soil. Accordingly, all the computed values of CF for Cd and most of the CF values of Sb indicated the high level of contamination, while the minimum CF of Sb indicated the considerable level of contamination.

Nemerow Integrated Contamination Factor. The nemerow integrated contamination factor (NICF) for 21 studied metals for dry and rainy season is presented in Figs. 12 and 13, respectively. Based on these figures, all the studied metal elements had showed that the NICF value was greater than 3, which indicated the high level of contamination in soil for both the dry and rainy seasons.

Pollution Load Index. The computed values of pollution load index (PLI) in soil both seasons was found as less than 1 and indicated that the soil was uncontaminated in the study area.

Modified Contamination Degree. The variation of mCD values in soil from 40 boreholes of dry season is shown in Fig. 14. The lowest value of mCD was to be found as 1.50 which for BH-39 in the selected disposal site location, goes to the class of low level of contamination ($1.5 < mCD < 2$). On the other hand, the highest value of mCD was observed as 5.34 in case of BH-1 in the selected area, which lies in the class of high degree of contamination ($4 < mCD < 8$). Most of the mCD values lie in the class of moderate degree of contamination in soil.

Similarly, Fig. 15 represents the mCD for 20 boreholes of soil in rainy season with the classification of soil. The lowest value of mCD was found to be 0.60 in case of BH-39 in studied area which belongs to the class of nil to very low contamination ($1.5 < mCD$). On the other hand, the highest value of mCD was
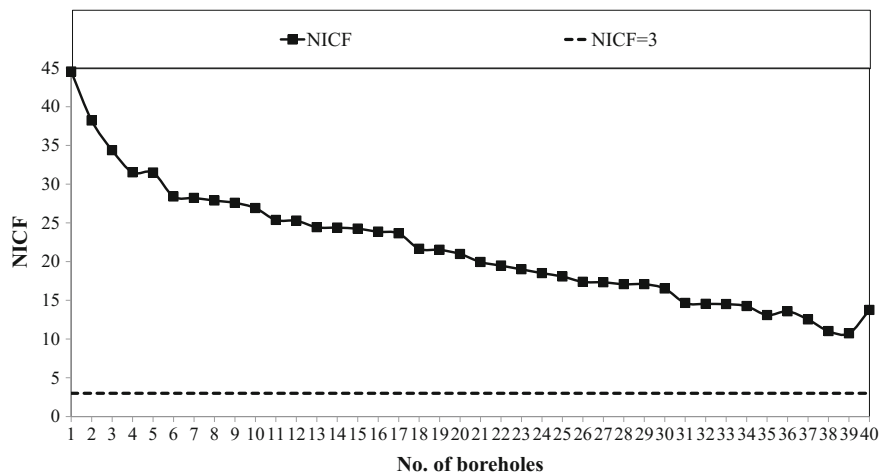
Fig. 12 Nemerow integrated contamination factor (NICF) of studied metals in dry seasons
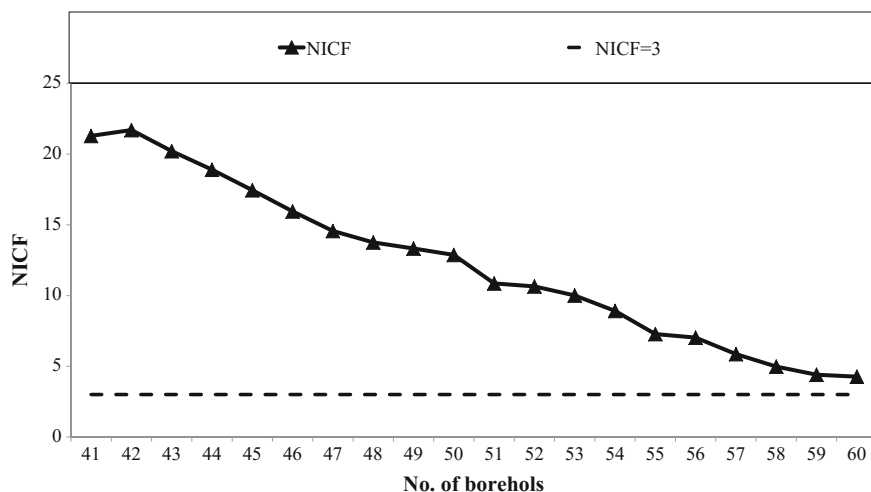
Fig. 13 Nemerow integrated contamination factor (NICF) of studied metals in rainy seasons

recorded 2.64 for BH-41 in the area which belongs to the class of moderate degree of contamination (2 < mCD < 4). However, most of the computed value of mCD lies in the class of nil to very low contamination of soil in the waste disposal site.

Enrichment Factor. In this assessment, aluminium (Al) used as the reference element because this normalizing element assumed less contamination with respect to the other metal elements in soil of the study area. As, Al was selected as reference element hence EF of Al was found 1 for both the seasons. The value EF varied across the sites following the sequence of Sb > Cd > As > Pb > Sc > Zn > Hg > V > Co > Ti >
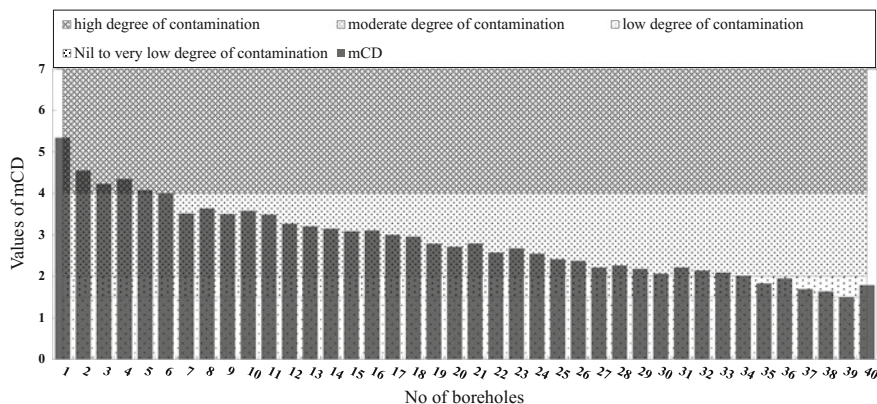
Fig. 14 Classification of mCD values of BH-1 to BH-40 (dry season)
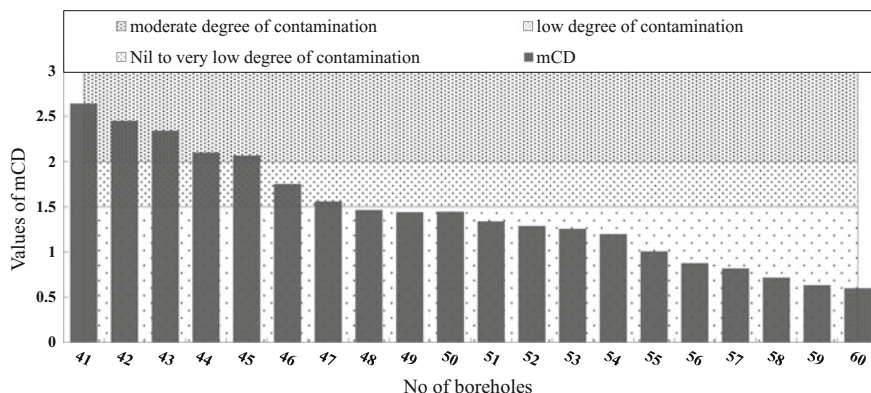
Fig. 15 Classification of mCD values of BH-41 to BH-60 (rainy season)

Ba > Cu > Sr > Ni > Cr > Fe > Mn > K > Ca > Na in dry season. In rainy season, the EF varied with the sequence of Sb > Cd > Pb > As > Sc > Zn > Co > Hg > V > Ti > Ba > Sr > Cu > Ni > Cr > Fe > K > Mn > Ca > Na. Figure 16 shows the mean value of EF of 20 elements (aluminium as reference element) measured for both the dry and rainy seasons. In dry season, the mean value of EF was calculated from EF of selected 40 boreholes (BH-1 to BH-40) where in rainy season, EF mean is the average of 20 (BH-41 to BH-60) boreholes. To make a comparison of EF for all the studied metal elements and it can be concluded that the values of EF were found to be very close for both the dry and rainy seasons. However, the dry season showed the highest value of EF than that of rainy season as well as vice versa. Figure shows that the values of EF for the elements of Pb, Zn, Cd, As, Hg, Co and Sb were greater than 50 and lie in the class of extremely severe enriched. Furthermore, the value of EF for Sb and Cd showed very high
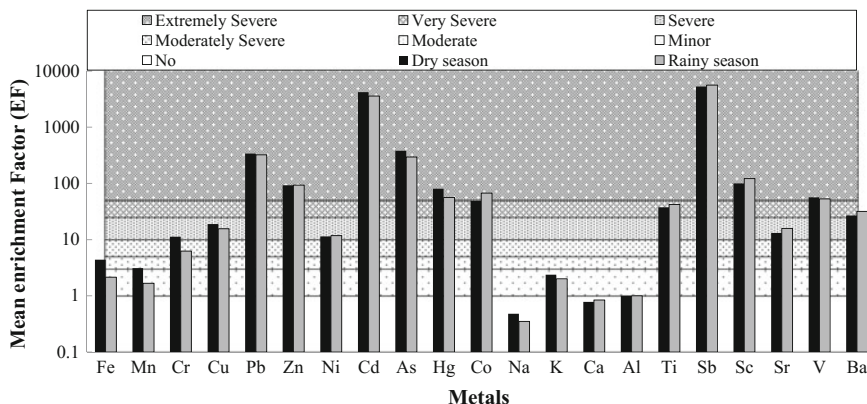
Fig. 16 Classification of mean EF values of soil samples

EF values. EF for Ti and Ba showed the class of very severe enriched ($25 < EF < 50$). The value of EF for Fe lies in the class of moderately enrichment ($3 < EF < 5$) for dry season. The EF of Fe (rainy season), Mn and K indicated minor enrichment and Na and Ca indicated no enrichment in soil of the site.

Figure 17 depicts the spatial distribution of EF values for four heavy metals (Cd, Sb, Pb and As) in soil for the dry season by the method of interpolation (kriging) using ArcGIS software. As illustrated by the figure, spatial variations of EF for Cd, Sb and Pb were found to be similar but different from the value of EF in case of the spatial variation of As. On the contrary, Fig. 18 depicts the spatial distribution of the EF values for Cd, Sb, Pb and As in rainy season. In rainy season, the spatial variations of EF for Cd and Pb were found to be similar but different from the spatial variation of Sb and As in soil.

Geo-accumulation Index. The mean value of I_{geo} and the level of contamination for different metals in soil are provided in Table 8. Figures 18 and 19 show the overall statistics of I_{geo} in soil over two seasons. Result reveals that the value of I_{geo} in case of Pb and As showed the uncontaminated to moderately contaminated level for dry season, while it showed the uncontaminated level for rainy season. In consideration of the metal of Cd, the value of I_{geo} for Cd showed the strongly contaminated as well as moderately contaminated in soil for dry and rainy season, respectively. Correspondingly, the mean value of I_{geo} for the metal of Sb indicated the strongly to extremely contaminated and strongly contaminated level in case of dry and rainy season, respectively.

In Fig. 18, the values of I_{geo} range for Fe, Mn, Cr, Cu, Zn, Ni, Hg, Co, Na, K, Ca, Al, Sc, Sr, V and Ba were found to be less than zero and it can be concluded that the soil is uncontaminated by these metals in soil.

Potential Ecological Risk Index. With regard to the assessment method [19], ecological risk index of a single element (ER) and comprehensive potential
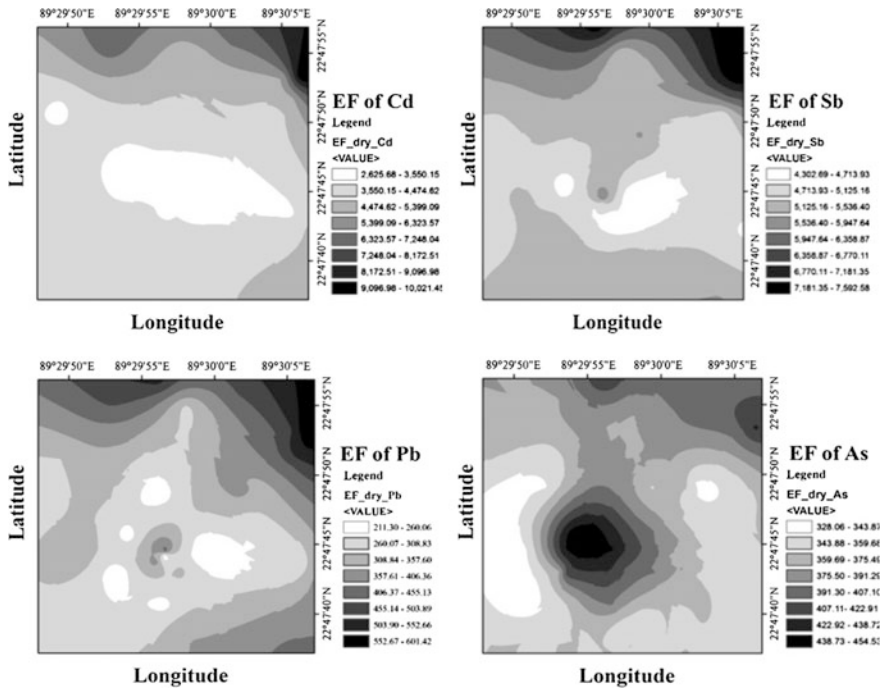
Fig. 17 Classification of mean EF values of soil samples

ecological risk index (PERI) were calculated for 40 boreholes, and the results of first 10 boreholes in dry season are shown in Table 9.

In terms of the maximum potential ecological risk indices of these nine metals, the potential ecological risk arrayed is in the order of ER(Cd) > ER(As) > ER(Hg) > ER(Pb) > ER(Co) > ER(Cu) > ER(Zn) > ER(Ni) > ER(Cr). Result depicts that Cd had the maximum value (1054.50) of ER with respect to the other counter metals in soil and it can be revealed that Cd was the key influence factor to cause the potential ecological risk in soil of waste disposal site. Furthermore, all of the boreholes have extremely strong potential ecological risk of Cd, whereas, other metals only showed slight ecological risk except As and Hg. These two metals have medium to slight ecological risk. In addition, comprehensive potential ecological risk indexes (PERI) for all boreholes were almost above 320. Hence, from PERI point of view risk degree is above very strong.

Besides, the values of ER and PERI were also computed for 20 boreholes in rainy season and first 10 boreholes are shown in Table 10. In terms of the maximum potential ecological risk indices of these metals, the potential ecological risk same as dry season arrayed in the order of ER(Cd) > ER(As) > ER(Hg) > ER(Pb) > ER(Co) > ER(Cu) > ER(Zn) > ER(Ni) > ER(Cr). The boreholes have extremely strong to very strong potential ecological risk of Cd, whereas other metals only showed slight ecological risk. Comprehensive potential ecological risk

Table 8 Contamination levels of soil classified by average I_{geo} in two seasons

Metals	Dry season		Rainy season	
	I_{geo} value	Contamination level	I_{geo} value	Contamination level
Fe	−6.00	Uncontaminated	−8.02	Uncontaminated
Mn	−6.56	Uncontaminated	−8.55	Uncontaminated
Cr	−4.67	Uncontaminated	−6.52	Uncontaminated
Cu	−3.92	Uncontaminated	−5.19	Uncontaminated
Pb	**0.25**	Uncontaminated/moderately contaminated	−0.81	Uncontaminated
Zn	−1.64	Uncontaminated	−2.60	Uncontaminated
Ni	−4.62	Uncontaminated	−5.58	Uncontaminated
Cd	**3.88**	Strongly contaminated	**2.68**	Moderately contaminated
As	**0.46**	Uncontaminated/Moderately contaminated	−0.96	Uncontaminated
Hg	−1.83	Uncontaminated	−3.41	Uncontaminated
Co	−2.51	Uncontaminated	−3.07	Uncontaminated
Na	−9.20	Uncontaminated	−10.65	Uncontaminated
K	−6.86	Uncontaminated	−8.12	Uncontaminated
Ca	−8.48	Uncontaminated	−9.36	Uncontaminated
Al	−8.10	Uncontaminated	−9.11	Uncontaminated
Ti	−2.89	Uncontaminated	−3.72	Uncontaminated
Sb	**4.25**	Strongly/extremely contaminated	**3.31**	Strongly contaminated
Sc	−1.49	Uncontaminated	−2.19	Uncontaminated
Sr	−4.41	Uncontaminated	−5.13	Uncontaminated
V	−2.30	Uncontaminated	−3.39	Uncontaminated
Ba	−3.38	Uncontaminated	−4.13	Uncontaminated

Bold colour highlights the significant values

indexes (PERI) for first 6 boreholes are above 320 so having very strong risk. From Tables 9 and 10, it is depicted that the ER and PERI are declining along the increasing borehole numbers or increasing distance. Hence, risk due to metals was more severe in dry season according to the variation in two seasonal PERI and ER values.

Furthermore, in Fig. 19, the ranges of I_{geo} value for Fe, Mn, Cr, Cu,Pb, Zn, Ni, Hg, Co, Na, K, Ca, Al, Sc, Sr, V and Ba were less than zero so the soil is uncontaminated by those metals. Only As has the maximum value greater than zero in rainy season (Fig. 20).
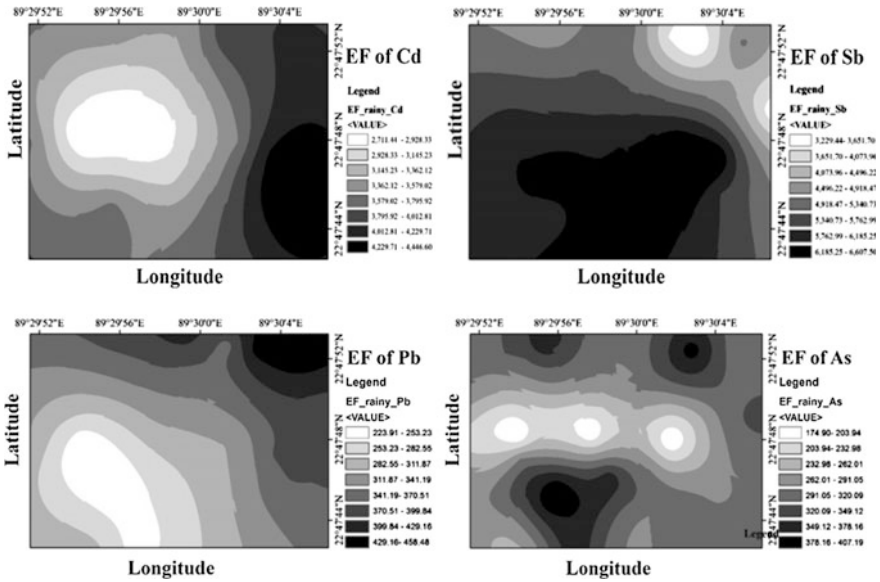
Fig. 18 Classification of mean EF values of soil samples
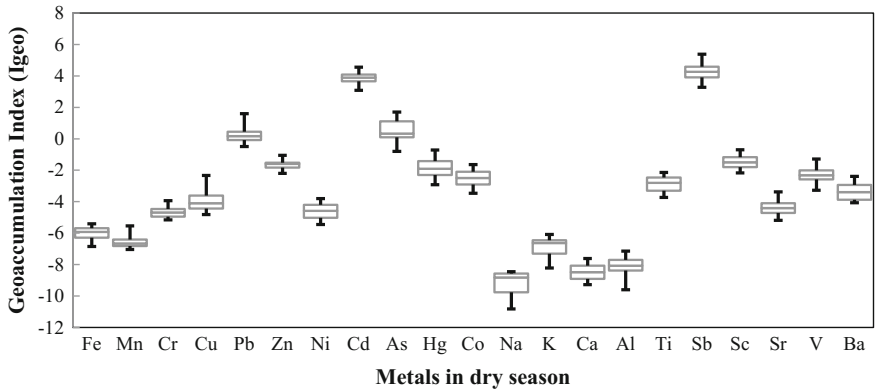
Fig. 19 Statistics of I_{geo} for metals in soil for dry season

3.4 Pearson's Correlations Analysis

In this study, Pearson's correlation coefficients were calculated for metal concentration present in soil of study area for soil quality assessment. The Pearson's relationship analysis is a fundamental process to evaluate the level of relationship among the factors considered. Analysed relationship is helpful to prompt new learning about causal association between the factors and decision making [33].

Table 9 Variation on ER and PERI in ten boreholes around study area in dry season

BH	ER									PERI
	Cr	Cu	Pb	Zn	Ni	Cd	As	Hg	Co	
1	0.12	1.23	22.64	0.73	0.54	1054.50	48.72	35.48	2.40	1166.36
2	0.12	1.50	12.72	0.73	0.52	903.00	43.83	36.80	2.10	1001.31
3	0.18	0.98	12.75	0.65	0.48	880.50	42.56	33.28	2.15	973.52
4	0.18	1.27	17.72	0.72	0.50	1042.50	41.06	34.36	2.24	1140.54
5	0.20	1.17	12.67	0.70	0.47	919.50	38.61	28.88	2.14	1004.34
6	0.16	1.39	15.19	0.65	0.45	993.00	37.22	32.04	2.14	1082.26
7	0.16	1.08	11.42	0.63	0.47	720.00	38.44	30.60	1.96	804.76
8	0.14	0.70	9.42	0.54	0.45	843.00	35.17	28.56	1.62	919.59
9	0.14	0.62	10.19	0.50	0.45	754.50	40.56	24.56	1.78	833.29
10	0.13	0.65	11.72	0.52	0.41	843.00	35.83	19.04	1.96	913.27

Table 10 Variation on ER and PERI in ten boreholes around study area in rainy season

BH	ER									PERI
	Cr	Cu	Pb	Zn	Ni	Cd	As	Hg	Co	
41	0.09	0.58	6.07	0.33	0.31	585.00	20.42	18.08	1.79	632.6602
42	0.06	0.38	5.45	0.33	0.34	465.00	17.97	14.76	1.80	506.0937
43	0.08	0.34	5.32	0.28	0.23	467.25	16.67	20.84	1.62	512.624
44	0.11	0.32	5.79	0.28	0.24	382.50	15.36	9.32	1.37	415.3056
45	0.05	0.28	6.02	0.25	0.21	441.75	10.44	7.66	1.28	467.9495
46	0.04	0.25	4.06	0.35	0.19	318.00	10.69	4.48	1.55	339.6169
47	0.03	0.18	5.19	0.25	0.18	265.50	6.17	4.44	1.61	283.5395
48	0.03	0.26	3.97	0.27	0.16	247.50	5.89	5.80	1.53	265.4128
49	0.03	0.28	4.17	0.26	0.20	256.50	5.67	4.08	1.06	272.2412
50	0.03	0.24	4.46	0.25	0.19	282.00	4.89	4.44	1.02	297.521

Correlation matrix between various metal parameters in soil of selected waste disposal site for dry season is shown in Table 11. Maximum metal parameters considered in the study were found to bear statistically significant correlation with each other indicating close association with each other. Correlation matrix (Table 11) of the metal data indicates positive correlations ($r^2 > 0.5$) among all elements without Cr–Mn (0.449). Based on the results of Pearson's correlations matrix on metal elements in soil during dry season, it was observed the most significant, viz. high positively correlated values between Fe and Ti (0.983), Mn and Pb (0.872), Cr and Co (0.797), Cu and Ba (0.888), Pb and Sr (0.867), Zn and V (0.906), Ni and Ba (0.963), Ca and Ba (0.926), As and Ca (0.975), Hg and Ca (0.882), Co and Sc (0.977), Na and K (0.950), K and Ti (0.963), Ca and Ba (0.992),
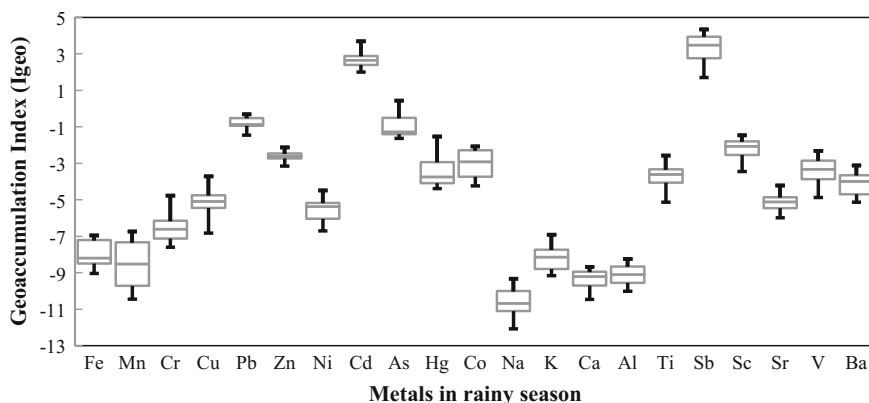
Fig. 20 Statistics of I_{geo} for metals in soil for rainy season

Al and Sc (0.980), Ti and Sc (0.987), Sb and Sr (0.988), Sc and Sr (0.986), Sr and V (0.984) and V and Ba (0.968). Such significant correlations between metal concentrations may reflect that these heavy metals had similar pollution level as well as similar pollution sources.

4 Concluding Remarks

This study describes the extent of heavy metal contamination in soil regarding distance and seasons of a selected waste disposal site in Bangladesh. Result reveals that the value of Cp for the metals of Sb and Cd for both the seasons indicated severe level of contamination in soil. Furthermore, the assessment results of CF indicated that the soil was highly contaminated for Cd and Sb, as well as moderately contaminated by Pb and As. Result also reveals that the values of EF in soil were extremely severe enriched by the element of Cd, As, Pb, Zn, Sc, Hg and Sb and varied across the sites following the sequence of Sb > Cd > As > Pb > Sc > Zn > Hg. Besides, results of PERI indicated that all of the soil sampling points have strong potential ecological risk including slight to strong ecological risk for Cd and Sb in study area. Based on the Pearson's correlation analysis, it can be observed that most of the metals in soil were significantly correlated with each other. Finally, it can be concluded that most of the indices, i.e. CF, mCD, I_{geo} and PERI showed that soil was polluted by heavy metals of Cd and Sb and it is detrimental for the surrounding environment and human health as well.

Table 11 Pearson correlation analysis comprising studied metal elements

ME[a]	Fe	Mn	Cr	Cu	Pb	Zn	Ni	Cd	As	Hg	Co	Na	K	Ca	Al	Ti	Sb	Sc	Sr	V	Ba
Fe	1																				
Mn	0.554	1																			
Cr	0.768	0.449	1																		
Cu	0.756	0.762	0.669	1																	
Pb	0.739	**0.872**	0.567	0.805	1																
Zn	0.845	0.708	0.711	0.887	0.800	1															
Ni	0.928	0.632	0.753	0.875	0.761	0.886	1														
Cd	0.889	0.741	0.747	0.815	0.825	0.797	0.880	1													
As	0.914	0.656	0.740	0.880	0.810	0.867	0.959	0.892	1												
Hg	0.760	0.727	0.575	0.882	0.789	0.789	0.855	0.807	0.886	1											
Co	0.949	0.653	**0.797**	0.856	0.811	0.879	0.942	0.918	0.955	0.832	1										
Na	0.942	0.462	0.738	0.633	0.621	0.753	0.818	0.817	0.785	0.635	0.880	1									
K	0.967	0.570	0.774	0.745	0.738	0.857	0.887	0.867	0.882	0.744	0.926	**0.950**	1								
Ca	0.948	0.658	0.750	0.884	0.812	0.881	0.958	0.920	**0.975**	**0.882**	0.970	0.850	0.919	1							
Al	0.952	0.645	0.776	0.866	0.799	0.888	0.952	0.902	0.974	0.868	0.960	0.862	0.948	0.979	1						
Ti	**0.983**	0.598	0.797	0.823	0.760	0.881	0.955	0.914	0.954	0.816	0.974	0.916	**0.963**	0.979	0.977	1					
Sb	0.952	0.687	0.713	0.852	0.841	0.895	0.943	0.901	0.953	0.830	0.956	0.848	0.926	0.972	0.965	0.967	1				
Sc	0.967	0.651	0.766	0.853	0.815	0.893	0.958	0.923	0.965	0.839	**0.977**	0.885	0.946	0.986	**0.980**	**0.987**	0.987	1			
Sr	0.938	0.709	0.701	0.849	**0.867**	0.883	0.946	0.912	0.966	0.862	0.957	0.832	0.915	0.975	0.968	0.959	**0.988**	**0.986**	1		
V	0.929	0.727	0.741	0.879	0.857	**0.906**	0.940	0.916	0.958	0.876	0.959	0.823	0.921	0.970	0.974	0.956	0.984	0.980	**0.984**	1	
Ba	0.943	0.668	0.753	**0.888**	0.814	0.887	**0.963**	**0.926**	0.971	0.867	0.971	0.835	0.903	**0.992**	0.964	0.976	0.975	0.983	0.973	**0.968**	1

[a]Metal element

Bold colour highlights the significant values

This study demonstrates that there is environmental contamination around dumping area and put emphasis on the necessity for a comprehensive public health approach to address environmental extortions in local communities. Finally, it can be established that it is obvious that a systematic and constant monitoring for heavy metal pollution should be established and certain remediation steps should be taken to decrease the rate and extent of pollution problems in future.

References

1. Rafizul, I.M., Howlader, M.K., Alamgir, M.: Construction and evaluation of simulated pilot scale landfill lysimeter in Bangladesh. J. Waste Manage. **32**(11), 2068–2079 (2012)
2. Murtaza, M.G.: Solid waste management in Khulna City. Plan Plus **1**(1), 6–15 (2012)
3. Scott, J., Beydown, D., Amal, R., Low, G., Cattle, J.: Land-fill management, leachate generation and leach testing of solid wastes in Australia and overseas. Crit. Rev. Environ. Sci. Technol. **35**(3), 239–332 (2005)
4. Srinivasa, G.S., Pradip, K.G.: Distribution of heavy metals in surface water of Ranipet industrial area in Tamil Nadu, India. Envi. Monit. Assess. **136**, 197–207 (2010)
5. Nriagu, J.O., Pacyna, J.M.: Quantitative assessment of worldwide contamination of air, water and soils by trace metals. Nature **333**, 134–139 (1988)
6. Yousuf, T.B.: Construction and operation of landfill: Experience of Dhaka City Corporation. In: 1st International Conference on Solid Waste Management: Technical, Environmental and Socio-economical Contexts-WasteSafe, Khulna, Bangladesh, 9–10 Nov 2009, vol. 2, pp. 517–524 (2009)
7. Esakku, S., Karthikeyan, O.P., Joseph, K., Nagendran, R.: Heavy metal fractionation and leachability studies on fresh and partially decomposed municipal solid waste. Pract. Periodical Hazard. Toxic Radioactive Waste Manage. ASCE **12**(2), 127–132 (2008)
8. Likuku, S.A., Mmolawa, K.B., Gaboutloeloe, G.K.: Assessment of heavy metal enrichment and degree of contamination around the copper-nickel mine in the SelebiPhikwe Region, Eastern Botswana. Environ. Ecol. Res. **1**(2), 32–40 (2013)
9. Guanlin, G., Qixing, Z., Lene, Q.M.: Availability and assessment of fixing additives for the in-situ remediation of heavy metal contaminated soils. Env. Monit. Assess. **116**, 513–528 (2006)
10. Ajah, K.C., Ademiluyi, J., Nnaji, C.C.: Spatiality, seasonality and ecological risks of heavy metals in the vicinity of a degenerate municipal central dumpsite in Enugu, Nigeria. J. Environ. Health Sci. Eng. **13**, 15 (2015). https://doi.org/10.1186/s40201-015-0168-0
11. Harrison, R.M., Chirgawi, M.B.: Sources of metals in the soil. Sci. Total Environ. J. **15** (1989), 13–34 (1989)
12. Ahmed, G., Uddin, M.K., Khan, G.M., Rahman, M.S., Chowdhury, D.A.: Distribution of trace metal pollutants in surface water system connected to effluent disposal points of Dhaka export processing zone (DEPZ), Bangladesh: A statistical approach. J. Nat. Sci. Sus. Technol. **3**, 293–304 (2009)
13. Mortula, M.M., Rahman, M.S.: Study on waste disposal at DEPZ. Bangladesh Environ. (BAPA) **2**, 807–817 (2002)
14. Islam, M.S., Tusher, T.R, Mustafa, M., Mamun, S.A.: Investigation of soil quality and heavy metal concentrations from a waste dumping site of Konabari industrial area at Gazipur in Bangladesh. IOSR J. Environ. Sci. Toxicol. Food Technol. (IOSR-JESTFT) **2**(1), 01–07. ISSN: 2319-2402, ISBN: 2319-2399 (2012)

15. Rahman, S.H., Khanam, D., Adyel, T.M., Islam, M.S., Ahsan, M.A., Akbor, M.A.: Assessment of heavy metal contamination of agricultural soil around Dhaka export processing zone (DEPZ), Bangladesh: Implication of seasonal variation and indices. Appl. Sci. **2**, 584–601 (2012). https://doi.org/10.3390/app2030584

16. Davaulter, V., Rognerud, S.: Heavy metal pollution in sediments of the Pasvik River drainage. Chemosphere **42**, 9–18 (2001)

17. Aprile, F.M., Bouvy, M.: Distribution and enrichment of heavy metals in sediments at the Tapacurá River Basin, Northeastern Brazil. Braz. J. Aquat. Sci. Technol. **12**(1), 1–8 (2008)

18. Krauskopf, K.B., Bird, D.K.: Introduction to Geochemistry, 3rd edn, 647 pp. McGraw Hill, New York (1995)

19. Hakanson, L.: Ecological risk index for aquatic pollution control. A sedimentological approach. Water Res. **14**, 975–1001 (1980)

20. Kalender, L., Uçar, S.C.: Assessment of metal contamination in sediments in the tributaries of Euphrates River, using pollution indices and the determination of the pollution source, Turkey. J. Geochem. Explor. **134**, 73–84 (2013)

21. Tomlinson, D.C., Wilson, J.G., Harris, C.R., Jeffery, D.W.: Problems in the assessment of heavy metals levels in estuaries and the formation of a pollution index. Helgoländer Meeresun. **33**, 566–575 (1980)

22. Harikumar, P.S., Nasir, U.P., MujeebuRahma, M.P.: Distribution of heavy metals in the core sediments of a tropical wetland system. Int. J. Environ. Sci. Technol. **6**(2), 225–232 (2009)

23. Abrahim, G.M.S.: Holocene sediments of Tamaki Estuary: Characterisation and impact of recent human activity on an urban estuary in Auckland, New Zealand. Ph.D. thesis, University of Auckland, Auckland, New Zealand, 361p (2005)

24. Sakan, S.M., Djordjevic, D.S., Manojlovic, D.D., Polic, P.S.: Assessment of heavy metal pollutants accumulation in the Tisza river sediments. J. Environ. Manage. **90**, 3382–3390 (2009)

25. Ackerman, F.: A procedure for correcting the grain size effect in heavy metal analyses of estuarine and coastal sediments. Enviorn. Technol. Lett. **1**, 518–527 (1980)

26. Taylor, S.R.: Abundance of chemical elements in the continental crust: a new table. Geochim. Cosmochim. Acta **28**, 1273–1285 (1964)

27. Wei, B., Yang, L.: A review of heavy metal contamination in urban soils, urban dust and agricultural soils from China. Michrochem J. **94**, 99–107 (2010)

28. Jarup, L.: Hazards of heavy metal contamination. Br. Med. Bull. **68**(1), 167–182 (2003)

29. Abrahim, G.M.S., Parker, P.J.: Assessment of heavy metal enrichment factors and the degree of contamination in marine sediments from Tamaki Estuary, Auckland, New Zealand. Environ. Monit. Assess. **136**(1-3), 227–238 (2008)

30. Nabholz, J.V.: Environmental hazard and risk assessment under the United States, Toxic Substances Control Act. Sci. Total Environ. **109**, 649–665 (1991). https://doi.org/10.1016/0048-9697(91)90218-4

31. Singh, A., Sharma, R.K., Agrawal, M., Marshall, F.M.: Health risk assessment of heavy metals via dietary intake of foodstuffs from the waste water irrigated site of a dry tropical area of India. Food Chem. Toxicol. **48**, 611–619 (2010). https://doi.org/10.1016/j.fct.2009.11.041

32. Douay, F., Pelfrêne, A., Planque, J., Fourrier, H., Richard, A., Roussel, H., Girondelot, B.: Assessment of potential health risk for inhabitants living near a former lead smelter, Part 1. Environ. Monit. Assess. **185**, 3665–3680 (2013). https://doi.org/10.1007/s10661-012-2818-3

33. Patil, V.T., Patil, P.R.: Physicochemical analysis of selected groundwater samples of Amalner Town in Jalgaon District, Maharashtra, India. E-J. Chem. **7**(1), 111–116 (2010)

Crop Phenology Study Based on Multispectral Remote Sensing

Supratim Guha, Teya Pal and Venkata Ravibabu Mandla

Abstract The study identifies various growing stages of rice crop using multi-spectral data through red edge analysis. The maximum reflectance values for 35, 66, 76, and 96 days which indicate vegetative phase, reproductive phase, reproductive phase and ripening phase are 0.17, 0.228, 0.231, and 0.266 respectively at the test site 1. For the test site-2, the same trends are followed. When the crop is in vegetative stage the reflectance values are less whereas, when the stage of crop is reproductive, adjacent to the vegetative, the values of reflectance are increasing significantly due to increase in trend in canopy. This type of spectral analysis approach can be adapted to generate spectral library which can be beneficial for future research purpose.

Keywords Multispectral · Phenology · Rice crop · Red edge · Sentinal-2 Spectral analysis · Spectral library

1 Introduction

Most significant components in foundation of Indian economy include agriculture. As agriculture is one of the major concerns, the crop monitoring should be taken cared properly to maintain good crop health. If crop misses possessing good health

S. Guha · V. R. Mandla (✉)
OS–GST Lab, Department of Environmental and Water Resources Engineering,
School of Civil and Chemical Engineering, VIT University, Vellore 632014, India
e-mail: ravi.mandla@gmail.com

S. Guha
e-mail: supratim.guha2010@gmail.com

T. Pal
School of Science, Technology and Knowledge Systems, Centre for Geoinformatics
Applications for Rural Development (CGARD), National Institute of Rural
Development and Panchayat Raj (NIRD & PR), Hyderabad 500030,
Telangana, India
e-mail: pal0teya@gmail.com

even any at least in one stage of its growth then also the overall growth and required yield will not be considered as proper as usually it should happen to be [1]. The comprehensive study is demanded to understand the growth and progress to improvement along with grain yield of a crop plant [2]. Study on crop phonology includes the factors serving as age of the crop, variety of the crop, genes along with environmental factors acting as weather conditions and climate, water supply may be natural or artificial and diseases can also be counted as influence for plant phenology [3]. Understanding crop phenology is also important for proper irrigation management, proper fertilization, yield prediction, and policy planning [1]. Spectral and temporal profiles which are extracted from the fields regarding same crop type can show some intra-yearly fluctuations (early or delayed phonological stages) even for local scales [4–7].

The stages of natural cyclic incidents of a crop can be observed practicing field observation, but when it comes to large areas it is very difficult to maintain the same procedure and due to this reason for large areas, remote sensing time series datasets are important for figuring out the phonological stages of crops [1].

Remote sensing and GIS approach plays a crucial role to the cost beneficial agricultural applications and practices [8]. One of the significant implementation is the spectral classification of the crop types from the satellite-based multispectral imageries, with which it is possible to form or update crop inventories when the field data is limited [9]. In vegetation, different species may show utterly similar spectral behavior, distinctively for some specific phonological stages and at the usual bandwidth along with spectral resolution of satellite-based multispectral imageries [10, 11]. So the issue can strongly limit accuracy of the crop types if classified by a single imagery dates [12–15].

Normalized Difference Vegetation Index (NDVI) imageries are often helpful to interpret crop biomass [16]. NDVI is formed by a red band (R) which is sensitive to content of foliar chlorophyll, and by a near infrared (NIR) band which is sensitive to canopy foliage amount or simply NDVI can be expressed as (NIR-R)/(NIR + R) [9]. Intra-yearly fluctuation in amplitude of NDVI profiles (temporal) of the two fields for the same crop type (when stage unaltered) point out several vegetation condition [9]. At the same time, intra-yearly fluctuations in the stage of the temporal profiles (when amplitude altered) of the fields of same crop type point out shifts in uplifting stages [17].

To enhance along with supporting the crop type categorizing which is based on NDVI temporal profiles, field data on crop phenology have been adopted as reference [8, 18–22].

But it has been explored that the NDVI saturates for high biomass and dense vegetative areas [23, 24]. In addition to the mentioned discovery, NDVI is critical to the canopy background and this comes with significant errors when the vegetation characteristics estimation is being done [25]. Furthermore, the utilization of NDVI values which can be derived from the multispectral spatial resolution sensors is limited for their blended pixels problems despite their huge utilization at the regional scale [26, 27].

The application of red edge is more effective [28] than the conventional ones such as contrast between NIR and Red bands [29].

The new favorable circumstances for the vegetation analysis include the availability of the extension of spectral ranges for instancing the red edge band which emerged with Rapid Eye and WorldView-2 launching [29]. The red edge reflectance possesses better sensitivity to the fluctuations of chlorophyll content and has been projected in the experimental studies as more effective for analyzing stress in vegetation [30, 31].

When it needs to be most accurate on earth observational data, vegetation structure estimating attributes for instance canopy storage capability and LAI hyper spectral data are the most preferable [25]. Hyper spectral data can detect even little vegetation traits which can be merged with mixed pixels while using broadband sensors with its narrow spectral pathways [32]. Due to being expensive, unavailable most of the time, limited with spatial coverage and complex for analysis due to low knowledge of skills such datasets are not agreeable all the time [33, 34]. Landsat datasets remain the most optimal source of the spatial data for the regions which have limited resources and it possesses the longest historic datasets, its readily available and free, with less complexities while processing and analyzing [25]. Enhanced Landsat 8 operational land imager, Landsat balanced spatial resolution along with the inadequacy of spectral channels for instance red edge, and sensitive vegetation mapping limits its benefits [35]. So the important was to search for other sensors which are having comprehensive spatial and spectral information and which could be utilized while mapping and the understanding sensitive water relevant issues like as canopy water storage capability and interception [25].

In this study, two test sites with rice crop fields taken near Vellore. The rice test fields variety is the same, i.e., ADT 43. Most of the nearby crop fields are farmed with the same variety of rice. The spectral analysis has been done with the data collected for the two crop fields. The different phonological stage of the crop has been analyzed with the utilization of red edge band.

2 Study Area

The study area (Fig. 1) is located in Vellore district, Tamil Nadu, India. The latitude and longitude of margining the study area are 12° 58′ 34″N to 12° 58′ 35″N and 79° 9′ 8″E to 79° 9′ 10″E, respectively. The maximum and minimum temperatures are 40.2 °C and 14.6 °C respectively for the plain areas of the districts [36]. The normal rainfall due to northeast monsoon is 392 and 501.3 mm due to southwest monsoon [36].
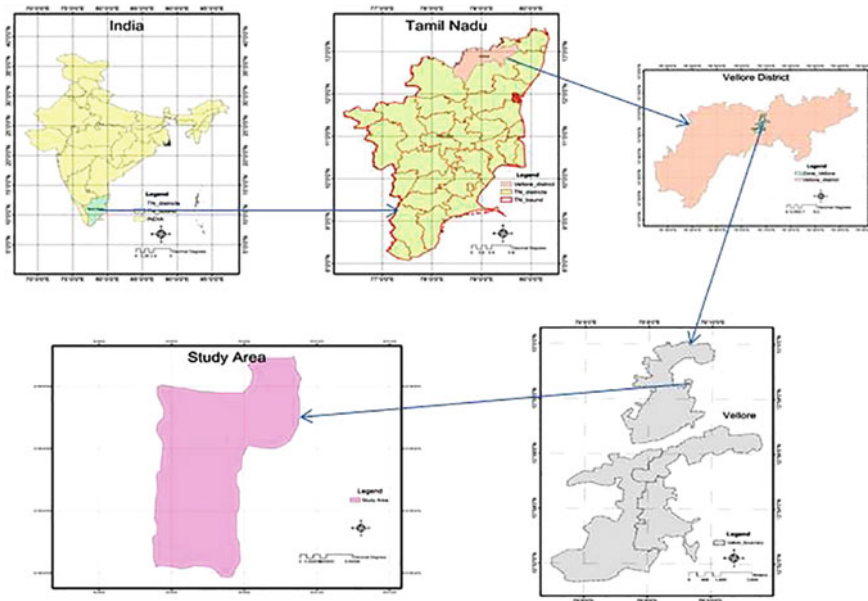
Fig. 1 Study area for the current work

3 Data Used and Methodology

Sentinel-2A satellite data has been used for this study which was launched in June of 2015. It is assembled with the identical multispectral instruments (MSI) a very wide field of view (a swath width of 290 km), which is skillful to acquire data with 13 bands in various spatial resolutions (within the range of 10–60 m). Estimated fact is sentinel-2A can supply at least one cloud free data image in each month on average

The MSI on Sentinel-2A can record data within the red edge spectral domain for vegetation which is one of the most useful remote sensing based description holders for chlorophyll content [37]. A 5-day Sentinel data has been taken for analysis consecutively for two test sites.

4 Red Edge Analysis

Red edge is the rapid transition zone within 680–760 nm as there occur a sudden increase from low red region of spectra to high infrared region of spectra due to intense pigment absorption close to 680 nm and high canopy scattering near 760 nm [38, 39]. Test site 1 had been taken for experimenting. The red edge first observed as for the vegetation analysis with satellite data red edge is more

significant. Then the cross verification is done by the other test site. The spectral signature of both the lands shows the same pattern when it comes to red edge portion.

5 Results and Analysis

5.1 Field Survey

The significant information pertinent with the experimental study was inventoried such as farming style, harvesting, composting, etc. The field inventoried data will not create any difference as the information about two test sites is similar only and the crop type is of short duration variety.

5.2 Spectral Analysis

Spectral signature of test site 1 for four available consecutive days is shown in Fig. 2. It shows the reflectance at visible and near infrared and the various stages pattern at difference growth stage, i.e., 5–96 days.

Figure 3 is similarly showing spectral signature of test site 2 and how the reflectance is changing and how this change is presenting different stages of rice (Tables 1 and 2).

In tropical environment, growth phases of rice plant take first 60 days as vegetative stage, next 30 days as reproductive phase, and last 30 days as ripening phase for a short duration variety [40]. So the reflectance is less in vegetative phase as the presence of water takes the absorption higher. In vegetative phase, tillers and more leaves are formed, plant heights increase whereas in reproductive stage, the plant is more matured and panicle formation takes place and in ripening stage the
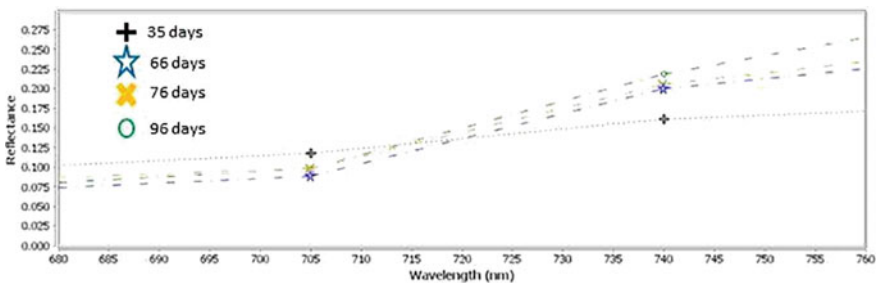
Fig. 2 Spectral signature of test site-1 for 4 days
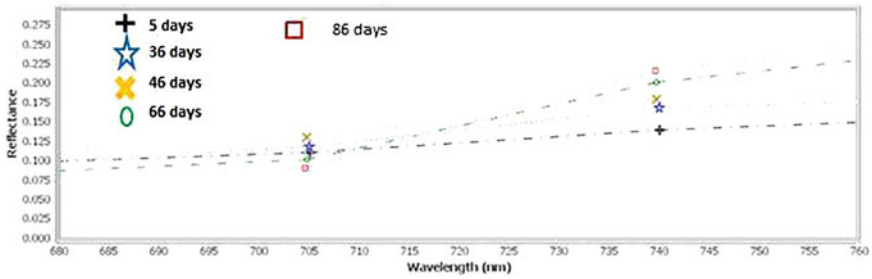
Fig. 3 Spectral signature of test site-2 for 5 days

Table 1 Phonological stages (daywise) analysis of test site 1

Age of the crops (in day)	Maximum reflectance	Growing stage
35	0.170	Vegetative phase
66	0.228	Reproductive phase
76	0.231	Reproductive phase
96	0.266	Ripening phase

Table 2 Phonological stages (daywise) analysis of test site 2

Age of the crops (in day)	Maximum reflectance	Growing stage
5	0.148	Vegetative phase
36	0.175	Vegetative phase
46	0.192	Vegetative phase
66	0.231	Reproductive phase
86	0.246	Reproductive phase

rice plant is in totally matured phase [40]. So the water absorption is no longer dominating in matured stages.

6 Conclusion

The study shows that depending on change in the age of the crop, the canopy of the crop also changes and based on this canopy change, remote sensing can identify crop stages with the red edge analysis. Current study's fruition is a new approach when it comes to crop monitoring. It is shown that multispectral data is also helpful for red edge analysis. This study shows the biophysical parameters analysis for the distribution of fertilization and nutrients through red edge concept. Further, the creation of spectral library can be considered which identifies the stressed vegetation, i.e., deceased crops for various rice varieties. This multispectral spectral

library can be compared with hyper spectral datasets for the further developmental implementation possibilities.

References

1. Jayawardhana, W.G.N.N., Chathurange, V.M.I: Extraction of agricultural phenological parameters of Sri Lanka using MODIS, NDVI time series data. In: International Conference of Sabaragamuwa University of Sri Lanka 2015 (ICSUSL 2015) Procedia Food Science, vol. 6, pp. 235–241 (2016)
2. Saichuk, J.: Chapter 4, Rice growth and development. In: Louisiana Rice Production Handbook, pp. 41–43 (1987)
3. Koch, E., Bruns, E., Chmielewski, F., Defila, C., Lipa, W., Menzel, A.: Guidelines For Plant Phenological Observations, WHO Technical Commission for Climatology, Open Program Area Group on Monitoring and Analysis of Climate Variability and Change (OPAG2) (2007)
4. Arvor, D., Jonathan, M., Simões, M., Meirelles, P., Dubreuil, V., Durieux, L.: Classification of MODIS EVI time series for crop mapping in the state of Mato Grosso, Brazil. Int. J. Remote Sens. **32**, 7821–7847 (2011)
5. Masialeti, I., Egbert, S., Wardlow, B.D.: A comparative analysis of phonological curves for major crops in Kansas. GIScience Remote Sens. **47**, 241–259 (2010)
6. Odenweller, J.B., Johnson, K.I.: Crop identification using landsat temporalspectral profiles. Remote Sens. Environ. **14**, 39–54 (1984)
7. Wardlow, B., Egbert, S., Kastens, J.H.: Analysis of time-series MODIS 250 m vegetation index data for crop classification in the U.S. Central Great Plains. Remote Sens. Environ. **108**, 290–310 (2007)
8. Zhong, L., Hawkins, T., Biging, G., Gong, P.: A phenology-based approach to map crop types in the San Joaquin Valley, California. Int. J. Remote Sens. **32**, 7777–7804 (2011)
9. Peña, M.A., Brenning, A.: Assessing fruit-tree crop classification from Landsat-8 time series for the Maipo Valley, Chile. Remote Sens. Environ. **171**, 234–244 (2015)
10. Esch, T., Metz, A., Marconcini, M., Keil, M.: Combined use of multi-seasonal high and medium resolution satellite imagery for parcel-related mapping cropland andgrassland. Int. J. Appl. Earth Obs. Geoinf. **28**, 230–237 (2014)
11. Galvão, L.S., Epiphanio, J.C.N., Breunig, F.M., Formaggio, A.R.: Crop type discrimination using hyperspectral data. In: Thenkabail, P.S., Lyon, J.G., Huete, A. (eds.) Hyperspectral Remote Sensing of Vegetation, pp. 397–421 (2012)
12. Jewell, N.: An evaluation of multi-date SPOT data for agriculture and land use mapping in the United Kingdom. Int. J. Remote Sens. **10**, 939–951 (1989)
13. Lo, T.H.C., Scarpace, F.L., Lillesand, T.M.: Use of multitemporal spectral profiles in agricultural land-cover classification. Photogram. Eng. Remote Sens. **52**, 535–544 (1986)
14. Murakami, T., Ogawa, S., Ishitsuka, K., Kumagai, K., Saito, G.: Crop discrimination with multitemporal SPOT/HRV data in the Saga Plains, Japan. Int. J. Remote Sens. **22**, 1335–1348 (2001)
15. Van Niel, T.G., McVicar, T.R.: Determining temporal windows for crop discrimination with remote sensing: a case study in South-Eastern Australia. Comput. Electron. Agric. **45**, 91–108 (2004)
16. Son, N.T., Chen, C.F., Cru, C.R.: Mapping major cropping patterns in Southeast Asia from Modis data using wavelet transform and artificial neural networks. ISPRS Int. Arch. Photogram. Remote Sens. Spat. Inf. Sci. **1**, 421–425 (2012)
17. Jakubauskas, M.E., Legates, D.R., Kastens, H.: Crop identification using harmonic analysis of time-series AVHRR NDVI data. Comput. Electron. Agric. **37**, 127–139 (2002)

18. Sakamoto, T., Yokozawa, M., Toritani, H., Shibayama, M., Ishitsuka, N., Ohno, H.: A crop phenology detection using time-series MODIS data. Remote Sens. Environ. **96**, 366–374 (2005)

19. Shao, J., Lunetta, R.S., Ediriwickrema, J., Liames, J.: Mapping cropland and major crop types across the Great Lakes Basin using MODIS-NDVI data. Photogram. Eng. Remote Sens. **75**, 73–84 (2010)

20. Sibanda, M., Murwira, A.: The use of multi-temporal MODIS images with ground data to distinguish cotton from maize and sorghum fields in smallholder agricultural landscapes of Southern Africa. Int. J. Remote Sens. **33**, 4841–4855 (2012)

21. Zheng, B., Myint, S.W., Thenkabail, P.S., Aggarwal, R.M.: A support vector machine to identify irrigated crop types using time-series Landsat NDVI data. Int. J. Appl. Earth Obs. Geoinf. **34**, 103–112 (2015)

22. Zhong, L., Gong, P., Biging, G.: Efficient corn and soybean mapping with temporal extendability: a multi-year experiment using Landsat imagery. Remote Sens. Environ. **140**, 1–13 (2014)

23. Huete, A., Didan, K., Miura, T., Rodriguez, E.P., Gao, X., Ferreira, L.G.: Overview of the radiometric and biophysical performance of the MODIS vegetation indices. Remote Sens. Environ. **83**, 195–213 (2002)

24. Mutanga, O., Skidmore, A.K.: Narrow band vegetation indices overcome the saturation problem in biomass estimation. Int. J. Remote Sens. **25**, 3999–4014 (2004)

25. Dube, T., Mutanga, O., Sibanda, M., Shoko, C., Chemura, A.: Evaluating the influence of the Red Edge band from RapidEye sensor in quantifying leaf area index for hydrological applications specifically focussing on plant canopy interception. Phys. Chem. Earth, 1–8 (2017)

26. Basuki, T.M., Skidmore, A.K., van Laake, P.E., van Duren, I., Hussin, Y.A.: The potential of spectral mixture analysis to improve the estimation accuracy of tropical forest biomass. Geocarto Int. **27**, 329–345 (2012)

27. Carreiras, J.M., Vasconcelos, M.J., Lucas, R.M.: Understanding the relationship between aboveground biomass and ALOS PALSAR data in the forests of Guinea-Bissau (West Africa). Remote Sens. Environ. **121**, 426–442 (2012)

28. Schuster, C., Förster, M., Kleinschmit, B.: Testing the red edge channel for improving land-use classifications based on high-resolution multi-spectral satellite data. Int. J. Remote Sens. **33**, 5583–5599 (2012)

29. Adamczyk, J., Osberger, A.: Red-edge vegetation indices for detecting and assessing disturbances in Norway spruce dominated mountain forests. Int. J. Appl. Earth Obs. Geoinf. **37**, 90–99 (2014)

30. Datt, B.: Remote sensing of chlorophyll a, chlorophyll b, chlorophyll a+b, and total carotenoid content in eucalyptus leaves. Remote Sens. Environ. **66**, 111–121 (1998)

31. Le Maire, G., Franc̜ois, C., Dufrene, E.: Towards universal broad leaf chlorophyll indices using PROSPECT simulated database and hyperspectral reflectance measurements. Remote Sens. Environ. **89**, 1–28 (2004)

32. Mariotto, I., Thenkabail, P.S., Huete, A., Slonecker, E.T., Platonov, A.: Hyperspectral versus multispectral crop-productivity modeling and type discrimination for the HyspIRI mission. Remote Sens. Environ. **139**, 291–305 (2013)

33. Adam, E., Mutanga, O., Rugege, D.: Multispectral and hyperspectral remote sensing for identification and mapping of wetland vegetation: a review. Wetl. Ecol. Manag. **18**, 281–296 (2010)

34. Dube, T., Mutanga, O., Ismail, R.: Quantifying aboveground biomass in African environments: a review of the trade-offs between sensor estimation accuracy and costs. Trop. Ecol. **57**, 393–405 (2017)

35. Sibanda, M., Mutanga, O., Rouget, M.: Comparing the spectral settings of the new generation broad and narrow band sensors in estimating biomass of native grasses grown under different management practices. GIScience Remote Sens. **53**, 614–633 (2016)

36. Brief Industrial Report, (2015–16): MSME, Government of India. Source: http://dcmsme.gov.in/dips/2016-17/DIP.VELLORE.2015.16.pdf. Accessed 15 April 2017

37. Curran, P.J., Dungan, J.L., Gholz, G.H.: Exploring the relationship between reflectance red edge and chlorophyll content in slash pine. Tree Physiol. **7**, 33–48 (1990)

38. Zhu, L.H., Chen, Z.X., Wang, J.J., Ding, J.Z., Yu, Y.J., Li, J.S., Xiao, N.W., Jiang, L.H., Zheng, Y.R., Rimmington, G.M.: Monitoring plant response to phenanthrene using red edge of canopy hyperspectral reflectance. Mar. Pollut. Bull. **86**, 332–341 (2014)

39. Smith, K.L., Steven, M.D., Colls, J.J.: Use of hyperspectral derivative ratios in the red-edge to identify plant stress response to gas leaks. Remote Sens. Environ. **92**, 207–217 (2004)

40. Growth phases, Ricepedia. Source: http://ricepedia.org/rice-as-a-plant/growth-phases. Accessed 15 April 2017

Comparison of Biomass in Natural and Plantation Dry Forests in India

Supratim Guha, Teya Pal, Dishi S. Nath and Bhaskar Das

Abstract The aim of this study is to compare the amount of aboveground biomass (AGB) for different diameter classes between natural forest and a well maintained plantation forest. The comparison of AGB is conducted in two different ways. In the first method, the AGB is calculated as to per unit forest area (Mg/Ha). In the second one, the AGB is expressed in terms of per unit basal area of trees (Kg/cm^2). From the first method the amount of AGB in natural forests and plantation forests are 248 Mg/ha and 294 Mg/ha respectively. AGB count in plantation forest is 18.54% higher than that of natural forest with the first method. For the second method, two species (Neem and Sal) were taken among all as they were ruling in number for both natural and plantation forests. In case when the second method was applied, the amount of AGB in natural and plantation forests for neem were calculated 0.31 kg/cm^2 and 0.32 kg/cm^2 respectively. For Sal AGB values for natural and plantation forests are 0.44 kg/cm^2 and 0.47 kg/cm^2, respectively. The study shows that for both the species when the diameter is lesser, the difference in AGB between two forests is more and in case of larger diameter, the difference between two forests is smaller. This happens due to silvicultural maintenance exists in plantation forest which is most important for younger trees. But for the natural forest, no silvicultural practices take place.

Keywords Biomass · Carbon storage · Carbon sequestration · Natural forest
Plantation forest · Silvicultural practice

S. Guha (✉) · T. Pal · D. S. Nath · B. Das
Department of Environmental and Water Resources Engineering,
School of Civil and Chemical Engineering, Vellore Institute of Technology,
Vellore 632014, Tamilnadu, India
e-mail: supratim.guha2010@gmail.com

T. Pal
e-mail: pal0teya@gmail.com

D. S. Nath
e-mail: dishinath@gmail.com

B. Das
e-mail: bhaskar.ju@gmail.com

1   Introduction

Tropical forests are significant for carbon stock who delivers 40% of terrestrial carbon storage [1]. The tropical forests accumulate huge quantity of carbon in vegetation and soil. Along with that carbon exchange with atmosphere through the photosynthesis and respiration also takes place [2]. Aboveground biomass (AGB) estimation is one of the most important parts of carbon stock studies and global carbon equalization [3]. Global carbon balance equation is getting unbalanced. Carbon dioxide emission by India in 2015 is also continuing the trend of increase in emission by 2.47 billion tones, 5.1% more than the previous year [4]. The main consequences of deforestation due to anthropogenic usage need come with huge amount of carbon dioxide emissions which is a conventional climate altering factor. The problem looks huge and devastating when the result is even extinction of species [5]. Tropical deforestation in particular is responsible for 25% of carbon emissions indirectly or directly by humans [5–7]. So along with renewable technologies, carbon sequestration can also be proved for mitigating the climate change in a large extent as capturing and storing carbon are also needed for balancing the climate condition. An estimation of 193–229 Mg/ha in aboveground biomass is typically stored in tropical forest [8] which is proved to be twenty times greater than the yearly emissions from total combustion and change in land use [9]. On the other hand, reducing emissions from deforestation and forest degradation (REDD) has now become a major concern for United Nations Framework Convention on Climate Change [10–12]. The funding of REDD is in a confused situation whether the mechanism of funding should be traditional or eventual market-based [13].

The actual data inventory to express C pool was almost nonexistent and if not then it used to be overestimated [14]. Decades passed but now also solution regarding the abovementioned problem is transparently unsolved. The field data related to carbon sequestration measurement is not reliable as the rate of deforestation and accurate database on standing biomass is not available [15].

We explored comparison study on above-ground-biomass calculation for carbon storage measurement between natural forest and plantation forest. The formation and analysis of carbon models on global scale require field data for estimating forest biomass [2]. The most trust worthy technique of estimating carbon stock in a forest is through field data of the forest followed by the procedure of developing allometric relationships between AGB of a tree and trunk diameter of the tree [16–18]. The equation from Chave et al. (2005) is convenient only with accurate height of trees for allometric modeling [19]. But the accuracy comes inaccessible for tree-height measurement for closed-canopy of natural forest [20, 21]. So avoiding the controversies about biased estimation of AGB Chave et al. (2014) introduced a little more convenient equation for AGB estimation in terms of field data availability [22]. Study areas we explored come under dry forest. Our study is to provide some useful field inventory regarding the above ground biomass for carbon storage measurement for some particular species. Among the plant biomass elements i.e.

AGB, below ground biomass (BGB) and dead wood the AGB is the most significant for regulation of atmospheric carbon and it also contributes 60% of the total phyto mass [2]. So the AGB estimation comes as the most important for the carbon sequestration studies [3].

2 Materials and Methods

2.1 Description of the Study Area

Our first study area (Fig. 1) is Vellore Institute of Technology's (VIT) Woodstock which is situated at Vellore district in Tamil Nadu, India. This is a plantation forest which lies between 12° 58′ 7″N to 12° 58′ 16″N and 79° 9′ 19″E to 79° 9′ 31″E. It is situated in Vellore taluk. Another study area selected was Yelagiri forest which is a natural forest. It lies between 12° 35′ 18″N to 12° 35′ 30″N and 78° 38′ 1″E to 78° 38′ 16″E belongs to in Thirupathur taluk. When evapotranspiration exceeds the rainfall for a time duration less than 30 days in a forest then the forest is called a "wet forest" Here, in this case, heavy rainfall (3500 mm/year) takes place. Where the rainfall is between 1500 and 3500 mm/year, the forest is called "moist forest". When the rainfall is below 1500 mm/year, the forest will be called "dry forest" [19]. Annual rainfall of the Vellore is 954 mm [23]. As the annual rainfall in our study area is below 1500 mm/year therefore our study area is "dry forest". Monsoon starts here generally from June due to both the south western and north eastern monsoon branches [23]. The average annual temperature of plantation forest is 27.9 °C [24]. The natural forest average annual temperature is 23.1 °C [25] with the annual average rainfall of 929 mm [26].

2.2 Forest Inventory

Field survey was done in summer of 2017. During the field survey, all the trees were inventoried for both the forests. For both the forests, total height of the tree and trunk diameter had been measured. The procedure we selected for the trunk diameter measurement was the diameter of the trunk at breast (DBH) height. In case where deformities showed up at the breast height, we simply took the measurement of diameter above the trunk deformities. The previously published studies could not provide any detailed procedure on how the tree heights were measured without the help of any completely advanced technology. Some error always may occur while tree height measuring procedures take place in any closed-canopy [20, 21]. Non-destructive way of measuring tree height does not always give the accuracy as the destructive procedure comes with [22]. Some experiments are conducted
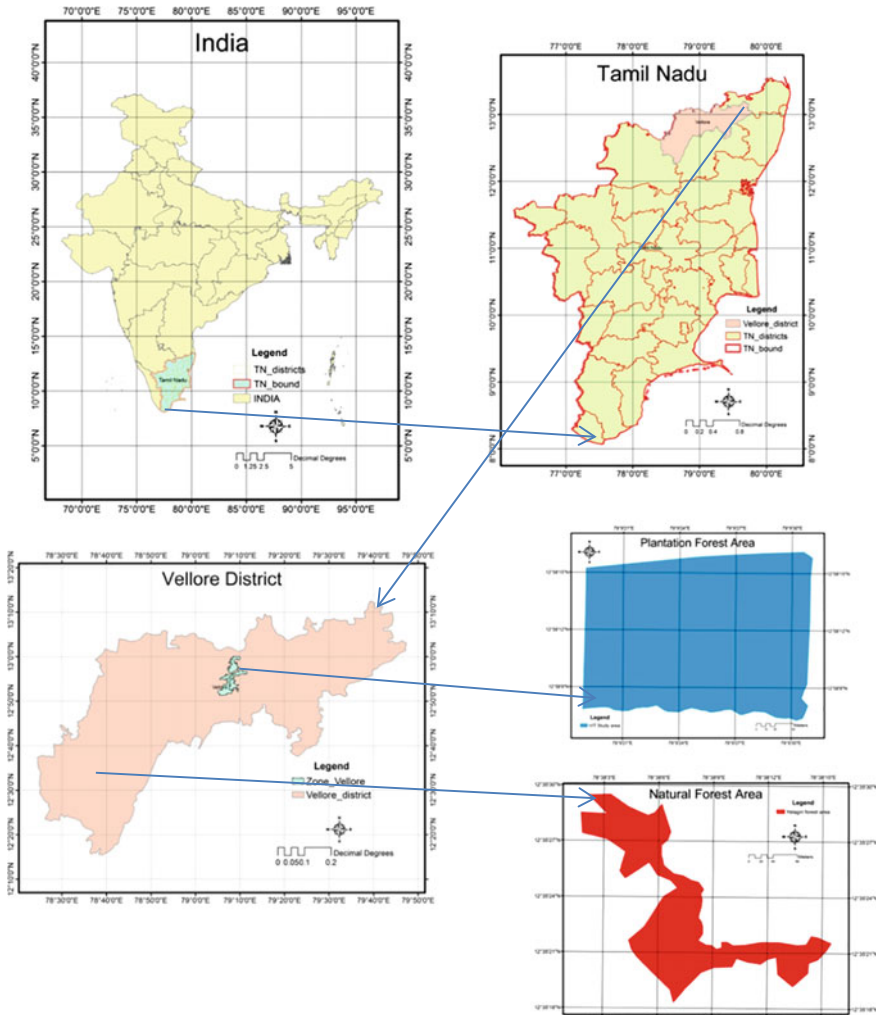
Fig. 1 Geographical location of the study sites

separately for leaves, branches and mass of the trunk until its first branching. But for dry forest areas like our study zone, it is difficult to measure leaf biomass for the deciduousness [22].

2.3 Analysis with Different Regression Models

To determine which model is more suitable for our study we had taken few models representing particular equation related to AGB formed by certain parameters.
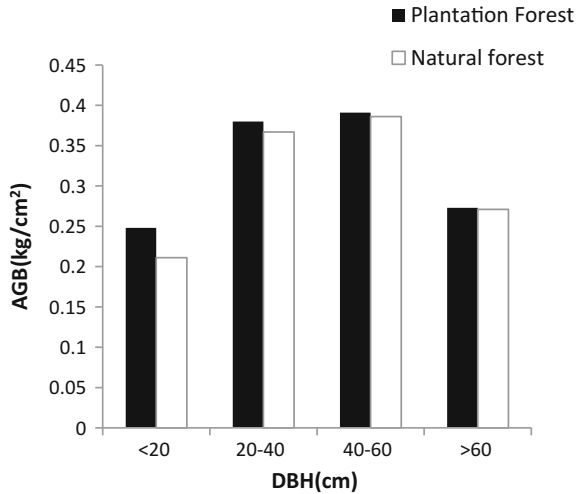
Fig. 2 Chart showing AGB distribution for both natural and plantation forests for different diameter ranges for Neem

Table 1 Different regression models to obtain the best fit for the estimation of biomass for both natural and plantation forests

Model	Equation	R^2	
		Natural forest	Plantation forest
Brown and Iverson [27]	$Y = 1.276 + 0.034(D^2H)$	0.84	0.87
Chambers et al. [28]	$Y = Exp[-0.37 + 0.33 \ln(D) + 0.933 \ln(D)^2\ 0.112 \ln(D)^3$	0.79	0.80
Chave et al. [29]	$Y = Exp(-2.00 + 2.42) \ln(D)$	0.88	0.83
Chave et al. [19]	$Y = \rho \times Exp[-0.667 + 1.784 \ln(D) + 0.207\ (\ln(D))^2 - 0.0281\ (\ln(D))^3]$	0.90	0.86
Chave et al. [19]	$Y = 0.112(\rho D^2H)^{0.916}$	0.97	0.97
Chave et al. [22]	$Y = 0.0559(\rho D^2H)$	0.96	0.96
Chave et al. [22]	$Y = 0.0673(\rho D^2H)^{0.976}$	0.97	0.99

From Table 1, we found R^2 for natural and plantation forests. For our study regarding data analysis, we had chosen the equation $Y = 0.673\ (\rho D_2H)^{0.976}$ formed by Chave et al. [22] as the R^2 are best by this equation for both the forests. These are 0.97 for natural forest and 0.99 for plantation forest. Where Y is the AGB in Kg, ρ is the wood density of the plant in gm/cm^3, D is the diameter of the plant at the breast height in cm and H is the height of the plant in m.

2.4 AGB Estimation

There were 25 types of species in the natural forest and 11 types of species in the plantation forest. The aboveground biomass are 248 and 294 Mg/ha for natural and plantation forests respectively. For detailed analysis of our study areas, it is more convenient to express AGB and carbon storage in terms of unit basal area than unit forest area.

After getting the best suitable equation comparing equations from Table 1, we proceeded with the equation attained for two species of trees who were governing in number for both the forests. They are Azadirachta Indica (common name "Neem") and Shorea Robusta (common name "Sal"). So, for the detailed analysis of AGB and carbon storage, we took different diameter ranges for both artificial and natural forests for AGB calculation for both the trees.

For carbon content calculation, the carbon is assumed to be taken as 50% of the total aboveground biomass [1, 15, 29–32].

Table 2 AGB calculations for different diameter ranges for Azadirachta Indica (Neem)

Plantation forest		Natural forest	
DBH (cm)	AGB (kg/cm^2)	DBH (cm)	AGB (kg/cm^2)
0–20	0.248	0–20	0.211
20–40	0.380	20–40	0.367
40–60	0.391	40–60	0.386
>60	0.273	>60	0.271

Table 3 Carbon storage for different diameter ranges for Azadirachta Indica (Neem)

Plantation forest		Natural forest	
DBH (cm)	Carbon storage (kg/cm^2)	DBH (cm)	Carbon storage (kg/cm^2)
0–20	0.124	0–20	0.105
20–40	0.190	20–40	0.183
40–60	0.195	40–60	0.193
>60	0.136	>60	0.135

Table 4 AGB calculation for different diameter ranges for Shorea Robusta (Sal)

Plantation forest		Natural forest	
DBH (cm)	AGB (kg/cm^2)	DBH (cm)	AGB (kg/cm^2)
0–20	0.471	0–20	0.382
20–40	0.474	20–40	0.459
40–60	0.467	40–60	0.469
>60	Not available	>60	0.437

Table 5 Carbon storage for different diameter ranges for Shorea Robusta (Sal)

Plantation forest		Natural forest	
DBH (cm)	Carbon storage (kg/cm^2)	DBH (cm)	Carbon storage (kg/cm^2)
0–20	0.235	0–20	0.191
20–40	0.237	20–40	0.229
40–60	0.233	40–60	0.234
>60	Not available	>60	0.2185

The trees with DBH (diameter at breast height) for above 60 m could not be found for the youngling plantation forest as the Sal had not grown that much to provide required diameter range when the field data was inventoried.

3 Results

3.1 AGB Distribution & Carbon Storage

Azadirachta Indica(Neem)

From the result of this study, the amounts of AGB in natural and plantation forests for Neem were calculated 0.31 and 0.32 kg/cm^2. As the results are reflecting, AGB (Fig. 2) and carbon storage (Fig. 3) for all the diameter classes are greater for the plantation forest. When the diameter range is less than 20 cm, the difference between AGB for natural forest and AGB for plantation forest is 17.53%. For the diameter range 20–40 cm, the difference is 3.54% and for diameter range 40–60 cm the difference is 1.29%. So when the diameter is lesser the difference in AGB between two forests are greater and in case of greater diameter the difference between two forests are lesser. For more than 60 cm diameter, the difference is very less, 0.73%. As the carbon storage is 50% of AGB (Tables 2 and 3), the plot of carbon storage for same diameter ranges and same number of trees follows the same pattern as of plot of AGB biomass distribution.

Shorea Robusta(Sal)

In case of Sal, AGB values for natural and plantation forests are 0.44 and 0.47 kg/cm^2, respectively. Now, for Sal when the diameter range is less than 20 cm, the difference between AGB for natural forest and AGB for the plantation forest is 23.29%. For the diameter range 20–40 cm, the above mentioned difference is 3.26% and for diameter range 40–60 cm the difference is 0.426%. So when the diameter is lesser the difference in AGB between two forests is greater and when the diameter is greater the difference in AGB between two forests is lesser. Similar to the Neem plant the carbon storage for Sal also is 50% of the AGB (Tables 4 and 5). Due to lack of data the difference between natural and plantation forests, difference in AGB for diameter above 60 cm cannot be shown (Fig. 4). Here also carbon storage plot (Fig. 5) is following the same pattern as of AGB distribution.

Fig. 3 Chart showing carbon
storage for both natural and
plantation forests for different
diameter ranges for Neem
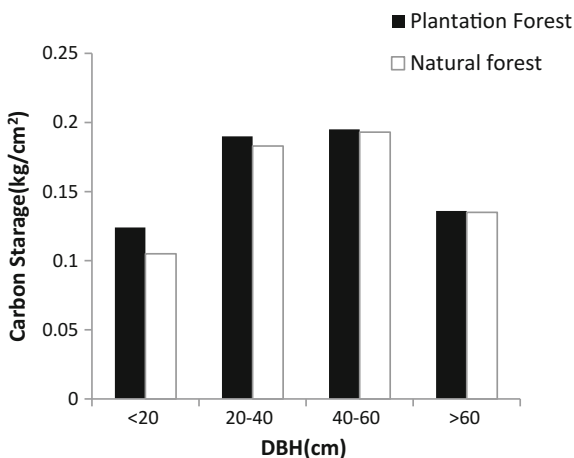
Fig. 4 Chart showing AGB
distribution for both natural
and plantation forests for
diameter ranges for Sal
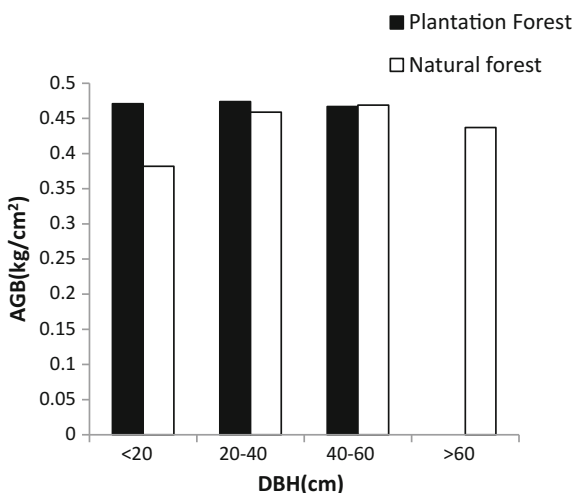
4   Discussions

The amount of carbon sequestration depends upon size of trees, type of forest, and
age of forest [33]. AGB value observed for natural forest in this study is 248 Mg/ha
a little less than 307 Mg/ha, the finding of Ramchandran et al. [35] on the tropical
evergreen forests in the eastern coast of Tamil Nadu, India [34]. However, the AGB
value of our study is very much less than 468 Mg/ha which is reported for the
tropical forest of semi evergreen type, situated in Western ghats of India reported by
Swamy [35]. AGB value of this study can be compared with the AGB value
275 Mg/ha which was reported by Terakunpisut et al. [34] by the study on the

Fig. 5 Chart showing carbon storage for both natural and plantation forests for different diameter ranges for Sal
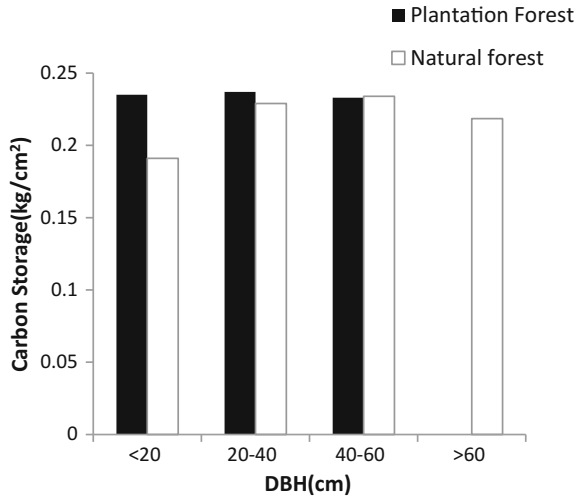
tropical rain forest in Thailand [33]. Brown and Lugo reported the AGB values of 260 Mg/ha for the tropical Africa, 150 Mg/ha for the total tropics, 170 Mg/ha for the forest of broadleaf type in tropical America and 215 Mg/ha for Asian tropic [36]. The obtained AGB value is much lower when it comes to not disturbed deciduous forests of Southern Appalachain Mountains [37]. The value of AGB of our study is little lesser than the AGB values found 304 Mg/ha for forests situated in Uttar Pradesh [38] and 261 Mg/ha which is for recovering tropical forest of Sal in eastern ghats of 10-year old [39]. The AGB value obtained for our study area is 248 Mg/ha for natural forest and 294 Mg/ha for the plantation forest which are less than 324 and 406 Mg/ha, respectively, found by Ratul et al. [2].

Higher amount of AGB is provided by mainly the trees having larger diameters but the trees of smaller diameters can also not be underestimated as they have the potential for high future carbon sequestration. The established fact is the forest has higher potential for carbon sequestration up to maturity depending on the type of forest but after being matured, the carbon sequestration amount is marginal [40].

5 Conclusion

In this study on Neem and Sal, the trees possessing smaller diameter are representing younger trees and the trees holding larger diameter are representing older trees. The difference in AGB between both natural and plantation forests is greater when the diameter range is smaller because silvicultural practices are predominating for younger trees and the difference in AGB between both the forests is lesser when diameter range is larger because silvicultural practices are very little effective for older tress. So this study concludes that silvicultural practices are more important

for younger trees. But in case of older trees, the effect of silvicultural practice seemed not to be that much important. Plantation forest has higher AGB than natural forest due to uniformity in arrangement and adaptation of silvicultural practices with a proper system of management.

References

1. Dixon, R.K., Brown, S., Houghton, R.A., Solomon, A.M., Trexler, M.C., Wisniewski, J.: Carbon pools and flux of global forest ecosystems. Science **263**, 185–190 (1994)
2. Baishya, R., Barik, S.K., Upadhaya, K.: Distribution pattern of aboveground biomass in natural and plantation forests of humid tropics in northeast India. Trop. Ecol. **50**, 295–304 (2009)
3. Ketterings, Q.M., Coe, R., van Noordwijk, M., Ambagau, Y., Palm, C.A.: Reducing uncertainty in the use of allometric biomass equations for predicting above-ground tree biomass in mixed secondary forests. For. Ecol. Manage. **146**(1–3), 199–209 (2001)
4. Olivier, G.J. (PBL), Janssens-Maenhout, G. (EC-JRC), Muntean, M. (EC-JRC), Jeroen, A.H. W., Peters (PBL): Trends in Global CO_2 Emissions: 2016 Report ©PBL Netherlands Environmental Assessment Agency the Hague, 2016 PBL Publication Number: 2315 European Commission, Joint Research Centre, Directorate Energy, Transport & Climate JRC Science for Policy Report: 103428 (2016)
5. IPCC (Intergovernmental Panel on Climate Change): Climate Change 2001: The Scientific Basis. Contribution of Working Group I to the Third Assessment Report of the Intergovernmental Panel on Climate Change. Cambridge University Press, Cambridge (2001)
6. Sala, O.E., Chapin III, F.S., Armesto, J.J., Berlow, E., Bloomfield, J., Dirzo, R., Huber-Sanwald, E., Huennke, L.F., Jackson, R.B., Kinzig, A., Leemans, R., Lodge, D.M., Mooney, H.A., Oesterheld, M., Poff, N.L., Sykes, M.T., Walker, B.H., Walker, M., Wall, D. H.: Global biodiversity scenarios for the year 2100. Science **287**, 1770–1774 (2000)
7. Thomas, C.D., Cameron, A., Green, R.E., Bakkenes, M., Beaumont, L.J., Collingham, Y.C., Barend, F., Erasmus, N., Ferreira de Siqueira, M., Grainger, A., Hannah, L., Hughes, L., Huntley, B., van Jaarsveld, A.S., Midgley, G.F., Miles, L., Ortega-Huerta, M.A., Peterson, A. T., Phillips, O.L., Williams, S.E.: Extinction risk from climate change. Nature **427**, 145–148 (2004)
8. Saatchi, S.S., Harris, N.L., Brown, S., Lefsky, M., Mitchard, E.T., Salas, W., Zutta, B.R., Buermann, W., Lewis, S.L., Hagen, S., Petrova, S., White, L., Silman, M., Morel, A.: Benchmark map of forest carbon stocks in tropical regions across three continents. Proc. Nat. Acad. Sci. USA **108**(24), 9899–9904 (2011). Epub 2011 May 31. https://doi.org/10.1073/pnas.1019576108
9. Friedlingstein, P., Houghton, R.A., Marland, G., Hackler, J., Boden, T.A., Conway, T.J., Canadell, J.G., Raupach, M.R., Ciais, P., Le Que´re´, C.: Update on CO2 emissions. Nat. Geosci. **3**, 811–812 (2010)
10. UNFCCC (United Nations Framework Convention on Climate Change): United Nations Framework Convention on Climate Change, Geneva, UNEP/WMO. Available at http://www.unfccc.int/ (1992)

11. UNFCCC (United Nations Framework Convention on Climate Change): Conference of the Parties, Third Session. Kyoto Protocol to the United Nations Framework Convention on Climate Change. FCCC/CP/1997/7/Add.1. Available at http://www.unfccc.int/ (1997)
12. UNFCCC (United Nations Framework Convention on Climate Change): Conference of the Parties, Eleventh Session. FCCC/CP/2005/L.2 Available at http://cdm.unfccc.int/ (2005)
13. Miles, L., Kapos, V.: Reducing greenhouse gas emissions from deforestation and forest degradation: global land-use implications. Science 320, 1454–1455 (2008)
14. Dadhwal, V.K., Nayak, S.R.: A preliminary estimate of biogeochemical cycle of carbon for India. Sci. Cult. 59(1), 9–13 (1993)
15. Ravindranath, N.H., Somashekhar, B.S., Gadgil, M.: Carbon flow in India forests. Clim. Change 35(3), 297–320 (1997)
16. Brown, S., Gillespie, A., Lugo, A.: Biomass estimation methods for tropical forests with applications to forest inventory data. Forest Science 35, 881–902 (1989)
17. Brown, S.: Estimating Biomass and Biomass Change of Tropical Forests: A Primer. FAO Forestry Paper 134, Food and Agriculture Organization, Rome (1997)
18. Clark, D.A., Brown, S., Kicklighter, D., Chambers, J.Q., Thomlinson, J.R., Ni, J.: Measuring net primary production in forests: concepts and field methods. Ecol. Appl. 11, 356–370 (2001)
19. Chave, J., Andalo, C., Brown, S., et al.: Tree allometry and improved estimation of carbon stocks and balance in tropical forests. Oecologia Ecosyst. Ecol. 145, 87–99 (2005). https://doi.org/10.1007/s00442-005-0100-x
20. Hunter, M.O., Keller, M., Vitoria, D., Morton, D.C.: Tree height and tropical forest biomass estimation. Biogeosciences Discuss. 10, 10491–10529 (2013)
21. Larjavaara, M., Muller-Landau, H.C.: Measuring tree height: a quantitative comparison of two common field methods in a moist tropical forest. Methods Ecol. Evol. 4, 793–801 (2013)
22. Chave, J., Rejou-Mechain, M., Burquez, A., et al.: Improved allometric models to estimate the aboveground biomass of tropical trees. Global Change Biol. 20, 3177–3190 (2014). https://doi.org/10.1111/gcb.12629
23. Rainfall data (Vellore), Geological Information. Source: http://www.velloreonline.com/Geologicalinfo.php. Accessed 25 Apr 2017
24. Temperature data (Vellore), Climate: Vellore. Source: https://en.climate-data.org/location/2185/. Accessed 25 Apr 2017
25. Temperature data (Yelagiri), Climate: Yelagiri. Source: https://en.climate-data.org/location/968045/. Accessed 25 Apr 2017
26. Rainfall data (Yelagiri), Climate: Yelagiri. Source: https://en.climate-data.org/location/968045/. Accessed 25 Apr 2017
27. Brown, S., Iverson, L.R.: Biomass estimates for tropical forests. World Resour. Rev. 4, 366–384 (1992)
28. Chambers, J.Q., dos Santos, J., Ribeiro, R.J., Higuchi, N.: Tree damage, allometric relationships, and aboveground net primary production in central Amazon forest. For. Ecol. Manage. 152, 73–84 (2001)
29. Chave, J., Rikra, B., Dubois, M.A.: Estimation of biomass in a neotropical forest of French Guiana: spatial and temporal variability. J. Trop. Ecol. 17, 79–96 (2001)
30. Brown, S., Lugo, A.E.: The storage and production of organic matter in tropical forests and their role in the global carbon cycle. Biotropica 14, 161–187 (1982)
31. Cannell, M.: Forest and the Global Carbon Cycle in the Past. Present and Future, European Forest Institute Report, Finland (1995)
32. Richter, D.D., Markewitz, D., Dunsomb, J.K., Wells, C.G., Stuanes, A., Allen, H.L., Ureego, B., Harrison, K., Bonani, G.: Carbon cycling in a loblobby pine forest: implication for the missing carbon sink and for the concept of soil. In: McFee, Kelly, J.L. (eds.) Carbon Forms and Function in Forest Soils, pp. 223–251. Soil Science Society of America, Madison, WI (1995)
33. Schroeder, P.: Carbon storage potential of short rotation tropical tree plantations. For. Ecol. Manage. 50, 31–41 (1992)

34. Terakunpisut, J., Gajaseni, N., Ruankawe, N.: Carbon sequestration potential in aboveground biomass of Thong pha phun national forest, Thailand. Appl. Ecol. Environ. Res. **5**, 93–102 (2007)

35. Ramachandran, A., Jayakumar, S., Haroon, R.M., Bhaskaran, A., Arockiasamy, D.I.: Carbon sequestration: estimation of carbon stock in natural forests using geospatial technology in the Eastern Ghats of Tamil Nadu, India. Curr. Sci. **92**, 323–331 (2007)

36. Swamy, H.R.: Study of Organic Productivity, Nutrient Cycling and Small Watershed Hydrology in Natural Forests and in Monoculture Plantations in Chikamagalur District, Karnataka, Sri Jagadguru Chandrashekara Bharti Memorial College, Sringeri, India (1989)

37. Brown, S., Lugo, A.E.: Biomass of tropical forests: a new estimate based on forest volume. Science **223**, 1290–1293 (1984)

38. Whittaker, R.H.: Forest dimensions and production in the Great Smoke Mountains. Ecology **44**, 233–252 (1996)

39. Singh, O., Sharma, D.C., Rawat, J.K.: Biomass and nutrient release in natural sal, eucalyptus and poplar plantations in Uttar Pradesh. Van Vigyan **30**, 134–140 (1992)

40. Behera, S.K., Misra, M.K.: Aboveground tree biomass in a recovering tropical sal (*Shorea robusta* Gaertn. F.) forest of Eastern Ghats. India Biomass Bioenergy **30**, 509–521 (2006)

Evaluation of Global Digital Elevation Model for Flood Risk Management in Perlis

Muhammad Faiz Pa'suya, Ami Hassan Md Din, Zulkarnaini Mat Amin, Kamaludin Mohd Omar, Amir Hamzah Omar and Noradila Rusli@Ruslik

Abstract In flood modelling process, Digital Elevation Models (DEMs) is a valuable tool in topographic parameterization of hydrological models. The release of the free-of-charge satellite based DEMs such as SRTM and ASTER prompted the accurate flood modelling process especially to propose flood mitigation in the Perlis region. In this research, the accuracy of SRTM DEM of spatial resolution 1 arc-sec and 3 arc-sec, as well as ASTER DEM are evaluated. The reference levels produced from GNSS observation and Earth Gravitational Model 1996 (EGM96), as well as local mean sea level are used to analyse the vertical accuracy of each GDEMs in Perlis, Malaysia. The total of 38 Benchmark (BM) and Standard Benchmark (SBM) around the Perlis region were observed by GNSS using static method and processed using TOPCON Tool software. A comparison with the local mean sea level height indicated that SRTM 1″ is the much greater absolute vertical accuracy with an RMSE of ±3.752 m and continued by SRTM 3″ and ASTER GDEMs where the obtained accuracy was ±4.100 and ±5.647 m, respectively. Also, by using orthometric height form the GNSS and EGM96 as reference elevation, the obtained accuracy was ±3.220, ±3.597, and ±5.832 m for SRTM 1″, SRTM 3″ and ASTER, respectively. Statistical results have also shown that

M. F. Pa'suya · N. Rusli@Ruslik
Green Environment & Technology (GREENTech), Centre of Study for Surveying
Science & Geomatics, Faculty of Architecture Planning & Surveying,
UniversitiTeknologi MARA Perlis Branch Arau Campus,
02600 Arau, Perlis, Malaysia

A. H. M. Din (✉) · Z. M. Amin · K. M. Omar · A. H. Omar
Geomatic Innovation Research Group (GIG), Faculty of Geoinformation
and Real Estate, Universiti Teknologi Malaysia, Johor Bahru, 81310 Johor, Malaysia
e-mail: amihassan@utm.my

A. H. M. Din
Geoscience and Digital Earth Centre (INSTEG), Faculty of Geoinformation
and Real Estate, Universiti Teknologi Malaysia, Johor Bahru, 81310 Johor, Malaysia

A. H. M. Din
Institute of Oceanography and Environment (INOS), Universiti Malaysia Terengganu,
Kuala Terengganu, Terengganu, Malaysia

SRTM 1″ has a good correlation with Hmsl and HGNSS where both correlations values are 0.9925, while the SRTM 3″ and ASTER show the correlation of 0.9873 and 0.9375.

1   Introduction

On the past few years, flash floods are becoming more common in the Perlis region and this situation has gained serious attention from the state government and federal, of which to propose a flood mitigation system in Perlis. Starting from 2005, followed by 2010 as well as in 2011, a series of serious floods events have hit the state and neighbouring state, Kedah. Two factors are believed to be the cause of this flood which are unusual rainfall distribution that causes water level of the rivers to increase and discharging water from Timah Tasoh Water Dam. Under flood risk mitigation plan to minimize the effect of flash flood in Perlis, the government has proposed to develop a flood bypass canal and a limestone tunnel to discharge the water during heavy rain into the Perlis River and finally into the Straits of Malacca.

In flood mitigation, identifying potential flash flood prone areas is one of the key solutions. By predicting the prone areas, a better plan management can be implemented by the authorities for the mitigation of the flood [1]. In order to accurately identify the flood prone areas, detailed elevation data are crucial [2]. In general, Digital Elevation Models (DEMs) providing basic information about the terrain relief [3] and in flood modelling process, DEMs is a valuable tool for the topographic parameterization of hydrological models There are various ways of generating DEMs such as photogrammetric method, topographic surveys, total station and GPS, airborne laser scanning, etc. However, the acquisition of high-resolution and quality elevation data over large area is costly and a challenging task. The release of the free-of-charge global DEMs (GDEMs) such as Global 30 Arc-Second Elevation (GTOPO30) and Global Multi-resolution Terrain Elevation Data 2010 (GMTED2010) as well as satellite based DEMs such as from Shuttle Radar Topography Mission (SRTM) and Advanced Space borne Thermal Emission and Reflection Radiometer (ASTER) prompted the accurate flood modelling process. However, the errors of GDEMs usually vary geographically due to the terrain condition [4] and any error in the DEMs will affect the accuracy of flood mitigation.

Therefore, the accuracy of GDEMs should be analysed to find out the most accurate accessible GDEMs [5, 6]. Therefore, the main objective of this study is to evaluate the accuracy of vertical GDEMs for the region in Perlis, situated between 100° 7′ 16.25″E–100° 22′ 11.77″E and 6° 15′ 38.24″N–6° 43′ 34.55″N as shown in Fig. 1 by comparing the elevation from each GDEMs and orthometric height derived from GNSS/EGM96 (HGNSS) and local mean sea level height (Hmsl).

Fig. 1 Study area

2 Global Digital Elevation Models (GDEMs)

The goal of this study is to analyse the error of three GDEMs that are Advanced Space borne Thermal Emission and Reflection Radiometer ASTER GDEM of spatial resolution 3 arc-sec, SRTM GDEM of spatial resolution 1 arc-sec and SRTM GDEM of spatial resolution 3 arc-sec. Details about the GDEMs are listed in Table 1 and all the DEMs can be downloaded via USGS website (http://earthexplorer.usgs.gov/).

2.1 ASTER GDEMs

The first version ASTER GDEM released in June 2009 was produced jointly by the Ministry of Economy, Trade, and Industry (METI) of Japan and the United States National and Space Administration (NASA). The GDEMs cover from 83° north latitude to 83° south, encompassing 99% of Earth's landmass. The first version of ASTER GDEM has been updated to second version (ASTER GDEMV2) and

Table 1 GDEM data input characteristics

DEM	Spatial resolution	Horizontal datum	Vertical datum
SRTM	1 arc-sec ($\sim$ 30 m), 3 arc-sec ($\sim$ 100 m)	WGS84	EGM96
ASTER	1 arc-sec ($\sim$ 30 m)	WGS84	EGM96

released on October 17, 2011. Compared to the first version which generated using stereo-pair images collected by the ASTER instrument, the ASTER GDEMV2 adds 260,000 additional stereo-pairs. Provided at a one (1) arc-sec resolution ($\sim$30 m), this GDEMs are referenced to WGS84 and EGM96 geoid model.

2.2 SRTM GDEM

The SRTM GDEM was generated from Shuttle Radar Topography Mission (SRTM), jointly by National Aeronautics and Space Administration (NASA), the National Imagery and Mapping Agency (NIMA), the German space agency (DLR) and Italian space agency (ASI). The GDEMs covers from 60°N to 56°S [7] and provides 3″ ($\sim$90 m) and 1″ (about 30 m) for any point on the earth. In the overall, the absolute and relative accuracy of SRTM GDEM is 20 and 16 m, respectively [7, 8]. As ASTER GDEMs, the horizontal and vertical reference of the SRTM DEMs is the WGS84 and EGM96 geoid, respectively.

3 Vertical Accuracy Assessment

In order to analyse the error and accuracy of GDEMs, the interpolated heights from GDEMs (HDEM) are compared with levelled heights (Hlevelling) and orthometric height derived from GNSS levelling (HGNSS/level). Krigging approach in SURFER (http://www.goldensoftware.com/) was used to interpolate the HDEM. In this study, a total number of 38 GNSS observations have been conducted on the Standard Benchmark (SBM) and Benchmark (BM) over the Perlis region (see Fig. 2) using static method with 2 h observation period, 1 s sampling rate and above 15° for elevation mask. The fieldwork was performed using TOPCON GR5 and Hyper GA. Two Malaysia Real-Time Kinematic GNSS Network (MyRTKnet) station were used as control stations and GNSS observation data were processed using TOPCON Tool software. Figure 3 illustrates the distribution of the GNSS levelling data for this study. The mean sea level value for each BM and SBM are provided by JUPEM. The ellipsoidal height derived from GNSS observation were transformed to orthometric height using EGM96 whereby consistent with the vertical datum of both GDEMs [9].

The relationship between orthometric and ellipsoidal heights is shown in Fig. 4 and the following relationship was used to transform ellipsoidal height to orthometric elevation using EGM96 geoid model:
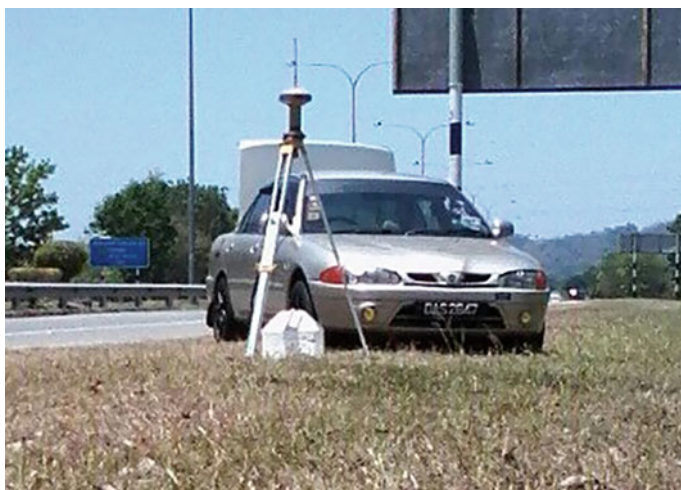
Fig. 2 GNSS observation on benchmark in the Perlis region
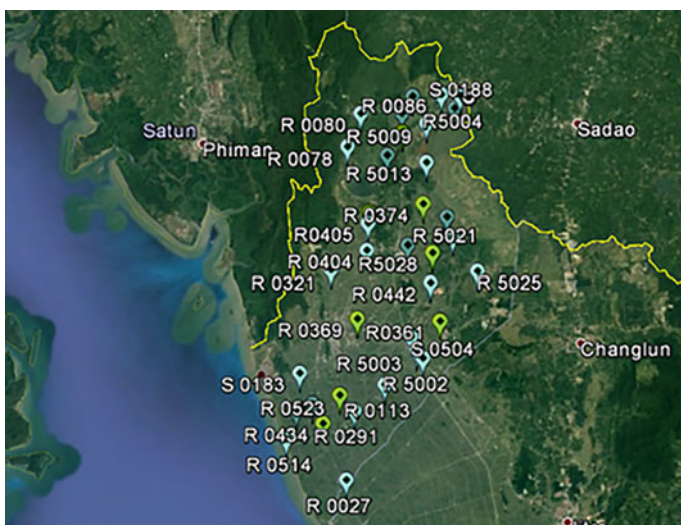
Fig. 3 Distribution of validation point
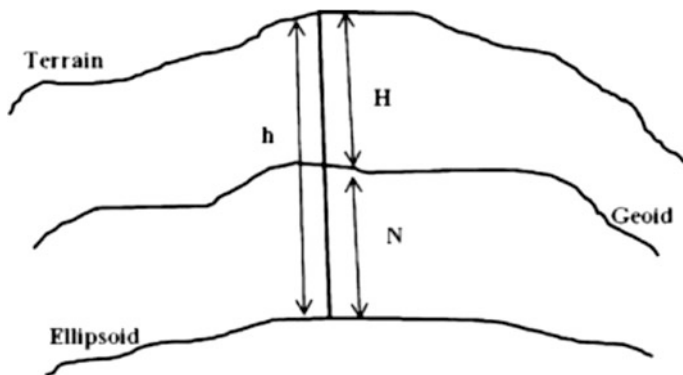
Fig. 4 Relationship between orthometric and ellipsoidal heights

$$H = h - n \tag{1}$$

where;

H = orthometric height,
h = WGS84 ellipsoid height and
N = EGM96 geoid undulation

The vertical accuracy is computed by Mean Error (ME) and vertical Root Mean Square Error (RMSE) by the following equation:
Mean Error (ME)

$$MRE = |Z^* - Z|/n \tag{2}$$

Root Mean Square Error (RMSE)

$$RMSE = \mathrm{sqrt}\left(\sum |Z^* - Z|\right)/n \tag{3}$$

where

Z^* = GNSS derived orthometric height,
Z = elevation from GDEMs and
n = total number of points

4 Results and Discussion

The discrepancies between orthometric heights derived from GNSS (HGNSS) and local mean sea level height (Hmsl) with ASTER GDEM, SRTM 1″ and SRTM GDEM 3″ for the 38 validation point are shown in Fig. 5. In general, the contour of SRTM GDEM was smoother than ASTER GDEM. There are large differences in the north and east of Perlis between ASTER GDEM and GNSS, as well as local mean sea level. Meanwhile, large discrepancies in the southeast and northeast of the Perlis can be seen from SRTM GDEM.

The summary of statistical analysis for the comparison of GDEMs with Hlevelling and HGNSS is shown in Figs. 6 and 7. A comparison with the local mean sea level height (Hlevelling) shows that SRTM GDEM of spatial resolution 1 arc-sec performs well compared with SRTM GDEM of spatial resolution 3 arc-sec and ASTER GDEM. As shown in Fig. 5, the mean error values and RMSE for SRTM 1″ were 3.268 and ±3.752 m, respectively when compared with the local mean sea level value.

Meanwhile SRTM GDEM with 3″ resolution showed better vertical accuracy than ASTER GDEM where the mean error values between the local mean sea level and the GDEM was 3.399 m. The estimated accuracy for the SRTM 3″ in the Perlis region is ±4.100 m, which is much better than with ASTER GDEM. ASTER GDEM exhibited the largest residual error where the RMSE value for the ASTER GDEM was calculated as ±5.657 m. The comparison of three GDEMs with orthometric height also exhibited that SRTM GDEM of spatial resolution 1 arc-sec performs well compared with SRTM GDEM of spatial resolution 3 arc-sec and ASTER GDEM with mean error values between HGNSS and SRTM 1″ GDEM was 3.220 m, respectively. From the statistical computation for the absolute vertical accuracy of SRTM 1″ elevations data gave the values of ±5.94 m.

Meanwhile, the absolute accuracy of SRTM 3″ GDEM is ±3.597, which is lower than SRTM 1″, but is believed to be better than ASTER GDEM. The mean error values between SRTM 3″ elevation and HGNSS were 2.795 m, respectively. The accuracy of ASTER GDEM elevations is the lowest of all the other GDEMs. The basic statistical analysis for these GDEMs highlighted that the accuracy of ASTER in the Perlis region of which is ±5.832 m.

The graphic plots of the Hmsl and HGNSS against the SRTM and ASTER DEMs is shown in Fig. 8. The results indicate that the three datasets show strong positive correlations with the Hmsl and HGNSS elevations. The results shows that SRTM 1″ has a good correlation with Hmsl and HGNSS where both correlation values are 0.9925, while the SRTM 3″ and ASTER show the correlation of 0.9873 and 0.9375, respectively as shown in Table 2.
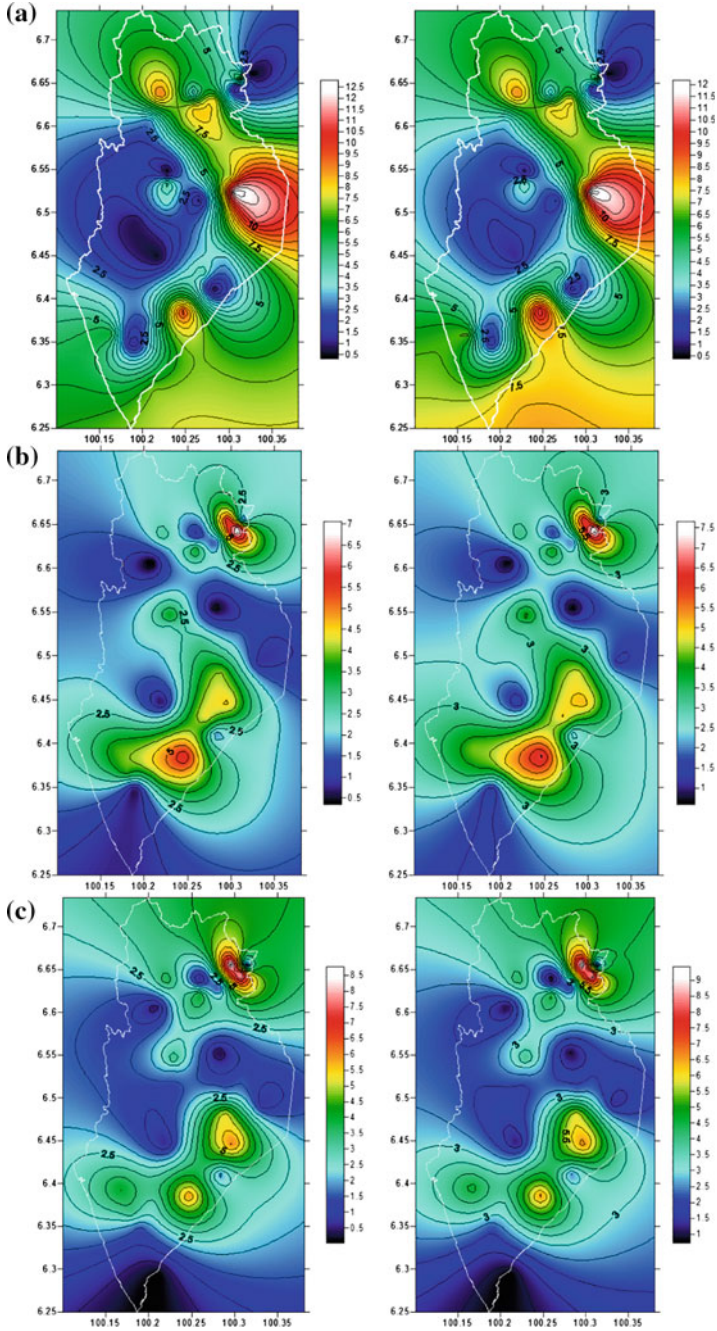
Fig. 5 Height errors between the orthometric height (left) and the H$_{levelling}$ (right) with **a** ASTER, **b** SRTM 1″ and **c** SRTM 3″ (unit in metre)
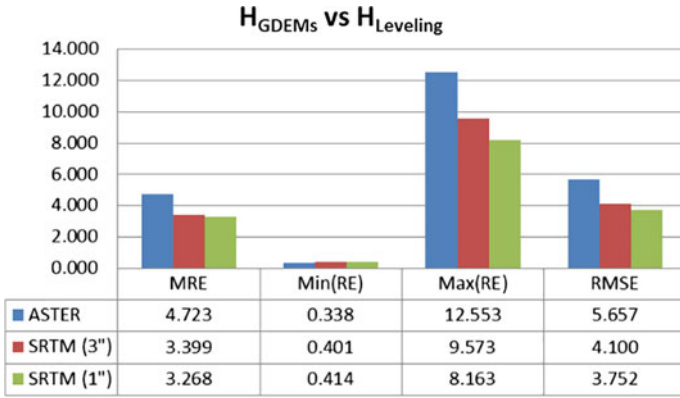
Fig. 6 Elevation differences between the local mean sea level height and GDEMs (units in metre)
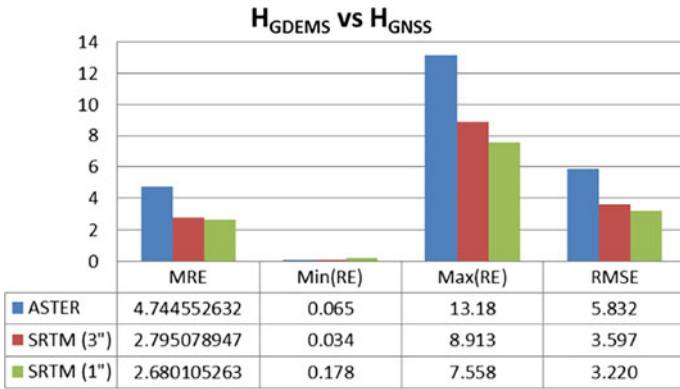
Fig. 7 Elevation differences between the orthometric height and GDEMs (units in metre)
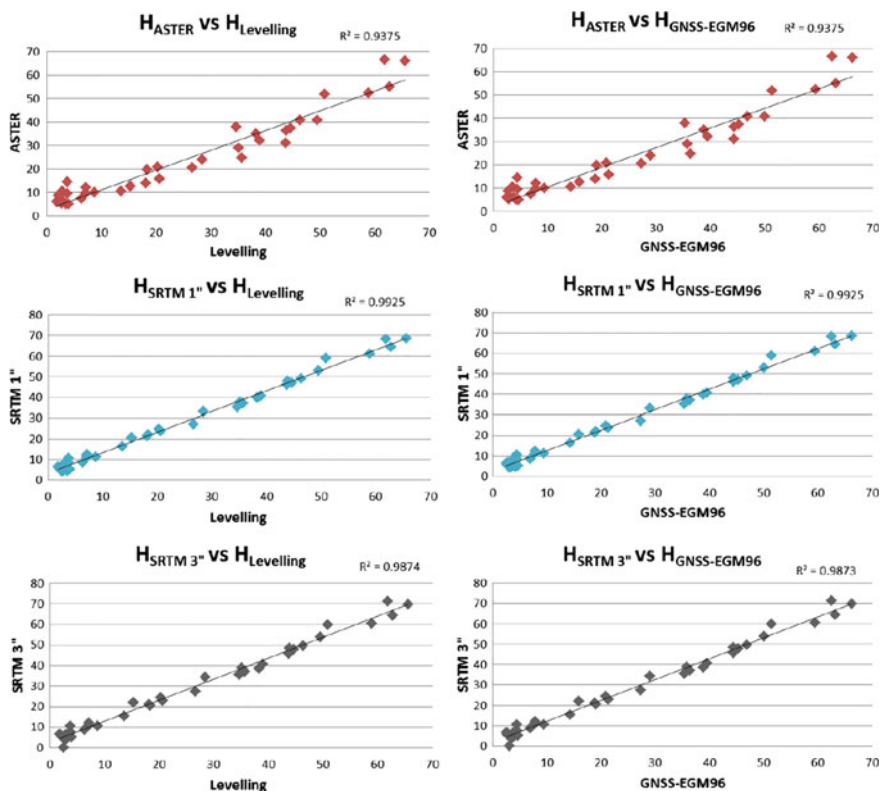
Fig. 8 Correlation between used DEMs with orthometric height and local mean sea level height

Table 2 Linear correlation, R^2 between $H_{LEVELLING}$, H_{GNSS} and GDEMs

No.	Model	GDEMs versus $H_{Levelling}$	GDEMs versus H_{GNSS}
1.	SRTM 1″	0.9925	0.9925
2.	SRTM 3″	0.9874	0.9873
3.	ASTER	0.9375	0.9375

5 Conclusion

Two free GDEMs; were investigated for two references elevation data that are orthometric height derived from GNSS observation and local mean sea level. Generally, the statistical computation for these DEMs highlights that the accuracy of SRTM 1″ is significantly more accurate compared to other GDEMs. By using the local mean sea level height as a reference for the elevation, the statistic shows that the accuracy of ASTER, SRTM 3″ and SRTM 1″ data for the Perlis region has

given the values of ± 5.657, ± 4.100 and ± 3.752 m, respectively. Meanwhile, the validation with orthometric height highlighs that the accuracy of SRTM 1″ is much better with RMSE of ± 3.220 m and ASTER GDEM exhibits the largest residual error with a RMSE of ± 5.832 m. The results from this investigation are crucial in order to determine the best GDEM for further analysis on flood risk management studies in the Perlis region.

References

1. Sarhadi, S., Soltani, S., Modarres, R.: Probabilistic flood inundation mapping of ungauged rivers: linking GIS techniques and frequency analysis. J. Hydrol. **458**(459), 68–86 (2012)
2. Garg P. K.: The role of satellite derived data for flood inundation mapping using gis. ISPRS—Int. Arch. Photogram. Remote Sens. Spat. Inf. Sci. XL-3/W3, 235–239 (2015)
3. Guth, P.: Geomorphometry from SRTM: Comparison to NED. Photogram. Eng. Remote Sens. **72**, 269–277 (2006)
4. Holmes, K.W., Chadwick, O.A., Kyriankidis, P.C.: Error in USGS 30-meter digital elevation model and its impact on terrain modelling. J. Hydrol. **233**, 154–173 (2000)
5. Kiamehr, R., Sjöberg, L.E.: The qualities of Iranian gravimetric geoid models versus recent gravity field missions. Stud. Geophys. Geod. **49**, 289–304 (2005)
6. Gorokhovich, Y., Voustianiouk, A.: Accuracy assessment of the processed SRTM-based elevation data by CGIAR using field data from USA and Thailand and its relation to the terrain characteristics. Remote Sens. Environ. **104**(4), 409–415 (2006)
7. Rabus, B., Eineder, M., Roth, A., Bamler, R.: The shuttle radar topography mission—a new class of digital elevation models acquired by spaceborne radar. J. Photogramm. Remote Sens. **57**, 241–262 (2003)
8. Smith, B., Sandwell, D.: Accuracy and resolution of shuttle radar topography mission data. Geophys. Res. Lett. **30**(9), 1467 (2003)
9. Hirt, C., Filmer, M.S., Featherstone, W.E.: Comparison and validation of the recent freely available ASTER-GDEM ver1, SRTM Ver4.1 and GEODATA DEM-9 s Ver3 Digital Elevation Models over Australia. Aust. J. Earth Sci. **57**, 337–347 (2010)

Land Use and Land Cover Mapping Using Rule-Based Classification in Karbala City, Iraq

Ahmed Abdulkareem Ahmed, Bahareh Kalantar, Biswajeet Pradhan, Shattri Mansor and Maher Ibrahim Sameen

Abstract Land use and land cover are important and useful geographic information system (GIS) layers that have been used for a wide range of geospatial applications. These layers are usually generated by applying digital image processing steps for a satellite image or images captured from an aircraft. Several methods are available in literature to produce such GIS layers. Image classification is the main method that has been used by many researchers to produce thematic maps. In the current study, a decision tree was used to develop rulesets at object level. These rules were applied and a thematic map of Karbala city was produced from SPOT image. The overall accuracy of the classification image was 96% and the kappa index was 0.95. The results indicated that the proposed classification method is effective and can produce promising results.

Keywords Land use/cover · Decision tree · GIS · Remote sensing

1 Introduction

Land use and land cover (LULC) are the basic layers for many geospatial applications including urban planning, change detection [1], environmental studies and risk assessments. Image classification is the main method used to produce such maps in GIS environments using remotely sensed data. In general, there are two types of image classification: pixel-based classification and object-based image

A. A. Ahmed · B. Kalantar · B. Pradhan (✉) · S. Mansor · M. I. Sameen
Department of Civil Engineering, Faculty of Engineering,
Universiti Putra Malaysia, 43400UPM Serdang,
Selangor Darul Ehsan, Malaysia
e-mail: Biswajeet24@gmail.com; Biswajeet.Pradhan@uts.edu.au

B. Pradhan
Faculty of Engineering and Information Technology, School of Systems,
Management and Leadership, University of Technology Sydney,
Building 11, Level 06, 81 Broadway, Ultimo, NSW 2007 PO Box 123 Australia

analysis (OBIA). In OBIA, image pixels are first grouped into a non-overlapped homogenous regions using a proper segmentation algorithm [2]. Then image objects are classified using some quantitative attributes. There are two ways to classify image objects which are: supervised and rule-based methods. In rule-based, several rulesets are developed to extract LULC features from remote sensing images. These rules either can be developed by expert opinions or using an automatic way such as by using decision tree algorithm.

In literature, several studies have been explored image classification using object-based classification methods and high-resolution satellite images such as SPOT, Worldview and QuickBird. Herold et al. [3] used OBIA classification method to classify an IKONOS image in an urban area. Through several image processing steps, a thematic map of nine classes was generated and evaluated. The overall accuracy of 79% indicated the effectiveness of the approach for classifying high resolution images. In addition, Myint et al. [4] compared pixel-based classification method with OBIA by using a very high resolution satellite images and an area of urban environment. The study revealed that OBIA outperforms pixel-based approaches. The object-based classifier achieved a high overall accuracy (90.40%), whereas the most commonly used decision rule, namely maximum likelihood classifier, produced a lower overall accuracy (67.60%).

This study develops a set of data-driven rules for classifying a SOPT image covers a part of Karbala city located in Iraq. A decision tree algorithm was used to generate ruleset that extract five LULC features from the image. Finally, a thematic map of Karbala city was generated by combining the classification image with several GIS layers extracted from GIS database of Karbala.

2 Study Area

The study area is the centre of Karbala city located in the middle part of Iraq. Karbala city is located about 100 km (62 mi) southwest of Baghdad. Karbala is the capital of Karbala Governorate, and has an estimated population of 572,300 people (2003). Figure 1 shows the geographic location of Karbala city. This subset was used to generate a thematic map for the area and to evaluate the ruleset developed in the current research.

3 Dataset

In this study, a SPOT 5 image was used to produce a thematic map of Karbala city. The spatial resolution of the image is 5 m which is considered as a suitable resolution for producing thematic maps at small scales. Figure 2 shows the SPOT image which covered main parts of Karbala city. The area is almost bare land, wet land and also contains water bodies, agriculture, and urban areas.
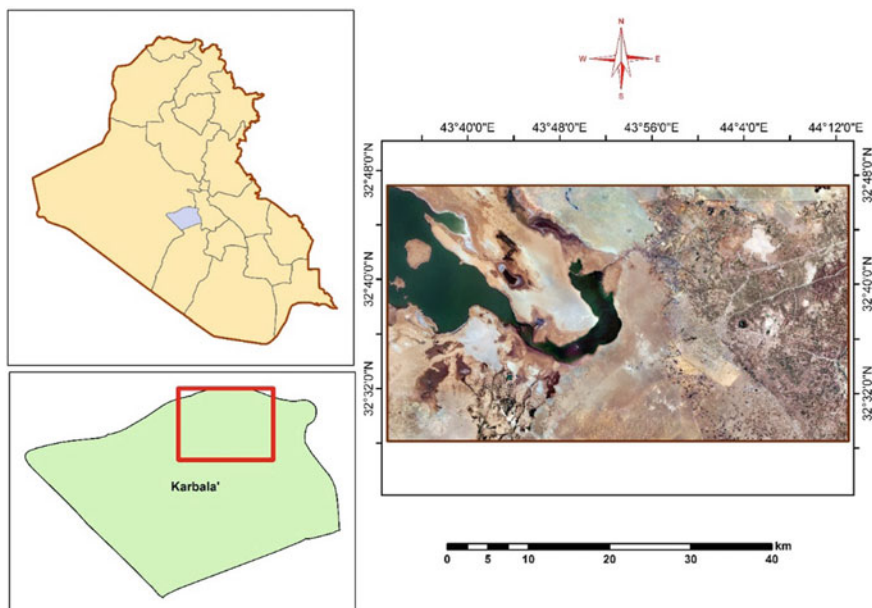
Fig. 1 The geographic location of the study area used in the current research
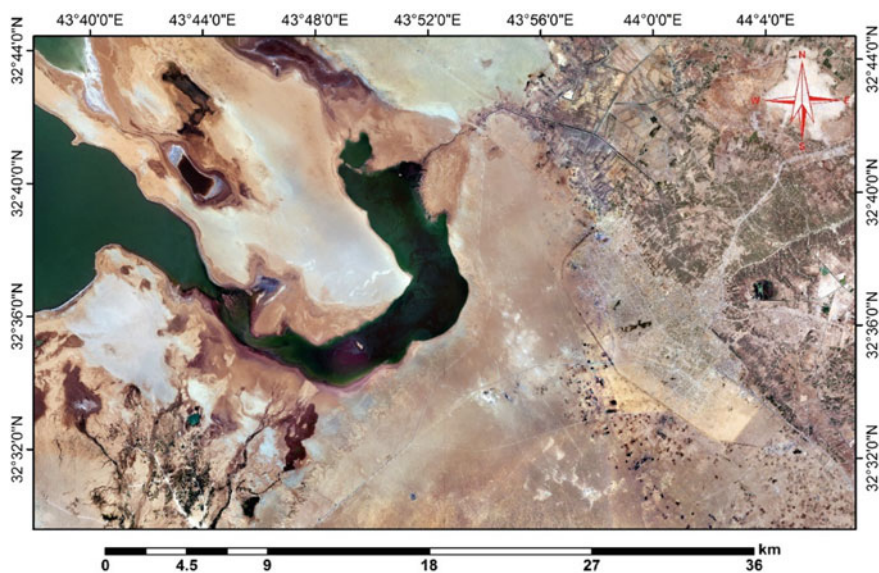
Fig. 2 The SPOT 5 image of Karbala city used in this study for LULC mapping

4 Methodology

The overall proposed methodology for LULC mapping using OBIA approach is presented in Fig. 3. First, the SPOT image was pre-processed to correct the radiometric and geometric errors existed in the image. These errors usually occur because of the malfunction errors or sensor degradation. Therefore, removing these errors was an important step before developing ruleset and generating classification maps for the study area. After that, the corrected image was segmented by using a well-known multiresolution segmentation algorithm. Then, the several samples from each LULC class were selected and a set of rule was developed by decision tree algorithm. Next, the image objects were classified based on the ruleset developed by decision tree. The results were evaluated by calculation the confusion matrix and accuracy indicators include overall accuracy and kappa index. Finally, a thematic map of Karbala was generated by combining the classification image and GIS layers.

4.1 Image Preprocessing

It is important to make sure that the remote sensing data is accurate and contains less noise before performing any image processing steps. In this study, the SPOT
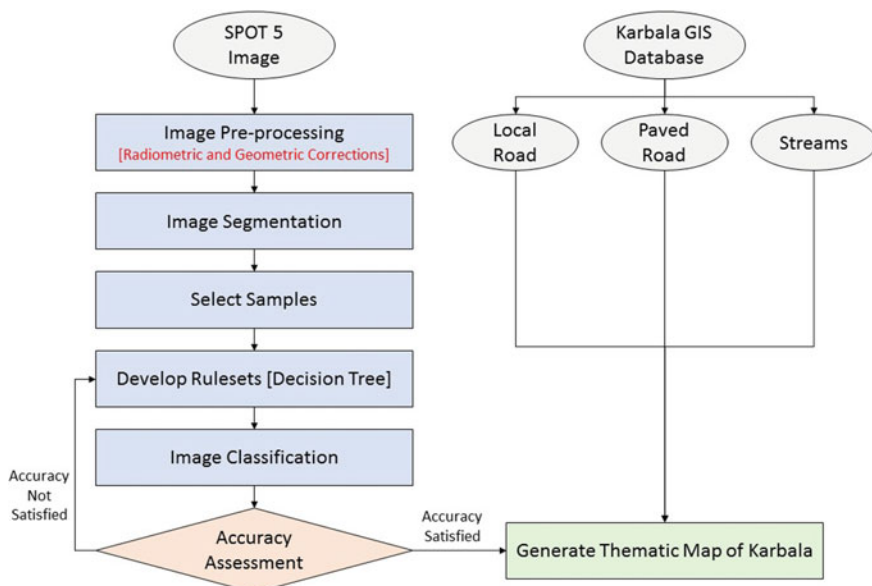
Fig. 3 The overall flow chart of proposed method for producing a thematic map for Karbala city

image was pre-processed in two main steps. The first step was to convert the digital numbers of the original image into reflectance. This step reduced the effects of sun light, atmospheric layer, and improved the spectral information of the image. In the second step, the image was geometrically corrected and projected with a proper projection system. This allowed to combine the GIS layers with the classified image for creating the final thematic map of Karbala. The SPOT image is ready to process after applying the pre-processing steps. The processed SPOT image was then used for image segmentation and image classification.

4.2 Image Segmentation

Once the SPOT image was prepared for analysis, the image was segmented into a non-overlapped and homogenous regions using multiresolution segmentation algorithm. This process was implemented in recognition software. In this algorithm, three parameters were required, namely, scale, shape and compactness. These parameters were selected by trial and error method. After several trails, it was found that scale of 100, shape and compactness of 0.5 were the best to use with our study area and dataset. Based on these values of user-defined parameters of multiresolution segmentation algorithm, the image was segmented and image objects were produced for classification process.

4.3 Ruleset Development Through Decision Trees

Based on the image objects created by segmentation process, it was possible to automatically develop ruleset by decision tree algorithm. First, several samples for each LULC class were selected and exported into excel sheets along with their quantitative attributes. These quantitative attributes were then used for classification. Ruleset were developed by using a cross-validation accuracy assessment technique implemented in Weka software. The ruleset was then generated after the application of decision tree in the software. The results of the ruleset that classify the five LULC classes are presented in Fig. 4.

5 Results

5.1 Image Segmentation

The results of image segmentation are shown in Fig. 5. In this figure, it is clear how the image objects were created from image pixels. The image pixels were grouped
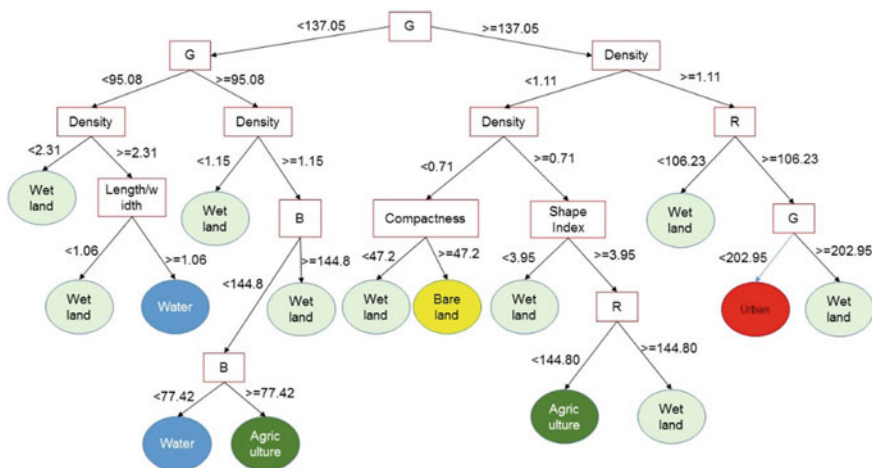
Fig. 4 Rulesets proposed for LULC mapping of SPOT image in Karbala city
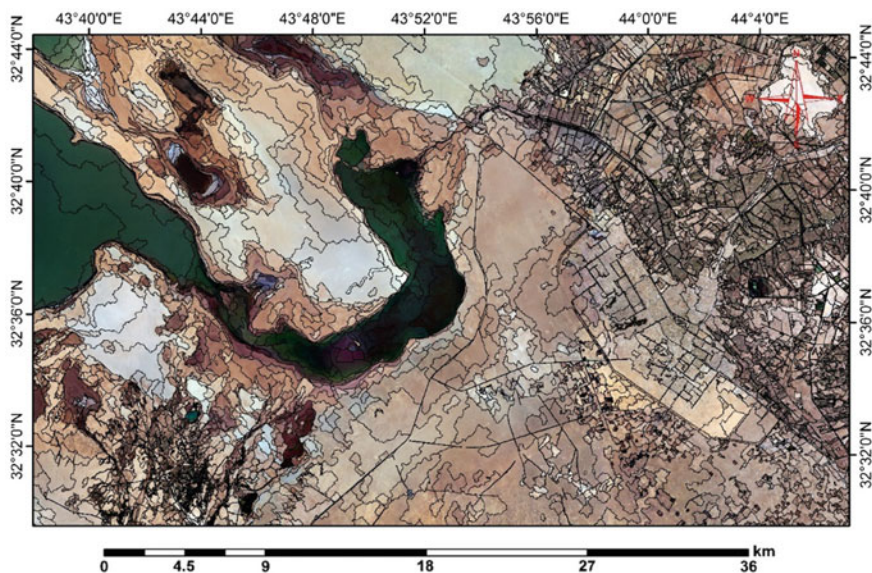
Fig. 5 Rulesets proposed for LULC mapping of SPOT image in Karbala city

and the objects were created based on spectral and spatial information of the SPOT image. These objects which are in vector format can be converted into GIS layer and used for further applications. In the current study, they were used to classify the image and produce the thematic map of Karbala city. These image objects contain several attributes calculated for each object using mathematical formulas.
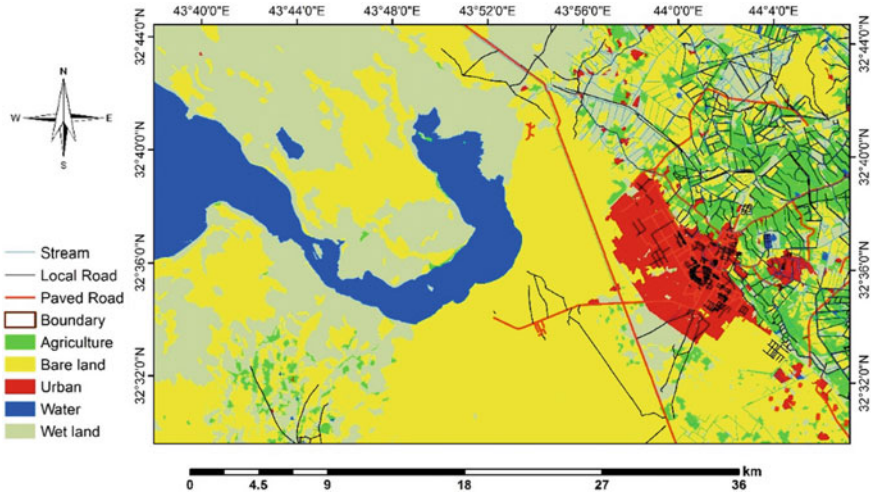
Fig. 6 The thematic map of Karbala city produced by the application of developed rulesets in GIS

The density, compactness and the ration of length over width are some examples of spatial attributers, the spectral bands of SPOT image (R, G, B) are the example for spectral attributes. These attributes were used to develop ruleset and classify the image for producing the thematic map of Karbala city.

5.2 Classification

The results of image classification are presented in Fig. 6. The thematic map of Karbala shown in Fig. 6 consisted of five LULC classes. These classes are water, wet land, bare land, agriculture and urban. If we compare these results of image classification and the original image, we can observe that the most of the image objects were accurately classified. The most parts of the area were classified as bare land, wet lands. The urban area was located in the east of the study area. These urban areas are almost residential areas. On the other hand, agricultural area located at the east part of the study area, however, they are distributed from the north to the south of that areas. Water bodies usually situated at the west part of the city. The wet and bare lands were distributed almost in the all parts of the study area.

5.3 Accuracy Assessment

The results of image classification were evaluated by calculating the confusion matrix. This matrix was then used to calculate the overall accuracy, kappa index,

Table 1 The confusion matrix and accuracy indicators that were calculated to evaluate the proposed classification framework

User class/sample	Wetland	Water	Bare land	Agriculture	Urban	Sum
Confusion matrix						
Wetland	425	0	2	0	3	430
Water	0	123	0	1	0	124
Bare land	6	0	456	5	15	482
Agriculture	4	3	2	321	0	330
Urban	1	0	4	0	81	86
Unclassified	0	0	0	0	0	0
Sum	436	126	464	327	99	
Accuracy						
Producer	0.974	0.9761	0.9827	0.9816	0.818	
User	0.9883	0.992	0.946	0.972	0.941	
Hellden	0.9815	0.984	0.964	0.9771	0.8785	
Short	0.9637	0.968	0.9306	0.955	0.778	
KIA per class	0.9641	0.974	0.9741	0.9762	0.8067	
Totals						
Overall accuracy	0.9683					
Overall accuracy	0.9573					

user and producer accuracy. Table 1 shows the confusion matrix along the estimated accuracies. In this figure, we can see that most of the LULC classes were extracted accurately and effectively. The overall accuracy was estimated as 96% and the kappa index was 0.95. On the other hand, the highest and lowest user accuracy was 0.99 (water) and 0.94 (urban), respectively.

6 Conclusion

This study produced a thematic map for Karbala city using SPOT 5 satellite image. Through several image pre-processing steps, the SPOT image was first prepared for actual analysis. The image was then segmented and exported into GIS. Ruleset was developed in Weka by using a decision tree algorithm. Ruleset was then applied and the image objects were classified. The classification image was combined with several GIS layers including roads and streams created the final thematic map of Karbala city. The results were also validated using overall accuracy which was over 95%. The results indicated the robustness of the proposed approach for classifying SPOT image and producing a thematic map that is useful for several geospatial applications.

References

1. Zhou, W., Troy, A., Grove, M.: Object-based land cover classification and change analysis in the Baltimore metropolitan area using multitemporal high resolution remote sensing data. Sens. **8**(3), 1613–1636 (2008)
2. Blaschke, T.: Object based image analysis for remote sensing. ISPRS J. Photogramm. Remote Sens. **65**(1), 2–16 (2010)
3. Herold, M., Scepan, J., Müller, A., Günther, S.: Object-oriented mapping and analysis of urban land use/cover using IKONOS data. In: 22nd Earsel Symposium Geoinformation for European-Wide Integration, pp. 4–6, 2002)
4. Myint, S.W., Gober, P., Brazel, A., Grossman-Clarke, S., Weng, Q.: Per-pixel versus object-based classification of urban land cover extraction using high spatial resolution imagery. Remote Sens. Environ. **115**(5), 1145–1161 (2011)

Frontier in Three-Dimensional Cave Reconstruction—3D Meshing Versus Textured Rendering

Mohammed Oludare Idrees and Biswajeet Pradhan

Abstract Underground caves and their specific structures are important for geomorphological studies. This paper investigates the capabilities of a new modelling approach advanced for true-to-life three-dimensional (3D) reconstruction of cave with full resolution scan relative to 3D meshing. The cave was surveyed using terrestrial laser scanner (TLS) to acquire high resolution scans. The data was processed to generate a 3D-mesh model and textured 3D model using sub-sampled points and full resolution scan respectively. Based on both point and solid surface representation, comparative analysis of the strengths and weaknesses of the two approaches were examined in terms of data processing efficiency, visualization, interactivity and geomorphological feature representation and identification. The result shows that full scan point representation offers advantage for dynamic visualization over the decimated xyz point data because of high density of points and availability of other surface information like point normal, intensity and height which can be visualized in colour scale. For the reconstructed surface, mesh model is better with respect to interactivity and morphometric but 3D rendering shows superiority in visual reality and identification of micro detail of features with high precision. Complementary use of the two will provide better understanding of the cave, its development and processes.

Keywords Terrestrial laser scanning · Cave · 3D model · Virtual reality
Geomorphology · Geovisualization

M. O. Idrees · B. Pradhan (✉)
Department of Civil Engineering, Faculty of Engineering,
Universiti Putra Malaysia, 43400 UPM Serdang, Selangor Darul Ehsan, Malaysia
e-mail: Biswajeet24@gmail.com; Biswajeet.Pradhan@uts.edu.au

B. Pradhan
School of Systems, Management and Leadership, Faculty of Engineering
and Information Technology, University of Technology Sydney,
Building 11, Level 06, 81 Broadway, Ultimo, NSW 2007 PO Box 123 Australia

1029

1 Introduction

The study of cave, its geomorphological processes and features have advanced understanding the events that have occurred underground during Earth's history over geologic timescale through the interaction of nature, animals and man. First and most important step in cave investigation is to produce digital replica of the cave in its exact three-dimensional geometry. In recent years, 3D model of a number caves has been generated using laser scanning surveys. Digital representation of enclosed surfaces from sampled points has been a subject of extensive research [1–4].

Most of the algorithms for freeform surface reconstruction employ triangular 3D mesh (tetrahedron) using topological data structure that partition the input *xyz* coordinates into regular polygonal mesh made up of assemblage of vertices, edges and faces. In cave where multiple elevation values occur at the same *xy* positions, generating polygonal model is a little more complicated and time consuming due to limitation of the computer systems in handling large volume of data acquired [5]. The usual approach is to decimate the data to a size that the computing capacity can efficiently convert into polygonal mesh based on Delaunay tetrahedrization [6, 7]. Meshing generates surface model that replicates the cave in its true 3D geometry but at low resolution.

Understanding the speleogenesis and use of any cave in the past requires detail true-to-life perception of the space in all dimensions. Since the work of [8], several investigations have been conducted to improve identification of detail features in the cave by taking advantage of laser scanning technology, usually in combination with short-range photogrammetry for 3D documentation [9–11]. However, the use of laser scanning and digital photogrammetry for virtual reality cave modelling is challenging. How to manage illumination variation in the photos, finding exact match between the photos and the geometric model, and handling the volume of data acquired are the main issues with this approach [8]. Besides, the procedure requires several manual operations and editing. Recently, Idrees and pradhan [12] introduced textured 3D modelling of cave based on the geometric data and intensity value using full resolution scan, a deviation from mesh-dependent cave reconstruction. This paper presents comparative assessment of the two approaches in terms of visualizing cave structure and its geomorphological features.

2 Laser Scanning Survey and Point Cloud Processing

In July 2014, Gomantong cave was surveyed using FARO Focus3D laser scanner [13]. The network of cave system intersects a 300 m thick tower-like limestone hill that sits within the 3000 hectares Sabah Forest Reserve (1180 04′E and 50 32′N). By road, the forest reserve is about 34 km south of Sandakan and about 26 km east
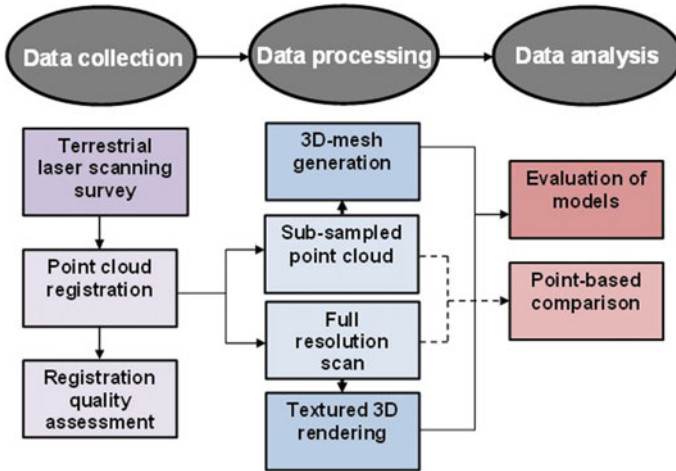
Fig. 1 Methodological workflow diagram

from the state capital, Kota Kinabatangan [14]. Schematic flow of the data processing and analysis steps is presented in Fig. 1.

Before the laser scanning survey, data collection plan was made, considering the general configuration of the cave to locate the best scan positions for good overlap and determine the scanning angle and scan resolution. The cave was scanned at ¼ scan resolution mode which allows recording 244,000 points/s.

From the two weeks of field work, a total of 203 scans amounting to over 6.09 billion points (∼38.0 GB) and RGB photograph. However, only the scans representing the upper level cave (Simud Putih) were processed. Data processing task started with scan alignment to obtain a global point cloud from the different scans. This was done in FARO SCENE-5.5 (www2.faro.com/downloads/training/Software) using the iterative closest point (ICP) [15] algorithm. The registration quality produced root mean square error of 0.0044 (4.4 mm) RMSE which is less than the 6 mm point spacing. This was followed by cleaning, filtering of the point clouds to remove noise and unwanted points [16] and exporting at two resolution scales as ASTM E57 File [17]—one for mesh generation and the other for textured 3D model.

3 Data Presentation and Analysis

3.1 Point-Based Visualization

The data was analysed with the sub-sampled and full resolution scan. During export from FARO SCENE, the aligned scans were decimated by sampling every 7th point

to optimize processing time [18]. Then, the decimated scans were imported to CloudCompare [19], a free and open source software, where they were merged into a single discontinuous point cloud of the cave. Furthermore, the resulting merged data was spatially sub-sampled using a horizontal and vertical distance spacing of 5 cm between points. The second dataset employs the full resolution scan.

The resulting point cloud is xyz representation of the cave surface that documents the exact dimensions, morphology and all the details of the walls. Nevertheless, point cloud does not offer continuous surface depiction of the cave for morphological structure and features. Figure 2 illustrates point visualization of a section of the cave's main hall. The point data provides far better information about the cave, in quantity and reliability, than the data obtained from traditional topographic surveys.

From the point model, basic metric measurements such as extraction of dimensional data (linear and angular, slopes) and cross sections (vertical and horizontal) can be obtained. Unlike the *xyz* point representation (Fig. 2a), availability of additional information such as point orientation (normal direction), height and intensity value (Fig. 2b–d) in the full scan data provides powerful dynamic visualization that enhances interpretation of the cave's channel morphology. The translation of these geometric and surface reflective properties into colours effective analytic tool makes visualizing and interpreting the 3D point representation of the cave easier. For example, major structural features are easily detectable by using colours to render the points in the point representation.
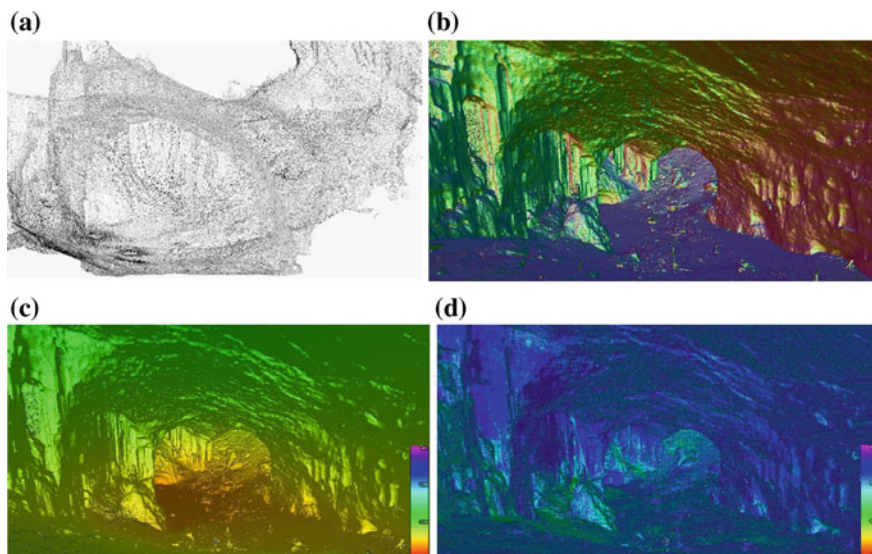
Fig. 2 Point cloud based representation of the cave using **a** decimated and **b–d** full resolution scan visualization specifying colour of points based on—**b** their normal direction **c** point height and **d** intensity value

3.2 Meshing Versus Textured 3D Models

Digital representation of the cave in 3D geometry was produced using the sub-sampled point and full resolution scan, respectively. First, 3D meshing was done in MeshLab 1.3.4BETA [20] using Poisson Surface Reconstruction algorithm. MeshLab is open source software for point cloud processing, advance mesh generation and editing. The meshing process considers the xyz coordinates of each point which makes it more suitable to model complex three-dimensional surfaces. Poisson surface reconstruction converts the point normal into solid 3D surface by defining a scalar function that best matches the vector field to build fitting iso-surface [1, 21]. The mesh model comprises of triangles, each with a face bounded by a set of three vertices (Fig. 3).

The surface obtained with Poisson surface reconstruction has a variable detail level depending on the input parameter of the octree depth. Here, octree depth of 10 generated 825,451 vertices and 1,650,604 faces. The choice of the octree depth was informed by compromise between level of details, visual reality and real-time interaction with the model [1, 16]. The meshing process produced digital model of the cave's structure and the complex irregular formations at coarse level (Fig. 4).

Advances in computational efficiency of point cloud processing software and 3D modelling capability are bringing a new dimension into cave investigation [12]. The textured 3D rendering was accomplished in Autodesk ReCap360 student license package [22]. ReCap360 creates complex 3D model with real-world visualization by combining the *xyz* point cloud with intensity information or RGB photograph (Fig. 5). The package computationally optimizes input files by indexing to its native
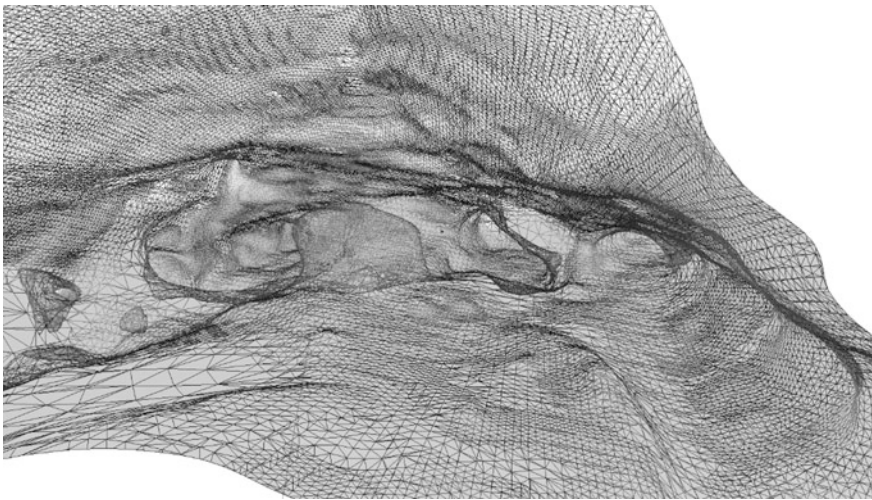
Fig. 3 3D mesh model generated in MeshLab v1.3.4BETA
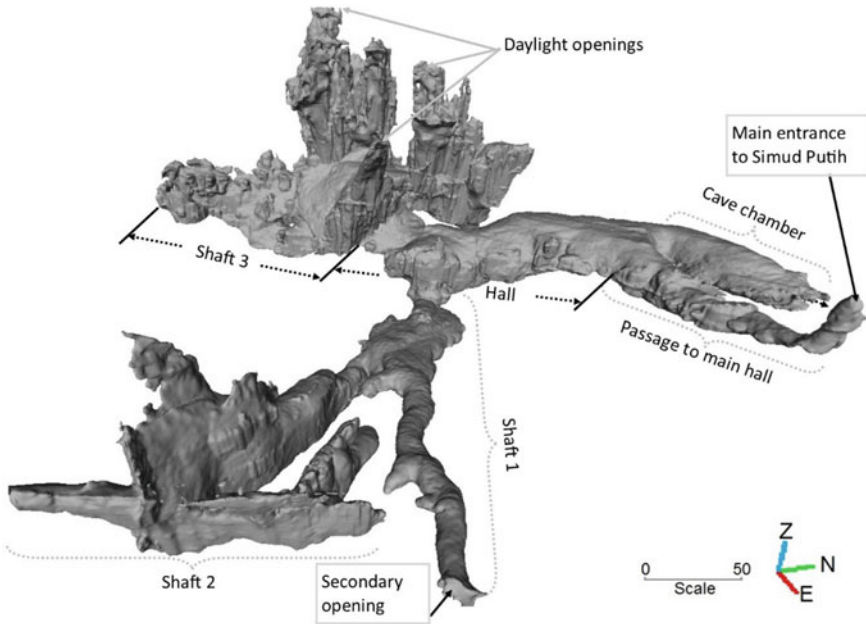
Fig. 4 General passage network structure of the upper section of Gomantong caves
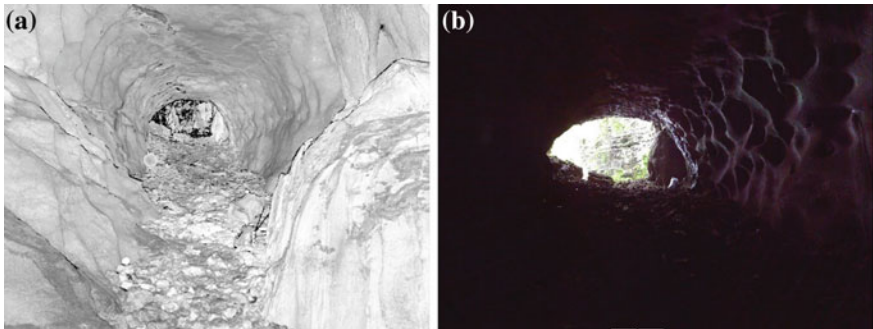
Fig. 5 Visualizing textured 3D models of cave interior close to the entrance of Shaft-1 where light outside the cave penetrates—**a** intensity and **b** RGB photograph

RCP file format for efficient processing, modelling and interactive visualization. It considers points normal and their vector fields to create watertight solid 3D surface.

One of the advantages of high-resolution texture 3D model is that it allows precise measurement of fine surface details down to 1 mm accuracy which is possible with mesh model (Fig. 6). It also permits capturing the degree of
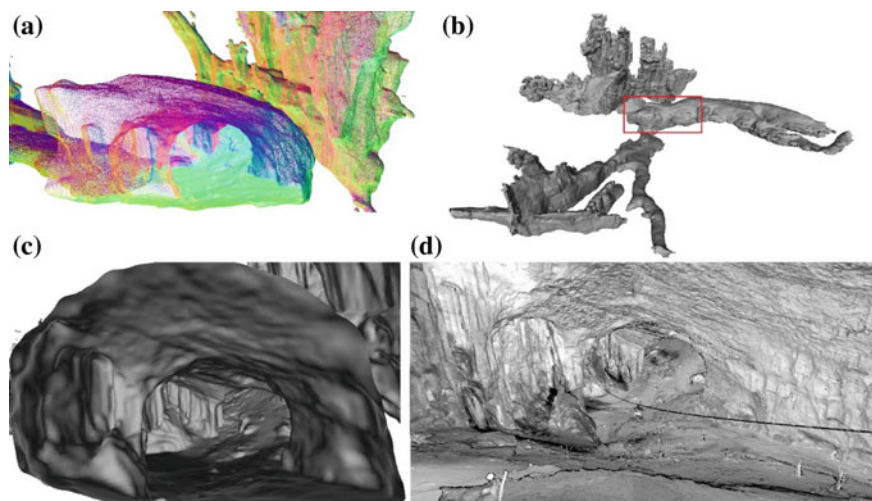
Fig. 6 Comparison of passage interior **a** triangular mesh **b** upper cave section **c** mesh model and **d** texture 3D rendering. The rectangular box in **3b** shows the display interior section

complexity of surface irregularities including the meso- and micro-morphological features and offers complete natural feel of the cave interior. Texturing with greyscale intensity image makes it possible to identify fine geologic rock details, swiftlet birds and bats, cave arts/engraving, etc. Structurally, it is possible to examine and quantify evolving phenomena within the conduit. A virtual tour of the cave reveals many phreatic and epiphreatic erosive features such as scallop, fluvial and torrential deposits, talus, flowstone, dripstone, gravity induced breakdown on the cave floor (Fig. 5a) and avens in the ceiling. It equally reveals old rock surfaces from recent ones which explain the condition and continuous process of passage deformation. All these are not possible with RGB photographic-based rendering (Fig. 5b) due to darkness in the cave.

3.3 Comparative Assessment

Exploiting the overlap and complementarities of the two modelling approaches, as highlighted in Table 1, will certainly deepen our knowledge about cave formation and development.

Table 1 Comparative assessment of meshing and textured 3D rendering

	Factors considered	Mesh model	Textured 3D model
1.	Processing time	Reasonably short, a matter of few hours	Takes several hours to days to load, index and render the point data
2.	Interactivity with model	Interaction with the model is efficient and in real-time	Interaction is much slower
3.	Navigation	Navigation is constraint to a particular pattern	Offers dynamic and multiple navigation modes such as real and 3D views
4.	Virtual reality	Not possible	Provides high resolution true-to-life visualization
5.	Feature detail/ identification	With sparse xyz points, only the general cave morphology is represented	Micro, meso and macro features can be identified and measured in the model
6.	Morphometry	Most suitable for quantitative measurements (volumetric, passage surface area, profile and sectional drawings, distance, slope, etc.)	Not efficient for quantitative measures

4 Conclusion

Texture 3D model shows superiority over mesh model, particularly in terms of visual perception and identification. This new approach is a progressive step that will assist scientists to visualize the cave interior with better understanding of the geomorphological structures and unfolding events. It reveals good outcropping condition and unique geological information like vertical and overhanging slopes. On the other hand, the mesh model is efficient for deriving morphometric and interactive navigation of the cave system generally. Comparative analysis reveals that the geometry and geomorphology of the cavities can be well understood by combining the potentials of the two models. Perhaps, such synergistic data exploration may allow linking the morphology of the conduits with the cave processes.

References

1. Silvestre, I., Rodrigues, J.I., Figueiredo, M.J.G., Veiga-Pires, C.: Cave chamber data modeling and 3D web visualization. Proc. Int. Conf. Inf. Vis. 468–473, (2013). https://doi.org/10.1109/iv.2013.103

2. Kanaya, I., Kadobayashi, R., Chihara, K.: Three-dimensional modelling of Shofukuji burial chamber. In: Seventh international conference on virtual systems and multimedia, pp. 113–120. (2001). https://doi.org/10.1109/vsmm.2001.969662

3. Roncat, A., Dublyansky, Y., Spötl, C., Dorninger, P.: Full-3D Surveying of Caves: A Case Study of Märchenhöhle (Austria). In: Marschallinger, R., Zobl, F. (eds.) IAMG 2011 proceedings: Mathematical Geosciences at the Crossroads of Theory and Practice, pp. 1393–1403, Salzburg, Austria, September 5–9 2011. https://doi.org/10.5242/iamg.2011.0074

4. Cosso, T., Ferrando, I., Orlando, A.: Surveying and mapping a cave using 3D laser scanner: the open challenge with free and open source software. ISPRS Arch. Photogramm. Remote Sens. Spat. Inf. Sci. **XL-5**, 181–186 (2014). https://doi.org/10.5194/isprsarchives-xl-5-181-2014

5. Höfle, B., Rutzinger, M.: Topographic airborne LiDAR in geomorphology: a technological perspective. Zeitschrift für Geomorphol. Suppl. Issues **55**(2), 1–29 (2011). https://doi.org/10.1127/0372-8854/2011/0055S2-0043

6. Fabio, R.: From point cloud to surface: the modeling and visualization problem. Int. Arch. Photogramm. Remote Sens. Spat. Inf. Sci. **34**, W10 (2003)

7. Idrees, M.O., Pradhan, B.: A Decade of modern cave surveying with terrestrial laser scanning: a Review of sensors, method and application development. Int. J. Speleol. **45**(1), 71–88 (2016). https://doi.org/10.5038/1827-806X.45.1.1923

8. El-Hakim, S. F., Fryer, J., Picard, M.: Modeling and visualization of Aboriginal rock art in the Baiame Cave. Proc. XXth Congr. Int. Soc. Photogramm. Remote Sens. 12–23 July 2004 Istanbul, Turkey. Comm. V, Work. Gr. V/2, pp. 990–995, 2004

9. Gonzalez-Aguilera, D., Rodriguez-gonzalvez, P., Mancera-taboada, J., Muñoz-nieto, A., Herrero-pascual, J., Gomez-lahoz, J.: Application of non-destructive techniques to the recording and modelling of palaeolithic rock art, In: Laser Scanning, Theory and Applications, Chau-Chang Wang, Ed. InTech, 2011, pp. 305–326. DOI https://doi.org/10.5772/14567

10. Gonzalez-Aguilera, D., Muñoz, a.L., Lahoz, J.G., Herrero, J.S., Corchón, M.S.m García, E.: Recording and modeling paleolithic caves through laser scanning. In: Proc. Int. Conf. Adv. Geogr. Inf. Syst. Web Serv. GEOWS 2009, 19–26, (2009). https://doi.org/10.1109/geows.2009.7

11. Lerma, J.L., Navarro, S., Cabrelles, M., Villaverde, V.: Terrestrial laser scanning and close range photogrammetry for 3D archaeological documentation: the Upper Palaeolithic Cave of Parpalló as a case study. J. Archaeol. Sci. **37**, 499–507 (2010). https://doi.org/10.1016/j.jas.2009.10.011

12. Idrees, M.O., Pradhan, B.: Characterization of macro-and micro-geomorphology of cave channel from high-resolution 3d laser scanning survey: case study of gomantong cave in sabah, malaysia. In: Savas, K., Mualla, C.C. (eds.) Cave Investigation, pp. 3–24. InTechOpen (2017). doi:http://dx.doi.org/10.5772/intechopen.69084

13. McFarlane, D., Roberts, W., Buchroithner, M., Van Rentergem, G., Lundberg, J., Hautz, S.: Terrestrial LiDAR-based automated counting of swiftlet nests in the caves of Gomantong, Sabah, Borneo. Int. J. Speleol. **44**(2), 55–60 (2015). https://doi.org/10.5038/1827-806X.40.1.2

14. Idrees, M.O., Pradhan, B., Buchroithner, M.F., Shafri, H.Z.M., Bejo, S.K.: Assessing the transferability of a hybrid Taguchi-objective function method to optimize image segmentation for detecting and counting cave roosting birds using terrestrial laser scanning data. J. Appl. Remote Sens. **10**(3), 1–16 (2016)

15. Besl, P., McKay, N.: A method for registration of 3-D Shapes. IEEE Trans. Pattern Anal. Mach. Intell. **14**(2), 239–256 (1992). https://doi.org/10.1117/1.JRS.10.035023
16. Canevese, E.P., Forti, P., Tedeschi, R.: New acquisition, 3D modeling, and data used methods: the laser scanning survey of retiberio cave, 16th International congress of speleology, **2**, 340–345 (2013)
17. Huber D.: The ASTM E57 File Format for 3D Imaging Data Exchange, *Proc. SPIE Vol. 7864A, Electron. Imaging Sci. Technol. Conf. (IS&T), 3D Imaging Metrol.* pp. 1–9 (2011)
18. Gallay, M., Hochmuth, Z., Kaňuk, J., Hofierka, J.: Geomorphometric analysis of cave ceiling channels mapped with 3D terrestrial laser scanning. Hydrol. Earth Syst. Sci. **2016**(February), 1–48 (2016). https://doi.org/10.5194/hess-2016-74
19. CloudCompareV2.8, "GPL software," 2016. [Online]. Available: http://www.cloudcompare.org/. Accessed 15 August 2016
20. P. Cignoni and G. Ranzuglia, "MeshLab. Visual Computing Lab," *ISTI – CNR*, 2014. [Online]. Available: http://meshlab.sourceforge.net/. [Accessed: 26-Dec-2016]
21. Silvestre, I., Figueiredo, M., Veiga-pires, C.: High-resolution digital 3D models of Algar do Penico Chamber: limitations, challenges, and potential. Int. J. Speleol. **44**(January), 25–35 (2015). https://doi.org/10.5038/1827-806X.44.1.3
22. Autodesk, Autodesk software for students, educators, and educational institutions, *Autodesk Education Community*, 2017. [Online]. Available: http://www.autodesk.com/education/free-software/featured. Accessed 04 Nov 2016

Feasibility Assessment of Tidal Current Along the Bay of Bengal to Generate Electricity as a Renewable Energy

Myisha Ahmad and G. M. Jahid Hasan

Abstract Electricity is the pinnacle of human civilization. At present, the growing concerns over significant climate change have intensified the importance of use of renewable energy technologies for electricity generation. The interest is primarily due to better energy security, smaller environmental impact and providing a sustainable alternative compared to the conventional energy sources. Solar, wind, biomass, tidal, and wave power are some of the most reliable sources of renewable energy. Ocean approximately holds 2×10^3 tW of energy and has the largest renewable energy resource on the planet. Various forms constitute ocean energy namely, encompassing tides, ocean circulation, surface waves, salinity and thermal gradients. Ocean tide in particular, associates both potential and kinetic energy. The study is focused on the latter concept that deals with energy due to tidal current. Tidal currents generate kinetic energy that can be extracted by marine energy devices and converted into transmittable electricity form. The study analyzes the extracted tidal currents from numerical model works at several locations in the Bay of Bengal. Based on current magnitudes, directions and available technologies, the most fitted locations were adopted and possible annual generation capacity was estimated. The paper also examines the future prospects of tidal current energy along the Bay of Bengal (BoB) and establishes a constructive approach that could be adopted in future developments.

M. Ahmad · G. M. J. Hasan (✉)
Department of Civil Engineering, Military Institute of Science
and Technology, Dhaka, Bangladesh
e-mail: jahid@ce.mist.ac.bd

M. Ahmad
e-mail: myisha.ahmad@gmail.com

1 Introduction

In today's world, adequate supply of energy is a focal obligation for comprehensive development and constructive advancement of human lifestyle in any country. However, effects of global climate change and depletion of traditional energy sources of fossil fuel due to excessive consumption seem to be influencing the development trend to a significant extent. Recent studies also suggest that by 2100, the global energy demand would escalate by five times the current demand. A constructive and sustainable solution of this acute problem can be incorporation and analysis of renewable energy sources, as an effective means of power generation. Renewable energy chiefly includes wind, biomass, solar, ocean, and geothermal energies. Covering around 71% of the earth surface, ocean embodies the largest unused renewable energy resource on the planet. Theoretically, ocean is capable of producing 20,000–92,000 tW h/year of electricity that can meet the current world consumption of 16,000 tW h/year [1]. Ocean energy is attainable in various forms including wave, thermal, salinity gradient, and tide. Tidal energy in particular scores highly compared to the other forms in terms of availability of resources, supply security, and most importantly, minimal environmental impact. The extraction of energy from ocean tides can be achieved by "tidal current" and "tidal barrage" technology. The former concept, which is the main focus of this study, involves deployment of tidal current devices to the seabed to extract energy from fast moving tidal current utilizing kinetic energy, i.e., current velocity. A tidal current energy converter extracts and then converts this mechanical form of energy into transmittable form. This study is concerned with the assessment of feasibility of tidal current energy potentials along the Bay of Bengal and possible power generation through analysis of available data.

Until 20 years ago, the only form of tide energy for electricity generation was a barrage which harnesses potential energy. But recently, interest has been shifted toward harnessing the kinetic energy of tidal flows by tidal current turbines, using the principles similar to wind energy. Conversion efficiency of tidal current technology is less but predictable power generation capacity and relatively lower environmental impact makes the tidal current turbine technology potentially more acceptable and preferable than tidal barrage concept.

A river current turbine project ran from 1976 to 84, marks the origin of the marine tidal current concept. Peter Fraenkel used a vertical axis Darrieus-type rotor for irrigation pumping, which was anchored to the bank of the river Nile in Juba, Sudan. The turbine operated well through a head of 5 m and a current of 1 m/s, pumping 2000 L/h. With further development, the design was then marketed with a horizontal axis rotor [2]. Since then, projects supportive of similar technology started to develop and active research has been ongoing in the United States, Canada, Europe and Japan. However, the technology has yet to be developed to a great extent and devices are at early stages compared to other renewable energy technologies. Most of the designs for this technology are still at an experimental stage. Their commercialization is still at its infancy and has not yet matured to the

extent of massive power generation. Many of them have great potentials for being used in large scale projects. The existing small-scale prototype models and some recent achievements of industrialized and pre-commercial large tidal current turbine (over 500 kW) technologies include: Open-hydro turbine-A 250 kW prototype installed in Orkney islands, Scotland, E-Tide turbine project (300 kW) installed in Norway, SeaGen S turbine installed in Strangford Lough, Northern Ireland-world's first grid-connected megawatt-level Marine Current Turbine (MCT) system, a 110 kW Voith Hydro Turbine has been operating since 2011 near the South Korean island of Jindo, and Sabella D10 turbines with a power capacity of 0.5–1.1 mW for current velocities of 3.0–4.0 m/s [3]. Moreover, a recent approach is the Deep Green—a 12 m diameter turbine mounted on a submerged anchored structure that intensifies the experienced water speed by a factor of 10, generating 220–500 kW units [4]. Studies and researches indicate huge potential of commercialization of these projects that are at prototype and testing phases.

Oceans are propitious resource, capable of providing clean energy on a grand scale. On the other hand, Bangladesh, with its 710 km long coast line, with suitable tidal range variations, and effective current speed, has promising renewable energy potential. Accelerated development of harnessing ocean energy along the Bay of Bengal can offer a wide sphere of long-term benefits including: identifying new prospects of de-carbonization of power supply, creating manifold energy generation portfolio, improved energy security in terms of production, distribution, and plausible economic development of the whole nation.

2 Tidal Current Technologies

2.1 Tidal Current

Tide is the result of mutual gravitational interaction among earth, moon and sun. Due to the floods and ebbs, the tides rises and falls generating horizontal movement of water called 'tidal current'. The current is not only influenced by tide but also by temperature, wind, salinity difference, relative positions of the sun and moon with respect to earth along with changing angles of declination. The extreme declination of the moon results largest currents, while lowest currents occur at zero declination. These astronomic characteristics results in periodic variation of tidal currents which can be predicted with high accuracy.

2.2 Harnessing Tidal Current Energy

The technique of harvesting current energy is to obstruct the free flowing water, trapping the kinetic energy and converting into transmittable electric energy.

The basic physical principle of extracting kinetic energy is virtually similar to that of wind. Tidal current devices are placed directly in stream to draw energy from tidal currents in a manner resembling wind turbine. In practice, tidal current devices are employed as fences or arrays of turbines in restricted channels and inlets, where the optimal tidal power is extractable with the option of few multiple rows. Tidal current power varies with density of the medium and cube of velocity. The density of water being 832 times of the density of air is capable of producing substantial power at lower tidal flow velocities, compared to wind speed. However, the tidal current technology is not yet adequately developed for large scale exploitation of energy resource. Some of the turbine designs have been developed to prototype stage for testing and some have been built to full scale for pre-commercial testing. The methods that have undergone prototype testing phases till date are highlighted as follows:

Vertical axis turbine technology. Vertical axis turbines typically consist of two or three blades attached to a vertical shaft forming a rotor. Incoming water flow hits the axis of rotation perpendicularly, as shown in Fig. 1a. The incoming flow generates a lift force to drive the rotor, which eventually rotates the generator and produce power.

Horizontal axis turbine technology. Horizontal axis turbines usually have two or three rotor blades which can generate lift and result axial rotation to drive a generator. These turbines ought to be aligned to the current either by rotating the device or by pitching the blades through an angle of 180° (Fig. 1b).

Oscillating hydrofoil turbine technology. This device consists of a hydrofoil connected to the end of a swing arm whose angle changes with the water stream as displayed in Fig. 1c. It rests on gravity-based foundation. The lift and drag force oscillates the arm, resulting in extension of the hydraulic cylinder. The cylinder is connected to the main arm and used to pump high pressure oil to a generator. Upon entering into the turbine of hydraulic design, the oil drives a generator and produce electricity.

Tidal kite. In this technology, the turbine is attached to a wing which moves forming loops in water. They are attached to the seabed with a moving wire, like a kite. The device moves through water at a speed higher than the water speed and are able to generate electricity from very low velocity currents (Fig. 1d).

Helical screws. Flumill's Helix screws' turbine is shaped like a screw. It has only one moving part and is slow-rotating. As water flows through the helix, the screws extract power from the tidal streams. The gearless turbine drives a permanent magnet synchronous generator and generates power (Fig. 1e).

Enclosed tip—venture. Enclosed tips (ducted) devices are enclosed within a shrouded structure. The funnel effect accelerates and concentrates on the fluid flow, allowing applicability of smaller rotor diameters. Moreover, ducted structures assist minimization of turbulence and alignment of the water flow into the turbine (Fig. 1f).
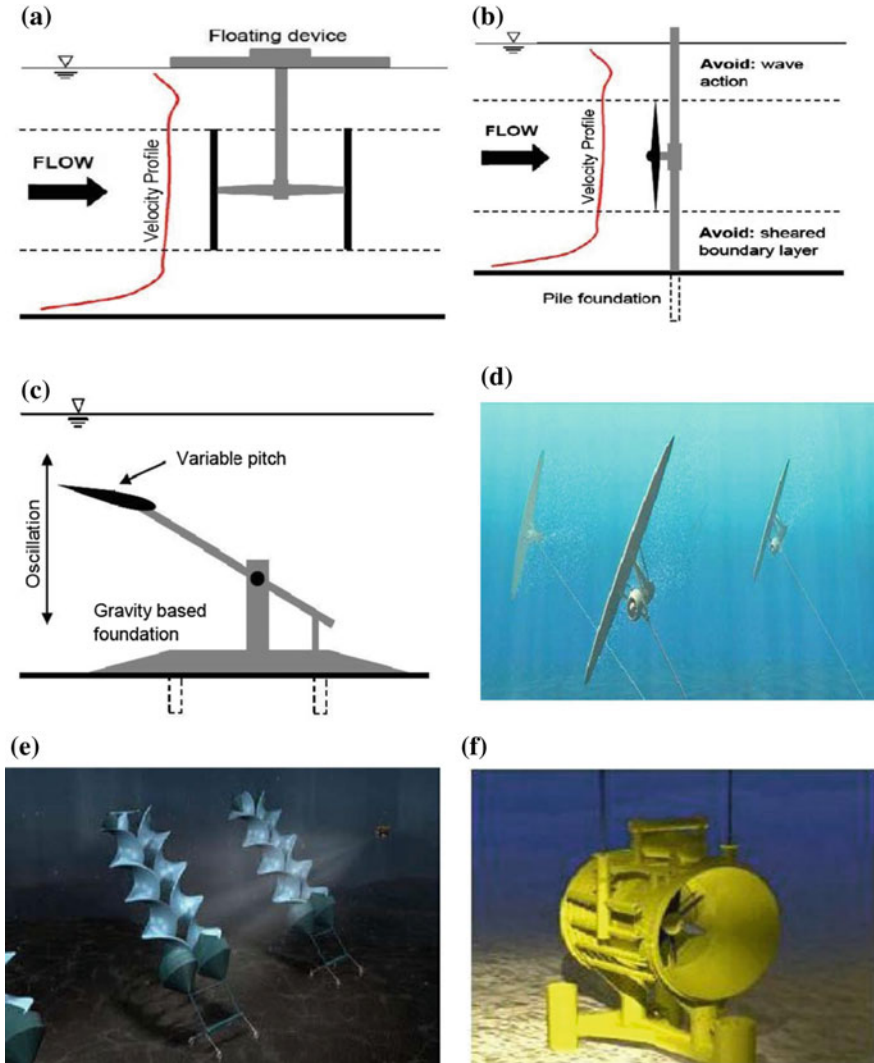
Fig. 1 Different types of available turbine technologies **a** vertical axis turbine, **b** horizontal axis turbine, **c** oscillating hydrofoil turbine, **d** tidal kite, **e** helical screws and **f** enclosed tip venture

3 Prospects of Tidal Energy in Bangladesh

3.1 Origin of Tides in the Bay of Bengal

The tides entering the Bay of Bengal originates in the Indian Ocean and gains access through two submarine canyons: the "Swatch of no ground" and the "Burma trench". There are six major entrances through which fresh water penetrate into the

waterway system in Bangladesh and these are: (a) The Pussur Entrance, (b) The Haringhata Entrance, (c) The Tentulia Entrance, (d) The Shahbazpur Entrance, (e) The Hatia River Entrance, and (f) The Sandwip Channel Entrance [5]. The tides are predominantly semidiurnal with large variation in range corresponding to seasons, particularly during the monsoon. They are affected by the local conditions like geomorphology, configuration and orientation of the coast, upstream flow of rivers, number of openings in the coast. In some places, the tidal stream can reach up to 5.5 knots (2.8 m/s) which is suitable for establishment of tidal current turbine deployment [6].

3.2 Potential Locations in the Bay of Bengal for Tidal Current Energy Extraction

High tidal flows commonly occur in areas with narrow straits, around headlands, and between islands, enhanced due to funneling effect. Some of the fundamentals and key criteria of site selection for tidal current turbine deployment can be given as considerable spring peak current, uniform and strong currents, close to coast, constricted channels [7]. Coastal areas in Hiron Points, Mongla, Char Changa, Cox's Bazar, Golachipa, Patuakhali, Sandwip, Barisal, etc., are some of the important and suitable locations along the Bengal coast. But assessing the coast line along the Bay of Bengal, the Sandwip channel tends to fulfill most of these criteria and possess huge potential of tidal current energy. Situated at the estuary of the Meghan River on the Bay of Bengal the non-navigable channel is surrounded by Sandwip Island on one side and Chittagong on the other. This geological criterion enhances the current speed of the location varying from approximately 0.1–2.5 m/s in the tidal channels [8].

3.3 Present Scenario and Future Goal of Renewable Energy Development in Bangladesh

Renewable energy shares only 1% of the total available energy in Bangladesh, while in the world it accounts for almost 19% of total energy consumption. It is high time to shift the dependency trend from conventional fossil fuel sources to alternative means. However, the country intends to rise electricity generation up to 10% through utilizing renewable energy, by the year 2020 (http://www.powerdivision.gov.bd). With that aim, the government is already working to reduce the dependency on natural gas in commercial energy consumption, declining to 42% in 2012 compared to 50% in 2009 [9].

With the recent ocean victory, Bangladesh has been assured rights over 118,813 km^2 of territorial sea. Now she has access to the open sea and sovereign

rights over 200 nautical miles exclusive economic zone that can be used and explored of marine resources including oil and gas [10]. So, huge potential energy is available in this large sea zone which can be utilized for generating electricity. Moreover, in order to promote the importance of replacing indigenous nonrenewable energy sources as well as to encourage different public and private investments in this sector, renewable energy is included in the national energy policy in year 2008. Although different forms of renewable sources are already being explored and utilized to extract energy, the vast potentials of the ocean renewable source of the Bay of Bengal is yet to be analyzed and studied.

4 Generation of Energy

4.1 Tidal Energy Estimation

The instantaneous power density P produced by a tidal current turbine can be calculated by Eq. (1) [11]

$$P = \frac{1}{2}\rho A V^3 C_P \tag{1}$$

where

ρ the water density (in kilogram per cubic meter),
A the cross-sectional area of the flow intercepted by the device, i.e., area swept by turbine rotor (in square meters),
V the flow velocity (in m/s),
C_P the turbine efficiency.

For each cycle of tidal current, V varies with time in a predictable manner and is characterized by the depth of water level as well as channel position and seasonal changes.

4.2 Methodology

A stepwise methodology has been adopted in this study that leads to an estimation of effective stream power potential of the site under investigation, presented by a flowchart as depicted in Fig. 2.

Initially, bathymetry data and satellite images of all suitable locations along the Bay of Bengal were analyzed and finally Sandwip Channel with an approximate width of 13 m and 12–16 m water depth variation was selected as stable and feasible location. Figure 3 displays Sandwip Channel which is located in between Chittagong district and Sandwip Island. Reason for selection of this location is due to its relatively
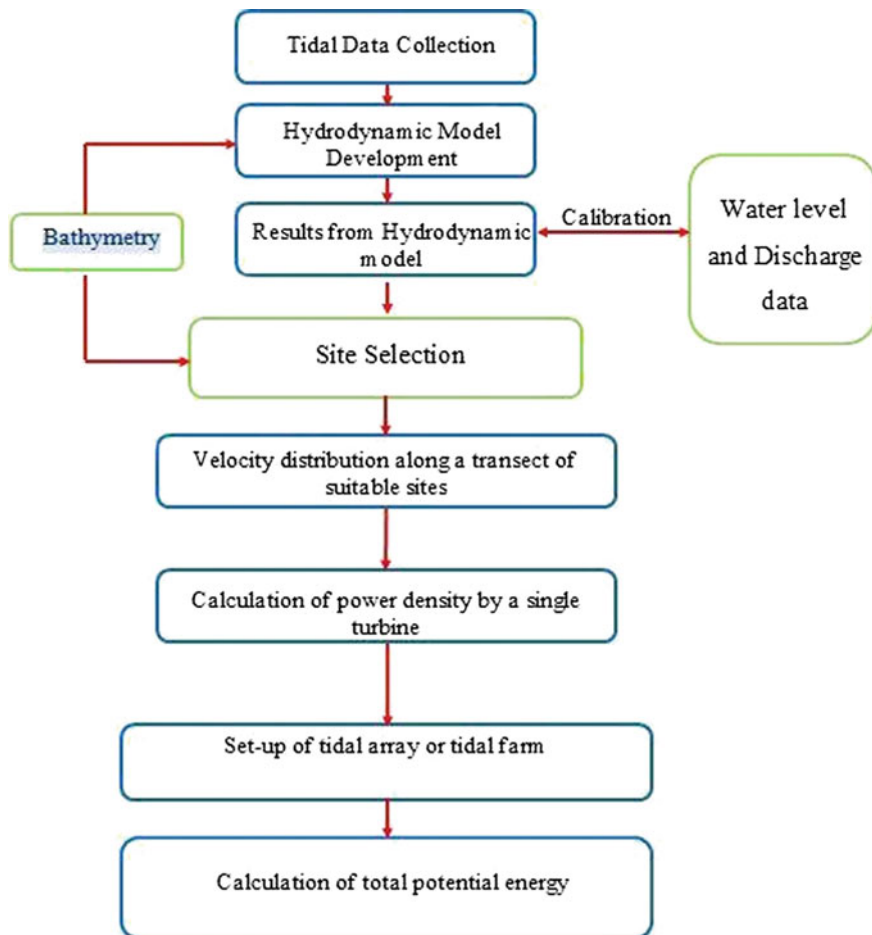
Fig. 2 Flowchart presenting stepwise methods followed for tidal current power potential calculation

stable channel, clean water, higher velocity, and it is nearer to the main land for connectivity. Then result from a hydrodynamic model obtained from a secondary source (developed by the Institute of Water Modelling) has been assisted in the analysis. The developed hydrodynamic model has been calibrated against measured water levels and discharges at different locations. Depth-average velocity and direction along a transect of Sandwip channel for a period of 14 days (covering spring-neap) during both monsoon (August) and dry period (March) for the year 2014 were extracted from the model results which were incorporated in the energy calculation procedure. During monsoon period, a maximum velocity of 2.41 m/s and minimum velocity of 0.19 m/s was observed. On the other hand, during dry period maximum and minimum velocity reached to 2.01 and 0.12 m/s, respectively.
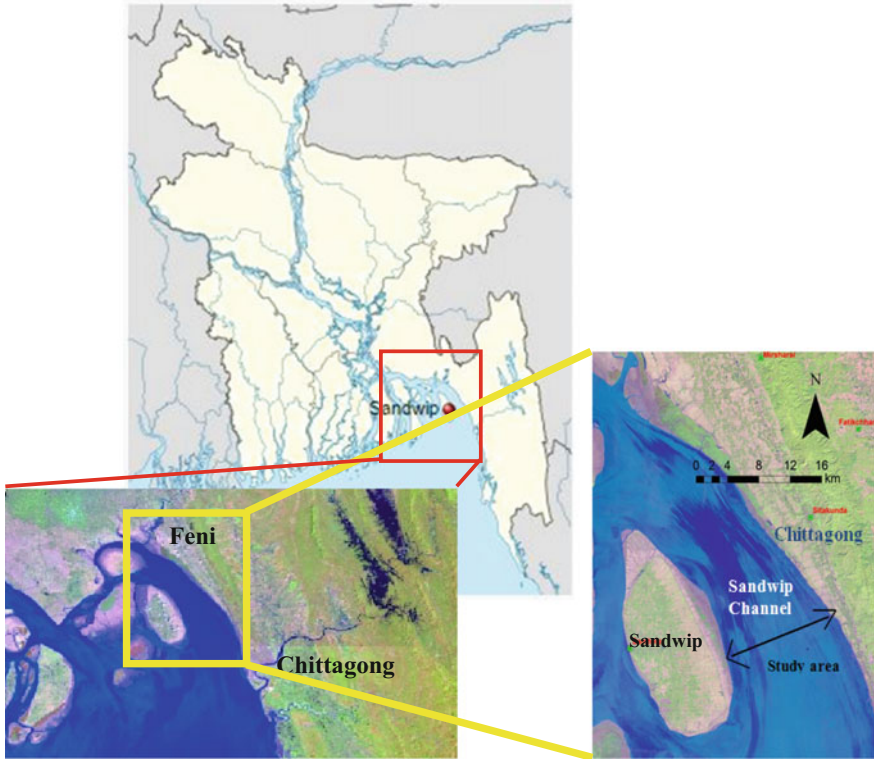
Fig. 3 Suitable study location along the Bay of Bengal. Main study location (Sandwip channel) is highlighted by a zoomed box

The developed hydrodynamic model divides the Sandwip channel into several grids. The depth-average velocities for each of the grids were taken from the 14 days modeled data of hourly variation. These data were averaged and the maximum value was taken into consideration for power calculation using Eq. (1). Figure 4 projects a graphical representation of change of generated power with the variation of velocity for both monsoon and dry period. An estimation of annual power generation has finally been made considering an array of turbines accommodated in a single row along the selected transects (Fig. 5).

For the purpose of this study, single-bed mounted horizontal axis turbine technology has been taken into consideration, given the fact that, it is the most efficient and practical concept and is most experimented among the existing technologies. Being similar to wind mill concept, it won't require exclusive technical expertise. Moreover, the bathymetry characteristics and sea bed nature of Sandwip channel prefers the deployment of the horizontal axis turbine.
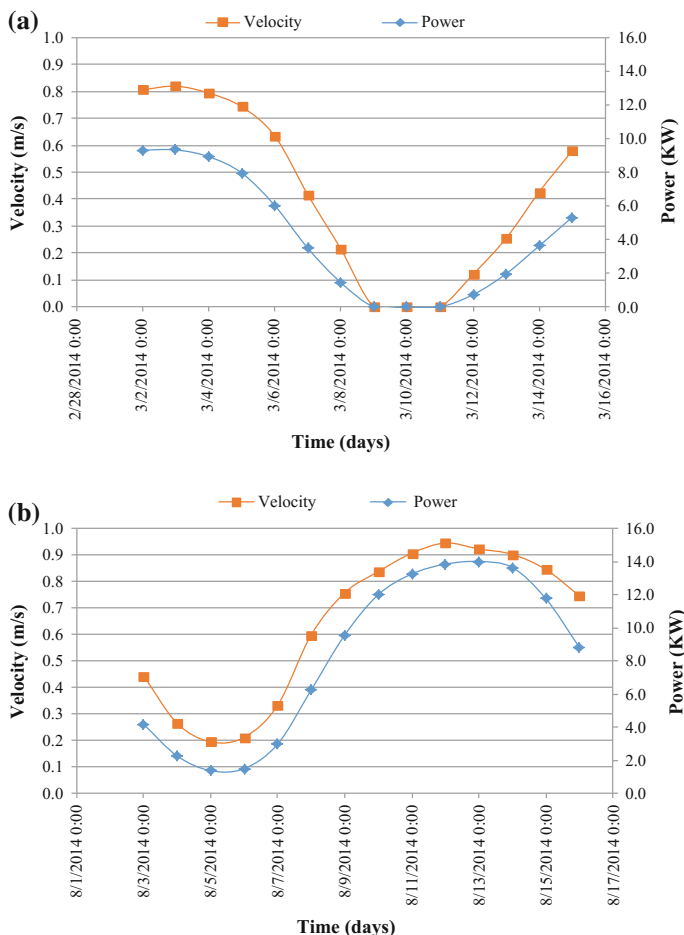
Fig. 4 Variation of daily average velocity and estimated power covering a spring-neap tidal cycle during **a** monsoon period and **b** dry period, for the year 2014

5 Result and Discussion

Total width of the Sandwip Channel is approximately 13 km. As the channel is bounded on both sides by stable landmass, naturally seabed is shallow at the corners and deeper at the center. Considering the fact, the effective width for tidal turbine deployment is selected to be 12 km. Spacing between subsequent turbine is considered as 10 times the diameter of a rotor. This spacing is required to reduce the wake effects of nearby turbines. Diameter of turbine rotor is considered as 6 m that yields a swept area of 28.274 m². Approximately 200 turbines can be deployed in a single row along a tidal stretch of 12 km and with a 35% turbine efficiency (i.e., $C_p = 0.35$), the total power output by all the turbines would sum up to 470 mW per
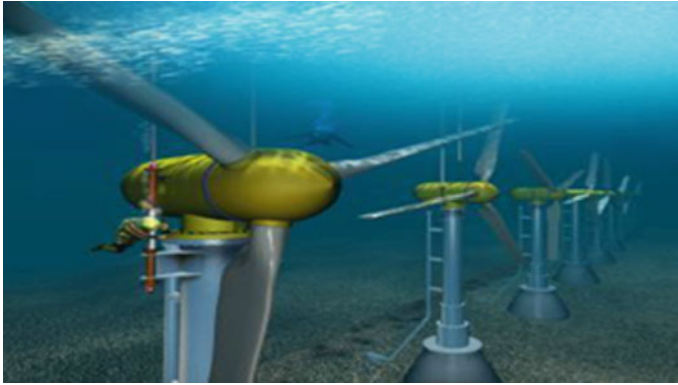
Fig. 5 Proposed arrangement of tidal current turbine array in the selected location (extracted from [12])

Table 1 Summary of annual generated power at the study location

Parameter	Dimension
Width of study location (Sandwip channel)	12 km
Turbine type	Submerged horizontal axis turbine
Turbine diameter and number of blades	6 and 3 m
Average daily power generation during monsoon period (per turbine)	8.25 kW
Average daily power generation during dry period (per turbine)	4.15 kW
Number of turbines	200 nos
Annual generated power (per turbine)	2.355 mW
Total annual generated power	470 mW

year. Each turbine is yielding an annual energy output of 2.355 mW. Table 1 summarizes the total annual power yield using tidal current turbine concept.

6   Concluding Remarks

Power demand is increasing rapidly in Bangladesh and there is no constructive plan yet, to meet the forthcoming power deficit by renewable energy. The traditional energy sources being limited and unsustainable, the country has to face a great challenge in upcoming days. In this respect, tidal power, as a renewable energy source with multifarious benefits, can be a fundamental provision for our future energy necessities. Fundamental of this paper is to highlight the prospects and

potentials of the Bay of Bengal for developing research focusing on tidal current technologies, in conjunction with assessment of the feasibility of the concept.

In order to quantify the tidal power potential of the Bay of Bengal, an extensive and elaborate investigate has been carried out in this study. Sandwip channel with its desirable geological location, a considerable channel width of 12–16 m, and a variable current speed of 0.12–2.4 m/s (approx) was found to be one of the most preferable locations for energy extraction. A set of depth-averaged velocity data for the study area was obtained through a hydrodynamic model study. The velocity varies higher during flood than ebb and the maximum value reached 2.41 and 2.01 m/s during monsoon and dry period, respectively. The magnitude of generated electricity being directly proportional to the cube of velocity and the area of water surface swept by the turbine suggests that power generation is more effective and maximum during monsoon than dry period, as available kinetic energy is more. The power density reached its maximum with a value of 8.25 kW daily, at mid-flood of a mean spring tide of monsoon period, whereas it accounted to 4.15 kW daily power during dry period for a single-bed mounted horizontal axis turbine. Due to ease of installment, and simpler technical features, horizontal axis turbine technology has been preferred over the other existing technologies to be used applied in the study area. Finally, theoretical design of deploying 200 tidal turbines in a single row sums up to 470 mW annual power generation.

The potential for progression of the techno economic ability of ocean power conversion technologies is enormous and propitious. Ocean energy conversion technologies are speculated to make appreciable contributions in achieving miscellaneous objectives of environmental, social, and economic policies in many countries around the world, after their integration into the world electricity market. Bangladesh too needs to keep pace with this advancing trend by exploring the renewable energy possibilities in the country. A comprehensive, holistic energy strategy should be developed to address the shortcomings related to research and studies acquainted with the suggested technology.

References

1. Esteban, M., Leary, D.: Current developments and future prospects of offshore wind and ocean energy. J. Appl. Energy **90**, 128–136 (2012). https://doi.org/10.1016/j.apenergy.2011.06.011
2. Thake, J.: Development, Installation and Testing of Large-Scale Tidal Current Turbine, p. 74. Report IT Power, Marine Current Turbines, Seacore, Bendalls Engineering, Corus (2005)
3. Zhou, Z., Scuiller, F., Charpentier, J.F., Benbouzid, M., Tang, T.: An up-to-date review of large marine tidal current turbine technologies. In: International Power Electronics and Application Conference and Exposition. IEEE Press, Shanghai, China, pp. 480–484. https://doi.org/10.1109/peac.2014.7037903 (2014)
4. Hammar, L., Ehnberg, J., Mavume, A., Cuamba, B.C., Molander, S.: Renewable Ocean energy in the Western Indian Ocean. J. Renew. Sustain. Energy Rev. **16**(7), 4938–4950 (2012). https://doi.org/10.1016/j.rser.2012.04.026

5. Mondal, M.A.M.: Sea Level Rise along the Coast of Bangladesh. Report, Ministry of Shipping, Dhaka (2001)
6. Ahmed, C.S.F.: Bathymetric Survey in the Coastal Area of Bangladesh—A Challenging Experience for the Surveyors. Report, North Indian Ocean Hydrographic Commission (NIOHC 16–14), 12p (2013)
7. Li, D., Wang, S., Yuan, P.: An overview of development of tidal current in China: Energy resource, conversion technology and opportunities. J. Renew. Sustain. Energy Rev. **14**, 2896–2905 (2010). https://doi.org/10.1016/j.rser.2010.06.001
8. Hasan. M. S.: A study on morphological change from Chandpur to Sandwip Channel in the Meghna Estuary. Masters Thesis, Department of Water Resource Engineering, Bangladesh University of Engineering and Technology, Dhaka, Bangladesh, 103p (2011)
9. Halder, P.K., Paul, N., Joardder, M.U.H., Sarker, M.: Energy scarcity and potential of renewable energy in Bangladesh. J. Renew. Sustain. Energy Rev. **51**, 1636–1649 (2015). https://doi.org/10.1016/j.rser.2015.07.069
10. Islam, M.A.: Second victory at sea. In: The Prothom Alo, 10 July 2014
11. Lim, Y.S., Koh, S.L.: Marine tidal current electric power generation: state of art and current status, Renewable Energy. In: Hammons, T.J. (ed.) ISBN:978-953-7619-52-7, InTech, 211p. https://doi.org/10.5772/7368 (2009)
12. Singh, T.: Retrieved from http://inhabitat.com/worlds-first-tidal-farm-successfully-installs-100-foot-subsea-turbine/hs1000-tidal-turbine-installation (2012)

Detection of Environmental Degradation of Satkhira District, Bangladesh Through Remote Sensing Indices

M. Tauhid Ur Rahman and Jannatul Ferdous

Abstract Satkhira is one of the most vulnerable coastal districts of Bangladesh due to both natural disasters and anthropogenic causes, which faces continuous environmental degradation. This study aims to explore the environmental changes in the Upazilas of Satkhira district by employing several remote sensing indices using the Landsat images of the year 2007, 2010, 2013, and 2016. NDVI, NDWI, NDSI, NDBI, and NDBaI are used to extract the spatial information regarding the condition of vegetation, wetlands, soil salinity, built up area and bare lands in the Upazilas respectively. Temporal change of these variables has been monitored and compared among and within the Upazilas on the basis of the threshold values of the indices. Analysis of NDVI has revealed that there was a drastic change in vegetation from 2007 to 2010, which was because of the cyclones. Though NDVI of 2013 showed a positive increase from 2010, it cannot restore its previous state not even in 2016. Analysis of NDBI and NDBaI have revealed that built up area has been increased day by day; whereas, a decreasing trend has been seen in case of bare lands, as the bare lands are occupied either by built up area or by shrimp farming area. Increasing NDWI and NDSI justify the increasing shrimp farming trend in Satkhira. These variables indicate the changing nature of land use land cover and the vulnerability due to environmental degradation in Satkhira district, which reveals a need for immediate land use planning. This study will help the policy makers and land use manager to promote substantial and sustainable development plan for Satkhira district.

Keywords Coastal Bangladesh · Environmental degradation · Shrimp farm Remote sensing indices

M. Tauhid Ur Rahman
Military Institute of Science and Technology, Dhaka, Bangladesh
e-mail: tauhid_cee@yahoo.com

J. Ferdous (✉)
Bangladesh University of Engineering and Technology, Dhaka, Bangladesh
e-mail: jannaturp10@gmail.com

1 Introduction

Environmental degradation is one of the most serious matters of concern worldwide, which is acuter in developing countries due to the lack of effective monitoring system and strong legislation [1, 2]. Environmental degradation or the damage of natural environment is occurred both by the effect of climate change and harmful human activities and results in loss of biodiversity and natural resources, which is a common phenomenon in the southwest coastal region of Bangladesh. Both natural hazards and major land use/land cover change exist together in this area and have significant and adverse effects on the environment [3]. Being one of the most vulnerable coastal areas around the world, this region has been observed to change rapidly since late of twentieth century. Degradation of soil and water condition due to increased salinity, destruction of mangrove forest, unplanned practices of land surface, etc., have been experienced in this region.

Change in land use/land cover has been established as one of the most useful methods to detect environmental degradation [4]. Significant change in the land use/land cover pattern has been observed the southwest region of Bangladesh, especially in Satkhira district. Cultivated land has been decreased about 20% and water bodies have been increased about 10% from 1980 to 2009 [5]. Shifting of occupation from agriculture to shrimp farming has been taken place due to the combined effect of climate change and salinity intrusion and 30% increase in shrimp farming has been seen in the past 13 years [3]. Satkhira district is recognized for its economic and environmental importance and it is now facing several environmental challenges caused by the anthropogenic activities like unplanned land use practices and demographic changes. Economic growth of this region has been proved as detrimental to the environment causing increased salinity both in soil and water, drinking water scarcity, decreased land fertility, increased health hazard, destruction of mangrove forest, and agricultural land loss [1]. Moreover, Satkhira district has been experienced a significant environmental change due to the devastating cyclone Sidr in 2007 and Aila in 2009.

For monitoring and assessing the environmental degradation, long-term prior information about the environmental components are required, which is now easily accessible in the form of satellite images. Remote sensing techniques have provided the opportunity of studying the pattern of environmental change for a long period of time. There are several indices for detecting the environmental change like Normalized Difference Vegetation Index (NDVI), Normalized Difference Water Index (NDWI), Normalized Difference Salinity Index (NDSI), Normalized Difference Built-up Index (NDBI), and Normalized Difference Bareness Index (NDBaI), which are used to extract the spatial information regarding condition of vegetation, wetlands, soil salinity, built up area and bare lands respectively.

The objectives of this study are to detect the environmental degradation of Satkhira district of Bangladesh in terms of change in different land uses/land covers and to present a comparative scenario of the Upazilas (Sub-districts) on basis of spatiotemporal change pattern. For this, satellite images of the year 2007, 2010,

2013, and 2016 have been employed. The change due to natural hazards (cyclone Sidr and Aila) has been revealed after analyzing the images of 2007 and 2010 and the change occurred in the recent years can be considered mostly due to anthropogenic causes.

2 Study Area

Satkhira District of Khulna division, Bangladesh has been selected as study area. This district is located on the southwest extremity of Bangladesh, in between 21°36′ and 22°54′ north latitudes and in between 88°54′ and 89°20′ east longitudes. It is bounded by Jessore district on the north, the Bay of Bengal on the south, Khulna district on the east, West Bengal State of India on the west. There are seven Upazilas in this district named Assasuni, Debhata, Kalaroa, Kaliganj, Satkhira Sadar, Shyamnagar and Tala. Of the seven Upazilas of the district, Shyamnagar is the largest and Debhata is the smallest (Fig. 1).

The total area of the district is 3817.29 km^2, of which 1534.88 km^2 is under mangrove forest (The Sundarbans). The rural economy of Satkhira is predominantly agricultural as 62.56% people are engaged in agriculture. Paddy, jute, sugarcane, mustard seed, potato, onion, betel leaf, etc., are the main crops in Satkhira. Besides, Prawn farming is one of the most important economic activities of the households and one of the main export items of Bangladesh, which is abundantly available in the district [6].

3 Methodology

3.1 Acquisition of Satellite Images

To detect the environmental degradation of Satkhira district through remote sensing indices, multi-temporal satellite images (WRS2: 138/44, and 138/45) were collected from the United States Geological Survey (USGS) website. All bands of Landsat Thematic Mapper 5 (TM) (dated 18 March 2007 and 6 February 2010), and Landsat 8 Operational Land Imager (OLI) (dated 28 April 2013 and 26 March 2016) were collected, and all the spatial data layers were registered to the same Universal Transverse Mercator (UTM) coordinate system and resampled to the same pixel resolution of 30 m. In order to use satellite images of different periods, it is essential to acquire images of same dates (especially the same plant growing seasons). Though the acquisition dates are ranged from the month February to April, it covers same plant (e.g., Boro rice and potato) growing seasons in Bangladesh.
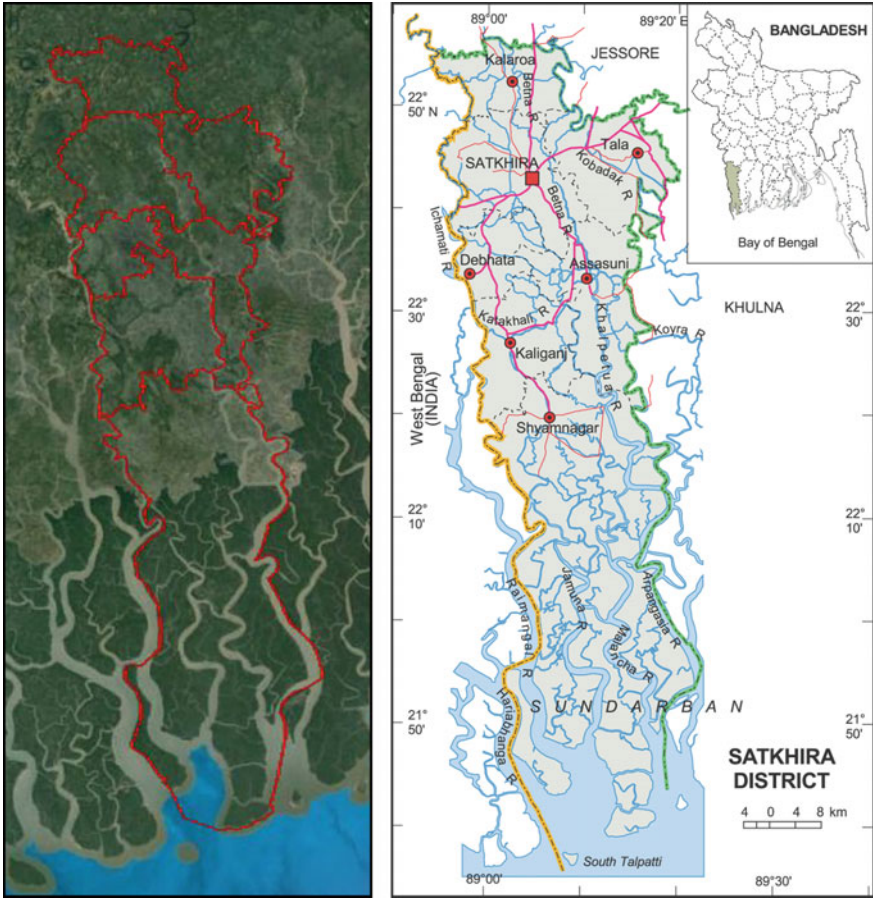
Fig. 1 Location of study area (Satkhira district) [6]

3.2 Processing of Satellite Images

As the raw satellite images are not best suited to calculate remote sensing indices, the radiometric correction has been performed and the Digital Number (DN) values have been converted into reflectance. For Landsat 5 TM, there is a two-step conversion process (Eqs. 1 and 2) and in Landsat 8 it can be done by a single step (Eq. 3). Spectral Radiance Scaling Method has been followed for radiometric correction of Landsat 5 TM. All the necessary data has been found in the header file (metadata) downloaded with the satellite images.

(a) **Radiometric Correction of Landsat 5 TM**

The formula used in the Spectral Radiance Scaling Method for Landsat 5 TM is as follows [7]:

$$L\lambda = ((LMAX\lambda - LMIN\,\lambda)/(QCALMAX-QCALMIN))^*(QCAL-QCALMIN)+LMIN\lambda \tag{1}$$

where

Lλ	the cell value as radiance
QCAL	digital number
LMINλ	spectral radiance scales to QCALMIN
LMAXλ	spectral radiance scales to QCALMAX
QCALMIN	the minimum quantized calibrated pixel value (typically = 1)
QCALMAX	the maximum quantized calibrated pixel value (typically = 255).

Then, the radiance value has been converted to reflectance value by using the following formula [8].

$$\rho\lambda = \pi^*L\lambda^*d2/ESUN\lambda^*\sin\theta z \tag{2}$$

where

ρλ	Unit less planetary reflectance
Lλ	Spectral radiance (from the earlier step)
d	Earth–Sun distance in astronomical units
ESUNλ	Mean solar exo-atmospheric irradiances
θz	Sun Elevation Angle.

(b) **Radiometric Correction of Landsat 8 OLI**

For Landsat 8 OLI, DN values have been converted to reflectance by using the following formula [9].

$$\rho\lambda = (M\rho\,Qcal + A\rho)/\sin\theta z \tag{3}$$

where

ρλ	Unit less planetary reflectance
Mρ	Band-specific multiplicative rescaling factor from the metadata
Aρ	Band-specific additive rescaling factor from the metadata
Qcal	Quantized and calibrated standard product pixel values (DN)
θz	Sun Elevation Angle.

The reflectance values have been used to compute the indices except for Normalized Bareness Index (NDBaI) as it uses the thermal band. For computing NDBaI, DN values of the respective bands have been used. Radiometric correction provides the more accurate result as noise from reflectance is 50% less than noise from DN value [10].

3.3 Calculation of Remote Sensing Indices

Normalized Difference Vegetation Index (NDVI), Normalized Difference Water Index (NDWI), Normalized Difference Built-up Index (NDBI), Normalized Difference Bareness Index (NDBaI) and Normalized Difference Salinity Index (NDSI) are used to extract the spatial information regarding condition of vegetation, wetlands, built-up area, bare lands, and salinity-affected areas in the Upazilas, respectively. Threshold values have been used to identify the areas with moderate vegetation, water features, salinity-affected areas, built-up area, and bare lands. Formulae and threshold values for these indices are given in Table 1.

G, R, NIR, SWIR, and T are the Green, Red, Near Infrared, Short Wave Infrared, and Thermal Bands, respectively. For Landsat 8 OLI image, band 10 has been used to compute the NDBaI, as NDBaI computed from band 10 and SWIR band gives the best-suited result for extraction of bare soil [11]. Threshold values for Landsat 5 TM and Landsat 8 OLI have been considered same as the DN values are converted to reflectance values. But the threshold values for NDBaI are different for different Landsat, as the DN values of thermal bands cannot be converted into reflectance [11] (Fig. 2).

Table 1 Corresponding remote sensing indices with the formulas and their threshold values

Index used	Formula	Threshold value of the index used
NDVI	$\frac{NIR-R}{NIR+R}$	>0.2
NDWI	$\frac{G-NIR}{G+NIR}$	>0
NDBI	$\frac{SWIR-NIR}{SWIR+NIR}$	0.1–0.3
NDBaI	$\frac{SWIR-T}{SWIR+T}$	>−0.15 (>−0.09 for Landsat 8)
NDSI	$\frac{R-NIR}{R+NIR}$	>0
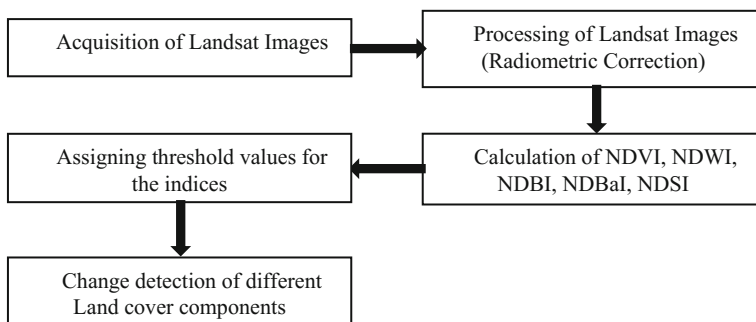
Fig. 2 Methodological approach for the study

3.4   Change Detection of Different Land Cover Components

Threshold values of the indices are the base of change detection analysis. Areas above the threshold values have been calculated and used to compare the changes among the Upazilas during the period 2007–2016.

4   Results and Discussions

The collected satellite images of the study area of the year 2007, 2010, 2013, and 2016 are as follows in false color composite (Fig. 3).

4.1   Spatiotemporal Dynamics of NDVI

For identifying the healthy vegetation area from the satellite images, NDVI has been used and the threshold value for NDVI is 0.2 as greater than this value indicates the vegetation area [12]. Table 2 shows the NDVI statistics for the Upazilas of Satkhira district for the selected years.

The analysis of NDVI has revealed that there was a significant reduction in vegetation area from the year 2007 to 2010, which can be said as the impact of the devastating cyclones Sidr and Aila. Every Upazila has faced a reduction in vegetation area to a great percentage, among which there is about 79% reduction in Assasuni Upazila and 81% in Debhata Upazila. Vegetation areas have been increased in 2013 and even in 2016, but it is not the same as the vegetation area of 2007 (Fig. 4).
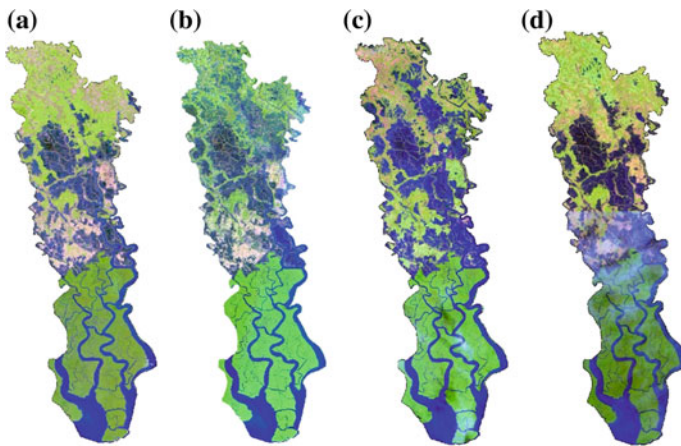
Fig. 3   Satellite images of study area in false color composite (R(SWIR), G(NIR), B(Red)) **a** in 2007; **b** in 2010; **c** 2013; **d** in 2016

Table 2 NDVI statistics of Satkhira district

Upazila	Vegetation area (in % of total area of the Upazila)			
	2007	2010	2013	2016
Assasuni	**37.2**	**7.8**	22.1	33.4
Debhata	**28.2**	**5.3**	21.7	23.7
Kalaroa	85.3	43.4	57.9	69.6
Kaliganj	30.5	12.2	23.9	27.9
Satkhira Sadar	79.3	49.5	53.7	55.7
Shyamnagar	74.9	49.7	52.4	56.3
Tala	75.6	46.3	52.5	66.2

The bold values represent the corresponding highest and lowest values
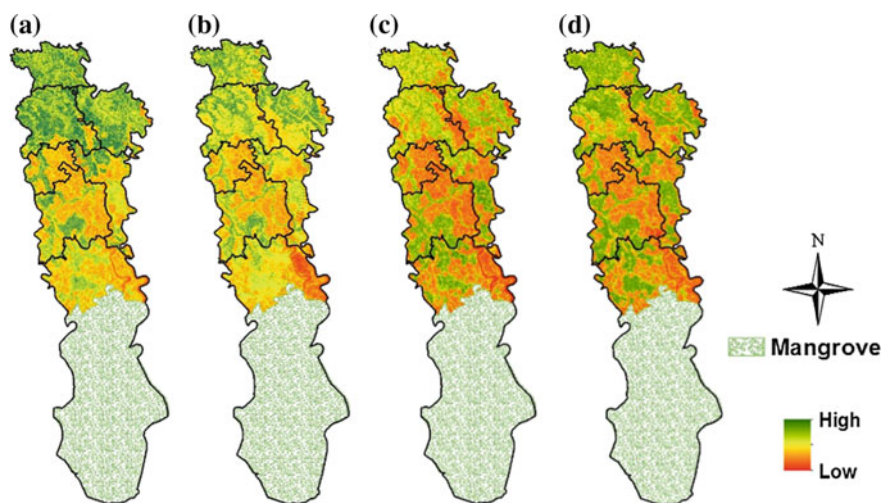
Fig. 4 Spatiotemporal pattern of NDVI **a** in 2007; **b** in 2010; **c** 2013; **d** in 2016

On an average, 20% reduction in vegetation cover has been observed in Satkhira after the cyclone Sidr and more than 30% reduction has been happened in Satkhira due to cyclone Aila in 2009, as Aila mainly hit the Satkhira and Khulna district and affect much on that area [13].

4.2 Spatiotemporal Dynamics of NDWI

For identifying the wetland areas, NDWI has been used and NDWI shows positive value in the areas with water [14].

Table 3 shows the NDWI statistics for the Upazilas of Satkhira district for the selected years. The increasing wetland areas from the year 2007 to 2010 are the

Table 3 NDWI statistics of Satkhira district

Upazila	Wetland areas (in % of total area of Upazila)			
	2007	2010	2013	2016
Assasuni	40.2	53.9	41.2	44.5
Debhata	56.7	69.2	61.7	65.1
Kalaroa	1.7	13.1	11.6	19.8
Kaliganj	52.4	68.9	49	80.5
Satkhira Sadar	**8.3**	35.3	27.9	**47.7**
Shyamnagar	85.3	86.2	85.1	82.4
Tala	**7.2**	32.7	31.6	**35.4**

The bold values represent the corresponding highest and lowest values
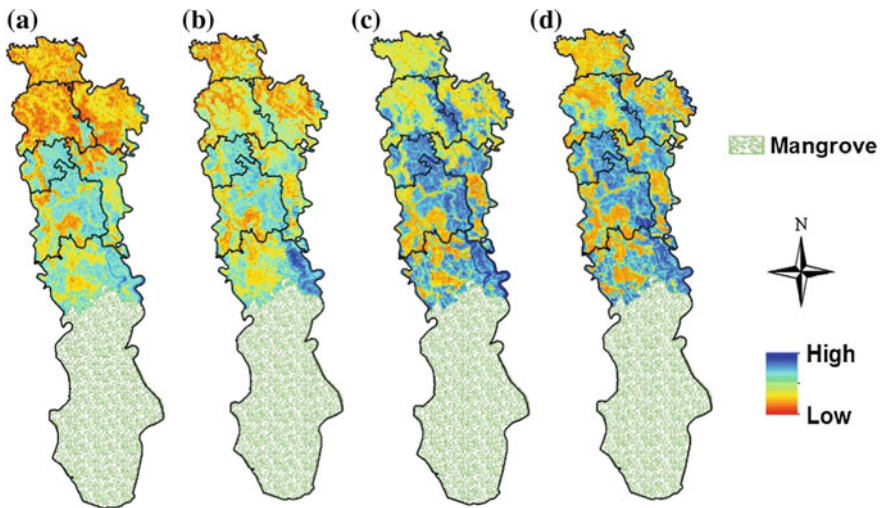
Fig. 5 Spatiotemporal pattern of NDWI **a** in 2007; **b** in 2010; **c** 2013; **d** in 2016

indication of the waterlogged areas due to the cyclones. Wetlands are increasing in all the Upazilas, as shrimp culture is one of the prominent occupations in Satkhira district. Satkhira Sadar Upazila and Tala Upazila have experienced significant increase among the Upazilas (Fig. 5).

4.3 Spatiotemporal Dynamics of NDBI

NDBI is a useful index to identify the built up areas from the satellite images, where the built-up areas have NDBI values ranged from 0.1 to 0.3 [15]. Table 4 shows the NDBI statistics for the Upazilas of Satkhira district for the selected years.

Table 4 NDBI statistics of Satkhira district

Upazila	Built up areas (in % of total area of Upazila)			
	2007	2010	2013	2016
Assasuni	20.6	18.2	22.2	25.3
Debhata	**8.8**	12.4	15.4	**18.2**
Kalaroa	**22.5**	**12.7**	18.7	20.3
Kaliganj	**15.3**	18.2	21.4	**24.5**
Satkhira Sadar	15.6	10.3	18.7	19.2
Shyamnagar	44.8	37.6	40.5	45.8
Tala	23.2	21.9	25.6	27.6

The bold values represent the corresponding highest and lowest values
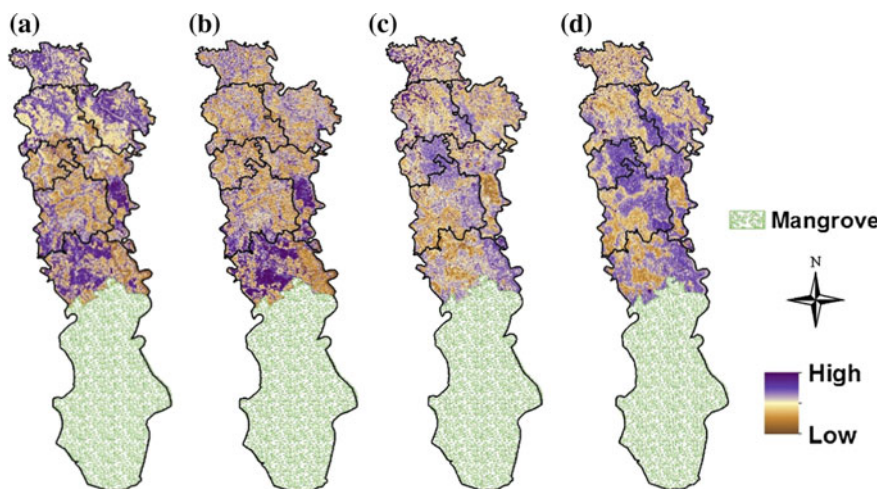
Fig. 6 Spatiotemporal pattern of NDBI **a** in 2007; **b** in 2010; **c** 2013; **d** in 2016

Overall increase in built up areas has been seen from the analysis of NDBI, though there is little reduction in built up areas from the year 2007 to 2010 due to the impact of the cyclones. Increase rate is higher in Debhata and Kaliganj Upazilas. Due to the cyclones, Kalaroa faced more reduction in built up areas due to the cyclones than other Upazilas (Fig. 6).

4.4 Spatiotemporal Dynamics of NDBaI

NDBaI is used to identify the bare lands from the satellite images. For Landsat 5 TM, it has threshold value greater than −0.15 and for Landsat 8 OLI it is −0.09 [11,

Table 5 NDBaI statistics of Satkhira district

Upazila	Bare lands (in % of total area of Upazila)			
	2007	2010	2013	2016
Assasuni	7.5	3.4	2.8	1.9
Debhata	**0.36**	0.22	0.16	**0.1**
Kalaroa	1.1	0.93	0.74	0.62
Kaliganj	2.9	1.55	1.2	0.95
Satkhira Sadar	**0.7**	0.44	0.4	**0.32**
Shyamnagar	16.1	13.16	10.4	8.9
Tala	1.7	1.14	0.87	0.65

The bold values represent the corresponding highest and lowest values
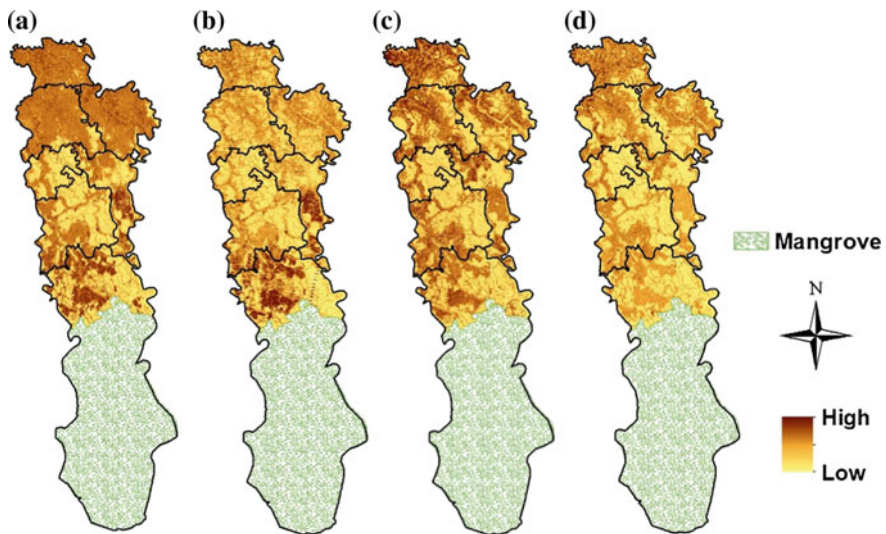
Fig. 7 Spatiotemporal pattern of NDBaI **a** in 2007; **b** in 2010; **c** 2013; **d** in 2016

15]. Table 5 shows the NDBaI statistics for the Upazilas of Satkhira district for the selected years.

Though there were fewer amounts of bare lands in all Upazilas, it shows a decreasing trend at present. Bare lands have been converted into either built-up areas or into shrimp farming lands. Satkhira Sadar and Debhata have the least amount of bare lands as they are close to the main urban area with high population density (Fig. 7).

4.5 Spatiotemporal Dynamics of NDSI

NDSI shows the salinity-affected area from the reflectance value of red and near infrared bands [2]. Table 6 shows the NDSI statistics for the Upazilas of Satkhira district for the selected years.

Analysis of NDSI has revealed that the areas near the water bodies are severely affected by salinity and value of NDSI is increasing. South part of the district (Shyamnagar Upazila) is severely affected due to the proximity to the sea and the salinity intrusion has been spread toward the north (Fig. 8).

Table 6 NDSI statistics of Satkhira District

Upazila	Salinity-affected areas (in % of total area of Upazila)			
	2007	2010	2013	2016
Assasuni	38.2	54.6	32.3	40.5
Debhata	52.1	67.1	52.8	62.8
Kalaroa	1.2	13	8.2	14.7
Kaliganj	50.2	59.5	42.6	47.3
Satkhira Sadar	7.2	31.7	22.9	25.4
Shyamnagar	**85**	**86.6**	**84**	**87.4**
Tala	7.3	30.8	27.2	32.6

The bold values represent the corresponding highest and lowest values
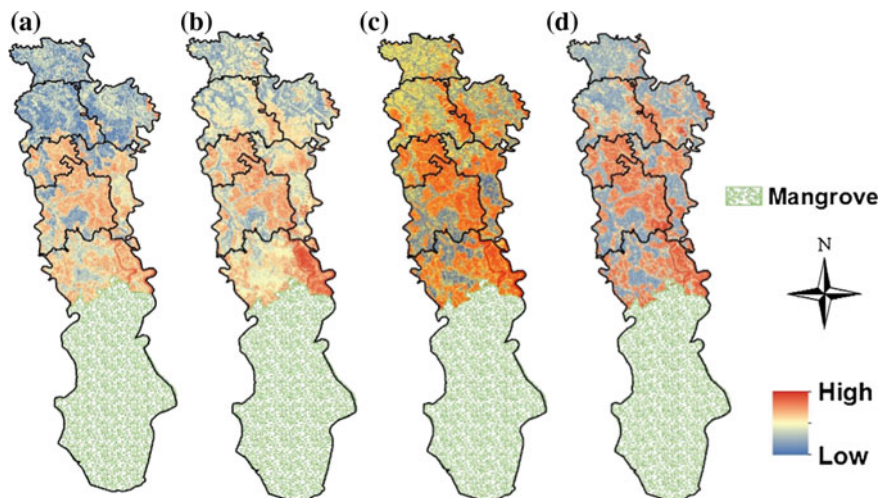
Fig. 8 Spatiotemporal pattern of NDSI **a** in 2007; **b** in 2010; **c** 2013; **d** in 2016

5   Conclusions

This study reveals the changing nature of the environment of Satkhira district, which is one of the most vulnerable coastal districts of Bangladesh. Through the remote sensing indices, it is very realistic to explore the long-term change in environmental components. The decreasing vegetation areas, increasing salinity-affected areas, decreasing bare lands with increasing built-up areas are the result of this study, which indicate the environmental degradation in the study area. To control the environmental degradation in this area, an effective sustainable development plan is in need. Policy makers should give focus on this regard and promote sustainable development in Satkhira district.

References

1. Ghosh, M.K., Falk, G.C., Ahmed, R.: Environmental impact of land-use change in the southwest coastal zone of Bangladesh. In: International Conference on Environment and Development. University of Rajshahi (2014)
2. Kundu, A., Dutta, D., Patel, N.R., Saha, S.K., Siddiqui, A.R.: Identifying the process of environmental changes in Churu district, Rajasthan (India) using remote sensing indices. Asian J. Geoinform. **14**(3), 14–22 (2014)
3. Khan, M.M.H., Bryceson, I., Kolivras, K.N., Faruque, F., Rahman, M.M., Haque, U.: Natural disasters and land-use/land-cover change in the southwest coastal areas of Bangladesh. Reg. Environ. Change **15**(2), 241–250 (2015). https://doi.org/10.1007/s10113-014-0642-8
4. Hadeel, A.S., Jabbar, M.T., Xiaoling, C.: Remote sensing and GIS application in the detection of environmental degradation indicators. Geo-spatial Info. Sci. **14**, 39–47 (2011). https://doi.org/10.1007/s11806-011-0441-z
5. Rahman, M.M., Begum, S.: Land cover change analysis around the Sundarbans Mangrove Forest of Bangladesh using remote sensing and GIS application. J. Sci. Found. **9**(1, 2), 95–107 (2011). http://dx.doi.org/10.3329/jsf.v9i1-2.14652
6. Banglapedia, Satkhira District. Retrieved from http://en.banglapedia.org/index.php?title=Satkhira_District. Accessed on 12 Feb 2017 (2015)
7. Chander, G., Brian, L., Markham, Julia, A.B.: Revised landsat-5 thematic mapper radiometric calibration. IEEE Geosci. Remote Sens. Lett. **4**(3). https://doi.org/10.1109/lgrs.2007.898285 (2007)
8. USGS, Earth Observing 1 (EO-1). Retrieved from https://eo1.usgs.gov/faq/question?id=21. Accessed on 9 Mar 2017 (2017)
9. USGS, Using the USGS Landsat 8 Product. Retrieved from https://landsat.usgs.gov/using-usgs-landsat-8-product. Accessed on 19 Mar 2017 (2017)
10. Huang, C., Yang, L., Homer, C., Wylie, B., Vogelman, J., DeFelice, T.: At satellite reflectance: a first order normalization of LANDSAT 7 ETM + images, USGS (2002)
11. Li, S., Chen, X.: A new bare soil index for rapid mapping developing areas using Landsat 8 data. Int. Arch. Photogrammetry, Remote Sens. Spatial Info. Sci. **XL-4**, 139–144 https://doi.org/10.5194/isprsarchives-xl-4-139-2014 (2014)
12. USGS, NDVI, the Foundation for Remote Sensing Phenology. Retrieved from https://phenology.cr.usgs.gov/ndvi_foundation.php. Accessed on 19 Mar 2017 (2015)

13. Islam, M.K., Chowdhury, S., Raja, D.R.: Assessment of ecological change due to cyclone using remote sensing technique. J. Bangladesh Inst. Planners **8**, 175–186 (2015)
14. McFeeters, S.K.: The use of the normalized difference water index (NDWI) in the delineation of open water features. Int. J. Remote Sens. **17**, 1425–1432 (1996)
15. As-syakur, A.R., Adnyana, W.S., Arthana, W., Nuarsa, W.: Enhanced built-up and bareness index (EBBI) for mapping built-up and bare land in an urban area. Remote Sens. **4**, 2957–2970 (2012). https://doi.org/10.3390/rs4102957

Snow Damage Prediction Model Using Socioeconomic Factors

H. Park, Y. R. Oh, J. W. Lee and G. Chung

Abstract Due to the climate change, the natural disasters have been occurred more frequently and the amount of damage has been increased as well. In South Korea, the number of snow disaster has been increased recently. In last 20 years, from 1994 to 2013, total snow damage was 1.3 billion dollars. In this study, the snow damage was estimated using historical damage data to response the possible heavy snow and mitigate the damage. The historical snow damage data from Annual Natural Disaster Report for the last 22 years were used to develop a multiple linear regression model. Input data for the model were daily maximum snow depth (or daily maximum fresh snow depth), daily highest temperature, daily lowest temperature, daily average temperature, relative humidity as meteorological factors, and also regional area, greenhouse area, number of farmers, number of farmers over age 60 were considered as socioeconomic factors. The developed model was applied in Jeolla-do, Chungcheong-do, and Kangwon-do which have the largest snow damage in the history. As the results, the model showed over 70% of accuracy in all of three cities.

Keywords Heavy snow damage · Socioeconomic factors · Snow damage forecast
Multiple regression analysis · Climate change

H. Park (✉)
Korea Institute of Civil Engineering and Building Technology, Goyang-si,
Gyeonggi-do, South Korea
e-mail: hspark90@kict.re.kr

Y. R. Oh · J. W. Lee · G. Chung
Department of Civil Engineering, Hoseo University, Asan-si,
Chungcheongnam-do, South Korea
e-mail: dudtla224a@nate.com

J. W. Lee
e-mail: wlsdn8592@nate.com

G. Chung
e-mail: gunhuic@gmail.com

1 Introduction

Due to the climate change, the natural disaster has been increased in South Korea. Snow disaster was the third major natural disaster in South Korea. In 2001, the roof top of Olympic Gymnastic stadium was fallen down by heavy snow. In 2004, the hall constructed by sandwich panel was collapsed by snow. In the accident, 103 people were injured and 10 people died. In Jan. 2016, the Jeju airport was closed for two days because of heavy snow and severe cold. It was an unexpected disaster because the winter daily average temperature in Jeju island was usually over 0 °C. Therefore, the necessity of snow disaster preparedness was increased. Many researches have been conducted to estimate snow damage in Korea. Oh et al. [1] said that the social and economic damage by heavy snow will be increased in South Korea.

Park et al. [2] conducted the vulnerability analysis by heavy snow in the Ulsan metropolitan city. The vulnerable area for the heavy snow was suggested for the disaster preparedness. Kim et al. [3] constructed snowfall forecasting model using neural networks and multiple regression analysis to consider nonlinear process of snowfall. Jeong et al. [4] estimated the snow damage using daily maximum fresh snow depth, snow days, population, GRDP, and area. Kwon and Chung [5] and Kwon et al. [6] also developed regression models to estimate snow damage using meteorological factors. Toya and Skidmore [7] developed a model to estimate the damage per GDP caused by natural disaster.

In this study, for the more accurate and applicable model, both of meteorological and socioeconomic factors were considered as input data to estimate snow damage. Regression models were developed using daily maximum fresh snow depth. The fresh snow depth was divided into six categories and different regression models were developed to improve the accuracy of the models.

2 Multiple Linear Regression Analysis

Multiple linear regression analysis is the linear model with more than two independent variables to estimate one dependent variable. The regression model to estimate Y with $X_0, X_1, X_2, \ldots, X_i$ (where i is the number of variables) independent variables were shown in Eq. (1).

$$Y = \beta_0 + \beta_1 x_1 + \beta_2 x_2 + \cdots + \beta_j x_j + \epsilon \tag{1}$$

where, $\beta_0, \beta_1, \beta_2, \ldots, \beta_i$ are regression coefficients, ϵ is the random error.

The accuracy of the regression model is estimated using adjusted-$R^2(R_a^2)$. The adjusted-R^2 is shown in Eq. (2).

$$R_a^2 = 1 - \left(\frac{n-1}{n-k-1}\right)\frac{SSE}{SST} \tag{2}$$

where n is the number of data, k is the number of independent variables. SSE and SST are the sum of squared error and total sum of squares.

3 Data

3.1 Snow Damage Report

The snow damage data from 1994 to 2015 was collected from the Annual Natural Disaster Report published by Ministry of Public Safety and Security (MPSS) in South Korea. The damages were categorized with 23 types of damaged facilities. The number of snow damages during 22 years (1994–2015) in the administrative districts were drawn in Fig. 1. The frequently damaged areas were located in the mountainous areas or near ocean. The most damaged districts were Jeonlla, Chungcheong, and Kangwon-do. Among the 23 types of facilities, 33% of snow damage was occurred in the greenhouse. Therefore, the greenhouse is shown as the most vulnerable facility to the snow disaster.

Fig. 1 The number of snow disasters for 22 years (1994–2015)
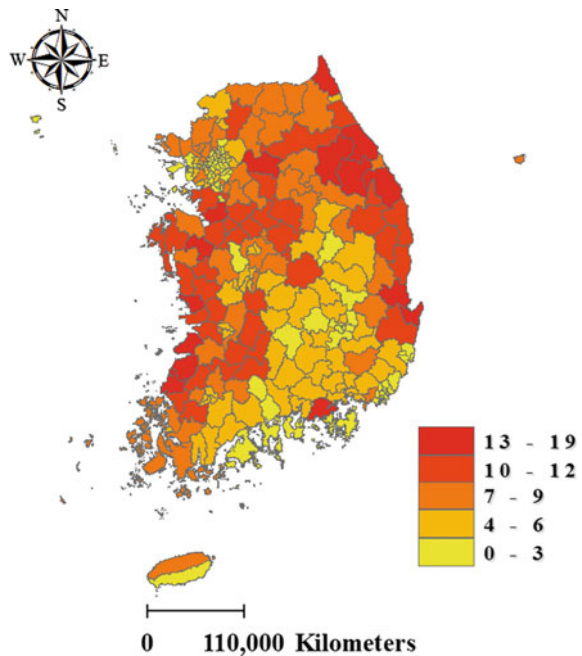
3.2   Meteorological Data

In South Korea, snow damage is mostly caused by the snow loads over the roof [8]. The snow loads could be significantly changed depending on the humidity. The weight of 1 foot of fresh snow ranges from 3 lb per square foot for light and dry snow to 21 lb per square foot for heavy and wet snow [9]. Yu et al. [10] proposed that the light and dry snow is formed below −10 °C and the heavy and wet snow is formed between −1 and 1 °C. Therefore, the snow density depends on the relative humidity and temperature. In this study, snow depth (daily maximum fresh snow depth), relative humidity, daily minimum temperature, daily maximum temperature, and daily mean temperature were applied as the meteorological input data.

3.3   Socioeconomic Factors

As mentioned earlier, the most vulnerable facility to the snow disaster is greenhouse which is located in the agricultural area. According to Statics Korea, the average age of the agricultural area is 66.5 years in 2016 and increases very rapidly. Therefore, it is important to consider the agricultural district and the greenhouse area for the snow damage estimation. As the socioeconomic factors, the area of administrative districts, greenhouse area, number of farmers, and number of farmers over age 60 were considered in the regression model.

4   Results

The multiple linear regression model was developed using 541 historical snow damage data for the three provinces in South Korea, Jeonlla, Chungcheong, and Kangwon-do. The snow damage data was collected for the lasts 22 years. However, some damages were happened when snow depth was less than 10 cm which was not heavy snow. Therefore, it was assumed that the snow damage data with low snow depth might be caused by the maintenance mistake and cannot present the real disaster situation. The snow depth causing damage should be defined.

To find the appropriate thresholds of the snow depth, six different regression models were developed as Table 1. Case 1 is the snow damage estimation model when the snow depth was higher than 10 cm, that is, the snow depth less than 10 cm was discarded. As the same manner, case 6 discards the data with snow depth less than 25 cm. After less than 25 cm of snow depth data was discarded, the number of data considered in a multiple regression model was only 91.

However, the expectation accuracy of the model is increased as the snow depth threshold become high. The most accurate model is case 6 with 0.7074 of adjusted R^2. Therefore, it is concluded that the reliable snow damage could be estimated

Table 1 The number of data considered in the regression models and adjusted R^2

Case	Threshold (cm)	Number of data	Adjusted R^2 (R_a^2)
1	10	342	0.256
2	13	278	0.356
3	15	229	0.449
4	18	184	0.526
5	20	162	0.562
6	25	91	0.707
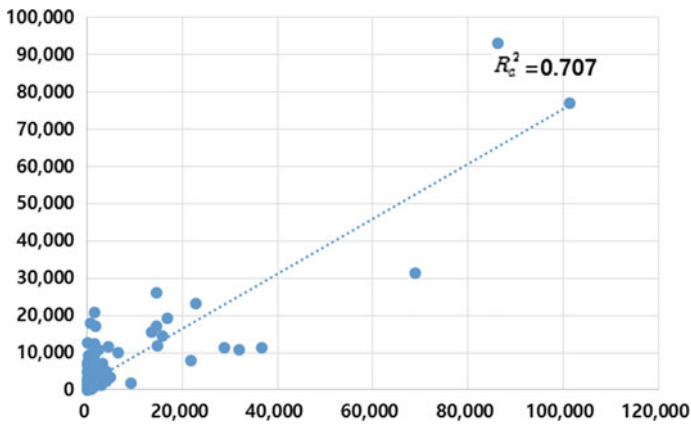
Fig. 2 Comparison of observed (*X*-axis) and calculated (*Y*-axis) snow damage using multiple regression model (case 6) (unit: thousand dollar)

when the fresh snow depth is higher than 25 cm in case of South Korea. In Fig. 2, the observed and calculated snow damage in case 6 model was shown.

The regression coefficients were listed in Table 2. The regression coefficients from the six different models did not have the regular sign for the dependent variables. For example, some of the models have the positive coefficients for the minimum temperature and relative humidity, whereas others do not.

Table 2 Regression coefficients of 6 models

Independent variables	Regression coefficients					
	Case 1	Case 2	Case 3	Case 4	Case 5	Case 6
Constant	−6,286,238.6	−10,908,407.7	−15,606,573.1	−23698,152.9	−23,374,841.4	−15,570,661.5
Snow depth	170,478.0	199,131.3	216,559.8	245,774.9	226,793.7	115,164.8
Maximum temperature	626,055.4	636,389.3	703,090.3	90,879.5	946,309.5	1,229,436.7
Minimum temperature	−76,258.6	−171,414.9	−139,806.2	−320,137.5	−146,532.1	534,184.8
Relative humidity	−53,469.2	−14,819.3	29,123.1	74,805.9	86,000.4	66,930.3
Area	14,567.1	20,840.3	27,131.0	35,046.1	38,246.7	45,232.5
Area of greenhouse	1413.8	1932.2	2798.7	3421.1	4331.5	4217.6
Farming population	−59.2	−103.2	−127.5	−144.4	−193.6	−21.1
Farming population older than 60	243.3	69.8	−51.1	−255.4	−145.9	−268.0

5 Conclusions

In this study, multiple linear regression models using both of meteorological and socioeconomic factors were developed to estimate snow damages. The snow depth thresholds were investigated using six different regression models for more accurate model estimation. Historical 541 snow damage cases from Jeonlla, Chungcheong, and Kangwon-do which had the largest snow damages were applied in the models. As the result, the regression models with higher than 25 cm of snow depth showed the most accurate estimation. However, the regression signs of the six models do not have consistency. The developed models are needed to be verified using the more number of data, however, the model could give the decision-maker the insight about the area or scale of the possible snow damage for the rapid disaster response.

References

1. Oh, S.M., Kim, G.H., Jung, Y.H., Kim, D.H., Kim, H.S.: Risk assessment of heavy snowfall using PROMETHEE—the case of Gangwon Province. J. Korean Soc. Hazard Mitig. **15**(1), 87–98 (2015)
2. Park, H.S., Lee, J.S., Yu, I.S., Jeong, S.M., Chung, G.H.: Snow disaster risk index in the Ulsan Metropolitan City. J. Korea Soc. Hazard Mitig. **14**(2), 97–106 (2014)
3. Kim, Y.S., Kang, N.R., Kim, S.J., Kim, H.S.: Evaluation for snowfall depth forecasting using neural network and multiple regression models. J. Korean Soc. Hazard Mitig. **13**(2), 269–280 (2013)
4. Jeong, J.H., Lee, S.: Estimating the direct economic damages from heavy snowfall in Korea. J. Clim. Res. **9**(2), 125–139 (2014)
5. Kwon, S.H., Chung, G.H.: Estimation of snow damages using multiple regression model—the case of Gangwon Province. J. Korean Soc. Civ. Eng. **37**(1), 61–72 (2017)
6. Kwon, S.H., Kim, J.H., Chung, G.H.: Snow damage estimation of Gangwon Province damages using regression analysis. Korean Soc. Hazard Mitig. **16**(2), 437–443 (2016)
7. Toya, H., Skidmore, M.: Economic development and the impacts of natural disasters. Econ. Lett. **94**, 20–25 (2007)
8. NEMA (National Emergency Management Agency): The Development of Heavy Snowfall Casualty Minimization Policies and Optimal Road Snow Removal Systems considering Climate Change (2012)
9. Gooch, C.A.: Heavy Snow Loads. Dairy Facilities/Environmental Management Engineering. Cornell University, Ithaca (1999)
10. Yu, I.S., Kim, H.Y., Imee V.N, Jeong, S.M.: Assessment and Improvement of Snow Load Codes and Standards in Korea. J. Korean Soc. Civ. Eng. **34**(5), 1421–1433 (2014)

Spatial Variability of Rainfall in Urban Catchment

H. Haris, M. F. Chow and L. M. Sidek

Abstract The rapid urbanization process has created massive pressure on the environment and interrupted the water balance. In this research, Penchala River was chosen as the research area. Spatial variability of rainfall can lead to significant error in rainfall–runoff processes and hydrological modeling, specifically in the urban area. Thus, one-way analysis of variance (ANOVA) was used to determine whether there are any statistically significant differences between the means of rainfall data from selected rainfall stations. The yearly and monthly data of all eight rainfall stations during the period of the year, 2012–2015 was used for this analysis. The post hoc test was used to identified, in which rainfall station differed among each other during the study. The null hypothesis (no significant difference) is accepted, when the computed p value is more than 0.05. The results showed that there is no significant statistical difference in the rainfall data between the rain gauges of S1–S8 with the p-values 0.945 (2012), 0.954 (2013), 0.342 (2014), and 0.427 (2015). It can be concluded that none of the gauge used for the determination of rainfall dataset contained systematic errors.

Keywords Spatial variability · Penchala river · Urban runoff · Rainfall analysis ANOVA analysis · Boxplot analysis

H. Haris
Department of Civil Engineering, Universiti Tenaga Nasional,
43000 Kajang, Selangor, Malaysia
e-mail: harizah.haris@gmail.com

M. F. Chow (✉) · L. M. Sidek
Center for Sustainable Technology and Environment (CSTEN),
Universiti Tenaga Nasional, 43000 Kajang, Selangor, Malaysia
e-mail: Chowmf@uniten.edu.my

L. M. Sidek
e-mail: lariyah@uniten.edu.my

1 Introduction

The urbanization with increasing population and development has extremely interrupted the balance of water in natural catchment. The variation in hydrological responses due to rainfall and land use changes increases the difficulty on rainfall–runoff modeling. In addition, large error in rainfall data can be a significant source of error in flood simulation.

Climate change in the past decades has significantly changed the rainfall pattern as well as its magnitude and interannual variability worldwide [1–4]. Tropical countries have experienced warmer climate, where the temperature was found to be increased by 0.7–0.8 °C over the last century. Much of this variability is driven by the El Nino-Southern Oscillation (ENSO), timescale based oscillation of the Indian Ocean Dipole (IOD) and the intra-seasonal Madden Julian Oscillation (MJO) [5]. Such increase in rainfall variability is always accompanied by shifting in its seasonal magnitude, timing, and duration. Department of Meteorology Malaysia [5] stated that there is a decreasing seasonal rainfall trend for Peninsular Malaysia in the year, 1998–2007 as compared to those in 1961–1990. Among the seasons, the wettest and driest seasons observed was in the month of June, July and August, and in the month of March, April and May, respectively.

West of Peninsular Malaysia also experienced higher rainfall than east of Peninsular Malaysia in December, January and February [5]. Meanwhile, east of Peninsular Malaysia experienced higher rainfall than the west of Peninsular Malaysia in September, October, and November. The climate change has brought in heavy rainfall and caused several floods event in Malaysia.

Climate change has changed the magnitude of the rainfall event, when the annual mean precipitation does not change significantly [6–13]. Increasing intensities and duration of rainfall during the monsoons have intensified the occurrence of flooding events and impacted many people in terms of loss of lives and property damage [14].

2 Study Site

In this study, Penchala River located in Petaling Jaya, Kuala Lumpur was chosen as the study area, as shown in Fig. 1. Penchala River catchment is located within the Klang River catchment in the state of Selangor. It is flowing through the district of Petaling and finally enters the Klang River.

The total length of Penchala River is about 12 km, which 4 km of its length is located within the Dewan Bandaraya Kuala Lumpur (DBKL) area while another 8 km is located within the Petaling district. The catchment area is about 35.41 km^2 and majority of the land use is hilly area with mainly medium to low density of residential development area.
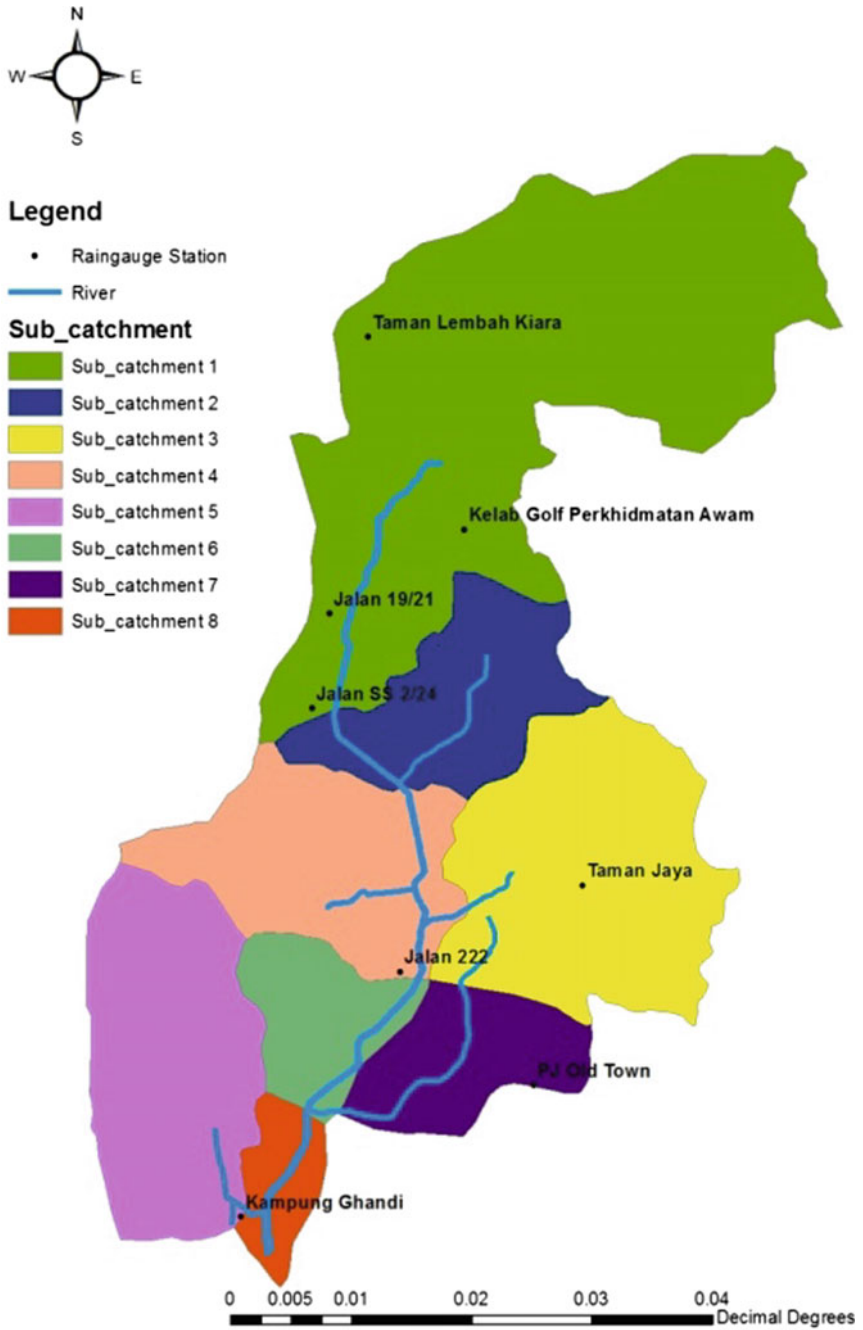
Fig. 1 Penchala river catchment (ARCGIS map)

Penchala River is one of the major contributors of pollution to the Klang River. The water quality index (WQI) at the upstream of Penchala River is classified as Class I. However, the WQI at the downstream is dropped to Class IV or Class V after it is flowing through 70% of channelized concrete channel in the Petaling district [15].

3   Rainfall Data

Rainfall data was collected by using a tipping bucket rain gauge with resolution of 0.5 mm in this study. The rain gauge was set up at a clear place in order to collect the total rainfall amount without any obstruction. Eight new tipping bucket rain gauges were installed at selected locations within the Penchala River catchment. The rainfall data was collected biweekly from the site from July 2012 to September 2015. Table 1 shows the details of installed rainfall stations.

4   Monthly Rainfall Distribution

Most of the studies have reported that spatial variability of rainfall is a main controlling factor for flood formation in urban areas [16, 17]. Thus, the variability of rainfall distribution in Penchala River catchment was investigated during this

Table 1 Details of newly installed rainfall stations

No.	Station number	Station name	Latitude (N)	Longitude (E)	Owner
1	3016080	Kg. Ghandi	03° 04′ 35.1″	101° 37′ 16.5″	DID
2	3016077	Jalan 222	03° 05′ 49″	101° 38′ 4.1″	DID
3	3116079	Jalan SS 2/24	03° 07′ 7.4″	101° 37′ 42.7″	iFFRM
4	3116076	Jalan 19/21	03° 07′ 35.8″	101° 37′ 42.7″	DID
5	3116075	Taman Lembah Kiara	03° 09′ 3.5″	101° 37′ 57.1″	JLN
6	3110016	Bukit Kiara Golf Resort	03° 08′ 1.7″	101° 38′ 23.2″	DID
7	3116078	Taman Jaya	03° 06′ 8.5″	101° 38′ 42″	MBPJ
8	3116080	PJ Old Town	03° 05′ 14.9″	101° 38′ 44.4″	MBPJ

DID Department of Irrigation and Drainage; *iFFRM* Integrated Flood and Rainfall Management; *JLN* Jabatan Landskap Negara
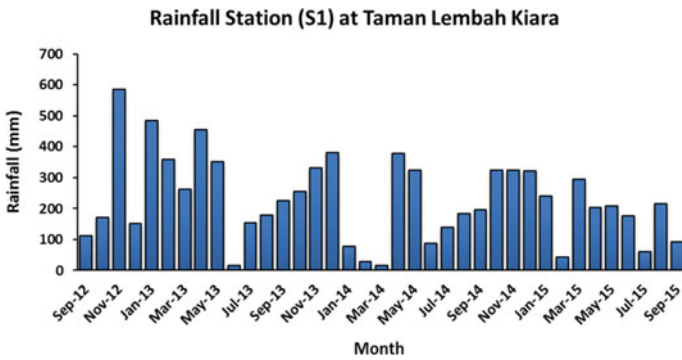
Fig. 2 Monthly rainfall distribution at Taman Lembah Kiara rainfall station
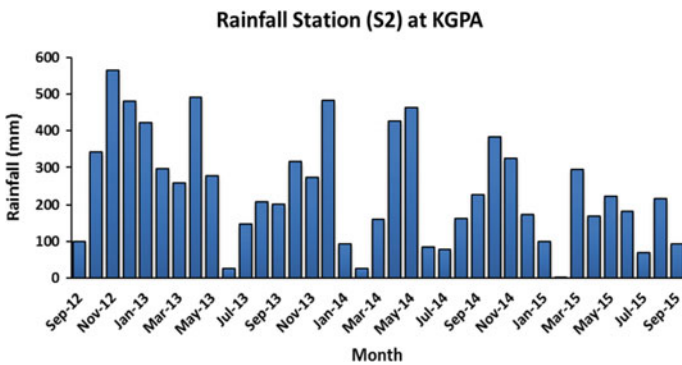
Fig. 3 Monthly rainfall distribution at KGPA rainfall station

study. The monthly rainfall distribution during the periods of 2012–2015 was plotted for eight rainfall stations within the Penchala River catchment as shown in Figs. 2, 3, 4, 5, 6, 7, 8 and 9.

The rainfall stations are denoted as S1-Tmn Lembah Kiara; S2-KGPA; S3-Jalan 19/21; S4-Jalan SS2/24; S5-Taman Jaya; S6-Jalan 222; S7-Jalan Othman; and S8-Kg. Ghandi, respectively. According to the monthly rainfall distribution in Table 4, the average monthly rainfall for Penchala River catchment is recorded to be as 249.50 mm. This value is slightly higher than the monthly mean rainfall (191 mm) as reported by Desa and Niemczynowicz [17] for Kuala Lumpur. The highest monthly rainfall occurred in November, 2012 at Kg. Ghandi station with total rainfall amount of 668.20 mm, whereas the lowest monthly rainfall occurred in February, 2015 at KGPA Station with the total rainfall of only 0.9 mm. The occurrence of monthly rainfall during the months of October to December was found to be relatively higher than other months due to the Northeast monsoon season.
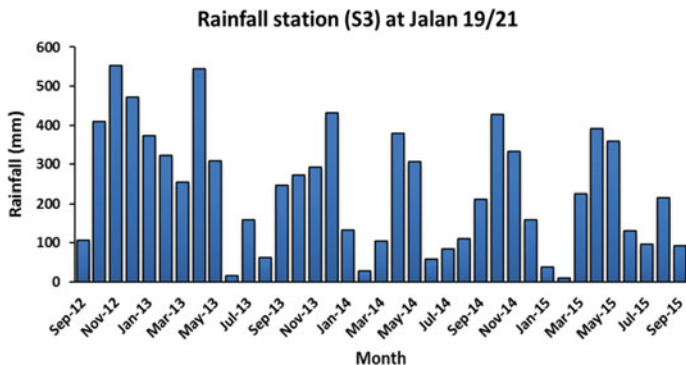
Fig. 4 Monthly rainfall distribution at Jalan 19/21 rainfall station
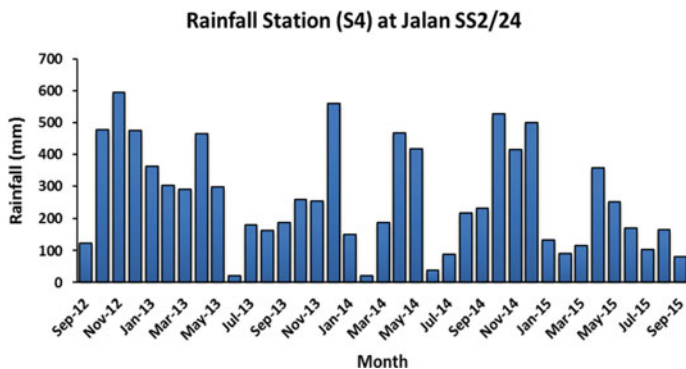
Fig. 5 Monthly rainfall distribution at Jalan SS2/24 rainfall station
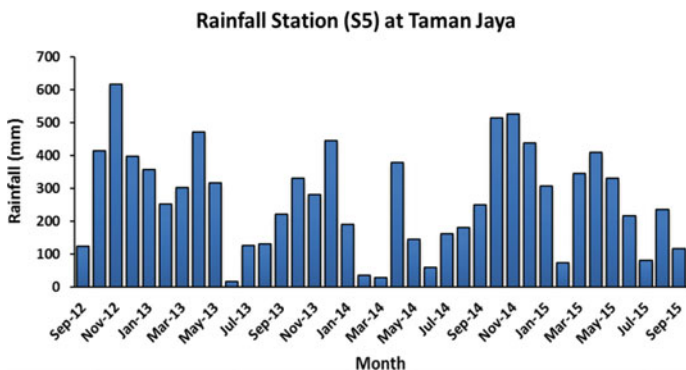
Fig. 6 Monthly rainfall distribution at Taman Jaya rainfall station
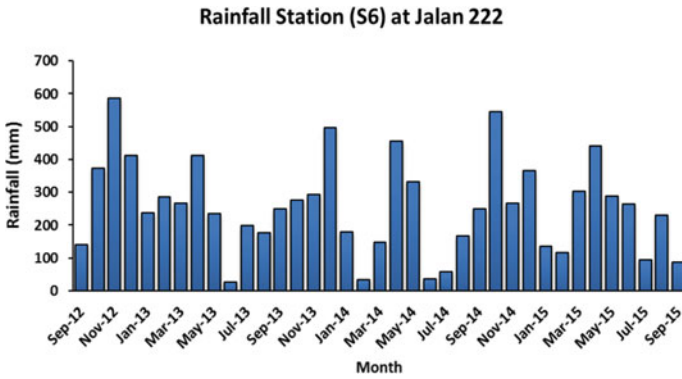
Fig. 7 Monthly rainfall distribution at Jalan 222 rainfall station
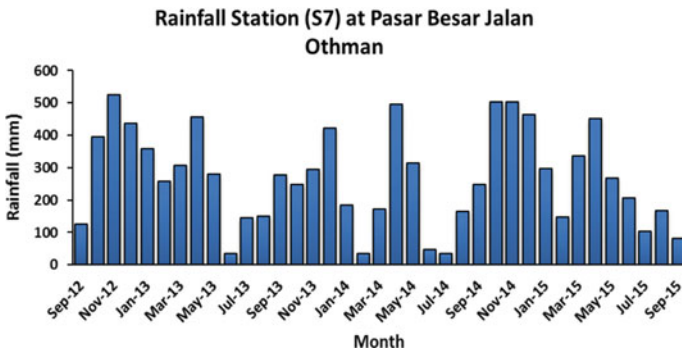
Fig. 8 Monthly rainfall distribution at Jalan Othman rainfall station
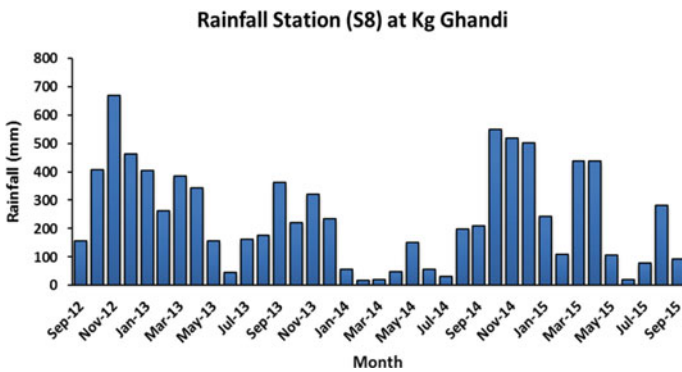
Fig. 9 Monthly rainfall distribution at Kg. Ghandi rainfall station

Table 2 Descriptive statistic summary for rainfall data at each rain gauge

Year	Rainfall (mm)					
		Sum of squares	df	Mean square	F	Sig.
2012	Between groups	793.9	7	113.4	0.319	0.945
	Within groups	170,647.4	480	355.5	–	–
2013	Between groups	1175.1	7	167.8	0.300	0.954
	Within groups	536,744.3	960	559.1	–	–
2014	Between groups	17,827.5	7	2546.7	1.13	0.342
	Within groups	1,820,873	808	2253.5	–	–
2015	Between groups	1698.1	7	242.5	1.005	0.427
	Within groups	108,144.6	448	241.3	–	–

The average annual rainfall obtained for all rainfall stations of S1, S2, S3, S4, S5, S6, S7, and S8 was 2765, 2910, 2869, 3212, 3230, 3107, 3271, and 2925 mm, respectively. The spatial variability of rainfall in the Penchala River catchment showed that the mean annual rainfall is found to be relatively higher in the central region (S4, S5, S6, and S7), when compared to the upstream (S1, S2, S3) and downstream (S8) regions. Central region with fully urbanized area is likely to have warmer climate than the upstream rural area, and to cause large increase in the amount of rainfall. Many studies have shown that amount and intensity of rainfall will increase along with urbanization due to urban heat island effect [18–20]. The average contribution of Northeast monsoon (October, November and December) to the annual rainfall in rainfall stations of S1, S2, S3, S4, S5, S6, S7 and S8 is 35.2, 38.7, 39.2, 42.5, 41.2, 38.8, 38.7, and 45.9%, respectively for the period between September 2012 and September 2015.

5 Boxplot Analysis of Monthly Rainfall

The rainfall dataset from each of the station was further investigated using boxplot analysis. The storm event is defined as rainfall depth greater than 1.0 mm. Similar definition for minimum rainfall depth of 1 and 0.8 mm was given by Pedersen et al. [21], Chow and Yusop [22] studies, respectively. The monthly data was compiled from daily rainfall data, while the annual data was derived from monthly data. Boxplots are useful for identifying outliers and comparing distributions based on five number summaries: minimum, first quartile (25%), median (50%), third quartile (75%) and maximum. The outliers of the rainfall data can be detected from the boxplot graph, where any of the point is located below minimum and above maximum. It was noted that great variability was observed for rainfall during the months of June and August.

The descriptive statistic summary of mean, median, standard deviation, minimum and maximum values for the monthly rainfall data from September 2012 to

September 2015 are shown in Table 2. It is seen from the table that the daily mean rainfall depth is about 24.1 mm. The maximum daily rainfall event is found to be 564 mm, which occurred during the monsoon season of December 2014.

6 One-Way Analysis of Variance (ANNOVA)

Spatial variability of rainfall can lead to significant error in rainfall–runoff processes and hydrological modeling, especially in urban area [23, 24]. Therefore, one-way analysis of variance (ANOVA) is used to determine, whether there are any statistically significant differences between the data of rainfall stations. The yearly and monthly data of all eight rainfall stations during the period of September 2012 to September 2015 was used for ANOVA analysis. The post-hoc test was used to define, in which rainfall station is differed from each other during the study. Tables 3 and 4 represent the results of statistical analysis for rainfall data from September 2012 to September 2015. The null hypothesis (no significant difference) is accepted, when the computed p value is greater than 0.05. The results show that there is no statistical significant difference in the rainfall data between the rain gauges S1–S8 with p-values of 0.945 (2012), 0.954 (2013), 0.342 (2014) and 0.427 (2015). It can be concluded that no gauge in any of the rainfall dataset contains systematic errors.

Table 3 ANOVA results for rainfall data between rain gauges

Year	Rain gauge	N	Mean	Median	Standard deviation	Min	Max
2012	1	61	23.9	23.9	15.5	1.2	73.4
	2	61	26.2	21.6	23.1	1.0	129.4
	3	61	24.4	19.2	20.0	2.2	100.4
	4	61	25.5	17.2	22.2	2.0	86.2
	5	61	21.9	17.2	15.3	1.0	65.6
	6	61	22.8	20.9	15.7	1.0	76.3
	7	61	24.3	21.8	17.2	1.2	69.4
	8	61	24.8	20.8	19.7	1.0	80.6
2013	1	121	24.3	15.4	27.1	1.0	156.8
	2	121	23.9	14.8	24.8	1.2	116.6
	3	121	24.5	16.8	22.5	1.0	92.2
	4	121	24.3	16.4	22.8	1.0	98.4
	5	121	24.1	14.6	25.6	1.0	141.3
	6	121	23.3	17	21.7	1.0	102.6
	7	121	23.0	16	22.4	1.0	114.8
	8	121	20.9	13.6	21.2	1.0	115.8

(continued)

Table 3 (continued)

Year	Rain gauge	N	Mean	Median	Standard deviation	Min	Max
2014	1	102	24.4	12.7	36.9	1.0	284.0
	2	102	20.0	13.4	19.9	1.4	106.0
	3	102	26.9	17.1	39.4	1.0	231.0
	4	102	35.9	16.9	74.1	1.0	564.0
	5	102	31.9	21.0	43.8	1.0	306.0
	6	102	29.1	15.8	41.0	1.0	231.0
	7	102	31.8	18.3	52.6	1.0	450.0
	8	102	30.9	15.7	53.1	1.0	402.0
2015	1	57	19.3	17.6	13.0	1.2	53.5
	2	57	17.5	13.6	13.6	1.0	58.0
	3	57	20.2	17.0	15.6	1.0	57.3
	4	57	20.4	19.8	12.4	2.3	53.5
	5	57	23.6	18.2	16.7	1.0	72.5
	6	57	23.1	19.6	15.8	1.8	73.0
	7	57	22.5	20.8	15.3	2.3	59.4
	8	57	20.8	12.9	20.0	1.0	69.7

Table 4 Correlation results of rainfall data among all rainfall stations

Rain gauge	Rain gauge							
	S1	S2	S3	S4	S5	S6	S7	S8
S1	1							
S2	0.825	1						
S3	0.767	0.906	1					
S4	0.753	0.866	0.874	1				
S5	0.798	0.762	0.843	0.854	1			
S6	0.741	0.843	0.888	0.916	0.866	1		
S7	0.767	0.801	0.843	0.912	0.928	0.912	1	
S8	0.645	0.600	0.664	0.682	0.815	0.699	0.781	1

The spatial correlation of rainfall data between the rain gauges was also investigated and the correlation results are shown in Table 3. All rainfall data between the rain gauges showed statistically positive correlation with most of the correlation coefficients are greater than 0.7. This indicated that all rain gauges have measured the same amount of rainfall over the period of September 2012 to September 2015. It is observed that correlation is reduced with increasing inter-gauge distance such as S1–S8 (Pearson correlation, $r = 0.645$). Therefore, the spatial variability of rainfall should be considered accordingly in a larger river basin.

7 Conclusion

Monthly rainfall analysis shows that the average contribution of Northeast monsoon (October, November and December) to the annual rainfall in rainfall stations of S1, S2, S3, S4, S5, S6, S7 and S8 is 35.2, 38.7, 39.2, 42.5, 41.2, 38.8, 38.7, and 45.9%, respectively. Meanwhile, the mean daily rainfall depth is about 24.1 mm. The maximum rainfall for daily event is 564 mm and it occurs during monsoon season in boxplot analysis. The rainfall data between all rain gauges showed statistically positive correlation with most of the correlation coefficient are greater than 0.7. This indicates that all rain gauges have measured the similar rainfall amount over the period of September 2012 to September 2015. It is observed that the correlation is reduced with the increasing inter-gauge distance, for example S1–S8 (Pearson correlation, $r = 0.645$). Therefore, the spatial variability of rainfall should be considered accordingly in the larger river basin.

References

1. Karl, T.R., Trenberth, K.E.: Modern global climate change. Science **302**, 1719–1723 (2003)
2. Allan, R.P., Soden, B.J.: Atmospheric warming and the amplification of precipitation extremes. Science **321**, 1481–1494 (2006)
3. IPCC: Climate change 2013: The physical science basis. Working group 1 contribution to the fifth assessment report of the Intergovernmental Panel on Climate Change (2013)
4. Gorman, P.A.: Precipitation extremes under climate change. Curr. Clim. Change Rep. **1**, 49–59 (2015)
5. Malaysian Meteorological Department (MMD): Climate change scenarios for Malaysia 2001–2099. Scientific report, Malaysian Meteorological Department, Ministry of Science, Technology and Innovation, Malaysia (2009)
6. Chow, M.F., Haris, H., Sidek, L.M.: Analysis of rainfall trend and temporal patterns: a case study for Penchala River basin, Kuala Lumpur. In: Proceeding of the International Symposium on Flood Research and Management (2015)
7. Peterson, T.C., Taylor, M.A., Demeritte, R., Duncombe, D.L., et al.: Recent changes in climate extremes in the Caribbean region. J. Geophys. Res. **107**, 4601 (2002)
8. Klein Tank A.M.G., Können, G.P.: Trends in indices of daily temperature and precipitation extremes in Europe, 1946–1999. J. Clim. **16**, 3665–3680 (2003)
9. Groisman, P.Ya., Knight, R.W., Karl, T.R., Easterling, D.R., et al: Contemporary changes of the hydrological cycle over the contiguous United States: trends derived from in situ observations. J. Hydrometeorol. **5**, 64–85 (2004)
10. Alexander, L.V., Zhang, X., Peterson, T.C., Caesar, J., and others: Global observed changes in daily climate extremes of temperature and precipitation. J. Geophys. Res. **111**, D05109 (2006)
11. Klein Tank A.M.G., Peterson, T.C., Quadir, D.A., Dorji, S., et al.: Changes in daily temperature and precipitation extremes in central and south Asia. J. Geophys. Res. **111**, D16105 (2006)
12. Trenberth, K.E., Fasullo, J.: Water and energy budgets of hurricanes and implications for climate change. J. Geophys. Res. **112**, D23107 (2007)
13. Groisman, PYa., Knight, R.W.: Prolonged dry episodes over the conterminous United States: new tendencies emerging during the last 40 years. J. Clim. **21**, 1850–1862 (2008)

14. Loo, Y.Y., Billa, L., Singh, A.: Effect of climate change on seasonal monsoon in Asia and its impact on the variability of monsoon rainfall in Southeast Asia. Geosci. Front. **6**, 817–823 (2015)
15. Sidek, L.M., et al.: Challenges for urban water management for resilient environment, crossing from crisis to sustainability. In: The 2nd International Symposium on Advanced Technology for River Management, pp. 7–12 (2013)
16. Obled, C.H., Wendling, J., Beven, K.: The sensitivity of hydrological models to spatial rainfall patterns: an evaluation using observed data. J. Hydrol. **159**, 305–333 (1994)
17. Desa, M.M.N., Niemczynowicz, J.: Spatial variability of rainfall in Kuala Lumpur, Malaysia: long and short term characteristics. Hydrol. Sci. J. **41**(3), 345–362 (1996)
18. Atkinson, B.W.: Urban effects on precipitation: an investigation of London's influence on the severe storm in August 1975. Occasional paper no. 8, Department of Geography, Queen Mary College, University of London, UK (1977)
19. Huff, F.A., Changnon Jr., S.A.: Potential urban effects on precipitation in the winter and transition seasons at St. Louis, Missouri. J. Climate Appl. Meteorol. **25**, 1887–1986 (1986)
20. Collier, C.G.: The impact of urban areas on weather. Q. J. R. Meteorol. Soc. **132**(614), 1–25 (2006)
21. Pedersen, L., Jensen, N.E., Christensen, L.E., Madsen, H.: Quantification of the spatial variability of rainfall based on a dense network of rain gauges. Atmos. Res. **95**, 441–454 (2010)
22. Chow, M.F., Yusop, Z.: Characterization and source identification of stormwater runoff at tropical urban catchments. Water Sci. Technol. **9**(2), 244–252 (2014)
23. O'Loughlin, G., Huber, W., Chocat, B.: Rainfall-runoff processes and modelling. J. Hydraul. Res. **34**(6), 733–751 (1996)
24. Syed, K.H., Goodrich, D.C., Myers, D.E., Sorooshian, S.: Spatial characteristics of thunderstorm rainfall fields and their relation to runoff. J. Hydrol. **271**, 1–21 (2003)

Analysing Petroleum Leakage
from Ground Penetrating Radar Signal

**Zulkarnaini Mat Amin, Norwahidatul Akma Kamal,
Norhazimah Husna Shokri and Amalina Yusop**

Abstract The current evolution of technologies and rapid development has influenced the pipeline construction all over the world. However, this development can be a risk to the surrounding environment, for example pipeline leakage. There are numerous incidents that caused by pipeline leakage, which includes petroleum pipeline leakage. The petroleum pipeline leakage is one of the very serious situations that can lead to the explosion and the worst it can cause disaster to the nearby area and loss of life. There are numerous methods that are used to detect underground pipeline leaks. One of the methods is Ground-Penetrating Radar (GPR). This study investigates the petroleum leakage and its impact to the surrounding soil. The objectives of this study are to determine the physical properties of the contaminated soil and to evaluate the numerical analysis of the electromagnetic wave for petroleum leakage diffusion in sand. The prototype of leakage model has been built for simulating observation. The data have been collected for every hour for 16 h to monitor the petroleum leakage diffusion. The software used to process and extract GPR data is Reflex 2DQuick. Furthermore, the Finite Difference Time Domain (FDTD) method was used for the simulation of the petroleum leakage diffusion by simulating the electromagnetic waves penetrating through different materials. GPR signal modelling and numerical analysis were done in MATGPR software. The result of this study indicates the changes of dielectric constant of sand from 3 to 5.3 when the sand is mixed with petroleum. The increase in dielectric properties of sand is due to its ability to store the electrical energy. Moreover, the result of GPR signal modelling proves that the content of petroleum has disturbed the signal attenuation which is transmitted by the antenna.

Z. M. Amin (✉) · N. A. Kamal · N. H. Shokri · A. Yusop
Geomatic Innovation Research Group, Faculty of Geoinformation
and Real Estate, Universiti Teknologi Malaysia, 81310 Skudai, Johor, Malaysia
e-mail: zulkarnaini@utm.my

1 Introduction

In the modern world, the infrastructure development is such a common thing. There are a lot of construction, excavation work and maintenance. All of this work needs a very high accuracy of geospatial data in order to avoid any mistake and serious problem during implementation. The pipeline leakage is one of the very serious situations that can lead to the explosion and the worst it can cause disaster to the nearby area and loss of life. The pipelines are used as a transportation medium of many resources such as water, gas, petroleum and others. The major reasons for pipeline leakage are erosion, mechanical failures, construction defeats, natural disaster and other reasons. There are numerous incidents caused by pipeline leakage all around the world especially the most dangerous pipeline which is petroleum pipeline leakage. It can lead to a very critical problem. Many cases of pipeline leakage are caused by excessive stress, corrosion and valve cracks and it is starts from small cracks [1]. Other contributors to the pipeline leakage are natural disaster and construction works. One of the cases was reported on April 2014 in Malaysia. According to *The Star Online*, the incident occurred in Gua Musang, Kelantan caused 11 injured and 4 cars were burnt. There was an explosion caused by leaking hose when a tanker was filling up its underground tank. The leaking fuel flowed to the nearby food stall before catching fire [2].

Various methods are used to detect underground pipeline leaks and breaks. The common method that was used is acoustic devices [3], gas sampling devices, pressure wave detectors, microphone leak detection [4]. Each method has their own capabilities and weaknesses depending on the type and size of case area and the stage of the leakage occurred. One of the sophisticated methods is detection using Ground-Penetrating Radar (GPR). The word radar itself represented that this method used radio detection and ranging. It is basically transmits the electromagnetic signals into the soil and the total time travelled of the emitted signals will be recorded [5]. GPR is a technology that is often used in various underground detections. It is a radar that generates an image based on the reflection of radar waves from soil, pipe or anything located underground. The advantage of using GPR for leak detection are it is known as a rapid measurement, noninvasive nature of the technique and its capability to detect defects before they reach an advanced phase. Unlike the other methods, application of GPR for leak detection is suitable for various type of pipe whether metal or non-metal. GPR is a higher potential method that can be used to avoid difficulties encountered with usually used acoustic leak detection [6]. Therefore, the underground detection by using GPR is the potential method that can be used for various cases. Besides, GPR serve as a non-destructive technique (NDT), which is very suitable for use in urban environments, as well as protecting the geological, environmental and archaeological [7].

As a rapid measurement technique, GPR directly gives a raw data after scans were done. The raw data must go through some processes of filtering before extracting the parameters. The interpretation and information from the GPR data

will be later used in numerical modelling known as Finite Difference Time Domain (FDTD) method. FDTD is one of the numerical modelling techniques, which implement the time domain method [8–10]. FDTD method is easy and simple, both conceptually and in terms of implementation, of the full-wave techniques is used to answer questions in electromagnetic problem [9].

In this study, data collection has been accomplished by using GPR. GPR can effectively locate metallic and non-metallic objects. However, it not suitable and cannot work in certain soil conditions, which contain high water such as clay. The penetration of GPR signal will be disturbed by the soil itself and thus the data obtained will be difficult to interpret. Soil is one of the elements of subsurface and it is defined as a top layer of the earth that also contains of mineral, water and decay organic. It can be considered as three phase mediums, which include soil matrix, air and water [11]. GPR signals are usually disturbed by water content in the soil. The detection ability of the objects and the contrast between dielectric value can be increased by the differences of water capacity in the background medium and the buried objects [12]. Soil properties parameters include the velocity and dielectric constant value. Each material has different value of velocity and dielectric constant. Even soil itself has different parameter based on different soil types.

2 Methodology

This study involved the design of special simulation tank to simulate the petroleum or specifically diesel leakage. The prototype laboratory model for this study which was shown in Fig. 1 was made up from fibreglass because of its less reflectivity, stability and strength. This prototype tank with a dimension of 2 m × 2 m × 2 m is filled with sand. A 1.8 m metal pipe was buried in this tank at 0.5 m depth. A hole was created at the middle of the pipe to simulate the pipe leakage situation. The
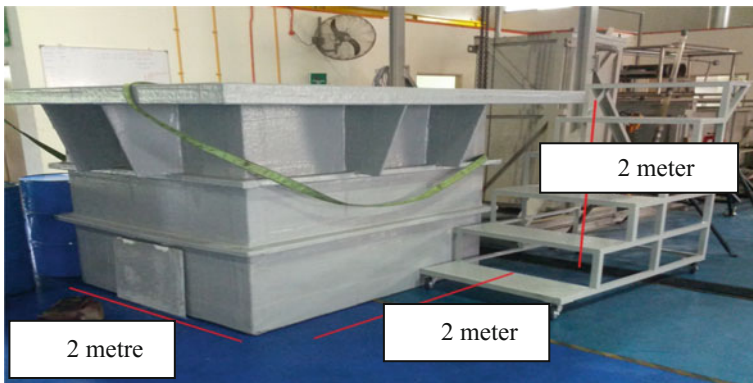
Fig. 1 Prototype laboratory tank

liquid flow into the pipe was controlled by the flow-line valve to monitor the volume of liquid pass into the simulation tank.

The equipment that was used in this study is GPR IDS Detector Duo. It is a multi-channel antenna with 250 and 700 MHz frequency, respectively.

2.1 Data Acquisition

Data collection for GPR survey was performed using grid method. Hence, grid lines were established at the top of the tank as shown in Fig. 2. Grid method consists of two scans which are longitudinal and transversal scan lines. Adoption of grid method for GPR survey is more systematic and as data was scanned along the designated lines at constant interval. Besides, a grid data can easily be used to create the three dimensional (3D) model.

2.2 Data Processing

Basic processing and filtering of GPR data were done using Reflex 2DQuick software [13]. In this study, the software was used to obtain the electromagnetic parameter of the contaminated soil and signal interpretation. The properties of contaminated soil by oil leakage are investigated by their physical behaviour. Therefore, the knowledge of soil properties is important in this study to differentiate the soil properties before and after contamination occurred. Further and advanced processing was executed using the MatGPR software [14]. The purpose of using this software is to create a FDTD simulation model and numerical analysis for this study.
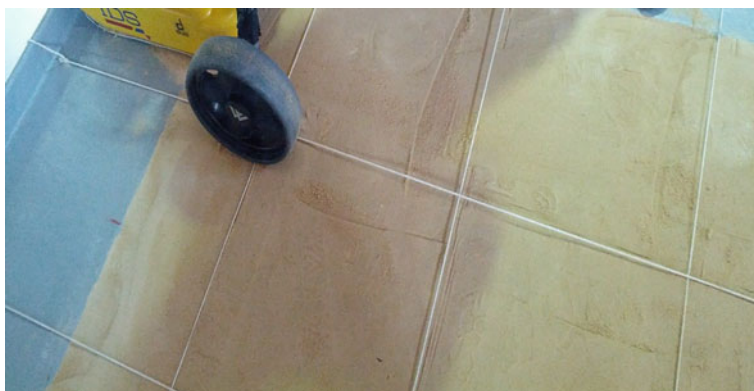
Fig. 2 Top view of the tank and the grid system

The visual interpretation of the input data can be done in various options via inspecting traces, trace spectra and attenuation characteristics. In this study, the details of every data was investigated and analysed correctly in order to understand the flow of the leakage. Time–frequency analysis are done for each individual traces to compute a time frequency of that data. This time–frequency analysis is very useful in dispersion flow and propagation characteristic. In this case, the focus of time–frequency analysis is only for longitudinal data because it shows the clear visualization of the dispersion compared to the transversal data. Other than that, data can also be analysed using attenuation characteristics. This attenuation analysis is used to determine the mean and median attenuation of all traces. Based on the attenuation analysis, it can obtain the best-fitting exponential decay curve and the best-fitting power-law decay curve.

3 Results and Analysis

3.1 Data Interpretation

GPR provides data in the form of radargram based on the signal propagation and properties of underground materials. The IDS Detector Duo GPR instrument used dual frequencies in data collection. In this study, the higher frequency was used focus to provide better resolution for 2 metres depth. The benefit of high frequency is it provides a good resolution data for data interpretation. Figure 3 shows the radargram of the observation data at 1 and 10 h. The change of the reflected signal can be seen in the radargram due to the existence of different materials from the soil. The reflection represents the content of the petroleum in the sand. The differences of the reflected signals, where the petroleum spill occurred can be seen in each radargram.
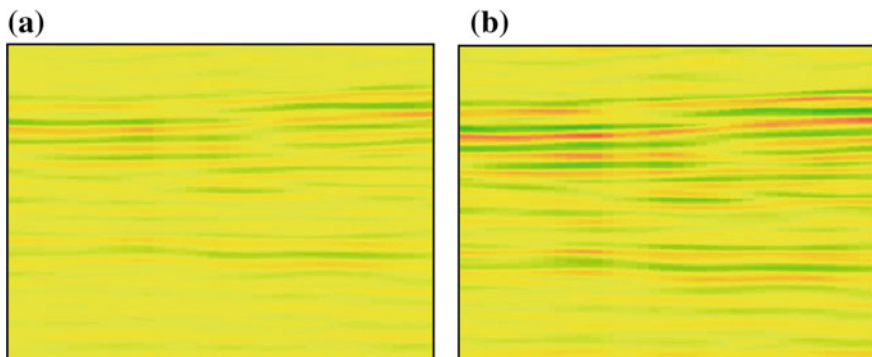
Fig. 3 Radargram of the petroleum leakage at 1 h (**a**) and 10 h (**b**)
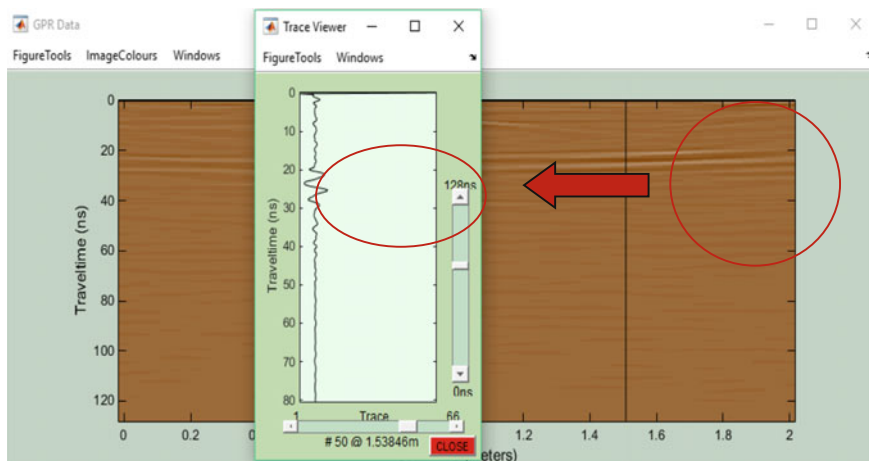
Fig. 4 Trace viewer at trace 50

The leakage occurrence has interrupted the propagation of the GPR signal. Therefore, the signal propagation at the spill area was analysed using trace viewer as marked in Fig. 4. The signal was disturbed at travel time 20–30 ns (see red circle), which are around 1.2–1.9 m depth.

3.2 Parameters Extraction from GPR Data

GPR transmits the electromagnetic signal into the ground and the signal will be reflected back to the antenna as it touches any underground material. Therefore, the time travel recorded from the signal can be used to define the depth and location of the object. Penetration of signal depth is influenced by the antenna frequency that has been used in data collection. The higher the antenna frequency, the shorter the signal penetration. All materials have their own dielectric constant value depending on the ability to store the electrical energy. The normal dielectric constant for sand is 3 and the value of the dielectric constant obtained after sand mixed with petroleum have changed. Table 1 shows the value of dielectric constant that is calculated from the observation data using Eq. 1. The dielectric constant is calculated for

Table 1 Parameters of the contaminated sand obtained from the radargram

Time (h)	Velocity (m/ns)	Soil dielectric constant
1	0.1702	3.1
4	0.1538	3.8
8	0.1499	4.0
12	0.1398	4.6
16	0.1302	5.3

every 4 h observation. Results show the value of dielectric increase as the observation hours increase. It can be concluded that dielectric constant of uncontaminated sand and contaminated sand are different and about 2.3 dielectric constant increase from its original value. The value of velocity is inversely proportional to the dielectric constant which is decreases as the dielectric constant increases.

$$v = \frac{c}{\sqrt{\varepsilon}}$$ (1)

where

v is the electromagnetic signal velocity
c is the speed of light in vacuum
ε is the dielectric constant of the material.

3.3   Signal Modelling

2D Model of the prototype tank was created in order to be used in the FDTD simulation. The properties of the 2D model that has been created follow exactly the real prototype with depth and distance 2 m each. Metal pipe was illustrated at the 0.5 m depth (Fig. 5).
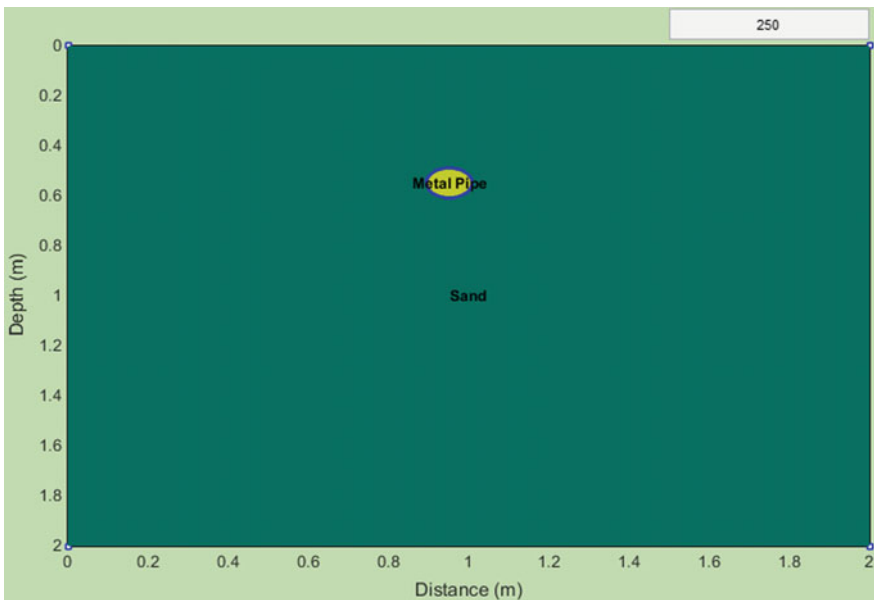
Fig. 5   2D model of the tank
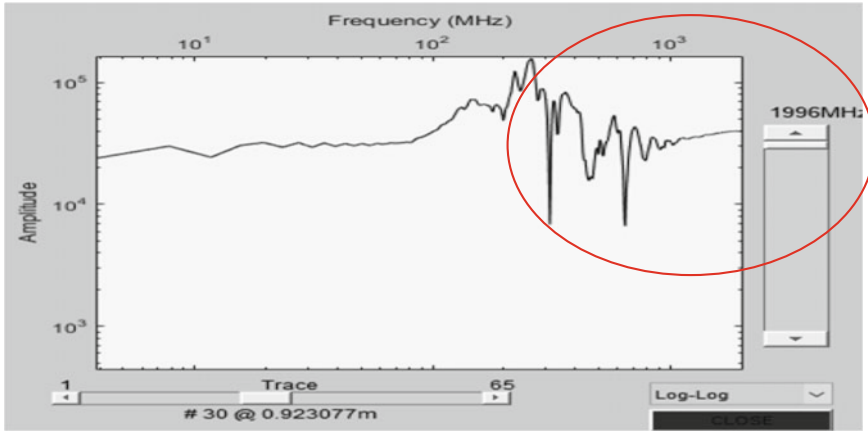
Fig. 6 Amplitude of the metal pipe at trace 30
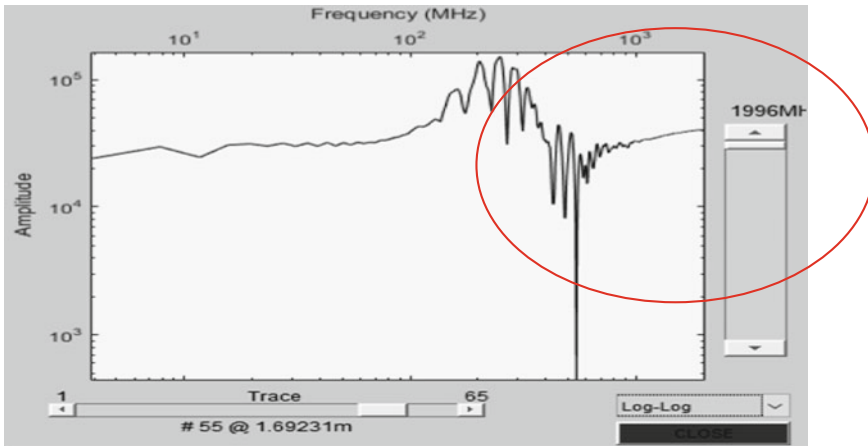
Fig. 7 Amplitude of the pipe leakage at trace 55

Figure 6 shows the amplitude of the signal fluctuation due to the metal pipe. This pipe which has a dielectric constant of 14 mostly impacts the amplitude. Conversely Fig. 7 shows the impact of petroleum in sand. As illustrated in the amplitude graph, the average of the fluctuated peak is varied. This is because the particles of petroleum and the sand was not completely mix together.

3.4 Analysing Electromagnetic Properties Between Contaminated and Uncontaminated Soil

The dielectric constant value represents the capability of a material to hold the electrical energy. Contaminated sand with petroleum has different dielectric constants because its structural and electromagnetic properties have been disturbed. Figure 8 shows the graph comparison between normal and contaminated value of sand dielectric constant. It can be seen in the graph that the dielectric value of contaminated sand increases with hour. At the end of observation, the dielectric constant goes up until 5.3 which is different from the normal value 2.3. The straight line represents dielectric constant for normal dry sand, while star symbol represents the dielectric constant for contaminated sand. Sample number 1 in *x-axis* is observed in the first hour of leakage, samples number 2, 3, 4 are observed at hour 4, 8, 12 after leakage occurred and sample number 5 was taken at the last hour of observation.

Conversely, the graph in Fig. 9 illustrated the differences in the relationship of velocity and observation time, dry and contaminated sand with petroleum. Straight line graph with a of value 0.17 m/ns represented the normal velocity in sand with dielectric constant 3. As can be seen in the figure, the graph continuously declines until sample 5 which is hour 16 of observation. The petroleum leakage flow increases for each hour which means the volume of the petroleum mixed with sand increased. Therefore, the higher volume of petroleum mixed with sand, the lower the velocity value.

3.5 Attenuation Characteristics Analysis

GPR collected underground data by transmitted electromagnetic wave into the ground. Every signal transmitted is differentiated by it trace number. The
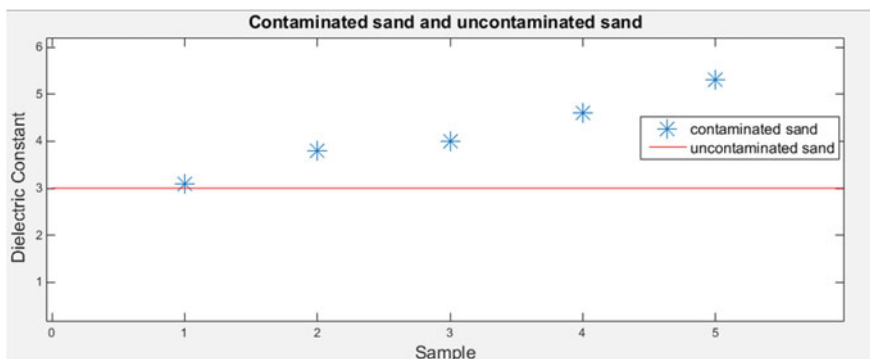
Fig. 8 The graph of comparison of dielectric constant between contaminated sand with petroleum and the normal value of dielectric constant
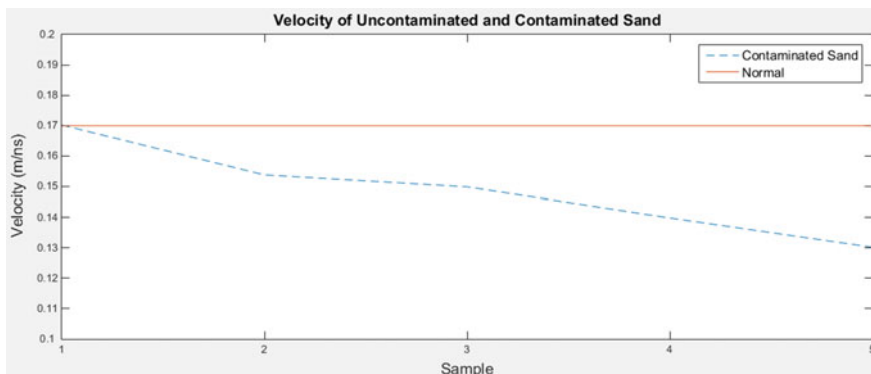
Fig. 9 The graph of comparison velocity between the signal in contaminated sand with petroleum and the uncontaminated sand
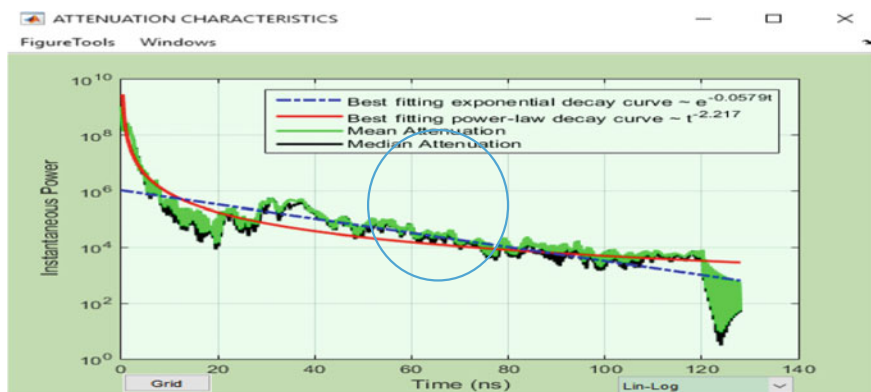
Fig. 10 Attenuation graph of instantaneous power against time (ns) at 1 h

attenuation of the electromagnetic signal is one of the important elements while investigating the flow of the petroleum leakage, since it will be used to obtain the optimal gain function. Figures 10, 11, 12 and 13 illustrate the attenuation characteristics graph of the GPR signal. As the signal goes further which increases in time, the power of the signal is decreased gradually. The mean and median attenuation at time around 20–30 ns are increased and slightly fluctuate due to signal interference. The interference is assumed to be occurring because of the leakage since the radargram of the observation data shows the reflection of the leakage are around time 20–30 ns. The differences of the attenuation between the observation data can be seen in those figures. The graph for signal fitting is also illustrated. The fitting model includes exponential decay and power-law decay. The process of fitting
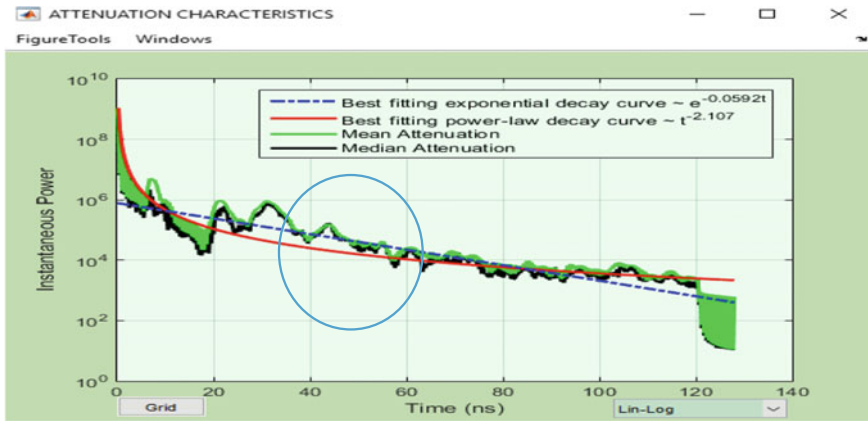
Fig. 11 Attenuation graph of instantaneous power against time (ns) at 5 h
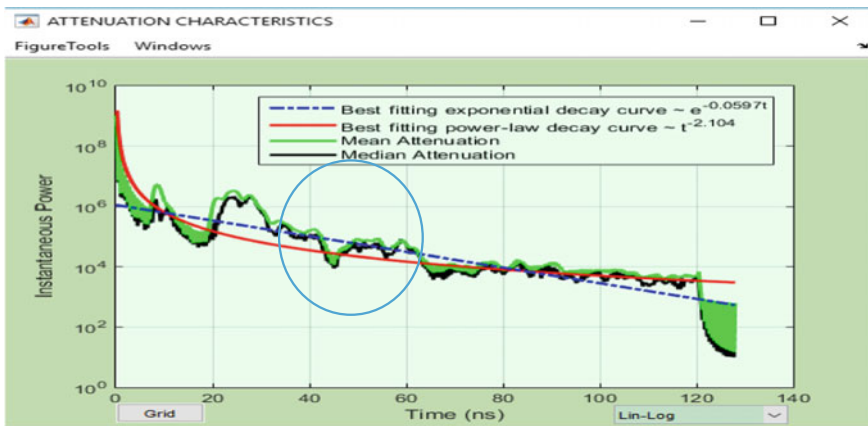
Fig. 12 Attenuation graph of instantaneous power against time (ns) at 10 h

exponential decay is one of the modelling data using exponential function. The best-fitting exponential decay curve at $e^{-0.0579t}$ of attenuation power is decrease with time travel of the signal as can be seen at 1 h observation data. Meanwhile, the best-fitting power-law decay curve at $t^{-2.217}$ drastically falls from time 0 to 20 ns, then it decrease slowly along the time.

The value of attenuation power at the last observation hour is higher compared to the hour before. As can be seen the highest peak of the attenuation at 1 h data is below 10^6. Then it increases along the observation time and the highest peak of the attenuation at 16 h is more than 10^6.
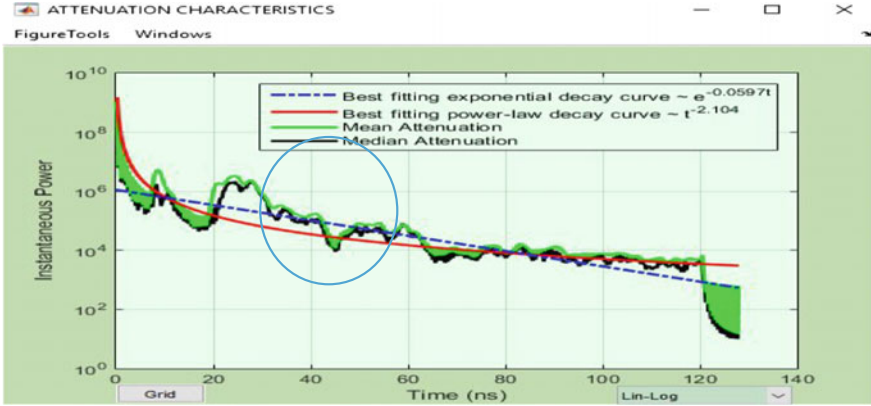
Fig. 13 Attenuation graph of instantaneous power against time (ns) at 16 h

3.6 Interpretation of Radargram Obtained from Simulation and GPR Survey

This study produces the theoretical prediction by implementing FDTD simulation. The comparison between results obtained from the simulation and the radargram can be used to enhance data interpretation, reduce the errors and even predict the reflection of the underground medium and materials. Radargram in Fig. 14 was obtained from the observation data carried out in this study using 250 MHz frequency. The parabola shape from the reflected signal of metal pipe can be seen clearly in the radargram. The 1 m metal pipe was buried at 0.5 m from the surface. The 2D model in Fig. 15 was created using MATGPR Model Builder. The metal pipe was placed exactly like the real prototype set up. The frequency which has
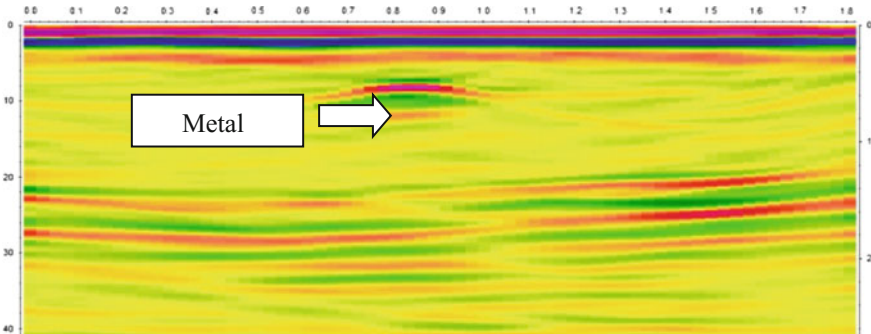
Fig. 14 Radargram data obtained from observation
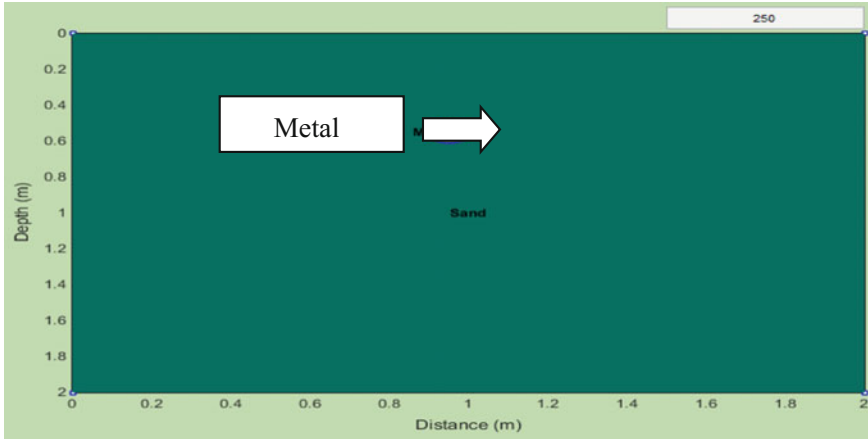
Fig. 15 2D model of the tank
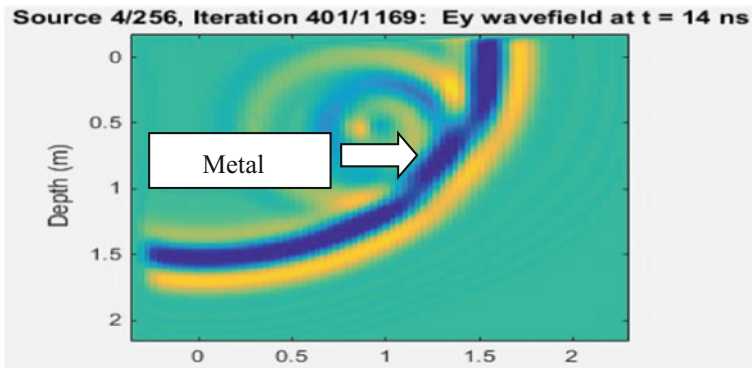
Fig. 16 FDTD simulation

been set for the whole model is 250 MHz and every detail object or medium in the model are created using their own electromagnetic properties. Dielectric value of metal pipe is 14 while sand is 3. FDTD simulation as shown in Fig. 16 is an animation of iteration process. The synthetic model was obtained from the FDTD simulation as the prediction of the scanned data. Therefore, the synthetic model must be identical with response from the radargram. The position of the metal pipe parabola is similar with the radargram with time travel of 10 ns. A noticeable dissimilarity between radargram and synthetic model is the presence of the other reflection due to the petroleum leakage flow (Fig. 17).
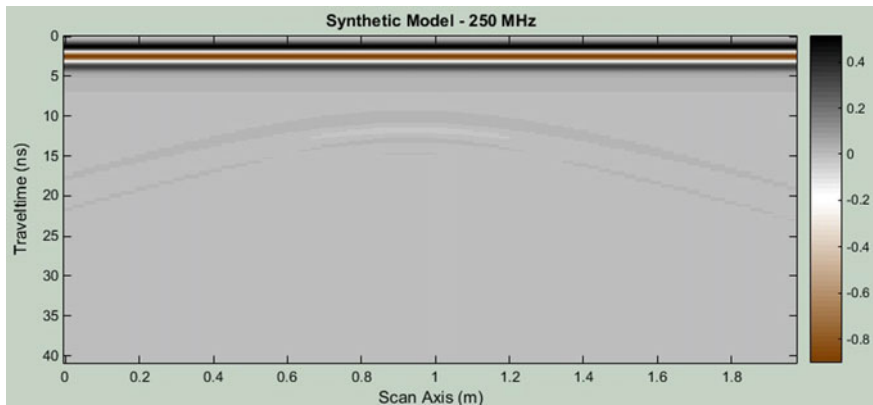
Fig. 17 Synthetic model obtained from FDTD Simulation of 2D model

4 Conclusion

Electrical properties of the soil influenced the applications of GPR. The interpretation of the GPR data requires the knowledge of the soil properties, electromagnetic characteristic of the materials in order to produce high-quality results as accurate as possible. Furthermore, the underground detection must be done accurately to avoid any hazardous in further works. Therefore, one of the objectives in this study is to determine the physical properties of the contaminated soil with petroleum. Even though, crude oil such as petroleum has less dielectric constant value and electrical conductivity than water, it still gives an impact to the electromagnetic signal. Consequently, GPR technique is capable to be used in detection flow of the petroleum leakage. Through this study, the physical changes of the soil properties when mixed with petroleum have been identified. Besides, the attenuation analysis also has been done for each data since it affects the propagation of the wave through a medium. Attenuation is directly proportional to the electrical conductivity. Therefore, the materials with high electrical conductivity will create high attenuation. In this study, the simulation was implemented to predict the flow of system and petroleum leakage. The simulation is a necessary step in some cases which could not implement the physical test due to the risk, cost and time consuming. The synthetic model obtained from the simulation has illustrated the same image as shown in observation data. The simulation result was compared with the radargram to improve the data interpretation and minimize errors. In addition, the numerical analysis was done to analyse the signal propagation and properties. The conclusion can be made from this study is GPR survey and basic filtering processes can be done by anyone but an experienced and knowledgeable operator for advance interpretation is required. The advance interpretations mentioned are the signal interpretation and modelling has been done in this study. Nevertheless,

further study can be pursued by applying real pressure equipment or system to create the real rate flow of the liquid and comparison of the pipe leakage detection in different types of soils.

References

1. Lilly, M.T., Ihekwoaba, S.C., Ogaji, S.O.T., Probert, S.D.: Prolonging the lives of buried crude-oil and natural-gas pipelines by cathodic protection. Appl. Energy **84**(9), 958–970 (2007)
2. Syed Azhar, C.A.Z.: 11 hurt in blaze at R&R stop. The Star Online. April 2014
3. Xu, Q., Zhang, L., Liang, W.: Acoustic detection technology for gas pipeline leakage. Process Saf. Environ. **91**(4), 253–261 (2013)
4. Shimanskiy, S., Iijima, T., Naoi, Y.: Development of microphone leak detection technology in Fugen Nuclear Power Plant. Saikuru Kiko Giho, 67–77 (2002)
5. Rebecca Ludwig, H.G., Klenk, P., Wollschlager, U., Buchner, J.: Electromagnetic Methods in Applied Geophysics (2011)
6. Hunaidi, O., Giamou, P. (eds.): Ground-penetrating radar for detection of leaks in buried plastic water distribution pipes. In: International Conference on Ground Penetrating Radar (1998)
7. Gamba, P., Lossani, S.: Neural detection of pipe signatures in ground penetrating radar images. IEEE Trans. Geosci. Remote Sens. **38**(2), 790–797 (2000)
8. Yee, K.S., Chen, J.S.: Impedance boundary condition simulation in the FDTD/FVTD hybrid. IEEE Trans. Antennas Propag. **45**(6), 921–925 (1997)
9. Schneider, J.B.: Understanding the Finite-Difference Time-Domain Method (2017)
10. Connor, S.: Introduction to the finite-difference time-domain (FDTD) technique. In: 2008 IEEE International Symposium on Electromagnetic Compatibility, vols. 1–3, 972–981 (2008)
11. Rebecca Ludwig, H.G., Klenk, P., Wollschlager, U., Buchner, J.: Electromagnetic Methods in Applied Geophysics, p. 64. CreateSpace Independent Publishing Platform (2014)
12. Lauro, S.E., Mattei, E., Barone, P.M., Pettinelli, E., Vannaroni, G., Valerio, G., et al.: Estimation of subsurface dielectric target depth for GPR planetary exploration: laboratory measurements and modeling. J. Appl. Geophys. **93**, 93–100 (2013)
13. Sandmeier, K.J.: ReflexW 7.2 Manual Book. Karlsruhe, Germany (2013)
14. Tzanis, A.: MATGPR, Manual and Technical Reference. Department of Geophysics UoA, editor (2013)

Surface Runoff Estimation and Prediction Regarding LULC and Climate Dynamics Using Coupled LTM, Optimized ARIMA and Distributed-GIS-Based SCS-CN Models at Tropical Region

Hossein Mojaddadi Rizeei, Biswajeet Pradhan and Maryam Adel Saharkhiz

Abstract The integration of precipitation intensity and LULC forecasting have played a significant role in prospect surface runoff, allowing for an extension of the lead time that enables a more timely implementation of the control measures. The current study proposes a full-package model to monitor the changes in surface runoff in addition to forecasting the future surface runoff based on LULC and precipitation factors. On one hand, six different LULC classes from Spot-5 satellite image were extracted by object-based Support Vector Machine (SVM) classifier. Conjointly, Land Transformation Model (LTM) was used to detect the LULC pixel changes from 2000 to 2010 as well as predict the 2020. On the other hand, ARIMA model was applied to the analysis and forecasting the rainfall trends. The parameters of ARIMA time series model were calibrated and fitted statistically to minimize the prediction uncertainty by latest Taguchi method. Rainfall and streamflow data recorded in eight nearby gauging stations were engaged to train, forecast, and calibrate the climate hydrological models. Then, distributed-GIS-based SCS-CN model was applied to simulate the maximum probable surface runoff for 2000, 2010, and 2020. The comparison results showed that first, deforestation and urbanization have occurred upon the given time and it is anticipated to increase as well.

H. M. Rizeei · B. Pradhan (✉) · M. A. Saharkhiz
Department of Civil Engineering, Faculty of Engineering,
Geospatial Information Science Research Center (GISRC),
Universiti Putra Malaysia, 43400 Serdang, Selangor, Malaysia
e-mail: Biswajeet24@gmail.com; Biswajeet.Pradhan@uts.edu.au

B. Pradhan
Faculty of Engineering and Information Technology, School of Systems,
Management and Leadership, University of Technology Sydney,
Building 11, Level 06, 81 Broadway, PO Box 123, Ultimo,
NSW 2007, Australia

Second, the amount of rainfall has been nonstationary declined till 2015 and this trend is estimated to continue till 2020. Third, due to the damaging changes in LULC and climate, the surface runoff has also increased till 2010 and it is forecasted to gradually exceed.

1   Introduction

Forecasting and time series analysis have become the main tool in varied environmental applications such as hydrology and watershed management. In order to have a sustainable watershed management system, it is essential to detect, monitor, and predict all the environmental contributing elements. There are some flood conditioning parameters which mainly would not change upon short time (i.e., within 50 years) namely; geology, soil type, and land morphology. However, there are other factors which are changing almost every season or year (e.g., land use/land use, rainfall magnitude, and temperature). The effects of climate and LULC dynamics have directly affected the surface runoff and flooding events.

Pluvial flooding or surface runoff events are highly nonlinear phenomena and subject to many conditioning elements such as the shape of natural meteorology, weather and climate, soil types, topography, land use/land cover (LULC), groundwater conditions and magnitude of rainfall intensity [1]. Land use plays a significant role in hydrological processes, such as infiltration, evapotranspiration and surface runoff [2]. Besides, observed evidence specifies that climate change affects directly the hydrological systems as well [3].

Particularly, the effect of climate and land use dynamics on surface runoff and flooding has always been under spotlight for hydrological modelling. Yet, hydrologists are still quite uncertain how much surface runoff generation will be changed by the diversion of these parameters to, mostly in monsoon basins [4].

By detecting the diversity of LULC and climate, there is an opportunity to forecast their behaviour using statistical, geospatial and machine learning approaches. So, comprehensive and modern understanding of LULC cover along with detailed rainfall magnitude are is essential for surface runoff monitoring and forecasting [5].

Although there have been many studies on the impacts of LULC on hydrology in different regions, still no united and accurate system has been developed to model the relationship of LULC and climate changes with surface runoff [6]. Upon the time basically, people tend to remove the forest areas and convert them into agricultural or urban lands. While forest area has higher leaf surface area, higher surface roughness, lower surface albedo, and deeper roots rather than agriculture and urban regions. All mentioned forest characteristics tend to contribute to a decline in

flooding and a rise in evapotranspiration [7]. Consequently, a decrease of dense vegetation area like forest canopy can trigger surface runoff [8].

LULC projection modelling detects the LULC changes over the time and predict the future LULC. Biophysical and socioeconomic matters, as well as scale, spatial distributions, and current LULC are the main influencing factors for LULC change [9]. Recently, there are several types of LULC computer simulation models and applications, which have been applied for different purposes such as GEOMOD, CLUE, and CA-Markov [10]. Yet in the current study, Land Transformation Model (LTM) was chosen to simulate land use change due to high efficiency with data scarcity, comprehensive simulation capability, modest calibration, ability to simulate future LULC regarding to deriving related parameters, and socio-economic patterns. Land Transformation Model (LTM) engages GIS along with artificial neural networks (ANNs) in order to predict the future LULC. Actually, ANN is applied to find the development patterns in a region, while GIS can play a great role to make the spatial predictor and implement the spatial analysis [11].

ANN is basically a self-learning computer model and it has been used for pattern recognition in many applications [11]. Lately, ANN protocol has been started to apply on the LULC modelling, which makes a bridge between past and future LULC as well as maps of suitability.

As written earlier, another inflected factor in the quantity of surface runoff was weather and climate dynamics. One of the common approaches to simulate and predict climate changes is time series analysis. Statistical techniques for analyzing the time series range from relatively straightforward descriptive methods to sophisticated inferential techniques [12]. Linear trends of a hydrological time series can be detected using different methods such as the *t*-test parametric method and linear regression as well as nonparametric statistical tests (e.g., seasonal Kendall, Spearman's rho, and Mann–Kendall) [13]. One of the recent and well-known methods in terms of forecasting precipitation is ARIMA model, which is a statistically and mathematically complex method [14]. It has received a great attention nowadays due to its capability of handling stationary and nonstationary observations, overcoming missing data distributions, and high forecasting accuracy [15]. Recently, Box–Jenkins ARIMA linear models have dominated many areas of time series forecasting. The ARIMA procedure analyzes and forecasts equally spaced univariate time series data, transfer function data, and intervention data using the autoregressive integrated moving average called "ARIMA" [16]. Efficiently, implementing the future runoff simulation is another challenge of this study.

According to previous works, many models have been developed for rainfall–runoff assessments including SWAT, HEC-HMS, etc. However, each model has its own pros and cons which should take them into account. The SWAT requires, for instance, too many detailed data (e.g. soil evaporation, infiltration and available water capacity) to simulate the runoff model while these sort of data are not always available [17]. Lumped HEC-HMS is another popular model which is not dependent on ancillary data like SWAT. Yet, it is a conceptual rainfall–runoff model which calculates a single value of runoff magnitude for the entire subbasin area. Perhaps, it is quite aggregated scale approach and might cause the uncertainties in

the analysis. In this study, we proposed the distributed-GIS-based soil conservation service-curve Number (SCS-CN) method to model the runoff magnitude for each individual pixel of the watershed basin.

Distributed-GIS-based SCS-CN was employed to examine the LULC and climate dynamics impact on surface runoff. The method is presenting a curve number to estimate the condition of a catchment. The CN index is taken into account, in a finite way, to determine the effects of LULC, soil types (infiltration condition) on surface runoff [18]. The GIS-based-SCS-CN method is selected in this study primarily, because it allows to model a large watershed basin in a very fine scale.

In this study, we proposed a full packaged model to monitor the dynamics of surface runoff and also forecast the future surface runoff regarding the simulated LULC and precipitation. LTM model was used to predict the 2020 land cover, optimized ARIMA also was engaged to forecast maximum rainfalls using 8 gauging stations. Then, distributed SCS-CN model was applied to simulate the 2020 maximum probable surface runoff.

1.1 Study Area and Datasets

The first step for any runoff and flood models is watershed basin analysis. The basin model represents the catchment morphology mainly extracted from digital elevation model (DEM). Hydrological and surface parameters should be developed using GIS analysis to delineate watershed basin analysis efficiently. In fact, the DEM spatial accuracy defines the degree of reliability of the derived watershed model [4].

The hydrogeomorphological characteristics of the study area, such as basin slope, area, and elevation, were calculated using GIS Spatial Analyst tools (Table 1). The watershed border was delineated using hydrology basin tool, which needs an accurate flow direction extracted from DEM. Main river length, upstream distance also was calculated by flow length option from GIS hydrology toolbox. Another important parameter is basin slope, which was calculated by the surface raster-based tool in percentage [19] (Fig. 1).

The Semenyih watershed basin was delineated which has a total area of 268.4 km^2. Basically, this watershed basin has one of the main rivers in the state of Selangor, which has been negatively influenced by industrial and urban wastes since the early 1990s [5]. In the past decades, Semenyih catchment has experienced excess surface runoff and flooding events usually, from November to February due to the monsoon season [20]. In addition, Semenyih basin has a mixed land cover

Table 1 Geomorphological information of Semenyih watershed basin

Basin	Area (km^2)	Min elevation (m)	Max elevation (m)	Mean elevation (m)	Mean slope (°)
Semenyih watershed	268.42	28.93	1060.26	224.18	12.5
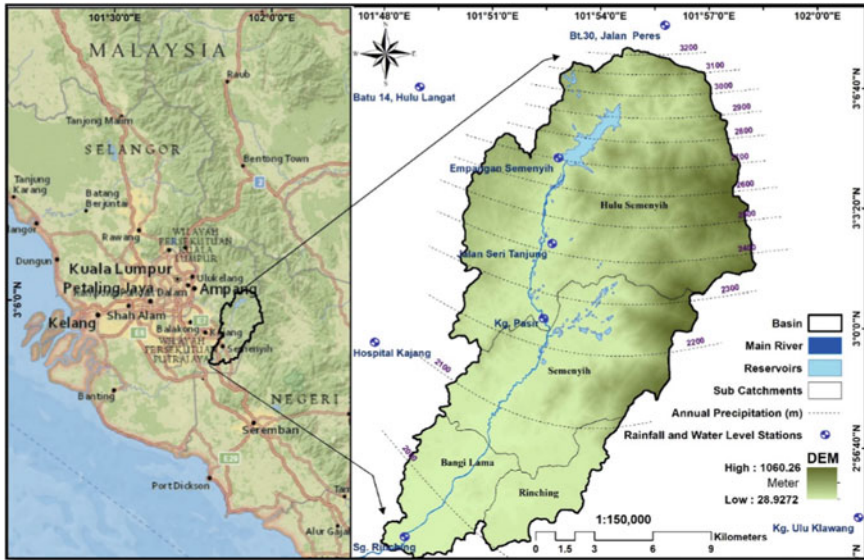
Fig. 1 Location of study area

pattern (e.g. urban, rural, agriculture and frost) which is suitable for a comprehensive runoff modelling. This region lies between longitude 101° 48′ 32.9″E to 101° 52′ 30.5″E and latitude 02° 54′ 14.9″N to 03° 03′ 23.1″N. The population of three districts (Semenyih, Hulu Semenyih, and Beranang) was about 25,480 in 1980 and 34,313 in 1991.

High-resolution SPOT-5 satellite images (5 × 5 m spatial resolution) were processed for two periods of time (2000 and 2010) to extract the LULC maps. In addition, SRTM satellite image (30 × 30 m spatial resolution) captured at 2010 was utilized to generate DEM. There are 1923 × 2615 pixels in columns and rows for both mentioned raster satellite images. Also, precipitation and streamflow data (since 2000 till 2017) were collected from the nearby eight metrological gauging stations.

2 Methodology

Three main parts of this study can be summarized as simulation modelling of LULC, climate, and surface runoff. There are some pre-considerations to do that; (a) collection of proper and accurate data, (b) define the logical time series (i.e. neither too short nor too long) and (c) measure and optimize the right variables of simulation models. In the current study, the authors tried to minimize the degree of distortion by implementing all the mentioned considerations. The overall flowchart of this study is shown in Fig. 2 step by step.
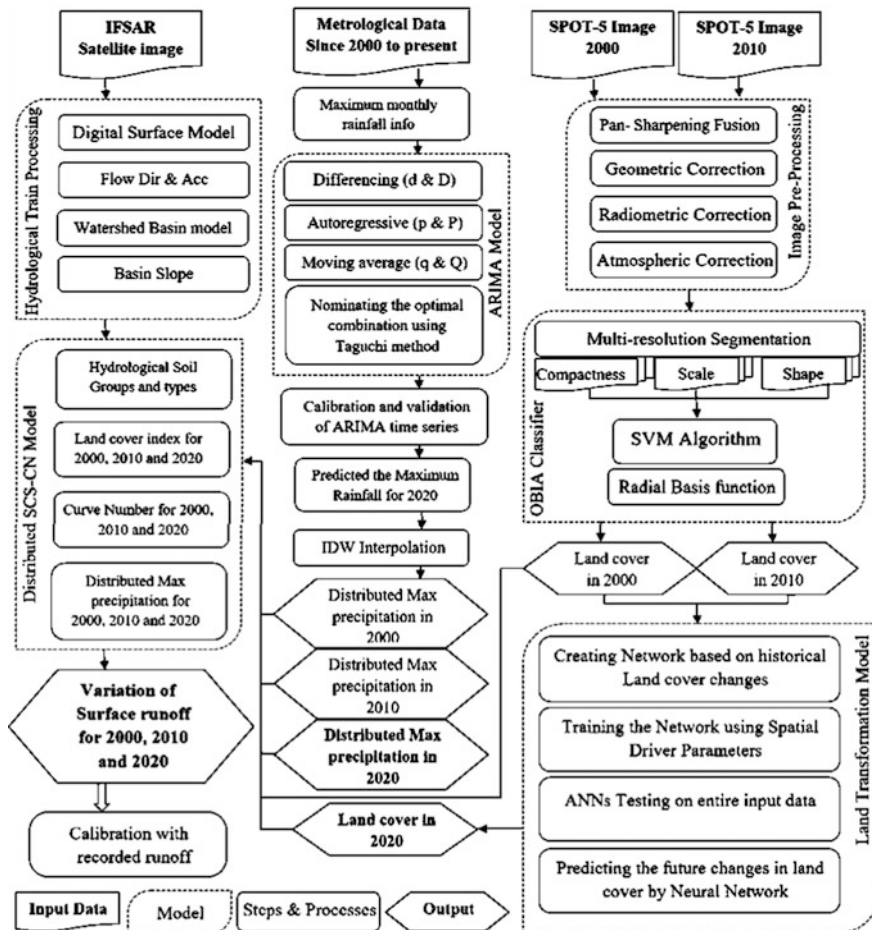
Fig. 2 The computational framework of this study

2.1 Satellite Image Processing

The very first stage of image analysis is preprocessing level. PAN-sharpening is one of the vital procedures to improve the satellite image spatial resolution by fusing the panchromatic band (PAN) with multispectral bands (MS) [21].

The atmospheric and topographic correction (ATCOR) model was applied on satellite imagery to correct the atmospheric distortion by retrieving surface reflectance and engage topographic correction as well as adjacency effect correction [22]. In the present study, ATCOR was applied to remove atmospheric uncertainties.

The output image was then projected to a Universal Transverse Mercator (UTM) coordinate system Zone 47 with the datum of WGS 1984, which was

geometrically checked by 58 well-distributed benchmarks over the study areas. Digital number (DN) values were converted to radiance in the radiometric correction stage then, the radiance values were converted to pure surface reflectance to enhance image capability and contrast [23].

The second stage of OBIA after preprocessing is image segmentation. The creation of optimal segmentation is still a matter of debate [24]. The multi-resolution segmentation algorithm successively merges image pixels with spectral, spatial, and textural similarities. Two basic approaches were integrated to optimize setting parameters in this study, multi-resolution (MRS), and spectral difference segmentation (SDS) [25]. MRS has four elements that should be defined by expert knowledge based on the image details, namely, layer weight, compactness, shape and scale. Having examined all possible MRS arrangements, the optimal percentages and weights of layer weight, compactness, shape and scale were derived from a satellite image (Table 2). Then, SDS allows segments to merge neighbouring objects if the spectral difference between their means is below a certain value of the maximum spectral differences.

Image analysis procedures were used to extract land cover information from satellite images. Basically, image analysis can be divided into two main categories; pixel-based image analysis (PBIA) and object-based image analysis (OBIA) [26]. Information from these approaches, such as textural, spectral and geometrical information, can be subjected to image analysis algorithms using the PBIA or OBIA [27].

Previous related studies indicated that pixel-based image classifiers are less impactful when accurate urban maps are developed from VHR satellite imageries [27, 28]. OBIA is a cooperative feature extraction method that starts with image segmentation to divide the image into similar segments [29]. Selection of an optimized segmentation is still one of the biggest challenges in OBIA. It depends on the size and scale of urban objects, which should be extracted from the image [30].

Object-based Support Vector Machine (SVM) classifier was applied to perform the classification. Six different land cover classes were categorized due to the scope of this study including, agriculture, forest, oil palm, barren land, urban, and water body. SVM is a supervised learning binary classifier and is based on the structural risk minimization principle [31]. The nonlinear structures can be modelled by transferring the space of input data into high dimension space through kernel trick [32].

The aim of SVM classifier is to yield a model based on the training info, which calculates the target values of the test sample. Assume a training dataset of instance–label pairs (x_i, y_i) with $x_i \in R^n$, $y_i \in \{1, -1\}$, and $i = 1, …, m$. The SVM needs the solution of the optimization problem in Eqs. 1 and 2:

Table 2 Optimized segmentation parameters

Spectral layer weights	Scale parameter	Shape	Compactness
Red = 1, Green = 1, Blue = 1, NIR = 2	55	0.3	0.5

$$\text{Minimize} \sum_{i=1}^{n} \alpha_i - \frac{1}{2} \sum_{i=1}^{n} \sum_{j=1}^{n} \alpha_i \alpha_j y_i y_j (x_i x_j) \tag{1}$$

$$\text{Subject to} \sum_{i=1}^{n} \alpha_i y_j = 0, 0 \le \alpha_i \le c, \tag{2}$$

where α_i signifies the Lagrange multipliers and C stands for the penalty parameter. The SVM model discovers a linear splitting hyperplane along with the maximal margin in the upper dimensional space. Basically, $C > 0$ is set as the penalty factor of the error. The kernel-type selection in SVM model can be considered as a vital step due to its direct impact on the successful training and classification accuracy [33]. In this study, we used Radial Basis Function (RBF) kernel type to classify the land cover map, which was suggested as the optimal kernel type in other research [19].

Radial Basis Function (RBF):

$$K(x_i, y_i) = \exp\left(-\gamma \|x_i - x_j\|^2\right), \gamma > 0. \tag{3}$$

where γ and r are the kernel parameters.

2.2   LULC Modelling by LTM

Changes in LULC have resulted from the composite interface of numerous factors such as; culture, human behaviour, policy, economics, management and the environment [34]. Majority of mentioned factors are intangible for computer modelling, so it is attempted to model the tangible environmental parameters in this study by using LTM approach. Basically, LTM uses four sequential steps to predict the future LULC: At first, processing or data coding to generate spatial layers which connect with predictor drivers. Second, performing spatial regulations in that connect predictors to LULC transitions for any possible location. Third, integrate all of the input grids by using ANN algorithm then finally, the amount of transitions should be scaled temporally to create a time sequence for the potential future LULC [11].

There are some factors which can positively influence the projected LULC growth known as "Driver layers". Also, there is another layer which demonstrate the areas where we do not want to include in predicting analysis, called exclusionary layer as shown in Table 3 [5].

To build a reliable system with enough predictive potential, ANN should be required to train and test by different inputs [35]. Training step involves expressing input values as well as modifying the weights which were applied to each node using the learning algorithm. In the testing stage, the system presents another dataset towards trained network to calculate the error value independently. There are four levels where ANNs used for prediction of land cover change: (i) network

Table 3 The LTM driver variables applied for LULC forecasting

Variable name	Description
Highway approximate	Distance to nearest highway
River approximate	Distance from rivers and streams
Secondary road approximate	Distance to nearest county road
Dam reservoir approximate	Distance from dam reservoir
Urban and agriculture approximate	Distance to urban and agriculture of 2000
Inland lakes approximate	Distance from a lake inside of the watershed basin
Exclusionary layer	Cells which do not want to include in predicting the analysis, for instance national parks or constrained area

and inputs design based on historical data; (ii) training the network by using a clipped input; (iii) ANNs testing using the full inputs dataset; (iv) using the neural network information in order to change prediction [11]. Having implemented all the mentioned procedures, LULC for 2020 was projected (see Fig. 4).

2.3 Precipitation Forecasting by ARIMA Model

Basically, ARIMA model is divided into three stages namely, Identify, Estimate, and Forecast levels [36]. The identify statement reads time series that are to be used in later statements, possibly differencing them, and computes autocorrelations, inverse autocorrelations, and cross correlations. Estimate stage is implemented to specify the ARIMA model to fit the variable specified in the previous identify account, and to evaluate the factors involved in the model. Then, the forecast statement was used to predict future beliefs of the time series and also confidence intervals for these forecasts were generated from the ARIMA model [37].

The Autocorrelation Function (ACF) is another important component of any prediction and time series analysis. The ACF calculates the amount of linear dependency between observations in a given time series that are separated by a lag k (interval value). The ACF plot also, assists to control how many autoregressive terms are required to expose of the following features: seasonality of the series, time lags where high correlations appear, trend either in the mean level or in the variance of the series.

A time series is said to be stationary or nonseasonal if it has constant mean and variance with the steady division, otherwise, it as considered as nonstationary or seasonal trend [16]. The ARIMA model is classified by two set of parameters (p, d, q) and (P, D, Q) that can have zero or positive integral values. The first set is nonseasonal parameters, which are the autoregressive (p), differencing passes (d) and moving average (q). But, the second set is seasonal parameters which

known as seasonal autoregressive (P), seasonal differencing passes (D) and seasonal moving average (Q) [38].

The nonseasonal ARIMA model may be written as

$$\varnothing(B)\nabla^d X_t = \theta(B)\varepsilon_t \tag{5}$$

where $\varnothing(B)$ and $\theta(B)$ = polynomials of order p and q, correspondingly.

$$\begin{aligned}\varnothing(B) &= \left(1 - \varnothing_1 B - \varnothing_2 B^2 - \dots \varnothing_p B^p\right) \text{ And } \theta(B) \\ &= \left(1 - \theta_1 B - \theta_2 B^2 - \dots \theta_q B^q\right)\end{aligned} \tag{5}$$

The nonseasonal can be described as

$$\varnothing_p(\mathrm{B})\varnothing_p\left(B^{12}\right)\nabla^d \nabla^D_{12} = \theta_q(\mathrm{B})\theta_q(B^{12})\varepsilon_t \tag{6}$$

where p is the order of nonseasonal autoregression, d the number of regular differencing, the order of nonseasonal ARIMA, P the order of seasonal autoregression, D the number of seasonal differencing, Q the order of seasonal ARIMA. B is the nonseasonal backward shift operator while B^{12} stands for seasonal backward shift operator. $\varnothing_p$ is autoregressive and θ_q is the moving average polynomials of order P and Q, respectively [16].

For instance, ARIMA (0, 1, 1) (1, 0, 1) defines a model that includes NO autoregressive parameter, one differencing passes and one moving average parameter as well as one seasonal autoregressive parameter, NO differencing passes seasonal and one moving average parameter. In order to achieve the ideal combination of ARIMA seasonal and nonseasonal variables, in this study Taguchi statistical optimization method was applied to select the best combination of these parameters to predict the future precipitation.

In this research, there are six variables (p, d, q, P, D, Q) and each one can be varied from 0 to 1 [16]. So, these parameters can produce 64 different combinations, which are to be examined by residual errors resulted from fitting plot to discover the most calibrated combination. However, this is a very time-consuming procedure when tested [39]. To overcome this issue, statistical Taguchi technique can substantially reduce the number of experiments to 7 times.

In order to develop the Taguchi optimization method, the first step is to define the possible values of the parameters, which can be defined by their domain (i.e., each parameter can vary from 0 to 1). After that, an orthogonal array was assigned to determine the number of experiments that measure the special effects of each parameter on the forecasting model. In this study, we define $L = 7$ for array design. Having selected the fitting array, the trials were performed, and the weight of each factor was measured on seasonal and nonseasonal ARIMA combination regarding POF index as well as SNR ratio. POF is the combination of a spatial autocorrelation index and a variance indicator. The optimal value of each factor was nominated when it has the highest value of SNR index [40].

$$\text{SNR} = -10 \log_{10} \left(\frac{1}{n} \sum \frac{1}{y_i^2} \right) \tag{7}$$

where n is the number of repetitions under the same test conditions ($n = 1$), and y signifies the POF values obtained from each ARIMA forecasting test. Lastly, the ideal combination of six parameters was achieved.

2.4 Runoff Simulation by SCS-CN Model

One of the reliable methods to calculate the precipitation excess (surface runoff), which cannot penetrate into the saturated soil based on the soil conservation service and curve number (SCS-CN), as a function of precipitation, soil types, soil moisture, and LULC [41]. The SCS-CN is one of the most accurate and well-known methods which can be applied to large regions and for the regions with evaluation variability at various spatial resolutions. The SCS-CN equation is shown in Eq. 8 [42].

$$Q(t) = \frac{(P(t) - I_a)}{P(t) - I_a + S} \tag{8}$$

$P(t)$ is the precipitation, I_a is the initial abstraction (the amount of water before runoff) such as infiltration, or rainfall interception by vegetation; previously, that I_a is generally assumed as $0.2S$. However, recently hydrologists have found that $I_a = 0.05S$ might be a more suitable relationship in urbanized watersheds, where the CN is updated to reflect developed conditions [43]. S is the potential maximum retention, which measures the ability of a watershed to abstract and retain storm precipitation. The runoff will be zero unless the accumulated rainfall exceeds the initial abstraction. The potential maximum retention S describes as

$$S = \frac{1000}{CN} - 10 \tag{9}$$

2.5 Curve Number Calculation

The CN index was projected as a function of LULC, soil types, and soil moisture of the watershed basin [44]. In this study, AMC III scheme was used to derive CN index which represents saturated soil with dormant season rainfall of over 27.9 mm and growing season rainfall over 53.3 mm. SCS runoff CN for hydrologic soil cover complex under AMC II condition for the study area is given in Table 4 [44].

Table 4 CN indices under AMC II conditions based on TR-55 table [20]

Land use classes	Hydrologic soil group			
	A	B	C	D
Forest	30	55	70	77
Rubber	61	70	77	80
Oil palm	71	80	87	90
Grassland	71	81	84	87
Paddy	60	72	80	84
Other agriculture	64	75	82	85
Bare soils	49	69	79	84
Urban	77	85	90	92
Water	97	97	97	97

In this study area, all types of hydrological soil groups are available which are described as Group A is sand, loamy sand or sandy loam types of soils. It has low runoff potential and high infiltration rates even when thoroughly wetted. Group B is silt loam or loam. It has a moderate infiltration rate when thoroughly wetted and moderately well to well-drained soils textures. Group C soils have low infiltration rates when thoroughly wetted and consist chiefly of soils with a layer that impedes downward movement of water and soils with moderately fine to fine texture. Group D soils have high runoff potential. They have very low infiltration rates when thoroughly wetted and consist chiefly of clay soils with a high swelling potential.

The AMC factors can be looked up in the reference Table 5. The CN value for AMC II should be multiplied by the adjustment factor based on the actual AMC III to determine the adjusted curve number.

Table 5 Adjustments to select CN for soil moisture conditions [45]

Curve number (AMC II)	Indices to convert CN from AMC II to AMC III
10	2.22
20	1.85
30	1.67
40	1.50
50	1.40
60	1.30
70	1.21
80	1.14
90	1.07
100	1.00

3 Results and Discussion

In general, runoff and flood are a result of heavy and continuous rainfall (high-intensity rainfall) beyond the adsorbent capacity of soil and the streamflow capacity of river bank [19]. This is the reason that we used the maximum amount of rainfall in each month from 60 min storm events to run the ARIMA and SCS-CN models. It is proved that both climate (precipitation) and LULC changes can dramatically influence water availability and surface runoff. Hence, based on the historical changes in climate and LULC their future scenarios have been simulated to forecast the probable amount of runoff in 2020.

3.1 LULC Change Detection and Prediction Analysis

Having trained every possible feature signature for each LULC class (i.e., at least 30 training sites) as well as the image preprocessing analysis, the object-based classification was implemented to extract the LULC from Spot-5 satellite images. The land cover classification results using SVM-OBIA approach for 2000 and 2010 were shown in Table 4. After that classified LULC maps for the mentioned years were compared to detect the real changes during that given time. Then seven predictor variables were considered along with detected changes to forecast the 2020 LULC map by using LTM approach. Figures 3 and 4 show the detailed information about LULC simulation results.

The following major important changes in LULC were detected during the considered time period (see Fig. 4). Basically, deforestation at the time can be clearly observed all over the area particularly on the upper catchment has occurred substantially. Approximately, 22 km^2 of forest areas have been removed within

	Agriculture	Forest	Oil Palm	Barren Land	Urban	Water Body
■ 2000	50.68	148.55	29.46	18.23	15.94	5.58
■ 2010	65.07	124.76	35.57	17.42	19.49	6.13
■ 2020	80.57	102.42	39.15	15.05	25.45	5.8
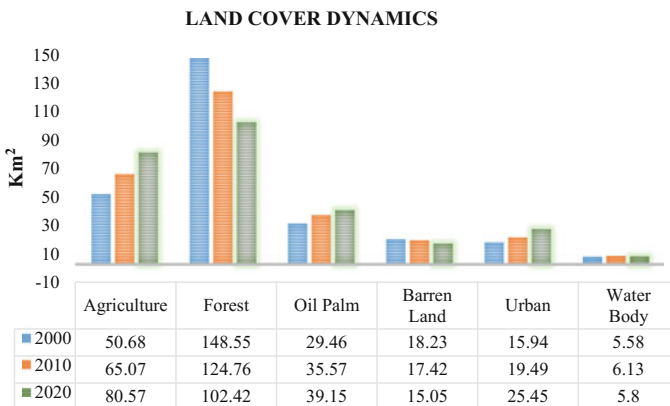
Fig. 3 Comparison of LULC dynamics in 2000, 2010, and predicted 2020
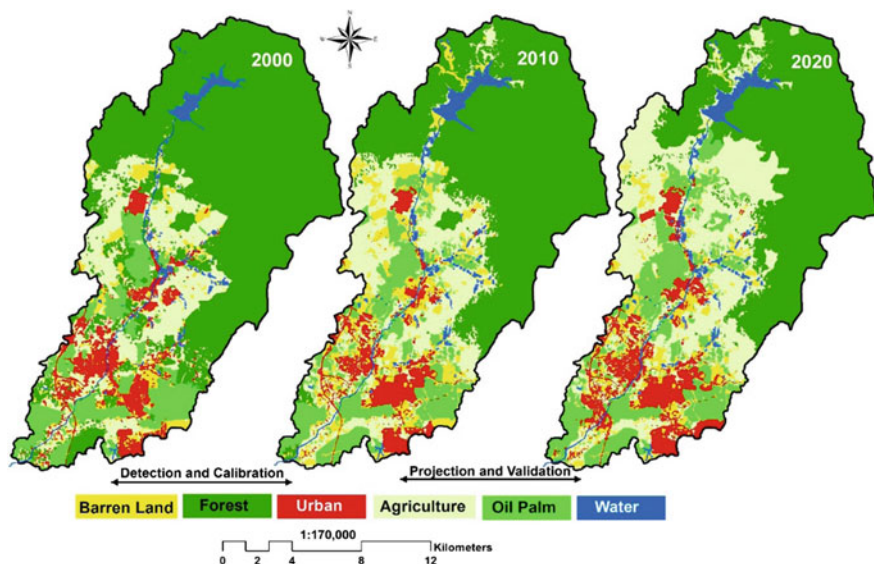
Fig. 4 LULC maps for 2000, 2010, and 2020

10 years and almost more 24 km^2 was expected to extinct by 2020 if there is no protection strategy. Mainly, the forest areas have been converted to agricultural and oil palm cultivation lands which might lead to increasing of flooding probability. Urban areas (e.g., built up and roads) have also shown increment up to 4 km^2 in the first 10 years, and it is anticipated to reach to 6 km^2 growth from 2010 to 2020. Oil palm plantation has been increased to 35.57 km^2 till 2010, and forecasted to continue this trend to reach to more than 39.15. In general, oil palm cultivated, agricultural and urban areas have been found to be expanded while forest and barren lands have been reduced over the given time.

In terms of classification accuracy assessment, the achieved land covers for 2000 and 2010 were checked by 250 ground control points (GCPs) in the region using confusion matrix method. The results indicated the high overall accuracy of 89.6 and 93.1% with 0.87 and 0.91 kappa coefficients for 2000 and 2010, respectively. Additionally, testing was completed for LULC simulation by comparing those cells that were observed for transition, "Real Change", with those cells with the highest likelihood of transition, based on the model. Percent Correct Metric (PCM) method can evaluate the accuracy of LTM model to predict the 2020 land cover as follows:

$$\text{PCM} = \frac{(\text{Number of cells predicted to change})}{(\text{Number of cells that transitioned to 2020})} \times 100 \qquad (10)$$

So, (156,024/212,026) × 100 = 73.56% and kappa index equal to 0.694. In argument with other literature, 60–80% is considered an exceptional model for prediction accuracy [10].

3.2 Climate Change Analysis

Time series plot was conducted to assess the stability of the data using the maximum monthly rainfall data for 60 min storm from eight gauged stations (Fig. 5). Since the data is monthly rainfall, there is a seasonal cycle of the series so this series is not stationary. First, the accuracy of our seasonal data which was obtained from Kg.Pasir gauging station was tested by Mean Absolute Percentage Error (MAPE) and Mean Squared Deviation (MSD) to ensure that it will be capable to run the time series analysis. Figure 5 shows the maximum of monthly rainfall from 2002 to 2015 recorded in Kg.Pasir gauging station.

As it can be clearly seen from Fig. 5, the rainfall general trend has been gradually decreased since 2000–2015. The calculated linear trend model is

$$Yt = 30.73 - 0.0840 \times t.$$

MAPE states accuracy as a percentage of the error. Because this number is a percentage, it may be easier to understand than the other statistics. The MAPE is almost 10 so it can be concluded that the forecasting analysis for such a data is off by almost 10%. MSD is also another commonly used measure of the accuracy of fitted time series values. In this method, outliers have more influence and then smaller values generally indicate a better fitting model. Furthermore, to discover whether the data is stationary or not, ACF was applied. Autocorrelation is the correlation between observations of a time series separated by k time units. According to the graph represented in Fig. 6, given data has a nonstationary pattern.

After that, the most ideal ARIMA combination of seasonal and nonseasonal parameters was calculated by using Taguchi method. The best seven fittest combinations were compared by statistical Taguchi model, then measured P-value, POF, and S/N ratio determine the most optimal combination (Table 6).
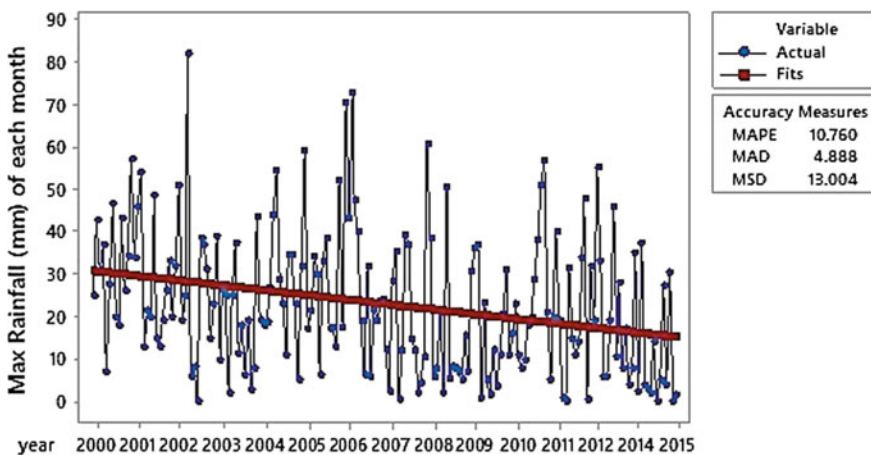
Fig. 5 Trend analysis plot for Kg.Pasir gauging station
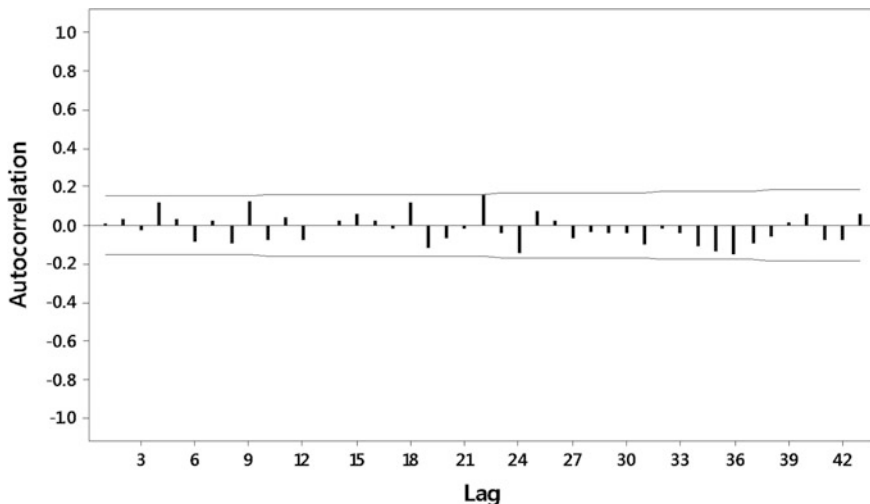
Fig. 6 ACF of residuals (with 5% significance limits for autocorrelations)

Table 6 ARIMA model statistical characteristics optimization results

Experiment of nominated combinations	P-values	POF	SNR
ARIMA (1, 0, 1) (1, 1, 1)	0.0907	0.77	−2.3752
ARIMA (1, 0, 0) (1, 1, 1)	0.0621	0.86	−1.4210
ARIMA (1, 1, 0) (0, 1, 1)	0.0758	0.63	−3.0645
ARIMA (0, 0, 0) (1, 0, 1)	0.1732	1.12	1.1831
ARIMA (1, 0, 1) (0, 0, 1)	0.2325	1.27	2.5684
ARIMA (1, 0, 0) (1, 1, 1)	0.0856	0.92	−2893
ARIMA (0, 0, 0) (0, 1, 1)	0.1004	1.05	0.6051

The highest POF and S/N ratio showed the optimum combination for forecasting and it was confirmed by P-value test (i.e. all the archived P-values are above 0.05 which is significant). Finally, ARIMA (1, 0, 1) (0, 0, 1) was selected as the optimal model forecasting fusion regarding its minimum error (Table 6).

In this model, rainfall data from 2000 to 2015 were used to train the model for forecasting for the next 5 years. Besides, 2016 and 2017 data were used to calibrate the ARIMA model. By applying model calibration, observed data were compared with predicted data for 2016 and 2017. The result of RMSE indicated 0.67, which is proved the degree of reality of ARIMA model.

Having calibrated the ARIMA parameters for one rainfall station (Kg.Pasir), it was extended to the other seven nearest stations to anticipate the probable maximum rainfall for 2020. The predicted maximum rainfall (forecast level) for 2020 in
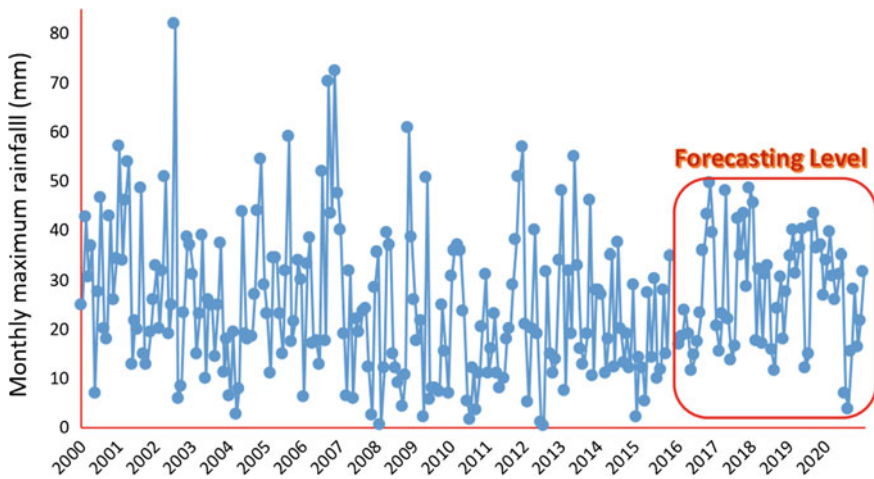
Fig. 7 Optimized ARIMA time series forecasting results till 2020 (95% confidence limits)

each gunging station was then interpolated by inverse distance weightage (IDW) along with 2000 and 2010 to create the distribution precipitation maps for those particular years (Fig. 7).

3.3 GIS-Based SCS-CN Model Results

A distributed-finite-elements-SCS-CN model measures the transformation of excess precipitation to runoff and to simulate the amount of direct runoff through a watershed basin for each individual pixel. In GIS-based SCS-CN model, the CN and maximum monthly rainfall values from 60 min storm were utilized to compute the relevant surface runoff for given time periods. The CN index was calibrated by LULC and HSC then adopted based on AMC III to estimate the most reliable runoff in our tropical watershed basins (Table 7).

The CN maps were derived using hydrologic soil group combined with land cover for each year. Then, using Eqs. 8 and 9 the maximum runoff depth (mm) for the considered 3 years were computed in GIS environment (see Fig. 8).

The maximum rainfall for 60 min storm was used to simulate the maximum runoff for 2000 and 2010 as well as forecasting 2020. GIS-based SCS-SN approach enables the expert to simulate the runoff magnitude for each individual pixel over the catchment basin. Dynamics in LULC and rainfall within the considered period of time were resulted in significant changes in runoff and flooding (see Fig. 8). The urban areas, barren lands, and temporary plantation areas tend to increase the amount of surface runoff especially during the monsoon season floods where high-intensity rainfall takes place.

Table 7 Calibrated and adapted CN look-up table

LULC class	Soil suitability	Soil type	Area (ha)	Soil description	HSG	CN	CN-AMCIII
Forest	2Gn	Seremban-Munchang Serdang and Kedah	16.37	Fine loamy	A	30	50
Forest	2Gnt	Rengam	61.94	Coarse sandy clay loam	A	30	50
Barren land	2Gn	Seremban-Munchang Serdang and Kedah	16.37	Fine loamy	A	49	69
Barren land	2Gnt	Rengam	61.94	Coarse sandy clay loam	A	49	69
Forest	5H(m)	Disturbed land—lack of structure	6.26	Clay	D	77	77
Barren land	2nT	Local alluvium colluvium association	23.74	Silt and clay	C	79	79
Oil palm	5G	Steep land	154.24	Silt and loamy	B	80	80
Agriculture	2nT	Local alluvium colluvium association	23.74	Silt and clay	C	82	82
Forest	5G	Steep land	154.24	Silt and loamy	B	55	82
Forest	5G	Steep land	154.24	Silt and loamy	B	55	82
Agriculture	2Gn	Seremban-Munchang Serdang and Kedah	16.37	Fine loamy	A	64	83
Agriculture	2Gnt	Rengam	61.94	Coarse sandy clay loam	A	64	83
Barren land	5G	Steep land	154.24	Silt and loamy	B	69	83
Barren land	5H(m)	Disturbed land—lack of structured	6.26	Clay	D	84	84
Agriculture	5H(m)	Disturbed land—lack of structured	6.26	Clay	D	85	85
Forest	2nT	Local alluvium colluvium association	23.74	Silt and clay	C	70	85
Urban	5G	Steep land	154.24	Silt and loamy	B	85	85
Oil palm	2Gn	Seremban-Munchang Serdang and Kedah	16.37	Fine loamy	A	71	86
Oil palm	2Gnt	Rengam	61.94	Coarse sandy clay loam	A	71	86
Oil palm	2nT	Local alluvium colluvium association	23.74	Silt and clay	C	87	87

(continued)

Table 7 (continued)

LULC class	Soil suitability	Soil type	Area (ha)	Soil description	HSG	CN	CN-AMCIII
Oil Palm	5H(m)	Disturbed land—lack of structure	6.26	Clay	D	90	90
Urban	2nT	Local alluvium colluvium association	23.74	Silt and clay	C	90	90
Urban	2Gn	Seremban-Munchang Serdang and Kedah	16.37	Fine loamy	A	75	91
Urban	2Gnt	Rengam	61.94	Coarse sandy clay loam	A	75	91
Agriculture	5G	Steep land	154.24	Silt and loamy	B	75	91
Urban	5H(u)	Urban land	15.50	Urban land	D	92	92
Urban	5H(m)	Disturbed land—lack of structured	6.26	Clay	D	92	92
Waterbody	WATER	Waterbody	271.0	Waterbody	D	97	97
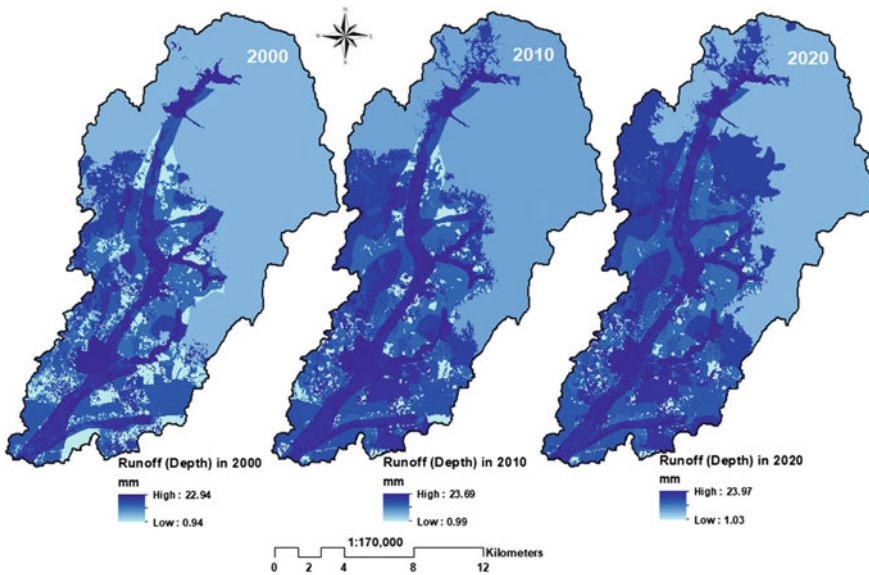
Fig. 8 Distributed maximum surface runoff in the three considered time periods

The amount of surface runoff has been increased steadily from 2000 to 2020 for more than 1 mm (Fig. 9). These phenomena happened due to deforestation in Semenyih basin. However, Forest mostly replaced by oil palm and agricultural lands where the infiltration of soil still high. As a result, the coverage of land
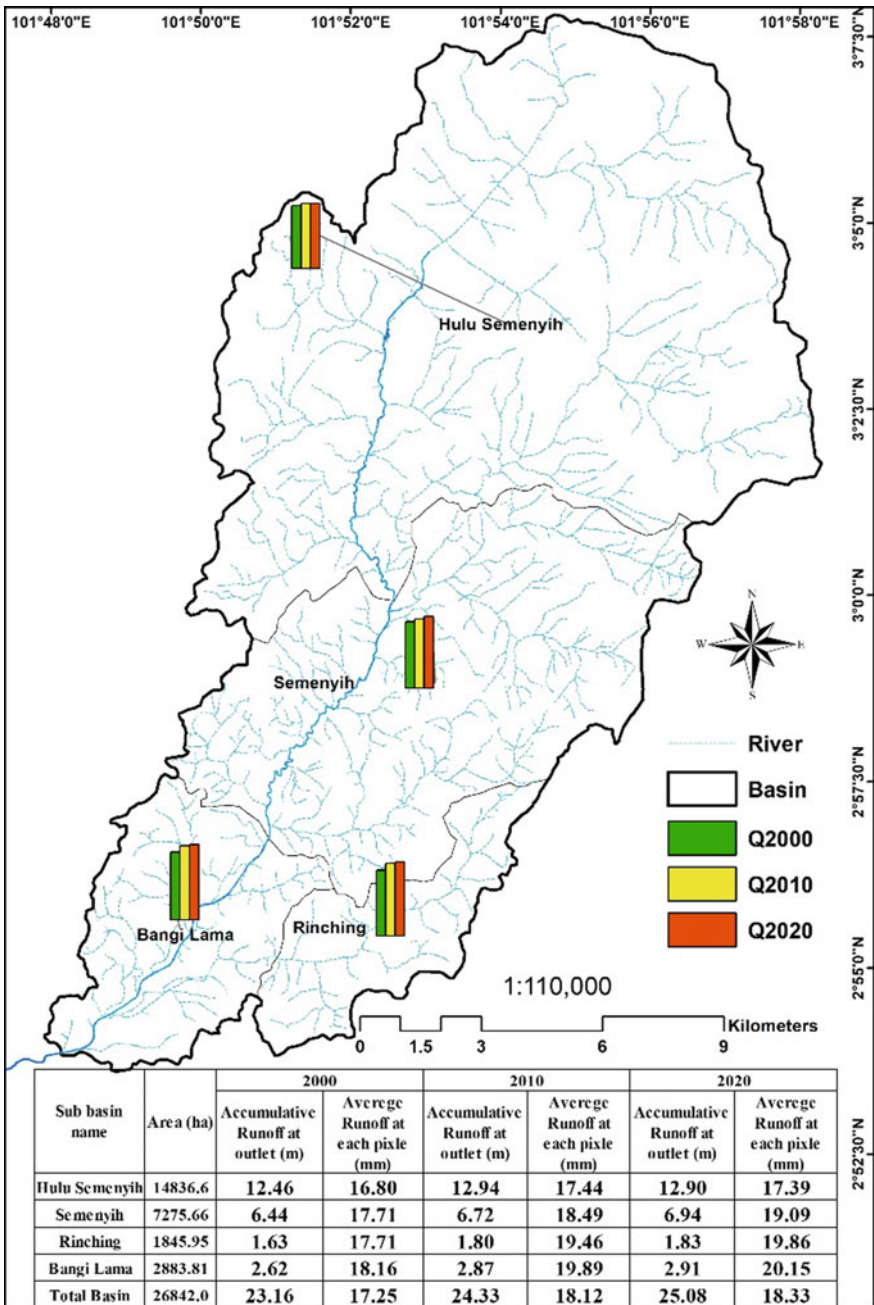
Fig. 9 Compared distributed-maximum surface runoff in three considered time periods within sub-catchments

protects the soil to get saturated with water and the excess water will not run through the area which causes a sustainable watershed area. In other words, although there is a wide range of deforestations in Semenyih since 2000, the runoff has not been changed dramatically. The simulated averaged runoff magnitude were extracted for each sub-catchments for the given time period as shown in Fig. 9.

To verify the implemented rainfall–runoff model, it is needed to run the model calibration which is a systemic approach for correcting the model parameters to achieve a desirable similarity between the observed and simulated hydrographs [4]. In the SCS-CN model, the degree of difference between observed and simulated runoff quantitatively was measured. The sensitivity analysis was applied for 12 iterations which attempt to achieve the optimum values for parameters (e.g., AMC-CN and I_a) to calibration the simulated runoff model. Regarding the observed streamflows in Sg. Rinching Station (monthly 2000–2015) the proposed model was calibrated by adjusting the mentioned parameter values till the minimum RMSE was achieved.

4 Conclusion

The present study demonstrates the interest of GIS techniques and remote sensing, and the utility of the estimation and prediction of the runoff for the watershed. Object-based SVM classification method was applied on Spot-5 satellite images to classify LULC classes for 2000 and 2010. This approach had an excellent performance where the overall accuracy was 89.6 and 93.1% with 0.87 and 0.91 kappa coefficients for 2000 and 2010, respectively. Then changes in LULC classes were detected and the future LULC scenario was simulated using LTM model. It should be noted that the LTM model considers all the contributing drivers (e.g., approximately from roads, river, and urban) deal with LULC classes for simulation using neural systems algorithm. As a result, the spatial accuracy of LULC prediction for 2020 was estimated 73.56% with the kappa index of 0.66 which shows a satisfactory level of accuracy.

Another purpose of this study was to simulate climate change in the foreseeable future 2020 and evaluate the impact of the precipitation on surrounding ecosystem. The ARIMA model was engaged to foresee and simulate rainfall magnitude based on the past trends. The maximum monthly rainfall data from 8 gauging stations were implemented to run ARIMA. The parameters of ARIMA time series model have to be calibrated and fitted statistically to minimize the prediction uncertainty. Therefore, the most optimal ARIMA combinations (i.e., seasonal and nonseasonal parameters) were calculated by recent Taguchi method. Having examined possible combinations of ARIMA (1, 0, 1) (0, 0, 1) was selected as the best model to forecast rainfall magnitude for 2020. Then, IDW interpolation model was applied in order to create the finite distributed rainfall maps.

For this study, the soil conservation service-curve number (SCS-CN), was used to simulate the amount of surface runoff within subbasins in GIS framework.

This method requires surface rainfall depths as well as CN index for the entire watershed. The CN maps were derived using hydrologic soil group combined with land cover regarding to AMC III scheme. Then, distributed SCS-CN model was derived for 2000, 2010, and 2020. The accumulative simulated runoff at the basin outlet for 2000 and 2010 were calibrated with absorbed-recorder streamflow to calibrate the integrity of the model.

The comparison results showed that the surface runoff from urban areas, bare soils, and some agricultural areas are dominant for a pluvial flooding compared with runoff from forest and oil palm lands in this study area. Basically, the urban areas with the impervious surface as well as barren lands where the soil prone to erosion, tend to increase for runoff particularly in terms of heavy rainfall. Deforestation and land clearing in the Semenyih watershed for agricultural, urbanization, and infrastructure development will result in the growth of surface runoff and flooding.

References

1. Bronstert, A.: Floods and climate change: interactions and impacts. Risk Anal. **23**(3), 545–557 (2003)
2. Liu, Z., Yao, Z., Huang, H., Wu, S., Liu, G.: Land Use and Climate Changes and Their Impacts on Runoff in the Yarlung Zangbo River Basin, China (2012)
3. Hanson, C., Rosenzweig, C., Casassa, G., Karoly, D.J., Imeson, A., Liu, C., Menzel, A., Rawlins, S., Root, T.L., Seguin, B., Tryjanowski, P.: Assessment of observed changes and responses in natural and managed systems. In: Contribution of Working Group II to the Fourth Assessment Report of the Intergovernmental Panel on Climate Change, Climate Change. Impacts, Adaptation and Vulnerability. Cambridge University Press, Cambridge, UK (2007)
4. Adnan, N.A., Ariffin, S.D.S., Asmat, A., Mansor, S.: Rainfall trend analysis and geospatial mapping of the Kelantan River Basin. In: ISFRAM, pp. 237–247. Springer, Singapore (2016)
5. Rizeei, H.M., Saharkhiz, M.A., Pradhan, B., Ahmad, N.: Soil erosion prediction based on land cover dynamics at the Semenyih watershed in Malaysia using LTM and USLE models. Geocarto Int. **6049**, 1–20 (2016)
6. Andréassian, V.: Waters and forests: from historical controversy to scientific debate. J. Hydrol. **291**(1–2), 1–27 (2004)
7. Farley, K.A., Jobbágy, E.G., Jackson, R.B.: Effects of afforestation on water yield: a global synthesis with implications for policy. Glob. Chang. Biol. **11**(10), 1565–1576 (2005)
8. Calder, I.R.: Forests and water-Ensuring forest benefits outweigh water costs. For. Ecol. Manage. **251**(1–2), 110–120 (2007)
9. Lambin, E.F., Geist, H.J., Lepers, E.: Dynamics of land-use and land-cover change in tropical regions. Annu. Rev. Environ. Resour. **28**(1), 205–241 (2003)
10. Koomen, E., Stillwell, J., Bakema, A., Scholten, H.J.: Modelling Land-Use Change: Progress and Applications, vol. 90, no. 2 (2007)
11. Pijanowski, B.C., Brown, D.G., Shellito, B.A., Manik, G.A.: Using neural networks and GIS to forecast land use changes: a land transformation model. Comput. Environ. Urban Syst. **26**(6), 553–575 (2002)
12. Heistermann, M., Müller, C., Ronneberger, K.: Land in sight? achievements, deficits and potentials of continental to global scale land-use modeling. Agric. Ecosyst. Environ. **114**(2–4), 141–158 (2006)

13. Kahya, E., Kalayci, S.: Trend analysis of streamflow in Turkey. J. Hydrol. **289**(1–4), 128–144 (2004)
14. Durdu, Ö.F.: Application of linear stochastic models for drought forecasting in the Büyük Menderes river basin, western Turkey. Stoch. Environ. Res. Risk Assess. **24**(8), 1145–1162 (2010)
15. Makridakis, S.: The M3-competition : results, conclusions and implications, vol. 16, pp. 451–476 (2000)
16. Brocklebank, J., Dickey, D.A.: SAS for Forecasting Time Series, pp. 191–299. SAS Institute (2003)
17. Yin, J., He, F., Xiong, Y., Qiu, G.: Effect of land use/land cover and climate changes on surface runoff in a semi-humid and semi-arid transition zone in Northwest China. Hydrol. Earth Syst. Sci. Discuss. **6**, 1–23 (2016)
18. Chu, X., Steinman, A.: Event and continuous hydrologic modeling with HEC-HMS. J. Irrig. Drain. Eng. **135**(1), 119–124 (2009)
19. Mojaddadi, H., Pradhan, B., Nampak, H., Ahmad, N., Halim, A.: Ensemble machine-learning-based geospatial approach for flood risk assessment using multi-sensor remote-sensing data and GIS. Geomat. Nat. Haz. Risk. **8**(2), 1080–1102 (2017)
20. Mishra, S.K., Pandey, A., Singh, V.P.: Special issue on soil conservation service curve number (SCS-CN) methodology. J. Hydrol. Eng. **17**(11), 1157 (2012)
21. Du, Q., Younan, N.H., King, R., Shah, V.P.: On the performance evaluation of pan-sharpening techniques. IEEE Geosci. Remote Sens. Lett. **4**(4), 518–522 (2007)
22. Pflug, B., Main-Knorn, M., Makarau, A., Richter, R.: Validation of aerosol estimation in atmospheric correction algorithm ATCOR. Int. Arch. Photogramm. Remote Sens. Spat. Inf. Sci. **XL**(5), 11–15 (2015)
23. Kay, S., Hedley, J.D., Lavender, S.: Sun glint correction of high and low spatial resolution images of aquatic scenes: a review of methods for visible and near-infrared wavelengths. Remote Sens. **1**(4), 697–730 (2009)
24. Kim, M., Madden, M., Warner, T.: Capítulo 3.2 Estimation of optimal image object size for the segmentation of forest stands with multispectral IKONOS imagery. In: Object-Based Image Analysis Spatial Concepts Knowledge-Driven Remote Sensing Applications, pp. 291–307 (2008)
25. Tiede, D., Li, M., Ma, L., Blaschke, T., Cheng, L.: A systematic comparison of different object-based classification techniques using high spatial resolution imagery in agricultural environments. Int. J. Appl. Earth Obs. Geoinf. **49**(4), 87–98 (2016)
26. Blaschke, T., Lang, S., Lorup, E., Strobl, J., Zeil, P.: Object-oriented image processing in an integrated GIS/remote sensing environment and perspectives for environmental applications. Environ. Inf. Plann. Polit. Public (1995), 555–570 (2000)
27. Blaschke, T.: Object based image analysis for remote sensing. ISPRS J. Photogramm. Remote Sens. **65**(1), 2–16 (2010)
28. Blaschke, T., Burnett, C., Pekkarinen, A.: Image segmentation methods for object-based analysis and classification. In: Remote Sensing Image Analysis: Including the Spatial Domain, vol. 211–236, no. 12 (2004)
29. Nikfar, M., Valadan Zoej, M.J., Mokhtarzade, M., Shoorehdeli, M.A.: Designing a new framework using type-2 FLS and cooperative-competitive genetic algorithms for road detection from IKONOS satellite imagery. Remote Sens. **7**(7), 8271–8299 (2015)
30. Hamedianfar, A., Shafri, H.Z.M.: Integrated approach using data mining-based decision tree and object-based image analysis for high-resolution urban mapping of WorldView-2 satellite sensor data. J. Appl. Remote Sens. **10**(2), 25001 (2016)
31. Nguyen, L.: Tutorial on support vector machine. Appl. Comput. Math. **6**(4–1), 1–15 (2016) (Special Issue: Some Novel Algorithms for Global Optimization and Relevant Subjects)
32. Jebur, M.N., Pradhan, B., Tehrany, M.S.: Optimization of landslide conditioning factors using very high-resolution airborne laser scanning (LiDAR) data at catchment scale. Remote Sens. Environ. **152**, 150–165 (2014)

33. Burges, C.J.C.: A tutorial on support vector machines for pattern recognition. Data Min. Knowl. Discov. **2**(2), 121–167 (1998)
34. Wilder, M.G.: Site and situation determinants of land use change: an empirical example. Econ. Geogr. **61**(4), 332–344 (1985)
35. Omrani, H., Tayyebi, A., Pijanowski, B.: Integrating the multi-label land-use concept and cellular automata with the artificial neural network-based Land Transformation Model: an integrated ML-CA-LTM modeling framework. GIScience Remote Sens. **54**(3), 1–22 (2017)
36. Taneja, K., Ahmad, S., Ahmad, K., Attri, S.D.: Time series analysis of aerosol optical depth over New Delhi using Box–Jenkins ARIMA modeling approach. Atmos. Pollut. Res. **7**(4), 585–596 (2016)
37. Momani, P.E.N.M.: Time series analysis model for rainfall data in jordan: case study for using time series analysis. Am. J. Environ Sci. **5**(5), 599–604 (2009)
38. AbbasAbd Allah Ibrahim, T.M.M.: Time series analysis of Baghdad rainfall using ARIMA method. Sust. J. Eng. Comput. Sci. **54**(4), 1136–1142 (2013)
39. Nagarjun, P.A., Rao, R.S., Rajesham, S., Rao, L.V.: Optimization of lactic acid production in SSF by Lactobacillus amylovorus NRRL B-4542 using Taguchi Methodology Optimization, no. 3 (2005)
40. Pradhan, B., Jebur, M.N., Zulhaidi, H., Shafri, M., Tehrany, M.S.: Data fusion technique using wavelet transform and Taguchi methods for automatic landslide detection from airborne laser scanning data and QuickBird satellite imagery. IEEE T. Geosci. Remote **54**(3), 1610–1622 (2016)
41. Nonglait, T.L., Tiwari, B.K.: Application of SCS-CN method for estimation of runoff in a humid micro watershed. Int. J. Curr. Agric. Sci. **6**(10), 121–127 (2016)
42. Bartlett, M.S., Parolari1, A.J., McDonnell, J.J., Porporato, A.: Beyond the SCS-CN method: a theoretical framework for spatially lumped rainfall-runoff response. Water Resour. Res. **6**(52), 4608–4627 (2016)
43. Woodward, D.E., Hawkins, R.H., Jiang, R., Hjelmfelt, Jr, A.T., Van Mullem, J.A., Quan, Q.D.: Runoff curve number method: examination of the initial abstraction ratio. World Water Environ. Resour. Congr. 1–10 (2003)
44. Faizalhakim, A.S, Nurhidayu, S., Norizah, K., Shamsuddin, I., Hakeem, K.R., Ismail, A.: Curve Number Determination for Kelantan River Basin, no. 9 (2016)
45. Ward, A.D., Trimble, S.W.: Environmental Hydrology. CRC Press (2003)

Three-Dimensional Stratigraphy View from Ground Penetrating Radar Attributes for Soil Characterization

Amalina Yusof, Muhamad Mubiin Abdul Manas, Zulkarnaini Mat Amin and Nurhazimah Husna Shokri

Abstract The Ground Penetrating Radar (GPR), a geophysical technique that uses non-destructive testing to detect objects and structure beneath the soil was a huge contribution in survey and engineering, especially in underground utility. GPR has been used since 1970 and the method is still undergoing upgrade alongside the sophisticated processing software. Nevertheless, soil is the principal medium which interferes with the signal penetration of GPR due to its physical and electrical properties. Thus, a study using soil stratigraphy is a prerequisite to understanding GPR radargram. In this study, a test bed was constructed to simulate different soil layers which consist of existing clay, sand, small stone, and crusher run stone. The GPR instrument with frequencies of 100, 250, 400, 750, and 900 MHz was used to collect the data. The processing was carried out using reflex software for image interpretation and three-dimensional (3D) visualizations. This study is expected to help surveyors in understanding the measurement, for example, soil composition, problems related to GPR underground surveying.

Keywords Three dimensional · Stratigraphy · Ground penetrating radar

1 Introduction

Malaysia is currently undergoing profound development and construction with an extensive underground utility installation such as for water reticulation, sewerage, electric, gas, and telephone [1, 2]. Thus, information on a particular location of utility installation is necessary to decrease any disturbance that would result in

A. Yusof · M. M. A. Manas · Z. M. Amin (✉) · N. H. Shokri
Geomatic Innovation Research Group, Faculty of Geoinformation
and Real Estate, Universiti Teknologi Malaysia, 81310 Skudai,
Johor, Malaysia
e-mail: zulkarnaini@utm.my

A. Yusof
e-mail: amalinayusup@gmail.com

property damages, design changes, service breakdown, and business disruption or even cause injuries [3].

Due to the capability of subsurface imaging and user-friendly features, Ground Penetrating Radar (GPR) is used in many engineering works such as civil engineering [4–6], archaeology [7–10], forensics [11–13], earth sciences [14], military, and environmental studies [15]. This underground utility mapping uses the principle of geophysics to detect, identify, and investigate subsurface object buried in the ground [6].

An object could be identified whether it is buried in shallow or deeper depths based on the correct radar antenna frequency [16]. As the technology develops, GPR had been featured in wide applications for the last 40 years with a continuously upgraded software to facilitate better results [17].

GPR has become a very important tool for non-destructive testing for underground exploration. In fact, it is capable to produce high-resolution images of the shallow subsurface and underground utilities. However, one of the obstacles in getting such information would revolve around the type of the soil [18]. Therefore, this study would like to identify the properties of the soil for better GPR image resolution.

Soil is an assemblage isolated unit of earth's layer deposit which includes mineral composition or organic source occasionally. Soil properties and characteristics could be identified from the GPR imaging data. The performance of GPR helps to differentiate types of soils [19, 20]. Therefore, the soil profile data and information could be collected. However, different soil and moisture condition affect the efficiency performance of GPR [21].

Various types of soils make the ground itself contain a number of soil layers. The stratigraphy of soil gives information of the soil profile, whereby measurement and study of the soil profile could be done by measuring the thickness of certain soil layer [22, 23]. Moreover, stratigraphic information is very useful for visualization of sedimentary structures, sand body geometry, and stratigraphic architecture [24, 25]. In that case, the visualization of stratigraphic structure could be upgraded to 3D visualization for better evaluation.

Lately, 3D model mapping has been used in the surveying field. Most of the maps, nowadays, are produced in 3D form which contain more details than two-dimensional (2D) maps. 3D map shows more details on the surface of the earth, as well as below the earth surface.

There are many benefits of the 3D view compared to 2D view. First, 3D view allows a concise picture of an object for higher resolution. Yet, the versatility allows users to easily understand the information given. Furthermore, 3D view enables instant calculations and interpolation such as coordinate computation and provide information of soil stratigraphy in order to correlate the soil strata [26]. The GPR data is analysed by using software to create and view 3D stratigraphy [27]. Therefore, 3D stratigraphy view gives more information than old existing stratigraphy view.

2 Methodology

2.1 Test Bed Simulation

The test bed is constructed at a selected site as shown in Fig. 1. The site is located at the Universiti Teknologi Malaysia cluster area and marked with a red flag. The test bed is built as a simulation for the imaging of soil stratigraphy. For this simulation, the test bed is built with a dimension of 2 m length × 1 m wide × 1.2 m depth. In order to create various types of soil layers, certain types of soil were selected such as smooth sand, small granite stone, and crusher run stone.

The test bed was divided into three layers. The deepest layer is the smooth sand followed by small granite stone, and crusher run stone. These entire layers are perfectly divided into same depth, 0.4 m, with the same dimension in length and width.

After the test bed is filled up with these soils, the soil then was compacted by using a compactor machine. The best common means for soil stabilization to meet the recommended road scheme necessity is through compaction. Soil compaction is used to compress the soil to the ground by eliminating the air voids, pore spaces between soil particles. Additionally, soil compaction is a recommended method to reduce error as the air gap between the soils becomes smaller. Therefore, the errors of radar images could be reduced. Figure 2 shows the three layers of the constructed test bed.
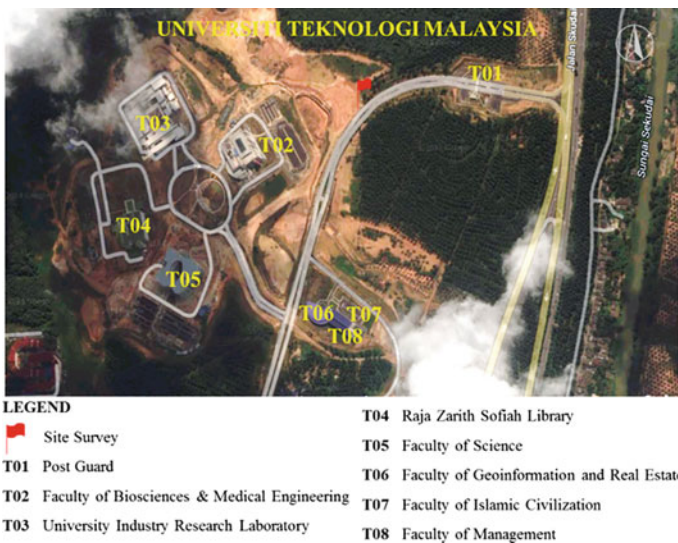
Fig. 1 Simulation site
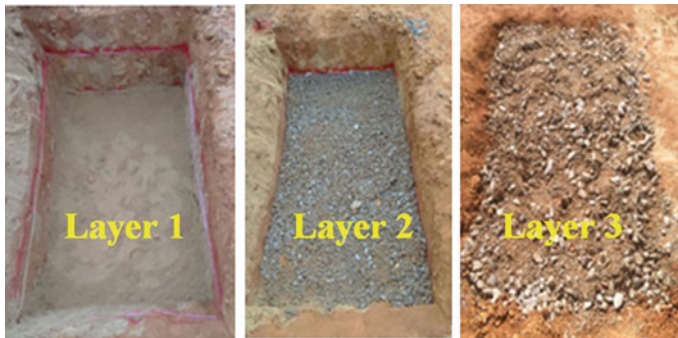
Fig. 2 Soil layers of the constructed test bed; layer 1 is the smooth sand, layer 2 is the small granite stone, and layer 3 is the crusher run stone

Data collection had been done by using GPR equipment with a variety of signal frequencies. The signal frequencies that had been used were 100, 250, 400, 750, and 900 MHz.

The extraction of the stratigraphy shows different resolution for different frequency. The low frequency creates a poor resolution, whereas the high frequency produces good resolution [28]. Hence, moderate frequency would best be employed.

The data collection surveys were performed by gridding method. It is commonly used to establish rectangular grids with 1 m or less line spacing, with interval of 0.5 m in this method [29–31]. The gridding sizes covered 3 m × 2 m area.

2.2 Data Processing

As for the data processing, the data underwent various stages before being presented as useful information. These stages include generalization, computation, adjustment, image filtering, and interpretation of raw radar data which validate the quality of the collected data. Then, the data is generated into 3D view. The software used to process this data is called Reflex2D and Reflex3D software. The result and analysis of the study is discussed in the next section.

3 Result and Discussion

3.1 Extraction of the Stratigraphy

The extraction of stratigraphy from the GPR images needs to be carried out according to several steps. The extraction of the stratigraphy is conducted by using
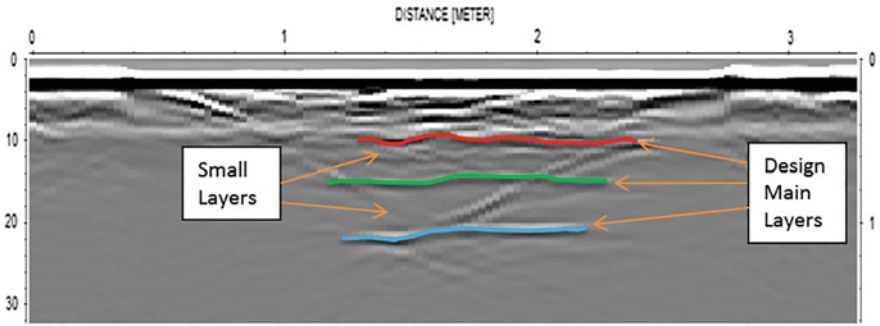
Fig. 3 Design of main soil layers on the radar image

Reflex2D software. In order to rectify and reduce errors, image filtering was employed. This software was used to process and identify the soil layers.

Then, the basic understanding of radar image interpretation is that the radar image would partially show the separation of the soil. Due to some blunders, the image would shows more small layers than what exactly the soil layer has. This is because the signal from the radar would reflect when it encounters different mediums. The signal detects too many different changes of conductivities and velocity. As a result, the best way to solve this problem is to design the main layers of the soil. Figure 3 shows a radar image with the design of the main soil layers. The soil layers stratigraphy were then extracted from the radar images.

Next, it is possible to identify and extract the soil stratigraphy based on their reflection velocity from the radargram. From the radargram, the soil stratigraphy which is based on soil conductivity and permittivity could be determined. Indeed, different types of soil have different properties. Figure 4 shows the extraction of soil layer based on soil velocity from the radargram.
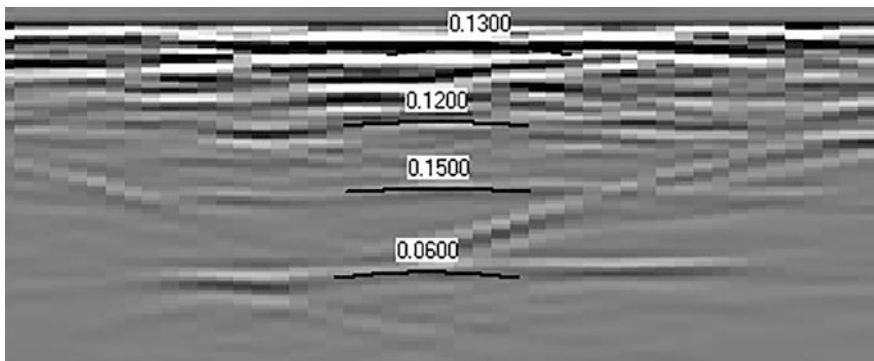
Fig. 4 Extraction of soil layer based on soil velocity

In this study, different frequencies of the GPR were used for the data acquisition. As we know, high-frequency signals would provide high resolution of radar images. As mentioned, the frequency involved in this study were 100, 250, 450, 750, and 900 MHz. The range of the frequency involved has covered both low and high frequency. As data was collected from different frequencies, a comparison of the data in terms of resolution of the data could be identified. The resolution is the depth or thickness of the soil layers.

There are different image resolutions between frequencies. The soil stratigraphy extraction was extracted from each image of different frequency, referred to the soil velocity of the radargram. After image analyses, the depths of different layers were slightly different based on their frequency. Therefore, the velocity readings of the different layers would prove the changes of soil stratigraphy. Table 1 shows the reading of soil layer depths and changes of soil velocity based on their frequency.

The signal velocity of the soil changes as the signal penetrates through different soil layers. In fact, based on Table 1, the velocity readings show that there is not much difference between the frequencies as the signal penetrates different soil layers. The outcome shows that the time gap between the construction of the test bed and the data acquisition was too long. The layers of soil were slightly mixed with the existing soils as the test bed was widely exposed to the weather conditions such as rain; thus, causing the thickness to vary in Table 1. The velocity reading for the first soil layer, which is the crusher runs stone, was almost the same for all the frequencies ranged between 0.130 and 0.135 m/ns. Despite that, from the evidence, it is proven that the soil layers have different velocity properties. The velocity reading for second and third layer similarly suits the test bed layers, which are small

Table 1 Soil layers velocity and depth based on their frequency

Frequency (MHz)	Soil layer	Velocity (m/ns)	Depth (m)	No. of traces
100	1	0.157	1.203	29
	2	0.128	0.808	
	3	0.135	0.414	
250	1	0.150	1.188	53
	2	0.120	0.788	
	3	0.130	0.364	
400	1	0.153	1.168	60
	2	0.128	0.791	
	3	0.132	0.382	
700	1	0.161	1.250	53
	2	0.120	0.785	
	3	0.132	0.402	
900	1	0.155	1.053	92
	2	0.120	0.712	
	3	0.133	0.402	

granite stone and smooth dry sand, respectively. Both soil velocities are ranged between 0.7 and 0.8 m/ns, and between 1.0 and 1.2 m/ns, respectively.

3.2 Generation of 3D View Stratigraphy

From the previous results (refer Sect. 3.1), the extraction of the soil stratigraphy would help in the interpretation of generating 3D view of the soil layers. Production of this 3D view would be carried out using Reflex3D software. The 3D view of stratigraphy would give better resolution; hence, interpretation of soil layers could be made. Consequently, 3D view would better demonstrate soil stratigraphy compared to 2D stratigraphy view. Besides that, the 3D view gives the overall view of soil profile. Figure 5 shows the 3D view of soil stratigraphy.

The soil layers shown in 3D view was extracted from the 2D radargram images based on the amplitude changes. Different medium would give different reflectance amplitudes and this is how the soil layers were separated. For this 3D view, the amplitudes changes were illustrated using changes of colors. The amplitude is shown through the color bars. The negative value of amplitude gives lower amplitude reading while the positive value shows high amplitude reading.

For the extraction of the stratigraphy, different frequencies were used to study the resolution of the images. The data from the variety of GPR frequencies were used to generate the 3D view with various resolution acquisitions, which includes 100, 250, 450, 750, and 900 MHz. Figure 6 shows the 3D view of soil layers and their extraction of stratigraphy slices powered by 900 MHz frequency GPR reading.

From the figure, it is concluded that higher frequency would generate a better 3D view resolution. Hence, the 900 MHz frequency for GPR signal creates the best resolution of soil stratigraphy as the soil layers could be clearly determined by its
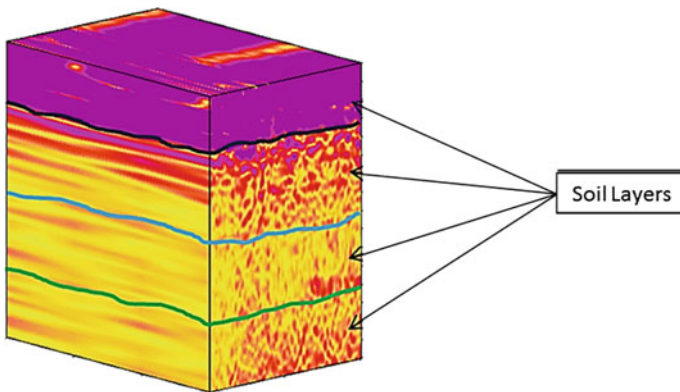
Fig. 5 The 3D view of soil stratigraphy
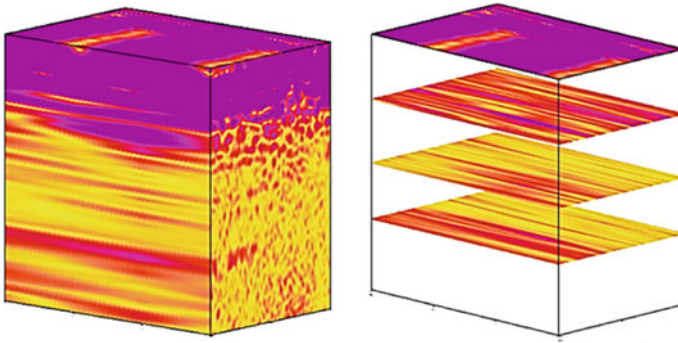
Fig. 6 The 3D view of soil layers and their extraction of stratigraphy slice powered by 900 MHz frequency GPR equipment

amplitudes color changes with the visualization being sharp and clear. In conclusion, 400 MHz would give best resolution between moderate and high frequency.

3.3 Real Site Stratigraphy

Instead of the simulated test bed mentioned earlier in this chapter, this study also utilizes an actual site data in order to create a realistic soil stratigraphy. For this study, the actual site in question was located at Sungai Batu, Merbok, Kedah. The National Heritage Department (NHD) with the cooperation of several agencies had discovered a stone structure (Fig. 7) that resembles a wall which bears historical structure. The data acquisition and data processing method applied were the same as the test bed before in order to extract the soil stratigraphy. Figure 7 shows the view

Fig. 7 The view of the actual site stratigraphy located in Sg. Batu, Merbok, Kedah
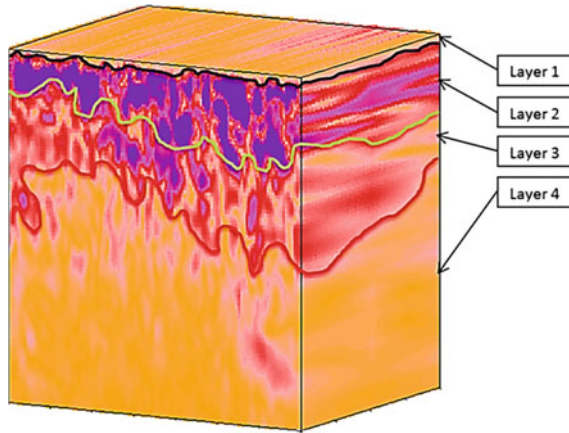
Fig. 8 The generated 3D view with the soil stratigraphy extracted
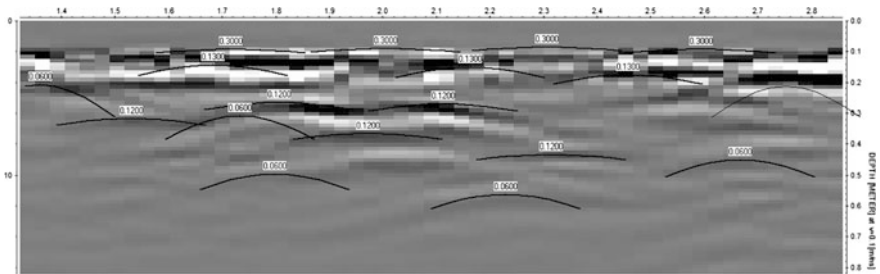
Fig. 9 The extraction of soil velocity from radargram image

of the real stratigraphy site while Fig. 8 shows the generated 3D view from the data with the soil stratigraphy extracted.

Based on Fig. 8, there were various types of soil layers at this site. The 3D view has clearly shown that the changes in the type of soil would result in obvious changes in amplitudes color. The reading of soil velocity helped in determining the soil types. Figure 9 shows the extraction of soil velocity from radargram image, while Table 2 shows the reading of soil velocity properties.

Layer	Velocity (m/ns)	Materials (m)
1	0.30	Air
2	0.12	Limestone
3	0.13	Granite
4	0.06	Clays

Table 2 Soil velocity at Merbok, Kedah

4 Conclusion

In this study, GPR has been used to produce a proper visualization for the internal structure of soil stratigraphy. With proper analysis of filtered techniques for the images, the soil stratigraphy could be interpreted and extracted. This study involved a variety of frequencies in data acquisition. The frequencies covered range between low and high frequencies of GPR, which are 100, 250, 400, 750, and 900 MHz.

From the previous section, this study has successfully identified and extracted the soil stratigraphy from the filtered radar images. The soil layers had been extracted and identified by detecting trace signals which have different reflectance for each medium.

As the test bed was constructed with the understanding of the depth of soil layers, the collected data was used to compare with the known information. From that comparison, it was determined that GPR could be used for soil stratigraphy interpretation instead of other existing equipment.

Moreover, high-frequency GPR would give the best resolution of radar images, with low penetration signal by employing the frequency from 400 to 750 MHz. Meanwhile, the low signal may penetrate deep but produces results in low resolution of the radar images. However, both low and high frequency have their pros and cons.

The 3D view of soil stratigraphy was generated based on the information and details obtained from analysis of the radar images. As shown in Fig. 6, the soil layers in 3D view mode were easier to analyse. The changes of amplitude color could be seen in this view.

The result of observation of soil stratigraphy was shown in 3D view. The soil stratigraphy is important in order to identify the medium of the ground. As discussed earlier, soil stratigraphy is not only important for the surveyors but also other users in different fields such as agriculture and construction. As a conclusion, this study is expected to help the surveyor to identify any underground utility mapping problem.

References

1. Yang, H.W., Yang, Z.k, Pei, Y.k: Ground-penetrating radar for soil and underground pipelines using the forward modeling simulation method. Optik—Int. J. Light Electron Opt. **125**(23), 7075–7079 (2014)
2. Fan, C., Zhi-Yuan, W., Lei, W., Yan-Bin, W.: Application of the ground penetrating radar ARMA power spectrum estimation method to detect moisture content and compactness values in sandy loam. J. Appl. Geophys. **120**, 26–35 (2015)

3. Qingqing, X., Laibin, Z., Wei, L.: Acoustic detection technology for gas pipeline leakage. Process Saf Environ. **91**(4), 253–261 (2013)

4. Alani, A.M., Aboutalebi, M., Kilic, G.: Applications of ground penetrating radar (GPR) in bridge deck monitoring and assessment. J. Appl. Geophys. **97**, 45–54 (2013)

5. Abujarad, F. (ed.): Independent factor analysis for clutter reduction in GPR data for landmine detection. In: IEEE 15th International Conference on Ground Penetrating Radar (GPR), 2014. Brussels, Belgium, 30 June 2014–04 July 2014

6. Clark, W.W., Burns, B.P., Ralston, J.M. (ed.): Soil effects on GPR antenna imaging quality. In: Proceedings of SPIE 5794, Detection and Remediation Technologies for Mines and Minelike Targets X, 968. Orlando, Florida, USA, 08 July 2005

7. Zhao, W.K., Tian, G., Wang, B.B., Shi, Z.J., Lin, J.X.: Application of 3D GPR attribute technology in archaeological investigations. Appl. Geophys. **9**(3), 261–269 (2012)

8. Nuzzo, L., Leucci, G., Negri, S., Carrozzo, M.T., Quarta, T.: Application of 3D visualization techniques in the analysis of GPR data for archaeology. Ann Geophys-Italy. **45**(2), 321–337 (2002)

9. Grasmueck, M., Weger, R., Horstmeyer, H. (eds.): Full-resolution 3D GPR imaging for geoscience and archeology. In: 10th International Conference on Ground Penetrating Radar, 2004 GPR 2004. Delft, The Netherlands, 21–24 June 2004

10. Golebiowski, T.: 3D GPR measurements for archaeological application with interpretation aided by numerical modelling. Acta Geophys. **54**(4), 413–429 (2006)

11. Whiting, B.M., Hackenberger, S. (eds.): Using 3D GPR to determine the extent of possible 17th and 18th century graves beneath a concrete driveway: bridgetown Synagogue, Bridgetown, Barbados. In: 10th International Conference on Ground Penetrating Radar, 2004 GPR 2004. Delft, The Netherland, 21–24 June 2004

12. Novo, A., Lorenzo, H., Rial, F.I., Solla, M.: 3D GPR in forensics: finding a clandestine grave in a mountainous environment. Forensic Sci. Int. **204**(1–3), 134–138 (2011)

13. Almeida, E.R., Porsani, J.L., Catapano, I., Gennarelli, G., Soldovieri, F. (eds.): GPR data analysis enhanced by microwave tomography for forensic archaeology. In: IEEE 15th International Conference on Ground Penetrating Radar (GPR), 2014. Brussels, Belgium, 30 June 2014–04 July 2014

14. Bradford, J.H.: Measuring water content heterogeneity using multifold GPR with reflection tomography. Vadose Zone J. **7**(1), 184–193 (2008)

15. Mahesh, V.S., Senthilkumaran, K., Jha, P.C. (eds.): 3D digitization of sub surface features using 3D GPR. In: ASME 2011 International Design Engineering Technical Conferences and Computers and Information in Engineering Conference. American Society of Mechanical Engineers, Washington DC, USA, 28–30 Aug 2011

16. Widodo, W., Aditama, I.F., Syaifullah, K., Mahya Ma, J., Hidayat, M.: Detecting buried human bodies using ground-penetrating radar. Earth Sci. Res. **5**(2), 59 (2016)

17. Wenke, Z., Emanuele, F., Michele, P., Gang, T.: Ground penetrating radar (GPR) attribute analysis for archaeological prospection. J. Appl. Geophys. **97**, 107–117 (2013)

18. Igel, J., Takahashi, K., Preetz, H. (eds.): Electromagnetic soil properties and performance of GPR for landmine detection: how to measure, how to analyse and how to classify? In: 6th International Workshop on Advanced Ground Penetrating Radar (IWAGPR), 2011. Aachen, Germany, 22–24 June 2011

19. Akturk, O., Doyuran, V.: Integration of electrical resistivity imaging (ERI) and ground-penetrating radar (GPR) methods to identify soil profile around Necatibey Subway Station, Ankara. Turkey. Environ. Earth Sci. **74**(3), 2197–2208 (2015)

20. Jonard, F., Weihermüller, L., Vereecken, H., Lambot, S.: Accounting for soil surface roughness in the inversion of ultrawideband off-ground GPR signal for soil moisture retrieval. Geophysics **77**(1) (2012)

21. Conyers, L.B. (ed.): Moisture and soil differences as related to the spatial accuracy of GPR amplitude maps at two archaeological test sites. In: 10th International Conference on Ground Penetrating Radar, 2004 GPR 2004. Delft, The Netherland, 21–24 June 2004

22. Al-Qadi, I.L., Lahouar, S.: Measuring layer thicknesses with GPR—theory to practice. Constr. Build. Mater. **19**(10), 763–772 (2005)
23. Xu, X.L., Peng, S.P., Xiao, W., Yu, Y.: Measuring soil layer thickness in land rearrangement with GPR data. Meas. Sci. Technol. **25**(7) (2014)
24. Bristow, C.S. (ed.): GPR in sediments: recent advances in stratigraphic applications. In: 10th International Conference on Ground Penetrating Radar, 2004. Delft, The Netherland, 21–24 June 2004
25. Ardekani, M.R., Druyts, P., Lambot, S., Coster, A.D., Neyt, X. (eds.): Recovering the structure of a layered soil, including layer thickness and dielectric permittivity, using the interfaces and objects backscatter detected in GPR B-scans. In: IEEE 15th International Conference on Ground Penetrating Radar (GPR), 2014. Brussels, Belgium, 30 June–4 July 2014
26. Farfán, J.N., García, E.G., Roque, D.C., Cambranis, W.K. (eds.): Integrating 20 years of geotechnical investigation using geostatistics: building a 3D model of soil stratigraphy, Campeche Bay, Gulf of Mexico. In: ASME Symposia Volumes OMAE. American Society of Mechanical Engineers, Hamburg, Germany, 4–9 June 2006
27. Beaupretre, S., Manighetti, I., Garambois, S., Malavieille, J., Dominguez, S.: Stratigraphic architecture and fault offsets of alluvial terraces at Te Marua, wellington fault, New Zealand, revealed by pseudo-3D GPR investigation. J Geophys. Res-Sol. Ea. **118**(8), 4564–4585 (2013)
28. Conyers, L.B.: Ground-penetrating radar for landscape archaeology: method and applications. In: Seeing the Unseen Geophysics and Landscape Archaeology, 245–255 (2009)
29. Gaffney, V., Patterson, H., Piro, S., Goodman, D., Nishimura, Y.: Multimethodological approach to study and characterize Forum Novum (Vescovio, central Italy). Archaeol. Prospection **11**(4), 201–212 (2004)
30. Yalciner, C.C., Bano, M., Kadioglu, M., Karabacak, V., Meghraoui, M., Altunel, E.: New temple discovery at the archaeological site of Nysa (western Turkey) using GPR method. J. Archaeol. Sci. **36**(8), 1680–1689 (2009)
31. Jurg, L.: Ground-penetrating radar: a modern three-dimensional prospection method. Archaeol. Prospection **10**(4), 213–240 (2003)

Geomorphometric Analysis of Landform Pattern Using Topographic Position and ASTER GDEM

Usman Salihu Lay, Gambo Jibrin, Ibrahim Tijani
and Biswajeet Pradhan

Abstract A number of research have been carried out on geomorphology using a conventional approach to classify the landform; this has a tendency of producing misleading result, due to ruggedness and inaccessibility of the terrain. Geographic Information System (GIS) and remote sensing techniques are capable of generating automated landform classes using Topographic Position Index techniques (TPI). This research is set to achieve the following objectives: to categorize landform elements and to illustrate the complexity of the terrain in Negeri Sembilan state based on ASTER GDEM with 30 m resolution. TPI-based algorithm for landscape classification was applied to slope position and landform classification automation. We used 300 and 3000 neighbourhood size on the TPI grids to determine the landform categories. To quantify the spatial pattern of topographic position, Deviation from mean elevation (DEV) is adopted. Maximum Elevation Deviation was selected to measure the spatial landscape pattern at the maximum (3000) scale of the absolute DEV value within the scale (DEV_{max}), and finally, high-pass filter algorithm was used to identify the extreme topography (ridges/valleys). The combination of the TPI and slope position of DEV that formed the landform classification results show four prominent landform classes these include canyons, U-shape valley, local ridges/ hill valleys, and mountaintops/high ridges. The slope position classes revealed only two (valley/cliff base and ridges/canyons edge) classes based on slope position index. The canyons had the maximum of 63% and minimum was U-shaped valley with 1.04% for the landform of the area of interest.

U. S. Lay · G. Jibrin · I. Tijani · B. Pradhan (✉)
Department of Civil Engineering, Faculty of Engineering,
University Putra Malaysia (UPM), Serdang, Selangor, Malaysia
e-mail: Biswajeet24@gmail.com; Biswajeet.Pradhan@uts.edu.au

B. Pradhan
Faculty of Engineering and Information Technology, School of Systems,
Management and Leadership, University of Technology Sydney,
PO Box 123 Building 11, Level 06, 81 Broadway, Ultimo, NSW 2007, Australia

To achieve better results, there is a need to utilize a high spatial resolution remotely sensed DEM derived data and sensitivity analysis need to be incorporated. For that, laser scanning data is capable of improving the results.

1   Introduction

The effect of global warming on climate change has exacerbated the intensity of gravitational disasters such as landslide, debris flow, and flood with expanding territorial vulnerability due to spatiotemporal landscape changes. Mitigating the impact of this menace requires understanding the spatially and temporally complex landscape systems that are subjected to changes due to natural and anthropogenic causes. Terrain-induced hazards have much negative impacts due to their rapid development associated with high velocities. This has made it difficult to predict their catastrophic impact and the degree of vulnerabilities to elements at risk. Knowing the variability of the surface topography and different landforms is important for enhancing spatial model for susceptibility mapping. Geomorphologic analysis of landforms has been widely used to understand numerous natural processes that affect man and the environment. Landforms are certain geomorphological structures found on the planet Earth's surface, stretching on different features sizes from major to minor features. These features include land comprises mountains, valleys, canyons, and oceanic water boundary features such as seas, peninsulas etc., as well as the characteristics of the terrain sub aqueous (volcanoes, ocean basins, and ridges). Classification of the landform has been considered as basic geo-relief descriptors in soil, vegetation, and land-use mapping. Landform affects our immediate environment in different ways such as sediment transformation, surface water flow, and soil formations and also, controls the local and regional climate. Blaschke and Strobl [3] noted that effects of landform patterns are directly pronounced on vegetation in a transversely relative position of the landscape.

Consequently, classification of landform has fascinated, unprecedented attention in geosciences and adjoining specialities. Geomorphic classification has variety of applications that comprises of mapping geomorphologic entities [34, 37], lithology representation, forest units and soil properties mapping and predictions [2, 24, 33, 38], landslide model [46], representations of wetland and estuarine morphology [7, 39], and precision farming [41]. In recent past, adoption of an automatic landform classification technique has increased as a result of paradigm shift in the geospatial science remote sensing industry. Iwahashi and Pike [20] mention that GIS and DEM contribute in the used landform simulation. Conversely, Drăguţ and Blaschke [9] stated that geomorphometric grouping of terrains surface has devoted

to certain features such as mountains, hills, and hill slope units or uniform areas [28], thus detract research on heterogeneous terrain. In previous studies, the means to determine terrain surface properties was conducted manually, by analysing the geometry of the landscape and the process is reported to be time-demanding. The availability of computers makes it possible to generate autonomous landscape characteristics statistically.

Various measures of geomorphometric can be extracted from a surface, with the usefulness of each of these steps being dependent on the type of surface and objectives. However, the elevations of the first and second derivatives (slope or gradient, aspect, and plan and profile curvature) are the most commonly used [13]. DEM integrates the methods of earth sciences, geoinformatics, and geostatistics. It examines the description and measurement of landform using a variety of approaches, including classification of morphometric parameters, filter techniques, cluster analysis, and multivariate statistics.

Geographical information system (GIS) facilitates the manipulation of digital elevation models (DEMs) and has provided valuable environments for the automated analysis of surface forms. A geomorphic or morphometric class, such as ridges, peaks, and passes, have been widely extracted from DEMs [6, 17, 31]. Weiss [43] introduced a GIS application tailored for semiautomated landform classification known as topographic position index (TPI). TPI measures topographic relative position as a central point of the difference between the elevation at this point and the mean elevation within a designated neighbourhood. Using TPI, landscapes can be classified into slope position classes. TPI is only one of the broad range of morphometric properties based on neighbouring areas that can be useful in analysis of topography and DEM. Topographic position compares the elevation of every cell in the DEM to the mean elevation of a specified neighbourhood around that cell. TPI has been applied to the fields of geomorphology [27, 29, 40]; geology [8, 30]; hydrology [14, 26]; agricultural science [36]; forest management [5, 12, 16, 18, 42, 47]; climatology [4, 10]; and risk management [35, 44]. The ability of TPI to subdivide landscapes into morphological classes based on topography makes this method essential for landscape research. Most of the previous geomorphological study on landform classification is basically on the homogeneous terrain. De Reu et al. [6] applied TPI in a geoarcheological research in northwestern Belgium, they pointed out that using this algorithm alone has led to erroneous landform classification in their study that is heterogeneous in nature. Also, in tropical Malaysia, there is not existing, comprehensive landform classification map, despite number of scientific researches in the country. Therefore, the purpose of this study is to classify the landform elements and to illustrate the complexity of the terrain based on ASTER GDEM. The main objective is to apply TPI-based (topographic position index) algorithm and slope position for landform classification and explore the higher order topographic position indices using high-pass filter to highlight the extreme topography of the neighbourhood (ridges/valleys). Also, quantify the spatial pattern of topographic position of the study area.

2 Study Area and Methodology

2.1 Study Area

The area selected for this study is Seremban, a capital of Negeri Sembilan state, Malaysia. Its geographic location lies between longitudes (101° 45′ 0″E and 102° 6′ 0″E) and latitudes (3° 0′ 0″N and 2° 30′ 0″N). The area extent of the city is roughly 936 km^2. The state constitutes eight districts, which include Ampangan, Labu, Lenggeng, Pantai, Rantau, Rasah, Seremban and Setu [1]. The area is selected because of its undulating and heterogeneity topography. The study was steered using elevation data, sourced from the Deva for Seremban state, Malaysia (Fig. 1). The choice for the study site was due to its size, it representativeness as the regional topography. The landscape of the area is typically agricultural plantation and built-up. Part of the north–west portion to the north–eastern topography in the area, established on high hill mountain region covered one-third of the study area. This could exacerbate landslide, debris flow and runoff. The southern part topography is made-up undulating gentle topography and slope to the centre. The highest and lowest elevation of the area ranges from 1184 to 8 m. The data used in this research is an open source ASTER GDEM of 30 m spatial resolution; sourced from the DEVA website www.deva.com for Malaysia, then area of interest (Seremban) was subset (Fig. 2).

2.2 Methods

2.2.1 Topographic Position Index (TPI)

TPI is a measure of change between altitude elevation on the principal point (Z_0) and the mean elevation all over the places surrounding its neighbourhood by a set radius (R) [6, 15, 23, 43]. In other words, the core of landform classification scheme laid on TPI approach is basically the change between an altitude pixel number and the mean elevation of the pixel that surrounds the neighbourhood [21]. The algorithm is suitable for landform classification and embraces concave features [32], which express this mathematically:

$$\text{TPI} = Z_0 - \bar{Z} \tag{1}$$

$$\bar{Z} = \frac{1}{N_R} \sum_{i \in R} Z_i \text{ or } \frac{\sum h_j}{n} \tag{2}$$

h_j height of cells that surrounds analysed cell,
n number of surrounding cells.
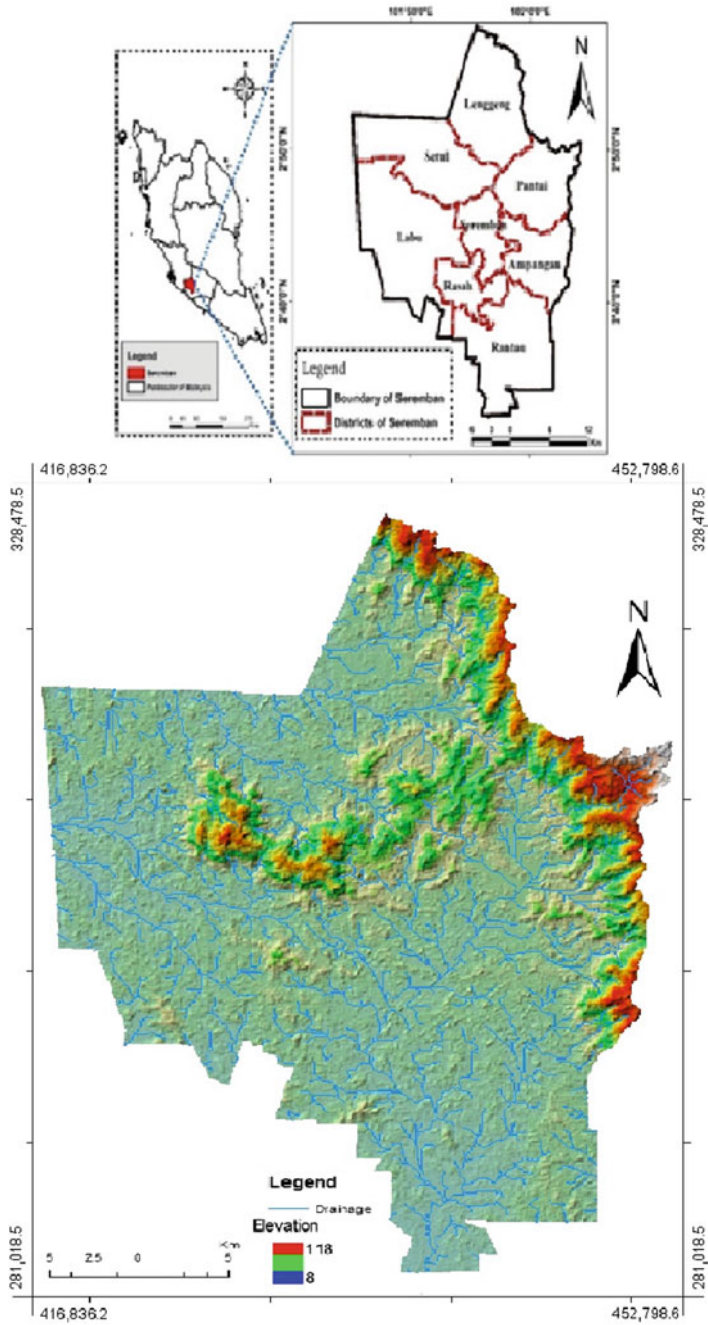
Fig. 1 The study area
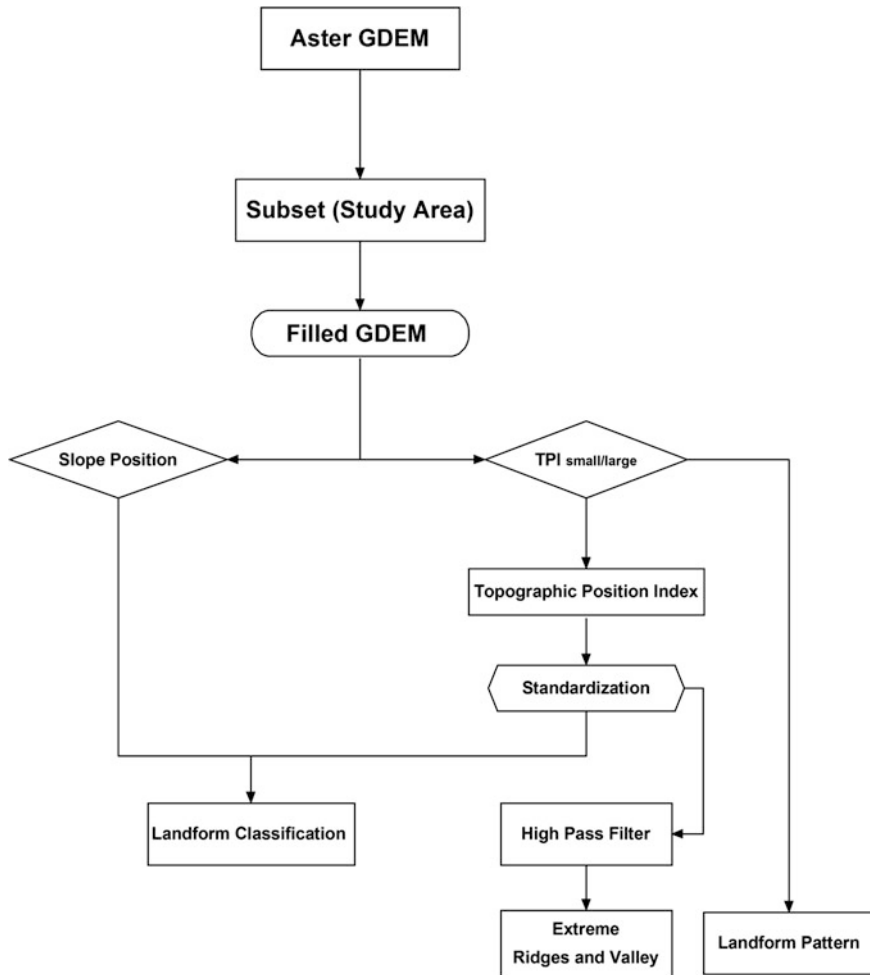
Fig. 2 Flowchart for the methodology for landform classification

If the TPI values are positive this means that its principal spot is situated higher than its mean location around it, however, the negative cell value signifies lesser spot than the mean [6]. The range of TPI depends not only on the elevation differences but also on R value.

TPI uses spatial autocorrelation for the elevation. With 300 and 3000 circle radius, TPI value range increases scale causing variation in the different scale. So, standardization of TPI grid is necessary (mean = 0, STD = 1).

$$\text{TPI}_D = \left(\frac{\text{TPI}_N - \text{MEAN}}{\text{STD}}\right) \tag{3}$$

The TPI grids, simply describe landform classes based on tangible slope position (SP) standards; here, the SPI standards are categorized into five class based on the threshold defined between −1 and 1. Furthermore, the slope position and the landform classification are based on these TPI values.

The two neighbourhood scales were combined to produce accurate basis for the classification of the landform, follow the standard deviation (SD) of the TPI. In this research classification are based on threshold criteria ten landform classes based on [21, 43] recommendations see Table 1.

2.2.2 Slope Positioning Index

By thresholding continuous TPI values at a given scale and checking the slope for values near 0, landscape can be classified into discrete slope position classes, i.e. defining thresholding, certain factors need to be taken into consideration such as the specific landscape, the scale of the index and the particular problems being addressed. Selected feature, particularly, important to a specific analysis could be

Table 1 Landform classification based on TPI

S/N	Classes	Description
1.	Canyons, deeply incised stream	Small neighborhood: $z_0 \leq -1$ Large neighborhood: $z_0 \leq -1$
2.	Midslope drainages, shallow valleys	Small neighborhood: $z_0 \leq -1$ Large neighborhood: $-1 < z_0 < 1$
3.	Upland drainages, headwaters	Small neighborhood: $z_0 \leq -1$ Large neighborhood: $z_0 \geq 1$
4.	U-shaped valleys	Small neighborhood: $-1 < z_0 < 1$ Large neighborhood: $z_0 \leq -1$
5.	Plains small	Neighborhood: $-1 < z_0 < 1$ Large neighborhood: $-1 < z_0 < 1$ slope $\leq 5°$
6.	Open slopes	Small neighborhood: $-1 < z_0 < 1$ Large neighborhood: $-1 < z_0 < 1$ Slope $> 5°$
7.	Upper slopes, mesas	Small neighborhood: $-1 < z_0 < 1$ Large neighborhood: $z_0 \geq 1$
8.	Local ridges/hills in valleys	Small neighborhood: $z_0 \geq 1$ Large neighborhood: $z_0 \leq -1$
9.	Mid-slope ridges, small hills in plains	Small neighborhood: $z_0 \geq 1$ Large neighborhood: $-1 < z_0 < 1$
10.	Mountain tops, high ridges	Small neighborhood: $z_0 \geq 1$ Large neighborhood: $z_0 \geq 1$

Source Weiss [43] and Jenness [21]

extracted by adjusting class elevation or slope in the neighbourhood of the target cell. Guisan et al. [17] classified slope position into six classes based on the standard deviation, which is adopted in this work.

1. Ridge > + 1 STD
2. Upper slope > 0.4 STD =< 1 STD
3. Middle slope > −0.4 STD, < 0.4 STD, slope > 6°
4. Flat slope > = −0.4, =< 0.4 STD, slope <= 6°
5. Lower slopes > = −1 STD < 0.4 STD and
6. Valley < −1 STD.

2.2.3 Landform Classification

A number of comprehensive geomorphological algorithms and approaches on morphological landscape classification exist; [6, 19, 20] in this research, we adopted Weiss [43] and Jennesse [21] methods in which the terrain surface is classified into classes of slope position. The parameter from two neighbourhood sizes (300 and 3000) are imperatively joined to ascertain multifaceted landscape features because such combination offers supplementary information on the topography [43]. Table 1 summaries ten generated landform classes.

Landform category was determined by classifying the landscape using one SPI grids at different scales. The strategy adopted in this research is a simple set of threshold values for the SPI grids; ten classes were defined based on the criteria shown in Table 1, relating to Weiss [43] approach in differentiating original slopes with the threshold values, which is a common practice [32, 40]. SPI values above a definite threshold are classified as ridgetops or hilltops, while TPI values below a threshold might be classified as valley bottoms.

2.2.4 Identification of Spatial Pattern of the Landscape

Elevation residuals are topographic indices derived from DEMs using spatial filtering techniques (i.e. a roving window of radius r is run on each grid cell in the DEM) to quantify the spatial pattern of topographic position within the context of a surrounding area. Gallant and Wilson [15] suggest that in defining neighbourhoods with circular shaped windows, although square windows are more commonly used in practice. These terrain attributes are based on characteristics of the statistical frequency distribution of the elevations within neighbourhoods defined by the moving window. All of the elevation residuals utilize location parameters (measures of central tendency) and/or scale parameters (measures of spread).

Numerous terrain features are used to quantify the spatial pattern of topographic position, in this research Deviation from mean elevation (DEV) is adopted. This is a unitless measure of topographic position and is the difference between the window centre's elevation and its mean elevation [15, 43] which is expressed as a measure

of topographic position of the central point (Z_0) using TPI and the standard deviation of the elevation, mathematically represented in Eq. (4). It has the same units as elevation and is either positive, indicating an elevated location, or negative, indicating a low-lying position, the elevation difference is normalized by s, such that

$$\text{DEV} = \frac{Z_e - \bar{Z}_d}{\text{SD}} \tag{4}$$

$$\text{SD} = \sqrt{\frac{1}{N_R - 1} \sum_{i=1} (Z_i - \bar{Z})^2} \tag{5}$$

$$D = 2n + 1 \tag{6}$$

where D is the size of the window, Z_e is the elevation of the window centre cell and $\bar{Z}_d$ is the window mean elevation. D is measured in grid cells. Since pixel-centred moving windows must have odd-numbered dimensions (3, 5, 7, etc.) [45] base (6), where ($n = 1, 2, 3, 4 \ldots n$); 5×5 moving gap is chosen because lower window value's elevation standard deviation is by comparison less sensitive to the extremes in elevation and is thought to better represent surface roughness properties [11, 22].

The input data is DEM and the neighbourhood size is specified in map unit (metre). DEV measures the topographic position as a fraction of local relief normalized to local surface roughness. Also, the output value is positive when the central point is situated higher than its neighbourhood and negative when it is situated lower. The output values mostly range between +1 and −1, the value outside this range may designate irregularities within the DEM. While DEV is essentially representing the spatial pattern of the local Z-scores, this fact does not imply that the index can be used to determine the statistical probability of a particular value occurring (i.e. outlier detection) because elevation distributions are often non-Gaussian. Nonetheless, values of DEV do tend to lie well within the range −3.0 to 3.0. Unlike DIFF, DEV is a measure of relative topographic position that is scaled by the local ruggedness [45]. This characteristic is particularly useful in applications involving heterogeneous landscapes [6]. Maximum elevation deviation was used to measure the spatial pattern of DEV at the scale of the maximum (3000) absolute DEV value within the scale (DEV_{max}). When window dimensions are large, the mean and standard deviation of the window become good estimates for the overall DEM mean and standard deviation. Thus, the convergence value for a location is equal to the difference in elevation between the site and the mean elevation of the DEM, normalized by the DEM's standard deviation, i.e. the DEM-wide z-score transformation [45].

With the standardized grids, the basic equations are used to classify the scaled combination of TPI grids to landform classification and slope position. To extract the extreme TPI, a spatial high-pass filtering algorithm is utilized because its preserve edge, smoothing, reduces noise, line detections, etc. of the features. Finally,

the output of the classified landform is overlaid on Google Earth image in order to visually validate the result and ascertain the underneath spatial relationship with land cover of the area.

2.3 Data Processing and Neighbourhood Size

TPI and DEV were calculated using a terrain analysis tools, based on elevation residuals in "Whitebox GAT" open source GIS software environment developed by Lindsay [25]. The most perceptive neighbour dimensions were selected from two contended radii scales (300 and 3000), are presented in this research. In this chapter, the scale levels (higher or lower) together with the cell slope, was considered in the cell classification process into various slope position. Depression filled DEM raster data is used in generating TPI grids and slope position scales, based on Deviation from mean elevation (DEV) was adopted in providing a modest pattern and repeatable process in classifying the area terrain surface into slope positioning index and then landform classes, adopting TPI approach. Choice of neighbourhood parameter and cell unit area is vital in this model. Small and larger scale units were applied in this research, 300 and 3000 (small and larger neighbourhood), respectively; circle cell unit neighbourhood size is utilized based on the maximum and minimum size of the elevation data. Thus, a higher scale is needed in order to highlight the extreme ridges in the neighbourhood, for this the maximum scale of 3000 radii was used together with high-pass filter/ different from the mean (DIFF) technique which preserved edges of the features. Therefore, a circular neighbourhood is defined by a radius length extending outwards from the cell centre. In theory, this neighbourhood is composed of all grid cells whose cell centre lies within that distance of the focal cell centre, but Spatial Analyst appears to have some kind of number rounding issue that sometimes includes or excludes cells that do not exactly fit this definition [25]. An outwards extension of radius length from the cell centre is explained by a circular neighbourhood. Theoretically, the neighbourhood is made up of complete grid cells that centred the focal cell centre, while Spatial Analyst tool is reported to handle certain values rounding concern which filter out or optimize cells that doesnot really fit the classification [25].

3 Results and Discussion

Figures 3 and 4 for the TPI-generated maps indicated the effect of neighbourhood sizes on the classifications landform in the study area; it reveals that smaller circle signify small features in low elevated area, while larger radius symbolize more features at high elevated area. The minimum radius provides detail landform information, however, it tends to overshoot/or representation of the landform pattern with an emphasis on valley noise (Fig. 3). Table 2 shows the extent of the
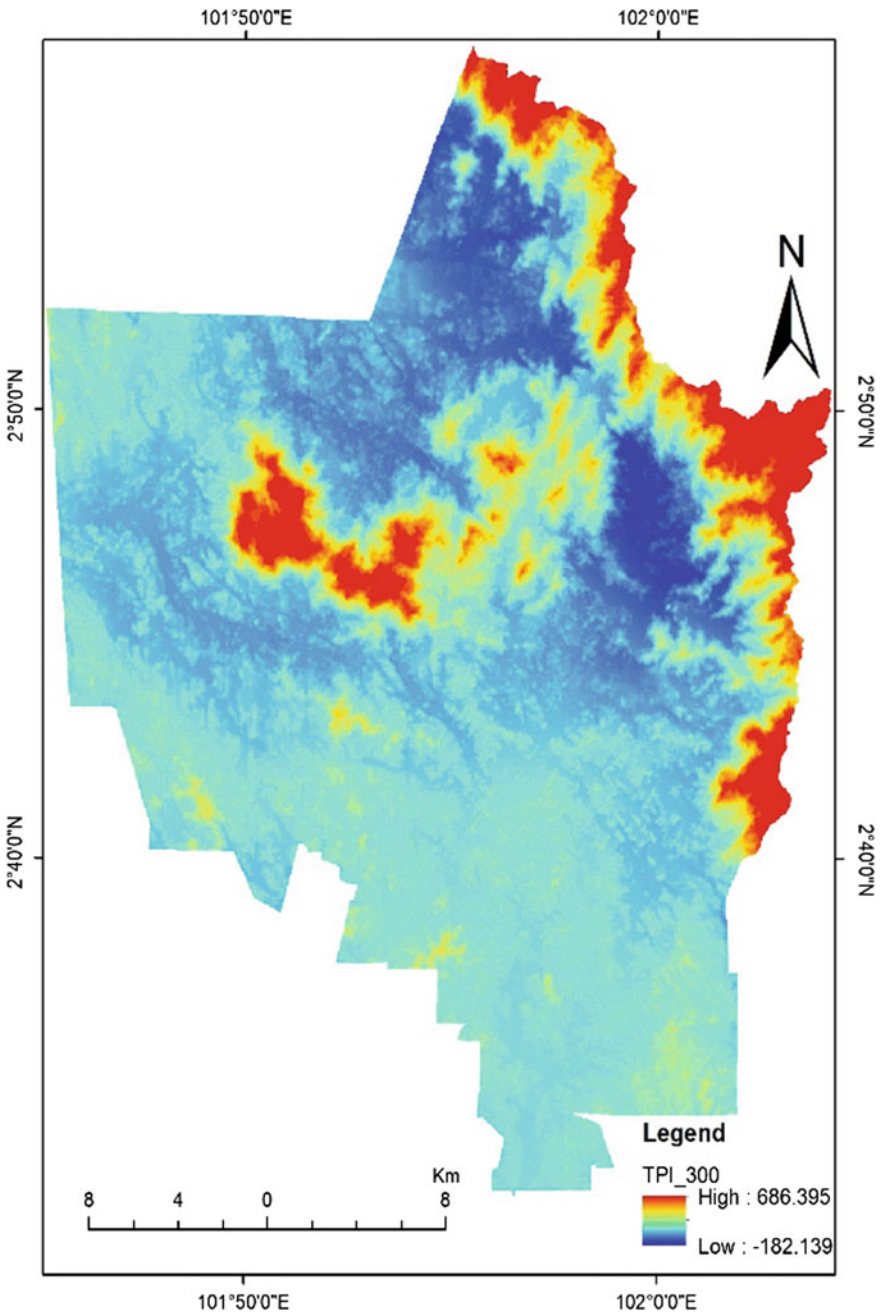
Fig. 3 Topography Position Index (TPI) 300 neighbourhood
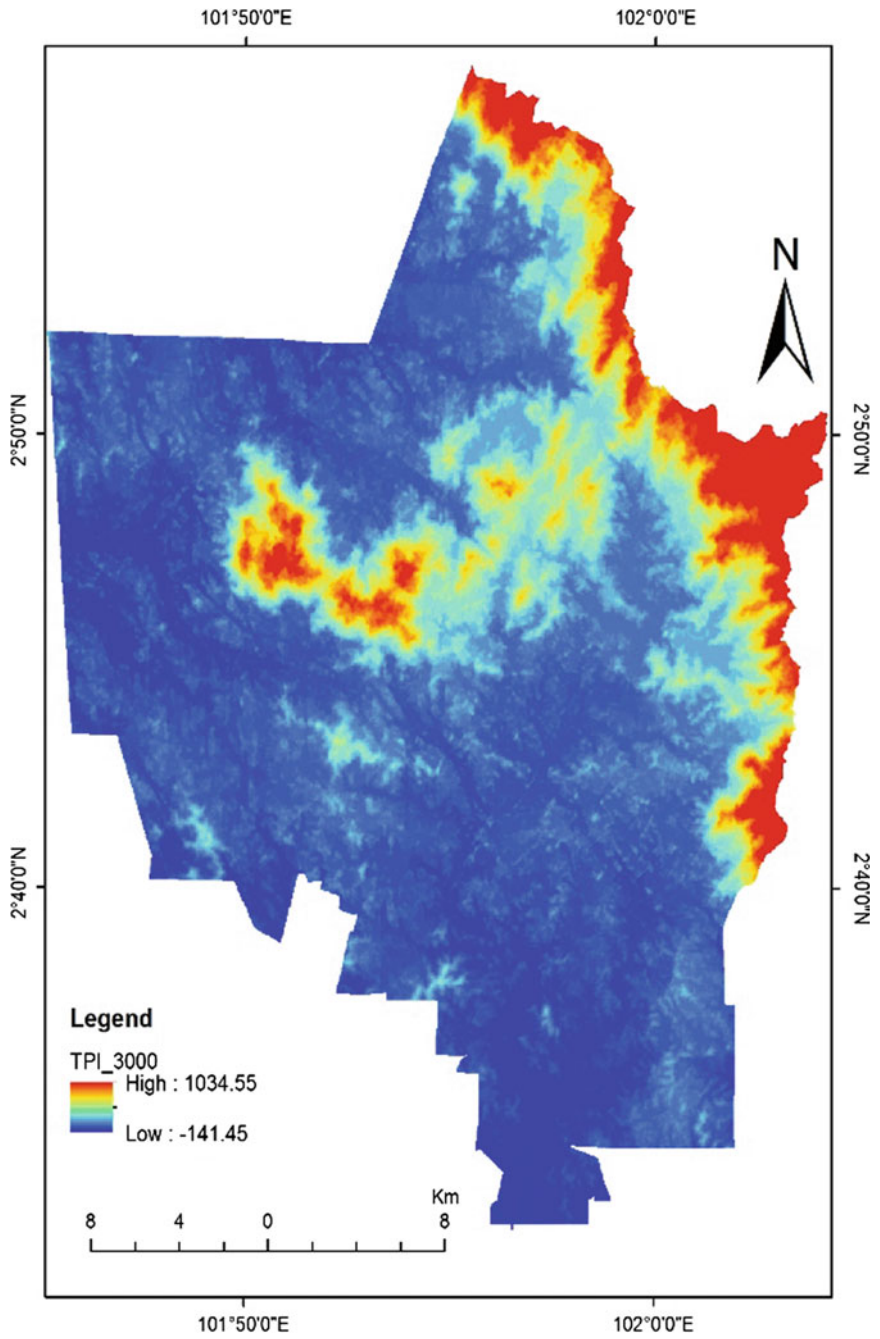
Fig. 4 Topography Position Index (TPI) 3000 neighbourhood

Table 2 Percentage of slope position class

Code	Classes	Area (%)	Area (m^2)
1	Ridge	68.20	14,139.24
2	Upper slope	0.30	62.55
3	Middle slope	0.15	31.92
4	Flat slope	0.45	93.37
5	Lower slopes	0.29	61.29
6	Valley	30.59	6343.29

classified slope position categories in percentages based on different sizes. Ridges category portray the largest spatial areas extend for about 68% (14139 m^2) and the lowest area is the middle slope class with about 0.15% and 32 m^2. Individual classes for the remaining four (Upper slope, Flat slope Lower slope and valley) were represented in area between 0.3 and 32% (63–6343 m^2). Though, the magnitudes for all neighbourhood and dispersal of these classes were connected mostly with the definite amount of landscape features (Figs. 5 and 8). The class ridges are regularly related by the upper portions of the Knolls in Northwest Seremban. Similarly, the class valley is virtually identified in these hilly provinces, connected by profound incised tributaries, and in the foremost valley's waterways of the study area. Small patches of ridges are detected in Fig. 5 and valleys were either anonymous or only to a very partial range of noise. These results are substandard and does not agree with the genuine landscape of the area.

Furthermore, integration of two scales neighbourhood and slope delivered a substantial outcome (Fig. 8). The area cover by individual landform class in percentage and square metre (m^2) is presented in Table 3; four prominent landform classes are exposed, include canyon (deeply incised stream), upland drainage, local ridges (hill in valleys) and mountaintops (high ridge). Area extent by each classes are about 63% (13,127 m^2), 05% (973 m^2), 09% (1893 m^2) and 21% (4435 m^2) of their area, respectively.

The derived DEV maps in Fig. 7, exhibits the impact of neighbourhood size spatially for different values of circle; displaying a diverse pattern extensively. The most upthrust and extreme classes were valleys and ridges emphases in Fig. 6, they cover spatial areas extent of about 74 and 26%, respectively. It reveals, that the generated results matched better with actual native terrain features of the area, meanwhile some terrain features were acknowledged. Valleys and ridges are recognized on the elusive landscape zones in the study area; the results are more convincing. Ridges are observed to correspond to the hills crest, valleys were ascribed only to the lowest zones areas and other classes are accurately recognized. Finally, more accurate spatial relationship between the land cover area and landform classes was established, see Fig. 9. Correlation between landforms classes, using TPI on the surface terrain agglomeration tallied with the distribution of the landform classes. This is shown especially in the hilly or ridges, valley areas and local ridges which supported drainages.
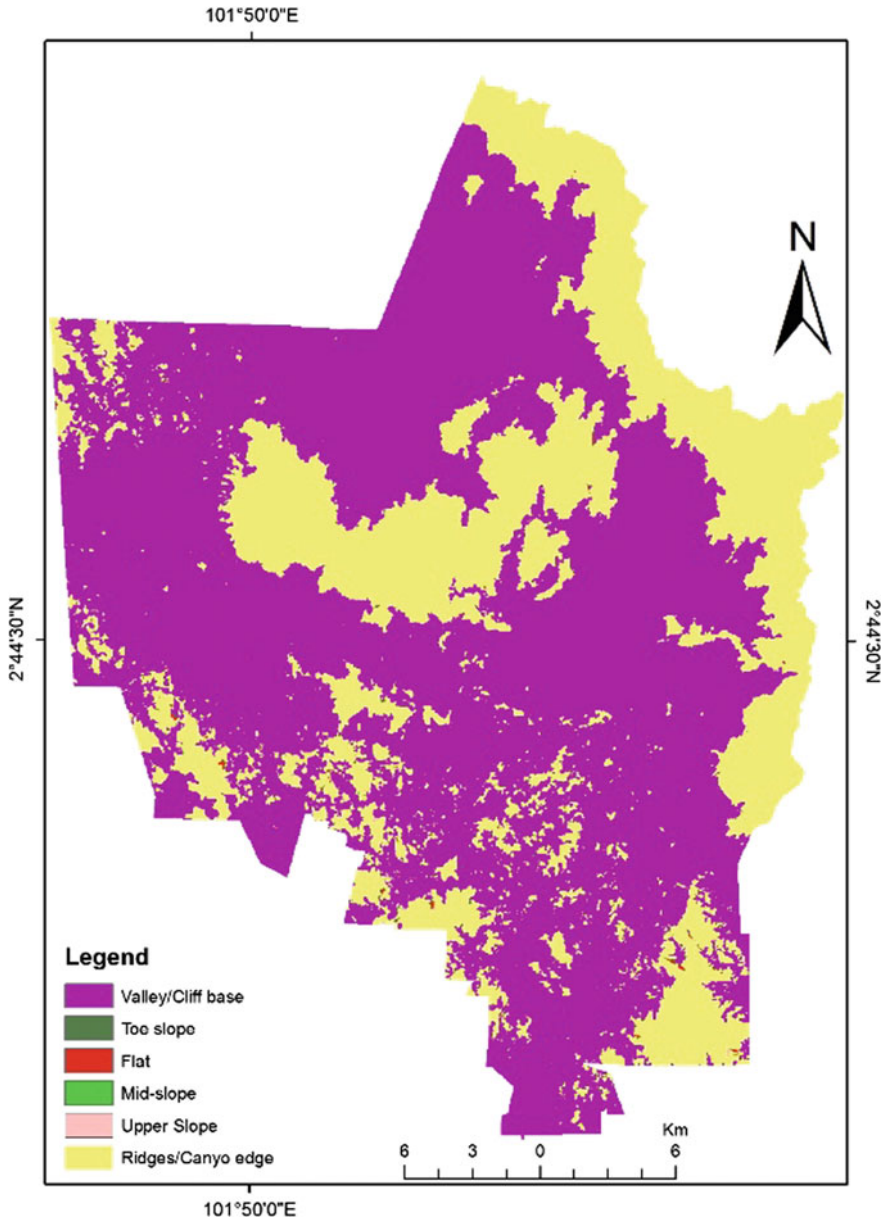
Fig. 5 Slope position classes

Table 3 Percentage of landform classification

Code	Classes	Area (%)	Area (m²)
1	Canyons, deeply incised streams	63.32	13126.90
2	Mid-slope drainages, shallow valleys	0.18	39.02
3	Upland drainages	4.69	973.31
4	U-shaped valleys	1.04	216.02
5	Plains small	0.00075	0.16
6	Open slopes	0.0034	0.71
7	Upper slopes	0.16	32.254
8	Local ridges/hills in valleys	9.13	1893.05
9	Mid-slope ridges, small hills in plains	0.072	14.84
10	Mountaintops, high ridges	21.39	4435.39

3.1 Slope Position

Using minimum scale of 300, many individual ridge line and valleys containing cross-section drainages of cutting edge in the foremost gulley and the bottom of the main canyons were grouped as flat zones. However, at the scale of 3000 TPI, it highlighted some important landform features (mountain, canyons, foremost ridgeline and valley); minor features vanish and canyons bottom are then classified. Figure 5 shows that there are two classes based on slope position index that consists of, valley/cliff base and ridges/canyons edge.

3.2 Landform Classification

Using spatial high-pass filter the generated landform map showed (Fig. 6) in detail the extreme elevated neighbour and it also preserved the edges, reduced the noise of the features.

Using the maximum TPI, we derived the landform pattern of the study area as shown in Fig. 7. The generated landform classification map (Fig. 8) showed that there are four landform types in the study area that consist of canyons, U-shape valley, local ridges/ hill valleys and mountaintops/high ridges.

In Fig. 9, the relationship with land use observed that most of the built-up areas are situated on the canyon/flat areas; the intermediate landform class (zone) that lie
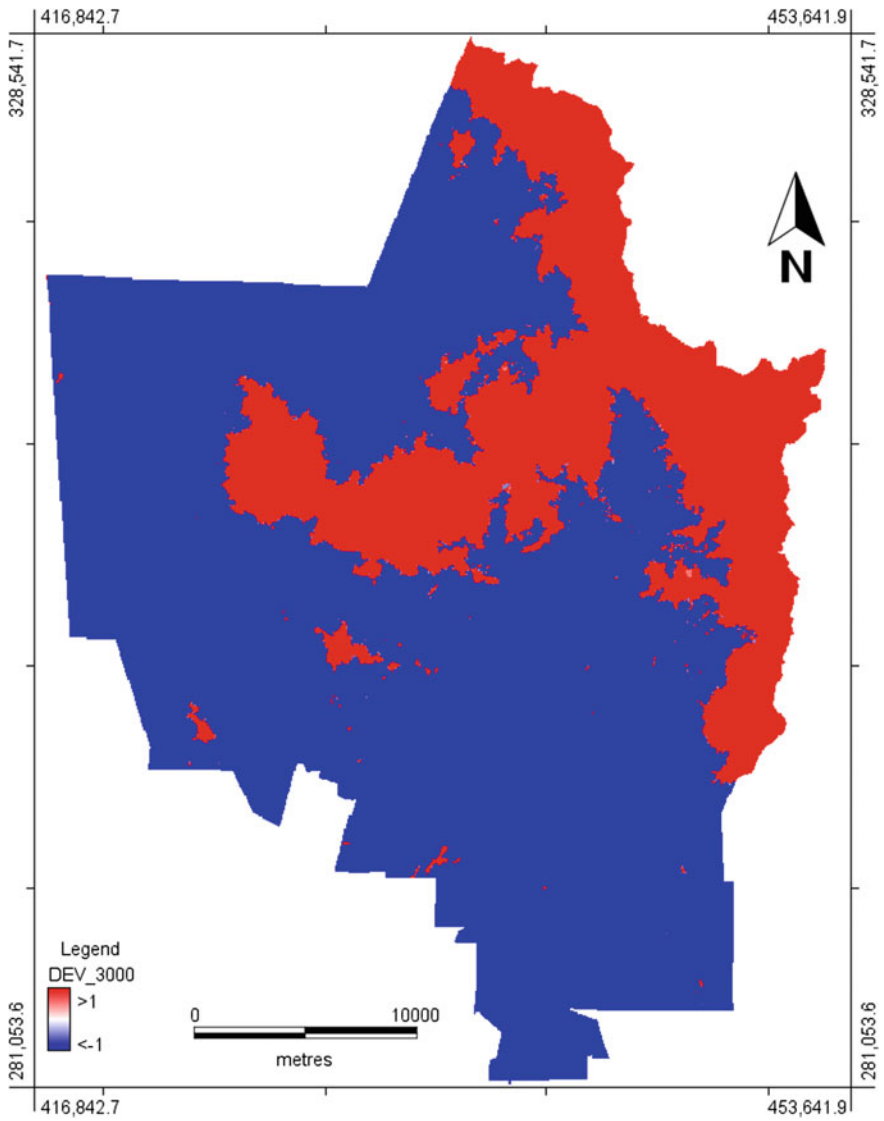
Fig. 6 Using high-pass filter for extreme topography for the study area
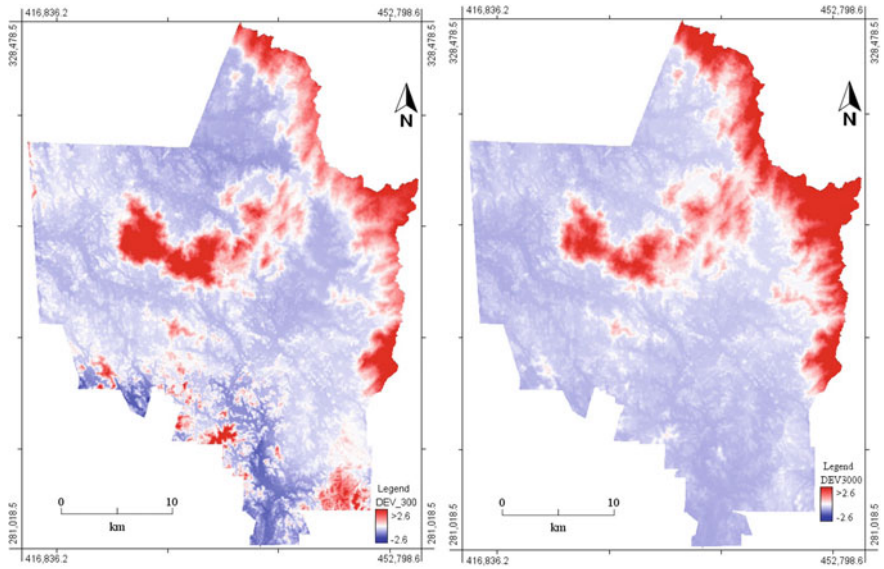
Fig. 7 Landform pattern for the study area

between class 1 and class 10 is the drainage capable of supporting agricultural activities, with few or absent of traces of human structures (buildings). The ridges/hilltops retain its natural physical condition of thick forest land cover, present of human-induced environmental or landscape change that has been manifested in the area especially in the local ridge (hill valleys) area as a result of urban growth.
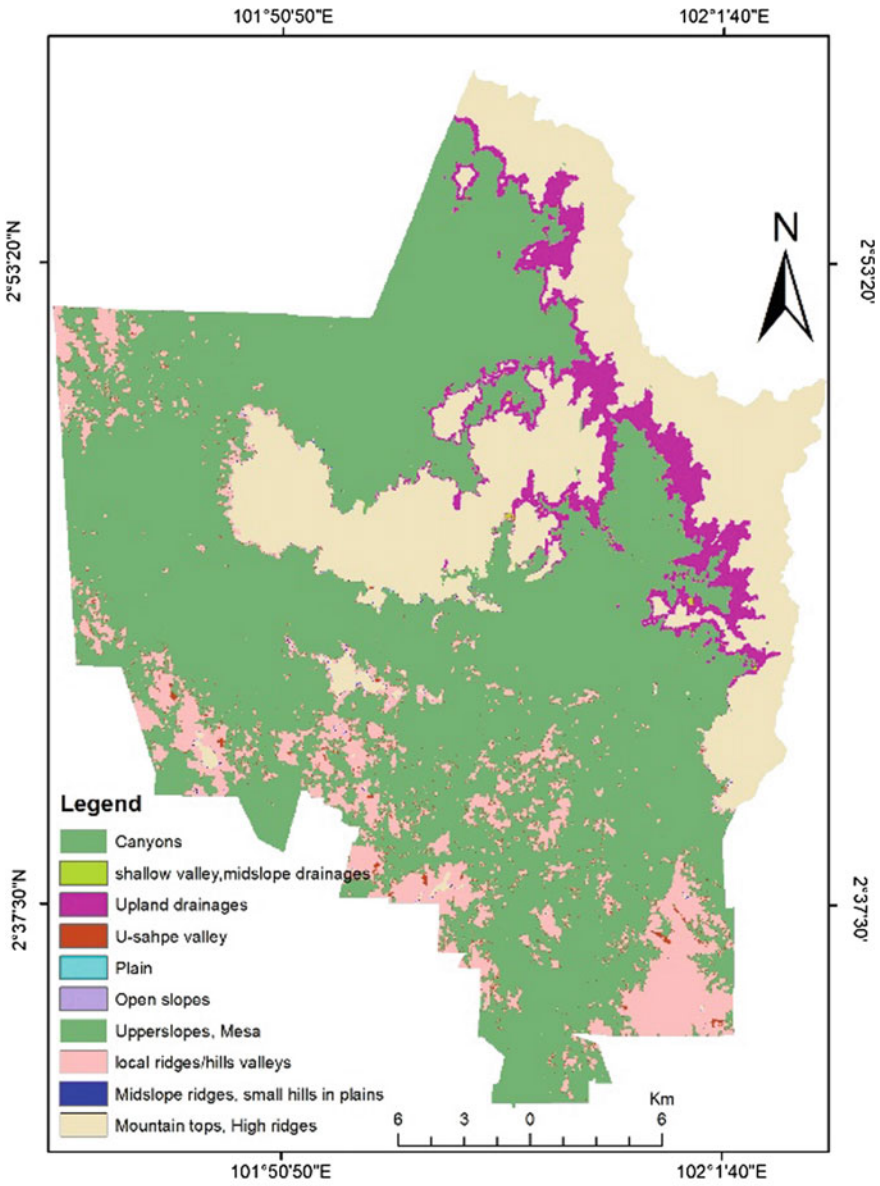
Fig. 8 Landform classification of the area
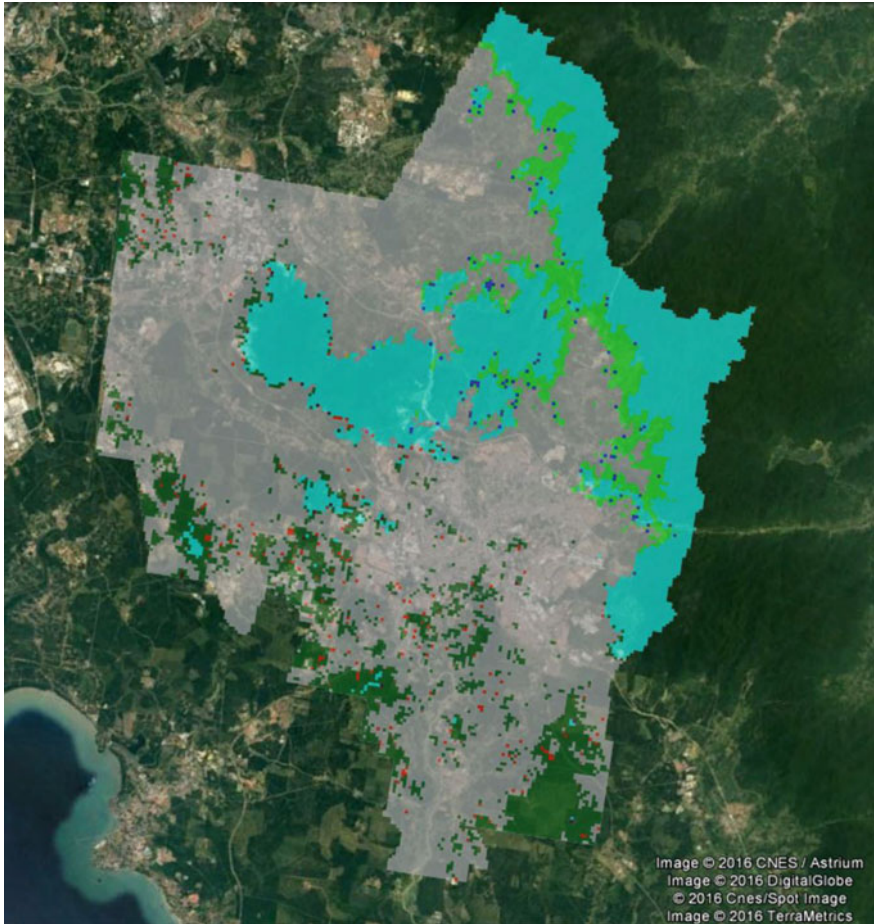
Fig. 9 Landform spatial relationship with land cover (Google Earth)

4 Conclusion

In this study, Aster Global digital elevation models (GDEM) are used as inputs data. Combining the TPI at smaller and larger scale with slope position the study area was classified into landform category; The result shows that there are four landforms that consist of canyons, upland drainage, local ridges/hill valleys and mountaintops.

- In this study, the input data considered is mostly Aster GDEMs; Combining the TPI at smaller and larger scale with slope position classified landforms into various categories.

- From the result, only four classes of landforms were manifested that includes, upland drainage valley, canyons local ridges/hill valleys and mountaintops/high ridges.
- Landscape change monitory challenges (open source data).
- Need for update terrain data to keep abreast spatiotemporal landscape dynamics.
- Need to correlate landform and land use with a high-resolution imagery.

References

1. Ahmed, G.B., Shariff, A.R.M., Balasundram, S.K., bin Abdullah, A.F.: Agriculture land suitability analysis evaluation based multi criteria and GIS approach. IOP Conf. Ser. Earth Environ. Sci. **37**(1), 012044. IOP Publishing (2016, June)
2. Barka, I., Vladovi, J., Máliš, F.: Landform classification and its application in predictive mapping of soil and forest units. GIS Ostrava 23–26, 1 (2011)
3. Blaschke, T., Strobl, J.: Defining landscape units through integrated morphometric characteristics. In: Ervin, E. (ed.) Landscape modelling: digital techniques for landscape architecture. Wichmann Verlag, Heidelberg (2003)
4. Bunn, A.G., Hughes, M.K., Salzer, M.W.: Topographically modified tree-ring chronologies as a potential means to improve paleoclimate inference. Clim. Change **105**(3), 627–634 (2011)
5. Clark, J.T., Fei, S., Liang, L., Rieske, L.K.: Mapping eastern hemlock: comparing classification techniques to evaluate susceptibility of a fragmented and valued resource to an exotic invader, the hemlock woolly adelgid. For. Ecol. Manage. **266**, 216–222 (2012)
6. De Reu, J., Bourgeois, J., Bats, M., Zwertvaegher, A., Gelorini, V., De Smedt, P., Chu, W., Antrop, M., De Maeyer, P., Finke, P., van Meirnenne, M., verniers, J., Crombe, P.: Application of the topographic position index to heterogeneous landscapes. Geomorphology **186**, 39–49 (2013)
7. Deepika, B., Avinash, K., Jayappa, K.S.: Impact of estuarine processes and hydro-meteorological forcing on landform changes: a remote sensing, GIS and statistical approach. Arab. J. Geosci. **8**(2), 711–726 (2015)
8. Deumlich, D., Schmidt, R., Sommer, M.: A multiscale soil–landform relationship in the glacial-drift area based on digital terrain analysis and soil attributes. J. Plant Nutr. Soil Sci. **173**, 843–851 (2010)
9. Drăguţ, L., Blaschke, T.: Automated classification of landform elements using object-based image analysis. Geomorphology **81**, 330–344 (2006)
10. Etienne, C., Lehmann, A., Goyette, S., Lopez-Moreno, J.I., Beniston, M.: Spatial predictions of extreme wind speeds over Switzerland using generalized additive models. J Appl. Meteorol. Climatol. **49**(9), 1956–1970 (2010)
11. Evans, I.: Correlation structures and factor analysis in the investigation of data dimensionality: statistical properties of the Wessex land surface, England. In: International Symposium on Spatial Data Handling, Zurich, pp. 98–116 (1984)
12. Fei, S., Schibig, J., Vance, M.: Spatial habitat modeling of American chestnut at mammoth cave national park. For. Ecol. Manage. **252**(1), 201–207 (2007)
13. Fisher, P., Wood, J., Cheng, T.: Where is Helvellyn? Fuzziness of multi-scale landscape morphometry. Trans. Inst. Br. Geogr. **29**, 106–128 (2004)
14. Francés, A.P., Lubczynski, M.W.: Topsoil thickness prediction at the catchment scale by integration of invasive sampling, surface geophysics, remote sensing and statistical modeling. J. Hydrol. **405**(1), 31–47 (2011)

15. Gallant, J.C., Wilson, J.P.: Primary topographic attributes. In: Wilson, J.P., Gallant, J.C. (eds.) Terrain Analysis: Principles and Applications, pp. 51–85. John Wiley & Sons Inc., New York (2000)

16. Giorgis, M.A., Tecco, P.A., Cingolani, A.M., Renison, D., Marcora, P., Paiaro, V.: Factors associated with woody alien species distribution in a newly invaded mountain system of central Argentina. Biol. Invasions **13**(6), 1423–1434 (2011)

17. Guisan, A., Weiss, S.B., Weiss, A.D.: GLM versus CCA spatial modeling of plant species distribution. Plant Ecol. **143**, 107–122 (Kluwer academic publishers) (1999)

18. Han, H., Jang, K., Song, J., Seol, A., Chung, W., Chung, J.: The effects of site factors on herb species diversity in Kwangneung forest stands. Forest Sci. Technol. **7**(1), 1–7 (2011)

19. Hengl, T., Reuter, H.I. (eds.): Geomorphometry: concepts, software, applications. In: Developments in Soil Science, p. 33. Elsevier, Amsterdam (2009)

20. Iwahashi, J., Pike, R.J.: Automated classifications of topography from DEMs by an unsupervised nested-means algorithm and a three-part geometric signature. Geomorphology **86**, 409–440 (2007)

21. Jenness, J.: Topography position index TPI landform slope classification standardization neighborhood statistics. Topographic Position Index (TPI), **1** (2006)

22. Klinkenberg, B.: Fractals and morphometric measures: is there a relationship? Geomorphology **5**(1–2), 5–20 (1992)

23. Kozioł, K.: Numeryczny model terenu dla wielorozdzielczej/wieloprezentacyjnej bazy danych przestrzennych. Geomatics Environ. Eng. **3**(1/1), 69–80 (2009)

24. Kühni, A., Pfiffner, O.A.: The relief of the Swiss Alps and adjacent areas and its relation to lithology and structure—topographic analysis from 250-M DEM. Geomorphology **41**, 285–307 (2001)

25. Lindsay, J.B.: Whitebox GAT: a case study in geomorphometric analysis. Comput. Geosci. **95**, 75–84 (2016)

26. Liu, H., Bu, R., Liu, J., Leng, W., Hu, Y., Yang, L., Liu, H.: Predicting the wetland distributions under climate warming in the Great Xing'an mountains, northeastern China. Ecol. Res. **26**(3), 605–613 (2011)

27. Liu, M., Hu, Y., Chang, Y., He, X., Zhang, W.: Land use and land cover change analysis and prediction in the upper reaches of the Minjiang River, China. Environ. Manage. **43**(5), 899–907 (2009)

28. MacMillan, R.A., Pettapiece, W.W., Nolan, S.C., Goddard, T.W.: A generic procedure for automatically segmenting landforms into landform elements using DEMs, heuristic rules and fuzzy logic. Fuzzy Sets Syst. **113**, 81–109 (2000)

29. McGarigal, K., Tagil, S., Cushman, S.: Surfacemetrics: an alternative to patch metrics for the quantification of landscape structure. Landscape Ecol. **24**, 433–450 (2009)

30. Mora-Vallejo, A., Claessens, L., Stoorvogel, J., Heuvelink, G.B.M.: Small scale digital soil mapping in southeastern Kenya. CATENA **76**, 44–53 (2008)

31. Mousavi, S.R., Pirasteh, S., Pradhan, B., Mansor, S., Mahmud, A.R.: The ASTER DEM generation for geomorphometric analysis of the central Alborz Mountains, Iran. Pertanika J. Sci. Technol. **19**, 115–124 (2011)

32. Oberski, T.: Methods of identification and delimitation of concave terrain features based on ISOK-NMT data. Tech. Sci./University of Warmia and Mazury in Olsztyn (2016)

33. Oltean, G.S., Comeau, P.G., White, B.: Linking the depth-to-water topographic index to soil moisture on boreal forest sites in Alberta. Forest Sci. **62**(2), 154–165 (2016)

34. Pirasteh, S., Pradhan, B., Safari, H.O., Ramli, M.F.: Coupling of DEM and remote sensing based approaches for semiautomated detection of regional geo-structural features in Zagrous Mountain. Iran. Arab J Geosci **3**(1), 91–99 (2013). https://doi.org/10.1007/s12517-011-0361-0

35. Platt, R.V., Schoennagel, T., Veblen, T.T., Sherriff, R.L.: Modeling wildfire potential in residential parcels: A case study of the north-central Colorado Front Range. Landscape Urban Plann. **102**(2), 117–126 (2011)

36. Pracilio, G., Smettem, K.R., Bennett, D., Harper, R.J., Adams, M.L.: Site assessment of a woody crop where a shallow hardpan soil layer constrained plant growth. Plant Soil **288**(1–2), 113–125 (2006)
37. Prasannakumar, V., Vijith, H., Geetha, N.: Terrain evaluation through the assessment of geomorphometric parameters using DEM and GIS: case study of two major sub-watersheds in Attapady, South India. Arab. J. Geosci. **6**(4), 1141–1151 (2012)
38. Qiu, Z., Pennock, A., Giri, S., Trnka, C., Du, X., Wang, H.: Assessing soil moisture patterns using a soil topographic index in a humid region. Water Resour. Manage. **31**(7), 2243–2255 (2017)
39. Riley, J.W., Calhoun, D.L., Barichivich, W.J., Walls, S.C.: Identifying small depressional wetlands and using a topographic position index to infer hydro period regimes for pond-breeding amphibians. Wetlands, 1–14 (2017)
40. Tagil, S., Jenness, J.: GIS-based automated landform classification and topographic, landcover and geologic attributes of landforms around the Yazoren Polje, Turkey. J. Appl. Sci. **8**, 910–921 (2008)
41. Verhagen, J., Verburg, P., Sybesma, M., Bouma, J.: Terrainmodelling as a basis for optimal Agroecological land management using dynamic simulation. In: Robert, P.C. (ed.) Site-Specific Management for Agricultural Systems. ASA, CSSA, and SSSA, Madison (1995)
42. Weber, T.C.: Maximum entropy modeling of mature hardwood forest distribution in four US states. For. Ecol. Manage. **261**(3), 779–788 (2011)
43. Weiss, A.: Topographic position and landforms analysis. In: Poster Presentation, ESRI User Conference. San Diego, CA (2001)
44. Wood, S.W., Murphy, B.P., Bowman, D.M.: Firescape ecology: how topography determines the contrasting distribution of fire and rain forest in the south-west of the Tasmanian Wilderness World Heritage Area. J. Biogeogr. **38**(9), 1807–1820 (2011)
45. Woodrow, K., Lindsay, J.B., Berg, A.A.: Evaluating DEM conditioning techniques, elevation source data, and grid resolution for field-scale hydrological parameter extraction. J. Hydrol. (2016, in press)
46. Youssef, A.M., Pradhan, B., Gaber, A.F.D., Buchroithner, M.F.: Geomorphological hazard analysis along the Egyptian Red Sea coast between Safaga and Quseir. Nat. Hazard Earth Syst. **9**, 751–766 (2009)
47. Zhang, Y., He, H.S., Dijak, W.D., Yang, J., Shifley, S.R., Palik, B.J.: Integration of satellite imagery and forest inventory in mapping dominant and associated species at a regional scale. Environ. Manage. **44**(2), 312–323 (2009)

Assessing the Spatial and Temporal Capacity of a Semi-Enclosed Gulf to Absorb and Release CO_2 Using GIS and Remote Sensing

A. Shanableh, R. Al-Ruzouq and G. Al-Khayyat

Abstract The increasing CO_2 level in the atmosphere is threatening oceans' ecosystems due to increased CO_2 absorption and potential oceans' acidification. In this study, we used geographic information system (GIS) and remote sensing (RS) techniques, coupled with chemical–mathematical models to evaluate the water capacity of a semi-enclosed gulf to absorb and release CO_2. The water of the gulf exhibits a wide range of spatial and temporal salinity and temperature variations due to the gulf location in a hot, arid region, the high water evaporation rate, and the unique water circulation pattern. In this study, GIS and RS data were used to assess the spatial and temporal distributions of surface temperatures and salinity of the gulf, which, in turn, were used to assess the capacity of the gulf waters to absorb and release CO_2. The results confirmed the profound impact of salinity and temperature on the CO_2 absorption and release capacity of the gulf, which highly influences potential acidification of the gulf waters.

Keywords Geographic information systems · Remote sensing · CO_2 absorption and release · Surface temperature · Surface salinity · Seawater Semi-enclosed gulf

1 Introduction

Prior to the industrial revolution starting the 1950s, CO_2 level in the atmosphere was in the range of 200–300 ppmv for hundreds of thousands of years [1–4]. Since then, the level of CO_2 rapidly increased reaching approximately 400 ppmv at the present time, or the year 2017. The CO_2 increase is mainly attributed to burning fossil fuels. About 30% of the CO_2 released to the atmosphere during the 1980s and

A. Shanableh (✉) · R. Al-Ruzouq · G. Al-Khayyat
Department of Civil and Environmental Engineering, Research Institute
of Sciences and Engineering, University of Sharjah, Sharjah,
United Arab Emirates
e-mail: shanableh@sharjah.ac.ae

1990s was absorbed by the oceans, with about 50% remaining in the atmosphere and 20% removed on land by the biosphere [5]. Others [6] estimated that the oceans absorbed about 50% of the CO_2 released during the past 200 years. Absorption of atmospheric CO_2 acidifies oceans [7–10], threatening to reduce $CaCO_3$ supersaturation and posing risk to calcifying organisms [11]. Acidification of seawater can significantly impact the biogeochemical transformations [6, 7, 11–14] in the sea. Acidification scenarios indicate that a sixfold increase of the preindustrial CO_2 level can potentially reduce the pH of oceans by about 0.7 units [6]. Direct observation between 1991 and 2006 indicated a pH decline of about 0.06 in the upper 0.5 km of the water of the North Pacific Ocean [15].

The Arabian Gulf (also referred as the Persian Gulf) is located between latitudes 23.5°–30°N (Fig. 1). It is about 800 km long, 300 km wide and 40 m average depth, with a total surface area of approximately 240,000 km^2. Water enters and exits the Gulf through the Strait of Hormuz, which connects the Arabian Gulf to the

Fig. 1 Location of the Gulf obtained from national geographic, ESRI

Gulf of Oman, Arabian Sea, and the Indian Ocean. The Gulf receives limited freshwater supplies, with rain not exceeding 150 mm/year [16, 17], and experiences high evaporation rate that exceeds 2000 mm/year [17–19], which increases its salinity.

The capacity of the Gulf to absorb and release CO_2 is highly affected by water temperature and water salinity. The water in the Gulf is generally saltier than waters of open seas, and experiences wide spatial and seasonal variations in temperature and salinity [17, 20–25]. These variations are due to the geographical extent of the Gulf, unique water circulation and stagnation patterns, evaporation, and disposal of brines from desalination plants.

In this chapter, we used GIS and RS to assess the spatial and temporal distributions of surface temperatures and salinity of the Gulf, then used the temperature and salinity distributions to assess the capacity of the surface water to absorb and release CO_2. This capacity plays an important role in determining potential acidification and influences the carbonate chemistry of the water of the Gulf.

2 Methodology

2.1 Chemical Equilibrium Model

The methodology used in this article was based on models developed during earlier work [20, 21]. Simple chemical-mathematical models representing CO_2 equilibrium between seawater and the atmosphere were used. Such models were based on preserving initial alkalinity (Alk_0) regardless of increased CO_2 absorption. Seawater alkalinity (Alk_0), including the borate ion, is presented in Eq. 1, and its simplified version excluding borate is presented in Eq. 2.

$$Alk_0 \cong [OH^-] + [B(OH)_4^-] + 2[CO_3^{2-}] + [HCO_3^-] - [H^+] \tag{1}$$

$$Alk_0 \cong [OH^-] + [HCO_3^-] + 2[CO_3^{2-}] - [H^+] \tag{2}$$

Using the pH-dependent carbonate speciation parameters ($\alpha_0, \alpha_1, \alpha_2$), Henry's equation ($[H_2CO_3] = k_H P_{CO_2}$), which is expressed in terms of Henry's constant (k_H), CO_2 pressure in the atmosphere (P_{CO_2}) and the water speciation constant (k_w), the initial alkalinity equation can be rewritten as

$$Alk_0 \cong \frac{k_w}{[H]} + (\alpha_1 + 2\alpha_2)\frac{k_H P_{CO_2}}{\alpha_0} - [H^+] \tag{3}$$

The water that enters the Gulf is subject to evaporation which concentrates the various water constituents. As such, a concentration factor R (i.e., $R = S/S_0$, where S = salinity, and S_0 = initial reference salinity) can be introduced in Eq. 3 to correct alkalinity as in Eq. 4.

$$R * \mathrm{Alk}_0 \cong \frac{k_\mathrm{w}}{[\mathrm{H}]} + (\alpha_1 + 2\alpha_2)\frac{k_\mathrm{H}P_{\mathrm{CO}_2}}{\alpha_0} - [\mathrm{H}^+] \tag{4}$$

Absorption and release of CO_2 can be evaluated from the concentration of total carbonates in water, C_T, noting that $[\mathrm{H_2CO_3}] = \alpha_0 C_\mathrm{T}$, $[\mathrm{HCO_3^-}] = \alpha_1 C_\mathrm{T}$, $[\mathrm{CO_3^{2-}}] = \alpha_2 C_\mathrm{T}$, then

$$C_\mathrm{T} = [\mathrm{H_2CO_3}] + [\mathrm{HCO_3^-}] + [\mathrm{CO_3^{2-}}] \tag{5}$$

The above equations rely on a number of constants, including the carbonate species dissociation constants, k_1, and k_2. The values of the various constants are dependent on water temperature and salinity as summarized in Table 1.

It should be stated that the suitability of the above models to predict pH and C_T was verified earlier [21] against [6] predictions relating to atmospheric CO_2 level of 280 ppmv up to sixfolds increase in CO_2 level to 1680 ppmv.

To estimate the pH and total carbonates (C_T) in the Gulf, the spatial and temporal distributions of salinity and water temperature were obtained from satellite images and an iterative procedure was used to estimate the pH and total carbonates for two CO_2 level in the atmosphere, 400 and 800 ppmv. The reference values required for solving Eq. 4 are provided in Table 2.

Table 1 Dependence[a] of the equilibrium constants (k_1, k_2, k_W, and k_H) on water salinity (psu) and temperature (k)

$\ln(k_\mathrm{w}) = \dfrac{-13,847.26}{T} + 148.9652 - 23.6521 * \ln(T)$ $\quad + \left(\dfrac{118.67}{T} - 5.977 + 1.0495 * \ln(T)\right) * S^{0.5} - 0.01615 * S$
$\ln(k_H) = \dfrac{9345.17}{T} - 60.2409 + 23.3585 * \ln(\dfrac{T}{100})$ $\quad + \left(0.023517 - 0.00023656 * T + 0.00000047036 * T^2\right) * S$
$pk_1 = \frac{3633.86}{T} - 61.2172 + 9.67770 * \ln(T) - 0.011555 * S + 0.0001152 * S^2$
$pk_2 = \frac{471.78}{T} + 25.9290 - 3.16967 * \ln(T) - 0.01781 * S + 0.0001122 * S^2$

[a]*Sources* [26–28]

Table 2 Initial values of parameters used in this study

Parameter	Value
Initial temperature (°C)	24
Reference salinity of surface water, S_0 (psu)	35
Initial alkalinity (eq/L)	0.0024
Reference (2016) CO_2 level in atmosphere (ppmv)	400[a]

[a]*Source* NOAA-ESRL
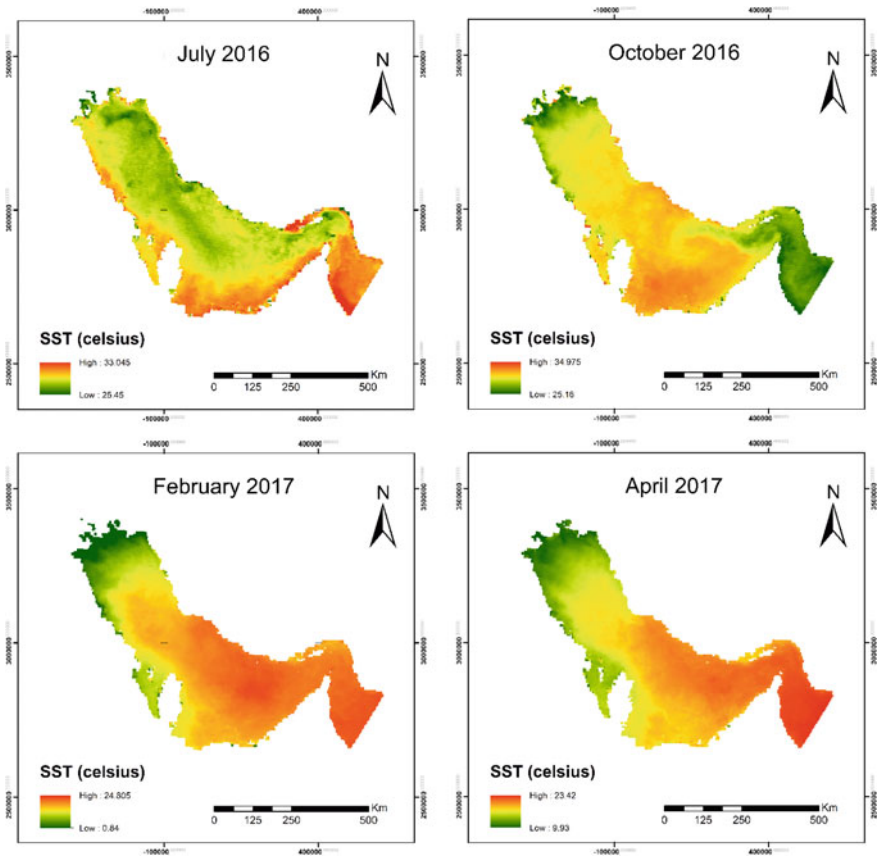
Fig. 2 Seasonal distribution of surface water temperature in the Gulf during 2017 as extracted from MODIS images by NASA

The spatial and seasonal distributions of temperature (Fig. 2) and salinity (Fig. 3) needed for estimating the various parameters in Table 1 were, respectively, extracted from the Moderate Resolution (4 km spatial resolution) Imaging Spectroradiometer (MODIS) on the Terra-satellite of NASA and from the Remote Sensing System (RSS) Company with 25 km resolution. For salinity, and as the obtained satellite images did not provide full coverage of the Gulf (Fig. 3), values in uncovered areas were estimated based on data available from a variety of other sources [17, 22–25].
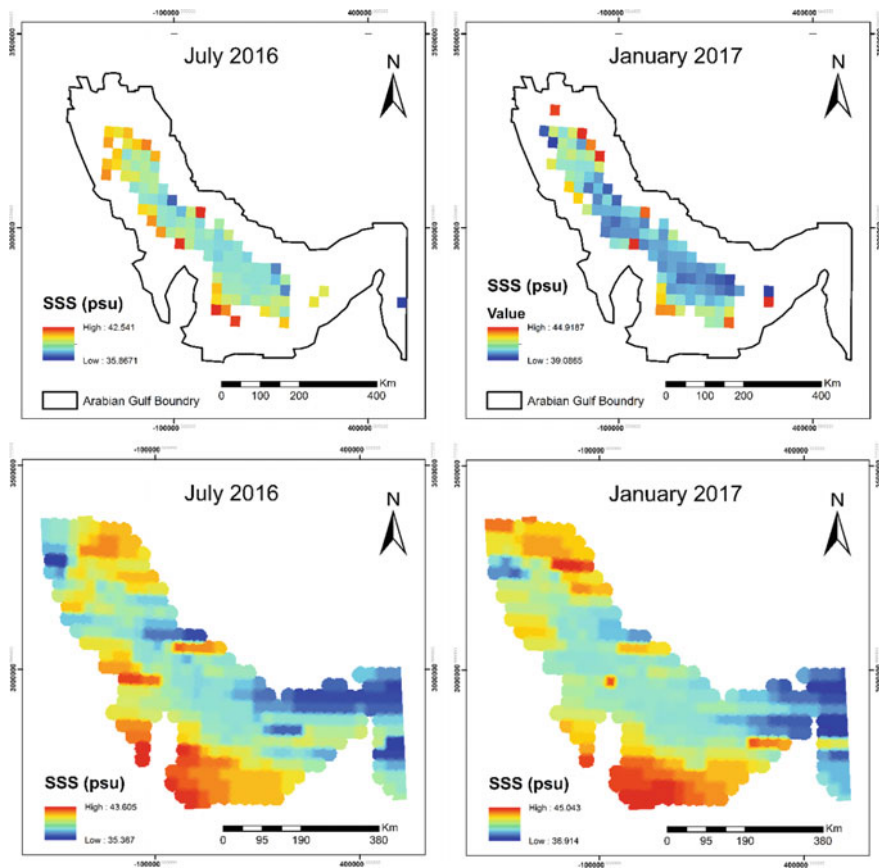
Fig. 3 Example seasonal distribution of surface water salinity in the Gulf during 2017 extracted from RSS by NASA

3 Results and Discussion

3.1 Spatial and Seasonal Distributions of Temperature and Salinity

The water temperature in July (summer) was in the range of 24–33 °C (Fig. 2), 25–35 °C in October (fall), 1–25 °C in February (winter) and 10–23 °C in April (spring). The water along the southern parts of the Gulf was the warmest in July and October and relatively warm in February and April. In February and April, warm waters entering from the Hurmuz straight kept the water along the northern coastline of the Gulf warmest. The February and April warm water entering the Gulf pushes northwest along the northern coastline of the Gulf but does not reach
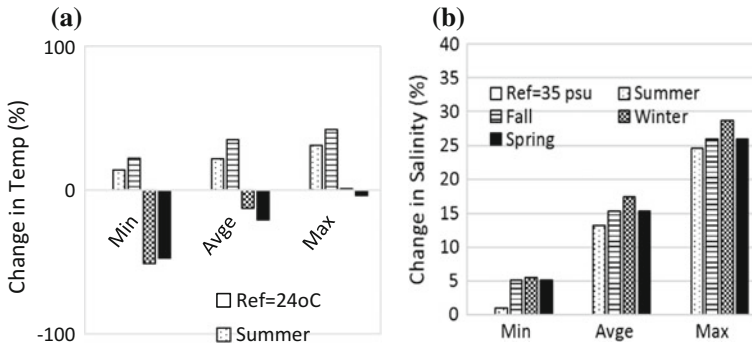
Fig. 4 Projected distribution of salinity and temperature in the Gulf compared to reference values (24 °C and 35 psu)

the northwestern part, opposite Iraq and Kuwait, which remains the coldest area in the Gulf during all seasons.

Although the satellite salinity data are incomplete, the general salinity distribution is generally affected by the water that enters from the Gulf of Oman, which generally has lower salinity than the water that exists the Gulf. The salinity is also affected by water circulation and evaporation in the Gulf. In general, the northern parts along the Iranian coast maintain the lowest salinity values while the southern parts along the coasts of the UAE and Qatar maintain the highest salinity values (Fig. 3).

A statistical summary of salinity and temperature variations in the Gulf compared to the reference values stated in Table 2 (i.e., 24 °C and 35 psu) is presented in Fig. 4. The data show that depending on the season, the temperature in some parts of the Gulf declined up to 50% or increased up to 42%. On the other hand, the salinity increased between 5 to about 27%, with an average increase of approximately 15%.

3.2 Capacity of the Gulf to Absorb/Release CO_2

The data in Fig. 5 show the impact of temperature and salinity on surface water alkalinity (Alk), total carbonates (C_T) and pH according to Eq. 4. At constant salinity, the Alk remains constant and C_T declines, as the water loses capacity to dissolve CO_2 with increasing temperature. As expected, the pH increases as the temperature increases up to 21°C, but then unexpectedly declines apparently due to the differences in the impact of salinity on the various constants in Table 1. On the other hand, both Alk and C_T increase as salinity increases at constant temperature due to concentration of constituents. The increase in alkalinity is equivalent to adding a strong base, which helps the water absorb more CO_2 but also results in increasing the pH.
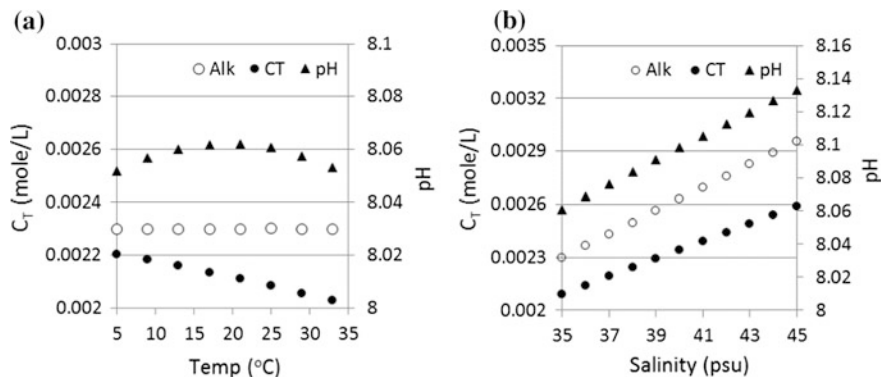
Fig. 5 Impact of temperature (at constant salinity of 35 psu) and salinity (at constant temperature of 24 °C) on pH and total carbonates (C_T) at atmospheric CO_2 = 400 ppmv

Clearly, the model suggests that lower temperatures and increased salinity increase the capacity of seawater to absorb CO_2 from the atmosphere. In terms of pH, the model suggests that increased salinity increases the pH despite absorption of additional quantities of CO_2 into the water. Therefore, the model predicts that increased salinity helps in absorbing excess atmospheric CO_2 and combating acidification of seawater.

The data suggest that water in the Gulf acted as a sink for CO_2 compared to water entering from the Gulf of Oman due to increased salinity. Furthermore, salinity was more important than temperature in deciding the level of CO_2 absorption as indicated by C_T. Therefore, the southern parts of the Gulf with high salinity achieved the highest CO_2 absorption levels followed by the somewhat saline and cold northern parts of the Gulf (Fig. 6). In general, the northern parts of the Gulf receiving water entering the Gulf from the Strait of Hurmuz showed lower CO_2 absorption levels than the saltier southern parts regardless of temperature.

Projected absorption of CO_2 into the surface water of the Gulf at double the current atmospheric CO_2 level (i.e., 800 ppmv) followed similar trends as absorption at 400 ppmv, except that the absorbed C_T quantities increased significantly (Fig. 7). The southern parts of the Gulf, which have the highest salinity are projected to experience the highest CO_2 absorption levels followed by the somewhat saline and colder northern parts.

The data in Fig. 8 present a statistical summary of the C_T variations in the Gulf compared to a chosen reference value (i.e., C_T = 0.00209 mol/L) defined at temperature of 24 °C and salinity of 35 psu. The data show that at atmospheric CO_2 level of 400 ppmv, C_T increased in the Gulf from 5 to about 25% above the reference C_T value, with an average increase of approximately 12%. The increase in C_T was consistent with increase in salinity shown in Fig. 4. At atmospheric CO_2 level of 800 ppmv, the data in Fig. 8 show projected C_T increase above the reference value between about 7 and 30%, with an average increase of approximately
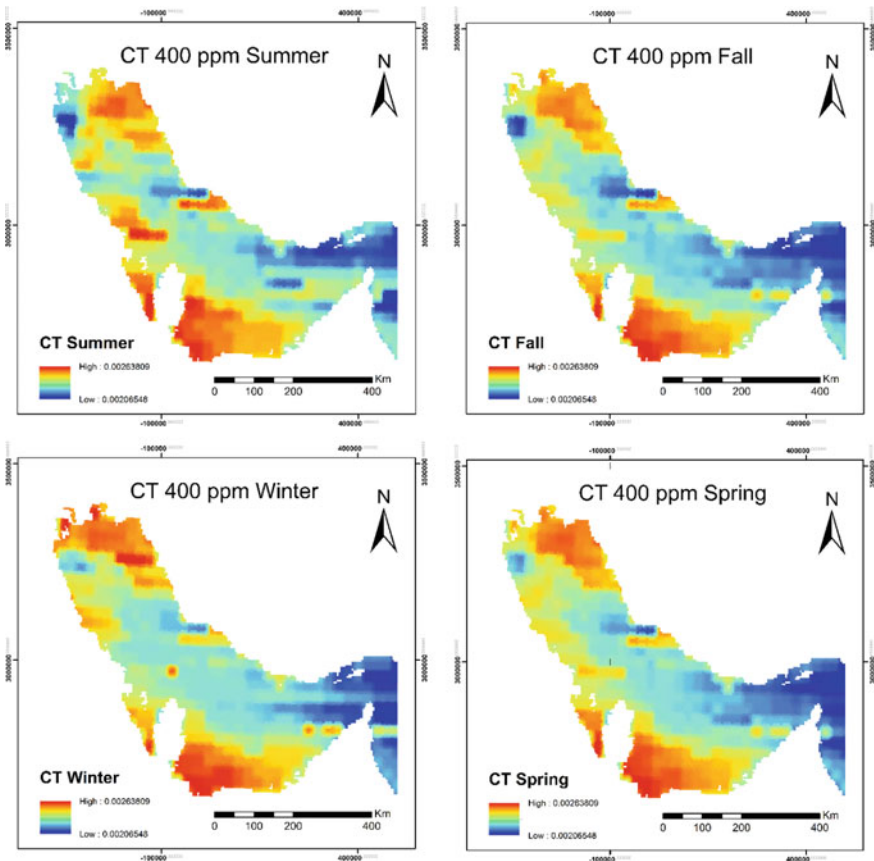
Fig. 6 Projected seasonal distribution of total carbonates (C_T) in the surface water of the Gulf at atmospheric CO_2 = 400 ppmv based on the salinity and temperature distributions in Figs. 2 and 3

20%. The data suggest significant increase in capacity of the Gulf water to absorb CO_2, which is mainly due to increased salinity.

3.3 Acidification of Surface Water

Absorption of CO_2 in the surface water of the Gulf increases as salinity and CO_2 in the atmosphere increase and declines as the temperature increases. Therefore, the temperature and salinity distributions in the Gulf have a significant impact on water acidification. In Fig. 5, it was shown that higher salinity resulted in higher alkalinity and more C_T absorption, which translated into pH increase. The data in Fig. 9 show that compared to the reference pH value of 8.061 at atmospheric CO_2 level of
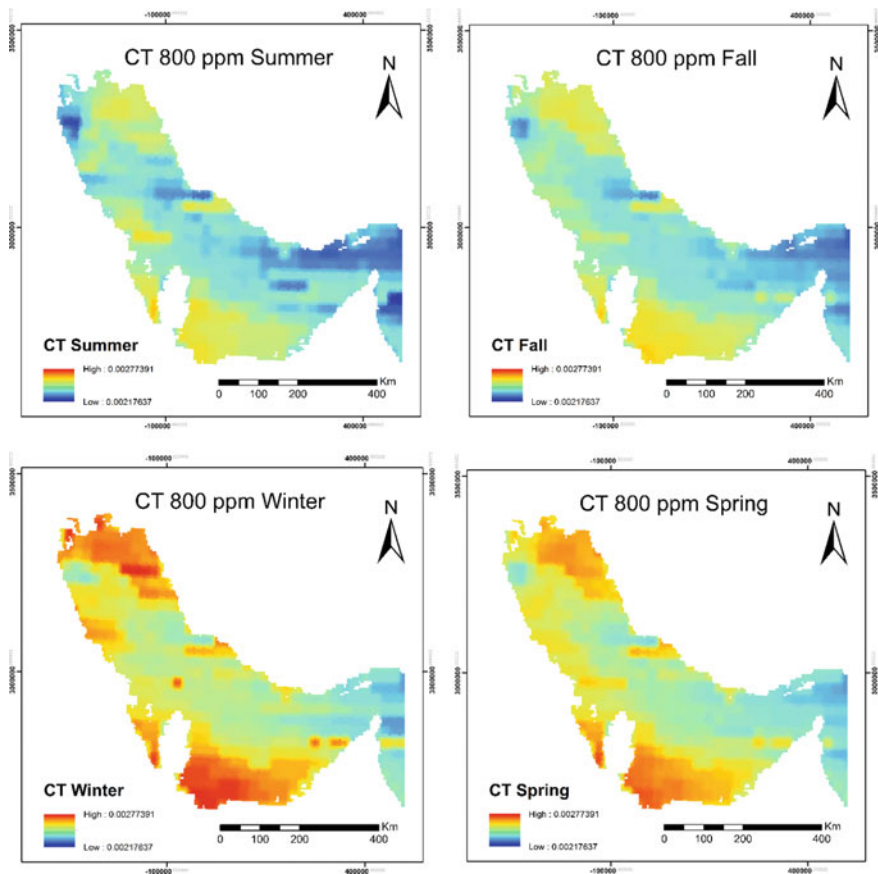
Fig. 7 Projected seasonal distribution of total carbonates (C_T) in the surface water at atmospheric CO_2 = 800 ppmv based on the salinity and temperature distributions in Figs. 2 and 3
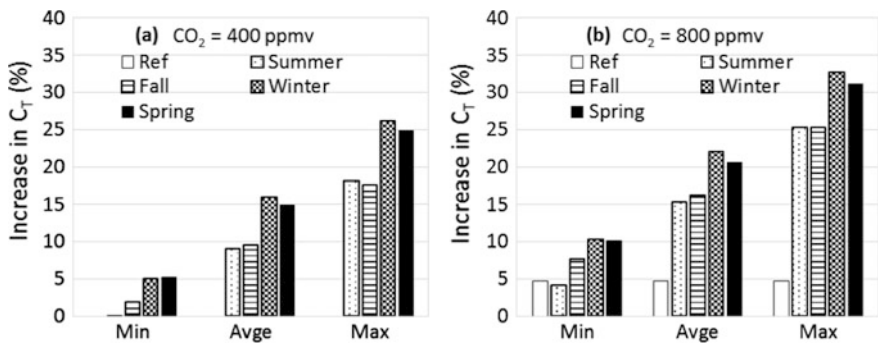
Fig. 8 Projected distribution of C_T in the Gulf compared to reference C_T value defined at 24 °C and 35 psu
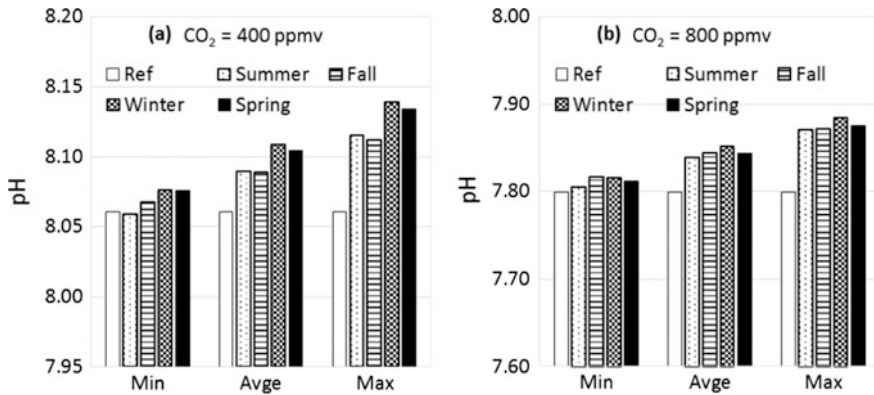
Fig. 9 Projected distribution of pH in the Gulf

400 ppmv and temperature and salinity values of 24 °C and 35 psu, the pH distribution in the Gulf ranged between 8.06 and 8.14 and average is 8.1, with more saline regions associated with the higher pH values. Similarly, compared to the reference pH value of 7.80, projected at atmospheric CO_2 level of 800 ppmv and temperature and salinity values of 24 °C and 35 psu, the pH distribution in the Gulf ranged between 7.80 and 7.89 (average of 7.84).

4 Summary and Conclusions

A simple mathematical–chemical equilibrium evaporation model was developed and used to assess the capacity of the surface water of the Arabian Gulf to absorb and release CO_2. The capacity of the surface water was found to be determined mostly by the salinization of the Gulf due to evaporation and other causes. Salinization increases the alkalinity of the water, which allows it to absorb more CO_2 and simultaneously increases the pH. As such, the salinization of the Gulf acts as a buffer that helps reduce projected acidification of the Gulf due to increasing atmospheric CO_2. The Gulf capacity thus to absorb and release atmospheric CO_2 is highly influenced by the distributions of the salinity and temperature in the Gulf waters, with the water releasing or absorbing CO_2 depending on its salinity and temperature levels.

References

1. Kleypas, J.A., Feely, R.A., Fabry, V.J., Langdon, C., Sabine, C.L., Robbins, L.L.: Impacts of ocean acidification on coral reefs and other marine calcifiers: a guide for futureresearch. In: Report of a Workshop held 18–20 April 2005. St. Petersburg, FL, p. 88 (2006)

2. Siegenthaler, U., Stocker, T., Monnin, E., Lüthi, D., Schwander, J., Stauffer, B., Raynaud, D., Barnola, J., Fischer, H., Masson-Delmotte, V., Jouzel, J.: Stable carbon cycleclimate relationship during the late Pleistocene. Science **310**, 1313–1317 (2005)

3. Augustin, L., Barbante, C., Barnes, P., Barnola, J., Bigler, M., Castellano, E., Cattani, O., Chappellaz, J., Dahl-Jensen, D., Delmonte, B., Dreyfus, G., Durand, G., Falourd, S., Fischer, H., Fluckiger, J., Hansson, M., Huybrechts, P., Jugie, G., Johnsen, S., Jouzel, J., Kaufmann, P., Kipfstuhl, J., Lambert, F., Lipenkov, V., Littot, G., Longinelli, A., Lorrain, R., Maggi, V., Masson-Delmotte, V., Miller, H., Mulvaney, R., Oerlemans, J., Oerter, H., Orombelli, G., Parrenin, F., Peel, D., Petit, J., Raynaud, D., Ritz, C., Ruth, U., Schwander, J., Siegenthaler, U., Souchez, R., Stauffer, B., Steffensen, J., Stenni, B., Stocker, T., Tabacco, I., Udisti, R., van de Wal, R., van den Broeke, M., Weiss, J., Wilhelms, F., Winther, J., Wolff, E., Zucchelli, M.: Eight glacial cycles from an Antarctic ice core. Nature, **429**, 623–628 (2004) (cited in Kleypas et al. 2006)

4. Petit, J.R., Jouzel, J., Raynaud, D., Barkov, N., Barnola, J., Basile, I., Bender, M., Chappellaz, J., Davisk, M., Delaygue, G., Delmotte, M., Kotlyakov, V., Legrand, M., Lipenkov, V., Lorius, C., Pèpin, L., Ritz, C., Saltzmank, E., Stievenard, M.: Climate and atmospheric history of the past 420,000 years from the Vostok ice core, Antarctica. Nature, **399**, 429–436 (1999) (cited in Kleypas et al. 2006)

5. Sabine, C.L., Feely, R., Gruber, N., Key, R., Lee, K., Bullister, J., Wanninkhof, R., Wong, C., Wallace, D., Tilbrook, B., Millero, F., Peng, T., Kozyr, A., Ono, T., Rios, A.: The oceanic sink for anthropogenic CO_2. Science **305**(5682), 367–371 (2004)

6. Royal Society: Ocean Acidification Due to Increasing Atmospheric Carbon Dioxide. Science Policy www.royalsoc.ac.uk (Section ISBN: 0 85403 617 2) (2005)

7. Caldeira, K., Wickett, M.E.: Anthropogenic carbon and ocean pH. Nature **425**, 365 (2003)

8. Zeebe, R.E., Wolf-Gladrow, D.A.: Seawater: equilibrium, kinetics, isotopes. In: Elsevier Oceanography Series, vol. 65. Elsevier, New York (2001)

9. Brewer, P.G.: Ocean chemistry of the fossil fuel CO_2 signal: the haline signal of 'business as usual'. Geophys. Res. Lett. **24**, 1367–1369 (1997)

10. Bolin, B., Eriksson, E.: Changes in the Carbon Dioxide Content of the Atmosphere and the Sea Due to Fossil Fuel Combustion, in the Atmosphere and the Sea in Motion, pp. 130–142. Rockefeller Inst. Press, New York (1959)

11. Doney, S., Fabry, V., Feely, R., Kleypas, J.: Ocean acidification: the other CO_2 problem. Annu. Rev. Mar. Sci. **1**, 169–192 (2009)

12. Orr, J.C., Fabry, V., Aumont, O., Bopp, L., Doney, S., Feely, R., Gnanadesikan, A., Gruber, N., Ishida, A., Joos, F., Key, R., Lindsay, K., Maier-Reimer, E., Matear, R., Monfray, P., Mouchet, A., Najjar, R., Plattner, G., Rodgers, K., Sabine, C., Sarmiento, J., Schlitzer, R., Slater, R., Totterdell, I., Weirig, M., Yamanaka, Y., Yool, A.: Anthropogenic ocean acidification over the twenty-first century and its impact on calcifying organisms. Nature **437**, 681–686 (2005)

13. Fabry, V., Seibel, B., Feely, R., Orr, J.: Impacts of ocean acidification on marine fauna and ecosystem processes. ICES J. Mar. Sci. **65**, 414–432 (2008)

14. Feely, R., Sabine, C., Lee, K., Berelson, W., Kleypas, J., Fabry, V., Millero, F.: Impact of anthropogenic CO_2 on the $CaCO_3$ system in the oceans. Science **305**(5682), 362–366 (2004)

15. Byrne, R.H., Mecking, S., Feely, R.A., Liu, X.: Direct observations of basin-wide acidification of the North Pacific Ocean. Geophys. Res. Lett. **37**, L02601 (2010)

16. Johns, W.E., Yao, F., Olson, D.B., Josey, S.A., Grist, J.P., Smeed, D.A.: Observations of seasonal exchange through the Straits of Hormuz and the inferred freshwater budgets of the Persian Gulf. J. Geophys. Res. **108**(C12), 3391–3407 (2003)

17. Kämpf, J., Sadrinasab, M.: The circulation of the Persian Gulf: a numerical study. Eur. Geosci. Union Ocean Sci. Discuss. **2**, 129–164 (2006)

18. Meshal, A.H., Hassan, H.M.: Evaporation from the coastal waters of the central part of the Gulf. Arab. Gulf Sci. Res. **4**, 649–655 (1986)

19. Ahmad, F., Sultan, S.A.R.: Annual mean surface heat fluxes in the Arabian Gulf and the net heat transport through the Strait of Hormuz. Atmos. Ocean **29**, 54–61 (1991)

20. Shanableh, A., Merabtene, T., Omar, M., Imteaz, M.: Impact of surface ocean acidification on the CO_2 absorption rate. Int. J. Glob. Warming **3**(1–2), 163–172 (2011)
21. Shanableh, A., Imteaz, M., Hamad, K., Omar, M., Merabtene, T., Siddique, M. (in press): Potential impact of global warming on whiting in a semi-enclosed gulf. Int. J. Glob. Warning
22. Alessi, C.A.: Hydrographic Data from the US Naval Oceanographic Office: Persian Gulf, Southern Red Sea, and Arabian Sea 1923–1996. Woods Hole Oceanographic Institution WHOI-99-02 (1999)
23. Alosairi, Y., Imberger, J., Falconer, R.A.: Mixing and flushing in the Persian Gulf. J. Geophys. Res. Oceans, **116**(C3) (March 2011)
24. Yao, F.: Water Mass Formation and Circulation in the Persian Gulf and Water Exchange with the Indian Ocean. Open Access Dissertations, Paper, p. 183 (2008)
25. Azam, M., Elshorbagy, W., Ichikawa, T., Terasawa, T., Taguchi, K.: A three dimensional model application to study the residual flow in the Arabian Gulf, ASCE. J. Water Way Port Coast. Ocean Eng. **132**(5), 388–400 (2006)
26. Lueker, T.J., Dickson, A.G., Keeling, C.D.: Ocean pCO_2 calculated from dissolved inorganic carbon, alkalinity, and equations for K1 and K2: validation based on laboratory measurements of CO_2 in gas and seawater at equilibrium. Mar. Chem. **70**, 105–119 (2000)
27. Millero, F.J.: Thermodynamics of the carbon dioxide system in the oceans. Geochim. Cosmochim. Acta **59**, 661–677 (1995)
28. Mucci, A.: The solubility of calcite and aragonite in seawater at various salinities, temperatures, and one atmosphere total pressure. Am. J. Sci. **283**, 780–799 (1983)

Part III
Geotechnical Engineering

Impact of Vertical Stresses on Geotechnical Properties of Sand

Aneel Kumar Hindu, Tauha Husain Ali and Agha Faisal Habib

Abstract Generally, before the construction of any construction project, the sub-soil investigations were carried out to evaluate the various geotechnical properties of soil like shear strength, permeability, etc. The sustainability of the projects largely depend upon the true prediction of the behaviour of the soil in long term and short term. However, due to the application of external loads, the stress induced on the soil increased and its effect remain high at shallow depths. This may cause the breaking of the soil particles particularly for coarse grained soils like gravel and sand. This chapter demonstrates the influence of induced stresses on the geotechnical characteristics of sand. The static normal stresses were induced in the range of 5–20 MPa with help of Universal Testing Machine (UTM). It is seen that with increase of static stresses the breaking of sand particles occurred. This possibly results in the decrease of permeability and shearing strength.

Keywords Particle breakage · Permeability · Sand · Shear strength

1 Introduction

It is a general practice that before the start of any civil engineering project the soil properties are evaluated and accordingly foundation or load-bearing stratum were designed/prepared. The stresses generated by dead and live loads ultimately transfer to the soil particles. The increase of stresses on soil particles may break the soil particles, particularly if underlain soil consists of coarse-grained soils like sand.

A. K. Hindu (✉) · T. H. Ali · A. F. Habib
Department of Civil Engineering, Mehran University of Engineering
and Technology, Jamshoro, Pakistan
e-mail: aneel.kumar@faculty.muet.edu.pk

T. H. Ali
e-mail: tauha.hussain@faculty.muet.edu.pk

A. F. Habib
e-mail: dr.faisal@faculty.muet.edu.pk

The breaking of soil particles can change the particle size distribution and other important geotechnical properties like strength and permeability. The ultimate outcome may be the faulty design of the foundations or load-bearing stratums, as the original geotechnical properties with which a foundation or load-bearing stratums were designed will change with the course of time. Therefore, it is of prime importance to understand the effect of increase of stress on the mechanical properties (like particle size distribution, strength and permeability) of coarse-grained soils like sand.

The effect of particle size crushing on engineering properties of soil was not only the research of interest in civil engineering but also in mineral engineering, mining engineering, powder technology, etc. [1–3]. It has been observed that the breakage of granular particles can alter the peak as well as residual stress-strain behaviour [1]. It is seen that the crushing of granular particles can result in the decrease of angle of shearing resistance [4, 5]. Previous researchers demonstrated that the breakage of soil particles depends upon induced stresses, porosity, moisture content, gradation, angularity, anisotropy and strength of soil grains [6–10]. Following the motivation from the results of previous researchers, this study was conducted to investigate the effects of increased stress on the various geotechnical properties of Bholari sand, like particle size distribution, shear strength and permeability. Bholari sand is commonly used as a borrow material for construction of load-bearing stratum and for manufacture of concrete by the local construction companies in the vicinity of Hyderabad and Karachi divisions of Pakistan.

2   Material

The sand was obtained from a natural source known as Bholari. To obtain the pure sand, the Bholari sand was, first of all, sieved through #4 sieve to separate gravels and cobbles, and then washed through #200 sieve to remove fine particles. Washed sand was then kept in thermostatically controlled oven for 24 h to make it dry.

3   Application of Stress

To induce the stresses in sand, the standard crushing value moulds were utilized. After filling the sand in the mould, it was placed in the Universal Testing Machine (UTM), where normal compressive stresses of 5, 10, 15 and 20 MPa were applied. The range of induced compressive stresses were based on the experimental work of previous researchers [6]. The applied compressive stress was kept constant for 45 min and then released. In each loading condition, the density of the sand was kept constant as 1.62 g/cm^3.

4 Result and Discussion

4.1 Particle Breakage

The influence of increase of stress on the crushing of sand particles is shown in Fig. 1. The D_{10}, D_{30} and D_{60} values for various loading conditions are given in Table 1.

It can be seen that the D_{10}, D_{30} and D_{60} values decreased gradually with the increase of stresses. This shows the breaking of particles occurred. The quantification of the breaking of particles was made by utilizing particle breakage factor (B_{10}) defined by Eq. 1 [11].

$$B_{10} = \frac{D_{10i} - D_{10f}}{D_{10i}}, \tag{1}$$

where D_{10i} and D_{10f} are the effective grain sizes of initial and final gradations, respectively.

Figure 2 shows the particle breakage factor with applied stresses. It is observed that breakage of particles increased with increase of induced stresses. It is necessary to mention that the application of normal compressive stress was only for 45 min.
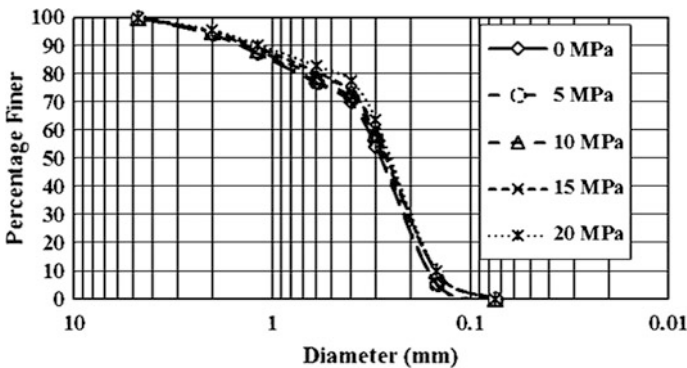
Fig. 1 Grain size distribution before and after inducing stresses

Table 1 D_{10}, D_{30} and D_{60} values of sand under various loading conditions	Applied stress (MPa)	D_{10} (mm)	D_{30} (mm)	D_{60} (mm)
	0	0.18	0.23	0.35
	5	0.17	0.21	0.32
	10	0.15	0.20	0.30
	15	0.14	0.20	0.29
	20	0.13	0.19	0.28

Fig. 2 Breakage of particles
due to induced stresses
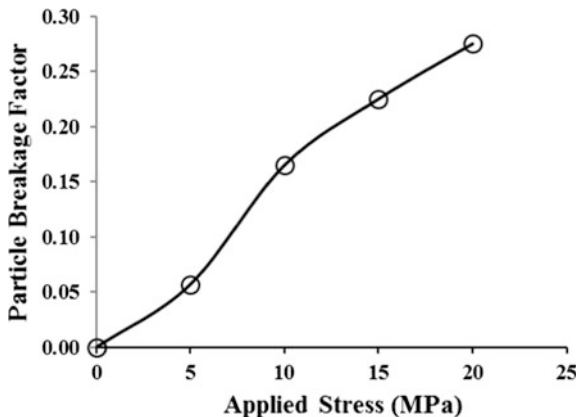
However, in the real conditions, the application of increase stresses may be for a
significantly long time. The breaking of particles may increase with increase in
loading time.

4.2 Effect on Permeability

Permeability of the soils was determined at different void ratios by utilizing stan-
dard constant head permeability test. Figure 3 shows permeability test results. It is
seen that the permeability of soil decreased when the stresses were induced in the
soil.

Fig. 3 Permeability versus
voids ratio before and after
inducing stresses
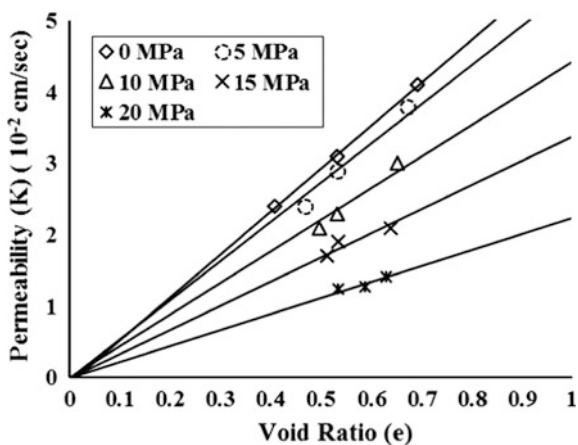
Fig. 4 Permeability at 0.6 void ratio before and after inducing stresses
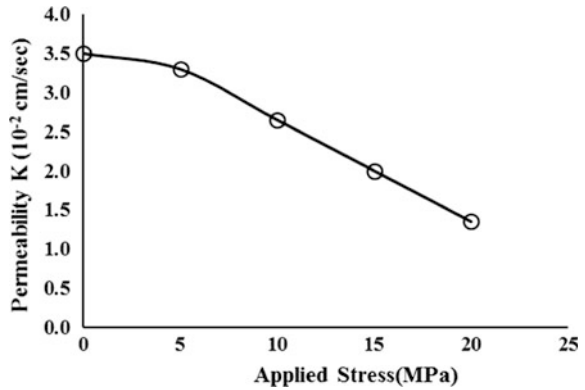
Figure 4 shows that even for the same void ratio, the permeability of the soil subjected to high stresses remains low. This may be attributed to the breakage of particles due to inducedstresses.

4.3 Effect on Shear Strength

Direct shear box test was performed to determine the influence of induced stresses on the shear strength of soil. Figure 5 shows the results of direct shear box test. Figure 6 shows the effect of induced stresses on angle of internal friction. It can be seen that with the increase of induced stresses the angle of internal friction is gradually decreased. This may be because of the breakage of sand particles. Breakage of sand particles, on one hand, causes the increased percentage of fine particles and on other hand, broken particles may have relatively smooth surfaces compared to their original ones.

Fig. 5 Shear stress versus normal stress before and after inducing stresses
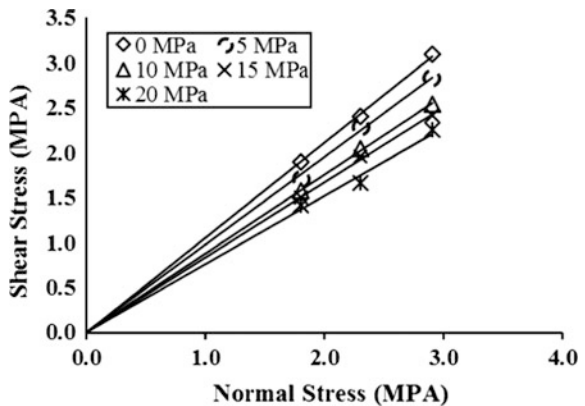
Fig. 6 Angle of internal friction before and after inducing stresses
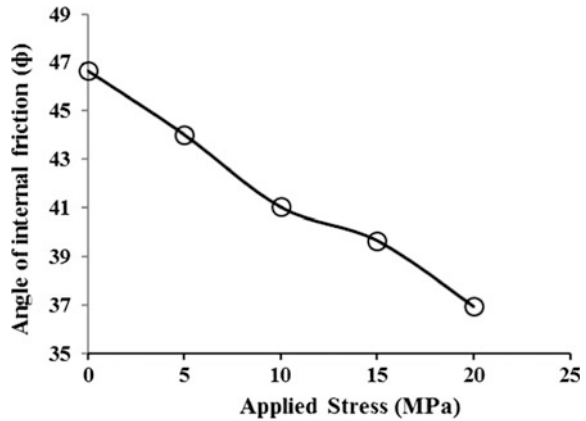
5 Conclusion

- The influence of induced stresses on geotechnical characteristics of the Bholari sand was investigated experimentally. The normal compressive stresses were induced by utilizing UTM and standard crushing value moulds. From the experimental results, it is seen that breaking of sand particles occurred by inducing stresses. Higher the applied stress, more the breaking of particle. Values of D_{10}, D_{30} and D_{60} decreased gradually with the increase of stresses.
- It is observed that the permeability of soil decreased with increase of applied stresses induced in the soil. It is further observed that even for the same void ratio, the permeability of soil subjected under high stresses remained the low and under low stresses remained high.
- It is also observed that the angle of shear strength of soil will decrease with the increase of induced stresses in soil.

References

1. Hattamleh, O.H.A., Al-Deeky, H.H., Akhtar, M.N.: The consequences of particle crushing in engineering properties of granular materials. Int. J. Geosci. **4**, 1055–1060 (2013)
2. Lim, M.S., Wijeyesekera, D.C., Zainorabidin, A., Bakar, I.: The effects of particle morphology (shape and sizes) characteristics on its engineering behaviour and sustainable engineering performance of sand. Int. J. Integr. Eng. **4**, 27–37 (2012)
3. Russell, A.R., Einav, I.: Energy dissipation from particulate systems undergoing a single particle crushing event. Granular Matter **15**, 299–314 (2013)
4. Feda, J.: Notes on the effect of grain crushing on the granular soil behavior. Eng. Geol. **63**, 93–99 (2002)
5. Bolton, M.D.: The strength and dilatancy of sands. Géotechnique **36**, 65–78 (1986)

6. Lee, K.L., Farhoomand, I.: Compressibility and crushing of granular soil in anisotropic triaxial compression. Can. Geotech. J. **4**, 68–86 (1967)
7. Hagerty, M.M., Hite, D.R., Ulrich, C.R., Hagerty, D.J.: One-dimensional high pressure compression of granular media. ASCE J. Geotech. Eng. **119**, 1–18 (1993)
8. Coop, M.R., Sorensen, K.K., Bodas-Freitas, T., Georgoutos, G.: Particle breakage during shearing of a carbonate sand. Géotechnique **54**, 157–163 (2004)
9. Valdes, J.R., Caban, B.: Monitoring the hydraulic conductivity of crushing sands. Geotech. Test. J. **29**, 322–329 (2006)
10. Erzin, Y., Yilmaz, I.: Case study of crushing resistance of anatolian sands at lower and higher density. Bull. Eng. Geol. Env. **67**, 71–77 (2008)
11. Lade, P.V., Yamamuro, J.A., Bopp, P.A.: Significance of particle crushing in granular materials. ASCE J. Geotech. Eng. **122**, 309–316 (1996)

Geotechnical Mapping of Seismic Risk for Sharjah City, United Arab Emirates

Maher Omar, Abdallah Shanableh, Samar Abduljalil, Khaled Hamad, Mohamed Arab, Moussa Leblouba and Ali Tahmaz

Abstract Seismic hazard and geotechnical microzonation maps of urban communities make it conceivable to describe potential seismic zones that should be considered when planning new structures or retrofitting existing ones. This study looked at a local site-specific ground response analysis, which is an important step in estimating the effects of earthquakes. The soil data from 200 boreholes up to 30 m depth were collected and analyzed using SHAKE2000 and NovoLiq in order to develop local site amplification and liquefaction potential maps for the city of Sharjah. In addition, Geographical Information System (GIS) was utilized to create amplification and liquefaction potentials maps at different areas in Sharjah. These maps show zones of high vulnerability earthquake risk used for earthquake-resistant design of structures. The city of Sharjah was divided into areas, according to the amplification factor, which ranged from 1.44 to 1.83. A high amplification factor was found near the central region of the city, while the rest of the city lies in low amplification potential and relatively low seismic risk. Finally, liquefaction risk of Sharjah estimated and expressed in terms of safety factor. The low values of the

M. Omar (✉) · A. Shanableh · S. Abduljalil · K. Hamad · M. Arab
M. Leblouba · A. Tahmaz
Department of Civil and Environmental Engineering and Research Institute
of Sciences and Engineering, University of Sharjah, Sharjah, United Arab Emirates
e-mail: momar@sharjah.ac.ae

A. Shanableh
e-mail: shanableh@sharjah.ac.ae

S. Abduljalil
e-mail: U00028467@sharjah.ac.ae

K. Hamad
e-mail: khamad@sharjah.ac.ae

M. Arab
e-mail: marab@sharjah.ac.ae

M. Leblouba
e-mail: mleblouba@sharjah.ac.ae

A. Tahmaz
e-mail: atahmaz@sharjah.ac.ae

safety factors against liquefaction were found in the north, northeastern, and southeastern portions of the city. Higher values were found in central and toward south central parts of the studied area. In these parts, the higher safety factor indicates low liquefaction potential of the soil and relatively low seismic risk.

Keywords Seismic · Risk · Microzonation · Amplification · Liquefaction GIS

1   Introduction

Seismic microzonation study is, for the most part, perceived as one of the viable procedures to assess the seismic hazard, evaluate the associated risk, which is defined as the zone with respect to ground motion attributes considering source, and site conditions [1]. Many lessons were learnt from earthquakes that repeatedly happened all over the world that have increased the awareness to public and government regarding the impacts of seismic risk on their structures.

According to [2], a preliminary microzonation study conducted in 2011 for the Abu Dhabi Island based on 245 borings out of approximately 1000 soil borings with average depth of 20 m provided and compiled for the selected area. In order to examine and assess the available geotechnical data, the selected areas within Abu Dhabi, Al Ain, and Western Region Municipalities divided into grids with dimensions of 250 m × 250 m. The locations of selected borings and the grid system are shown in Fig. 1. As it can be seen from Fig. 1, there are limited number of borings in major portion of the area, thus the reliability of microzonation maps for these sections are based on interpolation and extrapolation of the available borings. The reliability of the microzonation maps produced for Abu Dhabi, Al Ain, and Western Region Municipalities will also be dependent on the amount and quality of the available data.

In the review, microzonation concerning ground shaking intensity depended on average spectral accelerations computed between the 0.1 and 1 s, and peak spectral accelerations figured using equivalent shear wave velocities averaged at top 30 m [3]. In Fig. 2, the ground shaking intensity were zoned into three parts, where zone AGS demonstrates the ranges with low ground shaking intensity, zone BGS demonstrates the territories with low to medium ground shaking intensity, and zone CGS demonstrates the zones with high ground shaking intensity.

The susceptibility of liquefaction was calculated for each cell [4, 5]. The factors of safety were determined for each borehole comprising liquefiable sand or silt layers [4]. The liquefaction susceptibility guide map shown in Fig. 3 was created for three districts, where region AL shows very low susceptibility of liquefaction, zone BL shows regions with low to medium liquefaction susceptibility, and zone CL shows the regions with high liquefaction susceptibility. The produced map for the three areas demonstrates that in significant piece of Abu Dhabi Island, liquefaction susceptibly is low and in this manner irrelevant for Abu Dhabi Island.
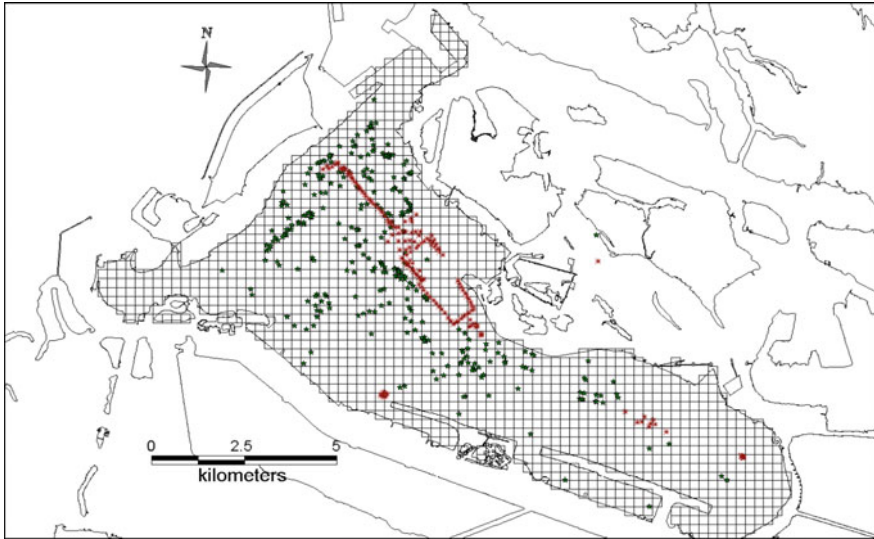
Fig. 1 Location of the borings selected as representative borings [2]
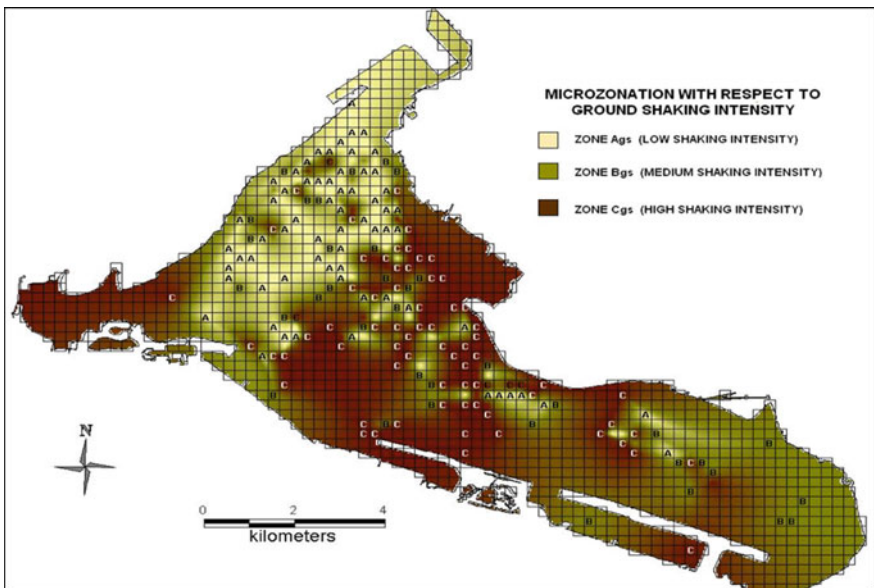
Fig. 2 Zones with respect to ground shaking intensity [2]

Comparative work was done in Dubai in 2008, as revealed by Ansal et al. [6], for which 1094 borehole information were analyzed and profiles for different soil types and shear wave velocity were created. Site response analysis was conducted
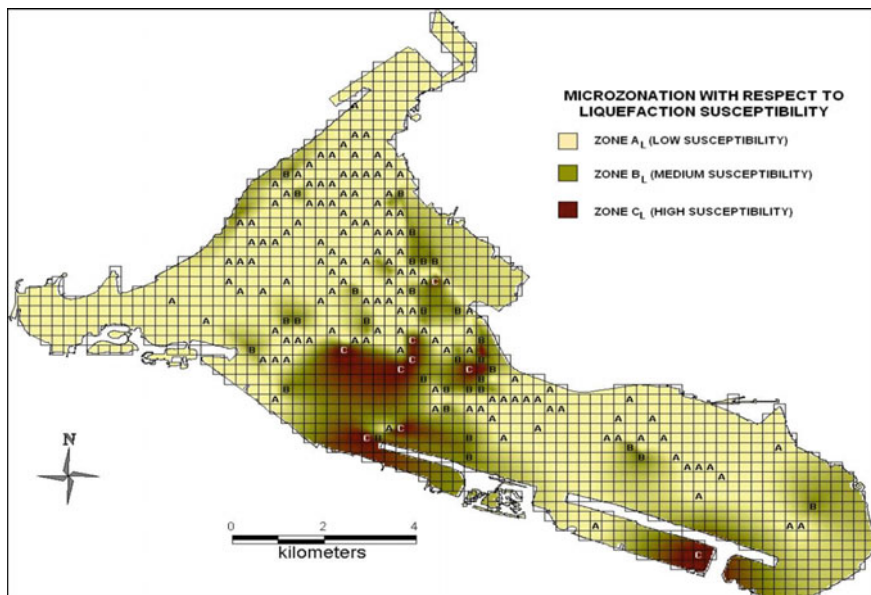
Fig. 3 Zonation with respect to liquefaction susceptibility for RT = 1000 years [2]

using PGA, scaled twelve records for the 1094 soil profiles considering two seismic hazard levels, corresponding to 2475 and 475-year return periods. A total of 25,256 site response analyses were performed and earthquake properties on the ground surface were estimated with respect to peak ground and spectral accelerations, peak ground velocity, and site amplification.

The selected area within the Dubai City was divided into 5110 cells with dimensions of 500 m × 500 m. Since some of the boreholes were shallow, 1094 borings out of 6101 with total depth D $\geq$ 15 m were selected as representative soil profiles. The locations of selected borings and the grid system are shown in Fig. 4. The microzonation area for Dubai City was limited based on the availability of data. There are no borings in major portion of the area, therefore, it would be more suitable to establish the microzonation maps based on 1094 borings for the most part situated in the north of Dubai city using the outer boundary.

The zonation regarding the intensity of ground shaking is produced with respect to three areas, where zone AGS shows the areas with very low intensity, zone BGS shows areas with low to medium intensity, while zone CGS shows the areas with high intensity as can be seen in Fig. 5.

The susceptibility of liquefaction was calculated for each cell [4, 7]. The factors of safety were calculated for each representative borehole containing liquefiable sand or silt layers [5]. The liquefaction susceptibility guide map shown in Fig. 6 was created for three districts, where region AL shows very low susceptibility of liquefaction, zone BL highlights regions with low to medium susceptibility of
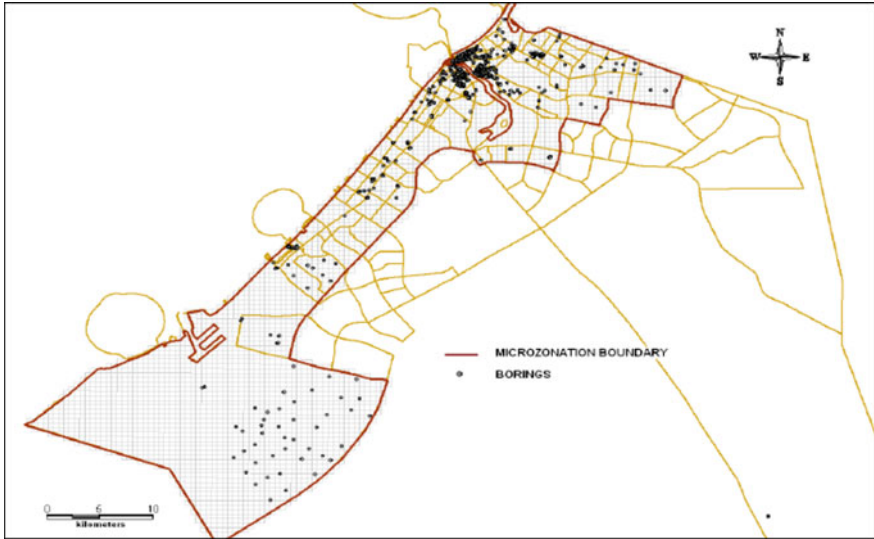
Fig. 4 The location of borings selected as representative borings [6]
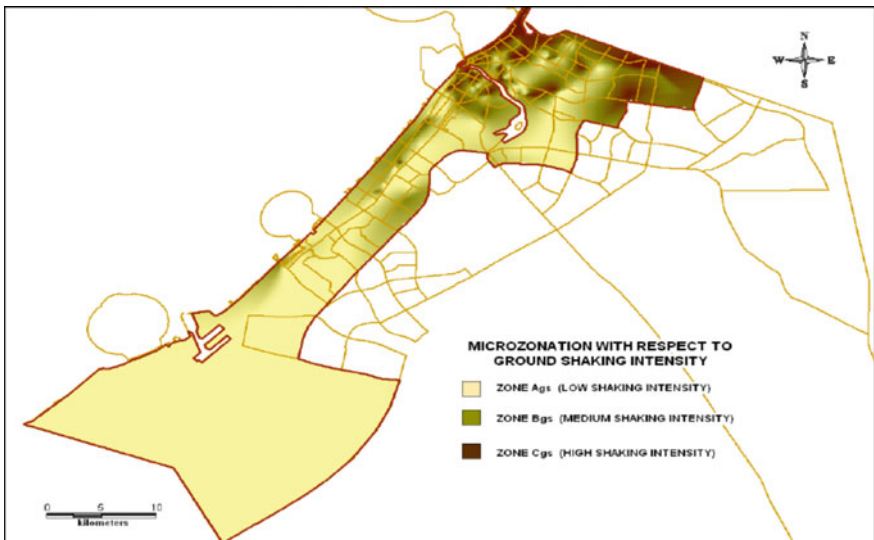
Fig. 5 Zonation with respect to ground shaking based on spectral acceleration [6]

liquefaction, and zone CL highlights the areas with high susceptibility of lique-
faction. The map produced for three areas demonstrates that in significant piece of
Abu Dhabi Island, liquefaction susceptibly is low and in this manner irrelevant for
Dubai.
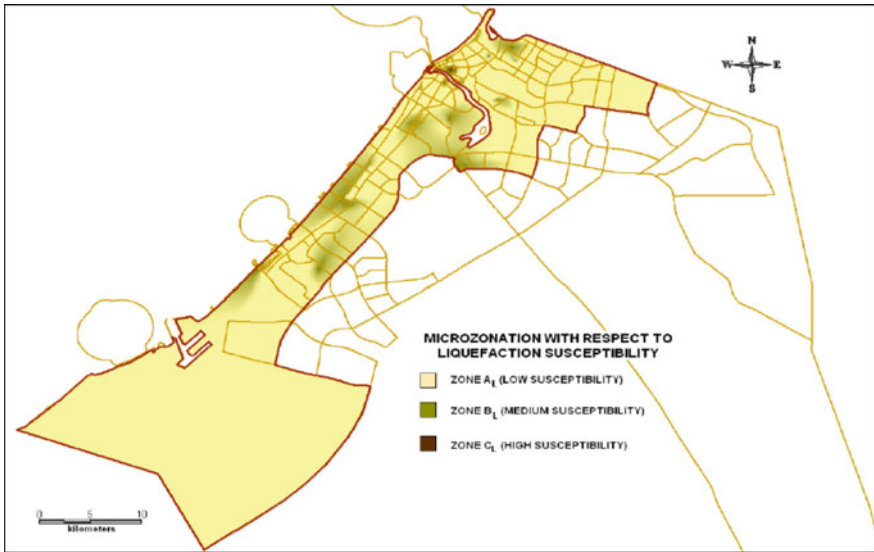
Fig. 6 Zonation with respect to liquefaction susceptibility [6]

In 2011, [8] performed analysis on the influence of local soil conditions on ground response during earthquakes at different areas in the Emirate of Sharjah, UAE estimating amplification potential and prepared a map indicating zones of high vulnerability to seismic hazard as shown in Fig. 7.
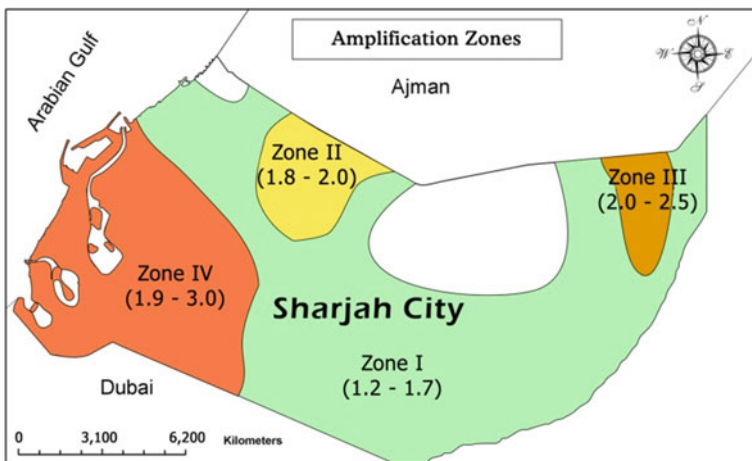
Fig. 7 Site amplification factor zonation map for Sharjah [8]

2 Geology and Seismicity of the Area

UAE has a mountain belt along the eastern coast of the Gulf of Oman; about one fifth of its land is desert. The western part of the UAE is facing the subduction boundary across the Arabian Gulf, opposite the Strait of Hormuz, one of the most seismically active zones in the world. The City of Sharjah faces the Zagros folded belt, one of the most active faults in the world. The main city lies on the Arabian Gulf and other parts of the Emirate lie on the Gulf of Oman. It is located in the geological window between altitudes (25° 25′N and 25° 14′N) and (55° 45′E and 55° 20′E).

It has been generally accepted that the UAE has little or no earthquake activity. However, the country is not as safe from earthquake disasters as often assumed. In March 2002, and according to Jamal and A-Homoud [9], an earthquake magnitude of five shocked al-Masafi area, northeast of UAE with its epicenter at 16 km depth. The strong motions recorded on December 10th, 2002 and April 25th, 2003 represents sufficient evidence of the existence of considerable seismic activity in the UAE.

3 Data Collection

Soil borehole logs from over 200 sites covering most parts of Emirates of Sharjah were utilized in this study. Boreholes selected were those with overburden thickness varying from 1 to 30 m representing typical geological features of Sharjah. The exact GPS locations for all boreholes obtained from Sharjah Directorate of Town Planning and Surveying are as shown in Fig. 8.

3.1 Shear Wave Velocity

Due to lack of availability of actually published shear wave velocities for the study area, Lyisan [10] used the following empirical model:

$$V_s = 51.5N^{0.516}, \tag{1}$$

where

N uncorrected SPT
V_s shear wave velocity, m/s
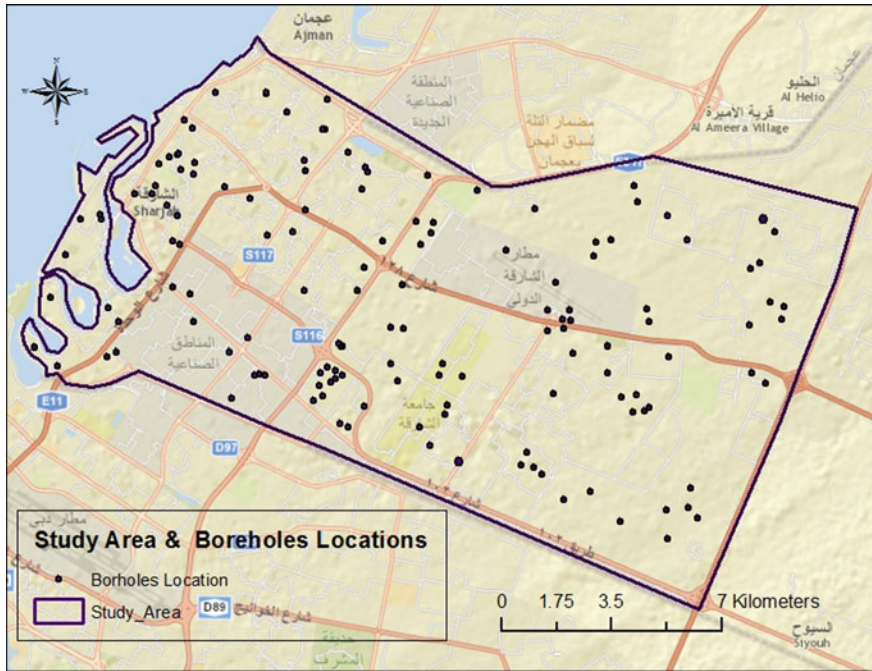
Fig. 8 Boreholes locations in Sharjah City

3.2 Earthquake Selection Procedure at Bedrock Level

Due to the lack of recorded earthquakes in the city, a set of artificial ground motions were generated to match a target response spectrum as shown in Fig. 9, where the minor Masafi earthquake in 2002 with (PGA = 0.03 g) was used as an envelope to the frequency response shown in Fig. 10. Seismosoft, 2016 program was used to perform artificial accelerogram generation following the work of [11].

The proposed analysis and response spectrum construction follows the same technique adopted by Bartlett et al. [12] and are consistent with site-specific ground response analyses and spectra outlined by MCEER/ATC-49 for highway bridge design, but the methods are general enough so that can also be applied to building design [12]. The following steps were followed [13]:

1. Generation of seven earthquakes
2. Performing spectral matching of candidate earthquake records to the target surface level spectrum as shown in Fig. 11
3. Deconvolution of the seven earthquakes using generic boreholes, Figs. 12 and 13, deconvolution of the generated earthquakes through generic boreholes representing different locations of the city to get the bedrock motion
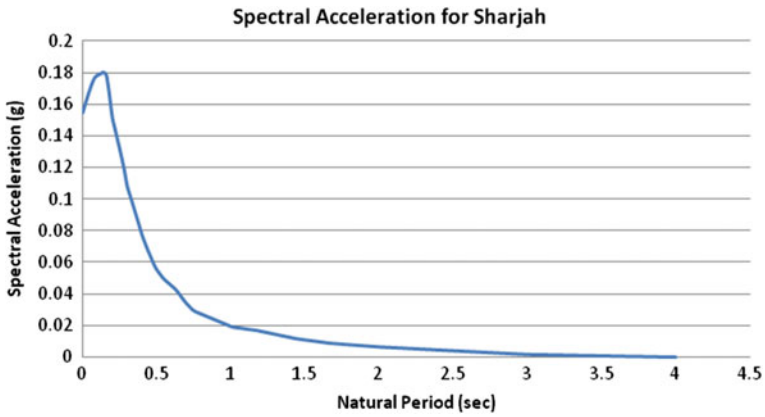
Fig. 9 Spectral acceleration for ($M = 5$) Sharjah for 50 years' exposure time and 0.1 probability of exceedance [22]
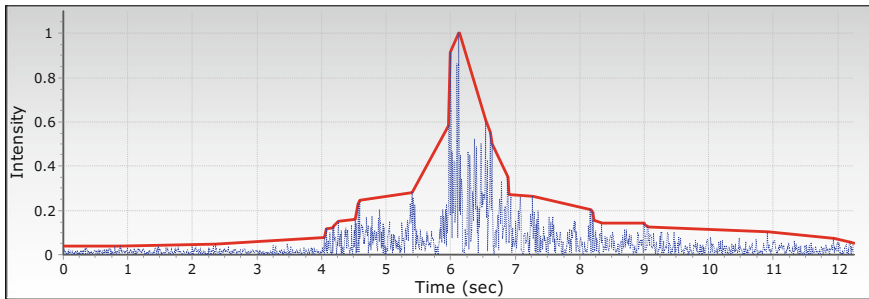
Fig. 10 Masafi, 2002 earthquake envelope
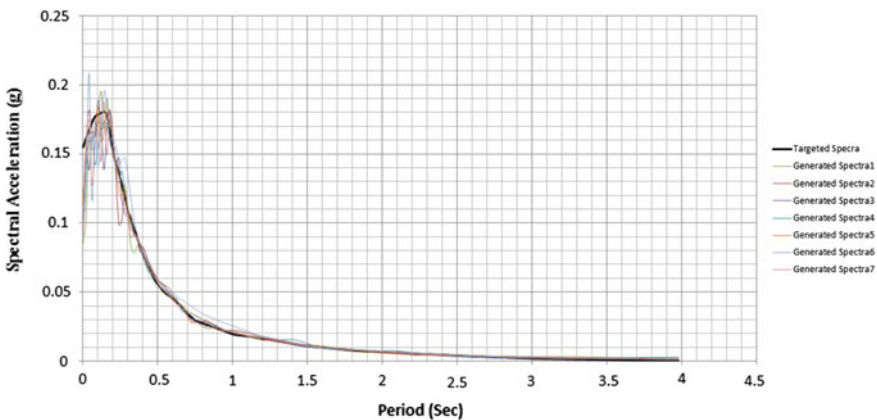
Fig. 11 Performing spectral matching of candidate earthquake records to the target rock spectrum
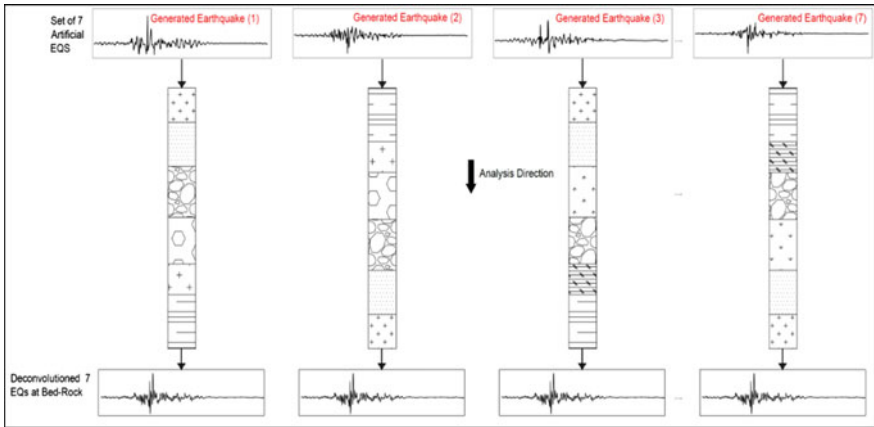
Fig. 12 Deconvolution of the generated earthquakes through generic boreholes
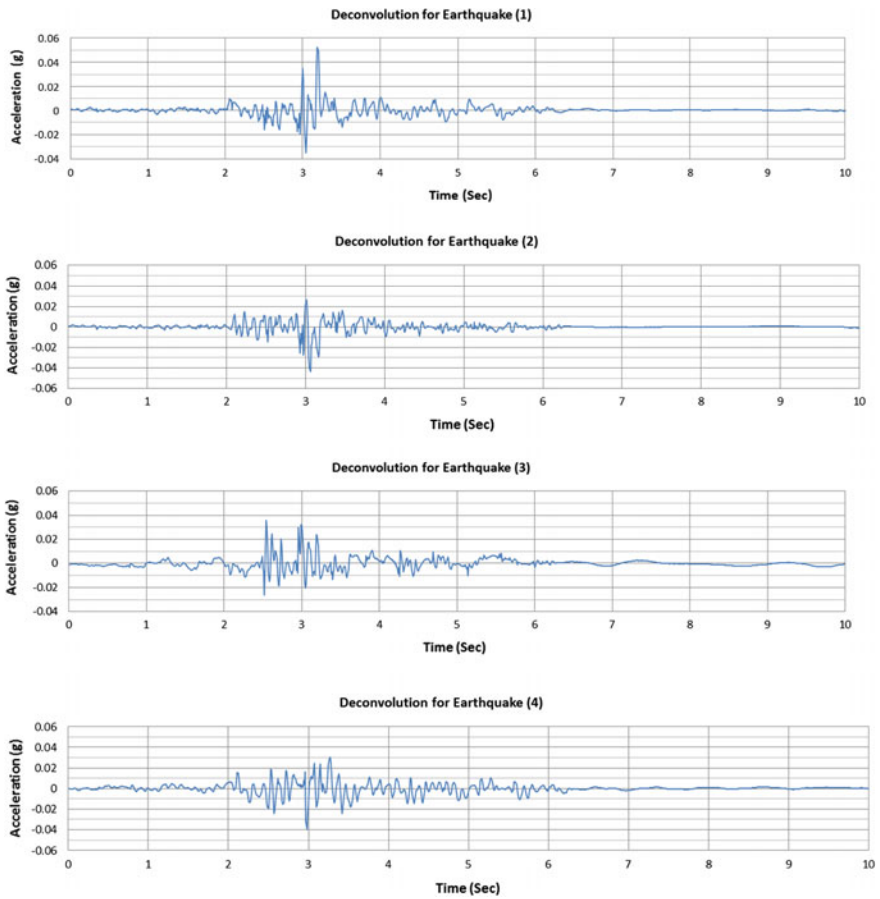
Fig. 13 Time history for deconvolution earthquakes
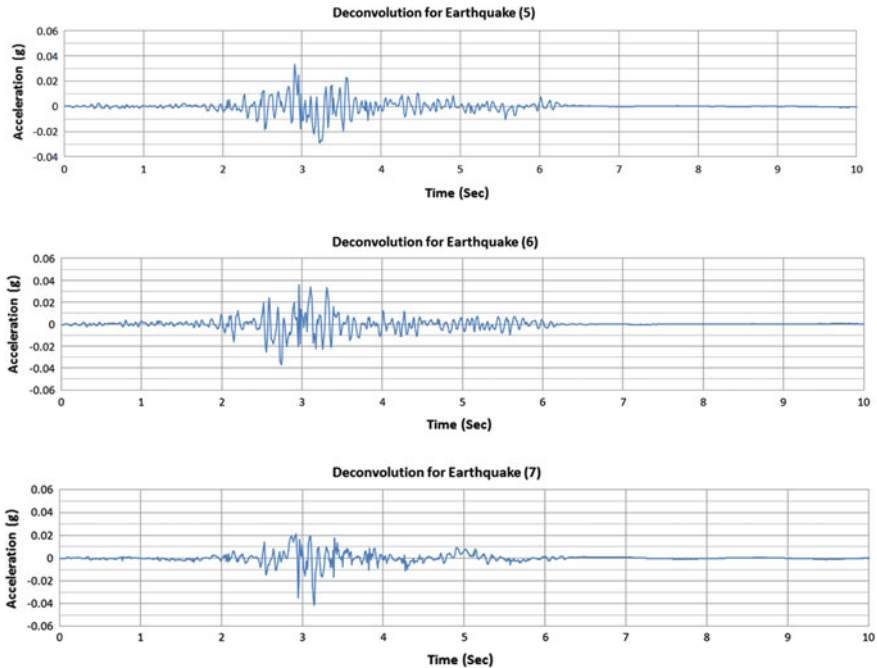
Fig. 13 (continued)

4 Results and Discussions

The estimation of soil amplification in this work is based on shear wave velocities, site periods, and amplification factors. A $V_{s(30)}$ map, site period and amplification factor maps were produced for the upper 30 m depth, in addition to peak ground acceleration at bedrock and surface maps. All maps were done depending on the average shear wave velocity to a depth 30 m.

4.1 Peak Ground Acceleration at Surface

PGA is the largest estimation of horizontal acceleration obtained from an accelerogram of that component. It is the most normally utilized measure of amplitude of a particular ground motion because the dynamic forces induced in structures closely related to the parameter PGA Value in this study is 0.15 g as discussed previously.

The PGA value at bedrock level amplified based on the soil profile at various locations. The acceleration-time histories at various depths obtained as output from SHAKE analysis. The peak acceleration value at the surface obtained for each
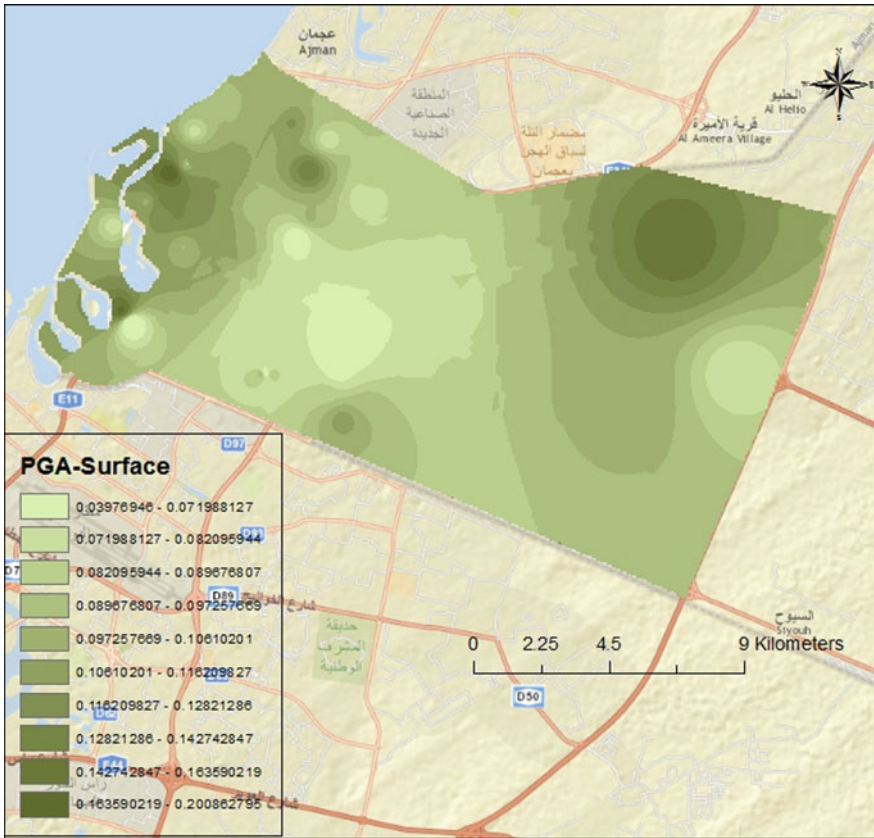
Fig. 14 PGA at surface

location plotted to obtain the Peak Ground Acceleration (PGA) map at ground surface as shown in Fig. 14. This PGA value at surface varies from 0.039 to 0.2 g and irregularly distributed due to variation in the soil profile at various locations.

4.2 The Shear Velocity Distribution

The elastic properties of materials located near the surface and their effect on the spread of seismic waves are critical in earthquake engineering. The increasing amplitude in soft-layered soils is one of the most influential parameters responsible for the amplification of an earthquake motion. For soil amplification and site response studies, the 30 m average shear wave is considered sufficient [14] and $V_s(30)$ can be obtained by the following relationship:

$$V_{s(30)} = \frac{30}{\sum_{i=1}^{N} \frac{d_i}{v_i}}, \tag{2}$$

where d_i and v_i represent ith layer's thickness and velocity.

Shear waves velocity distribution down to a depth of 30 m shown in Fig. 15. The determined average shear wave velocities categorized with respect to the NEHRP site classes and a map has been generated using ArcMap. Based on this, the study area is considered to consist of one class for seismic local site effects, which is site class C (180 m/s $< V_{s(30)} < 360$ m/s) that refers to Table 1 [15]. The map in Fig. 15 shows the average shear wave velocity distribution to a depth of 30 m.
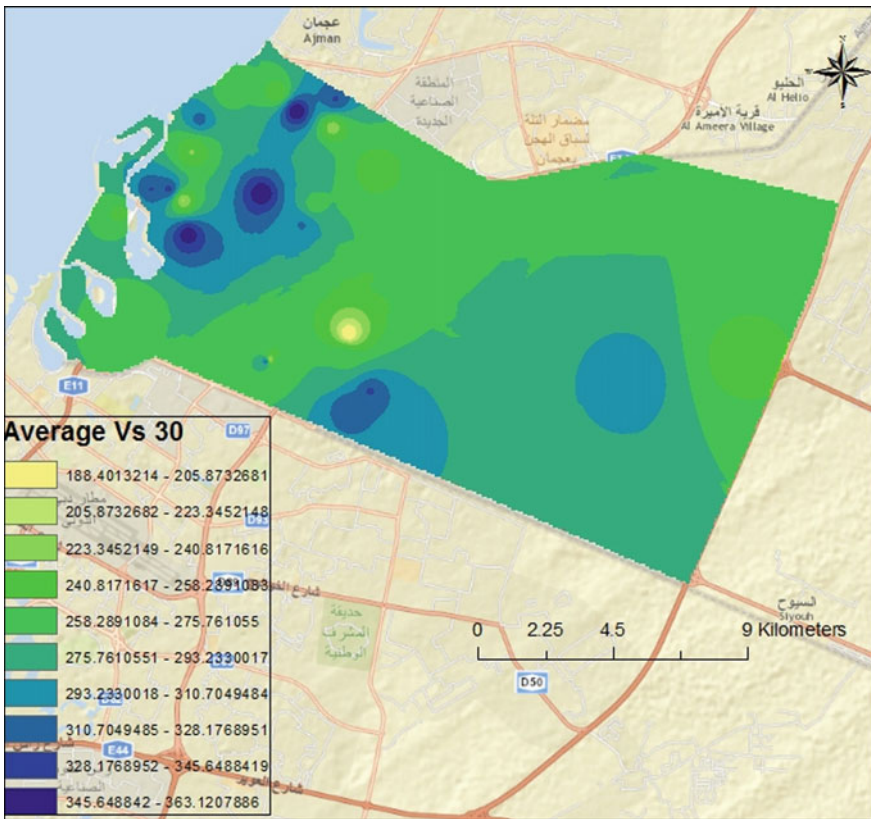
Fig. 15 $V_{s(30)}$ distribution map

Table 1 Site classes [15]

Site class	V_s in upper 30 m
A	>750/s
B	360–750/s
C	180–360/s

4.3 Amplification Factor

Amplification factor is a parameter that specifically identified with the seismic risk of the region. Initially, maximum factors of amplification obtained within the acceleration, velocity, and displacement controlled regions, which presented, generally, in such format in seismic design standards. The outcomes demonstrated that there was no genuine pattern with depth or shear wave velocity of the site when the amplification factors were obtained in such a manner. This is because the magnitude of the amplification factor highly depends on the shear wave velocity, while the location of the amplification is highly dependent on the site's period.

The amplification factor for specific period range is a function of $V_{s(30)}$. For periods greater than 0.5 s, the amplification factors are not very sensitive to period but are much greater than the short period amplification factor for the period less than 0.5 s. Two sets were used to calculate the amplification factors; one set for short periods ($T_s < 0.5$ s) and another set for long periods ($T_s > 0.5$) [16]. In the present study, the range of site period belongs to the short periods ($T_s < 0.5$). The period-dependent amplification factor was calculated using the following formula:

$$\text{AF} = \left(\frac{997}{V_{s(30)} \, \text{m/s}} \right)^{0.36},\tag{3}$$

where V is the average shear wave velocity to 30 m depth measured in m/s.

Based on this relation, the amplification factors for the study are shown in Table 2.

As it is seen in the graph below, there is inversely proportional relation between amplification factors and shear wave velocity values. That means, as the shear wave velocity increases the value of amplification factor also decreases and vice versa Fig. 16.

The calculated amplification factor in this study ranges from 1.44 to 1.83. The quantitative amplification factors obtained and these results were used to prepare the amplification factor map using ArcMap. The value of amplification factor for the study area is larger, where the value of $V_{s(30)}$ is low.

The site amplification factor map based on equations for the area is presented in Fig. 17. This map indicates that the north, northwestern, south, and southeastern (yellowish green to light green color) are characterized by low amplification factor values ranging between 1.44 and 1. The central part shown in dark green indicates medium amplification factor values; the range of this value is between 1.85 and 1.61. The third category is the light to dark blue colored part exposed in the central part of the area, where the amplification factor is high or more than 1.63.

Figure 18 shows amplification factor map for the area from SHAKE2000, slightly different in the amplification factor between equations and software, following Table 3 shows the results.

Table 2 Amplification factor values for each $V_{s(30)}$

$V_{s(30)}$ (m/s)	Amplification factor	$V_{s(30)}$ (m/s)	Amplification factor
363.6	1.44	267.3	1.61
359.2	1.44	265.1	1.61
357.2	1.45	265.1	1.61
333.0	1.48	263.5	1.61
332.8	1.48	260.1	1.62
330.4	1.49	258.0	1.63
329.9	1.49	253.6	1.64
329.3	1.49	251.0	1.64
323.9	1.50	250.8	1.64
317.1	1.51	242.7	1.66
315.1	1.51	242.6	1.66
312.1	1.52	230.6	1.69
304.6	1.53	221.7	1.72
287.5	1.56	215.3	1.74
286.3	1.57	212.0	1.75
286.1	1.57	206.1	1.76
286.0	1.57	194.0	1.80
274.4	1.59	188.2	1.82
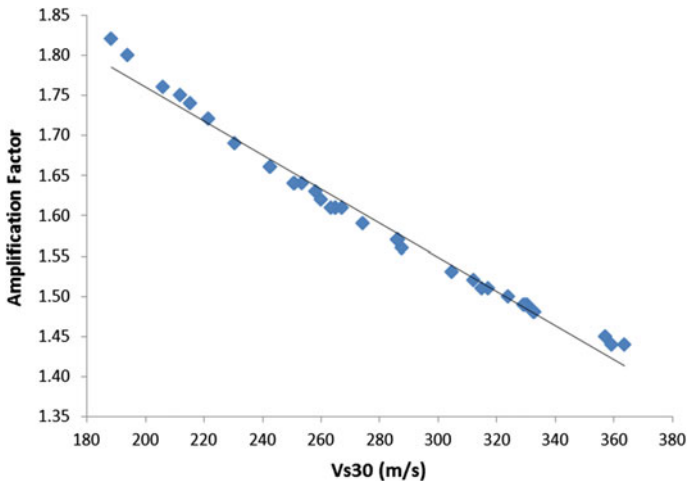
Fig. 16 $V_{s(30)}$ versus amplification factor
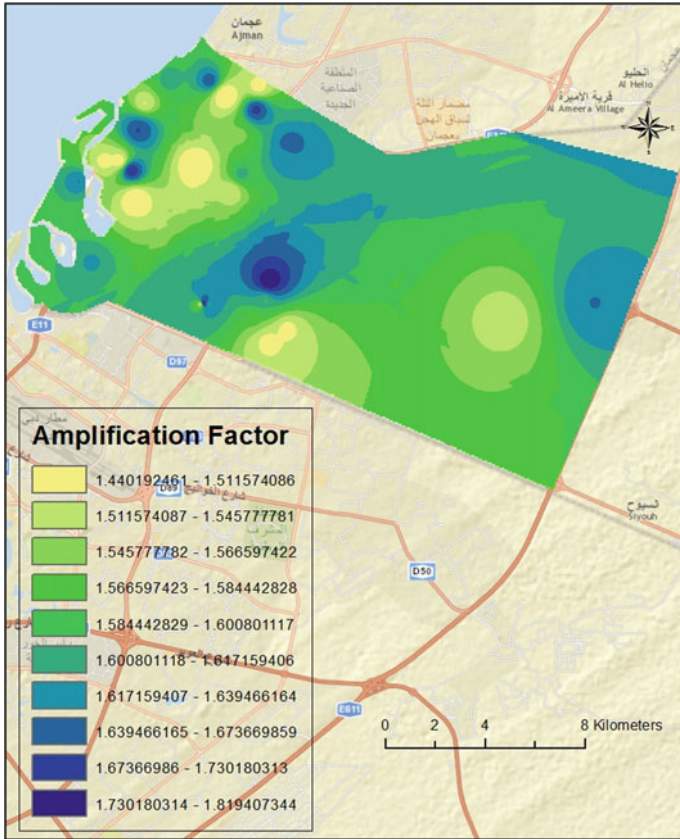
Fig. 17 Amplification factor map based on equations

4.4 Variability in Amplification Factors

Amplification factor varies as the value of $V_{s(30)}$ varies. Figure 19 plots amplification factor versus period for each of the $V_{s(30)}$ values. The factors of amplification for a given $V_{s(30)}$ are highly scattered. The amount of scatter varies with $V_{s(30)}$ and period.

4.5 Soil Liquefaction

It generally acknowledged that only recent sediments or fills of saturated, cohesionless soils at shallow depths would liquefy due to earthquake. The conditions required for liquefaction to occur are [17]:
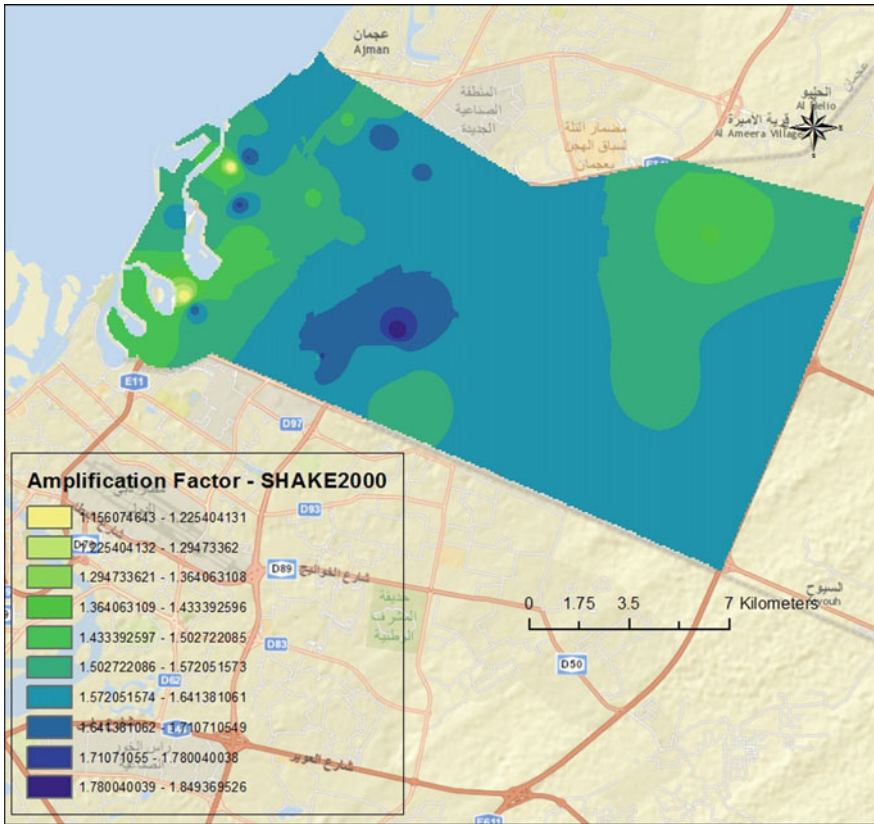
Fig. 18 Amplification factor map—SHAKE2000

a. the soil deposit is sandy or silty soil;
b. the soil is saturated or nearly saturated (usually below groundwater table);
c. the soil is loose or medium compact;
d. the soil is subjected to seismic stress (such as from earthquake, blast, etc.).

Earthquakes magnitude scaling factor (MSF) was taken 0.73 corresponding to highest earthquake magnitude M_w = 8.5, according to studies done for Dubai and Abu Dhabi [2, 6]. The safety factors figured along the entire profundity of the borehole for all liquefiable soil layers considering the accessible SPT-N blow count numbers utilizing the surface peak ground accelerations determined using site response analysis. For each borehole, the liquefaction potential was determined using the variation of the safety factors with depth. The factor of safety against liquefaction was grouped into four groups as shown in Table 4.

Microzonation maps in terms of the liquefaction for Sharjah city developed based on different method developed by researchers.

Table 3 Amplification factor equation versus SHAKE2000

AF (equation)	AF (SHAKE2000)	Difference	AF (equation)	AF (SHAKE2000)	Difference
1.57	1.17	0.40	1.49	1.57	−0.08
1.61	1.15	0.46	1.19	1.59	−0.40
1.69	1.5	0.19	1.82	1.63	0.19
1.52	1.43	0.09	1.41	1.65	−0.24
1.14	1	0.14	1.64	1.62	0.02
1.51	1.48	0.03	1.57	1.61	−0.04
1.49	1.44	0.05	1.56	1.68	−0.12
1.80	1.5	0.30	1.64	1.63	0.01
1.74	1.5	0.24	1.75	1.64	0.11
1.44	1.52	−0.08	1.50	1.66	−0.16
1.49	1.53	−0.04	1.72	1.6	0.12
1.45	1.51	−0.06	1.48	1.63	−0.15
1.48	1.52	−0.04	1.63	1.65	−0.02
1.51	1.56	−0.05	1.61	1.71	−0.10
1.61	1.55	0.06	1.44	1.73	−0.29
1.41	1.55	−0.14	1.66	1.75	−0.09
1.57	1.56	0.01	1.59	1.8	−0.21
1.76	1.6	0.16	1.66	1.81	−0.15
1.64	1.59	0.05	1.62	1.83	−0.21
1.53	1.58	−0.05	1.61	1.85	−0.24
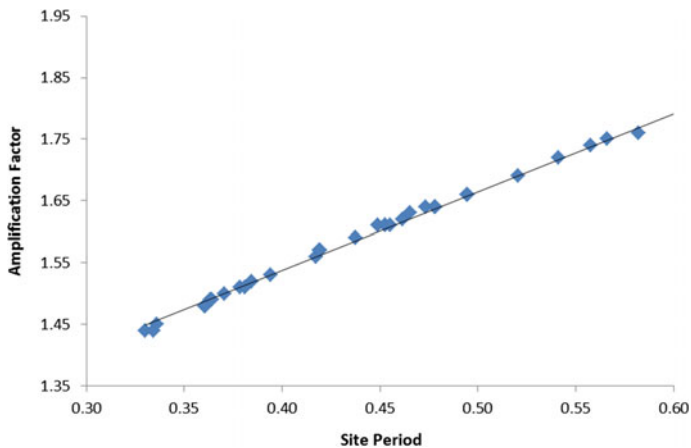
Fig. 19 Site period versus amplification factor graph

Table 4 Factor of safety against liquefaction groups [23]

Group	Factor of safety range	Severity index
1	<1	High
2	1–2	Moderate
2	2–3	Low
4	>3	Nil

Method Developed by Seed et al. [18]. Following Fig. 20 shows Liquefaction Safety Factor values based on Seed et al. for Sharjah City. The calculated safety factor following this method ranges between 0.56 and 6.42; refer to Table 4, most parts of the area is in the moderate range which is shown in orange color in the map, some parts of the area have nil liquefaction index displayed by yellow color, high severity index displayed by red color which quit few areas.

Method Developed by NCEER [19]. Figure 21 shows map of Safety factor against liquefaction based on NCEER [19]. This map indicates the north, northwest, and northeast (reddish orange color) characterized moderate severity index and low value of safety factor between 1 and 2. The south part of the area shown by yellow
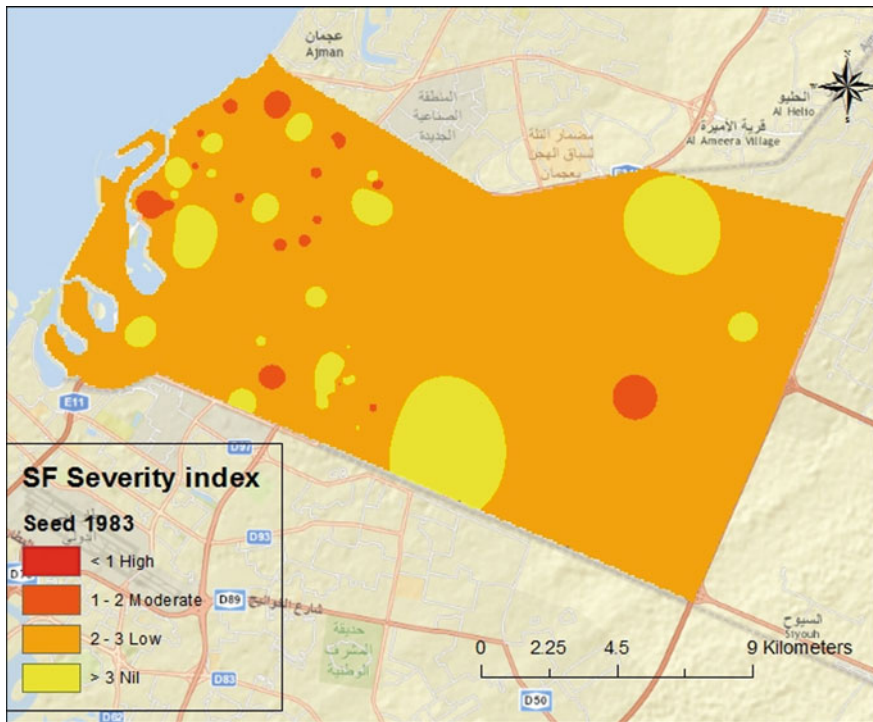
Fig. 20 Safety factor based on [18]
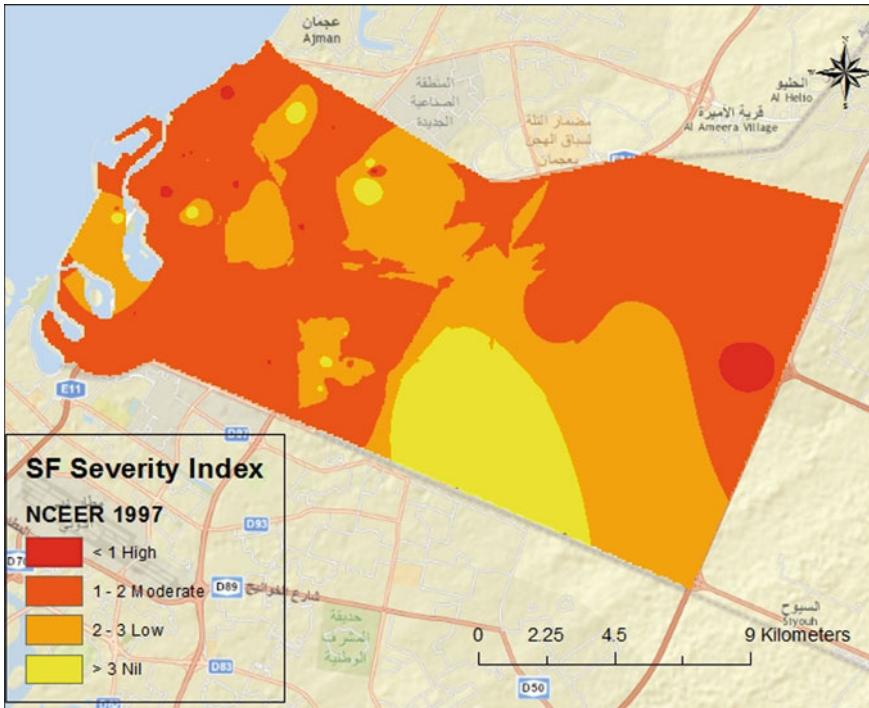
Fig. 21 Safety factor based on [19]

color indicates nil severity index and safety factor more than 3, some parts covered by orange color have low severity index and safety factor between 2 and 3.

Method Developed by Boulanger and Idriss [20]. Figure 22 indicates map based on Boulanger and Idriss [20] the south parts (yellow color) characterized nil severity index and high values of safety factor more than 3. The other parts of the area presented by reddish orange color indicates high to moderate severity index and maximum safety factor value of 2.

Vancouver [21]. Safety factor severity index map for the area is presented in Fig. 23. This map indicates that the north, northeastern, southeastern, and some parts of east (reddish orange color) are characterized by moderate severity index values of safety factor vary between 1 and 2. The central part shown in orange indicates low severity index and safety factor values between 2 and 3. The third category is the yellow colored part exposed in the south part of the area where the site safety factor against liquefaction is more than 3 which showed zero severity index.
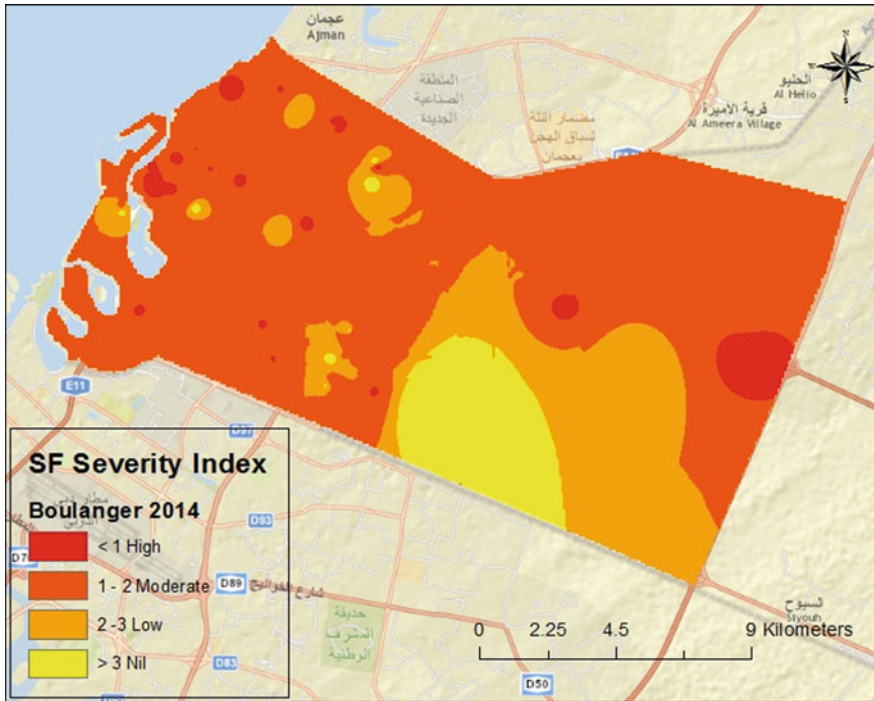
Fig. 22 Safety factor based on [20]

Combination of four methods. In this map, shown in Fig. 24, the previous four methods were used to prepare a map based on average of the four methods.

This map indicates that the north, northeastern, and southeastern (reddish-orange color) are characterized by moderate severity index values of safety factor which varies between 1 and 2. The central part shown in orange indicates low severity index and safety factor values between 2 and 3. The yellow colored part exposed in the south part of the area, where the site safety factor against liquefaction is more than 3, shows nil severity indexes. The following Table 5 shows a sample of soil liquefaction values of the previous methods.
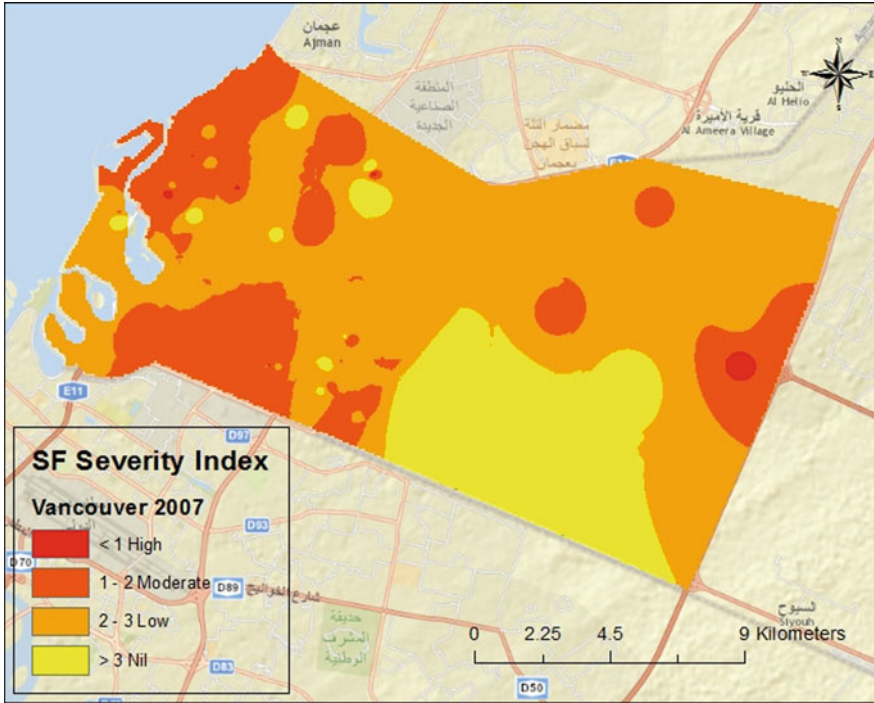
Fig. 23 Safety factor based on [21]
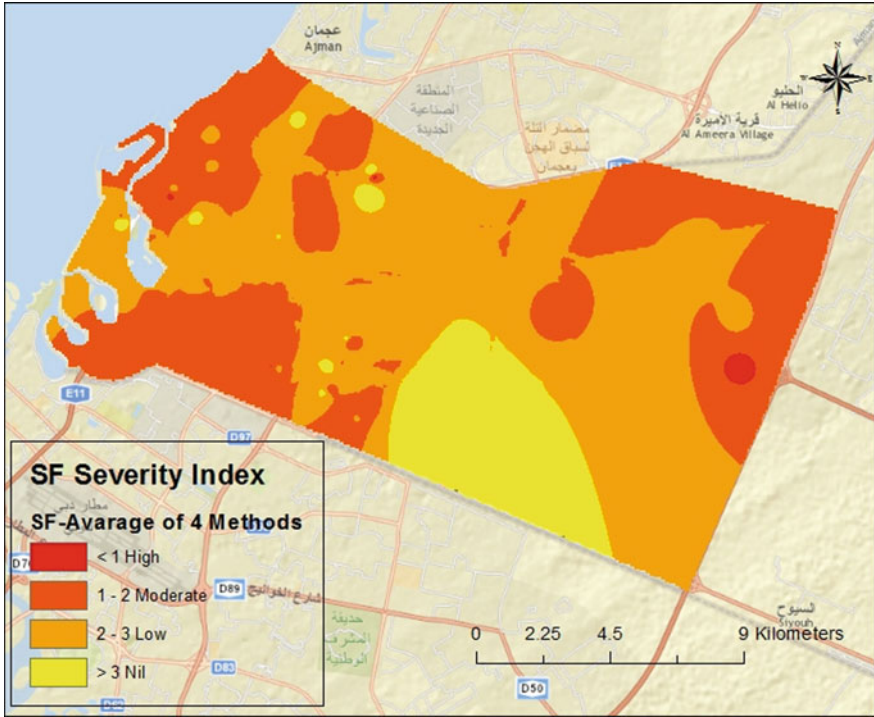
Fig. 24 Safety factor based on average of four methods

Table 5 Sample of soil liquefaction values of previous methods

BH_NO	NCEER workshop [19]	Boulanger and Idriss [20]	Vancouver task force [21]	Seed et al. [18]	Average
7	5.88	5.37	6.1	4.8	5.54
14	5.68	5.67	5.68	5.68	5.68
15	2.84	2.83	2.84	2.84	2.84
16	0.47	0.62	0.47	1.03	0.65
23	0.46	0.61	0.46	0.93	0.61
24	0.41	0.58	0.41	0.94	0.59
31	5.65	5.61	5.65	5.65	5.64
32	5.62	5.6	5.62	5.62	5.62
34	5.57	5.53	5.57	5.57	5.56
41	5.89	5.28	5.89	4.53	5.4
42	5.22	5.46	5.22	5.1	5.25
43	5.07	3.87	5.07	3.63	4.41
52	0.96	0.97	0.96	1.46	1.09
53	0.88	0.92	0.88	1.38	1.01
64	0.42	0.6	0.42	0.94	0.59
65	0.26	0.42	0.26	0.81	0.44
71	2.17	2.28	2.26	3.16	2.47
72	5.68	5.63	5.86	5.86	5.76
74	0.6	0.74	0.6	1.16	0.78
76	0.6	0.73	0.6	1.15	0.77
82	1.46	1.48	1.46	2.08	1.62
83	1.91	2.12	1.91	2.67	2.15
93	1.87	2.04	1.87	2.65	2.11
112	0.38	0.54	0.38	0.98	0.57
115	1.66	1.74	1.66	2.35	1.85

5 Conclusion

Soil amplification of the site expressed in terms of amplification factor. The calculated value of amplification factor for the site ranges from 1.44 to 1.83. The higher values of the amplification factors are located in the central portions and in these parts, the higher amplification factor shows high amplification potential and high seismic hazard. Lower values of amplification factor are found in all other parts of the study area. In these sites, the lower amplification factor indicates low amplification potential of the soil and relatively low seismic hazard. The damage due to seismic hazard is much higher on the unconsolidated soils than on solid rocks.

Soil liquefaction studies were carried out in Sharjah City. Soil liquefaction of the site was expressed in terms of safety factor. The calculated value of safety factor for

the site was divided into four categories, safety factor less than 1 indicates high severity index, SF value between 1 and 2 indicates moderate severity index, SF value between 2 and 3 indicates low severity index, and more than 3 indicates nil severity index. The low values of the safety factors against liquefaction are located in the north, northeastern, and southeastern portions and in these parts, the lower safety factor shows high liquefaction potential and high seismic hazard. Higher values of safety factor found in central and toward south central parts of the study area. In these sites, the higher safety factor indicates low liquefaction potential of the soil and relatively low seismic hazard. The damage due to seismic hazard is much higher on the unconsolidated soils than on solid rocks.

References

1. TC4-ISSMGE: Manual for Zonation on Seismic Geotechnical Hazard. Revised edition, Technical Committee For Earthquake Geotechnical Engineering (TC4) of International Society of Soil Mechanics and Geotechnical Engineering (ISSMGE), p. 209 (1999)
2. Assessment of Seismic Hazard and Risk in Emirate of Abu Dhabi Municipality (2011)
3. Borcherdt, R.D.: Estimates of site dependent response spectra for design (methodology and justification. Earthq. Spectra **10**(4), 617–654 (1994)
4. Youd, T.L., Idriss, I.M., Andrus, R.D., Arango, I., Castro, G., Christian, J.T., Dobry, R., Finn, W.D.L., Harder, Jr., L.F., Hynes, M.E., Ishihara, K., Koester, J.P., Liao, S.S.C., Marcuson, III., W.F., Martin, G.R., Mitchell, J.K., Moriwaki, Y., Power, M.S., Robertson, P.K., Seed, R. B., Stokoe, II., K.H.: Liquefaction resistance of soils: summary report from the 1996 NCEER and 1998 NCEER/NSF workshops on evaluation of liquefaction resistance of soils. ASCE J. Geotech. Geoenviron. (2001)
5. Idriss, I.M., Sun, J.I.: Shake91, a computer program for conducting equivalent linear seismic response analysis of horizontally layered soil deposits. Modified based on the original SHAKE program Published in December 1972 by Schnabel, Lysmer and Seed (1992)
6. Ansal, A., Kurtulus, A., Tönük, G.: Assessment of Seismic Hazard and Risk in Dubai. Department of Earthquake Engineering, University Istanbul, Turkey, UAE (2008)
7. Iwasaki, T., Tokida, K., Tatsuoka, F., Watanabe, S., Yasuda, S., Sato, H.: Microzonation of soil liquefaction potential using simplified methods. In: Proceedings of the 3rd International Conference on Microzonation, Seattle, vol. 3, pp. 1319–1330 (1982)
8. Omar, M., Shanableh, A., Balwan, M., Fattah, M.Y., Hamad, K.: Influence of local soil conditions on ground response—site amplification Sharjah, United Arab Emirates. Int. J. Mod. Eng. (IJME) **13**(2), 34–40 (2013) (ISSN: 2157-8052)
9. Jamal, A., A-Homoud, A.S.: Seismic hazard assessment of United Arab Emirates and its surroundings. J. Earthq. Eng. **8**(6), 817–837 (2004) (Imperial College Press)
10. Lyisan, R.: Correlations between Shear wave velocity and in-situ penetration test results. Teknik Dergi J. **2**(2), 1187–1199 (1996)
11. Halldorsson, B., Papageorgiou, A.S.: Calibration of the specific barrier model to earthquakes of different tectonic regions. Bull. Seism. Soc. Am. **95**, 1276–1300 (2005)
12. Bartlett, S.F., Ostadan, F., Abghari, A., Farnsworth, C.: Development of design spectra for deep and soft soil sites. www.civil.utah.edu/~bartlett/CVEEN6330/spectra.pdf
13. Baroud, M.: One Dimentional Dynamic Nonlinear Site Response Analysis. Sharjah City, United Arab (Case Study) (2016)
14. Kanli, A.I., Tildy, P., Prónay, Z., Pınar, A., Hermann, L.: VS30 mapping and soil classification for seismic site effect evaluation in Dinar region, SW Turkey. Geophys. J. Int. **165**(1), 223–235 (2006)

15. Boore, D.M., Joyner, W.B., Fumal, T.E.: Estimation of response spectra and peak accelerations from western North American earthquakes: An interim report (1993)
16. Ishihara, K.: Perspectives on earthquake geotechnical engineering. In: Geotechnical, Geological and Earthquake Engineering, 45 pp (2015)
17. Xiao, M.: Geotechnical Engineering Design. Wiley, United Kingdom (2015)
18. Seed, H.B., Idriss, I.M., Arango, I.: Evaluation of liquefaction potential using field performance data. J. Geotech. Eng. ASCE **109**(3), 458–482 (1983)
19. Youd, T.L., Idriss, I.M.: Proceedings of the NCEER Workshop on Evaluation of Liquefaction Resistance of Soils. Technical Report No. NCEER-97-0022, 31 Dec 1997
20. Boulanger, R.W., Idriss, I.M.: Evaluating the Potential for Liquefaction or Cyclic Failure of Silts and Clays. Report No. UCD/CGM-04/01, Center for Geotechnical Modeling, Department of Civil and Environmental Engineering, University of California, Davis, Calif (2004)
21. Vancouver Task Force Report: Task Force Report, Geotechnical Design Guidelines For Buildings on Liquefiable Sites in Accordance with NBC 2005 for Greater Vancouver Region, 8 May 2007
22. Malkawi, A.I.H., Barakat, S., Shanableh, A., Al Bdour, W., Omar, M., Altoubat, S.: Seismic Hazard Assessment and Mitigation of Earthquake Risk in the United Arab Emirates. Published Jointly by Jordan University of Science and Technology and the Deanship of Research and Higher Studies, University of Sharjah, United Arab Emirates (2007)
23. Sitharam, T.G., Anbazhagan, P., et al.: Seismic Hazarad Studies Using Geotechnical Borehole Data and GIS, pp. 23–24 (2005)

Sustainable Design of Compacted Laterite Soil Liner

Yamusa Bello Yamusa, Kamarudin Ahmad and Norhan Abd Rahman

Abstract Laterite soil, as one of the major groups of tropical residual soils, was investigated in application for engineered sanitary landfill liner. The laterite soil was used as a stand-alone material without any additives and subjected to different gradation to check its geotechnical potentiality as a sustainable material for liner. Specimens were prepared at different moulding water contents, i.e. optimum moisture content (OMC), dry of OMC and wet of OMC. Tests were carried out on natural soil 30, 40 and 50% fine content by dry weight of soil sample. The results showed that laterite soils should contain at least a minimum of 50% fine gradation to be used as liner. The outcome of this research is expected to serve as a sustainable guide to geotechnical/geo-environmental engineers in using laterite soil as a material in the construction of hydraulic barriers used for engineered sanitary landfill system in tropical countries of the world.

Keywords Sustainability · Gradation of laterite soil · Landfill liner

1 Introduction

Municipal Solid Waste (MSW) in landfills are associated with many potential environmental risks. These risks are often long-term, which include uncontrolled migration of landfill gas and leachate, generation of noise, visual nuisances, health hazards, landfill settlement, unpleasant odour, vegetation damage, surface and groundwater pollution, landfill fire and global warming [1, 2]. MSW in an unengineered landfill facilities contribute the principal sources of leachates in the

Y. B. Yamusa · K. Ahmad · N. A. Rahman
Faculty of Civil Enginering, Universiti Teknologi Malaysia,
81310 Skudai, Johor, Malaysia
e-mail: yamusabello@yahoo.com

Y. B. Yamusa (✉)
Department of Civil Engineering, Nuhu Bamalli Polytechnic,
810001 Zaria, Nigeria
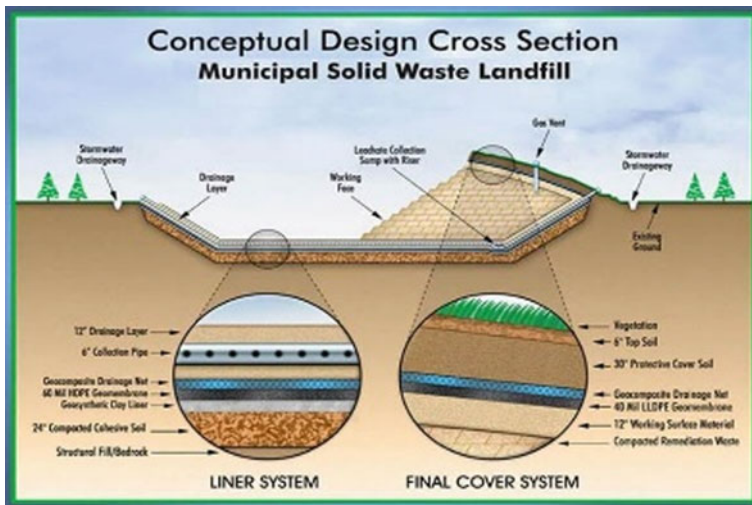
Fig. 1 Engineered sanitary landfill

environment. The leachate generated at landfill sites contains various organic and inorganic pollutants, which are considered as the most persisting contaminated effluent [3]. These leachates permeate the underlying aquifer, which affects the livelihood of the ecosystem [4, 5]. To prevent these issues, an engineered sanitary landfill liner is designed. Landfill liners provide an economically and environmentally safe disposal of MSW. The primary purpose of liner system for waste containment facility is to prevent or minimize infiltration of leachate through the hydraulic barrier. Liners provide the final line of defence against groundwater contamination [6] as shown in Fig. 1.

In this research, the material adopted for the design of liner is laterite soil, which is a residue of rock decay that is red in colour and has a high content of oxide of iron and hydroxide of aluminium and low proportion of silica. They are formed under weathering system productive of the process of laterization, the important characteristic of which is the decomposition of ferro-alumino silicate minerals and the prominent deposition of sesquioxides (Al_2O_3 and Fe_2O_3) within the profile to form the horizon of material called laterite [7]. The geotechnical characteristics and field performances of laterites are influenced by their mode of formation, degree of weathering (degree of decomposition, sesquioxides enrichment: laterization and dehydration desiccation/hardening), morphological characteristic, chemical and mineralogical composition as well as environmental condition [7]. Some researchers [8–11] have examined the geotechnical characteristics of laterite soil as hydraulic barrier material but did not specify the minimum percentage of fines to be adopted. This chapter considers the effects of fines at different gradation of laterite soil and recommends the percentage to be employed in order to achieve a sustainable design.

Sustainability relates to the notion of maintaining and enhancing the environmental, social and economic resources, which will not jeopardize the beneficiaries in order to meet the needs of current and future generations [12, 13]. A sustainable engineering design is necessary for an efficient integrated waste management system to maintain and minimize the adverse environmental and economic impacts. Careful design and management of landfills within the context of the available resources and local infrastructure can provide a cost-effective and safe disposal of waste [14].

2 Methodology

2.1 Materials and Methods

The laterite soil used in this study was extracted from Skudai campus (Johor), which is located at latitude 1° 33′ 39″N and longitude 103° 38′ 44″E of Universiti Teknologi Malaysia (UTM). Laterite soil samples are sieved into three different grading sizes (i.e. gravel, sand and fines). The gradation of laterite soil specimen investigated are

1. Laterite soil on its natural state with 30% fines, 40% sand and 30% gravel contents by weight of dry soil.
2. Laterite soil mixtures of 40% fines, 40% sand and 20% gravel contents by weight of dry soil.
3. Laterite soil mixtures of 50% fines, 40% sand and 10% gravel contents by weight of dry soil.

2.2 Index Properties

Laboratory tests were carried out to determine the index properties and particle size distribution of the laterite soil in accordance with British Standards (BS) [15] as shown in Table 1 and Fig. 2, respectively. From the particle size distribution shown in Fig. 2, the laterite soil contains 30% fines (<0.063 mm), 40% sand (2–0.063 mm) and 30% gravel (>2 mm). Furthermore, Atterberg limits results revealed a liquid limit of 76%, plastic limit of 42% and plasticity index of 34%. Based on these data, the laterite soil is classified according to the BS as sandy silt with gravel of very high plasticity (MV).

Table 1 Index properties of laterite soil

Property	Value
Natural moisture content, %	34
Specific gravity	2.7
% Passing BS 63 μm sieve	30
OMC, %	30
MDD, Mg/m^3	1.35
Liquid limit, %	76
Plastic limit, %	42
Plasticity index, %	34
BS classification	MV
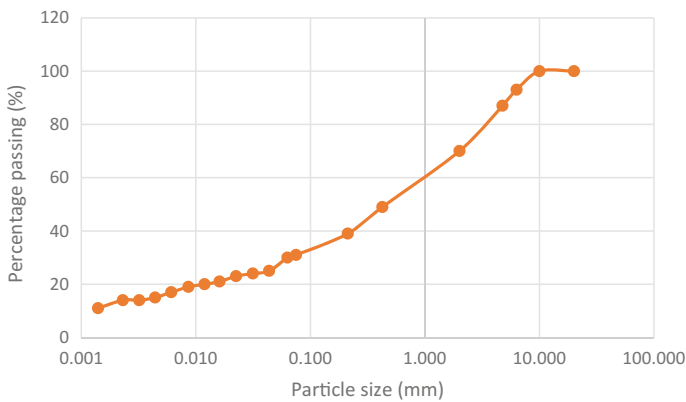
Fig. 2 Particle size distribution curve

2.3 Microstructural Properties

Field emission scanning electron microscopy (FESEM) technique was used to examine the morphology and microstructural properties of the laterite soil fabric. This was used in conjunction with Energy Dispersive X-ray Spectroscopy (EDX), which is a chemical microanalysis method to determine the elements present in the sample. Figures 3 and 4 shows the FESEM and EDX images, respectively. From the FESEM micrograph shown in Fig. 3, there is presence of kaolinite flakes and halloysitic tubes in the soil fabric. Moreover, EDX spectrum in Fig. 4 shows the presence of element of oxygen, iron, aluminium and silica, and the oxide composition of the soil, as given in Table 2 [16], revealed the sample to be laterite soil.
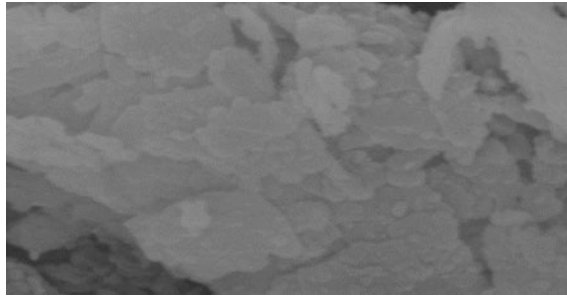
Fig. 3 Micrograph using FESEM
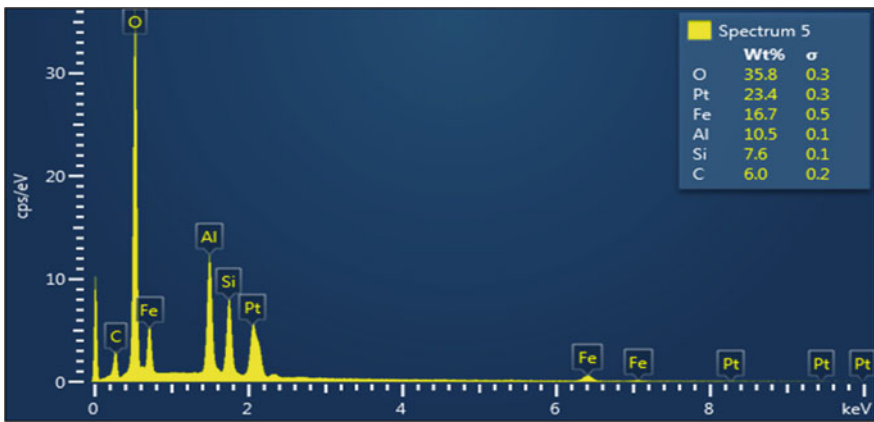
Fig. 4 EDX spectrum

Table 2 Oxide composition of laterite soil

Property	Value
SiO_2	25.46
Al_2O_3	31.10
Fe_2O_3	35.53
CO_2	7.91

The FESEM and EDX sample preparation is described as follows. Dry sample was prepared and placed on an aluminium stub, then covered with carbon tape and coated with platinum using a vacuum sputter to prevent charging effect and loss of resolution. Crossbeam 340 machine was used to analyze the sample connected to a computer as shown in Fig. 5.

Fig. 5 Crossbeam 340
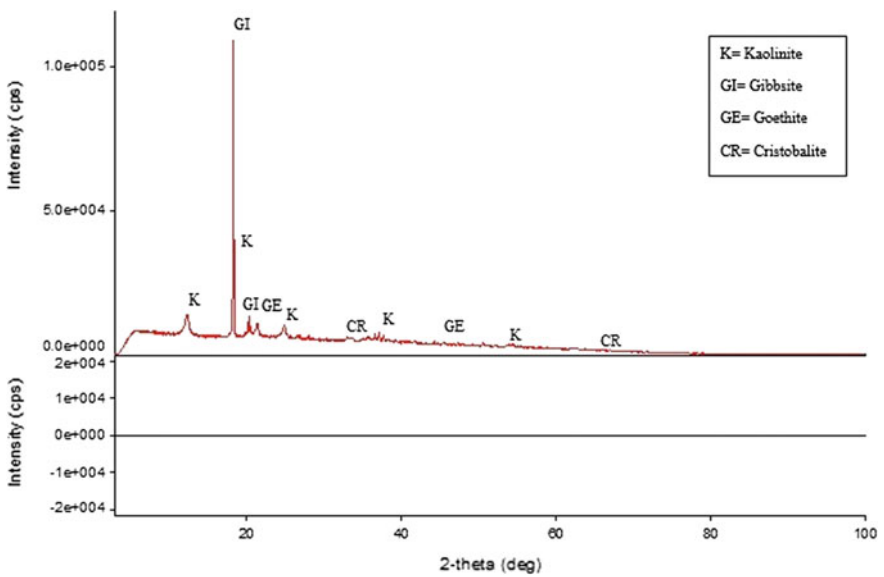
Fig. 6 XRD pattern

X-ray diffraction (XRD) technique is primarily used to identify and characterize compounds based on their diffraction pattern. The quantitative analysis using XRD determined the clay mineralogy of the soil sample to be kaolinite as shown in Fig. 6.

2.4 Compaction

In this research, the British Standard light compaction equivalent to Standard Proctor compaction is used as a baseline. This is because lesser compaction energies may not give the required minimum hydraulic conductivity for compacted laterite soil [8, 17].

The compaction test was performed to obtain the relationship between the dry density and the moisture content of the soils. The British Standard light (BSL) was performed in accordance with the recommended procedure outlined in BS 1377: Part 4: 1990. About 2 kg of dried sample that passed the 4.75 mm BS test sieve was thoroughly mixed with 26–34% of water. Then, the soil was put in a plastic bag for at least 24 h to allow proper distribution of moisture as shown in Fig. 7. The soil was then compacted into three equal layers. Each layer was given 27 blows of the 2.5 kg rammer falling freely through a height of 300 mm. At the end of compaction, the extension collar was removed and the top of the soil was trimmed off by means of a straight edge. The weight of the mould and the compacted soil were determined. The compacted soil was quickly extruded from the mould and a representative sample was taken for moisture content determination. The entire process was repeated at least four times within which the Optimum Moisture Content (OMC) and Maximum Dry Density (MDD) were determined by plotting a graph of dry density versus moisture content [15].

2.5 Hydraulic Conductivity

In this research, rigid wall permeameter under falling head condition was used to measure the hydraulic conductivity as recommended by [18]. Soil samples were compacted using the BSL at different fines contents (30, 40 and 50%) and different moulding water contents (−4, −2, 0, +2 and +4% of the OMC, respectively). Then, the samples were soaked for a minimum period of 48 h until no air bubbles are

Fig. 7 Moisture distribution

Fig. 8 Falling head
permeameter
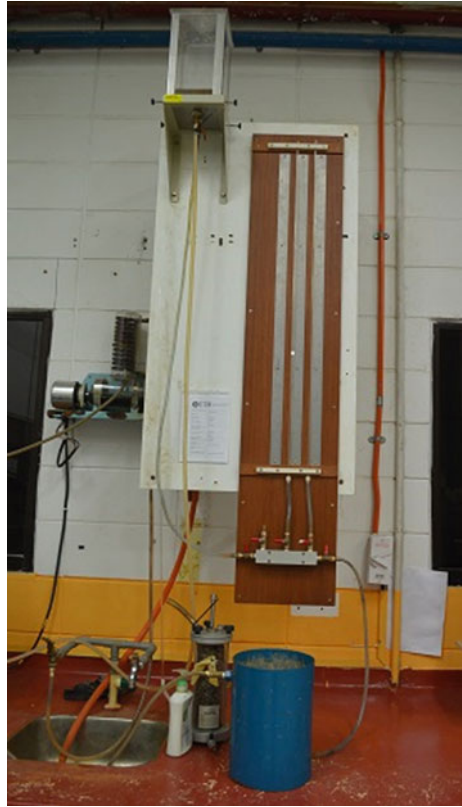
obviously observed to allow for full saturation inside a water tank. The fully
saturated test specimen was then connected to a permeant liquid (distilled water)
through a standpipe. Time and height/distance covered by water in the standpipe
were recorded. This was repeated for various moisture contents (−4, −2, 0, 2 and
4%) at different gradation (30, 40 and 50%) and the coefficient of permeability
(k) was calculated. Figure 8 shows the picture of hydraulic conductivity test
apparatus.

3 Discussion of Results

3.1 Compaction

The effect of gradation on the Maximum Dry Density (MDD) and Optimum
Moisture Content (OMC) of the laterite soil mixtures are shown in Fig. 9.
The MDD generally increased with higher fines content. This could be due to the
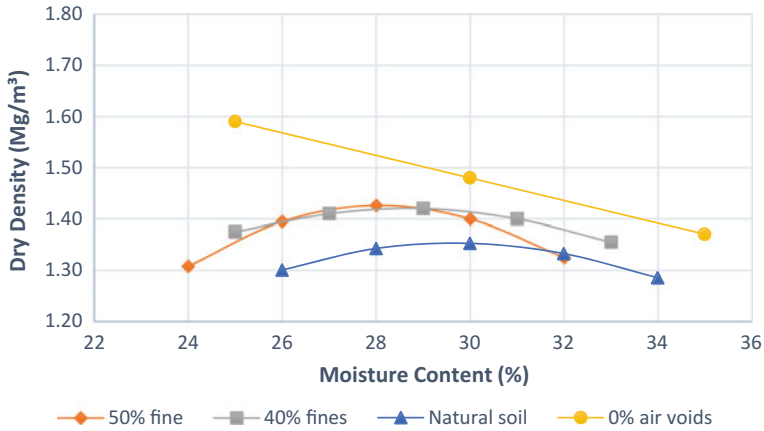
Fig. 9 Dry density versus moisture content

large amounts of fines having better cohesion and clogging the voids of the soil mixture. On mixing with 30, 40 and 50% fines content at OMC, the values of the MDD increased to 1.35, 1.42 and 1.43 Mg/m^3, respectively. On the other hand, the OMC decreased with higher fines content. The OMC reduced to 30, 29 and 28% for 30, 40 and 50% fines content, respectively. This could be due to the larger surface area which requires large amounts of water for the hydration of fines. This means that the higher the fines content the more the surface area.

3.2 Hydraulic Conductivity

There is a general decrease in hydraulic conductivity with higher moulding water content and fines content as shown in Figs. 10 and 11 respectively. Hydraulic conductivity of OMC decreased to 2.5×10^{-6}, 3.78×10^{-8} and 2.44×10^{-9} m/s with 30, 40 and 50% fines, respectively. Compaction with higher moulding water content (wet of OMC) resulted in soil grading that was devoid of macropores which conduct flow. It decreased to 1.55×10^{-7}, 8.13×10^{-9} and 1.02×10^{-9} m/s with 30, 40 and 50% fines, respectively. On the dry side of OMC, hydraulic conductivity with higher fines content did not give the required result like that of the OMC and wet of OMC. The values ranged are 9.87×10^{-6}, 5.08×10^{-8} and 9.1×10^{-9} m/s with 30, 40 and 50% fines, respectively. The laterite soil gradation attained the maximum regulatory hydraulic conductivity value of 1×10^{-9} m/s at 50% fines content. More pronounced result at the 50% fines is obtained on the wet side of OMC. Low hydraulic conductivity is likely to be achieved when the soil is well graded, and the clay fraction governs the hydraulic behaviour of the matrix [19].
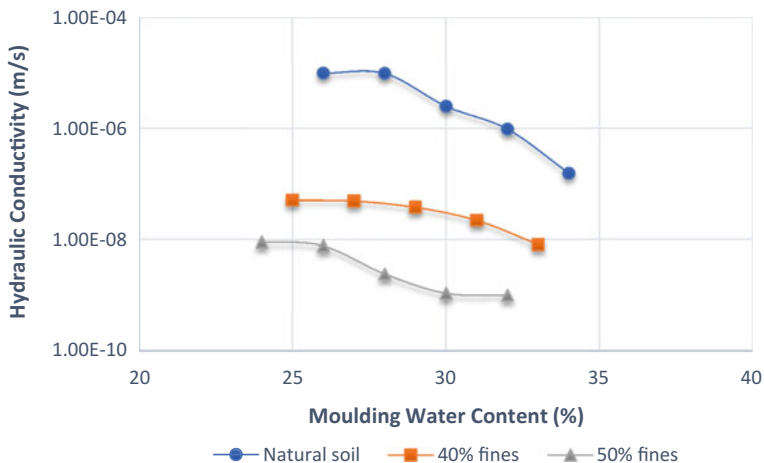
Fig. 10 Hydraulic conductivity versus moulding water content
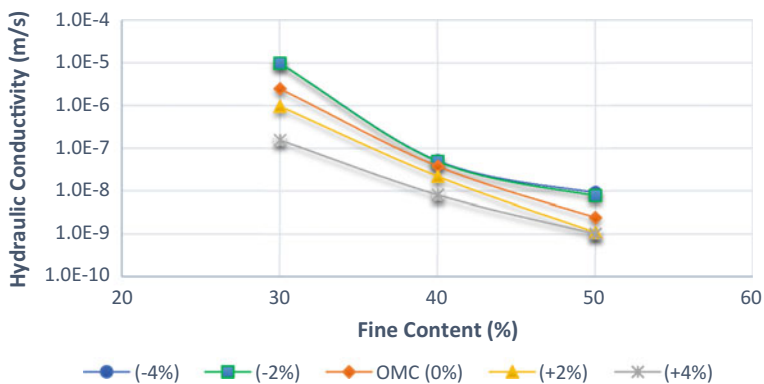
Fig. 11 Hydraulic conductivity versus fines content

The fines in soil have a higher impermeabilizing effect if they are well distributed so they can most effectively plug voids among the larger particles. Mechanical mixing distributes fines and breaks down some of the soil aggregates, thereby supplying fines for void-plugging and destroying large voids [20].

4 Summary and Recommendation

Laterite soil sieved and mixed at different gradation was compacted using the BSL (equivalent to Standard Proctor) compaction at five different moulding water contents (-4, -2, 0 +2 and +4%) of OMC to evaluate its suitability in engineered sanitary landfill system. The hydraulic conductivity values for specimen typically decreased with higher fines content and moulding water content. 50% fines content recorded the maximum permissible value of hydraulic conductivity.

The criteria for most regulatory agencies (guidelines) and researchers for assessing the technical suitability of materials meant for hydraulic barriers in waste disposal facilities are low hydraulic conductivity of 1×10^{-9} m/s, low volumetric shrinkage of 4%, acceptable shear strength of 200 kN/m^2 and a minimum of 30% fines with respect to gradation [8, 9, 21–29]. This showed that laterite soils which are found in the tropical regions exhibit different sets of physical and engineering properties from temperate region soils, particularly with respect to gradation. Thus, a minimum of 50% fines content is recommended for laterite soil to be used in waste containment facilities in order to achieve a sustainable design.

References

1. Amritha, P., Anilkumar, P.: Sustainable solid waste management through landscaped landfills. Indian J. Sci. Technol. **9**(29), 1–8 (2016)
2. EPA, Landfill Manuals, Landfill Site Design: An Ghníomhaireacht um Chaomhnú Comhshaoil. Johnstown Castle Estate, Co. Wexford, Ireland (2000)
3. Kallel, A., Attour, A., Trabelsi, I.: Electro-coagulation treatment of raw and autoclaved landfill leachate with aluminum electrodes: case study of Djebel Chakir (Tunisia). Arab. J. Geosci. **10**(4), 85 (2017)
4. Parameswari, K., Padmini, T., Mudgal B.: Assessment of soil contamination around municipal solid waste dumpsite. Indian J. Sci. Technol. **8**(36) (2015)
5. Rong, L., et al.: Assessment of the potential utilization of municipal solid waste from a closed irregular landfill. J. Clean. Prod. **142**, 413–419 (2017)
6. Daniel, D.E.: Geotechnical Practice for Waste Disposal. Springer Science & Business Media, Berlin (2012). https://doi.org/10.1007/978-1-4615-3070-1
7. Gidigasu, M.: Laterite Soil Engineering: Pedogenesis and Engineering Principles, vol. 9. Elsevier, The Netherlands (2012)
8. Osinubi, K.J., Nwaiwu, C.M.: Design of compacted lateritic soil liners and covers. J. Geotech. Geoenviron. Eng. **132**(2), 203–213 (2006)
9. Bello, A.: Acceptable zone for reddish brown tropical soil as liner material. The Pac. J. Sci. Technol. **16**(1) (2015)
10. Osinubi, K.J., et al.: Influence of molding water content on shear strength characteristic of compacted cement kiln dust treated lateritic soils for liners and covers. Niger. J. Technol. **34** (2), 266 (2015)
11. Aziz, H.A., et al.: Investigations on the hydraulic conductivity and physical properties of silt and sludge as potential landfill capping material. Int. J. GEOMATE **10**(22), 1989–1993 (2016)

12. Rahman, F.A., et al.: Pollution to solution: capture and sequestration of carbon dioxide (CO_2) and its utilization as a renewable energy source for a sustainable future. Renew. Sustain. Energy Rev. **71**, 112–126 (2017)
13. Fragaszy, R., et al.: Sustainable development and energy geotechnology—potential roles for geotechnical engineering. KSCE J. Civ. Eng. **15**(4), 611–621 (2011)
14. Jha, J.N., Singh, H., Gill, K.S.: Waste and waste characterization. In: Proceeding of the National Conference on 'Geotechnical and Geoenvironmental Aspects of Wastes and Their Utilization in Infrastructure Projects', pp. 25–33, Guru Nanak Dev Engineering College Ludhiana, India, 15–16 Feb 2013
15. BS1377: Methods of Testing Soil for Civil Engineering Purposes. British Standards Institute, London (1990)
16. Marto, A., Latifi, N., Eisazadeh, A.: Effect of non-traditional additives on engineering and microstructural characteristics of laterite soil. Arab. J. Sci. Eng. **39**(10), 6949–6958 (2014)
17. Bello, A.A.: Hydraulic conductivity of three compacted reddish brown tropical soils. KSCE J. Civ. Eng. **17**(5), 939–948 (2013)
18. Head, K.H., Epps, R.J.: Manual of Soil Laboratory Testing, vol. 2. Whittles publishing, Dunbeath (2011)
19. Daniel, D.E., Benson, C.H.: Water content-density criteria for compacted soil liners. J. Geotech. Eng. **116**(12), 1811–1830 (1990)
20. Benson, C.H., Trast, J.M.: Hydraulic conductivity of thirteen compacted clays. Clays Clay Miner. **43**(6), 669–681 (1995)
21. Daniel, D.E., Wu, Y.K.: Compacted clay liners and covers for arid sites. J. Geotech. Eng. **119**(2), 223–237 (1993)
22. Osinubi, K., Moses, G., Liman, A.: The influence of compactive effort on compacted lateritic soil treated with cement kiln dust as hydraulic barrier material. Geotech. Geol. Eng. **33**(3), 523–535 (2015)
23. Amadi, A., Eberemu, A.: Characterization of geotechnical properties of lateritic soil-bentonite mixtures relevant to their use as barrier in engineered waste landfills. Niger. J. Technol. **32**(1), 93–100 (2013)
24. MHLG, Ministry of Housing and Local Government: Criteria for Siting Sanitary Landfills: National Strategic Plan for Solid Waste Management, vol. 3, Appendix 6B. Kuala Lumpur, Malaysia (2005)
25. USEPA: Design and Construction of RCRA/CERCLA Final Covers. Soils Used in Cover Systems, EPA/625/4-91/025, pp. 1–25. United States Environmental Protection Agency, USA (1991)
26. USEPA: Solid Waste Disposal Facility Criteria: Technical Manual. EPA 530-R-93-017, pp. 1–84. United States Environmental Protection Agency, USA (1993)
27. USEPA: Requirements for Hazardous Waste Landfill Design, Construction, and Closure. EPA/625/4-89/022, pp. 53–74. United States Environmental Protection Agency, USA (1989)
28. Jones, R., et al.: Selection of clays for use as landfill liners. Waste Disposal Landfill-Green **93**, 433–438 (1995)
29. Boynton, S.S., Daniel, D.E.: Hydraulic conductivity tests on compacted clay. J. Geotech. Eng. **111**(4), 465–478 (1985)

Removal of Rose Bengal Dye Using Low-Cost Adsorbent Material

Aswin Sriram and Ganapathiraman Swaminathan

Abstract The adsorption of Rose Bengal dye over activated carbon prepared from *Calotropis gigantea* was investigated. SEM and FTIR characterization was carried out to evaluate the feasibility of adsorbent. The activated carbon was amalgamated into a polymeric bead and was coated with chitosan to increase the removal efficiency. Adsorption experiments were done at optimized equilibrium conditions and the absorbance was checked at 547 nm to calculate the removal percentage. The adsorption dynamics, isotherm kinetics were evaluated to interpret the removal efficiency of the dye. The rate kinetics were determined through the Ho's pseudo-second-order model, which fitted perfectly for the present adsorption studies.

Keywords *Calotropis gigantea* · Activated carbon · Rose bengal Adsorption

1   Introduction

Xanthene class dyes pose a greater challenge in wastewater treatment. These classes of dyes have a distinctive high molecular weight with three or more aromatic cyclic chain which requires innovative treatment methods. Dye colours in wastewater as such are highly defiant to ordinary and typical treatment methods [1].

Adsorption of dye colours in adsorbent has been proven quite effective in partial or complete removal from the adsorbate. Everyday, new adsorbent materials are tailor-made to adsorb variety of dye materials, thus increasing the efficiency of the treatment process. Various adsorption models have been developed that provide a wider range of operating parameters, thus supporting in potent application.

A. Sriram (✉) · G. Swaminathan
Department of Civil Engineering, National Institute of Technology,
Tiruchirappalli, Tamil Nadu, India
e-mail: sriramphdnitt@gmail.com

Rose Bengal dye finds extensive usage in the medical applications as a tracer dye [2]. Although the dye concentration used is very low, the extensive usage has toxic effects on the skin when it comes in contact. *Calotropis gigantea* is a weed plant typically found in the southern parts of India. The extract from the flowers has medicinal capability. The plant is found in abundance and it has no immediate usage as wood fuel. Little research has been carried out in utilizing the stem and leaves of *C. gigantea* as biosorbent and as activated carbon.

The aim of the present work is to produce low-cost activated carbon from *C. gigantea* and utilize it for the decolourization of Rose Bengal dye in aqueous solution. The efficiency of the sorption is studied by varying different parameters like pH, adsorbent dosage, initial dye concentration of the dye in aqueous solutions. The data from the optimum equilibrium conditions were fitted into different adsorption isotherm models and studied for their applicability.

2 Materials and Methodology

2.1 Preparation of Activated Carbon

The source of activated carbon used in the present study for removal of Rose Bengal dye is the stem of *C. gigantea*. The average stem thickness of 8–12 mm was collected from the plant and washed with distilled water. The top layer of the stem was scrubbed to remove impurities. The stem was cut into small equal pieces and saturated with H_2SO_4 in the ratio 1:1. The carbonized stem was washed with distilled water several times. The clean charred stem was placed in hot air oven for 343 K for 24 h to be void of moisture. The dried bark was grounded and the sieved material (150–350 μm) was placed in muffle furnace at 723 K for 1 h and at 1073 K for 0.5 h for activation. Activated carbon polymeric beads were prepared by ionic polymerization route [3]. The gel beads formed after the interaction of carbon impregnated alginate beads and 0.2 M $CaCl_2$ solution. The polymeric beads were subsequently washed with distilled water to remove excess $CaCl_2$ solution. The polymer beads were soaked in 2% chitosan solution for 12 h. 0.2 M ammonium persulphate and 1.2 N HCl were added to the soaked solution [4] as oxidants and kept for 4 h, thus enabling chitosan doping over the polymeric beads.

2.2 Preparation of Aqueous Dye Solution

Rose Bengal dye (C.I. 45440; molecular formula—$C_{20}H_2Cl_4I_4Na_2O_5$; Molecular weight—1017.65 g/mol) was used to prepare a stock solution of 1000 mg/L in double distilled water. The stock solution was kept in dark coloured glass bottle to prevent degradation through encompassing light.

2.3 Adsorption Process

Adsorption experiments were carried out in an incubating shaker at 120 RPM. Different concentrations of Rose Bengal dye solution viz. 4, 8, 12, 16 and 20 mg/L were prepared from 1000 mg/L stock solution. The experiments were carried out by optimizing the pH, contact time and adsorbent dosage. Samples were withdrawn at fixed time intervals and the absorbance of the supernatant was checked in UV—spectrophotometer at 547 nm wavelength. The adsorbent dosages were varied from 0.1 to 0.5 g with wet beads. The initial pH values ranging from 2 to 11 were altered with 0.1 N HCl and 0.1 N NaOH. All the experiments were conducted in 100 ml Erlenmeyer flasks and at room temperature.

3 Results and Discussion

3.1 Fourier Transform Infrared Spectroscopy (FTIR)

The FTIR study was carried out to confirm the existence of different functional groups before and after adsorption. The prepared activated carbon (CGAC) was analyzed and a weaker peak was resolved at 1591 cm^{-1}, thus reflecting the presence of C=C alkene groups (Table 1). An alkoxy C–O peak at 1115 cm^{-1} and aromatic C–H bend peak at 613 cm^{-1} were noted which indicate the presence of residue biomass material which may not have been converted to activated carbon. The FTIR spectrum (Fig. 1) of dye-loaded beads (RB-CH-SA-CGAC) was also analyzed and a distinctive–OH peak was resolved at 3364 cm^{-1}. Further, the FTIR spectrum revealed two peaks, at 1731 and 1631 cm^{-1}, which are characteristic amide and C=C stretch, thus confirming the doping of chitosan over activated carbon and their adsorption of Rose Bengal dye molecules. The reduction in peak positions and shift in the functional groups confirm the adsorption of rose Bengal dye on CH-SA-CGAC polymeric beads [5].

Table 1 FTIR spectra of adsorbents and adsorbed polymeric beads

Functional groups	Bands (cm^{-1})	FTIR spectrum	
		CGAC	RB-CH-SA-CGAC
Alcohol O–H stretch	3500–3150	–	3364
Aldehyde C=O, aldehyde C–H	1730–1680	–	1731
C=C alkene, N–H amide	1675–1625 1600–1550 1500–1450	1591	1631
Acyl C–O, phenyl C–O	1350–1200	–	1224
Alkoxy C–O	1150–1000	1115	1031
Aromatic sp^2 C–H bend	920–600	613	–
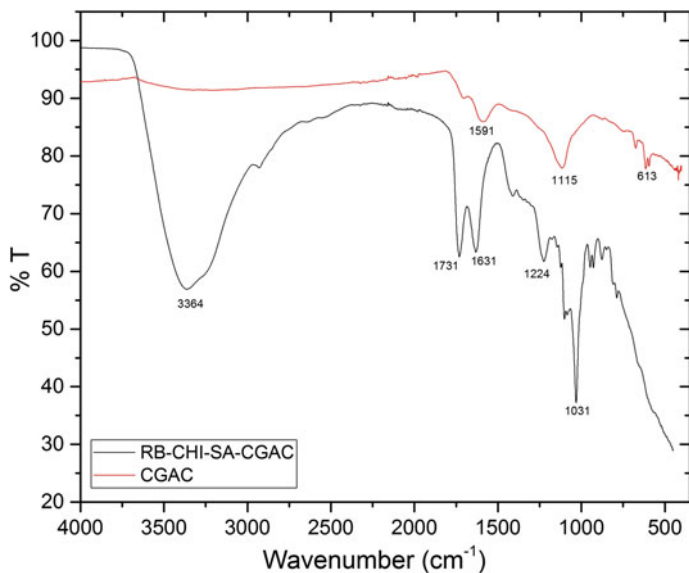
Fig. 1 FTIR spectrum profile of activated carbon (CGAC) and dye-loaded polymeric beads (RB-CH-SA-CGAC)

3.2 Scanning Electron Microscope (SEM)

The surface morphology of the chitosan-coated activated carbon beads and the dye-loaded beads were studied under scanning electron microscope (SEM). From the SEM image (Fig. 2), porous structures could be observed that are responsible for trapping the dye molecules. The SEM image of the dye-loaded polymeric beads show that the pores have been completely entrapped with the dye molecules [6].
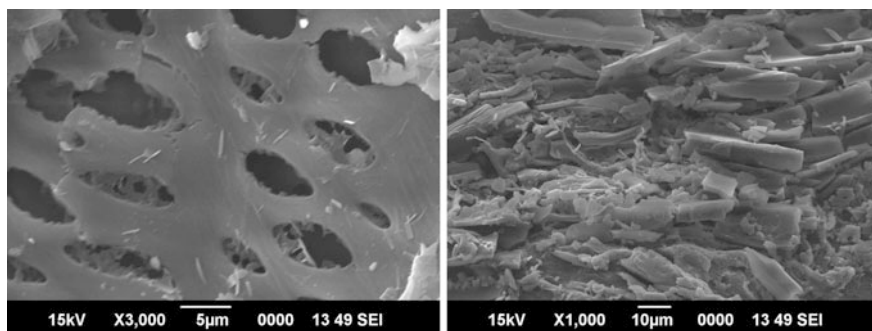
Fig. 2 SEM images of activated carbon (CGAC) and dye-loaded polymeric beads (RB-CH-SA-CGAC)

3.3 Adsorption Studies

3.3.1 Adsorbent Dosage Optimization

The effect of adsorbent dosage ranging 0.1, 0.2, 0.3, 0.4 and 0.5 g on the equilibrium dye removal capacity was also conducted with alginate beads to find the control adsorption. For the adsorbent dosage experiment, the dye concentration (4 mg/L) and pH (neutral) was kept constant (Fig. 3). Out of the various dosages, 0.2 g of CH-SA-CGAC had overall maximum removal efficiency of 91.67%. The equilibrium dye adsorption capacity tends to decrease with the increase in adsorbent dosage.

3.3.2 Effect of pH

The pH of the adsorption plays a compelling role in the efficiency of the process [7]. The effect of pH was studied through wide range of pH (2–11). From the experimental results, the equilibrium dye capacity was found to be maximum at pH 6 (Fig. 4). It can also be noted that the maximum adsorption removal was found to be 90–92%, while it was 85–90% at the pH range 7–8. The adsorbate tends to amass positive charge in the lower pH, while its surface is being negatively charged [1].
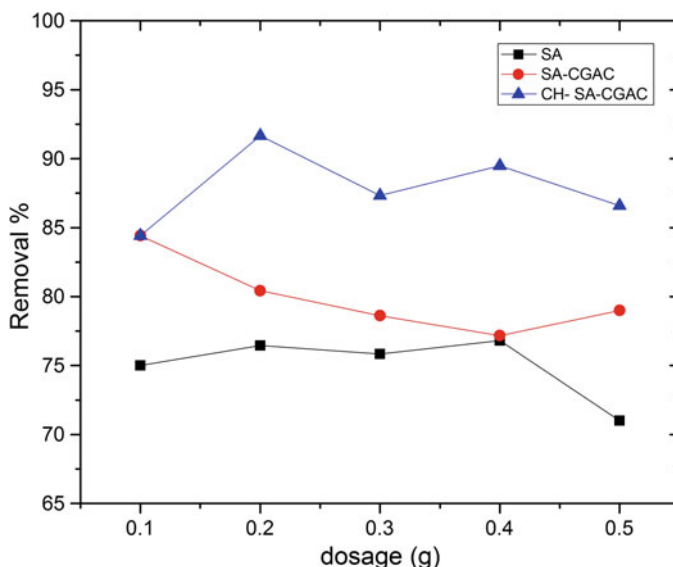
Fig. 3 Effect of adsorbent dosage of Sodium alginate (SA) control beads, sodium alginate and activated carbon (SA-CGAC) and chitosan-coated activated carbon alginate beads (CH-SA-CGAC) over adsorption of Rose Bengal dye
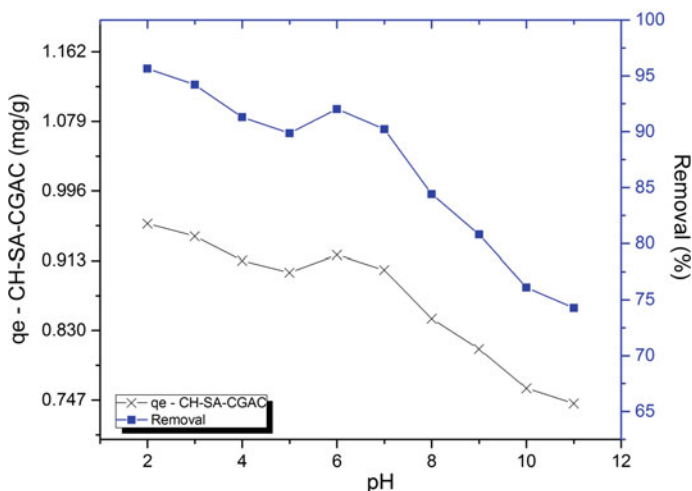
Fig. 4 Effect of pH in removal (%) of Rose Bengal dye and equilibrium capacity of CH-SA-CGAC

This generally leads to increase in adsorption of dye. But it is essential to keep the pH of the solution neutral to facilitate ionic equilibria in the aqueous solution.

3.3.3 Effect of Contact Time and Initial Dye Concentration

The effect of contact time for the removal of Rose Bengal dye by CH-SA-CGAC was investigated with varying contact time (0, 2, 5, 15, 30, 45, 60, 75, 90 and 12 min) for different dye concentrations (4, 8, 12, 16 and 20 mg/L) at neutral pH (Fig. 5). The equilibrium dye uptake capacity of CH-SA-CGAC increase with the increase in dye concentration [8]. Nevertheless, the efficiency peaked at 92% for 4 mg/L dye concentration at contact time of 60 min. Therefore, 4 mg/L initial dye concentration, 60 min contact time were selected as the optimum operating conditions for the adsorption of Rose Bengal dye on CH-SA-CGAC at neutral pH.

3.4 Isotherm Studies

To predict the type of adsorption occurring inside the system, many mathematical adsorption models have been developed. Out of these, Langmuir and Freundlich isotherm models are extensively used in understanding the solid–liquid adsorption. The Langmuir model considers a monolayer adsorption on to the adsorbent surface with definite number of indistinguishable adsorption sites [9, 10]. The linear mathematical expression of the Langmuir model is as expressed below.
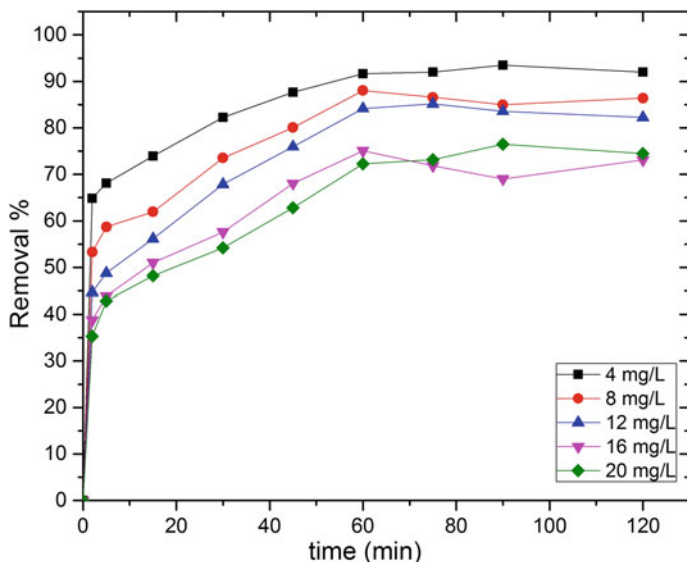
Fig. 5 Effect of contact time and initial dye concentration over adsorption of Rose Bengal dye on CH-SA-CGAC

$$\frac{C_e}{q_e} = \frac{1}{q_m}C_e + \frac{1}{K_a q_m} \tag{1}$$

The data from the equilibrium uptake capacity experiments were plotted against two different Langmuir isotherm plots (Fig. 6) and the results are tabulated (Table 2). The results indicate that out of the two different plots, Langmuir 1 plot was best suited with r^2 value of 0.992 for 4 mg/L initial dye concentration.

A proportionality relationship is established between the adsorbate concentration and dye uptake capacity in Freundlich isotherm [11]. The linear mathematical expression of the Freundlich model is as expressed below.

$$\log(q_e) = \log(K_F) + \frac{1}{nF}\log(C_e), \tag{2}$$

where K_F is the Freundlich adsorption constant with respect to the sorption capacity.

The Freundlich model parameters were calculated from the regression plot (Fig. 7) of log q_e vs log C_e and the values are tabulated (Table 2). On comparing with Langmuir isotherm model, Freundlich fitted slightly poorer, thus revealing that the monolayer adsorption is predominant.
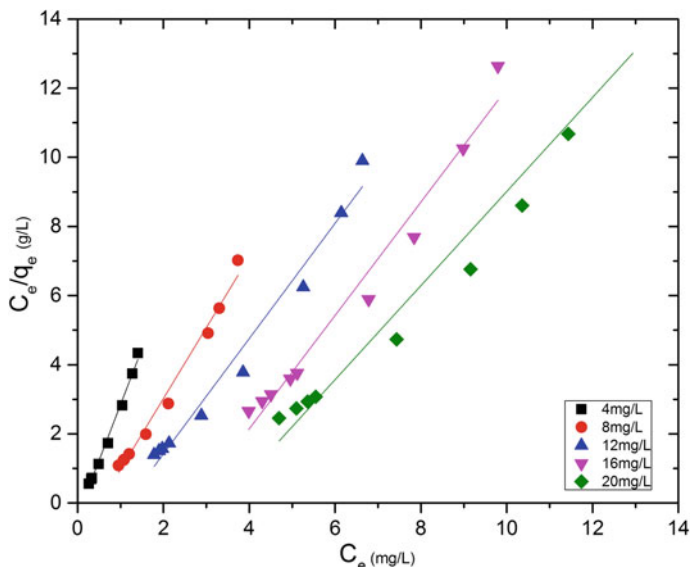
Fig. 6 Langmuir 1 isotherm model for adsorption of Rose Bengal dye on CH-SA-CGAC

Table 2 Langmuir and Freundlich isotherm parameters calculated from isotherm plots

Isotherm plot	Parameter	Rose Bengal dye concentrations (mg/L)				
		4	8	12	16	20
Langmuir 1	q_m	0.300	0.468	0.568	0.575	0.681
	k_a	7.147	1.673	0.768	0.343	0.266
	r^2	0.992	0.986	0.976	0.971	0.952
Langmuir 2	q_m	0.318	0.497	0.616	0.615	0.748
	k_a	9.981	2.057	0.935	0.375	0.306
	r^2	0.795	0.828	0.806	0.856	0.809
Freundlich	$1/n$	0.220	0.372	0.494	0.748	0.758
	k_F	0.645	0.956	1.301	1.937	2.298
	r^2	0.945	0.954	0.946	0.963	0.948

3.5 Adsorption Dynamic Studies

The rate controlling step for adsorption of rose Bengal dye on CH-SA-CGAC polymeric bead was determined through Lagergren's pseudo-first-order [12] and pseudo-second-order kinetic models [13] were used. The linear mathematical expression of the first order equation is as expressed below.
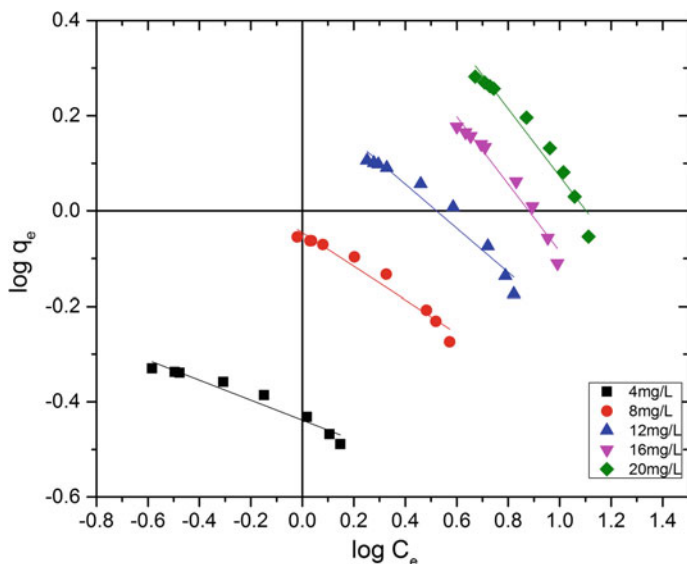
Fig. 7 Freundlich isotherm model for adsorption of Rose Bengal dye over CH-SA-CGAC

$$\log(q_e - q_t) = \log q_e - \frac{K_1 t}{2.303}, \tag{3}$$

where q_t is the amount of Rose Bengal dye at time t, q_e is the amount of Rose Bengal dye adsorbed at equilibrium concentration and K_1 is the pseudo-first-order rate constant. A linear fit (Fig. 8) of $\log(q_e - q_t)$ vs t shows the pertinency of the model through which the correlation r^2 coefficients are determined tabulated in Table 3.

The linear mathematical expression of the pseudo-second-order equation is as expressed below.

$$\frac{t}{q_t} = \frac{1}{k_2 q_e^2} + \frac{1}{q_e} t \tag{4}$$

Here, k_2 is the pseudo-second-order rate constant for the adsorption process. The values of k_2 and q_e are given in Table 3. The calculated coefficients of the pseudo-second-order model were found to fit better (Fig. 9) when compared with pseudo-first-order model in the adsorption of Rose Bengal dye on to CH-SA-CGAC polymeric beads.
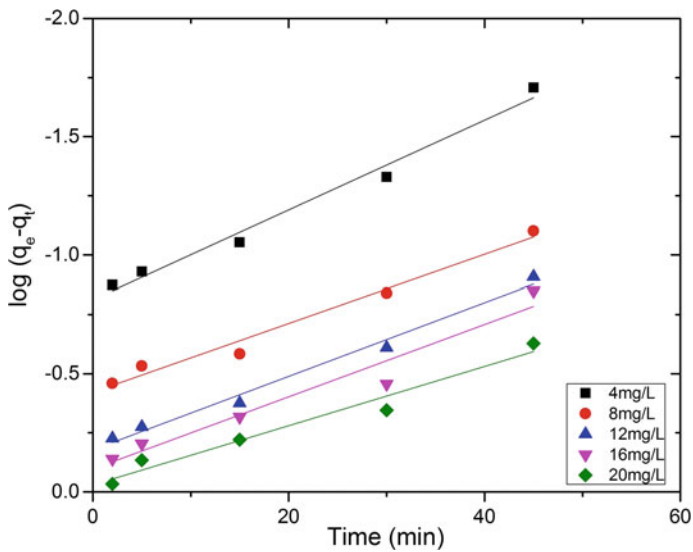
Fig. 8 Lagergren's pseudo-first-order plot for adsorption of Rose Bengal dye over CH-SA-CGAC

Table 3 Pseudo adsorption parameters calculated from the adsorption dynamic studies

Isotherm plot	Parameter	Rose Bengal dye concentrations (mg/L)				
		4	8	12	16	20
Pseudo 1st order	k_1	0.044	0.033	0.036	0.035	0.029
	q_e	0.444	0.656	0.837	0.908	0.971
	r^2	0.979	0.973	0.983	0.936	0.956
Pseudo 2nd order	q_e—exp	0.458	0.880	1.263	1.502	1.806
	k_2	0.614	0.223	0.118	0.110	0.052
	q_e—cal	0.474	0.893	1.307	1.466	1.989
	r^2	0.999	0.997	0.995	0.994	0.990
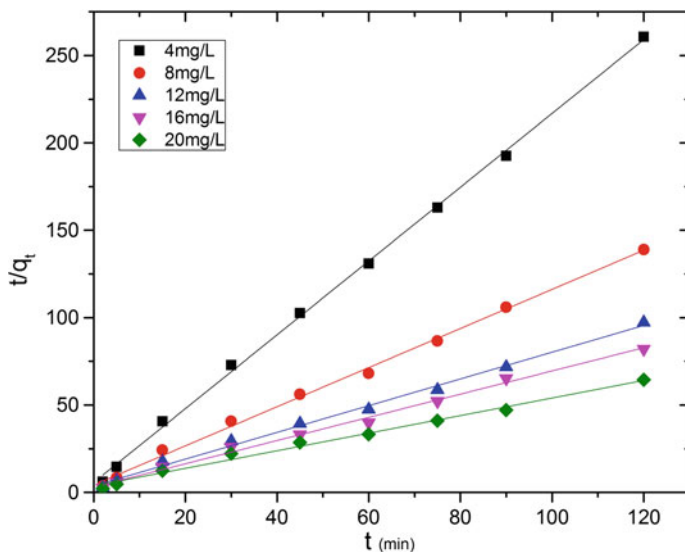
Fig. 9 Pseudo-second-order plot for adsorption of Rose Bengal dye over CH-SA-CGAC polymeric beads

4   Conclusion

Low cost activated carbon was prepared from *Calotropis gigantea*, a weed plant commonly found in the southern parts of India. The prepared activated carbon was amalgamated into polymeric beads using sodium alginate and subsequently coated with chitosan. The chitosan-coated beads were used as a viable adsorbent material and their feasibility was checked by conducting batch studies of adsorption of Rose Bengal dye. Operational parameters like dosage, dye concentration and pH were varied to arrive at an optimum equilibrium conditions. The equilibrium data suited well with Langmuir isotherm, thus indicating that the adsorption is monolayer in nature. The dynamic studies were also performed and the equilibrium uptake data was fitted with Lagergren's and Ho–Mckay model. In comparison, the pseudo-second-order model fitted very well with the experimental data. FTIR studies and SEM studies were carried out for the activated carbon and dye-loaded beads to confirm the adsorption of Rose Bengal dye.

References

1. Naveen, N.: J Environ. Sci. Eng. **57**, 183–189 (2015)
2. Gupta, V.K.: RSC Adv. **2**, 8381–8389 (2012)

3. Kumar, M.: Removal of Victoria blue using prosopis juliflora bark carbon: kinetics and thermodynamic modelling studies. J. Mater. Environ. Sci. **5**(2), 510–519 (2014)
4. Gopal, N.: Fixed bed adsorption studies of Rhodamine-B dye using polymer bound adsorbent. Adv. Appl. Sci. Res. **6**(7), 65–73 (2015)
5. Gopalakrishnan, L.: Ellagic Acid Encapsulated Chitosan Nanoparticles, as Antihemorrhagic Agent, *Carbohydrate Polymers* (2014)
6. Renganathan, S.: Chem. Prod. Proc. Model **3**, 1–15 (2008)
7. Geetha, A.: Desalination and Water Treatment, pp. 1–15 (2015)
8. Naveen, N.: J. Taiwan. Inst. Chem. Eng. **42**, 463–469 (2011)
9. Langmuir, I.: The adsorption of gases on plane surfaces of glass, mica and platinum. J. Am. Chem. Soc. **40**, 1361–1403 (1918)
10. Weber, W.J.: Physicochemical process for water quality control. Wiley, New York (1972)
11. Freundlich, H.M.F.: Ueber die Adsorption in Loesungen. Z. Phys. Chem. Leipzig **57A**, 385–470 (1906)
12. Lagergren, S.: About the theory of so-called adsorption of soluble substances. Kungliga Svenska Vetenskapsakademiens, Handlingar **4**, 1–39 (1898)
13. Ho, Y.S.: Pseudo-second order model for sorption, processes. Proc. Biochem. (Oxford) **34**(5), 451–465 (1999)

Effect of Wet and Dry Conditions of MUF Polymers on Strength Properties of Treated Peat Soil

Mohd Nazrin Mohd Daud and Nik Norsyahariati Nik Daud

Abstract Peat soil is one of the abundant soft soil material vastly found in east costal area of Peninsular Malaysia. Soft soil can be treated using wet and dry mixing method for the purpose of deep stabilization method. It is either mixed thoroughly with conventional or nonconventional binder. Among other properties of concern in soil, stabilization is a strength of treated peat medium which is much likely dependant on condition of wet and dry mixture between binder and treated soil. Essentially, nonconventional binder such as Melamine Urea Formaldehyde (MUF) polymer resin has recently found a fresh look in this study intendedly for future possible application, especially for rapid application stabilization technique. This chapter presents the performance of two types of MUF resin, namely MUF powdered (MUF-P) and MUF liquid (MUF-L) resin which were tested to treat peat soil for determination of unconfined compressive strength (UCS), and elasticity modulus. Both type of resins were mixed with peat specimens as wet and dry binder for stipulated periods of curing times (1–7 days). Results showed that MUF-P resin had performed significantly to improve UCS of initially high moisture content of treated peat soil specimens for up to 287 kPa in a week. Improvement of elasticity modulus, E_{50} in term of secant modulus also noticeable within 7–14 days of curing periods. However, MUF-L has significantly improved UCS of treated specimens particular for air curing application at lower range of moisture content with significant improvement of up to 500 kPa within 7 days curing period.

Keywords Peat soil · Wet condition · Dry condition · Melamine urea formaldehyde · Unconfined compressive strength

M. N. M. Daud (✉) · N. N. N. Daud
Department of Civil Engineering, Faculty of Engineering,
Universiti Putra Malaysia, Selangor, Malaysia
e-mail: hassan_seth@yahoo.com

N. N. N. Daud
e-mail: niknor@upm.edu.my

1 Introduction

Constructions of foundations of any engineering structure on soft soils, in particular, always involves excessive settlements and deformations, and not to mention other stability problems. Such problems can be avoided or minimized throughout several engineering measures such as soil improvement and stabilization. Generally, it is a broad field which may include different methods and techniques [1]. Among other properties of concern in stabilization of soil, strength of treated medium is very much dependant on condition of wet and dry mixture between binder and treated soil. Study on effect of wet and dry condition of mixtures is very important in search of new material and method that could be applied easily and quick in response to rapid reaction of strength development between binder and soft soil, in particular.

Study by Naeini and Masoud [2] on soils stabilized with epoxy resin polymer have suggested that compressive strength and modulus elasticity were significantly improved under dry condition. Consequent results of test by Naeini et al. [3] indicated that the waterborne polymer significantly improved the strength behavior of unsaturated clayey soils. Santoni et al. [4] has revealed that the polymer emulsions do provide significant strength gain under both wet and dry conditions on treated silty-sand soils. Ajayi-Majebi et al. [5] managed an experiment planned to determine the effects of stabilizing clay-silt soils with the combination of an epoxy resin and a polyamide hardener with positive results to increase load-bearing capacity of treated materials. Previously, Gopal et al. [6] has performed comparative studies to stabilize dune sand using Urea-Formaldehyde (UF) and its copolymers. Though, none of these treatments using polymeric reaction were studied on highly compressible material with high level of moisture content of peat soil.

Nonetheless, the good results of polymer treatment in stabilization of soil as nontraditional binder as described in previous research is still considered limited in both study and application, considering the lack of publication in particularly on peat soil stabilization. Indeed, this approach suffered several disadvantages particularly in wet clay considering difficulty in providing adequate mixing additives that require special equipment, much energy, and time and not to mention high material cost [7]. Studies on peat soil stabilization using polymeric substances have been rare and nearly nonexistence due to the fact that attention began to refocus on traditional binder including Portland cement, lime, and fly ash through pozzolanic reaction, especially for soft clay soils stabilization.

Traditionally, excavation—displacement or replacement, ground improvement, and reinforcement through preloading and vertical drains, stone columns, piles, and lightweight foundation system are among considerable options for peat soil stabilization [8]. In general, [9] suggested three optional method construction techniques that can be adopted, which was based on the depth of peat deposit. Deep stabilization techniques of soft soil stabilization such as clay and peat using soil column are not new as the methods have been available for decades with various configurations techniques and standard across the world. In Malaysia, the application of

soil column method of stabilization on tropical peat using traditional binders has been studied and reviewed adequately in various literatures [10–12]. It was also learnt that method of stabilization such as surface treatment using bamboo—geotextile surface mattress method for housing development was sufficiently adopted in some embankment and building platform over soft to very soft peat and/or clay in Malaysia. It is by creating buoyancy and hence a reduction in the magnitude of vertical stress applied [13]. This application may also be combined with surface treatment using binders as studied by Kalantari and Huat [14] under dry condition.

As a matter of fact, peat soil composed of fibrous organic matters that are organic residues of plants formed through incomplete decomposition process. Literature suggested that peat soil has wide range of variation in properties including its moisture content, organic content, liquid limit, specific gravity, and unit weight among others. Hemic peat in Johor, Malaysia, for example, has natural moisture content in the range of 230–500% [15]. Ling et al. [16] also had conducted several moisture content test on hemic peat soil in Johor and found that moisture content varies at different depth, in which were recorded between 119.03 and 103.68%. Practically, upper surface of peat medium may hold considerable lower amount of moisture primarily during dry season, as opposed to extremely high moisture content during wet season in tropical condition of Malaysia. In addition, study on polymeric admixture such as formaldehyde resin has been nearly nonexistence to peat soil treatment. Recent study by Daud and Daud [17] on strength of peat soil treated by MUF has shown promising result at lower range of moisture content using liquid form of MUF resin. In this chapter, the objective is primarily to investigate the effect of wet and dry condition of hemic peat soil treated with MUF polymer resins on strength within designated curing periods.

2 Research Methodology

2.1 Materials

Peat soil used in this study was obtained from Senggarang, Batu Pahat, Johor, Malaysia. Disturbed samples were collected at palm oil tree plantation area on relatively dry season with occasional rain recorded during May 2015 and December 2015, during rainy season. The peat was characterized in Table 1 by its typical physical properties from previous laboratory test by Daud and Daud [17]. Peat specimens were prepared based on its moisture content level to suit different mixing application with polymer resins. Relatively dry peat specimens were prepared through compaction test procedure to provide optimum moisture content (OPC) specimens that was purposely to be mixed with liquid MUF resin. On the other side, disturbed wet specimens of peat at natural moisture content were prepared to be mixed with both liquid MUF and powdered MUF resins.

Table 1 Physical properties of untreated peat soil [17]

Typical soil properties	Description
Peat soil classification	H5 (Hemic)
Moisture content (%)	303–550
pH	3.15
Specific gravity	1.4
Organic content (%)	76
Ash content (%)	24
Liquid limit (%)	153.8
Plasticity index (%)	47.7

Generally, polymers such as melamine urea formaldehyde (MUF) is obtained as industrial mass product in forms of liquid and solid powder. MUF used in this study was resourced from two key chemical industrial suppliers; Malayan Adhesive Corporation Sdn. Bhd and AL Asia Chemical Industries Sdn. Bhd for both liquid and powder forms, respectively. Commonly, formaldehyde emission concern on urea formaldehyde resin was lessened by incorporation of various portion of melamine resin in the composition. Additionally, at higher melamine content levels, the acidic pH yielded substantially lower formaldehyde emission than that of alkaline pH [18]. Manufacturer specification and details are provided and shown in Table 2.

Table 2 Properties of liquid and powdered MUF polymer resins

Properties	MUF polymer	
	MUL 600L	MUF 907-P
Generic Name	Melamine Urea Formaldehyde—liquid (MUF-L)	Melamine Urea Formaldehyde—powder (MUF-P)
Appearance	Milky white liquid	White powder
pH @ 30 °C	9.0–10.0	8.5–9.5
Viscosity	0.8–1.5	1750–3250 cP (mixed at 1:0.4 water ratio)
Specific gravity	1.21–1.29	Nil
Percentage volatile	0–5%	>3%
Solubility	<40%	Soluble in water
Chemical formula	$HO(CH_2-NH-CO-NH)_nCH_2O$	Nil

2.2 Sample Preparations and Procedures

In this study, wet and dry conditioning of treated peat mixtures in form of liquid and powder MUF resins were analysed based upon unconfined compressive strength characteristics at designated samples preparation and curing methods. Variations of moisture condition of treated mixtures were also affected by both liquid and powdered types of MUF resin. Initially, two group of peat specimens were prepared in association with peat soil moisture conditioning; wet and dry peat soils. Those wet peat specimens at natural moisture conditions were treated by both liquid and powdered MUF resins, while dry peat sample at OMC was treated only by liquid MUF resin to represent relatively dry moisture condition of the peat soil. Initially, relatively dry OMC peat samples were hardly mixed, became crumbly and difficult to be mixed with powdered MUF resin, thus excluded in the test schedule.

Essentially, wet conditioning of treated peat specimens were in reference to liquid type of MUF resin used in the mixture which was MUF-L and also high moisture content of peat soil. While dry conditioning term may refer to powdered MUF resin (MUF-P) and relatively reduced moisture content of OMC peat samples. Generally, liquid MUF (MUF-L) treated samples were cured under both air-dried and water submerging method, while specimen treated with powdered MUF resin only cured underwater submersion method. Dry conditioning of treated OMC peat sample treated with MUF-L resin was cured under air-dried curing method. On the other words, natural peat specimens with high moisture content were treated by both wet and dry conditioning form of MUF-L and MUF-P resins, respectively. In contrast, peat specimen at OMC only treated with MUF-L resin.

2.3 Mixing Methods

Natural peat soil was preliminarily sieved to separate organic particles such as roots and stones larger than 2 mm for wet conditioning procedures. One of the batches of peat soil specimens, with or without additional, sand filler were then mixed with liquid MUF (MUF-L) proportion of 350 kg/m^3, which was equivalently about 25% as per weight of peat soil and 12.5% MUF proportion for specimen with 50% of sand filler. Another batch of peat soil specimens only were treated with 15, 25 and 35% liquid MUF (MUF-L) resin by weight before cured at different methods of curing procedure. Third batch of natural wet peat specimens were mixed with powdered MUF (MUF-P) resin at proportion of 125, 250, and 350 kg/m^3. This mixture might also add with additional sand filler measured in ratio by weight to volume of peat similar to MUF-P polymer resin proportions. In cocntrast, dry conditioning treated peat specimens were initially prepared through Standard Proctor Test to obtain its OMC before mixed with liquid MUF resin of 10, 15, and 25% proportion. Practically in this study, powdered MUF polymer (MUF 907-P) only used to treat wet peat samples at natural moisture content after discovering it

Table 3 Test properties of liquid and powdered MUF polymer resins

Test properties	Type of binders (MUF polymer resin)	
	MUF 600L	MUF 907-P
Initial MC of Peat	OMC, natural MC	Natural MC
Mixing method	Dry, wet mixing	Wet mixing only
Curing method	Air-dry, water submerging	Water submerging
Compaction	Static compaction, surcharged load	Surcharged load

was difficult to handle the mixture after mixed with lower moisture content of peat soil. Table 3 shows test properties of both MUF- and MUF-P treated peat soil designed for this study.

2.4 Curing Method

Initially, two separate curing procedures involved for all types of treated specimen; air-dried and water submerging (wet) procedures. First batches of wet conditioning specimens with liquid MUF mixtures were cured following water submerging procedure for 1, 3, 7, and extended up to 14 days for both liquid MUF mixtures only and liquid MUF mixture with sand filler. Though, following batch of treated specimens with liquid MUF mixtures were cured under air curing procedures for 7 and 14 days. Consequently, experiment batch, with powdered MUF resin mixtures, was cured under water submerging procedures for 1, 3, 7, and 14 days period. In contrast, treated peat specimens mixed with liquid MUF resin at OMC condition were specifically cured under air-dried procedures for 1, 3, 7, and 14 days. In this study, both mixtures of MUF-L and MUF-P with peat soil cured using water submerging method were surcharged with 18 kPa of load to resemble on-site application which is practically imposed with additional surcharge up to 1 m.

2.5 Strength Characteristic and Testing Method

Peat soil commonly tested in laboratory by different types of shear strength test such as unconfined compressive strength (UCS), undrained shear strength, direct shear and direct simple shear, and ring shear test. The use of the UCS at different curing period and mixing condition allow for a rapid screening of a variety of different stabilizers and soil types along with other properties such as moisture content and modulus of elasticity. Essentially in this study, elastic modulus parameter based on Secant Modulus establishment was also examined accordingly. Though, UCS tests may tend to give conservative values of E_s as the computed value is too small resulting in measured value of ΔH being large compared with any

measured value [2]. UCS test was performed using a strain rate of approximately 1.5 mm per minute throughout of all specimens.

3 Results and Discussions

3.1 Development of Strength with Relation to MUF-L Proportion at Their Respective OMC—Air Curing Method

Figure 1 shows curves of UCS against 14 days curing period (air curing method) based on Optimum Moisture Content (OMC) samples of 15 and 25% MUF-L proportion. As noticed in the figure, development of strength in term of UCS for each sample at their respective OMC is correspondingly proportional to curing period and MUF-L content increased. In particular, higher MUF-L proportion with lower OMC value is proven to be significant in providing more strength gain effectively. Correlation between UCS and curing period for each MUF-L proportion based on their respective OMC can be established using power equation with respectable R^2 values, as shown in the figure.

3.2 Development Strength of Peat Soil Varied by MUF-L Proportion to Natural Moisture Content—Air Curing Method

UCS values of treated peat soil with MUF-L using air curing method under initial natural moisture content can be described in Fig. 2. From the graph, it shows that
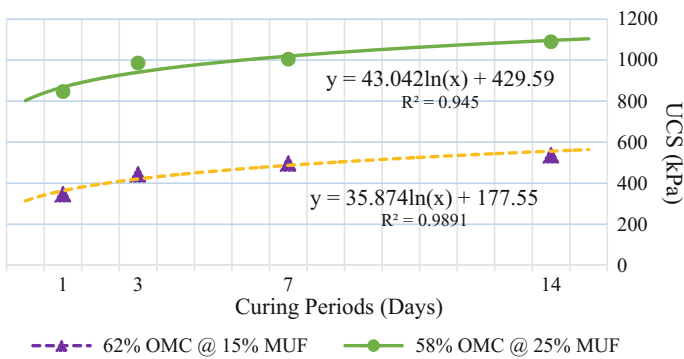
Fig. 1 UCS curves of treated peat soil with MUF-L at their respective OMC using air curing method
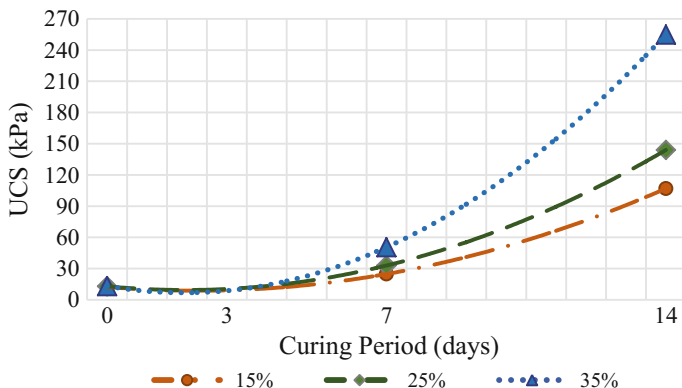
Fig. 2 UCS curves of treated peat soil with MUF-L at natural moisture content using air curing method

development of UCS for MUF-L treated samples is consistently increase up to 255 kPa through specified curing periods. This correlation can be explained by polynomial equation for all proportions of MUF-L. However as shown in the figure, improvement of UCS strengths at natural moisture content are lower if compared to OMC samples (Fig. 1) and insignificant during first week of curing periods.

3.3 Strength of Treated MUF-L Peat Soil with or Without Sand at Natural Moisture Content—Water Submerging Curing Method

Figure 3 compares curves between UCS of treated peat with MUF-L with and without sand as a filler against curing periods. From the graph, it shows that
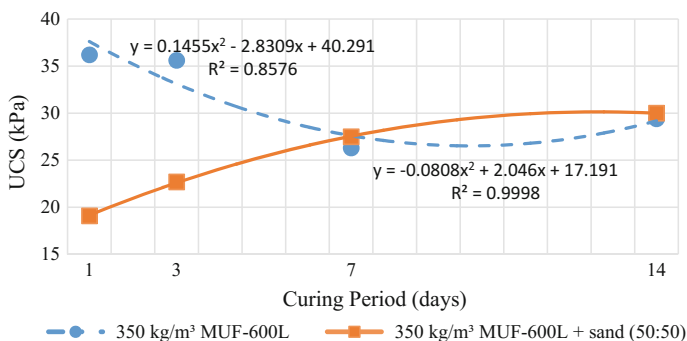
Fig. 3 UCS curves of treated peat soil with MUF-L at natural moisture content using water submerging curing method

development of UCS for MUF-L treated samples with sand filler was consistently increased up to 30 kPa through specified curing periods. This correlation can be explained by polynomial equation with satisfying R^2 value as shown in the figure.

However, strength curve for treated peat soil with only MUF-L shows decrease of UCS following similar polynomial relationship. Though, correlation of established equation is compromised by lower R^2 value. Lower UCS gain for MUF-L treated samples with sand filler was expected at the beginning of curing period as proportion of MUF in the mix was only around 175 kg/m^3 compared to MUF-L-only proportion. Evidently, through better inter particles and fabric bonding of treated sample with considerable increase of density due to addition of sand filler, UCS gain was improved at the end of targeted curing period.

3.4 Strength of Treated MUF-P Peat Soil with or Without Sand at Natural Moisture Content—Water Submerging Curing Method

In Fig. 4, improvement of UCS values is shown to be more significant for peat soil treated with MUF-P without additional sand filler. At 3 days of targeted curing period, UCS improvement was achieved at 90 kPa and further increased about 143 kPa after 7 days of curing. Noticeably, at slightly lower proportion of 125 kg/m^3, MUF-P only treated samples, UCS gain was equivalent to 350 kg/m^3 MUF-P treated sample with sand filler from the very beginning of curing period. In contrast, similar application of additional sand filler to peat soil treated with MUF-L was shown to be positive for greater UCS improvement as described in previous Fig. 3.
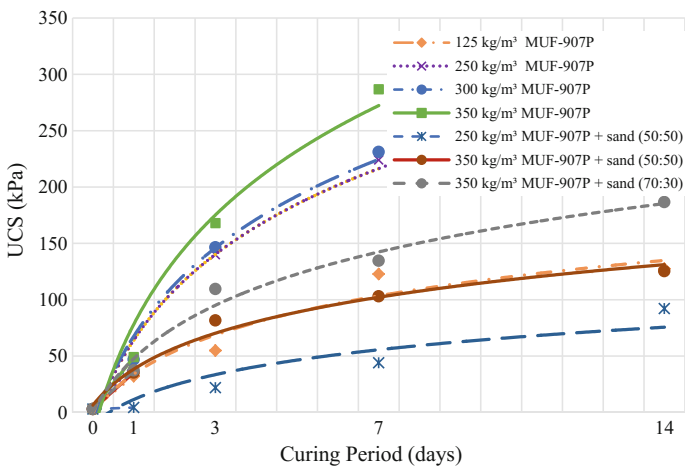
Fig. 4 UCS curves of treated peat soil with MUF-L at natural moisture content using water submerging curing method

3.5   Elastic Modulus of Peat Soil Treated with MUF-P Polymer Resin

In Fig. 5, elastic modulus of treated peat samples with both 250 and 350 kg/m^3 MUF-P polymer resin are shown correspondingly as determined using Secant Modulus (E_s). From the graph, elastic modulus of treated peat samples developed from stress–strain relationship is proportionally improved with both MUF-P content and curing periods. Using higher proportion of MUF-P at 350 kg/m^3, greater elastic modulus was achieved particularly at 3 and 7 days of curing periods. Tested samples treated with 250 kg/m^3 MUF-P shows significant improvement of elastic modulus at 10515 kPa after 14 days of prolonged curing period.
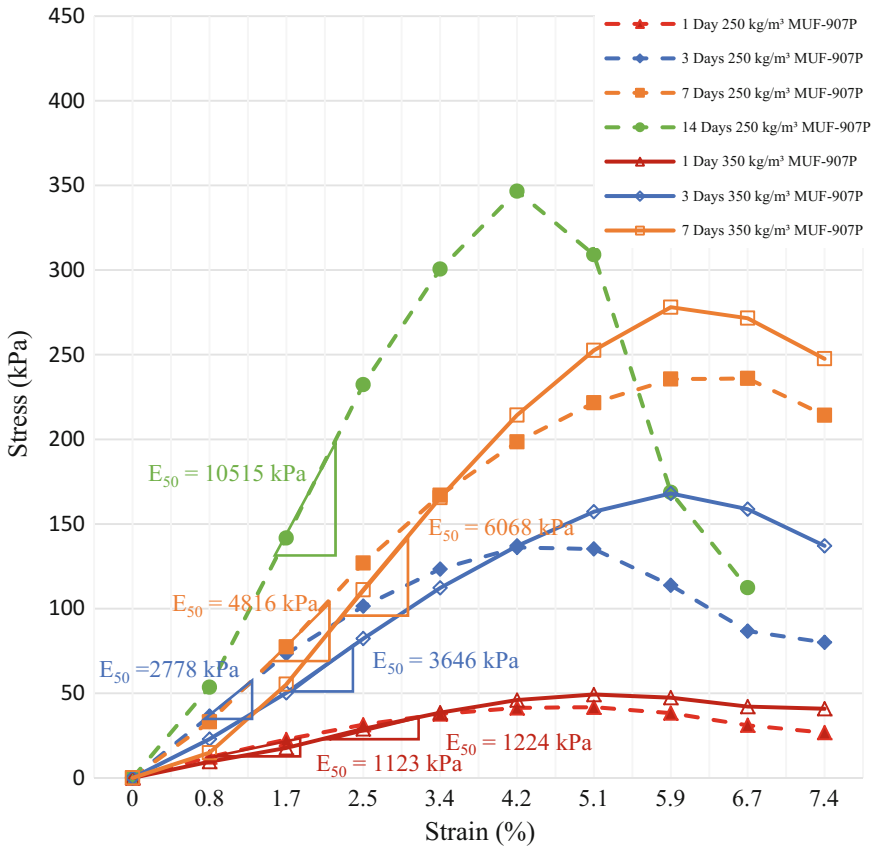
Fig. 5 Elastic Modulus, E_s of treated peat soil with MUF-P at natural moisture content using water submerging curing method

4 Conclusion and Recommendation

Study on peat soil samples treated with MUF polymer resins under both dry and wet mixing condition has advanced the knowledge on the strength characteristic particularly in term of UCS values. Consequently, conclusions of the study can be drawn as follows:

- Unconfined Compressive Strength (UCS) of peat soil can be improved significantly when treated with MUF-L polymer resin using dry mixing method up to 1090 kPa within 14 days of air-dry curing period. Apparently, high strength of stabilized peat using liquid MUF was achievable with OMC peat samples benefiting from lower range of moisture content in the samples due to preparation method in order to achieve its target strength.
- Peat soil with natural moisture content has also exhibited considerable increase in UCS when mixed with wet MUF-L polymer resin and cured using air-dry method without any compaction during 14 days of curing periods. Maximum 255 kPa of UCS can be achieved at day 14 but with considerable amount of MUF polymer resin. The need for higher proportion of MUF-L was mainly caused by high content of moisture in the natural samples if compared to OMC peat samples.
- On the other hand, UCS of treated peat with MUF-L (with and without sand as a filler) has exhibited considerably weak characteristic of strength gain. Although improvement of UCS was noticeable during 14 days of curing period, the increment was fairly insignificant. This can be explained by the nature of wet mixing method using liquid-type MUF polymer resin with naturally wet peat sample of very high moisture content. Noticeably, additional sand filler may only have improved density of the treated samples, but not the strength characteristic of the wet peat soil.
- However, UCS of treated peat soil using dry mixing method utilizing MUF-P has apparently improved the strength characteristic of naturally wet peat soil with high moisture content. Conclusively, powdered-type of MUF polymer resin such as MUF-P used in this study had significantly improved peat soil strength in term of UCS and elastic modulus, E_s with high moisture content for at least 3–7 days of rapid curing periods under water submerging curing method.

References

1. Kempfert, H.G., Gebreselassie, B.: Excavations and Foundations in Soft Soils. Springer, Berlin (2006)
2. Naeini, S.A., Masoud, G.: Effect of wet and dry conditions on strength of silty sand soils stabilized with epoxy resin polymer. J. Appl. Sci. **22**, 2839–2846 (2010)
3. Naeini, S.A., Naderinia, B., Izadi, E.: Unconfined compressive strength of clayey soils stabilized with waterborne polymer. KSCE J. Civ. Eng. **16**(6), 943–949 (2012)
4. Santoni, R.L., Tingle, J.S., Nieves, M.: Accelerated curing of silty sand using non-traditional additives. J. Transp. Res. Board **1936**, 34–42 (2005)
5. Ajayi-Majebi, A., Grissom, W.A., Smith, L.S., Jones, E.E.: Epoxy- resin-based chemical stabilization of a fine poorly graded soil system. Transp. Res. Rec. **1295**, 95–108 (1991)
6. Gopal, R.J., Singh, S., Das, G.: Chemical stabilization of sand comparative studies on urea-formaldehyde as dune sand stabilizer and effect of compaction on strength (Part IV). Indian Soc. Desert Technol. **8**(2), 13–19 (1983)
7. Brandon, T., Brown, J., Daniels, W.: Rapid stabilization/polymerization of wet clay soils. Lit. Rev. (2009)
8. Edil, T.B.: Recent advances in geotechnical characterization and construction over peats and organic soils. In: Huat et al. (eds.) Proceedings of 2nd International Conference on Advances in Soft Soil Engineering and Technology, pp. 3–25. Putrajaya, Malaysia (2003)
9. Mc Manus, K., Hassan, R., Sukkar, F.: Founding embankments on peat and organic soils. In: Huat and Bahia (eds.) The Proceedings Conference on Recent Advances in Soft Soil Engineering, pp. 351–367. Sarawak (1997)
10. Hashim, R., Islam, M.S.: Properties of stabilized peat by soil-cement column method. Electron. J. Geotech. Eng. **13J** (2008)
11. Kazemian, S., Huat, B.B.K.: Compressibility characteristics of fibrous tropical peat reinforced with cement column. Electr. J. Geotech. Eng. **14C** (2009)
12. Kalantari, B., Huat, B.: Precast stabilized peat columns to reinforce peat soil deposits. Electron. J. Geotech. Eng. **14**, 1–15 (2009)
13. Guidelines for Construction on Peat and Organic Soils in Malaysia. Construction Research Institute of Malaysia (2015)
14. Kalantari, B., Huat, B.B.K.: Peat stabilization using ordinary Portland cement, polypropylene fibers, and air curing techniques. Electron. J. Geotech. Eng. **13**, 1–13 (2008)
15. Zainorabidin, A., Bakar I.: Engineering properties of in-situ and modified hemic peat soil in Western Johore. In: Proceedings of 2nd International Conference on Advances in Soft Soil Engineering and Technology, Putrajaya, Malaysia, pp. 173–182 (2003)
16. Ling, F., Kassim, K., Karim, A., Tarmizi, A.: Geotechnical properties of Malaysian organic soils (case study: Batu Pahat, Johor). Int. J. Integr. Eng. **6**(2), 52–59 (2014)
17. Nik Daud, N.N., Daud, M.N.M.: Characterization of peat soil treated with polymer resin by unconfined compressive strength test. J. Adv. Civ. Eng. Prac. Res. **1**(1), 11–17 (2015)
18. Chung-Yun, H., Feng, F., Hui, P.: Melamine-modified urea formaldehyde resin for bonding particleboards. For. Prod. J. **58**(4), 2008 (2008)

Screw Plate Load Test in the Estimation of Allowable Bearing Capacity in Cohesive Soil Deposit

Sarah Tahsin Noor, S. M. Bodrul Haider and Shamsul Islam

Abstract Allowable bearing capacity is often indirectly estimated from the measurements of field tests without conducting further laboratory tests on undisturbed soil samples. Standard penetration resistance (SPT N-value), widely practiced all over the world, can give reliable indication about the strength or bearing capacity of cohesion-less soil strata only. However, in clay strata, SPT N-values obtained may be too small (e.g., 1 or 2), though the strata is not actually as weak as the degree indicated in SPT. In this respect, screw plate load test (SPLT) can be considered an advantageous means for obtaining load-settlement curve in undisturbed field condition at any depth below the ground. In this study, SPLTs at three different depths and unconfined compressive strength tests conducted on the undisturbed samples collected from the cohesive strata under consideration were conducted. This chapter presents the performance evaluation of SPLT in determining allowable bearing capacity as compared to the ones obtained by using undrained cohesion in the bearing capacity equation. As compared to the SPLT results, the bearing capacity equations are found in close agreement for stiff clay (Location-1), overestimating for firm clay (Location-2) and slightly underestimating for very stiff clay (Location-3). SPLT is found to indicate more representative q_a values, as the strengths of the soils below the test depth are reflected in the result.

Keywords Allowable bearing capacity · Screw plate load test · Bearing capacity equation

S. T. Noor (✉) · S. M. B. Haider
University of Asia Pacific, Dhaka 1215, Bangladesh
e-mail: sarah@uap-bd.edu

S. M. B. Haider
e-mail: parvez660@yahoo.com

S. Islam
Prosoil Foundation Consultant, Dhaka 1205, Bangladesh
e-mail: prosoil_9@hotmail.com

1   Introduction

Allowable bearing capacity is often indirectly estimated from the measurements of
in situ tests without performing undisturbed soil sampling for laboratory testing.
Undisturbed sampling of sand soft clay is difficult. In this respect, standard pene-
tration test is widely practiced all over the world. Standard penetration resistance
(SPT N-value) can give reliable indication about the strength or bearing capacity of
cohesion-less soil strata only. However, in clay strata, SPT N-values obtained may
be too small (e.g., 1 or 2), though the strata is not actually as weak as the degree
indicated through the results of SPT. Nowadays, the use of historical empirical
correlation between SPT N and undrained shear strength (or) cohesion is questioned
for fine-grained soil [1]. In such cases, the allowable bearing capacity determined
from SPT N-value may not be reliable.

Instead, screw plate load test (SPLT) is the means that can provide
load-settlement curve in undisturbed field condition at any depth below the ground.
Therefore, allowable bearing capacity can be evaluated reliably and directly at
different depths in both cohesive soil and cohesion-less deposits through conducting
SPLT [2]. An advantage of SPLT system is that the load test can be performed at
various depths in a borehole without removal of the soil. SPLT has added advan-
tages over ordinary plate load test (PLT) [3–8].

This chapter presents the results of screw plate load test and unconfined com-
pressive strength tests on the undisturbed samples collected from the same test site.
The performance of SPLT in estimating allowable bearing capacity was evaluated
and found in good agreement with those obtained by using strength parameter
(cohesion), as determined from unconfined compressive strength (UCS) tests, in
bearing capacity equations.

2   Test Program and Test Site

In this study, three SPLTs were carried out at the test site—Ghorashal, Bangladesh.
Three different depths (2, 3 and 3.5 m), within the cohesive soil layers of the test
site, were considered for conducting these tests. In addition, undisturbed soil
samples were collected from each depth for conducting unconfined compressive
strength (UCS) test in the laboratory.

3   Screw Plate Load Test and Results

A helical shaped plate is screwed into the ground to the depth of test without
disturbing the soil. A typical arrangement of SPLT is shown schematically in
Fig. 1. The test setup of this study is shown in Fig. 2.
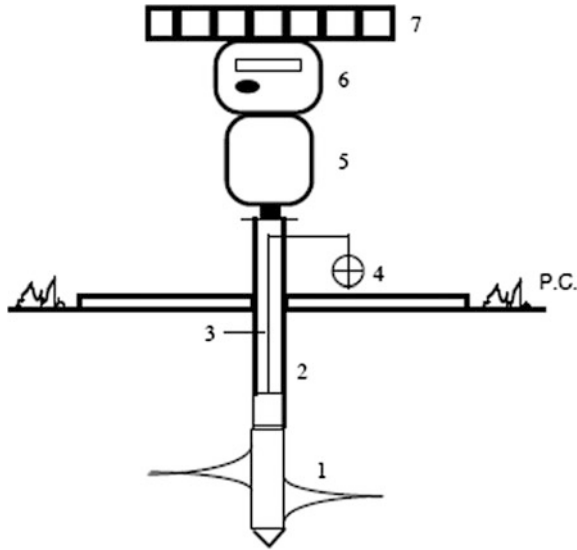
Fig. 1 Schematic diagram of screw plate load test arrangement; 1-plate, 2-external rod, 3-rod, 4-internal comparator, 5-hydraulic jack, 6-load cell, 7-contrast

Fig. 2 Screw plate load test setup

The helical plate, with a diameter 200 mm and equivalent area 315 cm^2, was connected to the other arrangements (namely loading device, data logger, etc.) at the ground surface with a system of coaxial rods that allow plunging. The pitch of the propeller was synchronized with the speed of rotation of the system of plunging.

A hole that was approx. 254 mm in diameter and slightly larger than the plate, was bored by drilling. The helical plate was lowered to the base of the hole and then advanced further about 300 mm (i.e. 1.5 times the plate diameter) by rotation to reach the test depth. A hydraulic jack was provided between the load cell and the rod. The load was applied by the hydraulic jack and measured by a digital data logger connected to a load cell. Two dial gauges (sensitive to measure 0.01 mm) were used to measure the settlement of the helical plate, as shown in Fig. 2. A load of 100 kg is applied for seating the plate and then released after 15 min. The load was then applied with increment of 0.5 ton.

For each load, the settlement of the plate was recorded from both the dial gauges in different intervals, such as 1, 2, 5, 10 and 20 min and the average reading was considered the settlement of the plate for that load. The loading continued up to the maximum load of 4 tons and followed by unloading in an increment of 1 ton.

The load intensity and settlement observations of the SPLTs are plotted in the form of pressure-settlement curve. The pressure-settlement curves obtained at Locations 1–3 are shown in Figs. 3, 4 and 5, respectively. From the pressure-settlement curve, ultimate bearing capacity of the soil below the test depth is taken as the stress corresponding to settlement of 25 mm.

The ultimate bearing capacity was obtained 6.25, 3.74 and 15.25 kg/cm^2 at locations 1–3, respectively. The allowable bearing capacity was calculated 2.1, 1.25 and 5.1 kg/cm^2 at locations 1–3, respectively, by applying a factor of safety 3.
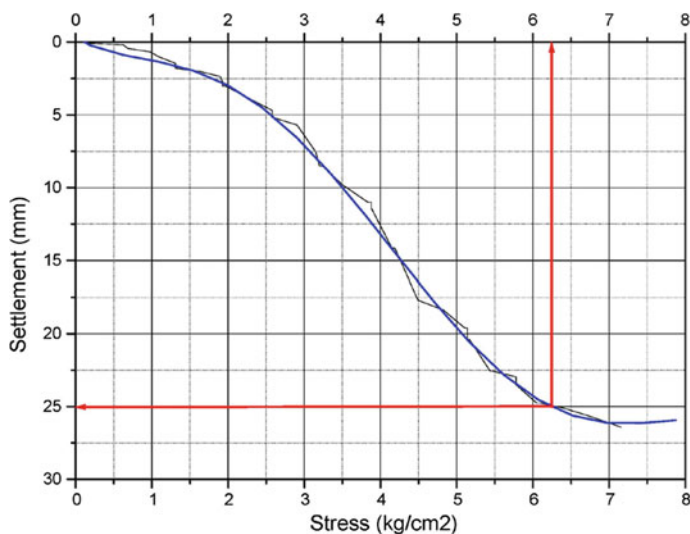
Fig. 3 Stress versus settlement curve from SPLT at 3.5 m depth of location-1
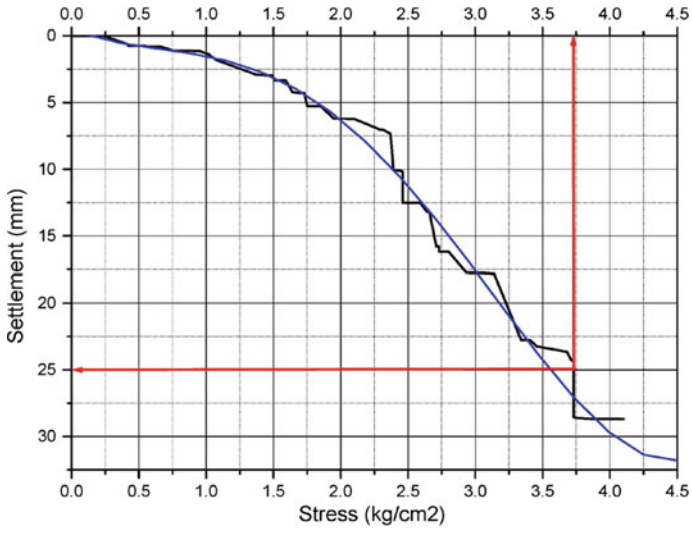
Fig. 4 Stress versus settlement curve from SPLT at 3 m depth of location-2
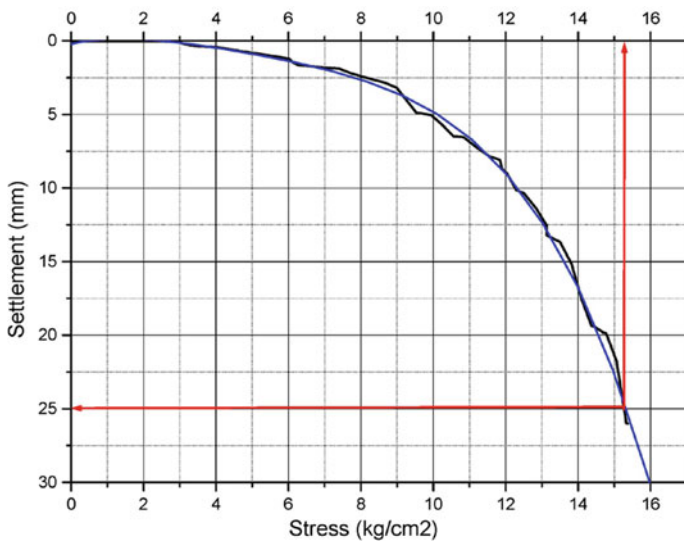
Fig. 5 Stress versus settlement curve from SPLT at 2 m depth of location-3

4   Allowable Bearing Capacity from Undrained Cohesion

Allowable bearing capacity (q_a) is determined using the following equation.

$$q_a = c_u \cdot N_c / \text{ F.S},\qquad(1)$$

where

c_u undrained cohesion
N_c bearing capacity factor with 'c' term
F.S   factor of safety.

Undisturbed samples were collected from the test depths for determining undrained cohesion by conducting unconfined compressive strength tests. The laboratory test setup of unconfined compressive strength test is shown in Fig. 6.

The stress–strain curve is drawn from the data recorded during each test, as shown in Figs. 7, 8 and 9.

From the stress–strain curve, the unconfined compressive strength (q_u) is determined at 15% strain and the values of q_u are obtained 180, 150 and 443 kPa for Locations 1–3, respectively. Consequently, the undrained shear strengths

Fig. 6 Unconfined compressive strength test set up

Fig. 7 Stress–strain curve for the sample from 3.5 m depth (location-1)
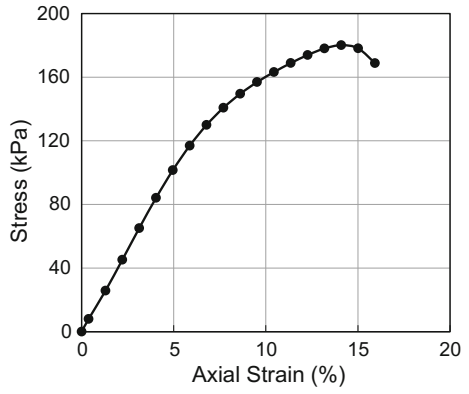
Fig. 8 Stress–strain curve for the sample from 3 m depth (location-2)
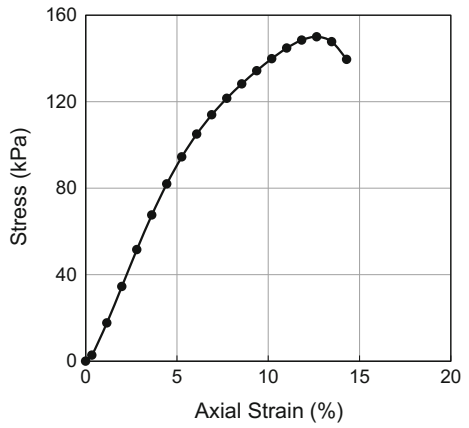
Fig. 9 Stress–strain curve for the sample from 2 m depth (location-3)
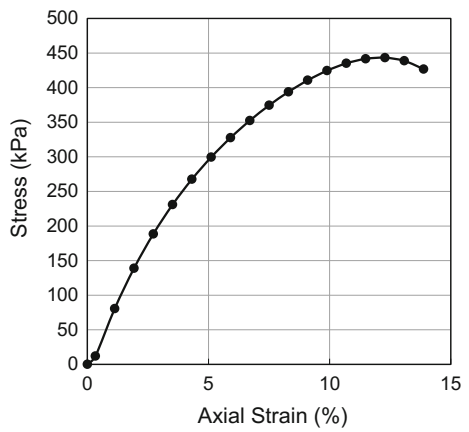
Table 1 Comparison of results

Location	References	Allowable bearing capacity		
		Strip footing (BC-equation) (kg/cm^2)	Square footing (BC-equation) (kg/cm^2)	SPLT (kg/cm^2)
1	Skempton [9]	2.20–1.87	2.60–2.24	2.10
	Meyerhof [10]	2.30–1.81	2.77–2.18	
	Hansen [11]	2.85–2.00	3.75–2.64	
2	Skempton [9]	1.76–1.53	2.13–1.83	1.25
	Meyerhof [10]	1.84–1.49	2.20–1.78	
	Hansen [11]	2.22–1.61	2.93–2.13	
3	Skempton [9]	4.96–4.27	5.89–5.17	5.10
	Meyerhof [10]	4.90–4.21	5.88–5.06	
	Hansen [11]	5.68–4.48	7.40–5.84	

(i.e. undrained cohesion,) of the samples are obtained 90 kPa (stiff clay), 75 kPa (firm clay) and 221 kPa (very stiff clay) for Locations 1–3, respectively. The dry unit weights were determined 1.65, 1.62 and 1.81 gm/cm^3, and the moisture contents were determined 26, 25 and 20% at the test depths in Locations 1–3, respectively.

These values of c_u are used to estimate q_a employing Eq. 1 for each case. The values of N_c obtained from [9–11] are used in estimating q_a. While using the value of N_c from [10], depth factor is also applied. For each location, the values of q_a are calculated for both strip and square footings, as given in Table 1. For each case, footing width was varied up to 2.5 m. Therefore, a range of q_a is obtained for each case.

5 Comparison of Results

The q_a values calculated from undrained cohesion and SPLTs are compared in Table 1 for all three locations. In calculating q_a, the factor of safety was considered 3.

It can be noted that the q_a value from SPLT falls within the range of values calculated from the equation using c_u for strip footing in Location-1. However,

in Location-2, the equation gives greater values of q_a than SPLT. On the other hand, the q_a from SPLT is greater than those obtained from the equation in Location-3. SPLT is found to indicate more representative q_a values, as the strength of the soils below the test depth are reflected in the result. Instead, while estimating q_a using the equation that solely depends on the c_u, several undistorbed samples from the depths below the test depth were needed to be determined through a lengthy process. There is a possibility of having more weak soils than that at the test depth in Location-2 and opposite case is noted in Location-3. It is found that the soils collected from Locations-1, 2 and 3 are stiff, firm and very stiff clays, respectively. Hence, the performance of the equation in estimating q_a is found the best for stiff clay (Location-1), overestimates for firm clay (Location-2) and slightly underestimates for very stiff clay (Location-3).

6 Conclusions

In this study, q_a obtained from SPLT is found in close agreement with the one estimated using c_u for strip footing in stiff and very stiff clays. Moreover, in firm soil, SPLT gives q_a values smaller than that obtained from the Eq. 1. For increased footing width, the deviation increases for strip footing but decreases for square footing 3. For stiff organic clay, pressure-settlement curve from SPLT indicates that the soil is significantly weak to resist load. Given the difficulty of performing sampling undisturbed in many soils (sand, heterogeneous terrains etc.) and the obvious problems of rehash connected to the same sampling (stress release), the test Screw plate arises as a valid alternative instrument for the assessment of certain characteristic parameters of the soil.

References

1. Reid, A., Taylor, J.: The misuse of SPTs in fine soils and the implications of Eurocode 7. Ground Eng. **43**(7), 28–31 (2010)
2. Noor, S.T., Islam, S., Haider, S.M.B.: Screw plate load test and SPT in the estimation of allowable bearing capacity. In: 1st International Conference on Advances in Civil Engineering. Infrastructure and Construction Materials, pp. 730–737 (2015)
3. Marr, W.A. (ed.): A History of Progress: Selected U.S. Papers in Geotechnical Engineering. ASCE Publications (2003)
4. Blight, G.E.: Unsaturated Soil Mechanics in Geotechnical Practice. CRC Press (2013)
5. Huat, B.B.K., Prasad, A., Asadi, A., Kazemian, S.: Geotechnics of Organic Soils and Peat. CRC press (2014)
6. Lee, Y.S., Hwang, W.K., Choi, Y., Kim, T.H.: Development and calibration of screw plate load tests. In: Proceedings of 19th International Offshore and Polar Engineering Conference. International Society of Offshore and Polar Engineers (2009)
7. Kim, T.H., G.C. Kang, G.C., Hwang, W.K.: Developing a Small Size Screw Plate Load Test. Marine Georesour. Geotechnol. **32**(3), 222–238 (2014)

8. Rowe, R.K. (ed.): Geotechnical and Geoenvironmental Engineering Handbook. Springer Science & Business Media (2012)
9. Skempton, A.W.: The bearing capacity of clays. Proceedings of Building Research Congress **1**, 180–189 (1951)
10. Meyerhof, G.G.: Some recent research on the bearing capacity of foundations. Can. Geo-tech. J. **1**(1), 16–26 (1963)
11. Hansen, J.B.: A General Formula for Bearing Capacity. Danish Geotechnical Institute, Copenhagen, Denmark. Bulletin 11, pp. 38–46 (1961)

Effect of Lime Stabilization on the Alteration of Engineering Properties of Cohesive Soil

Sarah Tahsin Noor and Rokon Uddin

Abstract The scarcity of land is ever increasing all over the world. Thus, ground condition is often improved through different techniques (such as soil stabilization using admixtures, compaction sand drains, etc.) if the shear strength and bearing capacity of the subsoil is inadequate. Highway construction projects often demand soil stabilization at the construction site to attain the design specifications related to shear strength and CBR. In the present context, an experimental program was carried out to investigate the influence of two different admixtures (namely, cement and lime) on different geotechnical parameters (such as maximum dry density, optimum water content, liquid and plastic limits) of the original soil characteristics and also in improving the soil's shear strength and CBR. The admixtures are found to have significant influence in modifying the soil's properties. The lime (%) mixed with the soil does not influence optimum moisture content and maximum dry density but shows significant effects on shear strength and CBR. The outcome of this study will be useful in roads, highways and airfield pavement constructions.

Keywords Lime stabilization · Unconfined compressive strength
California bearing ratio

1 Introduction

Lime has a history of more than 2000 years for being used as construction material because the Romans used to apply lime in road construction, since the ancient time. Today, lime is widely applied in different construction projects of highways, railways, airports, embankments, etc. [1–3] for stabilizing, controlling erosion and improving the engineering properties of fine-grained soil. Due to the lack of good

S. T. Noor (✉) · R. Uddin
University of Asia Pacific, 1215 Dhaka, Bangladesh
e-mail: sarah@uap-bd.edu

R. Uddin
e-mail: rokonuddin1964@gmail.com

quality soil and the urge for reutilizing the poor quality excavated materials (e.g. clay), lime stabilization is now globally recognized as one of the most common soil stabilization methods because of its ease of construction and economy as well. Several researchers paid attention to investigate the influence of lime in improving the soil performance in terms of strength, stiffness and compressibility [4–10].

Addition of lime for soil stabilization can modify the properties of soil significantly, as four basic reactions (such as cation exchange, flocculation/agglomeration, carbonation and pozzolanic reaction) that take place in the soil–lime mixture [11, 12]. The alteration of long-term soil properties (e.g. improvement in strength and deformation behaviour of soils) is caused by pozzolanic reaction that might depend on the type and amount of clay minerals and duration of interaction [4].

Hence, in this study, the effects of the reactions, between clay minerals (present in the Dhaka clay) and lime, on the alteration of engineering properties of soil were investigated for different percentages of lime over a period of a month. The effect of additional pozzolanic agent (i.e. local fly ash) along with lime was also investigated.

2   Experimental Program

In this study, natural clay collected from Dhaka, Bangladesh was chosen. Different percentages of lime were added to Dhaka clay as stabilizing agent, and its effects were investigated on different engineering properties of soil. The untreated soil and the soil treated with lime were tested for the determination of liquid limit, plastic limit, optimum moisture content, maximum dry unit weight, unconfined compressive strength and CBR. While investigating unconfined compressive strength, the effect of fly ash that was added to the soil as an additional pozzolanic agent along with lime was also investigated.

In conducting liquid limit, plastic limit and standard Proctor tests, soil and lime (of predetermined quantity) were added with water and mixed thoroughly to form a mixture of uniform consistency and then waited for 1 h before conducting tests. Liquid limit test was conducted using Cassagrande's apparatus, and plastic limit test was conducted by thread rolling method.

The soil–lime mix was compacted at optimum moisture content in cylindrical metallic mould of 38 mm in diameter and 76 mm in length. Unconfined compressive strength test was conducted on the prepared samples after desired time periods (i.e. 3, 14 and 28 days). Soaked CBR tests were conducted for both untreated and treated soils.

3   Experimental Results and Discussions

When lime was added to Dhaka clay, improvement in workability was immediately observed. In literature, this immediate effect is believed to depend on the cation exchange capacity and the type of exchangeable ions present in the soil [3].

Liquid limit (LL), plastic limit (PL) and plasticity index (I_p) were determined for Dhaka clay with different percentages of lime varying from 0 to 12%, as shown in Fig. 1. According to Cassagrande's plasticity chart, the untreated Dhaka clay is classified as CL, while the soil with any percentage of lime changes the classification to ML. This implies that the natural clay soil is transformed to a silty soil due to lime stabilization. Similar observation was noted for black cotton soil studied by [3].

Unlike the residual soil studied in [2], both LL and PL of Dhaka clay increase with the increase of lime content. However, plasticity index (I_p) decreases for both the soils due to the increase in lime content. According to [3], index properties indicate that lime treatment will be favourable for Dhaka clay.

Standard Proctor compaction tests were carried out to determine the optimum moisture content of Dhaka clay in untreated natural composition and also that with different percentages of lime. The compaction curves obtained from this investigation are presented in Fig. 2.

It can be noted that percentage of lime added to the natural Dhaka clay does not show any significant influence on the maximum dry unit weight $\gamma_{d(max)}$ obtained from standard Proctor test. For addition of 8% or more lime, almost the same value of $\gamma_{d(max)}$ was obtained. The experimental results also show that the optimum moisture content increases from 15.5 to 21% due to the increase in lime content from 4 to 16%, respectively. Similarly, increase in optimum moisture content was also obtained even for silt soil [8], as lime changes the soil characteristics significantly. However, silt soil showed decrease in $\gamma_{d(max)}$ due to lime treatment.

In natural composition, the unconfined compressive strength of Dhaka clay as compacted at optimum moisture content was determined about 300 kPa. This chapter presents the unconfined compressive strength of Dhaka clay when

Fig. 1 Effect of different percentages of lime on the consistencies of Dhaka clay
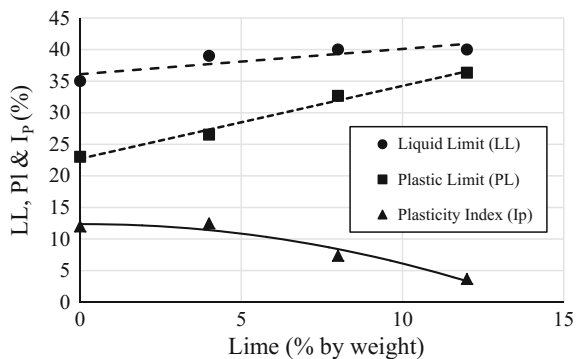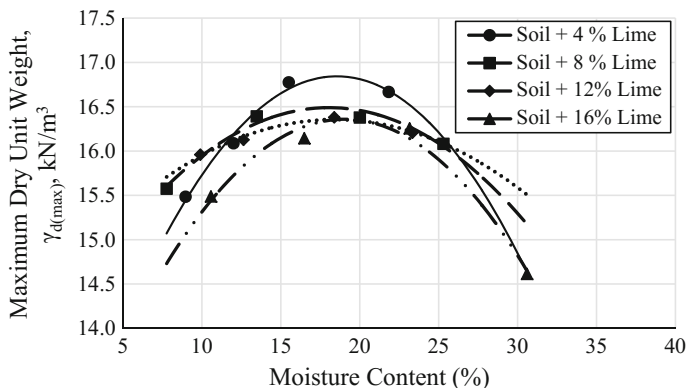
Fig. 2 Effect of different percentages of lime on compaction characteristics of Dhaka clay

stabilized with different percentages of lime and fly ash. The effect of ageing upon stabilization and compaction was also investigated at the same moisture content.

Figure 3 presents the stress–strain behaviour of the Dhaka clay stabilized with 4% lime at three different ages (3, 14 and 28 days) from unconfined compressive strength test results. It can be noted that the stabilized and compacted soil takes about a month to attain significant increase in undrained shear strength. At the age of 3 and 14 days, similar stress–strain behaviour was observed. The soil showed brittle behaviour at the age of 3 days but exhibit ductile type behaviour at the age of 14 or 28 days. Similar increase in unconfined compressive strength was observed in previous studies [6]. In addition, strain at failure had reduced below 1% after lime treatment in both cases.

Further, the effectiveness of lime admixture with/without additional pozzolanic agent, fly ash, was studied in terms of stress–strain behaviour in unconfined
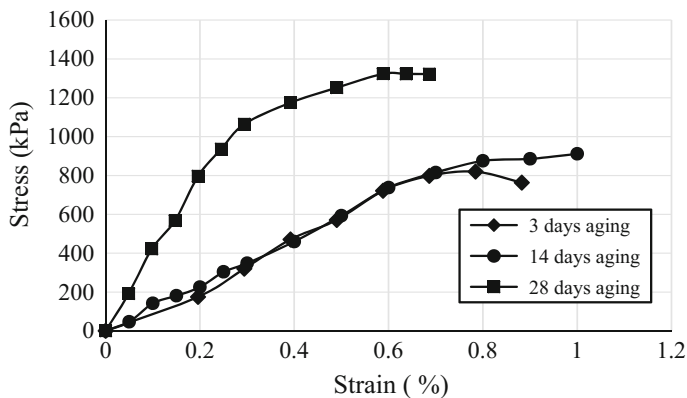
Fig. 3 Effect of ageing on unconfined compressive strength of Dhaka clay with 4% lime
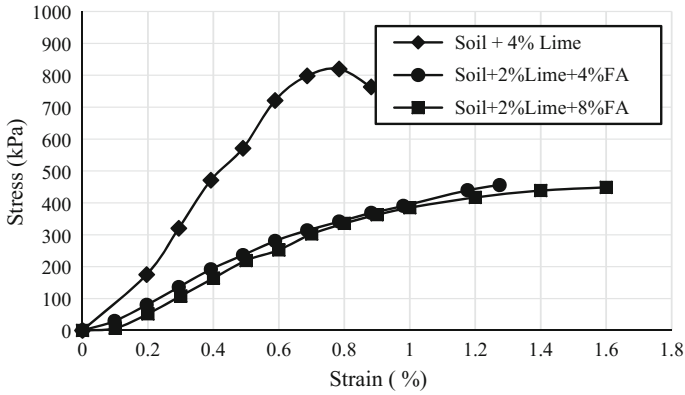
Fig. 4 Effect of different admixtures on unconfined compressive strengths of Dhaka clay at the age of 3 days

condition at the age of 3, 14 and 28 days, as shown in Figs. 4, 5 and 6. For this comparison, three different combinations of lime and fly ash admixtures, such as only 4% lime, 2% lime & 4% fly ash and 2% lime and 8% fly ash, were considered.

For all cases of stabilized soil, strain was observed below 1.5% at failure. At the age of 3 days, the percentages (4 or 8%) of fly ash with 2% lime did not show significant influence on the stress–strain behaviour.

Ultimately, soil stabilized with 2% lime with 8% fly ash showed greater undrained shear strength than that stabilized with 2% lime and 4% fly ash. In any case, soil stabilized with 4% lime gave significantly higher undrained shear strength than other two cases. Inclusion of additional pozzolanic agent was not found significant in increasing strength over a period of a month.
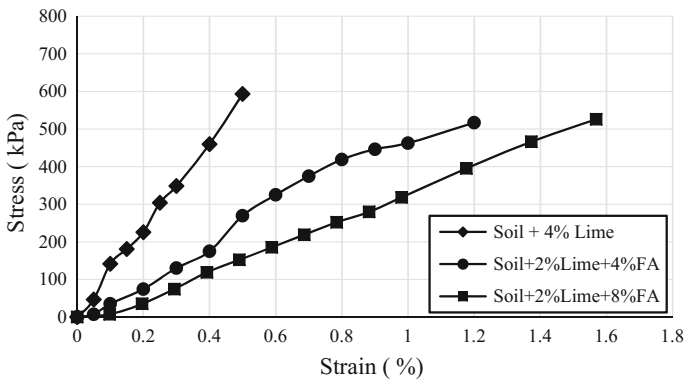
Fig. 5 Effect of different admixtures on unconfined compressive strengths of Dhaka clay at the age of 14 days
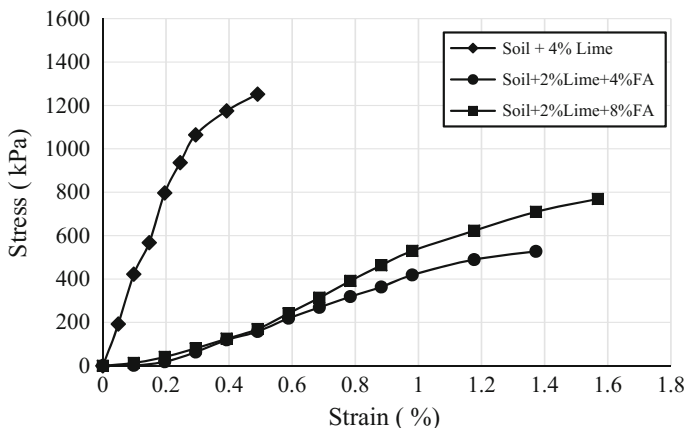
Fig. 6 Effect of different admixtures on unconfined compressive strengths of Dhaka clay at the age of 28 days

CBR tests were conducted on the soil samples in natural composition and also with different percentage of lime admixture. The stress versus penetration results are presented in Fig. 7. The CBR values are presented in Fig. 8.

It can be noted that though CBR of Dhaka clay (in natural composition) was obtained 4.5%, CBR values are greatly increased after stabilization with both 2% lime and 4% lime. CBR is found to vary linearly with the percentage of lime added to the soil for stabilization.
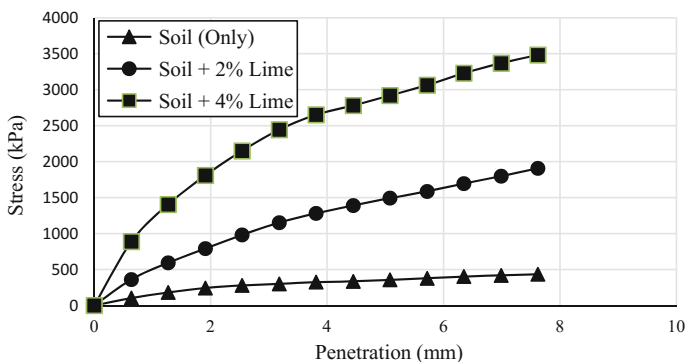
Fig. 7 Stress versus penetration curves from CBR tests

$$y = 7.3075x + 2.4583$$
$$R^2 = 0.9764$$
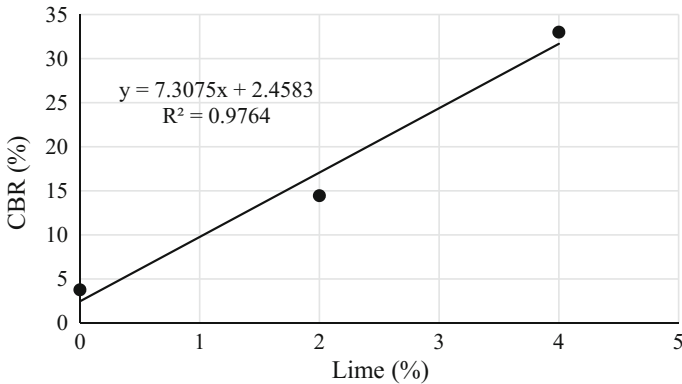
Fig. 8 Effect of lime admixture on CBR

4 Conclusions

Based on the experimental results and analysis, the following conclusions are drawn:

1. Addition of lime with Dhaka clay (i.e. CL) can significantly change the type of soil to low plastic silt according to unified soil classification system.
2. The optimum moisture content increases with the percentage of lime added to Dhaka clay for stabilization. The lime content has not shown any significant improvement in terms of $\gamma d(\max)$.
3. When the Dhaka clay is stabilized with 4% lime, the undrained shear strength can be obtained about four times higher than that in natural composition.
4. When fly ash is added in combination with lime, the rate of gaining undrained shear strength was observed slow.
5. CBR values were found to vary linearly with the lime content for Dhaka clay. Lime stabilization can be considered advantageous for improving the ground proposed for roads and highways.

References

1. Wilkinson, A., Haque, A., Kodikara, J., Adamson, J., Christie, D.: Improvement of problematic soils by lime slurry pressure injection: case study. J. Geotech. Geoenviron. Eng. **136**(10), 1459–1468 (2010)
2. Dash, S.K., Hussain, M.: Lime stabilization of soils: reappraisal. J. Mater. Civ. Eng. **24**(6), 707–714 (2012)
3. Sivapullaiah, P.V., Sridharan, A., BhaskarRaju, K.V.: Role of amount and type of clay in the lime stabilization of soils. Proc. Inst. Civ. Eng. Ground Improv. **4**(1), 37–45 (2000)

4. Manual, L.: Lime-Treated soil construction Manual-Lime stabilization and lime modification. Nat. Lime Assoc. USA Bulletin. 326 (2004)
5. Locat, J., Berube, M.A., Choquette, M.: Laboratory investigations on the lime stabilization of sensitive clays: shear strength development. Can. Geotech. J. **27**(3), 294–304 (1990)
6. Kavak, A., Akyarh, A.: A field application for lime stabilization. Environ. Geol. **51**(6), 987–997 (2007)
7. Rajasekaran, G., Rao, S.N.: Lime stabilization technique for the improvement of marine clay. Soils Found. **37**(2), 97–104 (1997)
8. Beeghly, J.H.: Recent experiences with lime-fly ash stabilization of pavement subgrade soils, base, and recycled asphalt. In: Proceedings of international ash utilization symposium, pp. 435–452 (2003)
9. Amu, O.O., Bamisaye, O.F., Komolafe, I.A.: The suitability and lime stabilization requirement of some lateritic soil samples as pavement. Int. J. Pure Appl. Sci. Technol. **2**(1), 29–46 (2011)
10. Rao, S.M., Shivananda, P.: Role of curing temperature in progress of lime-soil reactions. Geotech. Geol. Eng. **23**(1), 79 (2005)
11. Thompson, M.R.: Lime reactivity of Illinois soils. J Soil Mech. Found. Div. ASCE **92**(SM5), 67–92 (1966)
12. Bell, F.G.: Stabilization and treatment of clay soils with lime part 1 Basic principles. Ground Eng. **21**, 10–15 (1988)

Numerical Study of the Bearing Capacity of Embedded Strip Footings on Non-homogenous Clay Under Inclined Load

Mohamed Younes Ouahab, Abdelhak Mabrouki, Mekki Mellas and Djamel Benmeddour

Abstract The present study investigates the undrained bearing capacity for embedded strip footings under inclined loading on non-homogeneous clay. Elasto-plastic finite-element analyses are carried out through Plaxis code for perfectly rough strip footings on Tresca material. This study examines the influence of strength non-homogeneity and footing embedment ratio D/B, on the bearing capacity factor N_c^* of rigid footings for different load inclinations α. The numerical results were compared with the available results published in the literature.

Keywords Bearing capacity · Inclined load · Non-homogeneous clay

1 Introduction

The undrained bearing capacity of a strip footing on homogeneous clay is one of the problems that are widely studied by various methods. However most of these studies were carried out for strip footings under vertical loading. The offshore foundations are generally founded on soft soil with linear increase of cohesion with depth and subjected to vertical and horizontal loads due to the self-weight of structures, wind and wave forces. Undrained vertical bearing capacity of shallow foundations on non-homogeneous soil has been studied through analytical and numerical studies (e.g. [1–7] and recently [8]). They found that the strength non-homogeneity has a significant effect on the bearing capacity of shallow footings.

M. Y. Ouahab (✉) · A. Mabrouki · M. Mellas · D. Benmeddour
Civil Engineering Laboratory, Biskra University, BP 145, 07000 Biskra, Algeria
e-mail: ouahabmy@gmail.com

A. Mabrouki
e-mail: a.mabroukii@yahoo.fr

M. Mellas
e-mail: m_mellas@yahoo.fr

D. Benmeddour
e-mail: benmeddourdj@yahoo.fr

The problem of bearing capacity of shallow foundations on clay with strength gradient under combined loading has received significant attention (e.g. [9–16]). They found that the normalised failure envelopes of shallow foundations, under combined loading are dependent on the embedment depth and strength non-homogeneity. Several methods can be found in the literature to evaluate the bearing capacity of a rigid strip footing. These include the method of characteristics (slip-line method), the upper bound plastic limit analysis, the limit equilibrium calculations and the elasto-plastic analysis using the finite-element method or the finite-difference method. The bearing capacity problem of strip and circular footings has been studied by numerous researchers using the finite-element code Plaxis. In these studies, the plane strain elasto-plastic finite-element analysis was used.

In this paper, a series of numerical computations using the finite-element code Plaxis [17] are carried out to evaluate the bearing capacity factor N_c^*, for embedded strip footings subjected to centred inclined load on clay with linear increase of cohesion with depth.

2 Problem Presentation

The problem studied in this paper considers the effect of embedment ratio and linear increasing of cohesion with depth on the bearing capacity of a strip footing under inclined loading (Fig. 1). The undrained bearing capacity, for inclined loaded embedded strip footing is calculated as follows:

$$q_u = c_{u0}N_c^* \tag{1}$$

$$N_c^* = N_c i_c d_c, \tag{2}$$

where c_0 is the cohesion at the surface of soil (Fig. 1), N_c is the vertical bearing capacity factor, i_c and d_c are the inclination factor and the depth factor respectively,
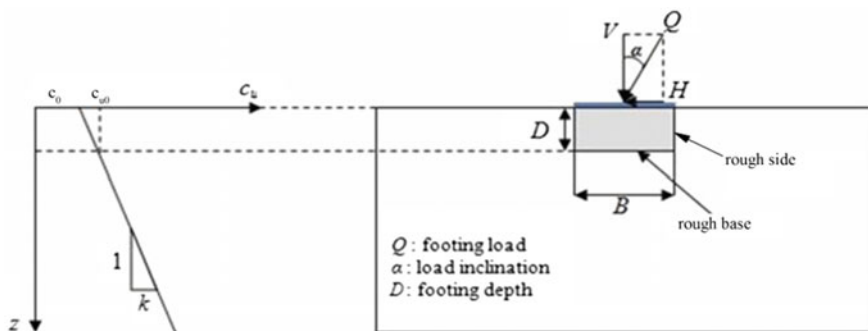
Fig. 1 Problem geometry

which represent correction factors, for the basic solution of pure vertical loading, that define the effects of load inclination and footing embedment respectively.

The undrained shear strength cu varies linearly with depth, expressed as follows:

$$c_u = c_0 + k \cdot z \tag{3}$$

$$c_{u0} = c_0 + kD, \tag{4}$$

where c_{u0} is the cohesion at the footing base level (Fig. 1) and k is the strength gradient with depth z, D is the depth of the footing.

The bearing capacity depends only on the degree of non-homogeneity represented by the dimensionless ratio $\kappa = kB/c_0$, and the embedment ratio D/B, where B is the footing width.

3 Numerical Procedures

In this paper, the finite-element code Plaxis was used, to evaluate the undrained bearing capacity for embedded strip footings on non-homogeneous clay under inclined loading, for practical range of non-homogeneity degrees ($\kappa = 0, 5, 10$ and 20) and the embedment ratios ($D/B = 0, 0.25, 0.5$ and 1). Because of the absence of loading symmetry, the entire soil domain of width 10B and depth 5B was modelled (Fig. 2).
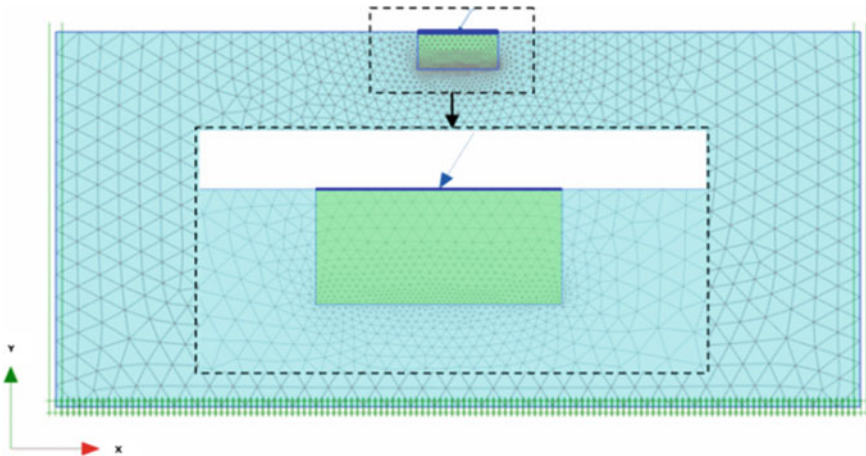
Fig. 2 Finite-element mesh with boundary conditions used in the analysis of rough strip footings, case of $\alpha = 30°$, $D/B = 0.5$

The soil domain is discretized as 15-node triangular elements. Several numerical tests have been carried out to examine the influence of the mesh size on the ultimate load. The effect of the mesh size on the ultimate load of strip footings was studied earlier by Frydman and Burd, [18]. The mesh around the footing edges is refined to capture significant deformations gradient. The right and left vertical sides of the models were constrained horizontally, while the base was constrained in all directions. The extent of the discretized domain is chosen to have no effect on the development of the failure mechanism. The boundary conditions and finite-element mesh for embedded strip footing are shown in Fig. 2.

In this study, the so-called "probe" loading technique is used (load control). The footing load is applied in increments up to failure under inclination angle α, ranges between 0 and 90°, with respect to the vertical. All finite-element analyses were carried out for embedded footings with rough bases and rough sides, so no detachment allowed in the interface between the soil and footings.

The soil was modelled as a Tresca material with increasing undrained shear strength and Young's modulus with depth ($v = 0.49$, $E_u = 500\ c_u$, $\gamma = 16$ kN/m^3). It was demonstrated by Mabrouki et al. [19] that the bearing capacity is insensitive to the elastic parameters of the soil.

It is worthwhile noting that the surface footing was modelled as a weightless rigid plate element (uniform settlement) with a significant Young's modulus and sufficient thickness, while the embedded footing was modelled as a rigid body with unit weight of 24 kN/m^3.

4 Numerical Results

4.1 Vertical Bearing Capacity (H = 0, V > 0)

The vertical bearing capacity factor N_c of 5.16 was predicted for a surface footing ($D/B = 0$) on homogeneous soil ($\kappa = 0$), using the elasto-plastic finite-element analysis. It is clear that the present bearing capacity factor only 0.4% higher than the exact value of 5.14 obtained by the analytical solution of Prandtl [20]. The elasto-plastic results obtained using Plaxis are in excellent agreement with those of Prandtl.

Figure 3 shows a comparison of the obtained N_c values with those of [8] for the cases of ($\kappa = 0$, D/B > 0) and ($\kappa > 0$, $D/B = 0$). The figure shows that N_c increases with increasing both of embedment depth and strength non-homogeneity. The numerical results from the present study are in good agreement with those of [8].
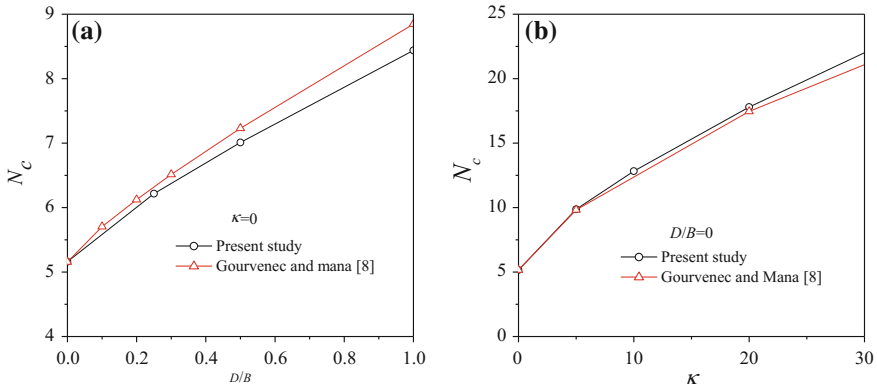
Fig. 3 Comparison of N_c values, for pure vertical loading ($\alpha = 0$)

4.2 Inclined Bearing Capacity (H > 0, V > 0)

The variation of N_c^* with increasing of load inclination (α), embedment ratio (D/B) and soil strength non-homogeneity is illustrated in Fig. 4. The influence of both α and D/B on N_c^* is evaluated through correction factors i_c and d_c that represent the influence of load inclination and embedment depth respectively.

For the case of homogeneous soil ($\kappa = 0$), Fig. 4a indicates that N_c^* increases with increasing footing embedment. On the other hand, for all values of κ and D/B,
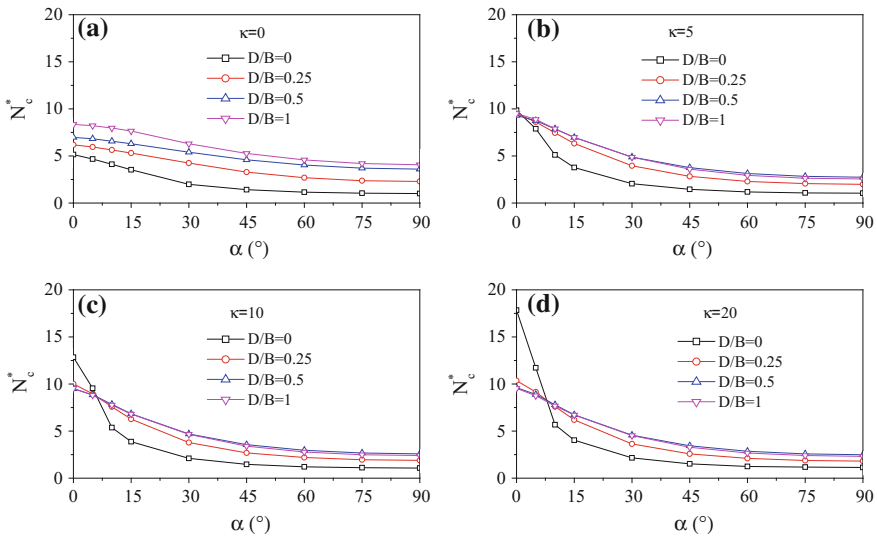
Fig. 4 Effect of κ and D/B on the variation of N_c^* with α

the factor N_c^* decreases with increasing of α. It is noted that for ($\kappa > 0$), the variation of N_c^* is found to depend on both c_{u0} and D/B. The general tendency is to increase with embedment ratio, with the exception of the cases where $D/B = 0$ and $\alpha = 0$.

5 Conclusions

The finite-element code Plaxis 2D was used to investigate the undrained bearing capacity of embedded strip footings in non-homogenous clay under inclined load. The aim of this paper was the evaluation of the bearing capacity factor N_c^* for a practical range of strength non-homogeneity and embedment D/B ratios. The elasto-plastic analysis gives an excellent estimate of the bearing capacity in the case of a strip footing subjected to a centred vertical load.

The N_c^* values depend on the load inclination, the strength non-homogeneity and the embedment depth. For all values of κ and D/B, the increase in the load inclination angle α reduces the N_c^* values. For the case of homogeneous soil ($\kappa = 0$), N_c^* increases with increasing footing embedment. The same tendency is observed for the case of $\kappa > 0$, with the exception of centrally loaded surface footing case.

References

1. Davis, E., Booker, J.: The effect of increasing strength with depth on the bearing capacity of clays. Geotechnique **23**(4), 551–563 (1973)
2. Griffiths, D.: Computation of bearing capacity on layered soils. In: Proceedings of the 4th international conference on numerical methods in geomechanics, Edmonton, Alberta, Canada, May. Balkema, Rotterdam, The Netherlands (1982)
3. Houlsby, G.T., Wroth, C.P.: Calculation of stresses on shallow penetrometers and footings. In: Proceedings of the IUTAM-IUGG symposium on seabed mechanics, Newcastle (1983)
4. Tani, K., Craig, W.H.: Bearing capacity of circular foundations on soft clay of strength increasing with depth. Soils Found. **35**(4), 21–35 (1995)
5. Kusakabe, O., Suzuki, H., Nakase, A.: An upper bound calculation on bearing capacity of a circular footing on a non-homogeneous clay. Soils Found. **26**(3), 143–148 (1986)
6. Al-Shamrani, M.A.: Upper-bound solutions for bearing capacity of strip footings over anisotropic nonhomogeneous clays. Soils Found. **45**(1), 109–124 (2005)
7. Yun, G., Bransby, M.: The undrained vertical bearing capacity of skirted foundations. Soils Found. **47**(3), 493–505 (2007)
8. Gourvenec, S., Mana, D.: Undrained vertical bearing capacity factors for shallow foundations. Géotechnique Lett. **1**, 101–108 (2011)
9. Ukritchon, B., Whittle, A.J., Sloan, S.W.: Undrained limit analyses for combined loading of strip footings on clay. J. Geotech. Geoenviron. Eng. **124**(3), 265–276 (1998)
10. Bransby, M., Randolph, M.: Combined loading of skirted foundations. Geotechnique **48**(5), 637–655 (1998)

11. Gourvenec, S., Randolph, M.: Effect of strength non-homogeneity on the shape of failure envelopes for combined loading of strip and circular foundations on clay. Geotechnique **53** (6), 575–586 (2003)
12. Bransby, M., Yun, G.J.: The undrained capacity of skirted strip foundations under combined loading. Geotechnique **59**(2), 115–125 (2009)
13. Gourvenec, S.: Undrained failure envelope for skirted foundations under general loading. Geotechnique **61**, 263–270 (2011)
14. Mana, D.S., Gourvenec, S., Martin, C.M.: Critical skirt spacing for shallow foundations under general loading. J. Geotech. Geoenviron. Eng. **139**(9), 1554–1566 (2012)
15. Vulpe, C., Gourvenec, S., Power, M.: A generalised failure envelope for undrained capacity of circular shallow foundations under general loading. Géotechnique Lett. **4**(3), 187–196 (2014)
16. Vulpe, C.: Design method for the undrained capacity of skirted circular foundations under combined loading: effect of deformable soil plug. Geotechnique **65**(8), 669–683 (2015)
17. Brinkgreve, R.B.J., Engin, E., Swolfs, W.M.: Plaxis user's manual., Netherlands: Plaxis, BV (2012)
18. Frydman, S., Burd, H.J.: Numerical studies of bearing capacity factor Nc. J. Geotech. Geoenviron. Eng. ASCE **123**(1), 20–29 (1997)
19. Mabrouki, A., Benmeddour, D., Frank, R., Mellas, M.: Numerical study of the bearing capacity for two interfering strip footings on sands. Comput. Geotech. **37**(4), 431–439 (2010)
20. Prandtl, L.: Über die härte plastischer körper. Nachrichten von der Gesellschaft der Wissenschaften zu Göttingen, Mathematisch-Physikalische Klasse, 74–85, (1920)

Evaluating the Compaction Behaviour of Soft Marine Clay Stabilized with Two Sizes of Recycled Crushed Tiles

Mohammed Ali Mohammed Al-Bared and Aminaton Marto

Abstract This paper focuses on stabilizing marine clay using recycled blended tiles (RBT) collected from construction sites at Johor, Malaysia. Marine clay is considered as problematic soil due to the existence of high moisture and organic contents, while RBT is a waste tile material produced in every construction area where those cracked or rejected tiles are dumped into landfills without any concern of the environmental impact. Hence, the suitability of RBT to treat marine clay is examined in this study. Standard proctor tests were conducted for all treated and untreated specimens. The compaction ability of treated and untreated marine clay was measured by adding two different sizes of RBT, i.e. 0.063 and 0.15 mm diameter. RBT for both sizes was added and tested in four different percentages (i.e. 10, 20, 30 and 40% of the dry weight of soil). The optimum moisture content (OMC) and Maximum Dry Density (MDD) for untreated samples were 22 and 1.59 Mg/m^3 respectively. Meanwhile, OMC and MDD varied from 18 to 16.5% and 1.66–1.72 Mg/m^3 respectively for those samples treated with 0.063 mm RBT. In addition, OMC and MDD for samples stabilized with 0.15 mm RBT varied from 18 to 17% and 1.70–1.74 Mg/m^3 respectively. For samples treated with 0.15 mm RBT, the higher is the percentage of additive, the higher the MDD and the lower the OMC. While for samples treated with 0.063 mm RBT, 30% was found to be the optimum value and further increment of RBT resulted in a reduction of MDD.

Keywords Soil stabilization · RBT · Sustainability

M. A. M. Al-Bared (✉) · A. Marto
Soft Soil Engineering Research Group, Faculty of Civil Engineering,
Universiti Teknologi Malaysia, 81310 Johor Bahru, Johor, Malaysia
e-mail: albared2009@yahoo.com

A. Marto (✉)
Malaysia-Japan International Institute of Technology,
Universiti Teknologi Malaysia, 54100 Kulala Lumpur, Malaysia
e-mail: aminaton@utm.my

1   Introduction

Development and high demand of construction at various civil engineering projects led to a corresponding reduction in all the natural resources, in particular, land resources. As a result, the limited availability of lands forced to build structures on weak soft soils. Soft soils are not suitable to be a structural support as they are not able to sustain the imposed loads [1]. Meanwhile, soft clayey soils are soils that are always associated with low shear strength and permeability, excessive settlement, high water content and high plasticity, and compressibility [2]. Soft soils absorb water extensively during wet or rainy season that make it swell under building and other structures foundations. On the other hand, during dry season, soft soils shrink resulting in the formation of cracks within the structures and other structural elements standing on top of soft soil. This problem costs a lot of money worldwide to repair the resulting defects from swelling and shrinking of soft soils. For instance, the average annual cost in UK was approximately 400 million Euro to repair the structural defects [3]. Furthermore, soft soils lack of many engineering properties required for construction such as strength and bearing capacity. Clay minerals such as montmorillonite are most responsible of the swelling behaviour of soft soils. The several engineering problems encountered with soft soils forced engineers and researchers to find new methods to improve those soils. Soft soil improvement depends largely on the type of construction, properties of soft soil, cost and environmental concerns [4]. High plasticity is also another poor characteristic of soft soil that make it undesirable for use as foundation for structures unless treated with proper stabilizer. Researchers investigated the suitability of conventional soil stabilizers (fly ash, lime, cement and cement kiln dust, etc.) and unconventional ones (chemicals, fibers, enzymes, etc.) long time ago [5]. Recent studies are looking for a stabilizing material that contributes to clean the surrounding environment and reduce the impacts created by those materials dumped in legal and illegal landfills.

Soil stabilization is a process at which one or more of the soil properties are modified or altered. The modification could be achieved chemically using traditional chemical additives, mechanically by compaction, biologically using bacteria, hydrologically by thermal processes or a combination of these methods. Due to the environmental considerations and hazards caused by using the chemical additives, nowadays researchers are into using stabilization methods that are environmental-friendly, economical and sustainable. Soil improvement by compaction is widely used in many geotechnical engineering applications. Soil compaction can be described as inducing increments in soil density with corresponding decrements in the air voids between the soil particles at a constant water volume. Soft clay soils can be compacted properly until it become nearly in an impermeable condition. Such condition may result in enhancing the shear strength of the soil and arrest the volume changes due to settlement [6]. According to Xia [7], soil compaction can be achieved by applying momentary loads (e.g. Vibrating and rolling) that result in decreasing the permeability and compressibility of soft soil. In geotechnical engineering, compaction is considered as one of the methods to enhance geomaterial's

strength. There is a considerable difference between cohesive and cohesionless soils, which is compacted by different methods. Cohesive soils generally contain silt and clay particles in sufficient amounts to provide nearly impermeable condition, when compacted using sheep foot compacter. Cohesionless soils contain sand and gravel which can be compacted using vibrating compacter. Moreover, compaction parameters are very important for all projects that need densification of soil. Highway and railway subgrades, foundation soils and landfills should take the compaction parameters into account [8].

Recycled materials are a matter of global concern of recent research in soil stabilization. In this paper, RBT refers to recycled blended ceramic tiles collected from construction sites to be used as stabilizing agent. Ceramic tile waste is generated at the manufacturing factories and during construction processes. Those ceramic tiles that are rejected at site create major environmental problems when it is accumulated in massive amounts in landfills. They affect the fertility of the soil and damage the growth of the vegetation at the accumulation areas. Hence, RBT is utilized to improve the mechanical properties of marine clay. Several standard proctor tests were conducted to assess the suitability of RBT to treat marine clay. The main focus of this study is to explore possible mix designs of the treated marine clay by monitoring the compaction parameters in terms of maximum dry density and optimum moisture content.

2 Materials Used

2.1 Soft Marine Clay

The marine clay used in this research was obtained about 1 m below the ground surface from a construction site at Nusajaya, Galang Patah, Johor, Malaysia. Figure 1 shows a Google map location of the area from which the marine clay was collected.

All marine clay in the site mentioned above is excavated, transferred and dumped into landfills as dredged soil. Marine clay used for this study was found to be in a black color (Fig. 2). It was transferred to the lab in black oil containers. Samples were collected in sealed air tight containers to measure the natural moisture content. Once the marine soil arrived into the laboratory, it was air dried for two week. Then, the soil was grinded using the grinder and stored in air tight containers. To conduct the index properties tests, soil sample was sieved to 2 mm size and oven dried at 105 °C for 24 h. The sieved sample was used to conduct specific gravity, liquid limit, plastic limit, organic content and natural moisture content in accordance with BSI 1924: Part 2: 1990 [9]. Table 1 illustrates the average values for all the index properties tests of the tested marine clay. The amount of organic contents was found to be less than 10% which according to Wong et al. [6] indicate that the soil is inorganic. According to BS 5930:1999 [10]

Fig. 1 Sampling site of marine clay

Fig. 2 Untreated marine clay sieved to 2 mm size

Table 1 Basic properties of untreated marine clay

Soil properties	Average value
Natural moisture content (%)	59
Specific gravity	2.52
Organic contents (%)	2.74
Liquid limit (%)	41
Plastic limit (%)	22
Plasticity index (%)	19
Optimum moisture content (%)	22
Maximum dry density (kg/m^3)	1590

and based on the liquid limit and plasticity index results, it can be interpreted from the plasticity chart that the soil is CLAY with intermediate plasticity with group symbol CI and the clay content was confirmed by the hydrometer analysis.

2.2 Recycled Blended Tiles (RBT)

Ceramic tiles wastes can generally be described as a solid, inorganic and non-metallic material. Pottery objects were the first ceramic made by human beings using clay and water only. Nowadays, ceramic tiles mainly made from clay, sand and feldspar mixed sometimes with silica. It is burned in ovens with a very high temperature in order to create a colourful and smooth texture. In this paper, recycled ceramic tiles were collected from three construction sites at Ponderosa, Impian Heights Golf and Country Club and Taman Pelangi, Johor, Malaysia. RBT used in this study were those rejected during construction due to design failures and appearance of cracks/smashes on the surface. Besides, the wastage generated by cutting tiles into specific sizes at site, especially those that have design errors. Figure 3 shows crushed RBT utilized for this research. Furthermore, RBT used in this study was prepared in several steps in order to obtain the required sizes. First, the tiles were cleaned by removing materials that stick on its surface such as

Fig. 3 RBT crushed into 5 mm using the crushing machine

cement, dust and others. Second, the tiles were crushed manually using hammer into smaller pieces that can fit into the crushing machine. Then, tiles were further crushed using the crushing machine into 5 mm size. After that, the tiles were blended into powder using Los Angeles Abrasion machine and this process took almost 48 h. The longer the tiles was kept rotating inside Los Angeles Abrasion machine, the finer it was blended. Finally, RBT were sieved through 0.15 mm sieve and those that passed were further sieved using 0.063 mm size. RBT retained on 0.063 mm sieve were used as 0.15 mm size while those that passed 0.063 mm sieve were used as 0.063 mm size.

2.3 Sample Preparation for Compaction Tests

The methods and procedures used to prepare the samples for standard proctor test followed the BSI 1924: Part 4: 1990 [11]. The untreated marine clay was first oven dried and approximately 90 kg of soil was taken to conduct the test. It was sieved through 2 mm mesh sieve in order to remove coarse particles, roots and plants from the soil. At the first place, sieved marine clay was mixed with specified amounts of water in a large tray and was thoroughly mixed until uniformity was observed. The mixture of marine clay and water was transferred into a plastic air tight bag and kept for a minimum of 24 h in order to make sure that the water is distributed properly within the marine clay sample. On the other hand, the standard proctor mold (Fig. 4) was 115.5 mm height with an internal diameter of 105 mm which was fixed on a steel detachable base plate before measuring its weight. A removable extension collar was attached to the top of the mold before placing the soil. Then, the soil was placed in three equal layers inside the standard proctor mold. Each layer of soil was compacted with 27 blows using 2.5 kg metal rammer that had a 50 mm diameter circular face and dropped vertically from a height of 300 mm. When the compacting process was completed, the extension collar was removed and the soil was trimmed and smoothed to eliminate the extra soil. The compacted soil together with the mold was weighted on a digital balance to the nearest three decimal places. Two samples of soil were obtained from the top and bottom of the compacted specimen for determining the moisture content. The soil was thrown after each compaction test as this soil was found susceptible to crushing.

The same procedure was repeated another four times in order to establish a proper curve from which the maximum dry density and optimum moisture content can be determined. Following the same procedures, standard proctor tests were performed on stabilized marine clay specimens. Two different sizes (0.063 mm diameter and 0.15 mm diameter) with four different percentages (10, 20, 30 and 40%) of RBT were used to establish a proper mix design.

Fig. 4 The standard compaction mold used for the test

3   Result and Discussion

Experiments were conducted on marine clay stabilized with RBT in order to obtain the maximum dry densities and optimum moisture contents of the various mix designs. The results of the standard proctor tests conducted on untreated and treated marine clay are discussed in this section.

3.1   Effect of 0.063 mm RBT on the Compaction Parameters

It is clearly shown in Table 2 the influence of different percentages of 0.063 mm RBT on marine clay compaction parameters. The highest value of MDD was achieved at 30% of 0.063 mm RBT while the OMC was reduced with further increments of RBT and the lowest OMC attained at 40% was 16.5%. The reason of the reduction of OMC was due to the replacement of the RBT particles by soil particles which reduced the attraction of the water molecules as explained by Sabat [12] who stabilized expansive soil with ceramic dust. Figure 5 demonstrates a

Table 2 Compaction parameters of marine clay treated with 0.063 mm RBT

Type	RBT (%)	Optimum moisture content (OMC) (%)	Maximum dry density (MDD) (Mg/m^3)
Marine clay	0	22	1.59
Marine clay—RBT	10	19	1.66
Marine clay—RBT	20	19	1.67
Marine clay—RBT	30	18	1.72
Marine clay—RBT	40	16.5	1.71
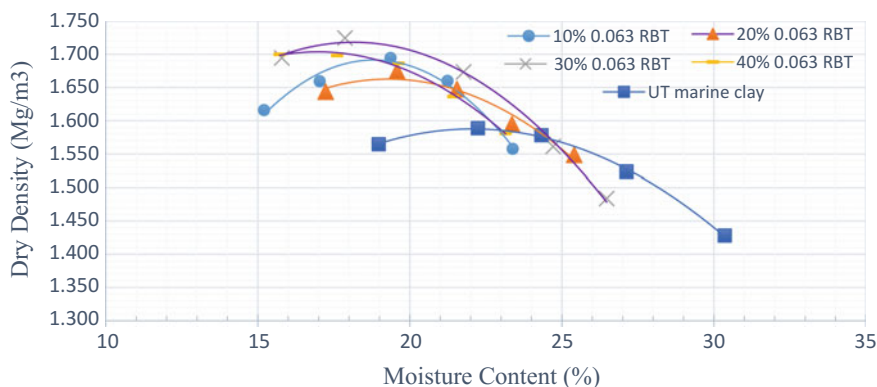
Fig. 5 Compaction curve for untreated and treated marine clay with 10, 20, 30 and 40% 0.063 mm RBT

comparison between the compaction curves of untreated and treated marine clay. A significant improvement of the compaction parameters can be observed when 10% RBT was added to the untreated marine clay. MDD increased from 1.59 to 1.69 Mg/m^3 while OMC was decreased from 22 to 19%. Further increments (20, 30 and 40%) of RBT resulted in a slight improvement of MDD and OMC.

3.2 Effect of 0.15 mm RBT on the Compaction Parameters

The effect of 0.15 mm RBT can be seen in Table 3 at which marine clay was treated by 10, 20, 30 and 40%. In terms of MDD, the influence of 10% 0.15 mm RBT was similar to that obtained by 10% 0.063 mm RBT which proves that the size of RBT did not induce much difference. Furthermore, as the percentage of RBT was increased, MDD also increased while OMC decreased. The obvious reduction of OMC with increments of RBT is due to the hydration reaction induced by RBT. It is observed from Fig. 6 that all the stabilized marine clay specimens with 0.15 mm RBT had similar compaction curves.

Table 3 Compaction parameters of marine clay treated with 0.15 mm RBT

Type	RBT (%)	Optimum moisture content (OMC) (%)	Maximum dry density (MDD) (Mg/m³)
Marine clay	0	22	1.59
Marine clay—RBT	10	18	1.7
Marine clay—RBT	20	18	1.71
Marine clay—RBT	30	17.8	1.74
Marine clay—RBT	40	17	1.74
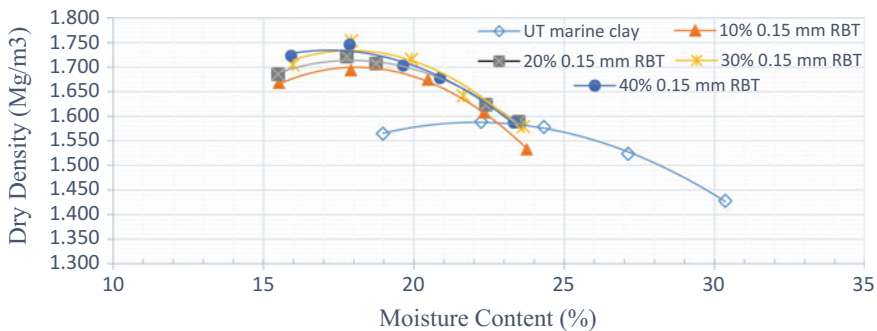
Fig. 6 Compaction curve for untreated and treated marine clay with 10, 20, 30 and 40% 0.15 mm RBT

3.3 Comparison of the Effect of RBT Size

The results of OMC for 0.063 and 0.15 mm RBT are shown in Fig. 7. For both sizes of RBT, the OMC decreased as the percentage of RBT was increased due to the replacement of the RBT particles by the soil particles that reduces the attraction of water molecules. These results were in agreement with Rani et al. [13] who used ceramic tiles dust to stabilize expansive soil. Izabel and Sangeetha [14] also found that OMC of treated marine clay was reduced as the amount of the additive was increased.

It is clearly seen in Fig. 8 that MDD of treated marine clay increased as the amount of RBT was increased. The optimum amount of RBT was 30% for 0.063 and 0.15 mm RBT and the same results were obtained by Sumayya et al. [15]. At 40% RBT, MDD was dropped slightly for 0.063 mm RBT, while MDD remained constant for 0.15 mm RBT. In addition, by comparing the effect of RBT size, 0.15 mm RBT was more effective. The highest value of MDD was 1.74 Mg/m³ at 30 and 40% 0.15 mm RBT. Ameta et al. [16] treated soil with different sizes of ceramic tiles (1.18, 2.0 and 4.67 mm) found that the bigger the size of ceramic tile, the higher the MDD. Although the difference of RBT sizes investigated in this paper was not significant, MDD highest value was obtained with the biggest RBT size.
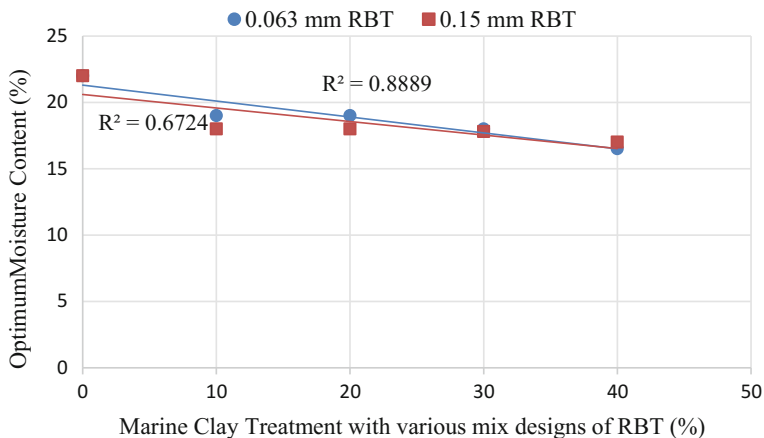
Fig. 7 Impact of 0.063 and 0.15 mm RBT on the optimum moisture content of marine clay
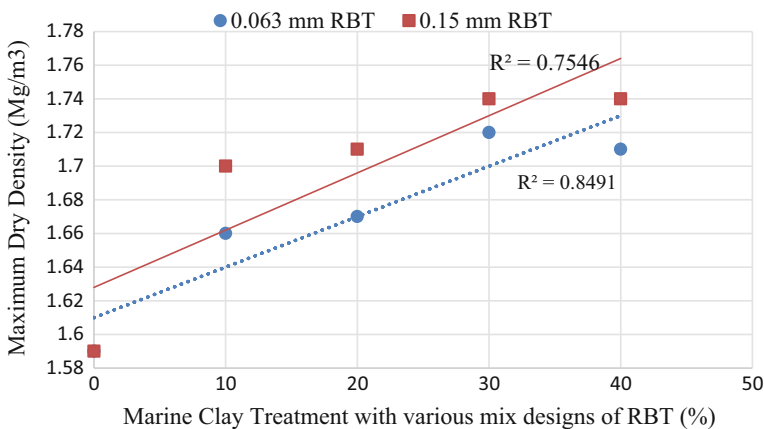
Fig. 8 Impact of 0.063 and 0.15 mm RBT on the maximum dry density of marine clay

By comparing the obtained results of 0.063 and 0.15 mm RBT, they almost had the same trend and the differences of results were very small. That was because both sizes were very fine particles. Moreover, Figs. 7 and 8 show a statistical observation of the results obtained for the compaction parameters. The value of the R^2 (Coefficient of determination) varied from 0.88 to 0.67 which indicates that the discrepancy of the linearity of observed results is small. This proves that the predicted percentages or mix designs of RBT were chosen appropriately.

4 Conclusion

This study examined the suitability of recycled blended tiles (RBT) to treat marine clay as environmental-friendly, cost-effective and sustainable stabilizer. It is observed from the results that RBT was found to be effective and resulted in significant improvement to the clay properties. By investigating the effect of RBT on the compaction parameters of marine clay using two different sizes and various mix designs, the following points can be drawn:

- For both sizes of RBT, by increasing the amount of RBT from 10 to 40%, the optimum moisture content decreased steadily.
- The optimum value of RBT was 30% for both sizes of RBT with respect to maximum dry density and the highest value was 1.74 Mg/m^3 for 0.15 mm RBT.
- Both sizes were able to make a noticeable improvement of compaction parameters when compared with the untreated marine clay.

References

1. Cai, Y., Shi, B., Ng, C.W.W., Tang, C.: Effect of polypropylene fibre and lime admixture on engineering properties of clayey soil. Eng. Geol. **87**, 230–240 (2006)
2. Al-bared, M.A.M., Marto, A.: Review on the geotechnical and engineering properties of Marine clay and the suitable common stabilization methods. In: International Conference on Separation Technology 2017 (ICoST 2017) I1–I3 (2017)
3. Dang, L.C., Fatahi, B., Khabbaz, H.: Behaviour of expansive soils stabilized with hydrated lime and bagasse fibres. Procedia Eng. **143**, 658–665 (2016)
4. Upadhyay, A., Kaur, S.: Review on soil stabilization using ceramic waste. Int. Res. J. Eng. Technol. **03**, 1748–1750 (2016)
5. Yilmaz, Y.: Compaction and strength characteristics of fly ash and fiber amended clayey soil. Eng. Geol. **188**, 168–177 (2015)
6. Wong, S.L., et al.: Comparative measurement of compaction impact of clay stabilized with cement, peat ash and silica sand. Measurement **94**, 498–504 (2016)
7. Xia, K.: Numerical prediction of soil compaction in geotechnical engineering. C. R. Mec. **342**, 208–219 (2014)
8. Ören, A.H.: Estimating compaction parameters of clayey soils from sediment volume test. Appl. Clay Sci. **101**, 68–72 (2014)
9. British Standards Institution.: British Standard Methods of Test for Soils for Civil Engineering Purposes: Part 2. Classification Tests. London (BS1377) (1990)
10. British Standards Institution.: British Standards Code of practice for site investigations, London (BS 5930). 3 (1999)
11. British Standards Institution.: British Standard Methods of Test for Soils for Civil Engineering Purposes: Part 4, Compaction-Related Tests. British Standards Institution, London (BS1377). 3 (1990)

12. Sabat, A.K.: Stabilization of expansive soil using waste ceramic dust. Electron. J. Geotech. Eng. **17**, 3915–3926 (2012)
13. Rani, T.G., Shivanarayana, C., Prasad, D.S.V., Raju, G.V.R.: Strength behaviour of expansive soil treated with tile waste. Int. J. Eng. Res. Dev. **10**, 52–57 (2014)
14. Izabel, K.J., Sangeetha, S.: Stabilization of marine clay using jerofix. Int. J. Sci. Eng. Res. **4**, 93–95 (2016)
15. Sumayya, K., Mohammed Rafeequedheen, K., Sameer, V., Firoz, T., Jithin, K.: Stabilization of expansive soil treated with tile waste. SSRG Int. J. Civ. Eng. **3**, 67–75 (2016)
16. Ameta, N.K., Wayal, A.S., Hiranandani, P.: Stabilization of dune sand with ceramic tile waste as admixture. Am. J. Eng. Res. **2**, 133–139 (2013)

Bearing Capacity of Eccentrically Loaded Strip Footings Near a Slope

Salah Zerguine, Djamel Benmeddour, Mohamed Younes Ouahab, Abdelhak Mabrouki and Mekki Mellas

Abstract This paper presents a numerical investigation into the behavior of eccentrically loaded strip footings adjacent to a cohesionless slope. In this study, the finite-element software Plaxis 2D was used to evaluate the influences of load eccentricity on the bearing capacity, soil pressure distribution underneath the footing and the pattern of failure mechanism. The results are presented using the failure envelopes in vertical and moment loading plan. The obtained results are compared with those found in the literature.

Keywords Bearing capacity · Finite element · Failure envelopes

1 Introduction

The evaluation of the bearing capacity for a surface strip footing on cohesionless soil under eccentric and/or inclined loading is an important problem in geotechnics. In the literature, there are two methods to determine the bearing capacity of strip footings subjected to eccentric and/or inclined loading: the classical method using correction factors and the advanced method using failure envelopes for the corresponding combined loading.

S. Zerguine (✉) · D. Benmeddour · M. Y. Ouahab · A. Mabrouki · M. Mellas
Civil Engineering Laboratory, Biskra University, BP 145, Biskra 07000, Algeria
e-mail: sa_zerguine@yahoo.fr

D. Benmeddour
e-mail: benmeddourdj@yahoo.fr

M. Y. Ouahab
e-mail: ouahabmy@gmail.com

A. Mabrouki
e-mail: a.mabroukii@yahoo.fr

M. Mellas
e-mail: m_mellas@yahoo.fr

Different studies have been devoted for the calculation of the bearing capacity of shallow footings under eccentric and/or inclined loads on horizontal ground (Saran and Agarwal [1], Gottardi and Butterfield [2], Ganesh et al. [3], Loukidis et al. [4], Krabbenhoft et al. [5]). By means of laboratory model tests, Okamura et al. [6] have proposed an empirical formula of reduction factor, that can be used to calculate the bearing capacity of shallow strip foundations embedded in sand and subjected to eccentric loaded. The case of a strip footing resting at the crest of slope is a particular configuration, frequently encountered in practice. Various studies treating this problem using analytical, empirical, and numerical methods are available. Maréchal [7], Maloum and Sieffert [8] and Magnan et al. [9] estimate the bearing capacity using correction factors where they took into account the relative distance between the crest of slope and the footing location. Furthermore, Georgiadis [10] and Baazouzi et al. [11] investigated the bearing capacity using failure envelopes in the corresponding loading plane for different parameters of slope geometry and soil properties.

In the present study, a series of numerical calculations, using the code Plaxis [12] are realized to estimate the bearing capacity of strip footings, resting on a cohesionless slope under eccentric loading. The results are represented in terms of failure envelopes, in combined vertical-moment loading plane (V-M) for rough strip footings. A practical range of the relative distance d/B that separates the footing location and the top of the slope is investigated. The obtained results are compared with those found in other studies.

2   Presentation of the Problem

The bearing capacity for a surface strip footing resting on a cohesionless slope under vertical eccentric load is evaluated using the following equation based on Terzaghi's equation [13]:

$$q_u = 0.5\gamma B N_\gamma i_{\gamma\beta} i_e, \tag{1}$$

where N_γ is the bearing capacity factor; i_e is a reduction factor that represents the effect of eccentricity; $i_{\gamma\beta}$ is a reduction factor defined as the following ratio:

$$i_{\gamma\beta} = \frac{q_{u\ (d/B,\ \beta)}}{q_{u(\beta=0)}}, \tag{2}$$

where $q_u(d/B,\beta)$ is the bearing capacity for strip footing resting on a slope and $q_u(\beta = 0)$ is the bearing capacity for strip footing resting on level ground.

In the case of a strip footing resting on sand slope under eccentric and/or inclined loading, the proposed reduction factor RF that takes into account the combined effect of eccentricity and inclination of load, and the depth of footing, is given by Ganesh et al. [3] as follows:

$$RF = \left[\left(1 - \frac{2e}{B} \right) \left(1 - \frac{\alpha}{\varphi} \right) \right]^{n}, \tag{3}$$

where $n = 2$ for $D/B = 0$ and $n = 1.15(D/B)^{-0.15}$ for $D/B > 0$. Where D is the depth, B is the width of footing, e is the load eccentricity, α is the load inclination angle, and φ is the internal friction angle of soil.

Gottardi and Butterfield [2] note that the failure surface for a strip footing on horizontal ground can be represented by a second-order equation as follows:

$$\frac{M}{BV_{max}} = 0.36 \frac{V}{V_{max}} \left(1 - \frac{V}{V_{max}} \right), \tag{4}$$

where V_{max} is the ultimate vertical load at the center of the foundation ($e = 0$), V is the vertical collapse load, determined from the results of eccentrically loaded footing ($e > 0$), B is the width of the foundation and M is the moment at foundation level.

The objective of the present study is to determine the failure loads V and M of a strip footing on a cohesionless slope, for different load eccentricities e/B. The geometry and loading conditions are illustrated in Fig. 1.

A strip footing of width B is located at a distance d from the crest of a slope with height H and slope angle β. The applied eccentric loads are marked to be positive or negative (Fig. 1). The slope angle $\beta = 26.56°$ and different relative footing distances from the crest of the slope $d/B = 0, 1, 2,$ and 3 were considered.

(a) Negative moment load   (b) Positive moment load

$M = V.e$

V : vertical load; e : load eccentricty

d : distance between the crest of the slope and the foundation, B : footing width

β : slope angle
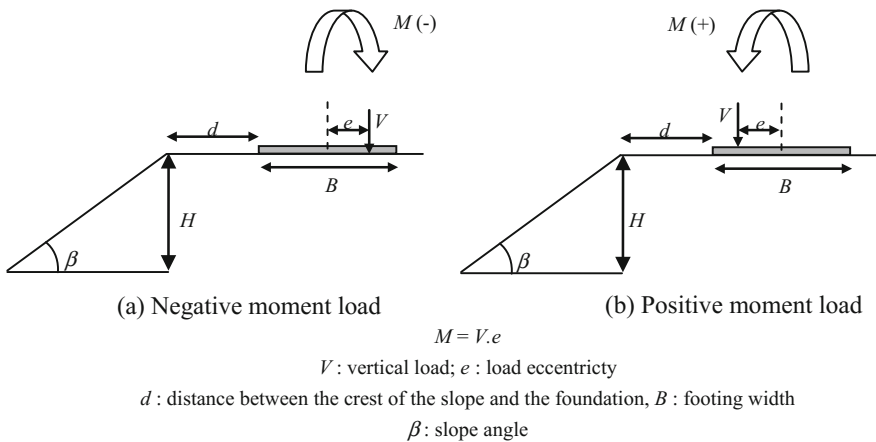
Fig. 1 Problem presentation

3   Numerical Procedures

In the present study, the software Plaxis based on finite-element was used to evaluate the bearing capacity for a surface strip footings resting on a cohesionless slope under eccentric loading.

The entire soil domain was modeled of width $20B$ and depth $7B$ (Fig. 2), the soil domain is discretized as 15-node triangular elements. In order to test the influence of the mesh size, a series of numerical calculations have been carried out. The mesh under the footing base and around the footing corners is refined in order to have smaller elements and graded mesh for which a more accurate solution was obtained. The right and left vertical borders of the model were blocked horizontally, whereas the base was blocked in all directions.

The boundary conditions and finite-element mesh for a surface strip footing resting at a distance $d = 1$ m from the crest of a cohesionless slope with height $H = 3$ m are shown in Fig. 2. The so-called "probe" loading technique is used in this study. The footing load is applied in increments up to failure under load eccentricity e/B, with respect to the reference point of pure vertical loading ($e/B = 0$). Each analysis using probe method leads to determine a single failure load which is marked as a point in the failure envelope (V-M). All numerical analyses were realized for rough footings.

The constitutive model used is an elastoplastic with plastic criterion of Mohr–Coulomb, an associated flow rule ($\varphi = \psi$) is adopted, the following parameters are used: the Poisson ratio $\upsilon = 0.3$, the unit weight of the soil $\gamma = 20$ kN/m^3 and the shear modulus $G = 20$ MPa, the frictional angle of the soil $\varphi = 30°$. It is noted that the elastic parameters of the soil had no influence on the bearing capacity (Mabrouki et al. [14]). The surface footing was modeled as a weightless rigid plate element (uniform settlement) with a significant Young's modulus and sufficient thickness.
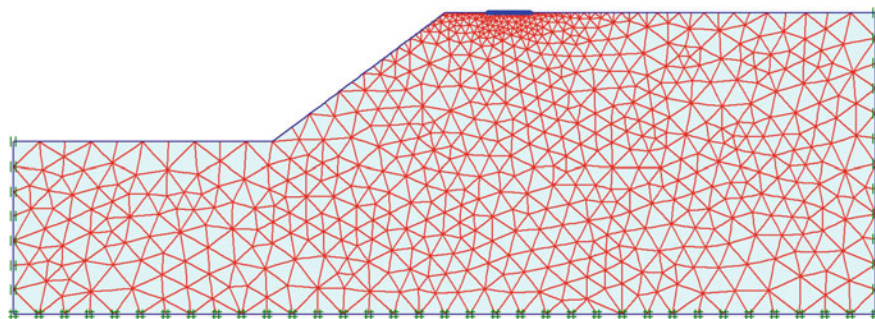
Fig. 2 Finite element mesh with boundary conditions used in the analysis of rough strip footings on sand slope, case of $d/B = 1$, $H = 3$ m

4 Results and Discussions

4.1 Strip Footing on Horizontal Ground (β = 0)

The failure envelope represents the surface that governs the failure of the foundation. The points in the failure envelope are obtained by the probe test analysis. The normalized failure envelopes (V/V_{max}-M/BV_{max}) for a strip footing on horizontal ground under eccentric loads are presented in Fig. 3.

The obtained results are compared with those of the Eq. (4) proposed by Gottardi and Butterfield [2] and with those of the lower bound values obtained by Krabbenhoft et al. [5]. It is found that the shape of failure envelopes is parabolic. The maximum value $M/BV_{max} = 0.082$ occurs at $V/V_{max} = 0.55$. The numerical results of the present study are in good agreement with those found by the application of the equation given by Gottardi and Butterfield [2], except for high values of M/BV_{max} where the numerical simulation underestimates the results. However, the present solution overestimates the results given by Krabbenhoft et al. [5] which represent lower bound values.

4.2 Strip Footing on Slope (β > 0)

Figure 4 shows the normalized failure envelopes (V/V_{max}-M/BV_{max}) obtained from the numerical analyses, for a strip footing with different values of a relative distance $d/B = 0, 1, 2$, and 3 from the crest of the cohesionless slope with $\varphi = 30°$ and $\beta = 26.56°$.
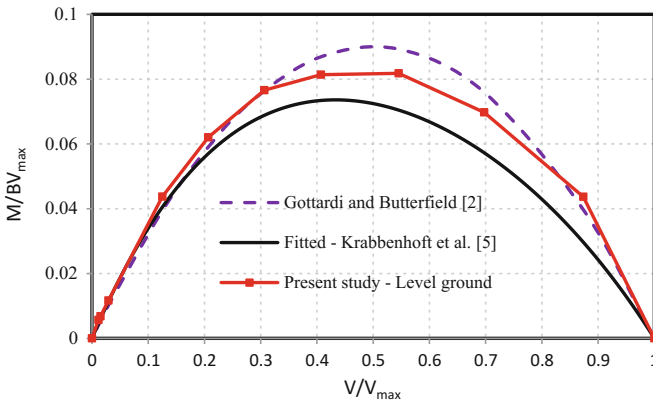
Fig. 3 Comparison of failure envelopes for footings under *V-M* loads for level ground with $\varphi = 30°$
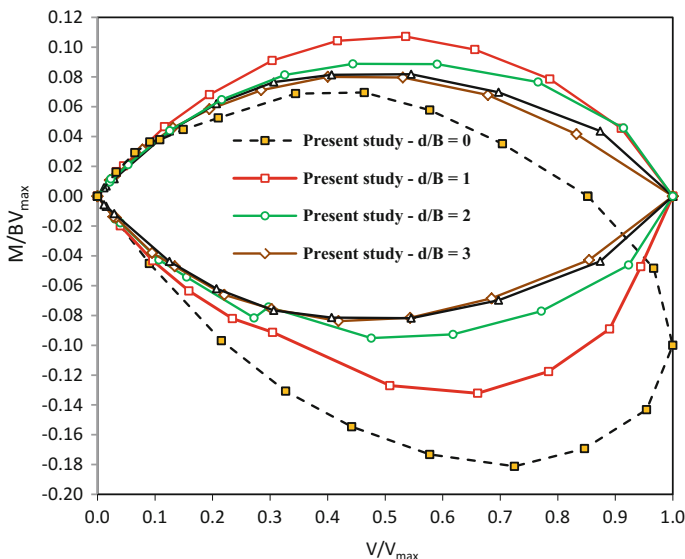
Fig. 4 Failure envelopes for strip footings under V-M loads ($\varphi = 30°$ and $\beta = 26.56°$)

It is seen that the increase in d/B leads to a translation of the failure envelopes towards the level ground curve ($\beta = 0$). This occurs in reason that the influence of slope on the bearing capacity vanishes at a certain distance of the footing from the crest of slope ($d/B = 3$). The shape and the size of the failure envelopes depend on the relative distance d/B.

4.3 Failure Mechanism

Figure 5 illustrates the vectors of the incremental displacements at failure, for strip footing under eccentric load of $e/B = -0.2$ resting at the crest of slope ($d/B = 0$). A non-symmetrical failure mechanism was observed. The vectors of incremental displacements move towards the slope inclination. The passive zone is imperfect in contrast to the footing position which leads to a reduction in the bearing capacity.

4.4 Distribution of Normal Stresses

The distribution of the normal stresses σ_n acting on the base of foundation from all analyses with associated flow rule ($\varphi = \psi$) using Plaxis, is plotted in Fig. 6. The stresses at the nodes of the footing base are calculated for the case of strip footing located at $d/B = 3$ from the crest of the slope. It is shown that, as the eccentricity
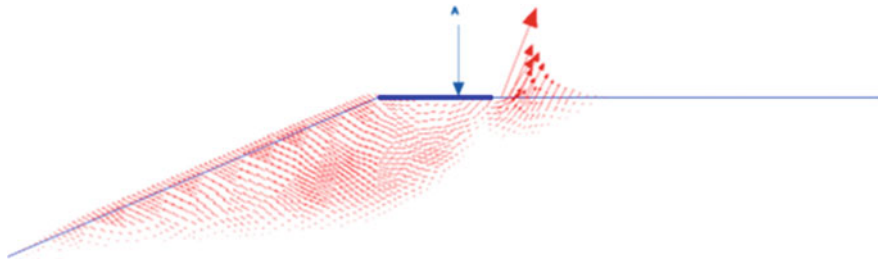
Fig. 5 Failure mechanism for $e/B = -0.2$
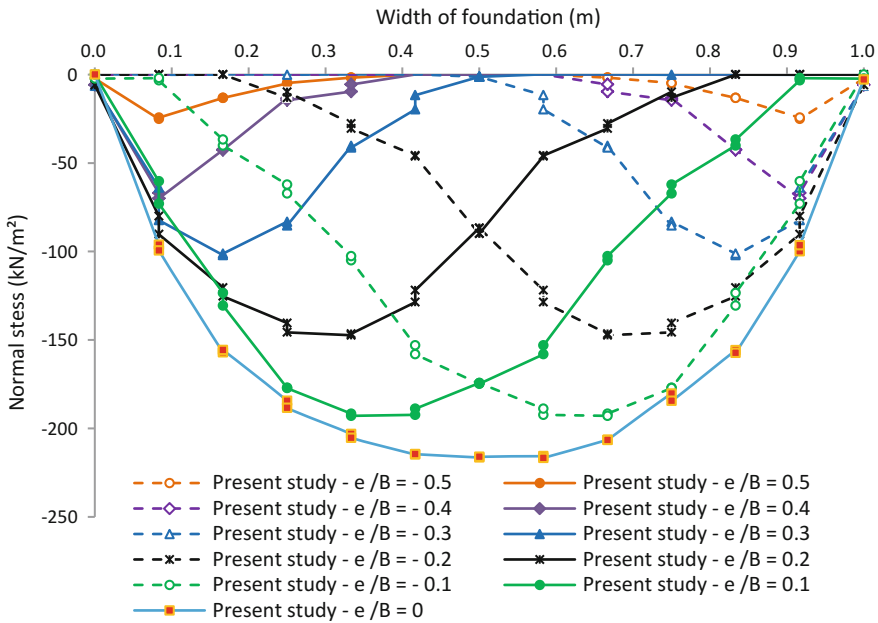
Fig. 6 Distribution of normal stress acting along the effective width of eccentrically loaded footing ($d/B = 3$ and $\varphi = 30°$)

increases, the distribution of the normal stresses σ_n changes in size and shape as indicated by Loukidis et al. [4]. It is seen that the distribution of the normal stress σ_n is symmetrical as in the case of level ground.

Figure 7 shows the normal stresses σ_n at the nodes of the footing base calculated for the case of strip footing resting on the crest of the slope. It is seen that the negative eccentricity e generates a high normal stresses than positive eccentricity and central loading ($e/B = 0$), the maximum stresses occur at $0.8B$ or $0.9B$, in the case of negative eccentricity e. On the other hand, for positive eccentricity, the normal stresses σ_n are distributed on the left half of the footing.
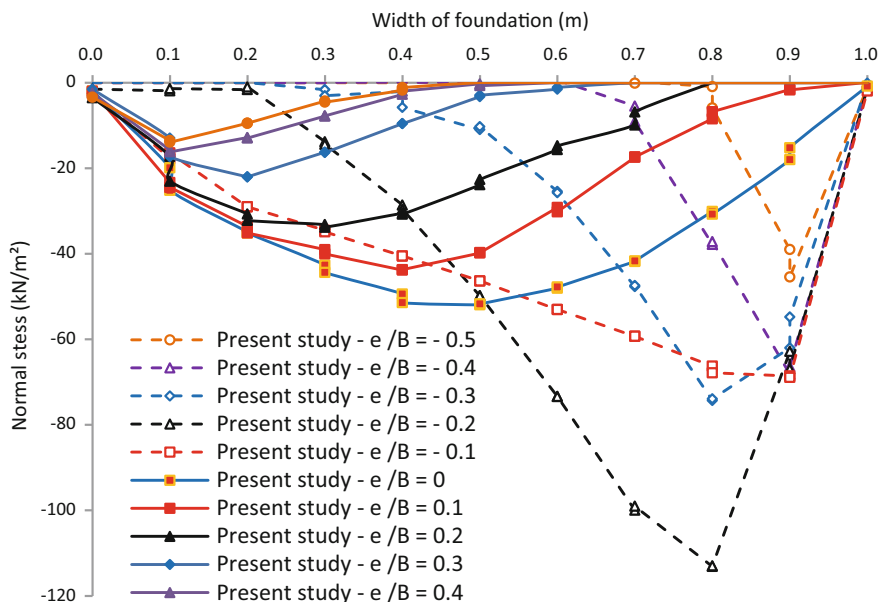
Fig. 7 Distribution of normal stress acting along the effective width of eccentrically loaded footing in the case of $d/B = 0$ and $\varphi = 30°$

5 Conclusions

Finite-element analysis calculations using Plaxis code are carried out for strip footings under vertical eccentric loads and located near a cohesionless slope with friction angle 30°, for different distances between the crest of the slope and the footing location. The obtained results are presented in terms of failure envelopes and compared with the available results published in other studies.

For the case of strip footing rested on horizontal ground, the present results are bracketed between the results of Gottardi and Butterfield [2] and those of Krabbenhoft et al. [5] that represent lower bound values. The obtained failure envelopes are symmetrical for both negative and positive moment loading cases. However, in the case of strip foundation rested on slope, the obtained failure envelopes are non-symmetrical for both negative and positive moment loading cases for values of $d/B \leq 3$. For the case of a strip footing rested on horizontal ground, the increase of negative or positive eccentricity leads to reduce the magnitude of normal stresses. For $e/B = 0$, the maximum normal stresses occur at the footing centerline. Moreover, in the case of strip foundation rested on slope, the increase in d/B reduces the influence of negative load eccentricity on the normal stresses.

References

1. Saran, S., Agarwal, R.: Bearing capacity of eccentrically obliquely loaded footing. J. Geotech. Eng. **117**(11), 1669–1690 (1991)
2. Gottardi, G., Butterfield, R.: On the bearing capacity of surface footings on sand under general planar loads. Soils Found. **33**(3), 68–79 (1993)
3. Ganesh, R., Khuntia, S., Sahoo, J.P.: Bearing capacity of shallow strip Foundations in sand under eccentric and oblique loads. Int. J. Geomech ASCE. https://doi.org/10.1061/(ASCE)GM.1943-5622.0000799
4. Loukidis, D., Chakraborty, T., Salgado, R.: Bearing capacity of strip footings on purely frictional soil under eccentric and inclined loads. Can. Geotech. J. **45**(6), 768–787 (2008)
5. Krabbenhoft, S., Damkilde, L., Krabbenhoft, K.: Lower-bound calculations of the bearing capacity of eccentrically loaded footings in cohesionless soil. Can. Geotech. J. **49**(3), 298–310 (2012)
6. Okamura, M., Mihara, A., Takemura, J., Kuwano, J.: Effects of footing size and aspect ratio on the bearing capacity of sand subjected to eccentric loading. Soils Found. **42**(4), 43–56 (2002)
7. Maréchal, O.: Portance des fondations superficielles établies à proximité d'un talus et soumises a des charges inclinées et excentrées. Thèse de doctorat, École Centrale de Nantes, 359 pages (1999)
8. Maloum, S., Sieffert, J.G.: Interaction sol-fondation superficielle au voisinage de la crête d'un talus: analyse de la capacité portante. Rev. Fr. Géotech. **100**, 83–89 (2002)
9. Magnan, J.P., Droniuc, N., Canepa, Y.: Les méthodes de calcul de la portance des fondations superficielles. In: Symposium international sur l'amélioration des sols en place (2004)
10. Georgiadis, K.: The influence of load inclination on the undrained bearing capacity of strip footings on slopes. Comput. Geotech. **37**(3), 311–322 (2010)
11. Baazouzi, M., Benmeddour, D., Mabrouki, A., Mellas, M.: 2D numerical analysis of shallow foundation rested near slope under Inclined loading. Procedia Eng. **143**, 623–634 (2016)
12. Brinkgreve, R.B.J., Engin, E., Swolfs, W.M.: Plaxis User's Manual. Plaxis, BV, Netherlands (2012)
13. Terzaghi, K.: Theoretical Soil Mechanics. Wiley, New York (1943)
14. Mabrouki, A., Benmeddour, D., Frank, R., Mellas, M.: Numerical study of the bearing capacity for two interfering strip footings on sands. Comput. Geotech. **37**(4), 31–439 (2010)

Granites in Malaysia: From Hard Rock to Clay Minerals

Z. M. Yusoff, Nik Norsyahariati Daud, Haslinda Nahazanan, Husaini Omar, Azalan Aziz and Mohd Shahriza Ab Razak

Abstract Tropical areas with extreme climates are host to extreme weathering processes and the weathered materials are normally left in situ with the absence of large-scale denudation processes such as glaciations. This research tries to understand the behaviour of the weathered granites in Malaysia, from hard rock to the final products, the clay minerals. Grade 1 or fresh granites were sampled from different locations in Malaysia and analysed. The residual soil above the fresh granites, which were formed from the weathering activities were also analysed. The types of clay minerals and clay-sized particle grains found from two study locations were compared. The bases of the comparisons were index properties, strength properties and the mineralogical properties. The parent rocks were also analysed to obtain the origin of the minerals formed at the later stages of weathering. It was found that the strength of the soil mass formed from the weathering processes generally depend on the clay-sized particle grains rather than the types of clay minerals. It should however be noted that only halloysites and smectites clay minerals were observed in the samples obtained from the two study locations.

Keywords Granite · Clay minerals · Weathering

1 Introduction

Residual soils are formed from the weathering processes on parent rocks, that is the in situ weathering of igneous, sedimentary and metamorphic rocks. Residual soils originating from granite are generally sandy, have lower water content and lower liquid limits compared to basaltic or gabbroic soils. The better-graded nature of the granitic soils produces higher compacted densities. Almost 80% of residual soil in

Z. M. Yusoff (✉) · N. N. Daud · H. Nahazanan · H. Omar
A. Aziz · M. S. A. Razak
Department of Civil Engineering, Faculty of Engineering,
Universiti Putra Malaysia, Serdang, Malaysia
e-mail: zmy@upm.edu.my

Peninsular Malaysia is granite residual soil. Gradual chemical weathering of granites forms different grades of residual soil. Several researchers have come up with different weathering grades [1–7]. In general, grade I is the fresh rock while grade V is the completely weathered rock and subsequently, grade VI is the residual soil.

Rocks are defined as an aggregate of minerals and granites in general, comprise of quartz, potassium feldspars, plagioclase feldspars, muscovite, biotite and other accessory minerals. Each mineral has its own hardness and generally, Mohr Relative Hardness Scale is used to compare the relative hardness of each mineral. Quartz is the hardest among the common minerals in granite rock and plagioclase feldspar being the softest in this scale. During the weathering processes, each mineral will degenerates at its own pace based on their relative hardness. The minerals will degenerate mechanically and/or chemically, depending on the ambience. When they degenerate mechanically, they will subsequently form clay-size minerals and when degenerate chemically, they will recrystallize to form secondary minerals or clay minerals. These minerals will exhibit regular crystal structures representing a particular mineral. Some clay minerals are swelling clays or expansive clays while some are not. Swelling clays are prone to large volume changes, either swelling or shrinking when exposed or devoid of water [8, 9]. Smectite group of clay minerals, which include montmorillonite and bentonite, have an interestingly huge shrink-swell capacity. This is due to the anion–cation exchange in their crystal structures. The kaolin groups of minerals, comprising clay minerals such as kaolinite and halloysite, are non-swelling clays [10, 11].

In some very slightly weathered rock, small amounts of clay minerals are formed as secondary minerals. These observations have led to two approaches in studying weathering. The first is the degree of weathering measured as the amount of weatherable primary minerals that have actually disappeared. In massive weathering, chemical decomposition affects all weatherable materials and they are replaced by large amounts of secondary minerals (gibbsite, kaolinite or smectite). During progressive weathering, differential leaching of primary minerals occurs and the resulting intermediate material tends to contain a large amount of coarse grains. The second approach is based on geochemical changes as recorded in the soil profile categorized soil profiles into two groups [12]. The first is soil covers that are in dynamic equilibrium, which have developed in conditions stable enough to keep the sequence of transformation from parent rock to soil surface constant. Secondly, soil covers that are in chemical disequilibrium. This is the transformation phase where the rock/soil will transform to another soil type, which tends towards a dynamic equilibrium [1, 13].

There is a school of thoughts saying that all failures in a soil mass are shear failures [14–16]. In general, when soil cannot withstand tension and compression, the internal structure will starts to shear apart leading to shear failures due to direct shearing forces acting on the soil mass. The shear strength of a soil is its maximum resistance to shear and is usually expressed as a stress. The stress–strain relationship in soil is usually nonlinear due to the un-homogeneity nature of soils, unlike many other engineering materials. However in some design calculations, it may be

assumed linear. The shear strength parameters measured are cohesion c, and friction angle, φ. The shear strength is a linear function of normal stress and shear strength parameters as expressed by Coulomb failure criterion.

Shear strength can also be expressed in terms of effective major and minor principle stresses σ_1' and σ_3' at failure. Cohesion c, is sensitive to water and pore-water chemistry and is directly related to the cohesiveness of the soil mass. Cohesive resistance develops quickly to the maximum value under small strains and decreases as strain increases. The frictional angle on the other hand, is derived from inter-granular contact and is not developed to its maximum value until significant amounts of strain have occurred.

2 Methodology

The study locations were in Balakong, Selangor (3° 2′ 0.28″N, 101° 44′ 33.95″E) and in Rawang, Selangor (3° 19′ 31.48″N, 101° 33′ 38.43″E) Fig. 1. Parent rock and residual samples were taken at appropriate intervals on a cut slope and on a vertical profile respectively (Fig. 2).

Fresh to completely weathered rock samples and residual soils were collected using thin-walled sampler where applicable on the slope surface of a hill in Balakong and a borehole were drilled and rock and soil samples were taken at a regular intervals in Rawang. These samples were used to study the index properties, mineralogical properties and strength properties.
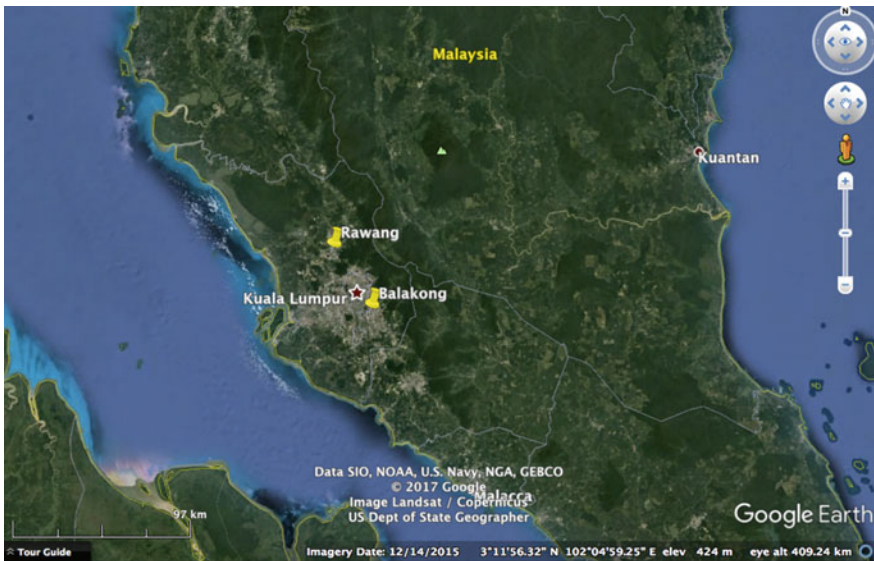
Fig. 1 A Google map showing the study locations
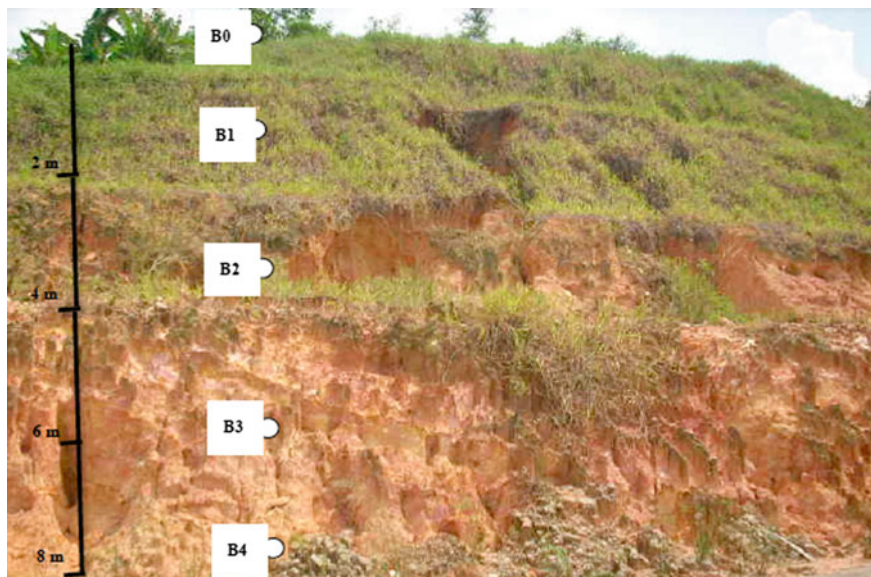
Fig. 2 The samples taken at selected depth in the profile in Balakong

Particle size distribution test is one of the index properties tests. For the course-grained particle determination (particles larger than 0.06 mm), sieve analyses were done while for the fine grained particles, hydrometer analyses were conducted as per the British Standards BS1377 (part 2). In hydrometer analyses, the principle of particles of same diameter settles in water at the same velocity was used.

Shear strength parameters for the soil mass were obtained from the shear box tests. A vertical force was applied to the specimen through a loading plate and shear stress was gradually applied on a horizontal plane by causing the two halves of the box to move relative to each other, the shear force being measured together with the corresponding shear displacement and change in thickness of the specimen.

For the petrographic studies, thin sections of the parent rocks were made and the mineralogical characteristics were analysed under a petrographic microscopy. The petrographic microscope transmits polarised light through the thin section and the light passes through two polarizing filters. The different types of minerals present can be identified and their characteristics can be studied.

The X-Ray diffraction (XRD) analyses were done on powders loaded into cavity holders. The powders were prepared as mixtures of 2.4 g of sample and 0.6 g of corundum (used as internal standard) using a spray-drying technique. Diffraction patterns were recorded on a Siemens D5000 instrument using cobalt radiation and with a diffracted beam monochromator. Quantitative analysis was made by a reference intensity ratio approach using the 20% added corundum as the reference and it was based on full patterns of reference minerals rather than individual peaks [17].

X-Ray fluorescence (XRF) analyses were carried out on a Philips PW2404 automatic X-ray spectrometer. The techniques used are similar to those described by Fitton et al. [18]. Major-element concentrations were determined after fusion with a lithium borate flux containing La_2O_3 as a heavy absorber. The samples were ignited at 1100° C to determine loss on ignition (LOI).

The scanning electron microscopy (SEM) study was done on a Philips XL30CP. The resolution of the microscope was 3.5 nm at 30 kV using the secondary electron (SE) detector while the backscatter (BSE) detector allows the formation of an image, which depends on the mean atomic number (Z) of the substance in the electron beam. Higher Z means more intense electron scattering so the image is brighter. Thus potassium feldspar appears brighter than plagioclase feldspar. Samples were gold coated for topographic imaging using SE and carbon coated for BSE studies Fig. 3.

Fig. 3 The samples taken from a borehole drilled on a flat land in Rawang

3   Results and Analysis

Particle size distribution tests were conducted on all the samples obtained and the results are tabulated in Table 1. In Balakong, the site was an exposed hill. The development or formation of gravel, when observed from the rock level upwards (from sample B5 at 16 m depth up to ground level), appeared only to 10 m depth (B3). It showed that the weathering processes had degenerated the gravels into sands and silts above this 10 m depth. However, the occurrence of sands and silts did not show any observable trends in terms of their increment nor their decrement. Clay-sized particles however, showed an increasing amount in the soil samples right above the rock (B4) upwards to sample B1. The B0 sample could not be used in the observation as the amount of organic materials were quite high, as shown in Table 3 as 19.3% LOI. In Rawang, the site was a flat land and samples were taken from a drill-hole. Right above the rock sample at 7 m depth (R5), gravels were observed in huge amount. The amount of gravel appeared to be decreasing drastically from 4.5 m depths upwards (sample R3). However, there was still gravel present right to the ground level as compared to those in Balakong. Again, the trends of the development of sand and silt from 6.0 m depth upwards were not obvious as in the samples in Balakong. However, the formation of clay-size minerals was the same as in Balakong.

   The formation of clay-size minerals as shown from the particle size distribution tests coincides, but vaguely, with the formation of clay minerals as shown in Table 2. The clay minerals formed very early during the weathering process. Clay minerals are defined as minerals having specific crystal structures regardless of their sizes while clay particles are defined as inorganic soil particles with diameters less than 0.002 mm, regardless of mineral type. Table 3 shows the chemical composition of the samples obtained from the XRF analyses. The results confirmed the

Table 1   The results of particle size distribution tests

Sample name	Depth (m)	Gravel (%)	Sand (%)	Silt (%)	Clay (%)
B0	0.0	0	70.3	5.1	1.3
B1	1.5	0	86.7	7.4	4.4
B2	5.5	0	81.4	9.2	3.6
B3	10.0	0.3	80.2	6.5	2.4
B4	14.0	1.4	78.7	4.2	1.4
B5	16.0	–	–	–	–
R0	0.0	9.0	32.6	41.2	4.3
R1	1.5	8.0	32.1	38.6	20.8
R2	3.0	5.7	24.8	37.1	30.2
R3	4.5	22.0	38.0	21.3	15.0
R4	6.0	26.0	49.3	17.6	1.0
R5	7.0	–	–	–	–

Table 2 The results of Quantitative X-ray diffraction analyses (XRD)

Depth below ground level (m)	Sample name	Quartz (wt%)	Plagioclase (wt%)	K-feldspar (wt%)	Gibbsite (wt%)	Muscovite (wt%)	Biotite (wt%)	Hematite (wt%)	Goethite (wt%)	Clay minerals (wt%)
0.0	B0	60	–	1	8	4	–	–	1	26
1.5	B1	61	–	1	13	2	–	–	–	24
5.5	B2	65	–	–	9	6	–	–	–	20
10.0	B3	60	–	6	–	9	–	–	–	25
14.0	B4	53	–	6	–	7	–	–	–	17
16.0	B5	31	20	42	–	6	6	–	–	2
0.0	R0	50	–	–	4	6	–	–	3	35
5.0	R1	45	–	–	25	–	1	–	2	23
8.0	R2	43	–	–	22	–	1	2	2	21
10.0	R3	56	–	–	14	–	2	1	1	24
13.0	R4	40	–	–	40	–	3	1	2	12
16.0	R5	33	25	25	N.D.	–	6	–	–	1

Table 3 The results of X-ray flouresence analyses (XRF)

Depth below ground level (m)	Sample name	SiO$_2$ (wt%)	Al$_2$O$_3$ (wt%)	Fe$_2$O$_3$ (wt%)	MgO (wt%)	CaO (wt%)	Na$_2$O (wt%)	K$_2$O (wt%)	TiO$_2$ (wt%)	MnO (wt%)	P$_2$O$_5$ (wt%)	LOI (wt%)
0.0	B0	60.2	18.3	1.7	–	–	–	0.3	0.2	0.0	0.0	19.3
1.5	B1	76.1	20.1	1.4	–	–	–	0.3	0.1	0.0	0.0	2.8
5.5	B2	79.2	18.3	1.4	–	–	–	0.7	0.2	0.0	0.0	1.3
10.0	B3	76.0	15.5	1.0	0.1	–	0.1	2.2	0.2	0.0	0.0	5.3
14.0	B4	72.7	18.0	1.1	0.1	–	0.1	1.7	0.1	0.0	0.0	5.8
16.0	B5	76.0	12.6	1.1	0.2	0.4	2.6	5.3	0.1	0.0	0.1	1.6
0.0	R0	64.4	20.5	5.3	–	–	–	0.1	0.9	0.0	0.1	8.6
5.0	R1	65.8	23.6	6.2	–	–	–	0.1	1.1	0.0	0.1	4.2
8.0	R2	70.3	19.9	4.2	–	–	–	0.5	0.7	0.0	0.1	4.8
10.0	R3	62.3	26.6	5.3	–	–	–	1.2	0.9	0.0	0.1	3.8
13.0	R4	55.9	35.3	4.4	–	–	–	0.6	0.7	0.0	0.1	2.7
16.0	R5	67.2	13.6	2.8	1.0	1.8	2.6	5.2	0.5	0.1	0.2	0.9
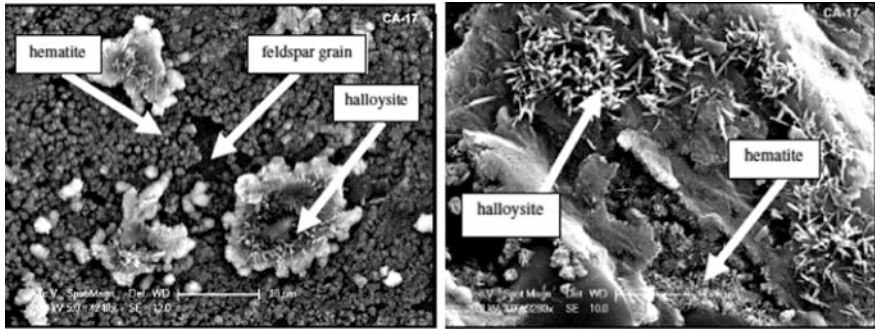
Fig. 4 The development of halloysite in granite (Balakong samples). Left: halloysite and hematite growing on feldspar grains. Right: high magnification of the clay minerals
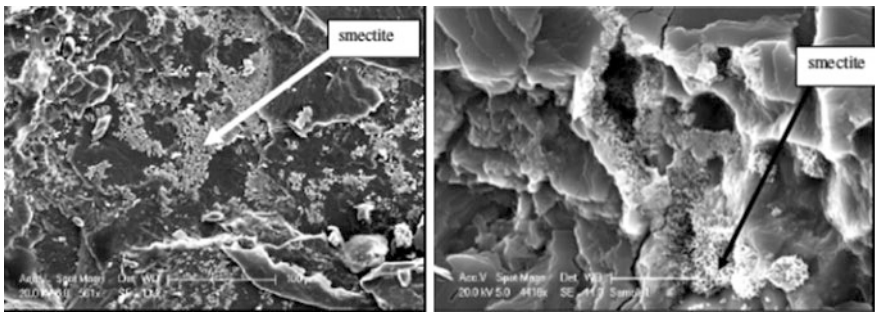
Fig. 5 The development of smectite clay minerals on feldspar minerals in the Rawang samples. Left: the lower magnification and right: higher magnification
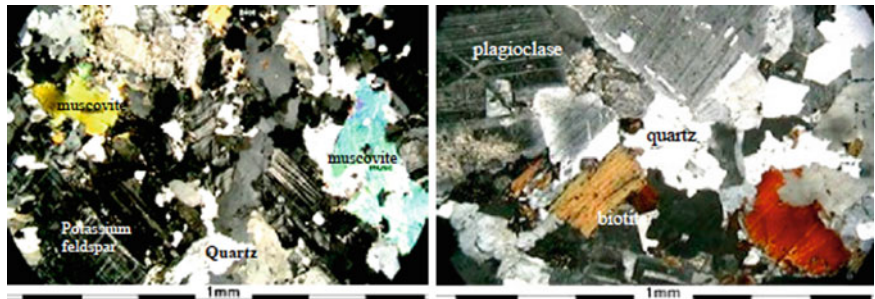
Fig. 6 Petrographic images showing the minerals present in Balakong (left) and Rawang (right)

formation of the clay minerals, as the basic chemical constituent of clays minerals is SiO_2 and Al_2O_3. SEM observations showed the initial formation of halloysite and smectites on the surface of feldspar minerals (Figs. 4, 5 and 6; Table 4).

Table 4 Shear strength parameters obtained using direct shear box tests

Depth below ground level (m)	Sample name	Cohesion, C (kN/m^2)	Friction angle, φ (°)
0.0	B0	–	–
1.5	B1	11.0	43.3
5.5	B2	11.3	44.2
10.0	B3	11.4	45.3
14.0	B4	12.4	41.2
16.0	B5	–	–
0.0	R0	–	–
5.0	R1	20.2	19.5
8.0	R2	18.8	20.3
10.0	R3	17.3	24.3
13.0	R4	19.5	22.3
16.0	R5	–	–

Upon comparing the presence of clay-sized particles, clay minerals and the shear strength parameters, it appears that cohesion within the soil mass was influenced by the amount of clay-sized particles present rather than the clay minerals. This can be inferred as the clay-sized particles provide the cohesive properties of the soil mass. However, the presence of clay minerals did not give any observable difference to the cohesion obtained. For the friction angle, no observable relation can be observed.

4 Conclusion

From the analyses conducted based on the findings of the above-discussed tests, it can be said that the presence of clay-sized particles are remarkably proportional to the increase in shear strength. However, the clay minerals do not give much impact on the shear strength parameters of the soil mass. This conclusion does not include the parameters that are directly related to the influence of water as the swelling and non-swelling types of clay minerals do act differently upon being soaked in water and not to forget the influence of pore-water pressures within particles in a soil mass.

References

1. Abad, S.A.N.K., Tugrul, A., Gokceoglu, C., Armaghani, D.J.: Characteristics of weathering zones of granitic rocks in Malaysia for geotechnical engineering design. Eng. Geol. **200**, 94–103 (2016)
2. Dearman, W.: Weathering classification in the characterisation of rock: a revision. Bull. Eng. Geol. Env. **14**(1), 123–127 (1975)
3. Goudie, A.: Quantification of rock control in geomorphology. Earth Sci. Rev. **159**, 374–387 (2016)
4. Irfan, T., Dearman, W.: Engineering classification and index properties of a weathered granite. Bull. Eng. Geol. Env. **17**, 79–90 (1978)
5. Komoo, I.: Engineering properties of weathered rock profiles in Peninsular Malaysia. Institution of Engineers Malaysia (1985)
6. Lin, D., Lou, F., Yuan, R., Shang, Y., Zhao, Y., Ma, J., Zhang, L., Li, K., Bao, W.: Rock mass characterization for shallow granite by integrating rock core indices and seismic velocity. Int. J. Rock Mech. Min. Sci. **93**, 130–137 (2017)
7. Raj, J.K.: Characterisation of the weathering profile developed over a porphyritic biotite granite in peninsular Malaysia. Bull. Int. Assoc. Eng. Geol.—Bull. de l'Association Internationale de Géologie de l'Ingénieur **32**(1), 121–129 (1985)
8. Deng, L., Yuan, P., Liu, D., Annabi-Bergaya, F., Zhou, J., Chen, F., Liu, Z.: Effects of microstructure of clay minerals, montmorillonite, kaolinite and halloysite, on their benzene adsorption behaviors. Appl. Clay Sci. **143**, 184–191 (2017)
9. Joussein, E., Petit, S., Churchman, J., Theng, B., Righi, D., Delvaux, B.: Halloysite clay minerals—a review. Clay Miner. **40**(4), 383–426 (2005)
10. Scarciglia, F., Critelli, S., Borrelli, L., Coniglio, S., Muto, F., Perri, F.: Weathering profiles in granitoid rocks of the Sila Massif uplands, Calabria, southern Italy. New Insights Formation Process. Rates: Sediment Geol. **336**, 46–67 (2016)
11. Tan, X., Liu, F., Hu, L., Reed, H., Furukawa, Y., Zhang, G.: Evaluation of the particle sizes of four clay minerals. Appl. Clay Sci. **135**, 313–324 (2017)
12. Arias, D., Pando, L., López-Fernández, C., Díaz-Díaz, L., Rubio, Á.: Deep weathering of granitic rocks: a case of tunnelling in NW Spain. CATENA **137**, 572–580 (2016)
13. Wray, L., Sauro, F.: An updated global review of solutional weathering processes and forms in quartz sandstones and quartzites. Earth-Sci. Rev. (2017)
14. Chen, A., Zhang, D., Yan, B., Lei, B., Liu, G.: Main types of soil mass failure and characteristics of their impact factors in the Yuanmou Valley, China. CATENA **125**, 82–90 (2015)
15. Ghandil, M., Behnamfar, F., Vafaeian, M.: Dynamic responses of structure–soil–structure systems with an extension of the equivalent linear soil modeling. Soil Dyn. Earthq. Eng. **80**, 149–162 (2016)
16. Khasawneh, Y., Bobet, A., Frosch, R.: A simple soil model for low frequency cyclic loading. Comput. Geotech. **84**, 225–237 (2017)
17. Hillier, S.: Quantitative analysis of clay and other minerals in sandstone by x-ray powder diffraction (XRPD). Inst. Assoc. Sedimentol. Spec. Publ. **34**, 213–251 (2003)
18. Fitton, J.G., Saunders, A.D., Larsen, L.M., Hardarson, B.S., Norry, M.J.: Volcanic rocks from the southeast Greenland margin at 63°N: composition, petrogenesis and mantle sources. Proc. ODP Sci. Results **152**, 331–350 (1998)

Investigation on Slope Stability Using Monte Carlo Simulation: A Case Study of Ulu Jelai Hydroelectric Project

Abdul Rahman Nurul Umibaiti

Abstract Slope safety and its monitoring are major concern for dam owners, especially if the slopes are adjacent to public highway or roads that experiences increase in traffic volume each year. If no proper assessment and maintenances are being done, there is potential for loss of life of public users. Deterministic design methods for the slope stability often depends on the interpretation of the geotechnical investigations by the geologist and civil engineers involved with the project. This method usually adopts conventional value of ground parameters and which then gives large safety factors. By performing probabilistic approach by utilising Monte Carlo Simulation, designers or owners are more confident with the results given and it will help in the decision-making, such as in deciding the best solution for the long-term maintenance and monitoring of the slopes at critical area. This paper described the probabilistic procedure and gave a distribution of Factor of Safety (FOS) rather than only one single calculated FOS for that critical slopes. The case study for the paper is the Ulu Jelai's dam located in Cameron Highlands, Malaysia. The analysis is done using both excel and software. At the end, proper mitigation plans are proposed for the critical slopes [1].

1 Introduction

Analysis of slope stability is usually consist of many uncertainties, which range from lack of accurate geotechnical parameters, inherent spatial variability of geo-properties, change of environmental conditions, unpredictable mechanisms of failure, simplifications and assumptions used in geotechnical models.

A. R. Nurul Umibaiti (✉)
Department of Civil Engineering, Universiti Tenaga Nasional,
43000 Kajang, Selangor, Malaysia
e-mail: nuruluar@tnb.com.my

Typical and conventional way of slope stability calculations usually will not consider many uncertainties in the process of getting the results. Also, several conservative safety factors are used to cover some uncertainties which in most cases are more than required, and in some cases are less. Actually, it is not possible to distinguish the accurate effect of these safety factors on safety level. By contrast, in probabilistic approaches the safety determination applies more accurately and clearly.

Monte Carlo Simulation is a useful tool that available for applying the probabilistic approaches in many fields. An iterative process using deterministic methods of slope stability analysis are applied in this technique. This method consists of five steps as follows:

- Selection of input variable for the calculation.
- Select a random variable for each input variable chosen earlier as per assigned probability density function.
- Calculate the factor of safety (Fellenius, Bishop Simplified Method, Janbu, etc.) based on the selected figure in Step 2.
- Step 1–3 is repeated for 500, 1000 or 1500 depends on the engineer.
- Determining distribution function of factors of safety and probability of failure.

The left bank of the Ulu Jelai Dam located in Malaysia has been considered as a case study, analysis has been accomplished using both software and excel calculation [2].

2 General Geology of Cameron Highlands

Ulu Jelai is located at the Cameron Highlands, Pahang, Malaysia. Cameron Highlands is located within the central part of the Main Range, which is underlined by Main Range Granite. The Main Range Granite consists predominantly of Late Triassic intrusive biotite granite and roof pendants of Lower Paleozoic sedimentary rocks intruded by minor quartz dykes. The main range granite crystallise in late Triassic is about 207–230 Ma (Fig. 1).

3 Salient Features Ulu Jelai Hydroelectric Project (Ulu Jelai HEP)

Ulu Jelai's dam was constructed on Susu river at Bertam Valley, Cameron Highlands, Pahang, Malaysia. The salient features of Ulu Jelai's Dam are represented in Table 1.

Fig. 1 General geology of Cameron Highland

Table 1 Salient features of dam

Item	Details
Dam type	Roller compacted concrete
Crest length	512.5 m
Maximum water level (MWL)	EL 548
Dam crest width	5 m
Reservoir gross storage	18.62 mm^3
Maximum operating level (MOL)	EL 548
Dam's height	88 m
Full supply level (FSL)	EL 540
Extreme minimum operating level (EMOL)	EL 524
1 in 100 year flood level	EL 548

4 JKR Road—Highway Adjacent to Dam

During the early stages of the design of Ulu Jelai's HEP, it was identified that drawdown of the reservoir during operation could possibly influence upon performance and stability of the Pos Betau—Lembah Bertam Road. This road is a highway class single carriageway road and wide shoulder in each direction. It

transverses along the rim of the Susu reservoir. The road completed in 2010, and it is under the responsibility of the Malaysian Jabatan Kerja Raya Authority (JKR). After this, the road is referred as the 'JKR Road'.

The slope on which the JKR Road has built are steep with local relief of several hundred metres. The height from the JKR Road to the bed of Sg. Bertam is about 100 m at the Susu Dam right abutment to about 20 m at the upper reach of the planned reservoir.

The road is about 60–80 m above the riverbed. These intervening slopes are at natural gradients of 20–40°. Normal operation of the Ulu Jelai HEP will result in rapid drawdown of the reservoir. There is potential that some of the slopes adjacent to the JKR Road, road embankments and road retaining structures are expected to be affected by the filling and operation of the reservoir.

4.1 Potential Modes of Instability for the Slope

The fluctuations from the reservoir could possibly affect the highway in a number of ways

- Undercutting of the toe of embankments and walls;
- Slope instability of road embankments;
- Instability of retaining structures;
- Differential settlement of the road;
- Culvert inundation may cause piping erosion of backfill.

Depending upon the setting, slope conditions, material types and the slope profile the modes of failure will vary. The following main modes of instability are considered possible:

- Rotation (or circular) slope failure;
- Non-circular slope failure;
- Retaining structure failure;
- Differential settlement;
- Debris (or mud) flow.

Rotational slope failure would be limited to generally uniform soil profiles where the slide surface does not reach the bedrock surface. Such a scenario could be on the long slopes both above the road and below the road, but both sites would likely have different driving mechanisms. A failure above the road may be due to the undercutting or removal of the supporting toe of the slope, whereas a failure below the road could be due to a raising of the groundwater table and consequent pore water pressure increase. Where the bedrock level is intersected by a failure surface the mode would change from a circular failure to a non-circular failure or a planar slide surface. Where large boulders are present in the slope face the failure mode could be due to a toppling mechanism or a rock fall.

If a retaining structure failed this may lead to a slump or driving wedge where a mass of material loads a lower part of the slope thus leading to a type of progressive failure. This may also be the case where differential settlement of the road surface causes a transfer of load down the slope and thus induces a type of progressive failure. The performance of this road is potentially affected by the filling of the reservoir and the fluctuations of reservoir level during operation of the dam. The raised water level and drawdown operation of the reservoir will affect the groundwater levels, causing increased pore pressure within the soil and weathered rock that can result in instability, in the slopes below and above the road and the road bench itself.

The road in its present state has exhibited significant signs of instability once groundwater or storm water increases the degree of saturation in the existing slope.

4.1.1   Design Considerations, Uncertainties and Limitations

It is considered that slopes that are flatter than 2H:1 V may experience some instability during reservoir operation but are unlikely to impact immediately on the performance of the JKR road.

In establishing a factor of safety criteria, a literature review has been undertaken of relevant references for highway and dam projects. The findings from this review include

  I. JKR Guidelines for Slope Design Table 2, Reinforced or treated slopes FOS = 1.5.
 II. Wilson and Marsel (1979—ICOLD)—Table 2:

Table 2 Geotechnical investigations and results of laboratory tests of the JKR's road

Material	Average thickness encountered along JKR road (m)	Interpreted seismic velocity (m/s)	Typical SPT N—Value range (blows/300 mm)	Results of laboratory tests
Fill	9	0 to 400	0 to 10	Sandy silt—sandy clay
Residual soil	5	0 to 800	0 to 10	Sandy silt—sandy clay
Completely weathered granite 1	5	800 to 1200	10 to 30 (with minor cored section)	Sandy silt or sandy clay, with gravel, cobbles and boulders
Completely weathered granite-2	6	1200 to 1600	20 to 50 (with numerous cored sections)	Bouldery silty sand
Granite bedrock	–	Greater than 1600	Continuous coring	–

- FOS = 1.5 using effective strength parameters and estimated flow net drawdown piezometric surface (as carried out in our JKR road stabilisation designs).
- FOS = 1.2 sudden drawdown from spillway crest—not considering flow nets calculating drawdown of piezometric surface during drawdown.

III. FHWA-NHI-10-024 'Design and construction of Mechanically Reinforced Stabilised Earth Walls and Reinforced Soil Slopes':

- FOS = 1.5 for slopes where limited and variable geotechnical information is provided or slopes support structures or where consequences of failure of supported structure are severe, (i.e. full or partial closure of a highway class road).
- FOS = 1.3 for slopes not supporting structure/slopes above infrastructure and only minimal to minor consequence of failure, i.e. movement of a sign foundation.

IV. United States Society on Dams USSD (Feb 2007)—'Strength of Materials for Embankment Dams', considering effective strength parameters:

- USACE—FOS = 1.3 for Sudden drawdown from Max storage pool crest.
- USACE—FOS = 1.4 to 1.5 Sudden drawdown when routine operating conditions.
- USBR—FOS = 1.3 rapid drawdown from normal pool.

The considerations and limitations of the design inputs and analyses that have been included in developing the determination of FOS and its slope treatment, but are not limited to

I. The JKR road slopes are supporting public R5 standard highway road infrastructure of 80 km/h speed limit.
II. The original JKR road is understood to have been designed for a FOS of 1.5 in accordance with JKR guidelines.

4.1.2 JKR Road Investigations Results

See Table 2.

5 Geohazard Map—Further Assessment on Potential Instability of the Slope

Susu Dam fo the Ulu Jelai HEP has a hilly topography. Due to the construction of the dam, some slope within the study area had been cut for access road during the development of the dam. The cutting of a few slopes is steep with angle more than

45°. The minimum elevation of access road is 525 m around the dam crest area while the maximum elevation of the access road is 546 m located around kg Leryar. As the project advanced, geohazard mapping has been performed to further assess the potential instability and the most hazard areas that need particular attention.

From the map, it is found that no major fault is identified in the study area. The overall study area is underline by granite bedrock, weathered granite, residual soil and boulder at top of layer. While at certain areas of sub-surface there are areas with highly water content zone. kg Leryar, the nearest settlement, is not affected as it was not located at potential geohazard area and it is quite far from the potential geohazard area. Basically, the location potential geohazard area is, where there is cutting of slope more than 45° without proper erosion protection. Potential geohazard is identified at level 530–540 m due to fluctuation water level.

6 Factor of Safety (FOS) Results from SLOPE/W

The stability analyses using Slope/W have been carried out to find the factor of safety for the slope. The Morgenstern Price Analyses has been adopted in the analysis with the assumption that the soil will be saturated at the levels of MWL (EL 548). Short term and long-term slope stability analyses were carried out at 10 selected location (Fig. 2). The selected locations is in Appendix 1.

The minimum global FOS obtained was 1.989 at slope Slope L. The minimum global term FOS obtained was 1.475 at slope Slope C. Output from SLOPE/W
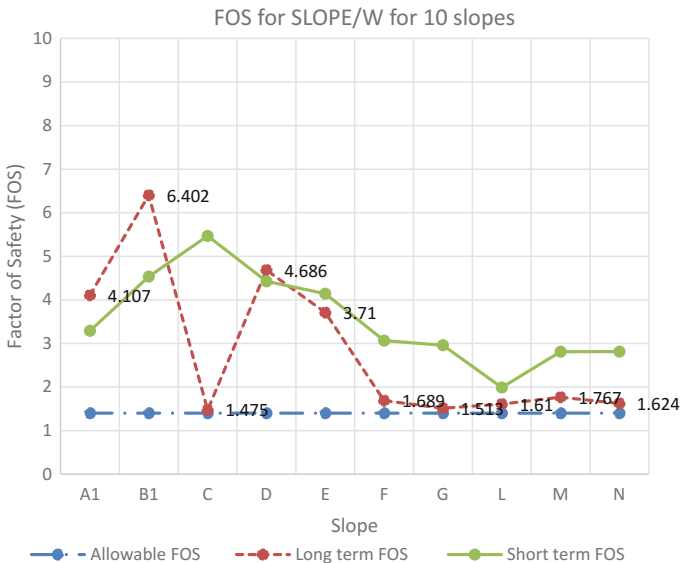
Fig. 2 FOS from SLOPE/W at 10 selected locations

shown that when the consolidated drained samples were soaked for 14 days suggest a decrease in the friction angle. From the experiment conducted, all slopes have sufficient stability, even with a drawdown of 6 ft/hr at extreme operation conditions, i.e. from MWL (548 m) to Extreme MOL (524 m). With intense rainfall of 100 mm/h for 1.5 days duration however, Slope C and L has FOS values, which are lower than allowed for slope stability. Thus, it is critical for Slope C and L to carry out further investigation on the slope stability using probabilistic approaches.

6.1 Variables of Pore Pressure

Pore pressure is determined from hydraulic tests result, and in some cases the result differ from the real values. Pore pressure is a direct reflection of variability in permeability, while permeability is usually highly uncertain. Below is the assumed drawdown scenario selected for the assessment (Figs. 3 and 4).
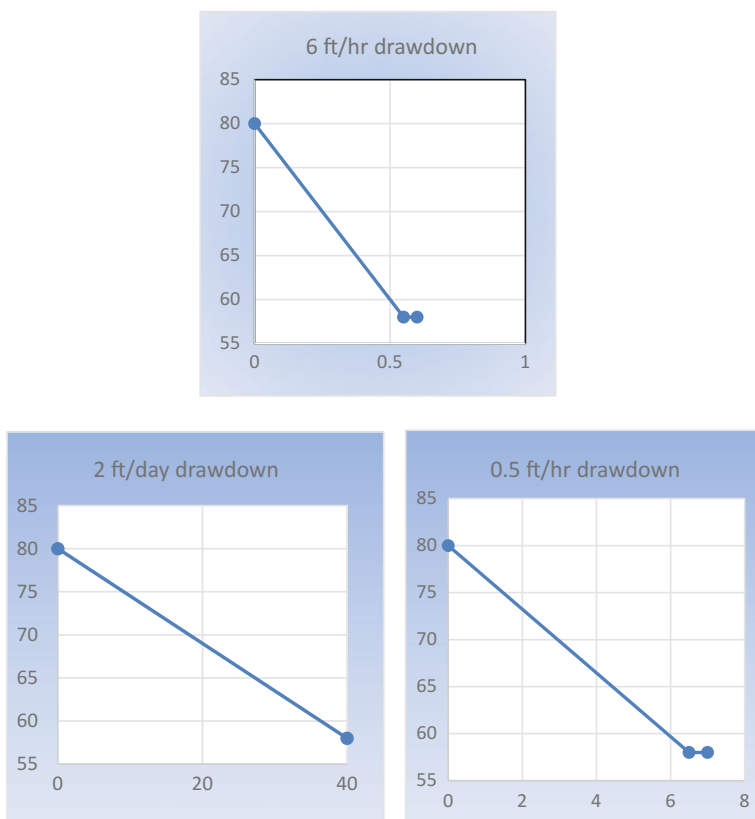
Fig. 3 Assumed drawdown scenario adopted for assessment
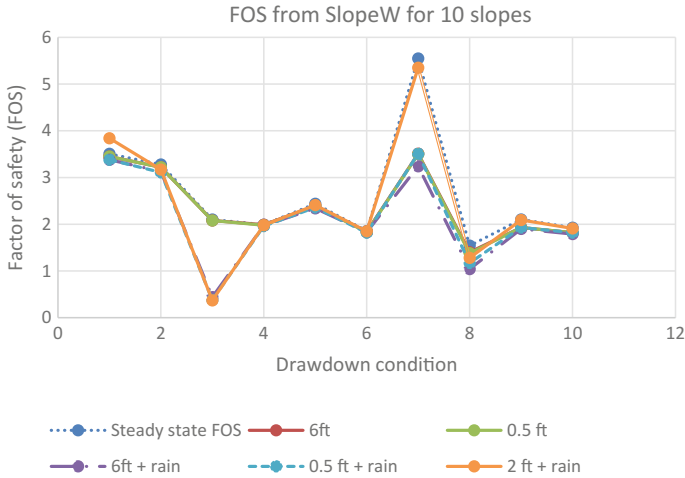
Fig. 4 Factor of safety relates to the drawdown scenario

7 Probabilistic Approach—Monte Carlo Simulation Method

Factor of safety (FOS) defined as

$$\frac{\text{Resisting forces}}{\text{Driving Forces}} = \frac{\text{Shear strength}}{\text{Shear Stress}} \tag{1}$$

In deterministic calculation, such as adopting SLOPE/W, often-single fixed values (mean values), strength parameters are used as the input in the calculation. Such calculations does not able to take into consideration for variation in slope parameters. The limits and assumptions used may pose some uncertainties in the result. Confidence of the decision maker to the output/results will be limit to that certain assumptions made.

Meanwhile, MCS simulation able to check the assumption made for the calculation (is it valid/not?) and explore the sensitivity of the results to the input parameters.

7.1 Material Properties

The strength envelope parameters obtained from site investigations for the left bank rim as in the Table 3.

Table 3 Strength envelope parameters

Parameters	Range	Mean	Standard deviation
cohesion	15–338	86.8	8.22
ϕ	22–75	29.75	7.6
τ	8–64	63.5	0.86
σ	6–98	33.9	24.27

8 Results

8.1 Monte Carlo Simulation (MCS) Output Analysis

Figures below is the probability of failure and the histogram data for the most critical slope, Slope C and L after 500 Monte Carlo trials using software RiskAmp (Figs. 5, 6, 7 and 8).

Referring to U. S Army Corps of Engineers (2006), for embankment dams, slopes with reliability index of more than 3 is stable. The probabilistic analysis gave a high reliability index (Fig. 9; Table 4).

9 Discussion

Based from the result of MCS output and previous assessment, the discussion came to these important points

- Slope stability is more sensitive to parameter—cohesion, but less sensitive to parameter—friction angle. As can be seen from the probability of failure graph

Fig. 5 Range of FOS (Slope L) related to the 500 MCS iteration for friction angle
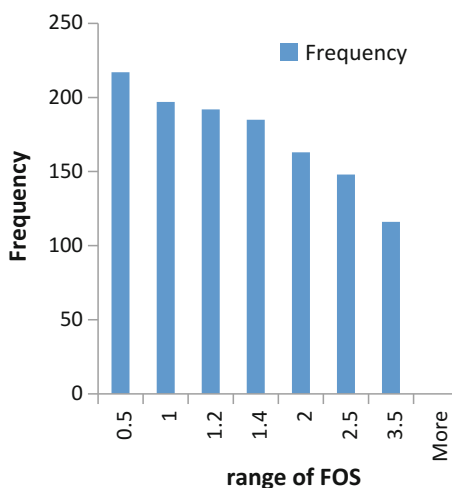
Fig. 6 Range of FOS (Slope C) related to the 500 MCS iteration for cohesion
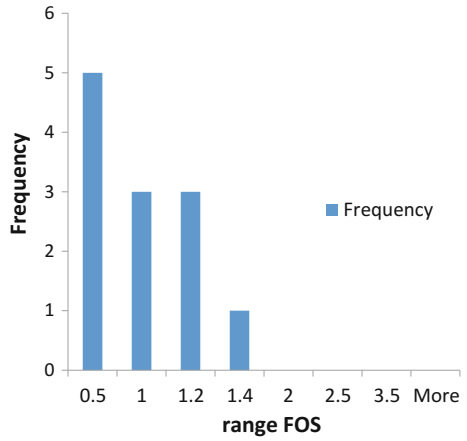
Fig. 7 Probability of failure Slope L 500 iterations of MCS
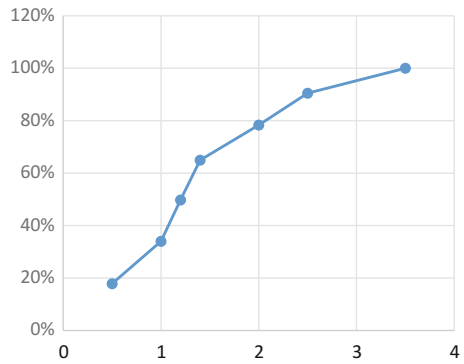
Fig. 8 Probability of failure Slope C 500 iterations of MCS
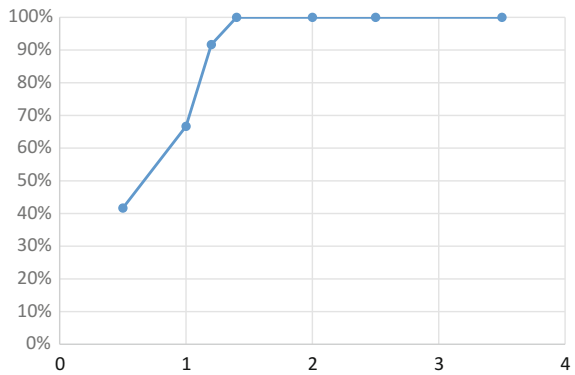
Fig. 9 FOS for different drawdown scenario
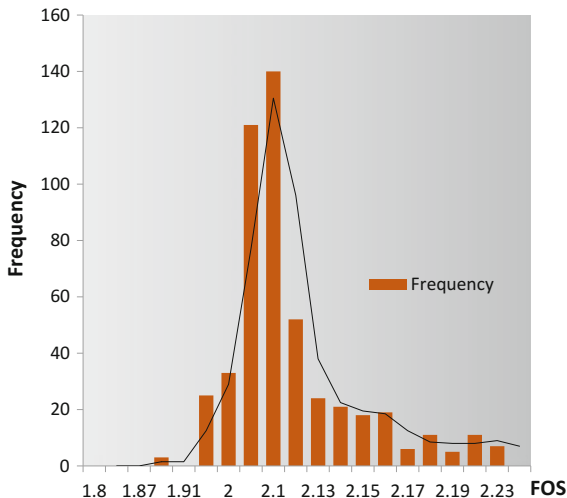
Table 4 Probability analysis results and reliability index

Probabilistic analysis results	Number of trials	500
	Min. FOS	1.94
	Max. FOS	2.12
	Mean FOS	2.076
	Standard deviation	0.068
	% failure	0
	Reliability index	15.705

for variables in cohesion, the probability of getting a FOS of less than 1.0 is more than 60%, compared to only 30–40% of obtaining FOS less than 1.0 for variables—friction angle. The decrease in the cohesion has negative effect on slope stability.

a. When the soil is saturated, the friction decreases and affected the shear strength of the soil. However, since the toe protection and sub-surface drainage have been installed before reservoir filling, the pore pressure is reduced and it increases back the shear strength.
b. The slopes throughout the study area are still intact with major areas still covered by thick trees and vegetation. Thus, the existing trees and vegetation helped with the overall stability of the slopes. The existing of deep roots from the trees will act as slope anchors deep into the hard layer and thick vegetation leaves will prevent heavy surface runoff from penetrating into the soil layer, which will weaken the soil. All these mitigations help to maintain the shear strength of the soil [3, 4].

10   Recommendation of Mitigations

Slopes next to watercourse need proper treatment and safety measure. Proper design of riprap or other protection measures is important due to fluctuating water levels. The exposed slopes (if exist) must be treated from running water and provide proper drainage.

10.1   Maintenance and Monitoring Program for Slope

Even though the slope conditions are safe based on the current conditions, the following recommendation are to be look in order to avoid the future risk of the area:

- To carry out inspection and maintenance of the slopes periodically;
- To monitor inclinometers and piezometers periodically; and
- To avoid any future development along the slope of the area as much as possible.

Follow complete guide for slope maintenance and monitoring shall be in accordance to JKR Cerun 1—Guidelines on Slope Maintenance in Malaysia. Remote sensing (RS) is possible to be considered for early warnings of slope failure.

10.2   Evaluation of Slope Stability

In the future, prove the slope repair had improved the stability of the slope, by checking/evaluating the stability of the left abutment slope by tool/software. The safety of the left abutment can be further verified. [5] Such database is valuable, and it is more economical to the dam owners, in making planning for slope maintenance in the future.

10.3   Conflicts of Development

Often if there is conflict of development, or there is other development concurrently with each other, communication and timing is an important thing to avoid waste of resources (time and money) fixing the damages that could be avoided if a proper plan and proper communication have been made.

When there is conflict of highway and dam, information that need to be pass to JKR are

- Elevation of the dam and the reservoir level along the important alignment adjacent to the reservoir;
- Slope characteristics—for rapid drawdown scenario;
- Operation rules of the dam need to be passed on those designing the highway;
- Early engagement and involvement in development of the highway with proper documentation as future reference, to cater for changing of the person in charge from time to time.

It is important for the dam operators/design team to be part of the highway design team, so that they can be actively involved in the design, as meetings, discussions and letters are not efficient in passing information that essential to avoid conflicts later. Sharing and discussing on the standard used for design is also an important thing to do. Maintain transparent and communicate often among all involved in the planning, design and construction of dams. Assessment of past event is essential so that the lesson learnt from past project is not repeated.

11 Conclusion

The model from the MCS is able to answer questions such as these:

'What if the parameters is such and such what will be the FOS of the slope?'
or 'Given all these parameters, what is the risk of slope failure?'

Its good to keep in mind that, the simulation will only be good as the estimates one made, like any other forecasting model. The simulation represents probabilities and not certainty. However, the Monte Carlo Simulation is one of power tool that useful when forecasting and unknown future [6–8].

Appendix 1

References

1. Paper, C., Power, M.M.: Probabilistic approach to assess dam slope stability utilizing monte carlo simulation, September 2012, (2016)
2. Huang, J., Fenton, G., Griffiths, D.V., Li, D., Zhou, C.: On the efficient estimation of small failure probability in slopes. Landslides **41572279**, 1–8 (2016)
3. Ross, S.M.: Introduction to Probability models, (2010)
4. Fei, Y., Yucheng, L.: Probabilistic slope stability analysis : the case study of a deposit slope in hydropower reservoir, (2013)
5. Journal, Q., Geology, E.: Safety monitoring and stability analysis of left bank high slope at Jinping-I hydropower station, November, (2016)
6. Matthews, C., Farook, Z.: Slope stability analysis—limit equilibrium or the finite element method ?, (2014)
7. Washington, T.G., Spring, S.: EX P L O R I N G M O N TE C ARLO, pp. 44–57 (2007)
8. Fearnside, P.M.: Brazil's Samuel Dam: lessons for hydroelectric development policy and the environment in Amazonia. Environ. Manage. **35**(1), 1–19 (2005)

The Effects of Coir Fibre
on Consolidation Behaviour of Soft Clay

Muneerah Jeludin and Nurafiqah Suffri

Abstract Natural fibres from coconut, bamboo, cane or palm are used in soil improvement techniques to enhance the behaviour of soft deposits. The main reason for utilising these natural fibres is that they are economically viable and environmental friendly. Coconut fibres or coir are locally available and in abundance in Brunei Darussalam. Experimental investigations into the use of these coir fibres (coconut fibres) in soft clay with regards to its consolidation behaviour were carried out. Kaolin of high plasticity of the following characteristics: LL of 61.5%, PL of 51.8% and PI of 9.7% was used. The Maximum dry density and Optimum moisture content was determined from compaction test to be used as a basis in preparing samples for the consolidation tests. The soil samples which were reinforced with various inclusions of coir that is at 1.0, 1.5, 2.0 and 2.5% and of different sizes of 10, 20 and 30 mm were tested to determine the effects on consolidation behaviour due to the inclusion of these fibres. The results were compared with that of the unreinforced soil sample and it was indicated that the coefficient of consolidation (c_v) is affected by the length of coir fibres. For inclusions of 10 mm coir fibres, the c_v increases with the increase of fibre inclusions up to a certain percentage and then decreases thereafter.

Keywords Soil reinforcement · Coir fibres · Consolidation

1 Introduction

Soft-clay deposits is known to be very sensitive, has low permeability, high compressibility and low shear strength. Construction on these types of deposits poses many challenges to the ground engineers especially in terms of its bearing

M. Jeludin (✉) · N. Suffri (✉)
Civil Engineering Programme, Universiti Teknologi Brunei,
Gadong, Brunei Darussalam
e-mail: muneerah.jeludin@utb.edu.bn

N. Suffri
e-mail: nurafiqah.suffri@gmail.com

capacity, settlement and stability. To overcome such problems, alternative means such as ground improvement techniques can be considered to enhance the engineering characteristics of these deposits, hence improving the performance. The function of the reinforcements in the soil matrix is to increase the strength and reduce deformation [3].

The primary advantages of randomly distributed fibres are the absence of potential planes of weakness that can develop parallel to oriented reinforcement [4]. Natural materials such as fibres from bamboo, coconut, cane, wheat and palm have been used as a reinforcing material to minimise settlement and to increase rate of consolidation [2, 5–8].

Over the past years, the use of natural fibres as soil reinforcement has gained attention for researches. Numerous laboratory investigations into the use of natural fibres as reinforcement in soils have been conducted. Based on the laboratory tests, previous researchers have shown that there was an increase in the strength and stability of soils reinforced with these natural fibres [3, 5]. Abdi et al. [1] worked on fibre-reinforced soils and concluded that consolidation settlements, swelling and crack formation reduced substantially. Nahta and Vibhakar [5] reported that the shear strength increases with the inclusion of coir fibre up to a certain coir content and then decrease beyond that point based on their CBR tests. Jha et al. [2] performed a series of laboratory tests to study the shear strength and bearing capacity of soft soil reinforced with randomly mixed human hair. Based on their experimental results obtained, the shear strength and the bearing capacity increases up to 2% inclusion of human hair fibre, and there is no more increment at 2.5% inclusion. Singh and Mali [7] used coir fibres, polypropylene fibres and scrap tire rubber fibres as the reinforcement. They carried out Tri-axial test, Direct Shear box test and unconfined compression test. Their Tri-axial test results indicated that by adding coir fibres in the silty soil, there was improvement in stress–strain behaviour. The major principle stress at failure increases when more fibres of constant length were added. There was only a small gain in strength when the fibre was added beyond 1% with an aspect ratio of 150. The shear strength of soil reinforced with polypropylene fibre also increases with fibres inclusion up to 0.4% inclusion and then decreases. The maximum increase was found at 20 mm length of fibre from the Direct Shear box test. They also reported that there was an increase in the soil's cohesion value when the amount of fibre content was added more. Their results also indicated that with increasing fibre content for the unconfined compression test, the compressive strength initially increased and then decreased when more fibres were added.

For any fibre content, however, 10–15 mm was observed to be the optimal fibre length at the optimum inclusion between 0.2 and 0.3%. But the optimum fibre length for tire rubber fibres is 10 mm with 2% inclusion. Qu and Sun [8] carried out consolidation test on reinforced and non-reinforced Shanghai clay using wheat straw fibre as their reinforcement element. They concluded that the Compression Index, C_c increases when the fibre contents were increased except for the 0.6% inclusion, where they reported that there is a decrease in soil stiffness beyond 0.5%.

2 Experimental Programme

A brief description of the materials and methods used in this investigation is given in the following paragraphs:

Materials

Test sample (soil): Kaolin with basic properties in Table 1 was used as representative of soft deposits. The sample is categorised as clay of high plasticity.

Reinforcement: Coir fibres are natural fibres extracted from the coconut husks which can either be brown or white fibres. Matured coconut contains brown fibres are generally strong, thick and have great resistance to abrasion whereas the white fibres obtained from young coconut are smoother, finer and also weaker. Brown coir fibres are preferable as the reinforcement materials on Kaolin. The properties of coir fibres vary and that may give difficulties to some construction due to the flexibility and rupture of the fibres which are easily affected by the ratio of length to diameter of the strand. In contrast, there are many advantages of using coconut fibres in such a way that the fibres are resistant to rot and fungi, not affected by moisture, durable and tough, readily available, cost-effective (cheap) and not easily flammable, i.e. flame-retardant. The coir fibres used in the investigation has a diameter of 0.4 mm and were obtained locally as they are easily available throughout Brunei Darussalam.

Sample Preparations: The fibres were extracted from the matured coconut husks and were cut into three different lengths of 10, 20 and 30 mm to be used for the tests. The cut fibres were then randomly mixed with kaolin to ensure that the fibres were spread homogenously as shown in Fig. 1. Water was then added to the mixture with an optimum water content and kept in an air tight bag in the laboratory for 24 h. The sample was then prepared for consolidation tests. The tests were performed on unreinforced and reinforced soil samples and the consolidation characteristics were compared.

Table 1 Properties of clay used

Properties	Values
Liquid limit (%)	61.5
Plastic limit (%)	51.8
Plasticity index (%)	9.7
Optimum moisture content (%)	13
Maximum dry density (kg/m^3)	13.93
Specific gravity (G_s)	2.6
Classification	High plasticity

Fig. 1 Coir to be mixed with kaolin

3 Results and Discussion

This paper aims to investigate the consolidation behaviour of high plasticity clay soil reinforced with coir fibres of length 10, 20 and 30 mm compacted using the standard Proctor's method. The testing programme is summarised in Table 2.

The results for the consolidation tests using automated Oedometer for the unreinforced and reinforced soil samples are presented in following sections.

3.1 Compression Index (C_c) Values and Coefficient of Volume Change (m_v) Unreinforced and Coir-Fibre-Reinforced Soil at Various Percentage Inclusions

It was found that the compression index (C_c) as shown in Fig. 2 for the unreinforced samples and samples with inclusions of coir decreases with the increase of coir fibre content up to 1.5% for 20 mm and 2.0% for 30 mm length of coir fibres. But for 10 mm fibre length, the compression index does not show any reduction

Table 2 Testing programme

Test no.	Length of coir (mm)	Percentage of coir inclusion (%)
1	None	0
2–13	10 20 30	1.0 1.5 2.0 2.5
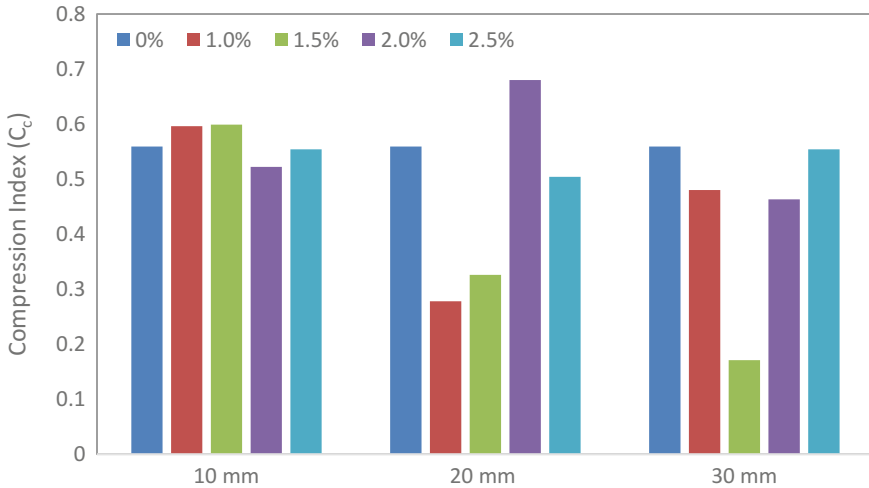
Fig. 2 Compression index chart of unreinforced and reinforced samples with various lengths and percentage inclusions of fibres

and only minimal reduction was seen in samples with 2.0% fibre inclusions. The coefficient of volume change (m_v) of the unreinforced soil and soil reinforced with different percentages of inclusions are shown in Fig. 3. It is observed that the values for coefficient of volume change (m_v) of soil also decreases with the inclusion of fibre content in soil up to 1.5% for 30 mm length of fibres, 1.0% for 20 mm. But for 10 mm no significant reduction is observed until 2.0%. The increase in C_c and m_v values at certain extent is when included with coir fibres is as a result from the coir acting as a binder to the soil particles and thus, increases the resistance of soil to compression.

3.2 Coefficient of Consolidation (c_v) and Time for 90% Consolidation (t_{90}) for Unreinforced and Coir-Fibre-Reinforced Soils

Taylor's (1948) method is used to determine the coefficient of consolidation (c_v) values of the unreinforced and soil reinforced with various amount of coir fibres. The result is shown in Fig. 4. It is indicated that for soils reinforced with 10 mm long fibres, the coefficient of consolidation increases up to fibre inclusions of 1.5%. Both 20 and 30 mm however the coefficient of consolidation c_v decreases with inclusion of coir fibres and subsequently starts increasing. The time taken for 90% consolidation (t_{90}) of reinforced soil samples is shown in Fig. 5. It is observed that t_{90} values for coir length of 10 mm in clay sample decreases with increase inclusions of coir fibre. This correlates well with observation from Kar et al. [3].
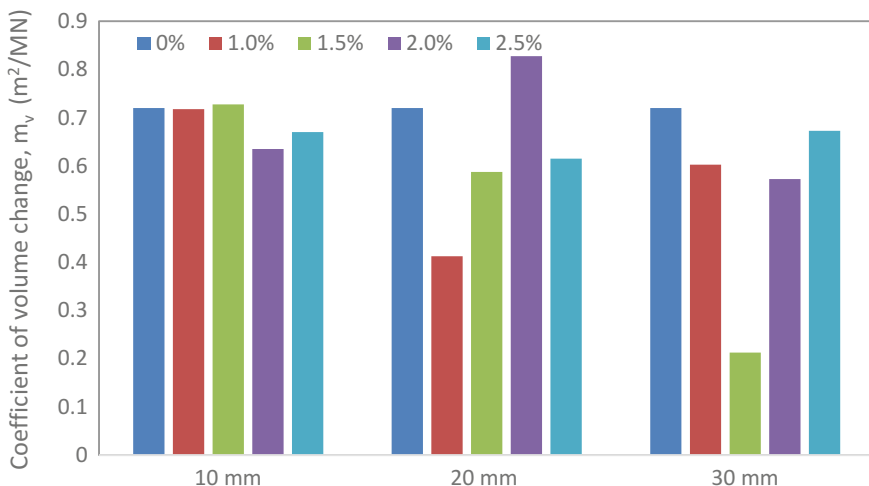
Fig. 3 Coefficient of volume change m_v for unreinforced clay sample and reinforced clay samples with coir inclusions at various length and percentage inclusions
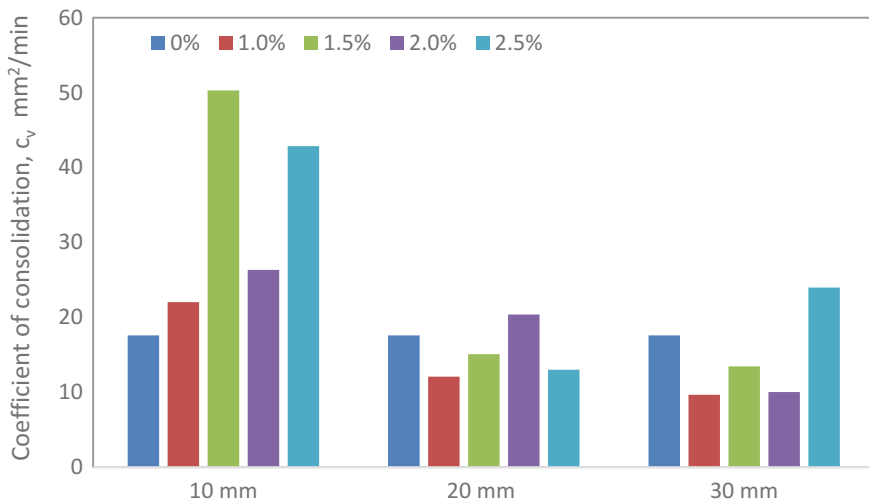
Fig. 4 Coefficient of consolidation (c_v) and time for 90% consolidation (t_{90}) for unreinforced and coir-fibre-reinforced soils

However, different observations were seen in clay samples reinforced with coir fibres of length 20 and 30 mm. This could due to the fact that length may cause uneven mixing due to insufficient friction and may cause overlapping leading to lower strength as indicated in the study by Qu and Sun [8].
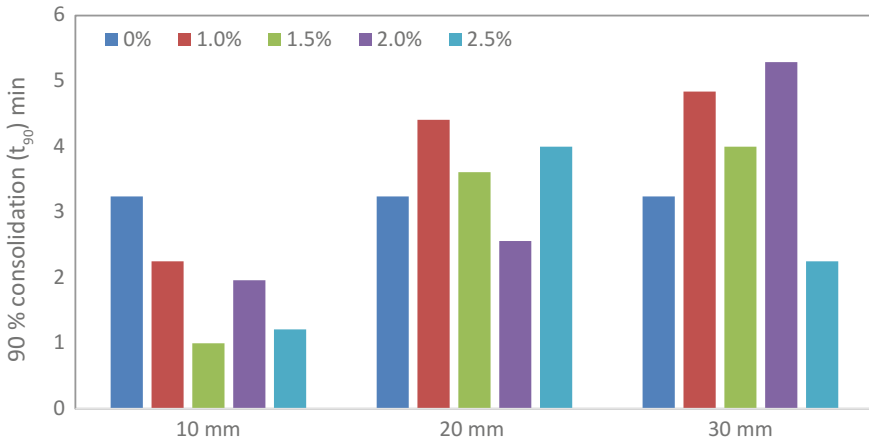
Fig. 5 Time taken for 90% consolidation for unreinforced and coir fibre reinforced clay samples

4 Conclusion

This study demonstrates the effects of coir fibre inclusion on the consolidation behaviour of clay samples. Consolidation test using automated Oedometer was conducted on several percentage inclusions of coir fibre with different lengths.

The experimental investigation indicated that for coir length of 10 mm, the compression index (C_c) and coefficient of volume change (m_v) does not show any significant reduction up to 1.5%. However, a reduction in C_c and m_v values was observed at 1.5 and 2.0% for 20 and 30 mm respectively. The values of coefficient of consolidation increase with the inclusion of coir fibres for length 10 mm. However, for 20 and 30 mm similar behaviour could not be seen. This, due to the longer length of coir, may cause uneven mixing due to insufficient friction and may cause overlapping leading to lower strength. The length of coir fibres does affect the behaviour significantly.

References

1. Abdi, M.R., Ali, P., Arjomand, M.A.: Effects of random fiber inclusion on consolidation, hydraulic conductivity, swelling, shrinkage limit and desiccation cracking of clays. Int. J. Civil Eng. **6**(4), 284–292 (2008)
2. Jha, J., Mir, B., Butt, W.: Strength behavior of Clayey soil reinforced with human hair as a natural fibre. Geotech. Geol. Eng. **34**(1), 411–417 (2015)
3. Kar, K.R., Pradhan, K.P., Naik, A.: Consolidation characteristics of fiber reinforced cohesive soil. EJGE **17**, 3861–3874 (2012)
4. Maher, M.H., Gray, D.H.: Static response of sands reinforced with randomly distributed fibres. J. Geotech. Eng. ASCE **116**(11), 1661–1677 (1990)

5. Nahta, S., Vibhakar, N.: Study of the effect of coir fibre reinforcement on the strength parameters and CBR value of clayey soil [online]. **3**(4) (April-2014) 2. Case, M.: Impulse compression using soliton effects in a monolithic GaAs circuit. App. Phys. Lett. **58**, 173–175 (2014)
6. Naik, A., Professor, P., Kumar, P., Professor, A., Kar, R.: Consolidation characteristics of fiber reinforced cohesive soil. Electronic J. Geotech. Eng. **17**, 3861–3874 (2012)
7. Singh, B., Mali, S.: Strength behaviour of cohesive soils reinforced with fibers. Int. J. Civil Eng. Res. **5**(4), 353–360 (2014)
8. Sun, Z., Qu, J.: Strength behavior of Shanghai Clayey soil reinforced with wheat straw fibers. Geotech. Geol. Eng. **34**(2), 515–527 (2015)

Part IV
Highway and Transportation Engineering

Effect of Compaction on the Degradation of Crushed Concrete Used as Partial Aggregate Substitute in Asphalt Mixtures

F. M. Jakarni, G. I. Safa Eldeen, R. Muniandy and S. Hassim

Abstract The amount of crushed cement concrete continues to grow every day from the demolition of old structures, causing more pollution. Hence, owing to the increase in environmental awareness and stringent regulations governing the disposal, as set by environmental protection agencies, more effective measures for the handling and disposal of crushed concrete must be implemented. Instead of simply disposing of crushed concrete, effective alternative efforts should be considered to utilise it as a reusable material. The objective of this study is to evaluate the possible utilisation of crushed concrete as an aggregate substitute in asphalt mixture for pavement construction applications. However, owing to the poor physical properties of crushed concrete in terms of absorption and abrasion, this study focuses on the degradation that happens in the aggregate after compaction. The recommendation is for crushed concrete to be mixed with conventional aggregates from natural sources. In this study, suitable mixtures of crushed concrete and conventional aggregates were determined based on the combinations of five types of gradation and six different proportions of crushed cement concrete (0, 20, 40, 60, 80 and 100%) from an aggregate passing and retained sieve size of 5 mm and 1.18 mm, respectively. Mixtures of the crushed concrete and conventional aggregates were subjected to compaction of 20, 40, 60, 80 or 100 blows, using a Marshall compactor. Based on the study, the mixtures of the crushed concrete with the recommended ranges of sieve sizes and conventional aggregates are suitable for roads with a medium traffic volume.

F. M. Jakarni (✉) · G. I. Safa Eldeen · R. Muniandy · S. Hassim
Department of Civil Engineering, Faculty of Engineering,
Universiti Putra Malaysia, 43400 UPM Serdang, Selangor, Malaysia
e-mail: fauzan.mj@upm.edu.my

1   Introduction

Recycled concrete aggregate (RCA) is generated by crushing old concrete structures. Owing to earthquakes, wars and the renewal of old structures waste concrete has increased. This waste material has increased over the past few years and has polluted the soil and water, and contributed to climate change [1]. Similarly, the increasing price of land in recent years has led to high dumping costs at landfill sites. Demolition contractors have discovered that it is now more expensive to dump demolition waste than to recycle it [2]. Each kilometre of flexible pavement uses 12,500 tons of natural aggregate [3]. Therefore highway construction projects represent the largest consumer of aggregate, which affects the amount of natural aggregates on earth [4]. Moreover, the primary benefits of using RCA include the reduction of demand for natural aggregate and environmental considerations.

Originally, studies focused on using RCA as a granular material in base and sub-base layers, because the lower layer specifications are less stringent than upper layers [5]. Then, it was discovered that RCA dissolves easily in water, which increases the pH of groundwater and affects the vegetation in the vicinity of the road [6]. Whereas, that is avoided in hot-mix asphalt because the aggregate was coated with asphalt.

In recent years, several studies examined the use of RCA in hot-mix asphalt (HMA). In these studies, the mortar attached to the RCA surface caused the properties of the RCA to differ from the natural aggregate [7]. The mortars give the RCA a lower density [8] and that feature is transferred to the asphalt mixture, giving the mixture a low specific gravity [9]. The attached mortar gives RCA a higher porosity value than the natural aggregate, which enables it to absorb more asphalt in the mixture [5], and endows the mixture with high optimum asphalt content [10]. The optimum asphalt content increases with the decrease of the RCA particle size [11], because specific surface area amount increases with decreases in particle size [12].

Moreover, RCA differs from natural aggregate in terms of abrasion value. RCA has a higher abrasion value, and cannot satisfy the abrasion requirements in some cases [13]. The aggregate which has high abrasion value in a Los Angeles machine, has a higher degradation value after compaction than other aggregate types [14]. Therefore it is expected that the RCA will have a high degradation value after compaction. Thus, studying degradation in RCA is crucial. In this study, the term 'degradation' is used to refer to aggregate breakdown owing to mechanical action. Breakdown in the aggregate particle could cause a loss of voids in the mineral aggregate (VMA) and air voids in the mix (VTM) [15], which may effect to the durability of the mixture [16]. Moreover, this breakdown can cause moisture damage in the pavement, because the binder film will break around the aggregate and water inlet to the mix [17]. Aggregate breakdown could occur in two ways: (1) the wearing of the aggregate, whereby small pieces of aggregate chips off; and (2) the actual fracturing of the aggregate. The first is affected by aggregate

angularity and abrasion value, whereas the second mechanism occurs when the applied stress is higher than the aggregate strength [18].

The most important factors affecting aggregate degradation are aggregate gradation and energy of compaction [18]. Suitable aggregate gradation prevents aggregate breakdown. The Marshall hammer exhibited more aggregate breakdown than other compactors [17]. Aggregate size is one of the important factors that influence degradation. Hence, a larger particle size has a higher degradation value. Moreover, a dense gradation has lower degradation. The aggregate shape also affects degradation. Increasing the amount of flat and elongated particle aggregates results in increased breakdown and fracture [19]. The degradation caused by shape can be controlled by select good gradation [20].

The present study was conducted with the following objectives: To compare the degradation between natural aggregate and RCA; To evaluate the effect of aggregate gradation on degradation and select the energy of compaction that generates less degradation.

In this study, aggregate degradation is evaluated without adding asphalt to the mixture. Five gradation types and the six different RCA percentages were used in this study. All samples were placed on a Marshall Compaction pedestal and subjected to 20, 40, 60, 80 and 100 blows.

2　Materials and Methods

In this study, two types of aggregates were used: RCA and natural aggregate. RCA was obtained from the demolition waste of different concrete members. The natural aggregate used was granite, which was provided by Kajang Rocks Quarry.

The properties of the RCA and natural aggregate were identified to ensure their compliance with the requirements. The properties are represented in Table 1.

Results indicate that RCA had lower specific gravity than granite. The specific gravity of RCA also increases as the RCA particle size decreases, along with water absorption. The Los Angeles abrasion values of RCA and granite were also determined. Results show that RCA had higher abrasion value than granite, and the abrasion value decreased with the decrease of RCA particle size. The aggregate gradations of all mixtures used in this study were based on the technical recommendations from the Malaysian Standard Specification for Road Works (JKR). In this study, hot-mix asphalt (HMA14) gradation was used because of its suitability for medium and light traffic volumes. Figure 1 and Table 2 present the used aggregate gradations. Five gradations are used in this study to reach adequate gradation (which represents lower aggregate degradation).

The RCA used in this study has a passing sieve size of 5 mm and a retained sieve size of 1.18 mm. The purpose of selecting these fractions is because an aggregate larger than this size has more abrasion value and less specific gravity. Moreover, the aggregate passing sieve size of 1.18 mm has a high absorption value.

Table 1 Aggregate properties results

Aggregate size (mm) passing—retained	Test		Specification
	Los Angeles abrasion value		ASTM C131
	Granite	RCA	
19–9.5	20	35	
9.5–4.75	20	36	30 max
4.75–2.36	19	28	
	Bulk specific gravity		ASTM C127
20–14	2.500	2.220	
14–10	2.550	2.320	
10–5	2.601	2.380	
5–3.35	2.618	2.360	
3.35–1.18	2.621	2.285	
	Absorption		ASTM C127
20–14	0.6	4	
14–10	0.5	6	
10–5	0.8	7	
5–3.35	0.9	10	
3.35–1.18	2.0	12	
	Granite	RCA	BS 812: Part 3
Flakiness index	18.1	16	20 max
Elongation index	7	5	20 max
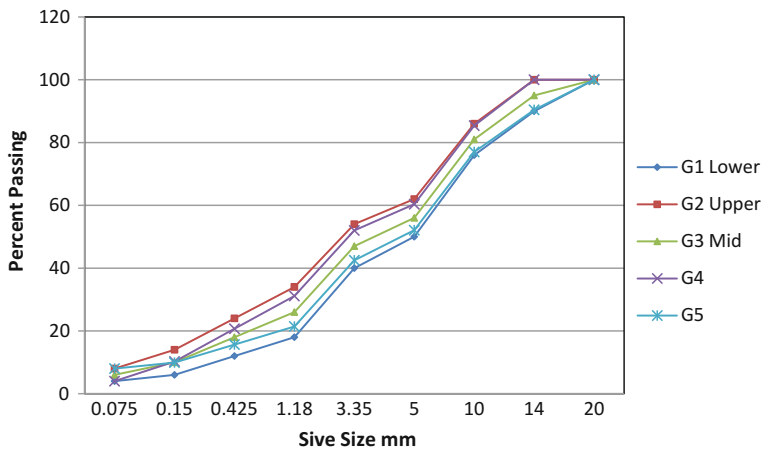
Fig. 1 Aggregate particle size distribution

Table 2 Aggregate gradation

Aggregate size (mm)	G1		G2		G3		G4		G5	
	P	R	P	R	P	R	P	R	P	R
20	100	0	100	0	100	0	100	0	100	0
14	90	10	100	0	95	5	100	0	90	10
9	76	14	86	14	81	14	85.4	14.6	77	13
5	50	26	62	24	56	25	60.3	25	52	25
3.35	40	10	54	8	47	9	52	8.35	43	10
1.18	18	22	34	20	26	21	31.1	20.9	21	21
0.425	12	6	24	10	18	8	20.7	10.4	16	6
0.15	6	6	14	10	10	8	10.3	10.4	10	6
0.075	4	2	8	6	6	4	4	6.26	8	2

P Percent Passing, *R* Percent Retain

Six different percentages of RCA (0, 20, 40, 60, 80, and 100%) from those fractions were blended with granite.

All samples were prepared according to the Malaysian Standard Specification for Road Works JKR specification. Each sample weighed 1200 gm. Then, each sample was mixed well to prevent segregation. Subsequently, each sample was placed in a Marshall mould of diameter 101.6 mm. Then, the mix was tamped with 30 blows by a new tamping rod to reach maximum density. (The tamping rod was manufactured for this study.) Afterwards, the mould was placed on a Marshal Compaction pedestal and was given 20, 40, 60, 80 and 100 blows. Finally, the mix was sieved in the same set of the sieves and the weight of retained aggregate on each sieve was calculated.

2.1 Tamping Rod

The tamping rod was made from steel as shown in Fig. 2, and consists of two cylindrical parts. The small part had a diameter of 45 mm and length of 40 mm. The other part had a diameter of 16 mm and length of 300 mm. The diameter of 45 mm was selected because it approximately half of the Marshall Mould diameter. The weight of the tamping rod was 957.9 g. The rod is inside a hollow cylinder. The hollow cylinder's internal diameter was 50 mm and the length was 280 mm. The first end of the hollow cylinder was open and the other end had a cap containing some holes. The first hole was located in the middle of the cap which the tamping rod was passed through. While the tamping rod was dropping, other small holes in the cap allowed the air to enter the cylinder. Moreover, there are five small holes on the bottom surface of hollow cylinder to allow air to exit from the cylinder when the tamping rod is dropping.

Fig. 2 Tamping rod

To determine the number of blows required for the mixture to reach maximum density, the aggregate was placed in the Marshall mould. Then, the tamping rod was placed on the mixture and allowed to drop freely on to the aggregate 5, 10, 15, 20, 25, 30 and 35 times around the perimeter. Afterwards, the surface of the mould was levelled by rolling the rod on the mould, as shown in Fig. 2. The weight of the aggregate was determined after each attempt. The air voids were calculated using the following equation [21]. This procedure was done using five aggregate gradations.

$$Va = [1 - (M/SV)]^*100 \qquad (1)$$

Va = voids in aggregate
M = average mass of the aggregate in the mould (g)
S = bulk specific gravity of the aggregate
V = volume of the cylindrical mould (ml)

Figure 3 shows that the air void percentage decreased with the increased number of blows, and then it became constant. That point represents the number of blows when the mixture reaches maximum density.

3   Results and Discussion

The changes in the passing percentage were determined for all fractions, gradations and mixes after compacting with the Marshal hammer with 20, 40, 60, 80 and 100 blows.

Figure 4 shows the average passing percentage of each gradation for each sieve size. Note that the passing percentage increases approximately with the increase in the number of blows. The passing percentage value is also higher for the sieve sizes 5, 3.35 and 1.18 mm. Moreover, gradation G3 is the best gradation, followed by
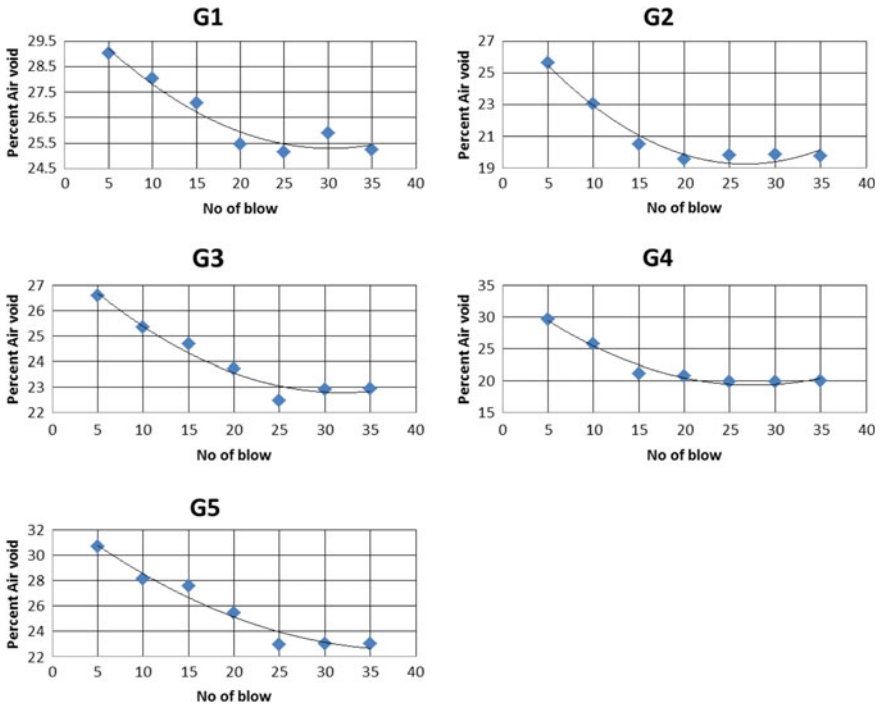
Fig. 3 Percent air void and number of blow
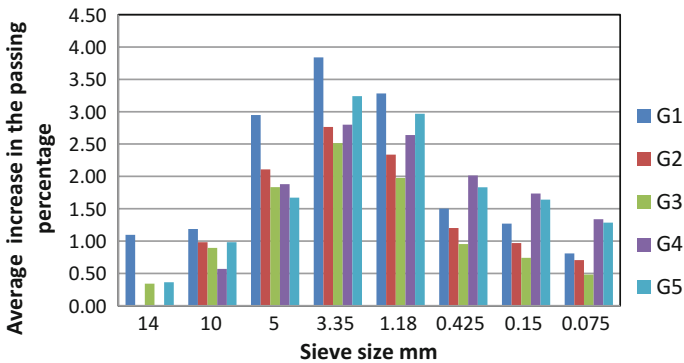
Fig. 4 Average increases in the passing percentage for each fraction

gradation G2 and gradation G4. Gradations G1 and G5 are the worst gradations. Such findings arise because gradation G3 represents the mid-gradation. Gradations G2 and G4 are better than gradations G1 and G5, because gradations G2 and G4 contain more fine aggregate, whereas gradations G1 and G5 contain more coarse aggregate. The fine aggregate protects the coarse aggregate from degradation.

Figure 5 shows the relation of the increase in the passing percentage for the sieve size 3.35 mm with the number of blows and the RCA percentage. Notably, the number of blows affected the passing percentage more than the RCA percentage. In order to compare gradations to select the best gradation, the average increase was calculated in the passing percentage with sieve size 3.35 mm, for all RCA percentages and the number of blows of each gradation. The calculated averages were 3.84, 2.76, 2.51, 2.80 and 3.24 for gradations G1, G2, G3, G4 and G5, respectively. Gradation G3 is the best gradation because it is a mid-gradation. Additionally, gradations G2 and G4 are better than gradations G1 and G5, because gradations G2 and G4 have more fine aggregate.

Figure 6 shows the relation of the increase in the passing percentage for the sieve size 1.18 mm with the number of blows and the RCA percentage. Note that the number of blows affected the passing percentage more than the RCA percentage. In order to compare all gradations to select the best gradation, the average increase was calculated in the passing percentage with sieve size 1.18 mm, for all RCA percentages and the number of blows of each gradation. The calculated averages were 3.28, 2.34, 1.97, 2.64 and 2.97 for gradations G1, G2, G3, G4 and
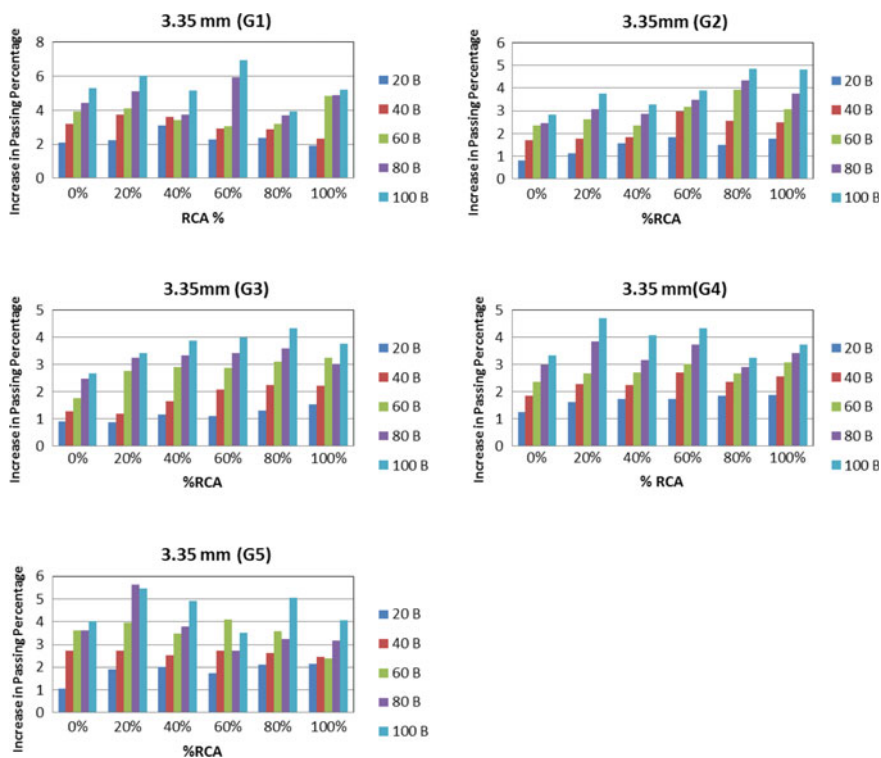
Fig. 5 Relations of RCA percentage and number of blow with increasing in the passing percentage for each gradation
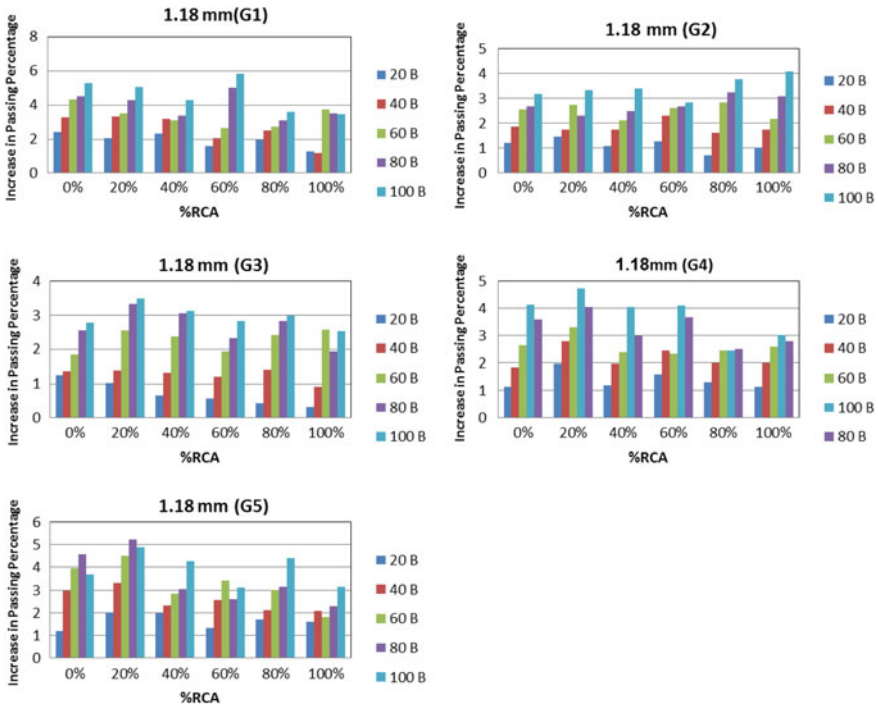
Fig. 6 Relations of RCA percentage and number of blow with increasing in the passing percentage for each gradation

G5, respectively. Gradation G3 is the best gradation because it is a mid- gradation, whereas, gradations G2 and G4 are better than gradation G1 and G5 because gradations G2 and G4 contain more fine aggregate. The highest amount of degradation occurred when compacting the mix with 100 blows.

3.1 Analysis of Variance (ANOVA)

To understand the main factors effecting aggregate degradation, all data were subjected to static analysis. Two-way ANOVA with replication was used. The significance level was assumed to be 0.05.

Table 3 displays the results of the analysis of the relation between the gradation and the number of blows with the increase in passing percentage from sieve size 3.35 mm. As the P-value for the gradation and number of blows is lower than 0.05, both factors have a significant effect on the increase in the passing percentage. Moreover, no interaction exists between the gradation and the number of blows. Table 4 shows the results of the analysis of the relation between the gradation and

Table 3 Effect of gradation and number of blow in increasing passing percentage for sieve size 3.35 mm

ANOVA						
Source of variation	SS	df	MS	F	P-value	F crit
Gradation	32.69	4	8.17	24.29	6.9E−15	2.444
Number of blow	123.52	4	30.88	91.78	3.0E−36	2.444
Interaction	2.79	16	0.17	0.52	9.3E−01	1.725
Within	42.06	125	0.34			
Total	201.06	149				

Table 4 Effect of gradation and number of blow in increasing passing percentage for sieve size 1.18 mm

ANOVA						
Source of variation	SS	df	MS	F	P-value	F crit
Gradation	31.6	4	7.9	23.3	2.1E−14	2.44
Number of blow	104.9	4	26.2	77.3	7.1E−33	2.44
Interaction	1.838	16	0.11	0.34	9.9E−01	1.73
Within	42.4	125	0.34			
Total	180.7	149				

the number of blows with the increase in passing percentage from sieve size 1.18 mm. Notice that gradation and number of blows have a significant effect on the increase in the passing percentage.

Table 5 presents the results of the analysis of the relation between the RCA percentage and the number of blows with the increase in passing percentage from sieve size 3.35 mm. A significant effect exists between the number of blows and the increase in passing percentage. However, the RCA percentage shows no significant effect on degradation. Moreover, no interaction exists between the RCA percentage and the number of blows.

Table 5 Effect of gradation and RCA percentage in increasing passing percentage for sieve size 1.18 mm

ANOVA						
Source of variation	SS	df	MS	F	P-value	F crit
Number of blow	32.69	4	8.17	6.65	7.2E−05	2.45
RCA percentage	6.43	4	1.29	1.05	3.9E−01	2.29
Interaction	14.48	16	0.72	0.59	9.1E−01	1.66
Within	147.5	125	1.23			
Total	201.1	149				

4 Conclusions

This study presented some conclusions obtained from mix crushed concrete with natural granite, and checked the degradation after compaction. The following was found:

1. The mortar attached to the RCA surface, make RCA of lower quality than conventional aggregates.
2. Aggregate gradation has a greater effect on aggregate degradation under the same level of compaction. When aggregate gradation becomes dense the degradation is decreased. Also, the fine aggregate protects the coarse aggregate from degradation.
3. Recycled concrete aggregate (RCA) is suitable for low- and medium-volume traffic, because the amount of degradation increases when the number of blow is higher than 50 blows.
4. The RCA percentages do not have a significant effect on the aggregate degradation. This means that with select adequate fraction, gradation and suitable traffic volume, RCA can easily be used in the mixes and satisfies the requirements.

References

1. Friend of the earth.: Recycling why it's important and how to do it. Website: www.foe.co.uk (2008)
2. Mahony, M.M.: Recycling of materials in civil engineering, Ph.D. Thesis, University of Oxford (1990)
3. Pourtahmasb, M.S., Karim, M.R.: Utilization of recycled concrete aggregates in stone mastic asphalt mixtures. Adv. Mater. Sci. Eng. (2014)
4. Symonds, A., Cowi, P.R.C.B.: Construction and demolition waste management practices, and their economic impacts. Report to DGXI European Commission (1999)
5. Pasandin, A.R., Perez, A.: Overview of bituminous mixtures made with recycled concrete aggregates. Constr. Build. Mater. **74**, 151–161 (2014)
6. Arabani, M., Azarhoosh, A.: The effect of recycled concrete aggregate and steel slag on the dynamic properties of asphalt mixtures. Constr. Build. Mater. **35**, 1–7 (2012)
7. Pasand, A.R., Perez, I.: Mechanical properties of hot-mix asphalt made with recycled concrete aggregates coated with bitumen emulsion. Constr. Build. Mater. **55**, 350–358 (2014)
8. Pasand, A.R., Perez, I.: Laboratory evaluation of hot-mix asphalt containing construction and demolition waste. Constr. Build. Mater. **43**, 497–505 (2013)
9. Pérez, I., Pasandin, A., Medina, L.: Hot mix asphalt using C&D waste as coarse aggregates. J. Mater. Des. **36**, 840–846 (2012)
10. Farias, M.M., Sinisterrra, F., Jemenez, M.: Influence of asphalt rubber on the crushing of recycled aggregates used in dense HMA. In: Proceedings of Asphalt Rubber, Munich. http://www.ra-foundation.org/wp-content/uploads/2013/02/044-PAP_049.Pdf (2012)
11. Bushal, S., Li, X., Wen, H.: Evaluation of effects of recycled concrete aggregate on volumetric of hot-mix asphalt. J. Transp. Res. Board **2205**, 36–39 (2011)

12. Shen, D.H., Du, J.C.: Application of gray relational analysis to evaluate HMA with reclaimed building materials. J. Mater. Civ. Eng. **17**, 4 (2005)
13. Bhusal, S., Wen, H.: Evaluating recycled concrete aggregate as hot mix asphalt aggregate. Adv. Civil Eng. Mater. **2**, 1 (2013) (Paper ID ACEM20120053)
14. Wen, H., Mclean, D.: Evaluation of recycled concrete as aggregate in new concrete pavements. Washington state department of transportation Lynn Peterson, Secretary. Research Project (2014)
15. Lynn, T., James, R., Wu, P., Jared, D.: Effect of aggregate degradation on volumetric properties of Georgia's Hot-Mix. Journal of the Transportation Research Board **17**, 123–131 (2007)
16. Roberts, F.L., Kandhal, P.S., Brown, E.R., Lee, D., Kennedy, T.W.: Hot mix asphalt materials, mixture design, and construction, 2nd edn. National Asphalt Pavement Association Research and Education Foundation, Lanham, Maryland (1999)
17. Gatchalian, D.: Characterization of aggregate resistance to degradation in stone matrix asphalt mixtures, Master Thesis, University of Texas A&M (2005)
18. Airey, G.D., Hunter, A.E., Collop, A.C.: The effect of asphalt mixture gradation and compaction energy on aggregate degradation. Constr. Build. Mater. **22**, 972–980 (2007)
19. Vavrik, W.R., Fries, R.J., Carpenter, S.H.: Effect of Flat and Elongated Coarse Aggregate on Characteristics of Gyratory Compacted Samples, vol. 99, p. 1338. Department of Civil Engineering, University of Illinois Urbana-Champaign (1999)
20. Aho, B.D., Vavrik, W.R., Carpenter, S.H.: Effect of flat and elongated coarse aggregate on field compaction of hot-mix asphalt, University of Illinois Urbana-Champaign, Department of Civil Engineering. J. Trans. Res. Board, 26–31 (2001)
21. ASTM D3398.: Standard Test Method for index of aggregate particle shape and texture. Annual Book of American Society for Testing Materials ASTM Standards (2003)

Damaging Effect of Tree Types on Roughness Progression Rates in Pavements Characterised with Alluvial Expansive Subgrades

Md Yeasin Ahmed, Robert Evans and Monzur Alam Imteaz

Abstract Any pavement founded on expansive soils subgrade is often subjected to non-uniform ground movement. Such ground movement originally initiates due to variation in soil moisture within pavement subgrade, which also results in development of shrinkage cracks, edge heaves and surface distresses. Moreover, development of alternative mounds and depressions (Gilgai) in surrounding areas can exacerbate such condition by creating undulating patterns on those subgrades. Due to the flexible behaviour of pavement, the undulation within pavement subgrade is also found to be reflected through its surface (known as roughness). It is commonly believed that trees can play a major part on subsurface moisture condition as they extract moisture from deep for photosynthesis. As withdrawal of moisture by trees can trigger expansive behaviour of soils, therefore it is expected that roadside vegetation can significantly contribute in moisture variation in subgrades and result in increased roughness progression rates. This study will evaluate the damaging effect of tree types (in terms of tree height) responsible for increased roughness progression rates in pavements characterised with medium to highly expansive subgrades. To do so, vegetation data (tree height) will be analysed against historical road roughness data for numerous sections for Borung Highway in north-western part of Victoria, Australia. Tree height of all available trees located on road reserve has been collected and analysed against historical roughness data. The outcome from this study has identified the tree categories (in terms of height) that are most responsible for increased roughness progression rates. The findings of this study can be used for efficient adaptation of improved and better pavement management strategies.

M. Y. Ahmed (✉) · R. Evans · M. A. Imteaz
Department of Civil and Construction Engineering, Faculty of Science
Engineering and Technology, Swinburne University of Technology,
Hawthorn, VIC 3122, Australia
e-mail: mdyeasinahmed@swin.edu.au

R. Evans
e-mail: robertevans@swin.edu.au

M. A. Imteaz
e-mail: mimteaz@swin.edu.au

1345

1 Introduction

Expansive characteristics of a soil are known as some of its specific behaviour that undergoes through significant volume changes with the variation in moisture content. The change in volume is also termed as shrink–swell behaviour of soil, as an increase in water content causes swelling in volume while a decrease in water content results in shrinkage. The presence of reactive clay particles (mostly montmorrilonite) was found to be the main reason for such shrink–swell characteristics. Many researches were conducted with the primary concentration on determining soil properties that significantly affect potential shrink–swell behaviour. The properties of soil that poses a significant relationship with shrink–swell behaviour includes clay mineralogy, soil structure, soil structure, soil-–water chemistry, soil suction and dry density [1–5]. Some other factors including climate, site drainage (topography), vegetation were also deemed as responsible for expansive behaviour of soil [6–10]. The combined effect of all these factors can also result in soil movement and associated change in soil volume.

Many regions of Australia have been reported to be affected by good distribution of expansive soil deposits [10–12]. To be specific, approximately 20% of Australian soil is characterised with expansive behaviour while almost 50% of Victoria is covered by moderately to highly expansive soils [13, 14]. Any light structure (i.e. pavements) that is established on this soil is highly vulnerable to premature failure, reduced life expectancy and performance degradation. For flexible pavements, rapid desiccation near pavement edges can enhance the development of shrinkage cracks and differential settlement may occur. Moreover, the moisture variation between centre of pavement and edge of the pavement can initiate development of tensile stress. Such initiation of tensile stress can result in development of longitudinal cracks, which further helps in creeping water through these cracks and upscaling moisture imbalance within pavement structure. This process can trigger in development of Gilgai beneath pavement structure.

Gilgai, the term originally came from the Australian aboriginal word meaning 'small waterhole'. Gilgai (often termed as Gilgai Phenomenon) is an undulating pattern of alternative mounds and depression of wavelengths ranging from 3 to 30 m. Gilgai was first reported in Australia by Aitchison [15] but the best possible description can be found in Australian Handbook of soils [16]. Gilgai usually manifests in expansive soils and can cause significant damage to flexible pavement by causing undulating pattern in pavement subgrade. It is noteworthy to mention that both Gilgai and long wavelength roughness maintain similar range of wavelength (3–30 m) and the presence of Gilgai has successfully been identified beneath pavements experiencing long wavelength roughness over years [17, 18].

In Australia, it is a common practice of planting trees on road reserve. It is believed that such plantation practice is an efficient way of roadside management, which also offers aesthetic peace to monotonous driving. Current literature suggests that trees do have some detrimental effects on subsurface moisture condition. The deciduous effect of trees can initiate expansion and contraction during wet and dry period respectively, hence result in premature failure in pavements. Richards et al. [14] found that trees can influence ground moisture conditions up to 10 m below the ground and horizontally up to 1.5–2 times the height of the tree. During dry season, these ranges have found to be extended further below the ground and around the trunk [19]. Therefore, this paper will present the potential relationship between tree height and pavement roughness (in IRI). The findings of this paper will also present a scale of measurement for deciduous tree height ranges that is responsible for excessive roughness progression over time.

2 Site Description

The Borung highway, located in north-western part of Victoria has been chosen for this study. The Borung highway is a 137 km long two-lane flexible rural highway running from St. Arnaud to Dimboola via the townships Litchfield and Warracknabeal. Two sections of the Borung highway: one running from Litchfield to Warracknabeal (41.8 km in length) and other running from Warracknabeal to Dimboola (39 km in length) were selected as test site location. These sites are located near Horsham and founded on cracking clay soils (alluvial type). The yellow to dark orange regions are alluvial expansive soils and the pink regions are residual expansive type soils (weathered basalt). Usually, light yellow and light pink represent areas of moderately to highly expansive soils where dark orange and dark pink areas are highly expansive in nature. All the selected test sites for this research fall into the dark orange region. Moreover, in some location of these sites, gilgai is predominantly found and well developed. In addition, availability of roughness data (IRI) for the sites and good density of roadside vegetation were also the deciding factors for choosing these sites. The location of the sites are presented and labelled in Fig. 1.

3 Data Collection and Methodology

The data collection of this study comprised of two parts: (a) pavement roughness data collection and (b) roadside vegetation data collection. VicRoads usually conduct detailed road surveys every two years for rural highways across the State of Victoria, which consists of measuring longitudinal road profiles and calculating the International Roughness Index (IRI) at 100 m intervals. A multi-laser profilometer is used to collect the profile data which is stored as an Engineering Research

Highway Section	Location	Length
Borung Highway (Section 2)	Litchfield to Warracknabeal	41.8 km
Borung Highway (Section 3)	Warracknabeal to Dimboola	39 km
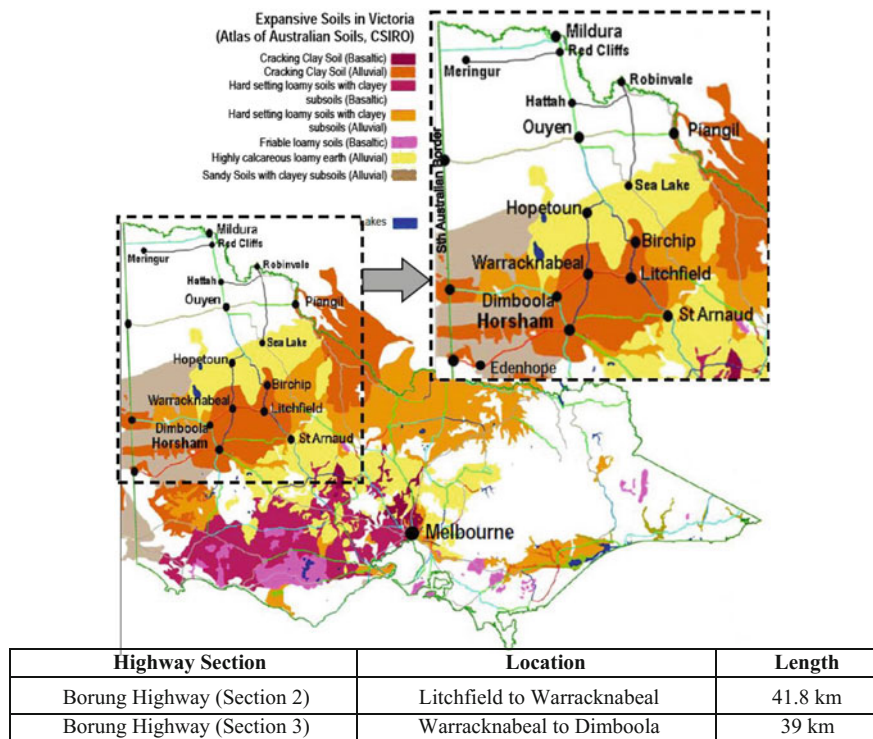
Fig. 1 Location of test site and expansive soil map of Victoria [17]

Division (ERD) file. The ERD file contained elevation values (roughness) for left wheel paths (LWP) and right wheel paths (RWP) for individual 100 m sections. For the Borung highway, consecutive road roughness data was available from 1995 to 2009, with the exception in 2003. This is a common scenario that roughness data are not synchronised which poses a great challenge for data preparation. Alignment of roughness data becomes necessary to make sure that the same sections are assessed over time. A detailed procedure of roughness data alignment and synchronisation can be found in Evans [17]. For Borung highway, alignment and synchronisation of roughness data for both LWP and RWP was performed. In addition, roughness progression rate (RPR) over time was calculated for both LWP and RWP using simple spreadsheet. Since, lane roughness progression rate is the overall representation of a pavement condition data; it was calculated, prepared and arranged for further analysis. From the 80 km of potential Borung highway to select, 201 sections (each 100 m in length) were selected as they showed positive growth in roughness levels over time. The selected test sites were identified according to Victoria's State Road Referencing System (SRRS), which is based on chainages. This was essential for the proper identification and management of the test site data.

Google Earth Pro was used to collect the roadside vegetation data as it offers recent satellite imagery with acceptable precision and accuracy. Tree data was collected using both satellite view and street view. For this study, tree height and distance between tree and pavement were collected from satellite and street view imagery options. An illustration of data collection procedure can be found in Fig. 2.
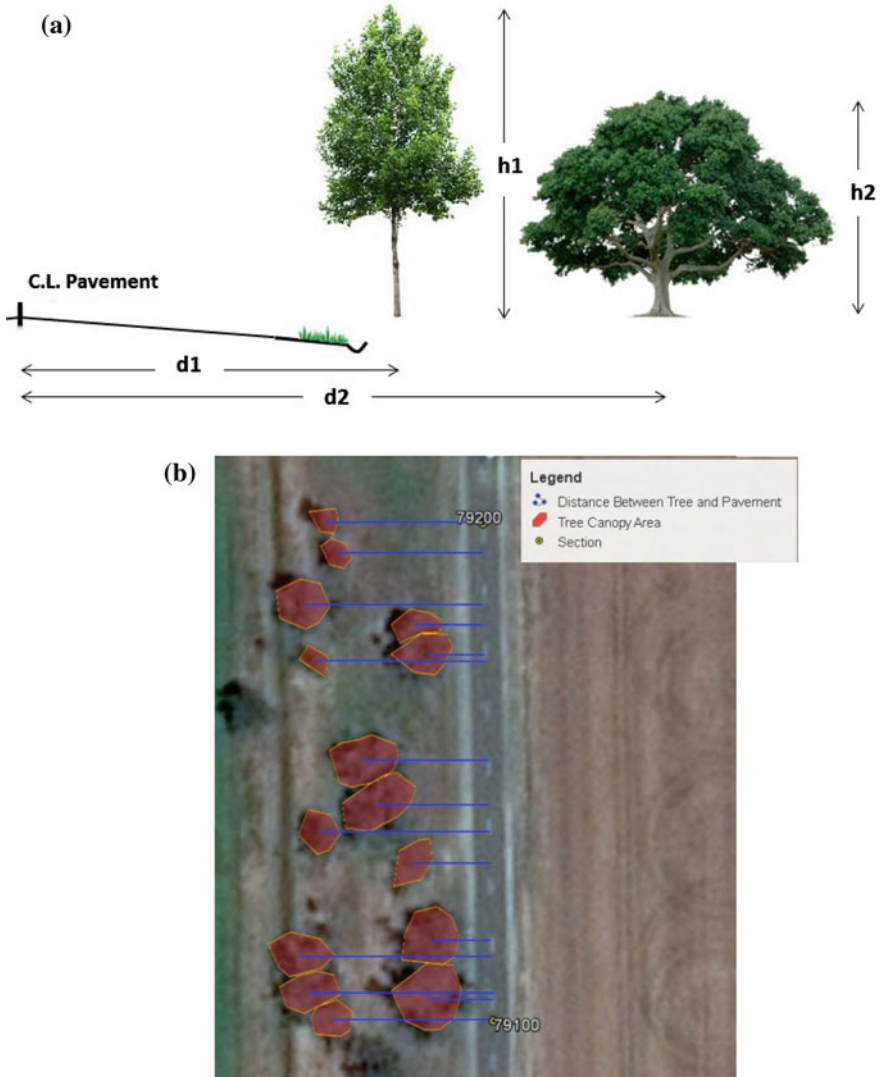
Fig. 2 Identification of tree data measurements **a** an illustration, **b** an example of distance measurement using satellite imagery, and **c** an example of tree height measurement using street view imagery
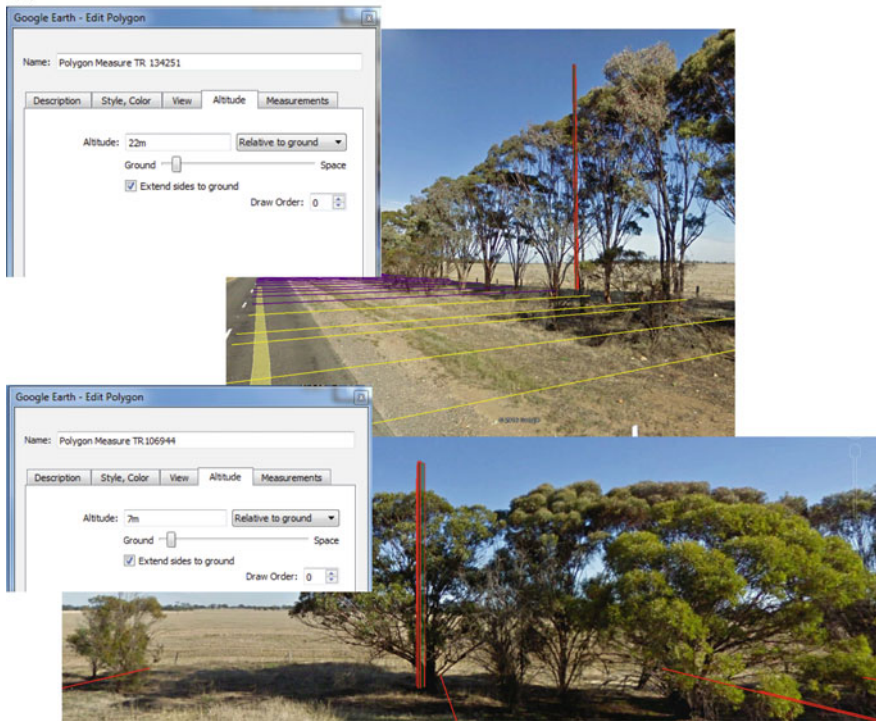
Fig. 2 (continued)

Individual tree heights were measured using the 3D polygon method available in 'ruler' tab. It is advised that a slender polygon to be placed at the base of the tree. This is because a slender polygon is easy to setup at the base while positioning a wide polygon could be troublesome. The base of the polygon was extended to the ground to get the elevation of the tree. Trial-and-error method was applied at the cell named 'Altitude', to revise and recheck the height of the polygon until it perfectly matches with the visible tree height. In Fig. 2c, it can be clearly seen that the trees are identified with an approximate height of 22 and 7 m respectively.

4 Data Analysis and Results

In order to evaluate and quantify the effect of tree height on pavement roughness progression rates (RPR), all collected tree height data was set up in tabular form and an average tree height data for individual sections were calculated. All these tree height data was then analysed against historic RPRs (in IRI). A frequency
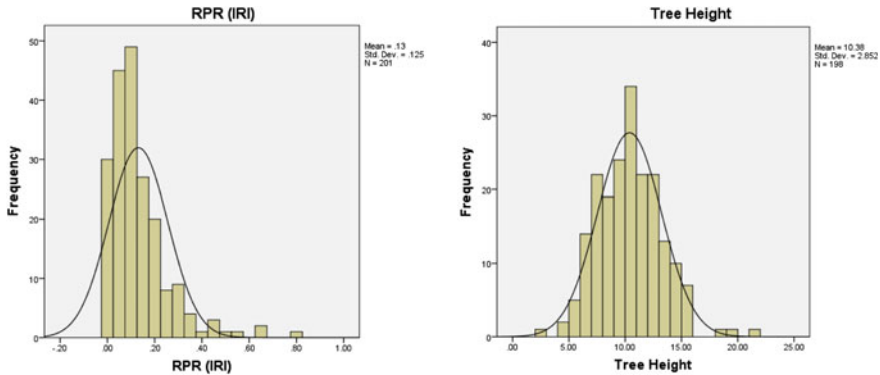
Fig. 3 Frequency distribution of RPR and tree height

distribution of analysed data and relevant descriptive statistics can be found in Fig. 3 and Table 1 respectively.

From the descriptive statistics, it is evident that the minimum value for RPR is zero for some sections and the RPR data distribution is positively skewed. This is because, whenever the RPR was calculated, any negative growth in RPR between any studied years was considered as a definite period of treatment. These treatments may include sealing, resurfacing and pavement overlay. Moreover, since RPR is the roughness growth over time, it is unrealistic that the growth of the slope becomes negative at any stage before any significant treatment activity. Therefore, all negative slopes were replaced with zero (i.e. no growth). Furthermore, RPRs for the studies sections were calculated for pretreatment phases only, while the pretreatment phase was identified from any sudden drop in roughness levels for the immediate year.

While tabulating the tree height data for respective pavement sections, care was taken for sections having no trees but experiencing good roughness growth. For these specific sections, the tree data was set as 'blank', because, an input of 0 (zero) m tree height can cause an unexpected influence in analysis.

In conjunction with analysing the total tally of tree height against RPRs, tree height data was also arranged as a function of distance between tree and pavement. A simple spreadsheet was used to arrange the data using 'IF' function available in excel. This allowed segregating the trees present within a certain boundary. Finally, bivariate correlation analysis was run against the prepared data to identify and measure the correlation between the variables. The findings of the correlation analysis have been presented in Table 2.

From the correlation statistics, it was evident that both RPR and average tree height (considering all trees) maintains a significant negative correlation. Even though the correlation is poor, it is statistically significant at 5% level. Since the stepwise elimination of trees outside a certain boundary was conducted, the correlation and associated significance level changed accordingly. However, elimination of trees outside a boundary (i.e. 16 m), has significantly made the correlation

Table 1 Descriptive statistics for variables (RPR and tree height)

Descriptive statistics

	N	Range	Minimum	Maximum	Mean		Std. deviation	Variance	Skewness		Kurtosis	
	Statistic	Statistic	Statistic	Statistic	Statistic	Std. error	Statistic	Statistic	Statistic	Std. error	Statistic	Std. error
RPR (IRI)	201	0.79	0.00	0.79	0.131	0.009	0.126	0.016	2.12	0.17	6.25	0.341
Tree height	198	18.45	2.71	21.17	10.38	0.203	2.85	8.13	0.39	0.17	0.75	0.344

Valid N (List wise): 198

Table 2 Correlation statistics

Roughness indices	Tree data type	Boundary of location	Sample size (N)	Significance	Correlation
RPR (IRI)	Average tree height	**All trees** within the road reserve	198	0.026	−0.08[a]
		Trees located within **40 m** from pavement centre	198	0.265	−0.08
		Trees located within **35 m** from pavement centre	198	0.338	−0.068
		Trees located within **30 m** from pavement centre	198	0.438	−0.055
		Trees located within **25 m** from pavement centre	196	0.446	−0.055
		Trees located within **20 m** from pavement centre	195	0.343	−0.068
		Trees located within **19 m** from pavement centre	189	0.453	−0.055
		Trees located within **18 m** from pavement centre	188	0.196	−0.095
		Trees located within **17 m** from pavement centre	187	0.108	−0.118
		Trees located within **16 m** from pavement centre	184	0.04	−0.151[a]
		Trees located within **15 m** from pavement centre	179	0.126	−0.115
		Trees located within **14 m** from pavement centre	170	0.039	−0.158[a]
		Trees located within **13 m** from pavement centre	160	0.065	−0.146
		Trees located within **12 m** from pavement centre	149	0.041	−0.168[a]
		Trees located within **11 m** from pavement centre	123	0.128	−0.138
		Trees located within **10 m** from pavement centre	101	0.029	−0.218[a]

[a]denotes correlation is significant at 5% level

strong and significant compared to the previous stages (the boundary between 16 and 40 m from the pavement centre). It is also noteworthy to mention that approximately half of the assessed sections (to be specific, 100 sections) has no trees inside of 10 m range from the pavement centre, even though the maximum correlation (−0.218) was obtained for the average height of the trees located within 10 m distance from the pavement. A trend of correlation between tree height and RPR with distance between tree and pavement being controlled is presented in Fig. 4.
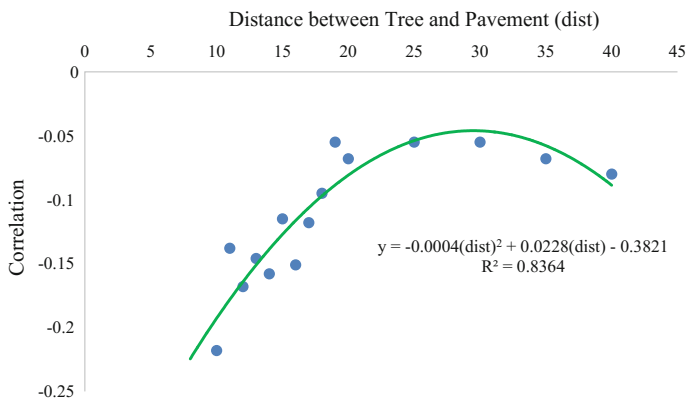
Fig. 4 Trend of correlation between RPR and average tree height with stepwise distance between trees and pavement being controlled

From Fig. 4, it can be clearly seen that the correlation between RPR and average tree height maintains a steep negative slope with the distance between tree and pavement being controlled from 25 m inwards. The opposite is evident for a distance from 25 m outwards, however, the slope is nearly flat.

5   Conclusion

The findings of this study have indicated that tree heights do maintain significant negative correlation with roughness progression rates. In other words, the smaller the trees, the higher the effect, which has also been discussed in Ahmed et al. [20, 21, 22]. Meanwhile, whenever stepwise elimination of trees outside a certain boundary was conducted, the correlation statistics changed subsequently. An increase in negative correlation was found to be evident for tree heights versus RPR for trees being present within a distance of 25 m and inwards. A rapid growth in correlation was identified once elimination of trees outside the 17 m range being started. Hence, negative correlation exists between tree height and RPR for all studied stages, it is also a clear indication of smaller trees being younger trees are contributing more in roughness progression rates if located at closer proximity to the pavement. The highest significant negative correlation was achieved for trees located within 10 m range from the pavement. Therefore, the findings of this study also suggest that plantation of trees within 10 m distance from the pavements should be discouraged.

References

1. Anderson, J., Fadul, K.E., O'connor, G.: Factors affecting the coefficient of linear extensibility in Vertisols. Soil Sci. Soc. Am. J. **37**, 296–299 (1973)
2. Finn, W., Strom, B.: Nature and magnitude of swell pressure. In: Highway Research Board Proceedings (1958)
3. Franzmeier, D., Ross, S.: Soil swelling: laboratory measurement and relation to other soil properties. Soil Sci. Soc. Am. J. **32**, 573–577 (1968)
4. Komornik, A., Zeitlen, J.: An apparatus for measuring lateral soil swelling pressure in the laboratory. In: Proceedings of the 6th International Conference on Soil Mechanics and Foundation Engineering, 278–281(1965)
5. Simic, D.: Evaluation of roadbed potential damage induced by swelling/shrinkage of the subgrade. In: 18th International Conference on Soil Mechanics and Geotechnical Engineering, Paris, France (2013)
6. Hammer, M., Thompson, O.: Foundation clay shrinkage caused by large trees. J. Soil Mech. Found. Div. **92** (1966)
7. Krohn, J. P., Slosson, J. E.: Assessment of expansive soils in the United States. Expansive Soils ASCE, 596–608 (1980)
8. Lambe, T.: The character and identification of expansive soils, soil PVC meter. Federal housing administration, technical studies program, FHA, 701 (1960)
9. Mathewson, C.C., Castleberry, J., Lytton, R.: Analysis and modeling of the performance of home foundations on expansive soils in central Texas. Bull. Assoc. Eng. Geol. **12**, 275–302 (1975)
10. O'malley, A., Cameron, D.: Street trees influence on soil moisture, urban dwellings and pavements and Walkley heights as a unisa-treenet research site. In: Treenet Proceedings of the 2nd National Street Tree Symposium (2001)
11. Delaney, M., Li, J., Fityus, S.: Field monitoring of expansive soil behaviour in the Newcastle hunter region. J. Aust. Geomech. **40**, 3–14 (2005)
12. Fityus, S., Smith, D., Allman, M.: Expansive soil test site near Newcastle. J. Geotech. Geoenviron. Eng. **130**, 686–695 (2004)
13. Holland, J., Richards, J.: Road pavements on expansive clays. Aust. Road Res. **12** (1982)
14. Richards, B., Peter, P., Emerson, W.: The effects of vegetation on the swelling and shrinking of soils in Australia. Geotechnique **33**, 127–139 (1983)
15. Aitchison, G.: The mechanics of gilgai formation. In: Proceedings of Conference on Soil Science, Adelaide, pp. 1–3 (1953)
16. Hallsworth, E.: A handbook of Australian soils. Rellim Public, Adelaide (1968)
17. Evans, R.: Synchronisation of road profile data and the assessment of road roughness using waveband analysis. Ph.D. Thesis, Swinburne University of Technology, Melbourne (2013)
18. Evans, R.P., Arulrajah, A., Horpibulsuk, S.: Detecting gilgai relief beneath sealed flexible pavements using road profile and road roughness measurements. Indian Geotech. J. **45**, 431–440 (2015)
19. Nelson, J., Miller, D.: Expansive Soils: Problems and Practices in Foundation and Pavement Engineering. (1992)
20. Ahmed, M.Y., Evans, R., Imteaz, M.: Vegetative influence on roughness levels for pavements founded on alluvial expansive soil deposits. In: Sixth International Conference on Geotechnique, Construction Materials and Environment. Bangkok, Thailand (2016)
21. Ahmed, M.Y., Evans, R., Imteaz, M.: Influence of roadside vegetation on roughness progression for pavements founded on expansive soils. In: 2nd IRF Asia Regional Congress and Exhibition. Kuala Lumpur, Malaysia (2016)
22. Ahmed, M.Y., Evans, R.: Effect of roadside vegetation on waveband roughness levels for pavements founded on expansive soils. In: World Conference on Pavement and Asset Management. Milan, Italy (2017)

Probability of Fire Spread Between Vehicles in Car Parking Buildings

Mohd Zahirasri Mohd Tohir and Michael Spearpoint

Abstract Over recent years, performance-based design approach has gained acceptance in the engineering community around the world. This has prompted an expanded demand in engineering approaches to the assessment of fire safety in structures. Two arising questions in designing car parking buildings are (1) if there had been another vehicle parked next to or a space away from the van would the fire have spread given no interruption by firefighters and/or fire suppression systems? (2) If so, what is the probability that the spread occurs? This work quantitatively assesses these questions using recent research into the risk-based design of car parking buildings. The probability of fire spread is formulated using the knowledge of the possible rate of heat release outputs from single passenger vehicles coupled with a prediction of time to ignition. There are two scenarios considered for the assessment, either where the vehicles are parked next to each other or where the vehicles are parked one space apart. The analysis shows that the probability of fire spreading to a vehicle in an adjacent space 0.63–0.90 while when there is a space in between, the highest probability of fire spread is 0.23 but spread may not occur at all.

Keywords Vehicle fire · Car parks · Probability · Fire spread
Performance based design

M. Z. M. Tohir (✉)
Department of Chemical and Environmental Engineering,
Universiti Putra Malaysia, Serdang, Malaysia
e-mail: zahirasri@upm.edu.my

M. Spearpoint
Department of Civil and Natural Resources Engineering,
University of Canterbury, Christchurch, New Zealand
e-mail: michael.spearpoint@canterbury.ac.nz

1 Introduction

On 27 February 2015, a van caught fire in a shopping mall's car park in Auckland, New Zealand, as depicted in Fig. 1. Questions arise: 'Should there be a vehicle parked next to or a space away from the van, will the fire be able to spread? If so, what is the probability of the fire to spread?' Up until recently, these questions are left unanswered due to lack of studies on the probability of fire spread between vehicles. Therefore, these questions become the main drive for this work which is also a part of a larger research project. The research project investigates into risk-based fire safety of passenger road vehicles in car parking buildings which was initiated in the University of Canterbury, New Zealand.

The initial work of the research project has attempted to study the probability of fire spread between vehicles using limited statistics of vehicle fires from several sources [1]. The study was limited to the assumption that all vehicles involved in a scenario are burned simultaneously therefore yielding high accumulation of heat release rate which is unrealistic.

This leads to further research on fire spread between vehicles was conducted. As a result, a simulation tool named UCVFire is developed for the spread of fire between vehicles in car parks [2]. The tool has been written using Microsoft Excel and Visual Basic for Applications (VBA) in which its main feature is its ability to conduct probabilistic analysis of multiple vehicle fire spread on a single row arrangement of parked vehicles. The tool is able to predict the time of ignition of subsequent vehicles, given a vehicle is already burning, using a heat release rate fire curve for a single passenger vehicle generated from an appropriate probability distribution. Times to ignition are calculated using a point source model (PSM) [3] for the radiation from the flames from a burning vehicle and the flux time product approach [4] with appropriate properties for critical heat flux, etc.

Fig. 1 Burnt van inside a shopping mall parking in Auckland, New Zealand (Retrieved from stuff. co.nz [5])

With the availability of the simulation tool, now the questions discussed earlier can be attempted to be answered. First step of the attempt can be done by quantitatively assess the probability of fire spread from a burning vehicle to another vehicle within its vicinity, with the assumption of no interruption to the fire by firefighters and/or fire suppression systems. The probability of fire spread is formulated using the knowledge of design fire of a single passenger vehicle, and the prediction of time of ignition approach, which has been combined into the UCVFire simulation tool. However, prior to the attempts, there are several points that must be discussed.

1.1 Parking Space Dimensions

When considering the probability of fire spreading between vehicles, one important parameter to analyse is the distance between vehicles. Based on the PSM flame radiation model, the shorter the distance, the higher the heat flux received by the target item, thus, increasing the possibility for the fire to spread between vehicles. In a car park, the common closest distance would be that of vehicles parked in parking spaces next to each other.

Therefore, a study on parking space dimensions is conducted based on the literature. Chrest et al. [6] describes that dimensions of a parking space vary depending on the level of service (LOS) and classification of vehicles. While, Hill [7] mentioned that parking dimensions depend on the timing of a single vehicle parked in a space. This shows that different sources have different approaches of considering the dimensions of a parking space. Hence, a summary of parking dimensions are collected for comparison purpose. Table 1 shows the summary of parking dimensions from accessible resources.

Table 1 Summary of parking dimensions from different resources

Source	Parking space dimensions		References
	Width (m)	Length (m)	
Parking structures: planning, design, construction, maintenance and repair	2.2–2.7	N/A	[6]
Car park designers' handbook	2.3–2.5	4.8	[7]
County of San Diego parking design manual	2.7	5.5	[8]
Asphalt paving design guide	2.7–2.8	5.6	[9]
Information bulletin/public-zoning code: Parking design	2.3–2.6	4.5–5.4	[10]
USAF landscape design guide	2.75	6	[11]
Parking design standards	2.5–3.2	N/A	[12]
Parking standards design and good practice supplementary planning document	2.5–2.9	5.0–5.5	[13]
Parking structures: recommended practice for design and construction	2.3–2.7	N/A	[14]

Based on the summary, it appears that the parking space width is in the range of 2.2–3.2 m, and the parking space length is in the range of 4.8–6 m.

1.2 Probability of Fire Spread Method

For the formulation of the probability of fire spread, considering a scenario of two vehicles parked in a space next to each other, this study performs a prediction of ignition for the second vehicle after the first vehicle already burning using the UCVFire simulation tool.

The algorithm for UCVFire is adjusted for the purpose of this work. The simulation process flowchart per iteration run is shown in Fig. 2, where at the end of the iteration, the user is informed if the second vehicle is ignited or not. The selection of vehicle classification and design fire is performed using the Monte Carlo algorithm, where it randomly selects a value from each distribution plot (fire growth coefficient, peak heat release rate and fire decay coefficient). It is assumed that there are no fire suppression systems installed in the car park, thus, there will be no intervention on the fire once it grows.

The design fire of a vehicle is dependent on the classification, where each classification has its own distribution of design fires. In addition, each classification is also dependent on the vehicle fleet distribution on the road. Thus, by performing the prediction model over a certain number of iterations with various distribution inputs, the results are able to show how many times the second vehicle ignited or not ignited. Therefore, the probability of fire spread from the first vehicle to the second vehicle can be calculated.

2 Approach

Two scenarios are examined: (1) vehicles parked next to each other, and (2) vehicles parked one parking space away from each other. These scenarios are simulated using the UCVFire simulation tool. Further explanation on the inputs for each scenario and the simulations are discussed in this section.
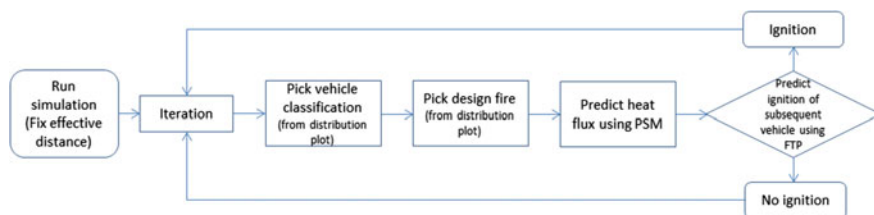
Fig. 2 Simulation process flowchart

2.1 Simulation Input

All input parameters such as numbers of iterations, the first component to be ignited and number of vehicles involved, are fixed, except for the main variable for this work, which is the effective distance. The width of the vehicle is unimportant, since the effective distance has already incorporated the width of the vehicle and the distance between one vehicle and another. The simulation model allows the user to vary the effective distance before running the simulation.

The probability of the fire spread from one vehicle to another is able to be calculated from a certain number of iteration runs, therefore 10,000 iteration runs is selected per simulation. This iteration number is deemed to be enough after series of 10,000 iterations were carried out for the same effective distance, and the results were similar due to the convergence of the iteration sequence. Also, the first component to be ignited is fixed to the bumper trim, as suggested in [15]. The work also suggests a power law index of 2 (thermally thick), an FTP value of 21,862 $\frac{kW\,s^n}{m^2}$, and a critical heat flux of 3.1 kW/m^2 is selected as the first component to ignite on a vehicle.

2.1.1 Scenario 1: Vehicle Parked Next to Each Other

This scenario represents the common closest distance in a car park, where two vehicles are parked next to each other. It is assumed that each vehicle is parked in the middle of the parking space, which makes the distance to both sides of the parking line symmetrical. In this scenario, the effective distance is the vehicle width of the burning vehicle, i.e., the heat source plus the distance between the edge of one vehicle to another, which is represented by *a* and *2b* respectively (Fig. 3). Since different works in the literature consider different widths of parking spaces, a range

Fig. 3 Vehicle parked next to each other
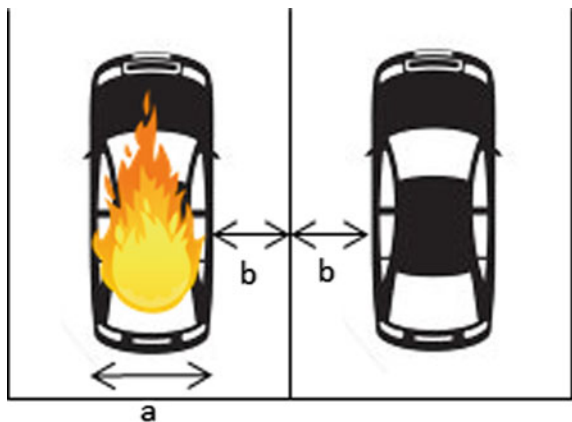
with a minimum parking space width of 2.2 m, and a maximum of 3.2 m, are used. Thus, this will be the range of effective distances used in the simulation.

2.1.2 Scenario 2: Vehicle Parked One Space Away

This scenario is chosen to study the effect of having an empty space in between a burning vehicle and another vehicle. Consistent to the assumption for Scenario 1, each vehicle also assumed to be parked in the middle of their parking space. In this scenario, the effective distance is the vehicle width of the burning vehicle, i.e. the heat source plus an empty parking space plus the distance between the tip of one vehicle to another vehicle, which is represented by a, c and $2b$ respectively (Fig. 4). Using the same range of parking space width 2.2–3.2 m, and adding another parking space width, this makes the range of effective distance for this scenario 4.4–6.4 m.

3   Results and Discussion

3.1   *Scenario 1: Vehicle Parked Next to Each Other*

Figure 5 shows the plot of results of probability of fire spread for Scenario 1. According to the results, the shortest effective distance of 2.2 m yields the highest probability of fire spread, with 0.90, and the longest effective distance of 3.2 m yields the lowest probability, with 0.63. The results show that, if a vehicle is parked next to a burning vehicle, there is a chance of 0.63–0.90 for the fire to spread to another vehicle.
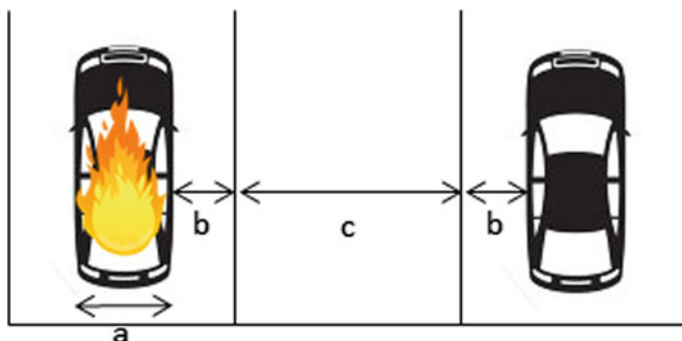
Fig. 4 Vehicle parked a space away from each other
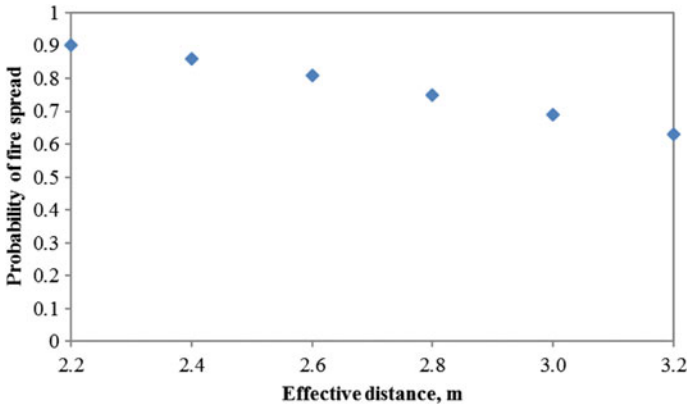
Fig. 5 Plot of results of probability of fire spread for Scenario 1

3.2 Scenario 2: Vehicle Parked One Space Away

Figure 6 shows the plot of results of probability of fire spread for Scenario 2. The results for this scenario show a lower probability than that of Scenario 1. The results show that the shortest effective distance of 4.4 m yields a 0.23 probability of fire spread, and the longest effective distance of 6.4 m results in no possibility of the fire spreading. The analysis suggests that having an empty parking space in between two vehicles lowers the probability of at least 0.40 in comparison to Scenario 1.
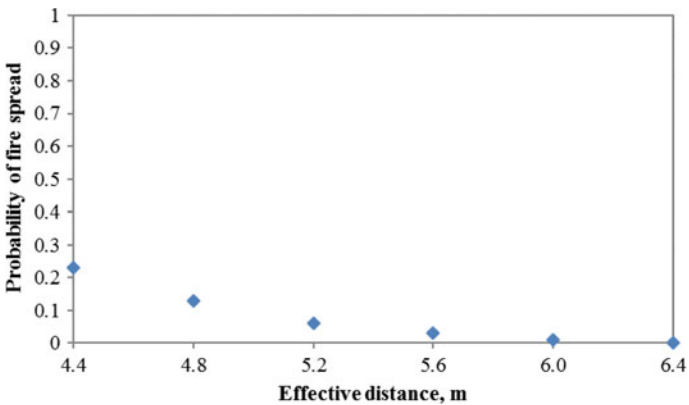
Fig. 6 Plot of results of probability of fire spread for Scenario 2

3.3 Estimation of Probability of Fire Spread for Other Distances

Essentially, the difference between Scenario 1 and Scenario 2 was only the distance between vehicles, which is the input for the simulation. Therefore, this section presents the combination of probability of fire spread results for Scenario 1 and 2 in a plot in order to fit a trendline which one can use to estimate the probability of fire spread for any distance. This combination is shown in Fig. 7 where a polynomial trendline with the order of two was fitted to the results. An equation of

$$y = 0.045x^2 - 0.62x + 2.11 \tag{1}$$

with the R^2 value of 0.99 is obtained. This equation can be used to estimate the probability of fire spread at different effective distances in between 2.2 and 6.4 m.

3.4 Sensitivity Analysis—Varying Vehicle Fleet Distribution Datasets

A sensitivity analysis on varying the vehicle fleet distribution datasets in the simulation was performed, and the results are shown in Fig. 8. Two different datasets; Tohir and Spearpoint [16], and Anderson and Bell [16] were used in the analysis. The results show that Anderson and Bell's dataset produces a higher overall probability of fire spread as compared to Tohir and Spearpoint's dataset. This is because Anderson and Bell's data has a higher portion of heavier vehicles compared to Tohir and Spearpoint's. One notable example is Anderson and Bell's portion for Passenger Car: Mini class is 0.1%, while for Tohir and Spearpoint it is
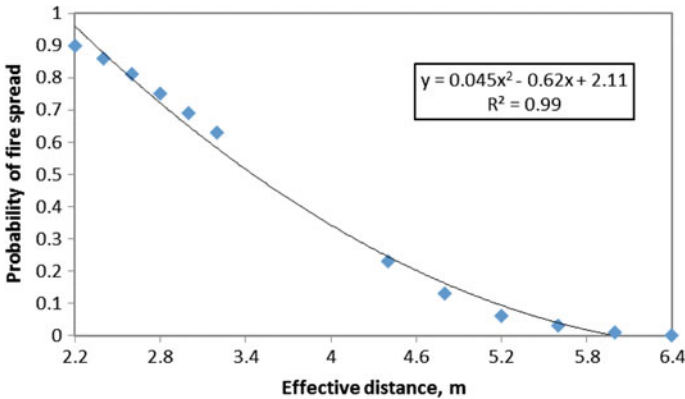
Fig. 7 Combination of probability of fire spread results for Scenario 1 and 2
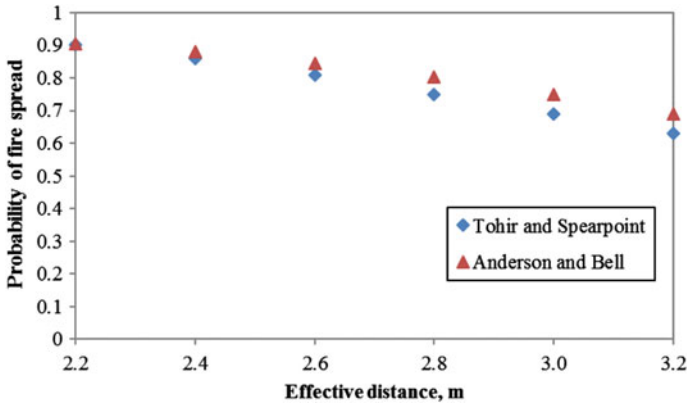
Fig. 8 Sensitivity analysis of using different vehicle fleet distributions

9.0%. A higher portion of heavier vehicles means a higher possibility of getting higher peak of heat release rate, thus, a higher possibility of igniting the neighbouring vehicle. Thus, the sensitivity analysis study shows that different vehicle distributions affect the probability of fire spread between vehicles.

4   Conclusion

This study was undertaken to quantitatively assess the probability of fire spread from a burning vehicle to another vehicle within its vicinity, given no interruption of the fire by firefighters and/or fire suppression systems. Using the specified inputs, this study has shown that, for Scenario 1, the probability of fire spreading to the neighbouring vehicle is 0.63 – 0.90, depending on the effective distance.

For Scenario 2, the highest probability of fire spreading for the shortest effective distance is 0.23, and probability for the longest effective distance (6.4 m) is 0. It is also found that the empty space between two vehicles is able to reduce the probability by at least 0.40.

Using the combination of results for Scenario 1 and 2, an equation of $y = 0.045x^2 − 0.62x + 2.11$ is obtained to estimate the probability of fire spread for different effective distance between 2.2 and 6.4 m.

Using different vehicle fleet distributions datasets affect the selection of design fire, thus, produces different sets of results. For more specific investigation, a different dataset of vehicle distribution fleet can be adopted in future analysis. However, this study is limited to only one vehicle initially burning. The effect of having two vehicles burning could have been different due to the higher intensity of energy released from the two vehicles.

It is to note that the work in this chapter excludes the intervention of firefighters and fire suppression systems to the fire. The intervention to the fire could have given a different effect to the probability of the fire spread to other vehicles. This is subject to future work where potential research such as the introduction of fire sprinkler systems into the model can be made.

References

1. Mohd Tohir, M.Z., Spearpoint, M.: Development of fire scenarios for car parking buildings using risk analysis. Fire Saf. Sci. **11**, 944–957 (2014)
2. Mohd Tohir, M. Z. Multiple Vehicle Design Fire Scenarios in Car Parking Buildings. PhD thesis, Department of Civil and Natural Resources Engineering, University of Canterbury, New Zealand (2015)
3. Fleury, R., Fleischmann, C.M., Spearpoint, M.: Evaluation of thermal radiation models for fire spread between objects. In: Fire and Evacuation Modelling Technical Conference (2011)
4. Smith, E.E., Satija, S.: Release rate model for developing fires. J. Heat Trans. **2**(105), 281–287 (1983)
5. Pratt, C.: Auckland Mall Shoppers Evacuated Because of Van Fire. Stuff NZ. http://www.stuff.co.nz/national/66735453/Auckland-mall-shoppers-evacuated-because-of-van-fire (2015)
6. Chrest, A.P., Smith, M.S., Bhuyan, S., Iqbal, M., Monahan, D.R.: Parking Structures: Planning, Design, Construction, Maintenance, and Repair, 3rd edn. Chapman and Hall, New York (2000)
7. Hill, J.: Car Park Designers' Handbook. ICE Publishing (2005)
8. Department of Planning and Land Use: Parking Design Manual (2013)
9. Asphalt Paving Association of Iowa: Parking Lot Design in Asphalt Paving Design Guide. Iowa, USA (1990)
10. City of Los Angeles—City Council: Parking Design. P/ZC 2002-001 (2010)
11. US Air Force: Parking areas in USAF Landscape Design Guide (1998)
12. Council, Fife: Parking Design Standards in Development Guidelines. Fife, Scotland (2006)
13. Rochford District Council: Parking Standards Design and Good Practice Supplementary Planning Document (2010)
14. Precast Concrete Institute: Parking Structures: Recommended Practice for Design and Construction (1997)
15. Mohd Tohir, M. Z., Spearpoint, M., Fleischmann, C.M.: Prediction of Time of Ignition in a Multiple Vehicle Fire Spread Experiment. Submitted to Fire and Materials
16. Spearpoint, M., Tohir, M.Z.M., Abu, A.K., Xie, P.: Fire load energy densities for the risk-based design of car parking buildings. In: Case Studies in Fire Safety (2015)

Effect of Crumb Rubber Modifier on the Fatigue Performance of Warm Mix Asphalt

Saeed Modibbo Saeed, Mohammad Yusri Aman,
Kabiru Abdullahi Ahmad, Ahmad Batari,
Ahmad Tijjani Ahmed Yero and Adamu Umar Chinade

Abstract Crumb rubber from waste tires is incorporated into asphalt mixtures as one of the successful strategies of improving the fatigue resistance of asphalt pavement. However, the degree of effectiveness and the percentage of CRM that gives the best fatigue resistance has not been firmly established. In this study, the effect of percentage crumb rubber on fatigue of rubberised warm mix asphalt mixtures was evaluated. A Pen-grade of 80/100 bitumen, crush granite aggregate with 9.5 mm NMAS, Sasobit at 2.5% by weight of the binder was blended with the bitumen to achieve a warm mix binder. Crumb rubber of size passing 0.150 mm sieve was incorporated into the WMA mixes at 0, 10 15 and 20% by weight of the virgin bitumen using wet process of modification. Indirect Tensile Fatigue Test (ITFT) was performed on the specimens at a temperature of 25 °C. The test was conducted at three levels of stresses (500, 600 and 700 kPa). The laboratory results findings indicate that the CRM significantly influence the fatigue life of the

S. M. Saeed · A. Batari · A. T. A. Yero · A. U. Chinade
Faculty of Engineering, Department of Civil Engineering,
Abubakar Tafawa Balewa University, PMB 0248, Bauchi, Nigeria
e-mail: abukhadijatsms@gmail.com

A. Batari
e-mail: ahmadbatari@gmail.com

A. T. A. Yero
e-mail: tijjaniyero@yahoo.com

A. U. Chinade
e-mail: adamuuc@gmail.com

M. Y. Aman · K. A. Ahmad (✉)
Faculty of Civil and Environmental Engineering, University Tun Hussein
Onn Malaysia, 86400, Parit Raja, Batu Pahat, Johor, Malaysia
e-mail: kabiruaahmad@gmail.com

M. Y. Aman
e-mail: mdyusre@gmail.com

K. A. Ahmad
Faculty of Engineering, Department of Civil Engineering, Bayero University
Kano, Bayero 3011, Kano State, Nigeria

mixtures. Based on the fatigue predictive life model, the 20% CRM have the highest fatigue life compared to other CRM percentages considered in this study.

Keywords Crumb rubber · Fatigue · ITFT · Sasobit

1 Introduction

Hot Mix Asphalt which is the conventional way of producing asphalt mixtures normally at a temperature of 150–180 °C. This high production temperature have resulted in a lot of environmental, economic, and health-related problems such as high energy consumption, greenhouse gases emission, excessive fuel consumption, air pollution, high-production cost, fumes, smoke, odor, and delay in traffic. These problems have contributed in the rapid increase of environmental awareness over the past few years.

Warm mix technology is the most effective strategy employed to alleviate the adverse effect caused by HMA production at high temperatures. This technology is now most widely used by pavement industries to reduce the environmental problems associated with the production of HMA under high temperatures. It was originated in Europe, and is referred to as the technology which lowers the binder's viscosity thereby reducing the production temperature of asphalt mixes considerably. One of this technologies is the use of Organic Additive, and the most widely used additive is Sasobit, which is a form of Fischer–Tropsch (FT) wax [1]. It was shown that Sasobit remarkably effects the complex modulus, (G^*) of both aged and unaged binders modified with crumb rubber modifier (CRM) [2]. Liu and Li [3] reported that the cracking temperature of both unaged and long-aged binders increased slightly with increasing Sasobit content. The fatigue life of Sasobit warm mix asphalt compacted at 100 and 110 °C were equal to and better than HMA respectively, while lower than HMA when compacted at 130 °C [4].

However, this reduction of temperature that is achieved through the use of WMA additives [4–6], has potential influence on the performance of asphalt mixtures which requires to be studied adequately. Cases such as the presence of residual moisture due to the incomplete drying of the aggregate under this low heating temperature will affect the pavement performance such as fatigue [7].

Fatigue cracking is an asphalt distress that is associated with the long-term performance of the asphalt pavement. This distress depends on some variables such as thickness of pavement layers, stiffness modulus, and process of fabrication among others with several other external causes like, environmental conditions, continuous passing of overweight trucks and poor quality control [8], and the material properties of the asphalt mixtures are the main influencing factor of fatigue cracking [9]. Laboratory fatigue test are commonly conducted using two mode of testing: Constant Stress and Constant Strain mode. Based on the interpretation of

many laboratory results, Finn et al. [10], derived these hypotheses relating pavement thickness, stiffness modulus, and fatigue performance: For thin asphalt pavement, low stiffness mixes should be used and fatigue life evaluation should be conducted under constant strain mode of testing but the stiffness should not be very low that will trigger rutting effect, while for thick asphalt pavement above 125 mm, high stiffness mixes should be utilized and the fatigue life be evaluated in a constant stress mode of testing. Many efforts have been employed in order to deal with this distress at the design stage, one of this effort is the use of modifiers in asphalt pavement production.

Many research efforts were focused on the use of Crumb Rubber obtained from used tires to modify asphalt pavement in improving pavement performance. Wang et al. [2], reported that warm mix asphalt incorporating CRM shows an influence on the softening point and the penetration index of a CRM binder, reduce its viscosity at high temperatures, increase stiffness of the binder, decrease traffic noise, reduce overall maintenance cost, and increase pavement life by increasing the fatigue resistance of the asphalt pavement.

In Malaysia, the use of rubber as an additive for pavement construction started as far back as 1940s, but this has not been officially recorded [11]. The first recorded trial was in 1988, the wet process was used with the mix of rubber additive in form of latex into asphalt binder [12]. There are two most widely used processes of incorporating CRM into asphalt mixtures. The first is Wet process, in which the CRM is blended with asphalt binder whereas the latter is known as Dry process, whereby CRM replaces a small portion of the mineral aggregate. The addition of crumb rubber into asphalt mixtures can enhance the anti-fatigue property of the mixture based on the following two reasons. One is that the presence of anti-aging element in the crumb rubber powder, such as carbon black, increases the aging resistance of the mixtures when added and the other reason is that crumb rubber increases the viscosity and the elasticity of the asphalt binder thereby, improve the asphalt film thickness on the aggregates surface and subsequently increases the asphalt mixtures aging resistance [13]. It was found that adding crumb rubber could significantly improve the intermediate temperature fatigue life of asphalt binders [4, 14–16]. Another study conducted by Wang et al. [13], on fatigue cracking property of CRM asphalt mixture using the SCB test, indicated that crumb rubber concentration plays a significant role in CRM asphalt mixture's fatigue property. When the crumb rubber concentration was 20%, CRM asphalt mixture had the best anti-fatigue property, the fatigue life was the longest and crack grew the slowest.

Although, many researches have been conducted on the use of crumb rubber in asphalt modification, but the degree of improvement and the cost effectiveness of using crumb rubber in asphalt mixtures is yet to be firmly established.

However, this study aims at investigating how crumb rubber concentration affects the fatigue life of rubberized warm mix asphalt mixtures.

2 Materials and Methodology

2.1 Materials

The penetration grade of 80/100 asphalt binder with characteristic properties as shown in Table 1 was used and Sasobit is added to the binder as a warm mix additive. A single-source crushed granite aggregate was used throughout the study.

The aggregate was oven dried at a temperature of 110 °C for 8 h, and then sieved into various sizes in accordance with AASTO T27-99, Table 2 shows the aggregate properties and also 1.5% of hydrated lime, by weight of the aggregate was gradually added and properly mixed with the aggregate serve as an anti-stripping agent [17–19].

The aggregate gradation was selected based on the Superpave gradation requirement using 0.45 gradation power chart, 9.5 mm was chosen as the Nominal Maximum Aggregate Size (NMAS) as illustrated in Fig. 1.

In this study, the size of the crumb rubber, passing 0.150 mm sieve was selected. The density of the crumb rubber is approximately 1.15 (g/cm^3). The crumb rubber modifier was obtained from Miroad Rubber Industries Sdn. Bhd Malaysia. Different percentages of crumb rubber (0, 10, 15, and 20%) by weight of the binder were used. The elastomeric compositions of the CRM are natural rubber 30%, Butadiene rubber 30%, and styrene-butadiene rubber (SBR) 40%.

Table 1 Properties of base binder (80/100 Pen-grade)

Test properties	Values	Test standard
Softening point @ 25 °C	45	AASHTO T53-96
Penetration @ 25 °C	88	AASHTO T49-03
$G^*/\sin\delta$ @ 64 °C (kPa)	1.262	AASHTO T315-1
RTFO-$G^*/\sin\delta$ @ 64 °C (kPa)	4.009	AASHTO T315-1
PAV-aged $G^*\sin\delta$ @ 25 °C (kPa)	3258.4	AASHTO T315-1

Table 2 Properties of the Crushed Granite Aggregate

Test properties	Values	Test standard
Specific gravity	2.658	AASHTO T85
Absorption (%)	0.8	AASHTO T85
Los Angelo's' Abrasion	50	AASHTO T96
Impact value (%)	14.86	BS 812: part 3
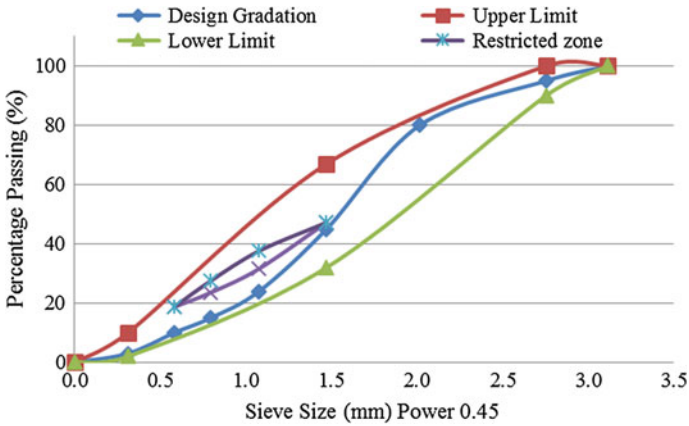
Fig. 1 NMAS 9.5 mm gradation using 0.45 power chart

2.2 Fabrication of Samples

In this study, Sasobit was added and blended at 2.5% of the weight of the bitumen to achieve a warm mix bitumen. The Sasobit was blended using shear mixer at a speed of 1000 rpm for 10 min at a temperature of 120 °C. To incorporate the crumb rubber in bituminous binder, the wet process of crumb rubber modification was selected, the CRM was added directly to the binder before mixing with aggregate. The crumb rubber was blended with the bitumen using shear mixer at 177 °C with mixer speed of 700 rpm for a period of 30 min. The Optimum bitumen content (OBC) was obtained using Superpave mix design method. The compaction was done to achieve 4% air void using Superpave Gyratory Compactor (SGC) at gyration levels of 8, 100 and 160 for $N_{initial}$, N_{design}, and $N_{maximum}$ respectively for 3 to <30 ESALs as recommended by AASHTO PP28. The OBC was chosen by examining the volumetric properties of the specimens conforming to the criteria set by Superpave mix design criteria. Four various amounts of OBCs were used for the four various CRM contents: 6.5, 7.2, 7.48, and 7.8% by weight of aggregate for 0, 10, 15, and 20% of CRM contents, respectively. Mixed aggregate weighing 1200 g was used for producing the asphalt mixtures, it was kept in an oven for 2 h at 140 °C and the bitumen was also heated for 1 h at the same mixing temperature and then added to the aggregate. Mixing temperature was maintained constant at 140 °C. The mixture was then conditioned for 1 h at the compacting temperature of 130°C and then transferred into a SGC mold of 100 mm diameter for compaction. All samples were compacted at N_{design} of 100 gyrations.

3 Test Methods

3.1 Indirect Tensile Fatigue Test

One of the methods used to determine the fatigue characteristics of HMA is Indirect Tensile Fatigue Test. It has a benefit of using specimens that can be cored directly from the asphalt pavement or easily produced in the SGC. This test uses a repeated controlled stress pulse to assess the specimen and the accumulated vertical deformation is plotted against the number of load pulse. It uses the same setup as that of the ITSM setup. In controlled stress mode, the results for the test is presented by plotting the log of the cycle counts to failure against the log of the stress imposed using Eq. 1 whereas the controlled strain mode, the result is presented by plotting the cycle counts to failure against the strain imposed using Eq. 2. When the strain and or stress was plotted against cycle counts to failure of each specimen in a logarithmic scale, the relationship observed was a linear-type and a predictive fatigue life model was established. The experimental setup is same as that of Indirect Tensile Stiffness Modulus (ITSM) only that failure occurs under condition of repeated loading. For this research work, the test was performed at a temperature of 20 °C because fatigue is a pavement distress that occurs at intermediate temperature and a three cyclic loading stresses were used at 500, 600, and 700 kPa, respectively. The test condition used in this research study is illustrated in Table 3, the tensile strain was calculated using the assumed poison ratio at the center of the sample as a function of the stress being used and the stiffness modulus of the sample specimen using Eq. 3. The failure of material as a result of fatigue loading consist of three stages; first stage has to do with condensation of the material, second stage is the gradual increase in deformation caused by repetitive load cycle, and the final stage is the material reaches it failure point [14].

The fatigue behavior is characterized by relating the number of load cycles to failure. This is expressed using the following equations:

$$N_f = a\left(\frac{1}{\sigma}\right)^b \qquad (1)$$

$$N_f = k\left(\frac{1}{\varepsilon}\right)^n, \qquad (2)$$

Table 3 Input parameters used for ITFT

Test condition	Test requirements
Stress level	Between 10 and 700 kPa
Target rise time	124 ms (equivalent to a frequency of 1.33 Hz)
Failure criterion	9 mm vertical deformation
Test temperature	25 °C

where N_f is the cycle counts to failure, σ is applied stress, ε is initial strain, and a, b, k and n are regression coefficients called the fatigue parameter, which are related to the properties of the mixture. The horizontal tensile strain is calculated using

$$\varepsilon_{max} = \frac{\sigma_{max}(1+3\mu)}{S_m} \tag{3}$$

whereas ε_{max} is the highest strain, σ_{max} is the highest stress, S_m is the stiffness modulus and μ is the poisson ratio.

4 Results and Discussion

4.1 Indirect Tensile Fatigue Test (ITFT) Result

Result of the Indirect Tensile Fatigue Test shows that at all level of stresses, the samples containing crumb rubber modifier have more number of cycle counts to failure as compared to the unmodified (control) samples with zero percent CRM. Table 4 shows the fatigue characteristics relating the applied stress, stiffness modulus, and the accumulated strain with the cycle counts to failure for all the specimens (with and without CRM) with their corresponding fatigue predictive model.

The relationship between the fatigue life and the accumulated strain illustrated in Fig. 2 indicates that CRM addition into warm mix asphalt mixtures improved the fatigue life of the mixtures and also reduce their strain accumulation [11]. This shows that adding crumb rubber into warm mix asphalt mixtures has beneficial

Table 4 Input parameters used for ITFT

Percentage CRM	Stress (σ) (kPa)	Strain, ε_f	N_f	Fatigue model	R^2	P-value
0% CRM	500	686.728	2823	$N_f = 6.05\text{E} + 08(1/\varepsilon)^{1.871}$	89.83	0.207
	600	824.074	2399			
	700	961.419	1489			
10% CRM	500	644.182	3337	$N_f = 1.39\text{E} + 07(1/\varepsilon)^{1.642}$	99.33	0.052
	600	773.019	2570			
	700	901.855	1916			
15% CRM	500	611.484	3824	$N_f = 5.18\text{E} + 06(1/\varepsilon)^{1.837}$	96.85	0.114
	600	733.781	3005			
	700	856.078	2050			
20% CRM	500	592.400	3920	$N_f = 1.87\text{E} + 09(1/\varepsilon)^{2.047}$	99.81	0.028
	600	710.880	2768			
	700	829.360	1966			
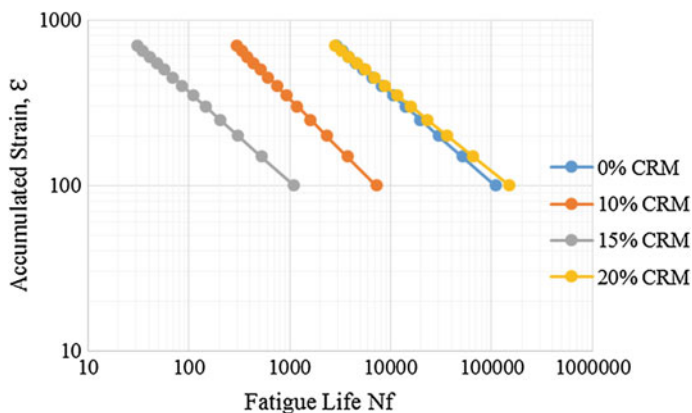
Fig. 2 Accumulated strain versus Fatigue life

effect on its fatigue life. It was also noted that the fatigue life decreases as the stress level is increased, the higher the stress is, the lower is the resulting fatigue life. It can be seen from the result obtained and the basic fatigue predictive model that the samples modified with 20% CRM have the higher fatigue life with low value of strain. This finding is in agreement with previous researches on the effect of crumb rubber on fatigue [4, 11, 13–16]. This shows that crumb rubber modifier has beneficial effect in sustaining higher tensile strains within asphalt concrete.

It is evident that incorporating crumb rubber into asphalt binder causes an increase in the viscosity and elasticity of the asphalt binder and the presence of anti-aging element in the crumb rubber powder such as carbon black increase the aging resistance of the binder and also improve the elastic recovery of the modified mixture and therefore, enhance the binder asphalt film thickness on the aggregates surface and subsequently increase the asphalt mixtures aging resistance and prevent crack initiation [13, 20]. The high elasticity and the improved tensile strength evident in the modified mixtures help in preventing cracks formation and propagation [16].

It can be seen in Fig. 2 that the lower percentages of crumb rubber (10 and 15%) considered in this study displayed negative effect on the fatigue life of the samples. Based on ANOVA analysis conducted, the lower CRM percentages recorded an effect that is insignificant in improving the fatigue life of the specimens having P-values greater than the assumed $\alpha = 0.05$, while the 20% CRM displayed a highly significant effect on the fatigue life with p-value of 0.028.

5   Conclusion

Based on the study conducted, conclusion can be stated as

The addition of crumb rubber into warm mix asphalt improved the fatigue life of the samples significantly which may be due to the increase in the viscosity,

elasticity, and the aging resistance of the modified samples. It can also be seen that the 20% CRM significantly influences the fatigue style of the WMA samples with p-value of 0.028 and it resulted in the longer fatigue life as compared to the other percentages considered in this study.

References

1. Rodríguez-Alloza, A.M., Gallego, J., Pérez, I., Bonati, A., Giuliani, F.: High and low temperature properties of crumb rubber modified binders containing warm mix asphalt additives. Constr. Build. Mater. **53**, 460–466 (2014)
2. Wang, H., Dang, Z., You, Z., Cao, D.: Effect of warm mixture asphalt (WMA) additives on high failure temperature properties for crumb rubber modified (CRM) binders. Constr. Build. Mater. **35**, 281–288 (2012)
3. Liu, J., Li, P.: Low temperature performance of sasobit-modified warm-mix asphalt. J. Mater. Civ. Eng. **24**(1), 57–63 (2011)
4. Goh, S.W., & You, Z.: Evaluation of warm mix asphalt produced at various temperatures through dynamic modulus testing and four point beam fatigue testing. In: Pavements and Materials: Recent Advances in Design, Testing and Construction, pp. 123–130 (2011)
5. Batari, A., Aman, M.Y., Saeed, S.M., Ahmed, T.Y., Chinade, A.U.: Rutting assessment of crumb rubber modifier modified warm mix asphalt incorporating warm asphalt additive. Int. Res. J. Eng. Technol. **4**(2), 1239–1244 (2017)
6. Zaumanis, M.: Warm Mix Asphalt Investigation (Master of Science thesis). Technical University of Denmark, Kgs. Lyngby, Denmark (2010)
7. Xu, Y.: Investigation of Effects of Moisture Susceptibility of Warm Mix Asphalt (WMA) Mixes on Dynamic Modulus and Field Performance. Diss. Worcester Polytechnic Institute (2012)
8. Roberts, F.L., Kandhal, P.S., Brown, E.R., Lee, D.Y., Kennedy, T.W.: Hot Mix Asphalt Materials, Mixture Design and Construction (1991)
9. Lv, J., He, X.: Finite element analysis on fatigue cracking of sisal fiber asphalt mixture. ICCTP 2010: Integrated Transportation Systems: Green, Intelligent, Reliable, pp. 3845–3851 (2010)
10. Finn, F.N., Nair, K., Hilliard, J.M.: Minimizing premature cracking in asphaltic concrete pavement. In: NASA STI/Recon Technical Report N 79 (1978)
11. Mashaan, N.S., Ali, A.H., Karim, M.R., Abdelaziz, M.: A review on using crumb rubber in reinforcement of asphalt pavement. Sci. World J. (2014)
12. Sufian, Z., Mustafa, M.S.: Prospects of rubberised bitumen pavement Malaysia roads and highways. In: Proceedings of the Conference on the Use of Rubberised Bitumen in the Road Construction (1997)
13. Wang, H., Dang, Z., Li, L., You, Z.: Analysis on fatigue crack growth laws for crumb rubber modified (CRM) asphalt mixture. Constr. Build. Mater. **47**, 1342–1349 (2013)
14. Kim, S., Lee, S.J., Yun, Y.B., Kim, K.W.: The use of CRM-modified asphalt mixtures in Korea: evaluation of high and ambient temperature performance. Constr. Build. Mater. **67**, 244–248 (2014)
15. Xiao, F., Zhao, P.W., Amirkhanian, S.N.: Fatigue behavior of rubberized asphalt concrete mixtures containing warm asphalt additives. Constr. Build. Mater. **23**(10), 3144–3151 (2009)
16. Arabani, M., Ferdowsi, B.: Laboratory evaluating and comparison of the SCB Test results with other common tests for HMA mixtures. Adv. Charact. Pavement Soil Eng. Mater. **1** and **2**, 151–164 (2007)

17. Aman, M.Y., Hamzah, M.O.: Evaluation of anti-stripping agents on warm porous asphalt mixtures. Aust. J. Basic Appl. Sci. **8**(10), 438–446 (2014)
18. Lee, S.J., Akisetty, C.K., Amirkhanian, S.N.: The effect of crumb rubber modifier (CRM) on the performance properties of rubberized binders in HMA pavements. Constr. Build. Mater. **22**(7), 1368–1376 (2008)
19. Hurley, G.C., Prowell, B.D. Evaluation of Sasobit for use in warm mix asphalt. In: NCAT report 5.06 (2005)
20. Hamed, F.K.M.: Evaluation of Fatigue Resistance for Modified Asphalt Concrete Mixtures Based on Dissipated Energy Concept (2010)

Evaluation of Aramid Fibre-Reinforced Asphalt Mixtures

Adham Alnadish and Yusri Aman

Abstract Continuous efforts by scientists and researchers are made to offer high-performance asphalt mixtures with longer service life, thus minimizing negative impacts to the environment, environmental sustainability, costs resulting from the rehabilitation, and maintenance of roads. In this regard, fibers can provide a distinct material in the enhancement of asphalt mixture performances. Fibers have been used in asphalt mixtures for decades due to their abilities in improving of asphalt mixtures performance. Aramid fibers are synthetic fibers with high-performance properties. This study is aimed to assess the ability of Aramid fiber in improving asphalt mixtures performance. Aramid fibers were added to the asphalt mixtures in different contents; i.e., 0.05, 0.1, 0.2, and 0.3% by total weight of the aggregate. Asphalt mixtures were performed by resilient modulus test at two temperatures 25 and 40 °C that indicates the mixture's resistance to fatigue and rutting resistance, respectively. Response Surface Methodology (RSM) using Design Expert 6.0 software was used to analyze data obtained. The results indicated that introducing of the Aramid fibers to mixtures increased the performance of mixtures in terms of resilient modulus by around 25% at 25 °C and 20% at 40 °C; compared to the control mixtures without fibers. The optimum content of Aramid Fibers was at 0.05% to the total weight of the aggregate.

Keywords Asphalt · Aramid fiber · Resilient modulus · RSM
Fatigue · Rutting

A. Alnadish · Y. Aman (✉)
Faculty of Civil and Environmental Engineering,
Universiti Tun Hussein Onn Malaysia, 86400 Parit Raja, Malaysia
e-mail: mdyusri@uthm.edu.my

A. Alnadish
e-mail: adhmalnadish@gmail.com

1   Introduction

Asphalt mixture is a combination of aggregates and binder, which is used in the paving and rehabilitation of roads [1]. Asphalt mixtures are characterized by their lower costs and greater flexibility than concrete [2]. Therefore, there are vigorous efforts by researchers and scientists to improve the performance of asphalt mixtures either by using additives to improve binder or using material to improve the mixtures [3]. One of the common material, which have been widely used are fibers [4]. Using fibers in asphalt mixtures have been used for decades due to their abilities in improving asphalt mixtures performance in terms of increasing resistance to cracking, increase-rutting resistance, and durability of the asphalt mixtures. In addition to that, it offers a longer service life compared to the traditional asphalt mixtures without fibers [5–7]. Polypropylene, polyester, and aramid are the most widely used fibers, which fall within polymer fibers [8]. Aramid fiber is a type of synthetic fibers, which is synthetic polyamides of long-chain, and what distinguishes it from other types of fibers its high tensile strength and melting point [5]. Many researchers have in depth investigated their properties and their effectiveness as a 3D reinforcement in asphalt mixture. Abtahi et al. [9] investigated the effect of polypropylene and fiberglass by different content in asphalt mixtures. The polypropylene fiber contents were 2, 4 and 6% by total weight of the binder, the fibers length were 12 mm. In view of that, the mixing method adopted by researchers was wet method. In term of fiberglass, the content were 0.05, 0.1, and 0.2% to the weight of aggregate, its length was 12 mm. In this aspect, asphalt mixtures performance was evaluated by Marshal's method. The results indicated that the higher polypropylene content results in lowering penetration and ductility exceptionally higher penetration in term of properties of bitumen tests. Besides that, the polypropylene content increased the stability and air voids and the flow has decreased with regard to Marshal tests. On the other hand, addition of fiberglass to the mixtures contributed in increasing of asphalt mixture performance at 0.1% fiberglass content. The optimum combination content for polypropylene and fiberglass were at 6 and 0.1%, respectively, that showed better outcome compared to the reference mixtures.

In similar content, Xu et al. [10] studied the effect of four types of fibers, which includes polyester, polyacrylonitrile, Lignin, and asbestos. Researchers conducted a comparison of the properties, proportions, and effects. The polyester was added at varying content, which range from 0.20 to 0.50% and the others were added at fixed content 0.3% by total weight of the mixture. These fibers were evaluated in the dense mixtures; the results indicated that all fibers increased slightly the performance of asphalt mixtures in terms of resistance to rutting and fatigue cracking and indirect tensile strength compared to the reference mixture. On the other hand, the lignin and asbestos fibers achieved slightly better results compared to other fibers types. Additionally, Kaloush et al. [5] assessed the effect of aramid and polypropylene fibers in the asphalt mixtures, these fibers were evaluated in the dense mixtures, and the content of the fibers was 1 Ib/ton. Triaxial shear testing was

used to evaluate failure shear and rutting resistance. The results indicated that addition of fibers increased the performance of the mixtures concerning of failure shear compared to the reference mixtures. On the other hand, flow number of the mixtures was 15 times greater than reference mixtures, flow number corresponding to the permanent deformation test. Furthermore, dynamic modulus test indicated in results that mixtures containing aramid and polypropylene fibers improved the performance of the mixtures with regard to the moduli compared to the control mixtures without fibers at different temperatures and different frequencies. Moreover, the results of fatigue cracking and indirect tensile strength at low temperatures (0, −10, and −20 °C) showed that mixtures containing fibers had better results compared to the control asphalt mixtures. However, the performances of the mixtures with fibers were higher than reference mixtures in terms of permanent deformation, fatigue cracking, fracture energy, thermal cracking, and indirect tensile strength.

2 Materials and Method

A penetration grade 80/100 of the bitumen produced by Petronas obtained from UTHM highway laboratory was used. Table 1 shows the physical properties of the binder. Crushed granite aggregate with a nominal maximum size aggregate 12.5 mm were used, Table 2 and Fig. 1 show the properties and gradation of the

Table 1 Physical properties of bitumen

Properties	Test value	Standard
Penetration at 25 °C, 1/10 mm	87	ASTM D 36–06
Ductility at 25 °C (cm)	>100	ASTM D 113–07
Softening point	49	ASTM D 36–06
Specific gravity at (25 °C) (g/cm^3)	1.02	ASTM D 70–09
Viscosity @ 135 °C (cP) Viscosity @ 165 °C (cP)	487 144	ASTMD44
Mixing temperature Compaction temperature	160 °C 150 °C	ASTM D4402

Table 2 Physical properties of the aggregates

Testing	Value	Standard	Speciation (%)
Loss angles abrasion	19.75%	ASTM C 131	≤25
Aggregate crushing value	23.6	IS: 2386 (Part IV)	≤25
Specific gravity: Coarse aggregate Fine aggregate	2.63 2.74	ASTM C127	
Water absorption	0.743%	ASTM C127	≤2
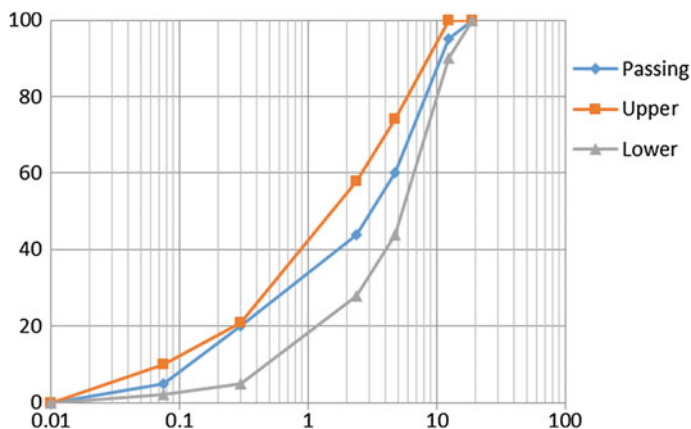
Fig. 1 Gradation of designed aggregate

Table 3 Aramid fibers physical properties

Material property	Measure
Material	Para-aramid fiber (50–52% by weight)
Density	1.45 (g/cm^3)
Tensile strength	>2.758 (GPa)
Modulus	>95 (GPa)
Decomposition temperature	>450 °C
Treatment type	Sasobit wax (48–50% by weight)
Treatment melting temperature	>80 °C
Length	19 mm
Form	Filament yarn

aggregate, respectively. Aramid fibers supplied by Surface Tech, Portland, United States of America were used. The Aramid fibers are lightweight, and it is difficult to introduce it to the mixture in its original state. For that, a creative solution by Surface tech was applied through soaking the fibers in wax binder to prevent them from blowing away when it is introduced to the mixture. Table 3 and Fig. 2 shows the physical properties and the shape of the Aramid fibers, respectively.

3 Specimens Preparation

In this study, control specimens without fibers were prepared, and four proportions 0.05, 0.1, 0.2, and 0.3% of Aramid fibers to the total weight of aggregate were introduced to the mixtures as a three dimensional (3D) reinforcement.

The specimens of the asphalt mixtures were produced using Superpave gyratory compactor in accordance with AASHTO T312. Mixing and compaction temperature were determined based on the viscosity of the binder in accordance with ASTM D4402, Table 1 shows mixing and compaction temperature results. Prior to compaction of the specimens, the aggregate were heated for four hours at mixing temperature 160 °C according to the specifications of Superpave, this is to insure equilibration temperature is reached, then the heated bitumen at 150 °C was added to the heated aggregate, and then they mixed for 3 min using automatically mixer. Thereafter, the aramid fibers were introduced to the mixtures, and then they were all mixed for another 3 min. The procedures of introducing Aramid fiber to the mixtures called composite method, which is a mix of dry-and-wet method. To simulate the short-term aging in accordance with Superpave specifications, the specimens were aged in the oven for 2 hours at compaction temperature (150 °C) prior to the compaction. Thereafter, the specimens were compacted by applying 100 gyratory. The extent of gyratory compaction effort was selected based on the level of traffic that is in this study, <30 million ESALs. Table 4 represents the volumetric properties of the mixtures, which were achieved in accordance with Superpave requirement.

Table 4 Volumetric properties of the mixtures

Mixtures properties	Result	Requirement	Status
OBC	4.78	4–9	Pass
AV	4	4	Pass
VMA	17.2	14 minimum	Pass
VFA	75.5	65–75	Pass
Dust proportion ratio	1.142	0.6–1.2	Pass

4 Test Method

4.1 Resilient Modulus

Ability of the material to absorb energy in the elastic range references to the resilient modulus [11]. Value of the resilient modulus can be considered as one of the important parameter, which used in the design of asphalt pavements, based on the theory of elasticity [12]. In this study, resilient modulus test carry out in accordance with ASTM D4123 using UTM-5P machine. Prior to the testing the samples were kept in the climate chamber of UTM-5P machine for 2 h, at each test temperature, this is to ensure a uniform distribution of temperature within the specimens. This test was conducted at two temperatures, testing at 25 °C related to the resistance of mixtures to fatigue cracking, while testing at 40 °C refers to the resistance of mixture to rutting [13]. Three specimens with 100 mm diameter and 65 mm in height were tested per each mixture, and each sample was tested at two different directions, the first direction was at the 0° angle then the specimen rotated by 90°. The test consists of applying a repetitive haversine compressive load pulse of 1000 N based on 10% by indirect tensile strength, this load was selected to be non-destructive. The load width was 0.1 s, and the rest period was a 0.9 s rest period (1 Hz) to simulate movement of the vehicle at high speed. The Poisson's ratio was assumed at 0.35. The resilient modulus of the mixtures was calculated automatically using UTM-5P software based on the recoverable vertical and horizontal deformations, which measured using a set of two LVDTs, aligned in the diametric plane.

5 Statistical Analysis

In this study, response surface methodology (RSM) and Design Expert 6.0 software were used to analyze data obtained. RSM is a statistical tool, which gives an indication about the relationship and interaction between factors and responses as well as generates a mathematical equation [14]. Additionally, two factors with one response were analyzed. Over and above, the outputs of Design Expert were evaluated using ANOVA. Furthermore, Proportion of Aramid fibers (0.05, 0.1, 0.2, and 0.3%) were the first factor and temperatures (25 and 40 °C) were the second

Table 5 Experiment matrix and obtained resilient modulus results

Run	Factors		Response
	Aramid fibers (%)	Temperature	Resilient modulus (MPa)
1	0	25	5760
2	0	40	865
3	0.05	25	7585
4	0.05	40	1070
5	0.1	25	5430
6	0.1	40	922
7	0.2	25	5125
8	0.2	40	885
9	0.3	25	4597
10	0.3	40	832

factor, while the resilient modulus was the response. Ten runs were analyzed that represents the average value of resilient modulus per each mixture. Table 5 represents inputs data of design Expert 6 software, which are outcomes of this study.

6 Result and Discussion

6.1 Resilient Modulus

Resilient modulus is considered as an important test due to its ability to give an indication about the resistance of the asphalt mixture to the cracking and permanent deformation (rutting). In addition, the value of resilient modulus is the main input in the mechanistic empirical pavement design, which used to determine strain and stress in asphalt layer that generated from the applied load of vehicles [15]. However, Fig. 3 shows the resilient modulus of the mixtures at 25 and 40 °C that
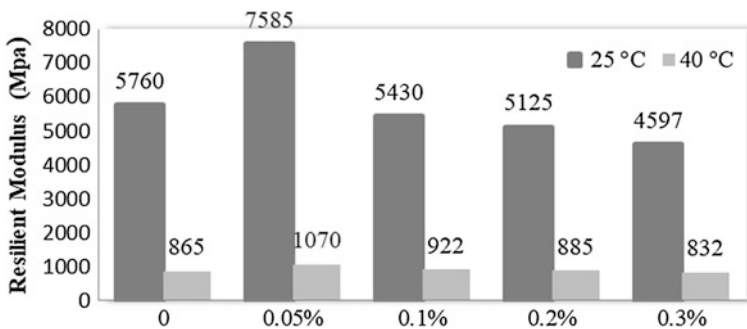
Fig. 3 Resilient modulus of the mixtures at 20 and 40 °C

indicates the resistance of the mixture to cracking (fatigue) and rutting (permanent deformation). As can be seen in Fig. 3, the asphalt mixtures containing a high content of aramid fiber (0.1, 0.2 and 0.3%) have decreased resilient modulus at the two-temperature test (25 and 40 °C) compared to the others, this was attributed to the high content of the aramid fiber, which increased thickness of the specimens by around 1–1.5 mm. On the other hand, the asphalt mixtures that containing 0.05% of aramid fiber exhibited the highest resulted in terms of resilient modulus at 25 and 40 °C compared to the other mixtures. This is because that 0.05% of aramid fiber represents the optimum content, which showed its ability to resist the indirect tensile load due to that aramid successfully, reinforced the asphalt mixtures. However, it can be seen that resilient modulus indicated that mixtures containing 0.05% of aramid fiber have increased resistance of mixture to cracking by around 25% at moderate temperature (25 °C), while it has enhanced the mixture resistance to permanent deformation by around 20% at high temperature (40 °C) compared to the control mixtures.

6.2   Statistical Analysis

Response surface methodology (RSM) is a statistical tool that used to investigate how different properties related to each other, and this is described based on the correlation between the factors and responses. On the other hand, factors represent parameters of the test, which are temperatures test and proportion of the aramid fiber, while the response corresponds to output of the test, which is value of the resilient modulus [16, 17]. However, Table 5 shows the inputs of Design expert 6 software that consists the factors and response. In this paper, four-regression models; .i.e., Two-factor interaction (2FI), Linear, Quadratic and Cubic were assessed in order to determine the best regression model that can describe the correlation between the factors and response as well as to generate a mathematical equation in order to predict the resilient modulus (response). However, the appropriate model was chosen based on some parameter; i.e. Lack of fit (DF), Prop > F, and R-Squared. Lack of fit assesses the model in terms of fits the data, this assessment is determined based on the differences between errors of sum and pure of squares. In similar content, the Prob > F is considered as the most important parameter in selecting the suitable model [18]. Prob > F value less than 0.05 indicates significant factors and considerable interaction between the factors and response [19, 20]. Based on the analysis of the obtained data in Table 6 that represents the ANOVA analysis, the linear regression model was suggested with the suitable model. The lack of fit for the models of Linear, 2FI, Quadratic and Cubic were 2, 1, 1 and 2, respectively. As can be observed in Table 6 the lower Prob > F was significant at linear model, which was less than 0.05, this indicated that linear model fits data well, while the other models showed not significant Prob > F that indicates the other models are not suitable to describe the correlation between factors and response. Moreover, R-squared used to describes how data is close to

Table 6 Summary on ANOVA analysis of aramid fiber content and test temperatures (factors) versus resilient mosulus (response)

Sequential model sum of squares						
Model type	Sum of squares	DF	Mean square	F value	Prob > F	Performance
Linear	58,614,306	2	293,07,153	53.59188	<0.0001	Suggested
2FI	1,092,183	1	1,092,183	2.395294	0.1727	
Quadratic	57,195.4	1	57,195.4	0.106762	0.7571	Aliased
Cubic	449,407.9	2	224,704	0.302398	0.7592	Aliased
Residual	2,229,220	3	743,073.3			
Total	1.72E + 08	10	17,181,142			

Model summary statistics						
Model type	Std. Dev.	R-squared	Adjusted R-squared	Predicted R-squared	Press	
Linear	739.4986	0.938695	0.92118	0.874304	7,848,760	Suggested
2FI	675.2559	0.956186	0.93428	0.891742	6,759,906	
Quadratic	731.9328	0.957,102	0.922784	0.859,166	8793977	Aliased
Cubic	862.017	0.9643	0.892899	0.503473	31,004,286	Aliased

the fitted line, and the adjusted R-squared has the same meaning of R-squared with the difference in explaining the variation percentage, while the predicted R-squared illustrates how data is closed to the fitted line based on the predicted model [18]. As can be concluded from Table 6, R-squared of Linear, 2FI, Quadratic and Cubic was more than 90%, which indicates that the data were close to the fitted line and the correlation between factors and response is strong. On the other hand, the predicted R-squared of the predicted model was 0.87; in other words, the predicted response (equation) for the linear model is favorable to predict the response. The suggested equation for the prediction of resilient modulus (response) in the asphalt mixtures containing aramid fibers is expressed by Eq. 1, which is a linear equation. Through regression coefficients of this equation, it can be concluded that an increase in Aramid fibers and temperature offset cause a decrease in resilient modulus. It can be seen from Fig. 4 that increasing Aramid fibers content leads to the decrease the resilient modulus, as well as the increase in the temperature causes reduction in the resilient modulus. As shown in Fig. 5, the points of data are approximately linear, which indicates that the data are normally distributed for the linear model, and the selected Aramid fibers proportions were almost proper.

$$\text{Resilient Modulus (MPa)} = 14125.80230 - (3462.06897 * \text{Aramid Fibers}\,(\%))$$
$$- (319.05333 * \text{Temperature(C)})$$

$$(1)$$
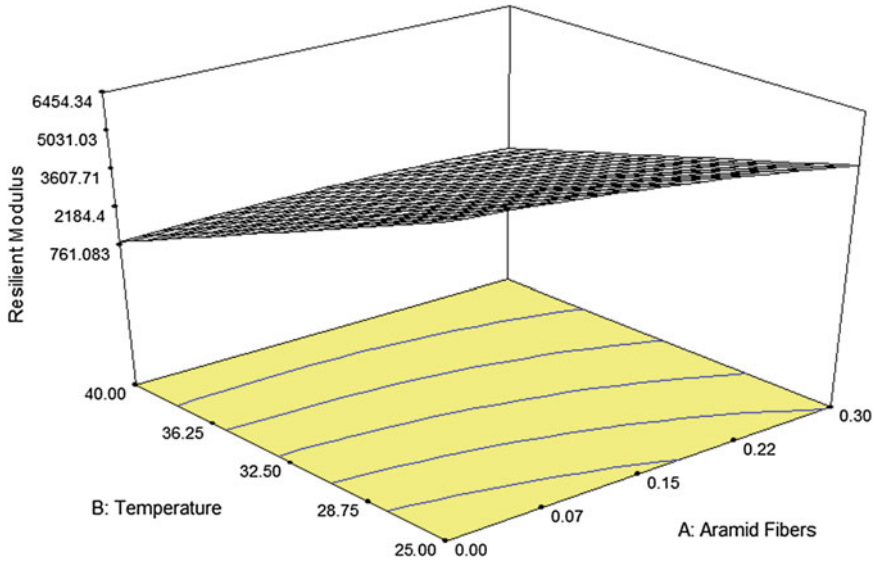
Fig. 4 3D counter plot of aramid fiber and temperature versus resilient modulus
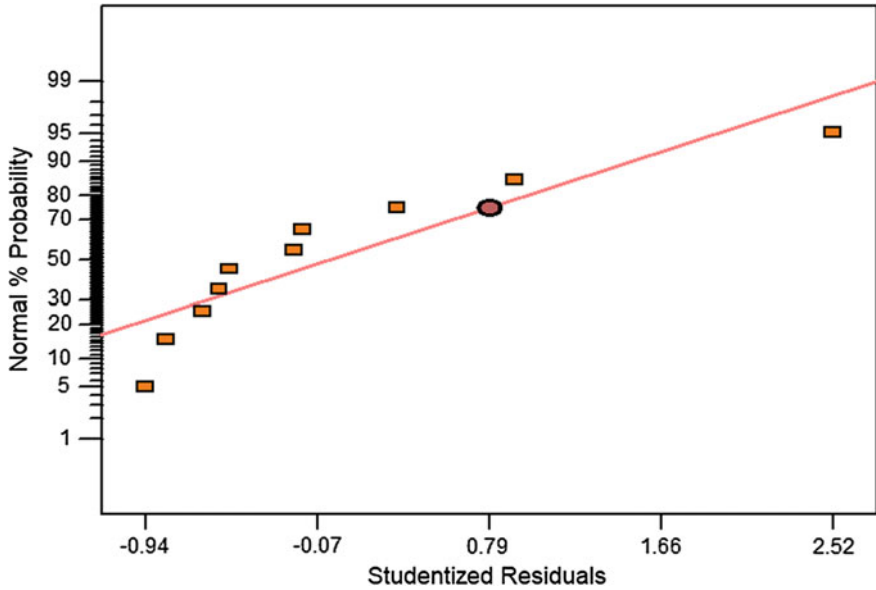
Fig. 5 Normal probability of resilient modulus

7 Conclusion

The aim of this study is to investigate the ability of Aramid fiber in increasing asphalt mixtures performances. The data obtained were analyzed using response surface methodology. The Aramid fiber has increased the performance mixtures of asphalt in term of fatigue cracking and rutting resistance, which were indicated by the results of resilient modulus. The optimum content of aramid fibers was at 0.05% by total weight of the aggregate. On the other hand, introducing aramid fiber into the mixture at the optimum content will increase the service life of asphalt layer, thus minimizing rehabilitation and maintenance costs.

References

1. Marienfeld, M.L., Guram, S.K.: Overview of field installation procedures for paving fabrics in North America. Geotext. Geomembr. **17**(2), 105–120 (1999)
2. Airey, G.D., Collop, A.C., Zoorob, S.E., Elliott, R.C.: The influence of aggregate, filler and bitumen on asphalt mixture moisture damage. Constr. Build. Mater. **22**(9), 2015–2024 (2008)
3. Airey, G.D.: Fundamental binder and practical mixture evaluation of polymer modified bituminous materials. Int. J. Pavement Eng. **5**(3), 137–151 (2004)
4. Busching, H.W., Elliott, E.H., Reyneveld, N.G.: A state-of-the-art survey of reinforced asphalt paving. In: Proceedings of the Association of Asphalt Paving Technologists (1970)
5. Kaloush, K.E., Biligiri, K.P., Zeiada, W.A., Rodezno, M.C., Reed, J.X.: Evaluation of fiber-reinforced asphalt mixtures using advanced material characterization tests. J. Test. Eval. **38**(4), 400–411 (2010)
6. Chen, H., Xu, Q., Chen, S., Zhang, Z.: Evaluation and design of fiber-reinforced asphalt mixtures. Mater. Des. **30**(7), 2595–2603 (2009)
7. Gibson, Nelson, Li, Xinjun: Characterizing cracking of asphalt mixtures with fiber reinforcement: use of cyclic fatigue and direct tension strength tests. Transp. Res. Rec. J. Transp. Res. Board **2507**, 57–66 (2015)
8. McDaniel, R.S.: Fiber Additives in Asphalt Mixtures. Project No 20-05, Topic 45-15 (2015)
9. Abtahi, S.M., Esfandiarpour, S., Kunt, M., Hejazi, S.M., Ebrahimi, M.G.: Hybrid reinforcement of asphalt-concrete mixtures using glass and polypropylene fibers. J. Eng. Fabr. Fibers (JEFF) **8**(2) (2013)
10. Xu, Q., Chen, H., Prozzi, J.A.: Performance of fiber reinforced asphalt concrete under environmental temperature and water effects. Constr. Build. Mater. **24**(10), 2003–2010 (2010)
11. Schmidt, R.J.: A practical method for measuring the resilient modulus of asphalt-treated mixes. Highw. Res. Rec. **404** (1972)
12. Hainin, M.R., Yusoff, N.I.M., Mohammad Sabri, M.F., Abdul Aziz, M.A., Sahul Hameed, M. A., Farooq Reshi, W.: Steel slag as an aggregate replacement in Malaysian hot mix asphalt. ISRN Civ. Eng. (2012)
13. Read, J., Whiteoak, D.: The Shell Bitumen Handbook. Thomas Telford (2003)
14. Kushwaha, J.P., Srivastava, V.C., Mall, I.D.: Organics removal from dairy wastewater by electrochemical treatment and residue disposal. Sep. Purif. Technol. **76**(2), 198–205 (2010)

15. Papagiannakis, A.T., Masad, E.A.: Pavement Design and Materials. Wiley, New Jersey (2017)
16. Golchin, B., Mansourian, A.: Evaluation of fatigue properties of asphalt mixtures containing reclaimed asphalt using response surface method. Int. J. Transp. Eng. **4**(4), 335–350 (2017)
17. Usman, N., Masirin, M.I.B.M., Ahmad, K.A., Wurochekke, A.A.: Reinforcement of asphalt concrete mixture using recycle polyethylene terephthalate fibre. Indian J. Sci. Technol. **9**(46) (2016)
18. Khuri, A.I., Mukhopadhyay, S.: Response surface methodology. Wiley Interdisc. Rev. Comput. Stat. **2**(2), 128–149 (2010)
19. Hussain, T., Ahmad, M., Masood, R.: Modelling the properties of pigment-dyed polyester/cotton sheeting fabrics by response surface methodology. Color. Technol. **129**(4), 274–278 (2013)
20. Dean, A., Voss, D., Draguljić, D.: Response surface methodology. In: Design and Analysis of Experiments, pp 565–614. Springer International Publishing, Berlin, ISO 690 (2017)

Investigating the Rheological and Physical Properties for Unaged of Crumb Rubber-Modified Binders Containing Warm Mix Asphalt Additive

Munder Abdullah Mohamed Bilema, Mohamad Yusri Aman and Kabiru Abdullahi Ahmad

Abstract The growing usage of crumb rubber modified in flexible pavements justification and the requirement for a good comprehension of its physical and rheological properties as well as its elastic behaviors. However, crumb rubber asphalt mixtures demand rising product temperatures than traditional asphalt binder due to the high viscosity of asphalt rubber binder. The main points of this research are to investigate the unaged rheological and physical properties of crumb rubber modifier (CRM) asphalt. In this study, crumb rubber-modified percentages was 0, 5, 10, and 15% from the binder weight, with adding 1.5% warm mix asphalt additive (Sasobit). The wet method was used to mix the CRM with bitumen, the CRM conducted at 177 °C for 30 min whit 700 rpm, and Sasobit conducted at 120 °C for 10 min with 1000 rpm. The results display that various crumb rubber contents have important impacts on modified binder properties. The result shown that increase the complex shear G^* and decreased the phase angle δ at high temperature with increased the CRM contents. The rutting resistance parameter was rising with increased CRM percentages at 70 °C. The softening results in rise in the temperature with adding the CRM and the penetration results in reduction with the growing CRM contents. The elastic recovery increased with higher CRM content. The storage stability was within the range for unmodified and 5% of CRM but for 10 and 15% the result was over the range. From the results we conclude that the CRM improves the elasticity and improves the stiffness of the modified binder.

Keywords CRM · WMA · Rheology and Physical properties

M. A. M. Bilema (✉) · M. Y. Aman · K. A. Ahmad
Department of Highway and Traffic Engineering, Faculty of Civil Engineering
and Environmental, University Tun Hussein Onn Malaysia, 86400 Parit Raja,
Batu Pahat, Johor, Malaysia
e-mail: mondo199131@gmail.com

M. Y. Aman
e-mail: mdyusri@uthm.edu.my

K. A. Ahmad
e-mail: Kabiruaahmad@gmail.com

1 Introduction

In highway pavement industry, the usage of crumb rubber in flexibility asphalt pavements is considered as a brilliant resolution for sustainable evolution by recycling rubbish material. Previous researchers believed that crumb rubber modifier (CRM) can be an alternate polymer material in improvement of the warm mix asphalt execution properties. Tire rubber is a blend of anti-oxidants, natural rubber, carbon black, synthetic rubber, extender type of oils and fillers which are soluble in warm paving grade. Reclaimed rubber, crumb rubber, and scarp rubber are various terms used to describe recycled rubber; car and truck tires are the largest recycled rubber sources. Car tires are primarily made of styrene butadiene rubber (SPR) or polyisoprene and carbon black. Truck tires on the other hand, consist of a higher percent of natural rubber comparing to vehicle tires up to 30% of the combined polymer content [1]. Rubberized bitumen binders are gained by blend the crumb rubber from the rubbish tires in bitumen binder under specific conditions of time and temperature. There are few methods to mix up the crumb rubber with bitumen and previous researchers' summarization in three various processes to product bitumen rubber: the dry process, the terminal blending, and wet process [2]. Crumb rubber is preparing by shredding scrap tires that is a particular material free of steel and fiber. The rubber particle is graded and found in numerous shapes and size. Crumb rubber is described or measurement by the mesh screen or sieve size through which it passes during the product process. To product crumb rubber, basically, it is important to minimize the size of the tires. There are two kinds of techniques to produce the crumb rubber: ambient grinding and cryogenic process [1]. Two various methods use mix the crumb rubber with the bitumen; first, it can be mixing the crumb rubber in the bitumen as binder modifier. Second, it can be by substituting a portion of a fine aggregate with ground rubber that completely reacts with bitumen. Few factors can affect the modification impacts which include the base bitumen constituents, temperature, mix time, type of mixing, percentages of crumb rubber, gradation of crumb rubber, and grinding process method [3]. Reference [4] concluded from his study, that the crumb rubber can be employed as modifier for bitumen to reduce waste tires pollution and enhance the engineering properties of bitumen mixes.

The elasticity or elastic recover describes the ability of the bitumen binder to elongate when tension is applied and it will be back to the original shape when the tension is released. The degree of the elasticity was used as an indicator of permanent deformation in asphalt material [5]. The elasticity properties are very significant factors that affect at both fatigue and rutting resistance selection and evaluation. The elasticity is a property that indicates the quality of the crumb rubber ingredients in bitumen binders [6]. According to [7], the elasticity of crumb rubber-modified binders leads to an increase as the rubber particle size reduction.

Reference [8] reported that applying the crumb rubber to the flexible mixture should also take into consideration its impact on chemical, physical, and rheological features of the bitumen binders modified by the crumb rubber. The improvements

achieved in the properties of the binders modified by the crumb rubber depend on the interactive relationship between the bitumen and crumb rubber. According to [9] rutting is essential measure of the performance of pavements in multiple pavements design process. Rutting can occur as a result of problem at sub-grade and unbound base course. The rutting inability is a consequence of heavy truck-loads with high tire pressures and high asphalt temperature. Hence, considerable option of bitumen binders and aggregate combination will assist in providing optimum performing asphalt pavements. Reference [10] concluded in his study, that the use of crumb rubber modified has important effect to enhance the mixture resistance of rutting deformation. In a study conducted by Sun et al. [11], the addition of crumb rubber modified rises the rutting resistance of asphalt binders. The outcome from the lab test study gives some important result such as higher stiffness and hardness at 60 °C than the unmodified binders.

2   Material and Method Use

In this study, bitumen binder 80\100 penetration grade was used. Crumb rubber powder of 20 mesh sizes (passing 0.15 mm) used. The crumb rubber was obtained from a Malaysian Supplier (Miroad Rubber Industries Sdn Bhd) the CRM was produced by mechanical shredding and then grinded at ambient temperature. The sasobit® was fixed addition by 1.5% from the binder weight. Some tests were done such as penetration test ASTM D4, softening test ASTM D36, elastic recovery ASTM D-6084, storage stability test, and the dynamic shear rheometer (DSR) ASTM D4.

The modified binders used in this study were prepared by blending the Original 80/100 bitumen with Sasobit® and crumb rubber, this process is known as "Wet Process" because the additive(s) were added to the bitumen. The unmodified penetration grade bitumen 80/100 (Original or virginal "A") was blended with the additives to produce three additional binders; B, C, and D depending on the binder composition, Table 1, shows the matrix of binder identity and composition.

CRM was added at 5, 10, and 15% by weight of the base binder to produce crumb rubber modified binders; CRM blending was conducted at 177 °C and mixed continuously for 30 min, using mechanical mixer at 700 rpm [12]. The 1.5%

Table 1 Binder identity and composition matrix

Binder identity	Constituent materials (%)		
	80/100 Bitumen	Sasobit® (%)	Crumb rubber (%)
A	100	–	–
B	100	1.5	5
C	100	1.5	10
D	100	1.5	15

Fig. 1 Binder blending with shear mixer

Sasobit® by weight of the base binder which is within the recommended dosage of 0.8–3% [13]. The sasobit® was added at 120 °C and was blended the same way the CRM was blended only that the mixing speed and time was 1000 rpm and 10 min respectively. The prepared binders were used immediately after modification, to avoid segregation upon storage due to its poor storage stability. Figure 1 show the mixer shear.

3   Result and Discussion

3.1   Penetration Test

The results of penetration for the original (virgin), and CRM-modified warm asphalt binders are shown in Table 2. The virgin binder has an average penetration value of 96 mm and is therefore 80–100 grade.

Figure 2 display the penetration result. The penetration values for warm asphalt binder with 5% CRM are 69 mm, with 10% CRM is 58 mm, and with 15% CRM is 46 mm. The penetration values gradually decrease as the additive content increases, [14] attributed the decrease in penetration values to increase in the viscosity and stiffness. With respect to the virgin binder, it was observed that modification with 1.5% Sasobit® and with further addition of: 5, 10, or 15% CRM, so the 15% of

Table 2 Result for penetration of asphalt binders

Binder	Penetration values			
	Trial 1	Trial 2	Trial 3	Average
Virgin	100	96	92	96
5% CRM	66	70	72.3	69
10% CRM	57	57.8	60.6	58
15% CRM	48.1	46	44.3	46
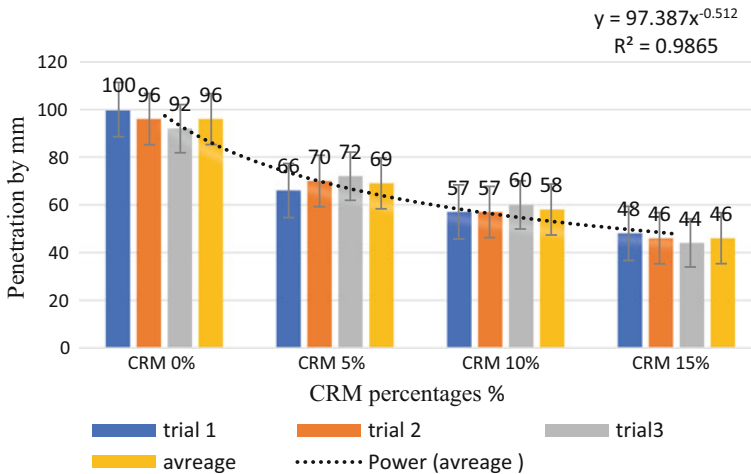
Fig. 2 Penetration result chart

CRM is the highest penetration result. There is reduction at result and the reduction percentages were calculated from original binder to the other modified percentages. The highest reduction happened, it was from original to 15% of CRM and it was 52%. The penetration result was analysis by (ANOVA). The significant effect shown that p-values of 0.001, 0.004 and 0.009 for original binder compare with the different percentage of modified binders. The influence respectively so the values less than the assumed $\alpha = 0.05$ at 95% confidence level. The correlation coefficients R^2 was 0.9865 that means that the quality of correlation is excellent.

3.2 Softening Test

The result obtained for this test is presented in Table 3 and Fig. 3. It can be seen from the results that the modified binders have higher softening points than the original unmodified binder. The softening point of the virgin binder was obtained as 48.25 °C. Therefore adding CRM leads to increase the softening point which

Table 3 Result for softening point of asphalt binders

Binder	Softening point degree (°C)		
	Trial 1	Trial 2	Average
Virgin	47	49.5	48.25
5% CRM	54	54.8	54.4
10% CRM	55.8	57.5	56.65
15% CRM	60	62.2	61.1
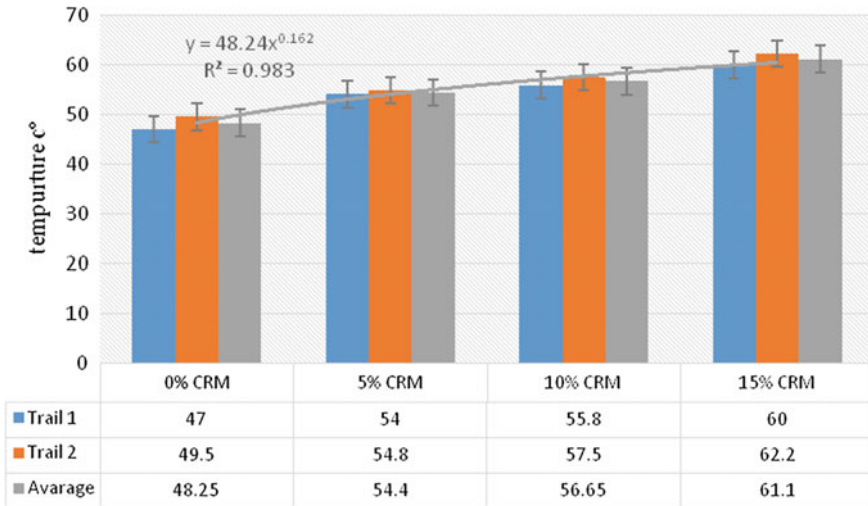
Fig. 3 Chart for softening point result of binders

improves stiffness. It is reported that higher crumb rubber content leads to increase the softening point [10]. Table 4 shows that softening point increases with the addition of CRM with a significance level 0.035 is 5% of CRM, 0.012 of 10% of CRM, and 0.002 of 15% of CRM. The correlation coefficients R^2 was 0.983, the result was excellent according to the percentage of the response variable variation that is the analysis by a linear model.

There is rise in temperature between the original binder and the modified binder at softening points and the increase happened with add the CRM to the binder. The increase was 11.3% between the original and the 5% of CRM and the increment between the original binder and 10% of CRM was 15%. The highest increase happened at 15% of CRM and it was 21%. In addition, the crumb rubber increases the stiffness of the binder and more temperature is required to make the binder soft, as this can be advantageous to prevent the distress at pavements modified.

This finding agreed with results obtained by Kim et al. [15], that the crumb rubber addition influenced the softening point and cause increase in the stiffness of the binder. The correlation coefficients R^2 was 0.983, the result was excellent according to the percentage of the response variable variation that is analysis by a linear model.

3.3 Storage Stability Test

It was conducted after modification and before in order to ensure the blending process were effective and the crumb rubber modified are in stable condition during the storage period. The storage stability of binders is evaluated by comparing the values of softening point of one-hird top and bottom cut sections of the binders. Table 4 displays the result of storage stability test.

As illustrated in Fig. 4, softening point from top section of storage tube was less than the bottom section of storage tube. The difference of softening point value between the top and the bottom section of control binder was 0.8 and this result was within the range which is less or equal to 2.2 °C for unmodified binder the result showed an increasing value of difference as the crumb rubber content increased. The proper result was obtained only for 5% sample, considered as stable storage blend as the differences value of the top and bottom section are less than 2.2 °C. For percentages 10 and 15% the binder was unstable due to the high crumb rubber content, the result was 4.6 and 7.6 °C respectively.

Table 4 Display the result of storage stability test

CRM (%)	Trial	Top temperature (°C)	Average	Bottom temperature (°C)	Average	Differences
0	1	46	46	47	46.8	0.8
	2	46		46.6		
5	1	53.8	54	55	56	2
	2	54.3		57		
10	1	60.3	59.9	63.9	64.5	4.6
	2	59.6		65		
15	1	64.2	63.5	70	71.3	7.6
	2	62.7		72.6		
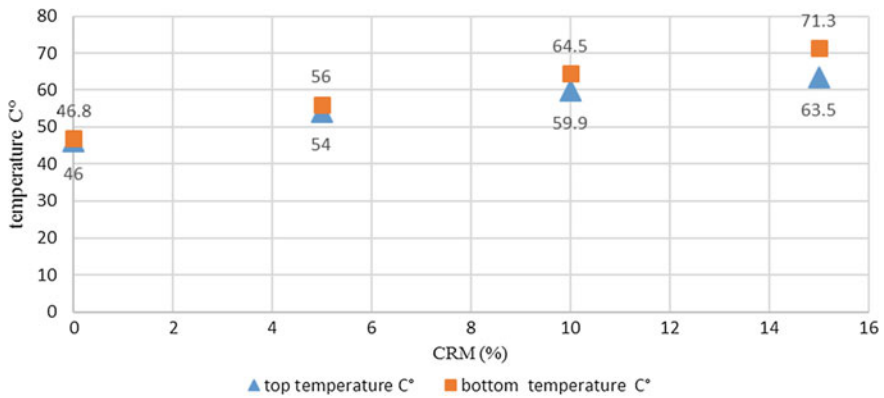
Fig. 4 Storage stability chart result

Table 5 Elastic recovery test result

CRM (%)	Initial length (cm)	Final length (cm)	Average	Elastic recovery (%)
0	20	14.2	14.6	27
		15		
5	20	9.9	10.2	49
		10.4		
10	20	6	7.3	63.5
		8.5		
15	20	2.5	2.2	89
		1.8		

3.4 Elastic Recovery Test

It is measured using a ductilometer to elongate an asphalt specimen at a constant rate. This test is conducted according to ASTM D-6804 at 25 °C the elastic recovery value was increased as the crumb rubber content rising and the Table 5 display the result of elasticity test.

Figure 5 displays the elastic recovery test result. Elasticity result showed that high content of crumb rubber has significant effect on the modified binder, which represented the consistency with binder elasticity and recovery after deformation move. Hence, the rutting resistance improves for the binder. The elastic recovery values increased from 27% for control binder to 89 for 15% of crumb rubber modified, indicating the ability of the binder recovers its original shape following application and release of the stress. An addition, the crumb rubber consists of the elastomers and it is well known that the synthetic rubber increases the elastic behaviour of crumb rubber modified binder.
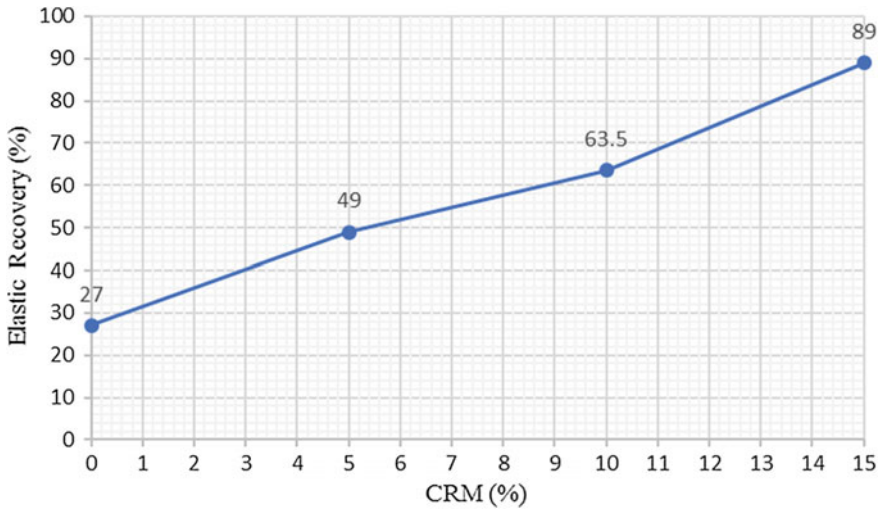
Fig. 5 Elastic recovery result chart
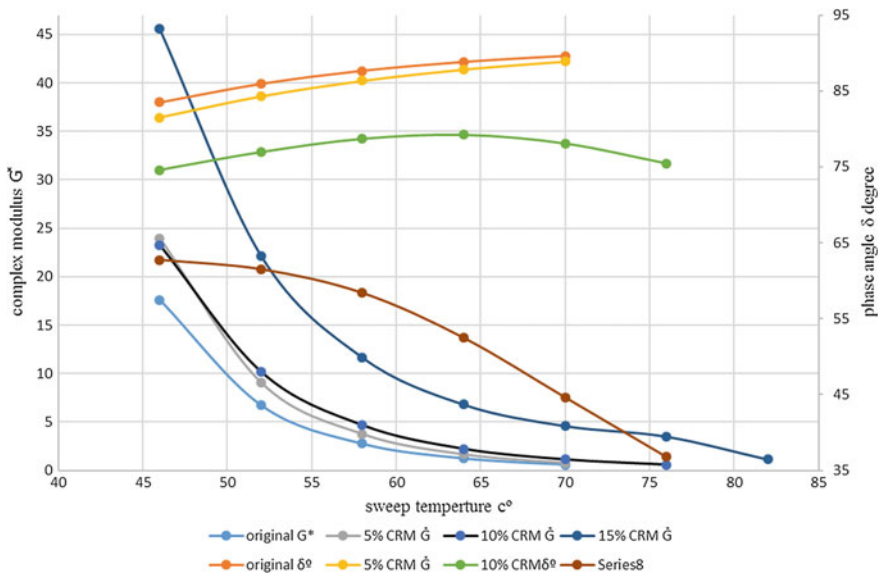
Fig. 6 Effect of CRM on complex modulus "$G*$" and Phase angle "δ"

3.5 Dynamic Shear Rheometer

The rheology or viscos-elastic properties of asphalt binders are best defined by two parameters; complex modulus "$G*$"and phase angle "δ" [16]. The $G*$ gives an idea of the binder stiffness at different temperature and loading rate, while δ is the phase angle

Table 6 DSR result for complex modulus and phase angle

Temp. (°C)	Virgin		5% CRM		10% CRM		15% CRM	
	G^* (kPa)	δ	G^* (kPa)	δ	G^* (kPa)	δ	G^* (kPa)	δ
46	17.6	83.5	23.98	81.5	23.29	74	45.55	62.67
52	6.73	85.93	9.08	84.26	10.14	76.98	22.16	61.52
58	2.76	87.64	3.76	86.35	4.68	78.74	11.67	58.47
64	1.25	88.8	1.66	87.85	2.24	79.26	6.81	52.47
70	0.61	89.59	0.77	88.91	1.15	78.11	4.6	44.62
76	–	–	–	–	0.61	75.46	3.51	36.77
82	–	–	–	–	–	–	1.15	28.21

between stress and strain, its values range from 0° to 90°, from some perfectly elastic materials to a perfectly viscous material respectively, this means the smaller value of δ is the higher elastic. Figure 6 and Table 6 presents the viscos-elastic properties of the virgin and warm asphalt binders modified with different CRM content.

The (original or virgin) binder is the lower G^* and the higher δ, also it was look out that warm asphalt modification with 5 and 10% further almost the same G^*, But with 15% CRM content, the G^* values was the highest test temperature. Meantime, the higher G^* values of the modified binders compared to the original shows that their stiffness raises with crumb rubber modified addition [17].

Based on these outcomes the highest get better in G^* was achieved with 15% crumb rubber-modified content. Furthermore, phase angle "δ" which is a measurement of the elasticity of the binders the δ values for the modified binders are mostly bring down (more elastic) compared to the original binder.

The binder with 5% CRM is more elastic than (original binder) without crumb rubber modified but is minimal elastic than the binder with 10% crumb rubber modified, and the binder with 15% crumb rubber modified content was found to be the most elastic over the entire range test temperatures considered.

In superpave® instruction, high temperature grade has been defined as the failure temperature, the $G^*\backslash \sin \delta$ parameter was to evaluated the rutting resistance which is more than 1 kPa. Figure 7 display the effect of crumb rubber modified on rutting resistance and failure temperature.

According to Fig. 7 obtained results indicate that for unaged specimens, at 70 °C the rutting parameter was increased with higher crumb rubber modified content that due to the elastic properties of the crumb rubber particles which is back to original shape after release it from the loading. For the failure temperatures, the unmodified binder and 5% of crumb rubber modified was the lower failure temperature with 64. On the other hand, the 10% of crumb rubber modified have higher failure temperature with 76 °C. The 15% of crumb rubber modified was over the range of failure temperature which is reach to 82 °C and the failure not happened yet that because two reasons; first, the crumb rubber need high temperature to melting. Second, the high crumb rubber content 15%.
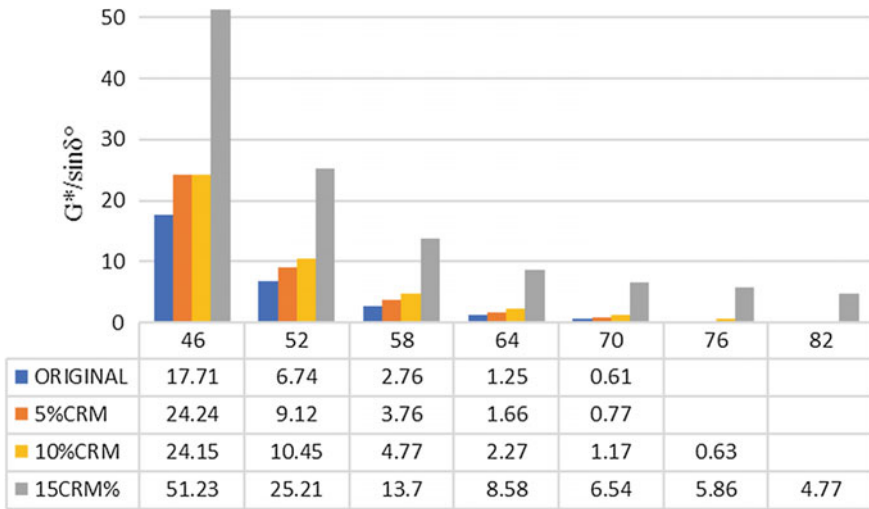
Fig. 7 The effect of crumb rubber modified on rutting resistance and failure temperature

4 Conclusion

Based on the study outcome, the following conclusions were drawn:

- The result of softening point test was identical with others researches was done the temperature was increased with rise the CRM percentages and when the crumb rubber increases the stiffness of the binder rise and more temperature is required to make the binder soft.
- The penetration test result shows significant decrease in the penetration values of modified binder due to high crumb rubber content in the binder. With increased the crumb rubber percentages the binder was more hardness and stiffness because lower penetration values.
- The elastic recovery test was important to discover the elastic properties of crumb rubber modified, the result showed that the elasticity growing with increased the crumb rubber content.
- The storage stability test was to conduct if the binder stable and can use it at mixtures, the result displayed that for original and 5% of crumb rubber the binder was stable and under the range but for 10, 15% of crumb rubber the binder was unstable and over the range.
- The rheology properties of asphalt binders are better defined by two parameters; complex modulus "$G*$"and phase angle "δ". For complex modulus $G*$ increased with higher crumb rubber content and phase angle δ decreased with rise the crumb rubber content. All thus, the crumb rubber has elastic properties and these elastic properties transform to the binder.

– The DSR test was conduct to investigate the rutting parameter $G^*\backslash\sin\delta$ and the failure temperatures, the result was the rutting resistance up with rising the crumb rubber content. For the failure temperature was increased with increased the percentages of crumb rubber.

References

1. Becker, Y., Mendez, M.P., Rodriguez, Y.: Polymer modified asphalt. Vision Tecnologica **9**(1), 39–50 (2001)
2. Takallou, H.B., Takaollu, M.: Effect of the mixing time and temperature on the viscose-elastic properties of asphalt rubber binders. In: Asphalt Rubber Conference, Brazil (2003)
3. Huang, Y., Bird, R.N., Heidrich, O.: A review of the use of recycled solid waste material in asphalt pavements. Resour. Conserv. Recycl. **52**, 58–73 (2007)
4. Hanson, D.I., Foo, K.Y., Brown, E.R., Derson, R.: Evaluation and characterization of rubber modified hot mix asphalt pavements. Transp. Res. Rec. J. Transp. Res. Board **1436**, 98–107 (1994)
5. Yildirim, Y.: Polymer modified asphalt binders. Constr. Build. Mater. **21**(1), 66–72 (2007)
6. Jensen, W., Abdelrahman, M.: Crumb rubber in performance-graded asphalt binder (2006)
7. Oliver, J.W.: Research on asphalt rubber at the Australian Road Research Board. In: National Seminar on Asphalt-Rubber, 1981, San Antonio, Texas, USA, Oct 1981
8. Green, E.L., Tolonen, W.J.: The chemical and physical properties of asphalt rubber mixtures. Part I. Basic Mater. Behav. **14**(162) (1977)
9. Sousa, J.B., Weissman, S.L.: Modeling permanent deformation of asphalt-aggregate mixes (with discussion). J. Assoc. Asphalt Paving Technol. **63** (1994)
10. Mashaan, N.S., Ali, A.H., Karim, M.R., Abdelaziz, M.: An overview of crumb rubber modified asphalt. Int. J. Phys. Sci. **7**(2), 166–170 (2012)
11. Sun, D., Ye, F., Shi, F., Lu, W.: Storage stability of SBS-modified road asphalt: preparation, morphology, and rheological properties. Pet. Sci. Technol. **24**(9), 1067–1077 (2006)
12. Xiao, F., Amirkhanian, S., Juang, C.H.: Rutting resistance of rubberized asphalt concrete pavements containing reclaimed asphalt pavement mixtures. J. Mater. Civ. Eng. **19**(6), 475–483 (2007)
13. Hurley, G.C., Prowell, B.D.: NCAT Report 05-06—Evaluation of Sasobit for Use in Warm Mix Asphalt, (June), 32 (2005)
14. Aman, M.Y., Shahadan, Z., Ruhania, M.Md., Buhari, R.: Effects of aging on the physical and rheological properties of asphalt binder incorporating Rediset®. Jurnal Teknologi **70**(7), 111–116 (2014)
15. Kim, Y., Im, S., Lee, H.D.: Impacts of curing time and moisture content on engineering properties of cold in-place recycling mixtures using foamed or emulsified asphalt. J. Mater. Civ. Eng. **23**(5), 542–553 (2010)
16. Brown, E.R., Kandhal, P.S., Roberts, F.L., Kim, Y.R., Lee, D.Y., Kennedy, T.W.: Hot Mix Asphalt Materials, Mixture Design and Construction (Third). NAPA Research and Education Foundation, Lanham, Maryland (2009)
17. Akisetty, C.K.K.: Evaluation of warm asphalt additives on performance properties of CRM binders and mixtures. PhD Thesis, Clemson University (2008)

Application of Recycled Polyethylene Terephthalate Fiber in Asphaltic Mix for Fatigue Life Improvement

Nura Usman, Mohd Idrus Mohd Masirin, Kabiru Abdullahi Ahmad
and Ahmad Suliman B Ali

Abstract The study aim is to determine the suitability of recycled polyethylene terephthalate (PET) fiber in fatigue life improvement of asphalt concrete mix. Fatigue crack is among the principal distresses that shortens the life span of flexible pavements. The aim was achieved through laboratory experiments (indirect tensile stiffness modulus and fatigue tests) to determine the fatigue characteristics of reinforced and neat asphalt mixtures. The reinforced mixtures were prepared using recycled PET fiber at 0.3, 0.5, 0.7, and 1.0% by total weight of mixture. The result was analyzed through regression analysis and fatigue life-prediction models were developed. The stiffness modulus of reinforced mixtures was improved by 19% at 0.3%, 34% at 0.5%, 4% at 0.7% and decreased by 34% at 1.0% recycled PET fiber reinforcement compared to neat mixture. The developed fatigue life-prediction models are statistically significant with p-values < 0.05. The fatigue life of recycled PET fiber reinforced mixtures at higher strains was highly improved at 0.3% reinforcement, while 0.5% reinforcement exhibited higher fatigue life at lower

N. Usman (✉) · M. I. M. Masirin · K. A. Ahmad · A. S. B. Ali
Faculty of Civil and Environmental Engineering, Universiti Tun Hussein
Onn Malaysia, 86400 Parit Raja, Malaysia
e-mail: nuragafai@gmail.com

M. I. M. Masirin
e-mail: idrusmas@gmail.com

K. A. Ahmad
e-mail: kabiruahmad@gmail.com

A. S. B. Ali
e-mail: algowel@yahoo.com

M. I. M. Masirin
Research Center for Soft Soil (RECESS), Universiti Tun Hussein
Onn Malaysia, 86400 Parit Raja, Malaysia

N. Usman
Department of Civil Engineering, Hassan Usman Katsina Polytechnic,
PMB 2052 Katsina, Nigeria

strain levels compared to neat mixtures. Therefore from the result and analysis conducted, recycled PET fiber has proved to be effective in fatigue life improvement of asphalt concrete.

Keywords Fatigue · Improvement · Asphalt concrete · Polyethylene terephthalate · Fiber

1   Introduction

Asphalt concrete mixture is a visco-elastic material made up of aggregates, bitumen, filler, and additives for enhancement of performance which is used as road surface layer in flexible pavement. Fatigue cracking is among the principal distresses that shorten the life span of flexible pavement, it usually occurs due to successive tensile strain induced by wheel loads at the bottom of asphalt mix layer [1]. In other words, vehicular loads cause the growth of micro- and macro-cracks which are the fatigue failure mode in asphalt pavements. A number of factors such as temperature, moisture, and aging do also contribute to flexible pavement fatigue failure [2].

The fatigue resistance of flexible pavement is its capability to stand against the repeated bending without cracks or fracture; the minor cracks developed are the beginning of major fatigue distress under traffic loads. Fatigue cracks are first initiated at the base of asphalt layer due to tensile train and then propagate to the surface [3]. Fatigue cracks are initiated when the level of applied wheel loads are lower than ultimate stress failure level which in turn bring about cracks and finally cause pot holes that may lead to accidents by road users [4].

The laboratory characterization of asphalt concrete fatigue resistance is usually conducted under either constant stress or constant strain loadings. Characterization using constant strain loading is more difficult than constant stress. Fatigue failure under constant stress is defined base on failure occurrence after the test when the sample fails due to excessive tensile strain [5]. To decrease the fatigue failure and construct a durable pavement, several options have been drawn by engineers and researchers [6]. Among the options for asphalt concrete improvements is the use of fiber as reinforcing agent, different types of fiber are being used.

Shukla et al. [7] used a glass fiber of 10 mm in length and 1 mm in thickness to reinforce asphalt concrete mixture. Their result indicated a maximum dosage of 0.15% glass fiber; it improved fatigue resistance by 37% compared to the neat asphalt concrete mixture. Herraize et al. [8] checked the potentiality of Posodonia Oceanica (Algae) fiber for reinforcement of stone mastic asphalt (SMA), they used hemp and polyester fiber as control. In their conclusion, 1.5–2% addition of algae fiber resulted in excellent improvement in stiffness and fatigue life.

Otuoze et al. [9] recommended a dosage of 0.5% waste high-density polypropylene (HDPP) fiber for reinforcement of asphalt concrete mixture, which according to them fatigue resistance and thermal cracking were improved.

Park et al. [10] studied the crack resistance of steel fiber-reinforced asphalt concrete at 20 °C and compared to asphalt mixtures reinforced with carbon and polyvinyl alcohol fiber at the same temperature. Their result demonstrated that steel fiber can significantly reduce low temperature cracking base on length of the fiber and its diameter. Xiong et al. [11] recommended the use of 0.45% brucite fiber for effective enhancement of stability of mixture at high temperature, its resistance to crack at low temperature and develop more resistance to moisture damage.

In another related studies conducted by Xue and Qian [12], performance of epoxy asphalt mix reinforced with mineral fiber was evaluated. The findings revealed that 8 mm length and 9% mineral fiber can reduce cracks at low temperature and improve tensile strength, but mineral fiber reduces the construction time for epoxy asphalt concrete mixture. In their contribution, Vadood et al. [13] developed a model for fatigue life prediction of hybrid (polypropylene/polyester) fiber-reinforced hot mix asphalt mixture. Based on their research, 10 mm length of fiber was recommended with the best fatigue life improvement at 1% polypropylene fiber reinforcement.

In view of the above, it is obvious that most of the researches conducted on fiber modification of asphalt concrete have focused on synthetic and expensive fibers, with a little trial on recycled polymeric fibers. Therefore, it is desirable to search for affordable and useable fiber for strength improvement of asphalt mixes against fatigue cracking. The study's aim is to determine the suitability of recycled polyethylene terephthalate (PET) fiber for the fatigue life improvements of asphalt concrete mixture.

2 Materials

The selection for the materials used in asphalt concrete needs to be based on quality [2], therefore the materials used in this study were selected based on their performance in control tests. For aggregates, the tests conducted were aggregates impact value, flakiness index, elongation index, fine aggregates angularity, and sand equivalent tests. The results for aggregates tests are presented in Table 1.

Quality test such as penetration, softening point, flash point, fire point, ductility, and viscosity tests were conducted on the bitumen binder, the result is presented in Table 2. In all the tests conducted, the property of the bitumen binder is with the acceptable range provided by ASTM standard specifications.

Table 1 Properties of aggregates used

Property	Method	Value (%)	Requirement (%)
Flakiness index	BS-812-105-1	15	<20
Elongation index	BS-812-105-2	17	<20
Aggregates impact value	BS-812-112	21	<30
Fine aggregates angularity	AASHTO T304	49.5	Min 45
Sand equivalent	AASHTO T176	51.3	Min 45

Table 2 Properties of bitumen used

Test	Method	Value	Specification
Penetration (dmm)	ASTM D5-97	83	80–100
Softening point (°C)	ASTM D36	47	47–52
Flash point (°C)	ASTM D92-5	259	Min 232
Ductility (cm)	ASTM D113-99	>100	Min 100
Loss on heating (%)	ASTM D 2872	0.033	Max 0.5
Viscosity at 135 °C (Pas)	ASTM D4402	0.487	Max 3

Aggregates gradation was conducted based on Superpave mix design criteria using maximum nominal aggregates size (NMAS) of 12.5 mm. Figure 1 shows the designed aggregates gradation which avoided restriction zone as recommended by superpave system [14].

The recycled PET fiber used in this study was made using used PET bottles. PET is a ubiquitous thermoplastic polymer used for packaging of soft drinks, drinking water, and other daily household needs. At a temperature of 175 °C, PET can bear a shear stress and possesses toughness [15].

Recycled PET fiber was produced using shredder, recycle PETs were collected, washed and cut to sheets then shredded to the size of 0.78 mm × 10 mm (Fig. 2). The size is similar to fiber sizes used by Usman et al. [2], Xue and Qian [12], and Vadood et al. [13] in strength improvement of bituminous mixes. The properties of recycled PET fiber are presented in Table 3.

Fig. 1 NMAS 12.5 mm aggregates gradation
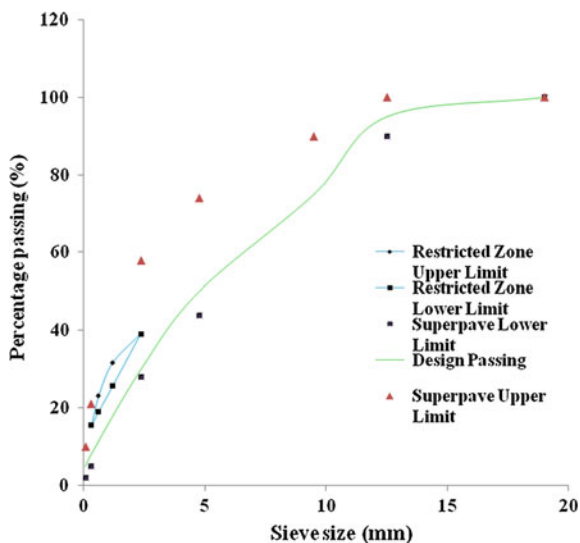
Fig. 2 Recycled PET fiber

Table 3 Physical and mechanical properties of recycled PET fiber

Property	Method	Value
Tensile strength (MPa)	ASTM C1557	192.4
Stiffness (N/m)	ASTM C1557	27,693
Young's modulus (MPa)	ASTM C1557	3924.2
Elongation at break (%)	ASTM C1557	34.2
Water absorption (%)	ASTM D570	0.2
Specific gravity (g/cm^3)	ASTM D792	1.356

3 Mixture Design and Experimental Methods

3.1 Mixture Design

Mix design is the next step in asphalt concrete production after material selection. In this study, Superpave method was used for mixture design. Five different mixes containing 0, 0.3, 0.5, 0.7, and 1.0% recycled PET fiber were designed and prepared using AASHTO-T312-11 [16] and compacted using gyratory compactor. The design was based on medium to high category of traffic load, i.e., between 3 and less than 30 million ESALs in which the mixtures' design density was achieved at N_{design} of 100 gyrations.

From rotational viscosity test of the bitumen binder used, the mixing and compaction temperatures were 165 and 155 °C respectively. Aggregates were heated at 165 °C for 2 h then mixed and blended with recycled PET fiber, this

Table 4 Properties of asphalt mixture

Property	Value (%)	Criteria (%)
Air void	4	4
VMA	16	Minimum 13
VFA	75	65–76
Bitumen content	4.7	4–11

Table 5 Air void and bitumen content of recycled PET fiber modified mixtures

Percentage of recycled PET fiber (%)	Air void (%)	Optimum Bitumen content (%)
0.30	4	4.7
0.50	4	4.9
0.70	4	4.9
1.00	4	5.2

mixing technique is called dry process [17]. Finally, bitumen was added to aggregates-recycled PET fiber mixture.

Table 4 is a summary of volumetric properties of designed mixture, and Table 5 shows the optimum bitumen contents and air voids of recycled PET fiber-modified mixtures.

3.2 Experimental Tests

3.2.1 Indirect Tensile Fatigue Test (ITFT)

Indirect Tensile Fatigue Test (ITFT) is widely used in the United Kingdom. The test uses a specimen in cylindrical shape prepared in the laboratory or cored from field pavement. The advantage of ITFT is that it is simple to conduct and suitable to evaluate the stiffness and fatigue characteristics of asphaltic mixes for construction sites. In this research, the test was conducted according to BS EN 12697-24-2012 [18] under stress control mode [19].

This was performed on both recycled PET fiber-modified and unmodified asphalt mixtures, the test involves the measurement of indirect tensile fatigue resistance of the mixtures using IPC UTM-5 universal testing machine (UTM). A uniform tensile stress was applied at 20 °C to the specimen [20]. This would simulate the field condition in which repeated loading and other environmental factors tend to undermine the strength of the pavement by means of fatigue cracks.

The asphalt concrete samples were prepared at 4% air voids using respective optimum bitumen contents. Samples and other testing accessories were cured at 20 °C for 2 h in the environmental chamber to ensure the uniformity of test temperature throughout the samples [21]. After 2 h, the samples were loaded with a

repeated compressive haversine wave shape load of 500, 600, and 700 kPa stress levels. Cycle pulse width was 124 ms and cycle pulse period was 1000 ms. The tests were terminated when samples' vertical deflections reached 10 mm or when the sample failed and disintegrated into two parts and the number of cycles were recorded [20].

3.2.2 Indirect Tensile Stiffness Modulus Test (ITSM)

ITSM is a non-destructive test and was conducted according to BS: DD 213: 1993 [22]. The stiffness modulus of a mixture is evaluated by applying a repeated load pulses with rest periods along the vertical diameter of cylindrical samples. IPC UTM-5 Universal Testing Machine (UTM) was used for the determination of the stiffness modulus in this research. The test samples were cured at 20 °C for 2 h prior to the testing time [21]. The samples were then subjected to a cyclic load in the haversine wave shape, the samples were initially preconditioned at 50 count pulse, the loading pulse width was 100 ms and pulse repetition period was 1000 ms. Stiffness modulus is very important in fatigue life prediction of asphalt concrete mixtures. The test setup is similar to indirect tensile resilient modulus test as indicated in Fig. 3, each sample was tested at 0° and at 90° and the average value was considered. The deformation was measured using linear variable displacement transducers (LVDT) shown in Fig. 3. The Stiffness Modulus was calculated using Eq. 1.

$$S_{\mathrm{m}} = \frac{P(v + 0.27)}{(zH)}, \tag{1}$$

Fig. 3 Stiffness modulus experimental setup
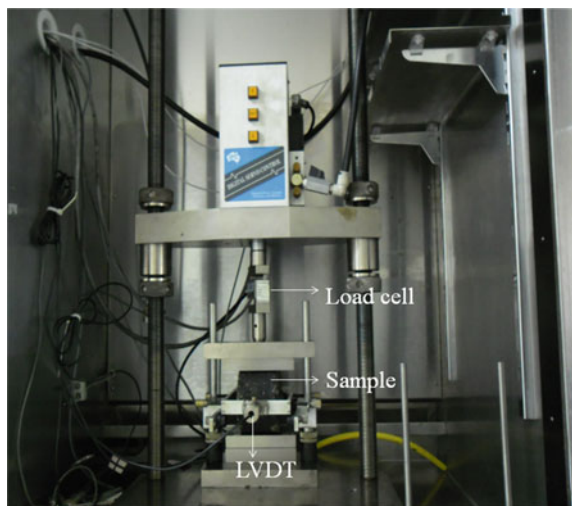
where S_m is stiffness modulus, P is the peak applied load (N), z is the value of horizontal deformation (mm), H is the average thickness of the sample (mm) and v is the assumed poison ratio.

4 Results and Discussion

4.1 Indirect Tensile Fatigue Test

Figure 4 presents the load cycles to failure of neat and recycle PET fiber reinforced asphalt mixtures for ITFT. The mixtures were subjected to 500, 600, and 700 MPa stress levels and the number of cycles to failure was determined. From Fig. 4, the number of cycles to failure in mixtures reinforced with 0.3 and 0.5% are greater than that of neat mixture. This shows that recycled PET fiber can improve fatigue life of bituminous mixes like polyester, polyacrylonitrile, lignin, and asbestos fibers as reported by Xu et al. [23].

The improvement was due to tensile strength, stiffness, good bonding characteristics, and higher storage modulus of recycle PET fiber at lower temperatures. The result of ITFT and indirect tensile stiffness modulus are very useful in fatigue life prediction of asphalt concrete mixture [24].

4.2 Indirect Tensile Stiffness Modulus

Stiffness modulus test was conducted on both neat and recycled PET fiber-reinforced asphalt mixtures. The test was conducted in accordance to BS DD 213:1993 test method at 20 °C [25], Fig. 5 presents a graphical representation of results obtained from stiffness modulus test. The stiffness moduli of mixtures

Fig. 4 Number of cycles to failure of neat and recycle PET fiber reinforced mixtures
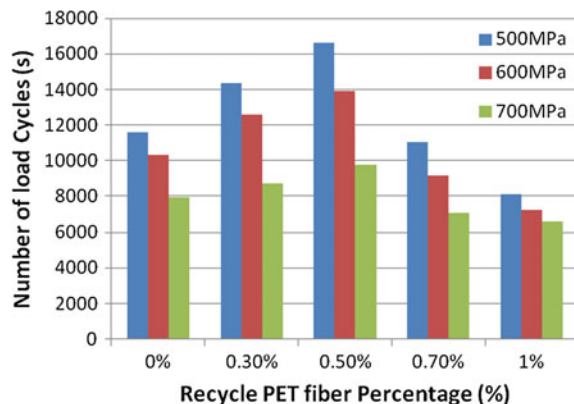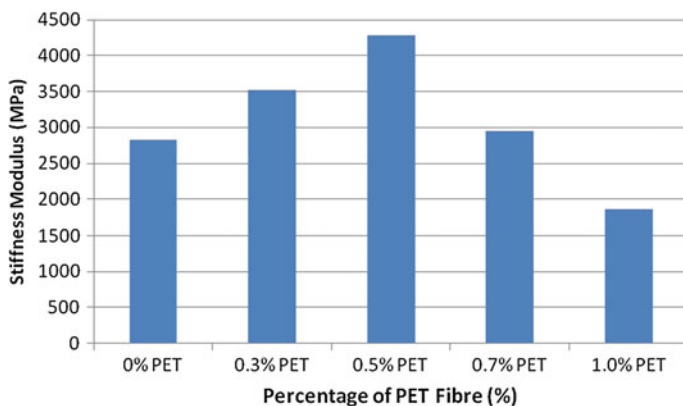
Fig. 5 Stiffness moduli of mixtures at various percentage addition of recycle PET fiber

containing 0.3, 0.5, and 0.7% recycled PET fiber are higher than that of neat mixture. This shows that recycled PET fiber increases mixture stiffness at lower temperature which in turn prevents fatigue cracks.

When the percentage of recycled PET fiber was increased to 1.0%, the stiffness modulus decreased compared to neat mixture. This effect was observed by Moghaddam et al. [26] in which PET was used as fine aggregates replacement. The reduction in the stiffness is caused by excess recycle PET fiber which has a less surface friction when lapped each other, this would eventually reduce internal friction of the reinforced mixtures [27].

4.3 Fatigue Life Prediction

The fatigue life prediction was performed based on phenomenological approach in which fatigue life is expressed as relationship between initial strain or stress and the number of repetitive load cycles to failure [28]. The main cause of fatigue cracking is the horizontal tensile strain induced by repeated loading at the base of asphalt layer, therefore the fatigue prediction was performed as a function of applied tensile strain using regression equation shown as Eq. 2 [29].

$$N_f = k \left(\frac{1}{\varepsilon_t} \right)^n, \tag{2}$$

where N_f is the predicted fatigue life, ε_t is the tensile strain, k and n are the intercept and slope of linear regression coefficients respectively.

Using values obtained from stiffness modulus test presented in Sect. 4.2, the maximum strain at each stress level was determined using Eq. 3 and the result is presented in Table 6.

Table 6 Strain values at various stress levels and percentage of recycled PET fiber reinforced and unreinforced mixtures

Mixture	Stiffness	ε (μ)		
	Modulus	Strain at	Strain at	Strain at
	Mpa	500 MPa	600 MPa	700 MPa
0% PET fiber	2821	363.35	436.02	508.68
0.3% PET fiber	3518	291.36	349.63	407.90
0.5% PET fiber	4280	239.49	287.38	335.28
0.7% PET fiber	2955	346.87	416.24	485.62
1.0% PET fiber	1856	552.26	662.72	773.17

$$\varepsilon_{\max} = \frac{\delta_{\max}(1+3v)}{S_{\mathrm{m}}} \times 1000, \tag{3}$$

where $\varepsilon_{\max}$ is the maximum horizontal strain, $\delta_{\max}$ is the maximum horizontal applied stress, v is the poison ratio (0.35), and S_{m} is the stiffness modulus.

The number of cycles to failure obtained from fatigue test was used to determine the coefficients (k and n) of the empirical model via regression analysis. Then these regression coefficients were substituted in Eq. 2 to obtain the predicted fatigue life models shown in Table 7. The models were used to predict the fatigue life of reinforced and unreinforced mixtures at various strain values shown in Fig. 6.

In Table 6, estimated strains shown a lesser strain in mixtures reinforced with recycled PET fiber due to its strong binding effect to bitumen and aggregates.

Table 7 contain a prediction models developed in this study, the models are statistically acceptable due to their strong regression coefficients (R^2). The R^2 coefficient obtained ranges between 99.4 and 99.9 in all the models which are statistically significant [2]. Another important statistical significance validation tool is p-value [30], the p-values of all the models are <0.05 which is statistically significant [31].

Figure 6 is a fatigue life-prediction plot using the developed models of this research, the fatigue life versus strain showed a strong correlation with a linear relationship. At higher strain levels, the predicted fatigue lives of mixtures

Table 7 Fatigue life-prediction models for reinforced and unreinforced recycled PET fiber asphalt concrete mixtures

Mixture	Model	R^2	p-value
0% PET fiber	$N_{\mathrm{f}} = 7.4593e5*(1/\varepsilon)^{0.7058}$	99.6	0.038
0.30% PET fiber	$N_{\mathrm{f}} = 1.3642e6*(1/\varepsilon)^{0.8019}$	99.4	0.045
0.50% PET fiber	$N_{\mathrm{f}} = 4.1562e6*(1/\varepsilon)^{1.0073}$	99.9	0.008
0.70% PET fiber	$N_{\mathrm{f}} = 2.3659e6*(1/\varepsilon)^{0.9190}$	99.4	0.047
1.00% PET fiber	$N_{\mathrm{f}} = 4.0188e5*(1/\varepsilon)^{0.6182}$	99.9	0.019

N_{f} predicted fatigue life, ε tensile strain
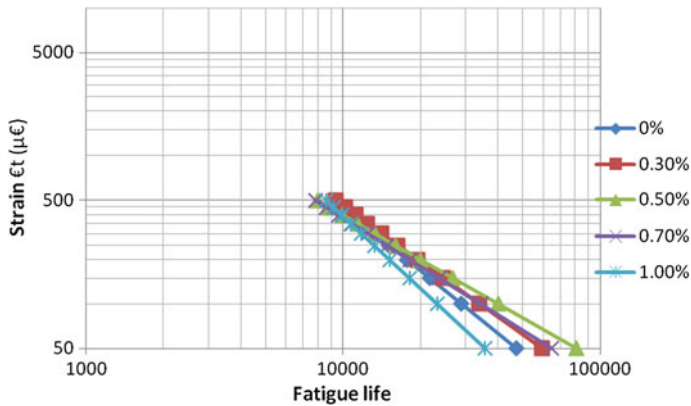
Fig. 6 Plot for predicted fatigue lives of reinforced and unreinforced recycled PET fiber asphalt concrete mixtures

containing recycled PET fiber at 0.3% are higher than that of neat mixture and at other PET fiber percentages. This is similar to result obtained by Gibson and Li [32] in which synthetic fiber modified asphalt mixes performed excellently at higher strains. Nevertheless, at lower strain levels 0.5% PET fiber reinforcement yielded a higher fatigue life compared to fatigue lives of neat mixture and other percentages of PET fiber reinforcements. The fatigue life improvement of recycled PET fiber-reinforced mixtures is the indications of good reinforcing effect of recycle PET fiber.

5   Conclusion

It is concluded that the recycled PET fibers have shown some potential in its application. Stiffness modulus and number of cycles to failure of recycled PET fiber were significantly improved at 0.5% reinforcement. Reinforcement of asphalt concrete mixture using 0.5% recycled PET fiber improves fatigue life at lower strain and 0.3% composition at higher strain. Recycled PET fiber has proven to be effective in fatigue life improvement of asphalt concrete mixture. Thus, the objective of this paper was achieved by performing the necessary laboratory investigations on the fatigue characteristics of neat and recycled PET fiber-reinforced asphalt mixtures as presented in this paper. Finally, the fatigue life-prediction model developed from linear regression was validated statistically as discussed in Sect. 4. With these results, it is hoped that better understanding on fatigue life improvement of recycled PET bituminous mixes will contribute towards road construction quality enhancement.

References

1. Eluozo, S.N., Nwaobakata, C.: Model predition of tensile stress and strain on mix stiffness modulus to determine fatigue on pavement. Am. J. Eng. Sci. Technol. Res. **1**(5), 96–103 (2013)
2. Usman, N., Masirin, M.I.B.M., Ahmad, K.A., Wurochekke, A.A.: Reinforcement of asphalt concrete mixture using recycle polyethylene terephthalate fibre. Indian J. Sci. Technol. **9**(12) (2016)
3. Daghighi, A., Nahvi, A.: Effect of different additives on fatigue behaviour of asphalt mixtures. In: Ekolu, S.O., Dundu, M., Gao, X. (eds.) Construction Materials and Structures : Proceedings of First International Conference on Construction Materials and Structures, pp. 601–607. IOS Press, Amsterdam (2014)
4. Samsuddin, N., Mohd Masirin, M.I.: Assessment of road infrastructures pertaining to Malaysian experience. MATEC Web Conference. **47**(3010), 1–7 (2016)
5. Tayebali, A.A., Rowe, G.M., Sousa, J.B.: Fatigue response of asphalt-aggregate mixtures. J. Assoc. Asphalt Paving Technol. **61**, 333–360 (1992)
6. Allam, M.A.A., Masirin, M.I.B.M., Abdullah, M.E.: Influence of using Batu Pahat soft clay on the mechanical properties of hot mix asphalt mixture. ARPN J. Eng. Appl. Sci. **11**(4), 2380–2386 (2016)
7. Shukla, M., Tirawi, D., Sitaramanjaneyulu, K.: Performance characteristics of asphalt concrete mix modified with glass fibre. In: Proceedings of IJPC-International Journal Pavements Conference, São Paulo, Brazil, pp. 1–10 (2013)
8. Herráiz, T.R., Herráiz, J.I.R., Domingo, L.M., Domingo, F.C.: Posidonia oceanica used as a new natural fibre to enhance the performance of asphalt mixtures. Constr. Build. Mater. **102**, 601–612 (2016)
9. Otuoze, H.S., Amartey, Y.D., Joel, M.: Assessment of dynamic modulus of high density polypropylene waste fiber reinforcement in asphalt concrete. Leonardo Electron. J. Pract. Technol. **27**, 13–30 (2015)
10. Park, P., El-tawil, S., Park, S., Naaman, A.E.: Cracking resistance of fiber reinforced asphalt concrete at À 20 °C. Constr. Build. Mater. **81**, 47–57 (2015)
11. Xiong, R., Fang, J., Xu, A., Guan, B., Liu, Z.: Laboratory investigation on the brucite fiber reinforced asphalt binder and asphalt concrete. Constr. Build. Mater. **83**, 44–52 (2015)
12. Xue, Y., Qian, Z.: Development and performance evaluation of epoxy asphalt concrete modified with mineral fiber. Constr. Build. Mater. **102**, 378–383 (2016)
13. Vadood, M., Johari, M.S., Rahai, A.R.: Relationship between fatigue life of asphalt concrete and polypropylene/polyester fibers using artificial neural network and genetic algorithm. J. Central South Univ. **22**, 1937–1946 (2015)
14. Kandhal, P.S., Cooley, Jr. L.A.: NCHRP REPORT 464—The Restricted Zone in the Superpave Aggregate Gradation Specification, pp. 1–45 (2001)
15. Venkatachalam, S., Nayak, S.G., Labde, J.V., Gharal, P.R., Rao, K., Kelkar, A.K.: Degradation and recyclability of poly (ethylene terephthalate). Polyester (2012)
16. AASHTO-T312-11: Standard Method of Test for Preparing and Determining the Density of Hot-Mix Asphalt (HMA) Specimens by Means of the Superpave Gyratory Compactor. American Association of State Highway Transportation Officials, Washington (2011)
17. Yoo, P.J., Kim, T.W.: Strengthening of hot-mix asphalt mixtures reinforced by polypropylene-impregnated multifilament glass fibres and scraps. Constr. Build. Mater. **75**, 415–420 (2015)

18. British Standards Institution: Bituminous Mixtures—Test Methods for Hot Mix Asphalt: Resistance to Fatigue, BS EN 12697-24-2012, London (2012)
19. Soltani, M., Moghaddam, T.B., Karim, M.R., Baaj, H.: Analysis of fatigue properties of unmodified and polyethylene terephthalate modified asphalt mixtures using response surface methodology. Eng. Fail. Anal. **58**, 238–248 (2015)
20. Yan, J., Ni, F., Yang, M., Li, J.: An experimental study on fatigue properties of emulsion and foam cold recycled mixes. Constr. Build. Mater. **24**(11), 2151–2156 (2010)
21. Wang, Y., Wong, A.S.T., Wen, Y., Chen, L., Chong, D., Wang, H.: Characterization of the distress modes and in situ material properties of highway asphalt pavement with long service life. J. Perform. Constr. Facil. 1–11 (2015)
22. British Standards Institution: Bituminous Mixtures—Test Methods for Hot Mix Asphalt-Stiffness: BS: DD 213: 1993, London. (1993)
23. Xu, Q., Chen, H., Prozzi, J.A.: Performance of fiber reinforced asphalt concrete under environmental temperature and water effects. Constr. Build. Mater. **24**(10), 2003–2010 (2010)
24. Silva, H.M.R.D., Oliveira, J.R.M., Peralta, J., Zoorob, S.E.: Optimization of warm mix asphalts using different blends of binders and synthetic paraffin wax contents. Constr. Build. Mater. **24**(9), 1621–1631 (2010)
25. Abreu, L.P.F., Oliveira, J.R.M., Silva, H.M.R.D., Fonseca, P.V.: Recycled asphalt mixtures produced with high percentage of different waste materials. Constr. Build. Mater. **84**, 230–238 (2015)
26. Moghaddam, T.B., Karim, M.R., Soltani, M.: Utilization of waste plastic bottles in asphalt mixture. J. Eng. Sci. Technol. **8**(3), 264–271 (2013)
27. Moghaddam, T.B., Karim, Soltani, M., Rehan, M., Baaj, H.: Optimization of asphalt and modifier contents for polyethylene terephthalate modified asphalt mixtures using response surface methodology. Measurement **74**, 159–169 (2015)
28. Norouzi, A., Sabouri, M., Richard, Kim Y.: Fatigue life and endurance limit prediction of asphalt mixtures using energy-based failure criterion. Int. J. Pavement Eng. **8436**(February), 1–14 (2016)
29. Fallah, S., Khodaii, A.: Reinforcing overlay to reduce reflection cracking; An experimental investigation. Geotext. Geomembr. **43**(3), 216–227 (2015)
30. De La Cueva, Bueno P., Gillerman, L., Gehr, R., Oron, G.: Nanotechnology for sustainable wastewater treatment and use for agricultural production: a comparative long-term study. Water Res. **110**, 66–73 (2016)
31. Hossain, K.F.B., Sikder, M.T., Rahman, M.M., Uddin, M.K., Kurasaki, M.: Investigation of chromium removal efficacy from tannery effluent by synthesized chitosan from crab shell. Arab. J. Sci. Eng. **42**(4), 1569–1577 (2017)
32. Gibson, N., Li, X.: Characterizing cracking of asphalt mixtures with fiber reinforcement. Transp. Res. Rec. J. Transp. Res. Board **2507**, 57–66 (2015)

An Expert System for the Dimensioning of Flexible Carriageways

Mouloud Belachia and Nadjette Bouacha

Abstract The use of expert systems in civil engineering and especially in road construction has become a necessity due to the structure's specificity in dimensioning, which is completely different from other structures. The parameters involved in road structure dimensioning are multidisciplinary in their values and behaviors; the road structure is complex and composed of heterogeneous materials, and its behavior is unpredictable due to the nature of the soil, the influence of climate, and different loads it supports. This expert system proposes different thickness, stress, and strain solutions by comparing them with the allowable values based on different mechanical models and formulates the methods and data sheets and then provides choices of body composition for the road based on the new version of the Algerian pavement catalog (2003). This tool is organized in the following forms: (1) rules derived from the experiences of professionals in the field. For our case, these rules are drawn from one side on the catalog of new pavements (version 2003) and another on a set of theoretical and practical method. (2) The property of GURU to call external programs of course that it is compatible. This property will help us to automate some models of flexible pavement sizing "Boussinesq Model, Westgaard Model, Odemark Model" with the Dev C++ language "which is a recent version of C". (3) The Algerian method outlined in the catalog.

Keywords Flexible pavements · Pavement body · Artificial intelligence Expert system

M. Belachia (✉)
Faculty of Technology, Department of Civil Engineering,
20 Aout 1955—Skikda University, Skikda, Algeria
e-mail: belachia@yahoo.fr

N. Bouacha
Faculty of Technology, Department of Civil Engineering,
Souk Ahras University, Souk Ahras, Algeria
e-mail: n.bouacha@yahoo.fr

1 Introduction

The computer in its classical form has acquired a central role in most businesses and human activities. When a task is repetitive and well defined by an algorithm, it can be entrusted to a computer.

The notion of algorithm involving a sequence is the basis of most classical programs. Artificial intelligence is the discipline which tries to understand the nature of intelligence by building computer programs imitating human intelligence.

Characterized by a large surface area, Algeria has contrasting regions in terms of topography, climate, economic, and agricultural potential as well as density of population. This diversity has generated the need to travel. In our country, 90% of travel and exchanges of goods is done by road, hence the need for a new coherent and pragmatic policy in regard to maintenance and modernization of the existing road network and construction of new roads.

The project of the catalog "New Pavement dimensioning" is important, since it is a recent document that summarizes the results of the behavior of materials that have allowed rational dimensioning of structures.

Our work is based on this document which is the result of close collaboration between Algerian and French experts and researchers (ENPC, SETRA, and LCPC) [1, 2].

The computer tool used for the validation of this work is the expert system generator GURU [3].

The approach in the implementation of expert systems is based on the specific geological and climatic conditions of the country as well as resource materials available for each region. It gives the users the choice among several alternative dimensioned structures according to the local and regional techno-economic data of the project.

2 Flexible Pavement Dimensioning Methods

2.1 Principle of Design

The role of pavements is to distribute the pressure exerted by the tire to bring it to a level compatible with what can be supported by the ground support. This level of stress is evaluated by a mechanical model of the pavement, which the researchers try to develop, to make it more representative of physical reality, especially as the theory requires many simplifying assumptions. The pavement design is to meet the following two points: lower cost and optimal conditions of comfort and security. To do so, there are two very different approaches to dimensioning the pavement: one is empirical and another theoretical. The application of a repeated rolling load on foundation soil causes bending strains of the structure layers. The latter leads to compressive stresses perpendicular to the load and tensile stresses at the base layers of the foundation [4].

This system consists in developing methods and data sheets from the Algerian catalog of new pavements, as well as offering suggestions and choices of body composition for the road. This proposal is based, of course, on the mechanical characteristics of the foundation soil (bearing capacity, composition, sensitivity to water, frost, thaw, etc.) [5, 6], types of loads, and availability of materials around the project site. The implementation of such a system will provide a significant gain in computing time for engineers and owners to avoid taking costly bad decisions.

2.2 The Parameters Affecting the Dimensioning of Pavement

The difference between these models lies in the assumptions, including the adopted approach and the mechanical behavior of materials of pavements and soil foundations [7]. In addition, the other parameters affecting the dimensioning of pavements are as follows:

– The ability of the pavement layers to bear and spread loads,
– Soil-foundation sensitivity to water, and
– The effect of temperature (season) and freezing–thaw cycles.

The load on the floor is represented by q_0 pressure on a circle of radius a.

• The floor support is a semi-infinite solid assumed homogeneous linear isotropic elastic Young modulus E_2 and Poisson's ratio v_2.
• Soil cannot endure without deforming a vertical stress (σz) below the allowable pressure q_0.
• Research the depth H for the vertical pressure σz which does not exceed σz eligible.
• Thickness H can be likened to the floor thickness or make him a match floor thickness $H' < H$ by a simple rule into account the E_1 module granular body and E_2 module ground support.

H' to assimilate H returns to assimilate E_1 to E_2. It is still necessary to realize this dimensioning, to know precisely how the diffusion of the vertical pressures is carried out, inside the solid mass (E_2, v_2).

Knowing the distribution of vertical pressure inside the massif is required to achieve the design.

Boussinesq could solve this problem (Eq. 1) and to identify constraints; hence, z vertical stress is shown in Fig. 1.

The vertical stress σz is maximum in the spread of line with the load circle.

At z-depth, it takes the following value:

Fig. 1 Pressure diffusion in Boussinesq massif
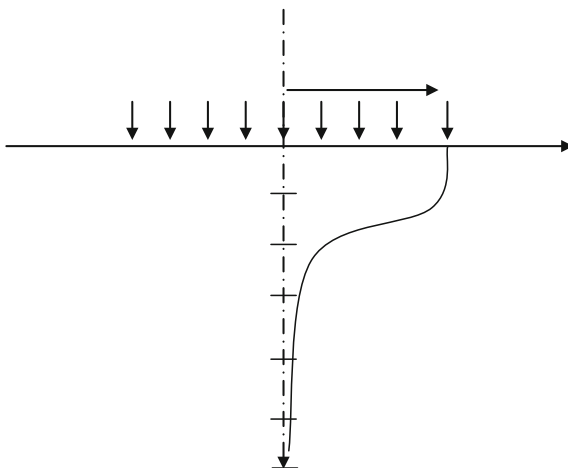
$$\sigma_Z = q\left[1 - \frac{Z^3}{(a^2 + Z^2)^{\frac{3}{2}}}\right] \tag{1}$$

Radial stress:

$$\sigma_r = \frac{q}{2}\left[(1 + 2V_2) - \frac{2Z(1 + V_2)}{(a^2 + Z^2)^{\frac{1}{2}}} + \frac{Z^3}{(a^2 + Z^2)^{\frac{3}{2}}}\right] \tag{2}$$

The maximum shear:

$$\begin{aligned}\tau_{\max} &= \frac{\sigma_Z - \sigma_r}{2} \\ &= q\left[\frac{(1 - 2V_2)}{4} + \frac{Z(1 + V_2)}{2(a^2 + Z^2)^{\frac{1}{2}}} - \frac{3Z^3}{4(a^2 + Z^2)^{\frac{3}{2}}}\right]\end{aligned} \tag{3}$$

Determination of displacement:

The displacement in the massif at any point on the axis of the load at a depth z is expressed by the following equation:

$$W = \frac{q}{E_2}\left[2(1 - V_2^2)(a^2 + Z^2)^{\frac{1}{2}} - \frac{(1 + V_2)^2}{(a^2 + Z^2)^{\frac{1}{2}}} + Z(V_2 + 2V_2^2 - 1)\right] \tag{4}$$

on the surface "for $z = 0$"

$$W_0 = \frac{2aq}{E_2}\left(1 + V_2^2\right) \tag{5}$$

2.3 Rolling Load Damages

Damages caused by heavy loads on the pavement surface are of various natures:

1. The subgrade layer composed of untreated materials records on each passage of a load a permanent strain versus applied vertical stress. The accumulation of strains, at least for traditional pavement with treated foundation layer with hydraulic or hydrocarbon binders, is sufficiently low on the vertical support so that permanent deformations are moderate.
2. The road structure with bonded layers bends at each load passage. This bending causes, at the base of the road structure, tensile stresses; the repetition of these stresses leads to an accumulation of fatigue damage which ultimately causes the breakdown of the road (cracks).
3. The pavement (surface layer) under rolling load leads to damages of the surfacing, which becomes slippery (tangential forces) or causes significant rutting (creep).

One of the tools implementing these approaches is the software ALIZE, developed by LCPC-SETRA. ALIZE is a computation software tool for stresses created by road traffic on pavement structures [2].

3 Expert System

Expert system is a rational approach to pavement design, in the interests of realizing a uniform road network. It is a coherent method, based on the computation of the resilient stresses and strains in road structure. The design is carried out by comparing these calculated values in all the layers, to the admissible stresses and/or strains values which are evaluated according to the fatigue characteristics of the materials and their rutting behavior caused by the untreated materials and soils. In addition, it takes into account the cumulative traffic particular to the pavement.

3.1 General Structure of an Expert System

An expert system is generally composed of three modules (Fig. 2):

Fig. 2 Expert system structure
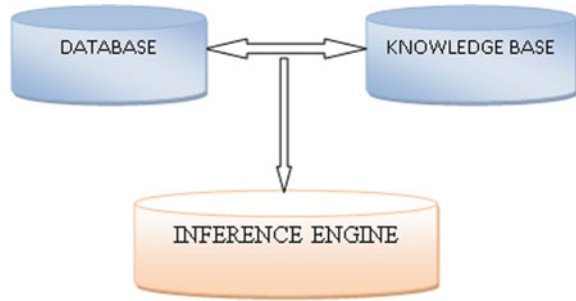
(a) The knowledge base is given in declarative form; its function is to accommodate the specific information of the field of application. It is divided into two parts:

- Database: the set of facts defining the problem to the system, as well as all the facts deduced by the system during the progression of reasoning.
- Knowledge base: proper, that which gathers together all of the information provided by the expert system on a specific domain.

(b) The inference engine is the central part of the expert system, designed as a rather general program that exploits the knowledge base by considering it as data (and therefore subject to change).

It is software responsible for exploiting given knowledge and for making deductions. It gives the impression that the expert system reasons. These rules take the form of "IF" premise "THEN" conclusion.

3.2 Development Tools

Artificial intelligence (AI) aims to make computers smart. A fundamental aspect of intelligence is the ability to understand and respond to questions raised by humans in natural language.

A second aspect is the ability to reason using facts, propositions, and relationships to solve problems. The tool used for the development of our prototype assistance system for the choice of pavement is the GURU system.

Building an expert system with GURU requires the construction of a rule base. This base consists of rules from expert reasoning knowledge on how to solve a typical problem.

The GURU module is optimal for the construction of expert systems. This is due to its synergistic integration with all classical modules of professional computing [3].

3.3 Architecture of GURU Expert System

The database is all the information available during the analysis of a particular problem.

The knowledge base consists of a set of "IF" … "THEN" … describing ways known to the expert to analyze the information from the database (Fig. 3). The "IF" part of the rule is generally named "condition".

The inference engine is the reasoning program responsible for situation assessment as described in the knowledge base, and triggers actions associated with each situation. A basic evaluation/trigger treatment done by the inference engine is called an inference.

The user acts on the database by introducing the problem hypothesis (1) and reading the results (2). The user has access to all the tools exploited by the expert system. The expert acts on the knowledge base by introducing his or her own experience (6). The inference engine uses the expert's knowledge (5) and information from the database (3) to complete the database with facts obtained through conclusions (4).

3.4 Expert System Operation

The forward chaining or deductive reasoning exhaustively traverses the knowledge base without a priori and triggers all that is possible, the conclusions drawn from a rule trigger can be used immediately for the triggering of other rules. At the end of the course, GURU decides whether or not to undertake a new course, so that all possible rules are triggered. For a new course to be undertaken, there must remain untriggered rules but also that the previous course had provided new elements, i.e., that at least one rule was triggered.

Fig. 3 GURU architecture
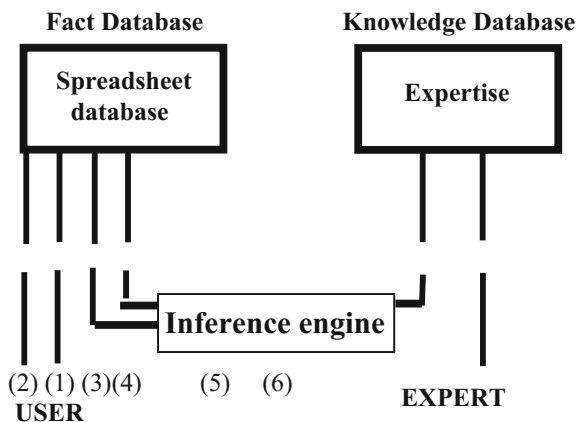
Backward chaining: backward chaining or inductive reasoning aims to dismantle a result; it is therefore only interested in rules that can assist it in this task. A "Candidate Rule" is a rule that contains in its conclusion a reference to a result, "This result is called during the research a goal". In backward chaining, GURU searches among all goals' "Candidates Rules", those that can be triggered.

Mixed chaining: it is the combination of the two types, forward and backward.

4 Implementation of Expert Systems

Based on the basic definitions of the concepts of an expert system:

An expert system, a tool for developing expert systems, is a software that facilitates the construction of expert systems.

A rule database manager is a software for building and maintaining specific rules for each type of problem.

A generalized inference engine can reason with any rule database.

Thus, the task of creating an expert system is reduced to building its own rule database. The inference engine that can run in the background is used primarily to find a goal or find out the cause of a real situation.

The formulation of the expertise can be done in several steps generating rule packets [8, 9].

A first set of rules allows the definition of the geographical area; we have selected three main areas characterizing Algeria:

– Littoral zone,
– Highland zone, and
– Saharan zone.

A second rule package allows the introduction of the geotechnical characteristics of the foundation soil according to climatic zones (Table 1).

Following that and according to the road classification by climatic zones (different from geographic zones, which are four (04)) are defined in function of hydrometric, as well as drainage quality (Table 2).

We adopted this classification of soils for Algerian roads (Table 3). The classification contains seven (07) soil families, which are gravel, sand, alluvium, clay, tufa, marl, and silt. Each of these families is divided into further subfamilies, to better specify the soil [1].

Table 1 Climatic zones

Annual precipitation in mm	Climatic zones
$P > 600$	I
$350 < P < 600$	II
$100 < P < 350$	III
$P < 100$	IV

Table 2 Load carrying capacity classification of soil

Categories	CBR index (%) of maximal density modified PROCTOR (4 day immersion) applicable to flexible pavements
S0	>40
S1	25–40
S2	10–25
S3	5–10
S4	<5

Table 3 Classification of soil

Family	Nature of soil	Road classification by climatic zone					
		I and II		III		IV	
		Quality of soil drainage					
		Good	Poor	Good	Poor	Good	Poor
	Clean, well, poorly calibrated	S1	S1	S1	S1	S1	S1
Gravel	Silty	S1	S2	S1	S2	S1	S1
	Clayey	S2	S3	S1	S3	S1	S1
	Clean, well calibrated	S1	S1	S1	S1	S1	S1
Sand	Clean, poorly calibrated	S2	S2	S1	S2	S1	S1
	Course, well, poorly calibrated	S2	S3	S2	S3	S1	S1
	Fine silty clayey	S2	S3	S2	S3	S1	S1
Alluvium	Slightly plastic	S2	S2	S2	S3	S1	S2
	Highly plastic	S3	S4	S3	S3	S1	S2
	Slightly plastic	S3	S4	S2	S3	S1	S2
Clay	Highly plastic	S3	S4	S2	S3	S1	S2
	Salted bottomland	S3	S4	S2	S3	S1	S2
Tufa	Encrustation	S1	S1	S1	S1	–	–
	Granular horizon	S1	S2	S1	S2	–	–
Marl	Structure	S3	S4	S2	S3	S1	S2
Silt	Organic soil	S4	S4	–	–	–	–

A third rule package is designed to help decide on the choice of layers which concord with the foundation soil that is classified as one of four (04) categories, taking into account the cumulative traffic over 20 years of service (Table 4).

The road structure layers are selected according to regionally available materials for the road project.

The final rule package retains the layer thickness variants within the intervals established for each layer of the pavement body, all while taking into account the most economic propositions with respect to the use of materials.

Table 4 Traffic classification

Traffic classification	Accumulated heavy vehicle traffic over 20 years
T1	$T < 7.3 \times 10^5$
T2	$7.3 \times 10^5 < T < 2 \times 10^6$
T3	$2 \times 10^6 < T < 7.3 \times 10^6$
T4	$7.3 \times 10^6 < T < 4 \times 10^7$
T5	$T > 4 \times 10^7$

5 Presentation of Knowledge

The first question we must answer is to define which information is to be included into the fact database, which information to be put into the rule database and the specific information to obtain from the results, as well as its form with corresponding variables.

The user introduces the various data into the database through a question-based interface between him and the machine. The experiment is introduced into the information database through rule packages ("If" condition "Then" conclusion). The inference engine uses these two rule databases to trigger the conclusions of the problem, and then sends them back to the fact database to be displayed to the user as results during a consultation (Fig. 4). Modeling process steps are as follows:

Step 1: Introductory questionnaire; Through the questionnaire, we ask the user to enter data on the following points: climate region, precipitation quality of soil drainage "good or poor", soil type (size, color, nature, and family), type of network, and traffic intensity.
Step 2: Outcome 1: The tool uses its rule packages successively to determine the following parameters: zone, road soil classification, and traffic classification.
Step 3: Outcome 2: At this point, the tool has at its disposal the three parameters that will allow it to determine the choice of structure that corresponds to the settings, displayed as results to the user. With the properties of the GURU expert system, we can call upon external programs, including the program written in C language used to display the already calculated pavement thickness.
Step 4: Final Results: "The help tool displays: The pavement thickness".

Different structure choices proposed by the tool correspond to the different parameters that are "road soil classification, predicted traffic classification, and climate zone".

So according to these results, the user can make the right choice according to the materials that are in abundance in the vicinity of the project site.
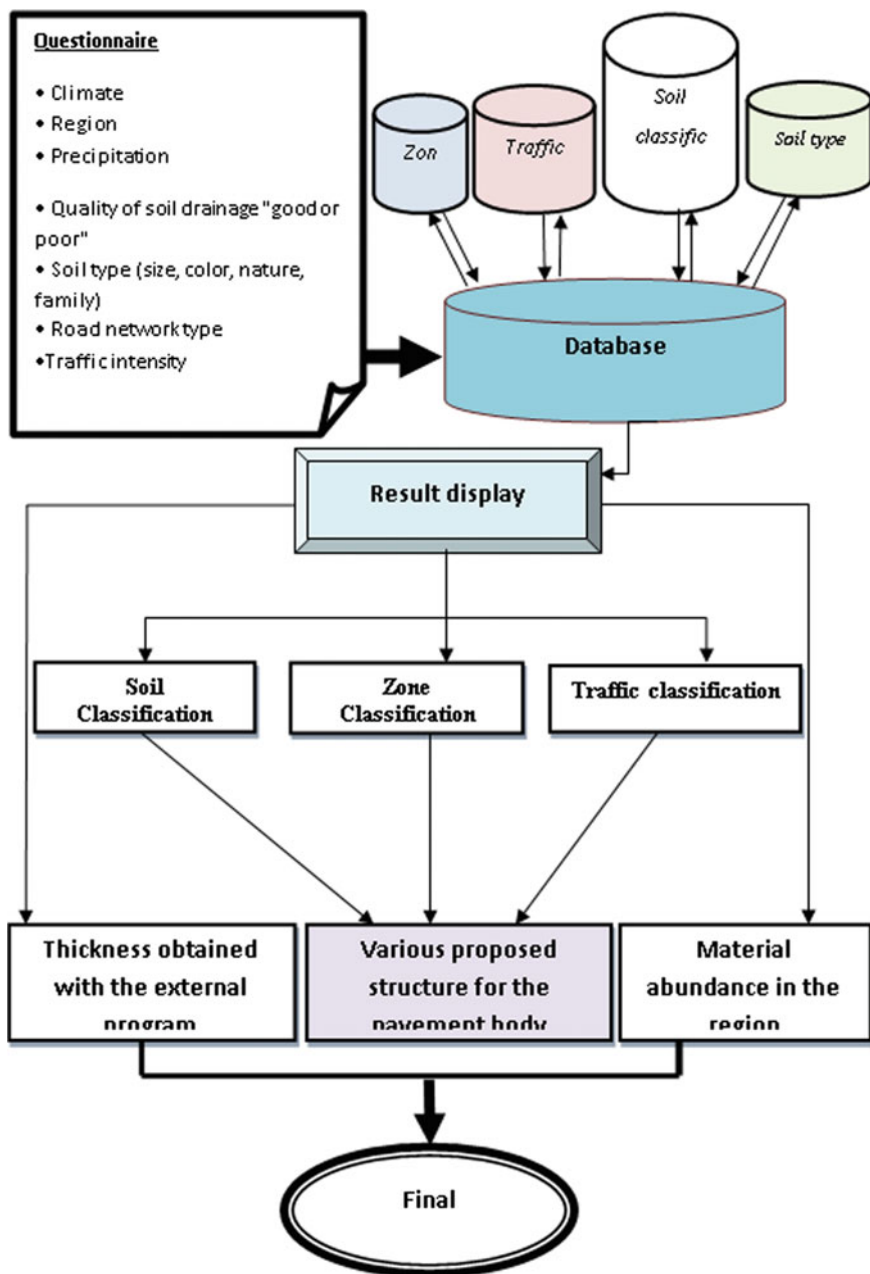
Fig. 4 Modeling process steps

6   Conclusions

This work involved the establishment of rules from the expert experience of professionals in the field. These rules are organized into rule packages so that the exploitation and enrichment are facilitated. At the other end of the expert system, the user will obtain proposals for body structure optimized for the pavement, either in the use of local materials or as economic solutions.

Second, we had to implement a tool for decision support. This tool is organized in the form of rules derived from the experiences of professionals on the subject. In our case, these rules are from the new pavement catalog (version 2003).

The rules are organized into packages so that the exploitation and the enrichment are eased. Then, the programs were completed by expert prototypes and were tested in order to ascertain their validity according to a number of cases presented in the catalog.

At our stage of this research, we have contented ourselves with establishing a non-exhaustive initial expertise which took a lot of time and effort, given the difficulty of going through all possible cases and introducing as many parameters as possible that influence the choice of pavement.

At first attempt, the validation has given us correct results, but much effort is needed to perfect the tool. This work will require a complete investigation of the tool being used, especially in the consideration of the expertise either human or documentary (dimensioning road catalogs). This work may require more research to make it operational [9].

References

1. CTTP: Critical study of different catalogs (AASHTO, Shell, France, Belgium, Switzerland, SETI, Spanish). Research Report No. 2 and 1st—Stage A: CTTP (1995)
2. LCPC: Design and measurements of pavement structures. Technical Guide, LCPC-SETRA (2014)
3. Guru v.2.0: User manual, Lafayette: Micro Data Base Systems Inc. (1990)
4. Jeuffroy, G.: Design and construction of roads, vol. 1, Edition Eyrolles (2013)
5. Autret, P., Boissoudy, A., Baucheron, J., Marchand, P.: Alize III practice. In: Proceedings of 5th International Conference on Structural Design of Asphalt Pavements (1982)
6. Boussinesq, J.: Potential application to the study of equilibrium and motion of elastic cops. Gauthier Villars, Paris (1985)
7. Peyronie, C., Caroff, G., Gilbert, C.: Road - Design of pavements In: Jeuffroy, G., Sauterey, R. (eds.) Presses de l'EcoleNationale des PontsetChaussées (1991)
8. Messabhia, A.: Using the definition of the technology and modeling structure works in a CAD system building. Ph.D. Thesis, University of Savoie in Chambery (1989)
9. Bouacha, N.: Dimensionnement and choice of the body of the supple roadways, Doctorate. Thesis, Dept. Civil. Eng., 20 Aout 1955 University Skikda, Algeria (2010)

An Investigation into the Use of Ultrasonic Wave Transmission Techniques to Evaluate Air Voids in Asphalt

Majid Zargar, Sourish Banerjee, Frank Bullen and Ron Ayers

Abstract Air voids and their distribution are very important factors that influence the structural performance of asphalt pavements under traffic loading. Several simple methods exist for the overall (macro) evaluation of air voids in asphalt mixture, however there are very few methods available to assess their micro-distribution within an asphalt matrix. While X-ray methodologies have historically been used by researchers to investigate the complex distribution of air voids in asphalt mixtures, both cost and ease of application do not support their widespread use. The use of non-destructive ultrasonic wave transmission techniques (UWT) is outlined in the paper as an accurate, rapid and economical alternative method. UWT is able to both estimate the total air voids and their distribution within laboratory compacted asphalt samples. Asphalt samples with 14 mm nominal aggregate size manufactured with three types of bitumen; Class 320 (C320), Multigrade (M1000) and a SBS Polymer Modified Bitumen (PMB-A5S) and with different air voids were analysed using UWT techniques. The results have shown that UWT testing has the potential of being a rapid and cost-effective method of estimating total air voids and their distribution in laboratory asphalt mixtures.

Keywords Ultrasonic velocity · Air voids distribution · Asphalt

M. Zargar (✉) · S. Banerjee · F. Bullen · R. Ayers
University of Southern Queensland, Toowoomba, QLD, Australia
e-mail: Majidzargar2009@gmail.com

S. Banerjee
e-mail: Sourish.Banerjee@usq.edu.au

F. Bullen
e-mail: Frank.Bullen@usq.edu.au

R. Ayers
e-mail: Ron.Ayers@usq.edu.au

1   Introduction

1.1   Air Voids and Their Effect on Asphalt Pavement Performance

Asphalt has been used as a pavement wearing surface for over 150 years [1]. An asphalt mixture (asphalt) is a complex distributed system of coarse aggregates, bitumen mastics (bitumen binder, fine aggregates and mineral powder) and air voids [2]. Its performance such as creep and fatigue under traffic loads depends on its component materials and compacted structural properties.

The properties of the component materials of aggregate and bitumen are normally well-known and controllable. The structural performance of the compacted asphalt is often a function of the construction processes related to the compaction temperature and effort and the resulting air voids and their distribution within the compacted mass [2]. It has been surmised that among all the key parameters that impact structural properties, air voids volume and distribution are the most important in pavement design [2].

Air voids below the minimum specification limit may lead to excessive creep (rutting) [3], flushing, bleeding and/or mix instability. In contrast, air voids above the maximum specification limit may lead to accelerated hardening of the binder through oxidation, ravelling and stripping of the asphalt layer [4]. However, high air voids content can also aggravate the rutting in the early age of pavement in the form of post placement compaction [3]. Fatigue damage, reduced strength and durability of asphalt may also result due to excessive air voids [2]. Pavement designers attempt to optimise the air voids percentage to obtain the best structural and serviceability behaviour.

1.2   Air Void Measurement in the Laboratory

In the laboratory, the accurate assessment of air voids within asphalt is a vital and critical component of quality assurance and control (QA/QC) procedures [4, 5]. There are a range of different methods (Table 1) employed to measure the air voids content dependent on the mix type (Dense Graded, Open Graded or Stone Mastic Asphalt), maximum aggregate size, compaction method and water absorption. The main difference across the various standards relates to the measurement method used for bulk specific gravity and maximum specific gravity as illustrated in Table 1.

All the laboratory techniques mentioned in Table 1 are useful when the overall air voids of the sample is required. However, not provide any information regarding air voids distribution within the laboratory sample. Investigating the impact of the air voids characteristics and distributions is thus difficult when using the methods provide in Table 1 [2]. A non-destructive technique, which could quickly evaluates

Table 1 Air voids measurement laboratory techniques (a part of data from Praticò and Moro [18])

Calculating air void content (%) in laboratory compacted specimens	AASHTO Or ASTM Or BU Or EN	Depends on the mix type, aggregate size, and water absorption one of the methods can be chosen for air voids calculation	Indicator	Standards
			Dimensional	AASHTO T 269-97 (2007) EN 12697-6:2003
			Parafilm	ASTM D 1188-07 (abs > 2%)
			Vacuum sealing device	ASTM D 6752-09/ AASHTO T 331-08 (2008)
			Paraffin	BU N40-1973 AASHTO T 275-07 (2007) A (abs > 2%) EN 12697-6:2003
			Saturated surface dry	AASHTO T 166-07 (2007) ASTM D 2726-09 (abs < 2%) UNI EN 12697-6:2003
			Bucket vacuum assembly	ASTM D 2041-11 AASHTOT-209–10-UL (rice method)
			Water displacement method	ASTM D 6857-09

the distribution and microstructure of air voids of compacted asphalt in the laboratory would be well received by industry [6].

Over the last few years research has focused on developing non-destructive laboratory techniques to evaluate the complexity of internal air void structures within asphalt samples. In 2010, Vincent et al. successfully used a gamma-densitometer to assess the influence of the compaction process on the air void homogeneity of asphalt samples [5]. Other non-destructive techniques such as X-ray Computed Tomography (CT) and image analysis methods [7–10] have been applied by other researchers and the research outcomes have shown that air voids within compacted asphalt are not uniformly distributed [7, 9]. In addition to the methods noted above, researchers have used Discrete Element Methods (DEM) for

modelling air voids in asphalt to assess the impact of air void distribution and microstructure on mechanical properties and pavement distresses [7, 10].

The research techniques outlined above required advanced equipment and/or modelling knowledge. The research reported here describes a simple technique using ultrasonic assessment for laboratory use to predict the air voids content and distribution in the asphalt samples. This technique will be useful for better evaluating some tests such as fatigue and creep where the applied load (dynamic or static) is localised at a specific part of the asphalt sample.

1.3 Ultrasonic Wave Velocity (UWT) and Asphalt Mixture

Non-destructive test have been successfully applied widely in civil engineering to obtain information on materials and structures. The Ultrasonic Wave Transmission (UWT) method is one widely used for determining the mechanical properties of anisotropic materials such as asphalt and concrete [10, 11]. This technique also has been used to evaluate and predict asphalt pavement fatigue [12, 13].

To date researchers have measured ultrasonic velocity in the centre of laboratory samples to assess material mechanical properties or asphalt distress [11, 12, 14–16]. However, none employ the technique to measure the air void volume and distribution in laboratory samples.

2 Experimental Details

2.1 Materials and Sample Preparation

Three commonly used hot mix asphalt (HMA) types in Queensland were selected and used in this study with the same dense aggregate grading (Fig. 1). The characteristics of the used aggregate and filler are provided in Tables 2 and 3. The three types of bitumen binders used were; Conventional (C320), Multigrade (M1000) and a SBS Polymer Modified (PMB-A5S), all at 5%. The physico-chemical properties of the used bitumen are provided in Table 4.

An asphalt shear box compactor using different compactive effort was used to produce asphalt slabs with a range of target air voids from 1 to 10%. Samples with a 150 mm diameter and 50 mm height were cored and cut from the compacted asphalt slabs. Specimens were washed, dried and preconditioned at the test temperature of 25 °C for 48 h before being subjected to the air void measurement test and UWT test.
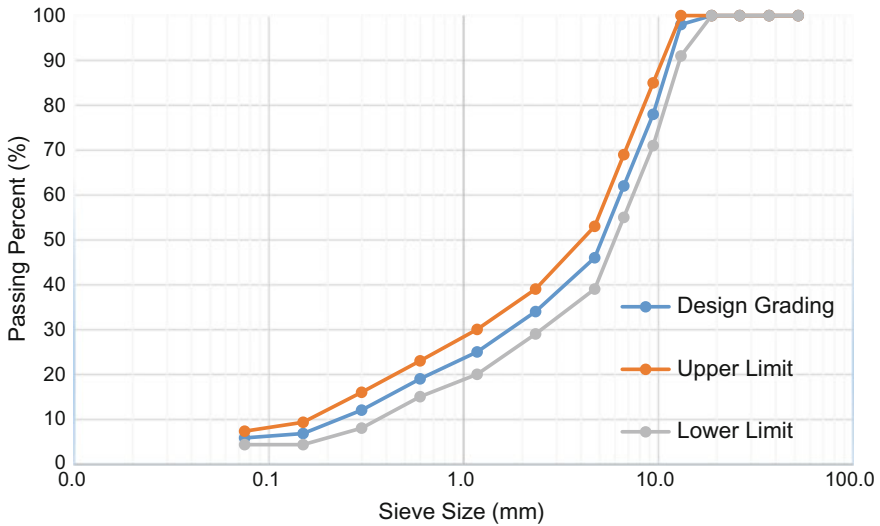
Fig. 1 BCC type III aggregate gradation

Table 2 Aggregate characteristics

Test method	Description	Limits	7 mm test result	9 mm test result	14 mm test result
AS 1141.11	Grading	–	Conforming	Conforming	Conforming
AS 1141.15	Flakiness	<30%	11.6	12.4	7.8
Q 214 B	Water absorption	Max 2%	0.68	0.39	0.5
Q 214 B	Particle density (Dry)	t/m^3	2.666	2.668	2.672
Q 215	Crushed particles	Min 80%	100	100	100
Q 217	Weak particles	Max 1%	0.7	0	0
Q 205 B	10% fines	Min 150 KN	296	272	239

Note Q refers to a Queensland Department of Transport and Main Roads test

2.2 Experimental Procedure

For all preconditioned samples, the air voids content of whole sample was calculated using the specimen's bulk specific gravity (Saturated Method) and the asphalt's theoretical maximum specific gravity (Rice Method) according to Australian standard (AS/NZS 2891).

Table 3 Filler characteristics

Test method	Description	Limits	Baghouse test result	Rockflour test result	Combined BH/RF test result
AS 1141.11	600 μm grading (AS 2357 limits)	100	100	100	100
AS 1141.11	300 μm grading (AS 2357 limits)	95–100	100	100	100
AS 1141.11	0.075 μm grading (AS 2357 limits)	75–100	92.8	97.1	97.1
AS 1141.17	Voids in compacted filler	Min 38%	48	49	46
AS 1141.7	Apparent particle density	TBR	2.706	2.756	2.729
	Products conforms	(Yes/no)	Yes	Yes	Yes

Table 4 Properties of bitumen binder class C320, M1000 and PMB-A5S

	Property	Test method	Limits	Test result
C320	Viscosity at 60 °C (Pa s)	AS 2341.2	260–380	328
	Penetration at 25 °C, 100 g, 5 s (pu)	AS 2341.12	Min 40	49
	Softening point (°C)	AS 2341.18	Report	51.2
	Viscosity at 135 °C (Pa s)	AS 2341.2	0.4-0.65	0.53
Multigrade	Viscosity at 60 °C (Pa s)	AS 2341.2	reported value	910
	Viscosity at 135 °C (Pa s)	AS 2341.4	1.5 max	0.78
	Softening point (°C)	AS 2341.18	Report	58.5
	Flash Point (°C)	AS 2341.14	250 min	348
PMB-A5S	Consistency at 60 °C (Pa)	AG: PT/T121	5000 min	11,254
	Stiffness at 25 °C (kPa)	AG: PT/T121	30 max	19
	Viscosity at 165 °C (Pa s)	AG: PT/T111	0.9 max	0.64
	Softening point (°C)	AG: PT/T131	82–105	103

The UWT technique used a Pundit 7 apparatus (Fig. 2a) applied according to BS EN 12,504-4 standard to generate the ultrasonic wave and to determine the ultrasonic pulse velocity of the asphalt sample. Two 54-kHz piezoelectric crystal transducers (transmitter and receiver) were placed in parallel at each side of the specimen to measure Ultrasonic wave transit time at 17 different locations at 25 °C

Fig. 2 a Pundit 7 with two 50 mm transducers. **b** Test locations for ultrasonic measurements
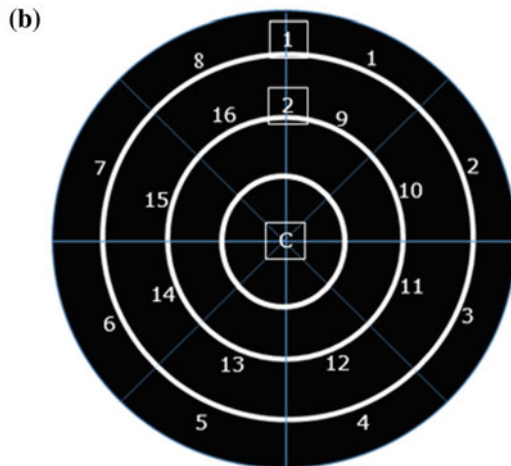
as shown in Fig. 2b. The transit time for the compression wave (*P*-wave) to pass the length of the asphalt sample was recorded to calculate the ultrasonic pulse velocity using the below formula

$$V = l/t \tag{1}$$

where,

V ultrasonic pulse velocity (km/s)
L length of specimen (mm)
T transit time (ms)

All asphalt samples surfaces were trimmed before UWT testing to ensure smooth and parallel surfaces with a maximum thickness and diameter variation of 1 mm.

The specimen's surface was divided into 17 areas as shown in Fig. 2b and ultra-sonic pulse velocity measured at the 17 locations.

Air void at the centre of samples was estimated using linear relationships between UWT results and air void results for each type of asphalt. The linear regression equations are as follows:

C320	$AV = -0.0168UV + 80.441$ (2)
M1000	$AV = -0.0109UV + 87.79$ (3)
PMB-A5S	$AV = -0.0214UV + 96.983$ (4)

UV ultrasonic velocity at centre
AV air void in center

3 Experimental Results and Discussion

3.1 Ultrasonic Velocity and Air Void in the Sample

The results for ultrasonic velocity and air void content (0–10%) for all asphalt mixes (C320, M1000 and PMB-A5S), calculated at the reference temperature of 25 °C, are summarised in Fig. 3 for the overall average of the 17 locations.

It can be clearly noted that the trend lines indicate that an increase of air void content from 0 to 10% results in a decrease in ultrasonic velocity for all three mix types when considering the average of all 17 locations. It can be concluded from the results that the higher the air void content in the sample, the lower the expected ultrasonic velocity. The data demonstrates the effective use of the non-destructive UWT test to estimate air void contents from 0 to 10% in laboratory compacted asphalt.

Figures 4, 5 and 6 show the air void in each type of asphalt at the centre (estimated from UWT technique) and at whole sample (measured by AS/NZS 2891 standard). The difference between the two indicates that the air void at the centre is different from that of the whole sample.

3.2 Air Void Distribution

Figure 7 shows the ultrasonic velocity across the 17 locations for C320, M1000 and PMB-A5S at their highest and lowest air void contents. The ultrasonic velocity at each point is an indicator of a special air void content on that point. From the
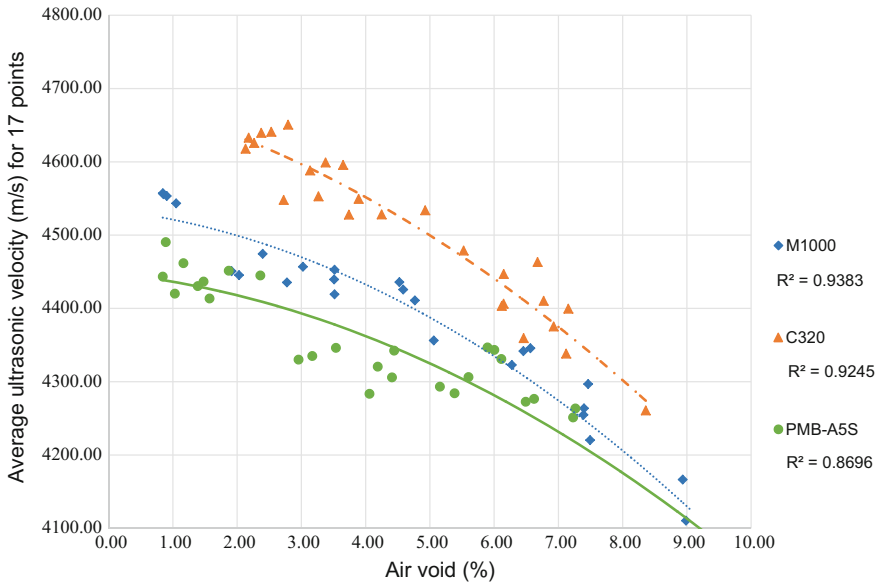
Fig. 3 Ultrasonic velocity versus air void content for mixtures with C320 and PMB in average 17 points
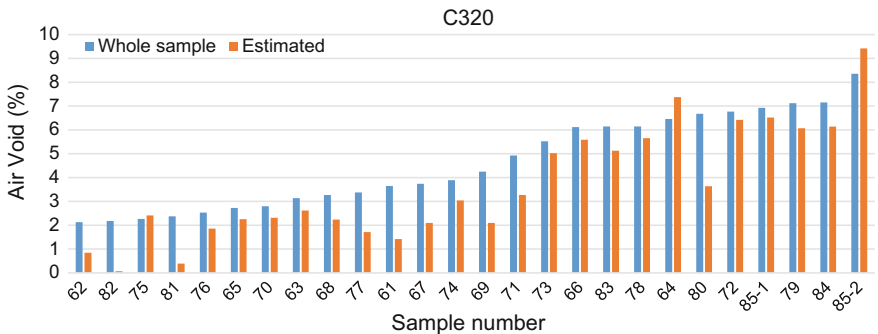
Fig. 4 Estimated Air void in the centre of samples for C320 samples

tolerance on ultrasonic results, it can be concluded that within the sample air void varies from one point to another. This outcome is similar to that obtained by other researchers using the X-Ray techniques [9, 17] as shown in Fig. 8 where the air voids distribution in an asphalt samples vertically and horizontally is seen.
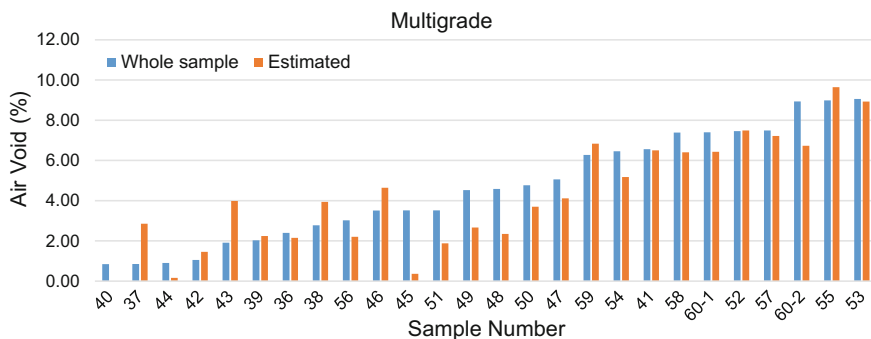
Fig. 5 Estimated air void in the centre of samples for M1000 samples
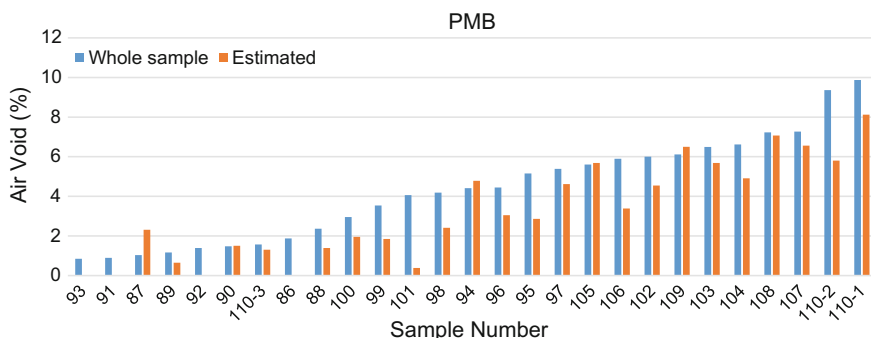
Fig. 6 Estimated air void in the centre of samples for PMB-A5S samples

3.3 Evaluating Asphalts Using UWT Method

The research results can have significant regarding test outcomes where localised air voids can contribute to the test results. This would apply where air voids at maximum tensile stress locations in fatigue beam testing are different from the overall voids of the beam. In the case of creep evaluation using localised compressive stresses such as in the European creep test (BS EN 12697-25:2005) knowledge of the air voids at the applied stress area is of more importance than the overall air voids of the sample. Such exact air void knowledge at maximum stress locations has the ability to improve experimental results, their correlation and predictive ability.
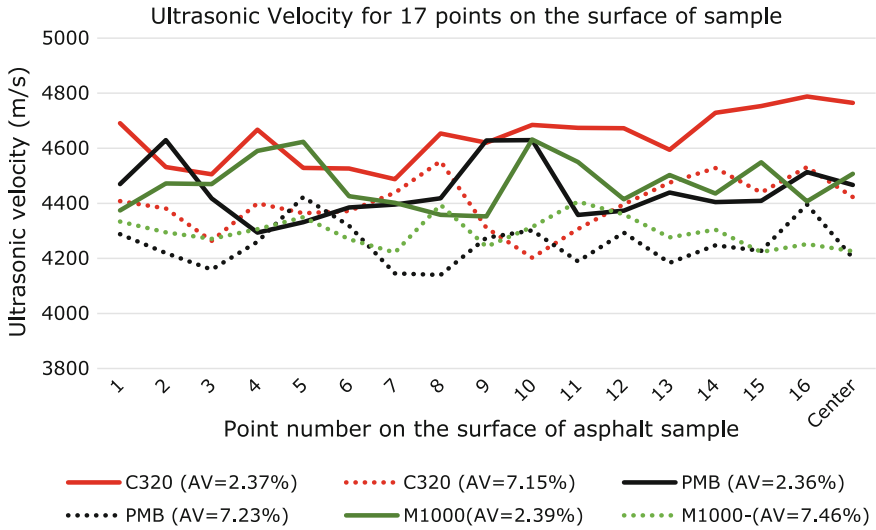
Fig. 7 Ultrasonic velocity for 17 points on the surface of samples with low and high air void content

Fig. 8 Vertical and horizontal air void distribution in gyratory specimen with 12.5 and 19 mm maximum aggregate size (a part of figure that was presented in Tashman et al. [17])
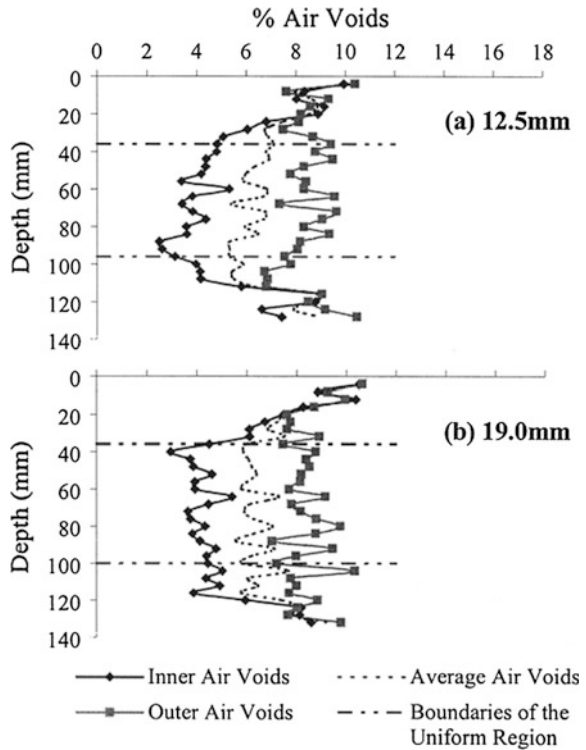
4 Conclusions and Comments

The research has shown that the UWT technique can be applied as a non-destructive tool to analyse and estimate the air voids content and their distributions in asphalt mixes. Air voids were found to be non-uniformly distributed along the horizontal directions in laboratory compacted asphalt samples. The technique can be applied to assist researchers in the analysis of asphalt test data involving air voids as an experimental variable. The next stage of the research will be to correlate air void measurement using X-ray and ultrasonic methods to further demonstrate the effectiveness and accuracy of ultrasonic techniques to measure air voids and their distributions.

References

1. Tarefder, R.A., Ahmad, M.: Effect of compaction procedure on air void structure of asphalt concrete. Measurement **90**, 151–157 (2016)
2. Ren, J., Sun, L.: Characterizing air void effect on fracture of asphalt concrete at low-temperature using discrete element method. Eng. Fract. Mech. **170**, 23–43 (2017)
3. Roy, N., Veeraragavan, A., Krishnan, J.M.: Influence of air voids of hot mix asphalt on rutting within the framework of mechanistic-empirical pavement design. Procedia Soc. Behav. Sci. **104**, 99–108 (2013)
4. MRTS30: Transport and main roads specifications MRTS30 Asphalt Pavements. Department of Main Road and Transportation (2016)
5. Dubois, V., De La Roche, C., Burban, O.: Influence of the compaction process on the air void homogeneity of asphalt mixtures samples. Constr. Build. Mater. **24**, 885–897 (2010)
6. Ma, T., Zhang, D., Zhang, Y., Zhao, Y., Huang, X.: Effect of air voids on the high-temperature creep behavior of asphalt mixture based on three-dimensional discrete element modeling. Mater. Des. **89**, 304–313 (2016)
7. Castillo, D., Caro, S.: Probabilistic modeling of air void variability of asphalt mixtures in flexible pavements. Constr. Build. Mater. **61**, 138–146 (2014)
8. Masad, E., Muhunthan, B., Shashidhar, N., Harman, T.: Internal structure characterization of asphalt concrete using image analysis. J. Comput. Civil Eng. **13**, 88–95 (1999)
9. Masad, E., Jandhyala, V., Dasgupta, N., Somadevan, N., Shashidhar, N.: Characterization of air void distribution in asphalt mixes using X-ray computed tomography. J. Mater. Civ. Eng. **14**, 122–129 (2002)
10. Partl, M.N., Bahia, H.U., Canesterari, F., De La Roche, C., Di Benedetto, H., Piber, H., Sybilski, D.: Advances in Interlaboratory Testing and Evaluation of Bituminous Materials: State-of-the-Art Report of the RILEM Technical Committee 206-ATB. Springer Science & Business Media (2012)
11. Stephenson, R.W., Manke, P.G.: Ultrasonic moduli of asphalt concrete. Highway Res. Rec. (1972)
12. Houel, A., Arnaud, L.: Damage characterization of asphalt in laboratory by ultrasonic wave propagation. Non Destr. Test. Civil Eng. (2009)

13. Tigdemir, M., Kalyoncuoglu, S.F., Kalyoncuoglu, U.Y.: Application of ultrasonic method in asphalt concrete testing for fatigue life estimation. NDT E Int. **37**, 597–602 (2004)
14. Jurado, M.C.: Quantifying Anisotropy in Asphalt Concrete Pavements Using an Ultrasonic Method. The University of Texas at El Paso (2008)
15. Mounier, D., Di Benedetto, H., Sauzeat, C.: Determination of bituminous mixtures linear properties using ultrasonic wave propagation. Constr. Build. Mater. **36**, 638–647 (2012)
16. Norambuena-Contreras, J., Castro-Fresno, D., Vega-Zamanillo, A., Celaya, M., Lombillo-Vozmediano, I.: Dynamic modulus of asphalt mixture by ultrasonic direct test. NDT E Int. **43**, 629–634 (2012)
17. Tashman, L., Masad, E., D'angelo, J., Bukowski, J., Harman, T.: X-ray tomography to characterize air void distribution in superpave gyratory compacted specimens. Int. J. Pavement Eng. **3**, 19–28 (2002)
18. Ratico, F., Moro, A.: Measurement of air void content in hot mix asphalts: method and core diameter dependence. Constr. Build. Mater. **26**, 344–349 (2012)

Chemical Analysis and Consistency Characterization of Domestic Waste Bio-asphalts

Sady Abd Tayh, R. Muniandy, S. Hassim and F. M. Jakarni

Abstract The objective of this paper is to characterize the chemical and consistency characterization of the bio-binder produced from domestic waste (DWBO) as compared with conventional petroleum–asphalt binder. A petroleum asphalt was modified with DWBO at 3, 6, and 9% by weight to prepare bio-binders, respectively. Samples of the DWBO-modified binders compared to base binder were tested by running the rotational viscosity (RV). Moreover, the fourier transform infrared (FTIR) spectroscopy as well as elemental analysis tests were utilized to validate the chemical compositions and bond initiations that caused changes in stiffness and viscosity of the asphalt modified with DWBO from those of base asphalt binders. This research has revealed that there are four factors to be influenced by the use of DWBO, (i) reducing greenhouse emissions and the toxic effect of binder compared with petroleum-based asphalt binders, (ii) increasing workability, (iii) reduction in viscosity of asphalt binders which led to reduction of asphalt pavement construction costs by reducing mixing and compaction temperatures, and (iv) increased the aging induces of the control asphalt binders. Bio-oil from domestic waste was found to be a promising candidate as a modifier for petroleum–asphalt binder.

Keywords Bio-oil · Bio-asphalt · Chemical properties · FTIR
Rotational viscosity

S. A. Tayh (✉)
Department of Civil Engineering, Mostansiriyah University, Baghdad, Iraq
e-mail: saabta75@yahoo.com

R. Muniandy · S. Hassim · F. M. Jakarni
Department of Civil Engineering, Universiti Putra Malaysia,
43400 Serdang, Selangor, Malaysia
e-mail: ratnas@upm.edu.my

S. Hassim
e-mail: hsalih@upm.edu.my

F. M. Jakarni
e-mail: fauzan.mj@upm.edu.my

1 Introduction

Generally, binders that are utilized for pavement construction are derived mainly from fossil fuels [1]. The most encouraging approaches to address the issue of rising costs of asphalt binder, restricting unrefined petroleum reserves, and demand for a more environmentally friendly, and energy-effective asphalt binders is by providing binders from renewable resources. Though, a number of important research works are being conducted worldwide to produce bio-binders from biomass resources. Since the bio-oil shows a great deal of rheological and performance similitude with crude oil bitumen, such as being cost-effective and simple to be produced locally on a regular basis, it can be a promising asset to provide bio-binder to be utilized as a part of asphalt pavement [1, 2]. Notwithstanding, work has been done demonstrating that the appropriateness of utilizing bio-oils as a bitumen modifier is an exceptionally encouraging option for the traditional asphalt binders [3].

Different specialists have showed that the use of bio-binder generated from artiodactyl mammal will decrease the binder stiffness and enhance the low-temperature characteristics [2, 4]. Wen et al. [5] have found that bio-oil from waste oil would cut back the fatigue and rutting resistance however enhances the thermal cracking resistance. Waste cooking oil was additionally observed to be a decent possibility to be a rejuvenator of matured asphalt binders [5].

The oxidization of asphalt binder will cause weakening in pavement structure attributable to long-run aging. Thus, create cracking. Consequently, bio-oil might presumably serve as an antioxidant agent in asphalt mixtures [6].

Disregarding some applicable analysis completed into utilizing bio-resources for bio-binder, still, considerably more ought to be accomplished for the asphalt paving business to fully cowl the use of bio-oil and to assess if it may be a good contrastive choice to petroleum-based asphalt binder in road pavement development.

For the first time a research as this is being conducted with main objective of investigating the viscosity performance and analysis of aging mechanism of a conventional asphalt binder (80/100) penetration grade binder modified by bio-oil generated from domestic waste. In addition, the aging mechanism of the produced DWBO-binders was studied using the FTIR. The chemical groups variation and chemical reactions throughout the aging were also studied as a result of it is not wide known for such new materials.

2 Methods and Materials

2.1 Generation of Bio-oil from Domestic Wastes

The fast pyrolysis method was followed to provide bio-oil from domestic wastes, wherever waste materials are quickly heated in an exceedingly vacuum to convert

them into fractures like vapors, aerosols, and bio-char. Before introducing the biomass into the transformation process, the domestic wastes materials were dried at concerning a 100 °C for a 24 h period, then the transformation process was done at about 500 °C. quick vaporization was then done on the product from the transformation stage to be condensed using cooling method to get the ultimate bio-oil product.

2.2 Bio-binder Production

The first stage was to upgrade the bio-oil. The DWBO to be tested is obtained from quick pyrolysis of domestic waste. In general, the initial bio-oil contains a high proportion of water (15–35%). Therefore, an upgrading method is critical to cut back the water content within the DWBO. Thus, thermochemical dehydration processes by indirectly heating the DWBO through the vacuum rotary evaporator device was performed. The DWBO was heated at the minimum water evaporation temperature to minimize the excessive aging.

The second step is to mix the treated bio-oil with the base binder to provide DWBO-binder. The DWBO was mixed with the base binder at 3 concentrations (3, 6, and 9%) by weight.

The blending process of the DWBO with the base binder is conducted at steady speed of 1000 rpm using a medium shear laboratory mixer at a temperature of (120–125 °C), until steady state conditions were achieved.

2.3 Laboratory Experimental Program

The experimental program was done to work out the consistency of each the control and the modified asphalt binders. The DWBO has been added to the base asphalt binder at proportions of 3, 6, and 9% by weight and tested as unaged, Rolling Thin Film Oven aged, and Pressure Aging Vessel aged.

The second role of this research consists of using of the elemental composition test (CHNS) and Fourier Transform IR (FTIR) spectrometry characterization technique to investigate the variations in chemical composition before and after the addition of DWBO to assess the aging and also the change in consistency of the modified binders. The roadmap of this research is as shown in Fig. 1.
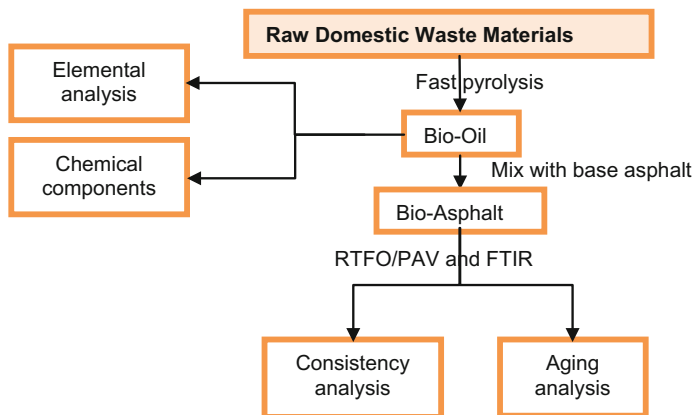
Fig. 1 Roadmap of the study

3 Results and Discussion

3.1 Rotational Viscosity Behavior

Brookfield rotational viscosity (RV) hardware was used in step with ASTM D4402 (2011) method. The rotational viscosity test was made at temperatures of 135, 150, and 165 °C to check up the pattern of viscosity values over a variety of temperatures.

Table 1 shows the average percent differences in viscosity between the unmodified asphalt binder and the DWBO-modified samples. Under all testing conditions, the samples have fulfilled the Superpave most critical viscosity specification of 3 Pa s at 135 °C. The unaged modified samples have lower consistency than the unmodified binder. For RTFO-aged samples, the DWBO-modified samples incontestable less decrease in viscosity compared with control binder specimens. The viscosity test results showed that the addition of DWBO to the base binder will lower mixing and compaction temperatures by lowering the viscosity of the base binder.

For additional analyzation for effect of using DWBO on aging of asphalt binders, the term aging index has been used, as appeared in Eq. 1:

$$\text{Aging Index} = \frac{\text{Viscosity of Aged Binder}}{\text{Viscosity of Unaged Binder}} \tag{1}$$

The aging indexes of the DWBO-binders were calculated and showed in Table 1. It is seen that the aging indexes of DWBO-binders were greater than the control binder.

Table 1 Rotational viscosity differences

Aging status	Temperature (°C)	Binder type			
		AB-80BO0	AB-80BO3	AB-80BO6	AB-80BO9
		Decrease in rotational viscosity (%) at different temperatures			
Unaged	135	0	13.4	33.9	39.7
	150	0	7.3	30.6	34.1
	165	0	7.6	29.5	30.7
RTFO aged	135	0	10.5	26.1	35.4
	150	0	11.6	22.7	29.7
	165	0	9.2	21.9	27.1
Aging index		1.50	1.55	1.59	1.61
Decrease in mixing temperature (°C)		0	3.5	11.5	13.5
Decrease in compaction temperature (°C)		0	4.25	11.3	14.8

3.2 Elemental Composition Characterization

Elemental composition of the asphalt binders were determined by utilizing elemental analysis process (carbon, hydrogen, nitrogen, and sulfur) CHNS.

The CHNS elemental analysis of domestic bio-oil and bio-asphalt contains 6% bio-oil, compared with two representative crude asphalt cement, 80/100 and 60/70 asphalt binders as a comparative analysis are shown in Table 2.

It is clear from Table 2 that DWBO has the highest amount of carbon and nitrogen elements and the lowest amount of hydrogen and sulfur elements. It is evidence that DWBO has a very small portion of sulfur that it can be negligible. The most effect is on nitrogen and sulfur amounts. Six percent of DWBO in the base asphalt has significantly increased nitrogen amount. The increase in nitrogen and oxygen elements could result in increasing the polarity of the base binder and this reciprocally causes the increase in adherence to aggregate surface. Whereas the

Table 2 CHNS elemental analysis of bio-asphalt with representative petroleum asphalts

Asphalt type	Carbon (%)	Hydrogen (%)	Nitrogen (%)	Sulfur (%)
Petroleum asphalt 80/100 penetration grade	80.75	7.87	2.11	5.80
Petroleum asphalt 60/70 penetration grade	82.12	7.86	1.20	4.27
80/100 + 6% house hold bio-oil	81.84	7.95	4.10	4.32
Domestic waste bio-oil	84.58	5.82	4.76	0.96

decrease in sulfur content could result in decreasing the toxic fume and vapors emitted from the binder throughout storage, mixing, transportation, and compaction processes.

3.3   Chemical Characterization Utilizing FTIR

Fourier transform spectrometry measures the infrared (IR) light absorbed by a particular material. This absorption relies upon its constituents and especially on the chemical functions displayed in the material. The FTIR spectroscopy of the DWBO-binder tests was directed using Perkin Elmer Spectrum 100 FTIR framework, utilizing the universal attenuated total reflectance (UATR) furnished with Gee crystal with a wave length of 650–3000 cm^{-1}, the scan rate of 4 cm^{-1}, and a scan time of 4 s.

FTIR setup was used to measure the functional and structural indexes of the DWBO-binders on unaged, RTFO-aged, and PAV-aged samples.

Infra Red (IR) spectra for the DWBO-binders and relating crude asphalt (80/100) are shown in Fig. 2. The functional groups between the 600 and 2000 cm^{-1} were indicated [7]. Comparative and symmetrical absorbance peaks were recognized between the control and modified asphalt binders. Aromatic and heteroaromatic rings, carbonyl, sulphoxides, methylene (aliphatic), and methyl (aliphatic) functional groups were recognized for the DWBO-binders specimens at the unaged, RTFO-, and PAV-aged conditions.

To decide the oxidation condition of a bituminous binder specimen, the crests for carbonyl, and sulfoxide can be determined at 1700 cm^{-1} denoted as ($I_{c = o}$), and
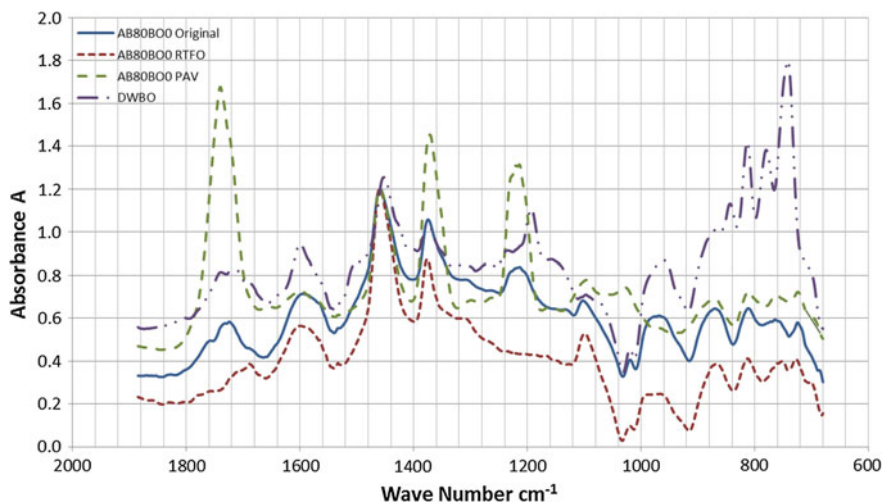
Fig. 2 Comparative FTIR spectra of the base and aged 80/100 DWBO-binders

1030 cm^{-1} denoted as ($I_{s = o}$), respectively, hence the integral bounds used are 1819–1668 cm^{-1} and 1035–1010 cm^{-1}, respectively [8–11]. For the DWBO-binders, there are extra peaks at 1110 cm^{-1} representative for ethers and 1220 cm^{-1} representative for acids and esters [12].

A quantitative examination of the carbonyl, sulphoxide, ethers, esters, and chloroform indexes is ascertained from an average FTIR spectrum range on an asphalt binder as in the following equations:

$$I_{c=o} = \frac{\text{Area of the carbonyl band around } 1700 \, \text{cm}^{-1}}{\text{Area of the spectral band between } 2000 \text{ and } 600 \, \text{cm}^{-1}} \tag{2}$$

$$I_{s=o} = \frac{\text{Area of the sulfoxide band around } 1030 \, \text{cm}^{-1}}{\text{Area of the spectral band between } 2000 \text{ and } 600 \, \text{cm}^{-1}} \tag{3}$$

$$I_{SD1} = \frac{\text{Area of acids and esters band around } 1220 \, \text{cm}^{-1}}{\text{Area of the spectral band between } 2000 \text{ and } 600 \, \text{cm}^{-1}} \tag{4}$$

$$I_{SD2} = \frac{\text{Area of the chloroform band around } 764 \, \text{cm}^{-1}}{\text{Area of the spectral band between } 2000 \text{ and } 600 \, \text{cm}^{-1}} \tag{5}$$

$$I_{C-O-C} = \frac{\text{Area of the ethers band around } 1110 \, \text{cm}^{-1}}{\text{Area of the spectral band between } 2000 \text{ and } 600 \, \text{cm}^{-1}} \tag{6}$$

The calculation of Oxidation Index (OI) was using the Eqs. (7 and 8)

$$\text{Oxidation Index after RTFO} : \text{OI}_{RTFO} = \frac{\sum I_{\text{after RTFO aging}}}{\sum I_{\text{before aging}}} \tag{7}$$

$$\text{Oxidation Index after PAV} : \text{OI}_{PAV} = \frac{\sum I_{\text{after PAV aging}}}{\sum I_{\text{before aging}}}, \tag{8}$$

where

$\sum I_{\text{after aging}}$ is the sum of bond indexes after aging
$\sum I_{\text{before aging}}$ is the sum of bond indexes before aging

Table 3 demonstrates the functional groups of the approximate absorption wave numbers in Fig. 3. The results showed that there was no considerable difference in functional groups after adding DWBO to the base binder.

The bond indexes and oxidation indexes for the DWBO-binders are shown in Table 4. There was almost a decrease or no change in band area of the bond ratios after RTFO aging. The oxidation indexes are only 0.25, 0.30, 0.54, and 0.66 for 0, 3, 6, and 9% DWBO by weight of the base asphalt binder 80/100.

However, it is noticed that there is slight increase of Oxidation Index (OI) after RTFO with the increase of bio-oil proportion. This indicates that little oxidation occurred during the RTFO aging. For the DWBO-binders, most of the bond indexes

Table 3 IR absorbance for representative functional groups for DWBO and asphalt

Wavenumber (cm^{-1})	Molecular motion	Functional group
1700	C = O stretch	Aldehydes and ketones (Carbonyl)
1600	C = C and C = O stretch	Aromatics
1460	CH$_2$ bend	Alkanes (methylene)
1375	CH$_3$ bend	Alkanes (methyl)
1220	C–C, C–O and C = O stretch	Acids and esters
1110	C–O–C stretch	Ethers
1030	S = O	Sulfoxides
764		Chloroform band
700–900	C–H bend	Aromatics
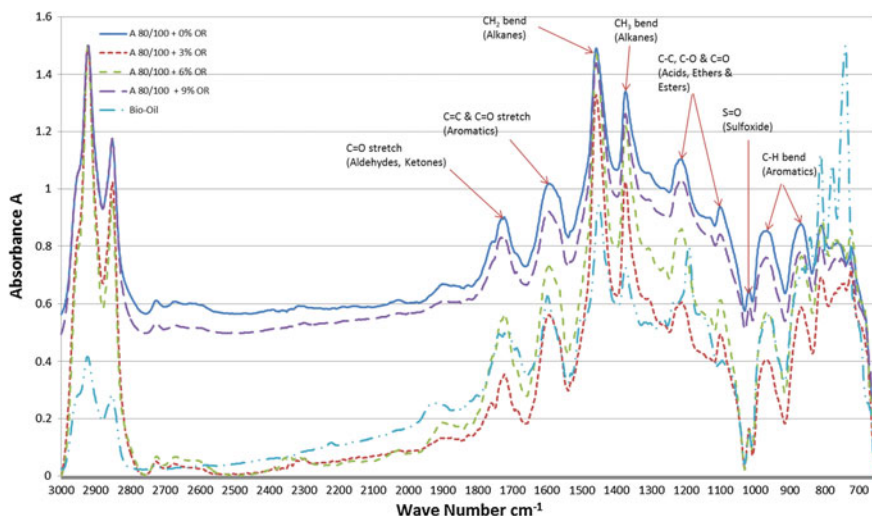
Fig. 3 FTIR spectra of the unaged 80/100 binder and the corresponding DWBO-binders

diminished after the RTFO aging, indicating a decrease in alcohol, ester, ether, and carbonyl groups concentration after RTFO aging. Therefore, the FTIR results showed no noteworthy oxidation after RTFO. This is often reliable with the viscosity test results, whereas there was a large chemical reaction for the DWBO-binders after PAV aging, despite the actual fact that this oxidation has lowered by the increase of DWBO percentage. It is believed that the long-term aging characteristics will be enhanced in the field on the base that the temperature and the air pressure are relatively low, compared by the test in lab conditions.

Table 4 Band areas of representative bonds before and after aging

Binder type	Aging state	Bond location (cm^{-1}) and bond index ($\times10^{-3}$)				Oxidation index (OI)
		C = O (1700)	C–O (1220)	C–O (1110)	S = O (1030)	
AB-80BO0	Original	32.90	13.79	2.03	1.47	–
	After RTFO	7.74	0.08	3.73	1.03	0.25
	After PAV	224.68	100.89	2.08	2.09	6.57
AB-80BO3	Original	38.46	17.13	3.73	3.75	–
	After RTFO	15.06	1.95	0.06	2.05	0.30
	After PAV	217.02	80.16	1.74	3.19	4.79
AB-80BO6	Original	46.61	22.13	3.57	2.48	–
	After RTFO	34.46	3.15	0.40	2.47	0.54
	After PAV	180.96	94.83	2.41	2.50	3.75
AB-80BO9	Original	66.16	25.77	1.84	1.61	–
	After RTFO	52.35	1.84	0.12	1.92	0.59
	After PAV	153.47	65.17	5.65	2.19	2.37

It is noticed in Table 4, that DWBO has the biggest portion of carbonyl, alcohol and sulfoxide, which is means more oxygen component. However, there is no noteworthy increment of carbonyl, alcohol or sulfoxide ratios observed after the RTFO aging. This could be due to the escape of lightweight compounds which have higher carbonyl and sulfoxide content.

However, the rotational viscosity results demonstrated that the consistency will increase after RTFO aging. Thus, the most reliable reason for the aging is because of the molecular loss of lightweight compounds within the DWBO-binders. After PAV aging, the bond ratios of alcohol and carbonyl for control asphalt binder and DWBO-binders increased. This is practically verified by oxidation, and this proves that the oxidation is the main cause of aging during PAV test.

Generally, the aging indexes for the DWBO-binders after PAV aging minimized with the rise in the DWBO content. This implies less susceptibleness for long-term aging, whereas the result of adding DWBO to the base binders is to decrease the viscosity and this might lead to improve fatigue cracking resistance of the binders and asphalt mixtures at intermediate temperatures.

4   Summary and Conclusions

Based on the analysis of the proposed characterization tests in this research, the main findings and conclusions are summarized as below

1. According to elementary test results, the DWBO has less content of Sulfur part than the base binder which can cause lower toxicity;
2. The DWBO forms a consistent chemical compounds with typical asphalt binders;
3. The results from FTIR analysis indicate that each DWBO and the base asphalt binder consist of saturated hydrocarbons and aromatic hydrocarbons. These parts are within the continuous phase embracing the asphaltene molecules and attribute to the liquidity in asphalt materials. Thus, DWBO does have the potential to soften the asphalt binder;
4. The DWBO-binders are more susceptible to be aged contrasted with the control binder;
5. The DWBO-binders rate of oxidation, measured by OI, when PAV aged, is smaller than that when RTFO-aged, inferring a good aging characteristics at the long-run service life.

It is clear from the result and conclusions in this study that the DWBO asphalt binders have similar physical and chemical properties compared by the traditional control binders and might be utilized in asphalt pavement industry with cautions associated with blending conditions the base binders, and mixing and compaction temperatures.

All of the aforementioned changes have an influence on the physical and rheological characteristics of DWBO-binders and consequently on the mechanical performance of asphalt mixtures. However, aging is the most crucial concern for asphalt binders during the construction and service life, the aging of DWBO-binders ought to be well addressed when employed in the asphalt pavement industry. Additionally, during aging process, some chemicals are produced whereas some are decreased, hence, the result of those chemicals on the environment and also the field paving crew ought to be extremely evaluated to conform to the safe construction environment of pavements incorporating DWBO-binder modifier.

References

1. Airey, G.D., Mohammed, M.H.: Rheological properties of polyacrylates used as synthetic road binders. Rheol. Acta **47**(7), 751–763 (2008). https://doi.org/10.1007/s00397-007-0250-3
2. Fini, E., Kalberer, E., Shahbazi, A., Basti, M., You, Z., Ozer, H., Aurangzeb, Q.: Chemical characterization of biobinder from swine manure: sustainable modifier for asphalt binder. J. Mater. Cvil Eng. **23**(11), 1506–1513 (2011). https://doi.org/10.1080/14680629.2016.1163281

3. Raouf, M., Williams, R.C.: Development of Non-Petroleum Based Binders for Use in Flexible Pavements. Institute for Transportation, Final Report. Iowa State University (2010)
4. Mills-Beale, J., You, Z., Fini, E., Zada, B., Lee, C.H., Yap, Y.K.: Aging influence on rheology properties of petroleum-based asphalt modified with biobinder. J. Mater. Civ. Eng. **26**, 358–366 (2014). https://doi.org/10.1061/(ASCE)MT.1943-5533.0000712
5. Wen, H., Bhusal, S., Wen, B.: Laboratory evaluation of waste cooking oil-based bioasphalt as an alternative binder for hot mix asphalt. J. Mater. Civil Eng. **25**(10), 1432–1437 (2013). https://doi.org/10.1061/%28ASCE%29MT.1943-5533.0000713
6. Tang, S.: Asphalt Modification by Utilizing Bio-Oil Esp and Tall Oil Additive. A thesis of master degree, Iowa State University (2010)
7. Karlsson, R., Isacsson, U.: Application of FTIR-ATR to characterization of bitumen rejuvenator diffusion. J. Mater. Civ. Eng. **15**, 157–165 (2003). https://doi.org/10.1061/(ASCE)0899-1561(2003)15:2(157)
8. Belgian Road Research Center: Bitumen Analysis by FTIR Spectrometry : Testing and Analysis Protocol. Brussels (2013)
9. Kanabar, A.: Physical and Chemical Aging Behavior of Asphalt Cement from Two Northern Ontario Pavement Trials. MSc. thesis, Queen's University Kingston, Ontario, Canada (2010)
10. Hagos, E.T.: The Effect of Aging on Binder Properties of Porous Asphalt Concrete. Ph.D. thesis, Delft University of Technology (2008)
11. Wu, S., Pang, L., Mo, L., Chen, Y., Zhu, G.: Influence of aging on the evolution of structure, morphology and rheology of base and SBS modified bitumen. Constr. Build. Mater. **23**(2), 1005–1010 (2009). https://doi.org/10.1016/j.conbuildmat.2008.05.004
12. Yang, Xu.: The Laboratory Evaluation of Bio Oil Derived From Waste Resources as Extender for Asphalt Binder. Master's thesis, Michigan Technological University (2013)

Part V
Water Engineering

Heavy Metal Contamination in Environmental Compartments of Buriganga River in Dhaka City

Md. Isreq Hossen Real, Asef Redwan,
Md. Mosheur Rahman Shourov, Hossain Azam and Nehreen Majed

Abstract Numerous textiles-/tanneries-/pharmaceutical-based industrial processes along with anthropogenic sources, discharge hazardous waste/wastewater into nearby water bodies. These untreated or poorly treated waste streams contain heavy metals that come into contact with sediment/aquatic systems and become part of the food chain. Heavy metals, many of which are persistent, bioaccumulative, and toxic, have a significant impact on environment and ecosystem. Buriganga has been accumulating alarming levels of heavy metals, and currently, it is one of the most polluted rivers in Bangladesh. This study evaluated the levels of selected heavy metals in different environmental compartments of the Buriganga river. Accordingly, three significant locations along the river stretch were selected. The plant (*Enhydra fluctuans*) and phytoplankton (*Lemnoideae*) samples and four different species of fish such as *Heteropneustes fossilis*, *Channa striata*, *Corica soborna*, and *Wallago attu* were collected from the river. Laboratory analysis of cadmium (Cd), chromium (Cr), lead (Pb), nickel (Ni), and zinc (Zn) was performed in all the sediment/plant/river water/fish samples. Contamination factor and plant concentration factors were determined. Concentrations of Cd, Zn, and Ni in the river water were obtained within acceptable ranges, whereas Cr and Pb exceeded the toxicity reference values for surface water standards for aquatic life. Notable concentration levels of heavy metals were measured in the sediments and plants. Specifically, Cr was obtained at an alarming level of 103 mg/kg in soil and 163 mg/kg in the plants near Hazaribagh area, where tannery waste mixes with the river water. Bioaccumulation of the analyzed metals was evidenced in the biological samples.

Md. I. H. Real · Md. M. R. Shourov · N. Majed (✉)
Department of Civil Engineering, University of Asia Pacific, Dhaka, Bangladesh
e-mail: nehreen23@gmail.com

A. Redwan
Department of Civil, Environmental and Construction Engineering,
Texas Tech University, Lubbock, TX, USA

H. Azam
Department of Civil and Environmental Engineering, Manhattan College,
New York, NY, USA

1 Introduction

Urban environmental pollution has intensified in recent years attributable to the advancement in urbanization, industrialization, and modern technology. Rapid urbanization and industrialization in Bangladesh have negatively affected the environment drastically since last two decades [1, 2]. These industries have limited effluent management system and reported to alter the physical/chemical/biological characteristics of the marine environment [3]. The inappropriate disposal and discharge practices of wastes cause severe pollution of water bodies. Contaminants due to poor control of effluents from textiles, tanneries, pharmaceutical industries, and release of toxic solid waste/wastewater come across with aquatic systems. Besides, sludge released in aquatic systems from the wastewater treatment process comprises a high proportion of poisonous substances like heavy metals and persistent organic pollutants (POPs) [4, 5]. Heavy metals exert genotoxic consequences on marine organisms [6, 7] and the marine food sources constitute important position in the human food chain [8, 9].

Heavy metals are cogitated as pollutants due to the perniciousness and persistence of those in the natural environment and strong linkage with different food chains [10, 11]. Uptake of certain heavy metals at elevated levels can damage gastrointestinal system, kidneys and nervous system [12], while some might cause cancer. Heavy metals also adversely impact ecological balance in soil/water, agricultural production, and surface/groundwater quality. The concentration of these pollutants seems to be very low, but these accumulate and get absorbed by lower organisms in the food web such as fish/earthworms/plants. These phenomena ultimately lead to serious harm to human health.

Heavy metal contamination is widespread, and it has become an inevitable challenge in recent times. So, it was addressed through multiple studies in river water, sediment, and fish [2, 13–15]. Heavy metals pollution has become a foremost hazard to public health in Bangladesh. The Buriganga river that flows past Dhaka, has an enormous capacity to accumulate heavy metals [16]. The massive volume of wastes contain a vast amount of heavy metals, and other poisonous contaminants are releasing to the water bodies directly or after accomplishing partial treatment from the city's enormous houses and industries, e.g., tannery, electronic, textile. Hence, organic and inorganic pollutants keep contaminating the river thus promoting depreciation of the environmental ecosystem. Heavy metals that are released into the Buriganga with these pollutants are eventually assimilated into the riverside soil, plants and sediments. Even fishes accumulate these heavy metals. Thus water, sediments and aquatic organisms are not entirely innocuous for the human health and the environment. This necessitates determining the present contamination scenario of heavy metals and the distribution of the metals in water, plant, sediment,

and aquatic organisms of the Buriganga river. There are only a few studies concerning the heavy metal contaminations of different environmental compartments in Buriganga river. However, no study is available until now that comprehensively analyze each of the major environmental compartments individually and shows the connection between the heavy metal contaminations of each compartment to the others. This study intended to evaluate the heavy metal pollution of the Buriganga river by estimating the heavy metal levels (Cr, Cd, Pb, Ni, and Zn) in water, riverside soil, sediment, plant, phytoplankton, and aquatic life, e.g., fish. It has also assessed the pollution status of the area by calculating parameters such as contamination factor (CF), plant concentration factor (PCF), and bioconcentration factor (BCF), and has highlighted relationships among metals pollution.

2 Methodology

2.1 Study Area

Buriganga is a severely polluted river in Bangladesh because of frequent discharge of natural/anthropogenic wastes. The river water is currently such severely polluted that the lives of aquatic organisms are at stake; sediments and plants beside the river are acutely becoming contaminated by heavy metals. With the intention to evaluate the contamination level of this river; water, sediment, plant, phytoplankton, and fish samples were collected and processed for analyzing heavy metals. The study area was split into three consecutive compartments; each located at least 2 km away from adjacent sampling station. Sampling locations were significant along the river stretch for their ill reputation for being polluted by several sources.

Sampling locations 1 and 3 (Basila and Babu Bazar) are heavily populated zones with industries, power plants, and numerous discharge points of municipal effluents (Fig. 1). Sampling location 2 is placed in Hazaribagh, where hundreds of tanneries are situated, and their effluents are often discharged into Buriganga river without noteworthy treatment. This division, therefore, enabled a qualitative identification and comparison of enrichment of heavy metals in particular location with a view to getting the representative indices of river water quality. Multiple sampling was accomplished in 2016 from three of the sampling locations as displayed in Fig. 1.

2.2 Sample Collection and Analysis

Water samples from Buriganga river were collected from three locations by laboratory prepared bottles of 500 ml (rinsed couple of times with river water beforehand) and acidified immediately according to APHA method [17]. Collected samples were preserved in a refrigerator at below 6 °C until analyzing.

Fig. 1 Three sampling locations of Buriganga river 1, 2, and 3 represent Basila, Hazaribagh, and Babu Bazar respectively

The sediment samples were collected by following the approach suggested by USEPA [18]. Plant species, *E. fluctuans*, were partially submerged in water. They were rooted out from the soil meticulously. Plants were rinsed with distilled water, collected in plastic bags and preserved at below 6 °C until analyzing. Phytoplankton (*Lemnoideae*) was sampled from the river surface using phytoplankton net. Nine samples of water, sediments, phytoplanktons, and plants (three samples per location) of each component were collected. Four different species of fish such as *Heteropneustes fossilis* (Shing), *Channa striata* (Shole), *Corica soborna* (Kachki) and *Wallago attu* (Boal) were captured from different locations at Buriganga river by the fishermen.

Five heavy metals chromium (Cr), cadmium (Cd), lead (Pb), nickel (Ni), and zinc (Zn) were selected to analyze for this study. Fish, phytoplankton, and plant samples were homogenized and ground into fine powder. To eliminate suspended materials, water samples were filtered using 0.45 μm filter paper. All samples were individually digested (at up to 105 °C) in a hot plate using perchloric and nitric acid. Standard solutions for each metal were prepared beforehand and were calibrated to measure the error. Heavy metal levels in the digested samples of water, riverside sediment, phytoplankton, and plant were examined using an atomic absorption spectrophotometer; Shimadzu, (AAS)—6800 model using flame photometry techniques described by Isaac and Kerber [19]. The fish samples were examined following the method suggested by Price [20] using the same AAS.

2.3 Calculation of Contamination Factor, Plant Concentration Factor, Bioconcentration Factor

CF_{metals} is defined as the ratio of the concentration of analyzed metal in the sediment to that in the geochemical background (the average shale value),

$$CF_{metal} = C_{metal}/C_{background} \qquad (1)$$

The contamination factor (CF) is used to determine the purity classes of the sediment samples. To monitor the contamination of metal, CF has been categorized into four classes: low contamination (CF < 1), moderate contamination (1 ≤ CF < 3), considerable contamination (3 ≤ CF < 6), and very high contamination (CF ≥ 6) [21]. Therefore, CF values provide an idea of the increase/decrease of a certain metal in sediments over a given period of time.

Transfer of metal from soil to plant is a key component of determining human exposure to metals through the food chain. The plant concentration factor (PCF), also known as transfer coefficient was estimated as follows:

$$PCF = C_{plant}/C_{soil}, \qquad (2)$$

where, C_{plant} and C_{soil} are the concentrations of analyzed heavy metal of plant and soil, respectively [22]. Higher PCF values suggest greater efficiency of plants to absorb metals from the soil, whereas lower values represent the strong sorption of metals to the soil colloids [23].

Bioconcentration factor (BCF) is used for the identification of bioaccumulative substances and provides a valuation for a specific concentration ranges for water bodies to maintain the pollutant concentration below the acceptable daily intake. By comparing BCF, a comparison could be made on the ability of those organisms to uptake metal from water. The bioconcentration factor (BCF) was calculated as follows:

$$BCF = C_{organism}/C_{water} \qquad (3)$$

According to EU regulation 253/2011 [24] in the context of assessing persistent, substances are bioaccumulative with a BCF > 2000 and very bioaccumulative with BCF > 5000. It is commonly considered that chemicals with BCFs < 1000 are low bioaccumulative [25].

3 Results

3.1 Heavy Metal Pollution Load in Water

Five types of heavy metals were analyzed in each sampling points. The levels of Cd, Cr, Pb, Ni, and Zn in the river water were compared with standards to check whether they were present within their permissible limits. The concentration ranges of these metals were observed to be 0.007–0.224 mg/l for Cr, below detection limit (BDL) to 0.0014 mg/l for Cd, BDL to 0.028 mg/l for Pb, 0.015–0.024 mg/l for Ni 0.028–0.12 mg/l for Zn. A decreasing order of concentrations was observed with Zn with the highest concentration and Cd with the lowest concentration
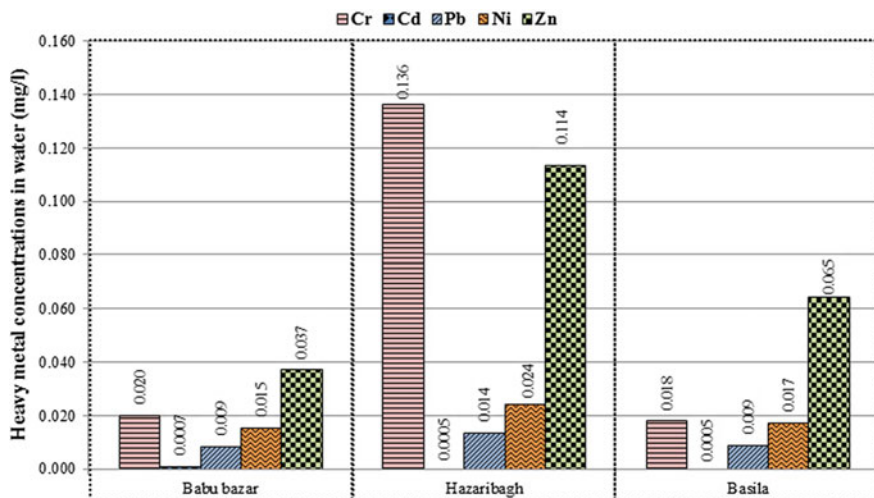
Fig. 2 Mean concentrations of heavy metals in Buriganga river water

(Zn > Cr > Ni > Pb > Cd). Chromium in water was observed to be more than five times greater than the tolerable limit at Hazaribagh (Fig. 2). In other locations, levels of chromium nearly matched the tolerable limit given by WHO standard for drinking water [26]. The mean Cr concentration in water was reported as 0.058 mg/l which greatly exceeded the toxicity reference value (TRV) for safe water (0.011 mg/l) proposed by USEPA [27]. Studies on Buriganga river water showed the similar level of Cr analogous to this study [16, 28, 29]. The highest (0.0244 mg/l) concentration of Pb was found in Hazaribagh.

In this study, the mean concentration of Pb in water (0.01 mg/l) exceeded the TRV (0.003 mg/l). The concentration of Pb was similar to different Buriganga River related studies carried out by Khan et al. [30] and Alam et al. [31]. The concentration levels of Cd, Zn, and Ni in the water were detected within acceptable ranges. The surface water quality standard to protect aquatic species in water bodies for both Cr and Pb is 0.001 mg/l established by CCME [32]. Hence, Cr and Pb exceeded the limit of toxicity reference values and surface water quality standards for aquatic life, indicating that water from this river require significant treatment if it is intended for domestic use like drinking and/or cooking.

3.2 Heavy Metal Pollution Load in Sediment

The mean concentrations of heavy metals identified in the sediment samples of Buriganga river are shown in Fig. 3. The unregulated presence of different industries and their waste treatment and dumping systems influenced the heavy metal concentrations at different locations sampled [31]. For the sediments,
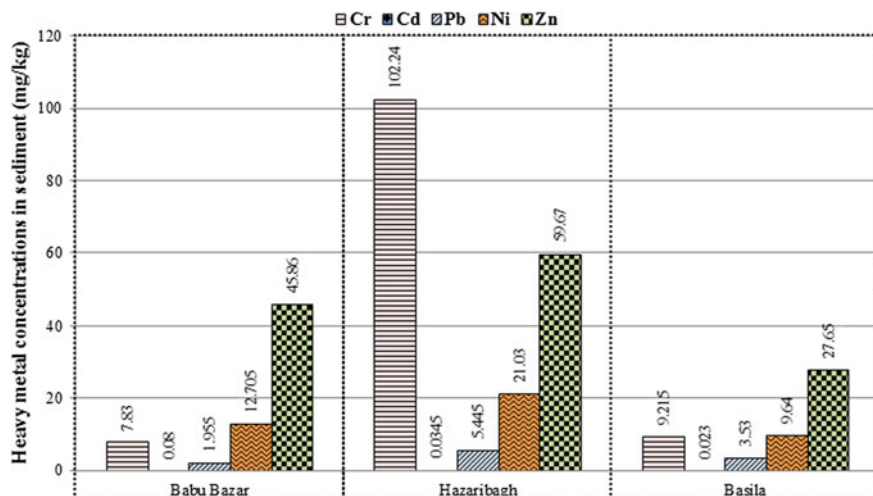
Fig. 3 Mean concentrations of heavy metals in Buriganga river sediments

the toxicity order based on the levels of heavy metal can be assigned as Cr > Zn > Ni > Pb > Cd in Buriganga river. Cd concentration was the lowest ranging from BDL to 0.16 mg/kg among the metals analyzed, whereas, a significant level of Cr (103.58 mg/kg) was observed in the sediments at Hazaribagh area (Fig. 3). Ni and Pb concentration in sediments were also the highest at Hazaribagh. Average Ni concentration exceeded the sediment quality guideline (16 mg/kg) suggested by USEPA [27]. Sediment samples showed elevated levels of Zn at every sampling point though they did not exceed the permissible limit. The levels of Cr in sediments ranged from 5.53 to 103.58 mg/kg with a mean value of 39.76 mg/kg. Unregulated and untreated Cr discharge from leather industries into the river could be the reasons behind the high levels of Cr [27]. The concentration of Cr in the majority of the sediment samples exceeded the permissible limit set for sediment. Cd, Pb, and Zn in the Buriganga river sediments were found to be lesser than the acceptable limit for sediment set by USEPA [27].

3.3 Heavy Metal Pollution Load in Plant

Plant samples, e.g., *Enhydra fluctuans*, collected from the study area showed alarming concentrations of heavy metals. The mean concentration levels of heavy metals detected in plants are presented in Fig. 4. Significant levels of Cr, Pb, Cd, Zn, and Ni were identified in the plant species. The average levels of heavy metals in *E. fluctuans* are in the descending order with Zn with highest concentrations and Cd is lowest concentrations (Zn > Cr > Ni > Pb > Cd) similar to the observation of Zhang et al. [15].
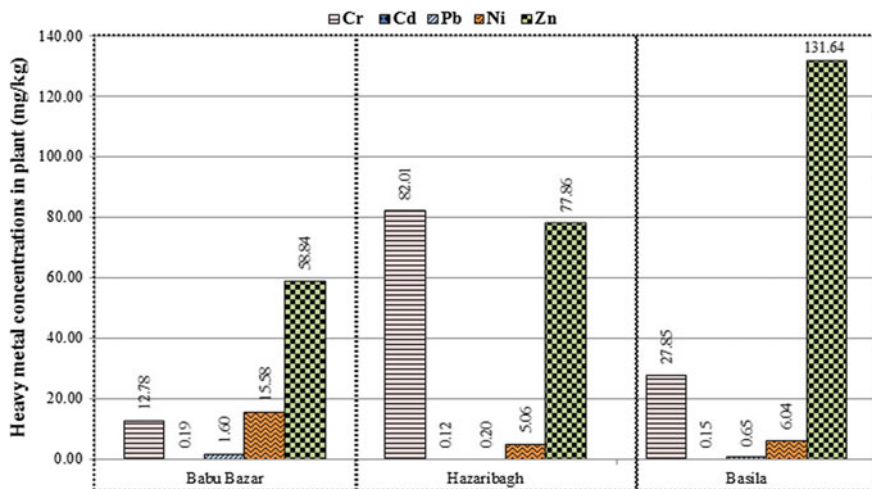
Fig. 4 Mean concentrations of heavy metals in plant beside Buriganga river

Cr concentration varied between 0.95 and 163.06 mg/kg. The maximum level of Cr was observed at Hazaribagh. This can be attributed to the tannery industries beside the Hazaribagh location. The mean concentration of Cr in plant exceeded the permissible limit for plant set by WHO [33]. Mean concentration levels of Cr in plant samples observed were 40.88 mg/kg while the allowable limit of Cr in plants by WHO had been specified as 1.5 mg/kg. Cd has potential to biomagnify and can be toxic to microorganisms. The Cd levels in various plants grown in unpolluted soils typically vary from 0.05 to 0.2 mg/kg [34]. Cd was accumulated the least in plants among the metals. The levels of Cd in the plant samples were BDL to 0.37 mg/kg. The average Pb content (2.55 mg/kg) in the present study is higher than the acceptable limit. The highest Ni concentration in the plant was observed at Babu Bazar (27.75 mg/kg). Plant samples exceeded the acceptable limit for Ni suggested by WHO [33] which is 10 mg/kg.

The maximum concentration of Zn (244.60 mg/kg) in *E. fluctuans* was found in Basila. Almost all plant samples exceeded WHO's recommended limit in each of the observed periods for Zn [35]. It is clear that *E. fluctuans* has stronger ability to accumulate for observed metals.

3.4 Heavy Metal Pollution Load in Fish

Long-term uncontrolled and untreated industrial wastes disposal could pollute the marine life (e.g., fish) having a significant impact in the food chain. Several point and non-point sources have been polluting the Buriganga river for a long time. Aquatic organisms living in Buriganga river must have been experiening negative

Table 1 Concentrations of heavy metals in fish samples in Buriganga river

Sample types	Cr	Cd	Pb	Ni	Zn
Corica soborna	1.04	BDL	2.92	BDL	23.61
Heteropneustes fossilis	0.35	0.035	0.765	0.245	6.83
Channa striata	0.57	0.015	0.52	0.13	12.675
Wallago attu	BDL	BDL	BDL	BDL	32.35
WHO Standards for aquatic life (Sudhira and Kumar [37])	0.1	0.0002	0.025	0.025	0.03

BDL Below detection limit

impacts, which eventually may cause the extinction of these organisms. In this study, the level of Cr in the fish samples was 0.29–1.04 mg/kg. The highest level of Cr was found in *Corica soborna* (1.04 mg/kg) and the lowest in *H. fossilis* (0.29 mg/kg). Concentrations of Cd in fish samples were below the permissible limit. Permissible limit of Cd for fish is 0.05 mg/kg established by Codex Alimentarius Commission [36]. The maximum concentration of Cd was observed in *H. fossilis* (0.04 mg/kg). No Cd was found in the muscle tissue in most of the fish samples. Pb content in fish samples was found up to 2.92 mg/kg. Except for *Wallago attu,* Pb was seen to accumulate in all other analyzed fish samples exceeding the WHO Standards for aquatic life (0.025 mg/kg). Nickel concentrations found in fish were BDL to 0.26 mg/kg and Zn concentrations were 5.77–32.35 mg/kg (Table 1).

3.5 Assessment of Metal Pollution (CF, PCF, BCF)

The values of contamination factor (CF) for all the metals revealed low contamination in sediments for all the sampling locations except for Cr which indicated moderate contamination in Hazaribagh (Table 2). Trend of CF was different for sediments of different locations. Babu Bazar followed the order of: Cd > Zn > Ni > Cr > Pb; Hazaribagh followed: Cr > Zn > Ni > Pb > Cd; Basila followed: Zn > Ni > Pb > Cr > Cd. The average CF values of Zn, Ni, Cd, Cr, and Pb were 0.40, 0.36, 0.33, 0.54, and 0.19 respectively.

The transport of metals from the soil to plants can be determined well by looking into plant concentration factors (PCF) of this study. The PCF of the studied heavy

Table 2 Summary of CF for sediments of different locations

Location	CF					PCF				
	Cr	Cd	Pb	Ni	Zn	Cr	Cd	Pb	Ni	Zn
Babu Bazar	0.14	0.57	0.07	0.32	0.32	1.63	2.33	0.82	1.23	1.28
Hazaribagh	1.32	0.24	0.34	0.52	0.54	0.80	3.36	0.04	0.24	1.30
Basila	0.17	0.16	0.18	0.24	0.35	3.02	6.71	0.18	0.63	4.76

Table 3 Bioconcentration factor (BCF) of heavy metals in different species

Source/species	Zn	BCF (l/kg)	Pb	BCF (l/kg)	Cr	BCF (l/kg)
Water (mg/l)	0.046		0.014		0.018	
Primary producers		405.43		1758.57		195.28
Lemnoideae [mg/kg]	18.65		24.62		3.515	
Primary consumers		513.26		208.57		57.78
Corica soborna [mg/kg]	23.61		2.92		1.04	
Secondary consumers		404.13		74.29		43.33
Channa striata [mg/kg]	18.59		1.04		0.78	
Tertiary Consumer		703.26		–		–
Wallago attu [mg/kg]	32.35		BDL		BDL	

metals are presented in Table 2. The PCF showed that Cd was adsorbed significantly among all metals followed by Zn, Cr, Ni, and Pb respectively (Table 2). The highest PCF was obtained at 6.71 for Cd and the lowest was found 0.04 for Pb. This signifies that the plant, *E. fluctuans* absorbs a higher concentration of Cd from the soil compared to other metals. Very low transfer of Pb suggests that the plant is less likely to absorb Pb.

The results obtained from the biological samples are shown in Table 3. In most of the cases, bioaccumulation of all the analyzed heavy metals was evidenced as the metal concentration seems to have a greater contribution in biological samples than that in water. However, the BCF values indicated that any of the heavy metals seem to be neither persistent nor very bioaccumulative (according to EU regulation) as BCF ranges are less than 2000. The BCF values for *Lemnoideae* confirmed that the species is a hyperaccumulator for lead. Higher BCF value for lead (>1000) indicates *Lemnoideae* as a suitable species for phytoremediation purposes.

4 Conclusions

Evaluation of heavy metals from the different compartments along the river stretch provided adequate information to assess the current environmental and ecological health of the river and riverside environment concerning heavy metal contamination. Although the heavy metals concentrations in water were not significant to impose severe risks, the sediments, plants and the fishes accumulate heavy metals even at frightening levels in certain cases. The significant accumulation of metals was observed in fish followed by soil, plant, and water. All metals present in water, except for Cr and Pb, were less than the toxicity reference values for safe water and the surface water quality standard for aquatic life. The contamination indices (CF, PCF, BCF values) did not exhibit alarming ranges or significant concerns; nevertheless, the sources of heavy metal contamination of the Buriganga river should be controlled to prevent further deterioration of the quality of river water and its surroundings.

References

1. Chowdhury, M.H.I.: Urban diversity and changes under globalization: a management perspective on beneficial urban development with a special reference to Dhaka megacity. Paper submitted to T.U., Berlin, Germany (2006)
2. Islam, M.S., Ahmed, M.K., Raknuzzaman, M., Habibullah-Al-Mamun, M., Islam, M.K.: Heavy metal pollution in surface water and sediment: a preliminary assessment of an urban river in a developing country. Ecol. Indic. **48**, 282–291 (2015). https://doi.org/10.1016/j.ecolind.2014.08.016
3. Huq, E.: A Compilation of Environmental Laws of Bangladesh. Department of Environment, Government of Bangladesh, Bangladesh (2004)
4. Paxéus, N.: Organic pollutants in the effluent of the large wastewater treatment plant in Sweden. Water Res. **30**, 1115–1122 (1996). https://doi.org/10.1016/0043-1354(95)00278-2
5. Singh, K.P., Mohan, D., Sinha, S., Dalwani, R.: Impact assessment of treated/untreated wastewater toxicants discharged by sewage treatment plants on health, agricultural and environmental quality in the wastewater disposal area. Chemosphere **55**, 227–255 (2004). https://doi.org/10.1016/j.chemosphere.2003.10.050
6. Medina, M., Correa, J.C., Barata, C.: Micro-evolution due to pollution: possible consequences for ecosystem responses to toxic stress. Chemosphere **67**, 2105–2114 (2007). https://doi.org/10.1016/j.chemosphere.2006.12.024
7. Frenzilli, G., Nigro, M., Lyons, B.P.: The Comet assay for the evaluation of genotoxic impact in aquatic environments. Mutat. Res. **681**, 80–92 (2009). https://doi.org/10.1016/j.mrrev.2008.03.001
8. Chakraborty, C., Huq, M.M., Ahmed, S., Tabassum, T., Miah, R.: Analysis of the causes and impacts of water pollution of Buriganga river: a critical study. Int. J. Sci. Technol. Res. **2**(9) (2013)
9. Majed, N., Real, M.I.H., Akter, M., Azam, H.M.: Food adulteration and bio-magnification of environmental contaminants: a comprehensive risk framework for Bangladesh. Front. Environ. Sci. **4**, 34 (2016). https://doi.org/10.3389/fenvs.2016.00034
10. Hapke, H.J.: Heavy metal transfer in the food chain to humans. In: Rodriguez-Barrueco, C. (ed.) Fertilizers and Environment: Proceedings of the International Symposium "Fertilizers and Environment", held in Salamanca, Spain, 26–29 Sept 1994. Springer Netherlands, Dordrecht (1996)
11. David, X.S., Romero, R., Esperanca, G., Jordi, C.: Differential accumulation of mercury and other trace metals in the food web components of a reservoir impacted by a chlor-alkali plant (Flix, Ebro River, Spain): implications for biomonitoring. Environ. Pollut. **159**, 1481–1489 (2011)
12. NRC (National Research Council), Drinking Water and Public Health: Safe Drinking Water Committee, pp. 237–245. National Academy Press, Washington (1977)
13. Öztürk, M., Özözen, G., Minareci, O., Minareci, E.: Determination of heavy metals in of fishes, water and sediment from the Demirköprü Dam Lake (Turkey). J. Appl. Biol. Sci. **2**(3), 99–104 (2008). https://doi.org/10.1007/s11274-015-1903-5
14. Praveena, S.M., Radojevic, M., Abdullah, M.H., Aris, A.Z.: Application of sediment quality guidelines in the assessment of mangrove surface sediment in Mengkabong lagoon, Sabah, Malaysia. Iran. J. Environ. Health. Sci. Eng. **5**(1), 35–42 (2008)
15. Zhang, H., Cui, B., Xiao, R., Zhao, H.: Heavy metals in water, soils and plants in riparian wetlands in the Pearl River Estuary, South China. Procedia Environ. Sci. **2**, 1344–1354 (2010). https://doi.org/10.1016/j.proenv.2010.10.145
16. Das, M., Ahmed, M.K., Islam, M.S., Islam, M.M., Akter, M.S.: Heavy metals in industrial effluents (tannery and textile) and adjacent rivers of Dhaka city, Bangladesh. Terr. Aquat. Environ. Toxicol. **5**(1), 8–13 (2011). https://doi.org/10.1016/j.envpol.2011.03.017

17. APHA-AWWA (American Public Health Association, American Water Works Association): Standard Methods for the Examination of Water and Wastewater, 20th edn. American Public Health Association, American Water Works Association, Washington, DC, USA (1998)

18. USEPA: Methods Manual for Bottom Sediment Sample Collection. Chicago, Illinois (1985) (EPA 905/4-85-004)

19. Isaac, R.A., Kerber, J.D.: Atomic absorption and flame photometry techniques and uses in soil, plant and water analysis. In: Walsh L.M. (ed.) Instrumental Methods for Analysis of Soils and Plant Tissues'. Soil Science Society of America, Inc., Madison, Wisconsin, USA (1971)

20. Price, W.J.: Spectrochemical Analysis by Atomic Absorption. Heyden, London (1979)

21. Loska, K., Cebula, J., Pelczar, J., Wiechuła, D., Kwapulinski, J.: Use of enrichment and contamination factors together with geoaccumulation indexes to evaluate the content of Cd, Cu, and Ni in the Rybnik water reservoir in Poland. Water Air Soil Pollut. **93**, 347–365 (1997). https://doi.org/10.1023/A:1022121615949

22. Kananke, T.C., Wansapala, J., Gunaratne, A.: Pb and Cr contaminations of irrigation water, soils and green leafy vegetables collected from different areas of Colombo district, Sri Lanka. Pak. J. Nutr. **14**, 593–602 (2015). https://doi.org/10.3923/pjn.2015.593.602

23. Alloway, B.J., Ayres, C.D.: Chemical Principles of Environmental Pollution, 2nd edn. Blackie Academic and Professional, London (1997)

24. EU Commission Regulation (EU) No 253/2011 of 15 March 2011 amending Regulation (EC) No 1907/2006 of the European Parliament and of the Council on the Registration, Evaluation, Authorisation and Restriction of Chemicals (REACH) as regards Annex XIII. European Commission, Brussels (2011)

25. Organisation for Economic Co-operation and Development (OECD): OECD Guideline for Testing of Chemicals No. 305 A-E: Bioaccumulation. Paris, 12 May 1981

26. WHO: Guidelines for Drinking Water Quality, 3rd edn, p. 515. World Health Organization (2004)

27. USEPA: Screening level ecological risk assessment protocol for hazardous waste combustion facilities, Appendix E: Toxicity reference values. United States Environmental Protection Agency (1999)

28. Ahmad, M.K., Islam, S., Rahman, S., Haque, M.R., Islam, M.M.: Heavy metals in water, sediment and some fishes of Buriganga river, Bangladesh. Int. J. Environ. Res. **4**(2), 321–332 (2010). https://doi.org/10.22059/IJER.2010.24

29. Mohiuddin, K.M., Alam, M.M., Ahmed, I., Chowdhury, A.K.: Heavy metal pollution load in sediment samples of the Buriganga River in Bangladesh. J. Bangladesh Agril. Univ. **13**(2), 229–238 (2015). https://doi.org/10.3329/jbau.v13i2.28784

30. Khan, Y.S.A., Hossain, M.S., Hossain, S.M.G.A., Halimuzzaman, A.H.M.: An environment of trace metals in the GBM Estuary. J. Remote sensing. Environ. **2**, 103–113 (1998)

31. Alam, A.M.S., Islam, M.A., Rahman, M.A., Siddique, M.N., Matin, M.A.: Comparative study of the toxic metals and non-metal status in the major river system of Bangladesh. Dhaka Univ. J. Sci. **51**(2), 201–208 (2003)

32. Canadian Council of Ministers of the Environment (CCME): Canadian Environmental Quality Guidelines. Ottawa, Canada (1999)

33. WHO: Permissible Limits of Heavy Metals in Soil and Plants. World Health Organization, Geneva, Switzerland (1996)

34. Peng, K.J., Luo, C.L., Lou, L.Q., Li, X.D., Shen, Z.G.: Bioaccumulation of heavy metals by the aquatic plants Potamogeton pectinatus L. and Potarnogeton malaianus Miq. and their potential use for contamination indicators and in wastewater treatment. Sci. Total Environ. **392**, 22–29 (2008). https://doi.org/10.1016/j.scitotenv.2007.11.032

35. FAO/WHO: Contaminants. In: Codex Alimentarius, vol. XVII, 1st edn. FAO/WHO, Codex Alimentarius Commission, Rome (1984)

36. CODEX Alimentarius Commission: Report of the 21st Session of the Codex ALINORM 89/12A. Committee on Food Additives and Contaminants, Geneva, Switzerland (1989)

37. Sudhira, H.S., Kumar, V.S.: International Symposium on Restoration of Lakes and Wetlands. CSIC Auditorium, Indian Institute of Science, Bangalore, India, 27–29 Nov 2000

Estimation of Sediment Concentration of River Dagga, Chanchaga Basin, Niger State, Nigeria

Muhammad Nda, O. D. Jimoh and Mohd Shalahuddin Adnan

Abstract Sedimentation is a concern to water resources project globally; water flows along with certain degree of sediment naturally, and when the natural flow regime of a river is altered by a dam, the reservoir stores both water and sediment which settles in the reservoir and reduces the storage capacity. Reduction in storage capacity of a reservoir beyond a limit hampers the purpose for which it was designed. River Dagga is proposed to be dammed for water supply purpose, but there is no consistent monitoring of sediment inflow into the rivers in Nigeria. This research aims to study the suspended sediment-laden water carried by River Dagga, Niger State Nigeria. Though most methods of estimating the rates of sedimentation are quite cumbersome, time-consuming and expensive but the availability of some data, (the sediment and flow rating curves) ease these difficulties. In this study, the direct method of sediment sampling data approach has been used to estimate the rate of sediments carried by river Dagga. The result shows that River Dagga sediment inflow is low as water flows only during the raining season, the bed material soil transported along the river bed is classified. The suspended sediment estimates are expected to increase if the upstream of the catchment area is subjected to further urbanization, farming, and animal grazing activities.

Keywords Reservoir sedimentation · Suspended sediments · River bed soil

M. Nda
Department of Civil Engineering, Federal Polytechnic Bida, Niger State, Nigeria

O. D. Jimoh
Department of Civil Engineering, Federal University of Technology Minna, Niger State, Nigeria

M. Nda (✉) · M. S. Adnan
Faculty of Civil and Environmental Engineering, Universiti Tun Hussein Onn Malaysia, 86400 Parit Raja, Johor, Malaysia
e-mail: muhdnda@gmail.com

1   Introduction

A river is a body of flowing sediments as well as flowing water. Sediment moves in rivers and streams as suspended load as well as bedload, i.e., fine particles and larger particles respectively. When this natural flow process is stilled behind a dam or an embankment, the sediments settle to the bottom of the reservoir [1]. Sedimentation of reservoirs is caused by the accumulation of the suspended and bed material load transported by running waters of the rivers. Sedimentation is mainly the result of erosion of hilly or semi-hilly tracts of natural streams and channels caused by heavy rains. Due to the very large quantity of sediment load transported by rivers, the rate of sedimentation is high and reduces reservoirs storage capacity [2].

Dams and reservoirs are developed to cope with the variability of water supplies over time. As of today, there are nearly 39,000 large dams (over 15 m tall) in the world [3]. Similarly, in Nigeria, there are over 264 dams of varying capacities constructed, 210 of which is owned and operated by the Federal Government, 34 by the States and 20 by private owners [4]. These dams produce several benefits including water supply and irrigation purposes, hydropower generation, flood control, and for recreational activities [5]. Sediment transport governs or influences many situations that are of importance to humanity. Deposition of sediments does not only reduce the capacity of reservoirs but, also interferes with harbor operation, reduces useful flood storage volume, changes underground water conditions, affects normal workings of low-level outlet gates and closes or modifies the path of watercourse [6, 7].

Sediment transport occurs when there is an interface between a moving fluid and an erodible boundary. The activity at this interface is extremely complicated. Once the sediment is being transported, the flow is no longer a simple fluid flow, since two or more materials are involved. Sediment movement within river channels is usually referred to as sediment transport [8]. Sand and silt particles move as solid material, but clay particles adhere like flocs which change in size and shape during motion. Hillslope transport of sediment from landslides and debris flow may dominate sediment supply in some watershed, locally forcing changes in channel gradient and grain size [9, 10]. Most sediments mobilized on hill slopes must pass through these streams before reaching lower gradient channels. Steep channels have wide grain size distributions that are composed of finer, more mobile sediment and large, rarely mobile grains. The large grains can bear a significant portion of the total shear stress and thereby reduce the stress available to move the finer sediment [11].

Rivers and stream are associated with basically two types of sediment load; suspended load and bedload. Since both the suspended load and bedload are found within the river channel, there combination is known as "bed material load" [12]. Estimating soil loss from measurements of sediment movement in streams and rivers faces several problems. Taking the measurements is time-consuming and expensive; the accuracy of the measurements is likely to be poor, and even if there

are reliable data on the movement in a river or stream it is challenging to know exactly where the soil came from and when [13].

In Nigeria, reservoir sedimentation has hampered so many dam operations for instance in Shiroro and Tiga dam where the reservoirs are used for hydroelectric power generation and water supply respectively. According to Jimoh [14] Shiroro reservoir is highly threatened by the accumulation of sediments deposit which has reduced the rate of power generation based on the author findings there is need to control the menace of sedimentation in the reservoir. Likewise, Tiga dam in Kano State Nigeria is not an exception in its case the sediments were trapped behind the dam and growth of typha plants in the river course, and irrigation canals were encouraged. The presence of typha plants in the channels reduces the flow rate. The Komadugu Yobe Basin Project (KYBP) offered a link between cause and consequence. The water audit highlighted the nature of the problem which led to the pilot clearing of sediments, though tedious and labor-intensive demonstrated a practical and cost-effective way of desilting [15]. Another similar study on reservoir sedimentation was carried out at College of Agriculture and Animal Science, Kaduna by Owolabi [16], using survey technique to estimate sediment rate with the aid of an echo sounder device. From the results, it was concluded that it would take about forty-two (42) years to have sediment concentration of 0.62 Mm^3 in the reservoir. The objectives of the present research are; (i) to provide reliable and dependable estimate of rate of sediment inflow of River Dagga that can be used to estimate the lifespan of the reservoir as well as its maintenance; (ii) to develop a sediment rating curve for River Dagga; and (iii) to determine the geometric mean particle size (D_{50}) of the river bed before and after rain events.

2   Methodologies

2.1   Study Area

River Dagga originates from the highland of Bosso, runs south and joins River Chanchaga at Sabon Dagga. The gauging station for this research work is located at Latitude 9.4728° and Longitude 6.3722° (Fig. 1). The study area is about 21 km from the Federal University of Technology, Minna Gidan Kwano campus the entire area is drained by River Dagga. River Dagga has a few tributaries. The catchment area of River Dagga is about 122 km^2. The flow pattern of the river is a function of the rainfall and geology over which the river flow. The river is seasonal with some granitic rocks along its channel and very low flow in the dry season. Peak flows occur in August, September, or October.
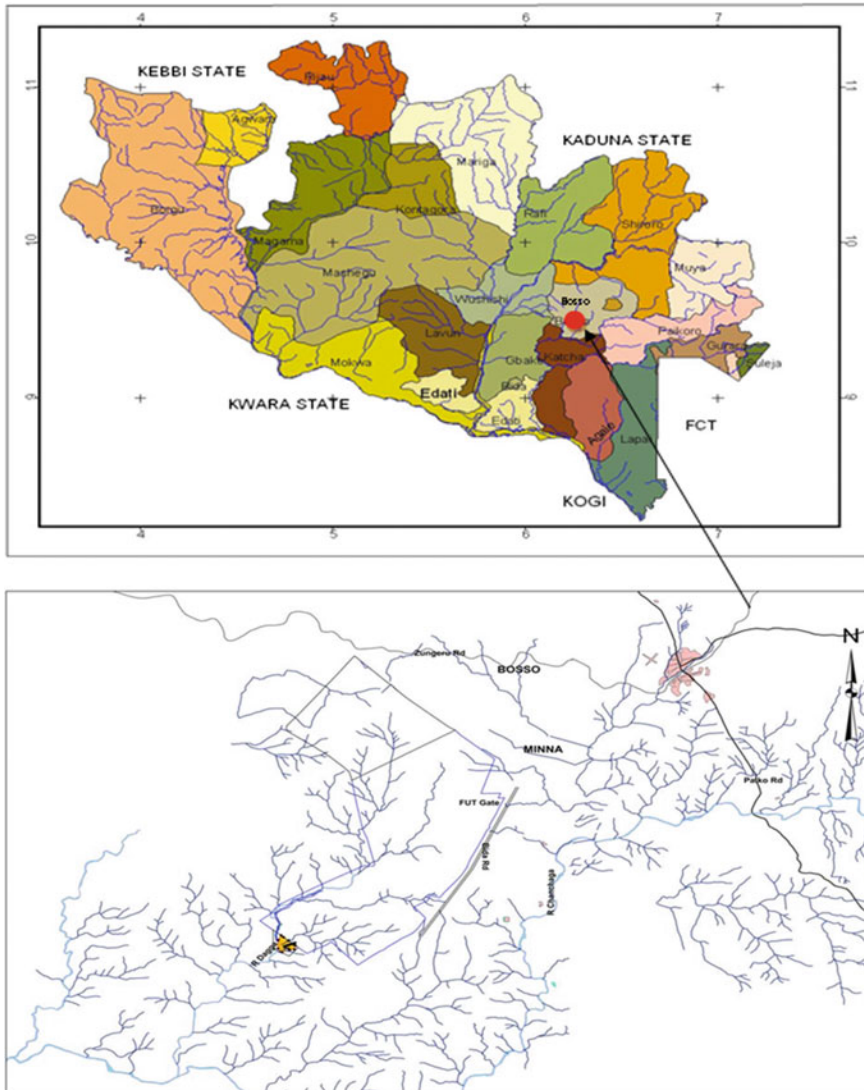
Fig. 1 Location of study area

2.2 Sampling Method

Data collection is an essential part of completing this study. The data were collected from the established gauging station, the station was established at that point where the river flow is relatively uniform and free of obstructions. The point lies on Latitude 9.4728° N and Longitude 6.3722° E. The data was collected in 2013 and

2014 raining season between July and November. The following data were collected from the field; flow rate, cross-sectional area, suspended sediment, river stage height, river bed soil sample.

2.2.1 Stream Gauging

For the stream discharge of the gauging station was determined based on area velocity method, the river flow rate was measured using MGG/KL—DCB Electric magnetic water current and speed meter. This was done by dividing the river into small elemental strips across the cross-section. Equations 1, 2, 3, and 4 were used to calculate; velocity at the first and the last strips (near the banks) where the depth is shallow, intermediate strip (with deep water), discharge in each strip and total discharge respectively.

$$V = v_{0.6d} \tag{1}$$

$$V = \frac{v_{0.2d} + v_{0.8d}}{2} \tag{2}$$

$$\Delta Q = (bd)v \tag{3}$$

$$Q = \sum \Delta Q, \tag{4}$$

where

V   average velocity in each strip
b   strip width
d   strip mean depth
Q   discharge

2.2.2 Sediment Sampling

Suspended sediment samples refer to the particles that the flowing river carries along, in this study only suspended sediment is considered. Suspended sediment samples were taken at the same location where discharge measurements were taken between 2013 and 2014. 0.75 l containers were lowered into the river to grab flowing water with the sediment along the cross-section at mid-depth and equal increments at verticals ¼, ½, ¾ of the river cross-section.

For this study, a total number of 27 samples were collected in 2013 and 18 samples in 2014 raining season, respectively. Each sample was filtered in the laboratory through a weighed filter paper and oven dried at a low temperature of 105 °C and reweighed. Sediment weight was then divided by sediment volume, the average concentration (mg/l) is multiplied by water discharge (Q_w) in cubic meters

per second and a multiplier 0.0864 which converts it to tones per day. The relationship between water discharge and suspended sediment load was plotted on logarithm graph paper with water discharge, (Q_w) in cubic meters per second, against suspended sediment load, (Q_s) in tons per day. The sediment rating curve from a continuous record of streamflow provides a rough estimate of sediment inflow carried by the river. The relation between the suspended sediment transport (Q_s) and streamflow (Q_w) *is* given by Eqs. 5 and 6

$$Q_s = kQ_w^n \tag{5}$$

$$\log Q_s = \log k + n \log Q_w. \tag{6}$$

2.2.3   Bed Material Samples

Soil samples taken from the river channel bed were taken to the laboratory for analysis and classification. The particle size distribution for fine and coarse-grained soil characterization was carried out in accordance with the procedures in BS 1377. The unified soil classification system (USCS) was used to classify the soil type.

3   Results and Discussion

3.1   *Sediment Concentration*

Figure 2a and b are graphs showing the variation of discharges measured with time. Graph a. represents measurements for 2013 while b. is plotted for the year 2014 data respectively. These figures indicate the minimum and maximum flow recorded in 2013 to be 6.72 and 104.03 m^3/s similarly it can be observed that the 2014 data as 19.668 and 86.30 m^3/s.

Figure 2 c and d these are graphs showing the average suspended sediment concentration carried out for three different samples collected for each date in 2013 and 2014. River Dagga sediment inflow from the result as represented on graphs below clearly shows low sediment concentration as water flows only during the raining season. The average suspended sediment concentration for 2013 season was 0.02855 and 0.05498 g/l for 2014 raining season. The rise in sediment concentration in 2014 may be due to higher rainfall depth and intensity, increase in farming activities and animal grazing upstream.

The result of sediment concentration are compared with similar studies carried out by Jimoh [14] in Kaduna and Sarkin Pawa river feeding shiroro dam, also compared with is another sedimentation study by Ezebuiro [17] in Mulenda river feeding Kilankwa reservoir in Nigeria as shown in Table 1.

From the comparison, river Sarkin Pawa has the highest concentration of suspended sediment inflow. This can be attributed to the soil type and unstable bank
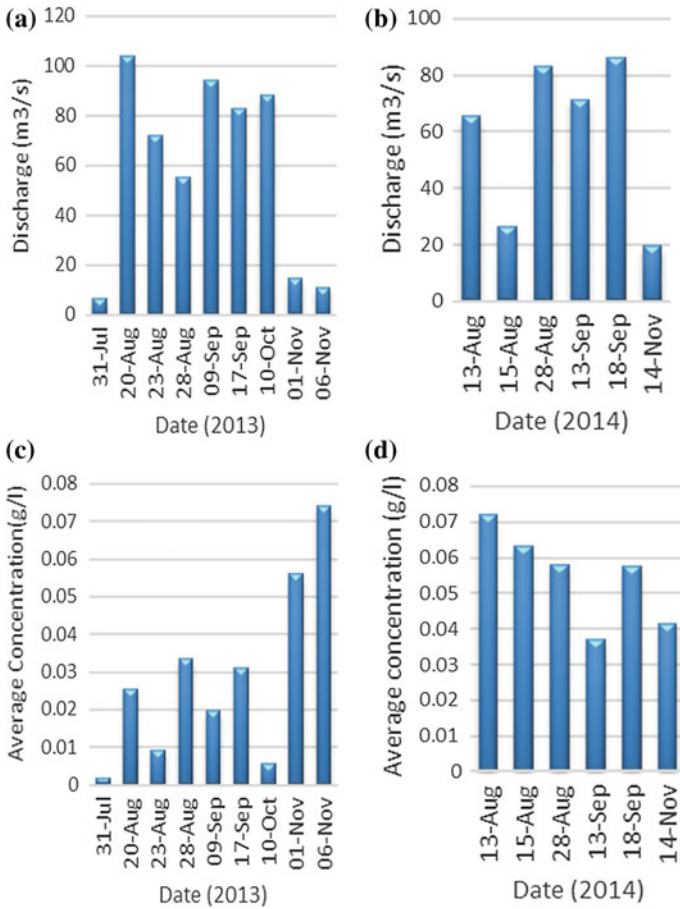
Fig. 2 River discharge (**a** and **b**) and average sediment concentration (**c** and **d**)

present. River Dagga can be seen to have the lowest sediment concentration this can be attributed to the vegetation, the river channel being relatively stable and the geology which is rocky.

Suspended sediment rating curve for any river is developed by the log-log plot of the river discharge Q_w and suspended sediment load Q_s. This is used to estimate sediment inflow when the discharge is known, provided there is no notable change in the river flow pattern and sediment characteristics. Figure 3 as presented below is the sediment rating curve of River Dagga using the 2014 results. The suspended sediment rating curve equation for River Dagga is written as Eq. 7 with a coefficient of determination R^2 of 0.880 which indicates a high positive correlation. The constant K and n are 3.413 and 1.077 respectively.

Table 1 Comparing the results with similar studies

|	River Dagga (2013)	River Dagga (2014)	Mulenda River	Kaduna River	Sarkin Pawa River
Sediment concentration (g/l)	0.02855	0.05498	0.3527	0.4	1.6
Vegetation	Presence of shrubs and trees	Presence of shrubs and trees	Presence of shrubs and trees	Presence of shrubs and trees	Presence of shrubs and trees
Period of estimate	Raining season	Raining season	Raining season	Dry season	Dry season
Characteristics of river channel	Outcropping rocks and fairly stable	Outcropping rocks and fairly stable	Rocky surface and fairly stable	Rocky surface and fairly stable	Unstable bank deposit of clayey, loamy and sandy soil
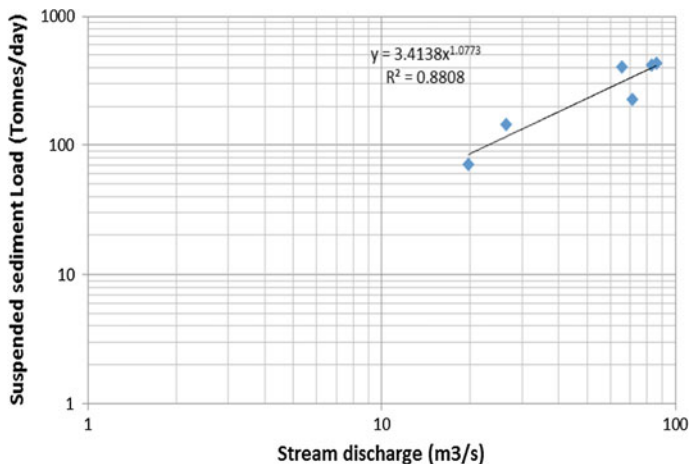
Fig. 3 Suspended sediment rating curve for River Dagga

$$Q_s = 3.413 Q_w^{1.077}. \tag{7}$$

3.2 Bed Material Characterization

Bed material sampling was carried out to characterize the grain size distribution of the soil in the river bed channel before and after rain to know the type of soil transported by the river flow. Sieve analysis was carried out for bed materials

collected for the sampling period between the year 2013 and 2014. Figure 4a
(before rainfall event) and b (after rainfall event) shows the particle size curve for
2013 also, Fig. 4c and d (before and after rainfall event) is the sieve analysis plots
for samples collected for the year 2014. The grain size distribution analysis showed
that in the 2013 raining season. River Dagga bed material had a geometric mean
particle size D_{50} of 0.70 mm, and consequently, the river transported a smaller
material when it rains with smaller size D_{50} of 0.51 mm. Similarly, in the 2014
raining season it had a geometric mean particle size D_{50} of 0.52 mm and trans-
ported a bit smaller material with D_{50} of 0.51 mm. This shows that the bed material
composition carried by the river flow does not vary much between the 2 years.

Based on Unified soil classification system for well-graded sands, gravelly sands
with little or no fines (SW). River Dagga bed material gradation analysis does not
meet the SW classification criteria hence the soil can be classified as poorly graded
sand (SP).
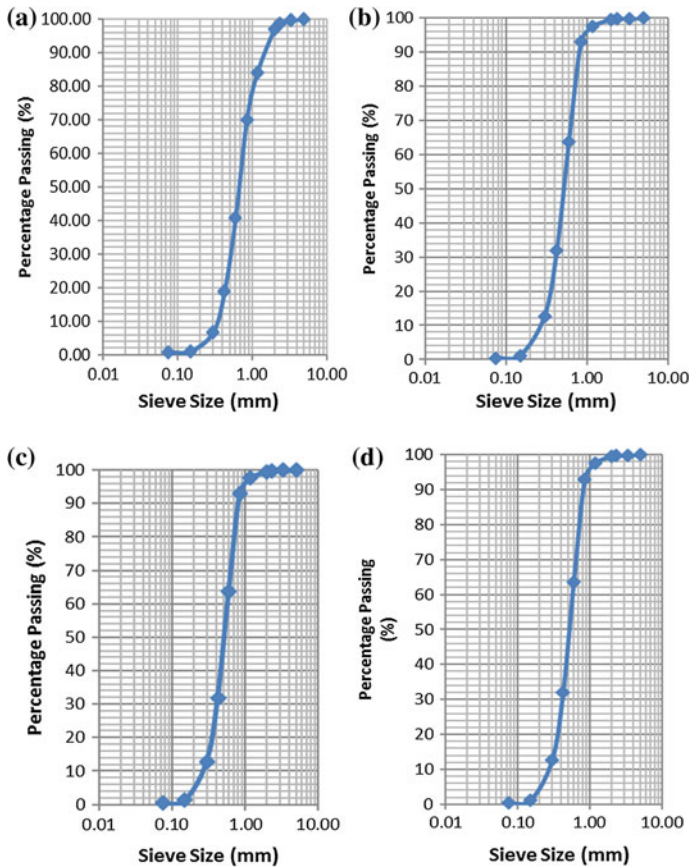
Fig. 4 Particle size curve before and after rainfall event (2013a, b; 2014c, d)

4 Conclusion

The results obtained from this study was taken during the rainy season thus, do not have an extended period records. Therefore, limited to determining the long-term average sediment yield, though extrapolation method was used to get the annual sediment inflow of the river. The annual sediment yield of River Dagga was computed to be 0.0005583×10^6 m^3. The result will provide reliable and dependable data that can be used to estimate the lifespan of the reservoir as well as its maintenance.

References

1. Latosinski, F.G., Szupiany, R.N., García, C.M., Guerrero, M., Amsler, M.L.: Estimation of concentration and load of suspended bed sediment in a large river by means of acoustic doppler technology. J Hydraul Eng (2014)
2. Kondolf, G.M., Gao, Y., Annandale, G.W., Morris, G.L., Jiang, E., Zhang, J., et al.: Sustainable sediment management in reservoirs and regulated rivers: experiences from five continents. Kondolf Earth's Future. https://doi.org/10.1002/2013ef000184 (2014)
3. Palmieri, R., Shah, F., Dinar, A.: Reservoir sedimentation and the sustainable management of dams. doi:10.1.1.377.5104 (1998)
4. Ezie, J.: Compendium of Dams in Nigeria. Committee on Large Dams (NICOLD) Symposium and AGM, Nigeria (2014)
5. Yüksel, I.: Hydropower for sustainable water and energy development. Renew. Sustain. Energy Rev. (2010)
6. Jansen, T.: The effect of tidal currents and storm surge to sediment transport in the North Ariake Sea, Japan [Internet]. Dissertation, Saga University (2015)
7. Dike, C., Agunwamba, J.C.: Modelling of sediments concentration distribution in dredged canals of the niger delta Estuarine Region, Nigeria. J. Urban Environ. Eng. (2013)
8. Kay, M.: Practical Hydraulics, 2nd edn. CRC Press, Boca Raton (2007)
9. Mueller, E.R., Pitlick, J.: Sediment supply and channel morphology in mountain river systems. J. Geophys. Res. Earth Surf. https://doi.org/10.1002/2013jf002843
10. Grabowski, R.C., Droppo, I.G., Wharton, G.: Erodibility of cohesive sediment: the importance of sediment properties. Earth Sci. Rev. (2011)
11. Yager, E.M., Dietrich, W.E., Kirchner, J.W., McArdell, B.W.: Prediction of sediment transport in step-pool channels. Water Resour. Res. (2012). https://doi.org/10.1029/2011WR010829
12. Wilcock, P., Pitlick, J., Cui, Y.: Sediment transport primer: estimating bed-material transport in gravel-bed rivers. http://www.treesearch.fs.fed.us/pubs/32966
13. Ladewig, M.: Sediment transport rates in the lower Muskegon River and tributaries. Unpublished thesis, university of Michigan. Available from: https://deepblue.lib.umich.edu/handle/2027.42/48710
14. Jimoh, O.D.: Sustainable Water Resources Management in Nigeria, vol. 18. Inaugural Lecture, Federal University of Technology Minna, Nigeria (2010)

15. Vulegbo, A.A., Schoeneich, K., Alagbe, S.A.: Measurement of the Remaining Storage and Rate of Siltation of Tagwai Impounding Reservoir, Niger State, Nigeria. J. Hydrogeol. Hydrol. Eng. **4** (2015)
16. Owolabi, B.C.: Reservoir Sedimentation Studies. A Case Study of College of Agriculture and Animal Science, Kaduna. Nigeria Technical Report, pp. 14–6 (2004)
17. Ezebuiro, U.A.: Estimation of Sediment Inflow to KilankwaI Reservoir in Gwawalada Area Council, Abuja-Nigeria. Unpublished thesis, Federal University of Technology Minna (2012)

Potential of Pineapple Waste Extract (PWE) as Co-substrate in Anaerobic Digestion of Rice Straw Washwater (RSWW): Enhancement of Biogas Production

Nurul Shafiqah Rosli, Syazwani Idrus, Azmir Md Dom and Nik Norsyahariati Nik Daud

Abstract This study aims to investigate the potential methane yield by mono-anaerobic digestion of rice straw washwater (RSWW) and pineapple waste extract (PWE) as well as the co-digestion of both RSWW and PWE at a ratio of 50:50 (v/v). The experiment was conducted at a controlled mesophilic temperature of 37 °C in Upflow Anaerobic Sludge Blanket (UASB) reactor for a period of approximately 55 days. The process performances were evaluated based on the efficiency of COD removal and methane production in relation to other parameters such as pH, organic loading rate (OLR) and alkalinity ratio. This study confirmed that the rate of COD removal for RSWW, PWE, and RSWW:PWE (50:50) were achieved the stable condition at 81, 89, and 86% respectively. The alkalinity ratio value and pH throughout the experimental period remained below 0.30 and kept in the range of 6.5–7.0 indicated the stable and good environment existed for anaerobic digestion within the UASB reactor. This study implies that the co-digestion of RSWW:PWE found to improve the efficiency of COD removal and production of methane during the mono-digestion of RSWW from 81 to 86% and 0.093 to 0.13 LCH_4/g COD_{rem} by the increment of 6.2 and 40%, respectively.

N. S. Rosli · S. Idrus (✉) · A. Md Dom · N. N. Nik Daud
Department of Civil Engineering, Faculty of Engineering,
University Putra Malaysia, 43400 Serdang, Selangor, Malaysia
e-mail: syazwani@upm.edu.my

1 Introduction

Agricultural-based industries are becoming more significant in the economy of Malaysia as it is the one that raises the raw agricultural products' value through downstream processing so that the product are consumable and profitable. Among the available plantation crops, paddy industry has recently received a new interest among the agriculture policy makers in the country. Succeeding to oil palm and rubber, paddy has become the third most extensively planted crop in Malaysia. In the year 2013, including those that are planted twice a year, 674,332 ha land were planted with paddy (Paddy Statistics of Malaysia 2013). In addition, due to the demand for rice based on population, the paddy plantation area and yield of paddy per metric tons has also increased consistently every year. Nevertheless, about 1.35 tons of rice straw will remained in the field for every ton of rice harvested, and approximately 80% of the rice straw in the world was employing the improper disposal method and management system [1]. Conventionally, rice straw is disposed of by the common practice; which is open burning as it is the most convenient, cheapest, and fastest way for rice straw disposal, especially in irrigated paddy field. However, the burning of rice straw in the field eventually is an incomplete combustion in nature that releases a significant amount of air pollutants including the toxic gases (such as carbon dioxide, carbon monoxide, methane, nitrogen oxide, and non-methane volatile organic carbon emissions) and fine or inhalable particles [2, 3].

In addition, the rice straw burning also has been reported to affects the public health as the increased of asthma attacks in children. Meanwhile, the large-scale burning of agricultural wastes in numerous Asian countries may significantly contribute to the formation of the Atmospheric Brown Cloud that can deteriorate the local quality of air, atmospheric visibility and thus Earth climate [2]. Besides, rice straw was also usually tilled back into the soil to be used as compost for the crops. Nevertheless, the decaying of rice straw in soil often releases gases such as nitrogen, ammonia, hydrogen, methane, and hydrogen sulfide. Thus, indirectly it could increase the methane emissions towards the atmosphere which can worsen the global warming phenomenon. In addition, among these released gases, methane, and nitrous oxide are those which contribute significantly to global warming and thus changing the climate at regional and global level [4].

On the other hand, according to Malaysian Pineapple Industry Board (MPIB), pineapple industry is one of the main agricultural sectors in Malaysia which contributed for the country's earnings as one of the world pineapple suppliers. In fruit processing industries, usually, pineapples are being processed for finished products such as juices, chips, slices, and others. However, this industry emanating large quantities of solid wastes (such as pineapple skin and pith) where it was used as an alternative food for livestock or disposed of as they are. Pineapple wastes generally consist of organic substances, therefore the disposal problem could be attenuated by anaerobic digestion and composting thus causing a serious environmental pollution problem when they were naturally degraded and release the greenhouse gases [5, 6].

In this context, anaerobic digestion was selected as an optimal alternative for the biomass waste treatment as it require a low operating cost in addition to green energy production (methane) as a by-product. Moreover, the use of agricultural waste as the biomass resource is more desirable because of its high availability and its potential to mitigate the greenhouse gases released into the atmosphere when the waste products are utilized rather than being left in the field to decompose [7].

Thus, concerning the best solution for the disposal management for rice straw and pineapple waste, anaerobic digestion could become one of the promising sustainable alternatives due to the production of renewable energy (methane) as a by-product [8]. Rosli et al. [9] have reported the potential of rice straw leachate as a source of biomass for biogas production. However, at a higher concentration, the low degradability and insufficient of the nitrogen content of rice straw leachate have caused the limitation in the production of biogas. Meanwhile, the study that was done by Bardiya et al. [5], suggesting that the pineapple processing wastes could potentially and suitable for anaerobic digestion as they are highly biodegradable, have a high moisture content and rich in organic matter. Thus, the co-digestion between the rice straw washwater and pineapple waste could synergistically improve the mono-anaerobic digestion of rice straw which was reported to be restricted due to its high lignin content which causes the difficulties for the anaerobic microorganisms to degrade [10]. However, there is still a lacking for the research on biogas potential from both rice straw washwaster (RSWW) and pineapple waste extract (PWE). Therefore, this study was conducted to assess the potential of using the agricultural waste such as RSWW and PWE for mono-digestion as well as co-digestion of both substrates as a feedstock to improve methane production, thus allow the application of agro-waste to be used widely as a source of green energy recovery.

2 Methods and Materials

2.1 Feed Substrates

Five kilograms of fresh rice straw was collected from the paddy field around Sekinchan, Selangor. It was preselected to remove the particulate components which include fine stones. The rice straw was cut up to a small size (roughly uniform in size) and was soaked with tap water for approximately 2 weeks period time with one liter of water to 18 g of rice straw. The RSWW was extracted by removing the rice straw, leaving only the liquid for anaerobic digestion.

Pineapple waste was collected from Juice Processing Factory organized by Pertubuhan Peladang Negeri Johor (PPNJ) located in Ayer Itam Johor. Waste consisted of the skin and pith of pineapple. PWE was prepared by blending both skin and pith until it well mixed with fine pulp appeared. The PWE was obtained by

Table 1 Compositions of synthetic wastewater preparation in 1L volume [11]

Materials	Amount
Yeast (granular form)	23 g
Urea	2 g
Sugar	11.5 g
Full cream milk	144 mL
Blood	5.75 mL
Tap water	Make up volume until 1 L

filtering any solid part, as the liquid will be used as a substrate fed in the UASB digester.

Synthetic wastewater will be used as a surrogate material as it allowed the use of a consistent ingredient of control feedstock which is high biodegradability without the risk of exposure to pathogens present in real sewage. The materials used for synthetic wastewater preparation are shown in Table 1. On the other hand, the activated sludge used as inoculum was collected from wastewater treatment plant of engineering faculty, University Putra Malaysia.

2.2 Reactor Setup and Experimental Design

The laboratory scale of anaerobic digestion RSL and DS was conducted in a 6.5 L working volume of upflow anaerobic sludge blanket (UASB) reactor. UASB reactor consisted of an opaque polyvinyl chloride (PVC) sheet solid column immersed in a water bath with a heater to heat up the water to mesophilic condition at $37°C \pm 2$. The reactor has two ports for each influent and effluent at its bottom part. Solenoid driven dosing pump was used to feed the substrate into the reactor. The effluent was collected into a sealed container and connected with Tedlar gas sampling bag for gas sampling purposes. The UASB reactor was inoculated with 3 L activated sludge and brought up to the reactor operating condition. The digester was operated for the period of 55 days including the acclimatization period. The hydraulic retention time (HRT) remained unchanged and was maintained at 24 h throughout the experimental period. The diagrammatic drawing of the UASB reactor is shown in Fig. 1.

Table 2 represents the phases of anaerobic digestion with types of components substrates and the corresponding concentration performed in this study. Synthetic wastewater was fed during phase A and B during the acclimation period to allow the anaerobic microorganisms to feed on the high biodegradability substrate. Same goes during phase E and H. A short period time was required to feed on the synthetic wastewater into the UASB reactor to recover the activity anaerobic microorganisms before starting with the new feeding of the other substrates. In addition, the experiment on the sludge morphological study was conducted at the end of the operational period.
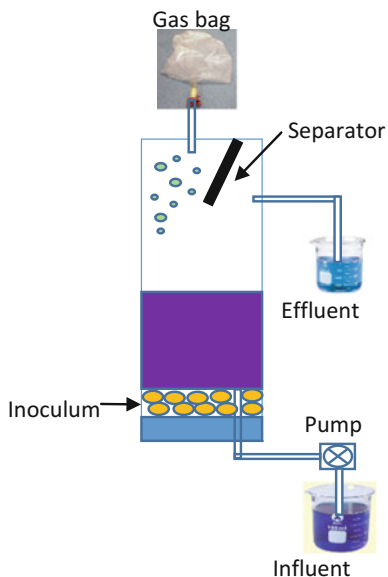
Fig. 1 Diagrammatic drawing of UASB [11]

Table 2 Component and concentration of feedstock

Operation time (Day)	Phase	Feedstock	
		Components	Concentration (gCOD/L)
1–18	A	Synthetic wastewater	0.70, 0.80 & 1.2
19–23	B	Synthetic wastewater	0.80
24–28	C	RSWW	0.80
29–34	D	RSWW	1.20
35–37	E	Synthetic wastewater	0.80
38–42	F	PWE	0.80
43–48	G	PWE	1.20
49–50	H	Synthetic wastewater	1.20
51–55	I	50% RSWW + 50% PWE (v/v)	1.20

2.3 Analytical Method

pH was measured using pH meter (Delta 320, Mettler Toledo Group). Salinity, total dissolved solid (TDS) and electrical conductivity (EC) were measured using TRACER PockeTester probe. COD was measured using Closed Reflux, Titrimetric Method recommended by Standard Methods for the Examination of Water and Wastewater. Total alkalinity was also determined per standard method for the examination of water and wastewater (APHA 2005). Total ammonia nitrogen (TAN) and Total nitrogen (TN) were measured using DR/890 Colorimeter HACH

equipment. The biogas composition (methane and carbon dioxide) was analyzed by gas chromatography (GC), Agilent Technology, 6890 N Network Gas Chromatography System. The sludge inoculum surface morphological was analyzed using Hitachi S-3400 N Scanning Electron Microscope (SEM).

3 Results and Discussion

3.1 Substrates Characterization

Table 3 presented the main characteristics of substrates used as a feedstock for this study.

3.2 Organic Loading Rate (OLR)

Figure 2 represented the OLR applied for approximately 8 weeks of experimental period. The OLR of the synthetic wastewater was increased gradually from 0.3 gCOD/L/day to 0.43 g/L/day and 0.65 g/L/day during the phase A, and reduced

Table 3 Components of feedstock used in the experiment

| Parameters	RSWW	PWE	50% RSWW + 50% PWE
pH	6.8	3.76	3.9
COD (g/l)	1.92	35	16
Suspended Solid (mg/l)	65	165	282
Turbidity (NTU)	56	800	390
TAN (mg/l)	17.5	48	55
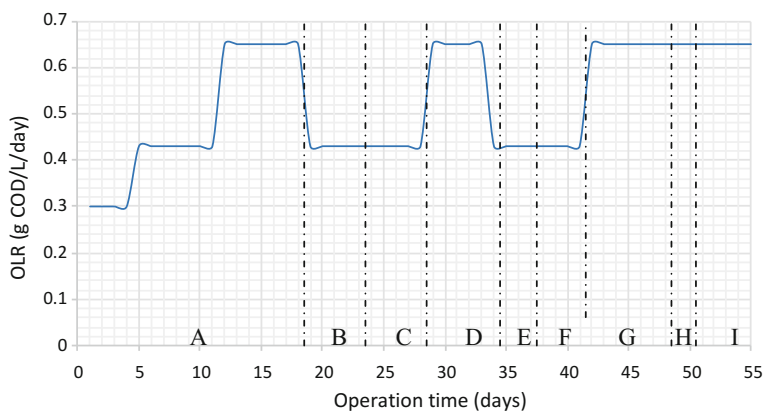
Fig. 2 Organic loading rate distribution

to 0.43 gCOD/L/day at phase B. The adjustment of OLR during this period was to determine the applicable and relevant organic loading to be fed into the reactors as for reactor startup, to avoid any instability for the proceeding anaerobic digestion process. In this experimental work, the OLR used for the feeding were 0.43 g/L/d and 0.65 g/L/d with the corresponding feedstock's concentration of 0.80 and 1.2 g/L. The maintained of operating condition at OLR 0.43 and 0.65 gCOD/L/day, was to remain the steady production of methane yield at a stable operating condition, as when the higher OLR was applied, the reduction in pH value and fluctuation in COD removal rate was observed and which might cause the instability for the upcoming anaerobic digestion process.

3.3   PH Value

The understanding of pH, and the factors that initiating or resisting to pH changes were critical to be controlled and secured for a successful operation in an AD system. Figure 3 shows the distribution of pH values for 55 days of an operational period in the UASB reactor. In general, the pH values were maintained at pH 6–7 at all phases. Phase A and B are known as the adaptation period where the reactor was only fed with synthetic wastewater for the anaerobic digestion process. In the early phase, the pH value was increased gradually from 5.50 to 6.76 indicating the good environment for anaerobic microorganisms which may be due to the application of low OLR value of 0.43 gCOD/L/day for the startup process. The reduction in pH value was detected at day 16 which might be due to the sudden increase of the OLR to 0.65 g/L/d that resulted in the acid accumulation in the reactors [12]. The pH increased and maintained in the range of 6.66–6.68 when the OLR was reduced to 0.43 g/L/day during phase B.

The gradual increase in pH from 6.61 to 6.91 was observed in phase C and D when the feedstock was switched to RSWW at OLR of 0.43 and 0.65 gCOD/L/day.
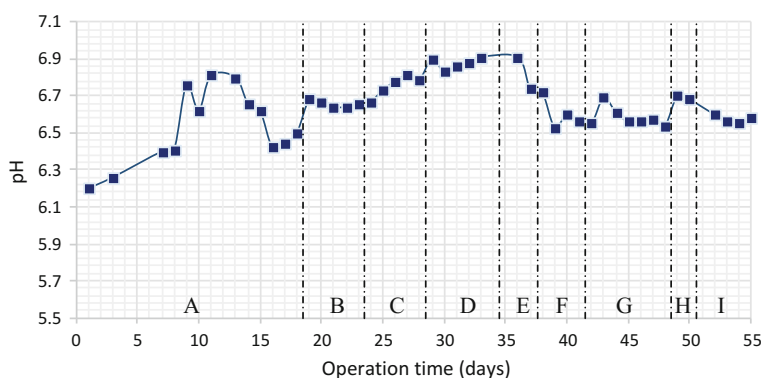

Fig. 3 pH distribution for 55 days of operating period

However, the pH values reduced to 6.53 and remain fluctuated around 6.54–6.60 during phase F and G, when the feedstock was switched to PWE at OLR of 0.43 and 0.65 gCOD/L/day. Generally, the trend of pH values from phase B to I was observed to fluctuate with pH values lies in the range of 6.5–7. The pH values can represent the current state of the anaerobic digester and become the indicator for the formation of volatile fatty acid. In order to obtain a good quality of granular sludge, a stable pH is required in the range of 6.3–7.8. In a mixed-culture anaerobic digester, the optimal pH range is 6.6–7.8 [13]. Hence, referring to the pH observation for this study, it indicates the stable anaerobic digestion process in UASB throughout the experimental period at all type of feeding.

3.4 Alkalinity Ratio and Ammonia

Figure 4a shows the distribution of alkalinity ratio values. Generally, the value of alkalinity ratio was recommended to be less than 0.30, for a good state indication of the anaerobic digestion process [14, 15]. For this study, the alkalinity values were maintained below 0.3 throughout the experimentation period, indicating that the reactor is having enough buffering capacity for the digestion process, at a stable anaerobic digestion operation.

On the other hand, the distribution of total ammonia nitrogen (TAN) is shown in Fig. 4b. TAN values were observed maintain in the range of 12.5–18.5 mg/L which indicated the stable condition of the feeding with various substrates conducted in this study. In addition, the values are far from the inhibition range which was reported by the previous studies. Instead, at the value lower than 200 mg/L, ammonia were reported as beneficial to anaerobic process since it was used for growth of anaerobic microorganisms [16]. It is important to mention that at a low ammonia concentration, it was generally utilized by methanogens organism as their
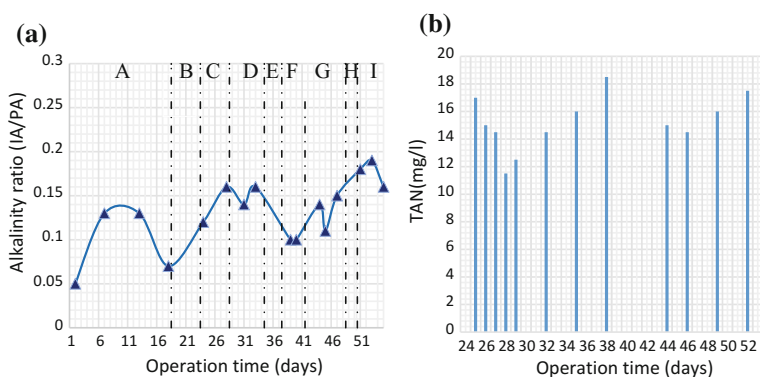

Fig. 4 Alkalinity ratio and TAN distribution graph over 55 days of feedings

source of nutrients which will give more acceleration for granules activities in the methanogenic phase thus increasing the biogas production.

3.5 Chemical Oxygen Demand (COD) Removal

Figure 5 indicated the distribution of COD removal efficiency in the UASB reactor. In Phase A, for the consecutive eleven days of synthetic wastewater feeding, the COD removal efficiency was observed to fluctuate in the range of 65–70%. This could be due to the adaptation of anaerobic populations towards the variation of the incoming organic loading of the feedstocks. Eventually, at the end of phase A, the COD removal efficiency has become steady and maintain at 84%. During the early stage of Phase C, the COD removal was decreased to 80% due to the adjustment of anaerobic microorganisms to adapt to a different type and concentration of the new substrate. The addition of RSWW that consist of small straw flakes could create the difficulties for the degradation and digestion process in the reactor. Providentially, after a week of RSWW feeding, the anaerobic population able to adapt towards the incoming RSWW with COD removal efficiency remained stable at 79–82%. The same trend was also observed during Phase D where the OLR of RSWW was raised to 0.65 gCOD/L/day. At this phase, the COD removal efficiency was increased and remains in the range of 84–85%, indicating the adapted of the anaerobic microorganisms towards the RSWW feeding. The increase of OLR presented a higher organic content in the substrate to be digested during the anaerobic digestion process which could also result in the increment of biogas production. In addition, the pH stability indicator showed no sign of overloading as pH was maintained above 6.60 and thus indicating the stability of process at the applied OLR.

The starting of Phase F showed a small reduction in COD removal efficiency from 84 to 82% due to the sudden change of the feedstock from synthetic wastewater to PWE. Nevertheless, the COD removal efficiency was observed to
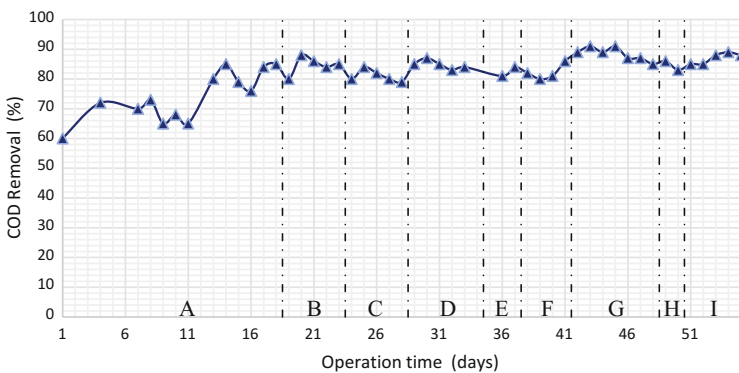

Fig. 5 The distribution of COD removal efficiency for 55 days operation period

increase gradually as the day of feeding with PWE going on until the OLR was raised to 0.65 gCOD/L/day (Phase G). As the concentration of PWE was increased to 1.2 gCOD/L in phase G, the COD removal efficiency was also gradually increased to 91% and remained stable at 87% from day 46 until 49. The higher removal of COD during the feeding of PWE compared to RSWW could be attributed to the characteristics of PWE which was highly biodegradable, rich in reducing sugar, and proteins content as compared to RSWW [5, 17]. Therefore, in order to investigate the potential improvement in the efficiency of anaerobic digestion of RSWW, the co-digestion of RSWW with PWE was conducted in phase I with the ratio of 50:50 (v/v). The COD removal efficiency found to increase by 11% during the co-digestion process compared to mono-digestion of RSWW, and the stable removal of COD was detected at day 55 with 88% of COD removal. Hence, this indicates that the co-digestion of feedstock with a higher degradability characteristic can actually promote the ability of anaerobic microorganisms to degrade or digest the organic materials which result in a higher efficiency of COD removal [18]. The co-digestion of RSWW with PWE was found to be a suitable approach to support and improve the degradation of biomass from both feedstocks.

3.6   Biogas Production

Following the assumption of all incoming COD is converted into methane, and that the growth of biomass and cell maintenance was considered insignificant, the theoretical methane produced should be 0.35 LCH$_4$/gCOD [19]. Table 4 represents the deviation of actual methane production in the UASB reactor from the theoretical values at all phases. Overall, it can be concluded that the deviation of methane yield was higher during the mono-anaerobic digestion of RSWW compared to PWE. This was as expected due to the differences in the characteristics of both substrates itself. The biogas production recorded during the mono-digestion of RSWW was increased at the increasing OLR, corresponded to the increment of COD removal efficiency from 79 to 84%. However, the observed specific methane yield during phase D (0.093 LCH$_4$/gCOD$_{rem}$) is slightly low than in phase C (0.103 LCH$_4$/gCOD$_{rem}$) was. This could be due to an advanced hydrolysis but less of methanogenesis, as hydrolytic bacteria are more robust towards environmental condition [12]. Moreover, the presence of lignin that tends to accumulate in the digester as the OLR was increased could also result in the difficulties for the anaerobic microorganisms to degrade the RSWW [20]. On the other hand, the specific methane production from PWE at OLR of 0.43 gCOD/L/day and 0.65 gCOD/L/day in both phase F and G showed a better methane yield compared to mono-anaerobic digestion of RSWW with the production of specific methane of 0.128 and 0.150 LCH$_4$/gCOD$_{rem}$ respectively. This indicated that the complex composition of pineapple could be digested more easily than that of RSWW, and suggesting the good potential of PWE as the source of biomass for green energy production. This is consistent with the study conducted by Bardiya et al. [5], whose

reported that the anaerobic digestion of fruit wastes is the best-suited waste treatment as it could produce energy in the form of methane and results in a highly stabilized effluent which is odorless and almost neutral in pH.

Therefore, to improve the degradation of RSWW and the production of biogas, co-digestion between RSWW and PWE were conducted in Phase I as the implementation of this concept was reported could successfully enhance the anaerobic digestion process by overcoming the drawbacks of mono-digestion [21]. This study found that the co-digestion of RSWW with PWE has the potential in improving the mono-anaerobic digestion of RSWW with the increment of 40% of specific methane yield from 0.093 to 0.13 $LCH_4/gCOD_{rem}$. This showed the synergistic effect of both substrates when mixed together during the co-digestion which could be attributed to a high degradability and the organic matter that present in PWE, that provides a better nutrient balance to create a favorable conditions for the methanogens [5, 22, 23]. In addition, the obtained results were in line with the previous study on the co-digestion of rice straw (RS) with food waste (FW) which is highly biodegradable and rich in protein content. It was reported that the anaerobic co-digestion of FW and RS does not only improved the system stability but also greatly enhanced the volumetric biogas production in comparison with mono-digestions of both substrates with the highest methane yield of 60.55 $mLCH_4/gVS/day$ at a ratio of FW to RS of 3:1 based on total solids.

In addition to the production of methane from the anaerobic digestion for both PWE and RSWW, the wastes of washed rice straw and solid residue of PWE could be fully utilized for other purposes. Washed rice straw was reported by several studies to possess a good quality trait as compared to the raw rice straw for burning application due to a significant improvement in its thermal behavior since the ash content and sintering formation was reduced. Moreover, it has an advantage in high energy conversion efficiency such as for electricity generation. Not only it could save the energy utilization, but also preserves the environment and reduce the open-field burning pollution at once increases the farmers' income [23, 24]. On the

Table 4 Comparison of methane production in UASB between the theoretical and actual yield

Days	Phase	Feedstock	COD_i (g)	COD_f (g)	Theoretical CH_4 ($LCH_4/gCOD_{rem}$)[a]	CH_4 produced ($LCH_4/gCOD_{rem}$)	CH_4 (%)	CH_4 deviation (%)[b]
26	C	RSWW	2.4	0.453	0.283	0.103	45.2	63.6
33	D	RSWW	3.6	0.528	0.298	0.093	46.0	68.8
40	F	PWE	2.4	0.450	0.284	0.123	48.5	56.7
47	G	PWE	3.6	0.417	0.309	0.141	50.4	54.2
55	I	50% RSWW + 50% PWE	3.6	0.498	0.302	0.130	50.0	57.0

[a]calculated by assuming 1 g COD = 0.35 LCH_4
[b]calculated from the difference between theoretical yield and actual yield per gram of COD removed

other hand, the solid residue of PWE could also be used for several applications such as fertilizer or animal feed in agricultural sector [25], bio-sorbent for heavy metals removal and anti-dyeing agent [26] and others [6].

3.7 Surface Morphological of Sludge Inoculum

The surface morphological of inoculum sludge was analyzed after completing the 55 days of experimental periods, using the scanning electron microscope (SEM) image to look for any differences or changes on the sludge inoculum after fed on several types of substrates. Figure 6a and b represent the images of the inoculum sludge before the feeding started and after 55 days of feeding. From Fig. 6b, the increment of anaerobic bacteria colonies were spotted with the increment of inoculum sludge particles as compared to the sludge before used as the inoculum inside the UASB digester. Generally, the anaerobic populations found in the anaerobic reactors are wide in range and vary depending on the substrates and
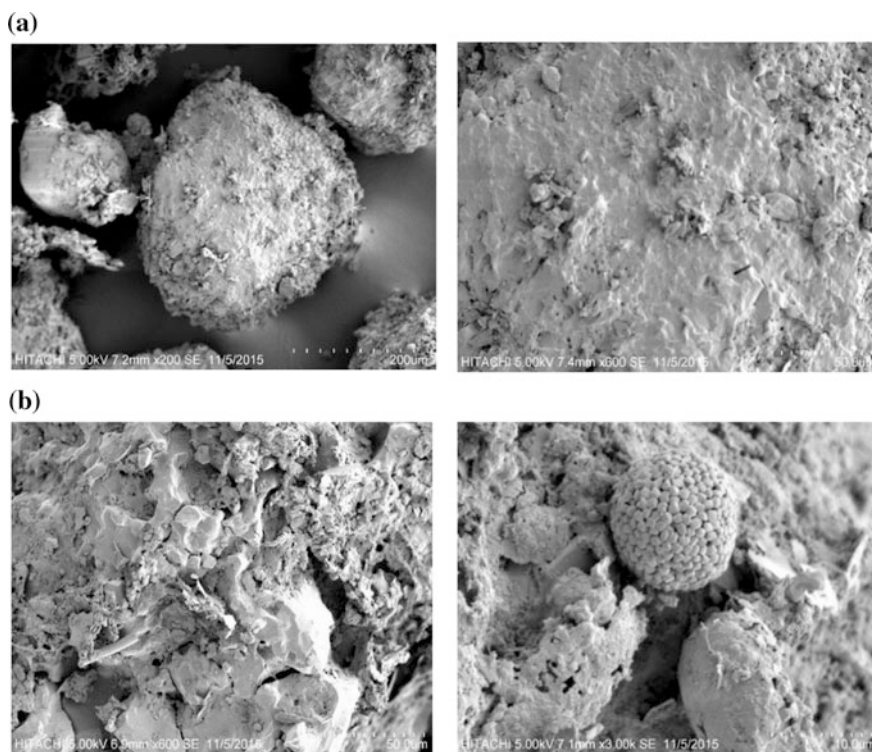

Fig. 6 SEM image on the sludge inoculum **a** before the feeding start **b** after the feeding complete for 55 days

operating condition of the digester used [27] which includes nutrient, minerals content, and operational period. These parameters can determine the degree of extracellular polymeric substance within granule which can improve granulation process thus improve biodegradation of AD system. In addition, due to the formation of granules, the reduction in sludge washout was observed, thus resulted in a better performance of UASB in specifically in COD removal and methane production efficiency.

4   Conclusions

Generally, the results indicate that RSWW and PWE were found to hold the potential for biogas production. However, the low degradability and the low nitrogen content of RSWW might cause a restriction towards the optimum production of biogas. The process anaerobic digestion of RSWW and PWE at OLR of 0.43 gCOD/L/d and 0.65 gCOD/L/day was able to maintain the stability of a system operated in UASB reactor with indicator of pH, TAN, and IA/PA ratio that always maintain in the range of 6.5–6.8, below 200 mg/L and 0.3 respectively. During the feeding of RSWW at OLR 0.65 gCOD/L/d, the COD removal efficiency was found stable in the range of 82–84% with specific methane production of 0.093 LCH$_4$/gCOD$_{rem}$. In contrast, the anaerobic digestion of PWE showed a better result both in COD removal efficiency and specific methane production of 89% and 0.141 LCH$_4$/gCOD$_{rem}$ respectively. PWE was found to be a promising raw material for biogas production since it is highly biodegradable and rich in carbohydrate and protein. Thus, a higher biogas volume was produced during the mono-anaerobic digestion of PWE. Meanwhile, the co-digestion of RSWW with PWE at a ratio of 50:50 (v/v) resulted in the synergistic effect with 86% of COD removal efficiency and 0.130 LCH$_4$/gCOD$_{rem}$ of specific methane yield with the corresponding increment of 6.2 and 40% respectively, compared to the mono-digestion of RSWW. SEM analysis showed the changes in a surface structure of the inoculum sludge by the increment in the inoculum sludge size with the existence of anaerobic population colonies.

References

1. Binod, P., et al.: Bioresource Technology Bioethanol production from rice straw: an overview". Biores. Technol. **1011**(13), 4767–4774 (2010)
2. Tipayarom, D., Oanh, N.T.K.: Effects from open rice straw burning emission on air quality in the Bangkok metropolitan region. Sci. Asia **33**(3), 339–345 (2007)

3. Arai, H., Hosen, Y., Hong Van, N.P., Nga, T.T., Chiem, N. H., Inubushi, K.: Greenhouse gas emissions from rice straw burning and straw-mushroom cultivation in a triple rice cropping system in the Mekong Delta. Soil Sci. Plant Nutr. **61**, 1–17 (2015)

4. Gadde, B., Menke, C., Wassmann, R.: Rice straw as a renewable energy source in India, Thailand, and the Philippines: overall potential and limitations for energy contribution and greenhouse gas mitigation. Biomass Bioenerg. **33**(11), 1532–1546 (2009)

5. Bardiya, N., Somayaji, D., Khanna, S.: Biomethanation of banana peel and pineapple waste. Biores. Technol. **58**, 73–76 (1996)

6. Upadhyay, A., Lama, J.P., Tawata, S.: Utilization of pineapple waste: a review. J. Food Sci. Technol. Nepal **6**, 10–18 (2013)

7. Mussoline, W., Esposito, G., Lens, P., Giordano, A.: Enhanced methane production from pilot-scale anaerobic digester loaded with rice straw. Open Environ. Eng. J. **6**, 32–39 (2013)

8. Menardo, S., Cacciatore, V., Balsari, P.: Batch and continuous biogas production arising from feed varying in rice straw volumes following pre-treatment with extrusion. Biores. Technol. **180**, 154–161 (2015)

9. Rosli, N.S., Idrus, S., Nik, Daud N., Ahsan, A.: Assessment of potential biogas production from rice straw leachate in upflow anaerobic sludge blanket reactor (UASB). Int. J. Smart Grid Clean Energy **5**(3), 135–143 (2016)

10. Mussoline, W., Esposito, G., Giordano, A., Lens, P.: The anaerobic digestion of rice straw-a review. Crit. Rev. Enviro. Sci. Technol. **43**(9), 895–915 (2012)

11. Idrus, S., Banks, C.J., Heaven, S.: Assessment of the potential for biogas production from wheat straw leachate in upflow anaerobic sludge blanket digesters. Water Sci. Technol. **66**(12), 2737–2744 (2012)

12. Babaee, A., Shayegan, J.: Effect of organic loading rates (OLR) on production of methane from anaerobic digestion of vegetables waste. In: World renewable energy Congress 2011, pp. 411–417. Bioenergy Technology, Sweden (2011)

13. Lay, J.J., Li, Y.Y., Noike, T.: Influences of pH and moisture content on the methane production in high- solids sludge digestion. Water Res. **6**(31), 1518–1524 (1997)

14. Drosg, B.: Process monitoring in biogas plants, IEA Bioenergy (2013). [Online]. Available: http://www.iea-biogas.net/files/daten-redaktion/download/Technical Brochures/Technical Brochure process_montoring.pdf. Accessed 24 Mar 2017

15. Martín-González, L., Font, X., Vicent, T.: Alkalinity ratios to identify process imbalances in anaerobic digesters treating source-sorted organic fraction of municipal wastes. Biochem. Eng. J. **76**, 1–5 (2013)

16. Cheng, J.: Anaerobic digestion for biogas production in biomass to renewable energy processes. In: Cheng, J. (ed.) CRC Press, New York, pp. 151–208 (2009)

17. Chong, H. C.: Nutritional characteristics evaluation of Malaysian commercial pineapple cultivars. Universiti Teknologi Malaysia (2013)

18. Khalid, A., Arshad, M., Anjum, M., Mahmood, T., Dawson, L.: The anaerobic digestion of solid organic waste. Waste Manag. **31**(8), 1737–1744 (2011)

19. España-Gamboa, E.I., Mijangos-Cortés, J.O., Hernández-Zárate, G., Maldonado, J.D., Alzate-Gaviria, L.M.: Methane production by treating vinasses from hydrous ethanol using a modified UASB reactor. Biotechnol. Biofuels **5**(92), 1–9 (2012)

20. Hills, D.J., Roberts, D.W.: Anaerobic digestion of dairy manure and field crop residues. Agric. Wastes **3**(3), 179–189 (1981)

21. Somani, D., Srivastava, H., Sabumon, P.C., Anjali, G.: A short review of anaerobic co-digestion and feasibility of anaerobic co-digestion of sewage and food waste for sustainable waste management. Int. J. Earth Sci. Eng. **9**(3), 55–70 (2016)

22. Zhan-jiang, P., et al.: High-solid Anaerobic co-digestion of food waste and rice straw for biogas production. J. Northeast Agric. Univ. **21**(4), 61–66 (2014)

23. Jenkins, B.M., Bakker, R.R., Wei, J.B.: On the properties of washed straw. Biomass Bioenerg. **10**(4), 177–200 (1996)

24. Said, N., Bishara, T., García-Maraver, A., Zamorano, M.: Effect of water washing on the thermal behavior of rice straw. Waste Manag. **33**(11), 2250–2256 (2013)

25. Saravanan, P., Muthuvelayudham, R., Viruthagiri, T.: Enhanced Production of cellulase from pineapple waste by response surface methodology. J. Eng. (United States), (2013)
26. Senthilkumaar, S., Bharathi, S., Nithyanandhi, D., Subburam, V.: Biosorption of toxic heavy metals from aqueous solutions. Biores. Technol. **75**(2), 163–165 (2000)
27. Levén, L., Eriksson, A.R.B., Schnürer, A.: Effect of process temperature on bacterial and archaeal communities in two methanogenic bioreactors treating organic household waste. FEMS Microbiol. Ecol. **59**(3), 683–693 (2007)

Effects of Cross-Section on Infiltration and Seepage in Permeable Stormwater Channels

Ahmed Mohammed Sami Al-Janabi, Abdul Halim Ghazali and Badronnisa Yusuf

Abstract Factors affecting the infiltration rate have been studied fairly well by many researches; however, the effects of the cross-section of a permeable stormwater channel on the surface water depth reduction due to infiltration and seepage have largely been neglected. In the present study, towards improving the efficiency of permeable channels, the effects of the three components of a trapezoidal section, namely, the water depth, side slope, and base width, on the infiltration and unsteady seepage rates were investigated. Laboratory studies using models of the channel with unsaturated soil were performed under ponding condition using various initial water levels, base widths, and side slopes for two soil textures, namely, sandy loam and loamy sand. The results showed that the rate of surface water depth reduction by infiltration and seepage increases with increasing water level irrespective of the base width and side slope. In addition, an increase of the side slope increases the infiltration rate, with the effect becoming more significant with increasing initial water level, while the effect of varying the base width is insignificant.

Keywords Stormwater · Channel section · Infiltration · Seepage
Physical modeling

A. M. S. Al-Janabi (✉) · A. H. Ghazali · B. Yusuf
Department of Civil Engineering, Faculty of Engineering,
University Putra Malaysia, 43400 Upm Serdang, Selangor, Malaysia
e-mail: huffad@yahoo.com

A. H. Ghazali
e-mail: ahahalim@gmail.com

B. Yusuf
e-mail: nisa@upm.edu.my

1 Introduction

The construction of permeable stormwater channels such as grassed swales is one of the methods commonly used for sustainable urban stormwater management. Swales are shallow channels with mild longitudinal slops and water depth near to their vegetation height. They may also be known as vegetated swales, grass channels, bio-retention swales, and wetland swales [1]. Swales can be categorized under the slow transport group of sustainable urban drainage (Fig. 1), as they link several on-site control systems, delay rapid runoff, and reduce its volume by their infiltration function [2]. They are also used for improving the stormwater quality through infiltration, sedimentation, and filtration [3].

Stormwater infiltration, unlike other approaches, is capable of solving urban runoff-related problems, such as peak flow reduction, increasing base flow, stream bank erosion, groundwater recharge, and water quality [4]. Reducing the volume of runoff by infiltration through porous surfaces at the source lessens the effort needed to control the remaining runoff at the downstream basin [4].

A good understanding of how infiltration and seepage rates are affected by surface conditions helps in choosing the optimal channel cross-section that maximizing the infiltration and seepage rates. In the present study, physical channel models were developed in the laboratory and used to investigate the effects of the permeable channel section on surface water reduction by infiltration and seepage under the unsaturated soil condition. Since trapezoidal cross-section is the preferred shape for unlined stormwater channel due its ample capacity with a limited depth and ease of construction [5], the effects of the three components of a trapezoidal section, namely, the water depth, side slope, and base width, on water loss by infiltration were investigated.

2 Factors Influencing Infiltration in Permeable Channels

Factors that affect the rate of infiltration have been studied fairly well by many researches (e.g., [4, 6–11]) and can be summarized as the amount and characteristics of rainfall, hydraulic conductivity, initial soil moisture, soil characteristics, surface and subsurface conditions.

Fig. 1 The four groups of sustainable urban drainage [2]
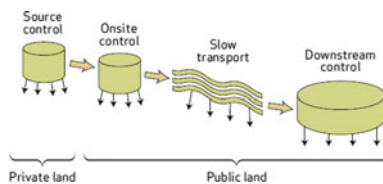
Although there are some studies about how the infiltration rate is affected by the ponding depth of water (e.g., [12–16]) and surface slope (e.g., [17–21]), the effect of channel cross-section on infiltration rate seems to be ignored. Ponding depth and slope may not be sensitive infiltration factors in some hydrologic models, but the water level in a channel and its side slope may be very important when the channel cross-section is considered for maximizing infiltration rate.

3 Seepage as a Function of Time

Figure 2 shows the three basic seepage conditions in unlined irrigation canals [22]. Figure 2a, b, and c show the seepage loss at the startup stage of a dry canal, steady-state seepage into a shallow water table, and seepage from a channel with a clogged bed respectively. The seepage rate at the startup stage was significantly higher than the steady-state seepage rate, which occurs when the soil becomes saturated [22].

Numerous studies have been conducted on the use of the section of an irrigation canal to minimize the seepage loss (e.g., [23–26]). However, the focus of these studies was on the steady-state seepage loss, while the unsteady seepage was usually neglected. For example, [23] used an optimization procedure to investigate the trapezoidal cross-section for minimum seepage loss in a canal with a deep groundwater table and homogeneous and isotropic soil. Their analysis was based on the following equations:

$$q_s = ky_n F \tag{1}$$

$$F = \left[\left(\{4\pi - \pi^2\}^{1.3} + \{2m\}^{1.3} \right)^{\frac{0.77 + 0.462\,m}{1.3 + 0.6\,m}} + \left\{ \frac{b}{y_n} \right\}^{\frac{1 + 0.6\,m}{1.3 + 0.6\,m}} \right]^{\frac{1.3 + 0.6\,m}{1 + 0.6\,m}}, \tag{2}$$

where q_s is the seepage discharge per unit length of the canal (m^2/s.m); k is the hydraulic conductivity (m/s); y_n is the canal normal flow depth (m); F is the seepage function (dimensionless), which is a function of the channel geometry; b is the base width (m); and m is the side slope (dimensionless).

Figure 3 presented the summary of their findings. From Fig. 3, it can be seen that an increase of the channel side slope has little effect on the seepage for a slope m of less than 1.5, while the effect is significant for m values of 1.5–5. In addition, the seepage loss slightly increases with increasing base width.

In stormwater channels, soil may not attain saturation during the storm, (except when there is ponding water with a shallow groundwater table), and hence seepage may not reach the steady-state and usually stay unsteady and rapidly decreases with time. Seepage rate under the unsaturated soil conditions was not considered in their study.
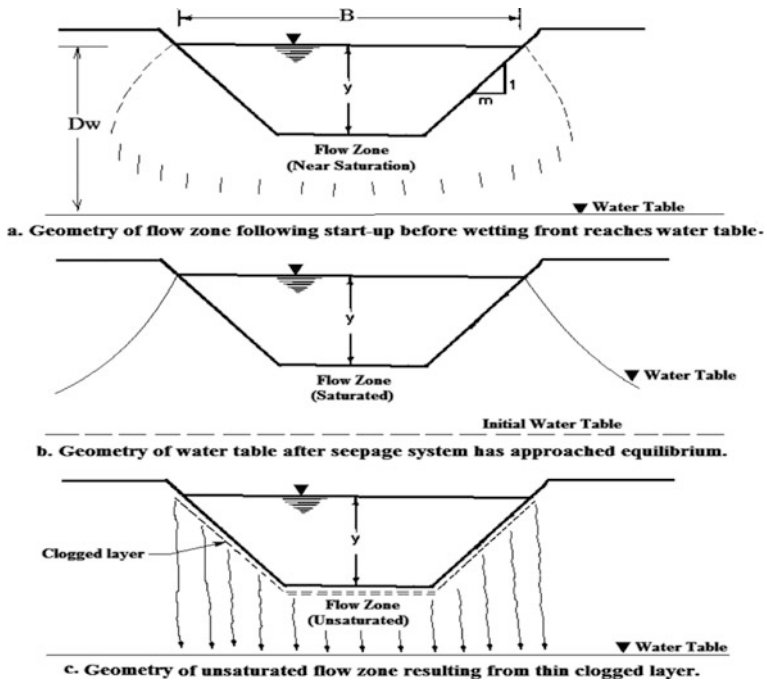
Fig. 2 Canal seepage geometry for different boundary conditions [22]

Fig. 3 Variation of the
seepage loss with the bed
width for different side slopes
"[23], © ASCE"
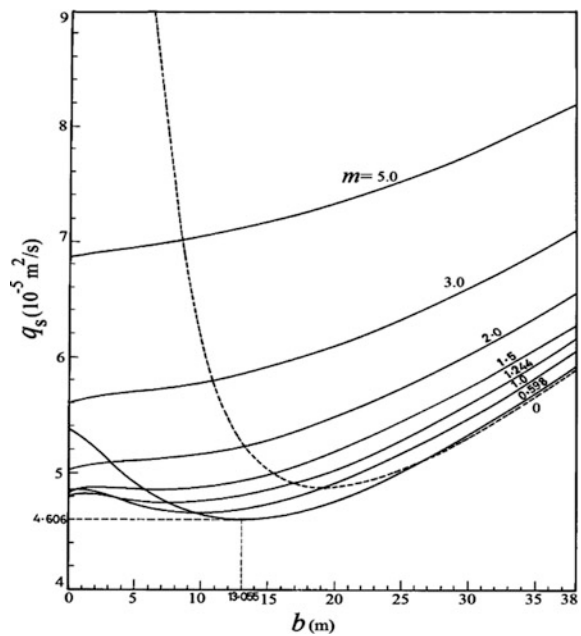
4 Design of a Swale Cross-Section

The issue that needs a designer attention is that some stormwater management practices are sized based on the peak flow of a design event, while others are sized based on the volume of the design event [1]. The grassed channels are a flow-rate-based design [27], and the principles of open channel flow are then used in the design of a swale cross-sectional flow area [1]. Therefore, there is usually a focus on the runoff conveyance and quality requirements, with less attention given to the best section for maximizing runoff reduction by infiltration and seepage. However, if the infiltration rate is taken into consideration, the Manning's equation

$$Q = \frac{1}{n} A R^{2/3} S^{1/2}, \tag{3}$$

where Q is the flow rate (m³/s), n is Manning's roughness coefficient, A is the cross-sectional area of the swale (m²), R is the hydraulic radius (m), and S is the channel slope (m/m).

and infiltration flow

$$Q_f = \frac{f}{100} PL, \tag{4}$$

where Q_f is the infiltration flow rate (m³/h), f is the infiltration rate (cm/h), P is the wetted perimeter (m), and L is the length of the swale (m) are usually used in the design of the cross-sectional flow area of a permeable stormwater channel. Infiltration rate f in Eq. (4) is estimated using either empirical test such as double ring or literature values of infiltration based on soil type and water content.

To verify the efficacy of the infiltration and adjust the swale cross-section, the flow and infiltration flow rates should be converted into volume for comparison with the required infiltration volume. The effects of the cross-sectional flow area on the surface water reduction and infiltration rate are usually neglected.

For the determination of the length of a swale required for a given total infiltration, [28] derived design equations for trapezoidal and triangular swales by combining Manning's equation (Eq. 3) and the infiltration flow rate equation (Eq. 4). The infiltration flow rate Q_f was replaced with the flow rate in Manning's equation as follows:

$$L = \frac{Q}{Pf} \tag{5}$$

For consistency of the infiltration rate units, the flow rate in the swale, Q, should be converted into (m³/h). For the considered trapezoidal channel, the wetted perimeter in Eq. (5) was substituted based on Manning's equation and the concept of the most efficient hydraulic section. The following equation was thus obtained,

Table 1 Swale length formula constant K as a function of the side slope m

M	K (SI Units) (i = cm/h, Q = m^3/s)	K (U.S. Units) (i = in./h, Q = ft^3/s)
1	98,100	13,650
2	85,400	11,900
3	71,200	9900
4	61,200	8500
5	54,000	7500
6	48,500	6750
7	44,300	6150
8	40,850	5680
9	38,000	5255
10	35,760	4955

$$L = \frac{360,000Q}{\left\{ b + 2\left[\frac{n\,Q(1+m^2)^{1/3}}{S^{1/2}\,m^{2/3}\,2\left[(1+m^2)^{1/2}-m\right]} \right]^{3/8} (1+m^2)^{1/2} \right\} f.} \tag{6}$$

Equation (6) was further simplified as follows by [29], who introduced the constant K:

$$L = \frac{KQ^{5/8}S^{3/16}}{n^{3/8}f}, \tag{7}$$

where K is a function of the side slope m (Table 1), which is only a mathematical simplification of the hydraulic relationship with the side slope m, without considering its effect on the infiltration rate.

In addition, only one value of the infiltration rate is employed and multiplied by the wetted perimeter in Eqs. (6) and (7). This implies that the variation of the infiltration rate with the channel cross-section is ignored. When the swale is intended for infiltration enhancement, it is necessary to consider the effect of the cross-sectional flow area on the infiltration rate.

5 Materials and Methods

5.1 *Experimental Setup*

The study was conducted using physical models of channels made from Perspex clear sheets with half-trapezoidal cross-sections. The length L of channel models was 0.5 m; the bottom width b values were 1, 0.5, and 0.2 m, respectively; and the side slope m values were 2, 3, and 4. To simulate the permeable boundaries, a
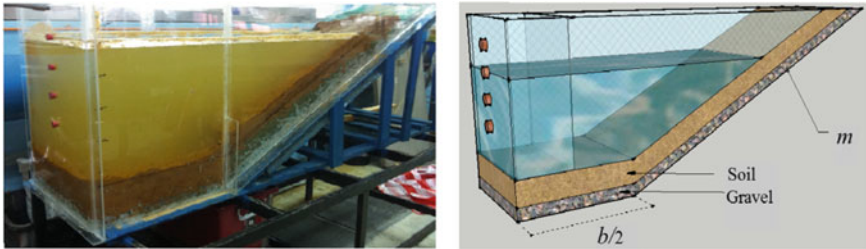
Fig. 4 Half-trapezoidal channel models with different base widths and side slopes

10-cm top soil layer was placed on a 5-cm-thick gravel filter (Fig. 4). Holes spaced at 10 cm were drilled in the bottom and side of the models to drain water infiltrating through the soil.

5.2 Soil Samples

Two soil samples with different texture, namely, natural soil and modified soil were used in this study. The natural soil sample was collected from the farm of the Universiti Putra Malaysia. A previous survey of the farm soil identified four major soil series, namely, the Melaka, Munchong, Bungor, and Serdang Series [30]. Laboratory tests revealed that the characteristics of the soil sample were comparable to those of the Serdang series, which have textures ranging from fine sandy loam to sandy clay loam [31].

The modified soil sample was prepared by mixing the natural soil with well-graded sand (100% sand). A 50 kg of sand was added to the 100 kg sandy loam and the final soil texture became loamy sand soil. Properties of the soil samples are described in Table 2. Saxton and Rawls [32] recommend the use of the USDA soil texture classifications for assessing soil properties in the context of infiltration study. Figure 5 shows that both soil textures are within the shaded area in USDA Textural Triangle which represents the soil textures that applicable for design of infiltration facilities [5].

5.3 Experimental Method

The ponding method, which involves filling the channel model to the target level and measuring the decrease in the water depth over time, was used for the infiltration tests. The present tests involved the effects of the three parameters of the cross-sectional flow area of a trapezoidal channel, i.e., the water depth, base width,

Table 2 Properties of the soil samples

	Units	Natural soil	Modified soil
Texture		Sandy loam	Loamy sand
Sand	(%)	77	84.7
Silt	(%)	4	2.7
Clay	(%)	19	12.6
Porosity[a]		0.453	0.437
Effective porosity[a]		0.412	0.401
Hydraulic conductivity[a]	(cm/h)	1.09	2.99

[a]Rawls et al. [33]

Fig. 5 The soil textures based on USDA Textural Triangle [34]

✳ **Natural Soil Sample**   ✳ **Modified Soil Sample**
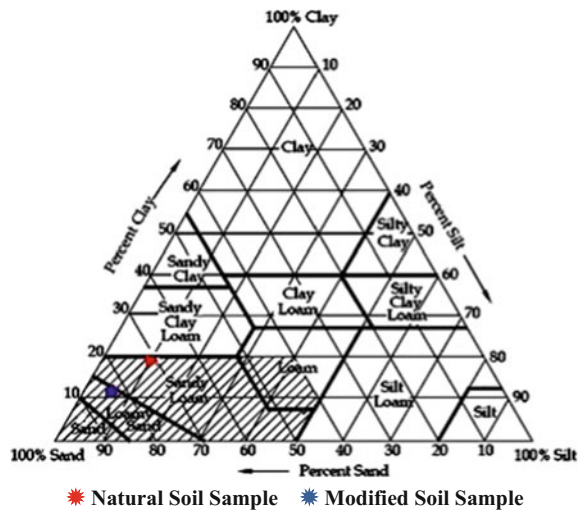
and side slope on water reduction by infiltration and seepage. The loss of water from the channel models by evaporation was considered insignificant and ignored.

The details of the laboratory tests for the different considered conditions are presented in Table (3). Same experimental tests were repeated for the two soil textures to generalize the results. The decreasing water level for each condition was measured at 10 min intervals over 8 h.

The initial water content of soil was set to the field capacity of the soil (unsaturated), and hence the soil was allowed to fully saturate before each test trail and then drain for 2–3 days to attain the field capacity. Seepage discharge per unit length in the unsaturated condition was calculated using the measured decrease in the cross-sectional area of the water with respect to time during the ponding test

Table 3 Details of the laboratory experiments

Case	Side slope (m)	Base width b (m)	Initial water depth y (m)
1	2	0.2	0.15, 0.25, 0.35, 0.45
2		0.5	0.15, 0.25, 0.35, 0.45
3		1	0.15, 0.25, 0.35, 0.45
4	3	0.5	0.15, 0.25, 0.35
5	4	0.5	0.15, 0.25, 0.35

$$q_s = \frac{\Delta A}{\Delta t},\tag{8}$$

where q_s is the seepage discharge per unit length (m²/h), and $\frac{\Delta A}{\Delta t}$ is the decrease of the cross-sectional flow area with respect to time (m²/h).

6   Results and Discussion

Figures 6 and 7 show the variation of the seepage rate with time for sandy loam and loamy sand soil textures respectively for different water levels, base widths, and side slopes.

From Figs. 6 and 7, it is clear that the seepage in the unsaturated condition is unsteady, and the seepage rate initially decreasing sharply with time, followed by a gradual decrease until it becomes constant (the basic seepage rate) after about 4 h.

On the other hand, a comparison of the seepage rates shown in Figs. 6 and 7 reveals that the seepage rates for the modified soil sample (loamy sand) are higher than those for the natural soil sample (sandy loam) for a given initial water level, base width, and side slope. The figures show that the seepage rates were approximately doubled when soil was modified. Rawls et al. [35] stated that the typical hydraulic conductivity of loamy sand is about 2.7 times higher than its value for sandy loam (Table 2). The increase on seepage rates after modification was only by 2 times because of the high percentage of clay contents (see Fig. 4 and Table 2).

The effect of water level on the seepage rate is also clear from Figs. 6 and 7, as the seepage rate increases with increasing water level for both soil textures, irrespective of the base width and side slope.

To investigate the effect of the base width on the seepage rate the base width was varied for a given initial water level and side slope. The results for sandy loam and loamy sand soil textures are shown in Figs. 8 and 9 respectively. From Fig. 8, it can be seen that for the sandy loam soil, the seepage rate for a base width b of 0.2 m is always the lowest for a given water level. However, there is very
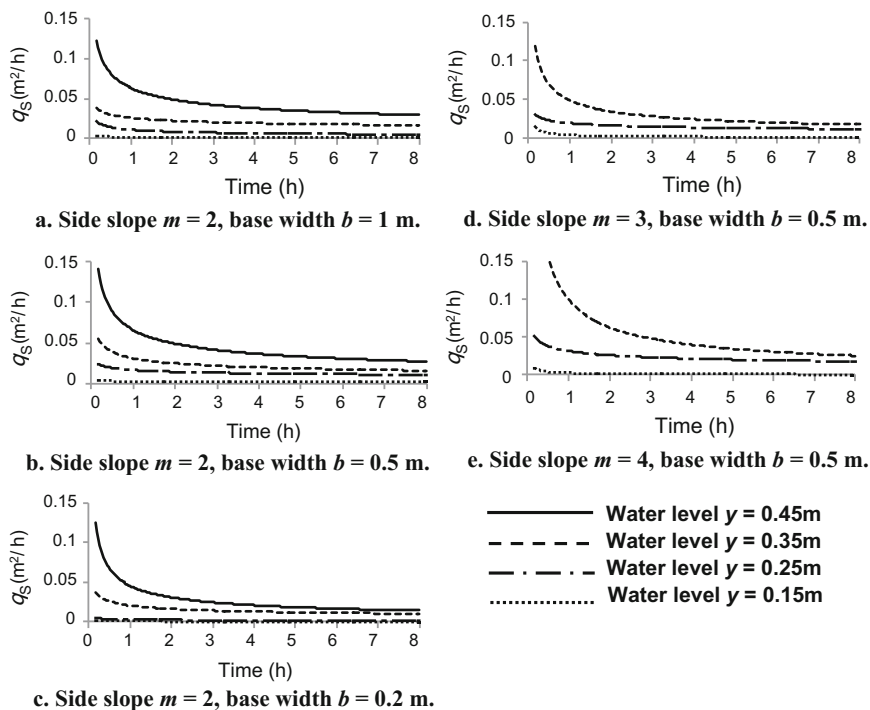
Fig. 6 Variation of the seepage rate with time for sandy loam soil for different initial water levels, base widths, and side slopes

little increase on the seepage rate when the base width is changed from 0.5 to 1 m for all the considered initial water levels. For loamy sand soil, the results which are shown in Fig. 9, indicated that the seepage rate increases slightly with increasing base width.

Moreover, to investigate the effect of the side slope on the seepage rate, the side slope was varied for a given initial water level and base width. The results are shown in Figs. 10 and 11 for sandy loam and loamy sand soil textures respectively, which show that the side slope has negligible effect on the seepage rate for a low water level h of 0.15 m for both soil textures. The effect, however, increases with increasing water level from 0.25 to 0.35 m. The results therefore indicate that an increase of the side slope for both soil textures increases the unsteady seepage rate, with the effect becoming more significant with increasing initial water level.
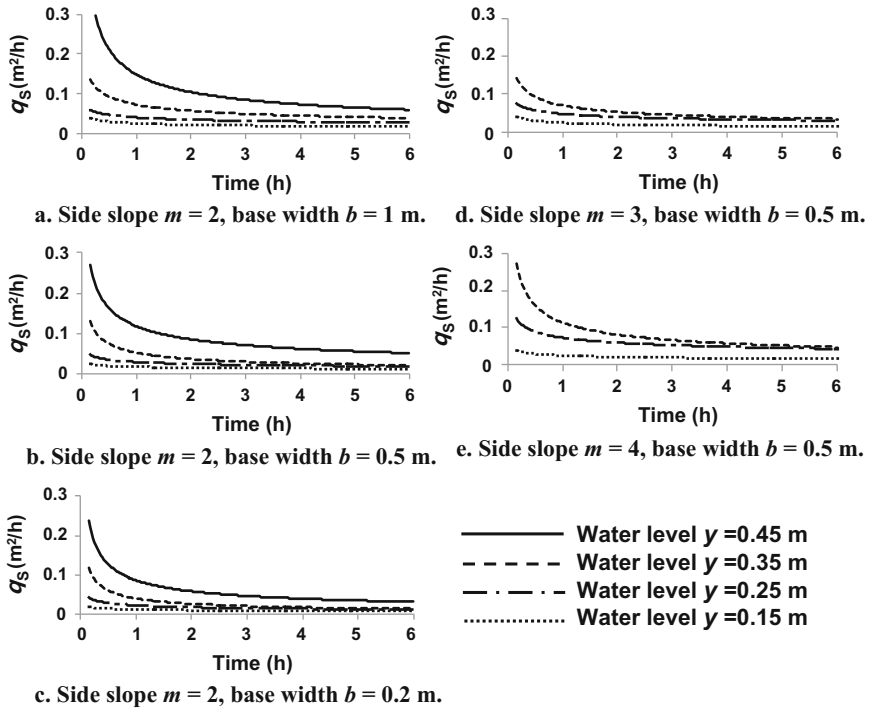
Fig. 7 Variation of the seepage rate with time for loamy sand soil for different initial water levels, base widths, and side slopes
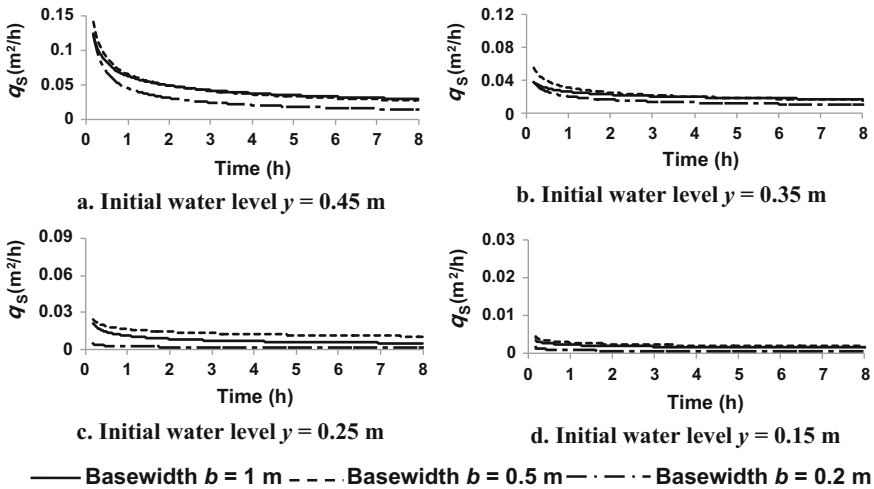
Fig. 8 Comparison of the seepage rates for sandy loam soil for base widths of 1, 0.5, and 0.2 m with respect to the initial water level
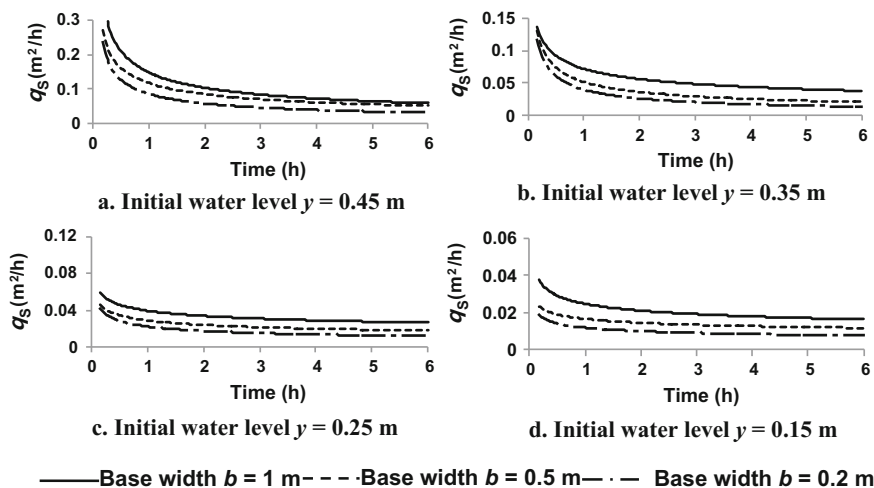
Fig. 9 Comparison of the seepage rates for loamy sand soil for base widths of 1, 0.5, and 0.2 m with respect to the initial water level
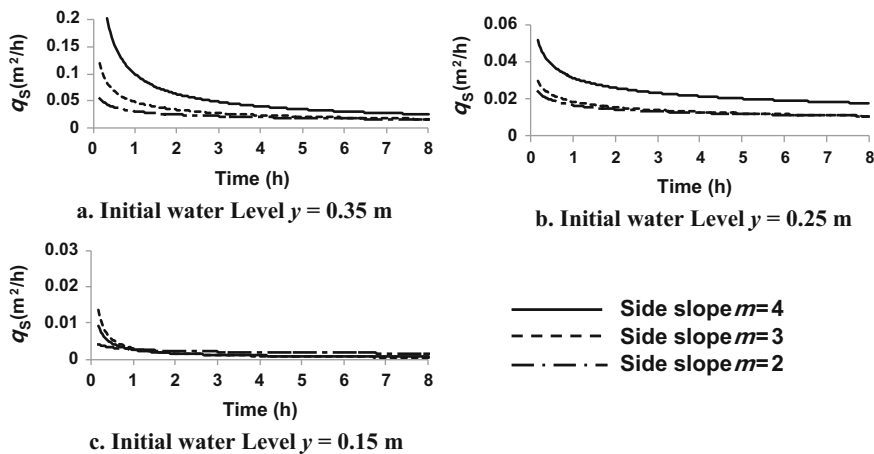
Fig. 10 Comparison of the seepage rates for sandy loam soil for side slopes of 2, 3, and 4 with respect to the initial water level

a. Initial water Level $y = 0.35$ m

b. Initial water Level $y = 0.25$ m

c. Initial water Level $y = 0.15$ m
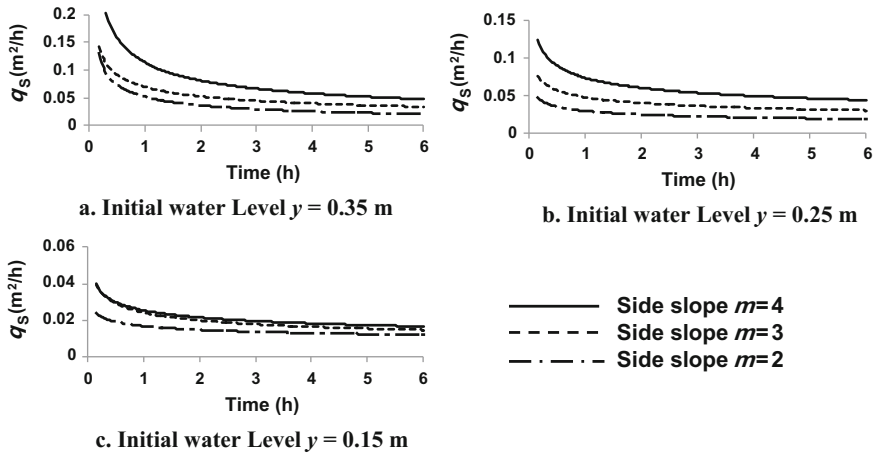
Fig. 11 Comparison of the seepage rates for loamy sand soil for side slopes of 2, 3, and 4 with respect to the initial water level

7 Conclusions

The effects of the three components of a trapezoidal section, namely, the water depth, side slope, and base width, on infiltration and seepage rates were investigated in the present study using physical permeable channel models. The study involved two sets of experiments, one using the original natural soil (sandy loam) and the second using the modified soil (loamy sand). Comparison of the results from the variation of the seepage rate with time for different water levels, base widths, and side slopes shows that the seepage rate increases with increasing initial water level irrespective of the base width and side slope. In addition, an increase of the side slope increases the infiltration rate, with the effect becoming more significant with increasing initial water level, while the effect of varying the base width is insignificant. The findings of this study confirmed that it is necessary to consider the effect of the cross-sectional flow area on the infiltration rate when the channel is intended for infiltration enhancement.

References

1. Water Environment Federation (WEF) Design of Urban Stormwater Controls: MOP 23, McGraw Hill Professional, USA (2012)
2. Stahre, P.: Blue-Green fingerprints in the city of Malmo. VA SYD, Sweden, Sweden (2008)
3. Boogaard, F.C., Lucke, T., Sommer, H., De Beer, J., Van De Giesen, N.C., Van De Ven, F.H.M.: Lessons learned from over two decades of global swale use. In: 13th International Conference on Urban Drainage, Sarawak, Malaysia, 7–12 September 2014
4. Ferguson, B.K.: Stormwater Infiltration, LEWIS Publishers, CRC press, Inc (1994)
5. Department of Irrigation and Drainage (DID): Urban Stormwater Management Manual for Malaysia, 2nd edn. Malaysia (2012)
6. Lewis, M.R., Powers, W.L.: A study of factors affecting infiltration. Soil Sci. Soc. Am. Proc. **3**, 334–339 (1938)
7. Horton, R.E.: An approach towards a physical interpretation of infiltration capacity. Soil Sci. Soci. America **5**, 399–417 (1940)
8. Fletcher, J.E.: Some properties of water solutions that influence inflltration. Trans. Am. Geophys. Union **30**, 548–554 (1949)
9. Parr, J.F., Bertrand, A.R.: Water infiltration into soils. Adv. Agron. **12**, 311–358 (1960)
10. Hillel, D.: Environmental Soil Physics. Academic Press, San Diego, CA (1998)
11. Brady, N.C., Weil, R.R.: The Nature and Properties of Soils, Upper Saddle River. Prentice Hall, Inc, NJ. (1999)
12. Philip, J.R.: The theory of infiltration. 6. Effect of water depth over soil. Soil Sci. **85**, 278–286 (1958)
13. Schmid, B.H.: On overland flow modelling: Can rainfall excess be treated as independent of flow depth? J. Hydrol. **107**, 1–8 (1989)
14. Wallach, R., Grigorin, G., Rivlin, J.: The errors in surface runoff prediction by neglecting the relationship between infiltration rate and overland flow depth. J. Hydrol. **200**, 243–259 (1997)
15. Warrick, A.W., Zerihun, D., Sanchez, C.A., Furman, A.: Infiltration under variable ponding depths of water. J. Irrig. Drain. Eng. ASCE. **131**(4), 358–363 (2005)
16. Elhanafy, H., Copeland, G.: The effect of water stage on the infiltration rate for initially dry channels. Strathclyde University, UK (2007)
17. Everett, S.R., Dutt, G.R.: Length and slope effects on runoff from sodium dispersed, compacted earth microcatchments. Soil Sci. Soc. Am. J. **49**, 734–738 (1985)
18. Haggard, B.E., Moore Jr., P.A., Brye, K.R.: Effect of Slope on Runoff from a Small Variable-Slope Box. J. Environ. Hydrol. **13**: 25 (2005)
19. Huat, B.B.K., Ali, F.H.J., Low, T.H.: Water infiltration characteristics of unsaturated soil slope and its effect on suction and stability. Geotech. Geol. Eng. **24**, 1293–1306 (2006)
20. Chen, L., Young, M.: Green-Ampt infiltration model for sloping surfaces. Water Resour. Res. **42** (2006)
21. Mishra, S.K., Chaudhary, A., Shrestha, R.K., Pandey A., and Lal, M.: Experimental Verification of the Effect of Slope and Land Use on SCS Runoff Curve Number. Water Resour. Manage. **28**:3407–3416 (2014). https://doi.org/10.1007/s11269-014-0582-6
22. Engineering, Keller-Bliesner: Critique of the conservation program's lateral canal lining verification plans and procedures. Prepared for Imperial Irrigation District, USA (1992)
23. Swamee, P.K., Mishra, G.C., Chahar, B.R.: Design of minimum seepage loss canal sections. J. Irrig. Drain. Eng., ASCE, **126**(1), 28–32 (2000)
24. Ghazaw, Y.: Design and analysis of a canal section for minimum water loss. Alexandria Eng. J. **50**, 337–344 (2011)
25. Adarsh, S.: Design of minimum seepage loss irrigation canal sections using probabilistic search. Int. J. Optim. Civ. Eng. **2**(1), 15–28 (2012)
26. Saha, B.: A critical study of water loss in canals and its reduction measures. Int. J. Eng. Res. Appl. **5**(3) (Part 4), 53–56 (2015)

27. Center for Watershed Protection (CWP): Design of stormwater filtering systems. Prepared for the Chesapeake Research Consortium, Solomons, MD, and USEPA Region V. Chicago, IL, by the Center for Watershed Protection, Ellicott City, MD, (1996)
28. Wanielista, M.P., Yousef, Y.A., Avellaneda, E.: Alternatives for the treatment of groundwater contaminants: infiltration capacity of roadside swales, Technical report, University of Central Florida, Department of Civil Engineering and Environmental Sciences, USA (1988)
29. Wanielista, M.P., Yousef, Y.A.: Stormwater Management. Wiley, USA (1993)
30. Shamsuddin, J., Darus, A.: Mineralogy and genesis of soils in Universiti Pertanian Malaysia, Serdang, Selangor. Pertanika **2**(2), 141–148 (1979)
31. Paramananthan, S., Zauyah, S.: 'Soil landscapes in Peninsular Malaysia. Geol. Soc. Malaysia Bull **19**, 565–583 (1986)
32. Saxton, K.E., Rawls, W.J.: Soil Water Characteristics Estimates by Texture and Organic Matter for Hydrologic Solutions. Soil Sci. Soci. Am. J. **70**, 1569–1578 (2006)
33. Chahar, B.R., Graillot, D., Gaur, S.: Storm-water management through infiltration trenches. J. Irrig. Drain. Eng., ASCE, **138**(3), 274–281 (2012)
34. USDA (United States Department of Agriculture): Soil Taxonomy—a basic system of soil classification for making and interpreting soil survey. USDA Handbook No. 436. Wash. D.C. (1999)
35. Rawls, W.J., Brakensiek, D.L., Miller, N.: Green–Ampt infiltration parameters from soils data. J. Hydraul. Eng. **109**(1), 62–70 (1983)

Contributions of Dry and Wet Weather Runoffs to Annual Pollutant Loading in Tropical Urban Catchments

Ming Fai Chow and Zulkifli Yusop

Abstract This study compares the relative contributions of potential contaminants discharged in dry weather flow (DWF) and wet weather flow (WWF) from typical type of catchments in Malaysia. A total of 52 storm events were monitored for WWF quality evaluation. Hourly DWF samples were also collected manually during selected weekday (Wednesday) and weekend (Saturday and Sunday). All water samples were analyzed for TSS, COD, BOD, oil and grease (O&G), NO_2–N, NO_3–N, NH_3–N, soluble P, total P and Zinc. The results indicate that TSS, BOD, COD and O&G were mostly transported in WWF than in DWF. More than 70% of the total annual load of TSS and O&G were transported in storm water runoff. Conversely, annual loadings of NH_3–N and soluble P were mainly evacuated by DWF at the commercial and industrial catchments. Storm water runoff contributes greater loadings of N and P in the residential catchment. In general, each pollutant and land use would give different relative contributions to the annual pollutant loadings. In conclusion, this study have recognized the relative pollutant loading contributions by dry and wet weather flows in typical urban catchments in Malaysia. This findings will help the decision makers to develop better target specific pollutant treatment strategies to reduce the urban water pollution.

M. F. Chow (✉)
Center for Sustainable Technology and Environment (CSTEN),
Universiti Tenaga Nasional, 63000 Kajang, Selangor, Malaysia
e-mail: Chowmf@uniten.edu.my

Z. Yusop
Water Research Alliance (Water RA), University of Technology
Malaysia (UTM), Johor Darul Ta'zim, 81310 Johor Bahru, Malaysia

1 Introduction

Rapid urbanization can cause the increased pollutant loading as well as runoff to receiving waters during both wet weather flows (WWF) and dry weather flows (DWF) [1–3]. Urban wet weather flow has long been recognized that contributes significant pollutants and causes the water-quality degradation in the receiving waters. For the past recent years, more concerns were focused on controlling WWF rather than DWF in the urban runoff management. However, the published literature shows that the discharge of dry weather pollutant may consider to have a major effect to the receiving water quality [4–8]. Volume of dry weather flow from storm drains is comprised mostly of nuisance flows (i.e., exfiltration from leaky sanitary sewers, illicit connections from sewerage, permitted discharges from industrial or municipal area [9–14].

Dry weather pollutants for example solids, metals and nutrients can be generated from natural sources and anthropogenic sources [15]. These pollutants may present in dry weather with low concentrations flow but there are certain dangerous pollution that could influence the marine life [16]. Furthermore, DWF can give a significant quantity of the annual elements load for instance, nutrients as well as metals during years through low rainfall volume [17]. McPherson et al. [8] has investigated the long term weather flow and pollutant loading at Ballona Creek watershed. The result showed that between 100 and 500 kg/year of trace metals load discharged annually during dry weather periods.

In order to mitigate adverse impacts from urban watersheds, an understanding of the relative pollutant contributions and characteristics from urban DWF and WWF is essential because management approaches may contrast for these two sources. The prediction of annual pollutant loads is required to formulate and fulfill the planning and management objectives. Evaluations of annual pollutant loads from a watershed to estimate future annual loads are also needed in order to determine the influence of watershed's urbanization process. Data on both concentration and discharge are required to calculate the annual loads and fluxes (e.g., [18]). The data of average annual pollutant concentration (dry and wet condition) can be found by direct measurement or from previous studies. However, there are no previous studies have been found on relative sources of dry weather loading in tropical urban catchments. Necessary data is required by researcher to determine the estimated loads and concentrations throughout dry weather condition and possible sources. Therefore, this study compares the relative contributions of potential contaminants discharged in dry weather flow (DWF) and wet weather flow (WWF) from typical type of urban catchments in Malaysia.

2 Methodology

2.1 Area of Study

This study was conducted in Skudai, Malaysia as shown in Fig. 1. Three typical types of land uses specifically residential, commercial, and industrial were selected within the Skudai river basin for wet and dry weather loading investigation. The annual rainfall in the Sg. Skudai river basin is approximately 2400 mm. Heavy rainfall is normally occurs between November and January [19] and dry and wet weathers could be determined accordingly. The details characteristics of each catchment were summarized in Table 1.

2.2 Water Quantity and Quality Measurements

Storm water runoff was measured and sampled at the main outlet of studied catchment. The flow depth in the storm drain was determined by using a stage gauge manually. A stage–discharge curve was established to convert the flow depth
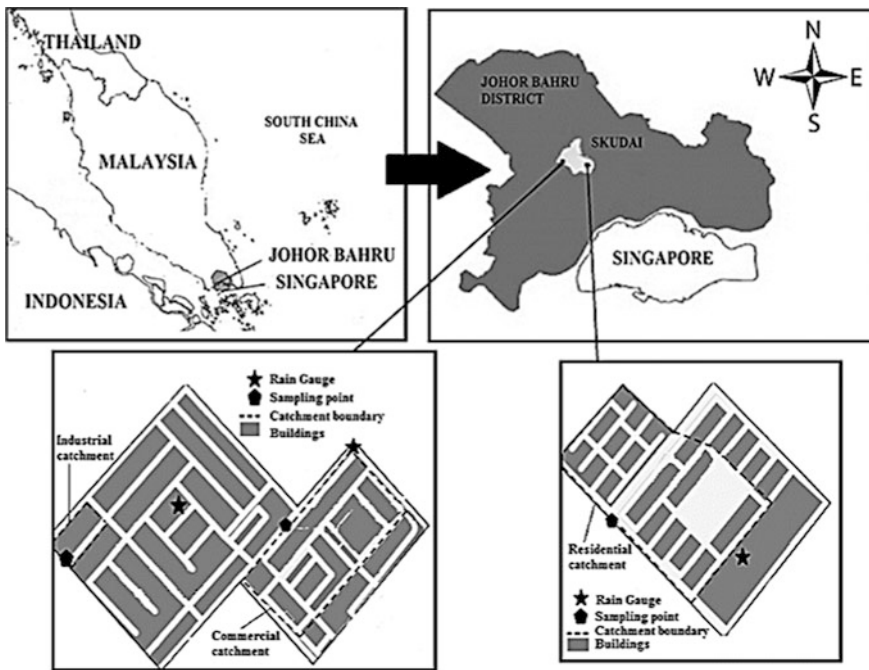

Fig. 1 Selected sampling location for this study

Table 1 Catchments characteristic in this study

Characteristics	Taman Impian Emas	Taman Universiti	Taman Perindustrian Universiti
Land use	Residential	Commercial	Industrial
Area	32.77	34.21	4.38
No. of shops/houses/factories	473	597	25
Impervious area (%)	85	95	93
Average daily traffics (cars/day)	7811	33286	3148

data to volumetric flow rate. After that, hydrograph was generated for individual storm runoff event. The area under the hydrograph was determined as the runoff volume that discharged during the storm event. Storm water samples were taken manually throughout the storm events. Although this method was considered more laborious than automatic water sampler, but it is suitable for small urban catchment that subjected to rapid increasing of water level in short period when the storm runoff has begun. Furthermore, grab sampling is able to reduce the risk of oil and grease from attaching to the container and the internal surfaces of the sampling tube in the automatic sampler. The total number of samples collected for each storm event differs from 8 up to 15 based on the storm size. The sampling protocol was followed the procedure outlined by Caltrans [20]. The intervals for each sampling were set between 10 and 20 min during the falling limb of the hydrograph. Meanwhile, 1–10 min was determined as the sampling interval during the rising limb of hydrograph. More acute sampling on the rising limb of the hydrograph is required in order to evaluate the first flush effect. Approximately 1 L of runoff volume was collected for each sample. In addition, hourly dry weather samples were collected manually for 24 hours during one day of weekdays (Wednesday) and the weekend (Saturday and Sunday). From each site, a total of 72 samples were collected in order to determine the standard dry weather concentration of selected water-quality parameters. Flow rate for every sample was measured in order to calculate the dry weather's pollutant loading. Rain samples were taken manually at an open arena in order to determine the quality of rainwater at study area. Three rainwater samples were taken from each storm event and analyzed for the average pollutant concentration. The standard method for the examination of water and wastewater [21] have been used as guidelines to conduct the stormwater quality analysis for every sample. The analytical number used are as follow: BOD (5210B), COD (5220B), TSS (2540D), oil and grease (O&G) (5520B), NO_2–N (4500-NO2 B), NO_3–N (4500-NO3 B), NH_3–N (4500-NH$_3$ F), total P (4500-P B), soluble P (4500-P E), and Zinc (3120 B).

2.3 Analysis of Data

Event Mean Concentration (EMC) has been used to determine the average pollutant concentration, which is defined as the total constituent mass M discharged during an event divided by the total runoff volume, V during the event [22], expressed as

$$\text{EMC} = \bar{C} = \frac{M}{V} = \frac{\int Q(t)C(t)\mathrm{d}t}{\int Q(t)\mathrm{d}t}, \tag{1}$$

where M is total mass of pollutant during the entire runoff (kg); V is total volume of runoff (m^3); $C(t)$ is time varying pollutant concentration (mg/L); $Q(t)$ is time variable flow (L/s); and t is total duration of runoff (s).

Generally, Site Mean Concentration (SMC) is required to estimate the annual discharge of urban wet weather's pollutant loading. The SMC value is calculated based on the average of EMC values for each catchment. In this study, annual pollutant loadings were calculated by using the method defined by Schueler [23] as

$$L = P \cdot P_j \cdot R_v \cdot C, \tag{2}$$

where, L is the normalized annual pollutant load (kg/ha/year), P is the annual precipitation (mm/year), P_j is the dimensionless correction factor that adjusts for storms without runoff, R_v is the dimensionless average runoff coefficient, C is the flow-weighted average concentration (mg/L).

The annual rainfall depth, P was determined from rainfall records collected at the study catchments. A mean annual rainfall of 2523 mm was recorded at the studied catchments and this value was used for the annual precipitation (P). A rainfall correction factor (P_j) of 0.9 was used as recommended by Schueler [23]. This value is supported by rainfall-runoff analysis for all catchments whereby runoff makes up about 90% of the annual rainfall. The runoff coefficient, R_v, was calculated using the equation as below

$$R_v = 0.05 + 0.009(\mathrm{I}), \tag{3}$$

where R_v is runoff coefficient; and I is the imperviousness catchment percentage. The baseflow annual loading of pollutant from each catchment was calculated as follows [6]

$$W = n \times \sum_{j=1}^{n} C_m \times Q_j, \tag{4}$$

where, W is the total load during the sampling period, n, C_m (mg/L) is the median concentration, and Q (m^3/s) is the dry weather flow on day j.

3 Results and Discussion

The descriptive statistics of dry weather's pollutant concentration (mg/L) in all catchments is summarized in Table 2. The average concentrations of pollutants are highest for the commercial catchment except for O&G which is the lowest among the three catchments. The industrial catchment is two folds lower than commercial catchment for NH_3–N concentration and the lowest in the residential catchment. Chow and Yusop [24] implied that car-washing station is the potential source of NH_3–N at the commercial catchment. The high standard deviation suggests that the pollutants concentration fluctuates significantly (Table 2). The mean concentrations of various constituents in rainwater and dry weather discharge are shown in Table 3 together with the EMCs at three types of urban catchments. The rainwater quality (first row) suggests that most of the constituents have very low concentrations. As a result, the pollutant contents in the wet weather discharge would not be influenced by rainwater quality except for NO_3–N. It showed that rainfall sample is a key source of NO_3–N at the urban catchment. The EMC of wet weather flow for all studied catchments are generally lower than mean pollutant concentration of dry weather flow, except for O&G and TSS from commercial and industrial catchments. Chow et al. [25] suggested that O&G and TSS were deposited temporarily in the drain and will be transported during the next large storm event. Similar observation found by Francey et al. [26] that TSS concentration in dry weather flow is lower than storm flow while nitrogen concentration is generally lower in storm flow. It is suggested that dry weather flow and small storm event should be treated instead of bypassing.

The dry weather flow concentrations at the residential catchment are relatively lower than those reported by Nazahiyah [27] and Mamun [28] for BOD, COD, TSS, O&G, and NH_3–N (Table 4). The separate underground stormwater drainage system used in this residential catchment could possibly prevent illegal or direct disposal of wastewater into the storm drain and thus reduces the pollutant concentration in the dry weather discharge. Again, the mean concentrations of major pollutants at the commercial catchment are generally lower than results reported by [27] except for NO_3–N and NH_3–N. Comparison was also made with the Effluent Standards A and B recommended by Department of Environment Malaysia [30]. The BOD and COD concentrations in all catchments exceeded the Standard A limits. The dry weather flow qualities at the commercial and industrial catchments are categorized as Class V according to the Interim National Water Quality Standard (INWQS). BOD concentrations are five times above the class V standard whereas the COD concentrations were higher by three orders of magnitude for the commercial and industrial catchments. In addition, NH_3–N concentration from the commercial catchment is approximately two folds greater than the Class V limit. The residential catchment shows relatively lower concentration of TSS when compared to the EQA Standard A. TSS concentration in the commercial catchment, however, exceeds this limit. These results indicate that dry weather flows are significant sources of non-point source pollution in the urban areas. As such,

Table 2 Descriptive statistics of pollutant concentrations (mg/L) for dry weather flows from respective catchments

Catchment		Flow rates (m³/s)	Dry weather flow concentration (mg/L)								
			BOD	COD	TSS	O&G	NO₃–N	NO₂–N	NH₃–N	Soluble P	Total P
Residential	Min	0.0004	3.5	6	1	0.2	0.10	0.001	0.01	0.02	0.09
	Max	0.0040	73.0	146	54	12.4	6.20	0.083	1.72	1.34	3.10
	Mean	0.0020	21.2	55	15	3.1	1.35	0.010	0.19	0.31	0.62
	Median	0.0024	15.5	47	12	2.9	1.05	0.004	0.10	0.27	0.44
	Std. dev	0.0010	15.6	34	11	2.3	1.10	0.016	0.30	0.23	0.53
Commercial	Min	0.0035	11.8	91	9	0.2	0.10	0.001	0.62	0.07	0.24
	Max	0.0091	80.0	608	209	8.0	18.60	0.092	24.80	2.36	4.45
	Mean	0.0053	68.1	342	59	2.7	3.10	0.019	5.22	0.87	1.82
	Median	0.0050	72.5	340	51	2.3	1.20	0.011	3.23	0.71	1.68
	Std. dev	0.0011	16.1	117	40	1.7	4.05	0.020	4.96	0.56	0.84
Industrial	Min	0.0001	2.3	2	6	0.2	0.10	0.001	0.01	0.01	0.57
	Max	0.0075	80.0	1281	457	16.0	22.40	0.090	21.30	2.40	6.19
	Mean	0.0010	62.6	294	49	3.8	2.86	0.013	2.96	0.64	1.55
	Median	0.0005	70.8	172	31	3.0	1.35	0.007	2.37	0.46	1.26
	Std. dev.	0.0014	19.5	303	63	3.0	4.38	0.015	3.36	0.55	1.05

Table 3 Average EMC values of pollutants in rainwater, wet weather and dry weather flows at the study sites

	Concentration (mg/L)									
	BOD	COD	TSS	O&G	NO_3–N	NO_2–N	NH_3–N	Soluble P	Total P	Zinc
Rainwater	3.1	5.0	2.0	ND	0.9	0.004	0.37	0.03	0.08	–
Residential catchment										
Wet weather	6.5	36	21	2.32	0.90	0.011	0.19	0.07	0.38	0.04
Wet weather (median)	6.5	39	26	2.28	0.94	0.008	0.17	0.07	0.41	0.05
Dry weather	21.2	55	15	3.14	1.35	0.010	0.19	0.31	0.62	–
Commercial catchment										
Wet weather	81.1	225	167	3.66	0.93	0.006	0.71	0.11	0.69	0.08
Wet weather (median)	58.1	196	124	3.89	0.80	0.006	0.70	0.08	0.73	0.05
Dry weather	68.1	342	59	2.72	3.10	0.018	5.22	0.87	1.82	–
Industrial catchment										
Wet weather	42.6	117	91	4.47	1.20	0.009	0.58	0.08	0.59	0.24
Wet weather (median)	44.8	97	91	4.52	1.14	0.009	0.46	0.08	0.62	0.29
Dry weather	62.6	294	49	3.78	2.86	0.013	2.96	0.65	1.55	–

Note – not available

pretreatment are important for controlling the pollution from dry weather discharge into the receiving waters.

3.1 Annual Pollutant Loading

Figure 2 shows the proportions of annual pollutant loads carried by wet weather and dry weather flows from residential, commercial, and industrial catchments. As noted before, annual pollutant loading of Zn is not discussed here because its dry weather flow concentration was not measured in the study. In overall, a large portion of the annual loading of various pollutants was transported in wet weather flow than in dry weather flow especially for TSS, BOD, COD, and O&G. More

Table 4 Comparison of dry weather flow quality with other studies

Land use/ standard	References	Dry weather flow concentration (mg/L)						
		BOD	COD	TSS	O&G	NO_3-N	NO_2-N	NH_3-N
Residential	Mamun [28]	49.3	120	38	13.0	–	–	4.85
Residential	Nazahiyah [29]	77	470	72	–	0.8	0.02	1.4
Commercial	Nazahiyah [29]	140	710	169	–	0.4	0.07	1.1
Residential	Current study	21.2	55	15	3.1	1.35	0.010	0.19
Commercial	Current study	68.1	342	59	2.7	3.10	0.019	5.22
Industrial	Current study	62.6	294	49	3.8	2.86	0.013	2.96
EQA standard A	DOE [30]	20	50	50	–	–	–	NA
EQA standard B	DOE [30]	50	100	100	10	–	–	NA
INWQS class V	DOE [30]	>12	>100	300	NA	–	–	>2.70

– no data, *NA* not available
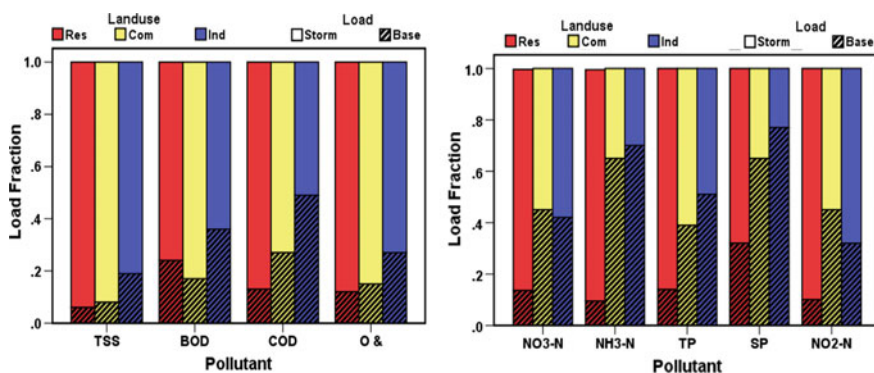
Fig. 2 Proportion of annual pollutant loadings carried by storm runoff and baseflow for different catchments

than 70% of the total annual loading of TSS and O&G were transported in storm water runoff. Since the average number of rain days in this area is high (175 days per year), the bulk of annual pollutant loading must have been discharged by more frequent and short duration storms. Conversely, annual loadings of NH_3-N and SP are mainly evacuated by dry weather flow at all studied catchments except for residential catchment. It showed that daily activities in commercial and industrial catchments have generated large amount of NH_3-N and SP. Problems of dry weather discharge from urban land use should be addressed more seriously in order to control the pollution into the receiving waters. Malik [31] showed similar observation that dry weather flow in storm channels are significant sources of ortho-P and NH_3-N. On the other hand, storm water runoff transported greater

loadings of N and P in the residential catchment. This may be associated with fertilizer application on gardens and lawns. Malik [31] also concluded that wet weather flow at residential catchment was the major contributor of nutrients into the receiving waters. Interestingly, the commercial and industrial catchments showed almost equal proportions of annual NO_3–N loading in wet and dry weather flows.

4   Conclusions

This study compares the relative contributions of potential contaminants discharged by dry weather flow (DWF) and wet weather flow (WWF) from typical type of catchments in Malaysia. The results indicate that TSS, BOD, COD, and O&G are mainly transported in stormflow than in dry weather flow. More than 70% of the total annual load of TSS and O&G were transported in storm water runoff. Conversely, annual loadings of NH_3–N and SP are mainly evacuated by dry weather flow at the commercial and industrial catchments. Storm water runoff contributes greater loadings of N and P in the residential catchment. In general, the relative contribution to the annual pollutant loading varied significantly among types of land use and each pollutant. Better target specific pollutant treatment strategies are suggested to be developed in order to reduce the urban water pollution in Malaysia.

References

1. Davis, A.P., Shokouhian, M., Ni, S.: Loading estimates of lead, copper, cadmium, and zinc in urban runoff from specific sources. Chemosphere **44**, 997–1009 (2001)
2. Chow, M.F., Yusop, Z.: A review of event mean concentration for urban storm water runoff. In: Proceedings International Conference on Environmental Research and Technologies (ICERT' 08), Parkroyal hotel, Penang (2008)
3. Chow, M.F., Yusop, Z., Toriman, M.E.: Level and transport pattern of faecal coliform bacteria from tropical urban catchments. Water Sci. Technol. **67**(8), 1822–1831 (2013)
4. Ackerman, D., Schiff, K.: Modeling storm water mass emissions to the Southern California Bight. J. Environ. Eng. **129**(4), 58–71 (2003)
5. Stein, E.D., Tiefenthaler, L.: Dry-weather metals and bacteria loading in an arid, urban watershed: Ballona Creek, California. Water Air Soil Pollut. **164**, 367–382 (2005)
6. McPherson, E.G., Simpson, J.R., Peper, P.J., Maco, S.E., Xiao, Q.: Municipal forest benefits and costs in five U.S cities. J. For. **103**, 411–416 (2005)
7. Piechota, T.C., Bowland, L.: Characterization of wet and dry weather flows from urban runoff in an arid region. In: Proceedings of the World Water and Environmental Resources Congress, May 20–24, 2001, Orlando, Florida, American Society of Civil Engineers, Washington DC (2001)

8. McPherson, T.N., Burian, S.J., Turin, H.J., Stenstrom, M.K., Suffet, I.H.: Comparison of the pollutant loads in dry and wet weather runoff in a southern California urban watershed. Water Sci. Technol. **45**(9), 255 (2002)

9. Li, T., Zhou, Y.C., Li, H.: Quantifying non-stormwater discharges to stormwater systems with model analysis. J. Environ. Eng. **134**, 928–932 (2008)

10. Lau, S.-L., Stenstrom, M.K.: Metals and PAHs adsorbed to street particles. Water Environ. Res. **39**, 4083 (2006)

11. Sercu, B., Van De Werfhorst, L.M., Murray, J., Holden, P.A.: Storm drains are sources of human fecal pollution during dry weather in three urban southern California watersheds. Environ. Sci. Technol. **43**, 293–298 (2009)

12. Hoes, O.A.C., Schilperoort, R.P.S., Luxemburg, W.M.J., Clemens, F.H.L.R., van de Giesen, N.C.: Locating illicit connections in storm water sewers using fiber-optic distributed temperature sensing. Water Res. **43**, 5187–5197 (2009)

13. Ana, E.V., Bauwens, W.: Modeling the structural deterioration of urban drainage pipes: the state-of-the-art in statistical methods. Urban Water J. **7**, 47–59 (2010)

14. Fenner, R.A.: Approaches to sewer maintenance: a review. Urban Water. **2**, 343–356 (2000)

15. Seiler, R.L., Zaugg, S.D., Thomas, J.M., Howcroft, D.L.: Caffeine and pharmaceuticals as indicators of waste water contamination in wells. Ground Water **37**, 405–410 (1999)

16. Stein, E.D., Tiefenthaler, L.L., Schiff, K.: Watershed-based sources of polycyclic aromatic hydrocarbons in urban stormwater. In: 2005–2006 Southern California Coastal Water Research Project Annual Report (2006)

17. Stein, E.D., Ackerman, D.: Dry weather water quality loadings in arid, urban watersheds of the Los Angeles basin, California, USA. J. Am. Water Resour. Assoc. **43**, 1–16 (2007)

18. Horowitz, A.J.: An evaluation of sediment rating curves for estimating suspended sediment concentrations for subsequent flux calculations. Hydrol. Process. **17**(17), 3387–3409 (2003)

19. Chow, M.F., Yusop, Z., Teo, F.Y.: Evaluation of stormwater runoff quality during monsoon and inter-monsoon seasons at tropical urban catchments. Int. J. River Basin Manage. **14**(1), 75–82 (2016)

20. Caltrans: Guidance Manual: Stormwater Monitoring Protocols. Report No. CTSW-RT-00-005. Department of Transportation, California (2000)

21. APHA (American Public Health Association), AWWA (American Water Works Association), and WEF (Water Environment Federation): Standard Methods for the Examination of Water and Wastewater, 21st edn. APHA/AWWA/WEF, Washington, DC (2005)

22. Huber, W.C.: Contaminant transport in surface water. In: Maidment, D.R. (ed.) Handbook of Hydrology. McGraw Hill, New York (1993)

23. Schueler, T.R.: Controlling Urban Runoff: A Practical Manual for Planning and Designing Urban BMPs. Washington Council of Governments, Washington, DC (1987)

24. Chow, M.F., Yusop, Z.: Characterization and source identification of stormwater runoff in tropical urban catchments. Water Sci. Technol. **69**(2), 244–252 (2014)

25. Chow, M.F., Yusop, Z.: Quality and first flush analysis of stormwater runoff from a tropical commercial catchment. Water Sci. Technol. **63**(6), 1211–1216 (2011)

26. Francey, M., Fletcher, T., Deletic, A., Duncan, H.P.: New insights into the quality of urban storm water in South Eastern Australia. J. Environ. Eng. **136**(4), 381–390 (2010)

27. Nazahiyah, R., Yusop, Z., Abustan, I.: Stormwater quality and pollution load estimation from an urban residential catchment in Skudai, Johor, Malaysia. Water Sci. Technol. **56**(7), 1–9 (2007)

28. Mamun, A.A.: Nonpoint source pollution from a tropical urban residential area. Ph. D. Thesis, Universiti Putra Malaysia, Malaysia (2005)

29. Nazahiyah, R.: Modeling of non-point source pollution from residential and commercial catchments in Skudai, Johor. Master Thesis. Universiti Teknologi Malaysia, Malaysia (2005)

30. Government of Malaysia: Environmental Quality Regulations (Sewage and Industrial Effluents) (1979)

31. Malik, U.: Nonpoint source pollution during dry and wet weather flows in an urbanized watershed. Master Thesis, University of Nevada, Los Angeles (2003)

Part VI
Construction Management

Environmental Benefits of Green Roof to the Sustainable Urban Development: A Review

Ming Fai Chow and Muhammad Fadhlullah Abu Bakar

Abstract With rapid growth of population and the increasing demands for higher living standards, the development of urban infrastructures and buildings are likely to increase the impervious surfaces in the river basin. Green roofs have a famous strategy in the sustainable urban development strategies in recent decades. Green roof is a viable means of increasing the amount of vegetation in urban cities, where the open space at ground level is limited but roof tops are largely unused yet remain impervious and contribute to storm water runoff. This paper is aimed to review comprehensively the types, components, and environmental benefits of green roofs to the sustainable urban development. Generally, green roofs provide a lot of advantages for example decreasing consumption of energy by reducing heating and cooling loads, increase building standards, provide aesthetic value and amenity, improves urban air quality, increase storm water runoff mitigation, decrease air temperatures, decrease noise in urban environments, support in urban storm water pollutant removal, and mitigate urban heat island effects. This paper also reviewed the development and application of green roofs in different countries. In conclusion, more implementation of green roofs in the urban city should be promoted in order to ensure the sustainability of the urban development.

Keywords Environmental benefits · Green roof · Sustainable development
Urban · City · Storm water management

M. F. Chow (✉)
Center for Sustainable Technology and Environment (CSTEN),
Universiti Tenaga Nasional, 43000 Kajang, Selangor, Malaysia
e-mail: Chowmf@uniten.edu.my

M. F. A. Bakar
Department of Civil Engineering, Universiti Tenaga Nasional,
43000 Kajang, Selangor, Malaysia
e-mail: feddy91@gmail.com

1 Introduction

In recent decades, industrialization and population have grown tremendously and the total of land use also increase for development purposed. Urbanized of natural catchment transformed green surface to impervious surface such as roadway and rooftops which increased significantly the overall hydraulic efficiency of catchment [1, 2]. Changing in the hydrological condition of catchment normally caused the increase of peak flow and runoff size [3]. After that, frequency and magnitude of urban flooding would be increased as well [4], contaminant transport [5, 6], and erosion of soil [7]. Stream degradation occurs when almost 10% or more of a watershed is transformed to impervious surfaces [6]. As a watershed turn from a forested state to 10–20% impervious surfaces, runoff would increase twofold; 35–50% impervious cover increases runoff threefold; and 75–100% impervious cover increases surface runoff volume more than fivefold over forested catchments [8]. As imperviousness increases, less rainwater infiltrates into the ground and reducing the groundwater for wetland, riparian vegetation and river base flow [8]. Relatively, low infiltration rates combined with low plant coverage reduce transpiration; evaporation and groundwater recharge fluxes [9]. According to the study by Choi et al. [10], a 30% of growths in city development caused decreasing in natural direct groundwater recharge approximately 30–40%. The combined effects of increased input from precipitation, increased drinking water imports, decreased precipitation losses, and hydraulically improved drainage systems have significantly cause an increase in urban runoff volumes of up to six times of pre-development runoff volumes. Increased rainfall and changes of rainfall distribution associated with climate change have imposed greater challenges to the urban cities [11]. According to the study by Mansell [12] it showed that the increase of precipitation amount in urban areas can be up to 15% under climate change impact. Meanwhile, rainfall intensity also increase by 15–20% by year 2050 [13].

As the developments are progressing, greater challenges are imposed on managing and reducing the storm water runoff in urban areas. Rooftop and transport systems commonly account for 80% of all the impervious surfaces in the urban area [14]. Rooftop runoff poses a greater threat to water quantity in urban catchment than rural catchment as the runoff can enter the receiving water bodies more rapidly due to the greater connectivity of roofs to gutters and drainages. Best management practices (BMP) such as retention ponds, vegetative swales, riparian buffers, and porous pavements have been implemented successfully in reducing storm water runoff volume and rate in many developed countries. However, BMPs require open space to be installed, which is limited in established urban cities. In view of this, green roof becomes a popular strategy for urban storm water management as it addresses the space issue and provides a promising mitigation solution to urban runoff problems [15, 16]. Green roofs take advantage of already existing rooftop space to decrease the source of urban storm water runoff by retaining and detaining the rainwater. In addition, plant species have the ability to evaporate additional water from substrate as it will provide additional spaces to absorb and retain more

rainwater in the following storm event [17]. Therefore, this paper is aimed to give a complete review on the green roof benefits to the sustainable urban city development.

2   Type of Green Roof

There are several green roofs type which including intensive, extensive and semi-intensive. The main differences between extensive and intensive green roofs are the depth of substrate and the vegetation type planted [18]. The typical characteristics of both types of green roofs can be assessed in term of purpose, maintenance requirement, vegetation type, irrigation requirement, substrate thickness, and supporting structural requirements. The comparison of the typical characteristics of extensive and intensive green roofs is summarized in Table 1. Extensive green roof consist of thin growing media, roughly 20–150 mm deep, and planted with sedum, succulents, grasses or low-lying vegetation which have capability to survive on drought condition, low-nutrient and thin substrate. Due to finite substrate depth, extensive green roof experiences limited moisture condition and plant stress during continuous dry periods. Usually, low cost is required to install the extensive green roof and is always cheaper to maintain due to little or no irrigation required. Extensive green roof only requires inspection and maintenance once or twice a year. Extensive green roof has a light weight structure and can be established over a larger roof area without requires additional structural support. Extensive green roof's vegetation can be developed in several techniques such as through, shot planting, prefabricated vegetation mats, spontaneous self-established vegetation, and seed sowing. Normally, extensive green roof consists of low saturated weight between 60 and 150 kg/m^2 and can be installed on a slope up to 30° [19]. Extensive green roof has more ability to adopt wide-scale condition instead of other type of green roof, where the loading on the structure would be the main factor that restrict the intensive green roof application on building. This type of green roof also would be the most popular choice when retrofitting existing roofs due to lower installation cost and requires the least maintenance. In Germany, more than 80% are extensive green roof [20].

Intensive green roof also popular as the garden on the roof that has a deeper layer of substrate with minimum 150 mm deep and allowing for the inclusion of larger vegetation types or small tree. The intensive green roofs are similar to open area at ground level and in type can be assessed by people as well. Due to the higher amount of substrate materials and vegetation, intensive green roofs normally consist of high saturated weight between 200 and 500 kg/m^2. As a result of higher amount of substrates and vegetation with its high water retention, as well as allowing human access to these areas, intensive green roofs normally require additional structural supports and only established at large-scale development such as high-rise building, airport, apartment, etc. Intensive green roofs also require higher cost for installation, fixed irrigation, applications of fertilizer, and maintenance.

Table 1 The characteristics for each green roofs type

Intensive	Semi-intensive	Extensive
For park/garden	For designed green roof	For ecological protection layer
Intensive maintenance required	Periodically maintenance	Extensive maintenance required
Accessible	Partly accessible	Inaccessible
Deeper growing media required (min 150 mm)	Medium growing media required (between 150 and 500 mm)	Shallow growing media required (between 20 and 150 mm)
Heavy weight (saturated weight between 200 and 500 kg/m^2)	Medium weight (saturated weight between 120 and 200 kg/m^2)	Low weight (saturated weight between 60 and 150 kg/m^2)
Varied selection of trees, shrubs, and other herbaceous plants	Certain selection of grass, herbs and shrubs	Restricted selection of low growing, drought tolerant plants and hardy
Require regular irrigation	Periodically irrigation	No or little irrigation
High cost	Medium cost	Low cost
Additional structural support required	Additional structural support required	Load can be carried by most existing structures

Semi-intensive green roof consists of substrate depth ranges from 150 to 500 mm and vegetation used includes grasses, herbaceous plants, and shrubs. The human access to the green roof area is very restricted. The saturated weight of semi-intensive green roofs normally ranges between 120 and 200 kg/m^2 and substantial reinforcement of roof structure is required. Periodically irrigation, fertilization, and maintenance are required for semi-intensive green roofs.

3 Components of Green Roof

Generally, conventional green roofs consist of five major components: vegetation (plant), growing media (substrate), filter fabric, drainage layer, and water proofing membrane/root barrier. The detailed green roof design system as shown in Fig. 1. Each layer plays different function and role in the green roof system. For example, filter membrane can filter the rain water from growing media as the water flowing toward the bottom of green roof and flowing out through the drainage layer. The green roof can be installed either by modular systems, pre-cultivated systems or complete systems.

Fig. 1 Components of green roof [36]

3.1 Vegetation Layer

The vegetation layer in green roof plays an important role in retaining rainwater, reduces wind erosion, provides shading for the substrate and reduces the temperature during daylight hours [21, 22]. The functions of vegetation or plant in green roof is to restore the water storage volume of the substrate through transpiration while the canopy provides the interception storage. The plant selection is typically based on several criteria such as weight, plant coverage, level of maintenance and tolerance to the tough environmental conditions such as, thin growing media, high sun exposure, limited water sources, increased wind speeds and prolonged dry periods [23]. *Sedum* spp., a succulent ground cover, has become very famous to be used in green roofs as this plant would be able to endure in challenging environments situation [24]. However, Snodgrass [25] suggested that green roof plant selection in most cases should be restricted to native plant species. The vegetation normally can be established in a green roof through plug planting, seeds and cuttings, vegetation mats or natural colonization methods.

3.2 Growing Media

The growing media of green roof is functions to provide open pore structure, nutrient, mechanical strength, drainage properties, and chemical composition that

required by the plant species. The characteristics of growing media such as high nutrient and water holding capacity, low density, well-drained material and will not break down overtime [26]. High levels of compost are not suggested due to decomposition factor and it also causes shrinkage on substrate [27], and increases levels of P and N in storm water runoff [28]. The depth of substrate is always depends on the water availability, seasonal low temperatures and the vegetation type [29].

Boivin et al. [30] recommended the suitable depth for substrate is 100 mm in order to provide sufficient defense for vegetation especially on low temperature area. Durhman et al. [31] stated that increasing the substrate depth could improve the plant growth rate, increase the insulation efficiency to the structure [26] and improve the retention performance of storm water [32, 33]. However, the storm water retention capacity is maximized at a certain depth of growing media and only achieves minimal improvement beyond this threshold depth. A typical substrate is consists of almost 20% organic matter and 80% non-organic material [27]. Examples of growing media include expanded clay, perlite, domolite, and expanded slate. These materials can be mixed and make up the growing media composition. The bulk densities of mixture is between 400 and 900 kg/m^3 for dry mixture where water absorbencies is between 15 and 210% by weight. The compositions of growing media have significant effects on the water retention performance of green roof [34].

3.3 Filter Fabric

The filter fabric is installed in between of drainage and growing media layers. Filter paper would retain growing media while allows water to flow through green roof system and filter paper also role as a root barrier as well. The filter paper normally consist of few layer of non-woven geotextile and one of it could be as root inhibitor (i.e., mild herbicide or copper). A part form that, filter fabric have capability to manage erosion issues at the surface of growing media in green roof.

3.4 Drainage Layer

The drainage layer is installed in between the growing medium and roof membrane which facilitates the outflow of rain water from green roofs to the drainage system of building. Certain green roof application may implement an expanded clay with large diameter as a layer, but most green roof application today prefer to use a corrugated plastic drain mat with a structural pattern that landscape paver or resembling an egg carton. The thickness of drainage layer normally not more than 20 mm, but a denser mat could provide extra insulation to root. Miller [34] stated

that the importance of drainage layer to eliminate the possibility of flooding in green roofs and also, to ensure the vegetation in green roof is not sink in water as a lot of plants cannot stand.

3.5 Water Proofing Membrane/Root Barrier

The water proofing membrane/root barrier is installed at the last layer of green roofs in order to avoid vegetation and water from flown into the existing roof layer. Usually, non-organic materials for example polyvinyl chloride (PVC), butyl rubber, or ethylene propylene diene monomer (EPDM), are used for water proofing/root barrier layer [35]. However, the types of water proofing/root barrier used are always depend on the types of system and plants used for green roofs.

4 Benefits of Green Roofs

4.1 Reduce Stormwater Runoff Volume

Green roofs are role as storm water retainer and have ability to delay the flow during heavy storm event. Rain water can be absorbed by the substrates and taken up by the plant, where it is either stored in plant tissues or returned to the atmosphere through evapotranspiration [36]. Green roofs have been found out that may reduce the storm water runoff volume by 60–100% [26, 32, 37, 38]. Nevertheless, the runoff volume reduction efficiency is greatly depends on the substrate depth, substrate composition, plant species, initial soil moisture content, slope of green roof, rainfall characteristics, and climate conditions. More than 958 million liter of storm water can be collected yearly in Washington, DC, USA if 25% of the buildings installed the green roofs [39]. Peck [40] in Toronto, Canada also suggested that the effect on retention of storm water would be equivalent to building a 60 million storage tunnel if 6% of the roof surface areas were green roofs. Mentens et al. [41] in Germany also described that intensive green roofs showed reduction of annual runoff equivalent to 65–85% of annual rainfall volume (100%) while the corresponding values for extensive green roofs were 27–81%, respectively.

4.2 Delay and Reduce Peak Flow of Stormwater Runoff

When the rainwater fill up the pore spaces within the substrate or drainage layers, this process will delay the flow and reduce the peak flow rate into storm drains. Numerous studies had proved that green roofs can effectively decrease the peak flow and extend the delay of storm water runoff [24, 26, 28, 42–44]. The runoff can

be postponed between 10 min [32, 45] and 4 h [28] using the green roofs instead of using conventional roofs of which the runoff is nearly instantaneous. Carter and Rasmussen [46] observed 57% of peak flow in a vegetated roof was delayed up to 10 min in contrast with that from a conventional roof. Liu [42] stated that preliminary rainfall from 2.8 mm/h after green roof installation runoff volume could decrease to 0.5 mm/h. Meanwhile, Moran et al. [28] in North Carolina, USA found 60–90% reduction of flow rates from a green roof. Fassman-Beck et al. [47] peak flow could be reduce from 73 to 89% compared to control green roof (depth 5–15 cm) in New Zealand. Alfredo et al. [48] also found 22–70% reduction in peak discharges from green roofs compared to the control roof.

4.3   Mitigate the Effect of Urban Heat Island (UHI)

Heat island effect (UHI) is a major environmental issues in most urban area. Green roofs can mitigate the UHI effect by decreasing the maximum air temperature through evapotranspiration. Installation of green roofs with large scale is required to reduce the UHI consequence in the urban city. Kinouchi and Yoshitani [49] reported that the implementation of green roofs by 3.4 and 16.4% of surface area in Tokyo can reduce the maximum air temperatures by 0.1 and 0.6 °C, respectively. Shaharuddin et al. [50] stated that green roofs can decrease the ambient air temperature as maximum as 1.5 °C throughout a day and slightly pronounced during non-rainy day (1.6 °C) as compared to rainy day. Smith and Roebber [51] in Chicago, USA also concluded that green roofs if used widely would reduce the ambient temperatures in the city by up to 3 °C.

Santamouris [52] had carried out the simulation studies on city-scale green roofs application and the outcomes showed that the potential ambient temperature reduction can be achieved between 0.3 and 3 °C. A climatic study done by Rosenzweig et al. [53] in the New York City region reported that conversion of all roof area to green roofs was comparable to converting all available street areas to tree planting, which reducing the temperature nearly by 0.6 and 0.7 °C, respectively. The green roofs were found that can reflect 27% of total solar radiation while 60% been absorbed by the plants and substrates, and only 13% was transmitted into the substrate medium [36]. Green roof's vegetation can utilize up to 60% of the incoming solar radiation for photosynthesis in the plant tissues and thus reducing the heat to the buildings [54].

4.4 Reduce Energy Consumption for Cooling and Heating of Building

The consumption of energy could be reduce by implementation of green roofs technology at building roof and can recover the standard building temperature especially during cold and hot season. Peck et al. [55] green roofs are also capable to reduce the internal temperature by 4–5 °C when outside temperatures are between 25 and 30 °C. A study conducted in British Columbia reported that total heat flow through a green roof was only 0.7 kW/m^2 compared to a control roof of 2.634 kW/m^2 [56]. Dunnett and Kingsbury [35] stated that electricity usage for air-conditioning may reduce up to 8% as the decrease of 0.5 °C in the air temperature of internal building. Wong et al. [57] in Singapore found 1–15% annual energy consumption saving when 17–79% reduction in the cooling load for buildings with green roofs. A green roof experiment in Minnesota, USA also found a 16% reduction in energy demand from cooling units [58]. On the other hand, Lui [42] found 75% reduction in daily energy demand for space conditioning in a test building in Toronto, Canada. Park and Hawkins [59] also observed more pronounced cooling of 8.1 °C in less compact buildings compared to that of 4.6 °C in compact buildings. The buildings with green roofs were also warmer by 0.7 °C during night time due to increased insulation [60]. Alcazar and Bass [61] described that, one of advantages of insulation resulted from cooling as range of heating decreasing between 0.13% until 0.2% while range for cooling reduction is 6.3–6.5%.

4.5 Reduce Noise Pollution

The noise pollution in urban areas can be solved by green roofs as it can absorb sound and reduce the noise. Studies have proved that green roof growing media (12 cm) can decrease sound level by 40 dB while a growing media (20 cm) layer can decrease sound level between 46 and 50 dB [62]. A solid concrete wall normally requires 100 mm thick layer for the typical sound reduction of 43 dB. Green roof normally can decrease sound level for whole building by 8 dB or more instead of a conventional roof [63]. Dunnett and Kingsbury [35] found that green roof with 10 cm depth can reduce the 5 dB of noise level at the airport in Frankfurt, Germany.

4.6 Increase Life Expectancy of Building

Growing media and plant in green roofs are able to protect roof layer from ultraviolet radiation and solar exposure could affect the traditional bituminous roof

layer. These green roof component also decrease fluctuations of temperature night and day at the roof layer, which can reduce the stress of daily expansions and contractions. A research conducted by Connelly and Liu [56] demonstrated that the green roof diurnal fluctuation is about 3 °C instead of for non-green roof could be as high as 50 °C. Liu and Baskaran [64] in Toronto, Canada also found that the conventional roof easily reached 70 °C in the afternoon whereas the green roof was only 25 °C. Peck et al. [55] estimated that the temperatures moderation resulted from green roofs can increase the roof layer life between two and three times. Some studies claimed that green roofs can increase the life period of water proofing membrane from a 10–20 year to 50 years [65, 66].

4.7 Improving Aesthetic Values

Green roofs or roof gardens can serve as an oasis within the busy city for building residents. The greenery view at the rooftop of buildings has a good impact towards people working and living in the green building instead of in buildings that are less environmentally friendly in term of worker productivity. Viewing green plants has many positive health effects for example, releasing muscle tension, reducing blood pressure, lowering stress, and improving good feeling [67, 68]. These advantages can be transformed into employee productivity and better-quality health. Kaplan and Herbert [69] described that workers who had natural view, for example flowers and trees, reduce stressed, increase job satisfaction, and less illness reported compared those who had no natural view. Ulrich [70] noted that patients faced earlier recoveries from surgery when they have a natural view.

4.8 Mitigating Air Pollution

Green roofs play a significant function in reducing the air pollution problem especially urban area. Plants in green roofs can act as a filter to remove carbon dioxide, carbon monoxide, nitrogen oxides, air-borne ammonia, sulfur dioxide, ozone, and other harmful gases [71–73]. Tan and Sia [74] stated that 21 and 37% decreasing of nitrous and sulfur dioxide can be observed at a newly setup green roof, respectively. Numerous studies also found a variation of pollutants on air can be relieved by green roofs system [75, 76]. Peck and Kuhn [77] expected that green roofs can eliminate dust particle on the order of 0.2 kg of particular per year per square meter of grass roof. Deutsh et al. [39] stated that same amount of air pollutant can be removed as the impact of planting 17,000 street trees if 20% of building roof areas in Washington DC were installed with green roofs. An air quality model study conducted by Laberge [78] proposed that greening all roofs in Chicago would result in a decreasing of 517,100.61 kg of sulfur oxide and 417,309.26 kg of nitrogen oxide emissions per year. More than 800,000 kg per

year NO_2 (or 0.5% of that area's emissions) would be removed if 25% of all commercial and industrial roof layers in Detroit, Michigan were transformed into extensive green roofs [79].

4.9 Provide Habitat and Increase Biodiversity

Extensive green roofs also can function as an undistubed habitat for insects, microorganisms, birds and small creatures [17, 68]. Brenneisen [80] stated that research in Basel, Switzerland about biodiversity of 17 green roofs had found 254 beetles and 78 spiders species, with 18% of those spiders and 11% of the beetles were registered as endangered or rare species. Darius and Drepper [81] stated that the research about 50 years old of green roof in German fond that beetles, white grubs, grasshoppers, and a large amounts of mites. In Northeastern Switzerland, more than five orchid types and other endangered or rare plants species were found lived in a 90 years old of green roof [80]. Besides, a lot of birds' species have been noted using green roofs in, England, Switzerland, and Germany [80, 82].

Green roofs could provide home for insects and birds. Coffman and Davis [83] in Dearborn, Michigan successfully identified 29 insects species, seven spiders species, and two birds species at a 42,900 m^2 greened roof within 2 years of initial plants establishment. Some researchers also suggested that green roofs can serve as a possible alternative to increase native plants species to a city area. Dewey et al. [84] assessed 35 wildflowers and native grasses in an irrigated intensive green roof and they found that more than 20 species were acceptable for a meadow mixture with a 1.0 m depth of growing media. Green roof consisted of native plant community would offer more biodiversity compared to a typical sedum based green roof [85].

5 Application of Green Roofs

Applications of green roofs in the building construction are well established in many developed countries. Well-developed countries, for example, United Kingdom, Hong Kong, and Singapore have implemented green roof as their alternative to reduce storm water runoff and increase green vegetation in urban area. These countries have developed advance knowledge and proper implementation guidelines for green roof system. On the other hand, the developing countries still facing land constraints issues that lead to the increasing competition for land between infrastructure developments and greenery area.

In Singapore, population growth is expected to increase from current 4.2 to 5.0 million over next 4–5 years [74]. In order to encourage green roofs application in this country, the National Parks Board and the Housing Development Board of Singapore have jointly initiated a preliminary project that installed a green roof on

the current roof of a multi-story car park in a residential area. This project is the first significant green roof installation project in Singapore. The result showed that the installed green roof have decrease the visible radiation significantly which recorded on the facades of residential area. The uses of thermocouple temperature sensor and infra-red thermal imagery had indicated there is significant difference in external temperature between planted covered and visible surfaces. The greatest challenge for green roof application in a tropical region like Singapore is the selection of plant species that can survive in the harsh rooftop environment conditions [74]. The study conducted by Vergroesen and Joshi [86] in Singapore was aimed to determine and quantify the runoff process in green roof that planted with sedum species. The experiment was set up to determine the comparison of runoff retention performance between green roofs and conventional reference roof. The results showed that a difference of delay runoff volume (0.2–20.2%) reduction in runoff volume (13.6–98.8%), reduction in peak flow (41.9–98.9%) and were observed for green roofs.

Rapid urbanization processes that spreading across China has caused the significant decreases of usable area for urban greening. Application of green roof in newly established building is started relatively late in this country compared with other developed countries. With the technology advancement on development and more focus on green roof, it had resulted in increasing number of green roof constructions in the recent years. The government of China also announced new guidelines to implement green roof constructions especially in Beijing, Shanghai, Guangdong, Chongqing, and Zhejiang provinces [87]. As in 2011, a total of 1,500,000 m^2 green roof area have been developed in Beijing. According to Zhang [88] stated that more than 3,000,000 m^2 of green roof area have been developed by more than 500 companies which specialize in roof greening in Chengdu, China.

In Taiwan, policies that promoting green roof have increased significantly in the recent years. Development of green roof is believed that it is a sustainable solution to reduce carbon emissions in Taiwan. In 2011, government of Taipei City has approved a new rules to added more environmental facility especially green roof system which able of retain and detain stormwater. In 2010, New Taipei City has started the Green T.A.I.B.E. project (Green Traffic, Green Architecture, Green Industry, Green Base and Green Economic) that planned to transform the existing city into an environmental friendly city [89].

Australia also one of developed countries that adopted green roof application. Alexandria and Jones [90] stated that most of the major cities in Australia have hot and dry summer season which is very suitable for green roof development as it will reduce the city temperature and decrease energy consumption as well. There are only few extensive green roofs projects in these country compared to the European countries. Extensive green roofs have great opportunity to be developed as a strategy to overcome climate issues as existing roof can be converted to green roof without major upgrades for building structure. But, there is certain difficulties on technical issues related to growing vegetation in shallow growing media especially on hot and dry rooftop condition has retarded the green roof development.

Implementation of green roof is also challenging in this country as there is no expert in green roof plant as well as substrate supplier that can provide advices and materials for green roof installation [91].

6 Conclusions

With rapid growth of population and the increasing demands for higher living standards, the development of urban infrastructures and buildings are likely will increase the impervious surfaces in the river basin. Green roofs have become a famous strategy in the sustainable urban development strategies in recent decades. Green roof is a viable means of increasing the amount of vegetation in urban cities, where the open space at ground level is limited but roof tops are largely unused yet remain impervious and contribute to storm water runoff. Extensive literature review has been conducted to explore the types, components and environmental benefits of green roofs to the sustainable urban development. Green roof have been recognized that it can give a lot of advantages, for example, decrease consumption of energy by reducing heating and cooling loads, increase building standards, generate amenity and aesthetic value, increase mitigation of storm water runoff, improve urban air quality, lower air temperatures, contribute on removal of urban stormwater pollutant, lower noise level in urban environments and reduce urban heat island effects. More implementation of green roofs in the urban city should be promoted in order to enhance the sustainability of the urban development.

References

1. Putnam, A.L.: Effect of Urban Development on Floods in the Piedmont Province of North Carolina, p. 87. United States Geological Survey, Open-file report (1972)
2. Johnson, S.L., Sayre, D.M.: Effects of Urbanization on Floods in the Houston. Texas Metropolitan Area, pp. 3–73, 50 pp. United States Geological Survey Water Resources Inventory (1973)
3. Yusop, Z., Chow, M.F.: A review of event mean concentration (EMC) for urban stormwater runoff. In: Proceeding of International Conference on Environmental Research and Technology, pp. 1–6 (2008)
4. Field, R., Masters, H., Singer, M.: Porous pavement: research, development, and demonstration. J. Transp. Eng. **108**(3), 244–258 (1982)
5. USEPA: Our built and natural environments: a technical review of the interactions between land use. Transp. Environ. Qual. **2001**, 4 (2001)

6. Doyle, M., Harbor, J., Rich, C., Spacie, A.: Examining the effects of urbanization on streams using indicators of geomorphic stability. Phys. Geogr. **21**, 155–181 (2000)
7. Schueler, T.: Environmental Land Planning Series: Site Planning for Urban Streams Protection. Center for Watershed Protection Publication No. 95708. Metropolitan Washington Council of Governments, Washington, DC (1995)
8. Chester, Jr., L.A., Gibbons, CJ.: Impervious surface coverage: the emergence of a key environmental indicator. J. Am. Plann. Assoc. **62**(2), 243–258 (1996)
9. Marsalek, J., Jimenez-Cisneros, B., Karamouz, M., Malmquist, P.A., Goldenfum, J., Chocat, B.: Urban Water Cycle Processes and Interactions. UNESCOHP Urban Water Series. Taylor and Francis, Leiden (2008)
10. Choi, H., Lee, W., Byun, W.: Determining the effect of green spaces on urban heat distribution using satellite imagery. Asian J. Atmos. Environ. **6**, 127–135 (2012)
11. Li, Q., Zhang, C., Miao, S.: The distribution characteristics of rainfall and the effect of land use in Beijing area (in Chinese with English abstract). J. Desert Res. **25** (Suppl.), 60–65 (2005)
12. Mansell, M.G.: Rural and Urban Hydrology. Thomas Telford, London (2003)
13. Zwiers, F.W., Kharin, V.V.: Changes in the extremes of the climate simulated by CCC GCM2 under CO2 doubling. J. Clim. **11**, 2200–2222 (1998)
14. Slonecker, E.T., Tilley, J.S.: An evaluation of the individual components and accuracies associated with the determination of impervious area. GISci. Remote Sens. **41**(2), 165–184 (2004)
15. Chow, M.F., Bakar, M.F.A.: A review on the development and challenges of green roof systems in Malaysia. Int. J. Civil Environ. Struct. Const. Architectural Eng. **10**, 16–20 (2016)
16. Moran, A., Hunt, B., Jennings, G.: A North Carolina field study to evaluate green roof runoff quantity, runoff quality, and plant growth. In: Proceedings of the ASAE Annual International Meeting, Paper no. 032303, pp. 1–15. Las Vegas, Nevada, USA, 27–30 July 2003
17. MacIvor, J.S., Lundholm, J.: Performace evaluation of native plants suited to extensive green roofs conditions in a maritime climate. Ecol. Eng. **37**, 407–417 (2011)
18. Cavanaugh, L.M.: Redefining the green roof. J. Architectural Eng. **14**, 4–6 (2008)
19. Environmental Protection Agency: Reducing Urban Heat Islands: Compendium of Strategies. Chapter 3: Green Roofs. Environmental Protection Agency. Washington, D.C., United States (2008)
20. Carter, T., Keeler, A.: Life-cycle cost-benefit analysis of extensive vegetated roof systems. J. Environ. Manage. **87**, 350–363 (2008)
21. Dhalla, S., Zimmer, C.: Low Impact Development Stormwater Management Planning and Design Guide, CVC & TRCA, 300 (2010)
22. Voyde, E.A.: Quantifying the Complete Hydrologic Budget for an Extensive Living Roof. Doctoral dissertation, University of Auckland (2011)
23. Compton, J.S., Whitlow, T.H.: A zero discharge green roof system and species selection to optimize evapotranspiration and water retention. In: Proceedings of 4th North American Green Roof Conference: Greening Rooftops for Sustainable Communities (2006)
24. Chow, M.F., Bakar, M.F.A., Roslan, M.A.A., Fadzailah, F.A., Idrus, M.F.Z., Ismail, N.F., Mohd, S.L., Basri, H.: Hydrological performance of native plant species within extensive green roof systems in Malaysia. ARPN J. Eng. Appl. Sci. **10**(15), 6419–6423 (2015)
25. Snodgrass, E.: The function of green roof vegetation. In: Mid Atlantic Green Roof Science and Technology Symposium. University of Maryland (2014)
26. Kok, K.H., Mohd, S.L., Chow, M.F., Zainal Abidin, M.R., Basri, H., Hayder, G.: Evaluation of green roof performances for urban storm water quantity and quality controls. Int. J. River Basin Manag. **14**, 1–7 (2016)
27. Beattie, D., Berghage, R.: Green roof media characteristics: the basics. In: Proceedings of the 2nd Greening Rooftops for Sustainable Communities Conference, pp. 411–416. Portland, OR (2004)

28. Moran, A., Hunt, B., Jennings, G.: A North Carolina field study to evaluate green roof quantity, runoff quality, and plant growth. In: 2nd Greening Rooftops for Sustainable Communities Conference, pp. 446–460. Portland, 2–4 June 2004

29. Köhler, M., Schmidt, M.: Study of Extensive Green Roofs in Berlin: Part III Retention of Contaminants (Saskia Cacanindin, Trans.). Technical University of Berlin, Berlin, Germany (2003)

30. Boivin, M., Lamy, A.Gosselin, Dansereau, B.: Effect of artificial substrate depth on freezing injury of six herbaceous perennials grown in a green roof systems. HortTechnology **11**(3), 409–412 (2001)

31. Durhman, A., Rowe, D.B., Rugh, C.L.: Effect of substrate depth on initial growth, coverage, and survival of 25 succulent green roof plant taxa. HortScience **42**(3), 588–595 (2007)

32. VanWoert, N.D., Rowe, D.B., Andresen, J.A., Rugh, C.L., Fernandez, R.T., Xia, L.: Green roof stormwater retention: effects of roof surface, slope, and media depth. J. Environ. Qual. **34**, 1036–1044 (2005)

33. Jarrett, A.R., Hunt, W.F., Berghage, R.D.: Annual and individual-storm green roof stormwater response models. In: Proceedings of the American Society of Agricultural and Biological Engineers Annual International Meeting. Portland OR. Paper # 062310 (2006)

34. Miller, C.: Moisture management in green roofs. In: Proceedings of the 1st Greening Rooftops for Sustainable Communities Conference, pp. 177–182. Chicago, IL (2003)

35. Dunnett, N.P., Kingsbury, N.: Planting Green Roofs and Living Walls. Timber Press, Portland (OR) (2004)

36. Vijayaraghavan, K.: Green roofs: a critical review on the role of components, benefits, limitations and trends. Renew. Sustain. Energy Rev. **57**(C), 740–752 (2016)

37. Rowe, D.B., Rugh, C.L., VanWort, N., Monterusso, M.A., Russell, D.K.: Green roof slope, substrate depth, and vegetation influence runoff. In: Proceedings of 1st North American Green Roof Conference: Greening Rooftops for sustainable communities, pp. 354–362 (2003)

38. Stovin, V., Vesuviano, G., Kasmin, H.: The hydrological performance of a green roof test bed under UK climatic conditions. J. Hydrol. **414–415**, 148–161 (2012)

39. Deutsch, B., Whitlow, H., Sullivan, M., Savineau, A.: Re-greening Washington, DC: a green roof vision based on environmental benefits for air quality and storm water management. In: Proceedings of 3rd North American Green Roof Conference: Greening Rooftops for Sustainable Communities. Washington, DC (2005)

40. Peck, S.: The Greening of North America. Building Envelope Forum (2005)

41. Mentens, J., Raes, D., Hermy, M.: Green roofs as a tool for solving the rainwater runoff problem in the urbanized 21st century. Landscape Urban Plann. **77**, 217–226 (2006)

42. Liu, K.: Engineering performance of rooftop garden through field evaluation. In: Proceedings of the 18th International Convention of the Roof Consultant Institute, pp. 93–103 (2003)

43. Bengtsson, L.: Peak flows from thin sedum-moss roof. Nord. Hydrol. **36**, 269–280 (2005)

44. Bengtsson, L., Grahn, L., Olsson, J.: Hydrological function of a thin extensive green roof in southern Sweden. Nord. Hydrol. **36**(3), 259–268 (2005)

45. Simmons, M.T., Gardiner, B., Windhager, S., Tinsley, J.: Green roofs are not created equal: the hydrologic and thermal performance of six different extensive green roofs and reflective and non-reflective roofs in a sub-tropical climate. Urban Ecosyst. **11**, 339–348 (2008)

46. Carter, T.L., Rasmussen, T.C.: Hydrologic behavior of vegetated roofs. J. Am. Water Resour. Assoc. **42**(5), 1261–1274 (2006)

47. Fassman-Beck, E., Voyde, E., Simcock, R., Hong, Y.S.: 4 living roofs in 3 locations: does configuration affect runoff mitigation? J. Hydrol. **490**, 11–20 (2013)

48. Alfredo, K., Montalto, F., Goldstein, A.: Observed and modelled performances of prototype green roof test plots subjected to simulated low- and high-intensity precipitations in a laboratory experiment. J. Hydrol. Eng. **15**(6), 444–457 (2010)

49. Kinouchi, T., Yoshitani, J.: Simulation of the urban heat island in Tokyo with future possible increases of anthropogenic heat, vegetative cover and water surface. In: Proceedings of the 2001 International Symposium on Environmental Hydraulics (2001)

50. Shaharuddin, A., Noorazuan, M.H., Yaakob, M.J.: Green Roof as best management pratices for heat reduction and strom water flow mitigation. World Appl. Sci. J. **13** (Sustainable Development Impact from the Socio-Environmental Perspective), 58–62:1818–4952 (2011)
51. Smith, K.R., Roebber, P.J.: Green roof mitigation potential for a proxy future climate scenario in Chicago, Illinois. J. Appl. Meteor. Climatol. **50**, 507–522 (2011)
52. Santamouris, M.: Cooling the cities—a review of reflective and green roof mitigation technologies to fight heat island and improve comfort in urban environments. Sol. Energy (in press) (2012)
53. Rosenzweig, C., Solecki, W., Parshall, L., Gaffin, S., Lynn, B., Goldberg, R., Cox, J., Hodges, S.: Mitigating new york city's heat island with urban forestry, living roofs, and light surfaces. In: Presentation at 86th American Meteorological Society Annual Meeting. Atlanta, Georgia, 31 Jan 2006
54. Weng, Q., Lu, D., Schubring, J.: Estimation of land surface temperature–vegetation abundance relationship for urban heat island studies. Remote Sens. Environ. **89**, 467–483 (2004)
55. Peck, S., Callaghan, C., Kuhn, M., Bass, B.: Greenbacks for Green Roofs: Forging a New Industry in Canada: Forging a New Industry in Canada. Status Report on Benefits, Barriers and Opportunities to Green Roof and Vertical Garden Technology Diffusion. Canada Mortgage and Housing Corporation, Ottawa, Canada (1999)
56. Connelly, M., Liu, K.: Green roof research in British Columbia: an overview. In: Proceedings of 3rd North American Green Roof Conference: Greening rooftops for sustainable communities, pp. 4–6. Washington, DC (2005)
57. Wong, J.K.W., Lau, L.S.K.: From the 'urban heat island' to the 'green island'? A preliminary investigate into the potential of retrofitting green roofs in Mongkok district of Hong Kong. Habitat Int. **39**, 25–35 (2013)
58. Leonard, T., Leonard, J.: The green roof and energy performance—rooftop data analysed. In: Proceedings of the 3rd North American Green Roof Conference: Greening rooftops for sustainable communities. Washington, DC (2005)
59. Park, G., Hawkins, T.W.: An examination of the effect of building compactness and green roofs on indoor temperature through the use of physical models. Geogr. Bull. **56**, 93–101 (2015)
60. Pompeii II, W.C., Hawkins, T.W.: Assessing the impact of green roofs on urban heat island mitigation: a hardware scale modeling approach. Geogr. Bull. **52**, 52–61 (2011)
61. Alcazar, S., Bass, B.: Energy performance of green roofs in a multi storey residential building in Madrid. In: Greening Rooftops for Sustainable Communities. Washington, DC (2005)
62. Kang, J., Yang, H.S., Choi, M.S.: Acoustic effects of green roof systems on a low-profiled structure at street level. Build. Environ. **50**, 44–55 (2012)
63. Kang, J., Huang, H., Sorrill, J.: Experimental study of the sound insulation of semi-extensive green roofs. In: Proceedings of INTER-NOISE (2009)
64. Liu, K., Baskaran, B.: Thermal Performance of Green roofs through Field Evaluation—Ottawa. Ottawa (Canada): National Research Council Canada, Institute for Research in Construction. Report no. NRCC-46412 (2003)
65. Niu, H., Clark, C., Zhou, J., Adriaens, P.: Scaling of economic benefits from green roof implementation in Washington, DC. Environ. Sci. Technol. **44**(11), 4302–4308 (2010)
66. Sproul, J., Wan, M.P., Mandel, B.H., Rosenfeld, A.H.: Economic comparison of white, green, and black flat roofs in the United States. Energy Build. **71**, 20–27 (2014)
67. Ulrich, R.S., Simons, R. F.: Recovery from stress during exposure to everyday outdoor environments. In: Proceedings of 17th Annual Conference Environmental Design Research Association, pp. 115–122 (1986)
68. Getter, K.L., Rowe, D.B.: The role of extensive green roofs in sustainable development. HortScience **41**(5), 1276–1285 (2006)
69. Kaplan, R., Herbert, E.J.: Culture and sub-culture comparisons in preference for natural setting. Landscape Urban Plann. **14**, 281–293 (1987)

70. Ulrich, R.S.: Aesthetic and effective response to natural environments. In: Altman, I., Wohlwill, J.F. (eds.) Behavior and the natural environment, pp. 85–125. Plenim Press, New York (1983)
71. Akbari, H., Pomerantz, M., Taha, H.: Cool surfaces and shade trees to reduce energy use and improve air quality in urban areas. Sol. Energy **70**(3), 295–310 (2001)
72. Wu, T., Smith, R.E.: Economic benefits for green roofs: a case study of the skaggs pharmacy building, university of Utah. Int. J. Des. Nat. Ecodyn. **6**(2), 122–138 (2011)
73. Speak, A.F., Rothwell, J.J., Lindley, S.J., Smith, C.L.: Reduction of the urban cooling effects of an intensive green roof due to vegetation damage. Urban Clim. **3**, 40–55 (2013)
74. Tan, P.Y., Sia, A.: A pilot green roof research project in Singapore. In: Proceedings of 3rd North American Green Roof Conference: Greening Rooftops for Sustainable Communities, pp. 4–6. Washington, DC (2005)
75. Liesecke, H.J., Borgwardt, H.: Abbau von luftschadstoffen durch extensive dachbegrünungen (Degradation of air pollutants by extensive green roofs). Stadt und Grün. **46**, 245–251 (1997)
76. Currie, B., Bass, B.: Estimates of air pollution mitigation with green plants and green roofs using the UFORE model. Urban Ecosyst. **11**, 409–422 (2008)
77. Peck, S., Kuhn, M.: Design Guidelines for Green Roofs. National Research Council Canada, Toronto, Canada (2001)
78. Laberge, K.M.: Urban oasis: Chicago's City Hall green roof. In: Proceedings of 1st North American Green Roof Conference: Greening Rooftops for Sustainable Communities, Chicago, pp. 194–203. The Cardinal Group, Toronto, 29–30 May 2003
79. Clark, C., Talbot, B., Bulkley, J., Adriaens, P.: Optimization of green roofs for air pollution mitigation. In: Proceedings of 3rd North American Green Roof Conference: Greening Rooftops for Sustainable Communities, pp. 482–597. Washington, DC, 4–6 May 2005
80. Brenneisen, S.: The benefits of biodiversity from green roofs: key design consequences. In: Proceedings of 1st North American Green Roof Conference: Greening Rooftops for Sustainable Communities, Chicago, pp. 323–329. The Cardinal Group, Toronto (2003)
81. Darius, F., Drepper, J.: Rasenda¨cher in West-Berlin. Das Gartenamt **33**, 309–315 (1984)
82. Gedge, D.: From rubble to redstarts. In: Proceedings of 1st North American Green Roof Conference: Greening Rooftops for Sustainable Communities, Chicago, pp. 233–241. The Cardinal Group, Toronto, 29–30 May 2003
83. Coffman, R.R., Davis, G.: Insect and avian fauna presence on the Ford assembly plant ecoroof. In: Proceedings of 3rd North American Green Roof Conference: Greening Rooftops for Sustainable Communities, Washington, DC, pp. 457–468. The Cardinal Group, Toronto, 4–6 May 2005
84. Dewey, D., Johnson, P., Kjelgren, R.: Species composition changes in a rooftop grass and wildflower meadow. Native Plants **5**, 56–65 (2004)
85. Monterusso, M.A., Rowe, D.B., Rugh, C.L.: Establishment and persistence of sedum spp. and native taxa for green roof applications. HortScience **40**, 391–396 (2005)
86. Vergroesen, T., Joshi, U.M.: Green Roof Runoff Experiments in Singapore Ruissellement des toitures végétalisées : expériences à Singapour, pp. 1–10 (2010)
87. Xu, S.: Green roofing–preliminary investigation on the environmental greening in the residential area in Shanghai. J. Shanghai Jiaotong Univ. **30**(1), 129–134 (1996). (in Chinese)
88. Zhang, C.: Cost-Benefit Analysis for Greening in Beijing. Beijing Forestry University Press, Beijing (2010)
89. Feng, C.C.: Performance evaluation and development strategies for green roofs in Taiwan: a review. Ecol. Eng. **52**, 51–58 (2013)
90. Alexandria, E., Jones, P.: Temperature decrease in an urban canyon due to green walls and green roofs in diverse climate. Build. Environ. **43**, 480–493 (2008)
91. Williams, N.S.G., Raynor, K.J.: Green roofs for wide brown land: opportunities and barriers for rooftop greening in Australia. Urban forest Urban Green **9**(3), 245–251 (2010)